ICF10

Honolulu (USA)

2001

Vol. B

ORAL/POSTER REFERENCE: ICF100602OR

DOUBLE COHESIVE ZONE MODEL AND PREDICTION FOR MICRO-SCRATCH TEST ALONG SOLID SURFACE

M. Zhao[1], Y. Wei[1,2] and J. W. Hutchinson[2]

[1]LNM, Institute of Mechanics, Chinese Academy of Sciences, Beijing 100080, China
[2]Division of Engineering and Applied Sciences, Harvard University, Cambridge, MA 02138, USA

ABSTRACT

A new double cohesive zone model describing the failure of ductile film in the micro-scratching test is presented in this paper. The failure behavior and adhesion work in the micro-scratch test is simulated and predicted based on the model. In the present analyses, the thin film is treated as the elastic-plastic material, and substrate is elastic material, and three-dimensional elastic-plastic finite element method is adopted. In order to simplify the analyses, the total problem will be divided into two sub-problems. One problem is that elastic-plastic large bend deformation of scratched film is considered, and an analytical solution can be obtained. Another problem is that the thin film is delaminated plastically along the interface with the elastic substrate, for which a special three-dimensional finite element method is used. The parameter relations of the horizontal driving force for the scratch test with the separation strength of thin film/substrate interface and the material shear strength, as well as the material parameters are developed. As an example of the application, the prediction result is applied to a scratch test for the Pt/NiO material system given in the literature, and both results are fairly agreement with each other.

KEYWORDS

Micro-scratch test, driving force, double cohesive zone model.

INTRODUCTION

The micro-scratch test is an important approach for determining the interfacial strength, toughness and adhesion properties for the thin film or coating layer on the substrate interface [1]. Its principle can be described as follows: On the material or specimen surface along the vertical direction an indentation force is exerted and indenter tip penetrates inside the material, then the indenter is moved in the horizontal and vertical directions simultaneously according to a fixed proportion. When the indenter tip moves near the film/substrate interface, a region of the thin film or coating layer near the indenter tip will be delaminated along the interface. Through measuring driving forces, the scratch depth, and the failure geometry, one will obtain the material or interface adhesion properties. According to usual experimental observations, there are two main kinds of failure characters in the scratch tests [1-5] depending on the material property of thin film or coating, whether ductile or brittle. One kind of failure character can be described as that for the ductile film case, a delaminated film strap is formed before the end of the scratch test and the delaminated film will be curved into a circular shape. The geometry of the delaminated area is fan shaped. Another failure character is that when film is brittle. A damage zone is formed near the indenter tip, inside which the film will be pressed to break into many small pieces and also delaminated from the substrate. In the present research, our attention will be focused on the metal film/ceramic substrate case. The ductile failure character will be simulated and analyzed in detail.

On the research of the material surface properties and adhesion work and strength of thin film or coating

layer along the substrate interface, many experimental researches based on the scratch methods have been carried out in past decade [1-5]. However, theoretical analyses connected with the scratch experiments are very few [1]. This is because that any theoretical study must deal with on the complicated failure geometry of the scratch test. It is obvious that a three-dimensional elastic-plastic deformation problem must be solved, and a robust theoretical model for describing the scratch failure behavior is needed. Must theoretical researches have been based on the simple geometry of the scratch failure strap and the simple mechanics equilibrium to simulate the scratch failure behavior [1-5]. However, it is difficult to use a simple model to describe the strong influence of plastic deformation on the micro-scratch behavior. It is well known that plastic deformation has a strong shielding effect on the interface cracking [6-8]. So that in an elastic-plastic failure process more energy is dissipated than that in a pure elastic failure process. Therefore, it is important to develop a reasonable mechanics model for scratch test simulation.

The failure characteristics of the scratch test for ductile thin film materials[2-4] are somewhat similar with the thin film peeling problems. Therefore, in micro-scratch test research, the analytical method for the thin film peeling problem [8] is relevant. It is important to obtain a reasonable relation between the critical driving force and the parameters of the materials and scratch strap geometry.

In the present research, based on the three-dimensional character of failure strap, a new mechanics model describing the interface separation and the thin film shear failure, i.e., a double cohesive zone model will be presented. Using the new model, a relation between the scratch horizontal driving force and the parameters of the materials will be set up and used to predict the scratch work. Finally, the simulation results will be applied to an experimental result for Pt/NiO from [4].

FUNDAMENTAL DESCRIPTION AND SIMPLIFICATION

From failure characteristics for ductile film scratching, the scratch test process can be described by figure 1. This process can consist of two stages. One stage is a normal scratch before thin film delamination occurs along interface. With the indenter moving forward and downward with scratch depth increase, especially when indenter tip is near the interface, a region of thin film or coating layer near the indenter tip will be delaminated from interface. Thereby, the scratch process is transferred to another stage. The failure character changes from the indenter tunnel growth to the delaminated film strap formation and growth (or post-scratch process). For simplifying the analysis, the problem is divided into two sub-problems. One problem is "plate bend" under elastic-plastic large deformation for the delaminated thin film part BCD, see figure 1. This sub-problem has been solved successfully in [8]. Another problem is a three-dimensional delaminating problem for a part of thin film BA and jointed substrate. In the present research, our attention will focus on the latter problem. The solution of the former problem [8] will be taken as the boundary condition and exerted on the section B directly. For simplification, we present and adopt a new double cohesive zone model to simulate the film failure process and the scratch work for the post-scratch process. The new model is shown in figure 2. In this model, there are three cohesive zones, one is the separation-dominated cohesive zone and other two are shear-dominated cohesive zones.

DOUBLE COHESIVE ZONE MODELS AND MECHANICS DESCRIPTIONS

In figure 2, the thin film delaminates from interface of thin film/substrate (plane x_2=0), and this failure process can be simulated by a separation-dominated cohesive zone surface. Simultaneously, the curved film layer is cut off from two sides of the delaminated region (planes x_3=-W and 0). The cutting process for each plane can be described by the shear-dominated cohesive zone deformation. In figure 2, δ_{cn} and δ_{ct} are critic relative displacements for the separation and shear cohesive zone surfaces, respectively. The separation cohesive zone model under plane strain case has been widely adopted and completely formulated in [6-8]. In the following, we shall discuss and give a brief description and generalization for the two kinds of cohesive zone models for the three-dimensional case.

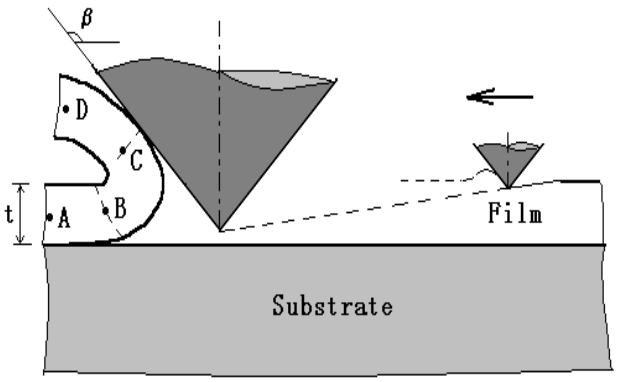

Figure 1: Scratch test geometry and ductile failure

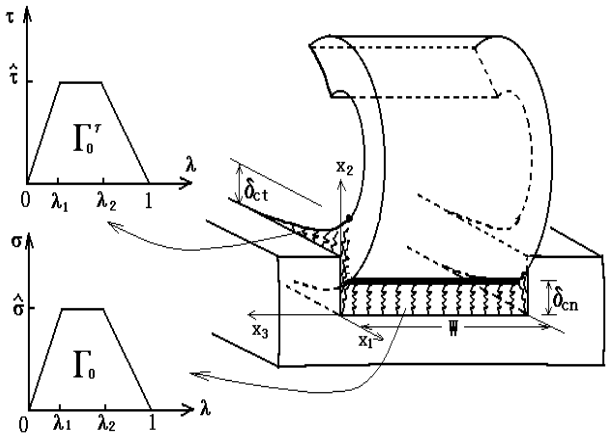

Figure 2: Double cohesive zone model

Let $(\delta_1,\delta_2,\delta_3)$ be relative displacements at each cohesive surface along direction (x_1,x_2,x_3), respectively, and define a normalized displacement quantity

$$\lambda=\delta_c^{-1}\sqrt{\delta_1^2+\delta_2^2+\delta_3^2}\quad , \tag{1}$$

The critical condition for the cohesive zone is, $\lambda=1$. For the separation-dominated cohesive zone case, $\delta_c=\delta_{cn}$, while for the shear-dominated cohesive zone case, $\delta_c=\delta_{ct}$. The traction relations, $\sigma(\lambda)$ and $\tau(\lambda)$, on the cohesive zone surfaces are sketched in figure 2.

The traction component expressions can be formulated in detail as follows. Define a potential function

$$\Pi(\delta_1,\delta_2,\delta_3)=\delta_{cn}\int_0^{\lambda}\sigma(\lambda')d\lambda' \tag{2}$$

then, one will derive out the traction expressions easily

$$(T_1,T_2,T_3)=(\frac{\partial\Pi}{\partial\delta_1},\frac{\partial\Pi}{\partial\delta_2},\frac{\partial\Pi}{\partial\delta_3})=\frac{\sigma(\lambda)}{\lambda\delta_{cn}}(\delta_1,\delta_2,\delta_3) \tag{3}$$

Similarly, for the shear-dominated cohesive surface, one reads

$$(T_1,T_2,T_3)=\frac{\tau(\lambda)}{\lambda\delta_{ct}}(\delta_1,\delta_2,\delta_3) \tag{4}$$

Adhesion work per unit area along the cohesive surface can be written as

$$\Gamma_0=\tfrac{1}{2}\hat{\sigma}\delta_{cn}(1+\lambda_2-\lambda_1) \tag{5}$$

for the separation zone, and

$$\Gamma_0^{\tau}=\tfrac{1}{2}\hat{\tau}\delta_{ct}(1+\lambda_2-\lambda_1) \tag{6}$$

for the shear cohesive zone. Earlier work has shown that the shape parameters (λ_1 and λ_2) of cohesive zone model have the secondary influence on the analytical results. In the present analysis, we take $(\lambda_1,\lambda_2)=(0.15,\ 0.5)$. Moreover, for reducing the number of governing parameters, we take $\delta_{cn}=\delta_{ct}=\delta_c$, then from (5) and (6), one have $\Gamma_0^{\tau}/\Gamma_0=\hat{\tau}/\hat{\sigma}$.

ENERGY BANLANCE AND ELASTIC-PLASTIC MECHANICS METHOD

The double cohesive zone model has been sketched by figure 2. The variation equation for the total system can be written as

$$\int_V \delta\varepsilon_{ij}.\sigma_{ij}dV = \int_V \delta\varepsilon_{ij}.D^e_{ijkl}\varepsilon^e_{kl}dV = \int_V \delta\varepsilon_{ij}.D^e_{ijkl}(\varepsilon_{kl}-\varepsilon^p_{kl})dV$$

$$= \sum_{k=1}^{3}\{\int_{S_k^+}\delta u_i.t_i dS + \int_{S_k^-}\delta u_i.t_i dS\} + WQ.\delta|\Delta_1| = -\sum_{k=1}^{3}\int_{S_k}\delta|u_i^+ - u_i^-|.|T_i|dS + WQ.\delta|\Delta_1|$$

$$= -\sum_{k=1}^{3}\int_{S_k}\delta|\delta_i|.|T_i|dS + WQ.\delta|\Delta_1| \qquad (7)$$

Where S_k $(k=1,3)$ are cohesive surfaces, (u_i,t_i) are the displacement and traction components on the cohesive zone surfaces, (δ_i,T_i) are the relative displacement and traction on the cohesive surfaces, see formulas（1）to（4）. Δ_1 is the displacement of the point acted by horizontal driving force Q.

Based on (7), one can develop the finite element method for scratch test problem. The incremental constitutive relation of plasticity usually is expressed as

$$\dot{\sigma}_{ij} = \frac{E}{1+\nu}\left\{\delta_{ik}\delta_{jl} + \frac{\nu}{1-2\nu}\delta_{ij}\delta_{kl} - \frac{(3/2)\Omega}{[1+(2/3)(1+\nu)H/E]\sigma_e^2}\sigma'_{ij}\sigma'_{kl}\right\}\dot{\varepsilon}_{kl} \qquad (8)$$

σ'_{ij} is deviator stress, $\sigma_e = \sqrt{3\sigma'_{ij}\sigma'_{ij}/2}$ is effective stress; for plastic loading $\Omega = 1$, otherwise $\Omega = 0$. H is plastic modulus. In uniaxial tension the film material has

$$\varepsilon = \sigma/E, \text{ for } \sigma < \sigma_Y; \quad \varepsilon = (\sigma_Y/E)(\sigma/\sigma_Y)^{1/N}, \text{ for } \sigma \geq \sigma_Y \qquad (9)$$

so that
$$H = E\{(1/N)(\sigma_e/\sigma_Y)^{1/N-1} - 1\}^{-1} \qquad (10)$$

Strap advance is assumed to occur in steady-state such that the stress and strain increment components can be expressed as
$$(\dot{\sigma}_{ij}, \dot{\varepsilon}_{ij}) = V(\partial\sigma_{ij}/\partial x_1, \partial\varepsilon_{ij}/\partial x_1) \qquad (11)$$

where V is velocity of crack tip during film delamination in x_1 direction. The formula（8）is independent of V. Plastic strain components can be expressed by stress and total strain as

$$\varepsilon^p_{ij} = \varepsilon_{ij} - D^e_{ijkl}{}^{-1}\sigma_{kl} \qquad (12)$$

A numerical method [9] which employs iteration to satisfy condition (11) is used to directly obtain the steady-state solution. Similarly, in the present analyses, adopting the fundamental relations of tensors and matrixes, (7) can be changed into the finite element relations. The steps of solving the problem can be described as follows: (1) Adopting a plastic strain distribution (in first step, take $\varepsilon^p_{ij} = 0$), find displacement and strain. (2) Find stress distributions in plastic zone and unloading zone using (8), (11) and yielding condition $\sigma_e = Y$ (Y is current flow stress). (3) Find plastic strain by (12). Repeat procedures until a convergent solution is obtained.

Consider that the substrate material is elastic and Young's modulus and Poisson ratio are E_s and ν_s respectively. For further simplification, neglect the effect of mismatch of film and substrate materials, so that we take $(E_s,\nu_s) = (E,\nu)$ in the present analysis. During the steady-state advance of delaminated film strap, total work per unit length is QW; dissipated work per unit length along the separation cohesive surface is $\Gamma_0 W$; and along two shear cohesive surfaces it is $2t\Gamma_0^\tau$. Let plastic dissipation work be $W\Gamma_P$. According to energy balance under steady-state advance, we have

$$Q = \Gamma_0 + \tfrac{2t}{W}\Gamma_0^\tau + \Gamma_P \qquad (13)$$

For elastic case, $\Gamma_P = 0$. In principle, the interface separation work (interface fracture toughness) Γ_0 and the material shear work (or material shear strength) Γ_0^τ could be determined by experimental measurement. The normalized horizontal driving force Q during the steady-state advance of failure strap can be

expressed by the related independent parameters as follows

$$\frac{Q}{\Gamma_0} = 1 + (\frac{2t}{W})(\frac{\hat{\tau}}{\hat{\sigma}}) + \frac{\Gamma_P}{\Gamma_0} = f\left(\frac{E}{\sigma_Y}, \frac{\hat{\sigma}}{\sigma_Y}, \frac{\hat{\tau}}{\sigma_Y}, \frac{t}{R_0}, \frac{t}{W}, N, \nu, \beta\right) \tag{14}$$

In（14）a reference length parameter has been introduced, whose definition is $R_0 = E\Gamma_0 / [3\pi(1-\nu^2)\sigma_Y^2]$, characterizing the plastic zone size in small scale yielding.

SOLUTIONS AND ANALYSES

Three-dimensional elastic-plastic finite element calculation for the scratch test problem is carried out based on the concepts implemented in previous sections. The results and analyses are shown in the following.
Figure 3 shows the relation of the normalized horizontal driving force (or applied work per unit area) to the maximum strength of separation and shear for two kinds of cohesive zones. The driving force changes with shear strength and separation strength are very sensitive, especially for large values of separation strength or

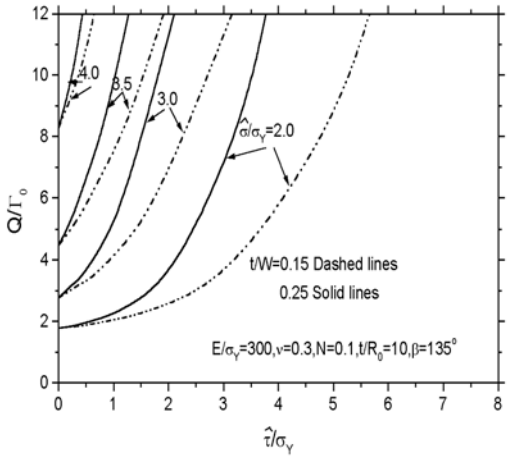

Figure 3: Scratch work vs. material parameters for low hardening film

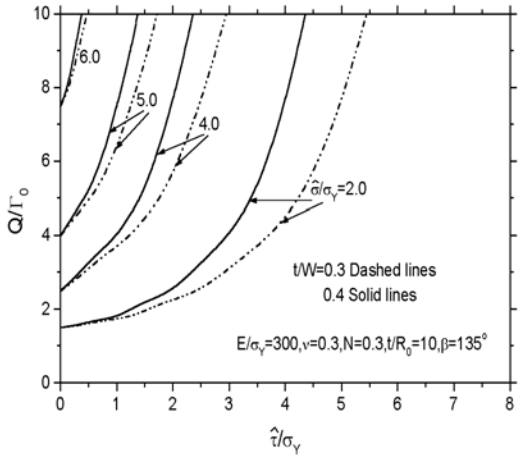

Figure 4: Scratch work vs. material parameters for high hardening film

shear strength. For the lower separation strength case, the horizontal driving force changes with the material shear strength slowly as shear strength increases, then sharply increases. For the higher separation strength, even a lower material shear strength will make the horizontal driving force increase very quickly. In the figure 3, the results of two different ratio of thin film thickness with the delaminated film width are compared. Clearly, the horizontal driving force changes sensitively with the ratios. The results correspond to the lower strain hardening exponent material, i.e., N=0.1. The separation cohesive energy along interface is taken as the normalized quantity. When the shear strength of material is zero and the elastic case is considered, the value of the normalized horizontal driving force (applied work per unit area) equals to unity. When the material shear strength is not zero, the normalized horizontal driving force will change linearly with the

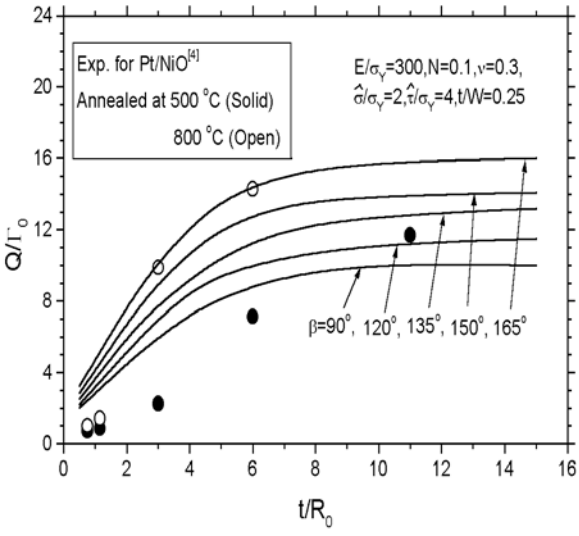

Figure 5: Scratch work vs. film thickness and indenter angles

shear strength from (14) for elastic case. Obviously, from figure 3, the energy contributed from plastic deformation is very high.

Figure 4 shows the results for the higher hardening thin film material case, N=0.3. The variations of the horizontal driving force with the material shear strength and the interface separation strength are similar to those of the lower hardening material. Clearly, the work dissipated in the plastic deformation for higher hardening material is lower than that for lower hardening material.

Figure 5 shows the relation of the driving force (applied work) changing with normalized thin film thickness. The curves are for different direction angles of indenter surface, $\beta = 90^o$, 120^o, 135^o, 150^o and 165^o. In the figure, the experimental results for the Pt/NiO film/substrate system and for the two kinds of techniques annealed at 500°C and 800°C from [4] are also shown. From figure 5, the horizontal driving force increases as thin film thickness increases and as the indenter angle increases. The indenter shape with the largest β corresponds to the high driving force. The simulation results are roughly consistent with the experiment results.

CONCLUDING REMARKS

By the detailed analyses in the present research, some important conclusions are obtained as follows: (1) Thin film plastic deformation has the important influence on the advance of delaminated film strap in the scratch test. (2) The interface separation strength and material shear strength have important influence on the failure of thin film/substrate system. (3) The horizontal driving force depends on the thin film or coating layer thickness. With the thin film thickness increase, the horizontal driving force increases and asymptotes to a stable value, which corresponds to the small scale yielding case.

When either the interface separation strength or the material shear strength is large, a strong shielding effect from plastic deformation can be produced when the failure strengths are increased. In other words, with any cohesive strength increase, it is difficult or even impossible to make a film failure strap advance due to the strong plastic shielding. Such a prediction from using the conventional elastic-plastic theory seems somewhat contradictory. Actually, for the strong separation strength of interface or for the high shear strength, or for both, a strong plastic strain gradient effect could dominate the crack tip fields [10]. A reasonable simulation for this behavior might be obtained by using the strain gradient plasticity theory. A success application of the strain gradient plasticity to the crack growth problem has been shown in [11].

Acknowledgements

The work is supported by National Science Foundations of China through Grants 19891180 and 19925211; and jointly supported by Fundamental Research Project from Chinese Academy of Sciences through Grant KJ951-1-201 and "Bai Ren" Project. The work is also supported by NSF Grants CMS-96-34632 in USA.

References

1. Blees, M.H., Winkelman, G.B., Balkenende, A.R et al.(2000). *Thin Solid Films*, 359,1.
2. Pistor, C.and Friedrich, K. (1997). *J. Appl. Polymer Science*, 66, 1985.
3. Maekawa, H., Ikeda, T. and Horibe, H., et al.(1994). *Quart. J. Japan Welding Society*, 12, 262.
4. Venkataraman, S., Kohlstedt, D.L. and Gerberich. W.W. (1996). *J. Mater. Res*., 11, 3133.
5. Thouless, M.D. (1998). *Eng. Frac. Mech.*, 61, 75.
6. Tvergaard, V. and Hutchinson, J.W. (1993). *J. Mech. Phys. Solids*, 41, 1119.
7. Wei, Y. and Hutchinson, J.W. (1997). *J. Mech. Phys. Solids*, 45, 1137.
8. Wei, Y. and Hutchinson, J.W. (1998). *Int. J. Fracture*, 93, 315.
9. Dean, R.H. and Hutchinson, J.W. (1980). In: *Fracture Mechanics*, ASTM STP700, p.383.
10. Fleck, N.A. and Hutchinson, J.W. (1997). *Advances in Applied Mechanics*, 33, 295.
11. Wei, Y. and Hutchinson, J.W. (1997). *J. Mech. Phys. Solids*, 45, 1253.

DUCTILE DAMAGE ACCUMULATION UNDER CYCLIC DEFORMATION AND MULTIAXIAL STATE OF STRESS CONDITIONS

N. Bonora[1] and A. Pirondi[2]
[1]DiMSAT – Dept. of Mechanics, Structures and Environment, University of Cassino
03043 Cassino, Italy
[2]Industrial Engineering Department, University of Parma
43100 Parma, Italy

ABSTRACT

The possibility to develop reliable predictive tools for the design of components undergoing plastic deformation is connected to the capability to incorporate damage mechanics into the constitutive model of the material. Even though many damage models for ductile failure are available in the literature, none of them, as far as the authors are aware of, is extended to reversal plastic flow occurring under compressive stress states. In this paper the damage model proposed by Bonora (1997) has been reformulated in order to account for compressive loading introducing a new internal variable associated to damage. The model has been implemented in a commercial finite element code and used to predict single element performance under cycling loading and damage accumulation in a round notch tensile bar. Some preliminary experimental results are also presented.

KEYWORDS

Ductile damage, cyclic loading, fatigue, CDM

INTRODUCTION

In the last decades it has been shown that local approaches have a great potential in predicting the occurrence of failure in specimens, components and structures. Today it is well assessed that ductile failure occurs as a result of microvoids nucleation and growth at inclusions. The local approach is based on the assumption that, if the microscopic mechanism of failure is known, the modification of the material constitutive response can be predicted from micromechanical considerations. Consequently, direct transferability from material to structure, without any geometry effect, would be one of the key features. Many theoretical models have been proposed in the literature that can be grouped in two main sets: continuum damage mechanics (CDM) based models and porosity models. Porosity models, derived from the Gurson type model, are based on the modification of the yield function as a result of the increasing porosity with plastic strain. Here, porosity plays the role of a softening variable that progressively implodes the yield surface in order to account for damage effects. CDM models are developed in the framework of continuum mechanics. Here, damage effects are accounted by a thermodynamic variable, D, that reduces material stiffness. Thus, the complete set of constitutive equations for the material undergoing damage is derived. Both approaches suffer major limitations. Porosity models usually require a large number of material parameters, none of which has a physical

meaning, that have to be identified using coupled numerical simulation and experiments. On the other side, CDM model performance depends on the assumed form for the dissipation potential from which damage evolution law can be derived by normality rule. All the models proposed in the literature show material dependency, lack of performance under multi-axial state of stress conditions and temperature and strain rate effect is usually neglected. In 1997 Bonora [1] proposed a new non-linear CDM model for ductile failure that overcome material dependency and stress triaxiality effects. The model resulted successful in predicting notched and cracked components response using only information, such as damage parameters, identified in simple uniaxial state of stress condition, [2]. Later, Bonora and Milella [3] extended the damage model in order to incorporate temperature and strain rate effects.

Up to now, very little attention have been given to the mechanics of ductile deformation and damage under compressive state of stresses. This issue becomes very important in order to understand and predict component life under low cycle fatigue regime or under intense dynamic loading in which damage accumulation is related to the bouncing motion of strain waves into the body. Bonora and Newaz [4] demonstrated the possibility to predict low cycle fatigue life at ductile crack growth initiation discussing possible integration scheme for the non-linear damage law. At the moment, as far as the authors are aware of, no attempt to extend CDM model formulation to cyclic loading under variable stress triaxiality loading conditions has been made. In this paper, for the first time, the non-linear damage model proposed by Bonora has been extended to negative stress triaxiality loading condition, based on simple physical considerations, introducing a new internal variable associated to damage *D*. The model, implemented in form of user subroutine in the finite element code MSC/MARC, has been tested on single FEM element under simple loading conditions such a as normal and shear stress. Successively, it has been applied to round notched bar specimens loaded in tension. At the present time, an extensive experimental program is under investigation. Here, the promising preliminary results are presented and discussed.

NON-LINEAR CDM MODEL FOR DUCTILE FAILURE

Lemaitre [5] firstly defined the CDM framework for plasticity damage. Damage accounts for material progressive loss of load carrying capability due to irreversible microstructural modifications, such as microvoids formation and growth, microcracking, etc. From a physical point of view, damage can be expressed as

$$D_{(n)} = 1 - \frac{A_{eff}^{(n)}}{A_0^{(n)}} \tag{1}$$

where, for a given normal *n*, $A_0^{(n)}$ is the nominal section area of the RVE and $A_{eff}^{(n)}$ is the effective resisting one reduced by the presence of micro-flaws and their mutual interactions. Even though this definition implies a damage tensor formulation, the assumption of isotropic damage leads to a more effective description where the scalar D can be simply experimentally identified. Additionally, this assumption is not too far from reality as a result of the random shapes and distribution of the included particles and precipitates that trigger plasticity damage initiation and growth. The strain equivalence hypothesis gives the operative definition of damage as:

$$D = 1 - \frac{E_{eff}}{E_0} \tag{2}$$

where E_0 and E_{eff} are the Young's modulus of the undamaged and damaged material, respectively. The complete set of constitutive equation for the damage material can be derived assuming that:
- a damage dissipation potential f_D, similarly to the one used in plasticity theory, exists;
- no coupling between damage and plasticity dissipation potentials exists;
- damage variable, *D*, is coupled with plastic strain;
-the same set of constitutive equations for the virgin material can be used to describe the damaged

material replacing only the stresses with the effective ones and assigning a state equation for *D*.

Bonora [1] proposed the following expression for the damage dissipation potential,

$$f_D = \left[\frac{1}{2}\left(-\frac{Y}{S_0}\right)^2 \cdot \frac{S_0}{1-D}\right] \cdot \frac{(D_{cr}-D)^{\frac{a-1}{a}}}{p^{\frac{2+n}{n}}} \tag{3}$$

where, D_{cr} is the critical value of the damage variable for which ductile failure occurs, S_0 is a material constant and n is the material hardening exponent. α is the damage exponent that determines the shape of the damage evolution curve and is related to the nature of the bound between brittle inclusions and the ductile matrix. Thus, the constitutive equation set for isotropic hardening material is given by:

strain decomposition

$$\dot{e}_{ij}^{T} = \dot{e}_{ij}^{e} + \dot{e}_{ij}^{p} \tag{4}$$

elastic strain rate

$$\dot{e}_{ij}^{e} = \frac{1+n}{E}\frac{\dot{s}_{ij}}{1-D} - \frac{n}{E}\frac{\dot{s}_{kk}}{1-D}d_{ij} \tag{5}$$

plastic strain rate

$$\dot{e}_{ij}^{p} = \dot{l}\,\frac{\P f_p}{\P s_{ij}} = \dot{l}\,\frac{3}{2}\frac{\dot{s}_{ij}}{1-D}\frac{1}{s_{eq}} \tag{6}$$

plastic multiplier

$$\dot{r} = -\dot{l}\,\frac{\P f_p}{\P R} = \dot{l} = \dot{p}(1-D) \tag{7}$$

kinetic law of damage evolution

$$\dot{D} = -\dot{l}\,\frac{\P f_D}{\P Y} = a \cdot \frac{(D_{cr}-D_0)^{\frac{1}{a}}}{\ln(e_f/e_{th})} \cdot f\left(\frac{s_H}{s_{eq}}\right) \cdot (D_{cr}-D)^{\frac{a-1}{a}} \cdot \frac{\dot{p}}{p} \tag{8}$$

Detailed description on the derivation of these Equations can be found elsewhere, [1]. In Equation (9) stress triaxiality effects are accounted by the function $f(s_H/s_{eq})$ defined as,

$$f\left(\frac{s_H}{s_{eq}}\right) = \frac{2}{3}(1+n) + 3\cdot(1-2n)\cdot\left(\frac{s_H}{s_{eq}}\right)^2 \tag{9}$$

that is derived assuming that ductile damage mechanism is governed by the total elastic strain energy, Lemaitre [5]. Here, $\sigma_H = \sigma_{kk}/3$ is the hydrostatic part of the stress tensor and n is the Poisson's ratio. The model requires five material parameters in order to be applied. The strain threshold (in uniaxial monotonic loading) e_{th}, at which damage processes are activated; the theoretical failure strain e_f, at which ductile failure under completely uniaxial state of stress conditions occurs; the initial amount of damage present in the material, D_0; the critical damage, D_{cr}, at which failure occurs and the damage exponent, α, that control the shape of damage evolution with plastic strain. Experimental procedure for damage parameters identification can be found elsewhere, [6].

EXTENSION TO REVERSAL PLASTIC FLOW

Ductile damage formulations available in the literature always address tensile loading configuration, since it is well known that positive stress triaxiality enlarges nucleating voids in the material microstructure. The possible effect on damage variable due to compressive loading is usually neglected in the theoretical formulations. The major consequence of this limitation is that the damage variable, *D*, has to be associated to the total effective accumulated plastic strain, usually indicated with *p*, that plays the role of the associated internal variable. In the literature, little attention is given to the effects on the

material constants, or constitutive response, due to plastic deformation under pure compressive loading. This knowledge is critical in order to develop a predicting model capable to account for plastic strain reversal as for low cycle fatigue. Few attempts based on the cyclic accumulation of damage, or its associated variable, always resulted in predicted very short lives as a consequence of the fact that *p* usually accumulates quickly. Porosity models, such as the Gurson model, are incapable to predict material failure since porosity effects are fully recovered during compressive loading resulting in a unrealistic healing-material behavior, [7]. These premises clearly indicate that additional hypotheses must be formulated in order to describe properly material behavior under compressive stress states. If ductile damage can be imputed to the formation and growth of microcavities that have the effect to reduce the net resisting area, and consequently material stiffness, thus the following scenarios can be speculated.

Scenario a). The material is initially stress-free and it is assumed that no strain history has modified its status from the one of "virgin material". Let us assume to start to load a material reference volume element, RVE, under pure compressive uniaxial state of stress avoiding any buckling phenomena. In this configuration, microvoids cannot nucleate since the ductile matrix is compressed around the brittle inclusions. If the local stress in the particle overcomes the particle strength, the particle itself can eventually break. This kind of damage should not affect material stiffness since no reduction of the net resisting area is occurred. The only effect that we would expect is probably an anticipated microvoids nucleation, due to an early void opening since the particle is broken, when the stress state is reversed in tension, (i.e. a lower strain threshold value). Even though an irreversible process such as particle breaking will eventually occur under compressive loads, the stiffness should remain unaffected indicating no damage in compression.

Scenario b). Let say that the virgin RVE is initially loaded in tension until some amount of damage. Then, the load is reversed in compression developing additional plastic strain. In this case, during the unloading from positive stress-state to zero, microvoids can close controlled by the large ductile matrix volume movement, (here, potential buckling of microcavities is neglected). Voids implode back to the particle from which they have nucleated. Void closure can eventually close to the zero displacement condition. During this phase the net resisting area is restored and the stiffness should be the same as for the virgin material. Continuing in the compressive ramp the stiffness, once again, should remain unaffected. Further compressive loads, will eventually breaks some particles, but no effects are expected on *E*. A new reload in tension would see both the opening of the previously grown voids plus the opening of the new ones nucleated at the broken particles. However, at this stage it can be assumed that compressive damage does not modify damage developed under positive stress states.

It follows that ductile damage can accumulate under positive stress state only, while total plastic strain will accumulate under both. Consequently, the associate damaged variable has to be a redefined as an "active accumulated plastic strain" $\boldsymbol{p}^+$, i.e. the plastic strain that accumulates if and only if, the actual stress triaxiality is greater than zero. Similarly, the damage effect on material stiffness will also be activated if and only if the current stress triaxiality is positive.

According to this, the damage model proposed by Bonora can be modified in terms of active damage $\boldsymbol{D}^+$ and active plastic strain $\boldsymbol{p}^+$ as follows:

$$\dot{D}^+ = -\dot{l}\,\frac{\partial f_D}{\partial Y} = \alpha \cdot \frac{\left(D_{cr} - D_0\right)^{\frac{1}{\alpha}}}{\ln(\varepsilon_f / \varepsilon_{th})} \cdot f\left(\frac{\sigma_H}{\sigma_{eq}}\right) \cdot \left(D_{cr} - D^+\right)^{\frac{\alpha-1}{\alpha}} \cdot \frac{\dot{p}^+}{p^+} \tag{10}$$

$$\dot{p}^+ = \frac{\dot{l}}{(1-D^+)} H\left\langle f\left(\sigma_m / \sigma_{eq}\right)\right\rangle \tag{11}$$

$$\tilde{E} = E(1-D^+) H\left\langle f\left(\sigma_m / \sigma_{eq}\right)\right\rangle \tag{12}$$

where

$$H\left\langle f\left(s_m / s_{eq}\right)\right\rangle = \begin{cases} 0 & s_m / s_{eq} < 0 \\ 1 & s_m / s_{eq} \geq 0 \end{cases} \tag{13}$$

FINITE ELEMENT ANALYSES

Damage model performance under cycling loading has been firstly checked on a single axisymmetric 4 node element. The element size is 1.0 x 1.0 mm. The material is a 22NiMoCr37 steel of German production for which damage parameters were previously determined by Bonora *et al.* (1998). A cyclic imposed displacement with zero mean value δ_m=0 and amplitude δ_a=0.2 mm has been applied until element failure. Response under isotropic and kinematic hardening is given in figure 1 together with the displacement evolution with time. Here, time is a fictitious variable since viscoplastic and time dependent behaviors have been neglected.

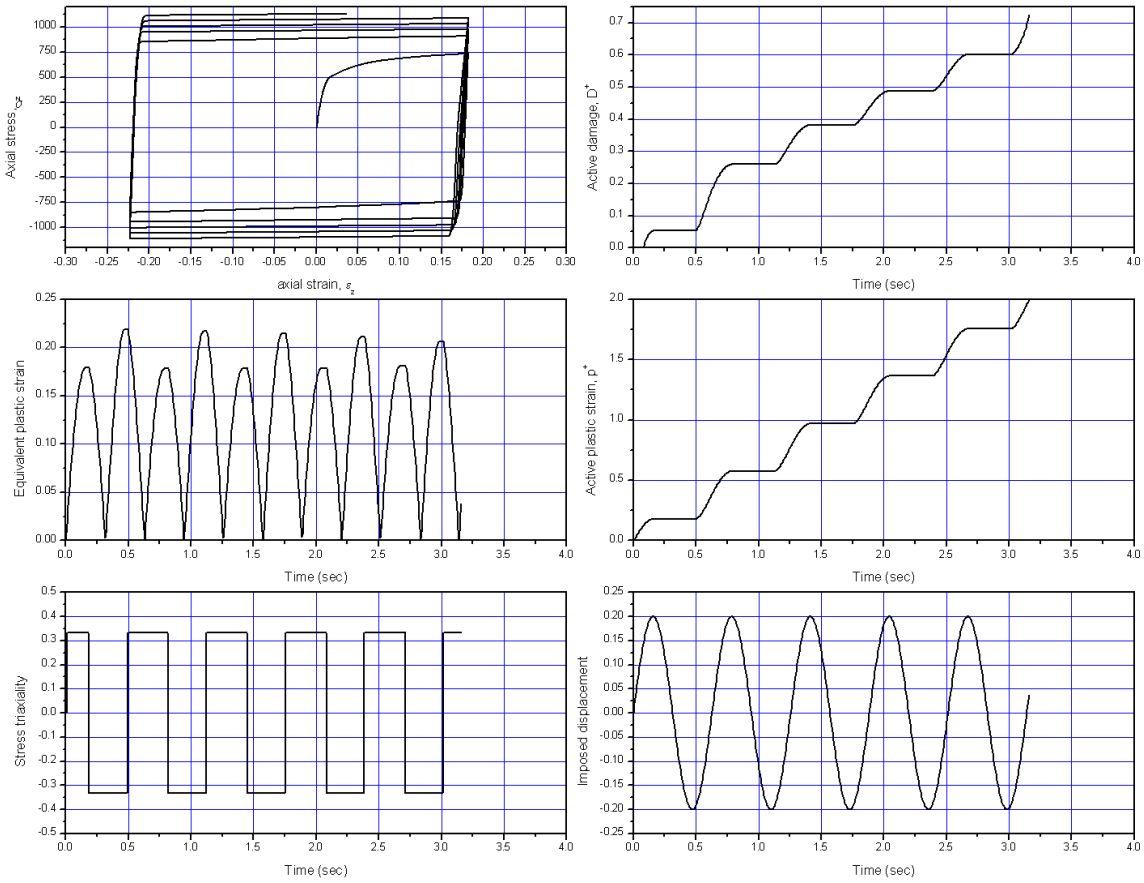

Figure 1 – Single element response under cyclic loading: a) axial stress vs axial strain; b) equivalent plastic strain vs time; c) stress triaxiality vs time; d) active damage vs time; e) active strain vs time; f) imposed displacement vs time

In figure 1 it is shown how the effective plastic strain, together with active damage, accumulates only when stress triaxiality is positive. In this case, where the imposed nominal strain amplitude is 20%, failure is expected to occur after 5 cycles. Subsequently, the model has been used to investigate damage evolution in round notched tensile bar (R = 2mm) under reversal plastic flow loading conditions, figure 2a. At the present time a single test has been performed on SA 537 steel. An initial monotonic ramp up to 0.2 mm has been applied followed by sinusoidal cycling with an amplitude of 0.125 mm. The cycling frequency was 0.0125 Hz. Local deformation field across the notch has been monitored using an extensometer with a gage length of 10 mm. In figure 2b, the comparison between the finite element results and the experimental data is given in term of applied load versus displacement at the gauge. It is important to note that the FEM model incorporating damage is capable to reproduce the load cycle in the near notch region pretty well if kinematic hardening is used. Isotropic hardening results in a very narrow

hysteresis loop. The major difference is given by the macroscopic ratcheting. A posteriori it has been found that this phenomenon can occur in SA537 steel under very low strain rate since at this deformation rate viscoplastic behavior becomes manifested. Experimental test has been stopped after 20 cycles. According to finite element prediction only a limited amount of damage should be generated in the specimen minimum section without failure in this cycling. In figure 3 the deformed mesh showing damage contours after 7 cycles is given as a sample.

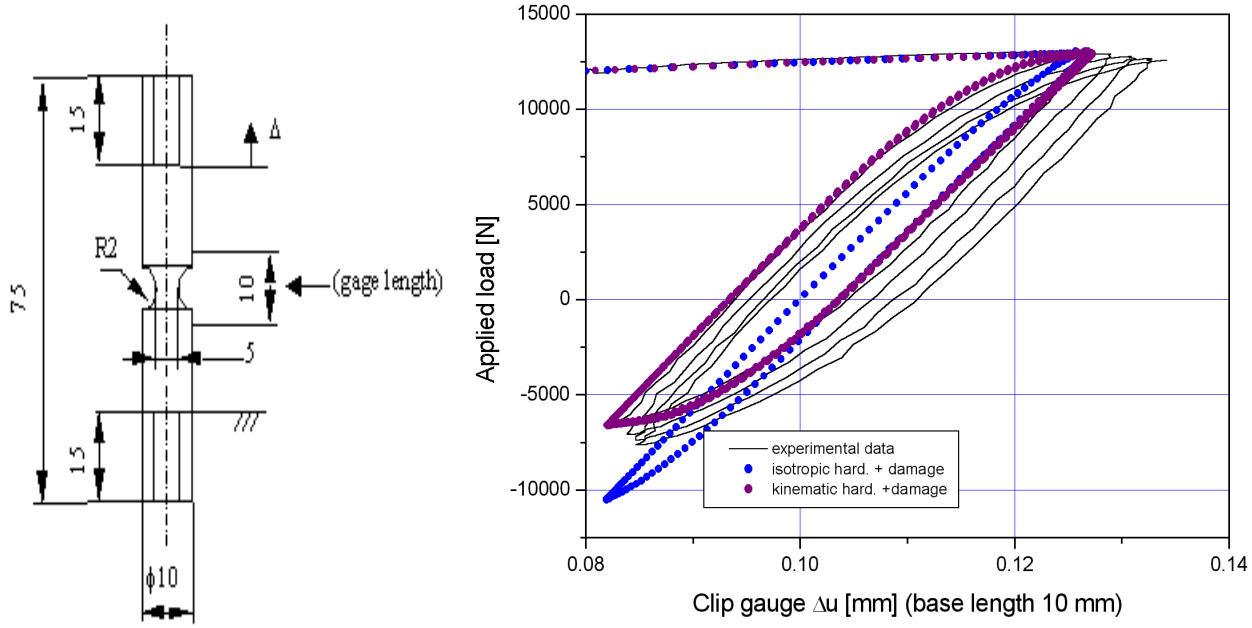

Figure 2a – RNB(T) specimen geometry and dimensions 2b- cyclic response: comparison between FEM results and experimental data

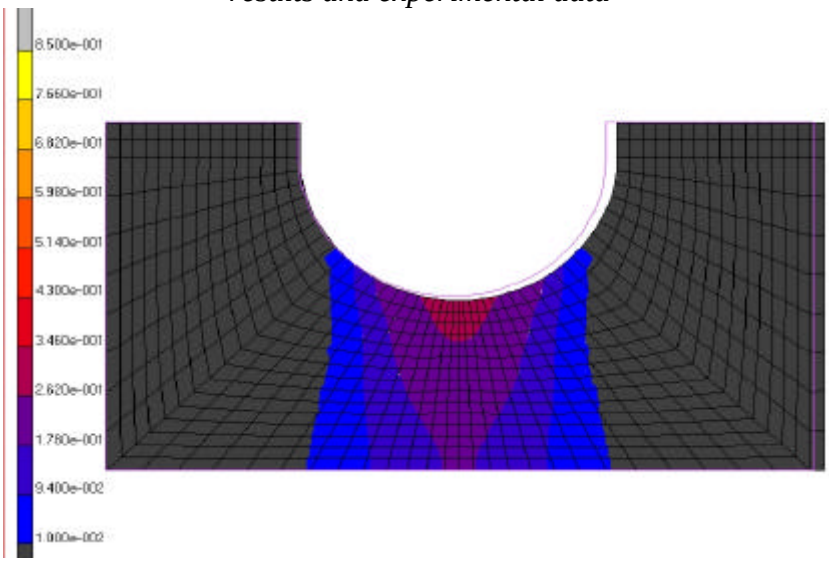

Figure 3 – Damage contours along the minimum section after 7 cycles.

REFERENCES

1. Bonora, N., (1997), *Eng. Frac. Mech.*,, **58**, pp. 11-28
2. Bonora, N., (1998), *Int. J. Frac.*, **88**, pp.359-371
3. Bonora, N., and Milella, P.P. (2001), *J. of Impact Engng.*, to appear.
4. Bonora N., and Newaz, G., (1998), *Int. J. Solids and Struc.*, **35** , pp. 1881-1894
5. Lemaitre, J., (1986), *Engng. Fract. Mech.*, **25**, No. 5/6, pp.523-537
6. Bonora, N, (1999), *J. Strain Analysis*, **34**, 6, pp. 463-478
7. Brocks, W., Bonora, N., O'Dowd, N. and Steglich, D., (2000), personal discussion at GKSS

DUCTILE DAMAGE AND CRACK GROWTH ANALYSIS IN 3D STRUCTURES
LIMITATIONS OF CDM APPROACHES

D. Gross and H. Baaser

Institute of Mechanics, Darmstadt University of Technology
Hochschulstrasse 1, D–64289 Darmstadt, Germany
gross@, baaser@mechanik.tu-darmstadt.de

ABSTRACT

Ductile crack initiation and growth is investigated by applying a three–dimensional finite element (FE) analysis in conjunction with a nonlinear damage model. This numerical procedure is formally restricted by the so–called "loss of ellipticity" due to a type change of the differential equations. A time–independent finite strain formulation is applied based on a multiplicative decomposition of the deformation gradient in an elastic and a plastic part leading to an efficient integration scheme. This formulation can be used as a general interface for the implementation of different constitutive models describing "damage" by a scalar quantity in an isotropic manner.
The general problem of describing on the microlevel strongly inhomogenious material behaviour by discretization methods using macroscopic mechanical field quantities, which are microscopic averages, is discussed. Often, typical discretization length scales fall obviously below the intrinsic material length scales, making the sense of the averaging structure of the applied numerical method doubtful.

KEYWORDS

3D–Finite–Element–Simulation, Finite Strain Plasticity, Ductile Damage, Loss of Ellipticity

INTRODUCTION

During the last years applications of models based on continuum damage mechanics (CDM) to ductile fracture mechanics become very popular. The computational evaluation and simulation of damage occurance by different models implemented in the framework of the FEM seems to be very promising, since lots of contributions have followed the first, fundamental publications such as [5], [11] or [7]. It is the common belief that the application of the FE method considering nonlinearities due to advanced constitutive damage models and finite deformations may be capable of simulating classical fracture specimens and test conditions. A well–known disadvantage in the numerical treatment of solid mechanics problems, where softening material behavior occurs, is the so–called *mesh–dependence* of numerical results. In a considerable number of investigations different methods have been proposed to overcome the mesh–dependence of finite element results. The common idea is to introduce a *characteristic* or *internal* length (scale) into the constitutive model or its evaluation, see [2], [3] or [4] and references therein, where a summary of different regularization techniques is outlined.
In this article some limitations and restrictions of ductile damage mechanics analysis in the scope of the finite element method and its nonlinear solution procedures are precisely pointed out at the example of a CT specimen. In order to resolve the highly nonlinear effects of stress and strain concentration occuring near notches, crack tips or due to shear band localization, the numerical discretization in these regions usually is refined without respecting minimal length scales limited by *inhomogenities* on the microscale of the material. Typical physically based length scales of ductile materials such as structural steel or aluminium alloys are in the magnitude of about 50μm – 200μm. But very often length scales resulting from FE discretizations of detailed simulations of damage and crack initiation and growth problems fall below these "natural" barriers. As a consequence, the basic assumptions of continuum mechanics such as continuity of mechanical quantities on the macroscale are violated definitely and the numerical results are highly questionable.
In this study 20–noded brick 3D elements are used with quadratic shape functions along the element edges. As a constitutive model, the ductile damage model of [7] is used. An advantage of this model is the description of material softening behavior due to damage by the influence of solely three material parameters. The second advantage is related to the numerical implementation of the constitutive law by means of an implicit integration scheme. The type of the constitutive equations leads to symmetric tangent material moduli, which is advantageous in computing and storing the matrix expressions. Simultaneously a localization analysis is performed during the iteration on every integration point by evaluation of the so called *localization* or *acoustic tensor* for all possible directions of localization in three dimensions. The fundamental derivation of the acoustic tensor in the case of finite strains is described in [10]. An essential result of this

load, but is restricted until the situation where loss of ellipticity occurs. The investigation is illustrated by a 3D discretization of a CT specimen considering ROUSSELIERs damage model.

3D FINITE ELEMENT FORMULATION

Starting point of any finite element discretization is the weak form of equilibrium $g(\mathbf{u}, \delta\mathbf{u})$ formulated in the current configuration, where $\mathbf{u}$ is the displacement and $\mathbf{t}_L$ are the prescribed tractions acting on the loaded boundary $\partial\mathcal{B}_\sigma$ of the body in the current configuration $\mathcal{B}$. Linearization with respect to the current deformation state and rearrangement leads (with $\mathrm{d}v = J\,\mathrm{d}V$) to the following representation of the element stiffness

$$Dg^{elmt}(\hat{\mathbf{u}}, \delta\mathbf{u}) = \int_{\mathcal{B}_0} J\ (\Delta\boldsymbol{\sigma} + \mathrm{grad}\Delta\mathbf{u}\cdot\boldsymbol{\sigma}) : \mathrm{grad}\,\delta\mathbf{u}\ \mathrm{d}V^{elmt}\,, \tag{1}$$

where $J = \det\mathbf{F}$ and $\mathcal{B}_0$ denotes the reference configuration. For further explanations on the implementation of the consistent linearization of the used algorithm see [9]. The discretization chosen in this paper is based on a 20–node–displacement element formulation with shape functions N_i, $(i = 1, 2, ..., 20)$, so that quadratic functions describe the element edges. As in [6], a $2 \times 2 \times 2$ integration scheme is used, which means an *underintegration* with respect to the quadratic shape functions N_i. It shall be pointed out that no *hourglassing* modes were detected like in the case of an 8–node–displacement element formulation and a $1 \times 1 \times 1$ integration scheme, see [2].

FINITE STRAIN PLASTICITY AND DAMAGE MODEL

Finite strain plasticity

At least in the crack tip region of elastic–plastic solids under sufficiently high load, finite deformations occur where the plastic part of the strains usually is large compared with the elastic part. The framework of multiplicative elastoplasticity is used, which is widely accepted in plasticity.. Its kinematic key assumption is the multiplicative split of the deformation gradient $\mathbf{F} = \mathbf{F}_{el}\cdot\mathbf{F}_{pl}$ into an elastic and a plastic part, providing the basis of a geometrically exact theory and avoiding linearization of any measure of deformation. As a further advantage, fast and numerically stable iterative algorithms, proposed and described in [9], can be used. In the following, only a brief summary of the algorithm in the context of a FE–implementation is given. The essential aspect of the multiplicative decomposition is the resulting additive structure of the current logarithmic principal strains within the return mapping scheme as $\boldsymbol{\epsilon}^{el} = \boldsymbol{\epsilon}^{tr} - \Delta\boldsymbol{\epsilon}^{pl}$. Here, $\epsilon_i = \ln\lambda_i$ $(i = 1, 2, 3)$ and λ_i^2 are the eigenvalues of an elastic trial state, described by the left CAUCHY–GREEN tensor $\mathbf{b}_{el}^{tr}$. The elastic strains $\boldsymbol{\epsilon}^{el}$ are defined by HOOKE's law and the plastic strain corrector $\Delta\boldsymbol{\epsilon}^{pl}$ can be derived by the normality rule of plastic flow. The elastic left CAUCHY–GREEN tensor can be specified with the multiplicative decomposition as $\mathbf{b}_{el} = \mathbf{F}_{el}\cdot\mathbf{F}_{el}^{\mathrm{T}} = \mathbf{F}\cdot\mathbf{C}_{pl}^{-1}\cdot\mathbf{F}^{\mathrm{T}}$, which clearly shows the "connection" between the elastic and plastic deformation measure by the occurance of the plastic right CAUCHY–GREEN tensor $\mathbf{C}_{pl} = \mathbf{F}_{pl}^{\mathrm{T}}\cdot\mathbf{F}_{pl}$. By means of the relative deformation gradient (see [9]) $\mathbf{f} = \partial\mathbf{x}/\partial\mathbf{x}_{n-1} = \mathbf{F}\cdot\mathbf{F}_{n-1}^{-1}$ which relates the current configuration $\mathbf{x}$ to the configuration belonging to the previous time step at t_{n-1}, an elastic *trial*–state $\mathbf{b}_{el}^{tr} = \mathbf{f}\cdot\mathbf{b}_{n-1}\cdot\mathbf{f}^{\mathrm{T}}$ is calculated for the current configuration with frozen internal variables at state t_{n-1}. If the condition $\Phi \leq 0$ (see Eqn. (2)) is fulfilled by the current stress state $\boldsymbol{\tau}$, this state is possible and it is the solution. If, on the other hand, $\Phi \leq 0$ is violated by the trial–state, the trial stresses must be projected back on the yield surface $\Phi = 0$ in an additional step, often called "return mapping".

Rousselier Damage Model

Following the ideas of [1] the stress and strain tensors are decomposed into scalar quantities, which is of advantage for the numerical implementation. Thus, the KIRCHHOFF stress tensor $\boldsymbol{\tau}$ is written as the weighted CAUCHY stress tensor as $\boldsymbol{\tau} = J\,\boldsymbol{\sigma} = -p\mathbf{1} + 2/3\,q^\tau\,\mathbf{n}^\tau$, where $J := \det\mathbf{F} = \mathrm{d}v/\mathrm{d}V = \rho_0/\rho$ and $p = -\tau_{ij}\delta_{ij}/3$ defines the hydrostatic pressure, $q^\tau = \sqrt{3/2\,t_{ij}t_{ij}}$ is the equivalent stress and $t_{ij} = \tau_{ij} + p\delta_{ij}$ are the components of the stress deviator. In this notation, an additional important quantity is the normalized stress deviator $\mathbf{n}^\tau = 3/(2q^\tau)\mathbf{t}$. The second order unit tensor $\mathbf{1}$ is defined as the KRONECKER symbol by its components δ_{ij} in the cartesian frame. In an analogous way the plastic strain rate can be written as $\Delta\boldsymbol{\epsilon}^{pl} = \frac{1}{3}\Delta\varepsilon_p\mathbf{1} + \Delta\varepsilon_q\mathbf{n}^\tau$, where $\Delta\varepsilon_p$ and $\Delta\varepsilon_q$ describe scalar rate quantities which are defined below. The constitutive model used in this study is the damage model proposed by [7]. Here, taking ductile damage processes into account, the yield function is written as

$$\Phi = q^\tau - \underbrace{\sigma_0\left[\frac{\varepsilon_{eqv}^{pl}}{\sigma_0}E + 1\right]^{1/N}}_{\sigma^*} + B(\beta)D\exp(-\frac{p}{\sigma_1}) = 0\,, \tag{2}$$

the damage (softening) behavior by the function $B(\beta)$ and an exponential assumption. Furthermore, D is the YOUNG modulus, σ_0 is the initial yield stress, N is the material hardening exponent, and D and σ_1 are *damage* material parameters. The function $B(\beta)$ is the *conjugate force* to the damage parameter β, defined by $B(\beta) = \sigma_1 f_0 \exp(\beta)/[1 - f_0 + f_0 \exp(\beta)]$. Here, the initial void volume fraction f_0 is the third damage–depending material parameter used in this constitutive set of equations. The macroscopic plastic strain rate $\dot{\boldsymbol{\epsilon}}^{pl}$ is determined by the classical associated flow rule

$$\dot{\boldsymbol{\epsilon}}^{pl} = \dot{\lambda} \frac{\partial \Phi}{\partial \boldsymbol{\tau}} = \dot{\lambda} \left\{ \frac{\partial \Phi}{\partial q^\tau} \frac{\partial q^\tau}{\partial \boldsymbol{\tau}} + \frac{\partial \Phi}{\partial p} \frac{\partial p}{\partial \boldsymbol{\tau}} \right\} . \tag{3}$$

Note that $\dot{\boldsymbol{\epsilon}}^{pl}$ coincides with the plastic increment $\Delta\boldsymbol{\epsilon}^{pl}$ for the algorithmic setting written in the principal axes. The last bracket on the right hand side of (3) shows a further advantage of this formulation following [1], since it is easy to determine the derivatives of Φ with respect to the scalar quantities q^τ and p. It can be seen with (3) that

$$\Delta\varepsilon_p = -\dot{\lambda} \frac{\partial \Phi}{\partial p} \quad \text{and} \quad \Delta\varepsilon_q = \dot{\lambda} \frac{\partial \Phi}{\partial q^\tau} . \tag{4}$$

These two equations allow the algebraic elimination of $\dot{\lambda}$. Thus, the increment of the plastic strain can be expressed by the two scalar quantities $\Delta\varepsilon_p$ and $\Delta\varepsilon_q$. Then the equivalent plastic strain ε^{pl}_{eqv} can be incremented directly by $\Delta\varepsilon_q$. The evolution equation for the damage parameter β is given by $\Delta\beta = \Delta\varepsilon_q D \exp(-\frac{p}{\sigma_1})$, which is obviously dependent on the deviatoric part of the strain rate $\Delta\varepsilon_q$ and the actual hydrostatic pressure p. With this the whole set of the constitutive equations is completed. The evaluation of the material model on the local level of integration points for a given load is realized by an implicit EULER backward integration scheme for the unknowns $\Delta\varepsilon_p$, $\Delta\varepsilon_q$ and $\Delta\beta$. The exact linearization of the set of equations follows the description in [1]. The variational expression

$$\delta\boldsymbol{\tau} = \mathbf{C} : \left(\delta\boldsymbol{\epsilon}^{tr} - \frac{1}{3}\delta\Delta\varepsilon_p \mathbf{1} - \delta\Delta\varepsilon_q \mathbf{n}^\tau - \Delta\varepsilon_q \frac{\partial \mathbf{n}^\tau}{\partial \boldsymbol{\tau}} : \delta\boldsymbol{\tau} \right) \tag{5}$$

leads, after some extended algebraic manipulations as described in [1], to the expressions $\delta\Delta\varepsilon_p$ and $\delta\Delta\varepsilon_q$ and finally to the material modulus for the implicit integration procedure at the end of the considered time interval $[t, t + \Delta t]$.

LOCALIZATION ANALYSIS

Acoustic Tensor

A steady evaluation of the "spatial localization tensor" $\mathbf{Q}$ is performed on every integration point during the iteration to check for material stability. The spatial localization tensor $\mathbf{Q} = \mathbf{n} \cdot \mathbb{D} \cdot \mathbf{n}$ is the contraction of the current fourth order material tensor $\mathbb{D}$ by the spatial surface unit normal vector $\mathbf{n}$ with respect to its second and fourth index. This derivation is introduced in [10] motivated by the assumption of spatially continuous incremental equilibrium across an arbitrary band of discontinuity, which implies that the nominal traction rate inside and outside the band is the same: $\overset{\circ}{\mathbf{t}}(\mathbf{x}^{out}) = \overset{\circ}{\mathbf{t}}(\mathbf{x}^{band})$. With the definition of the nominal traction rate $\overset{\circ}{\mathbf{t}} = J^{-1} \overset{\circ}{\boldsymbol{\tau}} \cdot \mathbf{n}$, the nominal rate of the KIRCHHOFF stress tensor $\overset{\circ}{\boldsymbol{\tau}}$ can be related to the spatial velocity gradient $\mathbf{l} := \dot{\mathbf{F}} \cdot \mathbf{F}^{-1}$ via $\overset{\circ}{\boldsymbol{\tau}} = \mathbb{D} : \mathbf{l}$. These relations become more evident by reformulation of the material rate of the first PIOLA–KIRCHHOFF stress tensor $\dot{\mathbf{P}}$ in terms of the KIRCHHOFF stress tensor $\boldsymbol{\tau}$ into $\dot{\mathbf{P}} = \mathbf{F}^{-1} \cdot \dot{\boldsymbol{\tau}} - \mathbf{F}^{-1} \cdot \mathbf{l} \cdot \boldsymbol{\tau}$. Relating $\dot{\mathbf{P}}$ to the rate of the deformation gradient $\dot{\mathbf{F}}$ via the tangent map $\mathbb{D}^{\mathrm{P}}$, yields

$$\overset{\circ}{\boldsymbol{\tau}} = \dot{\boldsymbol{\tau}} - \mathbf{l} \cdot \boldsymbol{\tau} = \mathbf{F} \cdot \mathbb{D}^{\mathrm{P}} : \dot{\mathbf{F}} , \tag{6}$$

which coincidences with the known *frame–invariant* (*objective*) OLDROYD rate $\overset{\triangledown}{\boldsymbol{\tau}}$ by $\overset{\circ}{\boldsymbol{\tau}} = \overset{\triangledown}{\boldsymbol{\tau}} + \boldsymbol{\tau} \cdot \mathbf{l}^{\mathrm{T}}$. Note that the derivations and the argumentation in [8] — depicted for the case of small strains — about loss of material stability by real or imaginary wave speeds very illustratively denote the term "acoustic tensor" for the double contraction $\mathbf{Q} = \mathbf{n} \cdot \mathbb{D} \cdot \mathbf{n}$ of the material tensor $\mathbb{D}$ by the normal vector $\mathbf{n}$ indicating a possible wave propagation direction. The condition for getting reasonable numerical results is the positive definiteness of the second order tensor $\mathbf{Q}$, which belongs to a positive value of the determinant $q = \det[\mathbf{Q}]$.

Numerical treatment

During the numerical analysis $q = \det[\mathbf{Q}] = \det[\mathbf{n} \cdot \mathbb{D} \cdot \mathbf{n}]$ has to be evaluated for all possible directions $\mathbf{n}$

spherical coordinates with the angles α and β characterizing the longitude and the latitude, respectively. To detect a possible critical direction, where q may vanish, one has to compute $q = \det[\mathbf{Q}] \rightarrow min$ for a set $\{\alpha, \beta\}$. This minimization procedure is synonymous to the evaluation of $\nabla q(\alpha, \beta) = \mathbf{0}$, which can be obtained by a classical NEWTON iteration scheme through

$$\begin{bmatrix}\alpha\\ \beta\end{bmatrix}_{k+1} = \begin{bmatrix}\alpha\\ \beta\end{bmatrix}_{k} - \begin{bmatrix}\frac{\partial^2 q}{\partial \alpha^2} & \frac{\partial^2 q}{\partial \alpha\, \partial \beta}\\ \frac{\partial^2 q}{\partial \alpha\, \partial \beta} & \frac{\partial^2 q}{\partial \beta^2}\end{bmatrix}^{-1} \cdot \begin{bmatrix}\frac{\partial q}{\partial \alpha}\\ \frac{\partial q}{\partial \beta}\end{bmatrix}, \tag{7}$$

and suitable initial conditions, e.g. $[\alpha, \beta]_0^{\mathrm{T}} = [0.1, 0.1]_0^{\mathrm{T}}$, where k indicates the iteration loop number. Because of the large number of operations, the expressions of the related FORTRAN code are obtained by the algebraic manipulation program MATHEMATICA exploiting some advanced methods for code generation.

EXAMPLE AND RESULTS

Model of a CT specimen

As example, a three–dimensional model of a CT specimen discretized by 20–node solid elements as shown in Fig. 1(1) is examined. Due to symmetry, just a quarter of the structure is modeled, for length dimensions

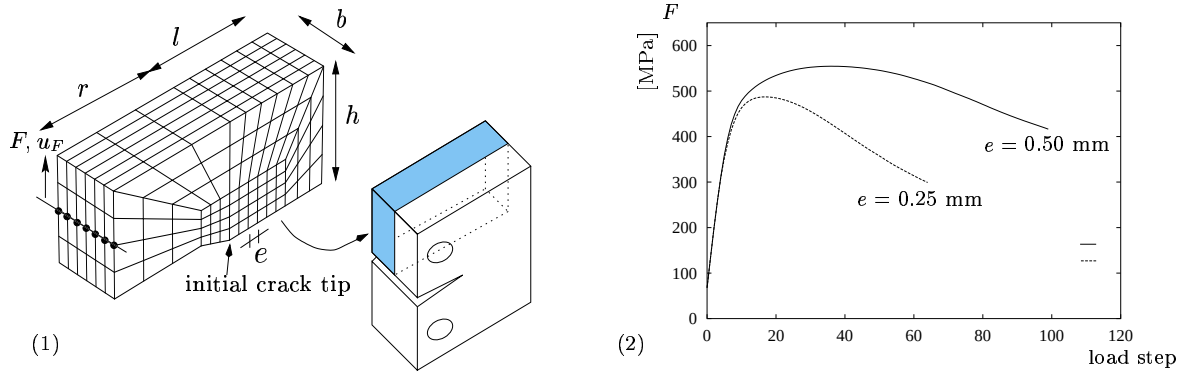

Figure 1: Model of CT specimen and typical load–deflection curve for different discretizations

see Tab. 1. The loading is applied by a prescribed displacement u_F (by 0.01 mm/step) of the nodes lying on the marked line, see Fig. 1(1). The chosen discretization is characterized by the typical element edge length e in front of the crack tip. In this investigation the element edge lengths $e = 0.50$ mm and $e = 0.25$ mm are used. Additionally the typical mesh sensitive results for a classical, local FE simulation using different discretizations are plotted as load–deflection curve in Fig. 1(2), where obviously the dependence of the reaction force on the finite element mesh can be seen. The set of material parameters used is shown in Tab. 1, where the first four parameters can be obtained by simple tensile tests, and D, σ_1 and f_0 are responsible for the damage representation of the constitutive model.

Table 1: MATERIAL PARAMETERS

E [MPa]	ν	σ_0 [MPa]	N	D	σ_1 [MPa]	f_0	r [mm]	l [mm]	b [mm]	h [mm]
210000	0.2	460	7	3	300	0.01	6	5	3	5

Results

A result for the load–displacement curves for different discretizations is plotted in Fig. 1(2) and can also be found in [3]. The mesh sensitivity is obvious, if no additional regularization technique is applied. In the following, we concentrate on computations resulting from the evaluation of the localization tensor $\mathbf{Q}$ and its determinant. The representation of the results is focussed on observations of the FE–integration point being located directly in front of the crack tip in the center of the specimen, which is the highest loaded point with the most increased damage parameter. Fig. 2 shows the normalized determinant of $\mathbf{Q}$ vs. the two spatial angles α and β parameterizing the normal vector $\mathbf{n}$ in each case by 20 steps (ROUSSELIER parameter set of Tab. 1 and $e = 0.50$ mm). Displayed is the situation for load steps 2, 4 and 8 ($u_F = 0.02, 0.04, 0.08$ mm), which represents directly the situation before the onset of localization ($q \rightarrow 0$). Obviously one can recognize the decrease of $q/|Q_{11}Q_{22}Q_{33}|$ during load steps 2–8.

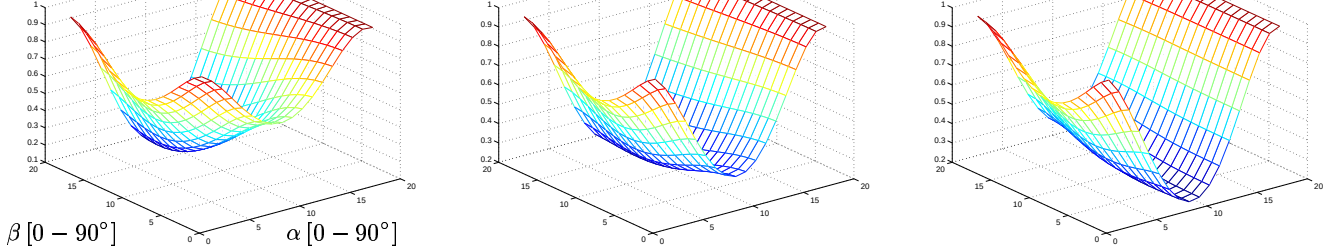

load step 2, $u_F = 0.02$ mm | load step 4, $u_F = 0.04$ mm | load step 8, $u_F = 0.08$ mm

Figure 2: Evaluation of the acoustic tensor

Because of the numerical costs determining these quantities during the iteration, we apply a NEWTON iteration scheme following Eqn. (7) for finding the minimum of these surfaces. For the integration point of interest, Fig. 3(1) shows the value of det $[\mathbf{Q}]$ vs. 30 load steps for two different discretizations with $e = 0.50$ mm and $e = 0.25$ mm and ROUSSELIER material, respectively. Additionally, the situation for a standard (non damaging) VON MISES material with the same power–hardening law σ^* and $e = 0.50$ mm is plotted. As expected, for the VON MISES material, the values of q decrease rapidly during the load incrementation over 30 steps, but never reach $q = 0$ indicating a possible localization.
In contrast, the curves for the ROUSSELIER damage material representation show precisely a zero–crossing and thus a localization occurance. Again, the mesh sensitivity is obvious through the results for $e = 0.25$ mm at load step 4, while the discretization with $e = 0.50$ mm reaches zero at load level 9. In Fig. 3(2) the equiv-

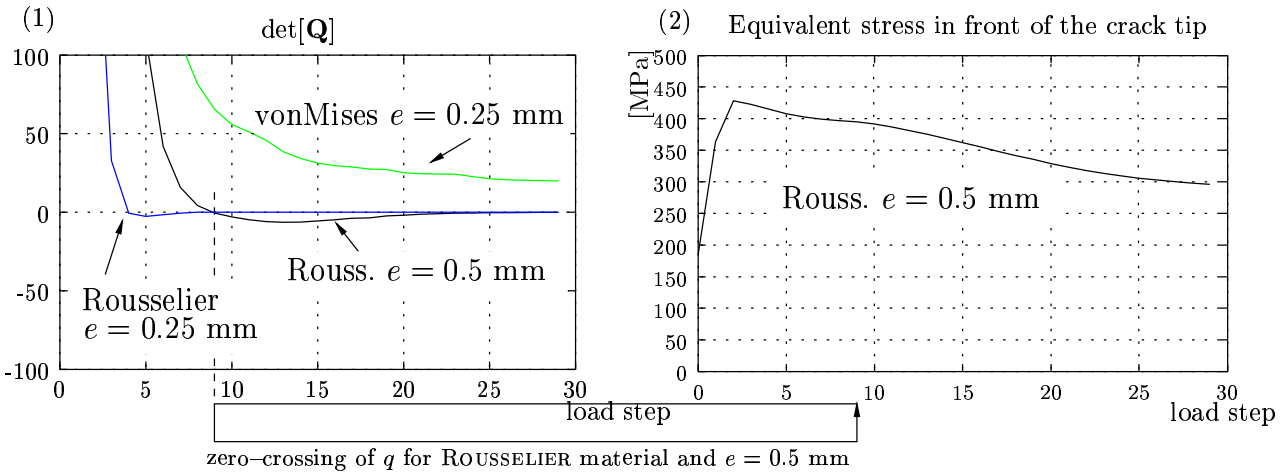

Figure 3: Determinant of acoustic tensor $\mathbf{Q}$ and equivalent stress in front of the crack tip

alent stress of the integration point in front of the crack tip is plotted vs. the applied load steps for the ROUSSELIER material and $e = 0.50$ mm. Note that the equivalent stress at the critical load level 9 ($u_F = 0.09$ mm) appears in the decreasing part of the load curve obviously after reaching the peak load.
Fig. 4 depicts the contours of integration points, where the determinant of the acoustic tensor reaches zero for the load steps 10, 20 and 30 in front of the crack tip. The contour lines in crack propagation direction are plotted over the discretized width b of the specimen using $e = 0.50$ mm and the ROUSSELIER material set of Tab. 1 demonstrating local loss of ellipticity in front of the crack tip during the computation. It should be emphasized, that the contour lines $q = 0$ must not be mixed up with the contour lines of lost load carrying capacity (crack growth) defined by a critical damage parameter. These crack growth contours follow the $q = 0$ contours far behind (at higher load steps), indicating that they are determined in inadmissible situations. These results show impressingly the close limits of the continuum damage mechanics using the FE method without additional regularization avoiding a type change of the leading differential equation. Mesh refinements resulting in the typical mesh sizes in the magnitude of the intrinsic material length scales can not represent the real, potentially inhomogenious, material structure on the microlevel.

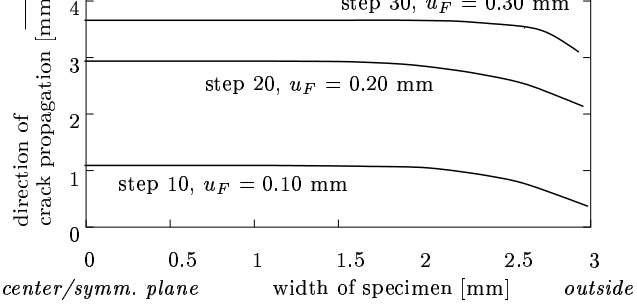

Figure 4: Contours of integration points on the ligament reaching $q = 0$ for load steps 10, 20, 30 using the ROUSSELIER material set and $e = 0.50$ mm

SUMMARY

In this contribution we present a study on ductile damage analysis by a 3D simulation of CT specimen using the ROUSSELIER damage model combined with a 3–dimensional finite element formulation based on 20–node–solid elements. The main attention is put to the limitations of the finite element method discretizing mechanical field equations by piecewise continuous functions, which are used to represent inhomogenious constituents of material on the microscale.
Typical FE analyses, resolving the situations in front of crack tips or in shear band regions as detailed as possible, are known to produce very mesh sensitive results because of the changing type of the basic differential equations. This "loss of ellipticity" is checked by a steady evaluation of the acoustic tensor and a stop of the overall computation reaching such a point of stability. It is worth mentioning that this critical situation is reached very early during the nonlinear iteration process, so that the subsequently determined numerical results become questionable, if no method of regularization is applied.

REFERENCES

[1] N. Aravas. On the numerical integration of a class of pressure–dependent plasticity models. *International Journal for Numerical Methods in Engineering*, 24:1395–1416, 1987.

[2] H. Baaser and D. Gross. Damage and strain localisation during crack propagation in thin–walled shells. In A. Bertram and F. Sidoroff, editors, *Mechanics of Materials with Intrinsic Length Scale*, number ISBN 2-86883-388-8, pages 13–17, Magdeburg, Germany, 1998A. EDP Sciences. Journal de Physique IV, **8**.

[3] H. Baaser and D. Gross. 3D Nonlocal Simulation of Ductile Crack Growth — A Numerical Realization. *European Journal of Finite Elements*, 2001. To appear.

[4] H. Baaser and V. Tvergaard. A new algorithmic approach treating nonlocal effects at finite rate-independent deformation using the ROUSSELIER damage model. *submitted to Computer Methods in Applied Mechanics and Engineering*, 2000. see also DCAMM Report 647, TU Denmark, Lyngby.

[5] A.L. Gurson. Continuum theory of ductile rupture by void nucleation and growth: Part I - yield criteria and flow rules for porous ductile media. *Journal of Engineering Materials and Technology*, 99:2–15, 1977.

[6] K.K. Mathur, A. Needleman, and V. Tvergaard. Ductile failure analyses on massively parallel computers. *Computer Methods in Applied Mechanics and Engineering*, 119:283–309, 1994.

[7] G. Rousselier, J.-C. Devaux, G. Mottet, and G. Devesa. A methodology for ductile fracture analysis based on damage mechanics: An illustration of a local approach of fracture. *Nonlinear Fracture Mechanics*, 2:332–354, 1989.

[8] H.L. Schreyer and M.K. Neilsen. Analytical and numerical tests for loss of material stability. *International Journal for Numerical Methods in Engineering*, 39:1721–1736, 1996.

[9] J.C. Simo. Algorithms for static and dynamic multiplicative plasticity that preserve the classical return mapping schemes of the infinitesimal theory. *Computer Methods in Applied Mechanics and Engineering*, 99:61–112, 1992.

[10] P. Steinmann, R. Larsson, and K. Runesson. On the localization properties of multiplicative hyperelasto–plastic continua with strong discontinuities. *International Journal of Solids and Structures*, 34(8):969–990, 1997.

[11] V. Tvergaard. Material failure by void growth to coalescence. *Advances in Applied Mechanics*, 27:83–151, 1989.

DUCTILE FRACTURE ANALYSIS OF STRUCTURAL STEEL USING MICROMECHANICAL MODELLING

M. Rakin[1], A. Sedmak[2], S. Sedmak[1], M. Zrilic[1], S. Putic[1]

[1]Faculty of Technology and Metallurgy, University of Belgrade, Karnegijeva 4,
11000 Belgrade, Yugoslavia
[2]Faculty of Mechanical Engineering, University of Belgrade, 27 Marta 80,
11000 Belgrade, Yugoslavia

ABSTRACT

Modelling of ductile fracture initiation on a precracked geometry, based on knowledge of the behaviour at tension of simple uncracked material, has been done within the scope of micromechanical analysis. Finite element calculation has been applied in two steps: first, on a tensile round smooth specimen and then, on the standard CT specimen. Analysis was performed on low-alloy structural steel as a part of Round Robin on Micromechanical Models, organised by European Structural Integrity Society (ESIS) - Technical Committee for numerical methods (TC8) [1].

Micromechanical model based on a particular criterion of flow in a porous solid has been applied. The model was initially established by Gurson, and later on modified by Tvergaard and Needleman (the GTN model).

The value of critical void volume fraction, f_c, was first determined on a smooth specimen, and then used for modelling of crack growth initiation in standard CT25 specimen. Four-node and eight-node isoparametric finite elements (FE) with reduced integration were used. Crack tip singularity of CT specimen has been modelled only using a rather fine mesh. The large strain analysis with updated Lagrangian formulation has been used in both calculations. Probably the most difficult part of ductile fracture analysis, to present physically void nucleation as accurately as possible, was carried out by quantitative metallographic analysis of size and number of non-metallic inclusions in steel.

The results obtained suggest that the critical values of micromechanical parameters according to GTN model may be used for approximate prediction of ductile fracture initiation on CT specimen for tested steel.

KEYWORDS

ductile fracture of steel, micromechanical modeling, finite element calculation, crack initiation, non-metallic inclusions, void volume fraction

INTRODUCTION

Micromechanism of ductile fracture of most metals and alloys includes void nucleation, growth and coalescence. Application of so-called global criteria of fracture mechanics such as COD and J-integral in characterisation of ductile fracture initiation does not provide satisfactory results for all cases of external

loading. The problems arising in solving the phenomenon of severe plastic strain at crack tips and application of the results obtained to account for the behaviour of various structures of different geometry are not insignificant. Micromechanical approach is introduced in an effort to describe the process of fracture in a way close to actual phenomena in a material. It means that it is necessary to define as accurately as possible the stress/strain fields, and at the same time the values of the variables describing material damage.

Micromechanical model based on plastic-flow function as formulated by Gurson [2] and modified by Tvergaard and Needleman [3,4] is most widely used for the analysis of initiation of ductile fracture of the alloys. Unlike traditional flow criteria (e.g. von Mises criterion), this one introduces the void volume fraction, f, variable. Numerical and experimental analysis of the modified Gurson model, most frequently referred to as Gurson-Tvergaard-Needleman (GTN) model, shows that the development of damage at microscopic level and plastic strain as a global, macroparameter affected by external loading can be well-described and determined [1,5,6,7].

In this paper, the round smooth specimen ϕ6 and compact tension specimen CT25 ($a_0/W = 0{,}56$) have been analysed according to ESIS TC8 Numerical Round Robin on Micromechanical Models, Phase II, Task A [1]. Void nucleation around non-metallic inclusions in tested low-alloy steel 22 NiMoCr 3 7 has been examined using quantitative metallographic analysis. Based on this analysis, initial void volume fraction, used as an input datum in FE calculation, was determined.

Criterion of crack initiation based on GTN model - critical void volume fraction, f_c - has been determined on smooth specimen and used in prediction of crack growth initiation on CT25 specimen. Fractography of smooth specimen has been performed and crack initiation site has been determined.

MICROMECHANICAL MODELLING OF DUCTILE FRACTURE USING THE GTN MODEL

Ductile fracture of structural steel is initiated by void nucleation, growth and coalescence around non-metallic inclusions and second-phase particles in metal matrix. Depending on the size, shape and quantity of these particles in steel, several models have been developed in an effort to describe complex micromechanism of void nucleation. The common point for all so far proposed models is the assumption that void nucleates when so-called critical stress within inclusion or at inclusion-matrix interface has been reached [8,9].

In the GTN model, void nucleation is most frequently defined using initial void volume fraction of non-metallic inclusions, f_0, with which so-called primary voids are defined, and using models that may describe their subsequent nucleation (secondary voids) during growth of the primary ones as matrix of material becomes deformed.

Growth of nucleated voids is strongly dependent on stress and strain state. The GTN model was based on the observation that the nucleation and growth of voids in a ductile metal may be described macroscopically by extending the classical plasticity theory to cover the effects of porosity [5]. Thus, void volume fraction variable f is introduced in plastic potential equation [2,3]:

$$\phi = \frac{3\sigma_{ij}^{'}\sigma_{ij}^{'}}{2\sigma^2} + 2q_1 f \cosh\left(\frac{3\sigma_m}{2\sigma}\right) - \left[1 + (q_1 f)^2\right] = 0 \qquad (1)$$

where σ denotes actual flow stress of the matrix of the material, $\sigma_{ij}^{'}$ is stress deviator, σ_m is mean stress and the parameter q_1 was introduced by Tvergaard [3] to improve the ductile fracture prediction of the Gurson model. It is obvious that material loses its load carrying capacity if f reaches the limit $1/q_1$, because all the stress components have to vanish in order to satisfy Eqn. 1. In order to take into consideration void coalescence mechanism, upon attainment of critical void volume fraction, f_c, the process of material failure should be "accelerated" so that in FE processing the following applies: 1) f for $f \le f_c$ and 2) $f_c + K(f - f_c)$ for

$f > f_c$. Parameter K defines slope of the sudden drop on the load - diameter reduction diagram and often is denoted as "accelerating factor".
Two parts contribute to the increase of the void volume fraction in FE calculation with incorporated GTN yield criterion: one is the growth of the existing voids and the other is the nucleation of new voids during the external loading:

$$\dot{f} = \dot{f}_{nucleation} + \dot{f}_{growth}, \text{ where } \dot{f}_{nucleation} = A\,\dot{\varepsilon}^{p}_{eq} \text{ and } \dot{f}_{growth} = (1-f)\,\dot{\varepsilon}^{p}_{ii} \quad (2)$$

$\dot{\varepsilon}^{p}_{eq}$ is equivalent plastic strain rate and $\dot{\varepsilon}^{p}_{ii}$ is the plastic part of the strain rate tensor. Nucleation of the secondary voids led by strain increase is most frequently tried to be described using two approaches. The first one was defined by Gurland [10], and is determined by the model of continuous nucleation of new voids, so that the parameter A is constant. The second one was proposed by Chu and Needleman [11] and is based on hypothesis that void nucleation follows normal distribution. Although the second one has been much more used in investigation, it has been shown [6] that both approaches give similar results.

RESULTS AND DISCUSSION

Critical value of void volume fraction f_c, corresponding to crack initiation in smooth specimen and crack growth initiation in CT specimen, was determined by combined experimental-numerical procedure. Void nucleation was defined by volume fraction of non-metallic inclusions. Initial void volume fraction f_0 was determined by quantitative metallurgical analysis; nucleation of the secondary voids was not taken into account due to rather low presence of non-metallic inclusions in tested steel. Using optical microscope, three prepared samples of test material were examined; 100 fields of vision were made for each sample.

Initial void volume fraction was determined as an average value of surface fraction of non-metallic inclusions for all fields of vision. For planimetric procedure of determination of volume fraction of non-metallic inclusions, a semi-automatic measuring method was applied. Contouring of inclusion profiles and determination of surface fraction for each of the fields of vision were carried out using computer software. The inclusions were classified according to the procedure described in [12].

Numerical calculations of tension of smooth round and CT specimen were made according to the true stress-strain curve at 0°C and in accordance with ESIS TC8 round robin project [1]. For both calculations the large strain analysis with updated Lagrange procedure was applied. Plastic flow of the material was determined by GTN yield criterion (eqn. 1) with isotropic hardening. FE calculations did not incorporated void coalescence effect. The calculations for smooth specimen were made in two ways: by applying quadrilateral 4-noded and 8-noded FE with reduced integration. CT specimen was modelled only with quadrilateral 4-noded FE; 8-noded FE were not used due to convergence problems. The calculation was made for plane strain conditions. Crack tip was modelled using refined mesh (0.4 x 0.4 mm), without singular FE. Dimensions of tested specimens and FE meshes are shown in Fig. 1.

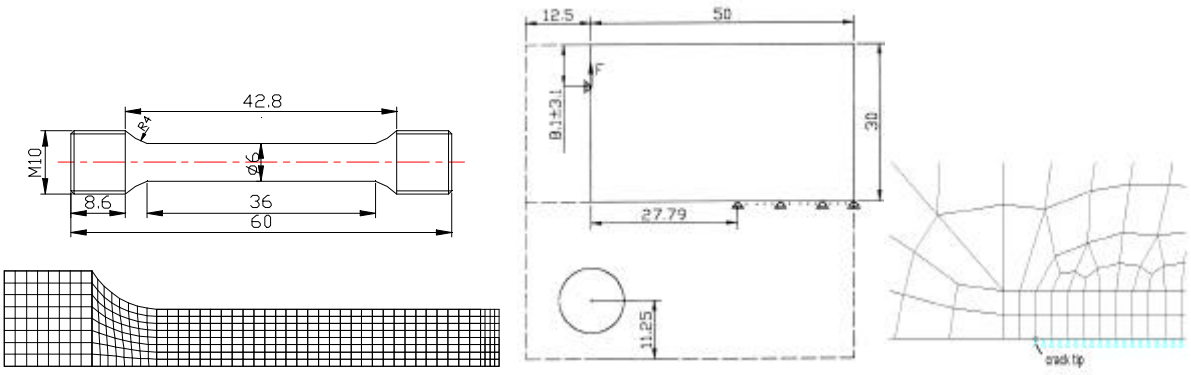

Figure 1: Tested specimens - dimensions and FE meshes

Force-reduction diagram of smooth specimen diameter is shown in Fig 2. Experimental and FE results are in good agreement. Force-specimen elongation curves are also in good agreement. Calculation with 8-noded FE gives somewhat lower position of tensile curve, and immediately in front of the experimental point of fracture, it gives certain further bending of the curve. Having in mind that the void coalescence effect is not used in the calculations and that sudden drop on force-necking diagram was not to be expected, the phenomenon of bending of tensile curve near the spot corresponding to experimental fracture is interesting. The reason for this phenomenon is significant softening of individual FE in the necking area, caused by an increase of void volume fraction f. The application of von Mises criterion does not indicate this phenomenon [13].

Critical void volume fraction f_c, was determined according to the diagram shown in Fig. 3, based on the increase of void volume fraction in finite element in the centre of the specimen and depending on reduction of the diameter of the minimum cross-section (in the region where necking occurred), for both calculations of smooth specimen. Certain difference between the values determined for f_c, is obvious, but the calculation using 4-noded FE gives for f_c a value which is in better agreement with previous researches and recommendations ($f_c = 0.05$ for the same steel [1] and $f_c = 0.045$ for the similar steel A508Cl.2 [7].

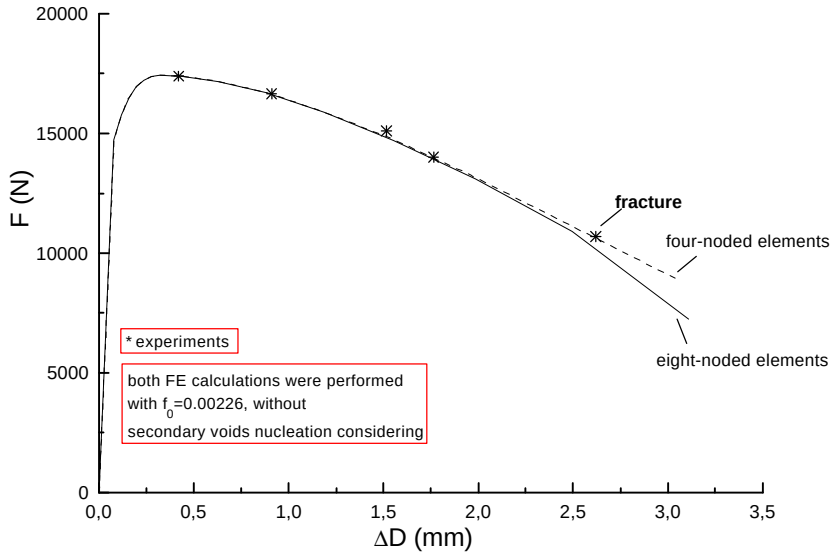

Figure 2: Load vs. reduction of diameter with four-noded and eight-noded FE calculation

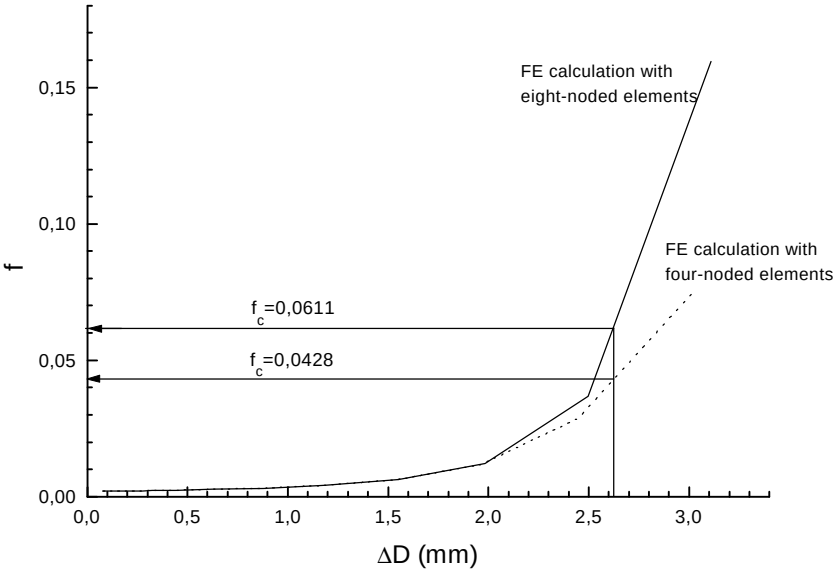

Figure 3: Determination of critical void volume fraction

Change of void volume fraction f (average value from 4 Gauss points) across the smallest cross-section of the specimen is given immediately before and after the fracture of the specimen (Fig. 4) for calculation

with 8-noded FE. One can clearly see from the figure that the fracture starts from the centre of the specimen. The change of f at cross-section in the necking area of the specimen obtained by the calculation using 4-noded FE is of the same character.

In Fig. 5 fractography of smooth specimen, obtained by SEM, is given. Crack initiation site in the centre of the specimen is shown in the left micrograph. The crack has initiated from dimple which had nucleated by cavity growth around sulphide, as suggested by its shape. Around crack initiation site, ledges of radial crack growth are noticeable. In micrograph to the right a larger cavity is noticeable, which has nucleated from a broken oxide, as also suggested by its shape.

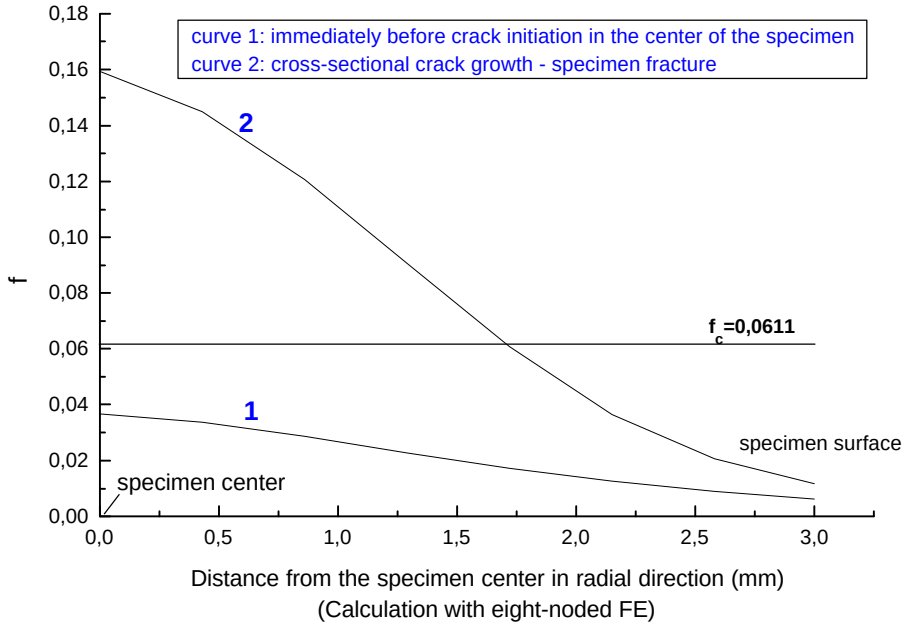

Figure 4: Distribution of void volume fraction f in necking zone

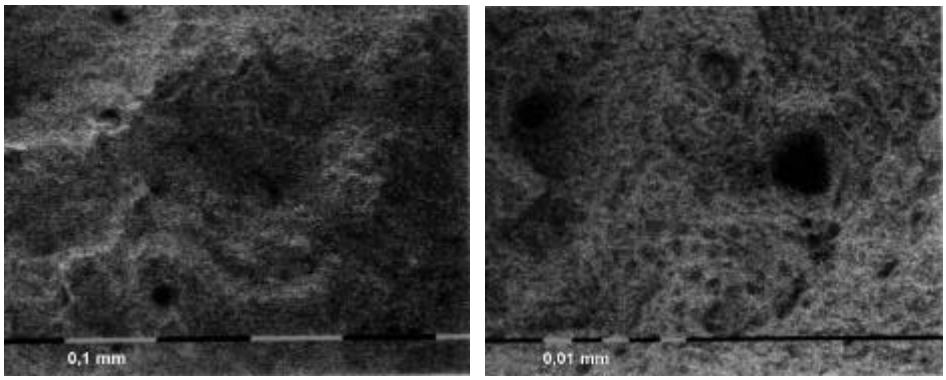

Figure 5: SEM micrographs of crack initiation in the center of smooth specimen

J-integral corresponding to the crack growth initiation in CT25 specimen was evaluated from the external work U according to the numerically obtained load – load line displacement curve [14]:

$$J_0 = \frac{\eta U}{B_n (W - a_0)} \quad \text{and} \quad \eta = 2 + 0.522\left(1 - \frac{a_0}{W}\right) \tag{3}$$

where B_n = 20 mm due to 20% side grooves. Load line displacement v_{LL} at the moment of the onset of crack growth was determined according to to the value f_c determined for smooth specimen. Failure of FE in front of a crack tip was conditioned by $f \geq f_c$. Based on the two values determined for f_c, two J-integrals corresponding to the crack growth initiation were calculated (Tab. 1)

TABLE 1
CALCULATED J_0 VALUES

Calculations of smooth specimen	f_c determined on smooth specimen	J_0 (kN/m) corresponding to the crack growth initiation in CT25 specimen
using 4-noded FE	0.0611	352.1
using 8-noded FE	0.0428	325.8

The values of J_0 determined in this way show certain deviation from the experimental value J_0 = 229 kN/m [1]. Possible reasons for this deviation are: a) use of 4-noded instead of 8-noded FE (the later were not used due to convergence problems); b) insufficient mesh refinement near the crack tip: further calculations should be made so that size of FE in front of a crack tip corresponds to the mean free distance between non-metallic inclusions $\lambda \approx 0.2$ mm determined by quantitative metallurgical analysis.

CONCLUSION

Based on the results of micromechanical modelling of ductile fracture of structural low-alloy steel, the following may be concluded:

- experimental values and results obtained by FE calculation according to GTN model for smooth specimen are in very good agreement; critical value of void volume fraction f_c was determined in the centre of the specimen in both calculations, using both 4-noded and 8-noded FE;
- quantitative metallurgical analysis is necessary for determination of initial void volume fraction f_0 and mean free distance λ;
- the value obtained for J_0 using both values determined for f_c exceeds experimental value and may be used for approximate prediction of ductile fracture initiation in CT specimen for tested steel; the calculations should be updated by more refined mesh and higher degree of FE interpolation functions.

REFERENCES

1. Bernauer G. and Brocks W. (2000). *Numerical round robin on micro-mechanical models - Results*, ESIS TC8, Institute for Materials Research - GKSS Research Center, Geesthacht
2. Gurson A.L. (1977). *Journal of Engineering Materials and Technology*, 99, 2.
3. Tvergaard V. (1981). *International Journal of Fracture*, 17, 389.
4. Tvergaard V. and Needleman A. (1984). *Acta Metallurgica*, 32, 157.
5. Zhang Z. L. (1996). *Fatigue & Fracture of Engineering Materials and Structures*, 19, 561.
6. Zhang Z. L. and Niemi E. (1994). *Engineering Fracture Mechanics*, 48, 529.
7. Sun D-Z., Kienzler R., Voss B. and Schmitt W. (1992). In: *Fracture Mechanics - Twenty - Second Symposium*, ASTM STP 1131, II, pp. 368-378, Atluri S.N., Newman J.C., Raju Jr.I. and Epstein J.S. (Eds.), American Society for Testing and Materials, Philadelphia.
8. Thomason P.F. (1990). *Ductile Fracture of Metals*, Pergamon Press, Oxford.
9. Argon A.S. and Im J. (1975). *Metallurgical Transactions*, 6A, 839.
10. Gurland J. (1972). *Acta Metallurgica*, 20, 735.
11. Chu C.C. and Needleman A. (1980). *Journal of Engineering and Materials Technology*, 102, 249.
12. Underwood E. E., (1970). *Quantitative Stereology*, Adison-Welsey, Reading, Mass.
13. Rakin M., Sedmak A., Matejic P., Zrilic M., and Sedmak S. (2000). In: *Proceedings of the ECF 13 'Fracture Mechanics: Applications and Challenges'*, printed on CD, M. Fuentes et al. (Eds.), ESIS Publication, Elsevier Science Ltd, Oxford.
14. ESIS P2/92 (1992), *Procedure for Determining the Fracture Behaviour of Materials*, ESIS Procedure

DUCTILE FRACTURE IN HIGH STRENGTH STEEL WELDMENTS

V. Olden [1], Z. Zhang [1], C. Thaulow [2]

[1]SINTEF Materials Technology, Trondheim, Norway
[2]Norwegian University of Science and Technology (NTNU), Trondheim, Norway

ABSTRACT

By using the modified Gurson model recently developed at SINTEF, the ductility behavior of high strength steel weldments, including base metal (BM), weld-metal (WM) and heat affected zone (HAZ) in longitudinal and transversal directions has been studied.

A fitting procedure based on smooth and notched cross weld tensile specimens which compares the strain predicted by finite element analyses to the actual strain at coalescence in the experiments, has been applied to determine the initial void nucleation parameter. Two simple models for void nucleation are used in the fitting procedure. Ductility behavior for the weldment has been described as a function of specimen geometry (stress triaxiality) and initial void volume fraction.

Increased stress triaxiality by decreasing notch radius generally results in higher tensile stress and lower ductility. The HAZ ductility level both in longitudinal and transversal direction was slightly lower than for base metal but clearly higher than the WM ductility level. The modified Gurson model, with a void nucleation model describing a sudden initiation of all voids at the early stage of plastic strain (cluster model), gave satisfying description of the ductility behavior for medium sharp notched specimens. The obtained void nucleation parameter f_0 (initial void volume fraction) was 0.0001 for BM and HAZ, and 0.001 for WM.

KEYWORDS

High Strength Steel, weld, ductile fracture, FE-Analysis, Gurson model, notch tensile

INTRODUCTION

Thermo-mechanical production methods have resulted in a new class of high strength construction steels, so called TMCP-steels, low in carbon content with excellent weldability and fracture toughness.

Classical fracture mechanics theory based on brittle fracture will not give a satisfying description of fracture behavior of these steels and welded joints. Failure acceptance criteria based on linear elastic or elastic-plastic relationships are conservative because they fail to include that stress also will be needed for plastic deformation of the material. Hence, there is a need to include a description of ductile fracture in the evaluation of the fracture behavior of TMCP steels.

The Gurson model [8] is a widely known micro-mechanical model for ductile fracture. With modifications by many authors, however, the Gurson model can only simulate void nucleation and growth but not predict ductile fracture. In the modified Gurson model proposed by Z. Zhang [1], ductile fracture is linked to one single void nucleation parameter. Once this void nucleation parameter has been determined, the remaining characteristic length parameter, which describes the inclusion spacing, can be fitted from fracture mechanics tests. The void nucleation parameter and the resulting length parameter are the transferable parameters for ductile fracture.

THE MODIFIED GURSON MODEL

The modified Gurson combines the Gurson-Tvergaard [2] model and the void coalescence criterion by Thomason [3] .

Two simple void nucleation models representing two extreme situations were used. The cluster nucleation model assumes that all the initial voids nucleate suddenly when the plastic strain level, $\bar{\varepsilon}^p$, has reached a certain critical value, $\bar{\varepsilon}_c^p$. This condition can be written as:

$$df_{nucleation} = f_o \delta(\bar{\varepsilon}^p - \bar{\varepsilon}_c^p) d\bar{\varepsilon}^p \qquad (1)$$

f_o is the initial void volume fraction that has to be fitted. $\delta(\bar{\varepsilon}^p - \bar{\varepsilon}_c^p)$ is the unitary impulse function (Kronecker function) and the position of the impulse are determined by the critical value $\bar{\varepsilon}_c^p$. In this work the commonly used critical value $\bar{\varepsilon}_c^p = 0$, is adopted.

The second nucleation model proposes that voids nucleate continuously during plastic loading. The nucleation rate is constant. Such simple continuous nucleation model can be written as:

$$df_{nucleation} = A d\bar{\varepsilon}^p \qquad (2)$$

The constant A is the damage parameter to be fitted. Equations 1 and 2 have greatly simplified the nucleation modelling and reduced the number of the unknowns of the nucleation process into one.

TENSILE TESTING

The material investigated was a welded joint in a 70 mm TMCP steel plate, welded by double-sided SAW. Yield strength level was 500 MPa and the main alloying elements were C (0.07%), Mn (1.5%), Ni (0.43%), Al (0.035%) and Nb (0.020%). Microstructure of the steel was polygonal ferrite and bainite. Areas subjected to investigation were the base metal (BM) the heat-affected zone (HAZ) and the weld metal (WM). Ductile crack initiation behavior was determined by using the multi specimen approach, including both smooth and notched round bar tensile specimens. HAZ and WM were tested in longitudinal and transversal direction, base material in longitudinal direction only.

Both smooth and notched specimens had a cross sectional diameter of 6.0 mm. Four different notch geometries with notch radiuses of 3.0 mm, 2.0 mm, 1.0 mm and 0.4 mm respectively, were prepared to represent different levels of stress triaxiality.

The tensile specimens were extracted from four different locations with respect to the plate surface as shown in Figure 1. Notch bottom of the HAZ transversal specimens was located 1.0 mm outside the horizontal fusion line.

Tensile testing was conducted in a 250 kN INSTRON 1126 testing machine. The crosshead speed during the tests was 0.01 mm/s for the smooth specimens, and 0.005 mm/s for the notched specimens. Accurate measurement of diameter reduction during the tensile test is essential for the establishment of the Bridgman corrected true stress-strain curve.

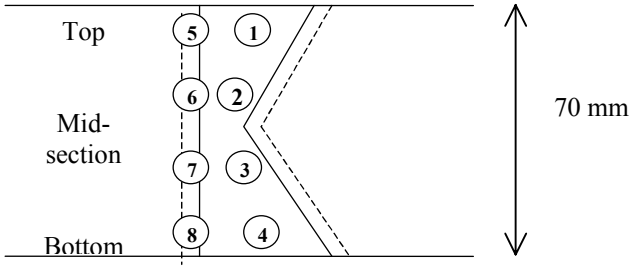

Figure 1: Location of longitudinal tensile specimens in WM and HAZ

This was performed by direct measurements of the diameter reduction during testing. The measurements were performed in two orthogonal directions normal to the tensile axis using 4 displacement gauges in a special designed fixture.

FINITE ELEMENT ANALYSES

FE Analyses were carried out to investigate the stress-strain state and the void coalescence (ductile fracture). The modified Gurson model were implemented into the FE Program ABAQUS version 5.8. All the specimens were modeled with axisymmetric quadratic 8 node elements. A reduced integration scheme was adopted. Due to symmetry conditions, only one quarter of the specimens was modeled. The nodes at the top end of the model were used to prescribe a monotonic vertical displacement to simulate the uniaxial loading situation.

The material models were defined by representative Bridgeman corrected true stress strain data from the smooth specimens, with modulus of elasticity E=210000 MPa and Poisson's ratio ν=0.3. Since no Bridgeman corrected stress strain curve could be obtained for the transversal direction the transversal fitting procedure was carried out using stress-strain curves from the longitudinal direction.

RESULTS

Base material

Figure 2a shows and overview of load vs. diameter reduction for all base material specimens. Figure 2b shows simulated curves for notch radius R = 1.0 mm fitted by different values of the Gurson parameter f_0. The results clearly show that increased stress triaxiality represented by decreasing notch radius causes a rise in the load level and a lowering of the diameter reduction at fracture. The fitted curves for R=1.0 mm agrees well with the experiment for f_0 = 0.0001.

After performing the fitting procedure for all geometries, the results were evaluated in ductility diagrams, comparing the measured and simulated strain at the beginning of final fracture, ε_c (Figure 3) In the experiments the critical strain was taken as the strain at maximum true stress. In the FE-analysis ε_c was represented by the strain at the initiation of failure, represented by a sudden load drop. Critical strain is plotted as a function of notch radius. Black points represent experimental values. Simulated results are represented by curves.

The best fit for the base metal was obtained for the cluster nucleation model with f_0 = 0.0001. The continuos model with A= 0.0005 also fitted the experimental results reasonably well, except for the smooth and sharpest notched specimens. It can be noticed that the model predicts higher ductility for the R0.4 than for the R1.0 specimens. The experimental results, however, showed relatively similar ductility values for these two geometries.

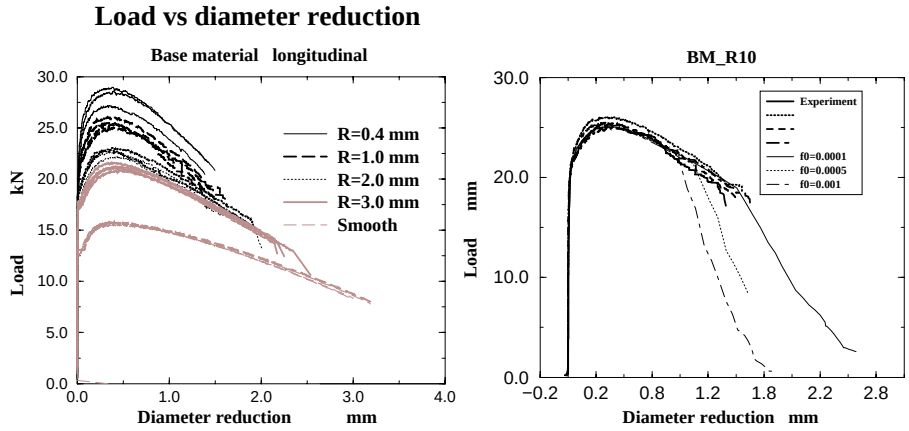

Figure 2: Load vs diameter reduction for base metal a) overview of all results b) f_0 fitted curves for R=1.0mm

The level of non-metallic inclusions in the base metal has been evaluated by Olden [5]. By counting of particles larger than 1 μm a volume fraction of 0.00014 was found. If one assume that voids primarily nucleate from these inclusions, the obtained f_0 value of 0.0001 matches the inclusion level very well.

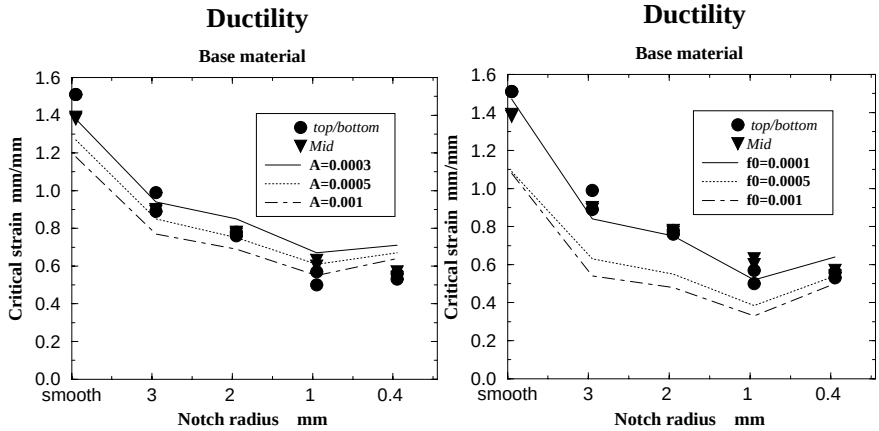

Figure 3: Ductility diagrams for the base metal. Continuos nucleation model (left) and cluster nucleation model (right)

Weld Metal

Weld metal was tested in longitudinal and transversal direction. In longitudinal direction the specimen geometries were smooth and notched with R=3.0 mm, R=1.0 mm and R=0.4 mm. In the transversal direction smooth specimens were omitted and the notch geometry R=2.0 mm was included in the test program.

Weld metal results were more scattered than the base metal results. The results also showed more scatter in the transversal direction than in the longitudinal direction. The transversal mid-section specimens had the overall lowest ductility, with a critical strain of about 0.2 for all notched geometries (Figure 4). This may indicate that other factors than the stress triaxiality level have influenced the ductility. Investigations of the welded joint [5] have revealed coarse dendrite austenite grain boundaries in weld metal. Measured hardness was also somewhat higher in the mid-section (230 - 250 HV) than in the "top" and "bottom"-region (200 - 220 HV). Accordingly there is a possibility that the brittle nature of the microstructure has influenced the results more than the stress conditions.

The tensile testing produced a large scatter in ductility results. The mid section R0.4 longitudinal specimens (all weld) achieved clearly lower ductility values than the R1.0 specimens, while the top/bottom specimens showed the same or slightly higher values.

In the longitudinal direction, the best fit was achieved for the cluster nucleation model with f_0=0.001 (Figure 4 left).

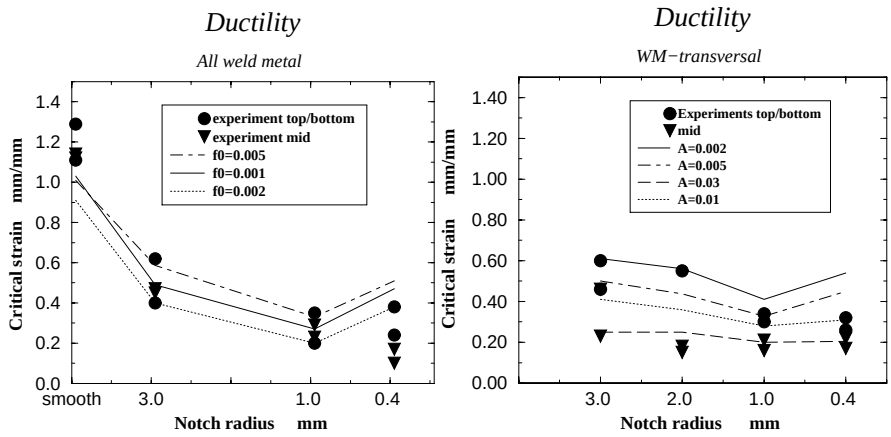

Figure 4: Ductility diagrams for WM. Longitudinal direction and cluster model (left), transversal direction and continuos model (right).

Both nucleation models, however, gave poor fit for the smooth and R=0.4 mm notched specimens with respect to ductility.

In the transversal direction, good fit for the mid-section specimens was achieved for the continuos model with A = 0.03 (Figure 4 right), and for the cluster model with f_0 = 0.005. Volume fraction of non-metallic inclusions in weld metal was measured in the range of 0.002 - 0.004 [5], which is approximately in the same range as the void volume fraction established by the model. Regarding to these results the cluster model with f_0= 0.001 gives a good description of longitudinal weld metal. In the transversal direction f_0=0.005 gives better representation of the ductility behavior.

The obtained values for f_0 in BM and WM agrees well with the findings in a previous SINTEF investigation of a welded joint in X-65 pipeline steel [6].

Heat affected zone

As for weld metal, there is a tendency of higher load levels and lower ductility for the mid section specimens (Figure 5). This tendency is slightly more pronounced in the transversal than in the longitudinal direction. However, comparing the tensile testing results of the longitudinal and transversal direction, the overall load and ductility level is quite similar.

Higher hardness values were found in the mid-section HAZ than in the top and bottom area. Higher hardness and lower ductility in the mid-section is proposed related to the welding procedure. Welding of the first passes (on both sides) were performed with lower heat input (1.5 MJ/m) compared to the rest of the weld (3.0 MJ/m). This will give shorter $\Delta t_{8/5}$ in the mid-section HAZ, and influence hardness and tensile properties [5][7].

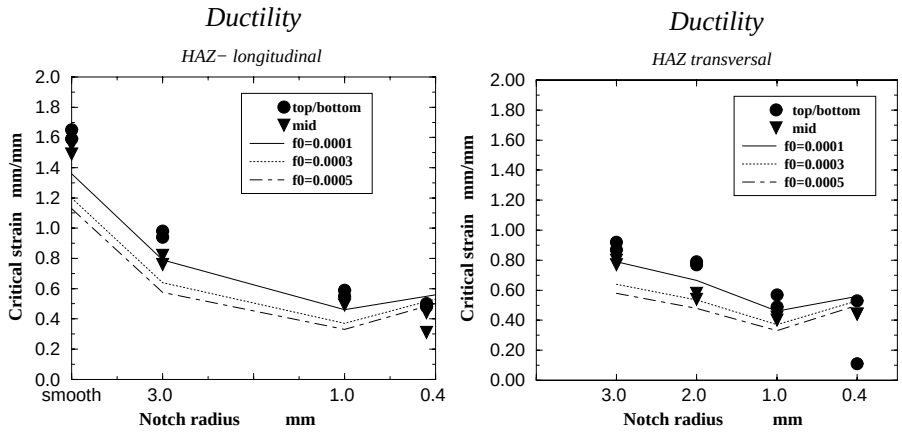

Figure 5: Ductility diagrams for HAZ. Longitudinal direction and cluster model (left), transversal direction and cluster model (right).

The cluster model with f_0 =0.0001 gives the best fit both in longitudinal and in transversal direction, see Figure 5. The level of non-metallic inclusions is the same in base metal and HAZ. Consequently the obtained level of f_0 could be expected. As for base metal and WM the model tends to overestimate the ductility of the R0.4 specimens and to underestimate the ductility of the smooth specimens.

EVALUATION OF THE MODEL

The modified Gurson model predicts higher ductility for the sharpest notched (R=0.4 mm) specimens than the R=1.0 mm specimens. This is based on a shift in damage process from stress to strain controlled initiation of fracture [6]. Strain controlled plastic initiation allows more plastic deformation and the ductility level will rise. The experiments show, however, that the model overestimates the critical deformation in the sharpest notched specimens.

When evaluating the model one must bear in mind that several simplifications are made. The model is based on the assumption that the material behaves like a continuum, and that the plastic strain happens in a distributed manner. If the plastic strain varies locally caused by defects or weak zones in the matrix, the critical plastic strain will be lower. The ductility level of the R=0.4 mm tensile specimens may well reflect the effect of non-homogeneity in the matrix. It can be noted that the ductility level of the R0.4 specimens in weld metal, which has the highest level of non-metallic inclusions, varies the most.

Both the cluster and the continuos void nucleation models are simplifications of the nucleation process. Perhaps does a more detailed void nucleation model better describe the process of void nucleation.

The material, as described by the Bridgeman corrected plastic stress strain-curve for smooth specimens, is supposed to represent all geometries. This may not be the best representation of the material behavior for the sharpest notched specimens. One can argue also that the longitudinal stress-strain curves do not represent the correct material behavior in the transversal direction. As presented the model seems well suited to describe the ductility behavior of medium sharp notched tensile specimens in the range $\frac{D_0(\textit{Initial diameter})}{R(\textit{notch radius})} = 2 - 6$.

ACKNOWLEDGEMENTS

The experimental and FE-simulation work presented in this paper, is performed as a part of the ESCS Multinational Research Project PRESS (Prediction of Structural Behavior on the Basis of Small Scale Specimen Testing). The project is partly financed by the Norwegian Research Council.

REFERENCES

[1] Z. L Zhang, C. Thaulow and J. Ødegård (2000):“A complete Gurson model approach for ductile fracture”, Eng. Fract. Mech., 67, 155 - 168.

[2] V. Tvergaard and A. Needleman (1984): "Analysis of the cup-cone fracture in a round tensile bar" Acta Metallurgica. 32, 157-169

[3] P.F. Thomason (1990):"Ductile fracture of metals" Pergamon Press, Oxford

[4] Z. Zhang, M. Hauge, C. Thaulow, J. Ødegård (*2000)*: “A notched cross weld tensile testing method for determining true stress strain curves for weldments”, submitted paper to the *Engineering fracture Mechanics*

[5] V. Olden (2000): “Ductile fracture in high strength steel weldments”, Diploma thesis, NTNU (In Norwegian)

[6] M.P. Loria (1999):”Determining damage parameters for a X-65 steel”, SINTEF Report STF24 A99281

[7] ”Acceptance criteria and level of safety for high strength steel weldments, Summarizing reports” SINTEF Report STF24 A97210, 1997

[8] AL. Gurson (1975), "Plastic flow and fracture behavior of ductile materials incorporating void nucleation, growth and coalescence, Ph.D. Diss., Brown University.

DUCTILE RUPTURE OF ALUMINUM SHEETS

W. Brocks [1], J. Besson [2], O. Chabanet [3], D. Steglich [1]

[1] *Institute of Materials Research, GKSS Research Centre, D-21502 Geesthacht, Germany*
[2] *Centre des Materiaux, Ecole des Mines de Paris, France*
[3] *Pechiney CRV, Parc Economique Centr'Alp, F-38341 Voreppe, France*

ABSTRACT

Crack growth resistance of thin aluminium sheets under monotonic loading is studied and numerically simulated. A phenomenological cohesive zone model and the micromechanically based damage model of Gurson are applied. The yield curve is determined from tensile tests on smooth flat specimens, the model parameters describing separation and damage, respectively, are fitted for a Kahn specimen. Both models guarantee transferability of the respective parameters from the small Kahn specimen to a large M(T) specimen. The respective contributions of elastic, plastic and separation energy to the total external work differ significantly for the two specimens. Crack growth is predicted as normal fracture if the common assumptions of symmetry are applied to the FE mesh, whereas the tests show a transition from normal to slant fracture. The general ability of damage models to simulate slant fracture is demonstrated on a Hill specimen.

KEYWORDS

aluminium sheets, fracture resistance, damage models, cohesive zone model, parameter identification, numerical simulation, slant fracture

INTRODUCTION

A realistic assessment of the residual strength of sheet materials, e.g. aluminum panels and shells in aircraft structures, with defects requires methods to experimentally characterize crack growth resistance as well as numerical simulation tools capable of predicting crack initiation and propagation. The global approach to failure uses macroscopic parameters like *J*-integral, CTOD, CTOA, energy disspation etc. [1]. These quantities suffer from a general lack of transferability of fracture resistance data obtained from specimens to large scale structures. The damage mechanics approach, on the other hand, provides a solution for the transferability problem by describing the degradation of the material by additional internal state variables, such as void volume fraction, porosity, micro-crack density, etc. [2]. These models have been applied successfully to predict crack growth in thick-walled structures [3] where a high stress triaxiality triggers the growth of voids. Their application to thin-walled high strength aluminum alloys, however, faces some specific problems:

- the stress triaxiality is much lower than required for the applicability of the respective models,
- the fracture plane often shifts from a normal to a 45° inclined orientation to the applied load,

- rolled sheets generally show an anisotropic behavior with respect to both plastic hardening and void nucleating particles.

In the present contribution, the plasticity and rupture behavior of thin aluminum sheets is characterized by using smooth tensile specimens and Kahn specimens. Three-dimensional finite element simulations of ductile rupture of small specimens are performed using the Gurson-Tvergaard-Needleman model. As this approach does not appear suitable for modeling crack extension in large structures, a two-dimensional simulation using a cohesive zone model is adopted. Finally, the conditions for simulating slant fracture are addressed. Model modifications accounting for anisotropic behavior are applied in [4] but will not be considered here.

MATERIAL AND SPECIMENS

The investigations were performed on rolled 1.73 mm thick sheets of an aluminum alloy of the 2000 series, which is mainly used in aircraft and space industry. The base material is coated by a 50 ÷ 80 μm thick layer of pure aluminum as a protection against corrosion. Second phase particles have been identified by a chemical analysis as iron and copper together with $Al_{12}Mn_2Cu$ segregations, with a total volume fraction of 0.12 %.

Various specimens have been tested to characterize the deformation and fracture behavior of the material, namely smooth, U- and V-notched flat tensile specimens, Kahn-specimens, see Figure 1, and large M(T) specimens. Kahn-specimens have originally been proposed for the investigation of fracture behavior in ship steel plates [5] and were applied for the determination of fracture properties of aluminum sheets, later [6]. They are C(T) like specimens without fatigue crack, $a/W = 0$, of dimensions 35×60 mm^2. Their advantage is their small size which reduces test and material costs in relation to the M(T) specimens of dimensions 760×1350 mm^2. All specimens were loaded in longitudinal orientation. Whereas smooth and notched tensile specimens failed macroscopically unstable, Kahn- and M(T) showed stable crack growth. The crack initiated normal to the loading direction but changed to slant fracture incliced by 45°, see right hand side of Figure 1. The same mechanism was observed on the M(T) specimens.

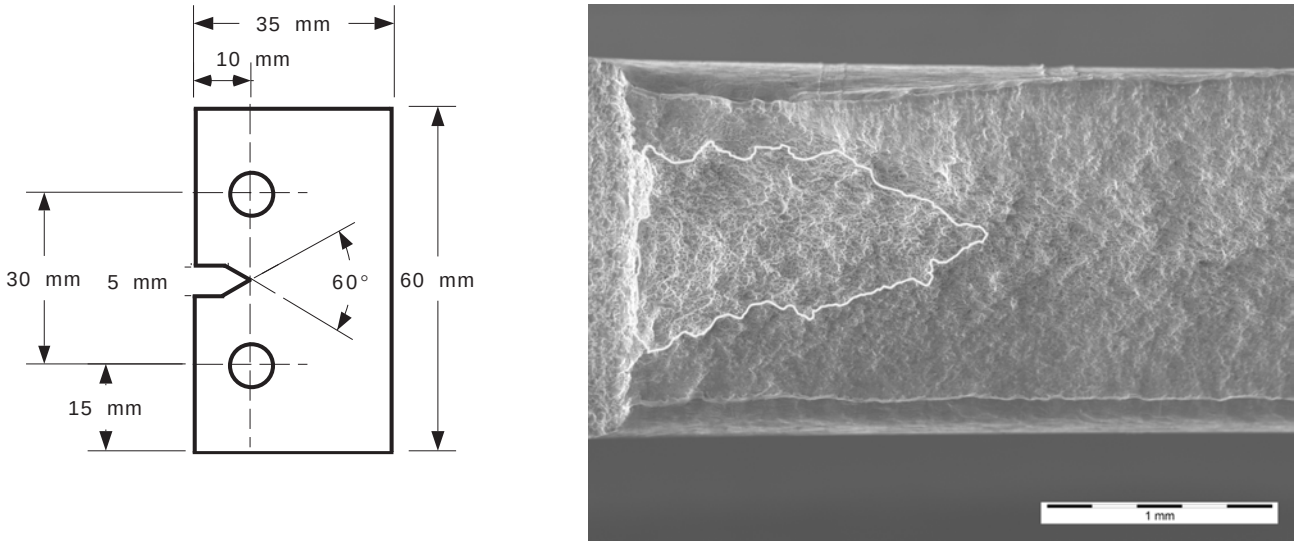

Figure 1: Kahn specimen: size and geometry (left),
fracture surface with normal and slant fracture (right)

MODELS FOR DESCRIBING DUCTILE DAMAGE

The Gurson-Tvergaard-Needleman-Model (GTN)

The model of Gurson [7] for porous metal plasticity with extensions by Tvergaard und Needleman [8] modifies the von Mises yield potential by introducing a damage parameter, f^*, which is a function of the void volume fraction, f,

$$\Phi(\sigma_e,\sigma_h,f,\sigma_Y)=\frac{\sigma_e^2}{\sigma_Y^2\left(\varepsilon^p\right)}+2\,q_1 f^*\cosh\left[q_2\frac{3\,\sigma_h}{2\,\sigma_Y\left(\varepsilon^p\right)}\right]-1-\left(q_1 f^*\right)^2=0 \quad ,$$
$$f^*=\begin{cases} f & \text{for} \quad f\le f_c \\ f_c+\kappa(f-f_c) & \text{for} \quad f>f_c \end{cases} \quad , \tag{1}$$

where σ_e is the von Mises effective stress, σ_h the hydrostatic stress, and $\sigma_Y(\varepsilon^p)$ the actual yield stress of the matrix material. The model was implemented as a "user supplied material" (UMAT) of the FE program ABAQUS.

In accordance with metallographic observations, it is assumed in the present simulations that voids have nucleated with beginning plastic deformation, $f(t=0) = f_0$, and damage evolution occurs due to the growth of

these voids, only. This reduces the number of parameters to five, namely q_1, q_2, f_0, f_c, κ. The parameters $q_1 = 1.5$ and $\kappa = 4$ have the usual values known from literature, whereas $q_2 = 2$ was assumed here for the thin panels with low triaxiality, which differs from common simulations of thick structures. The initial void volume fraction was taken to equal the volume fraction of inclusions, $f_0 = 0.0012$. Coalescence of voids takes place if a critical void volume fraction, f_c, is exceeded, and macroscopic crack growth results from $f^* = 0.6 \approx 1/q_1$. The only adjustable parameter is the critical void volume fraction, f_c.

The Cohesive Zone Model (CZM)

Whereas the GTN model results in constitutive equations governing inelastic deformation and evolution of damage in the continuum, the cohesive zone model intruduces a traction-separation law, $\Sigma(\delta)$, at the "interface" of continuum elements. Hence, the crack has to follow a presecribed path along the element boundaries where cohesive elements have been placed. A decohesion law based on a potential proposed by Rose [9] and applied by Xu and Needleman [10] has been used in the present simulations:

$$\Sigma_n = \sigma_{max}\, e\, z\, \frac{\delta_n}{\delta_c} \exp\left(-z\frac{\delta_n}{\delta_c}\right), \tag{2}$$

with maximum normal stress, σ_{max} and separation length, δ_c , being model parameters; $e = \exp(1)$ and $z = 16\,e/9$ are just numbers. This decohesion law is for pure "mode I" separation, but shear components can be added easily [10]. As the present FE model is 2D and accounts for crack growth in the ligament, only, which is assumed to be a plane of symmetry, no shear stresses can occur and the simulation is restricted to normal fracture. During the separation process, the mechanical work

$$\Gamma_0 = \int_0^{\delta_c} \Sigma_n \,\mathrm{d}\delta_n = \frac{9}{16}\sigma_{max}\,\delta_c \tag{3}$$

is "released". Hence, a crack has grown by one element length if $\delta_n = \delta_c$ or, equivalently, $\Gamma = \Gamma_0$. The CZM has been implemented as "user supplied element" (UEL).

MODELING OF MATERIAL AND SPECIMEN BEHAVIOR

Yield Curve

The yield curve of the material, $\sigma_Y(\varepsilon^p)$, was determined from tensile tests and fitted by a power law,

$$\sigma_Y = \sigma_0 + C\left(\varepsilon^p\right)^n \tag{4}$$

with $\sigma_0 = 343$ MPa, $C = 670$ MPa and $n = 0.67$. Young's modulus was taken as 65 GPa from literature.

Finite Element Models

The global deformation of thin specimens can be well described by plane stress models. The local triaxiality at a crack tip, however, is much higher than in plane stress, $T = 0.66$, as 3D analyses show. As void growth is significantly influenced by stress triaxiality, no damage evolution occurs under plane stress conditions [11] and the GTN model cannot be applied for plane stress elements. Plane strain conditions will overestimate damage evolution on the other hand. Hence, crack growth simulations using the GTN model require a 3D simulation at least in the vicinity of the crack tip and the ligament. In addition, the parameter q_2, which governs the influence of stress triaxiality, see eq. (1), and is commonly set to 1., has to be increased to a value of 2. in the present situation of thin panels. A fourfold symmetry is introduced to reduce the number of elements and unknowns in the FE simulation. Due to this symmetry, damage evolution and crack growth are restricted to a plane normal to the external load, and no slant fracture can be obtained in the simulations.

A 3D model as required for the GTN model is not very convenient for simulations of large amounts of crack growth. The phenomenological CZM offers the advantage of modeling in 2D, as the separation law is not dependent on the local triaxiality. The FE mesh now consists of three regions:

- a process zone where separation occurs, which is modeled by a layer of cohesive elements in the symmetry line, i.e. the ligament,
- a layer of elastic-plastic plane strain elements which allow for higher triaxiality and thus prevent localization of plastic deformation and necking adjacent to the cohesive elements,
- elastic-plastic plane stress elements all over the rest of the specimens, which guarantee the overall plane stress deformation behavior.

Neither of the two models can account for slant fracture. This is due to the symmetry conditions imposed to the 3D simulation with the GTN model, and the restriction to a 2D mesh in the model applying cohesive elements. The simulations have been run under displacement control.

Calibration of Damage Parameters by Simulation of the Kahn Test

The parameters f_c of the GTN model and σ_{max} und δ_c of the decohesion law, respectively, were adjusted to meet the experimental load vs displacement and load vs crack growth curves of the Kahn specimen, see Figure 2. The latter was measured from three specimens for which tests have been stopped at different amounts of crack growth. Both curves are met with satisfactory accuracy by both models, taking $f_c = 0.018$ and $\sigma_{max} = 580$ MPa, $\delta_c = 0.08$ mm, or $\Gamma_0 = 26.1$ N/mm, respectively.

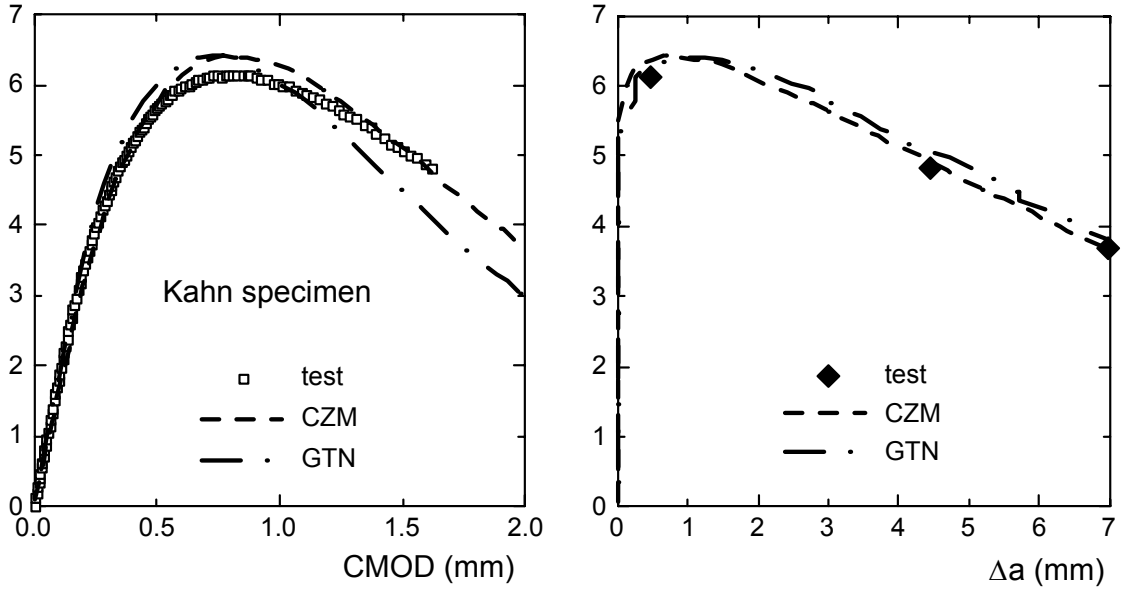

Figure 2: Kahn test and simulation by GTN and CZM

Verification by Simulation of the M(T) Test

The M(T) has now been simulated, taking these parameters, see Figure 3. No perfect agreement between test and simulation results could be obtained. Maximum load is overestimated and reached too early with respect to elongation v_L. On the other hand, crack growth is too fast in the simulation. Keeping in mind that there is a factor of 20 in size between the Kahn and the M(T) specimen, and the former is notched whereas the latter is cracked, the numerical prediction is not too bad. Some additional studies of the involved elastic and dissipated mechanical energies will further elucidate the transfer problems arising between small and large specimens.

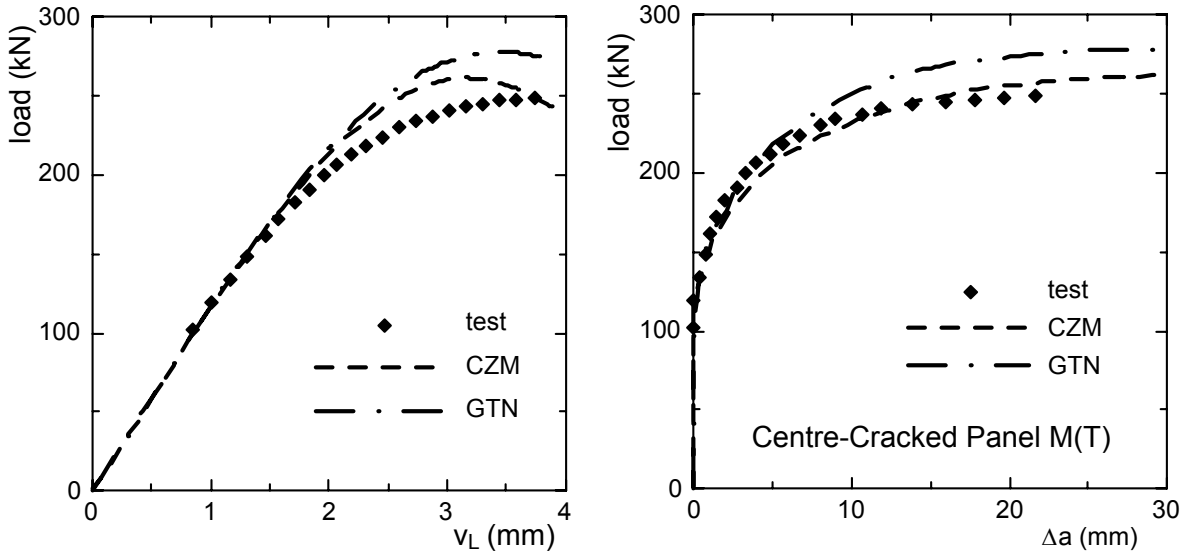

Figure 3: M(T) test and simulation by GTN and CZM

Energy Balances for Kahn and M(T) Specimen

The total external work is either stored as elastic energy or dissipated as work of plastic deformation or work of separation,

$$W = W_{\mathrm{el}} + W_{\mathrm{pl}} + W_{\mathrm{sep}}, \tag{5}$$

with

$$W_{\mathrm{el}} = \int_V \int_0^t \sigma_{ij}\, \dot{\varepsilon}_{ij}^{\mathrm{el}}\, \mathrm{d}t\, \mathrm{d}V, \quad W_{\mathrm{pl}} = \int_V \int_0^t \sigma_{\mathrm{e}}\, \dot{\varepsilon}_{\mathrm{e}}^{\mathrm{pl}}\, \mathrm{d}t\, \mathrm{d}V, \quad W_{\mathrm{sep}} = B\,\Gamma_0\,\Delta a\ . \tag{6}$$

The special advantage of the CZM is that the latter can be separated from the overall work of plastic deformation [12]. An analysis of these contributrions now shows, that plastic work constitutes more than 50 % and up to 70 % of the total mechanical work in the Kahn specimen whereas it is less than 20 % in the M(T) specimen, see Figure 4. Elastic energy amounts to 90 % in the M(T) specimen, but plays a minor role, 20 ÷ 40 %, in the Kahn specimen. Work of separation contributes only 4 % in the Kahn specimen and 0.6 % in the M(T) specimen at maximum crack growth. Thus, what is measured primarily in a J_{R}-curve is plastic work in the Kahn and elastic energy in the M(T) specimen. No wonder that any attempt of transferring these data is senseless. And the really interesting material property of separation energy is not captured at all by the respective tests.

The high amout of elastic energy stored in the M(T) specimen will result in a high influence of Young's modulus on the numerical result. As described above, the panels are not homogeneous but coated with a corrosion protection which comes up to 9 % of the total thickness. A parameter study showed that a reduction of Young's modulus by 9 % reduces maximum load by approximately the same factor. Any influence of the cladding on plastic deformation and dammage has not yet been studied.

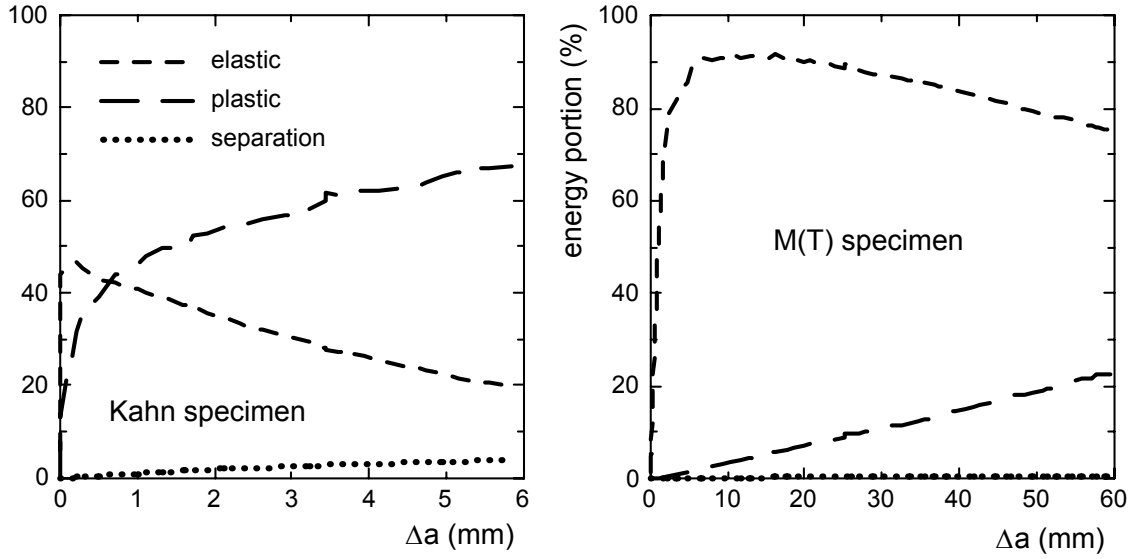

Figure 4: Recoverable and dissipated portions of total external work for Kahn and M(T) specimens

MODELING OF SLANT FRACTURE

As mentioned above and shown in Figure 1, the actual crack plane shifted from a normal to a 45° inclined orientation, which was not accounted for in the two simulations. Damage models as well as cohesive zone models are capable of simulating slant fracture under appropriate modeling conditions, namely

- a full 3D analysis is necessary and no symmetry conditions must be imposed in the ligament,
- the number of elements over the thickness has to be large enough for the models of continuum damage,
- a mode III component has to be added to the separation law and cohesive surface elements have to be placed along the faces of tetrahedral 3D elements to allow for 45° crack paths.

Further details on the influences of meshing and element formulations on the localization behavior of the Gurson [7] and the Rousselier [2] models in the context of modeling slant fracture in flat specimens and cup-cone fracture in round bars are discussed in [4, 13], and an example for modeling slant fracture in a M(T) specimen using cohesive elements is given in [14]. Figure 5 just shows an example of the numerical simulation of slant fracture in a Hill speciman [4] applying the Rousselier model.

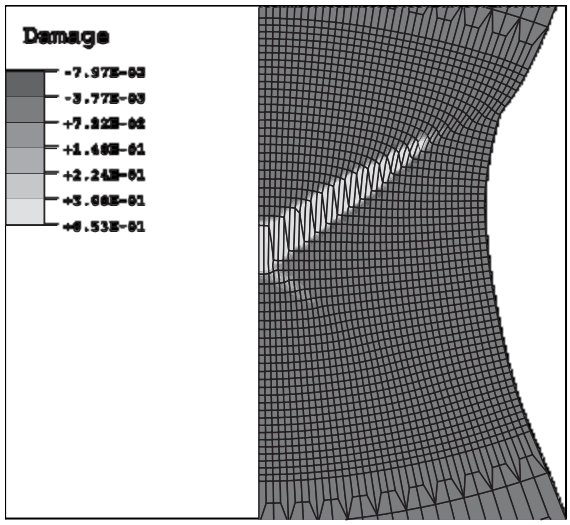

Figure 5: Modeling of slant fracture in the necking section of a Hill specimen by the Rousselier model

CONCLUSIONS

Finite element models with continuum elements incorporating damage evolution as well as cohesive zone elements are capable of simulating ductile rupture of thin aluminum panels. The respective model parameters can be determined from tests on comparably small and simple specimens, namely the Kahn specimen. Both models guarantee transferability over a large range of specimen sizes, though the global balances of mechanical energies differ significantly.

Crack growth is predicted as normal fracture if the common assumptions of symmetry are applied to the FE mesh, whereas tests on thin structures show a transition from normal to slant fracture. In general, damage models as well as cohesive zone models are capable of simulating slant fracture under appropriate modeling conditions. The computational consumption is considerable, however, and inhibits simulation of large amounts of crack growth.

ACKNOWLEDGEMENT

The presented results have been obtained in a cooperation project between PECHINEY CRV and GKSS Research Centre. The authors thank J. Ch. Ehrström, J. Heerens und D. Hellmann for providing the test data.

REFERENCES

1. Harris, C., Newman, J., Piascik, R. and Starnes, J. (1989). J. Aircraft 35, pp. 307-317.
2. Rousselier, G., Devaux, J. C., Mottet, G. and Devesa, G. (1989). Nonlinear Fracture Mechanics: Volume II - Elastic-Plastic Fracture, ASTM STP 995, pp. 332-354.
3. Brocks, W., Klingbeil, D., Künecke, G. and Sun, D.-Z. (1995). in: Second Symp. on Constraint Effects, ASTM STP 1224, pp. 232-252
4. Besson, J., Brocks, W., Chabanet, O. and Steglich, D. (2001). Europ. J. of Finite Elements, to be published.
5. Kahn, N. and Imbembo, E. (1958). The Welding Journal 27, pp. 169-184,.
6. Kaufman, J. and Knoll, A. (1964). Materials Research and Standards 4, pp. 151-155.
7. Gurson, A. L. (1977). J. Engng. Materials and Technology 99, pp 2-15.
8. Needleman, A. and Tvergaard, V.(1984). J. Mech. Phys. Solids 32, pp 461-490.
9. Rose, J., Ferrante, J. and Smith, J. (1981). Phys. Review Letters 47, pp. 675-678.
10. Xu, X. and Needleman, A. (1994). J. Mech. Phys. Solids 42, pp. 1397-1434.

11. Sun, D.-Z., Kienzler, R., Voss, B. and Schmitt, W. (1992). Fracture Mechanics: Twenty-Second Symposium (Volume II), ASTM STP 1131, pp 368-378.
12. Siegmund, Th. and Brocks, W. (2000). Fatigue and Fracture Mechanics: 31st Vol, ASTM STP 1389, pp. 475-485.
13. Besson, J., Steglich, D. and Brocks, W. (2001). Int.. J. of Plasticity, to be published.
14. Brocks,W. (2000). in: Advances in Computational Engineering & Sciences, ICCES 2K, pp.1037-1042.

ORAL REFERENCE: ICF100557OR

DUCTILE TEARING FROM INTERACTING SURFACE BREAKING DEFECTS

B. Bezensek and J.W. Hancock

Department of Mechanical Engineering, University of Glasgow, Glasgow, Scotland, UK

ABSTRACT

The interaction of coplanar surface breaking defects has been studied numerically and experimentally. Attention has been focussed on the behaviour of the re-entrant sectors which form as adjacent cracks coalesce in fatigue. Fatigue studies and numerical modelling shows that such sectors exhibit enhanced values of the stress intensity factor. The line spring technique [9,10] was used to analyse a series of evolving configurations, which originate from the interaction of two adjacent semi-elliptical cracks in monotonic loading. Under elastic-plastic conditions amplified values of J-integral were found in the re-entrant sectors, which also exhibit loss of crack tip constraint, as parameterised by T [7,8]. The numerical work is compared with ductile tearing experiments performed on a plain carbon–manganese steel. The experiments show that ductile tearing initiates from the re-entrant sector and the crack develops towards a bounding shape. The evolution of the shape of the coalescing defect in ductile tearing is initially similar to the development in fatigue. The conservatism of codified recharacterisation procedures is demonstrated for defects with re-entrant sector(s) in fatigue and ductile tearing conditions.

KEYWORDS

fatigue, fracture, crack interaction, coalescence, ductile tearing, recharacterisation

INTRODUCTION

Defects in real engineering structures frequently have complex shapes. Defect assessment procedures such as ASME, Section XI [1] and BS 7910 [2] recommend recharacterising the defect with a simple shape, which is amenable to analysis. Fracture mechanics assessments are performed for the recharacterised defect and structural integrity is assured when the recharacterised defect meets specified safety criteria. The validity of the procedure has been extensively studied in fatigue [3-5]. In fatigue adjacent surface breaking defects interact and form a single defect with a re-entrant sector, which exhibits accelerated crack growth rates [3]. The number of cycles in this stage may constitute a significant portion of fatigue life of the component, before the crack evolves into a bounding shape. The recharacterisation process is thus inherently conservative for fatigue. However for defects which fail in a brittle manner on the lower shelf, the presence of the amplified stress intensity factor values in the re-entrant sector presents significant concerns for the recharacterisation process [6]. The current work investigates the evolution of complex defects exhibiting a re-entrant sector in ductile tearing. Numerical analysis used the line spring concept [9,10] to evaluate crack tip parameters, including the J-integral and the non-singular T stress [7,8]. A related experimental programme studied the coalescence process in fatigue, ductile tearing and in brittle fracture [6] for defects with re-entrant sectors.

GEOMETRY AND TEST PROCEDURE

A rectangular plate of plain carbon-manganese steel defined as grade 50D in BS 4360, was machined to the geometry shown in Figure 1 and subject to three point bending. At the mid-length of the plate two coplanar notches were cut with a slitting wheel 70mm in diameter and 0.15mm thick. The two notches were used to initiate two surface breaking semi-elliptical cracks in fatigue. The evolving crack profiles in fatigue are schematically shown in Figure 2. These comprise seven configurations with neighbouring semi-elliptical cracks, seven coalesced cracks with re-entrant sectors and five bounding semi-elliptical cracks. The configurations are defined by the crack depth at the line of coalescence (position A). The current work considers the coalescence phase where the two adjacent crack tips merge to form a single crack with a re-entrant sector, as illustrated in Figure 2. The re-entrant sector initially has a highly concave profile which rapidly evolves to the convex shape of a bounding defect.

Error! Not a valid link.

Error! Not a valid link.

The experimental procedure evaluated two sets of tests. In the first set the development of adjacent defects in fatigue was examined. The second set used fatigue crack growth to develop characteristic profiles with re-entrant sectors which extended by ductile tearing in three point bending.

NUMERICAL ANALYSIS

A finite element numerical analysis based on the line spring concept of Rice and Levy [9], extended to deformation plasticity by White and Parks [10] was employed to assess the fracture mechanics parameters for a series of coalesced profiles which form re-entrant sectors. The geometry was modelled by thick shell elements in ABAQUS [11] and the surface breaking crack was represented by non-linear line spring elements. The model was subject to displacement controlled three point bending. The material was

represented with a Ramberg-Osgood power hardening law with a yield stress of 350 MPa, a hardening exponent of 9, a Young's modulus of 200 GPa and Poisson's ratio of 0.3.

Numerical results

The crack driving force was monitored through the development of the J-integral and is presented in Figure 3 for the shallowest part of the re-entrant sector and the deepest crack segment of the coalesced crack. J is normalised by the yield stress (Y) and the local ligament length ($t\text{-}a_{local}$). J is presented for a series of crack depths in the re-entrant sector for the same remotely applied load. The applied load is normalised with the limit load of an uncracked geometry (P_0). Amplified values of J are found in the re-entrant sector compared to the deepest crack segments for all applied loads favouring crack advance from the re-entrant sector.

Error! Not a valid link.

Crack tip constraint was quantified with the T stress [7,8] derived from the local bending moments and reaction forces in the line spring model. The interest was focused on the re-entrant sector which develops enhanced crack driving forces in elasticity and plasticity. Figure 4 presents T as a function of crack depth for the re-entrant sector. T is normalised with the yield stress and presented for five values of applied load, normalised with the limit load of the uncracked geometry. The magnitude of T depends on the extent of coalescence. Pronounced re-entrant sectors exhibit a compressive T stress in the initial stages of coalescence, indicating significant constraint loss. As the crack depth increases, T becomes more positive due to the bending dominated fields. Figure 4 shows that the T stress distribution saturates as the re-entrant ligament develops large scale plasticity.

Error! Not a valid link.

COALESCENCE IN FATIGUE

Fatigue crack growth tests were conducted at a frequency of 4 Hz and at a stress ratio of 0.1. The development of fatigue cracks was monitored with a "beach mark" technique. The processes of interaction and coalescence to form a bounding defect is presented in the fractograph of Figure 5. The spacing between consecutive beach marks in the re-entrant sector indicates accelerated crack growth during the process of coalescence. Use of the Paris fatigue crack growth law obtained from standard three point bend specimen, demonstrates that amplified values of the stress intensity factor exist in the re-entrant sector of the complex defect. Conversely the closely spaced beach marks in the deeper segment indicate reduced crack growth rates, until the re-entrant sector evolves into a bounding shape. The bounding crack then evolves towards a stable aspect ratio [12].

COALESCENCE IN DUCTILE TEARING

Ductile tearing tests were performed on two configurations, shown in Figure 6. These comprise a configuration with adjacent semi-elliptical defects before coalescence and a coalesced profile. The development of the re-entrant sector was monitored by heat tinting followed by a final brittle fracture after large amounts of stable displacement controlled ductile tearing. The test configurations are presented schematically in Table 1 with corresponding fractographs in Figure 6. Crack depths in the re-entrant sector and at the deepest segments are given in Table 1 for each tearing stage of the experiment.

Error! Not a valid link.

Extensive plasticity was observed in the re-entrant sector for both test profiles, followed by a stable ductile tear confined to the re-entrant sector, as indicated by a dark blue heat tint mark and a dark grey tear in Figure 6, followed by a brittle fracture. The remainder of the crack front underwent crack tip blunting and experienced only minor amounts of crack advance.

DISCUSSION

Analysis of the fatigue crack growth data confirmed the amplified stress intensity factors determined by the numerical analysis in the re-entrant sector. A numerical analysis of the development of plasticity on the upper shelf also showed amplified values of J-integral in the pronounced re-entrant sector. Experimental ductile tearing of a crack with a re-entrant sector showed substantial amounts of tearing in the re-entrant sector, agreeing with the line spring analysis and the experimentally observed rapid fatigue crack growth of the re-entrant sector. Constraint loss did not effect the tearing resistance in the moderate re-entrant sectors in bending dominated fields. The experimental studies show that in bending the shape of complex defects initially develop in similar ways for the distinctly different crack advance mechanisms of fatigue and ductile

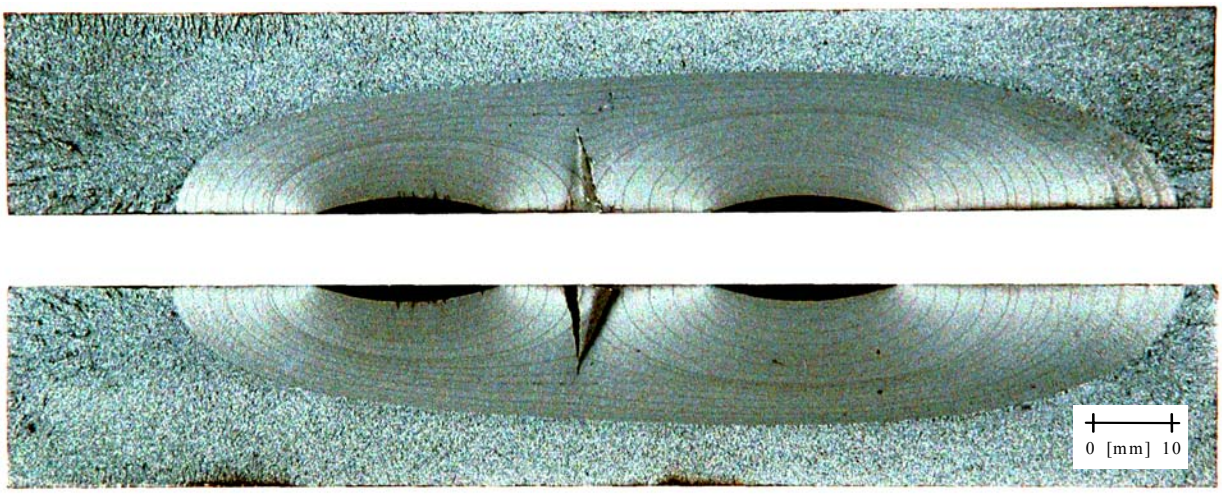

Figure 5: Coalescence in fatigue

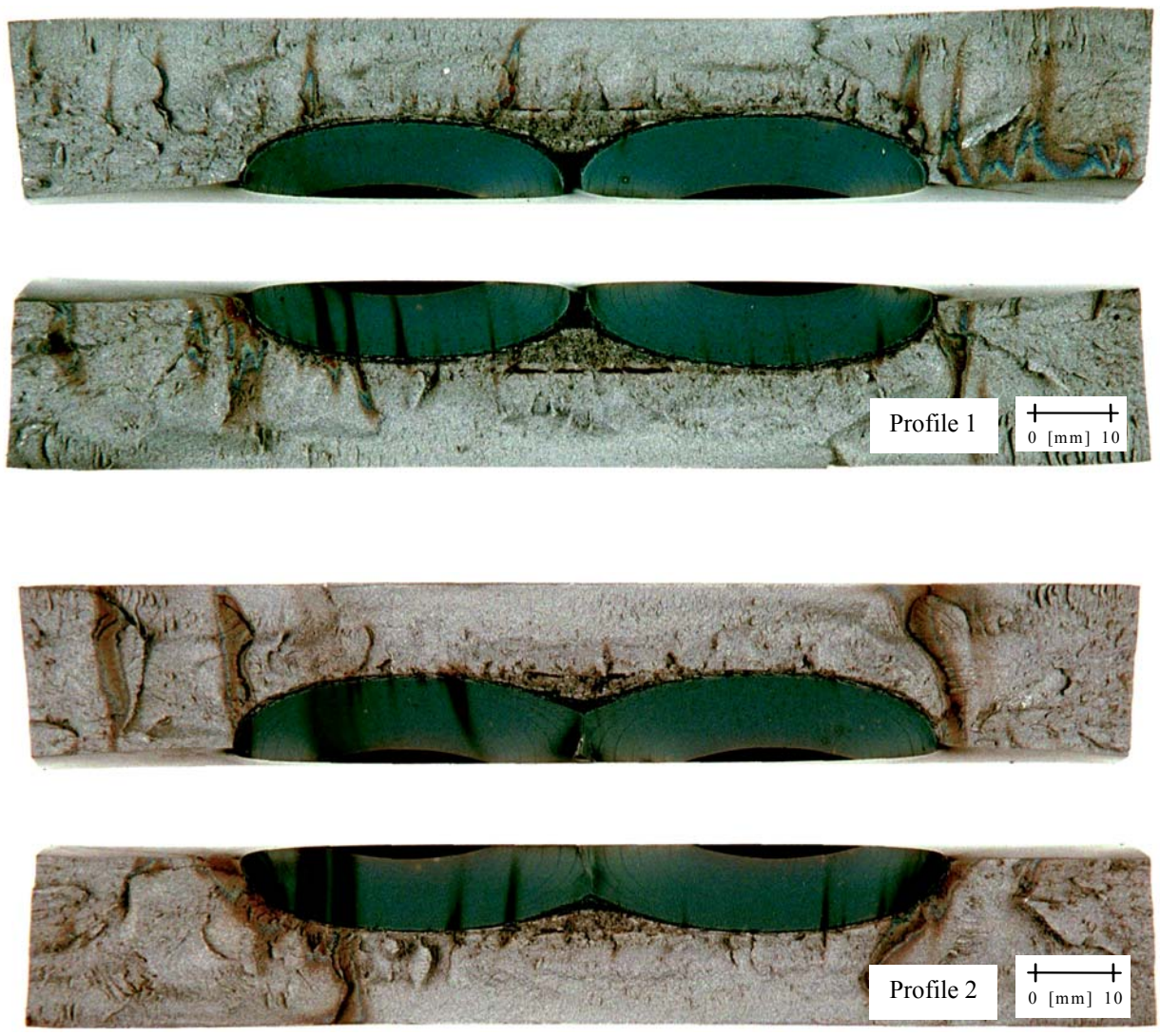

Figure 6: Coalescence in ductile tearing

tearing. Following the formation of a bounding defect of a low aspect ratio the major crack advance by tearing occurs near the free surface, in contrast to the fatigue where consistent crack advance along the crack front towards a stable aspect ratio was observed [12].

Codified recharacterisation procedure [1,2] for defects with re-entrant sectors recommends the evaluation for a bounding semi-elliptical defect. The conservatism of such procedure has been demonstrated for both, fatigue and ductile tearing. The coalescence phase amounts to the significant fatigue life of the component before the bounding profile develops. Although replacing the re-entrant crack with a bounding crack may incur premature repairs and expenses, the process is inherently conservative. Applying the recharacterisation procedure to cracks with re-entrant sectors in bending dominated ductile tearing is also conservative, since tearing starts in the re-entrant sector and the defect develops to the bounding shape of a recharacterised defect. For re-entrant cracks subject to conditions near the ductile-brittle transition regime a low fracture toughness was found [6] and a potentially non-conservative situation exists, when applying the codified recharacterisation procedure to such defects failing on the lower shelf.

ACKNOWLEDGEMENTS

The authors are thankful to Hibbitt, Karlsson and Sorensen for access to ABAQUS under Academic License. The support of British Energy Generation plc and discussions with Dr. R.A. Ainsworth is gratefully acknowledged.

REFERENCES

1. ASME, (1992), *Boiler and pressure vessel design code, Section XI* , American Society of Mechanical Engineers, Philadelphia, Pa.
2. BS7910:1999, *Guide on methods for assessing the acceptability of flaws in metallic structures,* British Standard Institution, London, 1999
3. Twaddle, B.R. and Hancock, J.W., (1986), *Fatigue of Offshore Structures*, EMAS
4. Leek, T.H. and Howard, I.C., (1996), Int. J. Press. Ves. and Pip., **68**, p: 181
5. Lin, X.B. and Smith, R.A., (1997), Int. J. Fract., **85**, p: 283
6. Bezensek, B. and Hancock J.W., (2001), Proc. ASME PVP2001, Atlanta, Ga.
7. Betegón, C. and Hancock, J.W., (1991), J. Appl. Mech.-T ASME, **58**, p:104
8. Hancock, J.W., Reuter, W.A. and Parks, D.M., (1993), *Constraint effects in fracture*, ASTM STP 1171, American Society for Testing and Materials, Philadelphia, p: 121
9. Rice, J.R. and Levy, N., (1972), J. Appl. Mech.-T ASME, **39**, p: 185
10. Parks, D.M. and White, C.S., (1982), J. Press. Vess. – T ASME, **104**, p: 287
11. HKS, (1998), ABAQUS/Standard Theory Manual, V 5.8, Hibbitt, Karlsson and Sorensen, inc, Providence, Rhoad Island
12. Scott, P.M. and Thorpe, T.W., (1981), Report R-10104, Atomic Energy Research Establishment, Harwell, UK

ORAL/POSTER REFERENCE: ICF 100580OR

DYNAMIC COMPRESSIVE BEHAVIOR OF CLOSED-CELL ALUMINUM FOAMS*

J. Lankford, Jr., A. E. Nicholls, and K. A. Dannemann

Mechanical and Materials Engineering Division, Southwest Research Institute™,
San Antonio, TX 78228, USA

ABSTRACT

Compression experiments were conducted on a closed-cell aluminum foam at strain rates ranging from $10^{-5}s^{-1}$ to 2000 s^{-1}. The materials demonstrated a strain-rate effect over the range of strain rates investigated; in particular, a marked strength increase at high strain rates is attributed to the stabilizing influence of the gas (i.e., air) pressure within the closed-cell structure. This was confirmed by testing samples with holes drilled through their cell walls to permit intercellular gas flow. An ultrahigh speed imaging system was used to capture the damage development sequence at high strain rates. Evaluation of sectioned microstructures following interrupted testing at a series of strains provided further insight on the deformation mechanism. The strain-rate sensitivity of the foam material appears to be related to sequential (time dependent) rupture of the cell walls that control the exit of cell-wall stabilizing gas from the structure. This conclusion was supported by the results of identical experiments involving a similar foam with very small pre-existing cell wall flaws.

INTRODUCTION

The contributions of intrinsic strength and relevant material properties to quasistatic deformation resistance of foam metals has been modeled by various authors [1-3]. Further theoretical analysis [4,5] suggests that cell wall imperfections (waviness; variation in wall thickness; non-uniform cell shape) probably are significant factors in local (initial) foam deformation. Experiments have shown [6] that such deformation proceeds by the formation of macroscopic deformation bands that initiate well below the steady-state flow stress.

Recently, several investigators have reported [7-10] strain-rate strengthening of Alporas closed-cell Al foam. Several mechanisms have been proposed to explain such behavior, including microinertial cell wall effects [11] on the kinetics of gas flow through broken cell walls [9]. The work reported here was aimed at defining the specific factors that control the strength-strain rate dependence of closed-cell metal foams.

* The authors appreciate the support of the Office of Naval Research under ONR Contract N00014-98-C-0126. They also greatly appreciate the advice and encouragement of their ONR technical monitor, Dr. Steven Fishman.

EXPERIMENTAL PROCEDURES

Two nominally closed-cell Al foams were investigated: (1) Alporas; relative density 0.15; cell size 2-3 mm; (2) Fraunhofer; relative density 0.24; cell size 1-2 mm. Cylindrical test samples (2.54 cm long x 2.36 cm diameter) were EDM-sectioned from blocks of each material. High strain rate ($\dot{\varepsilon} = 400$ s^{-1} to 2000 s^{-1}) tests were conducted using a split Hopkinson pressure bar system, while low strain rate (10^{-5} s^{-1} to 1 s^{-1}) tests were achieved using a servo-controlled hydraulic test machine.

In some of the Alporas samples, 300 μm holes were drilled through the sample in order to produce interconnected cells. The spacing between the holes (4 mm) ensured that virtually all cells were thus penetrated.

A high-speed camera was utilized to capture the deformation sequence for the Alporas foam during SHPB testing at high strain rates. Strain levels were determined within the sample using the recorded images and the Southwest Research Institute (SwRI™) displacement mapping (DISMAP) system. This automated stereo-imaging technique, developed at SwRI, measures material deformation by mapping the displacements within the material [12].

Some high strain-rate compression tests were stopped at predetermined strain levels to allow evaluation of the deformed microstructures at a series of increasing strains; this was accomplished using metal spacers to limit the strain response. Samples were evaluated prior to testing, and after high strain-rate compression to approximately 3-4% and 9-10% strain. The 3-4% strain level was chosen since it represents a region on the stress-strain curve below the onset of the plateau region, while the 9-10% strain level is more representative of deformation throughout the plateau region.

Following high strain-rate testing, samples of both foams were longitudinally sectioned by EDM for optical and scanning electron microscopy evaluation. Compressed samples were evaluated to determine the extent of cell wall deformation and the associated damage modes.

RESULTS

Both foams display a strain-rate dependence, examples of which are shown as stress-strain plots in Figures 1 and 2. For the Alporas, a significant increase in both yield and flow (plateau) stress ($\varepsilon \cong 5\%$) is evident at high strain rates; for example, at $\dot{\varepsilon} = 700$ s^{-1} (Figure 1). Under the same test conditions, the Fraunhofer material behaves differently (Figure 2). In this case, the material responds to the high strain-rate loading ($\dot{\varepsilon} = 700$ s^{-1}, Figure 2) by experiencing a high stress pulse, which quickly drops to a plateau level that lies within the data band for quasistatic (10^{-5} $s^{-1} \leq \dot{\varepsilon} \leq 1$ s^{-1}) experiments. Such peaks were never observed in any quasistatic tests, but were always present in high rate tests of Fraunhofer foam.

For Alporas samples with EDM-interconnected cells, no high strain-rate sensitivity was observed (Figure 3). Moreover, comparison of Figure 3 with Figure 1 shows that apart from the typical high strain rate closed-cell test at $\dot{\varepsilon} = 700$ s^{-1}, all of the data lie within essentially the same scatterband.

The results of multiple tests at several strain rates are shown in Figures 4 and 5 for both foams, with strength plotted versus strain rate. For Alporas Al, the plateau strength for closed-cell samples clearly is strain-rate dependent at high loading rates (Figure 4), but it is essentially strain-rate independent for the drilled (interconnected cells) state. For the Fraunhofer material (Figure 5), strength enhancement at high loading rates is observed only if the height of the transient pulse is taken as the measure of strength. On the other hand, if the post-pulse (plateau) flow stress is plotted, it is found to be essentially strain-rate independent (Figure 5).

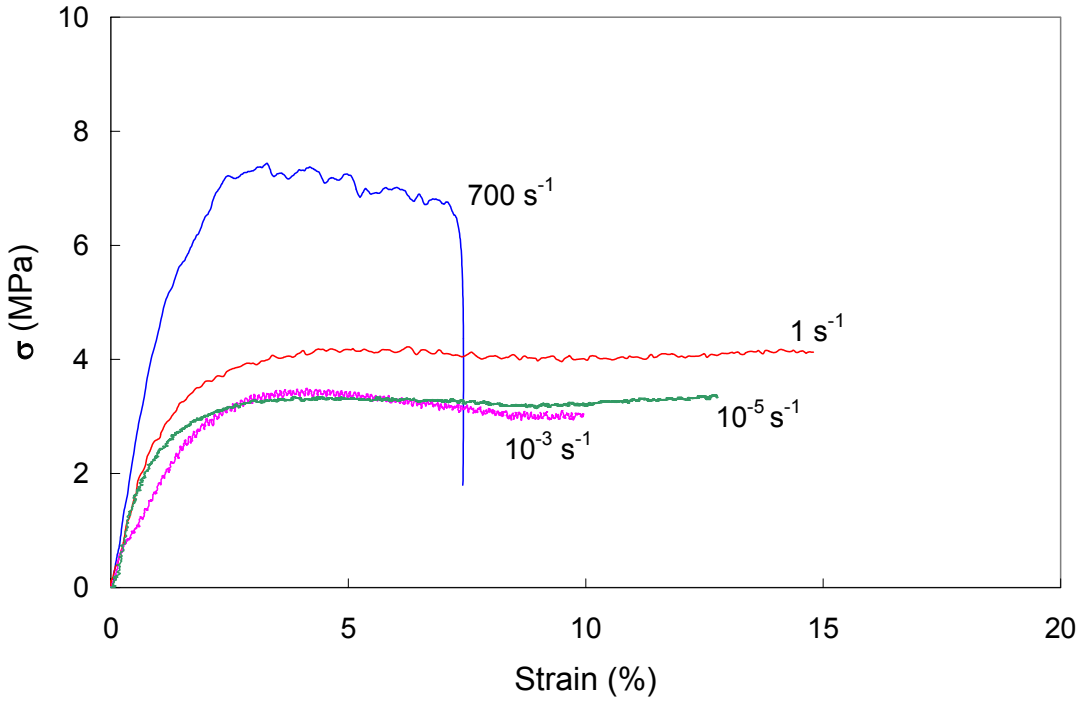

Figure 1: Stress-strain response of Alporas foam, showing marked increase in flow stress at a strain rate of 700 s^{-1} versus lower strain rates.

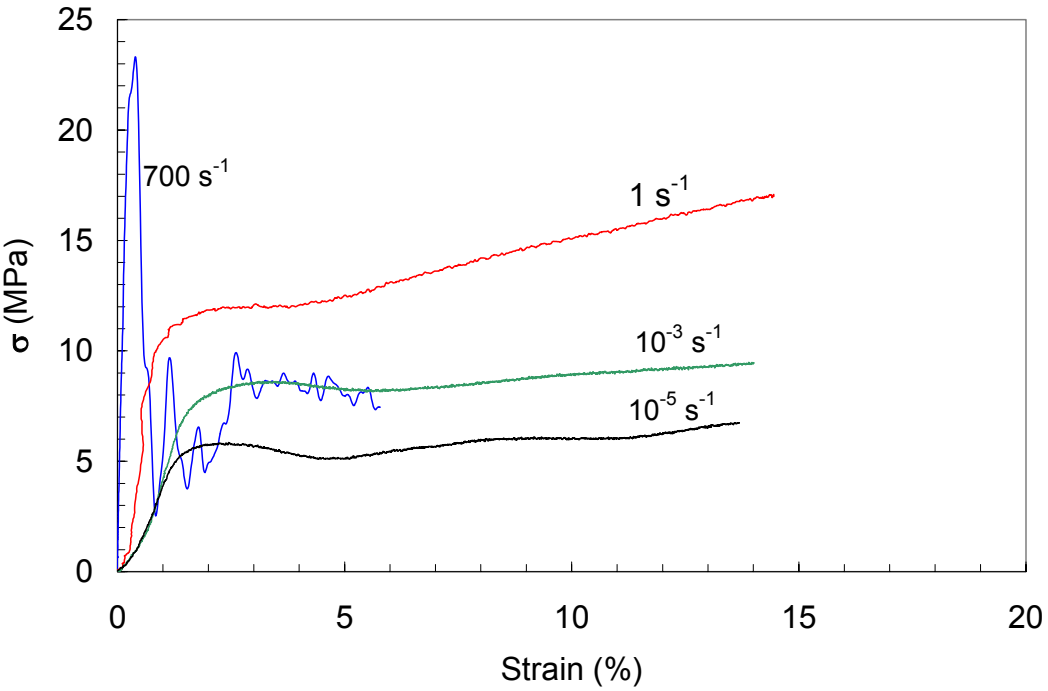

Figure 2: Stress-strain response of Fraunhofer foam, showing transient increase in strength at a strain rate of 700 s^{-1}.

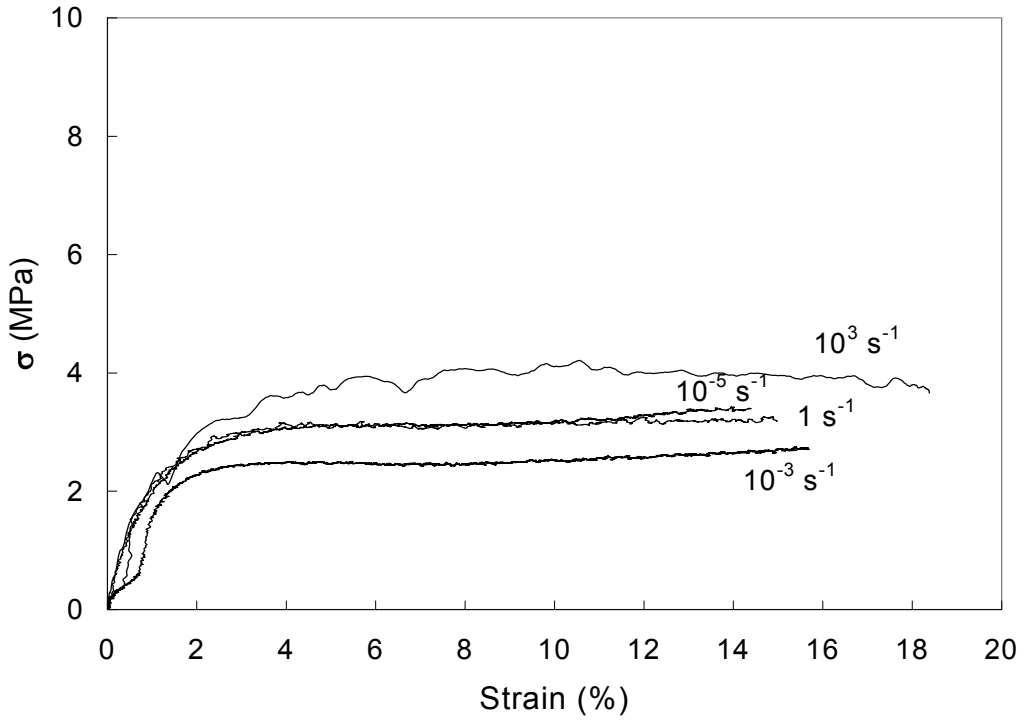

Figure 3: Stress-strain response of Alporas foam with EDM holes (interconnected cells).

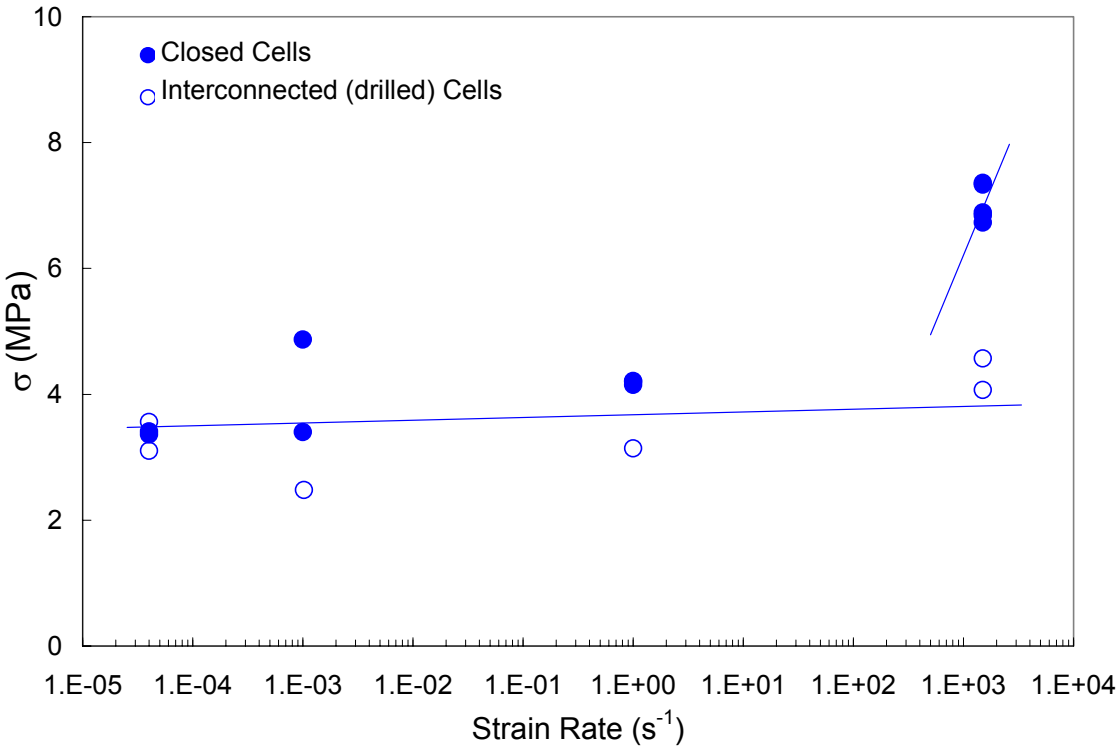

Figure 4: Flow stress (ε = 5%) versus strain rate for Alporas foam in the closed and interconnected cellular states. Lines are drawn to indicate trends.

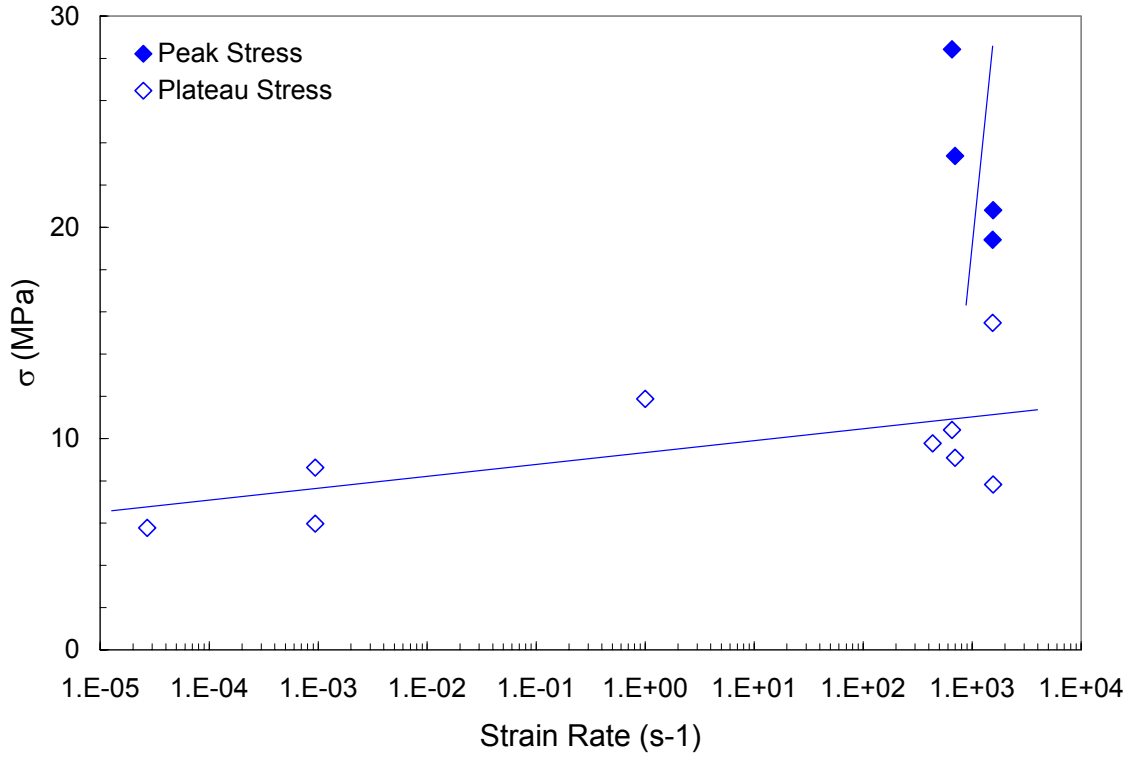

Figure 5: Flow stress (ε = 5%) and initial peak stress versus strain rate for Fraunhofer foam. Lines are drawn to indicate trends.

Analysis of high-speed photos of SHPB tests [12] showed that, as for quasistatic tests [6], isolated deformation/damage bands nucleate early in Alporas foam, at stress levels well below the plateau flow stress. Local strains in these bands approached 50%, and lead to flexing, kinking, and buckling of cell walls. Within the local buckled zones, explosive rupture ("blowout") of the cells was observed for samples tested at high ($\dot{\varepsilon} > 400\ s^{-1}$) strain rates, versus more stable tearing at lower strain rates.

Microstructural investigations demonstrated that Fraunhofer foam also fails via discrete deformation bands, which likewise form under both quasistatic and dynamic loading conditions. However, local failure at high strain rate generally seems to be a consequence of the growth (tearing) of pre-existing cell wall flaws, rather than through cellular "blowout." Microscopic examination of untested specimens appeared to reveal tiny (~ 10 μm) holes, whose existence was verified by flotation experiments. Identical samples of Alporas and Fraunhofer foam were immersed in water; the former floated for days, while the latter sank irreversibly in less than 30 minutes.

DISCUSSION

The implication of the Alporas results is that buildup of gas pressure within cells eventually causes some of the cell walls to rupture. Specimen collapse occurs when there are no longer sufficient cell walls intact to support the compressive load.

This view is supported by the absence of strain rate strengthening (other than what is probably a mild intrinsic material contribution) in the drilled versus the closed-cell specimens tested in the SHPB. Clearly, it is not the rate of gas flow that is paramount since the average strength of drilled samples essentially coincides with that of closed-cell ones. Thus, the fact that the cell walls must rupture sequentially in order to permit the internal gas to exit the structure must account for the strain-rate sensitivity of the closed-cell structure. Such a surface-to-interior rupture sequence obviously is not required for the collapse of the drilled foam metal.

In the case of Fraunhofer foam, it appears that at high loading rates, all of the cells must be able to release pressure as the load increases. This controlled release forestalls to a much higher overall stress level the formation of the first unstable deformation band, whose presence then drops the stress to that (flow stress) needed to continue its propagation/expansion. The instability point may be related to the pressure-driven growth of the natural flaws, an intrinsically rate-dependent process.

This behavior contrasts with that of the artificially interconnected (drilled) Alporas foam. Evidently 300 μm holes are sufficient to permit virtually unimpeded (rate-insensitive) egress of internal gas, while the more than order-of-magnitude smaller natural flaws in the Fraunhofer foam require rate-dependent growth before gas loss is sufficient to destabilize the foam structure.

It should be noted that the two foams are fabricated via entirely different processes, i.e., Alporas through foaming an alloy melt by adding a foaming agent (TiH_2), and Fraunhofer through the powder-metallurgical mixing of alloy powder with a metal hydride foaming agent, followed by compaction heating of the precursor material. Hence, it is reasonable that the relative porosities of their respective cell walls might differ, and that Alporas foam could be more truly closed-cell than the Fraunhofer material.

REFERENCES

1. Gibson, L. J. and Ashby, M. F. (1997). *Cellular Solids: Structure and Properties*, 2nd edition, Pergamon Press, Oxford.

2. Sugimara, Y., Meyer, J., He, M.Y., Bart-Smith, H., Grenestedt, J. and Evans, A. G. (1997). *Acta Mater*. 45, 5245.

3. Banhart, J. and Baumeister, J. (1998). *J. of Mat. Sci*. 33, 1.

4. Simone, A. E. and Gibson, L. J. (1998). *Acta Mater*. 46, 11, 3929.

5. Grenestedt, J. L. (1998). In *Porous and Cellular Materials for Structural Applications*, pp. 3-13, Schwartz, D. S., Shih, D. S., Evans, A. G., Wadley, H. N. G. (Eds.). Materials Research Society Symposium Proceedings, Vol. 521.

6. Bart-Smith, H., Bastawros, A. F., Mumm, D. R., Evans, A. G., Sypeck, D. J., Wadley, H. N. G. (1998). *Acta Mater*. 46, 3583.

7. Mukai, T., Kanahashi, H., Miyoshi, T., Mabuchi, M., Nieh, T. G. and Higashi, K. (1999). *Scripta Met.* 40, 921.

8. Paul, A. and Ramamurty, U. (2000). *Mat. Sci. & Engr.* A281, 1.

9. Dannemann, K. A. and Lankford, J., Jr. (2000). *Mat. Sci. and Engr*. A293, 157.

10. Dannemann, K. A., Lankford, J., Jr. and Nicholls, A. E. (2000, in press). "The Effect of High Strain Rate Compression on Closed-Cell Aluminum Foams." In *Proc. of Mtls. Conf. on Fundamental Issues and Applications of Shock Wave and High-Strain-Rate Phenomena,* Explomet™ 2000, Albuquerque, NM.

11. Park, C. and Nutt, S. R. (in press). *Mat. Sci. & Engr.*

12. Davidson, D. L., Chan, K. S. and Page, R. A. (1989). AMD-Vol. 102, *Micromechanics: Experimental Techniques,* Sharpe, W. N., Jr. (Ed.) Book No. H00539.

ICF100326OR

DYNAMIC DELAMINATION IN THROUGH-THICKNESS REINFORCED DCB SPECIMENS

N. Sridhar[1*], I. J. Beyerlein[2], B. N. Cox[1] and R. Massabò[3]

[1]*Rockwell Science Center, 1049 Camino Dos Rios, Thousand Oaks, CA 91360, U.S.A.*
[2]*Los Alamos National Laboratory, New Mexico, U.S.A*
[3] *Department of Structural and Geotechnical Engineering, University of Genova, Italy*

ABSTRACT

Bridged crack models using beam theory formulation have proved to be effective in the modeling of quasistatic delamination crack growth in through thickness reinforced structures. In this paper, we model dynamic crack propagation in these structures with the beam theory formulation. Steady state crack propagation characteristics unique to the dynamic case are first identified. Dynamic crack propagation and the energetics of steady state dynamic crack growth for a Double Cantilever beam (DCB) configuration loaded with a flying wedge is examined next. We find that steady state crack growth is attainable for this loading configuration provided certain conditions are satisfied.

KEYWORDS

Dynamic, Delamination, Crack, Bridging, DCB, Stitching, Energy Release Rate

INTRODUCTION

Through thickness reinforcement of various kinds, including stitched or woven continuous fiber tows and metallic or fibrous short rods, has been developed to address the delamination problem in structural composite laminates. Substantial experimental evidence shows that through thickness reinforcement dramatically alters the delamination characteristics for the better under both static and dynamic loading conditions. For static loading, a fundamental theory based on observations of essential mechanisms is now mostly in place [1-6]. The mechanics of crack bridging by the through thickness tows have been mapped out, with governing length scales and material parameters identified [1-6]. However, equivalent fundamental knowledge and models for dynamic delamination do not exist.

This paper deals with the delamination mechanics for through thickness reinforced structures under dynamic crack propagation conditions. A beam theory formulation is adopted and certain crack

propagation characteristics are identified for mode I conditions. In the next section, we examine the energetics of crack growth for a through thickness reinforced DCB specimen loaded by a flying wedge. The double cantilever beam (DCB) specimen loaded dynamically by a flying wedge offers a relatively simple experimental approach to analyzing the mode I dynamic delamination problem. Regions of stable crack growth as a function of the material properties of the through thickness reinforcement, the size of the DCB specimen and the velocity of the wedge have been identified.

Beam Theory Formulation and Solution Characteristics:
For a beam element, the equations of motion are:

$$\frac{\partial N}{\partial x} = \rho B h \frac{\partial^2 u}{\partial t^2} \tag{1a}$$

$$\frac{\partial Q}{\partial x} - p(w,t)B = \rho B h \frac{\partial^2 w}{\partial t^2} \tag{1b}$$

$$\frac{\partial M}{\partial x} - Q = \rho I \frac{\partial^2 \psi}{\partial t^2} \tag{1c}$$

where $u(x,t)$ and $w(x,t)$ are the in-plane and transverse displacements of the neutral plane respectively, $\psi(x,t)$ is the clockwise rotation of the cross-section, t is the time variable, N is the axial force, Q is the shear force, M is the bending moment, $2h$ is the total thickness of the DCB specimen, B is the width of the specimen, ρ is the density, $I\ (= Bh^3/12)$ is the moment of inertia and $p(w,t)$ is the bridging traction corresponding to the opening mode. In this work, the time dependent bridging traction p corresponding to the opening mode is assumed to depend only on the transverse displacement w. In the absence of an axial force N, $u = 0$.

For a Timoshenko beam, the equations for steady state motion can be reduced to [7]:

$$\frac{\partial^4 w}{\partial X^4} + \frac{c_l^2}{(R - c_l^2)(1 - c_l^2)} \frac{12R}{h^2} \frac{\partial^2 w}{\partial X^2} - \frac{1}{(R - c_l^2)} \frac{1}{Eh} \frac{\partial^2 p}{\partial X^2} + \frac{1}{(R - c_l^2)(1 - c_l^2)} \frac{12R}{Eh^3} p = 0 \tag{2a}$$

$$\frac{\partial \psi}{\partial X} = \frac{p}{REh} - \frac{(R - c_l^2)}{R} \frac{\partial^2 w}{\partial X^2} \tag{2b}$$

where $X = x - v\,t$, $c_l^2 = \rho v^2 / E$, $R = \kappa G / E$, v is the (constant) steady state velocity, G and E are the shear modulus and the Young's modulus of the laminate and the dimensionless shear coefficient κ=5/6 for a beam with rectangular cross section. For steady state dynamic delamination, the velocity v is the delamination crack tip velocity.

For an Euler-Bernoulli (E-B) beam, where both shear deformation and rotational inertia are ignored, the equation for steady state motion reduces to a simple form given by:

$$\frac{\partial^4 w}{\partial X^4} + \frac{12 c_l^2}{h^2} \frac{\partial^2 w}{\partial X^2} + \frac{12}{Eh^3} p = 0 \tag{3}$$

Let us now consider a linear bridging law of the following type to represent the bridging action of the through thickness reinforcement:

$$p = p_0 + b_3 w \tag{4}$$

The linear law particularizes to the Dugdale law $p = p_0$ (for $\beta_3 = 0$) and to the proportional linear law $p = b_3 w$ (for $p_0 = 0$). In the results that follow, we non-dimensionalize the variables by the laminate thickness h ($w \equiv h W$, $u \equiv h U$ and $X \equiv h x$). Thus, the transverse displacement obeys:

$$\frac{\partial^4 W}{\partial \xi^4} + \beta^2 \frac{\partial^2 W}{\partial \xi^2} + b^2 W + d^2 = 0 \tag{5}$$

For Timoshenko beam:

$$\beta = \sqrt{\frac{12\, c_l^2\, R}{(1-c_l^2)(R-c_l^2)} - \frac{b_3 h}{(R-c_l^2)E}}; \qquad b = \sqrt{\frac{R}{(1-c_l^2)(R-c_l^2)}\frac{12 b_3 h}{E}};$$

$$d = \sqrt{\frac{R}{(1-c_l^2)(R-c_l^2)}\frac{12 p_0}{E}}; \tag{6a}$$

For Euler-Bernoulli (E-B) beam:

$$\beta = \sqrt{12\, c_l^2}\,; \qquad b = \sqrt{\frac{12 b_3 h}{E}}\,; \qquad d = \sqrt{\frac{12\ p_0}{E}}\,; \tag{6b}$$

The general solution to Eqn. 5 is:

$$W(x) = -\frac{d^2}{b^2} + K_1 e^{-\sqrt{-\frac{\beta^2}{2} - \frac{1}{2}\sqrt{\beta^4 - 4b^2}}\,x} + K_2 e^{+\sqrt{-\frac{\beta^2}{2} - \frac{1}{2}\sqrt{\beta^4 - 4b^2}}\,x} + K_3 e^{-\sqrt{-\frac{\beta^2}{2} + \frac{1}{2}\sqrt{\beta^4 - 4b^2}}\,x} + K_4 e^{+\sqrt{-\frac{\beta^2}{2} + \frac{1}{2}\sqrt{\beta^4 - 4b^2}}\,x} \tag{7}$$

There are three regimes to the solution behaviour that are independent of the boundary conditions, and they have been identified below (Note: $S = \beta_3 h / (12\, kG)$):

- Case 1: $\beta^2 < 0$ and $\beta^4 > 4b^2$ => Exponential behavior
  - For Timoshenko beam, this is true provided:

$$\frac{r v^2}{E} \le \frac{S}{1+S} \quad \text{and} \quad 3(S(1-c_l^2) - c_l^2)^2 \ge S(1-c_l^2)(R-c_l^2) \tag{8a}$$

  - For the E-B beam, the above condition is never satisfied.
- Case 2: $\beta^2 > 0$ and $\beta^4 > 4b^2$ => Oscillatory and non-decaying behavior
  - For Timoshenko beam, this is true provided:

$$\rho v^2 / E > S/(1+S) \quad \text{and} \quad 3(S(1-c_l^2) - c_l^2)^2 \ge S(1-c_l^2)(R-c_l^2) \tag{8b.1}$$

  - For the E-B beam, this condition is satisfied when: $\rho v^2 / E \ge 2\sqrt{S\ R}$ (8b.2)
- Case 3: $\beta^4 < 4b^2$ => Oscillatory with exponential decay behavior
  - For the Timoshenko beam, this is true when:

$$3(S(1-c_l^2) - c_l^2)^2 < S(1-c_l^2)(R-c_l^2) \tag{8c.1}$$

  - For the E-B beam, this is true when: $\rho v^2 / E < 2\sqrt{S\ R}$ (8c.2)

The conditions determined above give us insight into when dynamic effects can significantly alter the mechanisms of deformation and the resultant bridging phenomena. For instance, if the crack tip velocity exceeds the condition prescribed in Eqn. 8a, oscillatory displacement fields will be introduced in the wake of the crack, and these multiple oscillations could lead to crack face interpenetration. When such oscillations are present, the mechanics of bridging and the efficacy of through thickness bridging ligaments on the energetics of crack growth will be considerably altered. For example, stick-slip propagation modes would appear to be possible, as contacting fracture surfaces bounce. The complex details of such a possibility will be considered elsewhere. Here, we model the arms of the DCB specimen as an EB beam and study propagation characteristics up to the point of fracture surface contact, which is a simpler problem. (Constants β, b and d are given in Eqn.6b)

Wedge-Loaded Double Cantilever Beam

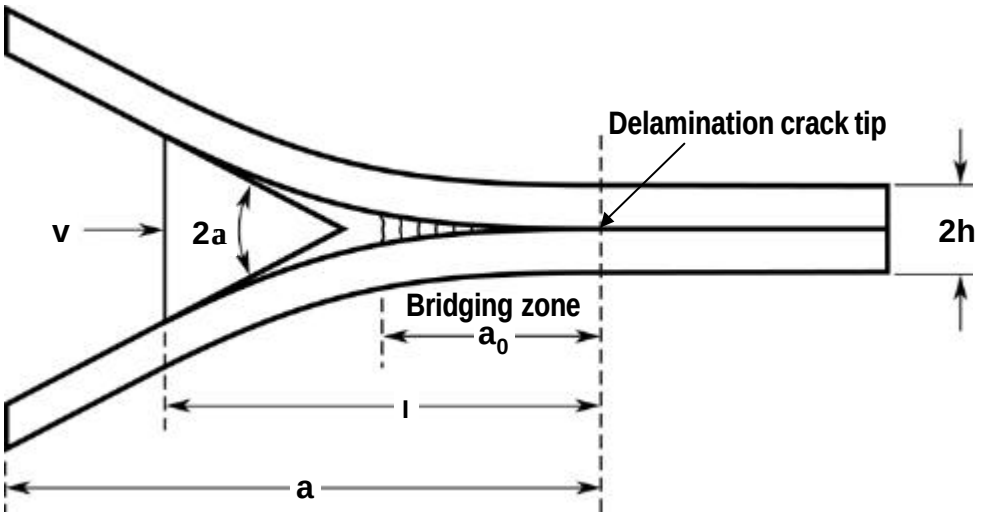

Figure 1: Schematic of through thickness reinforced DCB specimen loaded with a flying wedge

The double cantilever beam (DCB) specimen loaded dynamically by a flying wedge, of constant velocity v, offers a relatively simple experimental approach to studying the mode I dynamic delamination problem (Figure 1). The test is especially attractive for studying the bridging effects supplied by through-thickness reinforcement (e.g., stitches or rods) in laminates. In figure 1, 2α is the wedge angle, l is the distance between the wedge and the crack tip and a_0 is the length of the bridging zone. In non-dimensional form, $l \equiv h\,L$, and $a_0 \equiv h\,A_0$. The role of the bridging on the crack energy release rate is determined in this section. We assume that the crack propagates under steady state conditions and confirm the possibility of steady state propagation by finding consistent solutions. Further, we assume the bridging zone size is invariant and translates with the crack tip.

For the unbridged portion, the deflection profile ($w_u \equiv h\,W_u$) is obtained by setting $b = d = 0$. Therefore:

$$\frac{\partial^4 W_u}{\partial x^4} + \beta^2 \frac{\partial^2 W_u}{\partial x^2} = 0 \qquad \text{for } (-L \le x \le -A_0) \tag{9a}$$

$$\frac{\partial^4 W}{\partial x^4} + b^2 \frac{\partial^2 W}{\partial x^2} + b^2 W + d^2 = 0 \qquad \text{for } (-A_0 < x \le 0) \tag{9b}$$

The relevant boundary conditions are:

$$W(x=0) = 0\,,\; W'(x=0) = 0\,,\; W_u'(x=-L) = -a\,,\; W_u''(x=-L) = 0\,. \tag{10}$$

The governing Eqn. 9 together with the boundary conditions (10) and the continuity conditions at the end of the bridging zone ($x = -A_0$) will determine the deflection profile of the beam. Note that the bridging zone length (A_0) will be dictated by the critical crack opening displacement ($w_c \equiv h\,W_c$) required for failure of the bridging ligament. The crack energy release rate (G_{Total}), as determined through the total energy balance is:

$$G_{Total} = \frac{1}{B}\left(\frac{\partial U_{ext}}{\partial a} - \frac{\partial U_s}{\partial a} - \frac{\partial U_k}{\partial a}\right) \tag{11}$$

where U_{ext} is the work done by the applied load, U_s is the strain energy, U_k is the kinetic energy, B is the uniform width of the DCB specimen, and a is the crack length. For steady state crack extension $a = vt$, where v is the crack velocity and t is time. For the DCB specimen loaded with a flying wedge this reduces to:

$$G_{Total} = \frac{a\,E\,h}{6}\frac{\partial^3 W_u}{\partial x^3}\bigg|_{x=-L} - \rho\, h v^2 a^2 \tag{12}$$

In addition, by application of the dynamic J-integral, the energy released at the crack tip is related to the bending moment M by [8]:

$$G_{Tip} = \frac{12}{E\,h^3}\left(M_{x=0}\right)^2 = \frac{E\,h}{12}\left(\frac{\partial^2 W}{\partial x^2}\bigg|_{x=0}\right)^2 \tag{13}$$

Comparing G_{Total} and G_{Tip} for the displacement fields derived for the linear bridging law, one finds that

$$\Delta G_b = G_{Total} - G_{Tip} = 2\int_0^{w_c} p\; dw \tag{14}$$

where ΔG_b represents the work that must be done against the bridging ligaments along the bridged zone. This result is identical to that for the quasi-static case for small scale bridging conditions. Since there is no rate dependence to the bridging law, it is not surprising that the small scale bridging limit relationship is obeyed.

Since we limit our analysis to small scale bridging, tow failure must occur in the wake of the crack. Small scale bridging is ensured provided the displacement profile monotonically increases within the bridging zone from the crack tip and the pull-out required for tow failure is less than the maximum crack opening displacement within the bridging zone. This condition determines a criterion for the maximum allowable bridging zone length, A_{max}, which is obtained by solving $\partial W(x = -A_{max})/\partial x = 0$. Therefore, if $A_0 \le A_{max}$, then $W_c \le W_{critical}\,(\equiv W(x = -A_{max}))$, and hence small scale bridging condition is ensured.

Detailed calculations of the deflection profile, the crack energy release rate and the maximum allowable bridging length can be computed with the formalism presented above for both the Dugdale

bridging law and the proportional bridging law. For instance, when the bridging ligaments obey the Dugdale bridging law, steady state crack propagation with small scale bridging is provided $A_0 \le A_{max}$, where A_{max} is given by:

$$\begin{aligned} &-2\,l\,(\,Cos(\,l\,) - Cos(\,l\,(1-\hat{A}_{max}\,))\,) \;+\; 2\,l\,D\,\hat{A}_{max}\,(\,Cos(\,l\,(1-\hat{A}_{max}\,)) - 1\,) \\ &+ D\,(\,Sin(\,l\,(1-2\hat{A}_{max}\,)) + Sin(\,l\,\hat{A}_{max}\,)\,) + D\,(\,Sin(\,l\,\hat{A}_{max}\,) - Sin(\,l\,)\,) = 0 \end{aligned} \tag{15}$$

and where $\lambda = \beta L$, $D \equiv d/\lambda$, and $\hat{A}_{max} \equiv A_{max}/L$. Regions of steady state stable crack growth under small scale bridging condition can thus be deduced as a function of the material properties of the through thickness reinforcement, the size of the DCB specimen and the velocity of the wedge.

CONCLUSIONS

The dynamic delamination cracking behavior and the energetics of crack growth in through thickness double cantilever beam (DCB) specimens has been analyzed. The role of bridging by stitches or rods in dynamic crack growth was computed by solving the bridged crack problem within the framework of beam theory. For steady state crack growth conditions, different regimes of the solution behavior have been identified which would correspond to different crack propagation characteristics. Regions of steady state crack growth under small scale bridging condition can be deduced as a function of the material properties of the through thickness reinforcement, the size of the DCB specimen and the velocity of the wedge. This provides guidelines for design of experiments to probe the efficacy of bridging on improving the dynamic fracture toughness of through thickness reinforced structures.

ACKNOWLEDGMENTS: All four authors are grateful for support from the U.S. Army Research Office through contract number DAAD19-99-C-0042, administered by Dr. David Stepp. IJB is grateful for support from U.S. Dept. Of Energy through contract W-7405-ENG-36 and RM for support from the Italian Department for the University and for Scientific and Technological Research

REFERENCES:

1. Cartié, D. D. R., and Partridge, I. K., "Z-Pinned Composite Laminates: Improvements in Delamination Resistance", *Proc. DFC5 Conference*, I. Mech. E., March, 1999.
2. Jain, L.K., Mai, Y-W. (1994), "Analysis of stitched laminated ENF specimens for interlaminar mode-II fracture toughness", *Int. Journal of Fracture* **68**(3), 219-244.
3. M. He and B. N. Cox, "Crack Bridging by Through-Thickness Reinforcement in Delaminating Curved Structures", *Composites **A***, 29[4] 377-93 (1998).
4. R. Massabò and B. N. Cox, "Concepts for Bridged Mode II Delamination Cracks," *J. Mech. Phys. Solids*, **47**, 1265-1300 (1999).
5. B. N. Cox, "Constitutive Model for a Fiber Tow Bridging a Delamination Crack", *Mechanics of Composite Materials and Structures*, in press.
6. R. Massabò and B. N. Cox, "Unusual Characteristics of mixed mode delamination fracture in the presence of large scale bridging", *Mech. Comp. Mater. Structures*, in press
7. N.Sridhar, I.J.Beyerlein, B.N.Cox and R. Massabò, "Delamination mechanics in Through-Thickness Reinforced Structures under dynamic crack growth conditions", *in prepn.*
8. L.B.Freund, "Dynamic Fracture Mechanics", *Cambridge University Press*, New York (1993)

SLOW BRITTLE FRACTURE

C. J. McMahon, Jr.

Department of Materials Science and Engineering
University of Pennsylvania, Philadelphia, PA 19104

ABSTRACT

In contrast to the catastrophic types of brittle fracture in which cracks propagate unstably at hundreds of meters per second, brittle fracture can occur in a stable fashion at speeds that are many orders of magnitude slower. This occurs as a result of surface contamination by a mobile embrittling element that is induced to diffuse into a solid, usually along grain boundaries, under the influence of an applied stress. Examples are common in various engineering structures, but it is not widely recognized that they all belong to the same generic form of brittle fracture.

KEY WORDS: dynamic embrittlement, brittle fracture, intergranular fracture

INTRODUCTION

The term “brittle” is used here to denote fracture by decohesion that occurs apart from any plastic process. That is, plasticity may occur concomitantly, but it is not an essential part of the decohesion process. In the familiar fast brittle fracture in metals by transcrystalline cleavage or intergranular decohesion, plasticity is usually essential to crack nucleation, but is only incidental to crack propagation. The same applies here to slow brittle fracture.

Slow brittle fracture involves the propagation of a crack in a solid the surface of which is contaminated by an element that, when concentrated in the solid, would reduce the local cohesive strength. The application of a tensile stress to a solid in which a crack has nucleated both stretches bonds and causes the embrittling element to diffuse inward at the tip of the crack. This allows the crack to spread at a rate dependent upon the rate of diffusion of the embrittling element from the surface into the region ahead of the crack tip. This process has been termed “dynamic embrittlement” [1,2].

The phenomenon of dynamic embrittlement can be categorized according to the available concentration of embrittling element at the crack tip. The three categories being studied systematically in alloys are the following:

> (i) Low concentration. The embrittling element comes by way of surface segregation from the alloy itself.

(ii) Moderate concentration. The element comes from the vapor phase around the alloy.

(iii) High concentration. The embrittling species is in a liquid phase.

EMBRITTLEMENT FROM SURFACE SEGREGATION

The phenomenon was first recognized in the context of stress-relief cracking of alloy steels [3]. This is sometimes found in the coarse-grained heat-affected zone of welds, usually in thick sections. During the welding process, the HAZ reaches temperatures high enough to allow some dissolution of sulfides in the steel. During cooling, the dissolved sulfur segregates to austenite grain boundaries and then re-precipitates as very fine (probably metastable) sulfides in these boundaries. When the structure is later heated to allow relief of the residual stresses by creep, cavities can nucleate around large intergranular particles, like oxides or sulfides. If the stress is high enough, brittle cracks can grow from these cavities. This is caused by the presence of elemental sulfur that is segregated on the surfaces of the cavity and the subsequent crack and is then induced to diffuse into the grain boundary ahead of the crack by the tensile stress normal to the grain boundary, as illustrated schematically in Fig. 1. Sulfur is a very potent embrittling element in iron, and the concentration needed for decohesion at the stresses involved is probably less than one atom in ten [21].

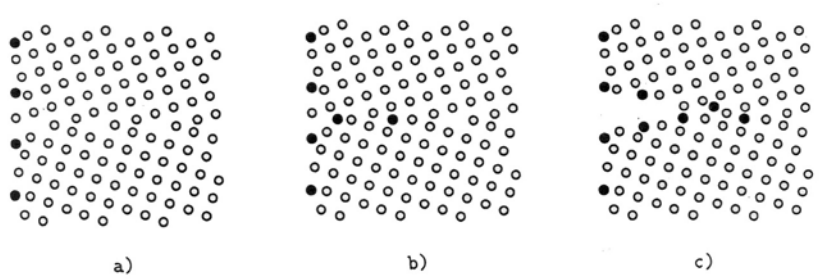

Fig. 1 Schematic representation of (a) surface adsorption of an embrittling element, (b) inward diffusion driven by a tensile stress, (c) decohesion in the diffusion zone.

The process depicted in Fig. 1 is analogous to the classical Hull-Rimmer mechanism of diffusive growth of creep cavities [4], which is the reverse of the sintering process. The stress across the grain boundary provides a gradient in chemical potential of atoms on the surface *vs*. in the bulk solid. That is, the stress does work when surface atoms diffuse into the bulk in exchange for lattice vacancies. Unlike in creep-cavity growth where the diffusing atoms are the same as in the bulk, in dynamic embrittlement the surface atoms are a mobile (i.e., low-melting) element that is adsorbed on the cavity/crack surface.

In a detailed study of stress-relief cracking using a simulated HAZ in a NiCrMnMo steel cooled rapidly from a high temperature [1], the following characteristics were found:

(i) The initial crack growth is macroscopically discontinuous, occurring in bursts, as indicated by the results from a compact-tension specimen under a constant load at

550˚C in vacuum, as shown in Fig. 2. Fractography by SEM showed that each burst represented cracking of a number of grain boundaries.

(ii) The local rate of crack advance is highly variable, depending on the grain-boundary structure, which determines the rate of diffusion of the surface element into the boundary. This results in a highly irregular crack front and in slow-cracking ligaments left behind the main crack front.

(iii) The tip of the growing crack is so sharp that no appearance of blunting could be found by examination of the fracture surface at the highest available resolution in the scanning electron microscope.

To test the hypothesis that this is a generic form of brittle fracture, similar experiments were carried out on a Cu-8%Sn alloy (without the prior high-temperature treatment). Compact-tension specimens loaded at 265˚C in vacuum exhibited behavior essentially similar to the steel [5], including intergranular decohesion and cracking in bursts. In this model material the tin played the role of sulfur in the steel. It is surface active [6], and it is a low-melting embrittling element in steel [7]. The conclusion is that the low creep ductility [8] and the hot shortness [9] exhibited by Cu-Sn alloys are both analogous to stress-relief cracking in steels.

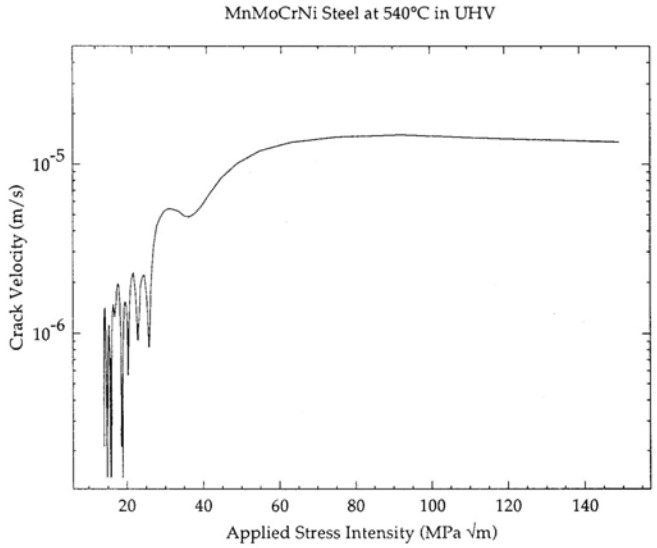

Fig. 2 Example of crack growth in bursts in the early stages of sulfur-induced dynamic embrittlement (stress-relief cracking) [1].

To test the idea that dynamic embrittlement requires diffusive penetration of the solid, which depends on the grain-boundary diffusion rate and thus grain-boundary structure, experiments were done on Cu-Sn bicrystals [10]. In specimens with Σ=5 (031)[100] symmetrical tilt boundaries made by diffusion bonding and loaded in vacuum at 265˚C, it was found that a crack could be grown easily along the tilt axis, but not transverse to the tilt axis. This corresponds to cracking along the fast-diffusion direction but not the slow-diffusion direction.

In the initial set of experiments, the boundaries had a residue of sub-micron-size alumina particles from metallographic polishing. Later, specimens were prepared without this residue [10], and still later by growth from the melt, also without particles [11]. The boundaries in this set of specimens were found to be difficult to crack, even along the fast-diffusion direction. Two conclusions were drawn from this. The first is that dynamic embrittlement may well follow the pattern of other types of grain-boundary failure [12-14] in which boundaries with Σ-value less than about 29 are particularly resistant to failure. The second conclusion is that the presence of particles probably enhanced the surface concentration of tin by decohering ahead of the crack and allowing tin to segregate to the new surfaces thereby created. They would thus have served a role analogous to that of the small sulfides in the steel. The influence of grain-boundary particles is an area that deserves further study.

EMBRITTLEMENT FROM THE ENVIRONMENT

Motivated by reports of oxygen-induced intergranular cracking in Cu-0.25%Be [15] and in nickel-base alloys, particularly alloy 718 [16], experiments were carried out to see if these types of cracking were analogous to the phenomena described above. When the steel and the Cu-Sn alloy were loaded at fixed displacement as notched bars in vacuum at elevated temperatures and the Cu-Be and alloy 718 were loaded similarly in oxygen, essentially the same behavior was found in all cases. The crack velocity could be calculated from the load-relaxation curve and the relation between specimen compliance and crack length. An example of the effect of oxygen pressure is given in Fig. 3.

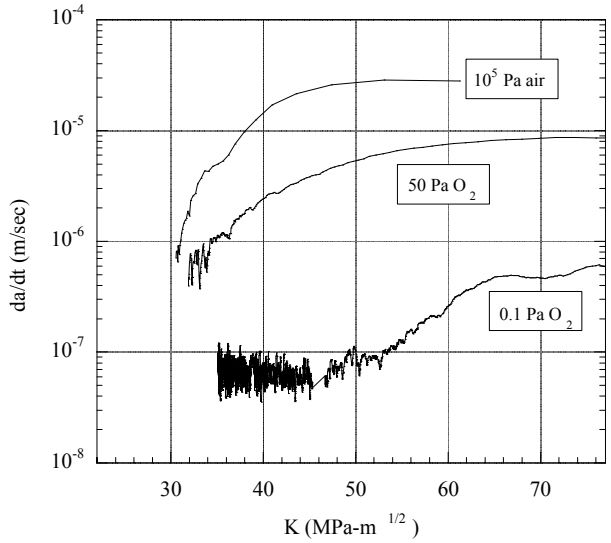

Fig. 3 Crack velocity *vs*. stress intensity curves derived from the load-relaxation curves and the compliance-calibration curve for alloy 718 at 650˚C in various pressures of oxygen [17].

Examination [17] of the fracture surfaces of the alloy 718 showed the typical decohesion appearance when the oxygen pressure was high enough. However, at very low pressures the growth rate dropped by several orders of magnitude, and the fracture appearance changed to a series of striations marked by strings of oxide, indicating that the cracking occurred in jumps at time intervals long enough for significant oxidation at the crack tip. The cracking at

higher oxygen pressures was also discontinuous (on the sub-micron scale), but the time intervals were much shorter, and the crack remained essentially sharp. Similar crack-arrest marks have been seen in all cases of dynamic embrittlement in polycrystalline specimens, but the cracking of the Cu-Sn bicrystals was continuous [10].

Our interpretation [17] of the fracture-surface observations was as follows: Cracking in polycrystals at sufficiently high surface concentration of the embrittling element occurs by the advance of sharp intergranular cracks caused by oxygen-induced decohesion, but at different rates along the crack front, depending on the local grain-boundary diffusivity. At any instant the main crack is advancing in some places, but not in others, and the load is therefore carried by the non-cracking regions. This shields the cracking regions from stress and allows the existence of sharp crack fronts. However, at any region of cracking the local stress relaxes as the crack moves forward, and the crack then has to stop and wait for creep of the non-cracking regions to raise the stress again. Thus, the cracking of a polycrystal is discontinuous because of the constraint imposed by non-cracking regions at any moment in time. The result is that large stress intensities are borne by the specimen (Fig. 3), but this does not reflect the stress intensity at the points of sharp-crack advance. In addition, the temperature dependence of cracking is found [17] to be consistent with that of self-diffusion in the alloy, rather than with the intergranular diffusion of the embrittling element in from the surface, because the cracking is constrained by the rate of power-law creep in the non-cracking regions.

Continuing this interpretation, in the case of cracking at very low oxygen pressures, oxygen atoms arrive at the crack tip so slowly that they have time to diffuse away along the grain boundary, down the gradient of chemical potential provided by the local stress. The crack then has time to blunt, and the oxygen collects in the region of maximum stress ahead of the blunt crack. When the concentration becomes high enough, cracking occurs back to the crack tip, and the process is repeated.

Oxygen-induced cracking in nickel-base alloys has been studied mainly in the context of cyclic loading and the effects of hold-time and loading rate on intergranular fatigue-crack growth [16,18]. The results obtained under fixed displacement conditions [17] indicate that the cyclic nature of the loading in the previous studies is incidental to the crack-growth process.

Experiments to study cracking in liquid metals using the same fixed-displacement, load-relaxation approach as outlined above have been only partly successful. It has been found with mercury and several copper-base alloys that the cracking is either too rapid to control or is so slow that it has to be driven with a moving cross head on the testing machine [19,20]. Much more work is needed in this area.

SUMMARY

It is now evident that dynamic embrittlement is a generic form of brittle fracture that involves decohesion caused by the inward diffusion of surface-adsorbed embrittling

elements, driven by an applied tensile stress. The source of the embrittling element can be the alloy itself (e.g., sulfur in steel and tin in Cu-Sn alloys) or the surrounding environment (e.g., oxygen in Cu-Be or in nickel-base alloys). Liquid-metal-induced cracking is thought to be a form of dynamic embrittlement, but this has not yet been demonstrated satisfactorily.

ACKNOWLEDGEMENTS

The work reviewed here was supported by the National Science Foundation under grants no. DMR 96-34718 and CMS 95-03980 and by the U.S. Department of Energy under grants no. CR-19314-429146.

References

1. Bika, D. and McMahon, C. J. Jr. (1995). *Acta Metall.* 43**,** 1909.
2. Liu, C. T.and White, C. L. (1987) .*Acta Metall.* 35**,** 643.
3. Shin, J. and McMahon, C. J. Jr. (1984) *Acta Metall.,* 32, 1535.
4. Hull, D. and Rimmer, D. E. (1959) *Philos. Mag.,* 4, 673.
5. Barrera, E. V., Menyhard, M., Bika, D., Rothman, B. and McMahon, C. J. Jr., (1992) *Scripta Metall.*, 27**,** 205.
6. Hofmann, S. and Erlewien, J. (1976) *Scripta Metall.* 10, 857.
7. Steven, W. and Balajiva, K. (1959) *J. Iron Steel Inst*. 193, 141.
8. Kanno, M. and Shimodaira, N. (1987) *Trans. Japan Inst. of Metals*,28, 742.
9. Metals Handbook, American Society for Metals, (1948) p. 860.
10. Muthiah, R. C., Pfaendtner, J. A., Ishikawa, S. and McMahon, C. J. Jr., Acta Mater. 47 (1999) 2797.
11. Woods, Seamus S. and McMahon, C. J. Jr., (2001) submitted for publication.
12. Palumbo, G., Lehockey, E. M. and Lin, P. *JOM* **50(2)** 40 (1998).
13. Was, G. S. Thaveeprungsriporn, V. and Crawford, D. C. *JOM* **50(2**) 44 (1998).
14. Kumar, M., King, W. E. and Schwartz, A. J. *Acta Materialia*, **48** 2081 (2000).
15. Guha, A. Brush-Wellman Inc., private communication 1993
16. Chang, K-M, Henry, M. F. and Benz, M. G. (1990), *JOM*, 42, 29.
17. Pfaendtner,. J. A. and McMahon, C. J. Jr, (2001) *Acta Mater.* in press.
18. Molins, R. Hochstetter, G. Chassaigne, J.C. and Andrieu, E. (1997) *Acta Metall.* 45 663.
19. Lerner, Jeffrey, Woods, Seamus S., Peng, Edward and McMahon, C. J. Jr. (2001) submitted for publication.
20. Lerner, Jeffrey and McMahon, C. J. Jr. (2001) submitted for publication.
21. Shin, K. S. and Meshii, M. (1983) *Scripta Metall.* 17, 1121.

ICF100240PR

DYNAMIC FRACTURE AND FRAGMENTATION OF BRITTLE SPHERES SUBJECT TO DOUBLE IMPACT TEST

K.T. Chau , S.Z.Wu and X.X. Wei

Department of Civil and Structural Engineering, The Hong Kong Polytechnic University, Kowloon, Hong Kong, China

ABSTRACT

This paper presents a new model for dynamic fracturing of a brittle sphere subject to the "double impact test", in which the sphere is crushed dynamically between two flat rigid platens. The dynamic tensile stress field in the specimen is calculated analytically using a superposition approach by Valanis [1]. The calculated local tensile field is imposed on vertical microcracks. The crack growth velocity is established in terms of the static stress intensity factor, the dynamic fracture toughness, and the Rayleigh wave speed. The dynamic strength corresponds to the crack growth velocity becoming unbounded. Double impact tests done on plaster spheres were used to verify the present model. Experimental results show that the impact energy required for fracturing in double impact test is about 150% of that required by the static counterpart (i.e. the diametral compression test).

KEYWORDS

Dynamic crack growth, Impact loads, Compression and fragmentation, Spheres

INTRODUCTION

The dynamic fragmentation of brittle spheres under impact loads has a wide range of engineering applications. It is also one of the most fundamental problems in applied mechanics. It relates to phenomena covering a wide range of length scales, from a large length scale of the collisional evolution of asteriods to shorter length scale of the degradation of materials in process industries, such as pharmaceuticals, chemical, fertilizers and detergents. In civil engineering and rock mechanics, its application has been in the mining industry, involving grinding, crushing, and impact comminution (Chau et al. [2]). Fragmentation of boulders during the impact phase of rockfall can also be modeled by dynamic impact of spheres (Chau et al. [3-5]).

Extensive experimental and theoretical efforts have been made to estimate the required energy and force to fracture a brittle solid into fragments with desirable size distribution. In the experimental approach, one of the most popular tests is the compression test of spheres, either statically or dynamically, between two flat rigid platens. Under quasi-static loads, compression of spheres between two flat platens has been proposed for testing the deformability of elastic materials, hardness of ductile materials and crushing strength of brittle materials. For example, the crushing of spheres between the flat platens can also be used to estimate the tensile strength of brittle spheres. A comprehensive review is given by Chau et al. [2] and by Darvell [6]. Although there are numerous experimental studies, stress distribution within a sphere under compression between two rigid platens has not been studied comprehensively. The most popular theoretical model is that proposed by Hiramatsu and Oka [7], which has been applied by various authors. Chau et al. [2] also provided a extension of Hiramatsu-Oka solution to incorporating the Hertz contact stress under compression. For the dynamic impact of spheres between two rigid platens, although a informative crater analysis was also suggested by Chau et al. [2]. However, due to mathematical complexity, Chau et al. [2] did not consider the exact solution for the stress distribution within spheres under the double impact test. Therefore, the dynamic stress inside the sphere and its relationship to the final fragmentation is not well understood.

Therefore, this paper outlines a new approach in which the Valanis [1] superposition principle for dynamic problems and the dynamic crack growth results considered by Freund [8] are combined to investigate the problem of dynamic fragmentation in spheres. The analysis is still on-going, only the essential idea and preliminary results will be reported.

VALANIS (1966) SUPERPOSITION PRINCIPLE

By applying the superposition principle put forward by Valanis [1], the problem of double impact test on spheres can be decomposed into two associated problems: the static problem and the free vibration problem of a sphere.

Static Compression of Spheres

The static solution for sphere can be generalized from that of Hiramatsu and Oka [7] (see Chau et al. [2]). In particular, by incorporating the Hertz contact stress, the static problem of compression of sphere between two rigid platens are:

$$\sigma_{rr} = \sum_{n=0}^{\infty} P_{2n}(\cos\theta)\left\{-\frac{\left(4n^2-2n-3\right)\lambda+2(2n+1)(n-1)\mu}{4n+3}A_{2n}r^{2n}+4n(2n-1)\mu C_{2n}r^{2n-2}\right\} \tag{1}$$

$$\begin{aligned}\sigma_{\theta\theta} = &\sum_{n=0}^{\infty} P_{2n}(\cos\theta)\left\{\frac{(2n+3)\lambda-2(n-1)\mu}{4n+3}A_{2n}r^{2n}+4n\mu C_{2n}r^{2n-2}\right\}\\ &+\ 2\frac{\partial^2}{\partial\theta^2}P_{2n}(\cos\theta)\left\{-\frac{(2n+3)\lambda+(2n+5)\mu}{2(2n+1)(4n+3)}A_{2n}r^{2n}+\mu C_{2n}r^{2n-2}\right\}\end{aligned} \tag{2}$$

$$\sigma_{r\theta} = \sum_{n=0}^{\infty}\frac{\partial}{\partial\theta}P_{2n}(\cos\theta)\left\{-\frac{4n(n+1)\lambda+\left(4n^2+4n-1\right)\mu}{(2n+1)(4n+3)}A_{2n}r^{2n}+2(2n-1)\mu C_{2n}r^{2n-2}\right\} \tag{3}$$

where the unknown constants can be obtained from the boundary condition as

$$\begin{cases} A_{2n} = \dfrac{E_{2n}}{a^{2n}}\left\{\dfrac{(4n+3)(2n+1)}{(8n^2+8n+3)\lambda + 2(4n^2+2n+1)\mu}\right\} & A_{2n+1} = 0 \\ C_{2n} = \dfrac{E_{2n}}{a^{2n-2}}\left\{\dfrac{4n(n+1)\lambda + (4n^2+4n-1)\mu}{2\mu(2n-1)[(8n^2+8n+3)\lambda + 2(4n^2+2n+1)\mu]}\right\} & C_{2n+1} = 0 \\ E_{2n} = -\dfrac{3(4n+1)F\sqrt{a^2-a_0^2}}{2\pi a_0^3}\int_{\cos\theta_0}^{1}\left(\dfrac{x^2}{\cos^2\theta_0}-1\right)^{1/2} P_{2n}(x)\,dx & \\ \cos\theta_0 = \dfrac{\sqrt{a^2-a_0^2}}{a} \qquad a_0 = \left(\dfrac{3Fa(1-\nu^2)}{4E}\right)^{1/3} & a_0 = a\sin\theta_0 \end{cases} \tag{4}$$

Free Vibration Problems of Spheres

Instead of using wave potential approach (Chau [11]), the Helmholtz decomposition theorem will be used here to solve the following "reduced dynamics problem" (Achenbach [12]):

$$(\lambda + 2\mu)\nabla\nabla\times\vec{V} - \mu\nabla\cdot\nabla\cdot\vec{V} = \rho\frac{\partial^2\vec{V}}{\partial t^2} \tag{5}$$

$$\sigma_{rr} = 0 \qquad \sigma_{r\theta} = 0 \quad on \quad r = a; \qquad V_i = U_i, \quad \frac{\partial V_i}{\partial t} = 0 \quad at \quad t=0$$

In particular, we can assume the displacement vector as

$$\vec{V} = \nabla\phi + \nabla\cdot\vec{\psi} \tag{6}$$

These scalar and vector potentials satisfy

$$\nabla^2\phi = \frac{1}{c_1^2}\frac{\partial^2\phi}{\partial t^2} \qquad \nabla^2\vec{\psi} = \frac{1}{c_2^2}\frac{\partial^2\vec{\psi}}{\partial t^2} \tag{7}$$

For our axisymmetric problem, the second of these becomes

$$\nabla^2\psi - \frac{\psi}{r^2\sin^2\theta} = \frac{1}{c_2^2}\frac{\partial^2\psi}{\partial t^2} \qquad (i.e.\ \vec{\psi} = (0,0,\psi)) \tag{8}$$

The general solutions for and are:

$$\phi = \sum_{n=1}^{\infty} A_n r^{-\frac{1}{2}} J_{n+\frac{1}{2}}\left(\frac{k}{c_1}r\right) P_n(\cos\theta) f_n(t), \quad \psi = \sum_{n=1}^{\infty} B_n r^{-\frac{1}{2}} J_{n+\frac{1}{2}}\left(\frac{k}{c_2}r\right) P_n^1(\cos\theta) f_n(t) \tag{9}$$

Substitution of these solutions to the displacement-strain and stress-strain relations leads to

$$\sigma_{rr} = \sum_{n=1}^{\infty} 2\mu A_n F_n(r,k) P_n(x) f_n(t) \tag{10}$$

$$F_n(r,k) = \left\{ n(n-1) - \frac{1-n}{1-2n}\left(\frac{k}{c_1}r\right)^2 \right\} J_{n+\frac{1}{2}}\left(\frac{k}{c_1}r\right) + 2\frac{k}{c_1} r J_{n+\frac{3}{2}}\left(\frac{k}{c_1}r\right) \Big] r^{-\frac{5}{2}}$$
$$+ \frac{B_n}{A_n} n(n+1)\left[(n-1) J_{n+\frac{1}{2}}\left(\frac{k}{c_2}r\right) - \frac{k}{c_2} r J_{n+\frac{3}{2}}\left(\frac{k}{c_2}r\right) \right] r^{-\frac{5}{2}} \tag{11}$$

$$\sigma_{rq} = \sum_{n=1}^{\infty} \mu A_n G_n(r,k) P_n^1(x) f_n(t) \tag{12}$$

$$G_n(r,k) = -2\left[(n-1) J_{n+\frac{1}{2}}\left(\frac{k}{c_1}r\right) - \frac{k}{c_1} r J_{n+\frac{3}{2}}\left(\frac{k}{c_1}r\right) \right] r^{-\frac{5}{2}}$$
$$+ \frac{B_n}{A_n}\left[-2n^2 + 2 + \frac{k^2}{c_2^2} r^2 \right] J_{n+\frac{1}{2}}\left(\frac{k}{c_2}r\right) - 2\frac{k}{c_2} r J_{n+\frac{3}{2}}\left(\frac{k}{c_2}r\right) \Big] r^{-\frac{5}{2}} \tag{13}$$

$$\sigma_{qq} = \sum_{n=1}^{\infty} 2\mu A_n \left(H_{n1} P_n(\cos\theta) + H_{n2} \frac{\partial^2}{\partial\theta^2} P_n(\cos\theta) \right) f_n(t) \tag{14}$$

$$H_{n1} = \left\{ \frac{n}{-1+2n}\left(\frac{k}{c_1}r\right)^2 + n \right\} J_{n+\frac{1}{2}}\left(\frac{k}{c_1}r\right) - \frac{k}{c_1} r J_{n+\frac{3}{2}}\left(\frac{k}{c_1}r\right) + \frac{B_n}{A_n} n(n+1) J_{n+\frac{1}{2}}\left(\frac{k}{c_2}r\right) \Big] r^{-\frac{5}{2}}$$
$$H_{n2} = \left\{ J_{n+\frac{1}{2}}\left(\frac{k}{c_1}r\right) + \frac{B_n}{A_n}\left[(n+1) J_{n+\frac{1}{2}}\left(\frac{k}{c_2}r\right) - \frac{k}{c_2} r J_{n+\frac{3}{2}}\left(\frac{k}{c_2}r\right) \right] \right\} r^{-\frac{5}{2}} \tag{15}$$

By applying the traction free conditions on the spherical surface (i.e. $\sigma_{rr} = 0, \quad \sigma_{rq} = 0 \quad$ on $r = a$), the following characteristic equations is obtained:

$$2n(n+1)\left[(n-1) J_{n+\frac{1}{2}}\left(\frac{k}{c_2}a\right) - \frac{k}{c_2} a J_{n+\frac{3}{2}}\left(\frac{k}{c_2}a\right) \right] \left[(n-1) J_{n+\frac{1}{2}}\left(\frac{k}{c_1}a\right) - \frac{k}{c_1} a J_{n+\frac{3}{2}}\left(\frac{k}{c_1}a\right) \right]$$
$$+ \left\{ n(n-1) - \frac{1-n}{1-2n}\left(\frac{k}{c_1}a\right)^2 \right\} J_{n+\frac{1}{2}}\left(\frac{k}{c_1}a\right) + 2\frac{k}{c_1} a J_{n+\frac{3}{2}}\left(\frac{k}{c_1}a\right) \Big]$$
$$\left[-2n^2 + 2 + \frac{k^2}{c_2^2} a^2 \right] J_{n+\frac{1}{2}}\left(\frac{k}{c_2}a\right) - 2\frac{k}{c_2} a J_{n+\frac{3}{2}}\left(\frac{k}{c_2}a\right) \Big] = 0 \qquad (n = 1, 2, 3, \cdots) \tag{16}$$

The full details of analysis and the numerical results will be presented in our forthcoming publication. Nevertheless, a new approach has been outlined here to solve the problem of dynamic compression of sphere.

DYNAMIC CRACK GROWTH IN SPHERE

The solution considered in the previous section for dynamic tensile along the center-line of the sphere can be used to estimate the dynamic mode I stress intensity factor of a vertical microcrack as shown in Fig. 1 (Deng and Nemat-Nasser [13]; Freund [8]):

$$K_{ID} = \sigma_{hoop}(t)\sqrt{\pi a}\left(1 - \frac{\dot{l}}{c_R}\right)\left(1 - \frac{\dot{l}}{2c_R}\right)^{-1} \tag{17}$$

where K_{ID} is the dynamic stress intensity factor, $\sigma_{hoop}(t)$ is the maximum hoop stress along the center-line of the axis of compression obtained in the previous section, $\dot{l}$ is the velocity of crack growth, a is the half size of the microcrack and c_R is the Rayleigh wave speed. It has been assumed that the microcrack is relatively small comparing to the size of the sphere such that local tensile field can be considered as a far field uniform stress. The speed of crack growth can be non-uniform. We should also emphasized that the speed of crack growth should not exceed the Rayleigh wave speed. It can be shown that the speed of crack growth can be determined as (Deng and Nemat-Nasser, [13])

$$\dot{l} = c_R \frac{K_{IS} - K_{IC}}{K_{IS} - \frac{1}{2}K_{IC}} \tag{18}$$

where K_{IS} is the static mode I stress intensity factor and K_{IC} is the dynamic fracture toughness.

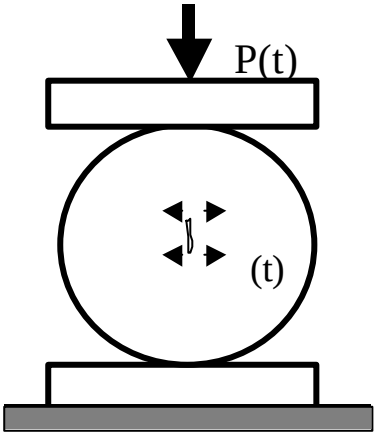

Figure 1: Dynamic growth of vertical microcrack in sphere under double impact test.

Chau et al. (2000) showed that the dynamic energy required for fragmentation can be estimated as 1.5 times of that required for static compression. Figure 2 was extracted from Chau et al. (2000).

FUTURE WORK TO BE DONE

In the case of double impact test, the present approach described needs to be combined with the dynamic motion of the drop weight attached to the upper platen. The application of the contact force during the dynamic impact needs to be evaluated by applying Newton second law to the falling rigid upper platen.

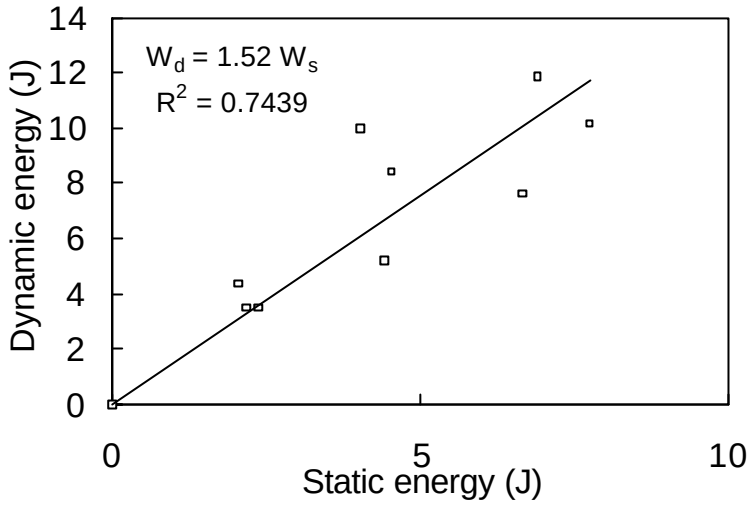

Figure 2: Dynamic energy versus static energy required for fragmentation of sphere (after Chau et al. [2])

CONCLUSION

The present paper summarizes a new theoretical approach to consider the dynamic stress within a sphere under double dynamic test. The application of this tensile stress to dynamic fracture in the sphere is also outlined. More elaborated numerical analysis remains to be done and will be presented at a later time. Nevertheless, the present framework should be very useful to investigate the dynamic fragmentation problem of spheres under dynamic compressions.

ACKNOWLEDGMENTS

The work was supported by the Research Grants Council of the Hong Kong SAR government with a CERG Grant No. PolyU 5044/99E to The Hong Kong Polytechnic University through KTC, by the PolyU studentship Project G-V946 to SZW, and by Post-doctoral Project No. G-YW39 to XXW.

REFERENCES

1. Valanis K.C. (1966). *J. Appl. Mech.* 33, 888.
2. Chau, K.T., Wei X.X., Wong R.H.C. and Yu T.X. (2000). *Mech. Mat.* 32, 543.
3. Chau, K.T., Wong, R.H.C. and Lee, C.F. (1998). *Int. J. Rock Mech. Min. Sci.*35(4-5), 662, Paper No. 007.
4. Chau, K.T., Wong, R.H.C., Liu, J., Wu, J.J. and Lee, C.F. (1999). In: *The 9th International Congress on Rock Mechanics*, Vol. 1, pp.541-544.
5. Chau, K.T., Liu J., Chan, T.C.P., Yu, T.X. and Chen, X.W. (1999). In: *Sixth Pan American Congress of Applied Mechanics (PACAM VI)*, pp. 967-970.
6. Darvell, B.W. (1990). *J. Mat. Sci.* 25, 757.
7. Hiramatsu, Y. and Oka, Y., (1966). *Int. J. Rock Mech. Min. Sci* 3, 89.
8. Freund L.B. (1989). *Dynamic Fracture Mechanics,* Cambridge University Press, Cambridge.
9. Chau, K.T. and Wei, X.X. (1999). *Int. J. Solids Struct.*36, 4473.
10. Wei, X.X. and Chau, K.T. (1998). *Int. J. Rock Mech. Min. Sci.*35(4-5), 623, Paper No. 006.

11. Chau, K.T. (1998). *J. Appl. Mech.ASME*, 65(1), 59.
12. Achenbach J.D. (1973). *Wave Propagation in Elastic Solids*, North-Holland, Amsterdam.
13. Deng H. and Nemat-Nasser S. (1992). *Mech. Mat.* 14, 83.

DYNAMIC FRACTURE BEHAVIOR OF COMPOSITES

S. Ravi[1*], N.G.R. Iyengar[1], N.N. Kishore[1] and A. Shukla[2]

[1] Indian Institute of Technology, Kanpur 208 016, India
[2] University of Rhode Island, Kingston, RI 02881, USA
[*] Presently at RIAM, Kyushu University, Kasuga 816-8580, Japan

ABSTRACT

Dynamic fracture behavior of glass-polyester composites subjected to dynamic loads has been studied. The aim is to study the effect of reinforcement type, fiber volume fraction, initial notch orientation and fiber orientation. Cranz-Schardin type multi-spark high speed recording system has been used to record the initiation and propagation history at a pre-determined short intervals of time. It has been observed that the damage grows normal to the loading direction irrespective of the type of reinforcement, initial notch orientation and fiber orientation. The damage propagates at higher velocity than in the unreinforced polyester matrix. Further, for a given energy input, the damage area reduces with increase in fiber volume fraction.

KEY WORDS

Dynamic fracture, stress waves, high speed recording, damage zone, glass-polyester composite.

INTRODUCTION

The fracture behavior of composite materials under various loads is of significant practical importance in terms of its service performance. It is known that the fracture process in composites precedes with the formation of a zone, often referred to as *damage zone*, ahead of the crack tip. The damage zone consists of many micromechanisms like fiber fracture, matrix cracks, interface failure etc. Further, as the damage propagates, these failure modes may interact with each other resulting in a complex fracture process. Shukla and Khanna [1, 2] have investigated the effect of fiber-matrix interface on dynamic crack growth and associated fracture energy in a brittle matrix material reinforced with discrete fibers. The results indicate that the fiber reinforcement reduces fracture energy available at the crack tip as calculated from the instantaneous stress intensity factor and results in small crack jump distance. Agarwal et al. [3] used Cranz-Schardin camera to study the dynamic damage growth in glass/polyester composites. Their results show that the dynamic damage in composite, propagates with a slightly lower velocity than the crack propagation velocity in a polyester resin. In the present study, we attempt to study the fracture behavior in glass-polyester composites having reinforcements in the form of cloth and chopped strand mat loaded with stress waves.

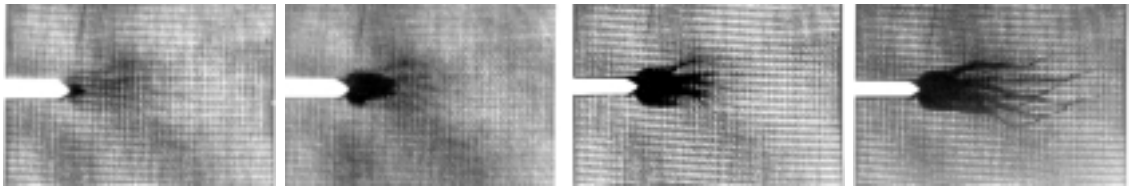

97.5 μsec 114.0 μsec 127.5 μsec 205.5 μsec

Figure 1: Damage growth pattern in glass/polyester composite MSEN ($V_f = 5.3$ % and 0° notch)

EXPERIMENTAL PROCEDURE

Material

Optically transparent glass/polyester composite plates have been fabricated in the laboratory from sheet grade polyester resin(Parikh Chemicals, Kanpur 208016, INDIA) and glass fibers in the form of cloth (balanced weave) and chopped strand mat (Harsh-Deep Industries, Ahmedabad 380023, INDIA). The refractive index of the polyester resin is modified to match with that of the glass fibers by adding 5% di-butyl pthalate and 2% di-vinyl benzene. The resin mixture has been cured using 1% MEKP and 0.03% cobalt octate at room temperature for $24\,h$ and post cured at $80^\circ C$ for $8\,h$. The plate thus fabricated with 33% fiber volume fraction shows a transmission ratio of 69.5%.

Testing

Dynamic damage growth in fiber composites have been studied using modified single edge notched (MSEN) specimens containing an initial notch length of 0.25 times the width. The specimen is mounted on the optical bench of Cranz-Schardin high speed camera. Dynamic loads are produced by the simultaneous detonation of two explosive charges on both side-shoulders of the specimen. For the present study, 50 mg and 25 mg of PETN explosive charge with lead azide as explosion initiator have been used respectively for cloth and mat composites. Detonation generates compressive waves which get reflected as tensile waves from the free end. The end shape of the MSEN has been selected in such a way that the reflected tensile waves propagate as a planar wave front. It has been established [4] that a plane fronted loading tensile wave can be achieved with the specimen configuration considered for the present analysis. The planar wave loads the notch and initiates the damage.

Damage Zone Measurements

The detonation simultaneously sends signal to the high speed camera to start recording twenty pictures of damage initiation and propagation history at 5 μsec interval. Image processing tool, IDRISI has been used to obtain the useful informations, like the damage area etc., from the recorded images.

RESULT AND DISCUSSION

Damage in Woven Fabric Composites

The damage pattern and the propagation history in woven fabric (cloth) composite specimen having $V_f = 5.3$ % with $\theta = 0^\circ$ are shown in Figure 1. The dark area ahead of the machined notch are the 3 dimensional damage occurred as the notch is loaded with the stress waves. Similar images have been obtained for all the cases considered. From these images, it is observed that the damage propagates perpendicular to the loading direction and parallel to the notch plane. In homogeneous materials, single crack propagates with possible crack branching under appropriate loading conditions, while in composites, a damage zone is formed ahead of the notch and this damage zone propagates. Further, it is observed that for a given energy, the damage zone size reduces as the fiber volume fraction increases.

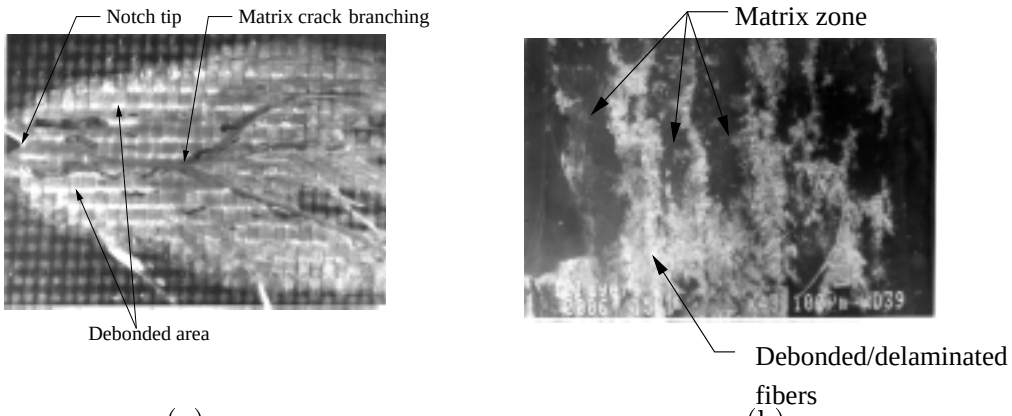

Figure 2: Microscopic picture showing (a) debonded area and matrix crack with branching in MSEN specimen having $V_f = 2.4$ % and 0° notch (b) delaminated and debonded fibers as bright spots in MSEN specimens having $V_f = 33.0$ % and 0° notch

Table 1: Damage propagation velocity and rate of growth of damage in glass/polyester composites

Volume fraction %	Notch orientation deg	Velocity (m/s)		Rate of growth (m^2/sec)	
		Initial	Final	Initial	Final
Woven fiber cloth composite					
2.4	0	460	260	3.49	–
	15	400	210	3.35	–
	30	420	320	3.21	–
	45	470	150	3.42	–
5.3	0	490	0	2.50	0.45
	30	380	0	2.22	0.13
	45	450	0	2.92	0.98
Chopped strand mat composite					
10.0	0	500	0	–	–
	15	250	0	–	–

Another important feature observed in specimens with low fiber volume fractions is the damage zone splitting, analogous to the crack branching in homogeneous materials. For low fiber volume fractions, the mechanisms involved in the formation of damage zone are, the matrix cracking, fiber-matrix interface debonding and branching in matrix region (Figure 2a). On the other hand, the mechanisms involved in high fiber volume fraction are matrix cracking, fiber-matrix interface debonding and delamination (Figure 2b).

Table 1 gives the damage velocity for different specimens studied. It is observed that the initial velocity is approximately same for both $V_f = 2.4$ % and 5.3 %. But during the end of the observation period, the damage slows down in single layer composites ($V_f = 2.4$ %), while it gets arrested in two layer composites ($V_f = 5.3$ %). Further investigations revealed that the damage traveled to the entire width of the specimen in single layer composite which is not seen in other specimens. This lowering and arrest may be due to the unloading of the damage zone as the trailing part of the stress wave passes over and due to the increased resistance due to rise in fiber volume fraction.

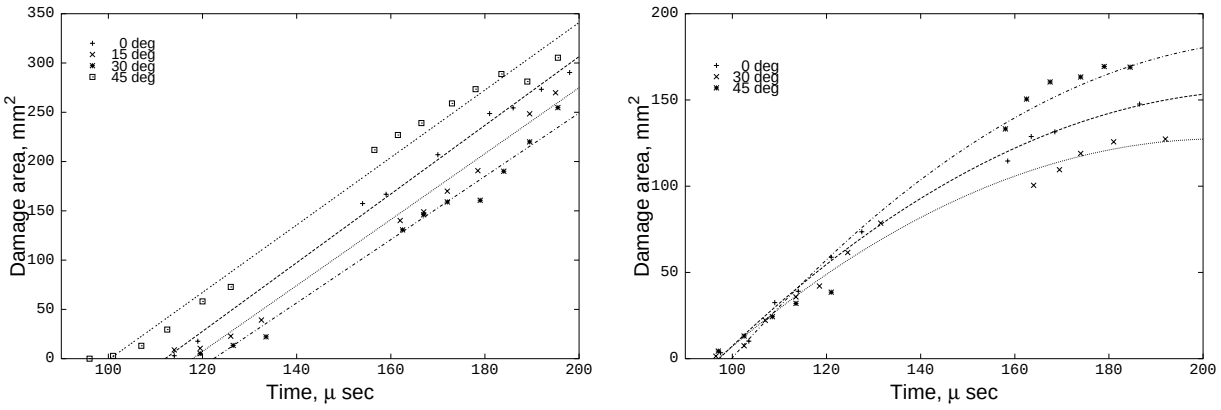

Figure 3: Propagation of damage zone during the observation period (a) single layer ($V_f = 2.4\%$) and (b) two layer ($V_f = 5.3\%$) composites

Figures 3a and b show the variation of damage area with respect to time for the composites specimens studied. Table 1 also presents the damage growth rate calculated from the above figures. From the figures and table, it is seen that for single layer composites, irrespective of the initial notch orientation, the damage zone grows at a constant rate. On the other hand, the damage has to overcome the resistance by the increased fiber and so the damage zone grows at a slower rate during the end of the observation period in two layer composite specimens.

Damage in Chopped Strand Mat Composites

Figures 4 and 5 shows damage sequences in short fiber composites with $V_f = 10\%$ and 0° notch. It is noted that the overall damage is perpendicular to the loading direction as observed in woven cloth composite specimens. In mat composites, the damage zone is formed due to multi-directional micro-cracks in the matrix, at the interface and due to fiber fracture. The damage zone initiates at the crack tip and grow perpendicular to the loading direction in a narrow band. Damage zone splitting, as seen in woven fabric composites, is not observed in mat composites. However, *secondary damage*, away from the notch tip and independent of main damage, has been noted. Some time this secondary damage is from the corner of the 'V' notch (Figure5). The energy absorbing mechanisms in mat composites are the matrix cracks and interface debonding at the ends of the short fibers. As the stress waves passes over, the dynamic load increases, which leads to an increase in the stress intensity around the notch. This raise in stress level leads to the concentration of stresses at the ends of the fibers, ultimately leading to the initiation of the debonding.

Table 1 also gives the the velocity of damage in chopped strand composites. It is observed that the initial propagation velocities are in the range of $250 - 500\ m/sec$. These damage velocities are higher than the crack velocity of 240 m/sec for glass-polyester composite model [3]. It is observed that in all the damage propagation velocity reduces and gets arrested. This reduction in velocity is analogous to the reduction in crack velocity with decrease in stress intensity factor in Homalite-100.

It may be pointed out here that the above definition of damage propagation velocity may provide a method for analyzing the results of dynamic fracture experiments on composite materials. However, the difference between this damage propagation velocity and the crack velocity in homogeneous materials should be recognized and properly accounted for in developing the analysis procedures and interpreting results. Actual damage in composites consists of numerous 3D micro damages in the form of fiber–matrix interface debonding, fiber, matrix cracks, etc., which is quite different from through-the-thickness cracks. On the other hand, the Cranz-Schardin camera records the 2D

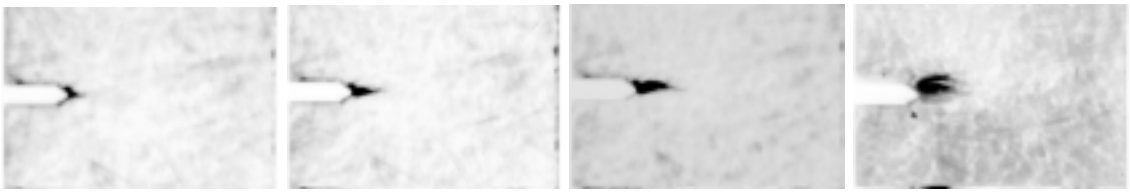

100.0 μsec 110.5 μsec 163.0 μsec 200.0 μsec

Figure 4: Damage sequence in random mat composites, $V_f = 10\%$, 0° notch, 25 mg PETN charge

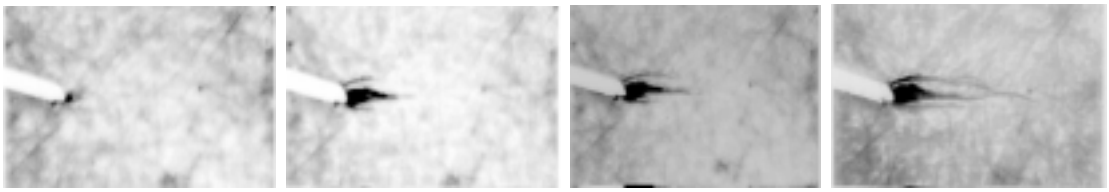

99.0 μsec 126.5 μsec 150.0 μsec 205.0 μsec

Figure 5: Damage sequence in random mat composites, $V_f = 10\%$, 15° notch, 25 mg PETN charge

projection of the 3D damages. Establishing the relationship between the shadow areas and the 3D fracture surface area is quite challenging and requires further work.

ACKNOWLEDGMENT

The partial financial support from National Science Foundation, USA and Aeronautics Research and Development Board (Structures Panel), Govt. of India are gratefully acknowledged.

References

[1] Shukla, A. and Khanna, S.K. (1993) Trans. ASME J Eng. Mat. Tech. 115, p140.

[2] Khanna, S.K. and Shukla, A. (1994) Exp. Mech. 34, p171

[3] Agarwal, B.D., Sharma, R. and Bajpai, K.K. (1995) Mech. Comp. Mat. Struct. 2, p295

[4] Ravi, S., Iyengar, N.G.R., Kishore, N.N. and Shukla, A. (Accepted for publication) App. Comp. Mat.

DYNAMIC FRACTURE SURFACE ENERGY VALUES AND FRUSTRATED MICRO-BRANCHES DURING RCP IN AN IMPACT MODIFIED POLYMER

C. Fond and R. Schirrer

Institut Charles Sadron, 6, rue Boussingault, F67083 Strasbourg.
fond@ics.u-strasbg.fr, schirrer.ics.u-strasbg.fr, http://ics.u-strasbg.fr/

ABSTRACT

The fracture behaviour of materials for which the fracture energy decreases near the Raleigh wave speed, c_r, is investigated using an impact modified polymer. An experimental device based on strip band geometry has been designed to explore the brittle behaviour of such polymers during rapid crack propagation (RCP). The macroscopic crack speed is found to be quasi-constant along an entire rubber toughened polymethylmethacrylate (RT-PMMA) specimen, even in the case of crack branching and until arrest, if any. As the material behaviour tends to accelerate the crack – the fracture energy decreases near c_r - whereas mechanical inertial effects tend to limit the rate of crack propagation – due to crack branching -, the macroscopic crack speed stabilizes at approximately $å_{mb} = 0.6\ c_r$, which is the macroscopic crack branching speed for RT-PMMA. Consequently, at the macroscopic crack branching velocity, the experimental fracture surface energy and the fracture surface roughness have no single value in such materials. In fact, the macroscopic fracture surface energy value increases with the number of instabilities or frustrated micro-branches.

INTRODUCTION

While the dynamic fracture behaviour of materials for which the fracture energy increases near the Raleigh wave speed, c_r, has been largely explored and is now relatively well understood – the speed of the cracks decrease at crack branching – the case of materials for which the fracture energy decreases near c_r is still to be investigated on real materials. Most polymeric materials exhibit a brittle fracture mode at high crack propagation speeds and experiments have revealed that crack propagation in rubber toughened-polymethylmethacrylate (RT-PMMA) is unstable between approximately 0.001 and 0.6 c_r, where c_r is the Raleigh wave speed. As the fracture surface energy decreases with increasing crack speed, the propagation velocity jumps from 1 to about 600 m/s when an increasing load initiates propagation of a crack. Crack branching occurs, as expected, at a crack tip speed of nearly 0.6 c_r. However, unlike in many other polymers such as for instance PMMA, the macroscopic crack speed ($å_m$) does not change after branching during rapid crack propagation (RCP) in RT-PMMA. In fact, at nearly 0.6 c_r, inertial effects modify the crack tip stress field and induce branching [1]. It is noticeable that branching is made easier by the rubber toughening particles, which perturb the micro-mechanical fields. Subsequently, as the material behaviour tends to accelerate the crack whereas mechanical inertial effects tend to limit the rate of crack extension, the crack speed stabilizes at approximately $å_{mb} = 0.6\ c_r$, which is the macroscopic crack branching speed for RT-PMMA.

EXPERIMENTAL SYSTEM

The experimental system (Fig. 1, left) was designed to enable a steady state regime of brittle fracture and a simple mechanical analysis of the fracture energy, even for RCP [2, 3]. The geometry is that of a strip band specimen (SBS) of typical dimensions $L \approx 200$ mm, $25 \text{ mm} < H < 45$ mm, $a_0 \approx 3\,H$, $B \approx 2$ mm. The location of the crack tip during propagation is determined by measuring the resistance of a metallic layer at a sampling rate of 250 kHz [4]. A loading device (Fig. 1, right) ensures uniform and constant displacement of the strip band boundaries and the symmetry of the loading is checked by strain measurements on the sides of the specimen.Crack propagation is started by an impact of low energy on a razor blade placed in contact with an initial blunt notch and the crack propagates symmetrically. Only one of the twin specimens undergoes fracture. Owing to the weight of the grips and the short fracture time, typically 200 μs, we assume that the boundary conditions are fixed during crack propagation. Crack branching can be obtained by increasing the mechanical potential energy of the specimen and the crack branches are generally symmetrical for polymethylmethacrylate (PMMA) and RT-PMMA specimens. RT-PMMA is a blend of PMMA and spherical rubber particles, in these experiments of diameter 200 nm and volume fraction approximately 40 %.

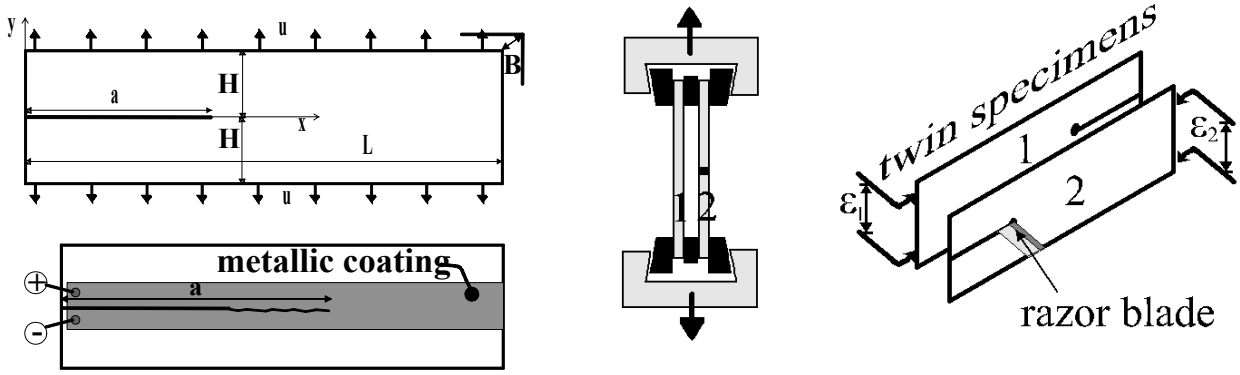

Figure 1: (left) Schematic representation of the strip band geometry uniformly loaded and the conducting layer used to record the crack tip position during propagation. (right) Experimental device ensuring symmetrical loading.

DYNAMIC ENERGY RELEASE RATE COMPUTATION AND VALUES OF THE FRACTURE SURFACE ENERGY

During RCP tests, no significant variation of the macroscopic crack speed has been observed for a given specimen at a given temperature, whether branching occurs or not (Fig. 2). Since the crack tip position during propagation and the stress state at initiation are known, the energy release rate G_{ID} may be calculated by means of a transient dynamic finite element procedure, using the software Castem2000©. Outside the singularity, thermo elastic effects are expected to be negligible since the mean stress is about 15 MPa [5]. Owing to the high strain rate, the fracture mechanics is assumed to display linear elastic behaviour [6]. The energy release rates were computed by differentiating the elastic energy integrated on the whole structure. As the geometry ensures a quasi-steady state regime of propagation, it is assumed that a specific treatment of the singularity is not necessary since the error done concerning the energy integration at the crack-tip singularity is eliminated by the differentiation. It has been shown experimentally that the impact on the razor blade influences the crack propagation only over the first few millimetres. Nevertheless, this crack initiation is simulated by imposing an initial crack tip opening, corresponding to the action of the razor blade at the crack lips.

Figure 3 shows that the dynamic correction factor is generally of the order of 0.7 to 0.8 for macroscopic crack speeds of about $0.6\,c_r$. This specimen geometry in fact induces a low dynamic correction factor [3, 7] and the remote stress field at the crack tip is not strongly influenced by inertial effects in this range of crack speeds. To simplify the results, as G_{ID} displays relatively small

oscillations during crack propagation, the mean value of the fracture energy $< G_{ID} >$ was calculated for each specimen before branching, if any. In practice, $< G_{ID} >$ concerns the steady state regime and does not take into account the first 1.5 mm of propagation in RT-PMMA. $< G_{ID} >$ varies from 0.49 to 2.1 KJ/m² and for a single straight line crack with smooth crack surfaces is typically 0.57 ± 0.12 KJ/m². In the case of a single straight line crack with crack surfaces showing small aborted but visible branches of length less than about 1 mm (Photo1), $< G_{ID} >$ is typically 0.8 ± 0.15 KJ/m². When macroscopic crack branching occurs, the crack surfaces are very rough before branching and $< G_{ID} >$ is of the order of 1.45 ± 0.7 KJ/m². The experimental mean dynamic fracture surface energy $< G_{ID} >$ for a crack propagating at several hundred metres per second is substantially lower than the fracture energy G_{Ic} at the onset of propagation, which is typically close to 10 kJ/m^2 at low or medium stress intensity loading rates. The crack speed is not correlated with $< G_{ID} >$ and lies in the range 550-610 m/s at temperatures between 19 °C and 27 °C.

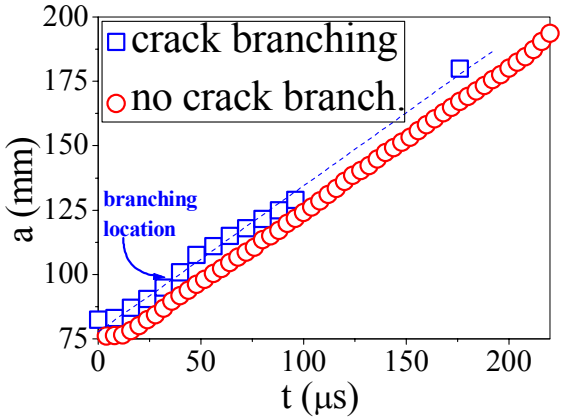

Figure 2: Crack length vs. time in the presence of crack branching (double branch at a = 99 mm) and in the absence of macroscopic crack branching. Note the similarity of the crack speeds and the quasi absence of crack speed variation.

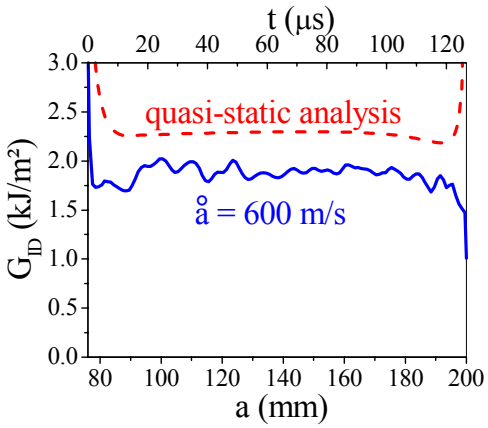

Figure 3: Quasi-static and transient dynamic finite element analyses: typical results for crack propagation without branching.

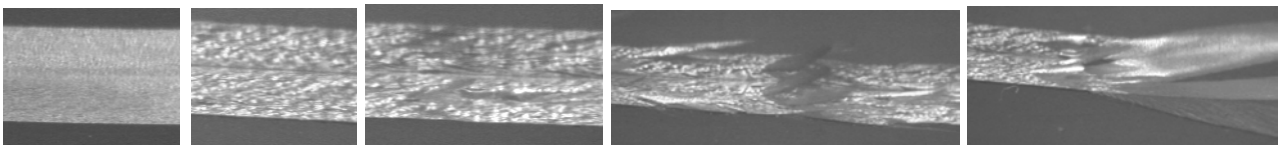

Photo 1: Photos showing different sizes of the frustrated micro-branches, increasing from left to right and corresponding to a RCP at about 0.6 c_r in an RT-PMMA. The cracks propagated from left to right. The entire specimen thickness, 2 mm, is visible and reflected on the metallic coating which acts as a mirror. The right hand photo shows a macroscopic crack branching (three branches) and a sudden change in the fracture surface roughnesses.

FRACTURE SURFACE ROUGHNESS

The fracture surface roughness displays a sharp change at branching, visible in the left and right parts of Photo 2. Optical microscopy reveals here a relatively coarse surface texture a few millimetres before branching (left) and a finer texture after branching (right). Figure 4 shows atomic force microscopy images of a fracture surface (left) a few millimetres before macroscopic crack branching, which corresponds to a high fracture surface energy and (right) just before crack arrest, which corresponds to the lowest fracture surface energy. It can be seen that also on a microscopic scale the surfaces are rougher prior to crack branching than before arrest at a similar crack speed. One notes further that the fracture surface does not pass through the rubber particles of RT-PMMA.

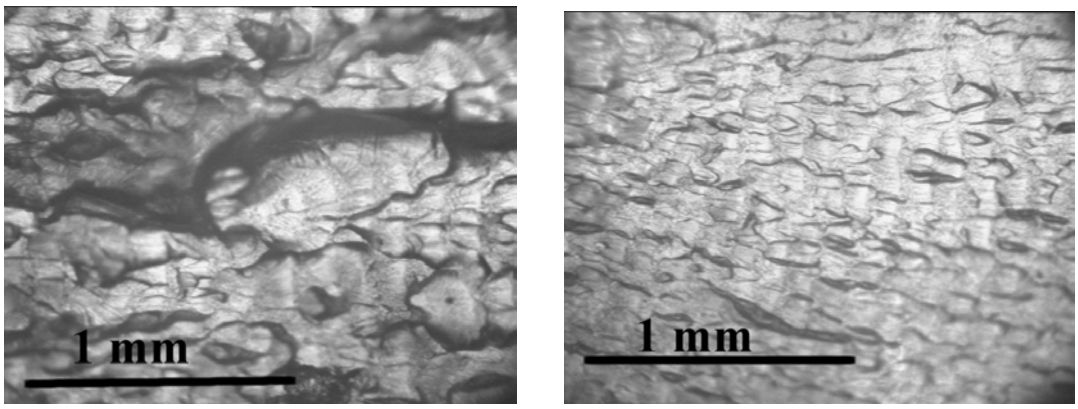

Photo 2: Optical micrographs showing the roughness change at branching: propagation from left to right in an RT-PMMA specimen of thickness 2 mm, (left) 9 mm before the onset of crack branching and (right) 7 mm after crack branching.

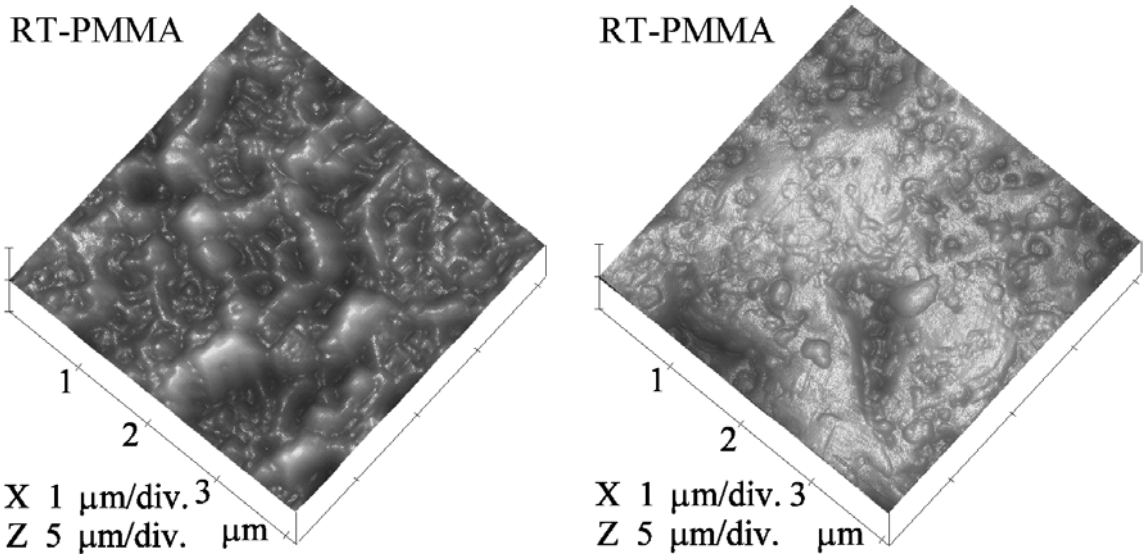

Figure 4: Atomic force microscopy images of a fracture surface: (left) rough surface before crack branching, åm > 500 m/s, and (right) smooth surface just before crack arrest, åm > 500 m/s.

Since the crack forms branches even though the experimental crack speed and the energy released inside the specimen remain quasi constant, two or sometimes three branches must consume the same energy as a single crack propagating at the same speed. The variable parameter at crack branching is thus the roughness of the fracture surface, which means the total surface created (S_{Ft}). As this may be approximately the same for two smooth crack branches as for a master rough crack, the usual planar crack surface (crack length increase multiplied by width, B Δa) cannot be employed. In the case of a smooth crack created at speed $å_{mb}$, as in Figure 4 (right), the fracture energy is G_{IDmin}. If the energy release rate is greater than G_{IDmin}, the propagating crack may produce microscopic instabilities since the inertial effects are sufficient to allow crack branching. These small instabilities are themselves

smooth and frustrated micro-branches. If the energy release rate exceeds twice G_{IDmin}, then two macroscopic smooth branches may appear. SBS fracture tests were also performed using pure PMMA specimens. In these samples, optical microscopy revealed mirror like fracture surfaces, while as expected [8, 9] the experimental fracture energy increased with crack speed. Figure 5 shows that G_{IDmin} is similar for PMMA and RT-PMMA at the equivalent crack speed. The fracture energy of RT-PMMA at a crack speed of $\mathring{a}_{mb}$ varies from 1 to 4 times G_{IDmin}, which corresponds to smooth crack surfaces, and we sometimes observed triple branching. Hence the fracture energy might be expected to be directly correlated with the ratio S_{Ft} / (B Δa) and the fracture energy of pure PMMA.

CONCLUSION

RT-PMMA represents an interesting model material to study the micro mechanisms of dynamic fracture processes. The present work shows experimentally and explains why the measured fracture surface energy has no single value at the macroscopic branching velocity, at least in materials in which the fracture energy decreases during RCP.

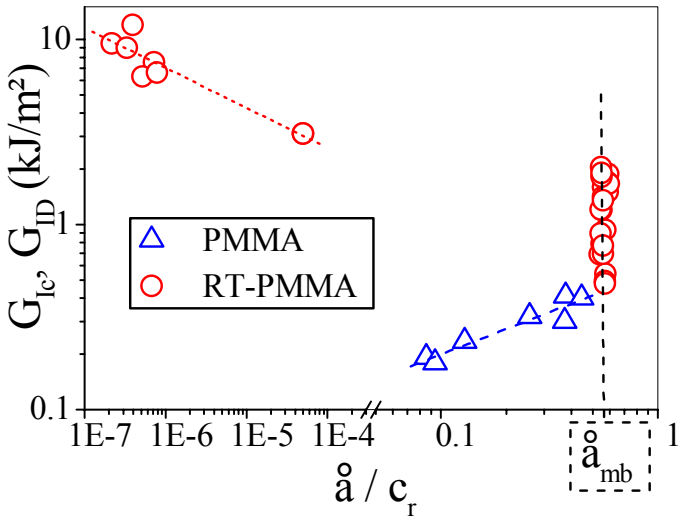

Figure 5: Fracture surface energy vs. normalized crack speed for PMMA and RT-PMMA.

REFERENCES

1. Yoffé, E. H., *Phil. Mag.*, **12**, (1951), p 739-750.
2. Fond, C. and Schirrer, R, *Journal de Physique IV*, (1997), p. C3-969-C3-974.
3. Nilsson, F, *Int. J. Fract. Mech.* **8**, (1972), p.403-411.
4. Thesken, J. C, The Aeronautical Research Institute of Sweden, FFA-TN, **57**, (1994).
5. Rittel, D., *Int. J. Solids Structures*, **35**, 22, (1998), p. 2959-2973.
6. Ferrer, J. B., Fond, C., Arakawa, K., Takahashi, K., Béguelin, P. and Kausch., H.-H., *Letters in Fract. and Micromech.* **87,** (1998), L77-L82.
7. Popelar, C. H. et Atkinson, C., *J. Mech. Phys. Solids*, **28**, 14, (1980), p. 77-93.
8. Williams, J. G., *Int. J. Fract.* **8**, (1972), p. 393-401.
9. Carlsson, J., Dahlberg, L. and Nilsson, F., *Proc. Int. Conf. Dyn. Crack Propag.*, (1972), ed. 1973, p. 165-181.

POSTER REFERENCE: ICF100346PR

DYNAMIC FRACTURE TESTING USING CHARPY INSTRUMENTED PENDULUM

Z. Radakovic [1], Gy. B. Lenkey [2], V. Grabulov [3], A. Sedmak [1], D. Radakovic [4]

[1] Department of Mechanical Engineering, University of Belgrade,
27. marta 80, 11220 Belgrade, Yugoslavia
[2] Bay Zoltán Institute for Logistics and Production Systems, Department for Structural Integrity
Iglói u. 2, 3519 Miskolc, Hungary
[3] Military Technical Institute, Niska bb, 11132 Belgrade, Yugoslavia
[4] Methode Electronics Malta Ltd., Mriehel Industrial Estate, Mriehel QMR09, MALTA

ABSTRACT

Charpy impact testing of a high strength low-alloyed (HSLA) steel has been performed by simultaneously recording two independent signals. The magnetic emission (ME) and potential drop (PD) techniques were used to determine critical crack initiation properties on standard V-notched and pre-cracked three-point bending specimens at room temperature. Both signals (ME and PD) were recorded and compared, with the purpose of more precise identification of critical fracture mechanics parameters determining the onset of ductile crack growth. Standard Charpy specimens made of HSLA steel, oriented perpendicular to rolling direction were tested by a modified instrumentation of the Charpy machine, which included the original magnetic emission, and the potential drop techniques. The strain gauges and emission probes, located on the hammer tup, measured the force, thus both the magnetic and electric potential drop signals were monitored and recorded as a function of time. The obtained results indicate good agreement between ME and PD techniques on evaluation of ductile crack growth initiation point.

KEYWORDS

Dynamic fracture, crack initiation, impact tests, fracture toughness, magnetic emission, potential drop

INTRODUCTION

The instrumentation of the Charpy testing machine by two independent techniques has been successful for dynamic fracture testing of the high strength micro-alloyed steel. The magnetic emission (ME) technique has been used for dynamic fracture testing by depicting the stable and unstable crack initiation [1], and has been applied for impact testing of certain types of steels, including railroad and reactor pressure vessel steels [2,3,4], as well as the HSLA steel [5]. In the case of ductile, or ductile/cleavage fracture, at temperatures well above nil-ductile, or at lower impact energies, it is sometimes difficult to distinguish the crack initiation event directly from the ME signal, and even the integrated ME signal sometimes has a slower rate of change, resulting in a plateau-like region without clear discontinuity. Alternatively, the potential drop method (PD) was also applied for the same purpose by recording the change in electrical resistance by drop in electric potential (PD) in the vicinity of the crack tip [6,7]. Results have also been obtained by applying this

technique on a single specimen with a particular method for evaluating the R-curve for HSLA steels [8,9]. Stable crack initiation in this case is similarly depicted from the local minimum (or maximum) of the potential drop value and, as in the case of ME technique, may not give clear local extreme values when conditions of fracture change from brittle to ductile [5]. As expected, results obtained from testing specimens at several loading rate (or impact velocity) have shown that the change of slope in the PD-t diagram can be used to evaluate critical crack behaviour, and if compared to similar changes of slope in the MF-t diagram, or vice versa, can eliminate doubts and provide a better understanding of both diagrams and measurement techniques. Some preliminary investigations have already been discussed [10].

Therefore, the two techniques were implemented in a Charpy instrumentation that gave independent and simultaneous records of ME and PD signals and the results were not only compared to check their validity, but to portrait the essence of superimposing all the benefits that characterize a certain testing technique.

MATERIAL AND EXPERIMENT

Micro-alloyed steels have a wide range of use in gas and oil pipelines, storage tanks, pressure vessels, vehicles, cranes, and metal structures in general. The tested steel is micro-alloyed with Nb and Ti and is obtained by controlled rolling and accelerated cooling, providing a ferrite-pearlite microstructure. With a yield stress of 411 MPa, the material is very ductile, even at lower temperatures, with a nil-ductility temperature below -80°C. The chemical composition (in wt. %) is shown in Table 1.

TABLE 1

CHEMICAL COMPOSITION IN WEIGHT PERCENT

C	Si	Mn	P	S	Al	Cu	Cr	Ni	Mo	Nb	Ti
0.08	0.20	1.12	0.027	0.011	0.033	0.065	0.027	0.019	0.010	0.026	0.017

The ferritic-pearlitic steel exhibits upper shelf values for ductile type of fracture at room temperature. This type of fracture is evident from load-time or load-displacement data. All the tests were performed at room temperature, owing to certain limitations of the PD technique [9]. The specimens were tested using initial energy levels in the range of E_o=26÷70 J, enabling different impact loading rates between v_o=1.69÷2.75 m/s. The fracture toughness of the material is affected by the impact velocity, and in ductile materials, the fracture mechanism is controlled by the strain field. This property may increase or decrease, depending on the loading rate [9,11]. The introduced fatigue cracks, that also influence the fracture toughness, are within the range: a/W=0.47÷0.57.

The standard V-notched Charpy specimens were cut from a 12 mm plate perpendicular to rolling direction. All specimens were pre-cracked by high frequency fatigue. Since potential drop measurement requires additional specimen preparation, specimens were prepared in the manner explained by Grabulov [9]. Fig. 1 shows the prepared specimen on the anvil of the Charpy machine with the required instrumentation. Very thin wire connections for potential signal output were resistance-spot-welded to the specimen at asymmetric positions in respect to the notch (locations A, Fig. 1), being the optimal position. Apparently, the spot welding technique was performed by selecting inadequate welding parameters, resulting in loose contacts. The output wires were produced of steel, Ni, or Ni-Cr alloy, so some connections had to be re-connected in an unfavourable manner, by soldering. The heavier input Cu-wires originating from the DC power source were connected to the specimens by bolts (position III), securing a firm contact. The nominal input DC electric current of 30 A was required in order to produce output potential drop values ranging from several to at least 10 mV. This input DC value was selected as a minimum, and for some specimens it was increased up to 40 A, and even 50 A in order to amplify the weak output PD signal. Another limiting effect appeared from these wire connections as well. Being rather large and massive, they influenced the inertia characteristic of the specimens, and produced a problem that has yet to be solved – interrupted specimen fracture at higher loading rates, because of mutual contact and/or collision of these wire-connections with the inclined anvil

wall surface when gradual specimen bending commences during impact. However, this appeared much later after crack initiation, and did not produce any unwanted effects within the investigated time window.
The magnetic emission probe (ME) on the hammer tup recorded changes in the external magnetic field in the vicinity of the propagating crack, Fig. 1. The calibrated strain gauge on the tup acted as a load transducer. Sophisticated data acquisition equipment consisted of a DC signal amplifier and voltage supply, both tied to a TEKTRONIX TDS 420A digital oscilloscope. The transient recorder, with an interior circuit amplifier, was tied to the remaining channel on the oscilloscope. The load was measured by strain gauges and emission probes on the hammer, and both magnetic and electric potential drop signals were monitored and recorded in real sampling time intervals of 2, 4, 10 and 40 microseconds. All acquired data was then handled by PC spreadsheet procedures, including the evaluation of absorbed energy (U) and the critical dynamic J-integral.

In order to check whether the ME instrumentation influenced PD measurements, and vice versa, the first two specimens were tested by applying techniques separately. The other specimens were tested simultaneously, with no record of signal interference, or other disturbing effects on the recorded signals. The high noise ratio in the PD signal is probably due to the poor grounding or it may have originated from nearby installations, but did not influence the character of the signal. This was minimized to a certain degree by toggling the input coupling impedance on the PD channel from 1 MΩ to 50 Ω, and also by analysing the diagrams and several multi-point linear trendlines in spreadsheet analyses. On the other hand, the ME signal retained good quality, having much less noise.

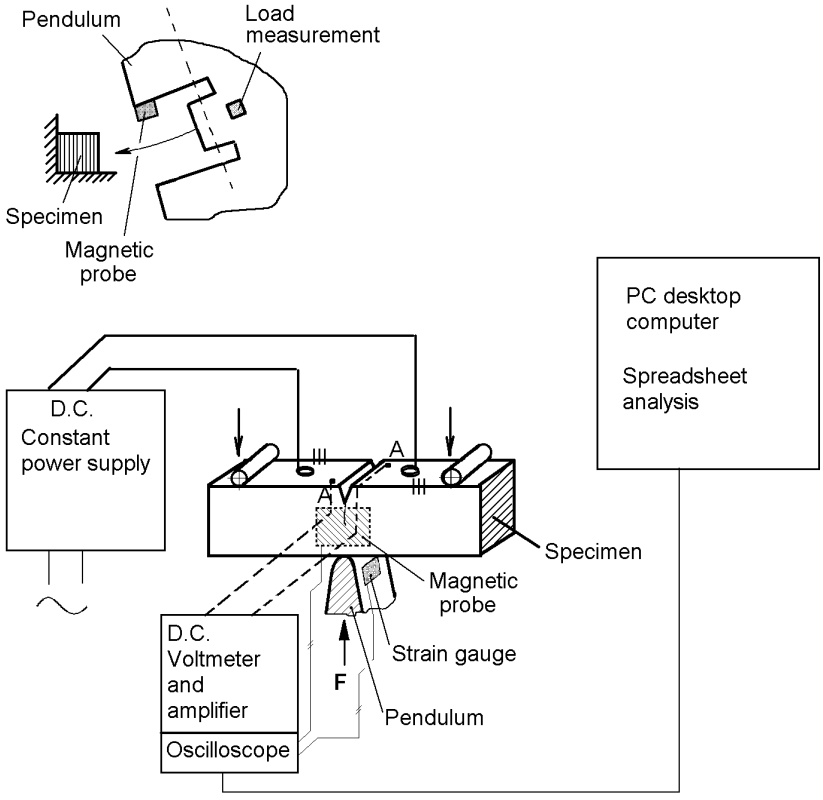

Figure 1. The Charpy pendulum instrumentation

RESULTS AND DISCUSSION

In the case of complete ductile fracture, the fracture toughness is calculated from the J-integral values under dynamic conditions (J_c^d), and is denoted by K_{Id}, whereas in the case of mixed fracture, especially when the ratio of elastic strain energy is not negligible, calculations should then include brittle and ductile fracture, separately ($J_{el} + J_{pl}$). In these tests fracture was generally ductile ($J_{el} < 0.03\ J_{pl}$). The obtained results shown in Table 2 and in Figs. 2 and 3 clearly indicate a satisfying agreement between ME and PD tests on the evaluation of ductile crack growth initiation for this type of HSLA steel.

The J-integral at the initiation of the stable crack growth under dynamic conditions (J_I^d) is determined from Eq. (1), given below

$$J_{Ii}^{d} = \frac{2U_i}{B_n(W-a)}, \quad \text{where} \quad i = \begin{cases} \text{m}, & \text{with results from ME tests} \\ \text{pd}, & \text{with results from PD tests} \end{cases} \tag{1}$$

The released energy – U_m or U_{pd}, is integrated from the load–displacement curve F(t)-f(t) by using

$$U_i = \int_0^{f_c} F(f)\,df \tag{2}$$

where the displacement at stable crack growth initiation $f_c(t)$ is determined at a time-to-stable crack initiation interval (t_i) or by time-to-fracture (t_F), whose determination is sometimes a difficult task, especially in the case of complete ductile fracture, when recorded diagrams, ME(t) and PD(t), do not always show a clear discontinuity. In these circumstances, it is necessary to analyze and compare all other diagrams as well: F(t), integrated-ME(t) (or MF(t)), or several multi-point linear or polynomial PD(t)-trendlines. This is a crucial moment when simultaneous implementation of two independent techniques is a benefit. In cases when diagrams acquired from a single technique cannot be distinguished, as an alternative, the other testing technique gave complementary diagrams.

As an example of good agreement, specimen C11 results are shown on diagrams F(t)-MF(t) and F(t)-PD(t) in Figs. 2 and 3. Table 2 contains relevant data for some HSLA steel specimens, tested at 20°C. Columns include: pre-crack length–a_o; impact load rate–v_o; maximum impact load–F_{max}; time to stable crack initiation –t_i (or time-to-fracture–t_F), and calculated relative time difference between ME and PD tests–$\Delta(t_i)$; released energy–U; calculated dynamic J-integral from ME and PD tests–J_{cm}^d, J_{cpd}^d, and the relative absolute difference between dynamic J-integrals calculated from ME and PD tests–$|\Delta(J_c^d)|$.

Table 2 - Measured and calculated results from ME and PD impact tests

Specimen id.	a_o	b_m	v_o	F_{max}	t_i, μs		$\Delta(t_i)$	U, J		J_c^d, kJ m^{-2}		$\|\Delta(J_c^d)\|$
	mm	mm	m s^{-1}	kN	ME	PD	%	ME	PD	ME	PD	%
A4 Ni *	5.60	7.03	1.69	4.59	920	940	-2.2	3.68	3.81	167.3	173.2	7.7
B1	5.37	6.77	1.81	5.62	1160	1190	-2.6	4.59	4.84	198.2	208.9	14.1
B3 Ni	5.70	7.65	1.82	4.96	540	500	7.4	3.56	3.27	165.4	152.0	5.5
B14	5.30	6.83	1.82	5.84	610	530	13.1	4.78	4.08	203.2	173.6	4.5
A7 NiCr	5.57	7.75	1.82	5.16	800	790	1.3	4.35	4.28	196.4	192.9	3.5
C10 Ni	4.70	6.62	2.09	6.17	1160	1040	10.3	6.77	5.45	255.4	205.7	0.0
C15	5.12	7.93	2.22	5.67	640	640	0.0	4.51	4.51	184.8	184.8	0.0
C11	4.83	7.72	2.33	6.54	800	770	3.8	4.88	4.51	188.9	174.6	0.0
B16	5.27	9.40	2.55	5.60	460	452	1.7	4.71	4.61	198.9	194.7	2.1
B17	5.37	9.40	2.55	5.59	530	480	9.4	5.03	4.42	217.1	190.8	10.9
A5 Ni	5.47	9.35	2.56	5.37	528	440	16.7	4.95	3.93	218.4	173.3	2.0
A6 NiCr	5.38	9.37	2.56	5.14	460	458	0.4	4.39	4.36	190.1	189.1	0.5
B20	5.30	9.17	2.56	5.43	640	684	-6.9	4.85	5.37	206.5	228.7	4.1
B19	5.37	9.27	2.75	5.66	490	490	0.0	4.48	4.48	193.4	193.4	5.5
C2	5.22	9.35	2.75	5.77	560	550	1.8	5.17	5.03	216.0	210.2	2.7

*) Some specimen identification also notes the material type of the PD output wire connections

Some diagrams, F(t)-ME(t) or F(t)-PD(t), may not provide exact information about stable crack initiation time, and so they were averaged, Figs. 2 and 3. Usually, the change of slope in the F(t)-MF(t) diagram, and the local extreme point in the F(t)-PD(t) diagram (normal or average) is used instead (Fig. 3). This is also in agreement with the physical meaning of ME and MF quantities [2,3]. In the case of PD signal, stable crack initiation time is evaluated directly [9].

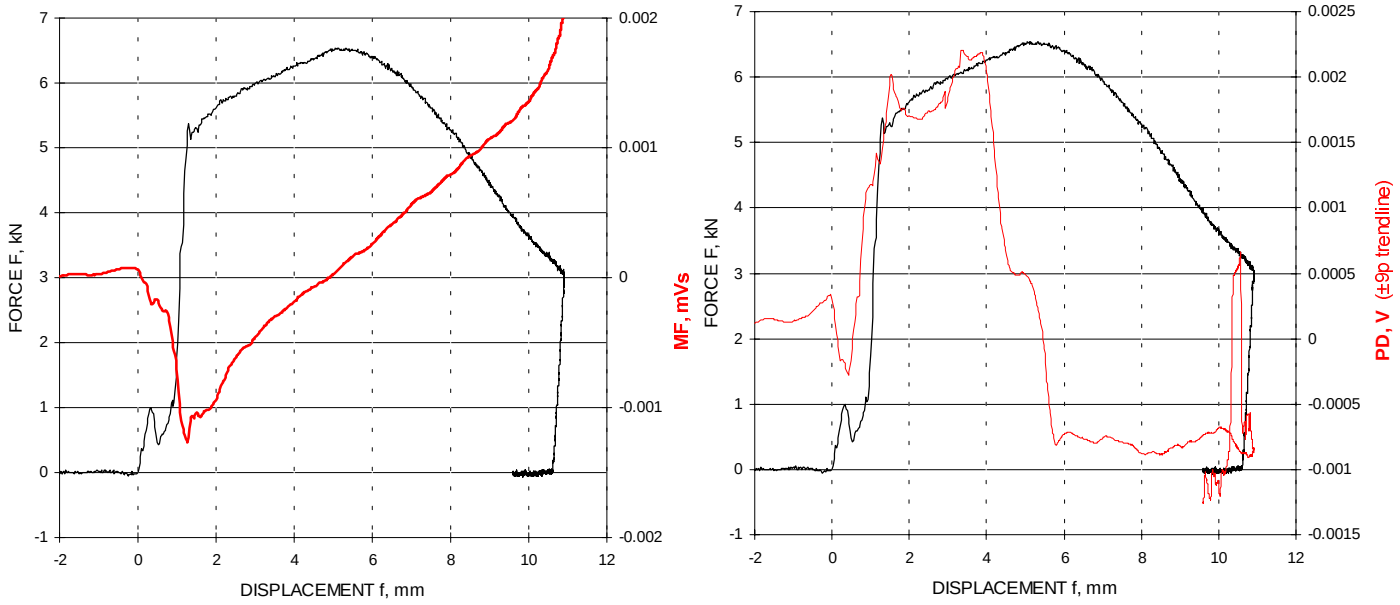

Figure 2. F(t)-f(t) diagrams with MF and PD signals for specimen C11 (E_o=50 J; a_o/W=0.48; PD input 50 A; insulated)

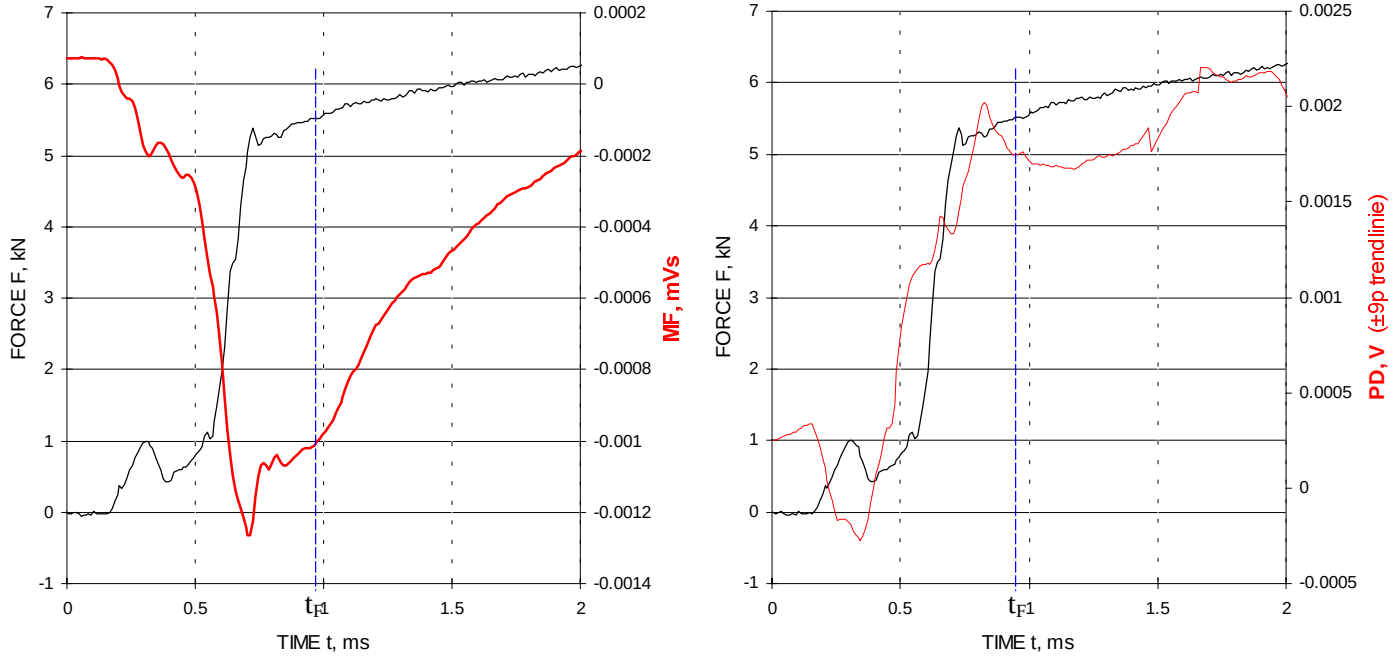

Figure 3. F(t) diagrams with MF and PD signals for specimen C11, indicating time-to-fracture (t_F)

The relative difference between critical values of dynamic J-integral is very low, with an absolute average $|\Delta(J_c^d)|_{aver.}$=7.3%, and standard deviation $|\Delta(J_c^d)|_{st.dev.}$=6.9%. Results are even better for the relative difference and standard deviation in crack initiation time: $\Delta(t_i)_{aver.}$=3.6%, $\Delta(t_i)_{st.dev.}$=6.5%. Indeed, both techniques were successful in evaluating crack initiation, although some major difficulties in performing the tests were:

- stability of the specimen, because of the massive PD-input wire connections;
- selection of the optimal PD-input electric current and voltage, because it affects the output signal quality;
- specimen insulation from direct contact of the anvil and tup, in order to reduce amplitude noise probably developing from the power source and eddy currents;
- special attention should be made to the quality of the acquisition device, since the adequate selection of the coupling impedance of the input signal and proper grounding on all electric devices decreases noise.

The curves in Figs. 4 and 5 show J-integral vs. loading rate, and J-integral vs. initial crack length, respectfully.

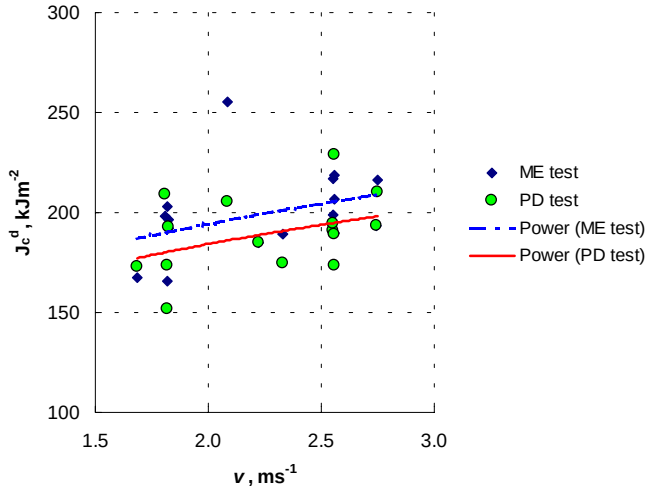

Figure 4. J_c^d–v dependence for MF and PD tests

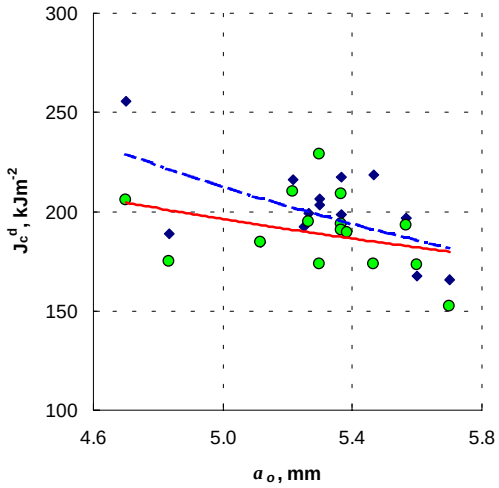

Figure 5. J_c^d–a_o dependence for MF and PD tests

CONCLUSIONS

Results shown in Figs. 4 and 5 have been statistically interpreted by power curves, although the result is the same if fitted by a linear, exponential, or logarithmic curve. This indicates an increasing tendency of the dynamic J-integral (J_c^d) with impact load rate (v), and a decreasing tendency for larger initial cracks (a_o). Fitted power curves $J=f(v^x)$, $J=f(a_o^x)$, show very small difference in J-integral, indicating good agreement between ME and PD techniques on evaluation of ductile crack growth initiation.

The ME power curve is constantly located above the PD power curve indicating slightly higher J-integral. In the average this is true, since PD evaluated time-to-fracture (t_i) is usually shorter than its ME equivalent (Table 2). So, the released energies U(t) are smaller, and dynamic J-integral values are smaller too, Eq. (1). Multiple peaks in F(t)-ME(t) and F(t)-PD(t) diagrams are probably related to complex development of crack initiation and propagation. Analyses indicate that ME peaks follow PD peaks by a small delay, and both peaks usually precede F(t) peaks. This is still not clear, but the delay is probably related to specimen–strain gauge, or specimen–probe interaction, or hysteresis in electric and magnetic properties of the tested material.

ACKNOWLEDGEMENTS

The authors gratefully acknowledge the support of the OTKA T 030057 project.

REFERENCES

1. Winkler, S.R. (1990). ASTM STP 1074, Philadelphia, pp.178-192.
2. Lenkey, Gy.B. (1997). In: 7th Summer School of Frac. Mech., Velika Plana, Yugoslavia, pp.39-50
3. Lenkey, Gy.B. and Winkler, S.R. (1997) *Fatigue and Fract. of Engng. Mater. and Struct.* 20, 143.
4. Lenkey, Gy.B. and Tóth, L. (2000). In: *Fracture Mechanics: Applications and Challenges*, Fuentes, M., Elices, M., Martin-Meizoso, A., and Martínez-Esnaola, J.M. (Eds.), Elsevier, Oxford.
5. Radakovic, Z., Lenkey, Gy.B. and Sedmak, A. (1998). In *Fracture from Defects*, Vol.III, pp.1267-1272, Brown, M.W., Rios, E.R. and Miller, K.J. (Eds.)
6. Glover, A.P., Johnson, F.A., Radon, J.C. and Turner, C.E. (1977). In: *ASM Int. Conf. on Dynamic Frac. Tough.*, Vol. 1, pp.63-75, The Welding Institute.
7. MacGillivray, H.J. and Turner, C.E. (1989). In: *Fourth Int. Conf. on the Mech. Properties of Mater. at High Rates of Strain*, Oxford.
8. Grabulov, V., MacGillivray, H.J., Tomic, D. and Jovanic, P. (1992). In: *Reliab. and struct. integ. of adv. materials*, pp.315-320, Sedmak, S., Sedmak, A. and Ruzic, D. (Eds.), EMAS, Warley West Midlands.
9. Grabulov, V. (1995). PhD Thesis, University of Belgrade, Depart. of Tech. and Metallurgy, Yugoslavia.
10. Radakovic, Z., Lenkey, Gy.B., Grabulov, V. and Sedmak, A. (1999) *Internat. Jour. of Frac.* 96, L23.
11. Yoon, J.H., Lee, B.S., Oh, Y.J. and Hong, J.H. (1999). *Inter. Jour. of Pres. Vessels and Piping* 76, 663.

POSTER REFERENCE: ICF100359PR

DYNAMIC J_R CURVES FROM INSTRUMENTED IMPACT TEST OF UNPRECRACKED CHARPY V-NOTCH SPECIMENS OF AUSTENITIC STAINLESS STEEL

P. R. Sreenivasan, S. K. Ray and S. L. Mannan

Materials Development Group, Indira Gandhi Centre for Atomic Resaearch, Kalpakkam, Tamilnadu-603 102,India
Telephone:04114-40202/40232/40222
Fax.: 04114-40360/40396/40381/40356/40301
E-mail: mannan@igcar.ernet.in

ABSTRACT. A new (shift) procedure has been suggested for obtaining the J_R (J fracture resistance) curves of ductile alloys from the load-displacement traces of (unprecracked) CVN specimens (with CVN energy > 30 J) and demonstrated using instrumented impact test results from Charpy V-notch (CVN) and precracked CVN (PCVN) specimens of AISI 316 stainless steel. This involves generating the **pseudo-J_R curve** from CVN specimens using a key-curve method and also by the procedure due to Schindler (**Schindler curve**). Then the **pseudo-J_R curve** is shifted uniformly downward to bring it into coincidence with or slightly above the **Schindler curve**. This shift can be expressed as $J_{\text{pseudo}} + Q.p$, where p is the exponent in the power-law fitted to the **pseudo-J_R curve** and Q takes values of – 2 to – 4. The **shift-J_R curves** more truly reproduce the slopes of the PCVN-J_R curves (hence tearing resistance) than the **Schindler curves**, though the latter are easy to generate. However, the range of applicability, size restrictions applicable and other aspects (like influence of loading rate, use of blunting line) need further validation using tests on different materials. When validated, the new method will obviate the need for expensive and time-consuming precracking, at least for select materials and test conditions. These methods will be useful not only for quality control purposes, but even for conservative engineering design.

KEYWORDS. Stainless steel, Charpy V-notch, dynamic J_R curve, key-curve, pseudo-J_R curve, Schindler procedure

1. INTRODUCTION

Austenitic stainless steels (SSs) are widely used structural materials in fast reactors. Owing to the high toughness of austenitic SSs, measurement of their fracture toughness requires the use of elastic-plastic methods [1,2]. Though, for very accurate evaluation of toughness, precracked and large size specimens are necessary, there is continuing interest and effort in obtaining conservative estimates of J_{id} (dynamic fracture (initiation) toughness) or J_R (J fracture resistance) curves using small and blunt notched specimens, particularly Charpy V-notch (CVN) specimens [2-4]. These methods, when validated, will be useful not only for quality control purposes, but even for conservative engineering design.

In this paper, instrumented impact test results obtained at room temperature from CVN and precracked CVN (PCVN) specimens of AISI 316 SS in various aging and cold-work (CW) conditions are reported. J_R curves obtained for CVN and PCVN specimens by key-curve procedure [2] are compared with each other and with those obtained using the procedure proposed by Schindler [4]. A new (shift) procedure is suggested for obtaining J_R curves from unprecracked CVN specimens. This seems to be promising, but its range of validity and applicability needs further validation and verification by tests on materials with different toughness levels.

2. MATERIAL AND EXPERIMENTAL DETAILS

Material tested was AISI 316 SS in the solution-treated (ST), ST + 1073 K/50 h aged (H5), ST + 1073 K/1008 h aged (H8), ST + 20% cold-work (CW) and CW + double age (GT) conditions (see [3] for full details). Initial crack aspect ratio (a/W, where a is the crack length and W is the specimen width) varied from 0.2 (CVN) to 0.8. The CVN and PCVN specimens were tested at room temperature on a 358 J capacity Tinius Olsen Model 74 instrumented impact machine. Full details of the material, precracking, test and data reduction procedure are reported elsewhere [2,3]. All tests reported here were done at the maximum impact machine velocity, $V_0 = 5.12\ m.s^{-1}$.

3. J_R CURVE REDUCTION PROCEDURES

3.1. Key-curve and Shift Methods

The J_R curves are obtained from the test records of both CVN and PCVN specimens using the power-law key-curve procedure described by Sreenivasan et al. [2] . The J_R curve obtained from CVN specimen is much higher than the PCVN-J_R curve (which is mostly conservative and most likely to approximate the true material property). Hence, in this, the J_R curves obtained using (unprecracked) CVN specimens are referred to as **pseudo-J_R curves**. However, the key-curve J_R curves from CVN and PCVN specimens seemed to show similar slopes [2]. This suggests the possibility that the PCVN-J_R curves can be obtained by applying a suitable scaling or translation to the **pseudo-J_R** curves (**shift method**). This aspect is explored in this paper.

Assuming a power-law relation, J_R is given by the following relation:

$$J = C\ (\Delta a)^p \tag{1}$$

where C and p are fit constants (C and p from CVN specimens are indicated as pseudo). For constant slope, dJ/da must be constant. Therefore,

$$\mathrm{d}J/\mathrm{d}a = C\ .\ p.\ (\Delta a)^{p-1} = \text{Constant} \tag{2}$$

This can be true only if the new J_R curve is represented by:

$$J = C\ (\Delta a)^p + K\ (= Q.p) \tag{3}$$

where numerical constants K and Q are determined empirically by comparing the **pseudo-J_R curves** with the PCVN-J_R curves. Because of plasticity and notch-root effects, **pseudo-J_R curves** are much higher than the PCVN-J_R curves. Hence, for obtaining the PCVN-J_R curve from the **pseudo-J_R curve**, a negative shift must be applied to the **pseudo-J_R curve** and Q is negative (see, however, Section 4.3).

3.2. Schindler's Procedure for Obtaining J_R Curves

In recent analyses, Schindler uses only the power-law (Eqn. 1) for estimating the J_R curve as is done in the present paper. Schindler and coworkers [4] obtain constants C and p of the power-law (Eqn.1) from the following relations:

$$C = (2/p)^p\ .\ [\eta(a_0)/\{B.(b_0)^{1+p}\}].\ E_t^p.\ E_{mp}^{1-p} \tag{4}$$

$$p = (3/4).\ [1 + E_{mp}/E_t]^{-1} \tag{5}$$

E_{mp} is the plastic energy upto $P_{\max}$ (maximum load), E_t is the total energy for the impact test and $\eta(a_0)$ is the well known eta-factor. We have used $\eta(a_0)$ given in [2].

4. RESULTS AND DISCUSSION

4.1. Key-curve J_R Curves and Application of the Shift Procedure

The power-law constants for the key-curve J_R curves are given in Table 1. Only the constants for the mean curves from the multiple specimens are given (separate fits for CVN and PCVN results in each heat-treatment condition). In most cases, the specimen to specimen scatter is small enough to justify this procedure. In making the fit, for each specimen, the maximum Δa was chosen to be equal to be 10% of b_0, the initial remaining ligament depth (= $W - a_0$, where a_0 is the initial a). The ASTM size criteria have not been evaluated since only the results from same size specimens are being compared. In cases

where there is more than normal scatter, the curve from the specimen giving the lowest data is also shown in the figures. The J_{id} corresponding to the crack-initiation point (by the procedure in [2]) and $J_{0.2}$ (corresponding to a crack-extension of 0.2 mm) estimated from the mean key-curve power-law are given in Table 1 for comparison with the estimates by the Schindler procedure.

Figure 1 shows the key-curve results for the CW condition. The results from the PCVN specimens are close together and is well represented by the common fit curve shown (PCVN-J_R curve). The **pseudo-J_R curve** is much higher than the PCVN-J_R curve and to bring the **pseudo-J_R curve** into coincidence with the PCVN-J_R curve, the **pseudo-J_R curve** was shifted down using $Q = -4$ (Eqn. 3). The Q-factor used is shown in Figure 1 by the side of the arrow indicating the shift. The J_R curve obtained by this procedure is referred to as the **shift-J_R curve**.

4.2. J_R Curves by the Schindler Procedure

The constants of the power-law fit obtained by the Schindler procedure as also the estimated $J_{0.2}$ are given in Table 1. Application of the Schindler procedure to CVN specimens gives J_R curves that are higher than those obtained by applying the Schindler procedure to PCVN specimens (Sch,PCVN in Figure 1). In the following, **Schindler curve** refers to the J_R curve obtained by applying the Schindler procedure to (unprecracked) CVN specimen; this is almost in coincidence with or slightly lower than the key-curve PCVN-J_R curve. **Schindler curve** is poor in reproducing the slope of the PCVN-J_R curve. The **shift-J_R curve** better reproduces the slope of the PCVN-J_R curve.

4.3. General Discussion

Results for ST, H5 and GT material conditions are similar to those in Figure 1, but with different Q values as shown in Table 1. Figure 2 for the H8 material shows anomalous behaviour. This material has been aged for 1000 h at 1073 K and is expected to have extensive precipitation along grain boundaries. This results in intergranular ductile fracture with a very low impact energy (~ 28 J: see Table 1) [5]. In such cases, blunt-notched CVN specimen reportedly shows lower toughness than the PCVN specimen [6]. Hence the anomalous behaviour in Figure 2: CVN J_R curve is lower than the PCVN-J_R curve. Also, the Schindler curves from CVN specimens are lower than those from the Schindler curves from PCVN specimens. Moreover, the key-curve J_R curves from PCVN specimens show excessive scatter and odd behaviour. In this case, the **pseudo-J_R curve**, without any shift ($Q = 0$), is ultra-conservative (lower) with respect to the PCVN-J_R curves. Schindler has also stated that his procedure is applicable for CVN energies greater than 30 J [4].

From the above, it is evident that, when homogeneous deformation prevails and abnormalities like grain boundary fracture or other preferential fracture paths are not active, using a Q factor -2 to -4 for generating the **shift-J_R curve** from the **pseudo-J_R curve** gives conservative results. In the absence of the above mentioned abnormal deformation and fracture behaviour, the **shift-J_R curve** is in coincidence with or slightly

higher than the **Schindler curve**. When the above mentioned abnormal fracture behaviour operates, the **pseudo-J_R curve**, without any shift, is ultra-conservative.

The observation of the near coincidence between the **shift-** and the **Schindler-J_R curves**, offers a reliable method to choose an appropriate Q value for a material. From the CVN specimen, generate the **pseudo-J_R curve** and also the **Schindler curve**. Then, by appropriate shift, bring the **pseudo-J_R curve** into coincidence with or slightly higher than the **Schindler curve**. From this, the Q value can be obtained. Though, **Schindler curves** are easy to generate and satisfactory for quality control and ranking purposes, the shift procedure proposed here helps obtain J_R curves which reproduce reliably the slope of the PCVN-J_R curves.

5. CONCLUDING REMARKS

A new method has been suggested for obtaining the J_R curves of ductile alloys from the load-displacement traces of (unprecracked) CVN specimens, with CVN energy > 30 J. This involves generating the **pseudo-J_R curve** from CVN specimens using a key-curve method and also the **Schindler-J_R curve** (J_R curve by the application of Schindler procedure). Then the **pseudo-J_R curve** is shifted uniformly downward to bring it into coincidence with or slightly above the **Schindler curve**. This shift can be expressed as $J_{\text{pseudo}} + Q.p$, where p is the exponent in the power-law fitted to the **pseudo-J_R curve** and Q takes values of – 2 to – 4. The shift procedure generates J_R curves that more truly reproduces the slopes of the PCVN-J_R curves (hence tearing resistance) than the **Schindler curves**, though the latter are easy to generate. However, the range of applicability, size restrictions applicable and other aspects (i. e., influence of loading rate, use of blunting line) need further validation using tests on different materials and conditions. When validated, the new method will obviate the need for expensive and time-consuming precracking, at least for select materials and conditions.

REFERENCES

1. O'Donnell, I.J., Huthmann, H. and Tavassoli, A.A. (1991). *Proc. International Seminar on Fracture in Austenitic Components*, October 8-9, Saclay, France, pp. 2-27.
2. Sreenivasan, P.R. and Mannan, S. L. (2000). *Int. J. of Fracture*. **101**, 229.
3. Sreenivasan, P.R., and Mannan, S. L. (2000). *Int. J. of Fracture*. **101**, 250
4. Schindler, H.-J. (2000). In: *Pendulun Impact Testing: A Century of Progress*, **ASTM STP 1380,** Siewert, T. A. and Manahan, M. P., Sr. (Eds). American Sociey for Testing and Materials, Philadelphia, PA. pp. 337-353.
5. Samuel, K. G., Sreenivasan, P. R., Ray, S. K. and Rodriguez, P. (1987). *J. Nucl. Mater.* **150**, 78.
6. Ray, S.K., Sreenivasan, P.R., Samuel, K.G. and Rodriguez, P. (1984). In: *Advances in Fracture Research: Proc. Of the Sixth International Conference on Fracture (ICF-6*), Dec. 4-10, New Delhi, India, Valluri,S.R., Taplin, D.M.R., Rama Rao, P. ,Knott, J.F. and Dubey, R. (Eds). Pergamon Press Inc., pp. 3221-3228.

TABLE 1

POWER-LAW CONSTANTS AND Q VALUES FOR CVN/PCVN SPECIMENS OF 316 SS BY KEY-CURVE AND SCHINDLER PROCEDURES

Sp. Code	*Sp. Type*	E_t/J	*p (Sch)*	*C (Sch)*	$J_{0.2}/(J.mm^{-2})$ *(Sch)*	P/Key-curve	C/Key-curve	$J_{id}/(J.mm^{-2})$ *Test*	$J_{0.2}(J.mm^{-2})$ *Test*	*Q*
GT	CVN	82	0.546	0.591	0.339	0.22	0.940	0.316	0.66	-1.5/-2
"	PCVN	-	-	-	-	0.338	0.731	-	0.424	-
CW	CVN	102	0.529	0.787	0.378	0.146	1.207	0.605	0.955	-4
"	PCVN	-	-	-	-	0.303	0.634	-	0.389	-
H5	CVN	107.5	0.537	0.804	0.360	0.245	1.268	0.331	0.846	-2
"	PCVN	-	-	-	-	0.267	0.834	-	0.543	-
H8	CVN	28.5	0.569	0.188	0.290	0.185	0.272	0.12	0.202	0
"	PCVN	-	-	-	-	0.387	0.801	-	0.430	-
ST	CVN	159	0.514	1.300	0.413	0.266	1.997	0.532	1.301	-3
"	PCVN	-	-	-	-	0.182	1.076	-	0.803	-

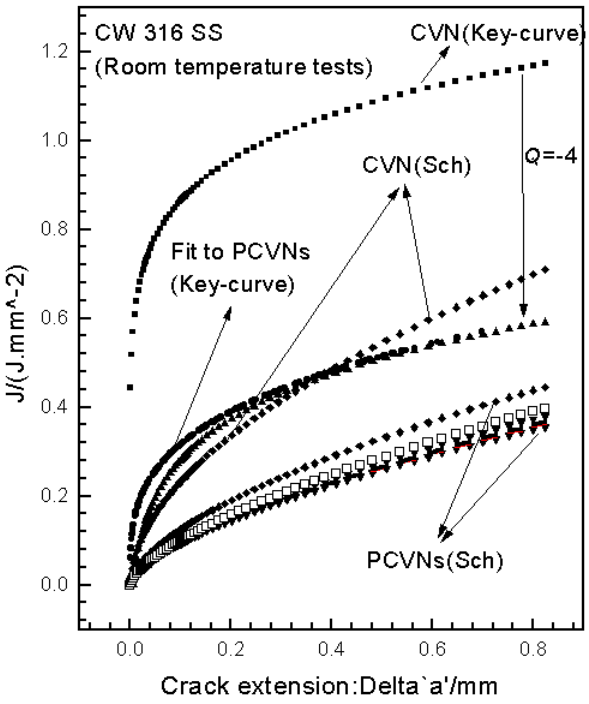

Figure 1. Shift and Schindler *J-R curves for CW 316 SS*

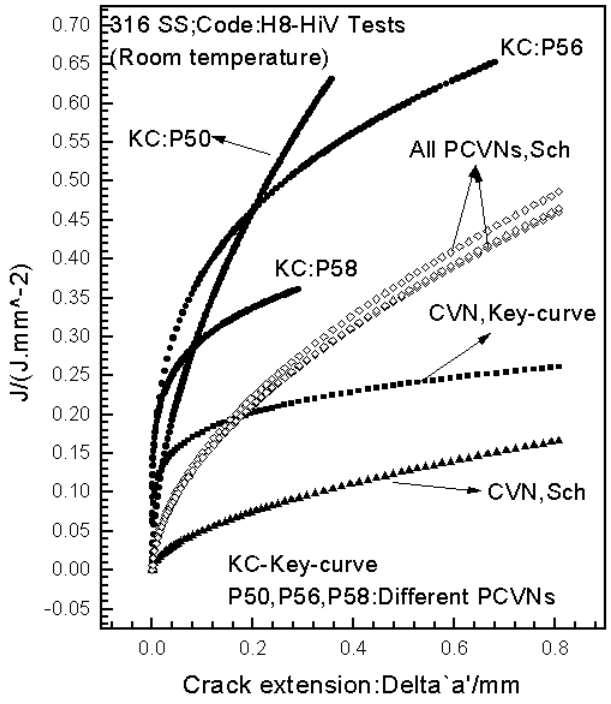

Figure 2. Shift and Schindler J-R curves for H8 316 SS

DYNAMIC STRESS INTENSITY FACTOR FOR UNSTEADY RAPID CRACK PROPAGATION

K. ARAKAWA, T. MADA and K. TAKAHASHI

Research Institute for Applied Mechanics, Kyushu University, Kasuga 816-8580, Fukuoka, Japan

ABSTRACT

Dynamic crack propagation in PMMA was studied using the method of caustics in combination with a Cranz-Schardin type high-speed camera. Four different types of specimen geometries were employed to achieve the crack acceleration, deceleration and re-acceleration process in one fracture event. Dynamic stress intensity factor K_{ID} and crack velocity $\dot{a}$ were evaluated in the course of crack propagation to obtain the relationship between K_{ID} and $\dot{a}$. The effect of crack acceleration and deceleration on the K_{ID}-$\dot{a}$ relations was examined.

KEY WORDS

Dynamic crack propagation, stress intensity factor, crack velocity, crack acceleration, caustic method, high-speed photography, PMMA

INTRODUCTION

Dynamic crack propagation in brittle materials has been investigated using many experimental techniques. Optical methods such as photoelasticity [1-4] and the method of caustics [5-9] have been widely employed for evaluating the state of dynamic stress field around a propagating crack tip, i.e. dynamic stress intensity factor K_{ID}. Crack velocity $\dot{a}$ was also estimated in crack propagation to correlate with K_{ID}. Many experimental studies have been made on the relation between K_{ID} and $\dot{a}$, however, different experiments derived significantly different types of K_{ID}-$\dot{a}$ relationships. Much discussion has taken place on the applicability of the methods employed for K_{ID} evaluation, the definition of the crack tip stresses, the influence of specimen geometries and loading conditions and so forth. In the case of brittle fracture, $\dot{a}$ generally changes with time, resulting in crack acceleration or deceleration according to the stress distribution in the specimen. The crack acceleration is an important parameter to understand the behavior of dynamic crack propagation, however, quantitative discussion on the effect of the crack acceleration and deceleration on K_{ID} has been limited.

The purpose of the present work was to study this problem in more detail using the method of caustics in combination with a Cranz-Schardin type high-speed camera[10,11]. Four different types of specimen geometries were employed so that cracks could undergo acceleration, deceleration and re-acceleration stages in one fracture process. Dynamic stress intensity factor K_{ID} and crack velocity $\dot{a}$ were evaluated in the course of crack propagation. The K_{ID}-$\dot{a}$ relations were determined for the stages of acceleration, deceleration and/or re-acceleration. Attention was focussed particularly on the effect of the crack acceleration and deceleration on the K_{ID}-$\dot{a}$ relations.

EXPERIMENTAL PROCEDURE

Specimen geometries used in this experiment are illustrated in Fig. 1, where (a) represents a single-edge-notched (SEN) specimen, (b) a uniaxially pin-loaded specimen, (c) a biaxially pin-loaded specimen and (d) a SEN with two circular holes specimen. These four types of specimens were selected to obtain the different behaviors of dynamic crack propagation. The

specimens were fabricated from a 5mm-thick sheet of PMMA (Acrylite S-001). A sharp precrack was generated by momentum-controlled chisel-impact into a pre-machined saw-cut on the specimen edge.

All specimens were tested under a displacement controlled condition using a tensile testing machine. Tests were performed at room temperature and at a constant crosshead speed of 1mm/min. The dynamic crack propagation was photographed using a Cranz-Schardin type high-speed camera with 30 sparks and a maximum frequency of 1.42×10^6 frames/sec [10,11]. This camera permitted a simultaneous record of two images with different focal distances. One focal distance was selected for specimen-focussed images and the other for caustic images.

EVALUATION OF K_{ID} AND CRACK VELOCITY $\dot{a}$

Figure 2 shows examples of high-speed photographs taken with a SEN specimen, where series (a) represents the specimen-focussed images and (b) the corresponding caustic patterns. As seen, size of the caustic changed with growing crack length. The stress intensity factor K_{ID} was determined from the following equation:

$$K_{ID} = (2\sqrt{2\pi}/3z_0 dc\eta^{3/2})(\phi/3.17)^{5/2} \quad (1)$$

where ϕ is the caustic diameter at a crack tip, z_0 is the distance between the specimen and the image plane, d is the specimen thickness and η is a convergency factor for incident light rays [9].

The values of K_{ID} and crack length a obtained for the four specimens are shown in Figs. 3-6 as a function of time t. The K_{ID} variations for the specimens were different. In the SEN specimen under uniform tensile loading, K_{ID} increased in the initial stage of crack propagation and gradually approached a constant value. The uniaxially pin-loaded specimen exhibited K_{ID} increasing and decreasing behavior. In both the biaxially pin-loaded and SEN (Holes) specimens, there existed three stages of recognizable K_{ID} increasing, decreasing and re-increasing regions.

To minimize data scattering in the evaluation of fracture parameters, a data-fitting procedure which was proposed in a previous work [9] was employed; obtained values of K_{ID} and a were expressed as ninth order polynomial of t based on the least-squares method so that they

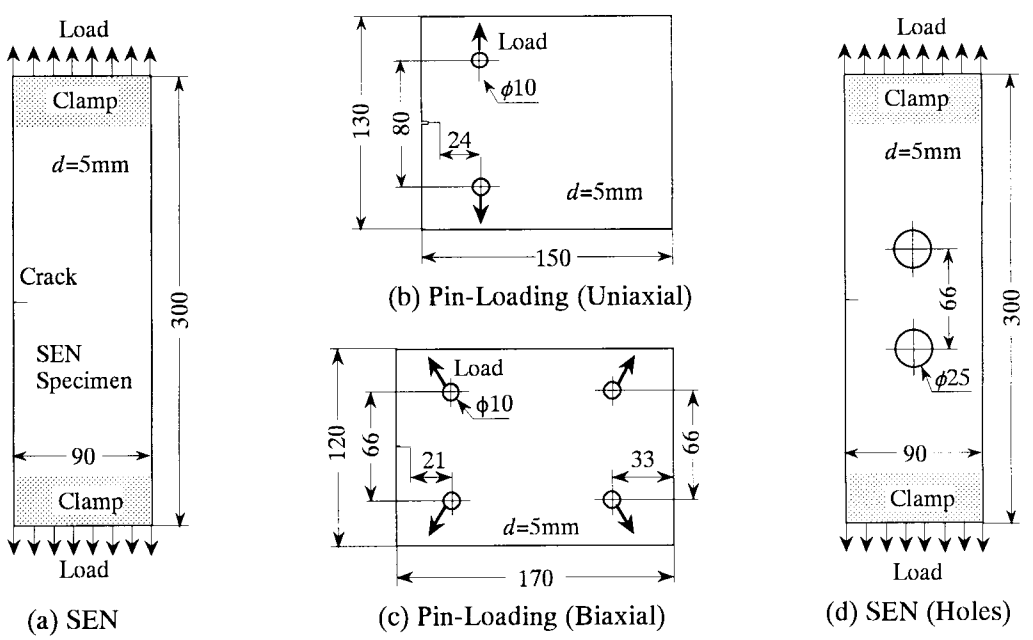

Fig. 1. Specimen geometries and loading methods

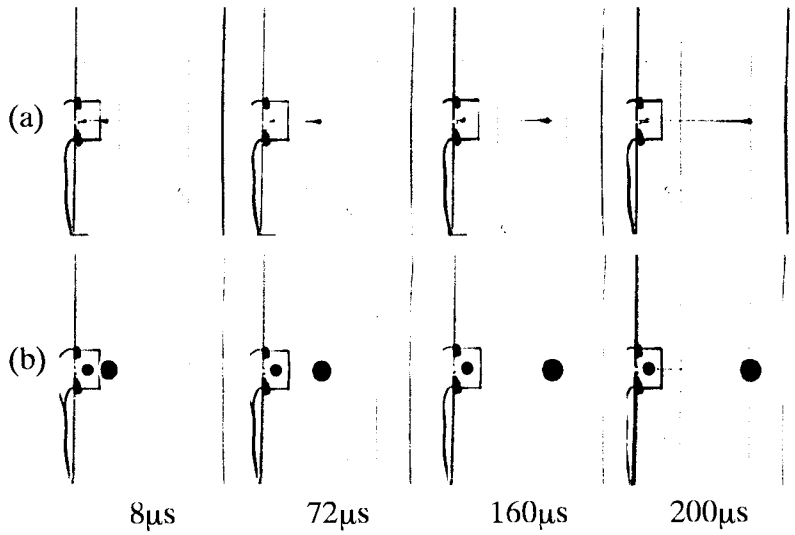

Fig. 2. Example of dynamic crack propagation in a SEN specimen. (a) specimen-focussed images, (b) caustic patterns

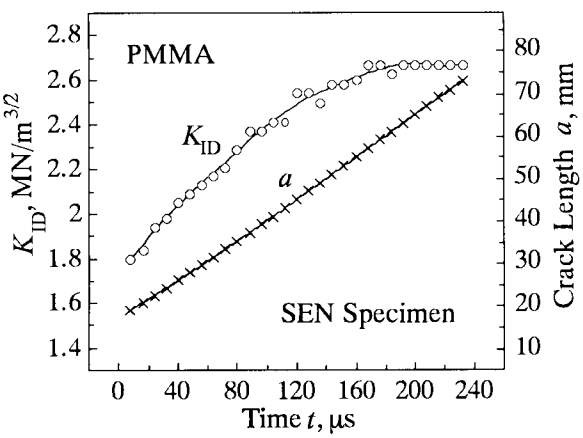

Fig. 3. Time variations of K_{ID} and crack length a for a SEN specimen

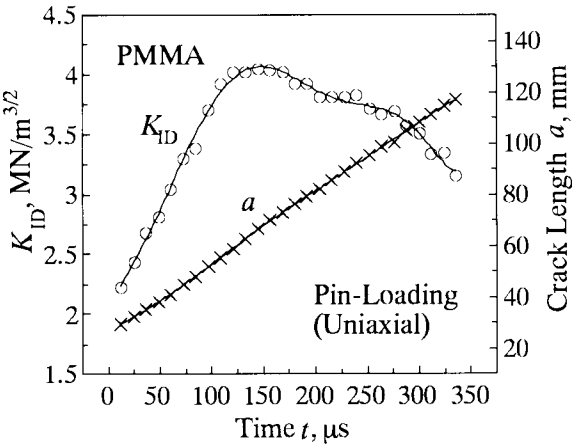

Fig. 4. Time variations of K_{ID} and crack length a for a uniaxially pin-loaded specimen

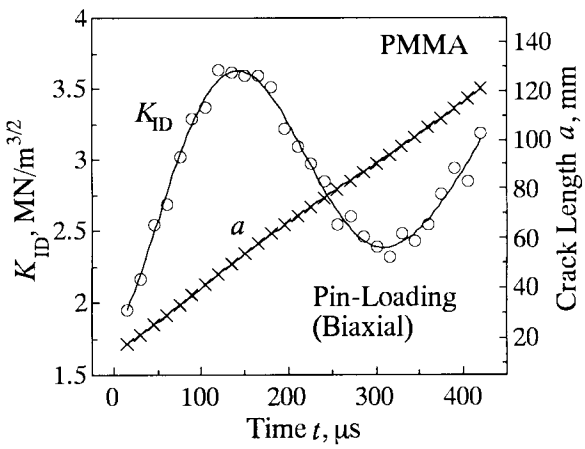

Fig. 5. Time variations of K_{ID} and crack length a for a biaxially pin-loaded specimen

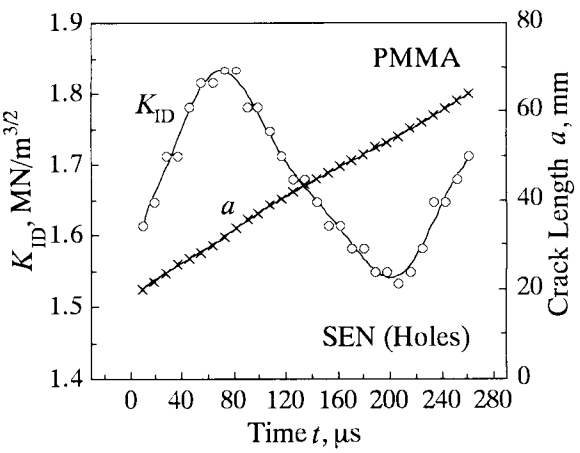

Fig. 6. Time variations of K_{ID} and crack length a for a SEN with holes specimen

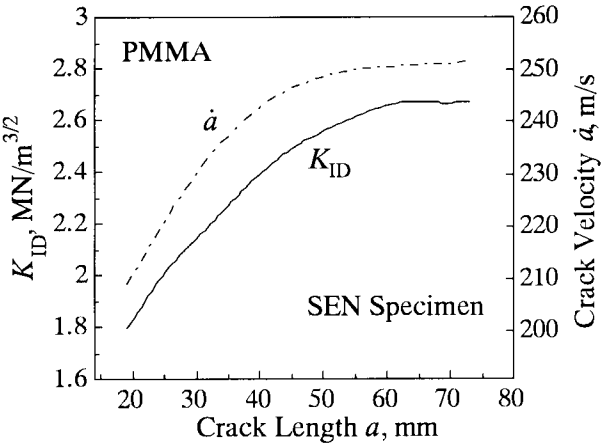

Fig. 7. K_{ID} and crack velocity $\dot{a}$ for a SEN specimen

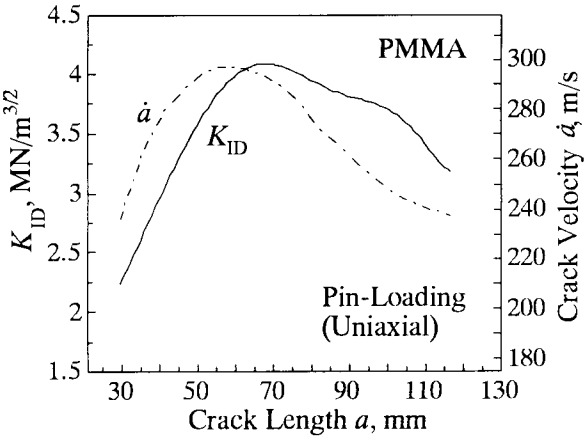

Fig. 8. K_{ID} and crack velocity $\dot{a}$ for a uniaxially pin-loaded specimen

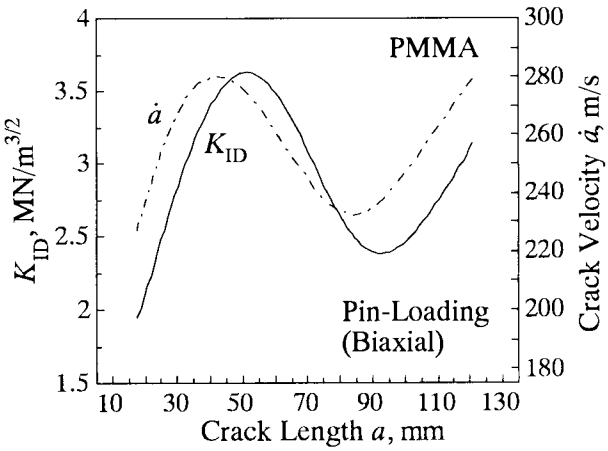

Fig. 9. K_{ID} and crack velocity $\dot{a}$ for a biaxially pin-loaded specimen

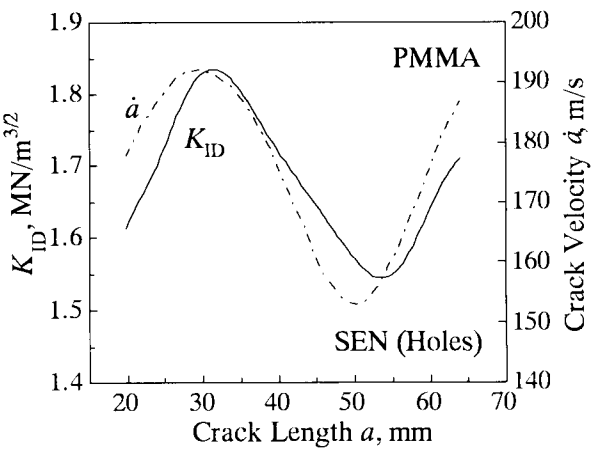

Fig. 10. K_{ID} and crack velocity $\dot{a}$ for a SEN with holes specimen

closely fitted their observed values (see Figs. 3-6). Crack velocity $\dot{a}$ was determined from the first time derivatives of the fitted curve $a(t)$. If $\dot{a}$ was determined simply from the first time derivative of increment Δa which was obtained from successive pictures taken on a film, large scatter in $\dot{a}$ was inevitably caused primarily by errors arising from visual identification of the crack tip position on film. Thus, the data-fitting procedure employed enabled us to determine crack velocity accurately.

RELATIONSHIPS BETWEEN K_{ID} AND $\dot{a}$

Figures 7-10 show values of K_{ID} and $\dot{a}$ as a function of crack length a. There are several interesting points in their relations. First, the change in $\dot{a}$ was qualitatively in accord with the one in K_{ID}. Second, $\dot{a}$ rose earlier than K_{ID} associated with a. Finally, K_{ID} for a constant $\dot{a}$ was larger when the crack was decelerated than when it was accelerated (see Figs. 8-10). Similar results were also obtained by the authors for epoxy and Homalite-100 specimens [12-15].

To study the effect of the crack acceleration and deceleration, the values of K_{ID} were expressed as a function of $\dot{a}$. Figures 11-14 show $K_{ID}(\dot{a})$ curves, where arrows indicate the direction of progress of the fracture. The open circles represent the acceleration-free points ($\ddot{a}$=0) obtained from the maximum and minimum velocity positions. There are several interesting points in the K_{ID}-$\dot{a}$ relations. First, $K_{ID}(\dot{a})$ for the SEN specimen only exhibited the increasing process so that it gradually approached a constant value. Second, distinct crack

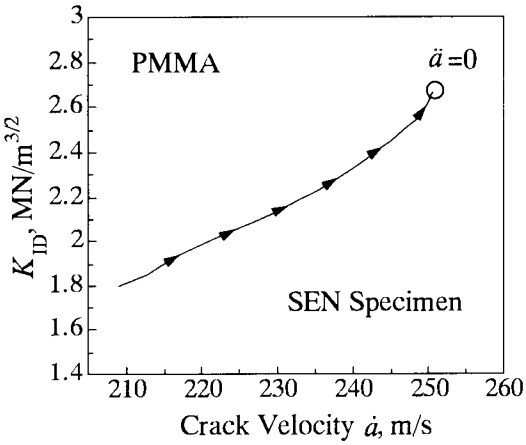

Fig. 11. K_{ID}-$\dot{a}$ relation for a SEN specimen under unifrom tensile loading

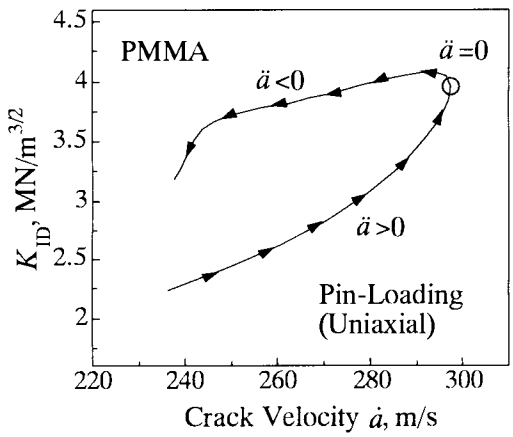

Fig. 12. K_{ID}-$\dot{a}$ relation for a uniaxially pin-loaded specimen

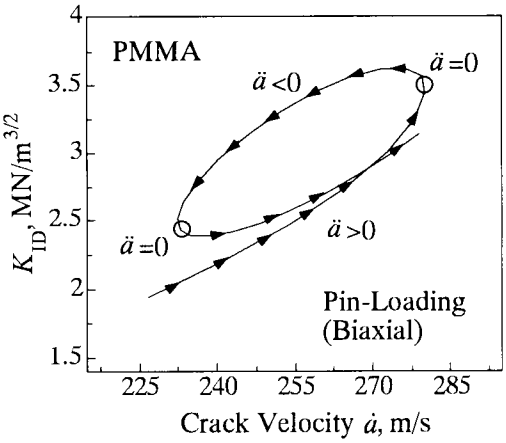

Fig. 13. K_{ID}-$\dot{a}$ relation for a biaxially pin-loaded specimen

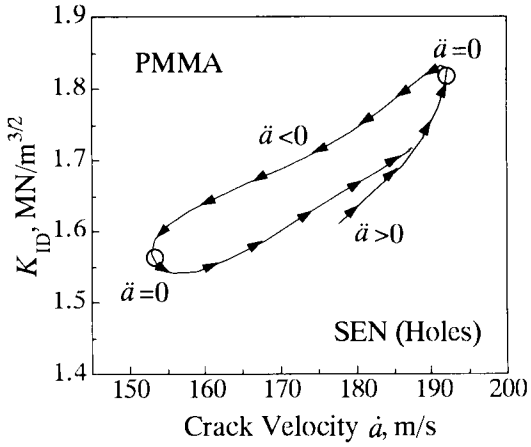

Fig. 14. K_{ID}-$\dot{a}$ relation for a SEN with holes specimen

acceleration ($\ddot{a}>0$) and deceleration ($\ddot{a}<0$) can be seen in the uniaxially pin-loaded specimen. Finally, in both the biaxially pin-loaded and SEN (Holes) specimens, three stages of distinct crack acceleration ($\ddot{a}>0$), deceleration ($\ddot{a}<0$) and re-acceleration ($\ddot{a}>0$) can be seen in one fracture process. Although $K_{ID}(\dot{a})$ is shown to increase with $\dot{a}$, it should be noted that their relation was not unique. For a constant $\dot{a}$, the decelerating crack had a larger value of K_{ID} than the accelerating or re-accelerating one. Such was also the case with other specimens tested.

The authors have suggested that K_{ID} was expressed as two parametric functions of $\dot{a}$ and $\ddot{a}$, i.e. $K_{ID}(\dot{a}, \ddot{a})$, and that $K_{ID}(\dot{a}, \ddot{a}$=constant) was uniquely related to $\dot{a}$ [9,12,13]. This was examined using the obtained results. Figure 15 shows the $K_{ID}(\dot{a})$ curves determined for the four specimens. The dotted curve of $K_{ID}(\dot{a}, \ddot{a}=0)$ connecting the acceleration free points can separate the acceleration ($\ddot{a}>0$) and deceleration ($\ddot{a}<0$) area in the K_{ID}-$\dot{a}$ diagram. As seen, $K_{ID}(\dot{a})$ for a constant $\dot{a}$ had a larger value when the crack was decelerated than when it was accelerated, i.e. $K_{ID}(\dot{a}, \ddot{a}<0) > K_{ID}(\dot{a}, \ddot{a}>0)$. It should be noted that $K_{ID}(\dot{a}, \ddot{a}=0)$ can be uniquely related to $\dot{a}$ as suggested in previous studies [9,13]. Hence, this clearly appears to indicate that $K_{ID}(\dot{a}, \ddot{a}=0)$ can be the material property, while the time variations of K_{ID} and $\dot{a}$ were strongly influenced by specimen geometries and loading methods as shown in Figs 7-10.

CONCLUSIONS

Dynamic crack propagation in PMMA was studied using the method of caustics and a Cranz-Schardin high-speed camera. Four different types of specimen geometries were employed to

achieve the crack acceleration, deceleration and re-acceleration process in one fracture event. Dynamic stress intensity factor K_{ID} and crack velocity $\dot{a}$ were evaluated, and the following findings were obtained:

(1) The variations of K_{ID} and $\dot{a}$ were strongly influenced by the specimen geometries and loading methods.
(2) $\dot{a}$ change was qualitatively in accord with the one in K_{ID}.
(3) K_{ID} for a constant $\dot{a}$ was larger when the crack was decelerated than when it was accelerated or re-accelerated.
(4) K_{ID} for acceleration-free can be uniquely related to $\dot{a}$.

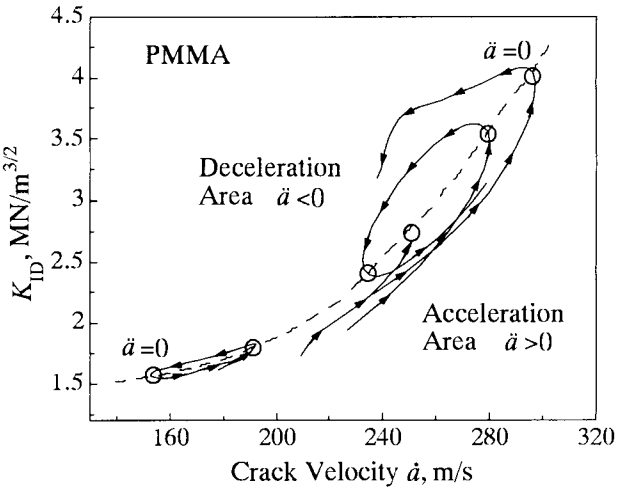

Fig. 15. K_{ID}-$\dot{a}$ curves for the four different types of PMMA specimens

REFERENCES

1. J.W. Dally, W.L. Fourney and G.R. Irwin (1985) "On the uniqueness of the stress intensity factor - crack velocity relationship", *Int. J. Fracture*, **27**, 159-168.
2. A.S. Kobayashi, M. Ramulu, M.S. Dadkhah, K.-H. Yang and B.S.J. Kang (1986) "Dynamicfracture toughness" *Int. J. Fracture*, **30**, 275-285.
3. A. Shukla and H. Nigam (1986) "A note on the stress intensity factor and crack velocity relationship for Homalite 100" *Engng Fracture Mech.*, **25**, 91-102.
4. J.W. Dally, R.K. Agarwal and R.J. Sanford (1990) "A study of hysteresis in the K_{ID}-$\dot{a}$ relation" *Exp. Mech.*, **30**, 177-183.
5. J.F. Kalthoff (1983) "On some current problems in experimental fracture dynamics" In W.G.Knauss (ed.), *Workshop on Dynamic Fracture,* California Institute of Technology, Pasadena,11-35.
6. W.G. Knauss and K. Ravi-Chandar (1985) "Some basic problems in stress wave dominated fracture" *Int. J. Fracture*, **27**, 127-143.
7. T. Nishioka, T. Murakami, H. Uchiyama, K. Sakakura and H. Kittaka (1991) "Specimen size effects on dynamic crack propagation and arrest in DCB specimens" *Engng Fracture Mech.*, **39**, 757-767.
8. A.J. Rosakis (1993) "Two optical techniques sensitive to gradients of optical path difference: the method of caustics and the coherent gradient sensor (CGS)" In J.S. Epstein (ed.), *Experimental Techniques in Fracture*, VCH Publishers, 327-425.
9. K. Takahashi and K. Arakawa (1987) "Dependence of crack acceleration on the dynamic stress - intensity factor in polymers" *Exp. Mech.*, **27**, 195-200.
10. K. Arakawa and K. Takahashi (1991) "Branching of a fast crack in polymers" *Int. J. Fracture*, **48**, 245-259.
11. K. Takahashi and T. Mada (1993) "Dual-focus high-speed photography and its application to fracture and impact studies" In J.M. Dewey and R.G. Racca (eds.), *20th International Congress on High-Speed Photography and Photonics,* SPIE 1802, 901-909.
12. K. Arakawa and K. Takahashi (1991) "Relationships between fracture parameters and fracture surface roughness of brittle polymers" *Int. J. Fracture*, **48**, 103-114.
13. K. Arakawa, D. Nagoh and K. Takahashi (1997) "Crack velocity and acceleration effects on the dynamic stress intensity factor in polymers" *Int. J. Fracture*, **83**, 305-313.
14. K. Takahashi, M. Kido and K. Arakawa (1998) "Fracture roughness evolution during mode I dynamic crack propagation in brittle materials" *Int. J. Fracture*, **90**, 119-131.
15. K. Arakawa, D. Nagoh and K. Takahashi (1999) "Dynamic Crack propagation and unloading behavior of brittle polymers" *Int. J. Fracture*, **96**, 345-358.

DYNAMIC TENSILE STRENGTH OF PMMA/AL PLATE BUTT ADHESIVE JOINTS

H. WADA[*1], S. KUBO[*1] K. MURASE[*2] and T. C. KENNEDY[*3]

*1 Daido Institute of Technology, 10-3 Takiharu-cho, Minami-ku, Nagoya, 457-8530 Japan
*2 Meijo University, Tenpaku, Nagoya, 468-8502 Japan
*3 Oregon State University, Corvallis, OR 97331-5001 USA

ABSTRACT

The impact strength was evaluated for a butt adhesive joint of Al alloy plate and PMMA plate. The materials were bonded together by cold-setting epoxy, commercial base adhesive. An impact tension test was carried out using a drop-weight testing machine. The fracture initiation time in the adhesive interface was determined from the measured strain gage signal. The impact tensile strengths of the adhesive joint were evaluated by the stress singularity field parameter and the average fracture stress. Fracture toughness in the dynamic stress field was determined from the stress distribution in the vicinity of the edge of the adhesive interface calculated by the finite element method at the fracture initiation time. The static fracture toughness was also determined by a similar method using the same type of specimen used in the dynamic test. It was found that the dynamic strengths exhibited considerably larger values than the static strengths.

KEYWORDS: Dynamic tensile strength, Butt adhesive joint, Adhesively bonded dissimilar butt joints, Loading rate, Stress singularity, Strain gage, Finite element method

INTRODUCTION

Recently, adhesive technology has been introduced into a wide variety of fields for the purpose of lightening and cost reduction of machine structures. However, the establishment of a fracture criterion for the adhesive interface which is useful for design is a difficult task, because of the wide variability of strength. So far, studies[(1)~(5)] on stress analysis and strength evaluation of the adhesive interface have been carried out mainly for the static problem with the development of the numerical analysis technology. In particular, the followings are reported for the strength evaluation: methods based on maximum stress, methods based the stress singularity field parameter at a joint of dissimilar materials, and methods based on fracture mechanics including a crack, etc. Generally it is known that a singularity in the stress appears in the vicinity of the edge in the adhesive interface between dissimilar materials. Therefore, a strength evaluation method based on the stress singularity field parameter[(3)] for the adhesive joint between dissimilar materials has been proposed for the static problem. The establishment of an impact strength evaluation method for an adhesive joint is needed for the case of severe loading of the structure. In this study, the dynamic tensile strengths are investigated for the dissimilar butt adhesive joints with the fracture toughness and the average fracture stress.

EXPERIMENTAL METHOD

MATERIALS AND SPECIMEN

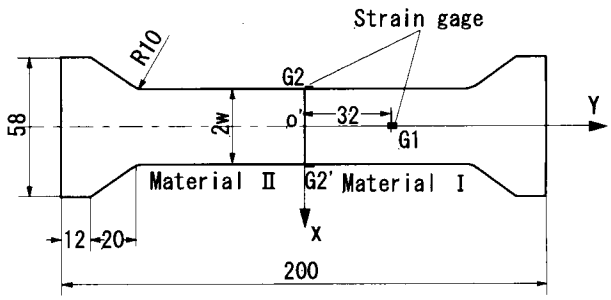

2w=30 h=6 (Dimensions in mm)

Fig.1 Specimen configuration and dimensions.

Table 1 Physical properties of materials.

		Young's modulus E (GPa)	Density ρ (kg/m^3)	Poisson's ratio ν
PMMA	Dynamic	4.87	1.18×10^3	0.388
	Static	3.50		
Al alloy	Dynamic	71.8	2.70×10^3	0.331
	Static			

The specimen configuration used in this experiment is shown in Fig.1. The specimen thickness was h=6mm. PMMA was used for Material I, and Al alloy (A6061P-T6) was used for Material II. The physical properties of both adherents are shown in Table1. A strain gage was bonded in the center (G1) of the Material I side (PMMA) shown in Fig.1 in order to measure the time-history of the stress in the specimen. Strain gages were also bonded in the vicinity of the edge of the adhesive interface (G2, G2') in order to measure the fracture initiation time. In this way, the time-history of strain measured by the strain gage (G1) was used as an external force for dynamic stress analysis by the finite element method. The two materials were bonded together using a special jig developed in this study in order to avoid slippage of the butt and non-uniformity of the thickness of the adhesive layer. The materials were bonded together by a cold-setting epoxy type adhesive (Epoxy resin 100%, Polyamide resin 100%). The specimen was used in the experiment after allowing the adhesive to set for 24 hours. Although the physical properties of the adhesive were not given by the manufacturer, the literature (3) gives physical properties for the same type of adhesive. Therefore, it was assumed that the physical properties of the adhesive used in this study were approximately equal to physical properties of the PMMA material of the adherent. Planes to adhere the two materials were polished in random directions by sandpaper. The surface roughness of the plane was measured with a surface roughness meter. As a result, the center line average roughness was R_a=0.12 μm for the PMMA material, R_a=0.14 μm for the Al alloy. By expanding with a projector by a factor of 20, the thickness of the adhesive layer of the joint was measured as about 50 μm.

IMPACT LOADING EQUIPMENT

The tension jig for impact tensile loading of the specimen is shown in Fig.2. It is constructed using 4 steel disks (ϕ160×30) and 8 steel pins (ϕ20×260), as shown in the figure. Steel disks 1 and 3, and 2 and 4 of the jig are respectively moved together by the pins. The specimen is installed in the center hole of steel disks 2 and 3. Disks 1 and 3 move downward when the falling weight collides with steel disk 1, and the specimen installed between disks 2 and 4 is dynamically pulled. The falling weight in the pipe is pulled up using a wire, and then, it is made to fall freely from some height in the tension jig. The largest height of the falling weight in this equipment is 1.6m. All experiments were carried out with the height of the weight at 0.8m. As the result, the velocity of the falling weight at

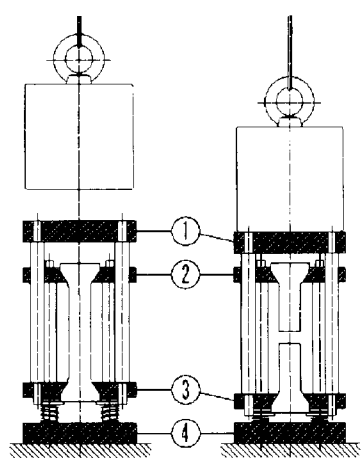

Fig.2 Impact tension jig.

the time of collision with the tension jig was about 4m/s. Also, a rubber plate of 5mm thickness was laid on disk 1 of the tension jig in order to reduce vibrations of high order caused by the collision of the falling weight.

DYNAMIC STRAIN MEASUREMENT

The dynamic strain measuring device system is shown in Fig.3. The output signal from the resistance strain gage which is bonded to specimen is converted into a voltage output by the bridge box, as shown in Fig.1. The voltage output is amplified by an amplifier (Signal conditioner CDV/CDA-230C, KYOWA). The time-history of the voltage output is recorded in the wave recorder (Transient converter TCL-005-DG, 6ch, 4096word/cha, 10bit smallest sampling time 50ns/W). It is also converted into strain after it is transferred to a personal computer. Incidentally, the strain measurement was carried out at a 200kHz digital sampling rate without using a filter in this experiment.

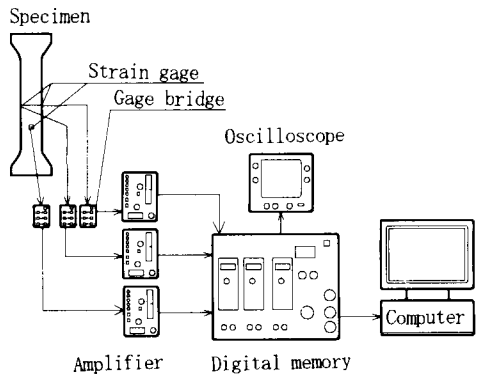

Fig.3 Recording system of dynamic strains.

DYNAMIC STRESS ANALYSIS BY FEM

Static and dynamic stresses in the adhesive joint between the dissimilar materials used in this experiment were analyzed using the general-purpose program ANSYS5.6. A second-order quadrilateral element with 8 nodes was used in the calculation, and the stress analysis was carried out with the assumption of plane stress conditions. Considering the symmetry of the specimen, only half of it was modeled. Fig.4(a) shows the boundary conditions on the specimen used to simulate the impact tension test in the FEM analysis. The time-history of the strain measured by the strain gauge G1 was used as a dynamic input load to the specimen. In this way, it was confirmed that the dynamic stress analyzed by the FEM agreed well with the measurement result. Therefore, numerical analysis by this method is appropriate. Fig.4(b) shows the element mesh of the specimen. The number of elements is 1571, and the number of the node is 4936. There is a singularity in stress at the edge of the adhesive joint interface, and it is necessary to divide this region into very small elements, since a large stress gradient exists. Fig.4(c) shows the details of the element mesh in the vicinity of the edge of the adhesive interface. The smallest element size is 19μm.

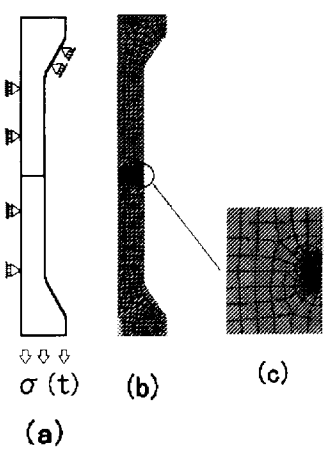

Fig.4 Boundary and meshing conditions.

STRESS SINGULARITY FIELD PARAMETER

The static stress distribution in the vicinity of the edge of an interface between dissimilar materials has been determined by Bogy[6]. Namely, the stress distribution is given in equation (1),

$$\sigma(x) = K / x^{\lambda} \tag{1}$$

where σ(x) is the stress component, K is the stress singularity field strength, and λ[7] is the exponent in the singular term which is determined by a combination of the properties of the dissimilar materials, and x is the distance along the interface from the singular point. The convenient technique shown next was used in order to determine the intensity K of the singular stress field. Namely, it is possible to obtain the theoretical resultant force F_y in a small region (a~c, a<b<c) in the vicinity of the singular point from Eq. (1) according to the following equation.

$$F_y = \int_a^c \frac{K}{x^{\lambda}} h \cdot dx \tag{2}$$

On the other hand, the stress in the 3 nodes of the 2 elements in the vicinity of the interface edge gives the resultant force F_{yf} from the finite element analysis by equation (3).

$$F_{yf} = \{\sigma_a + \sigma_b)(a - b) + (\sigma_b + \sigma_c)(b - c)\}h/2 \tag{3}$$

Equations (2) and (3) become equal, if the stress in the vicinity of the edge of the adhesion boundary is obtained accurately by the finite element method. Namely,

$$F_{yf} = F_y \tag{4}$$

Therefore, Eq.(5) is obtained from Eq.(4), and it is possible to conveniently obtain the intensity of the singular stress field from this equation

$$K = \{\sigma_a + \sigma_b)(a - b) + (\sigma_b + \sigma_c)(b - c)\}(1 - \lambda)/\{2(c^{1-\lambda} - a^{1-\lambda})\} \tag{5}$$

The value calculated by Eq.(5) was compared with the results from the extrapolation method in order to examine the accuracy of calculating the intensity K of the singular stress field. Good agreement was found, and it was confirmed that the convenient calculation formula given by Eq.(5) was effective.

RESULTS AND DISCUSSIONS

DYNAMIC STRESS

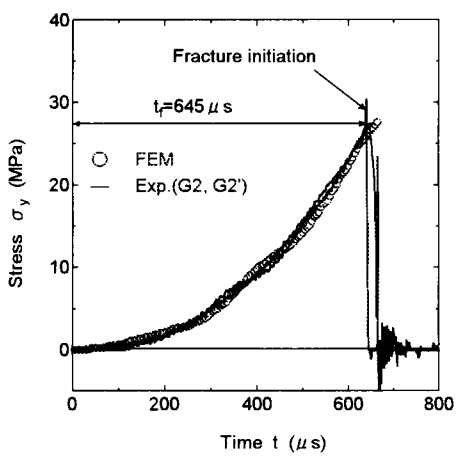

Fig.5 Dynamic stress response in adhesive joint

Figure 5 shows the results of simulating stress wave propagation in the specimen by the FEM. The measured results for the stress are also displayed in the figure for comparison with the calculation results. In the figure, the time-histories of stress measured by strain gages G2 and G2' are shown with the continuous line, and the calculation results by the FEM are shown with the mark o. Strain gages G2 and G2' were bonded on the edge of the PMMA material about 1.0mm from the adhesive interface. The two results are in good agreement until the stress rapidly decreases, as shown in the figure. Therefore, the dynamic stress which propagates in the specimen can be simulated by FEM accurately. In addition, the stress distribution at the adhesive interface at the fracture initiation time can be determined by the FEM analysis, as the strain gage signal yields the fracture initiation time value. Finally, the singular stress field parameter is obtained

from the stress distribution at the adhesive interface by FEM analysis.

IMPACT TENSILE STRENGTH

Fig.6 shows a Weibull plot[8] of the critical intensity of the stress field determined from stress component σ_y. A cumulative fracture probability F(%) of each data point was determined using the median rank method. There is considerable difference in the longitudinal modulus of elasticity of the PMMA material for the static value as compared to the dynamic one, as was shown in Table 1. Therefore, the value of the exponent λ of the singularity of the PMMA/Al adhesive joint specimen used in this experiment is different in the dynamic and static cases. Namely, it becomes λ=0.229 in the dynamic stress field, and it becomes λ=0.231 in the static stress field. The increase of λ becomes a factor which lowers the fracture strength. There is a difference evidently in the strength of the joint in the static case as compared to the dynamic one, as shown in the figure. The dynamic tensile strength of the PMMA/Al adhesion plate joint is considerably larger than the static strength. Namely, K_{yd} values are about 2.9 times those of K_{yc}. The interaction of the delay of the lateral deformation and the restraint of the deformation of PMMA material in the adhesive interface by the Al alloy, etc. appears to be the cause, since the velocity of the longitudinal wave is different from that of the transverse wave. Fig.7 shows critical intensities K_{xyc} and K_{xyd} of the singular stress field obtained from shearing stress τ_{xy}. Although K_{xy} is considerably smaller than K_y, the tendencies of the results in Fig.7 are similar to those of Fig.6 when comparing static and dynamic values. The dynamic tensile strength of the PMMA/Al adhesive joint is about 2.6 times that of the static strength.

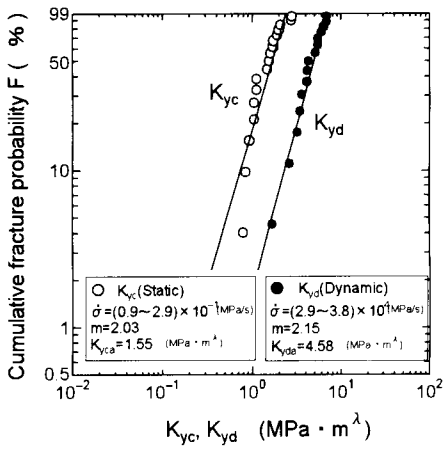

Fig.6 Weibull distributions of K_{yc}, K_{yd}

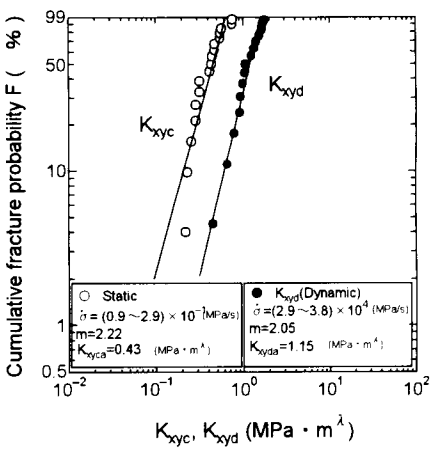

Fig.7 Weibull distributions of K_{xyc}, K_{xyd}

Fig.8 shows static fracture strengths of the joints for several combinations of materials on the average fracture stress on adhesive interface. The joint of Al/Al is highest strength due to the stiffening effect for adhesive layer by Al alloy. However, the strength of the PMMA/Al joint is lower than that of the PMMA/PMMA joint since it shows the stress singularity field. On the other hand, the dynamic strength of the PMMA/Al joint is higher than that of the PMMA/PMMA

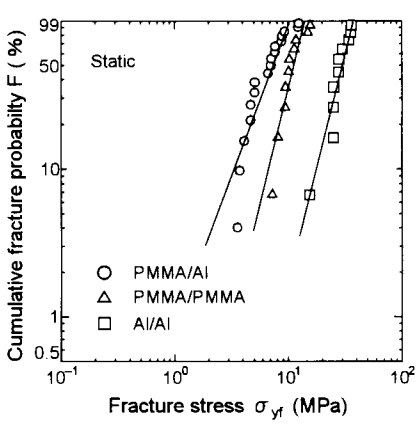

Fig.8 Weibull distributions of σ_{yc}

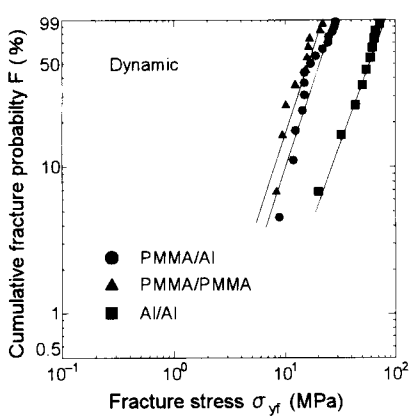

Fig.9 Weibull distributions of σ_{yd}

other hand, the dynamic strength of the PMMA/Al joint is higher than that of the PMMA/PMMA

joint slightly, as shown in Fig.9. Table 2 shows each numerical result relating both figures.

Table 2 Results of statistical analysis.

		Stress rate (MPa/s)	m	Average fracture stress σ_{yco}, σ_{yde} (MPa)
PMMA/Al	Static ○	$(0.9\sim2.9)\times10^{-1}$	2.04	6.97
	Dynamic ●	$(2.9\sim3.8)\times10^{4}$	2.27	18.98
PMMA/PMMA	Static △	$(0.9\sim1.2)\times10^{-1}$	3.09	10.78
	Dynamic ▲	$(1.8\sim4.0)\times10^{4}$	2.37	14.70
Al/Al	Static □	$(1.5\sim1.8)\times10^{-1}$	3.21	28.26
	Dynamic ■	$(1.8\sim8.0)\times10^{5}$	2.30	53.20

CONCLUSION

From the above results, the impact strength of a PMMA/Al plate butt adhesive joint was evaluated from a stress analysis by FEM and by measurement of fracture initiation time by strain gages, with the stress singularity field parameter and the average fracture stress. In addition, stress rate dependence of the strength of an adhesive joint between dissimilar materials was investigated in detail. Consequently, if some main clarified matters are considered, the following conclusions are derived.

(1) From the signal of a strain gage bonded to the specimen in the vicinity of the adhesive interface, it was possible to accurately determine the fracture initiation time in the specimen adhesive interface edge.

(2) In both the static and dynamic tests, fracture was observed to occur in the PMMA/epoxy adhesion interface.

(3) Using the fracture initiation time determined from the strain gage signal and the simulation results from the dynamic stress analysis by FEM, an effective technique for determining the singular stress field parameter at the fracture initiation time was developed.

(4) The dynamic tensile strengths of the PMMA/Al butt adhesion plate joint evaluated were about 2.9 times the static values for K_{yd}, and about 2.7 times the static values for σ_{yd}.

REFERENCES

(1) Sawa, T., K. Nakano, H. Toratani and M. Horiuchi, (1995). Two-Dimensional Stress Analysis of Single-Lap Adhesive Joints Subjected to Tensile Shear Loads. *Trans. of the JSME(A)*, **61**, 1994-2002.

(2) Tong, L., (1998). Strength of Adhesively Bonded Single-Lap and Lap-Shear Joints. *Int. J. Solids Structures*, **35**, 2601-2616.

(3) Hattori T., S. Sakata, T. Hatsuda and G. Murakami, (1988). A Stress Singularity Parameters Approach for Evaluating Adhesive Strength. *Trans. of the JSME(A)*, **54**, 597-602.

(4) Sato C., H. Iwata and K. Ikegami, (1997). Dynamic Strength of Adhesive Layer under Combined Impact Loading using Clamped Hopkinson Bar Method. *Trans. of the JSME(A)*, **63**, 341-346.

(5) Yokoyama T. and H. Shimizu, (1997). Determination of Impact Shear Strength of Adhesive Bonds with the Split Hopkinson Bar. *Trans. of the JSME(A)*, **63**, 2604-2609.

(6) Bogy D. B., (1971). Two Edge-Bonded Elastic Wedges of Different Materials and Wedge Angles Under Surface Tractions. *J. Appl. Mech.* **38**, 377-386.

(7) Dunders J., (1967). Effect of Elastic Constants on Stress in a Composite under Plane Deformations. *J. Composite Materials*, **1**, 310.

(8) Daimaruya M., H. Kobayashi, M. Chiba and H. Maeda, (1997). Measurement of Impact Tensile Strength of Concretes. *Trans. of the JSME(A)*, **63**, 2592-2597.

ORAL REFERENCE: ICF100833OR

DYNAMICS OF INTER-FACIAL CRACK FRONT PROPAGATION

Knut Jørgen Måløy[1], Jean Schmittbuhl[2], Arnaud Delaplace[3], and Jose Javier Ramasco[1,4]

[1] Fysisk Institutt, Universitetet i Oslo, P. O. Boks 1048 Blindern, N-0316 Oslo 3, Norway
[2] Laboratoire de Géologie, UMR 8538 École Normale Supérieure, 24 rue Lhomond, 75231 Paris Cedex 05, France.
[3] Laboratoire de Mécanique, et Technologie, École Normale Supérieure de Cachan, 61 Avenue du Président Wilson, F-94235 Cachan Cedex, France
[4] Instituto de Fisica de Cantabria (CSIC-UC) Facultad de Ciencias, Av de los Castros s/n 39005 Santander, Cantabria, Spain

Abstract. Here we report on *in situ* observations with a high speed CCD camera of an in-plane crack propagating through a transparent heterogeneous Plexiglas block. The toughness is controlled artificially and fluctuates spatially like a random noise. A stable crack in mode I was monitored by loading the system by an imposed displacement. We show that the movement of the fracture front is controlled by local instabilities triggered by the depinning of asperities even for very slow loading. Development of crack roughness is described in terms of a Family-Vicsek scaling with a roughness exponent $\zeta = 0.60$ and a dynamical exponent $\kappa = 1.2$.

Keywords: Inter facial fracture, roughness, depinning, local dynamics

Introduction

In this experiment we studied the dynamics of a slow inter-facial crack front line during its propagation through a transparent heterogeneous Plexiglas block. We found that the slip in the front line along the fracture interface is strongly correlated over scales much larger than the width of the fracture front and that the front moves in irregular bursts [1]. In contrast to the experiment presented here, most experiments are performed with unstable fractures which exhibit fast propagation of the order of the speed of sound. The fast propagation makes it very difficult to study dynamics. Direct observation of the crack front is usually impossible and an inverse description of the crack front obtained for instance from acoustic emissions is generally observed with a low spatial resolution.

Most studies on fractures have focused on homogeneous materials. The role of heterogeneities has been addressed more recently. Fracture surfaces have been found to exhibit self-affine long range correlations [2, 3, 4, 5, 6, 7, 8, 9]. However, the physical origin of it is still not fully understood. Static elasticity leads to long range interactions [8, 10] but in addition elastic waves specially recently observed crack front waves [11, 12, 13, 14, 15] may play an important role. In most modeling of fracture dynamics in heterogeneous materials the latter are ignored since a quasi static assumption is used. A recent quasistatic simulation presented by Hansen et. al [16] (see this proceeding) shows results consistent with our experiments.

Experimental method and results

In this work we present an experimental study of a stable slow fracture propagating along an annealed interface between two Plexiglas blocks [17, 18, 19, 1]. Crack fronts are directly observable because of the

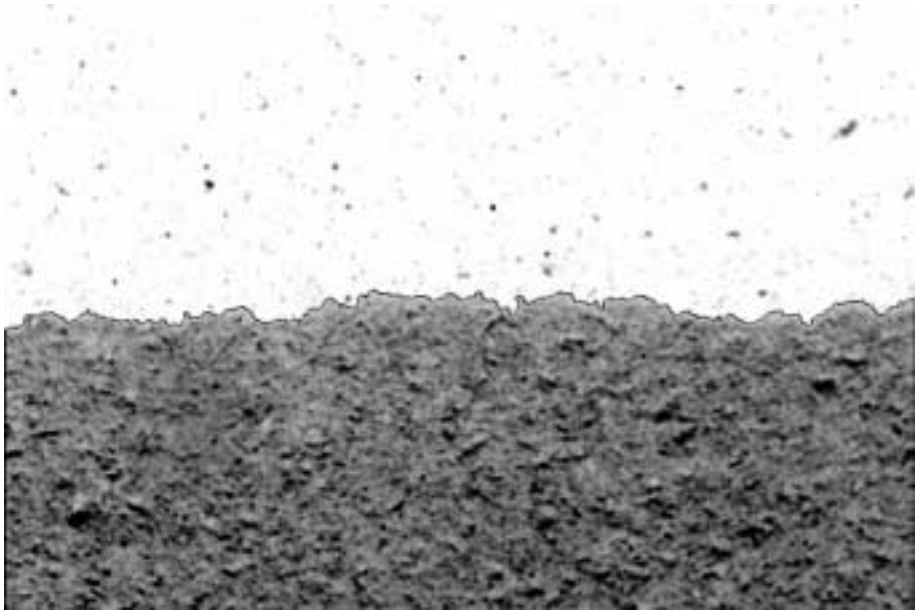

Figure 1: Sample of crack fronts. The background is an inverted raw image where the intact material appears white. In contrast, the cracked zone is dark. Crack propagates in this case from bottom to top because of a tensile load.

transparency of the material. Plates are : $32cm \times 14cm \times 1cm$ and annealed together at 205° C under several bars of normal pressure. The annealed surface corresponds to a weak plane which the fracture will propagate along. Before annealing, both plates are sand-blasted on the side to be annealed with $50\mu m$ steel particles. The sand-blasting procedure introduces a random roughness which induces local toughness fluctuations during the annealing procedure. Since the sand-blasting gives a cutoff of the structure in the plates of about $50\mu m$, we do not expect correlated toughness above this length scale. One of the plates is clamped to a stiff aluminum frame. A normal displacement is applied by a press to the other plate which induces a stable crack propagation in mode I at constant low speed ($68\mu m/s$). The fracture front is observed with a microscope linked to a high speed Kodak Motion Korder Analyzer camera which records 8.7s at 500 images per second with a 512x240 pixel resolution. We also performed experiments with a normal speed Kodak DCS 420 CCD camera which has a resolution of 1536x1024 pixels. This camera was used after loading when the fracture had come to rest. The visualization setup is mounted on a translation table with possible movement parallel to the propagation plane (x, y) controlled by two stepping motors.

In Fig. 1 is shown a sample image obtained with this setup. The uncracked part is seen as white while the gray region represents the open fracture. The front is defined as the contrast boundary. Let V be the local front velocity in the direction of the front normal. The velocities V at all front positions were calculated by measuring the distance δl, along the normal, to the intersection with the front that is $20ms$ later. The distributions of the velocity V is shown in Figure 2. The distribution have clear long tails at large velocities. Very high front velocities compared to the average crack speed are observed locally. Figure 3 shows the fluctuations of the crack front position : $h(x,t) - \langle h(t) \rangle_x$ in gray levels [1]. Light regions correspond to regions which are in advance of the average crack front. On the contrary, the dark gray correspond to pinned regions of the front that evolve slower than the average crack front. In the figure there are numerous sharp transitions which appear close to horizontal. These transitions are triggered after pinning periods (dark regions) and correspond to fast propagations or local instabilities along the front. The fracture front line only evolves during these fast instabilities or bursts. Apart from

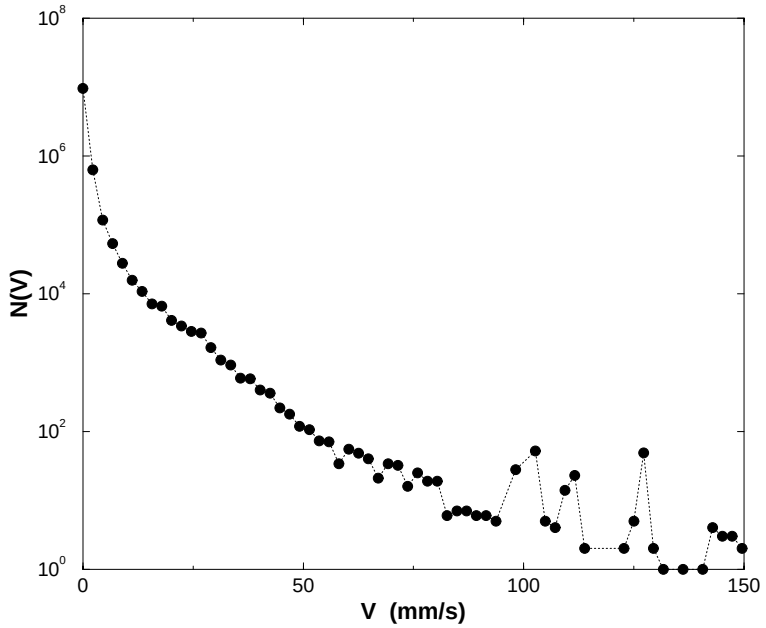

Figure 2: The distribution of the velocity V. The velocity V are calculated on the basis of fronts separated with a time interval of $\delta t = 20ms$. The largest measured local speeds are about three order of magnitude larger than the average front speed $V_f = 68\mu m/s$. It is important to note that the speeds V are average speeds within the time $\delta t = 20ms$. This means that even much higher speed fluctuations may be present with a higher resolution in space and time.

them there are almost no evolution of the front position.

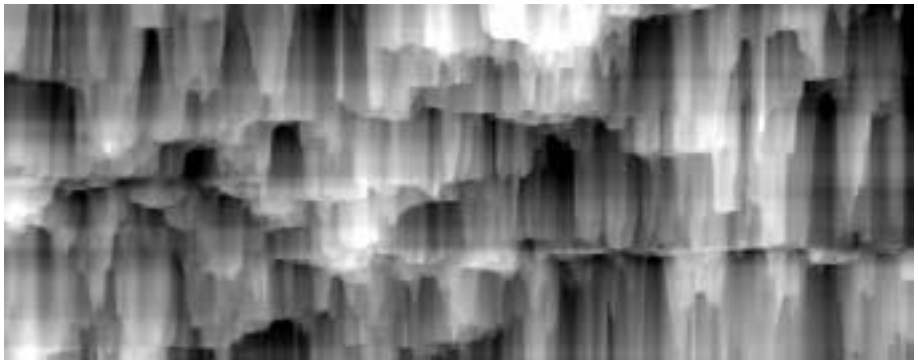

Figure 3: a) The figure shows the space (horizontal) and time (vertical) diagram ($5.12mm \times 8.7s$) of the position fluctuations $h(x,t) - \langle h(t) \rangle_x$. The gray level represents $h(x,t) - \langle h(t) \rangle_x$. Light gray corresponds to positive values of $h(x,t) - \langle h(t) \rangle_x$, while dark gray corresponds to negative values of $h(x,t) - \langle h(t) \rangle_x$.

The dynamic scaling of the fracture front has been checked by calculating the power spectrum $P(k,t)$ of the position difference $h(x,t) - h(x,t=0)$, where k is the wave-number and t is the time ($t = 0$ corresponds to the first image). The Family-Vicsek scaling [20] of the power spectrum $P(k,t)$ can be written as

$$P(k,t) = t^{(1+2\zeta)/\kappa} G(kt^{1/\kappa}) \; , \tag{1}$$

where $G(x)$ is constant for $x << 1$ and $G(x) \propto x^{-1-2\zeta}$ for $x >> 1$. The dynamic exponent κ gives the scaling with time of the horizontal correlation length $\xi_x \propto t^{1/\kappa}$.

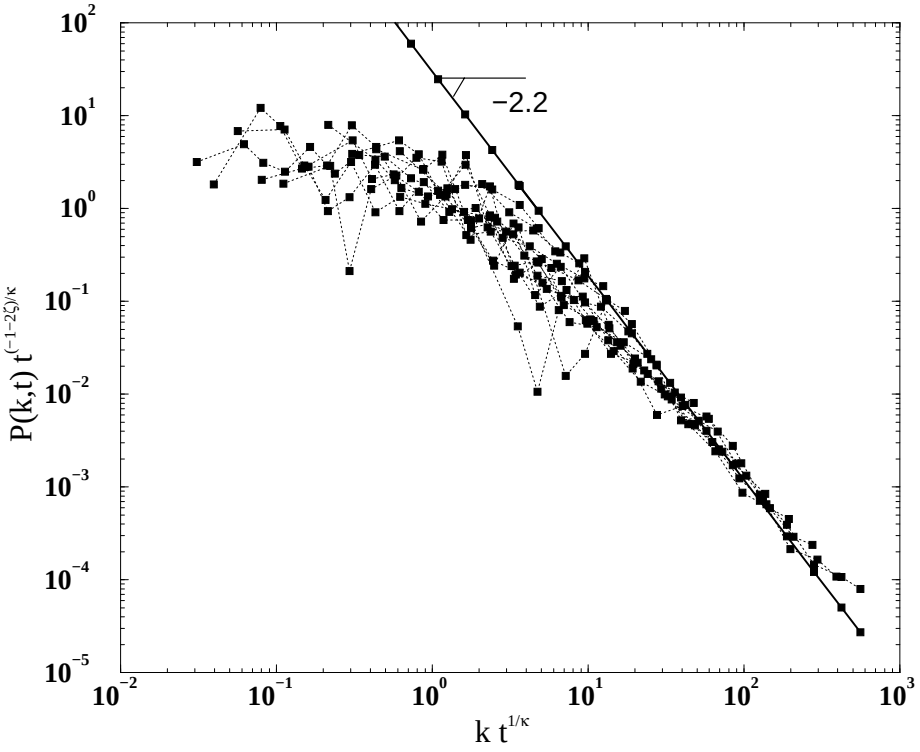

Figure 4: Family-Vicsek scaling: The dependence of the scaling function $P(k,t)t^{-(1+2\zeta)/\kappa}$ with $kt^{1/\kappa}$. This data collapse gives an estimate of the dynamic exponent $\kappa = 1.2$.

In Fig. 4, the scaling function $P(f,t)t^{-(1+2\zeta)/\kappa}$ is plotted as function of $kt^{1/\kappa}$ for different times from $0.03s$ to $7.11s$. This data collapse provides an estimate of the dynamic exponent $\kappa = 1.2$ and the roughness exponent $\zeta = 0.6$ [1]. We emphasize that the exponent may be different from the dynamic exponent obtained from an initially flat front. However the subtraction technique presented here is the only one experimentally accessible. The latter value of the roughness exponent has been extensively checked for fronts at rest over a larger range of scales ($5\mu m$ to $50mm$) [18].

The roughness exponent has also been measured after loading, when the fracture front had come to a complete rest. During each loading stop, the microscope was translated along the front and neighboring pictures were taken. By assembling up to 20 pictures we obtained front up to 2^{14} data points [18]. We found a self-affine crack front over more than three decades using several techniques[18]. The result of the power spectrum of the self-affine profile averaged over nine fronts is shown in Fig. 5. The fitted line corresponds to a roughness exponent of 0.64.

The roughness exponents obtained in our experiment is not consistent with most present theoretical models or simulations [8, 21, 11, 22]. However the theoretical model proposed by Ramanathan and Fisher [12] in which they solve the elastic problem of a planar tensile crack in a heterogeneous medium with a full elastodynamic description is consistent with our experimental work. In the ideal case where the toughness is not dependent of the velocity, they predict a roughness exponent of $\zeta = 0.5$ consistent with our experiments. This model contains elastic waves, and in particular crack front waves which will create stress overshoot along the fracture front. The results are also consistent with a recent quasi static simulation by Hansen et. al [16] (see this proceeding) who found $\zeta = 0.6$ and $\kappa = 0.9$.

Conclusion

The fast dynamics of the local scale is very different from the dynamics on large scale characterized by

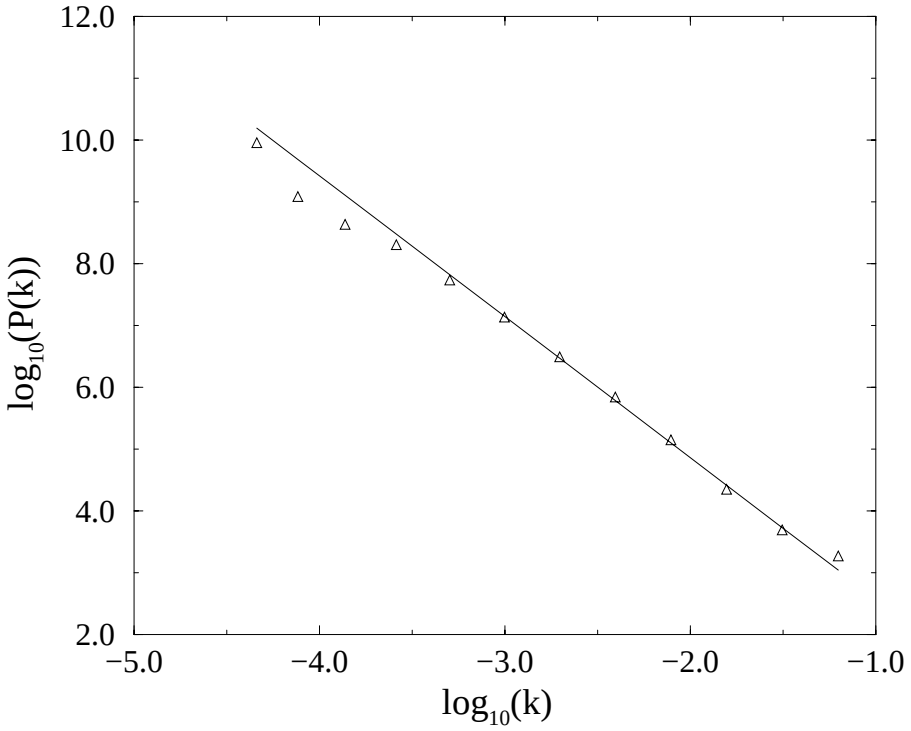

Figure 5: Average of the power spectrum analysis over nine fronts. The best fitted line has a slope of $-2.28 = -1 - 2\zeta$, where ζ is the roughness exponent.

a creeping motion. Very high front velocities compared to the average crack speed are observed locally. We show that the dynamics of the fracture is controlled by local instabilities or bursts which give rise to a self-affine fracture front line with roughness exponent $\zeta = 0.60$, and a dynamic exponent $\kappa = 1.2$. The slip along the front is found to be correlated on a length scale much larger than the asperity size.

References

[1] K. J. Måløy, and J. Schmittbuhl, and K. J. Måløy. *Preprint, 2001*

[2] B. B. Mandelbrot, D. E. Passoja, and A. J. Paullay. (1984) *Nature*, 308, 721.

[3] S. R. Brown and C. H. Scholz.(1985) *J. Geophys. Res.*, 90, 12575.

[4] E. Bouchaud, G. Lapasset, and J. Planés. (1990) *Europhys. Lett.*, 13, 73.

[5] J. Schmittbuhl, S. Gentier, and S. Roux. (1993) *Geophys. Res. Lett.*, 20, 639.

[6] B. L. Cox and J. S. Y. Wang. (1993) *Fractals*, 1, 87.

[7] K. J. Måløy, A. Hansen, E. L. Hinrichsen, and S. Roux. (1992) *Phys. Rev. Lett.*, 68, 213.

[8] J. Schmittbuhl, F. Schmitt, and C. H. Scholz. (1995) *J. Geophys. Res.*, 100, 5953.

[9] E. Bouchaud. (1997) *J. Phys*, 9, 4319.

[10] H. Gao and J. R. Rice. (1989) *ASME J. Appl. Mech*, 56, 828.

[11] S. Ramanathan and D. Fisher. (1998) *Phys. Rev. B*, 58, 6026.

[12] S. Ramanathan and D. Fisher. (1997) *Phys. Rev. Lett*, 79, 877.

[13] G. Perrin and J. R. Rice. (1994) *J. Mech. Phys. Solids*, 42, 1047.

[14] J. W. Morrisey and J. R. Rice. (2000) *J. Mech. Phys. Solids*, 48, 1229.

[15] J. W. Morrisey and J. R. Rice. (1998) *J. Mech. Phys. Solids*, 46, 467.

[16] A. Hansen, J. Schmittbuhl and G. Batrouni (2001) *See this proceeding*

[17] J. Schmittbuhl and K. J. Måløy. (1997) *Phys. Rev. Lett*, 78, 3888.

[18] A. Delaplace, J. Schmittbuhl, and K. J. Måløy. (1999) *Phys. Rev. E*, 60, 1337.

[19] J. Schmittbuhl, A. Delaplace, and K. J. Måløy., (2000) *In Physical Aspects of Fracture.* (eds E. Bauchaud), (Kluwer Academic Publishers)

[20] F. Family and T. Vicsek. (1985) *J. Phys. A*, 18, L75.

[21] J. P. Bouchaud, E. Bouchaud, G. Lapaset, and J. Planes. (1993) *Phys. Rev. Lett.*, 71, 2240.

[22] S. Roux and A. Hansen. (1994) *J. Phys. I*, 4, 515.

ORAL REFERENCE:ICF100517OR

EFFECT OF AQUEOUS ENVIRONMENT AND VISCID DROPLET ON DEFORMATION OF SPIDER THREAD

Masayoshi KITAGAWA

Department of Human & Mechanical Systems Engineering, Kanazawa University,
Kodatsuno 2-40-20, Kanazawa, 920-8667, Japan

ABSTRACT
As one of serial studies on the mechanical properties of spider threads, their amino acid compositions, the microstructure of dragline, the surface tension of the viscid droplet regularly spaced on capture thread and the effect of aqueous environment on the stress-strain curve were investigated. It was shown that (1) the dragline consisted of three layers at least, (2) the surface tension of the viscid droplet was about 65mN/m and (3) the shape of stress-strain curve was fairly affected by aqueous environment surrounding the thread.

KEYWORDS
Spider thread, Sticky droplet, Deformation, Rubber elasticity, Microstructure, Super contraction, Aqueous environment, Surface tension

1.INTRODUCTION

Some experiments on the structure and the strength of spider thread have been made on the analysis of amino acid composition, the crystalline structure, the microstructure, the mechanical properties, the effect of environment on the mechanical properties and so on using samples of spiders Nephila clavata and Argiope amoena [1,2,3,4,5,6,7].
It is interesting to note that the shape of stress-strain curve is very different between dragline and capture thread. The stress-strain curve of dragline shows a work hardening after steep yield point and breaks at small strain after elastic behavior. For capture thread, on the other hand, the curve which resembles that of rubber is upwardly concave (J-shaped) and the fracture strain, which amounts to 4 occasionally, is fairly large compared with that of dragline. The amino acid composition of capture thread without viscid droplets is nearly the same as that of dragline. Hence, the difference in the shape of the stress-strain curve between them may be attributed to the existence of viscid liquid attached to capture thread. In this paper, at first the fundamental properties of the droplet such as its shape and its surface tension are investigated, secondary the micro structure of dragline is observed using a urea super-contraction method developed by Vollrath et al. [8] and finally the effect of viscid droplet on the deformation behavior of the thread is shown.

2.EXPERIMENTAL

The spiders Nephila clavata and Argiope amoena who generally constructed orb webs were used for the test, since it was easy to collect threads from their living bodies and their webs.

Formation process of droplet

At first, how droplets were arranged at a regularly spaced row on capture thread was observed at an appropriate time interval. As soon as a spider constructed an orb web, a short part of the capture thread was cut out by means of a specially devised tool, and was subsequently set on an optical microscope. Furthermore, the shape of the droplets and their average spacing were measured for both spiders used here.

Surface tension

A collected quantity of viscid liquid is too small to measure the surface tension by a Du Nouy meter in which a large volume of test liquid was necessary. Therefore, a new machine was constructed as shown schematically in Fig.1. As illustrated in the enlarged view, the test liquid filled between the flat cylinders③ facing each other forms a symmetrical meniscus④. If the radii of meniscus curvatures are defined as r_1 and r_2, the surface tension T is calculated by Laplace equation

$$F = \pi r_1^{\,2} p, \quad p = T (1/r_2 - 1/r_1)$$

$$T = F/[\pi r_1^{\,2} p(1/r_2 - 1/r_1)] \qquad (1).$$

The shape of the meniscus and the applied force F was recorded by a video camera through an optical microscope. The values of r_1 and r_2 were measured by the radii at the necked region. The measurement was done at a humidity of about 60% and a temperature 20℃.

Microstructure

Since the diameter of dragline is 5 μm at most even for an adult female of Nephila clavata, it is difficult to observe its cross section by an optical microscope. A swelling technique by urea was used to investigate the microstructure. In urea, the thread diameter becomes more than 10 times bolder than the original one. A mixed solution of different concentrations of $CO(NH)_2$; 6-12M, NaOH(pH8); 0.05-1M and NaCl; 50mM was used. When threads shorter than about 5mm are placed in a swelling agent on a glass slide, they begin to swell immediately at their both ends.

Furthermore, a recoil test developed by Allen [9] was used to facilitate the observation of the interior structure of the thread.

Tensile test

How to prepare tensile specimens using samples collected from both spiders was stated elsewhere. When the dragline is wetted by water, it contracts after sufficient time. This phenomenon was named super contraction (SC) by Work [10]. The tensile samples for SC draglines were made as shown in Fig.2. The paper flame with a tight dragline set previously at its rectangular window was folded at the central part so that its ambient length might be obtained. After submersion during sufficient period, the thread became tight and the tensile specimen with an ambient SC ratio (SCR) was made. The super contracted ratio SCR was defined as SCR = $(L_0\text{-}Lc)/L_0$ where L_0 was the original length of the flame window and Lc was the shrinkage length after SC. Tensile tests were done for dry and wet draglines with ambient SCRs and capture threads.

3. EXPERIMENTAL RESULTS AND DISCUSSIONS

Formation process and geometry of viscid droplet

When a spider produced two core threads by a pair of flagelliform glands, viscid liquid produced by a pair of aggregate glands covered the core fibers simultaneously. Just after the capture threads were drawn out from the glands, the viscid liquid was still parallelepiped around the core threads. More than 10 minutes was necessary at least until some signs for the generation of regularly necked parts were recognized. After about 40minutes, a series of regularly spaced droplets formed completely along the core fibers.

The shape of the droplet is nearly the same for both spiders used as shown in Fig.3 where the dimensions are normalized by the maximum radius of the droplet. As shown by the solid curve in the figure, its shape is approximated well by a revolution ellipsoid.

Surface tension of sticky liquid

The load-time curves for the sticky liquid are shown in Fig.4. The liquid between the cylinders was pulled at a constant speed until their gap reached 0.25mm(point A), then the gap was kept constant for

a while (from A to C) and successively, it was pulled again at C. When stopping the machine, the meniscus is changing its curvatures very slowly due to its high viscosity and hence, the load drop occurs steeply. Using the curvatures at the stable period (B), the surface tension was estimated to be about 65±3 mN/m. This is nearly equal to that of water (73mN/m). This is plausibly due to the fact that the sticky liquid just after collected may contain a fairly large fraction of water.

Microstructure

As soon as urea liquid is dropped on the threads, swelling began at their both ends and moved to the central part. In the case where the concentrations of urea and NaCl are high, the interior substance becomes milky and flows out from the outer ring of the thread like a balloon. For the short thread, only the outer ring remains occasionally, the core material being solved out. This may indicate that the outer layer is stronger to swelling agents such as rain and fog than the core material. The observation of the short SC thread stained in a reagent of Coomassie Brilliant Blue shows that the thread consists of 3 layers, those are, the outer layer, the middle layer and the core.

The middle layer from which the outer layer is striped off at the recoil test can be seen in a fortunate case. This observation may show that the middle layer consists of numerous micro-fibrils parallel to the thread axis, which may be important for supporting the strength of dragline.

These features are illustrated schematically in Fig.5.

Tensile behavior Load(P)-draw ratio(λ) curves of dry and wet draglines with ambient SCRs are shown in Fig.6 (a) and (b). The value of P is calculated by (1-SCR) F where F is the actually recorded load, the cross sectional area being 1/(1-SCR) times larger than that of SCR=0. λ is defined as L/Lc where L is the length under deformation and Lc=(1-SCR)L_0 is the original length before deformation as defined above. P-λ curves in a dry state have a steep knee point denoting yield. The knee point tends to decrease with an increase in SCR. The P-λ curves after yielding are upwardly concave like rubber. But in a wet state, they are upwardly concave (J-shaped) without any distinct knee point. This may be similar to that of rubber.

Viscid droplets attached to capture threads were dissolved out into water. After the capture threads were soaked in water during 1 minute and more than 1 hours, they were sufficiently dried in air and were provided for tensile tests. If the capture thread was soaked in water during more than 1 hour, viscid droplets were completely removed from them and only the core threads remain. The dry core threads without any droplets were pulled. The P-λ curves for dry(②,③) and wet(①)capture threads are shown in Fig.7. The P-λ curves of wet capture threads has nearly the same shape as that of capture threads with viscid droplets. As the soaking time increases and the viscid droplets are much removed, the yield load increases. The P-λ curves of dry capture threads without any viscid droplet are very similar to those of dry draglines. This may be supposed by the fact that the amino acid compositions for both threads are nearly the same.

These behaviors may be explained well on the basis of a 3 elements model consisting of yield, rubber and spring elements as shown in Fig.8. The yield element does not move due to friction until the stress is lower than the yield stress Y. The rubber element shows rubber elasticity where the relationship between stress and λ is expressed by Langevin function. The spring element represents an elastic spring. If the applied stress exceeds Y, the behavior is governed by the rubber element. The yield stress Y is a function of SCR. In the case of wet thread, Y is chosen 0.

CONCLUSION

For the deformation behavior, it was shown that (1) the P-λ curve for capture thread without any viscid droplet was not different from that of dragline and (2) the capture thread with viscid liquid behaved like the dragline wetted and swollen by water sufficiently.

The author wishes to acknowledge Mr. T.Kitayama, Technical expert of Kanazawa Univ., and Mrs. M.Yasutomi and A.Furukawa, Master course student of Kanazawa Univ. for their technical assistance.

References

1. S.J.Lombardi and D.L.Kaplan,J.Arachnol.,**18**(1990)297.
2. M.A.Becker,D.V.Mahoney,P.G.Lenhert,R.K.Eby,D.Kaplan and W.W.Adams, in"Silk Polymers;Material Science and Biotechnology", ACS Symposium series, 544 (1993).
3. M.Kitagwa, S.Katsumi, Y.Wakoh, T.Yamamoto and M.Kimizu, J.Soc. Mater. Sci. Japan, **46**(1997) 4701.
4. D.T.Edmonds and F.Vollrath, Proc.R.Soc.London, **B248**(1992)145.
5. J.M.Gosline,M.E.Dumont and M.Denny,Euroarticle, **10**(1986)37.
6. M.Kitagawa and T.Kitayama, J.Materials.Sci., **32** (1997) 2005.
7. M.Kitagwa, S.Katsumi and Y.Wakoh, , J.Soc.Mater.Sci.Japan, **47** (1998) 55.
8. F.Vollrath and D.T.Edmonds, Nature, **340**(1989)305.
9. S.R.Allen,J.Materials Sci., **22**(1987)853.
10. R.W.Work,Textile Res.J, **47**(1977)650.

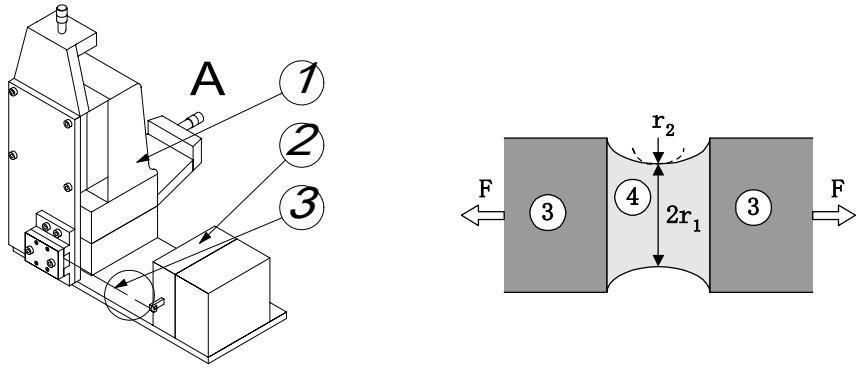

(a) (b)

Fig.1 Schematic illustration of a testing machine for measuring surface tension of viscid liquid. ①;cross table, ②;load cell, ③solid cylinders, ④;sticky liquid.

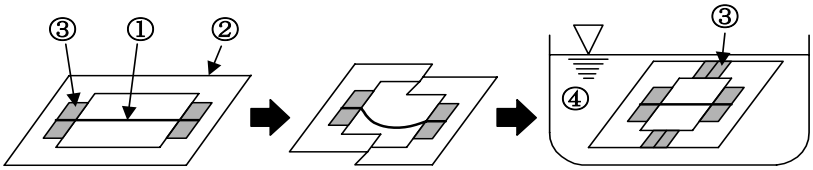

Fig.2 How to prepare tensile samples of dragline contracted by water. ①;dragline, ②;paper frame, ③;adhesive tape, ④;water.

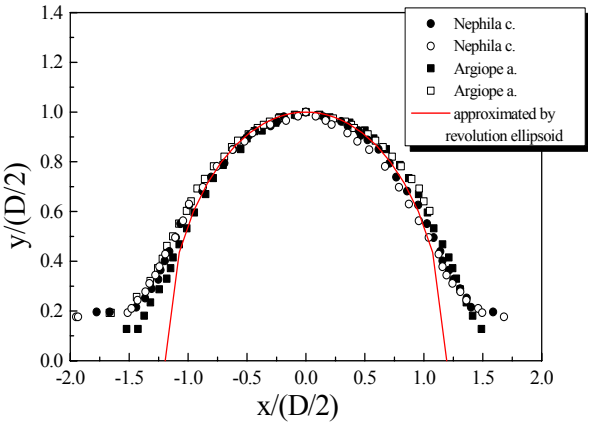

Fig.3 Shapes of viscid droplet for both spiders used in this experiment. The dimensions are referenced by the maximum radius of the droplet.

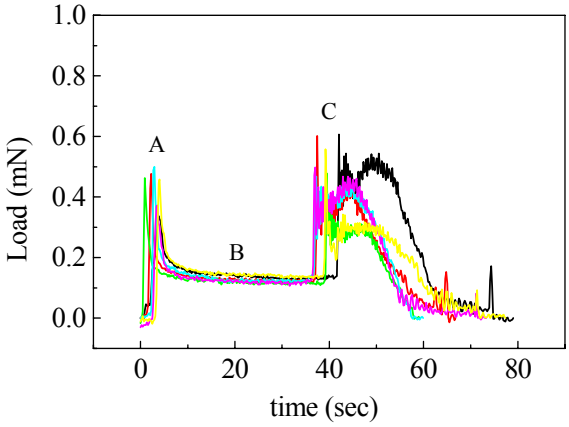

Fig.4 Load-time curves for spider viscid liquid tested using a home made surface tension meter.

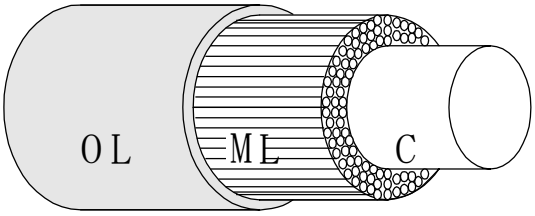

Fig.5 Schematic illustration of dragline microstructure.
OL; Outer layer insensitive to rain and fog, ML; Middle Layer with oriented micro-fibrils supporting strength, C; Core with amorphous substance.

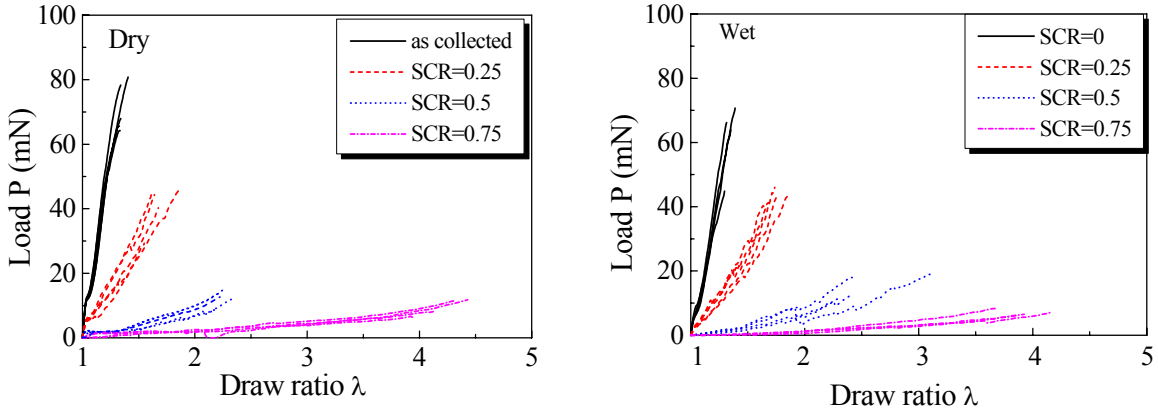

(a) dry state (b) wet state

Fig.6 Load-draw ratio curves for draglines with different SCRs under (a) dry and wet states.

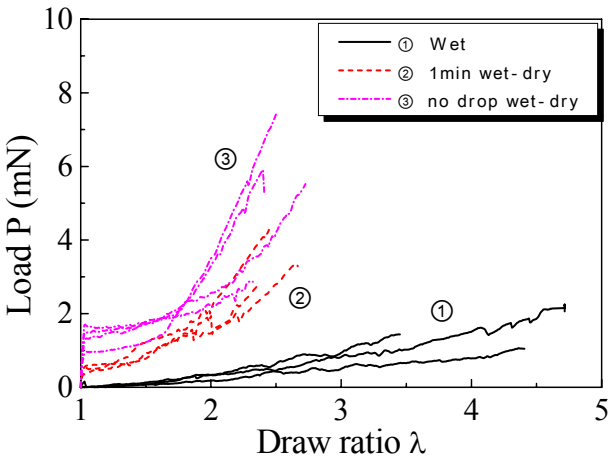

Fig.7 Load-draw ratio curves for capture thread under different conditions.

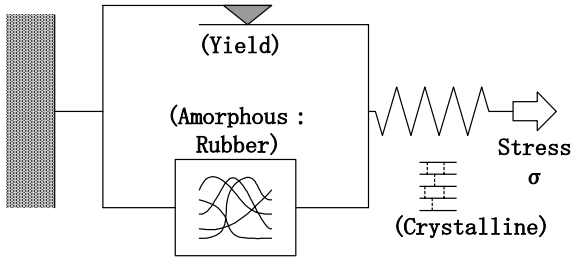

Fig.8 3-elements model for deformation of spider thread.

ORAL REFERENCE: 535

EFFECT OF BRIDGING LIGAMENTS UPON CRACK KINKING IN GRADED INTERFACES

Mark Hoffman[1], Lyndal Kidson[1] and Christoph Deneke[2]

[1]School of Materials Science & Engineering, University of New South Wales,
NSW 2052, Australia
[2]Department of Materials Science, Darmstadt University of Technology,
64287 Darmstadt, Germany

ABSTRACT

A graded interface involves a spatially changing composition gradient at an interface which removes the stress singularity which normally occurs at bimaterial interfaces. A number of analytical models have shown that, when a crack initiates perpendicular to the direction of a composition gradient, the cracks will kink as it propagates. This is a significant issue in the design of functionally graded materials. These existing analytical models show that the nature of kinking is controlled by the size and profile of the graded region and the elastic moduli of the two constituents. In this present work a model ceramic/polymer interface is constructed and the nature of fracture within this interface investigated experimentally. The sample developed ensures mixed-mode loading of the crack while ensuring no material composition gradient in the crack-tip field. Additionally, the choice of polyester and alumina means that there are negligible thermal residual stresses in the sample. It is found that the extensive crack bridging by the polymer phase occurs and that crack kinking is significantly less than that predicted by using existing analytical models which are based upon the elastic moduli of the ceramic and polymer. A numerical model is developed and demonstrates that it is the observed crack bridging which hinders crack kinking. An analytical model is then presented which confirms this hypothesis and also elucidates the influence of interface microstructure upon crack kinking in graded interfaces.

KEYWORDS

composite, graded, interface, kinking, fracture, crack, bridging

INTRODUCTION

Functionally graded materials often consist of a gradual spatial change from a ductile to a brittle material, e.g. a metal to ceramic. Often this results in the same type of structure as occurs in a ductile phase reinforced brittle material except, that in this case, there is a spatial change in the volume fraction of reinforcing phase. Because the 'matrix' and 'reinforcing' phases have different failure strains, the ductile phase leads to crack bridging and subsequent crack growth resistance or R-curve behaviour results.

A significant number of modelling studies have shown the effects of stiffness gradients upon strain energy release rate, G, in bodies containing a stiffness gradient for cracks which initiate both perpendicular and parallel to the gradient direction [1]. Crack deflection has also been considered where cracks initiate perpendicular to the gradient direction [2] and also observed experimentally, even in shallow stiffness gradients [3]. The majority of these studies however ignore two important aspects of fracture: (i) the effect of spatially changing fracture resistance, R, and (ii) the effect of an R-curve, which is an inevitable feature of many of the composite materials used in FGMs.

It has been shown that crack growth resistance behaviour may have a significant effect upon G for a crack which propagates parallel to the gradient direction from a brittle to a ductile composition or reverse [4, 5]. In this case no crack deflection occurs.

When a crack initiates perpendicular to the gradient direction both mode I and II stress intensity factors, K_I and K_{II}, result in a material containing a stiffness gradient. This leads to crack deflection. In many cases, it would appear advantageous for the crack to propagate towards the tougher material where, depending upon component shape, it may halt prior to ultimate failure. Crack bridging, however may cause significant reductions in mode I crack-tip stress intensity factors, and presumably has an effect upon mode II ones also. It is the purpose of this work to assist in elucidating the effects of R-curve behaviour, resulting from ductile phase bridges, upon crack deflection of a crack which initiates perpendicular to the gradient.

EXPERIMENTAL WORK

An experiment was devised which modelled the mixed-mode crack-tip loading in a gradient material. A piece of polyurethane foam was placed at one end of a mould into which an alumina slip was poured, penetrating the foam. This was then dried and sintered, during which time the foam pyrolised leaving a section at one end of the ceramic with interconnecting porosity. This was then placed into another mould and polyester resin poured in, penetrating the porous section of the ceramic. The sample was then machined into a single-edge tensile sample with a sharp-tipped notch placed perpendicular to the loading direction as shown in Fig. 1. The sample was ~40 mm wide by ~10 mm thick with the composite 'interface' region being ~10 mm high. Notches were placed at varying positions across the gradient with a notation of 0 closest the polymer and 1closest the ceramic, as shown in Figure 2. The composite region was measured to contain ~45vol% ceramic and was ~11% porous due to incomplete penetration of the polyester resin.

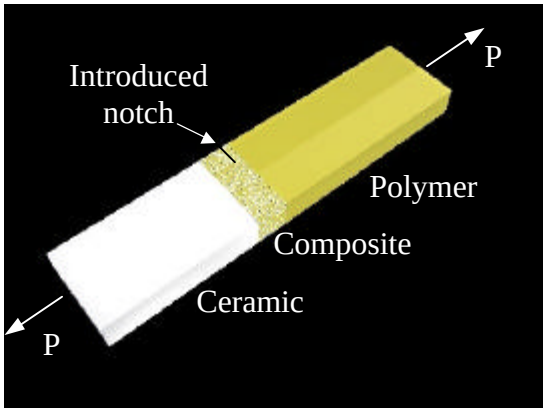

Figure 1: Schematic representation of single-edged tensile sample

The sample was then loaded to fracture. Figure 2 shows the nature of crack propagation and deflection, observed after failure. It was found that the fracture energy/area uncracked region was in the order of 650-900 J/m^2, depending upon initial crack position, compared to 55 J/m^2 for a similar bimaterial interface. Crack deflection occurred due to mixed mode loading resulting from the stiffness gradient along the sample and across the crack plane. The crack deflection angle, θ, was invariably positive and in the direction of the more compliant polymer. As intrinsic toughness was constant across the interface, this deflection could not be due to changing intrinsic fracture resistance. The deflection angle as a function of crack propagation in the initial crack plane was determined from a digitised post-failure image and results are shown in Figure 3.

It can be seen that as the crack propagates the deflection angle decreases. The fracture surface revealed evidence of crack bridging by the polymer phase with ligaments appearing to debond from the ceramic.

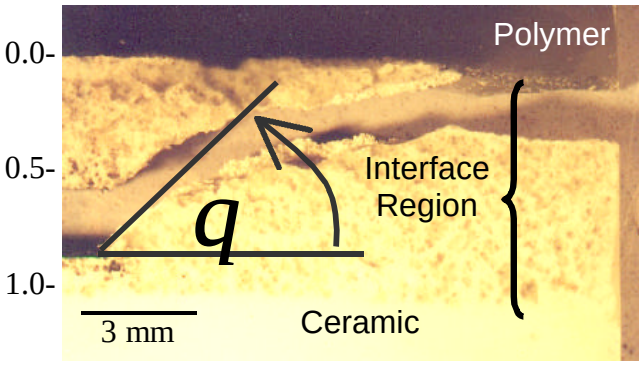

Figure 2: Fractured sample showing crack deflection, θ, with 'interface' and nomenclature used to define position of initial crack within the interface (0.0, 0.5 and 1.0 positions).

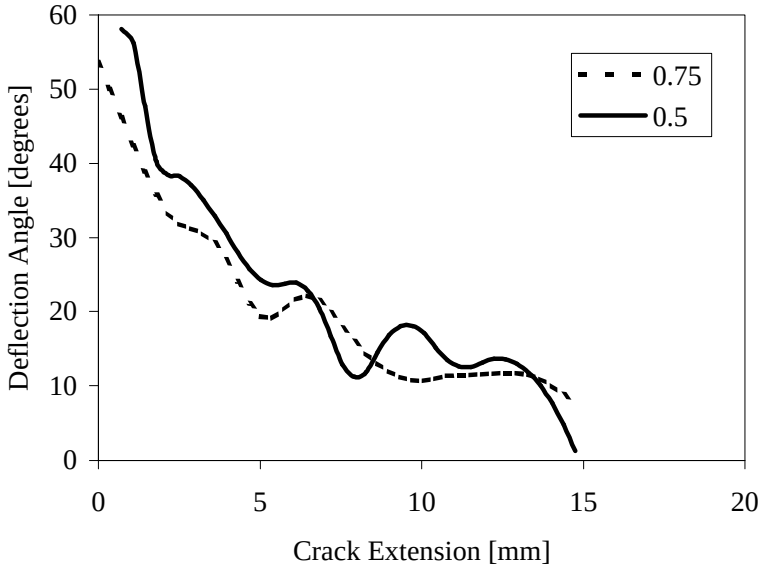

Figure 3: Experimentally determined crack deflection angle as a function of crack extension for initial cracks at the 0.75 and 0.5 position

FINITE ELEMENT MODELLING

A two-dimensional finite element model of the test piece was made using the Ansys FEM package. Plan2 elements were used in plane strain. These elements can handle the singularities associated with a crack tip. Cracks were introduced at 0.3, 0.5 and 0.7 positions with the Young's moduli of the Al_2O_3 and polyester taken to be 440 and 4.5 GPa, respectively, with Poisson's ratios of 0.4 and 0.22. An effective mean approximation was used to calculate the Young's modulus of the composite region, E_c, as 87.05 GPa and Poisson's ratio taken to be 0.3 with volume fraction of ceramic taken as 0.6. Crack bridges were introduced in the 0.5 crack position model as Beam3 elements with a diameter of 0.2 mm and initial length of 0.5 mm and with elastic properties of the polymer.

Using the co-ordinate system shown in Fig. 4, K_I and K_{II} for the crack were calculated from displacements of the crack face nodes in the directions perpendicular and in-plane to the crack direction, v and u, by solving:

$$v = \frac{K_I\left(1-\nu^2\right)}{E_c}\sqrt{\frac{8x}{\pi}} \quad (1)$$

$$u = \frac{K_{II}\left(1-\nu^2\right)}{E_c}\sqrt{\frac{8x}{\pi}} \quad (2)$$

where x is the distance from the crack tip. These were then used to determine the hoop stress around the crack tip:

$$\sigma_{\theta\theta} = \frac{1}{\sqrt{2r}}\left[K_I \cos^2\frac{\theta}{2} - \frac{3}{2} K_{II} \sin\theta \right] \cos\frac{\theta}{2} \qquad (3)$$

The angle of crack deflection, θ, was then determined by calculating the value of θ for which $\sigma_{\theta\theta}$ was maximum. Following this another model was constructed in which the crack was incremented ~1 mm in the direction of the calculated deflection and the process repeated.

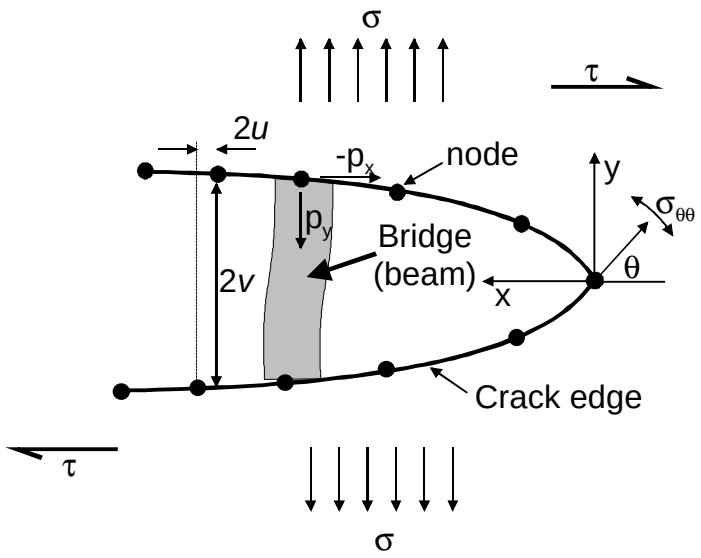

Figure 4: Model of crack showing bridging fibre and nomenclature used in calculations

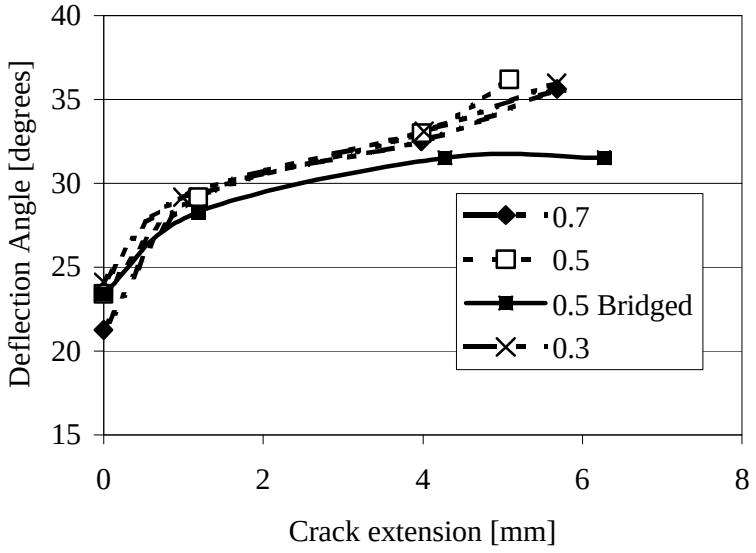

Figure 5: Crack deflection angles as a function of crack extension for bridged and unbridged cracks as calculated in FE model.

Figure 5 shows the calculated deflection angles as a function of crack extension for an unbridged crack with initial positions of 0.3, 0.5 and 0.7 and for a bridged crack with initial position of 0.5. It can be seen that the crack deflects towards the polymer as observed in the experiments. It can also be seen that for the unbridged crack models that the deflection angle *increases* as the crack propagates. This is in contrast to the experiment where the deflection angle *decreased* with crack extension. However, when crack bridges are incorporated into the model then the crack deflection is less than an unbridged crack and, as crack extension becomes large, begins to decrease. This analysis presents only a qualitative comparison with the experimental work as elastic constants and bridge geometry are dissimilar.

ANALYTICAL MODEL

In the FE model the effect of ligament diameter and stiffness and applied stress intensity were not considered. An analytical model is now developed to elucidate these effects upon crack defection for a bridged versus an unbridged crack.

A phase angle is used to describe the extent of mode mixity:

$$\psi = \tan^{-1}\left(\frac{K_{II}}{K_I}\right) \tag{4}$$

Considering Fig. 4, when a bridged crack is loaded in mixed mode then the bridge causes crack closure stresses both perpendicular, p_y, and parallel, p_x, to the crack plane. These lead to a resistance energy in both mode I and II directions according to:

$$R_{II} = 2\int_0^{u^*} p_x \, du \tag{5}$$

and

$$R_I = 2\int_0^{v^*} p_y \, dv \tag{6}$$

where u* and v* are crack face displacements at the position of the crack bridge furthest from the crack tip which was taken to be 20 times the fibre diameter in this example. This leads to crack-tip shielding, K_s, and Eq(3) becomes, for a bridged crack:

$$\sigma_{\theta\theta}^{br} = \frac{1}{\sqrt{2r}}\left[\left(K_I - K_s^I\right)\cos^2\frac{\theta}{2} - \frac{3}{2}\left(K_{II} - K_s^{II}\right)\sin\theta\right]\cos\frac{\theta}{2} \tag{7}$$

where $K_s = \sqrt{E_c R}$ separately for modes I and II.

To obtain the crack closure function, p, it is assumed that the bridging fibre acts as an elastic beam. There is assumed to be fibre delamination of length, L, equivalent to twice the fibre diameter, d, prior to loading. In Mode I the fibre acts as a beam loaded in tension while in mode II it is assumed to be fixed at the crack faces leading to a bending moment. Bending moments due to p_y in mode II are assumed to be negligible for simplification of calculations. The beam is assumed to be rectangular with width d and unit depth.

One then obtains:

$$p_y = \frac{E_f d}{L} \cdot v \tag{8}$$

and

$$p_x = \frac{E_f}{10} \cdot \left(\frac{d}{v}\right)^3 u \tag{9}$$

where v and u are defined in equations (1) & (2).

Figure 6 shows the calculated extent to which crack bridging reduces the deflection angle of a crack under mixed-mode loading. It can be seen that increasing the fibre diameter, and consequently the bridging length, and fibre stiffness reduces the deflection angle. It was also found (not shown) that, as applied stress intensity factor ($K^* = \sqrt{K_I^2 + K_{II}^2}$) is increased, the deflection angle decreases. It should be noted that this does not represent an equilibrium solution because for a bridged crack (1) and (2) are functions of (K-K_s) and not just K as taken here. Nevertheless, the relative effects of bridging upon $\sigma_{\theta\theta}^{br}$ should remain correct.

DISCUSSION

Crack deflection is a result of mixed-mode loading which is inherent to a crack propagating in a material containing a stiffness gradient. Numerical and analytical calculations show that decreasing crack deflection with crack extension, which was observed in the experiment, can be explained by the effects of the observed fibre bridging.

While the introduction of a graded interface may enhance the structural integrity of a material joint, the benefits that may be obtained by a crack deflecting into a more compliant and often tougher material, may be not fully realised. This is because crack bridges, inherent to a crack propagating in a composite of two materials with different failure strains, may reduce the extent of crack deflection such that the crack propagates through a more brittle region of the gradient structure.

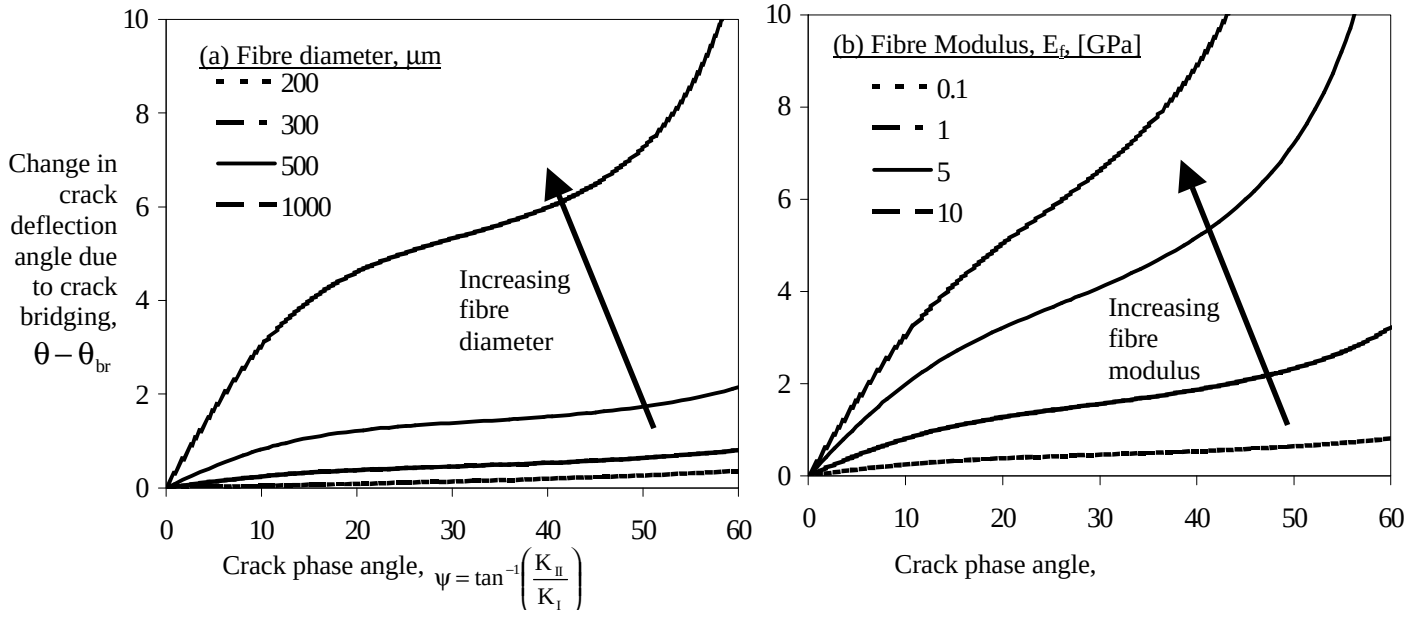

Figure 6 Effect of fibre (a) diameter and (b) modulus upon crack deflection (in degrees) as a function of phase angle (in degrees) of applied stress intensity factors.

CONCLUSIONS

From this work a number of conclusions can be made in regards to crack deflection of a crack propagating perpendicular to the direction of spatial material gradient which incorporates a stiffness gradient:

1. Crack bridging leads to a reduction in the extent of crack deflection and that
2. This is dependent upon the (a) diameter, (b) stiffness, (c) bridging length of the bridging fibres and also upon the (d) applied stress intensity factor.

ACKNOWLEDGEMENTS

A/Prof. Don Kelly of the Department of Mechanical Engineering, University of NSW, is thanked for his assistance with the FEM package. This work was supported by an Australian Research Council Large Research Grant.

REFERENCES

1. F. Delale and F. Erdogan (1983) *J. Appl. Mechanics,* **50** 609-14
2. N. Noboru and F. Erdogan (1994) *Eng. Fracture Mechanics,* **47**[4] 533-545
3. H. Li, J. Lambros, B. A. Cheeseman, M. H. Santare, Int. J. Solids Structures (2000) 37, 3715-32
4. Z.-H. Jin and R.C. Batra (1998) *Mat. Sci. & Eng. A,* **242** 70-6
5. T.-J. Chung, A. Neubrand, J. Roedel, and T. Fett. to be published in Proceedings of FGM2000, Estes Park, CO, USA 2000

POSTER REFERENCE: ICF10039OR

EFFECT OF CRACK ORIENTATION AND WELDING PROCESS ON J-INTRGRAL VALUES

Qingfen Li, Li Li, Shengshan Yang, Shanglin Yang and Shu-tong Yin

College of Mechanical & Electrical Engineering
Harbin Engineering University, Harbin 150001, China

ABSTRACT

A series of tests was performed with SENB specimens on a Titanium alloy. Results of seven groups of specimens show that the j-integral values of L-T direction specimens are much higher than those of L-S ones. The J-integral values of rolled ring are as : $J_{C-R} > J_{C-L} > J_{L-R}$. And that the J values of welded joint and HAZ are obviously smaller than those of the base metal. It signifies that the welding process can result in a reduced toughness of Ti-alloy and the effect of crack orientation on toughness value is not negligible for engineering applications.

KEYWORDS:

J-integral, Ti-alloy, crack orientation, welding process

INTRODUCTION

J-integral meathd plays a significant role in elastoplastic fracture mechanics. As an important fracture characteristic parameter, it is already well developed and extensively used in engineering prictice[1]. The heat affact zone (HAZ) is in many cases considered to be the most critical part of a welded structure with regard to unstable fracture. It is evident that the designers need to know the fracture toughness of welded joint, HAZ and parent plate as affected by the heat of welding, since the welded metal, the HAZ and the parent material normally have different fracture toughness. Studying the effect of welding process on J-integral value for Ti-alloy has been proved to be very useful for engineering applications. An experimental investigation is therefore carried out in this paper. Besides, the effect of crack orientation on J value is also investigated, because in some materials, such as forging, extrusions or plates, crack orientation can have an important bearing on fracture toughness measured.

EXPRIMENTAL PROCEDURE

material and Specimens

A chinese Ti-alloy plate and rolled ring were used. Their chemical composition is given in Table 1, and the mechanical

properties are given in Table 2.

Three-point sigle-edge noched bend (SENB) specimens were used for J-integral tests. The size is shown in Figure1. Based metal, welded joint and HAZ material were used to make different test specimens. Specimens made from the Ti-alloy plate were cut along L-T and L-S direction (see Figure 2). and those made from the Ti-alloy rolled ring were obtained along C-R, R-L and L-R dirrection respectively. (see Figure 3).

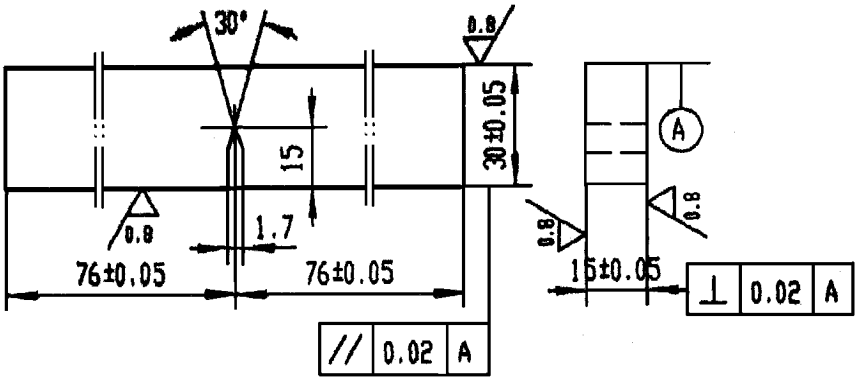

Figure 1: SENB specimen

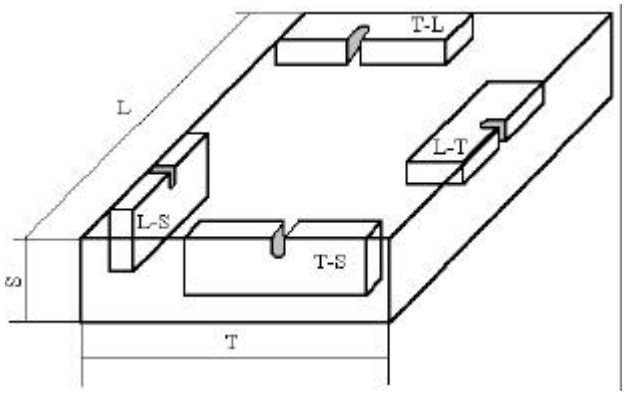

Figure 2: Specimen orientation for a plate

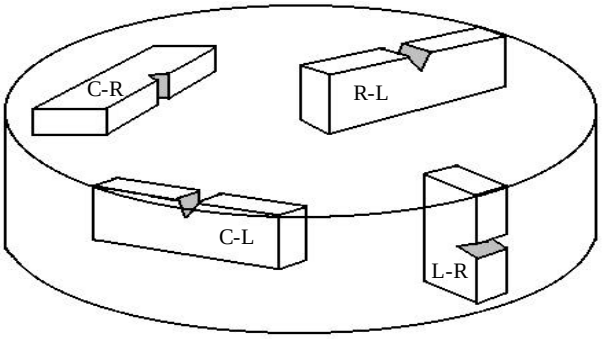

Figure 3: Crack plane orientation for a rolled bar

TABLE 1
CHEMICAL COMPOSITION

	Ti	Al	B	Fe	Si	C	N	H	O
Plate	95.57	4.0	0.005	0.23	0.05	0.025	0.024	0.005	0.084
Rolled ring	95.64	3.975	0.005	0.215	<0.05	0.016	0.023		0.073

TABLE 2
MECHANICAL PROPERTIES

	σ_b (MPa)	$\sigma_{0.2}$ (MPa)	$\delta\%$	E(MPa)	ν	a_{KU} (J/cm^2)
Plate	682	605	18.5	1.106×10^5	0.34	74.9
Rolled ring	712	615	16.3	1.310×10^5		71.4

Experimental Procedure

The J-integral tests were carried out on a Chinese WE-30 material testing machine of 300 KN capacity and in accordance with GB2038-91 standard[2]. Specimens have been precracked in fatigue. Load P versus load-point displesment Δ is recorded autographically. After off-loading, specimen crack fronts were marked by re-fatigue and then specimens were broken at low temperture. Crack length a and crack extension Δa measurements were made according to the nine-point-average procedure. A 50-fold enlargement optical micrometer was used to measure a and Δa. All tests were mdae at room temerature, approximately 22-26°C.

The J-integral values were calculated according to the following formula :

$$J_R = \frac{1-\nu^2}{E}\left[\frac{P_s}{BW^{\frac{1}{2}}}Y\left(\frac{a}{W}\right)\right]^2 + \frac{2U_P}{B(W-a)}$$

RESULTS AND DISCUSSIONS

The exprimental results of J-integral values of seven groups of specimens are shown in Figure 4-10. From Figure 4 and 5, we can see that the J values of L-T direction specimens are much higher than those of L-S ones. It can also be perceived from Figure 8, 9 and 10 that the J values of rolled ring are as follow :

$$J_{C-R} > J_{R-L} > J_{L-R}$$

This means that in Ti-alloy material, crack orientation has an important effect on fracture toughness. It is generally because of inclusions or intermetallic constituents which assist the crack by nucleating voids. Proper design and selection of crack orientation is therefore important for engineering strcture.

Figure 4, 6 and 7 shown that the J values of the welded joint and HAZ are obviously smaller than those of the base metal. it signifies that the welding process can result in a reduced toughness of Ti-alloy. Therefore, the inhomogeneity of the welded joint will bring about a problem in using Fracture Mechanics to assess welded structures. For example, cracks located in the welded joint or HAZ may grow to a critical size and propagate rapidly but then arrest when they enter the parent plate. Likewise, a slow-growing crack in the base metal could suddenly accelerate when entering the

welded joint or HAZ.

From our results, we can see that the fracture behaviour of the Ti-alloy is affeted by the welding process and also by the crack orientation. These effects are not negligible for engineering applications.

Because of space limitations, a further analysis and discussion will be conducted in a follow up paper.

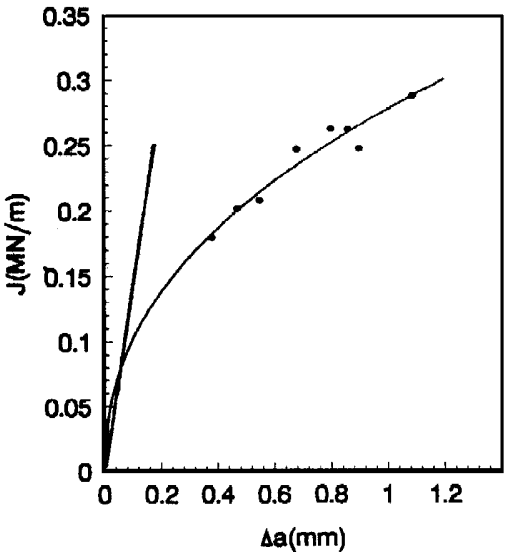

Figure 4: J vs a of base metal plate(L-T)

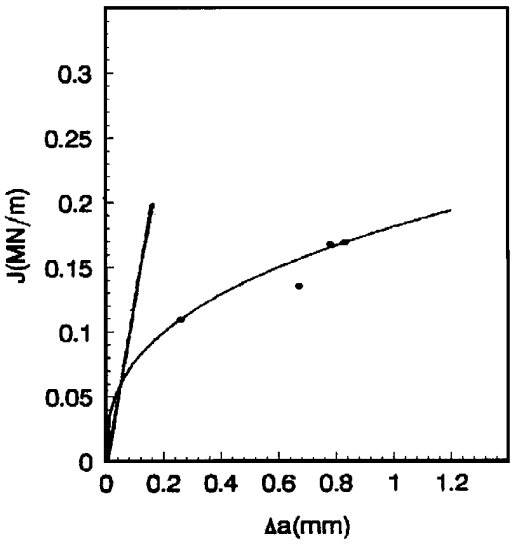

Figure 5: J vs a of base metal plate(L-S)

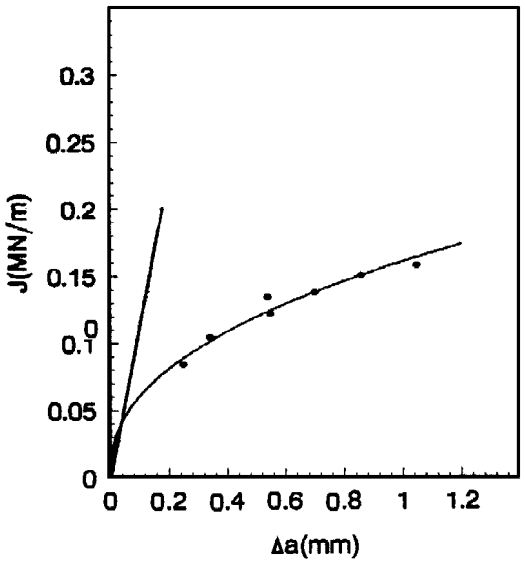

Figure 6: J vs a of HAZ plate(L-T)

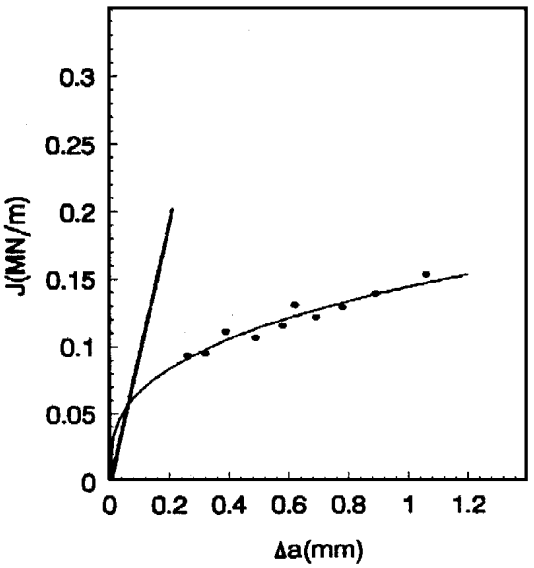

Figure 7: J vs a of welded joint plate(L-T)

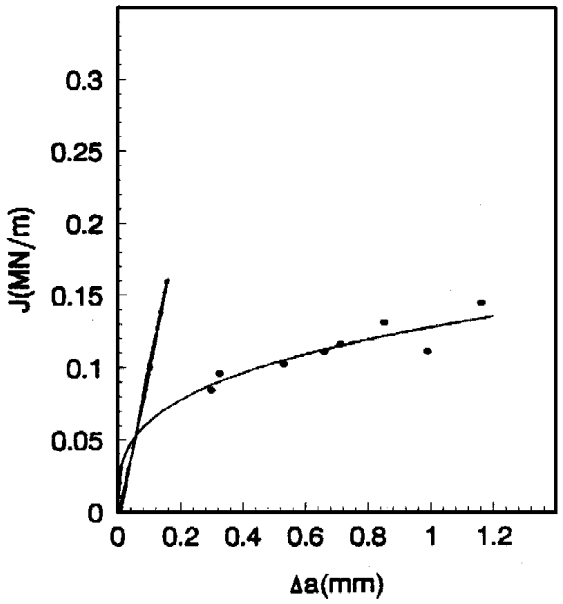

Figure 8: J vs a of rolled ring (C-R)

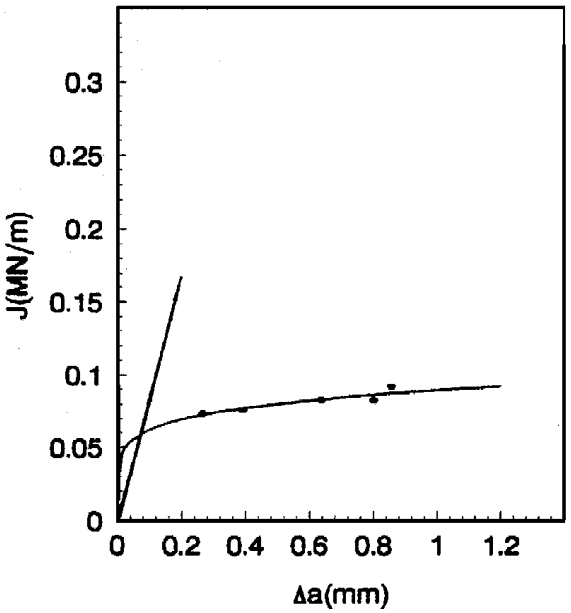

Figure 9: J vs a of rolled ring (L-R)

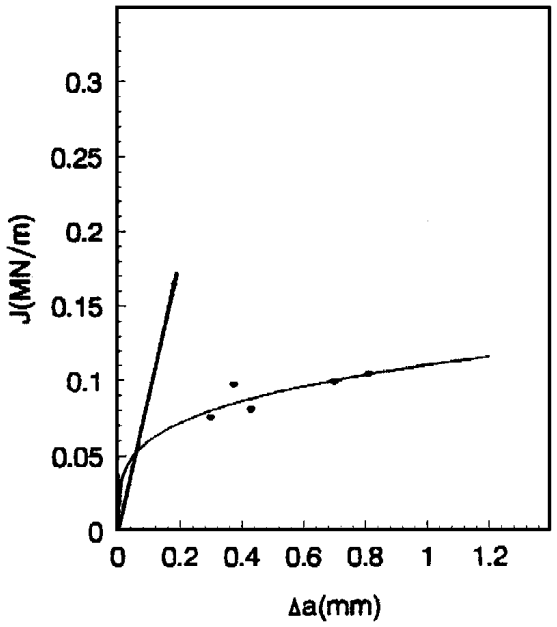

Figure 10: J vs a of rolled ring (R-L)

CONCLUSIONS

Crack orientation has an important bearing on fracture toughness. The J-integral values of Ti-alloy plate specimens taken along the L-T direction are much higher than those taken along the L-S direction. And the J values of rolled ring Ti-alloy are as follow:

$$J_{C-R} > J_{R-L} > J_{L-R}$$

The welding process can result in a reduced toughness of Ti-alloy. The J-integral values of the welded joint and HAZ

are obviously smaller than those of the base metal.

REFERENCES

1. Stanley, P.*Fracture Mechanics in Engineering Practice*, Applied Science Publishers Ltd, London, 1977.
2. *Standard Method of J-integral Testing, GB2038-91*, The Chinese Standard Institution, 1991.

ORAL REFERENCE: ICF100692OR

EFFECT OF CRACKING ON SERVICEABILITY OF FIBROUS CONCRETE

T. Ayano[1], M. A. Wafa[1] and K. Sakata[2]

[1]The Graduate School of Natural Science and Technology, Okayama University, 3-1-1, Tsushima-naka, Okayama 700-8530, JAPAN
[2]Department of Environmental and Civil Engineering, Faculty of Environmental Science and Technology, Okayama University, 3-1-1, Tsushima-naka, Okayama 700-8530, JAPAN

ABSTRACT

In many types of concrete structure loss the serviceability due to wide cracking or large deflection, and it should be repair it as early as possible. As very important structures, such as the tunnel of super express railway, which has a drop of concrete fragment, was a lead to severe social accident. The fiber is expected to be useful in order to improve the serviceability and to prevent a drop of concrete fragment. The performance of concrete with fibers is judged by the flexural toughness obtained by load-deflection curves. The flexural toughness of concrete is different by the different types of fiber and it can express well the toughness of RC members at failure. Sometimes, it is difficult to use the flexural toughness in order to judge the behavior of concrete structures under service load. From the result of cracking on concrete beam cyclic applied load, the necessity of adequate method to judge the performance of concrete with different types of fiber is discussed.

KEYWORDS

Cracking, serviceability, flexural toughness, polypropylene fibers, steel fibers

INTRODUCTION

There are several types of fiber for concrete. They have their own characteristic, such as, steel fibers has high dynamical performance, but it is rust [1, 2]. On the other hand, polypropylene fibers is elastic and flexible, it does not pierce the hands or the feet of the workers under construction. But concrete with polypropylene fibers can not be expected as high toughness at failure as concrete with steel fibers [3]. Because the Young's modulus of polypropylene fibers is about one tenth that of steel fibers, almost it is the same as that of concrete. If the fibers is used in order to improve the toughness of concrete structures at failure, steel fibers may be the best and the flexural toughness obtained by load-deflection curves is good remarks to express the performance of concrete with fibers.

The purpose of the usage of fibers is diversified. Sometimes, it is used to restrict the cracking due to drying, or it is used to prevent the spalling of concrete fragment [4, 5]. Recently, the fibers are also used in order to improve the serviceability of concrete structures. In these cases, it may be inadequate to use the flexural toughness to decide the type of fiber to be used.

TABLE1
MIX PROPORTIONS OF CONCRETE

Max size (mm)	Air (%)	Slump (mm)	W/C (%)	s/a (%)	Weight per unit volume (kg/m^3)				
					W	C	S	G	SP
20	2.0	150	46.0	45.0	159	350	800	1,040	1.75

SP: Superplasticizer

The concrete structures are continually subjected to oscillatory loads. The stresses due to the oscillatory loads cause fatigue in such structures. The phenomenon of irreversible and progressive damage in a material subjected to cyclic stress is called fatigue. Generally, concrete structures are designed as the reinforced steel is yielded. The failure of concrete structures by fatigue is also strongly affected by the yield of steel. On the other hand, a crack of concrete can form and then grow by fatigue and concrete structure loses the serviceability before the failure of concrete structure occurred. The growth of fatigue cracking in concrete is attributed to the inherent weakness of concrete in tension. Potentially useful improvements in the mechanical behavior of concrete can be affected by the incorporation of fibers [6].

In this study, the effects of the type of fibers that influence the composite behavior of reinforced concrete have been investigated under cyclic loading conditions. The aim was to quantify the delay in the fatigue crack initiation and further propagation in the concrete matrix due to the addition of fibers. In this study, two types of fiber was used, either polypropylene or steel fibers which are different especially in Young's modulus. The method to judge the performance of concrete with different types of fiber under service load is investigated.

EXPERIMENTAL PROGRAM

The proportioning of the concrete mixtures for testing is summarized in Table 1. Superplasticizer admixture was used as 0.5 % of the total cement. All concrete mixtures were prepared with ordinary Portland cement with 3.15 g/cm^3 density. The fine aggregate used in concrete was natural river sand with 2.55 g/cm^3 density and 2.3 fineness modulus. The coarse aggregate was crushed sand stone with 20 mm maximum size and 2.73 g/cm^3 density. Two types of fiber, either polypropylene fibers or steel fibers have generally been used in RC structural members with either 0.5 % or 1.0 % by volume. The fibers were replaced with a part of aggregate. The diameter and length of each fibers are 0.6 mm and 30 mm, respectively. The densities of steel and polypropylene fibers are 7.65 g/cm^3 and 0.92 g/cm^3, respectively.

In the test for flexural static and cyclic loading, four points loading was applied to the specimen. Deflection measurements were obtained using a dial gage accurate to 0.01 mm. Measurements were recorded at mid-span. Cracks width was measured at the bottom of specimen using a microscope reading to 0.02 mm. The RC T-Beam tested in flexural cyclic loading is shown in Figure 1. The load fluctuated between 10 % and 60 % of the ultimate load obtained in static flexure test, that is, between 147 kN and 49 kN. The test loads were applied at 300 cycles per minute (5 Hz). The crack width was measured when each T-Beam was loaded up to the upper limit, 147 kN statically.

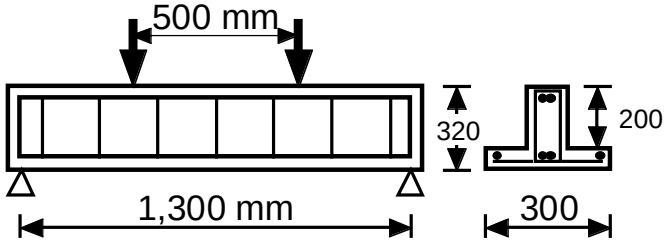

Figure 1: Set up of RC T-beam

EXPERIMENTAL RESULTS AND DISCUSSION

Figure 2 shows the load-deflection curves for concrete with different types of fibers. A significant difference in performance between steel and polypropylene fibers is found in the static flexural test. The flexural toughness is defined as the potential to absorb the energy with cracking. The area enclosed by load-deflection curve shows the flexural toughness. Japan Society of Civil Engineers recommends to use the flexural toughness factor σ_b obtained by Eqn. 1.

$$\sigma_b = \frac{T_b}{\delta_{tb}} \frac{l}{bh^2} \qquad (1)$$

where, δ_{tb}: 1/150 of span length, T_b: the area enclosed by load-deflection curves within the deflection equal to δ_{tb}, l: length of span, b: width of beam, h: height of beam.

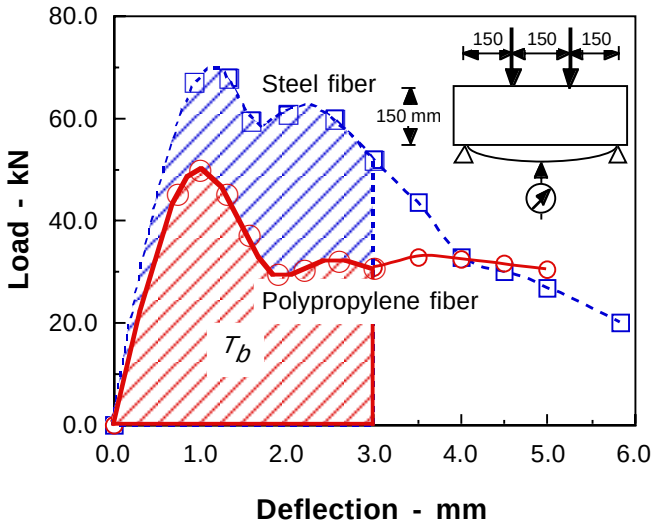

Figure 2: Load-Deflection curves for plain concrete reinforced with different type of fibers

The flexural toughness factors σ_b of concrete with polypropylene and steel fibers are 1.95 N/mm^2 and 4.36 N/mm^2, respectively. When the flexural toughness factor is used, the flexural toughness of concrete with polypropylene fiber is estimated as half as that with steel fiber. The load deflection curves of the two types of beam are shown in Figures 3 and 4. The results shown in Figure 3 and 4 were obtained from the beam with 2 stirrups and 4 stirrups, respectively. Irrespective of the number of stirrups, the largest increase in toughness was obtained when the concrete beams were reinforced with steel fibers followed by those reinforced with polypropylene fibers. It is clear that the flexural toughness factors σ_b can follow the toughness of concrete beams at failure.

Figures 5 and 6 show the number of cracks with load cycles. In Figure 5, the number of cracks of concrete with steel fibers is compared with that of control. It is noticed that, steel fibers have excellent performance in resisting crack initiation and propagation; thus; the ability of resistance to cyclic loading is increased greatly. In Figure 6, the number of cracks of concrete with polypropylene fibers is compared with that of control. The number of cracks of control specimen before the applying of cyclic load is more than that of specimen with fibers. The number of cracks of control specimen was increased rapidly after the applying of cyclic load and

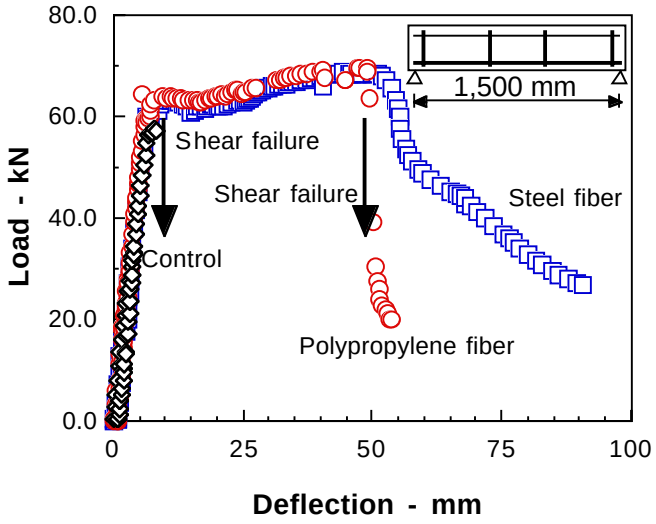

Figure 3: Load-Deflection curves for RC beam reinforced with different type of fibers

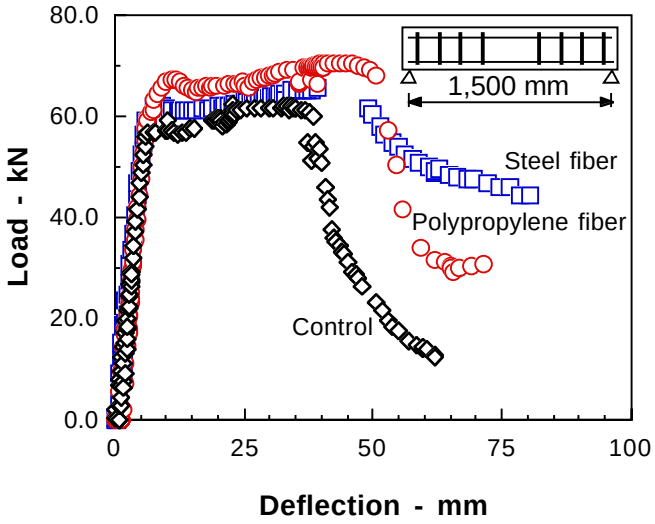

Figure 4: Load-Deflection curves for RC beam reinforced with different type of fibers

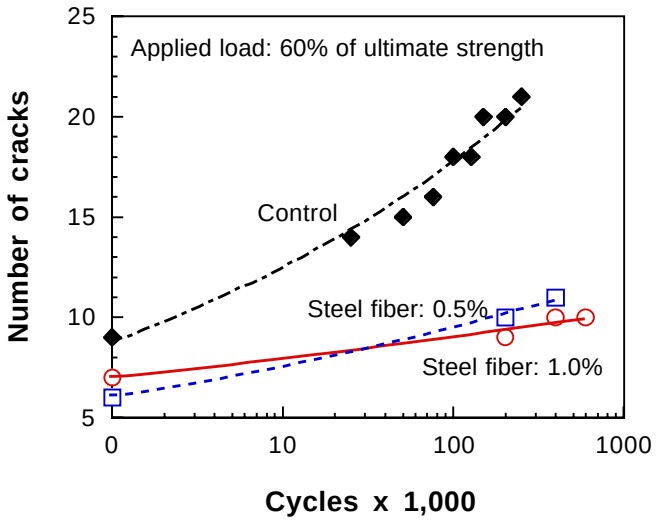

Figure 5: Effect of number of load cycles on number of cracks

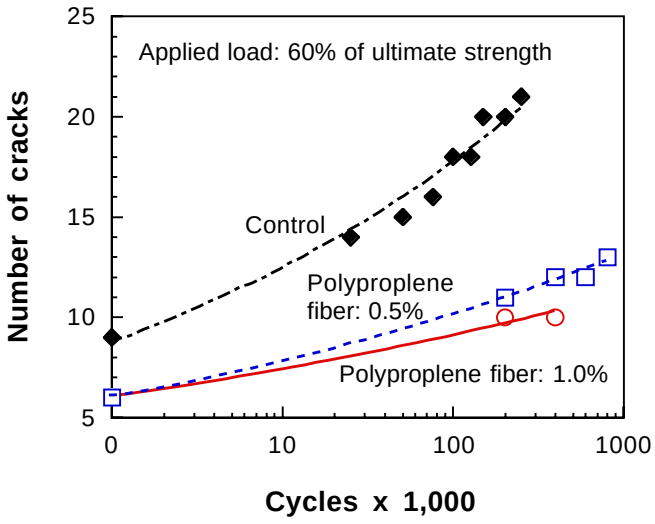

Figure 6: Effect of number of load cycles on number of cracks

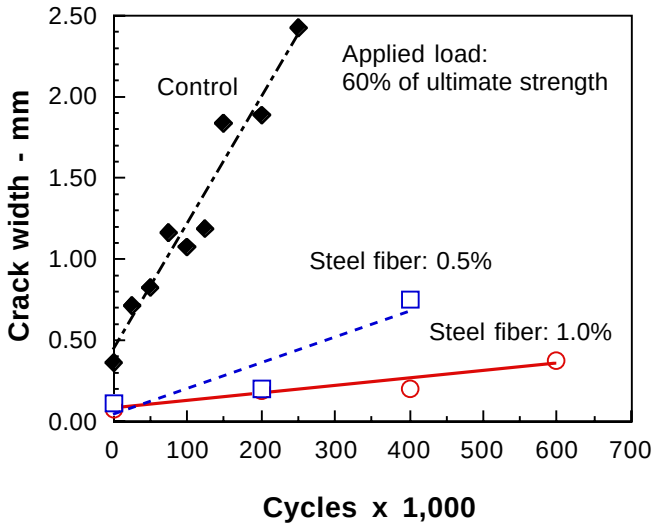

Figure 7: Effect of number of load cycles on crack width

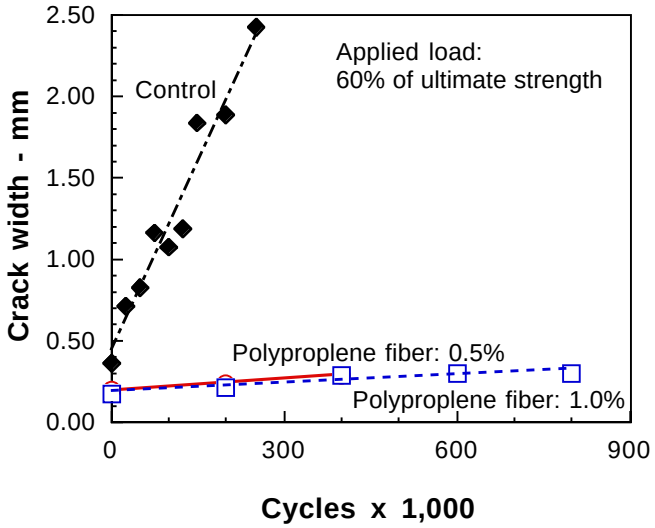

Figure 8: Effect of number of load cycles on crack width

broken at 250,000 cycles. On the other hand, the increase of the number of cracks of beams with fibers be less. The difference between concrete with polypropylene fibers and steel fibers in the number of crack is small.

Figures 7 and 8 show the crack width with the increase in number of load cycles. In Figure 7, the crack width of concrete with steel fibers is compared with that of control. In Figure 8, the crack width of concrete with polypropylene fibers is compared with that of control. Crack width which shown in these figures is average of the crack width for all cracks of each specimen. The development of crack width of control beam is quite different from that of beam with fibers. The crack width of control beam is over 5 times as wide as that of beam with fibers. The difference between concrete with polypropylene fibers and steel fibers in crack width is small, too.

Photos 1 and 2 show the control beam and polypropylene fibers beam just before failure. As clear from these photos, the decline of serviceability of control beam can be confirmed. The failure cycles of fiber's beams is between 500,000 and 800,000 cycles. It is not clear whether the fibers has played a role in prolonging fatigue life or increasing the capacity of fatigue load, because the fatigue is estimated by the order of cycles when concrete beam is broken not by the number of cycles itself. It is noticed that the number of cracks and crack

Photo 1: Mode of failure of control beam

Photo 2: Mode of failure of polypropylene fibers beam

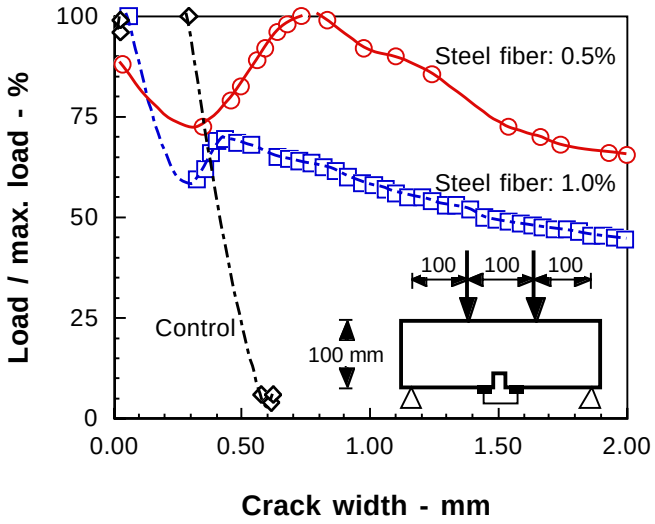

Figure 9: Effect of ratio of load / max. load on crack width

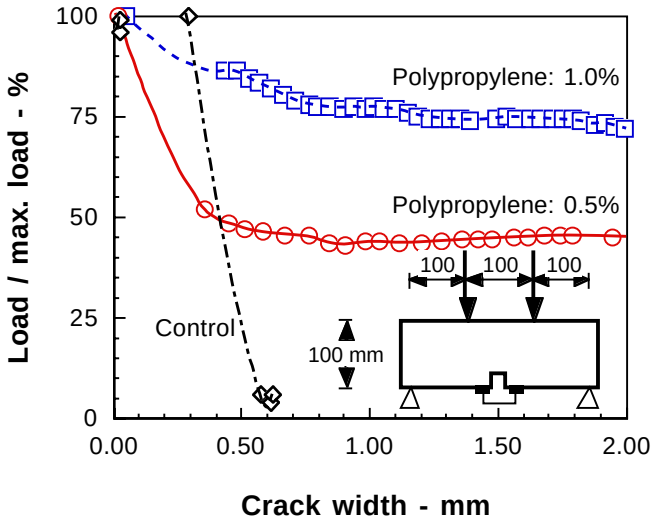

Figure 10: Effect of ratio of load / max. load on crack width

width is not increased so much when the fibers is used. The fibers can restrict the crack propagation under service load even if polypropylene fibers whose Young's modulus is about one tenth of steel fibers is used.

These results can not be explained the flexural toughness factor obtained by Eqn. 1. A number of previous experimental investigations have also established that cyclic loading not only affects the strength but also the serviceability, such as deflection and crack width, of reinforced concrete members [7].

Figures 9 and 10 show the relationship between crack width and load. The result shown in Figures 9 and 10 are obtained by using concrete with steel fibers and polypropylene fibers, respectively. The vertical line of these figures is the ratio between applied load and the maximum load. The crack width was measured at center of specimen. The specimen was made 5 mm raid to introduce the cracking. The control specimen was suddenly broken when the crack width reached at 0.5 mm. However, the concrete with fibers sustained the load of the half of maximum load at 2.0 mm crack width. The relationship between crack width and load of concrete with polypropylene fibers is almost same as that with steel fiber. The crack propagation under cycle service load may depend on the sustaining ability of load after cracking.

CONCLUSIONS

The load deflection curves indicated the advantage of fibrous concrete versus control concrete in obtaining higher toughness. Also, the development of crack width of specimen without fibers was quite different than those with steel fibers or polypropylene fibers.

By comparison between steel fibers and polypropylene fibers in performance of flexural toughness and crack propagation, it was found that, steel fibers have good performance in flexural toughness than that of polypropylene fibers, on the other hand, steel fibers and polypropylene fibers have the same performance in crack propagation.

In spite of the Young's modulus of polypropylene fibers is about one tenth of steel fibers, it was noticed that the number of cracks and crack width was not increased so much when even polypropylene fibers is used.

In spite of the flexural toughness can describe the toughness of concrete structural members with fibers at failure, it is not easy to use it in order to explain the propagation of cracking under service load.

It is necessary to express the sustaining ability of load after cracking by an adequate estimating method. In addition, the reliable and easy method to judge the performance of concrete with fibers is necessary that everybody can choose the adequate fibers in order to improve the serviceability of concrete structures.

REFERENCES

1. Sun, W., Gao, J. and Yan, Y. (1996) Study of the Fatigue Performance and Damage Mechanism of Steel Fiber Reinforced Concrete, ACI Materials Journal, Vol. 93, No.3, May-June, pp. 206-212.
2. S. P. Singh and S. K. Kaushik (2000) Flexural Fatigue Life Distributions and Failure Probability of Steel Fibrous Concrete, ACI Materials Journal, Vol. 97, No.6, November-December, pp. 658-667
3. Ayano, T., Abo El-Wafa, M., Yabuki, M., and Sakata, K., (2001), Resistance to Cracking due to Drying Shrinkage by Polypropylene Fiber, Proceedings of the Japan Concrete Institute, vol.22, No.2, pp.325~330
4. Hamada, T., Hikasa, J., Suemori, T. and Hirai T. (1999) Study on Concrete Reinforced by Vinylon Fiber, Proceedings of the Japan Concrete Institute, vol.21, No.2, pp.271~276
5. Kanemami A., Saeki N. and Horiguchi T. (1999) Cracking and Strength at Young age of Reinforced Concrete by Hybrid Fiber, Proceedings of the Japan Concrete Institute, vol.21, No.2, pp.259~264
6. Zhang, J. and Henrik, S. (1998) Fatigue Performance in Flexure of Fiber Reinforced Concrete, ACI Materials Journal, Vol. 95, No.1, Jan.-Feb., pp. 58-67.
7. Sun, W., Gao, J. and Yan, Y. (1996) Study of the Fatigue Performance and Damage Mechanism of Steel Fiber Reinforced Concrete, ACI Materials Journal, Vol. 93, No.3, May-June, pp. 206-212

ORAL/POSTER REFERENCE: 100340R

Effect of Electric Field Reversal on Crack Growth Behavior of Poled Piezoelectric Ceramic

G.C. Sih

Department of Mechanical Engineering and Mechanics, Lehigh University,
Bethelehem, PA 18015, USA
and
Institute of Engineering Mechanics, Hebei University of Technology, Tianjin 300130, China

ABSTRACT

A long standing unexplained crack growth behavior of poled PZT ceramics is that crack tends to grow longer under a positively applied electric field and shorter under a negatively applied field as compared to the situation when no electric field is applied. While this behavior was observed experimentally, the prevailing mathematical models have not been able to quantify the results. The attempted explanation speaks of separating the electrical and mechanical parts while realizing that the electromechanical energy field is coupled. The energy in a unit volume of material, once stored, could not distinguish the portion from the electric to the mechanical.

Based on the energy density criterion, an analytical approach is developed to show qualitatively the behavior of crack growth enhancement and retardation when the electric field is reversed. Crack growth segments are computed for the PZT-4 ceramic material to show that indeed a crack tends to grow longer and shorter depending on whether the applied electric is positive or negative. This confirms the experimental observation.

KEYWORDS: Piezoelectric, Crack Growth, Electromechanical

1. INTRODUCTION

Piezoelectric ceramics are prone to cracking because they are inherently brittle, an undesirable character that has limited the use of this class of materials. Much research has been done to understand how electrical and mechanical disturbances could lead to unexpected fracture. Indenters [1,2] have been dropped onto PZT (lead-zirconate-titanate) ceramic specimens to produce longer cracks when the poled direction coincides with that of the electric field. The opposite holds for electric field that is applied against the poled direction. The same phenomenon was observed in PZT-4 for a compact tension specimen with an edge crack [3]. Mathematical models have since been developed to quantify these observations without success. Controversies continue to prevail despite numerous unsuccessful attempts [4-6] of using the energy release rate or path independent integral as the fracture criterion. Only in recent times that the energy density criterion [7,8] was applied and resolved the long standing inconsistencies mentioned earlier [3,6].

In what follows, the energy density criterion shall be used to determine how crack growth would be

affected by reversing the direction of applied electric field with reference to the poled direction for a central crack in an infinite body made of PZT-4 material. The crack tip energy density function dW/dV is first computed using the equations of linear piezoelectricity. An energy density factor S near the crack tip can thus be defined; it has the units of energy release rate. The initiation of stable crack growth and rapid crack propagation correspond to dW/dV and S reaching their respective critical values, $(dW/dV)_c$ and S_c. Numerical results are presented to illustrate how the energy density factor is affected by sign change of the applied electric field while the energy release rate criterion has failed to account for such a behavior in the past.

2. THROUGH CRACK MODEL

Depicted in Fig. 1 is a central crack of length 2a in an infinite body. A remote electric field E and uniform mechanical stress σ are applied such that the macrocrack would extend along the x_1-axis while poling is directed in the positive x_3-axis. Plane strain in the x_1x_3-plane is assumed.

Figure 1: Line crack under electrical and mechanical load.

Figure 2: Crack tip decay of volume energy density

2.1 Coupling of electrical and mechanical effects

A complete description of cracking involves the process of initiation, growth and termination. For a solid subjected to both electrical and mechanical disturbances, the energy density function based on the theory of linear piezoelectricity can be computed as

$$\frac{dW}{dV} = \int_o^{\gamma_{ij}} \sigma_{ij} d\gamma_{ij} + \int_o^{D_i} E_i dD_i \quad . \tag{1}$$

In eq. (1), σ_{ij} and γ_{ij} are, respectively, the stress and strain components while E_i and D_i are components of the electric and displacement field. Even though the mechanical and electrical portion of the energy density function would appear to be separated in eq.(1), the equivalents forms of expressing eq. (1) in terms of stresses and electric displacements

$$\frac{dW}{dV} = \frac{1}{2}\sigma_{ij} H_{ijk\ell} \sigma_{k\ell} + \frac{1}{2} D_i \beta_{ij} D_j \tag{2}$$

or in terms of strains and electric fields

$$\frac{dW}{dV} = \frac{1}{2}\gamma_{ij} C_{ijk\ell} \gamma_{k\ell} + \frac{1}{2} E_i \varepsilon_{ij} E_j \tag{3}$$

show that the mechanical and electrical parts of dW/dV are always coupled. They cannot be separated as it was assumed in [3]. In eq. (2), H_{ijkl} and β_{ij} are the elastic and dielectric compliance constants while those in eq. (3) given by C_{ijkl} and ε_{ij} are the elastic and dielectric constants.

2.2 Energy density criterion

At the continuum scale level, the sharp crack tip is assumed to lie within a macroscopic size core region with radius r_o, Fig. 2. Mathematically speaking, the energy density function becomes unbounded as the crack tip is approached or as $r \to 0$ since

$$\frac{dW}{dV} = \frac{S}{r} \tag{4}$$

The relationship of eq. (4) is shown in Fig. 2 where S represents the area of the dW/dV versus r plot for a given level of dW/dV.

The form of eq. (4) does not limit the criterion of energy density to linear elasticity even though the inverse square root of r stress singularity would correspond to 1/r for dW/dV. Note from Fig. 2 that r adopts a much more general interpretation since it is simply the linear distance measured from the crack tip. The following hypotheses applied to dW/dV are in general valid for any nonlinear constitutive relations, large deformation theories with or without dissipation. When applied to a local region ahead of the crack tip, they can be stated as [9]:

- Hypothesis I: Location of crack initiation is assumed to coincide with the maximum of the minimum dW/dV or $(dW/dV)_{\min}^{\max}$.
- Hypothesis II: The onset of stable crack growth is assumed to occur when $(dW/dV)_{\min}^{\max}$ reaches a critical value $(dW/dV)_c$.
- Hypothesis III: Stable crack growth segments r_1, r_2, etc., are assumed to be governed by

$$\left(\frac{dW}{dV}\right)_c = \frac{S_1}{r_1} = \frac{S_2}{r_2} = \cdots = \frac{S_j}{r_j} = \cdots = \frac{S_c}{r_c} \tag{5}$$

The onset of rapid fracture is assumed to take place when

$$\left(\frac{dW}{dV}\right)_c = \frac{S_c}{r_c} \tag{6}$$

The ways with which S_c are related to K_{1c} for Mode I crack extension depends on the constitutive relations and the kinetics of cracks under consideration. For a crack under static load applied to an isotropic, homogeneous and elastic body, it has been shown in [9] that

$$S_c = \frac{(1+\nu)(1-2\nu)K_{1c}^2}{2\pi E_o} \tag{7}$$

in which ν is the Poisson's ratio and E_o the Young's modulus. For the PZT material considered in this work, the equivalent of eq. (7) takes the form

$$S_c = A_{11} + 2A_{14}\frac{g_{33}}{\beta_{33}} + A_{44}\frac{g_{33}^2}{\beta_{33}^2} \tag{8}$$

Here, A_{11} , A_{14} , A_{44} , g_{33} and β_{33} are complicated functions related to the elastic, piezoelectric and dielectric constants of the ferroelectric ceramics. The specific expressions can be found in [8]. Another set of B_{ij} connected with specifying electric field E can be defined instead of A_{ij} related specifying the electric displacements D.

2.3 Mode I crack extension

Referring to Fig. 1, both the applied stress σ and the electric field E are such that the crack would extend straight ahead along the x_1-axis where S possesses a relative minimum with reference to the angle θ in Fig.

1 such that Hypothesis I is satisfied. Under the above considerations, the work in [7,8] gives the expression of S for the present problem:

$$S = B_{11}K_I^2 + 2B_{14}K_I K_E + B_{44}K_E^2 \tag{9}$$

in which

$$K_I = \sigma\sqrt{\pi a} \qquad \text{and} \qquad K_E = E\sqrt{\pi a} \tag{10}$$

where both σ and E are constants. The quantities B_{11} , B_{14} and B_{44} for PZT-4 can be found in [7,8]. Substituting eqs. (10) into eq. (9), it can be shown that

$$S = K_I^2\left[B_{11} + 2B_{14}p + B_{44}p^2\right] \tag{11}$$

Defined in eq. (11) is a load parameter $p = E/\sigma$. It is now more pertinent to examine whether a crack would grow longer or shorter when the direction of the applied electric field is reversed by using the solution for no applied electric field as the base of reference.

3. ENHANCEMENT AND RETARDATION OF CRACK GROWTH

The phenomenon of crack growth enhancement and retardation due to applied electric field reversal has been known for sometime by experiments [1-3]. Attempts made in [3,6] to explain the observation have all failed because the energy release rate result could not distinguish a positive electric field from that of a negative one. Hence, the arguments presented for these unsuccessful attempts are also suspect.

3.1 Crack growth segments

Consider the situation in Fig. 1 where the crack is subjected to σ and E. The superscripts +, o and – will refer to, respectively, as the positive, zero and negative E field. The corresponding crack growth segments are r_1^+ , r_2^+ , …, r_1^o , r_2^o , …, and r_1^- , r_2^- , …, while the energy density factors are given by S_1^+ , S_2^+ , …, S_1^o , S_2^o , …, and S_1^- , S_2^- . Application of Hypothesis III governed by eq. (5) renders

$$\left(\frac{dW}{dV}\right)_c = \frac{S_1^+}{r_1^+} = \frac{S_2^+}{r_2^+} = \cdots = \frac{S_1^o}{r_1^o} = \frac{S_2^o}{r_2^o} = \cdots = \frac{S_1^-}{r_1^-} = \frac{S_2^-}{r_2^-} = \cdots = \text{const}. \tag{12}$$

For the jth segment of crack growth, eq. (12) gives

$$\frac{S_j^+}{r_j^+} = \frac{S_j^o}{r_j^o} = \frac{S_j^-}{r_j^-} \quad , \qquad j = 1,2,\cdots \tag{13}$$

What needs to be shown is that

$$S_j^+ > S_j^o \quad \text{and} \quad S_j^- < S_j^o \quad \text{for} \qquad j = 1,2,\cdots \tag{14}$$

and

$$r_j^+ > r_j^o \text{ and } \quad r_j^- < r_j^o \qquad \text{for} \qquad j = 1,2,\cdots \tag{15}$$

Refer to Fig. 3 for an illustration of eq. (15). Recall that positive and negative electric field refer, respectively, to E being in the same and opposite direction of poling.

3.2 Interaction of mechanical and electrical field

The interaction of mechanical and electrical field on crack growth can be exhibited by a plot of energy density factor and/or crack growth as a function of the parameter p or the ratio E/σ. Using the elastic,

piezoelectric and dielectric constants of PZT-4, numerical values of S in eq. (11) can be computed for $p \times 10^{-3}$ = -15, -10, -5, 0, 5, 10 and 15 Vm/N. Plotted in Fig. 4 are the normalized values of S as a function of p. The curve increases monotonically.

Figure 3: Enhancement and retardation of crack growth

Figure 4: Energy density and crack growth segment variations with positive and negative electric field strength

Once S can be computed numerically for situations where E changes sign, eq. (13) can be applied to show whether the inequalities in eqs. (15) would hold or not. The other curve in Fig. 4 corresponds to crack growth segments $r_j^{\pm}$ normalized to r_j^o. The point with coordinates $r_j^{\pm}$ = 1.0 and p = 0 corresponds to the crack growth segment r_j^o with E = 0. Summarized in Table 1 are the numerical values of r_j^+ and r_j^- normalized with reference to r_j^o. When E is positive r_j^+ / r_j^o is always greater than one.

TABLE 1

Normalized crack growth segments r_j^+ / r_j^o and r_j^- / r_j^o for PZT-4 and different $E/\sigma \times 10^{-3}$ values (Vm/N)

-15	-10	-5	0	5	10	15
0.765	0.814	0.894	1	1.132	1.290	1.474

Moreover, r_j^- / r_j^o is always less than one when E is negative. This implies that a crack would grow longer for a positive electric field. Shorter crack growth applies to a negative electric field. For comparing the relative magnitudes of r_j^+, r_j^o and r_j^-, the results in Table 1 are sufficient to validate the

experimental findings in [1-3]. There were no need to de-couple the electrical and mechanical effects nor was there the need to include nonlinear effects.

4. CONCLUSIONS

When material microstructure plays a role in failure analyses, the possibility of multiscale cracking should be considered even though it was not needed for illustrating the influence of electric field reversal on crack growth. For a quantitative assessment of the failure stress, however, microcracking would need to be modeled since the compliance of the specimen would be altered. The initiation and growth of the macrocrack would also be affected accordingly. Such a situation has been discussed in [8] where the interaction of micro- and macro-cracking was accounted for by introducing an additional length parameter.

Lacking at present is a knowledge of the initial states of the material microstructure, the behavior of which would depend sensitively on the stress/strain or energy density arising, say from the process of crystal nucleation and formation for metals. If the internal stresses trapped in the grains are of the same orders of magnitude as those induced by the applied loads, then the neglect of the influence of the initial states would leave any predictions in doubt. Such situations are no longer uncommon as the length scale of device components are being reduced to microns in size. Another seemingly innocent pitfall is the use of physical data extracted from test specimens that are orders of magnitude larger than the device under consideration. It appears that data correlation at the nano-, micro-, meso- and macro-scale requires extensive attention. Until the problem of scaling is better understood, the reliable use of ferroelectric ceramics in electronic devices leaves much to be desired.

References

[1] A. Tobin and Y. E. Pak, Effects of electric fields on fracture behavior of PZT ceramics, Smart Materials, ed. V. K. Varadan, 1916 (1993) 78-86.

[2] Y. E. Pak and A. Tobin, On the electric field effects in fracture of piezoelectric materials, Mechanics of Electromagnetic Materials and Structures, AMD-161/MD-42, ASME (1993)

[3] S. Park and C. T. Sun, Fracture criterion of piezoelectric ceramics, J. Am. Ceram. Soc., 78, (1995) 1475-1480.

[4] W. Yang and Z. Suo, Cracking in ceramic actuators caused by electrostriction, J. Mech. Phys. Solids, 42 (1994) 649-663.

[5] C. S. Lynch, W. Yang, L. Collier, Z. Suo and R. M. McMeeking, Electric field induced cracking in ferroelectric ceramics, Ferroelectrics, 166 (1995) 11-30.

[6] H. Gao, T. Y. Zhang and P. Tong, Local and global energy release rates for an electrically yielded crack in a piezoelectric ceramic, J. Mech. Phys. Solids, 45 (1997) 491-510.

[7] J. Z. Zuo and G. C. Sih, Energy density formulation and interpretation of cracking behavior for piezoelectric ceramics, J. of Theoretical and Applied Fracture Mechanics, 34(1) (2000) 17-33.

[8] G. C. Sih and J. Z. Zuo, Multiscale behavior of crack initiation and growth in ferroelectric ceramics, J. of Theoretical and Applied Fracture Mechanics, 34(2) (2000) 123-141.

[9] G. C. Sih, Mechanics of fracture initiation and propagation, Kluwer Academic Publishers, Boston, (1991).

ORAL/POSTER REFERENCE:

EFFECT OF FIBER COATINGS ON DETECTION OF TRANSVERSE CRACKS IN CFRP COMPOSITES USING FBG SENSORS

Y. Okabe, N. Tanaka, T. Mizutani, S. Yashiro, and N. Takeda

Graduate School of Frontier Sciences, The University of Tokyo
c/o Takeda Lab., Komaba Open Laboratories, The University of Tokyo,
4-6-1 Komaba, Meguro-ku, Tokyo 153-8904, JAPAN

ABSTRACT

FBG sensors have been applied to the detection of transverse cracks in CFRP cross-ply laminates using the sensitivity of the sensors to non-uniform strain distribution. However, there is the possibility that the resin coating of the FBG sensors will relax the non-uniform strain distribution and deteriorate the sensitivity of the sensors. Hence, in this study, the strain transfer from the 0° ply to the core of the optical fiber was calculated by a theory developed from the shear-lag model. As a result, it was found that the variation of axial strain in the core of a polyimide-coated FBG sensor was smaller than that of an uncoated FBG sensor. Nevertheless, the reflection spectra of the coated and uncoated FBG sensors calculated from the strain distributions were almost the same. This result shows that the coating of the optical fiber does not deteriorate the sensitivity of the FBG sensor for the detection of transverse cracks, and the coated FBG sensors can be used without removal of the fiber coatings.

KEYWORDS

Fiber Bragg grating sensor, CFRP, transverse crack, strain distribution, resin coating, shear-lag model.

INTRODUCTION

The authors have applied FBG sensors to the detection of transverse cracks in CFRP cross-ply laminates [1]. When transverse cracks appear in 90° ply under tensile loading, the longitudinal strain distribution in 0° ply becomes non-uniform. Since an FBG sensor is embedded in 0° ply, the reflection spectrum of the FBG sensor is distorted by the non-uniform strain distribution. Thus, the occurrence of transverse cracks can be detected from the change in the form of the reflection spectrum.

With regard to the application of this technique for practical use, the optical fibers without resin coatings have problems in handling for embedding, and the durability of the fibers is lower than that of coated optical fibers. Hence optical fibers coated with polyimide should be used. However, the coating relaxes the non-uniform strain distribution transferred from the 0° ply to the optical fiber, because the stiffness of the coating is much smaller than that of the glass optical fiber. This effect may decrease the sensitivity of the FBG sensor. Hence, in this research, the strain transfer from the 0° ply to the core of the optical fiber was calculated by a theory developed from the shear-lag model, and the effect of the fiber coating on detection of transverse cracks was

investigated.

STRAIN DISTRIBUTION IN 0° PLY OF A CFRP CROSS-PLY LAMINATE

The FBG sensor has been embedded in 0° ply on the border of 90° ply in a CFRP cross-ply laminates for the detection of transverse cracks that run through the thickness and width of the 90° ply, as shown in Figure 1(a) [1]. The occurrence of the transverse cracks can be detected from the change in the form of the reflection spectrum from the FBG sensor owing to the non-uniform strain distribution. Hence, the longitudinal strain distribution in 0° ply was calculated theoretically. As shown in Figure 1, McCartney's theory [2] was applied for each region between two neighboring cracks. In this analysis, generalized plane strain conditions are assumed, and calculated longitudinal strains in 0° ply are the values averaged through the thickness of the 0° ply.

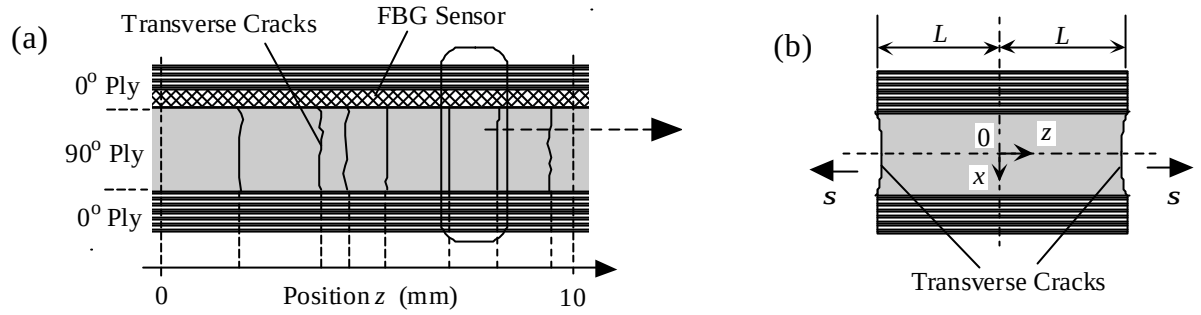

Figure 1: Schematic diagram for the calculation of the non-uniform strain distribution caused by transverse cracks: (a) positions of transverse cracks obtained from an experiment; (b) a region between two neighboring cracks where McCartney's theory is applied.

STRAIN TRANSFER TO THE CORE OF AN OPTICAL FIBER

Duck et. al. proposed a derivation that could predict the axial strain field of an embedded optical fiber sensor from a given arbitrary varying axial strain field in the surrounding material [3]. From the calculation results, they indicated that the in-fiber strain could not be assumed to be equal to the strain field present in the surrounding material. In this research, we modified the method to apply to multiple cylinder models and calculate the strain transfer more accurately.

The optical fiber coated with resin is assumed to be axisymmetric and divided into thin concentric cylindrical layers. The layers are numbered from the innermost core, so that the *i*th cylinder occupies the region $r_{i-1} \le r \le r_i$ for $i = 1 \ldots N$, where r_i denotes the outer radius of the *i*th cylinder and $r_0 = 0$. Figure 2(a) shows a free-body diagram of the *i*th layer. Since the radial and azimuthal stresses are assumed to be negligible, equilibrium equation is expressed as follows:

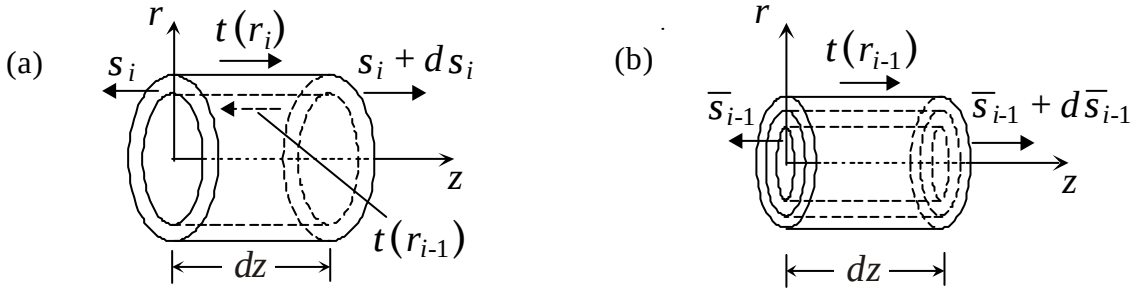

Figure 2: Free-body diagrams of a multiple cylinder model: (a) the *i*th layer; (b) the inner cylinder assembly of the *i*th layer.

$$\frac{\partial \sigma_i(z)}{\partial z}\pi\left(r_i^2 - r_{i-1}^2\right) + \tau(r_i, z)2\pi r_i - \tau(r_{i-1}, z)2\pi r_{i-1} = 0 \tag{1}$$

Figure 2(b) shows the inner cylinder assembly of the ith layer, where $\bar{\sigma}_{i-1}$ denotes the mean normal stress averaged over i-1 inner layers:

$$\bar{\sigma}_{i-1} = \sum_{j=1}^{i-1} E_j \varepsilon_j \frac{r_j^2 - r_{j-1}^2}{r_{i-1}^2} \tag{2}$$

Hence, the relationship of the stresses acting on the inner cylinder assembly is given by

$$\frac{\partial \bar{\sigma}_{i-1}(z)}{\partial z}\pi r_{i-1}^2 + \tau(r_{i-1}, z)2\pi r_{i-1} = 0 \tag{3}$$

The shear stress is expressed by

$$\tau(r, z) = G\left(\frac{\partial w(r, z)}{\partial r} + \frac{\partial u(r, z)}{\partial z}\right) \cong G\frac{\partial w(r, z)}{\partial r} \tag{4}$$

where u and w are displacements along r and z, respectively. From the Eqn.s 1-4, the following equation is obtained.

$$2G_i\left[\varepsilon_i(r_i, z) - \varepsilon_{i-1}(r_{i-1}, z)\right] + E_i\left[\frac{r_i^2 - r_{i-1}^2}{2} - r_{i-1}^2 \ln\left(\frac{r_i}{r_{i-1}}\right)\right]\frac{\partial^2 \varepsilon_i(r_i, z)}{\partial z^2} + \sum_{j=1}^{i-1} E_j\left(r_j^2 - r_{j-1}^2\right)\ln\left(\frac{r_i}{r_{i-1}}\right)\frac{\partial^2 \varepsilon_j(r_j, z)}{\partial z^2} = 0 \tag{5}$$

Then, the Fourier transform of $\varepsilon_i(r_i, z)$ is symbolized by $\hat{\varepsilon}_i(r_i, k)$, and $\hat{\varepsilon}_i(r_i, k)$ is related to $\hat{\varepsilon}_1(r_1, k)$ using a transfer function $H_i(k)$ as $\hat{\varepsilon}_i(r_i, k) = H_i(k)\hat{\varepsilon}_1(r_1, k)$. The Fourier transform of Eqn. 5 yields

$$\hat{\varepsilon}_i(r_i, k) = \frac{2G_i H_{i-1}(k) + \sum_{j=1}^{i-1}(2\pi k)^2 E_j H_j(k)\left(r_j^2 - r_{j-1}^2\right)\ln(r_i / r_{i-1})}{2G_i - (2\pi k)^2 E_i\left[\left(r_i^2 - r_{i-1}^2\right)/2 - r_{i-1}^2 \ln(r_i / r_{i-1})\right]}\hat{\varepsilon}_1(r_1, k) \tag{6}$$

Thus, $H_i(k)$ is expressed using the transfer functions $H_j(k)$ (j = 1…i-1). At first, $H_2(k)$ is obtained from $H_1(k)$ = 1. Next, $H_3(k)$ is calculated from the $H_2(k)$ and $H_1(k)$. Through the repetition of the calculation procedure, all $H_i(k)$ (i = 1…N) are obtained at discrete values of k.

From a given strain field at the outermost layer $\varepsilon_N(r_N, z)$, $\hat{\varepsilon}_N(r_N, k)$ is obtained by the Fourier transform. Then $\hat{\varepsilon}_1(r_1, k)$ is calculated from the $\hat{\varepsilon}_N(r_N, k)$ using the $H_N(k)$, and the strain field at the innermost core $\varepsilon_1(r_1, z)$ can be obtained by the inverse Fourier transform.

CALCULATION OF REFLECTION SPECTRA

According to the above procedure, axial strain distribution at the core of the FBG sensor embedded in a CFRP laminate was calculated. The CFRP laminate is T800H/3631 (Toray Industries, Inc), and the laminate configuration is cross-ply [0_2/90_4/0_2]. The optical fiber is made from glass whose Young's modulus is 73.1 GPa and whose Poisson's ratio is 0.16. The core and cladding are 10 μm and 125 μm in diameter, respectively. The length of the grating is 10 mm, and the grating period is about 530 nm. Strain distribution was calculated for an uncoated FBG sensor and an FBG sensor coated with polyimide, whose outside diameter was 150 μm. Young's

modulus and Poisson's ratio of the polyimide are 1.47 GPa and 0.45, respectively. In the analysis, the glass optical fiber was divided into seven concentric cylinders, and the polyimide coating into two cylinders.

Figure 3 shows the longitudinal strain distribution in 0° ply calculated from the positions of transverse cracks in Figure 1(a) obtained from a tensile test. The average tensile stress was 359 MPa. Furthermore, axial strain distributions at the cores of uncoated and polyimide-coated FBG sensors are shown in Figure 3. In the calculation, the strain distribution at the outermost layer was assumed to be the same as that in 0° ply. As shown in Figure 3, although the strain distribution in the uncoated FBG sensor scarcely changed from that in 0° ply, the variation of the strain in the polyimide-coated FBG sensor was attenuated and smoothed because of the soft coating.

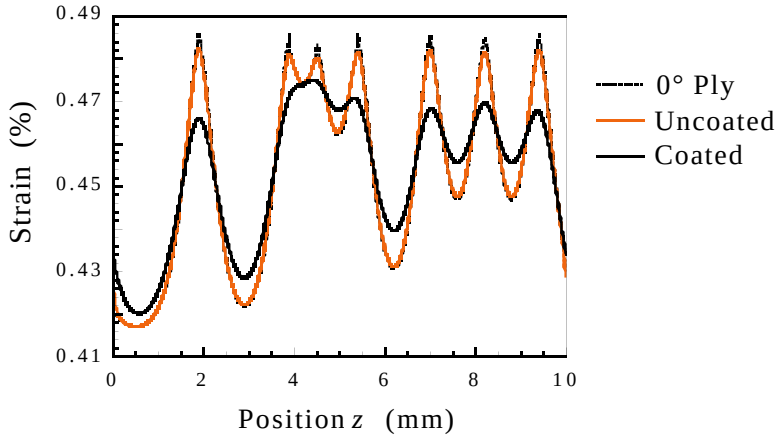

Figure 3: Longitudinal strain distribution in 0° ply calculated from the positions of transverse cracks in Figure 1(a) and axial strain distributions calculated at the cores of uncoated and polyimide-coated FBG sensors. The average tensile stress was 359 MPa.

From the axial strains, the distributions of the grating period and the average refractive index along the FBG sensors were calculated. Then, the reflection spectra were simulated from the distributions. This calculation was conducted using the software 'IFO_Gratings' developed by the Optiwave Corporation. This program can calculate the spectrum by solving the couple mode equations using the transfer matrix method. The reflection spectra calculated from the strain distributions in Figure 3 are shown in Figure 4. The deformation of the spectrum of the coated FBG sensor is slightly smaller than that of the uncoated FBG sensor. Peaks and dips of strain distribution in Figure 3 correspond to large wavelength and small wavelength components of the spectrum, respectively. Thus, the relaxation of the non-uniform strain distribution by the polyimide coating affects the intensity of the components away from the center wavelength of the reflection spectrum. However, the two spectra in Figure 4 are almost the same, so that the polyimide-coated FBG sensor can be applied to the detection

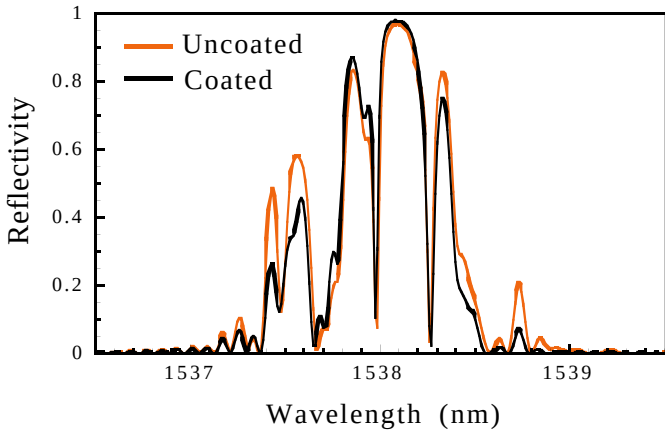

Figure 4: The reflection spectra of the uncoated and coated FBG sensors calculated from the strain distributions in Figure 3.

of transverse cracks. The agreement of the spectra between coated and uncoated FBG sensors were confirmed also in the cases that the crack density was very small or saturated, from theoretical calculations.

CONCLUSIONS

In this research, Duck's method was modified to be applied to multiple cylinder models and calculate the strain transfer from a surrounding material to the core of an optical fiber more accurately. From the analysis, it was found that the polyimide coating of an optical fiber relaxed the non-uniform strain distribution caused by the occurrence of transverse cracks in CFRP laminates. However, the reflection spectrum of a polyimide-coated FBG sensor, which was calculated from the relaxed strain distribution, was almost the same as that of an uncoated FBG sensor. Thus, the polyimide-coated FBG sensor can be applied to the detection of transverse cracks without removal of the fiber coating.

ACKNOWLEDGEMENTS

This research was conducted as a part of the 'R&D for Smart Materials Structure System' project within the Academic Institutions Centered Program supported by NEDO (New Energy and Industrial Technology Development Organization), Japan.

REFERENCES

1. Okabe, Y., Yashiro, S., Kosaka, T., and Takeda, N. (2000) *Smart Mater. Struct.* 9, 832.
2. McCartney, L.N. (1992) *J. Mech. Phys. Solids* 40, 27.
3. Duck, G. and LeBlanc, M. (2000) *Smart Mater. Struct.* 9, 492.

ICF100483PR

EFFECT OF FILM PLASTICIZING UNDER MULTISTAGE ULTIMATE STRAIN

Ata A. Miatiev* and Galina V. Khil'chenko

Pro Scientific & Technical Service, Prague, Czech Republic

ABSTRACT

The results refer to changes of mechanical properties of thin-walled nickel-chromium alloy tube specimens after multistage cold drawing. The goal was to analyze the possibilities of changing the kinetics of hardening and destruction under influence of deposited metal oxide films.
It has been noticed that under ultimate strain by drawing strength of coated tube specimens is much more than that of specimens without films. Specifically, the ultimate value of strain for coated tube specimens increases. At the same time the coated specimens have relatively high plasticity. The strength of coated specimens after ultimate strain is 14 – 23 % higher and plasticity is 4 times more. Specifically, that the ability of alloy to stand multistage ultimate strain can be increased more. It can be done by overlaying the film each time the specimen is drawn. In addition, there are the technological advantages of using the films under drawing. These advantages are the better quality of surface and decrease of drawing force. The possibility of effective application of plasticizing films to machining tools has been noted. The plasticity effect in this case is 50 – 70% of that when films are deposited on material. Besides, they work as solid lubricants, decreasing power consumption for working and wear of tool. In explosive stamping tests of titanium-base alloy coating with oxide films resulted in double increase of plasticity.

KEYWORDS

Film plasticizing, oxide films, ultimate strain, drawing, stamping, nickel–chromium alloy, films in metal working, solid lubricants.

INTRODUCTION

Amorphous oxide films, which are ideal elastoplastic bodies, are capable of essentially improving the plastic strain uniformity in the surface layers of engineering alloys under out-of-contact strain during mechanical tests [1]. Study of the effects caused by such films on the properties of alloys in working (drawing, rolling, stamping, extruding, and others) is of enormous interest for both science and practice. The process itself is of equal importance.

RESULTS

There is a special program for relevant research. This program involved: – drawing of thin-walled tubes, both uncoated and coated, through dies of various diameters without in-process and finish anneals; and– mechanical tests of the tubes.

The drawing conditions were standard, with spindle oil used as lubricant. All specimens of a nickel–chromium alloy were cut from one batch of as-received tubes 7.0 x 0.3 mm in diameter. The following sets of specimens were tested.

Set A. As-received (initial) tubes. The test procedure was the following: As-received tubes were drawn sequentially through dies of different diameters. After each drawing, three specimens were chosen from the set. The cross-sectional strain (the ratio of the reduction in the initial tube diameter to the inner diameter of the die) was controlled. These specimens were subjected to tensile tests at 573 K.

Set B. As-received tubes were coated by amorphous zirconia to a coating thickness of 1.5 μm. The drawing procedure, specimen selection, and mechanical tests were identical to those applied to Sets A.

Set C. Set B tubes, each time after being drawn but before being tested, were additionally coated by amorphous zirconia to form a 1.5-μm-thick film. The subsequent testing procedure was as in other sets.

We were also interested in achieving the highest possible reduction of the tube area.

The mechanical test data were processed in terms of ultimate tensile strength, offset yield strength, and total strain at fracture versus prior drawing strain (reduction of area).

Figures 1-3 present the results from mechanical tests at 573 K of tubes drawn to various extents. Tested were pieces of Set A (uncoated) tubes, Set B (zirconia-coated) tubes, and Set C tubes (Set B tubes with a zirconia coating overlaid after each drawing).

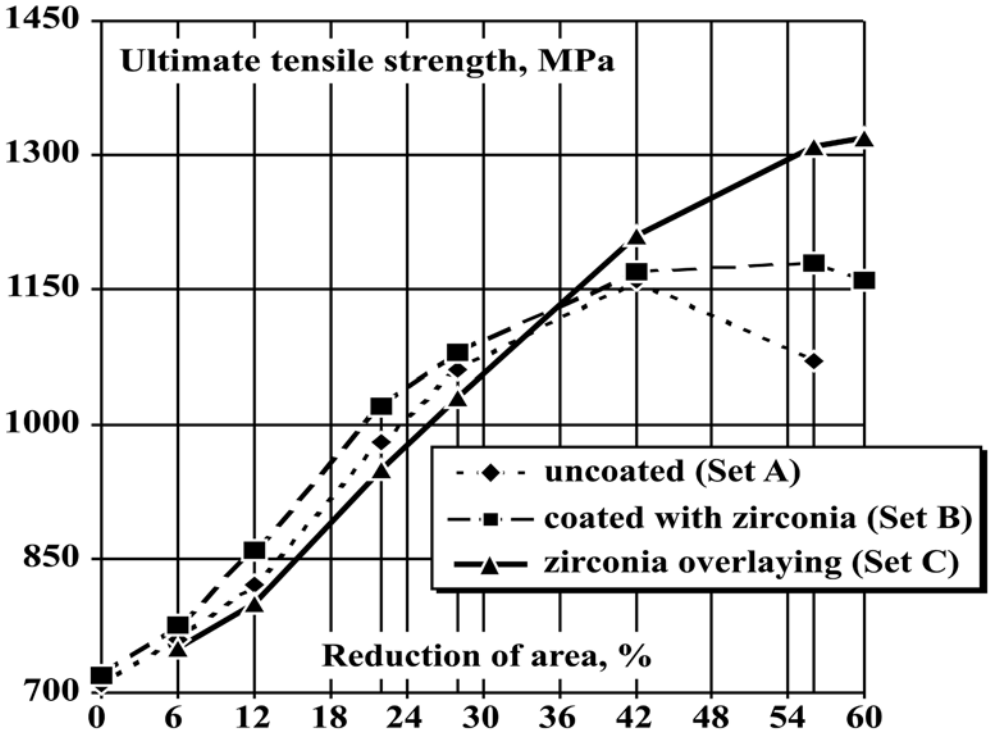

Fig.1: The plot of the 573 K ultimate tensile strength vs. reduction of area after drawing for nickel–chromium alloy tubular specimens of Sets A, B, and C. The film is zirconia 1.5 μm thick

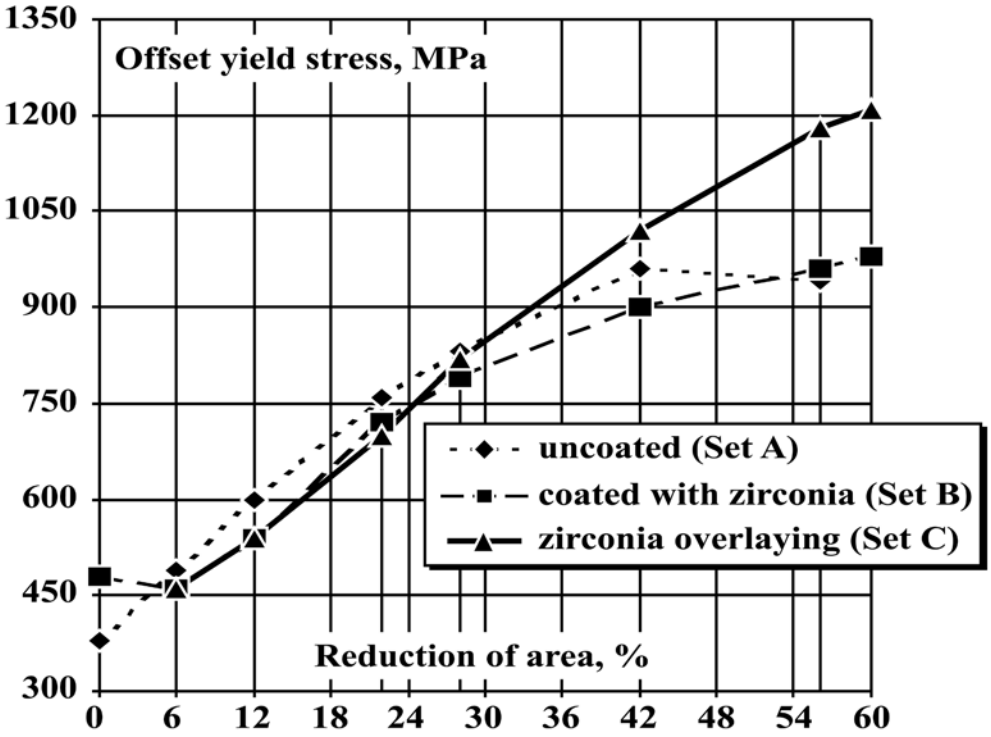

Fig.2: The plot of the 573 K offset yield stress vs. reduction of area after drawing for nickel–chromium alloy tubular specimens of Sets A, B, and C. The film is zirconia 1.5 μm thick

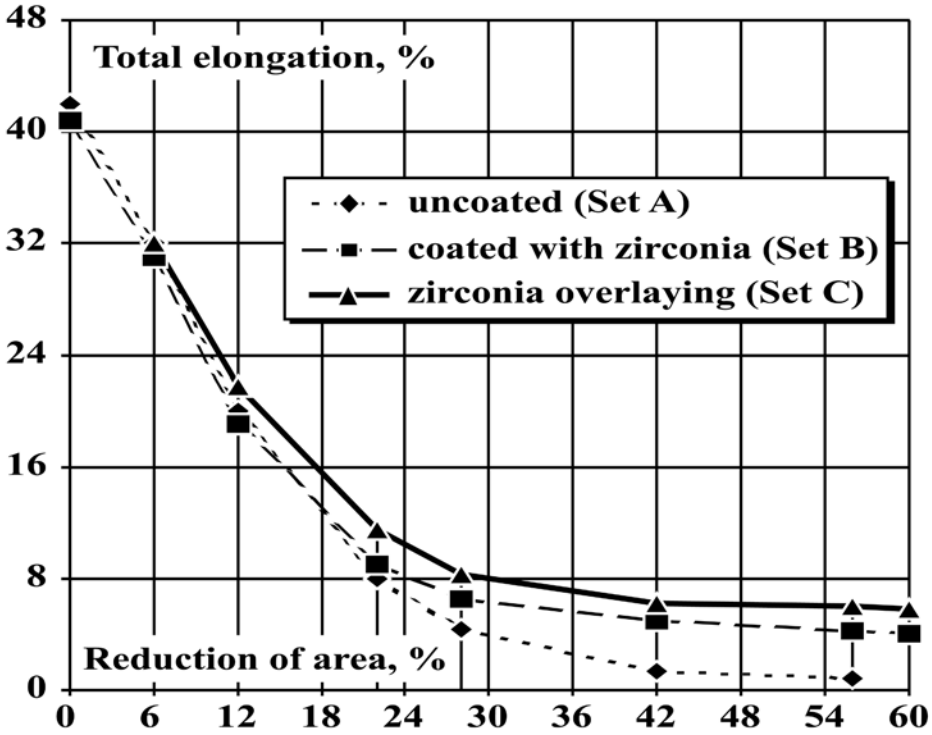

Fig.3: The ultimate strain in drawing vs. reduction of area at 573 K for nickel–chromium alloy tubular specimens of Set. A, B, and C. The film is zirconia 1.5 μm thick

For uncoated materials, the offset yield stress and ultimate strength increase to attain the maximum value when the reduction of area is 42%, then decreases; when the reduction of area is larger than 54%, the specimen is broken in drawing, being lengthwise separated into fibers. The yield stress values

for zirconia coated specimens are lower than for uncoated specimens. In addition, there is no peaks in the curve of Fig. 2, and the coated specimens do not break when the reduction of area is 60%. Of special interest are the results from zirconia-coated specimens on which zirconia was overlaid after drawing. For the reduction of area from 6 to 28%, the yield stresses in the coated specimens differ little from similar values in zirconia-coated Set B specimens. For the reduction of area larger than 28%, zirconia overlaying produces a substantial increment in the yield stress as compared both to the uncoated specimens and to the Set B specimens. The same trend is observed in the ultimate tensile strengths for the Set C specimens.

In this way, the application of zirconia to Ni–Cr tubes promotes hardening in work, and overlaying after each drawing operation considerably strengthens this effect. Characteristically, all deposited films gradually increase the alloy plasticity (Fig. 3). While the total elongation at ultimate strain hardening in drawing of the uncoated alloy is within 1%, its value for a coated alloy is substantially higher. Specifically, the elongation amounts to 4% for the specimens coated by zirconia before being repeatedly drawn. And for specimens on which zirconia films were overlaid each time they were drawn, the elongation is 6%.

The following questions arise: What is the reason for this? And which is the expression of this in terms of materials science?

Prior research, specifically, metallographic evidence, implies that the effects of amorphous deposited films are a consequence of the same physical processes in materials that were discovered earlier in mechanical tests [1]. The only distinction is that the role of the surface in working and under the contact action of the extrusion device becomes more significant. For example, under the contact action during drawing, films (that naturally possess a certain set of properties) can efficiently improve the uniformity of micro plastic strain in polycrystalline materials. Their effect in contact action becomes much stronger. As a result of the increased uniformity of plastic strain in every grain of the polycrystalline material (it was noted that additional crystallographic directions were involved in this [1]), the deformation defect structure becomes far more homogeneous and energy-balanced. A situation appears where grain boundaries; segregations (inclusion phases); the second, higher strength phase; texture; and other structural details of the initial material substantially loss their tendency to induce various local processes during deformation. Most likely, the weaker tendency of the polycrystalline material to locally accumulate structure defects is precisely the reason for the increment in the integral strength simultaneously with a relative increase in plasticity at ultimate strain hardening.

The results of the tests and studies on this set of specimens should be regarded as extraordinary, even if the effect of films on the mechanical properties [1] is taken into account.

Firstly, the films were applied on specimens before drawing. The observation that the effect characteristic of each type of coating is retained in multiple-draft (!) drawing is unexpected and very important in practice.

Secondly, the films after multiple-draft drawing substantially add to the plasticity at the ultimate extent of hardening (reduction of area). Note that the tests did not involve anneals, which is important.

Thirdly, not only the deposited films were strained together with the tube, but they were (at least, the film on the outer tube surface was) in direct contact with the extrusion device (die). However, the films each retained their distinctive effects on the mechanical properties of tubes in multiple-draft drawing. This provides grounds to suggest that not only are films conserved on the tube surface, but they even cause a certain influence on the mechanical properties of the substrate metal. Unlike the ordinary conditions of mechanical tests, there is a direct action of the extrusion device in this case. Therefore, the film may be regarded as a solid lubricant.

Lastly, the fact itself that the strength and plasticity increase in tandem in drawing is evidence that films are capable of substantially changing the conditions of contact micro plastic strain of the substrate metal. The most significant consequence of this is the lowering of the critical level of the deformation defect density in the substrate (the level that causes fracture of the material). The material after being drawn has a more perfect structure regarding its mechanical properties.

Based on experimental evidence (especially, from the sets of specimens on which an oxide film was overlaid each time they were drawn), we infer that the ability of the oxide coating to inhibit premature surface breakdown of the substrate is the dominant. In other words, the film creates a situation such that the surface layer remains more plastic than the metal bulk even under ultimate strain hardening. In this regard, the film

together with the surface layer of the substrate acts as an efficient solid lubricant in the device–metal system. The fact that such a lubricant can work under the increasing strength of the workpiece seems most significant. The possibility of surface softening due to the deposited film in metal working with a superhard contact action of the device is of enormous value for the engineering. This concerns not only rolling, stamping, drawing, and extruding, but also cutting, milling, drilling, etc. In addition, the surface softening of one of the partners of the contact pair can aid in solving many problems in tribology (friction and wear).

Oxide films might find extensive and diversified application in metal working. When the yield strength is reduced, especially in difficult-to-extrude alloys, energy requirements in metal working may be considerably reduced. The feasibility of reducing temperature and strain load goes along with this. The increment in plasticity makes it possible to attain deeper deformation in high-strength and low-ductility alloys, as well as an increment in the ultimate strain, which is usually controlled by work hardening and requires in-process anneals. The main conclusion from our tests and studies, which is very important in practice, is that the optimal effect of coatings in tube drawing, as assessed by the reduction in the drawing force, can reach 40–70% depending on the alloy and drawing conditions. Other achievements are high surface quality, structural homogeneity, and a set of mechanical properties. In particular, the scatter in the mechanical properties of coated tubes after drawing under the optimal conditions is reduced several times.

When drawing small-diameter thin-walled tubes, comparative tests of the efficiency of deposited oxide films were made on instrumental steel filaments. Pieces of stainless steel and a chrome–nickel alloy were drawn. The following control parameters were used: drawing force, chemical composition of the die surface, and state of the die surface as observed under a scanning electron microscope. Drawing with and without lubricants was performed, and various deposited oxide films were tested. This study showed the following results.

The general trend of the effect caused by films on the drawing force during unlubricated drawing fits the following pattern (regarding the reduction in the effect, all other conditions being equal):

amorphous oxide films >> crystalline oxide films,

multilayered films > single-layer films,

films on the tube and die > films on the die.

In addition, the drawing force versus film thickness relationship has the trend plotted in Fig. 4 and is characteristic of all film materials tested. The largest reduction in the drawing force on the die for various films ranges between 5 and 30%. It was concluded that, if the film is applied only to the tool, a softening effect, like that produced by the film on the workpiece, is observed. However, in this case, surface softening of a work or cut metal is 30–50% lower.

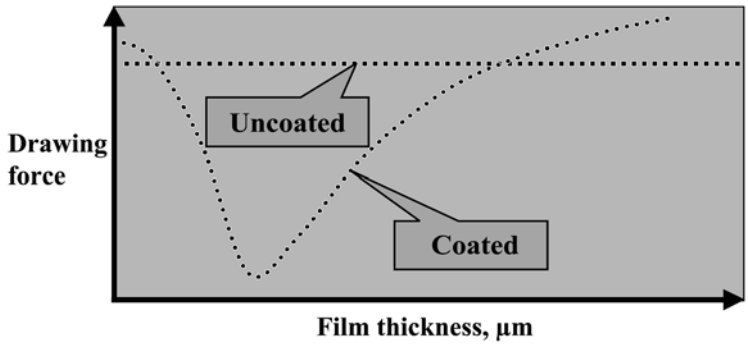

Fig.4: The effect of thickness of the deposited film on the drawing force

The general trend in the effect caused by films on the drawing force during lubricated drawing with organic lubricants (regarding the weakening of the effect, all other conditions being equal) depends strongly on the lubricant and film structure. Characteristically, all other conditions being equal, the drawing force varies as a function of film thickness as plotted in Fig. 4. The strongest effect is achieved in the case where films are applied to both the tube and the die. In contrast to dry drawing, the crystal and layered structure of the film are weaker factors in this case. We concluded that with liquid lubricants the ability of the film to retain the lubricant is of primary importance. In tests, the initial reduction of the

drawing force was as high as 50–70%. However, this effect weakens to the vanishing point with increasing the operation time of the die. An analysis of the chemical composition of the die and periodic examination of the surface with an electron microscope showed that, for any drawing conditions and material, there is mass transfer of chemical elements from the workpiece to the die surface. Under heavy drawing conditions with an uncoated die, mass transfer occurs in the first centimeters of drawing even if a lubricant is used. When there is a film on the die, the elapsed time (the number of meters drawn) until mass transfer to the working surface becomes evident increases by several orders of magnitude. Selective contamination of the film by the chemical elements from the workpiece is still observed, but the film continues operating until completely fretted.

Tests and study showed that for almost any working tool material and any work alloy, a film with optimal efficiency and wear resistance could be created. The practicality the wearlessness principle due to periodic renewal of the film is enormous. It has been noted that the higher the strength, hardness, and wear resistance of the tool material, the higher the efficiency of the periodically renewed coating.

Fig.5: An item manufactured by explosive stamping from a low-ductility titanium-base alloy coated with a plasticizing film

Another revealing example of the efficiency of softening films was a comparative explosive stamping test on titanium-base alloys. Sheet pieces were tested for manufacturing ring stampings with an overall strain of 12% at a strain rate of 7500 m s^{-1}. Previously, a high-ductile titanium-base alloy (1.5Al-1.0Mn; σ = 600 MPa, δ = 20%) was used to manufacture these stampings. There were no problems in one-stage stamping of this alloy. The titanium-base alloy (6.0Al-2.0Zr-1.0Mn-1.0V), which has higher strength but lower ductility (σ = 1000 MPa, δ = 6%), is evidently preferable in terms of performance. However, with this substitution, cracking and warping were observed during stamping, even under incremental loading. The application of a softening oxide film to the original titanium sheet resulted in a defect-free stamping, which is shown in Fig. 5.

References

1. Miatiev, A.A. (2000) NEW ADVANCES IN SURFACE PHYSICS, CHEMISTRY, AND MECHANICS: MATERIALS WITH DEPOSITED OXIDE FILMS, Findings, Effects, and Applications. Izd. Mosk. Gos. Univ. Pechati, Moscow.

ORAL REFERENCE: ICF100527OR

EFFECT OF FOREIGN OBJECT DAMAGE ON THE HIGH CYCLE FATIGUE STRENGTH OF TI-6AL-4V

Steven R. Thompson[1], John J. Ruschau[2] and Theodore Nicholas[1]

[1] U.S. Air Force Research Laboratory, Materials and Manufacturing Directorate, Wright-Patterson AFB, OH 45433 USA

[2] University of Dayton Research Institute, Dayton, OH 45469 USA

ABSTRACT

The role of residual stresses on the fatigue behavior of Ti-6Al-4V samples that had undergone foreign object damage was investigated. Real and simulated impacts were conducted using spherical projectiles launched at 300 m/s and quasi-static chisel indentation, respectively. A unique test specimen configuration that replicates the leading edge of a typical fan blade was ballistically shot at 30° with 1 mm diameter spheres, while rectangular plates were indented quasi-statically using a 2 mm diameter steel indentor at 0°. Fatigue strengths were developed for both geometries at 350 Hz. A number of specimens from both configurations were stress relief annealed, after impacting and before HCF testing, to remove residual stresses. Attempts were made to correlate the measured damage (macro-/microscopic) to the debit in fatigue strength. Results indicate that stress relief generally improves the fatigue limit stress, indicating that tensile stresses are present after both quasi-static and dynamic indentation. For the dynamic impacts, the damage induced is not as severe on the fatigue strengths as that predicted from conventional notch fatigue analysis.

KEYWORDS

high cycle fatigue, foreign object damage, residual stress, fatigue limit stress

INTRODUCTION

The fatigue behavior of airfoils in gas turbine engines that have been subjected to foreign object damage (FOD) is a complex issue due to many contributing factors. These factors include, but probably are not limited to, notch geometry causing a stress concentration, residual stress arising from plastic deformation, microstructural damage to the material from the impact event, and the formation of cracks during the impact event [1]. In addition, changes in the geometry of the airfoil edge and residual stresses due to plastic deformation may produce local stress ratios at the notch tip which are, in general, different than the far-field applied stress ratio and may drive the initiation location from surface to sub-surface [2]. This paper deals with the fatigue behavior of axial fatigue test specimens that have been

subjected to FOD, with a portion of the specimens having undergone a post-FOD event stress relief annealing in order to examine the effect of residual stresses.

EXPERIMENTAL PROCEDURES

Axial fatigue specimens were machined from a single Ti-6Al-4V forged plate that had been heat-treated to the STOA condition [3]. Two basic specimen configurations were used for this effort: a diamond cross-section tension (henceforth known as the LE, *i.e.* leading edge) specimen and a simple rectangular (flat) cross-section sample. The LE specimen was designed such that the edges of the gage section are tapered to radii representative of the leading edge on a fan blade. To span a range of leading edge configurations, two edge radii were examined: 0.38 mm and 0.127 mm. Details of the specimen geometries can be found in Ref [3]. Stress calculations for all samples were based on the gross area, excluding the slight loss in area due to the various FOD sizes.

The LE samples were ballistically impacted using a single-stage compressed gas gun. All of the samples were shot with a 1 mm glass sphere at a velocity of approximately 305 m/s. The glass sphere was chosen as being representative, in both size and properties, of sand or runway debris that is of concern in U.S. Air Force operational engines. It also produces damage which is geometrically similar to what is often observed in the field. Details of the ballistic impact procedures are likewise presented in Ref [3]. Quasi-static impact damage was performed on the flat samples. A hardened steel indentor with a 2 mm diameter round tip was used to induce damage to a specific depth on the thin side of the rectangular sample at a 0° angle [4].

To establish the fatigue strength, samples were fatigue tested using the step-loading procedures described by Maxwell and Nicholas [5]. Steps of 10^7 cycles were used in this investigation, while $\Delta\sigma$ was taken typically at 10 percent of the initial load block. This large increment (compared to 5 percent or less in other tests) was used to minimize the number of load blocks because of the wide scatter in fatigue strengths observed under FOD conditions. Testing was conducted at stress ratios (R) of 0.1 and 0.5 at a frequency of 350 Hz using an electro-dynamic, shaker-based test machine. All testing was performed under ambient laboratory air conditions.

The choice of tension-tension testing was made for several reasons. While a real blade may be subjected to combinations of bending and tension, it was felt that understanding one of the basic properties, tension fatigue, was important in characterizing FOD. Second, baseline data are available for the material tested to compare smooth [6] and notch [7,8] fatigue behavior. Finally, test apparatus is available to conduct high frequency axial fatigue testing whereas fully instrumented bend tests are more difficult to perform at high frequencies.

Prior to fatigue testing, the FOD sites of each LE sample were examined with a scanning electron microscope (SEM) to document the initial FOD defect. After test, the FOD site from which the fatigue cracking failure initiated, along with the fracture surface of each sample, were again examined to correlate the microstructural features with the ensuing fatigue strength. The flat samples were examined, prior to testing, under a standard optical microscope to determine the dimensions of the damage sites. Observations of whether there appeared to be material loss (chipping out) were noted. It should be noted here that during the testing process, the fracture faces tended to be crushed when the specimen failed. This action smeared the features on the fracture faces to the point that initiation sites were compromised.

Because of the expense of conducting ballistic tests, only a limited number of tests were carried out. In many cases, duplicate tests were not used. Because of this, as well as the scatter involved in this type of testing, only general trends are expected from the results.

A portion of the impacted samples, both from the ballistically impacted LE samples, and the quasi-statically impacted flat samples were stress relief annealed before fatigue testing. This process was performed to allow a comparison of fatigue limit stress of specimens impacted under identical conditions with and without residual stresses.

DISCUSSION OF RESULTS

Damage Characterization

The photos in Figures 1a and 1b show examples of ballistic impact damage on the LE samples. Although the conditions were the same for the ballistic impacting for these samples, the results were greatly different. Some of the impact sites exhibited a simple "dented" appearance with little or no loss of material evident (Fig. 1a), whereas other impact sites exhibited more damage with a much larger loss of material (Fig. 1b). The photos in Figures 2a and 2b show flat sample indents where there was no evidence of material loss (Fig. 2a) and where material loss occurred (Fig. 2b). The arrow in Figure 2b indicates an area where a crack occurred during the indenting process. A piece of material eventually chipped out during the handling of the sample. This behavior was typical in the samples with the large damage depths. LE samples were rotated in the SEM to provide the appropriate angle to measure the maximum depth of damage. These measurements (depth and width of impact notch) were used later to compute approximate values of the stress concentration factor, K_t, as well as a notch depth ratio, d/a. While the flat samples had a radius of the indent that was close to that of the quasi-static indentor, the LE specimens had notch root radii which had a larger amount of scatter. The scatter in these dimensions can be attributed to the scatter in the exact location of the impact on the thin LE samples and very small size of the projectile causing the impact.

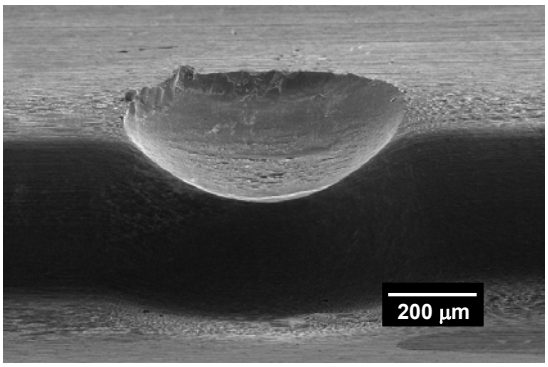

Figure 1a: Head-on view of a 30° ballistic impact FOD site for a 0.38 mm leading edge radius sample exhibiting little or no loss of material.

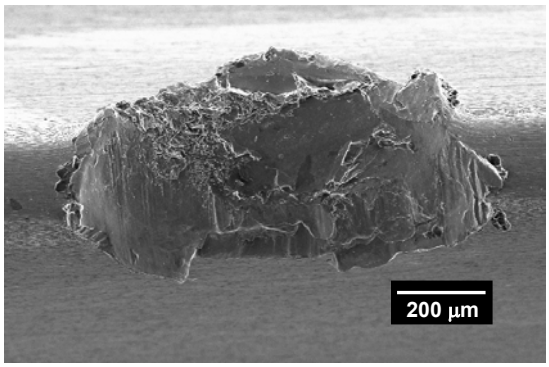

Figure 1b: Head-on view of a 30° ballistic impact FOD site for a 0.38 mm leading edge radius sample exhibiting a larger loss of material.

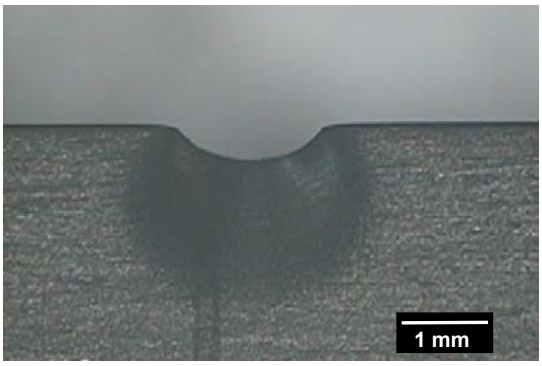

Figure 2a: Side view of a 0° quasi-static impact FOD site for a flat sample exhibiting no loss of material.

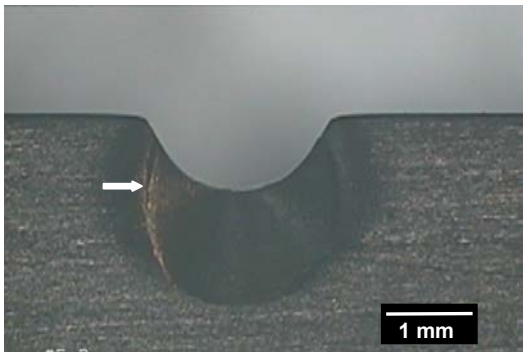

Figure 2b: Side view of a 0° quasi-static impact FOD site for a flat sample exhibiting a large crack (eventual loss of material).

Leading Edge (LE) Samples

The results for strength of ballistically impacted LE specimens are presented in Figure 3 where fatigue limit stress is normalized with respect to the smooth bar fatigue strength at the appropriate stress ratio. For this material, the maximum stresses for smooth bars are σ=568 MPa for R=0.1 and σ=660 MPa for R=0.5 [3,5]. It should be noted that in the figure, AR refers to specimens that were tested in the as-received (as-impacted) condition and SR refers to specimens that were tested in the stress-relieved condition. Symbols with upward arrows indicate notch geometries where failure occurred away from the notch at the indicated stress. From the data, it can be seen that the SR samples tend to have higher fatigue strengths than the samples tested in the as-impacted condition. Also shown in the figure are points that utilize a fatigue notch factor, K_f, which was calculated from the measured dimensions for radius and notch depth [4]. It can be seen that the SR samples lie above the predictions of large notch fatigue analysis, and many of the AR samples also lie above those points. It can only be concluded that the small size of the notches being dealt with here are not as severe as geometrically similar notches, a finding supported by the observations of Haritos, et al. [8] in notch fatigue studies on the same material. They observed that the detrimental effect of a notch decreased as the root radius became smaller for the same value of K_t, and attributed that finding to a size effect as formulated by other notch fatigue theories (*eg.* [9]).

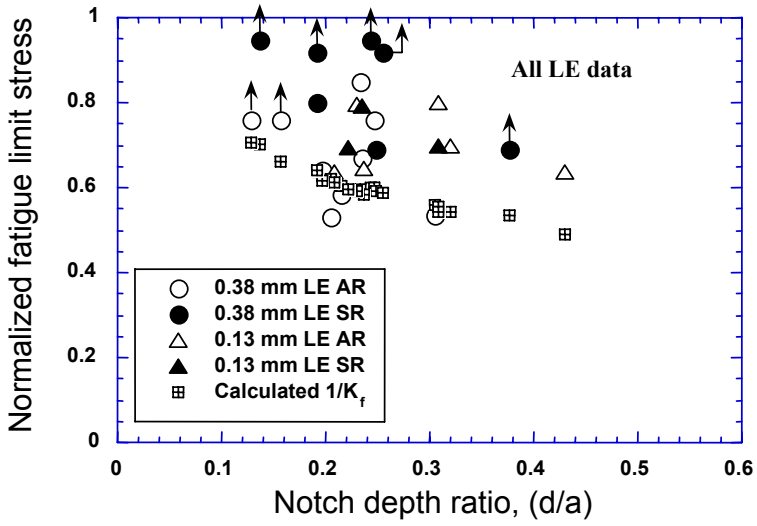

Figure 3: Effect of the notch depth ratio on the normalized fatigue limit stress for ballistically impacted 0.38 mm leading edge radius samples.

Flat Samples

Fatigue limit stress as a function of notch depth for the flat specimens subjected to a static indent with a 2 mm diameter chisel at a stress ratio (R) of 0.1 is shown in Figure 4. Data from this investigation, denoted MLS, are shown alongside those from a prior investigation using the same material and indentor, denoted AFIT [2]. While there are not many data points, it can be seen that the AR specimens (hollow symbols) clearly show a larger debit in fatigue strength. The greatest fatigue debit occurs in those specimens that exhibit a loss of mass through chipping, a finding consistent with prior observations by Kaufman and Meyer [10] and Martinez [11]. In the plot, the expected failure stress from a fatigue notch factor, K_f, is shown, based on the assumption that the radius of the indent is that of the indentor.

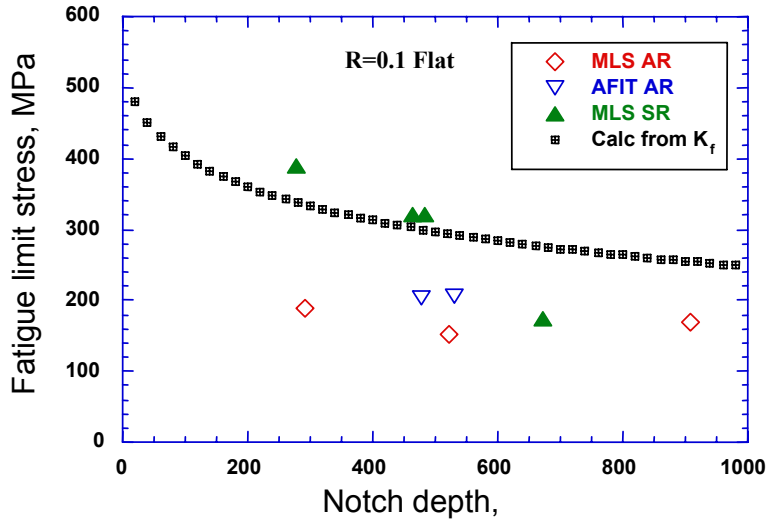

Figure 4: Effect of notch depth on the fatigue limit stress for R=0.1 on quasi-static impacted flat samples.

Role of Residual Stresses

Similar to what happens when compressive residual stresses are applied under surface treatments such as in laser shock peening [12], the beneficial effects of residual stresses seem to be more prominent at low stress ratios than at high ones. It is important to note that a residual stress superimposed on the stresses generated from fatigue loading does not change the stress range (or stress intensity factor range, ΔK, in the case of a cracked body) but, rather, changes the values of the maximum and minimum stresses by the same amount. Thus, compressive residual stresses superimposed on tensile fatigue stresses at a particular value of R will reduce the effective value of R for crack initiation. For low values of applied R, the effective R may be negative. Recent unpublished data from our laboratory indicate that the range of compressive stresses is much less effective than the same range in tension in high cycle fatigue. For the crack propagation phase after initiation, the compression region does not contribute to crack growth. For the situation where the residual stresses are in tension, the effective value of R increases although the stress range remains unchanged. In this case, tests at increasingly positive values of R can be detrimental because the magnitude of the fatigue limit stress decreases with increasing values of R, as evident in a Goodman diagram [5]. Further, any beneficial effects of compression for originally negative R can be removed.

SUMMARY AND CONCLUSIONS

Observations in this investigation and previous work [3,4] indicate that scatter in fatigue strength data involving FOD from ballistic impact, and even quasi-static indentations, have a tendency to obscure trends in causes of observed behavior. Nonetheless, the data obtained for fatigue limit strength on LE specimens indicate that the damage inflicted, excluding cases

where material was removed, was less severe than that predicted by notch strength analysis. A similar trend was also observed in the flat samples that were quasi-statically indented. While the generally observed lower strength of the as-impacted samples can possibly be attributed to tensile residual stresses below the notch surface, the stress relieved samples exhibit fatigue strengths above which one would expect for the geometry of the observed notches. It appears that the notches produced from the ballistically impacted FOD have effective notch fatigue strengths higher than predicted by their geometries using conventional notch fatigue analysis; however, most work on notch fatigue deals with notches that are considerable larger than those being dealt with in this FOD investigation. It is concluded, therefore, that FOD that produces notch geometries involving the dimensions discussed herein is not as detrimental as FOD with larger dimensions of geometrically similar notches. This conclusion is based on the detrimental effects of the notch geometry and the calculated large notch fatigue factor, and does not consider the effects of residual stresses nor of irregularly shaped indents that may involve loss of material, tears, or other geometric discontinuities. The most detrimental effects of FOD appear to occur when irregularly shaped notches are produced from conditions such as tearing or material removal. Finally, the role of residual stresses in tension can be blamed for the low fatigue limit stress in many cases based on observations in nearly identical impact events where stress relief annealing improves the fatigue strength. It can only be concluded, in these cases, that tensile residual stresses led to the degradation of the fatigue behavior.

REFERENCES

1. Peters, J.O., Roder, O., Boyce, B.L., Thompson, A.W., and Ritchie, R.O. (2000). *Metallurgical and Metals Transactions*, 31A, 1571.
2. Hamrick, J.L., Major, USAF (1999). Ph.D. Dissertation, Air Force Institute of Technology, USA.
3. Ruschau, J.J., Nicholas, T., and Thompson, S.R., (2001). *Int. Jour. Impact Engineering*, 25/3, 233.
4. Thompson, S.R., Ruschau, J.J., and Nicholas, T., (2001). *Int. Jour. Fatigue*, (in editing).
5. Maxwell, D., and Nicholas, T., (1999). In: *Fatigue and Fracture Mechanics: 29th Vol., ASTM STP 1321*, pp. 626-641, Panotin, T.L., and Sheppard, S.D. (Eds). American Society for Testing and Materials, USA.
6. Bellows, R.S., Muju, S., and Nicholas, T. (1999). *Int. Jour. Fatigue*, 21, 687.
7. Bellows, R.S., Bain, K.R., and Sheldon, J.W. (1998). In: *Mechanical Behavior of Advanced Materials, MD-Vol. 84*, pp. 27-32, Davis, D.C. et al (Eds). ASME, New York.
8. Haritos, G.K., Nicholas, T., and Lanning, D.B. (1999). *Int. Jour. Fatigue*, 21, 643.
9. Bannantine, J.A., Comer, J.J., and Handrock, J.L. (1990). *Fundamentals of Metal Fatigue Analysis*. Prentice Hall, Englewood Cliffs, New Jersey.
10. Kaufman, A., and Meyer, A.J. Jr. (1956*). National Advisory Committee for Aeronautics, Technical Note 3275*. USA.
11. Martinez, C.M., Capt., USAF (2000). M.S. Thesis, School of Engineering, University of Dayton, Dayton, OH, USA.
12. Ruschau, J.J., John, R., Thompson, S.R., and Nicholas, T. (1999). *ASME J. Eng. Mat. Tech.,* 121, 321.

Effect of Halogen Freeing on Fatigue Properties of Electronics Printed Plasitic Board

Masashi NAKAMURA[1], Hideto SUZUKI[1], Tetsuo MATSUMOTO[2] and Tomonari OHTSUKI[2]

[1] Ibaraki University, 4-12-1, Nakanarusawa, Hitachi-City, Ibaraki, 316-8511 JAPAN
[2] DDK Ltd., 14, Matsuyama, Mooka-city, Tochigi, 321-4393, JAPAN

ABSTRACT

Recently, it is important to develop new packaging technology that is gentle for environment and human body in electronic packaging fields. The printed circuit board of electronic equipment will be developed using materials for substrates without halide fire retarding material (that is halogen-free material) as dioxin does not arise. However, reliability assurance becomes an important problem for substrates using halogen-free fire retarding material, since there are fears that strength and heat-resistance are inferior to conventional circuit materials.

In this study, fatigue reliability of halogen-free substrate noticed as an environmental harmony type printed circuit board material was evaluated. The difference of fracture mechanism between halogen-free material and halogen material in fatigue fracture was demonstratively examined from mesoscopic viewpoint. Fatigue life of halogen-free material was longer than that of halogen material, though mechanical property of halogen-free material was almost equal to it of halogen material. From fractography using by SEM, it was indicated that the difference of fatigue life in halogen-free material and halogen material was controlled by the difference of a size of characteristic destruction pattern named "Unit Fracture Area". It was thought that difference of resinoid type between halogen-free material and halogen material appears in the difference in fatigue life, since matrix resin was a weakest link in fatigue fracture, on the other hand, strength of halogen material and halogen-free material was equal in static fracture, since the glass fiber was a strongest link.

KEYWORDS

Fatigue Reliability, Halogen-free- Electronics Substrate, Fractography, Reinforced Plastics

INTRODUCTION

Recently, the miniaturization is required in electronic equipment products. As the result, high-density packaging technologies such as buildup substrate have rapidly advanced. In the meantime, the environmental problem becomes serious, and they worry about the effect of pollution to environment and to human body. Therefore, it is important to develop the gentle packaging technology for environment, namely ecological design technology in electronic packaging fields.

There have been a series of research of fatigue reliability assurance of recycling engineering plastic material by authors, as it is shown in Fig.1 and Table 1. As the result, it was shown that the control of mesoscopic factor could improve the reliability of recycling engineering plastic materials.

At present, the use of halide fire retardant that is included in printed circuit board has been controlled. This is

because dioxin and furan of which the toxicity is high arise, when halide fire retardant burns. Therefore, the use of halogen-free system fire retardant such as phosphorus system fire retardant has increased year by year. However, the improvement of reliability of substrates using halogen-free system fire retarding material becomes an important problem, since there is fears that strength and heat-resistance are inferior to conventional substrates. . The safety assessment of halogen-free substrates is only to carry out simple evaluations by tensile test, etc. So the evaluation on fatigue reliability has not been almost carried out.

Then, fatigue reliability of halogen free substrate was evaluated in this study. Especially, this study was demonstratively carried out by investigating the difference of fatigue fracture mechanism between conventional halogen substrate and halogen-free substrate from a viewpoint of mesoscopic fracture mechanism.

EXPERIMENTAL METHOD

Sample materials used in this investigation were halogen free-laminated material MCL-RO-67G made by Hitachi Chemical Co., Ltd. New aromatic system addition reaction type thermosetting resin (RO resin) of which fire resistance was high had mainly been used for this laminated material. Therefore, fire-retardant UL94V-0 has been achieved, even if this material does not use the halide fire retardant such as halogen compound, antimony and red phosphorus. Especially, it has high elastic modulus and heat-resistance under the high temperature environment, since it mainly has the aromatic skeleton in molecular structure, (Table 2). And, the general FR-4 laminated material was prepared in order to compare characteristics of a conventional halogen laminated material. The molecular structure of halogen resin is shown in Fig.2. In either sample, the glass cloth has been used as reinforcement. Test specimens were machined in dambell-type. Fatigue test with a minimum/maximum load ratio R of 0.1 were carried out under 10Hz-loading rate at sine wave in ordinary-temperature. And the fatigue test equipment was computer control servo fatigue testing machine made of Shimadzu Co.,Ltd..

Tabel 1 A series of research result on reliability assurance of recycling engineering plastic

Matrix	Reinforcement material	Tested Method	Environment	Recycling property
PA66	Carbon fiber	Fatigue test	Above Tg/Bellow Tg	△
		Fatigue crack propagation test	Above Tg/Bellow Tg	△
	Glass fiber	Fatigue test	Above Tg/Bellow Tg	×
		Fatigue crack propagation test	Above Tg/Bellow Tg	×
PA46	Carbon fiber	Fatigue test	Above Tg/Bellow Tg	△
		Fatigue crack propagation test	Above Tg/Bellow Tg	△
	Glass fiber	Fatigue test	Above Tg/Bellow Tg	×
		Fatigue crack propagation test	Above Tg/Bellow Tg	×
	Aramid fiber	Fatigue crack propagation test	Room	△
PEEK	Carbon fiber	Fatigue test	Above Tg/Bellow Tg	◎
		Fatigue crack propagation test	Above Tg/Bellow Tg	◎
	Glass fiber	Fatigue test	Above Tg/Bellow Tg	○
		Fatigue crack propagation test	Above Tg/Bellow Tg	○
PPS	Glass fiber	Fatigue crack propagation test	Room	×
	Carbon fiber + Tetrapoded fiber	Fatigue crack propagation test	Room	△
PA·MXD6	Glass fiber	Fatigue crack propagation test	Room	×

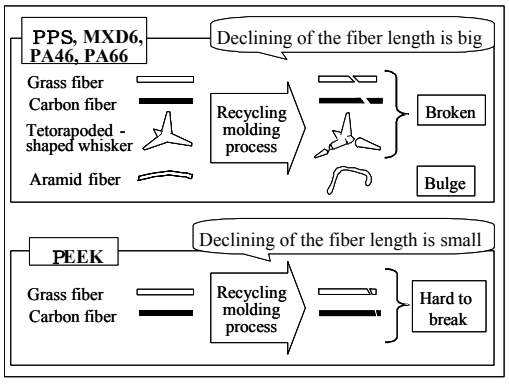

Fig.1 Schematic of influence of recycling molding process of FRTP on previous study

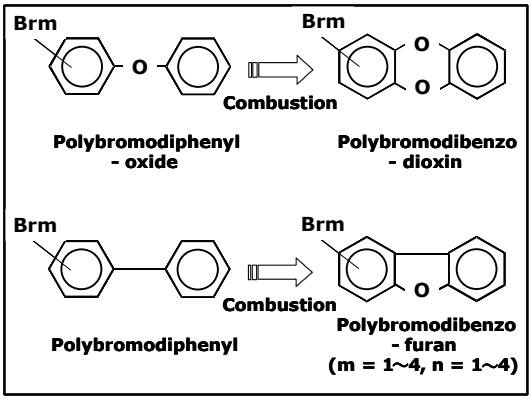

Fig.2 Formation of dioxin and furan

EXPERIMENTAL RESULT

A relationship between number of cycles to failure and stress amplitude in halogen free material and halogen material were shown in Fig.3. From Fig.3, it was proven that the fatigue life of halogen-free material is longer than that of conventional halogen material. That is to say, the fatigue life of halogen free material was longer than that of halogen material. Generally, the material of which the static strength shown by the stress-strain chart is similar becomes also similar on fatigue characteristics. However, there was a remarkable difference in fatigue life of both materials in spite of not recognizing the difference of static strength clearly. Then, in the following chapter, fatigue destructive mechanism are considered from a meso-scopic viewpoint, in order to clarify the difference of the fatigue characteristic of both material.

CONSIDERATION

Relationship between crack initiation life and fatigue fracture life

The relationship between crack initiation life and fatigue fracture life of sample materials is shown in Fig.4. Still, number of crack initiation cycles was decided when main crack length became 0.5 (mm) by visual observation. From Fig.4, it was proven that the crack initiation of halogen free material was comparatively an early time in fatigue life. On the other hand , it was proven that the crack initiation of halogen material was late in fatigue life, halogen material was immediately fractured after a main crack was initiated. Then, Fig.5 shows the relationship between crack initiation life ratio (NI ;Number of crack initiation life / Nf ; Number of failure life) and stress amplitude in both materials. From Fig.5, it was proven that the value of crack initiation life ratio of halogen free material was smaller than that of halogen

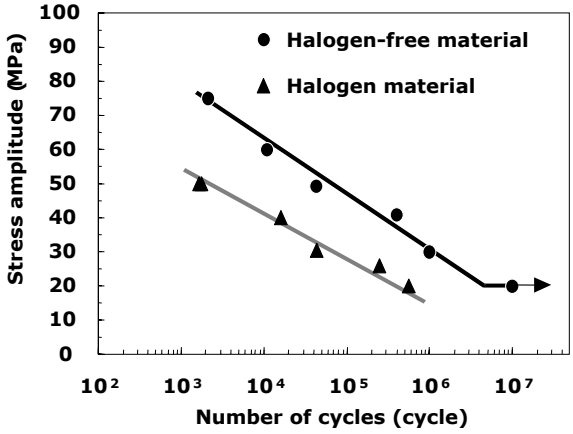

Fig.3 S-N curves

Table 3 Mechanical properties of Halogen-free and halogen material

Item	Halogen-free material	Halogen material
Elastic modulus(GPa)	1.51	1.44
Tensile strength(MPa)	363.7	364.7
Total elongation	3.36	3.32

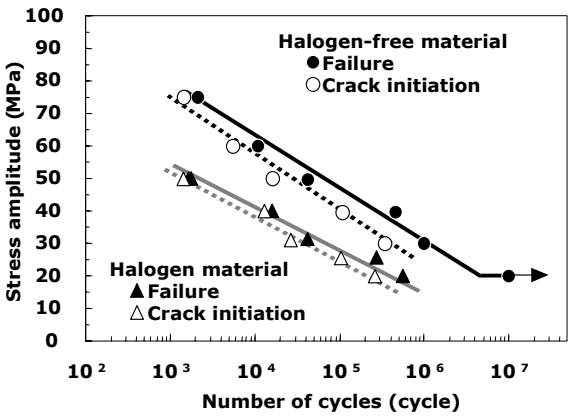

Fig.4 Relationship between number of cycles to failure and crack initiation

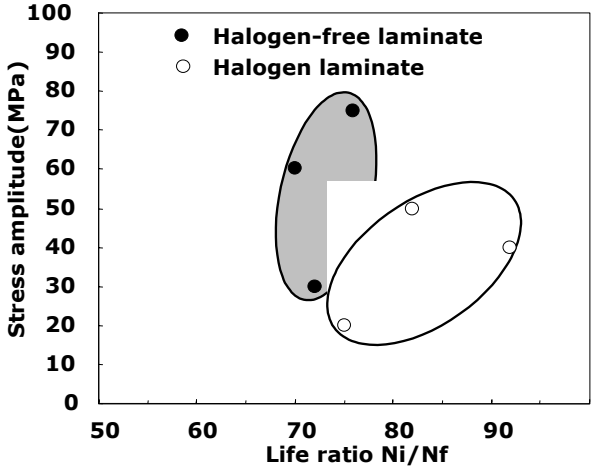

Fig.5 Ratio of number of cycles to crack initiation in fatigue life

material. That is to say, crack initiation life ratio of halogen free materials were 70～75%, and it of halogen materials were 80～90%.

Difference of destruction unit area in fracture surface of resin

Fig.6 (a) and (b) shows fracture surface photographs of halogen free material and halogen material by scanning electron microscope (SEM) at low magnification. In addition, fracture surface photographs at a high magnification are shown in order to compare the difference of fracture morphology of matrix resin of both materials. Examination of fracture surface by SEM revealed that a fracture surface of halogen free material differed from that of halogen material. It was proven that the fracture surface of matrix resin of halogen free materials have been formed in granular form, and a size of that grain was about 4 μm diameters, and the resin comparatively adheres to glass fibers from Fig.7 (a). In the meantime, it was proven that the fracture surface of matrix resin of halogen materials have been formed in the shell state form of about 100～200 μm diameters, and the resin does not adhere to glass fiber shown in Fig.7 (b). In

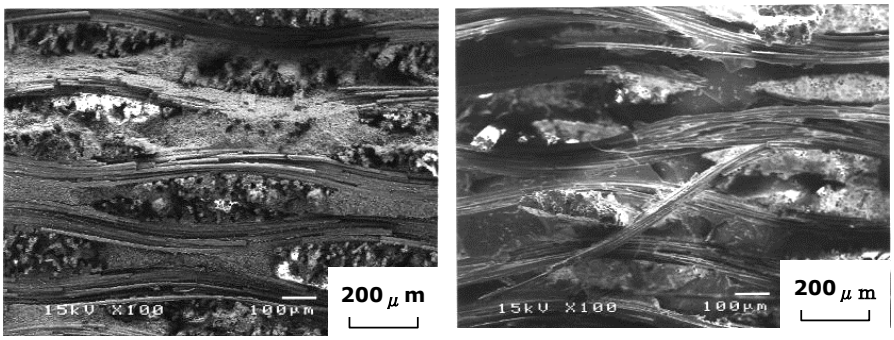

(a) Halogen-free material （×100） (b) Halogen material （×100）

Fig.6 Fracture surface of halogen-free material by using SEM

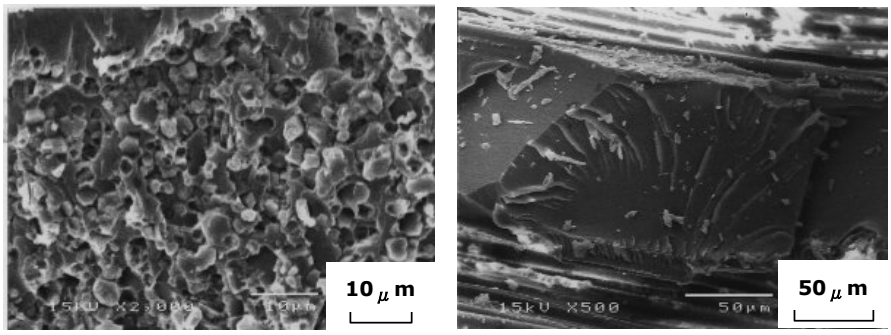

(a)Halogen-free material （×2000） (b)Halogen material （×500）

Fig.7 Difference of the pattern of fracture of resin in halogen-free and halogen mater

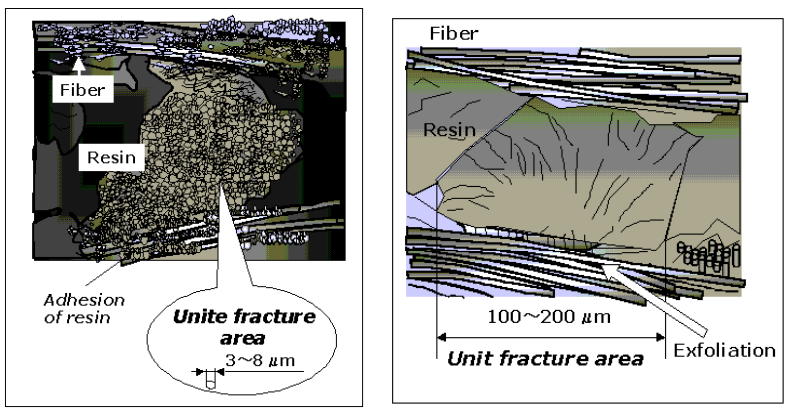

(a)Halogen-free material (b)Halogen material

Fig.8 Schematic of fatigue fracture mechanism of halogen-free and halogen material

addition, its fracture surface was flatter than halogen material, and it has shown frail fracture morphology. And, there was peeling between resin and glass fiber in the central region of the base of these shell state form. One region of the fracture surface pattern of matrix resin of each material like superscription was named Unit Fracture Area. The difference of this UFA seems to greatly affect the difference in fatigue life of each material. A cause of the difference of size of UFA between halogen material and halogen free material was considered to be due to the difference of a molecular structure of matrix resin.

Criteria of fatigue fracture in composite material

From this fatigue test result, the fatigue life of each material differs in spite of the equal of mechanical property. This was considered to be due to the difference of criteria of fracture between static fracture and fatigue fracture. Then, sample materials are caught as a resin/glass fiber composite in order to explain criteria of fracture.

Fig.9(a) shows a way of list of the element link of each material in static fracture. Each element link seems to parallelly range in static fracture. Therefore, the whole material was not fractured immediately, even if the weakest element was destroyed, because the material strength was kept by the more resistant elements. That is to say, its strength is dependent on the most resistant element in the static destruction. The glass fiber is the most resistant element in this material. So the static strength seemed to be equal, since an equal glass fiber has been used in sample materials.

Fig.9 (b) shows a way of list of the element link in fatigue fracture. Each element link seemed to ranks for the series in fatigue fracture. Fatigue fracture is caused by crack generating and developing at repeated stress that is smaller than yield stress (or, tensile strength). Therefore, a crack initiation and propagation is most important role in failure mechanism in fatigue fracture. Since a crack is generated from the weakest element in the material, its element decides the whole life in the fatigue fracture. So, it is considered that the fatigue life was controlled for the weakest link hypothesis. By the consideration to the previous paragraph, a weakest element in this material seemed to be an interface between resin and reinforced fiber or resin. That is to say, it is thought that a difference of the fatigue life of halogen material and halogen free material is based on a difference of the strength of the interface between glass fibers and resin by difference of the kind of resin. Fatigue cracks in halogen material were initiated from the interface of fiber and resin, and in addition, it develops, while the resin was exfoliated from fibers.

In the meantime, fatigue crack in halogen-free material develops inside of matrix resin, since adhesive property of the interface of fiber and resin was comparatively good. And since the resistance for fracture of the resin was bigger than halogen material, a fatigue crack comparatively slowly develops on the halogen free material. So, fatigue life of halogen-free materials seemed to be longer than that of halogen materials.

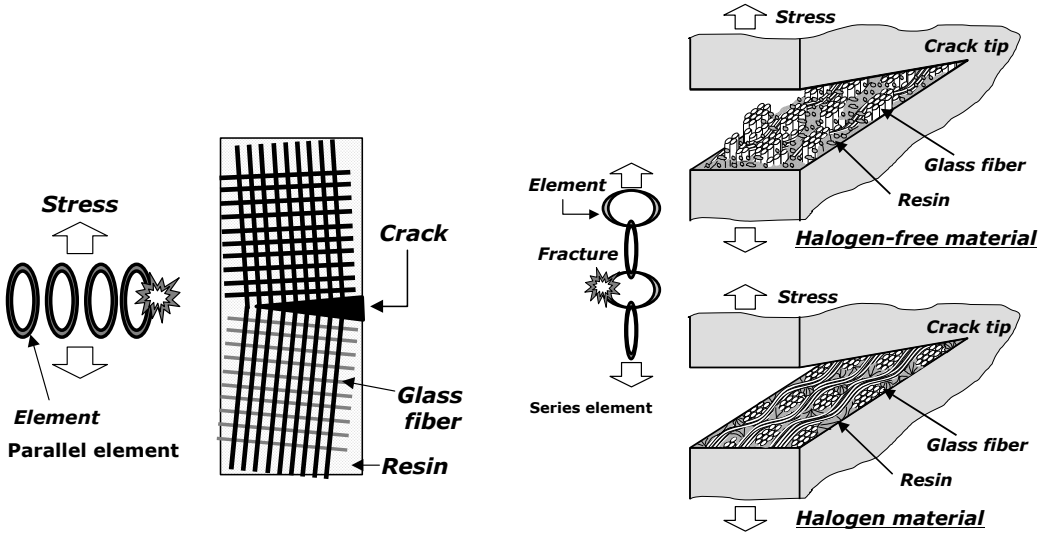

(a)Static fracture mode (b)Fatigue fracture mode

Fig.9 Criteria in static fracture and fatigue fracture , and fracture mechanism

CONCLUSION

In this study, fatigue reliability of halogen free substrate noticed as an environmental harmony type printed circuit board backing was evaluated. And, the examination was demonstratively carried out on the difference of fracture mechanism in fatigue fracture and static fracture from mesoscopic viewpoint. Main results were as follows; (1) Fatigue life of halogen free material was longer than that of halogen material, though mechanical property of both materials was same. (2) Fatigue crack of halogen-free material has comparatively been generated at the initial stage in fatigue life. In the meantime, halogen material was immediately broken , after the crack was generated, and the fracture morphology was brittle. (3) From the fractographic study, it was indicated that size of the characteristic destruction pattern; Unit Fracture Area influenced the difference of fatigue life between halogen free material and halogen material. (4) The difference of fatigue life between halogen material and halogen free material was explained in weakest link model in fatigue fracture. That is to say, the resin or the interface between fiber and resin is a weakest link in fatigue fracture. In the meantime, the effect of difference of resin didn't appear in the difference of static strength between halogen material and halogen free material, because the reinforcement glass fiber undertook the material strength in static fracture.

REFERENCE

(1) H.Suzuki, Fatigue reliability evaluation of the electronic component, (1997)
(2) T.Takahama,O.Hayashi,Journal of Japan adhesion institute,Vol.27,No.4(1991)
(3) "From the circuit to the mounting",Ccompiled by Japan Circuit Mounting Institute,pp15-23
(4) J.Sasaki,K.Hatakeda, High-density packaging technology symposium, Japan Circuit Mounting Institute,1-6,30-35
(5) S,Mizumoto,J.of JIEP,The 6th workshop proceeding,(1998),pp25-29
(7) K.Suga,H.hayashi, J.of JIEP,Vol.3, No.1(2000),pp22-23
(8) K.Yoshiki, "The plastic of the electronics field" Magazine plastic, separate volume, Japan industry investigating committee,(1997),49-54
(9) H.Suzuki, M.Nakamura, T.Kiyotomo, M.Kouhara, T.Haraguchi,Trans.JSME, 60-580,A(1996) pp.2695-2701
(10) M.Nakamura, T.Haraguchi, H.Suzuki,Trans.JSME, 62-600,A(1996) pp.1773-1778
(11) H.Suzuki, H.Fukunaga, A.Matsumura, T.Haraguchi, Trans.JSME, 62-596,A(1996), pp966-971
(12) H.Suzuki,A.Matsumura,H.Fukunaga,T.Haraguchi, Trans.JSME,62-603,A(1996) , pp689-694
(13) H.Suzuki,T.Haraguchi,M.Nakamura and S.Nishino Proceeding of International Workshopon Polymer Blends & Polymer Composites (1997), pp.128-135
(14)M.Nakamura, H.Suzuki, T.Haraguchi, Y.Watanabe,Trans.JSME,63-606,A(1997), pp.213-219,
(15) H.Fukunaga, A.Matsumura, K.yu, H.Suzuki, Trans.JSME, 63-608,A (1997), pp2501-2505
(16) H.Fukunaga, H.Suzuki, A.Matsumura, Trans.JSME, 63-613, A (1997), pp1874-1879,
(17) H.Fukunaga, H.Suzuki, A.Matsumura, T.Haraguchi, Trans.JSME, 63-613,A (1997), pp1880-1885,
(18) H.Suzuki, T.Haraguchi, M.Nakamura, Y.Okuno, Trans.JSME, 64-619, pp.590-596, A(1998)
(19) H.Suzuki, M.Nakamura, Y.Watanabe, T.Haraguchi, Y.Okuno,Trans.JSME, 64- 621,A(1998),pp.1244-1250
(20) S.Wang, Y.Okuno, M.Nakamura, H.Suzuki, T.Haraguchi, Trans.JSME, 65-637, A(1999), pp.1928-1934,
(21)K.Takano, T.Hukuda, M.Oze, Y.Murai, MES'99, Proceedings of the 9th microelectronics symposium, pp229-232
(22) K.Ohori,M.Yano,T.Aizawa,M.Kakiya, Technical report of Hitachi Chemical Co.,Ltd.. , No.33 (1999-7), pp27-30
(23) N.Honda, J.of JIEP, Vol.3, No.1 (2000),pp74-77
(24) T.Yasuda, Plastics, Vol.50, No.7 (1999), pp18-29
(25) A.Happoya,J.of JIEP, Vol.2,No.6(1999),pp481-484
(26) S.Honda, J.of JIEP, Vol.1, No.4 (1998), pp257-258
(27) R.Koterazawa, Zairyo, Need theory of material strength science, Asakura syoten (in Japanese), pp96-98

Effect of humidity on fatigue crack propagation of aluminum alloys

Yasuo Kobayashi, Yuzuru Ito, Kentaro Kido and Keisuke Ishikawa

Toyo University, Department of Mechanical Engineering,
2100 Kujirai, Kawagoe, Saitama, Japan 350-8585

Abstract

High specific strength materials are getting more important for saving energy in various kinds of transportation systems. Although high strength materials are sensitive to the environment, aluminum alloys are insensitive to the mild atmosphere. Aluminum alloy makes stable oxide film and has the resistance to the progress of oxidation. Since aluminum alloys do not show the clear fatigue limit, the information on the fatigue crack propagation behavior is essential for designing of the structure and estimating of the life of the structures. We carried out the fatigue tests on Al-Zn-Mg, 7075-T6 and Al-Mg, 5083-O alloys. They have quite different microstructure. The former has the strongest alloy among Al alloys and the strength is performed by the precipitation hardening. The latter has the strongest alloy among solid solution aluminum alloys. The fatigue crack propagation behavior was examined by compact tension specimen in two kinds of different environment. The atmosphere was controlled by dry and wet argon at ambient temperature. The dry argon did not contain water vapor and the humidity was almost 0%. The wet argon was added by water vapor and the humidity was kept more than 90%. The fatigue crack propagation properties for the steady state region, the second stage, were characterized by the Paris law, $da/dN = C(\Delta K)^m$. The exponent, m depends on the environment and is changed by the humidity. There is a relationship between C and m for both alloys. The relationship depends upon the environment alone. The crack propagation rate is usually accelerated by water vapor. The crack propagation test was also conducted in the dry argon with hydrogen gas. Since the fatigue crack propagation does not show any effect of hydrogen gas, the acceleration is due to the hydrogen atoms, which were produced on the fresh fractured surfaces. The chemical reaction on the fresh aluminum surface could produce hydrogen ions in the water on the surfaces. The difference in the oxides film formed on the aluminum surfaces would bring the clear change of the fatigue crack propagation. Besides, the crack closure effect was hardly observed for these alloys. The fractured surfaces in dry argon was typical striation pattern for both alloys. In wet environment, the surface was covered with fine structures for 5083 alloy.

Keywords: *fatigue crack propagation rate, humidity, aluminum alloy, Paris law, hydrogen embrittlement*

I. Introduction

Aluminum alloys with higher strength are focused for energy saving through the reduction of the weight of vehicles and the transportation systems. We are interested in two kinds of high strength aluminum alloys, which are 7075, Al-Zn-Mg and 5083, Al-Mg alloys. The former is precipitation-hardening alloy and the latter is solid solution hardening. Each alloy is the highest in the tensile strength among the respective categories. Fatigue crack propagation behavior of alloys would depend upon the microstructure and the environment. The microstructures of both alloys are quite different. The 7075 alloy contains the second phases and the 5083 is single phase. Fatigue behavior of materials depend upon the environment. An important parameter is humidity, moisture of water, which is ambient atmosphere. We carried out the experiments on both aluminum alloys in the environment, where the humidity and gas were controlled. The fatigue crack propagation behavior was evaluated based on Paris law [1].

II. Experimental procedures

2.1. Materials

The chemical composition of aluminum alloys used for this experiment is shown in Table 1. The specimen for fatigue crack propagation test is the modified compact tension type. The conventional heat treatment T6 was given to 7075, whose tensile strength was 500 MPa. The annealing was done to 5083 with the tensile strength of 300 MPa.

2.2. Fatigue test system

Fatigue crack propagation tests were conducted in the chamber with the controlled atmosphere. The humidity was always checked by the hygrometer. In this experiment, the humidity was selected less than 10 % and more than 90 %. The former is dry condition and the latter wet condition. The test temperature was controlled around 300 K.

Table1. Chemical composition of aluminum alloys. (mass %)

	Si	Fe	Cu	Mn	Mg	Cr	Zn	Ti	Al
5083-O	0.09	0.22	0.02	0.61	4.7	0.05	0.01	0.02	Bal.
7075-T6	0.08	0.18	1.2	0.02	2.4	0.18	6.3	0.01	Bal.

III. Experimental results

3.1. Effect of atmosphere on the fatigue crack propagation rate

The standard experiments were done in the dry argon, where there would be no effect on the fatigue crack propagation. The effect of the humidity on the fatigue crack propagation curves is shown Fig.1.

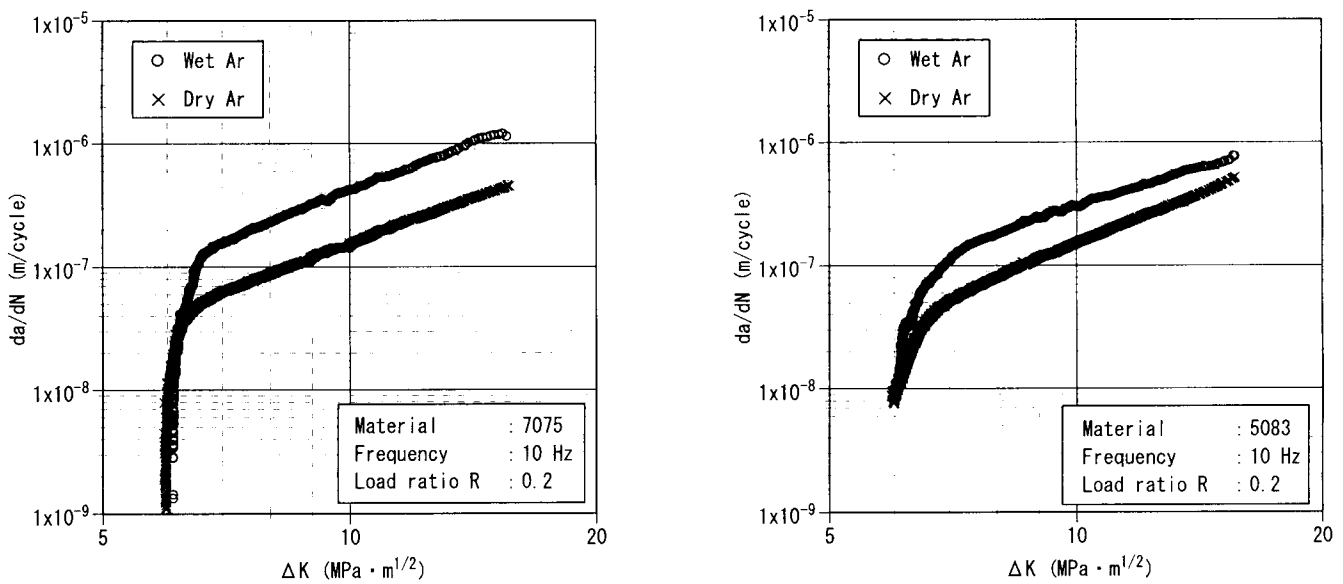

Fig.1. Effect of atmosphere on fatigue crack propagation rate of aluminum alloys.

The effect of the humidity on the fatigue propagation rate was larger for 7075 than for 5083. The effect depends upon the strength of the aluminum alloy. For 5083, the effect was reduced at the higher ΔK region. However, the definite difference was not recognized in the relationship of da/dN vs. ΔK of both alloys. In the inert gas, the fatigue crack propagation behavior would be similar for aluminum alloys regardless of the strength [2]. The mechanism would be controlled by ductile mode, which brings the striation pattern on the fatigued surfaces.

3.2. Effect of test condition on the fatigue propagation rate

The effect of the test condition, load ratio and frequency, was examined in the wet environment for both alloys. The interesting results were observed for both alloys. The effect of the frequency was neither recognized for 7057 nor 5083 alloys. When the reduction of the load ratio, $R = P_{min}/P_{max}$ was reduced, the apparent threshold ΔK was increased. When both alloys were fatigued at the higher load ratio, the crack took the discontinuous propagation behavior. Similar behavior was observed at the lower frequency. The discontinuity in the crack propagation was outstanding in the wet environment [3]. The existence of water vapor would be important for the phenomenon. The behavior is quite different from the results of magnesium alloys, which are chemically reactive to water [4]. The difference would be due to the chemical reaction and chemical product on the fresh surfaces introduced by the fatigue crack propagation [5]. The chemical product is oxide file formed through the chemical reaction of matrix metal and oxygen. The oxides are Al_2O_3 for aluminum alloys and MgO for magnesium alloys. The former is harder and denser than the latter.

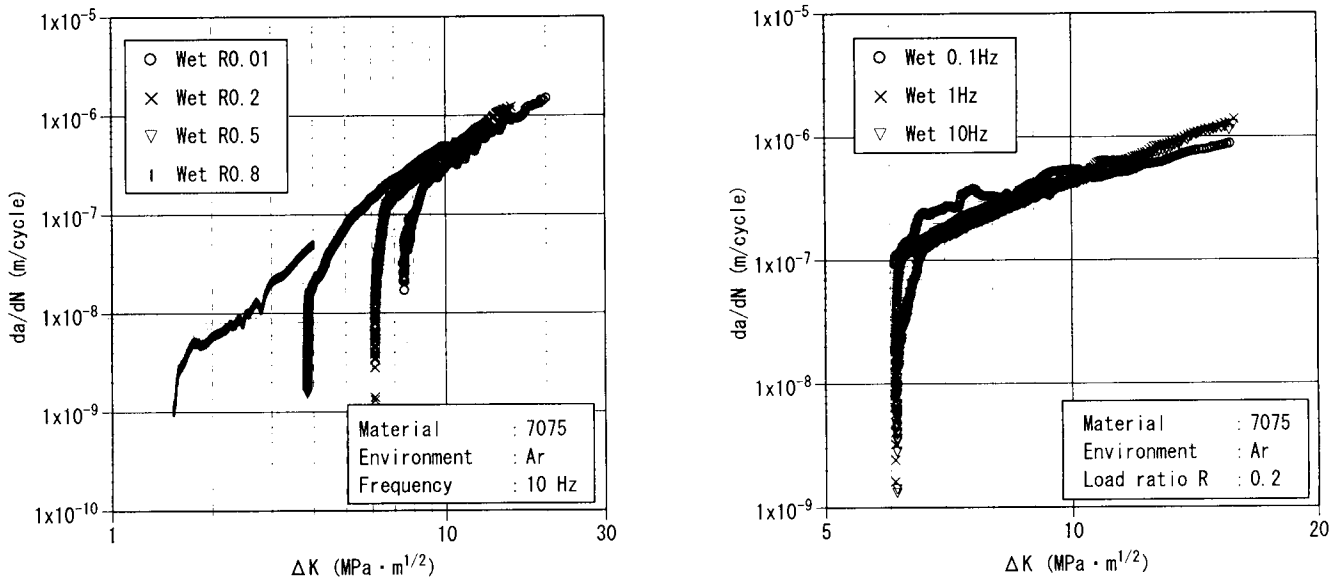

Fig.2. Effect of load ratio and frequency on fatigue crack propagation rate of 7075 alloy in wet argon atmosphere.

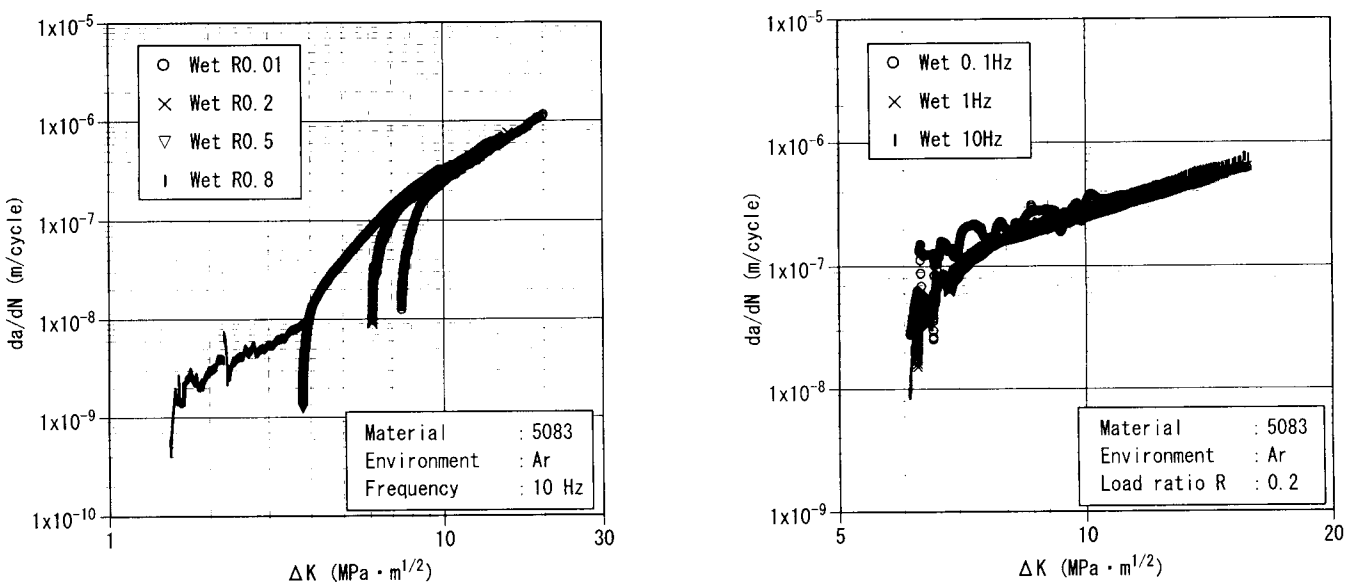

Fig.3. Effect of load ratio and frequency on fatigue crack propagation rate of 5083 alloy in wet argon atmosphere.

3.3. Observation of fractured surfaces

The fracture surfaces were observed to examine the difference of the fracture mechanism. The typical photos are shown for both alloys in Fig.4. The quite difference was observed between the wet and the dry environment for both alloys. In dry argon atmosphere, the fatigue crack propagates in the striation pattern for both alloys. The 7075 alloy with the higher strength shows the perpendicular cracking. However, in the wet environment, the chemical products were observed on the fatigue fractured surfaces. The fragmentation of the oxide is more remarkable for 7075 than 5085 alloy. The difference would result in the higher fatigue crack propagation rate. The brittleness of the oxide film would make the easy path for the penetration of hydrogen atoms.

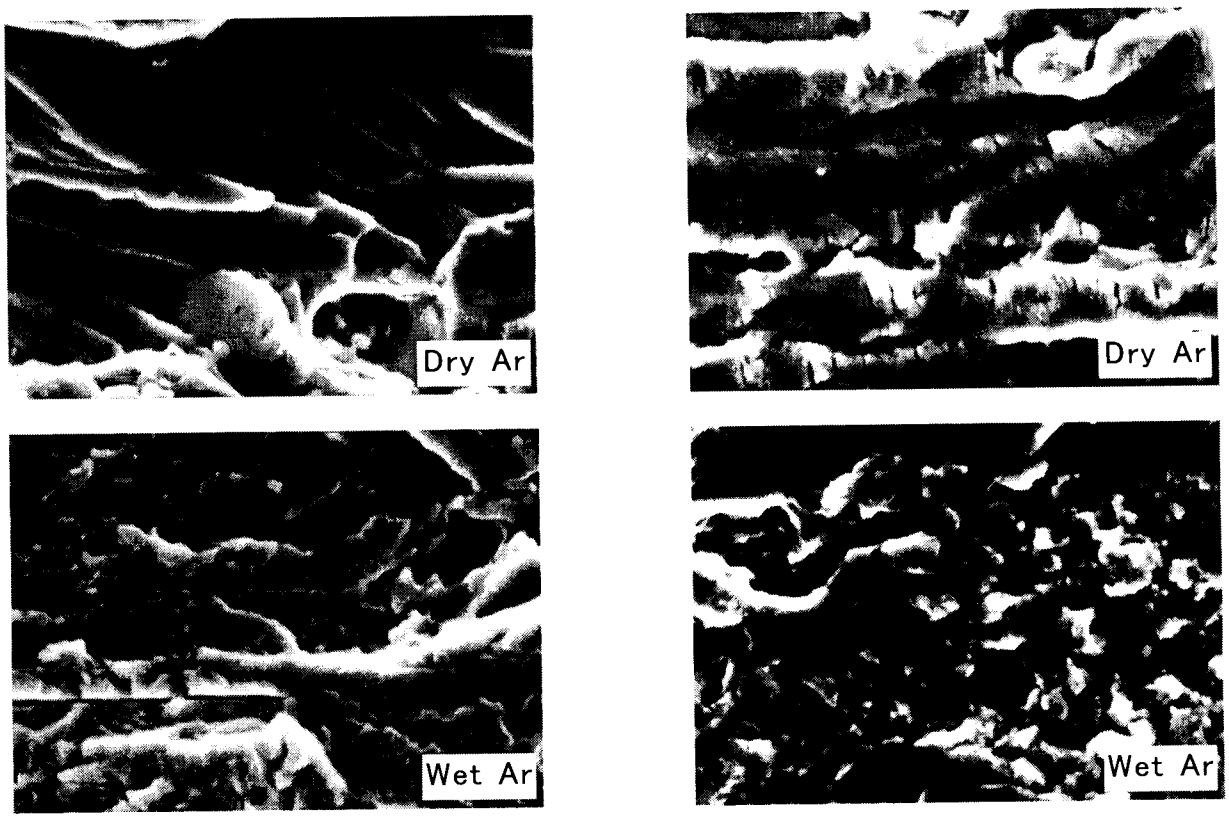

Fig.4. SEM micrograph of fatigue fractured surfaces of aluminum alloys in dry and wet argon atmosphere.

IV. Discussion

4.1. Paris parameters, m and C for the second stage

In this experiment, Paris law, $da/dN = C(\Delta K)^m$, was applied to evaluate the effect of the environment on the fatigue crack propagation behavior. The fatigue crack propagation behavior experimentally obeyed the above equation, where the parameter C and m are constant in the second region [6]. The constant, $m \approx 2$ is deduced by the energy criterion at the crack tip subjected to small scale yielding. In this experiment, we observed the values of C and m for both alloys under all experimental conditions. The results are shown in Fig.5, where the relationships between C and m are recognized. The relationships are divided into two groups, dry and wet condition. Humidity, water vapor accelerates the fatigue crack propagation of aluminum alloys through the increase in C and m at the second stage.

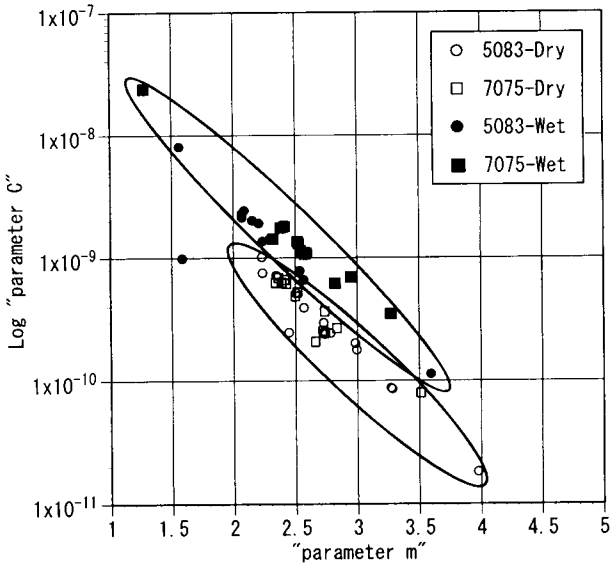

Fig.5. Paris parameters, C and m for 7075 and 5083 alloys.

4.2. Effect of humidity and hydrogen embrittlement

The following chemical reaction can take place on the fresh aluminum alloy surfaces in water.

$$2Al \rightarrow 2Al^{+3} + 6e \quad (1)$$

$$6H_2O \rightarrow 6H^{+1} + 6OH^{-1} \quad (2)$$

$$2Al^{+3} + 6OH^{-1} \rightarrow 2Al_2O_3 + 3H_2 \quad (3)$$

While aluminum oxide was formed, hydrogen ions were resolved in the water on the aluminum surfaces. The ions can easily penetrate into the aluminum matrix because of the extraordinarily small size. The hydrogen ions in the water on the aluminum surfaces should run through the aluminum oxide film formed on the fresh aluminum surface. The difference in the properties of the oxides is observed in the fatigue crack propagation behavior in wet environment. In Fig.1, the propagation rate of 7075 alloy is higher then of 5083 alloy. The oxide film of 5083 alloy is more dense and less brittle than of 7075 alloy. The hydrogen ions can easily diffuse in the aluminum alloys and make the matrix brittle and so hydrogen embitterment takes place. The acceleration of fatigue crack propagation in wet environment is due to the existent of hydrogen ions and the easiness of diffusion of the ions in the oxide film.

4.3. Effect of microstructure on fatigue crack propagation.

There is not found clear difference of the microstructures of the alloys in the parameters, C and m as shown Fig.5. The stable fatigue crack propagation at the second stage is independent of the microstructure, unless the materials are brittle [7]. Aluminum alloy in the mild environment never becomes brittle, because the fatigue crack propagation is actually controlled by the ductile striation mechanism. However, the properties of the oxide film formed on the fresh surfaces would depend upon the difference of the alloy composition. The heterogeneous structure, the 7075 alloy would make local cell on the surface and then the rough and thick film would be expected. The difference would also bring the closure effect. In this experiment, the effect was not observed definitely. But it was recognized slightly for the 5083 alloy.

V. Conclusion

We carried out the fatigue crack propagation tests for 7075 and 5083 aluminum alloys in dry and wet environment. The fatigue crack was accelerated in wet atmosphere, though the fatigue crack propagation rate was similar for both alloys in dry argon atmosphere. The crack acceleration was induced by hydrogen embrittlement. The hydrogen was ions which were in the water on the fresh aluminum surfaces. The hydrogen ions can easily penetrate the oxide film and the aluminum matrix. The difference of the properties of the oxide film formed on the aluminum surfaces was observed in the fatigue crack propagation behavior of the aluminum alloys. The fatigue fractured surfaces in wet atmosphere showed quite different features from that in inert atmosphere.

VI. References

[1] Suresh,S., Fatigue of Materials, Cambridge Press, Cambridge, (1998), p.341.

[2] Kobayashi,Y., Y.Ito and K.Ishikawa, "EFFECT OF GASEOUS ATMOSPHERE ON FATIGUE CRACK PROPAGATION BEHAVIOR OF Al-Mg ALLOYS", Proceedings of the 3rd International Conference on Mechanics of Time Dependent Materials, Erlangen, Germany, (2000), p.130.

[3] Ishikawa,K., Y.Kobayashi and T.Ito, "CHARACTERISTICS OF FATIGUE CRACK PROPAGATION IN HEAT TREATABLE DIE CAST MAGNESIUM ALLOY", Light Weight Alloys for Aerospace Applications III, Ed.by E.W.LEE, N.J.Kim, K.V.Jata and W.E.Franzier, The Minerals, Metals & Materials Society, (1995), p.449.

[4]Kobayashi,Y., T.Shibusawa and K.Ishikawa, " Environmental effect of fatigue crack propagation of magnesium alloy", Materials Science and Engineering A234-236, (1997), p.220.

[5] Barsom,J.M. and S.T.Rolfe, FRACTURE and FATIGUE CONTROL in STRUCTURES, *Applications of Fracture Mechanics*, Butterworth-Heinemann,Woburn, MA, (1999), p.305.

[6] Nishida,S., FAILURE ANALYSIS IN ENGINEERING APPLICATIONS, Butterworth-Heinemann, Oxford, (1992), p.27.

[7] Knott, J.F., Fundamentals of Fracture Mechanics, Butterworths, London, (1973),p.255.

EFFECT OF IMPACT LOADING ON TENSILE STRENGTH OF CONCRETES

M. DAIMARUYA, H. KOBAYASHI
H. SHIZAWA, R.A. SIREGAR and Y. ISHIHATA

Department of Mechanical Engineering Systems
Muroran Institute of Technology
27-1 Mizumoto, Muroran, Hokkaido 050-8585, Japan

ABSTRACT

The tensile strength and strain rate sensitivity of concretes under impact loadings were examined by means of the method of reflected tensile stress waves. The experimental method is conducted by the Hopkinson bar technique and it is based on the superposition and concentration of tensile stress waves reflected both from the free ends of a striking bar and a specimen bar. The impact tensile experiment for concretes was carried out and the tensile strength of concretes under impact loadings was discussed as well as the effect of strain rates. This study focused on the estimation and measurement of strain rates using crack gages. As a result, the impact tensile strength of concrete at the strain rate of 10^0 sec^{-1} was found to be approximately twice of the static tensile strength, and it was remarkably influenced by strain rates ranging from 10^0 to $10^1 sec^{-1}$.

KEYWORDS

Impact tensile strength, Concentration of tensile stress waves, Cumulative fracture probability, Strain rate, Crack gage, Concrete.

INTRODUCTION

The investigation of the mechanical characteristics and the fracture strength of concrete under high loading rate is increasingly important for the safe assessment of most engineering structures against impact loadings such as impingement of projectiles, explosions and enormous earthquakes [1-3]. Since concrete is inherently weak in tension, it is commonly used as a compressive member material in civil engineering structures. On the other hand, concrete is also used in protective structures designed to resist impulsive loads. Although impulsive loads are originally compressive, they may produce tensile stress waves in structural members developed at the free boundary and so on. It is difficult to isolate concrete structures from impact tensile stresses, even though static tensile loads on concrete members are avoided. Even in static tests, precise measurement of the tensile strength of concrete is known to be difficult as well as rocks and ceramics. For determining the static tensile strength of concrete materials, the splitting-tensile test is commonly used to avoid some difficulties associated with the direct tension. Many investigations on impact tensile strength of concrete materials

have been contributed by impact splitting-tensile test, together with impact direct tension test [4-7]. Recently an experimental method for dynamic tensile testing by spalling is reported [8,9]. However, it does not appear that there is a standard test method for measuring impact tensile strength of concrete materials [10].

This paper concerns with the measuring method for the impact tensile strength and strain rate sensitivity of concretes by means of the measuring method of reflected tensile stress waves. The experimental method has been proposed for brittle materials such as plaster, ceramics and concrete in our previous papers [11-15]. The impact tensile experiment is conducted by the Hopkinson bar technique and it is based on the superposition and concentration of tensile stress waves reflected both from the free ends of a striking bar and a specimen bar. The impact tensile experiment for concretes was carried out and the tensile strength of concretes under impact loadings was discussed as well as the effect of strain rates. This study focused on the estimation and measurement of strain rates using crack gages. Because the tensile stress region varies with time in this measuring method, it is necessary to find the beginning time when a specimen bar is broken after starting of tensile stress waves superposition, in other words, the gage length that the tensile stress waves have reached until the initiation of tensile break. Consequently, the impact tensile strength of concrete at the strain rate of 10^0 sec^{-1} was found to be approximately twice of the static tensile strength, and it was remarkably influenced by strain rates ranging from 10^0 to $10^1 sec^{-1}$.

STRESS WAVE PROPAGATION IN A CONCRETE BAR

The measuring theory had already been presented in the previous papers [11,13], but it is briefly explained here by means of a numerical simulation. Figure 1 (a) shows a concrete bar specimen with the length of l and an incident compressive stress σ_0 into the impact end of the bar. $T = t/t_0$ is the dimensionless time and $t_0 = l/c_0$ is the time of the wavefront reaching at the free end of the bar. c_0 is the velocity of stress wave in the concrete specimen bar. Assuming that the pulse length of an incident compressive stress has the same length with a concrete specimen bar, the numerical simulation was carried out under the condition of two-dimensional axisymmetric model using a FEM code, MARC.

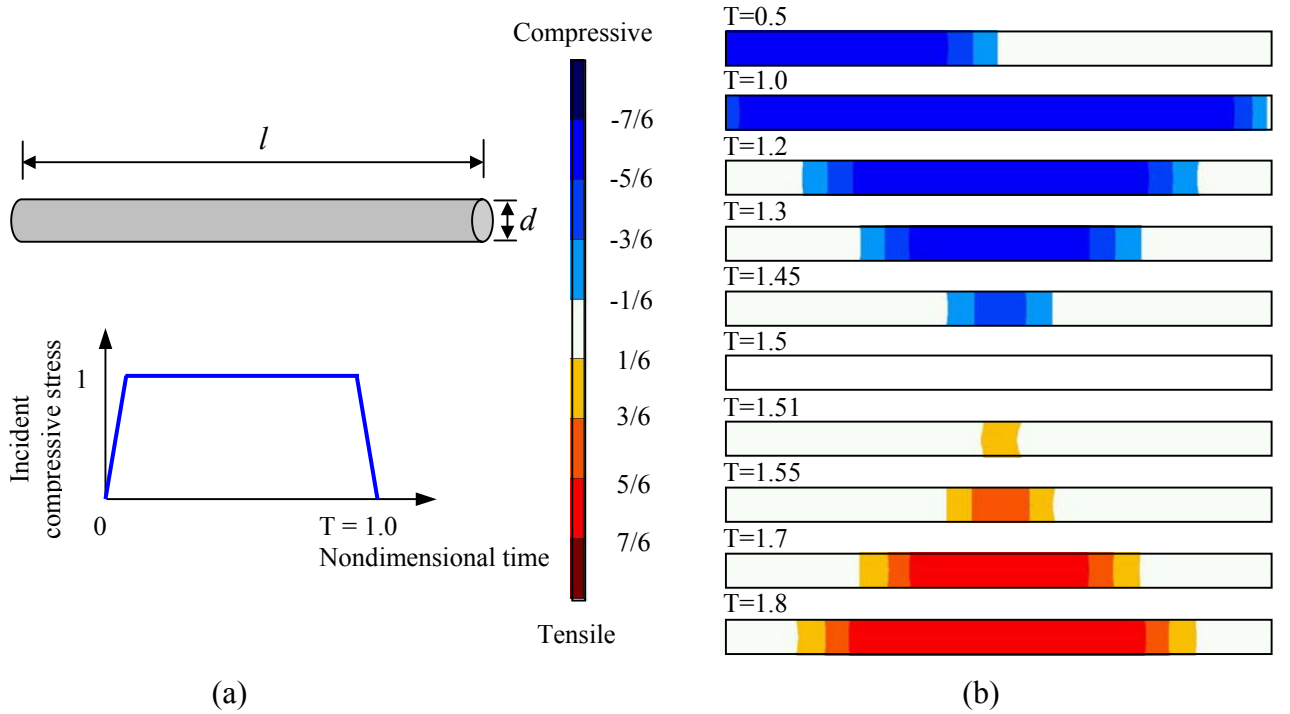

Figure 1: (a) Concrete specimen bar and an incident compressive stress in a numerical analysis.
(b) Propagation of incident compressive stress wave and development of tensile stress region produced by reflected tensile stress waves.

Figure 1 (b) shows the numerical results that illustrate the behavior of stress wave propagation in a concrete specimen bar. After the compressive stress wave propagation, the reflected tensile stress waves are superposed at the center of the specimen bar and the tensile stress region is developed. The blue denotes the compressive stress wave and region, and the red the tensile ones. By making use of this process of stress wave propagation, a simple measuring method for impact tensile strength of concrete materials was proposed. The impact tensile experiment is conducted by means of Hopkinson bar technique.

MECHANICAL PROPERTIES OF CONCRETE SPECIMEN

Concrete and mortar specimens were used for this study. In this paper, however, the results only concerning concrete specimens (with coarse aggregate) are presented. The concrete mix proportions are shown in Table 1. An ordinary Portland cement with fine and coarse aggregates was employed for the fabrication of concrete specimens. The maximum size of coarse aggregate was 10 mm. Concrete specimens cured for 10 months were used for this study. In the impact tensile strength experiment, cylindrical bar specimens of concrete with 750 mm length and 50 mm diameter were used. Static tests of splitting tension (Brazilian), 3-point bending and compression were also carried out to examine the static mechanical properties of the concrete specimen.

TABLE 1
MIX PROPORTIONS OF CONCRETE FOR A CUBIC METER

Material	Quantity
Water/cement ratio	0.5
Portland cement	370 kgf
Water	185 kgf
Fine aggregate	874 kgf
Coarse aggregate	874 kgf
Water-reducing admixture	0.74 kgf
Total weight per cubic meter	2303 kgf

TABLE 2
MECHANICAL PROPERTIES OF CONCRETE

Mechanical Properties	Value
Splitting tensile strength (σ_{ts})	2.9 MPa
Bending strength (σ_b)	5.4 MPa
Compressive strength (σ_c)	27.8 MPa
Elastic modulus (E)	35.1 GPa
Mass density (ρ)	2315 kg/m^3
Poisson ratio (ν)	0.2
Velocity of stress wave (c_0)	3894 m/s

In the static tests of splitting tension and compression, pieces of specimens with a length of 100 mm were cut from the long cylindrical bar specimens. To avoid some difficulties associated with the direct tension test such as specimen holing and proper alignment, the splitting tension test was carried out. The static splitting tensile test is an acceptable indirect method for determining tensile strength of concrete materials [6,10]. In the static bending test, the span was set to be 700 mm. All the static tests were conducted using an INSTRON (model 5586) material test machine at loading rates of 0.05 - 0.5 mm/min.

Table 2 shows the static mechanical properties of the mortar specimens obtained by the static tests. Each strength is the mean value of cumulative fracture probability, which is discussed later. Here, c_0 is the velocity of stress waves, given by $c_0^2 = E/\rho$, which almost corresponded to the experimental observation of elastic waves through the concrete specimen bar.

EXPERIMENTAL TECHNIQUE AND ARRANGEMENT

The Hopkinson bar technique is a widely used technique to determine the mechanical properties of materials at high loading rates. In this experiment, the setup consists of an air gun, a stainless-steel striking bar (SUS306), an aluminum alloy input bar (JISH4040), and a set of recording devices. The striking bar with 500 mm length and 20 mm diameter is chosen in order to initiate concentration of tensile stress at the center, C, of a specimen bar, shown in Fig. 2. The input bar is of length 1500 mm

and 50 mm diameter. It is adjusted to be collinearly impacted by the striking bar shot out from the air gun. Two sets of semiconductor strain gages, *a* and *b* , are cemented diametrically at a distance of 6*d* and 12*d* from the contact end the input bar with a specimen bar for measuring incident stress waves into the specimen bar [11]. One end of the concrete specimen bar is arranged in tight contact with one end of the input bar, while the other end of the specimen bar is released from stresses. The factors of reflection and transmission at the interface between the input bar and the specimen bar can be calculated using both the material properties of the input bar and the concrete specimen. In the present combination, α = - 0.25 and β = 0.75, where $1+\alpha = \beta$ on the assumption that all the incident stress, reflection stress and transmitted stress are taken to be compressive [2]. All specimens are equipped with two strain gages pasted diametrically at two locations 1 and 2, respectively, to measure directly stress waves propagated in a specimen bar. In order to specify the tensile break time, four crack gages (KYOWA, KV-5C) are also mounted at the center position of the specimens. The response signals trapped at those locations are passed through bridge boxes to a four-channel digital oscilloscope (Nicolet, Model 400).

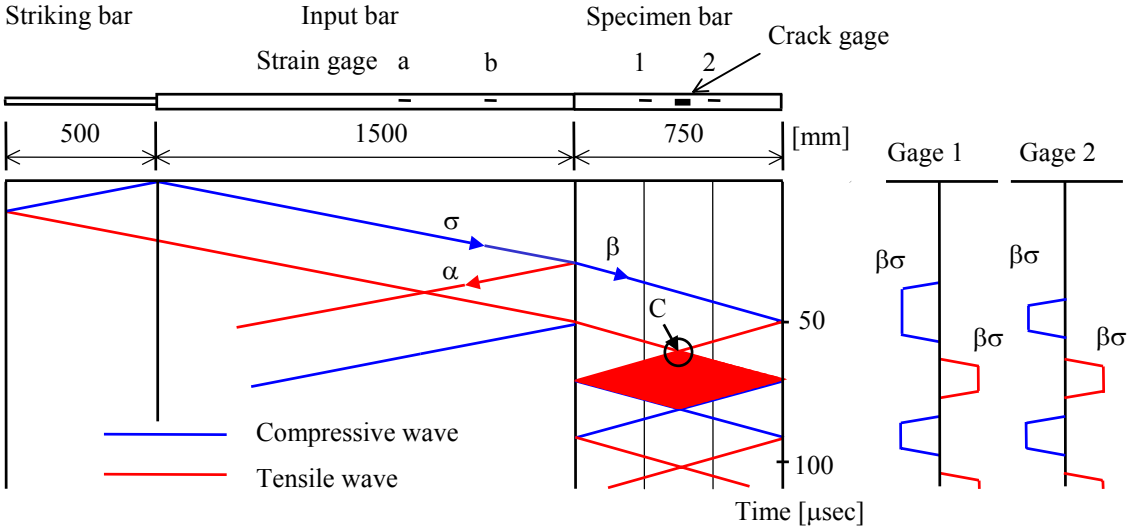

Figure 2: Experimental arrangement and superposition of tensile stress waves in concrete specimen.

IMPACT TENSILE STRENGTH AND STRAIN RATES

Cumulative Fracture Probability

The impact tensile strength is determined from reading off the intensity of the tensile stress waves measured by the strain gages cemented on the concrete specimen bar. Suitable statistical analyses may be required to treat the dispersion of the experimental data in relation to the concrete strengths. A Weibull distribution was applied to not only the impact tensile strength but also the static strengths of the concrete specimen, as shown in Figure 3. To plot the *i*-th ranked sample from a total of *n* number of fractured specimens, a median-rank position was adopted, which is the distribution function *Fi* expressed approximately in terms of $Fi = (i-0.3)/(n+0.4)$. The data plotted on the Weibull probability paper, i.e., $lnln[1/(1-Fi)]$ versus $ln(\sigma)$ lay on straight lines. The regression lines were drawn by means of the method of least squares. The Weibull modulus (shape parameter) *m* of each plot and the scale parameter ξ (fracture probability 63.2%) can be found from the Weibull distribution. The mean stress μ and the standard deviation *s.d.* can be calculated based on such data. The statistical results of the concrete used for this study are shown in Table 3. Comparing the impact tensile strength with the static tensile strength, it is worth noting that the tensile strength of the concrete is significantly influenced and increased by loading rates. Here the impact tensile strength, σ_{it} , in Table 3 denotes the minimum tensile stress to break the concrete specimen under impact loading in this experimental method. The impact splitting-tension test was also performed, but the detail is omitted.

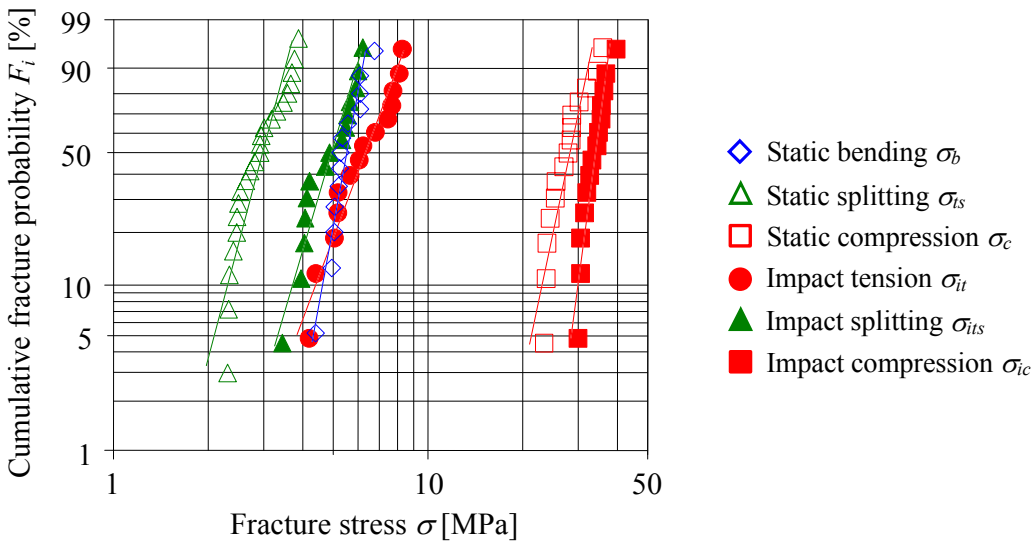

Figure 3: Cumulative fracture probability of concrete strengths.

TABLE 3
EXPERIMENTAL RESULTS OF STATISTICAL ANALYSIS BY WEIBULL PLOTS

Test		σ_b	σ_{ts}	σ_c	σ_{it}	σ_{its}	σ_{ic}
Number of samples	n	13	23	15	14	15	14
Shape parameter	m	10.6	6.3	9.8	5.2	6.5	14.6
Scale parameter [MPa]	ξ	5.7	3.1	29.3	6.8	5.2	36.9
Mean [MPa]	μ	5.4	2.9	27.8	6.2	4.9	33.7
Standard deviation [MPa]	*s.d.*	0.5	0.6	3.4	0.9	0.9	2.8

Strain Rate Sensitivity of Concrete

In this measuring method the tensile stress region developed in the axial direction of a specimen bar varies with time. Therefore it is necessary to find the beginning time when a specimen bar is broken after starting of tensile stress waves superposition, in other words, the gage length that the tensile stress waves have reached until the initiation of tensile break. The broken time of a specimen was measured using crack gages pasted on it, while the starting time of superposition of tensile stress waves was done by strain gages. A typical example of response signals measured by the strain and crack gages is presented in Figure 4. The solid blue line denotes the stress response at the broken position of a specimen bar, estimated from the stress response of the strain gage 2, while the red line denotes the response from crack gages. It can be found that the beginning time of tensile stress generation and tensile break is 431 μsec and 548 μsec, respectively, after an incident compressive stress is transmitted into the specimen bar. Then the gage length of tensile stress region is calculated as $l = 2c_0\Delta t = 0.85$ m, considering that the tensile stress region is initiated at the center of a specimen bar and progresses on both sides. Subsequently the strain rate can be found as, $\dot{\varepsilon} = v/l = 1.35$ sec^{-1} by making use of the relation between impact stress σ and particle velocity v, $v = \sigma / \rho c_0$. The corresponding impact tensile strength is about 9.2 MPa. Repeating the same procedure to each measuring result shown in Figure 3 and a series of experimental results on higher impact tensile stresses applied to concrete specimens, the relation of the impact tensile stress and the strain rate of the concrete used for the present test was obtained in Figure 5. The impact splitting tensile (Brazilian) results are also depicted in addition. The impact tensile strength of concrete at the strain rate of about 10^0 sec^{-1} may be found to be approximately twice of the static tensile strength, and it is remarkably

influenced by strain rates ranging from 10^0 to $10^1 sec^{-1}$. In addition, it is recognized that there are some differences between the results obtained by the present measuring method using reflected tensile stress waves and by the impact splitting-tension test.

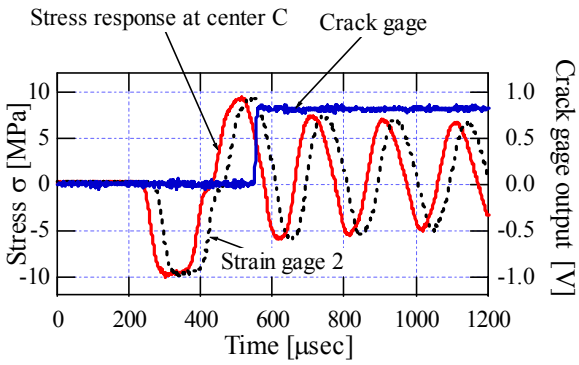

Figure 4: Responses of strain and crack gages.

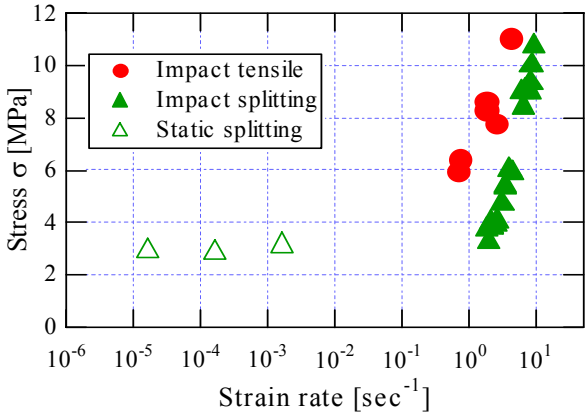

Figure 5: Strain rate effects on concrete strength.

CONCLUDING REMARKS

(1) In this paper the impact tensile strength and strain rate sensitivity of concrete was discussed by means of the measuring method using reflected tensile stress waves. The impact tensile experiment of concrete specimens was performed, together with the impact splitting-tension test. The experimental results were analyzed statistically by a Weibull distribution.

(2) The strain rates were estimated by specifying the gage length of the tensile stress region developed until the initiation of tensile break in a specimen bar, which was measured by using crack gages.

(3) The impact tensile strength of concrete used for the present study at the strain rate of 10^0 sec^{-1} was found to be approximately twice of the static tensile strength, and it was remarkably influenced by strain rates ranging from 10^0 to $10^1 sec^{-1}$.

REFERENCES

1. Goldsmith, W., (1960), *Impact*, Edward Arnold, London.
2. Johnson, W., (1972), *Impact Strength of Materials*, Edward Arnold, London.
3. Reinhart, H.W., (1986), In: *Cement Based Composites Strain Effect on Fracture*, pp.1-13.
4. Birkimer, D.L and Lindemann, R., (1971), J. American Concrete Institute, 68, pp.47-49.
5. Griner, G.R., Sierakowski, R.L. and Ross, C.A., (1975), Shock Vib. Bull., 45-4, pp.131-142.
6. Ross, C.A., Kuennen, S.T. and Tedesco, J.W., (1990), In: *Micromechanics of Failure of Quasi-Brittle Materials*, pp.353-363, Elsevier Applied Science.
7. Albertini, C. Cadoni, E. and Labibes, K., (1997), Journal de Physique IV, pp.C3- 915-920.
8. Brara A., Camborde F., Klepacko J.R., Mariotti C.(2001), Mechanics of Materials, 33, pp.33-45.
9. J.R. Klepaczko, A. Brara, (2001), Inter. J. Impact. Eng., 25, pp.387-409.
10. Japan Concrete Institute, *Handbook of Concrete* (2nd ed.), Gihoudo, 1996.
11. Daimaruya, M, Kobayashi, H. and Bustami, S., (1994), DYMAT Journal, 1-4, pp.289-305.
12. Daimaruya, M., Kobayashi, H., Bustami, S. and Chiba, M., (1996), J. Soc. Mat. Sci., Japan, 45-7, pp.823-828.
13. Daimaruya, M., Kobayashi, H. and Nonaka, T., (1997), EURODYMAT'97, J. de Physique III, pp.C3-253-257.
14. Daimaruya, M., et al., (1997), Trans. of Japan Society of Mech. Eng., 63-616, pp.2592-2597.
15. Daimaruya, M., Kobayashi, (2000), EURODYMAT 2000, J. de Physique IV, pp.Pr9-173-178.

ORAL: *xxxxx*

EFFECT OF MICROSTRUCTURAL CHANGE ON THE *R*-CURVE BEHAVIOR OF AN ALUMINA MATRIX COMPOSITE REINFORCED WITH SILICON CARBIDE WHISKERS

Takashi AKATSU, Yasuhiro TANABE and Eiichi YASUDA

Materials and Structures Laboratory, Tokyo Institute of Technology
4259 Nagatsuta, Midori, Yokohama 226-8503, Japan

ABSTRACT

The *R*-curve of an Al_2O_3 matrix composite reinforced with SiC-whiskers typically comprises two stages in response to crack face bridging processes. The microstructural change in the composite strongly affected the bridging processes, and resulted in a significant change in the *R*-curve.

KEYWORDS

R-curve, ceramic matrix composite, whisker, crack face bridging

INTRODUCTION

Tailoring the microstructure of ceramic matrix composites reinforced with ceramic whiskers to govern the rising *R*-curve behavior is important, because the initial rising gradient of the curve strongly affects their mechanical properties. A numerical simulation based on a series of probable crack face whisker bridging processes with a sound physical basis may be quite efficient to elucidate the dependence of microstructural change in the composite on the *R*-curve behavior. In this paper, the rising *R*-curve behavior of an alumina matrix composite reinforced with silicon carbide whiskers has been experimentally examined. On the other hand, an analytical simulation for a crack face whisker bridging model has been carried out. Comparison between the experimental and the simulated *R*-curves has been made to confirm the validity of the model. Analysis to derive crack closure stress σ_b from the observed *R*-curve has been accomplished to examine the effect of microstructural change on the *R*-curve.

EXPERIMENTAL

Two kinds of SiC whiskers named as TWS-400 of rather large size and as TWS-100 of relatively small size, respectively, were used as the reinforcement of alumina matrix composites. The

composites were fabricated by hot pressing [1], and were controlled to contain the whiskers with various volume fractions from 5 to 20%. Billets hot-pressed were cut into a flexural beam with a sharp single edge notch introduced to the center. Three-point flexural test of the SENB specimen was carried using an Instron-type test machine and a crack stabilizer [2] that was requisite for realizing stable crack propagation. The stable crack propagation was observed through an optical microscope to evaluate crack extension length Δa. Utilizing the crack length a, which is given by the addition of Δa to the initial crack length a_0, and the applied load P on the flexural beam with thickness B and width W, the critical stress intensity factor in mode I, K_{Ic}, as a function of a was determined.

SIMULATION FOR CRACK FACE WHISKER BRIDGING

Simulation based on a model with crack face whisker bridging was carried out in order to derive σ_b and crack tip opening displacement δ_b from an experimental R-curve. In the model, both frictional and pull-out bridging processes [3] were taken into account, and σ_b in each process was calculated on the basis of shear-lag theory. The δ_b-value was calculated in terms of the distance x from the tip using the Barenblatt relation [4] with σ_b thus calculated. The material parameters, such as the whisker volume fraction V_w, average radius of whiskers r_w, average length of whiskers l_w, elastic modulus of whiskers E_w and of matrix E_m, and tensile strength of whiskers σ_w were employed referring to the reports of the whisker supplier and of previous works [5,6]. The frictional shear stress at whisker/matrix interface τ_f was appropriately determined best-fitted to the experimental R-curve results. In the present composite system, σ_b was represented in the following formula;

$$\sigma_b(x) = \psi V_w \sqrt{2 \chi E_w \sigma_w \frac{\delta_b(x)}{l_w}} \tag{1}$$

for $0 < x < d$, where ψ was the orientation efficiency factor [7], $\chi = \frac{l_w}{r_w}\frac{\tau_f}{\sigma_w}\left\{1 + \frac{V_w E_w}{(1-V_w)E_m}\right\}$ and d was determined by $\delta_b(d) = \frac{l_w}{2\chi}\left(1 - \frac{1}{2\chi}\right)^2 \frac{\sigma_w}{E_w}$, and

$$\sigma_b(x) = \frac{2}{\chi}\psi V_w \frac{\frac{l_w}{4\chi} - \delta_b(x)}{r_w}\left\{1 - \frac{\frac{l_w}{4\chi} - \delta_b(x)}{r_w}\frac{\tau_f}{E_w}\right\}^{-1} \tau_f \tag{2}$$

for $d < x < b$, where b was given by $\delta_b(b) = \frac{l_w}{4\chi}$. Equations (1) and (2) were only available for the condition of $\chi \geq 1$. Finally, the critical stress intensity factor of the composite was estimated as a function of relative crack length α given as $\alpha = a/W$ under the condition that the length of bridging zone, l_b, is assumed to be much smaller than the total crack length a, as follows:

$$K_{Ic}(\alpha) = K_{Ic}{}^0 + \sqrt{\frac{2}{\pi}}\int_0^{\Delta a} \frac{\sigma_b(x)}{\sqrt{x}}\, dx \tag{3}$$

Details of the bridging model and the procedure of calculation are given in Ref.8.

RESULTS

The *R*-curves of the composites reinforced with the large whiskers (TWS-400) with various V_w were experimentally obtained as shown with closed circles in Fig.1. Each *R*-curve behavior typically comprised two stages divided at a bend in the curve. At the first stage of *R*-curve, $K_{Ic}(\alpha)$ steeply increased from 4 ± 0.2MPa$\sqrt{\text{m}}$ without a visible crack extension. The initiation of *R*-curve was, however, sensitively detected through the onset of nonlinear load-displacement relation in the bend test of SENB specimens. At the second stage beyond the bend, $K_{Ic}(\alpha)$ gradually increased as the crack macroscopically extended. The value of $K_{Ic}(\alpha)$ at the bend increased with V_w. In addition, the plateau of *R*-curve increased with V_w. The *R*-curves simulated for various values of V_w were shown as the solid lines in Fig.1. Good agreements between observed and simulated *R*-curves were confirmed, while the fitting is relatively insufficient for the composites having lower V_w-values. In addition, the bend was successfully reproduced in our *R*-curve simulation. The *R*-curve behavior of another composite reinforced with the small whiskers (TWS-100) of 20vol.% referred to as Compo-sw was shown with the closed squares in Fig.2 along with that of a composite with the large whiskers (TWS-400) of 20vol.% referred to as Compo-lw (closed circles) for comparison. A significant deference in their *R*-curves was seen: At the second stage of *R*-curve behavior, $K_{Ic}(\alpha)$ of Compo-lw showed a steeper increase and reached a higher plateau than that of Compo-sw, though the differences in $K_{Ic}(\alpha)$ at the initiation and at the bend in each *R*-curve are insignificant. The *R*-curves simulated for both the composites were shown as the solid lines in Fig.2. Good agreements between observed and simulated *R*-curves were demonstrated not only for Compo-lw but also for Compo-sw.

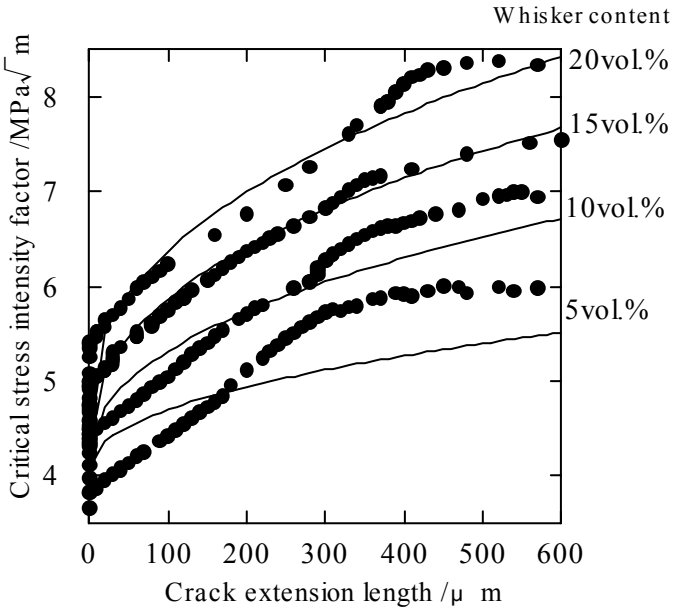

Figure 1: *R*-curves of an alumina matrix composite reinforced with silicon carbide whiskers (TWS400) for various whisker volume fractions. Closed circles are experimental and solid lines are simulated *R*-curves.

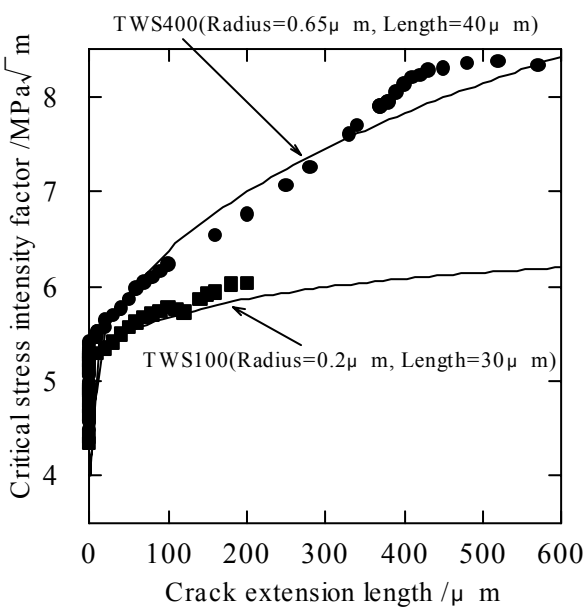

Figure 2: *R*-curves of the composite reinforced with whiskers of small (TWS100) and large (TWS400) sizes. The former and the latter are denoted with closed squares and circles, respectively. Solid lines are *R*-curves simulated for each composite.

DISCUSSION

Effects of whisker volume fraction on R-curve

The distribution of σ_b has been calculated for various values of V_w using the same whisker dimensions as TWS-400, as shown in Figs.3(a) and 3(b). As shown in Fig.3(a) where the relations of σ_b in the vicinity at a crack tip are demonstrated , the peak value of σ_b in Frictional Bridging (FB) [3,8] increases with V_w simply owing to the increase in the number of whiskers bridging a crack in FB. That is the main reason why $K_{Ic}(\alpha)$ at the bend of R-curve of the present composite system increases with V_w, as shown in Fig.1. In Fig.3(b) where a wide range view of bridging is depicted, the maximum σ_b in Pull-out Bridging (PB) [3,8] increases but the zone length l_b decreases with the increase in V_w. The former is also due to the increase in the number of whiskers bridging a crack in PB. In order to investigate the latter, we take δ_b into consideration, because l_b, which significantly affects $K_{Ic}(\alpha)$ at the second stage of R-curve as much as σ_b does, is geometrically determined through the combination of l_w and δ_b at the trailing edge of a bridging zone under crack propagation. The δ_b-values within the zone for various values of V_w have been calculated for the same whisker dimensions as TWS-400 in terms of the distance from crack tip. It is found that there is almost no difference in δ_b with various V_w at very close range from the tip; however, the δ_b-value of the composite with high V_w increases more progressively with the increase in the distance from the tip than that of the composite with low V_w. The progressive increase in δ_b is caused by the increase in nominal $K_{Ic}(\alpha)$ with V_w due to the stress shielding effect of σ_b, and results in the decrease in l_b with the increase in V_w at a constant l_w. The negative effect of the decrease in l_b on toughening is entirely overcome by the positive effect of the increase in σ_b with V_w. As a result, the minute increase in rising R-curve gradient at the second stage with V_w has been observed, as shown in Fig.1. We conclude that the increase in V_w is fairly effective for toughening the present composite system.

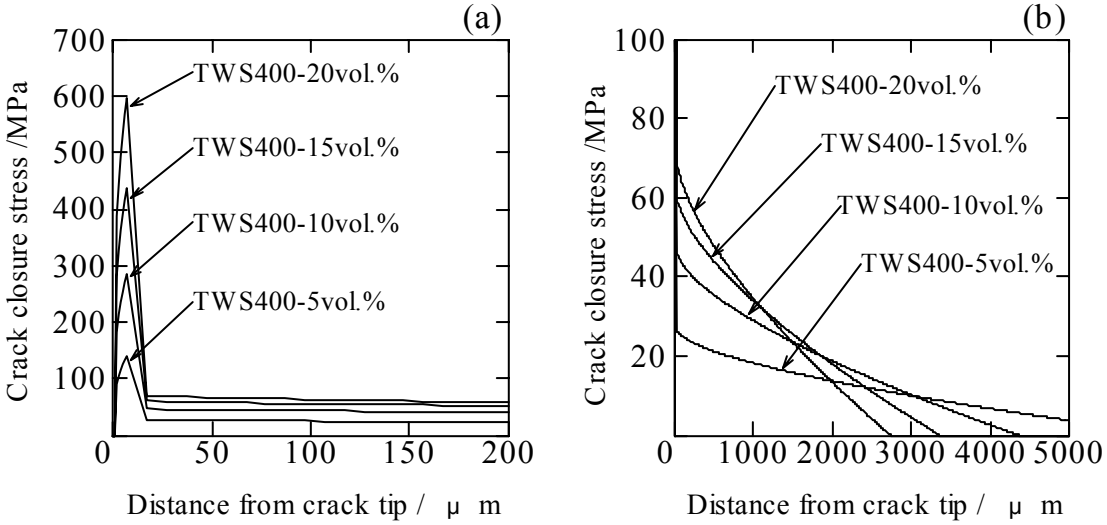

Figure 3: Distribution of crack closure stresses in the composite for various whisker volume fractions in the vicinity of a crack tip (a) and throughout bridging zone (b).

Effects of whisker dimensions on R-curve

As shown in Fig.2, there is a negligible small discrepancy in $K_{Ic}(\alpha)$ at the bend in R-curve between Compo-sw and Compo-lw, because of the insignificant difference between their peak values of σ_b. The simulation reveals that much larger values of σ_b and l_b in PB of Compo-lw than those of Compo-sw cause the significant difference in the rising behavior at the second stage of their R-curves. In order to examine the difference in R-curve between Compo-sw and Compo-lw in detail, the effect of the size and the aspect ratio A_w of whiskers on the R-curve behavior of the present

composite system should be taken into account individually, because they are expected to effect on the *R*-curve in different ways. The effect of whisker size on the rising *R*-curve behavior has, first, been examined with V_w of 0.2 and a constant A_w of 8.7 resulting in the constant χ-value of 1.0, where the effect of whisker bridging on the toughening of the present composite system has been optimized, as well as demonstrated in Fig.4. The increase in r_w and l_w with a constant A_w enhances the rising *R*-curve behavior in the second stage, while the difference in $K_{Ic}(\alpha)$ in the first stage of *R*-curve is hardly detected owing to the insignificant effect of whisker size on the peak value of σ_b in FB. The effect of whisker size on the maximum σ_b in PB is also insignificant, because it is principally given in terms of χ, V_w and σ_w. The simulation reveals that the increase in l_b with r_w and l_w at constant A_w is caused by the compensation of the increase in l_w for the increase in δ_b at the trailing edge of the bridging zone. Therefore, the increase in whisker size with constant A_w increases l_b, and results in the enhancement of rising *R*-curve behavior at the second stage in the present composite system. The effect of A_w on the rising *R*-curve behavior is, then, examined through the χ-value, because the use of χ, which is simply proportional to A_w, properly gives a general description of the change in *R*-curve behavior. The χ-value is given in terms of the ratio of l_w to r_w. Accordingly, we have employed r_w as a variable of χ. *R*-curves simulated for various values of χ with V_w of 0.2 were depicted in Fig.5. It is found that the decrease in χ down to χ=1 remarkably enhances the rising *R*-curve behavior at the second stage. However, the $K_{Ic}(\alpha)$-value at the bend in curve is very insusceptible owing to the insignificant dependence of χ on the peak value of σ_b in FB. The simulation of σ_b-values in PB for various values of χ with V_w of 0.2 reveals that both the maximum σ_b in PB and l_b increase with the decrease in χ down to χ=1. The increase in the maximum σ_b is caused by the increase in the number of bridging whiskers intact at the transition from FB to PB process; the tensile stresses on bridging whiskers decreases with the decrease in χ. Moreover, the decrease in the tensile stress increases the pulled-out whisker length resulting in the increase in l_b. We conclude that the decrease in A_w with the increase in r_w at constant l_w significantly enhances rising *R*-curve behavior at the second stage in the present composite system through the increase in both the maximum σ_b in PB and l_b. A significant difference in rising gradient at the second stage of *R*-curve between Compo-sw and Compo-lw is attributed to the difference in whisker size as well as aspect ratio.

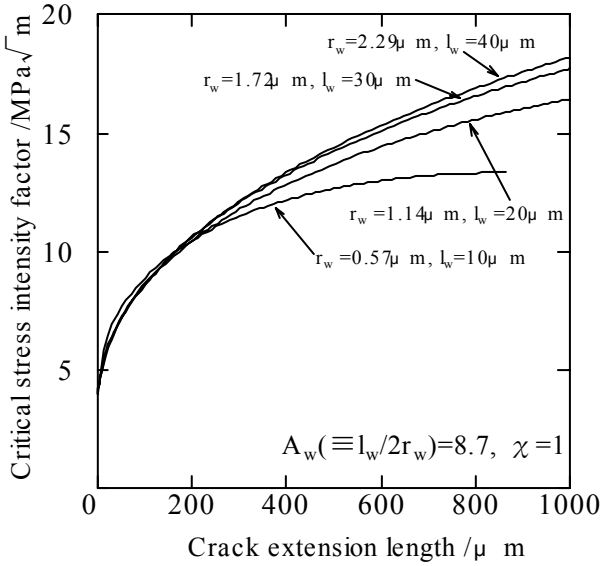

Figure 4: *R*-curves simulated for various whisker sizes with a constant whisker aspect ratio of 8.7 resulting in the constant χ-value of 1.0 and whisker volume fraction of 20%.

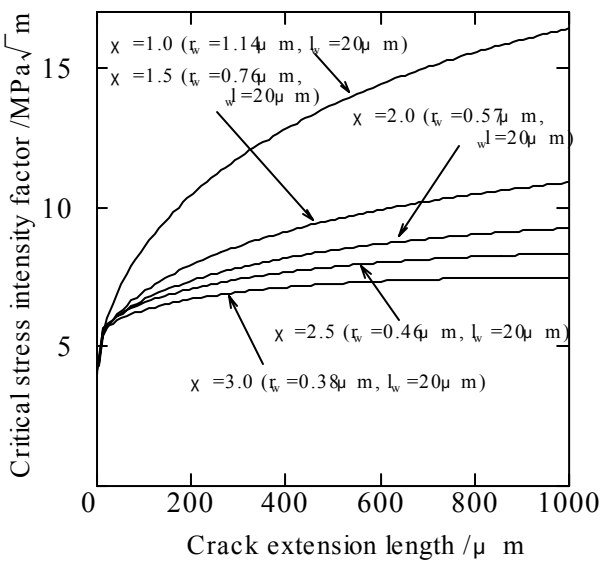

Figure 5: *R*-curves simulated for various values of χ with whisker volume fraction of 20%.

CONCLUSIONS

The effect of microstructural change on the *R*-curve behavior was examined for alumina matrix composites reinforced with silicon carbide whiskers, leading to the following conclusions:

(1) The increase in the volume fraction of whiskers increases crack closure stresses in both frictional and pull-out bridging processes through the increase in the number of whiskers bridging a crack, and results in the enhancement of rising *R*-curve behavior at both the first and the second stages.

(2) The increase in whisker size increases bridging zone length, whereas it does not cause any change in the maximum bridging stresses. In the present composite system, the decrease in whisker aspect ratio increases the maximum bridging stress as well as the zone length in pull-out bridging process. Therefore, the composite reinforced with whiskers of large size and small aspect ratio has an advantage for realizing the enhancement of rising *R*-curve behavior.

References

1. Yasuda, E., Akatsu, T. and Tanabe, Y. (1991) *J.Ceram.Soc.Jpn.*, **99**, 52-58.
2. Nishida, T., Hanaki, Y., Nojima, T. and Pezzotti, G. (1995) *J.Am.Ceram.Soc.*, **78**, 3113-3116.
3. Becher, P.F., Hsueh, C.H., Alexander, K.B. and Sun, E.Y. (1996) *J.Am.Ceram.Soc.*, **79**, 298-304.
4. Barenblatt, G.I. (1962) *Adv.Appl.Mech.*, **7**, 55-129.
5. Samanta, S.C. and Musikant, S. (1985) *Ceram.Eng.Sci.Proc.*, **6**, 663-672.
6. Petrovic, J.J., Milewski, J.V., Rohr, D.L. and Gac, F.D. (1985) *J.Mater.Sci.*, **20**, 1167-1177.
7. Akatsu, T., Tanabe, Y., Matsuo, Y. and Yasuda, E. (1992) *J.Ceram.Soc.Jpn.*, **100**, 1297-1303.
8. Akatsu, T., Tanabe, Y. and Yasuda, E. (1999) *J.Mater.Res.*, **14**, 1316-1324.

Effect of Microstructural Degradation on Crack Tip Stress Fields in Two-Phase Single Crystals

E.P. Busso, N.P. O'Dowd, S. Dumoulin, and D. Allen†

Department of Mechanical Engineering
Imperial College, London, UK
† ALSTOM Power Technology Centre, Whetstone, UK

ABSTRACT

A large proportion of the service life of high temperature single crystal components is taken up in initiating and growing surface cracks, which are driven by thermally induced stresses and environmental effects. In this work, the effect of a reduction in the volume fraction of the γ' precipitate phase in Ni-base superalloys on the time-dependent crack tip stresses is analysed numerically. Such variations can be related to the microstructural degradation caused by oxidation and diffusion processes around surface cracks in superalloy single crystals. The approach relies on a recently proposed multi-scale rate-dependent crystallographic theory to describe the macroscopic constitutive behaviour of the single crystal in terms of material parameters which depend explicitly on the characteristics of the precipitate phase at the microscale.

Results of a finite element study on a typical compact tension specimen reveal a strong dependency of the local crack tip stresses and strains on the local volume fraction of the precipitate population. The implications of these findings in relation to the microstructural degradation caused by oxidation at crack faces are discussed.

KEYWORDS

Single crystals; Superalloys; Oxidation; Crack Growth; Fracture.

INTRODUCTION

In two-phase single crystals such as Ni-base superalloys, heterogeneities exist at both the microscopic and mesoscopic levels. At the microscale, they are introduced by the presence of the 0.5-1 μm γ' precipitates and can become more pronounced due to the changing morphology of the precipitates during service and to inhomogeneous deformation patterns. At the mesoscale, e.g. in 10–100 μm sized regions, the presence of surface cracks also introduces a degree of heterogeneity in the local microstructure as a result of the local microstructural degradation caused by the oxidation of the crack faces [1][2].

Conventional single crystal models are unable to predict the effects of such heterogeneities as they generally treat the material as a homogeneous single crystal solid whose mechanical behaviour is uncoupled from inter-diffusion and oxidation processes. It is well known, however, that local variations in precipitate volume fraction strongly affect the local material behaviour. Although much work has been done to explain such volume fraction effects, it was not until recently that they were quantified for a range of temperature and strain rate conditions using periodic unit-cell techniques [3][4]. The results have been incorporated into a state variable crystallographic formulation to account for experimentally observed precipitate size and volume fraction effects in a Ni-base superalloy [5].

The main objective of this work is to quantify the effect of the reinforcing phase on the stress and strain fields at crack tip regions and to enhance the current understanding of the factors controlling short crack behaviour in Ni-base superalloys at high temperatures. The structure of the paper is as follows. First, a brief outline of the constitutive approach is presented. Then, the crack tip fields in a typical compact tension (CT) specimen are presented as a function of the volume fraction of the precipitate population. This is followed by a discussion of the results and the implications for crack growth predictions in single crystals.

MULTI-SCALE CRYSTALLOGRAPHIC FORMULATION

The average macroscopic stress-strain behaviour of the superalloy single crystal (SC) of interest, viz. CMSX4, is described by the multi-scale rate dependent crystallographic formulation recently proposed by Busso [5]. The flow rule relies on a stress-dependent activation energy expressed in terms of two internal state variables per slip system, α: a macroscopically average slip resistance S^α, and a internal or back stress B^α. Thus,

$$\dot{\gamma}^\alpha = \dot{\gamma}_o \exp\left[-\frac{F_o}{k\theta}\left\langle 1 - \left\langle \frac{|\tau^\alpha - B^\alpha| - S^\alpha \mu/\mu_0}{\hat{\tau}_0 \mu/\mu_0} \right\rangle^p \right\rangle^q \right] sgn(\tau^\alpha) \; , \tag{1}$$

where τ^α is the resolved shear stress, θ the absolute temperature, μ, μ_0 the shear moduli at θ and 0 K, respectively, and F_0, $\hat{\tau}_o$, p, q and $\dot{\gamma}_0$ are material parameters.

The evolutionary behaviour of the overall slip resistance is given by,

$$\dot{S}^\alpha \;=\; \sum_{\beta=1}^{n} \delta_S^{\alpha\beta} \left[h_s - d_D (S^\beta - S_0^\beta) \right] |\dot{\gamma}^\beta| \; , \tag{2}$$

where S_0^α is the initial value of S^α, d_D is a dynamic recovery function and n is the total number of slip systems. In Eq. 2, $\delta_S^{\alpha\beta}$ is the latent hardening or interaction function. Here, self-hardening is assumed so that $\delta_S^{\alpha\beta} = \delta_{\alpha\beta}$, the Kroneker delta.

The formulation contains an explicit link between the γ' precipitate population at the microscale and the behaviour of the homogeneous equivalent material at the macroscale. This link is introduced through the dynamic recovery function d_D and the initial microstructural state, S_0^α in Eq. 2 which, in turn, depend on the characteristics of the current precipitate population. Here,

$$d_D \;=\; \hat{d}_D \left\{ l/l_m, \, \mathrm{v}_f \right\} \quad , \tag{3}$$

$$S_0^\alpha \;=\; \hat{S}_0 \left\{ l/l_m, \, \mathrm{v}_f \right\} \quad , \tag{4}$$

where l/l_m is the precipitate size normalised by a mean reference value, and v_f the precipitate volume fraction. Equations 3 and 4 have been calibrated from FE analyses of periodic unit cells at the microscale containing the individual precipitates [4]. Note that the effects of the precipitate aspect ratio will not be quantified in this paper. For details, see [3] and [4].

The back stress evolves according to ,

$$\dot{B}^\alpha \;=\; h_B \dot{\gamma}^\alpha - r_D B^\alpha |\dot{\gamma}^\alpha|, \tag{5}$$

where h_B is the hardening coefficient, and r_D a dynamic recovery function expressed in terms of the current overall deformation resistance,

$$r_D \;=\; \frac{h_B \, \mu_o}{S^{(\alpha)}} \left\{ \frac{\mu_0'}{f_c \lambda} - \mu \right\} \; . \tag{6}$$

Here, f_c and λ are statistical factors, and μ_0' is the shear modulus in the slip plane. Note that the dependency of the back stress on the characteristics of the precipitate population is implicitly incorporated through S^α in Eq. 6.

The above crystallographic formulation has been implemented numerically into a material subroutine in a commercial FE code [6] using a large strain algorithm with an implicit time-integration procedure. It relies on the multiplicative decomposition of the total deformation gradient, $\mathbf{F}$, into an inelastic component, $\mathbf{F}^p$,

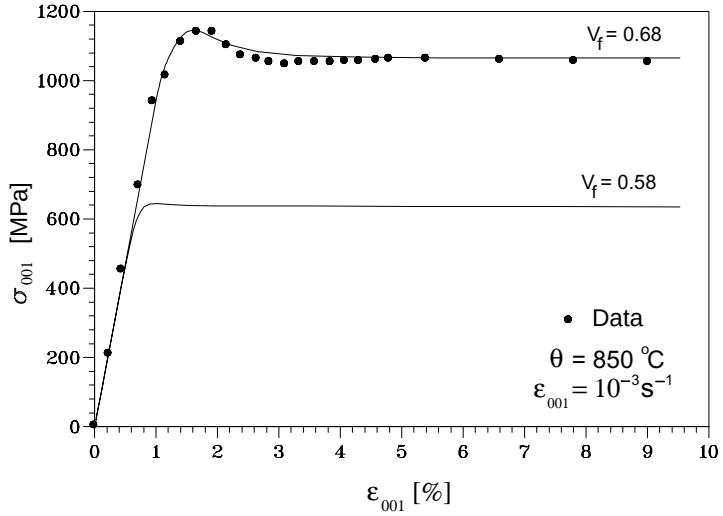

Figure 1: Effect of precipitate volume fraction on the $< 001 >$ monotonic response of CMSX4 at 850°C and 10^{-3} 1/s. Symbols represent experimental data for the $V_f = 0.68$ case

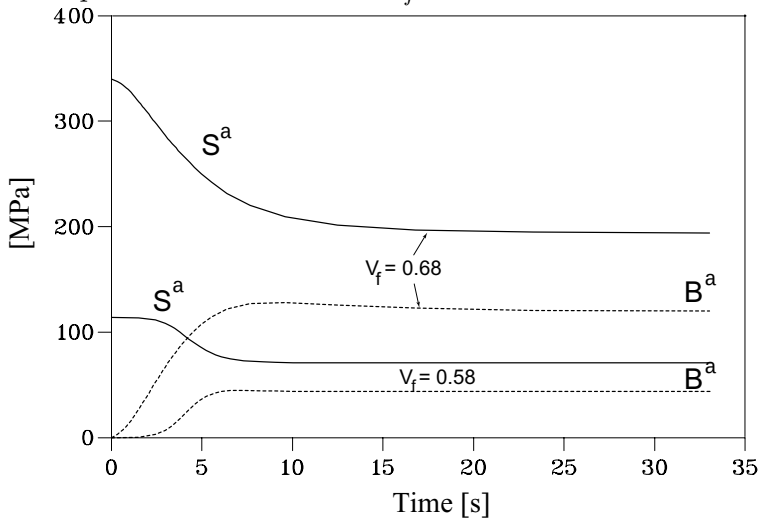

Figure 2: Predicted effect of the evolutionary behaviour of the $\{111\} < 011 >$ internal slip system variables for the monotonic stress-strain curves shown in Fig. 1

associated with pure slip, and an elastic component, $\mathbf{F}^e$, which accounts for the elastic stretching and rigid-body rotations. Thus, $\mathbf{F} = \mathbf{F}^e\mathbf{F}^p$. For details, refer to [4],[5].

The model calibration was carried out with the twelve octahedral ($\{111\} < 011 >$) and six cubic ($\{100\} < 011 >$) slip systems considered to be potentially active. The reference data to calibrate the model for $v_f = 0.68$ were obtained from uniaxial monotonic, cyclic and creep tests, and, the data for $v_f < 68\%$ from periodic unit cell analyses (see [3],[4]).

Typical predictions of the monotonic uniaxial behaviour of CMSX4 at 850°C and 10^{-3} 1/s are shown in Fig. 1 for two different γ' volume fractions, namely 58 and 68%, together with experimental data for the latter case. Figure 1 shows that a 10% reduction in volume fraction results in a 40% decrease in the superalloy steady state flow stress at this temperature and strain rate. The corresponding evolutionary behaviour of the internal slip system variables for each of the eight active (and equally stressed) $\{111\} < 011 >$ systems is shown in Fig. 2. The correspondence between the macroscopic softening and hardening behaviour and the steady state values of the slip resistance and the back stress can be clearly inferred from Figs. 1 and 2. For instance, the macroscopic softening observed for $v_f = 0.68$ is associated with a large decrease in the slip resistance, from its initial value of 338 MPa to its steady state value of 201 MPa. Even though a similar S^α softening trend is seen for $v_f = 0.58$, the macroscopic effect is negligible (see Fig. 1).

FINITE ELEMENT MODELLING

The three dimensional finite element mesh used to analyse the crack tip deformation of a typical compact tension specimen is shown in Fig. 3. A crack length of $a = 15.6$ mm and a crack length-to-specimen width ratio of $a/W = 0.6$ were used. Here, the specimen thickness and height are 12.5 mm and 31.2 mm, respectively, and the notch radius is 1.3 μm.

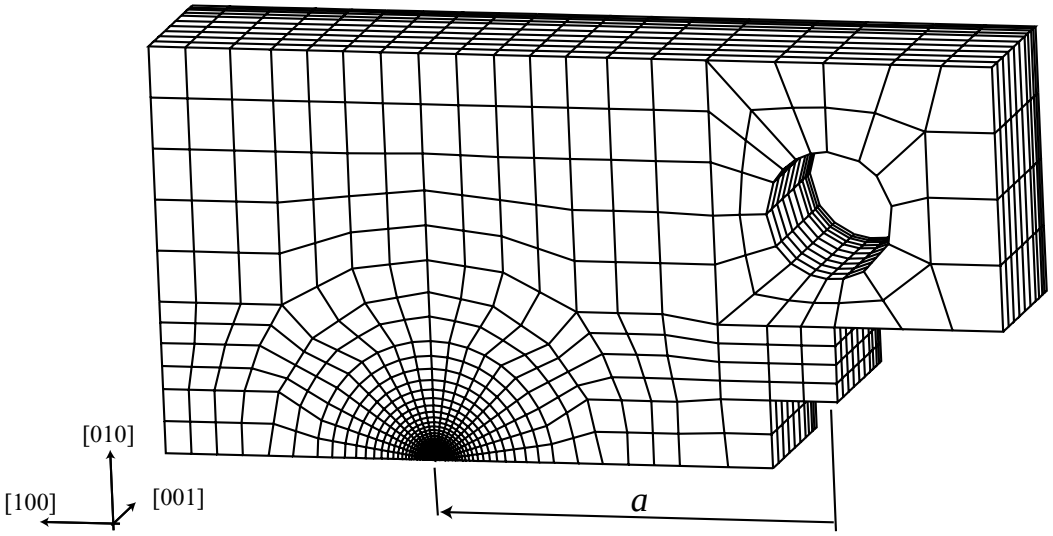

Figure 3: Finite element mesh of the CT specimen

The plane of the specimen is normal to the [001] crystallographic axis and the crack faces lie normal to the [010] axis. Note also that, due to the symmetries of the lattice and the specimen, only 1/4th of the specimen needs to be modelled. In total, 14000 linear brick elements are used in the analysis, with a focused mesh at the crack tip. The smallest element size in the model is 1.0 μm (or $\sim 6 \times 10^{-5} a$).

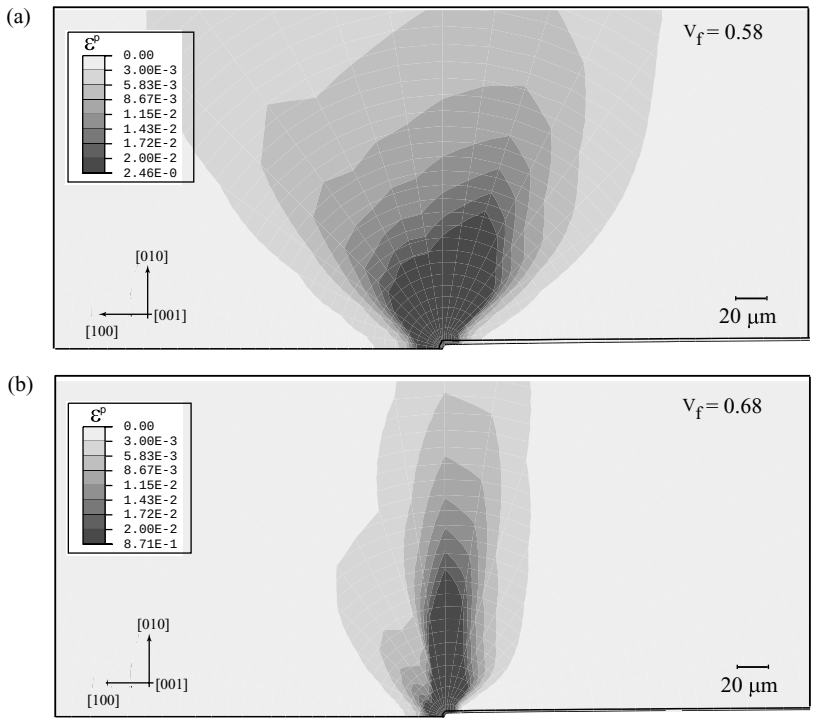

Figure 4: Contours of accumulated inelastic strain near the notch tip for: (a) 58% and (b) 68% γ' volume fraction after 320 hours exposure at 850°C

RESULTS AND DISCUSSIONS

The results to be discussed in this section are for CT specimens with a fixed content and uniform distribution of precipitates. Two cases are examined: an alloy with a precipitate volume fraction of 68%, which corresponds to that of CMSX4 at the start of life, and an alloy with a volume fraction of 58%, which is a typical volume fraction found near crack faces after long-term exposure to an oxidising environment. In on-going work, the effect of time and spatial evolution of the γ' volume fraction and size on the deformation and stress state is being studied.

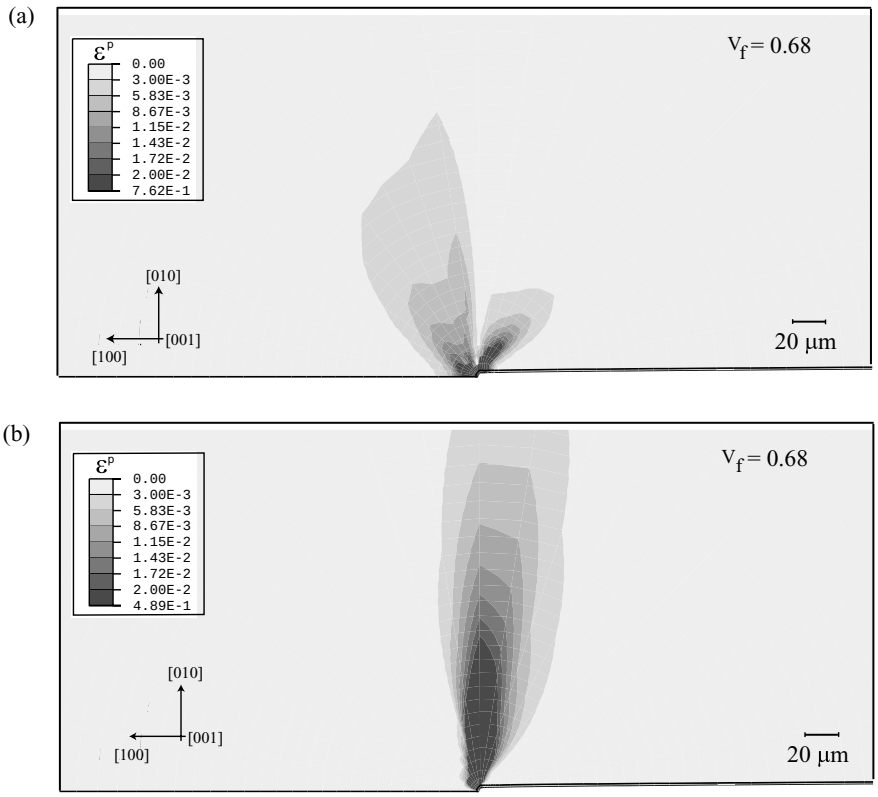

Figure 5: Contributions to the overall accumulated inelastic strain around the notch tip from the (a) octahedral and (b) cubic slip systems for the $v_f = 0.68$ case shown in Fig. 3

Figures 4 to 6 show results for the CT specimen loaded with a stress intensity factor of 10 MPa $\sqrt{\text{m}}$ at 850 °C. In Fig. 4, contours of accumulated inelastic strain are presented for (a) $v_f = 58\%$ and (b) $v_f = 68\%$ after 320 hours exposure. The contours are shown at the central notch root region of the specimen where fracture is expected to initiate. It is worth noting the greater magnitude and extent of the accumulated overall slip for the $v_f = 58\%$ case, which is a considerably softer material (see Fig. 1). The contributions to the overall accumulated inelastic strain around the tip of the sharp notch for the $v_f = 68$ % case (see Fig. 4(b)) from the octahedral and cubic slip system families are shown in Figs. 5 (a) and (b), respectively. Since the specimen is loaded along the [010] direction, one would expect the octahedral slip systems to be dominant, as it is the case under uniaxial $< 001 >$ (homogeneous) deformation. However, Fig. 5 reveals that the contribution from the cubic slip systems is equally important. This is a result of the multiaxial nature of the stress distribution near the notch region.

In Figs. 6(a) and (b), the distribution of the stress component normal to the crack faces, σ_{010}, and the mean hydrostatic stress, $\sigma_h = (\sigma_{100} + \sigma_{010} + \sigma_{001})/3$, respectively, are given in terms of the distance from the tip of the notch and the γ' volume fraction. The peak normal stress in Fig. 6(a), found at approximately 23 μm from the sharp notch root, decreases by 34% for a 10 % decrease in the precipitate volume fraction. Thus, the crack driving force for cleavage fracture is considerably reduced. It is known that the rate of growth of voids within the single crystal at high temperatures depends on the magnitude of σ_h and the local slip rates. Therefore, from the results of Figs. 4 and 6(b), the evolution of ductile damage could be inferred.

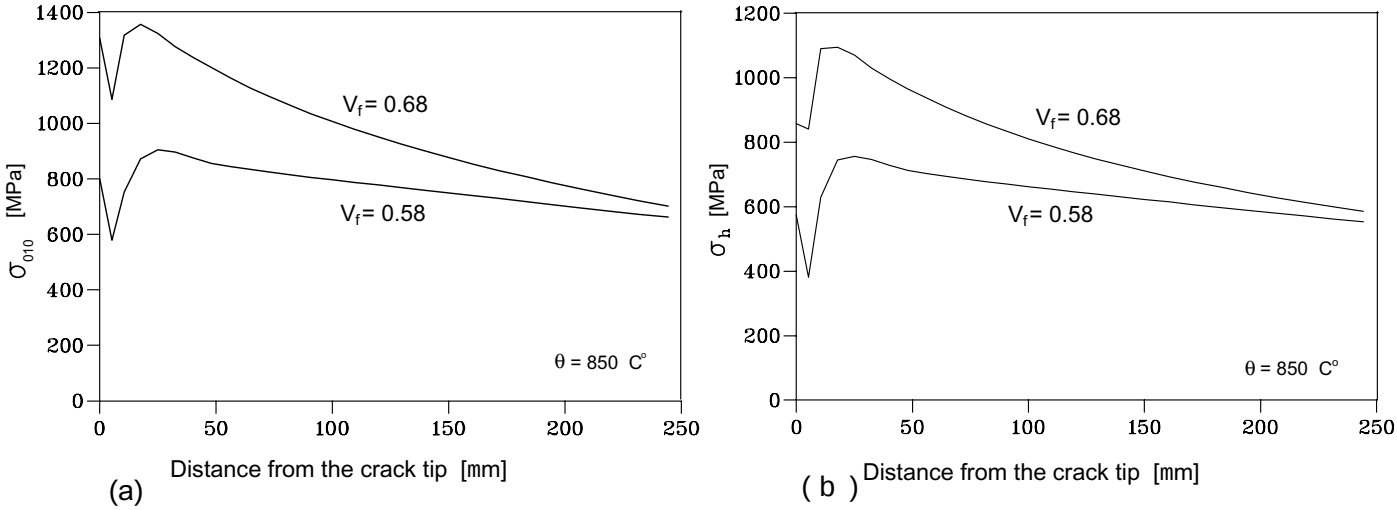

Figure 6: Distribution of (a) the stress component normal to the crack faces and (b) the mean hydrostatic stress (= $(\sigma_{100} + \sigma_{010} + \sigma_{001})/3$), as a function of the distance from the tip of the notch and the γ' volume fraction

In on-going work, parametric studies of the type shown here coupled with oxygen diffusion from the environment into the crack faces are being conducted and the resulting information used to formulate appropriate fracture mechanics-based formulation for crack growth predictions under creep-fatigue interaction.

CONCLUDING REMARKS

This work has shown that, in single crystal alloys reinforced with a high precipitate volume fraction, such as Ni-base superalloys, the decrease in the precipitate content due to environmental effects can have a strong effect on the local stresses responsible for both cleavage and stable crack growth. Such effects must be incorporated into fracture-mechanics based crack growth models to assure the accuracy of hot section component life assessments.

ACKNOWLEDGEMENTS

Financial support for this work by the EPSRC (UK) through grant GR/N12312 and by Alstom Power (UK) are gratefully acknowledged. The authors are grateful to Dr. F. Andrieux for her assistance in the calibration of the crystallographic model.

References

[1] Andrieu, E. and Pineau, A. (1999), Study of the Coupled Phenomena Involved in the Oxidation Assisted Intergranular Cracking in Ni-Base Superalloys, *J. de Physique IV*, V. 9 , pp. 3-12.

[2] Martinez-Esnaola, J.M., Martin-Meizoso, A., Affeldt, E.E., Bennett, A. and Fuentes, M. (1997), High Temperature Fatugue in Single Crystal Superalloys, *Fatigue Fract. Engng. Mater. Struct.*, V. 20 , pp. 771-788.

[3] Busso, E.P., Meissonnier, F., and O'Dowd, N.P. (2000), Gradient-Dependent Visco-Plastic Deformation of Two-Phase Single Crystals. *J. Mechanics Physics Sol.*, V. 48 , pp. 2333-2361.

[4] Meissonnier, F., Busso, E.P., and O'Dowd, N.P. (2001), Finite Element Implementation of a Non-Local Visco-Plastic Crystallographic Formulations. *Int. Journal of Plasticity*, V. 17, pp. 601-640.

[5] Busso, E.P., A Crystallographic Formulation for Superalloy Single Crystals with Explicit Microstructural Length Scales. Part I: Model Formulation. Submitted for publication.

[6] ABAQUS V. 5.8 (1999), Hibbitt, Karlsson and Sorensen Inc., Providence, RI.

invited paper for International Conference on Fracture, to be held Dec. 3-7, 2001, Honolulu, Hawaii, Hilton Hotel

EFFECT OF NANOTEXTURING ON INTERFACIAL ADHESION IN MEMS

M. P. de Boer[1], J. A. Knapp[2] and P. J. Clews[3]

Sandia National Laboratories
[1]Intelligent Micromachining, [2]Radiation Solid-Interactions, [3]Silicon Processing Dept.

www.mdl.sandia.gov/Micromachine

ABSTRACT

We demonstrate that the interfacial adhesion between microelectromechanical systems (MEMS) surfaces is in a regime not previously considered by standard models of rough surfaces such as the Fuller-Tabor [1] or Maugis [2] extensions of the theory of elastic contact of rough surfaces [3]. Our experiments and models show that at small roughness values, adhesion is mainly due to van der Waals forces across extensive non-contacting areas and is proportional to 1/(average surface separation)^2. At large roughness values, asperities that nearly bridge the gap become the dominating contributor to the adhesion. These van der Waals contributions to adhesion have been ignored in the above models. They cannot be ignored in MEMS because the surfaces are in close proximity over a long range as a result of the planar deposition technology.

KEYWORDS microcantilevers, interfacial adhesion, surface roughness, van der Waals forces, self-assembled monolayers

INTRODUCTION

MEMS is a recently developed technology in which free standing polycrystalline silicon (polysilicon) thin film structures are actuated electrostatically to form micron-scale complex mechanisms such as resonating sensors, gears, linear racks, pop up mirrors, and mechanical logic [4]. Because of the large surface-to-volume ratio in this regime, surface forces can dominate over inertial forces, causing mechanisms to adhere rather than perform their intended function.

It is well known that surface roughness reduces adhesion of two contacting bodies. Models describing the effect of roughness on adhesion consider only the adhesion at [1] or near [2] areas of real contact. A reduction in adhesion due to enhanced roughness has also been observed in MEMS. For example, polysilicon roughening techniques have been used to reduce the tendency towards adhesion under wet conditions [5,6]. Free standing cantilevers were actuated under dry conditions and the transition from adhered to free cantilevers was detected to estimate adhesion values [7,8]. It was observed that adhesion decreases with increasing surface roughness, and the authors suggested that $\Gamma \sim A/12\pi d_o^2$, where Γ is the adhesion (J/m^2), A is the Hamaker constant representing van der Waals forces, and d_o is the sum of the root mean square (rms) roughness of the two surfaces as measured by atomic force microscopy (AFM). Theoretical analysis considering the fractal nature of surfaces has also shown that adhesive forces decrease with increasing roughness [9,10].

In this work, we employ a joint experimental and modeling approach to address the effect of roughness on adhesion under dry conditions, allowing us to quantitatively address the following outstanding

questions: (1) To what degree is MEMS adhesion controlled by areas of real contact versus by van der Waals forces across non-contacting portions of the surfaces? (2) What is the minimum achievable value of adhesion for contacting bodies with rough surfaces? (3) What is the optimum value of roughness in MEMS?

SAMPLE PREPARATION

Cantilevers were fabricated according to a three mask level process, schematically represented in Fig. 1. Nanotexturing of the lower layer of polysilicon (poly 0 in Fig. 1(a)) was accomplished by thermal oxidation in dry O_2 at 900 °C for increasing times. Table I indicates the times and the rms roughness as measured by AFM. Fig. 2 shows SEM images of the surface textures achieved by this method after the release etch. Two features are noted. First, the main texturing effect is due to grains that protrude upwards from the surface. This occurs because the polysilicon grains are randomly oriented, and dry oxidation in the linear regime proceeds at different rates on different orientations of silicon [11]. Second, the grain boundaries are decorated at increasing oxidation times, giving rise to grooves. These do not contribute significantly to the desired texturing because they do not take up a large percentage of the surface area, and reach below the surface.

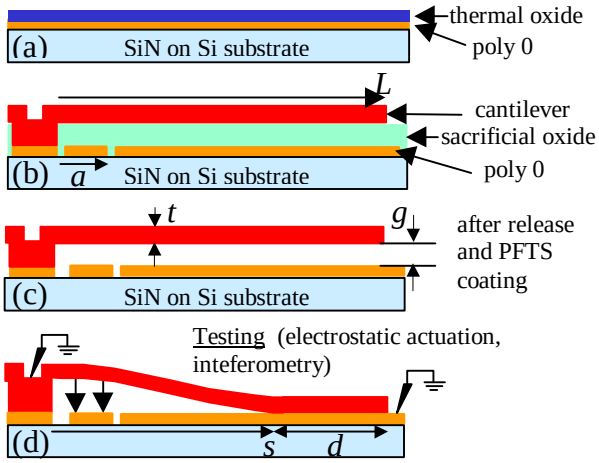

Fig. 1 (a) ground plane polysilicon (poly 0) oxidation (b) cantilever fabrication, (c) release and coating (d) testing

Table I Polysilicon roughness versus oxidation time

Oxdn. Time (min)	Target tox (nm)	rms roughness (nm)
0	--	2.8
20	10	4.5
136	30	7.8
400	60	12.1

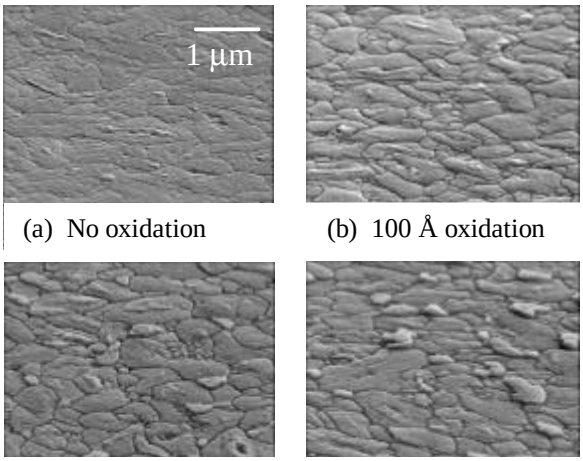

(a) No oxidation (b) 100 Å oxidation

(c) 300 Å oxidation (d) 600 Å oxidation

Fig. 2 Polysilicon ground plane surface textures versus oxidations times (SEM, 70° tilt).

Standard deposition, lithography and etch techniques were used to fabricate the cantilevers (Fig. 1(b)). They are supported on the left in Fig. 1 by a step-up support post, formed by filling a hole etched into the sacrificial oxide layer. A critical step is the release and coating of the cantilevers (Fig. 1(c)). We used a solvent-based coating procedure that applies a self-assembled monolayer coating of perfluorodecyltrichlorosilane (FDTS, ($C_8F_{17}C_2H_4SiCl_3$), similar to ref. [8]. Critical cantilever dimensions, as indicated in Fig. 1, include gap height g, thickness t, width w, length L, and actuation pad length a. After actuation (Fig. 1(d)), the length of the unattached region is used to denote the crack length s. Using profilometry, g=1.90 µm and thickness t=2.62 µm were determined from freestanding cantilevers. Mask dimensions were w=20 µm, a=81.5 µm and L ranged from 100 to 1635 µm.

ADHESION TEST RESULTS

Most cantilevers were free standing at lengths up to 1635 μm after the release and drying procedure as determined by interferometry. Some of these long cantilevers were contacting the substrate at their tips. In a few cases, cantilevers were attached over a relatively long length *d*, as indicated in Fig. 1(d). This latter group was excluded from further analysis.

Knowledge of Young's Modulus *E* and torsional support post compliance *b* are critical to assessing Γ [12]. We used a procedure previously described in detail [13] to determine *E*=163 GPa and *b*=1.25 μrad/(μN•μm). Also small curvatures *k* (caused by stress gradient through the thickness of the film) ranging from 0-1 m^{-1} were measured, and play a secondary role in determining adhesion values. These quantities are determined by electrostatically actuating the cantilevers, measuring the deflections and finding the best fit to finite difference models over a range of applied voltages.

Using a fracture mechanics analogy, a cantilever's adhesion to a substrate can be measured to high sensitivity and accuracy along its length [12,14]. In the adhesion testing procedure, free standing cantilevers are brought into contact with the substrate by modulating the voltage on the actuation pad. Using interferometry, the full deflection curve of the cantilevers is determined to better than 10 nm accuracy. At low to moderate voltages (up to 60V for this geometry), the deflections are highly sensitive to interfacial forces acting between the cantilever and the substrate.

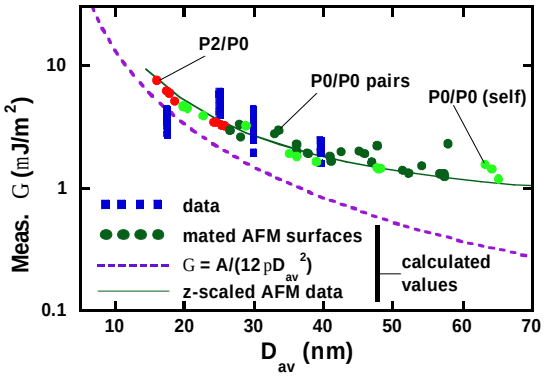

Fig. 3 Experimental and calculated results for adhesion verus average roughness

For different voltages applied to the actuation pad, corresponding to different points along the length of the beam, interferograms were taken and deflection curves were extracted. Knowing *a* and *w* from the mask layout and using the measured data for *E*, *t*, *g*, and *b* as input parameters, adhesion was determined by matching the model to each measured deflection curve. The only free parameter in the modeled curves is the adhesion Γ. A least squares fit between the model and measurement was used to determine its value. Typical minimum errors are less than 5 nm/pixel. Adhesion results for the different surface roughnesses are shown in Fig. 3, where the squares (data) correspond to the measured values of adhesion. The adhesion data is plotted versus D_{av}, the average separation between the surfaces. For each value of D_{av}, Γ values were determined from two different cantilevers at applied voltages of 0, 10, 20, 30, 40, 50 and 60 V. Small systematic errors in the input parameters limit the absolute accuracy of the Γ values to ~10%, but will not affect the relative values of adhesion in Fig. 3.

ANALYSIS

Adhesion testing was conducted in air at ~30% relative humidity (RH). A contact angle of 110° of the FDTS coating with water was measured, indicating a hydrophobic coating. We have observed no effect of RH on testing results up to 80% RH for these coatings [14]. Therefore, capillary condensation, which dominates adhesion of hydrophilic surfaces [15], does not play a role in these experiments. Furthermore, because the top and bottom surfaces are both grounded, electrostatic forces in the contact

zone *d* are insignificant. However, externally applied loads, van der Waals forces between the surfaces and contact at asperities must be considered to analyze our results.

To model the interfacial forces, we measured the topography of the top and bottom surfaces by AFM (double-sided tape applied to the cantilevers allows them to be removed from the substrate and placed upside down for imaging). A question arises as to the area of the contacting region that should be modeled. By considering the free body diagram of the loaded cantilever, there must be a short region of compressive contact just beyond the crack tip. From simple beam mechanics, a point reaction force exists, but from elastic considerations, this region has length ~2*t*, and therefore the contact area should be considered is ~2*tw*=80 μm^2. In fact, 10x10 μm^2 AFM images with 256 or 512 pixels in each direction (e.g., 40 or 20 nm lateral resolution) were used in our analysis.

The AFM topograph data was read into a finite element program, and the top and bottom surfaces were placed in contact in various ways as will be described below. An elastic-plastic model was created to describe the silicon material with *E*=165 GPa and hardness *H*=12 GPa. However, it was soon found that for any reasonable pressure as applied by the external modulation, only the first contacting asperity in the contact zone deforms, and then by less than 0.5 nm. At each pixel, a parallel plate law for van der Waals forces was used to model the adhesive forces, similar to the equation posed in the Introduction, e.g., $\Gamma = A/(12\,p\,D_o^2)$. However, D_o now replaces d_o, where D_o represents the gap at each individual pixel, and the adhesion energy is summed up over the individual pixels and divided by the total area. For the few pixels where there is actual contact, a cutoff value of D_{oc} =0.3 nm [16] was used. With $A=5 \bullet 10^{-20}$ J for a fluorocarbon surface, a surface energy of 15 mJ/m^2 is calculated in these regions. For comparison, values of 7 and 28 mJ/m^2 for advancing and receding surface energies respectively were recently determined by surface force apparatus measurements for a fluorocarbon surfactant (TAFC, $(C_8F_{17}C_2H_4)_2$-L-Glu-Ac-N^+-$(CH_3)_3$-Cl^-) applied to a mica surface.

The surfaces were placed in contact in various combinations. This included the original top and bottom measured layers with various random shifts in alignment, and pairs of the bottom layers including mating of the bottom layer to itself. The circles in Fig. 3 are the calculated adhesion results for the various combinations of the data. The solid line represents data from an individual placement combination, but with the roughness scaled to both lower and higher scales. The value of $D_{av} \approx 2d_o$ in Fig. 3 is determined by the finite element analysis for a given placement of the top and bottom surfaces.

DISCUSSION

The abscissa D_{av} in Fig. 3 is better used than d_o because it takes into account the actual alignment of the two surfaces, thereby reflecting the separation of the associated highest asperity pair. At small D_{av} values, $\Gamma = A/(12\,p\,D_{av}^2)$ is a good approximation for the calculated adhesion (circles in Fig. 3). Of course, this equation will always be a lower bound for the adhesion values because of the non-linearity in this equation. However, as indicated by both the data and the model, the adhesion does not fall off with $1/D_{av}^2$ at large D_{av} values. It is important to realize that for these deposited layers, there is no long range waviness to the surfaces. Therefore, surfaces can be near each other over large distances without contacting.

To qualitatively understand the results, we consider two conceptual extremes in the adhesion between rough surfaces. In one, the surfaces are relatively smooth and contact is at only one asperity point. Van der Waals forces across non-contacting portions of the surfaces, whose area is far greater than the

contacting area at the one asperity, will dominate the adhesion in this case. For example, at D_{av} =10 nm, Γ=13 μJ/m^2 is expected as seen in Fig. 3. At the other extreme, the surfaces are rough, and D_{av} is large. Only the single point of contact contributes to the adhesion. In this case, we would expect $\Gamma \sim (AR/(6D_{oc})/L_c^2)$, where *R* is the radius of the contacting asperities and L_c^2 is the area of adhesion that is being probed (the term $AR/(6D_{oc})$ is the van der Waals adhesion energy between two contacting spheres). With *R*=50 nm as a typical value for the polysilicon asperities in these experiments and L_c^2=100 μm^2 as discussed above, we expect a lower bound for adhesion to be 0.014 μJ/m^2. This latter extreme is a simplified expression of the Maugis model of rough surfaces [2], which takes van der Waals forces into account, but only at contacting asperities. That model is more appropriate here than the Fuller-Tabor approach because of the large *E* and small *R* of these surfaces. Note that the values of adhesion in Fig. 3 are much closer to the former than the latter extreme, implying that van der Waals forces over non-contacting areas dominate the adhesion. Negligible adhesion hysteresis measured in other experiments corroborates this notion [14].

To quantitatively understand the results, consider Fig. 4, where a histogram of the relative contributions from the range of D_o values is plotted for different surface roughnesses. At small D_{av}, most of the contribution to adhesion comes from non-contacting surfaces, whereas at large D_{av}, the contribution from surfaces nearly in contact begins to become the largest contributor.

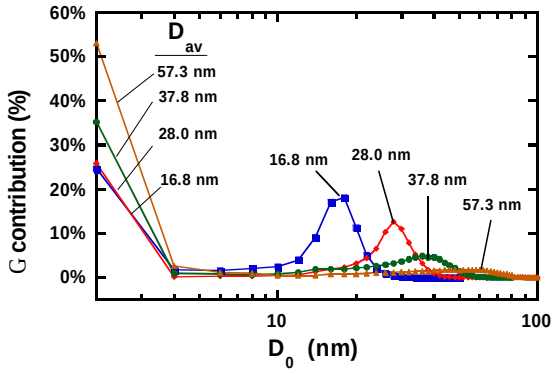

We can now address the questions posed in the Introduction. (1) Typically, MEMS surfaces exhibit D_{av} ~10-30 nm. Therefore, most adhesion in MEMS is due to van der Waals forces between non-contacting areas. Even for large D_{av} in Fig. 3, this remains true - the reason for the small reduction in Γ is that nearby non-contacting asperities begin to contribute significantly to adhesion. However, as D_{av} grows above 60 nm, the Maugis model will adequately describe the adhesion. (2) Adhesion as low as 0.01 μJ/m^2 should be possible by making surfaces rough. However, because of the weak dependence of Γ on D_{av}, extremely large roughness would be required. Given that MEMS structures are often used for optical reflection in mirror applications, this would be an unpopular choice. (3) There is a deviation in the calculated curve from $\Gamma = A/(12\,p\,D_{av}^2)$ beginning at D_{av} ~25 nm. We suggest this is a near-optimal separation value. For lower values of roughness, adhesion begins to increase significantly because of the close proximity of the surfaces, while for large values, optical reflectivity is significantly compromised.

Using the Greenwood-Williamson model [3], which applies reasonably well for these surfaces, the ratio of real to apparent contact area is found to be approximately 10^{-8} for the smoothest surfaces. The real contact area is greatly overestimated in the finite element formulation because of the pixel size limitation. Depending on the lateral resolution used in the AFM measurements, the smallest possible ratio is $(1/256)^2=1.5\bullet 10^{-5}$ or $(1/512)^2=3.8\bullet 10^{-6}$. Because the contribution to the total adhesion of the contacting point is still small, this causes only a small error in the adhesion calculation. However, this is further evidence that van der Waals forces in the vast area between contacts dominates the adhesion of these surfaces, especially when the average separation is small.

SUMMARY AND CONCLUSIONS

Understanding the effects of surface roughness on parameters such as adhesion, friction and wear is a central question in the tribology of MEMS. By combining deflection data from interferometry with computer-based models, the use of as-fabricated MEMS test structures provides a powerful means to the assess the interfacial adhesion between rough surfaces. In this work, we fabricated polysilicon cantilevers over textured surfaces of varying nm scale roughness, and measured the interfacial adhesion of the cantilevers to the surfaces. Contrary to expectations, the effect of roughness, when increased over a large range from 3 to 12 nm rms, reduced the adhesion only by a factor of 2, instead of by a factor of 16 as expected from previous literature models. The adhesion was studied by inputting 3-D data from AFM topographs of the surfaces into a finite element code, and mating the surfaces in the computer. It was found that at small roughness values, adhesion is mainly due to van der Waals forces across non-contacting areas and is proportional to 1/(average surface separation)^2. At large roughnesses, asperities that nearly bridge the gap are the dominating contributor to the adhesion.

ACKNOWLEDGMENTS

Sandia is a multiprogram laboratory operated by Sandia Corporation, a Lockheed Martin Company, for the United States Department of Energy under contract DE-AC04-94AL85000. We thank Aaron Hall for help in obtaining AFM data.

REFERENCES

[1] K. N. G. Fuller and D. Tabor, Proc. Roy. Soc. Lond. A. **345** 327 (1975).
[2] D. Maugis, J. Adh. Sc. Tech. **10** (2) 161 (1996).
[3] J. A. Greenwood and J. B. P. Williamson, Proc. Roy. Soc. Lond. A. **295** 300 (1966).
[4] J. J. Sniegowski and M. P. de Boer, Annu. Rev. Mater. Sci. **30** 297 (2000).
[5] R. L. Alley, P. Mai, K. Komvopoulos and R. T. Howe, Proc. 7th Int. Conf. Solid-State Sensors and Actuators, Transducers '93, Yokohama, Japan, 1993, pp. 288-291.
[6] Y. Yee, K. Chun and J. D. Lee, The 8th Int. Conf. on Solid-State Sensors and Actuators, Transducers '95, Stockholm, Sweden, 1995, pp. 206-209.
[7] M. R. Houston, R. T. Howe and R. Maboudian, J. Appl. Phys. **81** (8) 3474 (1997).
[8] U. Srinivasan, M. R. Houston, R. T. Howe and R. Maboudian, J. Micromech. Sys. **7** (2) 252 (1998).
[9] K. Komvopoulos and W. Yan, J. Trib. **119** 391 (1997).
[10] K. Komvopoulos and W. Wan, J. Appl. Phys. **84** (7) 3617 (1998).
[11] *VLSI Technology*; *Vol.* , edited by S. M. Sze (McGraw-Hill, New York, 1983).
[12] J. A. Knapp and M. P. de Boer, J. MEMS **to be submitted** (2001).
[13] B. D. Jensen, M. P. de Boer, N. D. Masters, F. Bitsie and D. A. LaVan, J. MEMS **10** (3) in press (2001).
[14] M. P. de Boer, J. A. Knapp, T. A. Michalske, U. Srinivasan and R. Maboudian, Acta Mater. **48** (18-19) 4531 (2000).
[15] M. P. de Boer, P. J. Clews, B. K. Smith and T. A. Michalske, Mater. Res. Soc. Proc., San Francisco, CA, 1998, pp. 131-136.
[16] J. Israelachvili, *Intermolecular and Surface Forces* (Academic Press, New York, 1992).

ABSTRACT REFERENCE NUMBER: ICF100277PR

EFFECT OF NOTCH SHARPNESS AND COLD EXPANSION ON THE FATIGUE CRACK ARREST

A.AMROUCHE*, G.MESMACQUE*, R.GHFIRI*, A.TALHA*, A.IMAD**

* Laboratoire de Mécanique de Lille URA CNRS 1441, IUT A GMP Le recueil. Rue de la recherche BP 179, 59653 Villeneuve d'Ascq France

** Laboratoire d'Etudes des Structures, Ecole des Hautes Etudes Industrielles, 13 rue de Toul, 59046 Lille Cedex, France

ABSTRACT

A fatigue crack can be stopped by a decrease of the notch sharpness and by residual compressive stresses at the crack tip [1]. The decrease of the notch sharpness is generated by a drilling at the crack tip and the residual compressive stresses by a cold expansion. This work is about two aluminium alloys which are used in land transport components. Three drilling radius and five expansion rate were performed at the crack tip. The required number of cycles to obtain a new crack initiation, the crack propagation rate and the crack tip opening displacement are studied and analysed from the different cases.
The necessary number of cycles to obtain a new crack initiation is called Time Life. The curves time life versus the applied stress are similar to the Wöhler curve and the same use can be done. The residual compressive stresses and the plastic zone size are determined from a numerical calculation code .

Without any cold expansion the fatigue life is controlled by the local stress concentration factor. In this case the fatigue life can be explained from a power law of the hole radius[2].
The crack propagation rate is minimum at the crack initiation and is depending on the hole radius too. After the new crack initiation we find again the crack propagation law of the initial material.

By practising a cold expansion, the time life is strongly improved and the minimum crack propagation rate is lower [3,4,5,6]. We can observe a limit in the time life improving exceptif the crack expansion degree become too high the time life strongly decreases. The cold expansion brings residual stresses, plastic deformations and the local microstructure is modified. The fatigue life depends on the cold expansion degree but it is difficult to identify the separated effect of residual stresses, of the plastic deformation and of the microstructure.

KEYWORDS

Notch sharpness, cold expansion, time life, residual stresses, crack propagation

INTRODUCTION

The propagation of fatigue crack often leads to fracture of components. Therefore it is possible to extend the time life by decreasing the notch sharpness and introducing residual compressive stresses [6]. An usual technique to decrease the notch sharpness is the drilling at the crack tip and to induce residual stresses is the cold expansion. The expansion degree is defined by the relation DCE % = 100*(3- $_{p)}$/ where $_{p}$ is the drilling radius.
By this way we can stop the crack propagation for a more or less time which is called "Time life". After a new crack initiation the crack propagation rate is lower than before drilling and that contribute to the security working.

In the present study, the hole drilling and cold expansion hole are investigated. Three radius value and five expansion degrees have been used. The hole radius successively were 1.0; 2.5 and 3.0 mm. In this case the time life is controlled by the local radius and the local stress concentration factor. The cold expansion has been performed in order to get a final radius of 3 mm, the initial radius were slightly smaller so the expansion degrees varies from 0% to 9.0%. As we'll see later there is a limit on top a certain level the cold expansion is damaging.

EXPERIMENTAL PROCEDURE

We used two aluminium alloys 60XX. that means its contents Magnesium and Silicium. These alloys are used for drawing at cold and mid temperature - working.
The composition and the main mechanical properties are respectively given in the table 1 . The true stress versus true strain shows a low stress hardening.

Alloy	Mg	Si	Fe	Cu	Mn	Cr	Zn	Ti		Re	Rm	E	A%	Hv50
60XX1	0.45	0.5	0.26	0.2	0.23	0.16	0.09	0.04		245	273	68	12	9010
60XX2	0.6	0.7	0.24	0.06	0.9	0.02	0.06	0.02		280	327	68	12	9510

TABLE 1 CHEMICAL COMPOSITION AND MECHANICAL PROPERTIES

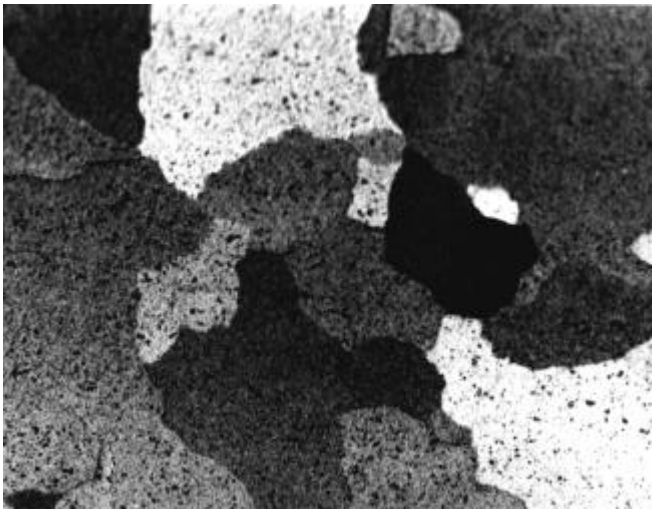

Photo 1 Microstructure Alloy 60XX1

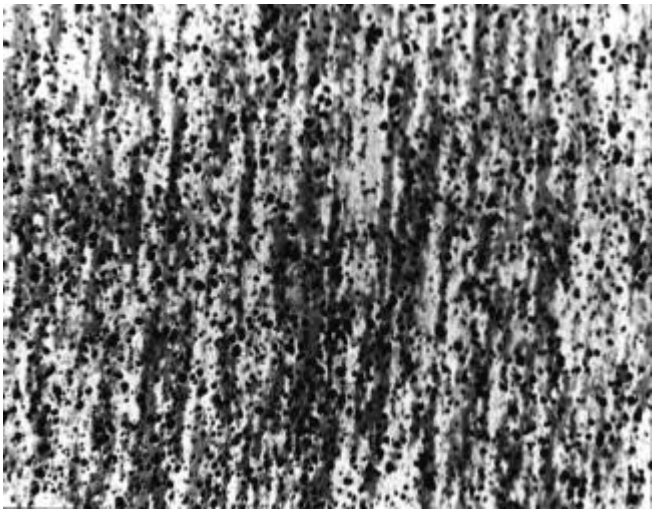

Photo 2 Microstructure Alloy 60XX2

The first alloy presents a constituted microstructure of coarse grains without any precipitates (photo 1) the microstructure of the second alloys presents fine grains where we can detect very small precipitates (photo 2).

The specimens were cut from aluminium alloys plates of 5mm thick, with the axe parallel to the rolling direction of the plates. A slit of 1mm in width and 15 mm in length was machined at one lateral side of specimen. A pre crack from the slit tip was introduced by cyclic loading and the total length of the slit and the pre-crack was (a_0 +) = 27.5 mm. A hole was machined at the pre-crack tip. The hole was first drilled conventionally and then carefully enlarged by a boring bar to a desired radius [2].

The cold working expansion process was realised by forcing a hard steel ball of 6mm in a diameter slightly smaller pre-drilled hole. A burnished surface of the expanded hole was obtained and the surface structure was refined by plastic deformation leaving at the hole surface.

The geometry and the dimensions of specimens are given on the figure 1

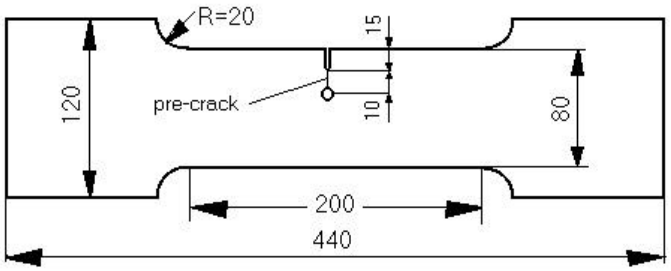

FIGURE 1: SPECIMEN SHAPE

The specimens were subjected to cyclic loading at room temperature with a sinusoidal waveform of a frequency of 30 Hz. For all tests the stress ratio (S_{min}/S_{max}) is the same and taken at the value 0.57. In this condition then crack is always opened.

EXPERIMENTAL RESULTS

From the curves crack length versus number of cycles fig(2) we can determine the time life and the minimal crack propagation rate versus hole radius and versus cold expansion degrees table 2. For each case the time life versus stress amplitude can be put in the form of power law in the same way that the well known Wöhler curves.

The fatigue limit corresponding to a time life of $2*10^6$ cycles can be expressed from the hole radius by a law $N = N_0*$. where N_0 corresponds with = 1.

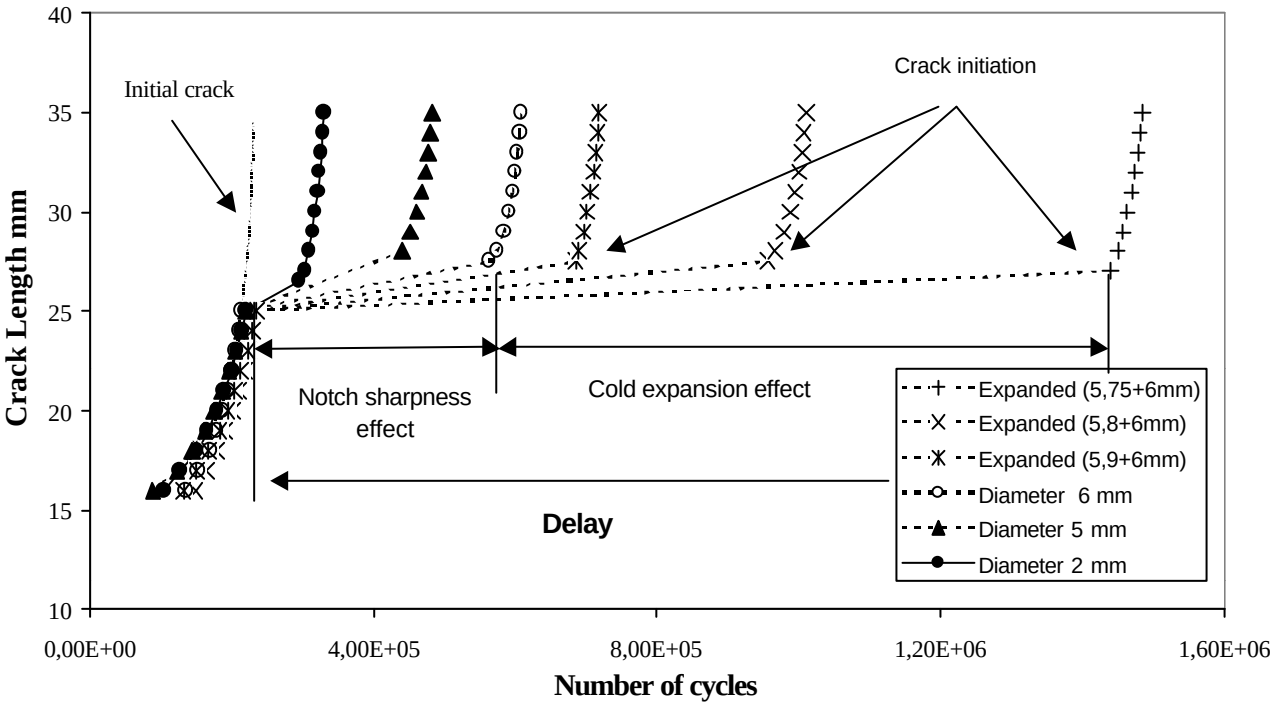

FIGURE 2: CRACK LENGTH VERSUS NUMBER OF CYCLES

The figure 2 shows clearly the crack arrest and the great time life gain we can get by modifying the notch sharpness and the cold expansion.

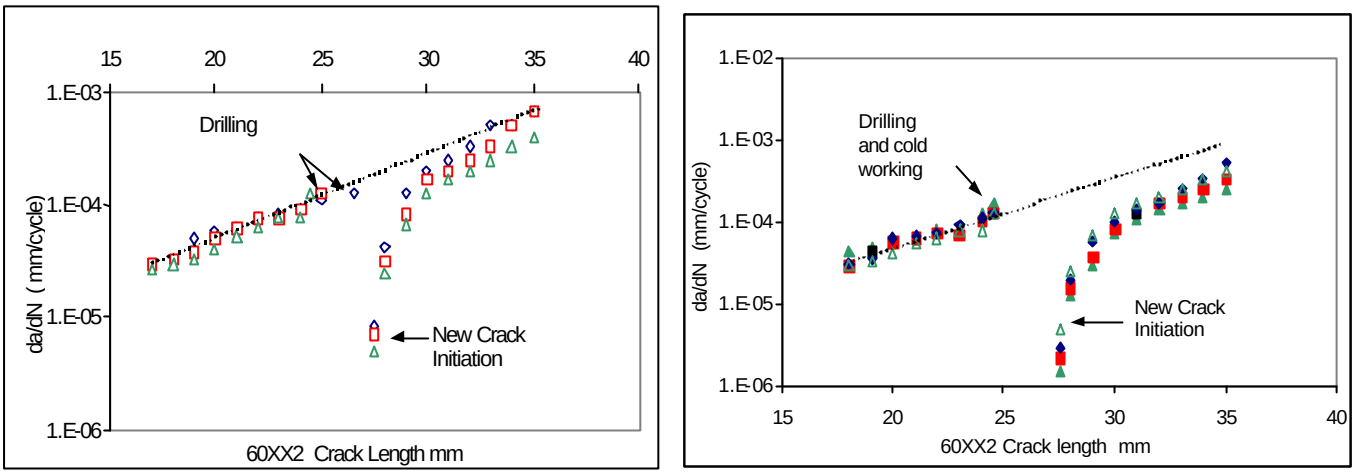

FIGURE 3: CRACK PROPAGATION RATE VERSUS CRACK LENGTH NOTCH SHARPNESS -COLD EXPANSION EFFECT

The figure 3 shows the evolution of crack propagation rate and bring out the notch sharpness effect (hole radius) and the cold expansion effect. A increase of the hole radius and of the cold expansion degree lead to a decrease of the crack propagation rate . We have to notice after cold expansion the crack propagation rate don't go back initial value, that means the parameters of the PARIS law have changed.

	Radius in mm					Radius 3 mm cold working Expansion degree %					
	1 .0	2.5	3.0			0	1.7	3.4	4.3	7.1	9.0
Time Life in kilocycles											
60XX1	75	220	340			340	450	720	1208	211	95
60XX2	119	335	611			611	1040	1420	2000	321	130
Minimum of crack Propagation Rate 10 $^{-6}$mm/cycle											
60XX1	13.6	11.5	8.80			8.80	6.65	4.20	2.50	14.21	31.60
60XX2	8.5	7.1	4.95			4.95	2.80	2.25	1.50	9.34	30.70

TABLE 2: TIME LIFE IN KCYCLES - CRACK PROPAGATION RATE SHARPNESS AND COLD EXPANSION DEGREE (NOMINAL STRESS 28.5 MPA)

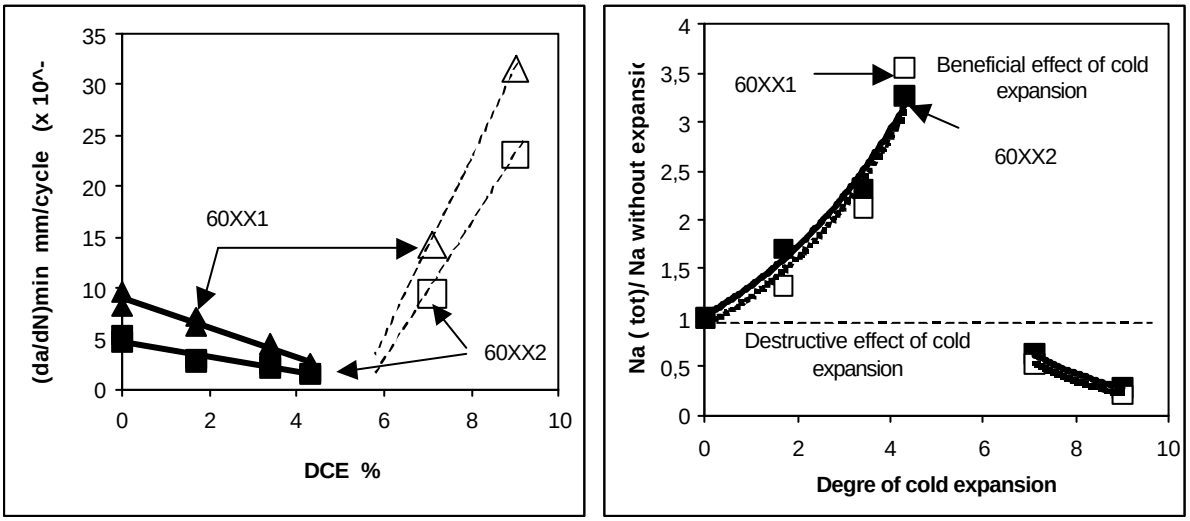

FIGURE 4: COLD EXPANSION EFFECT BRING OUT OF DAMAGING AFTER A TOO HIGH C.E.D

The figure 4 shows that over a value of the cold expansion degree, we clearly notice a decrease of the time life and an increase of the crack propagation rate. In these cases the expansion becomes disadvantageous compared with a single drilling. In our case for both alloys we find the behaviour inversion for a expansion of 5.5%.
The residual stresses and the plastic zone size were calculated from a numerical code (F.E.M IDEAS code in 3D). The results are given on the table 3.

	Residual stresses MPa			Plastic Zone Size mm		
	C.E.D 1.7%	C.E.D 3.4%	C.E.D4.3 %	C.E.D 1.7%	C.E.D 3.4%	C.E.D4.3 %
60XX1	295	317	335	4.38	5.68	6.39
60XX2	310	340	360	3.80	5.02	5.05

TABLE 3: RESIDUAL STRESSES AND PLASTIC ZONE SIZE VERSUS COLD EXPANSION DEGREE

The residual stresses act like a vice so the crack tip opening displacement is strongly dependents on the cold expansion degree. The results are given in three cases (table 4). We can notice a quasi stability in the absence of any expansion. In the presence of an expansion, the crack opening decreases in the first cycles of loading the a stability. Consequently, we can have a stresses redistribution during the first cycles.

Crack tip opening displacement mm			
	1 cycle	50000	10^5
Fatigue crack	0.624	-	-
Radius 3 mm	0.318	0.318	0.290
Expansion 4.3%	0.211	0.162	0.165

TABLE 4 CRACK TIP OPENING DISPLACEMENT

The Scanning Electron Microscopy shows the plastic deformation at the crack tip and into the zone near the crack tip we don't notice any micro crack the residual compressive stresses and the plastic deformation resulting from cold expansion closed these ones. On the other hand, far from the crack tip into the initial structure we notice a lot of micro-crack.

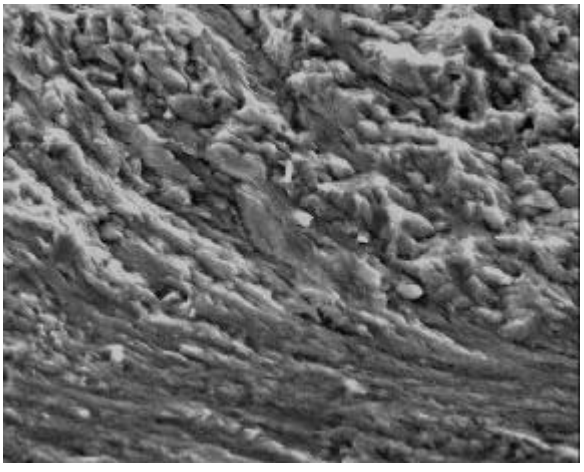

Near the crack Tip

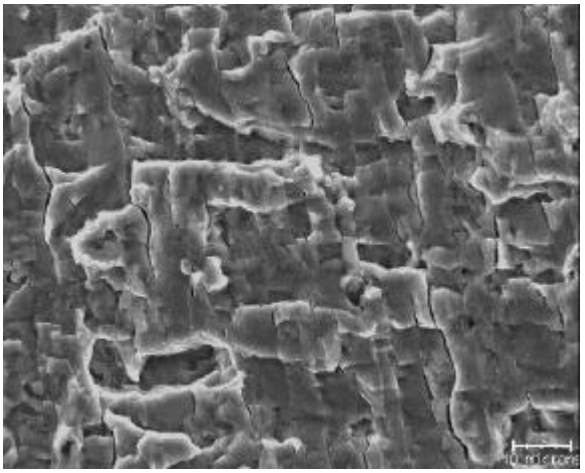

Far from the crack tip

PHOTO 3: SCANNING ELECTRON MICROSCOPY OF FRACTURE

CONCLUSION

The time life and the crack propagation rate minimum can be explained from a power law of the hole radius. The cold expansion bring a advantageous effect until a limit value, over this value the expansion is damaging. The advantageous effect can be explained in the same way that the hole radius effect. The time life versus the stress amplitude leads to similar curves that Wöhler curves and they can be used in the same way. The residual compressive stresses and the plastic zone size was calculated from three dimensions F.E.M. Alone Theses parameters can't explain the material behaviour . The local microstructure modifications must have a great part in the new crack initiation. The crack tip opening displacement can be used as a picture of the hole radius, of the cold expansion and of the residual stresses distribution.

BIBLIOGRAPHY

[1] Domazet Z, (1996) Engenering Failure Analysis, , 3 (2): 137-147

[2] R.Ghfiri, A. Amrouche, A.Imad, G. Mesmacque
(2000) International journal of fatigue and Fracture Engineering Materials and Structures Vol 23 pp911-916

[3] Landy.M.L, Armen.H.J, Eidinoff .H.L.(1986). Fatigue in Mechanically Fastened Composite and Metallic Joints. ASTM STP 927 pp 190-220.

[4] Bernard M, Bui-Quoc T. and Burlat M., Fatigue. Fract. Engng. Mater. Struct, (1995), No 18, pp765-775.

[5] Baker A.A., (1993), Fatigue. Fract. Engng. Mater. Struct.No 16, pp753-765.

[6].Cathey W.H and .Grandt A.F, (1980), J. Engng. Mat. Tech, No 102, pp 85-91.

ORAL REFERENCE: ICF100160OR

EFFECT OF PREDEFORMATION ON FATIGUE LIFE – EXPERIMENTAL CHARACTERIZATION AND DESCRIPTION BY MEANS OF A NEW PARAMETER

H.-J. Christ and K. Schoeler

Institut für Werkstofftechnik, Universität Siegen, D-57068 Siegen, Germany

ABSTRACT

Isothermal cyclic deformation tests were carried out on two nickel-base alloys (Nimonic 105 and Nimonic 75) after monotonic predeformation to various strains. The test temperatures ranged from room temperature up to 800°C, and plastic strain amplitudes between 0.025% and 0.25% were applied. The effect of predeformation was found to lose importance with increasing temperature, increasing plastic strain amplitude, decreasing prestrain and decreasing influence of particle strengthening. Appreciable changes in the crack initiation process and the dislocation arrangement resulted from predeformation. However, the change in the cyclic stress-strain response was identified to be the main reason for the effect of predeformation on fatigue life. Consequently, a new parameter S_{P_SWT} was derived which is based on the values of the Smith-Watson-Topper damage parameter obtained in fatigue tests on predeformed and not predeformed samples, respectively. It was shown that S_{P_SWT} is suitable to quantitatively describe the effect of loading conditions on the prehistory dependence and can successfully be applied for a simple and temperature-independent prediction of the influence of a predeformation on fatigue lifetime.

KEYWORDS

Predeformation, prehistory dependence, nickel-base alloys, cyclic stress-strain behaviour, microstructure, fatigue lifetime, damage parameter, high temperature

INTRODUCTION

Microstructure-related and mechanism-oriented studies on the cyclic deformation behaviour of metals and alloys mostly deal with materials in well-defined annealed starting conditions, in order to obtain results that are both definite and reproducible. Consequently, from all the parameters which are known to strongly influence cyclic stress-strain response and fatigue lifetime, such as loading amplitude, temperature and testing mode, least is know about the parameter mechanical prehistory. However, almost all engineering materials used in structural applications undergo a (thermo-)mechanical pre-treatment, either during the fabrication process or as a means to optimise the mechanical properties. Hence, the prehistory dependence of the cyclic deformation behaviour is on the one hand of high technical significance and on the other hand a complex scientific challenge.

Earlier studies which were focussing on single-phase fcc metals and alloys indicated the important role of the dislocation slip character [1-3]. In the case of planar slip, even a small monotonic prestrain gives rise to

an increase of the stress amplitude during strain-controlled cyclic loading. Since this stress increase retains until failure, the cyclic stress-strain curve (css curve) is shifted upwards by predeformation (prehistory dependent behaviour). As opposed to planar-slip materials, simple and general statements are not possible for materials showing wavy dislocation glide. The behaviour is determined not only by the extent of predeformation, rather the amplitude of the subsequent cyclic loading plays also a significant role. Tendentiously the dependence on a mechanical prehistory ceases at a small predeformation in combination with high plastic strain amplitude. It should be noted in this context that the term prehistory dependence relates only to the mechanical behaviour. As shown in [4], very similar stress-strain responses may result from different types of dislocation arrangements formed during cycling without and after predeformation, respectively.

The results presented are part of a comprehensive study aimed at a detailed understanding of the influence of a monotonic room-temperature predeformation on the high-temperature fatigue behaviour of nickel-base alloys [5]. The emphasis in this paper is put upon cyclic lifetime effects. A simple parameter is introduced which allows to quantify the degree of the influence of relevant loading parameters on both the cyclic stress-strain response and fatigue life and therefore applies to a prediction of predeformation-induced changes in the number of cycles to failure N_f. Microstructural aspects are only dealt with as far as they help to define the applicability range of this predeformation parameter. More details on the microstructural and mechanistic aspects are given in [6].

EXPERIMENTAL DETAILS

The materials studied were two polycrystalline nickel-base alloys, Nimonic 75 and Nimonic 105, which were tested in three different precipitation conditions. Nimonic 75 is a precipitate-free nickel-base superalloy and was used to represent the behaviour of the matrix of Nimonic 105 (precipitate-free condition). In order to improve the comparability to this particle-strengthened material, the mean grain size of Nimonic 75 was adapted to the one of Nimonic 105 by means of an annealing treatment that led to a mean grain size of 60µm. Nimonic 105 was used in two different heat-treated conditions. After a solution annealing with subsequent water quench, an ageing at 850°C for 16 hours was applied to establish the peak-aged condition that corresponds to the hardness maximum at RT. The over-aged condition resulted from an annealing at 1000°C for 500 hours. The peak-aged condition is characterised by spherical γ' precipitates of a mean particle diameter of 73 nm at a volume fraction of 43%. The over-ageing treatment led to a γ' volume fraction of 38%. In this condition, the γ' precipitates were present in three superimposed size distributions with mean sizes of 32nm, 138nm and 665nm. As a consequence of the existence of small precipitates in the over-aged condition, the cyclic deformation behaviour of both conditions was found to be very similar and will therefore be reported jointly.

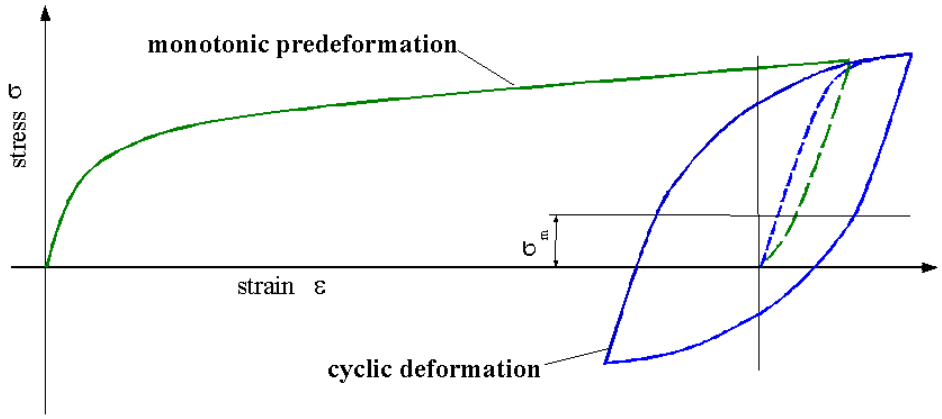

Figure 1: Effect of tensile predeformation on position of hysteresis loop

Specimens with a cylindrical gauge length of 6mm in diameter were tested in an electrohydraulic servocontrolled test system equipped with high frequency heating. The fatigue tests were performed at room temperature (RT), 400°C, 600°C and 800°C. True plastic strain control in combination with a triangular command signal was applied in all fatigue tests in such a way that the plastic strain rate was held constant at a absolute value of $5 \cdot 10^{-4}\ s^{-1}$. Plastic strain amplitudes $\Delta\varepsilon_{pl}/2$ ranging from 0.025% to 0.25% were used and were kept constant throughout the test (irrespective of a continuous change in Young´s modulus E) by means of a superimposed control of the plastic strain value at zero stress.

Predeformation was mainly carried out as monotonic tensile deformation up to certain levels of total strain ranging from 0% to 8% in steps of 2%. The basic effect of predeformation on the position of the hysteresis loop is illustrated in Figure 1. After tensile loading and unloading to zero stress the subsequent cyclic deformation leads to an asymmetric stress-strain hysteresis loop, since the deformation resistance is larger in tension as compared to compression. Hence, a positive mean stress σ_m results.

RESULTS AND DISCUSSION

The dislocation slip character in the matrix of Nimonic 105 and in the precipitate-free Nimonic 75 is planar, as expected for the Ni-Cr system [7]. Hence, dislocation glide during cyclic loading of Nimonic 75 is mainly restricted to single active slip planes. The main effects of prestraining seem to be a reduction of slip plane spacing and an increase of dislocation density within these planes [8]. The cyclic deformation behaviour of Nimonic 105 is governed by a strong dislocation/precipitate interaction. At low and moderate temperatures, cutting of γ′ particles by dislocation pairs prevails, while at high temperatures Orowan bypassing takes place and no slip bands are appreciable. Figure 2 illustrates the effect of predeformation on the dislocation arrangement of Nimonic 105 at 800°C. Since prestraining was carried out at room temperature, slip planes are introduced which seem to remain active during high-temperature cyclic deformation (Fig. 2b) in addition to the individually gliding dislocations and Orowan loops which are typical of this temperature range (Fig. 2a).

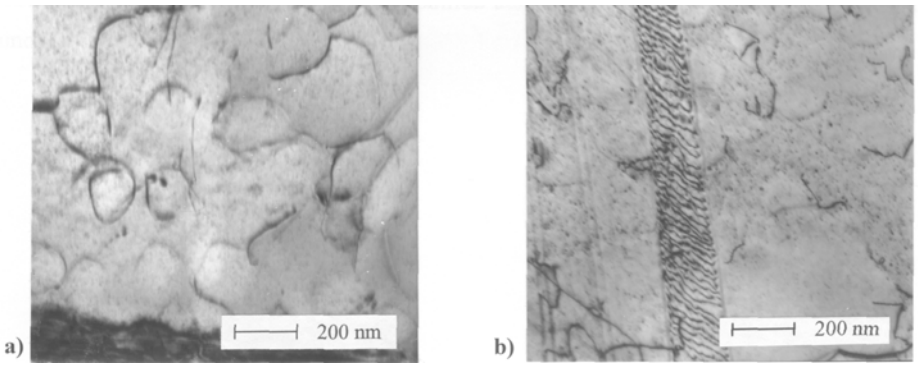

Figure 2: Dislocation arrangement in Nimonic 105 (over-aged) formed at 800°C and $\Delta\varepsilon_{pl}/2$=0.025% without predeformation (a) and after a tensile prestrain of 2% (b)

An example for the change of the location of crack initiation is given in Figure 3. In general, it was found that without predeformation crack initiation at low temperature takes place transgranularly at slip bands in the surface, whereas at high temperatures cracks form in the bulk of the material in the form of wedge cracks at grain boundary triple points and cavities. Predeformation gives rise to surface steps and therefore favours crack nucleation at the surface (Fig. 3b).

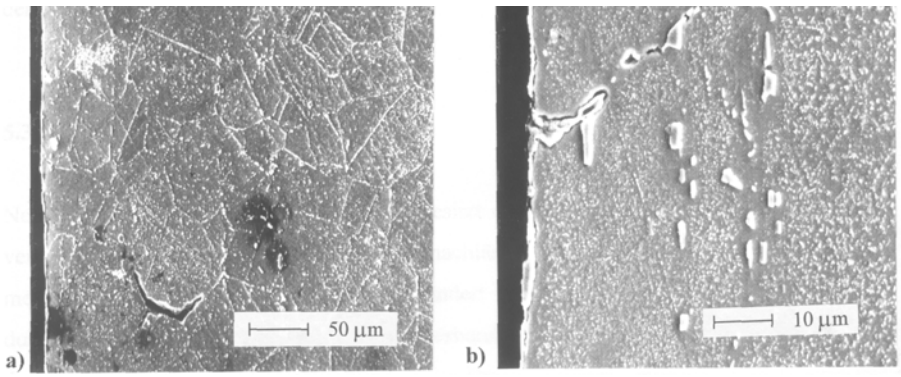

Figure 3: Cross sections showing fatigue crack initiation sites in Nimonic 75 (800°C and $\Delta\varepsilon_{pl}/2$=0.025%) without predeformation (a) and after a tensile prestrain of 8% (b)

As will be shown later by the successful application of the Smith-Watson-Topper damage parameter, these changes in dislocation arrangement and crack initiation site due to prestraining do not seem to strongly and directly affect cyclic life. Rather, the influence of predeformation on the cyclic stress-strain response, which however is at least an indirect consequence of the modified microstructure, appears to be mainly responsible for the life time alteration. As already pointed out by means of Figure 1, the type of predeformation used in this study leads not only to a change in the stress amplitude during subsequent plastic strain controlled cycling, but also gives rise to a positive mean stress, if prestraining is carried out in tension, and vice versa. The schematic respresentation given in Figure 4 documents that at a constant temperature and constant plastic strain amplitude both stress amplitude and mean

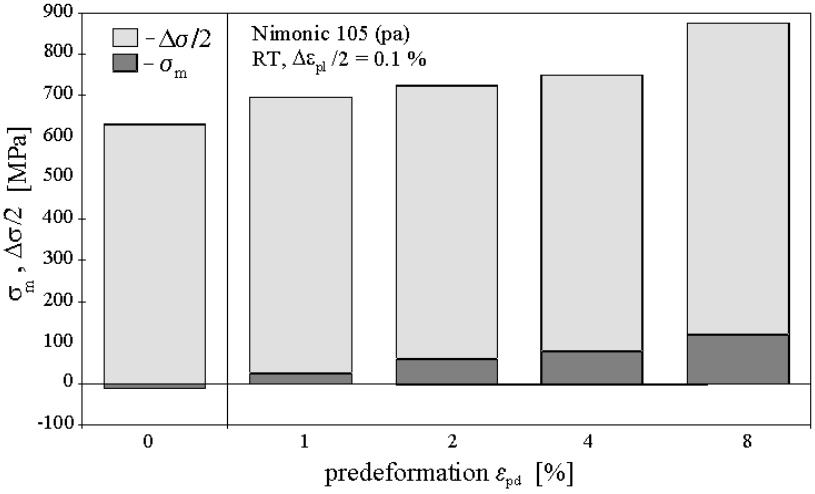

Figure 4: Effect of tensile prestrain on stress amplitude and mean stress at half fatigue life of Nimonic 105 (peak-aged) at $\Delta\varepsilon_{pl}/2$=0.1% and room temperature

stress usually increase with increasing degree of predeformation. However, it is important to mention that under certain conditions a decrease of $\Delta\sigma/2$ resulted from the mechanical prehistory.

A systematic evaluation of all the tests carried out showed the expected general trends that the extent of change in the stress-strain response (the history dependence) decreases with increasing temperature of subsequent cyclic loading, and with increasing plastic strain amplitude. Conversely the history dependence increases with increasing degree of predeformation (Fig. 4) and enhanced significance of particle strengthening.

The Smith-Watson-Topper parameter P_{SWT} [9] was appied to the cyclic stress-strain data at half life, since this damage parameter takes the predeformation-induced mean stress in a very simple and direct way into account.

$$P_{SWT} = \sqrt{\left(\frac{\Delta\sigma}{2} + \sigma_m\right)\frac{\Delta\varepsilon}{2}E} \tag{1}$$

P_{SWT} has shown in many earlier studies to be of similar capability of predicting cyclic life as those damage parameters which contain an adjustable variable [10]. A representation of P_{SWT} versus the experimentally observed number of cycles to failure is depicted in Figure 5 for all tests performed at room temperature. Irrespective of the extent of predeformation applied, rather narrow bands describe the correlation of P_{SWT} and cyclic life for each material. For each temperature a representation similar to Fig. 5 resulted. However, the shape and position of the respective P_{SWT} *vs.* N_f curves was found to depend on temperature. It must be emphasised that the predictive capability of P_{SWT} is rather surprising from a microstructural viewpoint. Obviously the effect of mechanical prehistory on the cyclic stress-strain behaviour determines the change in fatigue life that results from predeformation. Other aspects, such as surface roughening due to tensile prestraining, a different crack initiation site and a change in the dislocation arrangement of cyclic saturation, seem to have comparably small direct influence on N_f.

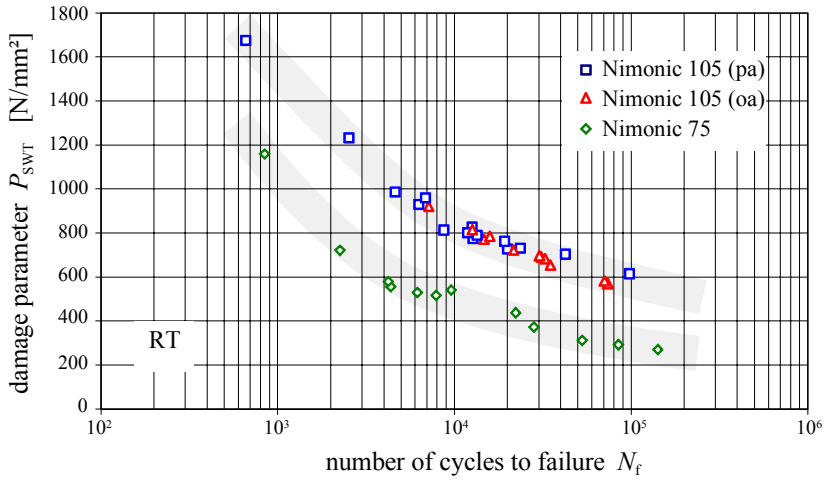

Figure 5: Description of cyclic lifetime at room temperature by means of the Smith-Watson-Topper damage parameter

The successful description of cyclic life by means of P_{SWT} allows the definition of a simple predeformation parameter S_{P_SWT}.

$$S_{P\_SWT} = 1 - \frac{P_{SWT}^{not\ predeformed}}{P_{SWT}^{predeformed}} \tag{2}$$

S_{P_SWT} approaches a value of 1, if the prehistory strongly affects P_{SWT} in such a way that P_{SWT} is tremendously increased as compared to the non-predeformed condition. A value of 0 corresponds to the situation

that the prehistory does not lead to a change in the cyclic stress strain response so that the value of P_{SWT} after predeformation equals the one of the non-predeformed (reference) behaviour.

Figure 6 shows that the parameter S_{P_SWT} turned out to be very helpful for a quantitative representation of the effect of loading parameters on the prehistory dependence. As already described above, increasing temperature decreases the influence of predeformation, whereas an increasing value of the prestain acts inversely. As a first approach, the linear relationships depicted in Figure 6 as dashed lines can be used to mathematically express these correlations. Linear relations are not obeyed as far as the effect of plastic strain amplitude and particle strengthening is concerned. However, the trends are clearly visible in corresponding representations (not shown here) that an increase of $\Delta\varepsilon_{pl}/2$ reduces the influence of predeformation and that prehistory dependence is the more pronounced the more effective the particle strengthening.

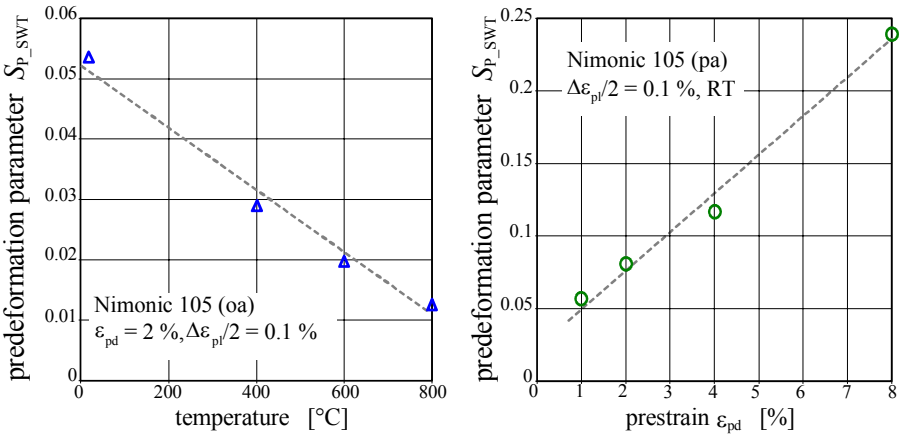

Figure 6: Effect of testing temperature (a) and value of prestrain (b) on the predeformation parameter for Nimonic 105

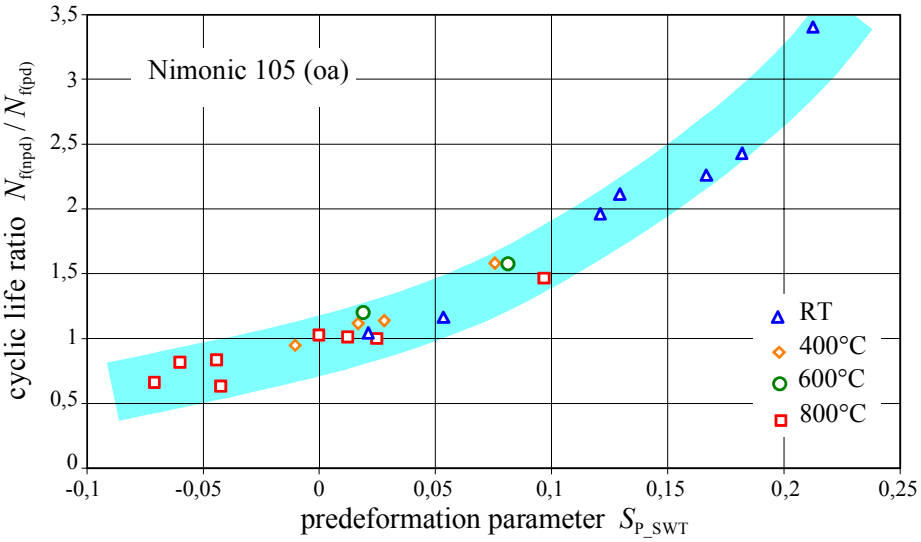

Figure 7: Description of cyclic lifetime of Nimonic 105 (over-aged) at various temperatures by means of the predeformation parameter

Since P_{SWT} works reasonably to describe the changes in cyclic life, also S_{P_SWT} is expected to be a suitable parameter for this purpose. As shown in Figure 7 for Nimonic 105, the main advantage of the application of S_{P_SWT} instead of P_{SWT} is that the correlation between the ratio of the number of cycles to failure of the non-predeformed condition $N_{f(npd)}$ to the corresponding value $N_{f(pd)}$ after predeformation (ordinate in Fig. 7) with S_{P_SWT} (abscissa) is independent of temperature. A very similar result was obtained for the particle-free alloy Nimonic 75. It should be noted that S_{P_SWT} can be both positive and negative. A negative value leads to cycle life ratios smaller than 1. That means that under the respective conditions predeformation extends cyclic life.

One reasonable application of the correlation shown in Figure 7 is the assessment of the extent of cyclic life change by prehistory. For this purpose, the corresponding value of S_{P_SWT} can be determined performing two fatigue tests at identical test parameters, one on the material in the reference (annealed) condition and one in the predeformed conditions. The tests only need to be run until cyclic saturation is established, since then P_{SWT} does not change any further (see Eqn. 1). S_{P_SWT} can easily be calculated from Eqn. 2, and the connection of S_{P_SWT} with the cyclic life ratio allows to predicted the change in cyclic life irrespective of the test temperature.

In order to define the range of applicability of the predeformation parameter S_{P_SWT}, fatigue life data obtained in an earlier study on the effect of predeformation on the room temperature fatigue behaviour of polycrystalline copper and α-brass [11] was evaluated. α-brass is known to show a very pronounced planar dislocation slip behaviour and behaves therefore microstructurally similar to Nimonic 75. This seems to be

the main reason why the S_{P_SWT} concept introduced by Figure 7 applies to this material as well. However, the dislocation arrangement in copper as a wavy-slip metal depends very sensitively on the plastic strain amplitude of cyclic loading and the degree of predeformation. Dislocation cells are formed at high values of $\Delta\varepsilon_{pl}/2$, but are also prevailing after strong prestraining and subsequent cyclic deformation even at low $\Delta\varepsilon_{pl}/2$. Single-slip dislocation arrangements, such as bundle/vein structure and persistent slip bands, are restricted to small value of $\Delta\varepsilon_{pl}/2$ and very low degrees of predeformation. Taking this strong variation in dislocation arrangement into account and considering that the S_{P_SWT} parameter ignores changes in microstructure and mechanism, it is not surprising that the data of copper can not be described by a single curve in the representation of the cyclic life ratio versus S_{P_SWT}. Consequently, a prerequisite for the application of the S_{P_SWT} concept is that no fundamental changes in the microstructure takes place within the range of predeformation and cyclic loading parameters considered.

CONCLUSIONS

The main results obtained in this study on the effect of a monotonic tensile prestrain on cyclic stress-strain response and fatigue life of Nimonic 75 and Nimonic 105 (over-aged and top-aged) at temperatures ranging from room temperature up to 800°C can be summarized as follows:

- The effect of predeformation on cyclic life can be described by means of the Smith-Watson-Topper damage parameter P_{SWT} despite a change in the microstructure and the favourable crack initiation site with room-temperature tensile prestraining
- Based on P_{SWT} the predeformation parameter $S_{P\_SWT} = 1 - \frac{P_{SWT}^{not\ predeformed}}{P_{SWT}^{predeformed}}$ is introduced.
- S_{P_SWT} successfully applies to quantitatively describe the effect of cyclic loading parameters, extent of predeformation and particle strengthening on the prehistory dependence.
- S_{P_SWT} correlates with the predeformation-induced cyclic life change in an unambiguous way. This correlation is independent of the temperature of cyclic loading.
- The applicability of S_{P_SWT} is restricted to materials and conditions which do not undergo a fundamental microstructural change.

Acknowledgement: The authors gratefully acknowledge financial support of this study by Deutsche Forschungsgemeinschaft.

REFERENCES

1. Feltner, C. E. and Laird C. (1967) *Acta met.* **15,** 1612-1632 and 1633-1653.
2. Lukáš, P. and Klesnil M. (1973) *Mater. Sci. Engng* **11**, 345-356.
3. Coffin, L. F. (1967) *Trans. ASME* **60**, 160-175.
4. Hoffman, G., Öttinger, O. and Christ H.-J. (1993). In: *Proc. Low Cycle Fatigue and Elasto-Plastic Behaviour of Materials (LCF3)*, pp. 106-111, Rie, K. T. (Ed.). Elesvier Applied Science, London.
5. Schöler, K. (1999) *Einfluß der Mikrostruktur auf das Wechselverformungsverhalten teilchengehärteter Legierungen bei hohen Temperaturen nach einer Vorverformung*. Doctorate Thesis, Universität Siegen.
6. Schoeler, K. and Christ, H.-J. (2000) *Intern. J. Fatigue*, in print
7. Gerold, V. and Karnthaler, H. P. (1989) *Acta met.* **37**, 2177-2183
8. Zheng, D., Rosenberg, A. and Ghonem, H. (1993) *Mater. Sci. Engng* **A161**, 13-21.
9. Smith, K. N., Watson, P. and Topper, T. H. (1970) *Journal of Materials, JMLSA* **5**, 767-778.
10. Nihei, M., Heuler, P., Boller, Ch. and Seeger, T. (1986) *Intern. J. Fatigue* **8**, 119-126.
11. Hoffmann, G. (1996) *Wechselverformungsverhalten und Mikrostruktur ein- und mehrphasiger metallischer Werkstoffe nach einer Vorverformung,* Doctorate Thesis, Universität Erlangen-Nürnberg

ORAL Presentation No. ICF101022OR

EFFECT OF REINFORCING PARTICLE MORPHOLOGY ON THE TENSILE RESPONSE OF 6061/SiC/25p DISCONTINUOUSLY-REINFORCED ALUMINUM

Jonathan E. Spowart[2] and Daniel B Miracle[1]

[1]Air Force Research Laboratory, Materials and Manufacturing Directorate,
AFRL/MLLM, Wright-Patterson AFB OH, USA
[2]U.E.S. Inc., Dayton OH, USA

ABSTRACT

In order to study the effect of particle morphology on the tensile response and fracture behavior of Discontinuously-Reinforced Aluminum (DRA), two P/M 6061/SiC/25_p materials were fabricated using established powder blending, compaction and extrusion techniques. One of the materials contained abrasive-grade SiC (F-600) whilst the second material was fabricated using a lower aspect ratio grain, selected to give an overall higher bulk density (HBD) in the as-blended form. Care was taken to ensure that each material contained the same size and volume fraction of SiC particles, and to ensure that each material experienced an identical processing route. Mechanical testing was completed at ambient temperature, in order to measure the effect of particle morphology (F-600 vs. HBD) on both the elastic and plastic tensile response of the DRA. Extensive microstructural and fractographic analyses were also carried out on the as-processed and as-tested specimens, using optical and electron microscopy. Future work includes both analytical and numerical modeling to relate the mechanical behavior to microstructural differences between the two materials.

KEYWORDS

Discontinuously-Reinforced Aluminum, DRA, SiC, ductility.

INTRODUCTION

Over the last decade, DRA materials based on the Al-SiC or Al-Al_2O_3 systems have been receiving increasing industrial interest[1, 2]. This can be attributed to more precise process control leading to well-characterized materials with better mechanical properties than those previously available, allowing them to be used in fracture-critical applications for the first time. The currently-available commercial DRA materials show great promise in terms of their specific stiffness (modulus ÷ density) when compared to conventional aluminum alloys, and are therefore seen as excellent candidates for further development as structurally efficient metallic materials. For example, an increase in specific stiffness of 1.5 x can be obtained using a reinforcement volume fraction of 50 %. However, this level of ceramic reinforcement typically reduces the ductility of the DRA around 20–60 % of the ductility of the matrix alloy, as shown in Figure 1.

Evidence from previous studies[3-6] suggests that angular particles can produce high localized hydrostatic stresses in response to external loads, especially at the particle corners. These localized stresses have been linked to void nucleation in the matrix adjacent to the particles during tensile loading. The incorporation of a less-angular reinforcement phase is therefore seen as a potential route to improving the ductility of DRA materials, by reducing the propensity for tensile failure by the commonly-observed void growth and coalescence mechanism. The present work can therefore be considered a first step toward the ultimate goal of producing a more ductile, high specific stiffness DRA.

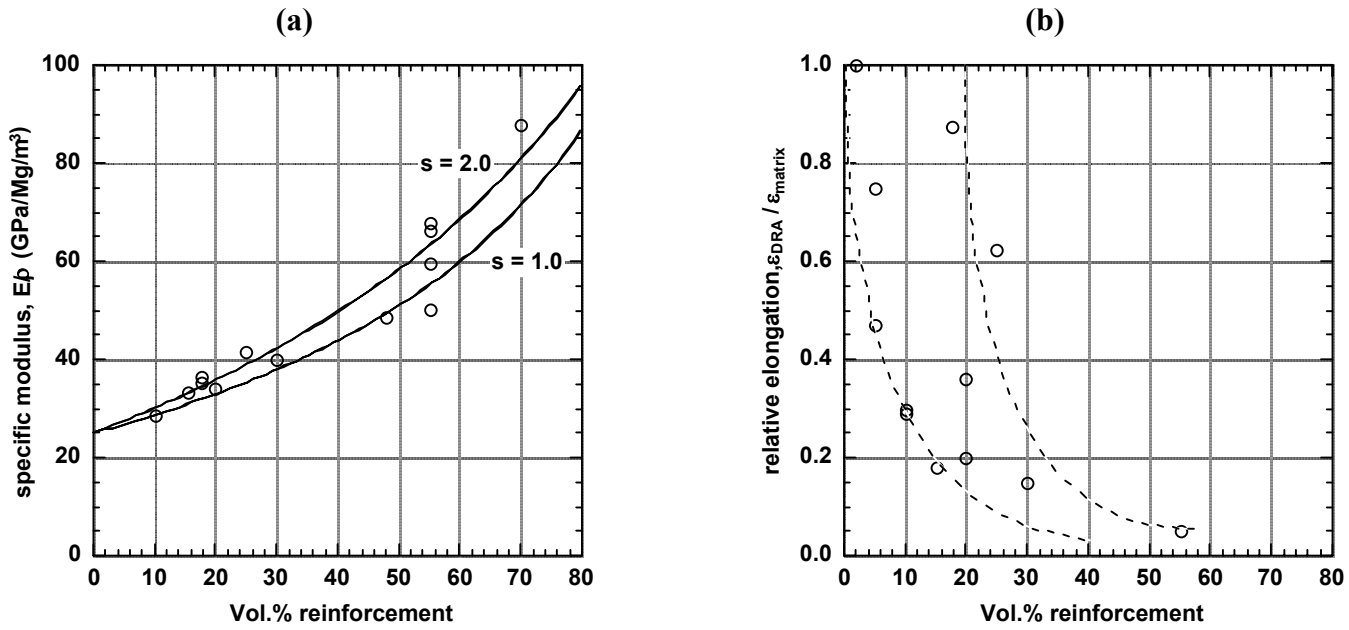

Fig. 1: Plot showing: **(a)** specific modulus, and **(b)** relative elongation vs. volume fraction of reinforcement for different DRA materials[7]. Solid lines are from Eshelby-type models[8], based on reinforcement aspect ratios s = 1.0 and s = 2.0. Broken lines are approximate upper and lower bounds on elongation data.

In order to quantify the effects of particle morphology on the tensile properties of the 6061/SiC/25$_p$ DRA materials, we required two morphologically different SiC particles. The lower aspect ratio HBD SiC particles used in the present study are produced by a proprietary milling process. The resulting particles have a size distribution similar to the standard abrasive grade F-600 SiC, but with a blocky appearance, Fig. 2. In addition, it is reasonable to conjecture that the HBD particles may have a higher intrinsic strength than the F-600 particles, due to their surviving the mechanical milling process. Both these features are attractive in terms of a ceramic reinforcement for DRA.

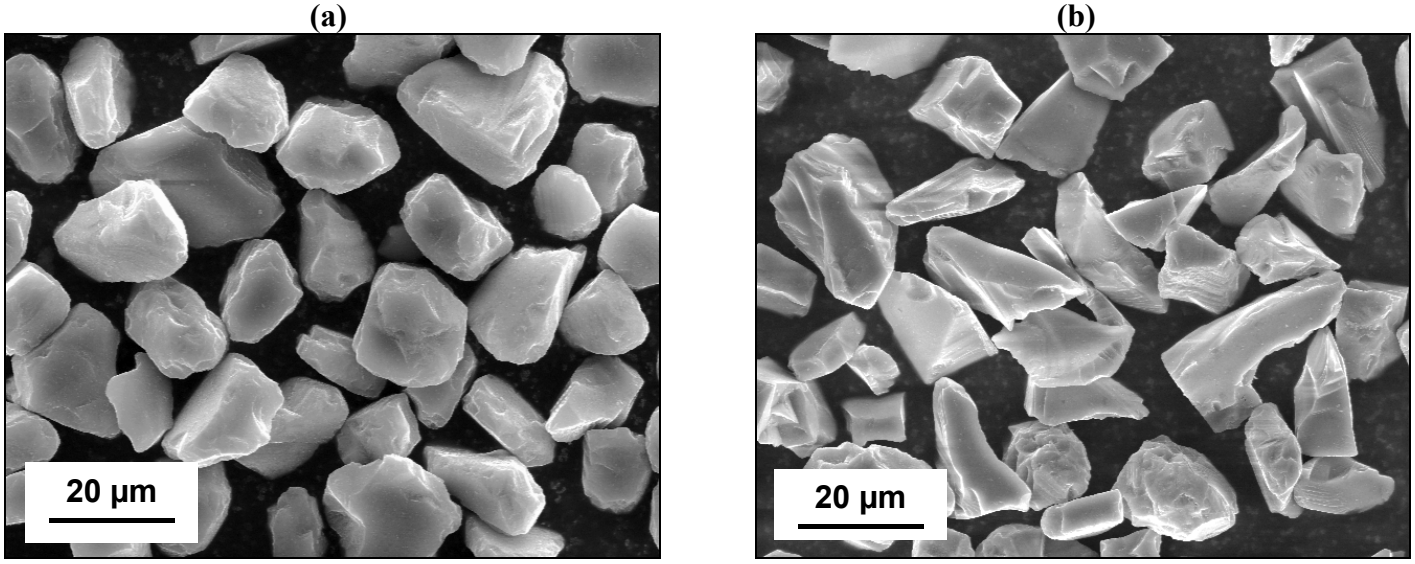

Fig. 2: SEM micrographs showing morphology of **(a)** High Bulk Density (HBD), and **(b)** F-600 SiC[1]. In each case, mean particle size ≈ 12 µm.

[1] "Green" SiC powder, obtained from Saint-Gobain Industrial Ceramics, Inc. Worcester, MA.

EXPERIMENTAL

Al-6061 matrix alloy powders (Al-0.27 Cu-0.26 Fe-0.97 Mg-0.56 Si)[2] were initially screened to -325 mesh prior to blending with the SiC reinforcement. During the blending stage, the matrix and reinforcement powders were suspended in a slurry using 1-butanol as the solvent, in order to reduce agglomeration due to electrostatic forces. After blending, the powders were carefully dried, re-screened to -325 mesh and placed in an extrusion can. An elevated temperature vacuum de-gas treatment was used to remove all traces of residual solvent from the powders, before sealing the cans for compaction and extrusion. Extrusion was carried out at 450˚C, with an extrusion ratio of 25:1 (round : round), followed by an air cool (F-temper designation).

Particle aspect ratios were measured from digital micrographs, using a commercial desktop image analysis package[3]. Around 200 particles were selected from each micrograph, at random, in order to perform a statistical analysis of the particle aspect ratios in each material, in both transverse and longitudinal orientations with respect to the extrusion direction. Particle size statistics for the as-received powders were obtained using a Coulter LS 230 Particle Size Analyzer, with small volume unit and associated software. Duplicate samples of each reinforcement were analyzed, using ethanol as the suspension medium.

Room-temperature tensile testing was carried out using a servo-hydraulic test frame under displacement control at a constant strain rate of 1.3×10^{-4}. A flat dog-bone specimen with a gauge length of 25.4 mm was used throughout. The oversize specimen ends were gripped between hydraulic jaws, and a clip-on extensometer was attached to the larger specimen faces for strain measurement. Each specimen was loaded to failure. The two specimen halves were then carefully separated and set aside for examination in SEM.

RESULTS

Microstructural Characterization

Figures 3(a) and 3(b) show longitudinal sections through each microstructure, with the extrusion direction horizontal. The two microstructures are very similar; especially in terms of the homogeneity of the spatial distribution of SiC particles. However, the F-600 material clearly contains a wider distribution of particle sizes, with many small, angular particles in the section. This qualitative statement agrees well with the particle size analysis results for F-600 SiC (d_p = 12.0 µm, s.d. = 4.0 µm) and HBD SiC (d_p = 11.5 µm, s.d. = 3.0 µm), in the as-received condition. No obvious porosity was observed in either microstructure.

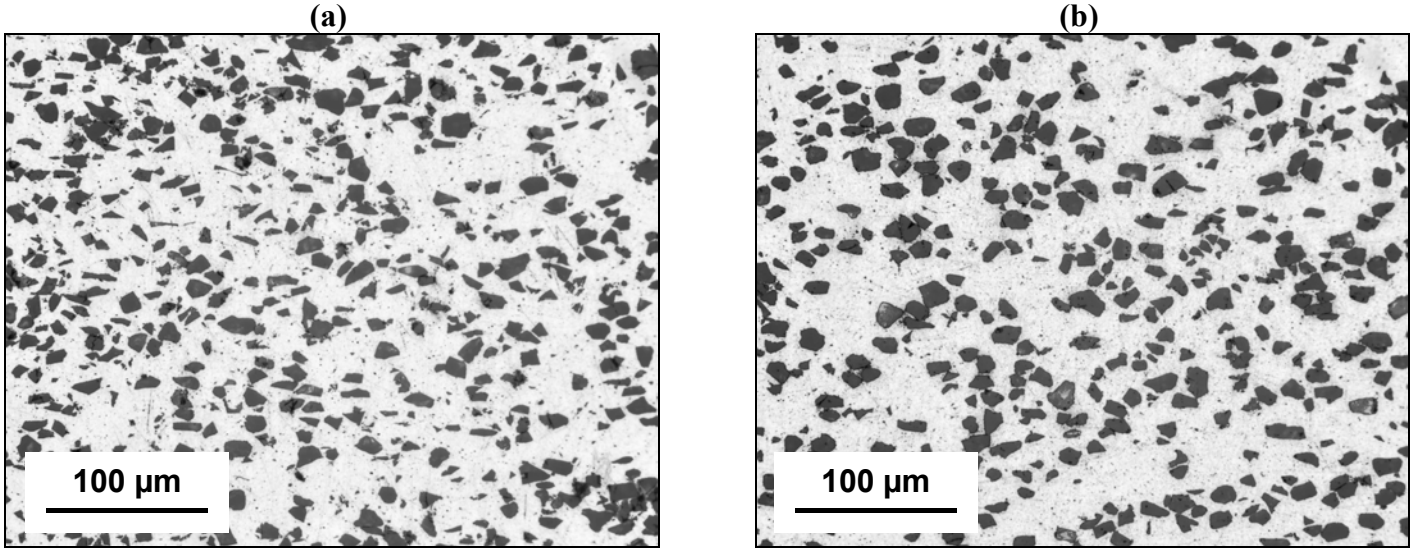

Fig. 3: Typical microstructures of **(a)** F-600 and **(b)** HBD DRA materials. Longitudinal sections, F-temper, unetched (extrusion direction is horizontal).

[2] spherical gas-atomized 6061-Al powder, obtained from Valimet, Inc. CA.
[3] Adobe Photoshop 5.5, running Image Processing Tool Kit, v2.10.

Figure 4 shows the results of measuring the aspect ratios of 200 particles selected from each of the longitudinal metallographic sections in Figure 3. The F-600 powder has slightly higher mean aspect ratio, with a greater spread in values. However, at these levels of reinforcement (25 Vol %), the effect of the higher particle aspect ratio on tensile properties is expected to be small. For example, interpolating between the curves for $s = 1.0$ and $s = 2.0$ on Figure 1(a) gives an increase in tensile modulus of only 3 % on increasing the particle aspect ratio from $s = 1.6$ to $s = 1.9$.

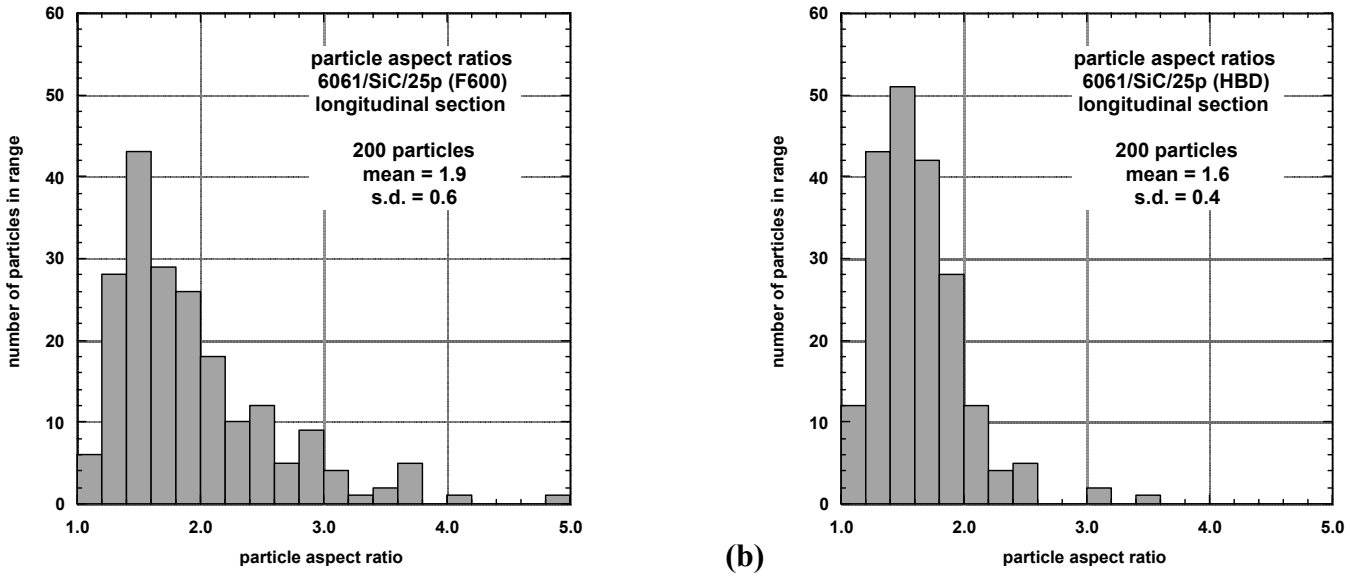

Fig. 4: Histograms of particle aspect ratio, *s*, for **(a)** F-600 and **(b)** HBD materials, as obtained from longitudinal metallographic sections taken parallel to the extrusion direction.

Mechanical Behavior

Figure 5 shows representative tensile stress/strain curves for each of the DRA materials. There is only a slight difference between elastic modulus and yield strength values measured in each material, which is well within experimental scatter, as shown in Table 1. However, there is a significant improvement in tensile ductility for the HBD material over the F-600 material. In the F-temper condition, an increase in ductility from 6.6 % to 9.5 % was observed on average, with 3 specimens of each material being tested.

TABLE 1
TENSILE PROPERTIES OF THE 6061/SIC/25P DRA MATERIALS

Material Designation	E (GPa)	σ_Y (MPa)[4]	σ_{uts} (MPa)	ε_{ult} (%)
6061/SiC/25$_p$ (F-600)	114 ± 10[5]	176 ± 3	224 ± 4	6.6 ± 0.8
6061/SiC/25$_p$ (HBD)	115 ± 9	173 ± 2	225 ± 1	9.5 ± 1.6

Fractography

Figure 6 shows details of the fracture surfaces of the two DRA materials. The HBD material generally shows a more ductile failure mode than the F-600 material. The HBD SiC particles are largely intact, and often associated with large, deep dimples on the fracture surface, with ductile failure and finer-scale dimpling in the surrounding matrix. Conversely, the lower-relief fracture surface of the F-600 material suggests a more brittle character, with more fractured particles at the surface, and considerable particle debris.

[4] 0.2 % offset yeild.
[5] average of 3 specimens, ± S.D.

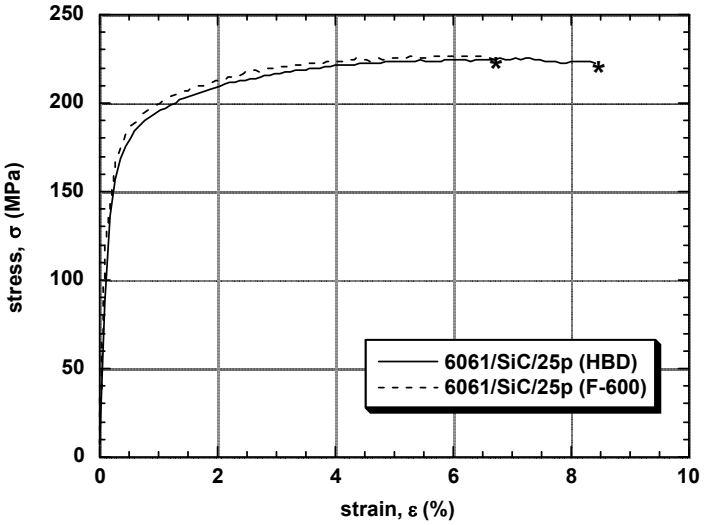

Fig. 5: Representative stress-strain curves for the two different 6061/SiC/25_p DRA materials: solid line, HBD material; broken line, F-600 material. Asterisk indicates failure. Specimens tested in as-fabricated condition (F-temper).

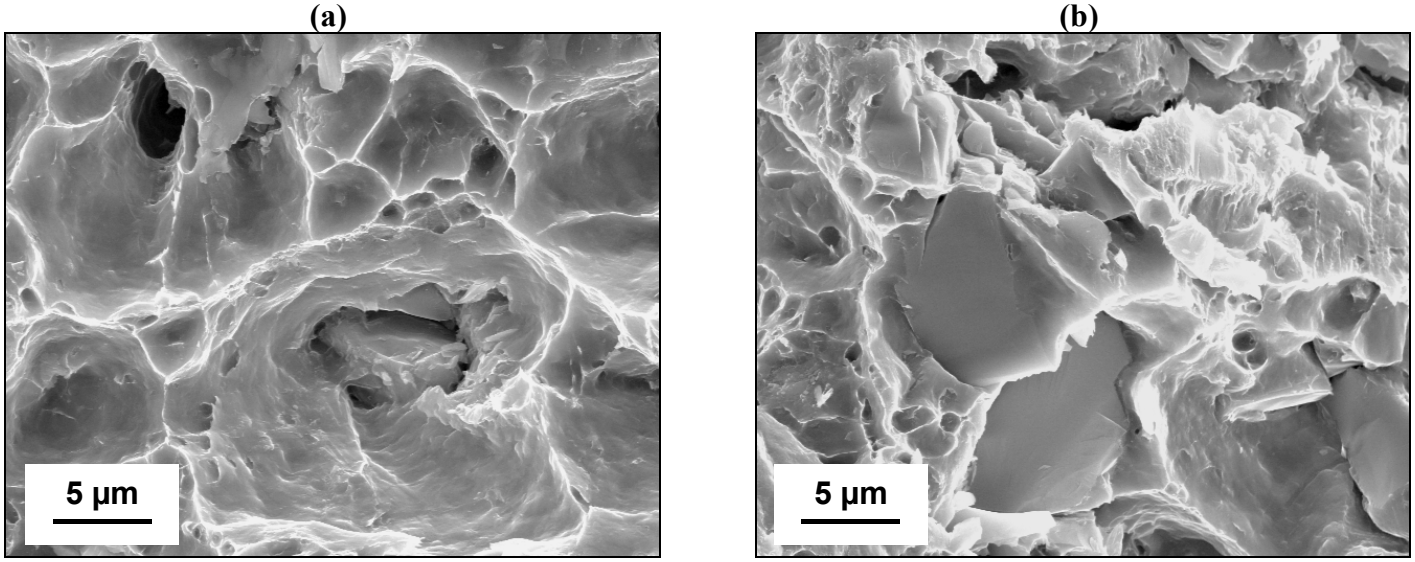

Fig. 6: SEM micrographs showing detail of fracture surfaces of DRA tensile specimens: **(a)** HBD SiC DRA that failed at ε_{ult} = 11.4 %, showing extensive matrix plasticity and large dimple associated with SiC particle **(b)** F-600 SiC DRA that failed at ε_{ult} = 5.7 %, showing fractured SiC particles.

DISCUSSION

In a previous investigation, Song *et al*[9] studied the tensile properties of two different 6061/Al_2O_3/20_p DRA materials. One DRA material was reinforced with angular Al_2O_3 particles, whilst the other was reinforced with Al_2O_3/mullite spheres of a similar size. The spherical particle reinforced material showed a decrease both in elastic modulus and tensile yield strength, compared to the angular reinforcement, however, a marked increase in tensile ductility was also observed. In the present work, however, we observed no decrease in either elastic modulus or yield strength, with a similar increase in ductility for the HBD material. Although our current fractographic investigations are too preliminary to ascertain the precise failure mode(s) operating in each material, there are a number of different mechanisms worth mentioning here. Firstly, the increase in tensile ductility in the HBD material could be attributed to increased strength in the HBD particles

themselves. As the matrix plastic strain increases, load is transferred to the particles, thereby increasing the probability of particle cracking. If the particles are strong, other mechanisms such as interfacial debonding and/or void nucleation and coalescence must occur, at much higher levels of plastic strain. For the more angular F-600 SiC particles, higher localized hydrostatic stresses may exist at the particle corners, thereby increasing the propensity for void nucleation and leading to a lower tensile ductility. We also have the added complication that the weaker F-600 particles may fracture at lower stresses[6] than the HBD particles. The fractured particle fragments can then act as nucleation sites for further matrix voids[5], exacerbating the problem.

It is also worth noting that the results presented here are all based on F-tempered material. Further testing is underway to determine the effect of a peak aging heat treatment on the tensile behavior of the two DRA materials. The addition of a fine dispersion of matrix precipitates should increase the work-hardening rate. Higher matrix flow stresses will lead to higher stresses on the particles at the same level of plastic strain. Whether this in turn leads to a greater improvement in ductility for the HBD material, is a matter for further study.

ACKNOWLEGEMENT

This work was supported in part by the Air Force Research Laboratory, Materials and Manufacturing Directorate, under Air Force Contract No. F33615-96-C-5258.

CONCLUSIONS

- A lower aspect ratio, less-angular SiC particle (HBD) has been identified as a viable reinforcement for experimental high specific stiffness extruded P/M DRA materials.
- Preliminary tensile results show that there is a significant increase in tensile ductility for the HBD SiC DRA compared with the F-600 SiC DRA, with no concomitant loss of elastic modulus, yield strength or ultimate strength.
- Higher tensile ductility in the HBD material may be attributed to either higher strength or less angular morphology of the reinforcement particles.
- The incorporation of HBD SiC reinforcement is therefore seen as a potential route for increasing the ductility of current high specific stiffness DRA materials.
- Further work is planned to ascertain whether the reported increase in ductility is also seen in other heat-treatment conditions, and for different temperatures including cryogenic (LN_2) temperatures.

REFERENCES

1. B. Maruyama, W.H. Hunt Jr., JOM 51 1999 59.
2. W.H. Hunt Jr., B. Maruyama, JOM 51 1999 62.
3. T. Christman, A. Needleman, S. Suresh, Acta. Metall. Mater. 37 1989 3029.
4. J.R. Brockenbrough, S. Suresh, H.A. Wienecke, Acta. Metall. Mater. 39 1991 735.
5. A.F. Whitehouse, R.A. Shahani, T.W. Clyne, Metal Matrix Composites: Processing, Microstructure and Properties, 12th RISØ International Symposium, Roskilde, Denmark, 1991, RISØ, 1991, p. 741.
6. H. Luo, R. Ballarini, J.J. Lewandowski, J. Comp. Mats. 26 1992 1945.
7. A. Mortensen, Fabrication of Particulates Reinforced Metal Composites: Proceedings of an International Conference, Montréal, Québec, Canada, 17-24 September, 1990, ASM International, 1990, p. 217.
8. T.W. Clyne, P.J. Withers, An Introduction to Metal Matrix Composites, Cambridge University Press, 1993.
9. S.G. Song, N. Shi, G.T. Gray III, J.A. Roberts, Met. & Mat. Trans. A 27A 1996 3739.
10. P.M. Singh, J.J. Lewandowski, Met. Trans. A 24A 1993 2451.

[6] Furthermore, the F-600 particles will experience slightly higher stresses than the HBD particles at the same overall plastic strain, due to more efficient load-sharing at the higher aspect ratios[10].

ORAL/POSTER REFERENCE: ICF100861OR

Effect of Residual Stress on Fatigue Strength of Steel Modified by WPC Process

D. YONEKURA[1], H. AKEBONO[2], J. KOMOTORI[2],M SHIMIZU[2] and H. SHIMIZU[3]

[1]Dept. of Mech. Eng., The University of Tokushima,2-1 Minami-josanjima-cho, Tokushima, Japan
[2]Faculty of Science and Technology, Keio University, 3-14-1,Hiyoshi, Kouhoku-ku, Yokohama, Japan
[3]N.E. LTD., 4-5-12, Sagamidai, Kanagawa, Japan

Abstract
Rotational bending fatigue tests were carried out on low carbon Cr-Mo steel modified by a combination of Wide Peening Cleaning (WPC) and carburizing, with special attention focused on the effect of surface residual stress on fatigue properties. By combining the carburizing and the WPC process, it is possible to generate a high compressive residual stress near the surface, maintaining a deep layer of compressive residual stress associated with the carburizing. The notched specimens modified by the combined process show significantly higher fatigue strength compared to those modified by single process of carburizing. This is because the extremely high compressive residual stress remained after stress cycling at the surface of the specimens modified by the combined process.

Key Words: WPC process, shot peening, fatigue, residual stress, surface modification

1. INTRODUCTION

The Wide Peening Cleaning (WPC) process is one of the new surface modifying techniques. The features of the WPC process are as follows: (1) extremely fine and hard particles are used as shot particles and (2) the velocity of shot particles is much higher than that of conventional shot peening methods. The resulting product offers remarkable fatigue resistance relative to that modified by conventional technique. As a consequence, the application of the WPC process to machine parts such as gears and car shafts, has been intensively attempted. However, the reasons for the improvement of fatigue strength have not been well understood.

In our previous work [1], it was clarified that the residual stress formed by the WPC process alone has a maximum value close to the surface and is stable under cyclic loading. Such residual stress effectively prevents propagation of small fatigue cracks. However, the ability to suppress crack propagation is limited in a very shallow depth beneath the surface, since the compressive residual stress layer formed by the WPC is very shallow. Thus, the WPC process has a problem in that the fatigue strength is not improved as much as it is expected from the effect of work hardening and of high compressive residual stress at the surface.

To make the effect of WPC on fatigue strength of the steel more effectively, it is necessary to develop a new surface treatment technique in which compressive residual stress is distributed over a deeper layer, while keeping the features of the residual stress produced by WPC. In order to produce such residual stress distribution, it seems to be useful to combine WPC with other surface treatment method which can give a deeper compressive residual stress layer.

In this study, we selected the carburizing process in combination with WPC. Attention was focussed on the distribution of residual stress and the effect of residual stress generated by the combined process on fatigue properties.

2. EXPERIMENTAL

A low carbon Cr-Mo steel (JIS SCM420H) with a chemical composition as listed in Table 1 was used. A 20mm diameter steel bar was machined into shape, which is described in Figure 1, and then finished by electrochemical polishing. After the carburizing process, the WPC process was applied. Table 2 shows the process parameters used in this study.

A Vickers microhardness tester was used to measure the microhardness of samples. X-ray diffraction equipment was used to examine the residual stress distribution in hardened layers.

The fatigue tests were performed using a rotational bending fatigue testing machine (3000rpm) at room temperature in a laboratory environment. After the fatigue test, crack initiation sites were examined by using an optical microscope and a scanning electron microscope (SEM).

Table.1 Chemical Composition

C	Si	Mn	P	S	Cr	Mo	Cu	Ni
0.21	0.30	0.74	0.017	0.015	1.04	0.15	0.14	0.09

Table.2 Condition of WPC and Shot Peening

	Particle diameter (μm)	Air pressure (MPa)	Shooting time (sec)	Particle material
WPC	120-170	0.4	60	FHS

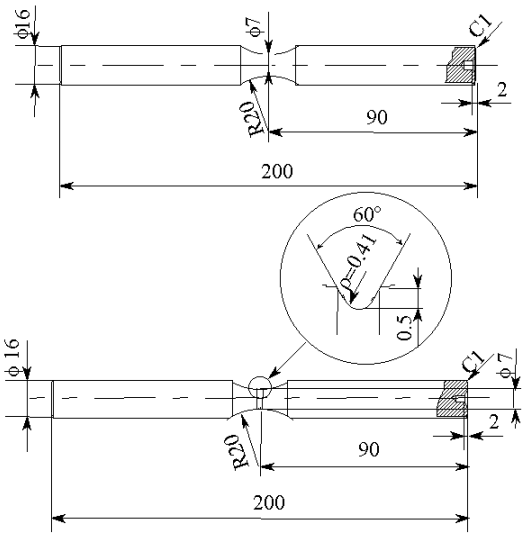

Fig. 1 Specimen configuration

3.RESULTS AND DISCUSSION

3.1 Characterization of hardened layer

Figure 2 shows Vickers microhardness distributions on the cross section of the carburized specimen and

the specimen modified by the combined process. By carburizing, a hardened layer has been formed in a wide region over 1000μm depth. With additional WPC process, remarkable increase in hardness can be observed in the shallow region at subsurface.

Figures 3 shows the distribution of residual stress near the surface. The carburized specimen shows a residual stress of -250MPa at the surface, and the depth of the compressive residual stress layer is over 200μm. In the specimen modified with the combined process, the existence of a large compressive residual stress over -1200MPa can be observed near the surface. It should be noted that such a region with the large compressive residual stress correspond to the region in which a remarkable increase in hardness has appeared in Fig.2.

From the results mentioned above, it is obvious that due to the combined process a high compressive residual stress can be generated near the surface while keeping a deeper compressive residual stress layer associated with the carburizing.

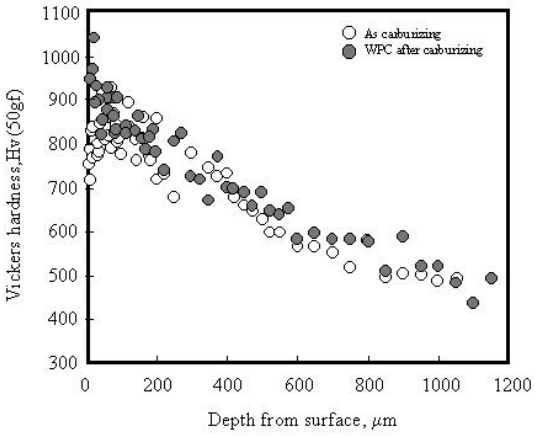

Fig. 2 Vickers hardness distribution

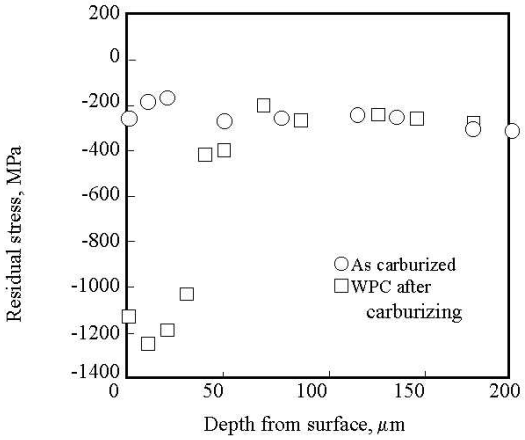

Fig.3 Residual stress distribution

3.2 Fatigue test of unnotched specimen

Figure 4 shows the results of fatigue tests of un-notched specimens. In this figure, the symbol "○" represents the results for the carburized specimen; the symbol "□" represents the combined processed specimen. If the effect of the residual stress on fatigue strength can be considered to be equivalent to that

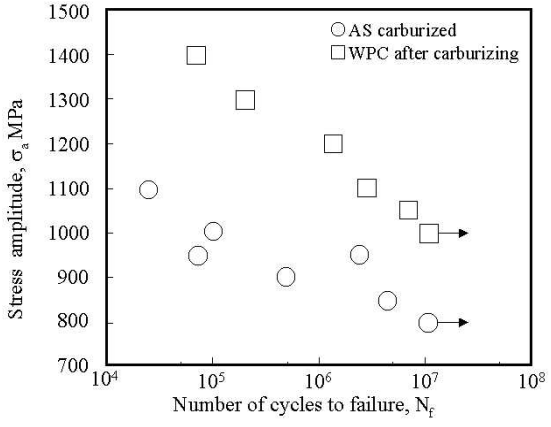

Fig.4 Results of fatigue tests

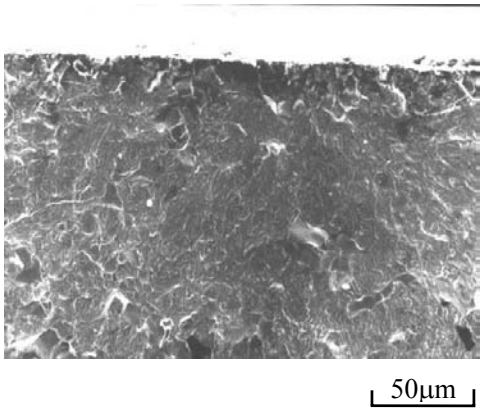

Fig.5 Typical feature of fracture surface
(as carburized σ_a=849MPa, N_f=4.24×10^6 cycles)

of the mean stress as proposed by Matsumoto[2], an increase in fatigue strength of about as much as 500MPa could be expected due to the combined process. However, the result is not true for the present case, where the increase of fatigue strength is about 200MPa. In order to examine the cause, SEM observation of the fracture surface was performed with special attention to the fracture origin in both types of specimens.

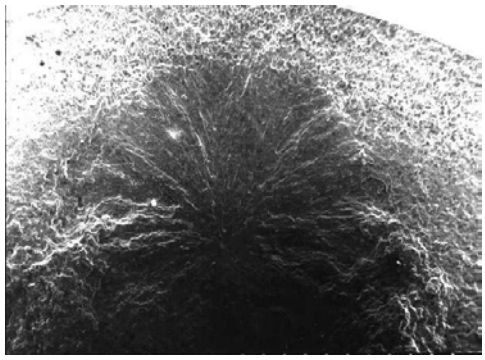

Fig.6 Typical feature of fracture surface
(WPC after carburizing,
σ_a=1050MPa, N_f=6.56×10^5 cycles)

Figure 5 and 6 show the fracture surfaces of the specimen treated by the carburizing and the combined process, respectively. In the carburized specimens, a fatigue crack initiated at the surface of specimen leads to the final fracture. In the combined processed specimen, however, the final fracture was resulted from the fatigue crack initiated from the inside of the specimen.

From the results mentioned above, it is clear that the surface modification due to the combined process is not effective for the improvement of the fatigue strength, because the fracture occurs inside the specimen without occurring in the surface modified layer as shown in Figure 6. Consequently, the small increase in fatigue strength due to the combined process can be attributed to the transition of the fracture mode from surface to internal one.

3.3 Fatigue tests of notched specimen

In order to examine the effect of the surface modified layer generated by the combined process on fatigue properties, it is necessary to study the fatigue properties of the notched specimen in which the fatigue crack starts at the specimen surface. Additional fatigue tests were carried out using notched specimen with a stress concentration factor of α=2.3.

The results are shown in Figure 7. In the case of notched specimens, the fatigue strength is remarkably improved by the combined process; the extent of improvement of fatigue strength for the notched specimen is much higher than that of the un-notched specimen. In this case, the fatigue crack started at

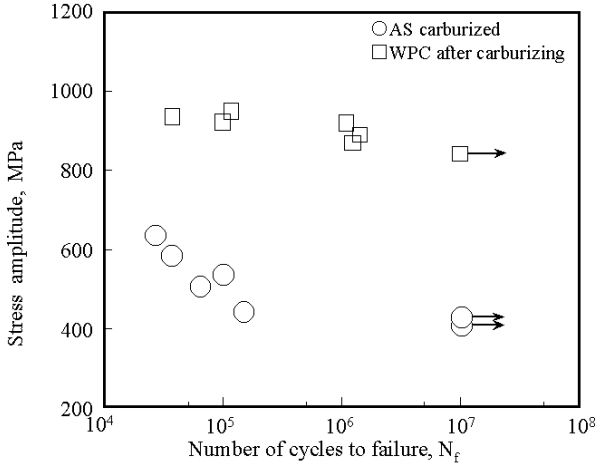

Fig.7 Results of fatigue tests for notched specimen

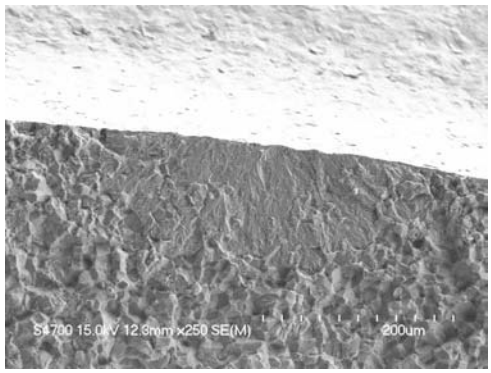

Fig.8 crack initiation site of notched specimen
(WPC after carburizing, σ_a= 950MPa, N_f=3.6×10^4)

the surface (notch root, Figure 8). This implies that the high compressive residual stress generated by the combined process results in an improvement of fatigue strength.

3.4. Residual stress under cyclic loading

In order to explain why the combined process is effective for the improvement of the fatigue strength of the notched specimen, the stability of residual stress within the surface modified layer was investigated. We measured the change in residual stress under cyclic loading. The results are shown in Figure 9, where the residual compressive residual stress remains unchanged after stress cycles $n=10^5$ in the specimen modified by the combined process.

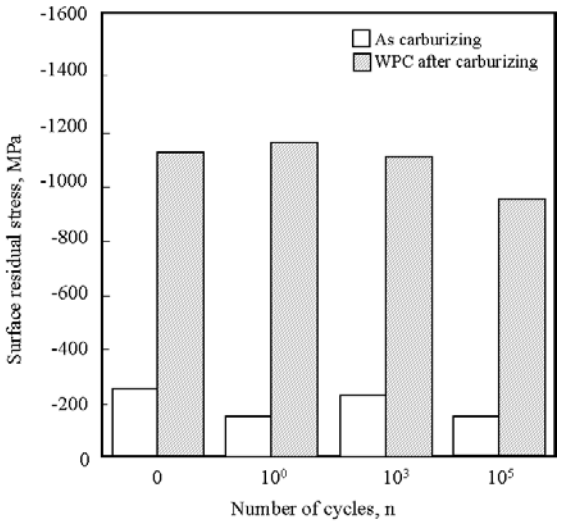

Fig.9 Release behavior of residual stress (σ_a=950MPa)

From the results, it could be concluded that the initiation and propagation of small surface crack can be suppressed by the compressive residual stress in the surface layer with a high hardness, resulting in a remarkable improvement of fatigue strength.

4. CONCLUSION

(1) By combining carburizing and the WPC process, it is possible to generate a high compressive residual stress near the surface, while keeping a deep compressive residual stress layer associated with the carburizing.

(2) In the specimens modified by the combined process, compressive residual stress maintains a high-level at the surface after stress cycling. The compressive residual stress in the surface layer with a high hardness effectively suppresses initiation and propagation of small surface cracks, and remarkably improves the fatigue strength.

(3) In the un-notched specimen where the stress gradient is gentle, the surface modified layer is not effective for the improvement of fatigue strength, because the fracture occurs from the inside of the specimen. In the notched specimens, however, the surface modifying effect for the improvement of the fatigue strength can act more effectively than in plain specimen, because the fatigue crack initiates at the specimen surface in notched specimen.

References

1. D. Yonekura, J. Noda, J. Komotori, M. Shimizu, Y. Miyasaka, Advanced Materials Development & Performance, Procs. of 2nd Inter. Conf. on Advanced Materials Development, Performance Evaluation and Application, Tokushima, Japan, Vol.1,Tokushima, Japan, Nov.23-26, 1999, pp.64-67

2. .K. Matsumoto, T. Sanpei, T. Toyota, T. Kanazawa, Proc. '90 M&M Conf. JSME, No. 900-86,1990, pp.275-277

EFFECT OF SURFACE CRACK GEOMETRY ON THE FATIGUE LIFE OF HIGH STRENGTH LOW ALLOY STEEL

A. Giassone[1,2], F.A. Darwish[1], M. V. Pereira[1], A. C. Vidal[2] and A. R. Martins[1,2]

[1]Department of Materials Science and Metallurgy (DCMM),
Catholic University of Rio de Janeiro (PUC-Rio), RJ 22453-900, Brazil
[2]Institute of Technology (ITUC), PUC-Rio

ABSTRACT

A study has been made concerning the effect of surface crack geometry on the fatigue life of a high strength low alloy steel connecting rod of a high power diesel motor. Connecting rods are usually designed to have "infinite" fatigue life but they may suffer premature failure in the presence of surface cracks which can be nucleated due, for example, to poor maintenance practice. Finite element calculations were carried out to determine the stress levels developed in the rod during its operational cycle. Using the mechanics of surface cracks, a design curve depicting the relationship between the length and depth for nonpropagating cracks was established. The results have indicated that semicircular cracks as small as 1.8mm in length (i.e. 0.9mm radius) are in fact capable of propagating and that fatigue life would drop by about an order of magnitude as the initial crack length was increased from 2 to 8mm. On the other hand, an 8mm long semielliptical crack was shown to be able to propagate only if it had an initial depth of at least 0.3mm. Increasing that initial depth from 0.3 to 2mm the fatigue life would drop by more than two orders of magnitude.

KEYWORDS

Fatigue limit, Semielliptical cracks, nonpropagating cracks, crack propagation, fatigue life.

INTRODUCTION

Fatigue fracture can occur in high strength low alloy steel motor connecting rods due to poor maintenance practice. Such practice can promote the nucleation of surface cracks, which may then propagate, leading to fatigue failure of these rods. As they are usually designed to work at stress levels below the materials endurance limit and therefore expected to last "indefinitely", their premature failure could have serious implications. Accordingly, the prediction of fatigue life in the presence of surface cracks should represent an important task that is closely related to economic as well as safety considerations. Primarily, fatigue life is determined by crack growth kinetics, which for a given loading condition, depends on the initial geometry and dimensions of the propagating crack.

In the present work, finite element calculations were performed to determine in-service stress levels developed in a steel connecting rod of a high power diesel motor used for offshore oil well perforation. As surface cracks were found to be present, apparently due to inadequate maintenance, eventual failure of the rod by fatigue was considered to be a real possibility. With this in mind, the mechanics of surface cracks proposed by Newman and Raju [1] was adopted and a design curve depicting the relationship between the length and depth for nonpropagating semielliptical cracks was established. Using the same mechanics, growth kinetics and hence fatigue life were estimated for propagating semielliptical as well as semicircular cracks of different initial dimensions.

FATIGUE LIMIT

The connecting rod under consideration was made of a BS 818M40 high strength low alloy forged steel, with a yield stress, σ_Y, and ultimate strength, σ_u, of 710 and 880MPa, respectively. As to the fatigue limit, this was estimated from [2,3]

$$\sigma_e = k_a k_b k_c k_d \sigma_u /2 \qquad (1)$$

k_a, k_b, k_c and k_d in the above equation are factors which take into account the effect, on the fatigue limit, of the degree of surface finish, size of the component, confidence limit and service conditions. For normal surface finish and ambient service conditions, it is proposed [2,3] that the factors k_a and k_d be taken as 0.9 and 1, respectively. The size factor k_b which corresponds to the cross sectional dimensions (12 x 42mm) of the rod was estimated following [2] as 0.77. Finally, for a survival probability of 0.99, a confidence limit k_c of 0.814 was adopted [2] and Eqn. 1 was then used to deliver a value of 248MPa for the fatigue limit of the rod. This value should be viewed as only a rough estimate of the steel's endurance limit, given the empirical nature of Eqn. 1. One may also add that Eqn. 1 is, in fact, valid for rotational (fully reversed) bending.

STRESS CALCULATION

The forces acting on the connecting rod during the operational cycle of the motor were estimated from appropriate data referring to both operational and dimensional aspects of the motor's components. The inertia force, driving force and frictional force were taken into account and were assumed to be uniformly distributed over the areas on which they respectively act. The connecting rod was then modeled in the X-Y plane by a number of finite elements (Figure 1), with their third dimension (along the Z axis) corresponding to the rod thickness. An ANSYS 5.1 ED software was used and stresses were calculated for various positions of the rod during its operational cycle. The results obtained have indicated that the region between the holes in the above figure is the most highly stressed area and that stresses there vary between a minimum of zero (no load) and a maximum of about 300MPa. This gives rise to a cyclic loading of stress amplitude, σ_a, and a mean stress σ_m of 150MPa.

The equivalent stress amplitude (σ_{ar}) for a completely reversed loading can be calculated from [3]

$$\sigma_{ar} = \sigma_a / (1 - \sigma_m/\sigma_u) \qquad (2)$$

resulting in a value of approximately 180MPa, which is less than the fatigue limit, σ_e, estimated earlier. One may thus conclude that the connecting rod was in fact appropriately designed. However, the presence of surface cracks capable of propagating under the cyclic stress state acting in the rod can lead to its failure and the prediction of fatigue life in this case becomes a necessary undertaking. Establishing a size criterion for nonpropagating cracks, though, should precede such an undertaking.

NON PROPAGATING CRACKS

A crack present in the connecting rod will remain stationary as long as the interval of the acting stress intensity factor, ΔK, is kept below the threshold level ΔK_{th} (taken as 7MPa$\sqrt{m}$ for the steel in question [4]). For semielliptical surface cracks (Figure 2), ΔK can be calculated from [1]

$$\Delta K = \Delta\sigma \sqrt{\frac{\pi a}{Q}}\, fgh \tag{3}$$

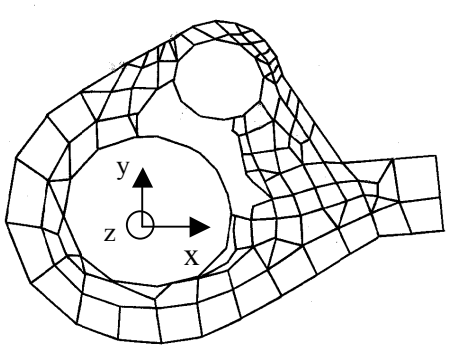

Figure 1: Finite element modeling of the connecting rod head.

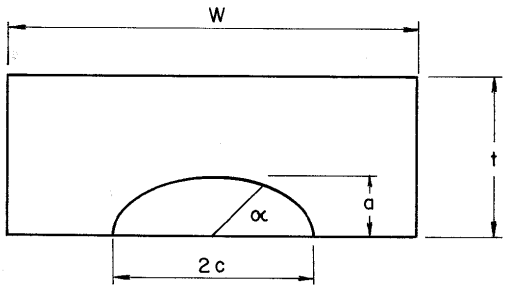

Figure 2: Geometric parameters of semielliptical cracks.

where $\Delta\sigma$ is the stress interval and Q, f, g and h are functions of a, c, t and W, and are given elsewhere [1,5,6]. As shown in Figure 2, the crack depth and crack length are represented by a and 2c, respectively. The angle α defines the angular position of the point on the crack tip where ΔK is to be calculated and t refers to the thickness. For a surface crack, which lies in the highly stressed area along the line of closest approach between the circular holes (Figure 1), W was taken as 52mm, which corresponds to the distance of closest approach measured along that line.

For a given crack depth a, one can determine the largest length such that the crack will not be able to propagate, a condition that is satisfied for $\Delta K = \Delta K_{th}$. Possible combinations of a and c for nonpropagating cracks can thus be obtained and are presented in Figure 3. An important conclusion that can be drawn from this figure refers to the strong influence of the crack depth on the maximum permissible length for values of a around 0.3mm.

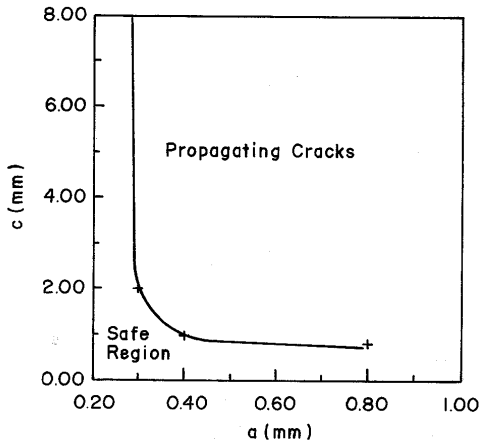

Figure 3: Limiting dimensions for nonpropagating cracks.

CRACK GROWTH KINETICS

Inspections have detected the presence of an 8mm long surface crack in the highly stressed region of the connecting rod. According to Figure 3, semielliptical cracks of that length would be expected to propagate under the cyclic stress acting in that region if they have a depth of at least 0.3mm. The crack propagation rate at the point on the crack front defined by $\alpha = \pi/2$ can be expressed as [4,7]

$$\frac{da}{dN} = C\,(\Delta K)^m \tag{4}$$

where N is the number of cycles and ΔK is given by Eqn. 3 for $\alpha=\pi/2$. The constants C and m for the steel in question were taken as 1.67×10^{-9} mm/cycle and 2.25, respectively, for ΔK in MPa [4].

Equation 4, which is not valid for near threshold crack propagation, is applicable (for ΔK levels far from ΔK_{th}) to all points on the crack front and dc/dN can therefore be obtained from the corresponding value of ΔK (calculated for $\alpha = 0$). One can thus obtain a and c as functions of N by simple integration and are presented in Figure 4 for an initial crack length of 8mm and three different initial crack depths. Notably, the number of cycles to failure was found to drop by two orders of magnitude as the initial value of a was increased from 0.3 to 1mm.

As ΔK varies along the crack tip, the propagation rate would do likewise. In fact the crack propagation is fastest for $\alpha=\pi/2$ and slowest for $\alpha = 0$. This leads to a situation where the crack front will eventually become semicircular (a = c) and the propagation rate will be the same in all directions. If one supposes that the initial crack is semicircular, similar calculations would show that the largest nonpropagating crack, for the cyclic stress under consideration, is of radius $a = c \approx$ 0,8mm. Cracks of larger size are obviously capable of propagating and the variation of crack radius with the number of cycles was determined for two different initial radii of 1 and 4mm (Figure 5). A decrease of about an order of magnitude in fatigue life is seen to be brought about as the crack radius was increased from 1 to 4.

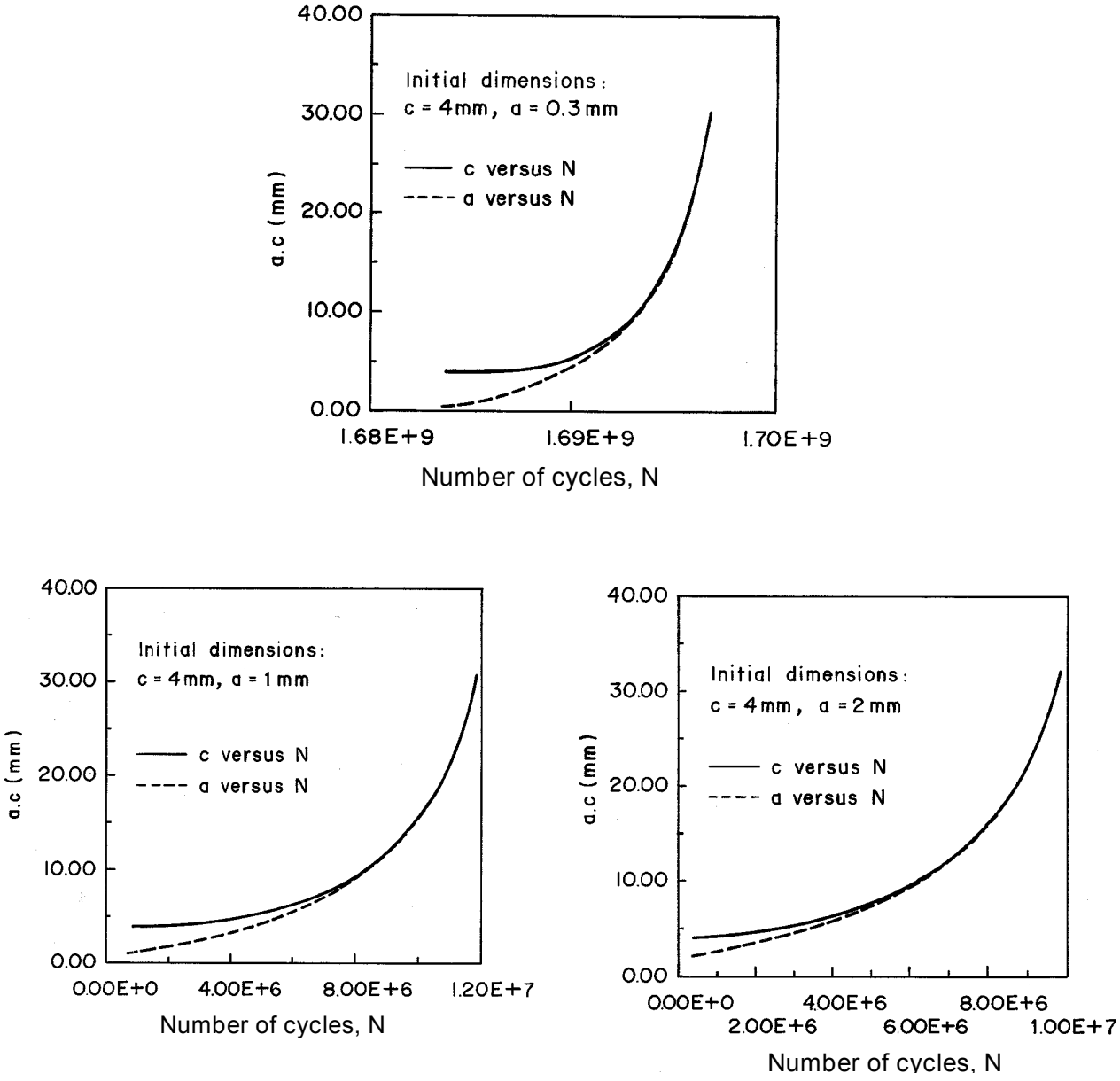

Figure 4: Variation of crack dimensions with N for nonpropagating cracks.

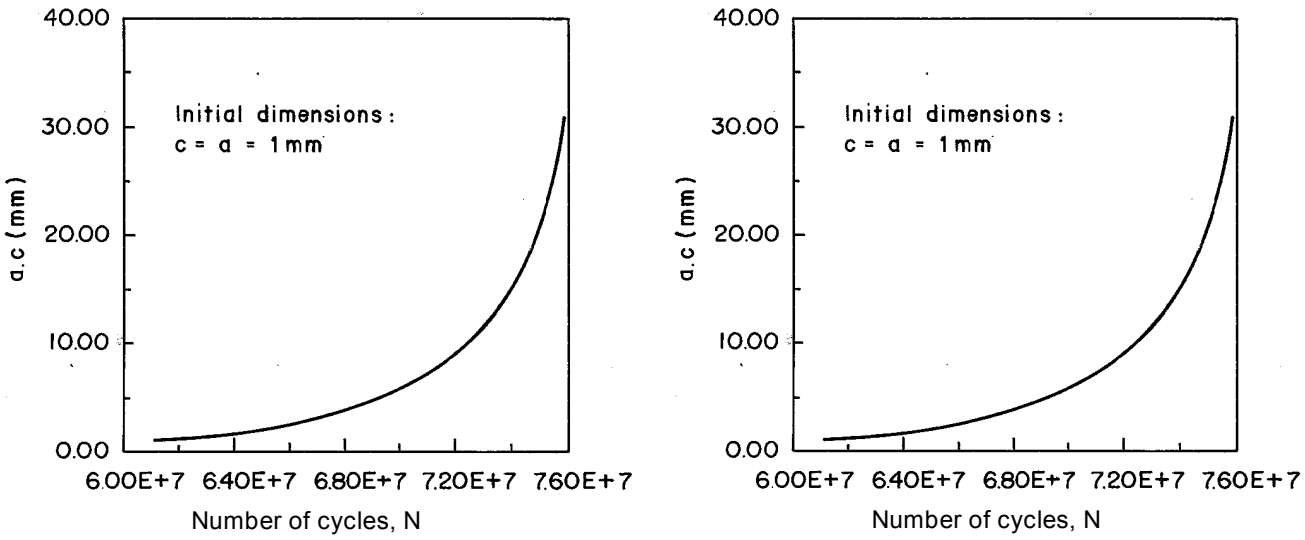

Figure 5: Variation of crack radii with the number of cycles for a semi circular crack of given initial radii.

CONCLUDING REMARKS

Based on the results presented above, the following conclusions can be drawn:

As the equivalent stress amplitude acting in the highly stressed region was found to be less than the steel's endurance limit, the connecting rod in question was considered to be appropriately designed. However irregular motor operation and/or poor maintenance practice can result in the nucleation of surface cracks and these may propagate leading to final failure after a limited number of cycles.

Semicircular cracks as small as 1.8mm in length were shown to be active, i.e., capable of propagating under the cyclic stresses acting in the rod. An 8mm long semielliptical crack would be active only if it has a depth of at least 0.3mm.

In the presence of active surface cracks, fatigue life was found to be strongly dependent on the initial crack geometry and dimensions. For the loading conditions in question, the number of cycles to failure was reduced by about an order of magnitude as the initial length of an existing semicircular crack was increased from 2 to 8mm. For an 8mm long semielliptical crack, fatigue life was found to drop by a factor close to 200 as a result of increasing the initial depth from 0.3mm to 2mm.

REFERENCES

1. Newman, J.C. and Raju, I.S. (1986). *Computational Methods in Mechanics of Fracture*, Alturi, S.N. (Ed). Elsevier North Holland, New York.
2. Shigley, J.E. (1986). *Mechanical Engineering Design*. McGraw Hill, New York.
3. Dowling, N.E. (1993). *Mechanical Behavior of Materials*. Prentice-Hall, Englewoud Cliffs, New Jersey.
4. Barsom, J.M. and Rolfe, S.T. (1987). *Fracture and Fatigue Control in Structures*. Prentice-Hall, Englewood Cliffs, New Jersey.
5. Newman, J.C. and Raju, I.S. (1984). *Stress-Intensity Factor Equations for Cracks in Three-Dimensional Finite Bodies Subjected to Tension and Bending Loads*. NASA TM 85793.
6. Anderson, T.L. (1995). *Fracture Mechanics* CRC Press, West Palm Beach, Florida.
7. Paris, P.C. and Ordogan, F. (1963) J. Basic Eng., Trans. ASME, 85, 528.

POSTER REFERENCE : ICF100722PR

EFFECT OF SURFACE ROUGHNESS ON CORROSION RESPONSE OF STAINLESS STEEL POLISHED BY ELID GRINDING METHOD

Jin Nagata [1], Jun Komotori [1], Kazutoshi Katahira [2], Hitoshi Ohmori [2]

[1] Department of Mechanical Engineering, Keio University, 3-14-1, Hiyoshi,
Kohoku-ku, Yokohama 223-8522, Japan
[2] The Institute of Physical and Chemical Research (RIKEN)

ABSTRACT

To clarify the corrosion resistance of a stainless steel having on ELID ground surface, electrochemical corrosion tests were carried out using a three electrode electrochemical cell connected to a computer driven potentiostat. After corrosion tests, morphologies of corroded surface and the corrosion products were analyzed by a Scanning Electron Microscope (SEM) equipped with an Energy Dispersive X ray analyzer (EDX). Excellent smooth surfaces can be achieved by the ELID grinding process when using extremely fine abrasives. The value of surface roughness (Ra) for the ELID ground sample is almost the same as that of the sample polished by using an alumina suspension. The corrosion properties of the ELID ground samples with smooth surface are superior to those of alumina polished specimen. This is attributed to the ELID grinding, producing a very thin and stable oxide layer which displays a superior corrosion resistance compared to that of the alumina polished samples. Consequently, the ELID process appears to offer significant future promise for use in bioimplant and other engineering components subjected to corrosion process.

KEYWORDS

Surface roughness, Corrosion response, Stainless steel, ELID grinding method

1. INTRODUCTION

The ELID (Electrolytic In-Process Dressing) grinding process, which incorporates in-process dressing of metal bonded superabrasive wheels, was applied for efficient and precision grinding of hard materials such as ceramic, optical

glass and hard metals[1][2]. This method is a relatively new process using a rigid metallic bond with the assistance of a special pulse electrolytic in-process method. The wheel is electrolytically dressed during the grinding process for continuous protruding abrasives from the grinding wheel. Until now, mirror surface machining of optical and electronic components mainly have been performed by polishing and lapping, but these methods provide poor machining accuracy and very low efficiency. Excellent smooth surfaces can be achieved by ELID with the use of extremely fine abrasives.

To apply this process for bio-implant materials, it is very important to study the corrosion resistance of the materials finished by the ELID grinding process. However, few works[3][4] have been published on corrosion of the ELID ground materials. In this study, corrosion resistance of a stainless steel having different surface characteristics was examined with special focus on the effect of surface roughness on corrosion response.

2. EXPERIMENTS

2.1 Materials and surface treatment

The chemical composition of the material (type 316 stainless steel) used in this study is given in Table1. The configuration of the test specimen is shown in Fig.1. Prior to surface finishing, all the specimens were carefully degreased using acetone, and dried with hot air. The test specimens were then subjected to two surface finishing processes; (1) ground by the ELID grinding method, and (2) ground and polished by emery paper (400 to 2000 grit) and alumina suspension (0.3μm). The rotating speed of the wheel for ELID grinding was 100 rpm and applied pressure was 150kPa. Three types of cast iron diamond wheels were used with different sizes of abrasives (#325, #2000 and #8000 wheel). Fig.2 shows the construction of the proposed ELID grinding system. Fig.3 shows the schematic illustration of the ELID-grinding mechanism in order to maintain ultraprecision finish grinding with fine abrasives.

2.2 Corrosion test

Electrochemical corrosion tests were carried out using a three electrode electrochemical cell connected to a computer driven potentiostat. The potentials were referred to as a saturated calomel electrode (SCE). Approximately 500

Table1 Chemical composition of type 316 stainless steel (wt%)

C	Si	Mn	P	S	Ni	Cr	Mo	Fe
0.05	0.30	13.1	0.39	0.26	10.59	16.36	2.01	Bal.

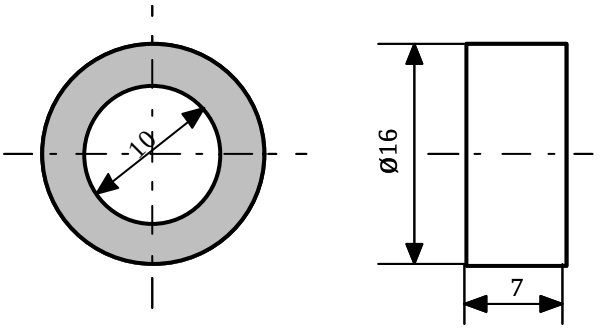

Fig.1 Specimen configuration

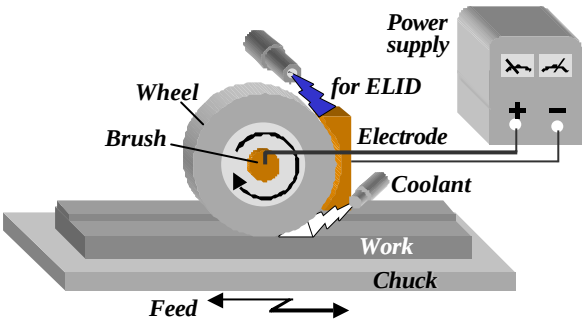

Fig.2 Principle of ELID grinding system[1]

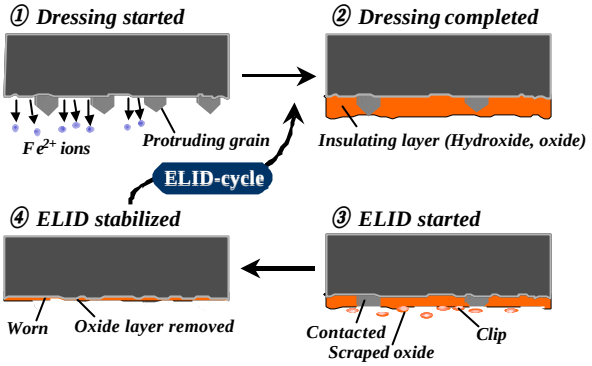

Fig.3 Schematic illustration of ELID-grinding mechanism[1]

ml of 3 wt% NaCl solution was used for potentiodynamic cyclic polarization testing. The corrosion potential (E_{corr}) of the sample was recorded without applying an external potential for 10 minutes. After holding the sample at the corrosion potential for 10 minutes, potentiodynamic cyclic polarization scans were commenced at a scan rate of 10mv/min. When the observed current density reached 1mA/cm^2, the anodic scan was stopped, the sample was then scanned in the cathodic direction, at the same scan rate, until the current density reached 0mA/cm^2. After corrosion tests, morphologies of corroded surface and the corrosion products were analyzed by a Scanning Electron Microscope (SEM) equipped with an Energy Dispersive X ray analyzer (EDX).

3. RESULTS

3.1 Surface characterization

Fig.4 shows a typical view of samples ground by the ELID grinding technique before corrosion test. A very smooth surface was observed for the specimen ground with a #8000 wheel (#8000 series). Detailed observations were also carried out using SEM. The surface ground with a #325 cast iron diamond wheel (#325 series) exhibited very distinct patterns due to the grinding grooves. In the case of the #8000 series, however, an excellent smooth surface finish was achieved.

To quantify the surface conditions, the surface roughness (*Ra*) was measured by using a Laser Scanning Microscope. Comparison of surface roughness for the specimen with different surface finishings is given in Fig.5. This result indicates that the surface roughness of the #8000 series is the same as that of the alumina polished specimen (alumina

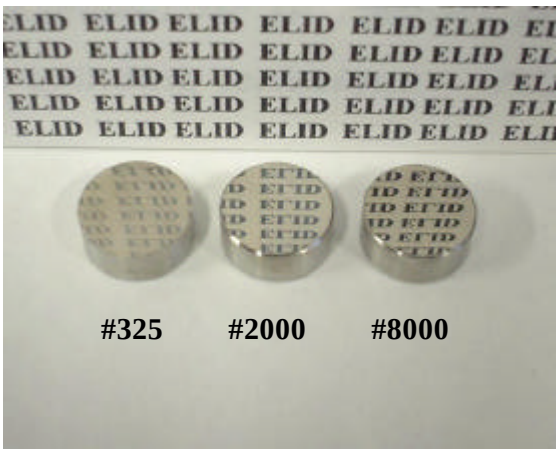

Fig.4 View of the resultant specimen (ELID series)

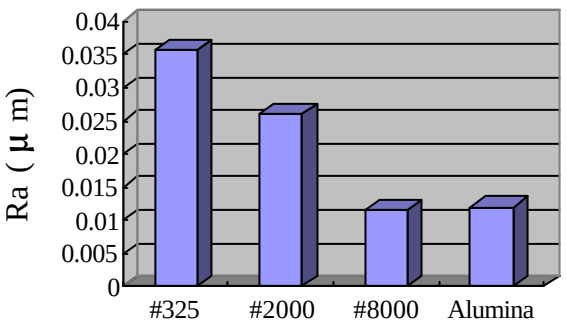

Fig.5 Comparison of surface roughness for the specimen with different surface finishings

series) ; these values are less than that of other ELID ground specimens.

3.2 Corrosion test

3.2.1 ELID ground specimen

Potentiodynamic polarization tests were carried out for the ELID ground specimen (Fig.6). During the anodic sweep of the test, the passive current densities of the specimens ground with the #2000 and the #8000 wheel, occurred in the applied potential range of 0.1 to 0.4 V vs S.C.E. The passive current density (I_{pass}) for #8000 series was higher than values observed for the #2000 series. No passive current density was observed for the #325 series with a relatively rough surface.

Pitting potential (E_{pit}) for the #8000 series was higher compared to the #325 and the #2000 series. Here, Epit is defined as the potential in which current density rapidly increased. This means that the corrosion property is superior with the scale of abrasives decreased. Fig.7 shows SEM micrograph of a pit observed after corrosion test. The corrosion pit generated along the grinding grooves. These results support the idea that the corrosion reaction is affected by the surface roughness.

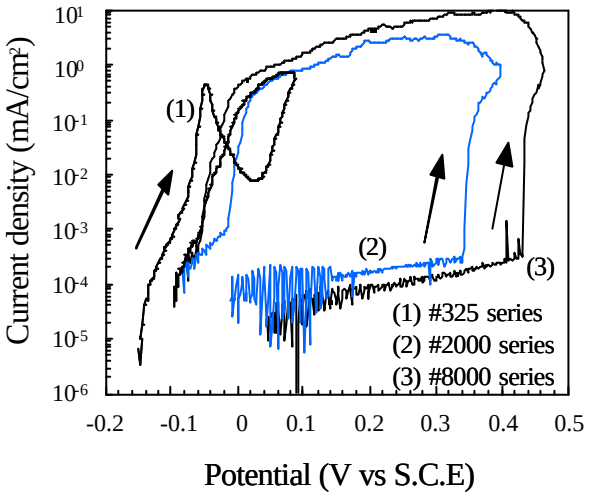

Fig.6 Anodic polarization curves of stainless steel for ELID ground specimen

Fig.7 SEM micrograph of the corrosion pit

3.2.2 Alumina polished specimen

Additional potentiodynamic polarization tests were carried out for the alumina polished specimen. Fig.8 shows the polarization curves, together with the results for the ELID ground specimens. This result indicates that the corrosion property of the #8000 series is more superior than that of the alumina polished specimen. Besides, the value of the surface roughness on the ELID ground specimen is the same as that on the alumina polished specimen.

4. DISCUSSION

Table2 summarizes the values of E_{corr}, E_{pit} and I_{pass} observed from the potentiodynamic polarization tests (Fig.6 and Fig.8). Remarkable differences in the values between the #8000 series and the alumina series are observed. To clarify the reason for this, a surface analysis was performed by using SEM and EDX. Fig.9 shows the results. The ELID ground sample had a high value of carbon and oxygen. This implies that the surface of the ELID ground sample was covered with some kind of oxide film ; existence of the film leads to an excellent corrosion property on the ELID ground specimen.

With ELID grinding, in the small clearance between the two poles, electrolysis occurs upon supply of a chemically soluble grinding fluid and an electrical current. It could be suggested that chemical reactions between oxygen and the heated specimen, due to the ELID grinding, results in the existence of oxide film.

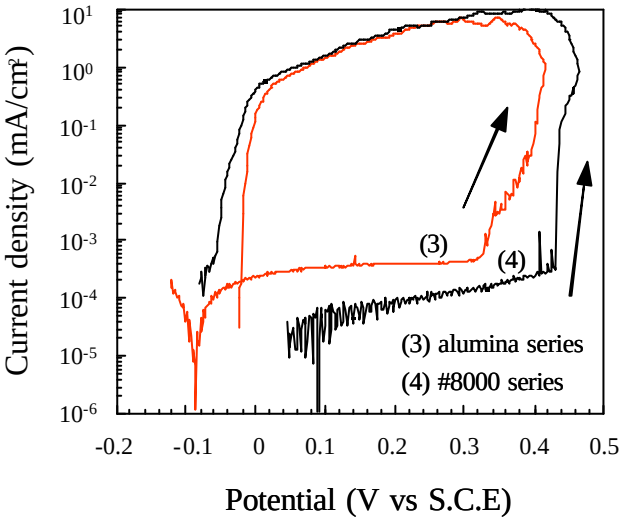

Fig.8 Anodic polarization curves of stainless steel for the specimen with different surface finishings

Table2 Polarization test results on surface finished stainless steel

	Ecorr (mV vs S.C.E)	Epit (mV vs S.C.E)	Ipass (10^{-4} mA/cm^2)
#325 series	-142	52	-
#2000 series	-23	330	2.00
#8000 series	43	427	0.86
alumina series	-131	310	3.32

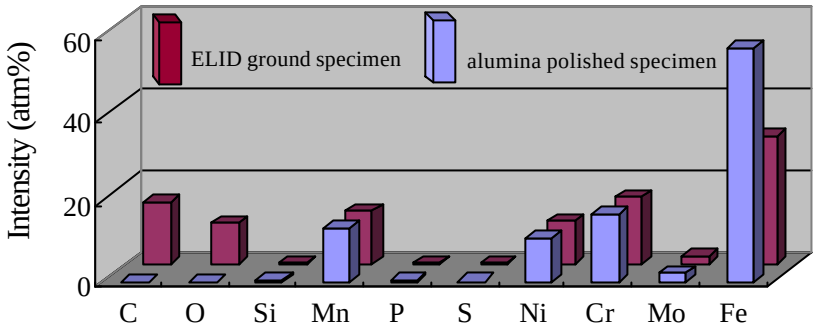

Fig.9 EDX pattern of the ground surface

5. CONCLUSION

In the present study, to clarify the effect of surface roughness on corrosion response of type 316 stainless steel, the ELID grinding method was used as the surface finishing process. Two surface finishing processes were evaluated: (1) the ELID grinding method, (2) alumina polishing method. Results are summarized as follows.

(1) Excellent smooth surfaces can be achieved by the ELID grinding process when using extremely fine abrasives. The value of surface roughness (Ra) for the ELID ground sample is almost the same as that of the polished sample by using an alumina suspension.
(2) The corrosion properties of the ELID ground samples with smooth surface are superior than those of the alumina polished specimen. This is attributed to the ELID grinding, producing a very thin and stable oxide layer which displays a superior corrosion resistance compared to that of the alumina polished samples.

REFERENCES

(1)H.Ohmori, Journal of the Japna Society for Precision Engineering , 9(1993), 59
(2)H.Ohmori and T.Nakagawa, Annals of CIRP, 44/1, (1995), 287.
(3)K.Kyo, Journal of the Society of Grinding Engineers, Vol.43, No.7 (1999), Jul. 321-326.
(4)K.Kyo, Journal of the Society of Grinding Engineers, Vol.43, No.11 (1999), Nov. 493-499.

ORAL REFERENCE:ICF0328

EFFECT OF TEST RATE ON TENSILE STRENGTH OF VARIOUS CONTINUOUS FIBER-REINFORCED CERAMIC COMPOSITES AT ELEVATED TEMPERATURES

S. R. Choi* and J. P. Gyekenyesi
NASA Glenn Research Center, Cleveland, OH 44135, USA

ABSTRACT

Ultimate tensile strength of three continuous fiber-reinforced ceramic composites, including SiC/CAS-II, SiC/MAS-5 and SiC/SiC, was determined as a function of test rate in air at 1100 - 1200°C. All three composite materials exhibited a strong dependency of strength on test rate, similar to the behavior observed in many advanced monolithic ceramics at elevated temperatures. Both the applicability of the preloading technique and the excellent data fit to log (*ultimate strength*)-vs-log (*test rate*) relation suggested that the overall macroscopic failure mechanism of the composites would be the one governed by a power-law type of damage evolution/accumulation, analogous to slow crack growth commonly observed in advanced monolithic ceramics.

KEY WORDS

Continuous fiber-reinforced ceramic composites (CFCCs), ultimate tensile strength, elevated-temperature mechanical testing, loading rate dependency of ultimate strength, failure mechanism, preload technique, constant stress-rate testing

INTRODUCTION

The successful development and design of continuous fiber-reinforced ceramic composites (CFCCs) depends on a thorough understanding of basic properties such as fracture and delayed failure (slow crack growth, fatigue, or damage accumulation) behavior. In particular, accurate evaluation of delayed failure behavior under specified loading/environment conditions is a prerequisite to ensue accurate life prediction of structural components.

This paper describes the effect of test (or loading) rate on elevated-temperature ultimate tensile strength of three different Nicalon™ fiber-reinforced ceramic composites such as SiC_f/calcium-aluminosilicate (CAS), SiC_f/magnesium-aluminosilicate (MAS) and SiC_f/silicon-carbide (SiC) ceramic composites. For each composite material, strength was determined in air as a function of test rate at elevated temperature of 1100°C (for SiC/CAS and SiC/MAS) or 1200°C (for SiC/SiC). This type of testing, when used for monolithic ceramics, is called "constant stress-rate" or "dynamic fatigue" testing [1-3]. The loading rate dependency of strength was analyzed with the power-law damage or slow-crack-growth propagation, conventionally utilized for monolithic ceramics and glass. Preloading tests were conducted to better understand the governing failure mechanism(s) of the materials. It should be noted that few studies on the subject of loading rate dependency have been done for continuous fiber-reinforced ceramic composites [4], particularly at elevated temperatures.

---

* NASA Senior Resident Research Scientist, Ohio Aerospace Institute, Cleveland, OH.

EXPERIMENTAL PROCEDURE

All the matrices of the three test composites were reinforced by ceramic-grade Nicalon™ fibers with a fiber volume fraction of about 0.39. The nominal fiber diameters ranged from 10 to 15 μm. The three composite materials tested included Nicalon™ unidirectionally (1D) fiber-reinforced calcium aluminosilicate (designated SiC/CAS-II), Nicalon™ cross-plied (2D) magnesium aluminosilicate (designated SiC/MAS-5), and Nicalon™ plain-woven (2D) silicon carbide composites (designated SiC/SiC). Both SiC/CAS-II and SiC/MAS-5 were fabricated by Corning, Inc. through hot-pressing followed by ceraming of the composites by a thermal process. The silicon carbide matrix in the SiC/SiC composites was fabricated by the DuPont Company through chemical vapor infiltration (CVI) into the fiber perform. SiC/CAS-II and SiC/MAS-5 laminates were 18 and 16 plies thick, respectively, with a nominal thickness of about 3 mm. The plain-woven laminates of the SiC/SiC composite were supplied 12 plies (normally 3.5 mm thick). More detailed information regarding the test composite materials can be found elsewhere [5]. The SiC/CAS-II material has been used in a previous, preliminary study on test rate-effect on tensile strength [6]. The dogboned tensile test specimens measuring 152.4 mm (length) x 12.7 mm (width) were machined from the composite laminates, with the gage section of about 30 mm long, 10 mm wide and 3.0-3.5 mm thick (as-furnished). The design of the dogboned tensile test specimen was the result of previous finite element analysis [7].

Monotonic tensile testing was conducted in air at 1100°C for both SiC/CAS-II and SiC/MAS-5 and at 1200°C for SiC/SiC, using a servohydraulic test frame (Model 8501, Instron, Canton, MA). A total of three to four different loading rates (in load control), corresponding to stress rates ranging within 50-0.005 MPa/s, were employed with typically 3 test specimens tested at each loading rate. Detailed experimental procedure on tensile testing and related induction-heating equipment can be found elsewhere [5]. Preload or accelerated testing technique, applied primarily to monolithic ceramics and glass [8], was also conducted at test temperatures using 0.5 MPa/s (for SiC/CAS-II) or 0.005 MPa/s (for SiC/MAS-5 and SiC/SiC) in an attempt to better understand the governing failure mechanism of the materials. Predetermined preloads, corresponding to about 80 to 90 % of the failure strength at 0.5 MPa/s or 0.005 MPa/s with zero preload (regular testing), were applied quickly to the test specimens prior to testing and their corresponding strengths were measured. Typically two to three test specimens were used in preload testing. Tensile testing was performed in accordance with an ASTM Test Method, ASTM C 1359 [9].

RESULTS

Constant Stress-Rate Testing

Results of monotonic tensile strength testing with different test rates are presented in Figure 1, where log (*ultimate strength*) was plotted as a function of log (*applied stress rate*) for each composite material. Each solid line in the figure indicates a best-fit regression line based on the log (*ultimate strength*) versus log (*applied stress rate*) relation. The decrease in ultimate strength with decreasing stress rate, which represents a susceptibility to damage accumulation or delayed failure, was significant for all the composite materials. The strength degradation was about 51, 31 and 62 %, respectively, for SiC/CAS-II, SiC/MAS-5 and SiC/SiC when stress rate decreased from the highest to the lowest. Fracture patterns for the SiC/CAS-II composite showed some fiber pullout with jagged faceted matrix cracking often propagating along the test-specimen length. For a given stress rate, however, the difference in strength between different fracture patterns was not obvious. No appreciable difference in the mode of failure was observed for SiC/MAS-5 and SiC/SiC, where most specimens tested at either high or low stress rate exhibited relatively flat fracture surfaces – possibly termed *brittle fracture*.

Preload Testing

The results of preload tests are also shown in Figure 1, where the ultimate strength with 80 to 90 % preloads is compared with that in regular testing with zero preload. The difference in strength between two preloads (0 and 80-90 %) was negligibly small for each material: 211 MPa (for 0 % preload) and 209 MPa (for a 85 % preload) for SiC/CAS-II; 142 MPa (0 and 80 % preload) for SiC/MAS-5; 77 MPa (0 %) and 80 MPa (90 %) for SiC/SiC. Hence, the maximum strength difference, exhibited by SiC/SiC, amounts to only about 4 %. This indicates that any significant damage that would control ultimate strength of the material did not occur before the applied loads up to 80 to 90 % of fracture load. Conversely, the damage to control final failure

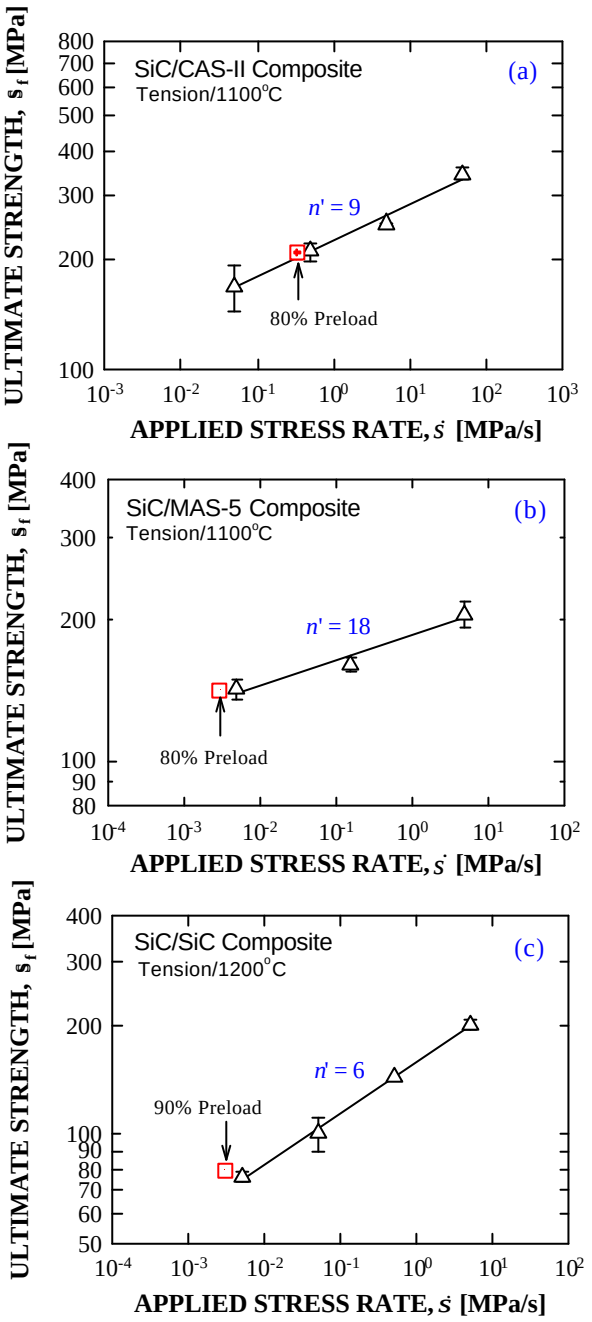

Figure 1. Ultimate tensile strength as a function of applied stress rate for (a) SiC/CAS-II, (b) SiC/MAS-5 and (c) SiC/SiC composites at elevated temperatures in air. The solid lines represent the best-fit regression lines based on Equation 3. Error bar indicates ± 1.0 standard deviation. Ultimate tensile strength with preload is also included for each material for comparison.

would have occurred when applied load or test time was greater than 80 to 90 % of fracture load or total test time. The theory explaining the results of preload testing will be described in the discussion section.

DISCUSSION

The strength dependency on test rate exhibited by the three composite materials (Figure 1) is very similar to that observed in advanced monolithic ceramics at ambient or elevated temperatures. The strength

degradation with decreasing stress rate has been known to be due to slow crack growth (delayed failure or fatigue) of an initial crack, typically governed by the following empirical power-law relation [1-3]

$$v = A(K_I / K_{IC})^n \tag{1}$$

where v, K_I and K_{IC} are crack velocity, mode I stress intensity factor and fracture toughness, respectively. A and n are called slow crack growth (SCG) parameters. Based on this power-law relation, the strength (σ_f) can be derived as a function of applied stress rate ($\dot{\sigma}$) [1-3],

$$\sigma_f = D\,[\dot{\sigma}]^{1/(n+1)} \tag{2}$$

where D is another SCG parameter associated with inert strength, n and crack geometry. Equation (2) can be expressed in a more convenient form by taking logarithms of both sides

$$\log \sigma_f = \frac{1}{n+1} \log \dot{\sigma} + \log D \tag{3}$$

Constant stress-rate ("dynamic fatigue") testing based on Equation (2) or (3) has been established as ASTM Test Methods (C1368 [2] and C1465 [3]) to determine SCG parameters of advanced monolithic ceramics at ambient and elevated temperatures. It has been recommended to use units of MPa for σ_f and MPa/s for $\dot{\sigma}$ [2-3]. As can be seen in Figure 1, the data fit to Equation (3) is very reasonable with the coefficients of correlation (r_{coef}) all greater than 0.980, indicating that the damage evolution/accumulation or delayed failure of the composite materials would be adequately described by the power-law type relation, Equation (1). Assuming this, the *apparent* parameters n' and D' for the composites were determined using a linear regression analysis based on Equation (3) with the data in Figure 1. Values of n' = 9.0 and D' = 226, n' = 18 and D' = 185, and n' = 6 and D' = 158 were obtained for SiC/CAS-II, SiC/MAS-5 and SiC/SiC, respectively (The prime was used here for composite materials to distinguish them from monolithic ceramic counterparts.). It is noteworthy that the value of n', a measure of susceptibility to damage, was very low for both SiC/CAS-II and SiC/SiC, but intermediate for SiC/MAS-5. Typical monolithic silicon nitrides and silicon carbides at high temperatures at $\geq 1200^{o}$C exhibit $n \geq 20$. Hence, compared with monolithic ceramics, the SiC/CAS-II and SiC/SiC composites exhibited a significantly higher susceptibility to damage evolution/accumulation.

The preloading or accelerated testing technique has been developed for monolithic ceramics in order to save test time in constant stress-rate testing [8]. Based on the power-law SCG relation of Equation (1) with some mathematical manipulation, strength of a test specimen under a preload (α_p) was derived as a function of preloading factor as follows [8,2,3]:

$$\sigma_{fp} = \sigma_f\,(1 + \alpha_p^{n+1})^{\frac{1}{n+1}} \tag{4}$$

where σ_{fp} is strength with a preload and α_p ($0 \leq \alpha_p \leq 1$) is a preloading factor (or percentage of preload) in which a preload stress (applied to the test specimen) is normalized with respect to the strength with zero preload. Equation (4) indicates that strength with a preload is sensitive to the magnitude of preload particularly at lower n and higher α_p values. A theoretical prediction of ultimate strength as a function of preload, based on Equation (4) with estimated values of n' from Figure 1, is presented in Figure 2. The prediction is in excellent agreement with the experimental data for all the three composite materials tested, as seen in the figure. This result obtained from the composite materials is also analogous to that observed in advanced monolithic ceramics and glass [8]. Damage, mainly SCG, of monolithic ceramics occurs substantially close to 90 % of total failure time because of their higher n ($\geq$20) value [8]. The applicability of the preloading analysis for the composite materials strongly suggests that major damage evolution/accumulation process would be the one governed by the power-law relation (Equation (1)) and that the damage would have occurred after a long incubation time, at least after 80 % of total test time.

The strength dependency on test rate, the very reasonable data fit to Equation (3) and the applicability of preloading technique all support that the damage evolution/accumulation of the composite materials tested was controlled by a process very similar, in principle, to the power-law type of SCG of monolithic ceramics.

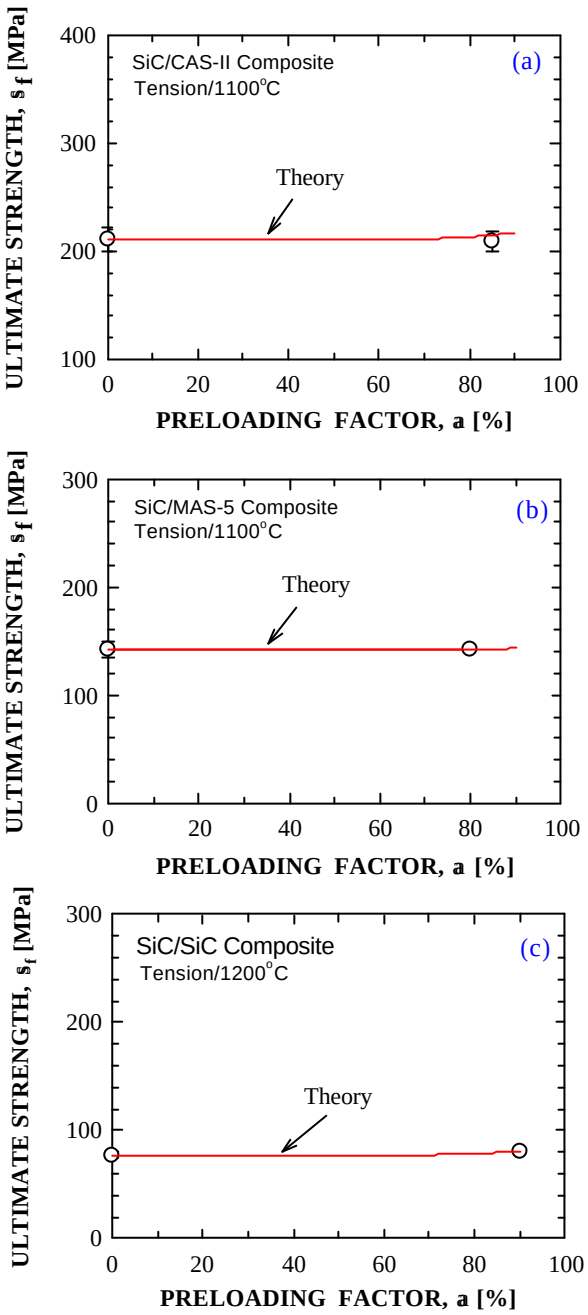

Figure 2. Results of preloading tests (ultimate strength as a function of preloading) for (a) SiC/CAS-II, (b) SiC/MAS-5 and (c) SiC/SiC composites at elevated temperatures in air. A theoretical line based on Equation (4) [8] is included for comparison for each composite material.

The previous results obtained from constant stress ("stress rupture") tensile testing for the same test materials also showed the power-law type of damage evolution/accumulation mechanism [10]. This all indicates that constant stress-rate testing, commonly utilized in determining life prediction parameters of monolithic ceramics, could be applicable even to composite materials as a means of life prediction test methodology. The merit of constant stress rate testing is enormous in terms of simplicity and test economy (shortened test time and less test specimens required) over other stress rupture or cyclic fatigue testing, especially for short lifetimes. A continuing effort to establish a database in elevated-temperature constant stress rate testing is in progress by adding more CFCC materials. At the same time, a more detailed understanding regarding microscopic failure mechanisms [4,11-14] associated with matrix/fiber interaction, matrix cracking and its effect on slow crack growth, and delayed failure of sustaining fibers near catastrophic fracture, etc. is also

needed. The results of this work also suggest that care must be exercised when characterizing elevated-temperature strength of composite materials. This is due to the fact that elevated-temperature strength has a relative meaning if a material exhibits rate dependency: strength is simply dependent on which test rate one chooses (Figure 1). Therefore, at least two test rates (high and low) are generally recommended to better characterize high-temperature strength behavior of a composite material.

CONCLUSIONS

Elevated-temperature strength of three continuous fiber-reinforced ceramic composites, including SiC/CAS-II, SiC/MAS-5 and SiC/SiC, exhibited a strong dependency on test rate, similar to the behavior observed in many advanced monolithic ceramics at elevated temperatures. The applicability of the preloading technique as well as the reasonable data fit to log (*ultimate strength*)-vs-log (*test rate*) relation suggested that the distinct, overall failure mechanism of the composite materials would be a process primarily governed by a power-law type of damage evolution/accumulation, analogous to the mechanism observed in monolithic counterparts.

Acknowledgements
This work was in part supported by the UEET Program, NASA Glenn Research Center, Cleveland, Ohio. The authors are grateful to R. Pawlik for the experimental work during the course of this work.

REFERENCES

1. Evans, A.G. (1974) *Int. J. Fracture*, 10 251.
2. ASTM C 1368, *Annual Book of ASTM Standards*, Vol. 15.01, American Society for Testing and Materials, West Conshohocken, PA (2000).
3. ASTM C 1465, *Annual Book of ASTM Standards*, Vol. 15.01, American Society for Testing and Materials, West Conshohocken, PA (2001).
4. Sorenson, B.F. and Holmes, J.W. (1996) *J. Am. Ceram. Soc*. 79 313.
5. Worthem, D.W. (1995) NASA CR 195441, NASA Glenn Research Center, Cleveland, Ohio
6. Choi, S.R. and Gyekenyesi, J.P. (2000) *Proc. of the 7th Annual International Conference on Composite Materials*, pp.299-300, Hui, D. (Ed), University of New Orleans, New Orleans.
7. Worthem, D.W. (1990) NASA CR 185261, NASA Glenn Research Center, Cleveland, OH (1990).
8. (a) Choi, S.R. and Gyekenyesi, J.P. (1997) *ASME Trans., J. Eng. Gas Turbines & Power*, 119 493; (b) Choi, S.R. and Salem, J.A. (1995) *Ceram. Eng. Sci. Proc.* 16[4] 87.
9. ASTM C 1359, *Annual Book of ASTM Standards*, Vol. 15.01, American Society for Testing and Materials, West Conshohocken, PA (2000).
10. Choi, S.R. and Gyekenyesi, J.P. (2001), to be published in *Ceram. Eng. Sci. Eng. Proc.* 22.
11. Curtin, W.C. and Halverson, H.G. (1999) *HITEMP Review: Advanced High Temperature Engine Materials Technology Project*, NASA/CP-1999-208915/VOL2, Paper 48, NASA Glenn Research Center, Cleveland, Ohio.
12. Lewinsohn, C.A., Henager, C.H. and Johns, R.H. (1998) *Ceram. Eng. Sic. Proc*. 19[4] 11.
13. Henager, C.H. and Jones, R.H. (1994) *J. Am. Ceram. Soc*. 77[9] 2381.
14. Spearing, S.M., Zok, F.W. and Evans, A.G. (1994) *J. Am. Ceram. Soc*. 77[2] 562.

EFFECT OF THE NOTCH SHAPE AND THE PRESENCE OF A CIRCULAR VOID IN FRONT OF A CIRCULAR NOTCH ON THE FAILURE MODE TRANSITION SPEED IN AN IMPACT LOADED PLATE

R. C. Batra, N. A. Jaber and M. E. Malsbury

Department of Engineering Science and Mechanics, M.C. 0219
Virginia Polytechnic Institute and State University
Blacksburg, VA 24061 USA

ABSTRACT

We study dynamic thermomechanical deformations of a prenotched plate impacted on the notched side by a cylindrical projectile of diameter equal to the distance between the notches, and made of the same microporous thermoviscoplastic material as the plate. For the ratio of the semimajor to the semiminor axes of the notch tip equal to 0.4, 1.0, 2.0 and 10.0, the impact speed at which the failure mode transitions from the brittle to the ductile is computed. For a circular notch-tip of radius r_0, we delineate the effect on the failure-mode initiation of the presence of a hole of radius r_0 and situated directly ahead of the notch tip at distances of $3r_0,\ 4r_o,\ 5r_o$ and $6r_o$.

1 INTRODUCTION

Kalthoff (2000) and Kalthoff and Winker (1987) have experimentally studied dynamic deformations of a rectangular high strength steel plate containing two notches, with circular notch tips, parallel to the top edge of the plate and extending to the middle of the plate. They found that, with an increase in the impact speed, the failure mode changed from a brittle failure in the form of a crack propagating at about 70° to the notch-axis to a ductile failure in the form of a shear band emanating essentially parallel to the axis of the notch. The failure mode transition speed was found to depend upon the notch tip radius r_0. Needleman and Tvergaard (1995), Zhou et al. (1996), Batra and Nechitailo (1997), Batra and Gummalla (2000), Batra and Ravisankar (2000) and Batra and Jaber (2001) have numerically studied the problem. Whereas Batra and Ravisankar analyzed the three-dimensional problem, other investigations scrutinized plane strain deformations of the plate. These works employed different thermoviscoplastic relations and obtained qualitatively similar results. The maximum principal tensile stress was found to occur at a point a little above the upper surface of the notch tip, and the shear band initiated from a point on the lower surface of the notch tip, which is closer to the impacted surface of the plate. Only Batra and Jaber (2001) computed the failure mode transition speed and found it to depend upon the thermoviscoplastic relation employed to characterize the material response. Here we explore the effect on the failure mode transition speed of the notch tip shape and the presence of a circular hole ahead of a circular notch tip.

2 FORMULATION OF THE PROBLEM

A schematic sketch of the problem studied is shown in Fig. 1. A rectangular plate with two parallel notches extending nearly to the vertical centroidal axis is struck at normal incidence on the notched side by a cylindrical projectile made of the same material as the plate. The diameter of the projectile equals the distance between the

notches, and its speed equals v_0. The plate is assumed to be made of a homogeneous and isotropic microporous thermoviscoplastic material, and it rests on a flat rigid smooth surface prior to being impacted. Batra and Ravisankar (2000) analyzed three-dimensional deformations of the plate and the projectile and found that the deformations of the central 75% of the thickness of the material closely resembled those obtained by the two-dimensional plane strain analysis. Here we do not study deformations of the projectile, replace its action on the plate by prescribing the normal component of velocity of the plate particles on the impacted surface, and presume that a plane strain state of deformation prevails in the plate. All of the contact surfaces are taken to be smooth, and the bounding surfaces including those of the notches thermally insulated. However, heat conduction is considered in the plate. Noting that the bottom edge of the plate is far away from the notch, we assume that deformations of the prenotched plate are symmetrical about the horizontal centroidal axis, and examine deformations of only the upper half of the plate. Thus at a point on the plane of symmetry, the vertical component of displacement, the tangential traction and the normal component of the heat flux are set equal to zero.

The thermomechanical deformations of the plate are governed by the balance of mass, linear momentum, moment of momentum and internal energy. The hypoelastic material of the plate is modeled by a linear relation between the Jaumann derivative of the Cauchy stress tensor $\boldsymbol{\sigma}$ and the elastic part of the strain-rate tensor $\mathbf{D}$ with Young's and the bulk moduli decreasing affinely with an increase in the porosity. The material obeys Gurson's (1977) yield criterion as modified by Tvergaard and Needleman (1984), the associated flow rule, Fourier's law of heat conduction with the thermal conductivity decreasing affinely as the porosity increases, and the Bodner-Partom (1975) thermoviscoplastic relation

$$\begin{aligned} \dot{\varepsilon}^p &= D_0 \exp\left[-\frac{1}{2}\left(\frac{K^2}{3\sigma_e^2}\right)^n\right], \\ K &= K_1 - (K_1 - K_0)\exp(-mW_p),\ n = \frac{\hat{a}}{\theta} + \hat{b}, \\ W_p &= \int_0^t tr(\boldsymbol{\sigma}\mathbf{D}^p)dt,\ \varepsilon^p = \int_0^t \left[\frac{2}{3}tr(\mathbf{D}^p\mathbf{D}^p)\right]^{1/2} dt. \end{aligned} \tag{1}$$

Parameters $D_0,\ n,\ K_1,\ K_0,\ m,\ \hat{a}$ and $\hat{b}$ characterize the material of the plate, θ is the absolute temperature, and $\mathbf{D}^p$ is the plastic part of the strain rate tensor. The material parameters were assigned the following values: Mass density $= 7860\ \mathrm{kg/m^3}$, specific heat $= 473\ \mathrm{J/kg^\circ C}$, thermal conductivity $= 49.73\ \mathrm{W/m^{2\,\circ}C}$, Young's modulus $= 208\ \mathrm{GPa}$, Poisson's ratio $= 0.3$, coeff. of thermal expansion $= 11.5 \times 10^{-6}/^\circ\mathrm{C}$, $\hat{a} = 1200\ \mathrm{K}$, $\hat{b} = 0$, $K_1 = 2950\ \mathrm{MPa}$, $K_0 = 2937\ \mathrm{MPa}$, $m = 3510\ \mathrm{MPa}$, $D_0 = 1.732 \times 10^8/\mathrm{s}$, yield stress σ_0 in a quasistatic simple tension test $= 702\ \mathrm{MPa}$. Values of material parameters in the yield criterion and the evolution equation for the porosity are the same as those given in Batra and Jaber (2001). Note that in the Bodner-Partom relation, the plastic strain rate is positive even when the effective stress is less than the pertinent yield stress of the material.

The plate is taken to be initially at rest, stress free, and at a uniform temperature. The normal velocity, v_1 imposed on the impacted surface is given by

$$v_1/v_0 = \begin{cases} 0.3t, & 0 \le t \le 2\mu\mathrm{s}, \\ 0.525 + 0.0375t, & 2 \le t \le 10\mu\mathrm{s}, \\ 0.9, & 10 \le t \le t_s, \\ 0, & t > t_s, \end{cases} \tag{2}$$

where t_s equals the time when the projectile separates from the plate. The expressions (2) for v_1 are derived by fitting straight lines to the data of Batra and Ravisankar (2000).

3 COMPUTATION AND DISCUSSION OF RESULTS

The aforestated problem is solved numerically by using an in-house developed finite element code. It employs constant strain triangular elements, lumped mass matrix obtained by the row sum technique, and the subroutine LSODE (Livermore Solver for Ordinary Differential Equations) for integrating the stiff set of coupled nonlinear ordinary differential equations. A reasonably fine mesh was employed in the region around the notch tip and the hole, and a coarse mesh elsewhere. Results presented herein have been computed with a fixed mesh.

A brittle failure is assumed to initiate at a point if the maximum principal tensile stress there exceeds $2.34\sigma_0$. The ductile failure in the form of an adiabatic shear band ensues at a point as soon as the effective stress there has dropped to 90% of its maximum value at that point and the material point is deforming plastically. The computation of the numerical solution is continued till an element has been very severely distorted. Once a shear band has initiated, the time step size continues to decrease rapidly. The subroutine LSODE adjusts the time step adaptively in order to compute the solution within the prescribed accuracy. We note that no failure criterion has been implemented in the code. Neither the failed elements are eliminated from the mesh nor values of their elastic moduli are reduced. However, elastic moduli decrease because of the increase in the porosity, and the radius of the yield surface decreases because of the rise in the temperature and the porosity.

For the four shapes of the notch tip considered herein, Fig. 2 depicts the dependence of the times of initiation of the brittle and the ductile failures upon the impact speed. For the blunt notch tip with $a/b = 0.4$, where a and b equal the semimajor and the semiminor axes of the elliptical notch tip, the two failure modes occur essentially simultaneously; $b = 0.15\text{mm}$. The failure mode transitions from brittle to ductile at an impact speed of about 19m/s for the circular notch tip, and the ductile failure mode precedes the brittle failure mode for elliptical notch tips with $a/b = 2$ and 10. It provides an explanation for the different failure modes observed by Kalthoff (2000) and Zhou et al. (1996) in their experiments on very similar steels. Since the notches were cut by different techniques, the notch shapes may not have been the same in the two experiments. However, when a circular hole of radius $r_0 = 0.15$ mm was located ahead of the circular notch tip of radius r_0 with the distance, d, between the centers of the circular notch tip and the hole equal to $3r_0,\ 4r_0,\ 5r_0$ and $6r_0$, the brittle failure always preceded the ductile failure. Whereas the brittle failure initiated from the point, P, on the lower surface of the circular hole that is closer to the notch tip, the ductile failure originated from a point either on the lower surface of the notch tip or on the upper surface of the hole. For the distance of $3r_0$ between the centers of the hole and the notch tip, the line joining point P to the center of the hole made an angle of 9° counterclockwise with the axis of the notch, this angle equaled 18° for the other three cases. Figure 3 illustrates the dependence of the times of initiation of the brittle and the ductile failures upon the impact speed for the four locations of the circular hole.

4 CONCLUSIONS

For the impact loaded prenotched plate with the blunt and the circular notch tips considered herein, the failure mode transitions from the brittle to the ductile with an increase in the impact speed. However, when a circular hole of radius equal to the radius of the circular notch tip is located ahead of the notch, the brittle failure always occurs first and it initiates from a point on the lower surface of the circular hole.

Acknowledgment: This work was partially supported by the ONR grant N00014-98-0300 to Virginia Polytechnic Institute and State University with Dr. Y. D. S. Rajapakse as the cognizant program manager.

REFERENCES

Batra, R. C. and Nechitailo, N. V. (1997). Analysis of failure modes in impulsively loaded prenotched plates. *International Journal of Plasticity* **13**, 291-308.

Batra, R. C. and Gummalla, R. R. (2000). Effect of material and geometric parameters on deformations near the notch tip of a dynamically loaded prenotched plate. *International Journal of Fracture* **101**, 99-140.

Batra R. C. and Ravisankar, M. V. S. (2000). Three-dimensional numerical simulation of the Kalthoff experiment, *International Journal of Fracture*, **105**, 161-186.

Batra, R. C. and Jaber, N. A. (2001). Failure mode transition speeds in an impact loaded prenotched plate with four thermoviscoplastic relations. *International Journal of Fracture* (to appear).

Bodner, S. R. and Partom, Y. (1975). Constitutive equations for elastic-viscoplastic strain-hardening materials. *Journal of Applied Mechanics* **56**, 527-

Gurson, A. L. (1977). Continuum theory of ductile rupture by void nucleation and growth. Part 1 Yield criteria and flow rules for porous ductile media. *Journal of Engineering Materials and Technology* **99**, 2-15.

Kalthoff, J. F. and Winkler, S. (1987). Failure mode transition at high rates of shear loading, in Chiem. C. Y., Kunze, H. D. and Meyer, L. W. (eds.), *Impact Loading and Dynamic Behavior of Materials*, Verlag, **1**, 185-195.

Kalthoff, J. F. (2000). Modes of dynamic shear failure in solids. *International Journal of Fracture* **101**, 1-31.

Needleman, A. and Tvergaard, V. (1995). Analysis of brittle-ductile transition under dynamic shear loading. *International Journal of Solids and Structures* **32**, 2571-2590.

Tvergaard, V. and Needleman, A. (1984). Analysis of the cup-cone fracture in a round tensile bar. *Acta Metallurgica* **32**, 157-169.

Zhou, M., Ravichandran, G. and Rosakis, A. J. (1996). Dynamically propagating shear bands in prenotched plates: II - finite element simulations. *Journal of the Mechanics and Physics of Solids* **44**, 1007-1032.

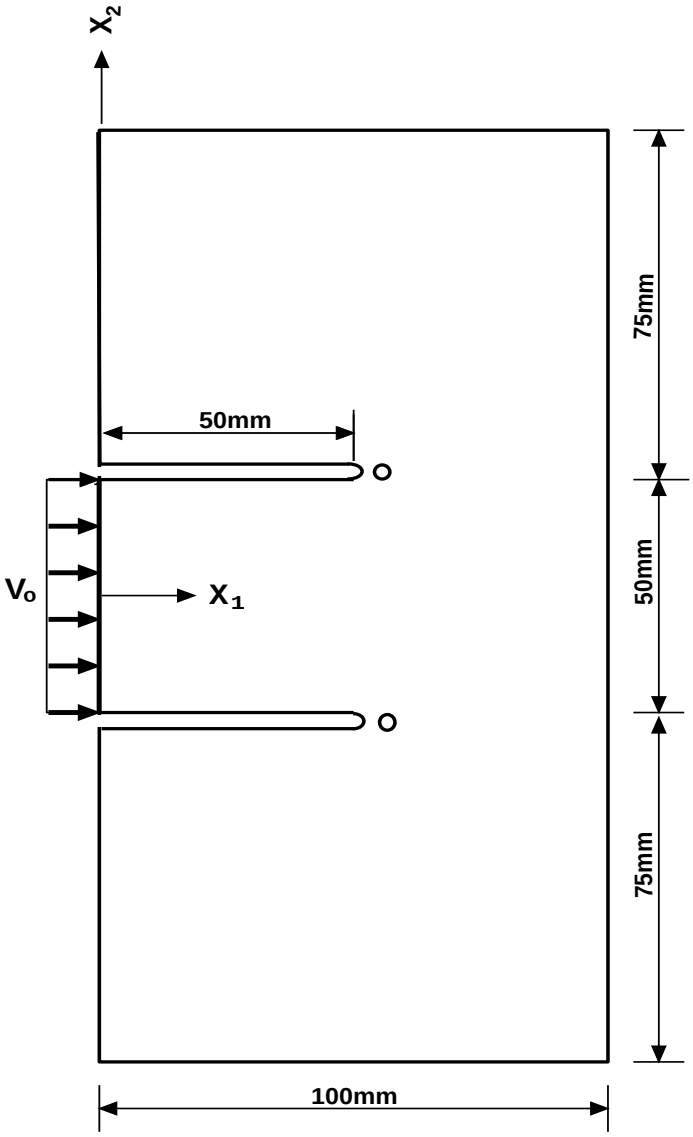

Figure 1: A schematic sketch of the problem studied.

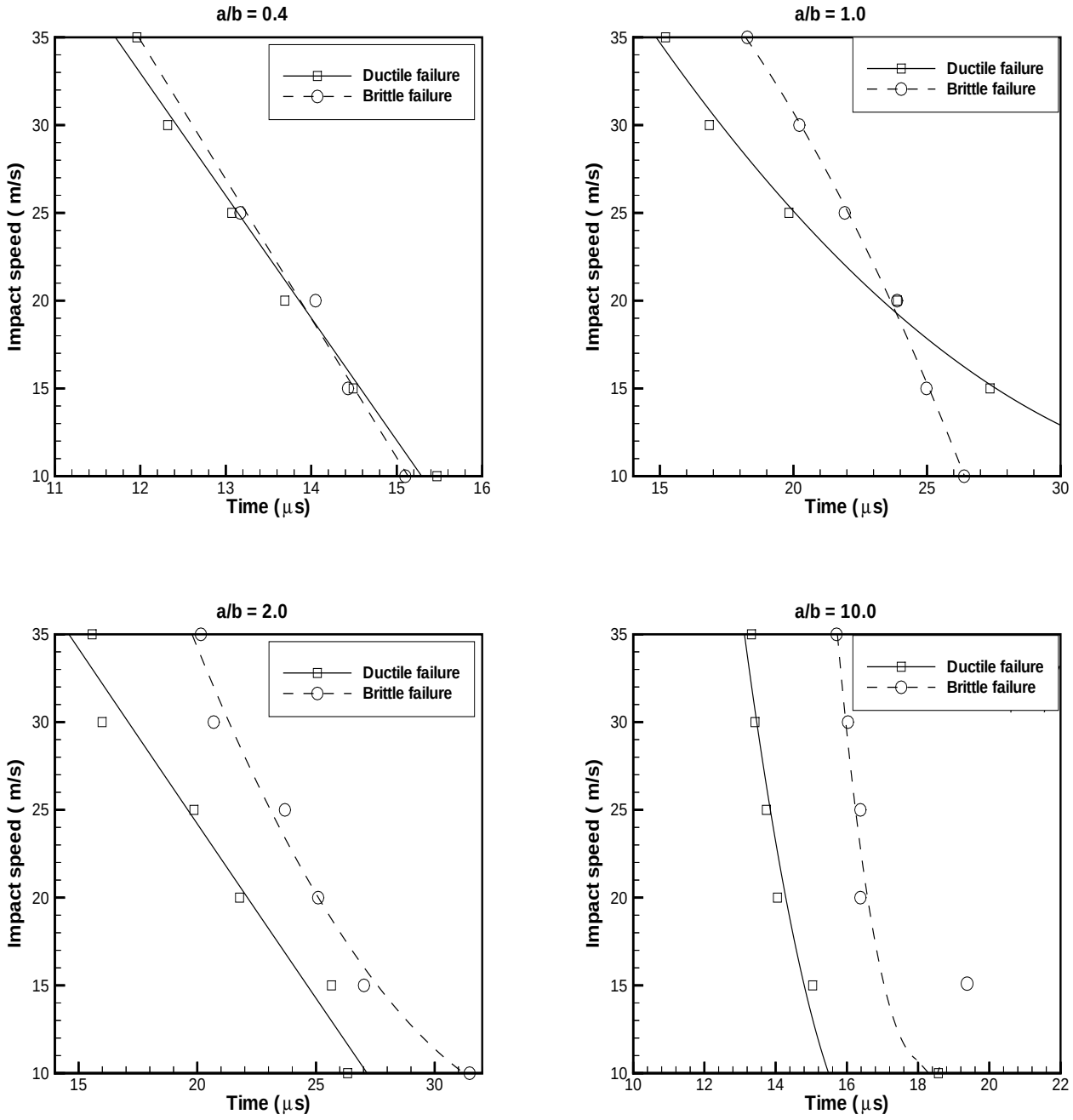

Figure 2: For the four shapes of the notch-tip, the dependence of the times of initiation of the brittle and the ductile failures on the impact speed.

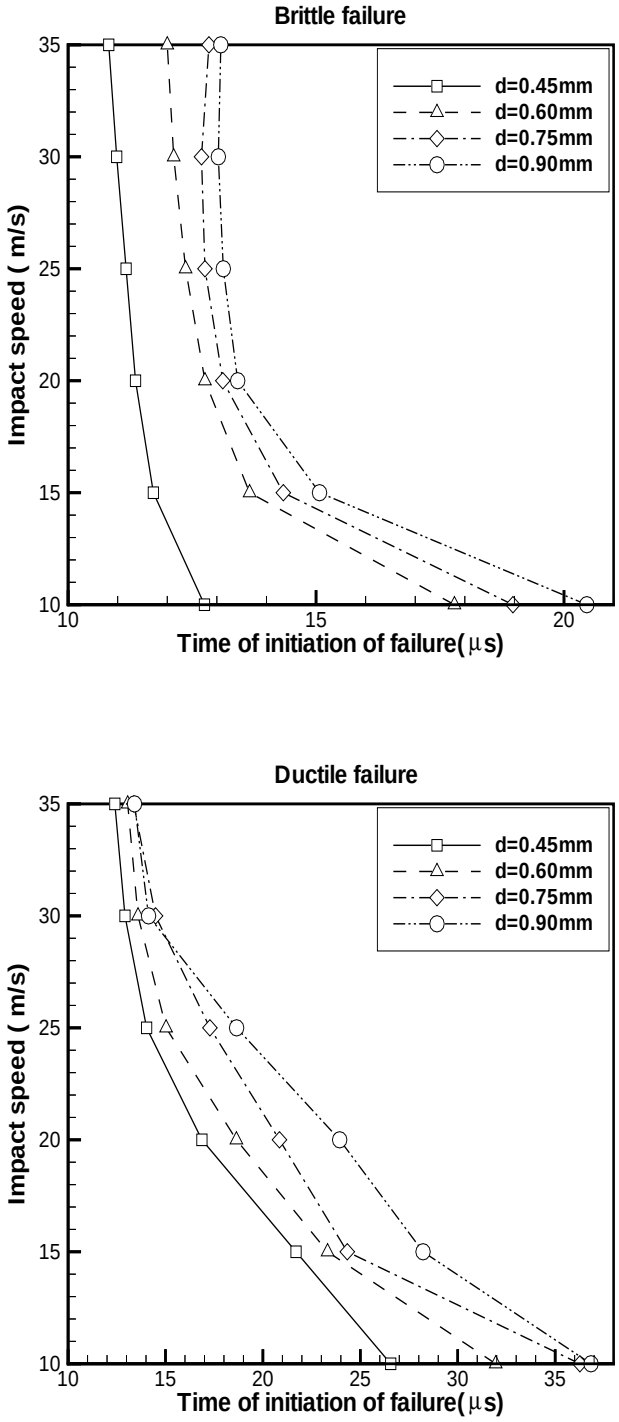

Figure 3: For the four locations of the circular hole, the dependence of the times of initiation of the brittle and the ductile failures on the impact speed.

The Effect of the Size of Surface Defects on the Fatigue Strength of Shot-peened Springs

B. Vargas-Arista[1], J. L. Gonzalez[1], J. M. Hallen[1], and A. J. McEvily[2]

[1]Instituto Politecnico Nacional, Dep. Ing. Metalurgica
Labs. De Metalurgica, Apdo. Post. 75-872,Mexico, D. F. 07300, MEXICO
[2]Metallurgy Dept. The University of Connecticut, Storrs, CT 06269, USA

ABSTRACT

The effects of simulated surface defects on the fatigue strength and on the crack initiation and crack propagation processes of a shot-peened AISI 9254 spring steel were investigated. The specimens were in the form of helical springs. Manufacturing defects representing die marks were simulated by creating surface notches which were 3.12 mm in length transverse to the spring wire, 0.8 mm in width, and varied from 115 μm to 570 μm in depth. Two different stress relieving and shot-peening procedures were used prior to fatigue testing. One group of specimens (Group 1) was stress relieved at 400 °C and then shot-peened for 30 minutes. The other group of specimens (Group 2) was stress relieved at 415 °C and then shot-peened for 45 minutes. X-ray stress analysis revealed that the shot-peening effect was less effective with increase in notch depth. It was also found that the compressive residual stresses induced for Group 2 were higher than for Group 1.

Fatigue test were carried out under axial loading at an R value of 0.44 and and a stress range of 451 MPa (65.5 ksi) at a frequency of 34 Hz. Group 2 specimens were found to have a higher fatigue resistance than did Group 1 specimens owing to a higher level of residual compressive stess induced by shot-peening. In both groups the fatigue resistance decreased with increase in defect depth as a result of both a decrease in residual compressive stress with depth as well to the increase in the stress concentration factor with depth.

EFFECT OF HYDROTHERMAL AGING ON FRACTURE PROPERTIES OF BONDED TITANIUM JOINTS

D. W. Rhymer[1] and W. S. Johnson[2]

[1] Department of Engineering Mechanics, U.S. Air Force Academy, USAFA, CO 80840, USA
[2] School of Material Science and Engineering, Georgia Institute of Technology, Atlanta, GA 30332-0245

ABSTRACT

Fatigue delamination is a major concern for titanium laminate composites, particularly at elevated temperatures. Research has been conducted to investigate the durability of bondlines in titanium laminates following long term hydrothermal exposure. In an effort to determine the optimal titanium-polyimide bond for high-temperature in adverse conditions, Ti-15-3 cracked lap shear specimens were tested with combinations of two different polymeric resins with three different commercially available titanium surface treatments in a variety of exposure environments. After 10,000 hours in both hot (177°C) dry and hot wet conditions, the specimens were fatigued at constant amplitude to demonstrate the optimal resin/surface treatment combination. As was determined by Cobb and Johnson [1] for higher temperature tests after 5,000 hours, Ti-15-3 treated with Boeing's Sol Gel surface preparation and subsequently bonded together using FM5 polyimide proved the most durable combination. Furthermore, as expected, most combinations exhibited more accelerated fatigue crack growth in the wet condition then the dry condition.

KEYWORDS

Fatigue, bond, titanium, surface treatment, delamination, elevated temperatures.

INTRODUCTION

Modern aerospace researchers still endeavor to design aircraft that fly faster and longer then ever before. Such advancement is contingent upon materials capable of operating at long lives (> 10,000 hours) and high temperatures while being fatigue resistant and damage tolerant. Hybrid Titanium Composite Laminates (HTCL) are a type of hybrid composite laminate

designed specifically for this purpose and these mechanical properties. Hybrid composite laminates consist of varying layers of metal alloy (in this case titanium for 177°C durability) bonded with layers of polymeric matrix composites (PMC) to produce a high-performance, fatigue-resistant material, retaining the strength-to-weight gains of fiber composites. However, for the damage tolerance to be realized in such a material, stable, controlled delaminations must be achieved. The development of hybrid composite laminates originated following the success of extensive lamination research. In 1967, J. Kaufman [2] proved that a laminate of adhesively bonded aluminum plies has nearly twice the fracture toughness of a single aluminum plate of the same overall thickness. In 1978, W. S. Johnson, et al. [3] demonstrated the increased fatigue and crack growth resistance of laminated aluminum. Johnson [4], in 1983, proved these increased damage tolerant properties also characterized adhesively bonded titanium. By the mid-1980's, Delft and ALCOA developed the first hybrid composite laminate called ARALL. [5] The material is composed of thin aluminum laminae with aramid fiber reinforcing the bondline. The premise of the design was to retain the damage tolerance and fracture toughness demonstrated in metal laminates, while incorporating the mechanical advantage the fibers offer to strengthen the material and contribute to crack growth resistance of the metal. After the initial success of ARALL, GLARE was developed in 1991, which uses R and S2 glass instead of aramid as the fiber [6]. These materials are now flying on several commercial and military aircraft. HTCL was developed by Johnson, Miller, and colleagues [7] in the mid-1990's for the same benefits, only for high-temperature (177° C) applications. With the preliminary testing proving successful, subsequent, extensive testing was started by Li and Johnson [8] in 1996 to demonstrate HTCL's fatigue resistance at elevated temperatures.

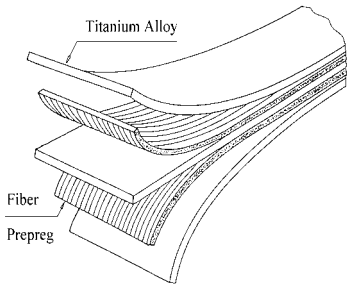

Figure 1. HTCL

However, the results showed that HTCL consistently debonded at the titanium/polymer interface following a fatigue crack forming in a titanium layer. For the fibers to adequately "bridge" the titanium crack, only a moderate amount of delamination can occur between the layers. In order to limit such damage, efforts began to determine ways to increase the strength of the titanium/PMC interface. The primary method to improve bond strength and durability is to prepare the surface of the titanium. The surface treatment produces a relatively continuous micro-rough surface on the titanium foil, which improves the mechanical interlocking between titanium and the polyimide. The improved mechanical interlocking results in not only a stronger bond, but also a more durable bond, as the interface does not solely rely on chemical bonds that are susceptible to failure with water infiltration.

Cobb and Johnson [1] conducted research to optimize the interface, to be used in a second-generation, advanced HTCL. Titanium cracked lap shear (CLS) specimens were tested with combinations of two different polymeric resins with three different commercially available

titanium surface treatments in a variety of exposure environments. Specifically, CLS specimens were constructed using the polyimides FM5 and LaRC-IAX to bond Ti-15-3 that had one of three commercially available surfaced treatments including: Pasa-Jell 107, Sol-Gel, and Turco 5578. These specimens were tested in constant amplitude fatigue and fracture toughness in one of three conditions: as received, after 5,000 hours at 177°C in dry air, and after 5,000 hours at 177°C in humidified air. The results showed the Ti-15-3/FM5/Ti-15-3 bond using Boeing's Sol-Gel surface treatment possessed superior fatigue durability in each environment over the other combinations. This work extends the previous research [1] to longer environmental exposures.

EXPERIMENTAL PROCEDURE

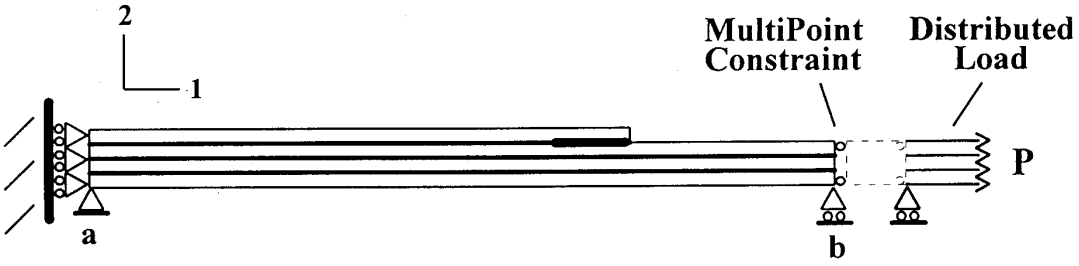

Figure 2. Cracked-Lap Shear Specimen

Panels were constructed using 50 mil thick sheets of Ti-15Al-3Cr-3Sn-3Al (Ti-15-3 – a metastable β-alloy) in the form of cracked lap shear specimens. As was used in Cobb's study, the three titanium surface treatments used were: Sol-Gel (Boeing), Turco 5578, and Pasa-Jell 107. The foils were then bonded together in the CLS specimens using either FM5 (Cytec Industries) or LaRC-IAX (NASA-LaRC) as the polymeric resin. The CLS specimen configuration was chosen due to its close approximation to the bonds commonly found in aerospace applications as well as the numerous studies that have demonstrated its viability for mixed-mode fracture. Each specimen was 0.5" wide with the "strap" portion being 6" long and the "lap" 4" long.

Specimens were exposed for 10,000 hours in either an arid (Hot-Dry) or humid (Hot-Wet) atmosphere, both at 177°C. They were subsequently tabbed and mechanically tested for fracture toughness and constant amplitude fatigue durability. A traveling microscope was used to determine and plot da/dN versus ΔG graphs.

RESULTS

The graphs in Figures 3 and 4 show that the FM5/Sol-Gel combination is the most durable in either the Hot-Dry or Hot-Wet environments. Additionally, data shows that while wet environment did greatly decrease the FM5/Sol-Gel or LaRC-IAX/Pasa-Jell bonds, a loss of durability was evidenced in the LaRC-IAX/Turco and LaRC-IAX/Sol-Gel combinations. The FM5/Pasa-Jell tests in the Hot-Dry and the FM5/Pasa-Jell and FM5/Turco tests in the Hot-Wet conditions either possessed little-to-no durability to graph or were not accomplished. However,

as determined by Cobb [1] in previous research, both combinations proved to have more limited durability than FM5/Sol-Gel.

Figure 5 shows the FM5/Sol-Gel combination in all environments tested. The graph shows that the bond does weaken with greater exposure, however the humid environment has only an insignificant effect at either 5,000 hours or 10,000 hours exposure.

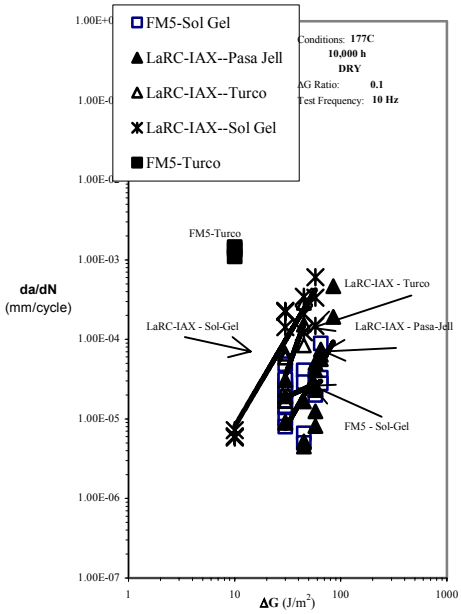

Figure 3. Mixed Mode Behavior of Ti-15-3 at 10,000 h Exposure in Dry, 177°C conditions.

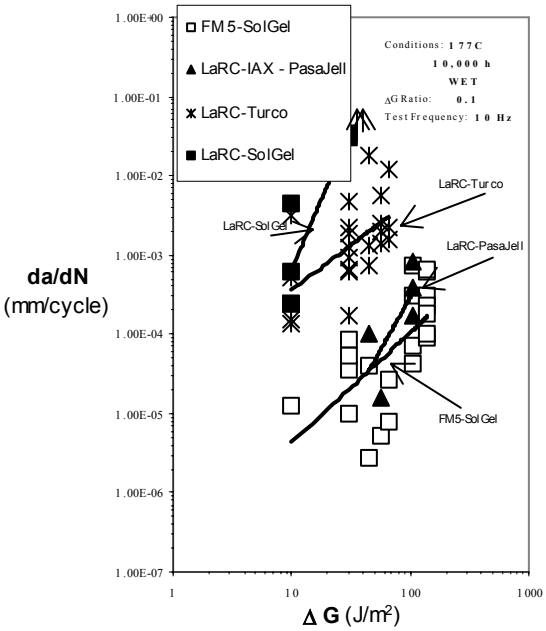

Figure 4. Mixed Mode Behavior of Ti-15-3 at 10,000 h Exposure in Humid, 177°C conditions.

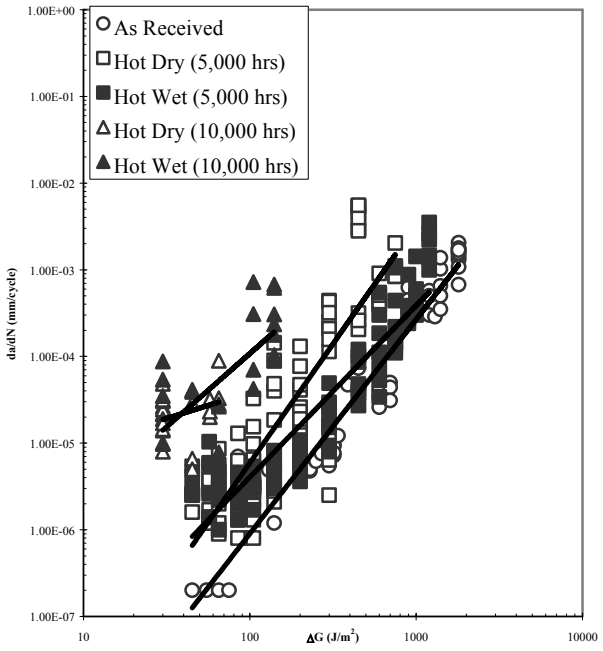

Figure 5. Mixed Mode Behavior of Ti-15-3/FM5-SolGel in all environments.

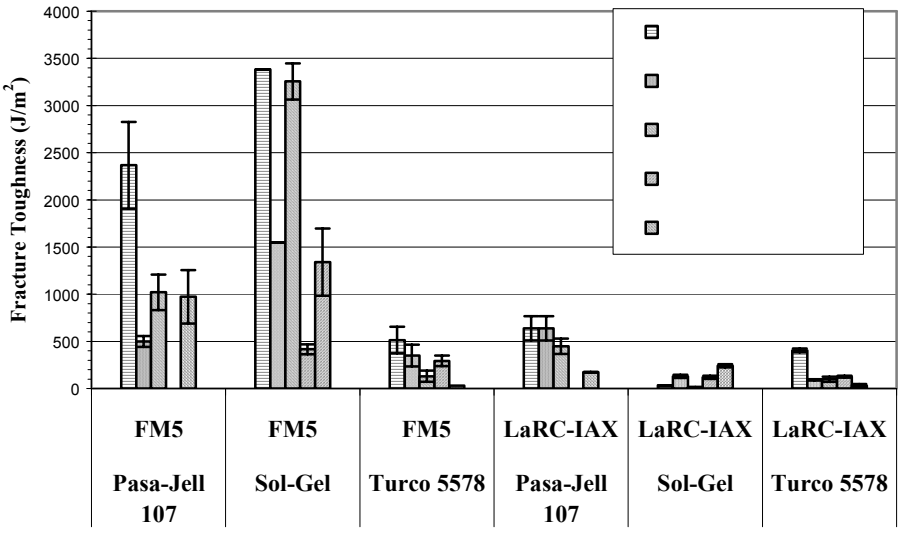

Figure 6. Fracture Toughness for all environments (95% confidence error bars shown)

Figure 6 depicts the fracture toughness properties of all combinations for all environments. Again, the FM5/Sol-Gel CLS surface proved the most durable for each exposure condition. Furthermore, after both 5,000 hours and 10,000 hours of exposure, the FM5/Sol-Gel actually possessed higher fracture toughness in the wet environment than the dry. This is probably due to a plasticization effect.

SUMMARY

Bonded titanium structure may offer several advantages, especially in elevated temperature applications. However, bond durability is a major concern. Several combinations of adhesive and surface treatment were evaluated in term of their fracture toughness and debonding resistance after exposure to 177°C. The FM5/Sol-Gel combination of polyimide and titanium surface treatment possesses the greatest fracture toughness and resistance to cyclic debond growth in both ambient and aggressive environments. Furthermore, in both 5,000 and 10,000 hours exposure time, the Hot/Wet environment produced a greater toughness in the FM5/Sol-Gel than the Hot/Dry condition.

REFERENCES

1. Cobb, T., Johnson, W.S., Lowther, S.E., St. Clair, T.L., Optimization of Surface Treatment and Adhesion Selection for Bond Durability in Ti-15-3 Laminates, Journal of Adhesion, Vol. 71, 1999, pp. 115-141.
2. Kaufman, J.G., "Fracture Toughness of 7075-T6 and –T651 Sheet, Plate and Multilayered Adhesive-Bonded Panels," *Journal of Basic Engineering*, Vol. 89, 1967, pp. 503-507.
3. Johnson, W.S., Rister, W.C. and Spamer, T., "Spectrum Crack Growth in Adhesively Bonded Structure," *Journal of Engineering Materials and Technology*, ASME, Vol. 100, 1978, pp. 57-63.
4. Johnson, W.S., "Damage Tolerance Evaluation of Adhesively Laminated Titanium," *Journal of Engineering Materials and Technology*, ASME, Vol. 105, 1983, pp. 182-187.
5. Verbruggen, M., "Aramid Reinforced Aluminum Laminates: ARALL," Report LR-503, Delft University of Technology, November 1986
6. Young, J.B., Landry, J.G.N., Cavoulacos, V.N., "Crack Growth and Residual Strength Characteristics of Two Grades of Glass-reinforced Aluminum 'Glare'," *Composite Structures* Vol. 27, 1994, pp. 457-469.
7. Johnson, W.S., Miller, J.L., Progar, D.J., St.Clair, T.L., "Preliminary Evaluation of Hybrid Titanium Composite Laminates," NASA Technical Memorandum 109095, National Aeronautics and Space Administration, Langley Research Center, Hampton, Virginia 23681-0001, April 1994
8. Li, E, An Investigation into the Fatigue of Hybrid Titanium Composite Laminates, *Journal of Composites Technology & Research*, JCTRER, Vol. 20, No. 1, January, 1998, pp.3-12.

EFFECTIVE MODE-II STRESS INTENSITY FACTOR FOR PARTIALLY OPENED NATURAL CRACKS UNDER MIXED-MODE LOADING

T. Fett

Institut für Materialforschung II, Forschungszentrum Karlsruhe,
Postfach 3640, 76021 Karlsruhe, Germany

ABSTRACT

Failure considerations under mixed-mode loading need knowledge about the influence of friction between partially closed crack faces in the case of a negative mode-I stress intensity factor. A simple relation is derived, which enables to compute friction contributions to the mode-II stress intensity factor K_{II} for the case of negative mode-I stress intensity factors K_I. The relation is exact for the limit case of an edge crack in a half-space. It can be shown that an adequate description of small natural cracks is possible. The effective stress intensity factor is computed for a contact loading problem between a flat bar and cylinders.

KEYWORDS

Crack closure, effective stress intensity factor, friction, mixed-mode loading.

INTRODUCTION

Under mixed-mode loading failure of a crack-containing component occurs, if a function f of the three stress intensity factors reaches a critical value f_c

$$f(K_I, K_{II}, K_{III}) = f_c \tag{1}$$

Several mixed-mode fracture criteria have been proposed. In most commonly used criteria only K_I and K_{II} are included in the function f. The most popular failure criterion is that of the coplanar energy release rate [1]. Under plane strain conditions it reads

$$\sqrt{K_I^2 + K_{II}^2 + \frac{1}{1-\nu} K_{III}^2} = K_{Ic} \tag{2}$$

This criterion makes sense only for positive K_I. For $K_I < 0$ the crack faces are under compression and no singular mode-I stress field exists. Nevertheless, a mode-II stress intensity factor can occur, caused by the superimposed shear loading. Due to friction between the crack faces, K_{II} has to be calculated with an effective shear stress [2].

$$\tau_{\text{eff}} = \begin{cases} \tau & \text{for} \quad \sigma_n > 0 \\ |\tau| + \mu\sigma_{\text{n}} & \text{for} \quad |\mu\sigma_{\text{n}}| < |\tau| \\ 0 & \text{for} \quad |\mu\sigma_{\text{n}}| > |\tau| \end{cases} \tag{3}$$

If the considered crack is small compared with the variation of normal stresses σ_{n} (i.e. if the effective shear stress is sufficiently constant over the crack size) it holds simply

$$K_{II} = \tau_{eff} Y \sqrt{a} \tag{4}$$

with the geometric function Y for constant shear stresses. Equation (4) is correct only for cracks with completely closed crack faces. The aim of the contribution is to compute the effective stress intensity factor also for partially closed cracks.

STRESS INTENSITY FACTORS FOR STRONGLY VARYING STRESSES

In the case of a crack size comparable to the variation length of normal stresses, the computation becomes more complex. Stresses with very strong gradients predominantly occur near contact loads. Figure 1a shows a rectangular bar symmetrically loaded by a pair of forces P acting via two cylinders. At the distance x from the symmetry line an edge crack of depth a is assumed to exist. The stresses occurring in the uncracked bar can be computed from [3]. The stress distributions along the cross section AA (Fig. 1a) are plotted in Figs. 1b and 1c for a contact width of $s/H = 0.1$, normalised on

$$\sigma^* = P/(HB) \tag{5}$$

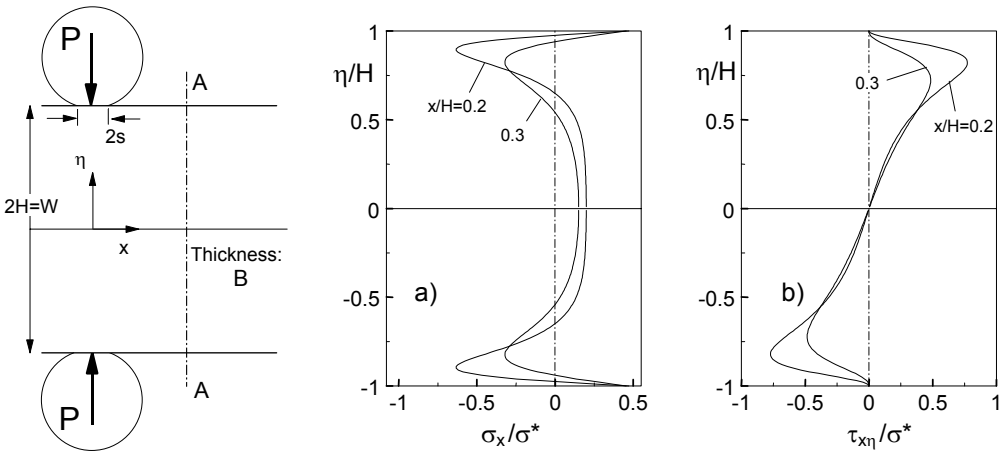

Figure 1: a) Geometric data for a bar loaded by two opposed cylinders, b) stress normal to cross section AA, c) shear stress in cross section AA.

COMPUTATION OF STRESS INTENSITY FACTORS

Natural surface cracks in ceramics are often modelled as edge cracks. An edge crack at the free surface of depth a orientated in y-direction is considered in Fig. 2a. From the stresses, present in the uncracked body, the applied stress intensity factors $K_{\text{I,appl}}$ and $K_{\text{II,appl}}$ can be computed according to [4]

$$K_{appl,I} = \int_0^a h_I(y,a)\,\sigma_x(y)\,dy \tag{6}$$

$$K_{appl,II} = \int_0^a h_{II}(y,a)\,\tau_{xy}(y)\,dy \tag{7}$$

with the weight functions h_I for mode-I and h_{II} for mode-II loading. The results obtained with the weight function solutions given in [5] are plotted in Figs. 2a and 2b.

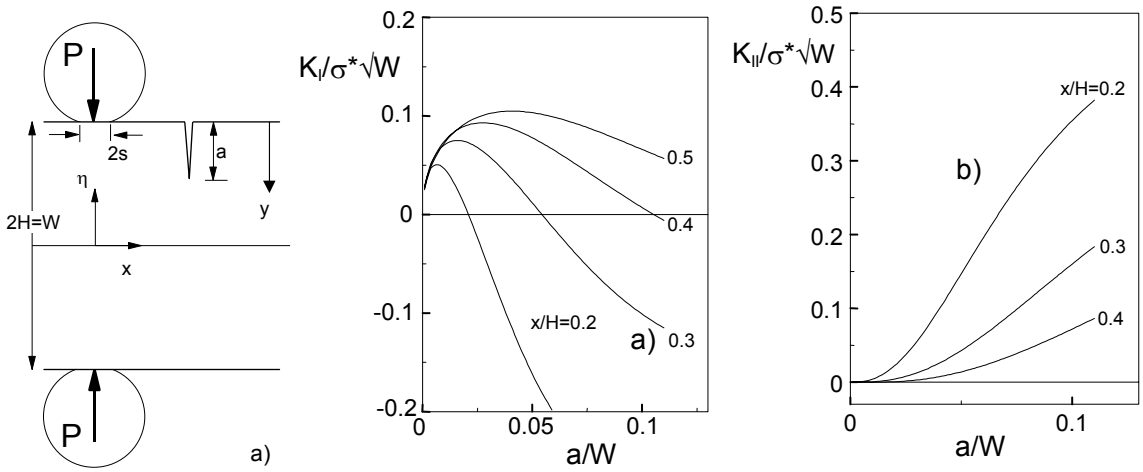

Figure 2: Stress intensity factors for edge cracks, a) mode-I and b) mode-II stress intensity factor.

From this representation it is obvious that the mode-I stress intensity factors are first positive due to the tensile stresses near the free surface ($\eta/H \to 1$ in Fig 1b) and then become negative at larger depths. In this case at least partial crack closure must occur. In order to predict failure by the remaining stress intensity factor K_{II}, it is necessary to determine that mode-II stress intensity factor contribution which reduces the applied stress intensity factor by crack surface friction.

Figure 3a shows the crack opening displacement δ_{appl} resulting from the applied stress $\sigma_{appl} = \sigma_x$. The penetration of the crack faces reflects the negative mode-I stress intensity factor. In a real structure crack-face penetration is not possible of course. The crack faces are in direct contact, producing contact stresses σ_{cont} as illustrated in Fig. 3b.

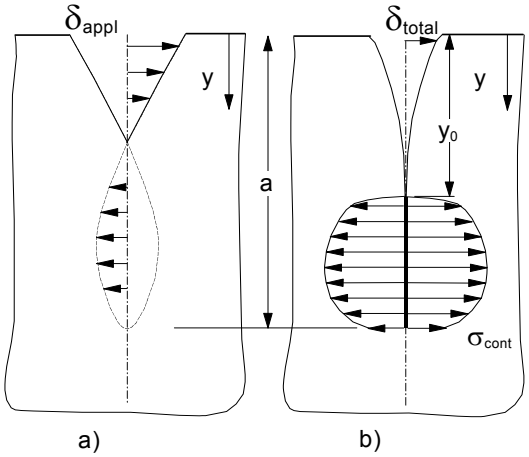

Figure 3: Schematic illustration of stresses and displacements: a) crack opening displacements from applied stresses (penetration allowed), b) crack closure and resulting contact stresses.

In the region where the crack is closed it holds

$$\delta_{total} = \delta_{appl} + \delta_{cont} = 0 \quad \text{for} \quad y_0 \le y \le a \tag{8}$$

The near-tip displacement must vanish, i.e.

$$\lim_{y \to a} \delta_{total} = \sqrt{\frac{8}{\pi}} \frac{K_{total}}{E'} \sqrt{a - y} \tag{9}$$

and, consequently, the total stress intensity factor must disappear, too

$$K_{I,total} = K_{I,appl} + K_{I,cont} = 0 \tag{10}$$

In weight function representation Eqn.(10) reads

$$K_{I,total} = \int_0^a h_I(y,a)\,\sigma_n(y)\,dy + \int_{y_0}^a h_I(y,a)\,\sigma_{cont}(y)\,dy = 0 \tag{11}$$

Due to the contact stresses σ_{cont} between the crack surfaces, friction is caused, resulting in a mode-II stress intensity factor contribution $K_{II,frict}$

$$K_{II,frict} = -\mu \int_{y_0}^a h_{II}(y,a)\,\sigma_{cont}(y)\,dy\,, \qquad K_{I,appl} \le 0 \tag{12}$$

where μ is the friction coefficient. Then the effective mode-II contribution is

$$K_{II,eff} = K_{II,appl} + K_{II,frict} \tag{13}$$

Numerical evaluation of the contact stresses needs the solution of the integral equation [5]

$$\delta_{total}(y) \times E' = \int_y^a h(y,a') \left[\int_0^{a'} h_I(y',a')\,\sigma_{appl}(y')\,dy' + \int_{y_0}^{a'} h_I(y',a)\,\sigma_{cont}(y')\,dy' \right] da' \tag{14a}$$

with

$$\delta_{total}(y) = 0 \quad \text{for} \quad y \le y_0 \le a \tag{14b}$$

In Eqn.(14a) E' is the plane strain Young's modulus. From the solution of the integral equation (14) the distributions of the contact stresses $\sigma_{cont}(y)$ and total displacements $\delta_{total}(y)$ are obtained. The solution of (14) can be determined by several numerical methods, for instance by the "iterative approximation". As an additional condition $d\delta_{total}/dy = 0$ for $y = y_0$ has to be satisfied. In Fig. 4 all displacement contributions are plotted for arbitrarily chosen values of y_0/W. The additional condition for the total displacements ($d\delta_{total}/dy = 0$ for $y = y_0$) is fulfilled here for $y_0/a \approx 0.7$, i.e. the correct solution is obtained for this y_0/W.

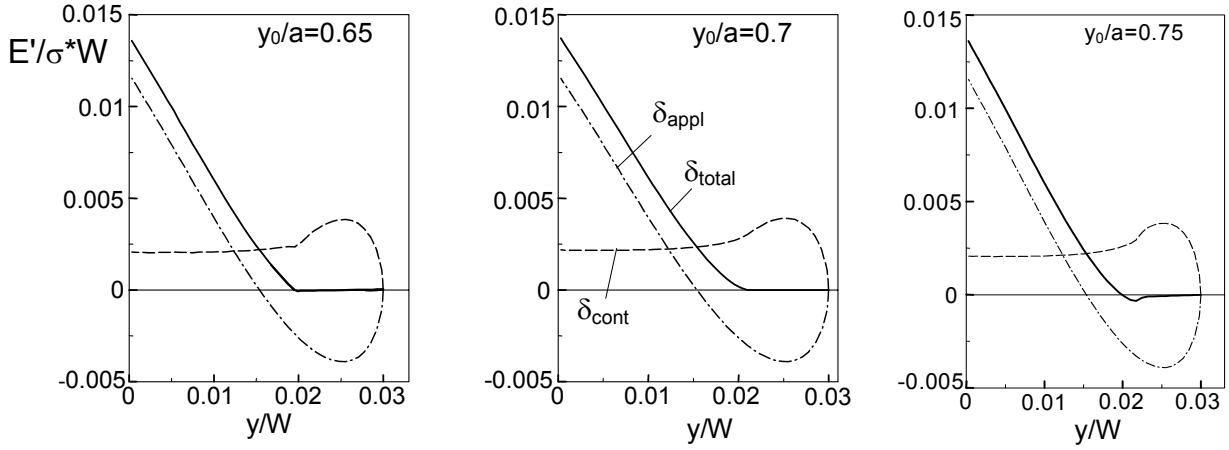

Figure 4: Displacements for a crack of depth $a/W = 0.03$ and differently chosen y_0/a.

The related contact stress distribution is plotted in Fig. 5a. From Eqn.(12) the friction part $K_{II,frict}$ and from Eqn.(13) the effective mode-II stress intensity factor can be determined. In Fig. 5b the friction stress intensity factor $K_{II,frict}$ (solid curve) is shown together with the applied stress intensity factor $K_{I,appl}$ (dashed curve). The two curves show a very good agreement for $0.02 < a/W < 0.06$, i.e. $K_{II,frict} \cong K_{I,appl}$.

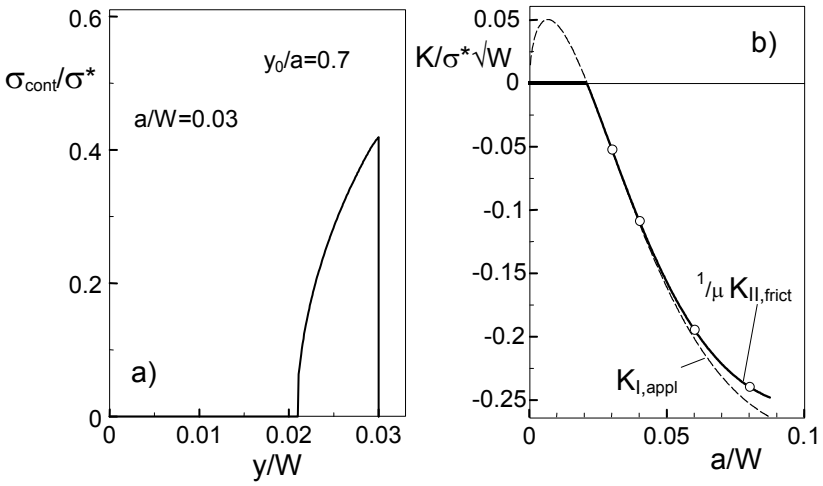

Figure 5: a) Distribution of contact stresses σ_{cont}, b) friction stress intensity factor $K_{II,frict}$ for $x/H = 0.2$.

EFFECTIVE K_{II} FOR SMALL CRACKS

Determination of the friction stress intensity factor is relatively complicated since it needs the solution of an integral equation. A useful approximation will be derived below. From Eqn.(11) it results

$$\int_{y_0}^{a} h_I(y,a)\,\sigma_{cont}(y)\,dy = -K_{I,appl} \tag{15}$$

For the evaluation of Eqn.(12) we need a very similar integral, namely

$$I = \int_{y_0}^{a} h_{II}(y,a)\,\sigma_{cont}(y)\,dy \tag{16}$$

Now let us use the fact that in the limit case $a/W \to 0$ (i.e. for very small cracks) the mode-I and mode-II weight functions are identical. Then, combining Eqs.(12), (15), and (16) provides the simple result of

$$K_{II,frict} = \mu K_{I,appl} \qquad for \quad K_{I,appl} \le 0 \tag{17}$$

Having this result in mind, we can conclude that the agreement of the two curves in Fig. 5b is not a feature of the specially chosen stress distribution.

In order to estimate the errors made by application of Eqn.(17) to larger cracks, one has to look for the deviations between h_I and h_{II}. In Fig. 6a the two weight functions proposed in [6] are plotted for several relative crack depths a/W. Figure 6b shows the ratio h_I/h_{II}. The crack depths of natural cracks in ceramic materials are in the order of 50 μm, the widths of commonly used test specimens are > 3mm in most cases. The relative crack size for standard tests therefore is $a/W < 0.02$. For cracks in this range of relative depths the maximum deviations between the two weight functions are less than 2%. The maximum deviations of the stress intensity factors are, of course, less than the maximum deviations of the weight functions. This is due to the integration of the weight function over a positive stress, by which the curves in Fig. 6b are averaged as a consequence of the mean value theorem for integrals.

The effective stress intensity factor K_{eff}, combining K_I and K_{II}, was computed by

$$K_{eff} = \begin{cases} \sqrt{K_I^2 + K_{II}^2} & \text{for} \quad K_I > 0 \\ K_{II} + \mu K_I & \text{for} \quad K_I < 0 \end{cases} \tag{18}$$

and is represented in Fig. 7. The coefficient μ was chosen as $\mu = 0.5$. At the crack depth for which $K_I = 0$ is fulfilled, the resulting K_{eff} is continuous but not smooth.

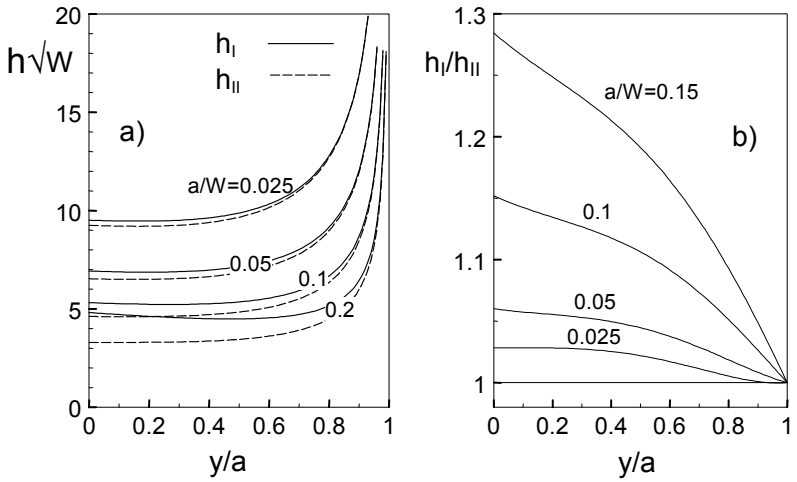

Figure 6: Comparison of the mode-I and mode-II weight functions.

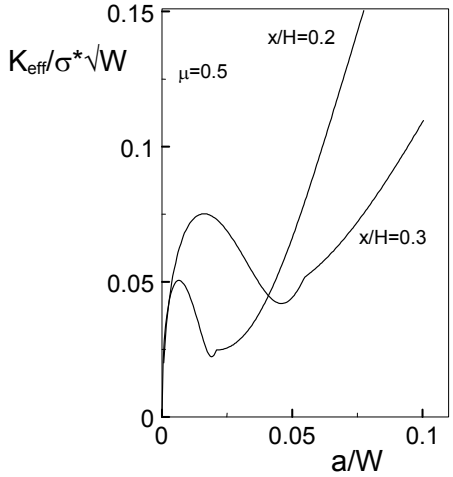

Fig. 7 Effective stress intensity factors for edge cracks perpendicular to the free surface at several distances from the load application cylinders.

References

1. Paris, P.C., Sih, G.C. (1965), ASTM STP **381**, 30–80.
2. Alpa, G. (1984) *Engng. Fract. Mech.* 19, 881–901.
3. Fett, T., Munz, D., Thun, G. (2001). *Journal of Testing and Evaluation*.
4. Bueckner, H. (1979). *ZAMM* 50, 529–546
5. Munz, D., Fett, T. (1999). *CERAMICS, Failure, Material Selection, Design*, Springer-Verlag, Heidelberg
6. Fett, T., Munz, D. (1997). *Stress Intensity Factors and Weight Functions*, Computational Mechanics Publications, Southampton, UK

EFFECTS OF CONSTRAINT AND GRAIN SIZE ON DUCTILITY AND TOUGHNESS IN TI ALLOYS

S.KANAMORI, E.ABE, T.TAGAWA AND T.MIYATA

Department of Materials Science and Engineering,Nagoya University,
Furo-cho,Chikusa-ku,Nagoya,464-8603,Japan

ABSTRACT

The effects of stress triaxiality on the process of micro-void coalescence type of fracture and ductility of α/β titanium alloys with equiaxed α phase were investigated. Materials tested were 3 types of titanium alloys (Ti-6Al-4V, Ti-4.5Al-3V-2Fe-2Mo, and Ti-10V-2Fe-3Al alloy) and two or three different heat treatments were conducted for these three alloys in order to obtain different grain size. It was shown that the most of micro-voids in α / β titanium alloys were nucleated at α / β interface, and the micro-structural parameter defined as the average distance between α/β interfaces was closely related to the dimple size on the fracture surface. The refinement of microstructure leads to the reduction of ductility and fracture toughness, though near- β titanium alloys with ultra-fine particle of α ($< 1\ \mu$ m) have exceptionally a different tendency from other α / β titanium alloys.

Fracture toughness testing was performed and J_{IC} values were evaluated. Correlation between the toughness and the ductility under the high triaxial stress state was investigated to clarify the dominant factors constructing the fracture toughness.

KEYWORDS

Micro-void coalescence type of fracture, Micro-void nucleation, Stress triaxiality, Dimple size, Fracture toughness, Local fracture criterion approach, Constraint effect, α / β Ti alloys

INTRODUCTION

Titanium alloys with $\alpha + \beta$ phase are attractive materials for commercial application because of well bal-

anced mechanical properties, in strength, ductility and fracture toughness. It is shown the fracture of α / β Ti alloys generally take micro-void coalescence type of ductile fracture [1] . Several studies by Niinomi and Kobayashi [2-4] and Teruo Kishi [5] have shown that the mechanical properties of α / β Ti alloys is quite sensitive to the variation of microstructure. In case of structural steels, micro-voids are nucleated at non-metallic inclusions and grown up to coalescence with the help of stress triaxiality and plastic strain [6] , and ductility is not sensitive to a little variation of microstructure but is influenced by the volume fraction of inclusions and strength of the materials. In the present work, tensile test and fracture toughness tests were performed for several types of α / β Ti alloys with different grain size. The effects of grain size and stess triaxiality on the ductility were investigated focusing the mechanisms of micro-void coalescence type of fracture. Then, the effect of grain size on the fracture toughness was investigated in relation to the ductility.

EXPERIMENTAL PROCEDURE

Materials tested were three types of titanium alloys of which chemical compositions were different (Ti-6Al-4V, Ti-4.5Al-3V-2Fe-2Mo, and Ti-10V-2Fe-3Al). Mill annealing and solution treatment with aging were performed to each materials to obtain different grain sizes with almost the similar equaxed microstructure. Hereafter, the materials are designated as 64-An, 64-STA, Fine-An, Fine-STA1, Fine-STA2, 10-2-3-STA1, !0-2-3-STA2, 10-2-3-STA3 (An=mill anneal., STA=solution treatment with aging) .Tensile tests were performed on smooth and 1mm radius notched round bar specimens with a diameter of 3.5mm. The equivalent strain at minimum cross section was taken as a measure of ductility and the stress triaxiality, $\sigma_m / \bar{\sigma}$, where σ_m = average value of the three principal stress, and $\bar{\sigma}$ =equivalent stress, was evaluated from Bridgman's formula [7]. The fracture toughness tests were performed on a half inch CT-specimens with 5 or 10mm thickness. The fracture toughness tests were carried out at the room temperature and the toughness and the resistance curve of crack growth were evaluated in terms of J integral and converted to K_C values as $K_C(J)$ in accordance with the JSME S001.

MICROSTRUCTURES

Figure 1 shows the microstructures of the materials observed by scannning electron microscope. All microstructures consist of the primary α phase which morphology is equiaxed and β matrix phase. For some of

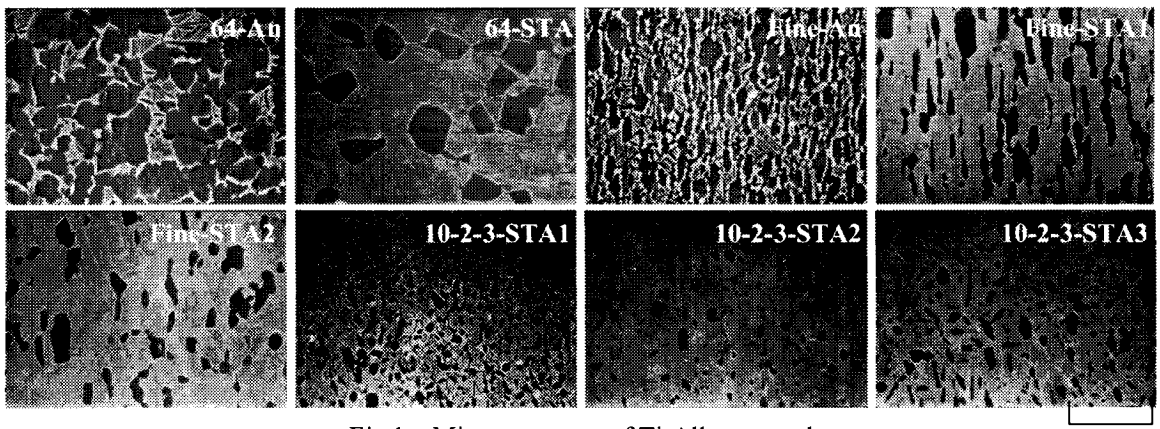

Fig.1 Microstructures of Ti-Alloys tested.

materials that are called STA materials, the high temperature solution treatment was followed by a low temprature aging treatment, that leads to the precipitation of fine secondary α phase in the β matrix.

RESULTS ON TENSILE TESTS

Figure 2 shows the failure elongation in smooth specimens in relation to the yield strength of materials, σ ys. Increase of the yield strength causes significant reduction of the ductility irrespective of the microstructure. Figure 3 shows examples of fractographs on the center part of smooth specimens. The fracture surfaces are occupied with equiaxed dimples, while the sizes of dimples are different in each material. The dimple sizes in Ti alloys are generally small in comparison with that of structural steels. In the case of Ti alloys, the most of void nucleation sites are the interface between primary α phase and β matrix as is shown in Figure 4. More than 80% of micro-voids in every materials are nucleated at α / β interface as is reported by K.H.Schwalbe [8] . The average distance between α / β interfaces is taken as a microstructural parameter, D. Figure 5 shows relations between D and the dimple sizes in the smooth specimens and the CT specimens. The dimple sizes are related to the distance of α / β interfaces especially in the CT specimens. It implies that the void nucleation sites in the α / β Ti alloys are closely related to the microstructure. The difference in dimple sizes

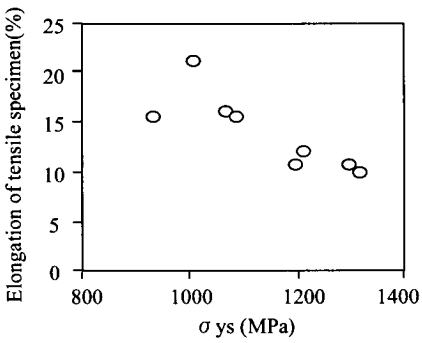

Fig.2 Relations between σ ys and elongation for materials tested.

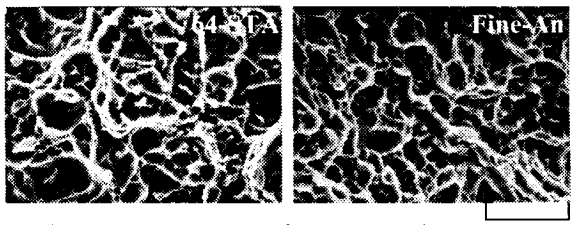

Fig.3 Fractgraphs s of 64-STA and Fine-An in smooth specimens.

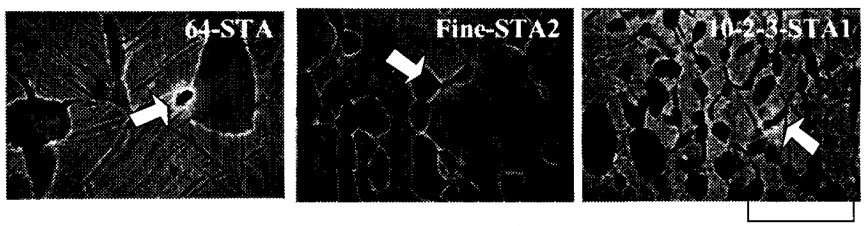

Fig.4 Micrographs of longitudinal sections of smooth specimens.

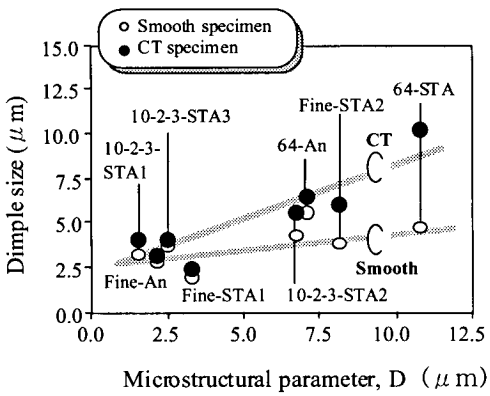

Fig.5 The relationship between Microstructural parameter and dimple size.

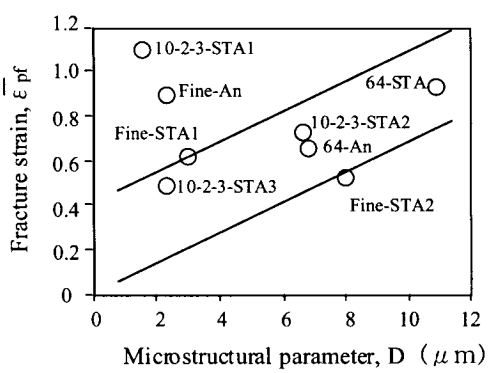

Fig.6 The relationship between microstructural parameter and fracture strain.

for the smooth specimen and the CT specimens are attributed to the difference of the stress triaxiality as is discussed later.

Figure 6 shows relation between fracture strain in the smooth specimen and the parameter, D. It should be noticed that the materials with fine microstructure show smaller ductility except for 10-2-3 STA1 and Fine-An. Exceptional results on both two materials in spite of their fine structure might be caused by the difference in void nucleation strain. As far as 10-2-3-STA1 is concerned, the particle size of α phase is smaller than 1 μm. The ductility must be governed with the void nucleation strain and void growth strain up to the coalescence. The critical stage of void coalescence is strongly depending on the number of voids or volume fraction of voids. An increase of the void nucleation sites generally leads to the reduction of ductility but not always the case.

Figure 7 shows the effect of stress triaxiality on the fracture strain obtained in the round bar specimens. Significant reduction of the fracture strain with the increase of the triaxiality is observed for every material. However, the reduction due to the high triaxiality is different in each material. The Fine-STA1,2 and 10-2-3-STA2,3 show small dependency. It arises from the difference in the void growth strain because void growth is strongly depending on the stress traxiality as is shown in Rice and Tracey Model [9] . Figure 8 shows the void nucleation strain and fracture strain for each material. The void growth strain in higher strength materials is relatively small and it results small dependency of the triaxiality on the ductility. In the Fine-An and 10-2-3-STA1, void growth strain are large, while the dimple sizes are small. This results indicate that the void nucleation strain is relatively large and the number of void nucleation from α phase is relatively small in the materials with ultra-fine microstructure, and result high ductility as shown in Figure 6.

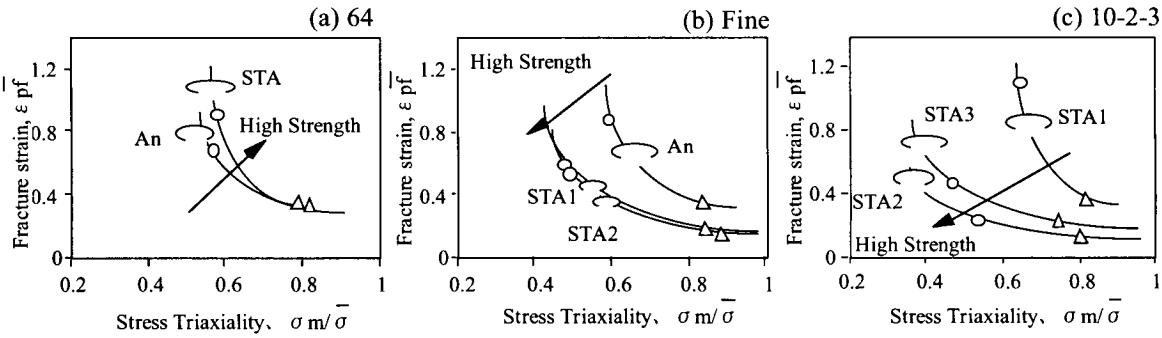

Fig.7 Effects of stress triaxiality on fracture strain.

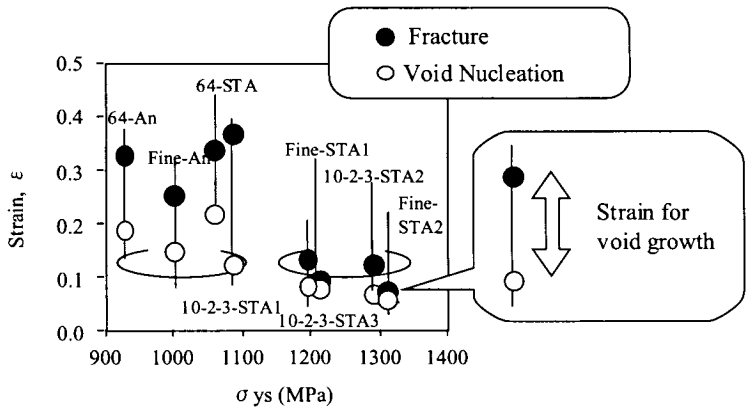

Fig.8 Void nucleation strain and fracture strain.

RESULTS ON FRACTURE TOUGHNESS TESTS

The fracture initiation toughness, $K_{IC}(J_{IC})$ are shown in Figure 9 in relation to the yield strength and the failure elongation of the materials, respectively. Correlation to the yield strength seems to be better though a few materials involving 10-2-3-STA1 doesn't fit in correlation. A description of the ductile fracture toughness in terms of mechanical properties is proposed by several authors. Ritchie and Thompson [10] have proposed

$$J_i = D_j \lambda \sigma_{ys} \bar{\varepsilon}_{pi} \tag{1}$$

, where λ is a material constant denoted as 'Characteristic distance' as is shown in Figure 10 , D_j is a material constant related to the strain hardening or so on, and $\bar{\varepsilon}_{pi}$ is the critical plastic strain under the high stress triaxiality. Taking the fracture strain in the notched specimens as the critical strain, $\bar{\varepsilon}_{pi}$ and the micro-structure parameter, D as the characteristic distance, λ , the fracture toughness in terms of J_{IC} is shown as a function of $\lambda\sigma_{ys}\bar{\varepsilon}_{pi}$ in Figure 11. Linear proportional relation is observed here again except for 10-2-3-STA1 and Fine-An. Exceptional two materials have fine microstructure and low strength.

The average sizes of dimples on the fracture surface at the crack tip are shown in Figure 5 in comparison with the results on the smooth specimens. The average sizes of dimples in the CT-specimens also show linear relationship with the microstructure parameter, D, though those are larger than that of the smooth specimens. It arises from the constraint effect, that is, the effect of the stress triaxiality. The high strength materials show a tendency of little difference in the size of dimples. It is noticed as a reflection of the results in Figure 8, since the void growth strongly depends on the stress triaxiality.

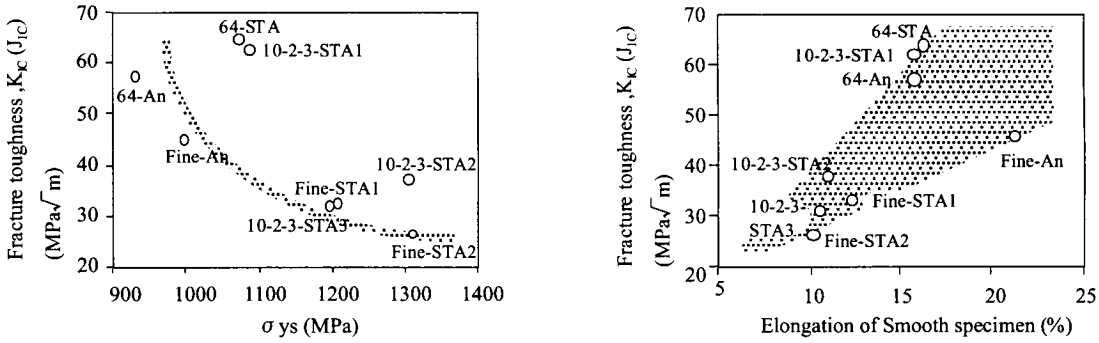

Fig.9 Relationship between fracutre toughness and mechanical properties of materials

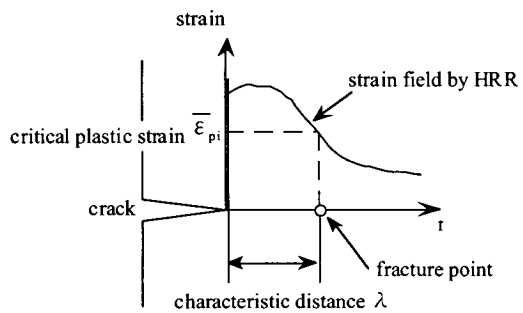

Fig.10 Characteristic Distance Model

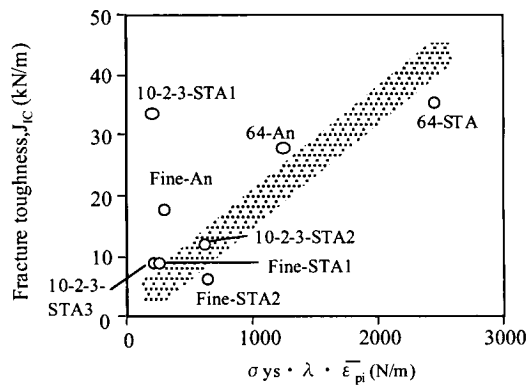

Fig.11 Fracture toughness and the toughness parameter according to Characteristic Distance Model

CONCLUSIONS

The effects of microstructure and constraint on the ductility and the fracture toughness of α / β Ti alloys with equiaxed α particles were investigated. The main conclusions are as follows; 1) The most of micro-voids nucleate from α / β interface and the dimple size on the fracture surface is related to the distance between α / β interfaces. 2) Refined microstructure leads to the increment of the nucleation sites of voids and high strength, then results low ductility. However, materials with extremely fine α particles show different behavior from other materials and high ductility. 3) The local fracture criterion approach, such as the characteristic distance model, can be applied to describe the toughness in terms of the strength and ductility of materials. A few exceptional materials are the same with the materials which show different tendency in the relation of the ductility and dimple sizes. 4) Conclusively, it is noticed that the improvement of ductility and toughness of the α / β Ti alloys can be achieved by the extreme refinement of α phase and decrease of the strength. Half done of refinement may cause reduction of the ductility and the toughness.

REFERENCES

[1] Harold Margolin and Yashwant Mahajan (1978) Matell. Trans. A, 9A, 781

[2] M.Niinomi, T.Kobayashi (1996) Meter. Sci. Eng. , A213, 16

[3] M.Niinomi, T.Kobayashi, N.Sasaki (1986) Tetsu-to-Hagane, 72, 633

[4] M.Niinomi (1996) Journal of Japan Institute of Light Metals, 46, 352

[5] Takao Horiya and Teruo Kishi (1998) Metal.Mater.Trans.A, 29A, 781

[6] A.Otsuka, T.Miyata, T.Sakurai, H.Iida (1984) Journal of the Society of Materials Science, 34, 622

[7] P.W.Bridgman (1952), 'Studies in large flow and fracture' Mc.Graw-Hill

[8] G.Terlindek, H.J.Rathjen, and K.H.Schwalbe (1988) Metall.Trans.A, 19A, 1037

[9] J.R.Rice and D.M.Tracy (1969) J.Mech.Phys.Solids, 17, 201

[10] R.O.Ritchie,A.W.Thompson (1985) Metall Trans. A, 16A, 233

ORAL/POSTER REFERENCE: ICF100428OR

EFFECTS OF DYNAMIC STRAIN AGING IN J-R FRACTURE RESISTANCE OF SA516-Gr.70 PIPING STEELS

Ji Hyun Yoon, Bong Sang Lee and Jun Hwa Hong

Korea Atomic Energy Research Institute,
Dukjin-Dong 150, Yusung, Daejon 305-353, Republic of Korea

ABSTRACT

J-R fracture resistance tests have been performed on two heats of SA516-Gr.70 carbon steels used for the elbows of nuclear piping. The tests covered a wide temperature range of ambient to 500℃ with various loading rates ranging from 0.3 to 1000 mm/min. The steep drops in fracture resistance of the SA516-Gr.70 steels were observed at certain temperature ranges at all loading rates. The temperature for the minimum fracture resistance moved to the higher temperature region as loading rates increase. Tensile tests were also carried out at temperatures of 100 to 316℃ with a range of strain rates of 2.5×10^{-5} to 1.33×10^{0}/s. The serrated flows were observed on some of the stress-strain curves. All these features indicated that the test materials were susceptible to DSA. However, some differences were founded in fracture resistances and DSA sensitivity between the two test materials. From the metallurgical analysis performed on them, it was deduced that microstructural characteristics such as grain size and pearlite fraction made quite a larger gap between the fracture resistance levels of the two materials and that the chemical composition, especially the contents of free interstitial atoms, were a main controlling factor for DSA sensitivity in SA516-Gr.70 steels.

KEY WORDS

J-R fracture resistance, dynamic strain aging (DSA), SA516-Gr.70 steel, loading rate, LBB

INTRODUCTION

SA516-Gr.70 steel has been widely used for elbows of nuclear piping. The leak-before-break (LBB) design concept [1] that has been applied to nuclear piping recently requires confirming fracture resistance of the piping materials through J-R tests. However, the systematic J-R test data obtained under various test conditions are very rare while a large database has been built for another piping material, i.e. SA106 steel by the International Piping Integrity Research Group (IPIRG) program.

It is well known that the fracture resistances of ferritic steels like SA516-Gr.70 steel are deteriorated in dynamic strain aging (DSA) region. Although some researchers like Miglin et al. and Marengo et al. reported DSA effect in J-R fracture resistance [2,3], their investigations were limited to J-R tests under static loading condition. Therefore, J-R fracture resistances were investigated in the present study at various temperatures ranging from ambient to maximum reactor operating temperature and various loading rates for SA516-Gr.70 steels. DSA effects in of J-R fracture resistances of two heats of SA516-Gr.70 steels with loading rates and temperatures were analyzed. Furthermore, differences of DSA behaviors and fracture resistances between two test materials of same specification were described and discussed with respect to microstructure and chemical composition.

EXPERIMENTAL

Materials and Specimen

Two heats of SA516-Gr.70 steels for elbow are used in this study. The chemical compositions are shown in Table 1. The ASTM standard 1T-C(T) specimens with T-L orientation were used for J-R tests. The specimens were side-grooved to a depth of 10% of the specimen thickness on both sides after fatigue pre-cracking.

TABLE 1

CHEMICAL COMPOSITIONS OF SA516-Gr.70 STEELS

wt.% / Material	C	Si	Mn	P	S	Cu	N	Ni	Cr	Mo	Al	V	Nb
Mat. A	0.22	0.31	1.14	0.005	0.002	0.10	0.0088	0.21	0.15	0.04	0.020	<0.005	<0.05
Mat. B	0.17	0.30	1.14	0.009	0.001	0.20	0.0024	0.36	0.03	0.10	0.031	0.028	0.016

J-R fracture resistance test

Direct current potential drop (DCPD) method that is applicable to the fast loading test was used for monitoring crack extension. The tests were conducted on a servo-hydraulic MTS 810 system. To insure signal integrity, the specimen and grip assembly was isolated from the rest of the load train. The details were reported elsewhere [4].

RESULTS AND DISCUSSION

Fig. 1 and Fig. 2 shows the J-R curves under various loading rates and temperatures. It was observed that the J-R fracture resistance of SA516-Gr.70 steels was very sensitive to the loading rate and temperature. The fracture resistances of Mat. A were superior to those of Mat.B under every test conditions.

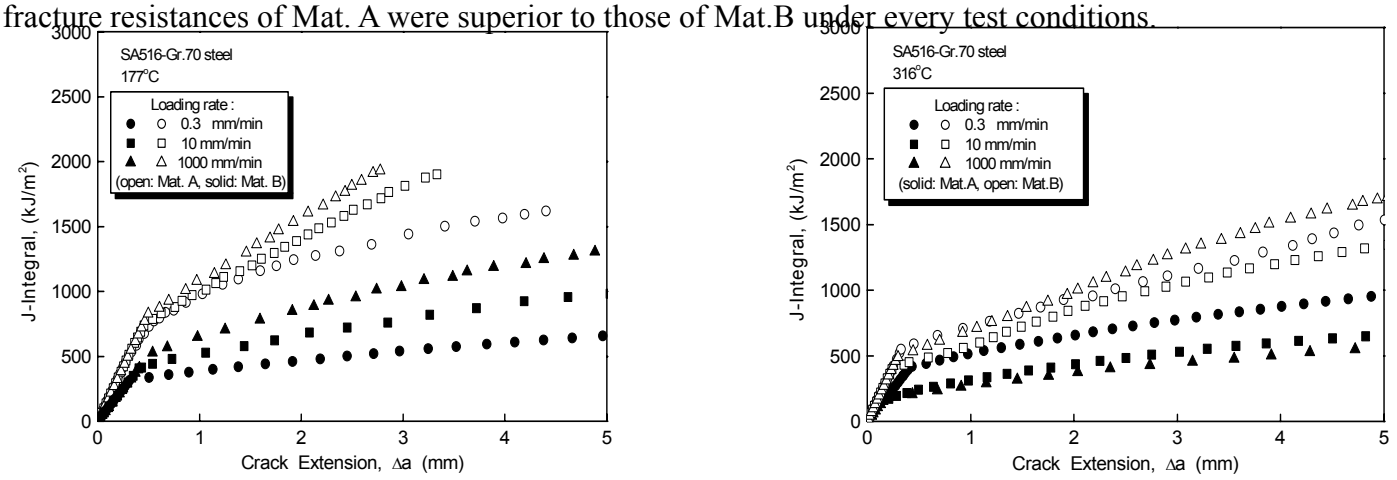

(a) (b)

Fig. 1 : J-R Curves at various loading rates for Mat.A and Mat.B at (a) 177℃ and (b) 316℃.

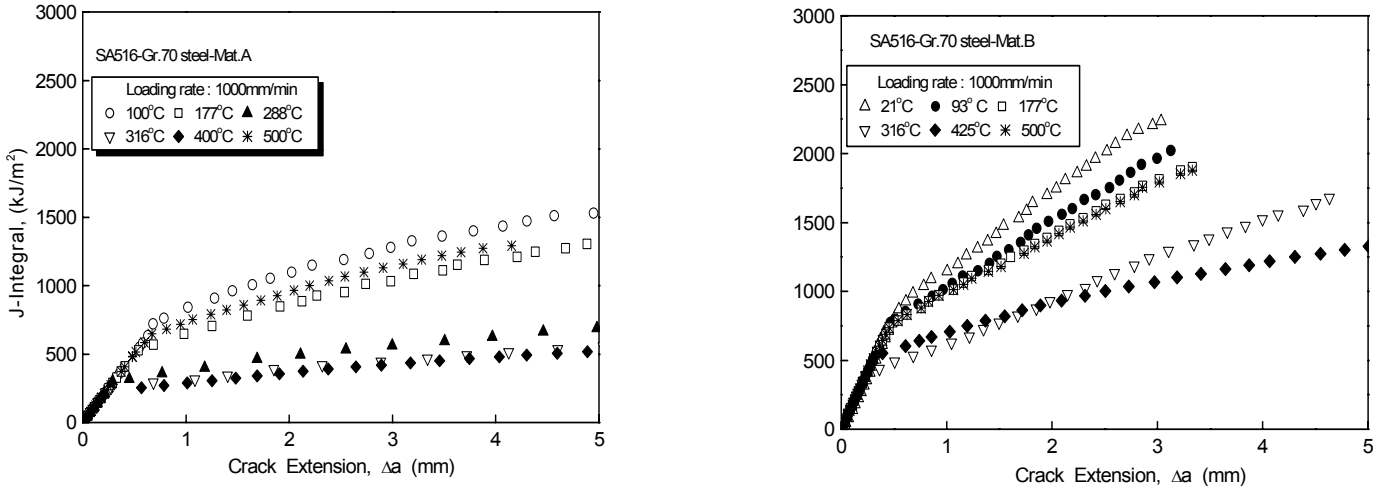

(a) (b)

Fig. 2 : Variations of J-R curves with test temperature ; (a) Mat.A, (b) Mat.B.

J integral values named as $J_{0.1}$ were obtained at Δa=0.1 inch (2.54 mm) on J-R curves to appreciate the dependence of the fracture resistance on the temperature and loading rate quantitatively as shown in Fig. 3.

As the loading rate increased, the temperature at which the fracture resistance became minimum or each loading rate shifted to higher temperature region. On the basis of previous research, the occurrence of the abrupt drop in J-R fracture resistance at a specific temperature and loading rate range is due to DSA [2]. In case of Mat. B, the temperature range which DSA occurred in was shifted to a higher temperature region and was narrower compared to Mat. A.

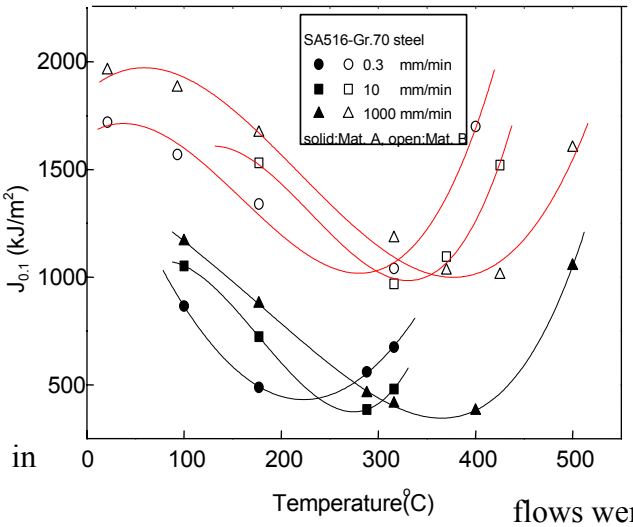

Fig. 3 : Variation of $J_{0.1}$ at various temperature and loading rate.

DSA phenomena was usually recognized by serrated flows in tensile stress-strain curve that is referred to Portevin-Le Chatelier effect [5]. Fig. 4 shows tensile test results for SA516-Gr.70 steels. The serrated flows were obviously observed in some test conditions. The serrations in Mat.A was more apparent than those in Mat.B. The conditions for the occurrence of serrated flows were expressed as a serration map in Fig. 5.

Since DSA is regarded as a thermally activated process, the activation energies of solute diffusion in test materials can be obtained from Arrhenius type plot.

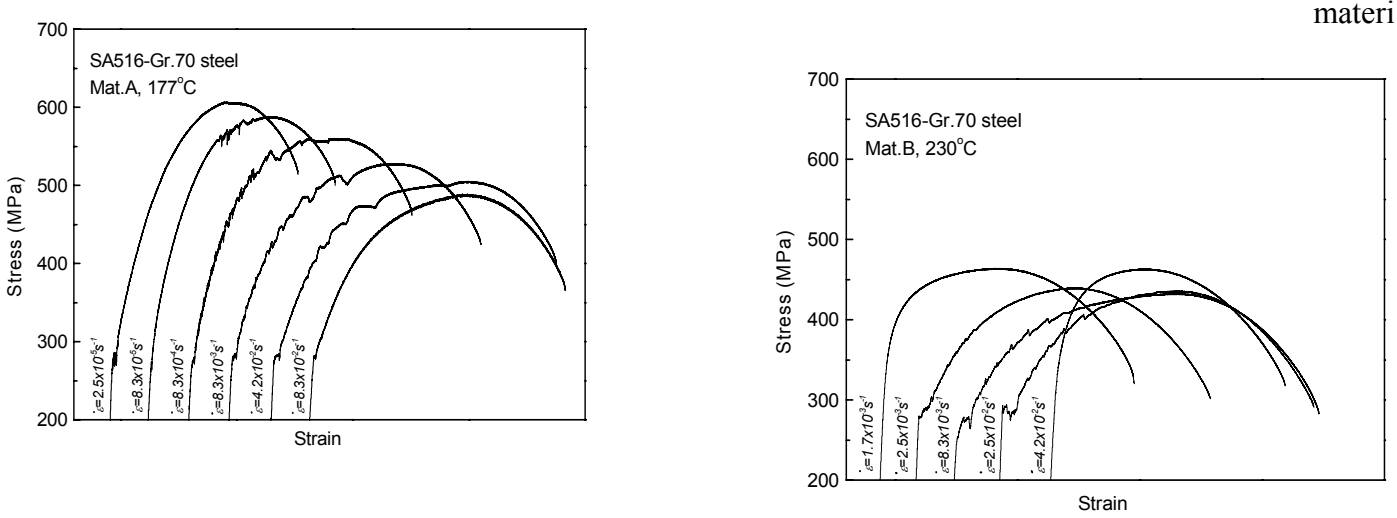

(a) (b)

Fig. 4 : Stress-strain curves at various strain rates for (a) Mat.A and (b) Mat.B.

The activation energies were determined as 65 and 92 kJ/mol for Mat.A and Mat. B respectively as represented in Fig. 5. The differences of fracture resistance and DSA behaviors between two heats of SA516-Gr.70 steels were analyzed with respect to chemical composition and microstructural factors. It was found that the comparatively high fracture resistance of Mat. B under all test conditions due to smaller grain size and lower pearlite to ferrite ratio compared to Mat. A. The concentrations of interstitials and activation energy for diffusion are main factors that affect on DSA behavior in steel [6]. The concentrations of carbon

and nitrogen in SA516-Gr.70 steels, in Mat A are higher than those of Mat. B. The solubilities of carbon and nitrogen in α-Fe can be calculated by the following equations, which were proposed by R. Stevenson [7].

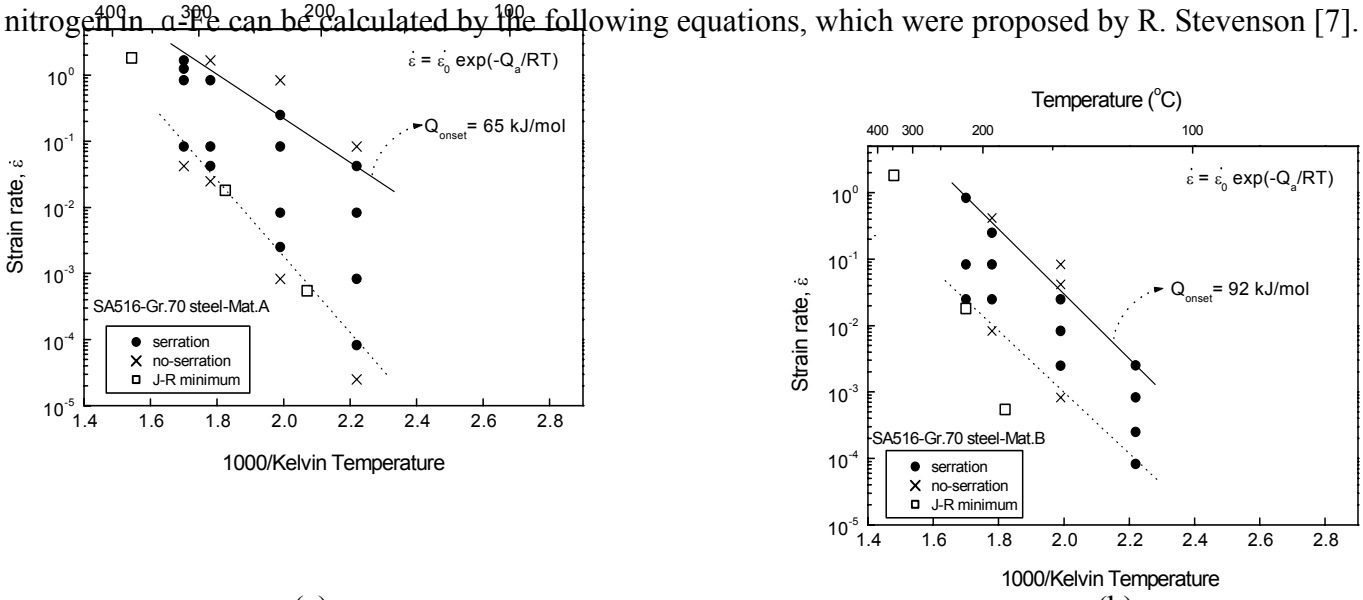

Fig. 5 : Serration map for SA516-Gr.70 steel ; (a) Mat.A, (b) Mat.B.

$$\text{wt\% C} = 2\exp(-38.07(\text{kJmol-1})/RT) \quad (1)$$

$$\text{wt \% N} = 12.3\exp(-34.73(\text{kJmol-1})/RT)$$ (R : 8.314 J/mol/K, T : Kelvin temperature)

Table 2 summarized the solubilities of carbon and nitrogen in an iron matrix in the test temperature range. It is expected that the solubility of nitrogen is higher than that of carbon in SA516-Gr.70 steels in the test temperature range. The nitrogen concentrations of Mat. A and B are 88 and 24 ppm, respectively. These are within the solubility limit in the matrix. On the other hand, carbon concentrations of Mat. A and B exceed the solubility limit in the matrix. It means that the difference of DSA sensitivities between Mat. A and B is mainly due to the difference of nitrogen concentration.

TABLE 2

Solubility of C and N in α-Fe (in ppm)

	293 K	373 K	473 K	573 K	673 K	773 K
C (ppm)	0.003	0.09	1.3	6.8	22.2	53.5
N (ppm)	0.079	1.68	18.0	89.3	249.7	553.3

Baird and Jamieson reported that carbon and nitrogen are bound more strongly to the substitutional impurities like Mo, Co, Ni and Mn than to dislocations [8]. DSA will be extended to a higher temperature range than in pure Fe-C or Fe-N due to the reduced mobility of the carbon and nitrogen atoms in steel containing Mo, Co, Ni and Mn. Cr, V, Nb, Ti and Zr were also pointed as substitutional impurities which

extend DSA to higher temperatures although they are less effective than Mo, Co, Ni and Mn. Chakravartty et al. reported that the nitride formers such as Al, Ti and V tie up a major fraction of nitrogen in the form of alloy nitrides and DSA is diminished in ferrictic-pearlitic steel [9]. As shown in Table 1, the concentrations of Mo, Ni, V, Al in Mat. B are even higher than those in Mat. A. From the previous studies, it is deduced that substitutional impurities such as Mo, Ni, V, Al also reduced DSA sensitivity in Mat. B.

CONCLUSIONS

J-R fracture resistance of SA516-Gr.70 steels is very sensitive to the loading rate and temperature due to dynamic strain aging.

The difference of J-R fracture resistance levels and DSA behaviors between two heats of SA516-Gr.70 steels are mainly due to differences of pearlite to ferrite ratio and chemical composition such as concentrations of interstitial solute atoms. It was presumed that substitutional solute concentrations also affected DSA behavior in SA516-Gr.70 steels.

ACKNOWLEDGEMENT

This work has been carried out as a part of Reactor Pressure Boundary Materials Project under the Nuclear R&D Program by MOST in Korea.

REFERENCES

1. USNRC (1987). *Leak Before Break Evaluation Procedure, USNRC Report NUREG-800, Standard Review Plan. 3.3.6.*
2. M. T., Migline et al. (1985). *Effects of Strain Aging in the Unloading Compliance J test, ASTM STP 856,* ASTM, Philadelphia,.
3. A. A., Marengo and J. E., Perez (1996). *Nucl Engng Des.* 167, 215-222.
4. J. H. Hong et al. (1997). *KAERI Report, KAERI/CR-35/97.*
5. A., Portein and F., Le Chatelier (1923). *Compt. Rend. Acad. Sci*., 176, 507-512.
6. A. S., Keh et al., (1968). *Dislocation Dynamics*, McGraw-Hill, New York,.
7. R. Stevenson : *Metall. Trans.* 11A (1980) 1909
8. J. D. Baird, A. Jamieson (1966). *J. Iron Steel Inst*., 204, 793.
9. J. K., Chakravartty et al. (1983). *J. Nucl. Mater*.,119, 51-58.

ORAL REFERENCE: ICF 1003060R

EFFECTS OF HETEROGENEITY ON THE STRENGTH OF 3D COMPOSITES

Sivasambu Mahesh[1], Irene J. Beyerlein[2], and S. Leigh Phoenix[1]

[1]Theoretical & Applied Mechanics, Cornell University, Ithaca NY 14853. USA.
[2]Materials Science & Technology, Los Alamos National Laboratory,
Los Alamos, NM 87545. USA.

ABSTRACT

Monte Carlo simulation interpreted with theoretical modeling is used to study the statistical failure modes in unidirectional composites consisting of a hexagonal array of elastic fibers embedded in an elastic matrix. Composite structure is idealized using the chain-of-bundles model in terms of bundles of length δ arranged along the fiber direction. Fibers element strengths in δ-bundles are taken to be Weibull distributed and Hedgepeth and Van Dyke load sharing is assumed for transverse fiber break arrays.

Simulations of δ-bundle failure reveal two regimes. When fiber strength variability is low, the dominant failure mode is by growing clusters of fiber breaks up to instability. When this variability is high, cluster formation is suppressed by a more dispersed fiber failure mode. Corresponding to these two cases, we construct simple models that predict the strength distribution of a δ-bundle. Their predictions compare very favorably with simulations in the two cases.

KEYWORDS

unidirectional fiber composites, brittle/ductile transition, extreme value problem, chain of bundles model, shear-lag model.

INTRODUCTION

Quasistatic failure of unidirectional composite materials, which consist of long aligned reinforcing fibers embedded in a matrix is a complex stochastic process. While complexity stems from the occurrence of various damage events preceding formation of a catastrophic crack, statistical variation in strength primarily arises due to the variability in fiber strength. Consequently composite tensile strength is itself a statistical quantity and methods to determine its distribution are of considerable significance in assuring composite reliability.

Idealization of composite structure and material properties are found to be inevitable before further analysis can be attempted. In this study we assume stiff linear elastic fibers arranged in

a hexagonal array and embedded in a relatively compliant linear elastic non-debonding matrix so that material damage in our idealized composite is limited to fiber breakages alone. The large fiber-matrix stiffness ratio implies that most of the applied load will be borne by the fibers and the role of the matrix is limited to conducting loads from broken fibers to nearby intact fibers. This load transfer occurs through shear deformation that tends to occur over a certain length scale δ. δ is typically only a few fiber diameters and is much less than the composite length L.

As has been common in the literature, we idealize the failure process in terms of a longitudinal partition into $m = L/\delta$ transverse slabs or short bundles of length δ, called δ-bundles. The failure process within a given δ-bundle is treated as mechanically and statistically independent of that in neighboring δ-bundles. The composite is then treated as a weakest-link arrangement of these δ-bundles; that is, the composite fails when the weakest δ-bundle fails. Thus the chain-of-bundles assumption converts the 3D problem of composite failure into the problem of failure of the weakest of several 2D δ-bundles. We also assume that fiber strength X is random and distributed according to the Weibull distribution

$$F(x) = \Pr\{X \leq \sigma\} = 1 - \exp\{-(\sigma/\sigma_\delta)^\rho\} \tag{1}$$

where σ is the stress experienced by the fiber, σ_δ is the scale parameter for a fiber element of length δ and ρ the shape parameter of the distribution.

We use Hedgepeth and Van Dyke's [1] local load sharing model (HVLLS) to determine stress concentrations in the plane of a tranverse array of fiber breaks. While we do not delve into the details of their approach, we note that under HVLLS, the stress concentration around a penny-shaped crack of r fiber breaks is approximately

$$K_r \approx \sqrt{\frac{2\sqrt{r}}{\pi^{3/2}} + 1} = \sqrt{\frac{D}{\pi} + 1} \tag{2}$$

where D is the effective non-dimensional diameter of the penny-shaped crack and $r = \pi D^2/4$. Also, as the crack size becomes large, the stress concentration decays as $1/\sqrt{t}$ in the near-field where t is distance from the crack tip and shares this characteristic of the near-tip stress field with LEFM.

In this work, we take our δ-bundles to be rhombus shaped. In every realization of δ-bundle failure, gradually increasing load is applied to it in the fiber direction until a fiber fails due to the applied load just exceeding its Weibull strength. This fiber breaks causes stress redistribution according to HVLLS which in turn may cause more failures. This back-and-forth process of fiber failures and stress redistribution is continued until either stability (i.e., no further fiber breakage) is reached or the δ-bundle fails. In the case of stability, gradual applied load increment is resumed until the failure of another fiber. Then the above process of stress redistribution and further fiber failures is repeated. Eventually, at some applied load(the δ-bundle strength), a cascade of fiber failures signifies catastrophic δ-bundle failure. We now proceed to describe dominant failure mechanisms of composite failure observed in simulations and to model them in order to analytically predict the statistical strength distribution of composite strength.

FAILURE MECHANISMS AND MODELS IN δ-BUNDLES

1. Small Variability in Fiber Strength (large ρ)

Snapshots of the damage evolution in the $\rho = 10$ median (among 500 simulations) δ-bundle en route to failure are shown in Figure 1. The last stage shown corresponds to the arrangement

of breaks immediately after the formation of an unstable system of fiber breaks and before the catastrophic failure of the remaining fibers. Note that the boundary conditions are periodic so that a break cluster appearing at one edge may be continued on the opposite edge. Cluster formation and growth is clearly the dominant failure mode in the specimen shown.

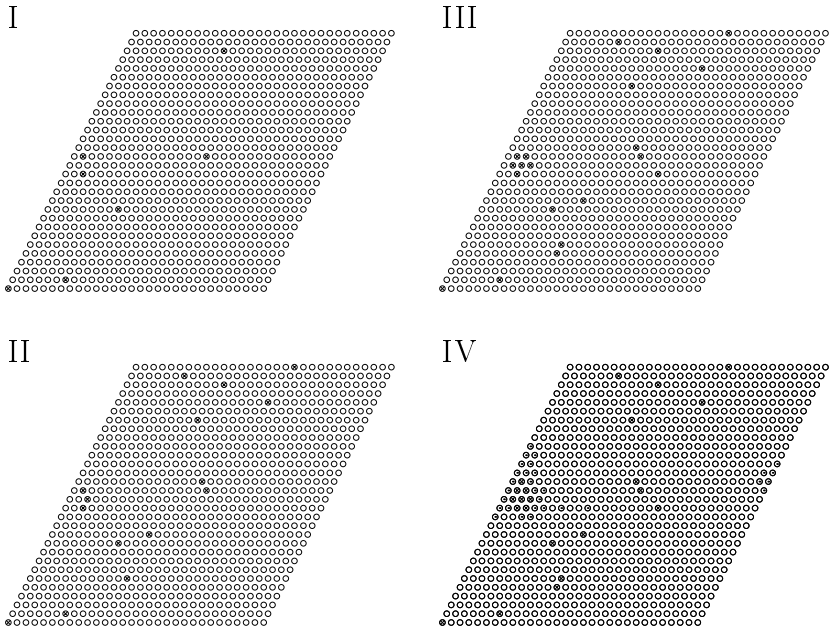

Figure 1: Snapshots of the failure process in the median (among 500 simulations) δ-bundle with 900 Weibull fibers of $\rho = 10$ under periodic boundary conditions. Open circles $\bigcirc$ denote intact fibers, $\bigotimes$ denote broken fibers.

Following Harlow and Phoenix [2], we have plotted the empirical weakest-link distributions

$$\hat{W}_n(\sigma) = 1 - [1 - \hat{G}_n(\sigma))]^{1/n} \tag{3}$$

on Weibull paper, in Figure 2 obtained from our Monte-Carlo simulations of failure of δ-bundles under HVLLS. Here $\hat{G}_n$ denotes the empirical strength distribution of the n-fiber δ-bundle. For $\rho \geq 2$ the $\hat{W}_n(\sigma)$ curves for $n = 225$, 625 and 900 collapse onto one characteristic curve $\hat{W}(\sigma)$. This n-independent collapse however fails to hold for $\rho = 1$. The collapse of $\hat{W}_n$ into a single curve for $\rho \geq 2$ suggests that the cluster growth failure mode is active for ρ range in the composite sizes that were simulated.

We model the cascade event defining $W(\sigma)$ as the formation of a break cluster at stress σ that goes unstable. The non-dimensional effective diameter D of a tight circular cluster of r breaks was defined earlier as $\pi D^2/4 = r$. The circumference of the circle, $\pi D = \sqrt{4\pi r}$ is approximately the number of intact fibers surrounding this r-cluster. Let N_r be the number of these neighbors that are severely overloaded. The first step is the failure of a given fiber in the δ-bundle under σ, followed by the failure of one of its $N_1 = 6$ equally overloaded neighbors under stress $K_1\sigma$. The resulting pair of fiber breaks has eight intact neighbors of which only $N_2 = 2$ are severely overloaded under stress $K_2\sigma$. The next likely event is the failure of one of these, to form a break triplet with $N_3 = 3$ severely overloaded neighbors, of which one fails, and so on. The critical event is thus the evolution of a growing "tight" r-cluster, with each added break being the failure of one of the N_r severely overloaded fibers surrounding it. We write this as

$$\begin{aligned} W_n(\sigma) \approx\ & F(\sigma)\{1 - [1 - F(K_1\sigma)]^{N_1}\} \\ & \times \{1 - [1 - F(K_2\sigma)]^{N_2}\} \ \cdots \ \{1 - [1 - F(K_{n-1}\sigma)]^{N_{n-1}}\}, \end{aligned} \tag{4}$$

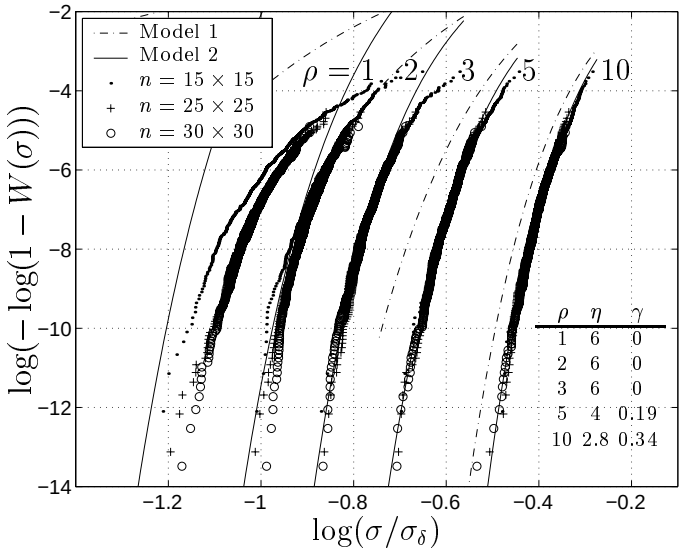

Figure 2: Comparison of the weakest link distribution predicted by the 2D cluster growth model with the empirical weak link distributions $\hat{W}(x)$ obtained from Monte-Carlo simulations. Model 1 assumes $\eta = \sqrt{4\pi}$ and $\gamma = 0.5$ for all ρ. In Model 2, we adjust the parameters η and γ so as to get the best fit with the simulated data. These values of η and γ are listed in the bottom right corner. Weakest link distributions corresponding to $\rho = 0.5$ are not shown because both Model 1 and Model 2 predict distributions that are out of the range of this plot. Also omitted is the Model 1 line for $\rho = 1$ which also lies outside the range of this plot.

where K_r is the stress concentration on the N_r most severely overloaded neighbors of a tight r-cluster and is given by Eqn. 2. We introduce two parameters, η and γ, to account for the actual number of fibers at high risk of failure. Let

$$N_r = \eta r^\gamma \tag{5}$$

be the number of severely overloaded neighbors around an r-cluster, where $\eta > 0$ and $0 < \gamma \leq 1/2$. We find this structure for N_r to be essential in order that $W_n(\sigma)$ in Eqn. 4 agree with the form of the simulated $\hat{W}(\sigma)$ distribution especially for small ρ. Taking $\eta = \sqrt{4\pi} \approx 3.55$ and $\gamma = 1/2$, implies counting all the fibers on the cluster periphery to be at risk of failure. Model 1 lines in Figure 2 correspond to this case and do not fit the simulated $\hat{W}(\sigma)$ very well. However model 2 lines in which we vary η and γ as functions of ρ fit the simulated $\hat{W}(\sigma)$ much better. A closed form approximation for $W(\sigma)$ is derived in [5].

2. Large Variability in Fiber Strength (small ρ)

When ρ is small corresponding to large variability in fiber strength, the cluster-driven breakdown mechanism is dominated by a dispersed, strength-driven breakdown mechanism of the δ-bundle. This is clearly seen in the failure snapshots of a δ-bundle for $\rho = 1$, as shown in Figure 3.

In the case of dispersed fiber failure in a δ-bundle, the details of the fiber load-sharing model may not be important provided that the model conserves load. Thus we consider behavior under the equal load-sharing rule or ELS. ELS assumes that the stress concentration factor for each intact fiber in an n-fiber δ-bundle with j broken fibers is $\kappa_{n,j} = n/(n-j)$. Applying a result due to Smith [3] which sharpens one due to Daniels [4] to an ELS bundle of Weibull fibers we find that the bundle strength distribution $G_n(\sigma)$ converges as $n \to \infty$, to the normal form $\Phi((\sigma - \mu_n^*)/s_n^*)$

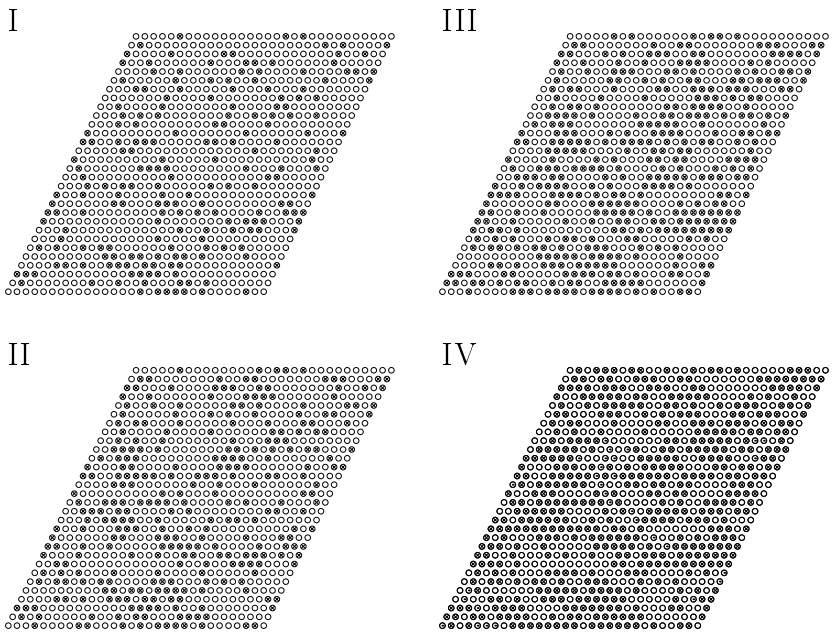

Figure 3: Snapshots of the failure process in the median (among 500 simulations) δ-bundle specimen with 900 Weibull fibers of $\rho = 1$ under periodic boundary conditions. Open circles $\bigcirc$ denote intact fibers, $\bigotimes$ denote broken fibers.

with asymptotic mean

$$\mu_n^* = \sigma_\delta (\rho e)^{-1/\rho} \left\{ 1 + 0.996 n^{-2/3} \left(e^{2/\rho}/\rho \right)^{1/3} \right\} \tag{6}$$

and asymptotic standard deviation

$$s_n^* = \sigma_\delta n^{-1/2} \rho^{-1/\rho} \sqrt{e^{-1/\rho}(1 - e^{-1/\rho})}. \tag{7}$$

2a. Global/Local Model

Unlike in ELS, wherein material damage accrues globally, we speculate that in HVLLS there is a ρ-dependent size scale within which damage accumulates in a dispersed manner and propagates catastrophically from there. That is, failure initiates over $\tilde{m} = n/\tilde{n}$ bundles of $\tilde{n}$ fibers in an ELS-like manner within a localized region and propagates catastrophically from there resulting in composite strength distribution

$$G_n(\sigma) = 1 - \{1 - \Phi[(\sigma - \mu_{\tilde{n}}^*)/s_{\tilde{n}}^*)]\}^{\tilde{m}}, \tag{8}$$

In Figure 4, for highly variable fibers with $\rho = 1$, 2, 3, and 5 we have plotted the strength distribution of the smallest sized δ-bundle ($n_1 \times n_1$) to which weak-linked distributions of larger bundles collapse. This smallest δ-bundle size approximately corresponds to the critical cluster size defined previously. We also show the distributions of larger bundles of size ($n_2 \times n_2$) or ($n_3 \times n_3$) weak-linked to the size ($n_1 \times n_1$). Note that as ρ decreases, these weak-linked distributions become increasingly Gaussian (indicated by the straightness of the strength distribution on normal coordinates) and are better approximated by the ELS asymptotic distribution. Despite the excellent agreement of the 900-fiber, weak-linked strength distribution with the 625-fiber,

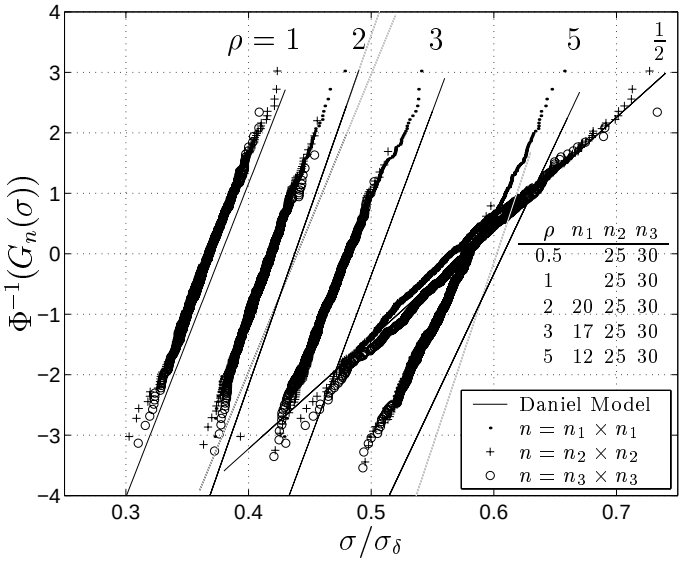

Figure 4: Comparison of $\Phi((\sigma - \mu_n^*)/s_n^*)$ given by Daniel's asymptotic formula for ELS bundles with simulated strength $G_n(\sigma)$ of an $n = n_1 \times n_1$ HVLLS δ-bundle. Also shown are empirical strength distributions of larger δ-bundles weak linked to the size $n_1 \times n_1$ in agreement with those of the $n_1 \times n_1$ δ-bundle.

weak-linked distribution when $\rho = 0.5$, it turns out that they do not agree with a 2500-fiber, weak-linked δ-bundle strength distribution. This suggests that the smallest catastrophic failure event of the bundle occurs over more than 625 or perhaps even 900 fibers.

CONCLUSIONS

In Eqn. 4, we give the weakest-link characteristic distribution function $W(\sigma)$ for δ-bundles. These bundles are links in the chain-of-bundles model for the failure of 3D unidirectional composites. For sufficiently large Weibull modulus ρ, say $\rho > 4$ in 3D composites, the strength distribution of a composite of length $L = m\delta$ and with n fibers is $H_{m,n}(x) \approx 1 - (1 - W(x))^{mn}$. For $\rho \leq 4$, however, we observe that the details of the load-sharing become increasingly unimportant, and the δ-bundle strength distribution for fixed n is not only increasingly Gaussian up to quite large n but also converges to that for ELS whose analytical form is known. For fixed ρ, however, this Gaussian nature is expected to persist only up to a δ-bundle size of the order of the critical cluster size. For composites beyond this critical size the distribution function for δ-bundle strength is that for a chain of Gaussian 'patches' of $\tilde{n}$ fibers in the δ-bundle. Thus the composite can be viewed as a weakest-link arrangement of $m\tilde{n}$ such Gaussian patches.

REFERENCES

[1] Hedgepeth, J.M and Van Dyke, P. (1967), *J. Comp. Mater.*, **1**, 294.

[2] Harlow, D.G. and Phoenix, S.L. (1978), *J. Comp. Mater.*, **12**, 314

[3] Smith, R.L. (1982), *Ann. Probab.*, **10**, 137.

[4] Daniels, H.E. (1945), *Proc. Royal Soc. London A* , **183**, 405.

[5] Mahesh, S., Phoenix, S. L., and Beyerlein I.J. (2001) In preparation.

POSTER REFERENCE:ICF100513PR

EFFECTS OF NOBLE GAS ENVIRONMENTS ON FATIGUE CRACK GROWTH IN TITANIUM ALLOYS

M. Shimojo[1], R. Kusama[1] M. Otsubo[1] and Y. Higo[1]

[1] Precision and Intelligence Laboratory, Tokyo Institute of Technology, Yokohama, 226-8503, Japan

ABSTRACT

The effects of gaseous environments on fatigue crack growth behaviour of metals have been studied by many researchers. However, most of them are limited to the effects of hydrogen and oxygen. It is generally understood that the effects of noble gases such as xenon are negligible as compared to vacuum environments in most metals such as steels. In our previous research we have found that noble gases including helium, argon and xenon do affect the fatigue crack growth behaviour of pure titanium. The noble gases increase the fatigue crack growth rate and change the fracture surface appearance as compared to those tested in vacuum. This peculiar behaviour may be due to the active nature or the hexagonal structure of titanium. In this study, fatigue crack growth tests were carried out on a β-titanium alloy, which has a bcc structure, in noble gas environments. It was found that argon and xenon increased the fatigue crack growth rate of the β-titanium in the Paris regime and changed the fracture surface appearance as compared to those tested in vacuum, however, helium did not. Striations were clearly observed on fracture surfaces of specimens tested in argon and in xenon, while no obvious striations were found on those tested in vacuum and in helium. This may indicate that the observed effects of noble gases are related to both the active nature of titanium and crystal structures.

KEYWORDS

gaseous environment, noble gas, titanium alloys, fatigue crack growth, fractography

INTRODUCTION

Gaseous environments generally affect fatigue crack growth behaviour of ductile metals and alloys. It is well recognised that fatigue crack growth rate in air and in oxygen is faster than in vacuum in most metals and alloys [1]. This phenomenon is explained by the adsorption of oxygen on exposed slip steps which are produced upon loading, and this leads to the reduction of reversible slip on unloading [1]. However, the

effects of gaseous environments other than oxygen and hydrogen have not been studied extensively.

Shimojo et al. [2] reported that fatigue crack growth rates of titanium increased in a pure nitrogen environment as compared to that in vacuum. Nitrogen is considered to be less aggressive than oxygen, but it can still react with titanium and, thus, could inhibit reverse slip. Though it is generally considered that noble gases do not affect fatigue crack growth, it is also shown that even noble gas environments can affect fatigue crack growth rate of pure titanium. Shimojo et al. [3, 4] showed that noble gas such as pure helium, argon and xenon increased fatigue crack growth rate as compared to that in vacuum. Fatigue crack growth rates in helium, argon and xenon were approximately twice that in vacuum and were almost the same as that in air. Additional findings showed that striations were clearly observed on fracture surfaces of specimens tested in helium and xenon, while less obvious striations were observed on those in vacuum and argon. These interesting results indicate that even noble gases may adsorb strongly on exposed slip steps and affect fatigue behaviour of titanium. However, most fatigue data obtained in noble gases, to date, are treated as reference data for more aggressive environments. Very little research has been carried out on the effects of noble gases themselves on fatigue behaviour of metals. Thus, the mechanism causing these effects of noble gases is still uncertain.

Noble gas atoms are less likely to form a strong bond with metals. But, on the other hand, titanium is a reactive metal, which means that titanium atoms form a bond easily with other atoms. The above-mentioned effects of noble gases on fatigue crack growth may result from the active nature of titanium and may appear on other titanium alloys, not limited to pure titanium (α-titanium, hcp structure).

In this research, fatigue crack growth tests are carried out on a β-titanium alloy, which has a bcc structure, in noble gases and the effects of noble gas environments on fatigue crack growth behaviour are discussed.

EXPERIMENTAL PROCEDURE

The material used was a hot-rolled and annealed β-titanium (Ti-15V-3Al-3Cr-3Sn) polycrystalline plate. This material has a microstructure that consists of equiaxial grains, the diameter of which was approximately 150 μm. Compact tension specimens of 50 mm width and 12.5 mm thickness were prepared from the material with an L-T orientation (the macroscopic crack plane is perpendicular to the loading direction, and the crack growth direction parallels to the transverse direction of the plate.)

Fatigue crack growth tests were performed under a sinusoidal loading control at a frequency of 10 Hz and a stress ratio of 0.1 using a servohydraulic fatigue machine with an environmental chamber made of stainless steel. The block diagram of the measurement system is shown in Fig.1. Crack length was monitored using a direct current potential drop technique. Some tests were carried out under constant load amplitude conditions and others were under constant stress intensity factor range (ΔK) conditions by feeding back the crack length measured. All tests were carried out at room temperature (approximately 24^{o}C) in an environment either vacuum or high purity noble gas of 1×10^5 Pa. Attention was paid especially to the purity of the gases and the contamination that might have occurred during the introduction of the gases to the chamber. (The effects of air contamination on fatigue crack growth rate and on fracture surface

appearance of α-titanium is discussed elsewhere [4].) The purities of the gases used are shown in Table 1. The chamber had been evacuated to vacuum (5×10^{-5} Pa) using a turbomolecular vacuum pump, before noble gas was introduced.

TABLE 1
PURITY OF NOBLE GASES USED

Gas	Purity (%)	Oxygen (ppm)	Nitrogen (ppm)
He	> 99.99999	< 0.05	< 0.05
Ar	> 99.9999	< 0.1	< 0.3
Xe	> 99.995	not detected	not detected

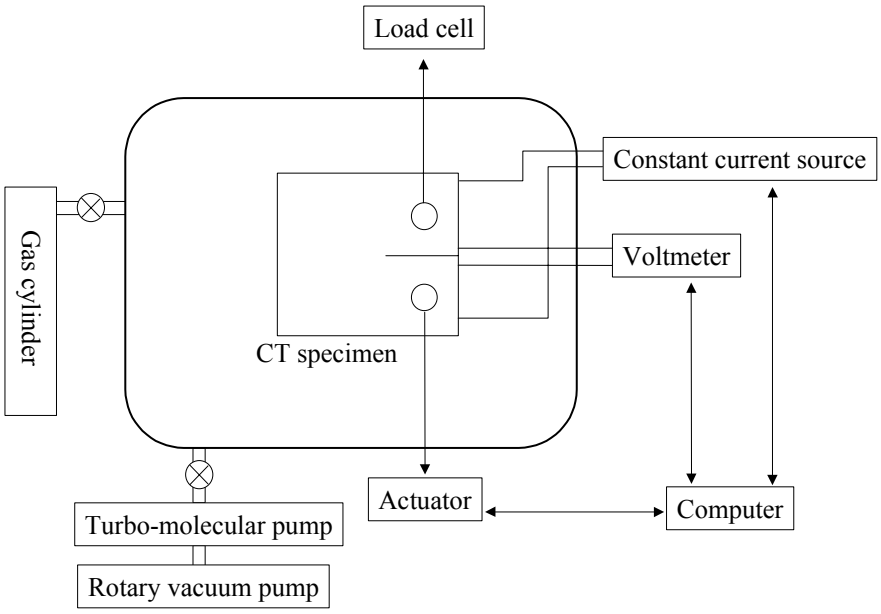

Figure 1: Block diagram of the measurement system

After the fatigue crack growth tests, fracture surface observations were carried out using a field emission gun scanning electron microscope.

RESULTS AND DISCUSSION

Figure 2 shows fatigue crack growth rate of β-titanium as a function of ΔK in vacuum and noble gases under both constant load amplitude and constant ΔK conditions. Fatigue crack growth rate measured in air is also included. Fatigue crack growth rates in air, argon and probably xenon are higher than those in vacuum. Fatigue crack growth rate of α-titanium in noble gases are approximately twice that in vacuum in the Paris regime [3, 4]. Irving and Beevers [5] showed that the fatigue crack growth rate of a titanium alloy in vacuum is slower than that in air by a factor of 2 to 3 in the Paris regime. These results agree with those shown herein. However, fatigue crack growth rate of β-titanium in helium showed different behaviour

from that of α-titanium. Fatigue crack growth rate of β-titanium in helium was almost the same as that in vacuum, while that of α-titanium in helium was approximately twice that in vacuum at a given ΔK.

Fractorgraphs of β-titanium specimens tested in vacuum, helium, argon and xenon at ΔK of 13 MPa $m^{1/2}$ are shown in Fig. 3. Striations are clearly observed on fracture surfaces of specimens tested in argon and xenon, while less obvious striations are found on those tested in vacuum and helium.

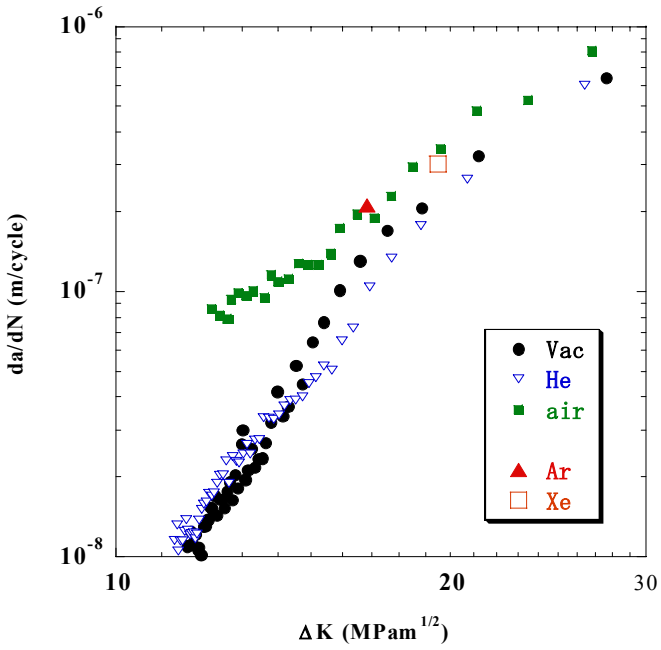

Figure 2: Fatigue crack growth rate of β-titanium in gaseous environments

Both an increase in crack growth rate and a change in fracture surface appearance indicate that even noble gases have interactions with a metal during plastic deformation. The difference in fracture surface appearance may be caused by the noble gas atoms entered the metal, not by simple adsorption on the surfaces. (Please note that the entrance of noble gas atoms has been confirmed on α-titanium [4].) The appearance of clear striations accompanies with an increase in crack growth rate. This may indicate that the entrance of noble gas atoms into the titanium matrix causes embrittlement and thus results in a change in deformation behaviour.

Fatigue crack growth rate of α-titanium increased in a helium environment as compared to that in vacuum, while that of β-titanium alloy did not. Fracture surface appearance of α-titanium tested in the helium environment was similar to that in the other noble gas environments, while that of the β-titanium alloy was similar to that in vacuum. These differences may be caused by the difference in crystal structure. The interaction between titanium matrix and entered noble gas atoms may be affected by the difference in crystal structure, that is the size of spaces among the titanium atoms. However, further studies are necessary to understand the details.

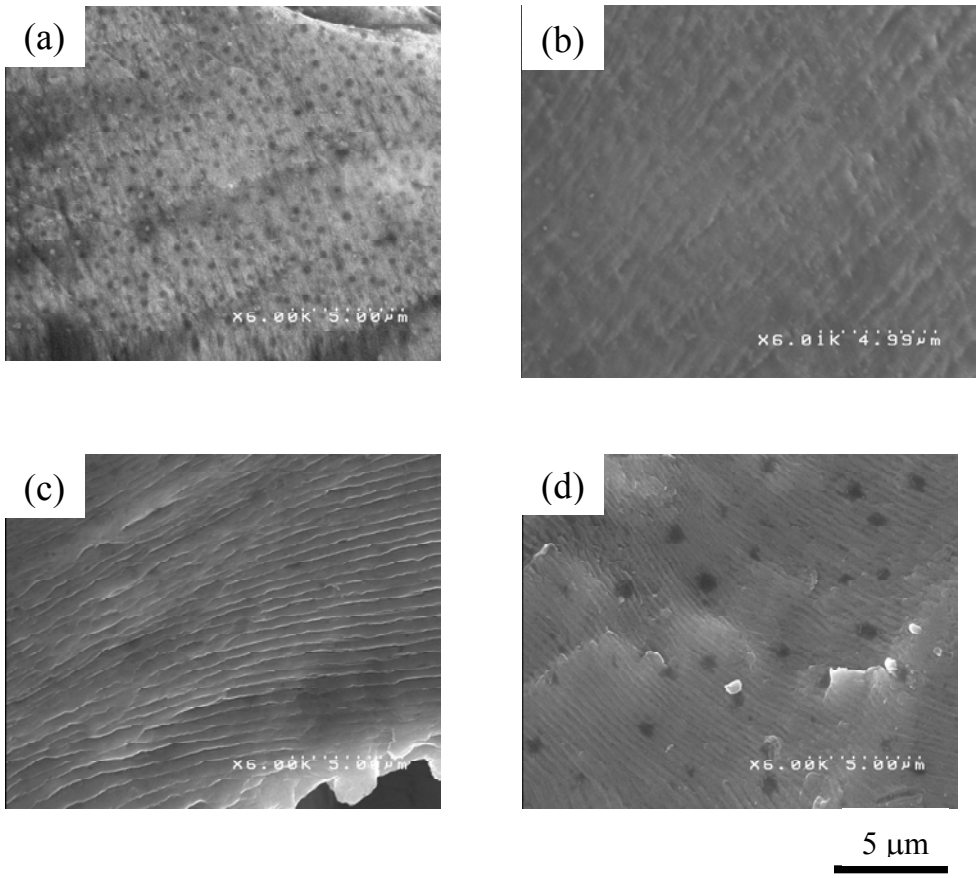

Figure 3: Fractgraphs of specimens tested in (a) vacuum,
(b) helium, (c) argon and (d) xenon

CONCLUSIONS

It was found that argon and xenon increased the fatigue crack growth rate of the β-titanium in the Paris regime and changed the fracture surface appearance as compared to those tested in vacuum, however, helium did not. Striations were clearly observed on fracture surfaces of specimens tested in argon and in xenon, while no obvious striations were found on those tested in vacuum and in helium. This may indicate that even noble gases have interactions with a metal during plastic deformation. These interactions are slightly different from those in α-titanium. Therefore, the interaction between titanium matrix and entered noble gas atoms may be affected by the difference in crystal structure, that is the size of spaces among the titanium atoms

Refereces

1. Suresh, S. (1994). *Fatigue of Materials*, Cambridge University Press, United Kingdom.
2. Shimojo, M., Iguchi, R., Myeong, T. H. and Higo, Y. (1997) *Metall. Mater. Trans. A, 28A*, 1341.
3. Shimojo, M. and Higo, Y. (1999) *Proc. 7th Int. Fatigue Congr. (Fatigue 99), 4*, 2311.
4. Shimojo, M., Higo, Y. and Oya-Seimiya, Y. (2000) *Metall. Mater. Trans. A, 31A*, 1435.
5. Irving, P. E. and Beevers, C. J. (1974) *Metall. Trans. 5*, 391

POSTER REFERENCE: ICF100481PR

EFFECTS OF PLASTIC STRAIN ON CLEAVAGE FRACTURE PREDICTIONS IN STEEL

S. R. Bordet [1,2], A. D. Karstensen [2], C. S. Wiesner [2] and D. M. Knowles [1]

[1] University of Cambridge, Department of Materials Science and Metallurgy, Pembroke Street, Cambridge, CB2 3QZ, U.K.
[2] TWI, Granta Park, Great Abington, Cambridge, CB1 6AL, U.K.

ABSTRACT

This work analyses the influence of plastic strain on cleavage fracture in a lower bainitic Grade 450EMZ steel. It is shown that a dual stress/plastic strain criterion is needed to describe the conditions of cleavage initiation and early propagation. This serves to explain why inconsistent and/or unrealistic shape factor estimates for stress-only Weibull distributions of cleavage strengths may be often encountered in the literature. The general ability of small-scale yielding expressions to describe the failure probability of toughness specimens is re-explained in terms of the plastic strain evolutions in fracture specimens.

KEYWORDS

Cleavage fracture, local approach, constraint, small-scale yielding conditions, bainitic steel, plastic strain

INTRODUCTION

The cumulative failure probability by cleavage is commonly expressed in terms of a Weibull distribution:

$$P_f = 1 - \exp\left(- \int_{V_p} \left(\frac{\sigma - \sigma_{th}}{\sigma_0} \right)^m dV \right) \quad \textbf{(1)}$$

where m, σ_0 are, respectively, the shape and scaling factors, σ_{th} is a threshold stress below which there is zero probability of failure, V_p is the plastic zone size (or some fraction thereof) and σ is generally the maximum principal stress [1-3]. In the particular case of small-scale yielding (SSY), the integration in Eqn. 1 can be solved as a closed-form expression, as shown by several authors [1-3].

$$P_f = 1 - \exp\left(- \frac{B}{B_0} \left(\frac{\delta_c}{\delta_0} \right)^\alpha \right), \quad \alpha = 2 \quad \textbf{(2)}$$

In Eqn. 2, B is the fracture specimen thickness corresponding to the critical Crack Tip Opening Displacement (CTOD) values, δ_c, B_0 is a reference thickness, α is the shape factor and δ_0 is the CTOD value at which a specimen of thickness B_0 will have a 63.2% failure probability. Eqn. 2 has the form of a Weibull distribution with a fixed value of 2 for the shape factor α. If expressed in terms of K_{JC} or *J*-Integral, α equals 4 and 2, respectively. Eqn. 2 can be modified to account for the existence of a threshold toughness δ_{min}:

$$P_f = 1 - \exp\left\{-\frac{B}{B_0}\left(\left(\frac{\delta_c}{\delta_0}\right)^2 - \left(\frac{\delta_{min}}{\delta_0}\right)^2\right)\right\} \quad (3)$$

However, Wallin and Anderson et al. [2,3] found that Eqn. 3 did not adequately describe the true fracture behaviour. They suggested [2,3] that a better fit to the δ_c-results was obtained if P_f was arbitrarily re-written as a three-parameter Weibull distribution:

$$P_f = 1 - \exp\left\{-\frac{B}{B_0}\left(\frac{\delta_c - \delta_{min}}{\delta_0 - \delta_{min}}\right)^{\alpha}\right\}, \quad \alpha = 2 \quad (4)$$

Eqns. 2, 3 and 4 serve as the foundation of many models to quantify size effects and address the inherent probabilistic nature of cleavage fracture [1-3]. Eqn. 4 has been extensively validated on a wide range of steels and forms part of the new ASTM E 1921-97 to describe toughness scatter and size effects. The less flexible Eqn. 2 has also proved to work reasonably well, even if strict SSY conditions are not satisfied [4]. The good consistency of Eqn. 2 contrasts with the difficulty in establishing typical values for the parameters (often called Weibull parameters) in Eqn. 1: in a recent round-robin, estimates for *m* were found to vary from 10 to 50 for similar structural steels [5]. As pointed out by many researchers [1-3], Eqn. 2 actually predicts that, under SSY conditions, the scatter of fracture toughness is independent of the cleavage initiator distribution. The only material characterizing parameter is J_0, since the scale factor of 2 results from the weakest-link and SSY assumptions. However, it was shown [6] that an infinite number of possible parameter pairs (*m*, σ_0) or sets (*m*, σ_0, σ_{th}) in Eqn. 1 lead to the same value of J_0 and this could explain the difficulty in finding consistent *m* values. Another answer, examined below, is likely to be that the special representation of the failure probability in Eqn. 2, derived from the assumption that the stress field is self-similar in the plastic zone, indirectly addresses the effects of plastic strain on cleavage fracture. The discussion is based on Eqn. 2 rather than Eqn. 4, because Eqn. 4 has no theoretical basis yet [3].

INFLUENCE OF PLASTIC STRAIN ON MODELS PREDICTIONS

The above proposal has been investigated using CTOD results from a Grade 450EMZ lower bainitic steel plate produced according to BS 7191. The microstructure of Grade 450EMZ is shown in Figure 1. The data sample consisted of eighteen small 10×10 mm^2 (referred to as Set 1) and twenty full-thickness 50x50 mm^2 (referred to as Set 2) Single Edge Notch Bend (SENB) specimens with a nominal crack depth to width ratio a_0/W of 0.5. The small and full-thickness SENB specimens were tested in

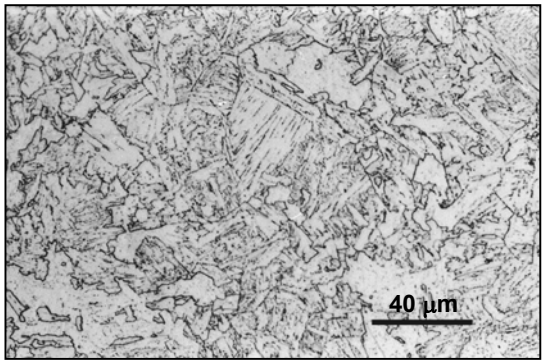

Figure 1: **Grade 450EMZ microstructure**

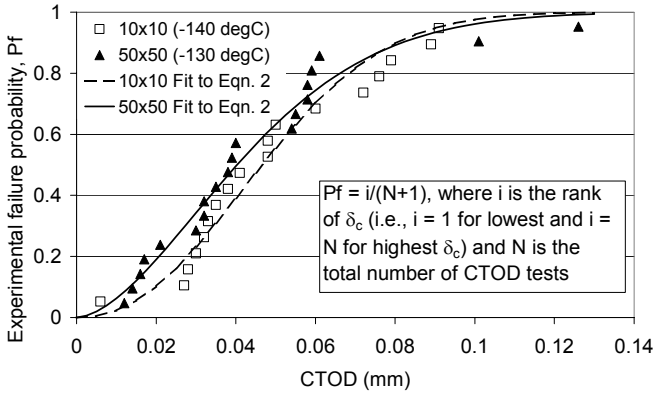

Figure 2: **δ_c-results for the SENB specimens**

three point bending, according to BS 7448, at temperatures of -140°C and -130°C respectively. The CTOD results are plotted in Figure 2. All specimens exhibited cleavage fracture without prior ductile tearing.

Fractographic analyses were carried out on a scanning electron microscope (SEM) to investigate the conditions of cleavage initiation. Most specimens of Set 1 and a few specimens of Set 2 were selected for comparison, particularly specimens that fractured at a high or a low CTOD. The main initiation point was determined using river lines patterns and its distance from the crack tip was measured. In all cases, it was found that cleavage initiated at grain boundaries. However, notable differences in the initiation conditions existed for specimens with toughness lying at the extremes of the CTOD values range. In Set 1, the very low toughness of one specimen (δ_c = 0.006 mm) is explained by an unexpected early intergranular failure that then changed into transgranular cleavage. For specimens with the highest CTOD values, the initiation points were found to be located closer to the crack tip than in most specimens with lower CTOD, in regions where microductile behaviour (microvoids) began to occur.

Finite element (FE) models for both geometries [7] were used to infer the original location of the initiation sites in the specimen before loading. For simplicity, the initiation points were assumed to lie in the plane of the fatigue crack. The distance from the crack tip to the peak stress occurring on the crack plane was also determined in the undeformed configuration at different CTOD values. Both distances are plotted against the critical CTOD values for both geometries in Figure 3 (no data point for specimen 2 of Set 1 is plotted, as no clear initiation point could be found in the intergranular fracture zone). Figure 3 clearly shows that initiation points can be divided into two groups with different nucleation conditions: one, containing most results (Group 1), the other one containing only the highest δ_c-values of the two geometries (Group 2). Group 1 lies above Group 2, expressing the tendency of cleavage nucleating nearer to the crack tip at higher CTOD. Secondly, all initiation points lie below the "peak stress lines", which indicates that all initiation points were located between the crack tip and the peak stress location. There is also a general tendency for the distances of both groups to increase proportionally with CTOD, or equivalently with peak stress location distances, so that both groups remain at an approximately constant distance from the peak stress position.

These observations confirm some well-known results [8]: cleavage is stress-controlled and sufficient plastic strain is needed to achieve nucleation. The fact that cleavage is stress-controlled implies that nucleation sites are to be expected around the maximum stress value, which is the case, since the initiation point location follows the peak stress location as it moves away from the crack tip as loading increases. However, initiation points are not found at the peak stress location, but closer to the crack tip, which expresses the necessity for sufficient plastic strain to nucleate a microcrack, yet still enough tensile stress to propagate it. Further supporting evidence is the fact that all initiation points have "experienced" the maximum stress at some time during the specimen loading, but this was not coincident with failure. Indeed, ahead of a blunting crack in SSY, the maximum tensile stress stays essentially constant as it spreads with increasing load. Any point of the specimen which "experienced" the peak stress will therefore have been subjected approximately to the maximum tensile stress value developing in the specimen. The CTOD value at which the peak stress position coincided with the later initiation point location can be inferred from Figure 3. It corresponds to the CTOD value at the intersection between the relevant peak stress line and a horizontal line passing through the data point of interest. For data point A (δ_c = 0.06 mm) in Figure 3, this gives a CTOD of 0.035 mm. Figure 3 links

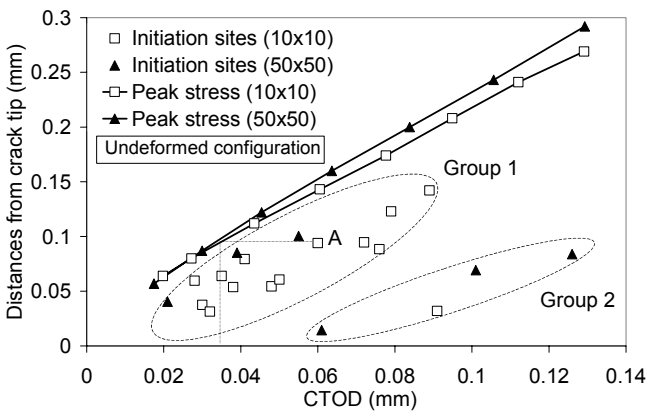

Figure 3: **Initiation site and peak stress distances v's**

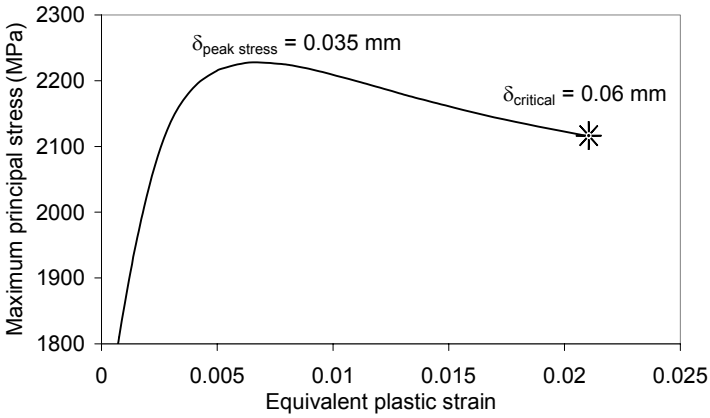

Figure 4: **$\sigma - \varepsilon_p$ history of data point A**

with Figure 4, showing the maximum principal stress – equivalent plastic strain history up to failure for point A evaluated from FE calculations. Finally, it is noted that a great deal of the δ_c-results scatter is due to the varying location of the critical nucleation sites relative to the crack tip, implying both that nucleation leading to total failure is rare and that the critical nucleators are scarce in the present material.

Although final fracture is still stress-controlled, the necessary attainment of a critical plastic strain level invalidates Eqn. 1, which does recognize the necessity of plastic strain in the cleavage process through V_p, but does not account for the determinant role of both its magnitude and build-up. The stress-only description of cleavage in Eqn. 1 inherently implicates that all potential nucleators are created at the onset of plasticity and that their number keeps constant with further plastic deformation [1]. Whilst this may have been a reasonable assumption for the steels investigated at the time, the present results indicate a significant difference for a more modern steel. They show that regions experiencing the highest tensile stresses may be less critical than regions with lower stresses but higher plastic strain levels. Interestingly, the invalidation of Eqn. 1 may explain the unrealistically high values that are sometimes obtained for the scale factor estimate $\hat{m}$. As the above results suggest, the actual risk of failure, P_f, rises with increasing plastic strain as well as with stress. If Eqn. 1 is applied to describe the toughness scatter for the present material, the left-hand side of Eqn. 1, given by the experimental results, would rise more quickly than predicted by the right-hand side, which scales with stresses only. The data set of stresses would therefore wrongly appear to be not very scattered relative to the evolution of P_f and this would be "corrected" through an unrealistically large value of $\hat{m}$. Application of Eqn. 1 to the 10×10 mm^2 toughness results e.g. lead to $\hat{m}$ = 44.7, which is certainly an overestimation if one believes the last argument, yet of a magnitude often encountered in the literature. Inconsistent values of $\hat{m}$ in different geometries could also be explained by the different evolutions of the plastic strain according to the constraint level.

Such plastic strain effects should also invalidate Eqns. 2 and 3, since they are based on the same assumptions as Eqn. 1. The maximum likelihood (ML) method was used to fit the δ_c-results to Eqn. 2, with B_0 equal to 10 and 50 mm for Set 1 and 2 respectively (that is δ_0-values are not size-corrected relative to any reference B_0 to be able to compare them directly). The two fitting curves are plotted in Figure 2. The ML estimates $\hat{\alpha}$ and $\hat{\delta}_0$ were found to be equal to 2.2 and 0.055 mm for Set 1 and 1.7 and 0.050 mm for Set 2. The 95% confidence intervals for $\hat{\alpha}$, $CI_\alpha^{0.95}$, were [1.5, 3.2] and [1.2, 2.4] for Sets 1 and 2, respectively. These results are in good agreement with the theoretical value of 2 for α under SSY conditions and illustrate the point raised in the introduction, i.e. the ability of Eqn. 2 to describe toughness data even if Eqn. 1 produces suspicious results. Note also that the δ_0-values are not very different, which indicates a low size effect. A qualitative explanation for both points is proposed below.

GENERAL APPLICABILITY OF CLOSED-FORM SSY EXPRESSIONS

For every specimen examined on the SEM, a unique fracture origin was found, which is a prerequisite to the correct application of Eqns. 1 to 4 to describe the scatter in toughness results. However, considering the small specimen fracture tests, at least three different nucleation processes could be identified, namely: an intergranular failure type transforming to cleavage, a transgranular type with moderate plastic strain (Group 1) and a transgranular type with large plastic strain and microductility (Group 2). It was mentioned in the previous section that Eqns. 1 to 4 were not derived to account specifically for the change in plastic strain inside the plastic zone. Also, each equation is meant to address only one nucleating process at a time, not all of them (as was done in the preceding section), unless they are modified to do so. Here, the choice is made to address only the δ_c-values originating from the main nucleation mechanism, i.e. these of Group 1. The specimens that were not analyzed on the SEM are assumed to belong to Group 1, given that their δ_c-values fall in its range. A fit to Eqn. 2 of these δ_c-values only gives the following ML estimates: $\hat{\alpha}$ = 2.72, $\hat{\delta}_0$ = 0.056 and $CI_\alpha^{0.95}$ =

[1.87, 3.94] for the 10×10 mm² specimens, $\hat{\alpha}$ = 2.46, $\hat{\delta}_0$ = 0.041 and $CI_\alpha^{0.95}$ = [1.67, 3.63] for the 50×50 mm² specimens. Once again, the estimated values for α approach the theoretical value of 2, but the size effect is this time more apparent.

Following the discussion in the previous section, the above verification of Eqn. 2 is clearly not due to the evolution of the stress field in the SENB specimens alone. An alternative explanation is proposed in terms of a dual stress - plastic strain criterion. The model retains the fundamental assumptions that cleavage follows a weakest-link principle, is stress-controlled and that plastic flow is necessary for nucleation. To simplify, it is assumed that nucleation is controlled only by plastic strain and that propagation is controlled only by tensile stress. It is considered here that the material fractures at a certain critical tensile stress, constant over the range of present testing temperatures, i.e. the scatter is expected to be due only to the initiators location and plastic strain. There is experimental evidence showing that the number of nucleated microcracks increase with plastic strain and decreasing temperature [9-11]. The number of cracked carbides was found to increase proportional with plastic strain by Gurland [9] and Brindley [10], results approaching proportionality were also obtained by Lindley et al. [11]. At some temperatures, interpolation by a power law was more appropriate [10]. It is considered here that, for a small range of critical plastic strain values, at a given temperature, a linear relationship can be used. The influence of temperature will be inferred later. The last assumption is that if a fresh nucleated microcrack is not propagated immediately, that is if the tensile stress is less than the critical tensile stress, σ_{crit}, it blunts and will not be able to contribute to failure anymore. The cumulative cleavage failure probability can then be written as:

$$P_f = 1 - \exp\left\{-\int_{V_p}\left[\int_0^{\varepsilon_p}\Phi(\sigma)\,d\varepsilon_p\right]dV \Big/ \Sigma_0(T)\right\} = 1 - \exp\{-\Sigma/\Sigma_0(T)\} \quad , \quad \text{where} \begin{cases}\Phi(\sigma)=1 & \text{if} \quad \sigma \geq \sigma_{crit}\\ \Phi(\sigma)=0 & \text{if} \quad \sigma < \sigma_{crit}\end{cases} \qquad \textbf{(5)}$$

ε_p is the equivalent plastic strain, $\Sigma_0(T)$ is a scaling factor dependent on temperature so that P_f = 63.2% if $\Sigma = \Sigma_0(T)$, T is the test temperature. Comparison with Eqn. 2 shows that under SSY, this occurs if $\delta = \delta_0$ (where δ_0 is no size-corrected, i.e. B = B_0). The double integral Σ, representing the risk of failure, increases in proportion to the plastic zone and the plastic strain. Note that only the fraction of ε_p, which was coincident with a stress above the critical value ($\sigma \geq \sigma_{crit}$), is integrated, such that only the nucleated microcracks capable of propagation are considered. $\Sigma_0(T)$ is introduced as a material parameter, which accounts for the effect of temperature on the microcracks nucleation rate. $\Sigma_0(T)$ is therefore expected to decrease with temperature. Σ was calculated numerically from FE results, at –140°C for the 10×10 mm² geometry and at –130, –140, –150 and –196°C for the 50×50 mm² geometry. σ_{crit} was chosen equal to 1800 MPa and only $\varepsilon_p > 0.2\%$ data were integrated. The Σ-values are plotted against CTOD in Figure 5: it can be shown that they are proportional to δ^2. Assuming the model is correct, this would explain why Eqn. 2 is systematically reasonably verified, while Eqn. 1 may not apply. The values larger than 2 for the α-estimates obtained here may be due to the use of the two-parameter Weibull distribution (δ_{min} = 0) [2]. Σ_0 was calculated for the 10×10 mm² geometry at -140°C, with δ_0 equated to the ML estimate $\hat{\delta}_0$ = 0.056 determined from the δ_c-values: it was found equal to 0.022 mm³. Knowing this value, $\hat{\delta}_0$ for the 50×50 mm² geometry tested at -140°C can then be inferred from Figure 5 and is equal to 0.024 mm. Using Eqn. 2 with α equal to the theoretical value of 2, the

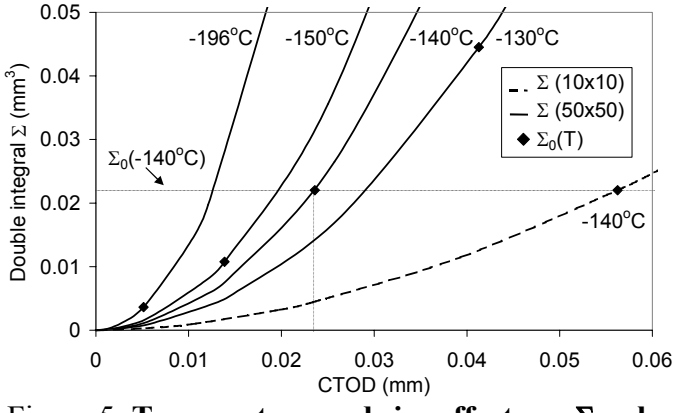

Figure 5: **Temperature and size effects on Σ-values v's**

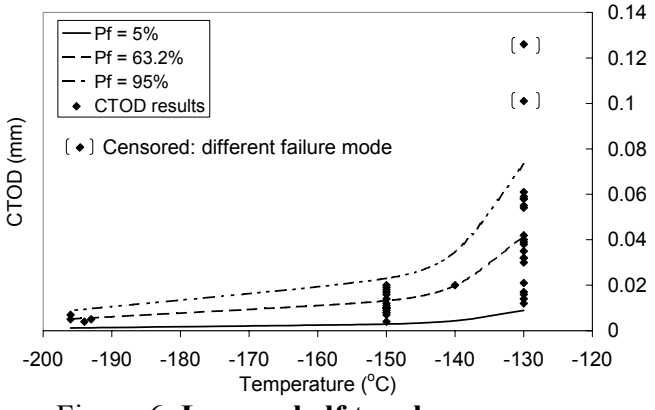

Figure 6: **Lower-shelf toughness**

model predicts a size effect of $(0.056/0.024)^2 = 5.44$, which is only just higher than the expected 5-fold increase. The difference may be explained by the slightly higher triaxiality developed in the 50×50 mm^2 geometry. The next step consists of predicting the toughness scatter at other temperatures (for specimens failing by the same initiation process). As the evolution of $\Sigma_0(T)$ with temperature is not known, it is interesting to predict the expression for $\Sigma_0(T)$, assuming the model is valid over the range of testing temperatures. CTOD measurements at –150 and –196°C were available for the 50×50 mm^2 geometry: all δ_c-values were considered to belong to Group 1's nucleation type and the calculated ML estimates for δ_0 were respectively 0.014 and 0.005 mm. This enabled the determination of $\Sigma_0(T)$ at –130, –150 and –196°C, and it was found 0.045, 0.011 and 0.0036 mm^3 respectively (Figure 5). Let $\kappa(T)$ be a temperature correction factor so that $\kappa(T)\times\Sigma_0(T) = \Sigma_0(T_0) =$ constant. Here, T_0 is arbitrarily fixed to -130°C, thus $\kappa(-130°C) = 1$ and $\Sigma_0(T_0) = 0.045$. It can be shown that, when plotted against temperature, the four values of $\kappa(T)$ at –130, –140, –150 and –196°C are approximately aligned, increasing with decreasing temperature. A linear interpolation gives $\kappa(T) \approx \kappa(T_0)-0.174(T-T_0)$, for $T \leq T_0$. Figure 6 shows the lower-shelf toughness curves for P_f equal to 5, 63.2 and 95% predicted from Eqn. 5 where $\Sigma_0(T)$ is replaced by $0.045/[1-0.174(T+130)]$. The good agreement with the experimental results is expected since $\kappa(T)$ was calculated to tune the model to the results. Note that the two 50×50 mm^2 censored specimens (that belonged to Group 2) lie well above the 95% toughness curve. The next stage to valid the present proposal would be to determine the expression for $\kappa(T)$ from direct microcracks nucleation rate measurements.

CONCLUSION

This work has clearly unveiled the existence of a dual stress/plastic strain criterion for cleavage fracture in Grade 450EMZ. This invalidates the stress-only description that is commonly used to derive the theoretical probability of fracture by cleavage in steel. It has been shown that discounting the effect of plastic strain on the risk of failure explains the inconsistent and/or unrealistic values that are sometimes obtained for the shape factor *m* when using Eqn. 1. Classical expressions for assumed SSY conditions such as Eqn. 2 remained valid to describe the distribution of Grade 450EMZ toughness values, but it is suggested that this is because they are able to indirectly address the effects of plastic strain on cleavage fracture. An alternative expression has been developed which allows for the effect of plastic strain. This shows potential to accurately predict fracture toughness transition.

ACKNOWLEDGEMENTS

Thanks are due to Professors A. H. Windle FRS and D. J. Fray FREng for the provision of laboratory facilities and TWI for the mechanical testing. The work reported here has been carried out under the PTP (Postgraduate Training Partnership) scheme which is funded by DTI and EPSRC.

REFERENCES

[1] **Beremin, F. M. (1983). *Met. Trans. A,* 14A, 2277-2287.**

[2] **Wallin, K. (1984). *Eng. Fract. Mech.*, 67, 1085-1093.**

[3] **Anderson, T. L., Stienstra, D. and Dodds, R. H., Jr. (1994). In: *Fracture Mechanics: Twenty-Fourth Volume, ASTM STP 1207,* pp. 186-214, Landes, J. D., McCabe, D. E. and Boulet, J. A. M. (Eds). American Society for Testing and Materials, Philadelphia.**

[4] **Pineau, A. (1992). In: *Topics in Fracture and Fatigue*, pp. 197-234, Argon, A. S. (Eds). Springer-Verlag, New York.**

[5] **Brocks, W. (1996). In: *Proceedings of the 11th European Conference on Fracture, Poitiers, France.* pp. 1-4, Petit, J et al. (Eds), EMAS, U.K.**

[6] **Gao, X., Ruggieri. C. and Dodds, R. H., Jr. (1998). *Int. Jour. Frac.*, 92, 2, 175-200.**

[7] Bordet, S. R., Karstensen., A. D., Wiesner, C. S. and Knowles, D. M. (submitted to *Comp. Mat. Sci.*).
[8] Chen, J. H., Wang, G. Z., Wang, Z., Zhu, L. and Gao, Y. Y. (1991). *Met. Trans. A*, 2287-2296.
[9] Gurland, J. (1972). *Acta Met.*, 20, 735-741.
[10] Brindley, B. J. (1970). *Acta Met.*, 18, 325-329.
[11] Lindley, T. C., Oates, G. and Richards, C. E. (1970). *Acta Met.*, 18, 1127.

ORAL/POSTER REFERENCE: ICF1001039PR

EFFECTS OF STATIC STRESS ON ANODIC POLARIZATION BEHAVIOR OF Ti-4.5Al-3V-2Mo-2Fe ALLOY

Nobukuni Hyakutake[1], Masashi Takagaki[1], Jun Komotori[1],
Atsushi Ogawa[2], Kuninori Minakawa[3]

1 Department of Mechanical Engineering, Keio University, 3-14-1, Hiyoshi, Kohoku-ku, Yokohama 223-8522, Japan
2 NKK Co. Ltd.; 3 NKK America Inc.

ABSTRACT

Corrosion behavior of implant metals having applied stress must be quantified because these metals are often used under stress *in vivo*. The aim of the present study is to clarify the effects of static stress on corrosion behavior of Ti-4.5Al-3V-2Mo-2Fe alloy in a simulated physiological environment. An anodic polarization procedure was performed with applied static stresses in Ringer's solution at 37°C, from a free corrosion potential up to a potential of 4.0 V higher than the free corrosion potential. Then the potential was scanned in the cathodic direction. The specimen surfaces were observed using a Scanning Electron Microscope.

We conclude that constant compressive stress up to –800 MPa and tensile stress of below 100 MPa have little effect on corrosion behavior because both of the anodic polarization curves and the features of corroded surfaces were similar to those under zero stress. With applied static tensile stresses of 200 ~ 800 MPa, current density increased suddenly at about 4 V vs. SHE, which is about 1 V higher than the breakdown potential. Before the sudden current density increase, the corrosion reaction seems to be the same as the corrosion reaction under zero stress because the anodic polarization curves and the features of corroded surfaces were similar to those without an applied stress. The observations of corroded surfaces indicate that sudden current density increase at about 4 V vs. SHE is due to great dissolution in a localized area.

KEYWORDS

Titanium alloy, Biomaterial, Passivity, Corrosion resistance, Corrosion fatigue

1. INTRODUCTION

Corrosion of implant metal is detrimental for two reasons. First, corrosion fatigue is a major risk factor in fracture of implant metals [1]. Second, released metallic ions may be toxic [2]. Therefore, corrosion of implant alloys is a serious problem. Not only simple corrosion behavior but also corrosion behavior with applied stress must be clarified because implant metals are often used under stress *in vivo*. In recent years, titanium alloys have been widely used as biomaterials. Although the effects of cyclic load on corrosion behaviors of titanium alloys have been reported [3], no detail work has focused on the effects of static stress on its' corrosion behavior [4]. In the present study, to clarify the effects, anodic polarization tests were carried out in constant stress condition.

2. EXPERIMENTAL

2.1. Materials

A β rich, α+β type titanium alloy (Ti-4.5Al-3V-2Mo-2Fe; with the commercial name of SP-700) was used. This alloy was annealed at 800°C for 8 hours. The configuration of the test specimens is shown in Figure 1. The surfaces of the specimens were ground and polished electrolytically. To avoid preferential corrosion of edges, the specimens were covered with inert coatings, leaving an exposed surface area of 1 cm^2 (Figure 1).

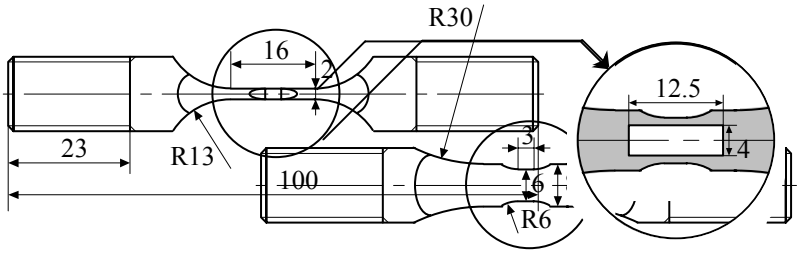

Figure 1: Configuration of the specimen

2.2. Corrosion test

Figure 2 shows the schematic of the corrosion test system; a platinum auxiliary electrode and an Ag/AgCl reference electrode were used. A Ringer's solution, a simulated physiological solution was used as the electrolyte. This solution was kept at a temperature of 37°C and was exposed to the atmosphere.

Fist, a specimen was mounted on a polarization cell and on the chuck of a servohydraulic test system. Then static stress was applied using the servohydraulic test system followed by filling the polarization cell with the solution. Cyclic, anodic, potentiodynamic polarization tests were carried out with an automatic polarization system. The open-circuit potential, i.e., the corrosion potential, was recorded after maintaining constant stress for 30 min. The potential was potentiostatically kept to the measured corrosion potential for 1 hour then scanned anodically at a scan rate of 0.167 mV/s, from the corrosion potential, up to the potential of 4.0 V higher than the corrosion potential. Then the potential was scanned in the cathodic direction at the same scan rate until the applied potential reached the corrosion potential. Such anodic polarization tests were conducted

without an applied stress, with applied compressive stresses of –800 and –200 MPa, and with applied tensile stresses of 100 ~ 800 MPa. The specimen surfaces were observed using a Scanning Electron Microscope (SEM) to examine corrosion reaction of the samples.

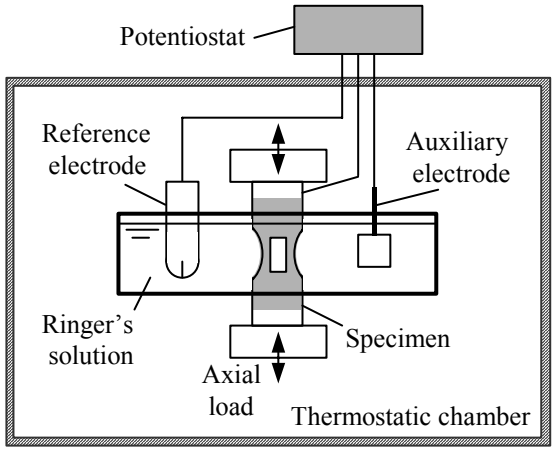

Figure 2: Schematic of the corrosion test system

3. RESULTS

3.1. Anodic polarization curve of the specimen without an applied stress

The solid line in Figure 3 (a) shows the anodic polarization curve of the specimen without an applied stress. It can be seen that passive current density is 3.0 $\mu A/cm^2$ (1 V vs. SHE) and breakdown potential is 2.5 V vs. SHE (We define the breakdown potential as the potential at which current density exceed 10 $\mu A/cm^2$). Above the breakdown potential, the current density increases significantly as the potential becomes more positive because pitting initiates and propagates. This region of the anodic polarization curve is called the transpassive region. The reverse sweep of the scan closely retraces the path of the forward scan. This indicates that the pitted region repassivates immediately. Consequently, Ti-4.5Al-3V-2Mo-2Fe alloy has a high corrosion resistance in Ringer's solution.

3.2. Anodic polarization curves of the specimens under applied compressive stresses

The Anodic polarization curves of the specimens with applied static stresses of –200 MPa (a dotted line in Figure 3 (a)) and –800 MPa were similar to the ones of the specimen without an applied stress. Figure 4 shows the passive current densities (solid squares) and breakdown potentials (open circles) of these tests. These values seem to be independent of stresses between 0 ~ -800 MPa. This implies that static compressive stress has no significant effect on corrosion behavior.

3.3. Anodic polarization curves of the specimens under applied tensile stresses

The anodic polarization curve of the specimen under an applied stress of 100 MPa is shown in the dotted line in Figure 3 (b). The curve is similar to the one without an applied stress. This suggests that static tensile stress of 100 MPa has no effect on corrosion behavior.

During the anodic sweep at below 3.8 V vs. SHE, the anodic polarization curve of the specimen under an applied tensile stress of 200 MPa (the broken line in Figure 3 (b)) is similar to the one of the specimen without an applied stress (the solid line in Figure 3 (a)). As shown in Figure 4, in this anodic polarization test, the passive current density (the solid square) and the breakdown potential (the open circle) are approximately the

same as those of the specimen without an applied stress. However, at 3.8 V vs. SHE in a transpassive region, the current density suddenly increased to 200 mA/cm^2, and stayed at a high value during the cathodic sweep. Such sudden current density increase was also found with applied tensile stresses of 400 ~ 800 MPa at 3.8 ~ 4.1 V vs. SHE. These results suggest that static tensile stress of 200 ~ 800 MPa has no effect on corrosion behavior at below or about 4 V vs. SHE. However, this stress greatly accelerates dissolution at this potential in a transpassive region.

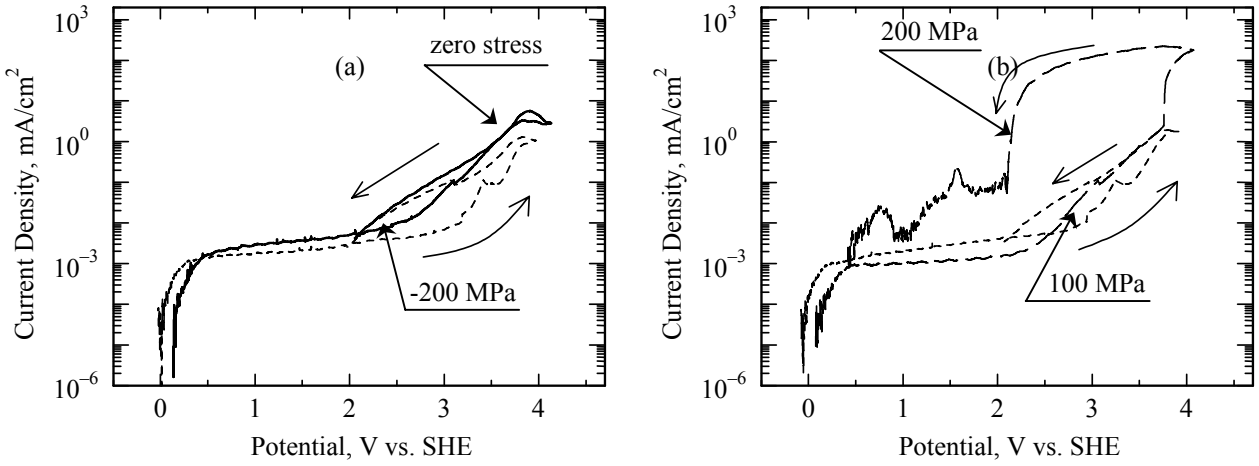

Figure 3: Anodic polarization curves for Ti-4.5Al-3V-2Mo-2Fe alloy in Ringer's solution at 37°C

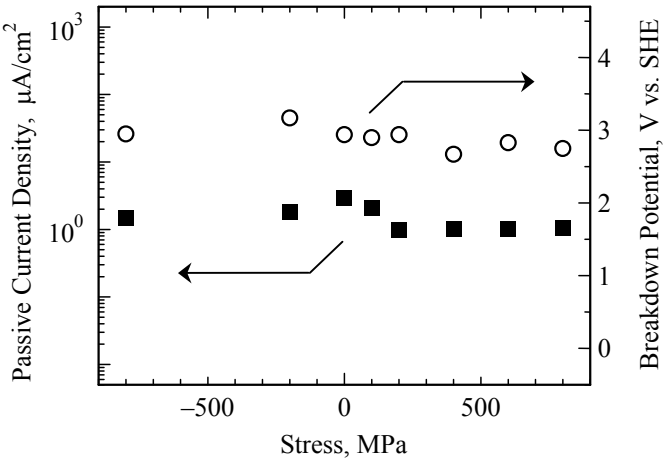

Figure 4: Passive current densities and breakdown potentials obtained by anodic polarization tests

3.4. Observation

In order to examine the corrosion reaction under tensile stress before the sudden current density increase at about 4 V vs. SHE, an anodic polarization test was conducted under an applied tensile stress of 400 MPa. After the current density reached 1 mA/cm^2, the test was terminated and the surface of the specimen was observed using SEM. A Typical feature of the corroded surface is shown in Figure 5. Dissolutions in the β-phase and corrosion products were found. Similar phenomena were also observed after the anodic polarization tests with compressive stress of –200 MPa and zero stress. Therefore, the corrosion reaction with either tensile stress or compressive stress turns out to be the same as the corrosion reaction under zero stress before sudden current density increase at about 4 V vs. SHE.

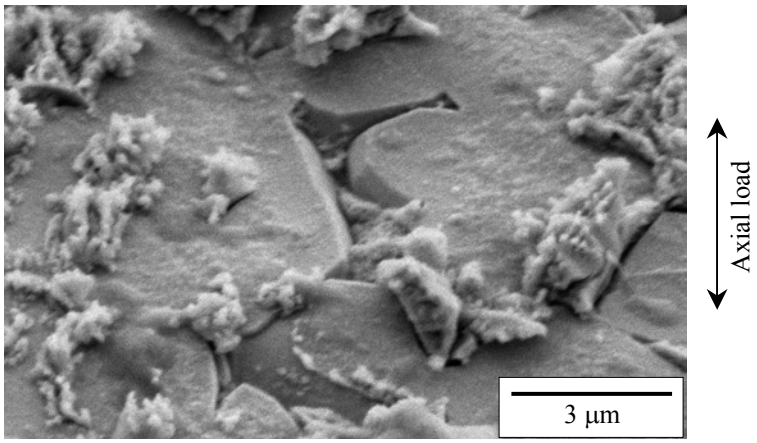

Figure 5: SEM observation of dissolutions in the β-phase and corrosion products

To explain the reason for the sudden current density increase at about 4 V vs. SHE, an additional anodic polarization test was carried out with a tensile stress of 400 MPa. The test was terminated 7 min after sudden increase, and the surface of the specimen was examined. Macroscopic damage at the center of the test surface was observed (Figure 6). However, the rest of the surface was similar to that of Figure 5. This means that the sudden increase in current density is probably because of a great dissolution in the localized area as shown in Figure 6.

Most of the test surfaces were damaged similarly and there was only one damage on one test surface after anodic poralization tests with constant stresses of 200 ~ 800 MPa.

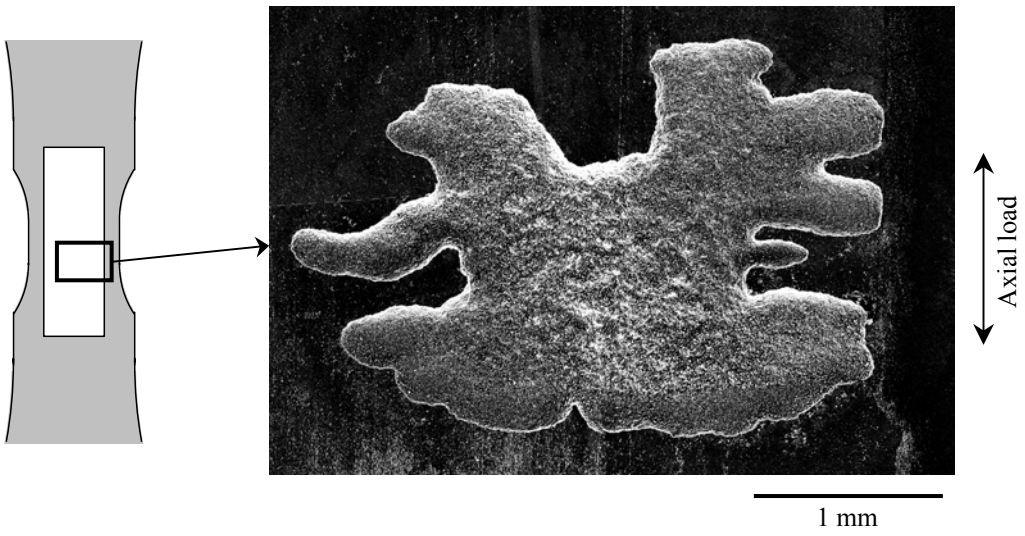

Figure 6: SEM observation of large damage at the center of test surface

4. DISCUSSION

In this study, the effects of static stress on corrosion behavior of Ti-4.5Al-3V-2Mo-2Fe alloy were investigated. We conclude that constant compressive stress and tensile stress of below 100 MPa have little effect on corrosion behavior because the anodic polarization curves and the feature of the corroded surfaces were similar to the one under zero stress (Figures 3 (a), and 4).

With applied static tensile stresses of 200 ~ 800 MPa at below or about 4 V vs. SHE, the anodic polarization curves and the surface feature were also similar to those without an applied stress (Figures 3, 4, and 5). Thus, we conclude that the corrosion reaction with static tensile stress of 200 ~ 800 MPa at below or about 4 V vs. SHE is the same as those under zero stress.

On the other hand, with static tensile stresses of 200 ~ 800 MPa, current densities increased suddenly at about 4 V vs. SHE in a transpassive region (Figure 3 (b)). To investigate the reason, anodic polarization with an applied stress of 400 MPa was conducted and terminated 7 min after sudden current density increase. Macroscopic damage was observed on the test surface (Figure 6) while the rest of the surface was similar to the one without an applied stress. From these results, static tensile stress of 200 ~ 800 MPa makes great dissolution in a localized area at about 4 V vs. SHE in a transpassive region. The shape of the damage (Figure 6) suggests that microscopic damage spread to the macroscopic damage. With these stresses, current densities kept at a high value after sudden current density increase and there was only one damage on each test surface after the anodic polarization tests. These results suggest that localized macroscopic damage propagates over most of the test surface.

In conclusion, static tensile stress of 200 ~ 800 MPa greatly accelerates dissolution at about 4 V vs. SHE in a transpassive region. This phenomenon might be the cause of corrosion fatigue and toxicity *in vivo*. Further study of the influence of stress on corrosion behavior of titanium alloy is needed to examine whether this phenomena would take place *in vivo*.

5. CONCLUSIONS

In the present study, anodic polarization tests were carried out in constant stress conditions to clarify the effects of static stress on corrosion behavior of Ti-4.5Al-3V-2Mo-2Fe alloy in Ringer's solution at 37°C. We conclude as follows.

Static compressive stress up to -800 MPa and tensile stress of below 100 MPa appears to have little effect on corrosion behavior.

With applied static tensile stresses of 200 ~ 800 MPa, current density increases suddenly during the anodic polarization tests at about 4 V vs. SHE, which is about 1 V higher than the breakdown potential for pitting. At below or about 4 V vs. SHE, the corrosion reaction is the same as the corrosion reaction under zero stress. On the other hand, great dissolution takes place in a localized area at about 4 V vs. SHE, while the rest of the test surface is similar to the one below this potential.

REFERENCES

1. Sumita, M. (1997) *Journal of Japanese Society for Biomaterials*, 15-5, 240
2. Kawahara, H. (1992) *Bulletin of the Japan Institute of metals*, 31-12, 1033
3. Yu, Q. W., Morita, M., Itoman, M., and Sasada, T. (1993) *Journal of Japanese Society for Biomaterials*, 11-1, 27
4. Bundy, K. J., Marek, M., and Hochman, R. F., (1983) *Journal of Biomedical Materials Research*, 17, 467

ORAL REF: ICF100191OR

EFFECTS OF STRESS RATIO ON STRIATION FORMATION UNDER CYCLIC LOADING CONDITIONS IN POLYMETHYL METHACRYLATE (PMMA)

C. Ishiyama*, M. Kobayashi, T. Asai and Y. Higo

Precision and Intelligence Laboratory, Tokyo Institute of Technology,
4259 nagatsuta-cho, Midori-ku, Yokohama, Kanagawa, JAPAN

ABSTRACT

The fatigue crack propagation tests were performed on an amorphous polymer, poly (methyl methacrylate) (PMMA) to investigate the striation formation mechanisms. A confocal scanning laser microscope was used to observe in-situ crack propagation in compact type (CT) specimens under tensile-tensile fatigue loading conditions. Fatigue cracks usually propagated within the craze which always existed at the crack tip at a relative humidity of 75% and an R-ratio of 0.1-0.5. Craze fragments were observed at the edges of the crack at the maximum load of a loading cycle. However, they disappeared in the subsequent cycle at the R-ratios. This may be because a part of the broken fibrils, which were situated just behind the crack tip, were pushed down by the contact between the fracture surfaces during unloading. This may mark fracture surfaces with striations. However, broken crazes did not disappeared in the subsequence cycle at an R ratio of 0.7. After these tests, fatigue fracture surfaces were observed using a field emission-gun scanning electron microscope (FE-SEM). With increasing R-ratio, striations become less obvious. These results support the contact model for striation formation. According to these results, a striation formation mechanism on PMMA is discussed.

KEYWORDS

striations, polymethyl methacrylate (PMMA), fatigue crack growth, stress ratio

INTRODUCTION

Recently many researchers have been studying crack propagation behavior of glassy polymers under static loading conditions [6, 12] or cyclic loading conditions [2, 3, 9-11] to clarify the mechanisms of crack

propagation.

Crack propagation is strongly affected by plastic deformation at the crack tip and the typical plastic deformation of polymethyl methacrylate (PMMA) is crazing. In our previous study, the vicinity of a crack tip, which was growing in PMMA, was observed in detail using a scanning laser microscope. It was found that the crack usually accompanied a craze and bright bands, which were made of broken craze, were remained along the crack wakes under monotonic loading conditions. Fracture surfaces were even in this case.

However, these bands were not observed under cyclic loading condition but successive ridges were sometimes observed along the crack wakes. Striations corresponded with the valleys between these successive ridges. These results suggest that striations were made by contacts between surfaces during unloading, in other words, closure produces striations on fatigue fracture surfaces of PMMA.

To clarify the effects of closure on striation formation in PMMA, fatigue tests were performed with changing stress ratio. A confocal scanning laser microscope was used to observe in-situ fatigue crack propagation in compact type (CT) specimens. These observations clarify the state of the crack wakes in PMMA at each stress ratio. Moreover, to clarify the effects of R-ratio on striation formation, fatigue fracture surfaces were observed using FE-SEM.

According to all the results, both of a striation formation mechanism and a crack propagation mechanism on PMMA are discussed.

MATERIAL AND EXPERIMENTAL PROCEDURES

Material

The material used in this study was a commercial acrylic cast sheet, 15 mm in thickness, Sumipex supplied by Sumitomo Chemical Co., LTD. Compact type (CT) specimens with dimensions shown in Figure 1(a) were cut from this sheet.

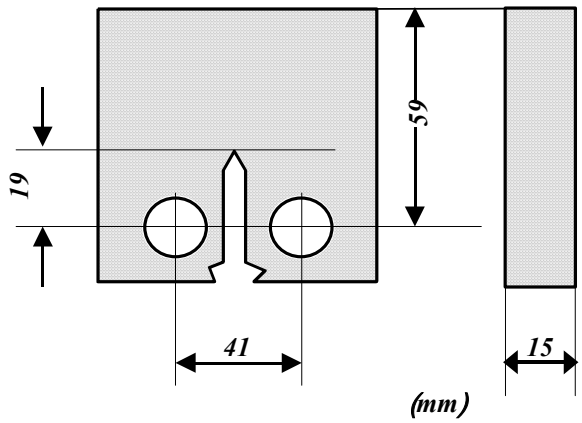

Figure 1: A schematic diagram of a compact type(CT) specimen

The specimens were heat-treated in an oven at a temperature of 363 K for 24 hours to dry and remove any

residual stress.

Prior to the tests, the specimens were kept under a 75% relative humidity condition at a temperature of 293 K for the purpose of adjusting the water content in the specimens, because the humidity condition is optimal for stable crazes growth according to our previous studies [4-5]. All the specimens had been stored in the humidity until the water content in the specimens saturated with the humidity, for more than a year [1].

Experimental procedure

A fatigue testing machine, which can be installed on a scanning laser microscope (SLM) (made by Lasertec Co., Ltd.), has been developed to observe in-situ the crack tip shape on a side surface. The details of the machine are shown in Fig. 2. An ultrasonic motor drives a screw to apply load on a specimen.

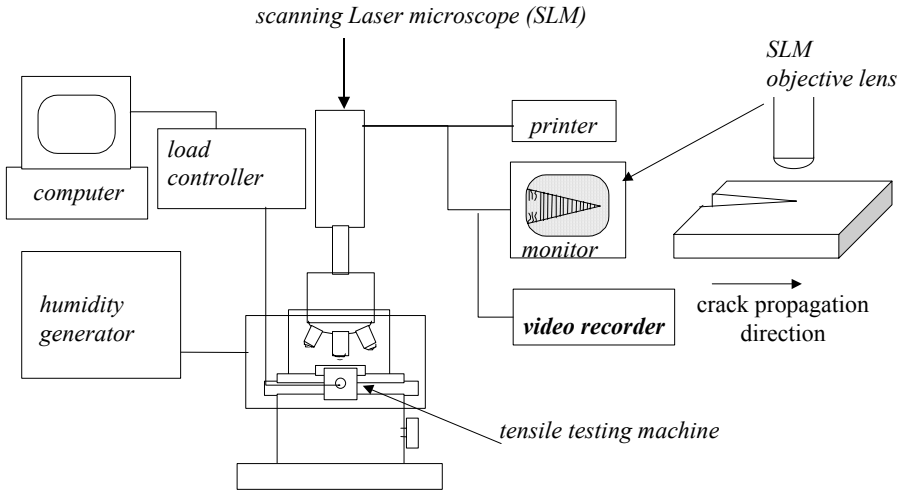

Figure 2: In-situ observation using scanning laser microscope(SLM)

Prior to the crack propagation tests, pre-cracks of 1mm had been introduced to the specimens under a cyclic loading condition (at a mean stress intensity factor (K_{mean}) of 0.26 $MPam^{1/2}$, at an R ratio of 0.1 and at a sinusoidal frequency of 1 Hz).

Tensile load was applied to a specimen until the main crack started to grow and then the load was decreased until the crack stopped growing. This threshold stress intensity for a monotonic loading was defined as K_{th}, which was 0.78 $MPam^{1/2}$, in this study.

Seventy percent of K_{th}, 0.55 $MPam^{1/2}$, was chosen for the maximum stress intensity factor (K_{max}) for the fatigue crack growth tests. Fatigue tests were performed at K_{max} of 0.55 $MPam^{1/2}$- using triangle waves at a frequency of 0.01 Hz and at stress ratios of 0.1, 0.3, 0.5 and 0.7, to clarify the effect of closure on the formation of striations on fracture surfaces. The vicinity of fatigue cracks was observed on a side surface of a specimen with changing R-ratio and the images were recorded using the a video recorder.

After the in-situ observations, the PMMA specimen was broke in two by overloading without unloading to observe the fatigue fracture surface. The fracture surfaces of the specimens were sputter-coated with

osmium and observed using a field emission-gun scanning electron microscope (FE-SEM).

RESULTS AND DISCUSSION

In-situ observation on propagating fatigue crack in PMMA

In this study fatigue crack mostly grew into the craze accompanied the crack and the craze was broken at the midrib. This suggests that fracture surfaces were covered with the fragments of the craze. Previous studies [7, 14] also pointed out that fracture surfaces in PMMA must have thin fracture layer, which was demonstrated by on the evidence that color interference fringes observed on the surfaces.

At low R-ratios of less than 0.5, however, fragments of the craze were hardly observed at the edges of the fatigue crack wakes. In further detail, when the crack just propagated at K_{max} in a loading cycle, fragments of the craze had still remained at the edges of the crack just behind the crack tip, but the fragments disappeared in the subsequent cycle. This may be because the craze fragments were pushed down by contact between the fracture surfaces, in other words, crack closure.

On the other hands, at an R-ratio of 0.7 the fragments remained at the edges of crack wakes after the subsequent cycles. Figure 3 shows the vicinity of the fatigue crack tip after the R ratio was changed from 0.5 to 0.7. This micrograph makes it clear that the craze fragments along the edges of the crack wakes disappeared at an R-ratio of 0.5 but remained at an R-ratio of 0.7. This result shows that closure should collapse the craze fragments layers on fatigue crack propagation in PMMA.

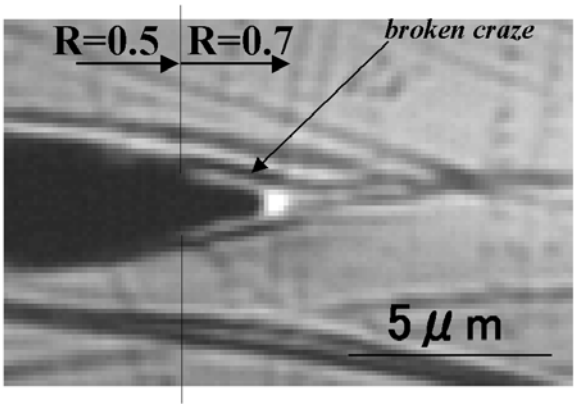

Figure3: A micrograph of a fatigue crack tip, after the stress ratio was changed from 0.5 to 0.7

Striations on the fatigue fracture surface in PMMA

In our previous study [15] we suggested that striations on fatigue fracture surfaces in PMMA might be formed by the contacts between fracture surfaces. This means that it is correct, pushing down the craze fragment layers in each cycle would make a striation.

In FE-SEM observations, striations become less obvious on the fracture surfaces in the material with increasing R-ratio. Figure 4 (a) shows a fatigue fracture surface at which R ratio was just changed from 0.5 to 0.7. At an R-ratio of 0.5 striations, which are partly shown by several arrows in the figure, were narrowly observed, but were not observed at an R-ratio of 0.7 in spite of high magnification as shown in figure 4 (b).

These FE-SEM observations also support that the contact between fracture surfaces should make striations on fatigue fracture surfaces.

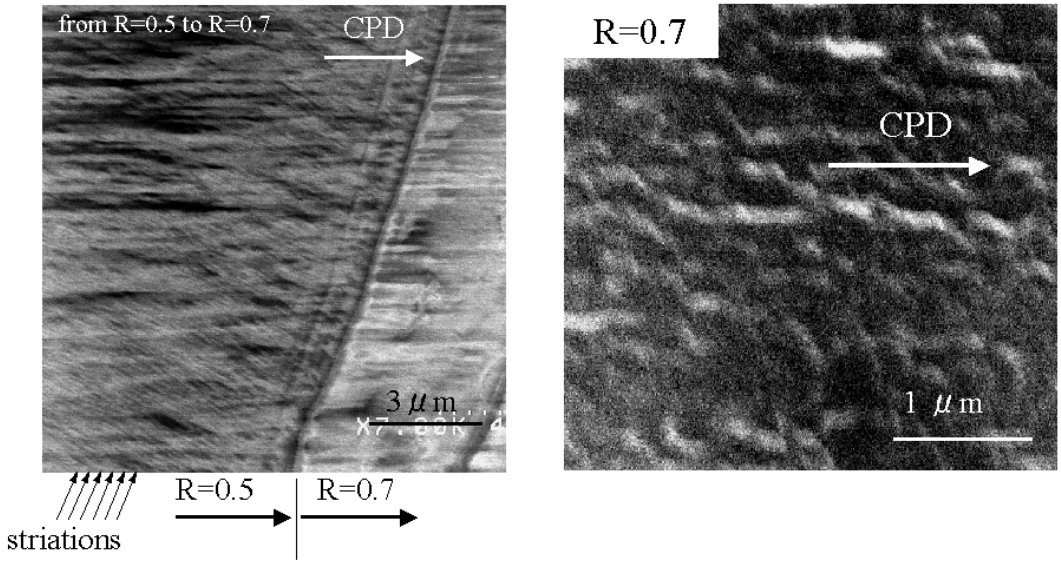

(a) when a stress ratio was changed from 0.5 to 0.7

(b) tested at the stress ratio 0.7

Figure 4: Micrographs of fatigue fracture surfaces

From these results a striation formation mechanism is proposed as follows. A fatigue crack propagates into the midrib of the craze accompanying the crack during a loading of a half cycles and new fracture surfaces are covered with these craze fragments. Then, the crack is closing with unloading of a half cycles and the craze fragments are pushed down by the closure in each cycle. Pushing down the craze fragments in each cycle produce the striations on the fracture surfaces.

Fatigue crack propagation mechanism

A crack does not propagate at a constant K_{max} condition, However, when the load is unloaded and reloaded a crack propagates. This may be because the craze fibrils of the crack tip become weak by unloading and/or reloading. Several researchers [8, 13] suggested that craze fibrils at the crack tip were entangled each other by unloading. This suggests that the critical length for failure of entangled fibrils might become shorter than the fibril length at K_{max} in the previous cycle. The entanglement of fibrils in the craze is one of the possible mechanisms for fatigue crack growth. There is another possible mechanism, which is creep deformation. The strength of the fibrils might decrease by creep deformation, because PMMA is a visco-elastic material. However, the crack did not propagate when the applied load was kept at K_{max} for more than half an hour. Thus, it is difficult to conclude that the creep deformation of fibrils is the main cause of fatigue crack growth in PMMA. It is thus considered that the main cause should be resulted from unloading and/or reloading, for example, the entanglement or any other cause for decreasing the strength of craze fibrils.

CONCLUSIONS

Crack growth behavior in PMMA was investigated by in-situ observation under a scanning laser microscope to clarify the crack propagation process under cyclic loading conditions. The following conclusions are reached;

1. A fatigue crack propagated into the midrib of the craze during loading in each cycle. However, the craze fragments did not remain at the edges of the crack wakes. This may be because the craze fragments on fracture surfaces were pushed down by crack closure and striations on fracture surfaces should be formed due to the closure.
2. The strength of the craze fibrils at the crack tip might become lower than that of the previous cycle. It should be due to the weakened fibrils by closure between fracture surfaces. The fibrils might be weakened mainly due to the entanglements of fibrils.

REFERENCE

1. Bokoi, Y. Ishiyama, C. and Shimojo, M. (2000) *J. Mater. Sci.* 35, pp. 5001-5011.
2. Bucknall, C.B. and Dumpleton, P. (1987) *Polym. Eng. Sci.* 27, pp. 110-115.
3. Clark, T.R. Herzberg, R.W. and Mohammadi, N. (1993) *J. Mater. Sci.* 28, pp. 5161-5168.
4. Ishiyama, C. Sakuma, T. Bokoi, Y. Shimojo, M. and Higo, Y. (1998) *Progress in Accoustic Emission IX* pp. 99-106.
5. Ishiyama, C. Shiraishi, Y. Shimojo, M. and Higo,Y. (1997) *Proc. of the 9th Inter. Conf. Fracture* 2, pp. 1029-1035.
6. Jud, K, Kausch, H.H and Williams, J.G (1981) *J. Mater. Sci.* 16, pp. 204-210.
7. Kambour, R.P (1966) *J. polym. Sci.* 4, pp. 349-358.
8. Konczol, L, Shinker, M.G and Doll, W (1984) *J. Mater. Sci.* 19, pp. 1605-1615.
9. Puros, G.C and Knauss, W.G (1998) *Int. J. Fract.* 93, pp. 161-185.
10. Puros, G.C and Knauss, W.G (1998) *Int. J. Fract.* 93, pp. 145-159.
11. Puros, G.C and Knauss, W.G (1998) *Int. J. Fract.* 93, pp. 187-207.
12. Ravi-chander, K (1995) *Int. J. Solids. Struct.* 32, pp. 925-938.
13. Schirrer, R (1987) *J. Mater. Sci* .22, pp. 2289-2296.
14. Ward, M.I and Brown, H.R (1973) *Polymer* 14, pp. 469-475.
15. Ishiyama, C. Asai, T. Shimojo, M. and Higo, Y. (1999) *Proc. of the seventh Int. Fatigue Cong.* pp. 1761- 1766

EFFECTS OF T–STRESS AND VOID NUCLEATION ON COHESIVE ZONE MODEL PREDICTIONS FOR DUCTILE FRACTURE

Viggo Tvergaard

Department of Mechanical Engineering, Solid Mechanics,
Technical University of Denmark, DK–2800 Kgs. Lyngby, Denmark

ABSTRACT

Special interface elements that account for ductile failure by void growth to coalescence are used to analyse crack growth under mode I loading conditions. The tangential stresses inside the interface are determined by requiring compatibility with the surrounding material in the tangential direction. Earlier applications of the model are here extended to consider the effect of a T–stress or effects of void nucleation inside the interface elements.

KEYWORDS

Cracks, voids, fracture, plasticity.

INTRODUCTION

For the analysis of crack growth by a ductile failure mechanism the fracture process zone is represented in terms of special interface elements in the crack plane ahead of the crack. The modified Gurson model is used in the interface elements to represent the nucleation and growth of voids to coalescence. In relation to the finite element mesh the initial width of the interface is taken to be zero, but the traction separation relations represented by the interface are based on assuming an interface width of the order of the void spacing.

The present interface element formulation is not based on assuming that the plastic strains or the stress state inside the interface are identical to the values of these field quantities in the material adjacent to the interface (as in Tvergaard and Hutchinson [1] or Sigmund and Brocks [2]) . Instead, the present model enforces the continuity of the longitudinal strain along the band, across the band interface. Thus, the stiffnesses of the cohesive zone element give a coupling between the displacement normal to the band and those tangential to the band.

Predictions of this cohesive zone model have been presented previously, for growth of pre–existing voids under mode 1 loading conditions (Tvergaard [3]). In the present paper the model is extended to account for the effect of void nucleation inside the interface elements. Furthermore, the model is used to estimate the effect of a T–stress on predicted crack growth resistance curves.

DUCTILE FAILURE MODEL FOR INTERFACE

In the computations the initial width of the special interface element is taken to be zero, as in other cohesive zone calculations [1]. However, the traction–separation properties of the interface element are calculated based on

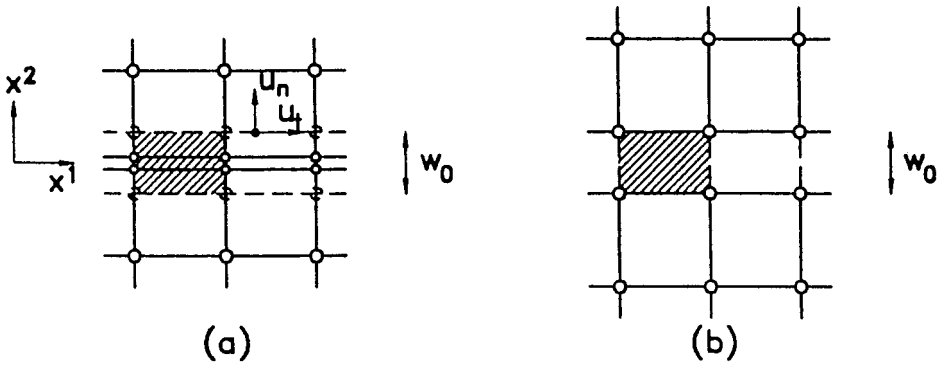

Fig. 1: Interface elements along the crack plane. (a) Shows the artificial overlap between interface elements and surrounding elements. (b) A corresponding configuration with no overlap.

a background element with the non–zero initial width w_0 . Fig. 1a illustrates the finite element mesh near the line of symmetry, with the background interface element sketched in, while Fig. 1b indicates the configuration if this interface element is attached to the surrounding elements as a common element. The displacement components u_n and u_t on the top side of the interface element (Fig. 1a) are required to be compatible with the displacements on the edge of the adjacent finite element. Then with the assumption that the displacements inside the interface element vary linearly through the element width (in the x^2–direction), the displacement gradients inside the element are

$$\frac{\partial u_1}{\partial x^1} = \frac{\partial u_t}{\partial x^1} \ , \ \frac{\partial u_2}{\partial x^2} = \frac{2u_n}{w_0} \ , \ \frac{\partial u_1}{\partial x^2} = 0 \tag{1}$$

Furthermore, when choosing to replace displacement gradients by their averages through the element width, we find $\partial u_2/\partial x^1 = 0$.

From these displacement gradients it is possible to determine the current metric tensor G_{ij} , the Lagrangian strain tensor η_{ij} and its increment η_{ij} in any point on the middle surface, $x^2 = 0$, of the interface element. Thus the evolution of stresses and of damage inside the interface can be calculated from a set of constitutive relations. These constitutive relations are based on the modified Gurson model [4,5] , which makes use of an approximate yield condition for a porous solid

$$\phi = \frac{\sigma_e^2}{\sigma_M^2} + 2q_1 f^* \cosh\left[\frac{\sigma_k^k}{2\sigma_M}\right] - 1 - \left(q_1 f^*\right)^2 = 0 \tag{2}$$

where $\sigma_e = (3s_{ij}s^{ij}/2)^{1/2}$ and $s^{ij} = \sigma^{ij} - G^{ij}\sigma_k^k/3$. The void volume fraction is f , and $f^*(f)$ is a function that approximately describes final failure by void coalescence. The change of the void volume fraction during an increment of deformation is taken to be given by

$$\dot{f} = (1 - f)G^{ij}\dot{\eta}_{ij}^P + \mathcal{A}\dot{\sigma}_M + \mathcal{B}\left(\dot{\sigma}_k^k\right)/3 \tag{3}$$

where the first term results from the growth of existing voids, and the two last terms model the increment due to nucleation [6] .

The numerical solutions are obtained by a linear incremental finite element method, based on the incremental principle of virtual work, with the material outside the interface represented by finite strain J_2 flow theory. The details of the computational method are given in [3] and shall not be repeated here. As described in [3] , an extra parameter r_0 is introduced, to be able to reduce the tangential components of the nodal forces calculated by the interface element procedure described above. Thus, if $(P_t)_{elm}$ denotes the interface element contribution to the value of the nodal force component tangential to the interface, as calculated by the interface element procedure, the tangential component P_t actually applied in the solution is taken to be given by

$$P_t = r_0(P_t)_{elm} \tag{4}$$

Here, $r_0 = 0$ will be used, as this gives the best representation of an initially sharp crack (see further discussion in [3]). The value of the initial width w_0 of the strip (Fig. 1) is non–zero, representing approximately 0.7 times the initial void spacing. In the small–scale yielding solution for crack growth, the value of the J–integral is calculated on a number of contours around the crack–tip to check agreement with the prescribed amplitude K of the edge displacements (i.e. $K^2 = JE/(1 - \nu^2)$) , and very good agreement is found. For the presentation of the results reference values for the J–integral and for the corresponding size of the plastic zone are defined

$$J_0 = \sigma_y w_0 \ , \ R_0 = \frac{1}{3\pi}\left(\frac{K_0}{\sigma_y}\right)^2 \tag{5}$$

where the value K_0 corresponds to J_0 .

According to the small strain linear elastic solution the in–plane stress components near the crack–tip are of the form

$$\sigma_{\alpha\beta} = \frac{K}{\sqrt{2\pi r}} f_{\alpha\beta}(\theta) + T\delta_{1\alpha}\delta_{1\beta} \tag{6}$$

where $(r \ , \ \theta)$ are polar coordinates, δ_{ij} is Kronecker's delta and T is a non–singular stress term, acting parallel to the crack plane. In the present analyses the T–stress is applied first, together with the corresponding transverse stress $\sigma_{33} = \nu T$ under plane strain conditions.

RESULTS

The elastic–plastic material parameters in the first case analysed are specified by $\sigma_y/E = 0.002$ and $\nu = 0.3$ with the power hardening exponent $N = 0.2$. Furthermore, in the porous ductile material model the initial void volume fraction is $f_I = 0.01$, and other parameter values in the model are $q_1 = 1.25$, $f_C = 0.15$ and $f_F = 0.25$. Fig. 2 shows predicted crack growth resistance curves for various values of the T–stress according to (6) . It is well knows from other fracture models, e.g. [7] , that positive values of T tend to have little effect on the fracture toughness, while negative values of T tend to increase the toughness. Therefore, Fig. 2 uses the curve for $T = 0$ as reference. The other three curves show that also the present interface model for ductile fracture predicts increasing fracture toughness for increasing negative values of T.

In Fig. 3 the level of strain hardening is lower, $N = 0.1$, but otherwise all material parameters are identical to those considered in the previous figure. It is seen that also here the negative T–stresses give a significant increase of the fracture toughness, in fact a relatively much larger increase than that found in Fig. 2. This in qualitative agreement with predictions of a more standard cohesive zone model [7] , where it was also found that the T–stress effect is stronger for the more low hardening material.

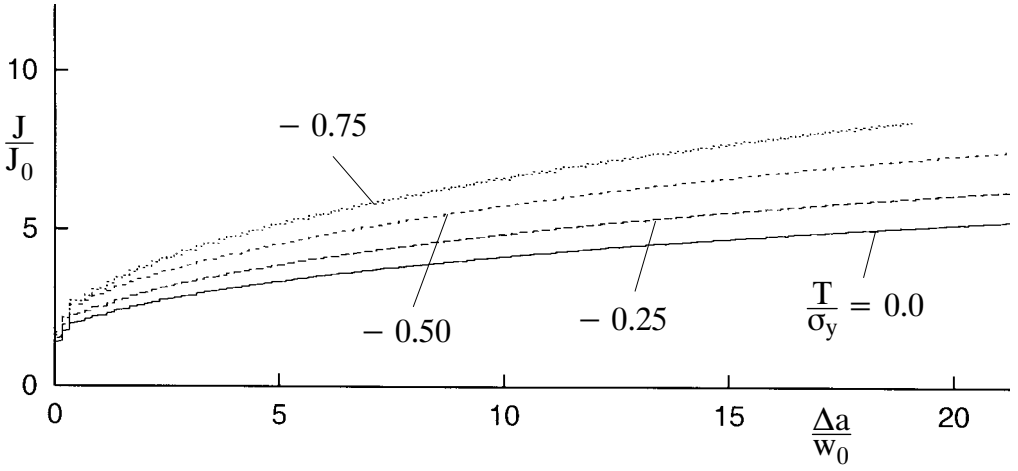

Fig. 2: Crack growth resistance curves for various values of the T–stress, when $f_I = 0.01$, $N = 0.2$ and $r_o = 0$.

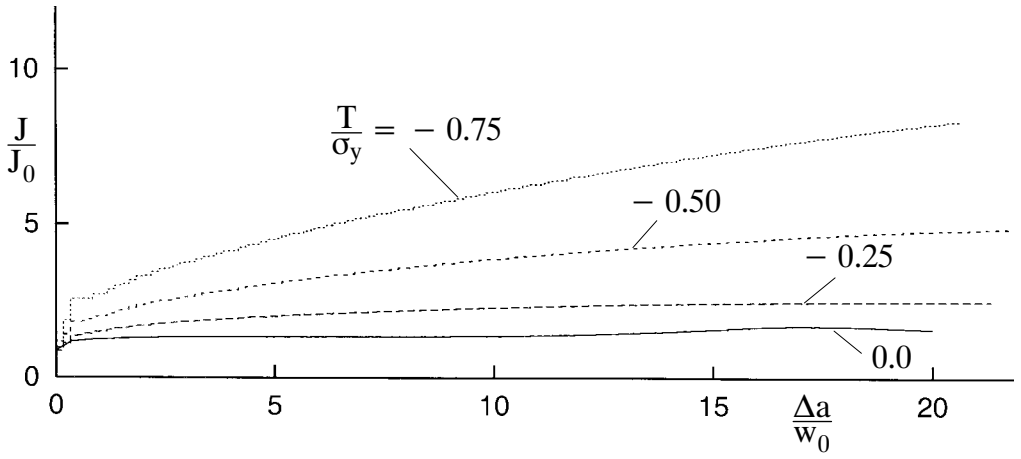

Fig. 3: Crack growth resistance curves for various values of the T–stress, when $f_I = 0.01$, $N = 0.1$ and $r_o = 0$.

The effect of void nucleation is not easily accounted for in interface elements or those of [2], where the dependence on stress triaxiality outside the interface is based on fitting with various cell model studies. However, in the present interface elements nucleation criteria can be specified in the usual manner for Gurson model elements, as the stress and strain fields in the interface elements are fully specified by the conditions of equilibrium and compatibility with neighbouring elements specified above. Nucleation is here taken to be plastic strain controlled, as modelled in terms of (3) by taking $\mathcal{A} > 0$ and $\mathcal{B} = 0$. The dependence of $\mathcal{A}$ on the effective plastic strain is specified such that nucleation follows a normal distribution [8], with the volume fraction f_N of void nucleating particles, the mean strain for nucleation ϵ_N, and the corresponding standard deviation s.

Fig. 4 shows two examples of crack growth resistance curves predicted with void nucleation in the interface. Both curves use the parameter values $f_N = 0.04$ and $s = 0.1$, so the only difference is that the lower curve has a smaller mean strain for nucleation, $\epsilon_N = 0.1$, than the value $\epsilon_N = 0.2$ used for the upper curve. It is

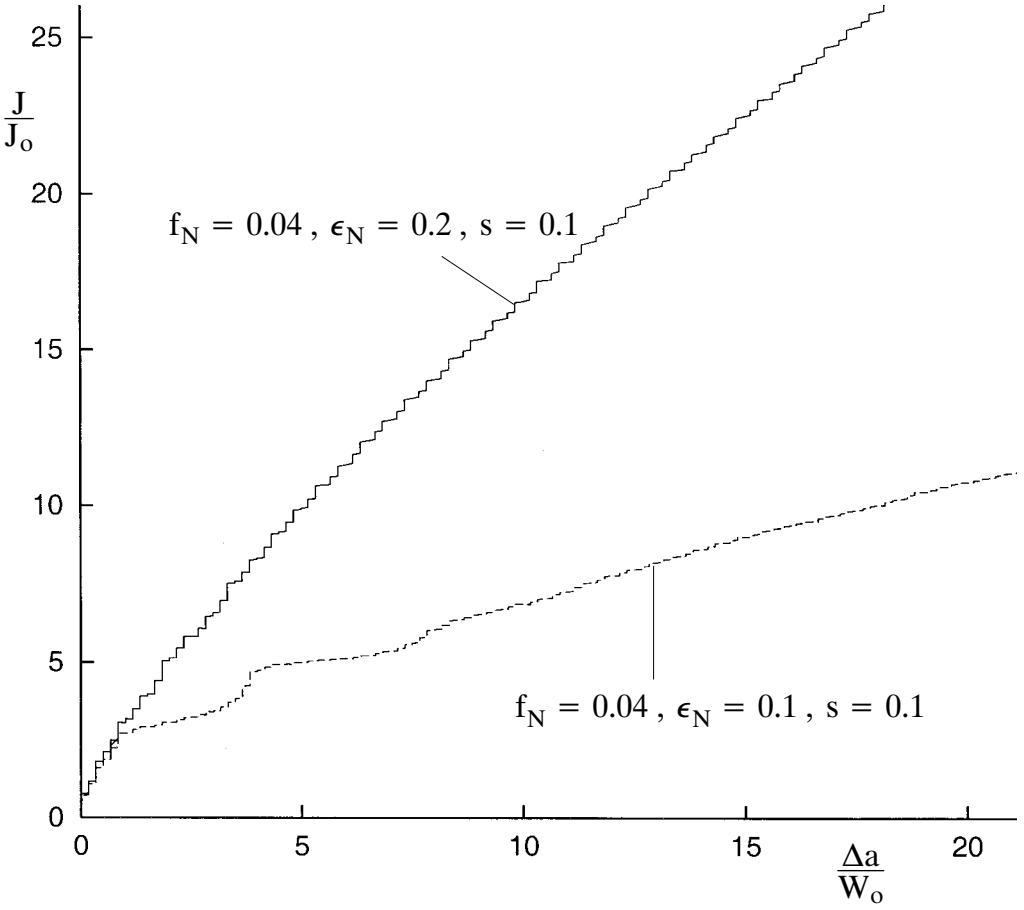

Fig. 4: Crack growth resistance curves for cases with plastic strain controlled nucleation in the interface elements, when $f_I = 0.0$, $N = 0.1$, $r_o = 0$ and $T = 0$.

seen that the material with no initial voids but with void nucleation can show a significantly higher crack growth resistance than that found in Fig. 3 for a material with voids present initially.

REFERENCES

1. Tvergaard, V. and Hutchinson, J.W. (1996) *Int. J. Solids Structures* 33, 3297–3308.
2. Sigmund, T. and Brocks, W. (1998) *J. Phys.* IV, 8, 349–356.
3. Tvergaard, V. (2000). Crack growth predictions by cohesive zone model for ductile fracture. *Danish Centre for Appl. Math. and Mech.*, Report No. 640, July 2000 (to appear in *JMPS*).
4. Gurson, A.L. (1977) *J. Engrg. Materials Technol.* 99, 2–15.
5. Tvergaard, V. (1990) *Adv. App. Mech.* 27, 83–151.
6. Needleman, A. and Rice, J.R. (1978) in *Mechanics of Sheet Metal Forming* (eds. D.P.Koistinen et.al.), 237–267, Plenum Publishing Corporation.
7. Tvergaard, V. and Hutchinson, J.W. (1994) *Int. J. Solids Structures* 31, 823–833.
8. Chu, C.C. and Needleman, A. (1980) *J. Eng.Materials Technol.* 102, 249–256

ELASTIC INSTABILITY OF ALLOYS BY HYDROGENATION: MOLECULAR DYNAMICS STUDY OF HYDROGEN-INDUCED AMORPHIZATION

M. Katagiri and H. Onodera

National Institute for Materials Science
1-2-1 Sengen, Tsukuba, Ibaraki 305-0047, Japan

ABSTRACT

The microscopic mechanism of Hydrogen-Induced Amorphization (HIA) in C15 Laves phases of AB_2 compounds is studied. Experimentally, compounds in which the AA internuclear distance is reduced and BB internuclear distance expanded compared to pure crystals show Hydrogen-Induced Amorphization which suggests that the relative atomic size is the controlling factor. We investigate the role of the size effect by static and Molecular Dynamics methods using Lennard-Jones potentials. Our simulations show that in such a compound, the bulk modulus is remarkably reduced by hydrogenation compared to the isotropic tensile load, so that elastic instability is facilitated. This situation is caused by the negative increase of the pressure-fluctuation contribution in the elastic constant. We also report the fracture process under isotropic tensile loading. An elastic analysis at sublattice level shows that one of the sublattices is less stable in the HIA material.

KEYWORDS

molecular dynamics, hydrogen, Laves phase, fracture, amorphous, softening, elastic instability

INTRODUCTION

Hydrogen-Induced Amorphization (HIA) is a phase transformation from crystalline to amorphous induced by hydrogenation. HIA is a potential method for preparing amorphous alloys since hydrogenation and dehydrogenation can be done easily and rapidly. In addition, HIA has a close relation with the structural change of hydrogen-storage alloys which determines their performance [1]. For effective materials design using HIA, it is important to understand the atomistic mechanism of this process. For this purpose, computer simulation is a powerful tool.

Aoki et al [2] studied HIA of C15 Laves phase AB_2 compounds experimentally. They found that the relative atomic size is the controlling factor of the occurrence of HIA. HIA does not occur when the ratio of the Goldschmidt radii of A and B atoms, R_A/R_B, is less than 1.37 (A = rare earth, B = Al). In this ratio, the internuclear distances between both AA and BB atoms contract compared to those in the pure crystals [2]. On the other hand, HIA occurs when the ratio is larger than 1.37 (A =

rare earth, B = Fe, Co, Ni). In this ratio, the AA internuclear distance contracts and BB internuclear distance expands. Thus it is known that the size effect is essential. Our goal is to reveal the role of the size effect at the trigger of HIA [3, 4, 5].

METHOD

Model

YAl_2 and $CeNi_2$ were modeled. YAl_2 is a non-HIA material and $CeNi_2$ is a HIA material. We used pair-wise Lennard-Jones (L-J) 12-6 potential to reveal the size effect. For different species pairs, the geometric combination rule was used. As for hydrogen, only repulsion was taken into account [4]. By the analysis of the equation of state using our potential, it is known that *both the YY and AlAl internuclear distances contract in YAl_2, while CeCe internuclear distance contracts and NiNi internuclear distance expands in $CeNi_2$*. This corresponds to experimental results reported by Aoki et al. [2]. The ratio R_Y/R_{Al} is 1.27 and R_{Ce}/R_{Ni} is 1.46 in our model. Details of the interatomic potentials are in a reference [2]. The total number of metal atoms in the simulation cell is 192 with three-dimensional periodic boundary condition. We compared non-hydrogenated systems under isotropic tensile load and hydrogenated systems at zero pressure.

Elastic Stability

We treat homogeneous systems which do not contain any surface or defect. The dynamical stability of homogeneous lattice can be discussed by elastic stability criteria [6]. We calculated elastic constants C^{ijkl} by fluctuation formula [7] from microcanonical molecular dynamics data.

$$C^{ijkl} = -\frac{\Omega_0}{kT}\delta(P^{ij}P^{kl}) + \frac{2MkT}{\Omega_0}(\delta^{il}\delta^{jk} + \delta^{ik}\delta^{jl}) + \frac{1}{\Omega_0} < \sum_a \sum_{b(>a)} (\frac{u'' - u'/r_{ab}}{r_{ab}^2}) r_{ab}^i r_{ab}^j r_{ab}^k r_{ab}^l > \qquad (1)$$

Each term shows the pressure-fluctuation, kinetic and potential contributions, respectively. Ω_0 is the total volume, T the temperature, k the Boltzmann factor and M the number of the metal atoms. The superscripts i, j, k and l are the Cartesian indices. P^{ij} is the pressure tensor, $<>$ the ensemble average and $\delta(P^{ij}P^{kl})$ the ensemble fluctuation. Note that the summations are taken over the metal atoms excluding hydrogen. By using the elastic constants obtained here, we calculated the elastic stability criteria for cubic symmetry at external pressure P [6].

$$B = \frac{1}{3}(C_{11} + 2C_{12} + P) \qquad (2)$$

$$G' = \frac{1}{2}(C_{11} - C_{12} - 2P) \qquad (3)$$

$$G = 4(C_{44} - P) \qquad (4)$$

Here, $P < 0$ for tension. All are finite and positive so that the crystal lattice is elastically stable [6]. The vanishing of the bulk-modulus B is the instability of lattice decohesion by pure dilation with no symmetry change. The vanishing of the tetragonal shear-modulus G' leads to symmetry breaking (bifurcation) with volume conservation. The vanishing of the rhombohedral shear-modulus G gives a simple shear instability along one of the symmetry directions with volume conservation [6].

ELASTIC INSTABILITY BY ISOTROPIC TENSILE LOAD

Molecular Dynamics

Figure 1 shows snapshots of the fracture for *non-hydrogenated* YAl_2 and $CeNi_2$ caused by an isotropic tensile load at temperature $T_s = 0.05$ and 0.06, respectively. Here the temperature is scaled by the melting one calculated by MD simulation [4]. YAl_2 shows a kind of cleavage by decohesion with maintaining

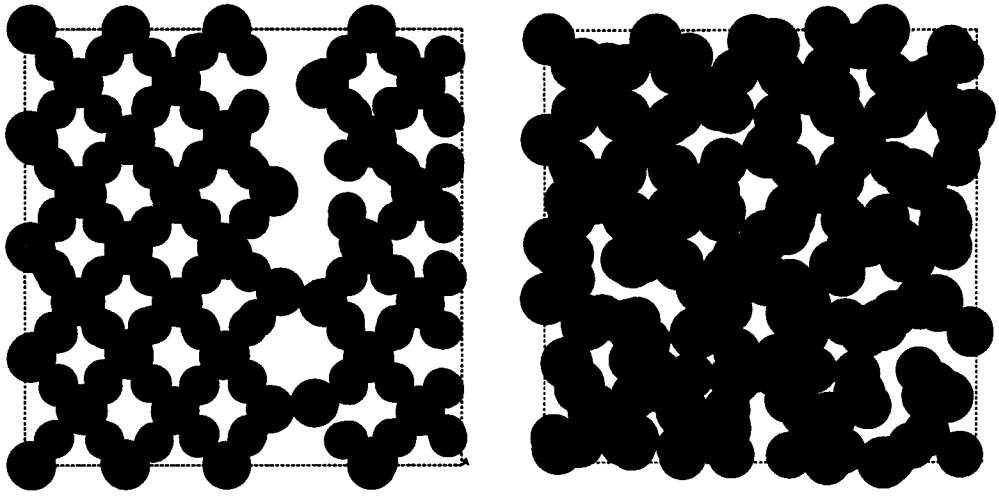

Figure 1: MD result of the fracture by isotropic tensile load. YAl_2 (left) shows cleavage fracture, while $CeNi_2$ (right) is collapsed to a amorphous-like structure.

the local lattice structure. On the other hand, $CeNi_2$ shows amorphous-like structure. By examining snapshots during the amorphization process it can be seen that the trigger of the amorphization is the movement of Ni atoms rather than Ce, as also seen in the HIA modeled by the embedded-atom potential [3]. A discontinuous potential-energy decrease is observed [4].

Static Calculations

We discuss the origin of the different fracture mode described above on the basis of the elastic stability criteria. For this purpose, we extend the definition of elastic constant of total lattice to the sublattice level. We define the potential part of the elastic constant of a sublattice as follows.

$$C^{ijkl}_{sub} = \frac{1}{\Omega_0} < \sum_{a \in sub} \sum_{b \neq a} \frac{1}{2} \left(\frac{u'' - u'/r_{ab}}{r^2_{ab}} \right) r^i_{ab} r^j_{ab} r^k_{ab} r^l_{ab} > . \tag{5}$$

Here *sub* means sublattice. Similar to the criteria for total lattice, the definitions are extended to sublattice level. Note that the sublattice also has cubic symmetry. Here, we consider only the potential contribution in the definitions. It is approximately valid for non-hydrogenated systems under the isotropic load, because the reduction of potential part in elastic constants contributes mainly in the elastic unstabilization of homogeneous lattice by the load.

$$B_{sub} = \frac{1}{3}(C_{11,sub} + 2C_{12,sub} + P_{sub}) \tag{6}$$

$$G'_{sub} = \frac{1}{2}(C_{11,sub} - C_{12,sub} - 2P_{sub}) \tag{7}$$

$$G_{sub} = 4(C_{44,sub} - P_{sub}) \tag{8}$$

Figure 2 shows the bulk-modulus stability under an isotropic load. In each simulation the simulation cell was expanded by rescaling the atomic positions. Figure 2(a) shows the stability change of YAl_2. The bulk moduli of total and sublattices become zero at almost the same cell length of 1.66nm, which means that the sublattice-instability points agree well with the instability point of the total lattice. The critical cell-length predicted by the instability point of total lattice is in good agreement with that obtained by MD simulations at low temperatures. Figure 2(b) shows the stability change of $CeNi_2$ at T=0K for homogeneous rescaling. The bulk modulus of the Ni sublattice becomes zero at about 1.50nm cell length. The total-lattice instability has not been reached at this length. However this critical cell-length of the Ni sublattice is in good agreement with the onset of amorphization seen in the MD simulations. Thus it seems that the instability of the Ni sublattice is the trigger for amorphization.

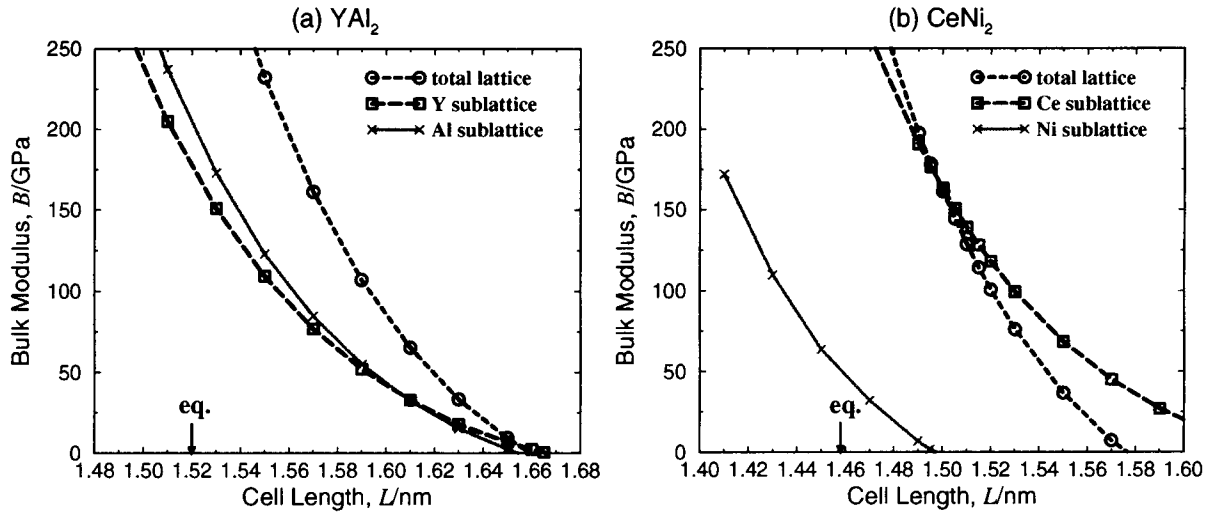

Figure 2: Static calculations of bulk-modulus stability at sublattice level under isotropic tensile load.

The different modes of fracture seen in the two MD simulations can be interpreted by such elastic stability argument. YAl_2 is fractured by the decohesion of the total lattice, since the instabilities of total and sublattice are realized together. When a cleavage fracture occurs at a local part of lattice by thermal fluctuation, it propagates to the whole region. On the other hand, for $CeNi_2$, the sublattice of Ni atoms becomes unstable, leading to amorphization. The instability of the Ni sublattice is associated with the expansion of the Ni-Ni distance in the Laves phase.

Note that shear-modulus G' and G-instabilities are not reached before the lattice instability for both YAl_2 and $CeNi_2$. In both cases, the bulk-modulus instability governs the fracture.

Equation of State

We have illustrated the fracture mode of YAl_2 and $CeNi_2$. To address the behavior for a general combination of atomic sizes, we calculated the inter-atomic contraction/expansion and the critical cell length at which the bulk modulus instability occurs, as shown in Figure 3. It was calculated by constructing the equation of state within the third neighbor interaction shell. In Figure 3(a), the negative (positive) value of $(r-R)/R$ means the atomic contraction (expansion). At 1.225, there is a contraction of both A and B interatomic distances giving geometrical ideal lattice. The lower and upper limits of the size ratio for sublattice stabilities at zero pressure are given by 1.01 and 1.55, respectively. In fact, all materials reported in a reference [2] exist in this range. The ratio of 1.225 gives the equivalent critical length of A and B-sublattices. Note that hard sphere model gives the ideal lattice at the ratio of 1.225. In the range of $1.225 < R_A/R_B < 1.33$, both A and B interatomic distances contract. The stability of the B-sublattice is lower than that of the A-sublattice. In the range of $1.33 < R_A/R_B$, A distances contract and B distances expand. The stability of B-sublattice is considerably lower than that of A-sublattice.

ELASTIC INSTABILITY BY HYDROGENATION

We consider the elastic response of the lattice to hydrogenation. Figure 4 shows the elastic stability of (a) YAl_2 and (b) $CeNi_2$ under hydrogenation at zero pressure. In the figure, $\times$ denotes the bulk-modulus B-stability in Eqn.2 and $+$ denotes the shear-modulus G'-stability in Eqn.3. For comparison, B and G'-stabilities of non-hydrogenated systems under isotropic tensile load are also shown by $\bigcirc$ and $\square$, respectively. In $CeNi_2$, the bulk-modulus B is reduced by hydrogenation (denoted by $\times$), leading to a lattice instability: Unlike B, G' does not soften. The elastic constants C_{11} and C_{12} decrease with hydrogenation, but for G' which is the difference between C_{11} and C_{12} (Eqn.3), the softenings are canceled. In YAl_2, we did not observe any evidence of such a softening effect. We found that hydrogenation and isotropic tensile loading gave similar elastic stability changes. This suggests that

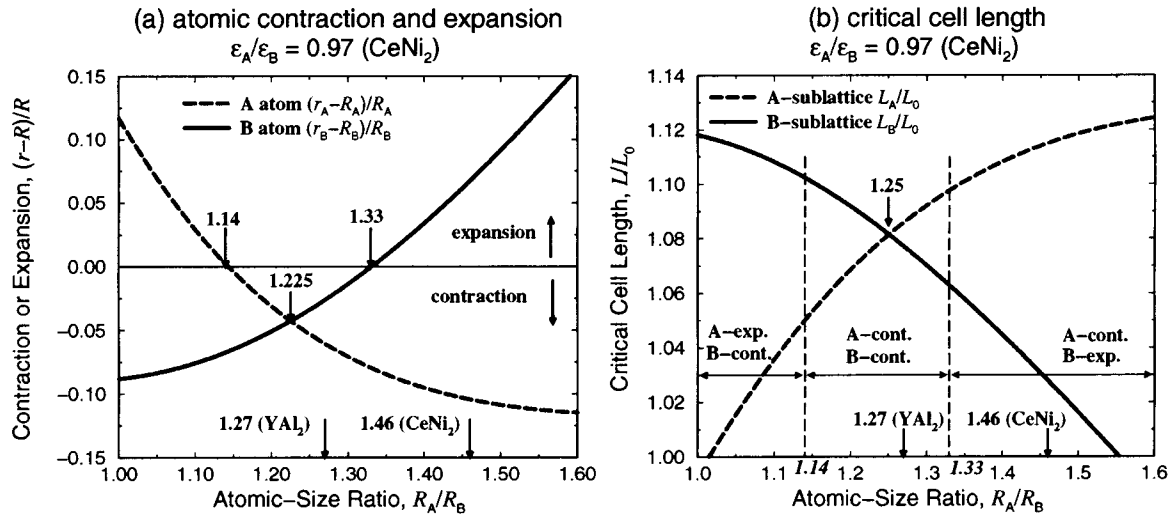

Figure 3: (a) Atomic contraction/expansion and (b) the critical cell length at the bulk modulus instability by the isotropic tensile load. ϵ is the Lennard-Jones energy parameter. R is the Goldschmidt radius of pure crystal state estimated by our potential. r is the radius in Laves phase. L_0 is the equilibrium cell length at zero pressure. The ratio of energy parameters ϵ is adjusted for $CeNi_2$ while that of the size parameters are varied.

hydrogenation simply causes a volume expansion, and the softening due to the volume expansion is observed. On the other hand, the softening by hydrogenation in $CeNi_2$ is caused by the negative increase of the pressure-fluctuation term in the elastic constant. The softening in a simple volume expansion of $CeNi_2$ is caused by the decrease of the potential term in the elastic constant as in Eqn.1. Such a softening by volume expansion needs a large expansion to reach the elastic instability for amorphization. However, amorphization by hydrogenation occurs at a lower volume. The reason for the reduction in the pressure-fluctuation term is that metal atoms in the neighborhood of hydrogen deviate locally from their equilibrium positions. Even if such a relaxation is energetically small, the change in the pressure fluctuations is large.

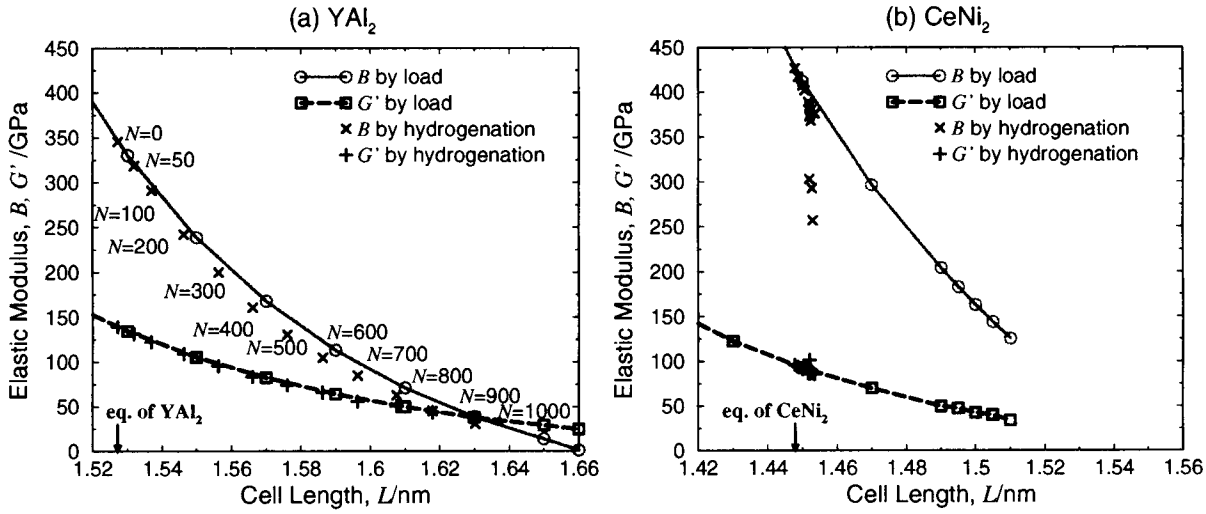

Figure 4: Elastic stability under isotropic tensile loading or by hydrogenation. N is the number of hydrogen atoms incorporated into $A_{64}B_{128}$ systems. As for $CeNi_2$, $N < 37$.

CONCLUSIONS

Hydrogen-Induced Amorphization (HIA) was simulated by static and molecular dynamics (MD) methods. We compared non-HIA and HIA materials, YAl_2 and $CeNi_2$, respectively. The changes of the elastic

stability by the isotropic tensile load and the hydrogenation were calculated.

The fracture process of non-hydrogenated systems by isotropic tensile load was simulated by MD. The lattice fractured at the cell length where the bulk modulus falls to zero. In YAl_2, the bulk moduli of total lattice and sublattices fall to zero at a similar volume, and a cleavage surface is created. On the other hand, in $CeNi_2$, the bulk modulus of Ni sublattice is relatively small and falls to zero first. The amorphous-like structure is obtained. Such a difference in the mode of fracture is caused by the size effect. Compared to the pure states, Y and Al internuclear distances contract, while Ce internuclear distances contract and Ni internuclear distances expand in Laves phase. In $CeNi_2$, the bulk-modulus stability of Ni sublattice is low due to the expansion of the internuclear distances and falls to zero first.

We incorporated hydrogen into the systems. YAl_2 did not show HIA. On the other hand, once the amount of hydrogen atoms exceeds a critical value, $CeNi_2$ showed HIA [4]. In YAl_2, hydrogenation simply increases the volume and the bulk modulus is reduced because of the non-linearity of the interatomic potentials. A similar reduction is observed under an isotropic tensile load. The main cause of the reduction is the potential term in the elastic constant. On the other hand, in $CeNi_2$, hydrogenation greatly reduces the bulk modulus. This reduction is mainly caused by the negative increase of the pressure-fluctuation term in the elastic constant. As a result, hydrogenation lead to the amorphization at a much smaller volume than under a load. The increase of the pressure-fluctuation is the result of the atomic relaxation induced by hydrogenation. In $CeNi_2$, the contraction and expansion are realized simultaneously, and relaxation can occur by hydrogenation. Even if the potential-energy change resulting from the relaxation is small, the change in pressure fluctuation is high.

These features can also be understood by the consideration of the equation of state for these compounds. When the size ratio exceeds 1.33, the bulk-modulus stability of the sublattice of B-atoms becomes low compared to that of A-atoms. However, there is no evidence that the ratio of 1.33 gives the critical ratio for HIA. The stability changes continuously as the ratio increases. This suggests that the mechanism of HIA cannot be understood by simple volume expansion and the atomic relaxations play an important role in it. When the internuclear distances of one sublattice expand and the other contract relative to pure crystals, relaxation occurs.

It is concluded that the role of the size effect in HIA is to allow the atomic relaxation on hydrogenation and to facilitate the elastic instability by the increase of pressure fluctuations.

Acknowledgement
We acknowledge Profs. Ruth Lynden-Bell at Queen's University of Belfast and Ali Alavi at University of Cambridge. Calculations were performed on Numerical Materials Simulator at NIMS.

REFERENCES

[1] Aoki, K. and Masumoto, K. (1995) *Materia Japan* **34**, 126.

[2] Aoki, K., Li, X. G. and Masumoto, T. (1992) *Acta Metall. Mater.* **40**, 1717.

[3] Katagiri, K. and Onodera, H. (1999) *Trans. MRS-J* **24**, 245.

[4] Katagiri, M. and Onodera, H. (1999) *Mater. Trans., JIM* **40**, 1274.

[5] Katagiri, M. and Onodera, H. (2001) *J. Phase Equilibria in press.*

[6] Wang, J., Li, J., Yip, S., Phillpot, S. and Wolf, D. (1995) *Phys. Rev.* **B 52**, 12627.

[7] Ray, J. R., Moody, M. C. and Rahman, A. (1985) *Phys. Rev.* **B 32**, 733.

ELECTROMECHANICAL MODELING OF UNIDIRECTIONAL CFRP COMPOSITES

T. Okabe[1], J. B. Park[2], N. Takeda[2] and W. A. Curtin[3]

1. Smart Structure Research Center, National Institute for Advanced Industrial Science and Technology (AIST), 1-1-1 Umezono, Tsukuba city 305-8568, Japan
2. Department of Advanced Energy
Graduate School of Frontier Sciences, The University of Tokyo,
c/o Komaba Open Laboratory (KOL), Takeda Lab.
4-6-1 Komaba, Meguro-ku, Tokyo 153-8904, Japan
3. Division of Engineering, Brown University
Providence, RI, USA, 02912

ABSTRACT

The electrical resistance behavior of conductive carbon fiber reinforced composites under the loading/unloading process is investigated experimentally and analytically. The well-known recovery of the conductivity in a multi-fiber composite during the unloading process is investigated using the single fiber composite, consisting of a single fiber in a polymer. Based on the experimental hysteresis curve of conductivity for a fragmented single fiber, the authors modify our previous discrete network model. Predictions for the electrical resistance behavior have good agreements with the experimental results.

KEYWORDS

Composite, Fiber break, Electrical sensing technique, Nondestructive inspection

INTRODUCTION

In the use of conductive carbon fiber reinforced composites, the insitu and nondestructive inspection should be clearly established. However, since fiber damages occur at the microscopic level (Fig. 1), the monitoring technique considering the micro-damages are required. As argued by some studies[1-6], the measurement of the electrical resistance change for the engineering application has been expected to be one of the promising techniques. Although experimental results imply that the electrical resistance change has a correlation with fiber breaks, the micro-mechanism and theoretical modeling have not been well discussed. The main reason is the

lack of understanding of the internal contacts between carbon fibers. Recently, we proposed a new theoretical model to account for the conducting path formed by the fiber contacts [7]. The present theoretical model assumes the concept of an electrical ineffective length as the finite length δ_{ec} over which a broken carbon fiber loses its current-carrying capacity. Therefore, as shown in Fig. 2, the conductive composite can be modeled as a series array of parallel fiber resistors of length δ_{ec} such that fiber damage within one length δ_{ec} does not affect the resistance of other sections of the composite.

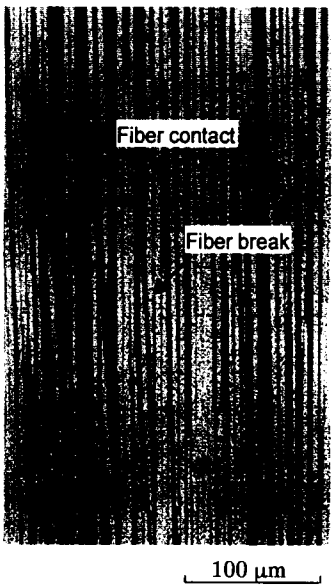

Figure 1: Photograph of CFRP composite

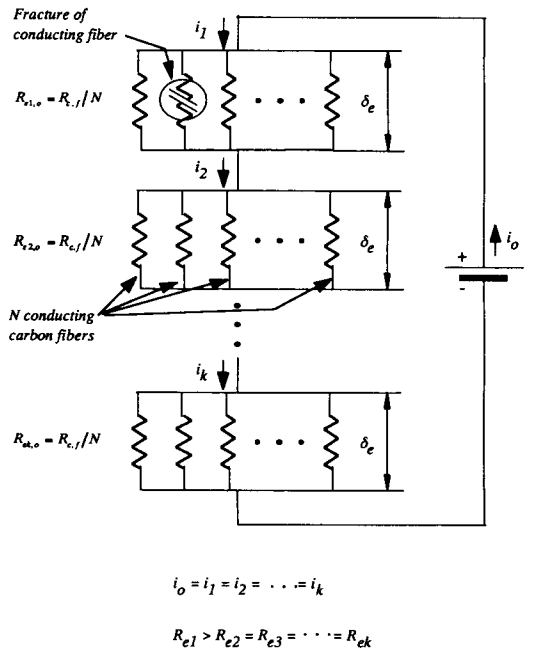

Figure 2: Schematic figure of discrete network model

Then, taking into account the linear dependence of fiber resistance as a function of the strain and the Weibull strength distribution over the length δ_{ec}, we have derived an expression for the resistance change ΔR_{total} normalized by the initial composite resistance $R_{total,o}$ as

$$\frac{\Delta R_{total}}{R_{0,total}} = \frac{(1+\alpha\varepsilon)}{1-P_f(\varepsilon)} - 1 \qquad (1)$$

$$P_f(\varepsilon) = 1 - \exp[-(\frac{\delta_{ec}}{L_0})(\frac{E_f\varepsilon}{\sigma_0})^m] \qquad (2)$$

where E_f is the fiber Young's modulus, α is the proportionality constant between single fiber strain and resistance, σ_o is the stress for one break to occur in Length L_o and m describes the statistical scatter. The above model can predict the resistance change during the tensile load. The δ_{ec} is also found to be the average distance between fiber contacts by the application of the percolation theory [8]. The insitu monitoring of cumulative microdamages during the cyclic load is also important. Some researchers [3,5] have pointed out that the residual electrical resistance is a useful parameter to detect the loading history of the composite. However, as argued by Arby et al.[5], the residual electrical resistance is remarkably reduced during unloading. In the present study, we measure the electrical resistance of a single fiber composite to investigate the basic mechanism for the recovery of an electrical conductivity in a multifiber-reinforced composite during the unloading process. Based on the

hysteresis curve of the single fiber composite after a first fiber break, we modify our previous theoretical model to explain the electrical resistance change of multifiber-reinforced composites under the cyclic load. Although the model requires further development and verification, **comparisons with experimental results** show good agreements.

EXPERIMENT

We measured the electrical resistance in T700S type carbon fiber/ 2500 epoxy matrix CFRP composites under the gradually increasing loading/unloading cycles. Using the applied maximum strain ε^{max}, the electrical resistance change is given as

$$\frac{\Delta R_{total}}{R_{0,total}} = \frac{(1+\alpha\varepsilon)}{1-P_f(\varepsilon^{\max})} - 1 \qquad (3)$$

As shown in Fig. 3, although the theoretical line has a reasonable agreement with the experimental results, the difference increases as the strain approaches to the perfectly unloading process.

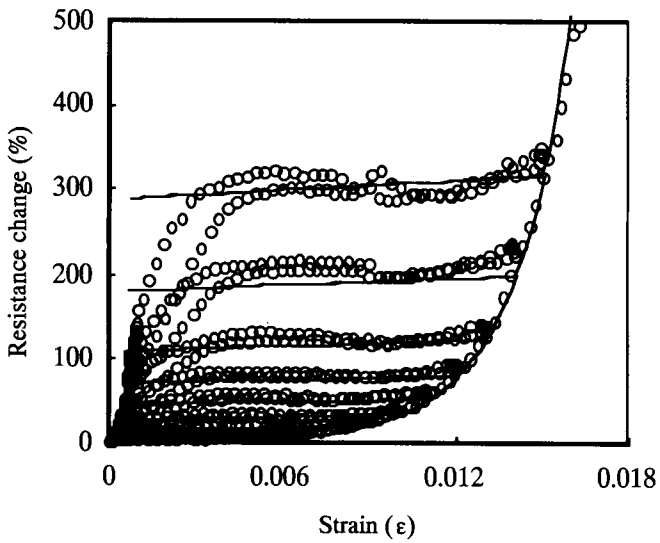

Figure 3: Resistance change curves of loading/unloading cycles

To investigate the mechanism of this difference between our model and experimental results, we measured the electrical resistance of a single fiber composite with the same specimen configuration to as multifiber-reinforced composites. Figure 4 shows the electrical resistance versus test time. As shown in Fig. 4, before a first break, the electrical resistance increases linearly. After that, the fiber becomes nonconductive. However, the electrical conductivity recovers during an unloading process. This behavior is also seen after the 2nd cycle. Therefore, the recovery of an electric conductivity in a multifiber-reinforced composite is originated from this recovery in a fragmented single fiber . This is the first main result of the present paper.

Figure 5 shows the relation between current i versus voltage V during the unloading process. The relation i-V is linear. Therefore, the conductivity in a broken part of the embedded single fiber is found to be ohmic. The fiber strain is still positive when the conductivity of a fragmented single fiber recovers, as shown in Fig. 6. Herein after, to remove the thermal residual strain in a single fiber, the fiber strain ε is used as

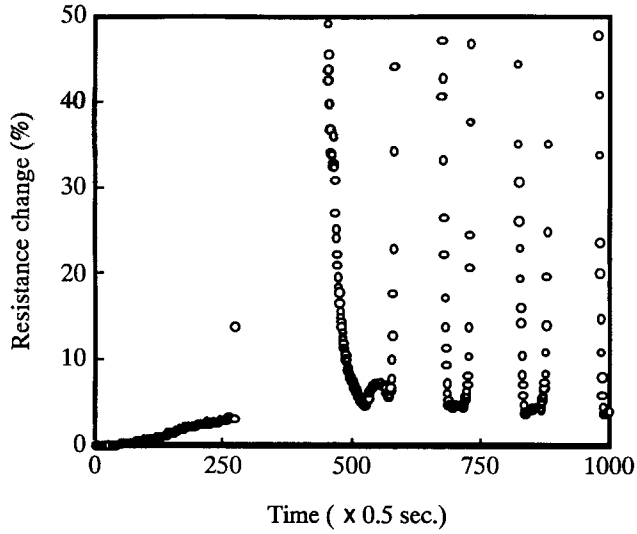

Figure 4: Electrical resistance change of a fragmented single fiber

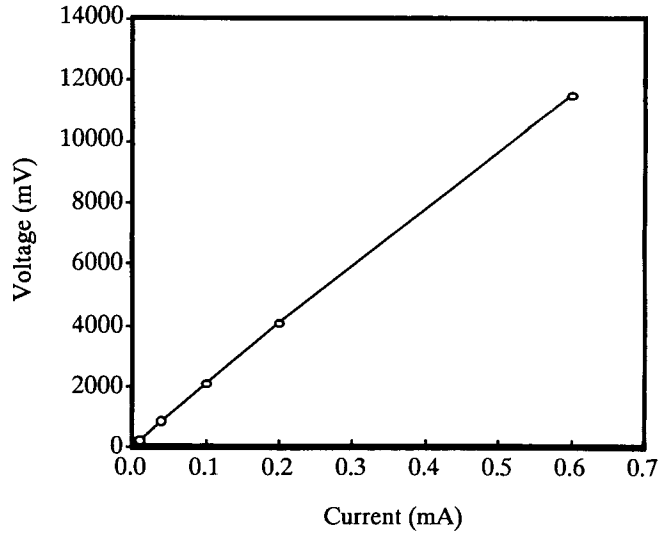

Figure 5: Experimental results for the relationship between current versus voltage

$$\varepsilon = \varepsilon_{comp} - \varepsilon_{thermal} \quad (4)$$

Since the direct contact of neighboring fractured planes is unrealistic, this conductive path in the fractured region is considered to be formed by carbon fiber flakes as shown in Fig. 7. These experimental results are very similar to the electrical response of the conductive thin film reported by Cairns et al.[9]. In their analytical model, the bridging block is assumed as a conductive path. However, we proceed below to analyze with the experimental relation between electrical resistance and strain and will address the mechanism for future study.

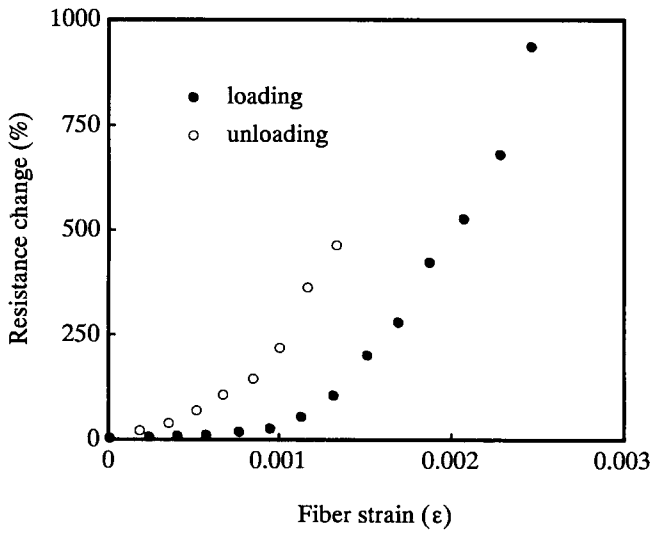

Figure 6: Electrical resistance change of a fragmented single fiber

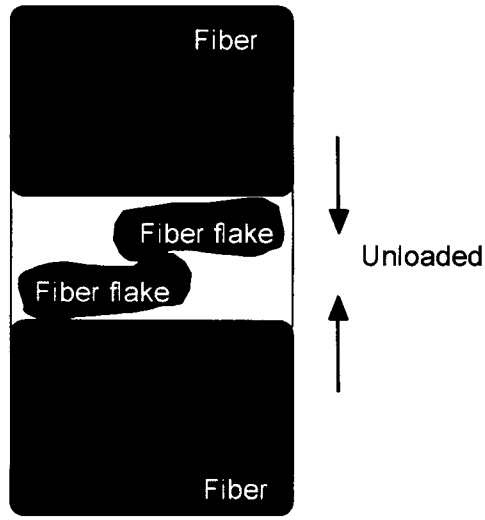

Figure 7: Schematic of electrical conductive path formed by fractured cabon flakes

ANALYTICAL MODEL AND DISCUSSION

As mentioned above, the electrical conductivity of a fragmented single fiber is recovered during the unloading process. Based on the experimental data, the electrical resistance R^{frag} of a fragmented single fiber can be described by

$$R^{frag} / R_0 = \exp(10^3 \times \varepsilon) \quad (5)$$

where R_0 is the initial fiber resistance Our previous model assumes that the conductivity of a broken fiber does not recover during the unloading process. However, the electrical resistance behavior of broken fibers should be considered. Based on the DC circuit model with series and parallel arrays of resistors, the electrical resistance of a multifiber-reinforced composite is modified as

$$\frac{\Delta R_{total}}{R_{0,total}} = \left[\frac{1 - P_f(\varepsilon^{max})}{(1 + \alpha\varepsilon(t))} + \frac{P_f(\varepsilon^{max})}{\exp(10^3 \times \varepsilon(t))}\right]^{-1} - 1 \qquad (6)$$

Prediction with Eq. 6 is shown in Fig. 8 and shows a good agreement with the experimental result. It is true that the internal strain distribution in the composite is more complicated than that of the single fiber composite. However, the electrical resistance behavior can be easily predicted with Eq. 6. Thus, Eq. 6 is the most important result of the present paper.

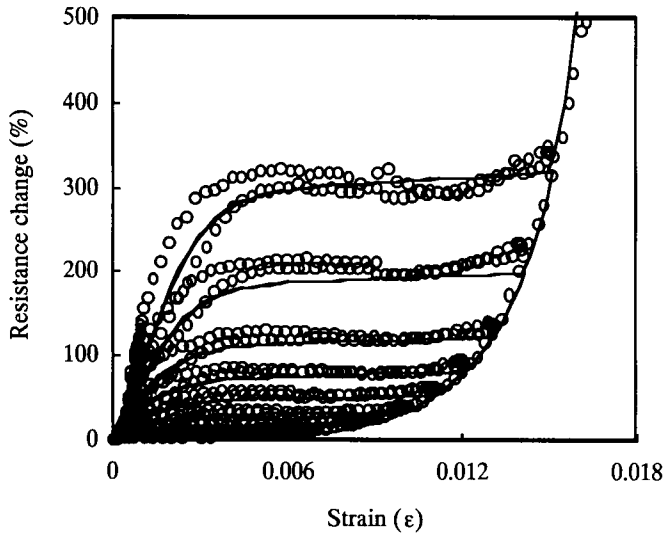

Figure 8: Prediction of electrical resistance curve of mulitfiber composite

CONCLUSION

In the present paper, we have discussed the electrical resistance behavior of conductive fiber reinforced composites. To consider the electrical resistance behavior of broken fibers, we modified our previous model by incorporating the experimental relationship obtained from a fragmented single fiber. The history of the electrical resistance change of the CFRP can be predicted with our modified model. In a view of application, the present technique can contributes to the insitu and nondestructive inspection of the composite structure.

REFERENCES

1. Schulte, K., Baron, C.h., (1989) Comp. Sci. and Tech., 36, 63.
2. Schulte, K., Wittich, H., (1995) Proc. of the ICCM-10
3. Muto, N., Yanagida, H., Nakatsuji, T., Sugita, M., Ohtsuka, Y., (1993) J. of the Am. Ceram. Soc., 76, 4, 185
4. Wang, X., Chung, D.D.L., (1997) Composites : Part B, 29, 63.
5. Abry, J.C., Bochard, S., Chateauminois, A., Salvia, M., Giraud, G., (1999) Comp. Sci. and Tech., 59,925.
6. Prabhakaran, R., (1990) Exp. Tech.,14, 1,16.

7. Park, J.B., Okabe, T., Takeda, N., and Curtin, W.A., Composites : Part A , in print.
8. Park JB, Okabe T, Takeda N and Curtin WA, Preparing for the publication
9. Cairns, D.R., Witte, R.P., Sparacin, **D.K., Sachman, S.M.**, Paine, D.C., Crawford, G.P. and Newton, R.R., (2000) Applied Physics Letters 76,11,1425.

ORAL REFERENCE: ICF100880OR

ELEVATED TEMPERATURE FRACTURE AND CRACK GROWTH IN TiAl BASE INTERMETALLICS

Bilal Dogan

GKSS Research Centre, Institute for Materials Research
Max-Planck-Str., D-21502 Geesthacht, F.R.Germany

ABSTRACT

New materials and processes are bringing about radical changes in the aerospace and transport industry. Due to the high premiums tied to weight reductions in advanced engines the application of TiAl base intermetallic alloys look especially attractive because of their high specific modulus, high specific creep strength, and good oxidation resistance at elevated temperatures. The fracture and high temperature crack growth behaviour of a γ-TiAl base intermetallic alloy, Ti48Al2Cr, with a duplex microstructure were studied at 700°C. Compact tension (CT) type specimens were tested both with EDM slit notches and fatigue precracks. The loading mode was varied to study the applicability of different test techniques.
The present investigation showed that the inhomogenity in microstructure needs to be considered in fracture toughness testing and crack growth assessment of TiAl base intermetallics. The starter sharp crack may be introduced by fatigue precracking and also by EDM provided notch root radius ρ is ≤ 0.05mm. The crack growth rate data showed loading mode dependence. Brittle fracture directs attention to the crack length measurement method that requires improvement. The crack growth rate data were correlated with K and $C^*_{(t)}$, and the applicability of the existing test method for crack growth characterisation of TiAl intermetallics is discussed. The emphasis is placed on the correlation between microstructure, fracture and crack growth behaviour of the alloys.

KEY WORDS: TiAl, Intermetallics, High Temperature, Fracture, Creep Crack Growth

INTRODUCTION

Enormous effort has been made in the field of intermetallic materials during the past two decades [1-3]. The work was concentrated on the light weight γ-TiAl base intermetallic alloys which are considered for future high temperature engineering applications to replace the current Ni and Ti base alloys. Several potential applications have been identified for TiAl-based alloys in the aerospace, automotive and turbine power generation markets. Aerospace industry is pursuing the implementation of these alloys in aircraft engine components [4]. Considering the potential application temperatures of about 700°C, the γ -TiAl base intermetallic alloys stand as promising materials for engineering applications provided the problems of relatively low fracture toughness and fast crack growth rates are overcome. The concern is that component life will then be limited in the presence of relatively small existing or in service-initiated defects or flaws. Therefore, the understanding of mechanisms of deformation, fracture and high temperature crack growth need be improved that has been recognised and being worked on intensively [2,5-9].

The fracture mechanics approach has not been fully developed in the research field of intermetallics. Therefore, the fracture toughness values reported in the literature reflect the various methods used for fracture toughness determination [5]. Furthermore, during fracture mechanics testing the crack deviation at lamellae may result in an invalid test [7]. Creep crack growth (CCG) testing of creep brittle materials, such as intermetallics, has been subject to an international effort [10], that produced recommendations to be incorporated in the only existing test method for creep crack growth rate testing of metals, ASTM E 1457-92 [11].

The present paper reports on a study of deformation, and crack initiation and crack growth in γ-TiAl base intermetallic alloys. Creep and crack growth data are determined at 700°. Some of the issues pertinent to fracture and CCG testing of creep brittle materials are highlighted using experimental data obtained on a TiAlCr alloy. The fracture behaviour strongly depends on the microstructural constituents and the orientation of the lamellae in the process zone of the crack tip. Microcracking and crack branching increases with temperature up to 700°C that affect the crack growth assessment.

EXPERIMENTAL PROCEDURE

Material and Metallography

A γ-TiAl base intermetallic alloy, Ti 48at%Al 2at%Cr, (TiAlCr), was investment cast (IC) and subsequently hot isostatically pressed (HIP) at 1200°C [5].
Metallographic specimens were prepared using conventional methods. The test specimens were sectioned from the IC+HIPed billets, some of which were heat treated at 1300°C in air.

Specimens and Testing

The tensile, creep and compact tension (CT) specimens were spark eroded (Electric Discharge Method, EDM) from investment cast near net shape forms and ground to final specimen dimensions. The CT specimens were 50mm wide and 10mm thick and side grooved 20% after precracking or machining of the EDM notches. The slit notches in CT specimens were introduced by EDM using a 0.1 mm diameter wire where the notch root radius, ρ, was 0.05mm.
The tensile properties of the material were determined at 700°C in air at cross head speed of 5mm/min. Creep tests were done at 700°C under constant load determined for an initial stress level to reach the test times that cover a wide stress-strain rate range.
Creep crack growth tests were carried out under displacement rate control at 1, 5 and 10 μm/h, and under constant load on an electro-mechanical machine. The load, displacement in the load line, V_{LL}, and the crack length were continuously monitored and recorded for further evaluation. The direct current potential drop (DCPD) method was employed to monitor crack initiation and crack growth in CT specimens. The crack length was evaluated from the electrical potential measurements and the crack growth rate, da/dt, was determined using 7 point incremental (second order) polynomial method, following the test standard [11].

CCG Data assessment

Due to the brittle fracture behaviour of TiAlCr at 700°C the crack growth data is correlated with K and $C^*_{(t)}$ following ASTM standards E399 [12] and E1457 [11]. For the tests where the load, the load-line deflection rates, and the crack size measurements is available, $C^*_{(t)}$ is determined from,

$$C^*_{(t)} = (F(dV/dt)/BW)\ \eta\ (a/W,n) \qquad (1)$$

where F is the applied load, B and W are the specimen thickness and width, respectively, dV/dt is the measured load-line deflection rate, n is the creep exponent, and η is a geometric function whose value depends on the crack size and n [11].

RESULTS

Tensile and Creep tests

The tensile and creep data determined at 700°C on materials as cast + HIPed (As Cast), and HIPed + heat-treated at 1300°C (HT 1300°C) are given in Table 1. The reported tensile data is an average value of two tests, which had a marginal scatter. The creep exponents reported in Table 1 are average values for the entire data set for a material condition.

TABLE 1: TENSILE AND CREEP DATA OF TiAlCr AT 700°C

Material	$R_{p0.2}$ (MPa)	R_m (MPa)	E-Modulus (MPa)	A_5 (%)	D_1	m	n
As Cast	372	522	152 450	0,03	8,0E-5	6,56	7,78
HT 1300°C	326	412	152 000	0,34	7,0E-5	9,13	9,19

Creep Crack Growth Tests

The scatter and pop-ins in recorded experimental data may be related to the mixed fracture mode with secondary cracking and crack front tunneling. The crack tip deformation and crack extension studied in a SEM on sectioned specimens.

The complete set of creep crack growth data obtained from CT specimens of both As Cast and HT 1300°C materials at 700°C are correlated with crack tip parameters K and C*(t) in Figures 1 and 2, respectively.

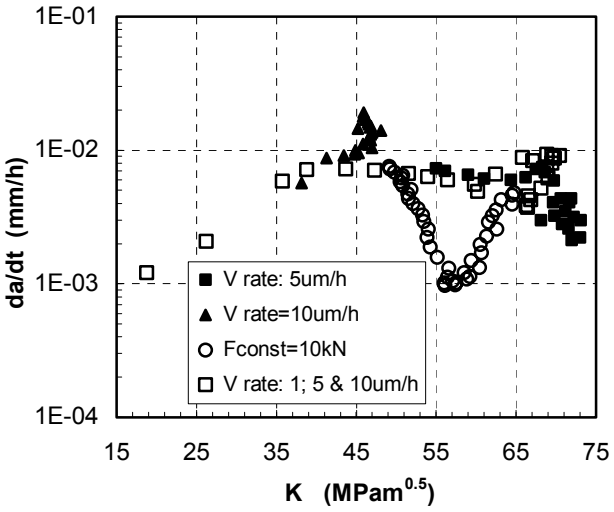

Fig.1.Crack growth rate as a function of K at 600°C (complete set of data).

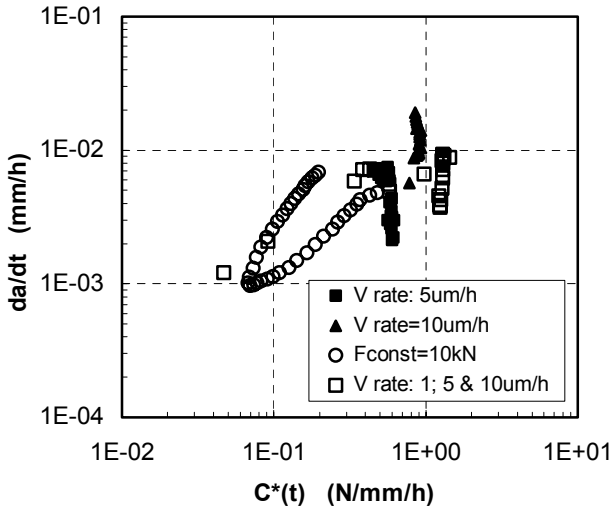

Fig.2.Crack growth rate as a function of C*(t) (complete set of data).

The CCG rate data correlated with K are reduced to transition range, i.e. $\Delta a<0.2$mm, showing a good correlation, as depicted in Figure 3. On the other hand, the crack growth data from displacement rate controlled tests (Vrate in Fig.2) showed decreasing C*(t) due to crack growth rate effect beyond F_{max}.

This data is reduced up to F_{max} in Figure 4, which gives a linear crack growth correlation. The data from constant load test, however, shows two parts that calls for study of effects of sharp starter crack and loading mode in CCG testing and validity of crack growth data. Therefore, the crack growth data is further analysed comparing the data from constant load and displacement rate control tests in Figures 5 and 6, respectively. Both tests showed the ratio of creep component of displacement rate, $\dot{V}_c$, to total displacement rate, $\dot{V}_t$, $\dot{V}_c / \dot{V}_t > 0.9$ for the whole range of tests (Figs.5 a and b), satisfying the validity requirement of the test standard [11]. However, the rather brittle fracture mode observed in SEM calls for

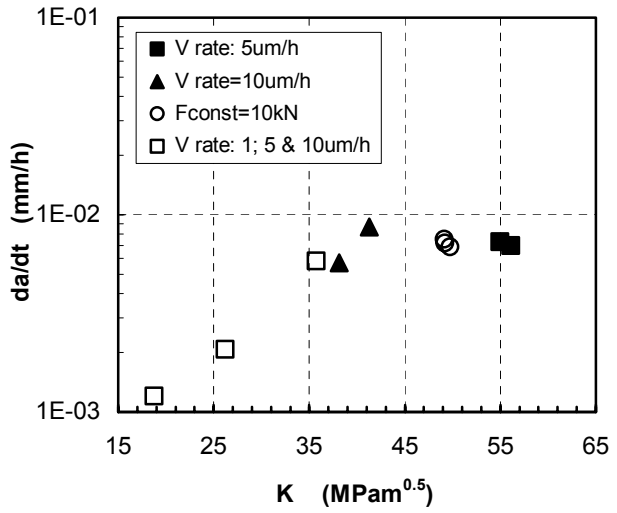

Fig.3. Crack growth rate as a function of K (reduced data for $\Delta a<0.2$mm).

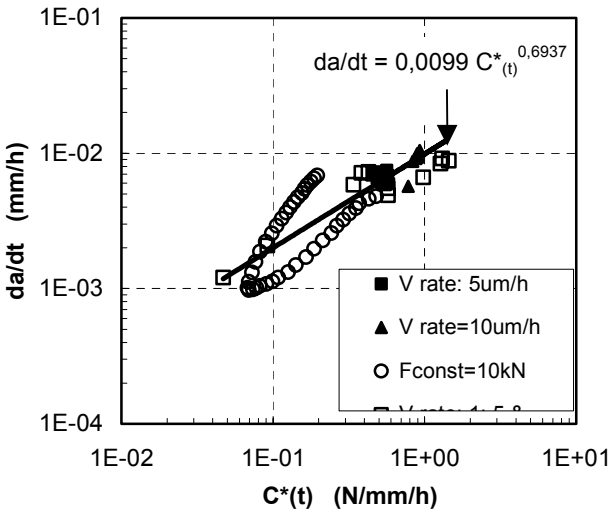

Fig.4. Crack growth rate as a function of C*(t) at 600°C (reduced data for $F<F_{max}$).

analysis of deformation and deflection rate partitioning. The total load line deflection, V_t, together with elastic, V_e, and creep components of deflection, V_c, are shown in Figure 6 a and b, for constant load and displacement rate control tests as a function of normalised time, t/t_f, respectively. A difference in the growth of creep deformation is noted from the variation of creep component of deflection, V_c, in the figures.

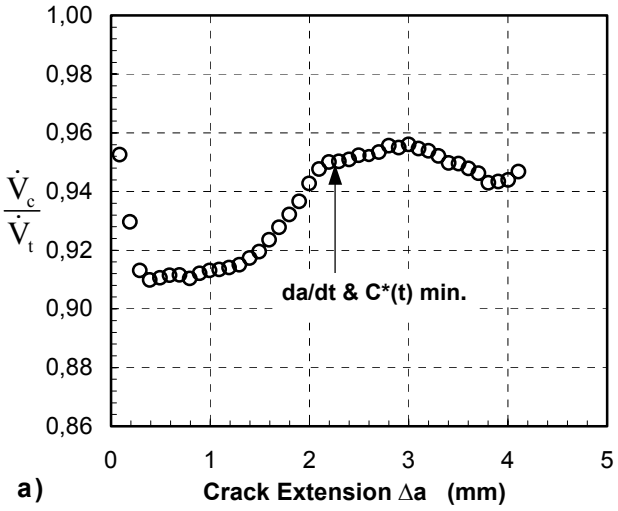

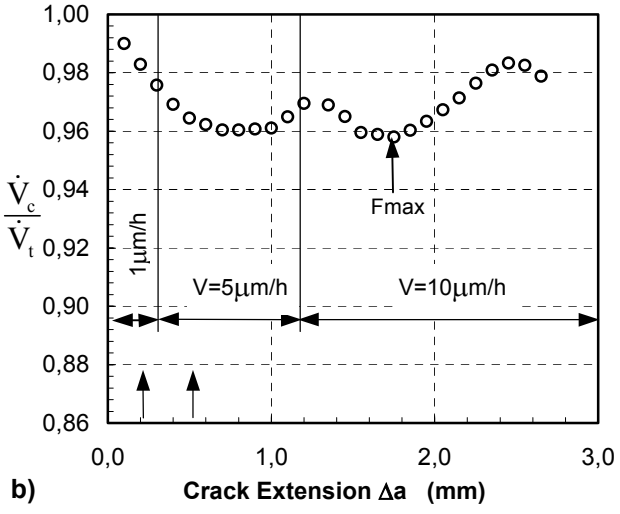

Fig.5. Ratio of load-line deflection rate due to creep (dVc/dt) to total load-line deflection rate (dVt/dt) as a function of crack extension (Δa) for HT1300°C TiAlCr tested at 700°C a) under constant load, b) displacement rate control.

DISCUSSION

The microstructure, particularly lamellar grain size and orientation, affects the fatigue crack initiation and fatigue crack growth leading to multi-crack initiation and crack branching [7], mainly affected by the lamellar orientation at the crack tip. The FCP load calculated from formulas given in the test procedures [11,12] overestimate the precrack loads by a factor of three. The difficulty faced with introduction of sharp starter crack may be overcome by spark erosion (EDM) of a fine, i.e. tip radius $\rho<0.05$mm [8], starter slit notch. The crack growth monitored during testing CT specimens using the DCPD method.

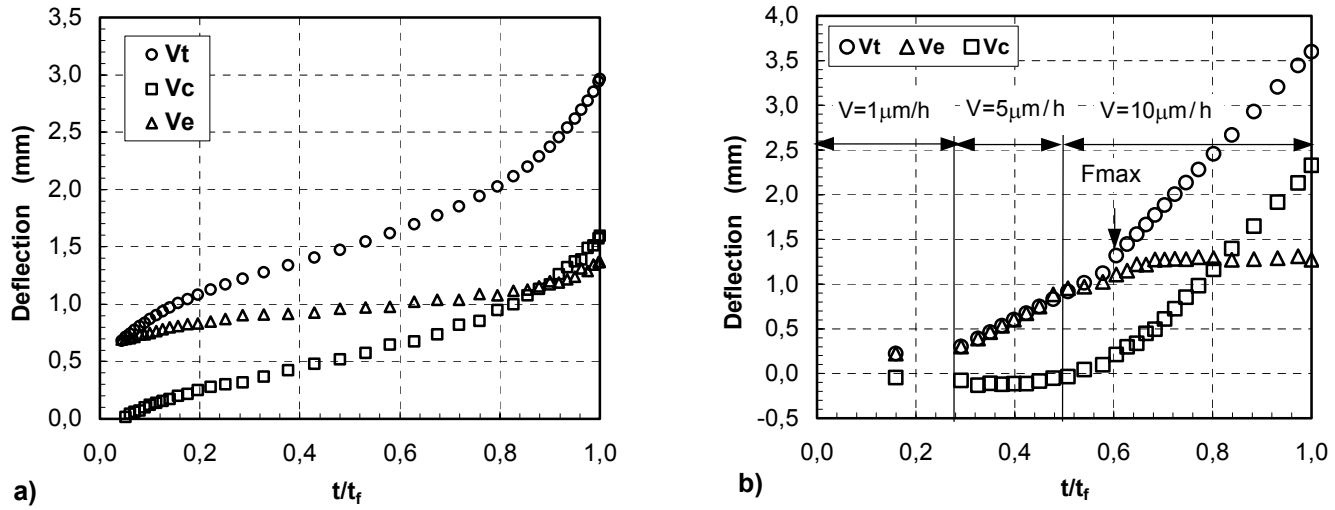

Fig.6.Load line deflection (Vc: creep component, Ve: elastic component, Vt: total load-line deflection) as a function of normalised test time, t/t_f, for HIPed + HT1300°C TiAlCr tested at 700°C a) under constant load, F=10kN, b) displacement rate control, Vrate=1,5&10μm/h.

Crack lengths determined from DCPD were compared with those determined from fracture surfaces. The difference was as high as 50 per cent, with those measured on fracture surfaces were higher, which also did not satisfy the standard requirement. In determining the crack lengths on fracture surfaces the unbroken shear ligaments were ignored, whereas crack lengths from the DCPD were erronous because of surface contacts and unbroken ligaments. The measurement of crack length in toughness testing of TiAlCr requires further study. Crack lengths measured on the side surfaces of specimens were smaller than those measured on fracture surfaces by up to 30 per cent. The crack fronts were uneven and the crack growth was non-uniform by more than 20 per cent or 0.15 mm that is not satisfying the standard test requirements [11]. Crack tunnelling and unbroken ligaments on fracture surfaces contribute to the discrepancy in crack length measurements. Crack branching and bifurcation lead to violation of the validity criteria.

Large grains and lamellae particularly promote the out-of-plane cracking. Out-of-plane cracking limits need to be specified for titanium aluminides similar to the one in Fig 8 of ASTM E647 [13]. The crack deflection at an excess of 20° may call for mixed-mode stress analyses to compute K as it is also suggested in ASTM E647.

The complete set of creep crack growth data is correlated with both $C^*(t)$ and K (Figs.1,2), followed by the reduced data (Figs.3,4) to shed some light on the applicability of the concepts of K and $C^*(t)$ in these materials. The data from transition range correlate only with K. This is because immidiately after loading, an elastic, or elastic-plastic stress distribution is generated ahead of a crack tip prior to the onset of creep. The criteria was set in the standard [11] to ensure the extensive creep stress distribution will be produced ahead of the crack for the data to correlate with $C^*(t)$. The complete CCG data satisfied transition time

$t_{test} > t_T$, and deflection rate ratio $\dot{V}_c / \dot{V}_t > 0.9$, although the material is brittle. The variation of deflection rate ratio in Fig.5 does not follow the predicted behaviour [14]. Similar discrepancy is also reported for creep brittle Al and Ti alloys [15]. As numerical work was not done in the present study, it may be noted that this aspect need further clarification particularly if the assessment of component made of TiAl is to be done and the crack tip parameter C_t [14] is considered.

The stationary stress state is achieved in the second part of constant load test (Fig.4). The decreasing part of the constant load test crack growth rate correlation is attributed to the transition of crack growth mode of a fatigue precracked specimen where initial crack growth follows the transgranular fatigue crack path that changes to creep crack mode with accumulation of grain boundary damage with time. This behaviour in TiAl is also reported by Fuji et al [9]. It is important to note that this transition occurs (Fig.5.a) over a period of finite crack extension, as large as 50% of the total test time, $t/t_f=0.5$.

The data from displacement rate controlled tests exhibited typical transition behaviour over a range of crack growth caused by change of stress state via changing applied load under displacement rate control in creep brittle material. This discussion is supported by the partitioned deflection in Figure 6, where creep component of deflection is 0 for a long period of time, $t/t_f>0.5$. It was followed by constant V_e and

increasing V_c, however, crack growth rate effect dominates after F_{max}. On the other hand the constant load test shows an increasing V_c from beginning of the test onwards as expected.

CONCLUSIONS

The microstructure influences the deformation and creep behaviour of TiAlCr alloys. The fracture mode in CT specimens at 700°C is brittle with microcracking observed in γ-phase and along lamellar interfaces. Large discrepancy, up to 50 per cent, between crack lengths measured on fracture surfaces and those determined using DCPD method were caused by unbroken lamellar ligaments, and crack branching and crack tunneling.
EDM slit notches with tip radius of 0.05mm can be used as sharp starter cracks.
Creep crack growth tests can be done both under constant load and displacement rate control provided the effects of crack growth on stress state is accounted for.
Crack growth data from displacement rate controlled tests beyond maximum load (F_{max}) may not be correlated with crack tip parameters.
The data from transition range i.e. $\Delta a<0.2$mm may be correlated with K.
The time dependent crack growth data assessed following the ASTM standard [11] correlates with $C^*_{(t)}$. However, much work is needed particularly for starter sharp crack requirement, crack length measurements and validity of data in order to assess the components made of creep brittle intermetallics.

ACKNOWLEDGEMENTS

The author would like to thank B. Petrovski for motivating discussions and scientific support and J. Granacher of T.U.Darmstadt for carrying out creep tests.

REFERENCES

1. Kim, Y.-W. (1995) Proc. Symp. Gamma Titanium Aluminides, Y.-W.Kim, R.Wagner and M.Yamaguchi Eds., TMS. Warrendale, Pa.,USA, pp. 637-654.
2. Appel, F. and Wagner, R. (1998) Materials Sci. and Engg., R22 (5), 187-268.
3. Yamaguchi, M., Inui, H. and Ito, K. Acta Mater. 2000, 48, pp.307-322.
4. Kim, Y.-W. JOM, TMS, 1995, 39-41.
5. Dogan, B. (2000) Proc. Int. Conf. Life Assessment of Hot Section Gas Turbine Components, 1999, R.Townsend et.al. Eds. IOM Book B731, pp.209-227.
6. Dogan, B., Schöneich, D., Schwalbe, K.-H. and Wagner, R. (1996) Intermetallics, 4 (1), pp.61-69
7. Dogan, B. and Schwalbe, K.-H. (1997) Engineering Fracture Mechanics, 56 (2), pp.155-165.
8. K.S.Chan and Y.-W.Kim, Met. Trans.A, 1993, 24A, pp.113-125.
9. Fuji, A., Tabuchi, M., Yokobori Jr., A.T. and Yokobori, T. (1999) Engineering Fracture Mechanics, 62 (1), pp.23-32.
10. VAMAS (Varsailles Project on Advanced Materials and Standards) TWA19: High Temperature Fracture of Brittle Materials, 1993-1998.
11. ASTM E1457-98, (1998), Standard Test Method for Measurement of Creep Crack Growth Rates in Metals. Annual Book of ASTM Standards, Philadelphia, 03.01., pp.1031-1034.
12. ASTM E399-90, (1990), Standard Test Method for Plane-Strain Fracture Toughness of Metallic Materials, Annual Book of ASTM Standards, 03.01., April 1991, pp.485-515.
13. ASTM E647-95, (1995), Standard Test Method for Measurement of Fatigue Crack Growth Rates, Annual Book of ASTM Standards, 03.01., April 1995, pp.485-515.
14. Saxena, A. Hall, D.E. and McDowell, D.L., (1999) Engineering Fracture Mechanics, 62, pp.111-122.
15. Kwon, O., Nikbin, K.M., Webster G.A. and Jata, K.V. (1999) Engineering Fracture Mechanics, 62, pp.155-165.

Oral/Poster Reference: ICF108920R

Embrittlement of High Strength β-Ti Alloys

R.P. Gangloff

Department of Materials Science and Engineering, University of Virginia, SEAS-Thornton Hall, Charlottesville, VA 22903-2442, USA

ABSTRACT

The outstanding strength of α-precipitation hardened β-Ti alloys is compromised by low plane strain fracture toughness, hydrogen embrittlement and perhaps elemental segregation. Solution treated all-β alloys are immune to hydrogen cracking for low to moderate H concentrations, but critical aging to form α triggers transgranular internal hydrogen embrittlement (TG IHE, along α/β interfaces) and intergranular hydrogen environment embrittlement (IG HEE, along β-grain boundaries). Increased strength does not explain this deleterious effect of aging. Rather, the aging dependence of TG IHE appears to be related to H enrichment in β and microscopic stress intensification at α/β interfaces arrayed continuously through β grains. Intergranular HEE is not explained by either grain boundary α formation or deformation localization due to aging. HEE persists when all α is dissolved, suggesting that elemental segregation of Si or impurities may be the requisite for IG cracking, but the offending species have not been resolved.

KEYWORDS

Titanium alloys, fracture toughness, hydrogen embrittlement, fracture mechanics, embrittlement.

INTRODUCTION

Titanium alloys based on a bcc (β) matrix that is hardened by fine precipitates of the hcp-α phase exhibit high strength to weight, excellent formability, and hardenability properties that enable high performance aerospace, marine, and land-based applications [1,2]. For example, a martensitic alloy steel must exhibit a tensile yield strength (σ_{YS}) of about 2400 MPa to exceed the strength-to-density ratio of the strongest β-Ti alloys (σ_{YS} ~ 1600 MPa). Results suggest, however, that fracture toughness and resistance to hydrogen (H)-assisted cracking are degraded substantially in concert with α strengthening of metastable β. The objective of this work is to examine the effect of α formation on the fracture resistance of modern β/α-Ti alloys, emphasizing deleterious hydrogen embrittlement and the crack tip damage mechanisms that govern damage tolerant properties.

EXPERIMENTAL PROCEDURES

Several β-Ti alloys were examined, including Ti-15-3 (Ti-15V-3Cr-3Sn-3Al in weight pct) [3-5], LCB (Low Cost Beta, Ti-7Mo-4.5Fe-1.5Al) [3], Beta-21S (Ti-15Mo-3Nb-3Al) [4,6], and Beta-C (Ti-8V-6Cr-4Mo-4Zr-3Al) [6-8]. Each alloy contained a total-dissolved H content of C_H = 25-200 ppm (parts-per-million by weight). High strength microstructures were developed by solution treatment (ST) above the β transus, air cooling to retain β only, and heating isothermally to precipitate α. This solution treated and aged (STA) microstructure is shown in Figure 1 for Ti-15-3 sheet where up to 60-volume pct of sub-micrometer α needles precipitate in the Burger's orientation of $\{110\}_\beta \parallel \{0001\}_\alpha, \langle 111\rangle_\beta \parallel \langle 11\bar{2}0\rangle_\alpha$ [9]. In addition to α, $(Ti,Zr)_5Si_3$ can precipitate at high aging temperatures and ω may be produced at low aging temperatures [9,10].

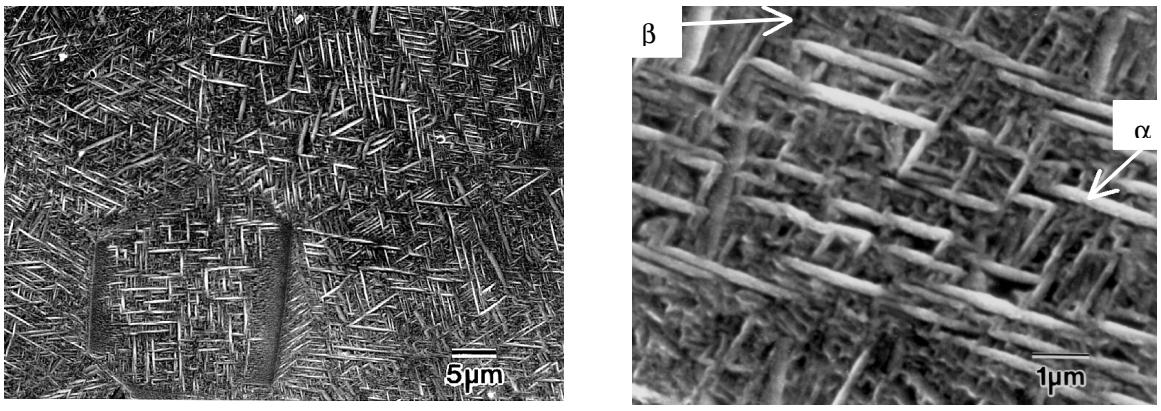

Figure 1: Optical (left) and scanning electron (right) micrographs of the deeply etched microstructure of STA Ti-15-3 sheet showing fine α needles precipitated with long axes that intersect to make angles of 0^o, 60^o and 90^o depending on the sectioning plane and consistent with the Burger's relationship.

Crack growth resistance was measured with a fatigue precracked specimen subjected to increasing crack mouth opening displacement (δ) at a fixed rate and using elastic-plastic J-integral fracture mechanics [11]. For cracking in moist air, the plane strain initiation toughness (K_{JIC} ~ K_{IC} [11]) was obtained for specimens with as-processed levels of H and the threshold K (K_{JTH} or K_{TH}) for the onset of H-assisted subcritical cracking was obtained for specimens electrochemically precharged to C_H of 100 to 10,000 ppm [3]. For specimens in aqueous chloride solution without H precharging, K_{TH} and stable crack growth rate (da/dt) were measured *vs* dK/dt [4,6].

RESULTS AND DISCUSSION

Fracture Toughness

The plane strain fracture toughness of high strength β/α-Ti alloys is deficient compared to martensitic steels at similar high strengths. The data compiled in Figure 2 show that the benefit of the 30% lower density typical of a β-Ti alloy is insufficient to compensate for the very high toughnesses achieved in steels such as AerMet 100 (K_{IC} ~ 120-170 MPa√m at σ_{YS} ~ 1800 MPa). Such steels exhibit up to an order of magnitude higher fracture toughness compared to K_{IC} approaching 25 MPa√m for very high strength β-Ti alloys.

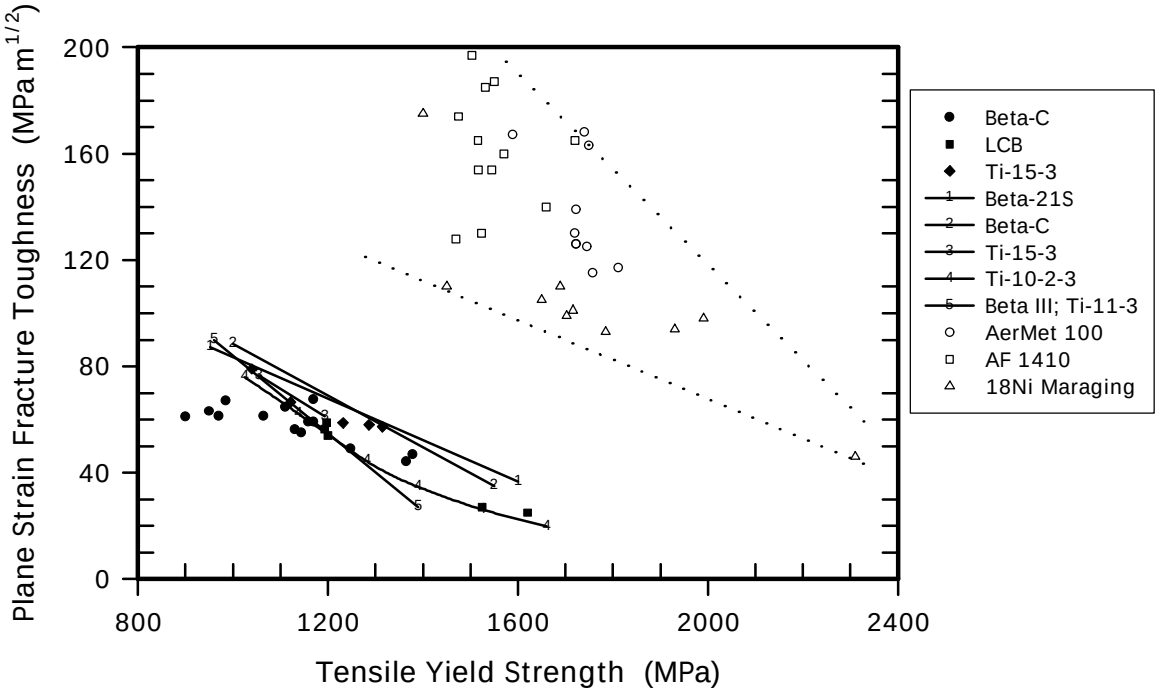

Figure 2: The yield strength dependence of plane strain fracture toughness for a variety of high strength β/α-Ti alloys and martensitic steels fractured in moist air at 25^oC.

Low fracture toughness in β-Ti is traced to the size and location of deformable α that localizes plastic strain and tensile stress to exacerbate microvoid nucleation, growth and coalescence [12-16]. For the lower strengths, α films or colonies precipitate heterogeneously at β-grain boundaries and large needles of α precipitate intragranularly; each provides preferred sites for microvoid damage and reduced K_{IC} [3,12,13,15]. To produce high strength, the size of α is reduced and the distribution is homogenized by low temperature aging with added nucleation sites such as dislocations, vacancies, or ω. The toughnesses of such microstructures are, however, low due to deformation banding and microvoid coalescence associated with the particularly high work hardening of fine α relative to β [14-16]. The dependencies of work hardening on α and β size and composition must be better understood, and local stresses from cooperative deformation in α and β must be incorporated into micromechanical models of fracture toughness [17].

Internal Hydrogen Embrittlement

Atomic hydrogen can dissolve in titanium during processing, fabrication, or service to degrade fracture resistance during subsequent deformation, so-called internal hydrogen embrittlement (IHE). Modern STA β/α-Ti alloys are prone to severe IHE for the tensile strengths in Figure 1 [3,5,8,18-20]. For example, experiments with H-precharged STA LCB (σ_{YS} = 1180 MPa) and Ti-15-3 (σ_{YS} = 1200 MPa) sheet showed that K_{TH} for IHE under rising-δ loading (dK/dt = 0.008 MPa√m/s) was reduced to 50% of K_{IC} at C_H levels of 400–500 ppm, and to 25% of K_{IC} at C_H = 750–900 ppm [3]. Absolute values of K_{TH} as low as 12 MPa√m were measured [3].

Aging and/or precipitation of α in β are a requisite for IHE in the moderate-C_H regime (< 2500 ppm) [5,8,18-20]. Figure 3 shows the aging time and strength dependencies of K_{JIC} for as-processed ST Ti-15-3 with 60 ppm H, and K_{JTH} for IHE of ST Ti-15-3 that was H-precharged electrochemically (C_H = 1300 ppm) [3]. ST Ti-15-3 is immune to IHE that only occurs for aging in excess of 5-6 h at 510°C. The reduction in K_{JTH} below K_{JIC} is accompanied by a change from dimpled rupture to transgranular-faceted cracking, as shown in Figure 3. Hydrogen cracking was likely along the interface between α needles and the β matrix, with facet surfaces reflecting the Burger's relationship between α and the multiple variants of {110} in β [3]. Intergranular (IG) cracking was never observed for IHE of STA LCB and Ti-15-3 for conditions typical of the data in Figure 3 [3].

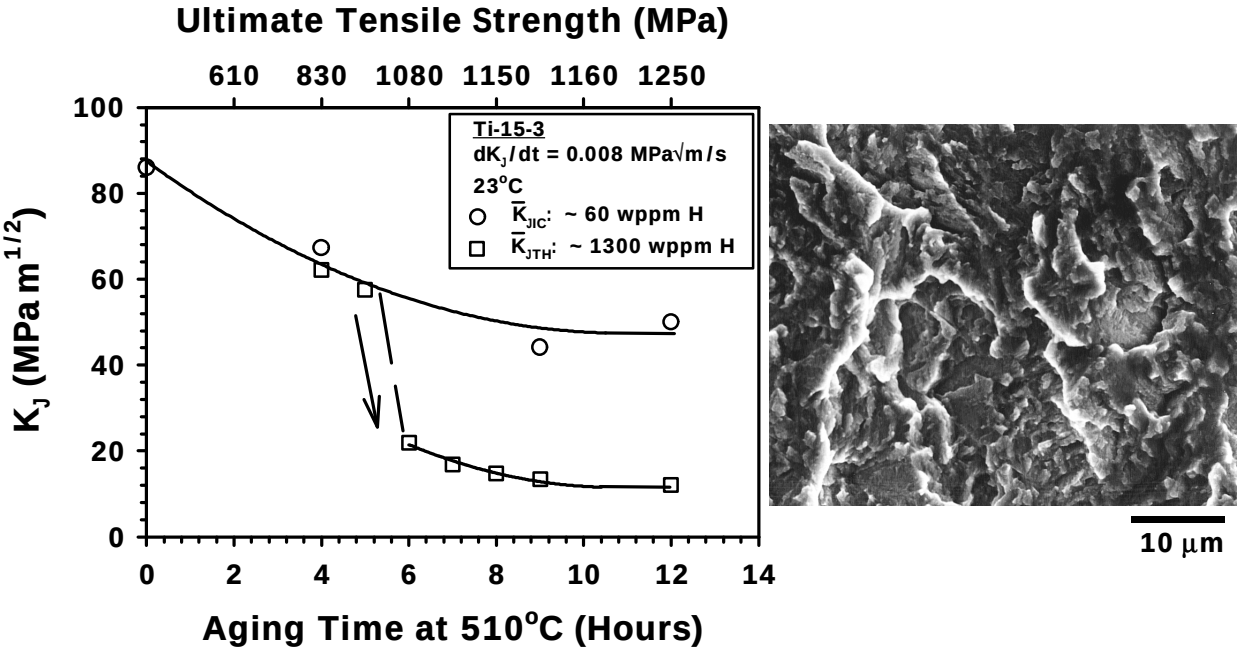

Figure 3: The isothermal-aging time and yield strength dependencies of plane strain fracture toughness at the as-processed H content of 60 ppm and the threshold stress intensity for IHE of H-precharged (C_H = 1300 ppm) ST Ti-15-3 stressed in moist air at 25°C. The SEM fractograph shows the morphology of transgranular IHE for the 12 h age case [3]. (The subscript, J, denotes K calculated from the J-integral and the bar indicates the average of 1st initiation and blunting-line offset definitions of crack growth [3,11].)

Generally, IHE of STA β-Ti alloys involves a variety of fracture modes depending on C_H, α/β microstructure, dK/dt, and constraint. The crack path in STA Beta-C changed from microvoid-based at low C_H, to intergranular along β boundaries (at 1300 ppm H), to crystallographic cleavage (2200 ppm H), to α/β-interface cracking at 3300 ppm H [8,19,20]. Intergranular cracking (1000 ppm H), slip plane cracking (4000 ppm H), and cleavage (5600 ppm H) were associated with IHE in Beta-21S [5,18]. ST β-Ti is susceptible to IHE by cleavage at very high C_H [21].

Hydrogen Environment Embrittlement in Aqueous Chloride Solutions

STA β/α-Ti alloys are susceptible to severe intergranular cracking when stressed in aqueous-NaCl solution [4,6,22-25] and the cracking mechanism was established with substantial certainty to be hydrogen environment embrittlement (HEE) [6,7,26,27]. H is produced exclusively at crack tip sites where the passive film is breached by concurrent plastic deformation and diffuses into the process zone to cause embrittlement. Locally large amounts of H can be introduced into Ti by this electrochemical scenario, provided that an occluded crack tip exists and crack tip strain rate conditions are favorable for H production and uptake [25-29]. Under such conditions, K_{TH} for HEE is as low as 15-20 MPa√m and da/dt is as high as 200 μm/s for STA alloys such as Beta-C and Beta-21S [22-25].

Aging and/or precipitation of α in β is a requisite for IG HEE. Figure 4 shows the strength and isothermal-aging time dependencies of K_{JIC} and K_{TH} for ST Beta-C stressed under rising δ (dK/dt = 0.004 MPa√m/s) in moist air and neutral-aqueous chloride solution, respectively [6,22]. ST Beta-C is immune to HEE that only occurs for aging in excess of 3-4 h at 500°C. The reduction in K_{TH} below K_{JIC} is accompanied by a change from microvoid to 100% IG cracking, as shown in Figure 4 and with no evidence of the brittle-transgranular cracking mode typical of IHE (Figure 3).

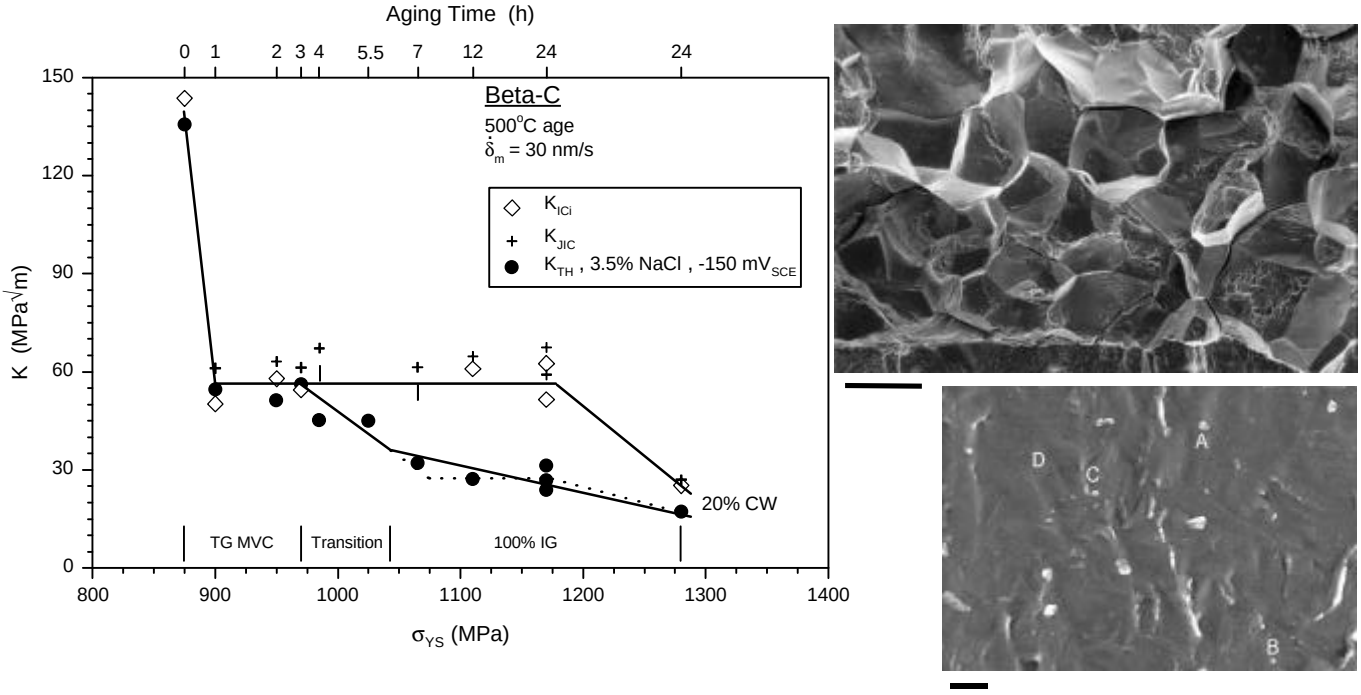

Figure 4: The strength and isothermal-aging time dependencies of fracture toughness and the threshold K for HEE of ST Beta-C stressed in moist air and aqueous-chloride solution at 25°C [6,22]. The highest strength and lowest K_{JIC} were achieved by 20% cold work prior to aging to stimulate fine-α precipitation. SEM fractographs show the morphology of 100% intergranular HEE for the 6 to 24 h age cases (top, 100 μm bar) and the high magnification view of an IG facet surface in these STA microstructures (bottom, 250 nm bar) [36].

Hydrogen Damage Mechanism and Metallurgical Culprit

Both IHE and HEE can be promoted by increasing yield strength since the magnitude of crack tip stresses increases proportionate to 3 to 5 σ_{YS} and H-damage mechanisms are exacerbated [30,31]. However, it is unlikely that strengthening explains the deleterious effect of aging on IHE (Figure 3) and HEE (Figure 4). For Beta-C, the ST β microstructure was immune to HEE for prior cold work levels from 0 to 80 pct, causing strength increases over the range typical of age hardening in Figs. 3 and 4 [22,23]. Experiments with notched-tensile specimens showed that cold worked Beta-C was also immune to IHE [19,20]. Yield strength increases are of secondary importance, perhaps because work hardening decreases with aging to offset the effect of rising σ_{YS}, and blunted crack solutions that equate crack tip stresses to 3-5 σ_{YS} may not be accurate for hydrogen embrittlement due to unique aspects of tip deformation for a crack localized to an interface or grain boundary [32].

Rather than strength, a metallurgical factor that changes during aging is responsible for the occurrence of IHE and HEE in β/α-Ti. Determination of the culprit is complicated by the multiple changes and fine scale of the α microstructure that evolve during aging of ST β-Ti. Additionally, the damage mechanism for hydrogen embrittlement is controversial, with possible contributions from hydride-phase transformation, hydrogen enhanced-localized plasticity, and interface decohesion [30,31,33].

IHE: Considerations of the kinetics of K_{TH} and da/dt *vs* dK/dt for IHE in Ti-15-3 suggest that H diffuses rapidly during loading and over a short distance (0.5-5 μm) through β in the fracture process zone to reach the α/β interface [3]. While brittle TiH may form in α [34], hydrides are less important in β alloys due to the high solubility of H in bcc Ti (~15,000 ppm at 25°C) [19,20]. H is enriched in β when α precipitates are present; local hydriding of α, at the interface with β, should occur for total C_H above 2500 ppm [19,20]. This hydriding was not observed experimentally and is not a likely cause of cracking at the C_H levels in Figure 3. The effect of locally high interface stresses on hydride precipitation is uncertain and this mechanism cannot be discounted. Fracture without H occurs at α/β interfaces in STA alloys such as Ti-15-3. It is reasonable to speculate that this fracture mode is promoted by H, trapped at this interface and with locally high tensile stresses, as envisioned in classic decohesion theory [30,31].

The aging dependence of TG IHE may be understood based on the need for a critical amount of intragranular α. Considering Figure 3, α precipitation was restricted to β-grain boundaries during 0-5 h of aging (α volume fraction of 0 to 0.48) and when Ti-15-3 was immune to IHE. H cracking correlated with α precipitation within many β at the 6 h age (0.52 α) and within all grains at 10-12 h (0.68-0.80 α) [3]. A critical amount of α in β may be required for: (1) a connected path for H cracking [35], (2) locally high tensile stresses from microscopic constraint adjacent to the α/β interface, or (3) H enriched in β and trapped at the interface with α. A connected crack path is not sufficient for IHE since the immune microstructures in Figure 3 exhibited α on all grain boundaries, but IG cracking did not occur.

HEE: Metallurgical variables could promote intergranular HEE by enhancing H production and uptake near β-grain boundaries at the crack tip, and by enabling brittle cracking of H-enriched boundaries within the process zone. Two factors constrain the governing metallurgical variable. The fully-IG fracture mode observed for susceptible STA Beta-C (Figure 4) dictates that the HEE mechanism and variable must operate at essentially every grain boundary, at least for some β-Ti alloys. Second, since H damage appears to occur within 0.1-1 μm of the crack tip surface contacting NaCl solution, the metallurgical variable must be sized and interconnected on this length scale [25,32]. Three microstructural factors may be consistent with these constraints and change during isothermal aging of the ST-β phase: grain boundary α, slip localization, and elemental segregation.

A study isolated these candidate explanations of aging-dependent HEE for the situation represented in Figure 4, but the results were not conclusive [36]. Two features, grain boundary α and H-enhanced slip localization, are not the cause of IG HEE in Beta-C stressed in NaCl solution. TEM and SEM analyses showed that α decorated less than 5% of the β-grain boundaries, but HEE was nearly-100% IG. High magnification examination of matching surfaces of IG facets, using an SEM with a field-emission gun and dual detectors to optimize topographic contrast and resolution, failed to evidence localized plasticity of the sort reported for IG IHE of β/α-Ti [19,20] and hydrogen embrittlement in general [33]. As illustrated by the high-magnification SEM fractograph in Figure 4, the only features resolved were perturbations of the cracked β-grain boundary surface by intersection of occasional α plates. The predominant feature was mildly undulating and featureless grain surfaces, consistent with interface decohesion.

Circumstantial evidence suggested that solute segregation to β-grain boundaries during aging, combined with trapped H, explained the onset of IG HEE in β/α-Ti (Figure 4). A similar explanation was adopted for IG IHE of STA Beta-C [20] and H embrittlement of steels [31]. Results implicated segregated Si as reducing boundary cohesion in β-Ti without H [37]. Experiments, where STA Beta-C was aged at higher temperatures to progressively dissolve α and remove segregation, support the importance of elemental segregation [36]. For example, a double aged and α-free microstructure was susceptible to IG HEE, confirming that grain boundary α and intragranular α are not required for embrittlement. Double aging at higher temperatures and longer times eliminated IG HEE in the all-β microstructure and restored the original ST immunity to cracking. The hypothesis was that HEE was precluded by elimination of boundary segregation, due to either reduced thermodynamic driving force or formation of $(Ti,Zr)_5Si_3$. Boundaries in HEE-immune and susceptible single and double ages of Beta-C were examined by small-probe STEM. No segregant was observed to correlate with the IG cracking tendency. Auger spectroscopy of intergranular facets produced by *in situ* fracture of H-precharged STA Beta-C failed to resolve segregation that correlated with severe IG IHE in long time single-aged specimens [20].

Similar aging times and α precipitation are required to trigger IHE and HEE of ST β-Ti, as shown by the similar K_{TH} relationships in Figures 3 and 4. As such, the mechanisms for these aging dependencies of TG *vs* IG H embrittlement may share a common feature. Elemental segregation to α/β interfaces during aging has not been considered for TG IHE, and enhanced-H trapping from enrichment in β or stress localization due to the presence of α have not been considered for IG HEE.

CONCLUSIONS

1. The outstanding strength capability of α-precipitation hardened β-Ti alloys is compromised by low plane strain fracture toughness compared to martensitic steels, and by both IHE and HEE.
2. All-β alloys are immune to hydrogen embrittlement for low to moderate H concentrations, but transgranular IHE (along α/β interfaces) and intergranular HEE (along β-grain boundaries) are triggered by a critical amount of aging to form α.
3. Increased strength does not explain the deleterious effects of aging on H embrittlement. The onset of TG IHE appears to be related to H enrichment in β and stress intensification at α/β interfaces continuous through β grains. For IG HEE, neither grain boundary α nor deformation localization explain the effect of aging. Segregation may be the requisite for IG cracking, but offending species were not resolved.

ACKNOWLEDGEMENT

This research was supported by the Office of Naval Research (Grant N00014-91-J-4164), with Dr. A. John Sedriks as Scientific Monitor. The author acknowledges the critical contributions of B.P. Somerday, S.P. Hayes and L.M. Young, as well as the collaboration with J.R. Scully.

REFERENCES

1. Boyer, R.R. and Rosenberg, H.W. (1984). *Beta Titanium Alloys in the 80's*, TMS, Warrendale, PA.
2. Eylon, D., Boyer, R.R. and Koss, D.A. (1993). *Beta Titanium Alloys in the 90's*, TMS, Warrendale, PA.
3. Hayes, S.P. (2000). PhD Dissertation, University of Virginia, Charlottesville, VA.
4. Young, L.M. (1993). MS Thesis, University of Virginia, Charlottesville, VA.
5. Young, G.A. (1993). MS Thesis, University of Virginia, Charlottesville, VA.
6. Somerday, B.P. (1998). PhD Dissertation, University of Virginia, Charlottesville, VA.
7. Kolman, D.G. (1995). PhD Dissertation, University of Virginia, Charlottesville, VA.
8. Gaudett, M.A. (1997). PhD Dissertation, University of Virginia, Charlottesville, VA.
9. Headley, T.J. and Rack, H.J. (1979) *Metall. Trans. A* 10A, 909.
10. Shen, G.Q., Wang, S.H., Liang, T.M., Luo, G.Z. and Xie, L.Y. (1996) *Trans. Metal Heat Treatment* 17, 10.
11. Haynes, M.J. and Gangloff, R.P. (1997) *J. Testing Eval.* 25, 82.
12. Froes, F.H., Chesnutt, J.C., Rhodes, C.G. and Williams, J.C. (1978). In: *Toughness and Fracture Behavior of Titanium, STP 651*, pp. 115-153, ASTM, West Conshohocken, PA.
13. Williams, J.C., Froes, F.H., Chesnutt, J.C., Rhodes, C.G. and Berryman, R.G. (1978). In: *Toughness and Fracture Behavior of Titanium, STP 651*, pp. 64-114, ASTM, West Conshohocken, PA.
14. Terlinde, G.T., Duerig, T.W. and Williams, J.C. (1983) *Metall. Trans. A* 14A, 2101.
15. Terlinde, G.T. and Schwalbe K.-H. (1987). In: *Microstructure, Fracture Toughness and Fatigue Crack Growth in Titanium Alloys*, pp. 97-109, Chakrabarti, A.K. and Chesnutt, J.C. (Eds.). TMS, Warrendale, PA.
16. Terlinde, G.T., Rathjen, H.-J. and Schwalbe K.-H. (1988) *Metall. Trans. A* 19A, 1037.
17. Haynes, M.J. and Gangloff, R.P. (1998) *Metall. Trans. A* 29A, 1599.
18. Young, G.A. and Scully, J.R. (1994) *Corrosion* 50, 919.
19. Gaudett, M.A. and Scully, J.R. (1999) *Metall. Trans. A* 30A, 65.
20. Gaudett, M.A. and Scully, J.R. (2000) *Metall. Trans. A* 31A, 81.
21. Nelson, H.G. (1992). *NASP Government Work Package #92*, NASA Ames Research Center, Moffett Field, CA.
22. Somerday, B.P. and Gangloff, R.P. (1998) *Matls. Sci. Engr. A* A254, 166.
23. Somerday, B.P. and Gangloff, R.P. (1998) *Matls. Sci. Engr. A* A254, 179.
24. Young, L.M., Young, G.A., Scully, J.R. and Gangloff, R.P. (1995) *Metall. Trans. A* 26A, 1257.
25. Somerday, B.P., Young, L.M. and Gangloff, R.P. (2000) *Fatg. Fract. Engr. Matls. Struct.* 23, 39.
26. Kolman, D.G. and Scully, J.R. (1998). In: *Effects of the Environment on the Initiation of Crack Growth, ASTM STP 1298*, pp. 61-73, Van der Sluys, W.A., Piascik, R.S. and Zawierucha, R. (Eds.). ASTM, West Conshohocken, PA.
27. Kolman, D.G. and Scully, J.R. (1997) *Metall. Trans. A* 28A, 2645.
28. Kolman, D.G. and Scully, J.R. (1999) *Phil. Mag. A* 79, 2313.
29. Kolman, D.G., Gaudett, M.A. and Scully, J.R. (1998) *J. Electrochem. Soc.* 145, 1829.
30. Oriani, R.A. (1987) *Corrosion* 43, 390.
31. McMahon, C.J., Jr. (2001) *Engr. Frac. Mech.* 68, 773.
32. Gangloff, R.P. (2001). "Diffusion Control of Hydrogen Environment Embrittlement in High Strength Alloys", In: *Hydrogen Effects on Material Behavior*, Moody, N.R. et al. (Eds.). TMS, Warrendale, PA, in review.
33. Robertson, I.M. (2001) *Engr. Frac. Mech.* 68, 671.
34. Nelson, H.G. (1973) *Metall. Trans. A* 4, 364.
35. Scully, J.R. (2000). In: *Environmentally Assisted Cracking, STP 1401*, pp. 40-69, Kane, R.D. (Ed.). ASTM, West Conshohocken, PA.
36. Somerday, B.P., Wilson, A.W., Howe, J.M. and Gangloff, R.P. (2001) "Microstructural Cause of Intergranular Hydrogen Environment Embrittlement of Aged Beta-Ti Alloys", *Metall. Trans. A*, in review.
37. Graham, D.E. and Koss, D.A. (1978) *Metall. Trans. A* 9A, 1435.

ENERGY BALANCE METHOD FOR PREDICTING CRACKING IN CROSS-PLY LAMINATES DURING BEND DEFORMATION

L. N. McCartney and M. J. W. Byrne

NPL Materials Centre, National Physical Laboratory
Queens Road, Teddington, Middlesex, UK, TW11 0LW

INTRODUCTION

Microstructural damage in composite structures arising from the application of mechanical and/or thermal loads is often unavoidable and its effects need to be taken into account when assessing structural performance, especially the occurrence of ply crack formation and delamination. For structures subject to fatigue loading it is desirable to avoid damage occurrence of any kind as it can act as nucleation sites for the growth of macroscopic damage (e.g. delaminations) that eventually leads to the catastrophic failure of the structure. As many structures experience some form of bend deformation during service it is vital that damage formation in the presence of bending is well understood. Of particular relevance to the performance of structures is the prediction of the occurrence of microstructural damage in complex loading modes where out-of-plane bending modes of deformation occur in conjunction with in-plane biaxial and through-thickness loading.

While a great deal of research has been devoted to the case of ply cracking in cross-ply laminates subject only to in-plane deformations, the practically important case of out-of-plane bending has received much less attention (e.g. [1-6]). One objective of this paper is to summarise the important results that have been derived using an energy balance method for predicting the conditions for the steady state growth of ply cracks in a cross-ply laminate subject to bending and thermal residual stresses. A second objective is to indicate how the methodology for ply crack formation can be developed without a detailed analysis of the stress transfer that is in fact needed only to estimate the thermoelastic constants of a damaged laminate (as described in [6]). The anti-clastic (i.e. biaxial) bending typical of deformed laminates will be taken into consideration.

GEOMETRY AND LOADING CONDITIONS

A cross-ply laminate of length 2L, width 2W and total thickness h consisting of perfectly bonded anisotropic layers is considered within a Cartesian coordinate system. The x-direction is taken as the through-thickness direction of the laminate, the y-direction is taken as the axial (longitudinal) direction and the z-direction as the in-plane transverse direction. The bending moments per unit area of loading cross-section for the axial and transverse directions are defined respectively by

$$M = \frac{1}{2hW}\int_{-W}^{W}\int_{0}^{h}\left(x-\frac{h}{2}\right)\sigma_{yy}(x,L,z)\,dx\,dz, \qquad M_T = \frac{1}{2hL}\int_{-L}^{L}\int_{0}^{h}\left(x-\frac{h}{2}\right)\sigma_{zz}(x,y,W)\,dx\,dy. \tag{1}$$

The moments are taken about the mid-plane of the laminate which might not correspond to the neutral axis if the laminate is unsymmetrical and/or damaged in the region of axial tension. The corresponding effective applied axial and transverse stresses are defined respectively by

$$\sigma = \frac{1}{2hW}\int_{-W}^{W}\int_{0}^{h}\sigma_{yy}(x, L, z)\,dx\,dz, \qquad \sigma_T = \frac{1}{2hL}\int_{-L}^{L}\int_{0}^{h}\sigma_{zz}(x, y, W)\,dx\,dy. \tag{2}$$

The faces of the laminate are assumed to be subject to a uniform applied tensile traction σ_t. The corresponding effective through-thickness strain ε_t for a laminate is defined by

$$\varepsilon_t = \frac{1}{4hLW}\int_{-W}^{W}\int_{-L}^{L}[u(h, y, z) - u(0, y, z)]\,dy\,dz, \tag{3}$$

and the effective applied in-plane axial and transverse strains $\bar{\varepsilon}$ and $\bar{\varepsilon}_T$ are defined by

$$\begin{aligned}\bar{\varepsilon} &= \frac{1}{4hLW}\int_{-W}^{W}\int_{0}^{h}[v(x, L, z) - v(x, -L, z)]\,dx\,dz,\\ \bar{\varepsilon}_T &= \frac{1}{4hLW}\int_{-L}^{L}\int_{0}^{h}[w(x, y, W) - w(x, y, -W)]\,dx\,dy,\end{aligned} \tag{4}$$

where u, v and w are respectively the x, y and z-components of the displacement vector.

In order to represent bending of the laminate for the axial and transverse directions it is assumed that the edge boundary conditions for the displacement components v and w are of the form

$$v = \begin{cases} L(\varepsilon + \hat{\varepsilon}x) & \text{on } x = L \\ -L(\varepsilon + \hat{\varepsilon}x) & \text{on } x = -L \end{cases} \qquad w = \begin{cases} W(\varepsilon_T + \hat{\varepsilon}_T x) & \text{on } z = W \\ -W(\varepsilon_T + \hat{\varepsilon}_T x) & \text{on } z = -W. \end{cases} \tag{5}$$

For infinitesimal deformations the radii of curvatures of the surface x = 0 of the deformed laminate are given by $R_1 = 1/|\hat{\varepsilon}|$ and $R_2 = 1/|\hat{\varepsilon}_T|$, so that $\hat{\varepsilon}$ and $\hat{\varepsilon}_T$ are respectively the curvatures of the surface x = 0 of the deformed laminate in the axial and transverse directions. Substituting the edge boundary conditions (5) into (4) and performing the integrations leads to

$$\bar{\varepsilon} = \varepsilon + \tfrac{1}{2}h\hat{\varepsilon}, \qquad \bar{\varepsilon}_T = \varepsilon_T + \tfrac{1}{2}h\hat{\varepsilon}_T. \tag{6}$$

It is clear that $\bar{\varepsilon}$ and $\bar{\varepsilon}_T$ are the axial and transverse strains on the mid-plane of the laminate subject to the edge conditions (5).

STRESS-STRAIN RELATIONS

It has been shown [6] that the effective stress-strain relations for a damaged cross-ply laminate are of the following form

$$\varepsilon_t = \frac{\sigma_t}{E_t} - \frac{\nu_a}{E_A}\sigma - \frac{\nu_t}{E_T}\sigma_T - \frac{\hat{\nu}_a}{\hat{E}_A}M - \frac{\hat{\eta}_t}{\hat{E}_T}M_T + \alpha_t\Delta T, \tag{7}$$

$$\bar{\varepsilon} = -\frac{\nu_a}{E_A}\sigma_t + \frac{\sigma}{E_A} - \frac{\nu_A}{E_A}\sigma_T - \frac{\hat{\nu}_A}{\hat{E}_A}M - \frac{\hat{\eta}_A}{\hat{E}_T}M_T + \alpha_A\Delta T, \tag{8}$$

$$\bar{\varepsilon}_T = -\frac{\nu_t}{E_T}\sigma_t - \frac{\nu_A}{E_A}\sigma + \frac{\sigma_T}{E_T} - \frac{\hat{\nu}_T}{\hat{E}_A}M - \frac{\hat{\eta}_T}{\hat{E}_T}M_T + \alpha_T\Delta T, \tag{9}$$

$$\hat{\varepsilon} = -\frac{\hat{\nu}_a}{\hat{E}_A}\sigma_t - \frac{\hat{\nu}_A}{\hat{E}_A}\sigma - \frac{\hat{\nu}_T}{\hat{E}_A}\sigma_T + \frac{M}{\hat{E}_A} - \frac{\hat{\delta}_A}{\hat{E}_A}M_T + \hat{\alpha}_A\Delta T, \tag{10}$$

$$\hat{\varepsilon}_T = -\frac{\hat{\eta}_t}{\hat{E}_T}\sigma_t - \frac{\hat{\eta}_A}{\hat{E}_T}\sigma - \frac{\hat{\eta}_T}{\hat{E}_T}\sigma_T - \frac{\hat{\delta}_A}{\hat{E}_A}M + \frac{M_T}{\hat{E}_T} + \hat{\alpha}_T\Delta T, \tag{11}$$

which defines the various thermo-elastic constants that characterise the properties of a damaged laminate subject to combined in-plane biaxial loading, out-of-plane through-thickness loading and bending.

REDUCED STRESS-STRAIN RELATIONS FOR CONSTRAINED TRIAXIAL LOADING

The damage-dependent stress-strain relations (10) and (11) are treated as a linear system of algebraic equations with unknowns M and M_T. For convenience, the following parameters are defined

$$\hat{\delta}_T = \hat{\delta}_A \frac{\hat{E}_T}{\hat{E}_A}, \qquad \Lambda = 1 - \hat{\delta}_A \hat{\delta}_T \ . \tag{12}$$

On solving (10) and (11) for M and M_T and substituting into the remaining damage-dependent stress-strain relations (7-9), the following reduced stress-strain relations are derived of the same form as those for a cross-ply laminate subject only to triaxial loading, without shear or bending

$$\tilde{\varepsilon}_t = \varepsilon_t + \frac{\hat{\nu}_a}{\Lambda}\left[\hat{\varepsilon} + \hat{\delta}_T \hat{\varepsilon}_T\right] + \frac{\hat{\eta}_t}{\Lambda}\left[\hat{\varepsilon}_T + \hat{\delta}_A \hat{\varepsilon}\right] = \frac{\sigma_t}{\tilde{E}_t} - \frac{\tilde{\nu}_a}{\tilde{E}_A}\sigma - \frac{\tilde{\nu}_t}{\tilde{E}_T}\sigma_T + \tilde{\alpha}_t \Delta T \ , \tag{13}$$

$$\tilde{\varepsilon} = \bar{\varepsilon} + \frac{\hat{\nu}_A}{\Lambda}\left[\hat{\varepsilon} + \hat{\delta}_T \hat{\varepsilon}_T\right] + \frac{\hat{\eta}_A}{\Lambda}\left[\hat{\varepsilon}_T + \hat{\delta}_A \hat{\varepsilon}\right] = -\frac{\tilde{\nu}_a}{\tilde{E}_A}\sigma_t + \frac{\sigma}{\tilde{E}_A} - \frac{\tilde{\nu}_A}{\tilde{E}_A}\sigma_T + \tilde{\alpha}_A \Delta T \ , \tag{14}$$

$$\tilde{\varepsilon}_T = \bar{\varepsilon}_T + \frac{\hat{\nu}_T}{\Lambda}\left[\hat{\varepsilon} + \hat{\delta}_T \hat{\varepsilon}_T\right] + \frac{\hat{\eta}_T}{\Lambda}\left[\hat{\varepsilon}_T + \hat{\delta}_A \hat{\varepsilon}\right] = -\frac{\tilde{\nu}_t}{\tilde{E}_T}\sigma_t - \frac{\tilde{\nu}_A}{\tilde{E}_A}\sigma + \frac{\sigma_T}{\tilde{E}_T} + \tilde{\alpha}_T \Delta T, \tag{15}$$

where the reduced strains $\tilde{\varepsilon}_t$, $\tilde{\varepsilon}$ and $\tilde{\varepsilon}_T$ can be interpreted as strains for a damaged laminate, subject to triaxial loading and constrained so that bending strains are zero, and where the reduced thermoelastic constants are defined by

$$\frac{1}{\tilde{E}_t} = \frac{1}{E_t} - \frac{1}{\Lambda}\left(\frac{\hat{\nu}_a^2}{\hat{E}_A} + \frac{\hat{\eta}_t^2}{\hat{E}_T} + \frac{2\hat{\delta}_A \hat{\nu}_a \hat{\eta}_t}{\hat{E}_A}\right) \qquad \frac{1}{\tilde{E}_A} = \frac{1}{E_A} - \frac{1}{\Lambda}\left(\frac{\hat{\nu}_A^2}{\hat{E}_A} + \frac{\hat{\eta}_A^2}{\hat{E}_T} + \frac{2\hat{\delta}_A \hat{\nu}_A \hat{\eta}_A}{\hat{E}_A}\right)$$

$$\frac{1}{\tilde{E}_T} = \frac{1}{E_T} - \frac{1}{\Lambda}\left(\frac{\hat{\nu}_T^2}{\hat{E}_A} + \frac{\hat{\eta}_T^2}{\hat{E}_T} + \frac{2\hat{\delta}_A \hat{\nu}_T \hat{\eta}_T}{\hat{E}_A}\right), \qquad \frac{\tilde{\nu}_a}{\tilde{E}_A} = \frac{\nu_a}{E_A} + \frac{1}{\Lambda}\left(\frac{\hat{\nu}_a}{\hat{E}_A}\left(\hat{\nu}_A + \hat{\delta}_A \hat{\eta}_A\right) + \frac{\hat{\eta}_t}{\hat{E}_T}\left(\hat{\delta}_T \hat{\nu}_A + \hat{\eta}_A\right)\right),$$

$$\frac{\tilde{\nu}_t}{\tilde{E}_T} = \frac{\nu_t}{E_T} + \frac{1}{\Lambda}\left(\frac{\hat{\nu}_a}{\hat{E}_A}\left(\hat{\nu}_T + \hat{\delta}_A \hat{\eta}_T\right) + \frac{\hat{\eta}_t}{\hat{E}_T}\left(\hat{\delta}_T \hat{\nu}_T + \hat{\eta}_T\right)\right),$$

$$\frac{\tilde{\nu}_A}{\tilde{E}_A} = \frac{\nu_A}{E_A} + \frac{1}{\Lambda}\left(\frac{\hat{\nu}_A}{\hat{E}_A}\left(\hat{\nu}_T + \hat{\delta}_A \hat{\eta}_T\right) + \frac{\hat{\eta}_A}{\hat{E}_T}\left(\hat{\delta}_T \hat{\nu}_T + \hat{\eta}_T\right)\right)$$

$$\tilde{\alpha}_t = \alpha_t + \frac{1}{\Lambda}\left[\hat{\nu}_a\left(\hat{\delta}_T \hat{\alpha}_T + \hat{\alpha}_A\right) + \hat{\eta}_t\left(\hat{\alpha}_T + \hat{\delta}_A \hat{\alpha}_A\right)\right], \quad \tilde{\alpha}_A = \alpha_A + \frac{1}{\Lambda}\left[\hat{\nu}_A\left(\hat{\delta}_T \hat{\alpha}_T + \hat{\alpha}_A\right) + \hat{\eta}_A\left(\hat{\alpha}_T + \hat{\delta}_A \hat{\alpha}_A\right)\right],$$

$$\tilde{\alpha}_T = \alpha_T + \frac{1}{\Lambda}\left[\hat{\nu}_T\left(\hat{\delta}_T \hat{\alpha}_T + \hat{\alpha}_A\right) + \hat{\eta}_T\left(\hat{\alpha}_T + \hat{\delta}_A \hat{\alpha}_A\right)\right].$$

The corresponding reduced stress-strain relations for an undamaged laminate are written:

$$\tilde{\varepsilon}_t^o = \frac{\sigma_t}{\tilde{E}_t^o} - \frac{\tilde{\nu}_a^o}{\tilde{E}_A^o}\sigma - \frac{\tilde{\nu}_t^o}{\tilde{E}_T^o}\sigma_T + \tilde{\alpha}_t^o \Delta T, \tag{16}$$

$$\tilde{\varepsilon}^o = -\frac{\tilde{\nu}_a^o}{\tilde{E}_A^o}\sigma_t + \frac{\sigma}{\tilde{E}_A^o} - \frac{\tilde{\nu}_A^o}{\tilde{E}_A^o}\sigma_T + \tilde{\alpha}_A^o \Delta T \ , \tag{17}$$

$$\tilde{\varepsilon}_T^o = -\frac{\tilde{\nu}_t^o}{\tilde{E}_T^o}\sigma_t - \frac{\tilde{\nu}_A^o}{\tilde{E}_A^o}\sigma + \frac{\sigma_T}{\tilde{E}_T^o} + \tilde{\alpha}_T^o \Delta T, \tag{18}$$

where a superscript 'o' denotes that the strains and laminate properties refer to their values for the undamaged state of the laminate.

FUNDAMENTAL INTER-RELATIONSHIPS BETWEEN THERMO-ELASTIC CONSTANTS

By considering the conditions for ply crack closure during uniaxial loading in the axial, transverse and through-thickness directions, it can be shown [7] that many inter-relationships between the thermoelastic constants of a damaged laminate can be derived. First of all define

$$\Phi = \frac{1}{\tilde{E}_A} - \frac{1}{\tilde{E}_A^o}. \tag{19}$$

It has been shown [7] that the thermo-elastic constants for a damaged laminate are related to those of the corresponding undamaged laminate according to the following simple relations

$$\frac{1}{\tilde{E}_t} - \frac{1}{\tilde{E}_t^o} = k'^2\Phi, \qquad \frac{1}{\tilde{E}_T} - \frac{1}{\tilde{E}_T^o} = k^2\Phi, \tag{20}$$

$$\frac{\tilde{\nu}_t^o}{\tilde{E}_T^o} - \frac{\tilde{\nu}_t}{\tilde{E}_T} = k\,k'\Phi, \qquad \frac{\tilde{\nu}_A^o}{\tilde{E}_A^o} - \frac{\tilde{\nu}_A}{\tilde{E}_A} = k\Phi, \qquad \frac{\tilde{\nu}_a^o}{\tilde{E}_A^o} - \frac{\tilde{\nu}_a}{\tilde{E}_A} = k'\Phi, \tag{21}$$

$$\tilde{\alpha}_t - \tilde{\alpha}_t^o = k'k_1\Phi, \qquad \tilde{\alpha}_A - \tilde{\alpha}_A^o = k_1\Phi, \qquad \tilde{\alpha}_T - \tilde{\alpha}_T^o = k\,k_1\Phi, \tag{22}$$

where the constants k_1, k and k' are easily obtained from the geometry and ply properties of the undamaged laminate. The results (20-22) indicate that the degradation of all the thermoelastic constants of a damaged laminate arising from ply cracking in the 90^o plies can be characterised by a single parameter Φ that is defined at the macroscopic laminate level by (19).

GIBBS FREE ENERGY FOR A CRACKED LAMINATE SUBJECT TO MULTI-AXIAL BENDING

It has been shown [7], for the case of uniform ply crack densities in one or more of the 90^o plies of the laminate, that the Gibbs free energy (equivalent to the complementary energy) per unit volume of laminate (averaged over the region V occupied by the laminate) may be expressed in the form

$$\begin{aligned}\bar{g} = &-\frac{\sigma_t^2}{2E_t} - \frac{\sigma^2}{2E_A} - \frac{\sigma_T^2}{2E_T} - \frac{M^2}{2\hat{E}_A} - \frac{M_T^2}{2\hat{E}_T} + \frac{\nu_a}{E_A}\sigma_t\sigma + \frac{\nu_t}{E_T}\sigma_t\sigma_T + \frac{\nu_A}{E_A}\sigma\sigma_T \\ &+ \frac{\hat{\nu}_a}{\hat{E}_A}\sigma_t M + \frac{\hat{\nu}_A}{\hat{E}_A}\sigma M + \frac{\hat{\nu}_T}{\hat{E}_A}\sigma_T M + \frac{\hat{\eta}_t}{\hat{E}_T}\sigma_t M_T + \frac{\hat{\eta}_A}{\hat{E}_T}\sigma M_T + \frac{\hat{\eta}_T}{\hat{E}_T}\sigma_T M_T + \frac{\hat{\delta}_A}{\hat{E}_A} M M_T \\ &- \left[\sigma_t\alpha_t + \sigma\alpha_A + \sigma_T\alpha_T + M\hat{\alpha}_A + M_T\hat{\alpha}_T\right]\Delta T \\ &+ \frac{1}{2}\left[\sigma_t^c\alpha_t + \sigma^c\alpha_A + \sigma_T^c\alpha_T + M^c\hat{\alpha}_A + M_T^c\hat{\alpha}_T\right]\Delta T - \frac{1}{2V}\int_V \sigma_{ij}^c\,\alpha_{ij}\Delta T\,dV + g_o(\Delta T).\end{aligned} \tag{23}$$

It should be noted that the stress-strain relations (7-11) for a damaged laminate may be obtained from (23) by differentiating with respect to $\sigma_t, \sigma, \sigma_T, M$ and M_T. It has been shown [7] that, on using (19-22) the complicated result (23) can be reduced to the simple form

$$\bar{g} - \bar{g}_0 = -\frac{\Phi}{2}\left[k'\sigma_t + \sigma + k\sigma_T - \bar{\sigma}^c\right]^2 - F(\hat{\varepsilon}, \hat{\varepsilon}_T) + F_0(\hat{\varepsilon}^o, \hat{\varepsilon}_T^o), \tag{24}$$

where $\bar{g}_0$ is the value of $\bar{g}$ for an undamaged laminate, $\bar{\sigma}^c$ is the crack closure stress for uniaxial in-plane loading constrained so that there is no bending, and where

$$F(\hat{\varepsilon},\,\hat{\varepsilon}_T) = \frac{1}{2\Lambda}\Big[\,\hat{E}_A\hat{\varepsilon}\Big(\hat{\varepsilon}+\hat{\delta}_T\hat{\varepsilon}_T\Big)+\hat{E}_T\hat{\varepsilon}_T\Big(\hat{\varepsilon}_T+\hat{\delta}_A\hat{\varepsilon}\Big)\Big], \qquad \Lambda = 1-\hat{\delta}_A\hat{\delta}_T\ ,$$
$$F_0(\hat{\varepsilon},\,\hat{\varepsilon}_T) = \frac{1}{2\Lambda_0}\Big[\,\hat{E}^o_A\hat{\varepsilon}\Big(\hat{\varepsilon}+\hat{\delta}^o_T\hat{\varepsilon}_T\Big)+\hat{E}^o_T\hat{\varepsilon}_T\Big(\hat{\varepsilon}_T+\hat{\delta}^o_A\hat{\varepsilon}\Big)\Big], \qquad \Lambda_0 = 1-\hat{\delta}^o_A\hat{\delta}^o_T\ . \tag{25}$$

PREDICTING DAMAGE FORMATION

Consider the special case where, during the formation of every ply crack, the fracture energy for ply crack formation has a unique value 2γ. The first objective is to determine the conditions for which it is energetically favourable for an array of equally spaced ply cracks having density ρ_0 to form quasi-statically in an undamaged laminate subject to fixed applied loads and temperature. For a macroscopic region V of the laminate, energy balance considerations and the fact that kinetic energy is never negative, lead to the criterion for crack formation having the form [8]

$$\Delta\Gamma \;+\; \Delta G \;<\; 0\ , \tag{26}$$

where the energy absorbed in a macroscopic volume V of laminate by the formation of the new ply cracks is given by

$$\Delta\Gamma \;=\; V\,\Gamma \;=\; V\,\frac{2\gamma\rho_0 h^{(90)}}{h}. \tag{27}$$

In (27) the parameter Γ denotes the energy absorbed per unit volume of laminate during the formation of new ply crack surfaces in the 90^o plies that have led to the initial damage state denoted by the ply crack density ρ_0, and $h^{(90)}$ is the total thickness of the 90^o plies in which the ply cracks have formed. The corresponding change of Gibbs free energy in the region V of the laminate is

$$\Delta G \;=\; \int_V \big[\,g - g_0\big]\,dV \;=\; V\,\big[\,\overline{g} - \overline{g}_0\big]. \tag{28}$$

In (28) g denotes the Gibbs free energy per unit volume when the damage in the laminate is characterised by the ply crack density ρ_0, and g_o denotes the corresponding value of g in the undamaged state. It follows from (24) that

$$\overline{g} - \overline{g}_0 = -\,\frac{\Phi(\rho_0)}{2}\Big[k'\sigma_t + \sigma + k\sigma_T - \overline{\sigma}^c\Big]^2 \;-\; F(\hat{\varepsilon},\,\hat{\varepsilon}_T,\,\rho_0) \;+\; F_0(\hat{\varepsilon}^o,\,\hat{\varepsilon}^o_T)\ , \tag{29}$$

where from (19)

$$\Phi(\rho_0) = \frac{1}{\widetilde{E}_A(\rho_0)} - \frac{1}{\widetilde{E}^o_A}\ , \tag{30}$$

and from $(25)_1$

$$F(\hat{\varepsilon},\,\hat{\varepsilon}_T,\,\rho) = \frac{1}{2\Lambda(\rho)}\Big[\,\hat{E}_A(\rho)\hat{\varepsilon}\Big(\hat{\varepsilon}+\hat{\delta}_T(\rho)\hat{\varepsilon}_T\Big)+\hat{E}_T(\rho)\hat{\varepsilon}_T\Big(\hat{\varepsilon}_T+\hat{\delta}_A(\rho)\hat{\varepsilon}\Big)\Big]\ ,$$
$$\Lambda(\rho) = 1-\hat{\delta}_A(\rho)\hat{\delta}_T(\rho)\ . \tag{31}$$

It then follows using (26-29) that ply crack formation is governed by the inequality

$$\frac{\Phi(\rho_0)}{2}\Big[k'\sigma_t + \sigma + k\sigma_T - \overline{\sigma}^c\Big]^2 \;+\; F(\hat{\varepsilon},\,\hat{\varepsilon}_T,\,\rho_0) \;-\; F_0(\hat{\varepsilon}^o,\,\hat{\varepsilon}^o_T) \;>\; \frac{2\gamma\rho_0 h^{(90)}}{h}\quad . \tag{32}$$

It is emphasised that the approach described above does not provide any information that indicates how the thermo-elastic constants depend upon ply crack density. A detailed stress analysis is required to provide this information (see [6]). Progressive ply crack formation can be analysed in a very similar way as described in [7].

CONCLUSIONS

The methodology that has been described for the prediction of ply crack formation in some or all of the 90^o plies of a multiple-ply cross-ply laminate subject to combined in-plane biaxial loading, out-of-plane through-thickness loading and bending about two orthogonal axes, and thermal residual stresses, has the following properties:

- the analysis is exact within the assumptions made,
- the stress-strain relations for a damaged laminate may be obtained by differentiating the Gibbs free energy with respect to the loading parameters, and the form of the stress-strain relations is identical to that for undamaged laminates,
- the consideration of ply crack closure conditions leads to the important result that the degradation of the properties of the thermo-elastic constants of the laminate is governed by a single parameter Φ that is dependent only on the axial moduli of the laminate in both the damaged and undamaged states,
- the form of the property degradation relations enables the complex expression for the Gibbs free energy of a damaged laminate to be written in a simple form,
- the results enable the derivation of a relatively simple criterion for the prediction of the loading and thermal conditions that are energetically favourable for ply cracks to form in some or all of the 90^o plies,
- the ply crack formation criterion may be used to develop a methodology for the prediction of progressive ply crack formation during loading.

REFERENCES

1. Li S, Reid S R & Soden P D, 'A finite strip analysis of cracked laminates', *Mech. Mater.* 18, (1994), 289-311.
2. McCartney L N & Pierse C, 'Stress transfer mechanics for multiple-ply laminates subject to bending', NPL Report CMMT(A)55, February 1997.
3. McCartney L N & Pierse C, 'Stress transfer mechanics for multiple ply laminates for axial loading and bending', Proc. 11th Int. Conf. on Composite Materials, Gold Coast, Australia, July 14-18, 1997, vol. V, 662-671.
4. Smith P A and Ogin S L, 'Characterisation and modelling of matrix cracking in a $(0/90)_{2s}$ GFRP laminate loaded in flexure', *Proc. Roy. Soc. Lond.* **A 456**, (2000), 2755 - 2770.
5. Smith P A and Ogin S L, 'On transverse matrix cracking in cross-ply laminates loaded in simple bending', *Composites Part A*, **30**, (1999), 1003 - 1008.
6. McCartney L N, 'Stress transfer mechanics for multiple ply cross-ply laminates subject to bending', summary in Proceedings of 6th International Conference on the Deformation and Fracture of Composites, Manchester, April 2001, pp. 57-66. Full details to be published.
7. McCartney L N & Byrne M J W, 'Energy balance method of predicting ply crack formation during bend deformation', to be published.
8. McCartney L N, 'Prediction of microcracking in composite materials', in "FRACTURE: A Topical Encyclopaedia of Current Knowledge Dedicated to Alan Arnold Griffith", (ed. G.P.Cherepanov), Krieger Publishing Company, Melbourne, USA, 1998, 905-916.

ENVIRONMENTAL EFFECTS ON CRACK GROWTH IN CONTINUOUS FIBER SIC-COMPOSITES

C. H. Henager, Jr., C. A. Lewinsohn, E. P. Simonen, and R. H. Jones

Pacific Northwest National Laboratory,*, Richland, WA 99352

ABSTRACT

A dynamic crack-growth model using discrete, two-dimensional fiber bridges developed for ceramic composites containing nonlinear, creeping fibers in an elastic matrix is used to develop a crack growth mechanism map. In addition to nonlinear creep, fiber oxidation and fiber/matrix interphase oxidation are treated and discussed. The model aids in the development of a crack-growth mechanism map based on available experimental crack growth data as a function of temperature and oxygen concentration and in terms of proposed crack-growth mechanisms; fiber relaxation (FR), interface removal (IR), viscous sliding (VS), oxidation embrittlement (OE), and fiber stress rupture (SR). Transitions between the various mechanisms are identified and discussed.

KEYWORDS

Dynamic crack growth, ceramic composites, mechanism map, modeling and simulation

INTRODUCTION

PNNL was among the first to identify and study time-dependent bridging in ceramic composites [1-3] and we have proposed a crack-growth mechanism map based on available experimental data as a function of temperature and oxygen partial pressure for continuous fiber composites with carbon interphases [4]. An approach to modeling dynamic time-dependent crack bridging has emerged from the work of Bückner [5] and Rice [6] based on the use of weight-functions to calculate crack-opening displacements [7]. Once a relationship [8,9] between crack-opening displacement and bridging tractions from crack-bridging elements is included, a governing integral equation obtains that relates the total crack opening, and the bridging tractions, to the applied load. The solution of this equation gives the force on the crack-bridges and the crack-opening displacement everywhere along the crack face [5-7,10]. Begley et al. [11] first developed a dynamic model and applied it to a variety of time-dependent bridging cases for linear creep laws [12-14]. Recently, a more appropriate bridging relation for creeping fibers has been developed by Cox et al.[9] that provides axial and radial stresses in creeping fibers with linear and non-linear creep laws.

* Pacific Northwest National Laboratory is operated for the U. S. Department of Energy by Battelle under Contract DE-AC06-76RLO 1830.

We have developed a similar bridging law for non-linear creeping fibers that also considers the case for interface removal due to oxidation. We treat discrete fiber bridges as opposed to a bridging force distribution and we employ a nonlinear (in time and stress) creep law to compute bridge extensions.

ENVIRONMENTAL EFFECTS: MODEL and MECHANISM MAP

Compliance of A Frictionally Bonded Fiber (Bridge)

We introduce an expression for the compliance of a bridging fiber, Φ_b, using the assumptions of frictional bonding with a weak, debonding interphase. The frictionally bonded fiber involves an unbonded or free length, l_{free}, and a debonded or frictionally bonded and sliding length, l_{deb}, for a fiber bridging a crack of opening u_t, as shown in Fig. 1.

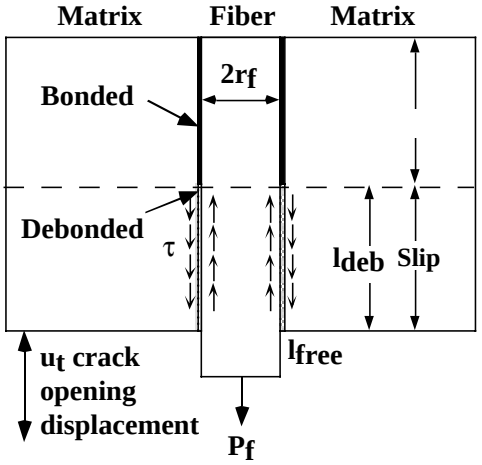

Figure 1. Schematic of frictionally bonded fiber acted upon by force P_f due to debonding and sliding across a Mode I crack with opening u_t. The lengths l_{deb} and l_{free} are shown.

The free length of fiber, which is not subject to frictional forces, is assigned a compliance, Φ_b^l, and the portion of the fiber subjected to a frictional sliding resistance along length l_{deb} due to P_f is assigned a nonlinear compliance, $\Phi_f{}^n$, such that $\delta_b = \Phi_b' P_b + \Phi_b'' P_b^2$ [15], where P_b is the 2D normalized bridge force and δ_b is the bridge displacement. As suggested by Cox et al. [9] one could include a time-dependent debonding from fiber contraction due to Poisson effect and creep deformation, which provides an additional time-dependent fiber compliance term.

Fiber Relaxation due to Creep (FR)

The time-dependent extension of a fiber bridge at elevated temperatures obeys a power-law creep equation [16] for Nicalon-CG and Hi-Nicalon fibers as

$$\varepsilon_f = A\sigma^n t^p \exp\left(\frac{-pQ}{RT}\right) = C(T)\sigma^n t^p \Rightarrow \dot{\varepsilon}_f = C(T)\sigma^n p t^{p-1} \tag{1}$$

where A is a constant, t is time, Q is an activation energy for creep, R and T have their usual meanings, n is the stress exponent, and p is the time-temperature exponent. The unbonded length given by l_{free} creeps at the bridging stress applied to the fiber. The debonded length of the fiber creeps at a stress that varies over the debond length, which is found by integration. The creep extension of a bridge becomes

$$\Delta l_{free} = C(T) p t^{p-1} \Delta t \left(\frac{P_b}{2r_f}\right)^n l_{free} \tag{2}$$

for the free length of fiber and

$$\Delta l_{deb} = C(T)pt^{p-1}\Delta t\int_0^{l_{deb}} \sigma^n(z)dz = C(T)pt^{p-1}\Delta t\left(\frac{P_b}{2r_f}\right)^n l_{deb}\left(1-\frac{1}{(1+\xi)^n 1+n}\right) \quad (3)$$

for the debonded length when the axial fiber stress is given by

$$\sigma(z) = \frac{P_b}{2r_f} - \frac{2\tau z}{r_f} \quad (4)$$

where t is the total creep time, Δt is the time step, and z is the axial distance along the fiber measured from the crack face. Time, t, is referenced to the inception of each bridge into the bridging zone and is tracked separately for each bridge.

Fiber/Matrix Interphase Removal by Oxidative Volatilization (IR)

When the fiber/matrix interphase is a material that can undergo a gaseous reaction with oxygen then interphase removal in oxygen-containing environments becomes important. Previous research has shown that the following interphase recession data applies to the typical 0/90 plain weave CVI-SiC/SiC_f materials with a CVI carbon interphase [17]

$$l_{ox} = 3.3\times10^{-4}e^{-6014/T}P_{O2}{}^{0.889}t = R(T,P_{O2})t \text{ thus } \Delta l_{ox} = R(T,P_{O2})\Delta t \quad (5)$$

where l_{ox} is the recession distance along the fiber/matrix interphase from the crack face into the composite in m/s, T is temperature in K, P_{O2} is fractional oxygen concentration, and t is exposure time. We assume that l_{deb} is maintained at its value determined by τ and the load on the fiber.

Oxidation of the Bridging Fiber (OE and VS/OE)

Exposed bridging fibers will undergo oxidation at elevated temperatures according to [18]

$$fib_{ox} = 1.84\times10^{-7}e^{-4016.8/T}P_{O2}t^{0.5} \quad (6)$$

where fib_{ox} is the oxide thickness grown on the fiber in m, T is temperature in K, P_{O2} is fractional oxygen concentration, and t is exposure time in s.

Fiber Stress Rupture (SR)

Exposed bridging fibers will obey time-dependent stress rupture relationships as [19]

$$\text{Ln}(\sigma_f) = 2.3E - (\beta/R)\left[RT(\text{Ln}(t)+C)\right] \quad (7)$$

where σ_f is fiber strength in MPa, and E, β, and C are fitted parameters from single fiber rupture tests in air.

Crack Growth Mechanism Map

The proposed mechanism map is shown in Fig. 2. Fiber creep relaxation (FR) dominates at high temperatures and low oxygen concentrations, as expected, since creep activation energies are high (~ 600 kJ/mol) and oxidation activation energies are low (~ 50 kJ/mol). Crack extension is dominated by interface removal (IR) for oxygen concentrations less than ~ 0.1 when the temperatures are not extreme. We observe both kinetic and activation energy changes in our experimental data consistent with this hypothesis. We define the transition from FR to IR by the locus of points where the crack growth from each mechanism is equal. At higher oxygen concentrations, the fiber/matrix interphase oxidizes and is replaced by a glass phase

and either oxidation embrittlement (OE) or viscous sliding (VS) mechanisms may occur. We propose that interphase glass formation and channel pinch-off (fiber-matrix bonding) at intermediate temperatures where the resultant glass phase is brittle results in OE and the fibers fail since they can no longer slide relative to the matrix. We define the transition from IR to OE as the locus of points where the fiber/matrix channel pinches-off and OE occurs in a finite crack growth increment (2.5 mm in this case). At higher temperatures the glass phase is viscous, not brittle and VS occurs. When the glass phase has a high viscosity, fibers can fail by rupture since the local fiber/matrix bonding leads to stress concentrations [20], rather like replacing an interface with a low frictional sliding stress with a higher one. It follows that there will be a temperature above which this stress concentration will not fail the fibers but this will depend on the details of the compositionally dependent glass viscosity. The transition from OE to VS/OE is schematic since we do not yet know the glass viscosity nor have we implemented a viscous sliding treatment for the model, although such treatments exist [21]. Fiber oxidation also results in loss of strength, which leads to embrittlement via fiber stress rupture (SR) [16,22,23]. Fiber stress corrosion should be accounted for by the SR mechanism since this data was obtained in air. Since predicted fiber stresses in the crack wake of a dynamic crack are on the order of 800 MPa or smaller, SR is difficult to achieve until temperatures above about 1400K.

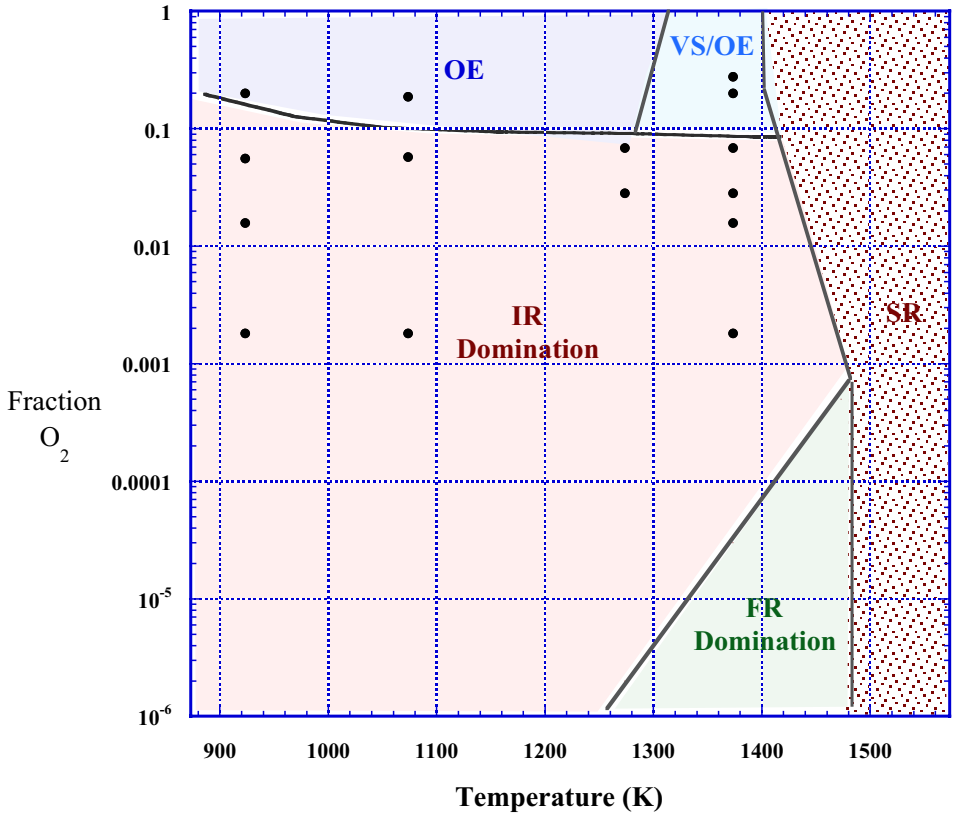

Figure 2. Suggested dominant crack growth mechanisms based on experimental data and model results. The plotted points correspond to experiments with Nicalon-CG composites and the map is fashioned using data appropriate for Nicalon-CG fibers.

DISCUSSION

The materials included in the map, and indicated by the plotted points (Fig. 2) are 2D woven SiC/SiC composites with Nicalon-CG fibers at ~ 40% by volume. Lewinsohn et al. [4] discuss the map concept, the materials, and the experimental data more fully. However, we have observed that temperature and oxygen concentration play the most important roles in determining the operable crack growth mechanisms.

Therefore, it was imperative to include oxidation in the dynamic crack model in addition to the nonlinear fiber creep. However, additional modeling remains and more experimentation is planned.

Crack growth appears to be controlled by FR above the composite matrix-cracking threshold at elevated temperatures in inert environments. PNNL and others have determined composite deformation rates[1,2,24-35] and activation energies under these conditions and they match quite well with activation energies for fiber creep, about 500 – 600 kJ/mol. Our dynamic crack growth model agrees reasonably well with measured crack growth rates and these activation energies.

When oxygen is introduced during the crack growth testing the deformation rates increase and the activation energy decreases to about 50 kJ/mol, in agreement with carbon oxidation processes. Significantly, the crack growth kinetics change from nonlinear to linear since now the bridge compliance is dominated by the linear portion as $l_{free} + l_{ox}$ approach and exceed l_{deb}. Again, our model agrees well with these changes in both kinetics and activation energies. The transition between the FR and IR mechanisms is defined as the locus of points where the crack growth rates of each mechanism are roughly equal. This was determined by choosing an oxygen concentration where the crack velocity doubled compared to the velocity without any oxygen. This curve is steep as shown in Fig. 2 due in part to the high activation energy of the fiber creep process. It is bounded at high temperatures by fiber stress rupture mechanisms.

Transitions from IR to either OE or VS/OE mechanisms are shown. We find that there is a competition between specimen failure due to IR relative to the time for pinch-off and OE to occur. The dynamics are handled by removing those fibers from the bridging zone that have an oxide thickness greater than some critical value, such as the interphase thickness. However, this transition is crack length (specimen size) and interphase thickness dependent. The size effect occurs since OE depends on total fiber exposure time, which is dependent on crack length. Interphase thickness effects arise due to our criterion that pinch-off occurs prior to the onset of OE. The computations shown here are for an interphase thickness of 150 nm. Other plausible OE mechanisms only require a critical oxide thickness that is not interphase thickness dependent [36,37]. However, such mechanisms will still exhibit a specimen size effect or history effect. Transitions from OE (pinch-off with brittle glass phase) to VS/OE (non-brittle, viscous glass phase) depend on the viscosity of the glass which is strongly dependent on glass composition. Thus, these transitions are not rigorously defined here and will have to wait for future work. By incorporating existing models of viscous interphase mechanics, we will be able to understand the effects of viscosity on fiber stress concentrations.

The database for fiber stress rupture is mainly limited to tests in air so dependence on oxygen concentration is lacking. SR competes with OE and IR at temperatures higher than about 1373K for oxygen concentrations near 0.2 The onset of SR occurs at 1373K in air during dynamic crack growth according to our model and this onset is predicted to shift to 1423K for lower oxygen concentrations. Without detailed data as a function of oxygen concentration, we cannot be more quantitative. The map suggests that SR shifts to higher temperatures as the oxygen concentration decreases. The boundary between FR and SR is suggested to occur at the fiber thermal limits. There is a need for additional stress rupture data as a function of oxygen concentration.

SUMMARY

We developed a dynamic crack-growth model with the following features: 1) it is based on the weight-function method using discrete fiber bridges, 2) it contains nonlinear bridge extension laws based on fiber-creep kinetics for Nicalon-CG and Hi-Nicalon fibers, 3) it contains bridge extension laws for the case of interphase removal, and 4) it provides fully dynamic crack tracking using a critical-stress-intensity propagation criterion. The model reproduces the time-dependent crack-growth kinetics observed

experimentally in specimens of Nicalon-CG and Hi-Nicalon 0/90 woven composites. The transition from nonlinear crack growth kinetics to linear growth kinetics is also reproduced by the model by comparing crack growth rates under FR or IR domination. By implementing a simple "fiber removal" algorithm, where the criterion for removal is based either on a critical oxide thickness or stress rupture threshold, we can also map out transitions between crack growth due to OE and SR. The model is useful in helping us develop and understand crack growth mechanisms and to design improved composite materials.

REFERENCES

1. C. H. Henager, Jr. and R. H. Jones, *Mater. Sci. Eng., A*, 1993, **A166** 211.
2. C. H. Henager, Jr. and R. H. Jones, *J. Am. Ceram. Soc.*, 1994, **77** 2381.
3. C. H. Henager, Jr., R. H. Jones, C. F. Windisch, Jr., M. M. Stackpoole, and R. Bordia, *Metall. Mater. Trans. A*, 1996, **27A** 839.
4. C. A. Lewinsohn, C. H. Henager, Jr., and R. H. Jones, *Ceram. Trans.*, 1999, **96** 351.
5. H. Bückner, *Z. Angew Math. Mech.*, 1970, **46** 529.
6. J. R. Rice, *Int. J. Solids Struct.*, 1972, **8** 751.
7. T. Fett, C. Mattheck, and D. Munz, *Engr. Fract. Mech.*, 1987, **27** 697.
8. D. B. Marshall, B. N. Cox, and A. G. Evans, *Acta Metall.*, 1985, **33** 2013.
9. B. N. Cox, N. Sridhar, and C. R. Argento, *Acta Mater.*, 2000, **48** 4137.
10. B. N. Cox and D. B. Marshall, *Acta Metall. Mater.*, 1991, **39** 579.
11. M. R. Begley, B. N. Cox, and R. M. McMeeking, *Acta Metall. Mater.*, 1995, **43** 3927.
12. M. R. Begley, A. G. Evans, and R. M. McMeeking, *J. Mech. Phys. Sol.*, 1995, **43** 727.
13. M. R. Begley, B. N. Cox, and R. M. McMeeking, *Acta Metall. Mater.*, 1997, **45** 2897.
14. B. N. Cox, D. B. Marshall, R. M. McMeeking, and M. R. Begley, *Solid Mech. Appl.*, 1997, **49** 353.
15. C. H. Henager, Jr. and R. G. Hoagland, *Ceramic Trans.*, 2001, **124** 315.
16. J. A. DiCarlo, *Ceramurgia*, 1998, **28** 88.
17. C. F. Windisch, Jr., J. Charles H. Henager, G. D. Springer, and R. H. Jones, *J. Am. Ceram. Soc.*, 1997, **80** 569.
18. Y. T. Zhu, S. T. Taylor, M. G. Stout, D. P. Butt, and T. C. Lowe, *J. Am. Ceram. Soc.*, 1998, **81** 655.
19. J. A. DiCarlo, H. M. Yun, G. N. Morscher, and J. C. Goldsby, *Ceram. Trans.*, 1995, **58** 343.
20. W. H. Glime and J. D. Cawley, *J. Am. Ceram. Soc.*, 1998, **81** 2597.
21. S. V. Nair, K. Jakus, and T. J. Lardner, *Mech. Mater.*, 1991, **12** 229.
22. H. M. Yun and J. A. DiCarlo, *Ceram. Trans.*, 1996, **74** 17.
23. R. E. Tressler and J. A. DiCarlo, *Ceram. Trans.*, 1995, **57** 141.
24. F. Abbe, J. Vicens, and J. L. Chermant, *J. Mater. Sci. Lett.*, 1989, **8** 1026.
25. J. L. Chermant, F. Abbe, and D. Kervadec, *Creep Fract. Eng. Mater. Struct., Proc. Int. Conf., 5th*, , 1993, 371.
26. X. Wu and J. W. Holmes, *J. Am. Ceram. Soc.*, 1993, **76** 2695.
27. G. Grathwohl, B. Meier, and P. Wang, *Key Eng. Mater.*, 1995, **108-110** 243.
28. A. G. Evans and C. Weber, *Mater. Sci. Eng., A*, 1996, **A208** 1.
29. D. R. Mumm, W. Morris, M. S. Dadkhah, and B. N. Cox, *ASTM Spec. Tech. Publ.*, 1997, **STP 1309** 102.
30. M. Mizuno, S. Zhu, Y. Kagawa, and H. Kaya, *Key Eng. Mater.*, 1997, **132-136** 1942.
31. B. Cox and F. Zok, *Brittle Matrix Compos. 5, Proc. Int. Symp., 5th*, , 1997, 487.
32. B. Wilshire, F. Carreno, and M. J. L. Percival, *Scr. Mater.*, 1998, **39** 729.
33. J.-L. Chermant and G. Boitier, *Adv. Compos. Mater.*, 1999, **8** 77.
34. S. Zhu, M. Mizuno, Y. Kagawa, J. Cao, Y. Nagano, and H. Kaya, *J. Am. Ceram. Soc.*, 1999, **82** 117.
35. R. E. Tressler, K. L. Rugg, C. E. Bakis, and J. Lamon, *Key Eng. Mater.*, 1999, **164-165** 297.
36. A. G. Evans, F. W. Zok, R. M. McMeeking, and Z. Z. Du, *J. Am. Ceram. Soc.*, 1996, **79** 2345.
37. F. E. Heredia, J. C. McNulty, F. W. Zok, and A. G. Evans, *J. Am. Ceram. Soc.*, 1995, **78** 2097.

ORAL REFERENCE:

ENVIRONMENTAL EFFECTS ON FRACTURE AND SUB-CRITICAL CRACK GROWTH FOR LIFETIME PREDICTION

Tetsuo SHOJI, Junhyun KWON, Qunjia PENG and Guangfu LI

Fracture Research Institute, Tohoku University
Aoba 01, Aramaki, Aoba-ku, Sendai/980-8579, Japan

ABSTRACT

In environmentally assisted cracking processes, various parameters in mechanics, chemistry and metallurgy have synergistic effects on fracture and are cross-linked each other. Purely theoretical formulations were developed from slip/oxidation mechanism to deal with the synergy of these parameters for quantitative prediction of crack growth and lifetime of structures in high temperature water environments especially for energy conversion systems The formulations were derived based on an equation of metal oxidation for cracking and analysis of crack tip strain rate for a growing crack in an elastic/plastic work hardening material, in which crack tip strain redistribution due to crack advance was taken into consideration as a crucial part of cracking processes.

The obtained formulations were solved numerically to get relations between crack growth rate da/dt and stress intensity factor K in various situation. The well-known phenomena of existence of threshold stress intensities and plateau growth rates in da/dt-K diagrams for many materials/environments combinations can be reproduced by the theoretical formulations from crack tip strain rate point, without any assumption on crack tip water chemistry for the threshold or on diffusion-controlled process for the plateau growth behavior. The effects of crack tip solution chemistry and stress state on the crack growth behavior are discussed in the paper.

KEY WORDS:

Theoretical prediction, environmentally assisted cracking, stress corrosion cracking, crack growth rate, threshold stress intensity factor, crack tip strain rate, crack tip solution chemistry

INTRODUCTION

Quantitative evaluation of lifetime of structural components of aged plants and structures is one of the critical issues for safety and reliability evaluation in connection with economics. Such a quantitative capability of life-time prediction needs to be established based on understanding of physical and chemical mechanisms of fracture and sub-critical crack growth where many parameters in mechanics, chemistry and metallurgy have synergistic effects on fracture and are cross-linked each other. In this work, purely theoretical formulations have been developed to deal with the synergy of these parameters for quantitative prediction of crack growth and lifetime of structures in high temperature water environments, especially for energy conversion systems such as light water reactors. Such

environmentally assisted cracking is controlled by various parameters, it is very tedious and difficult to elucidate cracking process and to outline controlling factors quantitatively by only experiments

CRACK GROWTH MODEL AND ITS FORMULATION

Environmentally assisted crack initiation and growth process in many cases especially in high temperature water environments can be described based upon a slip/oxidation mechanism [1]. This mechanism consists of the following three processes,

(1) Rupture of protective film by mechanical straining at crack tip or other sites with stress concentration,

(2) Enhanced anodic dissolution/oxidation of bare metal, causing crack growth,

(3) Covering of bare surface by oxide or other protective film that shows repassivation.

According to this mechanism, the crack growth rate is equivalent to the oxidation rate of the metal at the crack tip.

Quantitative evaluation of crack tip strain rate is one of the most important steps in crack growth rate evaluation. There are two ways. One is to develop based on Gao and Hwang' s work on crack tip plastic strain distribution [2], as approached by Shoji *et al* [3, 4]. According to Gao and Hwang's theoretical work and Gerberich *et al*'s experimental verification [5], crack tip plastic strain distribution along the crack line for a steady growing crack under quasi-static loading in an elastic plastic strain hardening material can be expressed as [2, 5]

$$\varepsilon_{ct} = \beta \left(\frac{\sigma_y}{E}\right)\left[\ln\left(\frac{R_p}{r}\right)\right]^{\frac{n}{n-1}} \qquad (1)$$

where $R_p=\lambda(K/\sigma_y)^2$ is the plastic zone size, β and λ are dimensionless constants, σ_y and E are yield strength and elastic modulus, respectively. r is distance from a growing crack tip, K, stress intensity factor, and n, strain-hardening exponent in power law hardening Ramberg-Osgood stress-strain relations.

Based upon this strain distribution expression, crack tip strain rate can be derived and expressed as follows by considering strain increment due to both, change in distance 'r' from crack tip with crack advance and change in K caused by load change and/or crack growth [3, 4], even though these situations are beyond the conditions which Gao and Hwang were assumed to derive Eq. (1) because of the experimental verification made beyond the theoretical assumption.

$$\frac{d\varepsilon_{ct}}{dt} = \beta \frac{\sigma_y}{E}\frac{n}{n-1}\left[\ln\left(\frac{\lambda \cdot K^2}{\sigma_y^2 r_0}\right)\right]^{\frac{1}{n-1}}\left(2\frac{\dot{K}}{K} + \frac{\dot{a}}{r_0}\right) \qquad (2)$$

where, $\dot{K} = dK/dt$, $\dot{a} = da/dt$, r_0 is distance ahead of the crack tip where strain rate is defined.

Another way to evaluate crack tip strain rate is based on J. R. Rice *et al*'s work on crack tip opening displacement rate for a growing crack under plain-strain condition in elastic-perfectly plastic solids (no strain-hardening) [6]. The crack opening displacement rate can be converted to crack tip strain rate by assuming a length parameter such as the total width of the active flow bands. This length parameter was also assumed to be the same as r in the calculation [7]. The validity of these assumptions, however, has not been verified.

Currently, Gao and Hwang's expression is the best available for evaluation of crack tip strain rate, as has been experimentally verified by Gerberich *et al* [5], and this expression takes into consideration the effects of strain hardening that is important for engineering materials, although it may have some limitations as it was developed for steady crack growth under quasi-static loading. More work on this issue should be focused by, for example, FEM in the future.

Based upon Eq. (2) and slip/oxidation mechanism, theoretical crack growth rate can be derived as follows for plane strain condition, with details described in Ref. [1, 3, 4]

$$\frac{da}{dt} = \frac{M \cdot i_0}{z\rho F(1-m)}\left(\frac{t_0}{\varepsilon_f}\right)^m \left\{\beta \frac{\sigma_y}{E}\frac{n}{n-1}\left[\ln\left(\frac{\lambda \cdot K^2}{\sigma_y^2 r_0}\right)\right]^{\frac{1}{n-1}}\left(2\frac{\dot{K}}{K}+\frac{\dot{a}}{r_0}\right)\right\}^m \quad (3)$$

where r_0 is a characteristic distance for which a strain rate is defined and can be assumed as a material property depending on the microstructure such as grain size.

Similar equation for crack growth rate can be derived for plane stress condition as shown below:

$$\frac{da}{dt} = \frac{Mi_0}{z\rho F(1-m)}\left(\frac{t_0}{\varepsilon_f}\right)^m \left\{\beta \frac{\sigma_y}{E}\frac{n}{n-1}\left\{1+\ln\left[\lambda\frac{\left(\frac{K}{\sigma_y}\right)^2}{r}\right]\right\}\left(2\frac{\dot{K}}{K}+\frac{\dot{a}}{r}\right)\left\{\ln\left[\lambda\frac{\left(\frac{K}{\sigma_y}\right)^2}{r}\right]+\frac{1}{2}\left\{\ln\left[\lambda\frac{\left(\frac{K}{\sigma_y}\right)^2}{r}\right]\right\}^2\right\}^{\frac{1}{n-1}}\right\}^m \quad (4)$$

These crack growth rate formulas are unique expressions for environmentally assisted crack growth rate as a function of stress intensity factor by combing a mechanism of crack growth and mechanics of crack tip stress/strain field. These equations also clearly show the synergistic effects of material parameters, mechanical properties and electrochemical properties. It is important to note here that the crack tip strain rate is a function not only of loading rate but also of crack growth rate for growing crack. Hence, as a typical case, crack tip strain rate does exist even under a constant load or a constant displacement as long as crack grows.

NUMERICAL SOLUTION AND RESULTS

General trend of crack tip strain rate as a function of K

Eq. (2) describes the crack tip strain rate as a function of K, dK/dt, da/dt, and mechanical properties. Eq. (2) can be solved numerically and some results are shown in Figs. 1 and 2 as examples. These plots demonstrate the effects of yield strength and crack growth rate upon the relationship between the crack tip strain rate and K. The crack tip strain rate strongly depends on K in a relatively low K range, whereas less dependence can be seen at the higher K values. As expected from Eq. (2), the crack tip strain rate shows a threshold depending on the yield strength and characteristic distance, r_0. Smaller yield strength tends to give a lower value of threshold K, which is shown in Fig. 1. In the vicinity of a threshold, the crack tip strain rate decreases rapidly with decreasing K to threshold stress intensity of K_{th}. Below K_{th}, the value in the logarithmic term of Eq. (2) becomes less than unity and the rate becomes a complex number. The physical meaning in such solutions is not clear at this moment.

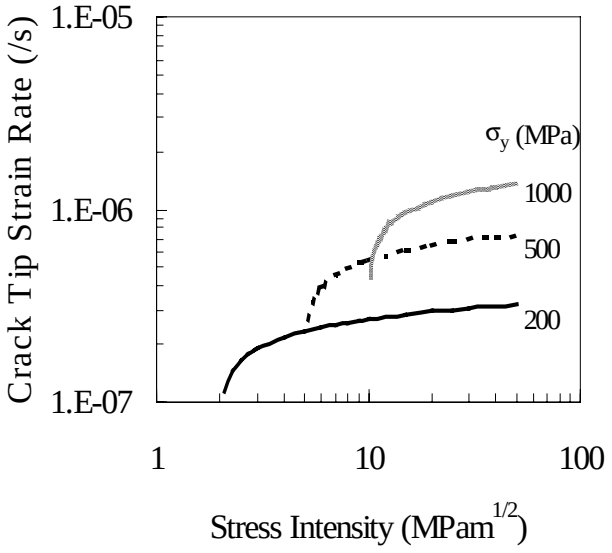

Fig. 1 Effect of yield strength on the crack tip strain rate for n = 5, da/dt = 10^{-9} m/s and dK/dt = 0.

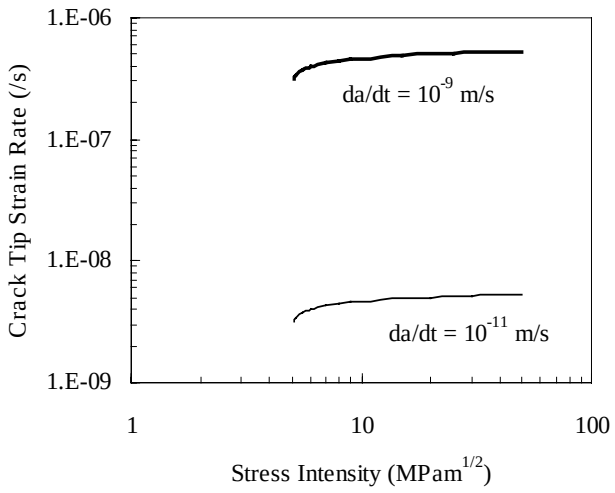

Fig. 2 Effect of crack growth rate on the crack tip strain rate for σ_y = 500 MPa, n = 10, and dK/dt = 0.

Significance of crack growth rate in crack tip strain rate evaluation under constant K/load tests

The effect of crack growth rate on the crack tip strain rate is shown in Fig. 2, which shows the crack tip strain rate as a function of stress intensity under static constant K test such as dK/dt = 0. Under constant K or load mode, a growing crack brings about the crack tip strain rate that shows a significant K-dependence. The behavior of the crack growth rate as a function of stress intensity factor is similar to that of crack tip strain rate with the same variable of K, showing a threshold behavior and a plateau crack growth region at the prevailing stress intensity level.

Sensitivity analysis of crack growth formulation

Eq. (3) can be used in estimating the crack growth rate in plane strain under dynamic and static loading conditions, which can be expressed in terms of dK/dt. In addition, important mechanical and electrochemical parameters affecting the cracking processes are included in Eq. (3). The last term in Eq. (3) in curly brackets, for example, stands for the strain rate, which has an interaction with parameter of "m". The parameter, m is determined by the film formation kinetics and the crack tip solution chemistry.

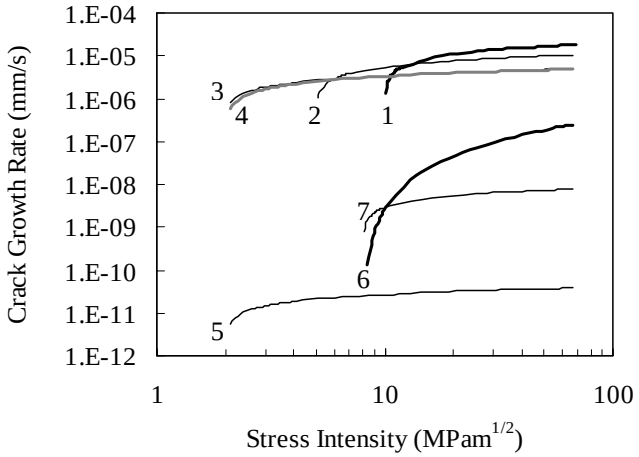

Fig. 3 Evaluation of crack growth rate as a function of K under RLT and constant K

Table 1 Summary of parameters used in the calculation of crack growth rate plotted in Fig. 3

Case #	m	n	σ_y (MPa)	dK/dt (MPam$^{1/2}$/s)
1	0.5	3	1000	1x10^{-5} (RLT)
2	0.5	3	500	1x10^{-5} (RLT)
3	0.5	3	200	1x10^{-5} (RLT)
4	0.5	3	200	0 (Constant K)
5	0.8	10	200	0 (Constant K)
6	0.8	3	800	0 (Constant K)
7	0.8	10	800	0 (Constant K)

Note: ----------

RLT: Rising Load Test. All other parameters used for calculation are as follows:
(β: 5.08, λ:0.5, M:55.85, z:2.67, ρ:0.00786 g/mm^3, F:96500 C, ε_f:0.001, r_o :0.03 mm, t_o:0.3 s, i_o:0.005 A/mm^2, E:210 GPa)

Figure 3 shows the effect of yield strength, strain hardening exponent "n", and repassivation kinetics parameter "m" on the crack growth rate as a function of K for given loading conditions, which are listed in Table 1. The profiles of crack growth rate as a function of K are close to the behavior of crack tip strain rate, both of which show a threshold and plateau region.

The general trend of crack growth response to yield strength is similar to that obtained from the calculation of crack tip strain rate. Higher yield strength results in higher crack growth rate at a given K level. While higher yield strength presents a higher threshold K value in crack propagation, the strain hardening exponent "n" does not affect the threshold K, which can be expected from Eq. (3). The repassivation kinetics parameter "m" has a strong impact on the crack growth behavior. Generally a lower value of "m", corresponding to slower repassivation kinetics, gives higher crack propagation.

The effect of yield strength on crack growth rate is significant irrespective of repassivation kinetics, which can be verified by comparing Case #1, 2 and 3 for m=0.5 and also Case #5 and 7 for m=0.8. This fact can be rationalized under the condition that all parameters are kept the same as shown above.

The crack growth behavior also is determined by the repassivation kinetic parameter "m", which is the slope of the current transient curve for a metal surface exposed to aqueous environment. Comparison of Case # 1 to 3 (m=0.5) and Case # 5 to 7 (m=0.8) illustrates the significance of the repassivation

behavior. At the higher value of m, the crack growth rate is several orders of magnitude lower than that at lower m. Besides, comparison of Case #3 and #4 presents the effect of loading rate on crack growth rate. In this particular case, no significant difference could be found between Rising Load Test (RLT, $dK/dt=1x10^{-5}$ MPa $m^{1/2}$/s) and Constant K Test.

The effect of strain hardening exponent "n" on crack growth rate can be seen from comparing Case #6 vs. 7 where n values are 3 and 10, respectively. Higher n value, corresponding to less strain hardening, gives rise to lower crack growth. Such a fact can be important to understand the behavior of irradiation-assisted stress corrosion cracking (IASCC) in that mechanical properties of materials such as yield strength and strain hardening exponent change due to the evolution of microstructure and grain boundary chemistry under irradiation.

DISCUSSION

Evaluation of crack tip solution chemistry and its implication for crack growth response

Figure 4 shows a clear evidence of how the crack tip solution chemistry controls the crack growth. Cracking completely comes to an arrest due to the removal of crack tip solution by microsampling. Microsampling extracts pre-existing aggressive crack tip solution containing anions, and the crack tip is replenished with bulk solution containing high dissolved oxygen. Consequently, the potential gradient and pH become in equilibrium. It takes time for the depletion of dissolved oxygen inside the crack and for the creation of potential gradient, which later causes the accumulation of anions at the crack tip. Once anions accumulate up to sufficient concentration, the quiescent crack might be activated again.

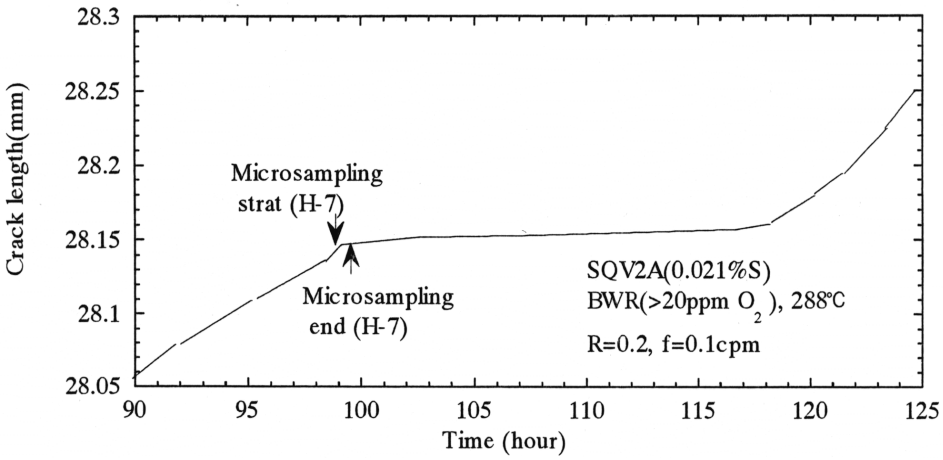

Fig. 4 Variation of crack growth behavior with microsampling for low alloy steel SQV2A (0.021%S)

Effects of stress state on crack growth behavior

Figure 5 shows the numerical results of crack growth rate that is calculated in plane strain and stress condition for three values of "m", 0.4, 0.5 and 0.6 [4]. In this calculation, the equations of (3) and (4) were used and parameters were kept the same as those listed in Table 1. It is clearly seen that under plane stress condition the crack growth rate in terms of K is higher than under plane strain one. Also, crack growth takes place at lower K level under plane stress condition. This trend can be understood from the fact that smaller plastic constraint at the crack tip provides a higher crack tip strain rate for a given K. Such a state becomes important for the plant lifetime prediction where defects are found as part-through cracks in most cases and the stress condition in near surface region comes close to a plane stress condition. Also, plastic constraint at crack front for small cracks would be small in plane stress because the stress state is close to uniaxial stress state. Very small cracks can cause high strain rate, which might be higher than that in plane stress. However, this situation becomes complicated when a strain concentration is taken into account. In order to explain this important problem, it is required to

analyze the strain distribution for a growing crack, particularly part-through cracks using 3D finite element method (FEM).

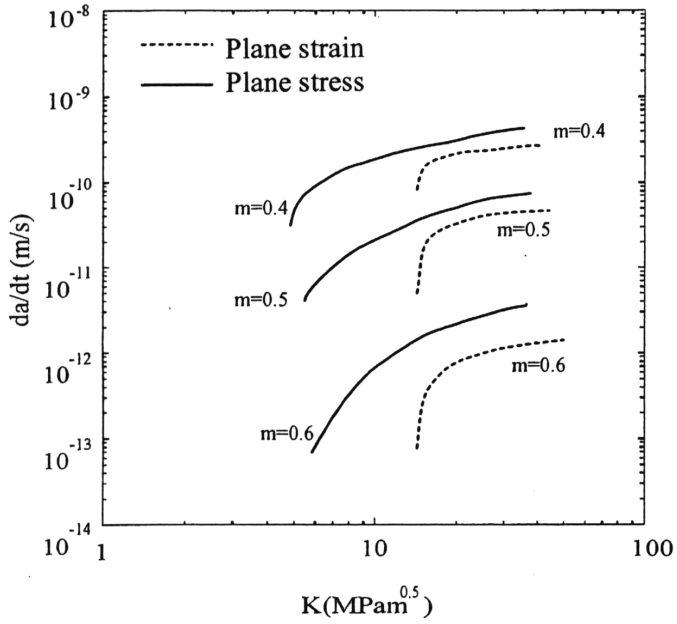

Fig. 5 Effects of stress state and repassivation kinetic parameter upon crack growth rate [4]

CONCLUSIONS

Based on slip-oxidation mechanism and crack tip mechanics, purely theoretical formulations have been developed to elucidate environmentally assisted cracking process and to outline controlling factors. The well-known phenomena of existence of threshold stress intensities and plateau growth rates in da/dt-K diagrams for many materials/environments combinations can be reproduced by the theoretical formulations from crack tip strain rate point.

ACKNOWLEDGEMENT

The partial support of this work by the Grant-in-Aid for COE (Center of excellence) Research (No.11CE2003), The Ministry of Education, Culture, Sports, Science and Technology is gratefully acknowledged.

REFERENCES

1. Ford, F. P. (1996) *Corrosion*, 52, 375.
2. Gao, Y. C. and. Hwang, K. C. (1982), In: *Proc. of the 5th International Conference on Fracture*, Pergamon, 669.
3. Shoji, T., Suzuki, S. and R. G. Ballinger, R. G. (1995). In: *Proceeding of the 7th Int. Symp. On Environmental Degradation of Materials in Nuclear Power Systems – Water Reactors*, Houston, TX: NACE, 881.
4. Suzuki, S. and Shoji, T. (1997). In: *Proc. of the 8th International Symposium on Environmental Degradation of Materials in Nuclear Power System-Water Reactors*, La Grange Park, IL: ANS, 685
5. Gerberich, W. W., Davidson, D. L. and Kaczorowski, M. (1990) *J. Mech. Phys. Solids*, 38, 87.
6. Rice, J. R., Drugan, W. J. and Sham, T.L. (1980) *ASTM STP 700*, 189.
7. Congleton, J., Shoji, T. and Parkins, R. N. (1985) *Corrosion Science*, 25, 633.

SPECIAL LECTURE

ENVIRONMENTALLY ASSISTED FRACTURE BEHAVIOR OF SILICON MICROELEMENTS

K. Komai[1], K. Minoshima[1] and T. Terada[2]

[1]Department of Mechanical Engineering, Kyoto University,
Kyoto, #606-8501, Japan
[2]Nomura Research Institute, Ltd., Tokyo, #100-0004, Japan

ABSTRACT

The influence of notch and water environment on the quasi-static and fatigue fracture behavior was investigated in single crystal silicon microelements. The tests were conducted in smooth and notched microcantilever beam samples. Single-crystal Si microelements deformed elastically until final failure, giving a brittle nature. The maximum fracture strength of a smooth microcantilever specimen reached about 7.7 GPa. However, the fracture strength decreased with an increase in notch depth, even though the notch depth was on the order of nanometer. In laboratory air, no fatigue damage was observed even though the surface was nanoscopically examined by an AFM. However, when the fatigue tests were conducted in pure water, the fatigue lives in water were decreased. Atomic force microscopy was capable of imaging nanoscopic cracks, which caused the failure in water.

KEYWORDS

Single-crystal silicon, Fracture, Fatigue, Notch, Focused ion beam, Water, Fractography, Atomic force microscopy

INTRODUCTION

In order to develop a reliable micromachine in a service operation, much care must be taken not only to processing methods, but also to micromechanical evaluation, i.e., mechanical properties of μm-sized microelements including fatigue and wear. For mechanical evaluation, Johansson and Schweitz [1] showed

that single-crystal silicon microelements on the order of μm have an extremely high bending strength over 10 GPa. The authors have also developed a specially designed testing machine for microelements [2], and have shown that bending strength increases with a decrease in specimen size, and the maximum bending strength obtained reaches about 8 GPa [3].

Beside these, fatigue behavior of microelements is also very important, when they are used in micromachines and micro electro-mechanical systems (MEMS) that are subjected to varying loads. The authors [3] have conducted fatigue tests in single-crystal Si microelement under three-point loading, and have shown that contact forces that work between a loading stylus and a sample promote crack initiation, and cause so-called fretting-fatigue. However, when a microelement is subjected to a simple bending in laboratory air, no fatigue damage is observed even though a sample surface is closely examined by an atomic force microscope. Note that fatigue behavior is observed when tests are conducted in water. Similar results such that water environments induce damage in single crystal silicon microelements were also demonstrated by Conally et al. [4, 5]. Our nanoscopic observation[3] showed that a crack of about 20 nm deep existed, which might be promoted by a synergistic effect of water and dynamic loading. Beside these, mechanical properties of single-crystal Si are very much sensitive to processing methods, and this is attributed to surface roughness. Therefore, it is very important to analyze the effects of nanometer-sized notch on the fracture behavior of a microelement.

In this investigation, mechanical tests including fatigue were conducted in single-crystal Si microelements, and special attention was paid to the effects of nanometer-sized notch and of water on the quasi-static and fatigue strength.

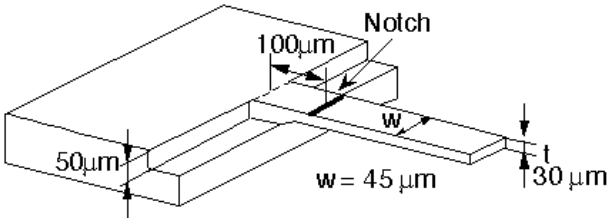

(a) Schematic view

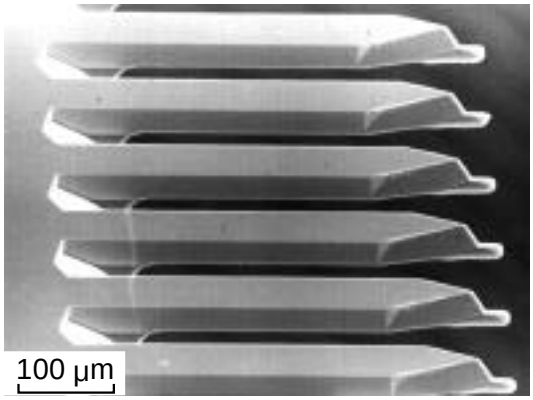

(b) SEM image

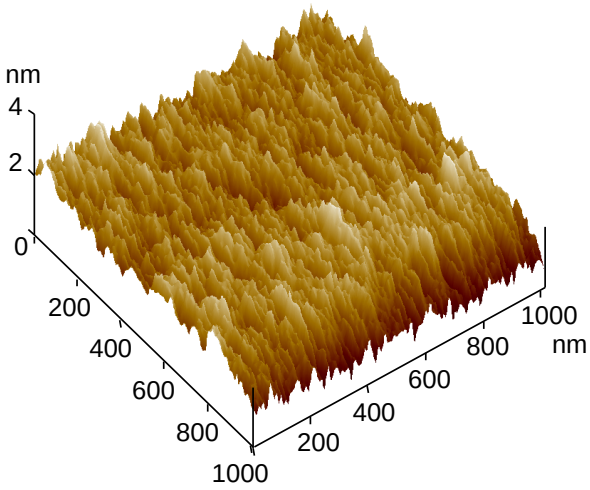

(c) AFM image of a microcantilever beam specimen (polished surface)

Fig.1 Microcantilever beam specimens.

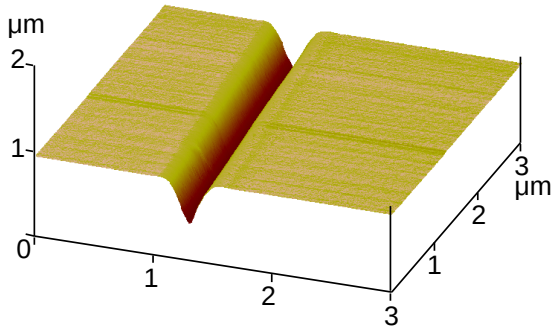

Fig.2 AFM image of V-shaped notch.

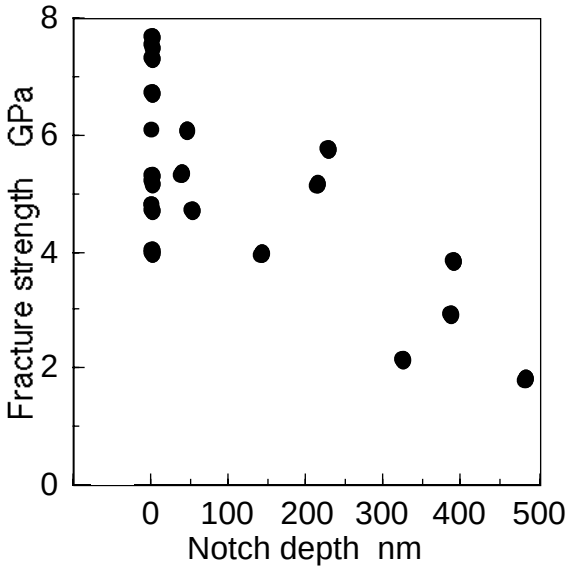

Fig.3 Fracture strength of single crystal as a function of notch depth.

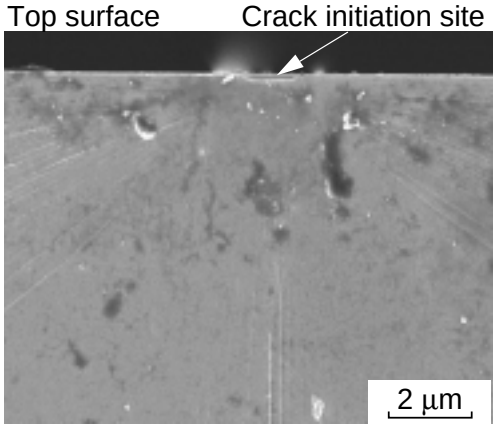

Fig.4 Quasi-static fracture surface of a notched specimen, imaged with SEM.

EXPERIMENTAL PROCEDURES

Single-crystal Si microcantilever beam specimens (Fig. 1) were prepared by micromachining (photo-etching) of (110) silicon wafers [3]. They were oriented along a <112> direction with a rectangular cross section. The sample used in this experiment was 30 μm thick, 45 μm wide, and 500 μm long. For some specimens, nanometer deep notch was milled 100 μm away from a sample root (Fig. 1(a)) by using a focused ion beam (FIB, ion source:Ga^+). Figure 2 illustrates AFM images of the cross-section of a V-shaped notch thus introduced by FIB milling. Bending force is applied to a microelement by a stylus positioned at the end of the actuator, which is a spherical diamond tip of 20 μm radius and 60° cone angle.

EXPERIMENTAL RESULTS AND DISCUSSIONS

Quasi-Static Fracture Strength and Influence of Notch

The load-displacement curve of a microcantilever with and without notch was linear until final catastrophic failure, indicating that single crystal Si microelement behaves elastically until final catastrophic failure. In the case of smooth microcantilever specimen [3], the fracture strength had large scatter band. The minimum fracture strength remained about 2 GPa, irrespective of specimen width ranging from 45 μm to 195 μm with thickness of 30 μm. However, the maximum or average fracture strength of each set of data increased with a decrease in specimen width. The maximum strength in all test results was 7.7 GPa, which was higher than that of mm order single crystal Si specimens machined by dicing which were subjected to four-point bending. The maximum fracture strength obtained in mm-sized sample was only 600 – 800 MPa [2].

Figure 3 shows the fracture strength as a function of notch depth. The fracture strength decreased with an increase in notch depth, even though the notch depth was on the order of nanometer.

Figures 4 shows the micrographs of the failed notched microcantilever sample. From the radial markings

we could thus trace back to the initiation site, where a notch existed. Beside these, the fracture surface was normal to the top surface of a sample, and the intersection of the fracture surface and the top surface was straight and was about 71 to 72 degrees against the longitudinal direction, or <112> direction. A crack that nucleated at a notch propagated on a {111} plane, resulting in normal crack to the top surface.

Fatigue Fracture Behavior in Air

Figure 5 shows fatigue lives of notched microcantilevers in laboratory air as a function of notch depth. The applied load was 100 mN or 50 mN, which was loaded 350 μm away from the specimen root. These gave the nominal maximum stress of 3.7 GPa and 1.9 GPa at a notch position, respectively. From this figure, it is shown that the fatigue lives were more than about 5 x10^4 cycles below a certain notch depth. However, it became extremely small when the notch depth exceeded a threshold value. The threshold value was smaller when an applied load was larger.

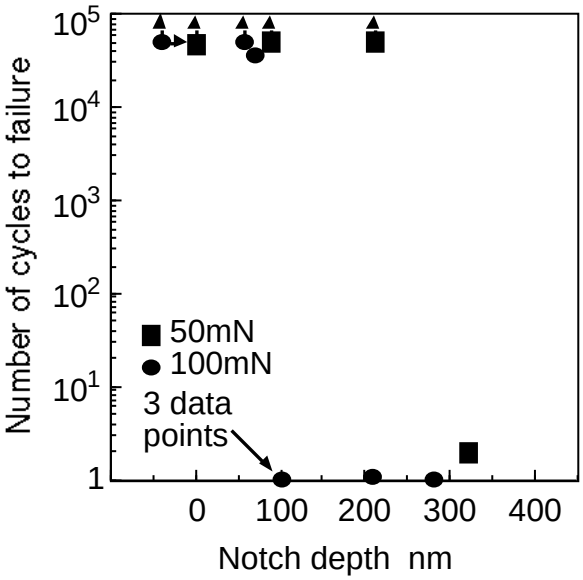

Fig.5 Fatigue strength in laboratory air as a function of notch depth.

Figure 6 shows an AFM image of top surface near and at a notch of a fatigued sample. The roughness of the fatigued sample surface was R_a=0.19 nm that was the same as that of the polished surface before fatigue tests. Nanoscopic fatigue damage could be seen neither near nor at a notch, indicating that single crystal Si might be immune to fatigue fracture in laboratory air.

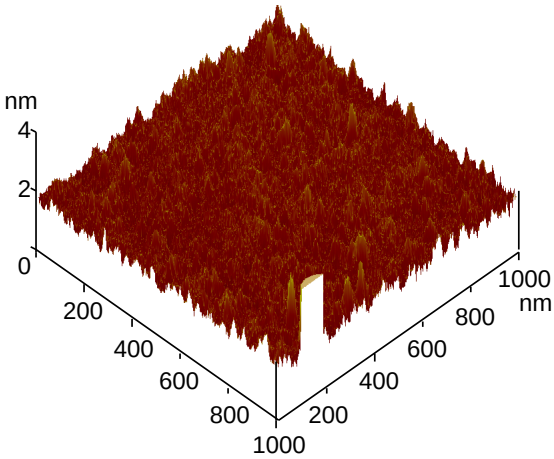

(a) top surface near a notch
(notch depth: 68 nm, N= 3.6 × 10^4)

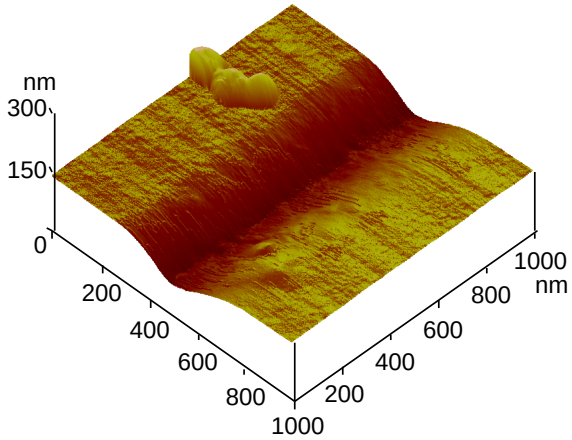

(b) notch (notch depth: 55 nm, N > 5 × 10^4)

Fig.6 AFM image of fatigued samples in laboratory air.

Influence of Water on Fatigue Fracture Behavior

Figure 7 shows fatigue lives in pure water of smooth and notched cantilever specimens as a function of pre-immersion time in water. The applied load was 100 mN, which gave the maximum stress of 3.7 GPa at a notch position. In this investigation, the water environment was achieved by placing wet absorbent cloth at a specimen root, and therefore, the adjacent microcantilevers to the testing one were also exposed to water. This means that the microcantilever fatigued later was immersed longer in water than the sample fatigued earlier. Therefore, the

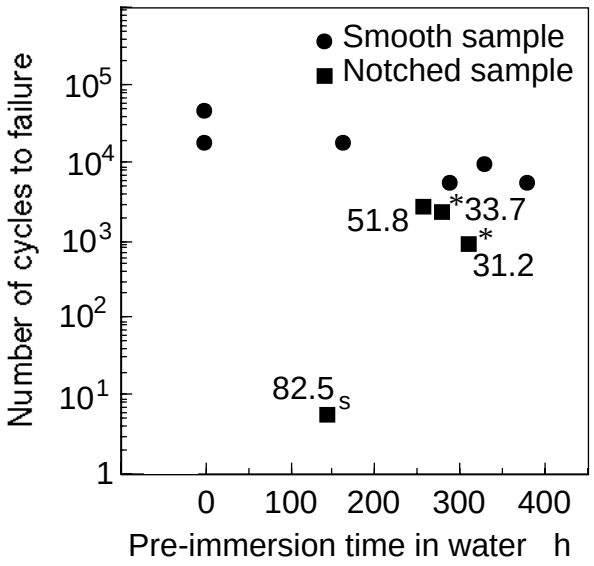

Fig.7 Fatigue strength in pure water as a function of pre-immersion time in water. (R = 0.1, f = 0.1Hz).

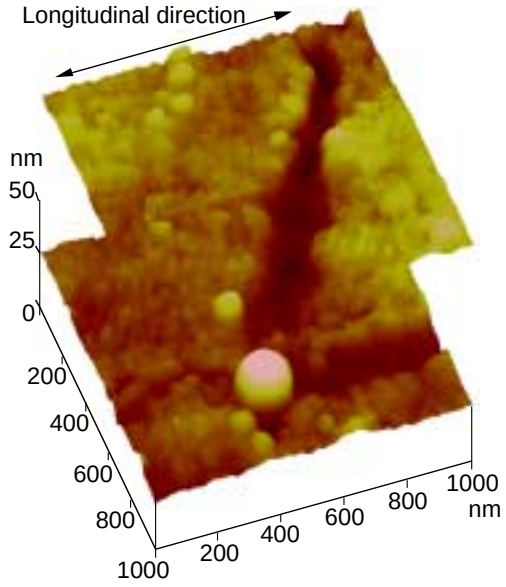

Fig.8 Fatigued sample imaged with AFM. The observed area is the smooth surface near a notch.

fatigue lives are plotted against pre-immersion time in water. The numbers in the figure indicate the notch depth in nm. Except the case with a superscript “s”, the notch depth machined was smaller than the threshold notch depth for fatigue in air.

For smooth cantilevers, the fatigue lives in water were shorter than those fatigued in air and became slightly shorter when the immersion time became longer. When a notch depth was large as is shown by a superscript “s”, the fatigue life was extremely short. In this case, the notch depth was almost equal to the threshold notch depth, above which static failure occurred, indicating that the failure was caused by the quasi-static one induced by stress concentration. Except this, similarly to the smooth microcantilevers, the fatigue lives of notched cantilevers were smaller than 3000 cycles, indicating shorter fatigue life than that conducted in air.

In the case of notched samples under quasi-static loading, a crack always initiated at a notch because of stress concentration. However, when a notch depth was smaller than a threshold depth below which no fatigue failure in air occurred, some sample failure in water was not associated with a notch. In Fig. 7, a superscript “*” is added when failure was not associated with a notch.

Figure 8 shows the notched sample surfaces fatigued in water, imaged by the AFM. The failure of the sample was not associated with a notch. The AFM tip used was a super sharp type with tip radius of about 5 nm. The groove type crack of about 16 nm in depth could be seen, and the direction of this crack was about 70 degrees against the longitudinal or <112> direction. This nanoscopic crack orientation agreed with that of the static failure, or {111} plane.

These observations indicate that a synergistic effect of fatigue loading and water environment caused a

nanoscopic crack, that oriented along {111} plane. The crack gradually propagated, and when its depth exceeded the critical depth, unstable or catastrophic failure occurred. Single-crystal Si was reported insensitive to water environment, and stress corrosion cracking does not occur [6]. In a microelement, however, we must note that crack initiation and propagation are promoted by a synergistic effect of fatigue loading and water environment [3, 4, 5].

CONCLUSIONS

Mechanical tests including fatigue were conducted in single-crystal Si microelements fabricated by photoetching using a specially designed testing machine that enables mechanical testing including fatigue. Special attention was paid to the effects of nanometre-deep notch machined by FIB and of water environment on fracture. The investigation yielded the following conclusion.

1. Focused ion beam is suitable processing method for machining a nanometre-deep notch. The cross-section is V-shaped, and the radius of the curvature decreases with an increase in notch depth. It ranges from about 20 nm to 100 nm, when notch depth exceeds about 100 nm.
2. Single-crystal Si microelements deform elastically until final failure, giving a brittle nature. However, they are sensitive to notch, and manometer-deep notch causes a decrease in the fracture strength.
3. For notched samples, a quasi-static fracture initiates at a notch, and a crack propagates in the direction normal to the sample surface on a {111} plane.
4. When fatigue load is applied in air, no fatigue damage is observed even though the surface is nanoscopically examined by an atomic force microscope. However, the fatigue lives in water are decreased compared with those conducted in air. An atomic force microscope is capable of imaging nanoscopic cracks on a {111} plane. Depth of a crack observed on a fracture surface was long enough to cause unstable fracture. These mean that a synergistic effect of fatigue loading and water causes a nanoscopic crack, and when its length, or depth, exceeds a critical length, catastrophic failure occurs, leading to lower fatigue lives in water.

REFERENCES

1. Johansson S. and Schweitz J.-Å.(1988) *J. Appl. Phys*, 63, 4799.
2. Komai K., Minoshima K., Tawara, H., Inoue S. and Sunako K.(1994) *Trans. Japan Soc. Mech. Eng., Series A*, 60, 52 (in Japanese).
3. Komai K. and, Minoshima K. and Inoue S.(1998) *Microsytem Technologies*, 5, 30.
4. Connally J. A. and Brown S. B.(1992) *Science*, 256, 1537.
5. Connally J.A. and Brown (1993). *Exp. Mech.*, 33, 81.
6. Wong B. and Holbrook R. J.(1987) *J. Electrochem. Soc.*, 134, 2254.

ICF100156OR

EQUILIBRIUM LENGTH OF A ZENER-BARENBLATT NANOCRACK WEDGED OPEN BY A DISCLINATION DIPOLE

Mao S. Wu

Department of Engineering Mechanics, University of Nebraska-Lincoln,
Lincoln, NE 68588-0526, USA

ABSTRACT

The aim of this paper is to investigate the equilibrium length of a stable, mode I nanocrack wedged open by a disclination dipole and subjected to a remote stress. The crack is assumed to be of the Zener type with its head coinciding with the negative disclination of the dipole. Also assumed is the Barenblatt model, in which cohesive zones carrying the theoretical tensile stress exist at the crack extremities. The resulting Zener-Barenblatt crack is modeled by edge dislocations. Exact equations for computing the crack length and cohesive zone lengths are presented. Numerical results show that for a stable nanocrack 10^{-9} to 10^{-8} m in length: (i) the cohesive zones constitute a significant portion of the crack, (ii) the traction-free zone length is significantly less than the predicted length of a purely elastic Zener crack with no cohesive zones, (iii) the traction-free zone length increases with the disclination dipole strength ω and arm length $2a$, and (iv) the cohesive zone at the crack head decreases in length with both ω and $2a$ while that at the crack tip increases in length with these parameters.

KEYWORDS

Zener-Barenlatt crack, disclination dipole, cohesive zones

1. INTRODUCTION

Disclinations have been used to model various dislocation ensembles in materials undergoing transformation plasticity, e.g., twinning and strain-induced martensitic transformation. In particular, the front of a deformation twin can be modeled by a wedge disclination dipole [1, 2]. When a twin is blocked by an intersecting twin, a very short crack (nanocrack with length 10^{-9} to 10^{-8} m) can nucleate from the negative disclination of the dipole.

The characteristics of such a nanocrack have only been recently predicted [3]. In this paper, a stable nanocrack subjected to remote mode I loading and wedged open by a disclination dipole is further studied. The wedge-shape crack is modeled as a Zener crack, which is characterized by the crack head opening b_T. For a very short crack with length 10 – 100 times the Burgers vector magnitude, however, the classical traction-free Zener crack may no longer be physically valid. Consequently, the Barenblatt model is invoked, in which atomistic cohesion exists at the crack extremities. Tractions, which for simplicity are taken to be constant and equal to the theoretical tensile stress, act over these cohesive zones. Of primary interests then are the total length of such a Zener-Barenblatt crack, the cohesive zone lengths, and their dependence on the disclination parameters, i.e., the dipole strength ω and the dipole arm length $2a$. Moreover, it is of interest to

compare the length of the classical (elastic) Zener crack with that of the Zener-Barenblatt (cohesive) crack, thus providing a basis for rejecting or accepting the classical model in lieu of the cohesive model.

The technique of solution relies upon the dislocation modeling of the entire Zener-Barenblatt crack. Exact closed-form expressions have been obtained for the density B of the modeling edge dislocations, the crack opening displacement v, and the normal stress $\sigma_y = \sigma$ on the crack line (subscript y indicates the crack normal direction) [3]. On the basis of exact closed-form expressions for v and certain consistency relations, the crack length and cohesive zone lengths are computed. These expressions are summarized in Section 2. The numerical results for B, v, the crack length and the cohesive zone lengths are presented in Section 3. A summary of the main findings is given in Section 4.

2. EXACT EXPRESSIONS FOR DISCLINATED ZENER-BARENBLATT CRACK

Figure 1 shows the dipole centered at the origin of the x-y coordinate frame. The negative and positive disclinations of the dipole are located at $x = a$ and $x = a$, respectively. The strength of each disclination is ω. The crack extends from $x = a$ to $x = a + 2c$ on $y = 0$. At the crack head $x = a$, the opening displacement Dv is b_T. The left cohesive zone is located in the interval $[a, a + l_1]$, and the right cohesive zone in $[a + 2c - l_2, a + 2c]$. The parameters $2a$, $2c$, l_1 and l_2 denote the dipole arm length, the total crack length, the left and right cohesive zone lengths, respectively. The remote stress σ_∞ is applied in the direction normal to the crack.

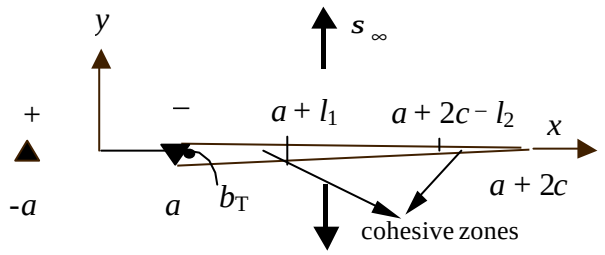

Figure 1: A Zener-Barenblatt crack subjected to disclination and remote loadings.

The entire crack is modeled by a continuous distribution of edge dislocations with density $B(x)$. As shown by the author in [3], $B(x)$ is given by:

$$B(x) = \frac{-\sqrt{x-a}\sqrt{a+2c-x}}{\pi^2 D} \int_a^{a+2c} \frac{\sigma_d(x') + \sigma_c(x')}{(x-x')\sqrt{x'-a}\sqrt{a+2c-x'}} dx', \tag{1}$$

where $D = G/2\pi(1-\nu)$ (G is the shear modulus and ν the Poisson's ratio), $\sigma_d(x')$ is the negative of the sum of remote stress and the y-component of stress due to the dipole, i.e.:

$$\sigma_d(x') = -\left(\sigma_\infty + D\omega \ln\left|\frac{a+x'}{a-x'}\right|\right), \tag{2}$$

and $\sigma_c(x')$ is the cohesive stress distribution in the intervals $[a, a + l_1]$ and $[a + 2c - l_2, a + 2c]$, i.e.:

$$\sigma_c(x') = \begin{cases} \sigma_c \cdot [H(a+l_1) - H(a) + H(a+2c-l_2) - H(a+2c)] \\ \sigma_c \cdot [-H(a+l_1) + H(a) + H(a+2c-l_2) - H(a+2c)] \end{cases}. \tag{3}$$

In Eqn. (3), H is the Heaviside function, and the cohesive stress is taken to be the constant σ_c. Also, the upper expression is used when the left cohesive zone is in compression, while the lower one is used when

the left zone is in tension. The right cohesive zone is always under tension. The left cohesive zone may be under compression or tension since the head of a Zener crack is in compression whereas the negative disclination at the head exerts a tensile stress in this region. Whether the left cohesive zone is in compression or tension is resolved by the sign of the stress intensity factor at $x = a$ of an elastic Zener crack subjected to the dipole and remote stress loading, see [3]. Substituting Eqns. (2) and (3) into Eqn. (1), a closed-form expression for $B(x)$ can be obtained. Integrating $B(x)$ with respect to x from x to $a + 2c$ yields $v(x)$, expressible also in closed-form. The crack length $2c$ and the cohesive zone lengths l_1, l_2 can be determined by equating $v(x)$ evaluated at $x = a + 2c - l_2$ to the critical value $_{cr}$, i.e.:

$$\pm\frac{\sigma_c}{\pi^2 D}\left\{\begin{array}{l}(c-l_1)\ln\left|\dfrac{c^2+(c-l_1)(c-l_2)-\sqrt{l_1 l_2(2c-l_1)(2c-l_2)}}{c(2c-l_1-l_2)}\right|+\\ (l_2-c)\ln\left|\dfrac{c^2+(c-l_1)(c-l_2)+\sqrt{l_1 l_2(2c-l_1)(2c-l_2)}}{c(2c-l_1-l_2)}\right|+\\ \sqrt{l_1(2c-l_1)}\left[-\tan^{-1}\left(\dfrac{c-l_2}{\sqrt{l_2(2c-l_2)}}\right)+\dfrac{\pi}{2}\right]\end{array}\right\}+$$

$$\frac{\sigma_c}{\pi^2 D}\sqrt{l_2(2c-l_2)}\left\{-\tan^{-1}\left(\frac{c-l_2}{\sqrt{l_2(2c-l_2)}}\right)+\frac{\pi}{2}\right\}+ \qquad , \qquad (4)$$

$$\frac{2w}{\pi}\left\{2\sqrt{a(a+c)}\tan^{-1}\sqrt{\frac{l_2}{2c-l_2}}-(2a+2c-l_2)\tan^{-1}\left(\sqrt{\frac{a}{a+c}}\sqrt{\frac{l_2}{2c-l_2}}\right)\right\}=\Delta_{cr}$$

and from the following consistency relations (see [3]):

$$\sigma_c\left\{\frac{\pi}{2}-\tan^{-1}\sqrt{\frac{2c-l_2}{l_2}}\mp\tan^{-1}\sqrt{\frac{l_1}{2c-l_1}}\right\}-\pi D w\tanh^{-1}\sqrt{\frac{a}{a+c}}-\frac{\pi}{2}\sigma_\infty=0, \qquad (5)$$

$$\tfrac{\sigma_c}{\pi D}\left[\pm\sqrt{l_1(2c-l_1)}+\sqrt{l_2(2c-l_2)}\right]+2w\left[\sqrt{a(a+c)}-a\right]=b_T\,. \qquad (6)$$

The upper and lower signs in Eqns. (4) - (6) correspond to the left cohesive zone being in compression and tension, respectively. These nonlinear equations can be solved numerically for c and l_1, l_2. The parameter $_{cr}$ equals twice the Burgers vector magnitude $2b$. The traction-free crack length $2c - l_1 - l_2$ can be compared to the crack length $2c$ of a purely elastic Zener crack (i.e., the classical crack with no cohesive zones).

3. NUMERICAL RESULTS

All the numerical results are obtained for the body-centered-cubic metal tungsten (W), except in the last figure where iron (Fe), aluminum (Al), silver (Ag), copper (Cu) and nickel (Ni) are also considered. The parameter b, taken from [4], and γ, G, ν, taken from [5], are summarized in Table 1. Also listed is the cohesive stress calculated from $\sigma_c = 2\gamma/_{cr}$, where γ is the crystal-vapor surface energy. For the elastic Zener crack, the crack length is computed by equating the mode I stress intensity factor to the fracture toughness K_{IC}. The latter is calculated from $K_{IC} = [4\gamma G/(1-\nu)]^{1/2}$, and the data are also shown in Table 1. Moreover, all numerical results in this paper are generated with $b_T = 4_{cr}$ and $\sigma_\infty = 0.02$ GPa.

TABLE 1
MATERIALS DATA (FROM [4, 5])

metals	b 10^{-10} m	g Jm^{-2}	G GPa	n	s_c GPa	K_{IC} MPa m$^{-1/2}$
Al	2.8635	0.98	26.5	0.347	3.422	0.399
Ag	2.8894	1.14	33.8	0.354	3.945	0.488
Cu	2.5560	1.725	54.6	0.324	6.749	0.747
Fe	2.4823	1.95	86	0.291	7.856	0.973
Ni	2.4919	2.28	94.7	0.276	9.150	1.092
W	2.7411	2.80	160	0.278	10.21	1.575

Dislocation Density and Crack Opening Displacement

Figure 2(a) plots $B(x)$ versus x for a stable Zener crack wedged open by a dipole of strength $w = 1^o$ and arm length $2a = 4$ nm. The solid and dashed lines correspond to the Zener-Barenblatt crack and the elastic Zener crack (crack tips at $x = a$, and $x = 2c$), respectively. Also predicted are $c = 12.5$ nm, $l_1 = 6.3$ nm, $l_2 = 8.1$ nm for the former, and $c = 7.9$ nm for the latter. It can be observed that $B(x)$ of the Zener-Barenblatt crack is singular at the boundaries between the traction-free zone and the cohesive zones, but is zero at the crack tip $x = a + 2c$ and has a finite value at the crack head $x = a$. These singular points and the minimum point correspond to inflection points on the crack profile. In contrast, $B(x)$ of the elastic crack is singular at both crack tips. Figure 2(b) plots $v(x)/2$ versus x. The Zener-Barenblatt crack has a complex shape with three inflection points as remarked above for Fig. 2(a). It also has a flattened shape at both crack ends. The elastic Zener crack, in contrast, has only one inflection point and has infinite slopes at the ends.

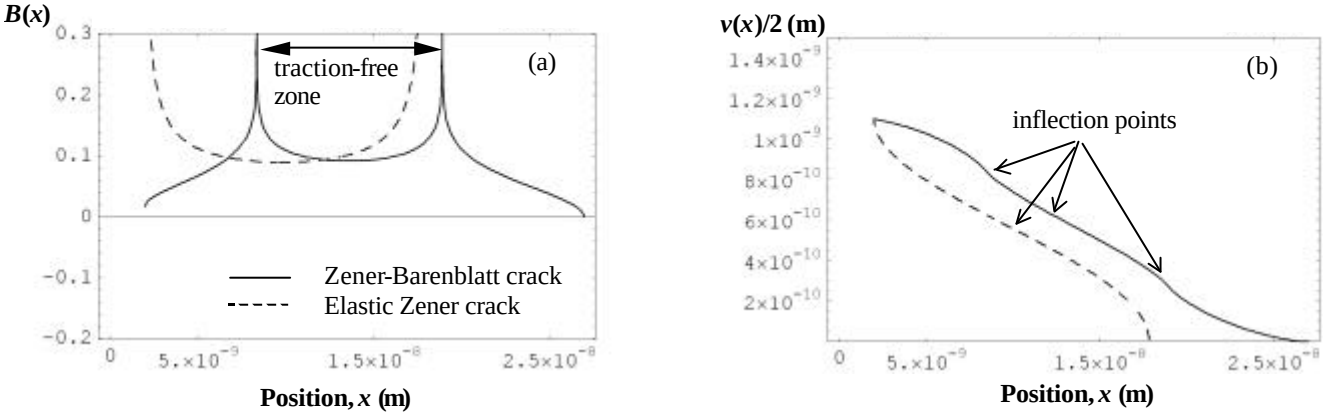

Figure 2: (a) Plot of the dislocation densities versus position for the stable Zener-Barenblatt and the elastic Zener cracks. (b) Comparison of the opening displacements of the two cracks.

Crack Length and Cohesive Zone Lengths

Figure 3 shows the dependence of the traction-free length ($2c - l_1 - l_2$), the total length $2c$ and the cohesive zone lengths of a stable Zener-Barenblatt crack on w and a. Since $2c - l_1 - l_2$ is of the order of 50% of $2c$, the cohesive zones make up a significant portion of the nanocrack. Second, the traction-free zone length increases with w and a. The total crack length has a more complex dependence on w and a: at the smaller values of w and a, $2c$ decreases with increase of these parameters; at the larger values of w and a, the reverse trend is evident. Third, the cohesive zone at the crack head (l_1) decreases in length with both w and a, whereas that at the crack tip (l_2) increases with these parameters. Fourth, no stable solutions can be found for sufficiently large w and a.

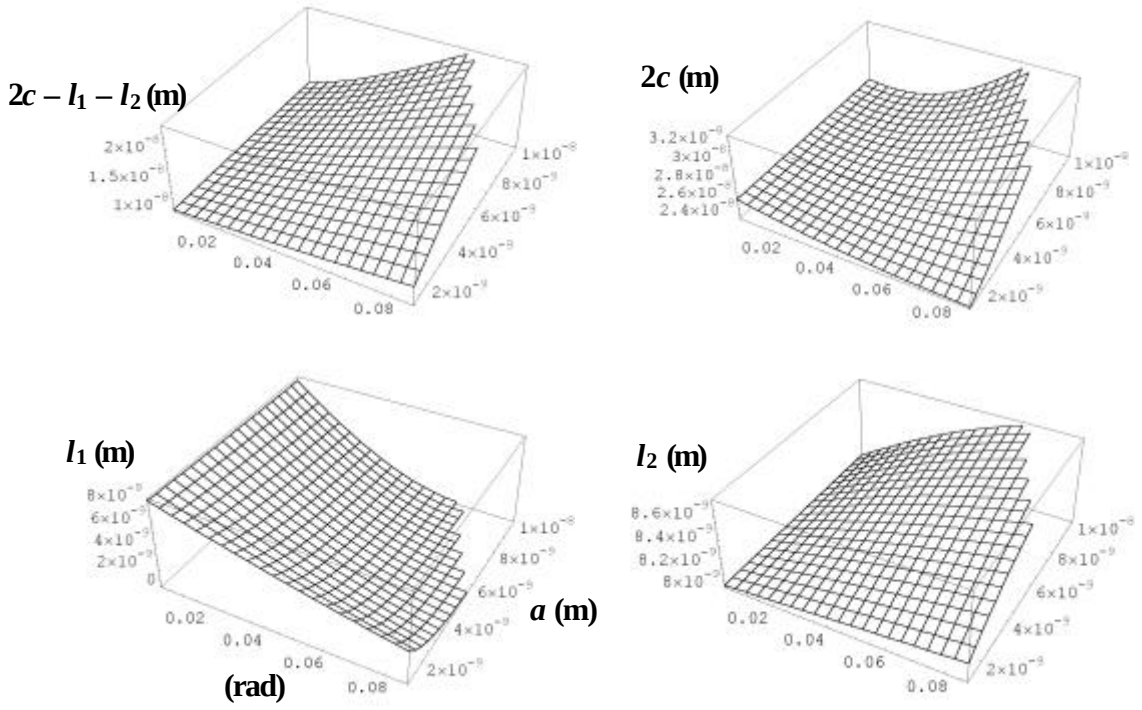

Figure 3: Dependence of the traction-free zone length, the total crack length, and the lengths of the cohesive zones at the crack head and crack tip on the disclination dipole strength and arm length.

Comparison of Cohesive and Elastic Cracks

Figure 4 compares the traction-free zone lengths of Zener-Barenblatt cracks to the crack lengths of elastic Zener cracks. The conclusion is that for the nanocracks considered here (with small crack head opening $b_T = 4_{cr}$) a significant discrepancy exists between the two predictions. The predicted elastic cracks are significantly longer than the predicted traction-free zones. Also, the discrepancy increases as ω and a *decrease* in magnitude.

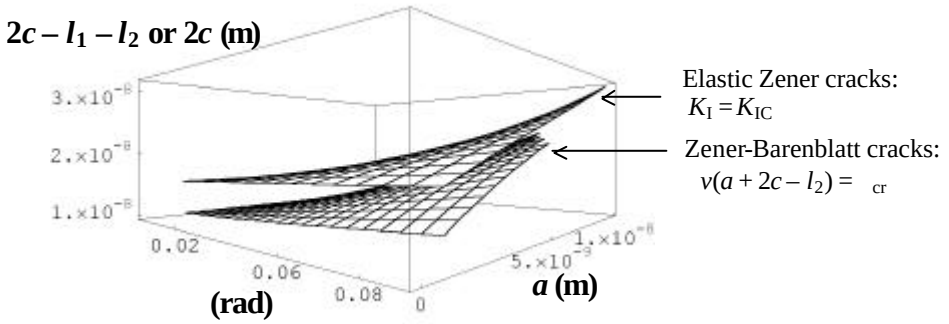

Figure 4: Comparison of the traction-free zone lengths of Zener-Barenblatt cracks with the lengths of elastic Zener cracks.

Dependence of Crack Lengths on Material

Figure 5 compares the traction-free zone lengths and the total lengths of cohesive cracks in various metals. The lengths of elastic cracks are also plotted in the figure. All lengths are plotted against the cohesive strengths $\sigma_c = 2\gamma/_{cr} = \gamma/b$ of the metals. In all cases, $\omega = 1^o$ and $2a = 4$ nm. The results show that the various lengths do not have a clear correlation with σ_c. Similarly, no clear correlation is found when they are plotted against γ, G or K_{IC}. In contrast, the length of an elastic Zener crack subjected to the opening b_T (no disclination loading) varies monotonically with the material parameters. The figure also shows that the predicted length of a disclinated elastic crack overestimates the traction-free zone length of the cohesive crack but underestimates the total length of the cohesive crack.

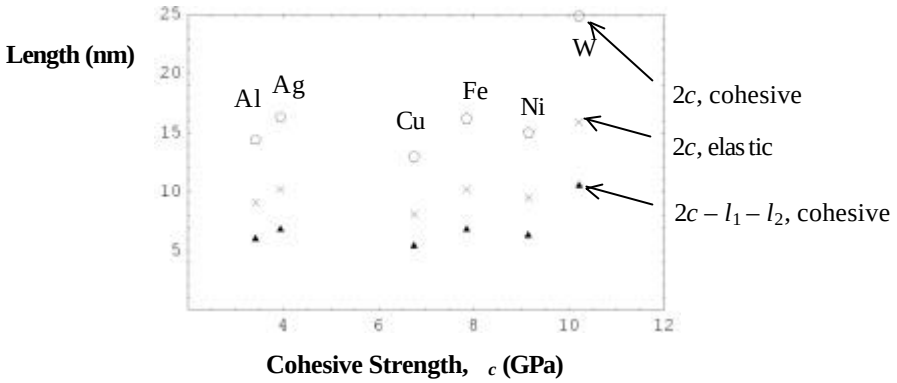

Figure 5: Comparison of the total crack lengths (pentagons), the traction-free zone lengths (triangles) of cohesive cracks, and the crack lengths (crosses) of elastic cracks.

4. SUMMARY

The equilibrium length of a stable mode I Zener-Barenblatt crack subjected to the loading of a disclination dipole is investigated in this paper. The crack length solutions are obtained by the method of dislocation modeling of the entire cohesive crack. Exact expressions constructed from the crack opening displacement and the consistency relations are solved numerically for the total crack length and the cohesive zone lengths. For small crack head opening displacement of the order of nanometers, numerical results indicate that: (i) the cohesive zones constitute a significant portion of the total crack, (ii) the elastic crack length, while significantly larger than the traction-free zone length, is significantly smaller than the total cohesive crack length, (iii) the traction-free zone length increases with the disclination dipole strength and the dipole arm length, and (iv) the cohesive zone at the crack head decreases in size with the disclination parameters, while that at the crack tip increases in size with these parameters.

REFERENCES

1. Müllner, P. and Kuschke, W.-M. (1997). *Scrip. Mater.* 36, 1451.
2. Müllner, P. (1997). *Mater. Sci. Engng.* A234-236, 94.
3. Wu, M. S. (2001). *Int. J. Engng. Sci.*, accepted.
4. Pearson, W. B. (1967). *Handbook of Lattice Spacings and Structures of Metals*, Vol. 2. Pergammon Press, Oxford.
5. Hirth, J. (1982). *Theory of Dislocations*, Second Edition. Krieger Publishing Company, Malabar.

POSTER REFERENCE:ICF100119PR

ERROR ESTIMATION OF SHAPE CHANGES DURING FATIGUE CRACK GROWTH

T. D. Righiniotis[1]

[1] Department of Civil and Environmental Engineering, Imperial College, London, SW7 2BU, UK

ABSTRACT

Accurate determination of the shape of a crack is important during fatigue. On the other hand, simulation may require a considerable number of fatigue evaluations that correspond to a wide range of crack shapes. Therefore, the numerical methods employed to carry out this task need to address the issues of accuracy, robustness and efficiency. In this paper, a fourth order Runge-Kutta scheme is used for crack shape evaluation and its accuracy is first assessed by comparison to closed form solutions for a surface cracked plate under tension and by means of a convergence study for the surface-cracked butt welded plate in tension. Finally, a convergence study is carried out on the fatigue lives of Monte Carlo samples of the latter geometry. This last study is carried out by assuming that crack growth follows a bi-linear law.

KEYWORDS

Semi-elliptical surface crack, fatigue, shape changes, Monte Carlo simulation

INTRODUCTION

Under fatigue, cracks grow while retaining a semi-elliptical shape. Accurate determination of the crack shape is important at all times during the crack evolution since accurate stress intensity factor determination and hence rate of crack growth is heavily reliant on the dimensions of the crack. For a two degree-of-freedom surface crack, and assuming that the Paris C parameters are the same in both directions [1], the pertinent equations are:

$$\frac{da}{dN} = C\left(\Delta K_A\right)^m \tag{1}$$

$$\frac{dc}{dN} = C\left(\Delta K_C\right)^m \tag{2}$$

Here, the point A refers to the deepest point of the crack border and the point C to its surface counterpart. The differential Eqns. 1 and 2 may be solved for a plate with thickness t by solving one of the two as a differential equation and integrating the other one thus,

$$\left(\frac{a}{c}\right)_f = f\left(\left(\frac{a}{c}\right)_{in}, \left(\frac{a}{t}\right)_{in}, \left(\frac{a}{t}\right)_f, m\right) \tag{3}$$

$$N = \frac{1}{C}\int_{a_{in}}^{a_f} \frac{da}{\left(S_r\ Y_A \sqrt{\frac{\pi\ a}{Q}}\right)^m} \tag{4}$$

where S_r is the stress range, Y_A is the stress intensity magnification factor for A, Q is the elliptical shape factor [1], and the subscripts *in* and *f* denote the initial and final values, respectively. Note that Y_A is a function of both a/t and a/c, the latter being calculated from Eqn. 3. Eqn. 4 may be solved using any numerical integration scheme and here the integral is calculated using 24-point Gauss integration. Eqn. 3 may be obtained by using any high order method. Here, the fourth order Runge-Kutta scheme is investigated using different number of steps. In order to demonstrate the robustness of the Runge-Kutta scheme, two geometries are investigated in this paper, both under tension. First, the case of the semi-elliptical surface crack in a plate under tension is investigated since analytical solutions of Eqn. 3 exist for different integer m [2] and these are directly compared with the results of the proposed numerical scheme. Then the case of the semi-elliptical surface crack in a butt-welded plate under tension is examined by means of a convergence study on the statistical characteristics of the crack shape and the fatigue lives while the latter are calculated based on a bi-linear crack growth law.

ERROR ESTIMATION

Semi-elliptical surface crack in a plate under tension

The factor Y_A used here is the Newman-Raju solution [3]. An analytical expression of Eqn. 3 in this case was supplied by Wu [2] for m=2 and m=3. The results for m=5 and m=6 are straightforward to derive and are given by Eqns. 5 and 6 for m=5 and 7 and 8 for m=6.

$$\frac{a}{c}=\left\{F\left(\frac{a}{t}\right)-\left[\frac{(a/t)_{in}}{(a/t)}\right]^{7/2}\left[F\left(\left(\frac{a}{t}\right)_{in}\right)-\left(\left(\frac{a}{c}\right)_{in}\right)^{-7/2}\right]\right\}^{-2/7} \tag{5}$$

where

$$F\left(\frac{a}{t}\right)=1.6105+1.6305\left(\frac{a}{t}\right)^{2}+0.7609\left(\frac{a}{t}\right)^{4}+0.1911\left(\frac{a}{t}\right)^{6}+0.0251\left(\frac{a}{t}\right)^{8}+0.0013\left(\frac{a}{t}\right)^{10} \tag{6}$$

$$\frac{a}{c}=\left\{F\left(\frac{a}{t}\right)-\left[\frac{(a/t)_{in}}{(a/t)}\right]^{4}\left[F\left(\left(\frac{a}{t}\right)_{in}\right)-\left(\left(\frac{a}{c}\right)_{in}\right)^{-4}\right]\right\}^{-1/4} \tag{7}$$

where

$$F\left(\frac{a}{t}\right)=1.7716+2.2547\left(\frac{a}{t}\right)^{2}+1.3451\left(\frac{a}{t}\right)^{4}+0.4565\left(\frac{a}{t}\right)^{6}+0.0908\left(\frac{a}{t}\right)^{8}+0.0099\left(\frac{a}{t}\right)^{10}+0.0005\left(\frac{a}{t}\right)^{12} \tag{8}$$

The robustness of the Runge-Kutta (R-K) scheme employed here was investigated by assuming different combinations of $(a/t)_{in}$, $(a/c)_{in}$ taken from the interval (0,1), calculating $(a/c)_f$ for $(a/t)_f$ = 1 by using Eqn. 3 and comparing with their analytically derived counterparts. In total, 400000 different combinations of these variables were used. The statistical characteristics of the differences between the numerical approximation of Eqn. 3 and the analytical solution are shown in Figure 1 and are presented in the form of mean and mean + standard deviation curves of the percentage difference between the proposed numerical scheme and the exact solution. The mean error lines demonstrate that, larger errors irrespective of the number of R-K steps used are observed for lower m values. However, the scatter is significantly smaller for low m values and decreases as the number of R-K steps increases.

Semi-elliptical surface crack in a butt-welded plate under tension

The factor Y_A used for this geometry is given in the Appendix. In this case, a closed form solution cannot be obtained as was done for the previous geometry. Consequently, differences are reported here with respect to the forty-step R-K scheme. Errors in $(a/c)_f$ were calculated again for the same values of $(a/t)_{in}$, $(a/t)_f$ (=1) and $(a/c)_{in}$ as in the previous section. The results are shown in Figure 2. The scatter, which is depicted by the solid lines, diminishes with decreasing m. The highest mean errors are here recorded for m=6, which drop below 5% for R-K steps greater than 10. The highest scatter is again

recorded for m=6 and this drops below 5% for R-K steps greater than 18. These results indicate that use of lower order schemes at the same small number of steps could result in unacceptably high errors. The convergence characteristics may also be investigated in a more comprehensive manner by looking at the fatigue lives calculated via Eqn. 4 in a probabilistic way. Here, the bi-linear crack growth law proposed in BS 7910 [1] is used.

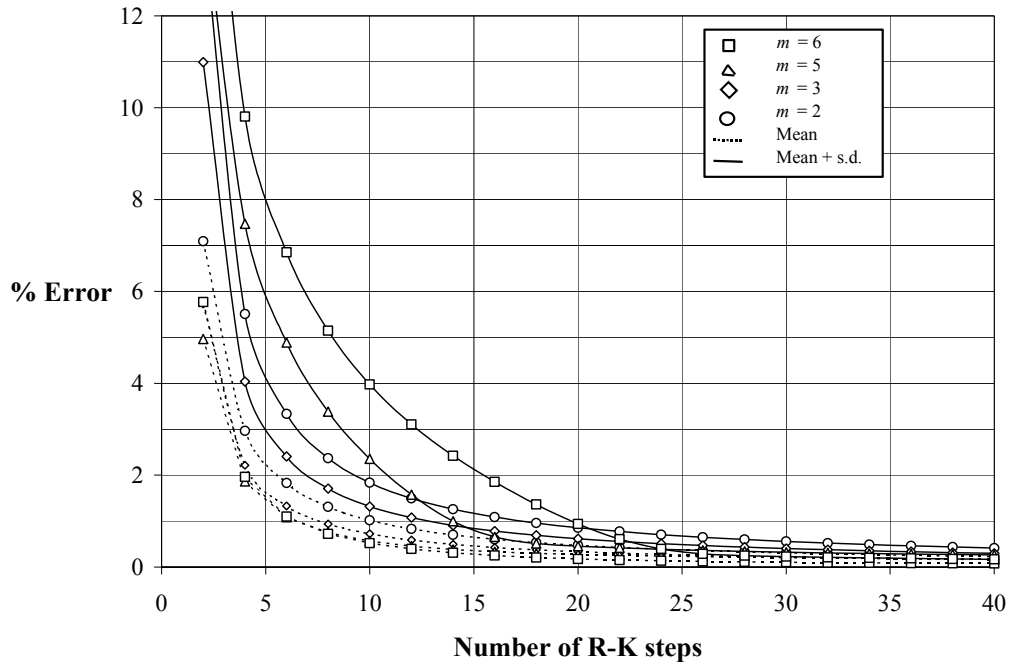

Figure 1: Mean and mean + s.d. curves of the errors in $(a/c)_f$ as functions of the R-K steps for a cracked plate

The crack growth model comprises two lines, each being described by its own Paris parameters. The crack growth law is described by the following equation

$$\frac{da}{dN} = \begin{cases} 0 & \Delta K \le \Delta K_{thr} \\ C_1(\Delta K)^{m_1} & \Delta K_{thr} < \Delta K \le \Delta K_{tr} \\ C_2(\Delta K)^{m_2} & \Delta K_{tr} \le \Delta K \end{cases} \tag{9}$$

where ΔK_{thr} is the threshold stress intensity range and ΔK_{tr} is the stress intensity range corresponding to the intersection of the two crack growth lines. The deterministic and probabilistic variables and their characteristics used here are the same as in Reference [4] with the added random variable of $(a/c)_{in}$, which was assumed to be lognormally distributed with mean 0.01 and coefficient of variation 0.5 . The Paris parameters m_1 and m_2 were taken to be deterministic and equal to 5.10 and 2.88, respectively, in accordance with BS 7910 [1]. Errors here were calculated with respect to the estimate arising from the application of the highest number of R-K steps (n_I, n_{II} = 10) in both crack growth regions. Results are shown in Figure 3. Additional information is given by the inset of this figure. The figure shows that in this case, the influence of the number of R-K steps in the near threshold crack growth region (I) is far more important than in the Paris region.

Consequently, it is quite clear that acceptable accuracy (error < 5%) may be obtained by using a $(3,n_{II})$ R-K with $n_{II}>1$.

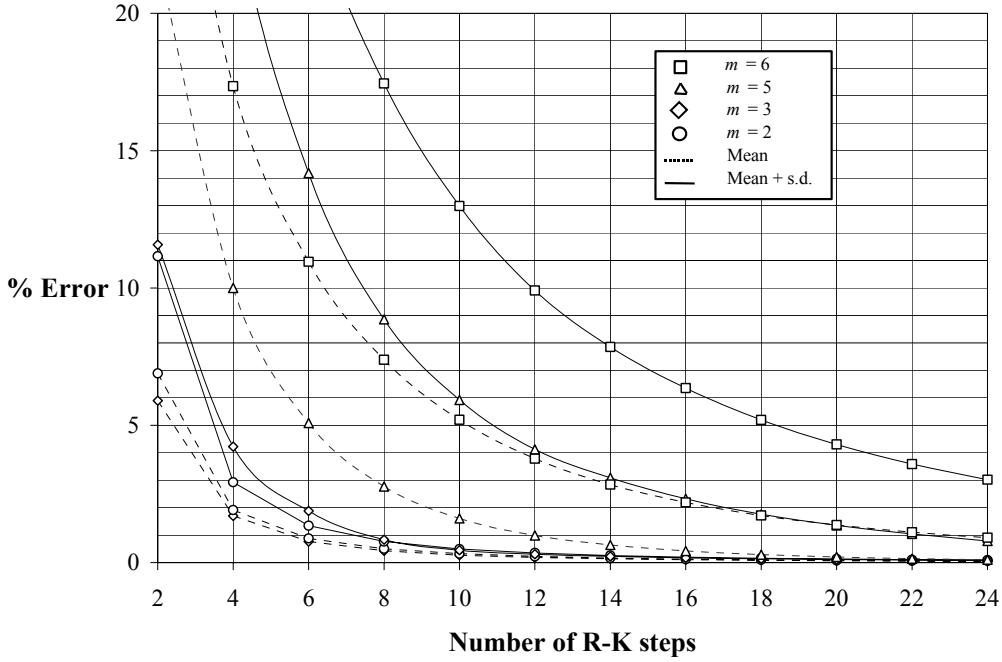

Figure 2: Mean and mean+s.d. curves of the errors in $(a/c)_f$ as functions of the R-K steps for a cracked butt-welded plate

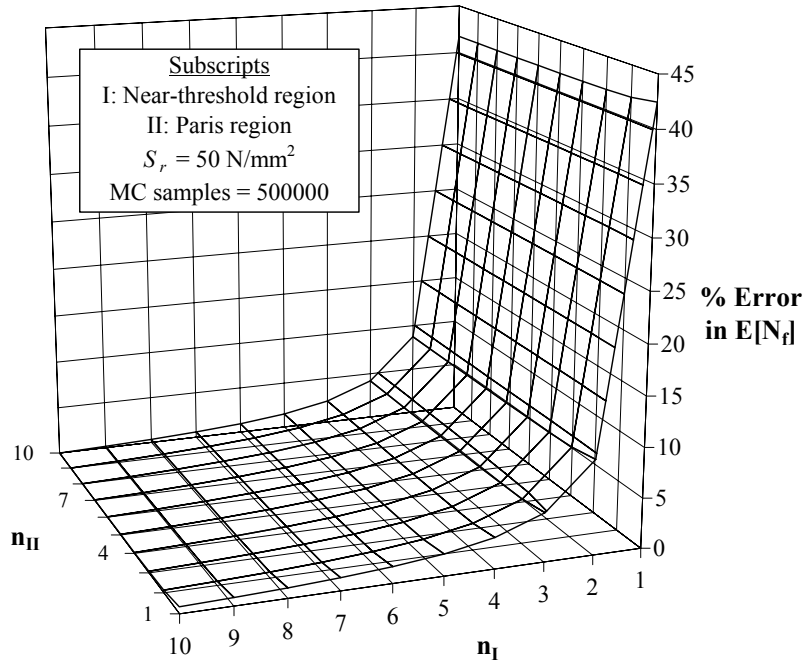

Figure 3: Variation of error in mean fatigue life with number of R-K steps in the two crack growth regions

CONCLUSIONS

The numerical characteristics of a fourth order Runge-Kutta scheme used to evaluate the crack shape during fatigue crack growth were presented in this paper. These were first compared against available analytical solutions for the case of a surface cracked plate under tension. Errors were then calculated in the form of a convergence study for a cracked butt-welded plate under tension. Both studies were carried out for a wide range of initial crack depths and shapes. The robustness of the scheme was also investigated with reference to fatigue lives as these were calculated using Gauss integration of a bi-linear crack growth law. Motivation for this work was supplied by the need to determine accurately fatigue lives within Monte Carlo simulation of the recently proposed bi-linear crack growth model of BS 7910 [1].

ACKNOWLEDGEMENTS

The author would like to thank Professor Chryssanthopoulos for his encouragement and support. This work forms part of a project, which is sponsored by the UK Highways Agency. Their support is gratefully acknowledged.

REFERENCES

1. BS 7910 (2000). Guide on methods for assessing the acceptability of flaws in metallic structures. BSI, London.
2. Wu, S.-X. (1985) *Eng. Fract. Mech.* 22, 897
3. Raju, I.S. and Newman, J.C. (1979) *Eng. Fract. Mech.* 11, 817.
4. Righiniotis, T.D. and Chryssanthopoulos, M.K. (2001). In: *Proc. 8th International Conference on Structural Safety and Reliability.* To be presented.

APPENDIX

For a welded plate, the factor Y_A is given by

$$Y_A = M_{km}\, M_m$$

where M_{km} is the magnification factor associated with the weld [1] and M_m is the Newman-Raju plate solution [3].

ESTIMATION OF CREEP CRACK GROWTH RATE FROM CIRCULAR NOTCHED SPECIMEN

T. Adachi[1], A. T. Yokobori, Jr.[2], M. Tabuchi[3], A. Fuji[4] and T. Yokobori[5]

[1]Faculty of Science and Engineering, Ishinomaki Senshu University, Japan
[2]Faculty of Engineering, Tohoku University, Japan
[3]National Research Institute for Metals, Japan
[4]Metallurgy Department, Research Institute, Ishikawajima-Harima Heavy Industries Co. Ltd, Japan
[5]School of Engineering and Science, Teikyo University, Japan.

ABSTRACT

A circular notched specimen was used to investigate the creep crack growth rate under multi-axial stress condition. A circular notch in a round bar specimen produces multi-axial stress field when uni-axial stress is applied in the axial direction. An electric potential drop method is adopted to measure crack length. In this paper, an equation for the relationship between the electric potential drop and the crack length of circular notch in a round bar is proposed and the accuracy of the measured length of a crack using this method was compared with the actual crack length. Using this equation, high temperature creep crack growth tests were conducted for a circular notched specimen of CrMoV steel.

KEYWORDS

Circular notch, multi-axial stress, electric potential drop method, creep crack growth, creep fracture life, thermal activated process

INTRODUCTION

The characteristics of crack growth rate under multi-axial stress condition have been investigated by many researchers using several methods[1-3]. Under the uni-axial tensile stress condition, a round bar specimen with a circular notch produces crack growth data under multi-axial stress condition[4]. We used a circular notched specimen to investigate the creep crack growth rate under multi-axial stress condition. An electric potential drop method was adopted to measure the crack length. The electric potential drop method bases on the fact that the potential distribution in the vicinity of a crack changes with crack growth[5]. A calibration curve is necessary to convert the value of electric potential drop into crack length. An equation which relates crack length to the electric potential has been obtained for CT specimen[5,6]. The equation can be applied to the measurement of a crack length for the center-cracked specimen, a single-edge notched specimen, a CT specimen and others, but it cannot be applied to the circular notched specimen. Therefore, the derivation of a relationship between the value of electric potential drop and the crack length for circular notch for a round bar specimen was conducted. The accuracy of the measured length based on this method was compared with the actual crack length[7].

High temperature creep crack growth tests were conducted for a circular notched specimen of CrMoV steel. The crack length was measured using the proposed equation in this paper and the law of creep crack

growth rate was derived on the basis of a thermal activation process.

MATERIAL AND SPECIMEN

Material used is a CrMoV steel. The chemical composition and mechanical properties at room temperature are shown in Tables 1 and 2, respectively. The material is used for a turbine rotor (400mm in diameter) and made by Japan Steel Works, Ltd.

TABLE 1 Chemical composition of CrMoV steel

(Wt%)

C	Si	Mn	P	S	Ni	Cr	Mo	V
0.3	0.22	0.74	0.005	0.0016	0.36	1.1	1.32	0.23

TABLE 2 Mechanical properties of CrMoV steel

0. 2% Y. S. Mpa	T. S. Mpa	EL. %	R. A. %
682	830	23.8	62.4

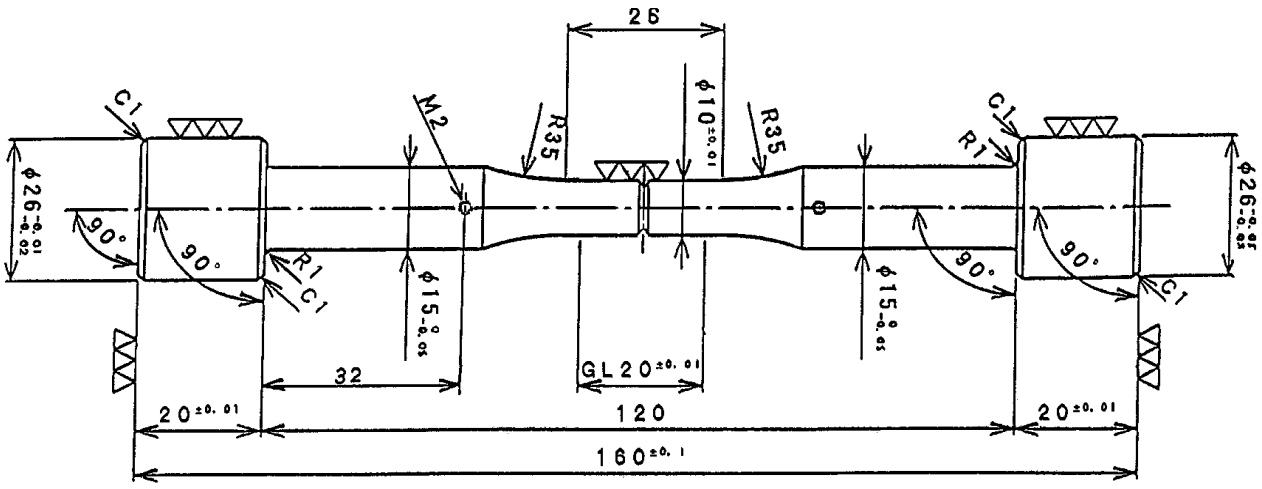

Fig. 1: Dimension of a circular notched specimen used in the creep test.

The geometry and dimension of a specimen is shown in Fig. 1. The circular notch is machined and notch tip angle, ϕ is 60º, notch depth, a_0 is 1.5mm and notch root radius, ρ is 0.25mm. The stress concentration factor is 3.85[8]. The stress intensity factor is given by Eqn.(1)[9],

$$K = \frac{1}{2}\sigma_{net}(\pi ad/D)^{1/2}\left(1+\frac{1}{2}\lambda+\frac{3}{8}\lambda^2-0.363\lambda^3+0.731\lambda^4\right)\left\{1+0.1\left(\frac{a}{D}\right)^{1/2}\left(1-\frac{2a}{D}\right)\right\}, \quad (1)$$

where σ_{net} is net stress, D is diameter of specimen, $d=D-2a$ (a is crack length which include notch depth), as shown in Fig. 3 and $\lambda=d/D$.

TEST METHOD

According to the electric potential drop method, an electric current is applied to the specimen and the value of electric potential drop is measured. The crack length of CT, CTT, SENT and SENB specimen can

be evaluated by Johnson's equation[5,6] as given by;

$$a = \frac{2W}{\pi}\cos^{-1}\frac{\cosh(\pi y/2W)}{\cosh\left\{(U/U_0)\cosh^{-1}\left[\cosh(\pi y/2W)/\cos(\pi a_0/2W)\right]\right\}} \tag{2}$$

where U_0 and a_0 are the initial values of potential and crack length, respectively. U and a are the actual values of potential and crack length, and y is one half of the gage span for U and W are shown in Fig. 2. For circular notched specimen, Eqn. (2) may not be applied. Thus, a calibration curve which converts the value of electric potential drop into the crack length is necessary to measure crack length initiated from a circular notch. The calibration curve which adjust to a circular notch was recently formulized by modifying Johnson's equation as follows[7]:

$$a = 0.973\exp\left[0.289\frac{D}{\pi}\cos^{-1}\frac{\cosh(\pi y/D)}{\cosh\left\{(U/U_0)\cosh^{-1}\left[\cosh(\pi y/D)/\cos(\pi a_0/D)\right]\right\}}\right] \tag{3}$$

where D is diameter of specimen, as shown in Fig. 3. The deviation of the measured crack length by Eqn. (3) from the actual crack length is 4% until crack length, $2a/D$ becomes 0.75[7].

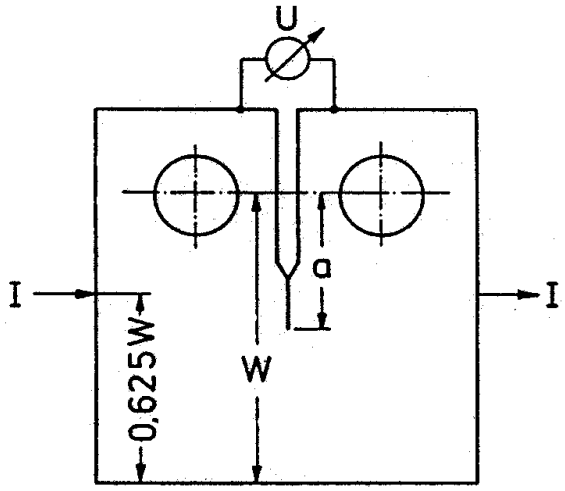

Fig. 2: Dimension of CT specimen.

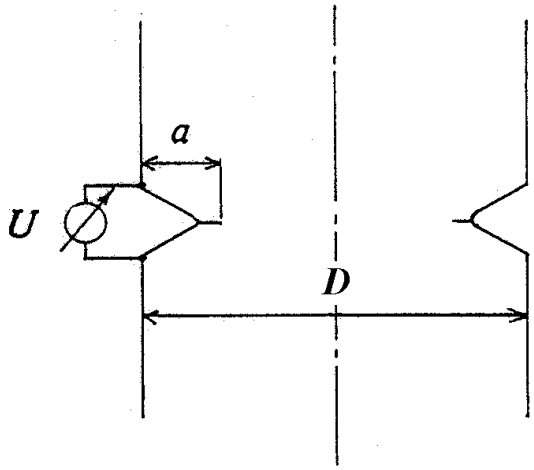

Fig. 3: Virtual Section of circular notched specimen.

To measure crack length by electric potential method, electrodes are connected to a specimen. Potential leads made of stainless steel wire (0.5mm in dia.) are welded on specimen in the vicinity of notch, as shown in Fig. 3. Current leads (2mm in dia.) made of stainless steel wire are attached to the shoulder part of specimen. The potential measurement and current input are located on a same centerline. The specimen with electrodes is heated up to test temperature. Creep tests are conducted at 538°C, 566°C and 594°C. Three applied loads, 13328N, 17640N and 21972N, are selected. The crack length is measured continuously during the creep crack growth test.

RESULTS AND DISCUSSION

The crack extension behaviour of a circular notch was in Fig.4. The crack front shows a circle of which center was almost identical with the center of the original round bar specimen with a circular notch, as shown in Fig. 4. From this result, the definition of a crack length in this paper is reasonable.

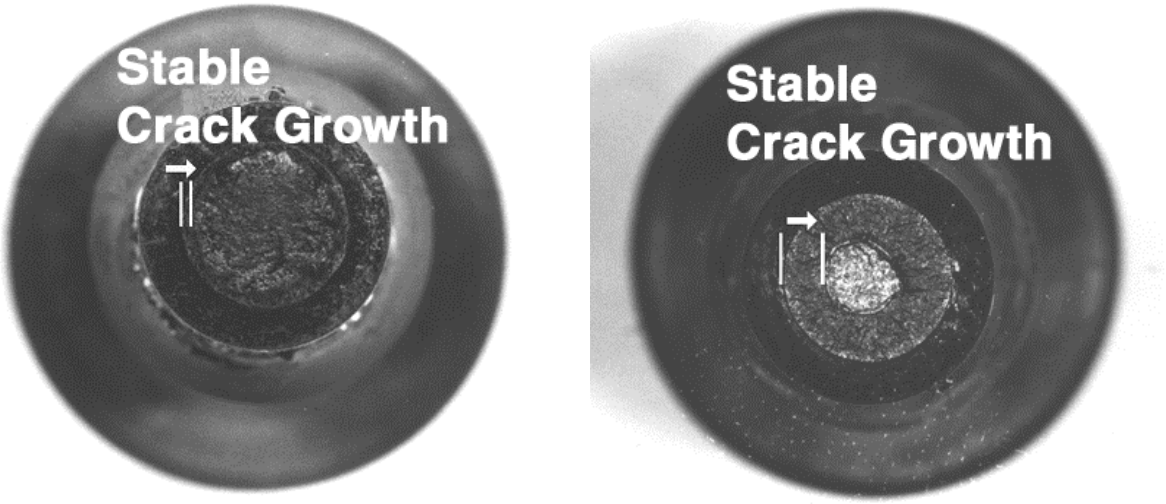

(a) The fracture surface tested under creep condition (17640N, 538°C). (b) The fracture sureface tested under strain controlled fatigue condition ($\Delta\varepsilon$ =0.4%, 594°C).

Fig. 4: The fracture surface of a circular notched specimen.

The creep crack extension from a circular notched specimen is plotted against the nondimensional time as shown in Fig. 5 (a), where t_f is the life of creep crack growth (fracture time). The region of constant creep crack growth rate (CCGR) accompanied by an accelerated process of CCGR occupies the main part of the total fracture life (90%). It is different from so-called the incubation process and is a creep brittle property such as IN100[10], however CrMoV steel itself is a creep ductile material. On the other hand, in the case of CT specimen, the accelerated region of CCGR occupies the main part of the total creep fracture life as shown in Fig. 5 (b) (80%). Therefore, the creep brittle property of the circular notched specimen will be due to the effect of multi-axial stress field by a circular notch.

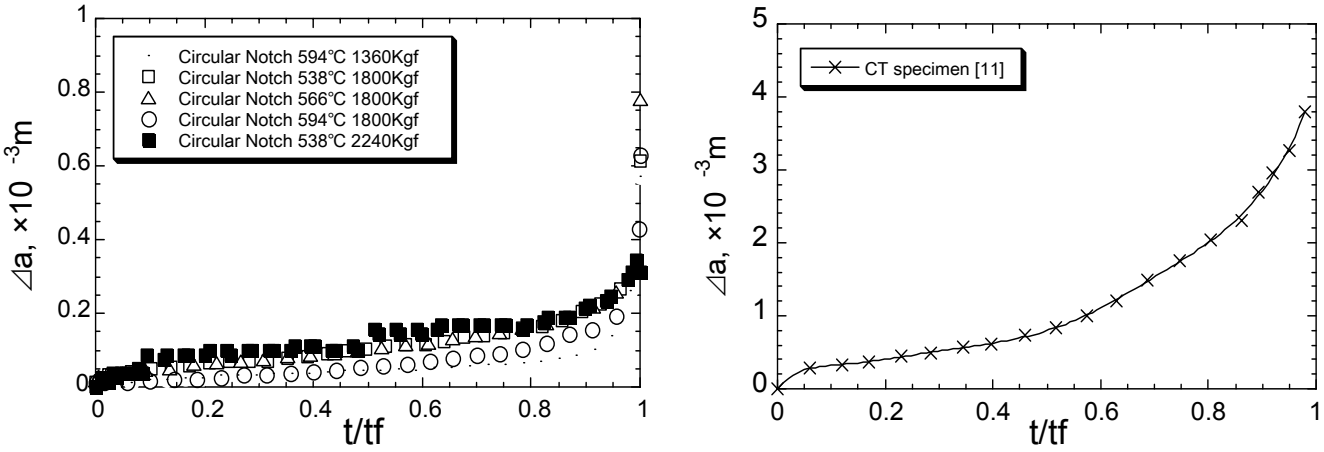

(a) Creep crack length of circular notched specimen. (b) Creep crack length of CT specimen.

Fig. 5: The relationship between creep crack length and the nondimensional time.

The CCGR was plotted against stress intensity factor as shown in Fig. 6. These results show that the CCGR increases with increasing in initial stress intensity factor and in temperature, and it is higher than those for CT specimens. The difference between circular notched specimen and CT specimen will be caused by the effect of multi-axial stress field due to the circular notch. As mentioned above, the constant CCGR region occupies the main part of the creep rupture life as shown in Fig.5, which corresponds to the circular region in Fig. 6. This region is defined as the first region of CCGR. Therefore, it is important to estimate the constant CCGR.

The relationship between CCGR in the first region, $CCGR_1$ and temperature is shown in Fig. 7. The results show that the CCGR is dominated by a thermally activated process. Furthermore, $CCGR_1$ is dominated by

the initial stress intensity factor, K_i, as shown in Fig. 8. On the basis of these results, $CCGR_1$ of circular notched specimen is given by:

$$\left(\frac{da}{dt}\right)_i = AK_i^{14.0}\exp\left(-\frac{384.4}{RT}\right) \qquad (4)$$

where *Ki* is initial stress intensity factor, *R* is gas constant (=8.314$Jmon^{-1}K^{-1}$) and *T* is absolute temperature. Eqn. (4) is similar as the CCGR law of IN100 alloy[10] which is creep brittle material.
On the other hand, the CCGR of CT specimen was given by[12]:

$$\frac{da}{dt} = 13.22\times10^{37}\sigma_g^{-9.626}\left(\frac{K}{70}\right)^{-34.90}\exp\left\{-\frac{304.3-363.9\ln(K/70)}{RT}\right\}, \qquad (5)$$

where σ_g is gross stress. The law of CCGR of a circular notched specimen is quite different form that of CT specimen. On the basis of Eqns. (4) and (5), the following results were found out. Eqn. (5) is stress dependent thermal activated process and it is seen in creep ductile materials. However, due to multi-axial stress, CCGR behaves in creep brittle manner as shown in Eqn. (4), even though material itself is creep ductile material.

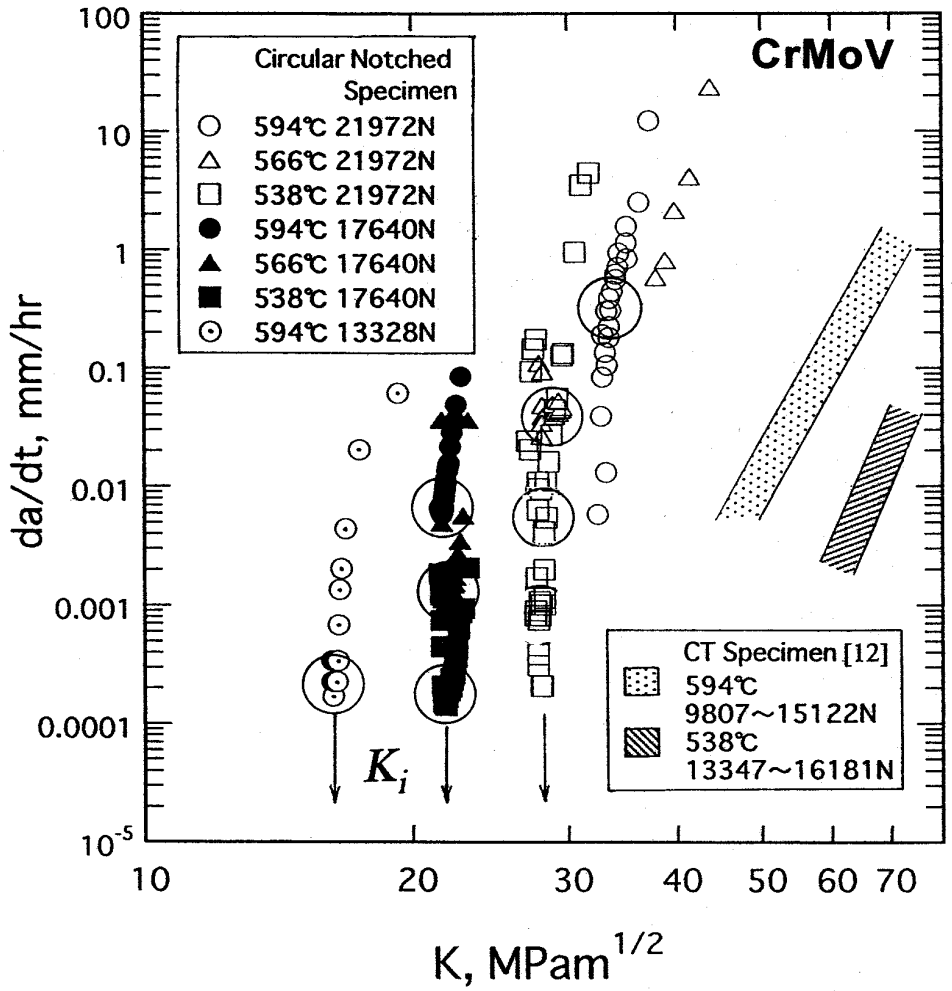

Fig. 6: Creep crack growth rate plotted against stress intensity factor

CONCLUSION

High temperature creep tests were conducted for a circular notched specimen of CrMoV steel. The electric potential drop method was adopted to measure the creep crack length. The proposed equation which relates the value of electric potential drop to crack length of a circular notched specimen was obtained.

Using this equation, the creep crack growth behaviour was investigated. The law of creep crack growth rate was derived on the basis of a thermal activation process. The law of CCGR for circular notched specimen was different from that for CT specimen and similar as that for creep brittle material, even though material itself is creep ductile. This will be caused by the effect of multi-axial stress field due to a circular notch.

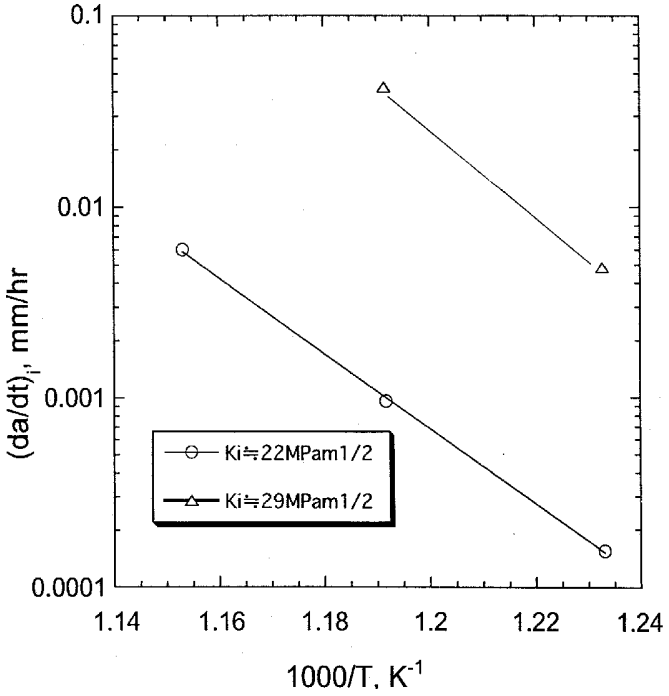

Fig. 7: The relationship between CCGR and the inverse value of absolute temperature.

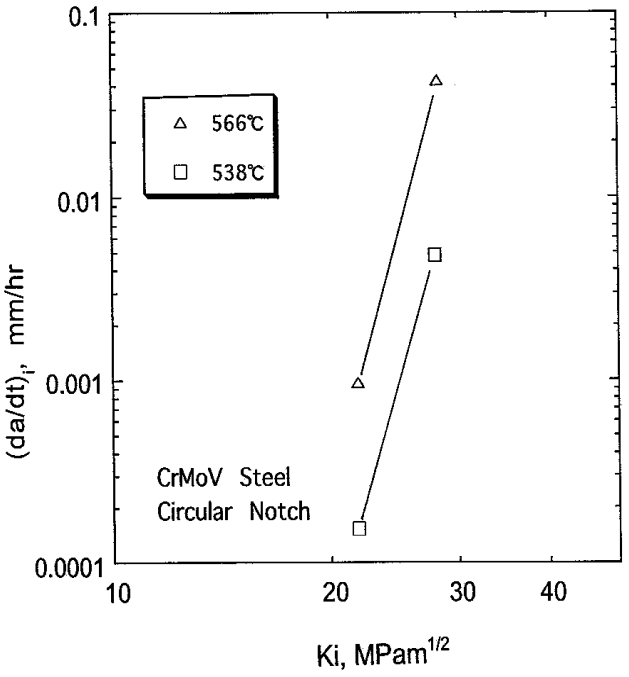

Fig. 8: The relationship between CCGR and the initial stress intensity factor.

ACKNOWLEDGEMENTS

Thanks should be made for financial aid to the Japan Society for Promotion of Science (JSPS) of the RFTF program 97R1201.

REFERENCES

1. Yokobori Jr., A.T., Yokobori, T., Sato, K. and Shoji, K.(1985) *Fatigue Fract. Eng. Mater.Struct.* 8, 4, 315.
2. Nelson, D. V. and Rostami, A. (1997) *ASME J. of Pressure Vessel Tech.* 119, pp.325-331.
3. Itoh, T., Sakane, M. and Ohnami, M. (1994) *ASME J. of Pressure Vessel Tech.* 116, pp.90-98.
4. Yokobori, T. (1974) *Strength of Mater.* 2nd Edition, pp.110-111, Iwanami, Japan.
5. Johnson, H. H. (1965) *Mater. Research and Standards,* 5, 9, pp.442-445.
6. Schwalbe, K. H. and Hellmann, D. (1981) *J. of Testing and Evaluation,* 9, 3, pp.218-221.
7. Adachi, T., Yokobori Jr., A. T., Tabuchi, M., Fuji, A. and Yokobori, T. (2001) *English J. of Japan Society for Strength and Fracture of Materials,* (to be published).
8. Peterson, R. E. (1953) *Stress Concentration Design Factors*, pp.33-5, John Willy & Sons.
9. JSME (1984) *JSME Mechanical Engineers' Handbook, A. Fundamentals, A4 : Strength of Materials,* p.107, JSME, Japan.
10. Yokobori Jr., A. T., Uesugi, T., Yokobori, T., Fuji, A., Kitagawa, M., Yamaya, I., Tabuchi, M. and Yagi, K. (1998) *J . of Materials Science*, 33, pp.1555-62.
11. Yokobori Jr., A. T. (1997) *Advances in Fracture Research,* ICF9, 1, pp.39-50.
12. Yokobori Jr., A. T. , Yokobori, T., Tetsuo, N. and Toshiaki, Y.(1992) *Mater. at High Temp.* 10, 2, pp.108-118.

POSTER REFERENCE: ICF100287PR

ESTIMATION OF DYNAMIC STRESS INTENSITY FACTORS FOR BEAM AND CYLINDRICAL SPECIMENS

S. Ye. Kovchyk[1], V. M. Boyko[1], I. V. Khodan[1], I. D. Skrypnyk[2]

[1] Karpenko Physico-Mechanical Institute, National Academy of Sciences of Ukraine,
5, Naukova st., 79601, Lviv, Ukraine

[2] Faculty of Design, Engineering and Production, Delft University of Technology
9, Jaffalaan, NL-2628 BX, Delft, the Netherlands

ABSTRACT

A simple numeric-experimental method for estimation of dynamic stress intensity factors (DSIF) at impact tests of cylindrical and beam specimens is proposed. For the case of solid cylindrical specimen the formulas are derived for estimation of DSIF from tensile impact tests (K_I) and impact torsion (K_{III}), while for a hollow cylindrical specimen only tensile impact tests are used (K_I). For the beam specimens symmetrical and eccentric three-point bending loading schemes are considered. The formulas derived contain parameters, estimated from modal analysis. They were evaluated using commercial Finite Element Analysis (FEA) package MARC. Based on the obtained numerical data and using the least square method, simple relations are derived for these parameters. These relations account also for some geometric parameters of specimens considered.

For use of these formulas the experimental loading diagram "applied force – time" is necessary. Therefore, special testing equipment was developed for every type of loading and type of specimen (named above). In order to verify the proposed formulas, the values of DSIF are estimated numerically using FEA package MARC and Newmark incremental integration method for all the cases considered. Good correlation between the results obtained numerically and based on proposed formulas is observed.

KEYWORDS

Impact test, modal analysis, experimental loading diagram, finite element analysis.

INTRODUCTION

Until recently the dynamic problems of fracture mechanics were studied only for idealized cases (for instance for infinite solid). Nowadays, using advanced numerical methods (namely, FE method [1, 2]) it became possible to find a solution to the dynamic problems for solid with more real shape.

For evaluation of dynamic stress intensity factors (SIF) one can use also experimental approach. One way is to use a small-spacing strain gage. However, the drawback of this approach is a necessity to glue every strain gage to the specimen with following calibration. Another way consists in use of the photoelasticity method. This method requires high-speed photography and, hence, is very cumbersome and is used only in for calibration.

Even very complex mathematical models describe only part of dynamic effects and still require introduction of experimentally estimated parameters. In the other words, currently combined experimental-numerical methods are widely used to solve dynamic problems. As an example the methodology [3-8] of data handling can be mentioned, which uses the "force – time" diagram, obtained from impact tests of beam specimens at one- and tree-point bending. In [9, 10] simple formulae for calculation of dynamic SIF for cylindrical specimens was proposed.

PROBLEM FORMULATION AND SOLVING

Tension of cylindrical specimen, weakened by surface circular crack. Let us consider cylindrical specimen with length $2h$ and radii r, which is contains an external circular crack of depth a at the middle. Two equal forces $P(t)$ are applied to the ends of the specimens. Approximating the function $P(t)$ by piece-wise linear function:

$$P(t)=\sum_{i=1}^{N}(k_i-k_{i-1})(t-t_{i-1})H(t-t_{i-1}), \tag{1}$$

where k_i are the slope coefficients ($k_0=0$); t_i denote the breaking points ($t_0=0$); $H(t)$ is the Heavyside function,
after simple transformations [9] one can write:

$$K_{\mathrm{I}}(t)=K_{\mathrm{IS}}^{(1)}P(t)-K_{\mathrm{IS}}^{(1)}\sum_{i=1}^{N}(k_i-k_{i-1})H(t-t_{i-1})\sum_{j=1}^{n}(\eta_i/\omega_i)\sin\omega_j(t-t_{i-1}). \tag{2}$$

Here ω_i are the circular frequencies of natural oscillations of half of cylindrical specimen; n is a number of modes of natural oscillations, which are accounted for in the analysis;

$$\eta_i=K_{\mathrm{I}i}u_{0i}\Big/\omega_i^2K_{\mathrm{IS}}^{(1)}\left(\sum_{i=1}^{n}\eta_i=1\right);$$

u_{0i} is the i^{th} component of the displacement vector of the point, where the force is applied; $K_{\mathrm{IS}}^{(1)}$ – is static SIF, when the specimen is loaded (in tension) by single force; $K_{\mathrm{I}i}$ denotes SIF in the specimen deformed by i^{th} normed mode of autonomous oscillations.

The frequencies of natural oscillations ω_i and the corresponding to them displacements (eigenvectors) are estimated from the generalized problems on eigenvalues [1, 11]

$$[K]\vec{\mathbf{u}}=\omega^2[M]\vec{\mathbf{u}} \tag{3}$$

and norming conditions

$$\mathrm{u}_i^{\mathrm{T}}[M]\mathrm{u}_j=\delta_{ij}, \tag{4}$$

where $[K]$ i $[M]$ are the stiffness and mass matrixes [11]; δ_{ij} is the Kroneker matrix; index "T" means transposition [11].
The formulae (2) represents the dynamic SIF as a sum of two additives: a quasistatic part and an inertial correction.

Dimensionless coefficients η_i and eigenfrequencies $\omega_i^*=\omega_i a\big/\sqrt{E/\rho}$ (here E is the Young modulus and ρ - material density) do not depend on the specimen dimensions, but they do depend on the ratio of specimen length to its radii, relative depth of crack and Poisson ratio ν [1].

In [9] simple relations are given for estimation of ω_i^* та η_i for a range $0.27\le\nu\le0.33$, and in [10] – for the range $0.2\le\nu\le0.4$ under the condition $4\le 2h/a\le 20$.

Tension of the hollow cylindrical specimen, weakened by external circular crack. We assume that a hollow cylindrical $2h$ - long specimen (with internal and external radii are correspondingly r_1 i r_2) is weakened by external circular crack, which radii is "a", and tensed by equally distributed forces, applied to the ends (along the ruling line).

If to represent the main vector of loading, applied to cylinder, as the piece-wise linear function (1), the dynamic SIF can be written in the form (2).

The dimensionless frequencies of natural oscillations $\omega_i^* = \omega_i r_2 / \sqrt{E/\rho}$ and the coefficients η_i were calculated numerically using commercial FEA package MARC for following values of geometric parameters: $9 \le 2h/r_2 \le 14$; $0.35 \le r_1/r_2 \le 0.80$; $0.2 \le (r_2 - a)/(r_2 - r_1) \le 0.5$. After the relation $\sum_{i=1}^{n} \eta_i = 1$ was analyzed we concluded that in this range of cylinder' relative length it is enough to restrict oneself by three modes of autonomous oscillations, in order to reach sufficient accuracy.

Making use of the least square method, following relations for ω_i, та η_i were obtained:

$$\begin{aligned}
\omega_1^* &= 0.2348 + 7.495\lambda - 10.4915\lambda^2 + \left(-0.8447\lambda + 1.6701\lambda^2 - 0.7952\lambda^3\right)\left(4.8875\sqrt{\gamma} - 0.5728\gamma\right) + \\
&+ \left[5.1393\lambda - 26.346\lambda^2 + 31.5317\lambda^3 + \gamma\left(-0.0109\lambda + 0.0403\lambda^2 - \right.\right. \\
&\left.\left. - 0.0437\lambda^3\right)\left(0.418 + 0.8312\gamma\right)\right]\left(1.0089\sqrt{t} - 0.726t\right), \\
\omega_2^* &= 0.6313 + 8.4907\lambda - 6.5496\lambda^2 + \left(-1.7829\lambda + 1.8045\lambda^2 - 0.4464\lambda^3\right)\left(2.004\sqrt{\gamma} - 0.1745\gamma\right) + \\
&+ \left[-11.139\lambda + 47.53\lambda^2 - 4.8197\lambda^3 + \gamma\left(-0.292\lambda + 1.2431\lambda^2 - \right.\right. \\
&\left.\left. - 1.2791\lambda^3\right)\left(0.0916\gamma - 3.7866\right)\right]\left(2.3233t - 2.9088\sqrt{t}\right), \\
\omega_3^* &= -0.4108 - 0.2956t + 0.7003t^2 + \left(4.3683 - 0.5161\lambda\right)\left(1/\gamma + 0{,}364/\sqrt{\gamma}\right)\left(2.1493 - 2.5253t\right) + \\
&\left(1/\gamma - 5.1156/\gamma^2\right)\left(44.945t - 18.849t^2\right).
\end{aligned} \tag{5}$$

$$\begin{aligned}
\eta_1 &= 1.2597 + \left(1.4352\lambda - 2.001\lambda^2\right)\left(0.7997\gamma^{-1} - 7.807\gamma^{-2}\right)\left(3.1391t - 0.0882t^2\right), \\
\eta_2 &= 0.2175 + 7.1996\lambda - 12.381\lambda^2 + 0.6053\lambda^3 + \left(1.7254 + 19.5782\lambda - 32.173\lambda^2\right)\times \\
&\left(26.804/\gamma^2 - 1.837/\sqrt{\gamma}\right)\left[1.4574\lambda - 2.337\lambda^2 + \left(18.09\lambda - 27.859\lambda^2\right)\times\right. \\
&\left.\left(17.058/\gamma^2 - 2.2894/\gamma\right)\right]\left(9.3297t - 10.541\sqrt{t}\right), \\
\eta_3 &= -4.3725 + 16.7274t - 11.967t^2 + \left(-8.3858 + 33.344t - 24.169t^2\right)\times \\
&\times \left(19.164/\gamma^2 - 2.2466/\sqrt{\gamma}\right) + \left[0.2475 + 0.136\lambda - 0.089\lambda^2 + \right. \\
&\left.\left(-4.9837\sqrt{\lambda} + 5.506\lambda - 1.5625\lambda^2\right)\left(5.388/\gamma - 1.5171/\sqrt{\gamma}\right)\right]\left(4.1364\sqrt{t} - 3.892t\right).
\end{aligned} \tag{6}$$

At the same time the static SIF under the loading with the main vector equal to unity was calculated. Processing the obtained data with a help of the least square method the following approximation for $K_{\mathrm{IS}}^{(1)}$ derived:

$$\begin{aligned}
K_{\mathrm{IS}}^{(1)} &= \left(-0.246 + 12.791\sqrt{\lambda} + 6.1363\lambda + 27.55\lambda^2 + \left(6.5745\sqrt{\lambda} + 4.4422\lambda + \right.\right. \\
&\left.\left. + 15.962\lambda^2 - 0.562\lambda^3\right)\left(-9.7118\sqrt{t} + 21.019t - 20.277t\sqrt{t} + 7.3759t^2\right)\right/ r_2\sqrt{r_2}
\end{aligned} \tag{7}$$

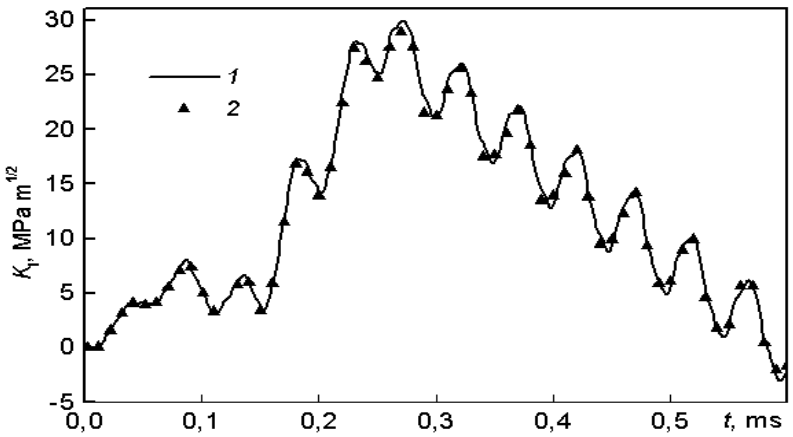

Figure 1: Dependence of the dynamic SIF vs. time for tension of the hollow cylindrical specimen (1 – dynamic SIF calculated using equations (1, 2); 2 – dynamic SIF calculated using FEA).

Using FEA (namely Newmark method) we estimated dynamic SIF for cylindrical specimen with following dimensions: $r_1 = 3\,\mathrm{mm}$; $r_2 = 8\,\mathrm{mm}$; $h = 60\,\mathrm{mm}$; $a = 5{,}5\,\mathrm{mm}$; $E = 200\,\mathrm{GPa}$, $\rho = 7870\,\mathrm{Mg/m^3}$,

$\nu = 0.3$. The loading diagram was obtained experimentally according to [12]. Based on these results, following parameters for approximation of the "force-time" diagram were chosen:
$k_1 = 11760\,\text{Pa}$; $k_2 = 8330\,\text{Pa}$; $k_3 = 53950\,\text{Pa}$; $k_4 = 0\,\text{Pa}$; $t_1 = 75\,\mu\text{s}$; $t_2 = 140\,\mu\text{s}$; $t_3 = 250\,\mu\text{s}$; $t_4 = 600\,\mu\text{s}$.
Comparison of the diagrams, obtained numerically (FEA) and one calculated using simplified formulae (2), (5) – (7) validates the approach developed.

Torsion of cylindrical specimen, weakened by surface circular crack. Let us consider cylindrical specimen with following dimensions: length is $2h$ and radii is a. At the middle the specimen has a circular crack of depth c. The load, which main vector is equal to T, is applied along the ruling line of the ends of specimens.

After the force T is represented by the piece-wise function (1), the dynamic SIF can be written as follows:

$$K_{\text{III}}(t) = K_{\text{IIIS}}^{(1)} P(t) - K_{\text{IIIS}}^{(1)} \sum_{i=1}^{N} (k_i - k_{i-1}) H(t - t_{i-1}) \sum_{j=1}^{n} (\eta_i / \omega_i) \sin \omega_j (t - t_{i-1}) \tag{8}$$

where ω_i are the circular frequencies of torsional natural oscillations of half of cylindrical specimen; n denotes number of modes of natural oscillations; $\eta_i = K_{\text{III}i} u_{0i} \Big/ \omega_i^2 K_{\text{IIIS}}^{(1)} \left(\sum_{i=1}^{n} \eta_i = 1 \right)$; u_{0i} is the i^{th} component of the displacement vector in the point, where load is applied; $K_{\text{IIIS}}^{(1)}$ means the static SIF for the specimen, loaded by the momentum, equal to a; K_{IIIi} is the SIF in the specimen, deformed with the i^{th} normed mode of autonomous oscillations.

For the range of specimen' dimensions $0{,}3 \le \lambda \le 0{,}7$ and $8{,}0 \le \gamma \le 13{,}0$ ($\lambda = c/r$; $\gamma = 2h/r$) for ν=0,3 making use of the Lancosh' blocks method we evaluated the circular frequencies of torsional natural oscillations and corresponding to them eigenvectors. The data were analyzed using the least square method with following dependencies as the result:

$$\begin{aligned}
\omega_1^* &= 0.158 - 1.113\lambda + 2.706\lambda^2 - 1.959\lambda^3 + \lambda\left(13.79 - 34.1\lambda + 21.94\lambda^2\right)/\gamma, \\
\omega_2^* &= 0.5295 - 3.376\lambda + 7.484\lambda^2 - 5.312\lambda^3 + \lambda\left(39 - 95.3\lambda + 68.1\lambda^2\right)/\gamma, \\
\omega_3^* &= 1.052 - 6.456\lambda + 13.317\lambda^2 - 8.916\lambda^3 + \lambda\left(60.1 - 135.9\lambda + 94.5\lambda^2\right)/\gamma, \\
\omega_4^* &= 1.5047 - 9.202\lambda + 18.602\lambda^2 - 12.198\lambda^3 + \lambda\left(81.68 - 176.16\lambda + 119.4\lambda^2\right)/\gamma.
\end{aligned} \tag{9}$$

$$\begin{aligned}
\eta_1 &= 1.058 + 1.9975\lambda - 5.5285\lambda^2 + 5.5249\lambda^3 + \left(-0.044 + 0.2144\lambda - 0.1977\lambda^2 + 3.5249\lambda^2\right)\lambda\gamma, \\
\eta_2 &= -0.0978 - 3.181\lambda + 9.64\lambda^2 - 7.033\lambda^3 + \left(0.0596 - 0.3317\lambda + 0.3315\lambda^2\right)\lambda\gamma, \\
\eta_3 &= 0.1894 + 0.9271\lambda - 4.3216\lambda^2 + 3.8868\lambda^3 + \left(0.954 - 0.131\lambda\right)\lambda^2\gamma, \\
\eta_4 &= -0.7987 + 3.9245\lambda - 6.412\lambda^2 + 3.481\lambda^3 + \left(0.046 - 0.3236\lambda + 0.6356\lambda^2 - 0.385\lambda^3\right)\gamma.
\end{aligned} \tag{10}$$

The accuracy of approximations (9, 10) does not exceed 2%. For calculations of the dynamic SIF using equations (2), (9) and (10) one must have the static SIF' value for the cylindrical specimen, loaded by torsion. There are several solutions to this problem, known from literature. For a range of λ parameter, based on the integral equations method, the SIF values have been obtained in [12]. Based on these values and using the least square method we got following dependence for $K_{IIIS}^{(1)}$

$$K_{\text{IIIS}}^{(1)} = \left(3{,}403 - 29{,}637\lambda + 104.613\lambda^2 - 156{,}12\lambda^3 + 89{,}14\lambda^4\right)/r\sqrt{r}\,. \tag{11}$$

Eccentric bending of a beam specimen. At the initial stage of the loading history the interaction between the specimen and beam seats does not influence the dynamic SIF value. In the other words, for the brittle materials and high-speed loading a crack propagation begins before the interaction between the specimen and the beam seats start and, as a result, the subcritical loading is not influenced. These conditions are called "one-point-bending" or "bending without support". First case is considered in [3]. Let us consider a case, when the crack is located not in the middle of the beam specimen (fig. 2).

As in the previous cases we represent the "force-time" diagram by piece-wise function. It is possible to show, that for such representation of the "force-time" diagram the dynamic SIF can be written as follows:

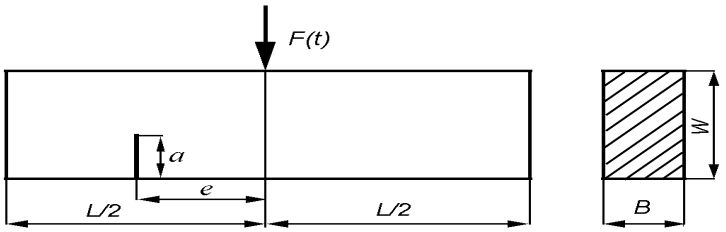

Figure 2: The loading scheme of the beam specimen with eccentric crack.

$$K_{\mathrm{I}}(t)=K_{\mathrm{IS}}^{(1)}F(t)-K_{\mathrm{IS}}^{(1)}\sum_{i=1}^{N}(k_i-k_{i-1})H(t-t_{i-1})\sum_{j=1}^{n_1}(\eta_{1i}/\omega_i)\sin\omega_j(t-t_{i-1})$$
$$K_{\mathrm{II}}(t)=K_{\mathrm{IIS}}^{(1)}F(t)-K_{\mathrm{IIS}}^{(1)}\sum_{i=1}^{N}(k_i-k_{i-1})H(t-t_{i-1})\sum_{j=1}^{n_2}(\eta_{2i}/\omega_i)\sin\omega_j(t-t_{i-1}) \qquad (12)$$

where ω_i denotes the circular frequencies of natural oscillations of the beam without support; n_1, n_2 mean the number of modes of natural oscillations, which are taken into account in analysis; $\eta_{1i}=K_{\mathrm{I}i}u_{0i}\Big/\omega_i^2K_{\mathrm{IS}}^{(1)}\left(\sum_{i=1}^{n}\eta_{1i}=1\right)$, $\eta_{2i}=K_{\mathrm{II}i}u_{0i}\Big/\omega_i^2K_{\mathrm{IIS}}^{(1)}\left(\sum_{i=1}^{n}\eta_{2i}=1\right)$; u_{0i} is the i^{th} component of displacement vector for the point of load' application; $K_{\mathrm{IS}}^{(1)}$, $K_{\mathrm{IIS}}^{(1)}$ are the static SIF for the tension of the specimen by force, uniformly distributed in the volume; $K_{\mathrm{I}i}, K_{\mathrm{II}i}$ are the SIF in the specimen, deformed by i^{th} normed mode of autonomous oscillations.

While calculating $K_{\mathrm{IS}}^{(1)}$, $K_{\mathrm{IIS}}^{(1)}$, the volume loading was substituted by equally distributed loading applied to the top and bottom part of specimen. For this the FEA approach was used. The mesh quality was verified by comparison with the results, obtained in [14]. The results in the range $4\le\gamma\le6$, $0.3\le\lambda\le0.7$; $\varepsilon=e/W=1$ can be described by equations (with error less than 1.5%):

$$K_{\mathrm{IS}}^{(1)}=L\sqrt{l}\Big[-1.3461+4.1651\lambda-6.2731\lambda^2+\gamma\big(1.5083\sqrt{\lambda}-1.9329\lambda+0.0333\lambda^2+ +2.3095\lambda^3\big)\big(1.0861-0.0606\gamma\big)\Big]\Big/BW^2,$$
$$K_{\mathrm{IIS}}^{(1)}=\lambda L\sqrt{l}\left[0.262-0.0861\lambda+\lambda\gamma\big(0.2024-0.4365\lambda+0.3122\lambda^2\big)\big(0.7705-0.1051\gamma\big)\right]\Big/BW^2. \qquad (13)$$

The dimensionless coefficients η_{1i}, η_{2i} and eigenfrequencies $\omega_i^*=\omega_i a\big/\sqrt{E/\rho}$ do not depend on the specimen dimensions. For $\varepsilon=e/W=1$, $0.3\le\lambda\le0.7$, $4.0\le\gamma\le6.0$ (here, $\lambda=a/W$; $\gamma=L/W$) and ν=0,3 using the Lancosh blocks method we found the circular frequencies of natural oscillations and corresponding to them eigenvectors. Analyzing the relations $\sum_{i=1}^{n}\eta_{ji}=1(j=1,2)$, we concluded that it is enough to chose $n_1=5$ and $n_2=6$ for evaluation of $K_{\mathrm{I}}(t)$ and $K_{\mathrm{II}}(t)$ correspondingly. Processing the numerical data using the least square method, following polynomial approximations were proposed for ω_i^*:

$$\omega_1^*=0.2935+4.617\lambda-6.2351\lambda^2-\lambda\gamma\big(1.1088-1.4685\lambda+0.0763\lambda^2\big)\big(1.4143-0.105\gamma\big),$$
$$\omega_2^*=0.8996+2.8588\lambda-4.0988\lambda^2-\lambda\gamma\big(0.7018-1.0621\lambda+0.3022\lambda^2\big)\big(1.7487-0.0096\gamma-0.0096\gamma^2\big),$$
$$\omega_3^*=0.6612+6.0468\lambda-5.6163\lambda^2-\lambda\gamma\big(1.2356-1.1247\lambda\big)\big(1.509-0.104\gamma\big),$$
$$\omega_4^*=1.2866+5.6316\lambda-6.4583\lambda^2-\lambda\gamma\big(0.5026-0.7079\lambda+0.2123\lambda^2\big)\big(4.2913-0.2151\gamma\big),$$
$$\omega_5^*=1.5634+8.5572\lambda-10.092\lambda^2-\lambda\gamma\big(0.7007-0.8957\lambda+0.1549\lambda^2\big)\big(4.1461-0.2309\gamma\big),$$
$$\omega_6^*=1.6014+10.416\lambda-13.535\lambda^2-\lambda\gamma\big(0.8715-1.2239\lambda+0.1916\lambda^2\big)\big(3.8153-0.2075\gamma\big). \qquad (14)$$

The approximations (14) describe the numerical data with the deviation less, than 2%. For coefficients η_{1i} following dependencies are proposed:

$$\eta_{11} = 1.1814 + 14.703\lambda - 19.443\lambda^2 + \lambda\gamma(1.4708\lambda - 1.122)(4.0276 - 0.3145\lambda),$$
$$\eta_{22} = 0.0175 - 6.5325\lambda + 25.07\lambda^2 - 15.82\lambda^3 + \lambda\gamma(0.6726 - 2.5323\lambda + 1.629\lambda^2)(2.9651 - 0.229\gamma),$$
$$\eta_{13} = 0.0471 + 0.6677\lambda - 0.7738 + \lambda\gamma(0.1183\lambda - 0.1073)(2.5695 - 0.2013\gamma), \quad (15)$$
$$\eta_{24} = 0.4548 - 2.0633\lambda + 2.1258\lambda^2 + \lambda\gamma(0.8861 - 0.816\lambda)(0.8801 - 0.0806\gamma),$$
$$\eta_{25} = 0.2915 - 8.2444\lambda + 36.28\lambda^2 - 36.92\lambda^3 + \lambda\gamma(0.5803 - 2.9915\lambda + 3.17\lambda^2)(3.0027 - 0.193\gamma).$$

For η_1, η_2 and η_4 the relative error does not excide 3%, but for approximations of η_3, η_5 the absolute error does not excide 0.003. Similar relations were obtained for η_{2i}:

$$\eta_{21} = 0.531 + 8.5372\lambda - 24\lambda^2 + 16.017\lambda^3 - \lambda\gamma(0.1678 - 3.227\lambda + 2.184\lambda^2)(1.4914 - 0.0439\gamma),$$
$$\eta_{22} = 0.0175 - 6.5325\lambda + 25.07\lambda^2 - 15.82\lambda^3 + \lambda\gamma(0.6726 - 2.5323\lambda + 1.629\lambda^2)(2.9651 - 0.229\gamma),$$
$$\eta_{23} = -0.2065 + 0.0792\lambda - 0.0076\lambda^2,$$
$$\eta_{24} = 0.4548 - 2.0633\lambda + 2.1258\lambda^2 + \lambda\gamma(0.8861 - 0.816\lambda)(0.8801 - 0.0806\gamma), \quad (16)$$
$$\eta_{25} = 0.2915 - 8.2444\lambda + 36.28\lambda^2 - 36.92\lambda^3 + \lambda\gamma(0.5803 - 2.9915\lambda + 3.17\lambda^2)(3.0027 - 0.193\gamma),$$
$$\eta_{26} = -0.026 + 0.2252\lambda - 0.4055\lambda^2 - \lambda\gamma(0.3281 - 2.358\lambda + 5.0185\lambda^2 + 0.4439\lambda^3 -$$
$$- 8.9764\lambda^4 + 5.3806\lambda^5)(8.3904 - 0.8796\gamma - 0.4054\gamma^2 + 0.0524\gamma^3).$$

For first five coefficients the deviation of proposed approximation is the same as in previous case, but for η_{26} parameter the absolute error does not exceed 0.004.

Using the dependencies (13) – (16) one can estimate the dynamic SIF for testing of beam specimen with eccentric crack.

REFERENCES

1. Parton V. Z., Boriskovski V. G. (1985). *Dynamic Fracture Mechanics*. Mir, Moscow (in Russian).
2. Chirino F., Dominguez J. (1989). *Eng. Fract. Mech.* **34**, 1051.
3. Andreykiv A. E., Rokach I. V. (1989) *Physicochemical mechanics of materials.* **25**, 42(in Russian).
4. Rokach I. V. (1990) *Physicochemical mechanics of materials,* **26**, 79(in Russian).
5. Kishimoto K., Fujino K., Aoki S., Sakata M. (1990) *JSME Int. J.*, Ser. 1. **33**, 51.
6. Andreykiv O. Ye., Kovchyk S. Ye., Khodan I. V., Bojko V. M. (1997) *The problems of machinebuilding and automatization*. 22 (in Russian).
7. Rokach I. V. (1998) *Fatig. Fract. Eng. Mat. Struct*. **21,** 1007.
8. Rokach I. V. (1998) *Fatig. Fract. Eng. Mat. Struct*. **21,** 1015.
9. Andreykiv O. Ye., Boyko V. M., Kovchyk S. Ye., Khodan I. V. (2000) *Physicochemical mechanics of materials*. 42(in Ukrainian).
10. Andreykiv O. Ye., Boyko V. M., Kovchyk S. Ye., Khodan I. V. (2000). In: *Abstract volume the 13th ECF: Fracture mechanics: Applications and Challenges*, p. 132, Fuentes M., Elices M., Martin-Meizoso A., Martinez-Esnaola J. M. (Eds). Elsevier, Oxford.
11. Zienkiewicz O. C. (1971). *The Finite Element Method in Engineering Science.* McGraw-Hill, London.
12. Kovchyk S. Ye., Khodan I. V., Zamora T. S. Zaydel B. M. (1994). *Physicochemical mechanics of materials*. **30**, 133(in Ukrainian).
13. Shibuya T., Koizumi T., Okuya T. (1979) *Bull. JSME.* **22**. 1049.
14. Jen Wang Ke, Lin Hsu Chi, Hua Kao (1977). In: *Adv. Res. Strength and Fract. Mater. 4th Int. Conf Fract.* . McGraw-Hill, New York.
15. MARC, Volume A: Theory and User information, Rev. K.7, 1998, MARC Analysis Research Corp.

ESTIMATION OF HIGH CYCLE FATIGUE LIMIT OF HARD SHOT PEENED AUSTENITIC STAINLESS STEEL

K. Masaki, Y. Ochi and T. Matsumura

Department of Mechanical Engineering and Intelligent Systems,
The University of Electro Communications Tokyo,
1-5-1, Chofugaoka, Chofu, Tokyo, 182-8585, Japan

ABSTRACT

It have been clear that Hard shot-peening (HSP) treatment is very successful for the improvement of the high cycle fatigue strength of austenitic stainless steel. The cause of the improvement is to give the surface hardening layer and compressive residual stress by the treatment, and also the effect of the change of the fracture type from surface crack origin fracture type to subsurface crack origin type. In this study, the fatigue limit at 10^8 cycles of the HSP treated Type 316L stainless steel was estimated by using the hardness distribution, the HVB (Half Value Breadth) distribution and the residual stress distribution of the specimen. The estimation by using the endurance fatigue limit diagram and the modified Goodman's diagram was not insufficient method, however. But the fatigue limit by the new estimation using the stress intensity factor was fairly good coincident with the experimental value.

KEYWORDS

Hard shot-peening, Residual stress distribution, Hardness distribution, Half value breadth, Stress intensity factor, High cycle fatigue strength, Austenitic stainless steel, Fatigue limit estimation

INTRODUCTION

The surface hardening treatment is a useful method for improving of fatigue properties. And it is also reported by some researchers that how to estimate the fatigue limit of the surface treated materials [1-3]. In generally, the fatigue limit was estimated from the relationship between the applied stress amplitude and the local fatigue limit distribution that was often obtained from fatigue test. However almost methods have been not useful practically because of using the information obtained from the fatigue testing.

One of the estimation methods, the suggestion by Murakami et al.[4],using the shot peened spring steel, is well-known because that it is not necessary for the estimation to have fatigue test. But one of the problems of this Murakami's method is that it needs the assumption in which the position of crack origin is depth range from the surface to 0.4mm [4].

In this study, the estimation method of fatigue limit at 10^8 cycles using the peening effects and fatigue limit diagram was supposed on the hard shot-peening (HSP) treated Type 316L austenitic stainless steel.

MATERIAL AND FATIGUE TEST

The material used in this study was Type 316L austenitic stainless steel, having the chemical compositions (weight %) of: 0.017 C, 0.39 Mn, 0.014 S, 12.17 Ni, 16.31 Cr and 2.06 Mo. The average of the austenitic structure was about 88μm. The shape and dimensions of specimens are shown in Figure 1. After machining, the center of the specimen was shot-peened using ϕ0.6mm steel shot with air pressure of 0.196MPa. The Almen intensity was 0.6mmA (hard shot-peening) and the coverage was 100% over.

Rotating bending fatigue tests at 50Hz under water-cooling condition by deionized water were carried out. The results of the fatigue tests were shown in Figure 2. The fatigue limit of the HSP treated specimen, about 370MPa, was remarkably improved in comparison with fatigue limit of the n.p. specimen, about 200MPa.

ESTIMATION METHOD

The fatigue limit was decided by the relation in the local fatigue limit distribution and the applied stress amplitude slope. If the applied stress amplitude slope intersects the calculated local fatigue limit distribution curve, the specimen will be broken. If these two curves do not intersect each other, the specimen will be not broken. And if these two curves intersect in a point, its applied stress amplitude is the fatigue limit of the surface-hardening specimen.

Calculation of Local Fatigue Limit Curve

In generally, the local fatigue limit σ_{wa} can be calculated from the endurance fatigue limit diagram as Eqn.1-a or the modified Goodman's diagram as Eqn.1-b [5].

Endurance fatigue limit diagram : $$\sigma_{wa} = \sigma_w(1-\sigma_m/\sigma_T) \quad \text{[MPa]} \tag{1-a}$$

Modified Goodman's diagram : $$\sigma_{wa} = \sigma_w(1-\sigma_m/\sigma_B) \quad \text{[MPa]} \tag{1-b}$$

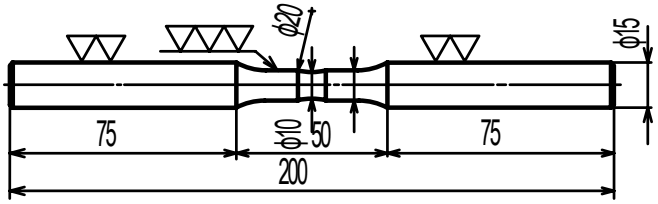

Figure 1: Shape of test specimen (mm)

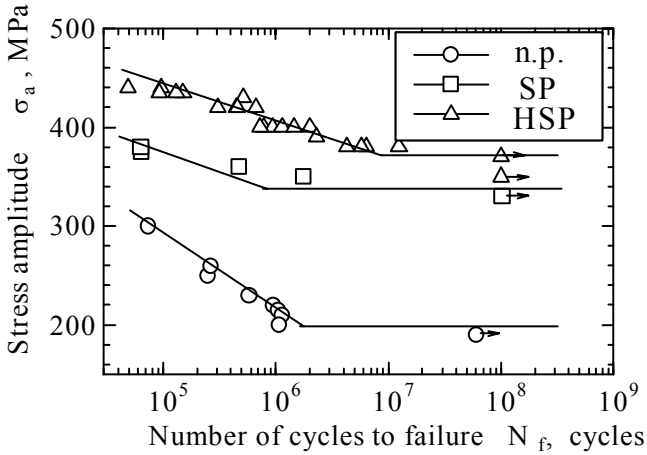

Figure 2: S-N curves under water-cooling condition.

Here, σ_m is the mean stress as the residual stress at the local position, σ_T is the true stress of fracture and σ_B is the tensile strength. The σ_w which is the local fatigue limit for the case of mean stress does not affect, can be calculated from local vickers hardness Hv. Next equation as shown Eqn.2 was supposed on the austenitic stainless steel [6].

$$\sigma_w = 0.16Hv \times 9.81 \qquad \text{[MPa]} \qquad (2)$$

However, an attention is necessary for following fact in the Modified Goodman's diagram. Although the true stress of fracture σ_T is not related to the matrix hardness, but the tensile strength σ_B is depended on the matrix hardness. Namely, the estimation of the fatigue limit by using the modified Goodman's diagram requires investigating of the relation between σ_B and Hv.

Peening Effects Measurements

In order to calculate the local fatigue limit from Eqn.1, the peening effects as the residual stress distribution and the hardness distribution, were measured of HSP treated Type 316L steel. Figure 3 shows the residual stress distribution of the HSP treated specimen using the X-ray diffract meter and the electro-polishing technique. Here, as the residual stress release by the electro-polishing, experimental values must be corrected. The corrected curve is also shown in Figure 3 by the solid line. This corrected curve is assumed as the mean stress.Figure 4 shows the vickers hardness distributions. Because of the scattering of vickers hardness value, the master curves of the hardness was obtained by converting from the half value breadth (HVB) distributions. This hardness master curve is used to calculate the σ_w distribution from Eqn.2.

FATIGUE LIMIT ESTIMATION

Using Endurance Fatigue Limit Diagram

At first, the estimation method of the fatigue limit by using the endurance fatigue limit diagram is shown as the followings.

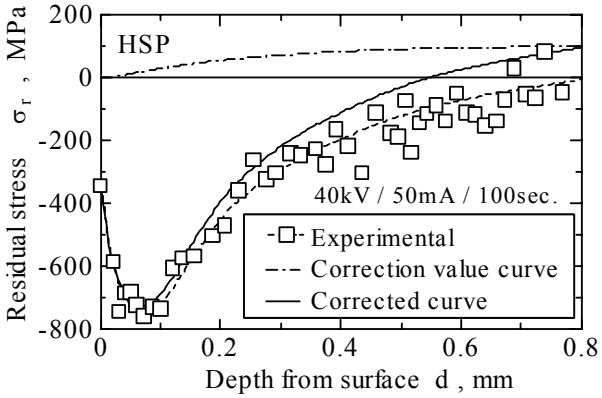

Figure 3: Residual stress distribution of HSP treated specimen

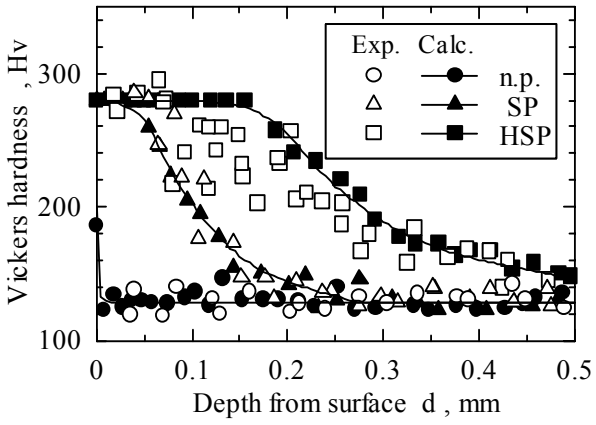

Figure 4: Hardness distribution

Figure 5 shows the local fatigue limit distribution calculated by using Figure 3 and Figure 4. Here, the value of 1811MPa was used at σ_T that obtained by the tensile test and that is not depended on the matrix hardness of Type 316L steel. The fatigue limit is estimated about 225MPa from Figure 5, however, the estimation value is not agreement with the experimental value as 370MPa.

Therefore next, the fatigue limit estimation of the n.p. specimen by using this method was carried out. When this method was applied to the n.p. specimen, the estimation value was obtained as 201MPa. In the n.p. specimen, the estimation value was good agreement with the experimental value of 200MPa.

The reason of disagreement between the estimation value and the experimental value in the HSP-treated specimen is for the assumption in which the threshold condition for the internal crack extension is identical with that of the surface crack. In short, the local fatigue strength that calculated from the fatigue limit diagram and Eqn.2 is assumed as the fatigue limit at internal portion, providing that fatigue limit at surface portion is equivalent to the fatigue limit at internal portion of the specimen.

In this study, the difference in the local fatigue limit between the internal portion of specimen and the surface portion of specimen is investigated by using the equation to calculate the stress intensity factor as a general theory. Figure 6 shows the stress intensity factor model of internal crack type in rotating bending loading [7]. In this case, the stress intensity factor was calculated from Eqn.3 at point B.

$$K_{Iin} = F\left\{\frac{1}{E(a,b)}\cdot\frac{s}{R} - f(a,b)\cdot\left(\frac{b}{R}\right)\right\}\sigma_{in}\sqrt{\pi b}$$

$$= C_{in}(a,b,d,s,R)\cdot\sigma_{in} \qquad [\mathrm{MPa}\sqrt{m}\,] \tag{3}$$

Here, F(a,b,d,R),E(a,b) and f(a,b) are function on the crack position as “d” and crack size as “a” and “b”.

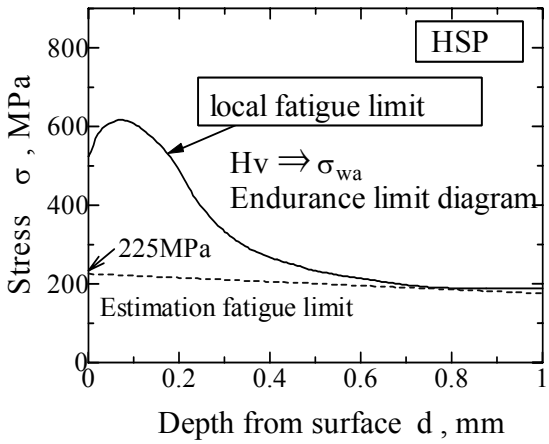

Figure 5: Local fatigue strength distribution inside the HSP treated specimen (using Endurance limit diagram)

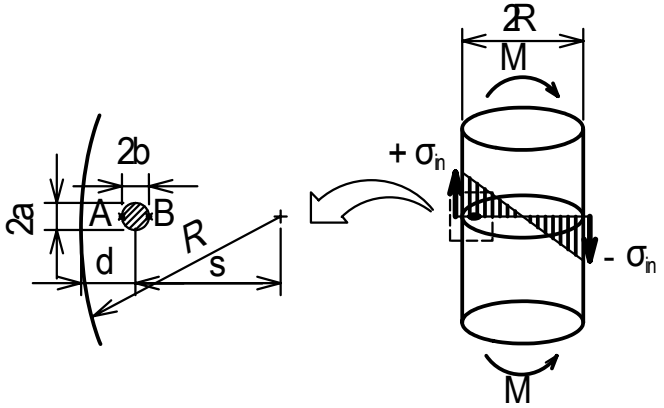

Figure 6: Stress intensity factor model of internal crack

On the other hand, the stress intensity factor of surface crack type was calculated from Eqn.4 [8].

$$K_{Isurf} = 0.65\sigma_{surf}\sqrt{\pi\sqrt{area}} = C_{surf}(a,b)\cdot\sigma_{surf} \quad [\mathrm{MPa}\sqrt{m}\,] \tag{4}$$

Here, the "area" is the fatigue crack area which is depended on the half crack length "a" and crack radius "b".

The values of the coefficient *Cin* of Eqn.3 is smaller than *Csurf* of Eqn.4, when the crack radius "a" of Eqn.3 and the one of Eqn.4 are the same, and 2a and 2b are the same also. M. Larsson et al [9] indicated that the fatigue limit of internal crack is explained by using the threshold of the stress intensity factor. In short, fatigue crack propagates when the stress intensity factor at crack tip reaches the threshold of the material. Here, because the threshold stress intensity factor does not vary with location in the specimen, the relationship between σ_{in} and σ_{surf} is indicated as next equation.

$$\sigma_{in} = (Csurf/Cin)\times\sigma_{surf} \tag{5}$$

There is two consideration points in this Eqn.5. One is that the local fatigue limit inside the specimen is *Csurf*/*Cin* times as the local fatigue limit at surface. And the other is that the coefficient ratio *Csurf*/*Cin* depends on the depth of the crack position and the local fatigue limit is dependent on the depth from surface. Figure 7 shows relationship between the coefficient ratio *Csurf*/*Cin* and the depth from the surface. Estimated local fatigue limit distribution can be modified by this value.

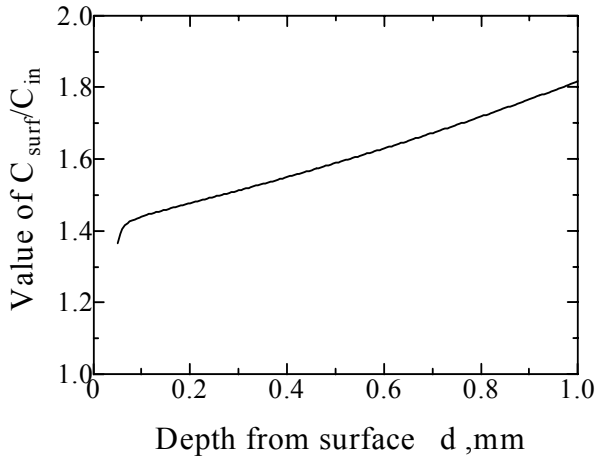

Figure 7: Relationship between coefficient ratio *Csurf*/*Cin* and depth from surface

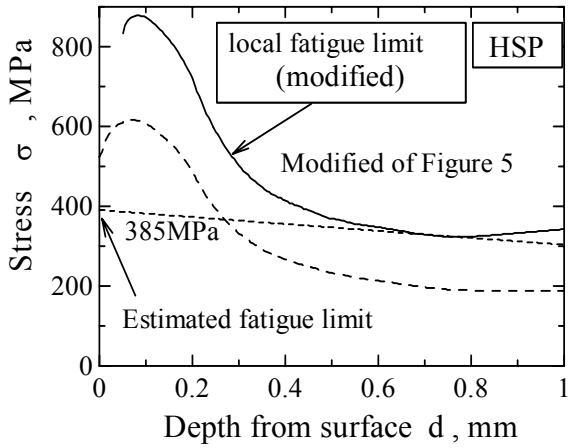

Figure 8: Modified local fatigue strength distribution inside the HSP treated specimen (using Endurance limit diagram)

Figure 8 shows the modified curve that was based on Eqn.5 for Figure 5. The fatigue limit was estimated as 385MPa from Figure 8, and this value agrees well with the experimental value of 370MPa.

In the other materials which authors have used in a series of research as the SP-treated Type 316L, the HSP-treated Type 316 and the HSP treated Type 304 etc., sufficient estimation results were obtained with the accuracy of 10% [10-13].

Using Modified Goodman diagram

In this paragraph, the estimation by using the modified Goodman's diagram as Eqn.1-b is investigated.

Since the tensile strength σ_B is depended on the hardness of matrix, relationship between the hardness and the tensile strength must be investigated of the Type 316L steel if the fatigue limit estimate by using the modified Goodman's diagram. In this study, the tensile test using pre-strain specimen was carried out. As a result, next equation was obtained.

$$\sigma_B = 356 + 1.378Hv \qquad \text{[MPa]} \tag{6}$$

The fatigue limit was estimated by using the Eqn.1-b as modified Goodman's diagram, Eqn.6 and the coefficient ratio *Csurf*/*Cin* as Eqn.5. As a result of this method, like the estimation using endurance fatigue limit, the fatigue limit of HSP-treated Type 316L was also estimated about 385MPa.

CONCLUSION

In order to estimate the rotating bending fatigue limit of the hard shot peening (HSP) treated Type 316L stainless steel, the method using the fatigue limit diagram, was applied. In this paper, it was clarified that there was the necessity to reconsider on these methods, and the new method to modified using the coefficient of equation to calculate the stress intensity factor was proposed. As a result of the investigation based on this modified method, the fatigue limit of HSP treated specimens was well estimated for the experimental values.

References

1. Mitsubayashi,M., Miyata,R. and Aihara,H. (1995). *Jpn. Soc. Mech. Eng.Ser.A,* 61, 1172.
2. Ohuchida,H., Nishioka,A., and Hayama,T. (1972). *Jpn. Soc. Mater. Sci.* 21,733.
3. Horikawa,T., Nakamura,H., Kawamura,M., Kawasaki,K. and Misaka,Y. (1997). *Jpn. Soc. Mater. Sci.* 46,1242.
4. Murakami,M., Konbayashi,M., Makino,Y., Toriyama,H., Kurihara,Y., Takasaki,S. and Ebara,R. (1994).*Trans. of JSSR*,7
5. Nakamura,H.,Tsunenari,T.,Horikawa,T. and Okazaki,S.(1983). *Fatigue Life Design of Machine*, Yokendo.Ltd,Japan.
6. Tanaka,T. (1983). *Reference of Fatigue Reliability Design on Metal.*
7. Murakami,Y., (1987). *Stress Intensity Factors Hand book Vol.3*, Pergamon Press.
8. Murakami,Y., (1993). *Metal Fatigue: Effects of Small Defects and Nonmetallic Inclusions*, Yokendo.Ltd
9. Larsson, M., Melander, A., Blom,R. and Preston, S. (1991). *Mater. Sci. Tech.* 7,11,998
10. Masaki,K., Ochi, Y.and Ishii,A.,Mater. Sci. Res.Int.Vol.4,1998,pp.200-205.
11. Masaki,K., Thoumyou,.H, Ochi,Y. and Matsumura, T., . (1999). *Jpn. Soc. Mech. Eng.Ser.A,* 65, 334.
12. Masaki,K., Ochi,Y. and Matsumura, T., . (1999). *Jpn. Soc. Mater. Sci.* 48,1124.
13. Ochi,Y., Akashi,A., Masaki, K., and Matsumura, T., . (2000). *Jpn. Soc. Mech. Eng.Ser.A,* 66, 320.

EVALUATION OF A BRITTLE FRACTURE ACCIDENT THAT OCCURRED AT THE HYOGO-KEN NANBU EARTHQUAKE

M. TOYOSADA, K. GOTOH, Y. WATANABE and S. NAKAYAMA

Department of Marine Systems Engineering, Kyushu University,
Hakozaki 6-10-1, Higashi-ku Fukuoka, 812-8581, Japan

ABSTRACT

Many fracture accidents of steel structures, which did not enable to occur under static loading, were found at the Hyogo-ken Nanbu Earthquake (17 January, 1995). Considering the strain rate effect on fracture toughness was required to evaluate these fracture accidents quantitatively. The evaluation concept of fracture toughness at arbitrary strain rate is explained briefly. An analysis on the brittle fracture accident of centrifugal cast steel bridge pier for railway was performed by means of this method. The result makes clear that vertical impulsive seismic wave is considered to be the major cause of the brittle fracture accident generated on this bridge pier at the Hyogo-ken Nanbu Earthquake.

KEYWORDS

brittle fracture, strain rate, impulsive seismic wave, dynamic loading, R prameter, cast steel bridge pier, Hyogo-ken Nanbu Earthquake

INTRODUCTION

Many fracture accidents of steel structures were found at the Hyogo-ken Nanbu Earthquake (17 January, 1995). In a design of structures, it was certificated that most of these accidents could not occur even though the same amount of static load acted on the structures. On the other hand, it is well known that fracture toughness decreases with increasing strain rate. Strain rate effect on fracture toughness was ignored on the design stage of the structures. Considering the strain rate effect on fracture toughness is necessary to evaluate the resisting ability on brittle fracture of steel structures.
Authors [1] had shown that fracture toughness is the function of strain rate-temperature parameter (R) proposed by Bennet et al. [2] under arbitrary strain rate and temperature condition. The estimation method of fracture toughness under arbitrary strain rate and temperature by using the results of static fracture toughness test had also stated in ref.[1] in detail. R parameter, which is derived from thermaly activated process of dislocation behaviour, is defined in Eqn. 1.

$$R = T \ln(A/\dot{\varepsilon}) \tag{1}$$

where T: temperature [K], A: frequency factor ($= 10^8[\mathrm{s}^{-1}]$), $\dot{\varepsilon}$: strain rate [s^{-1}]. In this study, an evaluation of brittle fracture accident occurred in the centrifugal cast steel bridge pier at the Hyogo-ken Nanbu Earthquake was performed by using the method in ref.[1]. An outline of the concept for

the quantitative evaluation method of strain rate effect on fracture toughness is explained to the next section. Refer to ref.[1] for more precise information concerning this procedure.

BASIC CONCEPT FOR THE QUANTITATIVE EVALUATION METHOD OF STRAIN RATE EFFECT ON FRACTURE TOUGHNESS

Yield stress of steel materials can be represented only by R parameter, because yield stress increases with the temperature drop and with the strain rate rise. R value under dynamic loading condition plays the same role as temperature under static loading condition for the constitutive equation of steels. Postulating the constitutive equation of materials followed by the n-th power work hardening ($\sigma = F\varepsilon^n$), it was also confirmed that strain hardening exponent (n) depends only on yield stress in case of static condition. Static loading in our researches was defined as the condition that no strain rate effect appeares in the constitutive equation and the value is equal to $5.0 \times 10^{-5}\mathrm{s}^{-1}$ [1].

Constitutive relation of steels under arbitrary strain rates, therefore, can be estimated only by the yield stress obtained from R value although R value usually changes throughout a loading process.

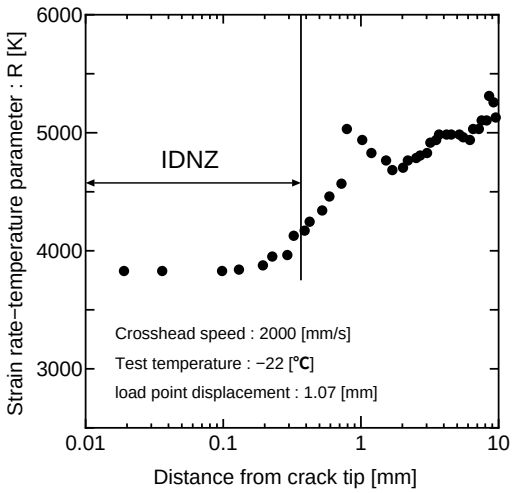

Figure 1 An example of R parameter distribution in the vicinity of a crack tip

Authors had presumed that fracture toughness is a function of R parameter under dynamic loading, because the fracture toughness is a function of temperature under static loading and R parameter performs a equivalent role of temperature under dynamic loading. Besides, R parameter considered the temperature rise generating by plastic work takes almost constant value in the fracture process zone at an arbitrary moment as shown in Fig. 1 [1] for example. This flat distribution could be appear as the additive effects obtained by combining temperature rise due to plastic work with strain rate distribution in the vicinity of a crack tip. In this figure, IDNZ defined by Rice and Johnson [4] corresponds to fracture process zone. This phenomenon and the hypothesis which fracture toughness is a function of R parameter enable to ignore identifying the precise fracture initiation point for evaluating strain rate effect on fracture toughness. R parameter which keeps almost constant value in fracture process zone denotes R_γ as follows. It can be recognized that fracture toughness is a function of R_γ under dynamic condition. Postulating that the relationship between R_γ and fracture toughness is the inherent characteristic of materials, fracture toughness under arbitrary strain rates can be quantitatively estimated from the results of static fracture toughness tests.

GENERAL ASPECT OF THE BROKEN CAST STEEL BRIDGE PIER

Some defects like shrinkage cavity existed in the inside layer of the broken cast steel bridge pier. These defects remained in service of this railway for the following reasons 1 and 2.

1. The inside layer was eliminated from load supporting member in structural design.
2. It was supposed that only compressive load acts on the section in service.

Figure 2 shows a fracture surface of the broken cast steel bridge pier. It is recognized that there were some large shrinkage cavities which played a role of the brittle fracture generating point in the bridge pier. Maximum depth and breadth of the shrinkage cavity were 18.8mm and 37.1mm respectively. To investigate the brittle fracture strength of this pier, this surface shaped defect was replaced by two dimensional infinite cracked body subjected to remote tensile stress, which the maximum value of stress intensity factor along the contour of the surface defect is equal [3]. The half crack length of one is equal to 18.3mm.

Figure 2 Fracture surface of the broken cast steel bridge pier

FRACTURE TOUGHNESS CHARACTERISTIC CURVE

Fracture toughness characteristic curve of the broken cast steel bridge pier must be prepared to evaluate the brittle fracture accident. This curve represents the relationship between R_γ and fracture toughness. Fracture toughness tests under three loading speed (0.01, 1, 100mm/s) and four ambient tempreature (0, -20, -40, -60 ˚C) had carried out to identfy the characteristic curve. Calculation procedure for R_γ is stated in ref.[1].

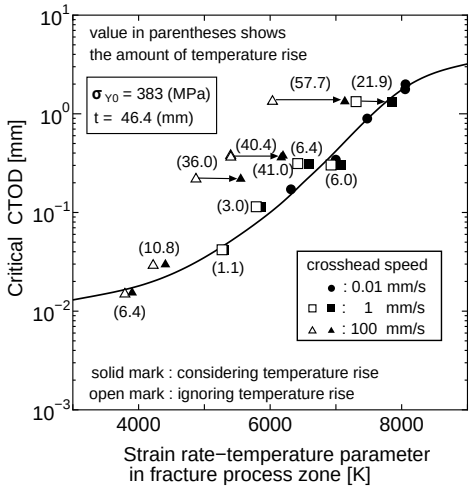

Figure 3 Relationship between R parameter in fracture process zone and critical CTOD

Figure 3 shows the characteristic curve of the broken steel material. Figures in parentheses in Fig. 3 indicate the estimated value of temperature rise (unit in degree) due to plastic work at the tip of IDNZ. R_γ in Fig. 3 were acquired by adding this temperature rise to the ambient temperature of fracture toughness test condition. It makes clear that fracture toughness can be recognized as the function of R_γ over the wide loading speed and temperature conditions by considering the temperature rise due to

plastic work. Bold curve in Fig. 3 could be recognized the fracture toughness characterisitic curve for the material of broken cast steel bridge pier.

THE BRIDGE PIER BEHAVIOUR UNDER SEISMIC LOADING

To estimate the applied load to the bridge pier, static elastic-plastic FE analyses were carried out at frist. Four nodal shell element was used to idealize this FE model. Shell thickness of FE model varied step by step to model the thickness variation of the pier. Total number of nodal point was 3017 and of element was 2912. Added vertical load derived from superstructure was inputted at bearing plate shoes of the pier. Yield stress of column material was 258MPa and of beam material was 235MPa. Stress-strain curve of both materials were approximated as a bi-linear (second modulus is equal to $E/100$, where E is Young's modulus).

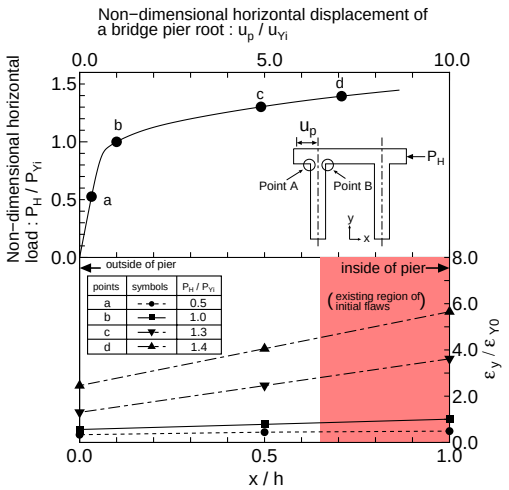

Figure 4 Displacement versus load curve at the pier top and strain distribution of vertical component through the reference cross section.

Figure 4 shows the calculation resutls. Upper side of Fig. 4 shows the horizontal displacement of the pier top undertaken the horizontal load illustrated in this figure. Both axes are normalized by the displacement and the load at the start of yielding on the reference cross section respectively, which is 400mm below the beam flange. Etou et al. [5] also estimated that the maximum horizontal displacement is equal to 21cm by means of elastic-plastic FE analyses. The displacement and load curve acquried by them was in good agreement with upper side of Fig. 4.

Lower side of Fig. 4 shows the vertical component of the strain distribution at the reference cross section in the column shell plate. a, b, c and d denote the appled load level respectively shown in upper part in Fig. 4. Shaded region of the graph means the initial flaw existing region. Ordinates is normalized by yield strain of column material and abscissa is done by shell thickness (h). This figure indicates that tensile strain generates at fracture generating region and that the value of strain exceeds yield strain by applying horizontal load at fracture generating.

Brittle fracture generating point was the area in which uniform strain distributed throughout shell thickness direction of the broken bridge pier. Besides, the reference strain to evaluate fracture parameter can be regarded as the average value of strain distribution on the defect position in no defect structures. Considering these condition, hilighted accident, namely brittle fracture generating from a large defect, can be evaluated by using average strain in the defect position from these FE analyses.

POSSIBILITY OF BRITTLE FRACTURE GENERATED BY HORIZONTAL SEISMIC WAVE

Brittle fracture genreating loads caused by horizontal seismic wave were estimated by inputting one pulse, which time duration equals 0.3s, to the FE model shown in Fig. 3. Supposed pulse time duration was almost equal to the average of observed time duration of horizontal seismic wave (north to south direction), which was equal to 034s, at the earthquake. Ambient temperature for the calculations was 4 ℃which was the same temperature at the day of earthquake.

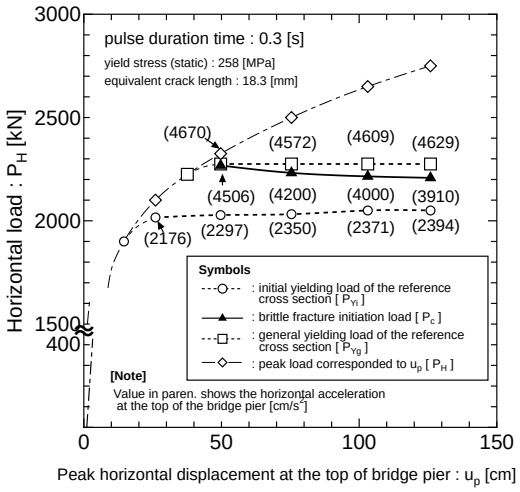

Figure 5 Estimation of brittle fracture generating load caused by horizontal seismic wave

Figure 5 shows the calculation results. Solid triangle marks represent the relationship between brittle fracture generating load and horizontal displacement at the pier top. Open circle marks represent the initial yielding load of the reference cross section and open square marks represent the genreal yielding load on the same section. Diamond shape marks mean the peak load in case of no defect. Figures in parentheses are equal to the horizontal acceleration of the pier top (unit in cm/s^2) at the each state. These result indicate that the brittle fracture accidents could be generated in case that the acceleration reached at least $4000cm/s^2$ and horizontal displacement of the pier top must exceed more than 40cm. Considering the observed maximum seismic wave acceleration of horizontal component equals $812.8cm/s^2$, it makes clear that the brittle fracture accident could not be generated by horizontal seismic wave.

POSSIBILITY OF BRITTLE FRACTURE GENERATED BY VERTICAL SEISMIC WAVE

To investigate the possibility of the brittle fracture accident generated by vertical component of the seismic wave, following analyses were carried out.

1. Time history response analyses of the bridge pier by applying the observed vertical seismic wave (maximum acceleration was equal to $333.3cm/s^2$).
2. Estimating the maximum amplitude of strain on the average of the reference cross section.
3. Calculation of time history of the relationship between R parameter in fracture process zone (R_γ) and CTOD by applying the half vertical pulse wave stated above.

Solid circle marks in Fig. 6 show this time history. Bold curve in Fig. 6 represents the fracture toughness characteristic curve of the bridge pier material, which is shown in Fig. 3. Cross point of the bold curve and the time history indicates the unstable fracture generating. This result implys that it was impossible to generate the brittle fracture accident by acting the observed vertical seismic wave to the bridge pier directly.

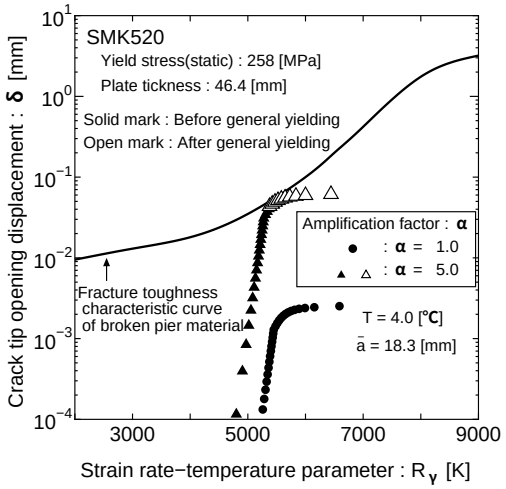

Figure 6 Estimation of brittle fracture caused by vertical seismic wave

Sonoda et al. [6] showed that the inputted vertical component of stress wave to the structures was amplified. The amplification factor (α) depends on the pulse period and velocity of the vertical seismic wave and the ratio of seismic wave acting area between ground and the bridge pier. Value of the amplification factor in case of our hilighted analysis condition (time duration equals 0.3s) was approximate to five [6].

Triangle marks in Fig. 6 show the R parameter in fracture process zone versus CTOD curve in case which the input vertical seismic wave was amplified to five times. Open marks of the triangle represent that the reference cross section reaches the general yielding condition.

By considering the following conditions (a) through (c), the brittle fracture accident caused by the vertical seismic wave could be understood as a natural phenomenon.

(a) Fracture toughness has a certain scattering.

(b) The fracture toughness characteristic curve of the bridge pier material corresponds to the average curve of one.

(c) Some specialists in seismology insisted that the stronger vertical short periodic pulse than the observed one could not be recorded because of the low ability of the recorders.

CONCLUDING REMARKS

Brittle fracture accident of centrifugal cast steel bridge pier at the Hyogo-ken Nanbu Earthquake was investigated by considering the strain rate effect on fracture toughness.

The result makes clear that vertical impulsive seismic wave is the major source to generate the brittle fracture accident on this bridge pier.

REFERENCE

[1] Toyosada,M. and Gotoh,K. (1996) *Memo. Eng. Kyushu University*, 56, 273

[2] Bennet,P.E. and Sinclar,G.M. (1966) *ASME J. Basic Eng.* 88, 2, 518

[3] The Japan Welding Engineering Society Standard 2805 (1994)

[4] Rice,J.R. and Johnson,M.A. (1970) *Inelastic Behavior of Solids*, McGraw-Hill, New York, 641

[5] Etou,O., Mihara,T. and Miki,C. (1998) *J. Japan Soc. Civil Eng.*, 591/I-43, 236

[6] Sonoda,K., Kobayashi,S. and Fukui,A. (1997) *Memo. Eng. Osaka City University*, Jan., 169

ORAL REFERENCE: 851

EVALUATION OF BOND PROPERTIES OF CRACK INJECTION REPAIR FOR CONCRETE STRUCTURES

M. Kunieda[1], T. Kamada[1] and K. Rokugo[1]

[1]Department of Civil Engineering, Gifu University, Yanagido, Gifu 501-1193, JAPAN

ABSTRACT

Bond quality is an important factor that affects the performance of repaired members. For crack injection repair, bond strength tests based on Japanese Industrial Standard (JIS) were carried out under conditions that were different from those normally encountered in the field (i.e. the tests involved smaller specimens, smoother surfaces and finer grained materials). Testing methods to evaluate the bond property of repair materials involve a plain concrete as the bulk one. Most repair materials were, however, used in reinforced concrete members. The behavior of repair materials in the members should be also evaluated appropriately. This paper presents the influence of injected surface roughness on the bond properties, in which the bond properties of crack injection materials were evaluated using fracture mechanics parameters. This paper also describes the results of bending tests for reinforced concrete beams repaired by crack injection techniques. The effects of the injected and un-injected parts on the mechanical behavior of repaired reinforced concrete were investigated.

KEY WORDS

Crack Injection Repair, Bond Property, Surface Roughness, Standard Tests, Flexural Bond Strength

INTRODUCTION

Good bonding between repair materials and bulk concrete is one of the basic performances required for repaired members. For crack injection repairs, good bonding may increase the stiffness of the repaired members and prevent the penetration of substance (e.g. chloride ions and water). In Japan, the bond property of crack injection materials has been evaluated with the flexural bond strength based on Japanese Industrial Standard (JIS) testing method, where smaller specimens with smooth surfaces for injection are used. This testing method helps to interpret the relative performance of repair materials. However, the evaluated values (indices) obtained from the standard tests depend on the testing methods, such as specimen geometry, loading manner and so on. There is few relation between the evaluated values and the performance of repair materials in existing concrete structures. Regarding the testing method for bond properties in repairs, the location of fracture might be more important (i.e. the fracture of bulk concrete or repair materials, or the delamination of repair materials should be observed).

The conventional indices to evaluate the bond property are the tensile bond strength, the flexural bond strength, the shear bond strength and so on. However, it is important to evaluate the bonding after the maximum load in order to estimate the failure process of repaired members. The fracture mechanics parameters, such as tension softening diagrams or fracture energy, were applied to the evaluation of the bond property on construction joint [1,2] and on repair material [3,4].

In the first part of this paper, the effects of the injected surface roughness on the bond property were investigated through the bending tests. The testing method using fractured surfaces of concrete as injection surfaces was proposed. In addition, the fracture mechanics parameters such as tension softening diagram and fracture energy were adopted as the indices. In the second part of this paper, the cracking behavior of reinforced concrete beams repaired by crack injection technique was described. The relationship between bond property of repair materials and mechanical behavior of repaired beams were discussed, in which the behavior of un-injected and injected cracks were investigated.

BOND PROPERTY OF CRACK INJECTION MATERIALS AND INJECTED SURFACE ROUGHNESS

Outline of Experiments

The test procedures are shown in Fig. 1. The size of the specimens was 100×100×400mm. The mix proportions of the concrete are tabulated in Table 1. The water to cement ratio was 50%. The compressive strength at the age of 47days was 52MPa. Four specimens were made for each series. The bulk concrete was cast and cured in water for 35days, and the wet curing (20°C) was carried out for 5days. A notch of 1/3 of the specimen depth was made by a concrete cutter. As shown in Fig. 2, the four point bending tests with the span of 300mm were carried out and the

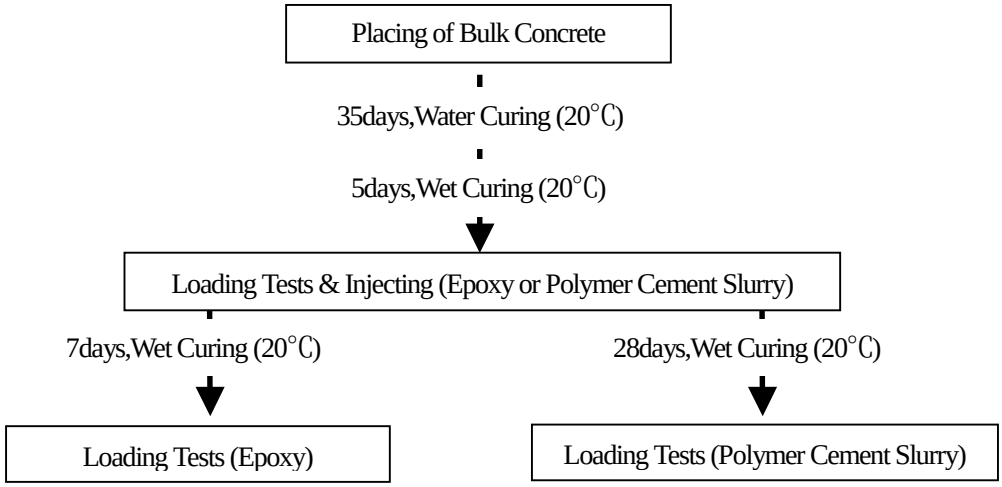

Figure 1: Test Procedures

TABLE 1
MIX PROPORTIONS OF BULK CONCRETE

W/C (%)	Slump (cm)	Air (%)	Units (kg/m^3)				
			Water	Cement	Fine Agg.	Coarse Agg.	Ad.*
50	13	4.1	165	330	765	1000	0.99

*Admixture (AE Water Reducing Agent)

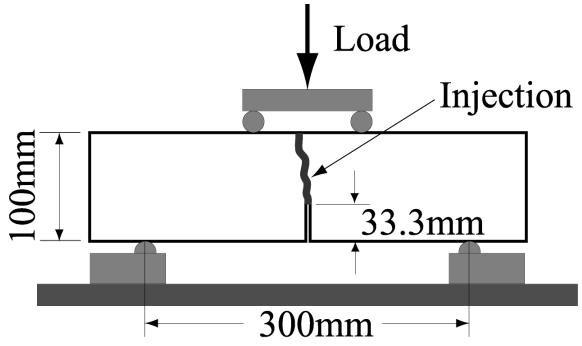

Figure 2: Test Setup

applied load and crack mouth opening displacement (CMOD) curves were measured. The fractured surfaces after bending tests and the smooth surfaces after removing the casting form were adopted for the injection surfaces. A clearance of 1.0mm thickness for injecting was made by using a spacer and the sides and bottom of the crack were sealed to prevent leakage. The epoxy or polymer cement slurry was injected into the clearance between the specimen halves. The material properties of the injections are tabulated in Table 2. For comparison, control un-cracked specimens were also made. The loading tests of the repaired specimens were carried out at 7 days (total: 47days) after injecting for the epoxy injected specimens, and 28days (total:
68days) for the polymer cement slurry injected specimens. The loading tests of the control specimens were also carried out at the age of 47days that was equal to the age of the epoxy injected specimens.

TABLE 2
MATERIAL PROPERTIES OF CRACK INJECTION MATERIALS (EXTRACTED FROM CATALOGS)

Properties	Epoxy	Polymer Cement Slurry
Shrinkage (%)	0.0	0.2
Young's Modulus (GPa)	2.9	9.7
Flexural Bond Strength (MPa) (JIS A 6024)	6.9	4.1
Viscosity (mPa･s) (JIS K 6833)	600	—
Consistency J14 (sec) (JSCE-F531)	—	2.4

The poly-linear approximation analysis method [5] combined with a fictitious crack model was used for the determination of the tension softening diagrams. In the repaired specimens, only one macro crack propagated and mainly consumed the energy that was indicated by the area of load-displacement relations. It was assumed that these back analysis concepts with the fictitious crack model could be applied to the determination of tension softening diagrams in the crack injection repair.

TABLE 3
TEST RESULTS

Injection Materials	Injected Surfaces	Number of Specimens	Flexural Bond Strength (MPa)	Fracture Energy* (N/m)	Location of Fracture
Epoxy	Smooth Surface	4	3.25	15.1	Interface & Injection
	Fractured Surface	4	4.41	27.6	Bulk
Polymer Cement Slurry	Smooth Surface	4	2.01	6.50	Interface & Injection
	Fractured Surface	4	2.43	12.8	Injection
Control	(Uncracked)	4	3.89	22.8	—

*Fracture Energy up to Crack Width of 0.01mm

Effect of Injected Surface Roughness on Bond Property in Plain Concrete Beams

The flexural bond strength of the each repaired specimens is shown in Table 3, along with those of the control un-cracked specimens. In all injected specimens with the smooth surfaces, the fracture occurred along the interface and within injection. The flexural bond strength of the these specimens was smaller than that of the control un-cracked specimens.

The tension softening diagrams of the injected specimens are compared with those of the control un-cracked specimens in Fig. 3. The difference in bond properties can be visually distinguished by the shape of the tension softening diagrams. In the case of the fractured surfaces, the tensile stress at each crack width was larger than that of the smooth surfaces. Especially, the tensile stress of the repaired specimens with epoxy injection was larger than that of the control un-cracked specimens. As shown in Table 3, the fracture energy of the specimens with injection on the fractured surfaces was twice as large as those with injection on the smooth surfaces. The fracture energy was a more sensitive

index than the flexural bond strength. In this study, the flexural bond strength and fracture energy of the repaired specimens with epoxy injection became larger than those of the control un-cracked ones. Because the crack path of repaired specimen, in which the injections have good bond properties, was longer than that of un-cracked specimen, the consumed energy was increased [4]. In addition, as the Young's modulus of the epoxy was smaller than that of concrete, the ductility of repaired members with epoxy became larger [3]. For repaired specimens with the epoxy injection on the fractured surfaces, a crack propagated in the bulk concrete. For repaired specimens with the polymer cement slurry injection on the fractured surfaces, a crack, however, propagated the injection material. These crack patterns, which depends on the difference of the injection materials, could be also observed in the repaired reinforced concrete, which will be described in the next part of this paper.

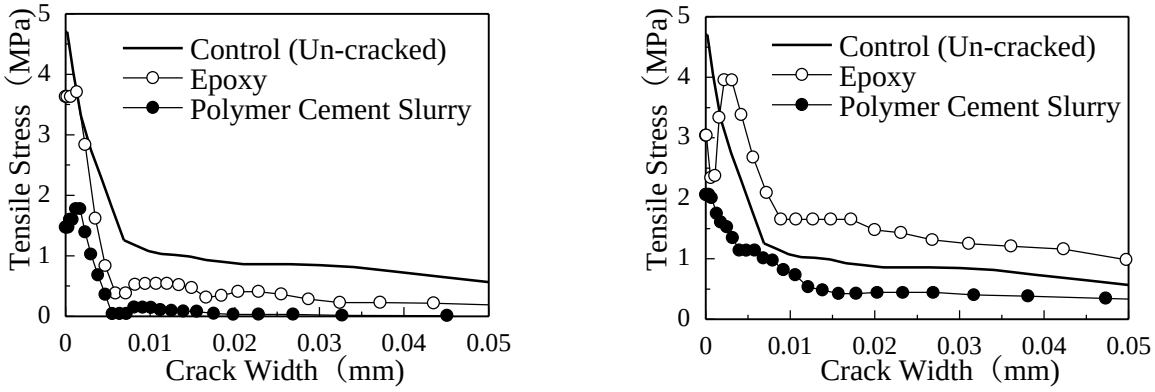

(a) Repaired with Smooth Surfaces (b) Repaired with Fractured Surface

Figure 3: Determined Tension Softening Diagrams

INJECTED REPAIR MATERIALS IN REINFORCED CONCRETE BEAMS

Outline of Experiments

The mix proportions of the concrete, which are used ones in the previous part, are shown in Table 1. The compressive strength at the age of 19 days was about 50MPa. The size of the specimens was 100×300×1800mm, as shown in Fig. 4. The reinforcement ratio, in which yield point of the re-bar was over 295N/mm^2, was 0.5%. After removing the casting forms, the wet curing (20°C) were carried out for 2 weeks. In order to obtain the dried specimens for the sealing, the specimens were exposed in the laboratory for 5 days.

The four point bending tests were carried out to induce cracks (first cracks) in original specimens. The applied load and relative displacement in the moment span were measured. The loading was continued up to the curvature of 1.5×10^{-4}(1/mm), and un-loaded to be the applied load of zero. The epoxy and polymer cement slurry, which are also used ones in the previous part, were used as the injection materials. Each material was injected into the first cracks that have dried injected surfaces in original specimens by means of the low-pressure injection method. The first cracks were, however, classified into two main groups; (a) injected cracks each having the crack width of 0.2-0.8mm were repaired by the crack injection techniques, (b) un-injected cracks each having the crack width under 0.04mm were not repaired. In

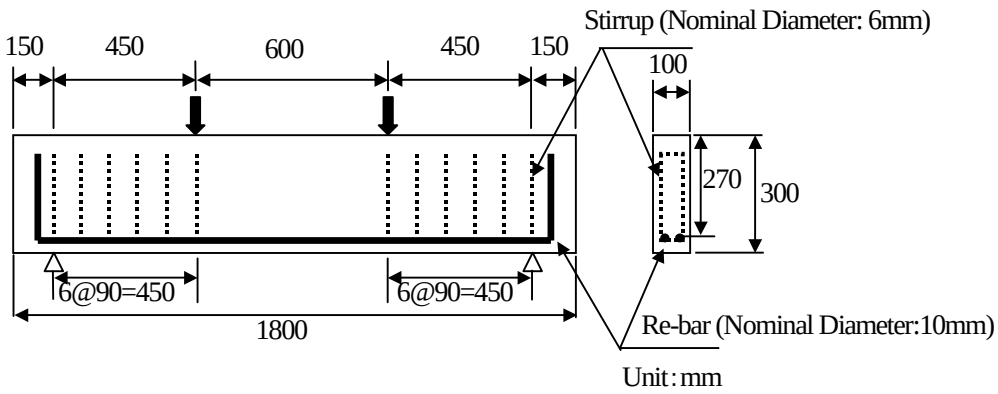

Figure 4: Test Setup

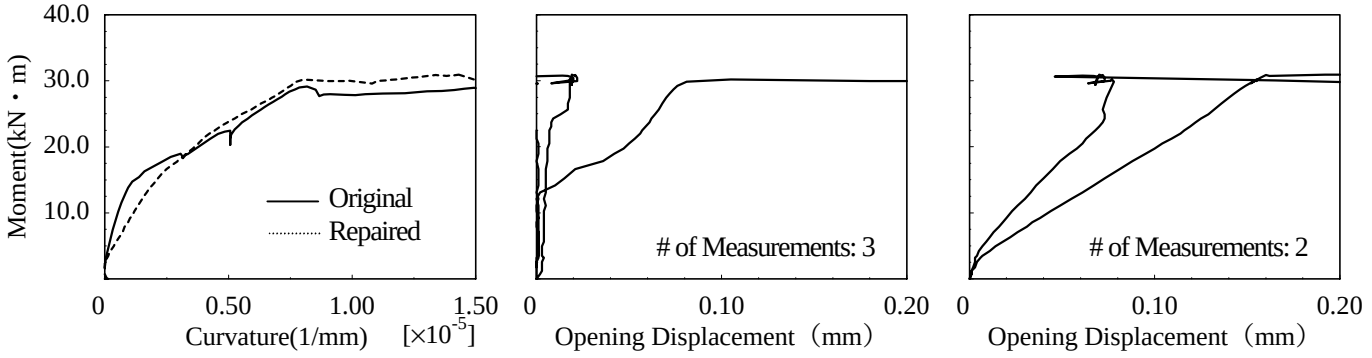

(a) Moment-Curvature (b) Opening Disp. of Injected cracks (c) Opening Disp. of Un-injected cracks

Figure 5: Mechanical Properties of Repaired Reinforced Concrete Beams with Epoxy Injection

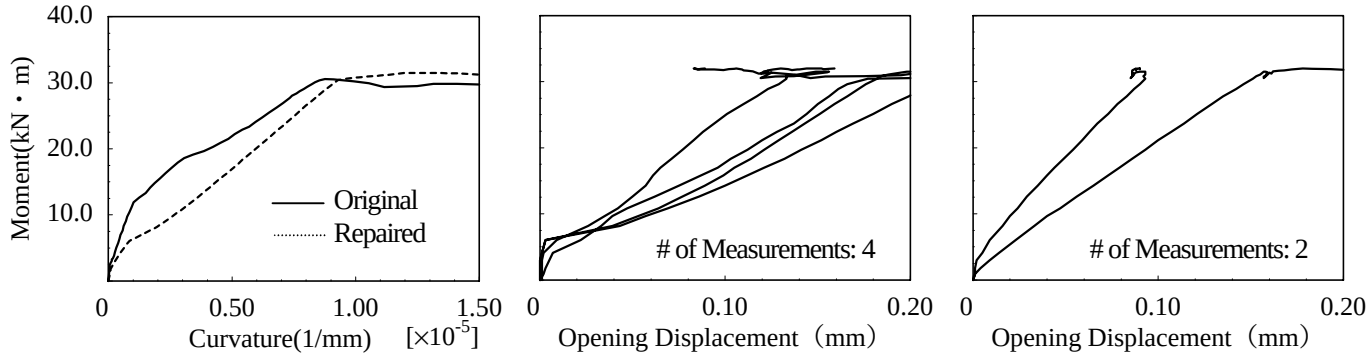

(a) Moment-Curvature (b) Opening Disp. of Injected cracks (c) Opening Disp. of Un-injected cracks

Figure 6: Mechanical Properties of Repaired Reinforced Concrete Beams with Polymer Cement Slurry Injection

these beam specimens, the crack having the crack width of 0.2-0.04mm could not be observed. After the injection repair, the bending tests used for the original specimens were also carried out, and the opening displacement of injected and un-injected cracks was measured through the crack opening displacement transducers.

Cracking Behavior of Repaired Reinforced Concrete Beams

The relationships between moment and curvature in each specimen are shown in Fig 5(a) and 6(a). The initial stiffness of repaired specimens using each injection material was lower than that of original specimens. The crack opening displacement of each crack in repaired specimens is shown in Fig. 5(b),(c) and 6(b),(c). For the un-injected cracks, the opening displacement became larger with increasing of the applied load. Especially, the opening displacement of the un-injected cracks was larger than that of injected cracks in lower loading level. The un-injected cracks imparted the lower stiffness to the repaired specimens. Figure 7 shows the crack patterns after the loading tests for the repaired specimens. As shown in Fig. 6(b), because the opening displacement rapidly increased at the moment of 6-7kN・m, the cracking would be occurred at the injected cracks with the polymer cement slurry injection. The new cracks (second cracks) in repaired specimens could be observed at the injected cracks. The cracking in the polymer cement slurry injection imparted the lower stiffness to the repaired specimens, as shown in Fig 6(a), because the each inflectional point in moment-curvature and moment-crack opening displacement relations was similar to each other. The opening displacement of injected cracks with the epoxy injection, however, suddenly increased at the moment of 14kN・m, which was higher than that of injected cracks with the polymer cement slurry injection. In addition, some of the injected cracks with the epoxy injections were not opened, as shown in Fig. 5(b). The second cracks in repaired specimens with the epoxy injection could be observed at the bulk concrete near the injected parts, as shown in Fig. 7.

These results show that the difference of bond properties of each crack injection material could be observed in not only load-displacement relations but also load-crack opening displacement ones. Especially, the un-injected cracks having larger crack width in each loading level would affect not only the mechanical behavior of repaired members but also the durability due to permeability of substance. The un-injected cracks in concrete structures should be detected, or injecting and coating techniques should be used jointly for a durable repair.

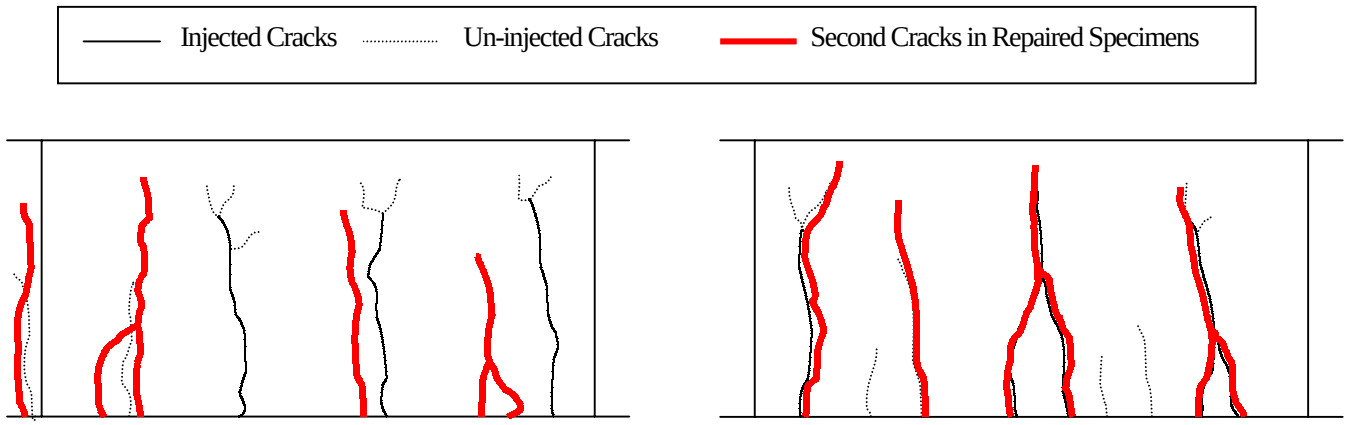

(a) Epoxy Injection (b) Polymer Cement Slurry Injection

Figure 7: Examples of Crack Patterns in Moment Span of Repaired Reinforced Concrete Beams

CONCLUSIONS

In the first part of this paper, the bond property in crack injection repair was investigated by using the plain concrete beams, and the following conclusions were obtained;

1 In order to evaluate the bond property in crack injection repair, the testing method with the fractured surfaces of concrete was proposed. The bond property of the injected specimens with fractured surfaces was better than that with smooth surfaces. Regarding this testing method with the fractured surfaces, the failure mode is one of the effective indices to evaluate bond properties of repair materials (i.e. good bonding and poor one gave the fracture of bulk concrete and the delamination of repair materials, respectively) .

2 The fracture mechanics parameters were applied to the evaluation of bond property in crack injection repair. Especially, the fracture energy of the repaired specimens with the fractured surfaces was twice as large as that with the smooth surfaces.

In the second part of this paper, the mechanical properties of the repaired reinforced concrete beams, which have injected and un-injected cracks, were discussed, and following conclusions were obtained;

3 The un-injected cracks impart the lower stiffness to the repaired reinforced concrete beams. Locally, the opening displacement of the un-injected cracks was larger than that of the injected cracks in lower loading level. This result shows that the un-injected cracks in concrete structures should be detected, and coating techniques might be effective in a durable repair.

REFERENCES

1 Wittmann, F. H. and Müller, T. (1994). In: *Adherence and Fracture Energy: Adherence of Young on Old Concrete*. pp.97-106, Wittmann, F. H. (ed.), AEDIFICATIO Verlag.
2 Kurihara, N., Kunieda, M., Uchida, Y. and Rokugo, K. (1999) *J. of Materials, Conc. Struct., Pavements* V-42, 309.
3 Kitsutaka, Y., Kamimura, K. and Nakamura, S. (1992) *J. of Struct. and Constr. Engng.*, AIJ, 432, 1. (in Japanese)
4 Kleinschrodt, H. D. (1989). In: *Evaluation of Force-locking Epoxy Resin Injections in Concrete Cracks by Means of Fracture Mechanics Parameters: Fracture of Concrete and Rock Recent Developments*, pp.537-548, Shah, S. P., Swartz, S. E. and Barr, B. (eds.) , ELSEVIER APPLIED SCIENCE.
5 Uchida, Y., Kurihara, N., Rokugo, K., and Koyanagi, W. (1995). In: *Determination of Tension Softening Diagrams of Various Kinds of Concrete by Means of Numerical Analysis: Fracture Mechanics of Concrete Structures*, pp. 17-30, Wittmann F. H. (ed.), AEDIFICATIO Publishers.

ORAL/POSTER PRESENCE:0441

EVALUATION OF FRACTURE TOUGHNESS OF CERAMICS/METAL FUNCTIONALLY GRADED MATERIAL BY THREE-POINT-BENDING TEST

K. Tohgo [1], T. Suzuki [1], H. Araki [1] and H. Ishii [1]

[1] Department of Mechanical Engineering, Shizuoka University
3-5-1, Johoku, Hamamatsu 432-8561 Japan

ABSTRACT

This paper dealt with fracture toughness and fracture behavior of ceramics/metal functionally graded material (FGM). The used material was fabricated by powder metallurgy using partially stabilized zirconia (PSZ) and stainless steel (SUS 304). The material had a functionally graded surface layer (FGM layer) with a thickness of 1mm or 2mm on SUS 304 substrate. On the FGM layer, a volume fraction of PSZ varied from 100% at the surface to 10% at the interface between the FGM layer and substrate. In order to evaluate the fracture toughness of the FGM layer, three-point bending tests were carried out on a rectangular specimen with a very short crack in the ceramics surface. On the three-point bending test, unstable crack growth occurred from a short pre-crack to some amount of crack length, and then the crack grew stably to the interface between FGM layer and substrate with increasing the applied load. Finally, the crack was arrested at the SUS 304 substrate, and the specimen deformed plastically. From the relationship between the applied load and crack length during the stable crack growth in the FGM layer, fracture toughness was evaluated. The fracture toughness increases with an increase in a volume fraction of SUS 304. It is concluded that the three-point bending test of the rectangular specimen with a short pre-crack is useful to evaluate the distribution of fracture toughness in FGM layer.

KEYWARDS

Functionally graded materials, Fracture toughness, Three-point-bending test, Stable crack growth, Ceramics/metal composite

INTRODUCTION

Functionally graded materials (FGMs) in which material components or their contents vary in some direction have a large amount of potentiality as engineering materials because of their unique performance [1-6]. An FGM plate consisting of ceramics and metals, for example, can be designed to reduce the thermal stress and to maintain the heat resistance and ductility. In order to apply FGMs to the engineering structure, it is necessary to estimate the strength and fracture mechanism not only under thermal loading but also under external loading such as static and cyclic loads [2-6].

This paper dealt with the evaluation of fracture toughness and fracture behavior of ceramics/metal functionally graded material (FGM). A possibility of stable crack growth in a three-point-bending specimen was discussed based on the crack driving force and the crack growth resistance of FGM. Then, on a FGM consisting of partially stabilized zirconia (PSZ) and stainless steel (SUS 304), three-point- bending tests were carried out on a rectangular specimen with a very short crack in the ceramics surface, and the details of fracture process were observed by a CCD camera and a scanning electron microscope. From the relationship between the applied load and crack length during the stable crack growth in the FGM layer, the distribution of fracture toughness along the FGM layer was evaluated. The influence of material composition on the fracture toughness in FGM layer and the fracture behavior of the FGM were discussed.

STABILITY OF CRACK GROWTH IN THREE-POINT-BENDING SPECIMEN

In this section, the stability of crack growth in a three-point-bending specimen as shown in Fig. 1 is discussed. It is assumed that the three-point-bending test is conducted by displacement-control of a load-point, and the compliance of the testing machine is negligible because of very high stiffness. The energy release rate G is given by the well-known equation

$$G = \frac{1}{2} P^2 \frac{dC}{dA} = \frac{1}{2} \frac{\delta^2}{C^2} \frac{dC}{dA} \tag{1}$$

where, C=δ/P is compliance of the specimen. P, δ and A are load, load-point displacement and crack area, respectively. On the displacement-control test, the stable crack growth occurs under the condition of

$$G = G_{mat} \ , \qquad \left(\frac{\partial G}{\partial A} \right)_{\delta} \le \frac{dG_{mat}}{dA} \tag{2}$$

where, G and G_{mat} show the driving force and material resistance to crack growth, respectively. The stability of crack growth in the three-point-bending specimen is examined based on the above condition. The left hand term of Eq. (2-$_2$) is written as follows

$$\left(\frac{\partial G}{\partial A} \right)_{\delta} = \frac{1}{2} \frac{\delta^2}{C^2} \left\{ \frac{d^2 C}{dA^2} - \frac{2}{C} \left(\frac{dC}{dA} \right)^2 \right\} \tag{3}$$

For the three-point-bending specimen, the stress intensity factor is given as

$$K_I = F_I(a/W) \sigma_0 \sqrt{\pi a} \quad , \quad \sigma_0 = \frac{3PS}{2W^2 B} \tag{4}$$

where, $F_I(a/W)$is the correction factor, and a, W, B and S are crack length, width, thickness and span length of the specimen. By introducing the non-dimensional crack length and compliance

$$\alpha = \frac{a}{W} \ , \qquad C_0 = \frac{\delta / S}{\sigma_0 / E'} \tag{5}$$

the following relations are obtained

$$\frac{d}{dA} = \frac{1}{WB} \frac{d}{d\alpha} \ , \qquad \frac{d^2}{dA^2} = \frac{1}{W^2 B^2} \frac{d^2}{d\alpha^2} \ ,$$

$$C = \frac{3S^2}{2W^2 BE'} C_0 \tag{6}$$

By considering these relations, Eq. (3) becomes as follows.

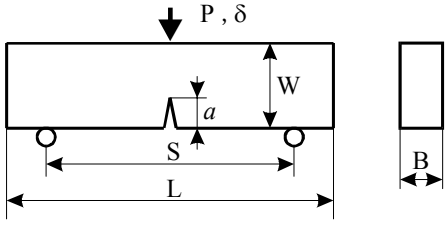

Figure 1: Three-point-bending specimen.

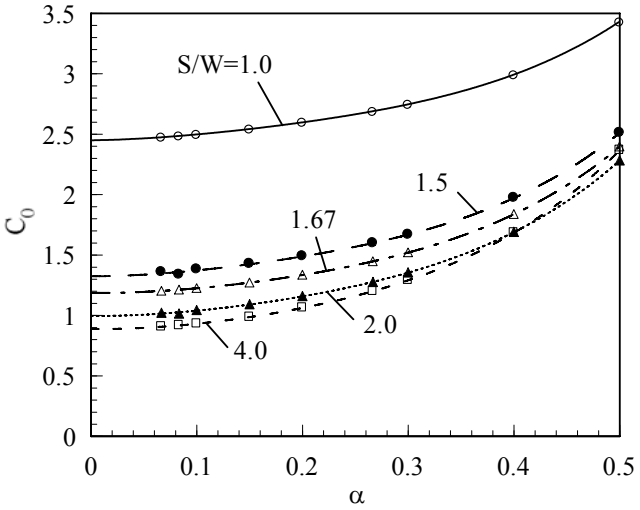

Figure 2: Nondimensional compliances of three-point-bending specimens.

$$\left(\frac{\partial G}{\partial \alpha}\right)_{\delta} = \frac{W}{3E'}\sigma_0{}^2\left\{\frac{d^2C_0}{d\alpha^2} - \frac{2}{C_0}\left(\frac{dC_0}{d\alpha}\right)^2\right\} \tag{7}$$

From the relation between the energy release rate and stress intensity factor

$$G = \frac{W}{3E'}\sigma_0{}^2\frac{dC_0}{d\alpha} = \frac{K_I{}^2}{E'} = \frac{W}{E'}\sigma_0{}^2\pi\{F_I(\alpha)\}^2\alpha \tag{8}$$

the following relation is obtained

$$\frac{dC_0}{d\alpha} = 3\pi\{F_I(\alpha)\}^2\alpha \tag{9}$$

By substituting Eq. (9) into Eq. (7), and considering Eqs. (2-$_1$) and (8), the following non-dimensional stability factor is obtained.

$$\frac{1}{G_{mat}}\left(\frac{\partial G}{\partial \alpha}\right)_{\delta} = \frac{1}{\{F_I(\alpha)\}^2\alpha}\left\{2F_I(\alpha)\frac{dF_I(\alpha)}{d\alpha}\alpha + \{F_I(\alpha)\}^2 - \frac{6\pi}{C_0}\{F_I(\alpha)\}^4\alpha^2\right\} \tag{10}$$

In the present investigation, Eq. (10) is evaluated based on the results of finite element analyses of the three-point-bending specimens with different ratio of span to width. Figures 2, 3 and 4 show the results of the non-dimensional compliance, correction factor of stress intensity and stability factor as functions of crack length for the three-point-bending specimens. From the condition of stable crack growth, the high value of the stability factor means that the unstable crack growth is easy to occur. As shown in Fig. 4, the stability factor in the region of short crack length is insensitive to the span to width ratio and it is higher for the shorter crack. When we consider the ceramics/metal functionally graded materials (FGM), the fracture toughness increases from ceramics surface to inside with an increase in a metal volume fraction. For example, the following linear relation is postulated for the distribution of fracture toughness.

$$K_{Imat} = K_{cer} + K\alpha \tag{11}$$

Since G_{mat} is obtained as

$$G_{mat} = \frac{K_{Imat}{}^2}{E'} = \frac{1}{E'}\left(K_{cer}{}^2 + 2K_{cer}K\alpha + K^2\alpha^2\right) \tag{12}$$

The gradient of material resistance is obtained as follows

$$\frac{1}{G_{mat}}\left(\frac{\partial G_{mat}}{\partial \alpha}\right) = \frac{2k + 2k^2\alpha}{1 + 2k\alpha + k^2\alpha^2} \quad , \qquad \frac{K}{K_{cer}} = k \tag{13}$$

In Fig. 4, the above equation is plotted for several k-values. This figure provides us with the information of stability of crack growth in the given specimen (S/W) and material (k). For example, if we conduct the

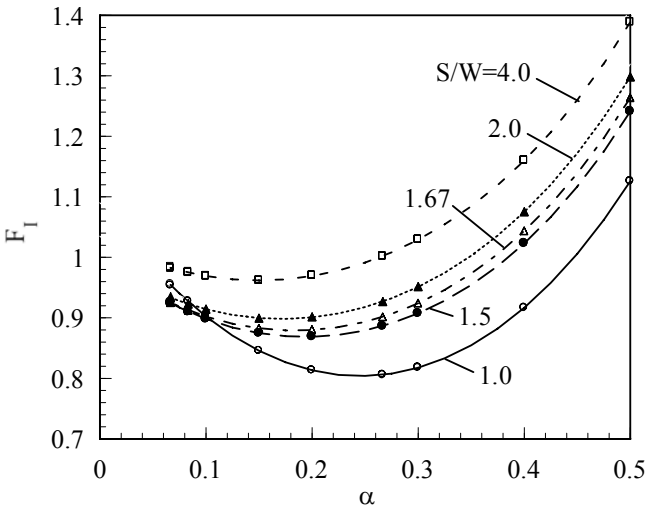

Figure 3: Correction factors of three-point-bending specimens.

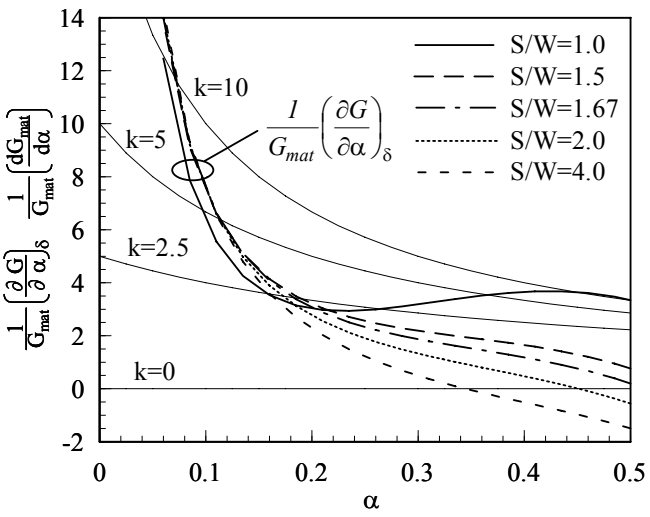

Figure 4: Stability of crack growth in three-point-bending specimens.

experiment for the material as shown by k=5 with the specimen with S/W=4, the crack growth becomes unstable to α=0.12 and then becomes stable for longer crack than α=0.12. Although the stable crack growth is obtained for longer crack than α=0.34 on the monolithic ceramics (k=0), the crack growth becomes stable in the wide region from shorter crack length on the FGM with high gradient of material resistance. Figure 4 is useful in the determination of the specimen size to obtain the stable crack growth in the given FGM.

MATERIALS AND EXPERIMENTAL PROCEDURE

The used material was fabricated by powder metallurgy using partially stabilized zirconia (ZrO_2-3molY_2O_3, PSZ) and stainless steel (SUS 304). The material has a functionally graded surface layer (FGM layer) on SUS 304 substrate. Figure 5 shows the configuration of three-point-bending specimen and the details of the FGM layer. The FGM layer consists of multi-layers in which a volume fraction of PSZ varies stepwise from 100% at the surface to 10% at the interface between the FGM layer and substrate. Two kinds of FGMs were fabricated, in which thickness of the FGM layers were designed to be about 1mm and 2mm; hereafter they are referred as FGM-1 and FGM-2, respectively. The SUS 304 particles were dispersed in the PSZ matrix in the layers from 100% PSZ to 40% PSZ, and on the contrary, the PSZ particles were dispersed in the SUS 304 matrix in the layers from 20% PSZ to 10% PSZ. The width of the specimen was 6mm, and the span length was changed in 24mm (S/W=4.0), 12mm (S/W=2.0) and 10mm (S/W=1.67). A series of median cracks by Vickers indentation were introduced as a starter-crack on the ceramics surface of the three-point-bending specimen. The depth of the median cracks was about 300μm.

Three-point-bending tests were conducted with 0.05mm/min crosshead speed at the room temperature and air. During test, the relation between load (P) and load-point-displacement (δ) was recorded, and the crack length and fracture process were observed on a side surface of the specimen by a CCD camera. The critical stress intensity factor was calculated from relationship between the load and crack length during stable crack growth. On the fractured specimen, the details of fracture surfaces were examined by a scanning electron microscope (SEM).

RESULTS AND DISCUSSION

Figure 6 shows an example of load-displacement relation obtained by three-point-bending test of FGM-2 and Fig. 7 exhibits the observation of a side surface of the specimen by CCD camera. As shown in Fig. 7, the stable crack growth is obtained in the FGM layer. The crack length measured on the video by a CCD

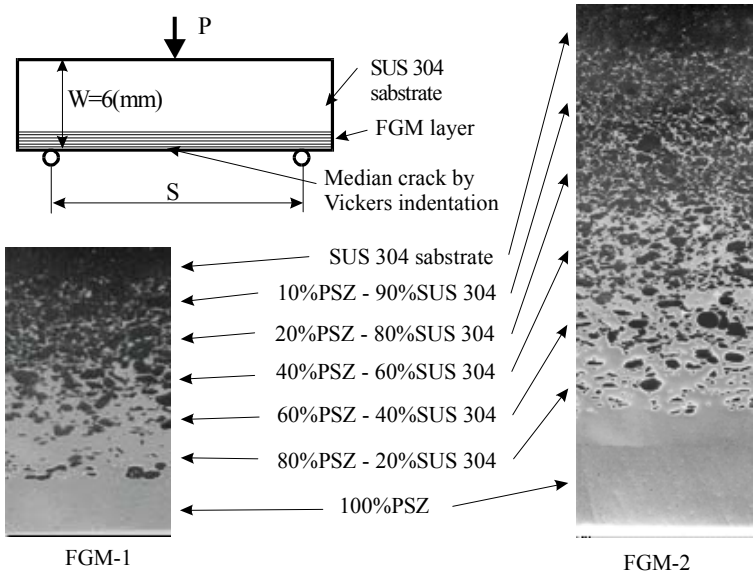

Figure 5: Specimen configuration and details of the FGM layer.

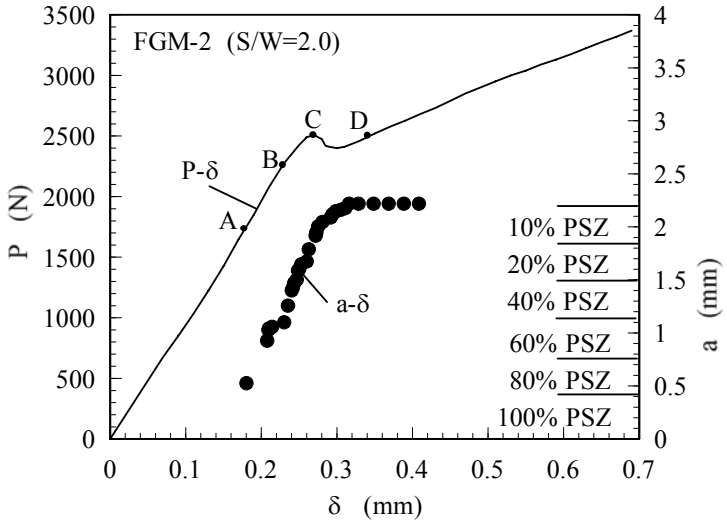

Figure 6: Load and crack length as functions of load-point displacement.

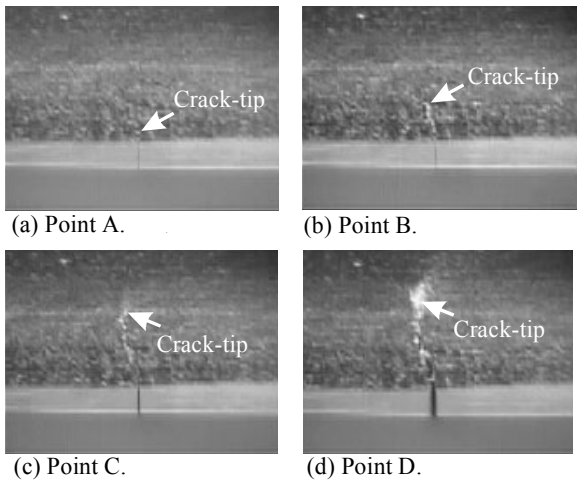

Figure 7: Stable crack growth in FGM layer.

camera is also plotted in Fig. 6. When the applied load reaches the critical value for the initial indentation crack at the point A in Fig. 6, the unstable crack growth occurs from the initial crack to 80% PSZ layer. However, any signal such as load drop is not observed on the load-displacement relation. Then, a crack grows stably to the interface between FGM layer and SUS 304 substrate with increasing the applied load. The load-displacement relation shows the slight nonlinearity before the growing crack reaches the 20% PSZ layer (Point C). At this point, the plastic zone spread out from the crack tip into the SUS304 substrate, and the applied load once drops then increases with increasing the displacement. The crack grows gradually into the plastically deformed 10% PSZ layer and finally is arrested at the SUS 304 substrate (Point D). This feature is almost the same as that observed in the FGM-1.

From the relationship between the applied load and crack length during the stable crack growth, the critical stress intensity factor K_{IC} is calculated for each specimen. Figures 8 and 9 show the critical stress intensity factor as a function of crack length in FGM-1 and FGM-2, respectively. These figures exhibit the distributions of fracture toughness through the FGM layers since the crack length means the distance from the ceramics surface. The fracture toughness linearly increases with an increase in the distance from ceramics surface through the FGM layer. Although the slight difference in the distribution among the specimens is observed even in the same kind of FGM, it may be attributed to the difference in the thickness of FGM layer, the distribution of the PSZ content, the residual stress created in the fabrication, the span-to-width ratio of three-point-bending specimen and so on. In order to clarify the difference, further investigations are necessary.

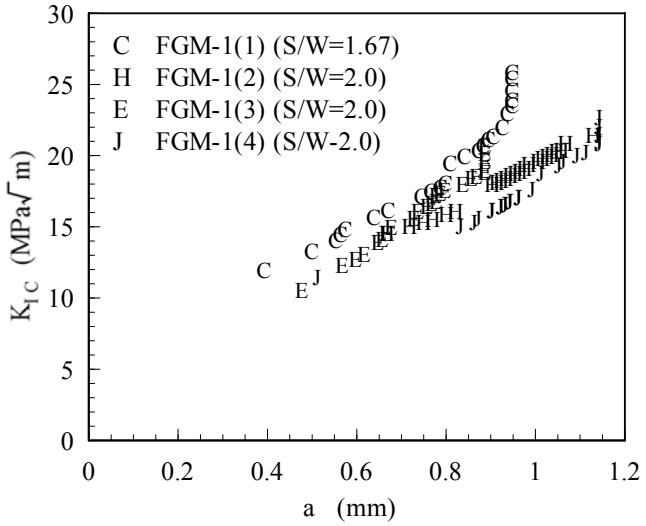

Figure 8: Distributions of fracture toughness in FGM-1 specimens.

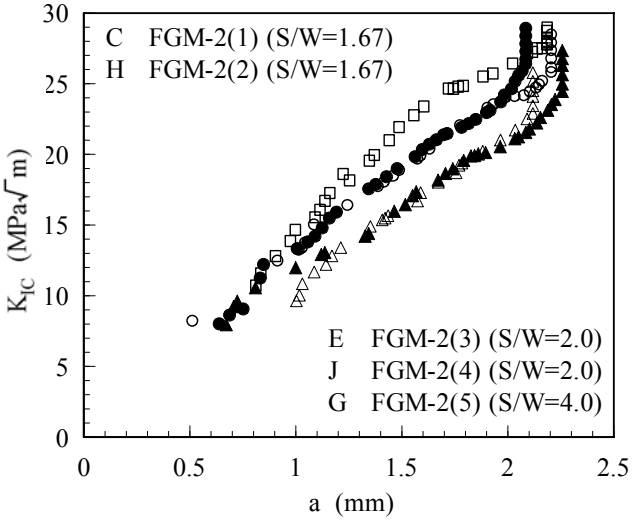

Figure 9: Distributions of fracture toughness in FGM-2 specimens.

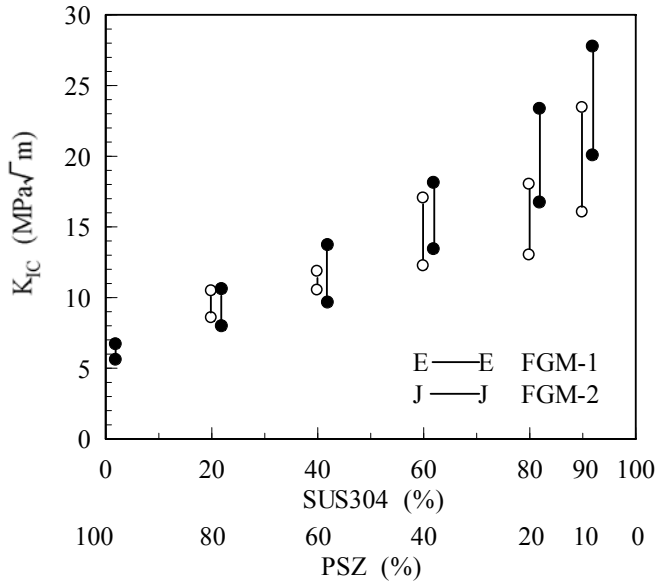

Figure 10: Fracture toughness as a function of material composition in FGM layer.

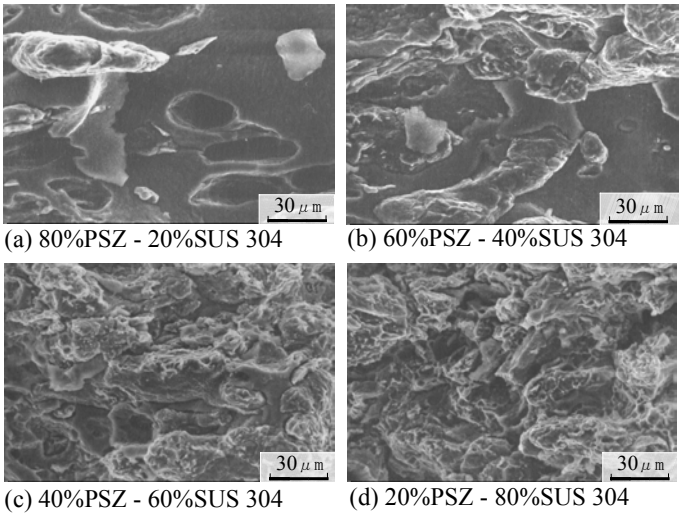

(a) 80%PSZ - 20%SUS 304 (b) 60%PSZ - 40%SUS 304

(c) 40%PSZ - 60%SUS 304 (d) 20%PSZ - 80%SUS 304

Figure 11: Micrographs of fracture surfaces of FGM layer.

In order to obtain the relationship between the fracture toughness and composition of PSZ and SUS 304 in the FGM layer, the experimental results in Figs. 8 and 9 are rearranged as in Fig. 10. The fracture toughness of the PSZ ceramics (FGM-2) and 80%PSZ layer (FGM-1) is evaluated from the unstable crack growth of the initial indentation crack with 300μm in length. The fracture toughness in FGM layer in both materials is well described by the unique relation, namely it linearly increases with an increase in SUS304 content up to 90%. It is concluded from Fig. 10 that the distribution of fracture toughness through the FGM layer is given as a function of the composition of PSZ and SUS 304. The fracture toughness in the FGM layer is at most 30MPa m at 90% PSZ layer, and is very low compared with the fracture toughness of 100% SUS 304. This might be caused by the intrinsic property of the FGM that the fracture toughness abruptly drops between 100% SUS 304 and 90% SUS 304 in addition to that the influence of the plastic deformation is not considered in the evaluation of the fracture toughness.

Micrographs of fracture surface of the FGM are shown in Fig. 11. In the layers with high content of PSZ as shown in Figs. 11(a) and (b), the debonded SUS 304 particles and their traces are observed in the brittle fracture surface of the PSZ matrix. This means that the interfacial strength between the SUS 304 particles and PSZ matrix is relatively low. On the other hand, the metal rich layers exhibit the brittle fracture surface of PSZ phase in the ductile fracture surface of the SUS 304 matrix as shown in Figs. 11(c) and (d). With increasing the content of SUS 304, the area of ductile fracture surface with dimple-pattern increases. This well corresponds to the distribution of the fracture toughness in FGM layer as shown in Fig. 10.

REFERENCES

1. For example, (1991). Functionally Gradient Materials, Kogyo Chosakai Publishing (in Japanese).
2. Finot, M., Suresh, S., Bull, C., Giannakopoulos, A.E., Olsson M. and Sampath, S. (1994). Proc.3rd Int. Symp. Struct. Funct. Grad. Mater., 229.
3. Kawasaki, A. and Watanabe, R. (1994). Proc. 3rd Int. Symp. Struct. Funct. Grad. Mater., 397.
4. Blumm, M., Dollmeler, K. and Ilschner, B. (1994). Proc. 3rd Int. Symp. Struct. Funct. Grad. Mater., 315.
5. Tohgo, K., Sakaguchi, M. and Ishii, H. (1996). JSME Int. J., Ser. A. 39, 479.
6. Tohgo, K. and Hadano, A. (1999). Proc. Exper. Comput. Mech., 81.

Evaluation of High-cycle Fatigue Life of Aluminum Cast Alloy from Meso-level Consideration

Hiroshi NOGUCHI [1] **and Tatsujiro MIYAZAKI** [2]

[1]Department of Mechanical Science and Engineering, Faculty of Engneering,
Kyushu University, 6-10-1 Hakozaki, Fukuoka 812-8581, JAPAN.
[2]Graduate School of Engneering, Kyushu University,
6-10-1 Hakozaki, Fukuoka 812-8581, JAPAN.

ABSTRACT

In this paper, a growth rate law of a small crack under a large scale yielding is proposed for a generic metal material. A method is also proposed for considering the size distribution of spheroidal defects which interest with the specimen surface. Both methods are used to predict the high-cycle fatigue life with the large scatter due to the presence of defects. Moreover, rotating bending fatigue tests are carried out on Aluminum Cast Alloy with eutectic Si, Fe compounds and porosities. The present method for predicting fatigue life reliability from the meso-level consideration is examined and confirmed by comparing the predicted fatigue life distribution.

KEYWORDS

Metal Fatigue, Aluminum Cast Alloy, Fatigue Life, Fatigue Crack Growth, Statistics, Defect, Porosity, Recycle

INTRODUCTION

From a necessity of light transportation machine with a high specific strength, Aluminum Cast Alloy has been used in the engine and so on. 80% of material fracture is due to the fatigue. Therefore it is important to evaluate the fatigue characteristics as mechanical properties for machine designs. Moreover the results are useful for the improvement of reliability and alloy design. In researches on aluminum cast alloy, although many researches especially on shape and quantity of eutectic Si have been carried out [1-6], there are few researches on the effect of Fe introduced during the recycling process [2,3]. Fe forms a coarse needle shaped metal compound, and the compound decreases the flow of the melts and the mechanical properties. In order to decrease the bad effect of Fe, transition metals (Mn,Cr,Be and so on) are added to the aluminum cast alloy to improve the fracture toughness and breaking elongation by changing the Fe-compound's structure from a needle type to a Chinese script type [8-11]. The changing ratio depends on the composition ratio of the transition metal to Fe [12] and amount of an improving element Sr [13,14]. It is necessary to evaluate the effect the various Fe-compounds on the fatigue characteristics simply and quickly.

As afore mentioned, although it is necessary for practical use of new materials to evaluate the fatigue characteristics, a traditional macro-scale materials testing is useless because of the required long testing time. In order to overcome the problem, a new evaluation system for fatigue characteristics is constructed in this paper from meso-level considerations. Then it becomes possible to evaluate the fatigue characteristics of practical structures rapidly and to point out the direction of the material design reasonably.

PREDICTION OF HIGH CYCLE FATIGUE LIFE

In this paper, the high-cycle fatigue life characteristics are divided into the fatigue crack growth characteristics and the maximum defect size.

Versatile fatigue crack growth law (stress ratio $= -1$)

Under a small scale yielding condition, for example $\sigma_{\mathsf{a}} < 0.5\,\sigma_{\mathsf{S}}$ [15,16], the fatigue crack growth rate $d\,\ell/dN$, where ℓ is the total crack length on the specimen surface and N is a number of stress repetitions, is expressed as a the power of the stress intensity factor range, ΔK, as follows.

$$\frac{d\,\ell}{dN} = C(\Delta K)^{\mathsf{m}} \tag{1}$$

Here, σ_{a} is the stress amplitude, σ_{S} the yield stress, ℓ the total crack length on the specimen surface and N a number of cycle. On the other hand, under a large scale yielding condition, for example $\sigma_{\mathsf{a}} > 0.6\,\sigma_{\mathsf{S}}$ [15,16],

the following law of fatigue crack growth rate [16-19] in case of steels is satisfied for $R = -1$, where R is a stress ratio.

$$\frac{d\ell}{dN} = C_3 \left(\frac{\sigma_a}{\sigma_B} \right)^n \ell \tag{2}$$

Here, n and C_3 can be estimated from a database if the heat treatment and steel type are known.

Although there is a lot of fatigue data for steels, non ferrous materials have a few data. This is one obstacle to wide usage of new materials in mechanical engineering. Therefore in this paper, a fatigue crack growth rate law will be proposed from the fatigue crack growth mechanism and a few fatigue data.

The mode I type of fatigue crack growth is based on the successive plastic blunting and resharpening of the crack tip. Then at first, in a non-work-hardening materials, crack growth due to the plastic blunting under a monotonic stress σ is obtained from the dimensional analysis as follows.

$$\Delta a \propto \frac{\sigma_S}{E} f \left(\frac{\sigma}{\sigma_S} \right) a \tag{3}$$

Here, E is Young's modulus, a the half crack length, and Δa the increment of a. The crack growth due to plastic blunting is expressed concretely from CTOD with the Dugdale Model as follows.

$$\Delta a \propto \frac{8\sigma_S}{\pi E} \ln \left[\sec \left(\frac{\pi \sigma}{2\sigma_S} \right) \right] a \tag{4}$$

It is supposed that the crack behavior due to the cyclic stress strain relation or load history can be represented by σ_S for steels. Although the differences of these factors among the materials are very important in the fatigue life near the non-propagating crack limit, the differences may be the secondary factor in $N_f < 10^6$ region. Hence the differences are neglected in this report. Therefore considering Eqn.2, the fatigue crack growth law is presented as follows, by approximating $\ln[\sec(\pi/2 \times \sigma/\sigma_S)]$ with $(\sigma/\sigma_S)^n$.

$$\frac{d\ell}{dN} = C_4 \frac{\sigma_S}{E} \left(\frac{\sigma_a}{\sigma_S} \right)^n \ell \tag{5}$$

Figures 1 and 2 show C_4 and n values in Eqn.5 obtained from small crack growth data of steels [15], aluminum cast alloy [4,20], rolled aluminum alloy [18], brass [21] and titanum alloy [22]. In steels whose mechanical properties are dependent on the alloy element and heat treatment, n and C_4 in Eqn.5 should be functions of σ_S, however for simple use, n is taken to be constant; $n = 6$ in this paper.

$$\frac{d\ell}{dN} = C_5 \frac{\sigma_S}{E} \left(\frac{\sigma_a}{\sigma_S} \right)^6 \ell \tag{6}$$

Figure 3 shows C_5 values of Eqn.6 obtained from Figs.1 and 2. The following expression is a curve through the center of the data.

$$C_5 = \begin{cases} \frac{\sigma_S}{2500} & (\sigma_S \geq 300\text{MPa}) \\ \left(\frac{\sigma_S}{510} \right)^4 & (\sigma_S < 300\text{MPa}) \end{cases} \tag{7}$$

Even if materials are changed, most data lie between twice and half of Eqn.7 except for low carbon steels.

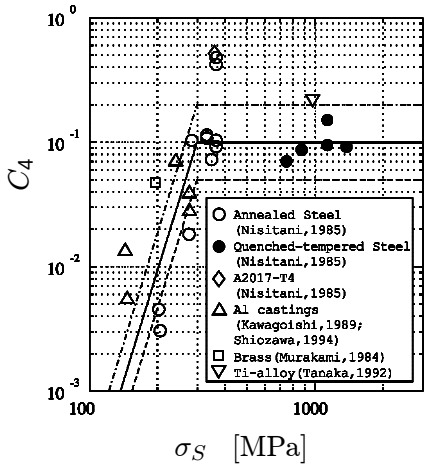

Figure.1: Relation between C_4 and σ_S

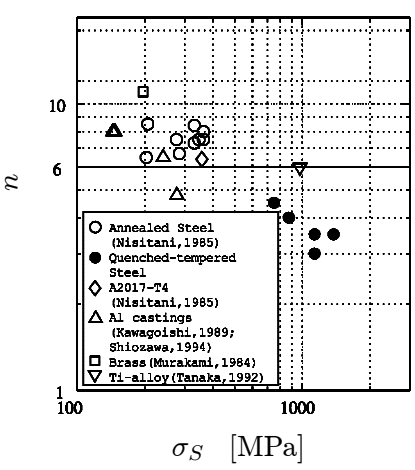

Figure.2: Relation between n and σ_S

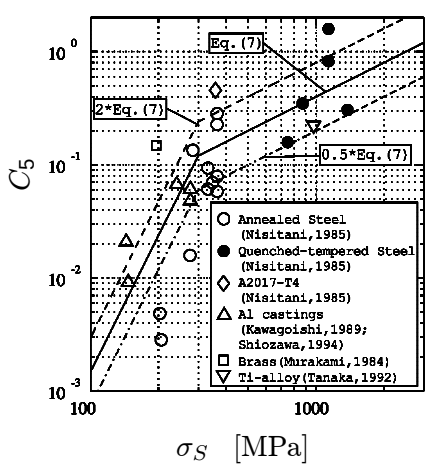

Figure.3: Relation between C_5 and σ_S

Particle size distribution

The authors [23] have proposed a method where a size distribution of particles in materials can be estimated from information on a cutting plane. The method is applied to eutectic Si, Fe compound and porosity in aluminum cast alloy. The size distribution of particles in materials can be assumed as follows.

$$M_{V0}(R_1) = \bar{N}_{V0} \exp\left\{-\left(\frac{R_1}{\lambda}\right)^{\nu}\right\} \tag{8}$$

Here, $M_{V0}(R_1)$ is the number of particles per unit volume whose radius, R, is larger than R_1, $\bar{N}_{V0}$ the total number of particles and λ and ν are the characteristic constants of the particle-size distribution.

According to the below-mentioned fatigue test, the fracture origins of the present materials were the surface defects. Therefore the characteristics of a particle cut by the specimen surface are examined from the size distribution of particles in the material.

The particle cut by the specimen surface is projected perpendicular to the first principal stress and the projected area is corrected on the basis of a fracture mechanics consideration. Then the corrected area is identified with $area_P$ as shown in Fig.4. The number of cut particles on the surface whose $\sqrt{area_P}$ is larger than $\sqrt{area_P}_1$, $M_{S0}(\sqrt{area_P}_1)$, can be expressed as

$$M_{S0}(\sqrt{area_P}_1) = \lambda \bar{N}_{V0} \int_0^1 \frac{t}{\sqrt{1-t^2}} \left\{\Gamma\left(1+\frac{1}{\nu}, \left(\frac{\sqrt{area_P}_1}{\lambda\sqrt{\theta^-}}\right)^{\nu}\right) + \Gamma\left(1+\frac{1}{\nu}, \left(\frac{\sqrt{area_P}_1}{\lambda\sqrt{\theta^+}}\right)^{\nu}\right)\right\} dt \tag{9}$$

$$\theta^+ = \frac{\pi}{2} + 2\sqrt{1-t^2}\,, \quad \theta^- = \arcsin(t) - t\sqrt{1-t^2} \tag{10}$$

Next, let us consider the probability distribution function of the maximum $\sqrt{area_P}$ value on area A, $\sqrt{area_P}_{max}$. The average number of particles whose $\sqrt{area_P}$ is larger than $\sqrt{area_P}_1$, is $A \cdot M_{S0}(\sqrt{area_P}_1)$. The probability that the $\sqrt{area_P}_{max}$ is smaller than $\sqrt{area_P}_1$, means the probability that there is no particle whose $\sqrt{area_P}$ is larger than $\sqrt{area_P}_1$. Using the Poisson's distribution, the probability is $\exp[-A \cdot M_{S0}(\sqrt{area_P}_1)]$. Therefore, the probability that the $\sqrt{area_P}_{max}$ is smaller than $\sqrt{area_P}_{max1}$, $F_{Smax}(\sqrt{area_P}_{max1})$, is expressed as follows.

$$F_{S\,max}(\sqrt{area_P}_{max_1}) = \exp[-M_S(\sqrt{area_P}_{max_1})] \tag{11}$$

Prediction of high-cycle fatigue life

Although the fatigue life consists of the fatigue crack nucleation life and growth life, it is supposed in this paper that the former life can be neglected and the main crack propagates from the maximum surface defect in the present materials. Moreover, although the scatter of the fatigue life consists of the scatter of the maximum defect size and the scatter of material properties in the crack propagation process, it is supposed in this paper that the former scatter can be considered as the main factor. That is; the fatigue life, N_f, is expressed from Eqn.6 as follows.

$$N_f = \frac{E}{C_5\,\sigma_S}\left(\frac{\sigma_S}{\sigma_a}\right)^n \ln\left\{\frac{d}{\frac{\pi}{8}\sqrt{area_P}_{max}}\right\} \tag{12}$$

Here, d is a diameter of a specimen. The scatter of the fatigue life depends on the scatter of $\sqrt{area_P}_{max}$ in Eqn.11 and it can be evaluated with Eqn.10.

Determination of C_5

With Eqn.7 for estimating C_5 in Eqn.6, the fatigue crack growth rate can be estimated within about $\pm 50\%$ error except for low strength steels. However, if the fatigue life data of the specimen with a small blind hole is measured under a certain stress amplitude, C_5 can be determined more accurately with Eqn.11. Moreover, if $d\ell/dN$ is measured under the stress amplitude, the validity of Eqn.6, where $n = 6$ is supposed, can be examined.

FATIGUE EXPERIMENT

A commertial JIS-AC4B alloy was used. The chemical compositions of the alloy is shown in Table 1. Figure 5 and Table 2 show the tensile properties and micro-Vickers hardness of α-Al after T6 treatment.

Fatigue tests were carried out on the plain specimen shown in Fig.6. For an examination of Section 2.4, a specimen with a small blind hole ($\phi 0.3 \times 0.15$mm) was used for an observation of fatigue crack growth. The specimen was machined, polished with fine emery paper, alumina(3μm) and diamond paste(1μm), and polished chemically. A Ono-type rotating bending fatigue machine, whose capacity was 15Nm and frequency was about 50Hz, was used for fatigue tests. The stress used in the analysis of experimental results is the nominal stress

at the minimum cross section.

Figure 7 shows S-N curves. The large scatter is particular in the present materials, compared with the usual materials. Therefore the measured $\sqrt{area_P}$ value of the fracture origin are added to the symbols in Fig.7. From Fig.7, it is found that the scatter of the fatigue life is small for the same $\sqrt{area_P}$ value of the fracture origin.

TABLE 1

CHEMICAL COMPOSITION (MASS %)

Si	Cu	Mg	Fe	Mn	Zn	Pb	Sr
6.79	2.93	0.17	0.59	0.49	0.17	0.05	138

Sr : ppm

TABLE 2

MECHANICAL PROPERTIES

σ_B	$\sigma_{0.2}$	δ	E	H_V of α(Al) 25g, 30 sec
349	292	1.50	74	124

σ_B :Ultimate Tensile Strength (MPa) $\sigma_{0.2}$:0.2% Proof Stress (MPa)
E: Young's Modules (GPa) δ:Elongation (%)
H_V :Micro Vickers Hardness (kgf/mm^2)

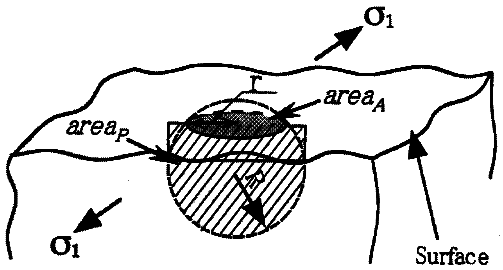

Figure.4: Shperoidal particle cut by surface

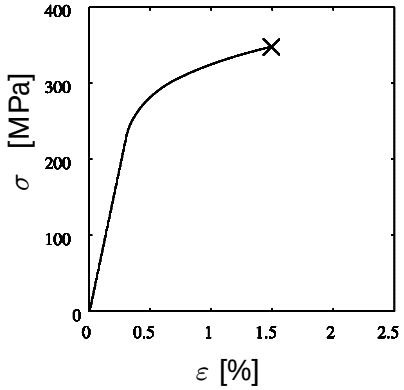

Figure.5: Stress-strain curve

PREDICTION RESULTS FOR ALUMINUM CAST ALLOY

Fatigue crack growth characteristics

Table 3 shows the C_5 values estimated from Eqn.7, using $\sigma_{0.2}$.

The fatigue test results for a specimen with a 0.3mm small hole under σ_a = 160 MPa are mentioned as follows. The C_5 values calculated from Eqn.11 under this stress level with the projected area of the drill hole, $\sqrt{area_P}_{max}$ = 180μm, are shown in Table 3. As the C_5 values from Eqns.7 and 11 agree with each other, it is confirmed that Eqn.7 as the first approximation is valid also in the present materials.

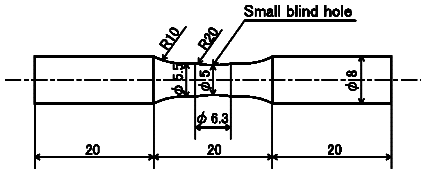

(a) plain specimen

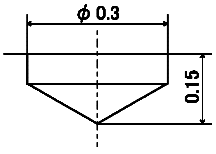

(b) small blind hole

Figure.6: Specimen configuration

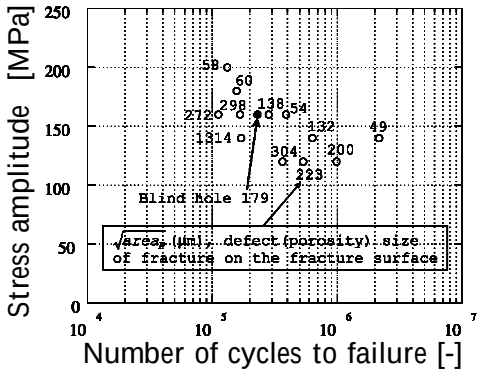

Figure.7: S-N curve

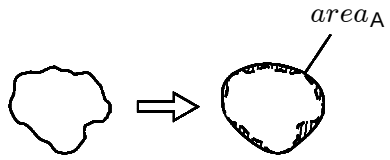

Figure.8: Definition of $area_A$

TABEL 3

C_5 VALUE OF PRESENT CAST ALLOY

Eqn.7	Eqn.11
0.11	0.14

Size distribution of particle

The actual particle or porosity is not a perfect sphere (for example, gas type and shrinkage type) and the cross-section of cut particle is not a perfect circle. Thus let's consider the measurement method of the cross-section radius, r. Surrounding an irregular cross-section with a smooth convex curve, the area is defined as $\sqrt{area_A}$

as shown in Fig.8. The r values are obtained from $\sqrt{area_A}$ values with the following relation.

$$r = \frac{\sqrt{area_A}}{\sqrt{\pi}} \tag{13}$$

Let us consider the radius of circle obtained from a cut sphere. The number of circles whose r is larger than r_1 per unit area, $M_{A0}(r_1)$, has a mutual relation with $M_{V0}(R_1)$ [23]. Especially if $M_{V0}(R_1)$ is supposed with Eqn.8, $M_{A0}(r_1)$ is expressed as follows.

$$M_{A0}(r_1) = \sqrt{\frac{2\pi}{\nu}} \lambda \left(\frac{r_1}{\lambda}\right)^{1-\frac{\nu}{2}} \bar{N}_{V0} \exp\left(-\left(\frac{r_1}{\lambda}\right)^{\nu}\right) \tag{14}$$

Figure 9 shows the experimental data for $M_{A0}(\sqrt{area_A})$ of eutectic Si, Fe compound and porosity of each material. The $\bar{N}_{V0}, \lambda$ and ν values of Eqn.8 were determined after drawing the curve of Eqn.8, which is an optimum fit to the data. Figures 12 and 13 show $M_{V0}(R)$ and $M_{S0}(\sqrt{area_P})$, respectively.

When the inspection area, A, is taken as the area whose stress is $(1 \sim 0.9)\sigma_{max}$ on the specimen surface, A=60 mm^2 in case of the present specimen. Figure 17 shows $F_{Smax}(\sqrt{area_P}_{max})$ on the present area. It is possible that the surface porosity is the fracture origin in AC4B-T6.

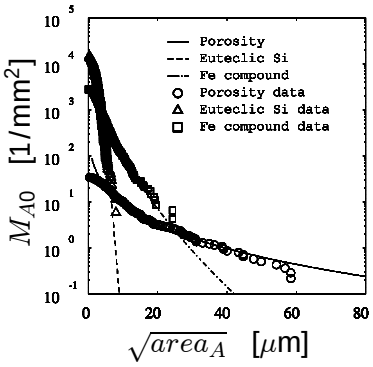

Figure.9: $M_{A0}(\sqrt{area_A})$

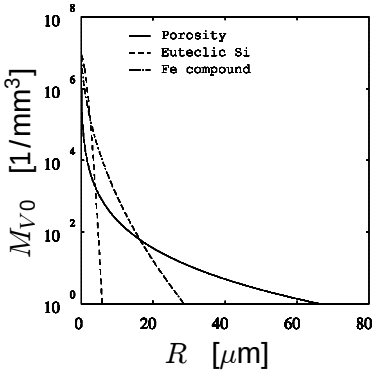

Figure.10: $M_{V0}(\sqrt{area_R})$

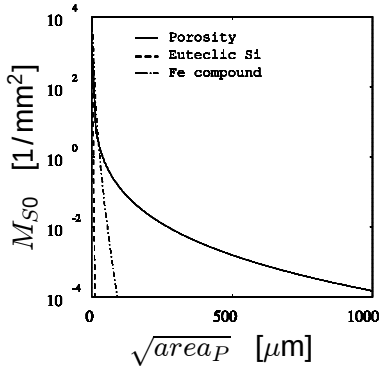

Figure.11: $M_{S0}(\sqrt{area_P})$

Comparison between predicted and experimental fatigue life

A cumulative distribution of $\sqrt{area_P}$ values observed on the fracture surface was obtained from Fig.7 using the mean rank method. Figure 13 shows both the cumulative distribution of porosity. As results of Fig.13, it is found that the estimation method for the probability distribution of $\sqrt{area_P}_{max}$ is valid and the maximum value of $\sqrt{area_P}$ of cut porosity with the specimen surface controls the fatigue strength of the present aluminum cast alloy.

Therefore the fatigue life reliability of the present specimen shown in Fig.5 can be estimated by using Eqn.10 which expresses the statistical characteristics of $\sqrt{area_P}_{max}$ of porosity, and Eqn.11 which expresses the fatigue life due to fatigue crack growth. Namely, the fatigue life reliability such that the fatigue life is greater than N_{f1}, F_{N_f}, is

$$F_{N_f}(N_{f1}) = F_{Smax}(\sqrt{area_P}_{max1}) \tag{15}$$

$$N_{f1} = \frac{E}{C_5 \sigma_S}\left(\frac{\sigma_S}{\sigma_a}\right)^6 \ln\left[\frac{d}{\sqrt{\frac{\pi}{8}}\sqrt{area_P}_{max}}\right] \tag{16}$$

Figure 14 shows the predicted results from meso-level data and experimental data.

As a result, the following is found. Although the fatigue life characteristic of AC4B cannot be evaluated quantitatively from the macro-scale fatigue characteristic of Fig.7, the characteristics can be evaluated quantitatively from the meso-scale material characteristics with Table 3, and Figs.12 and 13.

CONCLUSION

1. The prediction method for the data scatter of high-cycle fatigue life has been proposed with microscope observations for cross-section size distribution of particles cut by a cutting plane.
2. The predicted results have been confirmed for aluminum cast alloy.

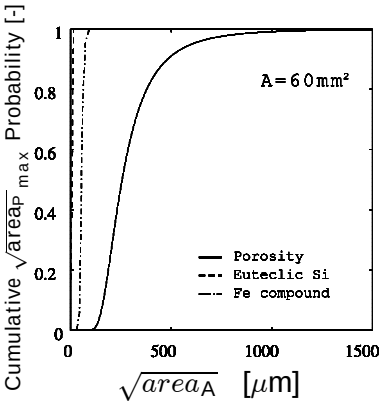

Figure.12: $F_{Smax}(\sqrt{area_P}_{max})$

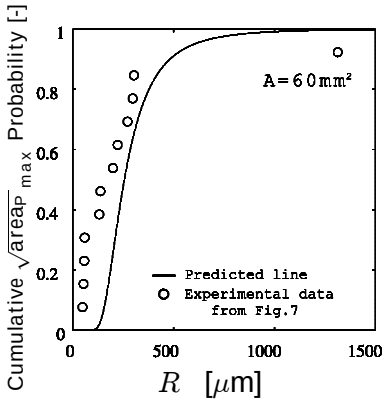

Figure.13: Cumulative $\sqrt{area_P}_{max}$

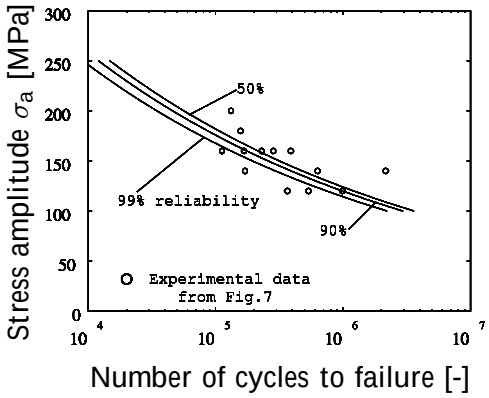

Figure.14: Estimated S-N reliability

REFERENCE

[1] Kobayashi,T., Niinomi,M. and Ikeda,K.,(1987). International Journal of Fracture, 37-12, pp.824-830.
[2] Egashira,H., Hirota,I., Kobayashi,T. and Sakai,S.,(1989). Journal of Japan Institute of Light Metals, 39-12, pp.878-885.
[3] Egashira,H., Hirota,I., Kobayashi,T. and Sakai,S.,(1989). Journal of Japan Institute of Light Metals, 39-12, pp.886-892.
[4] Shiozawa,K.,Nisino,S.,Higashida,Y. and Sun,S.M.,(1994). Jounal of Japan Institute of Light Metals, 38-4, pp.202-207.
[5] Lee,F.T., Major,J.F. and Samuel,F.H.,(1995). Metallurgical and Materials Trans. A., 26A, pp.1553-1570.
[6] Kobayashi,T., Ito,T., Kim,H. and Kitaoka,S.,(1996). Journal of Japan Institute of Light Metals, 46-9, pp.437-443.
[7] Kumai,S., Hu,J., Higo,Y. and Ninomura,S.,(1995). Journal of Japan Institute of Light Metals, 45-4, pp.198-203.
[8] Gobrecht,B.,(1976). Journal of Japan Institute of Light Metals, 39-12, pp.886-892.
[9] Couture,A.,(1981). AFS International Cast Metals Journal, 6-4, pp.9-17.
[10] Shimizu,Y. and Awano,Y., Nakamura,M.,(1988). Jounal of Japan Institute of Light Metals, 38-4, pp.202-207.
[11] Kato,E. and Murakawa,S.,(1994). Journal of Japan Foundry Engineering Society, 66-1, pp.10-14.
[12] Iwahori,H., Takamiya,H., Yonekura,H., Yamamoto,Y. and Nakamura,Y.,(1988). J. of Japan Foundry Engng. Soc., 60-9, pp.590-595.
[13] Sigworth,G.K.,(1987). Modern Casting, July, pp.23-25.
[14] Kang,H.G., Miyahara,H. and Ogi,K.,(1997). Journal of Japan Foundry Engineering Society, 69-5, pp.383-390.
[15] Nisitani,H.,(1981). Mechanics of Fatigue, AMD 47,ASME, pp.151-166..
[16] Nisitani,H., Kawagoishi,N. and Goto,M.,(1994). In Handbook of fatigue crack propagation in metallic structures (Edited by Carpinteri,A.),Elsevier,Amsterdam, pp.733-778.
[17] Nisitani,H. and Goto,M.,(1985). Transaction of Japanese Society of Mechanical Engineers, A51-462, pp.332-341.
[18] Nisitani,H., Kawagoishi,N. and Wakahara,M.,(1985). Transaction of Japanese Society of Mechanical Engineers, A51-464, pp.1017-1025.
[19] Goto,M. and Nisitani,H.,(1994). Fatigue and Fracture of Engng. Mater. Struct., 17, pp.171-185.
[20] Kawagoishi,N., Nisitani,H. and Tsuno,T.,(1989). Transaction of Japanese Society of Mechanical Engineers, A55-516, pp.1733-1739.
[21] Murakami,Y., Makabe,C. and Nisitani,H.(1984). Transaction of Japanese Society of Mechanical Engineers, A50-459, pp.1828-1837.
[22] Tanaka,S.,Nisitani,H.,Fujisaki,W.,Teranisi,T.,Honda,M.,(1992). Journal of Japanese Society of Material Science, 41-469, pp.1485-1491.
[23] Hashimoto,A., Miyazaki,T., Kang,H.G., Noguchi,H. and Ogi,K.,(2000). Jounal of Testing and Evaluation, 28-9, pp.367-377.

ORAL/POSTER REFERENCE: ICF100847OR

Evaluation of Stress Intensity Factors of Spot Welded Joints Using Meshless Method

Kengo SHIMIZU[1], Noboru TOMIOKA[2] and Akifumi OKABE[3]

[1]Mechanical Engineering major, Graduate school of Nihon University, Tokyo Japan
[2,3]Department of Mechanical Engineering, College of Science & Technology, Nihon University, Tokyo Japan

ABSTRACT

It has been required strongly to evaluate fatigue strength of spot welded joint accurately in the stage of designing automobile body structure. There is a evaluation method of fatigue strength based on stress intensity factors K in linear fracture mechanics. We applied Element Free Galerkin Method (EFGM) developed by T. Belytschko et al. to calculating stress intensity factors K of spot welded double cup specimen (is called DC for short) under multiaxial loads, and investigated the accuracy of the solutions. This paper shows that K obtained by using EFGM are appropriate results.

KEYWORDS

Meshless Method, Fractures, Stress Intensity Factors, Spot Weld

INTRODUCTION

It has been required strongly to evaluate fatigue strength of spot welded joint accurately in the stage of designing automobile body structure. There is a evaluation method based on stress intensity factors K in linear fracture mechanics. In order to obtain value of K accurately using finite element method (FEM), the detail division of elements on spot welded joint model is essential. In crack growth problem, the rearrangement of nodes and elements around a crack tip is needed through progress of crack. Especially, this rearrangement is the most difficult work in three-dimensional problems. Meshless method, which needs no elements on analytical model, is of great advantage to solving crack growth problem.

In this paper, we applied EFGM developed by T. Belytschko et al. [1] to calculating stress intensity factors K of double cup specimen (DC) under multiaxial loads, and investigated the accuracy of the solutions.

DC SPOT WELDED JOINT AND ANALYTICAL MODEL

The test specimen composed of two cups, called DC shown in Figure 1, is spot-welded at center in the bottom of the cups. Dieter Radaj et al. [2] suggested DC for fatigue strength under multiaxial load. We

consider the part around nugget as a ringshaped crack and apply EFGM to linear fracture mechanics and evaluate K of DC.

We consider analytical model as only bottom of the cups as shown in Figure 2. When we analyze DC acted on multiaxial loads, the DC is analyzed as superposition of the load which is divided into cross tension (β =90deg) and tensile shear(β =0deg). When cross tension(β =90deg) is acted on DC, the elastic stress analysis comes to be a axisymmetric problem. When tensile shear(β =0deg) is acted on DC, the elastic stress analysis comes to be a axisymmetric body problem.

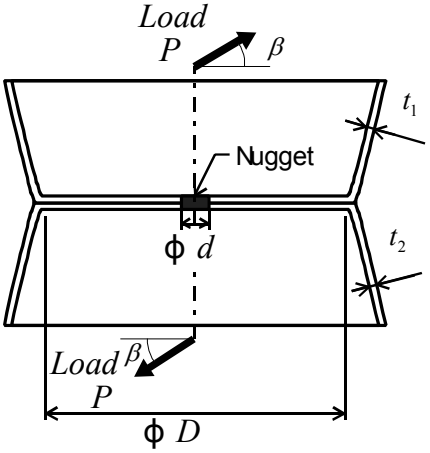

Figure 1: Double cup joint under out-of-plane

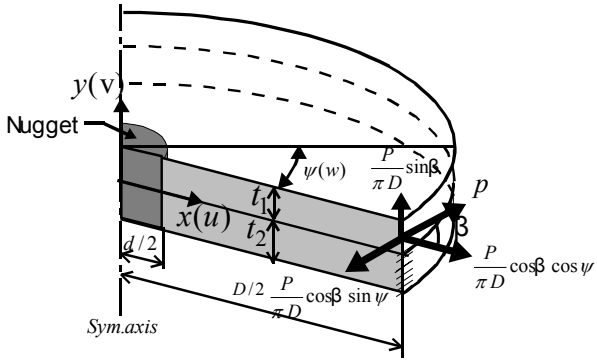

Figure 2: Analytical model

GOVERNING EQUATION AND BOUNDARY CONDITIONS

Analyzing stresses and strains of DC by theory of elasticity are boundary-value problems of partial differential equations expressed as following equations:

$$\sigma_{ij,j} + b_i = 0 \qquad \text{in}\,\Omega \tag{1-a}$$

$$u_i = \bar{u}_i \qquad \text{on}\,\Gamma_u \tag{1-b}$$

$$n_j \sigma_{ij} = \bar{t}_i \qquad \text{on}\,\Gamma_t \tag{1-c}$$

Where Eqn. 1-a is a governing equation of stress field, Eqn. 1-b is a fundamental boundary condition, and Eqn. 1-c is a natural boundary condition. The notation $,j$ represents partial different with respect to space coordinate $x_j \left(x_1 = x, x_2 = y\right)$. Eqn. 1-a is expressed by using Einstein's summation convention. σ_{ij} is stresses, b_i is a body forces, Ω is an analytical domain bounded by Γ , Γ_t is a boundary acted by given surface forces $\bar{t}_i$, and Γ_u is a boundary prescribed displacements $\bar{u}_i$. n_j can be considered to give the direction cosines of the unit normal of the interface on which the traction force is desired.

A equilibrium conditions for a linear elastic body are identical with minimizing total potential energy expressed in Eqn. 2:

$$\pi(u_i) = \int_\Omega \left(\frac{1}{2}\sigma_{ij}\varepsilon_{ij} - u_i b_i \right) d\Omega - \int_{\Gamma_t} u_i \bar{t}_i d\Gamma + \int_{\Gamma_u} \frac{\alpha}{2}(u_i - \bar{u}_i)^2 d\Gamma \tag{2}$$

Where ε_{ij} is component of strain. α is a penalty number which is a large positive number for reliving a fundamental boundary condition with a penalty method.

Interpolation function in FEM is set by each element but the one of EFGM is locally set by using moving least square method (is called MLSM for short) . In the MLSM of two-dimensional problem, the function u_0 of arbitrary evaluation point $\mathrm{x}^T = \lfloor x \; y \rfloor$ in the domain is approximately expressed as:

$$u_0(x,y) = p_j(x,y)c_j(x,y) \equiv \mathrm{p}^T(x,y)\mathrm{c}(x,y) \quad i,j = 1 \sim 3 \tag{3}$$

Where p_j are multinomial expression including space coordinates (x, y), c_j are coefficients undefined.

$$\mathrm{p}^T(x,y) = \lfloor p_1 \; p_2 \; p_3 \rfloor = \lfloor 1 \; x \; y \rfloor \tag{4-a}$$

$$\mathrm{c}^T(x,y) = \lfloor c_1 \; c_2 \; c_3 \rfloor \tag{4-b}$$

In the MLSM, the coefficients c_j are obtained by minimizing the following weighted square expression J.

$$J = \sum_i^n w(\|\mathrm{x} - \mathrm{x}_i\|)[u_0(\mathrm{x}_i) - u_i(\mathrm{x}_i)]^2 = w_i \Delta u_i^{\,2} \tag{5}$$

$$w_i = w(\|\mathrm{x} - \mathrm{x}_i\|) \tag{6-a}$$

$$\Delta u_i = u_0(\mathrm{x}_i) - u_i(\mathrm{x}_i) = p_{ji}(x_i, y_i) c_j(x,y) - u_i(x_i, y_i) \tag{6-b}$$

Where $\mathrm{x}_i = \lfloor x_i \; y_i \rfloor$ is the coordinate of a node i in the neighborhood of evaluation point x and u_i is the nodal value at $\mathrm{x} = \mathrm{x}_i$. n is the number of nodes in the neighborhood of x. $w(\|\mathrm{x} - \mathrm{x}_i\|)$ is a weight function defined in the neighborhood of x. We used four-dimensional spline function in Eqn. 7 as $w(\|\mathrm{x} - \mathrm{x}_i\|)$. $\|\mathrm{x} - \mathrm{x}_i\|$ is norm of vector $\mathrm{x} - \mathrm{x}_i$ and stands for the distance from the evaluation point x to node x_i.

$$w(r_w) = 1.0 - 6.0\left(\frac{r_w}{\rho}\right)^2 + 8.0\left(\frac{r_w}{\rho}\right)^3 - 3.0\left(\frac{r_w}{\rho}\right)^4 \; (0 \le r_w \le \rho) \tag{7}$$

Where $r_w = \|\mathrm{x} - \mathrm{x}_i\|$ and ρ is a radius of circular domain of influence in two dimensions. The stationary of J in Eqn. 5 with respect to $\mathrm{c}(\mathrm{x})$ leads to the following equation.

$$\mathrm{A}(x,y)\mathrm{c}(x,y) = \mathrm{B}(x,y)\mathrm{u} \tag{8-a}$$

or

$$\mathrm{c}(x,y) = \mathrm{A}^{-1}(x,y)\mathrm{B}(x,y)\mathrm{u} \tag{8-b}$$

Where A, B and u in Eqn. 8 are defined by following equations.

$$\mathrm{A} = [A_{ij}], \quad A_{ij} = w_k p_{ik} p_{jk} \qquad i,j = 1 \sim 3 \quad k = 1 \sim n \tag{9-a}$$

$$\mathrm{B} = [B_{ij}], \quad B_{ij} = w_i P_{ji} \qquad i,j = 1 \sim 3 \tag{9-b}$$

$$\mathrm{u}^T = \lfloor u_1 \; u_2 \; \cdots u_n \rfloor \tag{9-c}$$

Eqn. 8-a must be solved accurately to retain the accuracy of the MLSM interpolant. When the matrix A is not well conditioned, Eqn. 8-b cannot be solved with desired accuracy. However the necessity for solving Eqn. 8-a can be eliminated by diagonalizing the matrix A. To diagonalize the matrix A, we obtained orthogonal basis function $q_i(\mathrm{x},\mathrm{x})$ by using Schmidt orthogonalization procedure. The coefficients c_j can be expressed by using Eqn. 8-a with $q_i(\mathrm{x},\mathrm{x})$. Thus, by substituting the coefficients c_j for Eqn. 3, the MLSM interpolant approximation can be expressed as follows:

$$u_0(x,y) = w(\|\mathrm{x} - \mathrm{x}_i\|) \frac{q_k(\mathrm{x},\mathrm{x}) q_k(\mathrm{x}_i,\mathrm{x})}{w(\|\mathrm{x} - \mathrm{x}_j\|) q_k^{\,2}(\mathrm{x}_j,\mathrm{x})} u_i \tag{10}$$

By using a method developed by T. Belytschko et al, we divide the analytical domain into regular and

latticed domain named background cell. The cell has a unit which is integrated variation $\delta\Pi$ of integral equation 2. We apply Gauss integral to integrating each cell. We use MLSM for evaluating an integrand of Gauss integral point. We obtained stiffness equation by discreting variation $\delta\Pi$ on the value of node.

STRESS INTENSITY FACTORS

Stress intensity factors K_I, K_{II}, K_{III} can be obtained directly by using stresses or displacements around crack tip. We set newly a coordinate system which has a origin around crack tip as shown in Figure 3.The relation between $K, \Delta u$ which is a relative displacement in x_c direction and Δv which is relative displacement in y_c direction and Δw which is relative displacement of circumferential direction are expressed as:

$$\Delta u = \frac{8K_{II}(1-\nu^2)}{E}\sqrt{\frac{r}{2\pi}} \tag{11-a}$$

$$\Delta v = \frac{8K_{I}(1-\nu^2)}{E}\sqrt{\frac{r}{2\pi}} \tag{11-b}$$

$$\Delta w = \frac{8K_{III}(1+\nu)}{E}\sqrt{\frac{r}{2\pi}} \tag{11-c}$$

Where E is a young's modulus, ν is a Poisson's ratio, r is a distance from crack tip. K_I, K_{II}, K_{III} are obtained by substituting relative displacements $\Delta u, \Delta v, \Delta w$ calculated by EFGM for Eqn.11. We can obtain K by extrapolating K_I, K_{II}, K_{III} to $r \to 0$.

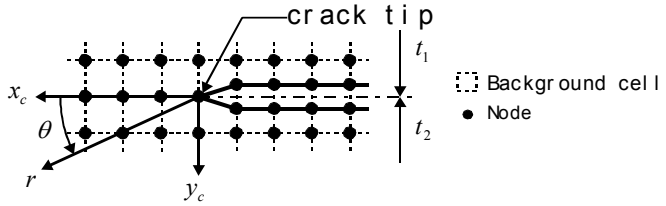

Figure 3: Distribution of nodes and background cells around crack tip

By adopting the maximum tangential stress criterion (F. Erdogan and G. C. Sih`s criterion), initial crack under K_I, K_{II} mixed modes grows in the direction of angle $\theta = \theta_0$ inclining to x_c axis in Eqn. 12. Maximum principal stress intensity factor $K_{\theta\max}$ is obtained by Eqn. 13.

$$K_I \sin\theta_0 + K_{II}(3\cos\theta_0 - 1) = 0 \tag{12}$$

$$K_{\theta\max} = \cos\frac{\theta_0}{2}\left(K_I \cos^2\frac{\theta_0}{2} - \frac{3}{2}K_{II}\sin\theta_0\right) \tag{13}$$

ANALYTICAL RESULTS

Before we calculate K of DC using EFGM, we apply EFGM to calculating K of finite flat plate named single edge crack of which exact solution has been known (Figure 4), and examine the accuracy of the solution. Table 2 shows the results of K of single edge crack using EFGM under the analytical condition shown in Table 1. We get analytical domain to be half of the total length. The K values of crack obtained by using EFGM are in agreement with the exact solutions.

TABLE 1
ANALYTICAL CONDITION

Height b(mm)	Width w(mm)	Load σ (N/mm^2)
30	20	1000
The number of nodes	The number of cells	Node distribution
29×43	20×30	Uniform distribution

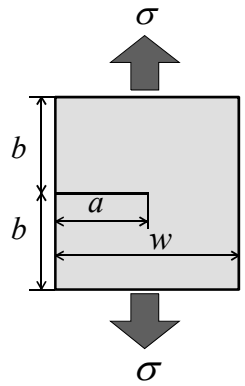

Figure 4: Finite flat plate with single crack subjected to uniform tension

TABLE 2
STRESS INTENSITY FACTORS OF SINGRE EDGE CRACK

Crack length		Stress intensity factors K(×10^{4}N/mm$^{3/2}$)		Error
a(mm)	a/w(-)	Analytical solution	Exact solution	e (%)
5	0.25	0.594	0.595	0.10
10	0.5	1.611	1.584	-1.68
15	0.75	5.800	5.799	-0.02

On the basis of the analytical results shown in Table 2, we will arrange nodes and background cells uniformly and calculate stress intensity factor K of DC by EFGM. Figure 3 shows the distribution of nodes and background cells around crack tip.

Because DC shown in Figire 1 has a crack in analytical domain, there is a possibility of including the boundary between nodes and evaluation point. Therefore giving equal weight to the nodes across and beyond a boundary causes to decrease accuracy of the solution and therefore we define the domain of influence around a boundary (crack) as shown in Figure 5.

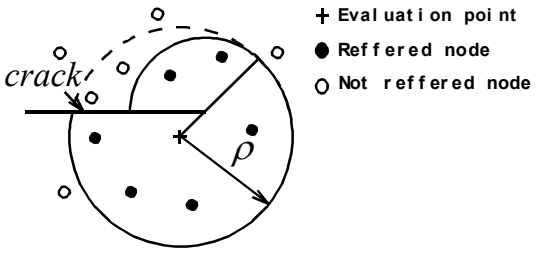

Figure 5: Domain of influence

Table 3 shows the analytical results of DC which is changed load direction β (from 0deg to 90deg) by using EFGM. We get diameter of nugget to be $5\sqrt{t}$.

TABLE 3
STRESS INTENSITY FACTRORS OF DC

Load direction β (deg)	Diameter D(mm)	Plate thickness t_1=t_2(mm)	Load P(N)	ナゲット径 d (mm)	Stress in K ($\times 10^3$ N/mm$^{3/2}$)				
					$K_I(\Psi=0)$	$K_{II}(\Psi=0)$	K_I / K_{II}	$K_{\theta\max}$	θ_0(deg)
0	34.2	0.8	1000	4.48	0.000	0.152	0.000	0.176	-70.5
15	34.2	0.8	1000	4.48	0.222	0.147	0.664	0.319	-46.0
30	34.2	0.8	1000	4.48	0.428	0.132	0.308	0.481	-29.7
45	34.2	0.8	1000	4.48	0.605	0.108	0.178	0.632	-19.1
60	34.2	0.8	1000	4.48	0.741	0.076	0.103	0.753	-11.5
90	34.2	0.8	1000	4.48	0.856	0.000	0.000	0.856	0.00

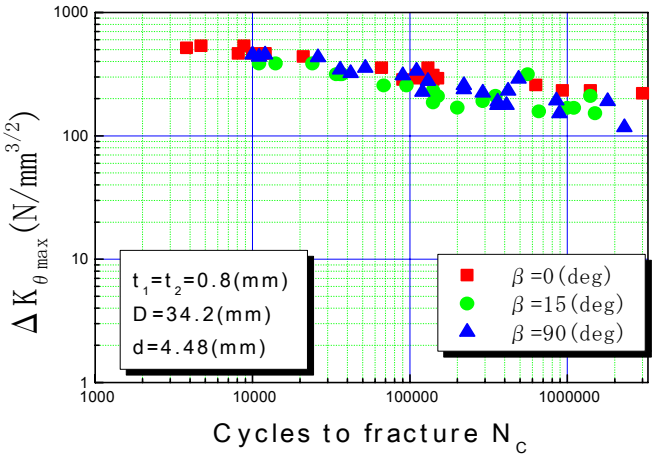

Figure 6: $\Delta K_{\theta\max} - Nc$ curve

Figure 6 shows $\Delta K_{\theta\max} - Nc$ which can be obtained by the data of fatigue test ($\Delta p - Nc$ curve) and $K_{\theta\max}$ obtained by EFGM. Figure 6 show the data are gathered in narrow range. So we can say K obtained by using EFGM are appropriate results.

CONCLUSIONS

We applied EFGM to calculating stress intensity factors K of DC under multiaxial loads, and investigated the accuracy of the solutions obtained.
Main results were as follows.

(1) In order to examine the accuracy of solutions of K obtained by using EFGM, finite flat plates named single crack under uniform tension were analyzed by applying EFGM as two dimensional elastic problem.
(1) The K values of cracks obtained by EFGM were in agreement with the exact solutions.
(2) When we analyzed DC acted on multiaxial loads, the DC was analyzed as superposition of the load which was divided into cross tension and tensile shear. From the value of K obtained by EFGM, the data of fatigue could be arrange systematically. So we could say K obtained by EFGM were appropriate results.

REFERENCES

1. Y.Y.Lu,T,Belytschko,L.Gu.(1994): "A new implementation of the element Galerkin method" , Computer methods in applied mechanics and engineering, Vol. 113, pp. 397-414
2. Dieter Radaj: "Spot-Welded Double-Cup Specimen", MATERIALPRUFUNG Vol.37(1995)1-2,pp.10-13
3. JSAE SYMPOSIUM No. 06-00: " New Proposals for Evaluation of Fatigue Durability of Automotive Body Structures".(Japanese)

OLAL/POSTER REFERENCE: ICF100930OR

EVALUATION OF THERMAL AND ELASTIC PROPERTIES FOR SOLID SURFACES USING TRANSIENT REFLECTING GRATING METHOD

K. Katayama [1], Q. Shen [2], A. Harata [3], and T. Sawada [1]

[1] Department of Advanced Materials Science, Graduate School of Frontier Sciences, The University of Tokyo, Tokyo 113-0033, Japan
[2] Graduate School of Electro-Communications, The University of Electro-Communications, Tokyo 182-0021, Japan
[3] Graduate School of Engineering Sciences, Kyushu University, 6-1 Fukuoka, 816-8580, Japan

ABSTRACT

Subnanosecond time-resolved transient reflecting grating (TRG) method has been developed and applied to various solid surfaces such as a DLC film on a multiplayer substrate and an Ar ion-implanted silicon. This method provides a depth profiling of thermal and acoustic properties by changing the observed depth which can be experimentally controlled, and has the least depth region of hundreds of nanometers. We propose a new microscopic method using the TRG method where the signal is measured at various delay times while scanning a sample. This gave a various kinds of images including thermal and elastic properties at local places in the surface and subsurface region. Further, for clarifying a fundamental mechanism of a heat generation, the TRG method has been improved to have a time resolution of hundreds of femtoseconds. In this time range, ultrafast carrier dynamics can be monitored and the energy transfer processes from carriers to phonons were detected clearly.

INTRODUCTION

Surfaces and subsurfaces of materials modified by means of ion implantation, chemical and physical vapor deposition, etc., sometimes show higher order structures such as gradient structures and multilayered structures. Their evaluation places some technical requirements on the measurement method being applied in manufacturing process, i.e., it should be noncontact, nondestructive, and *in situ*. Photothermal and related techniques can partially cover the requirements[1] and deduce thermal and elastic properties for thin films, multilayered films and surface-modified materials. In the latest device technology, device components get smaller and smaller to the size region of nanometers, and for example, thin films of several nanometers in thickness are practically used. Conventional photothermal methods cannot measure thermal or elastic properties for such thin films of nanometer thickness because the methods usually have the least depth resolution of several micrometers. Thus, measurement methods for evaluating thin films of nanometer thickness are required.

On the other hand, as the device size is reduced, the time of carrier transport between components also gets faster and faster to the time region of picoseconds. Ultrafast carrier transport generates heat in the nano-sized region, so that there are some local places with high temperature. To improve device

performance, the fundamental physical processes of such heat generation at a surface or interface must be clarified and
the temperature should be controlled. In order to clarify the origin of heat generation, the source process es, namely the photo-excited carrier dynamics should be studied.

For the last 10 years, we have developed new photothermal methods that allow sub-nanosecond time-resolved measurements and offer a nano-scale depth resolution. These methods are Transient reflecting grating (TRG) and Transient reflectivity (TR), and they were applied to various solid surfaces [2,3,4], solid-liquid interfaces [5,6,7,8], multi-layered films [9] and liquid surfaces [10]. In this paper, we will show some results obtained by applying the TRG method to thin films and multilayered films of nano-scale thickness. Also, a new type of microscope using the TRG method is proposed for investigating thermal and elastic properties at local places. Futher, the time resolution of the TRG method has been improved from sub-nanosecond to sub-picosecond, and the results are also shown about ultrafast carrier dynamics related to the fundamental processes of thermal generation.

Experimental

Schematic illustration of the principle for the TRG method is shown in Fig.1. In the TRG technique, two crossed pump pulses are incident at a solid surface and, as a result, the focused spot is irradiated with a pulse of an interference pattern. The complex refractive index at the spot changes due to a physical property change, or grating-patterned surface deformation occurs mainly due to a surface acoustic wave. After the pump pulses irradiation, a probe pulse is also incident there, and the complex refractive index change and the grating-patterned surface deformation are detected through the diffracted light of the probe light. A refractive index change due to photoexcited carriers is observed until several picoseconds, and that due to temperature rise and the following diffusion are observed from several picoseconds to nanoseconds. A surface deformation is detected in the time range of several nanoseconds.

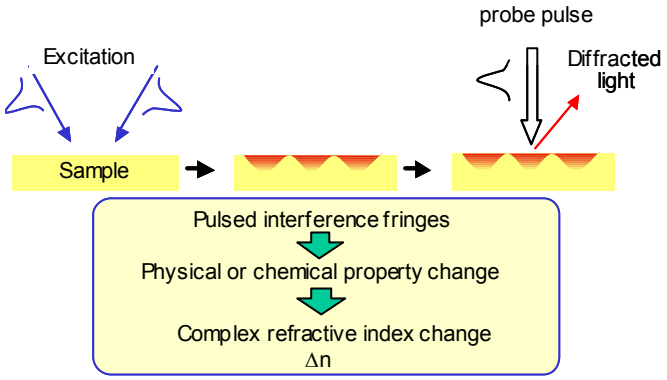

Figure 1 The principle of the transient reflecting grating method.

For measurement with a time resolution of sub-nanosecond, Nd-YAG laser (Pulse width :80 ps, Repetition frequency : 1 kHz, Wavelength : 1064 nm) was used as a light source. The wavelength was frequency-doubled to 532 nm. The pulse was separated into pump and probe pulses using a partial reflective mirror. The pump pulses were further divided into two pulses by a half mirror. The two pump pulses were crossed and irradiated onto the same spot of the sample surface, to coincide in time to form an interference pattern. The probe pulses were also incident at the spot after passing through a computer controlled optical delay line. The diffracted signal of the probe pulses were detected with a photomultiplier, and observed by a computer after averaging the signal with a box-car integrator.

In measurements with a time resolution of 200 fs, a regeneratively amplified titanium sapphire laser laser (CPA-1000; Clark-MXR Inc.) was used as a light source. The pulse train wavelength was 800 nm with a repetition rate of 1 kHz and pulse width of 200 fs in full width at half maximum. Only the pump pulses were frequency doubled to a wavelength of 400 nm. The probe pulses remain 800 nm.

Results and Discussion

TRG responses measured with the sub-nanosecond time resolution is shown in Fig.2. The signal had a small peak just after photo-excitation at the almost same time as incident pulse. The following signal shows an oscillating decay consisting of an exponential decay and an oscillating decay. The signal was separated to each component, which is shown in the right side of Fig.2. Considering the time range observed, the first peak corresponds to a refractive index change due to photo-excited carriers, and the exponential decay and the oscillating decay mean a thermal decay and a surface acoustic wave (SAW), respectively. It is very difficult to discuss the photo-excited carrier dynamic because the dynamics is considered to be faster processes than the used pulse width. About the thermal component, the decay occurs due to a thermal diffusion parallel to the interface, which disappears the temperature distribution like a grating pattern. Thus the decay time corresponds to the time during which heat diffuses for the length of the grating spacing. The grating spacing, $\Lambda$is expressed as $\Lambda = \lambda/2\sin(\theta/2)$, where λ is the wavelength of the pump pulses, and θ is the intersection angle of the two pump pulses. From the thermal decay time and the value of Λ, a thermal diffusion coefficient can be calculated, and this value is a property value in the depth region of Λ, which can be controlled by changing θ and has a typical length of 1 – 10 μm. Then, this signal provides a depth profiling of the thermal diffusion coefficient. The acoustic oscillation of the SAW originates in thermal expansion due to heat generation with a grating pattern. The wavelength of SAW must agree with the grating spacing, so that the SAW with a controllable wavelength can be generated and detected. Since a SAW have an elastic information in a surface region of the wavelength, this acoustic signal also offers a depth profiling of elastic properties. Actually the depth profiling of thermal and acoustic properties were applied to 10 keV nitrogen ion-implanted DLC films (40 nm) on multiplayer substrates, with Λ from 0.86 to 3.96 μm [9], and for 300 keV Ar ion-implanted Si wafers (ion-projected range, 0.31 ∓ 0.09 mm) with Λ from 1.65 to 3.66 μm [11]. Effective surface thermal conductivities and elastic constants were obtained. Effective thermal conductivities approached the real values for DLC films as the observed effective thickness is decreased, and the obtained value measured with the least depth resolution is good agreement with the real one. For the ion-implanted Si wafers, measurements of effective elastic constants revealed that the ion-implantation hardened the surface layer, though the surface-hardening mechanism is not clear yet.

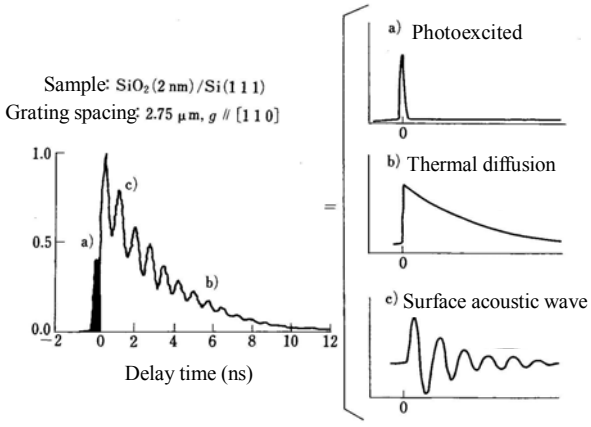

Fig. 2 A response of transient reflecting grating for a silicon (111) surface with a time resolution of 100 picoseconds. Three components comprising the response are also shown on the right side.

Furthermore, it is expected that this TRG method is used to investigate in-plane local properties for surface analysis in the depth range of nanometers because thermal and elastic properties at local places are very important for inhomogeneous surfaces including a partially ion-implanted region, structural defects, impurities and so on. The TRG method gives such properties at the focused spot of a probe light with a diameter of several micrometers. Imaging of the TRG signal can be obtained by measuring it while scanning a sample surface. This new type of imaging method features in providing a set of time-resolved images by changing delay times. By using the images, images for thermal relaxation rate or surface acoustic wave frequency can be deduced. We call this new microscope *Sazanami* imaging. *Sazanami* is a Japanese word that refers to the small rippling waves caused by a light wind blowing over a water surface. TRG looks like the *sazanami* ripples on a material surface, but are generated by light.

Time-resoled sazanami images are shown in Fig. 3. The sample was a Si wafer, partly 300 keV He-ion-implanted (dose, $10^{15}/cm^2$). The initial parts of the TRG responses for both non-implanted and implanted regions are shown at the top. The two arrows at t=0.0 and 0.5 ns indicate the photoexcited carriers' peak and the first acoustic peak, respectively. By using the two delay times, two different sazanami images were obtained. Although no sturucture apart from dust appears in the dark field image, the ion-implanted region is distinguishable in the sazanami images. The dark area in the 0.0 ns image indicates a small number of carriers. The bright area in the 0.5 ns image means that a large amount of heat is generated. The results are simple that, ion-implantation makes the carrier density small and heat generation large as a result of acceleration of carrier recombination. With time-resolved imaging we can easily grasp such dynamics.

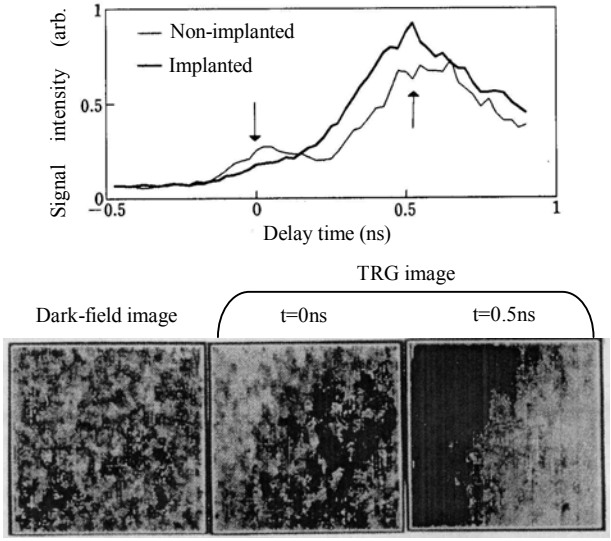

Fig.3 Top: TRG responses at He-implantated and non-implanted place. Bottom: A dark-field image and time-resolved TRG images of a partially He ion-implanted silicon.

Next, the photoexcited carrier dynamic was focused on. The dynamics was observed in the first peak of the sub-nanosecond time-resolved TRG signal. To clarify the temporal response, the TRG measurement with the time resolution of 200 fs was applied to the same sample. The TRG response is shown in Fig.4. The signal rose just after photo-excitation and decayed in 2ps. The photo-excited carriers lose their energy due to scattering by phonons, that is, an energy transfer from photo-excited electrons to phonons. The process is the origin of a temperature rise. In the literature [12], it was reported that the scattering due to phonons occurs about a few picoseconds. Thus it was concluded that the TRG signal in the picoseconds time range includes information on the origin of heat generation, that is, an energy transfer from photo-excited electrons to phonons.

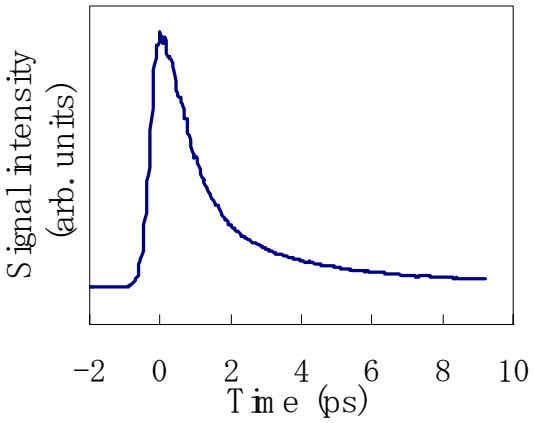

Fig. 4 A response of transient reflecting grating for a silicon surface with a time resolution of 200 femtoseconds.

Conclusion

The TRG method was applied to various solid surfaces in the time range from femtoseconds to nanoseconds. In a measurement with a time resolution of sub-nanoseconds, the signal gave information on thermal diffusion and SAW. This method provides a depth profiling of thermal and acoustic properties by changing the experimentally controllable observed depth. Also, we propose a new microscope using the TRG technique and it provide a thermal and elastic characterization at local places with a spatial resolution of several micrometers. Recently developed ultrafast time-resolved measurement with 200 femtosecond time resolution offers an investigation of an initial heat generation, that is, an energy transfer from electrons to phonon.

---

[1] *Photoacoustic and Photothermal Phenomena II*, edited by J. C. Murphy, J. W. M. Spicer, L. C. Aamodt, and B. S. H. Royce (Springer, Berlin, 1990), **Vol. 62,**

[2] K. Katayama, Q. Shen, A. Harata and T. Sawada, Appl. Phys. Lett. **69**, p. 2468 (1996).

[3] K. Katayama, Q. Shen, A. Harata and T. Sawada, Phys. Rev. B **58**, p. 8428 (1998).

[4] A. Harata, N. Adachi and T. Sawada, Phys. Rev. B **58**, p. 7319 (1998).

[5] A. Harata, T. Kawasaki, M. Ito and T. Sawada, Anal. Chim. Acta **299**, p. 349 (1995).

[6] A. Harata, T. Edo and T. Sawada, Chem. Phys. Lett. **249**, p. 112 (1996).

[7] A. Hibara, A. Harata and T. Sawada, Chem. Phys. Lett. **272**, p. 1 (1997).

[8] K. Katayama, T. Sawada, I. Tsuyumoto and A. Harata, Bull. Chem. Soc. Jpn. **72**, p. 2383 (1999).

[9] Q. Shen, A. Harata and T. Sawada, J. Appl. Phys. **77**, p. 1488 (1995).

[10] S. Ikeda, K. Katayama, I. Tsuyumoto, T. Tanaka, A. Harata and T. Sawada, J. Chem. Phys. **111**, p. 9393 (1999).

[11] A. Harata, Q. Shen, T. Tanaka and T. Sawada, J. Phys. Colloq. **6**, p. C7-159 (1994).

[12] A. Othonos, J. App. Phys. **83**, p. 1789 (1998).

REFERENCE: ICF 10069PR

EVOLUTION OF FRACTURE OF STEELS AT A TEMPERATURE OF 4.2 K AND UNDER THE ACTION OF ELECTRIC CURRENT PULSES

V.A. Strizhalo and L.S. Novogrudskii

Institute for Problems of Strength of the National Ac. Sci. of Ukraine
2 Timiryasevskaya str., Kiev, 01014 Ukraine

ABSTRACT

The authors studied specific features of the formation of a plastic zone at the crack tip at a temperature of 4.2 K and under the action of electric current pulses (ECP) of high density using steel 03Kh20N16AG6 with a stable austenite as an example. Employing the method of stereofractographic analysis, the results of investigations into specimen fracture surface microrelief, and analytical solutions, they demonstrate the formation of the plastic zone at the crack tip at a temperature of 4.2 K to follow the mechanism of discontinuous yielding. The influence of electric current pulses stimulates the process of the formation of the plastic zone to step up causing the plastic zone to reach its critical size at lower load levels. In the calculation of the stress intensity factor of materials characterized by non-monotonic development of elasto-plastic deformation at a temperature of 4.2 K it is recommended to choose the design load P_Q by the method of 5% secants.

KEYWORDS:

fracture, plastic zone, discontinuous yielding, electric current pulses

INTRODUCTION

The reason for the majority of unexpected fractures of high-stressed elements of structures is various design and manufacturing stress concentrators such as discontinuities, notches, recesses, holes, cracks, etc. The presence of such concentrators in the units of superconducting electromagnetic equipment operating at the temperature above 4.2 K and subject to powerful electromagnetic actions is responsible for significant nonuniformities of both mechanical and electromagnetic stress fields. These nonuniformities may result in the accumulation of energy in local regions of a material, where a crack is most likely to initiate and propagate. A rather strong electromagnetic action may give rise to deformation of the crack profile, which causes either its blunting or healing up, local thermal treatment and hardening through deformation due to electrodynamic loads, stimulation of the crack propagation as a result of the exhaustion of plasticity in the overstressed zone, etc. Electric current pulses passing through the loaded material plasticize it. In so doing at cryogenic temperatures and certain parameters of electric current pulses this plasticization is a consequence of the electron-dislocation interaction and occurs within the period of the electric current pulse action. At the instant the plasticity of the material increases, an abrupt reduction in the metal resistance to

deformation is observed that manifests itself as a sharp change of load on tensile diagrams [1]. The effect of the ECP on the metal with non-conducting defects of the crack type would have shown up most vividly at a temperature of 4.2 K since in the zone adjacent to the crack tip the concentration of electromagnetic, thermal, and force fields reaches its maximum.

Under conditions of subzero cooling (< 20 K) most metallic materials exhibit instability of plastic yielding that manifests itself in jump-like deformation (discontinuous yielding). The latter is recorded in the form of saw-tooth tensile diagrams. The initiation of the low-temperature discontinuous yielding and its character depend on a number of factors. One of the main factors is the volume of the material deformed. Strain constraint in the region of the material adjacent to the crack tip and nonmonotonic evolution of the plastic flow at cryogenic temperatures are responsible for specific features of the formation of the plastic deformation zone and the conditions of the evolution of fracture.

It is the foregoing that determined the objective of the present investigation – to establish specific features of the evolution of plastic deformation at the crack tip related to the action of the ECP and cooling down to 4.2 K.

EXPERIMENTAL RESULTS AND DISCUSSION

For the investigation we have chosen steel 03Kh20N16AG6, which exhibits stability of the phase composition in the temperature range from 293 to 4.2 K. Compact tension (CT) specimens of 12 mm thickness were fabricated from sheet billets of that steel. Analysis of fracture diagrams of CT specimens obtained at the temperature of liquid helium revealed the appearance of local load maxima to the left of the 5 % secant. In this case, we face the uncertainty in the determination of the design load P_Q [2, 3] because these local maxima can be indicative of both crack growth onset and discontinuous yielding of the material that is characteristic of the steels considered at 4.2 K in the process of plastic zone formation at the crack tip preceding its growth onset.

To verify this assumption, an experiment was performed according to the following scheme. Compact-tension specimens of steel 03Kh20N16AG6 were loaded at a temperature of 4.2 K until several local maxima appeared located to the left of the point of intersection of the load displacement (P –V) diagram with the 5 % secant. Then the specimens were unloaded. A possible crack extension increment was controlled by thermal painting. Ten specimens were tested in this way and no crack extension was observed. It is only after the maximum that coincided with the point of intersection of the 5 % secant with the P – V diagram or immediately following it that the crack growth onset was noted. Thus, the presence of a number of local maxima on the P – V diagrams to the left of the 5 % secant in testing CT specimens of the above steel is a result of the formation of a plastic zone prior to the crack growth onset that, under these temperature conditions, occurs by the mechanism of discontinuous yielding. The formation of a plastic zone due to discontinuous yielding is also confirmed by the fact that the stress values corresponding to the beginning of discontinuous yielding and determined on smooth specimens coincide with the values of nominal stresses in the weakened section of the CT specimen, σ_0, under the load corresponding to the first local maximum P_{D1}. The value of σ_0 is calculated by the following formula [3]:

$$\sigma_0 = \frac{P_{D1}}{(b-l)t}\left[1+\frac{3(b+l)}{b-l}\right], \qquad (1)$$

where t is the specimen thickness, $b = 2t$ is the distance from the line of load application to the specimen edge; l is the distance from the line of load application to the crack tip.

The stress of the beginning of discontinuous yielding determined on smooth specimens at a temperature of 4.2 K corresponds to the yield strength of the steel studied and is equal to 1440 MPa. The magnitudes of nominal stresses calculated by formula (1) for a batch of CT specimens are within 1400 – 1470 MPa. It is obvious that due to stress concentration in some region in the vicinity of the crack tip the stresses not only reach the level of the stresses corresponding to the beginning of discontinuous yielding, but exceed it.

When studying the influence of the ECP on the kinetics of plastic zone formation at the crack tip, electric current pulses were applied so that the current flew about the crack tip. This direction of the current causes local concentration of the electric and thermal fields [1] and also contributes to elasto-plastic deformation of the largest region of the material at the crack tip. The maximum value of the current density with the consideration of its concentration at the crack tip with its pulse amplitude being equal to 2800 A reached $18.5 \cdot 10^8$ A/m^2. The load levels, at which the specimens were exposed to the action of the ECP, produced nominal stresses equal to $0.6\sigma_{0.2}$, $\sigma_{0.2}$, and $1.2\sigma_{0.2}$.

Passing through the material at the nominal stress equal to $0.6\sigma_{0.2}$, the ECP does not change the run of the P-V diagram and the character of crack propagation as compared to the initial state. The influence of the ECP at the nominal stresses $\sigma_{0.2}$ and $1.25\sigma_{0.2}$ causes some deviation from the linear portion of the P-V diagram appearing as horizontal steps. However, the crack propagation is therewith not observed. At the same time, the first local maximum after the action of the ECP corresponds to the crack growth onset.

The estimation of the plastic zone radius r_n was performed on the basis of the Irvin approach [4] according to which $r_{p.stress} = \frac{1}{2\pi}\left(\frac{K}{\sigma_{0.2}}\right)^2$ in the case of the plane stress state, and $r_{p.strain} = \frac{1}{6\pi}\left(\frac{K}{\sigma_{0.2}}\right)^2$ in the case of the plane strain state. The estimation showed that on the exposure to the ECP at the instant of the crack growth onset $r_{p.stress}^{ECP} = 2.18...2.33$ mm and ($r_{p.strain}^{ECP} = 0.75...0.78$ mm). Also the values $r_{p.stress}^{ECP}$ ($r_{p.strain}^{ECP}$) are matched by the values of the plastic zone radii $r_{p.stress}$ ($r_{p.strain}$) calculated for the local maximum corresponding to the crack growth onset in the absence of the ECP action. Meanwhile, in the latter case for the first local maximum the size of the plastic zone radius is equal to $r_{p.stress} = 1.05...1.15$ mm and $r_{p.strain} = 0.35...0.40$ mm, i.e., under this load the plastic deformation zone at the crack tip does not reach its critical size.

The fracture kinetics of steels at the initial stage at a temperature of 4.2 K and under the action of the ECP has also been studied by the method of stereofractographic analysis following the procedure described in [5]. Two batches of specimens were loaded in the medium of liquid helium. One part of the specimens of the first batch was loaded until the first clear-cut local maximum appears on the P-V diagram and then unloaded. The second part of the specimens was loaded until the appearance of two local maxima.

The next batch of the specimens, which was divided into two parts, was exposed to the ECP and also loaded until the appearance of two maxima. The specimens of the second batch were unloaded as soon as the load reached the values corresponding to those attained in testing the first batch of the specimens. In this case, the only local maximum was observed at the load value corresponding to the appearance of the second local maximum for the specimens not exposed to the ECP. After unloading a possible crack extension increment was recorded and the specimens were fractured. Stereo pairs were photographed on the halves of the fractured specimen using a scanning electron microscope 'Stereoscan' at the convergent angle $\Theta = 5^0$ and magnification M=400. The stereo pairs were processed by a stereocomparator "Stecomoter".

The height difference between two points of the object was determined for the case of orthogonal projection by the formula $\Delta h = \frac{\Delta F}{2M \sin \Theta}$, where ΔF is the difference of distances between the images of two points of the object on two microfractograms of the stereo pair. In view of an appreciable nonuniformity of the stretch zone height along the crack front its size was obtained by averaging the results of measurement of no less than four profiles of fracture surfaces for each specimen.

It was established that even the appearance of two maxima recorded on the load vs displacement diagram does not imply the crack propagation since in this case the height of the stretch zone is 5×10^{-2} mm and no crack propagation is observed on the fractograms of fracture surfaces. After the appearance of the first local maximum, the height of the relief does not change at all as compared to the initial fatigue crack.
The action of the ECP results in an appreciable (1.4 fold) increase in the height of the stretch zone. The fact that there are no local maxima on the P-V diagram is likely to point to the change in the mechanism of its formation.

CONCLUSION

The investigations performed allow us to conclude that, when calculating the stress intensity factor in the case of discontinuous yielding of the material at a temperature of 4.2 K, the magnitude of the design load P_Q should be determined either from the load maximum, which coincides with the 5% secant, or from that immediately following the latter. On exposure to the action of the ECP, this should be done from the first maximum. The ECP contributes to the intensification of the process of the plastic zone formation at the crack tip. This makes the plastic zone reach its critical size at lower levels of the load, i.e., the ECP acts as an embrittling factor.

REFERENCES

1. Strizhalo V.A., Novogrudskii L.S., and Vorob'yov Ye.V. (1990). *Strength of Materials Used in Cryogenic Engineering under the Action of Electromagnetic Effects* (in Russian), Naukova Dumka, Kiev.
2. ASTM E399-74 (1975). *Test Method for Plane Strain Fracture Toughness of Metallic Materials.* Annual Book of Standards, Philadelphia, USA.
3. GOST 25506-85 (1986). *Methods of Mechanical Testing of Metals. Determination of the Characteristics of Crack Growth Resistance (Fracture Toughness) under Static Loading* (in Russian). Introduced 01.01.86.
4. Irvin Y.R. (1962). *J.Appl.Mech.*, No. 4, 651.
5. Krasowskii A.Ya., Kashtalyan Yu.A., and Krasiko V.N. (1982). *Investigation of Fracture Toughness of Pressure Vessel Steels under Sytatic and Dynamic Loading Considering the Size-Scale Effect of the Tested Specimens* (in Russian), Preprint, Inst. For Problems of Strength, Kiev, Ukraine.

ORAL/POSTER REFERENCE:ICF100819OR

EXPERIMENTAL AND ANALYTICAL STUDIES ON PEELING BEHAVIOR AND SPALLING RESISTANCE EFFECT OF CFS BONDED TO CONCRETE

Zhishen WU[1], Toshihiro ASAKURA[2], Hiroyuki YOSHIZAWA[3], Hong YUAN [4], Akira KOBAYASHI[5], and Toru TAKAHASHI[6]

[1] Department of Urban & Civil Engineering Ibaraki University, Hitachi city, 316-8511,Japan
[2,4]Department of Earth Resources Engineering Kyoto University, Kyoto city, 606-8501, Japan
[3,5] Nippon Steel Composite Co., Ltd., 3-8 Nihonbashikobuna-cho Chuo-ku, 103-0024,Tokyo, Japan
[6]Sho-Bond Corporation, 3-18 Kandanishiki-cho, chiyoda-ku, 101-8468, Tokyo, Japan

ABSTRACT

In this paper, the peeling behavior and the spalling resistance effect of externally bonded continuous fiber sheets (CFS) were firstly investigated experimentally through a series of punching shear tests. CFS applied concrete slabs with a hole in center were used for the test specimens. Specimens were varied in bonding length of CFS, diameters of spalling columnar concrete (indenter), types of fiber that were composed of CFS. Secondly, a fracture energy method was proposed for modeling the membrane peeling behavior and for evaluating spalling resistance effect of externally bonded CFS. It is realized that only one material parameter, interfacial fracture energy of CFS-concrete interface (G_c), was necessary to represent the interfacial behavior. Finally, the close agreement between the predicted results from the proposed analytical method and the experimental results was demonstrated by means of some numerical examples.

KEYWORDS

Continuous fiber sheet, Fracture energy, Peeling, Spalling resistance

1. INTRODUCTION

Today many of the existing tunnels need counter measures to prevent the peeling and spalling of their lining concrete caused by the action of ground pressure, the deterioration of concrete materials, etc. There are also road bridges and railway bridges which require counter measures to prevent the peeling and spalling of pieces of their concrete caused by the deterioration of concrete, the corrosion of steel reinforcement, etc.

In recent years, continuous fiber sheet (CFS) has been increasingly used to reinforce or repair tunnel linings and the slabs of viaducts. When CFS is applied to a concrete lining slab to prevent pieces of the

concrete from peeling and spalling, not only the in-plan shear stress but also the out-of-plane shear stress that makes the CFS peel off from the concrete surface are imposed on the interfacial crack tip between the CFS and the surface of concrete. In this case, the fracture mode in which a interfacial crack develops is considered to be a combination of the crack development of both Mode I and Mode II in terms of fracture mechanics.

We think that the fracture mechanism of peeling of CFS under the in-plane shear stress is different from the mechanism of that under the combination of in-plane and out-of-plane shear stress. Therefore, assuming that a piece of concrete spalls from the surface of concrete lining, we carried out a punching shear test of concrete slabs of which CFS bonded to the bottom surface. In the experiments, the bonding length of CFS, the diameter of concrete indenter were the experimental parameters[1)]. As a result, we proposed a new analytical technique using interfacial fracture energy, G_c, and compared the experimental results with the analytical results obtained using the new technique.

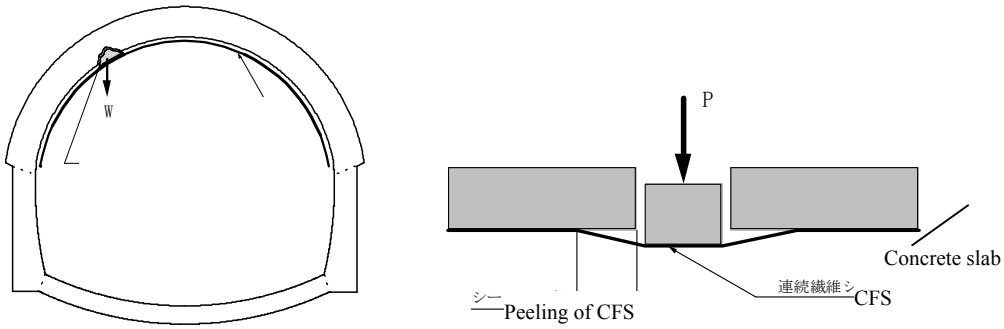

(a) Schematic diagram of spalling of concrete piece from concrete lining (b) Schematic diagram of present test

Figure 1: Schematic diagram of spalling of concrete piece and present test

2. SCHEME OF EXPERIMENT

2.1. Experimental apparatus

The experiments were carried out using a static load tester and concrete slab (W230 x L230 x H20 cm) provided with a hole in the center. CFS was bonded in two orthogonal layers (0/90) to the lower surface of the slab, and an indenter made of concrete was fitted in the hole. The CFS was bonded to the lower surface of the concrete slab and the indenter. The experiments were conducted under controlled displacement conditions. The load was applied to coerce the indenter into moving to force the CFS to peel off from the slab. In this way, CFS applied concrete slabs were subjected to a punching shear test in which a forced displacement was given to the indenter to peel the CFS off the concrete slab. The compression strength of the concrete used for the slabs was 28 N/mm^2. Displacement was measured at three points as shown in Figure 2. Mechanical properties of CFS using in this test are shown in Table 1.

2.2. Experimental cases

In the experiments, seven different cases were tested. Standard case (No. 1) is as follows. Hole diameter is 200 mm, Type of CFS is high strength carbon fiber. Bonding length is 500mm.

As the experimental parameters, fiber types, hole diameter, and bonding length are varied. The detail conditions are shown in Table 2 and Figure3.

Each specimen was subjected to surface preparation, coated with primer, and smoothed with epoxy putty before the CFS was bonded to it with epoxy resin. For specimen No. 3 with constraining plates, 4 steel plates, size of W50 x L600 x t3.2 mm, were arranged in a square at a distance of 30 cm from the hole center. Each of the plates was fixed with three M10 anchor bolts at a 250 mm pitch.

2.3. Experimental procedure

The test apparatus was controlled based on displacement and loading was conducted step-wisely. The loading speed was 1 mm/min and the pushdown rate was 0.5 mm per step. In consideration of the stress

relaxation right after the loading, the displacement and the load were measured two minutes after the loading.

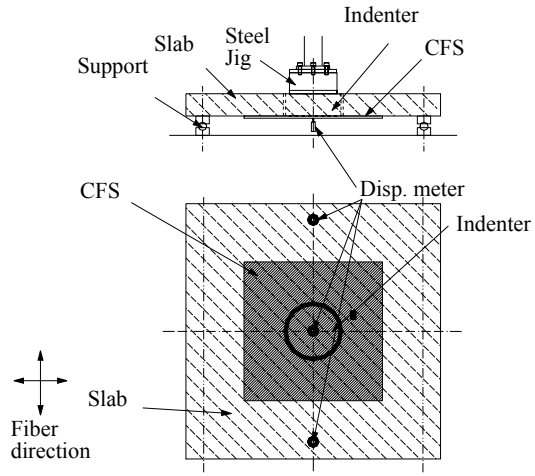

Figure 2: Experimental apparatus and specimen shape

TABLE 1
CHARACTERISTICS OF CFS

CFS type	Fiber areal weight g/m^2	Young's modulus E GPa	Tensile strength MPa	Design thickness t mm	Stiffness of CFS sheet E·t $*10^6$ N/mm
High-strength Carbon Fiber	200	235	4,150	0.111	26.1
Aramid Fiber	280	118	2,450	0.193	22.8
Glass Fiber	300	74	1,650	0.118	8.7

TABLE 2
EXPERIMNETAL PARAMETERS

NO.	Hole diameter mm	CFS type	Bonding length mm	Fiber areal weight g/m^2	Remarks
1	ϕ 200	High-strength Carbon Fiber	500	200	Standard
2	ϕ 200	High-strength Carbon Fiber	900	200	Bonding length
3	ϕ 200	High-strength Carbon Fiber	500	200	Constrained with plates
4	ϕ 500	High-strength Carbon Fiber	500	200	Hole diameter
5	ϕ 1000	High-strength Carbon Fiber	400	200	Hole diameter
6	ϕ 200	Aramid Fiber	500	280	Aramid Fiber
7	ϕ 200	Glass Fiber	500	300	Glass Fiber

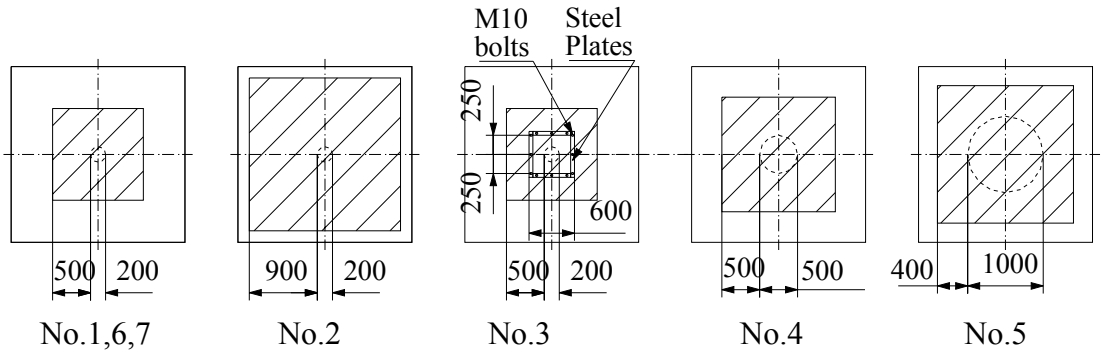

Figure 3: Scheme of specimens

3. EXPERIMENTAL RESULTS

Figure 4 shows the load-displacement curves obtained by the punching shear test. Here, the load values are those two minutes after load application. Photo.1 shows an example of expansion of the peeling zone of CFS. The white lines indicate the peeling zones of CFS when the indenter displacement was increased in increments of approximately 2 mm.

Table 3 shows the maximum load (load value measured two minutes after load application) for each of the specimens.

With the exception of the specimen bonded with glass fiber sheet (No.7), all the specimens showed maximum load right before the CFS peeled off completely (the CFS did not rupture at all).

In the early stages of peeling, the shape of peeling zone was circular. As the CFS continued peeling, the peeling zone became squarely shape because the continuous fibers were aligned diagonal orientations. In case of No.7 (glass fiber specimen), the sheets were ruptured at the edge of the concrete indenter right before they peeled off completely.

TABLE 3

EXPERIMENTAL RESULTS

NO.	Hole diameter mm	CFS type	Bonding length mm	Max. displace-ment mm	Max. load kN	Failure criteria
1	ϕ 200	High-strength Carbon Fiber	500	43.0	17.0	Debonding failure
2	ϕ 200	High-strength Carbon Fiber	900	71.0	23.9	Debonding failure
3	ϕ 200	High-strength Carbon Fiber	500	46.0	33.7	Bolt pull out Debonding failure
4	ϕ 500	High-strength Carbon Fiber	500	42.5	26.1	Debonding failure
5	ϕ 1000	High-strength Carbon Fiber	400	32.0	29.1	Debonding failure
6	ϕ 200	Aramid Fiber	500	48.0	24.6	Debonding failure
7	ϕ 200	Glass Fiber	500	48.0	16.4	Sheet rupture

Photo.1 Progress of peeling off zone (No. 2)

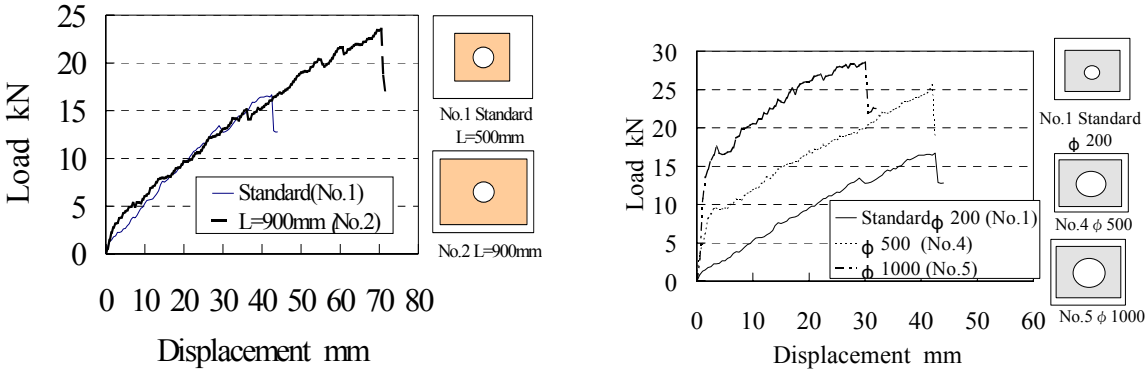

(a) effect of bonding length (b) effect of hole size

Figure 4: Load-displacement curves

a) Effect of sheet bonding length

As shown in Figure 4(a), with a given hole diameter, the maximum load increased as the sheet bonding length was increased. However, it was confirmed that the gradient of the load-displacement curve remained almost the same even when the sheet bonding length was changed.

b) Effect of hole diameter

As shown in Figure 4(b), the larger the hole diameter, the larger was the starting load (about 1 kN for No.1, about 9 kN for No.4, about 17 kN for No.5). However, even when the hole diameter was changed, the gradient of the load-displacement curve remained almost the same. As shown in Figure 5, the relationship between indenter vertical displacement and sheet peeling length is almost linear. With a given amount of vertical displacement of the concrete indenter, the larger the hole diameter, the greater is the sum of the sheet peeling length and the hole radius. Because of this, the larger the hole diameter, the higher was the maximum load of punching shear at a given amount of indenter vertical displacement.

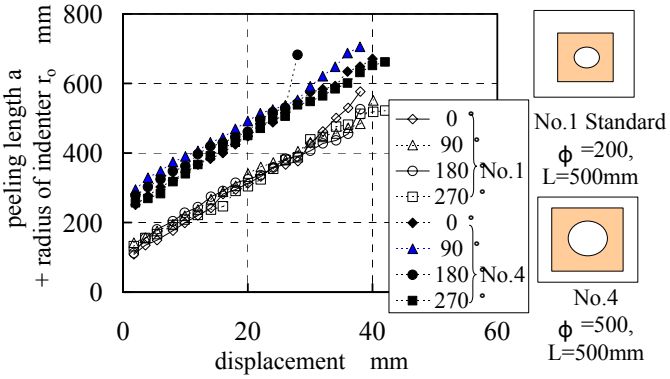

Figure 5: Relationship between peeling length and indenter vertical displacement (No.1,4)

4.COMPARISON BETWEEN ANALYTICAL AND EXPERIMENTAL RESULTS

4.1 Analytical technique

Figure 6 shows the equilibrium of forces between vertical load P applied to the indenter and tensile force of the CFS. In this figure, α, a, r_o, and L represent peeling angle in fiber orientation, sheet peeling length, indenter radius, and sheet bonding length respectively. Analyses were conducted on the assumption that when the sheet is bonded in two layers, one orthogonal to the other, the peeling zone becomes square in form when the steady state is reached. Using Young's modulus of CFS E, CFS thickness t, indenter radius r_o, sheet peeling length a, and indenter vertical displacement u, load applied to the indenter P, can be expressed as follows [2].

$$P = 4 \cdot E \cdot t \cdot (r_0 + a) \cdot \beta \cdot \left(1 - \frac{1}{\sqrt{1+\beta^2}}\right), \quad \beta = \frac{u}{a} = \tan\alpha \tag{1}$$

Fracture energy, G, can be obtained by the following equation.

$$G = E \cdot t \cdot \left(\frac{1}{2} \cdot \beta^2 + \frac{1}{\sqrt{1+\beta^2}} - 1\right) - E \cdot t \cdot \frac{a}{a + r_0} \cdot \left(\frac{1}{2} \cdot \beta^2 - \sqrt{1+\beta^2} + 1\right) \tag{2}$$

When the sheet peeling length is sufficiently greater than the indenter radius, fracture energy, G, can be expressed as follows.

$$G = E \cdot t \cdot \left(\sqrt{1+\beta^2} + \frac{1}{\sqrt{1+\beta^2}} - 2\right) \tag{3}$$

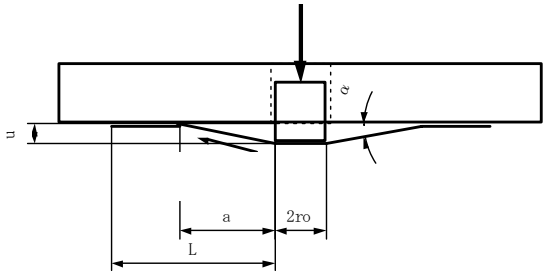

Figure 6: Equilibrium of forces between CFS and cylinder

4.2 Comparison between analytical results and experimental results

Table 4 shows the comparison between the analytical results and experimental results obtained with large specimens at G_c = 0.4 kN. In the analysis, it was assumed that the maximum load and the maximum displacement were reached when the sheet peeled off completely. In terms of both the maximum load and maximum displacement, the analysis values agree well with the experimental values.

TABLE 4

COMPARISON BETWEEN EXPERIMENTAL AND ANALYSIS VALUES (G_c = 0.4 kN/m)

Specimen No.	Analysis		Experimental		Experimental /Analysis	
	Max. Load kN	Max. disp. mm	Max. Load kN	Max. disp. mm	Max. Load kN	Max. disp. mm
L-1	20.0	43.5	17.0	43	0.85	0.99
L-2	34.2	78.8	23.9	71	0.70	0.90
L-4	23.7	42.6	26.1	43	1.10	1.01
L-5	26.5	33.3	29.1	32	1.10	0.96
L-6	21.9	44.8	24.6	48	1.12	1.07
L-7	15.2	57.4	16.4	48	1.08	0.84

4. CONCLUSIONS

In order to confirm the effect of CFS bonded to the surface of concrete to the prevention of concrete pieces from spalling from a concrete structure, we carried out a series of punching shear test experiments. In the experiments, the parameters such as CFS type, diameter of a cylinder simulating concrete piece which spalls, and bonding length of CFS were varied. And a new analytical technique that uses the interfacial fracture energy G_c was proposed. By comparing the analysis results with the experimental results, we could obtain the following conclusions.

1) When a CFS is bonded in two layers, one orthogonal to the other, the load of punching shear is almost proportional to the displacement of the concrete indenter or the peeling length of the CFS.
2) By applying our new analytical technique that uses interfacial fracture energy G_c between CFS and concrete (when the sheet is bonded in two layers, one orthogonal to the other), it is possible to accurately calculate the maximum load, maximum displacement, merely by determining the value of G_c experimentally.

REFERENCES

1) Asakura,S., Kojima,Y., Takahashi,T., Yoshizawa,H.: Experimental study on effect of continuous fiber sheet to prevent spalling of tunnel lining concrete, First-Australasian Conference on Composite Materials (ACCM-1), pp.106-1-106-4,1998 .
2) Wu,Z., Asakura,S., Yoshizawa,H., Yuan,.H., Kobayashi,A., and Takahashi,T.: Experimental and analytical studies on peeling behavior and spalling resistance effect of externally bonded continuous fiber sheets. J. Materials, Conc. Struct., Pavements, JSCE, No.662/V-49,pp.45-58, 2000.11.

ORAL/POSTER REF. ICF100104PR

Experimental and Finite Element Analysis of Fracture Criterion of Extra Deep Drawn Steel Sheets

Dhananjay M. Kulkarni [1] and Ravi Prakash [2]

1 Educational Hardware Division
Birla Institute of Technology and Science
Pilani, Rajasthan (333 031) India

2 Dean Research & Consultancy Division
Birla Institute of Technology and Science
Pilani, Rajasthan (333 031) India

ABSTRACT

The efforts made over the last three decades to understand fracture behaviour of structural material in elastic and elasto-plastic fracture mechanics regimes are numerous, whereas investigations related to fracture behaviour of materials in thin sheets or gross yielding fracture regimes are limited in number. The prevention of failure in stressed structural components currently requires fracture mechanics based design parameters like fracture toughness or critical crack-tip opening displacement. The present attempt would aim to fulfill this gap and generate more information thereby increased understanding on fracture behaviour of sheet metals. In the present investigation, using a recently developed technique for determining fracture criteria in sheet metals, results are generated on fracture toughness and verified with Finite Element analysis. At the end it is concluded that magnitude of fracture toughness of thin sheets increases with increase in thickness, unlike that for thick plates.

KEY WORDS

Extra Deep Drawn Steel Sheets, Fracture Criterion, Gross Yielding Fracture Mechanics, Crack-tip opening Displacement.

INTRODUCTION

In recent years, there have been considerable emphasis in the production of Deep Drawing and Extra Deep Drawing (EDD) steel in industries. The wide applications of EDD steel are not only well known for domestic appliances like storage containers, household utensils but also for automobile industries for manufacturing car bodies. With increasing global competition for quality materials, there is a need to understand the fundamentals of crack initiation in these bulk products. The characterization of thin sheets is presently being done with the help of empirical engineering simulative tests like Erichsen cup test, Olsen cup test and hole expansion test. The principle of the above tests, in general, attempt to search for an engineering parameter which indicates the mechanical environment for crack initiation and/or propagation [1] under the corresponding experimental conditions for each of these tests. The event of crack initiation and

propagation is commonly dealt with using fracture mechanics principles; but so far little attention has been paid in this direction.

OBJECTIVES

The insufficient attention on studies related to fracture behaviour of sheet metals originates from the fact that engineering materials with thinner sections are not considered as load bearing structural parts. Only Liu and his co-workers [2-4] have suggested some guidelines to assess fracture criteria of thin and tough plates of structural materials. The objectives of this study are (i) to present a simple technique for obtaining fracture criteria of EDD steel sheets in line with the studies of Liu [2], Ray [1] and verify the same with FE analysis. (ii) to examine the effect of the variation of thickness of such steel sheets on their fracture criteria.

BACKGROUND

The basic principle for obtaining fracture criteria of thin and tough sheets / plates according to Liu and his co-workers [2-4] is related to examinations of a strip necking zone which remains embedded inside the plastic zone ahead of a crack tip in a deformed specimen. The investigators have contended that such strip necking phenomenon is governed by the ratio of the plastic zone size and the plate thickness (B), and thus a physical parameter $(K/S_Y)^2/B$ controls the occurrence of crack tip necking. The parameter henceforth will be referred to as the strip necking parameter. In addition, Liu [2], and Liu and Kuo [4] have observed that the crack tip opening displacement in the strip necking zone is equal to the thickness contraction. This observation led them to conclude that the thickness contraction at the crack tip is equal to the crack tip opening displacement (CTOD), which in turn is related to the stress intensity factor. Thus, a measurement of the thickness contraction at the critical point of surface crack initiation leads to the assessment of a fracture criterion for thin and tough sheets and plates. But these investigations have not indicated any rationale for detecting the crack initiation event.

METHODOLOGY

The determination of fracture criterion for thin sheets in the present study was made using compact tension type specimens as per ASTM standard E399-91 [5] and with the help of a fabricated grip. The various tests are conducted to summarize the results.

SPECIMEN PREPERATION

Specimen is fabricated according to ASTM standard E399-91 [5] by wire electric discharge machining to maintain the exact relationship between all the dimensions. The configuration of the test specimen is shown in Fig.1. The specimens were ground with emery papers following 1/0 (coarse), 2/0, 3/0, 4/0 (fine). These were then polished first using alundum and finally using 0.25μm diamond paste. The mechanical grip was fabricated suitable to the Universal Testing Machine.

METALLOGRAPHIC AND MECHANICAL TESTS

The composition of the investigated steel is given as (C-0.06, Mn-0.38, S-0.03, P-0.017, Si-0.05, Fe-Bal., all in weight %). The microstructure of the material revealed ferrite plus pearlite (~5.1%), and the average ferrite grain size was found to be 7.2μm. The average tensile properties of the material were as follows: yield strength (S_Y) = 355.9MPa, ultimate tensile strength = 387MPa. The average hardness of the steel in the Rockwell-B scale was obtained as 71.3.

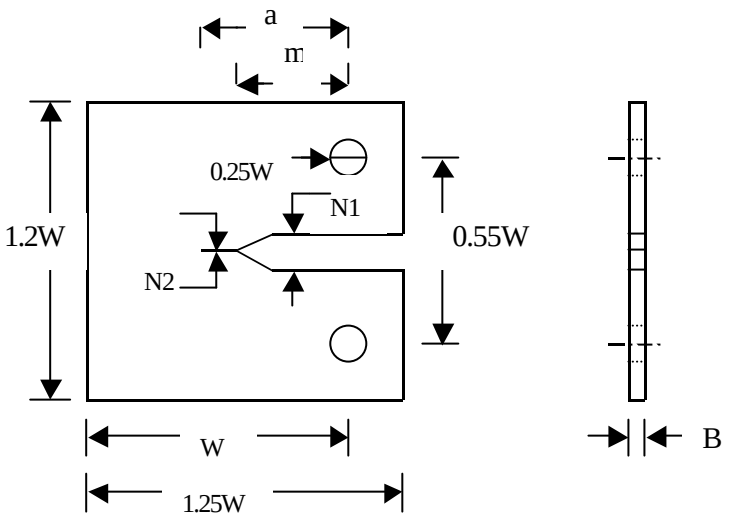

Fig.1. Geometry of the test specimens used for determining fracture criteria of thin sheets. (W = 24 mm, B = 1.18 - 1.69 mm, N1 = 0.8 mm, and N2 = 0.2 mm, a = actual crack length, m = major slot)

FRACTURE TEST

The fracture tests were carried out using an Instron (Model 4204) Universal Testing Machine with a loading rate corresponding to the constant crack head displacement of 0.2 mm/min at the room temperature of 300K. During such tests, the magnitude of load and displacement were recorded together with time. It was observed that load dropped at a particular instance during such a test, when butterfly-shaped surface cracks initiated. At that instance of time the loading of a specimen was discontinued, and the specimen was taken out for subsequent measurement of *CTOD* and analysis of alternate fracture criteria. Four specimens with thickness 1.18, 1.58, 1.64 and 1.69 mm were tested. The detailed dimensions of the specimens together with the critical loads (P_c) at the point of crack initiation obtained during their tests are given in Table 1.

Table 1.
Dimensions of the tested specimens and the Maximum Load (P_c) attained During the Fracture Tests.

Specimen Code	Thickness *B* (mm)	Crack Length *a* (mm)	Critical Load P_c (kN)
S1	1.18	10.16	1.194
S2	1.58	10.15	1.829
S3	1.64	10.22	1.773
S4	1.69	10.16	1.855

ESTIMATION OF FRACTURE TOUGHNESS

The critical crack-tip opening displacement during the loading consists of elastic CTOD (δ_e) plus plastic CTOD (δ_p) following report of You and Knott [6].

$$CTOD_c = \delta = \delta_e + \delta_p \quad (1)$$

$$\delta_e = [K^2(1-\nu^2)] / 4 S_Y E \quad (2)$$

where, the elastic modulus (E) and the Poisson's ratio (ν) were taken as 211 Mpa and 0.33, respectively. However, to know the value of δ_e the magnitude of stress intensity factor K needs to be estimated. The value of K is found from the Dugdale model [7] using the relationship:

$$G = K^2 / E = S_Y . CTOD \quad (3)$$

where, G = strain energy

The $CTOD$ is taken as δ_p, estimated with the help of an optical microscope and substituting this value in equation (3), the value of K is determined. Now the value of K gives the value of δ_e, which on substitution in equation (1) gives the value of critical CTOD (δ). Now the critical strain energy is given by

$$G_c = CTOD_c . S_Y = \delta . S_Y \quad (4)$$

and subsequently the value of fracture toughness K_c is calculated by:

$$K_c = \sqrt{(G_c . E)} \quad (5)$$

FINITE ELEMENT FORMULATION

The same study was simulated in ANSYS program using same dimensions, material and loading situation. The crack-tip deformation consists of elastic deformation and plastic deformation. Elastic deformation is based on linear analysis and plastic deformation is based on non-linear analysis.

SOLID MODELLING AND MESH GENERATION

A block is modeled with the dimensions as per ASTM standard, however one axes symmetry is considered for mode I type loading. Material properties are incorporated for linear & nonlinear analysis.

The solid model is then discertized into number of elements and nodes by automatic generation. Meshing is graded from fine at the crack-tip to coarse at the solid boundary. The element is defined by 20 nodes having three degrees of freedom per node: translations in x, y, and z directions. The element has plasticity, stress stiffening, large deflection and large strain capabilities. The most important region in a fracture model is the region around the edge of the crack. A prism shaped element may be formed by collapsing the top plane of a brick element along the surface diagonal. To pick up the singularity in the strain, the elements around the crack-tip should be quadratic, with the mid-side nodes placed at the quarter positions. Such an element called as a singular element was derived by Blackburn [8].

LOADING AND BOUNDARY CONDITIONS

In experiment, pins are inserted through the hole and are held through grip by the jaws of Instron machine. To simulate the practical situation, at the top of a cylindrical hole a line is defined and the total load is distributed along the line. To simulate the support condition, all the bottom face nodes are restricted for x and y direction movement.

LINEAR ANALYSIS

In this analysis, quarter shifting of the mid node is done to get singularity effect. For a particular specimen related critical load P_c is applied and the node of maximum displacement is located. For the particular node, 'θ', the angle made by the direction of maximum displacement with crack plane and the stress value, either σ_x or σ_y is noted. Then following the basic equation (5), the exact value of K is calculated.

$$\sigma_x = K_I / (2\pi r)^{1/2} \cos\theta/2 \, (1 - \sin\theta/2 \sin 3\theta/2) + \ldots$$
$$\sigma_y = K_I / (2\pi r)^{1/2} \cos\theta/2 \, (1 + \sin\theta/2 \sin 3\theta/2) + \ldots \quad (5)$$

where, r is the radius of the node from the crack tip. Now substituting value of K in equation (2), the value of elastic deformation δ_e is determined.

NONLINEAR ANALYSIS

Elastic-plastic finite element analysis can be considered as an extension of elastic analysis by incorporating extra conditions pertaining to nonlinear plasticity conditions. The elastic-plastic finite element analysis was carried out by Gdoutos et al [9]. Nonlinearity includes material nonlinearity and geometric nonlinearity. The elastic-plastic process requires a continuous assessment of stress and plastic strain at all points of the structure as the applied load increases. Hence the load is applied in sequence of relatively small increments, and within each step checks on stress and equilibrium are made. As the loading starts, the program starts to iterate the stress above the yield stress to consider the plastic effects. The whole nonlinear curve is considered to consist of number of straight lines, each being designated as a load step. With the help of this analysis, the value of plastic CTOD δ_p and crack-tip necking δ_n is determined at the same node considered in linear analysis to find the value of K_c. The values of δ_e and δ_p given by FE analysis are used in equation (1), (4) and (5) to find fracture toughness.

Table 2

Comparative Assessment of Experimental and FE Results on Different Fracture Parameters

Specimen Code No.	Thickness B (mm)	Crack-Tip Opening Displacement $CTOD_c$ (δ_c) (mm)		Fracture Toughness K_c MPa $m^{1/2}$	
		Experiment	FEM	Experiment	FEM
S1	1.18	0.631	0.640	211.5	212.8
S2	1.58	0.699	0.712	222.6	224.4
S3	1.64	0.778	0.783	234.8	235.4
S4	1.69	0.945	0.843	258.8	244.3

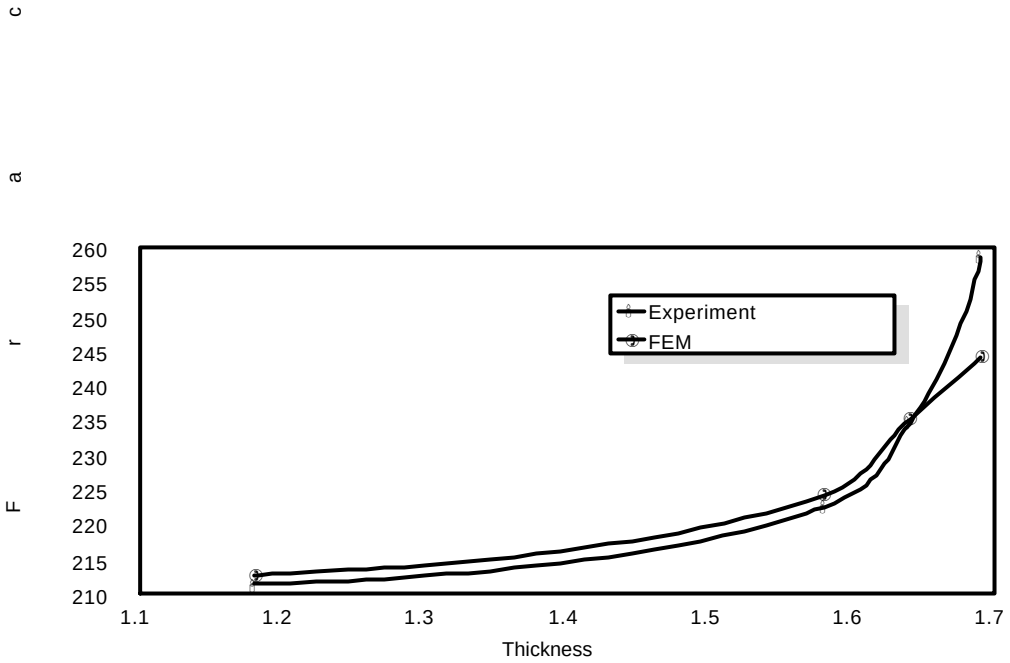

Fig. 2. Variation of Fracture Toughness for EDD (0.06%) Steel Sheet

CONCLUSIONS

1. The variation of δ and K_c with the thickness of steel sheets are given in Table 2. and Fig. 2. Figure 2 indicates that the trend of the present results by experiment and FE analysis is in agreement with those obtained by Liu [2], and in both the reports the magnitude of fracture toughness of thin sheets increases with increase in thickness, unlike that for thick plates as reported by Brown and Srawley [10].

2. One of the key observations in this study is the detection of the crack initiation in thin sheets from the phenomenon of load-drop, as illustrated with the help of Fig. 6. The detection of this event eliminates the elaborate effort required by Moire fringe technique for the estimation of $CTOD_c$ ($=\delta$) and replica technique for the estimation of crack tip contraction δ_n [2-3] because $CTOD_c$ can be simply estimated with the help of an optical microscope.

3. The plastic zone size for all the tested sheets extends upto the ligament boundary of the specimens.

4. The amount of crack-tip necking could be determined by FE analysis, which otherwise a difficult task to measure.

REFERENCES

[1] **Ray, K.K**. Fracture Criteria of Deep Drawn Steel Sheets. *International Journal of Fracture*, 70: R3-R8 (1995).

[2] **Liu, H.W.** Fracture Mechanics of Ductile and Tough Materials and its Applications to Energy Related Structures. Martinus Nijhoff Publishers, The Hague (1981) 189-198.

[3] **Liu, H.W.** and **Ke, J.S.** Engineering Fracture Mechanics 8 (1976) 425-436.

[4] **Liu, H.W.** and **Kuo, A.S.** *International Journal of Fracture* 14 (1978) R109-R112.

[5] American Society for Testing and Materials, E399-91, Philadelphia, PA (1991).

[6] **You, C.P.** and **Knott, J.F.** Fracture and the Role of Microstructure, 1, K.L. Maurer and F.E. Matzer, Chameleon Press Ltd., London (1982) 23-29.

[7] **Dugdale, D.S.** *Journal of Mechanics and Physics of Solids* 8 (1960) 100-108.

[8] **Blackburn**. On the Use of Singular Finite Elements in Linear Fracture Mechanics. *International Journal for Num. Methods in Engg.*, 10: 25-37 (1976).

[9] **Gdouts E.E.** and **Papakalitakis G**. Crack Growth Initiation in Elastic-Plastic Materials. *International Journal of Fracture*, 32: 143-156 (1987).

[10] **Srawley, J.E.** and **Brown, W.F.** Fracture Toughness Testing and its Applications. ASTM STP No. 381, Philadelphia, PA (1975) 133-198.

ORAL/POSTER REFERENCE: ICF100576OR

EXPERIMENTAL FAILURE MODES AND FEA OF LIGHTWEIGHT CERAMIC ABLATORS UNDER IOSIPESCU TESTING

S. Nagasawa, K. E. Parmenter, K. Shuman, and F. Milstein

Departments of Mechanical Engineering and Materials
University of California, Santa Barbara, CA 93106, USA

ABSTRACT

Lightweight ceramic ablators (LCAs) consist of fibrous ceramic substrates impregnated with organic resins. The ablators were developed at NASA Ames Research Center for use as heat shields to protect space vehicles during planetary entry. In the present work, the fracture characteristics of LCAs are determined by Iosipescu shear testing, and finite element analysis (FEA) is used to approximate the stress distribution in the Iosipescu tests. The experimental failure modes are interpreted in terms of the FEA results; it is shown that the LCAs fracture as a result of localized peak tensile stresses, rather than from the shear stress along the notch-root axis. Tests are made for two modes of load; i.e., parallel and perpendicular to the LCAs' preferred plane of fiber orientation.

KEYWORDS

SIRCA, PICA, Iosipescu, shear, FEA, LCA, ablator

INTRODUCTION

Lightweight ceramic ablators (LCAs) were developed at NASA Ames Research Center for use as heat shields to protect space vehicles during planetary entry [1]. The materials consist of fibrous ceramic substrates impregnated with organic resins. In this work, two material systems were investigated, in their virgin and charred states, viz., Silicone Impregnated Reusable Ceramic Ablator (SIRCA) and Phenolic Impregnated Carbon Ablator (PICA). SIRCA was the heat shield on the aft-plate of Mars Pathfinder and was chosen for the leading edges and nose cap of the X-34 Vehicle. PICA was chosen as the heat shield for Stardust Sample Return Capsule's forebody, and is a candidate for future sample return missions. The fibers in the substrates of the LCAs tend to be randomly and uniformly aligned parallel to a preferred plane (i.e., the fibers tend to lie normal to a preferred axis, but randomly oriented about the axis); hence the composites' mechanical properties

are anisotropic. Here we examine anisotropic fracture modes of the LCAs during Iosipescu shear testing, and interpret the results with FEA modeling.

EXPERIMENTAL IOSIPESCU SHEAR TESTS

Notched beam Iosipescu specimens [2] were loaded anti-symmetrically in an Adams and Walrath (A&W) fixture [3] as illustrated in Fig. 1. Load F_N was applied by a displacement-controlled Instron testing machine and measured with a compression load cell. Displacement y was determined from the Instron's internal displacement gage; the crosshead speed was set at 0.102 mm/min. Iosipescu tests were made on two types of LCAs, SIRCA 15F and PICA, in their virgin and charred states. To produce the charred materials, specimens were pyrolyzed in a tube furnace, in an argon environment, at 1000ºC for 10 minutes. Two modes of loading were employed (as illustrated in Fig. 2): (a) specimens were oriented with their preferred plane normal to the applied load, and normal to the notched cross-section (transverse loading), and (b) the preferred plane was parallel to the applied load, and parallel to the notched cross-section (parallel loading).

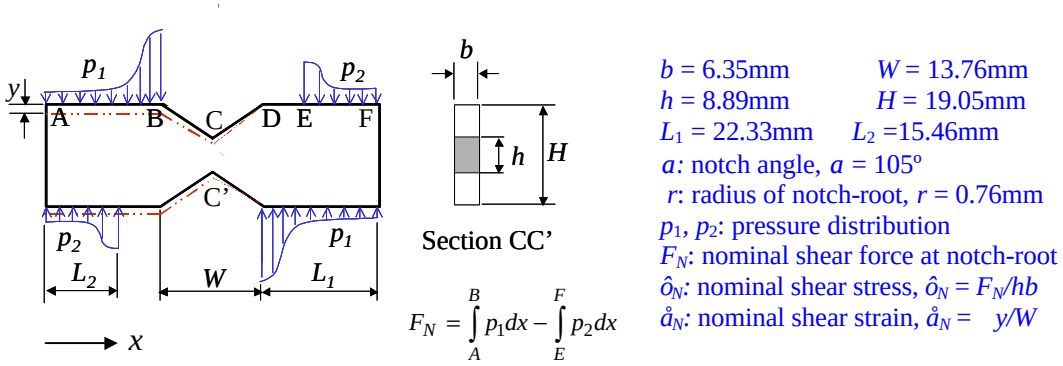

Figure 1: Boundary conditions and dimensions of Iosipescu specimen in A&W fixture

Figure 2 illustrates the predominant experimentally observed fracture patterns. Under transverse loading, cracks form at the surface, near top and bottom notch tips, at angles between 45º and 90º to the notch-root axis. This pattern was observed for virtually all of the transverse specimens, and is indicative of tensile failure. Under parallel loading, vertical cracks form at the surface at locations that are just to the left of surface points *E* and C'; the analyses presented in the next section suggest that these are locations of peak tensile stress. (The inverse scenario also occurred in which the cracks formed just to the right of surface points *E'* and *C*.)

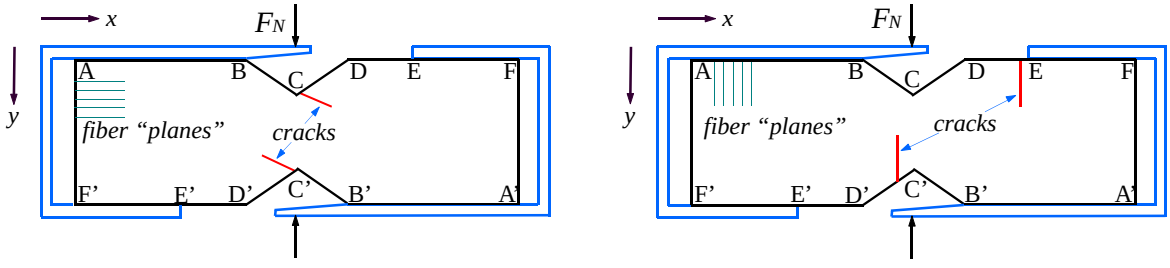

(a) Transverse loading **(b)** Parallel loading

Figure 2: Illustration of fracture patterns during Iosipescu testing of LCA specimens

Values of nominal maximum shear stress, $t_{N,max}$, and "nominal shear modulus," k_s, were determined experimentally, as indicated in Fig. 3. The values of $t_{N,max}$, for each test series, are listed in Table 1. Numerical values following +/- signs are standard deviations. Generally, the $t_{N,max}$ values are comparable for virgin and charred specimens, and are about 100% greater in the transverse than in the parallel mode; charred SIRCA in parallel loading is an exception.

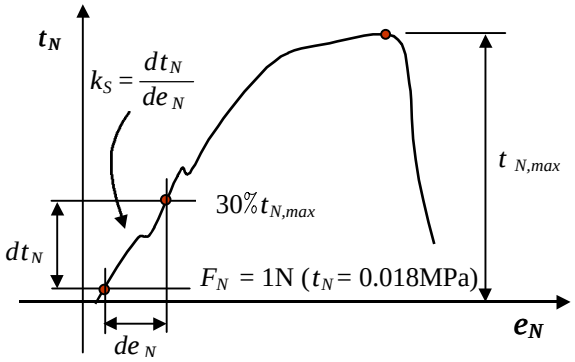

Material	Mode	k_s [MPa]
Virgin SIRCA	Transverse	12.3 +/- 3.5
Virgin SIRCA	Parallel	4.9 +/- 1.2
Charred SIRCA	Transverse	24.8 +/- 8.6
Charred SIRCA	Parallel	12.2 +/- 3.8
Virgin PICA	Transverse	6.3 +/- 1.2
Virgin PICA	Parallel	4.8 +/- 1.2
Charred PICA	Transverse	15.7 +/- 5.1
Charred PICA	Parallel	7.3 +/- 2.0

Figure 3: Illustration of Iosipescu Test Response and Determination of k_s

TABLE 1
MAXIMUM NOMINAL SHEAR STRESS $t_{N,max}$ DURING IOSIPESCU TESTING

Material	Density [kg/m^3]	Parallel Loading		Transverse Loading	
		No. of Tests	$t_{N,max}$ [MPa]	No. of Tests	$t_{N,max}$ [MPa]
Virgin SIRCA	240	9	0.39 +/- 0.05	9	0.80 +/- 0.04
Charred SIRCA	250	10	0.57 +/- 0.08	12	0.78 +/- 0.16
Virgin PICA	210	8	0.15 +/- 0.03	10	0.37 +/- 0.03
Charred PICA	190	9	0.17 +/- 0.03	10	0.38 +/- 0.05

FINITE ELEMENT ANALYSIS OF IOSIPESCU TESTS

In this section, we show that a relatively simple, anisotropic, linear elastic, model provides good qualitative understanding of the experimentally observed failure modes. In the analyses, the elastic properties of the model will be associated with two types of composites. In Type I, the fibers are unidirectional, and in Type II, the fibers are randomly and uniformly aligned parallel to a preferred plane. At this time, Iosipescu modeling of Type I is complete and is discussed here; modeling of Type II is in progress. For Iosipescu testing of both types of composites, under transverse loading, the load is normal to the fibers' axes and, under parallel loading, the composites may be envisioned as parallel planes of fibers that are parallel to the load; thus qualitative similarities may be expected among FEA results for both types. The FEA used an ANSYS meshed model, with geometric parameters shown in Fig. 1. The element library type is PLANE STRESS (quadrilateral, 8 nodes), the sizes of the elements and nodes are 1694 and 5377, respectively. The minimum side length of subdivided elements is 10.5% of the notch-root radius r, and the maximum length is 14.3% of the notched cross-section h. The computations employed a "standard" downward stroke, Δy = 0.1mm, of the left fixture, while the right fixture was fixed. For the CONTACT model, a friction coefficient

of 0.25 was assumed. For the Type I composites, if the fibers are aligned in the "1-direction," the 2-3 plane is the plane of isotropy, and there are five independent compliances: S_{11}, $S_{22} = S_{33}$, $S_{12} = S_{13}$, S_{23}, and $S_{55} = S_{66}$ (with $S_{44}/2 = S_{22} - S_{23}$) [4]. For modeling purposes, we take $S_{11} = 1/E_P$ and $S_{22} = 1/E_T$, where E_P and E_T are the experimental Young moduli of the LCAs under uniaxial loads, parallel and transverse, respectively, to the preferred plane [5]. Further simplifying assumptions are that the compliances S_{44} and S_{55} are equal and the Poisson ratios $\acute{\imath}_{12} = \acute{\imath}_{23} = 0.46$. With these assumptions and the known values of E_P and E_T, the remaining compliances are calculated from $S_{12} = -\acute{\imath}_{12}/E_P$, $S_{23} = -\acute{\imath}_{23}/E_T$, and $S_{44} = 2(S_{22} - S_{23}) = S_{55}$. The experimental values of E_P and E_T are listed in Table 2; the values of both moduli, E_P and E_T, were found to depend on whether the uniaxial load was tensile or compressive. FEA was carried out using both tensile and compressive values of E_P and E_T. As a check on the suitability of the modeling approximations, the nominal shear modulus k_s was calculated in the analyses and compared with the experimental values of k_s. There was generally good agreement between these quantities, with the calculated values tending to be somewhat greater than the corresponding experimental values when the tensile values of E_P and E_T were used in the FEA and vice versa when the compressive values of E_P and E_T were used; i.e., the experimental response was intermediate to the FEA responses computed with the tensile and compressive Young moduli (suggesting an "averaging" effect of the moduli in the Iosipescu experiments).

TABLE 2
EXPERIMENTAL VALUES OF YOUNG'S MODULUS USED IN THE FEA

Material	Under Uniaxial Tension		Under Uniaxial Compression	
	E_P [MPa]	E_T [MPa]	E_P [MPa]	E_T [MPa]
Virgin SIRCA	380	67	130	34
Charred SIRCA	630	170	138	89
Virgin PICA	N/A	N/A	143	12
Charred PICA	N/A	N/A	107	33

Earlier studies [6,7] have analyzed the shear stress in the notched cross-section for various composite materials. However, comparisons among the experimental failure modes and the normal stress contours calculated in the present work indicate that the LCA specimens fail in a tensile mode. Therefore, in addition to calculating the shear stress distribution along the notched cross-section *CC'*, we have focused on the principal stress distributions on the surface of the specimens. Since the FEA employs PLANE STRESS, the normal stress in the *z* direction, which is a principal stress, is always zero. The other two ordered principal stresses in the *xy* plane are $\acute{o}_{p1}$ and $\acute{o}_{p2}$. The maximum shear stress, $t_p = (\acute{o}_{p1} - \acute{o}_{p2})/2 \equiv t_p(y')$, was determined along the cross-section *CC'* (where $y' \equiv 0$ half-way between *C* and *C'* and $y' = +0.5$ and -0.5, respectively, at the notch-roots *C* and *C'*). In accord with earlier work [6,7] we found that $t_p(y')$ increases as $y' \rightarrow \pm 0.5$ under transverse loading and it decreases as $y' \rightarrow \pm 0.5$ in parallel loading. In transverse loading, t_p also exhibited a local maximum, t_{max}, at $y' = y'_{max}$. The normalized values of t_{max} and their locations are listed in Table 3 ($t_s \equiv t_N$ in the "standard" FEA, i.e., with $\Delta y = 0.1$mm); the maximum shear stress was observed to obey the relation $t_{max}/t_s \approx 0.028(E_P/E_T) + 1.05$, where $1.55 < E_P/E_T < 11.92$.

TABLE 3

NORMALIZED MAXIMUM SHEAR STRESSES $t_{max}/\hat{o}_s$ AND THEIR LOCATIONS y'_{max} IN FEA TRANSVERSE IOSIPESCU MODEL

Material	Modeling Parameters		E_P/E_T	$t_{max}/\hat{o}_s$	y'_{max}
	E_P [MPa]	E_T [MPa]			
Virgin SIRCA	380	67	5.67	1.211	0.469
Charred SIRCA	630	170	3.71	1.160	0.450
Virgin SIRCA	130	34	3.82	1.163	0.449
Charred SIRCA	138	89	1.55	1.088	0.419
Virgin PICA	143	12	11.92	1.385	0.487
Charred PICA	107	33	3.24	1.139	0.449

The Iosipescu principal stress distributions were investigated under parallel and transverse loading, using both the compressive and the tensile values of E_P and E_T of SIRCA and using the compressive moduli of PICA in the FEA. Attention was focused on the region along surface *BCDE*, since that is where cracking was observed in the experiments. Figure 4 shows a representative example of the normalized, ordered, principal stresses $ó_{p1}/t_s$ and $ó_{p2}/t_s$ along *BCDE*, for transverse and parallel Iosipescu tests. The compressive values of E_P and E_T of virgin SIRCA were used in the calculations of Fig. 4. The position on the surface s' is normalized by $2L_{CD}$ (twice the length of *CD*), so that s' = -0.5, 0, 0.5, and 0.9, respectively, correspond to positions at *B*, *C*, *D*, and *E* (s' = 0 is at the notch-root). During transverse loading (Fig. 4a), the tensile stress $ó_{p1}$ is highly concentrated in the neighborhood of the notch-root, where it reaches a peak value of $ó_{maxI}$ at $s' = s'_{maxI}$, while the compressive stress $ó_{p2}$ is concentrated on the opposite side of the notch-root; $ó_{p1}$ also reaches a secondary maximum $ó_{maxII}$ at s' = 0.900, which is at position E. The stress concentration at the notch-root explains why fracture occurs in a tensile mode near the notch tips during transverse loading (Fig. 2a). During parallel loading (Fig. 4b) $ó_{p1}$ is not peaked near the notch-root, but has a broad local maximum $ó_{maxI}$ at s'_{maxI} in the region between *C* and *D*; in this mode, $ó_{p1}$ also reaches a peak value, $ó_{maxII}$, at s' = 0.888 which is close to *E*. These results are consistent with fracture patterns observed under parallel loading (Fig. 2b). Normalized tensile stress maxima, $ó_{maxI}/t_s$ and $ó_{maxII}/t_s$, and the locations of $ó_{maxI}$ are listed in Table 4 for all of the materials and modeling conditions. During transverse loading, position s_{maxI} is at a distance of roughly 5% of L_{CD} from the notch-root, and in parallel loading it is at a distance of about 30% of L_{CD}. It was also found that the maximum stresses in the region *CD* of the notch could be expressed as $ó_{maxI}/t_s = 0.459\ln(E_P/E_T) + 1.530$, where $1.55 < E_P/E_T < 11.92$, in the Iosipescu modeling under transverse loading, and $ó_{maxI}/t_s = 0.0426\ln(E_P/E_T) + 1.638$, where $3.24 < E_P/E_T < 11.92$, in the parallel loading models.

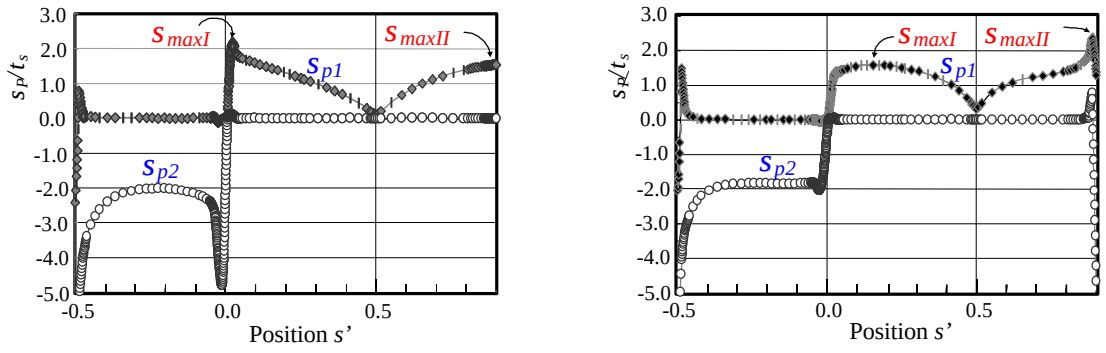

(a) Transverse loading **(b)** Parallel loading

Figure 4: Principal stress distribution on the surface *BCDE* of the Iosipescu specimen

TABLE 4

NORMALIZED MAXIMUM TENSILE STRESSES $\acute{o}_{maxI}$ AND $\acute{o}_{maxII}$ AND LOCATION s'_{maxI} OF $\acute{o}_{maxI}$

Material	Moduli [MPa]		Iosipescu Mode	$\acute{o}_{max}/\hat{o}_s$	s'_{maxI}	$\acute{o}_{maxII}/\hat{o}_s$
	E_P	E_T				
Virgin SIRCA	380	67	Transverse	2.344	0.024	1.691
Virgin SIRCA	130	34	Transverse	2.171	0.024	1.544
Charred SIRCA	630	170	Transverse	2.146	0.024	1.529
Charred SIRCA	138	89	Transverse	1.694	0.029	1.297
Virgin PICA	143	12	Transverse	2.633	0.024	2.072
Charred PICA	107	33	Transverse	2.082	0.024	1.485
Virgin SIRCA	380	67	Parallel	1.558	0.162	2.195
Virgin SIRCA	130	34	Parallel	1.584	0.149	2.394
Charred SIRCA	630	170	Parallel	1.584	0.147	2.367
Charred SIRCA	138	89	Parallel	1.531	0.117	1.633
Virgin PICA	143	12	Parallel	1.535	0.176	1.913
Charred PICA	107	33	Parallel	1.588	0.147	2.274

CONCLUSIONS

Iosipescu shear tests were conducted on composite LCA materials, under parallel and transverse loading conditions, and the experiments were modeled with anisotropic, linear elastic, FEA. The maximum nominal shear stress was measured, although the observed fracture patterns and FEA results indicated that the materials failed in a tensile mode rather than by shearing. The maximum values of principal stress in FEA occurred in regions where fracturing was observed in the experiments. The shear stress distribution along the notched cross-section was also computed.

ACKNOWLEDGEMENTS

NASA Ames Grant #NCC2-1049 provided financial support for this work. S. Nagasawa was an Overseas Research Scholar of the Japan Ministry of Education, Science and Culture, on leave from Nagaoka University of Technology. Support from K. Fields, C. Johnson, H. Tran, and D. Rasky is gratefully acknowledged.

REFERENCES

1. Tran, H.K. (1994). NASA TM 108798.
2. Iosipescu, N. (1963). *Rev. Mec. Appl.* 1, 147.
3. Adams, D.F. and Walrath, D.E. (1986). *Experimental Mechanics*. 27(2), 113.
4. Daniel, I.M. and Ishai, O. (1994). *Eng. Mechanics of Composite Materials.* Oxford Univ. Press.
5. Parmenter, K.E., Shuman, K., Milstein, F., Johnson, C.E., Tran, H.K. and Rasky, D.J. (2001). *Journal of Spacecraft and Rockets*. 38(2), in press.
6. Adams, D.F. and Walrath, D.E. (1987). *Journal of Composite Materials*. 21, 494.
7. Chiang, Y.J. (1996). *Journal of Testing and Evaluation, ASTM*. 24(1), 1.

ORAL/POSTER REFERENCE: *ICF1001064*

EXPERIMENTAL INVESTIGATION OF THE INERTIAL EFFECTS OCCURRING IN IMPACT TESTS ON PLASTICS WITH VARYING MASS DISTRIBUTION

A. Pavan[1] and G. Barbaglia[1]

[1]Dipartimento di Chimica Industriale e Ingegneria Chimica 'G. Natta',
Politecnico di Milano, Italy

ABSTRACT

Aim of the work is to elucidate some aspects of the phenomenology of impact tests in order to improve previously proposed modelizations. The experimental investigation focused on the influence of specimen dimensions and specimen mass distribution on the inertial effects observed in the initial part of an impact test. The experiments were carried out on single-edge notched specimens in the "one-point bending" mode. The flexural compliance of the notched specimens was varied by varying notch depth and specimen length and their mass distribution was varied by varying their length and by adding some concentrated masses. Analysis of the load-time traces recorded by the instrumented tup of the striker impacting the specimen at 1 m/s shows the distinct role played by the "contact mass" involved in the very first instants of the impact process, and by the inertia of the specimen wings. The "dynamic" one-point bend compliance of the specimen appears to be proportional to its "static" three-point bend compliance, if the specimen length in the former bending mode is equated to the span between the anvils in the latter bending mode. These results gave hints to the improvement of a previously proposed 'analogical' model for simulating the dynamics of the impact test.

KEYWORDS

Instrumented impact test, One-point bending, Inertial effects, Impact fracture, High rate of loading

INTRODUCTION

Use of instrumented impact testers is becoming commonplace and acquisition of the load vs. time response from a pre-cracked specimen makes the test amenable to fracture mechanics analysis, thus allowing an (intrinsic) value of fracture toughness to be extracted from the experimental data.

The analysis of the force-time trace recorded in an impact test, however, is complicated by the dynamic effects occurring when the test piece is loaded rapidly. Even at moderately high loading rates (speeds of the order of 1 m/s) the inertial forces set up by the accelerating masses produce effects that may mask the true

response of the material. These effects are reflected in the recorded force signal and need to be recognized and properly accounted for if the true impact resistance of the material itself is to be extracted from the experimental data.

In a previous work [1] we have demonstrated the usefulness of one-point bending impact experiments (same configuration as in a three-point bending test but without anvils) to elucidate the dynamics of the specimen deformation. Aim of the present work is to extend the investigation to non-standard specimen dimensions in order to elucidate the effects of varying the distribution of the masses involved in the impact process.

EXPERIMENTAL DETAILS

Impact tests were performed with an instrumented pendulum (Resil 25 by CEAST, Turin) in the Charpy configuration but with the two anvils removed (one-point bending mode). Built-in instrumentation consists of a strain-gauge load cell mounted in the tup of the striker to measure the force acting on its nose and a data acquisition system capable of capturing the force signal every 1 μs. A test speed (load-point displacement rate) of 1 m/s was applied and the impact energies used were far in excess of the energy subtracted by the specimen during the test, so that variations in the striker speed during the test were negligible. Standard (according to 2,3) and non-standard single-edge-notched (SE(B)) specimens of a rigid polyvinylchloride (PVC), were used. The specimen cross-section measured 8.1 mm in thickness (B) and 16.2 mm in width (W), while specimen length (L) and notch depth (a) were varied over wide ranges. The specimens were carefully machined to provide the best possible tup/specimen contact at impact so as to obtain reproducible measurements. An example of the degree of reproducibility generally obtained in this work is shown in Figure 1.

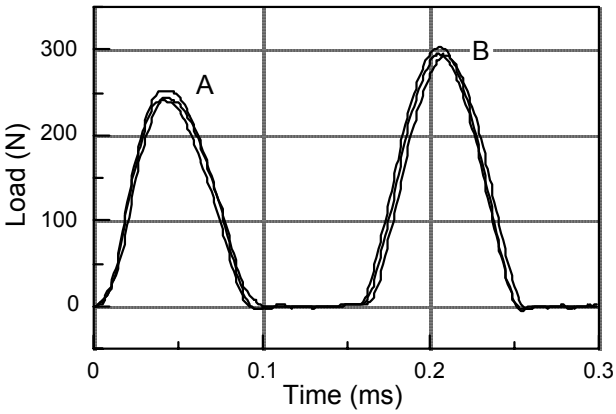

Figure 1 - Examples of load-time trace reproducibility: three replicates obtained from specimens with $L/W = 4.4$, $a/W = 0.5$.

To assess the effect of altering the mass distribution in the specimens, concentrated masses (lead tabs weighing 7.2 g each) were firmly glued either at the two ends of the specimens or at the two sides of the notch on the surface opposite to the impact point, as shown in Figure 2.

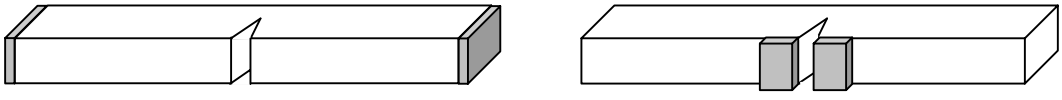

Figure 2 - Positions of added concentrated masses.

RESULTS AND DISCUSSION

Previous works [4,5,1] had already shown that the result of one-point bending impact tests is a series of peaks in the recorded force signal. We shall consider the first peak (often denoted as "*the* inertia peak") first and the subsequent peaks later on.

First peak

Previous observations [4,5,1] on specimens of standard dimensions ($W = 2B$, $L/W \approx 4$) but varying relative notch depth (a/W) had shown that the first peak recorded in the tests carried out at 1 m/s, with or without anvils, is nearly symmetrical (see e.g. in Figure 1) and invariant with a/W [5,1]. Since the notch depth affects the (static) flexural compliance of the specimen considerably, the latter observation suggested that the tup/specimen interaction reflected in the first peak involves only a limited portion of the specimen mass (the "contact mass"). By modelling the first tup/specimen contact as a simple mass-spring model ("contact mass" plus "contact stiffness") it appeared that the volume of the contact mass is constant (about 1.8 cm^3) for a wide range of test materials, specimen dimensions, test speeds and striker tup materials and geometries [6].

Results obtained with specimens of relative length L/W greater than the standard value of nearly 4 now show that only the ascending part of the peak is invariant with specimen geometry (Figure 3): the shape and the duration of the descending part is affected by a change in a/W and L/W.

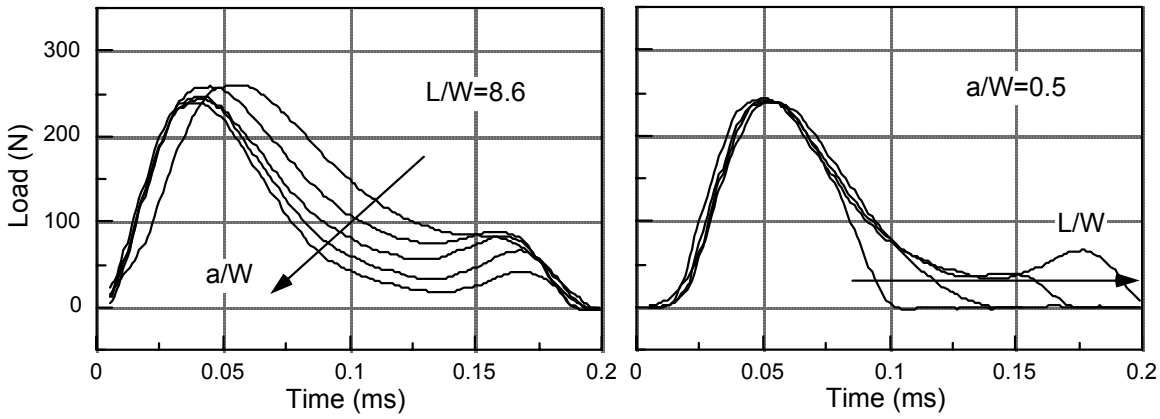

Figure 3 – Records of first peak obtained on specimens of relative length $L/W = 8.6$ and relative notch depth $a/W = 0.15$, 0.3, 0.4, 0.5, 0.6 (left) and specimens of relative notch depth $a/W = 0.5$ and varying relative length $L/W = 4.4$, 6.1, 7.5, 8.6 (right).

These results can be interpreted as follows. The ascending part of the peak reflects the acceleration of the contact mass, which is a limited portion of the specimen mass around the impact point. The remainder of the specimen is still at rest during this first stage: neither variation in length (L) nor in flexural compliance (through a/W) alter the specimen response to impact during this first stage. At the apex of the peak the speed of the contact mass reaches the speed of the striker and the force exerted on the tup (and sensed by the load cell) stops increasing. Afterwards, the speed of the contact mass keeps increasing [7] thus releasing the compressive force exerted on the tup (descending part of the force peak) until it reaches nearly twice a speed of the striker speed, as it can be predicted by an elastic analysis of a two-body impact. At this point the force acting on the tup of the striker vanishes, possibly reflecting loss of contact between tup and specimen.

During this stage of the impact process (descending part of the force peak) the reaction of the specimen to its bending starts to become appreciable, as indicated by the influence of the notch depth on the recorded load trace (Figure 3a): the greater the flexural compliance (as reflected in a/W) the shorter the duration of this stage. Consistently, also the wings of the specimen start moving, as indicated by the influence of the

specimen length on the recorded load trace (Figure 3b): the greater the specimen length, the greater the inertia of the wings, the longer the duration of this stage.

This interpretation is supported by observations drawn from the experiments performed on specimens bearing added concentrated masses. Placing the weights at the center of the test bar produces the same effect

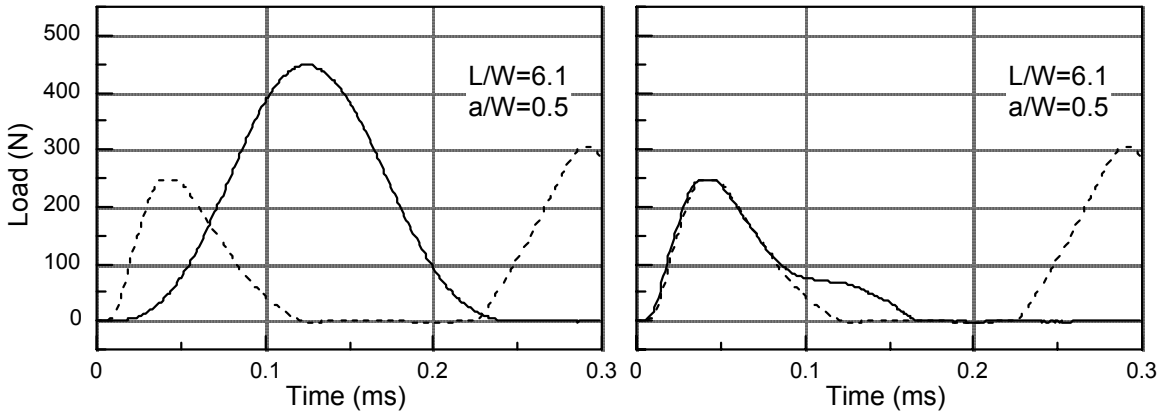

Figure 4 – Comparison of first peak records obtained from specimens of identical dimensions but with added concentrated masses placed either at mid-span (full line, left) or at specimen ends (full line, right). Dotted line: un-ballasted specimen.

as increasing the contact mass: both the intensity and the duration of the force pulse increase, as predicted by elementary mechanics (Figure 4, left). Placing the weights at the extremities of the test bar increases the inertia of the wings just as by increasing the specimen length, and the effect is an extension of the descending part of the force peak (Figure 4, right).

Subsequent peaks

It was shown previously [5,1] that number and separation of the subsequent peaks change by varying the notch depth a, and the time interval between two consecutive peaks turned out to be proportional to the square root of the "static" bending compliance in three-point bending, at least for specimens of "standard" three-point bend dimensions ($S/W = 4$ and $L \approx S$) [1].

The investigation has now been extended to consider the effect of increasing the specimen length and adding some concentrated masses. An example of the results so obtained is shown in Figure 5. Number, shape and separation of the force peaks are all affected. In an attempt to rationalize the dependence of the separation between the main peaks on specimen length, we have plotted the time interval between the first two main peaks A and B, T_{AB}, (assuming it is proportional to the fundamental vibrational period of the beam) as a function of the square root of the dimensionless "static" bending compliance in three-point bending, $\psi(a/W, L/W)$ calculated from [8,9] according to [2] with $S = L$ (Fig. 6). The diagram collects all data points measured in the present work, with a/W ranging from 0.15 to 0.75 and L/W ranging from 4.4 to 8.6. The points appear to fall nicely on a single straight line through the origin. This finding confirms (as to the a/W-dependence) and extends (as to the L/W-dependence) the validity of the argument set out in [1]: the "dynamic" one-point bend compliance is proportional to the "static" three-point bend compliance, as specimen wings inertia acts like a constraint on the wings movement just as the anvils do in the three-point testing mode.

This result further strengthens the data interpretation given in [1]: the series of force peaks observed during the test reflects successive impacts of the striker tup onto the specimen, resulting from flexural vibrations of the moving specimen.

A similar analysis of the minor peaks appearing in the force-time records, including the one arising in the descending part of the first peak (see Figures 3 and 5) when specimen length, L, is increased, shows that they can be interpreted as the effect of higher modes of vibration. As a matter of fact their distance from the major peaks turns out to be in a constant ratio to the fundamental vibrational period (T_{AB}).

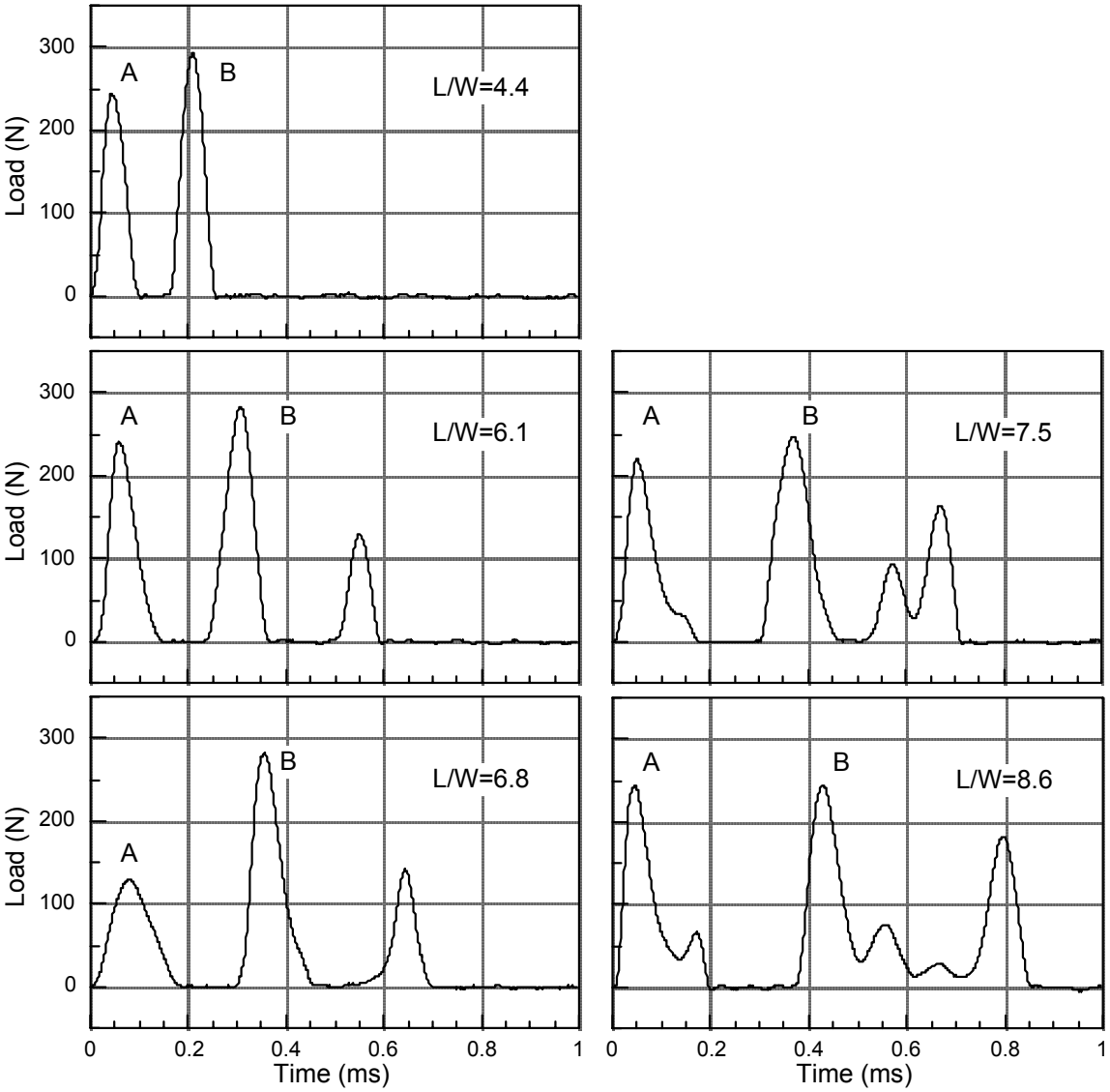

Figure 5 – Example of a load-time traces recorded in one-point bending impact tests on specimens with a/W=0.5 and varying relative specimen length L/W

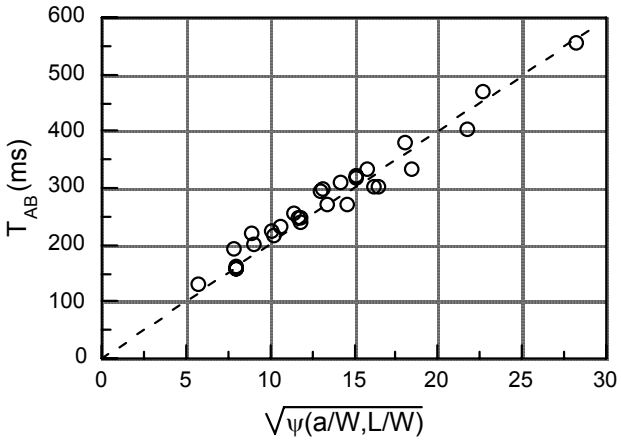

Fig. 6 – Time interval between the first two main peaks A and B of load-time traces recorded on specimens of varying relative notch depth a/W and relative length L/W, as a function

of the (dimensionless) three-point bending compliance $\psi(a/W, L/W)$

Modelization

In order to take into account the influence of specimen mass distribution and its variation with varying specimen length, a refinement of the model proposed in [1] was worked out [10]. Use of this model to extract the moment acting at the crack tip from the records of the apparent load measured at the striker tup is very promising. An example of its capability to simulate the test and reproduce the experimental load-time traces is shown in Fig.7.

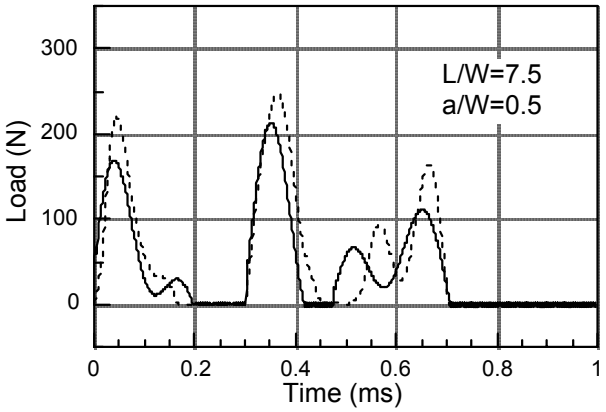

Figure 7 – Comparison of experimental (dotted line) and calculated (full line) load-time trace obtained from a one-point bending impact test on a specimen with a/W=0.5 and L/W=7.5.

CONCLUSIONS

The analysis of the force-time traces recorded in one-point bending impact tests performed on single-edge notched specimens of varying geometry and mass distribution allowed us to identify the origin of several features of the impact process. Based on these observations a further refinement of existing models for the test simulation was worked out, so that the model can be used to extract dynamic fracture toughness values from the impact test.

ACKNOWLEDGEMENTS

The impact instrument used in this work has been graciously loaned by CEAST, Turin. This work is part of the thesis submitted by G.B. to Politecnico di Milano for his diploma degree in Chemical Engineering.

REFERENCES

1. Pavan, A. and Draghi, S. (2000). In: *Fracture of Polymers, Composites and Adhesives, ESIS 27*, pp.347-361, Williams, J.G. and Pavan, A. (Eds). Elsevier, Amsterdam.
2. ISO 13586:2000. *Plastics - Determination of fracture toughness (G_{IC} and K_{IC}) - Linear elastic fracture mechanics (LEFM) approach.*
3. ASTM D 5045-93. *Standard Test Methods for Plane-Strain Fracture Toughness and Strain Energy Release Rate of Plastic Materials.*
4. Böhme, W. and Kalthoff, J. F. (1982). *Int. J. Fracture* 20, R139.
5. Zanichelli, C., Rink, M., Riccò, T. and Pavan, A. (1990) *Polym. Eng. Sci.* 30, 1117-1124.

6. Maurer, G. and Breuer, H. (1995). In: *Impact and Dynamic Fracture of Polymers and Composites, ESIS 19,* pp. 93-102, Williams, J. G. and Pavan, A. (Eds). MEP, London.
7. Venzi, S., Priest, H. A. and May, M. J. (1970). *Influence of Inertial Load in Instrumented Impact Tests, ASTM STP 466*, American Society for Testing and Materials, Philadelphia, PA, pp. 165-180.
8. Williams, J.G. (1984). *Fracture Mechanics of Polymers*. Ellis Horwood, Chichester
9. Bakker, A. (1990). *Fatigue Frac. Engng. Mater. Struc.* 13(2), 145.
10. Barbaglia, G. and Pavan, A., in preparation.

EXPERIMENTAL INVESTIGATION ON THE INFLUENCE OF SURFACE ENGINEERING ON THERMAL FATIGUE OF A HOT WORK TOOL STEEL

A. Persson [1], J. Bergström [1], C. Burman [1] and S. Hogmark [2]

[1] Department of Materials Engineering, Karlstad University, SE-651 88, Karlstad, Sweden
[2] The Ångström Laboratory, Uppsala University, SE-751 21 Uppsala, Sweden

ABSTRACT

Thermal fatigue is an important life-limiting factor in die casting moulds. It is observed as a network of fine cracks on the surface exposed to thermal cycling. The crack network degrades the surface quality of the tool and, consequently, the surface of the casting. Surface engineered materials are today successfully utilised to improve the erosion and corrosion resistance. However, their resistance when exposed to thermal cycling is not fully understood.

In this work, surface treatments (boriding and Toyota diffusion to give CrC) and physically vapour deposited (PVD) coatings of CrN, as single-layered or duplex-treated (nitriding followed by PVD coating), on hot work tool steel specimens were compared with the untreated reference material by experimental simulation of thermal fatigue. The test is based on induction heating and surface strain measurements by a non-contact laser speckle technique, which enables studies of the surface strain during thermal cycling.

Thermal fatigue cracking of a surface engineered tool steel is influenced by the modification of the mechanical properties of the substrate which occurs during the engineering process. With the exception of duplex-treatment, all variants of surface engineering show a tendency to decrease the resistance to thermal fatigue cracking as compared to the reference steel. However, the fact that the duplex-treated PVD CrN coating increased the resistance to thermal fatigue cracking as well as reduces the density of cracks as compared to the single-layered CrN coating, the potential to improve the life and performance in for example die casting applications still prevails.

KEYWORDS

Thermal fatigue, Heat checking, Die casting, Coating, Surface treatment, Hot work tool steel.

INTRODUCTION

During a die casting cycle, molten alloys of e.g. aluminium, zinc, magnesium or copper-based alloys are forced into an internally cooled mould by the application of pressure [1-3]. The molten metal flows with high velocity during injection and provides rapid filling of the die. A fill time in the order of milliseconds is a distinguishing characteristic of die casting. The high velocity injection allows high rate manufacturing of products in a wide range of thin-walled and complex shapes, typically 100 parts per hour. When the casting has solidified and cooled, the die is opened and the casting is ejected. Subsequently, the die may be

externally cooled and lubricated by spraying. The die is normally preheated to a temperature within the range of 150 to 350 °C, depending on the type of casting alloy. For aluminium and brass, the melt temperature is approximately 700 and 970 °C, respectively. During injection, the entrance velocity of the liquid metal is typically within the range of 20 to 60 m/s, but can be significantly lower (1 to 10 m/s) for brass. The metal pressure during injection can exceed 70 MPa. Hot work tool steels, such as AISI H11, H13, H21 and H22, are frequently used as die materials.

Thermal fatigue (or heat checking) is an important life-limiting factor in die casting moulds [1-3]. It is a fatigue process caused by the cycling of stress, strain and temperature in the die surface through the thermal cyclic nature of the casting process. Thermal fatigue of die casting moulds is a low cycle fatigue phenomenon basically controlled by the plastic strain imposed on the surface. However, both creep and oxidation may significantly contribute to damage and in some cases they can be the dominant failure mechanisms [4-7]. Thermal fatigue damage is often observed as a network of fine cracks on the surface exposed to thermal cycling. The crack network degrades the surface quality of the tool and, consequently, the surface finish of the cast products, and may eventually cause rejection of the casting. In addition to thermal fatigue cracking, gross fracture, erosion, corrosion and local adherence of the casting alloy (soldering) are other important failure modes which limit the life and performance of die casting dies.

Surface engineering is today successfully introduced to improve the erosion and corrosion resistance as well as to reduce soldering of dies and die materials [2, 8-13]. In addition, tests show that surface engineered materials may increase or decrease the resistance to thermal fatigue cracking as compared to an untreated material [11-13]. However, the resistance of surface engineered materials exposed to thermal cycling is not fully explored.

To increase the understanding of the thermal fatigue behaviour of surface engineered hot work tool steels exposed to thermal cycling it is necessary to perform experimental simulations. Since thermal fatigue cracks are usually limited to a thin surface layer of the tool, the surface response during the thermal cycling is of particular interest. In this study the following conditions of a hot work tool steel were evaluated: quenched and tempered (reference), treated by boriding and Toyota diffusion (CrC), CrN-coated and duplex-treated (CrN), respectively. The test is based on induction heating and surface strain measurements through a non-contact laser speckle technique. This enables studies of the changes of the response of the surface during thermal cycling.

EXPERIMENTAL

Materials

A hot work tool steel, Uddeholm QRO 90 Supreme, with the nominal chemical composition (wt. %) 0.38 C, 0.30 Si, 0.75 Mn, 2.6 Cr, 2.25 Mo, 0.9 V and Fe bal., was used as test material. The reference specimens were hardened and tempered (austenitizing 30 min at 1030 °C and tempering 2×2 h at 625 °C), followed by fine grinding to a surface roughness of (R_a-value) 0.38 ± 0.05 μm.

Prior to surface engineering, the specimens were ground and polished with 1 μm diamond paste in a last step to a surface roughness of (R_a-value) 20 ± 14 nm.

The specimens were surface treated by boriding (~25 h at ~850 °C), Toyota diffusion to generate CrC (TDP CrC) (6 h at 1030 °C) or plasma nitriding (15 h at 480 °C), to produce a diffusion zone without any iron nitride compound layer. The boriding process was followed by hardening and tempering (at 1030 °C and 2×2 h at 625 °C, respectively), while the TDP treatment was followed by tempering 2 h at 625 °C and 2 h at 600 °C. All plasma nitrided specimens were duplex-treated with a PVD CrN coating on top of the nitrided layer. The PVD CrN coatings were produced in a multi-arc process, with a deposition temperature of 300 - 400 °C. The five treatments resulted in different mechanical properties, see Table 1.

TABLE 1

MECHANICAL PROPERTIES OF THE MATERIALS

	Reference	Boriding	TDP CrC	PVD CrN	Nitriding + PVD CrN
Substrate hardness [HV_{30}]	507 ± 4	519 ± 2	522 ± 2	495 ± 1	507 ± 2
Surface hardness [$HV_{0.025}$]	-	1740 ± 100	1970 ± 70	2000 ± 100	2060 ± 100
Nitriding hardness [$HV_{0.025}$]	-	-	-	-	915 ± 15
Diffusion depth [µm]	-	29 ± 2	29 ± 1	-	159 ± 3
Coating thickness [µm]	-	-	-	6.1 ± 0.1	4.5 ± 0.2

Characterisation

Substrate hardness was assessed by macro-hardness (Vickers) measurements on polished cross-sections, using a load of 30 kg. Surface roughness (R_a-value) was measured using an optical surface profilometer.

For the specimens treated by boriding, TDP CrC and nitriding, the depth of the diffusion zone profiles were assessed by micro-hardness (Vickers) measurements on polished cross-sections, using a load of 25 g. The diffusion depth was defined as the depth beneath the coated surface at which the hardness was 50 $HV_{0.025}$ higher than the substrate hardness. For the specimens treated by boriding the depth is given excluding the outmost compound layer. PVD coating thicknesses were determined by light optical microscopy (LOM) on polished cross-sections.

Relative hardness of the surface treatments and surface coatings was assessed by micro-hardness (Vickers) indentations on polished cross-sections and in the surface of the coatings, respectively, using a load of 25 g. For the specimens treated by boriding, the surface hardness was measured below the compound layer.

Thermal fatigue testing

The test equipment is based on induction heating and surface strain measurements through a non-contact laser speckle technique, which makes it possible to calculate the strains induced in the specimen surface during thermal cycling. The test specimens are hollow cylinders with a diameter of 10 mm, a length of 80 mm and have a 3 mm axial hole for internal cooling. An induction unit (25 kW, 3 MHz) heats the specimen surface. Continuous cooling is performed by circulating silicon oil of 60 °C through the specimen, but also externally with argon, which also decreases oxidation during the thermal cycling. The specimen surface represents the surface of the die and the induction heating and cooling simulates the temperature cycles during die casting. More information is presented elsewhere [14].

Two temperature cycles were used to simulate aluminium and brass die casting conditions, respectively. They include a steep ramp to the maximum temperature, followed by a short hold time (<0.1 s), and subsequent cooling to the minimum temperature. To simulate aluminium and brass die casting, the maximum temperatures were set to 700 °C and 850 °C, respectively [14]. The minimum temperature for both cycles was set to 170 °C. The heating times in the 700 °C and 850 °C cycles were 0.4 and 2.5 s, respectively, and the total cycle times were 14.4 and 26.5 s, respectively.

Prior to testing, the specimens were pre-oxidised in order to get a thin oxide layer which facilitates pyrometer temperature control during heating. The reference specimens were pre-oxidised by electrochemical oxidisation in a NaOH-solution at 70 °C, followed by heat treatment, as described elsewhere [14]. All surface treated and surface coated specimens were pre-oxidised at 600 °C for 0.5 hour. In addition, a K-type (Chromel-Alumel) thermocouple with a wire diameter of 0.13 mm was welded to the specimen to measure the surface temperature during testing. Finally, to obtain a good speckle pattern for the surface strain measurements, an area of approximately 10×10 mm located in the middle of the specimens was roughened by a 1000 mesh abrasive paper or 3 µm diamond paste.

Evaluation of thermal fatigue

Induction heating using a frequency of 3 MHz give rise to heating of only a thin zone of the surface ('skin-effect'). During the thermal cycling, the total strain of the surface ε_{tot} is obtained by the laser speckle technique from the change in the specimen dimensions. The mechanical strain ε_{mech} generates the stress which is necessary for any surface cracking. It is due to the fact that the heat is inhomogeneously distributed through the specimen during thermal cycling. Through knowledge of the temperature cycle and the coefficient of thermal expansion of the tool material, it is possible to estimate the contribution from the thermal expansion/contraction ε_{th} of the unevenly heated/cooled specimen surface at any time. The mechanical strain is obtained as [15]:

$$\varepsilon_{mech} = \varepsilon_{tot} - \varepsilon_{th} \quad (1)$$

Crack propagation is represented as maximum crack length versus the number of thermal cycles. The thermal fatigue resistance (as maximum and mean crack length) and the crack density (the number of cracks per unit of length) was evaluated from crack length measurements after 5000 cycles to 700 °C. All evaluation of cracks is based on cracks larger than ~5 μm, where all measurements were performed on polished axial cross-sections by LOM. In addition, the crack pattern on the surface was studied using scanning electron microscopy (SEM). Finally, the mechanism of crack propagation was studied using LOM.

RESULTS AND DISCUSSION

Surface response

Typically, a linear increase in compressive ε_{mech} occurred with temperature, followed by a reduction of ε_{mech} during the first part of the cooling, see Fig. 1a and b. Subsequently, ε_{mech} moved toward an increasing or a decreasing compressive strain. The response of the surface during heating is a consequence of the constraint conditions due to the cooler bulk material, which retains the expansion of the surface. During the first part of the cooling, contraction of the surface occurs simultaneous with expansion of the bulk and, subsequently, both the surface and the bulk are contracting but at different rates. However, the response of the surface changes with increasing number of thermal cycles, represented by a decreasing residual mechanical strain range $\Delta\varepsilon_{residual}$, defined in Fig. 1a. Note that ε_{mech} at the peak temperature is approximately the same for all cycles.

Finally, each strain loop ends with a residual mechanical surface strain, which range is larger in the axial than in the tangential direction, see Fig. 1b. A difference in constraint conditions between the axial and tangential direction is probably the explanation. This indicates that the accumulated strain imposed on the surface during one thermal cycle is larger in the axial than in the tangential direction. Consequently, it is expected that the initial growth of the crack network is perpendicular to the axial direction of the specimen. The axial $\Delta\varepsilon_{residual}$, as normalised with respect to cycle 10, followed the same decreasing trend with increasing number of cycles for the surface engineered specimens as for the reference material, see Fig. 1c. The residual strain represents a cyclic creep strain and is governed by the plasticity of the material and the constraint conditions [16]. This indicates that the surface strain response during thermal cycling depends on changes of the mechanical properties of the substrate, as a consequence of for example cyclic and thermal softening, and a type of shakedown effect.

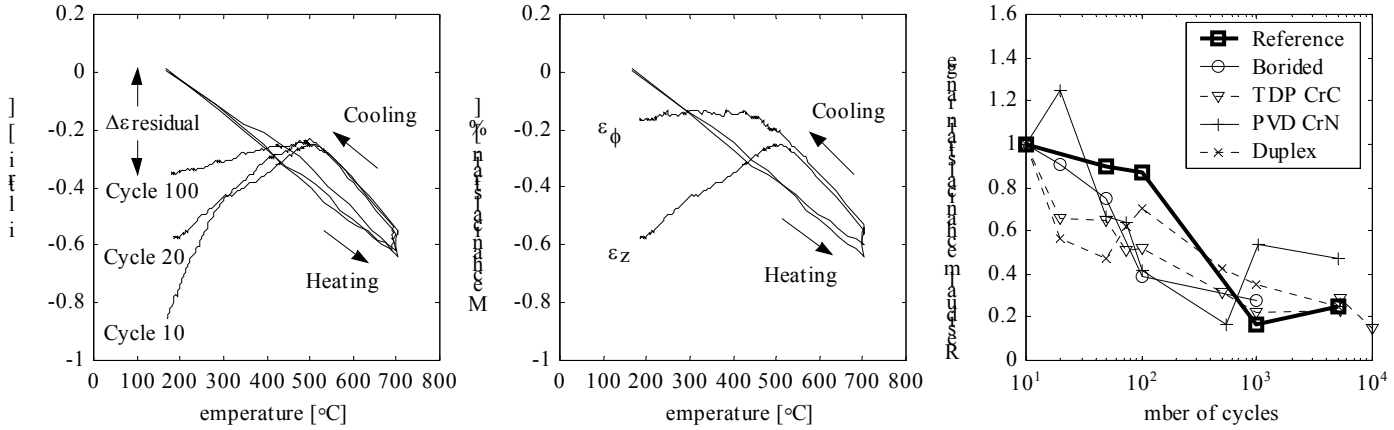

Fig. 1. Examples of the surface response during the 700 °C thermal cycling. a) Evolution of the axial ε_{mech}, including definition of the residual mechanical strain range ($\Delta\varepsilon_{residual}$). b) Comparison between axial strain (ε_z) and tangential strain (ε_ϕ) at cycle 20. c) Comparison between the normalised axial $\Delta\varepsilon_{residual}$ versus the number of cycles for the reference and the surface engineered specimens.

Development of the thermal fatigue crack network

This study indicates that the thermal fatigue cracks observed on the CrN coatings, after 5000 cycles to 700 °C, initiate at local coating defects, see Fig. 2a, followed by predominant growth perpendicular to the direction of the largest $\Delta\varepsilon_{residual}$, see Fig. 1b and 2b. Initially, the preferred circumferential crack growth is expected since the accumulated damage during one cycle is larger in the axial direction, as indicated previously. In addition, it was frequently observed that the crack network developed through the growth of cracks connected by local coating defects, see Fig. 2c, where the defects probably act as points of initiation in the coating. Crack initiation and propagation during thermal cycling to 10 000 cycles results in a random network of cracks, see Fig. 2d. This crack pattern corresponds well to that observed on die casting dies.

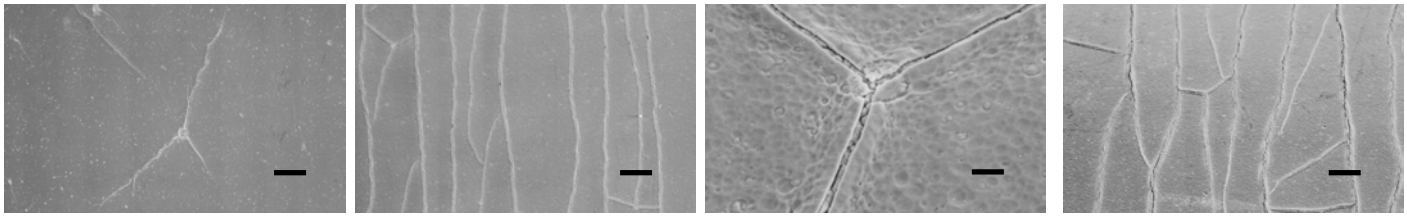

Fig. 2. Typical crack pattern observed using SEM on a CrN coated specimens after treatment with 700 °C cycles. a) Local surface crack at a local surface defect found on a duplex-treated specimen after 5000 cycles b) Cracks predominantly in the tangential direction observed on a CrN coated specimen after 5000 cycles. c) Close-up of b revealing coating defect as connection point for the cracks. d) Crack network observed on a CrN coated specimen after 10 000 cycles. (The axial direction is horizontal in all pictures.)

Crack growth

The crack growth was strongly dependent on the number of cycles and the maximum temperature during each cycle, see Fig. 3a. Since the crack propagation rate was very high during the 850 °C cycles, it was necessary to limit the number of these cycles to 1000. Studies of the mechanism of crack propagation using LOM on borided specimens revealed crack branching after exposure to the 850 °C cycles, whereas no branching of the cracks was observed after the 700 °C cycles, see Fig. 3b and c. The increased crack propagation rate for the 850 °C cycles is assumed to be an effect of increased plastic strain, increased effective crack driving force, or a decreased crack resistance.

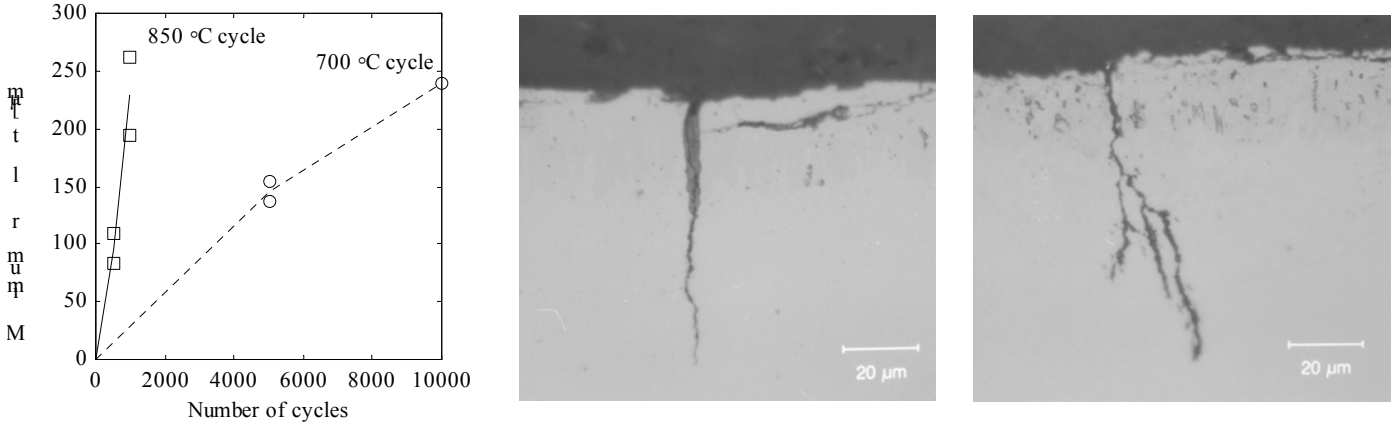

Fig. 3. Crack growth and mode of crack propagation of the borided specimens observed in LOM. a) Crack growth rate. b) Mode of propagation revealed after 5000 cycles to 700 °C. c) Crack propagation by branching revealed after 500 cycles to 850 °C.

In general, the boriding, TDP and CrN coating shows a tendency to decrease the resistance to thermal fatigue cracking as compared to the reference material, see Fig. 4. Additionally, the resistance to cracking among these seems to increase with the surface hardness. The density of cracks was significantly lower for the TDP than for the borided material which probably correlates to its higher surface hardness. To resist thermal cracking, a material should, for example, have a high hot hardness or hot yield strength, but also sufficient ductility, since the hot yield strength controls the plastic strain for a given temperature cycle, and the ductility represents the ability to resist plastic strain without cracking [2]. The engineered surfaces have higher hardness levels than the reference material, and it is expected that their hot yield strength is higher and their ductility is lower than for the reference material. However, the high deposition temperature of the boriding and the TDP processes probably affects the mechanical properties of the substrate differently as compared to that of the nitriding and PVD processes. When considering the maximum crack lengths in the borided and TDP treated materials, it is observed that they are well beyond the diffusion depths. This implies that the subsurface and substrate properties are different. However, the difference between the thermal fatigue resistance and the crack density between the two categories of surface engineerings is explained by the combined effect of differences in plastic response, residual stress state of the surface zone, as well as differences in these properties of the substrate.

Finally, it is clearly demonstrated that the duplex-treatment results in an increased resistance to surface cracking as well as a reduced density of cracks as compared to the single-layered CrN coating, see Fig. 4. This indicates that the plasma nitriding process prior to coating plays a dominant role to inhibit crack initiation and to slow down the crack propagation. The initiation and growth of cracks is probably slowed down as a consequence of the increased strength and the compressive stresses generated in a zone beneath the surface during plasma nitriding [16]. Simplified, this reduces the surface plastic strain and the tensile stress intensity range during thermal cycling and, consequently, the driving force for crack initiation and growth.

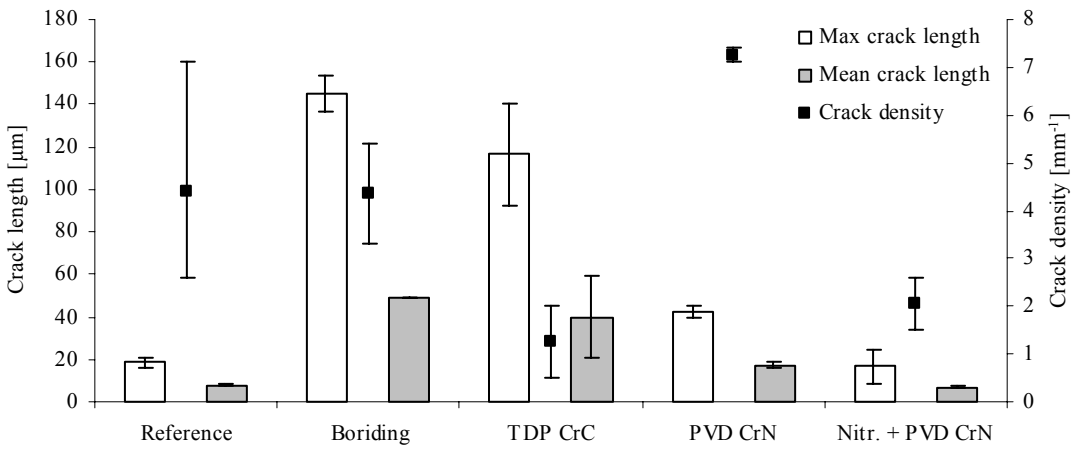

Fig. 4. Maximum and mean crack length as well as crack density after 5000 cycles to 700 °C. Three reference and two specimens of each treatment were tested. The error bars indicate the maximum and minimum value.

CONCLUSIONS

In this study, thermal fatigue of a tool during die casting of aluminium and brass was experimentally evaluated. A selection of surface treatments and PVD coatings of a reference hot work tool steel were included. The following conclusions can be drawn.

- Through induction heating the test equipment makes it possible to simulate failure of surface engineered tools during thermal cycling, as well as to deduce the surface strains responsible for the failure.
- Thermal fatigue cracking of a surface engineered tool steel is influenced by the modification of the mechanical properties of the substrate which occurs during the engineering process.
- With the exception of duplex-treatment, all variants of surface engineering show a tendency to decrease the resistance to thermal fatigue cracking as compared to the reference steel. However, the fact that the duplex-treated PVD CrN coating increased the resistance to thermal fatigue cracking as well as reduces the density of cracks as compared to the single-layered CrN coating, the potential to improve the life and performance in for example die casting applications still prevails.
- The initiation and progress of the crack network in CrN coatings on top of tool steel has been described.
- It is clearly demonstrated that the crack growth rate is rapidly increasing with the maximum cycle temperature above 700 °C. This indicates that an attempt to increase the life of tools exposed to thermal cycling should aim at decreasing the maximum temperature.

ACKNOWLEDGEMENTS

The financial and material support by the KK-foundation, Uddeholm Tooling AB, TA Hydronics AB and Bodycote Värmebehandling AB are hereby acknowledged. Special thanks to research engineer Anna Persson for all help with specimen preparation prior to light optical microscopy.

REFERENCES

1. Sully, L.J.D. (1988). In: *Metals handbook, Vol. 15*, pp. 286-295, ASM International, USA.
2. Davis, J.R. (ed.) (1995). *ASM speciality handbook, Tool materials*, ASM International, USA.
3. Allsop, D.F. and Kennedy, D. (1983). *Pressure diecasting, Part 2: The technology of the casting and the die*, Pergamon Press Ltd, Oxford.
4. Kovrigin, V.A., Starokozhev, B.S. and Yurasov, S.A. (1980) *Met. Sci. Heat Treat.* 22, 688.
5. Danzer, R., Sturm, F., Schindler, A. and Zleppnig, W. (1983) *Gisserei-Praxis*. 19/20, 287.
6. Zleppnig, W., Danzer, R., Fischer, F.D. and Maurer, K.L. (1986) *Proc. Euro. Conf. on Fract*. 6, 1139.
7. Schindler, A.M. and Danzer, R.B (1989) *Proc. Int. Conf. Step into the 90's*. 3, 905.
8. Chellapilla, S., Shivpuri, R. and Balasubramaniam, S. (1997) *Trans. 19th Int. Die Cast. Congr. Exp.* 295.
9. Arai, T. (1995) *Trans. 18th Int. Die Casting Congr. Exp*. 327.
10. Mitterer, C., Holler, F., Ustel, F. and Heim, D. (2000) *Surf. Coat. Technol*. 125, 233.
11. Starling, C.M.D. and Branco, J.R.T. (1997) *Thin Solid Films*. 308-309,436.
12. Wang, Y. (1997) *Surf. Coat. Technol*. 94-95, 60.
13. Faccoli, M., La Vecchia, G.M., Roberti, R., Molinari, A. and Pellizzari, M. (2000) *Int. J. Mat. Prod. Technol*. 15, 49.
14. Persson, A. (2000). Licentiate Thesis, Department of Materials Science, Uppsala University.
15. Sehitoglu, H. (1996). In: *ASM handbook, Vol. 19*, pp. 527-556, ASM International.
16. Suresh, S. (1998). *Fatigue of materials*, Cambridge University Press, UK.

ORAL/POSTER REFERENCE: ICF100237

EXPERIMENTAL RESEARCH ON FRACTURE AND FATIGUE OF SCT SPECIMEN SIMULATING HIGH-STRAIN REGION OF PRESSURE VESSEL NOZZLES

Chen Xuedong Yang Tiecheng Cheng Chuanqing
Hefei General Machinery Research Institute
No.888, West Changjiang Road, Hefei 230031, China

Jiang Jialing
Zhejiang University

ABSTRACT
This paper makes an in-depth analysis and research on the shaped compact tensile specimen (SCT), which simulates the high strain zone of pressure vessel nozzle. The elastoplastic FE analysis and test of SCT specimen show that SCT specimen fully possesses the characteristics of stress and strain simulation of high strain zone of pressure vessel nozzle, which is able to realize simulation of high strain zone of engineered structure with small test specimen and can conveniently change stress-strain field of the test specimen through changing the scale of geometric dimension, open size and shape of the test specimen. The rotational factor and crack tip opening displacement of SCT specimen are measured, The influence of local high strain plastic zone and the closing effect of the structure on fatigue crack propagation rate is studied and the engineering calculation method for COD of high strain zone and propagation rate of fatigue crack is proposed through theoretical analysis and calculation of fracture fatigue parameters of SCT specimen and experimental research and analysis of fracture fatigue crack propagation of SCT specimen, which provides a basis for fracture and fatigue assessment of high strain zone of pressure vessel nozzle.

KEYWORDS
pressure vessel, nozzle, high strain zone, SCT specimen, fracture, fatigue crack propagation

1. INTRODUCTION
High-strain zone of pressure vessel nozzle yields higher stress concentration due to continuous destruction of geometric structure, resulting in very high stress-strain level within local region. Meanwhile, complicated structure of nozzle location increases the degree of difficulty of fabrication inspection, therefore, occurrence of welding defects can not be thoroughly avoided. Moreover, the effect of welding residual stress and performance deterioration of material adjacent to welds make this location extremely susceptible to fracture and fatigue damage of pressure vessel[1].

In recent 30 years, many countries launched extensive research on the subject of fracture fatigue in pressure vessel nozzle. Man has been seeking medium and small-sized specimens that can simulate the characteristics of the nozzle location of the real-sized vessels for effective fracture fatigue analysis[2], models such as wide plate, flat-plate nozzle, shaped plate, shaped CT specimen(SCT), bi-directional loading cross shaped plate etc. Research results[3] show that SCT specimen has the advantage of compact structure, small test load etc, which provides a more effective way for fracture and fatigue research of high-strain zone of pressure vessel nozzle.

In this paper the plastic rotational factor and COD of SCT specimen are measured, the effect of local high-strain plastic zone and closing effect of the structure on propagation rate of fatigue cracks is researched and the engineering calculation method for COD and propagation rate of fatigue cracks of high-strain zone is proposed through theoretical analysis and calculation of fracture fatigue parameters of SCT specimen and experimental research and analysis on fracture and fatigue crack propagation of SCT specimen in combination with FE stress-strain analysis and test stress measurement of SCT specimen, thus providing a basis for fracture and fatigue assessment of high-strain zone of pressure vessel nozzle.

2. STRESS-STRAIN ANALYSIS OF SCT SPECIMEN

The characteristics of the stress-strain field of pressure vessel nozzle zone is the local high-strain zone and high-strain gradient zone are restrained by the wide elastic zone. SCT specimen is just proposed based on this feature of high-strain zone of the nozzle. SCT specimen is obtained by opening at the middle of CT specimen and local thinning variation. This variation realizes strong elastic restraint of high-strain zone of the opening periphery and reinforcement at external side of the specimen. The structural diagram and main dimensions can be seen in Fig. 1.

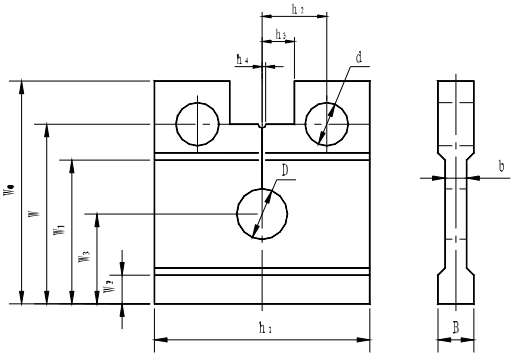

Fig. 1 Structural diagram of SCT specimen
W=90mm; h_1=1.2W; h_2=0.375W; h_3=0.2W; $2h_4$=2.5mm; W_0=1.25W; W_1=(5/6)W; W_2=(1/5)W; W_3=(2/3)W; b=(1/15)W; B=(1/5)W; d=12.5mm D=15,20,25mm

2.1 Elastoplastic FE analysis

In consideration of stress concentration due to opening on SCT specimen, the opening periphery of the specimen has already entered the state of local yield under the action of a certain load, therefore, the specimen adopts elastoplastic FE calculation method for the specimen.

For the specimens with opening diameter of 15mm, 20mm and 25mm, the strain distributions in Z-direction of the specimen without cracks along cracking line under the action of 10, 15, 17, 19 and 20kN respectively are shown in Fig. 2.

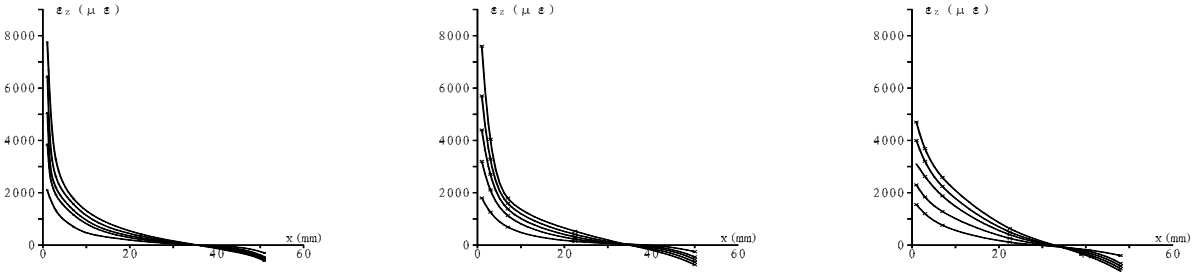

a. Φ15mm specimen b. Φ20mm specimen c. Φ25mm specimen

Fig. 2 Distribution of elastoplastic strain(Z-direction) of SCT specimen

2.2 Test stress-strain analysis of SCT specimen

In order to verify FE calculation results, the test stress-strain analysis is carried out on SCT specimen. Fig. 3 shows the distribution of measured strain e_z of the specimen with opening diameter of 15mm and 20mm respectively.

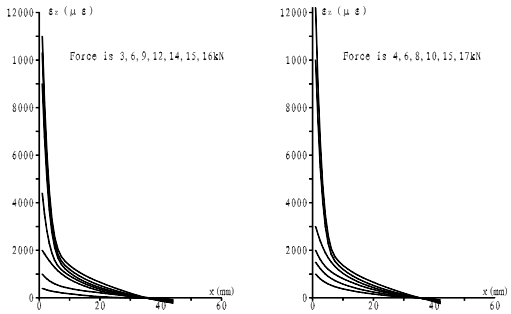

a. Φ15mm specimen b. Φ20mm specimen

Fig. 3 Distribution of measured strain of SCT specimen (Z-orientation)

It can be seen from measured results of FE calculation and strain that SCT specimen certainly has the three characteristics of high-strain zone of pressure vessel nozzle:

(1) **high-peak strain** when the load reaches P=17kN (equivalent to average cross- section stress σ_m=1700/541=31.4MPa=0.097 σ_y), the measured strain at the position 2mm away from the opening periphery has exceeded 10000 με, which is as high as $6e_y$. The peak strain extrapolated from strain distribution curve to the position X=0 of the opening periphery has already reached 13000 με, which is as high as $8.2e_y$.

(2) **high-strain gradient** with the increasing distance from opening periphery, the stress-strain value decreases very quickly. Measured results show that within the range of 8mm, strain value is reduced by about 50%, whereas within the range of 25mm, it is reduced by about 80%.

(3) **high-elasticity restraint** when the distance from opening periphery exceeds 20mm, the loading range for this test has already been under the state of elasticity. Particularly, for the reinforcement rib at right side of the specimen in Fig.1, its elastic restraining capability is stronger.

The above results show that the strain distribution law of SCT specimen is very similar to high-strain zone of engineered construction such as pressure vessel nozzle, etc., thus having a good simulation.

Both the strain peak and the size of yield zone of SCT specimen decrease with the increase of opening diameter, showing that the opening diameter is a more important structural parameter of SCT specimen.

3. FRACTURE RESEARCH OF SCT SPECIMEN

3.1 Calculation of fracture initiating force

Wells induced the empirical formula for COD according to the test results of wide-plate specimen with small crack:

$$\delta = 2\pi ea \tag{1}$$

In early 1980s, we found if the strain reaches several times the material yield strain when we conduct experimental research on fracture and fatigue of the nozzle, Formula (1) is too conservative, so we derived the formula below from Neuber relation[4]:

$$\delta = \pi ea \tag{2}$$

Cai Cigung[5] and Mercle[6] give the J-integral expression for full-yield model:

$$J = 2\pi a \int \sigma de \tag{3}$$

In recent 20 years, various forms of COD expression at high strain were all obtained based on the above expression by adopting an appropriate safety factor.

The COD expression adopted in PD6493－80, 91 for high strain:

$$\delta = 2\pi e_y a(e/e_y - 0.25) \tag{4}$$

Chinese CVDA Code adopts COD expression for high strain:

$$\delta = \pi a(e + e_y) \tag{5}$$

These COD expressions are all basically based on the wide-plate tests that seek full-yield state. Because the stress-strain field of wide plate is uniform, which is very different from high-strain zone of engineered construction such as pressure vessel nozzle etc., application of δ calculation method obtained from wide-plate test results to high-strain zone of practical engineered construction will yield a big deviation.

By deriving from Dugdale's COD expression for strip yield model and Cai Cigung's J-integral expression for full yield model, we get unified expressions for various states of stress within the entire range from low stress to high strain, i.e.:

$$\delta = \frac{\pi a e_y}{m}\left(\frac{\sigma}{\sigma_y}\right)^2 \qquad \left(\frac{\sigma}{\sigma_y} \le \frac{1}{\pi}\right) \tag{6}$$

$$\delta = \frac{1}{m} ae \qquad \left(\frac{\sigma}{\sigma_y} \text{或} \frac{e}{e_y} > \frac{1}{\pi}\right) \tag{7}$$

when $\sigma / \sigma y = 1/\pi$,

$$\delta_{(6)} = \delta_{(7)} = \frac{ae_y}{\pi m} \tag{8}$$

where m is COD reduction factor. For flat stress, m=1; for flat strain, m=2; for most practical constructions between them, m=1.5.

After considering 2 times safety factor, we get the following expressions:

$$\delta = \frac{2\pi a e_y}{m}\left(\frac{\sigma}{\sigma_y}\right)^2 \qquad \left(\frac{\sigma}{\sigma_y} \le \frac{1}{\pi}\right) \tag{9}$$

$$\delta = \frac{2ae}{m} \qquad \left(\frac{\sigma}{\sigma_y} \text{或} \frac{e}{e_y} > \frac{1}{\pi}\right) \tag{10}$$

3.2 Measured Results Of Rotational Factor Of Crack Mouth Opening Displacement And COD

3.2.1Test contents

(1) Based on strain measurement on SCT specimen without cracks, cut a manual notch at right side of the opening using linear cutting machine. Attach 5 pairs of cutting edge diagonally in front of crack tip, as shown in Fig. 4.

(2) Prefabricate fatigue crack at a load of 0~6kN, stop when we can see 1~2mm fatigue crack on the surface with our eyes.

(3) Take two pieces of specimen with respective Φ15mm and Φ20mm specially for test calibration of rotational factor r. Determine rotational factor r according to position of cutting edge, opening displacement and total length of cracks (calculate from position of loading line).

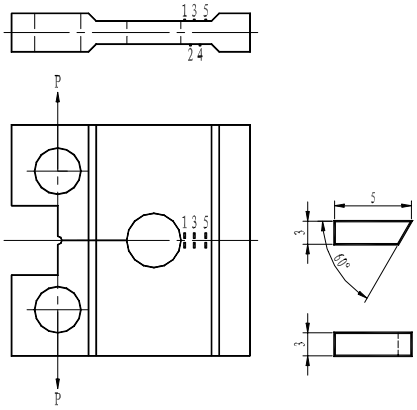

Fig. 4 Arrangement of lateral cutting edge for SCT specimen

3.2.2Test results and analysis

(1) Measured results of rotational factor for crack mouth opening displacement and COD

The conversion from crack mouth opening displacement V to COD δ can be carried out with the following formula:

$$\delta = \frac{r(W - a_t)V}{a_t + r(W - a_t) + Z} \tag{11}$$

where W——width of test specimen;

a_t——crack length calculated from loading line of the specimen, mm;

V——crack mouth opening displacement, mm;

Z——thickness of cutting edge, for SCT specimen, Z=0;

r——rotational factor, calibrated through test.

By conducting test calibration on SCT specimen with cracks of different length, the measured rotational factor r is about 0.28, yet this value basically does not vary with crack length and load.

With the clamp-type tensiometer fixed on the crack mouth, we measured the crack mouth opening displacement V at each load during loading process, the results are shown in Fig. 5. From the measured V and calibrated r, we can obtain COD δ according to formula (11).

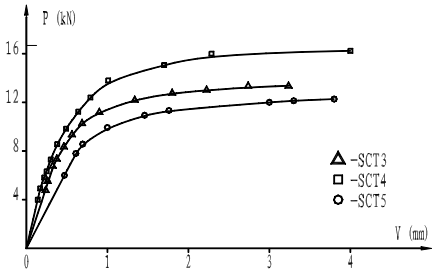

Fig.5 P-V curve of SCT specimen

(2) δ - e curve

Take δ measured on the specimen with cracks and the peak strain e (0.5mm away from opening periphery) measured on the specimen without cracks under the same load as the coordinates of δ - e curve, join the marked points that correspond to each load during the whole test process, they become δ - e curves, as shown in Fig. 6.

Plot expression (5), (9) and (10) onto the diagram at the same time, it can be seen that the test data points basically lie above the curves of expression (9) and (10), indicating that this expression can be taken as the calculation expression for fracture assessment of the cracks in high-strain zone.

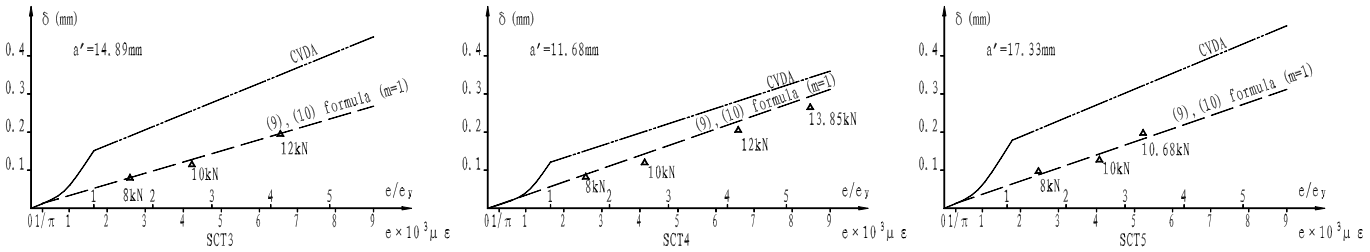

Fig. 6 δ - e curve of SCT specimen

4. EXPERIMENTAL RESEARCH ON FATIGUE CRACK PROPAGATION IN HIGH-STRAIN ZONE OF SCT SPECIMEN

4.1 Test Method And Conditions For Fatigue Of SCT Specimen

The test conditions for the fatigue of SCT specimen are listed in Table 1. The crack length is determined simultaneously by outlining method and unloading flexibility method. Outlining adopts load-reducing outlining method[7], the number of cycles is acquired and recorded automatically by computer.

TABLE 1
TEST CONDITIONS FOR FATIGUE OF SCT SPECIMEN

Specimen No.	Opening diameter mm	Max. load kN	Load ratio R	Loading frequency Hz	Length of prefabricated crack mm	Remarks
SCT6	25	8.0	0.05	8.0	1.31	17kN prestretching
SCT7	25	8.0	0.05	8.0	1.31	

4.2 Measurement Of Closing And Opening Force Of Fatigue Cracks

In the process of fatigue crack propagation, a residual tensile strain zone remains in front of crack tip, this residual deformation reduces crack opening displacement, the external elastic zone compresses the plastic zone of crack tip during unloading, making compression stress occur near crack tip after unloading, even reach reverse yielding. When reloading, load increase eliminates compression stress of crack tip, the crack fully opens. From this time the load indeed contributes to crack propagation. The closing effect of fatigue cracks in plastic zone has a bigger effect on fatigue crack propagation. Therefore, the closing and opening force of fatigue cracks of SCT specimen are measured during the test.

The methods for determining closing and opening force of fatigue cracks are Elber's[8] and Brahmaf's[9]test measurement methods and McCLung's[10] FE calculation method. In this paper the test method is adopted to measure closing and opening force of SCT specimen. In the test we use tensiometer and load sensor to measure P-COD diagram of the specimen, as shown in Fig. 7. It can be seen from Fig. 7 that the slope of P~COD curve between point A and B is bigger than the ones of other section, indicating the rigidity of the specimen is biggest and the crack fully closes; the slope of the curve between point B and C gradually decreases, the crack gradually opens and fully open at point C; after point C, the slope of the curve presents linear feature. Therefore, records below point C of the curve indicate the cracks does not fully open until point C is reached, therefore, the force corresponding to point C is the opening force. Also from Fig. 7 it can be seen that the return process also has the similar case, yet the opening and closing forces are basically equal. The value for opening force, COD δ and crack length corresponding to this value measured in the test are acquired and recorded automatically by computer.

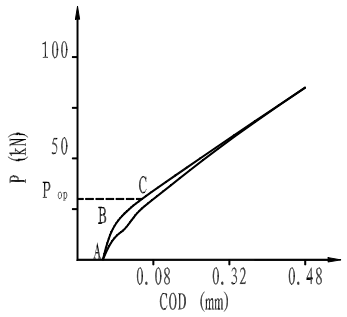

Fig. 7 SCT specimen vs. P-COD curve

The value of effective stress ratio U obtained through calculation is:

$$U = \frac{\sigma_{\max} - \sigma_{op}}{\sigma_{\max} - \sigma_{\min}} = \frac{p_{\max} - p_{op}}{p_{\max} - p_{\min}} \tag{12}$$

U-a relation can be seen in Fig. 8.

It can be seen from Fig. 8 that U values of the two specimens are bigger in the beginning, but they are quickly decreased to a certain value, and slowly increased to a stable value. The U value of prestretched specimen SCT6 is smaller than that of unprestretched specimen SCT7. When the crack propagates to a certain length, the U values of the two specimens gradually approach. At this time, crack has already propagated beyond the plastic zone of SCT specimen, the effect of prestretched plastic zone on crack closing has been eliminated.

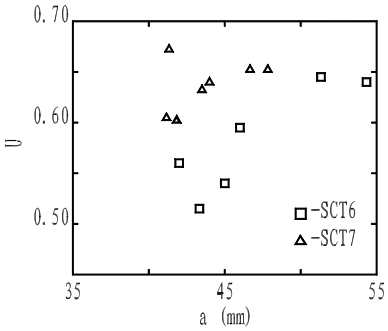

Fig. 8 Effective stress ratio of SCT specimen

4.3 Fatigue crack propagation rate

Within the elastic zone, fatigue crack propagation rate can be calculated by Paris equation:

$$\frac{da}{dN} = A(\Delta K)^m \tag{13}$$

Elastoplastic fracture parameter—COD δ is a simple and practical parameter, suitable for both elastic and elastoplastic conditions. The Paris equation is rewritten as follows after $\Delta\delta$ is taken as a fatigue parameter in the test:

$$\frac{da}{dN} = B(\Delta\delta)^n \tag{14}$$

Calculate COD as per formula (11).

The da/dN～$\Delta\delta$ relation measured in the test are shown in Fig. 9, by regression, the Paris equation is obtained:

$$\frac{da}{dN} = 2.683\ (\Delta\delta)^{3.21} \tag{15}$$

It can be seen from Fig. 9 that at the same $\Delta\delta$, the fatigue crack propagation rate of prestretched specimen is smaller than that of the unprestretched one. When the crack propagates to a certain length, their propagation rates approach. The data are diversely scattered. For smaller cracks, the phenomenon of short cracks occur although da/dN decreases, $\Delta\delta$ increases. It can be regarded that this phenomenon is mainly attributable to the influence of crack closing effect.

The presence of structural plastic strain zone makes the closing effect of the cracks more serious, resulting in reduction of $\Delta\delta_{\text{eff}}$ and slowdown of fatigue crack propagation rate. It can be seen from the effective stress ratio U (Fig. 8) that the U value of prestretched specimen SCT6 is lower than that of unprestretched specimen SCT7 due to existence of residual plastic zone. Therefore, production of residual plastic strain at the location of stress concentration such as the nozzle knee in conventional hydraulic test of pressure vessel is very favorable to reduction of fatigue crack propagation rate of these locations and extension of fatigue life.

Make closing effect correction to $\Delta\delta$:

$$\Delta\delta_{eff} = \frac{\Delta K_{eff}^2}{2E\sigma_y} \tag{16}$$

$$U = \frac{K_{max} - K_{open}}{K_{max} - K_{min}} = \frac{\Delta K_{eff}}{\Delta K_{max}} = \sqrt{\frac{2E\sigma_y \Delta\delta_{eff}}{2E\sigma_y \Delta\delta}} = \sqrt{\frac{\Delta\delta_{eff}}{\Delta\delta}} \quad (17)$$

$\Delta\delta_{eff}$～da/dN relation after taking into account the closing effect is shown in Fig.10. It can be seen from Fig. 10 that the two specimens have a good linearity for data and approach very much, which is expressed using unified fatigue crack propagation rate as follows:

$$\frac{da}{dN} = 5.827\ (\Delta\delta_{eff})^{2.56} \quad (18)$$

The crack fatigue propagation rate of standard CT specimen of the same material is:

$$\frac{da}{dN} = 4.905\ (\Delta\delta_{eff})^{2.06} \quad (19)$$

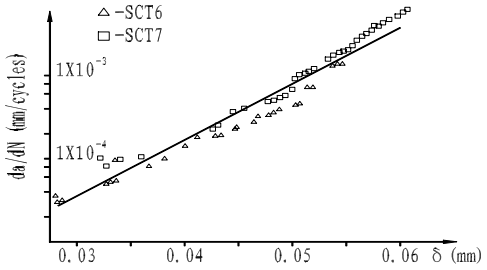

Fig. 9 da/dN-Δδ relation of SCT specimen

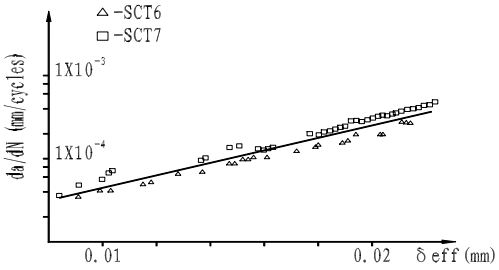

Fig. 10 da/dN-$\Delta\delta_{eff}$ relation of SCT specimen

It can be seen from the above equations that the fatigue crack propagation law of SCT specimen after closing effect correction is basically in agreement with the results of standard CT specimen.

5. CONCLUSION

(1) FE calculation and measured results on test stress of SCT specimen successfully repeat the main characteristics of high strain of engineered construction such as pressure vessel nozzle, the simulation of high-strain zone of engineered construction is realized using small test specimen, and by changing the scale of geometric dimensions, opening diameter and shape of the specimen, it is convenient to change its stress-strain field, thus providing an effective and convenient tool for fracture and fatigue research of pressure vessel with nozzles.

(2) Measured the plastic rotational factor of SCT specimen r=0.28, and measured the δ of COD by r and crack mouth opening displacement;

(3) Measured the opening and closing force of fatigue cracks in high-strain zone of SCT specimen, obtaining the effective stress ratio U;

(4) Proposed the engineering calculation method for COD in high-strain zone of SCT specimen and propagation rate of fatigue cracks corrected through closing effect, thus providing a basis for fracture and fatigue assessment of high-strain zone of pressure vessel nozzle.

REFERENCE

1. Decock, J., *Determination of Stress Concentration Factors and Fatigue Assessment of Flush and Extruded Nozzles in Welded Pressure Vessels, 2nd Int. Conference On Pressure Vessel Tech., Part 2*, pp.821-834(1973)
2. Li Zezhen, Soloms G., Lucia A.C., Volta G., 1988, *A Special Compact Tension Specimen for the Simulation of the Nozzle Corner Strain Field*, Commission of the European Communities, JRC-Ispra establishment, 21020 Ispra, Italy
3. Chen Xuedong, Yang Tiecheng, Li Zezhen, Wang Zhaowei, *Design Curves for Fracture Assessment in High-Strain Region of Pressure Vessel Nozzles, 9th International Conference on Pressure Vessel Technology*, Sydney Australia 9-14 April 2000
4. Zeng Guangxin, Li Zezhen, *The Two Basic Problems for the Defect Assessment Methods, Collection of Pressure Vessel Defect Assessment Materials* (No.5).
5. Cai Cigung, 1979, *Crack Propagation in Plastic Strain Zone*, J. of Mechanics
6. Mercle, 1976, *ASTM STP* 536
7. Gao Zengliang, Li Zezhen, *Research on Fatigue Propagation Law of Shaped Specimen Plate Simulating High-strain Zone of Pressure Vessel Nozzle*, Zhejiang Industrial University Bulletin, No.4, 1985
8. Elber Wolf, *The Signification of Fatigue Crack Closure, Damage Tolerance in Aircraft Structures*. ASTM STP 486, American Society for Testing and Materials, 1971, 230-243
9. Barhma, K. Et al, *Observation of Crack Closure Using a Crack Mouth Opening Displacement Gauge*, Int. J. Fatigue, 1989.11(1); 37-41
10. McClung, R. C. And Sehitoglu, H. *On the Finite Element Analysis of Fatigue Crack Closure -1, Basic Modeling Issues*, -2 Numerical Results, Engineering Fracture Mechanics, 1989, 33, 217-272

ICF100543OR

EXPERIMENTAL STUDY ON EFFECTS OF MECHANICAL PROPERTIES OF BEAM MATERIALS ON DEFORMATION CAPACITY OF BEAM/COLUMM CONNECTIONS

T.NAKAGOMI, K. MATOBA and Y. ICHIKAWA

Dept. of Architecture and Civil Engineering, Faculty of Engineering
Shinshu University
4-17-1 Wakasato, Nagano-shi, Nagano, Japan

ABSTRACT

The mechanical property of the beam flange influences the deformation capacity. When yield point, the yield ratio and strain hardening rate are low, deformation capacity of beam to column welded connection excels. 0℃ Charpy absorbed energy of heat affected zone which was the fracture starting point was 130J or more. The Charpy absorbed energy at 0℃ of the beam flange did not influence the deformation capacity. The specimen of the plastic region with a low yield ratio is larger than the specimen with a high yield ratio.

Keywords:

beam-to-column welded connection, mechanical property, fracture toughness, non-scallop method, deformation capacity

1.Introduction

HyogoKen-Nanbu Earthquake in 1995, brittle fracture to accompany beam-ends junction of an architectural iron frame the plastic deformation was confirmed. Absorbed energy (vEo) of 0℃ by the Charpy impact test of the steel material is thought by one of factors which influence brittle fracture at the edge of the beam[1]-[3]. In the SM material (B and C material) and SN materials (B and C material), the lower bound value of vEo is provided for. This research aims the examination of the mechanical property and vEo of the steel material used for the beam of the influence given to the deformation capacity of junction by using the specimen which models the beam-column welded connection.

2.Outline of experiment

2.1 specimen shape and experiment parameter

The specimen assumed the shop welding junction type. The size of the beam used six kinds of steel materials of B material of A material of rolling H shape steel RH-400×200×13×21, C

material, H material, and welding assembly H shape steel BH-400×200×12×25, E materials, and F materials. It indicates the mill sheet value of a mechanical property and a chemical element in Table 1. It assumed the beam-ends detail to be a scallop industrial method (Are of the scallop bottom was 10mm) and a non scallop industrial methods. Figure 1 shows the specimen shape. Of each of the scallop specimen and the non scallop specimen which used six kinds of steel materials at 0℃ in examination temperature; The non scallop specimen of five steel kind did the load testing room temperature (17℃-20℃).

Table 2 shows the experiment parameter. The loading was based on amount c δ p of the bending deformation at all plasticity yield strength (cPp) of obtaining the beam material all sections as effective. Figure 2 shows the loading pattern.

Table1. Mechanical property and Chemical element

beam	upY.P. (N/mm^2)	lowY.P. (N/mm^2)	ε st (%)	T.S. (N/mm^2)	ε u (%)	Y.R. (%)	EL. (%)
A	409	391	1.29	555	15.2	74	28
B	332	332	0.55	528	16.1	63	31
C	386	364	1.27	548	15.6	71	29
E	330	322	0.80	514	16.1	64	33
F	318	311	0.45	511	15.0	62	29
H	400	374	1.44	536	16.4	75	31
A(web)	441	414	2.01	552	16.0	80	30
B(web)	394	372	1.20	535	15.5	74	29
C(web)	442	416	2.31	550	15.9	80	30
E(web)	397	375	1.31	558	16.0	71	28
F(web)	399	382	1.39	555	15.6	72	27
H(web)	449	408	2.29	542	16.4	83	32

upY.P:Yield point LowY.P:Yield point in the under ε st:Strain when strain st
T.S:Tensile strength ε u:T.S . Strain at time Y.R:Yield ratio E

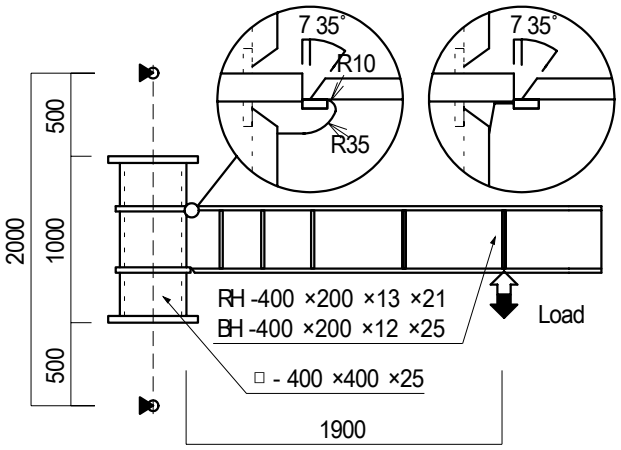

Fig.1. Specimen shape

Table 2 Experiment parameter

specimen	beam		detail	temp.
As0	A	RH	scallop	0℃
Cs0	C			
Hs0	H			
Bs0	B	RH	scallop	0℃
Fs0	F			
Es0	F			
An0	A	RH	non scallop	0℃
Cn0	C			
Hn0	H			
Bn0	B	RH	non scallop	0℃
Fn0	F			
En0	F			
Cn1	C	RH	non scallop	17℃ ~ 20℃
Hn1	H			
Bn1	B	RH	non scallop	17℃ ~ 20℃
Fn1	F			
En1	F			

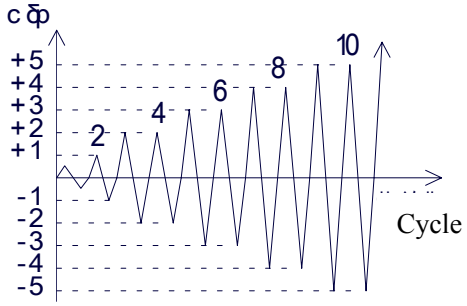

Fig.2 Loading plan

2.2 Material examination of steel material used for beam

It investigated the flange parent metal of each steel material and the material property in the weld with the butt weld splice. Table 3 shows the tension test result. H material and A material of yield

point were high, and, next, C material, B material, E material, and F material were low values. The yield ratio became a high result in order of H material >A material >C material >E material >B material >F material. Table 4 shows the Charpy impact test result. The specimen name shows the kind and the position where it gathers the steel material. S shows the parent metal, f shows fillet, and h shows HAZ.

Table.3 Tension test result

beam	upY.P. (N/mm^2)	lowY.P. (N/mm^2)	ε st (%)	T.S. (N/mm^2)	ε u (%)	Y.R. (%)	EL. (%)
A	409	391	1.29	555	15.2	74	28
B	332	332	0.55	528	16.1	63	31
C	386	364	1.27	548	15.6	71	29
E	330	322	0.80	514	16.1	64	33
F	318	311	0.45	511	15.0	62	29
H	400	374	1.44	536	16.4	75	31
A(web)	441	414	2.01	552	16.0	80	30
B(web)	394	372	1.20	535	15.5	74	29
C(web)	442	416	2.31	550	15.9	80	30
E(web)	397	375	1.31	558	16.0	71	28
F(web)	399	382	1.39	555	15.6	72	27
H(web)	449	408	2.29	542	16.4	83	32

upY.P:Yield point LowY.P:Yield point in the under ε st:Strain when strain stiffens
T.S:Tensile strength ε u:T.S . Strain at time Y.R:Yield ratio EL.:Elongation

Table. 4 Charpy impact test result

	specimen	vEo (J)	vBo (%)	Tre (℃)	Trs (℃)
parents (s)	A s	19	88	22	24
	B s	34	88	33	34
	C s	286	1	-51	-48
	E s	240	15	-39	-27
	F s	283	6	-28	-23
	H s	55	78	23	16
HAZ (h)	A h	199	7	-31	-28
	B h	160	47	-7	-1
	C h	250	2	-33	-33
	E h	200	33	-23	-13
	F h	260	10	-30	-27
	H h	130	47	3	-2
fillet (f)	A f	24	85	-	-
	C f	282	0	-	-
	H f	68	77	-	-
Weld Metal	RH Depo	80	60	3	8
	BH Depo	28	88	51	42

3. Experiment result

3.1 destruction properties

All specimens except Cn0 destroyed the brittleness from the edge of the width of the flange in the beam flange welding toe of weld part. Cn0 destroys the brittleness from the welding first layer neighborhood. The destruction is the following two types.

① In the direction of the width of the flange when the position becomes a starting point within 10mm. There are a lot of cases of 0℃.

② When the position at 10mm or more becomes a starting point in the direction of the width of the flange. There are a lot of cases of room temperature.

The P-δ curve of Fn1 and Hn1 decreases gradually when the load when maximum displacing increases the cycle, and the load has decreased obviously at the cycle to breaking.

3.2 skeleton curve and deformation capacity's indices

It requested from the P-δ curve, and it shows the method of calculating the skeleton curve and the accumulation plastic deformation irreversible deformation in Figure 3. The skeleton curve accumulated and obtained the P-δ curve for the load to have exceeded the maximum value of the pre-loop in the P-δ curve. Table 5 shows the experiment result list. Accumulation value (Σ W) of the energy requested from energy (Ws) requested from the skeleton curve shown in Figure 5 when it compares deformation capacities of junction and each loop of the P-δ curve is thought. The actual experiment requested by expression 1 and 2, and examines the result by η s and η w. It examines η sF and η wF obtained by expression 3 and 4.

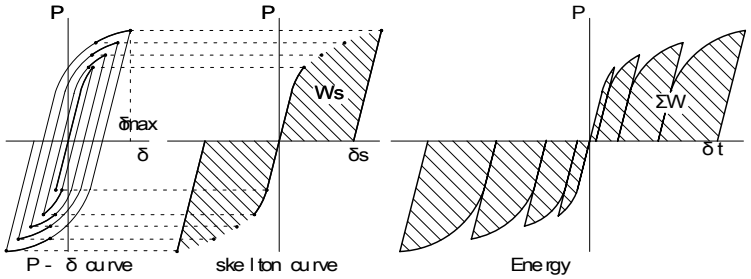

$$\eta_S = W_S / {}_C P_P \times {}_C \delta_P \quad \cdots (1)$$

$$\eta_W = \sum W / {}_C P_P \times {}_C \delta_P \quad \cdots (2)$$

$$\eta_S \mathrm{F} = W_S / {}_C P_P \mathrm{F} \times {}_C \delta_P \mathrm{F} \quad \cdots (3)$$

$$\eta_W \mathrm{F} = \sum W / {}_C P_P \mathrm{F} \times {}_C \delta_P \mathrm{F} \quad \cdots (4)$$

$${}_C P_P = Z_P \times Y.P./L, {}_C P_P \mathrm{F} = Z_P \times 325/L$$

Fig.3 Skeleton curve

Table.5 Experiment result

	Pmax	δ max	δ s	Ws	Σ W	δ t	Material examination result					※F= 1.3)					Fracture
	(kN)	(mm)	(mm)			(mm)	cPp	c δ p	η s	η w	α	cPpF	c δ pF	η sF	η wF	α F	Type
As0	-546	-46.3	-42.0	20075	81999	-194.9	439	16.13	2.8	11.6	1.2			4.7	19.1	1.6	①
Cs0	538	59.8	54.9	26038	120926	289.7	420	15.43	4.0	18.6	1.3	342	12.56	6.1	28.2	1.6	①
Hs0	-567	-54.8	-59.3	29247	133808	-304.1	434	15.92	4.2	19.4	1.3			6.8	31.2	1.7	①
Bs0	587	60.9	59.7	31025	128344	278.8	404	13.65	5.6	23.3	1.5			6.3	26.0	1.5	①
Es0	610	67.8	66.0	35827	191792	408.0	402	13.60	6.5	35.0	1.5	382	12.91	7.3	38.9	1.6	①
Fs0	-608	-59.2	-57.2	29957	146033	-322.3	391	13.22	5.8	28.3	1.6			6.1	29.6	1.6	①
An0	-594	-60.8	-67.5	35434	160711	-349.4	439	16.13	5.0	22.7	1.4			8.2	37.4	1.7	②
Cn0	-600	-69.0	-65.9	34208	182781	-405.3	420	15.43	5.3	28.2	1.4	342	12.56	8.0	42.6	1.8	①
Hn0	-615	-67.7	-70.0	37730	196350	-417.8	434	15.92	5.5	28.5	1.4			8.8	45.7	1.8	①
Bn0	623	72.3	90.0	50271	272380	544.8	404	13.65	9.1	49.4	1.5			10.2	55.2	1.6	①
En0	642	81.2	85.7	49216	265414	526.0	402	13.60	9.0	48.5	1.6	382	12.91	10.0	53.8	1.7	①
Fn0	-674	-70.5	-72.0	42081	246618	-487.4	391	13.22	8.1	47.7	1.7			8.5	50.0	1.8	①
Cn1	-585	-71.4	-66.6	34035	220174	-497.4	420	15.43	5.2	34.0	1.4	342	12.56	7.9	51.3	1.7	②
Hn1	574	94.1	99.6	52061	352284	767.6	434	15.92	7.5	51.1	1.3			12.1	82.0	1.7	②
Bn1	-646	-71.5	-81.3	45343	255987	-426.5	404	13.65	8.2	46.4	1.6			9.2	51.9	1.7	②
En1	631	94.7	101.1	57762	413220	814.8	402	13.60	10.5	75.5	1.6	382	12.91	11.7	83.8	1.7	②
Fn1	612	83.1	71.8	39490	330447	675.5	391	13.22	7.6	63.9	1.6			8.0	67.0	1.6	②

Pmax :maximum load δ max :maximum displacement δ s :Skeleton displacement (plasticity) Ws :Skeleton absorbed energy
Σ W :Accumulation absorbed energy δt :accumulation plastic deformation
cPp :All plasticity yield strength c δ p :bending deformation at all plasticity yield strength η s :Ws/ cPp·c δ p η w :Σ W/ cPp·c δ p α :Pmax/ cPp

4. Consideration

4.1 strain properties

It obtained load-skeleton strain (ε s) curve by the method of calculating the skeleton curve shown from load-strain (ε) curve in Figure 3. Figure 4 shows one example of the ε s- δ s curve obtained from P- ε s and P- δ s (70mm of Cs0). δ s compared ε s at 45mm(4c δ pF) with each specimen in the ε s- δ s curve.

Figure 5 shows the position where it affixes the strain gage used for the comparison.

Figure 6 shows the η sF- ε s relation between the scallop specimen and the non scallop specimen at 0℃. There is a tendency to which η sF becomes small when ε s is large from Figure 8(a) and (b). The skeleton strain becomes small a non scallop specimen compared with the scallop specimen. Moreover, the specimen with a low yield ratio of the beam material shows the tendency that ε s is small.

It can be said that the deformation capacity will grow by strain at the edge of the beam small. Moreover, it can be said that the specimen with a low yield ratio and the non scallop specimen extend the plastic region compared with the specimen with a high yield ratio and the scallop specimen, and strain at the edge of the beam has the tendency which becomes small.

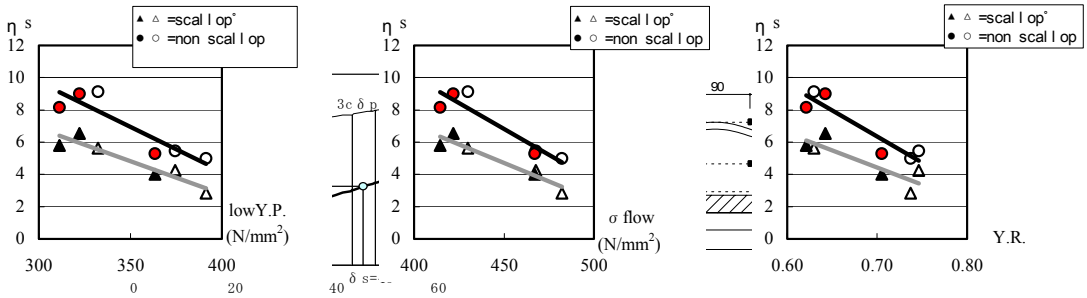

Fig.7 ηs－lowY.P.　　Fig.8 ηs－σ flow　　Fig.9 ηs－Y.R.

Fig.4　εs－δsCurve（Cs0，　　Fig.5　Gauge affixation position

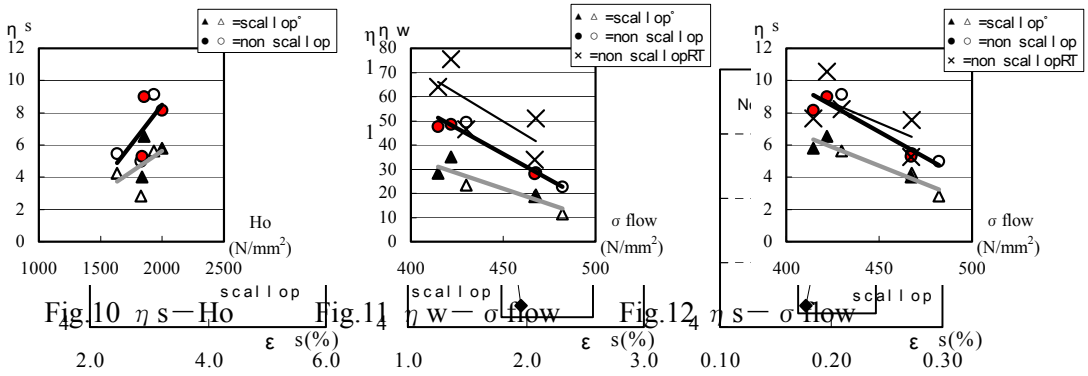

Fig.10 ηs－Ho　　Fig.11 ηw－σ flow　　Fig.12 ηs－σ flow

（a）30mm²Ave　　（b）70mm　　（c）550mm

Fig.6 ηsF－εs（at　0℃）

4.2　Influence of mechanical property of beam material

It shows the relation between ηs and the material property by which it makes Ws obtained from the skeleton curve dimensionless according to yield strength of the material examination result below. When it assumes the material property to be a parameter, yield point, tensile strength, the yield ratio, and the strain hardening rate etc. of the steel material are thought.

σ flow is a value divided by two adding yield point and tensile strength. Figure 7-Figure 10 shows ηs and each relation. LowY.P . There is a correlation in σ flow, Y.R, and ηs.

Moreover, ηs has the growing tendency as the strain effect rate of Figure 10 grows similarly. When it uses the same steel material for the beam, deformation capacities grow more than the scallop specimens as for the non scallop specimen. The influence of the mechanical property is larger in ηs. It considers it with ηw and ηs which makes accumulation plasticity absorbed energy (ΣW) of the specimen at room temperature dimensionless. Figure 11 and Figure 12 show the ηw-σ flow relation and the ηs-σ flow relation. There is a tendency which grows as σ flow becomes small ηw as well as ηs. In the experiment on room temperature, a tendency different from the ηs-σ flow relation is seen about the non scallop specimen. The difference between the specimen of room temperature and the specimen of 0℃ grows if it evaluates it with ηw.

5. Summary

a) Mechanical properties have significant influence on deformation capacity. Deformation capacity of beam to column welded connections is increased withthe decrease of the yield point, the yield ratio and the strain hardening rate of the materials.

b) The Charpy impact toughness has little influence on the deformation capacity provided that the absorbed energy of heat affected zone at 0℃, from which the fracture initiates, is 130J or more.

c) The plastically deformed zone of the components is larger in the materials of low yield ratio, and the skeleton strain at the end of beam is generally small in the low yield ratio materials.

d) The detail of connection, whether it has a scallop or not, has relatively smaller influence on the deformation capacity than the mechanical properties of materials used.

REFERENCE

[1] Tanaka.T et al. (1993) , “Effect of the Weld Details on the Behavior of Welded Tubular Column-to-Beam Connections Part .9 Effect of Scallop Shapes and Mechanical Properties of Beams” , *Summaries Of Technical Papers Of Annual Meeting Architectural Institute of Japan* , pp.1245～1246

[2] Fujimoto .M et al. (1996) ,”Plate Thickness , Strength and Nessessary Toughness of 500N/mm^2 Class Tensile Strength Steel.” *Summaries Of Technical Papers Of Annual Meeting Architectural Institute of Japan* , pp.619～620

[3] Hattori . K , et al (1999) , “Experimental study on effect which material of beam exerts on deformation capacity of beam-to-column welded joints.” *Summaries Of Technical Papers Of Annual Meeting Architectural Institute of Japan* , pp.529～530

ORAL REFERENCE: 040OR

EXPERIMENTAL STUDY ON THE EFFECT OF PLASTIC CONSTRAINT ON DUCTIAL TEARING

Qing-fen Li [1], Li Li [1], Shang-lin Yang [1], Ping Long [1], Xiu-ting Han [2] and Hua-qing Cao [2]

[1] College of Mechanical & Electrical Engineering, Harbin Engineering University
Harbin 150001, China
[2] Daqing Production and Technology Institute, Daqing 163453, Heilongjiang, China

ABSTRACT

The effect of plastic constraint on the initiation of ductile tears in four different alloy steels has been experimentally studied by measuring the crack opening displacement and J-integral at initiation in three-point bend specimens with deep and shallow notches in this paper. Experimental results of seven groups of different strength alloy steels show that both ì and Jì values of ductile tear from the shallow crack specimens which have less constraint flow field are significantly higher than deeply notched specimens. Slip-line- field analysis shows that, for shallow crack, the hydrostatic stress is lower than that from standard deeply cracked bend specimen, which develops a high level of crack tip constraint, provides a lower bound estimate of toughness, will ensure an unduly conservative approach when applied to structural defects, especially if initiation values of COD and J-integral are used.

KEYWORDS:

Ductile tearing, plastic constraint, slip line field, toughness, COD, J-integral

INTRODUCTION

Crack Opening Displacement (COD) and J-integral concepts of fracture are the accepted methods of estimating the significance of a crack or defect in structural steels. In design practice, the critical value at initiation $_i$ and J_i, are normally measured on three-point-bend specimens where the crack depth is approximately half the depth of the beam and the plastic flow is confined to the ligament. Since the plastic flow is constrained, the hydrostatic component of stress in these specimens is high. However, in practice many defects are shallow and the plastic flow associated with them reaches the surface of the component. In this case, the hydrostatic component of stress is smaller and the constraint is lower. As a consequence, the assessment for many shallow defects, the normal method is unduly conservative.

Experimental and theoretical study on the effect of the ratio of notch depth to specimen depth (a/w) on $_i$ and J_i is therefore necessary. Although many previous work have pointed out that shallow crack specimens give markedly higher values of $_i$ and J_i than deeply notched specimens [1-6], someone still doubt the correctness of it. In this paper, we examine the effect of shallow notches on ductile tearing in four Chinese alloy steels.

MATERIALS AND TESTING

Materials and Specimens

Steel 17CrNi4 was heat-treated to three different strength levels. Their mechanical properties are given in Table 1. Another alloy 18CrNiWA was heat-treated into two groups of different strength. The Properties are given in Table 2. The properties of steel 40Cr are given in Table 3. The properties of a structural steel are given in Table 4. Test specimens are of B=12.5mm, W=25mm, S=4W. The deep notch specimens are with a/W=0.5 and the shallow with a/W=0.1 or 0.2.

Experimental Procedure

Fatigue cracks were produced in all the specimens before they were tested. The toughness tests were carried out on a MTS-810 testing machine of 250 KN. Two clip gauges were used. One was to measure the crack mouth displacement V, the other was to measure the load-point displacement , P-V and P- plots were simultaneously recorded on an X-Y-Y recorder. After off-loading, specimen crack fronts were marked by heat tinting or re-fatigue. Then specimens were broken at low temperature. Crack length and crack extension a were measured with an optical micrometer with 0.001 mm per division and according to the seven-point average procedure. All tests were made at room temperature.

TABLE 1
MECHANICAL PROPERTIES OF STEEL 17CrNi4

Steel	group A	group B	group C
Yield strength(MPa)	932	864	736
Ultimate strength(MPa)	988	939	841
Work-hardening exponent n	0.051	0.057	0.068

TABLE 2
MECHANICAL PROPERTIES OF ALLOY 18CrNiWA

Group	A	B
Yield strength(MPa)	1045	1099
Ultimate strength(MPa)	1257	1415
Elongation	18.6	16.5

TABLE 3
MECHANICAL PROPERTIES OF STEEL 40Cr

Yield strength(MPa)	1043
Ultimate strength(MPa)	1252
Elongation(%)	12.5

For shallow crack specimens, the plastic flow spreads to the surface of the beam and the COD cannot be accurately obtained from a clip gage measurement at the mouth of a crack. Therefore, a replication technique was used. The values were measured by infiltrating the crack with a catalytically hardening silicone rubber Unitek Xantropren Blue dental impression material[1].

TABLE 4
COMPOSITIONS AND MECHANICAL PROPERTIES
OF THE STRUCTURAL STEEL

(a) Chemical analysis

C	Mn	Si	P	S
0.100	0.460	0.300	0.010	0.014

(b) Mechanical property

Ultimate strength(MPa)	1045
Yield strength(MPa)	715
Elongation to break(%)	19.20
Hardening exponent n	6.80

EXPERIMENTAL RESULTS AND DISCUSSION

Experimental results of three groups of different strength alloy steel 17CrNi4 are shown in Figure 1 and 2. Results of two groups of different strength steel 18CrNiWA are shown in Table 5. Results of COD and J-integral of alloy 40Cr with a/w=0.5 and a/w=0.1 are shown in Figure 3 and 4 respectively. Results of the structural steel are shown in Table 6.

All the results show that both $_i$ and J_i values of ductile tear from the shallow notches (a/w=0.1) are significantly higher than deeply notched specimens. As we have already seen in our previous works [3,4], the reason is that the plastic flow spreads to the top surface of the specimen and lead to a decrease in plastic constraint and stress triaxiality at the crack tip.

TABLE 5
RESULTS OF ALLOY 18CrNiWA

Group	$_y$(MPa)	*a/w*	J_i(MN/m)	$_i$(mm)
A	1045	0.5	0.0644	0.037
		0.1	0.0883	0.059
B	1099	0.5	0.0853	0.046
		0.1	0.1022	0.066

TABLE 6
RESULTS OF THE STRUCTURAL STEEL

a/w	J_i(MN/m)	$_i$(mm)
0.1	0.0921	0.093
0.2	0.0750	0.078
0.5	0.0582	0.065

The hydrostatic stresses for shallow cracks are smaller than for deeper cracks. Figure 5 shows a slip-line field in a three-point bend specimen containing a short crack. At the crack tip, the hydrostatic stress is given by:

$$s_H = 2kb + kp/2 - k(1 - 4w) \quad (1)$$

with decreasing a/W, the angle increased and the angle slightly decreased, the hydrostatic stress $_H$ therefore decreased. It explains the results that $_i$ and J_i values of shallow crack specimens are higher than

those of deep ones. As a consequence, the assessment of the significance of many shallow defects by the normal method is unduly conservative.

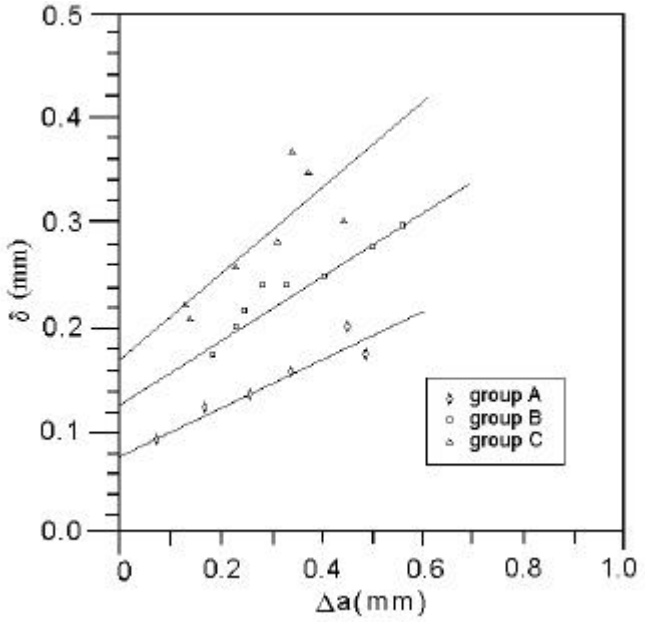

Figure 1: vs a of three groups of steel 17CrNi4 with a/w=0.5

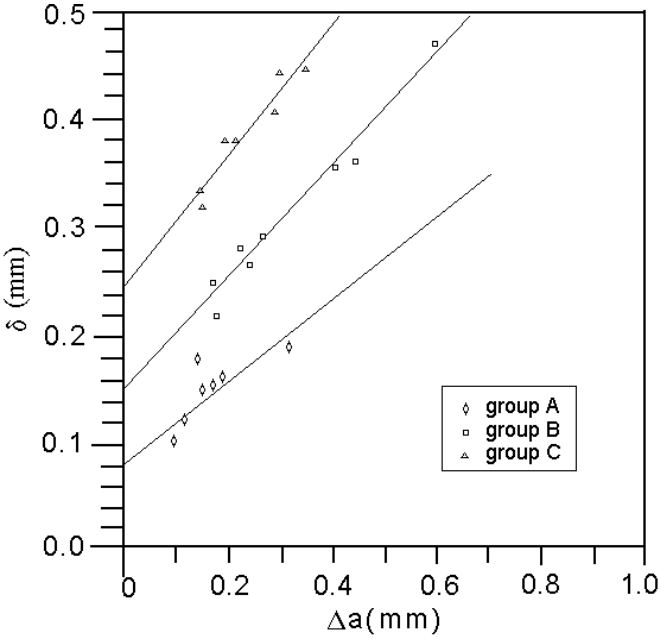

Figure 2: vs a of three groups of steel 17CrNi4 with a/w=0.1

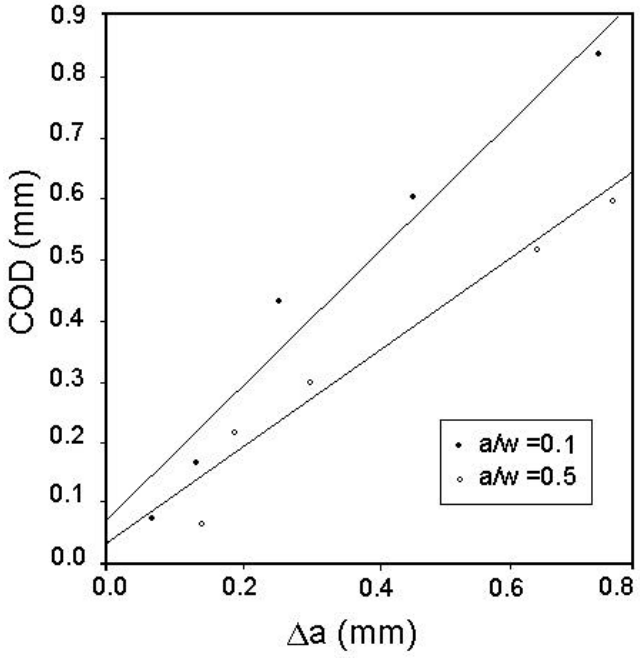

Figure 3: COD vs a of 40Cr steel

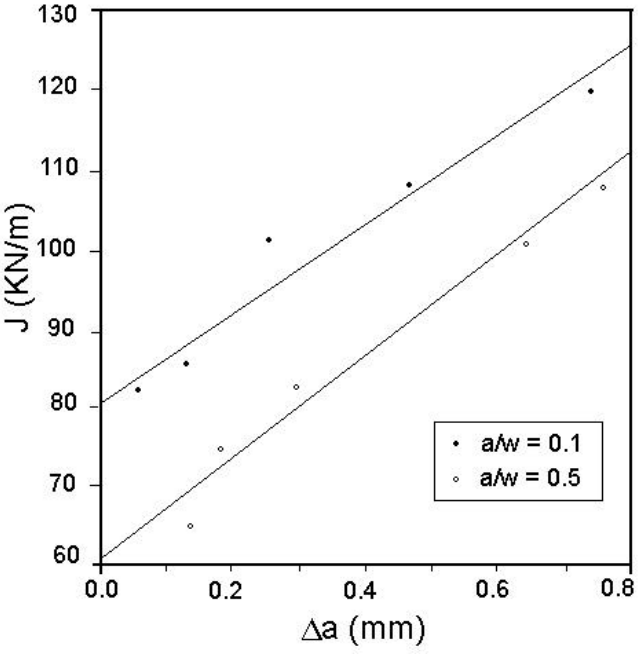

Figure 4: J vs a of 40Cr steel

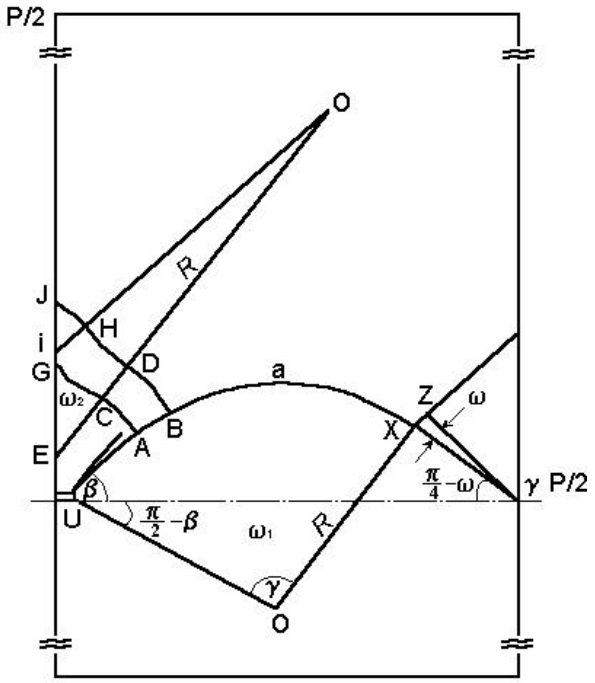

Figure 5: Slip-line field for a shallow crack in three-point bending

The theoretical developments [by J. W. Hancock et al] indicate that geometry dependent fracture toughness effects can be rationalized and united into one consistent scheme, through a two parameter characterization of elastic plastic crack tip fields and associated toughness [6,7].

Our experimental results are well in agreement with this Two Parameters Fracture Mechanics theory. Shallow cracked specimens (a/w<0.3) where T<0 exhibit increased toughness compared to deeply cracked ones, because their crack tip constraint is low. The state of constraint controls the triaxiality at the crack tip, and a low level constraint implies a low traixial stress field. The triaxiality controls the fracture process, and for specimens with a low triaxiality, the fracture toughness is known to be high.

We and some others, therefore, have pointed out that a typical fracture toughness obtained from a deeply cracked bend bar develops a high level of constraint, is known to be low. The standard fracture toughness test therefore provides a lower bound estimation, which ensure a safe but conservative value of the fracture toughness. It may lead to the imposition of prohibitive repair and inspection policies when applied to shallow cracks which are often found in structural components.
Therefore, the advantage of enhanced toughness for specimens with low levels of constraint should be taken into account for defect assessment, and a modified reasonable result should be taken for engineering applications.

CONCLUSIONS

1) Experimental results showed that shallow cracked specimens give markedly higher values of toughness than deeply notched ones.

2) Material data obtained from standard deeply cracked bend specimens which develop a high level of crack tip constraint, provides a lower bound estimate of toughness, will ensure an unduly conservative approach when applied to structural defects especially if initiation values of COD or J-integral are used.

3) Our experimental results are well in agreement with the Two Parameters Fracture Mechanics theory.

4) The advantage of enhanced toughness for specimens with low levels of constraint should be taken into account for defect assessment, and a modified reasonable result should be taken for engineering applications by using the TPFM method.

REFERENCES

1. Cotterell, B., Li, Q.F., Zhang, D.Z., and Mai, Y.W. (1985) *Eng. Fract. Mech.*, 21, 239.
2. Jie, L. (1987) *J.Harbin Shipbuilding Eng. Inst.* 8, 68.
3. Li, Q.F. (1985) *Eng. Fract. Mech.*, 22. 9.
4. Li, Q.F. and Shi, D.Y. (1991) *Proc. of the ISOPE-91*, 134.
5. Li, Q.F. and Zhang, L. (1996) *Eng. Fract. Mech.*, 53, 473.
6. Karstensen, A.D. and J.W.Hancock, J.W. (1996) *University of Glasgow Press.*
7. Du, Z.Z. and Hancock, J.W. (1991) *J. of Mechanics and Physics of Solids,* 39, 555.

ICF10098OR

Experimental Validation of $T^*_{\square}$ Integral

Albert S. Kobayashi* and Satya N. Atluri**

*University of Washington, Department of Mechanical Engineering,
Seattle, WA 98195-2600, USA
** University of California, Center for Aeronautical Research and Education,
Los Angeles, CA 90095-1597, USA

$T^*_{\square}$ integral, which includes J integral as a special case, is shown to be a material property suitable for characterizing crack propagation in thin 2024-T3 aluminum sheets. The $T^*_{\square}$ resistance curve, which was generated through stable crack growth tests of single edge-notched (SEN) and central notched (CN) specimens, were used to predict curved crack growth and crack link-up of in-line multiple cracks. $T^*_{\square}$ integral for rapid crack growth reached a maximum value at the terminal crack velocity.

Key Words: Ductile fracture, fracture resistance curve, stable and rapid crack growth, curved crack growth.

INTRODUCTION

The T^*_{ε} [1], *which is a path dependent integral based on incremental theory of plasticity*, circumvents much of the difficulties encountered by the *J*-integral as shown by Brust et. al. [2]. Recently, the author and his colleagues [3] used experimental, numerical and hybrid experimental/numerical techniques to demonstrate the utility of the T^*_{ε} integral in characterizing stable crack growth in thin aluminum fracture specimens. This study was followed by dynamic and curved crack growth and crack coalescence analyses. These results are summarized in the following.

*T** INTEGRAL

The numerical analyses by Brust et. al. [2] showed that the *T** integral in the very vicinity of the crack tip reaches a plateau with crack extension under creep and cyclic loading. In contrast, the local J-integral vanishes with crack growth. This local *T*,* which is designated as T^*_{ε} is [1]:

$$T^*_{\varepsilon} = \int_{\Gamma_{\varepsilon}} \left(W n_1 - t_i \frac{\partial u_i}{\partial x_1} \right) d\Gamma \tag{1}$$

where t_i is the surface traction on the contour Γ_{ε}, W is the strain energy density and n_1 is the first component of the normal to the curve. Γ_{ε} is an arbitrary small contour immediately surrounding the crack tip and more importantly it elongates together with crack extension. T^*_{ε}, as defined by Equation (1), is identical in form of the J integral and therefore T^*_{ε} coincides with J where the deformation theory of plasticity prevails. In terms of incremental theory of plasticity, T^*_{ε} integral at the end of the Nth load steps is the sum of ΔT^*_{ε} which is the incremental change of T^*_{ε} over a load step or

$$T^*_\varepsilon = \sum^{N} \Delta T^*_\varepsilon \qquad (2a)$$

where

$$\Delta T = \int_{\Gamma_\varepsilon} \left[\Delta W n_1 - (t_i + \Delta t_i) \frac{\partial \Delta u_i}{\partial x_1} - \Delta t_i \frac{\partial u_i}{\partial x_1} \right] d\Gamma \qquad (2b)$$

(2b)

The current T^*_ε, as defined by Equation (2), is thus dependent on the prior loading history, a property that is essential for elastic-plastic analysis under crack growth. Although such incremental analysis can be routinely conducted by finite element analysis, it is not practical in experimental analysis as the cumulative experimental errors per load step will eventually overwhelm the sought data. Fortunately, Pyo et al [4] have shown, through numerical experiments, that the total T^*_ε integral computed directly by using the stresses and strains based on the incremental theory of plasticity, was for practical purpose equal to the summed ΔT^*_ε of Equation (2). Thus Equation (1) can be used for crack growth study without the cumbersome incremental procedure provided the states of stress and strain are based on the incremental theory of plasticity. More recently, T^*_ε was also studied extensively by by Nishioka and his colleagues [5].

ε is governed by the plate thickness for a plane stress state to exist along the integration contour of Γ_ε. This distance, ε, is equated to the plate thickness after Narashimhan and Rosakis [6][1]. For a plane strain state, this characteristic distance could be several times the crack tip radius.

METHOD OF APPROACH

By restricting the integration contour very close to and along the extending crack, Okada and Atluri [7] have shown that the contour integration trailing the crack tip can be neglected by virtue of the closeness of Γ_ε to the traction free crack surface. Since the contour integral is now restricted to the frontal portion of Γ_ε, the deformation theory of plasticity can now be used to compute the stresses in the loaded portion of Γ_ε. The experimental procedure consisted of measuring the two orthogonal displacement fields surrounding a stably growing or a rapidly propagating crack in thin, single edge notched (SEN), central notched (CN) and compact (CT), 2024-T3 aluminum specimens. The strains and stresses, using the equivalent stress-strain and the measured uniaxial stress-strain data of the 2024-T3 sheet, were computed. Finally, Equation (1) was evaluated numerically along the contour, Γ_ε.

RESULTS

SEN and CN Specimens

Experimentally determined T^*_ε integral data of one SEN specimen and five CN specimens of different cracks lengths with saw cut or fatigued crack tip are shown in Fig. 1. For a contour size of Γ_ε = 1 mm, the T^*_ε data for the 152.4 mm and 254 mm wide specimens are approximately equal. Other than the 50.8 mm wide CN specimens, the experimental T^*_ε data of the SEN and CN specimens practically coincide thus suggesting that the T^*_ε is a geometry-independent material property of this material. The T^*_ε resistance curve represents the average of this data. As shown in Fig. 1, the T^*_ε resistance curve rises at the initial stage of crack growth and reaches a constant value during steady crack growth. In contrast, the global J resistance curve, J_R, continually rises with stable crack extension and includes energy from other sources.

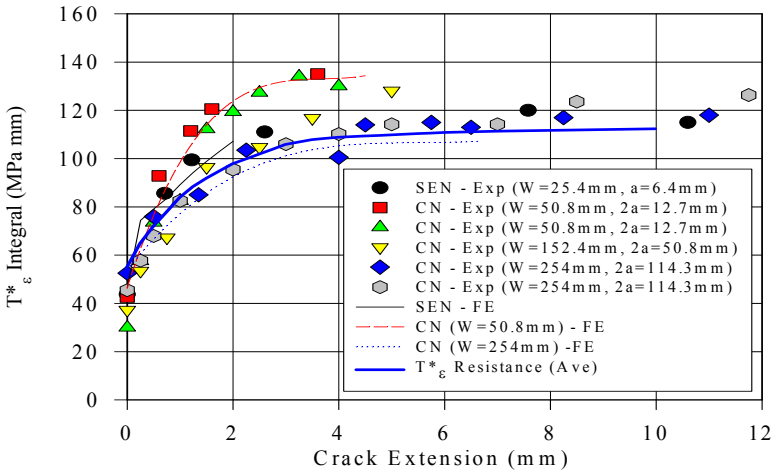

[1] The three-dimensional elastic-plastic finite element analysis of a flat crack in plate by Narashimhan and Rosakis [17] showed that the plane stress state prevailed at one half of the plate thickness from the crack tip. Since a 100 percent shear lip is the norm in ductile fracture, the minimum distance, ε, was conservatively picked as the plate thickness.

Fig. 1. SEN and CN experimental T^*_ε resistance curve (Γ_ε= 1mm)

While the J integral based instability criterion is determined on a global basis, the instability criterion for T^*_ε integral is locally based. During steady crack growth, the state of stress is in equilibrium and thus the parameter characterizing this phenomenon should be constant. When the driving force exceed the material's resistance, i.e. $T^*_\varepsilon > T^*_{\varepsilon R}$, instability will occur without an additional applied load or a displacement.

For crack growth simulation, a load or displacement was applied as the boundary condition and the crack was propagated when $T^*_\varepsilon > T^*_{\varepsilon R}$. With the prescribed load or displacement held constant, T^*_ε was evaluated again for the extended crack. If T^*_ε remained greater than $T^*_{\varepsilon R}$, the crack was extended again, and T^*_ε was re-evaluated. The crack continued to extend until T^*_ε dropped below $T^*_{\varepsilon R}$. Additional load/displacement was applied to the specimen until T^*_ε was equal to $T^*_{\varepsilon R}$ where upon another node was released to extend the crack. This procedure was repeated until no additional load or displacement was required to propagate the crack. At that point, instability was assumed to have occurred. The results identified as "FE" in Fig. 1 show that this simulation compared very well with the experimental data.

Curved Crack Growth

Twenty four biaxial test specimens were fabricated without or with bonded, bonded and riveted and integral pad-up tear straps and tested to failure. The results obtained in six tests, i.e. without tear straps, with bonded, bonded and riveted and machined pad-up tear straps are report in this paper. Figure 2 shows the variation in $T^*_{1\varepsilon}$, which corresponds to the mode I contour integral of Equation (1), along the frontal portion of Γ_ε at various crack tip locations of the curved cracks. The steady state $T^*_{1\varepsilon}$ in this study coincides with the corresponding T^*_ε resistance curve of Fig. 1. The increase in $T^*_{1\varepsilon}$ of Experiments B21 and B25, as the crack

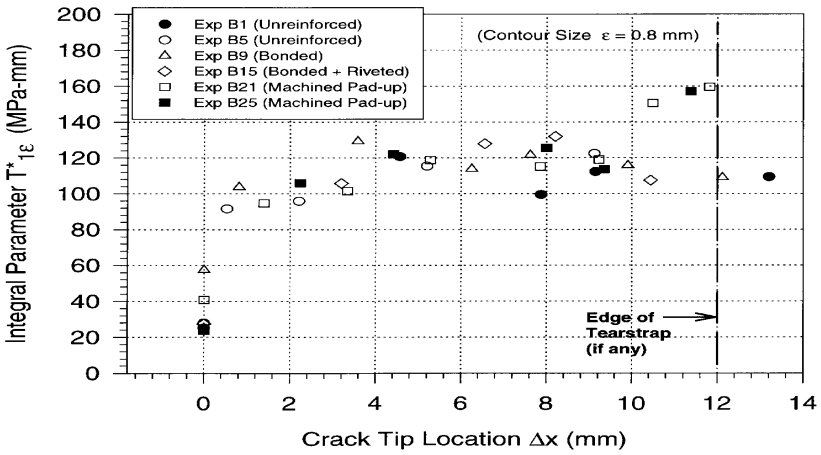

Fig. 2. $T^*_{1\varepsilon}$ variation with curved crack growth.

approaches the tear strap, represents the increased resistance to crack growth in these machined pad-up tear straps. Such an increase was not observed in Experiments B9 and B15, thus suggesting that the bonded and bonded-riveted tear straps may not be as effective as the machined pad-up tear straps in resisting curve crack extension. Indeed, the final load at fracture in the machined pad-up tear straps was 30 percent higher than that of the bonded and bonded-riveted tear straps.

$T^*_{2\varepsilon}$, which is the mode II equivalent of $T^*_{1\varepsilon}$, oscillated about its null value throughout the entire curved crack extension. These results suggest that $T^*_{1\varepsilon}$ is the resistance for a locally self-similar crack growth and that the crack curves in the direction of vanishing $T^*_{2\varepsilon}$. These results are the elastic-plastic counterpart to the vanishing K_{II} criterion for curved elastic crack growth [8,9]. The experimentally determined value of $T^*_{1\varepsilon}$ during stable crack growth is approximately 120 MPa-mm which is 5 percent higher than the $T^*_{1\varepsilon}$ resistance curve in Figure 1.

Crack Link-up

The feasibility of using the T^*_ε resistance curve of Fig. 1 to predict crack growth and linkup in the presence of mulitple site damage (MSD) was tested through a series of MSD experiments. The experimental procedure consisted of determining the T^*_ε integral experimentally and measuring the crack growth and linkup in MSD2 specimens with two cracks, MSD3 specimens with a center/lead crack approaching two holes with MSD cracks and MSD5 specimens with a center/lead crack and four holes. These specimens were machined from the same Al 2024-T3 clad aluminum sheet of thickness 0.8 mm. All cracks were oriented in the L-T direction and special buckling guides were used to prevent the out-of-pane buckling of the fracture specimen.

Specimens MSD5_08 (ligament = 12.7 mm and a_{msd} = 2.5 mm) and MSD5_13 (ligament 20.32 mm a_{msd} = 2.5 mm) failed simultaneously with the first crack linkup. The experimental T^*_ε versus crack extension for both specimens are shown in Figs. 3(a) and (b). In both cases, all the cracks exhibited stable crack growth at T^*_ε values similar to the CN specimen. Crack tips C and

D extended approximately 3 mm and 1.5 mm prior to linking up. Specimen MSD5_16, which had the same crack configuration as MSD5_08, was subjected to three cyclic loads. At each cycle, the load was increased until crack tip D extended approximately 0.8 mm. The specimen was then unloaded to 10% of the maximum load. Experimental T^*_ε was evaluated for each crack extension as the specimen was cyclic loaded. Figure 3(c) shows that T^*_ε values under cyclic and monotonic loads are the same during crack growth. Thus the T^*_ε generated from a monotonically loaded CN specimen may also be used to characterize low cycle fatigue crack growth.

Dynamic Crack Propagation

Dynamic T^*_ε has been previously determined experimentally using the laser caustic method by Nishioka et al in 1991 [10]. In this study [11, 12], dynamic moiré interferometry was used to determine the transient displacement fields perpendicular and parallel to the running crack in 7075-T6 aluminum alloy, single edge notch (SEN) specimen. The SEN specimen was either fatigue precracked or blunt notched for low and high crack velocity tests, respectively. By neglecting the contour integral behind the propagating crack, only a partial near-crack contour at ε = 2 mm from the crack was used in the integration process thus simplifying the T^*_ε computation. The measured crack tip displacement field was also used to compute the LEFM-based strain energy release rate, G.

Data in Fig. 4 identified as the first series is from Lee, Kokaly and Kobayashi [11] using fatigue precracked specimens and the second series refers to the data from the blunt notched specimens [12]. When plotted in terms of the crack velocity, the combined first and second series of tests, T^*_ε increased with increasing crack velocity and eventually leveled off at a terminal velocity of about 300 m/s as shown in Fig. 4. Literature on dynamic fracture show that the LEFM based dynamic strain energy release rate, G_{ID} with respect to crack velocity exhibits a characteristic gamma-shaped curve. The LEFM based G_{ID} for the dynamic fracture tests of 7075-T6 aluminum specimens and the blunt-notched 7075-T6 SEN specimens of Kobayashi and Engstrom [13] did yield this gamma-shaped curve. The LEFM approach results in a terminal velocity, which is insensitive to the variation in the driving force, G_{ID}, while the T^*_ε approach, based on elastic-plastic fracture mechanics (EPFM), suggests that the terminal crack velocity is a consequence of the saturation of the dissipated plastic energy.

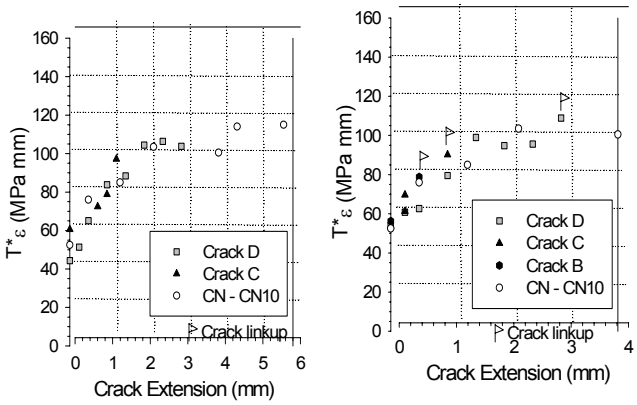

(a) MSD5_08. (b) MSD5_13.

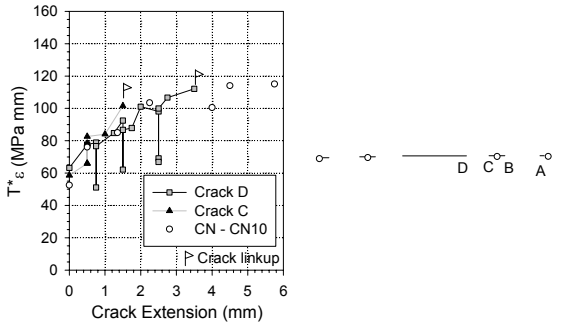

(c) MSD5_16. (d) Crack configuration.

Fig. 3. T^*_ε associated with stable crack growth.

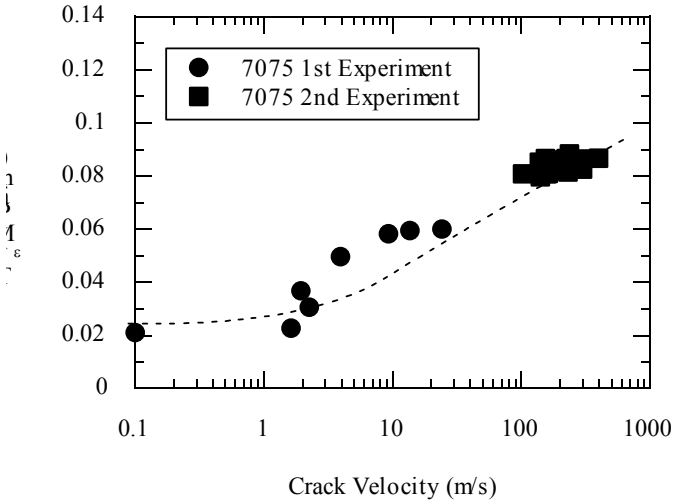

Fig. 4. T^*_ε versus crack velocity.

CONCLUSIONS

The experimental evidences accumulated over the past six years suggest that T^*_ε integral is a material property characterizing stable and dynamic crack growth. Specifically:

1. T^*_ε resistance curve reaches a plateau with static and dynamic crack growth
2. Crack curves in the direction of vanishing $T^*_{2\varepsilon}$ and grows with $T^*_{!\varepsilon}$ following the T^*_ε resistance curve.
3. A crack instability criterion based on the T^*_ε resistance curve was proposed and experimentally verified.
4. Dynamic T^*_ε value reached a constant value at terminal crack velocity.

ACKNOWLEDGEMENT

This paper summaries the cumulative efforts of the authors' colleagues of the past ten years. In chronological order, they are: Drs. Y. Omori, Pratt and Whitney Company, J. Lee, Republic of Korea Air Force, L. Ma, United Technology Research Center, P. Lam, Orbital Sciences Corporation and M. T. Kokaly, Fatigue Technology, Inc. This research was supported by FAA Grant No. 92-G-005 and ONR Contract N0001489J1276.

REFERENCES

1. Stonesifer, R.C. and Atluri, S.N., On a Study of the (ΔT) and C^* Integrals for Fracture Analysis Under Non-Steady Creep, *Engineering Fracture Mechanics*, Vol. 16 (1982), pp. 769-782.
2. Brust, F.W., Nishioka, T., Atluri, S.N. and Nakagaki, M., Further Studies on Elastic-Plastic Stable Fracture Utilizing the T^* Integral, *Engineering Fracture Mechanics*, Vol. 22 (1985), pp. 1079-1103.
3. Omori, Y., Okada, H., Ma, L., Atluri, S.N, and Kobayashi, A.S., T^*_ε Integral Under Plane Stress Crack Growth, *Fatigue and Fracture Mechanics, 27th Volume*, ASTM STP 1296 (1997), eds. P.S. Plasik, J.D. Newman, and N.E. Dowling, pp. 61-71.
4. Pyo, C.-R., Okada, H. and Atluri, S.N., An Elastic-Plastic Finite Element Alternating Method for Analyzing Wide Spread Fatigue Damage in Aircraft Structures, *Computational Mechanics*, Vol. 16 (1995), pp. 62-68.
5. Nishioka, T. and Yagami, H., Invariance of the Path Independent T^* Integral in Nonlinear Dynamic Fracture Mechanics, with Respect to the shape of a Finite Process Zone, *Engineering Fracture Mechanics*, Vol. 31 (1988), pp. 481-491.
6. Narasimhan, R. and Rosakis, A.J., Three-Dimensional Effects Near a Crack Tip in a Ductile Three-Point Bend Specimen: Part I—A Numerical Investigation," *ASME Journal of Applied Mechanics*, Vol. 57 (1990), pp. 607-617.
7. Okada, H. and Atluri, S.N., Further Study on the Characteristics of the T^*_e Integral Plane Stress Stable Crack Propagation in Ductile Materials, *Computational Mechanics*, Vol. 23 (1999) pp. 339-352.
8. Cottrell, B. and Rice, J.R., Slightly /curved or Kinked Crack, *International Journal of Fracture*, Vol. 10 (1980), pp. 155-169.
9. Sumi, Y., Nemat-Nasser, S. and Keer, L.M., On the Crack Path Stability in a Finite Body, Eng'g Fracture Mechanics, Vol. 22 (1985), pp. 759-771
10. Nishioka, T., Sakai, K., Murakami, T. Matsuo, S. and Sakakura, K., Measurement of Nonlinear Fracture Parameter T Integral under Impact Loading Using Laser Caustic Method, *Transactions of 11th International Conference on Structure Mechanics in Reactor Technology*, G13/1 (1991), Tokyo, pp. 321-326.
11. Lee, J., Kokaly, M.T. and Kobayashi, A.S., Dynamic Ductile Fracture of Aluminum SEN Specimens: An Experimental-numerical Analysis. *International Journal of Fracture*, Vol. 93 (1999), pp. 39-50.
12. Kokaly, M.T., Lee, J. and Kobayashi, A.S., Dynamic Ductile Fracture of 7075-T6 – An Experimental analysis, to be published in the *International Journal of Solids and Structures*.
13. Kobayashi, A.S. and Engstrom, W.L., Transient analysis in fracturing aluminum plates, *Proceedings of 1967 JSME Semi-International Symposium*, JSME (1967), pp. 172-181.

ICF10098OR

Experimental Validation of $T^*_{\square}$ Integral

Albert S. Kobayashi* and Satya N. Atluri**

*University of Washington, Department of Mechanical Engineering,
Seattle, WA 98195-2600, USA
** University of California, Center for Aeronautical Research and Education,
Los Angeles, CA 90095-1597, USA

$T^*_{\square}$ integral, which includes J integral as a special case, is shown to be a material property suitable for characterizing crack propagation in thin 2024-T3 aluminum sheets. The $T^*_{\square}$ resistance curve, which was generated through stable crack growth tests of single edge-notched (SEN) and central notched (CN) specimens, were used to predict curved crack growth and crack link-up of in-line multiple cracks. $T^*_{\square}$ integral for rapid crack growth reached a maximum value at the terminal crack velocity.

Key Words: Ductile fracture, fracture resistance curve, stable and rapid crack growth, curved crack growth.

INTRODUCTION

The T^*_{ε} [1], *which is a path dependent integral based on incremental theory of plasticity*, circumvents much of the difficulties encountered by the *J*-integral as shown by Brust et. al. [2]. Recently, the author and his colleagues [3] used experimental, numerical and hybrid experimental/numerical techniques to demonstrate the utility of the T^*_{ε} integral in characterizing stable crack growth in thin aluminum fracture specimens. This study was followed by dynamic and curved crack growth and crack coalescence analyses. These results are summarized in the following.

*T** INTEGRAL

The numerical analyses by Brust et. al. [2] showed that the *T** integral in the very vicinity of the crack tip reaches a plateau with crack extension under creep and cyclic loading. In contrast, the local J-integral vanishes with crack growth. This local *T*,* which is designated as T^*_{ε} is [1]:

$$T^*_{\varepsilon} = \int_{\Gamma_{\varepsilon}} \left(W n_1 - t_i \frac{\partial u_i}{\partial x_1} \right) d\Gamma \tag{1}$$

where t_i is the surface traction on the contour Γ_{ε}, W is the strain energy density and n_1 is the first component of the normal to the curve. Γ_{ε} is an arbitrary small contour immediately surrounding the crack tip and more importantly it elongates together with crack extension. T^*_{ε}, as defined by Equation (1), is identical in form of the J integral and therefore T^*_{ε} coincides with J where the deformation theory of plasticity prevails. In terms of incremental theory of plasticity, T^*_{ε} integral at the end of the Nth load steps is the sum of ΔT^*_{ε} which is the incremental change of T^*_{ε} over a load step or

$$T^*_\varepsilon = \sum^{N} \Delta T^*_\varepsilon \qquad (2a)$$

where

$$\Delta T = \int_{\Gamma_\varepsilon} \left[\Delta W n_1 - (t_i + \Delta t_i) \frac{\partial \Delta u_i}{\partial x_1} - \Delta t_i \frac{\partial u_i}{\partial x_1} \right] d\Gamma \qquad (2b)$$

(2b)

The current T^*_ε, as defined by Equation (2), is thus dependent on the prior loading history, a property that is essential for elastic-plastic analysis under crack growth. Although such incremental analysis can be routinely conducted by finite element analysis, it is not practical in experimental analysis as the cumulative experimental errors per load step will eventually overwhelm the sought data. Fortunately, Pyo et al [4] have shown, through numerical experiments, that the total T^*_ε integral computed directly by using the stresses and strains based on the incremental theory of plasticity, was for practical purpose equal to the summed ΔT^*_ε of Equation (2). Thus Equation (1) can be used for crack growth study without the cumbersome incremental procedure provided the states of stress and strain are based on the incremental theory of plasticity. More recently, T^*_ε was also studied extensively by by Nishioka and his colleagues [5].

ε is governed by the plate thickness for a plane stress state to exist along the integration contour of Γ_ε. This distance, ε, is equated to the plate thickness after Narashimhan and Rosakis [6][1]. For a plane strain state, this characteristic distance could be several times the crack tip radius.

METHOD OF APPROACH

By restricting the integration contour very close to and along the extending crack, Okada and Atluri [7] have shown that the contour integration trailing the crack tip can be neglected by virtue of the closeness of Γ_ε to the traction free crack surface. Since the contour integral is now restricted to the frontal portion of Γ_ε, the deformation theory of plasticity can now be used to compute the stresses in the loaded portion of Γ_ε. The experimental procedure consisted of measuring the two orthogonal displacement fields surrounding a stably growing or a rapidly propagating crack in thin, single edge notched (SEN), central notched (CN) and compact (CT), 2024-T3 aluminum specimens. The strains and stresses, using the equivalent stress-strain and the measured uniaxial stress-strain data of the 2024-T3 sheet, were computed. Finally, Equation (1) was evaluated numerically along the contour, Γ_ε.

RESULTS

SEN and CN Specimens

Experimentally determined T^*_ε integral data of one SEN specimen and five CN specimens of different cracks lengths with saw cut or fatigued crack tip are shown in Fig. 1. For a contour size of Γ_ε = 1 mm, the T^*_ε data for the 152.4 mm and 254 mm wide specimens are approximately equal. Other than the 50.8 mm wide CN specimens, the experimental T^*_ε data of the SEN and CN specimens practically coincide thus suggesting that the T^*_ε is a geometry-independent material property of this material. The T^*_ε resistance curve represents the average of this data. As shown in Fig. 1, the T^*_ε resistance curve rises at the initial stage of crack growth and reaches a constant value during steady crack growth. In contrast, the global J resistance curve, J_R, continually rises with stable crack extension and includes energy from other sources.

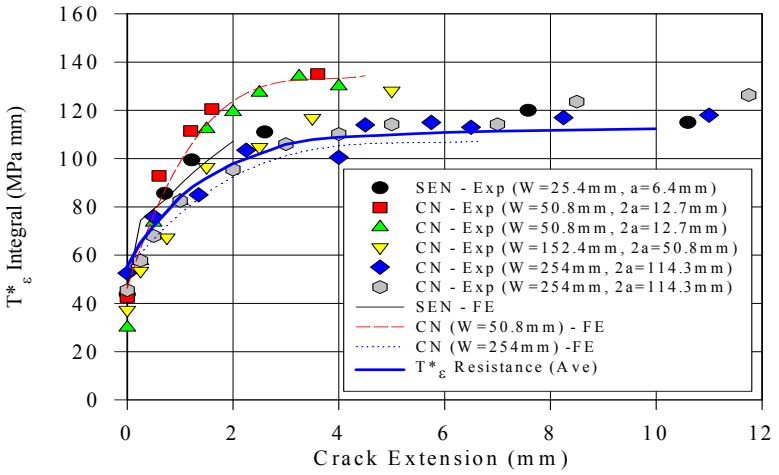

[1] The three-dimensional elastic-plastic finite element analysis of a flat crack in plate by Narashimhan and Rosakis [17] showed that the plane stress state prevailed at one half of the plate thickness from the crack tip. Since a 100 percent shear lip is the norm in ductile fracture, the minimum distance, ε, was conservatively picked as the plate thickness.

Fig. 1. SEN and CN experimental T^*_ε resistance curve (Γ_ε= 1mm)

While the J integral based instability criterion is determined on a global basis, the instability criterion for T^*_ε integral is locally based. During steady crack growth, the state of stress is in equilibrium and thus the parameter characterizing this phenomenon should be constant. When the driving force exceed the material's resistance, i.e. $T^*_\varepsilon > T^*_{\varepsilon R}$, instability will occur without an additional applied load or a displacement.

For crack growth simulation, a load or displacement was applied as the boundary condition and the crack was propagated when $T^*_\varepsilon > T^*_{\varepsilon R}$. With the prescribed load or displacement held constant, T^*_ε was evaluated again for the extended crack. If T^*_ε remained greater than $T^*_{\varepsilon R}$, the crack was extended again, and T^*_ε was re-evaluated. The crack continued to extend until T^*_ε dropped below $T^*_{\varepsilon R}$. Additional load/displacement was applied to the specimen until T^*_ε was equal to $T^*_{\varepsilon R}$ where upon another node was released to extend the crack. This procedure was repeated until no additional load or displacement was required to propagate the crack. At that point, instability was assumed to have occurred. The results identified as "FE" in Fig. 1 show that this simulation compared very well with the experimental data.

Curved Crack Growth

Twenty four biaxial test specimens were fabricated without or with bonded, bonded and riveted and integral pad-up tear straps and tested to failure. The results obtained in six tests, i.e. without tear straps, with bonded, bonded and riveted and machined pad-up tear straps are report in this paper. Figure 2 shows the variation in $T^*_{1\varepsilon}$, which corresponds to the mode I contour integral of Equation (1), along the frontal portion of Γ_ε at various crack tip locations of the curved cracks. The steady state $T^*_{1\varepsilon}$ in this study coincides with the corresponding T^*_ε resistance curve of Fig. 1. The increase in $T^*_{1\varepsilon}$ of Experiments B21 and B25, as the crack

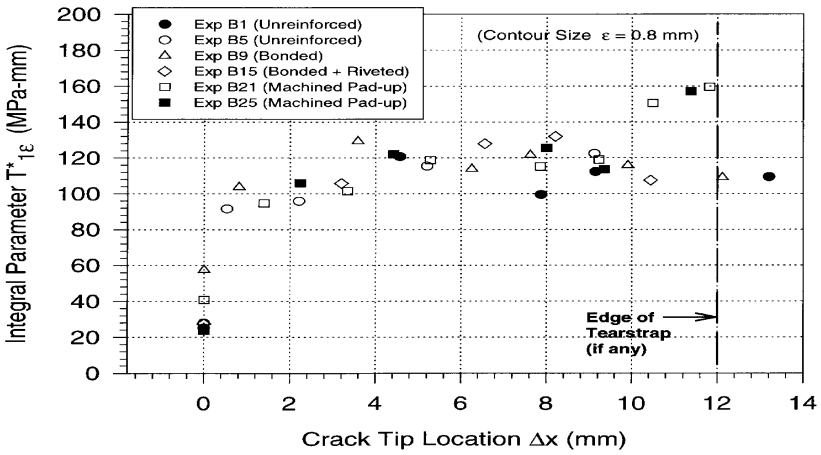

Fig. 2. $T^*_{1\varepsilon}$ variation with curved crack growth.

approaches the tear strap, represents the increased resistance to crack growth in these machined pad-up tear straps. Such an increase was not observed in Experiments B9 and B15, thus suggesting that the bonded and bonded-riveted tear straps may not be as effective as the machined pad-up tear straps in resisting curve crack extension. Indeed, the final load at fracture in the machined pad-up tear straps was 30 percent higher than that of the bonded and bonded-riveted tear straps.

$T^*_{2\varepsilon}$, which is the mode II equivalent of $T^*_{1\varepsilon}$, oscillated about its null value throughout the entire curved crack extension. These results suggest that $T^*_{1\varepsilon}$ is the resistance for a locally self-similar crack growth and that the crack curves in the direction of vanishing $T^*_{2\varepsilon}$. These results are the elastic-plastic counterpart to the vanishing K_{II} criterion for curved elastic crack growth [8,9]. The experimentally determined value of $T^*_{1\varepsilon}$ during stable crack growth is approximately 120 MPa-mm which is 5 percent higher than the $T^*_{1\varepsilon}$ resistance curve in Figure 1.

Crack Link-up

The feasibility of using the T^*_ε resistance curve of Fig. 1 to predict crack growth and linkup in the presence of mulitple site damage (MSD) was tested through a series of MSD experiments. The experimental procedure consisted of determining the T^*_ε integral experimentally and measuring the crack growth and linkup in MSD2 specimens with two cracks, MSD3 specimens with a center/lead crack approaching two holes with MSD cracks and MSD5 specimens with a center/lead crack and four holes. These specimens were machined from the same Al 2024-T3 clad aluminum sheet of thickness 0.8 mm. All cracks were oriented in the L-T direction and special buckling guides were used to prevent the out-of-pane buckling of the fracture specimen.

Specimens MSD5_08 (ligament = 12.7 mm and a_{msd} = 2.5 mm) and MSD5_13 (ligament 20.32 mm a_{msd} = 2.5 mm) failed simultaneously with the first crack linkup. The experimental T^*_ε versus crack extension for both specimens are shown in Figs. 3(a) and (b). In both cases, all the cracks exhibited stable crack growth at T^*_ε values similar to the CN specimen. Crack tips C and

D extended approximately 3 mm and 1.5 mm prior to linking up. Specimen MSD5_16, which had the same crack configuration as MSD5_08, was subjected to three cyclic loads. At each cycle, the load was increased until crack tip D extended approximately 0.8 mm. The specimen was then unloaded to 10% of the maximum load. Experimental T^*_ε was evaluated for each crack extension as the specimen was cyclic loaded. Figure 3(c) shows that T^*_ε values under cyclic and monotonic loads are the same during crack growth. Thus the T^*_ε generated from a monotonically loaded CN specimen may also be used to characterize low cycle fatigue crack growth.

Dynamic Crack Propagation

Dynamic T^*_ε has been previously determined experimentally using the laser caustic method by Nishioka et al in 1991 [10]. In this study [11, 12], dynamic moiré interferometry was used to determine the transient displacement fields perpendicular and parallel to the running crack in 7075-T6 aluminum alloy, single edge notch (SEN) specimen. The SEN specimen was either fatigue precracked or blunt notched for low and high crack velocity tests, respectively. By neglecting the contour integral behind the propagating crack, only a partial near-crack contour at ε = 2 mm from the crack was used in the integration process thus simplifying the T^*_ε computation. The measured crack tip displacement field was also used to compute the LEFM-based strain energy release rate, G.

Data in Fig. 4 identified as the first series is from Lee, Kokaly and Kobayashi [11] using fatigue precracked specimens and the second series refers to the data from the blunt notched specimens [12]. When plotted in terms of the crack velocity, the combined first and second series of tests, T^*_ε increased with increasing crack velocity and eventually leveled off at a terminal velocity of about 300 m/s as shown in Fig. 4. Literature on dynamic fracture show that the LEFM based dynamic strain energy release rate, G_{ID} with respect to crack velocity exhibits a characteristic gamma-shaped curve. The LEFM based G_{ID} for the dynamic fracture tests of 7075-T6 aluminum specimens and the blunt-notched 7075-T6 SEN specimens of Kobayashi and Engstrom [13] did yield this gamma-shaped curve. The LEFM approach results in a terminal velocity, which is insensitive to the variation in the driving force, G_{ID}, while the T^*_ε approach, based on elastic-plastic fracture mechanics (EPFM), suggests that the terminal crack velocity is a consequence of the saturation of the dissipated plastic energy.

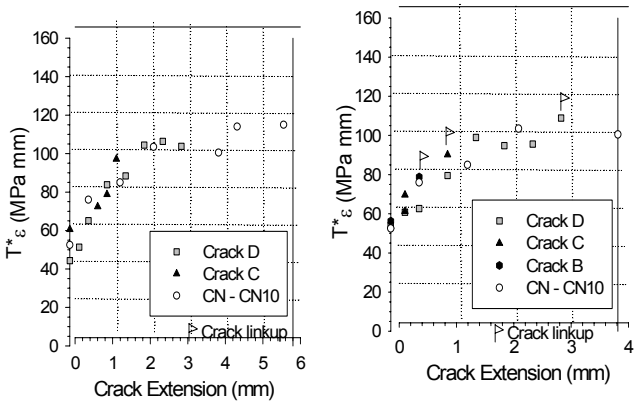

(a) MSD5_08. (b) MSD5_13.

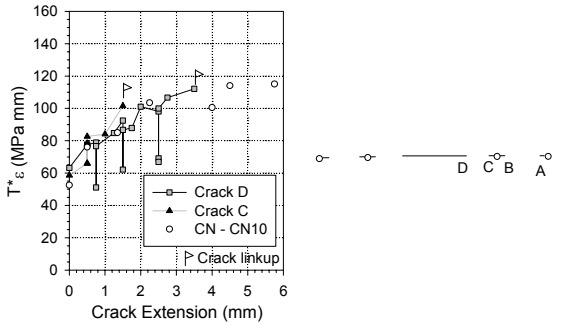

(c) MSD5_16. (d) Crack configuration.

Fig. 3. T^*_ε associated with stable crack growth.

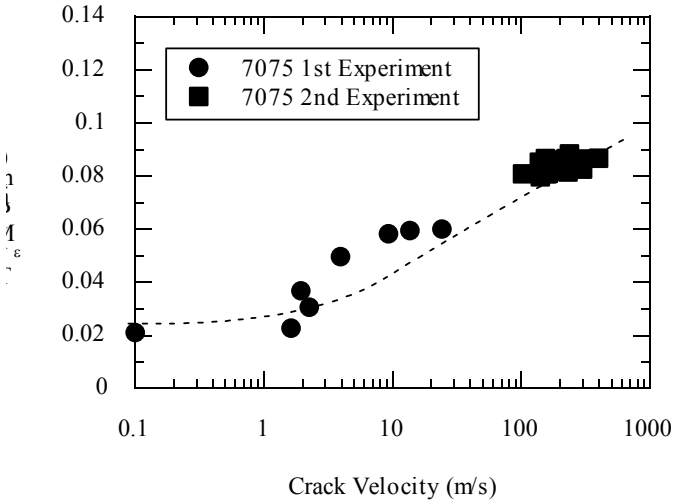

Fig. 4. T^*_ε versus crack velocity.

CONCLUSIONS

The experimental evidences accumulated over the past six years suggest that T^*_ε integral is a material property characterizing stable and dynamic crack growth. Specifically:

1. T^*_ε resistance curve reaches a plateau with static and dynamic crack growth
2. Crack curves in the direction of vanishing $T^*_{2\varepsilon}$ and grows with $T^*_{!\varepsilon}$ following the T^*_ε resistance curve.
3. A crack instability criterion based on the T^*_ε resistance curve was proposed and experimentally verified.
4. Dynamic T^*_ε value reached a constant value at terminal crack velocity.

ACKNOWLEDGEMENT

This paper summaries the cumulative efforts of the authors' colleagues of the past ten years. In chronological order, they are: Drs. Y. Omori, Pratt and Whitney Company, J. Lee, Republic of Korea Air Force, L. Ma, United Technology Research Center, P. Lam, Orbital Sciences Corporation and M. T. Kokaly, Fatigue Technology, Inc. This research was supported by FAA Grant No. 92-G-005 and ONR Contract N0001489J1276.

REFERENCES

1. Stonesifer, R.C. and Atluri, S.N., On a Study of the (ΔT) and C^* Integrals for Fracture Analysis Under Non-Steady Creep, *Engineering Fracture Mechanics*, Vol. 16 (1982), pp. 769-782.
2. Brust, F.W., Nishioka, T., Atluri, S.N. and Nakagaki, M., Further Studies on Elastic-Plastic Stable Fracture Utilizing the T^* Integral, *Engineering Fracture Mechanics*, Vol. 22 (1985), pp. 1079-1103.
3. Omori, Y., Okada, H., Ma, L., Atluri, S.N, and Kobayashi, A.S., T^*_ε Integral Under Plane Stress Crack Growth, *Fatigue and Fracture Mechanics, 27th Volume*, ASTM STP 1296 (1997), eds. P.S. Plasik, J.D. Newman, and N.E. Dowling, pp. 61-71.
4. Pyo, C.-R., Okada, H. and Atluri, S.N., An Elastic-Plastic Finite Element Alternating Method for Analyzing Wide Spread Fatigue Damage in Aircraft Structures, *Computational Mechanics*, Vol. 16 (1995), pp. 62-68.
5. Nishioka, T. and Yagami, H., Invariance of the Path Independent T^* Integral in Nonlinear Dynamic Fracture Mechanics, with Respect to the shape of a Finite Process Zone, *Engineering Fracture Mechanics*, Vol. 31 (1988), pp. 481-491.
6. Narasimhan, R. and Rosakis, A.J., Three-Dimensional Effects Near a Crack Tip in a Ductile Three-Point Bend Specimen: Part I—A Numerical Investigation," *ASME Journal of Applied Mechanics*, Vol. 57 (1990), pp. 607-617.
7. Okada, H. and Atluri, S.N., Further Study on the Characteristics of the T^*_e Integral Plane Stress Stable Crack Propagation in Ductile Materials, *Computational Mechanics*, Vol. 23 (1999) pp. 339-352.
8. Cottrell, B. and Rice, J.R., Slightly /curved or Kinked Crack, *International Journal of Fracture*, Vol. 10 (1980), pp. 155-169.
9. Sumi, Y., Nemat-Nasser, S. and Keer, L.M., On the Crack Path Stability in a Finite Body, Eng'g Fracture Mechanics, Vol. 22 (1985), pp. 759-771
10. Nishioka, T., Sakai, K., Murakami, T. Matsuo, S. and Sakakura, K., Measurement of Nonlinear Fracture Parameter T Integral under Impact Loading Using Laser Caustic Method, *Transactions of 11th International Conference on Structure Mechanics in Reactor Technology*, G13/1 (1991), Tokyo, pp. 321-326.
11. Lee, J., Kokaly, M.T. and Kobayashi, A.S., Dynamic Ductile Fracture of Aluminum SEN Specimens: An Experimental-numerical Analysis. *International Journal of Fracture*, Vol. 93 (1999), pp. 39-50.
12. Kokaly, M.T., Lee, J. and Kobayashi, A.S., Dynamic Ductile Fracture of 7075-T6 – An Experimental analysis, to be published in the *International Journal of Solids and Structures*.
13. Kobayashi, A.S. and Engstrom, W.L., Transient analysis in fracturing aluminum plates, *Proceedings of 1967 JSME Semi-International Symposium*, JSME (1967), pp. 172-181.

POSTER REFERENCE: ICF10033PR

EXPERIMENTAL-NUMERICAL ANALYSIS OF MECHANISMS OF DAMAGE INITIATION IN TOOL STEELS

L. Mishnaevsky Jr [1], N. Lippmann [2] and S. Schmauder [1]

[1] Staatliche Materialprüfungsanstalt (MPA), University of Stuttgart
Pfaffenwaldring 32, 70569 Stuttgart, Germany
Email: Leon.Mishnaevsky@mpa.uni-stuttgart.de

[2] Robert Bosch GmbH, FV/PLM, D-70442 Stuttgart, Germany

ABSTRACT

SEM in-situ investigations of the micromechanisms of damage initiation and fracture in tool steels are described. The critical state of the material and the damage growth were observed in the tests. It was shown that the initial microcracks in the steels are formed in primary carbides and then join together. A hierarchical finite element model of damage initiation, which included a macroscopic model of the deformation of the specimen under real experimental conditions and a mesomechanical model of damage in real microstructures of steels was developed. Using the hierarchical model, the conditions of local failure in the steels have been obtained.

KEYWORDS

High speed steels, damage, fracture, micromechanics, microstructure, finite elements, in-situ experiments

INTRODUCTION

The improvement of service properties of tool steels presents an important source of increasing the efficiency of metalworking industry. In order to develop a numerical model of damage or fracture in the steel, which should serve to predict the lifetime of the steel tool, or to improve the steel properties, one needs to know the mechanisms of damage and fracture in the steels [1-3]. The direct in-situ observation of the fracture mechanisms of the steels under microscope is quite difficult as compared with the case of more ductile materials, since the material fails very quickly. Then, not only qualitative parameters of fracture (like its mechanisms) but also quantitative ones (like critical damage parameters) are of interest. The purpose of this work was to study the mechanisms and conditions of damage initiation and growth in the tool steels both qualitatively and quantitatively. The work includes the

following steps:

- SEM-in situ experiments on 3-point bending of specimens with inclined notches,
- FE-Simulation of the deformation of the specimens on macro- and mesolevel, taking into account the real microstructure of the steels observed in the SEM-experiments.

The SEM in-situ observation of the damage initiation allowed to clarify the micromechanisms of damage initiation, whereas the developed hierarchical finite element model (macro- and mesomodel) made it possible to determine the failure conditions for steels constitutents using the real loading conditions and real microstructure of the steel.

SEM IN-SITU INVESTIGATIONS OF MICROMECHANISMS OF DAMAGE INITIATION

Conditions of Experiments

In order to clarify the mechanisms of damage initiation and growth in the steels, a series of SEM-in-situ-experiments was carried out. 3-point bending specimens with an inclined notch, as described in [4], were used in these tests. These specimens allow to observe the micro- and mesoprocesses of local deformation and failure of carbides and the matrix of steels during loading of macroscopic specimens in the SEM. The shape and sizes of the specimens are shown schematically in Figure 1. The advantage of the specimen with the inclined notch is that the most probable location of first microcrack initiation in the specimen notch can be simply predicted (which is not the case for the usual 3-point bending specimens). Therefore, one can observe this place with high magnification during loading and identify the load and the point in time at which the first microcracks form very exactly. Specimens made from the cold work steel X155CrVMo12-1 (in further text denoted as KA) and high speed steel HS6-5-2 (denoted as HS) have been used. In the experiments, the specimens with different orientations of primary carbide layers were studied. Since the tool steels are produced in the form of round samples and was subject to hot reduction after austenitization and quenching, they are anisotropic: the carbide layers are oriented typically along the axis of the cylinder (this is the direction of hot reduction). Therefore, the following designation of the specimen orientation was used: L – the direction along the carbide layers, R – radial direction in the workpiece, C – the direction along the workpiece axis. In the experiments, specimens with orientations CL, LC and CR have been used. The CR and CL specimens are shown in Figure 2. The specimens have been subjected to the heat treatment (hardening at 1070^{o}C in vacuum and tempering 2 times at 510^{o}C), and then polished with the use of the diamond pastes of different sizes till the roughness R_z of the surface of the specimens does not exceed 3 μm. The notch region of the specimens was etched with 3 % and 10 % HNO_3 until the carbides were seen on the surface.

Then, the specimens have been subjected to loading with simultaneous observation of the notch region in SEM. The scheme of loading is given in Figure 1 as well. Each loading test was repeated 3 times for each type of steel and specimen orientation.

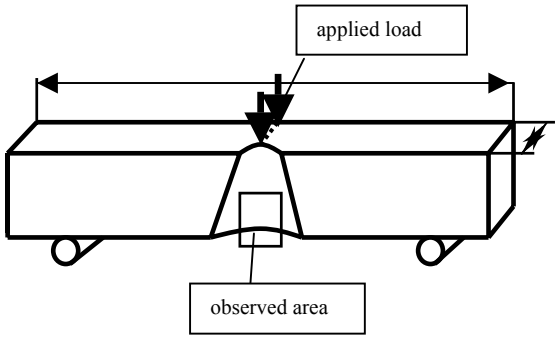

Figure 1. 3-point bending specimens

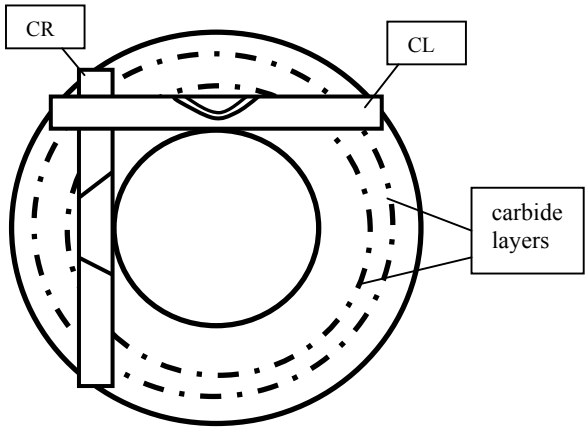

Figure 2. Orientation of CR and CL specimens as related to the carbide layers

Results of the Experiments

The force-displacement curves were recorded during the tests. The loading was carried out in small steps, with the rate of loading about 1 mm/s. The places in the specimen notch where the microcrack initiation was expected have been observed through scanning electron microscopy (SEM) during the tests. It was observed that the first microcracks formed only in the primary carbides, and not in the "matrix" of the steel. Also, no microcrack along the carbide/matrix interface was observed in the tests. The forces at which the failure of primary carbides was observed in each specimen are given in the Table 1.

TABLE 1. CRITICAL FORCES IN THE EXPERIMENTS .

Numbers of specimens	Type of the specimen	Force at which first microcrack was observed in the specimen, N	Force at which the specimen failed, N
1-3	KALC	95, 52, 37.5	155, 85,160
4-6	KACR	50, 55, 37.5	95, 95, 70
7-9	HSCR	45, 50 (several microcracks in both large and small carbides), 50	95, 80, 95
11-12	HSLC	50 (one microcrack), 72.5 (another microcrack), 127	200, 190, 195

Generally, the course of failure of the specimens was as follows: (1) formation of a microcrack at some carbide, (2) formation of several microcracks at many carbides in different places of observed area (in so doing, the microcracks are formed rather at larger carbides at some distance from the boundary of the specimen, than in more strained macroscopically areas in the vicinity of the lower boundary of the specimen; the local fluctuations of stresses caused by the carbides have evidently much more influence on the microcracking than the macroscopic stress field), and (3) after the failure of many carbides, the microcracks (or plastic zones in front of the microcracks) begin to grow into the matrix; just after this occurs, the specimens fail. The failure of many carbides was observed just before the specimens failed. The differences between the loads at which the microcracks are formed, and that at which the specimen failed was in most cases very small. Figure 3 shows

the SEM micrographs of a typical primary carbide in the notch region of steels before and after its failure. Comparing the values of critical forces from Table 1, one may conclude that the failing force for the specimens with orientation LC is much higher than with the orientation CR (more than twice). Then, the force at which first microcracks form and first carbides fail depends on the orientation of specimens much more for high speed steels than for the cold work steels.

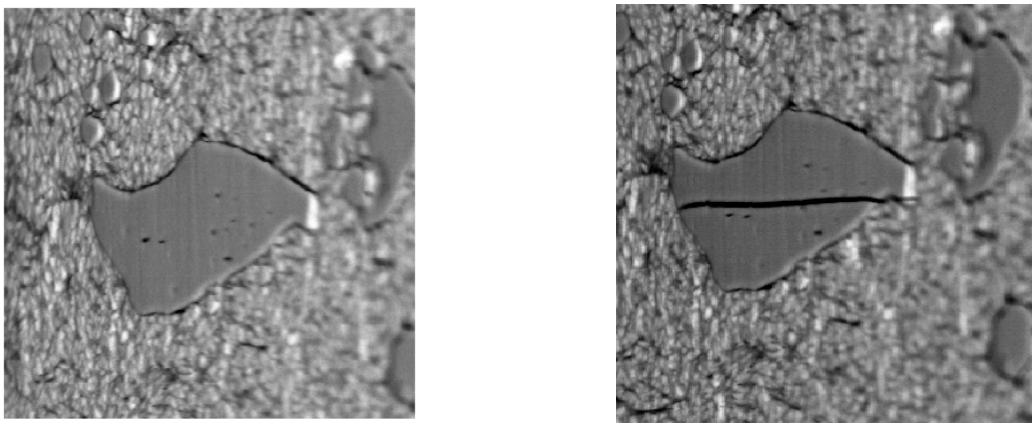

a) b)

Figure 3. A carbide grain before (a) and after failure (b). (Area size 40x100 μm).

MESOMECHANICAL SIMULATION OF DEFORMATION IN STEELS

To simulate the deformation of 3-point bending specimens with inclined notch, a three-dimensional FE model of the specimen was developed. Due to the symmetry of the specimen, only one half of the specimen was taken. The material was assumed to be homogeneous. The forces measured in the tests described above were applied in the simulations. The displacements from the boundary nodes of elements which are located in the vicinity of the symmetry plane and at the lower notch boundary are used as boundary conditions in the mesomechanical simulation of carbide failure. Then, the 2D mesomechanical simulations of carbide failure have been carried out for each microstructure and each load, measured in the experiments. The 2D-model was created, which represents the cluster of finite elements in the notch region of the specimen. The real structure region with 5000 elements of the plane strain type TRIP 6 and size 100 μm x 100 μm was located in the lower left corner of the model. As boundary conditions the displacements from the model of deformation of 3-point bending specimen were taken. Since the mesh density in the 2D case is higher, the calculated displacements have been linearly interpolated between the points which were available in the 3D simulation.

The mesomechanical simulation was performed with the use of the multiphase element method [5]. The micrograph of the carbide, obtained in SEM-in-situ experiments was digitized, and then automatically imposed on the region of the real structure. The micrographs to be digitized were chosen in such a way that they were representative enough for the given materials. Due to the inclined notch surface, the micrographs in Figure 3 have different scales in X- and Y-directions. To take that into account, the micrographs were scaled with the use of the image analysis software XView accordingly to their scales in both directions. The properties of carbide and matrix are as follows [3, 4, 6, 7]: (cold work steel) E_C=276 GPa, E_M=232 GPa, constitutive law of the matrix: σ_y = 1195 +1390 [1-exp (-ϵ_{pl}/0.0099)]; (high speed steels) E_C=286 GPa, E_M=231 GPa, constitutive law of the matrix: σ_y = 1500 + 471 [1-exp(-ϵ_{pl}/0.0073)], Poisson's ratio - 0.19 (carbides) and 0.3 (matrix).

FAILURE STRESS OF PRIMARY CARBIDES

Figure 4 gives the distribution of von Mises stress in the real microstructure of the cold work steel at the loads at which the carbide failed. Supposing that failure of the carbides is determined by the action of maximal normal stresses, one obtains the failure stresses of carbides for different steels and orientations (see Table 2).

TABLE 2. FAILURE STRESS OF CARBIDES

Type of the steel	KALC	KACR	HSCR	HSLC
Failure stress of carbides, MPa	1826	1840	1604	2520

It is of interest to compare the above results with some literature data. Lippmann et al. [8] and Lippmann [4] obtained the values 1863...1987 and 1200...2100 MPa, respectively, for the failure stress of carbides in cold work and high speed steels. One can see that our values for cold work steels are very close to those given in [4]; the values for high speed steels are about the higher boundary of the variation range.

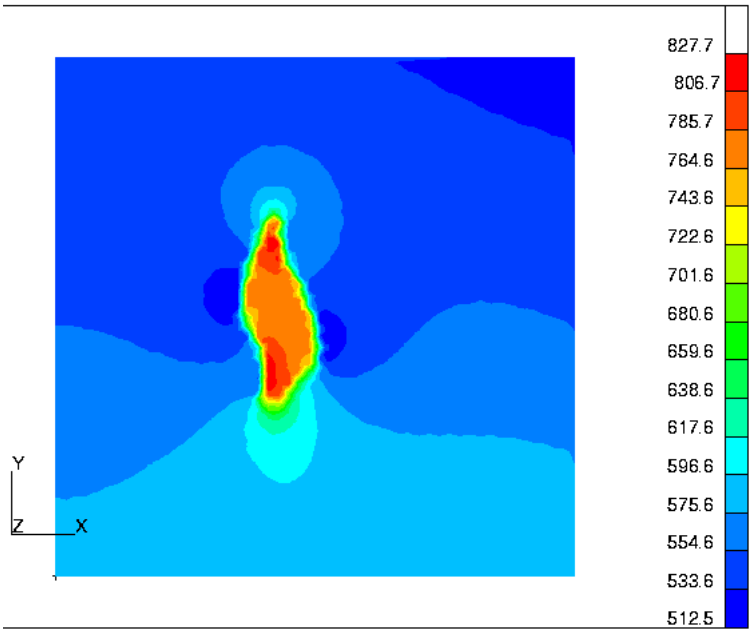

Figure 4. Von Mises stress distribution in the real microstructure of the steel in the notch of the specimen.

CONCLUSIONS

On the basis of the above analysis, one can draw the following conclusions:

1) The course of failure of the specimens was as follows: formation of one microcrack at some carbide, then formation of several microcracks at many carbides in different places of the observed area (in so doing, the microcracks are formed rather at larger carbides at some distance from the boundary of the specimen, than in more strained macroscopically

areas in the vicinity of the lower boundary of the specimen; the local fluctuations of stresses caused by the carbides have evidently much more influence on the microcracking than the macroscopic stress field), and, finally, after the failure of many carbides, the microcracks (or plastic zones in front of the microcracks) begin to grow into the matrix; just after this occurs, the specimens fail.

2) The initial microcracks in the steels are formed in primary carbides (i.e. not along the carbide/matrix interface and not in the matrix).
3) The failing force for the specimens with orientation LC is much higher than with the orientation CR (more than twice). The force at which first microcracks form and first carbides fail depends on the orientation of specimens much more for high speed steels than for the cold work steels.
4) The failure stresses of carbides (of approximately average sizes for given steels) determined from the SEM in-situ experiments and the FEM simulations are 1826 MPa (the specimen KALC), 1840 MPa (KACR), 1604 MPa (HSCR) and 2520 MPa (HSLC). The failing stress of carbides depends of the orientation of carbide layers in high speed steels much more than in cold work steels.

Acknowledgement: The authors gratefully acknowledge the financial support by the European Commission via the ECSC-Project 8834 ”Influence of micromechanical mechanisms on strength and damage of tool steels under static and cyclic loading”. The authors are grateful to the administration and specialists from the Technical University - Mining Academy Freiberg (TU BAF), who made it possible to carry out the SEM-in-situ experiments on their equipment and supported us during the experiments.

References

1. L. Mishnaevsky Jr and S. Schmauder (2001), *Appl. Mech. Rev*, 54, 1
2. L. Mishnaevsky Jr, N. Lippmann and S. Schmauder (2000), *In: Proc. 13th European Conference on Fracture “Fracture Mechanics : Applications and Challenges*”, CD-ROM
3. L. Mishnaevsky Jr, N. Lippmann and S. Schmauder, Computational Optimization of Materials by Varying the Microstructures: Some Recent Developments as Applied to the Improvement of Fracture Resistance of Tool Steels (submitted)
4. N. Lippmann (1995), Dissertation, Freiberg, Germany
5. L. Mishnaevsky Jr, M. Dong, S. Hoenle and S. Schmauder (1999), *Comp. Mater. Sci.,* 16, 1-4, 133-143
6. L. Mishnaevsky Jr and S. Schmauder, (2000), *Influence of Micromechanical Mechanisms of Strength and Deformation of Tool Steels under Static and Cyclic Load*, ECSC RTD Project Final Report, 2000, Creusot Loire, Frankreich
7. L. Mishnaevsky Jr and S. Schmauder (1999), *Pursuance and Analysis of SEM-in-situ-Experiments on the Deformation and Fracture of Cold Work and High Speed Steels,* MPA Report, 35 pp.
8. N. Lippmann, A. Lehmann, Th. Steinkopff and H.-J. Spies (1996), *Comp. Mat. Sci*., 7, 123-130

ORAL REFERENCE ICF100944OR

EXPLICIT MODELING OF DAMAGE INITIATION AND EVOLUTION IN OPEN-HOLE COMPOSITES

E.V. Iarve, [1] D. Mollenhauer[2] and R. Kim[1]

[1] University of Dayton Research Institute, 300 College Park Ave.,
Dayton, OH 45469-0168
[2] United States Air Force Research Laboratory, AFRL/MLBC,
2941 P Street Room 243, Wright-Patterson AFB, OH 45433-7750

ABSTRACT

The spline approximation approach for three-dimensional stress analysis in laminates containing open holes has been extended to account for matrix cracking in each ply. Crack surface where the displacement jump takes place is defined by using the domain Heaviside function approximated with higher order polynomial B-splines. It is shown that the spline approximation of the Heaviside function maintains the integral properties of the step function and that the gradient of the approximation maintains the integral properties of Dirac's delta function for any order of approximation. An advantage of the proposed method is that its implementation only involves integration of the products of original shape functions and their derivatives and does not require modification of the integration domains. Uniaxial tension of a unidirectional composite with open hole is considered. Fiber direction stress relaxation due to longitudinal splitting is successfully modeled by the method proposed. Observed by using incremental x-ray technique split origination and extension loads correlate well with predictions.

INTRODUCTION

Development of a high fidelity strength prediction tool for laminated composites with stress concentrations is an important problem for the aerospace industry as well as for less traditional areas of composite applications, such as rail-transportation and sports equipment industries. High fidelity modeling involves simulation of actual damage mechanisms such as matrix cracking, delaminations and their combined influence on the redistribution of fiber stresses, which determines the strength. Discrete modeling of transverse cracking represents a formidable problem. Normally the mesh configuration is dictated by the boundaries of the specimen, such as the presence of a hole. Transverse cracking directions in the plies are defined by fiber orientations and change from ply to ply. Higher order shape functions will be employed below to construct an efficient method for mesh independent discontinuity modeling.

The concept of partition of unity approximation by Babuska and Melenk [1], which encompasses the moving least square approximation approach, provides a powerful tool for building higher order

approximations for mesh independent field discontinuity modeling. Recently a novel method based on finite element approximation as a partition of unity basis was proposed for modeling crack propagation by Belytschko and Black [2], Moes, et al. [3], and Sukumar, et al. [4]. In this method the Heaviside step function is used for local enrichment. Practical implementation of this method involves several steps such as element partitioning and calculation of the cross integrals of the shape functions in the partitioned elements. Care also has to be taken to avoid crack trajectories generating near-zero volume partitions.

The method of mesh independent crack modeling by using higher order shape functions proposed below is based on replacing the Heaviside step function with its B-spline approximation. While an arbitrary crack face can be modeled in the limit of increased power of approximation, the implementation involves only standard Gaussian integration over original mesh cells (finite elements). Application of a three-dimensional B-spline approximation to stress analysis in laminated composites, including boundary conditions, implementation issues and asymptotic enrichments in the vicinity of stress singularities, are discussed in Iarve [5-7] and Iarve and Pagano [8].

VARIATIONAL FORMULATION

Consider an elastic volume V and a set of piecewise polynomial three-dimensional functions $X_i(\mathbf{x})$, which provide a partition of unity-type basis function for displacement approximation, so that

$$\mathbf{u}(\mathbf{x}) = \sum_{i \in \Omega} X_i(\mathbf{x}) \mathbf{U}_i , \tag{1}$$

where $\mathbf{U}_i$ are displacement approximation coefficients, not necessarily associated with nodal displacements except for the boundary ∂V where boundary conditions are imposed. All values of index i in equation (1) compose set Ω. Functions $X_i(\mathbf{x})$ are constructed from one-dimensional sets of B-spline basis functions of maximum order n and nodal defect k as standard tensor products. Nodal defect of spline designates maximum number of discontinuous derivatives in this node. If k=1 then $u_i(\mathbf{x}) \in C^{(n-1)}$; and in the case of k=n-1, one obtains C^0 continuous p=n approximation. In our present work a procedure based on polynomial representation (Iarve [5]) was used. Each function $X_i(\mathbf{x})$ possesses local support of no more than $(n+1)^3$ mesh cells and

$$\sum_{i \in \Omega} X_i(\mathbf{x}) \equiv 1, \ \ \mathbf{x} \in V .$$

The subdivision into mesh cells or finite elements in Figure 1 is essential for implementation because we assume that there is an integration procedure associated with these cells, which allows us to calculate volume integrals of shape functions, and their cross products and the products of their derivatives. Our goal is to model a displacement field discontinuous along a surface Γ_α for a given mesh configuration and approximation (1).

The step function enrichment of approximation (1) proposed in Belytscko and Black [2] for modeling the desired discontinuity for a bisected domain V can be written as

$$\begin{gathered} \mathbf{u}(\mathbf{x}) = \widetilde{H}(\mathbf{x}) \mathbf{u}^{(1)}(\mathbf{x}) + (1 - \widetilde{H}(\mathbf{x})) \mathbf{u}^{(2)}(\mathbf{x}) \\ \widetilde{H}(\mathbf{x}) = H(f_\alpha(\mathbf{x})) \end{gathered} , \tag{2}$$

where $\mathbf{u}^{(1)}$ and $\mathbf{u}^{(2)}$ are approximated by shape functions (1), $H(x)$ is the Heaviside step function, and $f_\alpha(\mathbf{x})$ is the signed distance function for the surface Γ_α . To extend equation (2) for a crack ending inside volume V in point B, we shall define the extension of the signed distance function for a given point, in the case when the point of the crack surface nearest to it is not the orthogonal projection of that point to the crack surface. The signed distance function, Belytschko and Black [2], is defined as

$$f_\alpha(\mathbf{x}) = sign(\mathbf{n}(\bar{\mathbf{x}})(\mathbf{x}-\bar{\mathbf{x}})) \min_{\bar{\mathbf{x}}\in\Gamma_\alpha} \left\|\mathbf{x}-\bar{\mathbf{x}}\right\|, \tag{3}$$

where Γ_α is the crack surface. In the case of the bisecting crack point, $\bar{\mathbf{x}}$ is the orthogonal projection of $\mathbf{x}$ on surface Γ_α . However, in the case when the crack ends in point B inside the region, we will find such $\mathbf{x}$ that $\bar{\mathbf{x}} = B$ according to (3), and $\mathbf{x}$- $\bar{\mathbf{x}}$ is not orthogonal to Γ_α . It is in this context that the signed distance function will be used below.
Let us denote the set of all index values in (1) for which the shape functions are nonzero at the crack surface by Ω_α , so that

$$\exists \mathbf{x} \in \Gamma_\alpha : X_i(\mathbf{x}) \neq 0 \Leftrightarrow i \in \Omega_\alpha .$$

The enriched approximation for the domain V and arbitrary crack is defined in the following form

$$\mathbf{u} = \widetilde{H}\mathbf{u}^{(1)} + (1-\widetilde{H})\mathbf{u}^{(2)} + \mathbf{u}^{(3)}, \tag{4}$$

$$\mathbf{u}^{(1)} = \sum_{i\in\Omega_\alpha} X_i \mathbf{U}_i^{(1)}, \quad \mathbf{u}^{(2)} = \sum_{i\in\Omega_\alpha} X_i \mathbf{U}_i^{(2)}, \tag{5}$$

and

$$\mathbf{u}^{(3)} = \sum_{i\in\Omega/\Omega_\alpha} X_i \mathbf{U}_i^{(3)} \tag{6}$$

We have also omitted the spatial argument for conciseness. Strictly speaking, the strains are assumed independently, as

$$\boldsymbol{\varepsilon} = \widetilde{H}\boldsymbol{\varepsilon}^{(1)} + (1-\widetilde{H})\boldsymbol{\varepsilon}^{(2)} + \boldsymbol{\varepsilon}^{(3)}, \tag{7}$$

where the strain tensors $\boldsymbol{\varepsilon}^{(1)}$, $\boldsymbol{\varepsilon}^{(2)}$ and $\boldsymbol{\varepsilon}^{(3)}$ are expressed through $\mathbf{u}^{(1)}, \mathbf{u}^{(2)}$ and $\mathbf{u}^{(3)}$ by using Konhsi equations, and the step function is not differentiated. Considering the elastic stress-strain relationship:

$$\boldsymbol{\sigma} = \mathbf{C}\boldsymbol{\varepsilon},$$

one can write the strain energy in the volume V as

$$W = \int_V \left\{ \frac{1}{2}\widetilde{H}\left[\boldsymbol{\varepsilon}^{(1)}\right]^{\mathrm{T}} \mathbf{C}\boldsymbol{\varepsilon}^{(1)} + \frac{1}{2}(1-\widetilde{H})\left[\boldsymbol{\varepsilon}^{(2)}\right]^{\mathrm{T}} \mathbf{C}\boldsymbol{\varepsilon}^{(2)} + \frac{1}{2}\left[\boldsymbol{\varepsilon}^{(3)}\right]^{\mathrm{T}} \mathbf{C}\boldsymbol{\varepsilon}^{(3)} + \right. \\ \left. + \widetilde{H}\left[\boldsymbol{\varepsilon}^{(1)}\right]^{\mathrm{T}} \mathbf{C}\boldsymbol{\varepsilon}^{(3)} + (1-\widetilde{H})\left[\boldsymbol{\varepsilon}^{(2)}\right]^{\mathrm{T}} \mathbf{C}\boldsymbol{\varepsilon}^{(3)} \right\} dV \tag{8}$$

The work of external traction **T** applied at the portion S_T of the boundary ∂V is expressed as

$$A = \int_{S_T} \mathbf{T}\mathbf{u} dS \,, \tag{9}$$

where the displacement is approximated by using equation (4). The minimum potential energy principle to obtain the equations for determining unknown displacement approximation coefficients can be expressed as:

$$\delta(W - A) = 0 \,. \tag{10}$$

The idea of the method proposed in this paper is to replace the step function in equations (4)-(10) by an approximation based on shape functions (1), so that

$$\widetilde{H}(\mathbf{x}) = \sum_{i \in \Omega} X_i(\mathbf{x}) h_i \tag{11}$$

In this case all integrals appearing in the system of equations resulting from (10) will contain products of unaltered original shape functions and their derivatives. The orders of polynomials to be integrated in the mesh cells are higher but always the same, thus a standard Gaussian quadrature can be employed. Equations (4)-(11) completely determine the displacement approximation coefficients in equations (5) and (6) provided that the coefficients h_i are defined. It is worth noting that extending the crack, i.e. changing the set Ω_α, the total number of degrees of freedom in equation (4) also changes, since duplicate degrees of freedom are required for each function with the index belonging to Ω_α .

RESULTS AND DISCUSSION

Cracks in a $[0°]_8$ IM7/5250-4 composite with a 0.25" hole were analytically examined using the mesh independent damage modeling technique proposed above. Axial tensile loading was applied through displacement boundary conditions $u_x(0,y,z)=-u_x(L,y,z)=u_0$. Other displacement components were zero at x=0,L. The crack orientation was parallel to fiber direction. The coefficients of the step function approximation (11) were determined for each crack according to the following rule: h_i=1 if

$$\int_V X_i(\mathbf{x}) dV > \int_V X_i^+(\mathbf{x}) dV$$

and h_i=0 otherwise, where

$$X_i^+(\mathbf{x}) = \begin{cases} X_i(\mathbf{x}), f_\alpha(\mathbf{x}) > 0 \\ 0, f_\alpha(\mathbf{x}) \le 0 \end{cases}$$

In this initial study assumptions regarding the crack length increment were made for ease of modeling. The specimen plane was subdivided into 20 regions, as shown by bold lines in Figure 1.a, and the cracks were incremented so that on each step they will bisect a new region. Maximum stress failure criterion was used to predict failure initiation and failure in the fiber direction. Initial crack length was defined by the near-hole region size shown in Figure 1.b, which is a close-up of the central region of the specimen. Crack growth was predicted by comparing the J-integral calculated around the crack tip to the Mode II critical energy release rate value G_{IIC}. Besides that the maximum stress criteria everywhere else in the laminate was checked to account for additional damage

origination or fiber breakage. In the present case crack growth resulted in complete cracking of the specimen into four separate sections. After that the fiber failure in the ligaments was predicted.

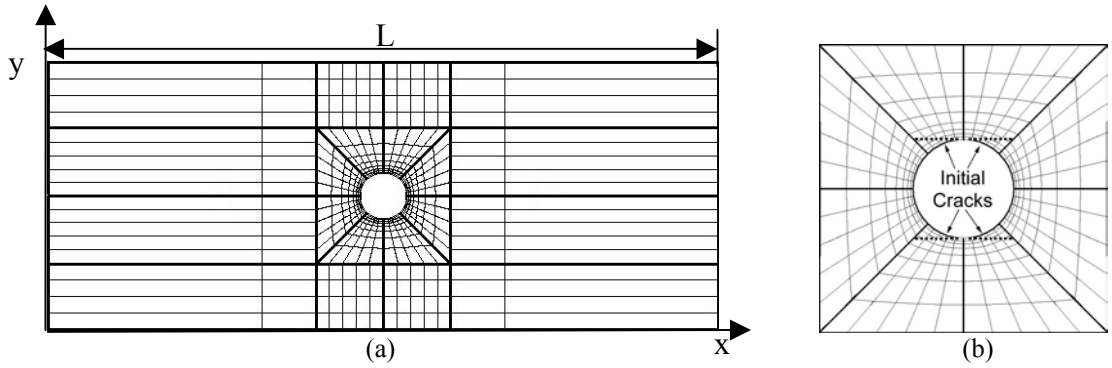

Figure 1: Specimen mesh and crack locations.

Axial stress results from this analysis are shown in Figure 2. These figures contain axial (fiber direction) stress distributions for the undamaged specimen (Figure 2.a) and that for two crack lengths for a close-up of the central region of the specimen. Of special interest is the reduction of the stress concentration at the hole edge as the cracks lengthen. When the cracks have extended to the ends of the specimen (Figure 2.c), the concentration is completely eliminated. This result is important in the sense that this effect can not be readily modeled by using finite element property degradation-based techniques. Extension of the splits eliminates the stress concentration as the physical reality of the situation demands.

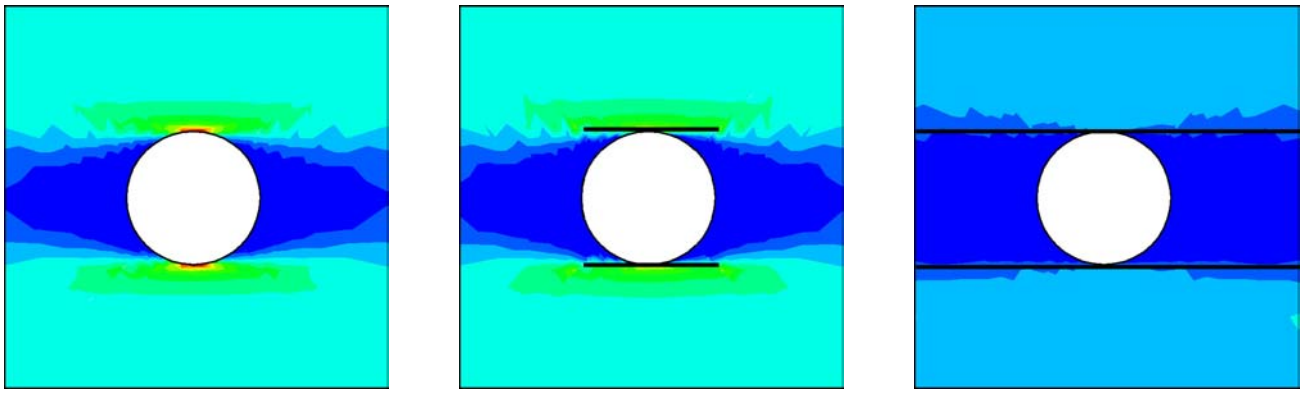

Figure 2: Axial stress distribution in a region close to the hole. (a) no crack; (b) initial crack (c) cracks split the specimen.

The progressive failure analysis-generated far field stress-strain curve and the experimentally measured one are shown in Figure 3. The stress value shown on the vertical axis represents average axial applied load divided upon specimen cross-section. Experimentally the applied load was obtained from the load sell data whereas in the analysis the applied load was calculated by integrating the axial stress over the lateral edge area. The far field strain on the horizontal axis of Figure 3 was measured using a strain gage located at the middle of strip between hole edge and specimen edge. The change in the slope of experimentally obtained stress-strain curve in Figure 3 indicates the vertical splitting emanating from the hole edge. As the vertical splitting extended to the end of the specimen, the stress in the strip increases while the stress in the region between the

vertical split decrease and eventually diminishes. The analytically generated curve is based on elongation equal to applied lateral displacement divided by length $2u_0/L$ and does not reflect explicitly the local stress change in the ligaments due to propagation of the splits. The load range in which the splits were experimentally observed and propagated through the near hole region (Figure(1.b)) is shown in Figure 3 as well. As can be observed, they are in good agreement with the prediction.

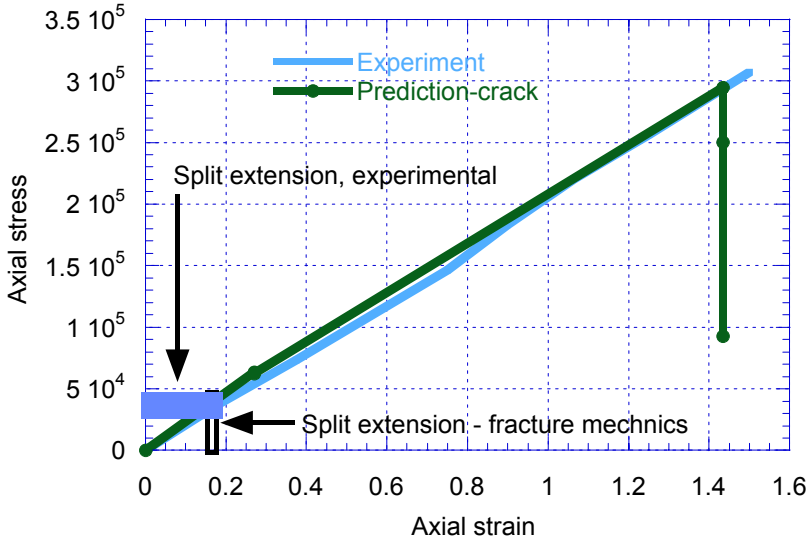

Figure 3: Progressive failure analysis generated and experimental stress strain curves for a unidirectional laminate with a hole.

Quasi-isotropic laminates were also considered, and the transverse cracks and delaminations modeled simultaneously. Moire' interferometry will be employed to obtain an accurate full-field distribution of in-plane strain on the face of the specimen as cracking progresses in order to verify the mesh independent damage modeling techniques proposed.

REFERENCES

1. Babuska, I. and Melenk, (1996), *Int. J. Numerical Methods Engineering*,
2. Belytschko, T. Y. and Black, T, (1999), *Int. J. Numerical Methods Engineering*, 45(5), pp. 601-620.
3. Moes, N., Dolbow, J., and Belytschko, T., (1999), *Int. J. Numerical Methods Engineering*, 46, pp. 131-150.
4. Sukumar, N., Moes, N., Moran, B., et al., (2000), *Int. J. Numerical Methods Engineering*, 48, pp. 1549-1570.
5. Iarve, E. V., (1996), *Int. J. Solids Structures*, 33(14), pp. 2096-2118.
6. Iarve , E. V., (1997), *Composites Part A*, 28(6), pp. 559-571.
7. Iarve, E. V., (2000), *Composites Science and Technology*, 60, pp. 2365-2374.
8. Iarve, E. V. and Pagano, N. J., (2001), *Int. J. Solids Structures,* 38(1), pp. 1-28.

ORAL REFERENCE: *ICF1001036OR*

FAILURE ANALYSIS OF A PARTICULATE COMPOSITE CUTOFF WHEEL WITH FIBER REINFORCING

Thomas J. Mackin and Helen M. Inglis

Department of Mechanical and Industrial Engineering, University of Illinois,
1206 W. Green Street, Urbana, IL 61802, USA

ABSTRACT

A failure analysis was undertaken after an abrasive particulate composite cutoff wheel failed in operation, injuring a worker. Compact tension tests and bend tests were performed on samples cut at various angles from the failed wheel and from unused wheels. Relative fracture toughness values calculated from the compact tension tests showed the dependence of plateau toughness on fiber orientation. Specimens with fibers normal to the crack direction exhibited a higher plateau toughness than those with mis-aligned fibers. Energy absorbed during fracture, calculated from the bend tests, reduced markedly with fiber orientation. Specimens with fibers parallel to the loading direction absorbed more energy during failure than those with mis-aligned fibers. It was determined that the catastrophic nature of this failure could be attributed to reduced fracture toughness resulting from the unfortuitous fiber orientation. In addition, the accident need not have been so severe had reasonable safety procedures been followed.

KEYWORDS

Failure analysis, composite, fracture toughness, brittle fracture, fiber bridging

INTRODUCTION

An abrasive cut-off wheel, used for cutting bronze bar into lengths, fractured during operation, seriously injuring a worker. A failure analysis was conducted to determine the contributory causes of failure. The emphasis of the discussion in this paper is on the mechanism of failure in a particulate composite with fiber reinforcing, and the implications for improved design of abrasive cutoff wheels. However, the failure analysis also showed that the severity of the incident was exacerbated by unsafe operating conditions. While this paper will not dwell on the issue of safety, it is important to note that, had reasonable safety procedures been in place, the failure need not have resulted in a serious accident.

Standards

The standard for the use and care of abrasive wheels [1] recognizes that abrasive wheels are easily damaged and liable to fail during operation, and recommends procedures to ensure that such failures should not cause injuries. These procedures are largely the responsibility of the operator of the equipment. Where relevant, the regulations are mentioned in the discussion following. There are no standards relating to the use of fiber reinforcing on abrasive wheels, or specifying the procedures which should be followed in the manufacture of a particulate composite abrasive wheel. For reasons that can only invite speculation, abrasive wheel manufacturers have not shown great willingness to develop fabrication standards.

Abrasive Cutoff Wheel Specification

The cut-off wheel in question is a 30" diameter abrasive wheel, ¼" thick, with a central arbor hole 1¾" in diameter. It is manufactured of particles of aluminum oxide embedded in a matrix of phenolic resin. This mixture is pressed between layers of loosely woven glass fiber cloth, resulting in a composite sandwich with one layer of glass cloth at the top and one at the bottom of the disk. The cloth is a 0°/90° weave with thicker fiber bundles in the warp direction than in the weft direction. The two glass fiber cloths are oriented at some random angle with respect to each other. The composite is subjected to a high pressure for a short time, and then cured for 48 hours at 170°C. Disks are speed-tested to 20% above the maximum rated speed before being shipped, as required by the standard [1].

Operation

The abrasive cut-off wheel was used to cut bronze bars into lengths in a continuous casting operation. Cartridge brass bar drops vertically through the cutting station and the wheel is hand-fed through the bar. Since the bar is moving while the wheel makes the cut, some amount of bending load is generated in the wheel during the cutting process.

The cut-off wheel is mounted horizontally over the motor shaft. A cupped mounting flange is placed on either side of the wheel, clamping the wheel along an annulus with an outer diameter of roughly 4". The ANSI standard [1] recommends, but does not require, that a compliant blotter be used between the mounting flange and the wheel to alleviate stress concentrations at the flange/wheel contact. A blotter was not used on the wheel that failed. A nut is used to securely clamp the wheel between the mounting flanges. Since there is no established tightening torque, the nut is tightened at the discretion of the individual mounting the wheel. Prior to and after mounting, the user is expected to conduct a subjective 'ring' test: the wheel is lightly tapped to excite vibrations. A skilled user is said to hear the difference between an undamaged and damaged wheel. When the user is satisfied with the 'sound' of the wheel, the wheel is put into use. This procedure was not followed in the present case.

To allow ease of manual cutting the cut-off wheel is mounted at about waist height. Unfortunately, this also enables a dangerous envelope for debris in the event of a wheel failure, with fragments flying horizontally at waist height. To reduce the threat posed by wheel fragments, a safety guard is required by the standard [1]. The guard in this case was designed to encircle the wheel, apart from an opening of 80°, allowing bar stock of diameter 10" to be cut. The subject manufacturer had 'modified' the guard to accommodate larger diameter bars, by increasing the opening. Additionally, the rotational speed of the wheel had been increased from the design speed of 1800 rpm.

The Failure Event

In the present failure, the wheel had been used for roughly one hour some time prior to the failure. Immediately before the failure the operator started the saw motor and allowed the wheel to come up to speed. The operator had initiated a cut when a 'popping' sound was heard, followed by wheel fragmentation. Unfortunately, an employee walking across the room, some 3 meters distant, was struck in the thigh by one of the wheel fragments, causing severe injury.

EXAMINATION AND ANALYSIS

Visual Examination of Failed Wheel

The fragments of the fractured disk were pieced together, as shown in the schematic diagram of Figure 1. Some key features are immediately visible.

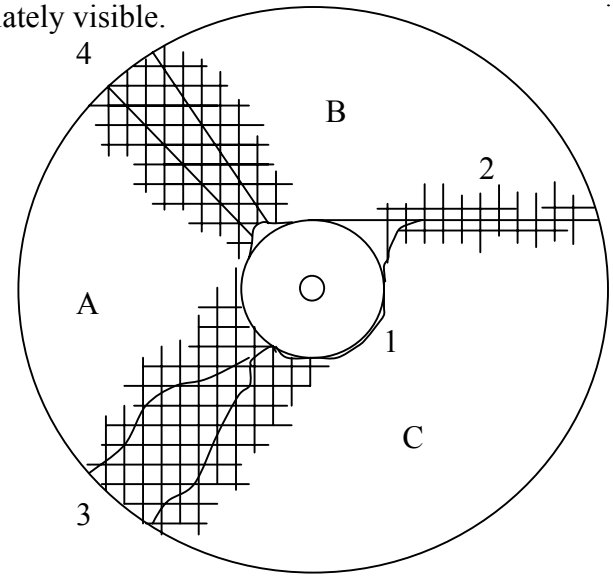

Figure 1: Schematic of the failed wheel.

There are four large cracks in the fractured disk. A circumferential crack (labeled "1" in Figure 3) runs completely round the disk along the circumferential footprint of the clamping washer. The fibers are cleanly broken. The other three cracks are radial cracks. Crack "2" runs at 90° to one fiber direction. The bridging fibers are cleanly broken along the length of the crack. Cracks "3" and "4" run at 45° to the fiber directions. They are characterized by large areas of fiber delamination and by considerable loss of the abrasive material. Crack "3" initiates in a non-radial direction, but changes direction to become a radial crack. As expected, therefore, all cracks show a preference for propagating in one of the directions of principal stress, that is, the radial or circumferential direction. The injury was caused by fragment "B".

Material Testing

Compact tension specimens and bend beams were fabricated from samples of the failed cut-off wheel as well as from two exemplar cut-off wheels. These samples were used to determine fracture toughness of the matrix material and the bending strength, taking into account the contribution of the fiber mats, and the effect of fiber orientation.

Samples were cut from each wheel at 0°, 45° and 90° with respect to the warp direction of the fiber weave pattern on the top surface of the disk. The relative orientations of the fiber patterns on either surface of the disk varied for each wheel. The fibers on the top and bottom surface of the failed wheel were nearly aligned with each other (relative angle ~6°) while those on the exemplar wheels where not aligned (relative angles ~25° and 60°). This was a consequence of the manufacturing procedure, which neither specified nor ensured the relative fiber orientation.

Compact Tension Tests

Compact tension tests were conducted to determine comparative measures of fracture toughness for the different wheels, and for different fiber orientations. The test sample geometry and dimensions are in accordance with ASTM E399 [2]. Typical load displacement curves from one wheel and specimen orientation are shown in Figure 2. In all cases, cracking initiates in the matrix. The toughness of the matrix

itself (given by the initiation toughness) is inferred from these tests and summarized in Table 1. The crack propagates across the entire remaining ligament of the test specimen, leaving an intact fiber-bridging zone behind the crack tip. Since the bridging zone is equal to the remaining width of the test sample, this becomes a problem of large scale bridging that is not properly treated using the concepts of linear elastic fracture mechanics [3,4]. Nonetheless, it is possible to calculate a peak load and an associated apparent (or plateau) toughness that can be used to compare samples of identical dimensions. It was observed that the initiation toughness did not show dependence on the fiber orientation, while the plateau toughness did show some dependence on the fiber orientation. This correlates with our understanding that the brittle matrix dominates crack initiation and propagation, but that final fracture occurs only once the bridging fibers have broken or become debonded. It is well known that the stresses exerted by bridging fibers will depend upon the orientation of those fibers, and that aligned fibers are more effective than mis-aligned fibers [5].

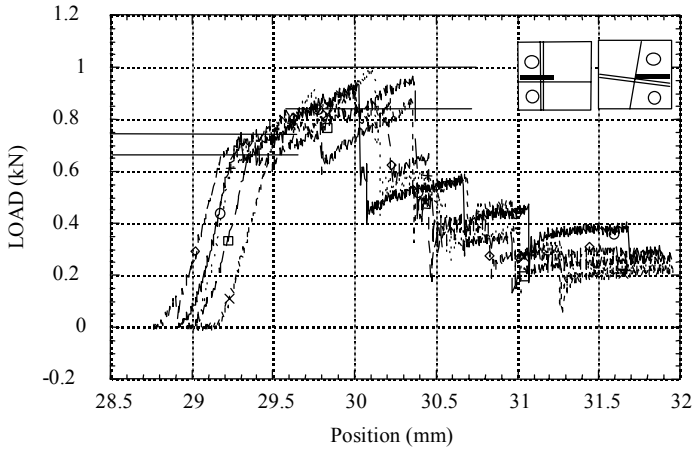

Figure 2: Typical results of compact tension tests. Inset shows the relative fiber orientation for these data.

TABLE 1
RESULTS OF COMPACT TENSION TESTS ON THE FAILED WHEEL SAMPLES

Wheel	**Loading Angle**	**Relative Angle**	**Initiation toughness**	**Plateau toughness**
	[°]	[°]	[Mpa√m]	[Mpa√m]
Failed wheel	0	6	3.5 (0.6)	6.6 (0.4)
	90	6	3.8 (0.2)	7.6 (0.5)
	45	6	3.5 (0.2)	5.8 (0.4)

Bending tests

Stress-displacement curves obtained from 4-point bending tests were compared for the different specimens and fiber orientations (Figure 3). There is a marked reduction in the amount of energy absorbed through cracking for different fiber orientations. In addition, the energy absorption of the failed wheel was lower than that of the exemplar wheels for all fiber orientations. Examination of the failed specimens showed that those samples with fibers in the loading direction failed by breaking the fibers, while those with fibers at 45° to the load failed by delamination of the fibers from the matrix.

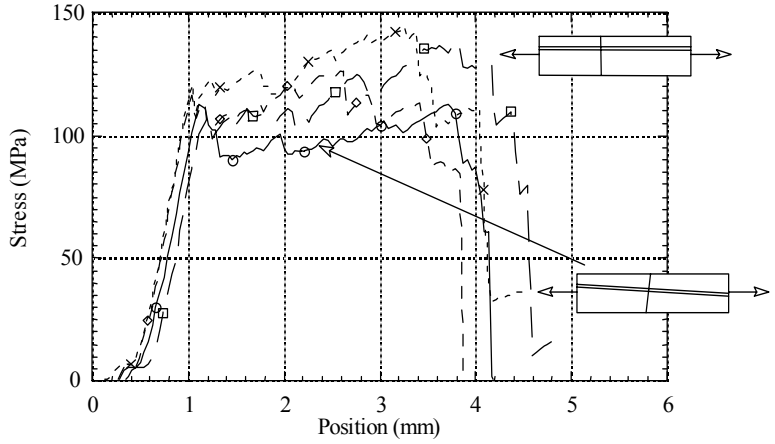

Figure 3: Typical results of bending tests. Inset shows the relative fiber orientation for these data.

DISCUSSION

Probable Failure Scenario

The clean fracture surface as well as the location and geometry of crack "2" support the hypothesis that the wheel fractured along crack 2 under application of a bending load as the wheel was cutting the brass bar. At the edge of the mounting flange, this stress would be concentrated due to sharp or uneven bearing surfaces between the flanges and the wheel. The cracking pattern suggests that failure initiated at the mounting flange and ran circumferentially around the flange. As the crack propagated it branched outward. It is important to emphasize, again, that a blotter pad was not used between the flange and the wheel. The circumferential stress concentration at the mounting flange damaged the fibers underneath the flange. These fibers are essential to the damage tolerance of the wheel, allowing for graceful failure, and large failure strains. In fact, if the fibers are properly utilized, the wheel fragments should hit the safety guard before any fibers have broken. The fibers are intended to pull-out and bridge the cracks in the underling matrix. However, the contact stress generated by the mounting flange damaged the fibers, causing localized fracture at the contact site. As a result, the fibers did not bridge the crack in the wheel and catastrophic failure ensued.

The effectiveness of fiber reinforcing to increase the fracture toughness of a brittle material is demonstrated through the experimental results reported above. The fracture tests presented in Figure 2 and summarized in Table 1 clearly show that the bulk of the toughness comes from fiber bridging stresses. Furthermore, that toughness was shown to depend upon the fiber orientation relative to the crack plane: perpendicular fibers offering the greatest energy absorption. The material testing clearly indicates the effect of fiber orientation on the energy which is absorbed during failure, and show the same trend in the effect of fiber orientation on comparative fracture toughness. The energy required to break fibers which are aligned with the load direction is much greater than that required to delaminate fibers which are at or near 45° to the load direction. If all the cracks in the abrasive wheel had been bridged by transverse fibers, the wheel would have failed, but in a safe manner. This requires redesign of the reinforcing fiber directions to ensure that there are fibers in the principal loading directions of the wheel.

CONCLUSIONS

Most probable cause

The wheel failed as a result of rapid crack propagation through the matrix, initiated at areas of concentrated stress due to the flanges bearing on the wheel. This failure became catastrophic when the layer of reinforcing fibers which bridged the cracks delaminated on two cracks and broke on a further two.

Remedial action

Redesign

It is desired that wheels should never fail. However, once they do fail, it is imperative that they should remain safe. Given the finite probability of failure which always exists when using a brittle material, emphasis should be given to damage tolerant design, to reduce the catastrophic effect of failure. In particular, design of cutoff wheels should be appropriate to the hostility of the operating conditions, and should assume a level of mishandling and abuse.

It is recommended that a different weave pattern should be used for the layer of reinforcing fibers on the abrasive wheel. A radial / circumferential weave pattern could be used with minimal increase in manufacture cost, resulting in a more damage tolerant product, with reinforcing fibers perpendicular to both principal loading directions.

Implement Safety Procedures

Crack initiation may not have occurred had the bearing surfaces on the flanges been properly maintained, or a blotter or compressible washer been used. Injury could have been prevented even in the case of catastrophic failure if the safety regulations laid down in the relevant standard [1] had been observed. Operators of abrasive wheels should recognize that there is always a risk of failure, and should take appropriate precautions.

REFERENCES

1. ANSI B7.1-1988 American National Standard – Safety Requirements for the use, care and protection of abrasive wheels
2. ASTM E-399. (1990). Annual Book of ASTM standards, Section 3, Metals Test Methods and Analytical Procedures, ASTM, Philadelphia.
3. Cox, B. N. and Zok, F. W., "Advances in ceramic composites reinforced by continuous fibers," Current Opinion in Solid State & Materials Science, vol. 11, No. 5, pp. 666-73, Oct. 1996.
4. Ewalds, H.L. and Wanhill, R.J.H. (1993). *Fracture Mechanics*. Edward Arnold Publishing, The Netherlands.
5. Chawla, K.K. (1987). *Composite Materials*. Springer-Verlag, Germany.

ORAL REFERENCE: ICF100311OR

FAILURE ANALYSIS OF THE GIRTH GEAR OF AN INDUSTRIAL BALL MILL

M. Mirzaei, A. Razmjoo, A. Pourkamali

Department of Mechanical Engineering, T.M.U, Tehran, Iran.

ABSTRACT

This paper describes the major activities carried out in the process of failure analysis of the girth-gear of an industrial ball mill. Three dimensional finite element modeling and analysis of the mill were performed under various loadings including: charge weight, dynamic loading due to the charge motion, centrifugal forces imposed by partial rotation of the charge, and the driving force imposed by the pinion. The results of the stress analysis conformed to various characteristics of the existing cracks. It was concluded that the charge weight and the dynamic effects due to the charge motion inside the mill were the main causes of the stress built-up in the gear, and the contribution of the forces imposed by the pinion was only 20 percent. Finally, semi-elliptical cracks were modeled and grown through a variable stress field and the crack driving forces were calculated. The calculated crack growth rates were compared with those monitored over a period of 21 months for real cracks.

KEYWORDS: Failure Analysis, Girth Gear, Ball Mill, Stress Analysis, Fatigue, Life Assessment, Finite Element.

INTRODUCTION

The Girth-Gears of industrial Ball-Mills are up to 12 meters in diameter and over 90 tones in weight, with a manufacturing cost exceeding $500,000 (see Fig.1a). These types of gears are expected to have fatigue lives of 20 years and more. In this case history, within the first two years of operation, a few cracks initiated from certain locations between the gussets and the gear flange, and propagated towards the lightening holes, as shown in Fig.1b. For some cracks, the propagation paths were almost identical on both sides of the gear, while there were several cases of crack propagation on one side. Since the premature occurrence of several similar cracks in certain locations could be interpreted as the possibility of a faulty design, it was decided to perform a complete stress analysis of the mill using the finite element method. In similar analyses reported in the literature the main charge with a flat surface has been considered as a major source of loading [1,2]. Accordingly, due to the symmetry of geometry and loading, only one half of the mill has been analyzed. In our analysis we considered various sources of loadings including the charge weight with a slanted surface, which required a complete 3-D modeling and analysis. The analysis results clearly revealed the cause of failure, i.e., high stress built-up in specific locations adjacent to the gear flange, and conformed to various characteristics of the existing cracks, including their propagation paths. This paper also describes the assessment of the remaining life of the gear through modeling of crack growth in the high-stress region. In these analyses, semi-elliptical cracks were modeled and grown through a variable stress field, and the crack driving forces were calculated. The calculated crack growth rates were compared with those monitored over a period of 21 months for real cracks.

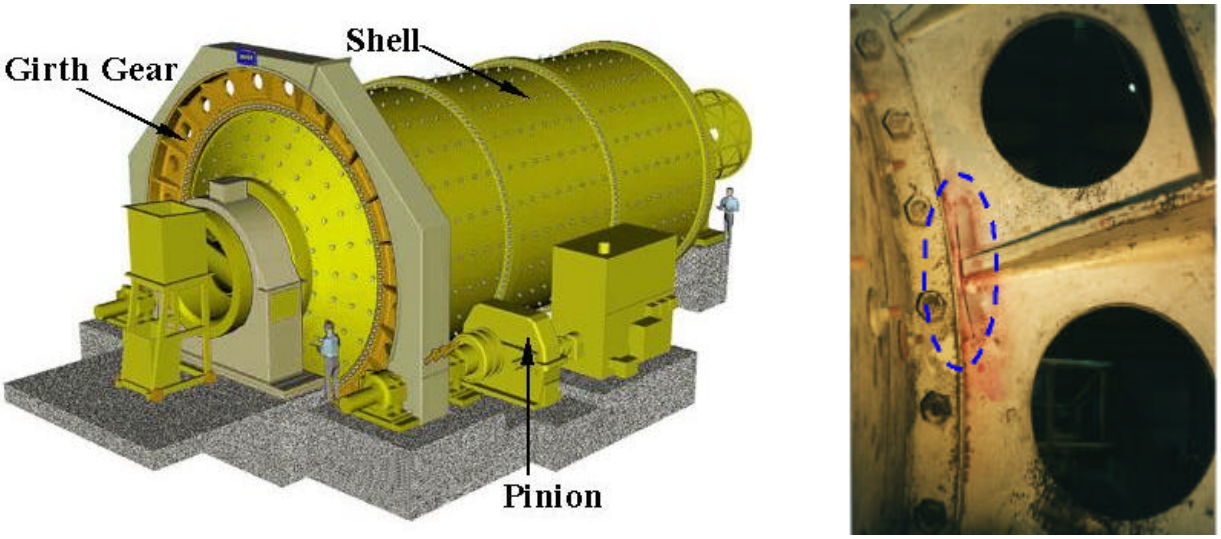

Figure 1: **a)** Schematic of an Industrial ball mill [5]. **b)** A typical crack in the rear side of the gear.

STRESS ANALYSIS OF THE GEAR

The modeling and analysis were performed using the LUSAS software. Figure 2a shows the three-dimensional finite element model of the mill, comprising of 8-noded brick elements. Figure 2b is a schematic presentation of the modeling of the charge motion inside the mill, which has been developed using the information presented in reference [3]. In general, the loadings included: charge weight, dynamic loading due to the charge motion, centrifugal forces imposed by partial rotation of the charge, and the driving force imposed by the pinion. The model was restrained in all directions at the location of the front trunnion (the gear side trunnion) while the rear trunnion was free to move only in the axial direction.

ANALYSES RESULTS

Figure 3 shows the distribution of the maximum principal stress component, S1, in the front face of the gear. The maximum amount of these stresses, 120MPa, occurs between the flat end of the gussets and the flange, at the location of 6 oclock. The distribution of this stress component conforms to the actual crack paths observed on the cracked gear (see Fig.1b).

The distribution of the minimum principle stress component, S3, in the front face of the gear showed a minimum amount of -65MPa, which occurred at the same region, but at a different location, i.e. at 4 o'clock. In fact the deflection of the shell, under the forces imposed by the charge motion, creates bending moments at different locations of the gear flange. These local bending moments cause tensile stresses at one side and compressive stresses at the opposite side of the critical region. As every point at the critical region around the mill, passes through these locations during the mill revolution, a cyclic loading is imposed which can lead to fatigue crack initiation and growth in this region. It is interesting to note that the charge weight and dynamic effects due to the charge motion inside the mill were the main causes of the stress built-up in the gear, and the contribution of the forces imposed by the pinion was only 20 percent.

Figures 4 shows the distribution of the maximum principal stress component, S1, in the rear side of the gear. It is clear that the stress levels are generally lower than the front side. However, the existence of two high tensile stress locations can create two loading cycles for every mill rotation.

Based on the results of the above analysis and considering the mechanical properties of the gear material shown in table 1, it is clear that the stress levels at the critical regions on the both sides of the gear are sufficient for fatigue crack initiation and growth in these regions. The results obtained from the above

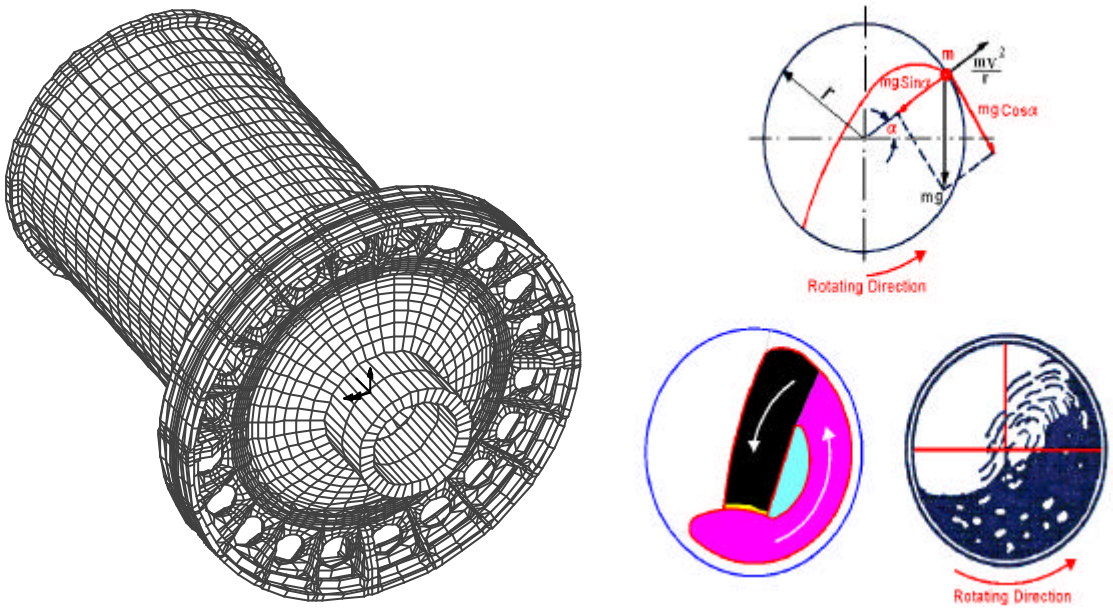

Figure 2: **a)** 3-D finite element model of the mill. **b)** Modeling of charge motion inside the mill.

analyses support the initial assumption of the cause of the crack initiation, and provide significant clues to the crack growth pattern and the shape of the final crack front. Based on the results of the above analyses, the remaining life of the gears were calculated using a Fracture Mechanics approach.

TABLE 1
Mechanical Properties of the Gear Material

Gear Material : Cast Steel (air quenched and tempered) C=0.35, Mn=1.5, Si=0.5, Mo=0.4
Hardness (Brinell) : 240, Tensile Strength : 800 MPa
Fatigue Endurance Limit (theoretical) : 300 MPa
Endurance Limit (after surface, size, and other corrections) : 75 MPa
Paris Law Coefficient, C : 1.2E-11 Paris Law Exponent, m : 2.7

LIFE ASSESSMENT OF THE GEAR

In order to assess the remaining life of the gear a failure criterion was required. The usual failure criterion in fracture mechanics is the onset of unstable crack growth. In this case, however, the stress built-up in the critical region was caused by deformation of the mill shell, which is in fact a displacement-controlled condition, where crack growth can give rise to stress relaxation. Hence, it was concluded that the cyclic crack growth would continue as far as the lightening holes. Accordingly, the remaining life was defined as the time required for the cyclic growth of the existing cracks up to the lightening holes, and was calculated by numerical integration of the Paris equation:

$$\frac{da}{dN} = C.(\Delta K)^m$$

Detailed investigation of crack growth in a variable stress field is time consuming, involving finite element determination of stress intensity factors (SIF) for a range of crack sizes. Hence, we started with an approximate method using the available SIF calibrations of semi-elliptical cracks, along with proper adjustments of the coefficients for the problem in hand. Figure 5 shows a comparison between the predicted crack growths using the above method with those measured over a period of 21 months on the real gear. It is clear that the calculated lives are significantly lower than the real life.

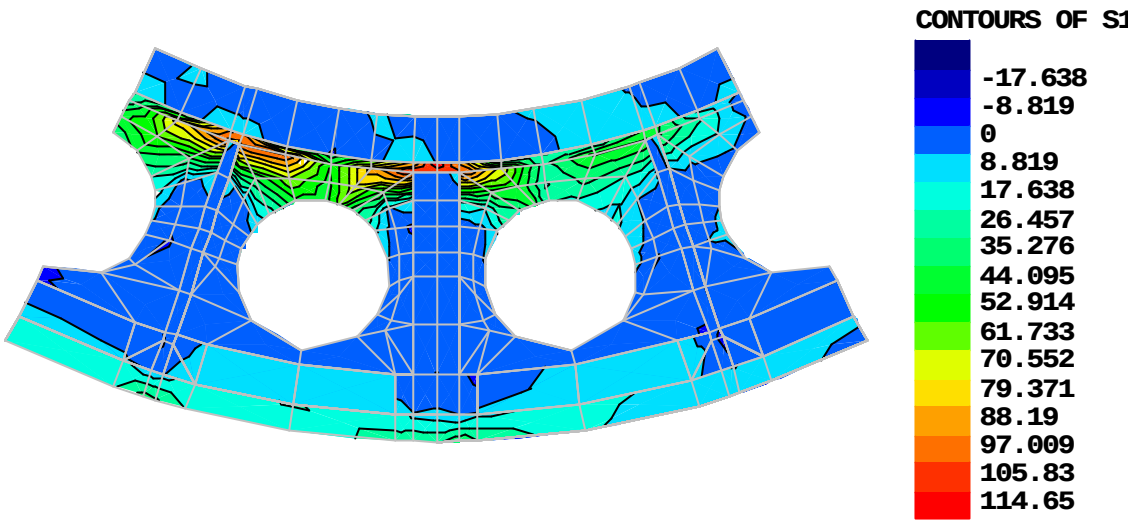

Figure 3: Contours of maximum principal stress component in the front side of the gear.

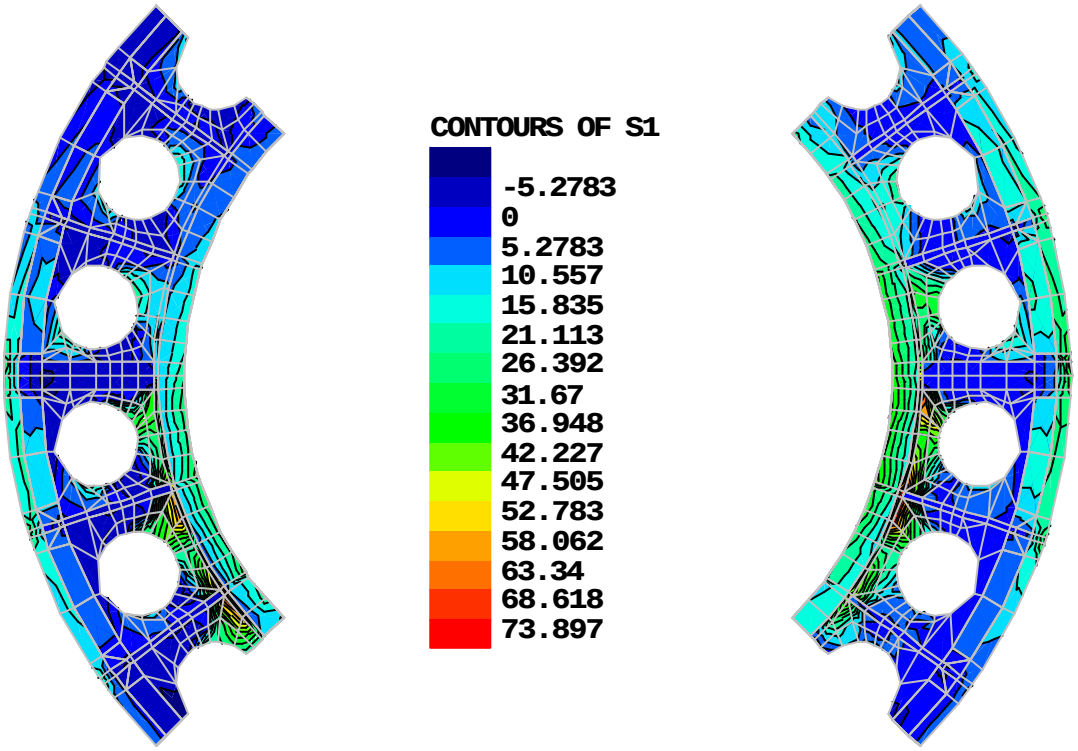

Figure 4: Contours of maximum principal stress component in the rear side of the gear.

In the next step, a numerical SIF calibration was obtained using the finite element method. Several procedures are available for numerical evaluation of stress intensity factors [4]. In this analysis we used stress and displacement point matching methods because of simplicity and consistency with our original model. As depicted in Fig.5, the calculated lives using the SIF calibration obtained from finite element analysis provided a better estimation of the real life. However, the fatigue lives predicted by both methods were quite shorter than the real life.

CONCLUSIONS

The problem of initiation and propagation of fatigue cracks in the girth gear of the ball mill under consideration was attributed to the existence of relatively high stress gradients at critical regions between the gussets and the flange. A 3-D finite element analysis of the mill revealed that the charge weight and dynamic effects due to the charge motion inside the mill were the main causes of the stress built-up in the gear, and the contribution of the forces imposed by the pinion was only 20 percent. The analysis results indicated that the stress built-up in the critical region was caused by deformation of the shell, which is in fact a displacement-controlled condition, where crack growth can give rise to stress relaxation. Hence, it was concluded that under normal operating conditions the crack growth would never become unstable and the cyclic crack growth would continue as far as the lightening holes. Accordingly, the remaining life, defined as the time required for the cyclic growth of the existing cracks up to the lightening holes, was calculated by numerical integration of the Paris equation. The calculated crack growths using an adjusted SIF calibration for semi-elliptical surface cracks were significantly higher than those measured over a period of 21 months on the real gear. Although the calculated lives using the SIF calibration obtained from finite element analysis provided a closer estimation of the real life, both methods overestimated the actual crack growth rates. This can be attributed to the inexact nature of our modeling and numerical analysis and/or the retardation phenomena like fatigue crack closure, which are operative in reality but were not considered in our analyses.

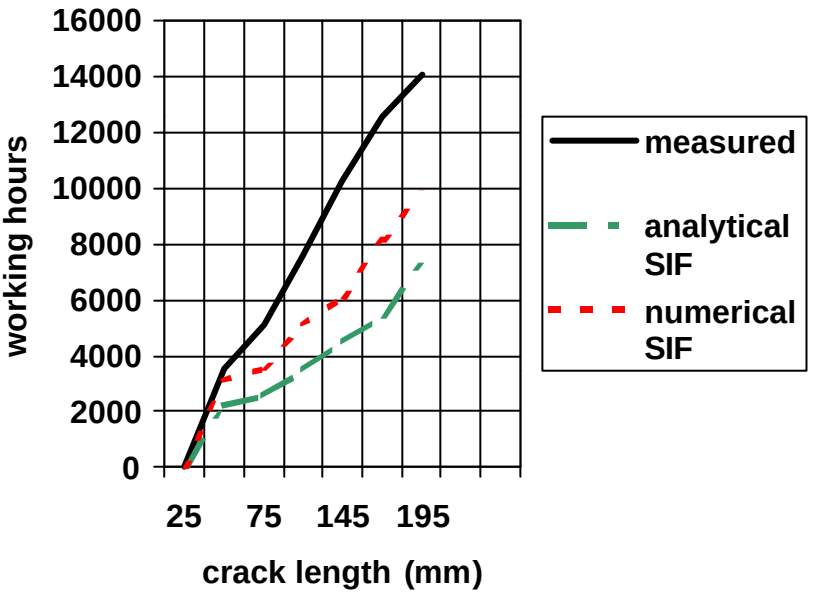

Figure 5: Measured and predicted crack lengths versus the working hours of the mill.

REFERENCES

1. Hadaway, J., Alden, J., and Hall, S., (1998) "Design Aspects of Large Ball Mills", ANI Grinding Mills- Technical Bulletin No. 8, 2-3, pp 1-12.
2. Hadaway, J., Alden, J., and Hecht, E., (1995) "Developments in the Use of Finite Element Analysis Models for Large Scale Non-linear Analysis of Bolted joints and Assessment of Manufacturing Non-Conformances", ANI Grinding Mills-Technical Bulletin No.4, pp 1-14.
3. Duda, W. H., (1985) Cement-Data-Book, Volume 1, International Process Engineering in the Cement Industry, 3rd Edition. Bauverlag GMBH, Berlin.
4. Anderson, T. L., (1995) "Fracture Mechanics Fundamentals and Applications." CRC Press, Florida.
5. http:/www.ani-mills.com.au/news/2243ball.jpg

FATIGUE AND FRACTURE BEHAVIOUR OF A LASER HEAT TREATED MARTENSITIC HIGH-NITROGEN TOOL STEEL

M.Heitkemper[1], C.Bohne[2], A.Pyzalla[2], A.Fischer[1]

[1]Werkstofftechnik, Universitaet Essen, 45117 Essen, Germany
[2]Hahn-Meitner Institut, Abt. Werkstoffe, 14109 Berlin, Germany

ABSTRACT

High nitrogen tool steels offer a superior corrosion resistance compared to conventional, Nitrogen-free tool steels at similar mechanical and tribological properties. For this reason they are nowadays applied for ball bearings in aircraft industry. A laser-surface treatment can lead to a further improvement of this combination of properties. The aim of a research project is to improve the tribological properties and at the same time keep up or enhance the corrosion resistance as well as the fatigue behaviour. The laser heat-treatment leads to a mixture of martensite and retained austenite. Thus, the martensitic regions show an increased hardness of about 700 HV10, while the austenitic regions are as soft as 400 HV10. To determine the influence of a laser-surface treatment on fatigue cyclic 4-point-bending tests in laboratory air as well an in artificial sea water (3%NaCl, 25°C) have been performed. The fatigue and fracture behaviour are mostly influenced by the refinement of the microstructure and the generation of compressive residual stresses. In addition the retained austenite and its stress induced transformation into martensite affects the fatigue behaviour. The residual stresses generated during heat treatment have a significant influence on crack initiation, while those generated during the transformation of the retained austenite have only a minor influence on crack propagation.

KEYWORDS

laser surface heat treatment, high-Nitrogen tool steel, fatigue, fracture mechanics, corrosion, residual stresses

INTRODUCTION

Martensitic high-Nitrogen steels (HNS) offer a favourable combination of tribological, chemical and mechanical properties. While the wear behaviour is comparable to conventional tool steels the corrosion resistance is significantly higher. For this reason they are already applied as materials for roller bearings of gas turbines and fuel pumps as well as for ball screws of thread gears in aerospace applications [1, 2, 3]. The good wear behaviour can be attributed to the fine dispersion of precipitates, which is governed by Nitrogen. The reason for the improved corrosion resistance is brought about by the high contents of Cr, Mo and N dissolved within the martensitic matrix. In many cases it is necessary to use cold-work tool steels in a tempered state in order to reduce the amount of retained austenite. In this heat treated condition Cr, Mo, and N are bound within precipitates. Within a DFG (German Research Council) funded research project the effect of a surface heat treatment by laser on microstructure and properties of HNS is investigated. During this kind of short time heat treatment nitrides are partly dissolved and new martensite is generated [4]. The dissolution of nitrides lays off some Cr and N and increases the resistance against pitting corrosion [5]. The

newly generated martensite brings about high compressive residual stresses and a higher surface hardness and distinctly improves the wear resistance under sliding wear in air as well as in artificial sea water [6]. Both should improve the life time of wear and corrosion resistant parts and tools. But, the endurance life might be limited by deteriorated fatigue and fracture properties.

In this paper the influence of the laser surface heat treatment on the fatigue properties is presented and discussed. With respect to the application of the HNS X30CrMoN15 1 (1.4108 = AMS5898) in aerospace industries the tests have been carried out in air as well as in artificial sea water.

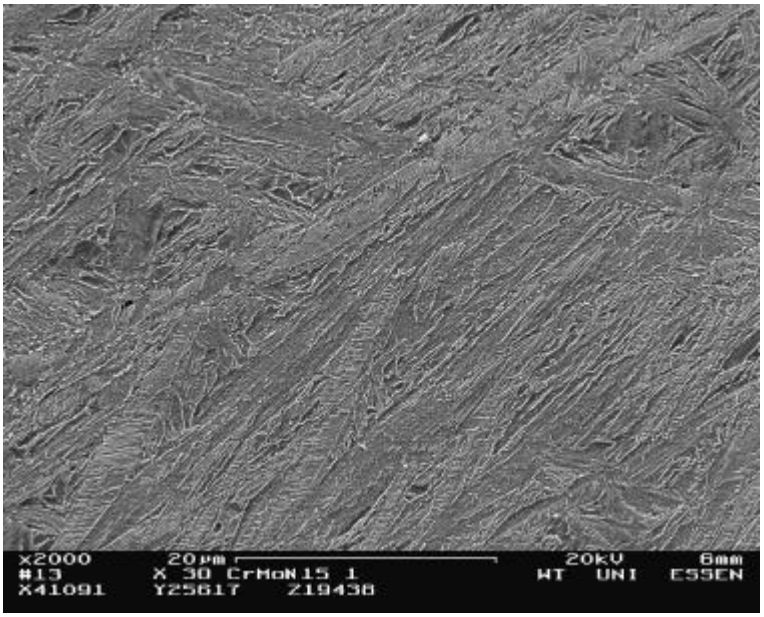

Figure 1: Tempered Martensite of Heat Treated X30CrMoN15 1 with less than 2 % Retained Austenite.

EXPERIMENTAL PROCEDURES

Materials and Heat Treatments

Before the laser treatments HNS discs of 100 mm diameter and 10 mm thickness were heat treated as

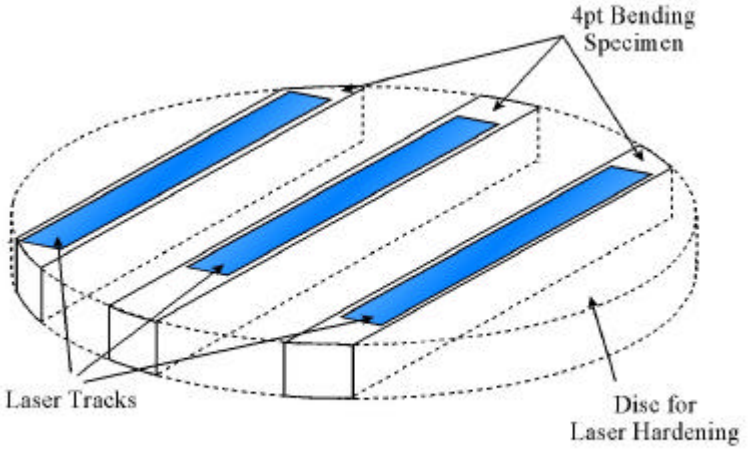

Figure 2: Design of the Specimens for Laser Surface Heat Treatment and Fatigue Testing.

follows: 30min/1200°C/oil+10min/-196°C/air+3x2h/620°C/air. The chemical composition of the HNS is given in Table 1. Figure 1 shows the microstructure, which consists of tempered martensite with less than 2 vol.-% of retained austenite (RA). Afterwards the specimens were laser-heat treated using a 3kW Nd:YAG-laser. The power of the laser was controlled by the maximum surface temperature T_{max} in the heat treated area. The beam had a cross section of 14 x 1,8 mm transversally to the moving-direction (Figure 2) and was moved with a speed of 100 mm/min over the surface under an atmosphere of 15 l/min N_2 and 0,13

l/min O_2. After this heat treatment all specimens were scrutinised as to their microstructures, residual stresses, wear, and corrosion properties which in detail is reported elsewhere [4, 5].

Table 1: Chemical Composition of the Martensitic High-Nitrogen Steel X30CrMoN15 1, 1.4108 = AMS5898 according to the Steel Manufacturers Specification.

Fe	C	Si	Mn	Cr	Ni	Mo	N
bal.	0.25-0.35	< 1	< 1	14-16	< 0.5	0.85-1.1	0.3-0.5

Fatigue Testing and Fractography

The fatigue specimens were cut out of the lasered discs by mechanical wet cutting and afterwards machined and ground on all areas - except the laser hardened surfaces – (Figure 1). It has to be noticed that two types of specimens were provided. One group contains specimens of 12 mm width, which comprise the hardened zones, only. The second group of 16 mm width embody the tempered zones as well. These bars were loaded cyclically in a 4-point bending (4PB) test device (Figure 3), which was mounted within a servohydraulic test rig. The load range of the constant stress amplitude tests was chosen between 225 and 630 MPa at 20 Hz and an R-value of 0.1. In order to carry out tests in artificial sea water (3 % NaCl in aqua dest.) at room temperature the specimens were placed inside a rubber tube. This set up allows a continuous flow of the artificial sea water brought about by a small aquarium water pump. The water temperature was measured by a thermocouple and scattered between 20 and 30 °C. Under both conditions (dry/3%NaCl) the specimens were fatigued to fracture and the results were plotted in Wöhler-diagrams (S-N curves). Afterwards the fracture surfaces were investigated in making use of a scanning electron microscope.

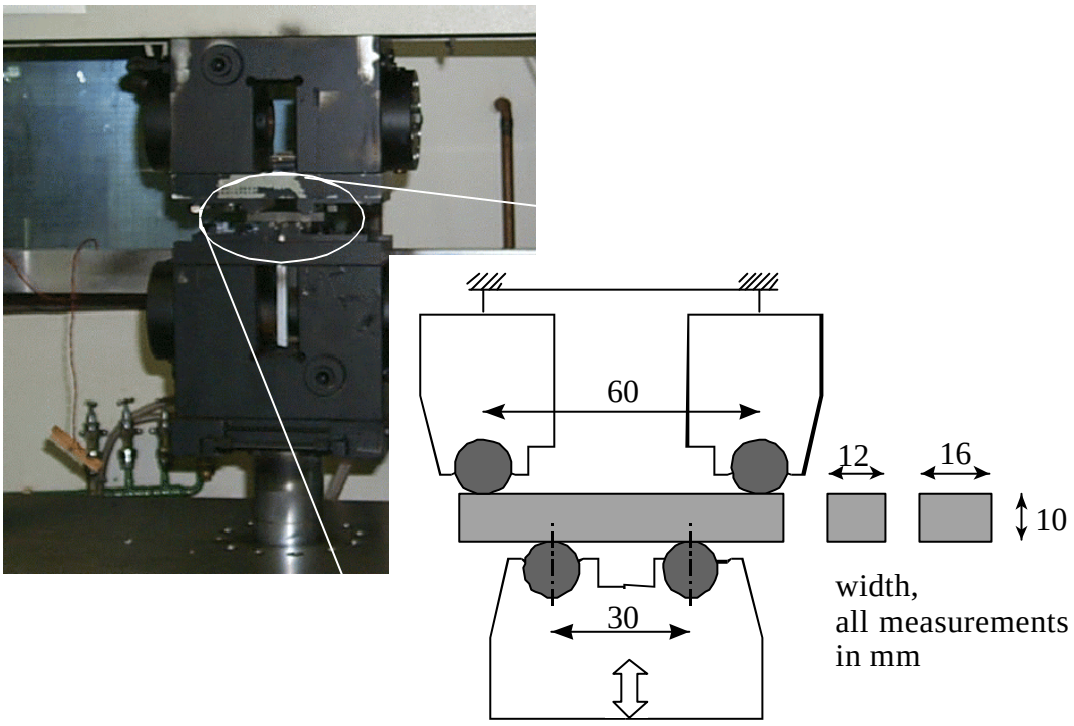

Figure 3: Test Rig for Cyclic 4-Point Bending in Air

RESULTS AND DISCUSSION

Microstructure and Residual Stresses

Figure 4 shows the results of the microstructural examinations after a series of laser heat treatments at different maximum temperatures [4, 5]. At about 950°C the surface hardness and the c_m/a_m-ratio, which represents the tetragonal distortion of the newly generated martensite, increase. The hardness reaches its maximum value slightly above 1000 °C as a result of the increasing distortion of the martensite. Above that temperature hardness decreases by the governing influence of the increasing amount of RA, which is markedly stabilised by N. According to the nature of the temperature field one has to distinguish between

two areas within a lasered track: The hardened zones in the middle of a track with compressive residual stresses and the softer tempered zones at the boundaries of the lasered tracks with tensile residual stresses.

In order to gain a high amount of RA directly at the surface, which has a beneficial influence on the chemical and tribological properties [4-6] T_{max} for the laser surface treatments of the specimens was chosen to 1100 °C. Thus, there is a gradient of RA, hardness and residual stresses with the distance from the surface. Due to the fact that there is 100 % RA at the surface, the maximum hardness value of 750 HV is at a depth of about 100 µm. The residual stresses alter from compression to tension at about 140 µm below the surfaces. One has to keep in mind that the beneficial effects of laser hardening might disappear at a distance of about 140 µm from the surface, if the laser heat treatment parameters are chosen as they have been in this study.

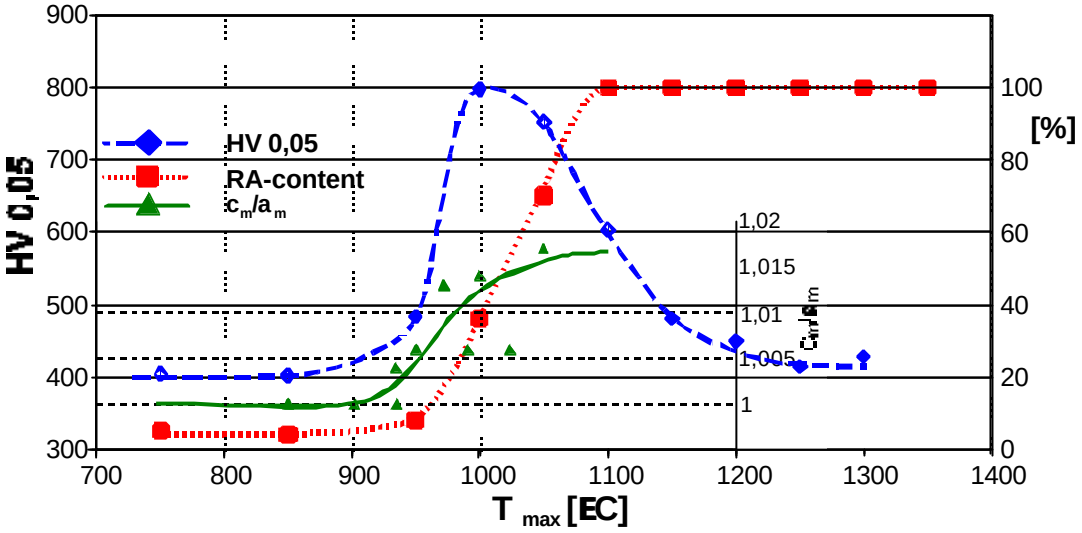

Figure 4: HV, c/a und RA vs. T_{max}

Fatigue Testing by 4-Point-Bending

Figure 5 presents the σ_a-N_f diagram of the 12 mm (T_{max}=1100°C, hardened zone, dashed line) and 16 mm (T_{max}=1100°C, hardened and tempered zones, dotted line) wide specimens in air in comparison to the base material (solid line). Obviously, the tensile residual stresses within the tempered zones have a detrimental effect on the fatigue properties. The number of cycles to failure (N_f) is about $6x10^4$ for the base material at

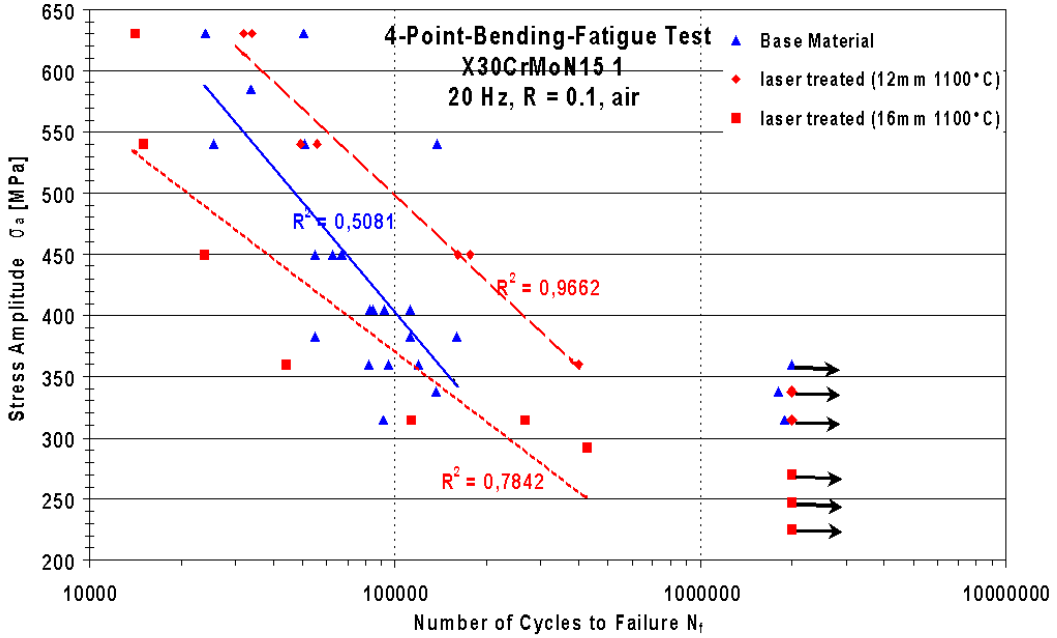

Figure 5: σ_a-N_f Diagram of 12 and 16 mm wide specimens

a stress amplitude of 450 MPa. The compressive residual stresses within the hardened zones bring about a N_f-value of $2x10^5$. This can be attributed to the fact, that the high compressive residual stresses distinctly decrease the effective stresses at the surface. Tensile residual stresses act in the opposite way and increase the effective stress. Thus, N_f drops down to a value of about $3x10^4$, which is a distinct loss of service life. The endurance limits of the base material and the hardened zones are similar and reach values of about 330 MPa, while the detrimental influence of the tempered zones brings about values below 270 MPa.

Artificial sea water seems to have a similar influence on fatigue as tensile residual stresses (T_{max}=1100°C, Figure 6). The trend lines of the narrow and the wide specimens are nearly equal and - within the accuracy available by the small number of data points - N_f ranges between 3 and $4x10^4$ for a stress amplitude of 450 MPa (dashed lines). The only measured endurance limit value is 270 MPa. Beside the fact that a higher number of tests will be necessary before one can draw a solid conclusion, it is obvious that the chemical attack by Cl-ions decreases the finite life as well as the endurance limit. This is true at least, if the surface consists of 100% RA supported by a hard subsurface martensitic layer, to which the compressive residual stresses are attributed. From potentiodynamic corrosion tests in aqueous 3%NaCl it is known, that the pitting potential just slightly differs between the base material and those laser heat treated at T_{max}=1100°C [5]. Thus, the chemical properties of the RA at the surfaces have no distinct influence on fatigue under corrosive environment. Other factors must, therefore, be more important.

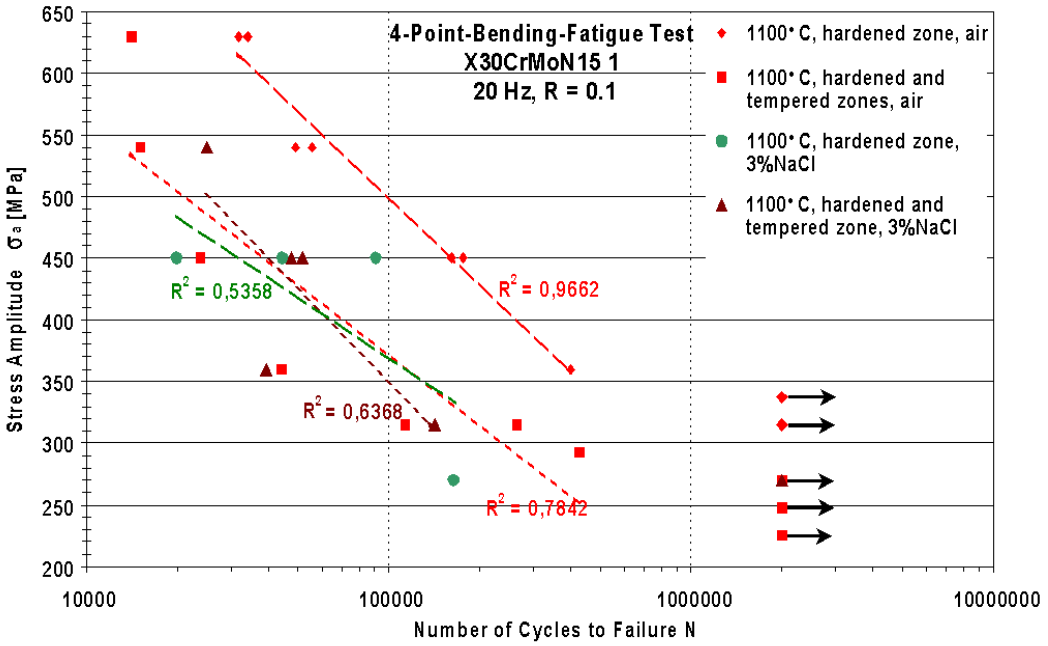

Figure 6: σ_a-N_f Diagram Comparison in Laboratory Air and 3%NaCl

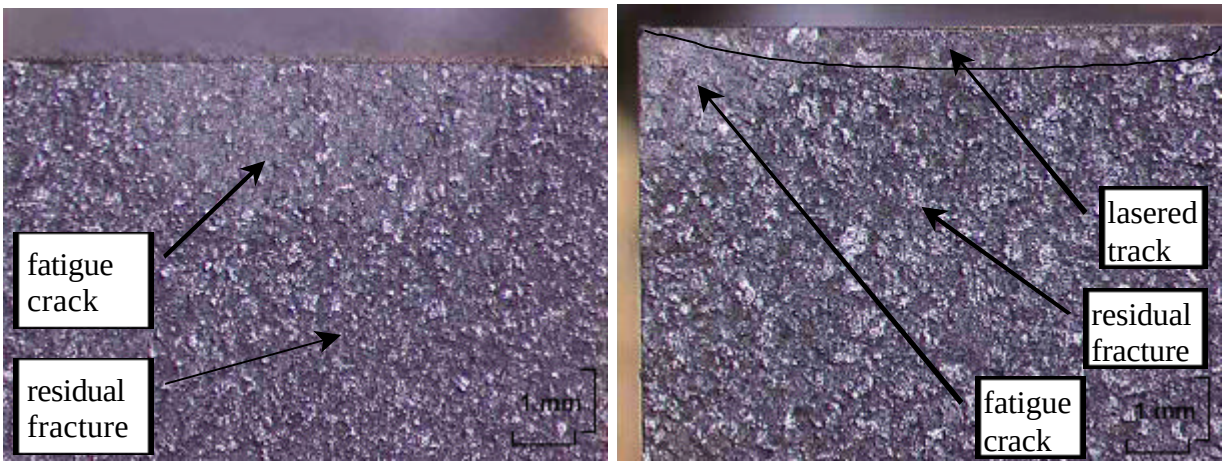

Figure 7: Fracture Surfaces with Edge and Half-Penny Shape Fatigue Cracks

Fractography renders, that crack initiations starts at or near the surfaces within the tempered zones (Figures 7a) or at the outer edge of the specimens (Figures 7b). The appearance of the fracture surfaces are typical for brittle fracture even though the fatigue crack area is somewhat smoother than the residual fracture. In

addition there is no difference between the appearances of the fatigue cracks generated in air compared to those generated under chemical attack. Nevertheless there is a difference in fatigue properties.
It is known from literature that martensitic tool steels often fail due to microstructural voids like coarse or eutectic hard phases, non-metallic inclusions, and pores, which act as internal local notches [7-10]. Due to the fact that the critical crack length a_c for unstable crack propagation is very small, it is concluded that the fatigue life of this type of tool steels is mainly governed by the number of cycles to crack initiation. If we examine those areas, where the fatigue cracks are likely to have started we find no signs of the common voids. But, there is some evidence that the former austenite grain boundaries act as notches (Figure 8). If we assume, that linear elastic fracture mechanics applies, ΔK_0 ranges from 3 to 5 MPa $m^{1/2}$ [7-11]. Now, a value of a_0 as a function of ΔK_0 and σ_a can be calculated, which is necessary to initiate stable fatigue crack growth [11, 12]. For an elliptical surface crack length a_0 might, therefore, range between 8 and 30 µm within the region of finite life. The compressive residual stresses should lower the values of σ_a and, thus, ΔK as well, bringing about higher critical crack length values. But, one has to keep in mind that the compressive residual stresses are only existing within the martensitic phase underneath the surface, while the austenite at the surface bares no or slight tensile residual stresses [13]. Due to the fact, that the former austenite grains have a size of about 100 µm they are likely to act as internal voids directly at and under the surface depending on the gradient of residual stresses and RA. Thus, crack initiation might take place at former austenite grains nearly independent of the measured residual stresses within the martensite, which might also relax during fatigue [14]. On the other hand it is known that the stress induced RA transformation brings about crack tip shielding effects [15]. This is most pronounced during crack propagation, which has a reported minor influence on fatigue life of martensitic tool steels.

But, this still does not explain the fact, that under 3%NaCl the numbers to failure are nearly independent of the residual stresses as shown in figure 6. The period of crack initiation must be similarly independent of the residual stress state at the surface. Otherwise, the measured values of N_f in 3%NaCl should differ distinctly between the 12 mm and the 16 mm wide specimens. This can only be attributed to the fact that ΔK_0 is lowered by corrosion as well. Thus, even smaller voids are critical and might act as cracks, which are able to propagate.

The influence of the competing mechanisms on crack initiation and propagation within the austenite is not clear, yet. There might be an early crack initiation, because of the tensile residual stresses within this phase. On the other hand the stress induced transformation of RA into martensite should distinctly slow down crack propagation. This has to be examined in detail in the future in order to be able to improve the fatigue life of parts and tools in air as well as under corrosive environment.

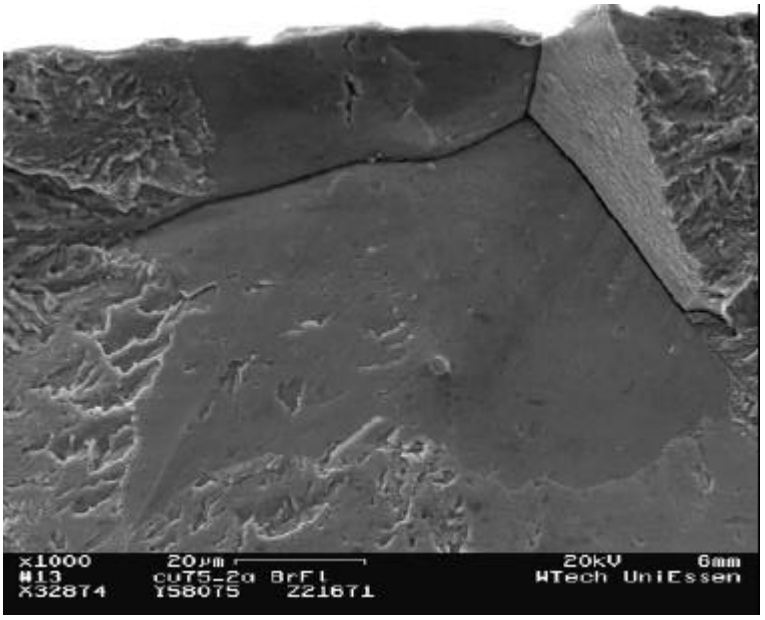

Figure 8: Crack Initiation at Former Austenite Grain Boundary

CONCLUSIONS AND OUTLOOK

An early crack initiation brought about by tensile residual stresses or stress corrosion cracking decreases finite fatigue life as well as the endurance limit.
Compressive residual stresses improve the fatigue behaviour in air, only.
More specimens are needed, because the coefficient of determination is often under 0.5.
Testing of specimens are necessary after grinding, because this changes the chemical, fatigue and wear properties due to the transformation of the RA bringing about additional compressive residual stresses within the surfaces.

ACKNOWLEDGEMENTS

The authors would like to thank the German research council (DFG) for sponsoring this work under contracts Fi451/4-3 and Re688/29-3. The 4PB tests have been partly carried out by Mr. Th.Dubreux of I.C.A.M., Toulouse, France during his stay at the University of Essen. In addition we are in debt to G.Stein, Dr.I.Hucklenbroich, and Dr.St.Koch of VSG GmbH, Essen, Germany for providing steel samples. We also would like to thank Prof.Dr.W.Reimers, Hahn-Meitner Institut, Berlin, Germany and Prof.Dr.H.Berns, Ruhr Universitaet, Bochum, Germany for their constant support and steady willingness for discussions.

REFERENCES

1. Berns, H., Lueg, J. (1990) *Neue Hütte* 36, 1, Pp.13-18.
2. Berns, H., Wang, G. (1993) in (Proc.Conf.) Bando, Y., Kosuge, K. (Eds.) Powder Metallurgy World Congress, Kyoto, Japan, Pp.513-516.
3. Berns, H., Escher, C., Streich, W.-D. (1998) *Ingenieur-Werkstoffe* 7, 3, Pp.36-39.
4. Bohne, C., Pyzalla, A., Reimers, W., Heitkemper, M., Fischer, A. (1998) in (Proc.Conf.) ECLAT ´98, Hannover, Germany, DGM-Informationsgesellschaft mbH, Frankfurt, Germany Pp.183-188
5. Pyzalla, A., Bohne, C., Heitkemper, M., Fischer, A. (2000) in (Proc.Conf.) Progress in Heat Treatment and Surface Engineering, E.J.Mittermeijer, J.Grosch (Eds.) 5th ASM Heat Treatment and Surface Engineering Conference, Gothenburg, Sweden. ASM, Metal Park, Ohio, USA, Pp.299-309
6. Heitkemper, M., Fischer, A., Bohne, C., Pyzalla, A. (2001) in (Proc.Conf.) Wear of Materials 2001, Vancouver, BC, Canada, D.Rigney et al. (Eds.) Elsevier, Amsterdam, The Netherlands, to be published
7. Berns, H., Trohjahn, W., Wicke, D. (1987) HTM 42, 4 Pp.211-216
8. Berns, H., Lueg, J., Trohjahn, W., Wähling, R., Wissell, H. (1987) Powder Met. Int. 19, 4 Pp.22-26
9. Berns, H. (1990) in (Proc.Conf.) 4th Int. Conf. on Fatigue 90, Honolulu, Hawaii, USA Eds. H. Kitagawa, T. Tanaka, Materials and Component Engineering Publications Ltd. Pp. 161 - 166
10. Melander, A. (1990) Int. J. of Fatigue 12, 3 Pp. 154-164
11. Schwalbe, K.H., (1980) Bruchmechanik metallischer Werkstoffe, Hauser, München, Wien Pp.646-654
12. Tada, H., Paris P.C., Irwin G.R., (1973) The Stress Analysis of Cracks Handbook, Del Research Corporation, St. Louis, MO, USA
13. Bohne, C., (2000) Mikrostruktur, Eigenspannungszustand und Korrosionsbeständigkeit des kurzzeitlaserwärmebehandelten hochstickstofflegierten Werkzeugstahls X30CrMoN15 1, Diss. TU Berlin, see also Berichte des HMI B572
14. Hauk, V., Nikolin, H.J. (1988) in (Proc.Conf.) ICRS 2, Nancy, France, 23.-25.11. 1988, Edited by G. Beck; S. Denis; A. Simon, Societe Francaise de Metallurgie, Elsevier Applied Science, Pp.895-900
15. Ritchie, R.O. (1987) in (Proc.Conf.) 5th Intern. Conf. on Mechanical Behavior of Materials, ICM 5, ASME, The Chinese Society of Metals, Beijing, China, Pp. 285-294

ORAL REFERENCE: ICF100301OR

FATIGUE AND FRACTURE OF Cu-SiO_2 BICRYSTAL WITH A [011] 18° TWIST BOUNDARY AT 673K

Hiromi Miura and Taku Sakai

Department of Mechanical Engineeringand Intelligent Systems,
The University of Electro-Communications, Chofu, Tokyo 182-8585, Japan

ABSTRACT

Fatigue and fracture behavior of a copper bicrystal containing dispersed SiO_2 particles and having a [011] 18° twist boundary has been investigated at a stress amplitude of 40MPa at 673K. The grain boundary was inclined 45 degrees to the loading axis to examine effect of grain-boundary sliding (GBS) on fatigue behavior. Crack nucleation took place initially at particle/matrix interface on the grain boundary. The nucleation of cracks at grain-boundary particles are caused by impediment of GBS and also by diffusional process especially near specimen surface. Because the crack seemed to propagate from the surface to the center in thickness, it was concluded that one of the cracks, nucleated on the grain boundary near the surface, propagated to rupture.

KEYWORDS

Fatigue, High temperature, Bicrystal, Copper, Dispersoids, Grain boundary, Grain-boundary sliding

INTRODUCTION

In spite of extensive use of dispersion-hardened alloys as high-temperature materials, studies on their mechanical behavior have been unfortunately limited to areas of creep and static strength. Most of studies on fatigue behavior of the dispersion-hardened alloys are carried out at ambient temperature. Recently, Miura et al. have investigated the temperature dependence of fatigue behavior of Cu-SiO_2 single crystals; easier formation of cell structures were observed with increasing temperature which contributes to fatigue hardening [1]. Furthermore, they have also reported from results using Cu-SiO_2 polycrystals that grain-boundary cracking (GBC) takes place more easily with increasing temperature and with decreasing stress amplitude [2]. The

occurrence of GBC reduces the fatigue life at elevated temperatures. Therefore, the role of grain boundary in high-temperature fatigue behavior must be more significant. In fact, grain boundary seems to strongly affect on fatigue behavior even at room temperature [3].

It is reported from static tensile test of dispersion-hardened alloy at high temperatures [4,5] that grain-boundary sliding (GBS) causes stress concentration around particles to form preferential nucleation of cracks because the particles impede the GBS. Therefore, it can be expected that GBS must also affect on the high-temperature fatigue behavior. This is the motivation of the present study. For simplicity of experimental system, orientation controlled copper bicrystal with dispersed SiO_2 particles was employed as a sample.

EXPERIMENTAL

Bicrystal of a Cu-0.1mass% Si alloy having [011] 18 ° twist boundary was grown by the Bridgman method using seed crystals. The grain boundary was microscopically straight. This bicrystal was internally oxidized at 1273K for 24h with mixed powder of Cu : Cu_2O : Al_2O_3 = 1 : 1 : 2 (mass ratio) to obtain dispersed SiO_2 particles both in grains and on grain boundary. By this treatment, we obtained Cu-0.82vol.%SiO_2 bicrystal. After a degassing treatment at 1273 K for 24 h in a graphite mold in vacuum, bicrystal specimen of 12 mm gage length and 4 x 2 mm^2 cross-section with a boundary inclined at 45 degrees to loading axis were cut by electric discharge machining (Fig. 1). Its crystallographic orientation is shown in Fig. 2. The slip planes and lines in the lower crystal are 18° rotated compared to the upper crystal around [011] axis. Before fatigue tests, surfaces of the specimens were mirror-finished by careful mechanical and electritical polishing.

Fatigue tests were carried out under stress control at a stress amplitude of 40MPa in a vacuum of 10^{-3} Pa at 673 K on a servo-hydraulic machine. Cyclic loading was applied in tension at 20Hz at a load ratio of R=0.1. Some of tests were stopped after cyclic deformation to some numbers of cycles to observe surface and microstructural changes during the cyclic deformation. In that case, the samples were removed immediately from furnace after the deformation to avoid structural changes. The microstructure and fractography were observed by using an orientation image microscopy (SEM-OIM). Yield stress of the bicrystal at 673K was 27MPa, when deformed statically on an Instron-type testing machine at a strain rate of 4.2×10^{-4} s^{-1}.

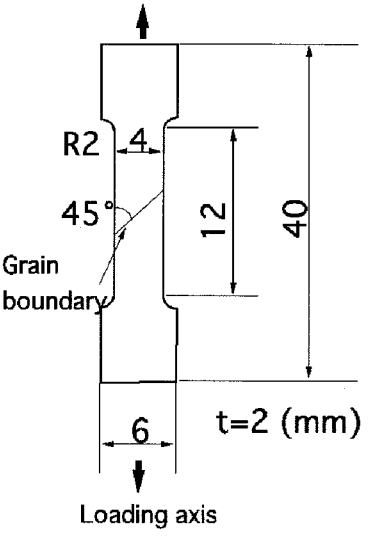

Figure 1 : Geometry of Cu-SiO_2 bicrystal fatigued.

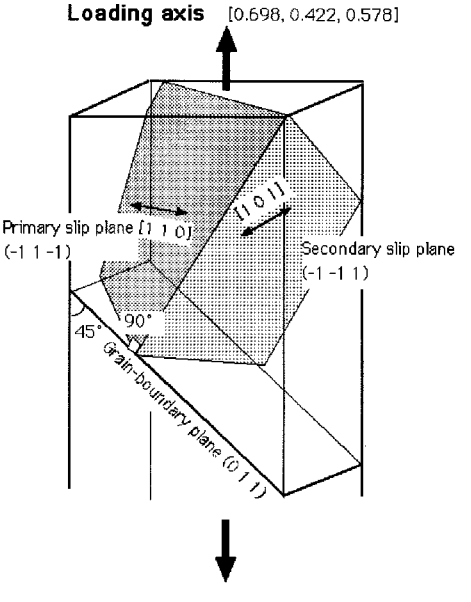

Figure 2 : Schematic illustration of crystallographical orientation of the bicrystal.

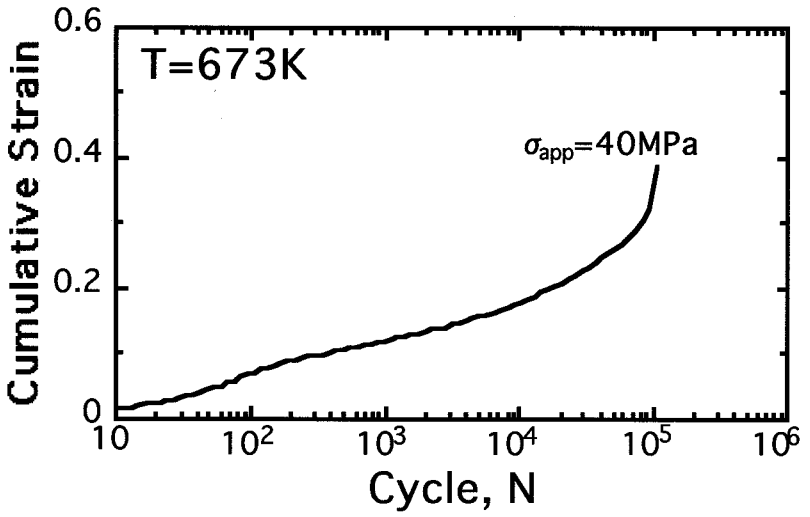

Figure 3 : Cumulative strain - number of cycle curve for Cu-SiO_2 bicrystal fatigued at 673K at a cyclic stress amplitude of 40MPa.

RESULTS AND DISCUSSION

Figure 3 shows cumulative strain against number of cycle (ε - N curve) for the Cu-SiO_2 bicrystal. The ε - N curve shows, after yielding, gradual increase in the cumulative strain at the steady-state work hardening stage and rapid increase to rupture. The ε - N curve of the Cu-SiO_2 bicrystal exhibits, therefore, typical tendency of cyclic creep.

Figure 4 shows microstructural changes with fatigue in processed SEM-OIM images scanned by 0.3μm step. The cycle, N = 10^5, is the cycle just before rupture. Image processing was carried

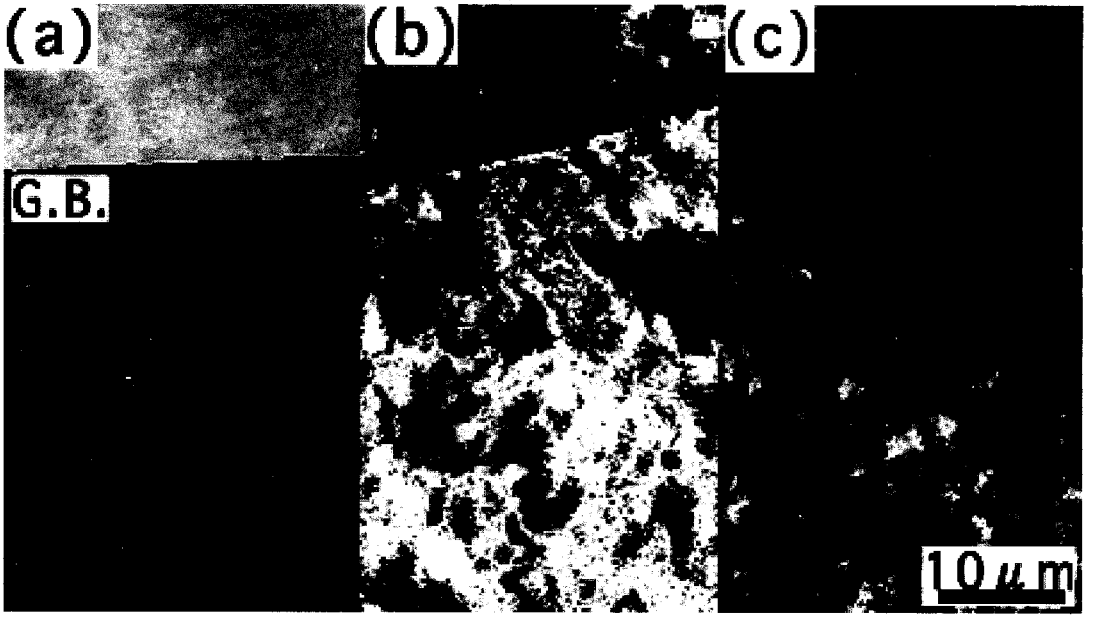

Figure 4 : Processed orientation image of the bicrystals fatigued to (a) N = 10^3, (b) N = 10^4 and (c) N = 10^5 cycles, respectively.

out to observe small change of substructures evolved in the bicrystals. The black lines seen upper sides of all the figures are the [011] 18° twist grain boundaries. Substructures develop gradually with increasing cycle. Such changes of the substructures were not detected in the original SEM-OIM images before the image processing. As can be seen in all the images, no specific structural development nor dynamic recrystallization occurred even near grain boundary while appearance of grain-boundary affected zone (GBAZ) was expected [3]. The hairlines of white contrast seen in Fig. 4 (c) are developed subboundaries. The absence of recrystallization in all the area of the samples even after deformation to a strain of $\varepsilon = 0.37$ at maximum (see Fig. 3) would be because of high-density distribution of the particles [6]. As the number of cycle increases, substructures developed more clearly and extensively. However, the substructure seems homogeneous and no GBAZ appeared to develop. This result suggests that macroscopic deformation concentration did not take place anywhere in the bicrystal under present experimental condition. This result may support the expectation that initial crack nucleates on grain boundary due to short range GBS but causes transgranular fracture, as will be shown later.

Surface morphology of the fatigued bicrystal to a number of cycle of $N = 10^3$ is shown in Fig. 5 (a). Only one slip traces perpendicular to the grain boundary seems to develop homogeneously. Slip traces of the primary and secondary slip systems are overlapped at the surface (see Fig. 2). Because the cumulative strain at this cycle is more than 0.1, both and further slip systems should work. However, change in slip morphology near the grain boundary, which corresponds to GBAZ, did not appear. What is more interesting, some small cracks are nucleated on the grain boundary. Miura et al. have reported from experimental results of static tensile tests of Cu-SiO_2 bicrystals that impediment of GBS by grain-boundary particles provides stress concentration site to promote preferential crack nucleation as schematically described in Fig. 5 (b) [4, 5]. We believe that the occurrence of GBS caused the crack nucleation also during high-temperature fatigue of dispersion-hardened alloy [7], because the [011] 18° twist boundary can slide easily at high temperature [8]. The mean particle radii in the grains and on the grain boundary measured by transmission electron microscopy were about 91 and 190 nm, respectively. The lager size of the grain-boundary particle would also attribute easier cracking around the particles due to larger stress concentration factor. The observed GBC on surface may be influenced also by diffusional process. However, rupture did not take place along the grain boundary. The crack propagated along the slip traces, as will be shown in Fig. 6. This would be due to homogeneous deformation

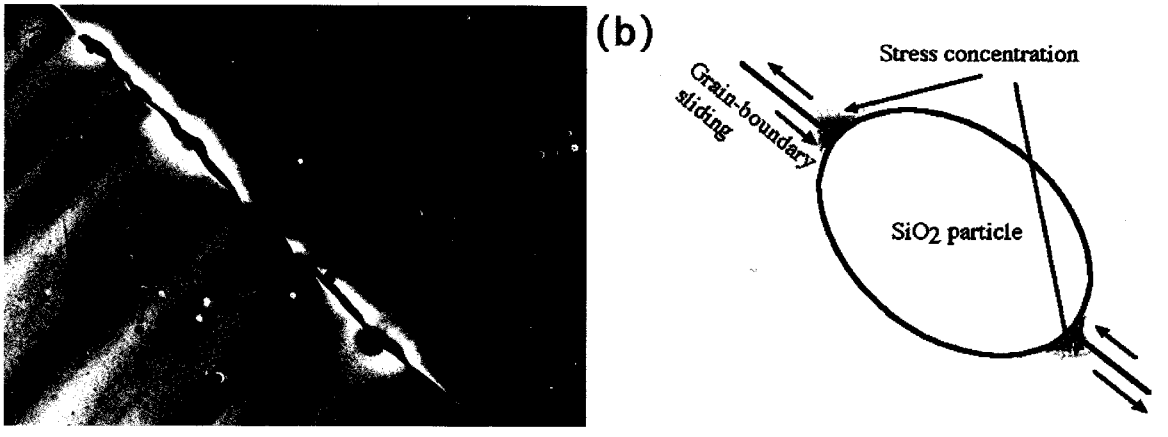

Figure 5 : (a) Surface morphology of the bicrystal fatigued to $N = 10^3$ cycles. (b) Schematic illustration of crack formation at the matrix/particle interface by stress concentration caused by grain-boundary sliding.

behavior during high-temperature fatigue of Cu-SiO_2 bicrystals. This result must not indicate that transgranular fracture occurs generally during cyclic deformation at elevated temperatures. Grain-boundary fracture would become dominant under such conditions of higher temperature and lower stress amplitude where GBS takes place more easily.

Observed typical features of fractographs are exhibited in Fig. 6. The macroscopic photograph of the fractured specimen (Fig. 6 (a)) shows that fracture occurred transgranularly. Grain boundary is pointed by arrow mark. The initiated crack on grain boundary did not propagated along the grain boundary. The SEM photograph in higher magnification shown in Fig. 6 (b) indicates that the fracture surface is composed of inhomogeneous morphologies; fine dimples around the center in thickness (Fig. 6 (c)) and relatively flat appearance of striation near the surface (Fig. 6 (d)). The existence of particles in the dimples implies that voids were formed at the particle/matrix interface. These fine dimples would be formed by ductile fracture manner just before rupture. The surface relief lines seen near the specimen's surfaces would be a striation (Fig. 6 (d)). The fractographs would imply that crack propagated from the surface to the center. It can be expected, therefore, that one of the grain-boundary cracks such as observed in Fig. 5 (a) is a starting point of crack propagation to cause rupture. This conclusion would be reasonable to think, because the crack nucleation and growth at the surface should be more acceralated by easier and faster supply of vacancy or gas atoms, when compared with part far from the surface. If fatigue test at higher temperature is carried out, it should be expected that crack propagation along grain boundary becomes easier because of much easier occurrence of GBS and vacancy supply.

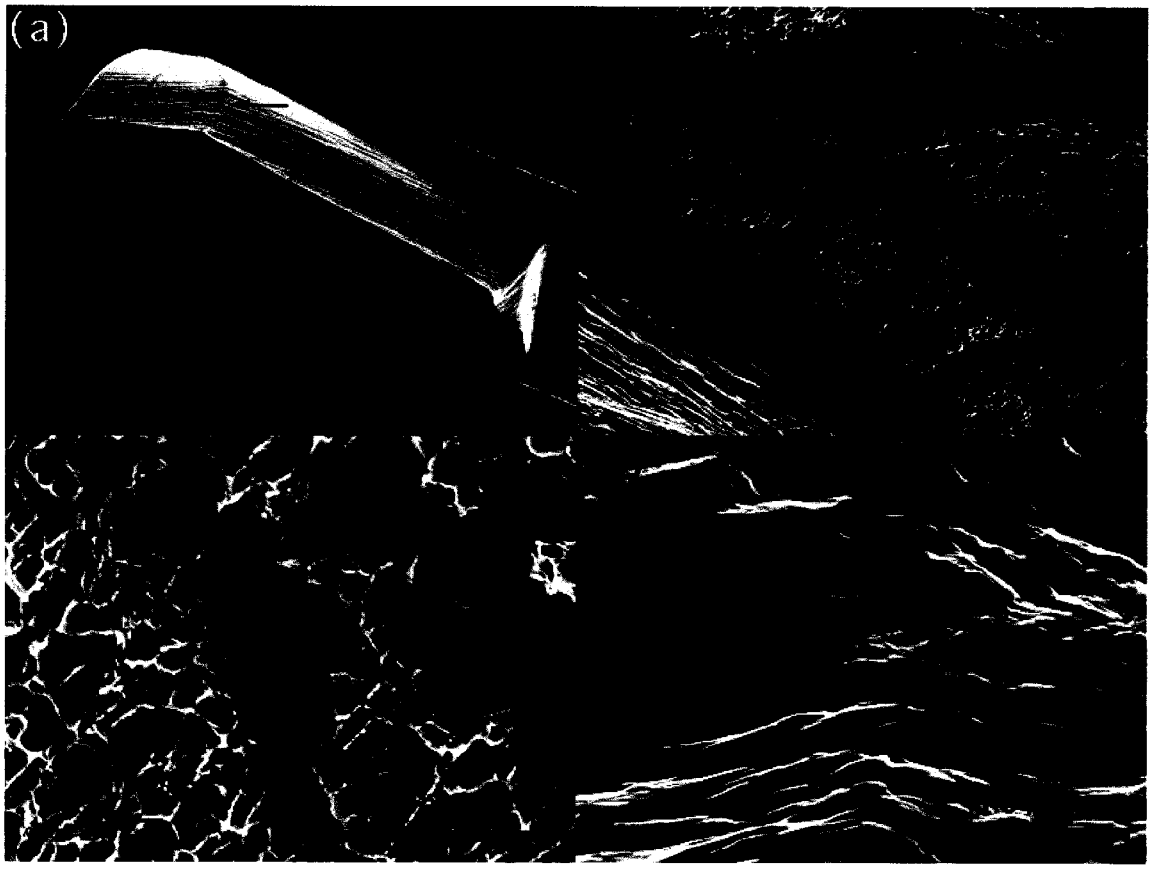

Figure 6 : Fractographs of the bicrystal; (a) whole view of the fracture surface, (b) further magnified image of a part of (a), (c) magnified image near the center of (b) and (d) magnified image of lower side of (b), respectively.

SUMMARY

Fatigue behaviour of a copper alloy bicrystal containing SiO_2 particles and having a [011] 18° twist boundary has been studied at 673K at a cyclic stress amplitude of 40MPa. Cracks were found to nucleate preferentially at grain boundary, probably around the grain-boundary particles. This is because of easy stress concentration by impediment of grain-boundary sliding by the particles. The fracture seemed to take place by crack propagation from surface to the center in thickness. Although preferential cracking took place initially on grain boundary, grain-boundary fracture did not occur under the present fatigue condition. This would suggest that homogeneous cyclic deformation took place in the bicrystal, and then, slip trace seemed to be comparably important route for crack propagation even at elevated temperature.

ACKNOWLEDGEMENTS

The authors acknowledge the financial support by Tanikawa Found Promotion of Thermal Technology, Japan and the material supplement from Nippon Mining and Metals Co. Ltd., Kurami Works, Japan.

REFERENCES

1. Miura, H., Kotani, K. and Sakai, T. (2001) Acta materialia, in press.
2. Miura, H. and Sakai, T. (2001) Proceedings of 9th IC on Creep and Fracture of Materials and Structures, Swansea, United Kingdom, 29.
3. Wang, Z.G., Li, W.X., Zhang, F.Z. and Li, X.S. (1999) Proceedings of Fatigue '99, China, 93.
4. Miura, H., Sakai, T., Tada, N., Kato, M. and Mori, T. (1993) Acta Metall. Mater., 41, 1207.
5. Miura, H., Sakai, T., Tada, N. and Kato, M. (1996) Phil. Mag. A, 73, 871.
6. Beden, I. (1986) Scripta Metall., 20, 1.
7. Miura, H., Ooi, T. and Sakai, T. (2001) Phil. Mag. Lett., 81, 293.
8. Monzen, R., Futakuchi, M. and Suzuki, T. (1995) Scripta Metall. Mater., 8, 1277.

ORAL/POSTER REFERENCE: ICF100231OR

FATIGUE AND FRACTURE PROPERTIES OF Co-Fe ALLOYS AT 150^0 C

V Filardi[1], E Guglielmino[2], S J Harris[3], T H Hyde[3], R V Major[4],

[1]DIIEM – Università degli Studi di Catania - Viale A. Doria, 6 – 95125 Catania - Italy
[2]DCIIM – Università degli Studi di Messina – S. Sperone 31 – 98166 Messina - Italy
[3]School of Mechanical, Materials, Manufacturing Engineering and Management – University of Nottingham -University Park -Nottingham, NG7 2RD UK
[4]CARPENTER Specialty Alloys UK, Crawley, Sussex, UK

ABSTRACT

The results of a series of fatigue tests performed on two Co-Fe alloys at 150^oC are reported. The ratio of the minimum to maximum load, R, in all tests was 0.1. Both materials behaved in a similar manner, with a fatigue limit (ie maximum stress to cause failure in 10^6 cycles) of 800 MPa (ie a stress range of 80 to 800 MPa). Following initiation, a short period of fatigue crack growth is followed by a fast fracture process. During fast fracture, the crack bifurcates; the bifurcation angles lie in the range 32^o to 39^o.

KEYWORDS

Fatigue, Co-Fe, Fast Fracture, Bifurcation.

INTRODUCTION

Cobalt iron alloys, are used in a wide variety of engineering applications, because they can be made with a combination of high mechanical strength and have a high level of magnetic saturation performance. In some situations, it is also necessary for these materials to operate at elevated temperatures and under variable loading conditions, such that fatigue must be considered as a possible failure mode. This paper contains the results of a series of tests performed on two Co-Fe alloys developed for use in a variable frequency generator for aeroengine applications. The materials, designated Rotelloy® 7 and Rotelloy® 8, were supplied by Carpenter Technology UK, as part of a DTI funded project managed by Lucas Aerospace.

TEST CONDITIONS, SPECIMEN GEOMETRY AND LOADING

The tests were performed on a 250kN Mayes, servo-electric machine, at 150^{o}C. Chromel-alumel thermocouples (TL (70, type)) were attached to each specimen to control the temperature of the three zone furnace; the specimen temperature was held constant to within $\pm$1^{o}C. The specimens were machined from 0.34mm thick (nominal) sheet; the other specimen dimensions are given in Fig 1. Because of the inevitable stress concentration features which results from the gripping arrangements, the waisted section at the centre of the specimen was included to ensure that fatigue failure would occur in the central, test section of the specimen, rather than at the grips or in the radii at the ends of the parallel sections of the specimens. Finite element analyses were performed to establish a suitable radius, r, for the "neck" section of the specimen; it was necessary to have as near to a uniform stress across the "neck" section as possible. The variation of the stress concentration factor, SCF, with r is indicated in Fig 2. A radius r = 50mm was chosen to simplify the manufacturing process and to ensure that a maximum SCF of 1.07 would occur. All fatigue tests were performed with a minimum load to maximum load ratio, R = 0.1.

TEST RESULTS

The results for the uniaxial fatigue tests are presented in Table 1 and are plotted in Fig 3. A schematic diagram of a typical fractured specimen is shown in Fig 4. It can be seen that the macroscopic fracture is characterised by a crack, of length a, which is perpendicular to the loading axis, followed by a bifurcation of the crack with bifurcation angle, θ_f. For those specimens in which the crack lengths, a, were clearly defined, the crack lengths were measured. Using published stress intensity factor data (1) together with the maximum load levels and crack lengths, a, estimates of the mode-I stress intensity factor, K_I, at which the bifurcation took place, were determined. The variation of the mode-I stress intensity factor, at bifurcation, with a/b for the two materials are shown in Fig 5, where b is the sample width. Also, the variations of θ_f with a/b for the two materials are shown in Fig 6.

From Fig 3 it can be seen that the two materials exhibit very similar fatigue behaviour. The results indicate that there is a fatigue limit at a maximum stress level of about 800 MPa (ie for stresses varying from 80-800 MPa). Hence, for maximum stresses less than about 800 MPa (with R = 0.1) more than 10^6 cycles is required to initiate a fatigue failure.

A scanning electron microscope (SEM) was used to investigate the fracture surfaces. Two distinct types of fracture surface were identified. Close to the crack initiation site near the edge of the specimen (see Fig 4), the fracture surface is flat and there are striations which indicate that a fatigue crack growth process is taking place; see Figs 7(a) and (b). For longer cracks, leading up to the bifurcation and beyond it, the surface is much more faceted and there are no striations, indicating that a fast fracture process is taking place as shown in Fig 7(c). Fig 7(d) shows a SEM view of the transition between the two types of fracture surface; this figure also shows that the transition is abrupt.

The spacing of the striations (see Fig 7(b) for example), indicates that the fatigue crack growth phase is short compared with the initiation phase. Also, the fatigue

crack lengths at the onset of fast fracture were generally in the range 0.15 to 0.3mm. This indicates (1) that, on the basis of an LEFM analysis, the fracture toughness K_{IC}, of the material is approximately 25 $MPam^{0.5}$. Using this value of the K_{IC} with a flow stress of 1000 MPa (2,3) leads to a crack tip plastic zone size of approximately 0.03mm. Although this is not insignificant compared with the crack length at the onset of fast fracture (0.15 to 0.3mm), it is small enough to ensure that it is reasonable to use K_{IC} = 25 $MPam^{0.5}$ as the fracture toughness to estimate the load bearing capacity of a component made from the Co-Fe alloys.

A detailed explanation of the fracture process will be the subject of a future paper. This will include an explanation of the relationship between K_{IC}, the bifurcation angle and the length of crack at the onset of branching.

CONCLUSIONS

- The fatigue limit for the alloys (with R = 0.1) is about 800 MPa.
- Fatigue initiation is followed by a relatively short period of fatigue crack growth.
- The K_{IC} for the materials is about 25 $MPam^{0.5}$.
- Following a short period of fatigue crack growth, fast fracture initiates, and the crack growths perpendicular to the applied stress axis.
- Crack branching occurs when the cracks have propagated to lengths in the range 0.5 to 1.5mm.

ACKNOWLEDGMENTS

The authors would like to thank the DTI, Lucas Aerospace and Carpenter Specialty Alloys UK for their financial support of the research reported in this paper and for granting permission to publish the paper. They also would like to acknowledge the advice given by Mr. K. Dinsdale for the SEM analysis of fractures.

REFERENCES

1. D P Rooke and D J Cartwright, "Compendium of Stress Intensity Factors", London, HM Stationery Office, 1976.
2. R V Major and W Gemmell, "Soft Magnetic Alloys Combining High Saturation and High Strength", Proceedings of conference on Soft Magnetic Materials 96, February 1996, San Francisco.
3. R V Major and V Samadian, "Physical Metallurgy and Properties of a New High Saturation Co-Fe Alloy", J Materials Engineering, Vol 11(1), 1989, pp 27-30.

Table 1

Results of Fatigue Tests of Co-Fe Specimens

Spec. (2)	Max Stress ÷ UTS	Crack length (a) at bifurcation (mm)	(a/b)	K_I ($MPam^{0.5}$) at bifurcation (1)	Cycles to Failure
1a	0.85	0.93	0.930	65.68	2.04E+04+
2a	0.78	2.05	0.203	104.58	4.80E+04+
3a	0.71	1.85	0.183	87.21	9.86E+04+
5a	0.63				3.40E+06+ (run out)
6a	0.84	1.29	0.128	79.64	1.39E+04+
7a	0.77	1.39	0.138	76.94	4.67E+04+
8a	0.74	1.42	0.140	74.33	6.90E+04+
9a	0.70				3.40E+06+ (run out)
10a	0.63				3.40E+06+ (run out)
1b	0.84	0.60	0.060	50.09	2.81E+04+
3b	0.76	0.83	0.082	54.88	4.01E+04+
4b	0.74	0.96	0.095	67.79	6.57E+04+
5b	0.89	0.55	0.055	51.12	0.52E+04+
7b	0.92	0.73	0.072	61.77	1.15E+04+
8b	0.89	0.60	0.060	53.63	1.55E+04+
13b	0.63				3.40E+06+ (run out)
14b	0.68	0.71	0.070	44.54	6.27E+04+

(1) Based on assumed LEFM behaviour using the formulation presented in reference 1.

(2) "a" designates Rotelloy® 7 specimen
"b" designates Rotelloy® 8 specimen

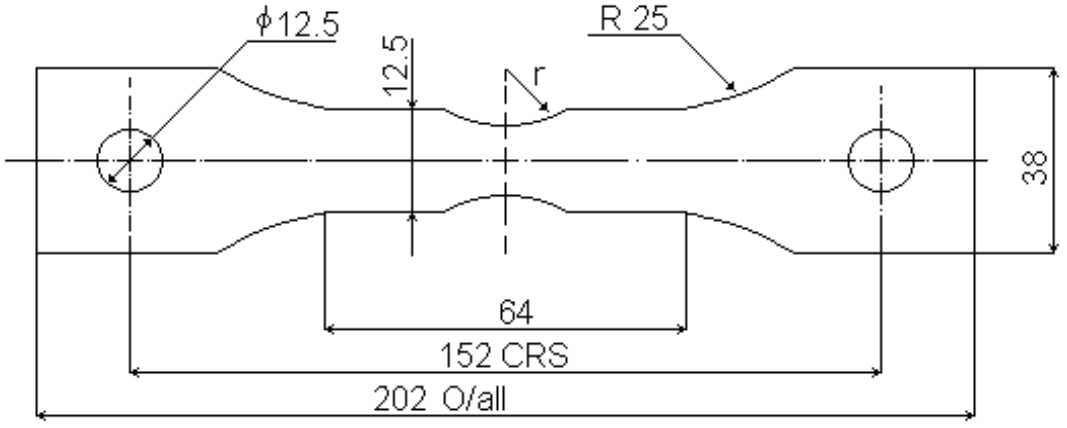

Minimun Specimen Width = 10 mm (Nominal)
Thickness = 0.35 mm (Nominal)

Fig. 1 Co-Fe Fatigue Specimen

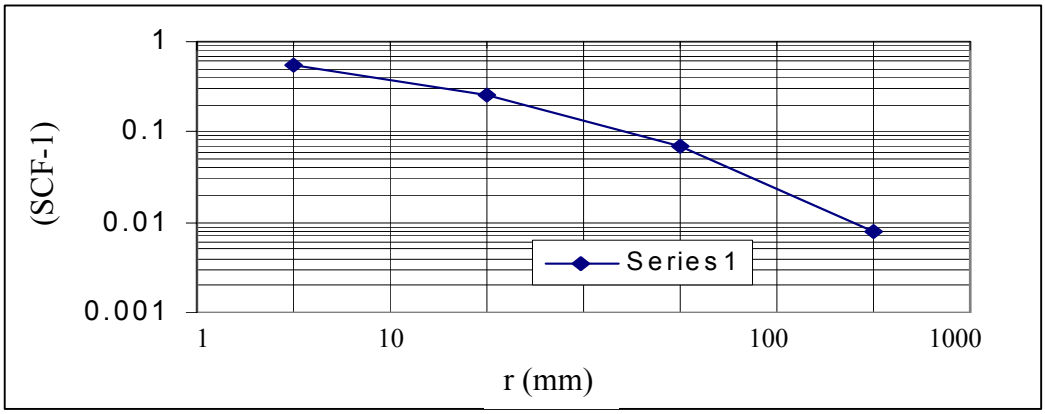

Fig. 2 Variation of SCF with r (obtained from FE Analysis)

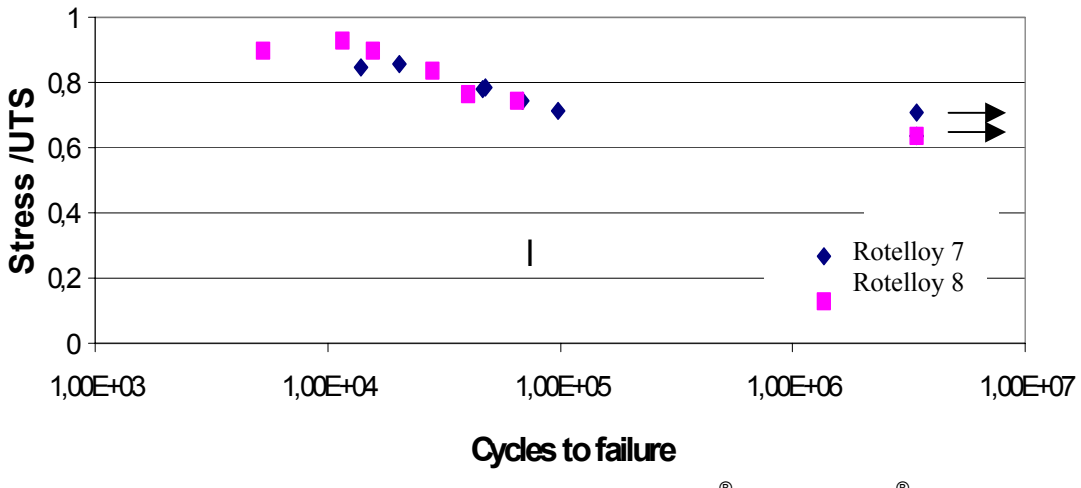

Fig. 3 Fatigue Data from Fe-Co Specimens (Rotelloy® 7 and Rotelloy® 8)

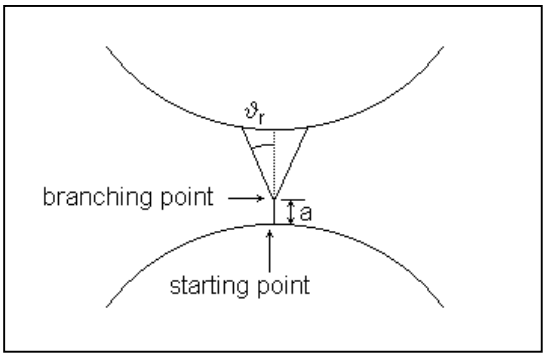

Fig. 4 Schematic Diagram of the fracture showing the bifurcation

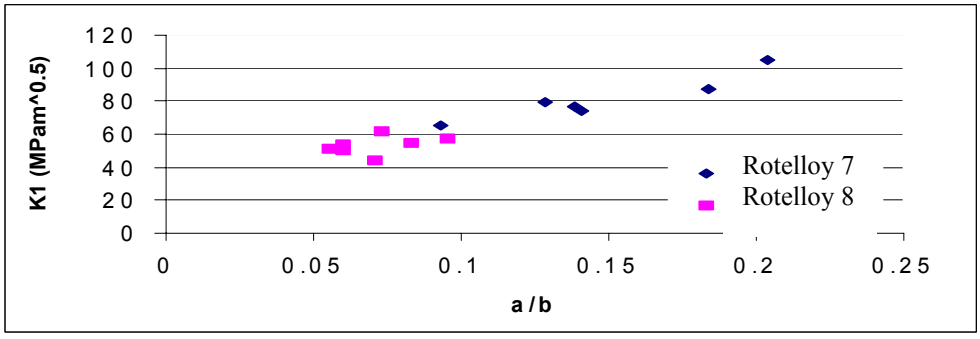

Fig. 5 K_1 at bifurcation for Fe-Co specimens based on LEFM assumption

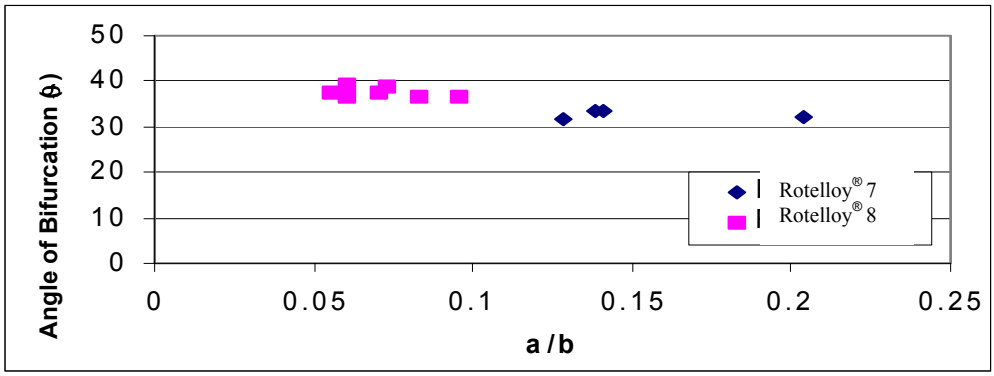

Fig. 6 Bifurcation angles ϑ_f obtained from the Co-Fe specimens

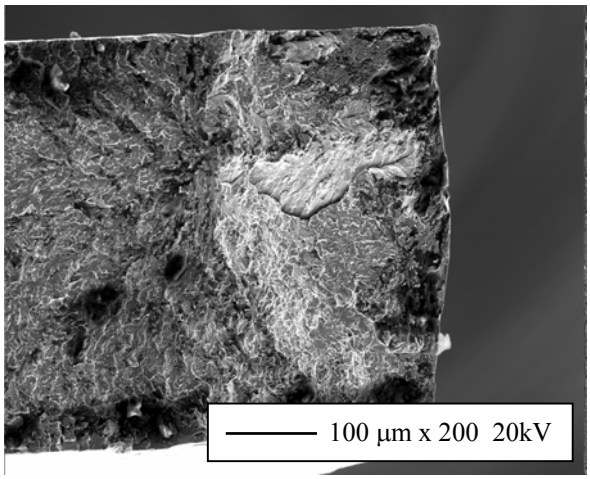

Fig. 7(a) Low magnification micrograph of fatigue crack initiating at the curve of the sample

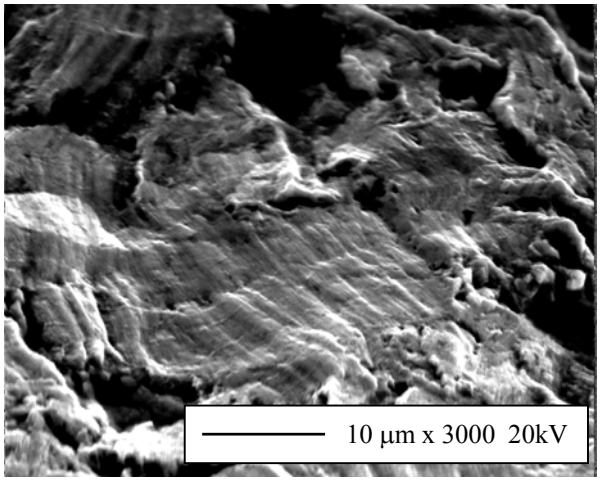

Fig. 7(b) High magnification micrograph of produced on fatigue fracture surface

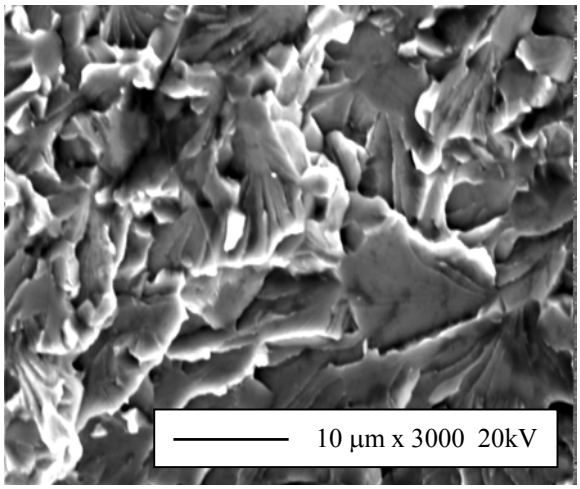

Fig. 7(c) Brittle facets on the fast fracture surface

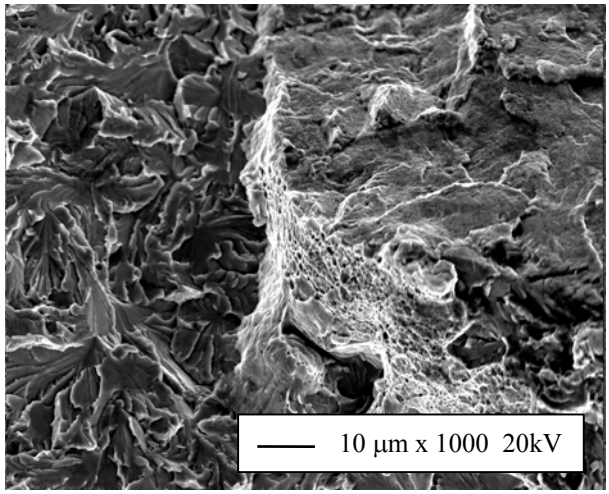

Fig. 7(d) Transition zone between fatigue and fast fracture surfaces

ORAL/POSTER REFFERENCE: ICF100986OR

FATIGUE AND HYDROGEN CRACKING IN CANNONS WITH MECHANICAL AND THERMAL RESIDUAL STRESSES

J. H. Underwood[1], A. P. Parker[2], E. Troiano[1], G. N. Vigilante[1], M. D. Witherell[1]

[1]Army Armament Research, Development and Engineering Center, Watervliet, NY 12189 USA
[2]Royal Military College of Science, Cranfield University, Swindon SN6 8LA UK

ABSTRACT

Bauschinger-modified autofrettage residual stresses are used to improve the *fatigue intensity factor* model for fatigue life of cannon pressure vessels. Effects of yield strength and initial crack size are included with applied and residual stress in a S-N description of cannon tube life that matches full-scale cannon fatigue test results with a R^2 correlation of 0.92. Thermally induced residual stress near the bore of a fired cannon is modeled by finite difference calculations of temperature and mechanics calculations of transient thermal stress and resulting residual stress. Temperature dependent thermal and physical properties are used, and the temperature distributions are validated by direct comparison with the known temperatures and the observed depths of microstructural damage and transformation in fired cannons. Calculations of fatigue life and yield pressure for a range of applied pressure, diameter ratio, yield strength and % autofrettage agree well with measurements from full-scale cannons. Increased life is predicted for increases in yield strength and % autofrettage, although the Bauschinger effect significantly reduces the amount of life increase for autofrettage above 50%. The combined effects of mechanically induced residual stress and thermally induced residual stress on cannon fatigue life are calculated, using an increased initial crack size to account for thermal residual stress. Calculations of fatigue life are presented for a range of applied pressure and for selected gas temperatures.
KEY WORDS: metal fatigue, pressure vessels, autofrettage, thermal stress, high strength steels, hydrogen crack

INTRODUCTION

The benefit of mechanically induced autofrettage residual stress in extending the fatigue life of a pressure vessel has been known for decades. Only relatively recently has comprehensive predictive analysis of autofrettage residual stress been available that can account for the actual material properties of pressure vessel steels, most importantly the significant reduction of compressive yield strength that occurs in an autofrettaged vessel, known as the Bauschinger effect. Measurements of the Bauschinger effect in the Ni-Cr-Mo steels commonly used in cannon pressure vessels have long been available [1]. Analysis of the Bauschinger strength reductions that are observed for different vessel diameter ratios and degrees of autofrettage was described by Chaaban et al [2], but they used a simple bilinear representation of the reduced compressive yielding, whereas a much more complex non-linear behavior is observed. Parker [3] has provided useful expressions that will be used here to calculate autofrettage residual stresses at the bore of pressure vessels with Ni-Cr-Mo type Bauschinger properties, accounting for diameter ratio, degree of autofrettage and non-linear behavior, the effects of concern here.

In the past decade a troublesome type of thermally induced residual stress has been found to affect cracking and service life of cannon pressure vessels. Underwood et al [4] showed metallographic evidence of a constant-depth array of cracks at the inner surface of fired cannon tubes that cannot be explained by a mechanical fatigue process. Finite difference calculations of the transient temperatures at the inner surface of a fired cannon tube predicted yield-level transient compressive stresses to about the same depth as the crack array, suggesting that tensile residual stress was present to this depth. Given that significant hydrogen is produced in cannon firing and cannon steels are highly susceptible to hydrogen cracking, the constant-depth cracks can be explained as

hydrogen cracks. In the work here additional finite difference temperature calculations and transient and residual stress calculations are performed, to determine the effect of thermally induced residual stresses and cracking on fatigue life of cannon pressure vessels. The fatigue life implications of both the mechanically induced autofrettage residual stresses and the thermally induced firing residual stresses will be described in the work here using the fatigue intensity factor (FIF) concept developed by Underwood and Parker [5]. This modified S-N approach gives a high correlation, single-expression description of fatigue life for a wide range of vessel configuration, stress concentration, applied and residual stresses, yield strength and initial crack size.

ANALYSIS

The residual stresses in a cannon pressure vessel that will be discussed here are those produced by a mechanical mandrel-swage autofrettage process during fabrication of the cannon tube and those produced by the transient convective heating of the inner surface (ID) of the tube during cannon firing. Transient heating of a cannon ID during firing has traditionally been important only because it would initiate fatigue cracking somewhat earlier than would otherwise be expected. However, with increases in cannon firing pressures, temperatures and duration, ID thermal damage is deeper and asserts a more significant control over cannon fatigue life than in the past. The finite difference method is used to calculate the near-ID transient temperature distribution, as the initial measure of the degree and depth of thermal damage. The temperatures are then used to calculate the biaxial transient compressive stresses and the tensile residual stresses in the locations of the steel substrate where the compressive stresses exceed the yield strength. The depth of a significant tensile residual stress is taken as the important final measure of thermal firing damage, because hydrogen cracking is expected to occur to this depth in the steel and thereby accelerate the fatigue failure process.

Autofrettage Residual Stresses and Yielding

The familiar Tresca-plane stress expressions for hoop residual stress in an autofrettaged tube were modified [3] to apply to the Mises-open end conditions that are more appropriate for cannon pressure vessels and also to include the effect of the Bauschinger reduced strength. These modified expressions are:

$$S_{\theta R} = R_S \left[-p_Y + S_Y [1+ \ln(r/a)] - p_Y a^2(b^2-a^2) (1+b^2/r^2) \right] \qquad \textit{for: } a < r < r_Y \qquad [1]$$

$$p_Y = R_P \left[S_Y [\ln(r_Y/a) + (b^2- r_Y^2)/2b^2] \right] \qquad [2]$$

where a and b are the inner and outer tube radii, r_Y is the autofrettage radius, S_Y is yield strength, p_Y is the equivalent pressure that would be required to accomplish the mandrel autofrettage, and R_S and R_P are the ratios that accomplish the modification for various degrees of autofrettage, n. At the critical ID, i.e., at r = a:

$$R_S = 1.669 – 0.165(b/a) – 0.730\, n^3 +1.984\, n^2 – 1.887\, n \qquad \textit{for: } 1.75 < b/a < 3.00; \quad 30\% < n < 80\% \qquad [3]$$

$$R_P = 1.155 / [\, 1+ 1 / 3(b/a)^{4 - 2.3\, n}]^{1/2} \qquad \textit{for: } n < 70\% \qquad [4]$$

Equations 1-4 are used here to calculate the mechanically induced hoop residual stresses at the ID of autofrettaged tubes, including the important effect of the Bauschinger reduced strength for the type of Ni-Cr-Mo steels used in cannons. Once the Bauschinger-modified hoop residual stresses are known, the Bauschinger-affected pressure, p*, at which the cannon tube re-yields when re-pressurized following initial autofrettage can be determined, using the Mises criterion in the notation here:

$$S_Y = \left[[(S_{\theta T} – p^*)^2 + (p^* - \nu\, S_{\theta R})^2 + (\nu\, S_{\theta R} - S_{\theta T})^2] / 2^{1/2} \right]^{1/2} \qquad \textit{for } r = a \qquad [5]$$

where $S_{\theta T}$ is total hoop stress (sum of applied and residual) and $\nu\, S_{\theta R}$ is an estimate of axial residual stress [3]. Equation 5 gives a Bauschinger-modified ID yield pressure, but it does not include any effect of additional re-yielding discussed by Parker [3] that can occur near the yield pressure. This will be considered in future work.

Transient Temperatures and Thermal Residual Stresses

Finite difference calculations of one-dimensional convective heat flow were used to determine the near-ID temperatures produced by cannon firing conditions. The calculations used increments of 0.02 mm in depth below the heated bore surface. About fifty increments were required for the temperature to drop from typically

1500 ^{o}K at the surface to within 1^{o}K of ambient (300^{o}K) at about 1 mm below the surface, for the few ms of convective heating typical of cannon firing. Temperature dependent material properties [6-8] of the 0.1 mm thick electro-plated chromium bore coating and the Ni-Cr-Mo steel substrate were used for the analysis, in the form $\delta(T) = C_0 + C_1 T$, with values of C_0 and C_1 as in Table 1. The inputs to the finite difference calculations, in addition to the chromium and steel properties, were: the initial ambient temperature, T_i , 300 ^{o}K; the duration of the convective heating pulse at the tube surface, 0.008 s; the convection coefficient, h, of the heating pulse, 193,000 W/m^2 ^{o}K; and the mean gas temperature of the pulse, with values as discussed in the upcoming results.

TABLE 1 – **TEMPERATURE DEPENDENT PROPERTIES OF CHROMIUM AND STEEL**

			Chromium		Ni-Cr-Mo Steel	
property	units	range; ^{o}K	C_0	C_1	C_0	C_1
thermal diffusivity, δ	m^2/s	300 - 2000	29.6 E-6	-12.6 E-9	11.7 E-6	-5.3 E-9
thermal conductivity, k	W/m ^{o}K	300 - 2000	97.2	-0.0266	43.6	-0.0097
elastic modulus, E	GPa	300 - 1000	--	--	248	-0.0968
thermal expansion, α	1/^{o}K	300 - 1000	--	--	13.5 E-6	0
yield strength, S_Y	MPa	300 - 1000	--	--	1740	-1.62

Expressions for the near-bore, transient, in-plane, biaxial compressive thermal stress, S_T, and the tensile residual stress, S_R, produced when the transient stress exceeds the material yield strength are:

$$S_T = - E \alpha [T\{x,t\} - T_i] / [1 - \nu] \quad [6]$$

where ν is Poisson's ratio; the transient temperature, T is for a given depth, x below the bore surface and time, t after the start of a heating pulse; the term [1 - ν] accounts for the biaxial nature of the temperature and stress distributions. Then S_R is determined directly using the linear unloading concept: $S_R = - S_T - S_Y$.

Fatigue Intensity Factor versus Life

The effects of autofrettage and thermal residual stresses on fatigue life will be described in the work here using the fatigue intensity factor (FIF) concept [5]. In brief summary, the FIF concept adds a quantitative measure of material yield strength and initial crack size to the stress parameter in a *log* stress vs *log* life description of fatigue life behavior of a structure. By adding material strength and initial crack size to S-N life descriptions, significant improvements in life modeling of cannon pressure vessels have been shown. The key expressions for an FIF description of ID-initiated fatigue life of a pressurized, autofrettaged cannon pressure vessel are:

$$\text{fatigue intensity factor} = \Delta S_{LOCAL} \times (S_{Y\text{-}NOM} / S_Y) \times (a_i / a_{i\text{-}NOM})^{1/6} \quad [7]$$

$$\Delta S_{LOCAL} = k_t S_{APPLIED} + S_{RESIDUAL} + p \quad [8]$$

Note that the local stress range for ID-initiated cracking includes: the familiar Lamé applied ID stress for the appropriate p and b/a, with stress concentration factor, k_t if one is present; the ID hoop residual stress, accounting for the Bauschinger reduced strength, using Eqs. 1-4, but no k_t even if present because it would be negated by the Bauschinger effect; and an added stress equal in magnitude to p, to account for the effects of pressure on the crack faces [5]. The second term in Eq. 7 accounts for the yield strength of a given vessel, when different from the nominal yield strength of the vessels under comparison. The third term accounts for the initial crack size of a given vessel, if different from the nominal initial crack size of the vessels under comparison. As will be seen in the forthcoming results, the effect of thermally induced tensile residual stresses in cannon vessels can be accounted for by using a_i values associated with the depth of the tensile residual stresses in cannons critically subject to hydrogen cracking.

RESULTS

Mechanical Residual Stress Effects on Fatigue Life

A baseline description of the effect of mechanical autofrettage residual stresses on ID initiated fatigue life for cannon tubes is available from prior results of full-scale cannon fatigue tests [5]. Four groups of the prior fatigue tests that were ID initiated and had well documented initial crack sizes will be used for a baseline fatigue life, see Table 2. Two of the groups were rifled cannons, with a k_t of 1.7 to account for the radius

TABLE 2 – **CANNON PRESSURE VESSEL FATIGUE LIFE TESTS WITH INITIATION AT THE ID**

group	mean yield strength S_Y; MPa	inner radius a; mm	outer radius b; mm	initial crack a_i; mm	stress concentration k_t; --	fatigue pressure p; MPa	degree of autofrettage n; %
75N	1280	89	187	0.01	1.7	345	0
75A	1020	89	187	0.01	1.7	345	50
55	1230	89	142	0.10	1.0	393	60
20	1120	79	155	0.10	1.0	670	60

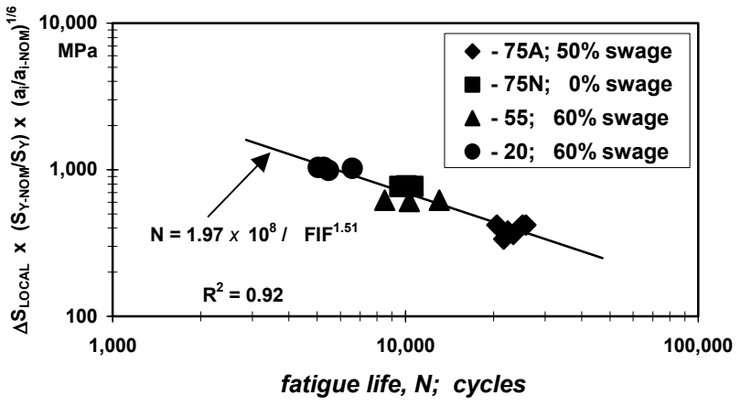

Figure 1: Lives for vessels with various % autofrettage

between the rifling land and groove. The measured fatigue lives of the sixteen tests from these four groups are shown in Fig. 1, using FIF as the stress parameter in the S-N plot. Referring again to Eqs. 7 and 8, FIF was calculated using: each of the sixteen values of S_Y ; $S_{Y\text{-}NOM}$ = 1134 MPa; $a_{i\text{-}NOM}$ = 0.10 mm; and values from Table 2. The high correlation of the linear regression expression shows that an FIF based S-N plot gives a good description of fatigue life for cannons, including the significant effect of autofrettage residual stress.

Thermal Residual Stress Verified from Thermal Damage

Inputs to finite difference calculations of near-bore cannon temperatures are, inevitably, somewhat uncertain. So, before the calculated temperatures are used to determine residual stress, they should be verified by metallographic observations of thermal damage. This has been done for a cannon after the firing of about 40 high temperature rounds [4], see Table 3. About two thirds of the 0.12 mm thickness of chrome showed a transformed microstructure associated with a temperature of about 1320 K. A more certain validation point is

TABLE 3 – **SUMMARY OF DAMAGE IN A FIRED CANNON**

thickness of chromium layer	depth of chromium damage layer	depth of steel transformation	depth of crack array; longitudinal section
0.12 mm	0.08 mm	0.19 mm	0.46 mm

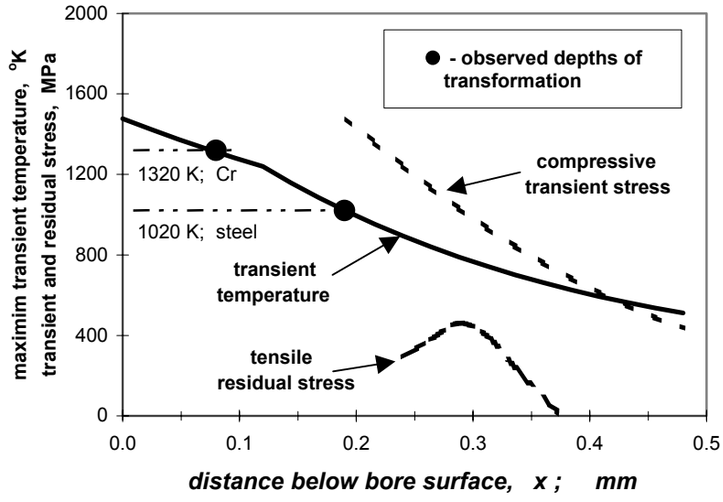

Figure 2: Firing temperatures and resultant stresses

the well-known 1020 K phase transformation for this type of low alloy Ni-Cr-Mo cannon steel, and metallographs show a consistent, clear depth of 0.19 mm. One further dominant damage feature observed was an ever-present array of constant depth cracks normal to the longitudinal orientation of the cannon, an orientation known to have no significant applied tensile stress. As discussed next, the crack array provides added verification of the calculated depth of thermally induced residual stress due to cannon firing.

Results of finite difference calculations of temperatures and solid mechanics calculations of transient and residual stresses, using the methods and validation already discussed, are shown in Fig. 2. The solid line shows the calculated maximum temperatures vs distance

below the bore surface, for the following input values: the δ and k properties for chromium and steel from Table 1; T_{gas} = 2160 K and 0.008 s pulse duration; and h = 193,000 W/m^2 ^{o}K. Note that the depths and temperatures of the 1320 K and 1020 K transformations of chromium and steel are well matched for the calculated temperature distribution, so it should be a useful basis for transient and residual stress calculations. These stress calculations are shown in Fig. 2 for selected ranges of depth somewhat below the bore surface; calculations very near the bore surface have little meaning due to the lack of information on material properties at the temperatures in this region. The significant region of tensile residual stress up to about 0.38 mm below the bore surface is alarming, considering the presence of hydrogen and the susceptibility of high strength cannon steel to hydrogen cracking.

Residual Stress Effects on Fatigue Life and Yielding

Fatigue lives calculated using the FIF concept for typical cannon conditions are shown in Fig. 3 for a range of fatigue pressure and various autofrettage conditions. Yield pressures for the cannon tube calculated from Eq. 5 are also shown. The results for 0% autofrettage, with the drastically lower lives and yield pressure, show how critical the autofrettage process is for cannon pressure vessels and similar high strength steel vessels. The lives and yield pressures for 30%, 50% and 70% autofrettage include the Bauschinger effect (BE) and show increases for increased autofrettage, but noticeably smaller increases in life and yield pressure are evident for additional autofrettage above about 50%. This diminishing return is a direct consequence of the progressive decrease in effective yield strength in steel vessels that accompanies an increase in degree of autofrettage. When the Bauschinger effect is not included in the calculation of fatigue life, such as the dashed curve example in Fig. 3, the decrease in yield strength is not accounted for, and dangerously non-conservative calculations of fatigue life and yield pressure are produced.

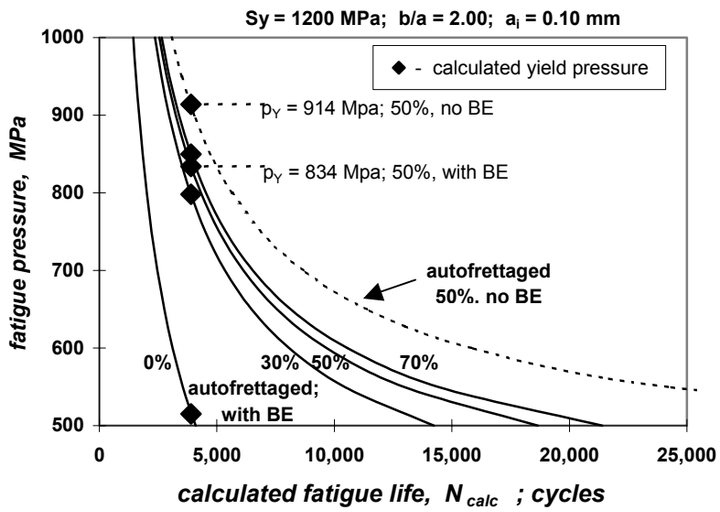

Figure 3: Life and yield pressure for various % autofrettage

Fatigue life and yield pressure calculations of a similar type to those of Fig. 3, but for actual cannon conditions, are shown in Fig. 4, typical of the chamber area of a tank cannon, with a b/a = 1.97, 60% autofrettage, and a_i = 0.10 mm. In contrast to the diminishing effect of % autofrettage in Fig. 3, there is no diminishing effect of increases in yield strength on either life or yield pressure. For the same degree of autofrettage, and thus the same relative reduction in effective yield strength by the Bauschinger effect, increases in material yield strength are rewarded with significant increases in life and yield pressure (but at the expense of decreased resistance to fast and environmental cracking). Results from one of the groups of cannon fatigue tests described earlier are also shown in Fig. 4, plotted at the 670 MPa pressure used in the tests and the mean and range of fatigue life from the tests. These results provide a good verification of the methods of life calculation described in the work here, because the mean life from the tests falls very close to the correct position, just to the right of the S_Y = 1100 MPa curve, as would be expected for the 1120 MPa mean yield strength of the tests. The test results also show, by their close proximity to the yield pressure for S_Y = 1000 MPa, that the 670 MPa fatigue pressure for the tests was close to the yield pressure.

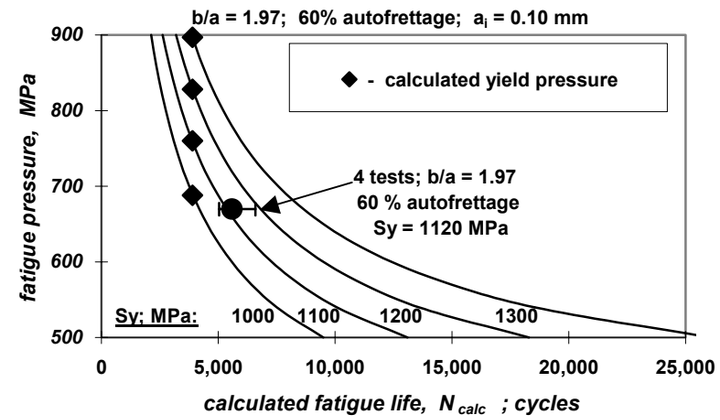

Figure 4: Life and yield pressure for various yield strengths

The effects of both mechanically induced autofrettage residual stress and thermally induced firing residual stresses on fatigue life are considered in the results of Fig. 5. The solid curve shows the close agreement between the fatigue tests and the life calculations, when the nominal initial crack size is used, a_i = 0.10 mm, which includes no effects of thermal residual stress. The dashed curves show the effects of two degrees of thermally induced residual stress, corresponding to two gas temperatures. Finite difference and mechanics calculations were performed in the same manner as those that gave the results in Fig. 2, except that arbitrarily chosen values of T_{gas}, 1500 K and 2500 K, were used to represent two levels of thermal damage. In these calculations, the maximum depths of the tensile residual stress were 0.29 mm and 0.41 mm, respectively. Our experience is that hydrogen cracks will readily grow to the depth of the tensile residual stress, so a fatigue life analysis with a_i values equal to these depths is appropriate. The result, at a 700 MPa fatigue pressure for example, is a 5000 cycle life for a_i = 0.10 mm and a 3510 cycle life for a_i = 0.41mm. Thus, the thermal residual stresses produced by a 2500 K gas temperature would cause cracks that would reduce calculated fatigue life by 30%, compared with the life with only autofrettage residual stress present.

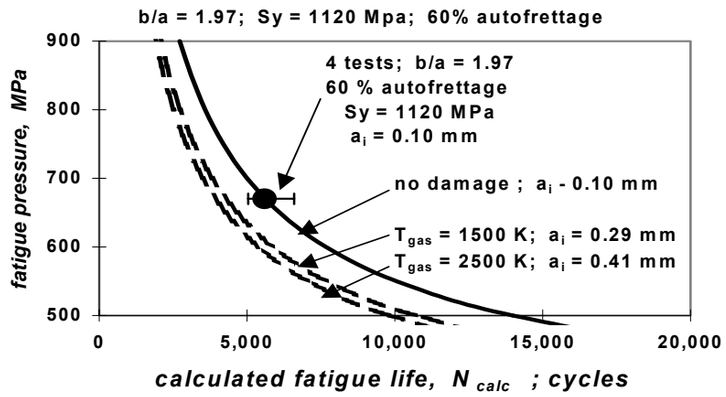

Figure 5: Life calculations with BE for various T_{GAS} and a_i

SUMMARY

[i] Bauschinger-modified autofrettage residual stresses improve the *fatigue intensity factor* model for fatigue life of cannon pressure vessels, matching full-scale cannon fatigue test results with an R^2 correlation of 0.92. There is need for additional measurements and analysis of Bauschinger effect in other high strength steels used for pressure vessels, in addition to the Ni-Cr-Mo steel in the work here.

[ii] Thermally induced residual stress in a fired cannon has been modeled by finite difference calculations of temperature and mechanics calculations of transient thermal stress and residual stress. Temperature dependent properties are used, and temperature distributions are validated by direct comparison with the known temperatures and the observed depths of microstructural damage and transformations in fired cannons.

[iii] Calculations of pressure vessel fatigue life and yield pressure, incorporating Bauschinger modified residual stress, are presented for a range of applied pressure, diameter ratio, yield strength and % autofrettage. Good agreement is demonstrated between calculations and measured lives from full-scale cannon fatigue tests. Significantly increased life is predicted for increases in yield strength and for % autofrettage up to about 50%.

[iv] The combined effects of mechanical autofrettage residual stress and thermal firing residual stress on cannon fatigue life are calculated, using a nominal initial crack size in association with autofrettage residual stress and larger crack sizes to account for added thermal residual stress. Hydrogen cracks can be expected to readily grow to the depth of the tensile thermal residual stress and thereby reduce the fatigue life.

REFERENCES

1. Milligan, R.V., Koo, W.H. and Davidson, T.E. (1966) *Trans ASME*, D, pp. 480-488.
2. Chaaban, A., Leung, K. and Burns, D.J. (1986) *ASME Special Pub., PVP Vol 110*, pp. 55-60.
3. Parker, A.P. (2001) *Journal of Pressure Vessel Technology*, Vol 123, to appear.
4. Underwood, J.H., Parker, A.P., Cote, P.J. and Sopok, S. (1999) *Journal of Pressure Vessel Technology*, Vol 121, pp. 116-120.
5. Underwood, J.H. and Parker, A.P. (1997) *Advances in Fracture Research, Vol. 1,* Pergamon, pp.215-226.
6. Incropera, F. P. and DeWitt, D. P. (1985) *Introduction to Heat Transfer*, Wiley, pp. 669-672.
7. Brown, W. F., Jr., Ed. (1970) *Aerospace Structural Metals Handbook, Volume IIA, Non-Ferrous Alloys*, Mechanical Properties Data Center, Traverse City, MI.
8. Smithells, C. J. (1962) *Metals Reference Book*, Butterworths, Washington.

POSTER REFERENCE: ICF100644PR

FATIGUE BEHAVIOR OF A MICRO-SIZED AUSTENITIC STAINLESS STEEL WITH FINE GRAINS

G. P. Zhang[1,2], K. Takashima[1], M. Shimojo[1] and Y. Higo[1]

[1] Precision and Intelligence Laboratory, Tokyo Institute of Technology
4259 Nagatsuta-cho, Midori-ku, Yokohama, 226-8503, Japan
[2] State Key Laboratory for Fatigue and Fracture of Materials, Institute of Metal Research
Chinese Academy of Sciences, 72 Wenhua Road, Shenyang 110015, P. R. China

ABSTRACT

A fine-grained (about 1-3 μm in diameter) austenitic stainless steel thin film was selected. Micro-cantilever beam type specimens were fabricated by focused ion beam (FIB) machining. The dynamic bending tests of the microbeams were carried out under constant load amplitude control. The cyclic strain hardening behavior was found in the material under two cyclic load amplitudes, ΔP=40 and 47 mN. At ΔP=47 mN, the significant intrusions formed on the sample surface due to the development of cyclic strain localization and provided the preferential site of microcrack initiation. Mode I fatigue crack propagation occurred in the fine-grained material by a transgranular mode. The dislocation microstructures of the fatigued micromaterial were investigated by TEM. The mechanism of fatigue damage in the material was discussed.

KEYWORDS

Micro-sized material, Austenitic stainless steel, Fine grain, Fatigue

INTRODUCTION

Great research interests on the measurement of Young's modulus, yield and fracture strength of all kinds of

micromaterials were brought about due to miniaturization of materials in microelectromechanical systems (MEMS) devices [1-3]. However, as many microcomponents, such as micro radio frequency switches, etc. are constantly subjected to a cyclic load with a high frequency during the period of their service, fatigue properties of micro-sized materials should be a more important factor for a long-term reliability of microcomponents [4,5]. On the other hand, fine- or super fine- grained materials are widely used in MEMS devices in the form of thin films, which are deposited on Si substrates. Therefore, the study on mechanical properties, especially fatigue properties of such a fine-grained material provides not only a database of mechanical properties for the design of MEMS devices, but also an insight into the fundamental fatigue mechanism.

In this study, a micro-sized austenitic stainless steel with fine grains was selected. Fatigue properties of the fine-grained material were investigated by dynamic bending tests.

EXPERIMENTAL

The material used in this study was a commercial 304 stainless steel thin sheet with fine grains. The microstucture of the material observed by Focused Ion Beam (FIB) machining system exhibited that the grain size was about 1-3 μm in diameter, as shown in Fig. 1. The micro-cantilever beam type specimens were fabricated at the center of a 3 mm-diameter disk with 25μm thickness by FIB machining [6]. The dimensions and shape of the microbeam is shown in Fig. 2. The distance from the loading point to the fixed end of the microbeam was 50 μm.

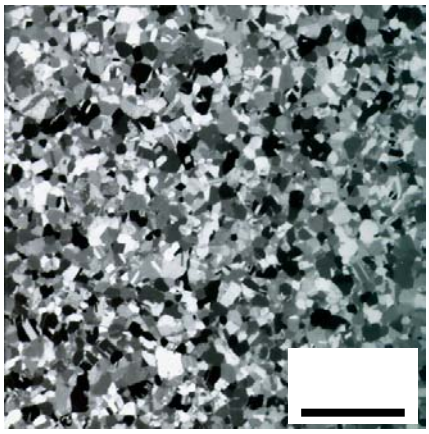

Figure 1: FIB observation of the grain size of the fine-grained austenitic stainless steel.

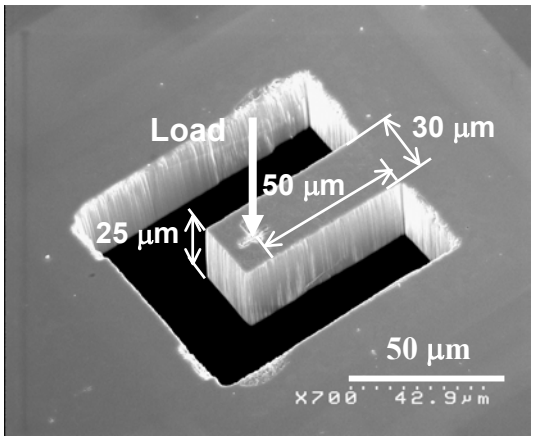

Figure 2: Dimensions and shape of the micro-cantilever beam type specimen fabricated by FIB machining.

Dynamic bending tests of the microbeams were carried out using a new type of fatigue testing machine for micro-sized specimens. This machine is of a displacement resolution of 5 nm and a load resolution of 10 μN [5]. The various waveforms for cyclic loading and frequencies up to 100 Hz can be applied using this machine. Before testing, the diamond tip was precisely located at the loading point by the repeated calibrations using the CCD camera, and then the micro-cantilever beam was dynamically bent under constant load amplitude control. The load ratio R ($R=P_{min}/P_{max}$) was 0.15 and the frequency was 10 Hz. All tests were stopped after about 4.5×10^5 cycles to examine fatigue damage on the specimen surfaces by scanning electron microscopy (SEM).

The deformed area of the microbeam was thinned by FIB machining to less than 0.1 μm to facilitate transmission electron microscopy (TEM) observations. The observation of dislocations was carried out with a Philips CM 200 type TEM at an accelerating voltage of 200 kV.

RESULTS AND DISCUSSION

1. Cyclic deformation behavior

The mean deflection δ_m ($\delta_m=(\delta_{max}+\delta_{min})/2$) of the microbeam at the first cycle was set to be zero ($\delta_m=0$), therefore, during cyclic loading if the microbeam moves downward gradually (the compliance of the beam increased), which is associated with the cyclic strain softening or cracking behavior of the material, δ_m will become negative. On the contrary, δ_m associated with the cyclic strain hardening behavior, will become positive, as schematically illustrated in Fig. 3(a). Figure 3(b) shows the variation of the mean deflection δ_m of the microbeam with cycles at both load amplitudes. It can be found that at ΔP=40 mN, the material initially experienced cyclic strain hardening and then cyclic hardening reached to a stable status gradually. The SEM examination on the top surface of the microbeam at the fixed end after 4.5×10^5 cycles exhibited that no microcracks initiated. When ΔP=47 mN, the material also exhibited the cyclic hardening behavior, but the maximum δ_m is higher than that at

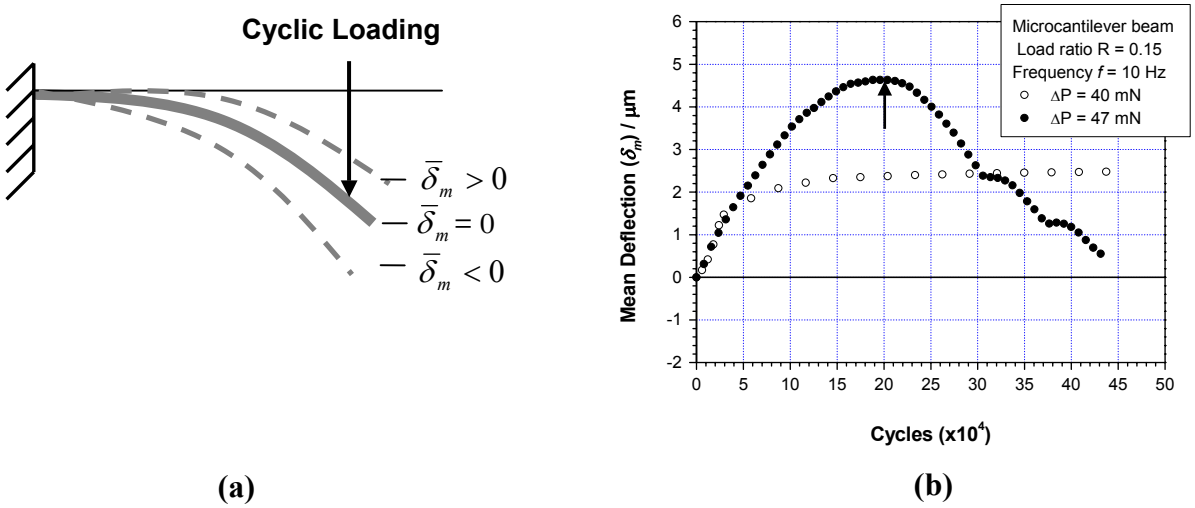

Figure 3: (a) A schematic illustration of the variation of the mean deflection; (b) The variation of the mean deflection with cycles at both different load amplitudes.

ΔP=40 mN. With increasing cycles, δ_m decreased gradually after 2.0×10^5 cycles. The decrease of δ_m was identified to result from microcrack initiation and propagation in the material, as reported in the next section.

The stainless steels with grain sizes from several hundred microns to several tens of microns at a low strain amplitude usually exhibited primary cyclic hardening followed by cyclic softening [7]. At a certain strain amplitude, primary hardening was followed by cyclic softening, which was then followed by secondary hardening. However, in the present study, only cyclic hardening was found in the fine-grained material at two load amplitudes. Figure 4 shows a comparison of dislocation microstructures before and after cyclic bending. Before deformation, the material showed a rather low density of dislocation, i.e. almost free dislocations (see Fig. 4(a)). But a high density of dislocation and strong interaction of dislocations within the grain could be

found after cyclic bending, as shown in Fig. 4(b). Therefore, dislocations rapidly multiplied and then interacted with each other by the to-and-fro motion under cyclic loading. This should be responsible for cyclic hardening observed here. Such an interaction of dislocations was also found in the same micromaterial subjected to static bending, which led to stage I hardening of stress-strain [6]. At ΔP=40 mN, the primary cyclic hardening and then gradually cyclic stability indicated that the cyclic plasticity caused by such a cyclic load amplitude was gradually exhausted by the interaction of dislocations within the fine grains. With increasing load amplitude, more hardening was naturally caused due to a larger cyclic plastic strain and the subsequent damage would be likely induced, as reported by follows.

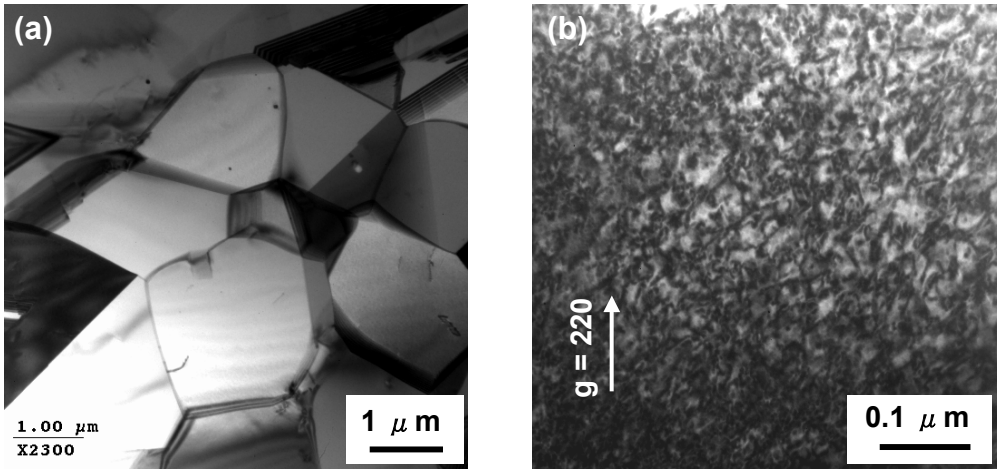

Figure 4: A comparison of dislocation microstructures in the fine-grained 304 stainless steel (a) before and (b) after cyclic bending.

2. Fatigue damage

The surface of the microbeam at ΔP=47 mN and about 4.5×10^5 cycles was examined by SEM. Figure 5 shows the whole view of the microbeam. A microcrack was found to initiate at the left corner of the fixed end and then gradually propagated toward the right side. The gradual decrease in δ_m at about 2.0×10^5 cycles was attributed to the microcrack initiation and subsequent propagation (see Fig. 3(b)). The crack propagation was perpendicular to the maximum tensile stress on the top surface and characterized by mode I cracking. A transgranular cracking was identified from the negative picture of the local area in Fig. 6(a), as shown in Fig.

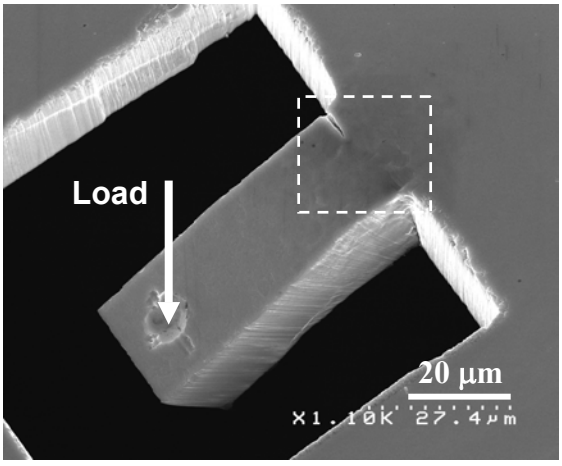

Figure 5: A whole view of the microbeam at ΔP=47 mN after about 4.5×10^5 cycles.

6(b). Especially, at the right corner of the fixed end circled by the white dot-line in Fig. 6(a), the slip traces within the grain became coarser and deeper preferentially. An enlargement of this area was presented in Fig. 7. Obviously, the strain localization developed in this area and resulted in some slip intrusions on the microbeam surface, as indicated by arrows. The depths of the intrusions **I** and **II** were about 0.56 and 0.24 μm measured by Scanning Laser Microscopy (SLM), respectively. The widths of the intrusions **I** and **II** were 0.38 and 0.22 μm, respectively.

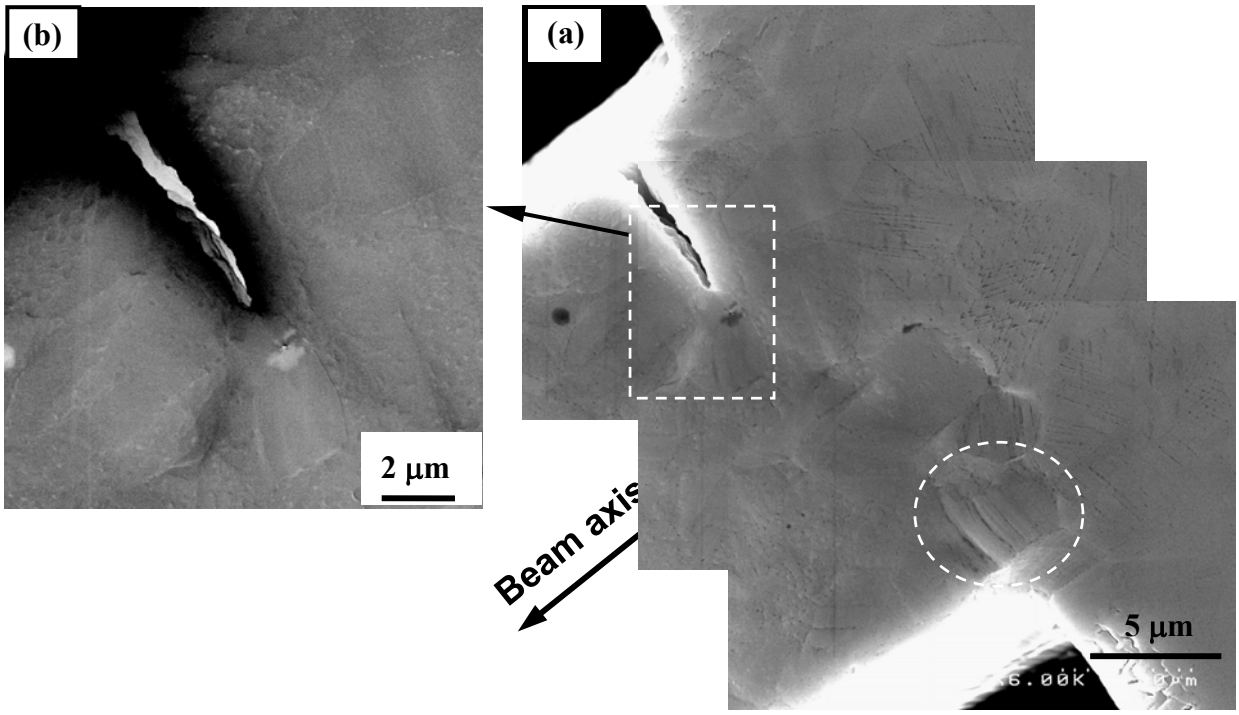

Figure 6: (a) A close observation of the surface of the microbeam cyclically bent at ΔP=47 mN after 4.5×10^5 cycles. (b) The negative picture shows a transgranular crack propagation.

The slip localization, which resulted in intrusions and extrusions on the specimen surface, are usually associated with the formation of PSB dislocation microstructures in single crystals, such as Cu, etc. under symmetrically cyclic plastic strain control [8]. However, at the present study, the slip intrusions on the micro-specimen surface were also found under asymmetrically cyclic load control, but no PSB microstructure

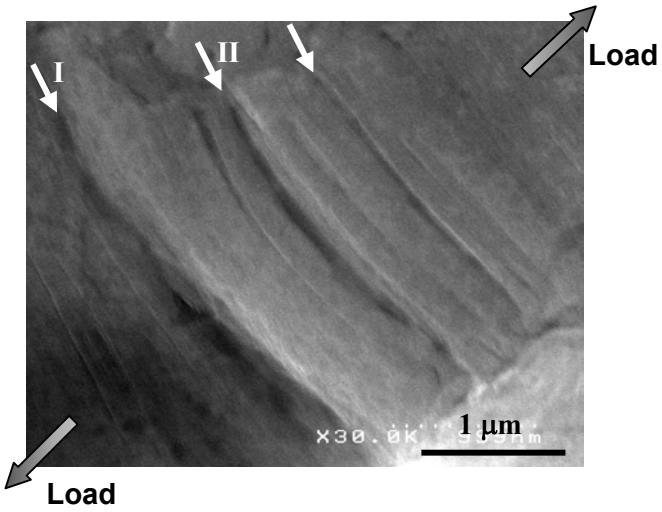

Figure 7: A high magnification of the strain localization within the grain developed at the fixed end of the microbeam circled by white dot-line in Figure 6(a).

was observed in the material, as shown in Fig. 4(b). Here, that a large number of dislocations slipped out of the specimen surface along preferentially oriented slip planes was suggested to be the reason for the formation of intrusions. While such coarse and deep slip traces were not observed in the same material subjected to static bending [6]. It is obvious that cyclic loading improved the strain localization. According to the measurement of the width and depth of the deepest intrusion **I**, it is reasonable to believe that such an intrusion with a depth of 0.56 μm and a root radius of 0.19 μm acted as a micro-notch. Therefore, the advancement of fatigue damage process in the micro-specimen with fine grains was as follows: under cyclic loading, some slip traces gradually developed to the coarse and deep slip traces, i.e. intrusions. These intrusions were of locally higher plastic strain at the intrusion root and more possibly became pre-sites of microcrack initiation. In general, cyclic strain localization still played an important role in microcrack initiation in the present micromaterial with fine grains and degraded the durability of the micromaterial.

CONCLUSTIONS

1. Cyclic strain hardening was found in the micro-sized austenitic stainless steel with fine grains. The strong interaction of dislocations was responsible for cyclic hardening.
2. The significant intrusions formed on the microbeam surface due to the development of cyclic strain localization. The microcracks were suggested to originate from the intrusions preferentially.
3. Mode I fatigue crack propagation occurred in the fine-grained material by a transgranular mode.

ACKNOWLEDGEMENTS

One of the authors (Zhang) would like to thank Japan Society for the Promotion of Science (JSPS) for the postdoctoral fellowship support (ID No. P99068).

REFERENCES

1. Ericson, F. and Schweitz, J. Å. (1990) *J. Appl. Phys*. 68, 5840.
2. Florando, J., Fujimoto, H., Ma, Q., Kraft, O., Schwaiger, R. and Nix, W. D. (1999) *MRS Symposium Proceedings. Materials Reliability in Microelectronics IX*. 353, 231.
3. Wilson, C. J., Ormeggi, A. and Narbutovskih, M. (1996) *J. Appl. Phys*. 79, 2386.
4. Schwaiger, R. and Kraft, O. (1999) *Scripta mater*. 41, 823.
5. Takashima, K., Higo, Y., Sugiura, S. and Shimojo, M. (2001) *Mater. Trans*. 42, 68.
6. Zhang, G. P., Takashima, K., Shimojo, M. and Higo, Y. (2000) *MRS Symposium Proceedings. Materials Science of Microelectromechanical Systems (MEMS) Devices III, edited by M. deBoer, M. Judy, H. Kahn and S. M. Spearing. 657, in press.*
7. Hennessy, D., Steckel, G. and Altstetter, C. (1976) *Metall. Trans*. 7A, 415.
8. Ma, B. T. and Laird, C. (1989) *Acta Metall*. 37, 325.

POSTER REFERENCE: ICF100257PR

FATIGUE BEHAVIOR OF A PULTRUDED GLASS-REINFORCED POLYMER-MATRIX COMPOSITE MATERIAL

L. B. Godefroid[1], W. A. Morais[1], G. P. Silva[1] and J. A. Martins[2]

[1] Dept. of Metallurgical and Materials Engineering, School of Mines, Federal University of Ouro Preto, Campus Universitário Morro do Cruzeiro – Ouro Preto – 35400-000 – MG – BRAZIL
[2] ENMAC Composite Materials Ltd. Rua Joaçaba,10 – São José dos Campos – 12238-530 – SP - BRAZIL

ABSTRACT

Most of the commonly used continuous fibers-reinforced polymer composite materials work with pultrusion. This process can produce a variety of reinforced solid, tubular or structural profiles, with very interesting chemical, physical and mechanical properties. Recently, the increase in the use of pultruded composites through critical applications in automobile and aerospace industries requires a complete and precise knowledge of its properties, mainly the fatigue resistance. This paper presents several aspects of the fatigue behavior of a glass-reinforced polymer composite, with particular emphasis on the Wöhler curve (S-N curve). Effects of R-ratio, frequency and overloads were studied. Damage by fatigue is measured by two different forms: residual strength obtained from tensile tests, and continuous measure of deformation of the composite material from fatigue tests.

KEYWORDS

Fracture, Fatigue, Damage, Composite Material.

INTRODUCTION

Without doubt fatigue is the most serious damage process in using engineering materials. With composite materials, as the same form of any other material, the major utilization problem is fatigue. However, in the most utilized composite material – fiber reinforced plastics –the formation and propagation of a crack or a few cracks does not happen, as in metals or ceramic materials. Due to its own inhomogeneity, these does not exist an unique (or few) crack propagating freely in the material's structure. A typical fiber reinforced composite continually damages under fatigue. The experimental verification of this dynamic fatigue response of composites can be found in many works [1-5]. The generated defects may reach a stable condition sometimes called [4] "characteristic damage stage" or CDS. In this condition the mechanical properties of the composite slightly change during the fatigue process. The alteration on mechanical properties is almost always easier and more representative to measure and to register than either a crack size or an effective crack size in fatigue of composites.

If we compare many processes, pultrusion is probably one of the most versatile composite processes [6]. It is a continuous process used to produce fiber-reinforced plastic structural shapes. The process involves pulling resin-impregnated fiber reinforcements through a preformer and a heated die to cure the resin. Pultruded composites exhibit all of the features produced by other composite processes, and also additional advantages inherent to this process.

With the support of a great industry of composite materials in Brazil, the authors made fatigue tests on a pultruded composite rod bar. Initially, tension-tension fatigue tests were executed to determinate a possible fatigue limit and the S-N curve for this material. Tests were made to verify the effects of R-ratio (low to high tension level ratio $_{min}/\ _{max}$), frequency and an overload. Cyclic deformation was measured and analyzed in conjunction of residual strength obtained from tensile tests. Similar methodology is mentioned in several references but almost always for non pultruded composites [2,4,5].

EXPERIMENTAL PROCEDURE

The materials used in this study were E-glass fibers and a polyester resin. The product was a unidirectional composite in the form of rod, 12.7mm in diameter, developed at the ENMAC by Martins [7]. The composite contains 70% fibers (about 0,016mm in diameter) by weight. Room temperature tensile strength was around 900MPa. Figure 1 illustrates the configuration of specimens used for fatigue tests, the tensile tests were done with the same only that these had smaller head. All tests were conducted on a closed-loop servo-hydraulic MTS testing machine with a capacity of 10tons. Tension tests were performed at room temperature under stroke control (displacement rate = 25mm/min).

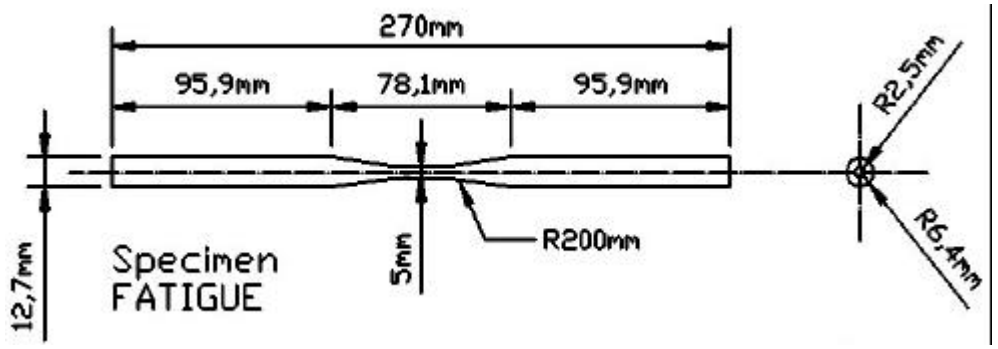

Figure 1 : Fatigue specimen configuration.

Fatigue tests were carried out in tension-tension with a sinusoidal waveform, at frequency ranging from 3 to 30Hz, at a stress ratio R ranging from 0.1 to 0.5, all tests at room temperature. Load, stroke and time data were collected and stored in a PC throughout the tests. These data were used to monitor the strain and the evolution of damage during fatigue tests. After the creation of a S-N curve of the composite, two extreme stress levels were fixed, to study the influence of mechanical parameters on fatigue life: frequency, stress ratio R and a single overload (overload ratio = 2.0). Damage propagation in fatigue was monitored by two different techniques: decrease of tensile strength and increase of strain with fatigue cycles. The specimens had their temperature observed during the test to confirm no heating on cycling.

RESULTS AND DISCUSSION

The plot of stress amplitude versus number of cycles of failure is showed in Figure 2 (S-N curve). A power-law correlation between the cyclic stress and fatigue life was observed. The corresponding life equation is of the form:

$$\sigma_a = \sigma_{uts} \left(2N_f\right)^b \quad (1)$$

where $_a$ is the stress amplitude, $_{uts}$ is the monotonic tensile strength, $2N_f$ is the number of reversals to failure and b is the fatigue strength exponent. The results obtained for b was –0.177 for $_{uts}$=910MPa. This type of correlation has been observed for other authors [8-10].

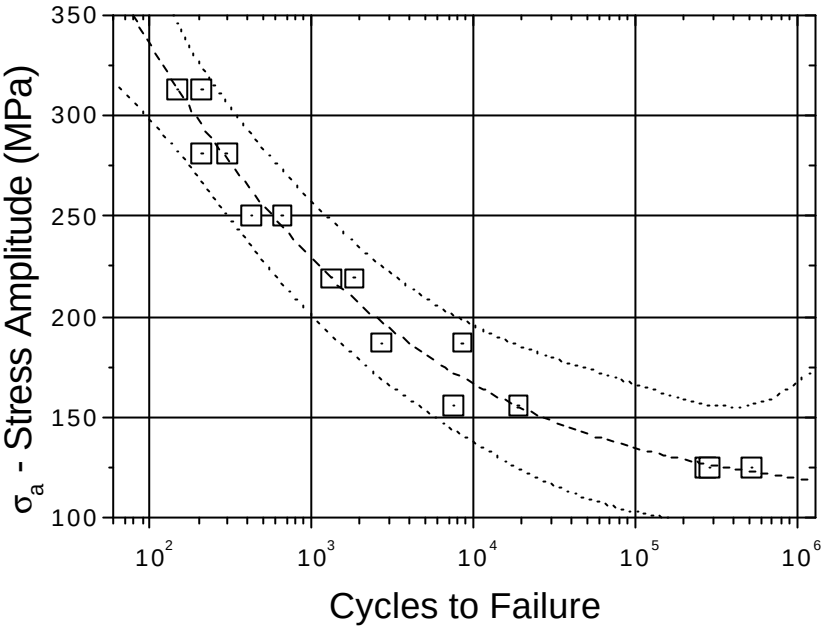

Figure 2: Stress amplitude versus number of cycles of failure.

The obtained results indicate a tendency of this material to not present a fatigue stress limit like some metals as aluminum alloys. This may be explained by the great presence of small defects in the matrix structure due the fabrication process. Obviously the $_a/N_f$ rate decreasing in high cycles of fatigue make the possibility of flaw more remote in these load levels.

The effect of stress ratio R in the composite fatigue life is showed in Figure 3. As we can see, fatigue life tends to increase with increasing stress ratio R. Many authors have showed the opposite result [8,11-13]. We explain this controversy by the fact that in our study the increasing R is made by increasing minimum load, at a constant maximum load. With this procedure we decrease the stress level and decrease the stress field in the fiber-resin system. Damage per cycle is then decreased, and fatigue life increases. This effect is more important when the stress amplitude is decreased (125MPa than 250MPa).

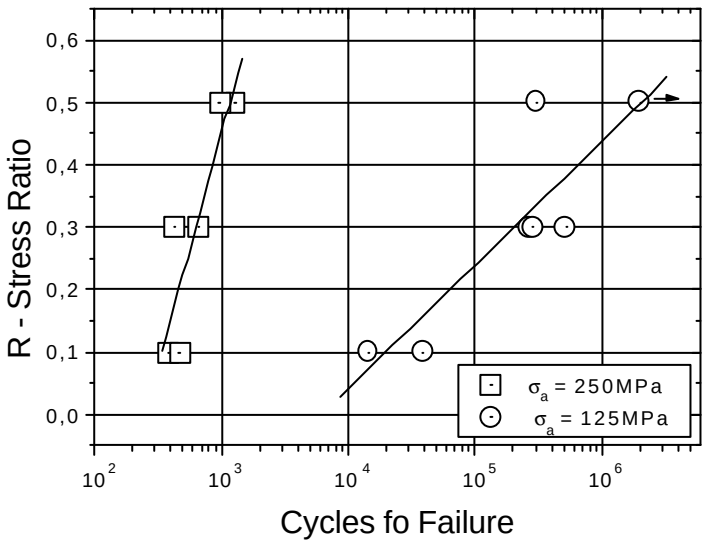

Figure 3 : Effect of stress ratio R in fatigue life.

The effect of frequency in the composite fatigue life is showed in Figure 4. As we can see, fatigue life tends to increase with increasing frequency. The effects of test frequency have been studied by several workers [14-17], who produced conflicting results. We believe that a low frequency induces a higher damage level in the fiber-resin system. This effect is again more important when the stress amplitude is decreased (125MPa than 250MPa).

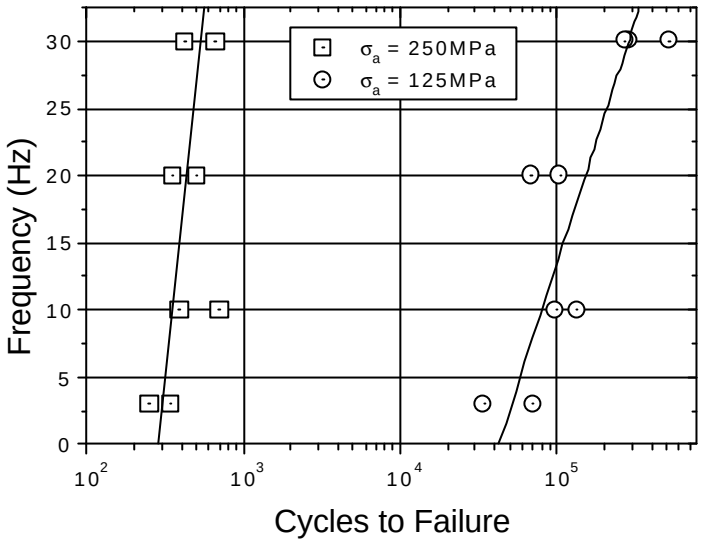

Figure 4: Effect of frequency in fatigue life.

The effect of a single overload in the composite fatigue life is showed in Figure 5. Three results are presented for a normal loading and two results after an overload. The overload stress was applied after 20% of fatigue life in 125MPa of stress amplitude. The value of this overload was equal to 250MPa. We can conclude that the effect of the overload is detrimental to composite life, due the generation of incremental damage in the fiber-resin system. This effect cannot be neglected.

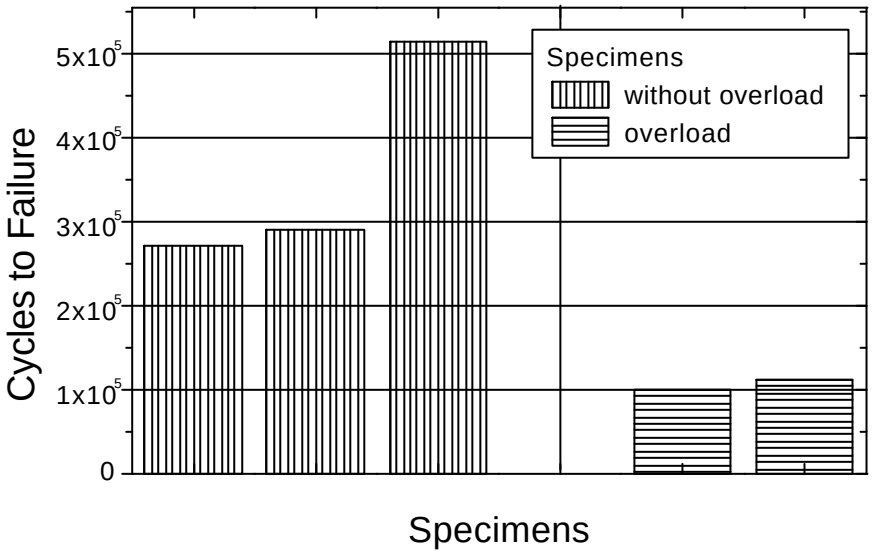

Figure 5: Effect of overload stress in the fatigue life.

Damage by fatigue is measured by two different forms : residual strength obtained from tensile tests, and continuous measure of deformation of the composite material from fatigue tests. A residual strength curve was obtained in tensile tests, with specimens cycled at stress ratio R of 0.3, frequency of 30Hz, stress amplitude of 125MPa and three different life fraction at this amplitude: 5%, 20% and 50%. Figure 6 shows this curve.

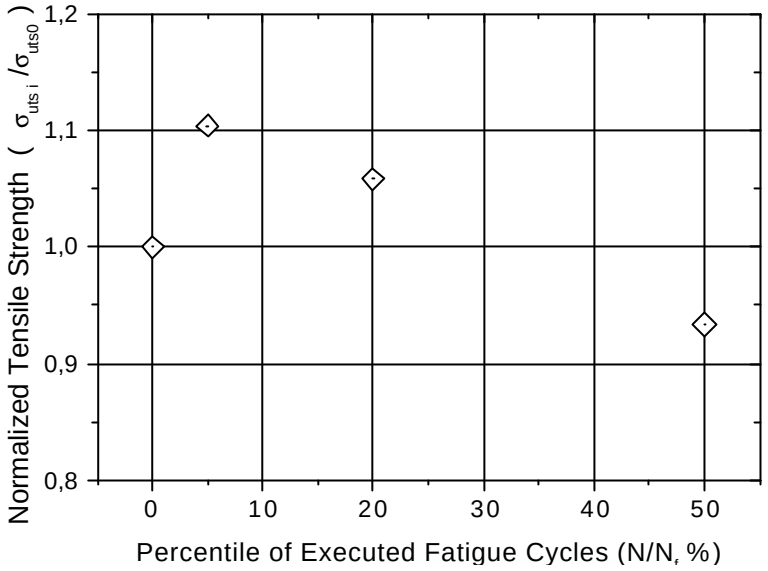

Figure 6: Residual strength results.

Tensile strength increases to a peak, then decreases with number of cycles. This technique is dangerous, because we can admit an erroneous conclusion that fatigue damage is good to the composite until the peak. In composite materials the initial evolution of fatigue damage promotes a stress redistribution in the fiber-resin system that dissipates energy. Consequently, tensile strength increases until a maximal damage concentration, that is enough to promote its further decrease. This result is observed by other authors [18-20]. We conclude that this method is not a good procedure to estimate fatigue damage.

In a load-controlled test, stroke response versus cycles will help understand the evolution of constitutive behavior during fatigue cycles. Figure 7 shows a typical plot of the displacement versus percentage fatigue life (both normalized) for three specimens tested on fatigue. The plot shows that displacement increases with cycling with a large CDS region. This observation is a good result that can be used to follow the fatigue damage progress. This result is observed also by other author [2].

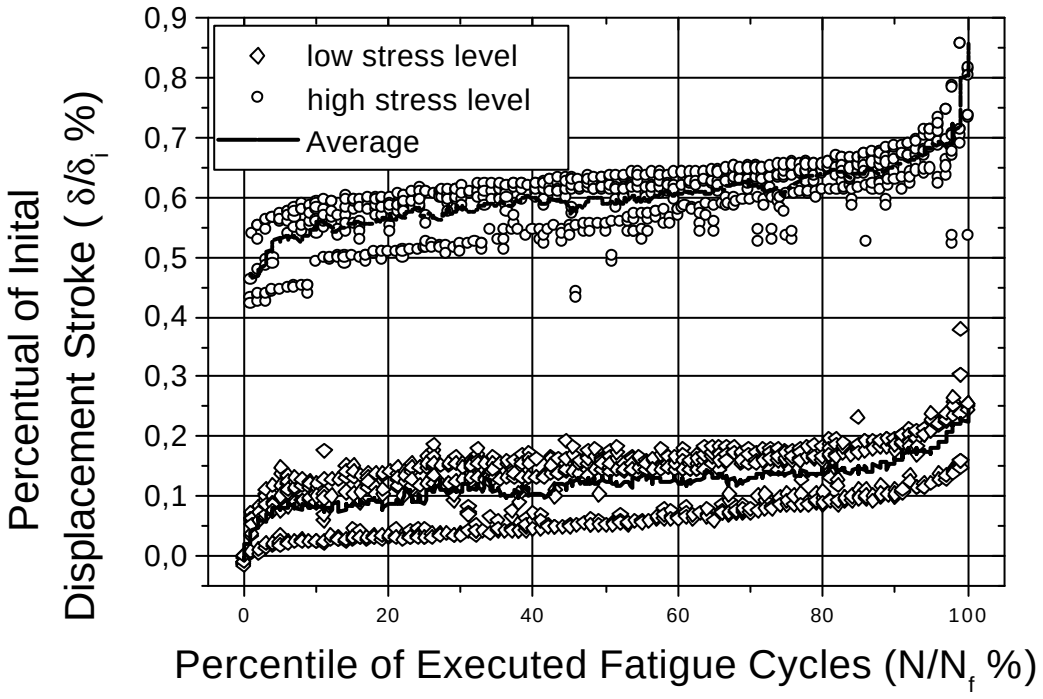

Figure 7: Stroke (%) versus fatigue cycles (%).

CONCLUSIONS

The fatigue life was found to decrease with increasing cyclic stress level. A power-law relationship of the form $_a = _{uts} (2N_f)^b$ was found to exist. The effect of R – maintaining constant the high stress level ($_{max}$) – was to decrease the fatigue life with the decrease of R (or increasing the $_a$). The frequency dependence was not obvious, but there are indications that decreasing the frequency decreases also the fatigue life. The application of an overload decreases the overall fatigue life of the composite. A way to accompany the fatigue life is to measure the apparent rigidity of the material by recording the lower and higher stroke (displacement) during the test.

ACKNOWLEDGEMENT

The authors wish to acknowledge FAPEMIG, FINEP, CNPq and Fundação Gorceix for financial support.

REFERENCES

1. Smith, T.R. and Owen, M.J. (1969) *Modern Plastics*. 128.
2. Ramakrishnan, V. and Jayaraman, N. (1993). *Journal of Materials Science*. 28, 5580-5591.
3. Schulte, K. (1996). In: *6th International Fatigue Congress*, pp.1531-1542.
4. Reifsnider, K.L. (1991). Composite Materials Series*: Fatigue of Composite Materials*. Elsevier, Oxford.
5. ASM Handbook (1999). *Fatigue and Fracture*. ASM International. Ohio, USA, p.905-919.
6. ASM Handbook (1987). Com*posites* . ASM International. Ohio, USA, p.533-544.
7. Martins,J.A. : private communication.
8. Dowling, N.E. (1993). *Mechanical Behavior of Materials***,** Prentice Hall, , p.339-396.
9. Bathias,C. (1997). *La Fatigue des Matériaux et des Structures***,** 2nd Ed., Hermes, p.645-664.
10. Chawla, K.K. (1998). *Composite Materials – Science and Engineering***,** 2nd Ed., Springer, p.404-426.
11. Branco, C.A.G.M. (1994). *Mecânica dos Materiais*, 2ª edição, Fundação Caloustre Gulbenkian, Lisboa.
12. Dieter, G.E. (1987). *Mechanical Metallurgy***,** 2nd ed.., McGraw Hill, p. 403-447.
13. Jang, B.Z. (1994). *Advanced Polymer Composites***,** ASM, p.199-211.
14. Dally, J.W. and Broutman, L.J. (1967). *J. Compos. Mater*, Vol. 1, p.424.
15. Mandell, J.F. and Meier, U. (1983). *Long-Term Behavior of Composites*, ASTM-STP 813, ASTM, p.55.
16. Sun, C.T. E Chan, W.S. (1987). *Composite Materials: Testing and Design***,** ASTM-STP 674, ASTM, Philadelphia, PA, p.418.
17. Saff, C.R. (1983). In: *Long-Term Behavior of Composites*, ASTM-STP 813, ASTM, Philadelphia, PA, p.78.
18. Ramani, S.V. and Williams, J.G. (1977). *Notched and unnotched fatigue behavior of angle ply graphite/epoxi composites***,** ASTM-STP 638, p.27-46.
19. Bakis,C.E and Stinchcomb,W.W. (1986). *Response of thick, notched laminates subjected to tension-compression cyclic loads***,** ASTM-STP 906, p.314-334.
20. Stinchcomb, W.W. and Bakis, E.C.(1991). *Fatigue of Composite Materials*, Edited by Reifsnider, K.L., Elsevier Science Publishers B.V., p.106-109.

Reference-No.: ICF10059OR

FATIGUE BEHAVIOUR OF A SINGLE CRYSTALL NICKEL SUPERALLOY USED IN HEAVY-DUTY GAS TURBINE BLADES WITH FILM COOLING

Y. Pan, R. Zimmer, B. Bischoff-Beiermann and D. Goldschmidt

Siemens AG Power Generation Group (KWU)
Mulheim, Germany

ABSTRACT

The low cycle fatigue property of a single crystal (SC) superalloy applied in heave-duty gas turbine blades with film cooling holes has been investigated. Special material tests have been carried out for evaluation of the crack behavior. This paper presents results of the testing and appropriate finite element (FE-) calculations. Advantages of SC blades can be revealed and a reliable fatigue life assessment can be achieved with the local approach concept.

KEYWORDS

Single Crystal Superalloy, High Temperature Low Cycle Fatigue, Heavy-Duty Gas Turbine, Film Cooling Hole, Crack Behaviour, FE-Calculation, Life Assessment

INTRODUCTION

A new generation of heavy-duty gas turbines with substantially increased output and efficiency has been developed by Siemens [1]. One of the important new technologies applied in this gas turbine, that is well proven in aircraft engines, is the application of single crystal turbine blades with an extensive film cooling.

The high temperature mechanical properties of superalloys are strongly dependent on the volume fraction and morphology of γ'-precipitation. In the investigated single crystal superalloy PWA 1483 there is a lower content of grain boundary strengthening elements compared with conventional cast superalloys, [2-3]. This causes a higher alloy melting point and permits a higher solution heat treatment temperature. Therefore a higher volume fraction of the γ'-precipitation's with proper morphology can be achieved. This is one of the important reasons for the better mechanical properties of PWA1483 blades.

The Laser-Drilling will be widely used in manufacturing of these cooling holes, as a precise hole pattern with exact relative positions can be thereby efficiently produced. However, micro cracks could, especially in a remelt-layer around of the internal hole surface, come into existence. The depth of these cracks must be within the manufacture tolerance.

The first-stage blading is illustrated in Fig. 1. As shown, a large number of cooling holes has been manufactured into the surface of blades and vanes, where cooling air will be discharged.

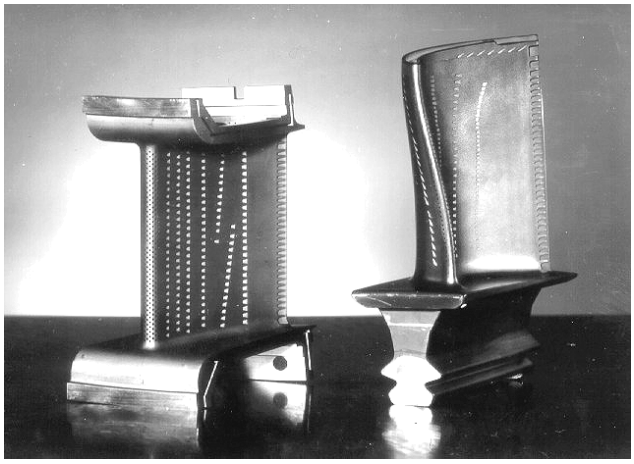

Figure 1: Blade and vane stage 1 with film cooling holes

The first stage turbine blades operate at high gas temperatures. There is a pronounced temperature gradient between outside and inside of blade walls due to an indispensable intensive cooling. This temperature difference will cause high thermal stresses. Additionally, the centrifugal force has also to be considered for the blade design.

The life prediction procedure for components with stress concentration can be carried out using the local approach concept, [4-5]. The applied material design curve is usually determined with standard cylindrical smooth samples under consideration of materials data scatter. However, for a reliable life prediction, not only the maximum local stress and strain is to be determined by elastic-plastic FE-calculations. Inhomogeneous stress states, manufacturing processes and surface quality should also be taken into account. In order to verify the local approach concept and to insure the long-term operational reliability of the SC blades in land based gas turbines for power generation, special LCF test specimen with holes on the gauge length has been used to determinate the life time and to investigate the crack behaviour under fatigue loading close to the operation conditions.

EXPERIMENTAL DETAILS

Fig. 2 shows the shape of the LCF-specimen. Holes were drilled by laser using the same tolerances and operating parameters as in blade manufacturing. The thickness of the specimens was similar to the wall of the blades.

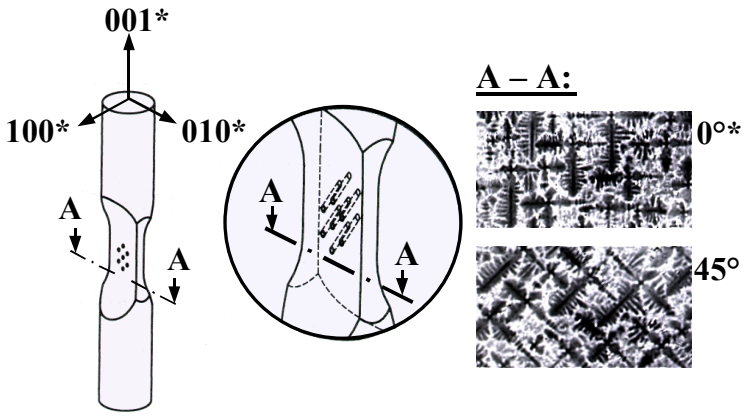

Figure 2: Special LCF test specimen with illustration of secondary orientation of 0° and 45°

The holes had a pattern with hole density, diameter and angel to surface as found in the leading edge, where a „shower head“ cooling is applied, giving the highest cooling hole density. Comparative specimens without holes had the same shape. To investigate the influence of different secondary orientations on the fatigue life some specimens were drilled with 45° secondary orientation in the planar gauge length (see Fig. 2).

The LCF tests were performed on a servohydraulic test machine with inductive heating under total strain control. The integral strain on the gauge length of the sample was taken as the control signal. The SC-Ni-basis superalloy PWA 1483 was investigated at temperatures of 900°C and 700°C, which are typical temperatures for material close to the outer and inner surfaces of the first stage blade.

The loading during gas turbine operation is predominately controlled by thermal strain. This results in compressive strains at the hot outer surface and tensile strains at the colder inner surface. Therefore the strain ratio $R=\varepsilon_{min}/\varepsilon_{max}$ was equal $-\infty$ for 900°C test temperature and equal 0 for 700°C test temperature.

A camera system was used to continuously observe the surface of the specimens during the fatigue tests. It was composed of two CCD-Cameras with specially developed control programs so that the crack initiation and propagation could be recorded automatically by computer.

After tests, an evaluation was made for crack behaviour relating to the hole pattern and to micro-cracks. The failure cycles N_f were defined as the cycle number after which a drop of the stress amplitude of more than 5% was found.

RESULTS AND DISCUSSIONS

Fatigue Test Results

Fig. 3 shows the LCF-life *in form of* the S-N-curves based on the integral strain range for specimens at 900°C and 700°C test temperature. Specimens with 45° secondary orientation are marked separately.

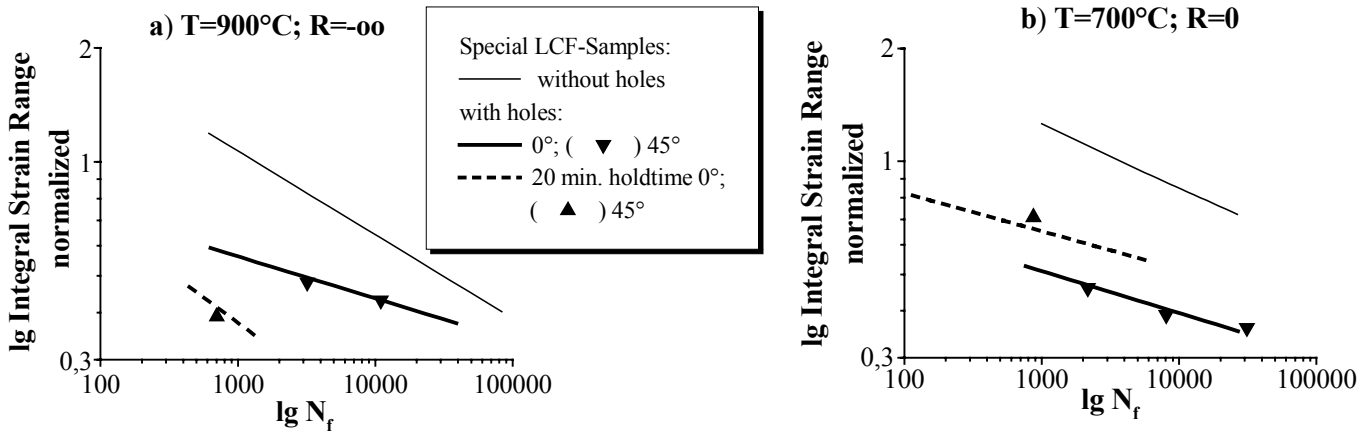

Figure 3: Influence of cooling holes and holdtime

For both temperatures it can be seen that the number of cycles to failure N_f for the samples with holes are lower at all strain levels. This is obviously due to the stress concentrations at the holes. The 45°-secondary orientation has hardly influence on the LCF-lifetime compared to the results of the mainly tested specimens with 0° secondary orientation.
In Fig. 3 a) a further reduction of the fatigue life was caused by a holdtime of 20 minutes at the maximum compressive strain. In contrast with that the tests with holdtime at maximum tensile strain for 700°C (Fig. 3 b)) reach a higher cycle number to failure than the tests without holdtime. This could be explained through mean stress relaxation.

In Fig. 4 the relaxation behaviour of 2 specimens cycled under the same strain range, but one of them with a holdtime, is compared. The holdtime at the maximum tensile stress caused a much stronger relaxation of the mean stress, which became negative after only 20% of the lifetime. The specimen without holdtime had a high positive mean stress and only about a third of lifetime compared to that one with holdtime.

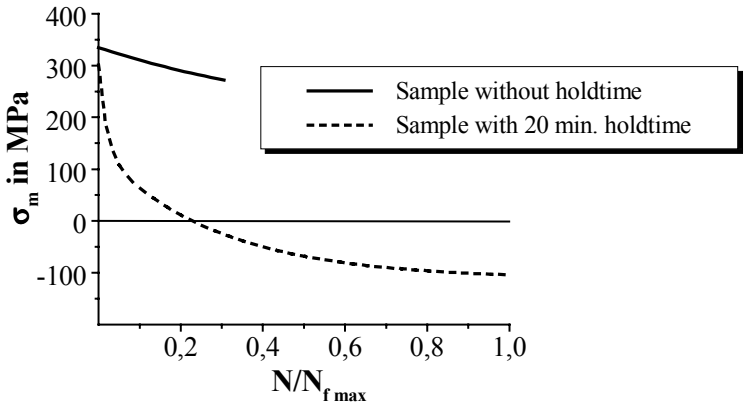

Figure 4: Example of mean stress development at 700 °C

The stress concentrations at the holes have been calculated with finite elements under the assumption of linear elastic material behaviour with cubic symmetry, see Fig. 5. Only the part of the test specimen between the extensometer has been modelled. Constant displacements have been applied to the corresponding cross sections between the extensometer to simulate the strain controlled LCF-test. The displacement is directly proportional to the nominal strain over the gauge length. The specimen is horizontally symmetrical with an additional axis of symmetry. Therefore, only one quarter of the specimen was modelled. Highest stresses are found along the curve where the holes intersect the outer surface of the specimen.

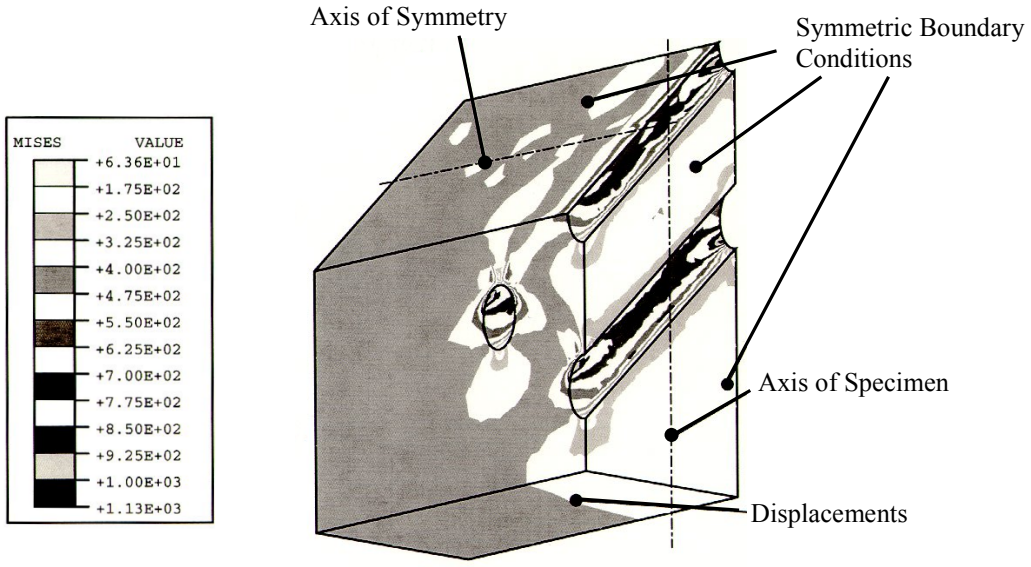

Figure 5: FEM-calculation of local stress

With the help of the FE-model the maximum local stresses were calculated as a function of nominal strain. Based on these results the maximum local total strain (with elastic and inelastic parts) is estimated with Neuber´s rule [6-8]. The cyclic stress-strain curve is used to take plastic deformations into account. From this the relation between the nominal strain over the gauge length and the local strain is derived.

S-N curves for specimens with holes at 900°C and 700°C test temperature, which are based on the local strain and compared with the normalised design curve, are presented in Fig. 6. In both cases the design curve under-estimates the cycles to failure so that a conservative, reliable life prediction using the local approach concept can be expected for the loading conditions considered here.

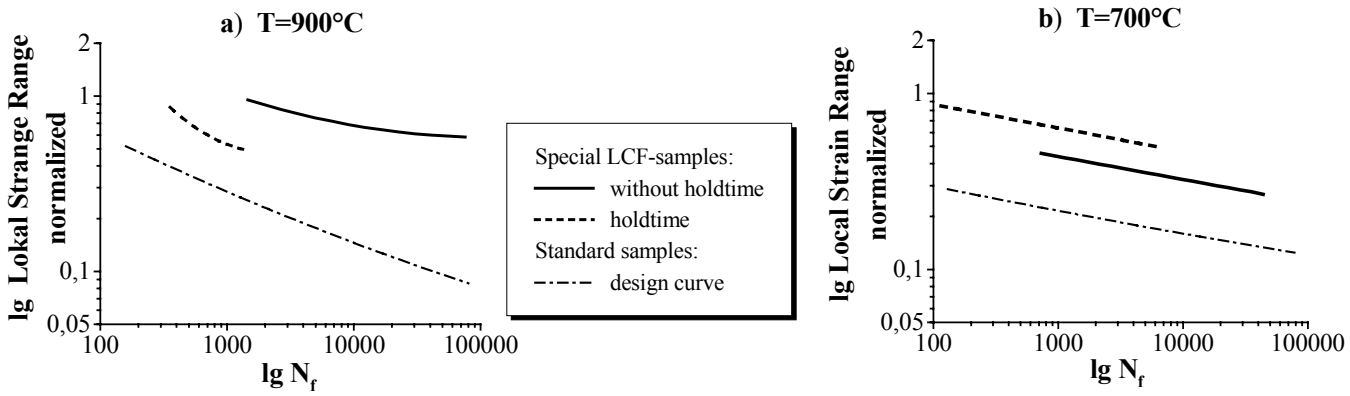

Figure 6: Comparison of results from cooling hole samples with design curve

In Fig. 7 results of an equiaxed conventional cast superalloy are compared with that of PWA 1483 SC. The PWA 1483 SC is generally better than the equiaxed material. Even with holes the integral strange range of SC-specimens is higher than that of the equiaxed samples for the same failure cycles. The application of SC-material brings therefore obviously a significant advantage for the gas turbine blades with film cooling holes. However the equiaxed material shows less relative decrease of the integral strange range due to cooling holes.

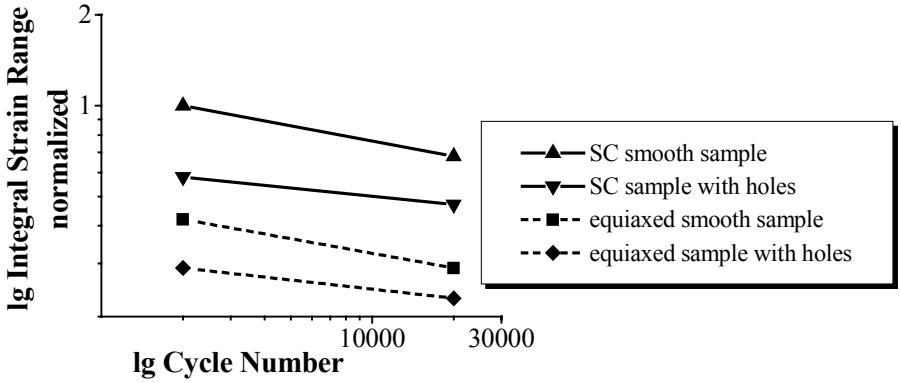

Figure 7: Comparison with a conventional cast superalloy

Crack Propagation

Metallographical investigations were carried out on samples after the tests. The most tests had more loading cycles than the defined N_f, (5% stress drop). The sample surface with cracks starting at the edges of the holes is shown in Fig. 8 a). The cracks grew perpendicular to the loading direction. After the final loading cycle there were still no direct links of cracks between the holes.

One typical example of crack history, happened during an LCF-test, is shown in Fig. 8 b).
A crack, initiated by cyclic loading, with a length of more than 0,3 mm on the sample surface could be recorded by the camera system in the fatigue test. After initiation the crack propagation of each crack slowed down while more and more cracks arose, some of them stopped before N_f. The samples were further loaded as usual until the test machine was automatically shut down by its control system.

When N_f had been reached at a 5% stress amplitude drop, all observed cracks were no longer than 1,5 mm and they were still in a stable propagation phase.

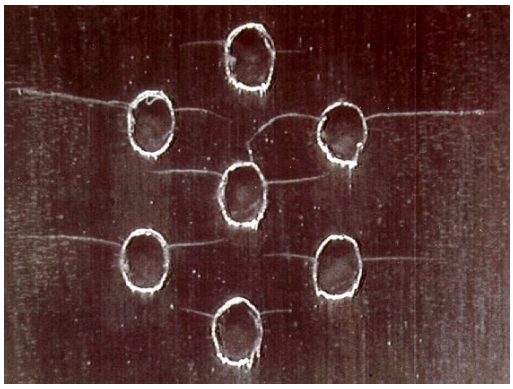

a) Cracks initiated from cooling holes

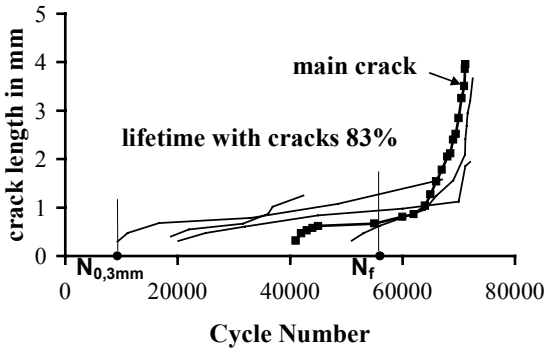

b) Typical crack initiation and propagation

Figure 8: Typical crack development within the hole pattern after LCF-test,

As shown the main crack initiated after some other cracks. In this case about 83% lifetime of the specimens was with cracks of more than 0,3 mm. The random distributed micro-cracks due to laser-drilling have obviously no major influence on the total lifetime.

CONCLUSIONS

A significant improvement of LCF property has been achieved through the application of the single crystal superalloy PWA 1483 SC for gas turbine blades with film cooling holes. The special LCF-fatigue-tests using specimens with laser-drilled holes have shown, that:

- SC-material can withstand higher strain ranges, even with holes, than an equiaxed material.
- Micro-cracks due to laser drilling have no significant influence on the total lifetime.
- After initiation the crack propagation of each crack will slow down while cracks at other locations will appear.
- With the local strain, determined by FE-Analysis, a conservative and reliable life assessment can be obtained by using the local approach concept.
- There won't be unstable crack propagation before the in design procedure used N_f has been reached.

REFERENCES

1. Becker, B., Schulenberg, T. and Termuehlen. H. (1995), The 3A Series Gas Turbines with HBR Combustors, ASME 95-GT-456, Turbo Expo. Houston, Texas
2. Stoloff, N. (1987), Superalloys II, pp. 87-95, Wiley&Sons, New York
3. Wege, R. and Wortmann, J. (1989), Mat.-wiss. Und Werkstofftech. 20, pp. 207-216
4. Seeger, T. and Heuler, P. (1980), Generalized Application of Neuber´s rule, J. Test, Eval. 3, pp. 199-204
5. Savaidis, G., Dankert, M. and Seeger, T. (1995), An Analytical Procedure for Predicting Opening Loads of Cracks at Notches, Fatgue Fract. Engng. Mater. Struct. Vol. 18 No. 4, pp. 425-442
6. Neuber, H. (1961), Theory of Stress Concentration for Shear-Strained Prismatical Bodies with Arbitary Nonlinear Stress-Strain Law, Journal of Applied Mechanics, 12, pp. 544-550
7. Chaudonneret, M. and Chaboche, J. L. (1988), Fatigue Life Prediction of Notched Specimens, Int. Conf. Of Fatigue of Engineering Materials ans Structures, Sheffield
8. Lemaitre, J. (1992), A Course on damage Mechanics, Springer Verlag

Oral Reference: ICF100378OR

FATIGUE BEHAVIOUR OF MULTIPHASE STEELS FOR AUTOMOTIVE APPLICATIONS

L. Tosal-Martínez, J. Keichel and N. Akdut

OCAS N. V., Research center of the SIDMAR Group,
ARBED Group Flat Products Division,
John Kennedylaan 3, 9060 Zelzate, Belgium
nuri.akdut@ocas.be

ABSTRACT

High strength steels are becoming more and more interesting for the automotive industry as they allow car weight reduction due to lower thickness ensuring the same performance and improved safety by higher energy absorption. A known way of improving the strength, ductility and formability of steels is to make use of additional strengthening and deformation mechanisms by introducing supplementary phases. It is evident that the fatigue behaviour of the materials used for automotive applications is a major point to be taken into account in design and material selection. In this paper the fatigue behaviour of different newly developed high strength multiphase steels (TS>600MPa) including ferritic-bainitic, ferritic-martensitic and TRIP steels is compared with the fatigue behaviour of the commercially available microalloyed steels used at the moment by the automotive producers. Results from laboratory research of pre-strained specimens, which were supposed to be representative for the preceding forming process, will be shown together with results of real components, e.g. wheel disks. Finally, the effect of paint baking on cyclic loading will be evaluated.

KEYWORDS

Fatigue behaviour, multiphase steels, microalloyed steels

INTRODUCTION

Car weight reduction has recently become a very important topic for the automotive industry due to the increasing requirements on fuel consumption efficiency that are related to energy savings and environmental restrictions. In this context, a great effort is being done in order to develop new high strength steels that combine both a good formability and a high strength, with the aim of reducing the material thickness of the different automotive parts without resulting in a loss of performance, especially passenger safety.

In this paper the fatigue behaviour of some newly developed high strength hot rolled multiphase steels to be used in the automotive sector for, e.g., wheel applications will be presented and compared with the fatigue behaviour of a microalloyed grade that is currently used by the wheel producers. Recently, first industrial wheel production trials have been carried out using those multiphase steels. E.g., it was possible to reduce thickness and thus weight by using a dual-phase grade, which led to a wheel lighter than one made of aluminium [1].

The product of tensile strength (TS) and rupture strain (A) is directly linked with the minimum sheet/wall thickness ensuring safety demands, i.e. the higher the TSxA value, the smaller the sheet thickness can be chosen [2] resulting in weight and cost reductions. The (TSxA)-value thus describes the materials formability, toughness and energy absorption capacity. Figure 1 shows the comparison of the TS and A value ranges of various hot rolled steel grades such as C-Mn steels and microalloyed steels as well as the new multiphase steels, like Dual-Phase (DP), Ferritic Bainitic (FB) or Complex Phase (CP) and Transformation Induced Plasticity (TRIP) steels. From Figure 1 it becomes evident that combining different constituents in the final microstructure of the steel, normally with a ferrite matrix, together with a certain fraction of bainite, martensite and/or retained austenite, strength levels up to 1000MPa can be reached without losing too much formability. The (TSxA)-value of a TRIP steel amounts about 22000 while the actual microalloyed grades are limited to 16000-17000.

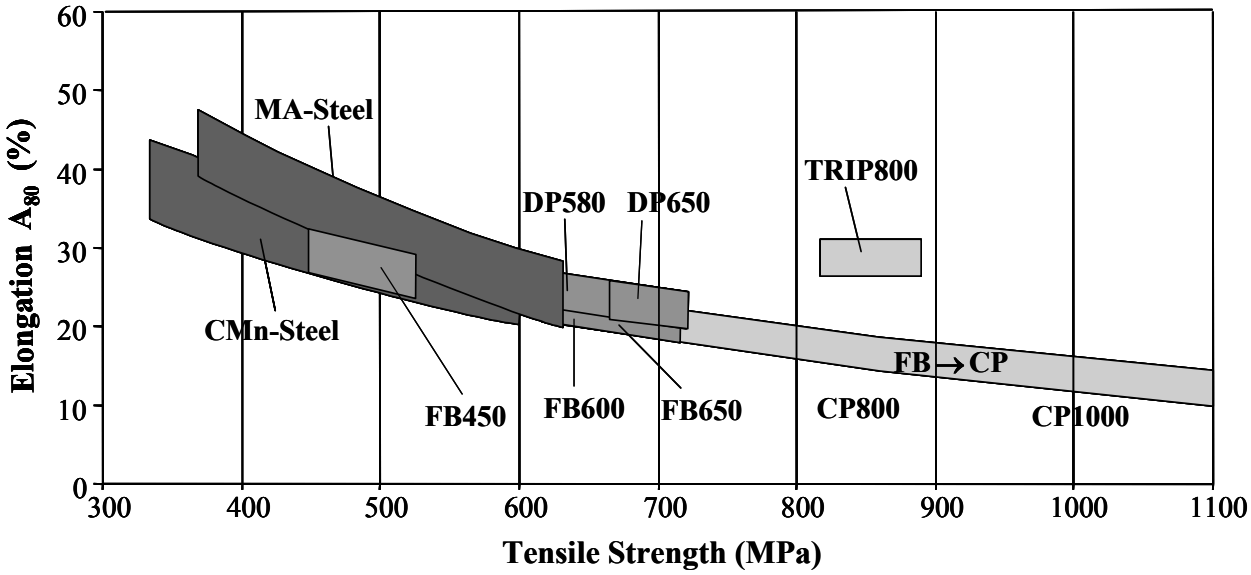

Figure 1: Schematic overview of TS and A80 of hot rolled carbon steel products

However, not only the formability and the energy absorption capability of these steels are important when it comes to applications. Especially in wheel applications fatigue resistance is a major characteristic due to the applied cyclic load. Therefore, in this paper the fatigue behaviour of the above mentioned multiphase steels will be presented, laboratory results under uni-axial loading and industrial fatigue results on wheels tested using an ex-centric rotating load will be shown.

MATERIALS AND EXPERIMENTAL PROCEDURE

The chemical composition of the industrially produced steels used for this study is shown in Table 1. Two ferritic-bainitic grades (FB600 and FB650) with different microalloying additions have been selected together with one ferritic-martensitic dual-phase steel (DP650) and a TRIP steel whose microstructure consists of ferrite, bainite and retained austenite. For comparison purposes the commercially available microalloyed grade S355MC (EN Standard 10149/2) was chosen.

TABLE 1
CHEMICAL COMPOSITION OF THE STEELS IN WEIGHT PERCENT

Grade	FB600	FB650	DP650	TRIP800	S355MC
C	0.08	0.07	0.08	0.2	<0.11
Mn	1.45	0.95	1.45	1.5	<0.8
other	Nb	Nb, Ti	Nb	Si, Nb	Nb

The microstructures of the multiphase grades in transverse direction are shown in Figure 2. Using LePera etching [3] in all steels the ferrite matrix is accompanied by bainite (black) in FB 600, FB 650 and TRIP, martensite (white) in DP 650 and retained austenite and/or martensite (white) in TRIP 800 while the Nital-etched single phased S355MC contains cementite (black) within the ferritic matrix.

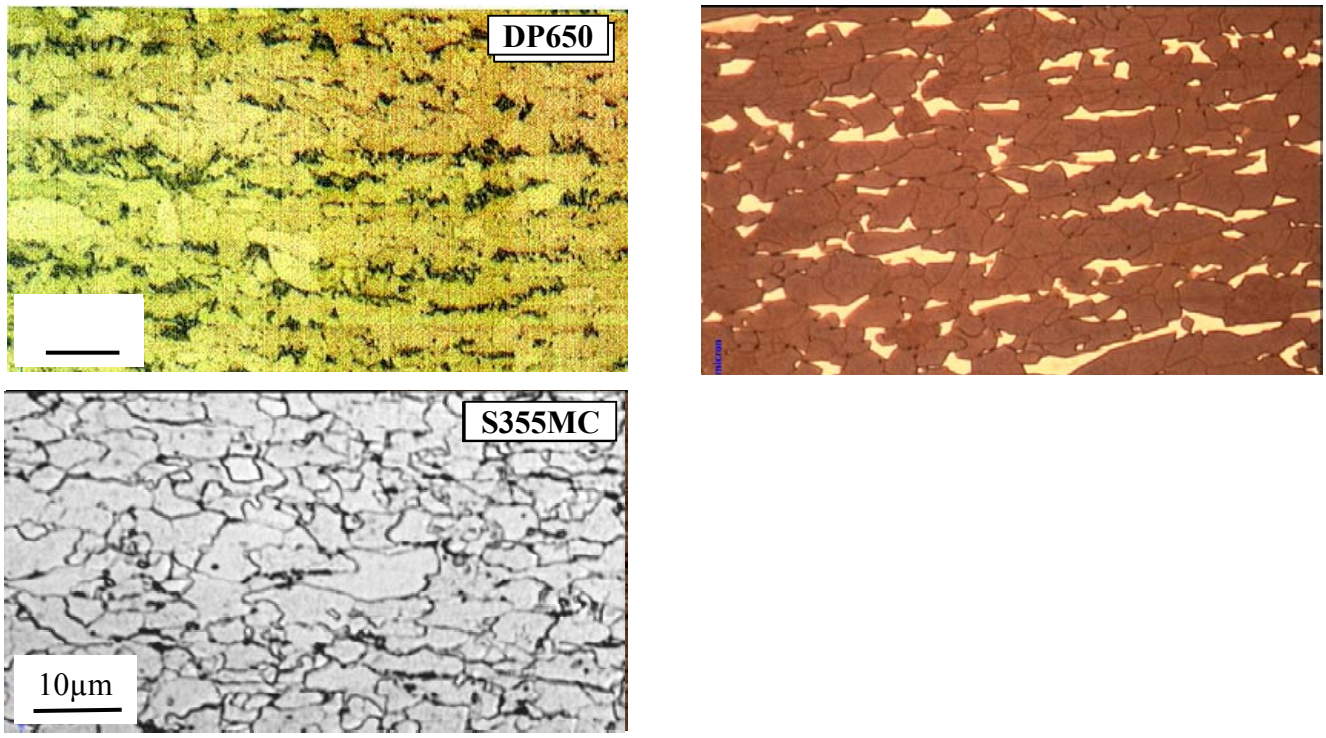

Figure 2: Longitudinal section of the investigated hot rolled grades (→ rolling direction)

The typical mechanical properties of those materials in rolling direction are given in Table 2. Here, the name of the new steel grades contains a number representing the minimum level of TS to be guaranteed.

TABLE 2
MECHANICAL PROPERTIES IN ROLLING DIRECTION OF THE DIFFERENT STEEL GRADES

Grade	YS in MPa	TS in MPa	A_{80} in %	YS in MPa after 10% pre-straining
FB600	520	620	24	572
FB650	610	670	20	660
DP650	520	695	21	692
TRIP800	617	840	28	790
QStE420 (S355MC)	400-470	480-550	22-29	469

For the fatigue tests, specimens were cut with their fatigue axis parallel to the rolling direction of the steel sheets using spark erosion. The laboratory fatigue tests were carried out on pre-strained material, which was used to represent a preceding forming process. The pre-strain of 10% was applied in rolling direction by means of an electro-mechanical closed-loop testing machine (INSTRON 4505) on non-proportional A_{80} tensile test specimens according to the EN10002 standard. The strengthening of the steels is represented by the yield strength (YS) after 10% pre-straining, see Table 2. The axial loading fatigue tests were carried out using a uni-axial closed-loop controlled servohydraulic test machine (MTS 810). All tests were performed at room temperature with a stress ratio $R=\sigma_{min}/\sigma_{max}=0$ and a load frequency $f\approx10$Hz (sine wave) up to fracture. In the case of the Dual Phase steel, additional fatigue tests were carried out on baked material (DP650+BH) in order to simulate the effect of the paint baking after the forming process. The specimens were baked after the pre-straining at 170°C for 20 minutes and were tested afterwards following the same procedure described above.

In Figure 3 a wheel made of FB600 is shown together with a schematic outline of the test method. In order to simulate the effect of the cars weight on the wheel disk, a whole wheel is clamped to the test equipment and subjected to fatigue by means of a rotating ex-centric load applied at the end of the axis. The test is carried out until the first crack appears.

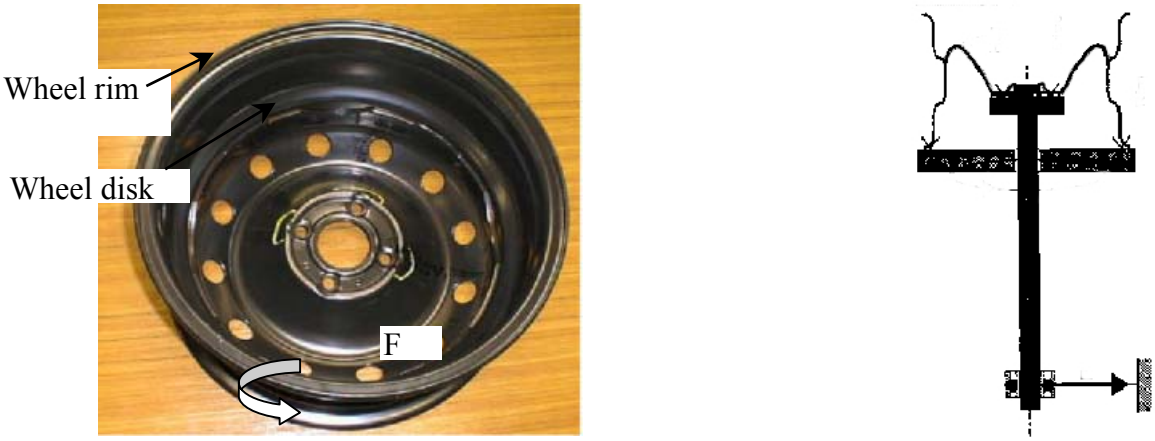

Figure 3: FB600 wheel and outline of the fatigue method

RESULTS AND DISCUSSION

The S-N curves (Wöhler diagram) of the different materials tested are shown in Figure 4, where σ stands for the maximum of the pure pulsating tensile stress (R=0) and N is the number of cycles at which the specimen fails. All curves corresponding to multiphase steels are shifted to clearly higher stress levels compared to the microalloyed S355MC, which is currently commercially used. That means, that for a given stress level the fatigue resistance of the multiphase steels is higher and, correspondingly, their fatigue limit also lies at higher stress values.

Generally, the tensile strength and the fatigue resistance are connected in such a way that with increasing tensile strength also the fatigue resistance increases [4]. This apparently is also valid for the ferritic-bainitic steels as can be deducted from Figure 4. Here, the curve of FB650 (TS=670MPa) is clearly placed above the one corresponding to FB600 (TS=620MPa). A different precipitation state due to a slightly different chemical composition is responsible for this strength increase and can explain also the increase in fatigue life. Comparing the yield strengths of FB600 and FB650 one can expect that the fatigue limit of FB650 will also be higher than the one of FB600. It must be noted that the presented results are part of an ongoing research and that the fatigue limits of the FB steels and of the S355MC grade are not yet determined. Contrary to the said above, the curves corresponding to DP650 (TS=695MPa) and TRIP800 (TS=840MPa) are placed slightly below the curve of FB650 (TS=670 MPa) despite the fact that both steels have a higher tensile strength, see Figure 4 and Table 2.

It can be assumed that the presence of a hard phase such as martensite will affect the fatigue performance of DP600 and TRIP800. Most probably, the effect of martensite is related to incompatibilities at the phase boundaries between martensite and ferrite [5]. These incompatibilities may lead to stress concentrations at the phase boundaries and thus to crack nucleation [5, 6]. Comparable effects were reported in ferritic-austenitic duplex stainless steels [6]. Since the incompatibilities and especially the difference in strength between ferrite and bainite are less pronounced than between ferrite and martensite in DP600 and TRIP800, the load transfer between ferrite and bainite can be expected to be less difficult [5].

Furthermore, while DP600 contains about 15% martensite from the beginning, in TRIP800 martensite only forms after strain induced transformation of the retained austenite during (pre-)deformation. Despite its high tensile strength the fatigue resistance of the TRIP grade at higher stresses is lower than expected. This might be due to the fact that its hardening mechanism, namely the austenitic-martensitic phase transformation, is strain dependent while the precipitation hardening of FB600, FB650 and DP650 is fully active from the be-

ginning. One also might argue with residual stresses stemming from the austenitic-martensitic phase transformation and the corresponding volume increase of 4%.

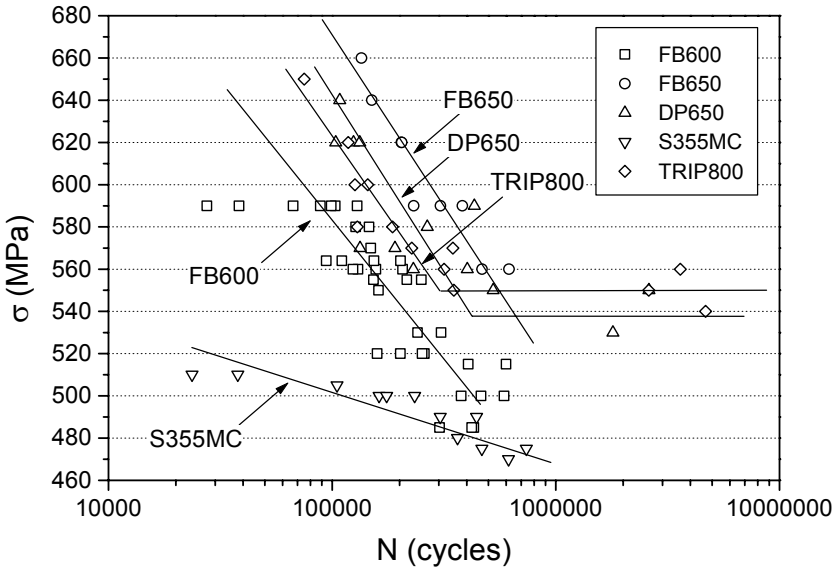

Figure 4: S-N curves of the different steels after 10% pre-straining

However, despite the assumed effect of martensite in the finite life range it is remarkable that the fatigue limit seems to correspond to the "high-strength – high-fatigue resistance" relation mentioned above. Since TRIP has the highest yield strength (Table 2) it also shows the highest fatigue limit, see Figure 4. In agreement with the literature [6, 7] the morphology of multiphase steels is responsible for retarding the crack nucleation and thus increasing the fatigue limit. The finer the microstructure the higher is the fatigue limit.

The results obtained by the industrially tested wheels according the earlier given procedure until the first crack appears are shown in Table 3. The average fatigue life of the microalloyed grade is about 100.000 cycles. It is evident that for the applied multiaxial state of strain all tested multiphase steels show a clearly better performance, i.e. an up to a twice as high fatigue life.

TABLE 3
FATIGUE LIFE OF WHEELS (AVERAGE CYCLES BEFORE CRACK INITIATION)

Steel Grade	FB650	DP650	TRIP800	S355MC
Fatigue Life in Cycles	192.700	176.000	205.050	100.000

It is important to point out that the fatigue tests were carried out using paint-baked wheels. The influence of such a paint baking on the fatigue life can exemplarily be seen for DP650 in Figure 5. The whole curve of the bake hardened steel DP650+BH shows higher values for the finite life range as well as for the fatigue limit, which increased about 60MPa compared to its non-baked state. The improvement of the fatigue performance through bake hardening (20 min. at 170°C) is caused by the diffusion of the C atoms to the dislocations created during the (pre-)deformation, resulting in an additional increase of YS, see Table 4. Simultaneously, the tensile strength increases. While the pre-straining accounts for a YS increase of 172MPa, after bake hardening the YS increased another 144MPa (=316-172), see Table 4. This extremely high value might be due to additional precipitation hardening of the ferritic phase by carbides with C stemming from the "C-saturated" brittle martensite before baking. An as such softened martensitic phase could improve the load transfer between the phases and thus contribute to the fatigue resistance increase. To clarify these assumptions, further research is needed. However, it should be paid special attention to the low cycle fatigue behaviour of multiphase steels, which show a large scattering of the results. This scattering is according to Vogt et al. [5] and Akdut [6] related to the phase morphology. Here parameters like grain size, phase size, phase volume fractions, orientation relationships between the phases, local stresses and the orientation of the phases with respect to the macroscopic sample directions play an important role. As said earlier, crack nucleation is generally retarded, but crack propagation might occasionally be enhanced leading to scattering.

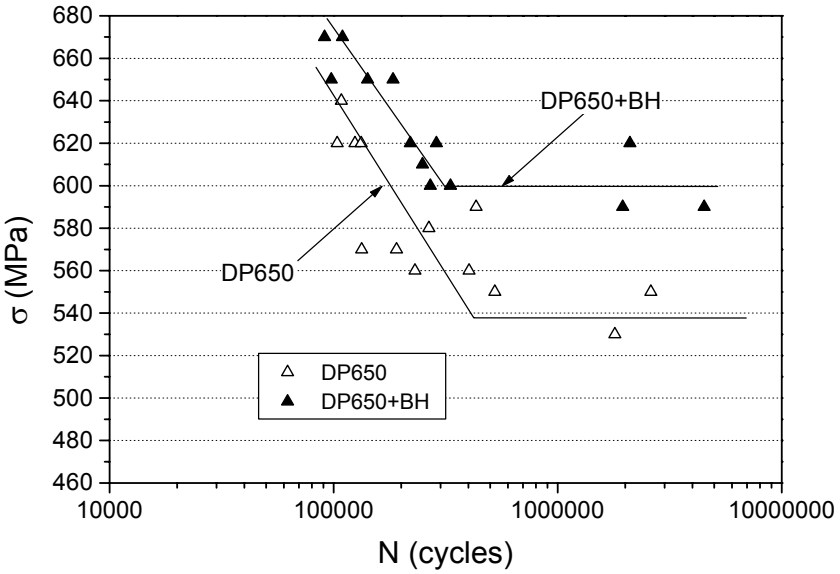

Figure 5: S-N curves of 10% pre-strained DP650 with and without paint baking simulation

TABLE 4
MECHANICAL PROPERTIES OF DP650 AND DP650+BH AFTER 10% PRE-STRAINING

	YS in MPa	TS in MPa	A_{80} in %	ΔYS in MPa
DP650	520	695	21	after pre-straining: 692-520=172
DP650+BH	836	837	6	after pre-straining and baking: 836-520=316

SUMMARY

The investigated multiphase high strength steels show qualitatively better fatigue properties than the commercially used microalloyed grade. Their higher finite life range and especially their higher fatigue limit allow a lightweight design for many automotive applications as shown here for wheels, which are subjected to high fatigue requirements.

The made assumptions concerning the effect of martensite and other phases as well as the effect of bake hardening on the fatigue behaviour of multiphase steels are still subject of investigation. Furthermore, the non-homogeneous loading sequences occurring in automotive structures during production and service have to be taken into account.

REFERENCES

[1] Theuwissen, J. (2000) Praktische toepassing van Slijtvaste Deklagen op Gereedschappen, internal report of the Ford wheel factory, Genk, Belgium
[2] Ludwig, J. and Schulz-Forberg, B. (1994) Sicherheitsniveaus von Transporttanks für Gefahrgut. Bundesanstalt für Materialforschung und –prüfung. Research report 203, Berlin (Germany), p.41
[3] Girault, E., Jacques, P., Harlet, Ph., Mols, K., Van Humbeek, J., Aernoudt, E. and Delannay, F. (1998) *Mater. Charact.* 111, p.40
[4] Fuchs, H. O. and Stephens, R. J. (1980). *Metal fatigue engineering*. John Wiley, New York.
[5] Vogt, J.B., Argillier, S., Leon, J., Massoud, J.P. and Prunier, V. (1999). *ISIJ International* 39, p. 1198
[6] Akdut, N. (1999) *International Journal of Fatigue* 21, S97
[7] In: *Light-weight automotive construction with steel* (1999) Technical Steel Research, Final Report, EUR 18412, Ed. and publisher: European Commission, Luxembourg, ISBN 92-828-5156-7, p. 222

REF NO: ICF100236OR

FATIGUE BEHAVIOURS OF A COMPRESSOR VALVE STAINLESS STEEL WITH SMALL AMOUNT OF RETAINED AUSTENITE

G. Chai[1], S. Olsson[1,2], P. Liu[1], and T. Larsson[1,3]

[1, 2]AB Sandvik Steel, [1]R&D Centre, [2]Strip Division, 811 81 Sandviken, Sweden
[3]Present address: Outokumpu Copper Partner AB, Copper R&D,
721 88 Västerås, Sweden

ABSTRACT

Impact and bending fatigue strengths are essential properties for compressor valve steels. The increase in efficiency of compressors requires higher performance valve steels. This paper describes the influence of retained austenite on the fatigue strengths in tension, bending and impact for a modified CrMo martensitic stainless compressor valve steel.

It is shown that the impact fatigue strength was significantly improved with increasing retained austenite. The bending fatigue strength was also improved, but reached a maximum value at about 4vol% retained austenite. However, the presence of retained austenite had little influence on the fatigue strength in tension. These different fatigue behaviours were discussed in relation to the microstructures and were interpreted in terms of fracture mechanisms.

KEYWORDS

Compressor valve steels, CrMo martensitic stainless steels, retained austenite, impact fatigue, bending fatigue, residual stresses, damping capacity, fracture mechanism.

INTRODUCTION

The change in service condition and increase in compressor efficiency require valve steel with even higher impact fatigue strength. CrMo martensitic stainless steel is a standard compressor valve steel. It usually contains small amount of retained austenite. It was reported that the presence of retained austenite has a positive influence on the impact fatigue properties [1, 2].

In the present study, the influences of retained austenite in a modified CrMo martensitic stainless steel on the fatigue behaviours in tension, bending and impact were systematically investigated. The material used contained much larger amount of retained austenite than the conventional one. Different fracture mechanisms were discussed concerning the different fatigue behaviours observed.

MATERIAL AND EXPERIMENTAL

The material used was Fe-0.37C-0.4Si-0.60Mn-13.5Cr-1.0Mo (wt%) martensitic stainless steel strip with a thickness of 0,38mm. Four variants with retained austenite from 0,4vol% to 14,3vol% were investigated. Table 1 shows amounts of retained austenite and the mechanical properties. The tensile strength and hardness were indirectly increased with increasing retained austenite, but reached maximum values at about 10vol% retained austenite. The plasticity (elongation and bendability) was also improved with increasing retained austenite.

TABLE 1
AMOUNT OF RETAINED AUSTENITE AND MECHANICAL PROPERTIES

Variants	Retained austenite (γ') (%)	$R_{p0.2}$ [MPa]	R_m [MPa]	A [%]	Bendability*	HV_1
Strip-A	0,4	1420	1783	7,4	17,6	555
Strip-B	4,4	1487	1910	7,6	16,6	570
Strip-C	10,1	1490	1948	9,5	13,7	582
Strip-D	14,3	1427	1930	11,4	9,5	577

*Bendability: the ratio of the minimum radius to the specimen thickness at which a strip does not fail when it is bent. This is usually called Wertzahl value.

The microstructure and fracture were investigated using SEM. For the microstructure investigation, the samples were etched in a solution consisting of 15 grams CuCl, 300 ml ethanol, 300 ml HCl and 300 ml H_2O. The precipitation states were investigated on the thin foils using Jeol 2000FX TEM/STEM equipped with Oxford ISIS EDX system. Residual stresses were measured with an X-ray diffractometer using CrKα radiation.

The damping capacity was determined using a simple experiment [3]. One end of the specimen was clamped horizontally and another was kept free. A steel ball with diameter of 17,5 mm and mass of 22 gram was dropped from a position of 300 mm above the sample. The changes in amplitudes of the free vibrations of the specimen were recorded using an oscilloscope. The damping capacity was evaluated by the following exponential approach:

$$U=U_o \exp(-bt) \quad (1)$$

where U is the amplitude at any vibration time, t is the time, U_o is the amplitude at t=0, and b is the damping index that is used to describe the damping capacity of material.

Three types of fatigue testing, namely pulsating tension, bending and impact, were performed in a laboratory environment at room temperature. Pulsating tensile fatigue test (R=0) was performed using a Amsler test machine with a frequency of about 150Hz. Reversed bending fatigue test (R=-1) was performed using a UMG test machine with a frequency of 25 Hz. Impact fatigue tests were performed using Sandvik Impact Fatigue Tester with a frequency of 250 Hz [3].

The fatigue strength was determined using the staircase method with 50 % fracture probability [4]. A series of 30 specimens were used. The specimen was tested at a given level of a stress until it failed, or till maximum $2 \cdot 10^6$ cycles for pulsating tension and bending and $1 \cdot 10^7$ cycles for impact. The impact fatigue strength is the impact speed (m/s) at which the specimen hits the seat [3].

RESULTS

Microstructure

Two groups of $M_{23}C_6$ particles were observed: larger ones with a mean size of 0,5μm and dense fine ones with a mean size of 0,1μm (Figure 1). With increasing retained austenite, the number and size of the larger particles were decreased, but those smaller ones were greatly increased (Figure 1a and b). However, the total fraction of $M_{23}C_6$ carbides was decreased (Figure 1c). It was found that the precipitation of these $M_{23}C_6$ carbides obeyed the Nishiyama-Wasserman (N-W) crystallographic orientation relation to martensite.

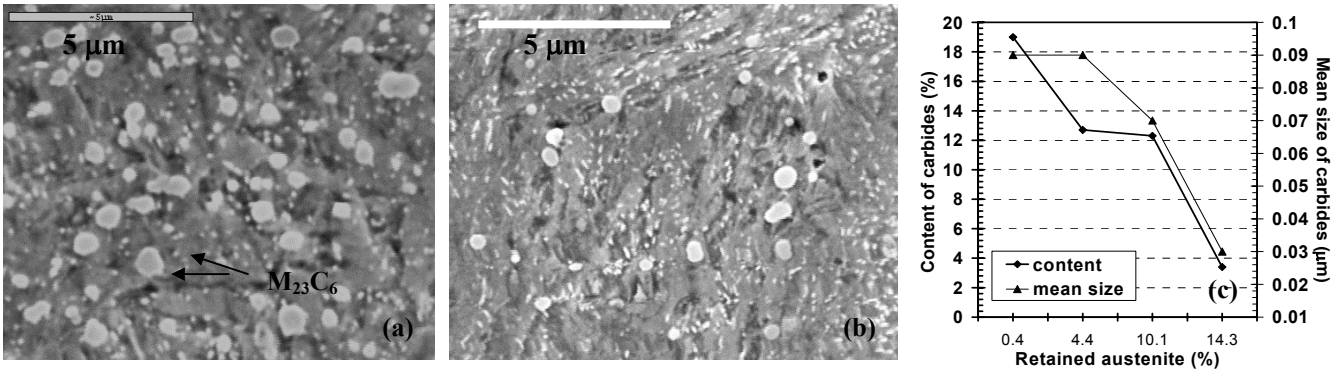

Figure 1: Precipitation of $M_{23}C_6$ in material with (a). 0,4vol% γ', (b). 14,3vol% γ'; (c). Relation between retained austenite and $M_{23}C_6$ carbides.

Another type of precipitate observed was very fine Fe_3C particles (with a typical size of 1nm) (Figure 2). It was found that its volume fraction was a function of retained austenite. In the strip with 0,4vol% retained austenite, very few Fe_3C particles could be observed (Figure 2a). With increasing retained austenite, the fraction of Fe_3C particles was increased (Figure 2b). In the strip with 14,3vol% retained austenite, very dense fine Fe_3C particles were observed (Figure2c). One of its crystallographic orientation relationships to martensitic matrix is shown in small picture in Figure 2c, which gives rise to a low energy interface through a low lattice misfit.

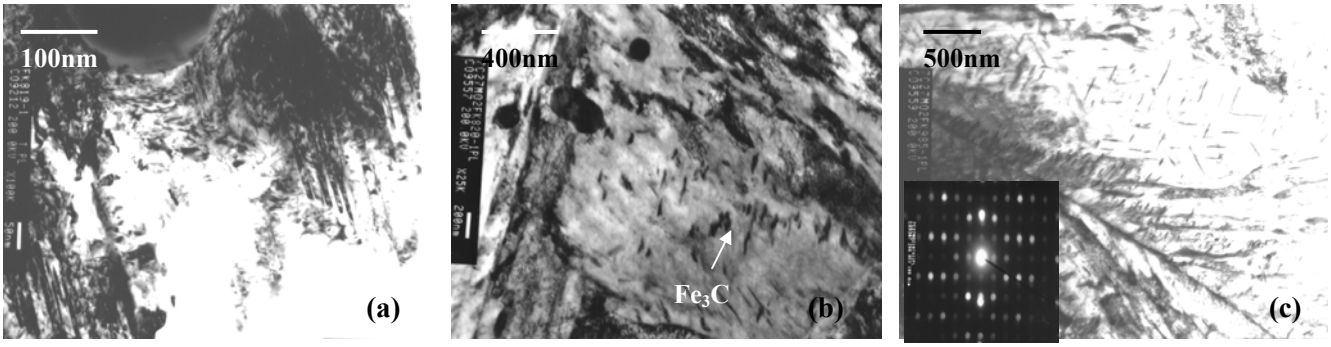

Figure 2: Precipitation of Fe_3C in material with (a). 0,4vol% γ', (b). 4,4vol% γ', (c). 14,3vol% γ', and composite electron diffraction pattern from the zone axes of $[010]_{Fe_3C}//[\bar{1}12]_{\alpha}$ (small picture).

Residual Stress and Damping Capacity

The relationship between the amount of retained austenite and the residual stress was plotted in Figure 3a and between the amount of retained austenite and damping capacity of the strips was plotted in Figure 3b. As can be seen the compressive residual stresses on the top surface of the strips were increased with the increase of the amount of retained austenite in the material. The depth of the compressive residual stresses from the surface was about 0,03 mm.

The damping capacity was also increased with increasing retained austenite (Figure 3b). This might be attributed to the increase of the total number of stacking-faults in retained austenite and the boundaries between retained austenite and martensite [5].

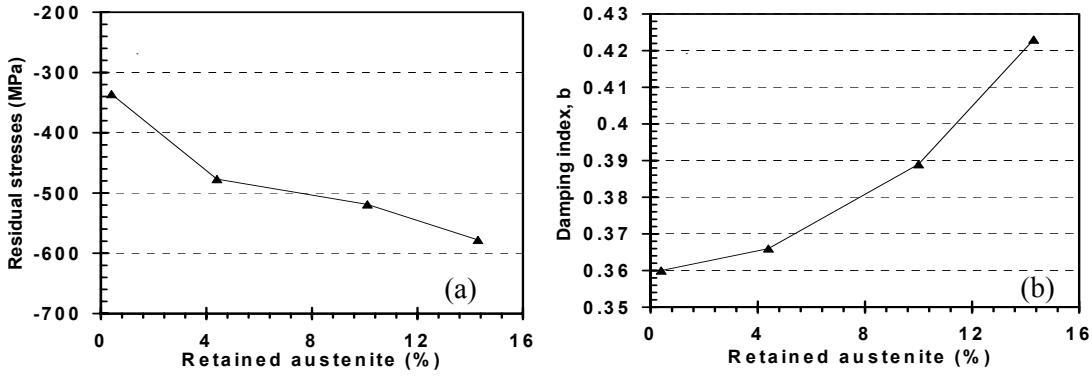

Figure 3: (a). Influence of retained austenite (vol%) on the compressive residual stresses; (b). Influence of retained austenite on the damping capacity.

Fatigue Strengths

The fatigue strengths from the different tests are summarised in Figure 4. The impact fatigue strength was significantly increased with the increase of the amount of retained austenite. However, increase of the amount of retained austenite had little effect on the pulsating tensile fatigue strength. For bending fatigue, the fatigue strength was increased with increasing retained austenite, and reached a maximum at about 4vol% retained austenite. However, the bending fatigue strength was still higher in the material with larger amount of retained austenite (or not lower in the material with 14,3vol% retained austenite) than in the material with 0,4vol% retained austenite.

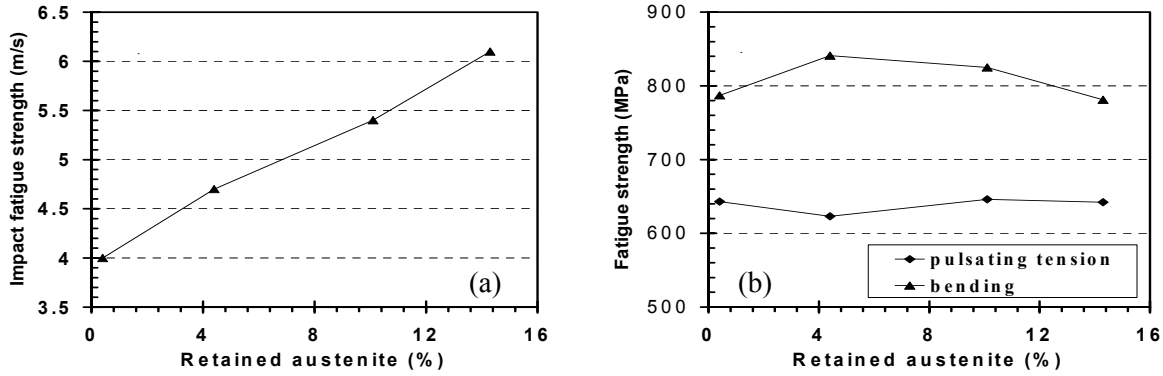

Figure 4: (a). Influence of retained austenite (vol%) on the impact fatigue strength; (b). Influence of retained austenite on the fatigue strengths in tension and in bending.

DISCUSSION

Precipitation Strengthening

In Table 1, it shows that the tensile strengths increased with increasing retained austenite in the strips. Austenite is a soft phase comparing with the matrix (martensite phase). It is unlikely that the presence of retained austenite could result in the increase of the tensile strength or hardness. The strengthening or hardening, therefore, could be attributed to the precipitation of densely dispersed fine $M_{23}C_6$ and Fe_3C particles as shown in Figure 1 and 2. Hence, the changes in the strengths or hardness were the resultant of the precipitation strengthening and softening due to the increase of retained austenite. It reached a maximum value at about 10vol% retained austenite. Slight decrease in the strength or hardness was owing to the large amount of retained austenite.

Influence of Retained Austenite on Fatigue Behaviours

As shown in Figure 4a, increase in retained austenite significantly improved the impact fatigue strength. This is quite promising since this property is very critical to compressor valve steels.

Different from other fatigue behaviours, the loading time of impact fatigue is very short. The specimen at each impact has suffered from very high strain rate. Fatigue-crack initiation results from plastic-deformation accumulation [6] and occurs at sub-surface [3]. The impact fatigue resistance mainly depends on both the strength and plasticity of the material [6]. In this investigation, the influence of the strength on the impact fatigue strength was relatively small. This was consistent with the earlier observations. The impact fatigue strength has shown little dependence on the tensile strength in the range of 1600-2500MPa [3]. One explanation is that the specimen at each impact has withstood very high strain rate, hence the impact fatigue strength should be compared with the tensile properties at high strain rate. On the other hand, the ductility (bendability or elongation) shows a great influence on the impact fatigue strength (Figure 5a).

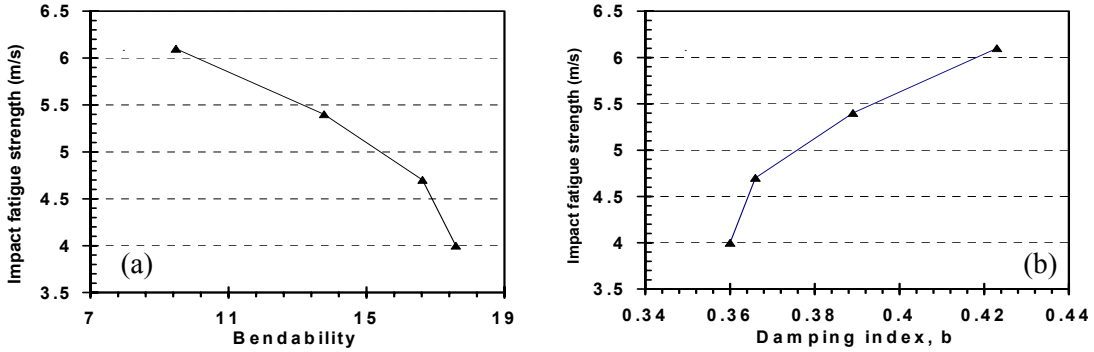

Figure 5: (a). Correlation between bendability and impact fatigue strength; (b). Effect of damping capacity on impact fatigue strength.

The impact of the specimen from this test was caused by high frequency flexural and torsional vibration [3]. This vibration can be more effectively damped in the steel with high damping capacity. Consequently, the impact stresses will become smaller, and the measured impact fatigue strength will be higher. This is shown in Figure 5b.

The above discussion indicates that the improvement of the impact fatigue strength of the valve steel strip can be attributed to the combination of its high strength and high absorption capacity of impact energy (plasticity and damping capacity).

As shown in Figure 3a, compressive residual stresses were increased with increasing retained austenite. This may also contribute to the improvement of the impact strength.

TABLE 2
DISTRIBUTION OF CRACK INITIATION OF FAILED SPECIMENS FROM EACH VARIANT [%].

Sample	Retained austenite (γ') (vol %)	Inclusion	Surface and edge	Corner
Strip A	0,4	73,3 (37%)*	6,7	20
Strip B	4,4	71,4(10%)	14,5	14,3
Strip C	10,1	71,4(10%)	28,6	0
Strip D	14,3	73,4(9%)	20,0	6,7

*: Probability of crack initiation at subsurface inclusion.

As known, the fatigue properties are correlated to the tensile strength and the compressive residual stresses in the materials. The results from the pulsating tension fatigue testing were therefore unexpected. Fracture investigation (Table 2) shows that most crack initiations started at inclusions. Increase in retained austenite could not change this distribution (see inclusion in Table 2). On the other hand, it seems that the increase of retained austenite could have facilitated the crack initiations at surface inclusion (comparing with subsurface inclusion) or other surface defects. This is contrary to the conventional phenomena where increase in compressive residual stress on the top surface will lead to crack initiation at subsurface inclusions. One explanation might be that the presence of relatively high amount of retained austenite near the surface

causes the crack initiation more easily [7]. The increase in compressive residual stresses and tensile strength might compensate for the reduced fatigue resistance due to softening by retained austenite.

Since the maximum stress in a bent strip is on its top surface, the bending fatigue strength is mainly dependent on the surface conditions and its strength. In spite of the fact that the compressive residual stresses and the tensile strength were increased with the increase of retained austenite, no continuous increase in the bending fatigue strength was obtained. This might also be attributed to the presence of retained austenite. The earlier experiences [7, 8] show that due to its weakness and easily slipping the presence of retained austenite near the top surface will facilitate the crack initiation during bending cyclic loading. In this investigation, however, very fine elongated retained austenite (about 0,1μm) was observed to have been embedded between two acicular martensite phases [2]. This might reduce the risk of retained austenite for crack initiation, and may also give an explanation why high bending fatigue strength can still be maintained in the material with large amount of retained austenite (14,3vol%).

CONCLUDING REMARKS

Increase in the strength or hardness of the material was the additive of the precipitation strengthening of fine dispersed $M_{23}C_6$ and Fe_3C particles and the softening due to the increase of retained austenite. It reached a maximum value at about 10vol% retained austenite.

The impact fatigue strength was significantly improved with increasing retained austenite. The presence of retained austenite however had little influence on the fatigue strength in tension. For the bending fatigue strength, it increased with increasing retained austenite and reached a maximum value at about 4 % retained austenite.

Increase in impact fatigue strength was likely attributed to the increase in its ability for impact energy absorption (damping capacity and plasticity) by increasing retained austenite and its tensile strength by precipitation strengthening. For fatigue in tensile, crack initiation at inclusion was the main fracture mechanism. For fatigue in bending, the presence of retained austenite near the top surface may facilitate crack initiation. High bending fatigue strength maintained in the material with large amount of retained austenite was owing to its high tensile strength and fine dispersed retained austenite.

ACKNOWLEDGEMENTS

This paper is published by permission of AB Sandvik Steel. The support of Dr T. Thorvaldsson, Mr H. Holmberg, Mr M. Lundström, and Mrs M. Sundqvist, and the technical assistance of Mr G. Svensk, Mr D. - E. Gräll, and Mr C. Lundemo are gratefully acknowledged.

REFERENCES

1. Olsson, S. (1992). *In: Proc. of the 1992 Inter. Compressor Engineering Conf. at Purdue*, pp. 909-918, Hamititon J. F. (Eds). Purdue University.
2. Nyström, M., Liu, P., Larsson, T., Olsson, S. and Svensk, G. (1996). *In: Proc. of the 1996 Inter. Compressor Engineering Conf. at Purdue*, pp. 511-516, Soedel, W. (Eds). Purdue University.
3. Svenzon, M. (1976). Ph. D Dissertation, Uppsala University, Sweden.
4. A guide for fatigue testing and the statistical analysis of fatigue data, ASTM Special Technical Publication No. 91-A, 1963.
5. Jun, J. and Choi, C. (1999). *J. Mater. Sci.*, 34. 3421.
6. Yu, J., Liaw, P. K. and Huang, M (1999). *JOM,* Apr. 15.
7. Inada, I., Hiroshi, Y. and Tsuyoshi, I. (1994). *Kobeco Technology review*, 17, 49.
8. Kumagaya, S. (1975). *Metals in Engineering*, 15, 15.

Reference No: ICF100434OR

FATIGUE CRACK GROWTH ACCELERATION EFFECTS UNDER HELICOPTER LOADING SPECTRA

V.Zitounis[1], P.E.Irving[1], R.Cook[2], S.Jenkins[3], D.Matthew[3]

[1] School of Industrial and Manufacturing Science, Cranfield University, Bedfordshire, MK43 0AL, UK
[2] Deceased; Formerly, MSS, DERA, Farnborough, GU14 6TD, UK
[3] GKN-WHL, Yeovil, Somerset, BA20 2YB UK

ABSTRACT

Fatigue crack growth tests have been performed under constant and variable amplitude loading spectra on pre cracked CT specimens of titanium alloy Ti-10V-2Fe-3Al. The variable amplitude spectra were simplified versions of those previously measured on a helicopter rotorhead. They consisted of constant amplitude loading at R values of 0.7 and 0.9, interspersed with excursions to zero load or intermediate tension loads. The number of underload cycles and their frequency were systematically varied, and the resulting growth rate increment produced by 10^6 cycles of the sequence was accurately measured. The starting ΔK of the high R cycles was at the constant amplitude threshold, ΔK_{th}. It was found that crack growth rates and crack growth increments were accelerated by factors between 1.6 and 2.7 with respect to calculated linear summations of crack growth made using constant amplitude crack growth data. This is a non conservative effect. The results are discussed with respect to previous work on load interaction models.

KEYWORDS

Fatigue, crack growth, load spectra, acceleration, underloads

INTRODUCTION

Damage tolerance design philosophy, based on fatigue crack growth, is well established and applied in fixed wing aircraft. In contrast, helicopter components have been traditionally designed using safe life approaches. Damage tolerant design of helicopters requires data and understanding of how fatigue cracks develop in helicopter materials under helicopter load spectra. The application of damage tolerance analysis to helicopters presents difficulties. Marquet and Struzik [1] provide a good summary. Two problems are a) lack of understanding of fatigue crack growth in the near-threshold region and b) lack of understanding of load interaction effects under helicopter load sequences. In particular, the effect of the ground-air-ground cycles on fatigue crack growth is not well documented [2]. The load spectra of many helicopter components consists of large numbers of load cycles at high R ratio (R>0.75). The rest of the spectrum consists of load cycles at R ratios between 0.4 and 0.7, with excursions to zero load. In cracked components, stress intensity ranges (ΔK) would be close to the threshold, ΔK_{th}. Prediction of fatigue crack growth rates requires an understanding of load interaction effects under these spectra.

The behaviour of fatigue cracks under variable amplitude spectra has been studied intensively over the past 20 years. [3,4] For many load sequences, delay effects are found, compared with the growth rates predicted by a linear summation. It is well known that fatigue crack growth rates caused by small cycles following larger load excursions are slower that the linear summation damage prediction. A linear summation of crack growth is that obtained by summing the crack growth increments for constant amplitude loading, assuming no interactions between succeeding load cycles. Fatigue crack acceleration effects have been reported previously, [5] and these were found when high R ratio cycles were followed by underloads and overloads. More recently Buller et al [2] have demonstrated crack acceleration effects, compared with a linear summation, when precracked CT samples of titanium alloy Ti-10-2-3 and aluminium alloy 7010 were subjected to helicopter rotorhead spectra consisting of large numbers of near threshold cycles of R between 0.7-0.83, interspersed with excursions to zero load.

To further investigate these effects, in this study, fatigue crack growth rates were measured under two different Simple Variable Amplitude Loading (SVAL) spectra. These are simplified versions of the real helicopter rotorhead spectrum. The spectra consisted of small cycles with R ratio of 0.7-0.9, and excursions to zero load. The sequence, number and R ratio of the cycles were systematically varied. The study was conducted on Ti-10-2-3 alloy. Experimental crack growth rates were compared with those calculated using a linear summation technique, with input data from constant amplitude testing on the Ti-10-2-3 alloy.

EXPERIMENTAL PROCEDURE

Tests were performed on Ti-10-2-3 which belongs to the near beta (β) or solute-lean beta alloy class where the body centred cubic (bcc) β phase is predominant [6]. Mechanical properties of the test material are shown in Table 1.

TABLE 1
NOMINAL MECHANICAL PROPERTIES OF THE Ti-10-2-3 TEST MATERIAL

Parameter	Description	Ti-1023
σ_{UTS}	Ultimate Tensile Strength	1146 MPa
σ_{YS}	Yield Strength	1048 MPa
K_{IC}	Fracture Toughness	63.9 MPa m^1/2

Compact tension (CT) specimens (W = 70.0 mm, t = 17.5mm) were used for the research. Constant amplitude and decreasing ΔK crack growth rate data for this alloy were measured at R ratios of 0.1, 0.4, 0.7 and 0.9. In addition, fatigue tests were performed using the two load spectra shown in figure 1.

In *SVAL-1*, constant amplitude cycles at R* ratios of 0.7 and 0.9 were applied for **n** cycles, followed by **n´** cycles of underloads at R=0 (figure 1a). The starting ΔK value of the R* cycles was equal to the threshold of 1.9 MPa $m^{1/2}$ at R* of 0.7 and 1.6 for R* of 0.9. The ΔK of the R = 0 cycles was 6.3 MPa $m^{1/2}$ for R* of 0.7, and 16 MPa $m^{1/2}$ for R* of 0.9. For R* = 0.7, the number of underloads **n´** was varied from 1 to 50, keeping n constant at 1000 cycles. Additional tests were performed with **n** values between 2,000 and 50,000. A further sequence applied 1 underload every 20 small cycles with R* = 0.7. For R*=0.9, the number of test sequences was reduced to 3, with **n** of 20, 1000 and 2000; **n'** being 1, 50 and 50 respectively. All sequences were repeated for a total of 10^6 small cycles.

In *SVAL-2*, CAL at R=0.9 was applied for **k** cycles followed by CAL at R=0.7 for **k''** cycles (figure 1b). The ΔK of cycles at R=0.9 and R=0.7 was the same and was equal to the threshold value of the stress intensity factor ΔK_{th} (=1.6 MPa $m^{1/2}$) at the beginning of the test. Tests were performed such that the ratio **(k''+1)/k** was 0.1. The range of small cycles **k** at R=0.9 was from 100 to 10,000. This sequence was repeated for 10^6 small cycles. Unlike *SVAL-1*, this sequence contained three cycle ranges. These were **k**

cycles at R =0.9, **k''** cycles at R = 0.7, and in each individual sequence, 1 cycle of R = 0.23, this cycle being formed by the transition between the other two R ratios. This cycle had a starting ΔK of 11.6 MPa $m^{1/2}$.

Crack lengths were measured to an accuracy of ±14 μm with a high precision electrical potential system described in [7]. Tests were conducted at between 8 and 20 Hz on a digitally controlled servo hydraulic machine which controlled test loads to better than 1 % of the maximum load applied during the test. All tests were carried out in a laboratory air environment at between 15-25°C.

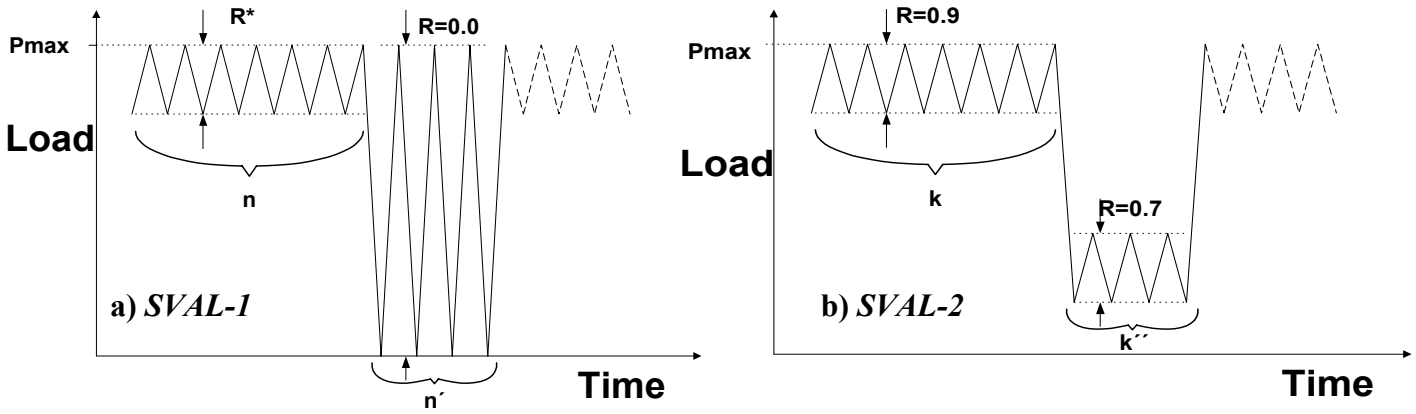

Figure 1: Definition of two different spectrums, *SVAL-1* and *SVAL-2* composed of small cycles in high R and underloads.

Crack length and cycles data were recorded automatically throughout the application of the test sequences. Crack growth rates da/dN were calculated by determining the total number of cycles of all ranges required to grow the crack successive increments of 0.1 mm. Thus the calculated da/dN was an average contribution from all types of cycle. Data were represented as crack growth increment (a) Vs total sequence cycles (N), and also as da/dN Vs ΔK. An acceleration factor γ, was defined as follows:-

$$\gamma = \frac{\text{final crack length increment measured in test } (\Delta a_t)}{\text{final crack length increment calculated by linear summation of the constant amplitude crack growth data } (\Delta a_f)}$$

The linear summation calculation required crack growth integration, and was performed by the AFGROW crack growth software model [8], with no load interaction effects. The model was provided with CAL data for Ti-10-2-3, which had been measured at R = 0.1, 0.7 and 0.9. The data were curve fit, and the fitted curves used to calculate the crack growth increment produced by the completed sequences, described above. It was established that the curve fits represented the original data to an excellent accuracy in the near threshold crack growth rate regions of interest (Figure 2). The excellent agreement between experimental data for R = 0.4 and predicted line for 0.4 may be observed. The line on the extreme right of the data is that predicted for R = 0.

RESULTS

It was found that under the *SVAL-1* spectra, acceleration effects were observed only for R* values of 0.9. No acceleration effects were found under any of the *SVAL-1* spectra for R* =0.7. As the number of underloads in a sequence at R* = 0.7 increased from 1 to 50 the average da/dN increased from 10^{-11} to 10^{-10} m/cycle. However, this was a consequence of the increases in the numbers of damaging cycles and no acceleration relative to a linear summation was observed. At R* = 0.9, significant accelerations were found relative to linear summation with γ values from 1.5 to 2.2 (table 2). Fatigue crack increments Vs cycles and crack growth rates can be seen in figure 3 for these tests. ΔK in figure 3 refers to the ΔK of the small cycles in the sequence. It can be seen that the value of the ratio **n**/**n'**, changes the observed growth rate. For example in

figure 3b, the ratio of **n**/**n'** has changed to half that used for 3a, and the growth rate is reduced by about a factor of two. However the growth rate overall is accelerated relative to the linear summation by 1.5-2.2 for all sequences at R*=0.9 (Table 2).

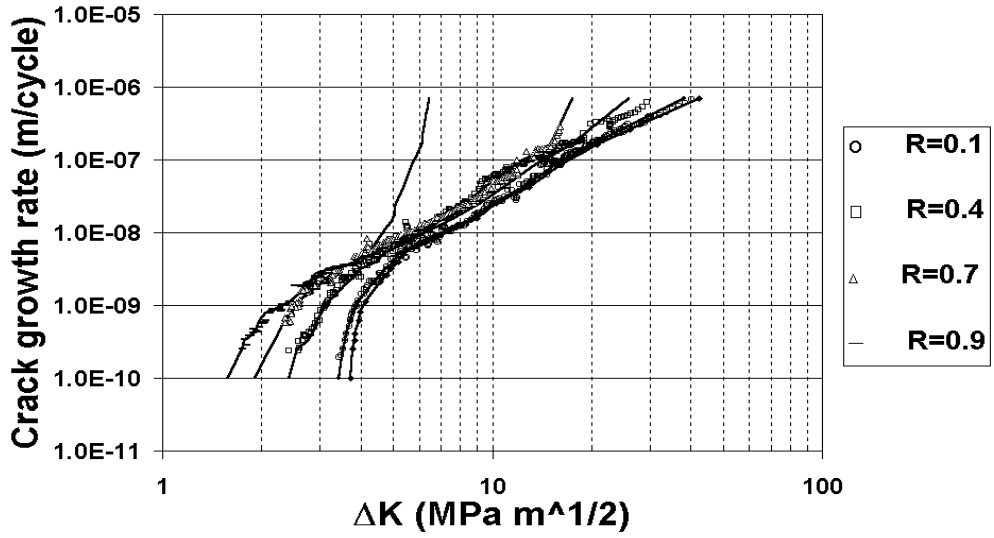

Figure 2: Fatigue crack growth rates measured experimentally (points), and curve fitted (lines)

TABLE 2
ACCELERATION FACTOR γ OBSERVED IN VARIOUS TESTS

Test condition	**n** = 20 **n'** = 1	**n** = 1000 **n'** = 50	**n** = 2000 **n'** = 50	**k** = 100 **k''** = 9	**k** = 1000 **k''** = 99	**k** = 2000 **k''** = 199
Acceleration factor $\gamma=\Delta a_t/\Delta a_f$	1.66	2.19	1.52	2.55	2.67	6.32

Crack growth rates recorded for *SVAL-2* tests are presented in figure 4. Data for linear summation calculations of growth rate are also shown. The data for the test with **k** = 10^4 are not shown as the growth rate increment was too small to be accurately measured. The value of γ = 6.3 recorded with **k** =2,000 is also subject to considerable error, as the recorded growth rate was only 10^{-10} m/cycle. The γ value calculated for each test is shown in table 2. For *SVAL-2,* there were fewer large cycles than in *SVAL-1.* Although the fraction of underloads was greater, it included the small R=0.7 cycles. γ values were 2.5-6.5 for *SVAL-2*, bigger than γ values of 1.5-2.2 calculated for *SVAL-1*. Figure 5a shows the γ factor for all tests plotted against the total growth increment obtained for each sequence. There is no clear relationship between γ and the total increment of growth obtained in 10^6 cycles. Figure 5b shows γ plotted against underload cycles expressed as a fraction of total cycles in the sequence. It shows a trend of increasing γ from 1.6 at a cycles fraction of 0.025, for *SVAL-1* to between 2.6-6 for *SVAL-2* at a cycles fraction of 0.1.

DISCUSSION

Under *SVAL-1*, only sequences with small cycles having R*=0.9 produced γ values greater than unity. No acceleration was detected for *SVAL-1* with small cycles of 0.7, despite the fact that the ΔK of the large underloads (6.3 MPa $m^{1/2}$), produced growth increments which were accurately measurable. It is concluded that acceleration effects under *SVAL-1* is confined to small cycle R ratios above R* = 0.7. Testing at R* = 0.9 produced much larger growth increments, and γ increased from 1.6 to 2.2 as the fraction of under loads increased. Testing under *SVAL-2* produced larger values of γ; despite the number of large underload cycles

being reduced. The three *SVAL-2* tests while having the same cycles ratio (0.1) differ in the frequency with which the largest cycle is applied. This appears to result in larger values of γ.

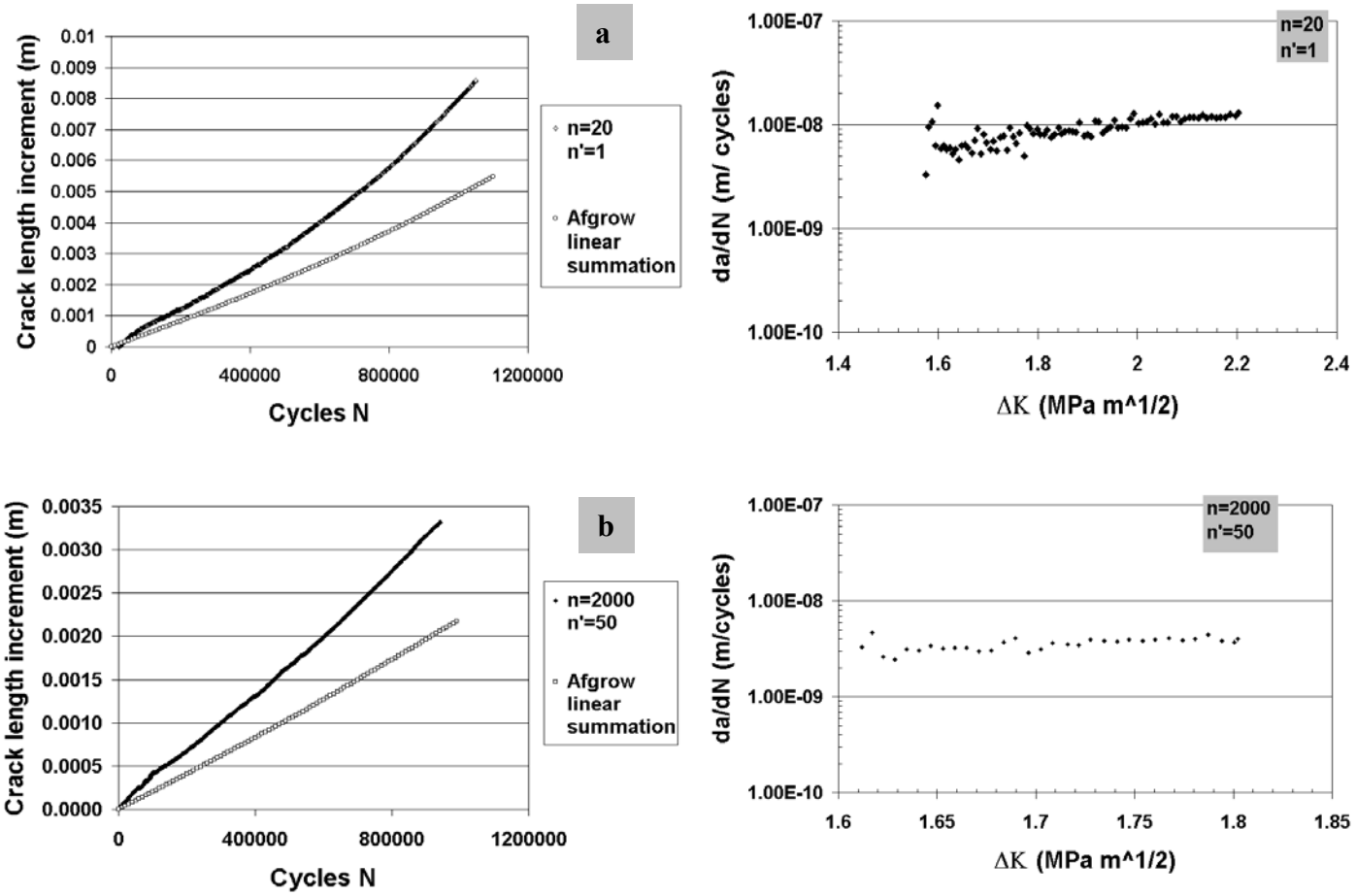

Figure 3: Comparison of measured and predicted fatigue crack growth rates under *SVAL-1* at R* = 0.9.

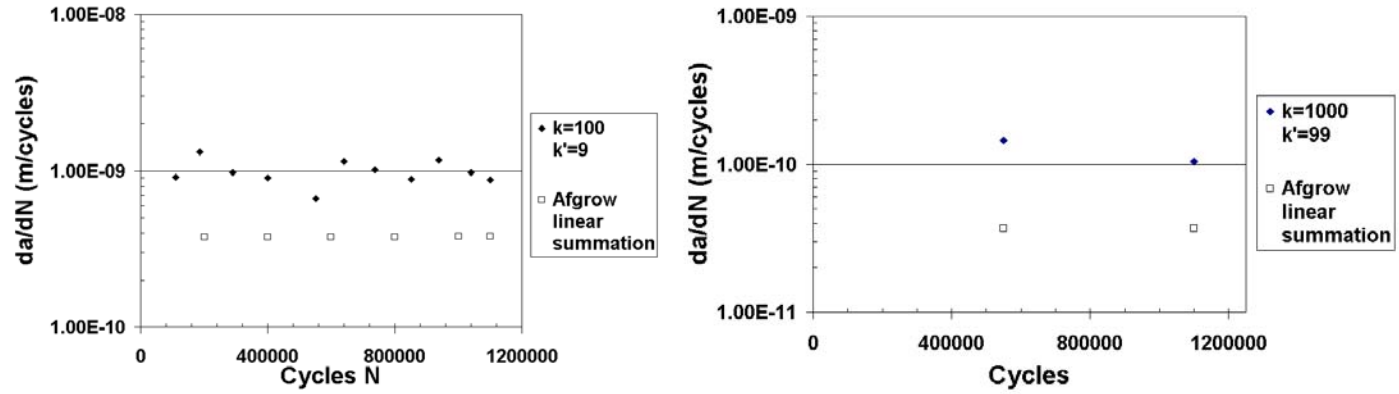

Figure 4: Comparison of measured and predicted fatigue crack growth rates under *SVAL-2* spectra.

It is unlikely that these results are a consequence of errors in constant amplitude data. Figure 2 shows excellent agreement of curve fits with the growth rate data points. In addition, the observation of changes in γ with the same cycles fraction of underloads suggests that these effects are a consequence of load interaction between low and high R cycles.

Underload effects on fatigue crack growth previously have been studied by a number of workers [5,9,10]. Acceleration effects were reported by Fleck [5], but under very different load conditions than those used in the present work. Dabeyeh & Topper [9], measured decreases in crack opening stresses as a consequence of transitions from compressive underloads to constant amplitude small cycles, up to R values of 0.8.

Accompanying transient increases in fatigue crack growth rates at R = 0.8 were found. It may be that the present results, although confined to tensile underloads, have their origin in a similar mechanism. Further work is in progress to identify the mechanism responsible and to develop adequate predictive models for fatigue crack growth under these conditions.

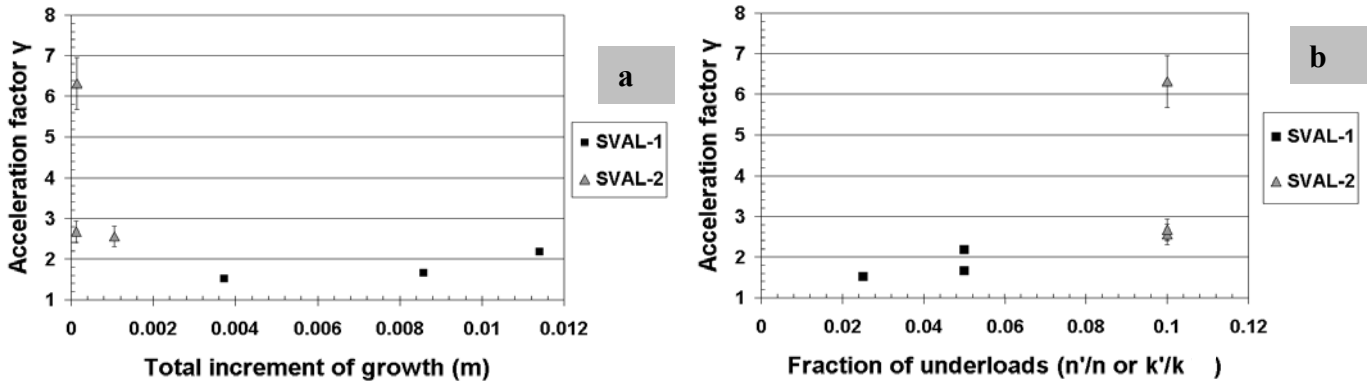

Figure 5: Variation of the acceleration factor γ with a) the total crack increment and b) Fraction of the underloads applied in each sequence of load.

Conclusions

(1) Fatigue crack growth rate testing under variable amplitude load sequences containing tensile underloads produces crack acceleration relative to a non interaction linear summation of constant amplitude crack growth rates.
(2) The acceleration relative to linear models is between 1.6 to 2.6, depending on the spectrum details.

Acknowledgements

This work was sponsored by the UK Civil Aviation Authority. Their financial support is gratefully acknowledged.

REFERENCES

1. Marquet, T., Struzik, A., (1998). *Damage tolerance applied to metallic components*, 24th European Rotorcraft Forum, Marseilles, France.
2. Irving, P.E., Buller, R. G., (1999). In: Fatigue and Fracture Mechanics 29th vol ASTM STP 1332, pp 727-742, Panontin, T.L., Sheppard. S.D. (Eds). American Society of Testing and Materials, USA
3. Kumai, S., Higo, Y. (1996). *Materials Science and Engineering A221*, 154
4 Sadananda, K., Vasudevan, A. K., Holtz, R. L., Lee, E. U, (1999). *Int. J. Fatigue 21*, 23
5. Fleck, N. A., (1985). *Acta Metall. Vol33, No 7,* 1339
6 Buller, R.G., Jenkins, S., (1998). Final report *WP320-Material Data and component tests on WHMS 640 (Ti-10V-2Fe–3Al)*, GKN Westland Helicopters, LR97,182 DTI-LINK RA/6/30/06
7. Wei, R. P., Brazil, R. L., (1981). In: *Fatigue Crack Growth Measurement and Data* Analysis ASTM STP 738, pp. 103-119, S.J. Hudak, Jr. and R. J. Bucci (Eds), American Society of Testing and Material, USA
8. Harter, James A., (2000) *AFGROW Users manual, Version 4.0001.11.8, Technical Memorandum,* AFRL-VA-WP-TR-2000-XXXX, AFWAL Flight Dynamics Laboratory, Wright-Patterson AFB, OH.
9. Dabayeh, A.A., Topper, T.H., (1995). *Int. J. Fatigue* 17, 261
10. Hackyard, M., Powell, B.E., Stephenson, J.M., McElhome, M., (1999). *Int. J. Fatigue* 21, S59

ORAL REFERENCE: ICF10 0192OR

FATIGUE CRACK GROWTH BEHAVIOR OF MICRO-SIZED SPECIMENS PREPARED FROM AMORPHOUS ALLOY THIN FILMS

K. Takashima[1], Y. Higo[1] and M. V. Swain[2]

[1] Precision and Intelligence Laboratory, Tokyo Institute of Technology,
4259 Nagatsuta, Midori-ku, Yokohama 226-8503, Japan.
[2] Faculty of Dentistry and Department of Mechanical & Mechatronic Engineering,
The University of Sydney, Australian Technology Park, Everleigh NSW 1430, Australia.

ABSTRACT

Fatigue crack growth tests have been performed on micro-sized Ni-P amorphous alloy specimens to investigate the size effects on fatigue crack growth behavior of such micro-sized specimens. Two types of cantilever beam type micro-sized specimens with different breadth (10 (B) × 12 (W) × 50 (L) μm^3 and 30 (B) × 12 (W) × 50 (L) μm^3) were prepared from an electroless plated Ni-P amorphous alloy thin film by focused ion beam machining. Notches with a depth of 3 μm were introduced in the specimens. Fatigue crack growth tests were performed using a newly developed fatigue testing machine for micro-sized specimens in air at room temperature under constant load amplitude and stress ratios of 0.1, 0.3, 0.5 and 0.7. Striations were observed on the fatigue fracture surfaces and fatigue crack propagation rates were estimated by careful measurements of the striation spacings. The fatigue crack growth rates at stress ratios of 0.3 and 0.5 were higher than that at 0.1. This suggests that crack closure may occur even in such micro-sized specimens. The fatigue crack growth resistance is also dependent on the specimen breadth. This suggests that the stress state ahead of the crack may affect the crack growth behavior. The results obtained in this investigation provide basic guidelines for designing actual MEMS devices.

KEYWORDS

Micro-sized specimen, Fatigue, Crack growth, Amorphous alloy, Thin film, Size effect

INTRODUCTION

Many micro-sized components are involved in microelectromechanical systems (MEMS) and these components are subjected to cyclic loading as they move. These micro-sized components are usually fabricated from a thin film deposited on a substrate using suitable surface micromachining techniques. The evaluation of fatigue properties for thin films is thus extremely important to design reliable and long-term durable MEMS devices. For example, the components used in micro-optical mirrors and switches are considered to experience extremely high number of cyclic loads (over 10^8 cycles). To date, fatigue tests for thin films and fatigue life of such films have been investigated [1-3]. However, there

have been no data for fatigue crack growth properties which are important for actual MEMS devices. This is partly due to the lack of suitable fatigue testing machine for micro-sized materials. In our previous investigations, we have designed a new fatigue testing machine for micro-sized specimens [4, 5], and fatigue life curves have been obtained for micro-sized specimens prepared from a Ni-P amorphous alloy thin film [6].

Amorphous alloy thin films deposited on substrates by sputtering or plating techniques are considered to be potential candidate materials for MEMS devices because of their isotropic mechanical properties and high corrosion resistance. Therefore, it is important to clarify the fatigue crack growth properties of these amorphous thin films. However, the fatigue properties of micro-sized amorphous specimens have not yet been studied apart from our previous investigation on the fatigue life of a micro-sized Ni-P amorphous alloy specimens [6]. In this investigation, fatigue crack growth tests have been performed on micro-sized specimens prepared from an electroless deposited Ni-P amorphous alloy thin film and the size effects on the fatigue crack growth behavior of micro-sized specimens have been discussed.

EXPERIMENTAL PROCEDURE

Preparation of Specimens

The material used in this investigation was a Ni-11.5 mass%P amorphous thin film electroless plated on an Al-4.5 mass%Mg alloy. The thickness of the amorphous layer was 12 μm and that of the Al-4.5 mass%Mg alloy substrate was 0.79 mm, respectively. A disk with a diameter of 3 mm was cut from the Ni-P/Al-Mg sheet by electro discharge machining. An amorphous layer was separated from the Al-Mg alloy substrate by dissolving the substrate with a NaOH aqueous solution. The amorphous thin film was fixed on a holder and two types of micro-cantilever beam specimens with dimensions of 10 (B) x 12 (W) x 50 (L) μm^3 and 30 (B) x 12 (W) x 50 (L) μm^3 were cut from the amorphous layer by focused ion beam machining. Figures 1 (a) and (b) show the specimens prepared by the above procedures. Notches with a depth of 3 μm were introduced into the specimens by focused ion beam machining. This notch depth is equivalent to $a/W = 0.25$, where a is notch length and W is specimen width. The width of the notch was 0.5 μm, and the notch radius is thus deduced to be 0.25 μm. The notch position was 10 μm away from the fixed end of the specimen. The loading position is set at 40 μm from the fixed end of the specimen.

Fatigue Crack Growth Test

Fatigue crack growth tests were performed in air at room temperature using the fatigue testing machine for micro-sized specimens. Fatigue tests were carried out at a frequency of 10 Hz and different stress ratios, R ($R = P_{min} / P_{max}$, where P_{min} is the minimum load and P_{max} is the maximum load applied over the fatigue cycle) of 0.1, 0.3, 0.5 and 0.7 under constant load amplitude ($\Delta P/2$, where $\Delta P = P_{max} - P_{min}$) of 2 mN. This fatigue test condition was determined from our preliminary experiments. Although the crack length was not able to be measured directly in this testing machine, the change in specimen compliance

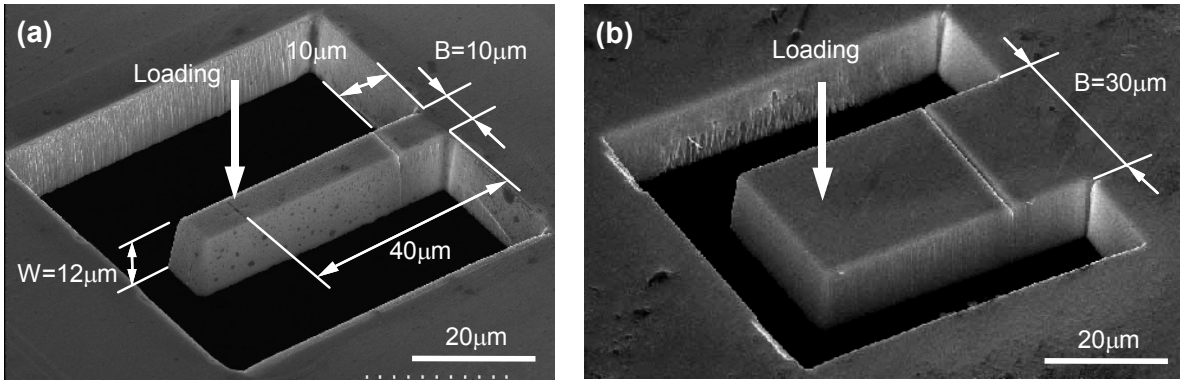

Figure 1: Two types of micro-sized cantilever beam specimens with different breadth (B) prepared by focused ion beam machining. (a) B=10mm and (b) B=30mm.

can be measured during fatigue tests. The initiation of crack growth was then determined by monitoring the specimen compliance. The fatigue surfaces after the tests were observed using a HITACHI S-4000 field emission-gun type scanning electron microscope.

RESULTS AND DISCUSSION

Fatigue Crack Growth Behavior

Figure 2 shows a scanning electron micrograph of fracture surface for the specimens with a breadth, B, of 10 μm after a fatigue crack growth test at a stress ratio of 0.5. The fracture surface is relatively flat and very fine equispaced markings are clearly visible ahead of the notch. These markings have been considered to be striations [7]. If the spacing between the striations on the fatigue surface is assumed to be equivalent to the fatigue crack growth rate, a fatigue crack growth resistance curves can be obtained from the measurements of the striation spacings. Careful measurements of the striation spacings were then made and fatigue crack growth rates ($\mathrm{d}a/\mathrm{d}N$) as a function of applied stress intensity factor range (ΔK) (where $\Delta K = K_{max} - K_{min}$) were obtained. Stress intensity factor (K) is calculated from the equation for a single edge notched cantilever beam specimen [8]. The crack length, a, was measured from scanning electron micrographs of the fatigue surfaces.

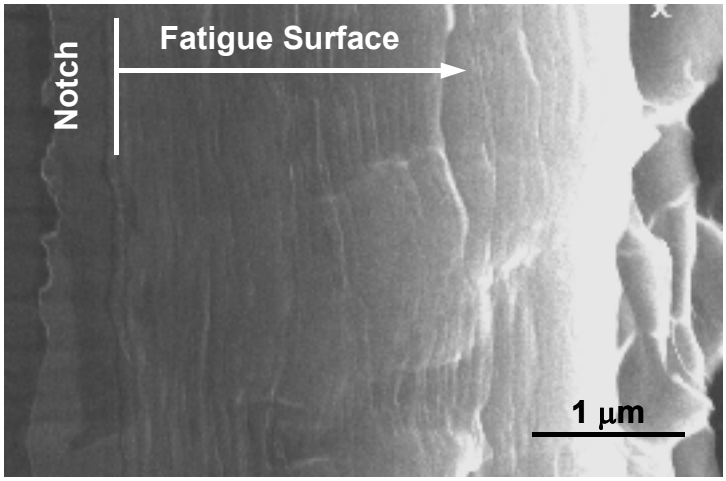

Figure 2: Scanning electron micrograph of fatigue surface. Fine equispaced markings considered to be striations are observed. Crack growth direction is from left to right.

Figure 3 shows the fatigue crack growth resistance curves for the specimens with B of 10 μm at different stress ratios. The fatigue crack growth rates at a stress ratio of 0.3 and 0.5 are almost the same. In contrast, the fatigue crack growth rate at a stress ratio of 0.1 is lower than those at 0.3 and 0.5 at a given value of ΔK. Generally, a decrease in fatigue crack growth rate at a low stress ratio can be explained by crack closure effects for ordinary sized specimens. This suggests that crack closure effects may occur even in such micro-sized specimens and may affect the fatigue crack growth behavior. The fatigue surface is relatively flat as shown in Fig. 2, so this crack closure is deduced to be a plasticity-induced crack closure.

On the other hand, the fatigue crack growth rate at a stress ratio of 0.7 is higher than those of 0.3 and 0.5. Figure 4 shows a fatigue surface at a stress ratio of 0.7. The fatigue surface is very rough and some vein patterned regions are observed in addition to the striation pattern. At this stress ratio, K_{max} was 6.8 $\mathrm{MPam}^{1/2}$ and this value is close to K_Q value of the specimen [9]. Therefore, the crack is deduced to extend by both cyclic and static mode, and this resulted in higher crack growth rate at a stress ratio of 0.7.

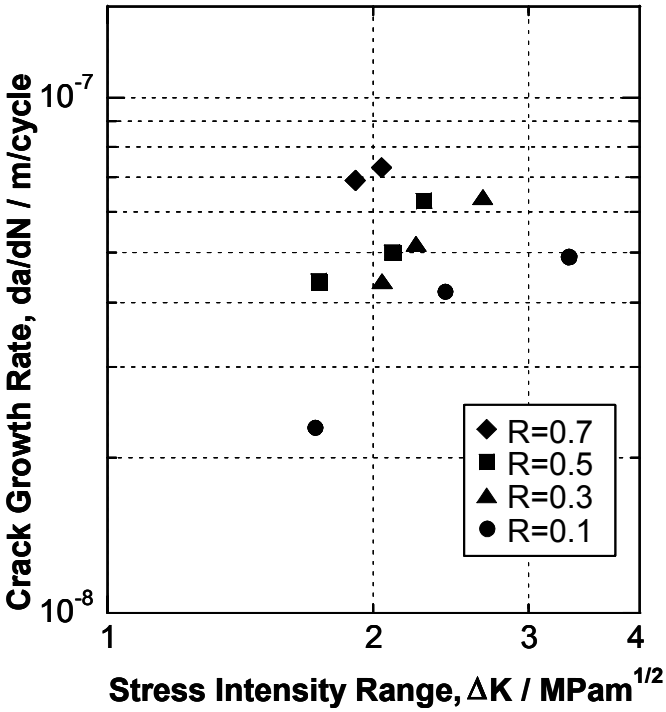

Figure 3: Fatigue crack growth resistance curves for micro-sized specimens at different stress ratios.

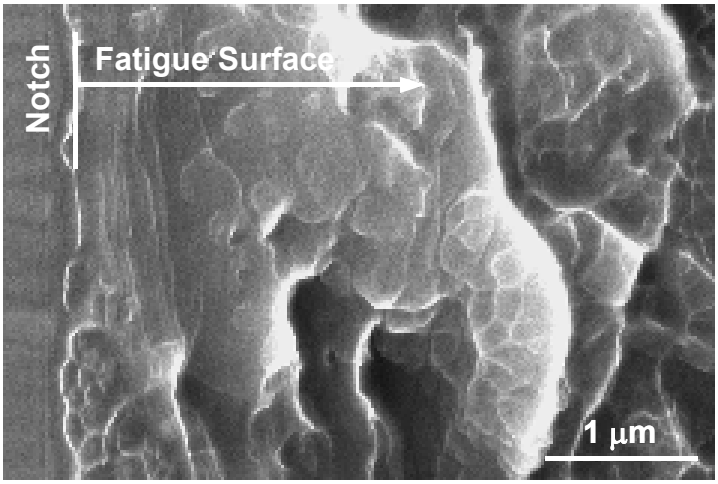

Figure 4: Scanning electron micrograph of fatigue surface tested at a stress ratio of 0.7. Crack growth direction is from left to right.

Effect of Specimen Breadth on Fatigue Crack Growth

In order to investigate the effect of stress state ahead of the crack tip on the fatigue crack growth behavior of micro-sized specimens, fatigue crack growth tests for specimens with different breadth (B) were carried out. Figure 5 shows a fatigue crack growth resistance curves at a stress ratio of 0.5, at which no closure effect is assumed, for the specimens with B of 10 and 30 μm, respectively. The fatigue crack growth rate with B of 10 μm is higher than that with B of 30 μm. In our previous investigations [9], plane stress and plane strain regions were observed on fracture surfaces even in micro-sized specimens. Thus, a decrease in crack growth rate with an increase in specimen breadth may be due to the difference in stress state ahead of the crack. It is interesting that the effect of specimen breadth on fatigue crack growth behavior was observed even in such micro-sized specimens.

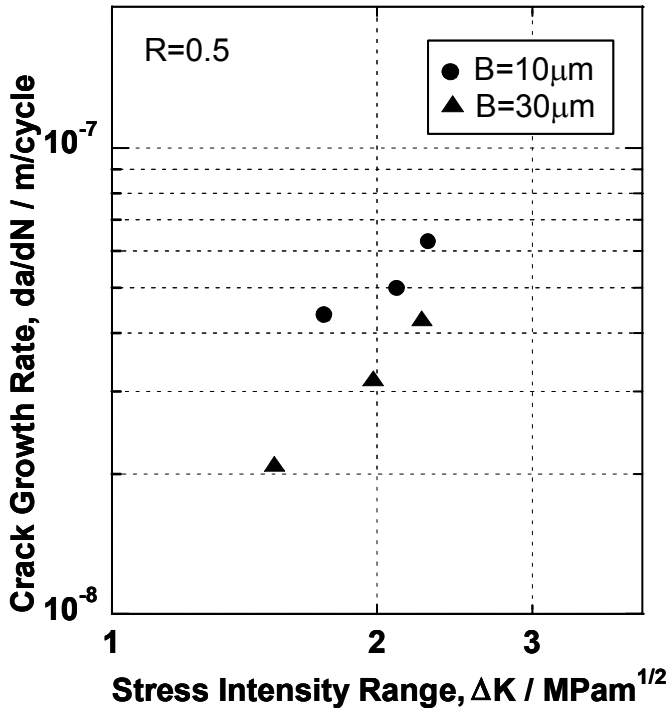

Figure 5: Fatigue crack growth resistance curves for the specimens with different *B* tested at a stress ratio of 0.5.

Effect of Specimens Size on Fatigue Crack Growth

As shown in Fig. 3, the effect of stress ratio on fatigue crack growth, which is deduced to be associated with a crack closure effect, is observed even for micro-sized specimens. The length of crack extended by fatigue loading in the micro-sized specimens used in this investigation was only 2 - 3 μm as shown in Fig. 2. Generally, crack closure effects are less pronounced for short cracks with length of less than 100 μm and almost no closure effects are observed for extremely short cracks with length in the order of microns [10]. However, these observations have been obtained for short cracks in ordinary-sized specimens. In contrast, the size of the specimen used in this investigation is three dimensionally small, so the normalized crack length is sufficiently long compared to the specimen size (actually, a/W is approximately over 0.5 at final fracture). Therefore, the crack length of 2 - 3 μm should be regarded as a long crack for this size of specimen, so the closure effects are deduced to be pronounced even for micro-sized specimens.

In this investigation, the fatigue crack growth behavior for micro-sized specimen was clarified. However, the detail of size effects on fatigue crack growth behavior is still unclear. Further investigation is required to quantify the size effect on fatigue mechanisms in micro-sized specimens.

CONCLUSIONS

Fatigue crack growth tests have been performed for micro-sized cantilever beam type specimens prepared from an electroless plated Ni-P amorphous alloy thin film to investigate the size effects on fatigue crack growth behavior of such micro-sized specimens.

Striations were observed on the fatigue fracture surfaces and fatigue crack propagation rates were estimated by a careful measurement of the striation spacing. The fatigue crack growth rates at stress ratios of 0.3 and 0.5 were almost identical, but the fatigue crack growth rate at stress ratio of 0.1 were lower compared to that at 0.3 and 0.5 at a given value of ΔK. This suggests that crack closure may occur even in such micro-sized specimens. In contrast, the fatigue crack growth rate at a stress ratio of 0.7 was

higher than those at 0.3 and 0.5. The fatigue crack was extended by both cyclic and static loading and this causes higher fatigue crack growth rate at a stress ratio of 0.7. The results obtained in this investigation are the first measurements of fatigue crack growth properties for micro-sized specimens and provide basic guidelines for design of actual micro-sized machine and MEMS devices.

Acknowledgement
This work was partly supported by the Grant-in-Aid for Scientific Research (B) (2) No. 12555186 from the Ministry of Education, Science, Sports and Culture, Japan. The authors would like to thank to Mr. S. Maekawa for his help in experiments.

REFERENCES

1. Read, D. T. and Dally, W. (1995) *J. Electronic Packaging*, **117**, 1.
2. Muhlstein, C. L. and Brown, S. (1998). In: *Tribology Issues and Opportunities in MEMS*, pp. 529-538, Bhusan, B., Klewer Academic Publications, Dordrecht.
3. Schwaiger, R. and Kraft, O. (1999) *Scripta Mater.*, **41**, 823.
4 Takashima, K., Kimura, T., Shimojo, M., Higo, Y., Sugiura, S. and Swain, M. V. (1999). In: *Fatigue '99 (Proc. 7th Int. Fatigue Cong.)*, pp. 1871-1876, Wu, X-R. and Wang, Z-G., (Eds). Higher Education Press, Beijing.
5. Higo, Y., Takashima, K., Shimojo, M., Sugiura, S., Pfister, B. and Swain, M. V. (2000). In: *Materials Science of Microelectromechanical Systems (MEMS) Devices II*, pp. 241-246, deBoer, M. P., Heuer, A. H., Jacobs, S. J. and Peeters, E., (Eds). The Materials Research Society, Pennsylvania.
6. Maekawa, S., Takashima, K., Shimojo, M., Higo, Y., Sugiura, S., Pfister, B. and Swain, M. V. (1999) *Jpn. J. Appl. Phys.*, **38**, 7194.
7. Maekawa, S., Takashima, K., Shimojo, M., Higo, Y. and Swain, M. V. (2000). In: *Materials Science of Microelectromechanical Systems (MEMS) Devices II*, pp. 247-252, deBoer, M. P., Heuer, A. H., Jacobs, S. J. and Peeters, E., (Eds). The Materials Research Society, Pennsylvania.
8. Okamura, H. (1976). *Introduction to Linear Fracture Mechanics*, Baifukan, Tokyo, (in Japanese).
9. Ichikawa, Y., Maekawa, S., Takashima, K., Shimojo, M., Higo, Y. and Swain, M. V. (2000). In: *Materials Science of Microelectromechanical Systems (MEMS) Devices II,* pp. 273-278, deBoer, M. P., Heuer, A. H., Jacobs, S. J. and Peeters, E., (Eds). The Materials Research Society, Pennsylvania.
10. Suresh, S. (1991), *Fatigue of Materials*, Cambridge University Press, Cambridge.

ORAL REFERENCE: ICF10071OR

FATIGUE CRACK GROWTH IN FERROELECTRIC CERAMICS DRIVEN BY CYCLIC ELECTRIC FIELD

D.N. Fang, B. Liu and K.C. Hwang
Department of Engineering Mechanics
Tsinghua University, Beijing 100084, China

ABSTRACT

In this paper, fatigue crack propagation of the ferroelectric ceramics with initial penetrated cracks under cyclic electric loading is investigated. The experimental results show that there are two distinct fatigue mechanisms. Under low electric loading, the emergence and growth of microcracks is major mechanism, while under a high electric field, the propagation of the macroscopic crack is dominant. It was found in experiments that the crack growth is in company with electric breakdown occurred inside the crack.

KEYWORDS

Ferroelectric ceramic, Electric Fatigue, Crack propagation, Cyclic loading

INTRODUCTION

Electric-field-induced fatigue refers to the deterioration of material properties associated with electric cycling. Experiments by Uchino and Furuta [1], Jiang and Cross [2], Cao and Evans [3], Lynch et al. [4], Hill et al. [5], Tai and Kim [6], Zhu et al. [7], Winzer et al. [8], have shown that cracks grow in ferroelectric ceramics under cyclic electric field. The performance of ferroelectric ceramics in smart structures is often hampered by crack propagation in the devices [1]. Does the crack grow by electric breakdown, or by the stress field near the crack tip? Based on the experimental observation and the analysis, the present paper provides both a physical mechanism analysis and a mechanistic explanation. In this paper, different from most work done by others, the propagation of an initial penetrated crack in ferroelectric ceramics instead of the growth of initial surface cracks produced by indentation is studied. Note that the surface crack belongs to a three-dimensional crack and there exists residual stress in the neighborhood of the indentation. The major obstacle in introducing a penetrated crack in the specimen is the brittleness of ferroelectric ceramics. On the other hand, considered that the ferroelectrics usually are used in the low electric loading, the authors try to investigate the fatigue behavior in a more wide loading range. It is more important to study the case of fatigue with low cyclic amplitude ($E \le E_c$).

EXPERIMENTAL PROCEDURE

The specimen is shown in Fig.1. The material used for the experiment was PZT-5, which has a tetragonal crystal structure at room temperature and an average 3 μm grain size. Specimens were

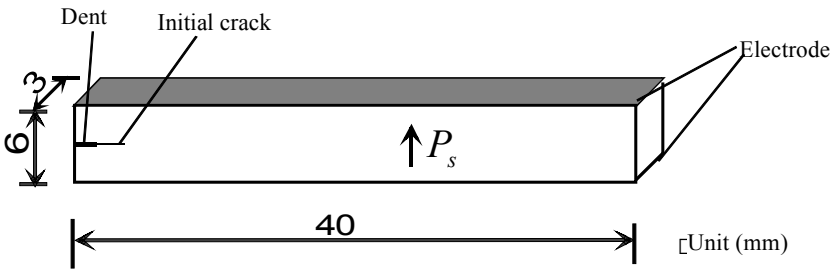

Fig. 1: Schematic of the specimen

cut and polished to dimensions of $40 \times 6 \times 3(mm)$. Gold electrodes were sputtered onto the upper and lower surfaces of the PZT-5 specimen. The specimens were poled in the direction perpendicular to the crack faces under an electric field of $3E_c$ (the coercive field, $E_c = 1000V/mm$) at a temperature of 130^oC. At first, a short notch with a width of 0.25mm was generated on the specimens. Then, by use of a Combined Load Device that was specially designed for producing pre-crack, the specimens were pre-cracked. For the details of this special technique, one can read the paper of Zhang et al [9]. The specimen was immerged in a silicon oil container that was made of transparent and insulating plexiglass and subjected to a cyclic electric field through the bolts that attach to the electrodes. The sine wave forms were applied to the specimens under a wide amplitude range of $0.8E_c$~$3.2E_c$. Because the specimen was plated on the upper and lower surfaces, if no crack existed in the specimen, the electric field in the specimen would be uniform. The power used in experiments was a voltage-adjustable alternating high voltage supplier, which can reach its highest output of $\pm$ 30 kV. There are five available frequencies which are 50 Hz, 4Hz, 3Hz, 2Hz and 1Hz.

RESULTS AND DISCUSSIONS

All specimens were observed through microscopy with 400 times amplification before loading. No obvious microcrack was found and the crack tips were very sharp. Fig. 2 exhibits that a crack propagates from an initial penetrated crack in the specimen. The experimental results [3] and the theoretical explanation [10] showed that there exists the anisotropy of fracture toughness in ferroelectrics. That is, the crack propagates along the direction perpendicular to the electric field more easily than along the direction parallel to the electric field. The reason that the main crack grows along the middle crack surface is due to the fact that the crack in the middle surface would bring the greatest disturbance for the electric and mechanical field. This may cause the strongest electric field and stress concentrations that induce the largest energy release rate.

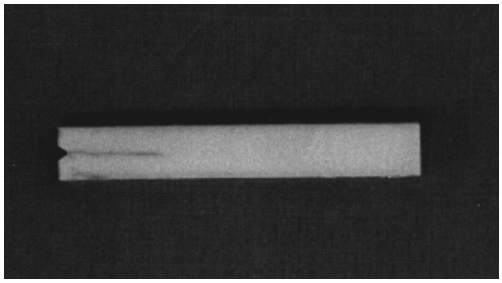

Fig. 2: The propagated macroscopic crack in the specimen

In the test, it was also found that the crack did not grow at once when the electric field was applied. It always frizzed for some time, then propagated quickly, especially under a low electric field. Moreover, there were some phenomena that occur before the crack grows. For example, some little bubbles produced from the main crack and the buzz noise can be heard. When the loading frequency was low, it can be found that sparks occurred inside the crack, and some black powder appeared on the crack faces. After a period of fatigue cycling, detached the specimen along the crack, we found that the crack surface generated by electric-field-induced fatigue was black. Note that the buzz always occurred and was independent of the crack length that would influence resonant frequency. Since the electric sparking was observed, it can be assumed that the electric breakdown occurred inside the crack. According the theory on electric breakdown [11], if there are bubbles in the liquid, since the electric fields in dielectrics under alternating current (AC) is inversely proportional to their permittivities, the electric field in the bubbles is always higher than that in the liquid. Because the electric field of electric breakdown in bubbles is less than that for liquid, the ionization

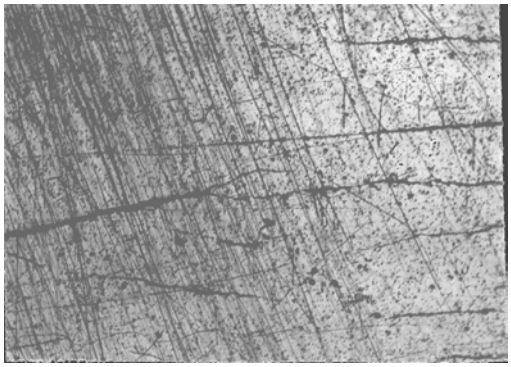

Fig. 3: Optical micrograph of a microcrack Distribution under E=0.8Ec observed by microscopy with 50 multiplication.

would happen in the bubbles first, which would lead to both the increase of temperature and the inflation of the volume of bubbles. On the other hand, the ionization produces many electrons with high energy, which collides with the molecules of the liquid, makes the liquid ionize and produces more bubbles. With the growth and birth of the bubbles, the Bubble Bridge would finally be formed between the crack surfaces, and the electric breakdown would occur locally. Moreover, the electric breakdown occurred in the bubbles would get off light and sound. Therefore, the theory on electric breakdown can be used to explain the experimental phenomena including the occurrence of bubbles, the buzz, the black crack surfaces as well as the sparking.

Another important phenomenon was that crack growth has two patterns in ferroelectrics under electric cycling. One is the case of the low electric field, i. e. $E < 0.83E_c$, in which the macroscopic crack stoped growing after it grew a little bit, and many microcracks in front of the macroscopic crack tip were found by microscopy. Furthermore, these microcracks would grow with the increase of the cycling number. The microcrack distribution near the macro-crack is shown in Fig. 3. Another crack growth pattern is corresponding to the case of high electric field, i.e. $E > 0.83E_c$, in which only macroscopic crack propagated and no micro-cracks were found as shown in Fig. 4. It is believed that the propagation of the electric-field-induced fatigue crack depends on the competition between two mechanisms. That is, one results in macroscopic crack growth and the other leads to produce microcracks. When the electric field is low, the macroscopic crack grows very slowly, and the long period of time in the process permits microcracks to emerge and grow. On the other hand, the microcracks near the macroscopic crack tip would weaken the electric field and thus the macroscopic crack would grow more difficult. Finally, as well known, the micro-cracks will produce a shield that impedes the propagation of the macro-crack. But for the case of high electric field, since the macroscopic crack propagated rapidly, the microcracks had no time to occur and grow. Besides, the electric field at the back wakes of the macroscopic crack was weakened due to the existence of

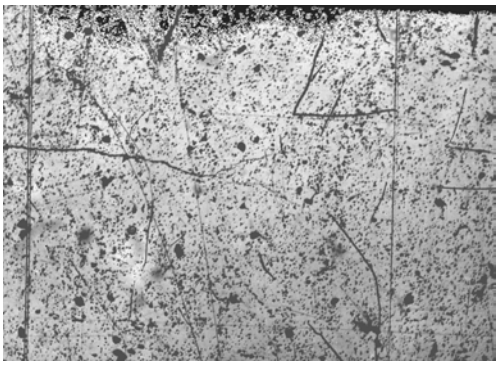

Fig. 4: Optical micrograph of a microcrack Distribution under E=1.0Ec observed by microscopy with 50 multiplication.

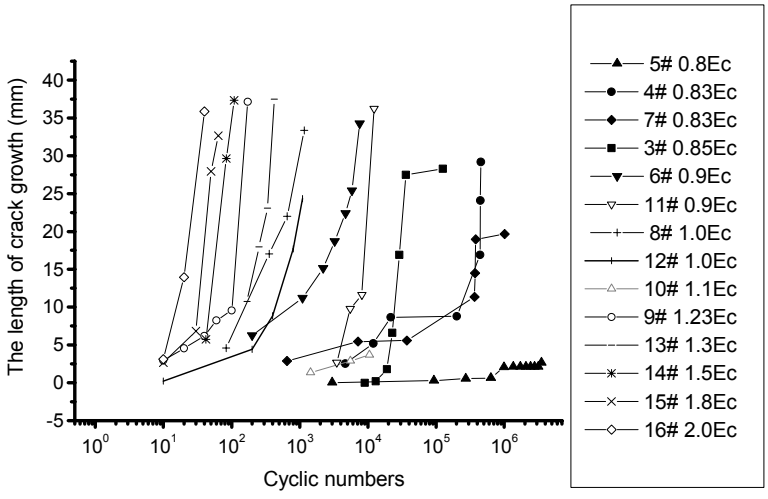

Fig. 5: Variation of crack growth length as a function of cyclic numbers

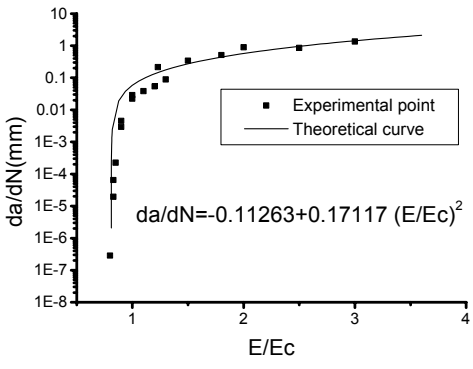

Fig. 6: Variation of crack growth rate as a function of electric field

the macroscopic crack, which can reduce the occurrence of microcracks as well. In Fig. 8, the curves between the loading numbers and the length of crack growth are presented. Note that although the crack growth rate varies significantly, they still almost are stable. The difference among the cyclic life corresponding to different amplitudes of the cyclic electric field can be considerably large. Fig.9 reveals the relationship between the electric loading and the crack growth rate. Although the logarithmic coordinate system is used, a nonlinear power relation between the electric field and the crack growth rate is obvious.

A THEORETICAL ANALYSIS OF THE CRACK GROWTH RATE

Fig. 7 shows the schematic of the proposed model. A voltage is applied on the upper and lower surfaces of the specimen. Consider the energy release rate between two regions (region I and region II), as shown in Fig. 7. The region I denotes the region far behind the crack tip while the region II denotes the region far ahead of the crack tip. Since the region I and the region II are far from the crack tip, the mechanical and electrical fields are uniform in them. Note that the energy release rate for crack growth is the difference of the unit length energy between the region I and the region II. The voltage at the upper surface of the specimen is V_2 and the voltage at the upper crack surface in region I is V_1. The height of the specimen is *2H* and the distance between crack surfaces in region I is *2h*. The permittivities of the specimen and the medium inside the crack are ε_m and ε_c, respectively. Next, in order to calculate the energy of the region I and the region II, we define D_1 and D_2 as the electric displacements of the region I and the region II, respectively. Because the electric displacement vector in the region I or in the region II is perpendicular to the middle surface, only one component of the electric displacement vector is not zero and written as D_1 or D_2. D_1 and D_2 can be calculated in the specimen subjected to an electric field as follows

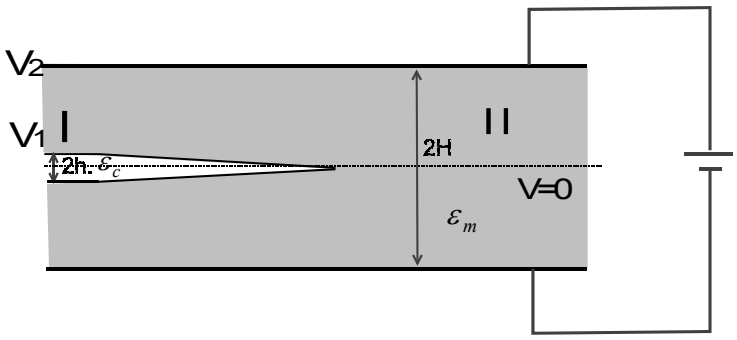

Fig. 7: Schematic of the analysis model

$$D_1 = \frac{-V_2 \varepsilon_c \varepsilon_m}{\varepsilon_m h + \varepsilon_c (H - h)}, \quad D_2 = \frac{-V_2}{H} \varepsilon_m \tag{1}$$

In order to calculate the total energy of unit length, the internal energy needs to be calculated at first. The internal energy of the region I and the region II is

$$U_1 = -V_2 D_1 = \frac{V_2^2 \varepsilon_c \varepsilon_m}{\varepsilon_m h + \varepsilon_c (H - h)}, \quad U_2 = -V_2 D_2 = \frac{V_2^2 \varepsilon_m}{H} \tag{2}$$

The external force potentials of the region I and the region II are

$$F_1 = 2V_2 D_1, \quad F_2 = 2V_2 D_2 \tag{3}$$

The total energy of the region I and the region II is

$$\Pi_1 = U_1 + F_1 = V_2 D_1, \quad \Pi_2 = U_2 + F_2 = V_2 D_2 \tag{4}$$

From equation (1)-(4), the energy release rate can be obtained as

$$\begin{aligned} G = \Pi_2 - \Pi_1 = V_2(D_2 - D_1) &= V_2^2 \varepsilon_m \left(\frac{\varepsilon_c}{\varepsilon_m h + \varepsilon_c (H-h)} - \frac{1}{H} \right) \\ &= V_2^2 \varepsilon_m \frac{(\varepsilon_c - \varepsilon_m) h}{H[\varepsilon_m h + \varepsilon_c (H-h)]} \end{aligned} \tag{5}$$

From equation (5) one can know that only when $\varepsilon_c > \varepsilon_m$, the energy release rate, G, is positive. So if the crack is impermeable, that is $\varepsilon_c = 0$, the energy release rate is negative and it seems that the crack should not be able to grow. However, it has been found in the experimental observation that there exists the electric breakdown. Thus, if we assume that the crack is a conducting crack in the electric breakdown process, i.e. $\varepsilon_c \to \infty$, the energy release rate becomes positive. In addition, note that the total energy for the conducting crack is lower than one for the permeable crack and thus the energy difference makes the electric breakdown happen. Substituting $\varepsilon_c \to \infty$ into equation (5) we get

$$G = V_2^2 \varepsilon_m \frac{h}{H(H-h)} \tag{6}$$

From equation (6), we note that if *h* equals zero, i.e. corresponding to the case of a crack without width or a mathematical crack, the crack could not propagate. Actually, cracks always have finite width, and equation (6) shows that the greater *h* the higher energy release rate. From equation (6) it is found that the relationship between the driven energy for crack growth and the electric voltage or the electric field is $G \propto V^2 \propto E^2$. It can be assumed that the fracture resistance energy consists of two parts. One is G_1, which represents the dissipated energy dependant on Δa (the crack growth in this step), and a further assumption of $G_1 \propto \Delta a$ is introduced. For example, the surface energy belongs to G_1. The other part is G_0, representing the dissipated energy independent of Δa or the least energy necessary to start fracture. The energy balance equation can be expressed as

$$AE^2 = G = G_1 + G_0 = B\Delta a + G_0 \tag{7}$$

where A and B are constants. From the above equation, we solve Δa as

$$\Delta a = -\frac{G_0}{B} + \frac{A}{B} E^2 = k_0 + k_1 E^2 \tag{8}$$

where $k_0 = -\frac{G_0}{B}$ and $k_1 = \frac{A}{B}$ are constants to be determined. They can be obtained by fitting the experimental data as shown in Fig.6. In Fig. 6, the theoretically predicted curve is presented. It is found that there is a good consistence between test points and theoretical curve. Moreover, since $k_0 = -\frac{G_0}{B} < 0$ and $k_1 = \frac{A}{B} > 0$, it is known from equation (8) that there will be a critical electric field $\widetilde{E}$ which makes $\Delta a = 0$ and corresponds to the minimum value of the electric field that can make the crack grow. When $E < \widetilde{E}$, Δa is negative, which means the crack could not propagate. The critical electric field can be obtained as $\widetilde{E} \approx 0.81E_c$ from the theoretical curve presented in Fig. 6, which approximately equals to the experimental result. As shown in Fig. 5, when $\widetilde{E} \approx 0.80E_c$, the cyclic number reaches four millions.

CONCLUSIONS

The electric-field-induced fatigue displays distinct characters under different magnitudes of electric loading. When $E < 0.83E_c$, the emergence and growth of microcracks is the major fatigue mechanism that impeds the macroscopic crack growing. Whereas, when $E > 0.83E_c$, the macroscopic crack growth is the dominant fatigue mechanism and no microcracks were found in experiments. The crack always propagates in company with the local electric breakdown occurred inside the crack. From the analysis, it is known that the electric field causes the positive energy release rate. The crack growth rate is nonlinearly related to the cyclic electric load.

REFERENCES

1. Furata A. and Uchino K. (1993) *J. Am. Ceram. Soc.,* 76:1615-1617.
2. Cao H.C., Evans A.G. (1994) *J. Am. Ceram. Soc.* 77:1783-1786.
3. Lynch C.S, Chen L., Suo Z., and McMeeking R.M., (1995) *J. of Intelligent Mater. Sysm. And Struc.* 6:191-198.
4. Hill M.D., White G.S., Hwang C.S., Lloyd I.K. (1996) *J. Am. Ceram. Soc.* 79(7)1915-1920
5. Jiang Q.Y., Cross L.E. (1993) *J. Mater. Sci.* 28:4536-4543
6. Tai W.P. and Kim S.H. (1996) *Mater. Sci. and Engng.* B38:182-185
7. Zhu T., Fang F. and Yang W. (1999) *J. Mater. Sci. Letters* 18:1025-1027.
8. Winzer H., Schneider G.A., Steffens J., Hammer M. and Hoffman M.J. (1999) *J. of the European Ceramic Society* 19:1333-1337.
9. Zhang J.S., Dong Z.X., Hua X. and Fang D.N., (1999) *Proceedings of IMMM'99, the fourth International Symposium on Microstructures and Mechanical Properties of New Engineering Materials*, Beijing, International Academic Publishers, pp.121-125.
10. Park S. B. and Sun C. T. (1995) *J. Am. Ceram. Soc.* 78: 1475-1480.
11. Dwyer O' (1973) The theory of electrical conduction and breakdown in Solid dielectrics, Oxford: Clarendon Press.

Paper Ref No: ICF100764OR

FATIGUE CRACK GROWTH PREDICTIONS IN AA 5083 AND AA 2024 USING A SIMPLE GEOMETRIC MODEL.

Ton Riemslag[(1)], Kees van Kranenburg[(1)], Saskia Benedictus-de Vries[(1)], Fred Veer[(2)] and Jan Zuidema[(1)(*)]

[(1)] Laboratory of Materials Science, Delft University of Technology
[(2)] Faculty of Architecture, Delft University of Technology
E-mail to: j.zuidema@tnw.tudelft.nl

Abstract

Constant amplitude fatigue crack growth tests conform ASTM E647 are performed on AA 5083-H321 for different R-values in air and seawater. Fatigue crack growth starts in the flat tensile mode, but after some crack advance shear lips start on both sides of the fracture surface. The shear lips grow in width on further crack growth until (almost) the total crack surface has become slanted. The start and growing in width of the shear lips is accompanied by a decrease in crack growth rate, resulting in a change to a lower slope of da/dN-ΔK on double-logarithmic scale. When the shear lips cover the total fracture surface the original slope of da/dN versus ΔK is almost restored. Crack closure relations for several parts of da/dN versus ΔK have been found. A simple macroscopic geometrical model is made in order to predict fatigue crack growth behaviour in the shear lip crack growing area. The model is also applied to a situation with underloads in AA 2024-T351.

Keywords

crack closure, shear lips, underloads, crack growth prediction

Introduction

The fatigue crack growth properties of two aluminum alloys, AA 2024 and AA 5083, are compared. The AlCuMg Aluminium Alloy AA 2024 is widely used in both civil and military aircraft because of its superior damage tolerance and fatigue properties. The AlMgMn Aluminium Alloy AA 5083 is increasingly used in shipbuilding, including high-speed ferries, because of its good mechanical properties and excellent corrosion (fatigue) resistance. Both materials have been fatigued in laboratory air and AA 5083 also in seawater. The difference in fatigue fracture behaviour is described in terms of differences in macroscopic fracture surface and different corrosion-fatigue behaviour. Crack closure was accounted for by varying the stress ratio. Especially transitions in the crack growth rate, that are accompanied by developing shear lips, form a subject of study. The shear lips grow in width as the crack length increases, but there exists no direct correlation between start of shear lips and transition in crack growth rate. It will be shown that suppression of shear lip initiation and growth also shows the same transitions.

For both materials the shear lip starts at about the same crack growth rate da/dN, at which value also the slope change in da/dN-ΔK occurs, but both events are dependent on the environment. When the shear lips cover the total fracture surface the original slope of da/dN versus ΔK is changed again. Crack closure relations for AA 5083 for some parts of da/dN versus ΔK have been found. A simple macroscopic geometrical model is made in order to

predict fatigue crack growth behaviour in the shear lip crack growing area, using crack growth rate data from the area without shear lips.. The principle of the calculation is that the K factor and the shear lip width are both influenced by the same, yet unknown (micro)mechanism. The shear lip width is then considered as a measure for K. The developing shear lip width rate is assumed to be proportional to the difference in actual shear lip width and the equilibrium shear lip width, being the width as would be found in a constant ΔK test after a large enough crack growth.
Furthermore the model is applied to a situation with underloads in AA 2024. The underloads are high enough to give rise to slanted crack growth. The crack growth behaviour after different numbers of underloads is both measured and predicted.

Experiments

The chemical composition of the materials is as shown in the table:

TABLE CHEMICAL COMPOSITION(WT %) OF AA 5083 AND 2024, REMAINDER AL

AA	Mg	Mn	Si	Fe	Cr	Cu	Zn	Ti
5083	4.5	0.65	0.26	0.22	0.09	0.09	0.06	0.03
2024	1.18	0.67	0.34	0.14	0.004	4.75	0.19	0.03

The center-cracked specimens have a length of 340 mm, a width of 100 mm and a thickness of 8 mm (AA 5083) or 6 mm (AA 2024). The fatigue crack growth experiments are performed on a computer-controlled servohydraulic fatigue machine. The loading program is

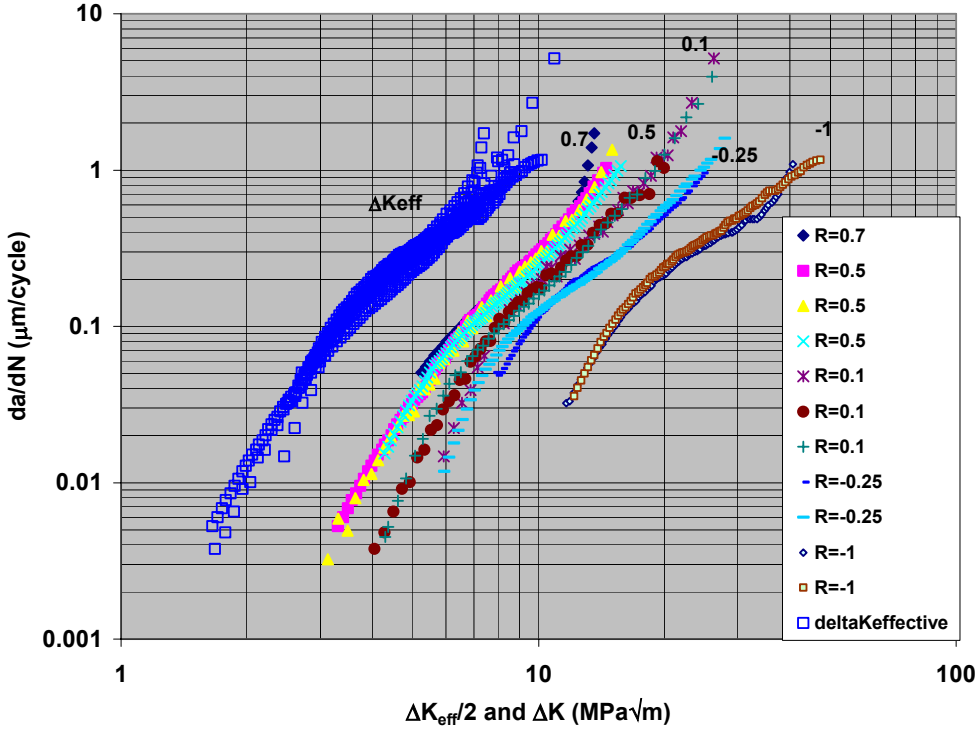

Figure 1. Results of 11 constant amplitude tests on AA 5083 at 5 different values of R and the corresponding da/dN-ΔK_{eff} (shifted a factor 2 to the left for clearness).

offered to the machine in the form of a load table where the maximum load, the minimum load, the crack length and the frequency are specified.. The crack length is measured using a pulsed direct-current potential drop measurement system. The frequency is 10 Hz.

Results

The results from 11 constant load amplitude tests on material AA 5083 in air are shown in figure 1. It can be noticed that at about da/dN = 0.1 μm/cycle, the crack growth rate curves change in slope. Observations of the different fracture surfaces revealed that at the corresponding ΔK-values the crack appearance started changing from flat to slant. At first the change in slope was attributed to a possible different crack closure situation due to the growing shear lips. But it was shown that suppression of shear lips leads to the same change of slope, thus extra closure due to shear lips probably doesn't exist in AA 5083. As the start of shear lips corresponds with different K_{max}-values (e.g. K_{max} = 8.8 and 13 MPa√m respectively for R = 0.1 and 0.5), it can be concluded that the start of the shear lips is also probably not a matter of plane stress/plane strain. The only obvious correlation is with the crack growth rate or, which is equivalent, with the ΔK_{eff}. This is in agreement with observations on AA 2024 [1]. In seawater the change in slope starts at about 0.2 μm/cycle, at 10 Hz [2].

Crack closure relations

For AA 2024 the well-known relation of Elber will be used, with U=0.5+0.4R for – 0.1 < R < 0.7. This relation fits the results for AA 5083 not very well. Crack closure for this alloy is not measured directly, but it is found by correlating 7 of the 11 constant amplitude da/dN versus ΔK results shown in figure 1. One test at R=0.7, one test at R=0.5, two tests at R=0.1, one test at R=-0.25 and two tests at R=-1. The best quadratic crack closure function $U= a+bR+cR^2$ is found by taking all combinations of a, b and c and calculating $\Delta K_{eff}=U\Delta K$ for all measurement points of the 7 tests. A power formula of type $da/dN=C\ \Delta K_{eff}^m$ is fitted through the da/dN-ΔK_{eff} points. The combination of a, b and c with a maximum value of the correlation coefficient, based on log(da/dN) and log(ΔK_{eff}), is considered the best combination. The combination is normalized, i.e. the normalized coefficients are found by dividing the best calculated coefficients by their sum, meaning that U=1 if R=1. The best crack closure formula found in this way for this material is $U=0.66+0.32R+ 0.02R^2$. The formula for the best power fit is given in equation 1, where da/dN in (μm/cycle) and ΔK_{eff} in (MPa√m):

$$da/dN=0.70*10^{-3}\ \Delta K_{eff}^{2.8} \qquad (1)$$

However the results in figure 1 show that the curves for R=0.5 and 0.7 are about the same, meaning that crack closure is not important above R=0.5. If it is assumed that U=1 already for R>=0.5, then this constraint can be added to the calculation procedure. The result of the calculation is now $U=0.80+0.39R+ 0.03R^2$ for R<=0.5 and U=1 for R>0.5. With this constraint da/dN can be calculated as:

$$da/dN=0.41*10^{-3}\ \Delta K_{eff}^{2.8} \qquad (2)$$

The same crack closure calculation was also applied using only datapoints without shear lips, i.e. for da/dN<0.1 μm/cycle. For the constraint situation with U=1 for R=1, the result is $U=0.65+0.32R+0.03R^2$ and

$$da/dN=0.80*10^{-4}\ \Delta K_{eff}^{4.16} \qquad (3)$$

The da/dN-ΔK_{eff} fit result for the constraint situation with U=1 for R=1, eq.1, is also shown in figure 1 for all data points at different R. A parallel shift is applied to better show the result, i.e. the corresponding ΔK_{eff} results have to be multiplied by a factor of 2.

The geometric crack growth prediction model

Although the start of shear lips is not the cause of the change in slope of the log(da/dN)-log(ΔK) line, it seems to be a consequence of another, not yet known (micro)mechanism, that results in both shear lip start and growth and also in a lower slope of the log(da/dN)-log(ΔK) relation. The shear lip width is chosen to represent this unknown mechanism. It was shown in

reference 1 that shear lips grow in width, even in a constant ΔK test, until an equilibrium width has been reached. A linear relation was found between equilibrium width and ΔK_{eff} for AA 2024. An equivalent behaviour for AA 5083 was assumed. In figure 2 a fatigue fracture surface is shown. The shear lip is suppressed on one side of the specimen by making a scratch with a depth of 0.1 mm along the crack growth direction.

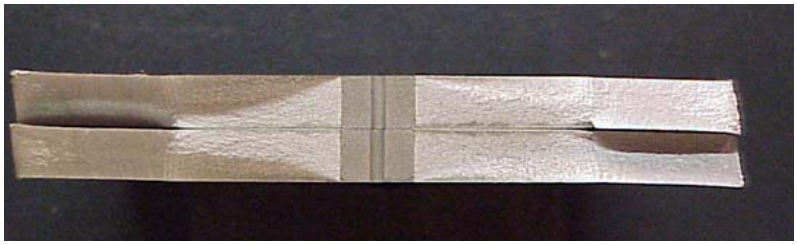

Figure 2. Shear lips suppressed on one side in AA 5083.

Hardly any difference was found in crack growth rate between specimens with scratches on both sides, where shear lips were fully suppressed, or specimens with shear lips on one side or specimens with full shear lips. Also the change in slope occurred equally, for da/dN=0.1 μm/cycle, in all three different kind of specimens. Based on a preliminarily study of the fracture surfaces the equilibrium shear lip width is estimated (for $t_{s,eq} > 0$):

$$t_{s,eq} = 0.90\Delta K_{eff} - 5 \text{ (mm)} \quad (4)$$

If the actual $t_{s,eq}$ and ΔK_{eff} do not fulfill this equation, the shear lip width will increase or decrease until the equilibrium situation is reached, according to the equation given above. The rate of change in shear lip width is taken proportional with the difference in actual width and equilibrium width, in formula form:

$$dt_s/da = C(t_{s,eq} - t_s) \quad (5)$$

For AA 5083 the C-value is estimated as:

$$C = 0.40/t_{s,eq} \quad (\text{mm}^{-1}) \quad (6)$$

In a constant amplitude test the ΔK_{eff} changes continuously and hence also $t_{s,eq}$ and t_s; t_s lags behind $t_{s,eq}$ for the growing crack. It is assumed that the crack driving force ΔK is influenced by the slope changing (micro)mechanism and that the shear lip width is a measure for it. The ΔK that is responsible for the lower da/dN increase in the shear lip area and beyond is called ΔK(shear). It is defined as:

$$\Delta K(\text{shear}) = \Delta K/(1+2(\sqrt{2})-1)t_s/t) \quad (7)$$

It means that the product of ΔK and the transverse crack length is assumed to be constant. If a shear lip angle of 45° is taken $\Delta K(\text{shear}) = \Delta K/\sqrt{2}$ for a complete slanted surface with $t_s = t/2$, and for $t_s = 0$ it gives $\Delta K(\text{shear}) = \Delta K$.

A computer program was written to calculate ΔK(shear) as a function of the crack length for constant amplitude tests. Also da/dN versus ΔK is calculated, using the da/dN-ΔK equation in the crack growth area without shear lips.

Result of the prediction

The prediction is tested on the crack growth rate result for R=0.1 as shown in figure 3. The slope of the results is about 5.5 for da/dN<0.1 μm/cycle, above which value it transforms to about 2.5 until da/dN =1 μm/cycle. From 1 to 10 μm/cycle the slope is again about 5. Above 10 μm/cycle static effects are probably superposed on the fatigue crack growth rate. For the calculation of ΔK the ASTM formula for a centre-cracked tension specimen (width w) is used:

$$K = \sigma\sqrt{\pi a}\sqrt{\sec\frac{\pi a}{w}} \quad (8)$$

The prediction is quite well in the shear lip developing area. Static effects have not been incorporated in the calculation.

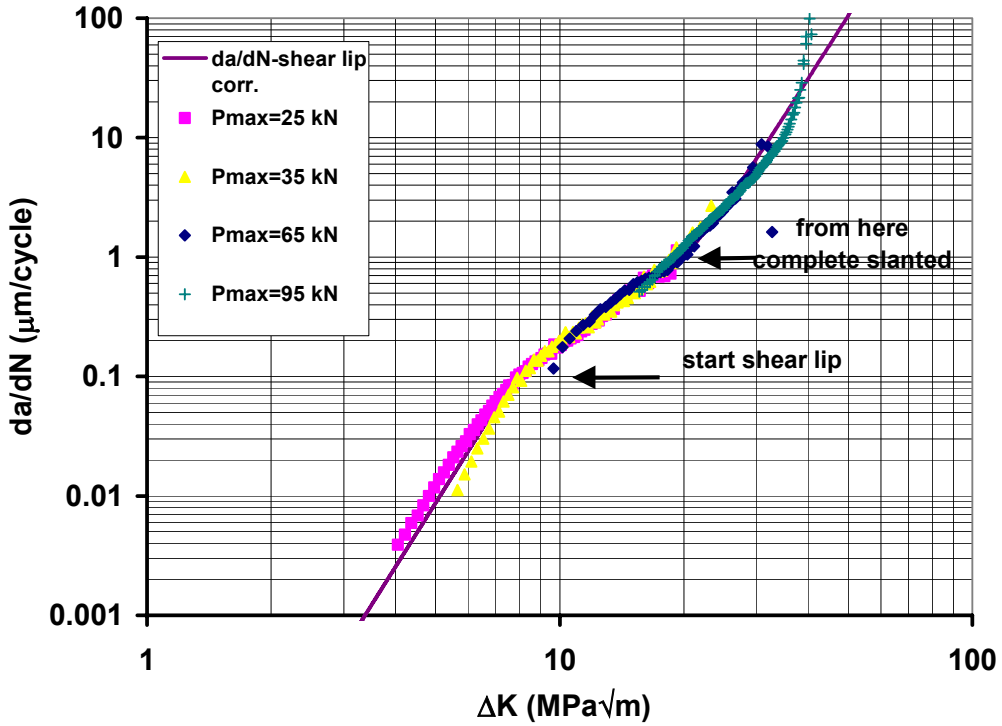

Figure 3 Experimental fatigue crack growth rate results and prediction for AA5083 at R=0.1

Underloads in AA 2024

Constant ΔK tests with constant ΔK underloads were performed in AA 2024. The underloads were high enough to lead to development of shear lips, while the ΔK before and after the underloads were to low for it. All K_{max} were the same to avoid plasticity induced crack closure at the loading transitions. A retardation in crack growth rate was measured after the underloads. The retardation was larger for higher ΔK of the underloads and for more underload cycles. The shear lips vanished quickly after the underloads, but the retardation of the crack growth rate lasted about three times as long, i.e. if there is an effect of the shear lips on ΔK, it extends outside the area where shear lips are really present. The same calculation is applied as on AA 5083, only now, in this situation of decreasing and vanishing shear lip width, ΔK is not assumed to be influenced by the real shear lip width at the crack tip, but by a mean of the shear lip width extending over some mm crack length after the tip. Calculations taking the actual shear lip width at the tip as a measure for ΔK, and calculations taking the mean shear lip width over 3 mm after the tip were applied and compared with a real test with underloads, see figure 4. The 3 mm was estimated using a potential drop measurement of the affected crack length by crack closure in this case.

A possible explanation of the change in slope.

The following explanation is rather speculative at the moment. It is found that in AA 5083 the change in slope starts at 0.1 µm/cycle in air and at 0.2 µm/cycle in seawater [2]. The change in slope is independent of K_{max} or ΔK. Earlier investigation on AA 2024 in vacuum did result in a change of slope at about 0.004 µm/cycle (for R=0.3). These results indicate that the reason of the change in slope is not due to mechanically causes alone, but that it more

depends on the environment. Suppose that a corrosion reaction is responsible for enhanced fatigue crack growth below the transition, i.e. below 0.1 μm/cycle in air.

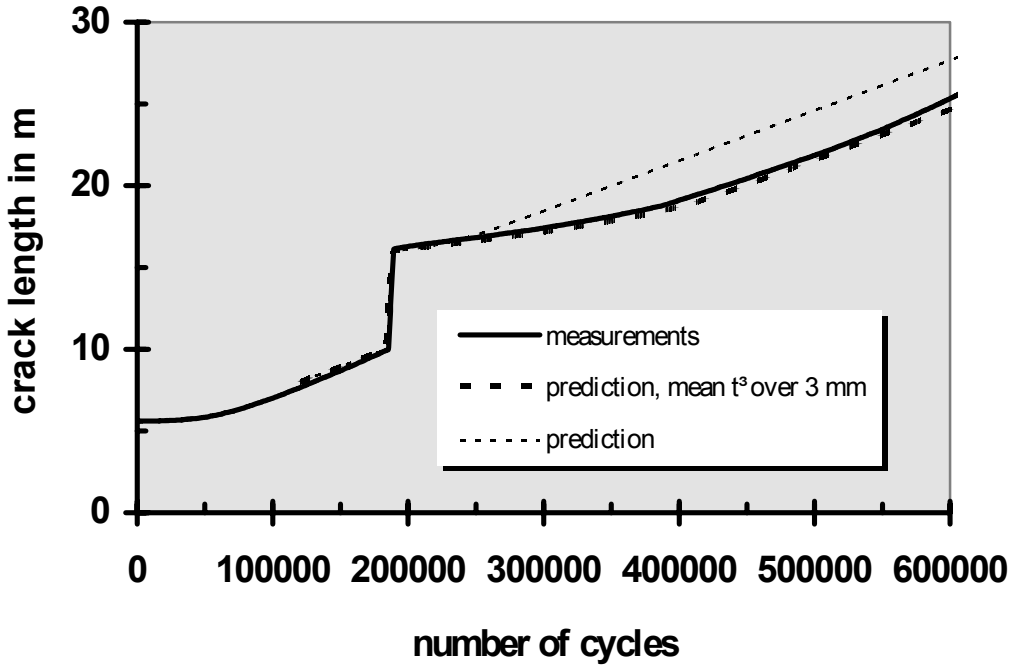

Figure 4. Measurements and prediction of the a-N curve in AA 2024 with 5000 underloads, underload sequence ΔK=5-16-5 (MPaŒm) at K_{max} = 29 (MPaŒm) and 10 Hz.

Above this crack growth rate the crack moves too fast for the corrosion assisted mechanism to take fully place, and the intrinsic fatigue crack growth rate will increasingly dominate, with a growing slanted crack surface as a result. Seawater is a more aggressive environment, and it can be expected that a higher crack growth rate than in air is needed to outrun the corrosion reaction speed. In vacuum the reverse is true and the transition will take place at a very low value of the crack growth rate. We will at the moment not speculate on the exact mechanism of the corrosion reaction, but following this rationale it is clear that the fatigue fracture situation with shear lips is the "normal" fatigue crack growth mode in these Al Alloys. When the fracture surface is flat, it is so by an environmental attack.

Conclusions

1) The shear lip width seems to be a good measure for the transition from fast crack growth rate due to environmental attack to slower intrinsic true fatigue crack growth rate after the transition point.
2) The enhanced crack growth rate at lower da/dN is due to environmental attack.

References

1) Zuidema, J. and M. Mannesse, *A model for predicting slant crack growth in Al 2024*. Engineering Fracture Mechanics 34 ,1989, 2, p.445-456'
2) Jan Zuidema, Saskia de Vries and Adirakhmantyo Hascaryantono,*The Accelerated ΔK Fatigue Crack Growth Test on AA 5083-H321 and Similitude Validation,*The 13th European Conference on Fracture ECF 13, 6th-9th september, 2000, San Sebastian, Spain.

PAPER REFERENCE: ICF100327PR

FATIGUE CRACK GROWTH UNDER SIMPLE VARIABLE AMPLITUDE LOAD SEQUENCES

L. P. Borrego[1], J. M. Ferreira[2] and J. M. Costa[2]

[1]Department of Mechanical Engineering, ISEC/IPC, 3030 Coimbra, Portugal
e-mail: luis.borrego@mail.dem.uc.pt
[2]Department of Mechanical Engineering/FCT, University of Coimbra, 3030 Coimbra, Portugal

ABSTRACT

Fatigue crack propagation tests with single tensile peak and periodic overloads, Hi-Lo blocks and Lo-Hi blocks have been performed in 6082-T6 aluminium alloy, either in load control or in constant ΔK conditions. The tests were carried out using Middle-Tension specimens in a servo-hydraulic machine at R=0.05 and a frequency of 20 Hz. Crack closure was monitored in all tests by the compliance technique using a pin microgauge. The observed transient post-load step behaviour is discussed in terms of the overload ratio, ΔK baseline levels and number of intermediate baseline cycles. The crack closure parameter U was obtained and compared with the crack growth transients. Plasticity induced closure seems to be the main mechanism in determining the transient crack growth behaviour in 6082-T6 aluminium alloy following the simple variable amplitude load sequences analysed.

KEYWORDS

aluminium alloys, fatigue crack propagation, overloads, crack closure

INTRODUCTION

The 6000 aluminium alloys series are very frequently used in structural applications under service conditions that involve random or variable amplitude rather than constant amplitude loading conditions, mainly due to the fact of allying a relatively high strength, good corrosion resistance and high toughness to a good formability and weldability. An accurate prediction of fatigue life requires an adequate evaluation of load interaction effects. However, fatigue crack growth under variable load amplitudes in this series of aluminium alloys is not as well understood as in the 7000 and 2000 series. Furthermore, the amount of data available for the material studied in this work is reduced.

The effects of crack growth retardation following single or multiple peak tensile overloads have been reported in many investigations simply because this type of loading can lead to significant load interaction effects [1-8]. Several mechanisms have been proposed to explain crack growth retardation, which include models based on residual stress [9], crack closure [10], crack tip blunting [11], strain hardening [12], crack branching [13] and reversed yielding [14]. The precise micromechanisms responsible for these phenomena are not fully understood. In spite of some controversy, the effect of

plasticity induced crack closure, has been identified as the main variable in explaining, fairly reasonably, the variation of the characteristic features of post-overload transients [1-5].

In recent work, the authors [15] concluded that crack closure was able to explain the influence of the stress ratio on the fatigue crack growth rate in 6082-T6 aluminium alloy, in both regimes I and II of crack propagation. Furthermore, for overload conditions, the influence of several load parameters could be correlated with the variation of crack closure. The present work intends to analyse the transient behaviour observed on crack growth rate following block loading and periodic overloads and to clarify if the observed behaviour can also be correlated with the crack closure phenomenon.

EXPERIMENTAL DETAILS

The material used in this research was an AlMgSi1 (6082) aluminium alloy with T6 heat treatment. The chemical composition (wt.%) of this alloy was 0.7-1.3 Si, 0.6-1.2 Mg, 0.4-1 Mn, 0.5 Fe, 0.25 Cr, 0.2 Zn, 0.1 Cu, 0.1 Ti, 0.05 other. The mechanical properties of the 6082-T6 aluminium alloy were as follows: 300 MPa tensile strength, 245 MPa yield strength and 9% elongation.

Fatigue tests were conducted, in agreement with the ASTM E647 standard, using Middle-Tension, M(T), 3 mm thick specimens with 200 mm and 50 mm length and width, respectively. The specimens were obtained in the longitudinal transverse (LT) direction from a laminated plate. The geometry of the M(T) specimen used in this study was presented elsewhere [15]. The notch preparation was made by electrical-discharge machining. After that, the specimen surfaces were polished mechanically.

All experiments were performed in a servo-hydraulic, closed-loop mechanical test machine with 100 kN load capacity, interfaced to a computer for machine control and data acquisition. All tests were conducted in air, at room temperature and with a frequency of 20 Hz. The specimens were clamped by hydraulic grips. The crack length was measured using a travelling microscope (30x) with a resolution of 10 μm. Collection of data was initiated after achieving an initial crack length $2a_0$ of approximately 12 mm.

Four different types of simple variable amplitude fatigue loading conditions were applied in this study, as shown schematically in Figure 1.

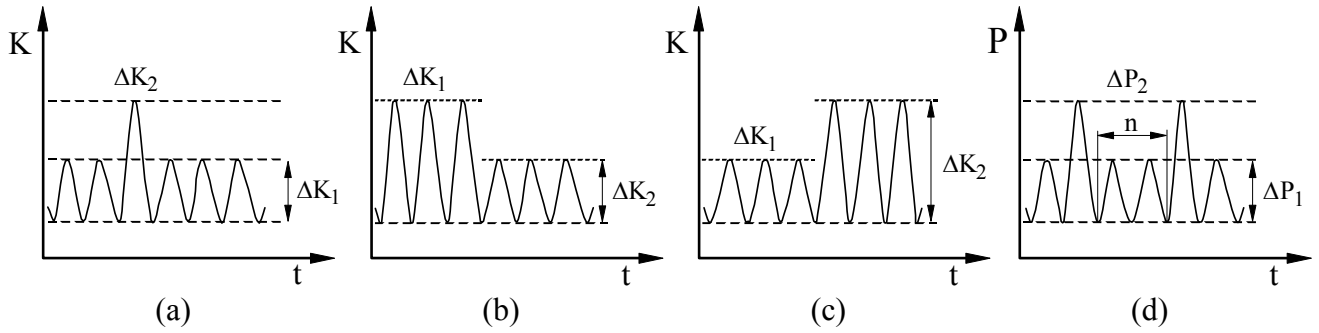

Figure 1: Applied simple variable amplitude loading sequences: (a) single peak overload; (b) Hi-Lo block; (c) Lo-Hi block; (d) periodic single overloads.

The single overload and the block loading tests where performed under constant ΔK and stress ratio R conditions, by manually shedding the load with crack growth. The load shedding intervals were chosen so that the maximum ΔK variation was smaller than 2%. The overloads were applied under load control during one cycle by programming the increase in load to the designated overload value. After the change of load, the associated transient crack growth behaviour was carefully observed. All loading conditions were investigated at R=0.05. The periodic overload tests were performed under load control and the

intermediate baseline cycles were previously programmed for each test. The crack growth rates were determined by the secant method.

Load-displacement behaviour was monitored at all crack measurements for each of the tests using a pin microgauge. The gauge pines were placed in the two drilled holes of 0.5 mm diameter located above and below the centre of the notch. The distance between these points was 3.5 mm. In order to collect as much load-displacement data points as possible during a particular cycle, the frequency was reduced to 0.5 Hz.

From the load-displacement records, variations of the opening load P_{op} were derived using the technique known as maximisation of the correlation coefficient [16]. This technique involves taking the upper 10% of the P-ε data and calculating the least squares correlation coefficient. The next data pair is then added and the correlation coefficient is again computed. This procedure is repeated for the whole data set. The point at which the correlation coefficient reaches a maximum can then be defined as P_{op}.

The fraction of the load cycle for which the crack remains fully open, parameter U, was calculated by the following equation:

$$U = \frac{P_{max} - P_{op}}{P_{max} - P_{min}} \tag{2}$$

The values of the effective stress intensity factor range, ΔK_{eff}, are given by the expression:

$$\Delta K_{eff} = K_{max} - K_{op} = U \Delta K \tag{3}$$

RESULTS AND DISCUSSION

Figure 2(a) illustrates the typical transient crack growth behaviour obtained when a specimen is subjected to a single tensile overload, a high-low block and a low-high block in a constant ΔK test. In this figure the crack length from the step load event, a-a_O, is plotted against the number of cycles from the point of load variation, N-N_O, where a_O and N_O are the crack length and the number of cycles at which the change in load is applied, respectively. Generally, the magnitude and extent of retardation are quantified by the crack growth increment affected by the step in load, Δa_O, and by the delay cycles, N_D. Δa_O is the crack growth distance between the point of load variation and the one at which the crack growth rate reaches the steady-state level corresponding to ΔK_2. N_D is the difference between the number of cycles at which growth to steady state level ΔK_2 is achieved and the number of cycles that would occur for the same loading conditions and crack length if no load variation was applied.

Figure 2(a) shows that there is a brief initial acceleration of crack growth rate immediately after the overload. The subsequent crack growth rate decreases until its minimum value is reached, followed by a gradual approach to the level of the baseline steady-state. The observed behaviour is usually referred to as delayed retardation of crack growth. The effect of the high-low block is similar to that observed for the peak overload. However, for this load sequence, the retardation is always immediate and not preceded by the acceleration phase. The low-high sequence produces an acceleration of crack growth rate, above the steady state level expected for the high block, followed by a gradual reduction to the corresponding steady-state level ΔK_2. These trends are consistent with the behaviour normally reported in the literature [3,5,17].

As expected, the magnitude and extent of crack retardation are higher for the high-low block than for an equivalent single tensile overload. For the overload Δa_O=0.65 mm and N_D=12900, while for the high-low block Δa_O=2.64 mm and N_D=277500, representing an increase in life of approximately fourteen times. Also, the minimum value of da/dN reached during the retardation phase decreases from 0.32 to 0.009 relative to the constant amplitude da/dN baseline level. Moreover, the crack retardation is even higher for the high-low sequence with ΔK_1=9 MPa $m^{1/2}$ and ΔK_2=6 MPa $m^{1/2}$**,** than for a 100% overload (Δa_O=2.52

mm and N_D=87400 cycles). The accelerated da/dN produced by the low-high block persisted for several thousands of cycles (approximately 2500 cycles and 0.35 mm affected crack increment).

The corresponding crack closure data are presented in figure 2(b), plotted in terms of the normalised load ratio parameter U, calculated by (4), against the crack growth increment from the point of the step in load. This plot presents the typical crack closure response, in 6082-T6 aluminium alloy, obtained following the load sequences (a) to (c) represented in figure 1.

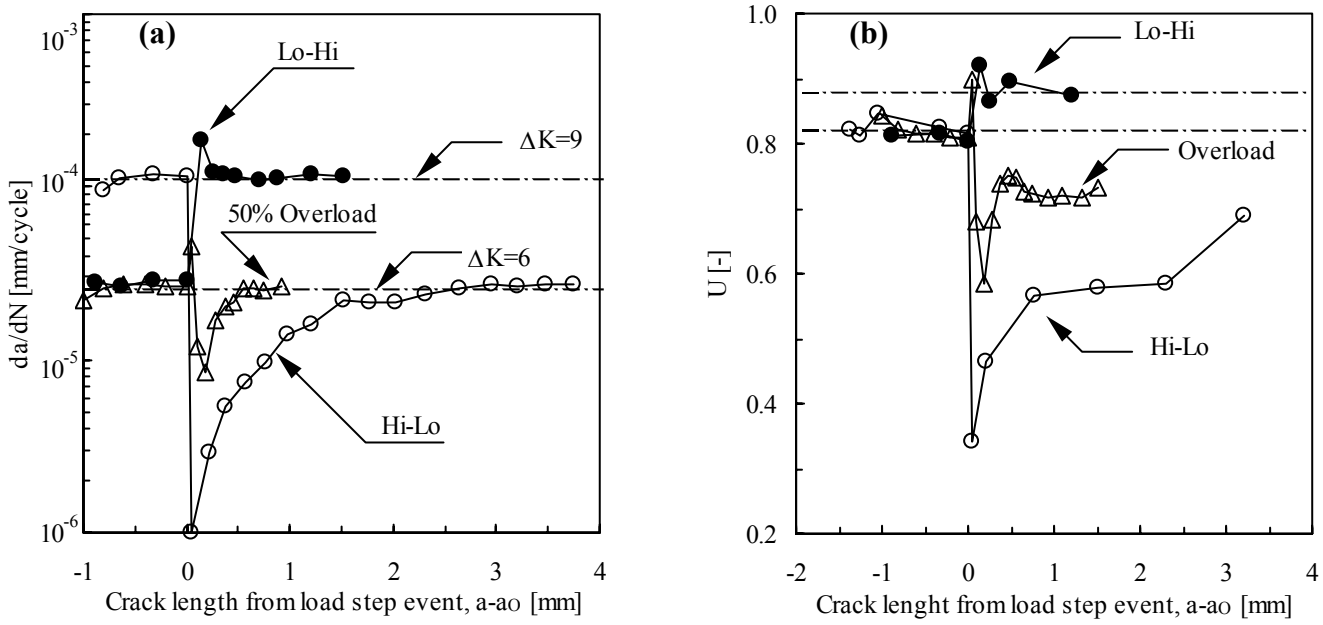

Figure 2: Transient behaviour following a single tensile overload, a high-low block and a low-high block. (a) crack growth rate response, (b) crack closure response.

It is clear from this figure that the crack closure data show basically the same trend as the corresponding experimentally observed crack growth rate response. Prior to the overload, the U parameter for the baseline loading level is relatively stable. Upon application of the overload, U rapidly increases followed by a decrease to a minimum value and then increases gradually towards the baseline level. It is important to notice that the decrease in U is not immediate after the overload application, but on the contrary decreases slowly towards the minimum value. This is in accordance with delayed retardation behaviour observed on the crack growth rate transients. For load step-down, the decrease in parameter U is immediate after the change in load and for low-high blocks there is a decrease of U until some crack length after load change. In general the minimum U value occurs at the same crack increment after load variation, where the minimum value of the crack growth rate is reached. Thus, the phenomenon of plasticity-induced closure seems to be the dominant cause of the post-overload crack growth transients in 6082-T6 aluminium alloy.

Figures 3(a) and 3(b) present the influence of the magnitude and position of the load step in block loading for high-low and low-high sequences, respectively. Figure 3(a) shows that increasing the initial stress intensity relative to the final stress intensity range increases crack growth retardation. For the step load from ΔK_1=12 MPa $m^{1/2}$ to ΔK_1=6 MPa $m^{1/2}$ the crack was arrested. This behaviour is in agreement with the experimental results of Sehitoglu and McDiarmid [17], where non-propagating cracks occurred for $\Delta K_1/\Delta K_2$ ratios less than 0.6. For the blocks with the same increase in load (3 MPa $m^{1/2}$), affected crack length increases from Δa_O=2.64 mm to Δa_O=5.23 mm when ΔK_1 and ΔK_2 increase from 9 to 12 MPa $m^{1/2}$ and 6 to 9 MPa $m^{1/2}$, respectively. However, N_D decreases from 277500 to 86100 cycles for the same loading conditions, indicating that fatigue live is enhanced by the decrease in the final ΔK, ΔK_2. Similarly Figure 3(b) shows that for low-high sequences, crack growth acceleration increases with the final ΔK.

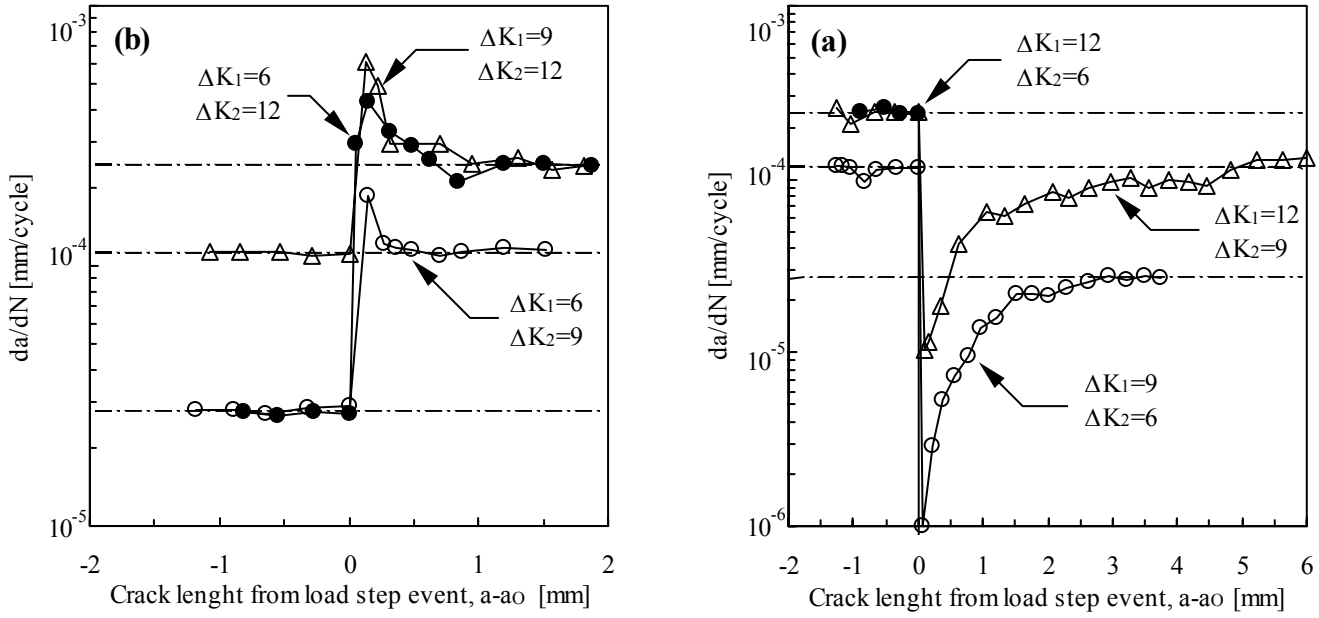

Figure 3: Influence of the magnitude and position of the load step in block loading. (a) high-low block, (b) low-high block.

The effect of periodically applied overloads after ΔK=6 MPa $m^{1/2}$ for several numbers of intermediate baseline cycles n can be seen in Figures 4(a) and 4(b). In Figure 6(a), the crack length is plotted against the number of cycles, and Figure 4(a) presents the correspondent crack growth response as a function of ΔK. For less frequently applied overloads (n>10) crack retardation is observed, while the results for overloads applied after 10 baseline cycles present crack acceleration. For a crack length of 10 mm N_D are 216282, 419308 and 475538 cycles for n=100, n=1000 and n=10000, respectively. The crack retardation represents a fatigue life increase of approximately 1.8 to 4, in comparison to constant amplitude loading, when n increases from 100 to 10000. For overloads applied after 10 baseline cycles the crack reach 10 mm at 94777 cycles, corresponding to a decrease in fatigue life of approximately 20%.

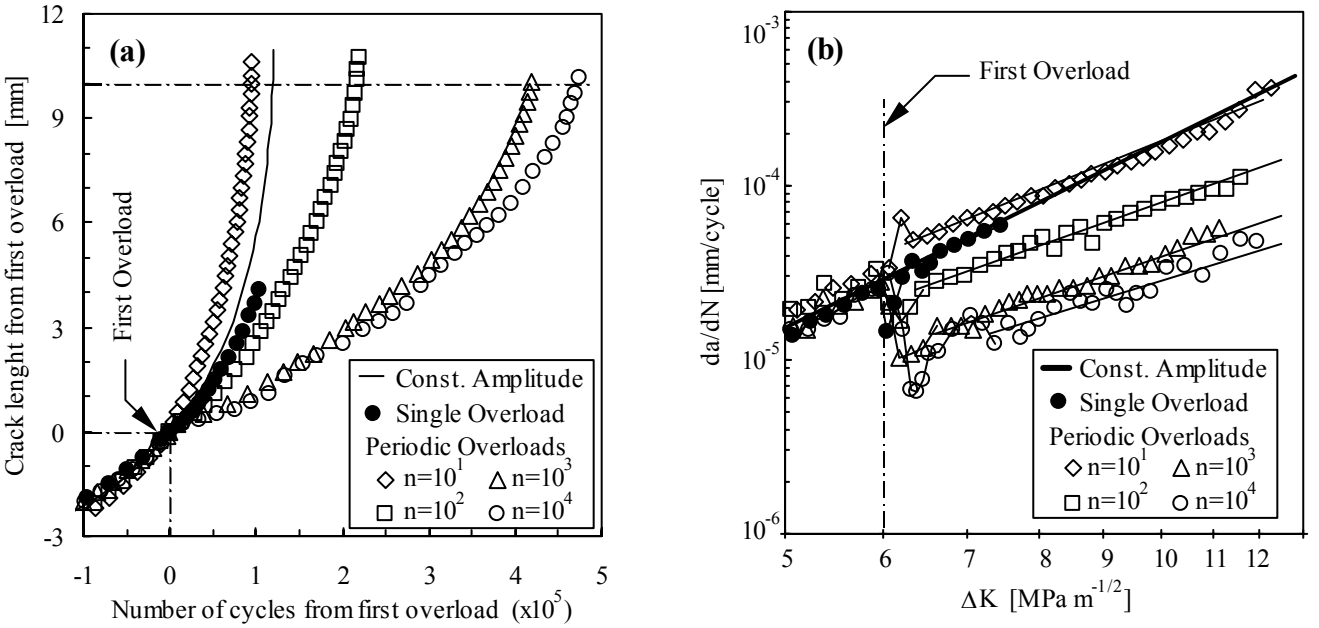

Figure 4: Transient fatigue crack growth behaviour following periodically applied single tensile overloads. (a) crack length versus cycles, (b) crack growth rate response.

It can be seen in figure 4(b) that the retardation in crack growth rate increases with ΔK for overloads applied after baseline cycles higher than 10. For overloads applied with 10 intermediate baseline cycles the acceleration in crack growth rate decreases with ΔK and for ΔK values above 10 MPa $m^{1/2}$ there is

even a small crack growth retardation. Similar experimental results were reported in [8]. This is not surprising because the monotonic plastic zone produced by the overloads increases with ΔK. An interesting feature that can be seen in figure 4 (b) is that after application of the first overload there was a delay retardation period that persisted for several thousands of cycles. During this period, the minimum crack growth rate was attained only after approximately 29000, 38000 and 55000 cycles for n=100, n=1000 and n=10000, respectively. Furthermore, crack growth rates lower than the following ones persisted for approximately 52000, 112000 and 125000 cycles for n=100, n=1000 and n=10000, respectively.

CONCLUSIONS

1. The effect of block loading is similar to that observed for peak overloads. However, for this load sequence the retardation is always immediate. Load step-down leads to a greater increase in fatigue life than overloads. High-low sequences produce crack acceleration.

2. The phenomenon of plasticity-induced closure seems to be the dominant cause of the post-load variation crack growth transients in 6082-T6 aluminium alloy.

3. Increasing the difference between the initial stress intensity and the final stress intensity range, for high-low blocks, increases crack growth retardation. Furthermore, for equal step-down in loads retardation increases with the decrease of the lower ΔK. For low-high blocks acceleration increases with the final ΔK.

4. For less frequently applied overloads (n>10) crack retardation is observed, while the results for overloads applied after 10 baseline cycles present crack acceleration.

ACKNOWLEDGEMENTS

The authors would like to acknowledge POCTI programme, project 1999/EME/32984, for funding the work reported.

REFERENCES

1. Shin, C.S. and Hsu, S.H. (1993) *Int. J. Fatigue* **15**, 181.
2. Shercliff, H.R. and Fleck, N.A. (1990) *Fatigue Fract. Engng. Mater. Struct* **13**, 297.
3. Fleck, N.A. (1988) *Basic Questions in Fatigue:* **Volume 1**, ASTM STP 924, 157.
4. Shuter, D.M. and Geary, W. (1995) *Int. J. Fatigue* **17**, 111.
5. Ng'Ang'a, S.P. and James, M.N. (1996) *Fatigue Fract. Engng. Mater. Struct* **19**, 207.
6. Ward-Close, C.M., Blom, A.F. and Richie, R.O. (1989) *Engng. Fract. Mech.* **32**, 613.
7. Fleck, N.A. (1985) *Acta Metall.* **33**, 1339.
8. Ohrloff, N., Gysler, A. and Lutjering, G. (1988). *Mechanics of Fatigue Crack Closure*, ASTM STP 982, 24.
9. Shijve, J. and Broek, D. (1962) *Aircraft Engng.* **34**, 314.
10. Elber, W. (1971). *Damage Tolerance in Aircraft Structures*, ASTM STP 486, 230.
11. Christensen, R.H. (1959). *Metal Fatigue*. MacGraw-Hill, New York.
12. Jones, R.E. (1973) *Engng. Fract. Mech.* **5**, 585.
13. Suresh, S. (1983) *Engng. Fract. Mech.* **18**, 577.
14. Nicoletto, G. (1989). *Nonlinear Fracture Mechanics:Volume I*, ASTM STP 995, 415.
15. Borrego L.P., Ferreira J.M. and Costa J.M. (2001) *Fatigue Fract. Engng Mater. Struct.*, in press.
16. Allison,J., Ku, C. and Pompetzki, A. (1988). *Mechanics of Fatigue Crack Closure*, ASTM STP982, 171.
17. Sehitoglu, H. and McDiarmid, D.L. (1980) *Int. J. Fatigue* **2**, 55.

ORAL/POSTER REFERENCE: ICF100983OR

FATIGUE CRACK GROWTH WITH TENSILE RESIDUAL STRESSES

Y Prawoto[1] and RA Winholtz[1, 2]

[1]Department of Mechanical and Aerospace Engineering, University of Missouri
[2]Research Reactor Center, University of Missouri

ABSTRACT

Cracks were grown in specimens with and without initial residual stresses under conditions of constant applied stress intensity factor. The specimens with initial tensile residual stresses showed acceleration of the crack propagation rates. The residual stresses were converted to stress intensity factors using the weight function and added to the applied stress intensity factors using the superposition principle. The plastic zone size was also measured utilizing diffraction line broadening and a small synchrotron x-ray beam. The results show that the weight function method, combined with the three-component model of crack growth, provides a good prediction of fatigue crack propagation rates in tensile residual stress fields.

KEYWORDS

Residual stress, fatigue crack propagation, weight function, plastic zone, x-ray

INTRODUCTION

Previous studies [1-5] have found that residual stresses can increase or decrease fatigue resistance. The Paris model predicts crack growth rate as a power function of the stress intensity factor (SIF) range, but cannot predict any influence of residual stresses on crack growth rate. The Walker [6] model includes an effect of load ratio, $R = K_{min}/K_{max}$, which is affected by residual stresses. The Walker equation may be written as shown in Table 1, where da/dN is the crack growth rate, ΔK is the SIF range, and γ is the Walker exponent, which captures the R dependence. This model only captures the Stage II crack growth regime. Later models also include crack growth in Stages I and III [7,8]. The three-component (TC) model of Saxena [7] was used in this study and is also given in Table 1.

The weight function method provides a powerful and simple means for calculating SIFs from the residual stresses. The SIF at any future crack length, a, is computed from the residual stress distribution, $\sigma(x)$, on the prospective crack line using the relation [9-11]

$$K_R = \int_0^a \sigma(x) \cdot m(a,x) dx \,. \tag{1}$$

Here the weight function, $m(a,x)$, depends only on the geometry of the component. A number of studies using the weight function have been conducted [12-19].

TABLE 1
FATIGUE CHARACTERIZATION RESULTS

Model	Equation	Constants*
Walker	$\frac{da}{dN} = C\left[\frac{\Delta K}{(1-R)^{(1-\gamma)}}\right]^n$	$C = 2.4\times10^{-10}$ $N = 4$ $\gamma = 0.8$
Three-Component	$\frac{1}{(da/dN)} = \frac{A_1(R)}{(\Delta K)^{n_1}} + A_2(R)\left[\frac{1}{(\Delta K)^{n_2}} - \frac{1}{(K_c(1-R))^{n_2}}\right]$ where $A_1(R) = C_1(1-R)^{\alpha}$ for $0.1 \le R \le 0.5$ $A_1(R) = C_2$ for $0.5 \le R \le 0.8$ $A_2(R) = C_3(1-R)^{\beta}$	$C_1 = 1.6\times10^{18}$ $C_2 = 1.5\times10^{12}$ $C_3 = 4\times10^{9}$ $\alpha = 20$ $\beta = 0.5$ $n_1 = 10.5$ $n_2 = 4$ $K_c = 83$

*The constants relate da/dN and ΔK when their units are in [mm/cycle] and [MPa√m], respectively.

EXPERIMENTAL PROCEDURES

Material and Specimen Preparation

Hot-rolled 1080 steel plate (12.7 mm thick) was austenitized for 30 minutes at 800 °C followed by a water quench and tempering at 700 °C for 3 hours. The average ferrite grain and cementite particle sizes were 5.6 μm and 1 μm, respectively. Electro-polishing was used to remove 0.5 mm from the surfaces, without introducing residual stresses, for accurate x-ray diffraction measurements. The specimens were machined into compact tension (CT) specimens [20]. Tapered interference pins (20.8 mm/m) were inserted in tapered holes in half the specimens along the future crack plane, as shown in Figure 1. In the other half of the specimens, no pin was inserted and no hole was drilled. An interference level between the specimen and pin of 0.125 mm was achieved by pressing the pin into the specimen.

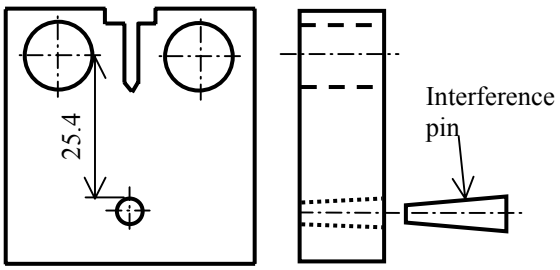

Figure 1: CT specimen with interference pin.

Initial Residual Stress Measurements

The initial residual stresses were measured using x-ray diffraction [21]. A chromium rotating anode source was used with x-rays of wavelength 2.2897 Å. A tapered glass capillary tube was used to focus the x-rays to a 210 μm spot. The stress component perpendicular to the future crack faces was measured along the prospective crack line.

Fatigue Crack Propagation Measurements

Fatigue cracking was performed under software control [22] using a sinusoidal waveform at 4 Hz. The crack length was measured using the compliance method [20] and was also monitored using a traveling microscope. First, the material constants for the Walker and TC models given in Table 1 were determined with residual stress free specimens. Next, two specimens were cracked at each of six different constant ΔK values, ranging from 17.5 to 25 MPa$\sqrt{m}$, one with and one without residual stresses, all with an applied load ratio of R=0.1.

Plastic Zone Size Measurements

The size of the plastic zone was determined from line broadening of the diffraction peaks using a 50 x 50 μm synchrotron x-ray beam. The method relies on the broadening of a diffraction peak with plastic deformation due to an increased dislocation density. The specimens were sectioned longitudinally to obtain the interior plastic zone size. The sectioned surface was metallographically polished and etched to remove the damage from sectioning. Experiments were performed at the SRI CAT 1-BM beamline at the Advanced Photon Source, Argonne National Laboratory. X-rays of 10 keV were used and the Fe-411 peak was studied. The crack surface was found by monitoring the iron fluorescence produced by the x-ray beam. The line broadening was monitored as the beam moved into the interior of the specimen perpendicular to the crack face. This procedure was repeated at a number of positions along the crack line to determine the plastic zone size as the crack grew through the specimen.

RESULTS AND ANALYSIS

Residual Stress Intensity Factor

Figure 2 shows the initial residual stresses on the specimen before fatigue cracking along the prospective crack line on both the front and back faces of the specimen. Near the pin interface, there are some differences between the front and back faces due to friction while inserting the pin. Finite element modeling of the insertion process gives comparable results for the faces and shows that the stress distribution in the interior of the specimen is similar [23]. The average of the front and back faces was used in further analysis. The residual stresses were converted to a residual SIF using the weight function for a CT specimen [11] and Eqn. 1. Figure 3 shows the result of these calculations.

Crack Growth Rates

Predictions of the crack growth rates were made as follows. Using the superposition principle, the effective load ratio was calculated as

$$R' = \frac{K_{\min} + K_R}{K_{\max} + K_R}. \tag{4}$$

The effective load ratio, R', changes from the original applied load ratio. Here, $K_{\min}$ and $K_{\max}$ are the minimum and maximum applied SIFs, and K_R is the residual SIF shown in Figure 3. Having calculated R', shown in Figure 4, the da/dN predictions were then made using the constants in Table 1. Figure 5 shows experimental and predicted crack growth rates for a specimen containing residual stresses loaded with a constant applied ΔK. The predictions based on the TC model fit best with the experiment results. Results for five other specimens, loaded at different ΔK values, show similar trends.

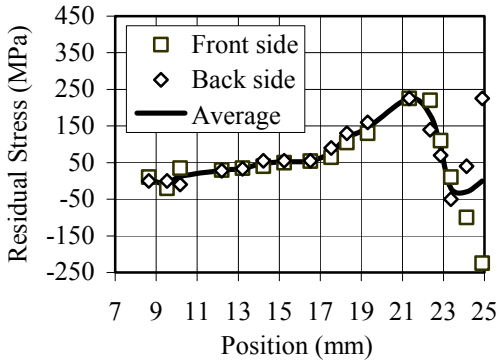

Figure 2: Initial tangential residual stress along the prospective crack line.

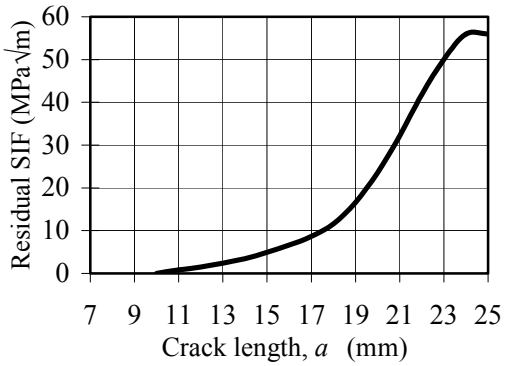

Figure 3: Residual SIF calculated using the weight function.

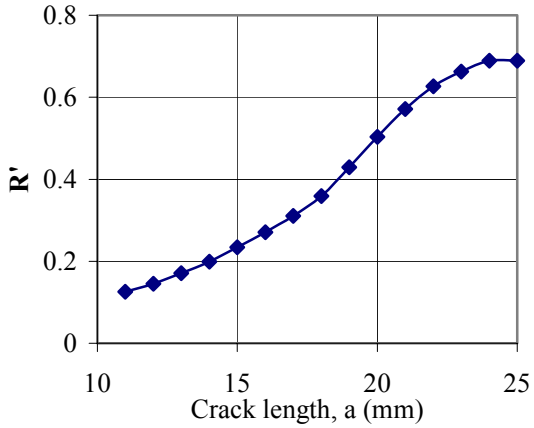

Figure 4: (a) Effective load ratio, R', as a function of crack length for residual stress specimens.

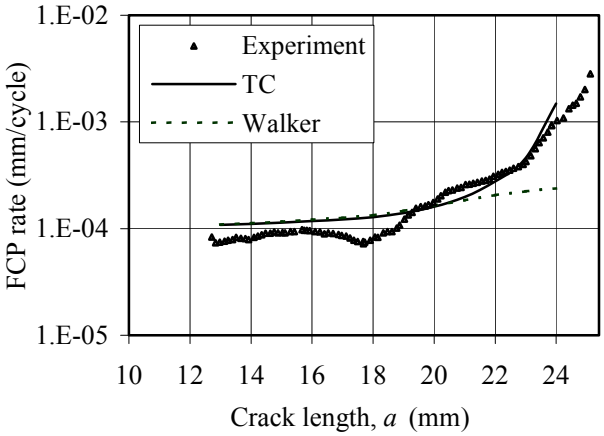

Figure 5: Comparison of predicted and experimental crack growth rates with Constant applied SIF range ΔK=25 MPa√m.

Plastic Zone Measurements

Experimental determination of the plastic zone size along the crack line is shown in Figure 6. Even though the specimen experienced a constant maximum applied SIF of 25 MPa√m, the plastic zone size was found to increase as the crack entered the residual stress field.

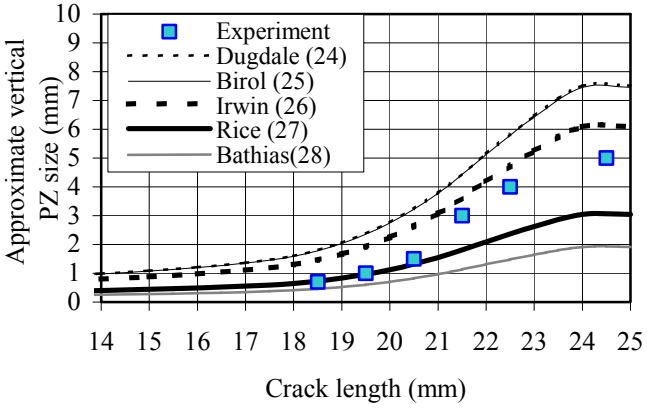

Figure 6: Vertical plastic zone sizes in the interior of the sample. Note the Dugdale and Birol solutions are nearly overlapped.

The results here are also compared with some analytical and experimental approximations available [24-28]. The predictions in the figures were made by assuming that the total maximum SIF is the superposition of the maximum applied SIF and the residual SIF. The experimental results obtained here fall in between the Rice and Irwin analytical solutions [26,27]. The experimental results are also shown compared to calculations based on constants experimentally obtained by Birol [25], which was based on an etching method, and Bathias [28], which was based on a microhardness method.

SUMMARY AND CONCLUSIONS

Accurate predictions of fatigue crack growth rates through residual stress fields were obtained from the superposition of residual stresses and applied stresses using the weight function approach. Both the residual stresses and the applied stresses were converted to stress intensity factors independently and then combined using the basic principle of linear elastic superposition. The specimens with initial tensile residual stresses show acceleration of the crack propagation rates, which compare well with predictions based on models. Evaluation of the results lead to the following conclusions:

1. The residual stresses in a specimen can be used, with the weight function, to compute a residual stress intensity factor that a crack will experience as it propagates through the residual stresses. Then, with a crack propagation law, one can predict the fatigue crack growth rate of a crack growing into a tensile residual stress field. Superposition may not work satisfactorily if either the residual or applied stress intensity factors are compressive. If the net stress intensity factor is decreasing as the crack grows, the plastic zone size is decreasing which can cause the crack to behave differently than the growth model.

2. Tensile residual stresses accelerate a fatigue crack by increasing the load ratio. This has two effects. First, materials display a load ratio sensitivity, usually quantified by the Walker exponent γ, such that cracks grow faster at a higher load ratio. Secondly, at a higher load ratio cracks will transition into the more rapid Stage III growth regime at a lower stress intensity range. This effect can be seen in Figure 5 as the point where the TC model deviates from the Walker model predicting higher crack growth rates and better representing the experimental data.

3. The three-component model of Saxena gives a good prediction of fatigue crack propagation rates when used with the superposition of the applied and residual stress intensity factors. It captures both of the load ratio sensitivity and the transition to Stage III growth and hence makes a better prediction for the crack growth rate than the Walker model.

4. The size of the plastic zone can be measured with a small synchrotron x-ray beam along a fatigue crack by measuring the diffraction line broadening of the material perpendicular to the crack faces. The superposition of the residual stress intensity factor and the maximum applied stress intensity factor during fatigue crack growth correctly predicts the shape of the plastic zone size variation as a fatigue crack grows into a tensile residual stress field. The measured size of the plastic zone falls between the theoretical predictions of Rice and Irwin, which give upper and lower bounds, respectively.

ACKNOWLEDGEMENTS

The authors would like to acknowledge the University of Missouri Research Board for funding this research. They also express thanks to J.D. Almer and J.B. Cohen for performing the initial residual stress measurement at Northwestern University. The assistance of D.R. Haeffner and P.L. Lee with the synchrotron x-ray measurements is gratefully acknowledged. The use of the

Advanced Photon Source was supported by the U.S. Department of Energy, Basic Energy Sciences, Office of Science, under Contract No. W-31-109-Eng-38.

REFERENCES

1. Underwood, J.H, Pook, L.P. and Sharples, J.K. (1977) *ASTM STP 631,* 402.
2. Underwood, J.H. (1995) *Exp. Mech.* 35, 61.
3. Elber W., (1971) *ASTM STP 486*, 230.
4. Nelson, D.V. (1982) *ASTM STP 776*, 172.
5. Parker, A.P. (1982) *ASTM STP 776*, 13.
6. Walker, K. (1970) *ASTM STP 462*, 1.
7. Saxena, A., Hudak, S.J. Jr., and Jouris, G.M. (1979) *Eng. Fract. Mech.*, 12, 103.
8. Miller, M.S. and Gallagher, J.P. (1981) *ASTM STP 738*, 205.
9. Wu, X.R. (1984) *Eng. Fract. Mech*., 20, 35.
10. Wu, X.R. and Carlsson, A.J. (1991) *Weight Functions and Stress Intensity Factor Solutions*, Pergamon Press, Oxford.
11. Fett, T. and Munz, D. (1997) *Stress Intensity Factors and Weight Functions*, Computational mechanics publications, Southampton.
12. Stacey, A. and Webster, G.A. (1988) *ASTM STP 1004*, 37.
13. Nguyen, N. and Wahab, M.A. (1996) *Welding Journal*, 75, 55s.
14. Itoh, Y.Z. (1989) Eng. Fract. Mech., 33, 397.
15. Okamoto, A. and Nakamura, H. (1990) *J. Pressure Vessel Tech.,* 112, 199.
16. Glinka, G. (1979) *ASTM STP 677*, 198.
17. Glinka, G. (1987) *Advances in Surface Treatments: Technology-Applications-Effects*, Pergamon, 413.
18. Todoroki, A. and Kobayashi, H. (1988) *Trans. Japan Soc. Mech. Eng.,* A-54 30.
19. Todoroki, A. and Kobayashi, H. (1990) *Proceeding of the LSME/JSME Joint Conference*, Seoul, Korea, 367.
20. ASTM Standards, ASTM E 647-95a.
21. Almer, J.D., Cohen, J.B., and Winholtz, R.A. (1998) *Metall. and Matls. Trans*, 29A, 2127.
22. MTS Systems Corporation (1993) '*759.40 Testware fatigue crack growth test operator's guide'*, MTS System Corporation.
23. Almer, J.D., Cohen, J.B., McCallum, K.R., and Winholtz, R.A. (1997) *Proc. of the Fifth International Conference on Residual Stress*, Soc. Exp. Mech., Bethel, CT, 1072.
24. Dugdale, D.S. (1960) *J. of Mech. and Phys. of Solids*, 8, 100.
25. Birol, Y. (1988) *J. of Mater. Sci*, 23, 2079.
26. Irwin, G.R. (1960) *Proc. of Seventh Sagamore Ordnance Materials Conference*, Syracuse University, IV 63.
27. Rice, J.R. (1972) *Int. J. Solids Structures*, *8*, 751.
28. Bathias, C. and Pelloux, R.M. (1973) *Metall. Trans.*, 4, 1265.

ORAL/POSTER REFESENCE:233PR

Fatigue Crack Initiation (FCI) Life Prediction for a Flat Plate with a Central Hole

Tso-Liang Teng[1], Cho-Chung Liang[2], Peng-Hsiang Chang[3]

[1,2]Department of Mechanical Engineering, Da-Yeh University
[3]University of National Defense Chung Cheng Institute of Technology

ABSTRACT

This work constructs an effective procedure that combines the finite element and strain-life methods in order to accurately predict fatigue crack initiation (FCI) life and then establish an estimated schedule of fatigue life. The proposed method is applied to a flat plate with a central hole to obtain predicted lives. Comparing the results from the proposed method is compared with those of Juvinall's stress-life method, Socie's local strain method and Bannantine's summary experimental data. Comparative results demonstrate that the fatigue life estimated by the novel procedure closely approximates the experimental results.

Keywords：Notch, stress concentration, finite element method, crack initiation life.

1. Introduction

Fatigue life prediction for notched members may be approached from several viewpoints. For crack initiation, many researchers have supplemented the traditional approach, which is based on nominal stresses and stress concentration factors. Peterson [1] initially used elastic stress concentration factors and nominal stresses to estimate the fatigue lifetime of notched members, but the later studies [2-4] used the Neuber's rule [5,6], which uses the relations between nominal stresses and strains to estimate the fatigue life of the material at the notch root. The above analyses assumed the crack propagation part of fatigue life to be extremely small. Meanwhile, Socie [7] used local stress-strain concepts and a cumulative-damage approach to predict fatigue-crack initiation in engineering structures subjected to random loading, and Newport et al. [8] used Neuber's rule and the equivalent strain-energy density method to predict fatigue-crack-initiation life. Furthermore, Costa [9] predicted fatigue crack initiation life for notched bend specimens with two different notch acuities and two stress ratios using the equivalent strain energy density method, while Giglio and Vergani [10] employed total strain energy

density numerically determined through elastic-plastic analysis to predict fatigue life. Yip et al. [11] investigated multi-axial fatigue crack initiation lives for solid cylindrical specimens with transverse circular holes.

This work constructs an effective procedure by combining the finite element and strain-life methods to predict fatigue crack initiation (FCI) life and then establishing an estimated fatigue life schedule. The proposed procedure can obtain the complete distribution of structural strains and strain-time history at the notch by using the finite element method, and can also obtain the fatigue life at any location in the structure by smooth specimens fatigue resistance. Additionally, this investigation considers interaction between loads, and Miner's rule can be used to calculate the cumulative damage in the FCI phase. The proposed procedure is then applied to a flat plate with a central hole, and the results compared with those of Juvinall's stress-life method, Socie's [7] local strain method, and Bannantine's summary experimental [13] data. Comparative results demonstrate that the fatigue life estimated by the novel procedure closely approximates experimental results.

2. Fatigue-analysis Procedure

The life prediction procedure involves two parts, as illustrated in Fig. 1. The structural analysis involves the stresses and strains calculated in a highly stressed area where slip concentrates from the input loads for a given material and geometry. The stresses and strains of critical areas are transformed into fatigue damage, and integrating the damage subjected to an empirical failure criterion produces a prediction for structural life.

In the structural analysis, the strains and stresses can be calculated at each time increment using a finite element method in which loading history is the input of the structural model. The service stress-strain field in these critical areas within the components can also be found by using the finite element method. The structural analysis assumed that the material followed the Von Mises yield criterion and the associated flow rules.

3. Analytical Model

To assess whether the use of the more accurate present calculation procedure improves fatigue-life prediction, predictions made with Juvinall's stress-life method, Socie's [7] local strain method and the method presented herein are compared with experimental results taken from Bannantine[13].

3.1 Specimen and material properties

The material used herein is medium strength steel [13], The length, width and thickness of the plate are assumed to be 1.00in, 10in and 0.30in, respectively, while the diameter of the central circle is 0.50in.

3.2 Finite element model for notched plates

This investigation develops a two-dimensional symmetrical plane stress model for converting a load-time history into a strain-time history by using the finite element method. The model employs two-dimensional four node plane elements. Figure 2 displays the finite element meshes for the notched plates, along with the refined meshes used in the stress concentration area. The symmetric model contains 280 elements and 339 nodes after meshing.

4.Results and Discussion

Stress acting along the loading direction is known as axial stress, and is denoted by σ_y. Figure 3 illustrates the contours of σ_y for load P=9.03 Kips. The critical areas of the stress-strain field of the notched plates were found by the finite element method. As Fig. 3 displays, a high tensile stress occurred at point 'a' along the central hole. Following analysis with the finite element method, specimens A-1~A-6 are into plastic scope while specimens A-7~A-10 remain in elastic scope. Figure 4 presents the cyclic stress-strain curve of specimens A-1~A-6 at point 'a', and Fig. 5 displays the strain-time history of specimens A-7~A-10 on point 'a'. Owing to hysteresis loops of specimens A-1~A-6 and the strain range of specimens A-7~A-10 having been determined, a fatigue life analysis for the amplitude history can be performed by using a strain life equation. Figure 6 presents the results of applying various techniques to predicting the endurance of the notch plates (specimen A) under zero mean loads, with the experimental lives being in terms of first crack (approx 0.02in). As Fig. 6 indicates, the prediction results obtained by the novel method showed a strong correlation with the experimental results.

5.Conclusion

1. The Juvinall's [24] stress-life method achieves the most accurate results for high cycle fatigue (HCF), where the notch strains are predominantly elastic and loading is essentially constant. This approach does not account for inelastic behavior at the notch and cannot properly account for changes in notch mean stresses.
2. The relatively conservative fatigue life estimates yielded by Socie's local strain method (Neuber's rule) result from over prediction of the notch strain in the notch tip.
3. Applying the approach method rather than Socie's and Juvinall's method leads to an improvement in improve fatigue-life predictions, and the predictions are equally accurate for both the low and high cycle fatigue-life regions.
4. The proposed life prediction procedure, which combines the finite element method (FEM) and convenient notch analysis, is presented herein. The suggested procedure is applied to various

specimens with different materials, geometries, and stress ratios, and the predictive results are successfully compared with experimental data.

Reference

1. Peterson, R. E. (1959) Technical Report 59-507, U.S. Air Force-WADC Symp. Fatigue Metals, Dayton, Ohio.
2. Topper, T. H., Wetzel, R. M., and Morrow, J. (1969) *J. Mater.*, Vol.4, No. 1, pp. 200-209.
3. Dabell, B. J., Hill, S. J., Eaton, D. E., Watson, P. (1977) *Journal of the Society of Environmental Engineers*, Vol. 16, No 4, Dec., pp. 3-11.
4. Truchon, M., ASTM STP 770, C. Amzallag, B. N. Leis, and P. Rabbe, Eds. (1982) *American Society for Testing and Materials*, pp. 254-268.
5. Neuber, H. (1946) Theory of Notch Stresses: Principle for Exact Stress Calculations, J. W. Edwards, Ann Arbor, Mich.
6. Neuber, H., J. (1961) *Appl. Mech, Trans. ASME,* Vol. E28, pp.544-560.
7. Socie, D. F. (1977) *Experimental Mechanics*, Vol. 17, Feb., pp. 50-56.
8. Newport, A., Glinka, G. (1990) *Experimental Mechanics*, Vol. 30, No. 2 Jun, pp. 208-216.
9. Costa, J.D.,Ferreira, J.M. (1993) *International Journal of Fatigue*, Vol. 15, No. 6, Nov, pp. 501-507.
10. Giglio, M., Vergani, L. (1995) *Journal of Engineering Materials and Technology*, Vol.117, Jan., pp. 50-55.
11. Yip, Ming-Chuen, Jen, Yi-Ming (1996) *International Journal of Fatigue*, Vol. 18, No. 2, pp. 111-117.
12. Juvinall, R. C. (1967) *Engineering Considerations of Stress, Strain and Strength*, McGraw-Hill, New York.
13. Bannantine, Julie A., Comer, Jess J. and Handrock, James L. (1990) Fundamentals of Metal Fatigue Analysis, Prentice Hall, Englewood Cliffs, New Jersey.

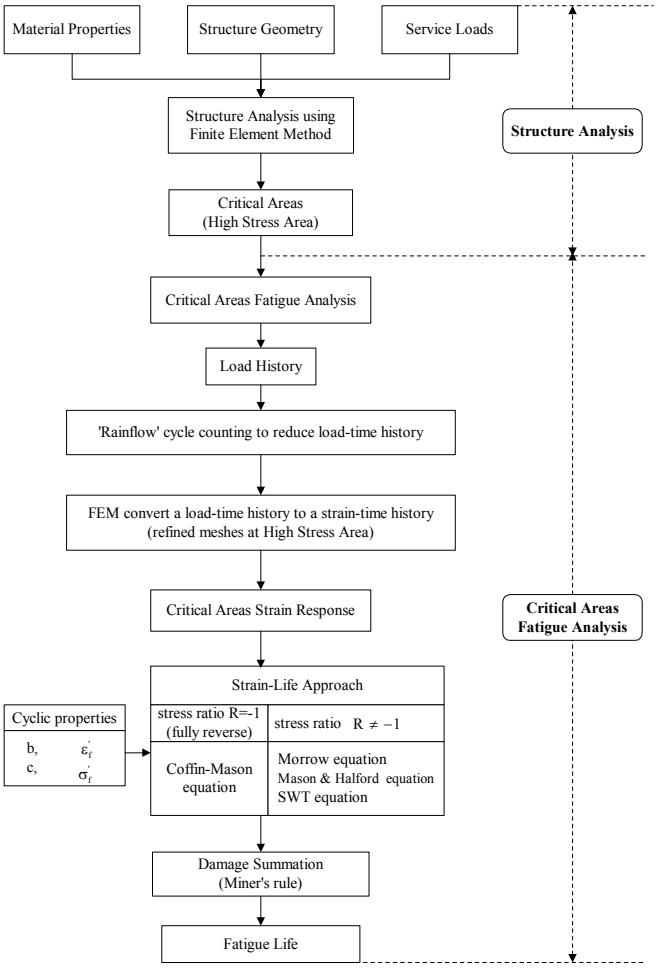

Figure 1: Life prediction flow chart

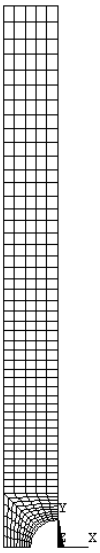

Figure 2: Refined mesh for the notched plates(325 elements)

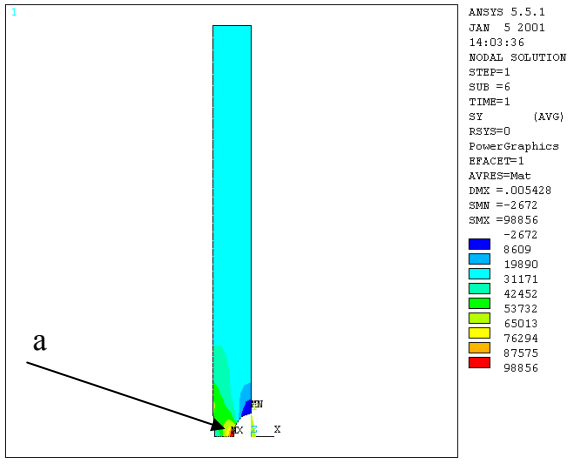

Figure 3: Contours of σ_y

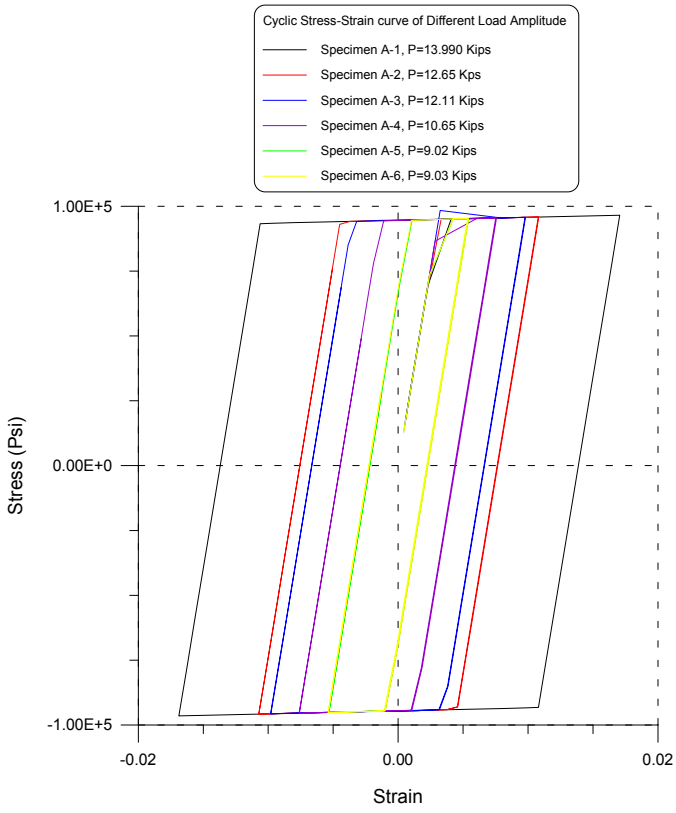

Figure 4: Cyclic stress-strain curve of specimen A-1~A-6

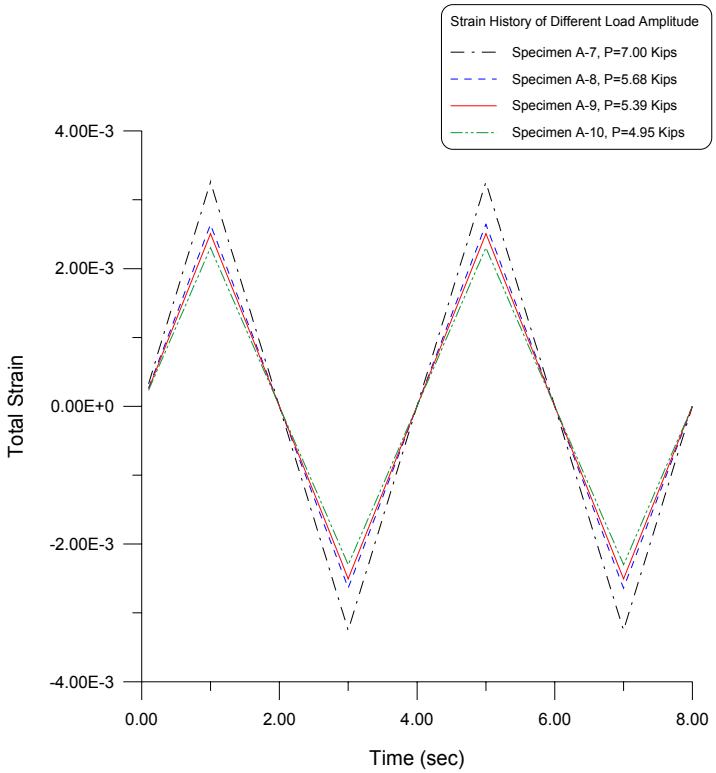

Figure 5: Strain-time history of specimen A-7~A-10

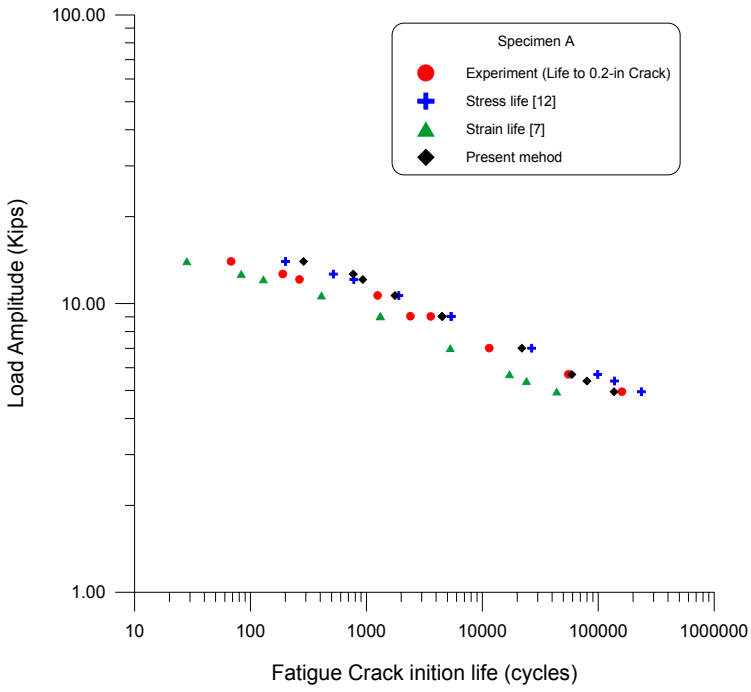

Figure 6: Various techniques for predicting the endurance of the notch plates (specimen A)

ORAL REFERENCE: ICF100940OR

FATIGUE CRACK INITIATION AND PROPAGATION FROM REINFORCEMENT FIBER ENDS FOR Ti-Alloy MATRIX COMPOSITES

Kazumi HIRANO [1], Hiroyuki YOSHIDA [2] and Shinji MIYAKE [2]

[1] National Institute of Advanced Industrial Science and Technology (AIST)
Namiki 1-2, Tsukuba-shi, Ibaraki-ken 305-8564, JAPAN
[2] Kobe Materials Testing Laboratory

ABSTRACT

The partial reinforcement is very useful concept for a wide practical use of continuous fiber reinforced metal matrix composites (MMCs). It follows the reinforcement fiber ends in MMCs components as a necessary consequence. It is therefore very important to examine the influence of reinforcement fiber ends on long-term durability performance for ensuring structural integrity of MMCs components. This paper investigates the fatigue crack initiation and propagation behavior and summarizes the influence of continuous reinforcement fiber ends on low-cycle fatigue behavior for Ti-alloy matrix composite. The reinforcement fiber ends specimen has shorter fatigue lives than those of standard specimen. In particular, the surface fiber ends specimen has shorter fatigue lives as compared with those of inner fiber ends specimen. Cyclic stress-strain and stress-inelastic strain curve measurements indicate a significant difference in the response of these materials depending on the specimen type and strain level. These differences in the response suggest that fatigue crack initiation and propagation mechanisms play different roles in defining fatigue life.

KEYWORDS: Ti-alloy Matrix Composites, SP700, Low-cycle Fatigue, Reinforcement Fiber Ends, Fatigue Crack Initiation and Propagation, Fractographic Examinations, Prediction of Fatigue Lives

INTRODUCTION

Continuous fiber reinforced metal matrix composites (MMCs) have been researched and developed because of light-weight and high temperature capability for the past twenty years and characterized fatigue damage tolerance based on fracture mechanics [1~6]. They have been applied to various high temperature structural components in the field of aeronautics, aerospace and power generation industries. The continuous fiber partially reinforced Ti-alloy matrix composite rotor bladed ring has also been successfully fabricated on the basis of the design requirements [7,8]. It has been widely recognized that the partial reinforcement is very useful concept for a wide practical use. It followed the reinforcement fiber ends in MMCs components as a necessary consequence. It is therefore very important to investigate the influence of these fiber ends on long-term durability performance for ensuring structural integrity of MMCs components.

The final goal of this research is to establish not only the materials database but also the design database also included materials testing and evaluation and damage tolerance fatigue design concepts for continuous fiber reinforced Ti-alloy matrix composite (TMCs) rotating parts in aircraft engines, such as impellers, disks, integrally bladed rotors or bladed disks, and bladed rings now primarily fabricated of nickel based super-alloys. This paper investigates the fatigue crack initiation and propagation behavior and summarizes the influence of

continuous reinforcement fiber ends on low-cycle fatigue behavior for Ti-alloy matrix composite.

MATERIALS AND EXPERIMENTAL PROCEDURE

Materials and Test Specimens

The materials investigated are unidirectional six- and seven-plies SCS-6/SP700 laminate composites. The composite panel was fabricated by hot isostatically pressing alternate layers of continuous SiC fibers, SCS-6 and thin Ti-alloy foils, SP700. Specimens used here are coupon-type with a dimension of 150 mm-long, 10 mm-width and 15 mm-gage length of 1.4~1.6 mm thickness as shown in Fig. 1. Taking account of the processing method of TMCs rotor bladed ring, two types of test specimen were prepared to examine the influence of reinforcement fiber ends on low cycle fatigue behavior. The simulated reinforcement fiber ends were introduced in the first ply layers light under specimen top surface (Type-I) and in the middle ply layer (Type-II) at the center of the gage section.

Experimental Procedure

The low-cycle fatigue tests lower than 10^5 cycles were performed at RT, 450 and 650℃ under strain-controlled mode at a frequency of 0.5 Hz with a constant strain ratio R_ε of 0.1 using a MTS 810 TestStar materials testing system. Measurements of cyclic stress-strain curves were conducted using extensometer with 10 mm gage length. Cycles to failure N_f was determined at a number of cycle of 25 % load-drop from the initial steady state. After the fatigue testing, fractographic examinations were performed on specimen surface and fracture surface in order to examine the low cycle fatigue crack initiation and propagation mechanism

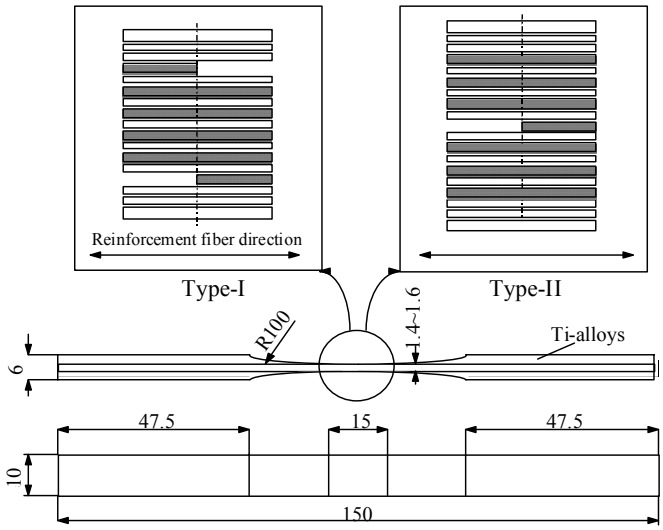

Figure 1: A schematic illustration of simulated reinforcement fiber ends and configuration and dimensions of fatigue test specimen.

EXPERIMENTAL RESULTS

Low-cycle Fatigue Lives

Relationships between total strain range $\Delta\varepsilon_t$ and cycles to failure N_f are shown in Fig. 2 for a comparison with standard specimen. These show the almost straight line in log-log plots and have same slope within the limits of this experiment, although there is a little scatter in fatigue lives at every type of specimen among the materials 11FY and 12FY. It can also be seen from this figure that the reinforcement fiber ends specimen has a shorter fatigue lives than those of standard specimen. It is fundamentally resulted from the difference in fatigue crack initiation and propagation behavior. Reinforcement fiber ends specimen has a shorter fatigue crack initiation lives as compared with standard specimen. And Type-I has a shorter fatigue lives than Type-II. It is concluded here that the reinforcement fiber ends near the surface is the most critical for the low cycle fatigue lives.

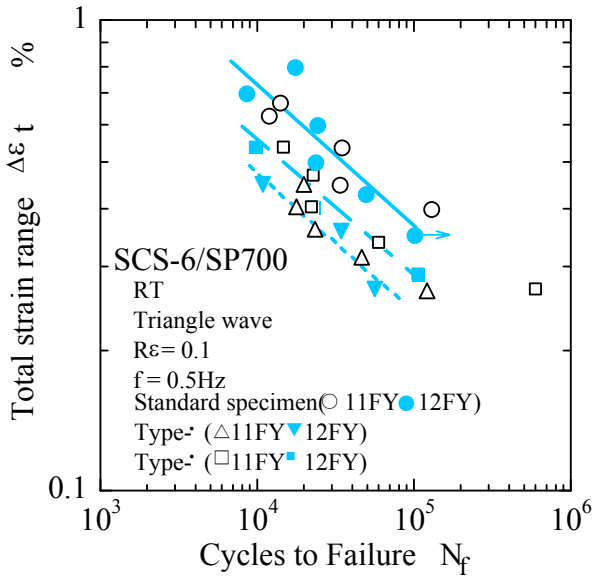

Figure 2: Relationships between total strain range $\Delta\varepsilon_t$ and cycles to failure N_f.

Also, Type-I, -II and standard specimen have different mechanical properties depending on fiber volume fraction and total number of laminates as cross section are shown in Fig. 1. Low-cycle fatigue lives curves normalized in terms of strain-to-failure ε_f are shown in Fig. 3. These curves have almost same slope. Reinforcement fiber ends specimen has smaller retention of strain-to-failure than those of standard specimen. In particular, there is a remarkable difference at high cycle region over 10^5 cycles. In a case of Type-I, the retention of strain-to-failure against the maximum low cycle fatigue strain determined at 10^5 cycles is the lowest, approximately 25 %. On the other hand, standard specimen kept at nearly 40 % level. Also, Type-I, that is, surface laminate layer reinforcement fiber ends specimen has smaller lives as compared with those of middle laminate layer reinforcement fiber ends specimen, Type-II. It should be noted here that TMCs have a lower design allowable in strain for low cycle fatigue, although they have also high strength characteristics.

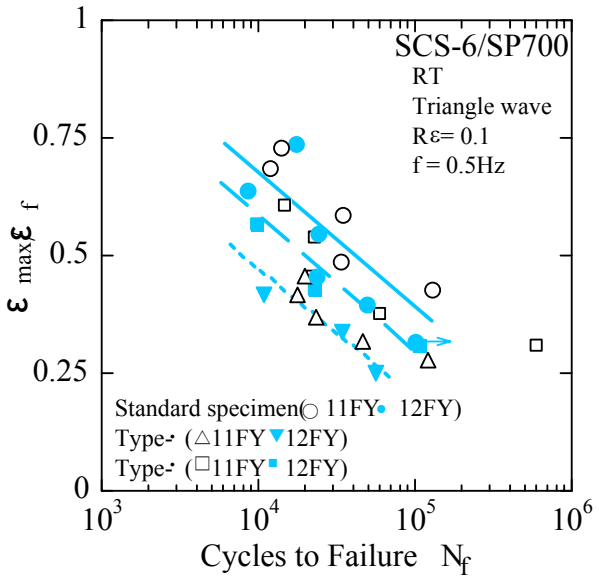

Figure 3: Normalized low cycle fatigue lives curves in terms of strain-to-failure ε_f.

Changes of Stress Amplitude during Fatigue Cycle

Changes of stress amplitude slightly depend on the maximum/minimum strain, strain amplitude and type of specimen. Generally, maximum stresses decreases with increasing of number of fatigue cycles, and then show the steady-state value. Finally, both maximum and minimum stresses decrease due to fatigue crack initiation and propagation, and then stress amplitude suddenly decreases near N_f cycles. Minimum stress is also reached to the negative value and the tension-compression fatigue behavior in the latter, although the strain ratio is controlled to the constant positive value. It is fundamentally resulted from the redistribution of residual stress

in the matrix metal due to the fatigue crack initiation and propagation. Accordingly, there is a much difference between strain-controlled fatigue lives and stress-controlled fatigue lives.

Measurements of Cyclic Stress versus Strain Curves

Cyclic stress-strain and stress-inelastic strain curve measurements indicate a significant difference in the response of these materials depending on the strain level and type of specimen. There is also a quite influence of test temperature on low-cycles fatigue lives. These differences in the response suggest that fatigue crack initiation and propagation mechanisms play different roles in defining fatigue life. Generally, the slope of S-S curves gentle with increasing of fatigue cycles, and gradually show the hysteresis loop along with the increment of inelastic strain. There is also the distinct knee point in the S-S curve due to the fatigue crack closure behavior. Fatigue crack initiation life can be determined from this knee point of S-S curve. The ratio of fatigue crack initiation life to the total fatigue life is relatively small, and the low cycle fatigue lives for both Type-I and -II are fundamentally controlled by fatigue crack propagation life.

Fractographic Examinations

There is the tendency that some fatigue cracks initiated near the reinforcement fiber ends at both edge side where the fibers were exposed, and then joined to a main fatigue crack. It has already reported [9] there is no remarkable effect of the fiber exposure on the load-controlled fatigue lives for standard specimen. Some cases are that the main fatigue crack finally surrounded the whole specimen but the specimen was not failure due to the reinforcement fiber bridging even at N_f cycles.

SEM examinations of fatigue fracture surface are shown in Figs. 4(a), (b) and (c) for Type-I tested at ε_{max} of 0.3 %. It is terminated at N_f=1.2x10^5 cycles and then residual tensile test was performed to reveal fatigue fracture surface. There is a difference between fatigue fracture and monotonic failure regions in the matrix metal. Fractograph(a) show the dimple pattern fractured during the residual tensile test. Fractographs (b) and (c) indicate that not only the fatigue cracks initiated in the reinforcement fiber ends laminates layer but also many fatigue cracks radially propagated from the breakage fibers were observed in the middle laminate layers where there is no reinforcement fiber ends. There also observed some steps formed by joining some fatigue cracks in the middle laminate layers. It is concluded here that the fatigue cracks are not always initiated in the fiber ends laminate layer but in the middle laminate layers where it is very high stress (strain) states due to the reinforcement fiber ends as discussed in details in the later section.

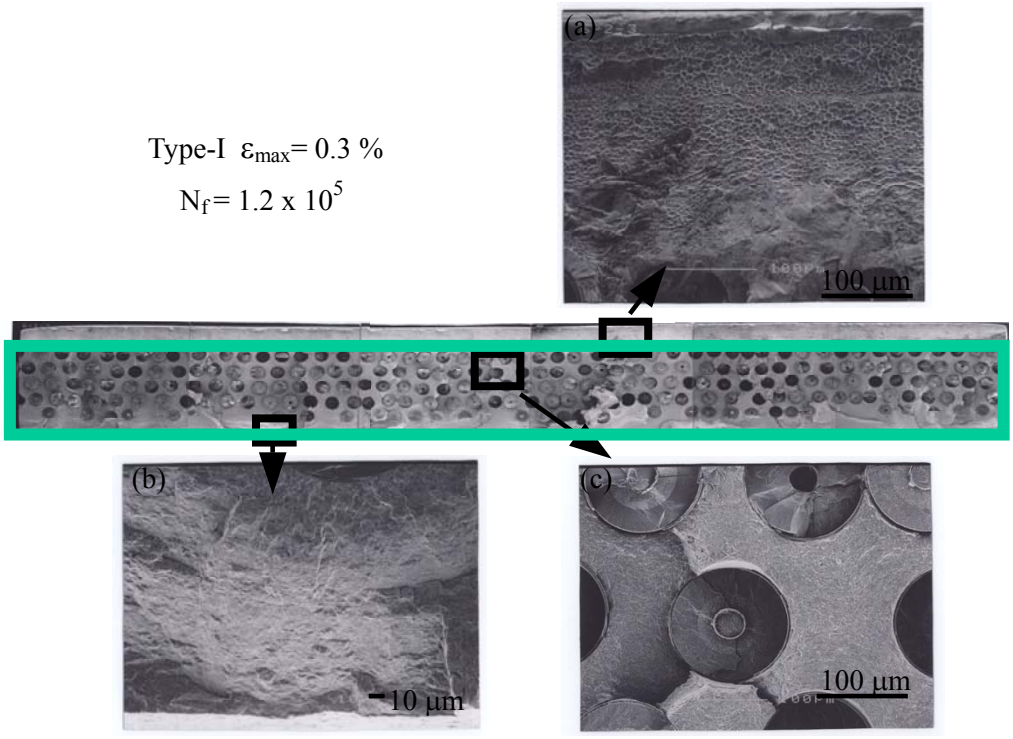

Figure 4: SEM examinations of fatigue fracture surface for Type-I tested at ε_{max}=0.3 %

DISCUSSION

Comparisons with Matrix Ti-alloys SP700

Comparisons of low cycle fatigue lives with matrix metals SP700 are shown in Fig. 5. There is little in-fluence of thermo-mechanical treatments on ultra-low cycle fatigue lives for SP700. It is shown from this figure that strain-controlled low cycle fatigue lives for TMCs are very small as compared with the extra-polation fatigue lives for SP700 shown by the solid line. It is presumed to be resulted from the residual tensile stress in the matrix metal induced during the fabrication process due to the mismatch of thermal expansion between the reinforcement fiber and matrix Ti-alloy.

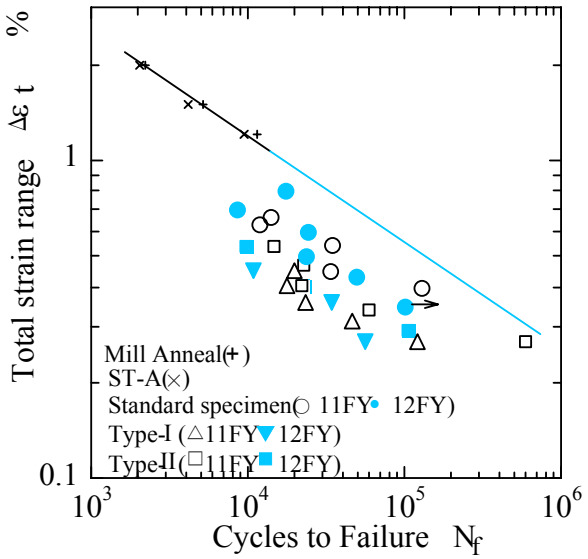

Figure 5: Comparisons of strain-controlled low cycle fatigue lives with matrix Ti-alloys SP700.

Analysis for Reinforcement Fiber Ends Specimen and Fatigue Lives Prediction

Fractographic examinations show that many fatigue cracks initiated and propagated even in the non-reinforcement fiber ends laminate layers. These are joined to the main fatigue crack. The fatigue crack propagation life mainly controlled low cycle fatigue life. There is fundamentally little difference in fatigue crack initiation and propagation mechanism between Type-I and -II specimens.

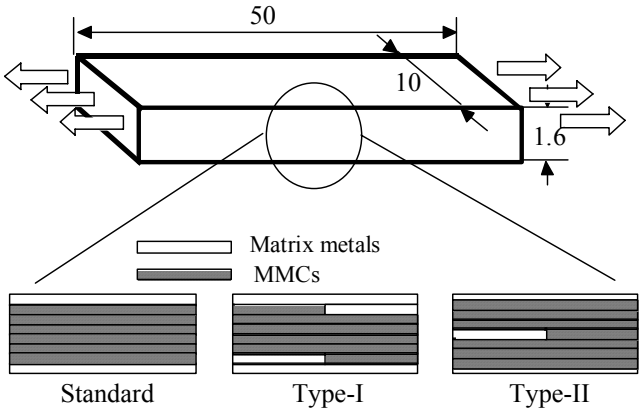

Figure 6: Schematics of analytical model

A macroscopic stress field of test specimen was analyzed based on a simple analytical model schematically shown in Fig. 6 [10]. These stress analyses show that the MMCs part of Type-I is highly stressed and quail-tatively corresponds to lower fatigue lives of Type-I. There is little difference in stress field of the MMCs part between standard specimen and Type-II. Accordingly, differences in low cycle fatigue lives between standard specimen and Type-II shown in Figs.2 and 3 cannot always rationalized by this macroscopic stress analysis. It is necessary for the future research to model fatigue crack initiation and propagation and consider the redistribution of residual stress for quantitative prediction of low cycle fatigue lives.

CONCLUSIONS

The influence of reinforcement fiber ends on low cycle fatigue behavior was investigated in order to establish the fatigue damage tolerance design concept for continuous fiber reinforced Ti-alloy matrix composite (TMCs) rotating parts in aircraft engines. The conclusions may be summarized as follows.

(1) Low cycle fatigue tests were successfully performed for the reinforcement fiber ends specimen simulated continuous fiber partially reinforced metal matrix composite components.

(2) There is a remarkable influence of reinforcement fiber ends on low cycle fatigue lives. The surface laminate layer reinforcement fiber ends specimen has the lowest fatigue lives. It is necessary for the fatigue damage tolerance design of continuous fiber partially reinforced metal matrix composites structural components to consider the influence of reinforcement fiber ends.

(3) Stress analyses of the reinforcement fiber ends specimen show that the lower fatigue lives of Type-I corresponds the highly stressed at the MMCs portion. It is also identical to the fractographic examinations that there are many fatigue cracks initiated and propagated in the laminate layers near the reinforcement fiber ends and joined by forming the steps to the main fatigue crack.

ACKNOWLEDGEMENTS

This research has been conducted as a part of R&D on Construction and Preparation of Database for High Temperature Structural Composite Materials(Ti-MMCs, TiB_2-TiAl and MGCs) in Agency of Industrial Science and Technology, MITI. The authors are highly appreciated all members of technical committee in Research Institute of Metals and Composites in the Future Industry (RIMCOF).

REFERENCES

1. Hirano, K., Current R&D Trends of Advanced Metallic and Inorganic Materials and Its Technical Problems, *Trans. JSME (A),* 58-550(1992) pp.817-823 (in Japanese)
2. Hirano, K., R&D Trends of Advanced Metal Matrix Composites and Fracture Mechanics Characterization, *ISIJ International,* 32-12(1992) pp.1357-1367
3. Hirano, K., High Performance Materials for Severe Environments in the Field of Aerospace and Power Generator Technologies in Japan (Invited Lecture), Metal Matrix Composites, *Proc. 9th Int. Conf. on Composite Materials,* 1(1993) pp.87-88
4. Hirano, K., Fatigue of Metal Matrix Composites, *J. Soc. Mat. Sci., Japan,* 43-493(1994) pp.1373-1378 (in Japanese)
5. Hirano, K., K. Etoh and M. Kikuchi, Fracture Toughness of Unidirectional Fiber Reinforced Titanium alloy and Titanium Intermetallic Matrix Composites, *LOCALIZED DAMAGE'96-Computer-Aided Assessment and Control-* Computational Mechanics Pub. (1996) pp.409-416.
6. Hirano, K., High Temperature Melt Point Ductile Metallic Fiber Toughening of γ-Type Titanium Aluminide Intermetallics, Progress in Mechanical Behavior of Materials(ICM8), Vol.III, (1999) pp.853-857
7. Natsumura, T., et.al, Component Design of CMC and MMC rotor for Turbine Engine Applications, *SAMPE COMPOSITE '99*, (1999)
8. Yamada, T., Tsuzuku T., Hirota, M., Kawachi, Y. and Yamamoto, S., Fabrication of Titanium Matrix Composite Blade, To be presented at *ICCM-13*, (2001-6)
9. Fukushima, A., Fujiwara, C., Kawachi, Y. and Yasuhira, K., Fatigue Properties of SCS-6/SP700 Titanium Matrix Composite, *Proc. of ICCM-12*, (1999)
10. Kohno, Y., et.al, Stress Analysis of Fatigue Test Specimen, RIMCOF Report on R&D on Construction and Preparation of Database for High Temperature Structural Composite Materials, (2001-3) (in-press)

ORAL/POSTER REFERENCE: ICF100424OR

FATIGUE CRACK PROPAGATION LIMIT CURVES FOR METALLIC AND NON-METALLIC MATERIALS

J. Lukács

Department of Mechanical Engineering, University of Miskolc
H-3515 Miskolc-Egyetemváros, Hungary

ABSTRACT

There are different documents containing fatigue crack propagation curves and rules for the prediction of crack growth. The research work aimed to develop a new method for determination of fatigue crack propagation limit curves and determination of limit curves for different metallic materials (steels, austempered ductile iron, aluminium alloys) and their welded joints and non-metallic materials (ceramic, polymer, composite), under different loading conditions, based on statistical analysis of test results and the Paris-Erdogan law. With the help of the characteristic values of threshold stress intensity factor range (ΔK_{th}), two constants of Paris-Erdogan law (C and n), fracture and fatigue fracture toughness (K_{Ic} and ΔK_{fc}) a new method can be proposed. The limit curves represent a compromise of rational risk and striving for safety.

INTRODUCTION

Reliability of a structural element having crack or crack-like defect is determined by the geometrical features of the structural element and the flaws, the loading conditions as well as the material resistance to crack propagation. There are different documents and standards containing fatigue crack propagation limit or design curves and rules for the prediction of crack growth [1, 2, 3, 4, 5]. The background of the limit curves and the calculations consists of two parts: statistical analysis of numerous experiments and fatigue crack propagation law, frequently the Paris-Erdogan law [6].

The research work aimed (i) to develop a new method for determination of fatigue crack propagation limit curves; (ii) determination of limit curves for different metallic materials and their welded joints, under mode I and mixed mode I+II loading conditions and for non-metallic materials under mode I loading condition.

EXPERIMENTS

Specimens made of micro-alloyed steel grades 37C, E420C and HSLA steel grade X80TM and their welded joints by gas metal arc (GMA) welding were tested. Specimens made of 10 Cr Mo 9 10 hot resistant steel and its welded joints by submerged metal arc (SMA) welding, specimens made of KL7D pressure vessel steel and its welded joints by manual metal arc (MMA) welding and specimens made of railway rail steel grade DO76 and HSLA steel grade QStE690TM were investigated, too. Welding of 37C steel was carried out with CO_2 gas, E420C steel with 80% Ar + 20% CO_2 gas mixture and X80TM steel with 82% Ar + 18% CO_2 gas mixture. Specimens made of austempered ductile iron (ADI) and specimens made of aluminium

alloy types AlMg3, AlMg5, AlMg4.5Mn and their welded joints by GMA and pulsed GMA welding were tested, too [7]. Mechanical properties of base materials (bm) and weld metals (wm) are shown in Table 1.

TABLE 1
MECHANICAL PROPERTIES OF THE TESTED METALLIC MATERIALS AND WELD METALS

Material	R_y N/mm^2	R_m N/mm^2	A_5 %	Z %	KV(20^{0}C) J	KV(0^{0}C) J	KV(-20^{0}C) J
37C bm	270	405	33.5	63.5	–	>27	–
10 Cr Mo 9 10 bm	374	510	≥20	–	≥34	–	–
KL7D bm	390	535	≥19.0	–	–	–	≥40
E420C bm	450	595	30.7	–	–	>40	-
X80TM bm(1)	540	625	25.1	73.1	–	–	≥243
DO 76 bm	582	954	7.6	–	≥7	–	–
QStE690TM bm(2)	780	850	18.3	–	130	90	95
VIH-2 wm	410-485	535-585	22.0-24.8	40.9-63.9		46-80	29-61
ESAB OK Flux 10.62/ OK Autrod 13.20 wm	450	590	–	–	≥100	–	–
EB 12 wm	420-510	510-630	≥22.0	–	–	–	–
Union K56 wm	≥500	560-720	≥22.0	–	–	–	≥47
Böhler X90-IG wm(3)	≥890	≥940	≥16.0	–	–	≥100	≥90
AlMg3 bm	112	224	21.4	–	–	–	–
AlMg5 bm	185	288	14.5	–	–	–	–
AlMg4.5Mn bm	230	296	18.0	–	–	–	–

(1) KV (-60°C) = 128-208 J.
(2) KV (-40°C) = 35 J, KV (-60°C) = 20 J.
(3) KV (-40°C) = 80 J, KV (-60°C) = 60 J.

The investigated non-metallic materials were as follows: silicon nitride ceramics (Si_3N_4, Re_2O_3, SiO_2 and additive component Y_2O_3 or Yb_2O_3 or Dy_2O_3)[8, 9]; polymethyl methacrylate (PMMA) [10]; unidirectional carbon fiber reinforced plastic (CFRP), carbon fiber/epoxy, T300/914 [11, 12]; injection-molded composite, glass fiber/nylon 6, 6 [10, 13].

Compact tension (CT) and three point bending (TPB) specimens were tested for base materials and welded joints, while for testing of weld metal TPB type specimens were used. CT type specimens were cut from the sheets parallel and perpendicular to the rolling direction, so the directions of fatigue crack propagation were the same. For testing of weld metals cracks which propagate parallel or perpendicular to the axis of the joint were also distinguished. Compact tension shear (CTS) specimens were used for tests under mixed mode I+II loading condition. The specimens were cut parallel to the rolling direction, so the cracks were propagated perpendicular to the rolling direction. Tests were carried out according to the ASTM prescription by an universal electrohidraulic MTS testing machine. Experiments were performed by ΔK-decreasing and constant load amplitude methods, at room temperature, in air, following sinus-type loading wave form. Stress ratio was constant (R=0.1), crack propagation was registered by compliance and/or optical method.

DETERMINATION OF FATIGUE DESIGN LIMIT CURVES

Values of threshold stress intensity factor range (ΔK_{th}) and two parameters of Paris-Erdogan law (C and n) were measured according to prescriptions [14], values of fatigue fracture toughness (ΔK_{fc}) were calculated from crack length measured on the fracture surface of the specimens by the means of stereo-microscope. Fatigue crack growth was determined by secant or seven point incremental polynomial method.

On the basis of these results, mathematical-statistical samples were examined for each testing groups. As its method, Wilcoxon-probe was applied [15], furthermore statistical parameters of the samples were calculated. The mathematical-statistical samples of tested metallic materials and their welded joints can be found in earlier works [16, 17] and the samples of non-metallic materials are summarised in Table 2.

TABLE 2
MATHEMATICAL-STATISTICAL SAMPLES OF NON-METALLIC MATERIALS AND THEIR PARAMETERS

Material	Parameter	Element number of sample	Average	Standard deviation	Standard deviation coefficient
Silicon nitride ceramics (Si_3N_4)	n	11	23.54	4.447	0.1889
	K_{Ic}	9	5.24	0.400	0.0763
Polymethyl methacrylate (PMMA)	n	4	6.38	1.299	0.2035
Carbon fiber/epoxy (T300/914)	n	4	14.70	0.979	0.0666
Glass fiber/nylon 6,6	n	13	6.20	1.650	0.2659

Afterwards it was examined, what kind of distribution functions can be used for describing the samples. For this aim, Shapiro-Wilk, Kolmogorov, Kolmogorov-Smirnov and χ^2- probe were used at a level of significance ε=0.05. It was concluded, that Weibull-distribution is the only function suitable for describing all the samples. Taking this into account parameters of three parameter Weibull-distribution function were calculated for all the samples.

Based on the calculated distribution functions, considering their influencing effect on life-time, characteristic values of ΔK_{th}, n and ΔK_{fc}, were selected. With the help of these values a new method can be proposed for determination of fatigue crack propagation limit curves:

- the threshold stress intensity factor range, ΔK_{th}, is that value which belongs to the 95% probability of the Weibull-distribution function,
- the exponent of the Paris-Erdogan law, n, is that value belonging the 5% probability of Weibull-distribution function,
- the constant of the Paris-Erdogan law, C, is calculated on the basis of the correlation between C and n (Figure 1),

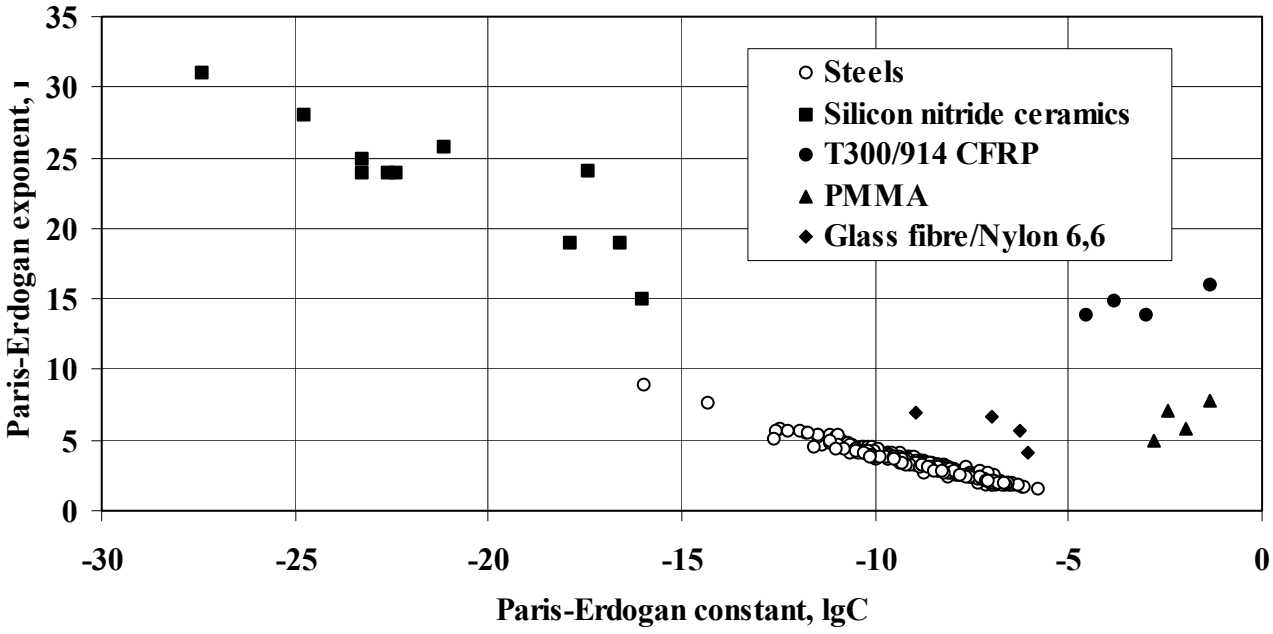

Figure 1: Connection between the exponent and the constant of Paris-Erdogan law

- the critical value of the stress intensity factor range or fatigue fracture toughness, ΔK_{fc}, is that value which belongs to the 5% probability of the Weibull-distribution function.

Figure 2 shows the proposed method shematically.

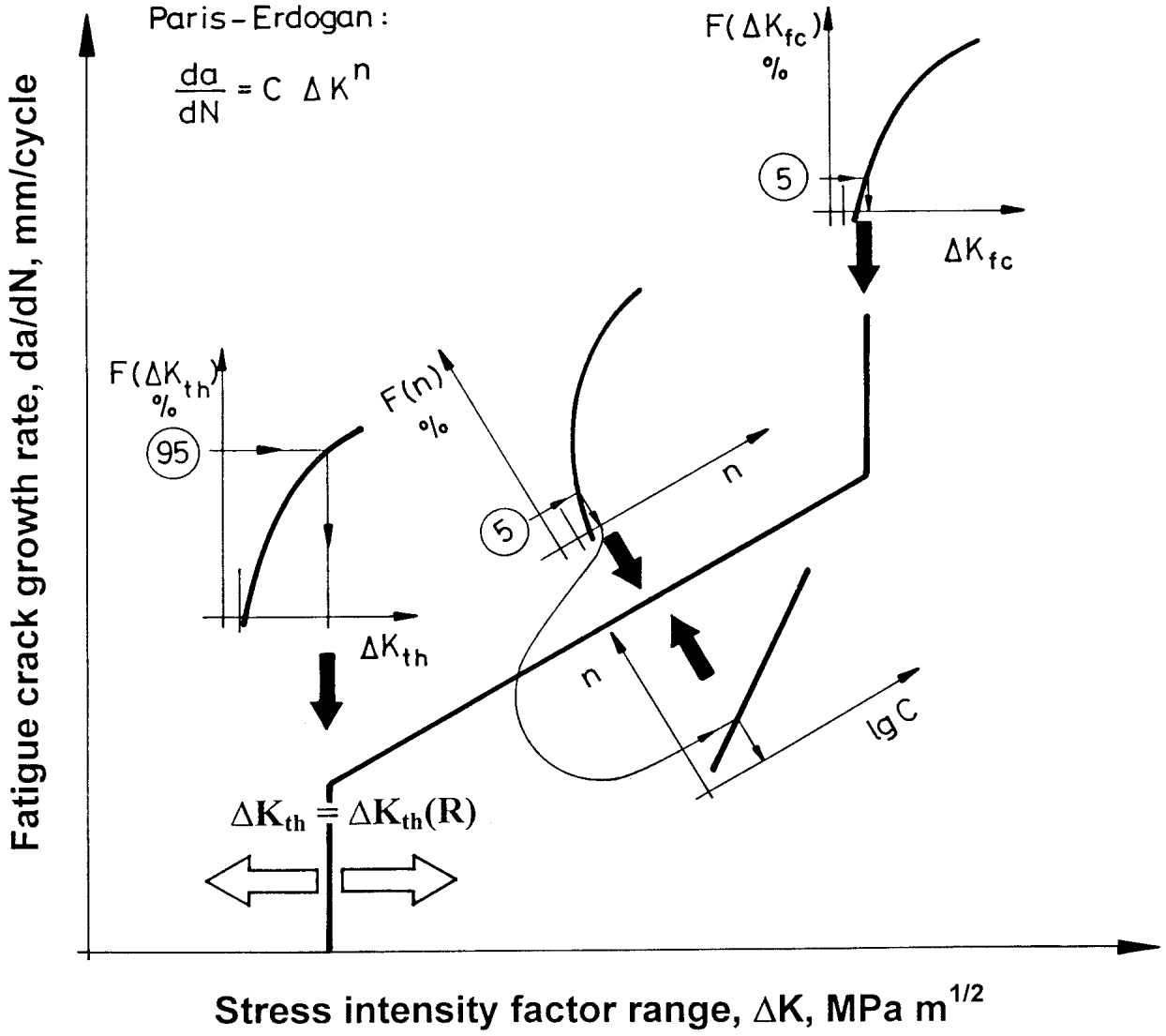

Figure 2: Schematic presentation of the proposed new method for determination of fatigue crack propagation limit curves

The details of fatigue crack propagation limit curves determined for non-metallic materials can be found in the Table 3 and for metallic materials and their welded joints are summarised in the Table 4.

TABLE 3
DETAILS OF FATIGUE CRACK PROPAGATION LIMIT CURVES FOR NON-METALLIC MATERIALS

Material	ΔK_{th} MPam$^{1/2}$	C	n	ΔK_{fc} MPam$^{1/2}$
		mm/cycle and MPam$^{1/2}$		
Silicon nitride ceramics	–	5.80E-17	16.21	4.9[3]
PMMA	–	2.89E-04	4.24	–
T300/914	–[1]	5.92E-06	13.54	–
Glass fiber/nylon 6,6	–[2]	2.11E-05	4.03	–

[1] $\Delta K_{th}(R = 0.1) = 0.73$ MPam$^{1/2}$.
[2] $\Delta K_{th}(R = 0\text{-}0.2) = 1.12\text{-}2.4$ MPam$^{1/2}$.
[3] Based on K_{Ic} distribution function.

TABLE 4

DETAILS OF DETERMINED FATIGUE CRACK PROPAGATION LIMIT CURVES FOR METALLIC MATERIALS

Material	ΔK_{th} MPam$^{1/2}$	n MPam$^{1/2}$	C and mm/cycle	ΔK_{fc} MPam$^{1/2}$
37C base material	10.4	2.98	8.22E-09	53
10 Cr Mo 9 10 base material	–[5]	1.40	1.33E-06	77
KL7D base material	–	2.65	2.04E-08	66
E420C base material	8.0	2.26	9.78E-08	92
X80TM base material	–	1.78	3.74E-07	129
DO76 base material	–	2.94	7.74E-09	76
DO76 base material[2), 3)]	–	4.01	2.16E-10	–
QStE690TM base material	–	1.82	3.27e-07	–
QStE690TM base material[2), 3)]	–	2.15	1.09E-07	–
37C welded joint	–[1), 6)]	3.16	2.42E-09	70
10 Cr Mo 9 10 welded joint	–[1), 7)]	1.76	4.54E-07	85
KL7D welded joint	–[1)]	3.72	2.98e-10	–
E420C welded joint	–[1), 8)]	2.74	1.16E-08	101
X80TM welded joint	–[1)]	1.86	3.13E-07	–
ADI base material	–	2.80	6.05E-07	–
AlMg3 base material and welded joint	4.5[4)]	2.75	3.94E-09	17
AlMg5 base material and welded joint	4.5[4)]	3.02	2.06E-09	19
AlMg4.5Mn base material and welded joint	4.5[4)]	3.06	1.87E-08	21

(1) It can be derived from data concerning to the base metal after the evaluation of characteristic and assessment of magnitude of residual stresses.

(2) Under mixed mode I+II loading condition.

(3) ΔK should be replaced by ΔK_{eff}.

(4) One distribution function was calculated from the test results of the three aluminium alloys.

(5) Average value of 2 tests: $\Delta K_{th} = 12.7$ MPam$^{1/2}$.

(6) Average value of 16 tests under compressive residual stress: $\Delta K_{th} = 16.9$ MPam$^{1/2}$.

(7) Average value of 3 tests: $\Delta K_{th} = 9.0$ MPam$^{1/2}$.

(8) Average value of 4 tests under compressive residual stress: $\Delta K_{th} = 16.3$ MPam$^{1/2}$.

DISCUSSION

For micro-alloyed steels and their welded joints both the threshold stress intensity factor range (ΔK_{th}) and the exponent of the Paris-Erdogan law (n) decrease with the increase of the strength of steel, while the fatigue fracture toughness (ΔK_{fc}) increases.

For metallic materials both the exponent of the Paris-Erdogan law (n) and the fatigue fracture toughness (ΔK_{fc}) for welded joints are higher than those of base materials.

The proposed method is suitable for determination of fatigue crack propagation design curves under mixed mode I+II loading condition. For this case stress intensity factor range (ΔK) should be replaced by effective stress intensity factor range (ΔK_{eff}).

The design curves of welded joints in the near threshold region are open. The threshold stress intensity factor range, ΔK_{th}, must be reduce by tensile residual stress field and may be increase by compressive residual stress field (e.g. welding residual stresses).

The limit curves of metallic materials locate among the design curves determined by various procedures.

CONCLUSIONS

Based on the results of our experimental tests, evaluated samples and data can be found in the literature the following conclusions can be drawn.

(i) The proposed method can be generally applied for determination of fatigue crack propagation limit curves for metallic materials and their welded joints under mode I and mixed mode I+II loading conditions and for non-metallic materials under mode I loading condition.

(ii) The limit curves represent a compromise of rational risk (not the most disadvantageous case is considered) and striving for safety (uncertainty is known).

(iii) Based on the determined fatigue design limit curves integrity assessment calculations can be done for operating structural elements and structures having cracks or crack-like defects.

(iv) Determination of fatigue crack propagation limit curves of non-metallic materials based on other fracture mechanical parameters (e.g. G, ΔG, ΔJ) requires further investigations

ACKNOWLEDGEMENTS

Author wish to acknowledge the assistance given by the National Scientific Research Foundation and the Hungarian Ministry of Education for supporting the research (OTKA F 4418, OTKA T022020 and MKM FKFP-0633/2000).

REFERENCES

1. Allen, R. J., Booth, G. S. and Jutla, T. (1988). *Fat. Fract. Eng. Mater. Struct.* 11, 45.
2. Allen, R. J., Booth, G. S. and Jutla, T. (1988). *Fat. Fract. Eng. Mater. Struct.* 11, 71.
3. Ohta, A. et al. (1989). *Trans. Jap. Weld. Soc.* 20, 17.
4. Merkblatt DVS 2401 Teil 1 (Oktober 1982). *Bruchmechanische Bewertung von Fehlern in Schweissverbindungen. Grundlagen und Vorgehensweise.*
5. Det norske Veritas, Classification Notes, Note No. 30.2 (August 1984). *Fatigue strength analysis for mobile offshore units.*
6. Paris, P. and Erdogan, F. (1963). *Journ. Bas. Eng., Trans. ASME.* 528.
7. Török, I. (1996). *Publ. Univ. Miskolc, Series C. Mech. Engng.* 46, 33.
8. Cornelissen, B. E. et al. (1994). *Acta Metall. Mater.* 42, 3055.
9. Sugeta, A., Jono, M. and Koyoma, A. (1966). In: *Proceedings of The Sixth International Fatigue Congress.* 3, pp. 1663-1668, Lütjering, G. and Nowack, H. (Eds.) Pergamon.
10. Hertzberg, R. W., Manson, J. A. and Wu, W. C. (1973). In: *Progress in Flaw Growth and Fracture Toughness Testing.* ASTM STP 536, 391.
11. Hojo, M. et al. (1986). In: *Proceedings of a Japan-US Joint Seminar on Advanced Materials for Severe Service Applications.* pp. 353-372. Elsevier.
12. Hojo, M. et al. (1994). *Eng. Fract. Mech.* 49, 35.
13. Mandell, J. F. (1990). In: *Fatigue of Composite Materials: Fatigue Behaviour of Short Fiber Composite Materials.* pp. 231-337. Elsevier.
14. ASTM E 647 (1988). *Standard test method for measurement of fatigue crack growth rates.*
15. Owen, D. B. (1973). *Handbook of statistical tables.* Vychislitel'nyjj Centr AN SSSR, Moskva. (In Russian).
16. Lukács, J. (1996). *Publ. Univ. Miskolc, Series C. Mech. Engng.* 46, 77.
17. Lukács, J.(2000). In: *Third International Pipeline Technology Conference.* 2, pp. 127-140, Denys, R. (Ed.) Elsevier Science B. V.

ORAL REFERENCE: ICF100589OR

FATIGUE CRACK PROPAGATION OF DISSIMILAR METAL WELDS

C.S. Kusko[1], J.N. DuPont[1], S. Spooner[2], and A.R. Marder[1]

1. Department of Materials Science and Engineering, Lehigh University, Bethlehem, PA 18015, USA
2. Oak Ridge National Laboratory, Oak Ridge, TN 37831, USA

ABSTRACT

The hard martensite layer that forms adjacent to the fusion line of austenitic/ferritic dissimilar metal welds has been investigated by microstructural characterization and mechanical testing methods. Residual stress measurements were made in the vicinity of the fusion line in both the substrate and overlay materials and fatigue crack propagation tests were performed as to allow the crack to propagate along the dissimilar alloy weld fusion line. This hard martensite layer was found to be non-detrimental to the fatigue crack growth response, as the majority of the fatigue cracks propagated across the martensite layer and fusion line and into the substrate. The compressive residual stresses within the substrate contributed to the enhancement of the growth response of the weld overlay specimens. Based on these results, the hard martensite layer should not be a major factor in causing failure along the fusion line in austenitic/ferritic dissimilar metal weld overlay applications.

KEY WORDS

fatigue crack propagation; microstructure; martensite; weld

INTRODUCTION

In the power generation industry, austenitic weld overlays are often used for erosion and high temperature corrosion resistance for ferritic carbon and low alloy steels [1]. Fabrication of such dissimilar metal welds can result in distinct problems. For example, rapid cooling and overlay/substrate chemical composition differences [2] lead to the formation of a martensite layer adjacent to the weld fusion line [3-11]. Figure 1 illustrates a typical martensite layer that forms along the fusion line of a 309L stainless steel/A285 carbon steel weld [11]. Previous research by Kusko [11] has provided a fundamental explanation for the formation of the martensite layer, which leads to steep microstructural and mechanical property gradients across the fusion line. For example, Figure 2 illustrates microhardness results conducted across the fusion line of the 309L stainless steel/A285 carbon steel weld [12]. As evidenced from this figure, the hardness in the martensite layer region can reach values that are approximately twice as large as the hardness values found in the bulk austenitic overlay and ferritic substrate. In addition to this detrimental microstructural gradient, the coefficient of thermal expansion mismatch between the overlay and the base material induces thermal stresses at the fusion line [2]. A post-weld heat treatment (PWHT), which is often incorporated in order to reduce the magnitude of residual stresses, can induce significant microstructural changes and thus, additional gradients in mechanical properties [3].

It is generally known that fatigue crack initiation often occurs more rapidly in welded structures as compared to non-welded structures due to welding defects and other stress concentrators. Consequently, a significant portion of a weld's fatigue life is spent in the propagation stage. The presence of such weld-related stress concentrators, in addition to the aforementioned hard martensite layer found adjacent to the fusion line, makes fatigue crack propagation a concern for dissimilar metal welds. In addition, residual stresses resulting from welding and

thermal expansion mismatch in the vicinity of a weld can significantly affect the fatigue behavior. Thus, knowledge of the fatigue crack growth behavior of such welds is of practical importance.

The objectives of this research are to investigate the fatigue crack growth behavior in the presence of the martensite layer found adjacent to the fusion line for as-welded (AW) 309L stainless steel/A285 carbon steel dissimilar metal welds. Included in this objective is an understanding of the residual stress pattern that can develop in such dissimilar metal weld overlay coatings. The results of this research should provide insight as to whether the martensite layer in such dissimilar welds should be of concern in the presence of cyclic loading conditions during service.

EXPERIMENTAL PROCEDURE

Carbon steel designation ASTM A285 Grade C, of dimensions 61 cm x 15 cm x 4 cm, was utilized as the substrate material. The austenitic overlay used was iron-based 309L stainless steel. The weld strip electrode size was 30 mm × 0.5 mm. Strip electrode and substrate compositions are provided in Table 1. Electroslag welding was used to deposit the strip electrode continuously along the top edge of the substrate at 565 A, 24 V, and 3.0 mm/s travel speed. The electroslag process was chosen because of its abilities to produce a relatively flat fusion line and to provide a uniform cladding with low dilution levels [8]. The resulting dilution level was 17 %.

Compact-tension (C(T)) specimens were fabricated from specimens comprised of bulk electroslag welds and electron-beam (EB) extensions of the overlay material. EB welding was chosen to produce a minimal heat affected zone, allowing the original dissimilar metal electroslag fusion line microstructure to remain unchanged during the process. The resulting C(T) specimens were of dimensions 63.5 mm x 60.96 mm x 12.7 mm. Starter notches having a 1.52 mm radius of curvature were inserted by wire electro-discharge machining (EDM) as close to the fusion line as possible as to enable crack growth along the fusion line (parallel to the welding direction). However, since the welding process resulted in a fusion line that was not perfectly flat, it was impossible to insert the starter notch perfectly along the fusion line. Figure 3 shows a photomacrograph of a typical C(T) specimen with starter notch.

Neutron diffraction measurements were utilized to determine the residual stress pattern in three orthogonal directions near the dissimilar alloy C(T) specimen weld fusion line. Measurements were performed on the 309L stainless steel AW specimens. Due to differences in crystal structure between the substrate and the overlay, the measurements could not be conducted directly on the fusion line. Thus, for each sample, strains were measured at distances of 1, 3, and 5 mm from the dissimilar alloy weld fusion line (into both the substrate and overlay) at the notch tip, 10 mm, and 20 mm from the notch tip, as illustrated in Figure 4.

Fatigue crack propagation tests, conforming to ASTM Standard E647 [13], were performed on AW specimens and on wrought 309L stainless steel and A285 specimens to provide a baseline. Instron servohydraulic fatigue testing equipment was utilized, along with constant amplitude loading and a sine waveform. All testing was performed at a frequency of 25 Hz. Software from Fracture Technology Associates was used to allow for computer-controlled testing. Constant R (equal to 0.10) tests were utilized to generate steady state and higher crack growth rate data. Constant K_{max} tests, during which the R ratio increased as the load decreased, were utilized to obtain low crack growth rate and threshold data. Crack lengths were determined by the compliance function and visually verified. Crack growth rates were calculated by the modified secant method. Stereomicroscopy and light optical microscopy were used to characterize the fracture surface and microstructure of the welds following testing.

RESULTS AND DISCUSSION

Residual Stress

Figure 4 shows the residual stress measurements for the 309L stainless steel/A285 carbon steel dissimilar metal weld in the AW condition for the normal (N), transverse (T), and longitudinal (L) directions of the stress. In this figure, the x-axis represents the magnitude of the residual stress, with positive values corresponding to tensile stresses and negative values corresponding to compressive stresses. The y-axis exhibits the distance from the fusion line, with positive values corresponding to locations within the austenitic overlay and negative values corresponding to locations within the ferritic substrate. The legend key illustrates the measurements taken at the notch tip and at 10 mm and 20 mm from the notch tip. From this figure, the residual stresses are tensile in the

309L stainless steel overlay and compressive in the ferritic substrate. Within the overlay, the magnitude of the stresses generally increase as the measurement location increases in reference to the notch tip such that the stresses at the notch tip are generally the smallest in magnitude. The residual stresses reach a maximum value of approximately 560 MPa, but are generally on the order of magnitude of 400 MPa or less for this dissimilar metal weld. Within the substrate, the compressive residual stresses reach a maximum value of approximately 130 MPa.

Fatigue Crack Propagation Testing

Figure 5 shows the C(T) specimens for the 309L stainless steel/A285 carbon steel samples in the AW (5a and 5b) condition following fatigue crack propagation testing. As evidenced from Figure 5a, which corresponds to test identification 309DMW3, the crack grew nearly parallel to and along the fusion line for this specimen. However, Figure 5b, which corresponds to test identification 309DMW2, illustrates that the fatigue crack grew across the fusion line and into the substrate and remained in the substrate during propagation.

Figure 6 exhibits the interaction of the crack with the fusion line microstructure for test specimen 309DMW3 (corresponding to Figure 5a), which macroscopically followed the interface. As evidenced from this figure, the extremely hard martensite layer, shown by Figures 1 and 2, does not appear to detrimentally affect the fatigue behavior as might be expected from such a hard layer. That is, propagation does not occur within the martensite layer. The interaction of the fatigue crack with the martensite layer in Figure 6a is representative of only a localized region of the crack growth. Figure 6b, which exhibits the fatigue crack in a different region of the same specimen as in Figure 6a, is more indicative of the entire crack path, such that little interaction exists with the martensite layer.

Crack growth rates for the two 309L stainless steel welds, in addition to wrought 309L stainless steel and A285 specimens, are plotted in Figure 7. As evidenced from this figure, the dissimilar metal welds exhibit increased fatigue resistance as compared to the wrought stainless steel and carbon steel specimens. Crack growth into the substrate, which experiences compressive residual stresses, most likely contributes to the enhanced fatigue response. Even the specimen that propagated a small distance through the martensite layer exhibited an improved response, indicating a possible retardation of the fatigue response caused by the martensite layer. Regardless, the main point to emphasize is that, as evidenced by this figure, in conjunction with Figures 5 and 6, the martensite layer does not appear to detrimentally affect the fatigue crack growth behavior of these austenitic/ferritic dissimilar alloy welds.

CONCLUSIONS

Residual stress measurements made within the vicinity of the fusion line for the dissimilar alloy welds indicated compressive behavior in the substrate and tensile behavior in the overlay. Fatigue crack propagation results indicated that crack growth either crossed over the martensite layer and fusion line and continued within the compressive substrate or continued in the vicinity of the martensite layer within the overlay. Regardless, the hard martensite layer did not negatively affect the fatigue response of the welded materials, as the cracks never propagated fully within the martensite layer. In addition, the crack growth rate curves for the weld overlay specimens exhibited increased fatigue crack propagation resistance as compared to the wrought specimens, most likely due to the compressive residual stresses within the substrate region in which the cracks propagated. Based on these results, the martensite layer does not appear to present a major concern for contributing to interfacial failure in weld overlay applications in austenitic/ferritic dissimilar metal welds.

ACKNOWLEDGEMENTS

The authors would like to thank Dr. C. Robino at Sandia National Laboratories for the electron beam welding, A. Benscoter for assistance with sample metallurgical preparation, G. Kozma for assistance with the testing equipment, and M. Rex for assistance with specimen machining. This research was sponsored by the American Welding Society Navy Joining Center Fellowship and a consortium of power generation companies.

REFERENCES

1. Nelson, T., Lippold, J., and Mills, M. (1998). *Science and Technology of Welding and Joining* 3, 249-255.

2. Wang, Z., Xu, B., and Cii, Y. (1993). *Welding Journal*. 72, 397s-402s.
3. Gittos, M. and Gooch, T. (1992). *Welding Journal*. 71, 461s-472s.
4. Ornath, F., Soudry, J., Weiss, B.Z., and Minkoff, I. (1981). *Welding Journal.* 60, 227s-231s.
5. Faber, G. and Gooch, T. (1982). *Welding in the World.* 20, 87-98.
6. Pan, C., Wang, R., Gui, J., and Shi, Y. (1990). *Journal of Materials Science.* 25, 3281-3285.
7. Pohle, C. (1991) *Welding International.* 5, 409-413.
8. Zhao, Q., Gao, Y., Devletian, J., McCarthy, J., and Wood, W. (1993). In: *International Trends in Welding Science and Technology*, pp. 339-343, David, S.A. and Vitek, J.M. (Eds). Gatlinburg, Tennessee.
9. Pan, C. and Zhang, Z. (1994). *Materials Characterization* 33, 87-92.
10. McPherson, N., Baker, T., and Millar, D. (1998). *Metallurgical Transactions A*. 29A, 823-832.
11. Kusko, C. (1999). MSc Thesis, Lehigh University, Bethlehem, PA.
12. Kusko, C. (1999). Unpublished research.
13. ASTM E647. (1993). *Annual Book of ASTM Standards. Section 3. Metals Test and Analytical Procedures*. 3.01, 565-601.

TABLE 1
SUBSTRATE AND FILLER METAL COMPOSITIONS

	Fe	Ni	Cr	Mo	Nb	Si	C	P	S	Al	Ti	Mn
A285	98.31	--	--	--	--	0.21	0.06	0.01	0.028	--	--	0.81
309L	60.33	12.62	23.44	--	--	0.40	0.013	--	--	--	--	--

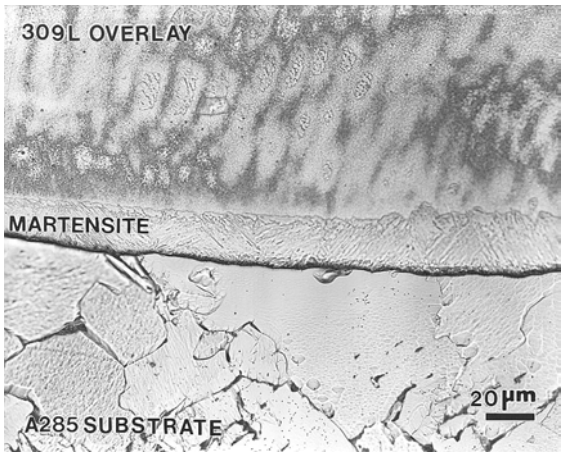

Figure 1. Martensite layer observed at fusion line of dissimilar metal welds (etchant: 90 ml methanol/ 5 g FeCl/ 4ml HCl, electrolytic preset at 6 volts for 3 seconds).

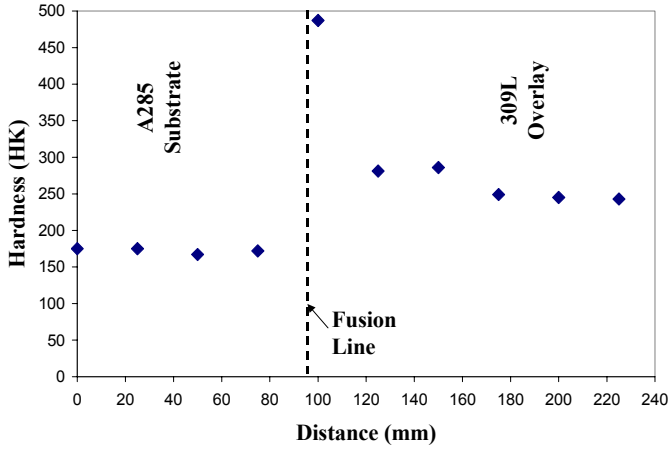

Figure 2. Microhardness results for 309L dissimilar weld (Knoop indenter, 10 g load for 10 seconds).

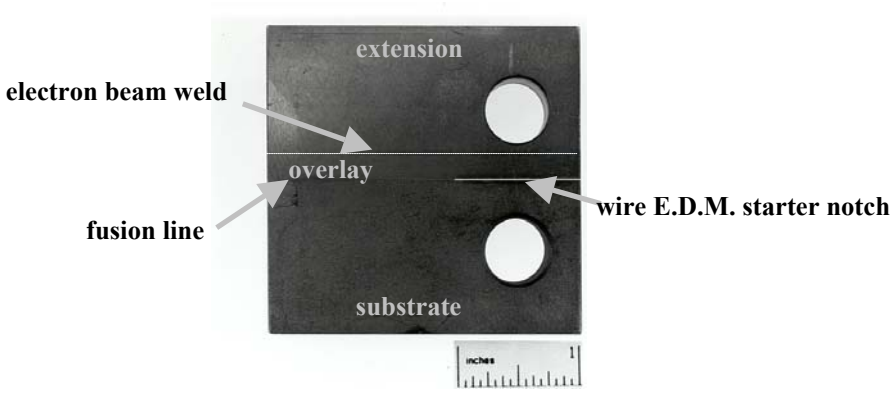

Figure 3. Photomacrograph illustrating typical C(T) specimen starter notch insertion.

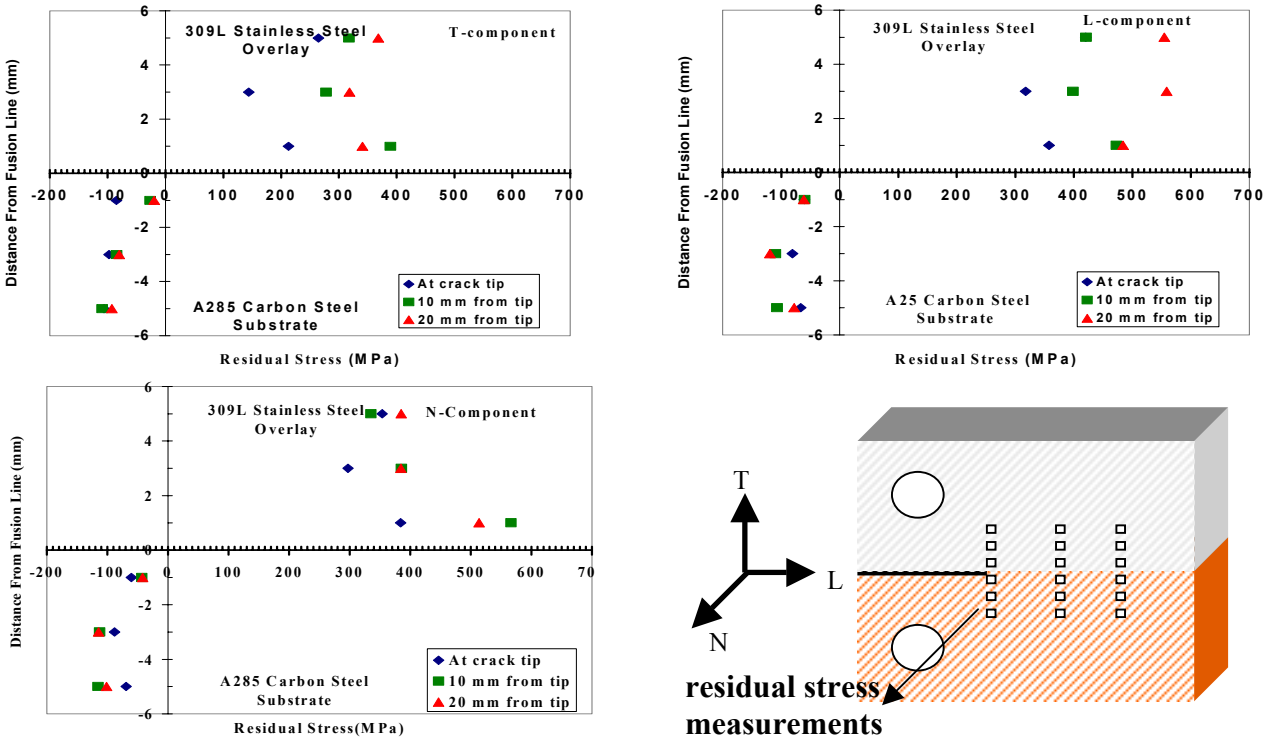

Figure 4. Residual stress measurements for 309L AW dissimilar metal weld specimen.

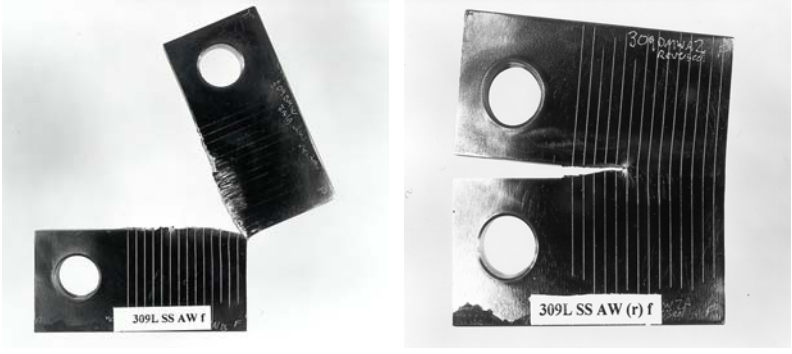

(a) (b)

Figure 5. Macroscopic crack growth directions for specimens a) 309DMW3 and b) 309DMW2.

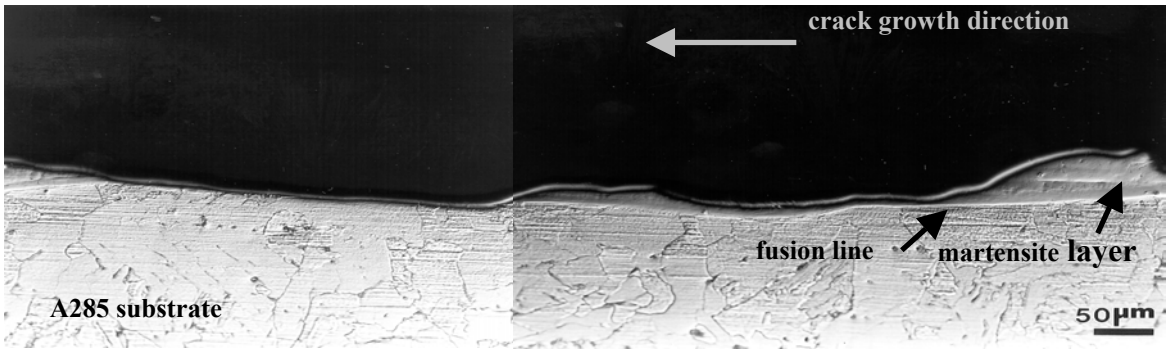

(a)

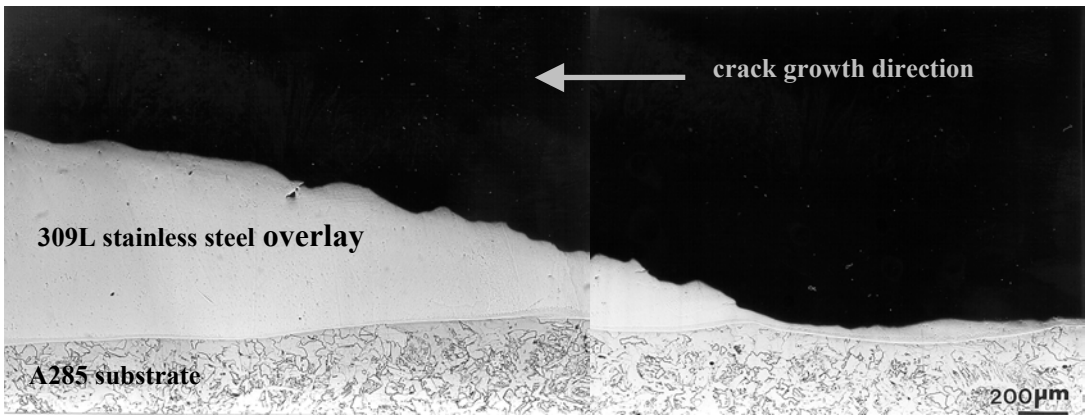

(b)

Figure 6. Crack growth interaction with the fusion line in 309L stainless steel dissimilar welds corresponding to test identifications 309DMW3 (AW).

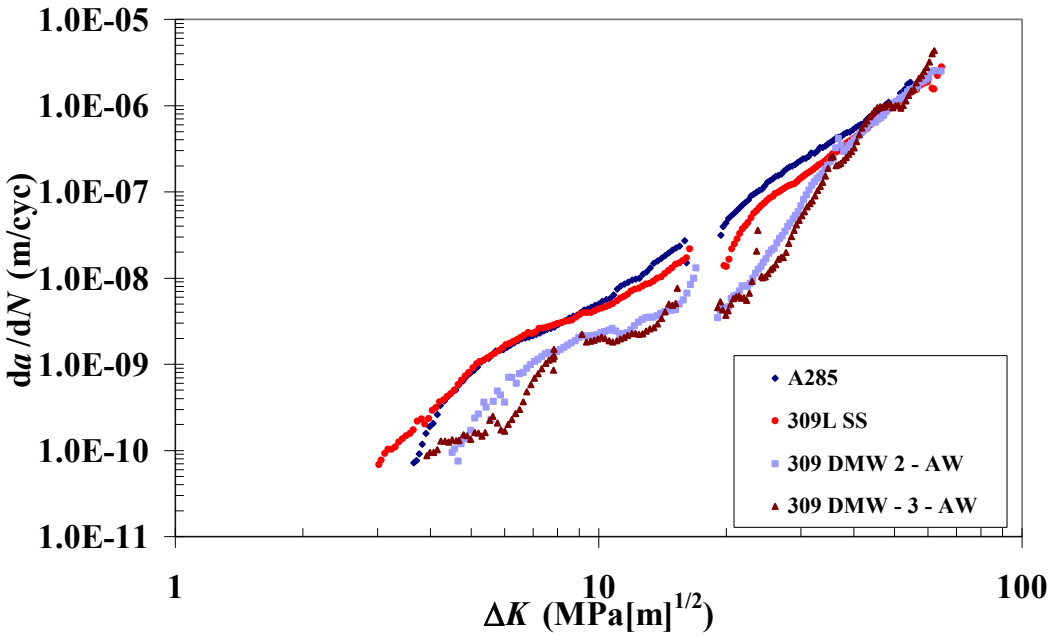

Figure 7. Crack growth rate curves for 309L stainless steel/A285 carbon steel dissimilar metal weld specimens and wrought A285 carbon steel and 309L stainless steel specimens.

ORAL REFERENCE: ICF100946OR

FATIGUE DAMAGE AND COMPRESSIVE RESIDUAL STRENGTH OF A WOVEN PMC SUBJECTED TO CYCLIC HYGROTHERMAL CONDITIONING

Michael G. Castelli and John C. Thesken

Ohio Aerospace Institute
NASA Glenn Research Center
Cleveland, OH 44135 USA

ABSTRACT

An experimental investigation was conducted to characterize the elevated temperature, fully reversed fatigue response of a hygrothermally conditioned carbon fiber reinforced epoxy composite. The material is a 5 harness satin weave in a high temperature epoxy matrix: AS4/PR500. Elastic modulus and residual compressive strength were recorded as a function of fatigue cycle. Unconditioned material is compared to material exposed to 12 khrs of hygrothermal cycle (HC) mission conditioning. Simulating the usage of a gas turbine propulsor component, the HC mission consisted of a 90 minute hold at 121 °C followed by a 22.5hr soak at 30 °C with 85 % nominal relative humidity. Specimens were then machined into a dogbone geometry that was developed and verified for fully reversed fatigue and static compression testing without anti-buckling supports. Fully reversed fatigue data revealed a deterministic stress-life response. The 12 khrs HC conditioned material experienced an 11 % strength degradation when compared to baseline data prior to mechanical fatigue loading. Residual compressive strength measurements were made at specified compressive modulus degradation levels. When correlated with compressive modulus, these strength data showed a clear degradation due to the HC conditioning. Work is underway to characterize material conditioned to 30 khrs.

KEYWORDS

Fatigue damage, hygrothermal conditioning, compressive properties, composites, residual strength.

INTRODUCTION

By improving their economy and quality, advances in fully automated composite fabrication techniques have led to wider use of 2-D and 3-D woven polymer matrix composite (PMC) materials in aerospace applications. However, predicting long term fatigue damage progression and durability of PMC materials under prototypical environments remains a challenge. Here, elevated temperatures, ambient moisture levels, and their combined synergistic effects can lead to enhanced degradation rates [1]. These issues are of particular concern for cases where the potential applications are primary/load bearing structures. Compensating for the lack of accurate

predictive methods in the area of fatigue durability has resulted in over-conservative designs that often mitigate the advantages of using PMCs in primary components.

To address these issues, an experimental investigation was made of the fatigue damage progression and damage tolerance of a 5-harness satin carbon fiber reinforced epoxy composite, AS4/PR500, subjected to fully reversed cyclic loading. Two datasets were created and examined. The first is the baseline data for the material behavior without environmental conditioning, i.e., 0 hrs. The second dataset consisted of material that underwent 12,000 hrs (12k hrs) of hygrothermal cycle (HC) conditioning. The elevated temperature fatigue behavior and damage progression was tracked through the measurement of the real-time tensile and compressive modulus. One unique feature of the work was to quantify the severity of fatigue damage via residual compressive strength measurements made at various degrees of *actual* compressive modulus degradation. Specifically, samples were subjected to residual compressive strength tests at approximately 0, 2.5, 5, and 7.5 % reductions of their initial compressive modulus. These data illustrate a relationship between fatigue damage progression as measured by the material's effective modulus and the material's damage tolerance while avoiding all assumptions with respect to the percentage of cyclic life. This detailed examination was completed on material from both datasets and then the data trends were compared.

MATERIAL AND EXPERIMENTAL DETAILS

All material was fabricated by a resin transfer molding (RTM) process at Dow U.T. (USA) from a single batch of resin and fiber mat into thick laminates (16 ply, 6.1 mm) with panel dimensions of 63.5 x 63.5 cm. Test coupons were machined using a diamond wheel grinding process. The HC conditioning, illustrated in Fig 1, was a nominal 85/30 (85 % relative humidity at 30 °C) exposure combined with a daily "mission cycle" consisting of a 90 minute exposure at 121 °C in a forced air convection oven. The cycle was selected as representative of a static component in the propulsor region of a gas turbine engine. The 12 khr conditioning was conducted on the material in large panel form prior to cutting the test coupons to avoid edge effects influencing the mechanical properties. The weight gain, shown in Fig. 2, was monitored using a traveler panel with a width to thickness ratio of 25 to 1. Note that the 90 min cycle at 121 °C was sufficient to prevent the material from reaching a moisture equilibrium state, even after 12k hrs. After conditioning and machining of the coupons, all material was vacuum dried for 48 hrs at 105 °C and stored in a dessicator until immediately prior to testing. Mechanical testing was performed on a computer controlled servohydraulic test frame. A radiant mini-furnace was used for specimen heating and strains were measured using edge-mounted extensometers with a 12.7 mm gage length. All mechanical testing was performed at 121 °C in a laboratory air environment.

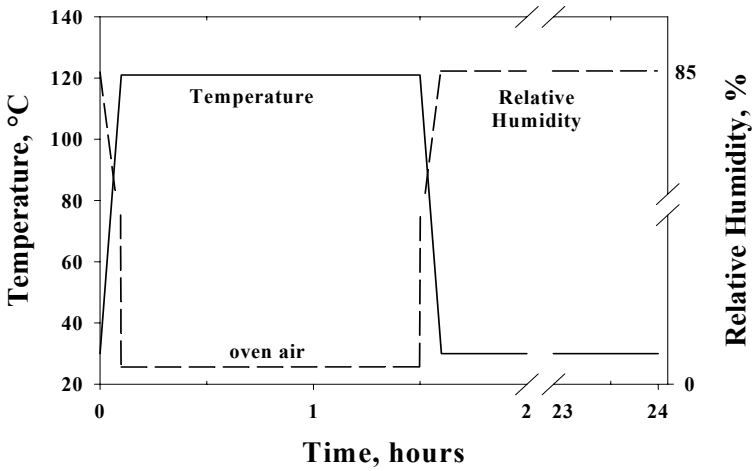

Fig. 1-Hygrothermal Cycle (HC)

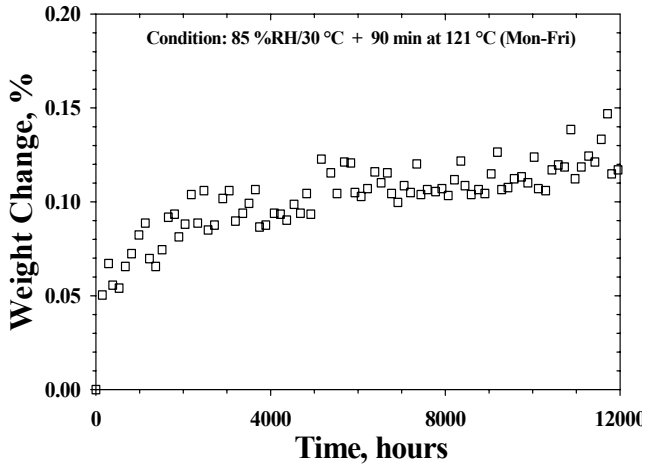

Fig. 2-Weight gain during HC conditioning.

All fatigue tests were conducted under fully reversed loading conditions. Fully reversed fatigue testing of composites is relatively uncommon due to buckling instability issues. Anti-buckling guides may be used, but problems like frictional ware and thermal influences at elevated temperatures are also formidable [2]. The current research used thick laminates with a refined dogbone specimen design (Fig. 3) and an experimental setup that served to significantly reduce specimen instabilities. The design viability was verified by comparing the compressive strength results to those obtained using the standardized Celanese fixture (ASTM Standard D 3410). Ultimate strength results showed good agreement [3]. The specimen stability and experimental set-up were further evaluated by examining the compressive behavior while monitoring the strains on opposite faces of the sample. Deviation of these two measurements is a good indicator of the most likely state of bending. This result is shown in Fig. 4 along with the extensometer strain measurement. The results indicate minimal bending until immediately prior to failure. Further, the maximum fatigue strain ranges examined do not exceed ±0.7 % which are well within the regime absent of significant bending.

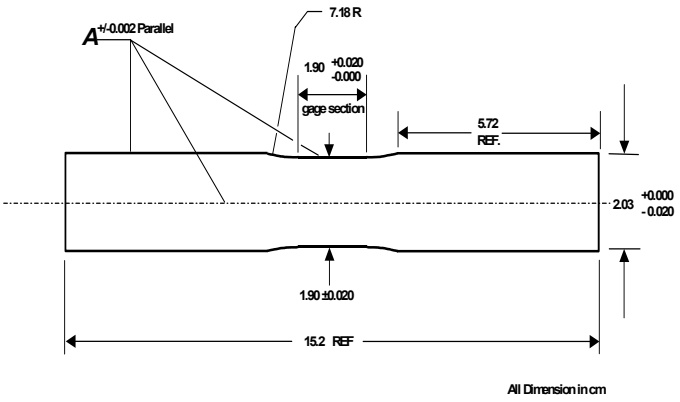

Fig. 3-Dogbone specimen geometry.

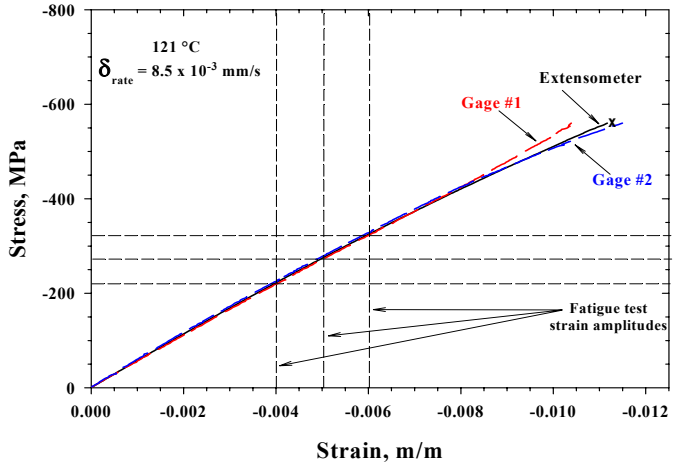

Fig. 4-Static tests indicating a lack of bending at strain ranges consistent with fatigue testing.

The fully reversed fatigue tests were conducted in load-control (R_σ = -1) with load levels selected to yield a specific initial strain range (±0.4, ±0.5 and ±0.6 %). This is consistent with the fact that the design criteria for the intended application is a limiting strain. Samples were subjected to a saw tooth waveform at a frequency of 2 Hz either until complete fracture or until a predetermined reduction in modulus. In the later case, cyclic fatigue was suspended and a residual compressive strength test was performed. All static residual strength tests were conducted at 121 °C with a controlled displacement rate of 8.5 x 10^{-3} mm/s.

FATIGUE LIFE AND MODULUS DEGRADATION RESULTS

The fatigue strength as a function of the number of cycles to complete failure is presented in Figs. 5 and 6. Figure 5 does this in terms of the initial applied cyclic strain range and Fig. 6 does this in terms of the applied cyclic stress range. Data are shown at the ±0.4, ±0.5 and ±0.6 %, strain range, in addition to a datum at ±0.3 % where failure did not occur and the test was terminated at approximately 6 million cycles. The data indicate that HC conditioning does not have a strong influence on the axial fatigue life though some deficit in life may be suggested at the lower load ranges. There appears to be some measure of increased scatter at the longer life/lower strain or stress ranges, as might be expected. One should note that the appearance of the data does not correspond with the 3-regime format generally observed in the results of PMC axial fatigue [4]. The first high stress/high scatter regime, traditionally associated with the probabilistic failure of the fiber, is not present in these results. Due to the fully-reversed loading conditions all of the samples ultimately failed in compression. Compressive loads drive the phenomenon of buckling induced delamination growth which control the compressive strength of the composite [5]. Note that there were clear distinctions between the 0

and 12k hrs samples regarding the failure morphologies and appearance of these buckled delaminations. This will be highlighted later.

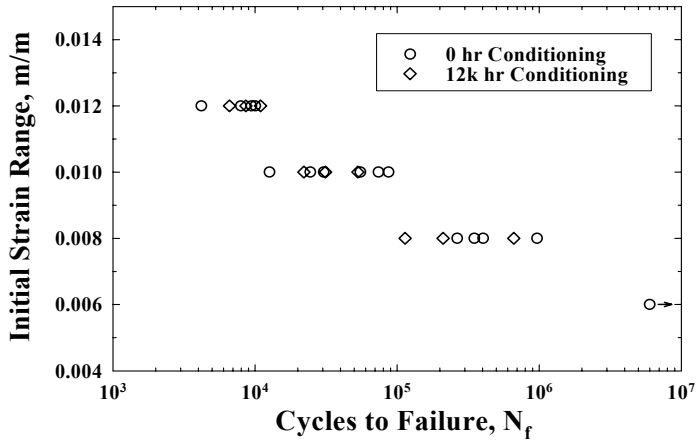

Fig. 5-Fatigue life plot based on initial strain range.

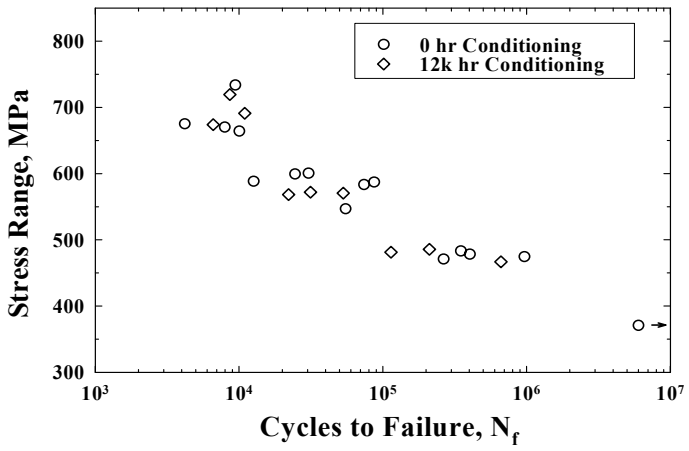

Fig. 6- Fatigue life plot based on stress range.

During fatigue tests, the elastic modulus (E) was checked periodically to determine its degradation or residual value. This was done in both tension and compression. Representative residual compressive modulus data plotted against fatigue cycle are shown in Fig. 7. Results for the 0 hr and 12k hr material are compared for the ±0.4% strain range. The modulus values are normalized with respect to the material's initial modulus (E_o) at the beginning of the fatigue test. The last cycle plotted for each of the two curves represents the point of complete specimen fracture. As illustrated, both the 0 and 12k hrs HC conditioned materials tended to maintain their initial modulus values over the first several thousand cycles. In general, the modulus of the HC conditioned material tended to degrade earlier. A number of samples experienced a slight "stiffening" trend prior to the measurable degradation, as illustrated by the 0 hr data. This may be a result of the woven fabric "locking-up" with the accumulation of deformation.

All observed trends in the modulus response were consistent between tension and compression with the difference being that the compression modulus measurements were generally 2 to 5 % lower for any given sample. In the range of approximately 50,000 cycles and up, the material begins to experience a gradual degradation of modulus that is relatively regular. At the ±0.4 % strain level, the material consistently experienced a minimum of 15 % loss in modulus prior to complete fracture. The following discussion of residual strength and modulus relationships focuses on the ±0.4 % initial strain range fatigue data.

RESIDUAL STRENGTH/MODULUS RELATIONSHIPS

There are several ways to view the material's response to the accumulation of the cyclic hygrothermal and mechanical fatigue damage and its ability to tolerate that damage under an ultimate compressive event. Using the 0 and 12k hr HC conditioned material results for the initial strain range of ± 0.4 %, three different permutations of the residual property fatigue data are presented in Figs.8-10. Fig. 8 shows the residual compressive modulus for each specimen as a function of its total number of fatigue cycles. As expected, the residual compressive modulus decreased in magnitude for specimens with a greater accumulation of fatigue cycles. While this trend is consistent with Fig. 7, the degree of degradation is masked in Fig. 8 by significant sample-to-sample modulus variation. Prior to fatigue cycling the compressive modulus of unconditioned material varied 7.6 % from 53.6 to 57.7 GPa and the HC conditioned material varied 5.8 % from 54.4 to 57.6 GPa. This is common to RTM fabricated woven composites, where variations in local fiber orientation and degree of waviness lead to local variations in properties. The average initial compressive modulus of all the samples were 55.4 GPa and 55.6 GPa for the 0 hr and the 12k hr data sets, respectively. This suggests that the

degradation associated with the 12k hrs of HC conditioning had little to no influence on this "effective" property. Subsequent fatigue cycling does not cause any observable difference in the rate of compressive modulus degradation between the two data sets.

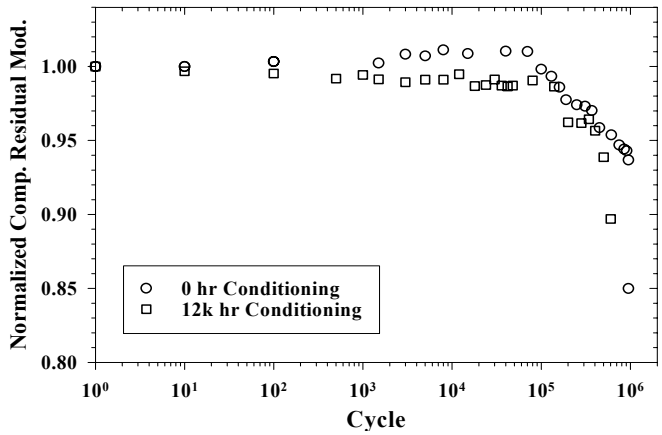

Fig. 7-Representative compressive residual modulus (normalized) during fatigue at the ±0.4 % range.

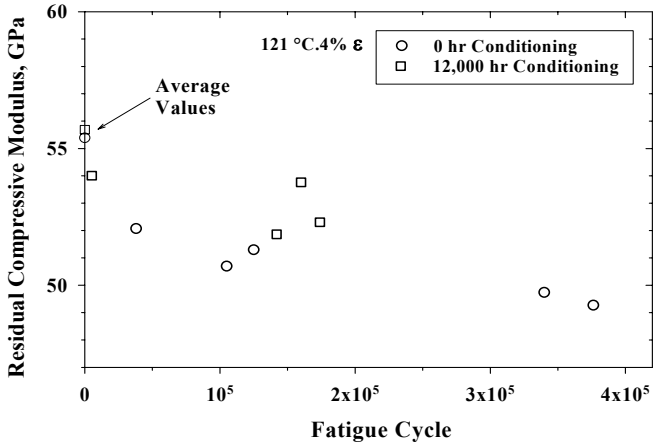

Fig. 8-Modulus values at cycle where fatigue test was suspended prior to residual strength.

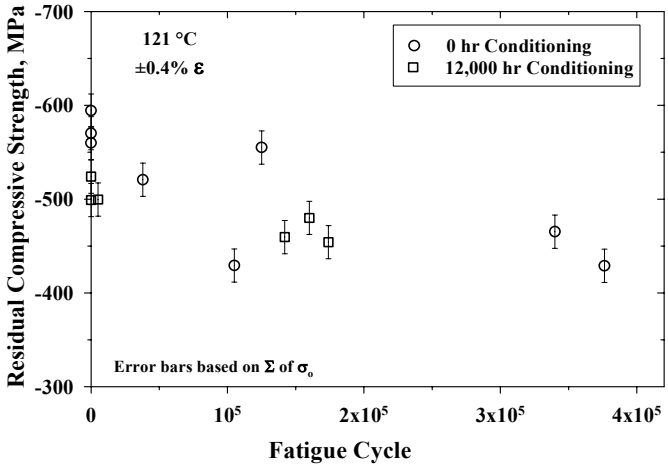

Fig. 9-Residual strength as a function of fatigue cycles.

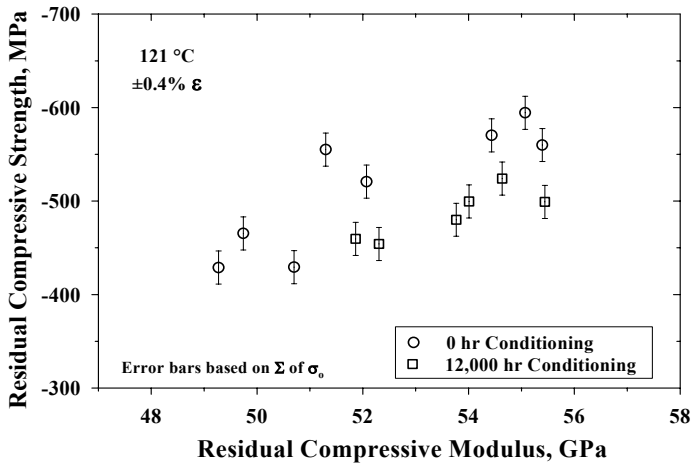

Fig. 10-Residual strength/modulus relationship.

Figure 9 illustrates the residual compressive strength as a function of fatigue cycles. Again, as expected this property reveals a degrading trend with cumulative fatigue cycling. The trends are relatively linear in cycles suggesting more regular "deterministic" response when the damage tolerance is examined as a function of residual compressive strength, as opposed to tensile. It is more common to examine the residual tensile strength properties of composites, and this, in response to tension-tension fatigue. In such cases, modest degrees of fatigue damage are difficult to assess due to the dominating effect of the fiber and its probabilistic failure characteristics [6]. In contrast, residual compressive strength is more likely controlled by the unstable growth of a critically sized buckling induced delamination [5].

Unlike the residual compressive modulus, the residual compressive strength reveals an 11 % on average knock-down due to HC conditioning alone. Damage associated with the HC conditioning may have a greater influence on the extreme values of a defect population (size, spacing) effecting strength, while having an indistinguishable influence on the average distribution of flaw characteristics effecting modulus. Indeed Lacy, McDowell, Willice and Talreja [7] show that different damage distributions may exhibit identical stiffness properties while having markedly different rates of damage evolution and tolerance to damage. The residual compressive strength of the 0 hr and 12k hr datasets are intermingled with the accumulation of mechanical fatigue. This is in spite of clear differences in the observed failure morphologies for the two datasets. Upon static failure, the 0 hr samples generally revealed clean transverse fractures, with only modest ply delamination at the most aggressive states of fatigue damage. In contrast, the 12k hr HC conditioned material revealed extensive delamination, both at the ply and bundle interfaces. This strongly indicates that the damage induced by the HC missions was most degrading to the fiber/matrix interface.

Fig. 10 takes the final step of comparing the compressive residual strengths with the corresponding residual compressive modulus values. Presentation of the fatigue data in this manner is believed to be relatively unique; empirically it infers a proportional relationship between residual strength and modulus. First, it can be stated that each of the datasets independently suggests a consistent relationship between these two properties. Furthermore the 0 hr data are layered above the 12 khr data with the similar proportionality. While the 0 hr and 12 khr material may exhibit similar compressive modulus response, the residual compressive strength of the 0 hr material tends to be greater. This relationship will be further examined with additional conditioning times ranging to 30k hours of the HC exposure.

CONCLUSIONS

In conclusion, an experimental investigation was conducted to examine the fatigue damage progression and damage tolerance of a high temperature graphite/epoxy PMC under fully reversed axial loading conditions with and without hygrothermal cycle conditioning. The specimen geometry performed well at elevated temperature without anti-buckling guides for fully–reversed fatigue and compressive strength testing. A deterministic relationship was found between the applied stress range and the number of cycles to failure; the resulting stress-life data in Fig. 6 maybe used to make design life predictions. Prior to mechanical fatigue loading, the 12 khr material experienced an 11 % strength degradation relative to the 0 hr material. No distinction was found between 0hr and 12 khr material when examining the residual compression modulus and residual compression strength as a function of fatigue cycle. Designers may find that the correlation of residual compressive strength and modulus in Fig. 10, give a clearer representation of compressive strength degradation due to HC conditioning. Evaluation of 30 khrs conditioned material is in progress to verify this trend.

ACKNOWLEDGEMENTS

The authors acknowledge Chris Burke for technical assistance in the laboratory, Rod Ellis for project guidance and oversight, and also Ron Cairo, Rajiv Naik, and Ken Tosi of Pratt & Whitney for numerous interactions on the project. The work was made under the NASA cooperative research grant NCC3-821.

REFERENCES

1. Cornelia., D.(1994). In: *39th International SAMPE Symposium*, pp. 917-929.
2. Bakis, C.E. et al. (1989). In: *Composites (2nd Vol), ASTM STP 1003*, pp.180-193.
3. Gyekenyesi, A.L. (1998). *ASME-98-GT-106*.
4. Talreja, R. (1981). In: *Proceedings of the Royal Society of London*, A378, pp. 461-475.
5. Nilsson, K. F., Thesken, J. C., Sindelar, P., Giannakopoulus, A. E. and Storåkers, B. (1993) *J. Mech. Phys. Solids* 41, 749-782.

6. Reifsnider, K. and Stinchcomb, W.W. (1986). In*: Composite Materials: Fatigue and Fracture, ASTM STP 907*, pp. 298-313.
7. Lacy, T.E., McDowell, D.L. Willice, P. A. & Talreja, R. (1997) *International Journal of Damage Mechanics,* vol. 6, pp.62-95.

ICF100208OR

FATIGUE DAMAGE AND REPAIR OF 250 kN PORTAL CRANE IN SHIPYARD

Z. Domazet[1], Z. Lozina[1] and T. Pirsic[1]

[1] Faculty of Electrical Engineering, Mechanical Engineering and Naval Architecture, University of Split
R. Boskovica bb, 2100 Split, Croatia

ABSTRACT

The paper presents fatigue damage analysis and repair procedure that was carried out after the cracks at 250 kN portal crane were detected. After few years of crane service, fatigue cracks occurred at several critical points – bottom of the tower and both legs of portal. Previous attempts of repair by simple welding of cracks were not successful, because new cracks were detected soon after the repair. When cracks reached the critical length, the exploitation of the crane was stopped and detailed analysis was carried out. The results of numerical analysis and strain gauge measurements showed the source of a crack propagation – high stress concentration due to inappropriate design of portal details. FEM models also showed that stress concentration could be reduced by applying the additional stiffeners. Having in mind this fact, critical crane areas were redesigned. Later measurements and examinations showed that this repair was successful – after two years of intensive service new cracks were not detected.

KEYWORDS: Fatigue cracks, repair, welding, FEM

INTRODUCTION

General rules for design the machine parts against fatigue are well known for many years, but still now the examples of inappropriate design can be found. This paper describes such example – heavy portal crane in shipyard: unusual portal box construction made of steel plates, Figure 3. The cracks occurred at transition areas from vertical to horizontal supports on both legs, growing from the corners and bringing into danger the whole construction, Figure 1. First cracks were detected soon after the crane was placed in the shipyard, so the allowed carrying capacity was reduced from 250 kN to 50 kN, but the cracks continued to grow. First attempt of repair by simple welding did not solve the problem – new cracks were detected in the same areas soon after the repair. When the cracks reached the critical values, the crane was stopped to avoid the risk of total failure. In order to find the source of crack initiation and growth, the complete manufacturer's documentation and calculations were checked. It was found that calculations were performed by using the simple beam elements, without taking into account the stress concentration, and the influences of inertial forces and wind were underestimated. Those facts led us to perform the complete static and fatigue analysis, to measure the real stresses during the typical manoeuvres of the crane, and to redesign the critical places to avoid stress concentration. The results of this work including the later stress measurements are presented in this paper.

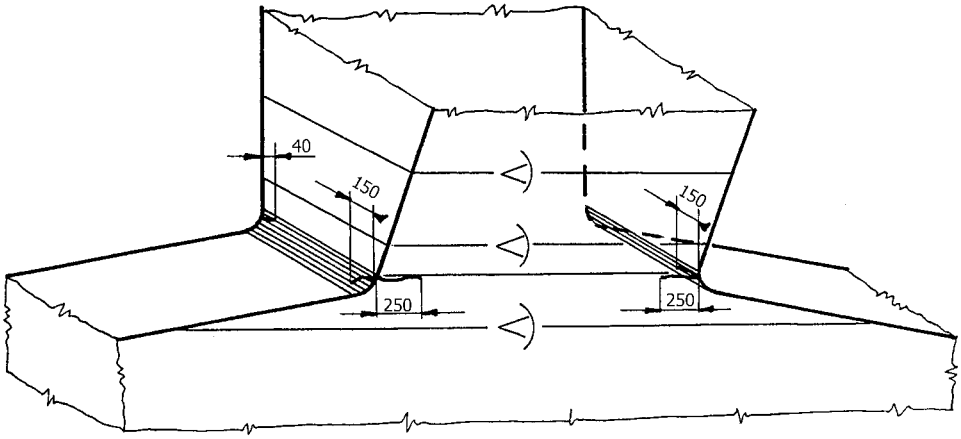

Figure 1: Detected cracks (measures in millimetres)

MEASUREMENT OF STRESSES, COD AND ACCELERATION

To determine the dynamic behaviour of the construction strain gauges, two induction transducers for displacement and capacitive transducer for acceleration were applied. Test load was 50 kN, and there were no wind during the measurement. All data were recorded during the typical working cycles of the crane and results were presented by great number of diagrams.

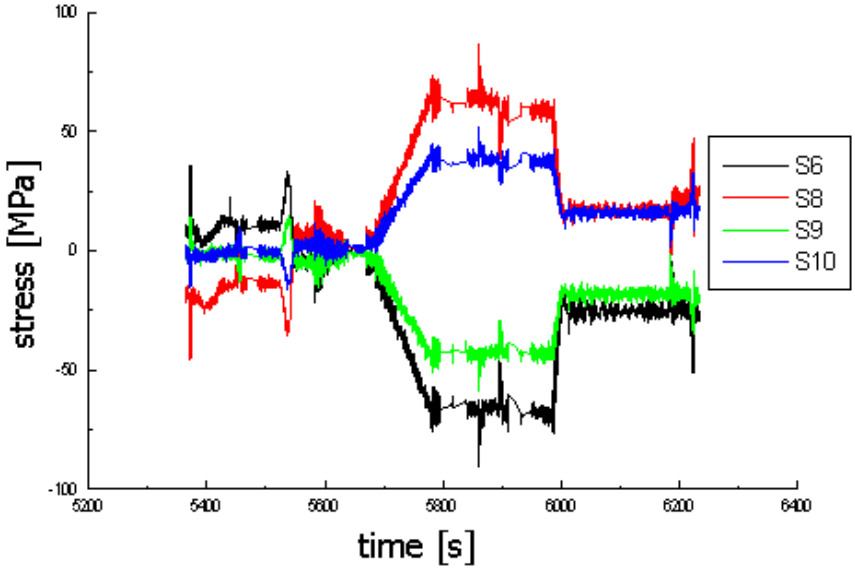

Figure 2: Measured stresses during typical manoeuvres

Based on the analysis of these diagrams, some general conclusions can be set:
- the highest measure stress amplitude were about 150 MPa, but in practice stresses can be higher, because of several reasons: - strain gauges were not attached at the places of highest stress concentration (access is not possible because of cracks)
- stress concentration factor α_k is about 2, what is not theoretical maximum
- during the measurement, the secondary stresses that reached up to 20 MPa were recorded, not connected with the nominal stresses, probably caused by swinging of the tower
- crack opening displacements reached 1.5 mm, what according to the Fracture Mechanics COD – concept indicates the stress of about 200-300 MPa

- measured values of acceleration were up to 0.2 m/s^2, what is acceptable, but during the test the crane was driven very carefully – in every day's use, with the influence of wind, these values can be higher.
- it is interesting to notice that the stresses were mostly caused by the manoeuvres of the crane – stresses caused by the loads were not significant. This result could be expected, because the maximum allowable load (250 kN) is less then 10% of the own weight of the construction.

FEM ANALYSIS

Finite Elements Method was used to determine the global stress distribution and to find out the weak points of construction that could cause high stress gradients and stress concentration. Linear elastic model and 3D-Plate elements with four or three nodes and six degrees of freedom was used.

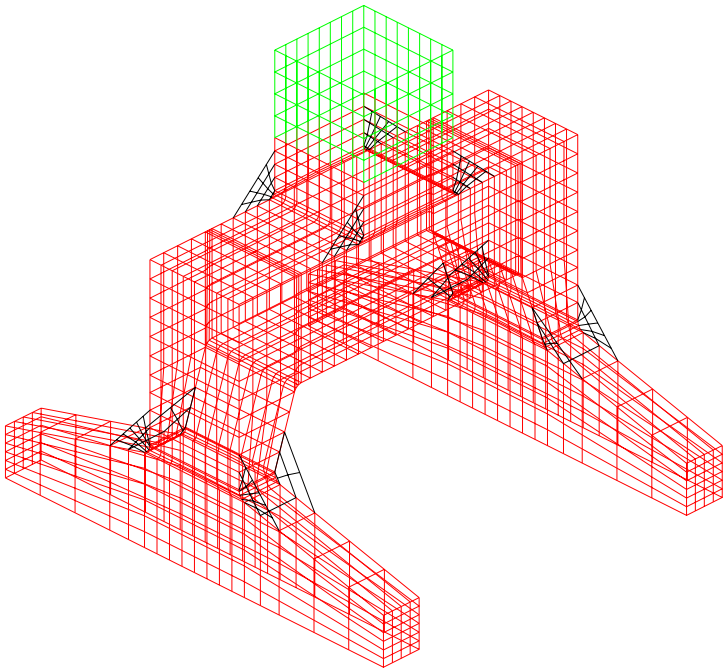

Figure 3: FEM model of the lower part of the crane (Variant with stiffeners)

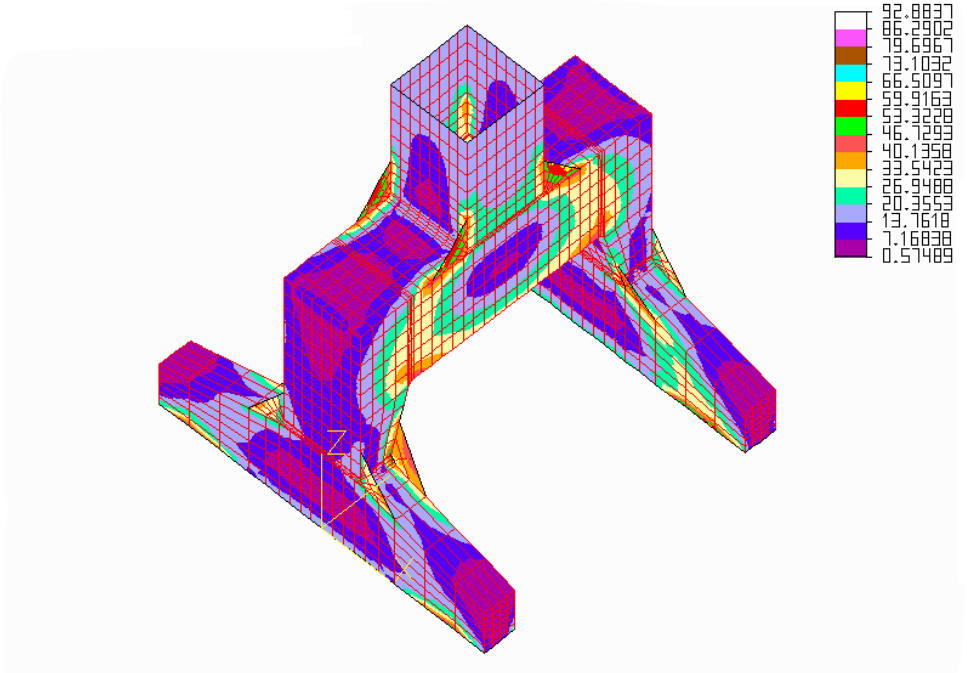

Figure 4: Typical stress distribution – visible areas of stress concentration

The geometry of the lower part of the crane was defined by 2191 elements (2327 elements in variants with stiffeners) were used, Figure 3. Boundary conditions were defined as follows:
- all six degrees of freedom on the nodes at the bottom contour of model were constrained,
- concentrated forces and bending moments are distributed along the nodes on the top of the model, representing the own weight of upper part of the crane and particular load case.
The complete analysis included 17 variants, with various loads, with or without stiffeners , with different orientation of crane branch and including the weight of construction. Typical results of FEM analysis are shown on Figure 4.

REPAIR PROCEDURE

Strain gauge measurement and FEM analysis showed the source of crack initiation – high stress concentration in the transition areas from vertical to horizontal part of the supports. At critical points those stresses exceeded the fatigue strength of material and caused the crack initiation and growth. Variable loads cannot be avoided, so the only solution was to redesign the critical areas in order to redistribute the local stresses. FEM analysis also showed the best way for redistribution of high stresses: application of triangle stiffeners that fit the existing construction (Figure 4 and Figure 5). Those stiffeners were welded by using MAG process. The heat treatment was used to minimize the residual stresses and fatigue limit of welds was increased by grinding the weld toes and roots.

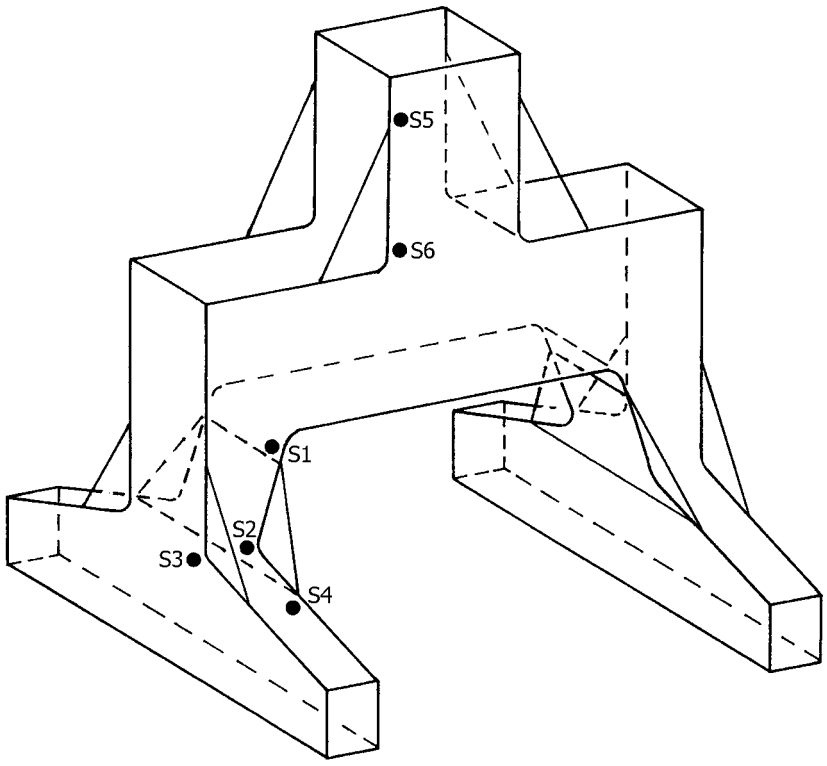

Figure 5: Positions of attached strain gauges

After the repair was completed, stresses at critical points were measured once again and compared to the values predicted by FEM. Places where strain gauges were attached are shown on Figure 5, and the results are shown in Table 1. Presented results are approximate, because the strain gauges cannot be attached perfectly at the same positions. According to data from Table 1., it is clear that the stresses at critical points are significantly lowered, especially in critical areas. All the stresses are under the fatigue limit, so the main source for crack growth is removed.

TABLE 1
COMPARISON OF STRESSES BEFORE AND AFTER REPAIR

Strain gauge	S1	S2	S3	S4	S5	S6
Max. stress without stiffeners (MPa)						
Measured	Not measured	Not measured (crack)	50-100	30	50	150
FEM	100	360	110	60	50-60	300
Max. stress with stiffeners (MPa)						
Measured	100	120	20	30	70	50-70
FEM	100	180	15-20	60	60-80	100

CONCLUSION

The paper illustrates the danger of inappropriate design in the case of variable loads. Sharp transition from vertical to horizontal plates at crane leg caused the initiation and growth of fatigue cracks that brought into danger the whole construction.
By replacing the plates that contained cracks and applying the stiffeners at the places of cracks initiation, the sources of fatigue damages are removed and the maximum stresses at redesigned construction are lowered to approximately one half of previous values. Having in mind important role of the own weight of construction and inertial forces, the application of electrical devices connected to all actuators was suggested. The purpose of these devices is to turn on the actuators gradually, without jerks, what will generally minimize the influence of inertial forces. Later examinations of the crane construction approved the success of this repair – two years after repair no new cracks were detected.

REFERENCES

1. Domazet, Z., Lozina, Z., Pirsic, T., Misina, N., Djukic, P. (1999). FESB Report No. 01/99

Oral/Poster Reference: ICF100285OR

FATIGUE DAMAGE IN ADVANCED POLYMER MATRIX COMPOSITES

H. E. Carroll[1], T. J. Matthams[1], D. M. Knowles[1] and A.J. Davies[2]

[1]Department of Materials Science, Cambridge University, Cambridge, CB2 3QZ, UK
[2]DERA Farnborough, Ively Road, Farnborough, Hampshire, GU14 0LX, UK

ABSTRACT

Advanced polymer matrix composites such as carbon fibre reinforced composites (CFRP) offer many advantages over more traditional materials such as metals. However, due to a lack of understanding of the materials behaviour, especially under in-service conditions such as fatigue, these materials are not being used to their full capability. This work investigates the fatigue response and damage mechanisms of a carbon fibre reinforced polymer with a quasi-isotropic lay-up, $[(\pm 45^{\circ}, 90^{\circ}, 0^{\circ})_2]_s$. Fatigue tests have been carried out at R ratios of +0.1 (tensile) and +10 (compressive) using thermography to identify damage. Results show that delamination is the major damage mechanism and that the main delamination occurs at a different interface for the different loading conditions. The interfaces highlighted in the fatigue tests are being investigated using a modified mixed-mode bend test.

KEYWORDS

Composite, Fatigue, Delamination.

INTRODUCTION

Advances have been made in the design, manufacture and application of composite materials. Much of this progress has been made in the field of Fibre-Reinforced-Plastics (FRP). FRP often have greater strength to weight and stiffness to weight ratios than traditional materials such as metals, which makes them ideal for use in many applications especially in the aerospace sector. However, there remain many unanswered questions regarding the behaviour of these materials especially under in-service conditions such as fatigue. There is an increasingly urgent need to gain an better understanding of how FRPs behave under fatigue load cases. Until recently the strains used in the design of aircraft structures have been so low (approximately 0.4%, but with a safety factor of 50% the expected peak is around 0.27%) that fatigue has not been considered an issue(1) and static properties have been used in design. This is now changing as designers want to use composite materials to their full capability and therefore

design strains are increasing to such a level that fatigue is now a real problem, particularly under compressive loading. To fully understand the fatigue of a material it is necessary to gain an understanding of how damage initiates and accumulates, and how this damage will affect the materials properties.

The complexity of composite microstructures means that the wide range of fatigue damage mechanisms are often diffuse throughout the laminate. Another major factor that restricts the understanding of damage initiation during fatigue testing of laminates is the scatter found in fatigue lives. This impedes the effectiveness of carrying out interrupted tests with destructive evaluation, since at a given number of cycles it is impossible to say what percentage of life has passed. There is the possibility of using thermography to overcome this problem and this is investigated here. The work carried out here identifies delaminations as the major damage mechanism. These need further investigation and hence work has begun to investigate the relationship between mixed-mode loading and delamination growth rates using a mixed-mode bending rig.

EXPERIMENTAL

The material used in the program was a composite system containing high strength continuous 919HF carbon fibres in HTA epoxy resin matrix. Cytec Fiberite supplied this in zero-bleed pre-preg form with a nominal fibre content of 55-wt%.

A single stacking sequence was used for all static and fatigue tests. This was a 16-ply laminate with the lay-up $[(\pm 45^{\circ}, 90^{\circ}, 0^{\circ})_2]_s$. This lay-up is a quasi-isotropic lay-up and it gives approximately uniform properties in the plane of the laminate. The composite panels were laid up by hand. The composites were then autoclaved following the manufacture's specifications. The cured plates were then C-scanned to check for any defects. Any faulty areas were avoided when preparing specimens. The panels were cut into specimens with final dimensions 250 mm or 200 mm long by 20 mm wide, unwaisted. This left a gauge length of either 150 mm or 100 mm for tensile and compressive fatigue tests respectively. The final thickness of the specimens was nominally 2 mm without end tabs and 6 mm with end tabs.

The MMB specimens have a balanced lay-up with a 0/45˚ interface at the centre. A PTFE film was used as a starter crack and edge inserts are also used to try and prevent fibre bridging. The specimens were then prepared in the same way as the fatigue specimens.

Static tests were conducted using a 100 kN screw machine at a loading rate of 1 to 2 mm per minute to bring failure within 90 seconds. Fatigue tests have been completed using an Instron servo hydraulic machine. Tests have been completed at R ratios 0.1 and 10. These represent a tension-tension and a compression-compression loading case respectively. All fatigue tests have been completed at a rate of 10 Hz. As has already been stated, thermography was used in the fatigue tests at R = 0.1 to investigate damage initiation and growth.

To investigate delaminations in more detail mixed-mode bend tests have been carried out using the modified MMB rig designed by Crews *et al*(2). A schematic diagram is shown in figure 1. Currently only static results are available.

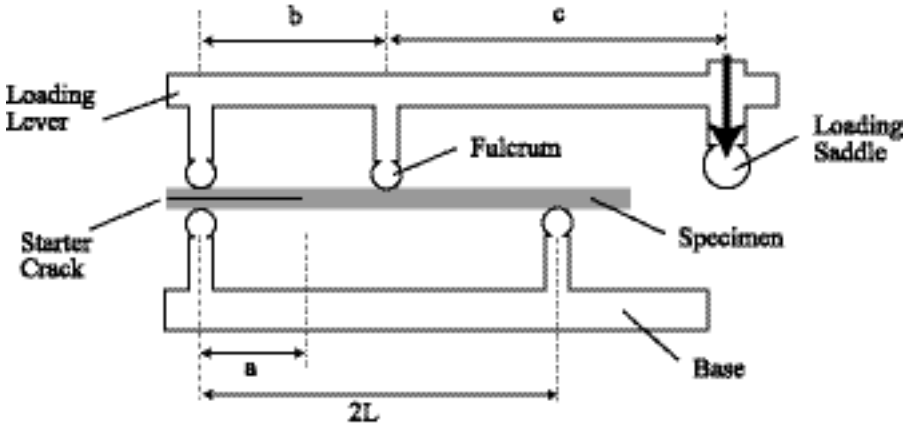

Figure 1. A Schematic of the Modified Mixed-Mode Bend Test Apparatus.

RESULTS AND DISCUSSION

Static Results

Two series of 5 tests were performed on 919HF/HTA to obtain values for the materials tensile and compressive strengths. The results are shown in Table 1. It can be seen that there is relatively little scatter in the results. The standard deviation of the mean tensile strength is 0.04 and of the compressive 0.03, which are approximately 5% of the mean value in both cases. The compressive strength is approximately 20% weaker than the tensile strength but that is to be expected.

TABLE 1. STATIC TEST RESULTS FOR 919HF/HTA

Test	Tensile Failure Stress (GPa)	Compressive Failure Stress (GPa)
1	0.760	0.545
2	0.762	0.608
3	0.710	0.592
4	0.750	0.620
5	0.679	0.587
Average (mean)	0.732	0.590
Standard Deviation (%mean)	5.46	5.08

Fatigue Results

Tensile fatigue tests

A series of tests were carried out at 90% and 80% of the laminates mean tensile strength and all were taken to failure. The fatigue lives for each test are given in Table 2.

The scatter in the results of 90% is significant; the standard deviation of the mean is 2682, which is 68% of the mean. It is not unusual to find this amount of scatter in fatigue results at higher stress levels due to the two elements which contribute to the scatter, i.e. the tensile scatter and the fatigue scatter. The scatter in the results at 80% is significantly lower than that for the tests conducted with a peak stress at 90%. The standard deviation is 31,472, which is 44% of the mean life. This reduction in the fatigue scatter agrees with the hypothesis of Barnard et al.(3) that as the peak stress is reduced the amount of static scatter as a proportion of the applied stress decreases and therefore scatter in the fatigue results will also decrease.

Alongside recording the cycles to failure for each specimen tested, a series of thermographic images were also taken. The change in temperature picked up by the camera has two causes 1) hysteresis heating and 2) local heating caused by friction induced by damage in the laminate such as crack faces shearing over each other. Figure 2 shows a typical thermographic image taken during a test and a schematic of the specimens "hot spots", where there is assumed to be the highest occurrence of damage.

TABLE 2.
FATIGUE LIVES AT, (A) 90% AND (B) 80% OF THE TENSILE FAILURE STRENGTH.

Test	Cycles to Failure
1	6600
2	1900
3	600
4	5700
5	5800
Average (mean)	3920

(A)

Test	Cycles to Failure
1	113,820
2	43,000
3	96,800
4	60,500
5	47,000
Average (mean)	72,224

(B)

All of the laminates in this series of tests showed varying degrees of delamination. These delaminations were visible with the naked eye at the outer 0/90˚ interface and were present from a very early stage of the laminates life. The images showed the progressive initiation and propagation of delaminations. However, the outer 0/90˚ interface had completely delaminated along the length and breadth of the specimen by approximately 50% of laminate life in all cases. The image in figure 2 is taken after the outer layer has fully delaminated and formed a sub-laminate. However, hot spots are still visible. This suggests that as there is a continued increase in temperature in the hot spot regions and that the early initiation of delamination in the outer 0/90˚ interface has induced some further damage mechanisms in this area such as delamination of the inner 0/90˚ interface or fibre fracture. This must be the case, as the laminates failed through the area of the hottest point in all cases and the delaminations alone were not enough to cause final failure or it would have occurred when complete delamination occurred. It is important to note here that all of the tests in the two series of experiments were conducted at an R ratio of +0.1, i.e. tensile-tensile fatigue. In this case the delaminations will not cause the final failure of the laminate. However, once fatigue moves into the compressive regime, the delaminations buckle and this may cause final failure of the laminate.

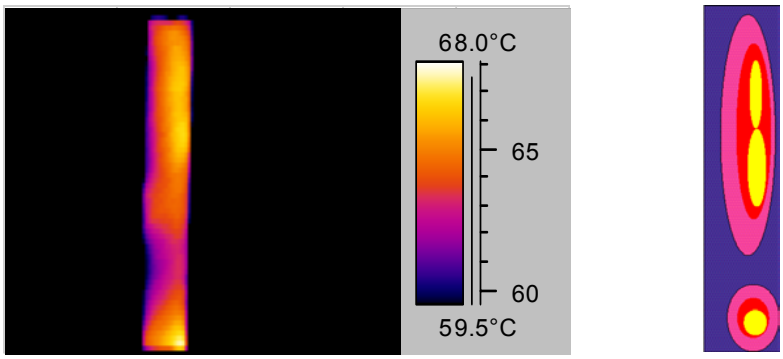

Figure 2. A Typical Thermographic Image Taken During a Fatigue Test and a Schematic of the Composite "Hot Spots" During Testing.

Compressive Fatigue Tests.

A series of compressive fatigue results have been completed at an R ratio of +10 at 10 Hz. The results are given in Table 3. The scatter in both sets of compression data is approximately 40% of the mean. This is a large number and as opposed to the tensile case the scatter had not decreased with decreasing peak load. It should also be noted that the peak loads are considerably lower in compression to produce comparable fatigue lives. This shows that compression-compression fatigue is much more damaging than tension-tension fatigue.

TABLE 3.
FATIGUE LIVES AT, (A) 70% AND (B) 60% OF THE COMPRESSIVE FAILURE STRENGTH.

Test	Cycles to Failure
1	4711
2	7064
3	12045
4	3658
5	6274
Average (mean)	6750

(A)

Test	Cycles to Failure
1	31,255
2	63,978
3	71,503
4	93,855
5	41,261
Average (mean)	60,370

(B)

Unfortuanatly, thermography could not be used during compression-compression fatigue tests due to the presence of antibuckling guides. However, post failure examination showed that the primary delamination occurred on the inner 0/+45˚ interface. This is different to the primary delamination interface in the tension tests and led to further investigations.

Mixed-Mode Bending (MMB) Tests.

To investigate the different delamination interfaces being highlighted in the fatigue tests a series of work has begun to investigate delamination growth rates using MMB tests. This work is at a very early stage. Initial tests have begun to investigate the 0/+45˚ interface at a mixed-mode ratio of 50% M_I and 50% M_{II}. A typical graph is shown in figure 3. This graph shows the load–displacement response to be almost linear up to a maximum load where it is assumed that the delamination begins to grow. In this case the fracture was sudden and grew quickly. This is a typical response where mode II is dominant(2). The average maximum load was 0.254 kN. The overall strain energy release rate, G_t, for this test is 408.2 J m^{-2}. This was calculated using Eqns. 1 and 2(4), where the total G is the sum of the strain energy release rate due to mode I and mode II loading.

$$G_I = \frac{3P^2\left(a+\chi_I h\right)^2}{\omega_s \omega_c h^3 E_{11}}\left[\left(1-\frac{c+b}{2L}\right)-\frac{c}{b}\right]^2 \qquad (1)$$

$$G_{II} = \frac{9P^2\left(a+\chi_{II} h\right)^2}{4\omega_s \omega_c h^3 E_{11}}\left[\left(1-\frac{c+b}{2L}\right)+\frac{c}{b}\right]^2 \qquad (2)$$

Where E_{11} is the axial stiffness, a the crack length, ω_c the width of the composite fracture surface, ω_s the specimen width, h is the half thickness of the specimen and χ_I and χ_{II} are the mode I and mode II end rotation correction factors. Tests will now continue investigating a range of mode I / II ratios and a range of interfaces.

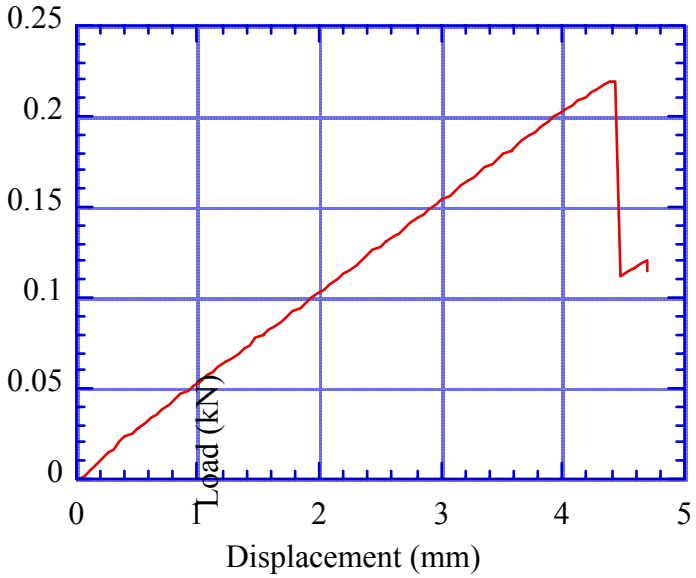

Figure 3. Graph of Displacement Against Load for Static MMB Test at 50% Mode I.

CONCLUSIONS

- The fatigue response of a quasi-isotropic CFRP has been investigated at two R ratios.
- Compression fatigue is more damaging than tensile fatigue.
- The tests completed identify delamination as the primary damage mechanism.
- Delaminations occurred at different interfaces for the different loading conditions. These were the -45˚/90˚ interface in the tension-tension fatigue tests and the 0/+45˚ interface for the compression-compression fatigue tests. The reasons for this trend to delaminate along a particular interface is now being investigated using MMB tests

REFERENCES

1. P. T. Curtis, A. J. Davies, Fatigue life prediction of polymer composite materials, *ECCM9* conference, Brighton, (2000),
2. K. Shivakumar, N, J. H. Crews, Jnr, V. S. Avva, *J. Comp. Mat.* **32**, 804-828 (1998).
3. P. M. Barnard, J. B. Young, DERA, Cumulative fatigue and life prediction of fibre composites : Final report (1986).
4. A. J. Kinloch, Y. Wang, J. G. Williams, P. Yayla, *Comp. Sci. Tech* **47**, 225-237 (1993).

FATIGUE DAMAGE IN UNIDIRECTIONAL COMPOSITE LAMINATES UNDER CONSTANT STRESS AND CONSTANT STRAIN LOADING CONDITIONS: A COMPARATIVE STUDY

N. Bonora[1], Newaz, G.[2] and Gentile, D.[1]
[1]DiMSAT – Dept. of Mechanics, Structures and Environment, University of Cassino
03043 Cassino, Italy
[2]Mechanical Engineering Department, Wayne State University
Detroit (MI) -USA

ABSTRACT

In this paper the approach to understand fatigue performance of composite laminates is reviewed in the light of a strain-based approach as proposed by the authors. Here, starting from the observation that damage in composite laminates is controlled by the effective strain applied during a fatigue cycle, constant stress fatigue is re-discussed. The strain-based approach allows accounting for the large experimental data scatter usually observed in composite laminates tested under cyclic loading and to give the basis for developing a rationale for reliable fatigue design tools.

KEYWORDS

FATIGUE, COMPOSITE , DAMAGE

INTRODUCTION

The possibility to understand and predict composite material performance under cycling loading has been deeply investigated in the last decades. In the majority of the published studies, fatigue behavior of composite materials has been approached as for metals. Large experimental effort has been spent in determining the S-N for different laminate configurations, stacking sequences, matrix-fiber choice, and so on. Mainly experimental data reported in the literature have been obtained under constant stress amplitude. Additionally, composite strength after cycling has been also used as a critical parameter to characterize material fatigue performance, Laws and Dvorak [1], Hashin [2-3], Allen *et al.* [4].

From all these studies, the following common features arise. Firstly, failure is not a unique concept for composite materials. Traditionally, final failure for metals represents the configuration at the end of life for which the imposed loading conditions are no longer sustained and specimen breaking into two or more parts occurs. On the contrary, complete specimen separation in composite laminates may not occur even under extremely severe damaging conditions. Here, failure intended as loss of performance with respect to the application for which the component is designed for, should be used as a more effective screening criterion in material characterization. A large data scatter always characterize the fatigue life under stress controlled conditions. Usually, small variation of the imposed maximum stress results in a very dispersed data at failure lives. The major consequence is the lack of reliability of the fatigue curve

available in published papers for design purposes. Additionally, it has to be noted that still today, the MIL Handbook procedure does not provide any detailed procedure for designing composite material components to fatigue. Finally, the damage development in composite laminates under cyclic loading usually follows clear sequences in the development of the basic damage modes, such as matrix cracking, interlaminar delamination, fiber failure, fiber-matrix pull up, and no new mechanism of failure with respect to quasi-static loading is generated under fatigue.

The presence of a large scatter in the representation of experimental measurement sometimes can be an indicator of low correlation between the dependent and independent variables.

The possibility to better understand the effective composite material performance has been initially offered by Talreja [7] reformulating constant stress amplitude data in terms of imposed strain.

In this paper, fatigue behavior of composite laminates is reviewed comparing material performance under constant stress and constant strain amplitude. This approach confirms the role of the effective applied maximum strain as a governing parameter for fatigue performance estimations. A major outcome is that strain can be actively, reliably and continuously controlled in composite components in service using embedded sensors.

CONSTANT STRESS AMPLITUDE AND CONSTANT STRAIN AMPLITUDE FATIGUE FEATURES

Fatigue testing for composite materials has been traditionally performed under constant stress amplitude loading condition following the same approach used for metals. When loaded, damage can occur in a composite laminate in the form of matrix cracking, fiber failure, interlaminar delamination and fiber-matrix debonding. The sequence of appearance of these basic failure modes is controlled by the lowest strain to failure of the composite constituents. An interesting feature is that no new damage mechanism is introduced by fatigue with respect to the monotonic quasi-static loading. Each of these basic damage modes modifies the material constitutive response. However, transverse matrix cracking, that is the first damage mode to appear both under quasi static and fatigue loading, is the responsible of the major reduction of the material stiffness. Transverse matrix cracking density increases with the increasing of the imposed strain (stress) until saturation occurs, a situation usually described as characteristic damage state (CDS).

According to this, damage in composite laminates has been addressed focusing the attention on the evolution of the matrix crack density with cycles. Even though the relation between the stiffness reduction due to a given crack density is well assessed, the damage kinetic evolution law with cycles still needs to be assessed. As previously stated, this job is made even more difficult due to the large experimental data scatter that arise from constant stress amplitude testing.

Bonora and Newaz [6] investigated fatigue performance of a number of composite laminates, varying stacking sequences, constituents, etc. They found that during constant stress fatigue, cyclic strain amplitude increases as a result of damage that lower material stiffness plus an additional strain ratcheting due to the non complete closure of generated cracks, Figure 1 . Additional strain accumulation can be also induced by visco-plastic material behavior.

If the dominating part of the total accumulated strain is the one due to damage, strain amplitude increases until CDS is reached. After this point, stress amplitude and strain amplitude will be both constant during cycling similar to metals under stabilized cycle loading conditions.

Newaz and Bonora [7] have found that this correlation between stress and damage is inadequate to describe the material damage evolution process as the assumption of uniform stress on the net section is

an unrealistic one. In reality, the stress field in a cracked laminate is quite far from being uniform. The multiple transverse cracks shield each other resulting in a very scattered stress field as can be observed experimentally using thermal wave image or photoelastic technique. In essence, this results in a large scatter in composite stress-strain response.

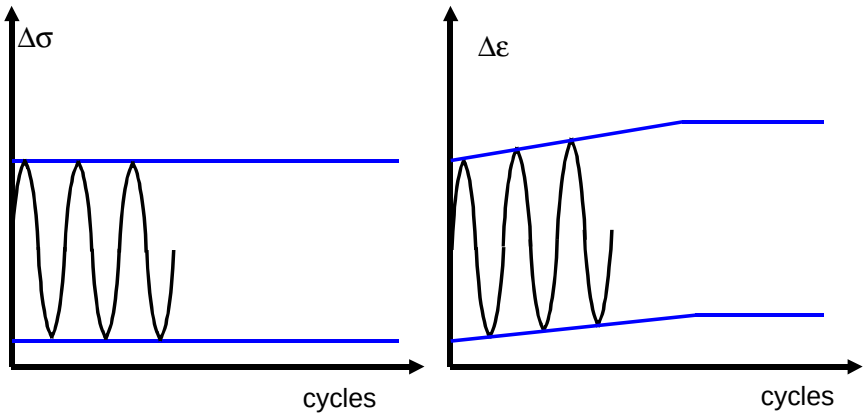

Figure 1 – Strain amplitude evolution under constant stress amplitude fatigue loading in unidirectional composite laminates.

Bonora and Newaz [6] proposed an approach to stiffness reduction in composites in term of the effective applied strain. They found that using strain as independent variable, the damage curve obtained from several specimens is characterized by a very low scatter confirming the fact that damage *D* as a function of strain, ε, is a reliable material property degradation indicator in fatigue. Here, damage evolution with strain , defined as the complementary normalized stiffness loss for the laminate, can be accurately described as:

$$D(e) = D_0 + \left[D_{cr} - D_0\right]\left[\frac{\ln\left(e / e_{th}\right)}{\ln\left(e_{CDS} / e_{th}\right)}\right]^{\frac{1}{M}} \qquad (1)$$

where D_0 is the initial damage, D_{cr} is the value of damage at CDS, ε_{th} is the threshold strain for which damage process, i.e. matrix cracking, is activated; ε_{CDS} is the strain at CDS and *M* is a material constant. This equation has been successfully verified for a large number of brittle composite systems both ceramic and polymeric.

In addition, it has been found that, if the effective accumulated strain is correlated with cycles, the damage curve resulting from fatigue is the same as for quasi-static loading, as given in figure 2, suggesting the absence of new damage mechanisms due to fatigue.

If the key parameter to understand damage accumulation in composite laminates is the effective applied strain it follows that damage evolution observed under constant stress amplitude is not a material feature or property.

Let us assume to apply a stress amplitude Ds on a given laminate. If the resulting maximum strain associated with the applied maximum stress overcomes the material strain threshold (0.025 in Figure 2), some damage is produced in the laminate in the form of transverse matrix cracking. Since the damage curve is very steep in the first part (lower strain), small strain changes generates large damage amounts.

At the end of the first cycle, the material stiffness is changed as a result of the damage and a residual strain can also be measured. In the following cycle, in order to reach the previous maximum stress with a lower stiffness, a larger maximum strain value will be reached and consequently new damage will be generated. This accumulation process will continue until CDS stage is reached. It follows that crack density accumulation has to increase faster in the early stage of fatigue life and slow down with the

increasing of cycles. This has to result in a concave accumulation curve as effectively observed in the experiment.

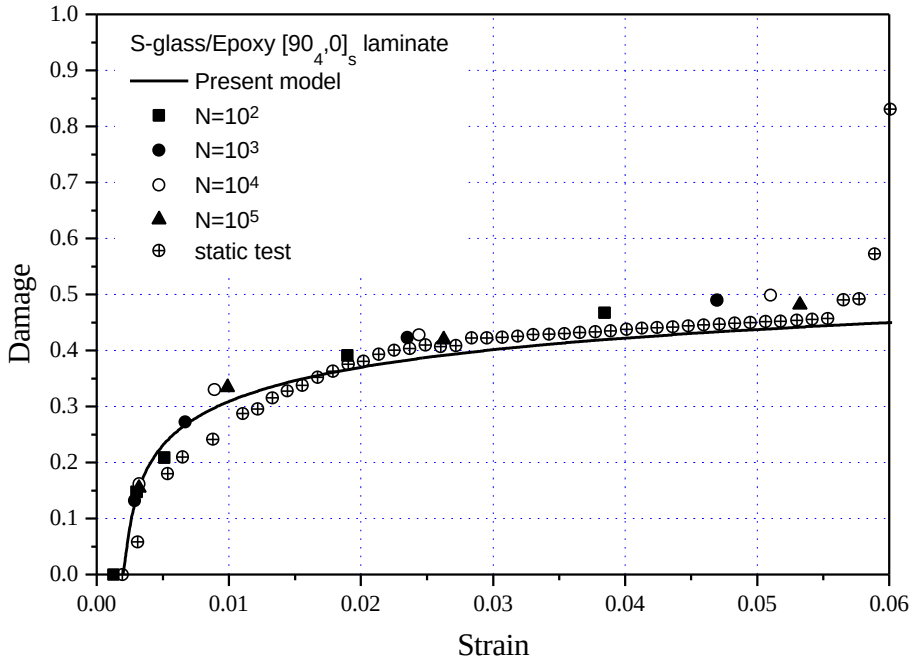

Figure 2 – Comparison between the quasi-static and the fatigue damage evolution with strain in glass/epoxy laminate

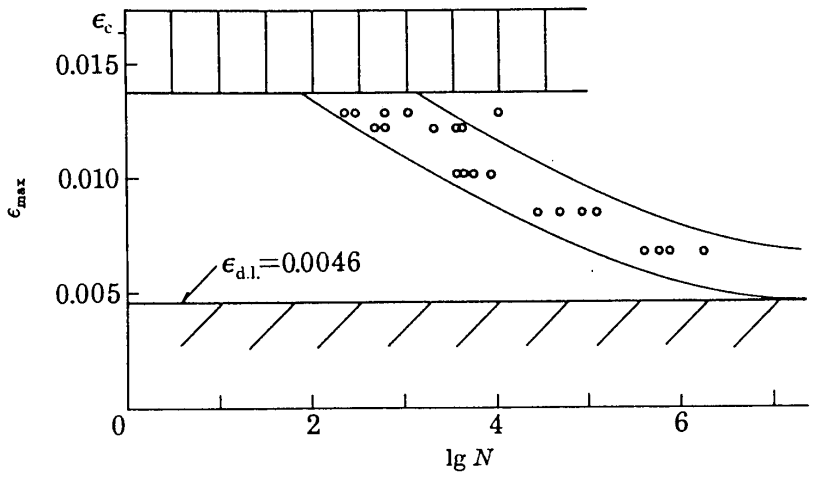

Figure 3 – Fatigue life diagram for glass/epoxy laminate (Talreja, 1987).

If the maximum strain associated with the stress amplitude is below the strain threshold no damage occurs and theoretical infinite life is expected. This value is characteristic for the material and stacking sequence since the laminate lay-up gives constraint condition for the occurrence of transverse matrix cracking. On the other side, if the maximum stress is high enough to develop CDS condition in the laminate during the first cycle, no further stiffness loss will occur in the following cycles due the already occurred saturation in the damage curve. In this case failure will occur as a result of fiber failure.
This scenario finds confirmation in the fatigue life diagram as proposed by Talreja and given for example in figure 3. The only objection comes from the possibility to convert constant stress amplitude data to strain. As discussed, this is only possible for stress above CDS, in the lower range strain accumulation with cycles need to be evaluated and accounted for.

If damage is associated to strain and fatigue does not introduce any new damage mechanism, it follows that constant strain amplitude cycling should not result in material fatiguing. Bonora *et al.* [8] have verified this assumption in glass/epoxy laminates. In addition, experimental tests performed on laminates previously damaged at different D values, shown the absence of evolution of damage state in the usual fatigue life range (< $5E10^6$ cycles). It has to be said that even though the under constant strain amplitude the damage generated in the first cycle does not growth, additional damage mechanism such as localized delamination can initiated as a result of internal friction. According to the authors experience these phenomena are activated in the very late part of the laminate life with a very weak effect on the material stiffness changes.

CONCLUSIONS

The strain-based approach proposed by the authors to describe fatigue performance of composite laminates seems to indicate a better way to understand material response under stress controlled conditions.

The experimental tests performed on different laminate stacking sequences confirm that under strain controlled condition no damage evolution occurs. Damage is controlled by the maximum strain in the first cycle.

Under constant stress amplitude, strain increases with cycles as a result of the change in stiffness, resulting in an apparent damage evolution, as usually observed in the literature where fatigue resistance is evaluated looking at the number of cycles before failure.

The proposed framework is consistent with the fatigue life diagram proposed by Talreja that represent a valid way for developing a reliable tool for fatigue design.

It is the authors' opinion that the evolution of strain under constant stress fatigue should be more thoroughly investigated in order to come up with a relationship to correlate strain evolution with cycles and damage.

REFERENCES

1 Laws, N., and Dvorak, G. J., 1985, in Proc. Of IUTAM Eshelby memorial Symp., Cambridge press, pp. 119-127.

2 Hashin, Z, (1986), Engineering fracture mechanics, **25**, pp:771-778.

3 Hashin, Z., (1985), Mechanincs of materials, **4**, pp:121-136.

4 Allen, D.H., Harris, C.E., Groves, S.E. and R.G:, Norvell, (1987), International Journal of Solids and Structure, **23**, pp:1319-1338.

5 Talreja, R., (1987), in Fatigue of Composite Materials, Lancaster, Technomic Publishing Co., pp. 113-122.

6 Bonora, N. and Newaz, G., (1997), ASME J. of Engineering Material and Technology, Vol. 119

7 Newaz, G. M., and Bonora, N., (1996), in *Thermal and Mechanical Test Methods. and Behavior of Continuous Fiber Ceramic Composites*, ASTM STP 1309, M. G. Jenkins, S. T. Gonczy, E. Lara-Curzio, N. E. Ashbaugh and L. P. Zawada, Eds., American Society for Testing and Materials

8 Bonora, N., Newaz,G., and Nusier S., Proc. of the 8th US-Japan Conference on Composite Materials, Sept. 24 and 25 , Baltimore, 1998

ORAL REFERENCE: ICF100321OR

FATIGUE FRACTURE PLANE DIRECTION ASSESSMENT THROUGH THE WEIGHT FUNCTION METHOD

Andrea CARPINTERI[1], Aleksander KAROLCZUK[2], Ewald MACHA[2]

[1] Department of Civil Engineering, University of Parma, Parco Area delle Scienze 181/A, 43100 Parma, Italy
[2] Technical University of Opole, Faculty of Mechanical Engineering, ul.Mikolajczyka 5, 45-271 Opole, Poland

ABSTRACT

In the present paper, the expected principal stress directions under proportional and nonproportional multiaxial high-cycle fatigue loading are determined by averaging the instantaneous values of the "principal" Euler angles. Such angles are employed to describe the position of the principal stress axes at the generic time instant, and the averaging procedure is performed through suitable weight functions. Three possible types of weight functions based on stress parameters are adopted and verified using available experimental results related to some metallic materials. It is shown that the fatigue fracture plane position under multiaxial loading may be established on the basis of the averaged direction of the maximum principal stress, by employing proper weight functions.

KEYWORDS

Multiaxial fatigue, weight function method, fatigue fracture plane

INTRODUCTION

According to several well-known stress-, strain- and energy-based models for multiaxial fatigue (for instance, [1-9]), the failure assessment is usually performed by referring to the "critical plane". The concept of the critical plane, which is related to the crack initiation phenomenon, was firstly proposed by Stanfield [1] in 1935, and has been developed since then.

On the other hand, from a review of fatigue test results under in-phase and out-of-phase cyclic multiaxial loading, it appears that the final fracture plane very often corresponds to:
(a) the plane on which the normal stress, or strain or strain energy density attain their maximum;
(b) one of the two maximum shear planes;
(c) an intermediate position between (a) and (b).

Case (a), case (b) and case (c) are typical for brittle materials, ductile materials and semiductile materials, respectively. The fracture plane for case (b) is one of the two maximum shear planes in which the highest normal stress, or strain or strain energy density occurs [4,6,8]. Case (a) is preferred when the ratio of the

shear stress amplitude τ_a to the normal one σ_a is less than 0.63 [10], or when the ratio of the shear strain range $\Delta\gamma$ to the normal one $\Delta\varepsilon$ is less than 1.5 [3]. Such ratios depend on the kind of material, stress or strain level and temperature. Some theoretical predictions of the fatigue fracture plane position have been presented by Kanazawa et al. [11], Findley [12] and Stulen and Cummings [13].

Numerous models of fatigue crack initiation and propagation for multiaxial cyclic loading do not take into account the change of the principal strain and stress axes. That is a possible reason why they can only be applied to some particular cases. Consequently, averaged principal stress directions should be determined, and the averaging procedure could be carried out, for instance, by employing suitable weight functions [14-17]. In the following, the position of the principal stress axes 123 at the generic time instant is described by the three "principal" Euler angles φ, θ, ψ.

The aim of the present paper is to verify whether the weight function method can allow us to determine the expected fatigue fracture plane position. The algorithm presented in [15–17] is applied to experimental data related to one steel and two cast irons [18,19].

AVERAGING PROCEDURE

The principal axes 123 system can be considered as a transformation of the XYZ system, fulfilling a condition of orthogonal conversion or specific rotation [20]. A transformation between two Cartesian systems can be described in different ways, but the direction cosines matrix is usually employed. On the other hand, such a matrix includes nine dependent components, and we cannot average all the matrix elements since the averaged matrix would not satisfy all the conditions of transformation. Moreover, we are not able to select which three independent elements of the direction cosines matrix should be averaged. Thus, the three independent Euler angles φ, θ, ψ are selected for description of the transformation from the XYZ system to the 123 system (Fig.1). Let us assume that the 1-axis and the 3-axis represent the directions of maximum and minimum principal stresses, respectively.

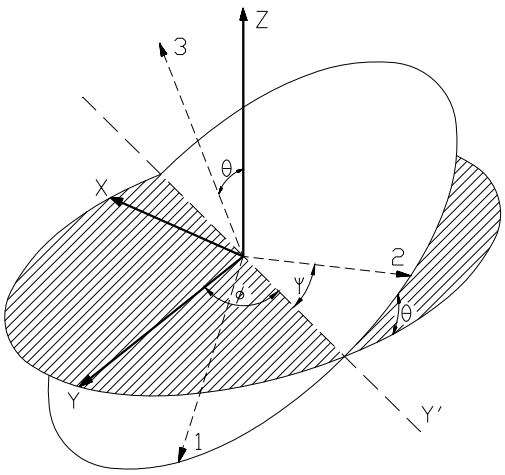

Figure 1: Principal stress axes 123 described by the Euler angles φ, θ, ψ

Under variable loading, the Euler angles are time-varying functions as well as the stress tensor components. Different sets of the Euler angles could describe the same position of the principal axes 123. Consequently, in order to average correctly the results determined for different time instants, the ranges of the Euler angles have to be reduced through a two-stage procedure, bringing them to $0 \le \varphi, \theta \le \pi/2$ and $-\pi/2 \le \psi \le \pi/2$. A detailed description of an algorithm to perform such a reduction can be found in Refs [15,16].

From a physical point of view, it seems logical to carry out the Euler angles averaging through suitable weight functions [14-17] in order to include various factors influencing the fatigue fracture behaviour (stress

amplitudes, exponents of the Wöhler curve and so on). Therefore, the mean directions of the principal stress axes may be described by the weighted mean Euler angles:

$$\hat{\varphi} = \frac{1}{W}\sum_{t_1}^{t_N}\varphi(t_k)\,W(t_k), \qquad \hat{\theta} = \frac{1}{W}\sum_{t_1}^{t_N}\theta(t_k)\,W(t_k), \qquad \hat{\psi} = \frac{1}{W}\sum_{t_1}^{t_N}\psi(t_k)\,W(t_k) \tag{1}$$

where $W = \sum_{t_1}^{t_N} W(t_k)$ is the summation of the weights, and N is the number of time instants considered.

Three kinds of weight functions are examined in the following:

Weight I

$$W_1(t_k) = 1 \tag{2}$$

According to such a weight function, each positions of the principal axes influences the mean position of the principal axes to the same degree, irrespective of the stress values. Application of this weight function gives us W = N, and leads to the arithmetic means.

Weight II

$$W_2(t_k) = \begin{cases} 0 & for \quad \sigma_1(t_k) < c\sigma_{af} \\ \left(\dfrac{\sigma_1(t_k)}{c\sigma_{af}}\right)^{m_\sigma} & for \quad \sigma_1(t_k) \geq c\sigma_{af} \end{cases} \tag{3}$$

where:

m_σ – exponent of the fatigue curve ($\sigma_a - N_f$)

σ_{af} – fatigue limit

c – constant

This weight function includes only those principal axes positions for which the maximum principal stress $\sigma_1(t_k)$ is greater than the product of c and the limit stress σ_{af}; the participation of such positions in averaging exponentially depends on the parameter m_σ of the Wöhler curve.

Weight III

$$W_3(t_k) = \begin{cases} \left(\dfrac{\sigma_1(t_k)}{\sigma_{af}}\right)^{\frac{m_\sigma}{2}} & for \quad \sigma_1(t_k) < \sigma_{af} \\ \left(\dfrac{\sigma_1(t_k)}{\sigma_{af}}\right)^{m_\sigma} & for \quad \sigma_1(t_k) \geq \sigma_{af} \end{cases} \tag{4}$$

This weight function is similar to the weight function II, but it includes all the principal axes positions and, when $\sigma_1(t_k) < \sigma_{af}$, the weight function exponent is divided in half.

RESULTS OF THE SIMULATION CALCULATIONS

The theoretical procedure above is applied to three metallic materials (Table 1). Fatigue test results including the actual position of the fatigue fracture plane are presented in Refs [18,19]. Thus, the position of the vector $\overline{\eta}_{exp}$ normal to the actual fracture plane can be compared with the calculated position of the vector $\overline{\eta}_{cal}$, assumed to be coincident with the averaged position of the maximum principal stress axis. In the following, the solid angle α between the X-axis and the vector $\overline{\eta}$ ($\overline{\eta}_{cal}$ or $\overline{\eta}_{exp}$) is considered. The parameter c for the weight function II is assumed to be equal to 0.5. The generated cyclic courses are similar to those of fatigue tests (N = 100 discrete values at wave period T of the sinusoid are applied).

TABLE 1
MECHANICAL PROPERTIES OF THE TESTED MATERIALS

Material	R_e[MPa]	R_m [MPa]	E[GPa]	ν	m_σ	σ_{af}[MPa]
GGG40	334.0	447.0	165	0.28	11.0	244.0
GTS45	305.0	449.0	160	0.27	18.5	250.0
18G2A	394.0	611.0	213	0.31	8.2	204.0

where R_e – yield point; R_m – tensile strength; ν – Poisson's ratio

Cast irons GGG40 and GTS45

Neugebauer [18] tested round specimens made of two cast irons: GGG40 and GTS45. The specimens were subjected to combined bending and torsion, with different amplitude ratio λ and phase difference δ (Tables 2 and 3).

TABLE 2
CALCULATION RESULTS FOR CAST IRON GGG40 [18]

No.	σ_a [M.Pa]	τ_a [MPa]	λ	δ	α_{exp} [rad]	$\alpha_{cal}(w_1)$ [rad]	$\alpha_{cal}(w_2)$ [rad]	$\alpha_{cal}(w_3)$ [rad]
1	200	200.00	1.000	0	0.144π	0.493π	0.176π	0.176π
2	200	200.00	1.000	π/4	0.217π	0.419π	0.177π	0.177π
3	220	220.00	1.000	π/2	0.183π	0.339π	0.138π	0.156π
4	215	123.63	0.575	0	0.113π	0.493π	0.136π	0.136π
5	220	126.50	0.575	π/4	0.129π	0.417π	0.125π	0.123π
6	265	152.38	0.575	π/2	0.010π	0.337π	0.080π	0.087π

TABLE 3
CALCULATION RESULTS FOR CAST IRON GTS45 [18]

No.	σ_a [M.pa]	τ_a [MPa]	λ	δ	α_{exp} [rad]	$\alpha_{cal}(w_1)$ [rad]	$\alpha_{cal}(w_2)$ [rad]	$\alpha_{cal}(w_3)$ [rad]
1	160	160.0	1.000	0	0.139π	0.493π	0.176π	0.176π
2	170	170.0	1.000	π/2	0.133π	0.339π	0.133π	0.142π
3	248	142.6	0.575	0	0.136π	0.493π	0.136π	0.136π
4	248	142.6	0.575	π/2	0.117π	0.334π	0.038π	0.052π

Steel 18G2A

Pawliczek [19] tested round specimens made of 18G2A steel under combined bending and torsion, with different values of amplitude ratio λ (Table 4).

TABLE 4
CALCULATION RESULTS FOR 18G2A STEEL [19]

No.	σ_a [Mpa]	τ_a [MPa]	λ	α_{exp} [rad]	$\alpha_{cal}(w_1)$ [rad]	$\alpha_{cal}(w_2)$ [rad]	$\alpha_{cal}(w_3)$ [rad]
1	464	0.0	0.0	0.005π	0.245π	0.000π	0.000π
2	374	0.0	0.0	0.004π	0.245π	0.000π	0.000π
3	447	224	0.5	0.137π	0.493π	0.125π	0.125π
4	364	182	0.5	0.142π	0.493π	0.125π	0.125π
5	315	157	0.5	0.129π	0.493π	0.125π	0.125π
6	298	149	0.5	0.110π	0.493π	0.125π	0.125π
7	447	447	1.0	0.162π	0.493π	0.176π	0.176π
8	403	403	1.0	0.160π	0.493π	0.176π	0.176π
9	368	368	1.0	0.150π	0.493π	0.176π	0.176π
10	344	344	1.0	0.167π	0.493π	0.176π	0.176π
11	338	338	1.0	0.170π	0.493π	0.176π	0.176π

ANALYSIS OF THE CALCULATION RESULTS

Table 5 presents the absolute values of the mean errors in determination of fatigue fracture planes for the examined materials. The results obtained by using of the weight functions II and III are almost identical since their mathematical forms are very similar (Fig.2). The agreement between calculation and experimental results is quite good for all the materials considered: the best results are found out for steel 18G2A, while the greatest error occurs for cast iron GGG40, i.e. 0.036 π (about 6^o). For the analysed materials, the fracture plane seems to be perpendicular to the weighted mean direction of the maximum principal stress.

TABLE 5.
ABSOLUTE VALUES OF MEAN ERRORS (IN [RAD]) IN DETERMINATION OF FATIGUE FRACTURE PLANE POSITIONS ACCORDING TO THREE WEIGHT FUNCTIONS

Material	Loading	W_1	W_2	W_3
GGG40	bending with torsion	0.284π	0.036π	0.034π
GTS45	bending with torsion	0.284π	0.029π	0.028π
18G2A	bending with torsion	0.326π	0.012π	0.012π

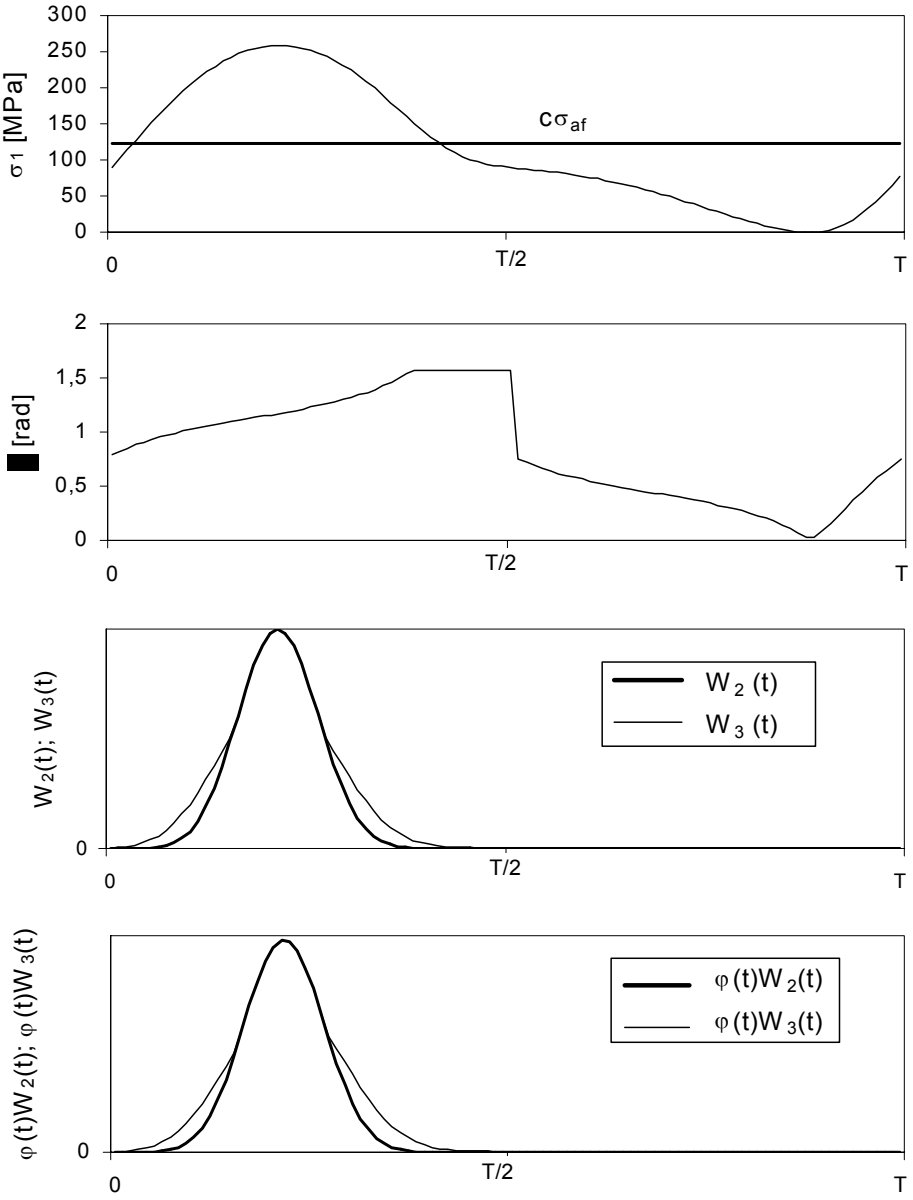

Figure 2: Modification of the Euler angle φ by the weight functions II and III (test No. 5 in Table 2)

CONCLUSIONS

Some experimental data related to one steel, 18G2A, and two cast irons, GGG40 and GTS45, under multiaxial high-cycle fatigue have been compared with the theoretical results of the expected principal stress directions. For the three materials examined, the fatigue fracture plane position is about perpendicular to the weighted mean direction of the maximum principal stress. Such a direction is determined by averaging the instantaneous positions of the principal stress axes through suitable weight functions. For each time instant, the most appropriate weight functions take into account whether or not the maximum principal stress is greater than a certain level dependent on the fatigue limit. Furthermore, such weight functions are influenced by the value of the Wöhler curve exponent.

REFERENCES

1. Stanfield, G. (1935) Discussion of „The strength of metals under combined alternating stresses", by H.Gough and H.Pollard. Proc. Inst. of Mechanical Engineers, Vol.131, p.93.
2. Brown, M.W. and Miller, K.J. (1973) A theory for fatigue failure under multiaxial stress-strain conditions, Proc. Inst. Mech. Engrs. 187 65/73, pp. 745-755.
3. Brown, M.W. and Miller, K.J. (1979) *Fatigue Engng Mater. Struct.* 1, 231-246.
4. Fatemi, A. and Socie, D.F. (1988) *Fatigue Engng Mater. Struct.* 11, 149-165
5. Lachowicz, C.T. and Macha, E. (1990) *Mat.-wiss. u. Werkstofftech.* 21, 450-458.
6. Socie D. (1993) Critical plane approaches for multiaxial fatigue damage assessement. In: *Advances in Multiaxial Fatigue, ASTM STP 1191*, pp. 7-36, McDowell D.L. and Ellis R. (Eds), American Society for Testing and Materials, Philadelphia.
7. Papadopoulos I. V. (1998) *Fatigue Fract. Engng Mater. Struct.* 21, 269-285.
8. Macha, E. and Sonsino, C.M. (1999) *Fatigue Fract. Engng. Mater. Struct.* 22, 1053-1070.
9. Carpinteri, A. and Spagnoli, A. (2001) *Int. J. of Fatigue* 23, 135-145.
10. McDiarmid, D.L. (1985) Fatigue under out-of-phase biaxial stresses of different frequencies. *Multiaxial Fatigue, ASTM STP 853*, pp. 606-621, Miller K.J. and Brown M.W. (Eds), American Society for Testing and Materials, Philadelphia.
11. Kanazawa, K., Miller, K.J. and Brown, M.W. (1977) *Journal of Engng Mater. Technology*, 222-228
12. Findley, W.N. (1959) *Journal of Engineering Industry*, 302-306
13. Stulen, F.B. and Cummings, H.N. (1954) A failure criterion for multiaxial fatigue stresses. Proc. ASTM, Vol. 54, pp. 822-835.
14. Macha, E. (1989) *Mat.-wiss. u. Werkstofftech.* 20, 132-136 and 153-163.
15. Carpinteri, A., Macha E., Brighenti R. and Spagnoli A. (1999) *Int. J. Fatigue* 21, 83-88.
16. Carpinteri, A., Brighenti, R., Macha, E. and Spagnoli, A. (1999) *Int. J. Fatigue* 21, 89-96.
17. Carpinteri, A., Brighenti, R. and Spagnoli, A. (2000) *Fatigue Fract. Engng Mater. Struct.* 23, 355-364.
18. Neugebauer, J. (1986) Fatigue strength of cast iron materials under multiaxial stresses of different frequencies, Report FB-175 Fraunhofer Institute fur Betriebsfestigkeit (LBF), Darmstadt.
19. Pawliczek, R. (2000) Fatigue fracture plane orientation under combined bending and torsion for 18G2A steel, Report No 1/2000, Technical University of Opole, Faculty of Mechanical Engineering, Opole, Poland, pp. 1-17 (in Polish).
20. Korn G.,A. and Korn T.,M. (1968) *Mathematical Handbook.* 2nd ed. New York: McGraw-Hill Book Company.

The paper realized within the research project 7 T07B 018 18, partly financed by the Polish State Research Committee in 2000-2002.

ORAL REFERENCE: ICF100124OR

FATIGUE LIFE CALCULATION OF FILLET-ROLLED COMPONENTS AT AXIAL CYCLIC LOADING

C. Richter, T. Seeger

Fachgebiet Werkstoffmechanik
Darmstadt University of Technology, Germany

ABSTRACT

Fillet rolling is a mechanical surface strengthening method. Residual compressive stresses induced in the surface layer of a component are able to increase significantly the fatigue limit and the fatigue life. It is known that the residual stresses cannot prevent crack initiation in fillet-rolled notched areas at load levels lower than the fatigue limit. However, in the crack propagation phase the main working principle of fillet rolling occurs. After crack initiation the residual compressive stresses retard or prevent further crack propagation. Hence the calculation of the fatigue limit and the fatigue life is possible by means of fracture mechanics. To account for plasticity effects an elastic-plastic crack growth model based on the effective *J*-integral is formulated. It can be applied at all phases of the fatigue process by combining the description of crack propagation with methods of the local strain approach. Particular attention has to be drawn to the crack closure phenomenon to describe the positive effect of residual stresses. A new method is presented to calculate the crack opening load-level in notched areas with residual stresses considering notch plasticity effects. The crack growth model and its modules are verified by experiments. The model can be applied in the case of constant and variable amplitude loading to calculate the fatigue limit and the life until fracture (fracture fatigue life) or crack growth stop.

KEYWORDS: fatigue life prediction, fatigue crack growth, fillet rolling, residual stresses, crack closure, *J*-integral, local strain approach, variable amplitude loading

INTRODUCION

Fillet rolling is a mechanical surface strengthening method. It is used with success particularly in the case of notched structural parts which are symmetric in respect to rotation. During the fillet rolling process a profiled roller is pushed around the notched component in a rolling motion bearing a constant pressure load. Plastic deformation of the surface area and the elastic reaction of the core lead to residual compressive stresses in the surface area while residual tensile stresses act on the core.

The fatigue life of notched components is usually subdivided into crack initiation and crack propagation phases. In fillet-rolled components the fracture fatigue life is mainly determined by the latter due to the effect of the residual stresses. Figure 1 demonstrates the special fatigue behaviour of fillet-rolled components for constant and variable amplitude loading. In comparison to the non-rolled component the crack initiation load-level can be increased by about 15% in the case of constant amplitude loading. In addition to the surface improvement the residual stresses reduce the local loading of the notch root by shifting the local stress-strain-path in the compressive region. But the changes in mean stress in the notch root cannot explain the high

endurance improvement, which can be reached by fillet rolling. This is in accordance with the experimental observation that crack initiation occurs at load levels lower than the fracture fatigue limit.

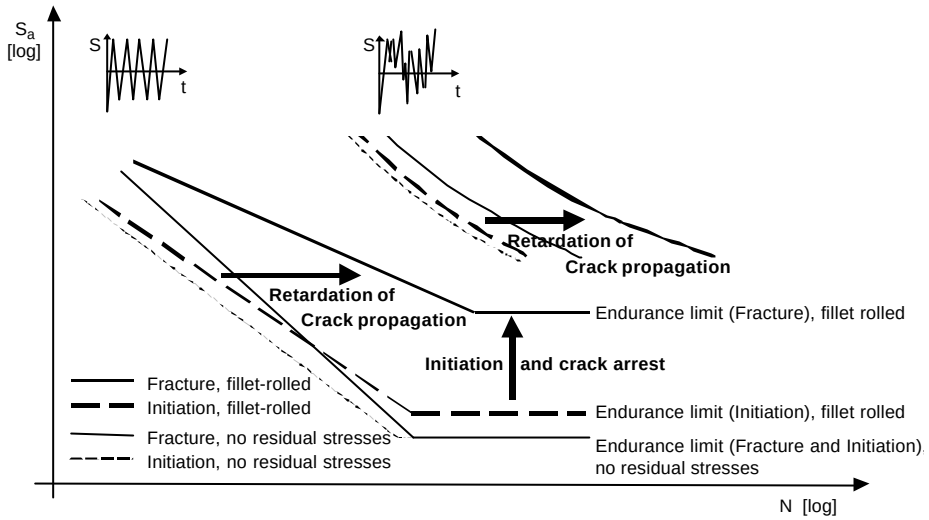

Figure 1: Enhancement of the fracture fatigue limit and the crack propagation fatigue lifetime due to fillet rolling in the case of notched components

The main working principle of fillet rolling occurs in the crack propagation phase because after fillet rolling the maximum of the residual stresses is beneath the surface. After crack initiation the residual compressive stresses retard or prevent further crack propagation which can be explained by the crack closure phenomenon. For the fillet-rolled component this leads to a reduction of the effective load amplitude in comparison to the non-rolled case, which causes a reduction of the effective fracture mechanical loading of the system. The effective load amplitude is regarded as the part of the total load amplitude in which the crack is fully open. From the description of the failure mechanism in fillet-rolled components it can be concluded that the calculation of the fatigue limit and the fatigue life can be predicted by means of fracture mechanics.
Even though there are a lot of models describing crack growth in residual stress fields little attention has been given to describe the phenomena in a unified way for the initiation and propagation phases considering the crack opening and closure behaviour in plastically deformed notches with residual stresses.

ELASTIC-PLASTIC CRACK GROWTH MODEL

The basis of the model is the equation

$$\left(\frac{da}{dn};\frac{dc}{dn}\right)=C\cdot\left(\Delta J_{eff}\right)^{m} \quad \text{if} \quad \Delta J_{eff} > \Delta J_{eff,th} \tag{1}$$

This describes the crack growth rate in a unified way for the initiation and the propagation phases. C and m are material constants from standard experiments, J_{eff} is the effective amplitude of the cyclic J-integral, a the crack depth, c the half surface crack length and $J_{eff,th}$ the effective threshold value of the cyclic J-integral. The value of J_{eff} is calculated by means of approximation formulae

$$DJ_{eff}=f\,(DS_{eff}\,,\text{geometry}\,,\text{cyclic}\ \acute{o}-\mathring{a}-\text{curve}\ ) \tag{2}$$

being dependent on the effective load amplitude for the crack depth and the crack length direction and on the notch geometry and the cyclic --curve . During the analysis the crack growth is determined incrementally in both directions starting from an initial crack length until the fracture of the component. As Eqn. 1 is formulated in terms of J_{eff} rather than J, the material parameters m and C are independent of the mean stress of the cyclic loading and therefore can be applied for the determination of crack propagation in areas with residual stresses.

A description of the developed model is shown schematically in figure 2, the essential elements of which are outlined below.

Calculation of the residual stresses due to fillet rolling.
Calculation of the elastic stress distribution in the crack propagation area.
Calculation of the redistribution of the residual stresses and the S--paths and --paths for the crack propagation area due to the applied cyclic loading by means of an approximation approach.
Calculation of the effective load amplitude considering the crack opening and closure behaviour in elastic-plastic, inhomogeneous loaded notched areas.
Calculation of the effective range of the *J*-integral by means of approximation formulae.
Calculation of the crack propagation.

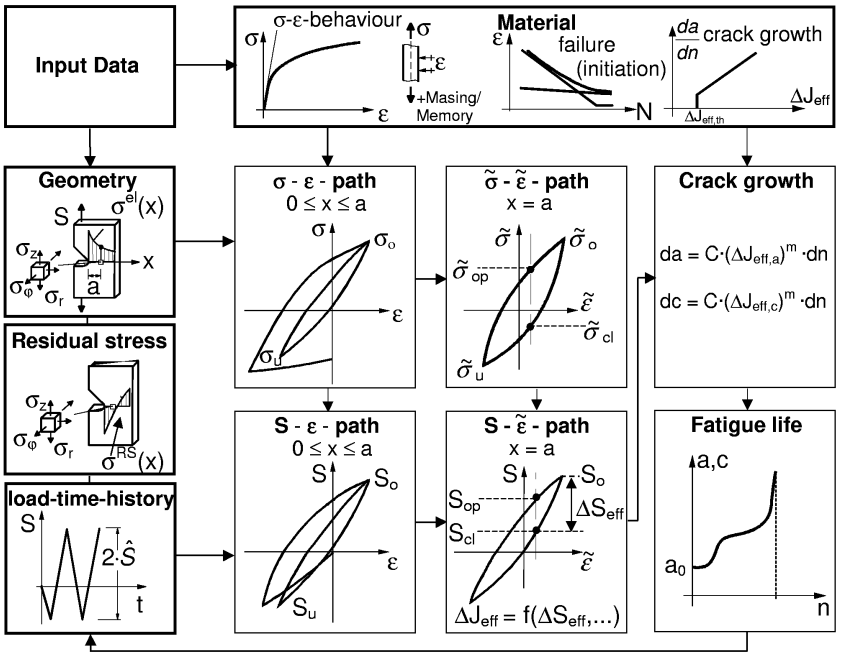

Figure 2: Crack growth model

Due to the improvements in computing power it is now possible to simulate the fillet rolling process and to determine the residual stresses after fillet rolling by Finite-Element-Analysis (FE-Analysis). The initial stress distribution changes due to the cyclic loading and the maximum of the residual compressive stresses is reduced and is pushed away from the surface. In the case of variable amplitude loading this redistribution occurs permanently. Therefore the load-strain curve and the corresponding local stress-strain curve due to the cyclic loading are calculated by approximation formulae, because a FE-analysis is not applicable for every cycle in a variable amplitude load sequence. As only axial loaded notched components symmetrical with respect to rotation are considered, a one-dimensional approach is sufficient. Therefore the crack propagation area is divided into k linear elements with $k+1$ nodes. The local stresses and strains are calculated at these nodes and are assumed to be linear between the nodes. At every reversal of the applied load a generalised Neuber Rule is applied. The increases of equivalent stress $_v$ and equivalent strain $_v$ at every node (i) are thereby formulated as:

$$E \cdot \Delta s_v^{(i)} \cdot \Delta e_v^{(i)} = p \cdot (\Delta s_{e,v}^{(i)})^2 \qquad i = 1,...,k+1 \tag{3}$$

where $_{ev}$ is the equivalent elastic stress at the node (i) and E the modulus of elasticity. So the elastic stress distribution in the crack propagation direction is essential for the application of the approximation formulae. The factor p is determined from the demand that the ligament stresses in the axial direction are in equilibrium with the applied load. For the application of Eqn. 3 it is assumed that the material is already cyclically stabilized. Hence Masing and Memory behaviour for the equivalent stress and strain is assumed to be valid. For the calculation of the increases of the stress and strain components the finite deformation law of Hencky is applied. To obtain the principal stresses and strains at the nodes further assumptions have to be made: In addition to Henckys law and the Mises yield criterion it is also assumed, as in [1], that $^{(i)}/_{z}^{(i)}$ = const. and

$r^{(i)}/z^{(i)}$ = const. is valid. The residual stresses after the fillet rolling process are considered by assigning every node (i) an equivalent stress and strain at the beginning of the load time history . Based on suggestions made by McClung [2] and Dankert [3], calculation of the local elastic-plastic loading path neglects the crack. In [4] it its shown that the procedure is able to describe the --paths as well as the residual stress reduction and removal in a fillet-rolled specimen subjected to cyclic loading.

Every closed hysteresis loop is regarded as a damaging event which causes crack propagation. The calculation starts with a semicircular surface crack with the radius a_0. Following Vormwald's local strain approach damage-parameter P_J [5] the value of a_0 is determined from the results of constant strain amplitude tests for an unnotched specimen without residual stresses by "backward" integration of the crack growth law, Eqn. 1.

In [6] it is shown that the determination of the crack opening load in notched areas can be done on the basis of approximation formulae which are originally formulated for the unnotched case. For this the formulae are applied using local stress and strain values at the point of the crack tip in the uncracked structure. However, if residual stresses lead to a high stress gradient in the crack growth area, the total stress and strain distribution acting on the crack surfaces have to be considered. In the case of small-scale yielding conditions this can be done by using a normalized stress intensity factor as proposed in [7] but at progressively higher stresses this parameter becomes less effective in characterizing the crack-tip stress and deformation fields. Therefore the Newman-formulae [8] is formulated in so called effective stress $\tilde{\sigma}$ and effective strain $\tilde{\varepsilon}$. For the crack depth direction (a-direction) they are computed from

$$\tilde{\sigma} = \int_0^a \sigma(x) \cdot G(x,a)\, dx$$
$$\tilde{\varepsilon} = \int_0^a \varepsilon(x) \cdot G(x,a)\, dx \qquad (4)$$

The local stresses (x) and strains (x) are determined by means of the approximation formulae Eqn. 3. For the crack length direction (c-direction) the effective stress and strain are equivalent to the local values. The function $G(x,a)$ is proportional to the weight function $m(x,a)$ used to determine the stress intensity factor for an edge crack in a semi-infinite plate. The factor of proportionality is determined from the demand that

$$\int_0^a G(x,a)\, dx = 1 \qquad (5)$$

is valid. So in the case of homogenous stress and strain loading in a unnotched component the effective stress and strain are equivalent to the local values.

Every time the local --hysteresis closes the corresponding S-$\tilde{\varepsilon}$- and $\tilde{\sigma}$-$\tilde{\varepsilon}$-hysteresis is calculated for the point of the actual crack tip by means of Eqn. 4. Then the effective crack opening stress $\tilde{\sigma}_{op}$ is calculated by means of Newman's approximation formula formulated in local effective values. Figure 2 shows that the crack closure load S_{cl} is determined with the aid of the equality of the effective crack opening strain and the effective crack closure strain $\tilde{\varepsilon}_{op} = \tilde{\varepsilon}_{cl}$ and the known S-$\tilde{\varepsilon}$ and the $\tilde{\sigma}$-$\tilde{\varepsilon}$-paths for the closed hysteresis. The validity of the equation $_{op} = _{cl}$ is proven experimentally for the case of notched specimens without residual stresses [9] but in the case of residual stresses the local values are regarded to be not representative for the description of the crack-tip stress and deformation fields. However, the application of local values ($_{op} = _{cl}$) is also possible as the deviations in the determined fatigue life are small.

Following [3] the effective load amplitude results from the difference between the maximum load of the closed hysteresis and the crack closure load, $S_{eff} = S_o - S_{cl}$. To obtain the value of the crack driving force per cycle, the approximation formulae (Eqn. 2), described and verified for circumferential and surface cracks in circumferentially notched round bar specimens [4] are applied. The basis of the approach is the superposition of the so-called elastic and plastic part of the J-integral.

VERIFICATION

Crack opening loads

The algorithm for the determination of the crack opening load is verified by experimental results for cracks growing from notches at CA loading at the nominal stress ratio R = -1 for two different materials and two notch geometries shown in Figure 3a. The measured values, material data and further details are reported in [6]. Figure 3b demonstrates that the developed algorithm is able to describe the crack opening behaviour. In accordance with the experimental results the calculated crack opening level (S_{op}) normalized with respect to the maximum load (S_{max}) increases the longer the crack grows and stabilises at a nearly constant level. Further examples show similar quality [4]. Following [5,8,10,11] the crack opening load is defined as the load level which opens the crack completely.

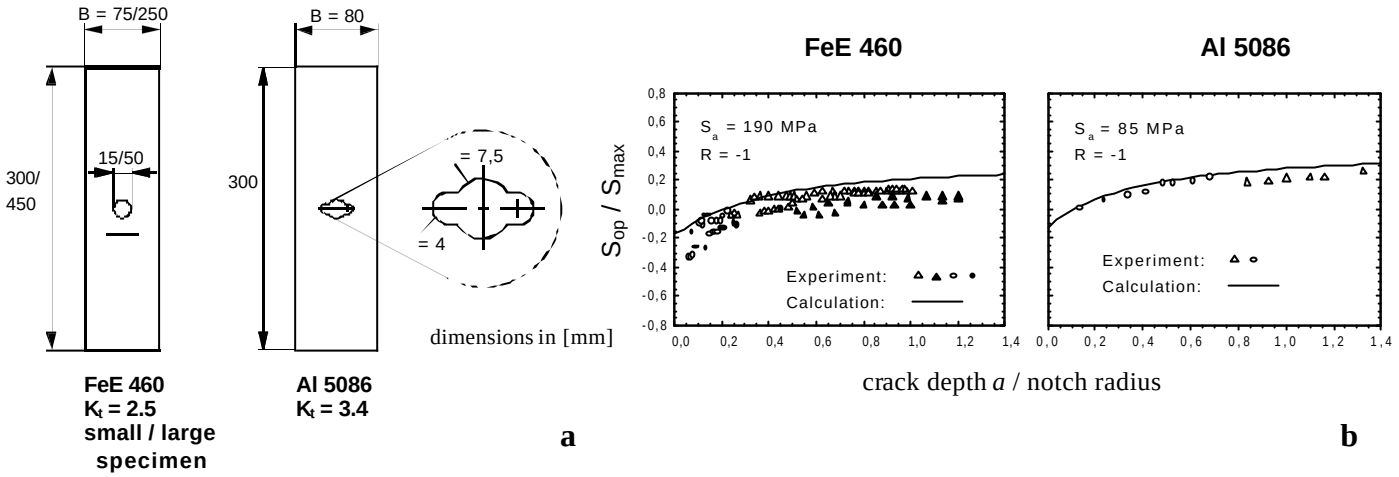

Figure 3: Specimen (a), Comparison of experimentally [6] and calculated crack opening loads (b)

Crack growth

The crack growth model is verified by experimental results described in [12]. The notched cylindrical specimen (material: German grade 42CrMo4, R_m=1065 MPa) is shown in Figure 4a. The fillet rolling force is F_w = 5 kN leading to compressive residual stresses of approx. –650 MPa at the notch root surface and a maximum of –1100 MPa approx. 0,4 mm beneath the surface after fillet rolling. These values are determined by FE-analysis performed by Schaal [13] and the residual stress distribution is employed as input data.

Figure 4b shows the result of the crack propagation calculation at the nominal stress ratio R = -1 in comparison to the experimentally determined crack propagation curve and describes the typical crack growth behaviour in notched fillet-rolled components. After crack initiation the crack grows with relative high crack growth rates, crack growth retardation occurs at the time the crack tip reaches the area of the maximum compressive stresses which are redistributed due to the cyclic loading. In the case of amplitudes which are lower than the fracture fatigue limit the crack stops. Otherwise the crack retardation phase is followed by a phase of crack growth acceleration ending in the fracture of the specimen. Figure 4c shows the results of the crack propagation calculation in the form of S-N-curves for different R ratios. The flat slope of the S-N-curves, which are typical for notched fillet-rolled components, and the endurance limit are quite accurately calculated by the developed model.

The crack growth model can also be applied in the case of variable amplitude loading. Load sequence effects are considered by an approach whereby the algorithm proposed in [5] is reformulated in terms of effective strains, in the way that the effective crack closure strain of the actual hysteresis depends on the effective crack closure strain of the actual hysteresis at CA loading and also on the effective crack closure strain of the previous hysteresis loops. Figure 5a shows the comparison between experimentally and numerically determined fracture fatigue life for a Gaussian load sequence (H_0 = 10^6, I = 0.99, $\overline{R}$ = -1). Figure 5b shows experimentally and calculated crack propagation curves for a blocked program test load sequence ($\overline{R}$ = -1). For all comparisons the measured crack growth can be fairly accurately described, particularly considering the high slope exponent of the S-N-curves for fillet-rolled components.

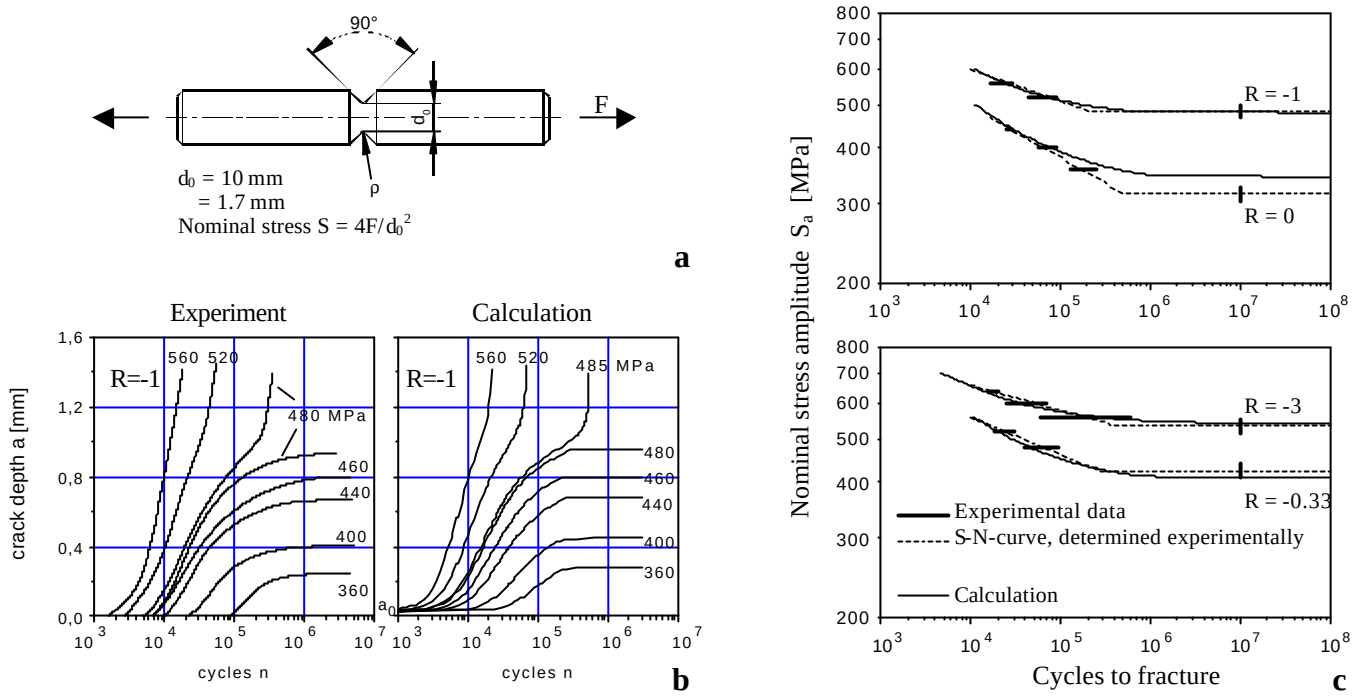

Figure 4: Specimen Geometry (a), Comparison of calculated and experimentally [12] determined crack propagation curves (b) and S-N-curves (c) for constant amplitude axial loading

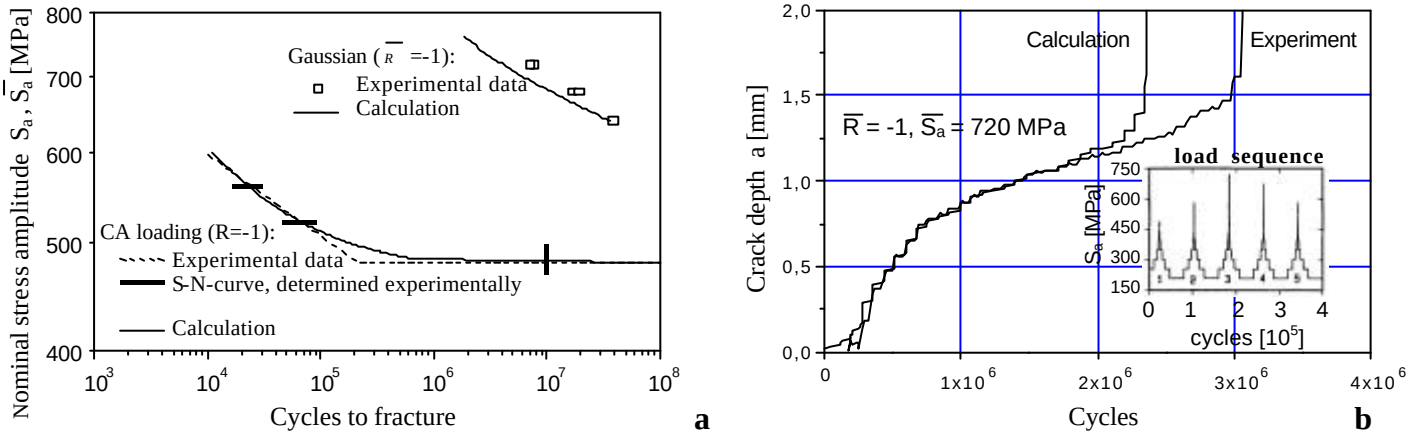

Figure 5: Comparison of calculated and experimentally [12] determined fatigue life curve for a Gaussian type random sequence (a), Comparison of calculated and experimentally [12] determined crack propagation curve for a blocked program test load sequence (b)

References

1. Hoffmann, M. and Seeger, T. (1985) Journal of Engineering Materials and Technology 107, 250.
2. McClung, R.C. (1991) Journal of Pressure Vessel Technology 113, 542.
3. Dankert, M., Greuling, S., Seeger, T. (1999) In: Advances in Fatigue Crack Closure Measurement and Analysis: Second Volume, ASTM STP 1343, pp. 411-426, McClung, R.C., Newman, J.C. (Eds). ASTM, West Conshohocken.
4. Richter C. and Seeger T. (2000) Report FB-1/2000, FG Werkstoffmechanik, TU Darmstadt, Germany.
5. Vormwald, M. and Seeger, T. (1991) Fatigue Fract. Engng. Mater. Struct. 14, 205.
6. Savaidis, G., Dankert, M. and Seeger, T. (1995) Fatigue Fract. Engng. Mater. Struct.18, 425.
7. McClung, R. C. (1994) Fatigue Fract. Engng. Mater. Struct. 17, 861.
8. Newman Jr.,J.C. (1984) Int. J. Fracture 24, R131
9. Savaidis, G. and Seeger, T. (1994) Fatigue Fract. Engng. Mater. Struct.17, 1343.
10. McClung, R.C. and Sehitoglu, H. (1986) In: ASTM STP 982, pp. 279-299, ASTM
11. Taylor, D. (1992) Engineering Fracture Mechanics 43, 109.
12. Kloos, K.H., Kaiser, B., Adelmann, J. (1992) Materialwissenschaft u. Werkstofftechnik 23, 423.
13. Schaal, R., Jung, U., Kaiser, B., Berger, C. (1999) In: DVM Report 231, pp. 287-295, DVM, Germany.

ORAL REFERENCE NO:ICF100187OR

FATIGUE LIFE EXTENSION OF AUSTENITIC STAINLESS STEEL USING NANO-SIZED MARTENSITES FORMED AT INTERSECTIONS OF DISLOCATIONS

T. Inamura, M. Shimojo, K. Takashima and Y. Higo

Precision and Intelligence Laboratory, Tokyo Institute of Technology
4259 Nagatsuta-cho, Midori-ku, Yokohama, 226-8503, Japan

ABSTRACT

A new fatigue strengthening method has been proposed. Dislocations are pinned at their intersections by the formation of nano-crystals after cold-work in this strengthening method. High cycle fatigue life of a cold-worked (tensile strain of 10%) 316-type austenitic stainless steel was extended by a cryogenic treatment and this is considered to be due to the pinning of dislocations by the formation of nano-sized α'-martensite particles. This fatigue strengthening did not decrease ductility of the material. This fatigue strengthening method is expected to be applicable for micro-sized materials.

KEYWORDS

fatigue life extension, dislocation pinning, ductility, nano-sized α'-martensite, micro-sized material

INTRODUCTION

Micromachines and/or MEMS devices have been intensively developed for the use in information technology, bio-medical technology and so on. The size of the components of these machines will be in the order of microns or sub-microns. Fatigue strength is one of the most important properties in micro-sized materials because the maintenance or the exchange of damaged elements is practically impossible in such tiny machines. Thus, the development of a fatigue strengthening method for micro-sized materials is extremely beneficial. It is necessary to construct a microstructure which is beneficial for the improvement in fatigue life in the order of nanometer, for the strengthening of micro-sized materials. Fatigue of metallic materials is mainly due to the accumulation of irreversible motion of dislocations. An increase in yield stress is, of course, fairly beneficial for fatigue strengthening. However, an increase in yield stress is generally accompanied by a decrease in ductility. We have already

revealed that micro-sized materials also fail by fatigue crack propagation as is observed in ordinary sized materials [1-2]. A decrease in ductility, which generally degrades crack propagation resistance, should be avoided also in micro-sized materials, as done for ordinary-sized materials. In addition, a microcrack, which is initiated in the earlier stage of fatigue process, is considered to become fatal damage in micro-sized materials [1-2]. Thus it is necessary to suppress crack initiation using a nano-order structure which does not degrade ductility but restrains the accumulation of microscopic plastic deformation under cyclic stress, for fatigue strengthening of micro-sized materials.

We have proposed a new fatigue strengthening method. Dislocation pinning at their intersections by nano-crystals after cold-work is considered to be an effective method for the suppression of the accumulation of microscopic damage. Figure 1 shows a schematic illustration of the concept of the pinning. The motion of pinned dislocations is expected to become bowing motion and not to cause re-arrangement of dislocations under cyclic stress. Nano-crystals are expected not to be a crack initiation site and higher stress may unpin the dislocations. The cyclic plastic deformation in this case should be homogeneously distributed, and the formation of stress concentrated fields should be suppressed. Consequently, crack initiation should be retarded and fatigue lives of materials are expected to be extended using this strengthening method. It should be noted that this strengthening method is not supposed to suppress plastic deformation, but to suppress the accumulation of the plastic deformation under cyclic stress. This strengthening method is considered to be effective on both the micro-sized materials and the ordinary-sized materials.

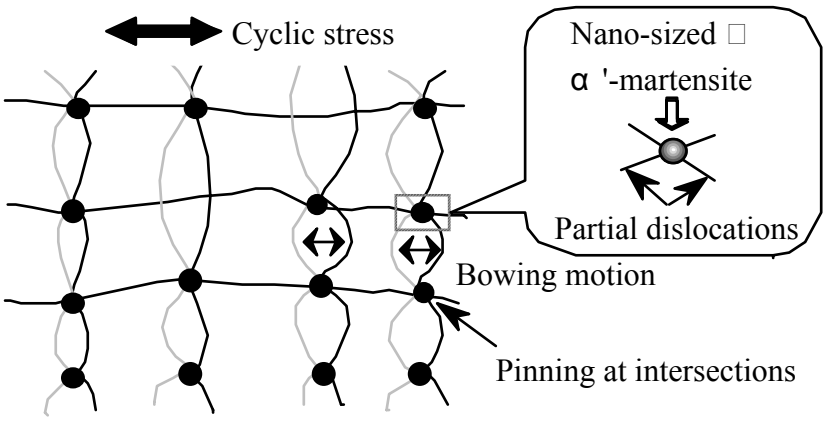

Figure 1: Schematic illustration of the concept of a new fatigue strengthening method. Dislocations are pinned at their intersections. Motion of pinned dislocations is considered to be bowing motion under cyclic stress. Our previous study using nano-sized α'-martensite particles indicates the validity of this strengthening method [x].

According to the model proposed by Bogers and Burgers [3], some of the intersections of partial dislocations in f.c.c. metals are expected to have b.c.c.-like stacking. It is well known that α'-martensitic transformation is caused by simple cooling and/or deformation in metastable austenitic stainless steels. In austenitic stainless steels, the b.c.c.-like stacking regions are considered to be preferential nucleation sites of α'-martensite. The b.c.c.-like stacking regions may transform into very fine α'-martensite particle by temperature control above $M_{s\alpha}^{b}$ during cooling. ($M_{s\alpha}^{b}$ is defined as the temperature at which spontaneous burst-like α'-martensitic transformation occurs during cooling in this study.) These very fine martensites are considered to be able to pin dislocations because b.c.c. stacking (nano-sized martensite) is incoherent to f.c.c. stacking (austenite).

We have partly verified the effects of this method on fatigue life extension using ordinary-sized austenitic stainless steel specimens. In our previous study [4], high cycle fatigue life of ordinary-sized 316-type

austenitic stainless steel specimens whose sub-surface area had been heavily cold-worked was extended by a cryogenic treatment above $M_{s\alpha}{}^{b}$. This fatigue life extension is considered to be due to the formation of nano-sized α'-martensites in the cold-worked sub-surface area of the specimens [4-5]. Observation of dislocation structure after fatigue loading suggested that the retardation of the rearrangement of dislocations is the origin of the fatigue life extension [4]. However, it has not been confirmed whether tensile properties (yield stress, UTS, fracture strain) are changed by the fatigue strengthening or not. The purpose of the present study is to investigate the tensile properties of a 316-type austenitic stainless steel specimen which have been fatigue strengthened by the pinning method.

EXPERIMENTAL PROCEDURE

The material used in this study were commercially available rods of 316-type(Fe-18Cr-10Ni-2Mn-0.06C) austenitic stainless steel (hot-rolled). Rotary bending fatigue specimens and monotonic tensile specimens were machined from the received rods after cold-work (tensile strain of 10 %) and thus, the entire specimen is cold-worked. Nano-sized α'-martensite should be formed and dispersed over the entire specimen by a cryogenic treatment at an adequate temperature. The cold-work of the received rods was performed at 573 K, not to cause any deformation induced martensitic transformation during this operation.

Nano-sized α'-martensites were formed by the cryogenic treatment at 195 K in the previous study [5]. However, the chemical composition of the received material is slightly different from that of used in the previous study [4-5]. Thus, formation temperature of the nano-sized α'-martensite may be different from that in the material used in the previous study. A cryogenic treatment at a temperature of either 240 K, 195 K, 175 K or 77 K for an hour was applied to each specimen to find adequate cryogenic temperature for fatigue life extension (adequate temperature for the formation of nano-sized α'-martensite). Microstructures of the specimens were observed using a scanning laser microscope (SLM) whose resolution is less than 1μm. The observation area was electrically polished using an acetic-perchloric acid solution and then, electro-etched using an oxalic acid solution.

Fatigue life tests were performed using an Ono-type four point rotary bending testing machine in air, at room temperature. The loading frequency was set to 2 ~ 10 Hz so that the temperature of the specimen surface did not exceed 313 K during the fatigue life tests. The stress amplitude under which specimen did not fail after 10^7 cycles was regarded as the fatigue limit in this study.

Monotonic tensile tests were performed using an Instron-type testing machine at room temperature. Strain rate , which was calculated from a cross head speed and the gage length of the specimen, was 8×10^{-4} / s.

RESULTS and DISCUSSION

No martensite phases (α' or ε martensite) were observed using the SLM after the cryogenic treatment at a temperature of either 240 K, 195K, 175 K. Figures 2 (a)~(c) show typical microstructures of (a) non-treated specimen, (b) 175 K-specimen and (c) 77K-specimen obtained by the SLM observation.

Non-treated specimens were fully austenite. A very small amount of martensites were observed in 77 K-specimen as shown in Fig. 2(c).

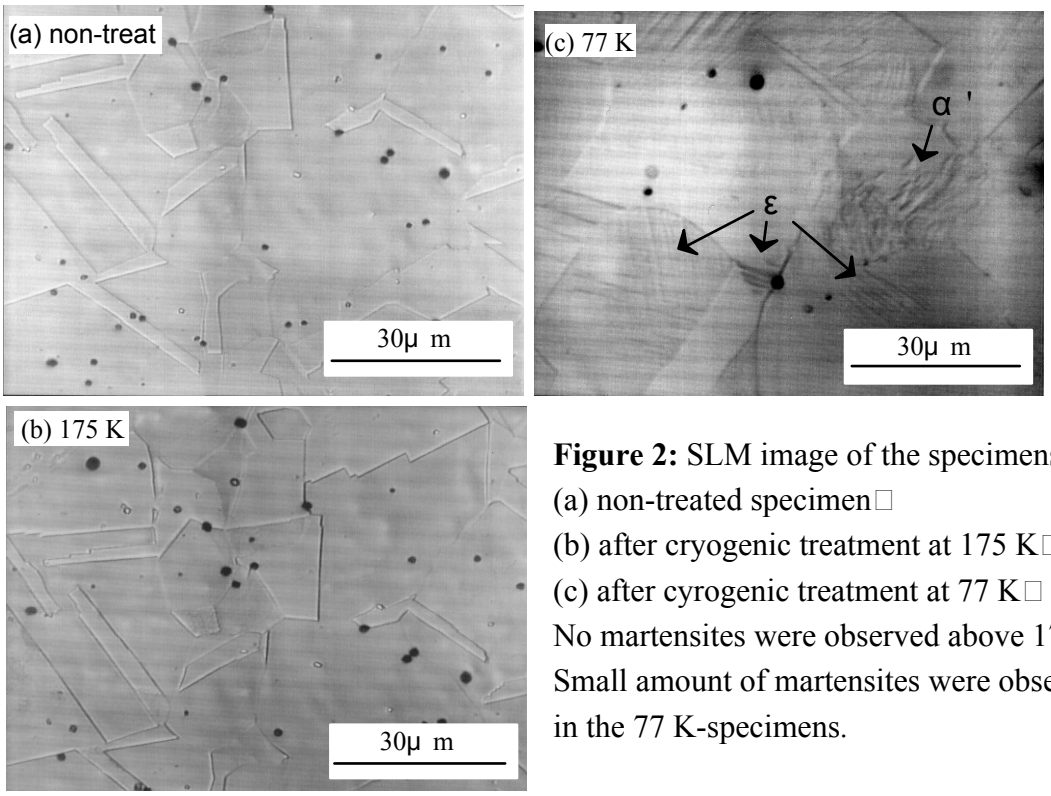

Figure 2: SLM image of the specimens
(a) non-treated specimen
(b) after cryogenic treatment at 175 K
(c) after cyrogenic treatment at 77 K
No martensites were observed above 175 K.
Small amount of martensites were observed in the 77 K-specimens.

S-N curves of non-treated, 175 K- and 77 K- specimens are shown in Fig. 3. The arrows indicate that the specimen did not fail after 10^7 cycles of loading. Fatigue lives of 240 K and 195 K specimens did not change compared to that of non-treated specimen. Thus, it is considered that no microstructural change was occurred by the cryogenic treatment at either of 240 K and 195 K (Fatigue data of 240 K and 195 K specimens are not plotted). No significant increase in fatigue lives was observed in 77 K-specimen. It has been reported that formation of α'-martensite which is optically visible has large influence on mechanical properties of austenitic stainless steels [6-9]. Small amount of optically visible α'-martensite (less than 30 volume % [6]) is beneficial, but large amount of it is detrimental [6-9] for fatigue life of an austenitic stainless steel. It is su… …en was so small that no significant change …

However, fatigue lives … …n-treated specimen especially in a high cy… …d by the cryogenic treatment at 175 K. Thi… …ble and effective on fatigue life has been … …agation in the 175 K-specimens is deduced … …earance which was accompanied by striatio… …results obtained in a 304-type austenitic st… …ispersed [4,10-11]. According to our previ… …re considered to be formed in the 175 K-specimens used in this study. In 77 K specimen, no nano-sized martensites were suggested to be formed.

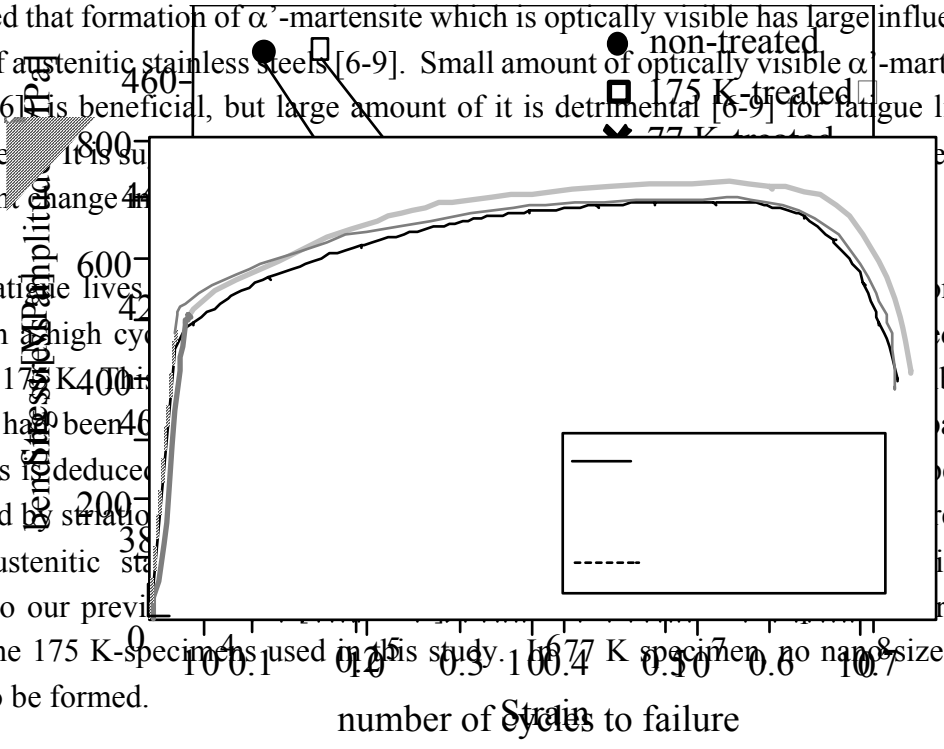

Figure 3: S-N curves of the 316 type austenitic stainless steel
Fatigue lives were extended especially in high cycle regime by the cryogenic treatment at 175 K.

Figure 4: Stress-strain curves of the specimens
No significant change in tensile property was observed in the 175 K specimen though fatigue life was extended by the cryogenic treatment.

Figure 4 shows stress-strain curves of a non-treated, 175 K and 77 K specimens obtained by the monotonic tensile tests. Large fracture strain of approximately 70 % was observed. This is due to TRIP (Transformation induced plasticies) effect which generally appears in austenitic stainless steels. No significant change in tensile properties (yield stress, UTS and fracture strain) was observed in 175 K and 77 K compared to non-treated specimen. It is therefore deduced that the ductility of the 175 K specimen is not degraded by the cryogenic treatment though fatigue life was extended. Thus, the pinning by nano-sized α'-martensite particles are considered not to obstruct the motion of dislocations under greater stresses. This results should explain the results of fatigue life tests in which low cycle fatigue life was not significantly extended, and the crack propagation manner was not changed in the175 K-specimens.

In the case of micro-sized materials, it has been pointed out that the deformation behavior and/or fatigue behavior of the materials may be different from those of ordinary-sized materials due to "size-effects" [1]. Our latest studies [1-2] using a micro-fatigue testing machine (MFT 2000) suggested that fatigue fracture of micro-sized materials is also driven by cyclic plastic deformation. Thus, essential mechanism of the fatigue fracture is supposed not to be changed in micro-sized materials and this strengthening method is expected to be applicable for micro-sized materials.

CONCLUSION

High cycle fatigue life of 10 % cold-worked ordinary-sized 316-type austenitic stainless steel specimens was extended by the cryogenic treatment at 175 K. This fatigue life extension is considered to be due to the pinning of dislocation by nano-sized α'-martensite, according to our previous study. The tensile properties of the material were not changed by the fatigue strengthening and thus, ductility of the specimen is deduced not to be decreased by this strengthening method. This fatigue strengthening method is expected to be effective also on micro-sized materials.

REFERENCES

[1]Maekawa,S., Takashima,K., Shimojo,M., Higo,Y., Sugiura,S., Pfister,B., and Swain,M.V. (1999) *Jpn. J. Appl. Phys*. **38**, 7194.

[2]Takashima,K., Higo,Y., Sugiura,S. and Shimojo,M. (2001) *Materials Transactions* **42**, 68.

[3]Bogers,A. J. and Burgers,W. G. (1964) *Acta Metall*. **12**, 255.

[4]Inamura, T., Shimojo, M., Takashima, K. and Higo, Y. *Proc. of the MRS 2000 fall met.* in press

[5]Shimojo,M., Inamura,T., Myeong,T. H., Takashima,K. and Higo,Y. (2001) *Metall. Mater. Trans. A* **32A**, 261.

[6] Maier,H. J., Donth,B., Bayerlein,M., Mughrabi,H., Meier,B. and Kesten,M. (1993) *Z. Metallkd.* **84**, 820.

[7]Srinivasan,V. S., Sandhya,R., Bhanu Sankara Rao,K., Mannan,S. L. and Raghavan,K. S. (1991) *Int. J. Fatigue* **13**,471.

[8]Horibe,S. Seki,Y., Fujita,T., Araki,T. (1980) *Transactions ISIJ* **20**, 398.

[9]Franke,G. and Altstetter,C. (1976) *Metall. Trans*. *A* **7A**, 1719.

[10]Myeong,T. H., Yamabayashi,Y., Shimojo,M. and Higo,Y. (1997) *Int. J. Fatigue* **19**, S69.

[11]Inamura,T., Abe,R. Myeong,T. H. Shimojo,M. and Higo,Y. (1999) *Proc. of the 7th Int. Fatigue Congress* **1**, p. 633

FATIGUE OF STEEL STRUCTURES

P. BROŽ

Klokner Institute, Czech Technical University,
Šolínova 7, 166 08 Prague 6, Czech Republic

The objective of the paper is to report about the main results and conclusions of a new stage of experimental research conducted in Prague on the coupled problem of a many times repeated loss of stability and cumulative damage in the slender webs of steel plate girders subjected to many times repeated loading. In so doing, the paper analyses the experimental data obtained, particularly from the point of view of the initiation and propagation of fatigue cracks in breathing webs, their failure mechanism and relation to the fatigue limit state of the whole girder.
Some comments concerning the issues of metal fatigue are added.

1. Introduction

Steel bridges, crane runway girders and similar systems are exposed to many times repeated loading and, if their webs are slender, they repeatedly buckle out of their plane. This phenomenon is now usually termed "web breathing" (see eg [1]), and generates pronounced cumulative damage in the webs, so that fatigue cracks usually occur in them. No reliable design procedure for the webs can then be established without the regime of crack initiation and growth in them having been thoroughly mapped.

2. Fatigue damage in thin-walled steel girders

The webs of the plate and box girders of steel bridges and like structures are subject to many times repeated loading; consequently, being usually slender, they exhibit many times repeated buckling, this process being now named web breathing. In is in the nature of this phenomenon that considerable cumulative fatigue damage is then generated in the girders, this very substantially affecting the limit state of the girders.
Designers of steel structures have for some time been aware of the importance of the breathing process and have been trying hard to incorporate it into design. Two simple approaches have been used to reach this objective:

(i) In the first of them, the depth - to – thickness ratio of the web is reduced so that all uncalled-for effects of web breathing may be neglected.
(ii) In the other, it is the load acting on the web that is reduced to achieve the some objective.

Both of the two aforementioned procedures are useful, but they hold out just part of the solution needed. They represent only a lower bound for this solution; a more economical approach, such as to go beyond this lower bound and to be profitable at least from part of the post-buckled reserve of strength of slender webs, is also very advisable.
With the importance of this approach to the breathing phenomenon for reliable and economical design of steel bridges and similar structures, extensive research, both theoretical and experimental, was started in Prague, several years ago, at both the Institute of Theoretical and Applied Mechanics of the Czech Academy of Sciences and Klokner Institute.
In the theoretical field, three studies are running or have already been closed:

(i) A large deflection theory analysis of stresses in crack – prone areas of breathing webs.
(ii) An analysis, based on Fracture Mechanics, of the propagation of cracks in breathing webs.
(iii) An ultimate load theory for fatigue – cracked webs subjected to predominantly shear.

The experimental investigation consists of several series of tests on steel plate girders under the action of many times repeated load, the geometrical characteristics of the test girders and the regime of the cyclic load being varied in them.

Two series of test girders were tested, by M. Zornerová and M. Škaloud, at the Institute of Theoretical and Applied Mechanics of the Czech Academy of Sciences in Prague.

(i) One series of girders with slender webs, whose depth–to-thickness ratio $\lambda = 250$.
(ii) Another series of girders with less slender webs, whose depth–to-thickness ratio $\lambda = 175$. This depth–to-thickness ratio was chosen so as to be lower than the maximum slenderness $\lambda^{n,b}_{max}$ of so-called non-breathing webs discussed above.

The former group to date comprised 71 test girders, the latter 22 girders, but experiments of other girders in both groups are running.

As it was demonstrated during static tests on the ultimate load behaviour of shear girders that these characteristics were fundamentally influenced by the flexural rigidity of girder flanges, one half of the test girders were equipped with very flexible flanges (50 x 5 mm) while the other half had more rigid flanges (50 x 10 mm).

Two other series of girders were tested at Klokner Institute of the Czech Technical University in Prague. In the first one, the web thickness $t_w = 4\ mm$ so that the web depth–to-thickness ratio $\lambda = 200$ (this means, that these girders were designed so as to have as good as non-breathing webs); in the other, $t_w = 2{,}5\ mm$ and $\lambda = 320$. Like the girders tested in the laboratory of the Institute of Theoretical and Applied Mechanics, even the above girders had two kinds of flanges being thin ($t_f = 8\ mm$) and for the others being thicker ($t_f = 20\ mm$).

The former series comprised 12 girders and is regarded as completed; the latter to date consisted of 13 girders, but other experiments are under way.

So, if looking at the general details of all the girders tested, it can be seen that the depth–to-thickness ratios of their web panels (which is beyond any doubt one of the main factors affecting web breathing) were of 175, 200, 250 and 320. Accordingly, they ranged from so-called non-breathing webs to very slender ones.

All the test girders were subjected to a point load $F = 2\ P$, located at mid-span and cycling between a minimum value $F_{min} = 10\ kN$ and a maximum value F_{max}, which varied from test to test. Both of the two web panels were then exposed to combined shear and bending, with the influence of shear predominating.

In addition to usual deflection and strain measurements, the main objective of the experiments was to study the initiation and propagation of cracks in the webs and the fatigue failure mechanism of the test girders. This was achieved largely by way of visual inspection checks of the breathing webs, aided by a magnifying glass. In several tests the acoustic emission method was also applied.

The strain measurements were used mainly to determine the zones of stress concentration in the crack-prone areas of the breathing webs, this being also supported by a theoretical study based on the finite element method.

Before every test, the initial curvatures of both web panels were cautiously gauged, and so was the plastic residue (including fatigue crack) in the web sheet and girder flanges after the termination of the experiment, this rendering it possible to study the collapse mechanism of the test girder.

As stated above, the main intendment of the experimental investigation was to study the initiation and propagation of fatigue cracks in the breathing webs, and their impact on the failure mechanism of the test girders.

It was seen that the fatigue cracks arose at the toes of the fillet welds connecting the web sheet panels with their boundary members (ie flanges and stiffeners). They initiated at the regions of maximum principal surface stress ranges and grew, with the number of load cycles increasing, along the boundary members and often diagonally across the corner of the web as well, so as in the end to “cut” the tension diagonal in the buckling web sheet.

The initiation and the character of crack propagation was as follows:

(i) Either a crack appeared in the diagonal tension band and rapidly advanced in a direction approximately perpendicular to that of the tension band. But still, this situation occurred only twice among the almost one hundred and twenty tests performed in Prague to date, and was probably owing to the presence of a manufacturing imperfection in the web material at the zone of crack initiation

(ii) Or a crack started close to the inner or outer transverse stiffener, namely near that portion of the stiffener into which the diagonal tension band in the web anchored, then propagated and rather at a slow pace – along this stiffener. Later on, as a rule, after several tens or hundreds of thousands of loading cycles (this depending on the magnitude of loading), the crack turned inside the web sheet.

(iii) Or a crack initiated in the close vicinity of the fillet weld connecting the upper flange with the web sheet, then propagated (at first in both directions) along the weld so that on one side it reached the adjacent web corner. Then it turned down along the vertical fillet weld joining the web sheet with the final stiffener, so that in the close the whole upper outer web corner tore away from the web peripheral frame. It was observed that the tearing off of the web sheet occurred in that portion of the web in which the diagonal tension bend developed and was anchored into the boundary frame.

(iv) In some cases, phenomenon (iii) interacted with process (ii), ie with a crack advancing (with a certain delay as far as the first crack) along the transverse stiffener.

An examination of strain gauge measurements indicated that the cracks initiated in those regions (near the transverse stiffeners or the upper flange) where the ranges of the principal surface stresses in the web sheet were maximum.

The number of load cycles to failure, ie the life of the test girder, was a function of load range, and varied from tens of thousands of load cycles when the load diapason was large to millions of load cycles when the load range was small.

The propagation of the fatigue cracks was a more or less continuous process. Never during the tests did we notice any sudden increase in the rate of crack propagation, such as to indicate an unstable crack growth and to announce a critical length phenomenon known from Fracture Mechanics.

The collapse of the girders was presented in a typical shear failure mode, well marked plastic buckles constituting along the tension diagonal of the web panels and plastic hinges developing in the flanges. In the end Stage of their fatigue lives, all the test girders conducted themselves like ones with an opening in their webs, the opening being represented by the developed fatigue crack.

The effect of web slenderness was studied by way of one series of experiments performed at the Institute of Theoretical and Applied Mechanics in Prague, namely via tests on girders of group (ii), described above, the main aim being to check whether there existed a maximum slenderness $\lambda^{n,b}{}_{max}$ such that for $\lambda \leq \lambda^{n,b}{}_{max}$ all effects of web breathing could be neglected.

In this regard it was found out that the problem was more complex and that it was impossible to define $\lambda^{n,b}{}_{max}$ independently of other factors, principally of the intensity of repeated loading and the magnitude of the initial imperfections of web panels.

The main conclusions of the experiments are dual:

(A) The webs of all the girders being part of this group (ii) exhibited pronounced breathing.

(B) Referring to the initiation and growth of fatigue cracks in them, it was observed that just in part of the experiments no cracks in the breathing webs were discovered. On the other hand, it was concluded that when (a) the maximum value F_{max} of the cycling load F was high and (b) the initial curvatures of the breathings webs were not small, the mechanism of fatigue crack growth was very like to that which was observed in the tests on group (i) test girders with web slenderness of 250.

It is normal practice in the fatigue analysis of civil engineering steel structures that this analysis is based on stress range only, the effect of the mean value of cyclic stress being completely disregarded. This is why ones of us wanted to verify whether this idea could also be applied for the fatigue assessment of breathing webs.

18 tests of this kind have hitherto been carried out at the Institute of Theoretical and Applied Mechanics.

Although the scatter of the results obtained was rather large (but this is the case with all web breathing tests), it was rendered that at least in some of the experiments, the influence of the mean value was quite marked, see Table 1. But still, more proofs in this principle is indispensable.

TEST GIRDER	MEAN VALUE OF LOAD F [kN]	LOAD RANGE [kN]	NUMBER OF LOAD CYCLES TO FAILURE
BTG 52	120	60	1 132 780
BTG 55	120	60	572 700
BTG 51	40	60	4 970 350

Table 1. Effect of the mean value of cyclic loading

A question now arises which value does the remaining carrying-capacity have, namely of the breathing girder webs being weakened by a fatigue crack. Since we have not observed any instabilized crack growth in the course of 1.test series, it remains to find a solution to the problem aforementioned, simply taking the equilibrium into consideration which several authors have resumed in the form of the so-called theory of tension field in the girder webs subject to shear. By virtue of test results and after introducing the tension field theory, the relationship was derived between the remaining shear carrying-capacity of the girders weakened by cracks and shear carrying-capacity of the unweakened ones, in the following form:

$$V_{res} = V_u \left\{ 1 - \frac{d_{ec}}{d_w} \right\} = V_u \left\{ 1 - \frac{d_c \cos\Theta + h_c \sin\Theta}{d_w \sec\Theta} \right\} \tag{1}$$

At that, the angle Θ of a diagonal of the tension field is equal to the two thirds of the angle Θ_d of the girder web diagonal. Eq. (1) be based on the assumption that the remaining shear carrying-capacity is linear in relation to the ratio d_{ec}/d_w, ie in terms of the ratio of the effective depth of a fatigue crack d_{ec} to the web depth d_w.

3. Metal fatigue considerations

Before as early as 1900 some authors specified that the application of a mean tensile stress would decrease fatigue resistance, this approach being later rated by fatigue tests implemented on plain specimens at various mean stress levels, together with static tensile test particulars. The relationship on a given subject adopted from [2] is indicated in Fig. 1. Notwithstanding the philosophical difficulty of related static to dynamic fracture phenomena, the mentioned approach is widely accepted by industry though at high mean stress levels arising in many components (eg pre-stressed bolts) serious contradictions can be ascertained that may be explained merely by a crack growth analysis.

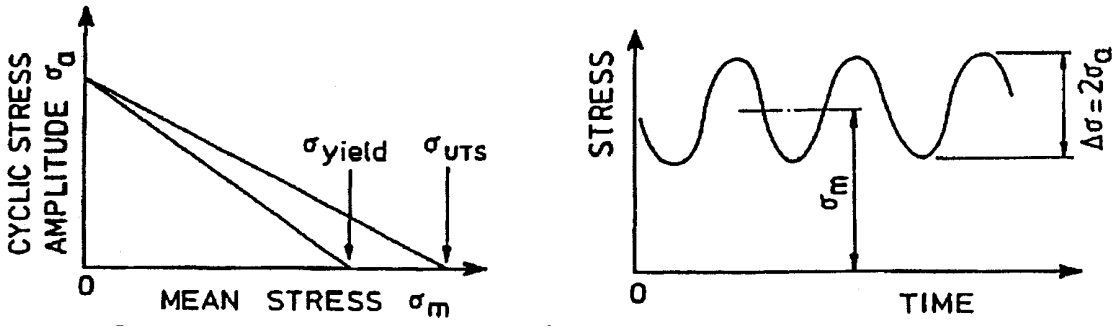

Fig. 1 Goodman diagrams and parameter specifications.

The reasons why a mean stress, σ_m can lessen fatigue resistance is that the maximum stress level in a constant $\Delta\sigma$ series of tests is increased and consequently the maximum crack tip opening displacement is enhanced; additionally the cyclic range of crack tip displacement is increased because crack closure on the elastic unloading part of a cycle can be excluded, and finally the environment has a much easier access and compensatory track to the plastically deformed zone at the crack tip. But still, giver cyclic torsion it is possible, with the crack sides of the Stage I shear cracks being left closed and thus the mean shear stress, τ_m, influence is not so outstanding and experimental results obey the depicted parabola more close at low R values ($R = \tau_{min}/\tau_{max}$). Of great attraction is the possibility of a periodic application of a tensile mean stress across the flanks of a shear directed crack since such loading conditions, frequently met in industrial components and structures (eg railway lines), may originate continuous Stage I crack growth without a transition to Stage II. To describe processes of crack initiation and propagation, six information entries are necessary:

1. Any sort of defect, no matter how small, represents a stress concentration (grain boundary, surface both inclusion and scratch) being at once a possible originator of the crack.
2. Fatigue crack are often watched below the fatigue limits of steels, these having grown but also subsequently arrested.
3. Micro- and macro-deformation responses with developed persistent slip bands may be immediately observed by optical and electron microscopes seeing that they are relatively large comparing to initial cracks which need only measure 0,1 x 0,1 microns but be difficult to find out.

4. The engineering definition of an initiated crack has been steadily reducing since the mid 19th century from a length of several millimetres, to one millimetre, to 100 microns, to the size of a single grain, to a few microns (and in the event 0,1 microns or less?).
5. A crack of any size demands plasticity (movement of dislocations) to grow and should not require to wait for the establishment of a permanent slip band.
6. The acoustic microscope of late introduced may differentiate between a slip band and a crack.

In 1970, K.P. Zachariah assumed that the crack initiation period was zero and that the whole of lifetime was concerned with two phases of propagation namely (i) a short crack propagation phase (the beginnings of Microstructural Fracture Mechanics) and (ii) a longer crack growth phase defined in terms of EPFM. For a starter crack of two microns, the older definitions of "initiation" were dependent on the resolution of currently available microscopes. On top of it, the early growth rate of a crack far removed from various form of microstructural barriers is rapid but decreases on approaching a barriers. In due course, should all obstacles be overcome, a ruling crack can continue its propagation to failure and be described by continuum mechanics. The "initiation" zone is an initially fast but small propagating crack that may either accelerate, decelerate and arrest to acceleration, or decelerate and arrest to give fatigue limit. It will also be recognized why cracks can and do grow below any of the LEFM definitions of a threshold state. In fact, any size of defect or fatigue crack can propagate if the cyclic stress range is highish.

3.1 Construction

All structures, in particular welded ones, embrace large defects, ie a > 0.5 mm, together with stress concentration characteristics. Thankfully Tables of Stress Concentration Factors and Stress Intensity Factors exist but always these are in the main applied after a failure incident when the regions of weakness are obvious to all.

Fortunately the condition da/dN = 0 for structures may be analyzed from simple LEFM threshold conditions if an initial defect size D can be precisely estimated (which seldom succeeds in large welded structures). The major issues with engineering construction are, as follows:

(i) small stress concentration regions being located in large stress concentration zones, eg notches situated at the structure of 3D formulation

(ii) 3D in-service loading patterns being random in intensity, in orientation and acting in- and out-of-phase at different occurances in time

(iii) critical region for crack initiation not being recognized; note that fatigue cracks do not have to initiate at the worst stress concentration locations

In the next century, for that reason more analyses will be demanded for structures holding complex stress concentration, with cracks ranging in size from round about one to a few millimeters. This will be primarily true for those industries that usually have not yet introduced fracture mechanics into their design interpretations. It is certainly probable that many metal construction will be replaced by composite structures which have the aptitude to turn cracks aside from dangerous track.

3.2 Materials

Betterments in metals must and will go ahead, in particular in the composites and multiphase substances. It is to be hoped that material scientists and physicists will develop materials with thicker, stronger and more closely packed obstacles to micro-crack propagation. One can anticipate specific materials being designed and developed for specific utilizations, ie hindering the growth of Stage I and/or Stage II fatigue cracks depending on the application.

Since it is hoped that more accurate and flexible systems will be discovered to gauge and monitor the propagation of micron and submicron sized cracks (the acoustic microscope can size cracks of a few microns in length-but is miles away from being a mundane implement for industrial use). Multi-failures in electronic devices will help urge these developments.

It is awaited that dislocation theory will find a use, acceptable to engineers, in the development of models for determining the growth characteristics of cracks that are of a comparable size to dislocation aggregations. Who can guess – we may ultimately have a new science of Dislocation Fracture Mechanics.

Eventually, a note on the scatter of fatigue data. In the next century serious attempts will have to be made to present scatter in a proper perspective probably starting with the influences of different test variables on the

three fundamental fatigue limits. That is why, for laboratory tests on materials, the scatter of microstructural variables on Stage I cracks such as grain size, barrier thicknesses and strengths, now demand more detailed studies.
Regarding components, effects of slight changes in surface profiles and the surface texture are in want of separation whereas for structures the effect of minor variations in initial defect / crack sizes and external loading variables are very important. It needs to be recognized that a few overload cycles, a transient change in the environment and /or temperature (including thermal shock) may have a far more serious effect on tests to specify material behaviour and Stage I growth than, say, for a structure already weakened by a noticeable Stage II crack.

4. Conclusion

The initiation of the first fatigue crack means usually very little for the exhaustion of the actual fatigue life of girders with breathing webs. Moreover, the post-initiation residual lifetime very considerably varies as a function of the web geometry and of the intensity of repeated loading: it is small for very slender webs and high loads, but can be very large for the other cases. For webs of usual depth-to-thickness ratios and subjected to usually encountered load ranges, a design base on crack initiation would be conservative and would substantially reduce the competitiveness of steel in bridge and similar construction. Fatigue failure appears to be a more rational basis for the definition of the fatigue limit state of breathing webs because, from the point of view of the cumulative damage process, it is equally "just" for all girders - their geometry and loading level notwithstanding. In its light it is required that no fatigue failure shall occur before the planned fatigue life of the girder is fully exhausted - which is the objective of fatigue analysis. In the case of webs under the action of many times repeated predominantly shear, the maximum depth-to-thickness ratio of those webs for which the effect of breathing can be disregarded for all loading ranges is less than 175, and will be specified by further research.
Knowledge of the characteristics of cracks has become increasingly important especially as for their size, shape, orientation and growth rate together with their initial and final geometries.
The relevant developments in metal fatigue to be accomplished in the next century will be pertinent to the development of techniques to measure and continuously monitor fatigue cracks, inclusive of particularly those of 10^{-7} to 10^{-9} mm in size inside the metal.
For engineering components, the major tendency will be concerned with improvements to the fatigue resistance of surfaces.
In the case of structures, crack detection systems will be improved and significant advancements made owing to the effect of changing structural compliance on local crack growth characteristics. Ageing aircrafts, nuclear plants, long-life oil rigs and pipelines, fast ground-transport and ships, will present ever-increasing matters, but we hope that fracture mechanics, in all its forms, will progress for its early development stages and be put into practice with appropriate imperativeness in every branch of engineering industry.

5. Acknowledgement

The author gratefully acknowledges the financial support of the presented research by the Grant Agency of the Czech Republic (project No. 103/00/0897).

6. References

[1] Škaloud, M., Roberts, T. M.: Fatigue crack propagation in slender webs breathing under repeated loading. *Journal of Constructional Steel Research, spec. issue: Second World Conference on Steel in Construction*, San Sebastian, 1998, pp. 417-419.

[2] Miller, K. J., ASTM STP 1296, *Fatigue and Fracture Mechanics: 27th Volume* (R.S. Piascik, J. C. Newman and N. E. Dowling, Eds.), 1997, pp. 267-286.

Improving of the fatigue lifetime prediction of screw for a large range of mean stresses

A. Duval, P. Robinet, F. Trivaudey and P. Delobelle
Laboratoire de Mécanique Appliquée R. Chaléat, UMR C.N.R.S. 6604
Université de Franche-Comté, 24 Chemin de l'épitaphe, 25000 Besançon, FRANCE

Abstract:

From a Finite Element analysis, the stress distribution in the notch of axisymmetric and highly loaded notched samples has been calculated. The samples are shaped like a thread root. We propose a simplified method of sizing screws for a large range of mean stresses.So, a local Haigh's diagram (at the thread root) is built from experimental the Haigh's diagram derived from smooth or notched samples.

I – Introduction

When trying to predict the fatigue lifetime of a screw used in a highly loaded assembly, the designer has to handle two types of difficulties. The first one is to include the effects of the mean stress on the damage. The second one, related to the geometry of the screw, is to know the influence of the notch effect on the damage in the thread root. The Haigh's and Goodman's diagram help us to solve the first problem when the mechanical properties of the material are known. Indeed, they give the endurance domain in which the applied and the mean stresses have to be located. The second difficulty is partly overcome thanks to Neuber's method or the method of the gradient since they take into account the effect of stress concentration inside the thread root.

Here, the method is based on an elasto-viscoplastic analysis leading to the knowledge of the local stress and strain components. Then, a multiaxial failure criterion derived from the damage rules is locally applied. This leads to a simple method of building the Haigh's local diagram. The global method follows four steps:

i) Determination for the considered steel of the elastoplastic behaviour rules under uniaxial loading with or without mean stress.
ii) Determination of the damage rules leading to the rupture criteria as well as to the cumulative calculations.
iii) Theoretical and experimental studies of notched axisymmetric samples shaped like a thread root.
iv) Study of the fully screw-bold assemblage.

We will present here the first three steps.

II – Materials and experimental methods

The screw steel studied here is a 38CD4 steel oil quenched from 850°C then stress relieved at 600°C for one hour. This results in a fully martensitic microstructure. Its weight composition is as follows:

C %	Mn %	Si %	S %	P %	Cr %	Mg %	Fe %
0.36	0.792	0.232	0.028	0.016	1.039	0.175	balance

$$K_t = \left[1 + \frac{1}{\sqrt{\left(\frac{1}{1.197K_p}\right)^2 + \left(\frac{1}{1.871K_q}\right)^2}} \right]^{\sqrt{\cos(\alpha/2)}} \quad \text{with} \quad K_p = \sqrt{\frac{t}{r}\frac{d/D}{1-d/D}+1} - 1, \quad K_q = \frac{1}{\sqrt{r/t}}, \quad t = \frac{D-d}{2} \qquad [1]$$

The whole set of tests were performed at room temperature, on smooth samples as well as on axisymmetric notched samples shaped like a thread root of a screw with a null pitch.

The dimensions of the notched samples with triangular profile (external diameter D = 6mm, diameter at the notch root d = 4.78mm, angle between the sides of the notch α = 60° and α = 120 ° and junction radius of the two sides at the notch root r = 0.35mm and r = 0.29mm) leads, following equations [1], to the geometric stress concentration factor K_t equal respectively to 2.41 and 2.1. Some specimens with circular notch leading to K_t = 1.5 were also tested.
For these samples, the applied and mean stresses $\Delta\sigma_E/2$, σ_{moyE} are calculated from the normal section at the site of the notch.

III – Results and Analysis

3.1) Main mechanical properties of the steel

This steel has the following characteristics :
A high yield stress $R_{0.2\%}$ around 1000 MPa and a failure stress R_m close to 1100 MPa together with a fairly good ductility at failure (>10%). Note that there is quite an important dispersion on these two values between the different sets of samples because of the low reproductibility of the heat treatment.

As far as the cyclic properties between symmetric imposed strains are concerned, a continuous softening is observed up to the failure. A plateau for the first quarter of cycle is visible together with the well curved form of the cycles related to an important Bauschinger effect. The cyclic curves measured at a quarter of cycle, at one cycle, at half failure number of cycles $N_R/2$ and at the failure number of cycles N_R are drawn in Figure 1. When the cyclic loading is no longer symmetric, an important progressive strain can be shown, when the maximal stress σ_{Max} is fixed at 990 MPa and when the mean stress σ_{moy} is less than 280 MPa (Fig. 2). The strong dispersion between the two sets of samples, due to the heat treatment, can also be noted.

At room temperature, the viscosity of this steel is too small to be considered. Indeed, after 48 hours, the relaxed amplitude related to the initial stress amplitude is always less than 10%.

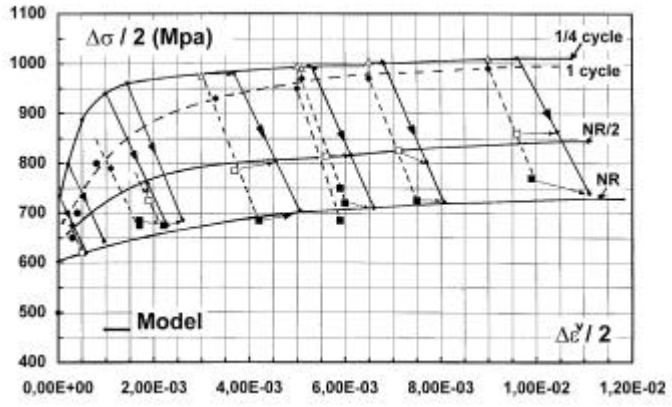

Fig.1*:Monotonic (1/4) and cyclic curves* $\Delta\sigma/2 = f(\Delta\varepsilon^v/2)$ *at one,* $N_R/2$ *and* N_R *cycles. Experiments and modelling*

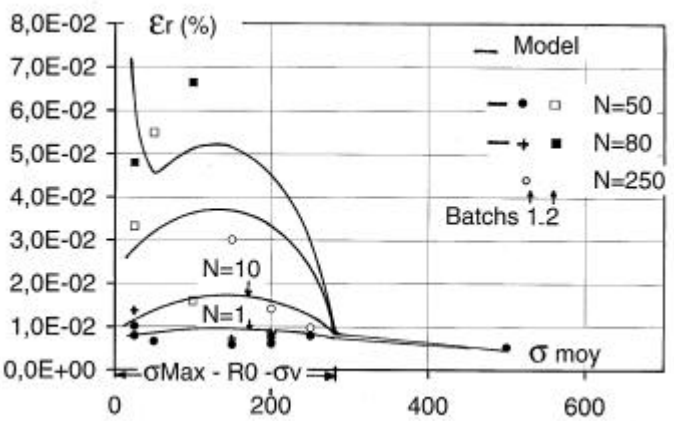

Fig.2 *: Ratchet strain as a function of* σ_{moy} *for different N. Experiments and modelling*

3.2) Formulation of the constitutive laws

According to the previous experimental observations, a unified viscoplastic formulation with a yield threshold, two kinematic hardening ($\alpha_{ij}^{(1,2)}$) and one isotropic hardening (Y) variables has been chosen. The general rules are :

$$\varepsilon_{ij}^{T} = \varepsilon_{ij}^{e} + \varepsilon_{ij}^{v} \qquad with \quad \dot{\varepsilon}_{ij}^{e} = \frac{1+\nu}{E}\dot{\sigma}_{ij} - \delta_{ij}\frac{\nu}{E}\dot{\sigma}_{kk}$$

$$and \quad \dot{\varepsilon}_{ij}^{v} = \frac{3}{2}\dot{\varepsilon}_{0}\left\langle \frac{J_2(\sigma - \alpha) - Y^{st}}{N} \right\rangle^{n} \frac{s_{ij} - \alpha_{ij}}{J_2(\sigma - \alpha)} \qquad where \quad \bar{\dot{\varepsilon}}^{v} = \left(\frac{2}{3}\dot{\varepsilon}_{ij}^{v}\dot{\varepsilon}_{ij}^{v}\right)^{1/2}$$

$$\alpha_{ij} = \alpha_{ij}^{(1)} + \alpha_{ij}^{(2)} \qquad [2]$$

$$\dot{\alpha}_{ij}^{(1)} = p_1\left(\frac{2}{3}Y_1\dot{\varepsilon}_{ij}^{v} - \alpha_{ij}^{(1)}\bar{\dot{\varepsilon}}^{v}\right) \qquad with \; \alpha_{ij}^{(1)}(0) = 0$$

$$\dot{\alpha}_{ij}^{(2)} = p_2\left(\frac{2}{3}Y_2\dot{\varepsilon}_{ij}^{v} - \alpha_{ij}^{(2)}\bar{\dot{\varepsilon}}^{v}\right) \qquad with \; \alpha_{ij}^{(2)}(0) = 0$$

$$Y^{st} = R_0 + Y \quad and \quad \dot{Y} = b(Y^{\infty} - Y)\bar{\dot{\varepsilon}}^{v} \qquad with \quad Y(0) = 0 \; and \; Y^{\infty} < 0$$

In these equations : $J_2(\sigma - \alpha) = \left(\frac{3}{2}(s_{ij} - \alpha_{ij})(s_{ij} - \alpha_{ij})\right)^{1/2} = \sigma_V + Y^{st}$ where s_{ij} *and* α_{ij} (*or* a_{ij}) are the deviators tensor components, δ_{ij} the Kronecker symbol, < > the Macauley brackets, that is <x>=xH(x), where H(x) is the Heaviside function.

The integration of the rules up to N_R (number of cycles to failure), with the identified model leads to the responses given in Figures 1 and 2. However, it is possible to choose a set of parameters, for a given number of cycles, that is, using new values for the parameters Y^{st} and p_1. Thus, at the ¼ of cycle, Y^{st} is equal to R_0 and at the stabilized cycle, Y^{st} is equal to $(R_0 - |Y^{\infty}|)$, at least for the greatest strain amplitudes. We can thus obtain directly the shape and the amplitude of the cycles at ¼ of cycle, for the cycle at $N_R/2$ and N_R , integrating the rules on only one cycle (Fig.1). For this steel with high yield stress, the progressive strain is on one hand due to the non-linearity of the kinematic variables (p_1 and p_2) and on the other hand to the cyclic softening. We can see in Figure 2, that the amplitude of the ratchet zone is fairly well modelled (ratchet zone $\approx \sigma_{Max} - R_0 - \sigma_v$) but although that the ratchet is compatible with experimental results even if its amplitude is over-estimated.

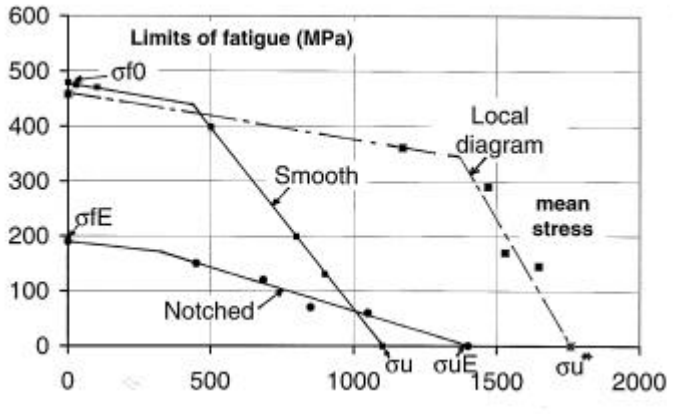

***Fig.3** : Different Haigh's diagrams for smooth and notched samples. Determination of the local diagram.*

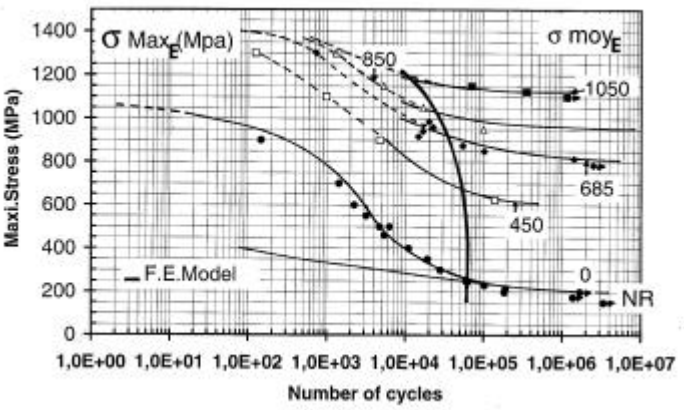

***Fig.4** : Woelher's curves of notched specimens for different mean stresses. Experiments and F.E. calculations.*

3.3 Fatigue properties and modelling

From the Woehler curves the Haigh's diagram can be built for smooth samples, giving the evolution of the endurance stress related to the mean stress $\sigma_f = f(\sigma_{moy})$ (Fig.3). From an uncoupled local approach, the damage variable D is taken with a formulation of the ONERA type {1}{2}:

$$dD = D^{a(\bar{p}, P_M, J_{2Max}, s_u^*, s_{f0})} \left(J_2\left(\frac{\Delta s}{2}\right) / M(\bar{p}) \right)^b dN \qquad [3]$$

Taking into account the non-linearity of the Haigh's diagram and the effect of the triaxiality on the ultimate stress s_u, the integration of equation [3] gives the number of cycles to failure N_R.

$$N_R = \frac{1}{aM_0^{-b}} \frac{\left\langle s_u^* - J_{2Max}(s) \right\rangle}{\left\langle J_2\left(\frac{\Delta s}{2}\right) - s_{f0}\, f(\bar{\bar{p}}) \right\rangle} \left\langle \frac{J_2\left(\frac{\Delta s}{2}\right)}{f(\bar{\bar{p}})} \right\rangle^{-b} \quad \text{with :}$$

$$\bar{p} = \frac{s_{ii}}{3}, \qquad p_M = Max(0, \bar{p}), \qquad \bar{\bar{p}} = (1-\lambda)\bar{p} + \lambda\, p_M - \frac{\lambda}{3} J_2\left(\frac{\Delta s}{2}\right),$$

$$J_2\left(\frac{\Delta s}{2}\right) = \frac{1}{2}\sqrt{\frac{3}{2}(s'_{ijMax} - s'_{ij\min})(s'_{ijMax} - s'_{ij\min})}, \qquad J_{2Max}(s) = Max(0, J_2(s)), \qquad [4]$$

$$J_2(s) = \sqrt{\frac{3}{2} s'_{ij} s'_{ij}}, \qquad f(X) = (1 - 3bX)^{\eta} + b'(s_u^* - 3X)(1-\eta) \quad \textit{where}$$

$$\eta = H\left(\frac{b' s_u^* - 1}{b' - b} - 3X\right) \quad \textit{with } X = \bar{p} \textit{ or } \bar{\bar{p}} \qquad \textit{and} \qquad s_u^* = s_u \exp\left(\frac{3\bar{p} + J_{2Max}\left(\frac{\Delta s}{2}\right)}{J_{2Max}(s)} - 1\right).$$

In equations [3] and [4], during each cycle, $\bar{p}$ and $\bar{\bar{p}}$ are the hydrostatic mean stress and the hydrostatic maximum stress, $J_{2Max}(s)$ the maximal equivalent von Mises stress, s_u the ultimate stress in a uniaxial tensile test and s_{f0} the endurance stress at null mean stress. Note that $s_u^* = s_u$ for uniaxial tests on smooth specimens and for symmetric cyclic tests ($\bar{p} = 0$) on notched samples. For $\bar{p} \neq 0$ on notched samples, $s_u^* \neq s_u$.

The whole experimental database let us identify all the coefficients involved in the relations [4], that is:

- tensile tests without mean stress, $\frac{1}{aM_0^b}$, b, s_u, s_{f0},
- tensile tests with mean stress, b and b',
- torsion tests, λ.

During the correlation analysis (N_R calculated = f (N_R experimental)), the experimental dispersion due to the heat treatment has been taken into account. Its single effect is to modify the experimental value of s_u. This leads to a fairly good correlation (factor 2) although the experimental dispersion on the database is important.

IV – Study of notched axisymmetric samples

Figure 4 shows the Woehler curves of notched samples, which lead to the Haigh's diagram for this geometry, $s_{fE} = f(s_{moyE})$ (Fig.3). For $s_{moyE} = 0$, we obtain something like $s_{f0} / s_{f0E} = 2{,}46 \approx K_t$. However, the uniaxial tensile tests up to the failure give $s_{uE} \approx 1400\, MPa$, which corresponds to the linear extrapolation of the experimental points with mean stress (Fig.3).

According to the different experimental applied loadings and using the rules [2], a lot of monotonic or cyclic F.E. calculations have been performed (integration over some hundreds of cycles). The calculated responses are then compared to the experimental results. The agreement is generally correct as shown in Figure 5 for a monotonic test. A study of the parametric sensibility of the results

shows that the isotropic hardening variable, describing the cyclic softening and responsible for the stress redistribution at the notch root, is the first component driving the progressive strain. This result is in opposition with the test on smooth samples. We note a strong geometric effect due to the quite high value of K_t.

Looking at the stress redistribution, for a symmetric loading, the profile of the von Mises stress $J_{2L}(\sigma)$ along the ligament is clearly continuously decreasing during the cyclic loading to reach the profile obtained for the stabilized cycle. This one can be quickly calculated by integrating on only one cycle the behaviour rules (Fig.1). These rules are directly identified for the number of cycles to failure N_R (Fig.1).
This results can be checked a posteriori in Figure 6 where the Woehler curves have been obtained by post-processing with the relations [4] and using the laws identified with one cycle, at $N_R/2$ and N_R (the elastic solution is also represented). The prevision of the number of cycles to failure is correct considering the rules for the stabilized cycle. Moreover, the good agreement of N_R on the whole curve related to elastic and plastic cycles shows that when $\Sigma_{f0E} < (R_0 + \Sigma_v)/K_t = 249\ MPa$, the cycles are elastic {3}.

Looking at the stress distribution for non symmetric loadings, it can be noted that for $\Sigma_{MaxE} < \Sigma_{moyE} + (R_0 + \Sigma_v)/K_t$ (this limit is drawn Fig.4), the cycles are elastic, $J_{2L}(\Delta\Sigma/2) = K_t(\Delta\Sigma_E/2)$ at the notch root, and the stress redistribution obtained at the end of the first quarter of cycle is stable during cycling. Thus, the prevision of N_R has been obtained by post-processing over one elastic cycle with the law identified at ¼ cycle. The results are correct as shown in Figure 4 (right part of the Woehler's curves).

For $\Sigma_{MaxE} > \Sigma_{moyE} + (R_0 + \Sigma_v)/K_t$, first the mean stress is fully relaxed at the notch root, and then, the amplitude $J_{2L}(\Delta\Sigma/2)$ starts to decrease and then increases again before remaining stable. This last period is related to the local ratchet (left part of the Fig. 4). The amplitude of the decrease can be easily estimated from F.E. calculations leading to the factors of stress intensity K_P as a function of $\Delta\Sigma_E/2$, respectively for the laws at the first cycle K_p^0 and at N_R, K_p^∞. The unknown amplitude $(K_p^0 - K_p^\infty)\Delta\Sigma_E/2$ can thus be obtained. However, the increase of $J_{2L}(\Delta\Sigma/2)$ is more difficult to evaluate. The only way to calculate it, is to use abacus built from F.E. calculations and to give the local ratchet rate at the notch root as a function of $\Delta\Sigma_E/2$ and Σ_{moyE}. Thus, the local stress state should be known, $\Sigma_{moyL} \neq 0$ and $J_{2L}(\Delta\Sigma/2)$ estimated with the previous method and then N_R is deduced from the Woehler's curve on smooth samples at $\Sigma_{moy} = 0$. For small values of N_R ($N_R < 10^3$) the previsions are good because the local ratchet rate is fairly well known. The extrapolation of the calculation is done on less than a decade. For higher values of N_R, ($N_R \neq 10^4$) the accuracy is not so good because of the ratchet rate is not precisely known anymore.

The F.E. method, using the law at ¼ of cycle of the evolution for a monotonic test, with the coefficients $K_m = 3p_{MaxL}/\Sigma_{MaxE}$ and $K_p = J_{2MaxL}(\Sigma)/\Sigma_{MaxE}$ as a function of Σ_{MaxE} (or Σ_{moyE}) let us estimate the local Haigh's diagram (Fig.3). Hence, for a given point of the global diagram of the notched specimens, its ordinate is multiplied by K_t and its abscissa by $K_m(\Sigma_{MaxE})$. The local rupture stress for a monotonic test is given by $\Sigma_u^* = \Sigma_u \exp\left(\frac{3p_{MaxL}}{J_{2MaxL}(\Sigma)} - 1\right) = \Sigma_u \exp\left(\frac{K_m}{K_p} - 1\right)$. Moreover, it could be shown (from the knowledge of $\Sigma_{f0}, \Sigma_{f0E}, \Sigma_u$ *and* Σ_{uE}) that a unique dimensionless Haigh's diagram can be built for smooth and notched specimens {3}. It is thus possible to work with a diagram (smooth) or the other (notched).

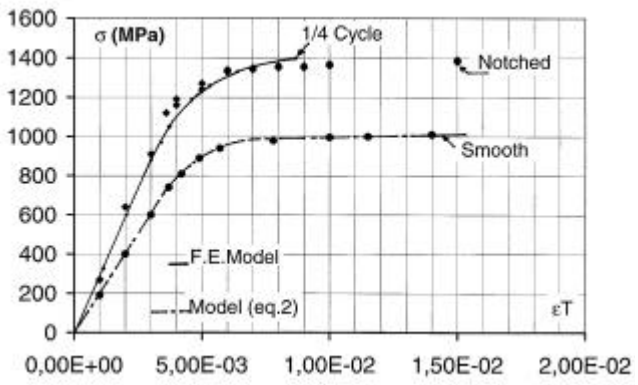

Fig.5 *: Monotonic stress-strain curves for smooth and notched specimen. Experiments and modelling.*

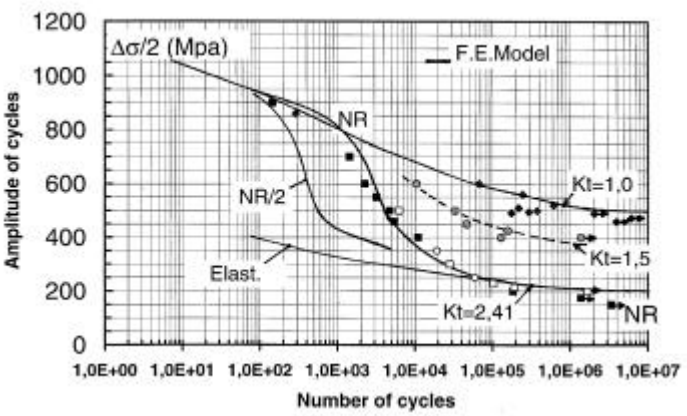

Fig.6 *: Woehler's curves for smooth and notched specimens ($\sigma_{moy} = 0$). Experiments and F.E. calculations.*

V – Conclusion

For the studied steel, the stress redistribution at the notch root has been shown to be mainly managed by the isotropic hardening variable describing the cyclic softening. Thus, a simple method is proposed, knowing the parameters K_t, K_p, K_m (F.E. calculations) and $\sigma_{f0}, \sigma_{f0E}, \sigma_u$ *and* σ_{uE} (experimental data), to deduce from the global diagram (smooth or notched specimen) the local Haigh's diagram at the notched root. In this case, the cycles are elastic.

When the cycles are plastic with $\sigma_{moyE} = 0$, the integration of the behaviour rules for the stabilized cycle following by the post-processing calculations of the failure rules allow us toestimate N_R. However, if $\sigma_{moyE} \neq 0$, the local mean stress is fully relaxed, the amplitude of the cycle starts to decrease and then increases because of the local ratchet strain. In this case, it is more difficult to estimate precisely N_R if the local ratchet rate is not precisely known.

Acknowledgments :

This study has been supported by the society FORMER-DELLE-90101.France.Cedex

References:

{1} - CHABOCHE J.L. Rev. Fr. Mec., n°9, 1974, 50.

{2} - CHAUDONNERET M. , J. Eng. Mat. Techn., Vol 115, 1993, 373-379

{3} - DUVAL A., ROBINET P., TRIVAUDEY F., DELOBELLE P., Rapport 7, contrat FORMER/LMARC, 1999

” Fatigue Reliability Evaluation and Fracture Analysis at Elevated Temperature related to Safety Guarantee of Industrial Use Pt Alloy”

Soichi HITOMI*, Hideto SUZUKI, Masashi NAKAMURA****

* Tanaka Kikinzoku Kogyo K.K. Isehara Works , 26, suzukawa ,
Isehara-city, Kanagawa, 259-1146 JAPAN
** Department of Engineering, Faculty of Engineering, Ibaraki University ,
4-12-1, Nakanarusawa, Hitachi-City, Ibaraki, 316-8511 JAPAN

ABSTRACT

Platinum and its alloys are widely used in the glass-melting industry because of their high melting point, high resistance to oxidation and inertness with molten glass. Since they are usually used above 1273K, it is important to improve their mechanical properties at high temperatures above 1273K. Alloying with rhodium is known as a conventional method to increase the strength of platinum. For the further improvement of high temperature properties, it is essentially important to clarify the basic mechanical properties of platinum and its alloys at elevated temperatures.

In this study, fatigue reliability at elevated temperature of platinum and its alloys were examined by the elucidation of fracture mechanism. Main results were follows ; (1)S-N characteristics of PtRh alloys were almost arranged in the straight line. (2) From the fractography using SEM, it was indicated that fatigue fracture mechanism was similar to the static destruction in the high stress side, on the other hand, that was effected by creep in the low stress side.

KEYWORDS

Fatigue fracture, Fractography, Platinum, High temperature, Creep

INTRODUCTION

Platinum is one of the precious metals which are representative as well as the gold. Platinum is used as not only decorative material but also industrial material. Platinum and its alloys are widely used in the glass melting industry because of their high melting point, high resistance to oxidation and inertness with molten glass. Therefore, platinum and its alloys are indispensable to the manufacturing of the high-grade glass.

Equipments used for glass melting generally be broken by creep rupture mechanism because it usually last for long time under high temperatures. Especially, the thermal fatigue by rapid temperature change occurs at temperatures higher than 1273K when raw materials are fed into the glass-melting crucible. However, the report on high temperature creep property and fatigue characteristics of platinum and its alloys are little still. Therefore, it is very important to grasp fracture characteristics of platinum and its alloys.

In this study, high temperature fatigue reliability of platinum alloy was demonstratively examined including the elucidation of fracture mechanism.

EXPERIMENTAL PROCEDURE

The materials used for the test are industrial grade purity platinum, industrial use Pt-10wt%Rh alloy and ZrO_2 dispersion strengthened platinum.

Industrial grade purity platinum and industrial use Pt-10wt%Rh alloy ingots were hot forged at 1473K. After they were forged, they were cold rolled to 10mm thickness and annealed at 1373K for half an hours. Then they cold rolled to 1mm thickness.

ZrO_2 dispersion strengthened platinum ingot was hot forged at 1473K. After it was forged, they were cold rolled to 10mm thickness and annealed at 1673K for an hour. Then they cold rolled to 1mm thickness.

Specimens were punched from the sheets. Their dimensions were 2.5mm wide and 20mm long. The surface was polished with alumina powder, and it was finished in the specularity.

The fatigue test was carried out in 20Hz frequency, sine wave of R=0.1 stress ratio, in the vacuum at room temperature and 1073K under the load control.

RESULTS AND CONSIDERATION

S-N chart

Relationship between rupture number of cycles (Nf) and stress amplitude (S) of the PtRh alloy explained above was measured in the vacuum at 293K and 1073K. The results are summarized in Figure-1. S-N characteristics of the PtRh alloy was regressed as the straight line. Fatigue strength of the specimen defined as stress amplitude at 10^7 cycles was 100MPa at 293K and 30MPa at 1073K.

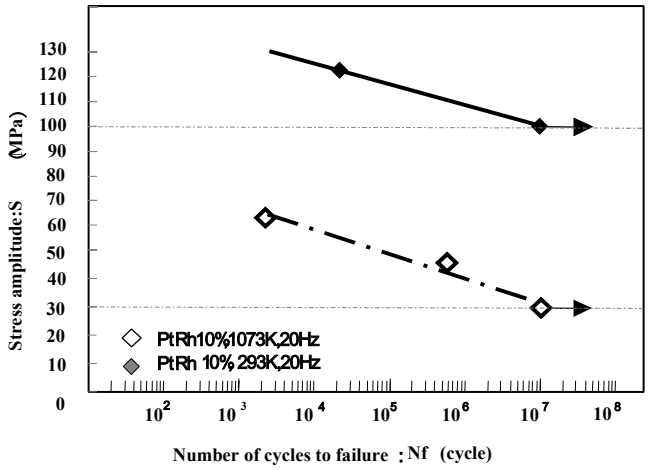

Fig.1 S-N curve of PtRh material

SEM observation and analysis of the specimen done fatigue breakdown at 1073K

Fracture surface analysis was carried out for the specimens after they broke in order to clarify high temperature fatigue characteristics of the PtRh alloy.

Fracture surface photograph in short life (S=60MPa, 1073K) is shown in figure 2. Figure 2(a) is low magnification, and (b) is a fracture surface of high magnification. From figure 2(a), there was sliding necking in the fracture surface, and it was proven to be the typical ductile fracture.

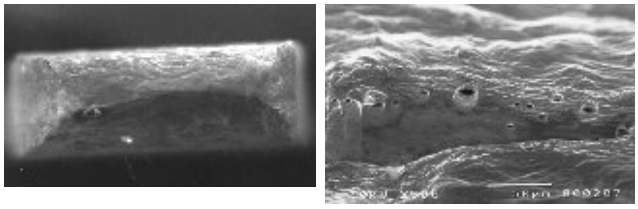

(a)Low magnification (b)High magnification

Fig.2 SEM photograph of fracture surface (S=60MPa)

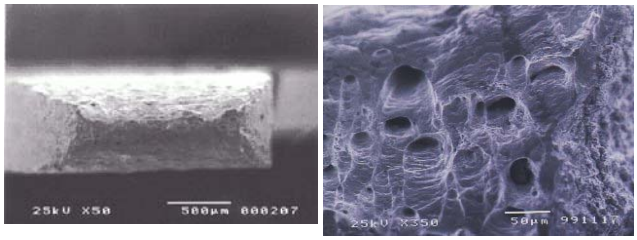

(a)Low magnification (b)High magnification

Fig.3 SEM photograph of fracture surface (S=45MPa)

Fracture surface photograph in long life (S=45MPa, 1073K) is shown in figure 3. Figure 3(a) is at low magnification, and (b) is a fracture surface of high magnification. From figure 3(a), there was sliding necking in the fracture surface, and it is considered to be ductile fracture. Different from the fracture surface of short life sample shown in figure 2(b), a lot of dimples were observed on entire fracture surface of long life sample as shown in figure 3(b).

It is assumed through the phenomena that creep deeply affected dimple generation and they were made under conditions of dynamic fatigue breakdown. There is a transition of the failure mechanism that effect of creep increases with decrease of stress. In other words, in the high stress

condition, it is similar to the static destruction, and it is indicated that the effect of the creep is big in the low stress condition. There was a difference of failure mechanism in high stress (short life) and low stress (long life).

The elucidation of the failure mechanism by the surface observation

Figure 4(a) and (b) show SEM photographs of the specimen surface which utilized in high stress (S=60MPa, 1073K) fatigue test. Figure 4(a) is at low magnification, and (b) is the specimen surface of high magnification. Slip lines were observed in the grains located up to around 800 microns from the rupture edge. Thickness of the specimen begun to decrease from the 800-micron point toward the rupture edge, namely necking occurred. In order for comparison with this, surface of sample ruptured at S=45MPa is shown in Figure 5. Figure 5 indicated that the thickness of the sample begun to decreased at around 300 micron away from the rupture edge. This result is different from the result of conducting at s=60MPa fatigue test. The effect of sliding in the grain differs in high stress (short life) and low stress (long life).
Rupture surface photograph of the high magnification is shown in figure 5(b). Opening of grain boundary that can be starting point of fracture was observed The high magnification rupture surface photograph at 30MPa is shown in figure 6. There was a grain boundary cracking, too. According to the result of rupture surface observation and fracture surface observation, the grain boundary fracture was generated by the effect of the creep in the lower stress side.

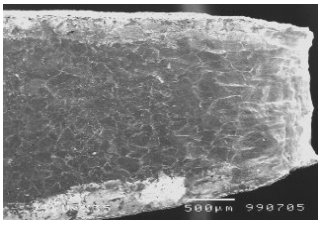

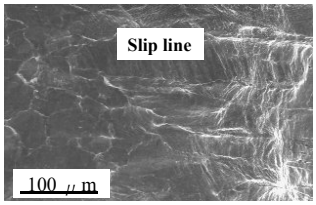

(a)Low magnification (b)High magnification

Fig.4 SEM photograph of the specimen surface (S=60MPa)

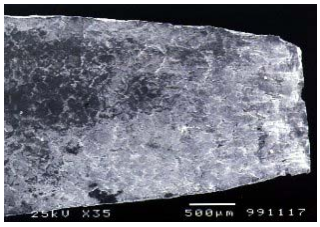

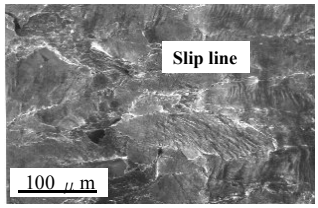

(a)Low magnification (b)High magnification

Fig.5 SEM photograph of the test piece surface (S=45MPa)

Fig.6 SEM photograph of the specimen surface (S=30MPa)

SEM observation and analysis of the specimen done fatigue breakdown at 293K

Specimen surface photographs in short life (S=120MPa) are shown in figure 7(a), (b), and fracture surface photographs are in figure 8(a),(b). As seen in figure 7(a) and (b), there was sliding necking. There was sliding in the grain on the fracture surface shown in figure 8(b). Therefore, this seems to be also the ductile fracture.

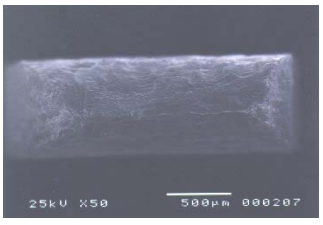

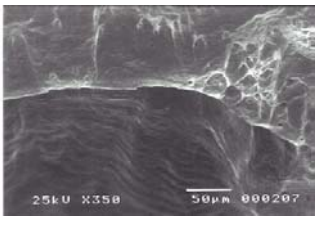

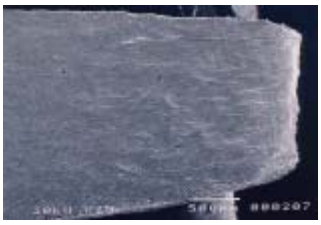

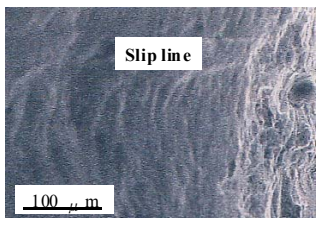

(a)Low magnification (b) High magnification (a)Low magnification (b) High magnification

Fig.7 SEM photograph of specimen surface (S=120MPa) Fig.8 SEM photograph of fracture surface (S=120MPa)

CONCLUSIONS

Fatigue test on the Pt-10wt%Rh alloy at 293K and 1073K were performed. Fatigue strength of Pt-10wt%Rh were 100MPa at 293K, and 30MPa at 1073K. It had broken in ductile fracture at both temperature range, and it was proven that the sliding in the grain was dominant for the deformation of the PtRh alloy. In low stress, high temperature side, there would be the effect of the creep, and there were crack and opening in the grain boundary.

Fatigue breakdown behavior of pure-Pt and ODS-Pt is under investigated.

REFERENCES

(1) K. Kikuchi, Y. Kaji, Y. Muto, S. Kitade, Trans.JSME, 59-557, A (1993-1), pp94-99
(2) R. Ohtani, T.Kitamura, M.Tsutsumi, H. Miki, Trans.JSME, 59-560, A (1993-4), pp933-938
(3) T.Kitamura, R. Ohtani, W. Zhou, M. Yamada, N. Iizuka, Trans.JSME, 59-566 A (1993-10), pp2234-2240
(4) H.Suzuki, S. Numata, K. Katahira, Trans.JSME, 63-616 A (1997-12), pp2679-2685
(5) H.Suzuki, S. Numata, S. Nishino, Trans.JSME, 63-610 A (1997-6) ,pp.1141-1146
(6) S. Numata, K. Katahira, H.Suzuki, Trans.JSME, 64-619, A (1998-3) pp.597-602
(7) T. Hamada, thesis, Osaka Univ. (1998)
(8) T. Hamada, S. Hitomi, T. Nishimori and S.Nasu, THERMEC'97 International Conference on Thermomechanical Processing of Steels and Other Materials, (1997), pp.1647-1653

PAPER REFERENCE: *ICF10010130R*

FATIGUE STRENGTH AND FRACTURE MECHANISM OF SILICON NITRIDES STUDIED BY AE WAVEFORM SIMULATION

A. Yonezu, T. Ogawa and M. Takemoto

Department of Mechanical Engineering, Aoyama Gakuin University,
6-16-1 Chitosedai, Setagaya, Tokyo 157-8572, Japan

ABSTRACT

In order to evaluate statistical characteristics of static and cyclic fatigue strength of a toughened silicon nitride, both the quasi-static loading test and ΔP-increasing-type cyclic loading test were conducted with simultaneous acoustic emission (AE) monitoring. Waveform matching of the zero-th order symmetric mode Lamb AE waves were attempted to study the fracture dynamics. Crack volumes estimated by the AE waveform simulation was compared with those computed by three dimensional FEM. Fracture mechanisms of toughened silicon nitride under static and cyclic fatigue were discussed in detail.

KEYWORDS

Silicon nitride, Static fatigue, Cyclic fatigue, Weibull distribution, Fatigue damage, Acoustic emission, Waveform matching, Fracture Mechanism

INTRODUCTION

It has been well recognized that sintered silicon nitrides, Si_3N_4, exhibit both static and cyclic fatigue behaviour [1]. Since the fatigue strength generally shows a large scatter, it should be evaluated by a statistical expression of *S-N* curve, namely *P-S-N* curve. However, the statistical evaluation requires a time-consuming and expensive work. One of the authors proposed a simple method to evaluate the fatigue strength statically under a mechanical condition where driving force for fracture is gradually increased [2]. This technique enabled us to study the statistic characteristics of fatigue strength and contribution of fatigue damage with respect to the testing conditions.

Mechanism of the fatigue damage of toughened silicon nitride is be caused by initiation and growth of small cracks [3]. However, the conventional optical observation is extremely difficult because crack initiation site is hardly predicted. Source location method of AE signals enables the estimation of crack initiation position. Further, the inverse processing or waveform simulation can study the fracture dynamics such as crack nucleation time, ΔT_r, and crack volume, ΔV [4], and supply us with information of damage mechanism. In the present study, both static and cyclic fatigue strength of toughened Si_3N_4 was studied utilizing new-type loading procedure and AE waveform simulation to monitor the behaviour of small cracks in the ceramic.

MATERIAL AND EXPERIMENTAL PROCEDURES

The material tested is a hot-isostatically sintered silicon nitride, Si_3N_4, developed by NGK Spark Plug Co. The density is measured as 3310 kg/m^3. Fracture toughness (SEPB) and four point bending strength are 9.8 $\mathrm{MPa}\sqrt{\mathrm{m}}$ and 729 MPa, respectively. Rectangular bar specimen (3x4x40 mm) was subjected to four point bending with inner span of 10 mm and outer spans of 30 mm, at room temperature in air using hydraulic testing machine with load capacity of 10 kN.

Figure 1(a) illustrates loading history of ΔP-increasing-type cyclic test. Stress ratio, R, of the cyclic loading is controlled as 0.1 and the cyclic loading frequency, f, is 20 Hz. Testing parameters of the ΔP-increasing test are the initial value, $\sigma_{max,i}$, of maximum stress, σ_{max}, and increasing rate of σ_{max}, $d\sigma_{max}/dN$(=2.8x10^{-4} MPa/cycle). Provided that the value of $\sigma_{max,i}$ is sufficiently lower than σ_{max} at failure, $\sigma_{max,f}$, all the specimens tested are broken by cyclic loading, and the $\sigma_{max,f}$ value is evaluated for the individual specimens, as schematically illustrated in Fig. 2, where the effect of $\sigma_{max,i}$ is investigated. When the $\sigma_{max,f}$ values are analysed by Weibull distribution, fatigue strength can be evaluated statistically. Similarly, static fatigue strength can be evaluated by P-increasing test as illustrated in Fig. 1(b).

Figure 3 shows AE monitoring system used. Two resonant-type AE sensors (Ch.1 and 2, PAC, PICO, center frequency of 0.58MHz) with a diameter of 4mm are mounted on the upper surface of the specimen opposite to the outer pins. Sensor outputs are amplified by a 40dB preamplifier and digitised by an A/D converter at a sampling interval of 50 ns with 1024 points at 10 bits. As the sensors monitor continuous noise with low frequency due to cyclic contacts of the specimen to two pins, trigger signal for AE events is prepared by using a new circuit. It has two functions of adding two sensor's output and of filtering out the lower frequency components (-20 dB at 100kHz and -2 dB at 1 MHz).

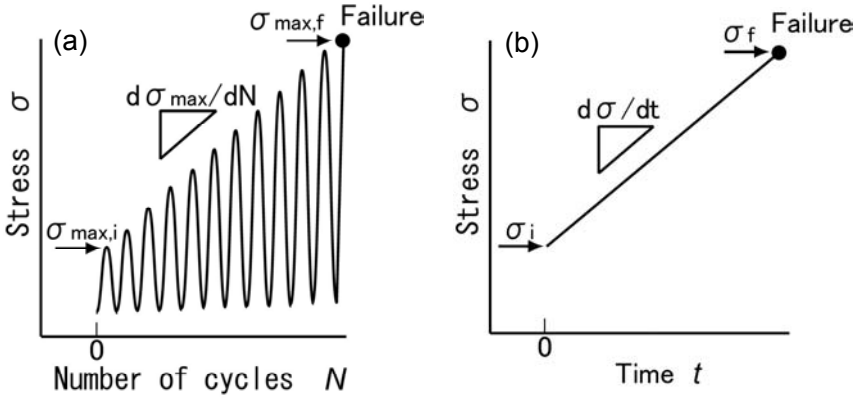

Figure1: Loading sequences of the (a)ΔP-increasing test (cyclic fatigue) and (b)P-increasing test (static fatigue).

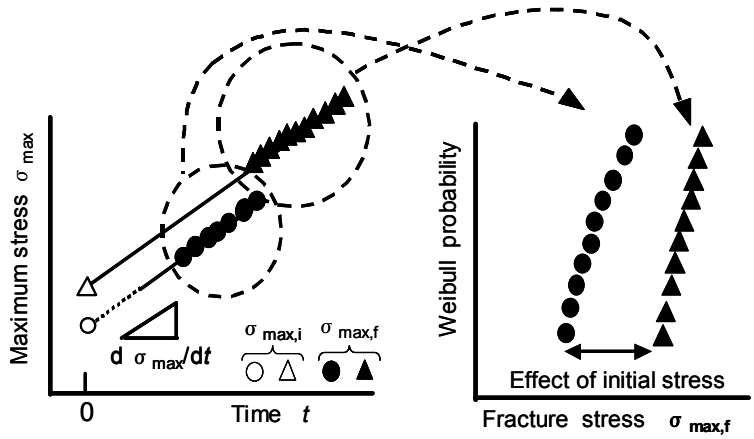

Figure.2: Schematic illustration of the ΔP-increasing tests and statistical analysis evaluating the effect of $\sigma_{max,i}$ on $\sigma_{max,f}$.

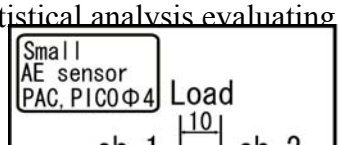

RESULTS AND DISCUSSION

Figure 4 presents the Weibull plots of σ_f and $\sigma_{max,f}$ for quasi-static and cyclic loading conditions, respectively. Also presented is a flexural strength measured under monotonic loading condition at the crosshead speed of 0.5 mm/min [5]. Despite the loading rate is 10^4 times lower, the σ_f values well agree with the flexural strength. This strongly suggests that there is no dependence of time, namely no static fatigue strength degradation. However, cyclic fatigue degradation clearly appeared in this material. ΔP-increasing tests with different $\sigma_{max,i}$ enabled us to evaluate the cyclic loading condition under which fatigue damage nucleated. The result suggested that $\sigma_{max,i}$ influenced the $\sigma_{max,f}$ values for statistically weak specimens and thus fatigue damage developed at lower stress levels.

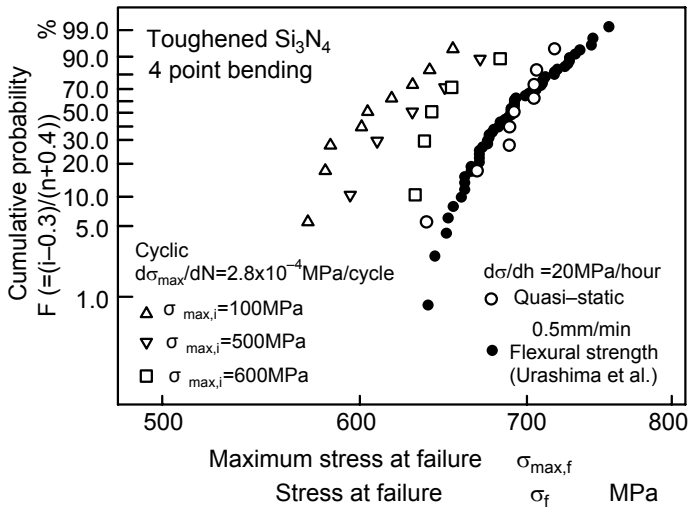

Figure 4: Weibull plots of σ_f and $\sigma_{max,f}$ in toughened Si_3N_4.

Detail signal analysis demonstrated that the AE events detected contain both symmetric (S_0) and anti-symmetric (A_0) mode Lamb wave of zero-th order. First arrival time and waveform of the S_0-Lamb mode were utilized for source location and fracture dynamics study. Source location results are shown in Fig. 5 for quasi-static (a) and cyclic (b) loadings. The location was estimated by using arrival time difference of So-mode and its group velocity for the specimens with average strength for these loading conditions. The abscissa is an axial location of specimens, where the origin is a left edge of specimen. Inner span and final fracture location are indicated by broken lines and solid line, respectively. The vertical axis represents stress values at fracture. The results revealed that a few AE signals were detected at stresses just below the final fracture value near the fracture locations.

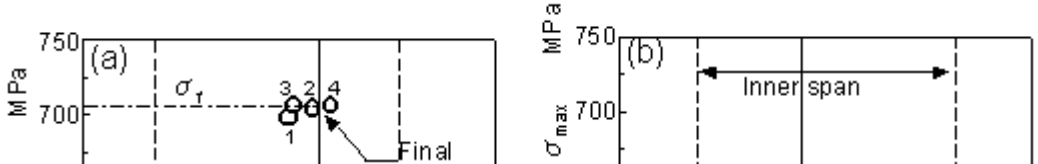

The fracture dynamics were studied by the S_0-packet waveform matching. Detail of this method can be found elsewhere [6]. The overall transfer function, including the sensor, medium and AE monitoring system, was determined by the method shown in Fig. 6. Lamb-wave AE signals were exited by a compression-mode PZT element, glued to a specimen and stainless steel block by epoxy, and were monitored by PICO sensor. Here, the out-of-plane displacement of PZT element was monitored by a laser interferometer and converted to time transient of crack volume. The overall transfer function for the Lamb-wave due to Mode-I crack opening was obtained by the time-domain Gauss-Zeidel deconvolution of the detected waves by the PICO sensor. Crack opening was represented by a sinusoidal rump function with rise time, ΔT_r, and crack volume, ΔV. They were determined by matching the simulated waveform of the S_0-packet to the detected one.

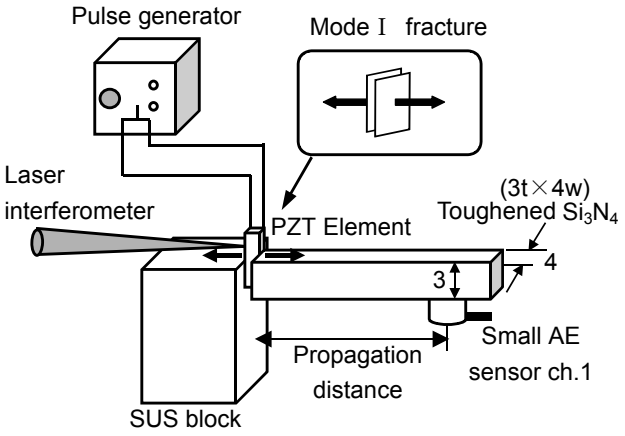

Figure 6: Experimental setup to determine the overall transfer function.

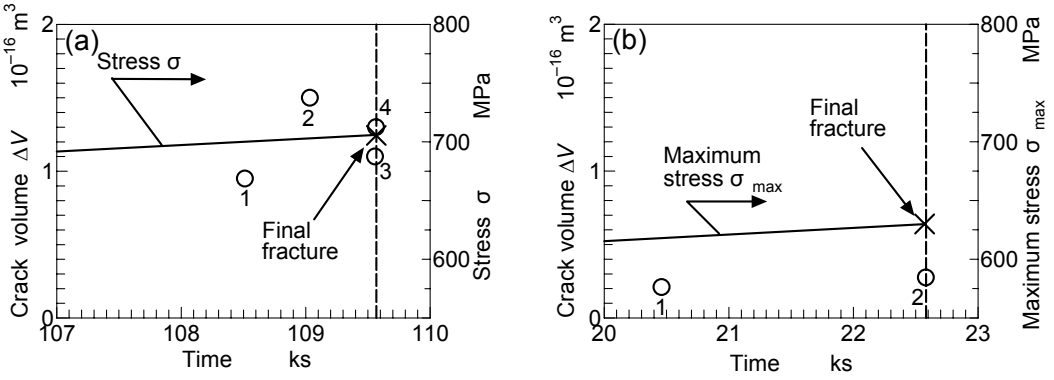

Figure 7: AE source volumes as a function of applied stresses for the quasi-static(a) and the cyclic(b) loading.

Figure 7 shows ΔV estimated for quasi-static (a) and cyclic (b) loadings with stress values as a function of testing time. The numbers in the figure indicate event count. The crack volume produced during the cyclic loading was estimated to be six times smaller than that produced during static loading at lower stress level.

Source rise time, ΔT_r, was estimated as 0.11 μs, which was the lower limit of our AE system. First AE signals for both loading conditions were monitored at more than 1 ks before the final fracture. These results suggest that cyclic loading enhances nucleation of small cracks.

The initial crack was observed at large-grown columnar β-Si_3N_4 under both loadings, as shown in Fig. 8. Sizes of the β-Si_3N_4 were about 90μm long and 20μm wide. Similar microstructure was observed on fracture surfaces of all the specimens tested. Next computed the crack opening displacement by three-dimensional finite element method (FEM) using MARC (K7-2). The model is illustrated in Fig. 9. Crack initiation location shown in Fig.8 (a) and (b) are modelled as in Fig. 9 (b) and (c), respectively. Total numbers of elements are 7168 (b) and 5488 (c). Displacements of axial direction on the tensile surface were constrained except the rectangular area surrounded by broken line. Axial displacements of the rectangular area are referred to a half of crack opening displacement and are used to determine the crack volume, ΔV, under the fracture load. The values of ΔV under quasi-static (b) and cyclic (c) loadings were calculated as 1.18×10^{-16} and 2.95×10^{-16} m^3, respectively. For the quasi-static loading, the crack volumes estimated by the AE waveform matching well agreed with that produced at columnar β-Si_3N_4, while those for the cyclic loading were ten times smaller than ΔV estimated by FEM. The cyclic loading appears to produce discontinuous small cracks along the columnar β-Si_3N_4.

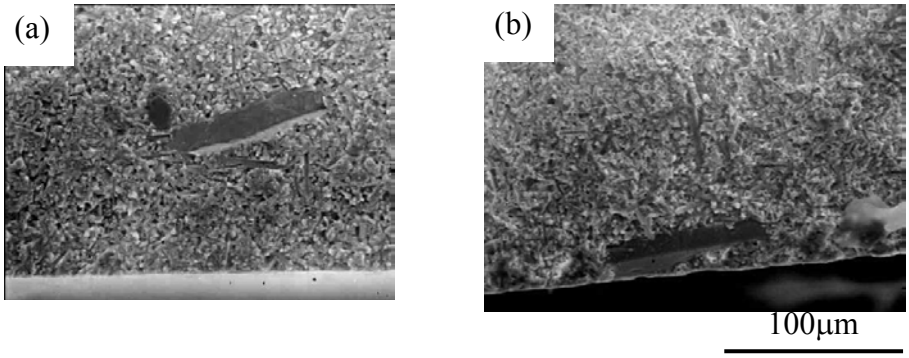

Figure 8: SEM photographs of fracture surfaces under the quasi-static loading(a) and the cyclic loading(b). AE analysis shown in Figure 7 and 11 was performed for these specimens.

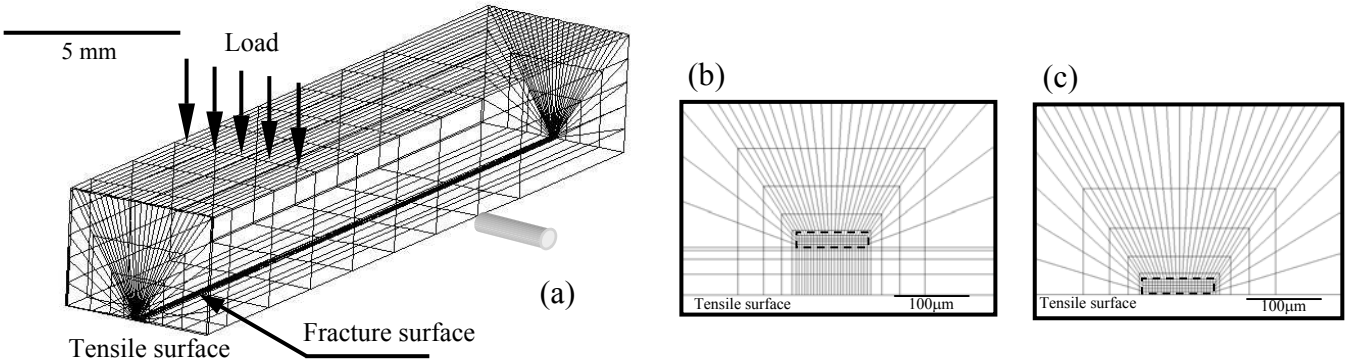

Figure 9: Three-dimensional finite element model (a) and initial cracks modeled for the quasi-static(b) and the cyclic(c) loadings.

Fatigue mechanism of the toughened Si_3N_4 is summarized as follows. Under the quasi- static loading, cracks with the size of large-grown columnar β-Si_3N_4 were initiated very quickly at the load level just below the fracture stress. Under the cyclic loading, crack initiation occurred under lower stress level with smaller initial size than under quasi-static loading. The small crack grew and led fast fracture. Cyclic fatigue damage can be regarded as the above small crack initiation, which developed under more than 100 MPa below the fracture stress level for statistically weak specimens. Early stage of the fatigue damage could not be detected by our AE monitoring system.

CONCLUSIONS

Both static and cyclic fatigue strength of toughened Si_3N_4 was investigated using new loading method and

AE waveform matching method. Results are summarized below:

1. No static fatigue strength degradation was found for this ceramic, while cyclic fatigue degradation appeared.
2. ΔP-increasing tests with different initial value of maximum stress, $\sigma_{max,i}$, enabled us to evaluate the cyclic loading condition under which fatigue damage nucleated. The result suggested that $\sigma_{max,i}$ influenced the maximum stress at failure, $\sigma_{max,f}$, for statistically weak specimens and thus fatigue damage developed at lower stress levels.
3. Crack volume produced during the cyclic loading was estimated by Lamb AE waveform matching method and found to be six times smaller than that produced during static loading.
4. Initial crack was observed at large-grown columnar β-Si_3N_4 under both loadings. For the quasi-static loading, the crack volumes estimated by the AE waveform matching method well agreed with that produced at columnar β-Si_3N_4, while those for the cyclic loading were ten times smaller than ΔV estimated by FEM.
5. Fatigue mechanism of the toughened Si_3N_4 is discussed based on the strength distribution and AE results.

ACKNOWLEDGEMENTS

Authors are grateful to Dr. Urashima, NGK Spark Plug Company, for supplying the toughened silicon nitride specimens.

REFERENCES

1. T. Yamada, T. Hoshide and H. Furuya, J. Soc. Mat. Sci., Japan, 33(364), 28-33(1983) [in Japanese].
2. T. Ogawa, Proc. The 13th European Conference on Fracture, Elsevier Science CD, 186C1.PDF, p.8 (2000).
3. O. Ritchie and H. Dauskardt, J. Ceramics Society Japan 99(10), 1047-1062(1991).
4. M. Takemoto, O. Tamura and H. Suzuki, Progress in Acoustic Emission IX, Ⅲ, 81-88(1998).
5. K. Urashima, Y. Tajima, M. Enoki and T. Kishi, Proc.11th Forum on Basic Science of High Temperature Ceramics, 66-70(1992).
6. T. Sato, M. Takemoto and K. Ono, Jpn Appl. Phys., 39, 3193-3200(1999).

Oral reference: ICF 100135OR

Fatigue-Creep Interactions in Solder Alloys.

J E Moffatt and W J Plumbridge.

Department of Materials Engineering, The Open University
Milton Keynes, MK7 6AA, UK

Abstract
Isothermal, low cycle, fatigue testing is a popular method of evaluating behaviour under thermomechanical fatigue conditions in many applications, such as power generation and, more recently, performance of interconnections in electronic equipment. In this latter context, strain-controlled fatigue tests, involving dwells at maximum strain limits, have been performed on bulk specimens of a eutectic lead-tin solder alloy and two lead-free solders (Sn-3.5 weight percent Ag and Sn-0.5 Cu) at room temperature and 75˚C. During continuous cycling, softening occurs at each temperature. The fatigue endurance is reduced by up to one third at the higher temperature in all alloys, with Pb-Sn showing the greatest reduction. The incorporation of a dwell of 10 or 100s into the cycle generally causes a reduction in fatigue life in comparison to that observed during continuous cycling, although for the Sn-0.5 Cu alloy, a 10s hold produces an increase in life at room temperature. Cycles containing balanced dwells at maximum and minimum strain limits are the most deleterious when lifetime debits of up to fivefold are observed at both temperatures. Generally, unbalanced compression-only cycle profiles tend to be the least damaging. The stress relaxation characteristics are similar in all dwells and at both temperatures, with the eutectic Pb-Sn exhibiting 80 percent relaxation and the lead-free solders up to 50 percent after 100s dwell. Metallographic observation of sectioned specimens reveals surface and intergranular cracking which is accentuated at higher-strain ranges and temperature but not dramatically affected by the cycle shape. These findings are considered in terms of the behaviour of other engineering alloys, and their significance for life prediction is discussed.

Keywords: solders, life prediction, electronics, lead-free alloys.

1 Introduction

The most common cause of failure in electronics equipment is thermomechanical fatigue (TMF) of soldered interconnections. This arises due to temperature fluctuations, either from power switching or from the external environment, and to the fact that the materials which constitute the joint (solder, substrate, board) have substantially different coefficients of thermal expansion, α. For example, α for common solder (Sn-37Pb) is 22×10^{-6} K^{-1} and for alumina (a common substrate) it is 6.5×10^{-6} K^{-1}. Cycling between temperature limits leads eventually to crack initiation, growth and failure, usually within the solder itself since this is the softest element of the joint. In practice, temperature excursions usually occur at different rates, and the overall cycle often contains a dwell during which the temperature is essentially constant. Continuous cycling data is of limited use for life prediction. Controlled thermomechanical fatigue testing is complex and expensive to perform, and the more common approach is to evaluate relevant mechanical properties isothermally.

Continued miniaturisation of devices has placed greater pressure on structural integrity, especially for surface mount configurations. Reliable design requires more sophisticated approaches, and this challenge is compounded by the emergence of a new generation of solder alloys that, for environmental reasons, do not contain lead. The present paper examines the performance of Sn-37 Pb solder and two lead-free alloys during high strain cycling with and without dwell periods.

2 Experimental Details

The materials used were commercial grade eutectic 63Sn-37Pb alloy, supplied in the form of rectangular ingots; the tin-3.5 silver and tin-0.5 copper were supplied as rods or bars. The alloys were heated to match the optimum reflow profile, to about 40˚C above their melting point, and cast into cylindrical aluminium moulds, preheated to the same temperature. The moulds were then rapidly quenched in water. The resultant surface finish on the specimen obtained after casting required no further treatment. Specimens were stored at -18˚C in order to minimise natural ageing. Prior to testing they were warmed to ambient for 2 hours. Their final dimensions were; gauge diameter of 11.28mm (cross sectional area 100mm^2) and a gauge length of 25mm.
Fatigue and fatigue plus dwell tests were carried out using an Instron 1342 servo hydraulic testing machine under total strain control. Dwell cycles were timed and controlled using a computer generated wave form. The test machine was fitted with an environmental chamber operating at 75˚C. Strain was measured using a contacting extensometer attached to the gauge length with coil springs. Tests were performed at a constant strain rate of $3.33 \times 10^{-3} s^{-1}$. The cyclic frequency therefore varied for each test depending on the strain amplitude. A triangular waveform was used with a strain ratio, R, of -1 (where R = ε_{min}: ε_{max}). The strain ranges employed in continuous cycling varied between 0.5 and 3.0 percent, and during cycling with dwells the strain range was 1.0 percent. Load and total displacement were continuously recorded. A tensile load reduction of 20 percent with respect to the first cycle was employed as the criterion of failure and then tests were terminated.
After testing, specimens were examined using both optical and scanning electron microscopy. Samples from the gauge length of the test pieces were sectioned longitudinally using electrical discharge machining to minimise surface damage, and subsequently polished to a 1μm surface finish.

3 Results

3.1 Cyclic Response

All hysteresis loops show a progressive drop in the load range necessary to maintain the constant strain limits, indicating cyclic softening. Saturation of the load range occurs at strain ranges of 1 percent and above, whereas, below this level, the plastic strain range continues to increase and saturation is not reached. A cyclic stress-strain curve, derived from the stress range during the first cycle and the total strain range may be described by the relationship,

$$\Delta\sigma = A\Delta\varepsilon^{\beta}$$

The values for the constants A and ß are presented in Table 1.

TABLE 1
VALUES OF CONSTANTS IN THE CYCLIC STRESS-STRAIN EQUATION

	Pb/Sn		Sn/Ag		Sn/Cu	
	RT	75	RT	75	RT	75
A	129	64	88.9	56	55.5	43.08
ß	25.2	22.1	30.85	20.3	4.5	8.7

A convenient means of depicting strength changes during high strain cycling is via the load drop parameter, Ø, (which is defined as Ø = 1 – (ΔP/ΔPm) where ΔP is the load range at any cycle and ΔPm is the load range during the first cycle). The variation in the load drop as a function of the fraction of fatigue life is shown in figure 1 for a strain range of 1 percent, with a dwell of 10 seconds incorporated at maximum tensile strain, at room temperature and 75˚C. The load falls (indicated by an increase in

load drop parameter) continuously from the first cycle, and the rate of cyclic softening with respect to total cyclic life is broadly similar in all three materials, at both temperatures and for all cycle profiles examined.

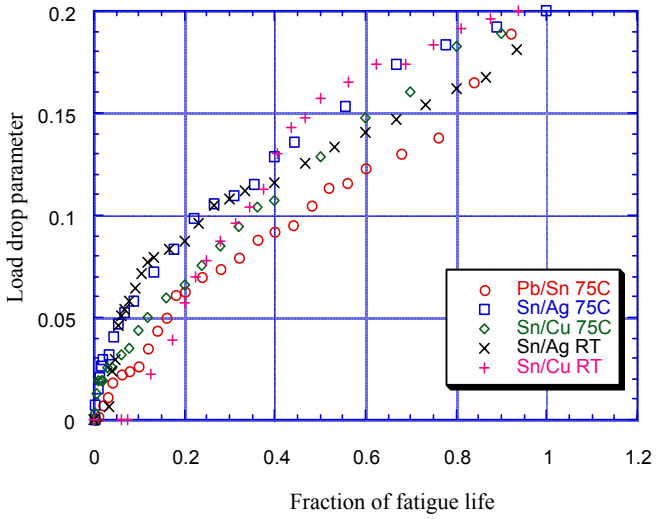

Figure 1. Load drop parameter v fraction of fatigue life during cycling with dwells of 10s at room temperature and 75ūC.

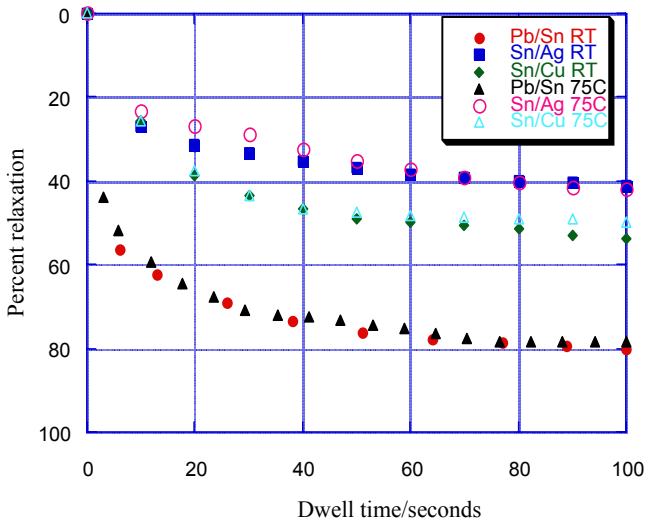

Figure 2. Stress relaxation during tensile dwell periods room temperature and 75ūC.

3.2 Stress Relaxation During Dwells

Stress relaxation ranges during dwells is substantial, ranging from 80 percent in Sn-37Pb to 40 percent in Sn-3.5Ag after 100s. It is independent of the temperature and cycle type. Figure 2 shows stress relaxation at room temperature and 75˚C during a tensile dwell cycle (designated t/0) of 100s. During other cycle profiles (compression-only, 0/t, and balanced dwells, t/t) the extent of stress relaxation varies by no more than 8 percent for any of the profiles, and at either temperature. The amount of stress relaxation is also independent of the cycle number. The equation

$$\sigma = A\, t^{m}$$

provides a good description of the relaxation process. The values of A and m are presented in Table 2.

TABLE 2
VALUES OF CONSTANTS IN THE STRESS RELAXATION EXPRESSION

	A	m
Pb/Sn	26.8	27.9
Sn/Ag	9.1	15.6
Sn/Cu	12.3	20.7

3.3 Fatigue Endurance - continuous cycling

In general, during continuous cycling the fatigue life at room temperature exceeds that at 75˚C, although the effect of temperature is not substantial. Figure 3 shows Coffin-Manson plots for the three alloys at both temperatures during continuous cycling. In all alloys at strain ranges equal to or below 1percent, continuous cycling at 75˚C exhibits up to 50 percent fatigue life reduction when compared to room temperature. At higher strain ranges the lives are reduced and the difference is less marked.

3.4 Cycles with dwells

Dwells produce a reduction in fatigue life when compared to the continuous cycling case. Figure 4 shows the load drop as a function of number of cycles for a dwell of 100s at the maximum tensile strain. Cycles containing balanced dwells are the most deleterious. Table 3 shows the number of cycles to

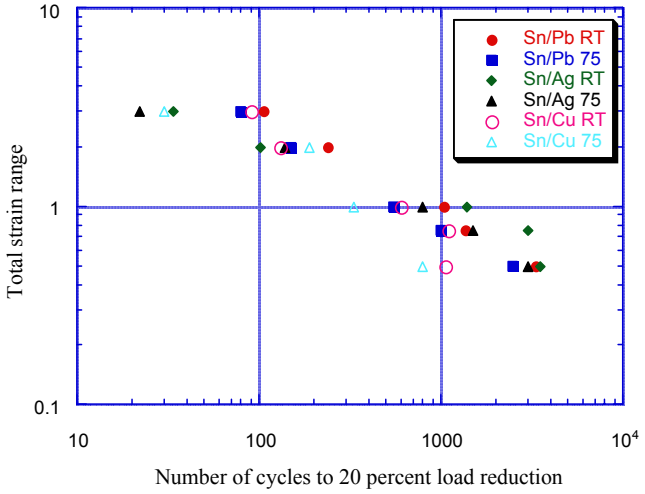

Figure 3. Cofin-Manson plot of total strain v number of cycles to 20 percent load reduction.

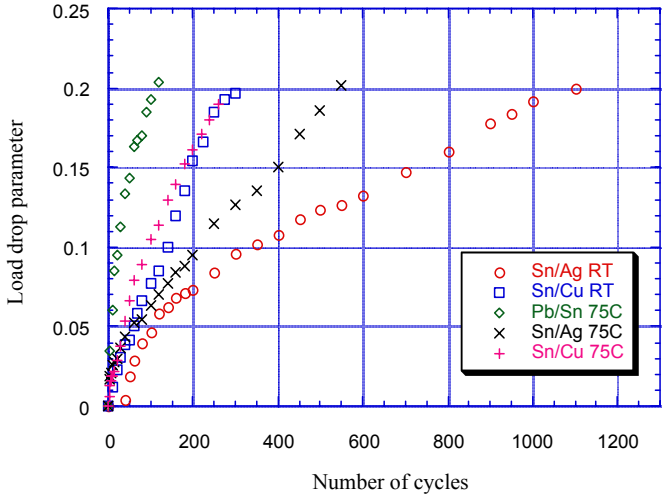

Figure 4. Load drop parameter v number of cycles with a 100s tensile dwell, 1 percent strain range.

failure for continuous cycling and for cycles containing dwell periods at 1percent strain range. These results follow a similar trend although at the lower temperature a dwell during the tensile cycle is the most damaging. The sensitivity to dwells, as defined by the Influence Ratio, which is the ratio of fatigue lives with and without dwells, is shown in figure 5. The Sn-0.5 Cu alloy is more resistant to short (10s) hold periods in the cycle but this superiority disappears when the dwell is extended to 100s. Apart from the short dwells for the Sn-0.5Cu, all other cycle profiles produced a deleterious effect on life.

TABLE 3
EFFECT OF DWELLS ON FATIGUE LIFE AT 75˚C AND ROOM TEMPERATURE (IN ITALICS) DURING DWELLS OF 10 AND 100 SECONDS.

Cyclic shape	zero dwell 0/0	10s dwell	100s dwell
Pb/Sn	550 / *1030*		
t/0		460 / *415*	125 / *150*
0/t		560 / *550*	300 / *340*
t/t		300 / *435*	120 / *282*
Sn/Ag	800 / *1400*		
t/0		400 /*1400*	500 / *1000*
0/t		450 / *700*	180 / *1000*
t/t		700 / *500*	145 / *550*
Sn/Cu	320 / *600*		
t/0		450 / *750*	240 / *325*
0/t		350 / *1400*	100 / *250*
t/t		200 / *300*	70 / *350*

3.5 Microstructure

In Sn-Pb, cracking around colony boundaries became more extensive at higher strain ranges and cycles with incorporated dwell periods. Figures 6(a) and 6(b) compares this cracking in Sn-Pb and Sn-Cu

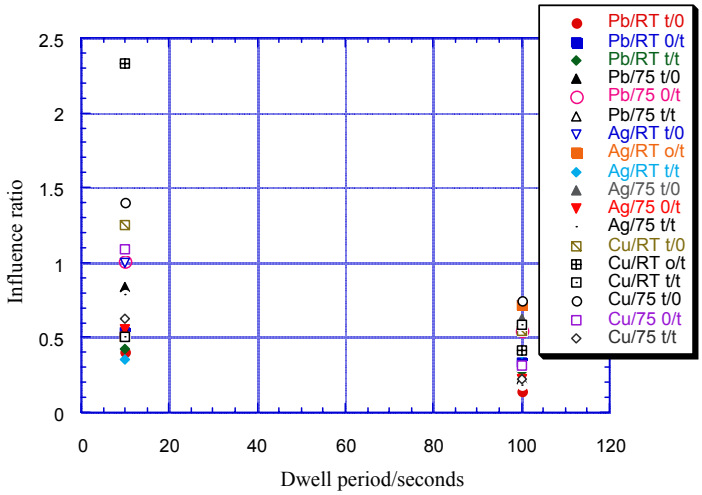

(Influence ratio is Nf(dwell):Nf(no dwell))

specimens tested at 75˚C, after being subjected to a 100s dwell at maximum tensile strain. Both Sn-Ag and Sn-Cu showed virtually no macroscopic cracking under the same conditions.

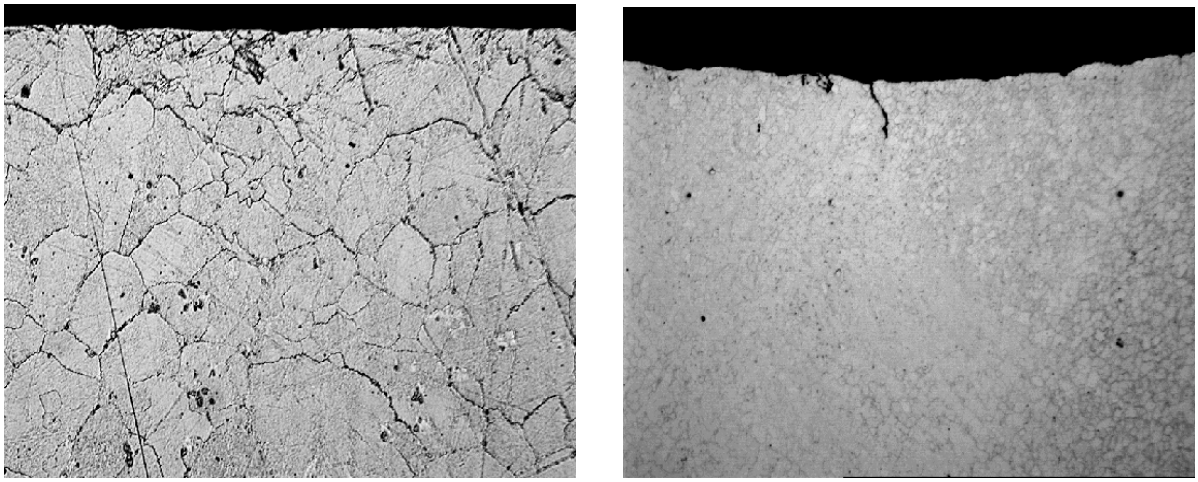

(a) Sn-Pb 75˚C (b) Sn-Cu 75°C

Figure 6. Comparison of Sn/Pb and Sn/Cu alloys after testing at 75˚C with a 100s dwell at the maximum tensile strain (magnification 200x).

Further investigation is planned. In Sn-Pb, intergranular cracking occurs throughout the bulk of the specimen. At low strain ranges (0.5 and 0.75 percent) cracking is confined to the surface layer, while at higher strain ranges, cracking is apparent throughout the bulk of the specimen although the majority of damage was found near to the surface. Specimens experiencing dwell cycles exhibited a higher crack density and the number of surface cracks was reduced. Cycle profile appeared to have little effect.

4 Discussion

This study has demonstrated that both lead-containing and lead-free solder alloys exhibit cyclic softening when subjected to high strain fatigue. The extent of softening is largely unaffected by temperature, strain range and the presence of dwell periods in the strain-time cycle. It is similar to that measured in a 1Cr-Mo-V steel at both room temperature and 565˚C [1]. Fatigue endurance is generally slightly lower at 75˚C than at room temperature. Insertion of hold periods in the fatigue usually causes a reduction in life by up to a factor of six for dwells of 100s duration. Post test metallographic examination reveals that fatigue produces macroscopic cracking in lead based alloys but not in lead free alloys. These findings are now considered in more detail.

A decrease in the load level can be caused by microstructural changes, fatigue crack nucleation or cavity formation. Some microstructural changes, for example those involving dislocation multiplication and sub grain formation, result in cyclic hardening. Since crack or void nucleation is associated with a reduction in load-bearing section, an immediate and continuous fall in load is observed unless the defects cease to grow. In the classic model of cyclic softening, microstructural changes produce a drop in load followed by a saturation level until fatigue cracking begins and results in a further load drop [2]. However, in a ductile material such as solder, it is likely that both processes, deformation and cracking, will occur simultaneously to some extent with the former predominant in the early stages. The balance between them will be influenced by the strain range and the ductility of the alloy. It is unlikely that in these alloys, crack initiation will occur immediately. Kariya and Otsuka [3] define three distinct stages in the load drop curve, in the first stage Ø increases rapidly, and crack initiation and propagation occur; the second stage is linear reflecting steady state growth, and the third state shows accelerating growth leading to failure. Most of the fatigue life is spent in the second steady state and the fatigue life is dominated by this steady load drop rate dØ/dN. In this study, since testing was terminated at 20 percent load drop the third state was not usually reached. Jiang et al [4] attributed similar load changes in a Sn-37 Pb alloy at room temperature to the predominance of cracking. Microstructural examination indicates progressive fatigue cracking taking place throughout all strain ranges but as yet observation of the very early stages is incomplete.

Stress relaxation in the Sn-37Pb alloy is significantly greater than that in the lead-free alloys. This cannot be explained on strength or melting point considerations. Temperature itself has negligible effect on the extent of relaxation in any of the alloys, and the strength of the Sn-0.5 Cu alloy over a range of strain rates is similar to that of the Sn-37Pb and significantly lower than that of the Sn-3.5Ag [5].

The fatigue endurance during continuous cycling is broadly similar for all the alloys examined. Since strength is not a good indicator of high strain fatigue resistance, this is not surprising. Indeed, it has been shown that this similarity extends to many engineering alloys [6]. Under total, as opposed to plastic, strain control some advantage might be expected to accrue to the stronger silver-containing alloy but this is offset by its lower ductility[5]. Endurance in the presence of dwells is reflected by the extent of stress relaxation with the Sn-3.5 Ag alloys exhibiting the longest life. However, the relative insensitivity of the Sn-0.5 Cu alloy to short dwells is difficult to explain. The alloy is ductile but not significantly more so than the Sn-37Pb, and a ductility argument would not account for the loss of relative resistance at longer dwells. It is possible that partitioning of the relaxed strain to different locations or into different mechanisms may be required to account for this apparent anomaly.

5 Conclusions

When the solder alloys, Sn-37Pb, Sn-3.5Ag and Sn-0.5Cu, are subjected high strain fatigue at 75˚C and room temperature, it has been found that:

- they exhibit cyclic softening to a similar degree which is independent of the strain range, temperature and cycle shape;
- their fatigue endurance is broadly similar, with fatigue at 75˚C being slightly more deleterious than at room temperature;
- during a dwell period in the cycle, stress relaxation occurs to an extent that is independent of temperature and location of the dwell, although it is significantly higher in the Sn-37Pb alloy;
- the endurance of all alloys is usually susceptible to the inclusion of dwells, and lifetimes may fall by up to six times after dwells of 100s duration.

6 References

1. Plumbridge, W. J. and. Bartlett, R. A. (1982) Int. J. Fatigue, 4, p 209.
2. Solomon H. D. (1986). Electronic Packaging - Materials and Processes, ASM p.29.
3. Kariya Y. and Otsuka M. (1998). J. of Electronic Materials, 27, 1229-1237.
4. Jiang, H, Hermann R, and Plumbridge W. J. (1996). J. of Materials Science, 31 p6455-6461.
5. Plumbridge W. J. and Gagg C. R. (1999). J Electronic Materials, 10, 461-468.
6. Plumbridge W. J. (2000) Materials at High Temperatures, ,17, 381-387.

ORAL/POSTER REFERENCE: ICF0705

FEM SIMULATION OF MIXED MODE CRACK PROPAGATION INDUCED BY HYDRAULIC FRACTURING

Kazushi Sato[1], Mikiyo Itaoka[2] and Toshiyuki Hashida[2]

[1] Department of Mechanical Engineering, Miyagi National College of Technology, 48 Aza–Nodayama, Shiote, Medeshima, Natori, JAPAN
[2] Fracture Research Institute, Tohoku University, 01 Aza–Aoba, Aramaki, Aobaku, Sendai, JAPAN

ABSTRACT

The hydraulic fracturing in a rock at great depth may induce a mixed mode (Mode I and II) crack propagation. In order to establish a design methodology for a geothermal energy extraction system, the prediction of the crack growth behavior is important. This paper presents a FEM model for hydraulic fracturing taking account of the mixed mode fracture.

In the FEM simulation model, the embedded crack (EC) element is employed to represent an arbitrary crack geometry due to the mixed mode crack propagation. The cohesive crack model is incorporated with a failure function for the mixed mode fracture in rock. This fracture model is implemented in the EC element. The failure function is verified by the comparison of the experimental data and numerical results.

Using the FEM model, the growth behavior of hydraulically induced crack is analyzed. The numerical results suggests that the fracture mode become the mixed mode at a great depth due to the tectonic stress. As the shear fracture mode is dominant, the crack growth tends to propagate toward the deeper direction.

KEYWORDS

Hydraulic Fracturing, Mixed Mode Fracture, Cohesive Crack Model, Embedded Crack Element

INTRODUCTION

The hydraulic fracturing is a key technology for developing a geothermal energy extraction system. In the geothermal energy system, the crack induced by the hydraulic fracturing is used for a heat exchanging surface. In order to design the geothermal energy system, a prediction of crack growth behavior induced by hydraulic fracturing is needed.

The hydraulic fracturing in a rock at great depth may induce a mixed mode (Mode I and II) crack propagation due to a tectonic stress. In order to predict the mixed mode crack propagation, the direction of the propagating crack must be analyzed. Furthermore, the crack growth is accompanied by a formation of fracture process zone.

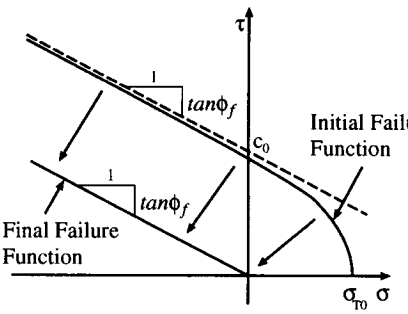

Figure 1: General shape of failure function

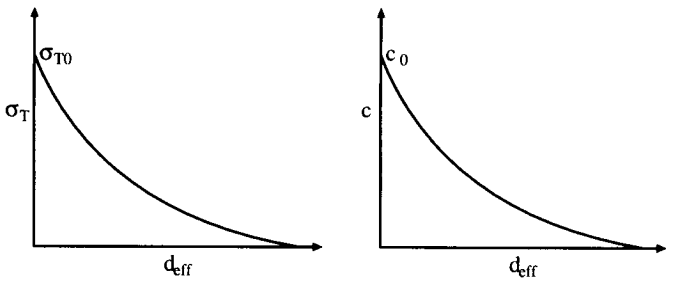

Figure 2: Softening behavior

The purpose of this study is the development of the numerical simulation code that can predict a mixed mode crack propagation with a fracture process zone during hydraulic fracturing in a deep rock mass. In order to handle both of an arbitrary crack geometry due to the mixed mode crack growth and a formation of the fracture process zone, a finite element analysis using an embedded crack (EC) element is adopted. This paper presents a FEM model for hydraulic fracturing taking account of the mixed mode fracture.

NUMERICAL MODEL

The FEM model used in this study consists of an EC element which is deal with an arbitrary crack geometry and a fracture model which represents a crack behavior of rock. This section presents a brief description of the FEM model. A detailed formulation is given in the literature [1].

The EC element has been proposed [2, 3, 4, 5] to deal with the strong displacement localization such as a crack and/or a shear bands in quasi–brittle materials. In the EC element, a crack is modeled as a displacement discontinuity within a continuum element. The major advantage of the EC element is that discrete cracks can be introduced anywhere and in any direction within the finite element mesh. According to this feature, an arbitrary crack growth can be handled without mesh refinement.

The fracture model represents the crack initiation and crack behavior in the EC element. Since the mixed mode (Mode I and II) fracture should be studied, the following failure function [6, 7] is employed as the fracture model.

$$F = \tau^2 - (c - \sigma \tan\phi_f)^2 + (c - \sigma_T \tan\phi_f)^2 \tag{1}$$

where τ and σ are the tangential and normal stress on the crack surface, respectively, c is the cohesion, ϕ_f is the angle of friction and σ_T is the tensile strength. A general shape of the failure function is shown in Figure 1. The crack initiation is determined by the initial state of the failure function. After the crack initiation, the rock exhibits a softening behavior. The softening behavior is characterized by the formation of the fracture process zone. The formation of the fracture process zone is well modeled by a cohesive crack model [8, 9]. The cohesive crack model represents the progress of fracture process by subjecting the cohesive stress to the crack surface according to the crack deformation. In this failure function, the cohesive crack model is incorporated through the parameter c and σ_T. c and σ_T are the function of a softening parameter d_{eff}, which is given by

$$d_{eff} = (d_t^2 + d_n^2)^{1/2} \tag{2}$$

where d_t and d_n are the tangential and normal relative displacement of the crack surface, respectively. The functions of c and σ_T represent softening behaviors in shear (Mode II) and tension (Mode I), as shown in Figure 2. These curves are often referred to as slip–weakening curve and tension–softening curve. As the parameters c and σ_T decrease with increasing the crack deformation, the failure function shrinks toward the final shape, which indicates a residual frictional force. During the cracking process, since the stress state on the crack surface must be maintained on the failure function, the crack follows the softening manner.

Mode II tractions generate crack slip and at the same time some induced crack opening or 'dilatancy' due to the irregularities of the crack surface. Figure 3 shows an example of the shear dilation behavior of a granite

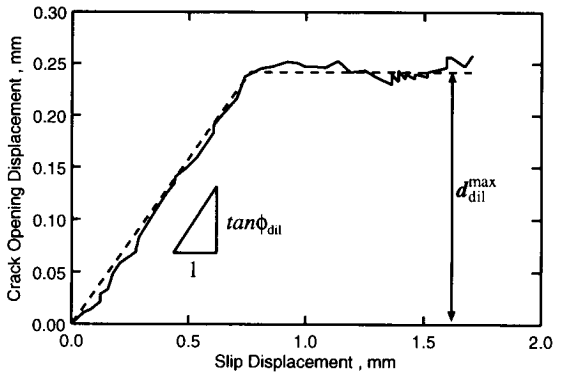

Figure 3: Shear dilation behavior

TABLE 1:
MATERIAL PROPERTIES USED

Young's modulus	41.7 GPa
Poisson's ratio	0.25
Density	2.6×10^3kg/m^3
Friction angle	40 deg
Tension–softening curve	Figure 4
Slip–weakening curve	Figure 5
Shear dilation angle	5 deg
Maximum dilatant disp.	0.60 mm

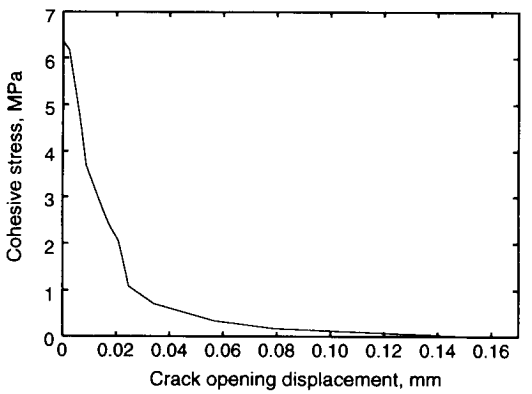

Figure 4: Tension–softening curve used

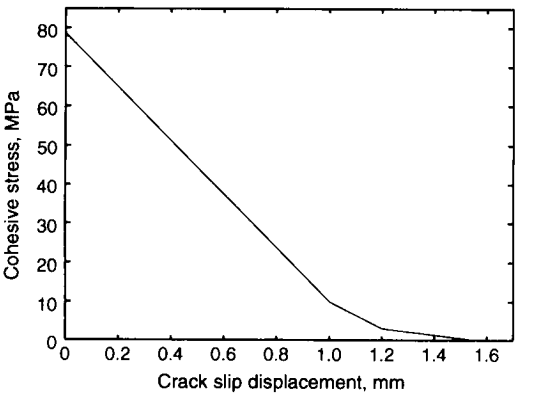

Figure 5: Slip–weakening curve used

observed in a laboratory test. It can be seen that the shear dilation indicated by the solid line in the figure is modeled as follows,

$$d_{dil} = \begin{cases} \tan\phi_{dil} \cdot d_t & (d_{dil} < d_{dil}^{max}) \\ d_{dil}^{max} & (d_{dil} \geq d_{dil}^{max}), \end{cases} \tag{3}$$

where ϕ_{dil} is the shear dilation angle and d_{dil}^{max} is the maximum dilatant displacement, as shown in the Figure 3. This shear dilation model is adopted in the fracture model in this study.

The FEM model is implemented in a 2D FEM code. A crack initiates when the stress state in an intact element reached the initial failure function. At this time, the intact element that is a generic element for an elastic analysis is replaced by the EC element with an internal crack. The crack direction can be calculated from both of the failure function and the stress state. The crack is introduced at the element centroid upon crack initiation and only one crack is allowed in each element. If the crack initiation criterion is satisfied at the centroid of a neighboring element, the crack propagates into that element. After the crack has been formed, the crack behavior is analyzed according to the fracture model.

CRACK INITIATION

Before analyzing a hydraulic fracturing, the numerical procedure used in this study should be verified. This section describes a comparison of numerical results with experimental data obtained by compression tests focusing on the crack initiation.

Numerical Procedure

A compression test under confining pressure was analyzed. Material properties used are shown in Table 1, Figure 4 and 5. These properties are measured by compression tests and direct tension tests using Iidate granite [10].

Plain strain condition was assumed. The analyzed geometry and boundary conditions are indicated in

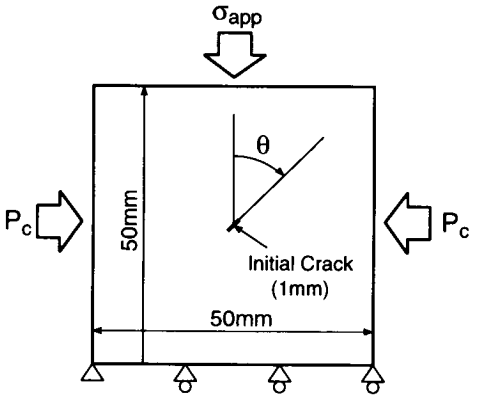

Figure 6: Boundary conditions for compression test analyses

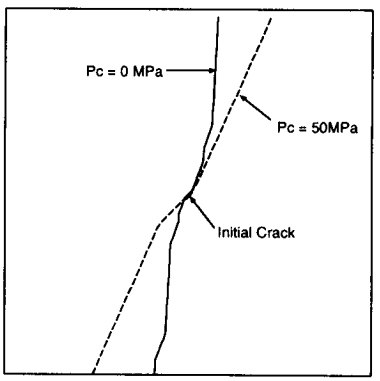

Figure 7: Final crack pattern

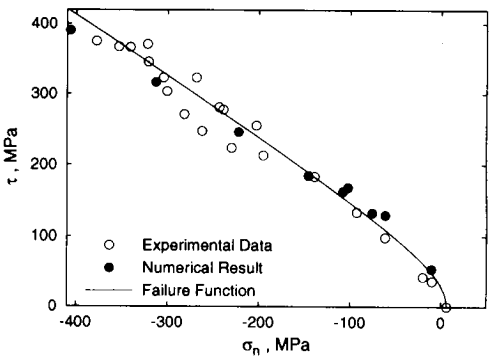

Figure 8: Crack initiation condition

Figure 6. The analyzed region was discretized using 4 node quadrilateral elements of 1mm × 1mm size. An initial crack is placed at the center of the region. The applied stress σ_{app} was raised stepwise until a crack propagate from the initial crack tip.

Numerical calculations were carried out for the condition of the confining pressure P_c varied from 0 to 200MPa and the inclination of the initial crack θ varied from 0 to 90 deg. for each confining pressure.

Failure Criterion

Crack patterns for θ = 45 deg. obtained by the numerical calculation for P_c = 0 MPa and 50 MPa are indicated in Figure 7. All the observed crack was propagated at the maximum applied stress. The crack pattern for P_c = 0 shows a growth in the direction toward the applied stress. For P_c = 50 MPa, the crack grows inclined direction, which indicates a shear fracturing. These crack growth behavior is consistent with that observed in compression tests of rocks.

A failure condition can be determined using a failure angle and a stress state when the failure was occurred. On experimental observations, the failure condition is deduced at the maximum applied stress point. Figure 8 shows a comparison of the failure condition deduced from the stress state and the crack angle observed at experiments for Iidate granite [10] and numerical results. The failure function used in the numerical calculation is also indicated for comparison. It can be seen that the failure function, which is determined by the independently measured parameters c, σ_T and ϕ_f, approximately represents the experimental data. And the numerical results follow the failure function, although small discrepancies are observed by the reason of either the softening behavior accompanied by the crack growth or the stepwise load control in the numerical procedure. These comparison results demonstrates a validity of the failure function as well as a validity of the numerical procedure. This evidence supports that the fracture behavior under high tectonic stress can be analyzed using the numerical procedure developed in this study.

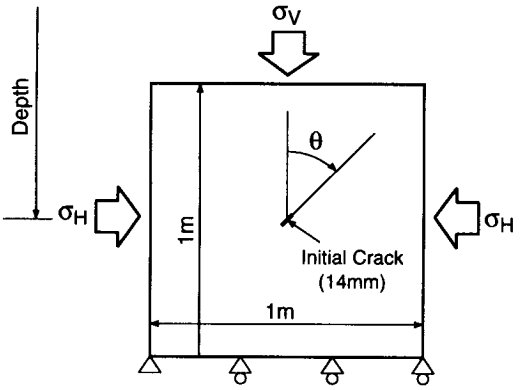

Figure 9: Boundary conditions for hydraulic fracturing analyses

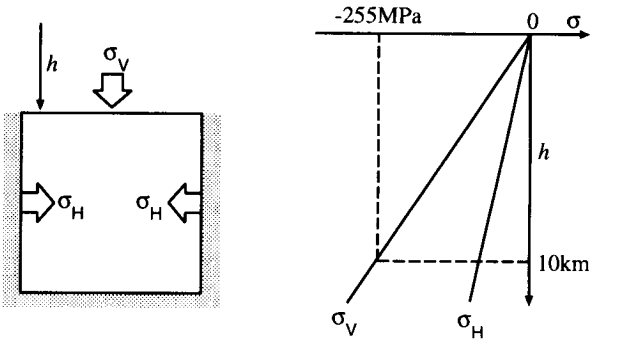

Figure 10: Tectonic stress model

HYDRAULIC FRACTURING

In order to analyze a hydraulic fracturing, a fluid flow in the rock should be calculated as well as the rock fracture. The fluid flow in the rock consists of a flow through the crack and flow into the rock mass. In this paper, the fluid flow through the crack is taken into account, although the flow into the rock mass is ignored. In this section, a growth behavior induced by hydraulic fracturing is examined focusing on the influence of tectonic stress.

Numerical Procedure

A small scall hydraulic fracturing was analyzed. Material properties are same as used in the previous section.

Plain strain condition was assumed. The analyzed geometry and boundary conditions are indicated in Figure 9. The analyzed region was discretized using 4 node quadrilateral elements of 14mm × 14mm size. An initial crack is placed at the center of the region. The inclination of the initial crack is 45 deg. The hydraulic pressure is applied into the initial crack. After the crack propagated, the fluid pressure distribution along the crack is calculated by a finite difference method.

The tectonic stress is assumed by the stress induced by the weight of rock, as follows,

$$\sigma_V = \rho g h, \tag{4}$$

$$\sigma_H = \sigma_V \cdot \nu/(1-\nu) \tag{5}$$

where ρ is the density of rock, g is the acceleration of gravity, h is the depth and ν is the Poisson's ratio. Therefore, the tectonic stress is proportional for the depth. Numerical calculations were carried out for the depth at 1, 4, 6, 8 and 10km.

Crack Growth Behavior

The crack growth pattern at 1, 6 and 10km is shown in Figure 11(a)~(c). At 1 km, the crack grows toward the vertical direction, and the upward crack is larger than the downward crack. At 10 km, the crack growth direction is inclined, and the upward crack is smaller than the downward crack. This differences of the growth behavior is the result of the change of fracture mode due to the tectonic stress.

Figure 12 indicates the stress condition at the advancing crack tip when the crack is nucleated. In the case of 1~4 km, the fracture mode is opening mode. If the opening mode dominated the fracture behavior, the crack may tend to grow upward, since the tectonic stress decreases gradually. At 6 km, the fracture mode is a mixed mode, but the opening mode seems to be dominant, according to the crack growth shown in Figure 11(b). In the case deeper than 8 km, the failure condition is on the compressive stress state. Therefore, it can be consider that the shear fracture mode dominates the crack growth behavior. As the result of this, it can be seen that the amount of the crack growth is larger in the deeper direction.

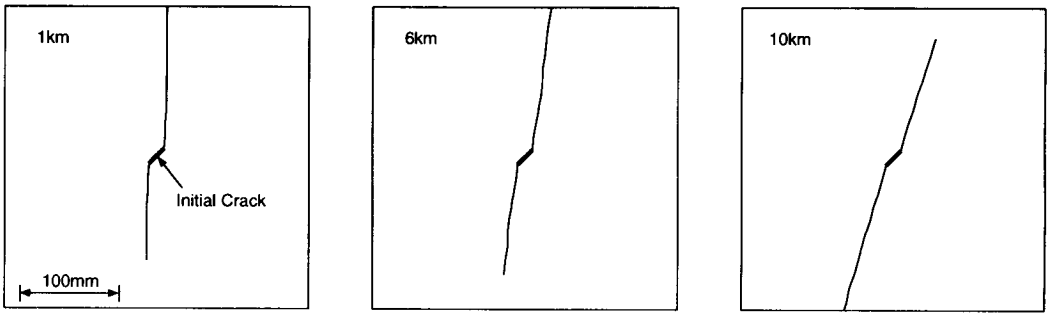

Figure 11: Crack growth pattern

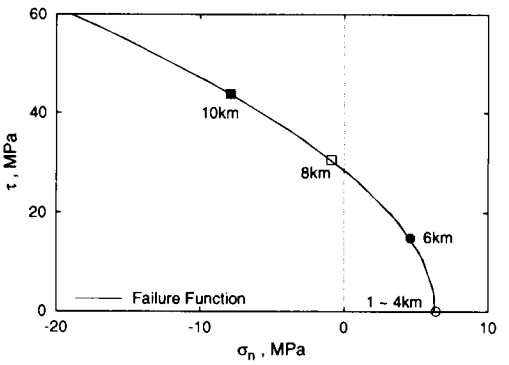

Figure 12: Stress conditions

CONCLUSION

This paper presents a brief description of a FEM model for analyzing a crack growth induced by hydraulic fracturing. In the numerical model, a mixed mode fracture is taken into account. The FEM model is verified by the comparison of the experimental data and numerical results. Using the FEM model, the growth behavior of hydraulically induced crack was analyzed. The numerical results suggests that the fracture mode become the mixed mode at a great depth due to the tectonic stress. As the shear fracture mode is dominant, the crack growth tends to propagate toward the deeper direction.

ACKNOWLEDGMENTS

The study presented in this paper was supported by The Japan Society for the Promotion of Science under "Research for Future" program (JSPS-RFTF 97P00901).

REFERENCES

1. Sato, K. and Hashida, T. (2000). *Proc. World Geothermal Congress 2000*, 3865–3870.
2. Dvorkin, E. N., Cuitino, A. M. and Gioia, G. (1990). *Int. j. Numer. Methods. Eng.*, 30, 541–564.
3. Klisinski, M., Runesson, K. and Sture S. (1991). *J. Eng. Mech.*, 117(3), 575–587.
4. Lotfi, H. R. and Shing, B. (1995). *Int. j. Numer. Methods. Eng.*, 38, 1307–1325.
5. Ohlsson, U. and Olofsson, T. (1997). *J. Eng. Mech.*, 123(10), 1027–1033.
6. Carol, I., Prat, P. C. and Lopez C. M. (1997). *J. Eng. Mech.*, 123(8), 765–773.
7. Červenka, J. (1994). PhD Thesis, Univ. of Colorado, Boulder.
8. Hillerborg, A. (1983). In: *Fractur Mechanics of Concrete*, F. H. Wittmann (Ed.)., Elsevier Science Publishers, B. V., Amsterdam, 223–250.
9. Rice, J. R. and Cleary, M. P. (1976). *Rev. Geophys. and Space Phys.*, 14, 227–241.
10. Takahashi, T. (2000). PhD Thesis, Tohoku University, Japan.

ORAL REFERENCE: ICF100572OR

FIDUCIAL MARKS AS MEASURES OF THIN FILM CRACK ARREST TOUGHNESS

Alex A. Volinsky[1], Michael L. Kottke[1], Neville R. Moody[3], Indira S. Adhihetty[1] and William W. Gerberich[2]

[1] Motorola, Digital DNA™ Labs, Process and Materials Characterization Lab, Mesa, AZ.
[2] University of Minnesota, Dept. of Chem. Eng. and Mat. Science, Minneapolis, MN.
[3] Sandia National Labs, Livermore, CA

ABSTRACT

Carbon fiducial marks are formed during thin film local delamination processes induced either by indentation, forming circular blisters, or by residual stress relief through telephone cord blister formations. Hydrocarbons are sucked into the crack tip during the delamination processes, outlining the crack tip opening angle (CTOA), which can be used to back calculate thin film adhesion using elastic or plastic analyses presented in the paper.

KEYWORDS

Fiducial marks, adhesion, fracture, delamination, crack arrest, crack tip opening angle, thin films

INTRODUCTION

Thin film adhesion can be measured by means of the superlayer indentation test [1-4]. Most good-adhered thin films can not be delaminated by means of regular indentation: films would rather deform plastically around the indenter by forming pileup. To prevent these problems a high modulus hard superlayer, capable of supporting and storing large amounts of elastic energy is deposited on top of the film of interest. Upon indentation a delamination blister forms around the indent, and its area is used to calculate the strain energy release rate (practical work of adhesion). This technique was shown to work with ductile metallic films (Al, Cu, Au, Cr) [2, 4-9, 15], ceramic (Ta_2N) [10, 12] and polymer films [16].

During indentation experiments into Cu thin films with a W superlayer it was found that the crack arrest marks form and correspond exactly to the blister size [13, 14]. Marks are formed of carbon, and outline the crack tip, representing its geometry [13, 14].

CRACK ARREST (FIDUCIAL) MARKS

Crack arrest marks were found after the blister removal with an adhesive tape. Scanning electron microscopy showed circles that correspond to the original blister diameter, and those were denoted as crack arrest fiducial marks [13, 14]. Atomic force microscopy was performed to measure the feature geometry, giving a width over 1 μm, and a height ranging from 5 to 15 nm. Contact and deflection AFM images of the partially removed blister showing the fiducial crack arrest marks are presented in Figure 1.

It was originally believed that the crack arrest mark is formed by crushed W and/or SiO_2 debris during the indentation [13]. More likely, however, radial cracking allowed laboratory air with moisture, hydrocarbons and surface debris to be sucked into the blister [14]. The exact source of contamination would be identified later, but whatever the source is, relatively mobile moisture, hydrocarbons and small debris particles were sucked into the crack tip leaving the fiducial mark detected in Figure 1.

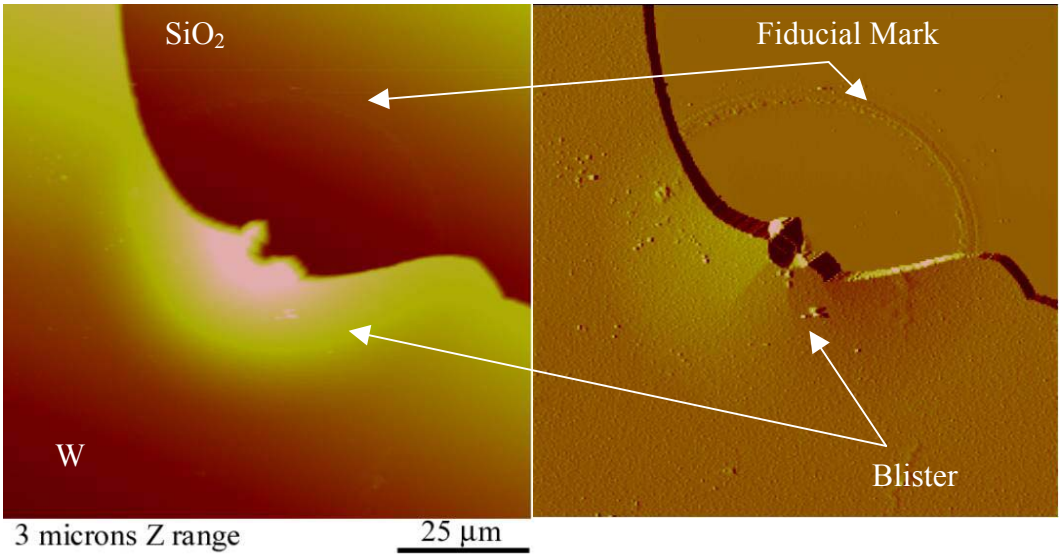

Figure 1. AFM height and deflection images of partially removed blister, showing fiducial mark underneath.

SLOW CRACK GROWTH ANALYSIS

Upon blister removal with a scotch tape the crack tip residue splits into two fiducial marks, leaving one on the film and substrate sides as shown in Figure 2. The substrate fiducial mark outlines the crack tip geometry, and its dimensions can be used to extract the thin film crack arrest toughness [13, 14].

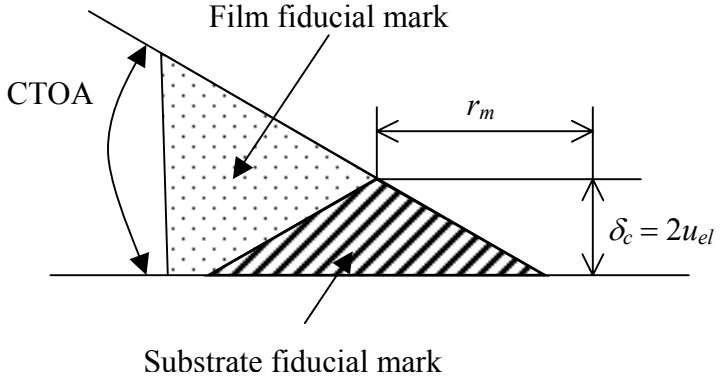

Figure 2. Fiducial mark geometry.

As discussed in [2, 4 and 15], brittle fracture is observed for thinner Cu films (< 100 nm) on Si substrates without a Ti underlayer. The majority of blisters in these films are buckled, so the crack is mostly under Mode I loading. This allows us to use the elastic crack tip opening displacement expressed for the plane stress tensile loading [17]:

$$u_{el}(r) = \frac{K}{E}\sqrt{\frac{8r}{\pi}} \tag{1}.$$

AFM measurements of the fiducial mark on the substrate side provide the height, $\delta_c=2u_{el}(r_m)$, and the half width of the mark, r_m (Figure 2), so K_I can be expressed as

$$K_I = \delta_c E\sqrt{\frac{\pi}{32r_m}} \tag{2}.$$

From equation (2), for δ_c = 8 nm and r_m = 1 μm one finds K_I = 0.3 MPa·m$^{1/2}$. This is close to the 0.33 MPa·m$^{1/2}$ value calculated from the actual G measurements (~0.9 J/m^2) for thinner Cu films using $K=(GE)^{1/2}$ for plane stress [2, 4, and 15]. Since the analysis is purely elastic, it indirectly proves that there is not much plastic energy dissipation at the crack tip for thin Cu films. Previously we also employed a plasticity-based slow crack growth approach based on the Rice, Drugan and Sham (RDS) analysis of the tearing modulus, T_0 [18] to show a similar result [13]. One can obtain a simple expression for strain energy release rate in terms of the crack-tip opening angle (CTOA in Figure 2):

$$J_{SS} = J_0 \exp\left(\frac{\alpha T_0}{\beta}\right) = J_0 \exp\left(\frac{E \cdot CTOA}{\sigma_{YS}\beta}\right) \quad (3),$$

where J_0 is the initial value of the J integral at crack initiation, T_0 is the tearing modulus, $\alpha \approx 1$, $\beta = 5.1$ from the mechanics description, E and σ_{ys} are modulus and yield strength. With 0.01 radians average value of the CTOA, a modulus of 120 GPa, a yield strength of 1 GPa and $\beta = 5.1$, one finds:

$$J_{SS} = J_0 exp\{0.23\} \approx 1.27 J_0 \quad (4),$$

which means that during slow crack growth the strain energy release rate has barely increased for this 120 nm thick copper film. This again agrees with the actual measured value of ~0.9 J/m^2 for the strain energy release rate.

CARBON CONTAMINATION SOURCE

There are three possible sources for carbon: adhesive tape, the diamond indenter and hydrocarbons from the atmosphere. In our previous studies the first two sources were eliminated [13-15], and hydrocarbons from the atmosphere were proposed as a source of fiducial mark formation.

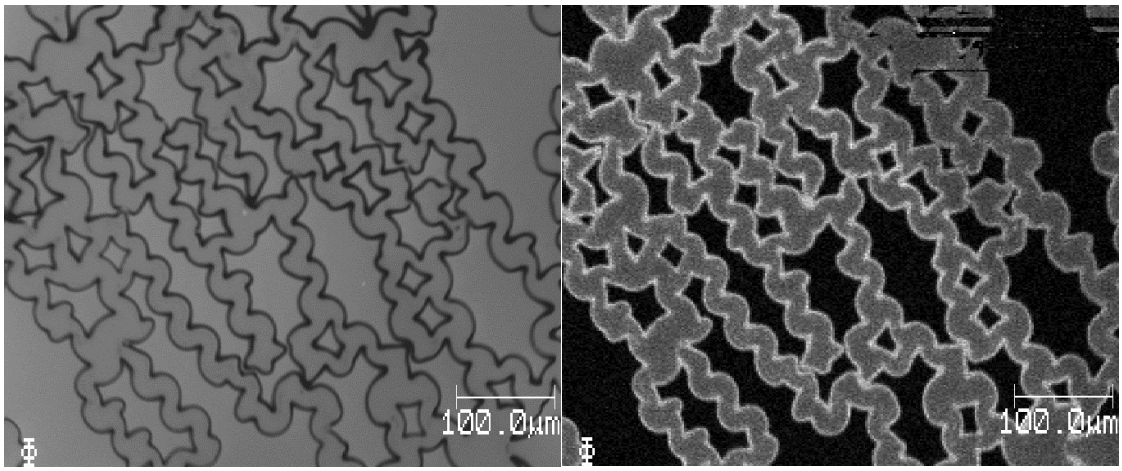

Figure 3. SEM micrograph and corresponding Carbon Auger map of a GaAs fracture surface upon TiW_XN_Y film removal.

During the course of this study it was found that a similar type of contamination is present in a different film system of Ti_XWN_Y on GaAs, where the telephone cord delaminations formed due to the high residual stress relief (Figure 3). The carbon traces noted both on the film and substrate surfaces mimic the original telephone cord delamination pattern. Fiducial crack arrest marks are like those observed in the Cu/SiO_2 system. Figure 3 also shows a carbon Auger map, where brighter areas correspond to

higher carbon concentrations. There is almost no carbon present between the original phone cord delaminated areas (black regions in Figure 3). Most of the carbon goes into the crack tip, outlining the telephone cord topography. Fiducial mark formation may also be associated with the local heating at the crack tip. The heat dissipates fast enough so that the whole sample is not heated up, although the local crack tip temperature may increase substantially. This is a very interesting phenomenon that requires further investigation

ACKNOWLEDGEMENTS

The authors would like to acknowledge support through DOE grants DE-FG02/96ER45574 and DE-AC04-94AL85000. We would also like to acknowledge W. Miles Clift and Bernice E. Mills from Sandia National Lab at Livermore for Auger analysis and Robert F. Cook from the University of Minnesota for valuable discussions.

REFERENCES

1. Kriese M.D. and Gerberich W.W., (1999) J. Mater. Res. 14 (7), pp. 3007-18
2. Volinsky A.A., Tymiak N.I., Kriese M.D., Gerberich W.W. and Hutchinson J.W., (1999) Mat. Res. Soc. Symp. Proc. Vol. 539, pp. 277-290
3. Gerberich W.W., Kramer D.E., Tymiak N.I., Volinsky A.A., Bahr D.F., and Kriese M., (1999) Acta mater., Vol. 47, No. 15, pp. 4115-4123
4. Tymiak N.I., Volinsky A.A., Kriese M.D., Downs S.A. and Gerberich W.W., (2000) Metallurgical and Materials Transactions A, Vol. 31A, pp. 863-872
5. Volinsky A.A., Moody N.R., Gerberich W.W., (2000) MRS Symp. Proc. Vol. 594
6. Moody N.R., Adams D., Volinsky A.A., Kriese M., Gerberich W.W., (2000) Mat. Res. Soc. Symp. Proc. Vol. 586
7. Schneider J.A., Guthrie S.E., Kriese M.D., Clift W.M., Moody N.R., (1999) Materials Science & Engineering A (Structural Materials: Properties, Microstructure and Processing), Vol.A259, No.2 pp.253-60
8. Kriese M.D., Gerberich W.W., Moody N.R., (1999) J. Mater. Res. 14 (7), pp. 3019-26
9. Schneider J.A., Guthrie, S.E.; Kriese, M.D.; Clift, W.M.; Moody, N.R. (1998) Fundamentals of Nanondentation and Nanotribology. Symposium p.347-52
10. Moody N.R., Medlin D., Boehme D., Norwood D.P., (1998) Engineering Fracture Mechanics, Vol.61, no.1 p.p107-18
11. Moody, N.R.; Hwang, R.Q.; Venka-Taramani, S.; Angelo, J.E.; Norwood, D.P.; Gerberich, W.W. (1998), Acta Materialia vol.46, no.2 p.585-97
12. Moody, N.R.; Medlin, D.; Norwood, D.P.; Gerberich, W.W.; Gao, H.; Sundgren, J.-E.; Baker, S.P. (1997) Thin Films: Stresses and Mechanical Properties VI. Symposium p.97-102
13. Volinsky A.A., Gerberich W.W., (1999) MRS Symp. Proc. Vol. 563, p.275-84
14. Volinsky A.A., Clift W.M., Moody N.R., Gerberich W.W., (1999) Mat. Res. Soc. Symp. Proc. Vol. 586
15. Volinsky A.A., (2000) Ph.D. Dissertation, University of Minnesota

16. Volinsky A.A., Vella J.B., Fowler B.W., Adhihetty I.S., Gerberich W.W., (2001) presented at 2001 Mechanics and Materials Summer Conference, San Diego
17. Lawn B., (1993) "Fracture of Brittle Solids", Cambridge University Press, Cambridge
18. Anderson T.L., (1991) "Fracture Mechanics: Fundamentals and Applications." CRC Press, Boston, p. 219

FINITE DEFORMATION ENERGY RELEASE RATE COMPUTATIONS IN A STEADY ROLLING TIRE

Sanjay Govindjee
Structural Engineering, Mechanics, and Materials
Department of Civil Engineering
University of California, Berkeley
Berkeley, CA 94720-1710, USA

ABSTRACT

The recent well publicized failures of the Firestone ATX/AT tires has brought to light the poor state of research into the basic physical causes of such failures and the poor state of research into analytic methods suitable for analyzing such failures. The essence of problems of this nature lies in the finite deformation fatigue fracture of elastomers at large strains. The definition of failure criteria is further complicated by the issue of material aging. The computational problem is rather demanding due to the truly 3-D nature of the tire system under load. Finding the failure forces (the singular energy momentum tractions) is made challenging by the spinning reference state normally utilized in computational tire analysis. A true analysis of such problems demands that one address all of these issues; this paper focuses on one aspect of this problem – viz., the formulation of suitable analytic expressions for the computation of the crack tip driving forces in spinning tires.

KEYWORDS

Tire mechanics, Energy release rates, Finite deformation

INTRODUCTION

In assessing the durability of tires a common physical phenomena to be investigated for steel belted radial passenger tires is belt edge cracking. The important physical quantity to be measured or computed here is the energy release rate. As is well known, energy release rate is the physical quantity introduced by Eshelby to characterize the driving force upon a singularity in the elastic field [2, 3] and it is intimately related to the pioneering fracture studies by Ingles [7], Griffith [6], Irwin [8], and Rivlin and Thomas [15]. In the context of fracture, this driving force or energy release rate is often associated with the J-integral criteria [14, 1]; under common conditions the two are of course synonymous. The application of these basic notions turns out to be a modestly complex undertaking for a spinning tire. If we leave aside the experimental aspects, we have available to us a variety of methods for the computation of energy release rates given mechanical loads. For the tire, one is for practical reasons restricted to methods associated with numerical approximations such as the finite element method[18]; see e.g. [11, 9] for a discussion on computational methods for energy release rates. As noted by Govindjee [4] these methodologies have

existed for many years, however, their direct application to the spinning tire in the open peer reviewed literature is amazingly scarce. In this paper we examine the extension of Steinmann's method [16, 17] for finite deformation elasticity to the case of an elastic spinning tire in steady rotation. Analysis in a steady spinning frame of reference is based upon the early work of Lynch [12] and the basic equations for such an analysis in finite deformation were first presented by Oden and Lin [13]; more recently see the discussions of LeTallec and Rahier [10] and Govindjee and Mihalic [5].

ENERGY RELEASE RATE

The issue of an energy release rate computation comes down to the computation of the following expression:

$$G_A = \lim_{\epsilon \to 0} \int_{\Gamma(\epsilon)} \Sigma^o_{AB} N^o_B \, d\Gamma(\epsilon) \,, \tag{1}$$

where $\Sigma^o_{AB} = W(\boldsymbol{F}^o)\delta_{AB} - F^o_{iA} P^o_{iB}$ is Eshelby's energy-momentum tensor, W is the strain energy density, F^o_{iA} is the deformation gradient, and P^o_{iA} is the first Piola-Kirchhoff stress tensor. The surface $\Gamma(\epsilon)$ with normal N^o_A surrounds the crack tip and is of radius ϵ. The result G_A is the crack tip driving force or energy release rate. Note that the result is zero unless the integrand is singular. Steinmann's method is based on the subtle observation that this quantity is in fact closely related to the "external work" terms in the weak form of the balance equation for the energy-momentum field. In the above and throughout we employ indicial notation with lower case Latin indices for the spatial frame and upper case Latin indices for the reference frame. The superscript o indicates quantities that are associated with the usual continuum mechanics definitions which are expressed in terms of a spatial and referential frame. Later on we will employ greek indices for quantities expressed in a rotating frame and also introduce transformed counterparts to our usual continuum mechanics machinery; these will appear with the same symbols modulo the superscript o.

STRONG FORM OF ENERGY-MOMENTUM BALANCE

The starting point for exploiting the observation of [16, 17] is to look at the governing balance equation for the energy-momentum tensor which can be expressed as:

$$\Sigma^o_{BA,A} - F^o_{iB} B^o_i = -F^o_{iB} \bar{\rho} \ddot{\phi}^o_i \,. \tag{2}$$

In the above, B^o_i represents any body forces (per unit reference volume), $\bar{\rho}$ the reference density of the body, and ϕ^o_i is the deformation (motion) map. The relation follows directly from linear momentum balance and an assumption on the smoothness of the motion. In what follows we will assume that $B^o_i = 0$ since the only direct body forces in the tire are gravitational and these can be safely neglected.

WEAK FORM OF ENERGY-MOMENTUM BALANCE

The weak form of this relation can be expressed with the aid of an arbitrary test function v_B and integration over the reference configuration of the body denoted as $\mathcal{B}$. After integrating by parts one has that

$$\int_{\mathcal{B}} v_{B,A} \Sigma^o_{BA} - \int_{\mathcal{B}} v_B F^o_{iB} \bar{\rho} \ddot{\phi}^o_i = \int_{\partial\mathcal{B}} v_B \Sigma^o_{BA} N^o_A \,. \tag{3}$$

The term on the right-hand side (RHS) is clearly related to the RHS of Eq. (1). In fact, Steinmann makes the observation that the RHS of Eq. (3) is the regular part of the "external virtual work" associated with the balance of energy momentum. For cases where this quantity is zero, the computation of the left-hand side of Eq. (3) will simply give the singular part. The reason the singular term does not appear on the RHS explicitly is that we have assumed no singularities during the application of the divergence theorem. In the case of the tire, the belt edge cracks are open when the cracks are rather short and possibly for points outside of the footprint; in theses cases the RHS will be zero. For longer cracks and in the footprint the crack faces are closed and driven in a shear type mode. In this case, the RHS of Eq. (3) (the non-singular part) will be non-zero. In particular, if we assume frictionless crack faces and a crack face contact pressure p, then we will have

$$RHS = \int_{\partial\mathcal{B}} v_B p N^0_A \delta_{AB} + v_B W N^0_B \,. \tag{4}$$

In order to compute the energy release rate (the singular part of the energy-momentum traction) this term needs to be subtracted from the LHS of Eq. (3). The feature that make this methodology attractive is that the machinery necessary for its computation is already built into almost all finite element programs. After solving for the deformed configuration of a body, one merely needs to evaluate the integrals in Eq. (3) to determine the energy release rates for any given crack tip.

WEAK FORM OF ENERGY-MOMENTUM BALANCE IN A SPINNING FRAME

The main complication in utilizing Eq. (3) is the inertial terms. However, in the case of steady state spinning this obstacle can be over come in a straightforward manner utilizing the formalism developed by Oden and Lin [13]; see also LeTallec and Rahier [10] and Govindjee and Mihalic [5]. In this formalism, a third coordinate system is introduced that rotates with the tire. In this frame of reference points are located by their coordinates X_α where $X_\alpha = R_{\alpha B}(t) X^o_B$ and $R_{\alpha B}(t)$ represents the steady rotation of the tire about its axis of circular symmetry. The mapping from X_α to x_i is given by ϕ_i. The deformation gradient from this spinning frame of reference to the spatial frame is given by $F_{i\alpha} = F^o_{iA} R_{\alpha A}$. Since we assume the tire is in a steady state rotation we have for the acceleration:

$$\ddot{\phi}^o_i = x_{i,\alpha\beta}\Omega_{\beta\gamma}X_\gamma\Omega_{\alpha\delta}X_\delta + x_{i,\alpha}\Omega_{\alpha\gamma}\Omega_{\gamma\delta}X_\delta \,, \tag{5}$$

where $\Omega_{\alpha\beta} = \dot{R}_{\alpha B} R_{\beta B}$ is the spin rate of the tire. It is also noted that the surface normals are mapped as $N_\alpha = R_{\alpha A} N^o_A$.

For isotropic materials we also have that $W(\boldsymbol{F}^o) = W(\boldsymbol{F}\boldsymbol{R}) = W(\boldsymbol{F})$ and through an abuse of notation that $W(\boldsymbol{C}^o) = W(\boldsymbol{C})$, where $C_{\alpha\beta} = F_{i\alpha}F_{i\beta}$. With these results we can now define an energy-momentum tensor relative to the spinning frame as $\Sigma_{\alpha\beta} = R_{\alpha A}\Sigma^o_{AB}R_{\beta B} = W(\boldsymbol{C})\delta_{\alpha\beta} - C_{\alpha\gamma}S_{\gamma\beta}$, where $S_{\alpha\beta}$ represents the second Piola-Kirchhoff stress tensor measured by the deformation from the rotating frame to the current frame. If now re-examine Eq. (3), we find that the singular part of the energy-momentum traction is given by

$$\begin{aligned} G &= \int_{\mathcal{B}} R_{\beta B} v_{B,\alpha}\Sigma_{\beta\alpha} - \int_{\partial\mathcal{B}} R_{\beta B} v_B \Sigma_{\beta\alpha} N_\alpha - \int_{\mathcal{B}} \bar{\rho} R_{\beta B} v_B F_{i\beta}\delta_{i\alpha}(\Omega^2)_{\alpha\theta}X_\theta & (6)\\ &+ \int_{\mathcal{B}} \bar{\rho} R_{\beta B} v_{B,\delta} F_{i\beta}\Omega_{\alpha\gamma}X_\gamma u_{i,\alpha}\Omega_{\delta\theta}X_\theta + \int_{\mathcal{B}} \bar{\rho} R_{\beta B} v_B F_{i\beta,\delta}\Omega_{\alpha\gamma}X_\gamma u_{i,\alpha}\Omega_{\delta\theta}X_\theta \,, & (7)\end{aligned}$$

where we have assumed that the boundary $\partial\mathcal{B}$ possesses circular symmetry.

To practically execute these integrals we now introduce a finite element approximation by expressing the motion ϕ_i as an element of a finite dimension functions space; *ie.* as $\phi_i = \sum_a x^a_i M^a(\boldsymbol{X})$ where x^a_i

are the nodal degrees of freedom and M^a is the shape function associated with node a. Likewise we approximate the space of test functions such that $v_B = \sum_a v_B^a M^a(\boldsymbol{X})$. From the arbitrariness of the test function we can now express the energy release rate for the steady rotation case upon any node a as:

$$G_\beta^a = \int_{\mathcal{B}} M^a_{,\alpha} \Sigma_{\beta\alpha} - \int_{\partial\mathcal{B}} M^a \Sigma_{\beta\alpha} N_\alpha - \int_{\mathcal{B}} \bar{\rho} M^a F_{i\beta} \delta_{i\alpha} (\Omega^2)_{\alpha\theta} X_\theta \tag{8}$$

$$+ \int_{\mathcal{B}} \bar{\rho} M^a_{,\delta} F_{i\beta} \Omega_{\alpha\gamma} X_\gamma u_{i,\alpha} \Omega_{\delta\theta} X_\theta + \int_{\mathcal{B}} \bar{\rho} M^a F_{i\beta,\delta} \Omega_{\alpha\gamma} X_\gamma u_{i,\alpha} \Omega_{\delta\theta} X_\theta \,, \tag{9}$$

In using these relations one needs to also consider the fact that the tire is composed of materials that are not isotropic. In particular the bead is effectively modeled as transversely isotropic and the steel belts as orthotropic. For the general conditions of transverse isotropy and orthotropy the above results do not hold. However, the anisotropy of the tire is very special in that the tire possess a global geometric invariance with respect to the spin of the tire. In this special case, and in this special case only, the expressions above also hold for general anisotropy without modification.

APPLICATION

The sequence of computational steps in computing the energy release rate at the tip of a circumferential belt edge crack is as follows. First one models the tire in circular symmetry. This implies that the cross tread grooves can not be modeled; only the circumferential tread grooves can be modeled. For a given tire inflation, speed, and axle force the deformation of the tire is computed by solving the linear momentum balance equations is a steady rotating frame using the method of Oden and Lin [13] as presented by Govindjee and Mihalic [5]. Once the deformation state has been computed it is a straightforward post-processing step to compute G_β^a using the relations from the previous section.

As an example consider the tire geometry of the Firestone P235/75R15 AT tire as described in Govindjee [4]. We demonstrate some of the types of analysis that can be performed with the method. Shown in Fig. 1 is the energy release rate at the tip of a 25.5mm circumferential crack for 4 different inflation pressures as a function of angular position where $-\pi/2$ represents the center of the footprint and $\pi/2$ the top of the tire. As can be seen from the figure there is very little effect of inflation pressure over this range of pressures (at 120 kph and a 4.4 kN axle load). Above 0 rad mesh coarsening reduces the accuracy of the reported results. As a second example, shown in Fig. 2 is the effect of belt edge crack length and axle load on the energy release rate increment $G_\beta(-\pi/2) - G_\beta(0)$. The figure also shows some results for the P235/75R15 ATX tire. Clearly such modeling capabilities are essential in analyzing belt edge crack durability issues.

References

[1] B. Budiansky and Rice. J.R., *Conservation laws and energy-release rates*, Journal of Applied Mechanics **40** (1973), 201–203.

[2] J.D. Eshelby, *The continuum theory of lattice defects*, Solid State Physics, Advances in Research and Applications (F. Seitz and D. Turnbull, eds.), vol. III, Academic Press, 1956, pp. 79–119.

[3] ———, *The elastic energy-momentum tensor*, Journal of Elasticity **5** (1975), 321–335.

[4] S. Govindjee, *Firestone tire failure analysis*, Tech. report, 2001.

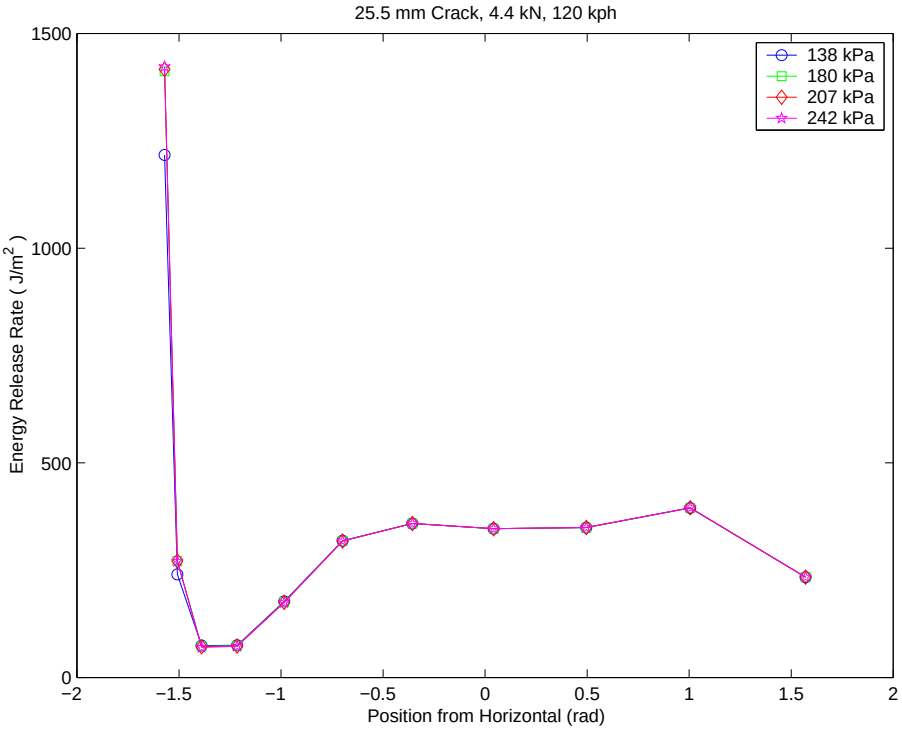

Figure 1: Energy release rate as a function of angular position from the horizontal for a 25.5 mm crack at 120 kph under a 4.4 kN load.

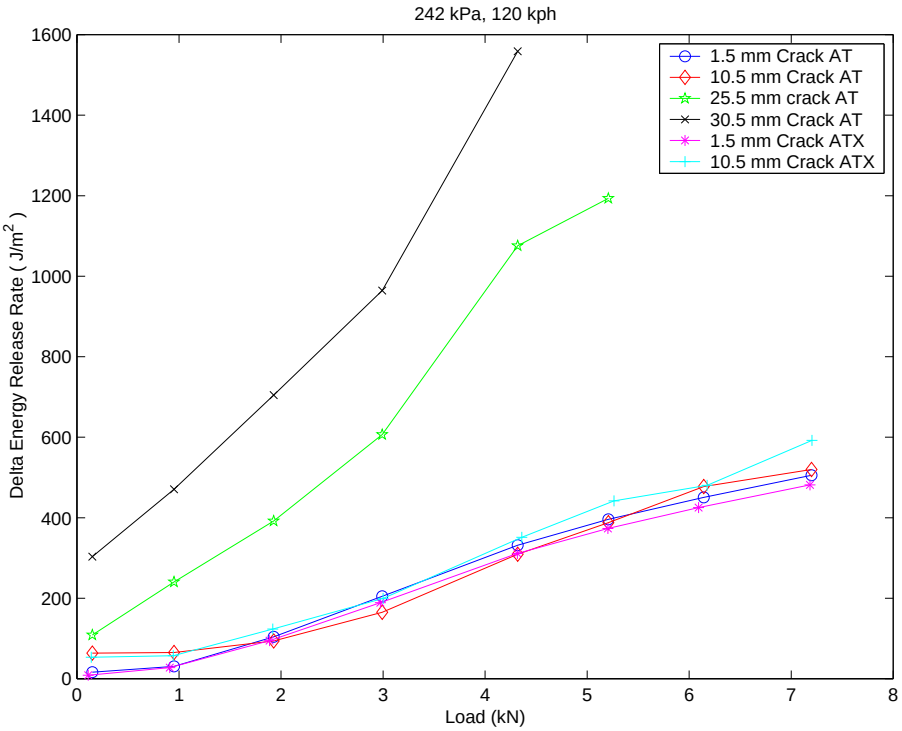

Figure 2: Energy release rate increments per revolution as a function of load indexed by crack length at an inflation pressure of 242 kPa and 120 kph.

[5] S. Govindjee and P.A. Mihalic, *Viscoelastic constitutive relations for the steady spinning of a cylinder*, Tech. Report UCB/SEMM-98/02, University of California Berkeley, Department of Civil Engineering, 1998.

[6] A.A. Griffith, *The phenomena of rupture and flow in solids*, Philosophical Transactions of the Royal Society of London **221A** (1920), 163–197.

[7] C.E. Ingles, *Stresses in a plate due to the presence of cracks and sharp corners*, Transactions of the Institute of Naval Architects **55** (1913), 219–241.

[8] G.R. Irwin, *Fracture dynamics*, pp. 147–166, American Society for Metals, 1948.

[9] K. Kishimoto, S. Aoki, and M. Sakata, *Dynamic stress intensity factors using $\hat{j}$-integral and finite element method*, Engineering Fracture Mechanics **13** (1980), 387–394.

[10] P. Le Tallec and C. Rahier, *Numerical models of steady rolling for non-linear viscoelastic structures in finite deformations*, International Journal for Numerical Methods in Engineering **37** (1994), 1159–1186.

[11] F.Z. Li, C.F. Shih, and A. Needleman, *A comparison of methods for calculating energy release rates*, Engineering Fracture Mechanics **21** (1985), 405–421.

[12] F. DE S. Lynch, *A finite element method of viscoelastic stress analysis with application to rolling contract problems*, International Journal for Numerical Methods in Engineering **1** (1969), 379–394.

[13] J.T. Oden and T.L. Lin, *On the general rolling contact problem for finite deformations of a viscoelastic cylinder*, Computer Methods in Applied Mechanics and Engineering **57** (1986), 297–367.

[14] J.R. Rice, *A path independent integral and the approximate analysis of strain concentration by notches and cracks*, Journal of Applied Mechanics **35** (1968), 379–386.

[15] R.S. Rivlin and A.G. Thomas, *Rupture of rubber 1. Characteristic energy for tearing*, Journal of Polymer Science **10** (1953), 291–318.

[16] P. Steinmann, *Application of material forces to hyperelastic fracture mechanics. I. Continuum mechanical setting*, International Journal of Solids and Structures **37** (2000), 7371–7391.

[17] P. Steinmann, D. Ackermann, and F.J. Barth, *Application of material forces to hyperelastic fracture mechanics. II. Computational setting*, International Journal of Solids and Structures (2001), (to appear).

[18] O.C. Zienkiewicz and R.L. Taylor, *The finite element method, volume 1*, 5 ed., Butterworth and Heinemann, 2000.

REFERENCE: ICF100497OR

FIRST PRINCIPLES MOLECULAR DYNAMICS CALCULATION ON THE TENSILE STRENGTH OF Al GRAIN BOUNDARY

Guang-Hong LU[1], Masanori KOHYAMA[2] and Ryoichi YAMAMOTO[1]

[1] Institute of Industrial Science, University of Tokyo, 7-22-1 Roppongi, Minato-ku, Tokyo 106-8558, Japan
[2] Department of Materials Physics, Osaka National Research Institute, AIST, 1-8-31 Midorigaoka, Ikedashi, Osaka 563-8577, Japan

ABSTRACT

The *ab initio* tensile test has been applied to Al $\Sigma 9(2\bar{2}1)/[110]$ tilt grain boundary by first principles plane-wave pseudopotential method based on density functional theory with local density approximation. Stress-strain relation shows that the maximum stress of the Al Σ9 grain boundary is 9.9GPa at the strain of 28%. The changes of the charge density and the bond length indicate that the bonds at the boundary break first.

KEYWORDS

first principles, tensile strength, aluminum, grain boundary

INTRODUCTION

It is possible now to investigate the strength and mechanical behavior of defect, interface and grain boundary directly through first principles calculations on large supercell, using the first principles molecular dynamics method[1-3]. Deyirmenjian et al.[4] first performed *ab initio* tensile test on aluminum with atomic-scale void. Kohyama[5] performed the calculation of the tensile strength and fracture of a tilt grain boundary in

cubic SiC by the same scheme. In both calculations the supercell is extended by a small increment and then relaxed to its ground-state configuration using the first principles pseudopotential method. The total energy and the average stress are obtained for each level of extension. By iterating this cycle, the maximum stress σ_{max} can be obtained at the corresponding strain ε_{max}. This should correspond to a real tensile test at zero temperature.

In this paper, we perform an *ab initio* tensile test on Al Σ9 grain boundary in order to investigate how aluminum containing the grain boundary fails as it is pulled apart at zero temperature.

COMPUTATIONAL METHOD

The unit cell is constructed as shown in Figure 1. Al $\Sigma 9(2\bar{2}1)/[110]$ tilt grain boundary is formed by rotating grain by 38.94˚ along the [110] axis, and $(2\bar{2}1)$ is set as the boundary plane. The coincidence site lattice (CSL) unit cell on the boundary plane is defined by $\frac{3\sqrt{2}}{2}a_0[1\bar{1}4]$ and $\frac{\sqrt{2}}{2}a_0[110]$. The size in the [110] direction is set twice that of the CSL, i.e. $\sqrt{2}a_0$. In the $[2\bar{2}1]$direction two symmetric boundaries are introduced to make the periodicity. The distance between the grains is determined by that the atom density in boundary is the same as that of the unit cell in the ref.[6].

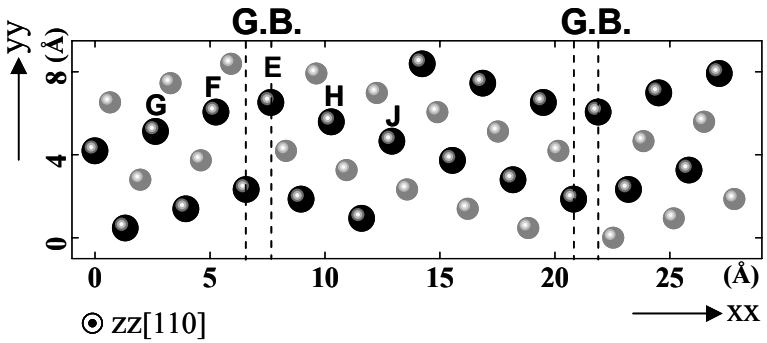

Figure 1: The cross section of zz[110] direction of the unit cell, Al Σ9(2-21)/[110] tilt grain boundary. There are four (110) atomic layers, A, B, C and D. The length of three sides are 28.469Å(xx), 8.379Å(yy) and 5.586Å(zz), respectively. There are 84 atoms in the unit cell. F, G, E, H and J are the atom positions of B layer marked for later discussions. The dark-grey spheres indicate the atoms of B(or D) layer in the unit cell. The light-grey spheres indicate the atoms of A(or C) layer in the unit cell.

Total energy, atomic forces and averaged stresses can be obtained quantitatively[7] by the *ab initio* plane-wave pseudopotential method[8] based on density functional theory (DFT)[9-10] with local density approximation (LDA)[11]. The pseudopotentials of Al is constructed[12] using Troullier-Martins scheme[13]. The separable form by Kleinman and Bylander[14] with the p orbital as the local component is used. The lattice parameters calculated by the pseudopotentials are 3.95Å for fcc Al, which is in good agreement with the corresponding experimental value of 4.02Å(0K)[15]. The electronic ground state is

obtained efficiently using the conjugate-gradient technique proposed by Bylander, Kleinman and Lee[16] with the Kerker mixing scheme[17]. The plane wave energy cutoff is 15Ry, and 32 k points in the Brilliouin zone are used. The electronic structure is determined by a real space grid of $256 \times 64 \times 32$ points.

In the tensile test, a uniaxial tensile strain is introduced into the stable configuration. The supercell is stretched by a small increment in xx direction that is normal to the boundary plane. The length of the yy and zz direction is fixed in order to save the computational time. This means Poisson's ratio has not been considered. The atomic positions are changed by uniform scaling. Then all the atoms are relaxed according to the Hellman-Feynman forces until all the forces are less than 0.15eV/Å. The total energy and stress tensor are calculated. This cycle is iterated until the stress reaches the maximum value. During the tensile test, the symmetric property of the system is naturally preserved.

RESULTS AND DISCUSSIONS

Figure 2 shows the change of the total energy with the increase of the tensile strain. It can be seen that the total energy decreases before the strain of 1%. After the strain of 1%, the total energy increases. This should be due to the boundary expansion after the initial relaxation (see Figure 3). Therefore there exists the compressive residual stress in the unit cell. When the unit cell is stretched, the residual stress will be relaxed at first, thus the system becomes stable and the total energy becomes lower.

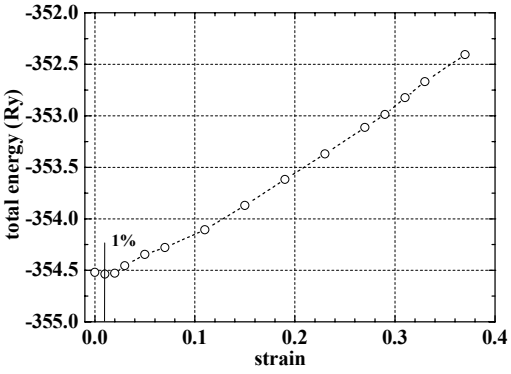

Figure 2: Total energy change with the tensile strain in the *ab initio* tensile test of the Al Σ9 grain boundary

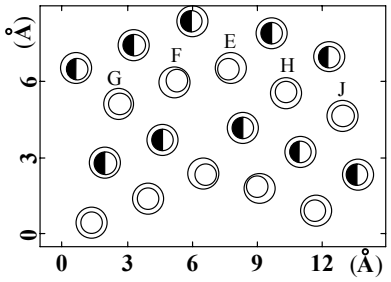

Figure 3: The relaxed configuration of the left half part of layer B and A in the unit cell. G, F, E, H and J correspond to the atoms marked in Figure 1. The atom positions before the relaxation are represented by the smaller circles, in which the unfilled and the half-filled ones represent the atom positions of B and A layer, respectively. The bigger circles indicate the atom positions after the relaxation.

The stress-strain curves of Al grain boundary are shown in Figure 4. Only those of xx($[2\bar{2}1]$), yy($[1\bar{1}4]$), zz([110]) direction are plotted. The stress in other directions is so small to be ignored. Figure 4(a) shows the stress-strain relation in xx direction. At the strain of 3%, the stress on the unit cell becomes positive, thus 3% is set as zero strain in the stress-strain curve. It is shown that the stress increases with the increase of the strain.

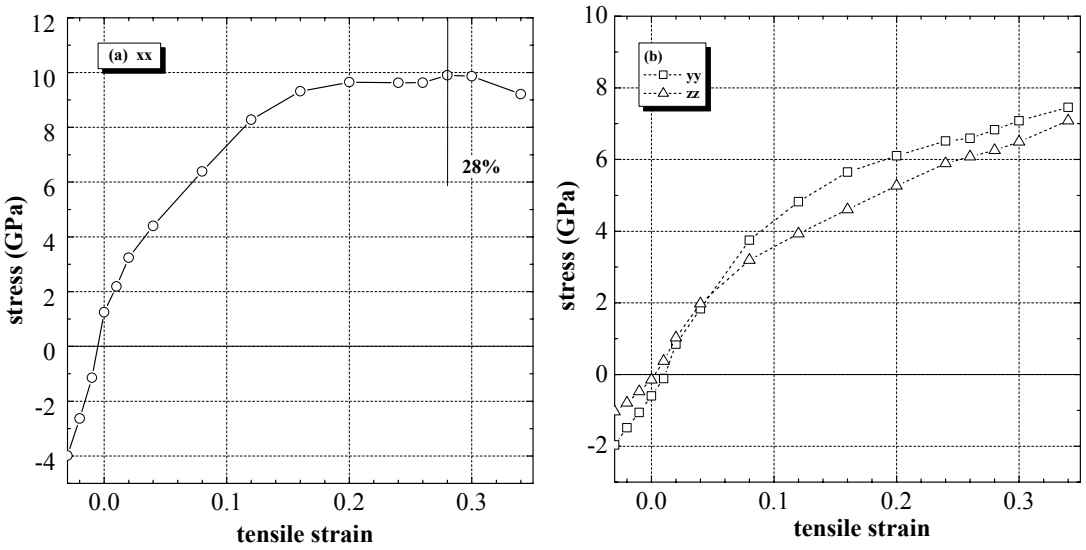

Figure 4: stress-strain relations of Al Σ9 grain boundary
(a) xx direction (b) yy, zz directions

At the strain of 28%, the stress is maximum, about 9.9GPa. After the strain of 28%, the stress decreases.

In real case, the size of yy, zz direction should decrease when the unit cell is stretched according to xx direction. Because the Poisson's ratio is not considered in this tensile test in order to save the computational time, there exists the stress also in the yy, zz directions (see Figure 4(b)).

TABLE 1

THE MAXIMUM STRESS σ_{max} AND THE CORRESPONDING STRAIN ε_{max}

	ε_{max}	σ_{max} (GPa)
Al boundary	28%	9.9
fcc Al [001][a]	20%	11
experiment [b]	2.9%	2.25

[a] ref.[4] [b] ref.[18]

Table 1 shows the maximum stress σ_{max} and the corresponding strain ε_{max} of Al single crystal by both the experiment and the calculation. The maximum stress of Al boundary in our calculation is a bit lower than that of [001] direction of Al single crystal calculated by Deyirmenjian et al.[4], i.e., 11GPa. This means Al grain boundary still bonds strongly. The maximum stress of single crystal of Al fiber tested by Gane[18] is about 2.25GPa, much smaller than that by this calculation. This should be due to:

1. Poisson's ratio is not considered in the calculation. The presence of Poisson's ratio generally decreases the maximum stress.

2. Dislocation is not considered in the calculation. In real crystals, the motion of dislocation usually results in a reduction in strength.

Furthermore, the changes of the charge density and the bond length with the increase

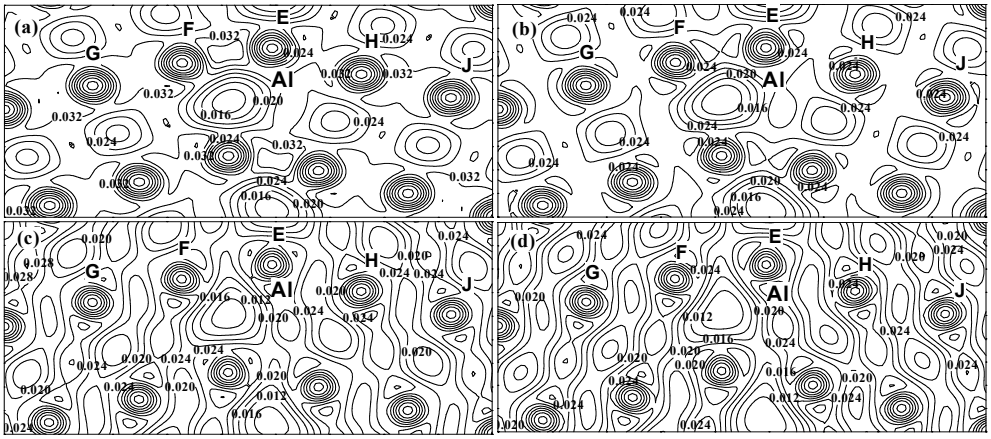

Figure 5: The charge density distribution of the left half part of the B layer in the unit cell (a) no strain (b) 2% (c) 20% (d) 28%

of the strain are investigated. Figure 5 shows the charge density with no strain, and at the strain of 2%, 20% and 28%, respectively, in the left half part of the B layer of the unit cell. It can be indicated that the charge density becomes lower with the increase of the strain. The charge density with no strain between EF bond is above 0.036/a.u.^{3}, and near 0.032/a.u.^{3} at the strain of 2%. Both values are the highest ones comparing to that between other bonds, such as FG, EH, HJ bonds. However, at the strain of 23% the charge density between EF bond is below 0.024/a.u.^{3}, and at the strain of 28% corresponding to the maximum stress, the charge density is below 0.016/a.u.^{3}. Both values are the lowest ones comparing to that between other bonds such as FG, EH, HJ bonds. Therefore it has high possibility that EF bond breaks first.

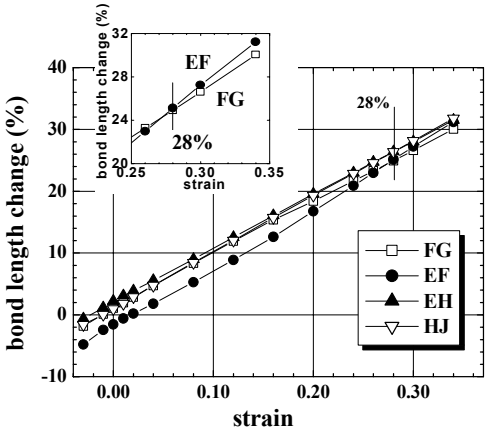

Figure 6: FG, EF, EH, HJ (B layer in the unit cell) bond length changes during the *ab initio* tensile test

Figure 6 shows FG, EF, EH, HJ bond-length changes during the tensile test. The vertical axis is set as:

$$\frac{l - l_{Al}}{l_{Al}} \times 100 \qquad (1)$$

Where l is the bond length of FG, EF, EH or HJ and l_{Al} is the bond length of fcc-Al, i.e. 2.80Å from our calculation. It is clear that the bond length increases with the increase of the strain. At first the four bonds increase in the same rate. However EF bond length increases more rapidly from the strain of 16%. On the contrary, FG bond length increase becomes slower. Therefore it can be concluded that EF bond breaks first with the increase of the strain. Notice EF bond locates just at the boundary, therefore the bond at the boundary breaks first.

CONCLUSIONS

The *Ab initio* tensile test has been applied to Al grain boundary for the first time by first principles molecular dynamics method. The maximum stress is 9.9GPa for Al Σ9 grain boundary at the strain of 28%. This is a bit lower than the maximum stress (11GPa) of [001] direction of Al single crystal calculated by Deyimenjian et al., which means Al grain boundary still bonds strongly. Because the Poisson's ratio and the dislocation are not considered in this calculation, the maximum stress of Al boundary is much higher than that of single crystal of Al fiber (2.25GPa). The changes of the charge density and the bond length indicate that the bonds at the boundary break first.

ACKNOWLEDGEMENTS

The research is supported by the Science and Technology Agency of Japan as the joint research with National Research Institute for Metals (NRIM), and also partly by the Science and Technology Promotion of Japan.

REFERENCES

1. Car, R. and Parrinello, M. (1985) Phys. Rev. Lett., **55**, 2471
2. Teter, M. P., Payne, M. C. and Allan, D. C. (1989) Phys. Rev. B, **40**, 12255
3. Payne, M. C., Teter, M. P., Allan, D. C., Arias, T. A. and Joannopoulos, J. S. (1992) Rev. Mod. Phys., **64**, 1045
4. Deyirmenjian, V. B., Heine, V., Payne, M. C., Milman, V., Lynden-Bell, R. M. and Finnis, M. W. (1995) Phys. Rev. B, **52**, 15191
5. Kohyama, M. (1999) Phil. Mag. Lett., **79**, 659
6. Mills, M.J., and Daw, M.S. (1990) Mat. Res. Soc. Symp. Proc., **183**, 15
7. Nielsen O. H. and Martin R. M. (1985) Phys. Rev. B, **32**, 3780; (1987) **35**, 9308
8. Pickett, W.E. (1989) Comput. Phys. Rep., **9**, 115
9. Hohenber, G P. and Kohn, W. (1964) Phys. Rev. B, **136**, 864
10. Kohn, W., and Sham, L.J. (1965) Phys. Rev. A, **140**, 1133
11. Perdew, J. P., and Zunger, A. (1981) Phys. Rev. B, **23**, 5048
12. Hoekstra, J., and Kohyama, M. (1998) Phys. Rev. B, **57**, 2334
13. Troullier, N., and Martins, J. L. (1991) Phys. Rev. B, **43**, 1993
14. Kleinman, L., and Bylander, S. M. (1982) Phys. Rev. Lett., **48**, 1425
15. Lam, P. K., and Cohen, M. L. (1981) Phys. Rev. B, **24**, 4224
16. Bylander, D. M., Kleinman, L., and LEE, S. (1990) Phys. Rev. B, **42**, 1394
17. Kerker, G. P. (1981) Phys. Rev. B, **23**, 3082
18. Gane, N. (1970) Proc. Roy. Soc. Lond. A, **317**, 367

ORAL/POSTER REFERENCE: ICF100514OR

FIRST-PRINCIPLE AND CLASSICAL MOLECULAR DYNAMICS STUDY ON TENSILE AND SHEAR STRENGTH OF SILICON NITRIDE

S.OGATA[1], H.KITAGAWA[1] and N.HIROSAKI[2]

[1] *Graduate School of Osaka University*
2-1 Yamada-oka, Suita-shi, Osaka 565-0871, Japan
[2] *National Institute for Research in Inorganic Materials*
1-1 Namiki, Tukuba-shi, Ibaraki 305-0044, Japan

ABSTRACT

The intrinsic tensile and shear strength of β- type silicon nitride were determined, using a first-principle molecular dynamics(FPMD) technique based on density functional theory. The results of this simulation were compared with the results obtained from a classical MD simulation, using a 3-body interatomic potential for silicon nitride. The agreement was satisfactory. The classical MD technique, based on the 3-body interatomic potential, was used to perform several simulations of crack propagation, slip and dislocation motion in α- and β- type silicon nitride. From the simulations an estimate of the critical stress intensity factor, the slip planes and directions, and the atomic structure of the dislocation were determined.

KEYWORDS

silicon nitride, tensile strength, shear strength, crack, stress intensity factor, slip plane, dislocation, classical molecular dynamics, first-principle molecular dynamics

INTRODUCTION

Currently, silicon nitride(Si_3N_4) is a very important material because of the inherent superior mechanical properties of the material. In general, Si_3N_4 is classed as polycrystalline, which means that the material properties of Si_3N_4 are determined by studying the single crystal and grain boundaries of Si_3N_4. However, existing experimental studies have used the polycrystalline material for experimental work since large single crystals are difficult to make. Hence, numerical methods are very important for studying the properties of the single crystal. In this study, the mechanical properties of Si_3N_4 are determined by specifically modeling the mechanical behavior of the single crystal.

Ching *et al.*[1] and Belkada *et al.*[2] have calculated the elastic constants, lattice constants and atomic structure of Si_3N_4 single crystals using first principle(FP) calculations based on density functional theory. Wendel and Goddard[3] did the same by using the method of linear combination of atomic orbitals (LCAO). Vashishta *et al.*[4] reported large-scale simulations of a sintering process and the mechanical behavior of a nanocrystal and amorphous Si_3N_4 using the classical MD method, introducing a 3-body interatomic potential for the materials in question.

In this paper, the intrinsic tensile and shear strength of β-Si_3N_4 are obtained using the FPMD simulation technique based on density functional theory. In addition, the slip planes and crack propagation of α- and β-Si_3N_4 are investigated using the classical MD simulation method, with the 3-body interatomic potential proposed by Vashishta *et al.*[5].

INTRINSIC TENSILE AND SHEAR STRENGTH OF β-Si_3N_4

In the FP calculation, a plane wave representation was used to obtain a solution of the Kohn-Sham equations. The local density approximation is adopted to describe the exchange-correlation energy as a function of the electron density. In addition, the pseudopotential approximation is used to estimate ion - electron interaction. The pseudopotentials are generated from the scheme of Troullier-Martins[6]. The pseudopotentials are given in the form used by Kleinman-Bylander[7] and the occupation of states is determined by the Fermi distribution function. Furthermore, the stress tensor is calculated from the explicit symmetric formulas proposed by Lee *et al.*[8].

The conjugate gradient algorithm proposed by Bylander, Kleinman and Lee[9] is employed to achieve a self-consistent electronic ground state. Each relaxed atomic configuration is obtained by the simulated annealing process.

Tensile Strength

The simulation performed to estimate the tensile strength was carried out using a 28 atom periodically repeated supercell($7.95 \times 13.155 \times 2.902 \times 10^{-10}$m) with a plane wave cutoff energy of 2.6×10^{-16}J (60 Ry). Five k-points were used for the Brillouin zone sampling. Uniaxial tensile deformations were simulated by increasing the uniaxial tensile strains along the z-direction, while the other supercell dimensions were fixed. The atomic configuration was relaxed at each strain level and this configuration was then used as the initial configuration for the next stain level. The tensile axis is defined to be parallel to the c-axis direction of the β-Si_3N_4 which is predicted to be the strongest direction. Calculated energy-strain and stress-strain curves are shown in Figure 1. The ideal tensile strength in this direction is estimated as 74 GPa. To examine the validity of the 3-body potential for the investigation of tensile properties, the result obtained using the 3-body potential was compared with this first-principle calculation(also shown in Figure 1). The energy values obtained from the 3-body potential are in good agreement with the values obtained from the FP calculation. However, calculated stress at large strain levels and the tensile strength are smaller.

Shear Strength

The supercell used in the calculation of the shear strength is shown in Figure 2. The x,y and z directions are defined as the <1000>, <01$\bar{1}$0> and <0001> directions of the β- crystal, respectively. This model contains 84 atoms, with the dimensions of the model

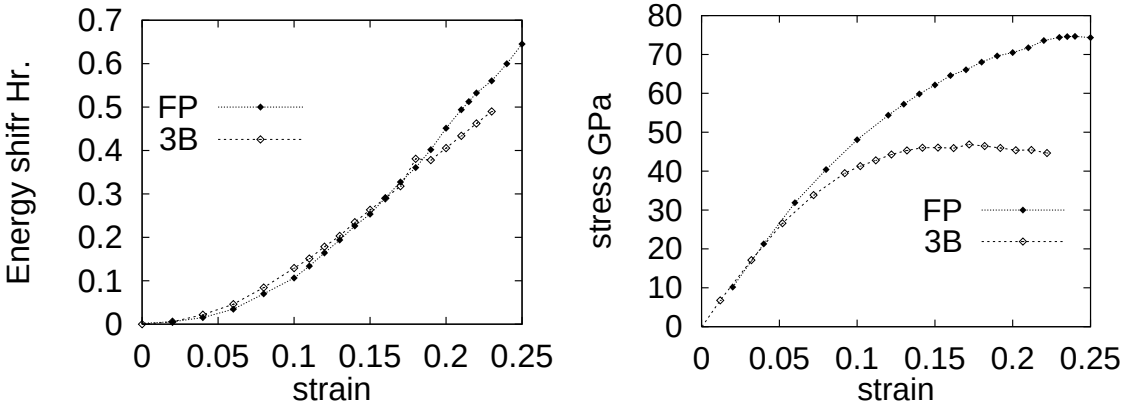

Energy-stain curve
(1Hr.=4.36×10^{-18} J)

Stress-strain curve

Figure 1: Energy-strain and stress-strain curve of β-Si_3N_4

shown in Figure 2. Shear deformation is simulated by means of a sliding procedure of the rigid center region as shown in Figure 2. The slip direction and plane orientation correspond to the primary slip system of β-Si_3N_4 proposed from experimental results. This was also confirmed using a MD simulation which will be discussed later.

For this simulation process, the relaxation of the atomic structure was not performed. The plane wave cut-off energy of 1.6×10^{-16}J (36 Ry) and four k-points are used for the FP calculation. The energy shift from a perfect crystal are estimated from the FP calculation and the 3-body potential (Figure 2). The results obtained from the 3-body potential are in good agreement with that of the first principle method. The ideal shear strength was estimated from the atomic force as approximately 22 GPa using the first principle method, and approximately 28 GPa using the 3-body potential. It is concluded that the 3-body interatomic potential is valid for the modeling of the shearing process.

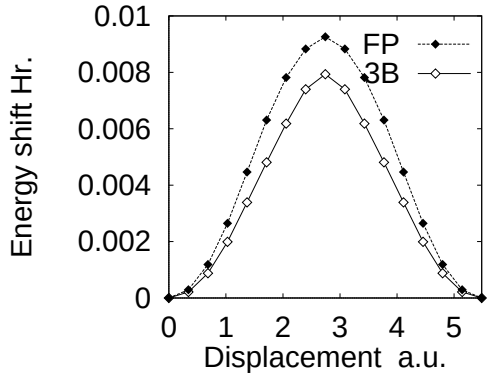

Model super cell

Energy-displacement curve
(1Hr.=4.36×10^{-18} J)
(1 a.u.=0.529×10^{-10} m)

Figure 2: Model super cell and energy curve of first principle shearing simulation

Four types of shear deformation are modeled, to examine the properties of the slip system, which are, α-$\{1\bar{1}01\}<11\bar{2}0>$ (Case 1), α-$\{10\bar{1}0\}<0001>$ (Case 2), β-$\{10\bar{1}0\}<0001>$ (Case 3), and β-$\{10\bar{1}0\}<1\bar{2}10>$ (Case 4). Cases 1 and 2 correspond to the possible primary slip systems which were reported by Suematsu *et al.*[10], and Niihara and Hirai [11], respectively. Case 3 corresponds to the primary slip system which was reported by Evans *et al.*[12], Kawahara *et al.*[13] and Milhet *et al.*[14]. Finally Case 4 corresponds to the secondary slip system reported by Kawahara *et al.*[13].

Snapshots of the atomic arrangement in the model under shear deformation are shown in Figure 3. The sliding directions are from left to right of the figures. The sliding speed was 10 m/s. The black and gray circles represent nitrogen and silicon atoms, respectively. Only those atoms which have a coordination number that differs from that of the perfect crystal are shown.

The shear stress was calculated as the sum of all the atomic forces of the fixed atoms along the shear direction divided by the initial area of the slip plane. The shear strength is estimated from the maximum shear stresses as 25 GPa(Case 1), 20 GPa(Case 2), 18.5 GPa(Case 3), and 17 GPa(Case 4).

In Case 1, no plastic deformation in the sliding direction was observed (Figure 3). However, Suematsu *et al.* [10] asserted that this direction is one of the possible slip systems from Knoop hardness testing. This discrepancy may be due to an effect of hydrostatic stress produced by Knoop hardness testing. However, slip deformation in Case 2, Case 3, and Case 4 was observed. In particular in Case 3 slip progresses by dislocation movement. The width of the dislocation is estimated to be approximately 8Å.

Case 1 Case2

Case 3 Case4

Figure 3: Atomic arrangements under shear deformation

CLASSICAL MD CRACK PROPAGATION IN α AND β-Si_3N_4

The MD crack propagation analysis was performed to determine the critical stress intensity factor. Cubic cells in which the a and c axes of α- and β-Si_3N_4 are along the x and z directions, respectively, were used. The cells contain approximately 10,000 atoms and the dimensions for the x, y and z axis were approximately 9 nm, 9 nm and 1.2 nm, respectively. Initially, a crack was inserted and the crack front was placed along the z axes. The initial atomic displacements were taken from the mode I linear elastic solutions corresponding to a stress intensity factor K_I. Following this the atomic configurations was relaxed for 1.2 ps, except for the outermost atoms within 0.6 nm of the cell boundaries. If the crack tip did not move after the relaxation process is complete, the critical stress intensity factor K_{Ic} can be estimated from K_I. Four cases were calculated, i.e. for the crack tip in the prism and basal plane of each α- and β- crystal. The results are listed in Table 1. Reimanis *et al.*[15] estimated the K_{Ic} for α- crystal as 1.5$\sim$2.0 MPa$\sqrt{\text{m}}$ from the Knoop tests and for β- as 1.3$\sim$1.4 MPa$\sqrt{\text{m}}$ from the theoretically calculated bond energy. The results presented in this paper are in good agreement with the estimations of Reimanis *et al.* However, it is possible that our estimated of K_{Ic} is somewhat smaller than the true K_{Ic} value because of the under estimation of stress and ideal strength by the 3-body potential.

Table 1: Critical stress intensity factors of silicon nitride

crystal type	crack plane	crack front	K_{Ic} MPa$\sqrt{\text{m}}$
α	(0001)	$[01\bar{1}0]$	1.5
α	$(01\bar{1}0)$	[0001]	1.3
β	(0001)	$[01\bar{1}0]$	1.7
β	$(01\bar{1}0)$	[0001]	1.4

CONCLUSION

The intrinsic tensile and shear strength of β-Si_3N_4 was found to be 74GPa and 28GPa, respectively. It is found that the 3-body potential used to calculate results for Si_3N_4 are of an acceptable accuracy. Furthermore, the primary slip system of α- and β- Si_3N_4 was determined as $\{10\bar{1}0\}<0001>$. The critical stress intensity factors for several mode I cracks were also calculated and are in good agreement with the data reported by Reimanis *et al.*

REFERENCES

1. W. Y. Ching, Y-N. Xu, J. D. Gale and M. Rühle (1998) "Ab-Initio Total Energy Calculation of α- and β-Silicon Nitride and the Derivation of Effective Pair Potentials with Application to Lattice Dynamics ",*J. Am. Ceram. Soc.*, **81**, pp.3189-3196.
2. R. Belkada, T.Shibayanagi, M. Naka and M. Kohyama (2000)"*Ab-initio* Calculation of the Atomic and Electronic Structure of β-Silicon Nitride",*J. Am. Ceram. Soc.*, **83**, pp.2449-2454.
3. J.A.Wendel and W.A.Goddard III (1992) "The Hessian Biased Force Field for Silicon Nitride Ceramics: Predictions of Thermodynamic and Mechanical Properties for α- and β-Si_3N_4",*J. Chem. Phys.*, **97**, pp.5048-5062.

4. P.Vashishta, R.K.Kalia and I.Ebbsjö (1995) "Low-Energy Floppy Modes in High-Temperature Ceramics",*Phys. Rev. Lett.*, **75**, pp.858-861.
5. R. Vashishta, R. K. Kalia, A. Nakano, and I. Ebbsjö (1996) "Amorphous Insulators and Semiconductors", Ed. by M.F.Thorpe and M.I. Mitkova, Kluwer, Dordrooht, pp.151-213.
6. N. Troullier and J.L. Martins (1991) "Efficient Pseudopotentials for Plane-Wave Calculations", *Phys.Rev.,B*, **43**, pp.1993-2006.
7. L. Kleinman and D.M. Bylander (1982) "Efficacious Form for Model Pseudopotentials", *Phys.Rev.Lett.*, **48**, pp.1425-1428.
8. I.H. Lee, S.G. Lee and K.J. Chang (1995) "Symmetric Stress Tensor in the Local-Density-Functional Framework using a Separable Nonlocal Pseudopotential", *Phys.Rev.,B*, **51**, pp.14697-14700.
9. D.M. Bylander, L. Kleinman and S. Lee (1990) "Self-Consistent Calculations of the Energy Bands and Bonding Properties of $B_{12}C_3$", *Phys.Rev.,B*, **42**, pp.1394-1403.
10. H.Suematsu, J.J.Petrivic and T.E.Mitchell (1996) "Plastic deformation of silicon nitride single crystal", *Mat. Sci. Eng., A*, **209**, pp.97-102.
11. K.Niihara and T.Hirai (1979) "Growth, Morphology and Slip System of α-Si_3N_4", *J. Mat. Sci.*, **14**, pp.1952-1960.
12. A.G.Evans and J.V.Sharp (1971) "Microstructural Studies on Silicon Nitride", *J. Mat. Sci.*, **6**, pp.1292-1302.
13. K.Kawahara, S.Tsurekawa and H.Nakashima (1996) "An Activated Slip Systems in β-Silicon Nitride during High Temperature Deformation", *J. Japan Inst. Metals*, **60**, pp.582-588.
14. X. Milhet, H. Garem, J. L. Demenet, J. Rabier, and T. Rouxel (1997), "Dislocation Studies in β-Silicon Nitride", *J. Mat. Sci.*, **31**, pp.3733-3738.
15. I.E. Reimanis, H. Suematsu, J.J. Petrovic and T.E. Mitchell (1996) "Mechanical Properties of Single-Crystal α-Si_3N_4", *J. Am. Ceram. Soc.*, **79**, pp.2065-2073.

ICF100749OR

FIRST-PRINCIPLES CALCULATIONS OF THE TENSILE STRENGTH AND FRACTURE OF COINCIDENCE TILT BOUNDARIES IN SiC

M. Kohyama

Interface Science Research Group, Special Division of Green Life Technology,
National Institute of Advanced Industrial Science and Technology,
Ikeda, Osaka 563-8577, Japan

ABSTRACT

Ab initio tensile tests have been applied to the polar and non-polar interfaces of the {122}Σ=9 coincidence tilt boundary in cubic SiC, where the tensile strength and fracture have been examined through the behavior of electrons and atoms based on the density-functional theory. The tensile strength of these interfaces is very large and over 80% of that of bulk crystal, because of the reconstruction of interfacial bonds. However, the presence of the interfacial C–C and Si–Si wrong bonds seriously affect the strength and fracture. The N-type polar interface with C–C bonds is the strongest. For the non-polar interface with both C–C and Si–Si bonds, the fracture starts from the back Si–C bond of the C–C bond because of local stress concentration at the atomic scale, and the fracture proceeds from bond to bond rather continuously. The P-type polar interface with Si–Si bonds does not reveal remarkable local stress concentration, because of the highly symmetric configuration. Thus this interface is stronger than the non-polar one, and the fracture occurs rather catastrophically. For the Si–C bond breaking, we have found the general critical bond stretching dominating the criterion of the fracture.

KEYWORDS

SiC, grain boundary, coincidence boundary, first-principles calculation, tensile strength, fracture, electronic structure

INTRODUCTION

SiC is a very important material as a high-performance ceramic. Grain boundaries dominate various properties of SiC ceramics. The understanding of mechanical properties of SiC grain boundaries is of great importance. For this purpose, it is essential to examine the behavior of grain boundaries under various tensile or shear stresses. In covalent materials like SiC, such mechanical behavior should be seriously dominated by the behavior of both electrons and atoms. Currently, by virtue of the development of the first-principles molecular-dynamics method [1] based on the density-functional theory [2], such complicated problems can be dealt with theoretically [3] in a similar way to recent theoretical studies of the mechanical behavior of bulk crystals [4,5] and defects [6]. In this paper, we investigate the tensile

strength and fracture of a coincidence tilt boundary in cubic SiC theoretically through the behavior of electrons and atoms [7].

THEORETICAL METHOD

We deal with the $\{122\}\Sigma=9$ boundary in cubic SiC. This is a typical coincidence tilt boundary frequently observed in chemical vapour-deposited SiC [8]. Two polar and one non-polar interfaces can be constructed by inverting the polarity of each grain as shown in Fig. 1 [9]. In each model, all the interfacial atoms are four-fold coordinated similarly to the same boundary in Si, and two sets of five-membered and seven-membered rings constitute one period along the $\langle 411 \rangle$ direction. However, the polar interfaces are non-stoichiometric and the non-polar interface is stoichiometric. The N-type polar interface contains two C–C wrong bonds and two interfacial Si–C bonds per period, although the P-type polar interface contains two Si–Si wrong bonds and two interfacial Si–C bonds per period. The non-polar interface contains both C–C and Si–Si wrong bonds and two interfacial Si–C bonds.

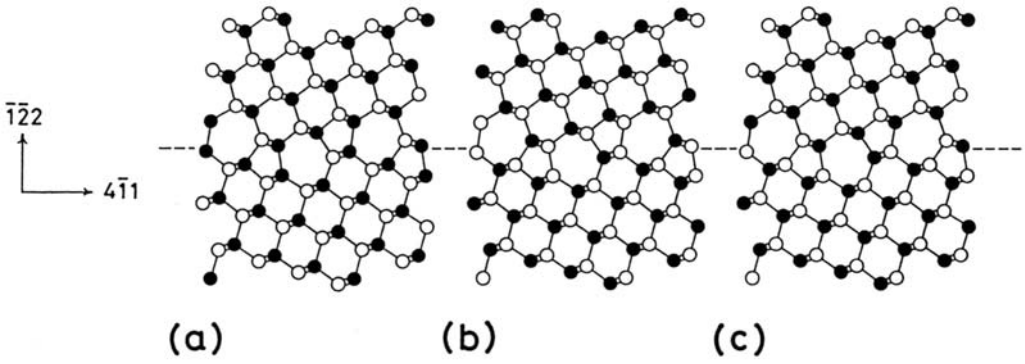

Figure 1: Atomic models of the $\{122\}\Sigma=9$ boundary in SiC. (a)N-type polar, (b) P-type polar, and (c) non-polar interfaces. Atomic positions are projected along the $\langle 011 \rangle$ axis. Empty and closed circles represent Si and C atoms, respectively.

We construct a 64-atom supercell. For the non-polar interface, the cell contains two equivalent interfaces with a distance of about $\frac{8}{3}a_0$. For the polar interfaces, it is necessary to stack two different polar interfaces alternately in the same cell by the geometric constraint. However, computations can be executed without any problems because the wrong bonds do not generate any extra carries or deep states in SiC.

Total energies, atomic forces and averaged stresses [10] can be obtained through the electronic-structure calculations of the supercell in the framework of the plane-wave pseudopotential method [11] with the local density-functional theory [12]. We use the conjugate-gradient technique [13] and the optimized pseudopotentials [14] for efficient computations. A plane-wave cutoff energy of 816 eV is used. We use the equilibrium lattice constant by the present theoretical method, which is 98.9% of the experimental one. Two special $\mathbf{k}$ points per irreducible eighth of the Brillouine zone are used. More details of the scheme are given in [7].

Initially, the stable configurations are obtained through relaxation from the models in Fig. 1. Then we perform the *ab initio* tensile test [6], where uniaxial tensile strain is introduced into the stable configuration. First, the cell is stretched in a small increment in the direction normal to the interface, and the atomic positions are changed by uniform scaling. Second, all the atoms are relaxed through iterative electronic-structure calculations until all the atomic forces are less than a tolerance value. Third, the total energy and stress tensor are calculated. This cycle is iterated until the interfaces are broken. This procedure corresponds to a real slow tensile test at T=0K [6]. For the non-polar interface, two equivalent interfaces in the cell are broken at the same time, because the symmetric property of the cell

is preserved in the calculation. For the polar interfaces, only a weaker interface in the cell is broken.

RESULTS AND DISCUSSION

In the stable configurations, all the interfacial bonds are well reconstructed within small bond distortions. Bond lengths and bond charges of C–C and Si–Si wrong bonds are rather similar to those in bulk diamond and Si. The bond-length and bond-angle distortions of the other Si–C bonds range from –2.9% to +2.9% and from –22.4° to +27.9°, respectively, for the non-polar interface. The bond distortions range from –2.7% to +2.5% and from –13.0° to +24.0° for the P-type polar interface, and from –2.7% to +2.0% and from –20.1° to +22.5° for the N-type polar interface. The boundary energy of the non-polar interface is 1.27 Jm^{-2}, which is very much smaller than that of two surfaces. The averaged boundary energy of the two polar interfaces is a little smaller (1.24 Jm^{-2}).

Fig. 2 shows the stress–strain curves in the tensile tests of the non-polar and polar interfaces. Stresses along the ⟨411⟩ and ⟨011⟩ directions parallel to the interfaces are also generated. Strictly speaking, the cell sizes along these two directions should be adjusted in each step so as to remove such stresses. However, this effect is not so serious, because such stresses are relatively small due to the low Poisson's ratio of cubic SiC. From the curves, the Young's modulus of the non-polar interface is 519 GPa, and the averaged value of the polar interfaces is 531 GPa. These are comparable with the bulk SiC value along the ⟨111⟩ direction, 558 GPa, by a similar first-principles calculation [4].

For the non-polar interface in Fig 2(a), the fracture starts at the strain of 12%. The maximum tensile stress is about 42 GPa at 14%, which is the strength of the non-polar interface. For the polar interfaces in Fig. 2(b), the P-type interface with Si–Si bonds is broken at the strain over 14%, and the N-type interface with C–C bonds is not broken. The maximum stress of about 48 GPa is the strength of the P-type interface. The fracture of this interface occurs rather catastrophically as seen in the sharp decrease of the stress in Fig.2 (b), which is in contrast to the gradual decrease in Fig. 2 (a).

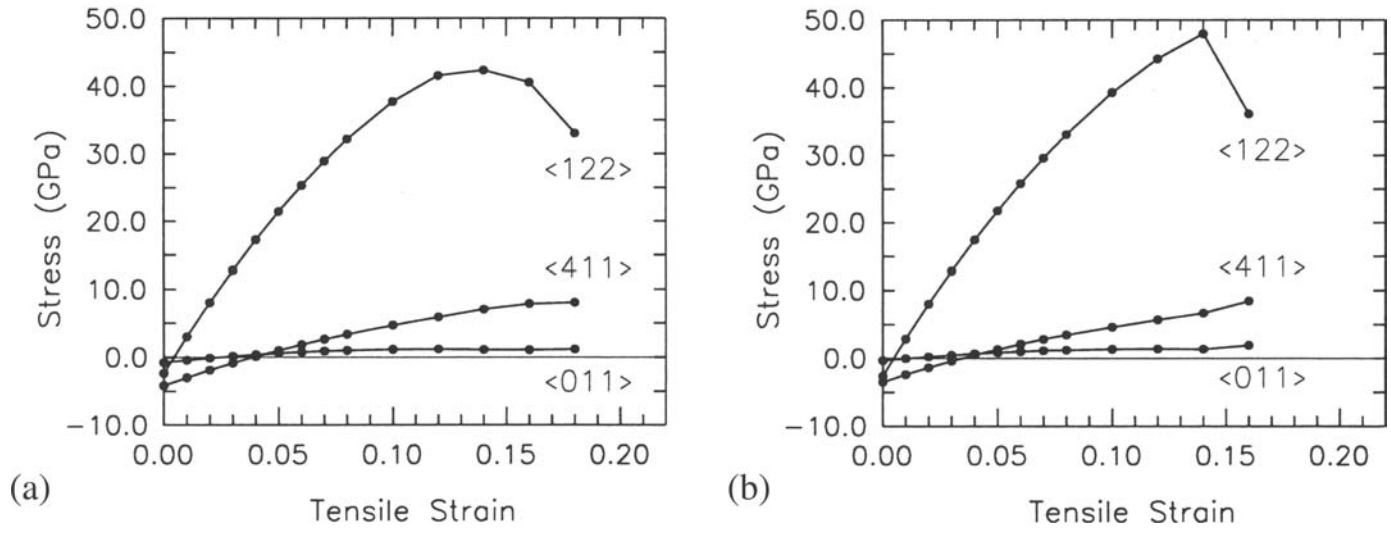

Figure 2: (a) Stress–strain curve of the non-polar interface. (b) Stress–strain curve of the polar interfaces.

The N-type polar interface is the strongest, and the non-polar interface is the weakest among the three interfaces. The tensile strength of these interfaces is very large because of the reconstruction of interfacial bonds. The strength is over 80% of the theoretical strength of bulk SiC along the ⟨111⟩ direction, 50.8 GPa [4], which is in good agreement with the experimental value of 53.4 GPa for a SiC nanorod [15]. The strength of these interfaces is very much larger than the observed macroscopic tensile strength of SiC ceramics, which is usually less than 1 GPa. In usual ceramics, fracture starts from pre-existing

cracks. Under lower macroscopic stresses, the stress concentration occurs at the crack tip. If the local stress at the crack tip exceeds some critical value, the crack should propagate. The present calculated strength of the interfaces and the bulk crystal should correspond to such critical local stress values for the crack propagation, which dominate the behavior of cracks. From the calculated results, the present interfaces should not act as an initial point of fracture, or not necessarily act as a preferential fracture path.

In the fracture of the non-polar interface shown in Fig. 3, the back Si–C bond of the C–C bond is broken first. This is due to the local stress concentration at the atomic scale caused by the special large strength and short bond length of the C–C bond like a diamond bond. At the tensile strain of 10%, the bond stretchings of the C–C bond and the back Si–C bond are +7.0% and +19.4% against the bond lengths of bulk diamond and SiC, respectively. At the strain of 12% shown in Fig. 3(a), the back bond is suddenly stretched into +27.8%, while the C–C bond shrinks into +6.4%. The C–C bond shrinks much more hereafter. Thus the back Si–C bond has been almost broken at this point.

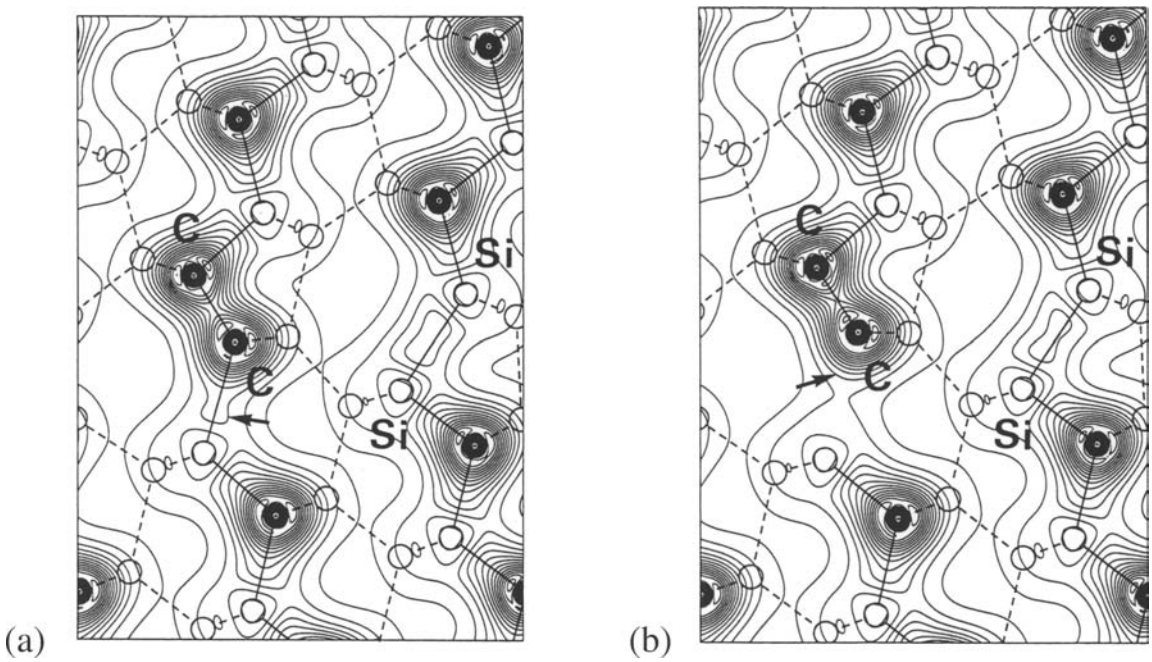

Figure 3: Atomic configurations of the non-polar interface for strains of (a) 12% and (b) 14%. Valence charge densities on the {011} plane are plotted by the contours from 0.015 to 0.275 a.u.$^{-3}$ with a spacing of 0.02 a.u.$^{-3}$. Arrows indicate contours of the same value at the back Si–C bond of the C–C bond.

At the strain of 14%, the stretching of the back Si–C bond is +46.3%, and the bond charge clearly disappears as shown in Fig. 3(b). At this point, the fracture proceeds to near interfacial Si–C bonds, where the stretchings of two interfacial bonds are +20.9% and +19.5%. At the strain of 16%, these two bonds are almost broken, and the breaking of the Si–Si bond starts. The fracture proceeds rather continuously from bond to bond. This feature is consistent with the shape of the stress–strain curve in Fig. 2 (a).

From the breaking of the Si–C bonds in the non-polar interface, we can deduce the critical Si–C bond stretching. Once the bond stretching exceeds about 20%, the Si–C bond cannot sustain the stress, and is rapidly stretched and broken. The bond charge clearly disappears whenever the stretching exceeds about 30%. This is consistent with results of bulk SiC [4]. Thus the criterion for the start of interfacial fracture is the generation of Si–C bond stretching over the critical value.

In the tensile test of the polar interfaces, there occurs no remarkable local stress concentration at the interfaces before the strain of 14%, because of the highly symmetric configurations. Thus the supercell is

stretched without any bond breaking till the strain of 14%, which results in the maximum tensile stress larger than that of the non-polar interface. At the strain of 14%, the stretching of the two Si–C bonds at the P-type interface indicated in Fig. 4(a) is +21.3%, which reaches the criterion of the Si–C bond breaking for the first time. The reason why these two Si–C bonds are greatly stretched is that the Si–Si bonds constituting seven-membered rings with these two Si–C bonds are long and easily stretched. At this point, the length of the Si–Si bond is +41.7% against the bulk SiC bond length. On the other hand, the maximum Si–C bond stretching is +17.3% for the N-type interface at this point. Therefore the two Si–C bonds at the P-type interface are broken rapidly during the relaxation at the strain of 16%. This means the breaking of a half of interfacial bond chains sustaining the stress in one period of the interface. Thus the two Si–Si bonds are also broken rapidly just after the Si–C bond breaking in the relaxation at 16%. At the same time, all the bonds at the N-type interface in the supercell shrink. In this way, the fracture of the P-type polar interface occurs rather catastrophically as shown in Fig. 4(b) and Fig. 2(b).

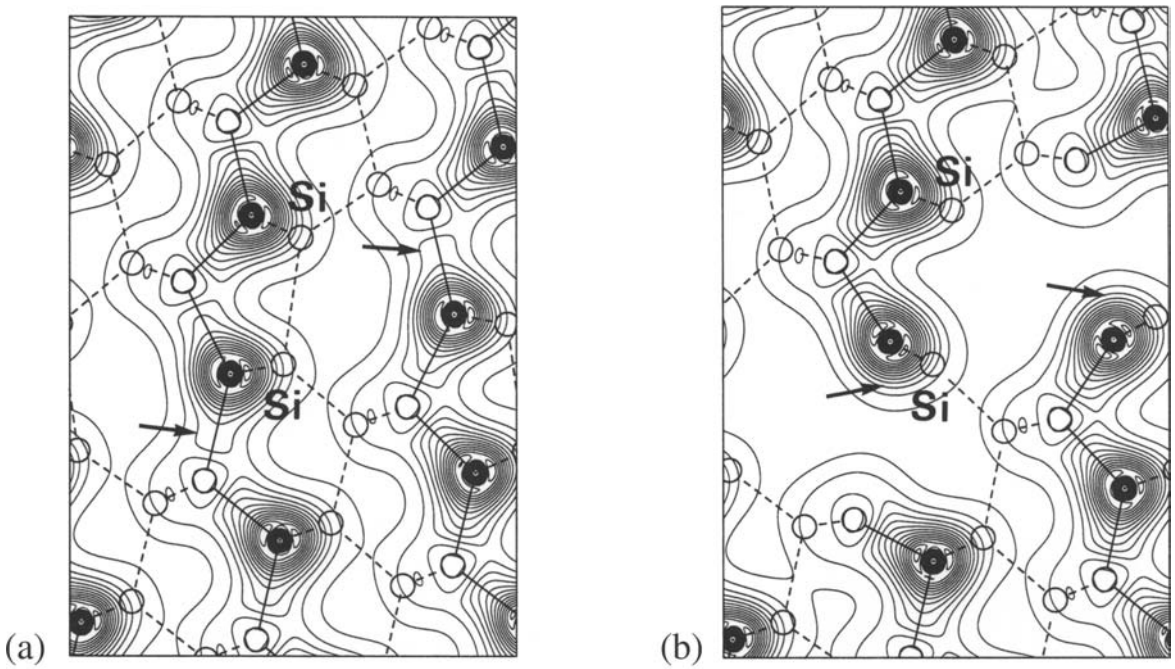

Figure 4: Atomic configurations of the P-type polar interface for strains of (a) 14% and (b) 16%. Arrows indicate contours of the same value at the Si–C bonds breaking first. Note that the Si–Si bond is located on the {011} plane other than that on which the densities are plotted.

The changes in the electronic structure during the tensile test have been examined in detail for the non-polar interface. The valence-band width and the band-gap width are gradually decreased. However, there seem to exist no dramatic changes associated with the bond breaking. The system is semiconducting even after the bond breaking. This feature can be explained as rather continuous changes of occupied and unoccupied weak-bond states into occupied C and unoccupied Si dangling-bond states, respectively, without generating deep gap states. This should be typical of compounds with both covalent and ionic characters.

About the effects of the cell size along the ⟨122⟩ direction, we think that the present cell size is sufficient. This is because the atomic layers in the bulk regions in the present cell seem to behave like a bulk crystal with a uniform expansion along the ⟨122⟩ direction. Concerning the effects of high temperature which are not included in the present calculations, thermal lattice dynamics and electronic excitation are important. The former may reduce the maximum strength, because bond stretchings over the criterion of breaking may occur locally associated with lattice dynamics. The latter may also reduce the strength, although this should be substantial only at very high temperature because of the large band gap.

CONCLUSION

The *ab initio* tensile test has been applied to polar and non-polar interfaces of a coincindence tilt boundary in SiC. The intrinsic tensile strength and fracture have been clarified through the behavior of electrons and atoms based on the density-functional theory. Coincidence tilt boundaries with reconstructed interfacial bonds should have large strength comparable with the bulk crystal, and should not act as an initial point of fracture or a fracture path. However, the kinds and arrangement of Si–Si and C–C wrong bonds seriously affects the strength and features of fracture. It seems that atomic-scale inhomogeneity or singularity by the presence of wrong bonds induces local stress concentration at the atomic scale, which should lower the strength. It is of great interest to apply the present kind of calculations to different kinds of boundaries or boundaries with impurities or dopants. The present kind of calculations are promising tools to investigate the basic mechanical properties of materials interfaces.

ACKNOWLEDGEMENT

The author is grateful to Dr. K. Tanaka and Dr. S. Tanaka for fruiteful discussions. The present study was supported by the Science and Technology Agency of Japan as the project 'Frontier Ceramics'.

REFERENCES

1. Car, R. and Parrinello, M. (1985). *Phys. Rev. Lett.* **55**, 2471.
2. Hohenberg, P. and Kohn, W. (1964). *Phys. Rev.* **136**, B864; Kohn, W. and Sham, J.L. (1965). *ibid.* **140**, A1133.
3. Molteni, C., Francis, G.P., Payne, M.C. and Heine, V. (1996). *Phys. Rev. Lett.* **76**, 1284.
4. Li, W. and Wang, T. (1999). *Phys. Rev. B* **59**, 3993.
5. Pérez, R. and Gumbsch, P. (2000). *Phys. Rev. Lett.* **84**, 5347.
6. Deyirmenjian, V.B., Heine, V., Payne, M.C., Milman, V., Lynden-Bell, R.M. and Finnis, M.W. (1995). *Phys. Rev. B* **52**, 15191.
7. Kohyama, M. (1999). *Phil. Mag. Lett.* **79**, 659.
8. Tanaka, K. and Kohyama, M. (1998). In: *Electron Microscopy 1998, Vol. II*, p.581, Benavides, H.A.C. and Yacamán, M.J. (Eds.), Institute of Physics, Bristol.
9. Kohyama, M., Kose, S., Kinoshita, M. and Yamamoto, R. (1990). *J. Phys.: Condens. Matter* **2**, 7809; Kohyama, M., Kose, S., Kinoshita, M. and Yamamoto, R. (1991). *ibid.* **3**, 7555; Kohyama, M. (1997). *Mater. Chem. Phys.* **50**, 159.
10. Nielsen, O.H. and Martin, R.M. (1985). *Phys. Rev. B* **32**, 3780.
11. Hamann, D.R., Schlüter, M. and Chiang, C. (1979). *Phys. Rev. Lett.* **43**, 1494.
12. Perdew, J.P. and Zunger, A. (1981). *Phys. Rev. B* **23**, 5048.
13. Payne, M.C., Teter, M.P., Allen, D.C., Arias, T.A. and Joannopoulos, J.D. (1992). *Rev. Mod. Phys.* **64**, 1045.
14. Troullier, N. and Martins, J.L. (1991). *Phys. Rev. B* **43**, 1993.
15. Wong, E.W., Sheehan, P.E. and Lieber, C.M. (1997). *Science* **277**, 1971.

ICF100509OR

Flow and Fracture of Free-Standing Thin Films and Multilayers

Haibo Huang, Denis Y.W. Yu and Frans Spaepen

Division of Engineering and Applied Sciences, Harvard University,
Cambridge, MA 02138, USA

ABSTRACT

Free-standing polycrystalline films of Ag, Cu and Ag/Cu multilayers were tested in tension using an optical diffraction grating for the measurement of the strain. The yield stress and the rate of work hardening both increase strongly with decreasing layer thickness. These effects combine to raise the stress for ductile fracture up to 700 MPa and to lower the maximum plastic strain.

KEYWORDS

Thin films, multilayers, yield stress, Hall-Petch, work hardening, fracture stress, ductile fracture.

INTRODUCTION

The study of the mechanical properties of thin films and multilayers is of considerable technological interest. At the same time, the microstructural control provided by the deposition processes of these films makes it possible to study systematically the effects on mechanical behavior of two length scales, the grain size and the individual layer thickness. These are not independent: if the deposition temperature is sufficiently high to allow extensive surface diffusion, the grain size is similar to the thickness of the film (if single component) or of the individual layer thickness in multilayers [1,2].

The main difficulty in the mechanical testing of thin films is the accurate measurement of the strain, which should be carried out directly on the deforming sample [3,4,5]. In our laboratory, we developed a technique based on optical diffraction from a lithographically

deposited grid [6]. It allows accurate determination of elastic strains as well as measurements of large plastic strains.

In this paper, we describe the technique and review the results obtained on Ag and Cu thin films, as well as Ag/Cu multilayers [7]. The dependence of the yield stress on the layer thickness is analyzed in terms of the Hall-Petch relation and compared to the results from hardness tests. The rate of work hardening strongly increases with decreasing layer thickness [2]. These results are used to interpret the trends observed in the fracture stress, the ductility and the fracture surface morphology.

EXPERIMENTAL METHODS

Thin film samples were deposited through a dogbone-shaped mask on glass substrates by electron beam deposition in high vacuum. Typical dimensions were a thickness of 3 μm, a gauge length of 10 mm and a width of 3 mm. The bilayer repeat length of the multilayers varied from 3 nm to 3 μm, depending on the number of layers. The thickness of the Ag and Cu layers was equal. Both the pure films and the multilayers had a strong <111> texture.

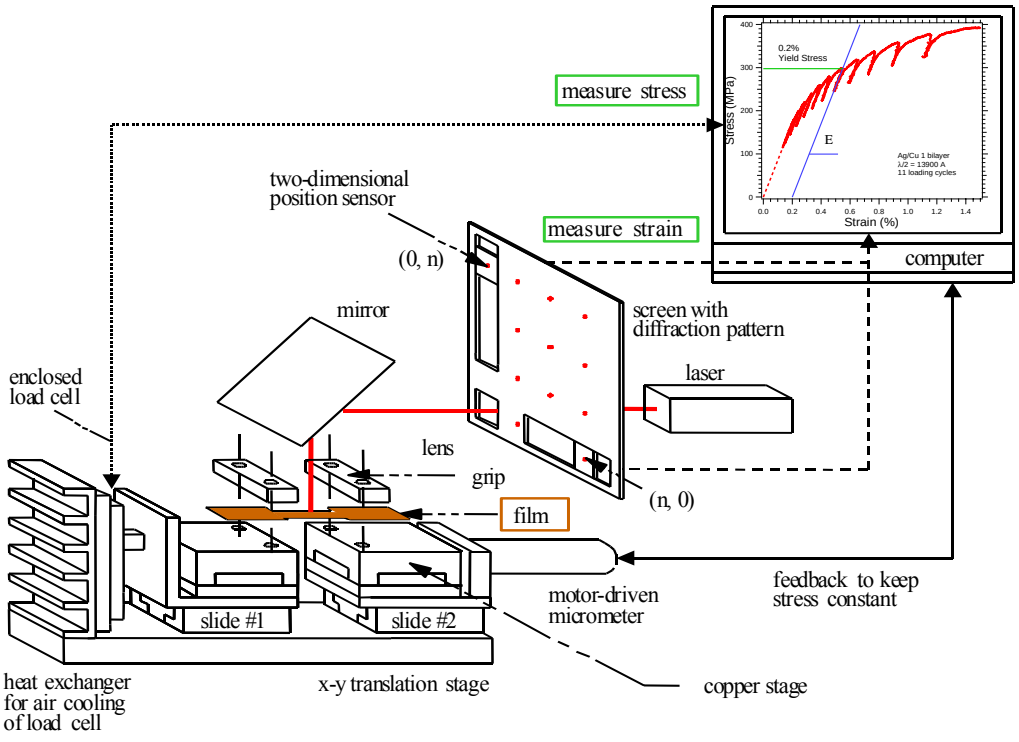

Figure 1: Schematic diagram of the tensile tester for thin film samples [7].

A thin, very compliant, two-dimensional square grid of photoresist dots (see Figure 4(a) for an oblique view) was deposited on the films by photolithography. The films were then removed from the substrate and placed in the grips of the tensile apparatus of Figure 1. The differences between the positions of two spots of the diffraction pattern produced by a

He-Ne laser, monitored by two-dimensional position-sensitive detectors, were used to determine the longitudinal and transverse strains. The transverse waviness that developed during plastic flow, however, made the measured transverse strains, and hence Poisson's ratio, unreliable.

The result of a typical test is shown on the computer screen of Figure 1. The initial stages of the tests did not yield meaningful data because it is impossible to mount the samples such that they are perfectly taut. It was therefore necessary to deform the sample first and to determine Young's modulus from partial unloading. The value of the modulus was then used to reconstruct the initial elastic loading line; its intersection with the zero-stress axis determined the origin for the strains. The yield stress, σ_y, was determined at the conventional value of 0.2% plastic strain. The full stress-strain curve is the outer envelope of the data. All tests were carried out at room temperature and at a strain rate of 1.1×10^{-5} s^{-1}.

RESULTS AND DISCUSSION

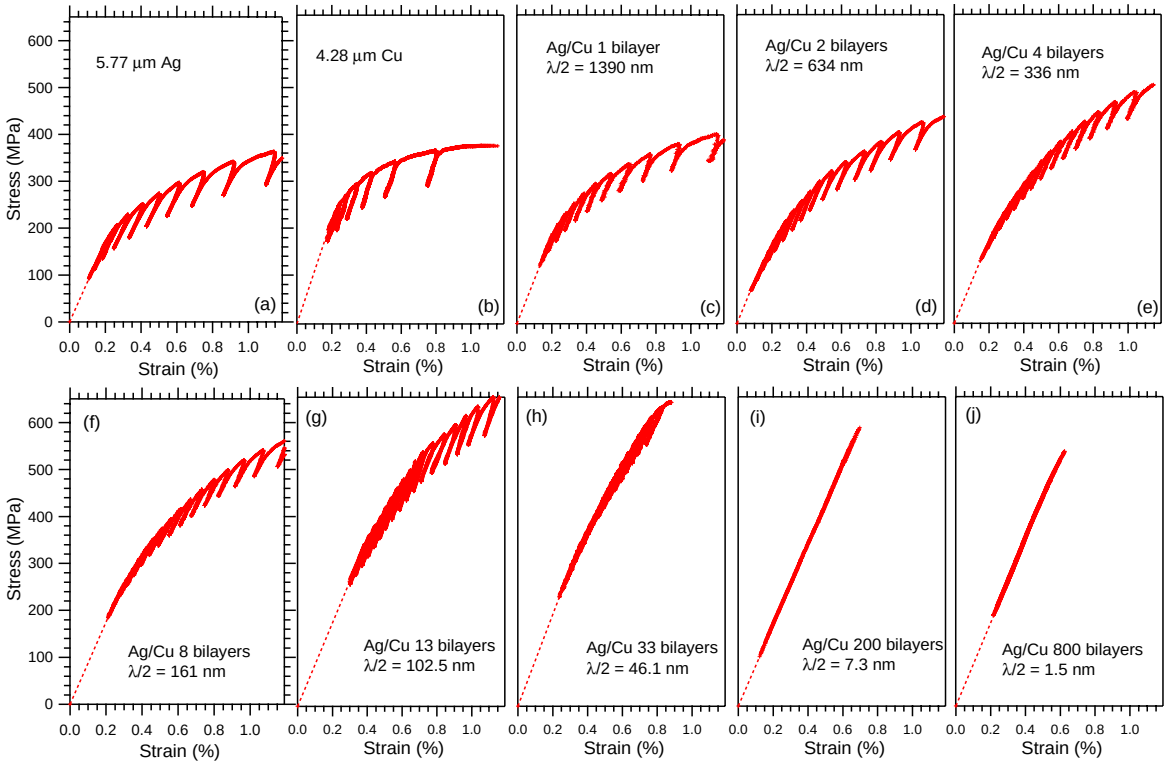

Figure 2: Stress-strain curves for films of pure Ag, pure Cu and Ag/Cu multilayers. The thickness of each film, or the number of bilayers and thickness (λ/2) of each layer are indicated [7].

Yield stress

Figure 2 shows the stress-strain curves for pure Ag, pure Cu and a series of Ag/Cu multilayers with decreasing bilayer repeat lengths, λ. For the shortest repeat lengths, no

yield stress could be determined because no macroscopic plastic flow could be measured before fracture occurred (see Figure 2(i) ad 2(j)). The yield stress clearly increases with decreasing λ. Traditionally, this dependence has been analyzed using a power law:

$$\sigma_y = \sigma_o + k\, d^{\,n} \qquad (1)$$

where d is the grain size and σ_o is the yield stress for very large-grained samples. For n = –0.5, Eqn. 1 reduces to the Hall-Petch relation. The yield data from our tests are shown as a log-log plot of (σ_y–σ_o) vs. grain size in Figure 3, together with nanoindentation data on the samples with the smallest repeat lengths [2] and microindentation data on coarse-grained copper [8]. The hardness data, H_v, were converted to yield stresses using the Tabor relation:

$$\sigma_y = H_v/3. \qquad (2)$$

σ_o for all data was 168 MPa, which was obtained from a Hall-Petch plot (σ_y vs. $d^{-1/2}$) of the microhardness data. The grain size in our samples was taken to be λ/2. The offset between the tensile and nanoindentation data on the multilayers arises from the inaccuracy of the Tabor relation for samples with strong work hardening.

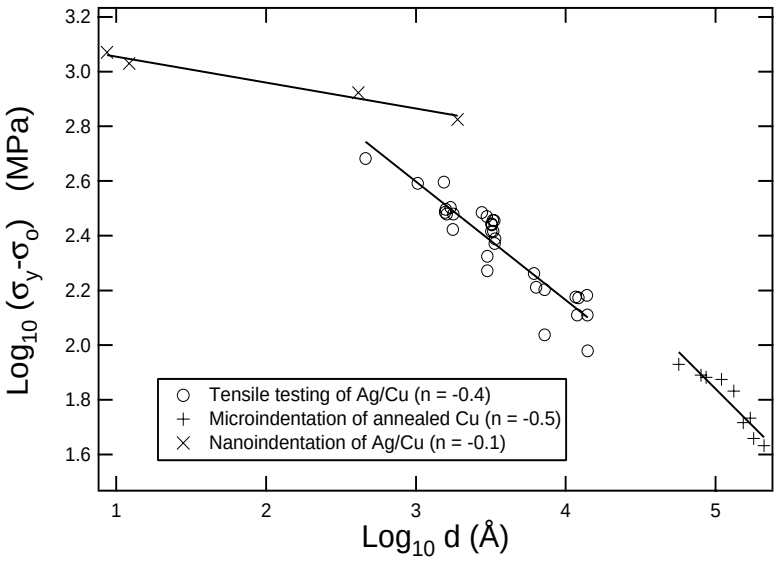

Figure 3: Comparison of the yield stresses of Ag/Cu multilayers (O) [7] with nanoindentation data on Ag/Cu multilayers (×) [2] and microindentation data on coarse-grained Cu (+) [8]. Hardnesses were converted to yield stresses by the Tabor relation (H_v/3). The value of σ_o, 168 MPa, was determined from a Hall-Petch plot of the microindentation data.

The slope of the lines in Figure 3 gives the exponent of Eqn. 1. For the microindentation data, n = –0.5. For the tensile data, n = –0.43, which is close to the classical Hall-Petch value. The slope of the line through the nanoindentation data, however, is n = –0.1. Such a deviation from Hall-Petch behavior has been seen in nanoindentation measurements on

other metallic multilayers [9] and has been attributed to changes in the dislocation dynamics when the number of dislocations in the pile-ups near the grain boundaries becomes small [10]. Importantly, however, the yield stress and hardness continue to rise with decreasing grain size even at the smallest sizes; no softening is observed.

Work hardening

The work hardening rate, $\theta = d\sigma/d\varepsilon$, of the stress-strain curves for the multilayers in Figure 2 has been analyzed [2] using the formalism developed by Kocks [11]. The initial work hardening rate is 10 to 20 times higher than the maximum work hardening rate, θ_{II}, in single crystal silver. This can be explained by the introduction of an additional set of dislocation obstacles with an effective spacing, D.

$$\theta = \theta_{II} + \frac{M^3 (\alpha G)^2 b}{2\sigma D} - \sigma\left(\frac{\theta_{II}}{\sigma_{sat}} + \frac{KM}{2D}\right) \qquad (3)$$

where M is the Taylor factor, G the shear modulus, b the Burgers vector, and σ_{sat} the saturation stress of the single crystal; α and K are constants.

D decreases with decreasing grain size but is substantially smaller than d. The dislocation structures built up as a result of the presence of interfaces could decrease the effective obstacle spacing provided by the layers [2].

Fracture and ductility

As shown in Figure 2, the fracture stress of the multilayers increases with decreasing λ as long as macroscopic yield can be observed. Values as high as 700 MPa have been measured. The plastic strain at fracture decreases continuously with λ and is only 0.16% in the strongest samples. For the shortest repeat lengths (λ < 80 nm) no macroscopic plastic strain is observed. In a few samples, with large repeat lengths, plastic strains up to 2.3% have been measured.

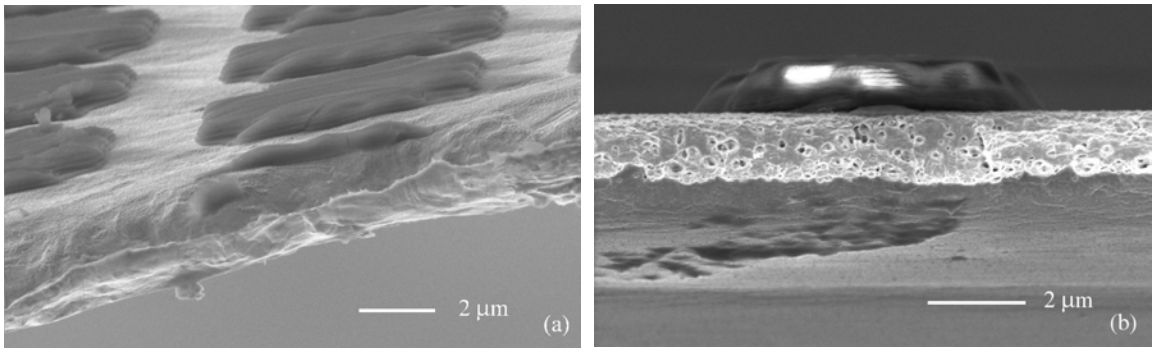

Figure 4: Scanning electron micrographs of the fracture surfaces of (a) a Cu thin film, (b) a Ag/Cu multilayer (bilayer repeat length 40 nm), both fractured in tension.

Figure 4(a) shows the fracture surface of a pure Cu film broken in the tensile tester. The overall ridge shape and the "vein" in the middle are clear indications of a simple, macroscopic ductile fracture. Figure 4(b) shows the fracture surface of a multilayer with a

bilayer repeat length of 40 nm. Although the overall shape of the surface is more planar than that in Figure 4(a), there are many "vein"-like features present that indicate the occurrence of extensive plastic flow. The edges of the pits also indicate that they were formed by local plastic flow.

The fracture of the Ag/Cu multilayers is intrinsically ductile. The fracture stress increases with decreasing repeat length due to the increase in, first, the yield stress, and then the rate of work hardening. The decrease in the ductility is directly attributable to work hardening as well. The absence of macroscopic yielding and the lower strength in the multilayers with the shortest repeat lengths is most likely due to the samples being more sensitive to alignment in the apparatus when there is less plastic accommodation.

CONCLUSION

The interfaces in metallic multilayers can be very effective obstacles to dislocation motion, leading to substantial increases in yield stress as well as in the rate of hardening. These effects combine to raise the resistance to ductile fracture in these materials.

ACKNOWLEDGEMENTS

We thank Warren MoberlyChan for assistance with the electron microscopy, and Marc Verdier, David Embury, Amit Misra and Harriet Kung for useful discussions. This work was supported by the Harvard Materials Research and Engineering Center under contract DMR-98-09363. HH and DYWY acknowledge support by a predoctoral fellowship from the AlliedSignal Corporation.

REFERENCES

1. Thompson, C.V. and Carel, R. (1996) *J. Mech. Phys. Solids* 44, 657.
2. Verdier, M., Huang, H., Spaepen, F., Embury, J.D., Hawley, M. and Kung, H. unpublished.
3. Read, D.T. (1998) *Meas. Sci. Technol.* 9, 676.
4. Sharpe, W.N. (1982) *Opt. Engineering* 21, 483.
5. Kretschmar, A., Kuschke, W.M., Baker, S.P. and Arzt, E. (1997*) Mater. Res. Soc. Symp.* 436, 59.
6. Ruud, J.A., Josell, D., Spaepen, F. and Greer, A.L. (1993) *J. Mat. Res.* 8, 112.
7. Huang, H. and Spaepen, F. (2000) *Acta mater.* 48, 3216.
8. Chokshi, A.H., Rosen, A., Karch, J. and Gleiter, H. (1989) *Scripta metall.* 23, 1679.
9. Misra, A., Verdier, M., Lu, Y., Kung, H., Mitchell, T.E., Nastasi, M.and Embury, J.D. (1998) *Scripta metall.* 39, 555.
10. Embury, J.D. and Hirth, J.P. (1994) *Acta metall. Mater.* 42, 2051.

11. Kocks, U.F. (1985). In: Dislocations and properties of real materials, Proc. 50th Anniversary of the Concept of Dislocations in Crystals, p.144, The Institute of Metals, London.

POSTER REFERENCE: ICF100508PR

FLOW STRESS OF STEEL AT LARGE STRAINS AND HIGH STRAIN RATES

G. Pape*, A. Bakker* and M. Janssen*

* Delft University of Technology, Laboratory of Materials Science,
Rotterdamseweg 137, 2628 AL, Delft, The Netherlands

ABSTRACT

In this study an experimental approach has been taken to investigate the strain rate influence on ductile behaviour of steel. A high-rate servo-hydraulic tensile machine has been used to perform experiments on steel. Deformation has been analysed using a high-speed drum-camera. Digital image processing techniques yielded geometry information, which has been used to derive the true stress-strain curve after localisation of deformation. Several correction procedures were applied to derive the von Mises flow stress of the material. Analytical procedures as well as a numerical technique have been used.
A modified Johnson-Cook relation has been applied to fit the experimental data. This relation gives a functional dependence of the material flow stress of the plastic strain and plastic strain rate. The influence of the temperature has been considered as well. The material flow stress increases at increasing strain rate for strains below necking, but tends to decrease at higher strains. The flow stress description used here can only be used for monotonic loading conditions, and does not provide a constitutive model for any deformation history. Modelling of tensile specimen experiments using the strain rate dependent flow stress shows good agreement with measurement data. Localisation behaviour is strongly influenced by the strain hardening and needs a proper description to account for the total deformation.

KEY WORDS

Flow Stress, High Strain Rate, Experiment, Model, Steel, Image Processing

INTRODUCTION

Research for the Royal Netherlands Navy on the vulnerability of warships has resulted in a detailed study on the failure behaviour of explosively loaded panels inside ship structures. This study contains on the one hand a determination of the material response to high strain rate deformation, and on the other hand an investigation of the failure behaviour of the material. Analysis of the failure behaviour was performed experimentally as well as numerically, and also the influence of the strain rate has been taken into account. This paper is concerned with the experimental determination of the flow stress of the material and a proper description of the flow stress as a function of plastic strain and strain rate. Failure investigations have been presented in an additional paper [1].

EXPERIMENTAL TECHNIQUES

The flow-stress of the material can be measured from tensile experiments on smooth round bars. To account for the influence of hydrostatic stress at the neck of the specimen a Bridgman [2], Siebel [3], and Bakker [4] correction procedure have been followed. For the experimental determination of the material flow stress as a function of strain and strain rate, two separate measurement systems have been applied. The first system was applied for strain rates up to 0.1 s^{-1}, the second system for strain rates beyond 10 s^{-1}. Both systems will be shortly discussed here as well as the techniques that have been applied for image processing.

Low Strain Rate Testing

For tensile tests at low strain rates a servo-mechanical machine has been used. Load measurement was provided by a strain gauge loadcell. Extension of the specimen has been measured by a strain gauge extensometer up to the strain at which localisation starts. For strains beyond the onset of necking digital camera images have been used to derive the true strain at the centre of the neck. The true strain ε has been taken from:

$$\varepsilon = \ln\left(\frac{A_0}{A}\right) \tag{1}$$

As the rolled plate material shows a slight anisotropy with respect to plastic flow in the plate thickness direction, initially round tensile specimen develop to an oval shape. Therefore two digital cameras were used to measure both diameters of the oval shape, which area has been estimated using an ellipse relation for the cross sectional area at the centre of the neck. Schematically, the camera set-up has been shown in Figure 1.

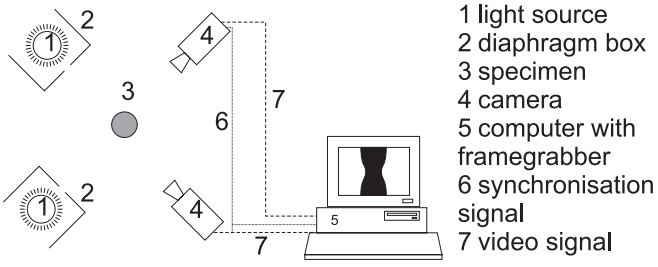

Figure 1: Top view of the camera set-up for the digital imaging system

From the camera images the diameter and radius of curvature of the neck has been derived using image-processing techniques. An anisotropy factor has been derived from the strains from both cameras defined as the quotient of two strain values. This factor appears to be independent of the strain level.

High Strain Rate Testing

The high strain rate testing equipment mainly consists of a hydraulic tensile machine, which can achieve speeds up to 10 m/s. During the experiment a rather constant speed has been maintained. A high-speed camera was used to monitor the deformation in the neck of a specimen. Two markers on the front side of the specimen have been used to measure the elongation during uniform deformation. Images from this conventional rotating drum camera have been developed and scanned with a high-resolution film scanner and subsequently processed with a computer. Image processing techniques will be treated in the next subsection. Load measurement using a piezo-electric loadcell resulted in a vibrating load signal caused by resonance phenomena. Investigations showed that the stresses in the specimen are hardly influenced by these resonances and may be assumed to be equally distributed and without resonance. Smoothing of the

load signal introduced relatively high inaccuracies for the decreasing part of the load curve, the localisation of deformation.

Image Processing

Image processing techniques have been applied to derive geometric data from the recorded images. As the low strain rate experiments have been monitored using digital cameras this resulted in good image quality, facilitating the processing techniques. The digital image was converted into black-white and detection of the specimen contours appeared to be rather simple. A sub-pixel technique was applied to increase the accuracy of the contour positions. Fitting of a circle at a small region of the neck of the specimen yielded an approximation of the radius of curvature, also the diameter has been measured from the images.

At high strain rates the quality of the scanned images was less compared with the digital images and more complicated techniques have been applied for detection of the specimen contours. The main technique consists of taking the second order derivative of the light intensity along a horizontal scan line perpendicular to the specimen axis. The specimen contour is located at a zero value of this derivative. Several smoothing techniques (moving average) were applied to reduce scatter in the derivatives and contour positions.

EXPERIMENTAL RESULTS

Flow Curves at Low Strain Rates

Mateman [5] performed tensile tests at strain rates up to 6.2 $.10^{-2}$ s^{-1} (engineering strain rate) using the low rate tensile test equipment. Specimens have been taken in the plate rolling direction, a diameter of 5 mm and gauge length of 35 mm has been chosen. The true failure strain according to Eqn. 1 is smaller for specimen perpendicular to the rolling direction compared to specimen in the rolling direction, respectively 1.0 and 1.46. No remarkable differences have been found in flow stress between the rolling direction and perpendicular to the rolling direction, except for a slightly increased initial yield stress. This means that only the rolling direction has to be examined with respect to flow behaviour. Figure 2 shows a comparison between the flow stress for two material directions taken from experiments.

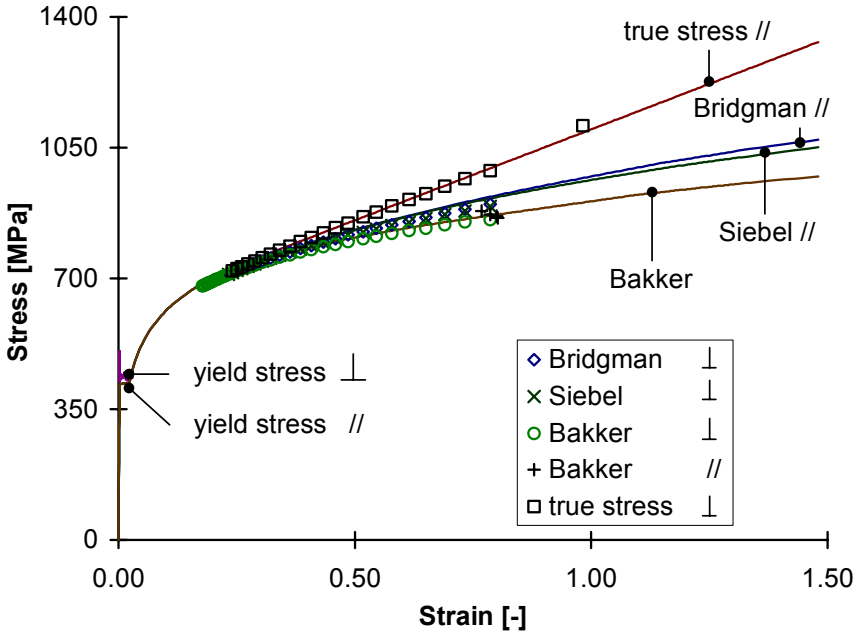

Figure 2. Comparison between flow-stress in parallel (//) and perpendicular (⊥) plate rolling directions

In Figure 2 the one direction is parallel to the rolling direction and shows the average curves for 4 experiments. The second direction is perpendicular to the rolling direction of the plate material and the markers shown in the figure represent only one experiment. To compare these results in both directions, the scatter in measurements for the parallel direction has been presented by plotting a few raw data points of the flow-stress according to Bakker into the graph. These points indicate that no remarkable differences were found between both plate directions. Only the Bridgman flow-stress and Siebel flow-stress deviate a little from the parallel direction. As the axial mean stress and Bakker flow-stress are practically identical and have been derived from load and diameter data only, one can conclude that the ratio a/R is slightly higher in the direction perpendicular to the rolling direction.

Flow Curves at High Strain Rates

For the experiments performed at high strain rate the results showed considerable scatter, as well the strain measurements from the camera images, as the load measurement from the piezoelectric signal. The scatter increased with increasing strain rate as the testing velocity largely influenced resonances. The failure strain appeared to be rather independent of the strain rate, a small reduction of failure strain in the rolling direction was found, yielding a failure strain of 1.3 and 1.4 at engineering strain rates of 60 s^{-1} and 200 s^{-1}, respectively. The correction procedures according to Bridgman [2] and Siebel [3] have been applied. However, the Bakker procedure showed some numerical problems, and an alternative approach has been applied to derive the flow stress at high strain rate. A finite element simulation has been performed using a preliminary flow curve. The flow-curve assumed did not yield to accurate similarity between numerical simulation and experiment. One could observe a premature localisation and deviation of axial stress compared with the experimental data. For this reason, the initial part of the flow-curve up to a strain of 0.2 has been adapted to prevent necking in an early stage of deformation. A simple powerlaw description gave satisfactorily results. For strains larger than 0.2 the coefficients have been adapted to fit the mean axial stress level from the experiment. Table 1 shows the values of the coefficients used in the powerlaw flow-curve. This resulted in a proposed flow curve as has been shown in Figure 3, engineering strain rate is 5.7 10^{+1} s^{-1}. Application of this flow-curve resulted in a better agreement between simulation and experiment, although the total elongation still has been underestimated by 10%.

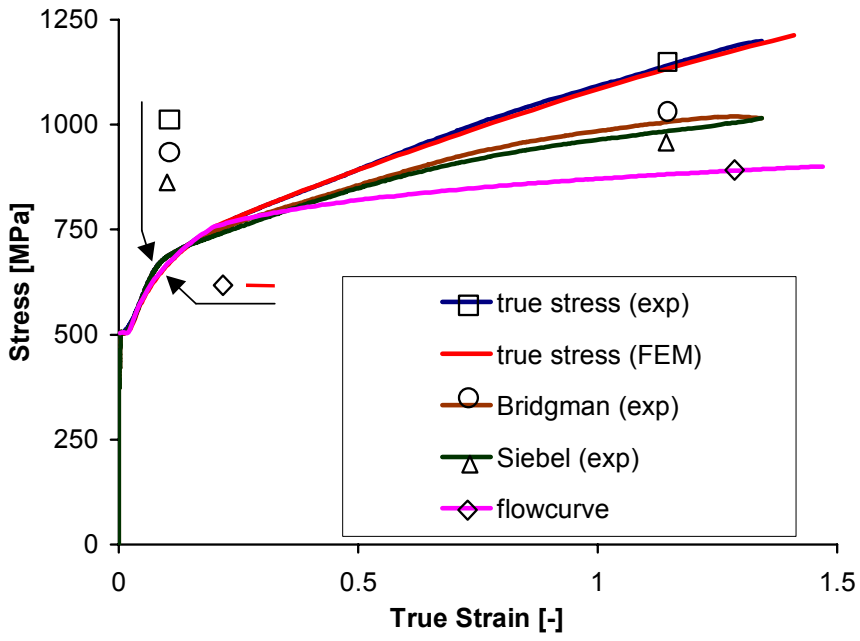

Figure 3: Flow-curve for FEM – simulation that fits experimental curve for the true stress at an engineering strain rate $\dot{e}$ = 5.7 10^{+1} s^{-1}

TABLE 1.

POWERLAW COEFFICIENTS FOR THE FLOWCURVE AT AN ENGINEERING STRAIN RATE OF $\dot{e} = 5.7\ 10^{+1}\ s^{-1}$

$\sigma_f = C\varepsilon^n$	C	n
Strain ≤ 0.2	1020 MPa	0.185
Strain > 0.2	871 MPa	0.087

An overview of the flow-stress, which has been derived with the Bakker correction procedure, has been shown in Figure 4. Increasing flow-stress has been observed for strains smaller than 0.4, for large strain values (> 1.4) the flow-stress decreases at increasing strain rate. Note that for strain values in the necking region (larger than 0.2) the strain rate increases at a constant tensile velocity due to necking.

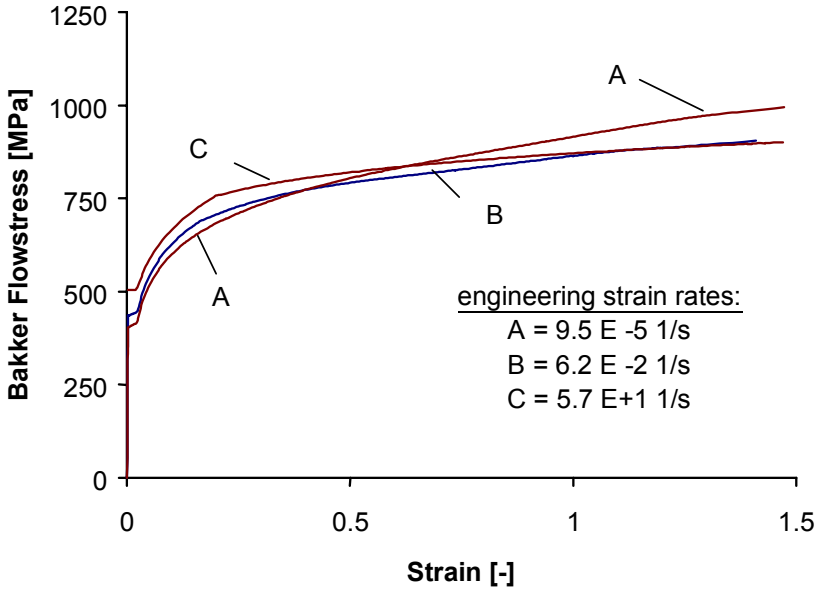

Figure 4: Flow-stress according to Bakker derived from experiments

CURVE FIT OF FLOW STRESS FOR SEVERAL STRAIN RATES

The experimental data has been used to fit a relation between flow-stress, strain, and strain rate. This relation was obtained by modifying the Johnson-Cook [6] relation for varying strain, strain rate, and temperature. We obtained:

$$\sigma_f = [905 + 127 \ln \varepsilon\,][1 + C_g (1 - \varepsilon) \ln \dot{\varepsilon}^*] \qquad [MPa]$$

$$\dot{\varepsilon}^* = \frac{\dot{\varepsilon}}{\dot{\varepsilon}_0}; \quad \dot{\varepsilon}_0 = 2.1 \cdot 10^{-3} [s^{-1}] \tag{2}$$

in which $\dot{\varepsilon}$ denotes the true strain rate, and $\dot{\varepsilon}_0$ is a reference value of the strain rate. For strain values varying from 0 to 0.02 a linear flow-stress has been taken, the level can be obtained by substituting the

strain value of 0.02 in Eqn. 2. Comparing experimental and model flow-stress – strain curves at several strain rates it appears to be a rather good approximation to use the coefficient $C_g = 0.0083$. However, for small strains the increase of flow-stress has been underestimated. A graph has been made for several flow-curves at constant strain rate, shown in Figure 5. Also the strain-hardening exponent derived from the derivative of the power-law function has been plotted into the graph. It has been shown that the necking strain, the intersection point of the hardening exponent and the stability line, decreases slightly with increasing strain rate.

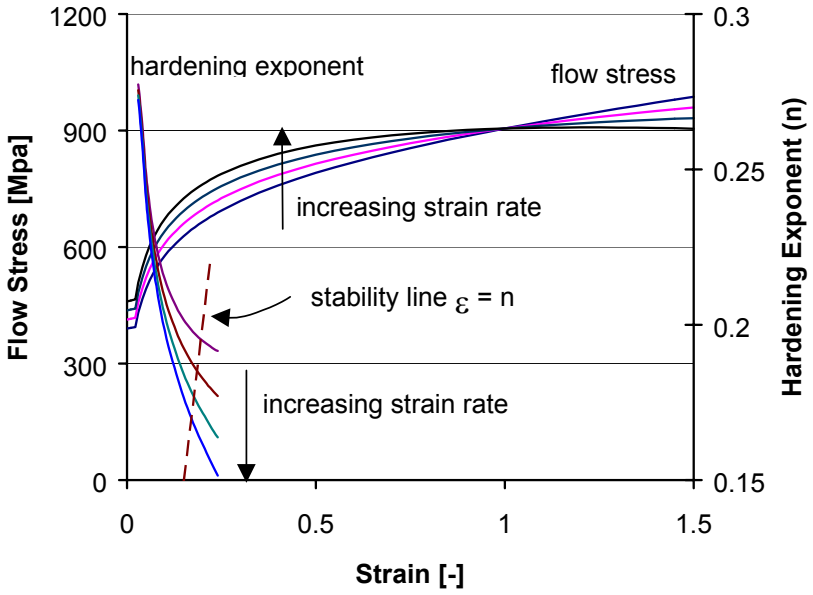

Figure 5: Flow-curves for increasing strain rate, respectively $1 .10^{-6}$, $1 .10^{-3}$, $1 .10^{+0}$, and $1 .10^{+3}$ s^{-1}. The hardening exponent has also been given for these strain rates.

ACKNOWLEDGEMENTS

This research was funded by the Technology Foundation STW, the TNO Prins Maurits Laboratory and the Delft University of Technology.

REFERENCES

1. Pape, G., Bakker, A., Janssen, M., (2001) *Fracture Predictions for Ductile Steel*, International Conference on Fracture, ICF 10, Conference Proceedings, Honolulu
2. Bridgman, P.W., (1952) Studies in Large Plastic Flow and Fracture, McGraw-Hill Book Company, New York
3. Siebel, E., (1925) Berichte der Fachausschüsse des Vereins Deutscher Eisenhüttenleute, Werkstofausschuß, Ber. 71
4. Bakker, A., (1990) *Influence of Material Flow Curve Modelling on Fracture Mechanics Evaluations*, in: Proceedings of the 5th International Conference on Numerical Methods in Fracture Mechanics, Eds. Luxmoore, A.R., Owen, D.R.J.
5. Mateman, G., (1997) *Determination of the Flow-curve of Constructionsteel (in Dutch)*, Graduate Report, Delft University of Technology
6. Johnson G.R. and Cook W.H., (1983) in: Proc. 7th Int. Symposium on Ballistics, The Hague, The Netherlands, 541

FLUID-STRUCTURE INTERACTION RELATED ASPECTS DURING THE GROUTING OF CRACKS IN CONCRETE

H.N. Linsbauer

Institute of Hydraulic Structures, Vienna University of Technology,
Karlsplatz 13/222, A-1040 Wien, Austria

ABSTRACT

Fluid Structure Interaction (FSI) processes in cracked systems generally may be assigned to "Hydraulic Fracturing", which in the field of petroleum-engineering is well understood by mathematical and numerical descriptions and utilisation in situ. However there is a further important aspect related to this technique but opposite in the objective – grouting of cracked concrete structures under the aspect of full rehabilitation. Unfortunately uncontrolled grouting may sometimes cause an opposite effect, e.g. creating of new cracks or further crack propagation. Based on the understanding of the closely coupled process between the injected fluid and the structural response especially the Stress Intensity Factor development at the crack front may serve as an efficient control parameter during the grouting procedure.

KEYWORDS

Concrete, cracks, grouting, repair, fluid structure interaction

INTRODUCTION

A certain category in the wide field of fluid structure interaction processes also has to be considered in civil engineering in all cases where an elastic structure in dynamic motion is in contact with a fluid at rest or vice versa. A wide class of problems stretching from flow induced vibrations in hydraulic engineering [1] to added mass concepts in dam engineering [2] may be assigned to this discipline. The injection procedure during the grouting of cracks in concrete structures also may be seen as an interaction between fluid penetration and structural response and basically is comprehended by the disciplines of fluid mechanics, structural mechanics and fracture mechanics. The closely coupled process is characterised by the time dependent fluid penetration as a function of the crack width and the herewith associated pressure development causing a further alteration of the cross section. In addition the stress intensity at the crack front, accountable for the stability (reliability) of the grouting procedure, is directly related with. The physical-mathematical formulation of these complex circumstances ever since has been a matter of special concern in the field of petroleum-engineering under the aspects of "hydro-fracturing ", to achieve optimal production conditions. Representative for the multitude of relevant treatises, Lit. [3,4,5,6] including recommendations for further readings, is specified. The grouting process of cracks mathematically may be exhibited similar to that one representative for hydraulic fracturing but with an essential difference concerning the crack (tip) behaviour. Opposite to the "hydraulic driven fracture" - a continuously moving fluid-fracture system – care has to be taken, strictly to avoid any instability of the system during grouting. Within this contribution a model both for a plane and a penny-shaped crack configuration is presented to comply with this demand.

MATHEMATICAL MODEL

Due to the intimately coupled process between the crack width-dependent fluid flow and the herewith pressure induced alteration of this flow-section as response of the structure (as shown in Figure 1), both fluid mechanics and structural mechanics principles have to be observed. Simultaneously, the stress development at the crack front has to be considered under the aspects of fracture mechanics methods.

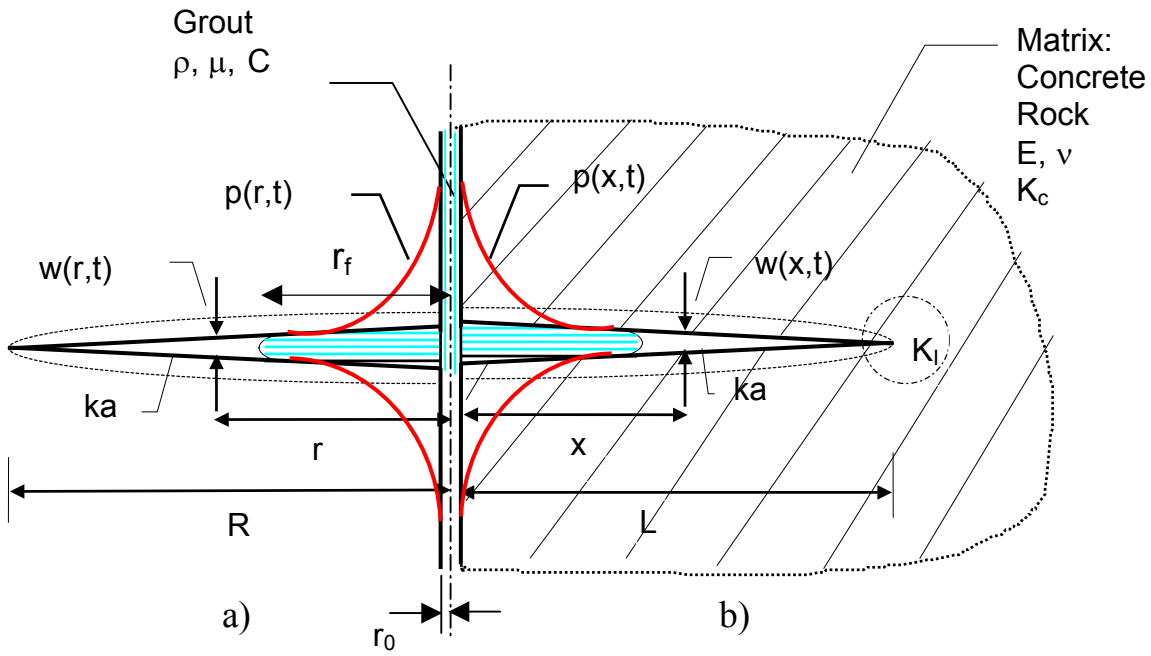

Figure 1: Scheme of the fluid-structure interaction process
a) penny shaped crack
b) wedge shaped crack

Fluid Mechanics Formulation

The physical description of fluid flow is based on the fundamental conservation principles – conservation of mass, momentum and energy, constitutive relationships and equations of state [7]. Disregarding the energy principle (which is not relevant for the present case), the characteristic equations for the conservation of mass and momentum are given by Eqn. 1 and Eqn. 2 (Cauchy equation of motion) respectively.

$$\frac{D\rho}{Dt} + \rho\nabla\cdot u = 0 \tag{1}$$

$$\text{——} = f - \nabla p + \nabla\cdot\tau \tag{2}$$

with ρ as the density of the fluid, u the velocity vector, ∇·u the divergence of the velocity, f the body force, ∇p the pressure gradient and ∇·τ the divergence of the surface forces (viscous stresses). D/Dt is the substantial derivative, representative for the Eulerian framework.

The constitutive relationship for a *Newtonian* fluid in the formulation of Stokes is shown in Eqn. 3,

$$= 2\left(\gamma - \frac{1}{}\nabla\cdot u\right) \tag{3}$$

where μ is the dynamic molecular viscosity and γ is the strain rate tensor. Postulating an incompressible fluid, the second term in the parenthesis of Eqn. 3 is equal to zero and the strain tensor τ then reads:

$$\tau = \mu\frac{1}{2}\left[\nabla u + (\nabla u)^t\right] \tag{4}$$

Combining the conservation equations Eqn. 1 and Eqn. 2 with the constitutive relationship Eqn. 4 results in the Navier-Stokes equation:

$$\frac{Du}{} = f - \nabla p + \mu \nabla^2 u \tag{5}$$

Flow in a gap (crack)

For a flow in a narrow gap or crack some specific attributes are significant. Under the physically admissible assumption that the velocity component in z-direction is zero, the continuity equation (Eqn. 1) results in $\delta u/\delta x = 0$, which means that the flow is unidirectional and such the convective term in the substantial derivative vanishes. Under these aspects and by neglecting the body force, the Navier-Stokes equation for the *steady state* case reduces to:

$$0 = -\frac{\delta p}{\delta x} + \mu \frac{\delta^2 u}{\delta z^2} \tag{6}$$

Integration under consideration of the boundary condition $u(z) = 0$ at $z = \pm w/2$ and averaging the velocity over the cross-section leads to

$$(z)_{av} \qquad \frac{1}{\cdot \mu} \quad (x)\frac{\delta p}{x} \tag{7}$$

For a slightly compressible injection fluid the following correlation between the density and the pressure is introduced

$$\begin{aligned} \rho(p) &= \rho_0 e^{C(p-p_0)} \Rightarrow \rho_0\left[1 + C(p - p_0)\right] \\ \frac{}{\delta t} &= \rho_0 C \frac{p}{\delta t} \end{aligned} \tag{8}$$

with C is the compressibility of the liquid.

Combining the continuity equation Eqn. 1 , the gap flow characteristic Eqn. 7 and the equation of state Eqn. 8, results in

$$\frac{p(\gamma, t)}{\delta t} = \frac{}{12 \cdot \mu \cdot C \cdot f(k_a)} \cdot \frac{}{\gamma^n} \; \frac{}{\delta \gamma}\left[\gamma^n \quad {}^2(\gamma, t) \cdot \frac{\delta p(\gamma, \;)}{\delta \gamma} \right] \tag{9}$$

with $\gamma = x$, $n = 0$ and $\gamma = r$, $n = 1$ for the planar crack and the axially symmetric crack configuration respectively. The function $f(k_a)$ is a friction coefficient considering the roughness of the gap surfaces.

The Eqn. 9 is a representative of diffusivity equations where the fluid flow equation Eqn. 7 also may be interpreted as a rate equation based on Darcy's law. Under consideration of characteristic boundary conditions (Dirichlet, Neumann) and certain global mass criteria this equation may serve for the assessment of the time dependent pressure distribution in a gap during a grouting procedure. A similar strategy was used in a case of hydraulic fracturing stress determination [8].

Structural Mechanics Representation

The response of the 'unbounded impermeable' elastic medium, surrounding the crack configuration, due to the flow induced pressure development is given by the crack opening displacements and the associated stress intensity factor growth rate at the crack front. An expression for the crack opening displacements is given in [9] for both cases and is represented by Eqn. 10 in a formulation according to Lit. [3]:

$$w(\gamma, t) = w(\gamma, 0) + \frac{8 \cdot \left(1 - \nu^2\right)}{\pi \cdot E} \cdot \int_{\gamma}^{\Gamma} \frac{s^{(1-n)}}{\left(s^2 - \gamma^2\right)^{1/2}} \cdot ds \cdot \int_{\chi}^{s} \frac{p(u, t)}{\left(s^2 - u^2\right)^{1/2}} \cdot u \cdot du \tag{10}$$

with $\gamma = x$, $\Gamma = L$, $n = 0$, $\chi = 0$ and $\gamma = r$, $\Gamma = R$, $n = 1$, $\chi = r_0$ for the planar crack and the axially symmetric crack configuration respectively. The surrounding medium is defined through the modulus of elasticity E and the Poisson ratio ν, r_0 is the radius of the bore-hole . The mode 1 stress intensity factor (SIF) expression for both cases reads:

$$I(t) = \quad - \quad ^{1/} \quad \frac{(\gamma, t)}{\left(\Gamma^2 - \gamma^2 \right)^{1/}} \left(- \right)^{n} \cdot d\gamma \qquad (11)$$

$$0$$

with the same labels as defined above.

NUMERICAL METHOD

The solution of the fluid flow equations Eqn. 9 under consideration of appropriate initial and boundary conditions and under direct compensation of Eqn. 10 at each time step (decoupling) was carried out by an implicit finite difference scheme. A detailed discussion weighing up the pros and cons compared to the explicit method may be found in Lit. [10] and is not discussed further here. An essential disadvantage lies in the fact that the 'propagation speed' is infinite and therefore the fluid front at each time step is adjusted due to a surface tension criterion and a global mass balance consideration. According to the particular boundary condition an associated tridiagonal algebraic system has to be solved. Additionally, at each time step the determination of the stress intensity factor is carried out via Eqn. 11.

SOLUTIONS (EXAMPLES)

Each method is as good as the correspondence to results of natural cases or experiments to be simulated with. Therefore a comprehensive investigation with the planar model has been carried out for in situ cases (grouting of cracks in the Koyna dam), block tests (repair of Zeuzier dam) and basic experiments with gaps formed by stiff steel plates. The results are documented in Lit. [11], which mainly is focussed on the engineering aspect of the procedure. A Fortran routine for the axial symmetric case is given in Lit. [12]. The pressure development for an open 'gap' , simulating an in situ procedure [13] is given in Figure 2, where also an extension up to a steady state behaviour is carried out, showing the typical logarithmic characteristic.

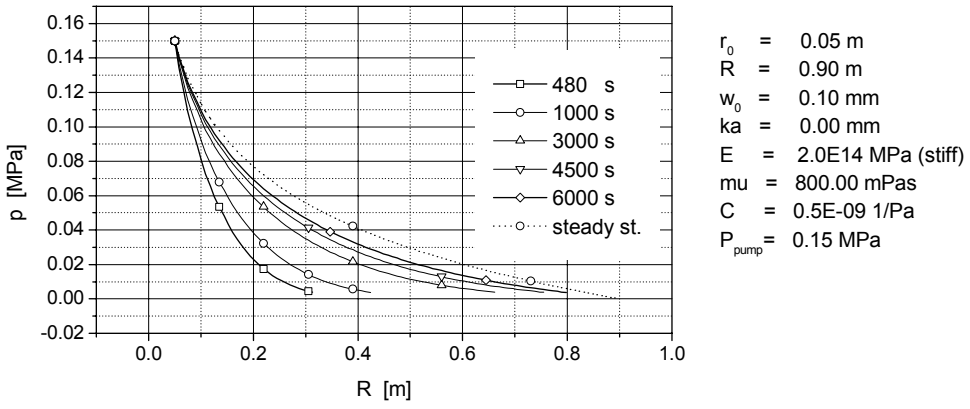

Figure 2: Pressure development in an open 'gap'

The pressure distribution and the associated time dependent Stress Intensity Factor (SIF) development in a radial crack configuration with wedge shaped geometry is documented in Figure 3a and in Figure 3b. The abrupt transition in the SIF-diagram up to the static pressure is typical for the fluid front approaching the crack tip. This analysis can be used for a save grouting procedure, to control the pressure according to a given limit of the fracture toughness K_{IC} of the concrete or rock [11].

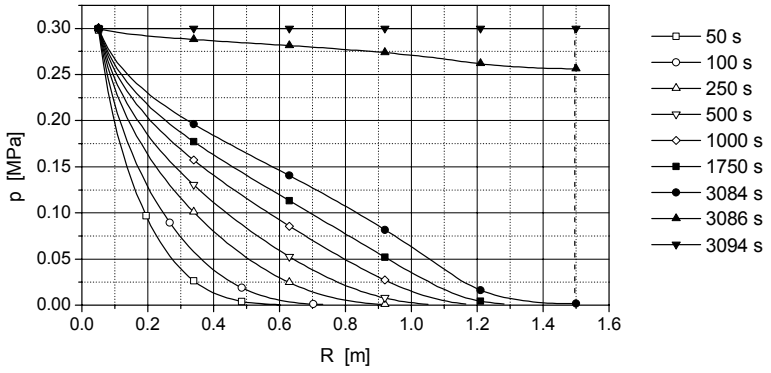

a)

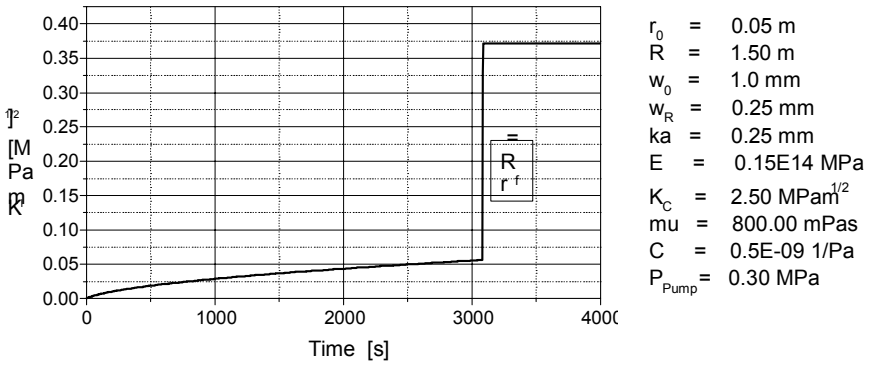

b)

Figure 3: Radial crack system - wedge shaped geometry
a) pressure development
b) associated Stress Intensity Factor

The influence of the crack environment on the fluid structure interaction process characterised by a variation of the Modulus of Elasticity, both on the pressure distribution, the crack profile and the SIF-development is shown in Figure 4a, Figure 4b and Figure 4c respectively.

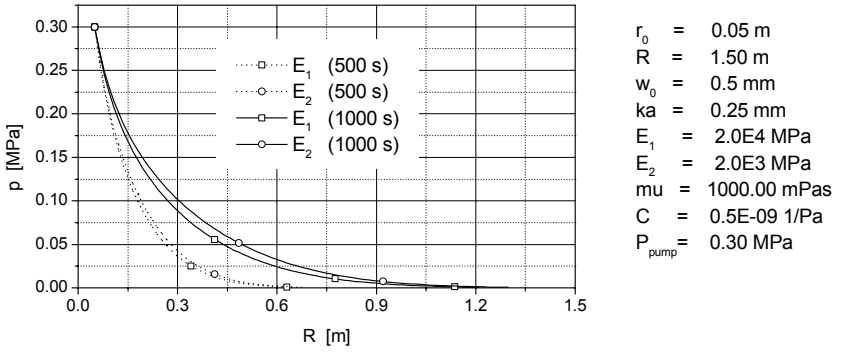

a)

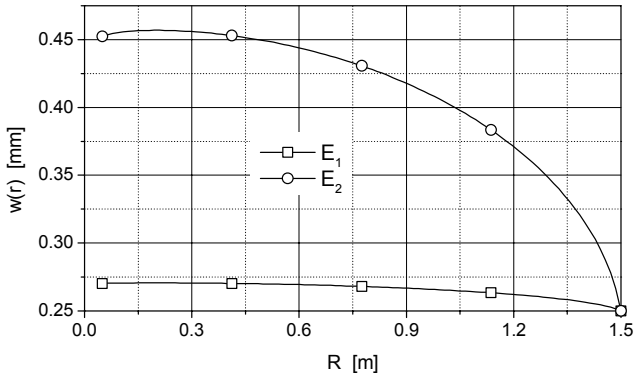

b)

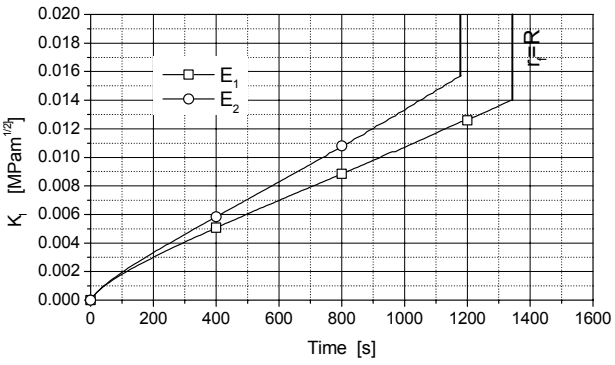

c)

Figure 4: Radial crack system with different moduli of elasticity (E_1/E_2=10)
a) pressure distributions
b) crack opening profiles
c) SIF-characteristics

Whereas for this special case the pressure distributions (Figure 4a) due to different moduli of elasticity with a ratio of E_1/E_2 =10 correspond quite well, naturally the crack opening profiles (Figure 4b) show significant discrepancies. The SIF-gradients (Figure 4c) are different, with a steeper inclination for the softer material.
.

CONCLUSION

The present investigation may be seen as an illustration of the physical process which is characteristic for the grouting of cracks. Especially parameter studies can serve the purpose of understanding the influence of fluid, matrix and geometrical attributes on a stable procedure.

REFERENCES

1. Naudascher,E. and Rockwell,D. (1994). *Flow-induced vibrations*. A.A. Balkema, Rotterdam.
2. Zienkiewicz,O.C. and Taylor,R.L. (2000). *The Finite Element Method*. Butterworth-Heinemann, Oxford
3. Nilson,R.H. (1986). *Int. Journal. f. Num. and Analyth. Meth. in Geomechanics*.10,191.
4. Detournay,E., Cheng,A.H-D. and McLennan,J.D. (1990). *Journal of Energy Res. Techn.*112,224.
5. Savitski,A. and Detournay,E. (1999). In: *Rock Mechanics for Industry ,*pp.851-858, Amadei,B., Kranz,R.L., Scott,G.A. and Smeallie,P.H. (Eds.).A.A.Balkema, Rotterdam
6. Abe,H., Mura,T. and Keer,M.L. (1976). J. of Geophys. Res. 81,5335.
7. Batchelor,G.K. (1991). *An introduction to fluid dynamics*. Cambridge University Press, Cambridge
8. Hardy,M.P. and Asgian,M.I. (1989). Int.J.Rock Mech. Min. Sci & Geomech. Abstr. 26,489.
9. Geerstma,J. and de Klerk,F. (1969). *J of Petrol. Techn.* 21,1571.
10. Jaluria,Y. and Torrance,K.E. (1986). *Computational Heat Transfer*. Springer, Heidelberg
11. Linsbauer,H.N. (1998). In: *Dam Safety*, pp.621-628, Berga,L. (Ed.). A.A. Balkema, Rotterdam
12. Bockhoff,N. (1996). MSc Thesis, Vienna University of Technology, Austria
13. Thomas,H.H. (1976). *The Engineering of Large Dams*.-PartII, John Wiley&Sons,London

ORAL REFERENCE ICF0744

FOREIGN OBJECT DAMAGE AND HIGH-CYCLE FATIGUE THRESHOLDS IN TI-6AL-4V

J. O. Peters[**], B. L. Boyce, J. M. McNaney and R. O. Ritchie

Department of Materials Science and Engineering,
University of California, Berkeley, CA 94720-1760

ABSTRACT

The objective of this study is to define limiting threshold conditions for high cycle fatigue (HCF) in the presence of foreign object damage (FOD) in an engine Ti-6Al-4V alloy. Impacts in the form of FOD were simulated by firing steel spheres onto tensile fatigue specimens at velocities of 200 to 300 m/s. Such FOD was found to reduce the fatigue strength of the alloy, primarily due (i) stress concentration, (ii) microcrack formation, (iii) impact-induced plasticity and (iv) tensile residual stresses associated with the impact damage. Two groups of fatigue failures could be identified. The first group initiated directly at the impact site, and can be readily described through a Kitagawa-Takahashi approach, where the limiting threshold conditions are defined by the stress-concentration corrected smooth-bar fatigue limit (at microstructurally-small crack sizes) and a "worst-case" fatigue crack growth threshold (at larger "continuum-sized" crack sizes). The second group of failures was caused by fatigue cracks that initiated at locations remote from the impact site in regions of high tensile residual stresses. By evaluating the effect of such residual stresses as a superimposed mean stress, specifically by conducting smooth-bar *S-N* tests at load ratios between -1 and 0.8, it was found that simple superposition of the applied and initial residual stresses provided a significant contribution to the FOD-induced reduction in fatigue strength by affecting the *local* load ratio. Such factors are considered in a modified Kitagawa-Takahashi approach to provide a basis for the effect of FOD on HCF failures in Ti-6Al-4V. To evaluate the role of surface treatments to enhance high-cycle fatigue resistance, fatigue specimens were also laser shock peened prior to FOD-impact and subsequent fatigue loading. The initial results of these HCF failures of laser shock peened samples are briefly discussed.

KEYWORDS

Ti-6Al-4V, foreign object damage, high cycle fatigue, residual stress, fatigue crack initiation, fatigue crack growth threshold

INTRODUCTION

High-cycle fatigue (HCF) of turbine engine disk and blade components represents one of the major concerns limiting with the readiness and safety of military aircraft. Since *in-flight* HCF conditions invariably involve high cyclic frequencies, small crack sizes and (depending on blade location) very high mean stress levels, a preferred approach for design against HCF can be considered in terms of the concept of a threshold for no fatigue crack growth [1-3]. Foreign object damage (FOD) by small hard particles has been identified as a key factor associated with such HCF related failures in titanium alloy blades [1,2]. Specifically, FOD has been found to reduce the fatigue strength of fan and compressor blades, principally by causing stress-raising notches and microcracks [2] at impact sites; this, in association with the plastic deformation and tensile residual stresses resulting from such impacts [1], can lead to the early nucleation and growth of fatigue cracks.

[**] Now with the Department of Physical Metallurgy and Materials Technology, Technical University Hamburg-Hamburg, 21071 Hamburg, Germany

Recent studies [4,5] on the HCF properties of a Ti-6Al-4V blade alloy, where FOD was simulated using high-velocity impacts of steel shot on a flat surface, have focused on the definition of threshold conditions for crack initiation and growth on subsequent fatigue cycling. The mechanistic effect of FOD was considered in terms of (i) the possibility of forming microcracks in the damage zone, (ii) the stress concentration associated with the FOD-induced notches, (iii) microstructural damage from FOD-induced plastic deformation, and (iv) the localized presence of tensile residual hoop stresses in the vicinity of the impact site. Although all these factors play an important role, a pivotal effect of FOD in reducing fatigue life in Ti-6Al-4V appears to be the formation, at high impact velocities, of damage-induced microcracks; on subsequent cycling, these act as preferred sites for the initiation of fatigue cracks in the pile-up of material around the rim of the impact crater, depending upon the relative magnitude of the residual stresses in the vicinity of the impact. For high applied stress ranges, HCF failures initiate directly *at* the impact site, whereas at correspondingly low applied stresses ranges, they initiate in locations *away* from the impact site.

In analyzing the high stress failures, it was found that FOD-initiated microcracks, together with the stress concentration of the indent, were the prime reasons that the HCF failures initiated at the FOD sites. The microcracks (some as small as 1 μm) grew at applied stress intensities as low as ΔK = 1 MPa√m, which is well below the "worst-case" ΔK_{TH} threshold in bi-modal Ti-6Al-4V [6] of 1.9 MPa√m for "continuum-sized" cracks, i.e., for cracks larger than the characteristic microstructural size-scales. Thus, although the "worst-case" threshold, which is determined at $R \rightarrow 1$ to minimize crack closure, provides a critical lower-bound for the growth of HCF cracks in bi-modal Ti-6Al-4V, it only applies for "continuum-sized" cracks, which in this microstructure are larger than ~50-100 μm in length. Since the microcracks associated with impact damage are more than an order of magnitude smaller than this, an alternative approach is proposed to describe the threshold HCF conditions in the presence of FOD based on a Kitagawa-Takahashi diagram, where the limiting conditions for HCF are defined in terms of the stress concentration-corrected smooth-bar fatigue limit (at microstructurally-small cracks sizes) and the "worst-case" threshold (at larger, "continuum-sized" crack sizes).

In contrast to HCF failures under high applied stresses, at low applied stress ranges failures were caused by fatigue cracks that initiated at locations remote from the impact site, specifically in regions of high tensile residual stresses. It is the purpose of this paper to examine the role of the relative magnitudes of the applied and residual stresses in dictating the sites for the initiation of HCF failures in impact-damaged Ti-6Al-4V, and to provide a methodology to describe the limiting threshold conditions for such failures at both low and high applied cyclic stresses. To achieve this objective, the residual stresses in the vicinity of the damage sites are computed numerically [7] and measured experimentally using synchrotron x-ray micro-diffraction. Such stresses are considered to affect the local load ratio for subsequent fatigue cracking, which is evaluated by determining smooth-bar stress-life (*S-N*) curves for load ratios from R = -1 to 0.8. Using such results, a modified Kitagawa-Takahashi approach is presented to provide a rational basis for the effect of FOD on HCF failures in Ti-6Al-4V at both high and low applied stresses.

Additionally, we briefly consider the effect of laser shock peening (LSP) as a surface treatment to improve resistance to FOD-induced failures under HCF cycling [1,8]. In this study, the flat surfaces of fatigue samples were prepared by LSP processing prior to FOD event, and the subsequent fatigue lives compared to of samples without such surface treatment.

EXPERIMENTAL PROCEDURES

The Ti-6Al-4V alloy investigated, of composition (in wt.%) Ti-6.3Al-4.19V-0.19Fe-0.19O-0.013N-0.0041H, was from the forgings produced specifically for the U.S. Air Force National HCF Program. The bi-modal (solution treated and overaged) microstructure of this material, consists of ~60 vol.% primary α (grain size ~20 μm) within a lamellar α+β matrix. The alloy has yield and tensile strengths of 915 and 965 MPa, respectively, with a reduction in area of 45%, based on tests parallel to the length of the plate [4].

Foreign object damage was simulated by firing 1.0 mm or 3.2 mm diameter chrome-hardened steel spheres onto a flat specimen surface of tensile fatigue (so-called modified K_B, details are given in Ref. [4]) specimens at an angle of 90º at velocities of 200 and 300 m/s using a compressed-gas gun facility. Impact velocities of 200 to 300 m/s represent typical in-service impact velocities on aircraft engine fan blades. The impact damage craters are also typical of those seen in service, with root radii similar to those of actual damage sites [2].

To evaluate the effect of surface treatments on the HCF resistance, the gauge and transition section of modified K_B specimens were laser shock peened to induce compressive residual stresses to approximately 500 μm deep on each side.

Following impacting with the steel spheres to simulate FOD, the damaged regions were examined in a high-resolution, field-emission scanning electron microscope (SEM), prior to cycling at maximum stress values between 225 and 500 MPa at R = 0.1 and 0.5 (with a sinusoidal waveform).

Stress-intensity threshold conditions for no crack growth of small cracks at the impact site were defined based on the relationship of Lukáš [9] for small cracks at notches; for further details see Ref. [5]. Because the FOD-initiated microcracks have lengths ($2c$ ~ 1 to 50 μm) that are comparable to the scale of local plasticity, there may be a degree of uncertainty in the calculation of their driving forces. However, maximum plastic zone sizes are only ~ 0.2 to 1 μm for 1 to 10 μm sized cracks at ΔK ~ 1 - 2 MPa√m, such that conditions are close to that of small-scale yielding. The contribution of the residual stresses is not included in this ΔK calculation since these stresses do not change the stress intensity *range*. They do, however, affect the mean stress and hence alter the local load ratio, as is examined below. Indeed, initial estimates of the magnitude and gradient of the residual stresses have been computed [7] and are experimentally measured in this study.

RESULTS AND DISCUSSION

Simulation of foreign object damage

Damage sites on the flat surface of the rectangular gauge section of K_B specimens, resulting from 300 m/s impacts with 1 and 3.2 mm steel shot, are shown in Figs. 1a,b. Increasingly severe damage states have been previously reported with increasing impact velocity for the bi-modal Ti-6Al-4V [4,5]. For impact velocities in excess of ~250 m/s, pile-up of material (Fig. 1) at the crater rim resulted in multiple formation of microcracking (insert in Fig. 2). Moreover, circumferentially-oriented intense shear bands were formed, emanating from the surface of the impact crater. The microcracks (~2 to 50 μm) were found to provide the nucleation sites for crack growth on subsequent cycling (Fig. 2), although such microcracking was not seen at slower 200 m/s impacts. For this reason, we believe that low velocity or quasi-static indentations do not provide a realistic simulation of FOD.

In addition to the formation of the FOD-induced microcraks, the presence of tensile residual stresses at locations remote from the impact site was also of importance for crack initiation, especially for failures in the 10^7 to 10^8 cycles regime. These tensile stresses, measured using synchrotron x-ray micro-diffraction techniques at the side faces of the K_B specimens, counterbalance the compressive residual stress field directly beneath the indentation, as predicted numerically [7]. The estimated distributions of these FOD-induced stresses in K_B specimens are shown in Figs. 3a and b for 300 m/s impacts using 1 mm and 3.2 mm steel shot, respectively, and display tensile residual stresses (in longitudinal direction) as high as ~220 MPa (σ_{33}/σ_y = 0.24) to 385 MPa (σ_{33}/σ_y = 0.42), where σ_y is the yield stress, and σ_{33} the normal residual stress in longitudinal direction. The effect of such residual stresses on fatigue crack initiation and the fatigue crack growth thresholds is discussed below.

Fatigue properties

Stress-life (*S*-*N*) data in Fig. 4 clearly show the detrimental effect of FOD on the fatigue strength of bi-modal Ti-6Al-4V. The reduced lifetimes following impact damage was seen for both projectile sizes and at both low and high load ratios (R = 0.1 and 0.5). As discussed previously [8-10], this detrimental effect of FOD can be considered in terms of premature fatigue crack initiation resulting from (i) the stress concentration of the indent, (ii) FOD-induced microcracking, (iii) plastically-deformed microstructure and (iv) tensile residual stresses that result from the impact.

Two groups of failures can be identified in Fig. 4, dependent upon the magnitude of the applied stresses relative to the tensile residual stresses. At high applied stresses, HCF failures initiate directly *at* the impact crater. For 300 m/s impact velocities where FOD-induced microcracks were formed, fatigue cracking initiated from these microcracks at the crater rim (surface crack lengths are indicated at groups of data points); at 200 m/s impact velocities, fatigue cracking initiated at the base of indent site where the stress concentration is higher (compared to that at the crater rim) [5]. In contrast, at low applied stresses (and lower impact velocities), where FOD-induced microcracks were not formed or were much smaller, fatigue cracks were found to initiate *away* from the indent crater, in regions of relatively high tensile residual stresses.

An example of fatigue crack initiation at low applied cyclic stresses (σ_{max} = 325 MPa, R = 0.1) in regions remote from the damage site in the interior of a K_B specimen is shown in Figs. 5a and b for 300 m/s impacts of, respectively, 1 and 3.2 mm diameter shot. A further example (at σ_{max} = 300 MPa, R = 0.1), where initiation occurred close to surface at the side face of the specimen is shown in Fig. 5c. In all cases, fatigue cracking initiated in regions of the high tensile residual stresses away from the indent; specifically, these stresses were ~300 MPa, based on synchrotron x-ray diffraction measurements [10] and numerical computations (Fig. 3).

The tensile residual stresses also elevate the load ratio, when simply superimposed on the applied far-field fatigue loading. Based on FOD-related failures at applied cyclic stresses of 270 to 300 MPa (R = 0.1) and 250 MPa (R = 0.5), superimposing a measured tensile residual stress of ~300 MPa increases these R-ratios from 0.1 to ~0.5 and from 0.5 to ~0.7, assuming no relaxation. The corresponding increase in the maximum stress by this superposition is marked by arrows in the *S*-*N* diagram shown in Fig. 4. From these *S*-*N* results it is

clear that simple superposition of initial tensile residual stress onto applied far-field stress provides a significant contribution to the reduction in fatigue life due to FOD through its effect in elevating the local *R*-ratio.

Threshold conditions based on the Kitagawa diagram

For high applied stress ranges (relative to the magnitude of tensile residual stresses) and in the presence of relatively large impact-induced microcracks (~ 30 to 50 μm), it was found that fatigue failures at 10^5 to 10^6 cycles initiated directly at the impact site. These fatigue failures (shown as closed symbols in Fig. 6) have been described in our previous work [5] through the use of fatigue crack growth threshold concept and the Kitagawa-Takahashi diagram [11]. Here, the limiting threshold conditions were defined by the stress-concentration corrected smooth-bar fatigue limit (at microstructurally-small crack sizes) and a "worst-case" fatigue crack growth threshold (at larger "continuum-sized" crack sizes). A more favorable representation of the failure envelopes for the two load ratios of 0.1 and 0.5 in Fig. 10 can be made using the El Haddad *et al*. [12] empirical quantification of Kitagawa approach, which introduces a constant, termed the intrinsic crack length, $2c_o$, such that the stress intensity is defined as $\Delta K = Y \Delta\sigma \, [\pi(2c + 2c_o)]^{1/2}$, where Y is the geometry factor.

To account for residual stresses in this approach to describe the limiting threshold conditions for FOD-initiated HCF failures in Ti-6Al-4V, the effective *R*-ratio in the diagram has to be corrected for the presence of such residual stresses. Using the fatigue failures plotted in Fig. 10 as data points at surface crack lengths of $2c$ = 1 μm, and superimposing the measured tensile residual stress of ~300 MPa, the *R*-ratios are increased from 0.1 to ~0.5 and from 0.5 to ~0.7 at far-field stress range of ~300 MPa. Accordingly, such failures at both load ratios can still be described by the proposed Kitagawa-Takahashi approach, provided the limited conditions are given by the stress concentration *and* residual stress corrected smooth-bar fatigue limit at small crack sizes and the "worst-case threshold" for larger crack sizes.

The full quantitative effect of the FOD-induced residual stresses on fatigue failures at 10^5 to 10^6 cycles, however, is still under study. Although simple superposition of the residual and applied stresses was considered above, our recent *in situ* x-ray micro-diffraction results have indicated that during the first few fatigue cycles, significant relaxation of the residual stresses occurs *at* the base and rim of the impact crater, but *not at* locations a crater diameter or so away where fatigue cracks initiate under low applied stresses. This effect is currently under investigation using both *in situ* x-ray studies and numerical computation.

Laser Shock Peening

Laser shock peening (LSP) has been proposed as an effective means to improve the fatigue strength of titanium turbine blades, especially to enhance the HCF resistance to FOD [1,8]. A prime cause for this effect is that LSP can induce significant compressive residual stresses below the surface, which inhibits the propagation of FOD-related surface fatigue cracks. The positive effect of LSP prior to 200 m/s (3.2 mm shot) impacts is shown in Fig. 7, where it can be seen that the LSP process resulted in fatigue life extension of more than one order of magnitude. However, at higher impact velocities of 300 m/s (3.2 mm shot), LSP had little influence on HCF resistance (Fig. 7). As the impact crater sizes were essentially identical for non-LSP and LSP treated fatigue samples at this velocity, the similar fatigue lives appear to be the result of the deep impact penetration compared to the depth of LSP-induced compressive residual stresses. Currently, both experimental and numerical studies are focused on quantifying residual stress gradients after the LSP process and following FOD in order to explain limited benefits of LSP for the high velocity impacts.

SUMMARY AND CONCLUSIONS

Based on a study of the role of foreign object damage in affecting the high-cycle fatigue of an engine Ti-6Al-4V alloy with bi-modal microstructure, the prominent conclusions are:

1. Foreign object damage, simulated by high-velocity (200-300 m/s) impacts of steel spheres (1 and 3.2 mm shot) on a flat specimen surface, markedly reduced the HCF resistance, primarily by inducing sites for the premature initiation of fatigue cracks on subsequent cycling.
2. Premature crack initiation was caused by a number of factors: (i) the stress concentration due to the FOD indentation, (ii) the creation (at highest impact velocities only) of microcracks at the impact crater rim, (iii) microstructural damage from FOD-induced plastic deformation, and (iv) the localized presence of tensile residual stresses around the indent.
3. Two groups of FOD-induced HCF failures could be identified. The first group involved fatigue crack initiation directly at the impact site and caused failures within 10^5 to 10^6 cycles. The proposed criteria for such failures has been described by a modified Kitagawa-Takahashi approach, where the limiting threshold conditions are defined by the stress-concentration corrected smooth-bar fatigue limit (at

microstructurally-small crack sizes) and a "worst-case" fatigue crack growth threshold (at larger "continuum-sized" crack sizes).

4. The second group of failures at 10^7 to 10^8 cycles initiated at locations remote from impact damage in regions of high tensile residual stresses. Accordingly, the modified Kitagawa-Takahashi approach proposed above must be corrected for the presence of tensile residual stresses, in a first approximation by simple superposition of applied and residual stresses, to account for such failures. With this correction, this approach provides a rational basis for the effect of foreign object damage on high cycle fatigue failures in Ti-6Al-4V.
5. Laser shock peening (LSP) prior to FOD event was found to improve the HCF resistance following FOD, but only for lower impact velocities (200 m/s); no beneficial effect of LSP was found for high velocity impacts (300 m/s).

ACKNOWLEDGEMENTS

This work was supported by the Air Force Office of Science and Research, Grant No. F49620-96-1-0478, under the Multidisciplinary University Research Initiative on "High Cycle Fatigue" to the University of California, Berkeley. Special thanks are due to Prof. J. W. Hutchinson and Mr. X. Chen for providing us with their results prior to publication, and to Dr. D. M. Corbly and Mr. S. R. Mannava (GEAE) for helpful discussions and for the laser shock peening of our fatigue samples.

REFERENCES

1. Nicholas, T. (1999) *Int. J. Fatigue* 21, S221.
2. Hudak, S.J., Chan, K.S., McClung, R.C., Chell, G.G., Lee, Y.-D., Davidson, D.L. (1999) *High Cycle Fatigue of Turbine Blade Materials*, Final Technical Report UDRI Subcontract No. RI 40098X SwRI Project No. 18-8653.
3. Ritchie, R.O. (1996). In: *Proc. ASME Aerospace Division.* Chang, J.C.I., Coulter, J., Brei, D., Martinez, W.H.G., Friedmann, P.P. (Eds). AD-Vol. 52, ASME, Warrendale, PA, pp. 321-333.
4. Peters, J.O., Roder, O., Boyce, B.L., Thompson, A.W., Ritchie, R.O. (2000) *Metall. Mater. Trans. A.* 31A, 1571.
5. Peters, J.O., Ritchie, R.O. (2000) *Eng. Fract. Mech.* 67, 193.
6. Ritchie, R.O., Davidson, D.L., Boyce, B.L., Campbell, J.P., Roder, O. (1999) *Fat. Fract. Eng. Mat. Struct.* 22, 621.
7. Chen, X., Hutchinson, J.W. (2001) Unpublished research. Harvard University.
8. Ruschau, J.J., John, R., Thompson, S.R., Nicholas, T. (1999) *Int. J. Fatigue* 21, S199.
9. Lukáš, P. (1987) *Eng. Fract. Mech.*26, 471.
10. Boyce, B.L., Chen, X., Hutchinson, J.W., Ritchie, R.O. (2001) *Mechanics of Materials*, 33, 441.
11. Kitagawa, H., Takahashi, S. (1976) In: *Proc. Second Intl. Conf. on Mechanical Behavior of Materials,* ASM, Metals Park, OH, pp. 627-31.
12. El Haddad, M.H., Topper, T.H., Smith, K.N. (1979) *Eng. Fract. Mech.* 11, 573.

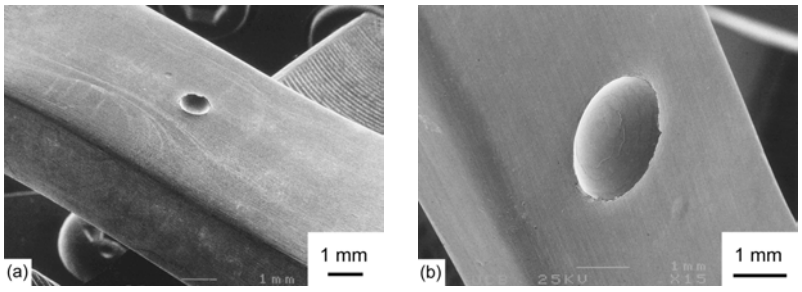

Fig. 1 Gauge section of modified K_B specimens for simulated FOD studies after high-velocity 300 m/s impact using (a) 1.0 mm diameter steel sphere and (b) 3.2 mm diameter steel sphere (normal impact angle).

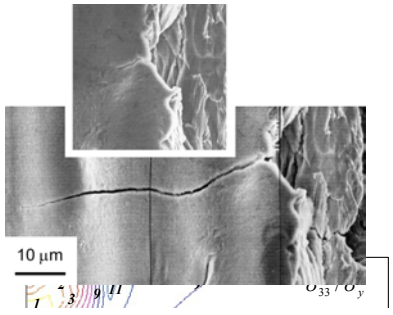

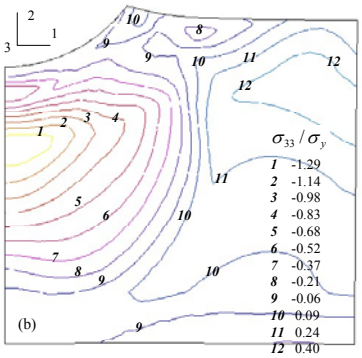

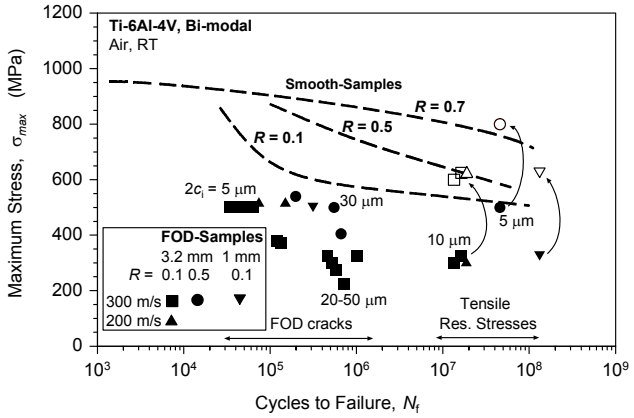

Fig. 4 *S-N* data show reduced fatigue life due to simulated FOD as compared to smooth-bar specimens. $2c_i$ is the surface crack length of FOD-induced microcracks. For failures at 10^7 - 10^8 cycles, the effect of local tensile residual stress (~300 MPa) in increasing the local maximum stress (and hence the local load ratio) has been illustrated by arrows and open symbols.

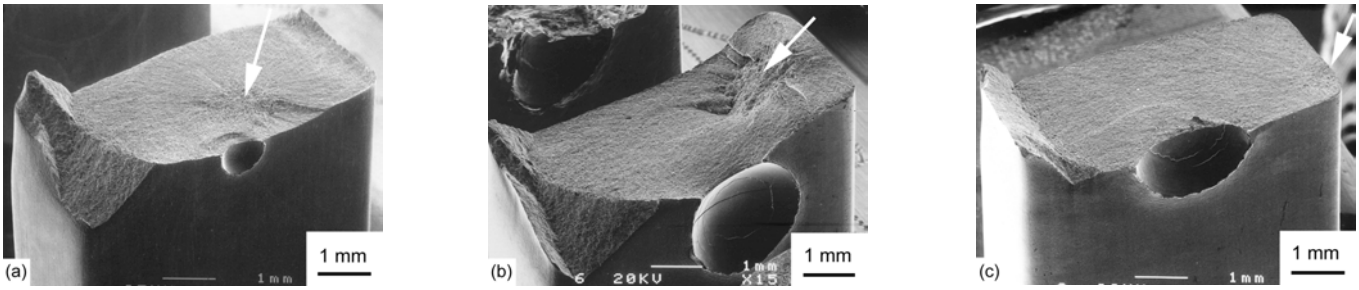

Fig. 5 Lower stress fatigue loading after 300 m/s impact using 1 mm or 3.2 mm diameter steel shot caused crack initiation away from the indent site (marked by arrows): (a) 1 mm steel shot, nominally applied σ_{max} = 325 MPa, R = 0.1, N_F = 1.3 x 10^8 cycles, (b) 3.2 mm steel shot, nominally applied σ_{max} = 325 MPa, R = 0.1, N_F = 1.6 x 10^7 cycles, and (c) nominally applied σ_{max} = 300 MPa, R = 0.1, N_F = 1.3 x 10^7 cycles.

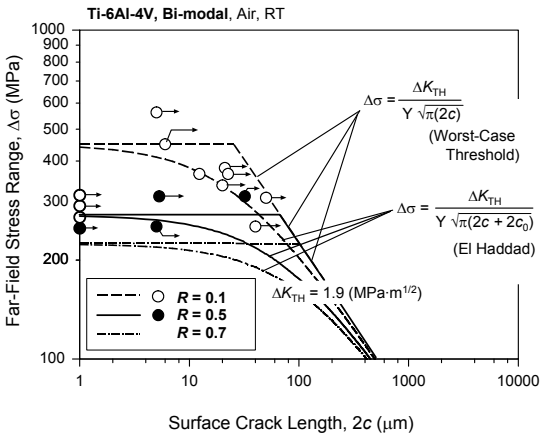

Fig. 6 Modified Kitagawa-Takahashi diagram representing the threshold crack-growth conditions (da/dN = 10^{-11}-10^{-10} m/cycle) at R = 0.1 and 0.5 for FOD-induced small-cracks in bimodal Ti-6Al-4V. Plotted is the threshold stress range as a function of surface crack length. Data points are corrected for the stress concentration of the FOD indents.

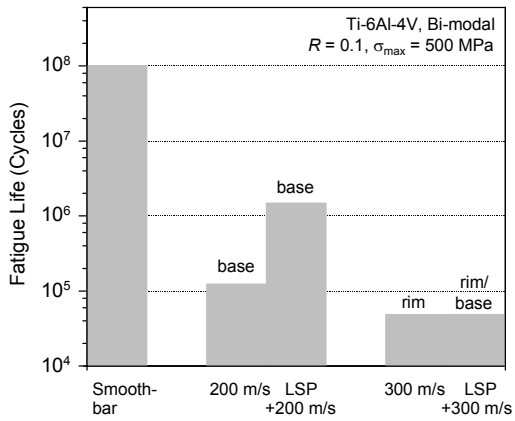

Fig. 7 Histogram showing the effect of laser shock peening (LSP) prior to the FOD event. FOD was simulated using 3.2 mm steel shot at velocities of 200 and 300 m/s. The sites of crack initiation, at base or rim at impact crater, are indicated.

FORMAL CONSIDERATIONS ABOUT FRACTURE: NUCLEATION AND GROWTH

James P. Sethna

Laboratory of Atomic and Solid State Physics,
Clark Hall, Cornell University, Ithaca, NY 14853-2501, USA

ABSTRACT

In this paper, we will answer several abstract, formal questions about the nature of crack growth and nucleation. Bringing a field theory point of view to fracture illuminates things in what I hope will be an entertaining way.

Formally, what is the crack nucleation rate? Fracture is an instability of elastic theory under tension. For thermally nucleated cracks, there is an analogy with supercooled liquids. Here the crack nucleation rate can be thought of as an imaginary part of the free energy - giving the decay rate of the metastable, stretched material. As an amusing consequence, we can formally calculate the asymptotic form for the high-order nonlinear elastic coefficients, and explicitly show that elastic theory has zero radius of convergence.

Formally, can we derive the the crack growth laws from symmetry? We can describe mixed-mode three-dimensional fracture as a moving curve in space, decorated with a description of the local crack plane, and driven by the stress intensity factors along the crack. Imposing the symmetries gives us the form of the crack growth laws in two dimensions, explaining the (well-known) fact that cracks under shear (mode II) abruptly turn until the stress becomes purely extensional (mode I). The form of the crack growth law in three dimensions will be derived, and linear stability analysis for mixed-mode fracture will be briefly summarized, with connection to factory-roof morphologies.

KEYWORDS

fracture, crack, nucleation, growth, thermal, evolution, factory roof

INTRODUCTION

In this paper, I will summarize formal work done in collaboration with Jennifer Hodgdon[1] and Alex Buchel[2, 3] on nucleation and growth of cracks in brittle, isotropic, homogeneous materials. This work is formal in the sense that bring to the problem the perspectives and approaches of theoretical physics: we'll be asking fundamental questions that most of the participants in this conference wouldn't think to ask. Sometimes answering very basic questions can be illuminating; in any case I hope it will be entertaining.

CRACK NUCLEATION

What is the crack nucleation rate? In a practical context, one may ask what the failure rate is of a component in a machine: the number of breakages per unit time. This definition depends on the size and shape of the object and the external loading. More generally, for a given material under a given load, there will be a rate of crack formation per unit volume per unit time.

the material (grain boundaries, surface heterogeneities, pre-existing microcracks, dislocation tangles). These heterogeneities usually evolve in time (fatigue, work hardening, electromigration, void formation). This makes the failure rate history dependent, and too complicated a problem to start with. So, we'll focus on brittle fracture, where we perhaps can assume that the material far from the crack tip does not irreversibly transform.

With this approximation, we have two cases. (1) The important case is when the failure is due to the inhomogeneities: distributions of microcracks[4], distributions of bond strengths[5], or other randomness[6]. In all of these cases, the rate is number of failures for a given increment of strain, not per unit time. Either the stress is large enough to trigger failure or not: a given sample, if it survives the initial loading, will survive forever. This leads to some elegant theories and simulations, but isn't what I'm focusing on today. (2) The case we study is when the material is homogeneous, and the failure is triggered by a thermal fluctuation. This basically never happens, but it's an interesting theoretical problem.

So, fundamentally, what is the fracture nucleation rate for our brittle, homogeneous material? This is actually a deep theoretical physics question. The basic problem is defining what is meant at finite temperature by a material under tension. The lowest energy state (free energy, to be pedantic) for a large cube of brittle material under external strain can easily be seen to be broken in two. The elastic energy released is proportional to the volume; the surface energy cost is proportional to the cross-sectional area; for fixed external strain there will be a length at which breaking wins. One should note that this breaking strain in real materials isn't very large: a cubic meter of iron will prefer to break in two when stretched by 10μm (140 μm if one includes the energy lost due to plastic deformation during fracture).

Crack nucleation is precisely the mechanism by which a material goes from the metastable stretched state to the state which is broken in two. There is a close analogy to the nucleation of crystals in supercooled liquids. In supercooled liquids[7] the liquid is a metastable state with a decay rate given by the thermal probability of generating a critical nucleus. For fracture, the stretched state is a metastable state with a decay rate given by the thermal probability of generating a crack of the size given by the Griffiths threshold.

(The analogy even extends to the practicality of the thermal nucleation mechanisms. Homogeneous nucleation of crystals in supercooled liquids almost never happens: the crystal almost always nucleates on a dust particle, or on the surface...)

Let's do this calculation explicitly, for a two-dimensional straight crack of length ℓ, in a medium under external hydrostatic tension (a pressure $P < 0$). One can solve the elastic equations to find the energy of this crack. Let α be the surface energy (energy per unit length, in two dimensions, of the crack surface), Y be the Youngs modulus, and σ be Poisson's ratio. If we define a critical crack length ℓ_c (the Griffiths[8] threshold) by

$$\ell_c = 4Y\alpha/\pi P^2(1-\sigma^2) \tag{1}$$

then the energy of the crack is

$$E = 2\alpha\ell - \alpha\ell^2/\ell_c. \tag{2}$$

It follows that cracks with $\ell > \ell_c$ will grow to lower their energy, and that cracks with $\ell < \ell_c$ will heal (at least in our model). The energy at the top of the barrier is $E(\ell_c) = \alpha\ell_c = 4Y\alpha^2/(\pi P^2(1-\sigma^2))$, and the probability for this critical crack to form by a thermal fluctuation is suppressed by the Boltzmann factor $\exp(-E(\ell_c)/k_BT)$. The fracture nucleation rate $\Gamma_{failure}$ per unit volume per unit time will be given by some prefactor times this Boltzmann factor:

$$\Gamma_{failure} = \Gamma_0 \exp(-E(\ell_c)/k_BT). \tag{3}$$

(Calculating this prefactor Γ_0 is quite a subtle problem[3].)

This calculation is precisely analogous to the corresponding one for a critical nucleus of solid forming in a supercooled liquid[7]. Indeed, the crack as it nucleates will be filled by a gas of vapor atoms (think of fracture in a piece of dry ice, where the vapor pressure isn't vanishingly small). The spontaneous fracture rate is precisely the nucleation rate of a gas forming in a super-stretched crystal.

Remember, though, that we claimed from a fundamental point of view the difficulty is defining the stretched material. A stretched piece of material is fundamentally a transient: how do we use equilibrium statistical mechanics to study what is only a metastable equilibrium? The precise definition of the stretched, metastable state is as an analytical continuation from the compressed state[7, 2]. In particular, suppose we study the

include the effects of thermal fluctuations producing small cracks, and then analytically continue $E(P)$ to negative pressure, one can show that it becomes complex! The decay rate (3) is proportional to the imaginary part of the energy:

$$\mathrm{Im}E(P) = C\Gamma_{failure}(P) = E_0 \exp\left(-4Y\alpha^2/\pi P^2(1-\sigma^2)k_BT\right). \tag{4}$$

Metastable states in statistical mechanics are defined by an analytic continuation of the (free) energy. The nucleation rate is defined as a particular dynamical constant prefactor Γ_0/E_0 times the imaginary part of this complex energy.

What can we derive from this formal imaginary part to the energy? The real part of the energy is related to the bulk modulus? Let's define the pressure-dependent bulk modulus $K(P)$ by

$$\frac{1}{K(P)} = -\frac{1}{V}\left(\frac{\partial V}{\partial P}\right)_T = -\frac{1}{PA}\left(\frac{\partial \mathrm{Re}(E)}{\partial P}\right)_T = c_0 + c_1P + c_2P^2\cdots + c_nP^n + \cdots \tag{5}$$

where the elastic material has cross-sectional area A. c_0 is the inverse of the normal bulk modulus, and the higher order terms c_n represent nonlinear elastic coefficients. These are normally ignored, because by the time they become important plastic deformation or fracture has set in, but in principle a careful experiment could measure them. Now, if $E(P)$ is an analytic function, then it obeys Cauchy's theorem,

$$E(-P) = 1/2\pi i \oint_\gamma E(T)/T + PdT = 1/2\pi i \oint_\gamma E(T)/T \sum_{n=0}^{\infty} (P/T)^n dT. \tag{6}$$

with γ circling $-P$ in the complex plane. Because it divides by i, it can be used to write the real part of the free energy $E(P)$ in terms of the imaginary part. Exchanging the sum and the integral, choosing contours and checking asymptotics, we can calculate the n-th nonlinear elastic constant in equation 5 asymptotically for large n:

$$c_n \to (-1)^n(n+2)/\pi A \int_0^B \mathrm{Im}E(T)/T^{n+1}dT \tag{7}$$

So because the (complex) energy is an analytic function, the high-order nonlinear elastic constants are related to the fracture rate.

We used this to answer an extremely formal question. What is the radius of convergence of nonlinear elastic theory? We can use the ratio test: the radius of convergence equals the ratio c_n/c_{n+1} as $n \to \infty$. Using (7) and (4) and doing the integrals, we find

$$c_n/c_{n+1} \to -n^{-1/2}\left(8\beta Y\alpha^2/\pi(1-\sigma^2)\right)^{1/2} \quad \text{as n} \to \infty. \tag{8}$$

(Doing the prefactor carefully[3] with various continuum limits leaves this expression unchanged, except that the surface tension α becomes the temperature-dependent surface free energy.) The ratio goes as $n^{-1/2}$, and the radius of convergence is zero.

Should we be concerned? Hooke's law is the first term of a series that doesn't converge? First, the physical origin of this is that our brittle material is in principle unstable as soon as the pressure P becomes negative. If you're not concerned about the fact that your bridges in theory will eventually fall down because of thermal crack nucleation, perhaps the associated non-convergence of Hooke's law shouldn't distress you. Indeed, thermal fluctuations are probably too weak to make observable effects in any measurement of the nonlinear elastic constants. Second, nonlinear elastic theory has lots of company: quantum electrodynamics[9] (the most quantitatively successful theory in physics) and Stirling's series for $n!$ also have zero radius of convergence.

Intellectual curiosity aside, what of practical importance can we glean from our calculation? First, perhaps the high-order nonlinear elastic constants of disordered materials might be computed by similar means, and (disorder being important to the fracture rate) might have effects large enough to measure. Second, the imaginary part of the frequency dependent elastic constants are related to viscosities: perhaps considering both external strain and frequency together might be illuminating (vibration-induced thermal fracture rates?)

and might relate to the plastic flow rate at very early stages (before work hardening sets in). The corresponding problem in two dimensions has been well studied,[10] but it seems likely that tangling of dislocations dominates in three dimensions.

CRACK GROWTH LAWS

What are the crack growth laws? On long length and time scales, most macroscopic systems obey simple laws of motion, which depend on the properties of the material only through setting constants (like density and elastic constants) or functions (like surface energies including the crystalline anisotropy). Can we deduce the laws describing the growth of a crack front, coarse-graining over all the atoms, grains, precipitates, and plastic deformation near the crack tip, to get relatively simple laws depending on only a few materials parameters or functions?

Jennifer Hodgdon and I studied this problem, inspired by conversations with Tony Ingraffea and members of his group. Ingraffea's group[11] solves the hard part of the problem: given a complicated, three-dimensional crack, they can tell us the stress intensity along the crack tip. All they wanted was the rules for advancing the crack forward in time. The simplest problem for us to study, and the one of most current interest to their group, was quasistatic fracture in an isotropic, homogeneous medium. Including crystalline anisotropy would lead us to the physics of cleavage along the crystalline planes. Including random inhomogeneities into theories of brittle fracture leads to logarithmically rough fracture surfaces[12], but not as rugged as the experiments[13]. Including the inertial dynamics of the growing front leads to interesting traveling waves along the crack front[14] that might improve the agreement with experiment. In ductile and intergranular fracture, the roughness reflects void growth and the presence of grains and inclusions.[15] Our work did not include any of these effects.

Naturally, Ingraffea's group already had a working solution. For mode I fracture, the material is described by a crack growth velocity $v(K_I)$. For mode II fracture, the crack turns abruptly until it is mode I (the principle of local symmetry[16]). There were two other rules in the literature for picking the crack growth direction: one maximizing the energy release[17], and one moving into the direction of minimum strain energy density[18]. All three rules seemed to predict crack paths which agreed well with one another[19]. At that time (around 1990) they were just moving into 3D fracture, and were quite interested in more crack growth laws for more general geometries.

Jennifer Hodgdon and I decided to try to write the most general crack growth law allowed by symmetry. Let us describe the local crack front with an orthonormal triad of vectors: $\hat{\mathbf{b}}$ perpendicular to the local crack face, $\hat{\mathbf{t}}$ tangent to the crack front, and $\hat{\mathbf{n}}$ pointing in the direction along which the crack was last growing. Our theory is valid on long length and time scales: in particular, we assume that the curvatures of the the radii of curvatures for the crack surface and crack front are large, so to zeroth order the crack is straight and flat (we'll expand in the curvatures). There are then three symmetries of the crack: the reflection R_{plane} in the $\hat{\mathbf{n}} - \hat{\mathbf{t}}$ plane of the crack, the reflection R_{cross} in the $\hat{\mathbf{n}} - \hat{\mathbf{b}}$ plane perpendicular to the crack front $\hat{\mathbf{t}}$, and the 180° rotation about $\hat{\mathbf{n}}$ (which is the product of the two other symmetries).

The first convenient thing to fall out of the symmetry analysis is the decomposition of the strain field into modes. The linear elastic solution near the crack tip can be decomposed into a superposition of solutions with definite symmetries under R_{plane} and R_{cross}. Mode I is symmetric under both transformations, mode II is antisymmetric under reflections in the plane but symmetric to reflections perpendicular to the front, and mode III is antisymmetric under both. Jennifer found that there was yet another mode (mode IV?) which is symmetric under R_{plane} and antisymmetric under R_{cross}. Presumably Hodgdon's mode IV is usually ignored because it does not introduce a crack opening.

We then assume that the body being cracked and the radii of curvature of the local crack front and crack surface are all large compared to the inhomogeneities in the material and the nonlinear zone around the crack tip. This is what is needed to ensure that there is a region around the crack tip where the elastic displacement fields scale with the square root of the distance r to the crack tip. (In general[1, 20] the displacement field for each mode can be expanded in a series of all half-integer powers of r. The less singular terms are important only far from the crack, and are determined by the boundary conditions and the crack shape; the more singular

for example, we describe ductile fracture only if the body is much larger than the plastic zone. We write the growth laws of the crack in terms of the three stress-intensity factors K_I, K_{II}, and K_{III} in this (so-called K-dominant) region, their gradients along the crack front, and the curvatures of the crack front and crack surface. We impose the symmetries of the problem described above, plus a gauge symmetry[21, 1] associated with reparameterization of the crack front, to find the most general law of motion allowed by symmetry.

In two dimensions, we found that the most general crack growth law was of the form

$$\partial \mathbf{x}/\partial t = v(K_I, K_{II}^2, K_{III}^2)\hat{\mathbf{n}}, \qquad \partial \hat{\mathbf{n}}/\partial t = -f(K_I, K_{II}^2, K_{III}^2)K_{II}\hat{\mathbf{b}}, \tag{9}$$

where $\mathbf{x}$ is the location of the crack tip, v is the velocity of the crack, and f represents the tendency for a crack to turn under the external load (hence changing the direction $\hat{\mathbf{n}}$ pointing along the crack).

What does this equation imply about the crack growth? If $K_{II} = 0$, the crack won't turn; otherwise it will turn (if $f > 0$) so as to reduce K_{II} in magnitude. Thus we agree with the principle of local symmetry, except that our cracks will turn gradually towards this direction, rather than jump abruptly to the new orientation. Over what turning radius does our crack turn? Using results of Cotterell and Rice[22], Hodgdon showed that if the angle of the crack differs from the angle that makes $K_{II} = 0$ by a small amount $\Delta\theta$, then $K_{II} = K_I \Delta\theta/2$; this implies that $\Delta\theta \ \exp(-fK_I x/2v)$, and the angle decays exponentially to pure mode I with a material-dependent decay length of $2v/fK_I$. We expect this length scale to be set by a microscopic scale characteristic of the material: the atomic size in a glass, the size of the nonlinear zone in a ductile material, etc. This means, in essence, that our analysis agrees with the traditional prescription that the crack turns abruptly. We think of writing the crack growth laws as differential equations replaces the atomistic short-distance cutoff with a smooth one.

Our analysis did not make any assumptions about microscopic mechanisms. We believe that arguing whether the crack turns to maximize the energy release or minimize the strain energy density is misguided: if you turn the crack according to the wrong rule, in the succeeding step it'll keep turning and you'll converge to the same final trajectory (making $K_{II} = 0$) with a radius of curvature given by the step size in your algorithm.

So much for reinventing what's already known. What about three dimensions? Now everything depends on where we are along the crack front. If we let s measure arclength along the crack front, then up to first order in gradients

$$\begin{aligned}
\partial x/\partial t = & \qquad v\hat{n} + w\hat{t} \\
\partial \hat{n}/\partial t = & -\left[\tfrac{\partial v}{\partial s} + w\tfrac{\partial \hat{t}}{\partial s}\cdot\hat{n}\right]\hat{t} + \Big[-fK_{\rm II} + g_{\rm I}K_{\rm III}\tfrac{\partial K_{\rm I}}{\partial s} + g_{\rm II}K_{\rm II}K_{\rm III}\tfrac{\partial K_{\rm II}}{\partial s} + g_{\rm III}\tfrac{\partial K_{\rm III}}{\partial s} + \\
& \qquad h_{tb}\tfrac{\partial \hat{t}}{\partial s}\cdot\hat{b} + h_{nt}K_{\rm II}\tfrac{\partial \hat{n}}{\partial s}\cdot\hat{t} + (h_{nb}K_{\rm II}K_{\rm III} + w)\tfrac{\partial \hat{n}}{\partial s}\cdot\hat{b}\Big]\hat{b},
\end{aligned} \tag{10}$$

where f, g_α, and h_{ij} are functions of $K_{\rm I}$, $K_{\rm II}^2$, and $K_{\rm III}^2$, and the velocity v can be a function of these and a number of gradient terms[1]. Only f among these constants, which gives the turning radius for mode II fracture, is expected to be large (as discussed above): the others should be all of the same order of magnitude.

What can we do with this expression? First, if the crack begins nearly flat and straight, we can do perturbation theory to see if the crack becomes flatter and straighter, or if it goes unstable. Jennifer Hodgdon[23] found that cracks under mode I are stable (as expected), but that cracks under mixed mode I and mode III (twisting) can be stable or unstable depending on the materials constants: in particular, if $g_I > 0$, steady-state mode III cracks are unstable to small perturbations. Experimentally, she found that cracks under mode III turned to form a helical crack surface: such turning wasn't allowed for in our perturbation theory, which assumed periodic boundary conditions. Others find, for longer cracks, that mode III fracture is unstable to the formation of a "factory roof" morphology. It wasn't possible at the time to test Hodgdon's results with realistic crack-growth simulations, and this work remains unpublished.[23]

Second, we can use it to propagate real 3D cracks in simulations, and compare to experiments and more microscopic simulations. I anticipate that our symmetry analysis will prove important and useful, but that there will be additional internal variables (perhaps crack-tip curvature[24]) that will be necessary for describing the crack, and which may induce crack branching and other effects missing in our existing theory.

1. Jennifer A. Hodgdon and James P. Sethna, *Phys. Rev. B* **47**, 4831 (1993).
2. Alex Buchel and James P. Sethna, *Phys. Rev. Lett.* **77**, 1520 (1996).
3. Alex Buchel and James P. Sethna, *Phys. Rev. E* **55**, 7699 (1997).
4. W. A. Curtin and H. Scher, *Phys. Rev. Lett.* **67**, 2457 (1991).
5. S. L. Phoenix and I. J. Beyerlein, Chapter 1.19 in Vol. 1 of *Comprehensive Composite Materials* (T.-W. Chou, ed., A. Kelly and C. Zweben, series eds.), Pergamon - Elsevier Science, pp. 559–639.
6. P. F. Arndt and T. Nattermann, "A New Criterion for Crack Formation in Disordered Materials", cond-mat/0012113, accepted for publication in *Phys. Rev. B.*
7. J. S. Langer, *Ann. Phys. (N.Y.)* **41**, 108 (1967); **54**, 258 (1969),
8. A. A. Griffith, *Philos. Trans. R. Soc. London Ser. A* **221**, 163 (1920).
9. F. J. Dyson, *Phys. Rev.* **85**, 631 (1952).
10. V. Ambegaokar, B. I. Halperin, D. R. Nelson, and E. D. Siggia, *Phys. Rev. Lett.* **40**, 783 (1978), and *Phys. Rev. B* **21**, 1806 (1980); P. Minnhagen, O. Wetman, A. Jonsson, and P. Olsson, *Phys. Rev. Lett.* **74**, 3672 (1995); M. Khantha, D. P. Pope, and V. Vitek, *Phys. Rev. Lett.* **73**, 684s (1994); R. L. B. Selinger, B. B. Smith, and W.-D. Luo, "Dynamics and Patterning of Screw Dislocations in Two Dimensions", cond-mat/0012447, to be published in the MRS Fall '00 Proceedings, Multiscale Materials Modeling.
11. Cornell Fracture Group, http://www.cfg.cornell.edu/.
12. S. Ramanathan, D. Ertas, and D. S. Fisher, *Phys. Rev. Lett.* **79**, 873 (1997).
13. E. Bouchaud, *J. Phys. Condens. Matter* **9**, 4319 (1993) and references therein.
14. S. Ramanathan and D. S. Fisher, *Phys. Rev. Lett.* **79**, 877 (1997); J. R. Rice, Opening Lecture at the 20th International Congress of Theoretical and Applied Mechanics, Chicago, Aug. 27, 2000.
15. T. L. Anderson, *Fracture Mechanics, Fundamentals and Applications*, CRC Press, Boca Raton, 1991, chapter 5.
16. R. V. Gol'dstein and R. L. Salganik *Int. J. Frac.* **10**, 507 (1974).
17. C. H. Wu, *J. Appl. Mech.* **45**, 553 (1978).
18. G. C. Sih, p. xv in *Mechanics of Fracture 2: Three Dimensional Crack Problems* (eds. M. K. Kassir and G. C. Sih), Noordhoof International, Netherlands, 1975.
19. P. A. Wawrzynek and A. R. Ingraffea, *Discrete Modeling of Crack Propagation: Theoretical Aspects and Implementation Issues in Two and Three Dimensions*, Ph.D. Thesis, Cornell University, 1991.
20. C. Y. Hui and Andy Ruina, *Int. J. Frac.* **72** 97 (1995).
21. S. A. Langer, R. E. Goldstein, and D. P. Jackson, *Phys. Rev. A* **46**, 4894 (1992).
22. B. Cotterell and J. R. Rice, *Int. J. Frac.* **16**, 155 (1980).
23. J. A. Hodgdon, *Three-Dimensional Fracture: Symmetry and Stability*, Ph. D. Thesis, Cornell University, 1993.
24. I. S. Aranson, V. A. Kalatsky, V. M. Vinokur, *Phys. Rev. Lett.* **85**, 118 (2000).

ORAL REFERENCE:ICF100569OR

FORMATION AND EVALUATION OF HAp FILMS BY ELECTROCHEMICAL METHOD

SHINOBU OZONE[1] and YUJI KIMURA[2]

[1]Graduate School, Kogakuin University
1-24-2 Nishishinjuku Shinjuku-ku, Tokyo, 163-8677, Japan
[2]Department of Materials Science and Technology,
Kogakuin University,

ABSTRACT

The calcium phosphate including Hydroxapatite ($Ca_{10}(PO_4)_6(OH)_2$: referred to as HAp) utilizes as a biomaterial, because that resembles the principal ingredient of the tooth and bone and have superior biocompatibilty. Through coating calcium phosphate on metallic biomaterial such as the commercially pure titanium, the biocompatible character can be given to the material together with its mechanical strength. Some trials have been conducted for applying these coated materials to the artificial bone and so on.

In this study, the optimum condition of the HAp films formation by electrochemical method was investigated by employing QCM(Quartz Crystal Microbalance), FE-SEM and EDX. Then, adhesive strength of coated HAp films was evaluated by the scratch test. Also, biocompatible character was examined by immersion test into guasi-human body fluid. As a result, the activation in precipitation of HAp was recognized at the electrode potential around –650mV[vs. SCE] due to the frequency change detected by QCM measurement and the cathodic current density increase. FE-SEM observation and EDX analysis on specimen surface used for QCM measurement revealed the uniform precipitation of HAp. Also, well developed crystal structure of HAp can be obtained under the condition detected by QCM measurement and the improvement in adhesion strength between HAp films and substrate metal was recognized.

KEYWORDS : HAp films, biomaterial, electrochemical method, biocompatibility, QCM, FE-SEM, EDX

INTRODUCTION

The calcium phosphate including HAp utilizes as a biomaterial, because that resembles the principal ingredient of the tooth and bone and have superior biocompatibilty. Through coating calcium phosphate on metallic biomaterial such as the commercially pure titanium, the biocompatible character can be given to the material together with its mechanical strength. Some trials have been conducted for applying these coated materials to the artificial bone and so on[1]. At present, Plasma-spray method was applied for making HAp coating. However, the temperature in the plasma-spray coating process becomes up to 5,000～20,000℃[2,3]. For this reason, the phase of calcium phosphate becomes amorphous. As a result, the problem of the biocompatible character of coated film being degraded is brought about. On the other hand, HAp coating made by electrochemical method can be obtained under relatively mild conditions compared with plasma-spray method. Also, more crystallized structure can be obtain by the electrochemical coating method. However, poor adhesion strength between coated layer and substrate metal and poor reproducibility of this coating method become problems to be solved.

Therefore, authors have been investigated reproducibility of HAp coating by electrochemical coating method. As a result, it was recognized that pitting corrosion of substrate Ti and poor adhesion strength between coated layer and substrate caused the delamination of coated HAp film. Therefore in this study, the optimum condition of the HAp films formation by electrochemical method was investigated employing QCM (Quartz Crystal Microbalance), FE-SEM and EDX. Then, adhesive strength of coated HAp films was evaluated by the scratch test. Also, biocompatible character of HAp film was examined by immersion test into guasi-human body fluid.

EXPERIMENTAL PROCEDURES

Determination of the optimum condition of the HAp films formation by QCM

Activating potential condition of HAp deposition on specimen surface can be detected by QCM, because of its ability to measure ng order precipitate through detecting the frequency change of quarts crystal vibration with the cathodic current density sweep. QCM measurements were conducted using three electrode method composed of Ti coated specimen (working electrode), Pt (counter electrode) and the saturated calomel electrode (S.C.E) (reference electrode). Then, optimum conditions of electrode potential for better HAp film formation was determined. Solution temperature was selected to be 310 K and the potential was swept from natural corrosion potential up to -1000 mV with the sweep rate of 20 mV/min. Detailed observation of specimen surface was conducted by FE-SEM. Also, the characterizasion of deposited materials were conducted by EDX.

Cathodic polarization curve measurement

It is difficult to conduct QCM measurement under the potential condition up to -1500 mV due to HAp precipitation on Ti electrode. Therefore, cathode polarization curve measurement were also conducted in the same solution using three electrode method composed of Ti (working electrode), Pt (counter electrode) and the saturated calomel electrode (S.C.E) (reference electrode). Solution temperature was selected to be 310 K

and the potential was swept from natural corrosion potential up to -2000 mV with the sweep rate of 20 mV/min. Detailed observation of specimen surface was conducted by FE-SEM. Also, the characterization of deposited materials were conducted by EDX.

Potentiostatic measurement

Potentiostatic measurement ware conducted under various peak potentials for HAp film formation obtained by QCM and cathode polarization curve measurement. Therefore, -700, -1200, -1500, and -2100 mV were selected as the constant potential condition for potentiostatic measurement. The measurements were continued up to 100 min. under above-mentioned various constant potential conditions.

Adhesion strength evaluation

To determine the optimum condition for HAp film formation, adhesion strength between coated HAp thin film and substhate Ti was measured using scratch testing machine of REVETEST made by Nanotec Co., Ltd. with testing conditions shown in Table 1.

The critical load Lc for initiation of microdelamination of thin film obtained by scratch test was determined employing the JSME (Japan Society of Mechanical Engineers) Standard S 010-1996 "Standard Method for Evaluating the Defects in the Coatings Made by Dry Processings"[4,5]. The value of Lc was synthetically evaluated from both changes in friction load and AE count and the morphology changes in scratch trace detected by microscopic observation.

Table 1 Condition of scratch test

Indenter	Tip radius	200 μ m
	Material	Diamond
Loading rate		100N/min
Sliding rate of Tip		10mm/min
AE sensitivity		5

EXPERIMENTAL RESULTS AND DISCUSSIONS

Determination of the optimum condition of the HAp films formation by QCM

The solution used in this study was deionized water in which $Ca(NO_3)_24H_2O$ and $(NH_4)2HP$ were dissolved with the mole ratio of Ca/P=1.67. By using this solution, the optimum condition for HAp film formation by electrochemical method was investigated employing QCM measurement whose specimen was Ti deposited electrode. Correlation between the cathodic potential vs. the current density and the cathodic potential vs. the vibrating electrode frequency was obtained by QCM measurement and shown in Fig. 1. From this figure, under the cathodic electrode potential condition around -650～-850 mV (S.C.E.), abrupt increase in cathodic current density and also sudden decrease in electrode vibration frequency were detected. For these reason, accelerated precipitation and deposition of HAp on Ti coated electrode can be expected. Under the potential range over -850 mV (S.C.E.), the frequency measurement of electrode was prohibited due to excessive precipitation of HAp on itself. Therefore, mophology of HAp deposited on QCM electrode was observed by FE-SEM and shown in Fig. 2. At the same time, examination of chemical composition of deposited film was conducted by EDX measurement. As a result, precipitation of HAp was recognized.

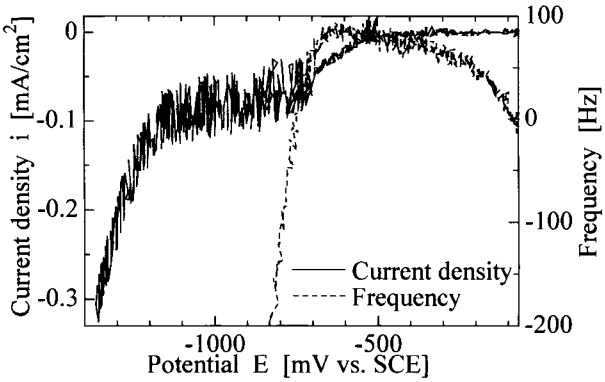

Fig. 1 Polarization Curve and QCM Data

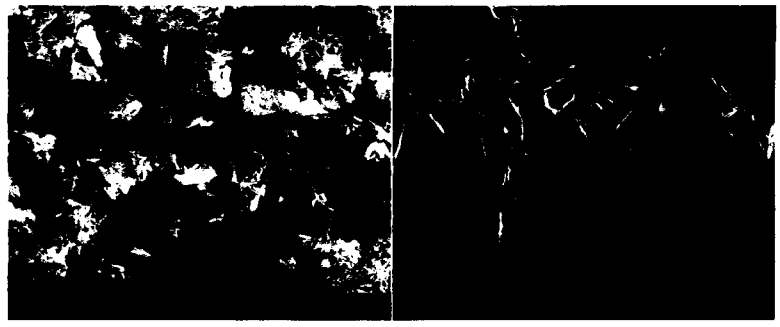

a) 5.0kV×500 **b)5.0kV×5.00k**

Fig. 2 Surface Morphology of HAp on QCM Electrode

Cathodic polarization curve measurement

To grasp the precipitation behavior of HAp under potential condition beyond -1500 mV, the cathodic polarization measurement was conducted employing the same Ti electrode. Obtained result was shown in Fig. 3.By comparing the results shown in Fig. 3 with those obtained by QCM measurement, the same trend of increase in the current density was recognized under the potential condition from about -650 mV up to -850 mV (S.C.E). The cathodic current density gradually increased up to the potential condition of -1250 mV. Then, abrupt decrease in the current density was recognized. After showing local minimum value in current density under potential condition around -1400 mV, the current density gradually increase again up to the potential condition of -2000 mV.

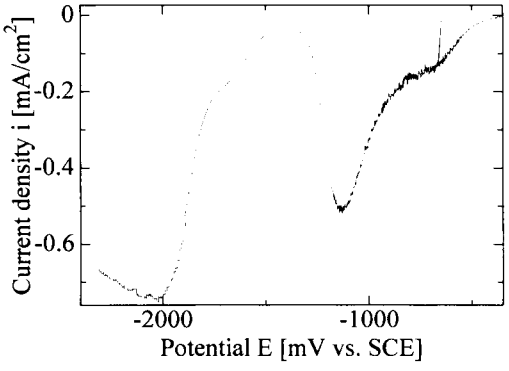

Fig. 3 Cathodic Polarization Curve

Constant potential measurement

-1200 mV, -1500 mV, and -2100 mV were detected as the local peak potential values from the cathode polarization measurement shown in Fig. 3. Constant potential measurements were conducted under these three kinds of potentials and also under -700 mV at which abrupt increase in cathodic current density and sudden change in vibration frequency of electrode were recognized in the QCM measurement.

The results of current density measurement were shown in Fig. 4. From these figures, only under the potential condition of E = -2100 mV (S.C.E), gradual increase in the current density was observed. Therefore, accelerating cathodic reaction was generated on the Ti substrate surface under the potential condition of -2100 mV. Out of other three potential conditions, at -700 mV the cathodic current density was recognized to be kept under relatively stable larger value state. It may result in excessive HAp precipitation on the substrate surface. Microscopic observation on the substrate surface after constant potential electrochemical test revealed that HAp uniformly precipitated on specimen surface under the potential condition of -700 mV. Under the potential condition of -1200 mV, precipitation of HAp was also recognized. In this case, double

layered HAp precipitation was observed by the microscopic observation on specimen surface. Under the potential condition of -1500 mV, delamination and precipitation of secondary HAp layer may be balanced.

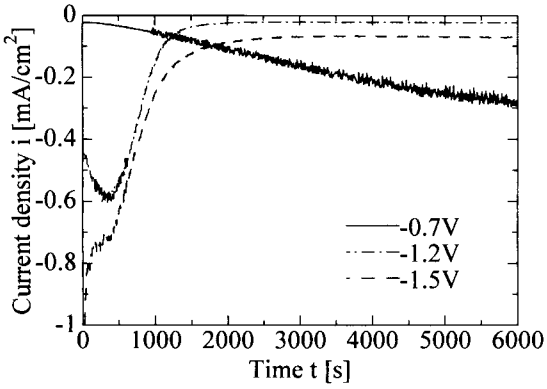

a) -0.7, -1.2, -1.5, -2.1 V

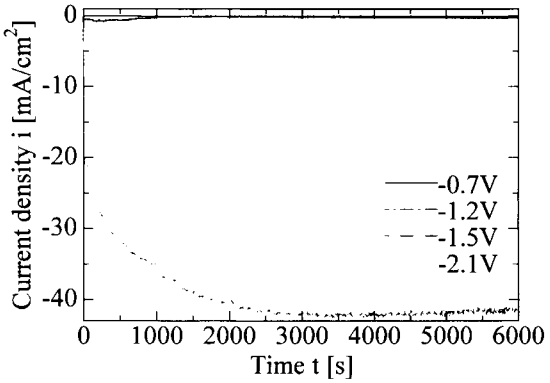

b) -0.7, -1.2, -1.5 V

Fig. 4 Current Density Change during Constant Potential Tests

a) -0.7V

b) -1.2V

c) -1.5V

d) -2.1V

Fig. 5 Surface Morphology of HAp

Adhesion strength evaluation

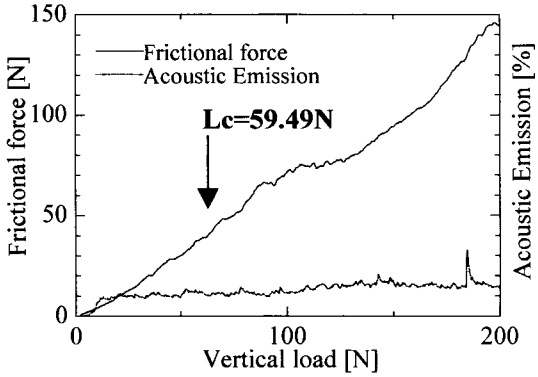

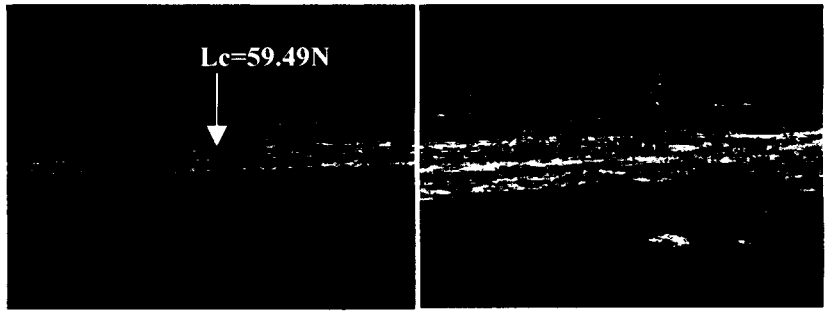

a) 59.47 [N]

b) 89.56 [N]

Fig.6 Result of scratch test of HAp film, Thickness of film : 280 μ m

Fig.7 Surface morphology of HAp film after scratch test, Thickness of film : 280 μ m

To evaluate adhesion strate of precipitated HAp film on Ti substrate, scrtch test was conducted. The result of

scratch test is shown in Fig. 6 and the surface morphology of HAp film after scratch test is shown in Fig. 7. In Fig. 6, the diagrams of frictional force and acoustic emission count changes depending upon vertical load were indicated. Fig. 7 shows the optical micrographs of scratch trace observed on 280 μ m thick HAp film that was formed under -700 mV. In this paper, the critical load of Lc for the initiation of micro delamination was mainly determined by examining the morphological changes in the scratch trace observed by optical microscope. At the same time, no aboupt change in AE count and also in frictional force were recognized as shown in Fig. 6. Therefore, critical load Lc was determined by the optical microscopic observation of the scratch trace and obtained to be 59.5 N in this case. This Lc value is almost the same revel as that of TiN/AISI304 coating obtained under the temperature condition of 900 ℃ by plasma CVD method[4].

CONCLUSIONS

The optimum condition of the HAp films formation by electrochemical method was investigated by employing QCM (Quartz Crystal Microbalance), FE-SEM and EDX. Then, a adhesive strength of coated HAp films was evaluated by the scratch test. As a result, the activation in precipitation of HAp was recognized at the electrode potential around -650 mV[vs. SCE] due to the frequency change detected by QCM measurement and the cathodic current density increase. FE-SEM observation and EDX analysis on specimen surface used for QCM measurement revealed the uniform precipitation of HAp. Also, well developed crystal structure of HAp can be obtained under the condition detected by QCM measurement and the improvement in adhesion strength between HAp films and substrate metal is recognized. Biocompatible character is expected to be examined through immersion test into guasi-human body fluid.

REFERENCES

1. Hyun-Min kim, Fumiaki MIYAJI and Tadashi KOKUBO, Preparation of Functionally Graded Bioactive Titanium and Its Alloys by Chemical Treatment, Japan Inst. Metals, Vol.62, No.11, pp1102-1107, 1998
2. Seiji NITTA and Yuji KIMURA, Journal of Material Testing Research Association of Japan, 42[1], pp.4-14, 1997.
3. Seiji NITTA and Yuji KIMURA, Trans. Japan Soc. Mechanical Engineers, 61[589], pp.1914-1920, 1995.
4. JSME standard S-010 "Standard Method for Evaluating the Defect in the Coatings Made by Dry Processing", JSME, 1996.
5. Yuji KIMURA and Tatsuya SHIRATO, Correlation between Interfacial State of Plasma CVD Coated TiN Film/Substrate and Pinhole Defect Ratio Evaluated by CPCD Method, Proc. of 13th ECF, CD volume. Ceramics, paper No. 8, pp.1-8, 2000, Elsevier Science.

ICF100340OR

FORMATION OF HIERARCHICAL ORDERED CRACK SYSTEMS AT FRACTURE

R. V. Goldstein and N. M. Osipenko

Institute for Problems in Mechanics,
Russian Academy of Sciences,
Prospect Vernadskogo, 101-1
117526, Moscow, Russia

ABSTRACT

Fracture processes in different materials, structural components and natural objects are often occured by formation and transformation of ordered systems of cracks or cracklike faults (structures of fracture). Scale interaction can lead to formation of a hierarchy of structures of fracture of different length scales. Ordered systems of cracks or cracklike faults are observed, e.g., at fracture of ceramics and rocks under biaxial compression, pipeline steels and titanium under the hydrogen absorption, ice cover under the wind action.

In the paper an approach is developed for modeling of processes of formation of hierarchical systems of structures of fracture. The approach implies, first, an analysis of a sequence of events leading to formation of separate elements of a structure of fracture of a certain scale (rank) taking into account local perturbations of the stress-deformation field caused by an influence of the initial structure and/or texture of the object under consideration. Then a set of such elements forms a basic element of a structure of fracture. In turn, a structure of fracture of a given scale can serve as a basic element for formation of a structure of fracture of another scale. The approach enables to take into account specific mechanisms of fracture and analyze formation of hierarchy of structures of fracture. Structures of fracture of long-range action and short-range action are considered. Coupled structures of fracture forming at smaller and larger scales relative to the scale of a basic structure of fracture are analyzed. The results of modeling different types of structures of fracture correlate with the available experimental data.

KEYWORDS

Odered systems, crack, cracklike faults, structure of fracture

INTRODUCTION

Fracture of materials, structures and nature objects is often accompanied by occuring ordered systems of faults-structures of fracture [1]. These structures can form hierarchical systems. The structures of fracture were observed at quasibrittle fracture of polymers and rocks, localization of plastic deformations [2,3,4], slip planes formation in quick media [5], energy dissipation on the deformation wave front [6], splitting off

fracture [7], etc. Structure of fracture formation occurs at small variations of the parameters near the limit equilibrium conditions for the media under consideration.

Several approaches were developed to analyze formation of structures of fracture within the framework of fracture mechanics. In particular, these processes are treated as an instability of deformation at a scale of a whole body [3,8]. Another approach, based on an analysis of a sequence of events associated with the fracture mechanism development and accompanied by formation of separate elements of the structure and the structure on the whole, was suggested by the authors [1,9,10,11]. In the paper we performed further development of this approach and considered some problems related to formation of a hierarchy of structures of fracture.

STRUCTURES OF FRACTURE

Conditions for increasing the rank of the structure

Remind necessary and sufficient conditions for increasing the rank of the structure of fracture, i.e. formation of a basic scale of a new structure having the elements larger than those of the "old" structure [1,9].

It is assumed that the medium has a structure (of rank i) which is active relative to the external loading. The response of the medium can be described by a distribution (field) of characteristics at the level of a structural element (SE) of rank i or a combination of such elements. The SE can attain a limit state at certain combinations of the values of these characteristics. Generation of a SE of rank (i+1) will be associated with the localization of response processes in the medium at the level of rank i, i.e. with the instability of a SE of rank i.

The formation of a structure of rank (i + 1) requires, on the one hand, the local instability of an SE of rank i to initiate the process of successive local changes in the structure of rank i and, on the other hand, the inhibition of this instability to complete the formation of the element of rank (i + 1). These two processes are necessary for the formation of a structure of rank (i + 1). In some cases, the formation of one element of rank (i + 1) does not lead to the formation of a system of such elements and, hence, does not lead to an increase in the rank of the entire structure. For these reason, we need also sufficient conditions for the change in the rank of the structure. To initiate the formation of the structure of rank (i + 1), it suffices that the perturbation caused by the appearance of the previous SE of rank (i -+- l)be able to lead to an instability necessary for the formation of the next SE of rank (i + 1).

The spatial configuration of the element of the new structure depends on the form of the initial structure and on the position of the site of generation of the local instability of a typical element of the initial structure. Since this position depends on the combination of the external field and the perturbation of this field by the element exhibiting instability, it is important that specific response mechanisms determining the spatial nonuniformity of the corresponding fields be considered in the model of the process. The basic mechanisms defining the change in the structure are the mechanism of excitation of the local instability of an element of rank i and that of instability restraint for the corresponding SE of rank (i + 1). Note that in some mechanisms restraining the instability, the spatial nonuniformity of the stress fields leads to the fracture of separate SE's of rank i. This provides the possibility of decreasing the rank of the structure combined with the increase of this rank (the combined formation of SE's of ranks (i + 1) and (i - 1)).

Fracture of a porous body

We will consider typical examples of structures of fracture. In [I], the increase in the rank of the structure of an elastic porous body is illustrated by the formation of the structure of rank i + 1 of crack elements interacting in short range in the tensile crack echelon. Similar constructions can be carried out also for other sorts of stress concentrators, for example, for inclusions or macrocracks. We will briefly consider the plane model of the process [1,9]. Let the body contains circular pores of radius R which are uniformly rarely arranged. Let the distance between the centers of the neighboring pores have an order of magnitude of 2L

(Fig. 1a*)*. The cracks formed by the external compression (i) came against the pore boundary in the

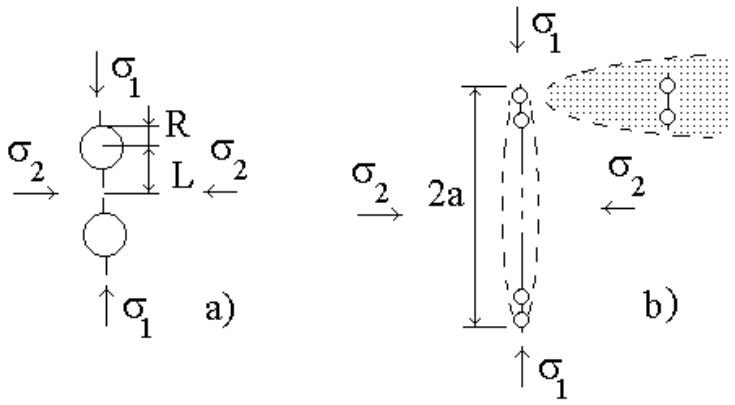

Figure 1: Fracture of a porous medium under uni-axial (a) and bi-axial (b) compression

diametrical direction, (ii) have identical lengths ℓ, and (iii) are oriented along the principal compressive stresses. The initiation of the main crack occurs by means of coalescence ofmicrocracks growing near typical pores, i.e., with the condition $\ell \sim L$ being satisfied. The propagation of the main crack under the uniaxial loading of the body is unstable. Hence, the stress intensity factor at the tips of the main crack exceeds that of an isolated microcrack of length $\ell \sim L$.

The effective value of the stress intensity factor for a main crack comprising several pores in the case of the uniaxial compression can be represented in the form

$$K_{Ia} = \sigma_1 \sqrt{R}\, f\left(\frac{R}{a}, n\right), \qquad f\left(\frac{R_0}{a}, n\right) \approx \frac{0.24 n^{1/3}}{1 - n^{1/3}\left(3\frac{R}{a} - 1\right)}, \quad \frac{a}{R} > 3. \tag{1}$$

where a is the half-length of the main crack and n is the porosity, R is a constant radius of curvature at the vertex of a narrow elongated ellipse equivalent to the main crack.

It was assumed that $\ell = L$ and $(L/R) \approx n^{1/3}$.

In a similar way, one can obtain the value of the stress intensity factors of isolated cracks having the lengths at which these cracks join together. Thus we obtain

$$K_{IR} = \sigma_1 \sqrt{R}\, f_1(n), \quad f_1(n) = \frac{8n^{1/3} - 1}{80(1 - n^{1/3})}. \tag{2}$$

If an additional lateral compression σ_2 acts, then the stress intensity factor can be expressed by the sum

$$K_I = K_I(\sigma_1) + K_I(\sigma_2). \tag{3}$$

For the case of an elongated ellipse mentioned above we have

$$K_I(\sigma_2) = \sigma_2 \sqrt{a}\, f_2\left(\frac{R}{a}, n\right), \quad f_2\left(\frac{R}{a}, n\right) = \left[\frac{1}{\sqrt{2}} + \left(0.32\sqrt{\frac{R}{a} - 0.05}\right)\frac{0.95n^{2/3} - 2n^{1/3} + 1}{n^{1/3}(1 - n^{1/3})}\right] \tag{4}$$

The functions f, f_1, f_2 were constructed on the basis of the results of the numerical solving the appropriate elasticity problems [12].

The size of the limit equilibrium crack is defined by the condition

$$K_I = K_{Ic} \tag{5}$$

It is apparent from Eqs. (3.2) and (3.3) that a porous material subjected to the uniaxial compression is fractured by main cracks intersecting the volume being loaded along the principal compressive stresses, since the inequality $K_{Ia} > K_{IR}$ is valid for any $a < 3R$. This statement is valid also for mechanisms of brittle fracture of heterogeneous materials with different stress concentrators [9-11]. It is in good agreement with the experimental data concerning the brittle fracture of rocks [12]. Main compression discontinuities represent one of the basic forms of brittle fracture of heterogeneous materials.

For a porous body subjected to the biaxial compression, main cracks are bounded in length. The occurrence of the unstable phase of the development of the main discontinuity formed by a chain of pores implies that the necessary condition for the generation of a higher-rank structure is satisfied. To satisfy the sufficient conditions, it is necessary that the perturbation of the stress field in the neighborhood of the main crack would initiate the unstable development of another main crack at a distance from the former crack. Depending on the parameters of the initial structure (for example, on the porosity) and loading condition, the stress field perturbation can initiate a fracture site in a short-range or long-range neighborhood of the main crack. The conditions for the generation of the fracture site near the tip of an arrested crack are most favorable in the neighborhood of a tensile crack at a distance of an order of magnitude of 2L from the crack tip [13]. At this distance, the shear perturbation zone covers two interacting pores (Fig. 1b*).* The condition for these pores to join together provides the sufficient conditions for an increase in the structural rank to be satisfied. The latter conditions imply the relations

$$\begin{aligned}
&K_{Ic} = K_{IR}(\sigma_1 + \Delta\sigma_1) + K_{IR}(\sigma_2 - \Delta\sigma_2), \quad \Delta\sigma_{1,2} \approx \pm \frac{K_{Ia}}{\sqrt{2L}}, \\
&K_{IR}(\sigma_1 + \Delta\sigma_1) = (\sigma_1 + \Delta\sigma_1)\sqrt{R}\, f_2(n), \\
&K_{IR}(\sigma_2 - \Delta\sigma_2) = (\sigma_2 - \Delta\sigma_2)\sqrt{R}\, f_3(n), \quad f_3(n) = \frac{5 + 8.4n^{1/3} - 13.4n^{2/3}}{n^{1/3}(22 - 21n^{1/3})}
\end{aligned} \tag{6}$$

If the boundary conditions specified in terms of stresses (σ_1, σ_2) are fixed, then the relations (6) define the basic parameters of the crack echelon in the volume being loaded. These parameters are the lengths of isolated main cracks in the echelon and the distance between parallel main cracks. The configuration of the echelon (the relative arrangement of main cracks) depends on the conditions of interaction of neighboring cracks in the echelon.

Note that the location of the fracture site in the neighborhood of the main fracture and the direction of the development of the next main fracture can be different and determined by stress fields in the long-range zone.

Echelon structures in ice cover

Necessary and sufficient conditions of structure of fracture formation can be provided by different mechanical processes.

As an example let us consider a type of largescale structures in the ice cover-formation of an echelonlike system of faults in thin level ice under uniform tension [14]. The velocity of growth of a single fault in a viscoelastic thin plate on a hydraulic foundation is changed with nonmonotone manner at increasing the fault length [8]

$$\frac{d\ell}{dt} \sim \frac{\vartheta^*}{f_1}\ell^{3/4}\left(1-\frac{bf_1}{\vartheta^*}\ell^{1/4}\right)^2 \qquad b=\frac{\eta}{E};\ f_1 = f(E, K_{Ic}, \overline{\sigma}) \tag{7}$$

where η is the ice cover viscosity, ϑ^* is the threshold rate of the fault surfaces displacement characterized by compensation of a mean stress $\overline{\sigma}$ by hydrodynamic resistance. Local instability is inherent for a small size of the fault, while fault growth arrest is related to its large size. Hence a necessary condition of a structural element formation is fulfilled. A sufficient condition occurs when the resulting stress in the vicinity of the fault tip becomes equal to the stress of new fault nucleation such that the size of a nucleous fault provides its growth with a larger velocity according to (7) than for the initial fault. One can show that the energy dissipation rate for an echelon of large size faults is larger than for a single fault of the same total length. As a result structure formation becomes the leading process at preparing large scale fracture in the conditions close to the limit equilibrium.

A possible role of structure formation in rocks was analyzed in [11] in case of preparing when the local instability is provided by the gas pressure in pores, while the arrest mechanism by the rock pressure.

A similar scheme of fracture characterized by formation of a system of microcracks under the action of the hydrogen diffusion is observed at the cracking of pipeline steels modeled in [15].

Basic and conjugate structures

Basic structures forming mechanisms of fracture at the initial stage of the medium deformation are of particular importance in the scheme of multiscale fracture. It seems that in the fragment of the hierarchy of structures which can be observed [8-10], the fracture structures play a leading role only within a limited range of scales, within the limits of the influence of certain basic structures. Note, that small perturbations of physical fields are important for occuring a basic structure in a quasihomogeneous body. One can show [11] that the interaction between the elements of this structure is implemented by means of long-range perturbations of stress fields.

The transformation of the basic structure into a higher-rank structure is not the only possible response of the medium to an input influence. Experiments with rocks and model media subjected to a quasistatic deformation reveal the process of combined change of the rank with respect to the initial block structure. This process involves the agglomeration of some blocks (formation of a structure of rank i + 1) combined with the refinement of other blocks (formation of a structure of rank i - 1).

This combined initiation of structures of rank i ± 1 can be activated by the mechanism of deceleration of the SE of rank i + 1 consisting of several elements of rank i in the effective medium determined by the basic structure of rank *i.* Additional stresses (stress concentration) in the vicinity of the growing element of rank i +1 can transfer some elements of rank i to the critical state, which leads to the local fracture of these elements and, hence, to a reduction in the rank of the structure. This, in turn, changes the boundary conditions on the scale of the growing element of rank i + 1, leading, in particular, to a stop of the element of rank i and initiation of the development of the neighboring structural element of rank i + 1. Note, that in this scenario of the development of the structures, the structure of rank i - 1 do not influence all elements of rank i and, hence, is not global for the medium subjected to a loading. The scheme of development of the structures just described cover three hierarchical levels. The further extension of the hierarchical systems of structures of fracture to cover all ranks can be implemented as a repetition of the three-stage procedure of formation of the hierarchical blocks. In each of these blocks, the basic structures for the formation of structures of higher ranks (i.e., the structures of rank i + 2, i + 3, etc.) have a rank which is lower by unity then the rank of the structure to be formed. The lower the rank, the less the volume covered by the local fracture process. The development of the process in accordance with such a scheme implies an increasing differentiation of the stress fields and geometrical parameters in the structures of the hierarchical system. This is due to the selective nature of the rank decreasing processes in space and also due to the fact that if the rank increases beyond level i + 1, the role of the lower rank structures in the three-stage hierarchical blocks,

is again played by separate portions of the hierarchical structure which has already been formed. However, these portions are subjected to additional local stress fields.

The relations between the sizes of similar elements of ranks i, (i - 1) and (i + 1) for a plane model of a three linked hierarchy of shear block structures were obtained in [11,16]

$$L_i / L_{(i-1)} \sim 1 + \frac{n^2}{4}, \quad n \sim L_{(i-1)}/L_i \tag{8}$$

The used model of shear fracture is similar to the aforedescribed model of fracture of a porous body at tension. The observed fragmentation effects [17,18] lead to $(L_i/L_{(i-1)}) \sim 3$ at $n \sim 3$ which correlates with (8).

The study was supported by the Russian Foundation for Basic Research (Grants 99-01-00925, 00-15-96066).

References

1. Goldstein, R.V. and Osipenko, N.M. (1978) *Doklady AN SSSR*. 240, 829.
2. Ryzhak, E.I. (1983) *Izv. AN SSSR. MTT*. 5, 127.
3. Nikitin, L.V. and Ryzhak, E.I. (1976) *Doklady AN SSSR*. 230, 1203.
4. Nikolaevskii, V.N. (1983). In: *Achievements in Science and Technology. Mechanics of Solids,* pp.149-230, VINITI, Moscow.
5. Revuzhenko, A.F., Stazhevskii, S.B. and Shemyakin, E.I. (1974) *Fiz.-Tekhn. Problemy Razrabotki Poleznykh Iskopaemykh.* N 3, 130.
6. Nikiforovskii, V.N. and Shemyakin, E.I. (1979). *DynamicFracture of Solids*. Nauka, Novosibirsk.
7. Morozov, N.F., Petrov, Yu.V. and Utkin, A.A. (1990) *Doklady AN SSSR*. 313, 276.
8. Rice, J. (1982). *Mechanics of the Earthquake Rupture.* Mir, Moscow (Russian translation).
9. Goldstein, R.V. and Osipenko, N.M. (1978) *Preprint N 110 IPM AN SSSR,* Moscow.
10. Goldstein, R.V. and Osipenko, N.M. (1992) *Doklady RAN.* 325, 735.
11. Goldstein, R.V. and Osipenko, N.M. (1999) *Izv. RAN. MTT.* N 5, 49.
12. Goldstein, R.V., Ladygin, V.M. and Osipenko, N.M. (1974) *Fiz.-Tekhn. Problemy Razrabotki Poleznykh Iskopaemykh.* N 1, 3.
13. Goldstein, R.V. and Kaptsov, A.V. (1981) *Preprint N 179 IPM AN SSSR.* Moscow.
14. Goldstein, R.V. and Osipenko, N.M. (1998) *Preprint N 632 IPM RAN,* Moscow.
15. Goldstein, R.V. and Osipenko, N.M. (1996) *Fiz.-Khim. Mekhanika Materialov.* 32, 25.
16. Goldstein, R.V. and Osipenko, N.M. (1993). In: *Construction of Models of Development of Seismic Processes and Earthquake Precursors*, pp.21-37, IFZ RAN, Moscow.
17. Sadovskii, M.A. (1979) *Doklady AN SSSR*. 247, 829.
18. Asatryan, Kh.O. and Sobolev, G.A. (1991). In: *Physics of Rocks Subjected to High Pressur,* pp.138-142, Nauka, Moscow.

A NEW APPROACH FOR IDENTIFYING THE HEAT SOURCES IN TWO DIMENSIONAL POTENTIAL PROBLEMS USING THE DISCRETE INTEGRAL METHOD

Hiroyuki Kisu[1], Yoshihiro Kondo[2] and Guiming Rong[1]

[1]Faculty of Engineering, Nagasaki University, Bunkyo-machi 1-14, Nagasaki 852, Japan
[2]Graduate School of Marine Science and Engineering, Nagasaki University

ABSTRACT

Analysis of inverse problems has already been performed in various fields. In many cases, it seems that a priori assumption for the solution are needed. This requirement causes a contradiction on the analysis.

On the other hand, we have developed the discrete integral method(DIM) utilizing the delta function. We have noticed that the DIM will become one of the excellent schemes to solve the inverse problem since it can naturally express the function of solution regardless of the type of function and can solve it without any assumptions. In this paper, we attempt to apply the DIM to the two-dimensional inverse problems. As one of the examples of two-dimensional inverse problems, we demonstrate a solving scheme for identifying the distribution of heat sources in the heat conduction problem.

Through some numerical verification, it is proved that the present scheme gives accurate and natural solutions without presumptions.

KEYWORDS

Boundary element method, Discrete integral method, Inverse problems, Potential problem

INTRODUCTION

One of the defaults in the analysis of inverse problem[1,2] is that usually a priori assumptions concerning the functional shape, the number of functions, definitive area of the function, and so on for the solution are required. As one of the consecutive studies to conquer this subject, this study is intended to establish and to suggest one of new solution schemes in the analysis of the inverse problems. We begin to introduce a way of functional approximation using the delta function. We develop the way to a new integral scheme named as the discrete integral method (DIM). In using the DIM, a domain integral can be converted to the sum of a boundary integral and values at some selected points utilizing the property of the delta function. We attempt to apply them to the identification of physical quantities expressed by an integration.

We have already established an analysis scheme for one dimensional inverse problem using this scheme[3, 4]. In this study, we try to expand this scheme to two dimensional cases. Here, the scheme for identifying heat source distribution in the heat conduction problem are demonstrated as an instance. The heat source

distribution is expressed as an inhomogeneous term in the governing differential equation, and is formulated as a domain integral term in the boundary element method (BEM). Therefore, it is convenient to combine the present identification scheme with the BEM.

1. INSTITUTION OF TWO DIMENSIONAL INVERSE PROBLEM

1.1 *Integral equation of heat conduction problem by BEM*

For the steady heat conduction problem with internal heat sources, the integral equation which gives temperature on a point p can be written as[7,8]:

$$u(p) = \int_\Gamma \Big[q^*(p,Q)\{u(Q) - u(P)\} - u^*(p,Q)\, q(Q) \Big] d\Gamma(Q) + \int_\Omega b(Q) u^*(p,Q)\, d\Omega(Q) + u(P) \qquad (1)$$

Here, u is the temperature, q is the flux, b is a function which expresses the distribution of heat source, P is a point on the boundary nearest to an internal point p, Q is a moving point within the range of integral, Γ indicates the boundary of the domain and Ω indicates the whole domain. u^*, q^* are fundamental solutions about temperature and heat flux, respectively, which are written as

$$u^*(p,Q) = -\frac{1}{2\pi} \ln r, \qquad q^*(p,Q) = \frac{\partial u^*(p,Q)}{\partial n} \qquad (2)$$

where r expresses the distance between two points of p and Q, n expresses outward normal on boundary Γ.

Inverse problem instituted in this paper is to estimate the heat sources distribution b in the second term on the right side of Eqn.1 using the information of the boundary condition and temperature distribution.

1.2 *Two dimensional discrete integral method utilizing the delta function*

First, we introduce a tool, named the discrete integral method(DIM), to solve the two-dimensional inverse problems. In the present problem, the domain integral term in Eqn.1. becomes the target.

Usually the heat source distribution function b included in that integral term is approximated by the isoparametric quadratic element, then the integration is performed by using the Gauss numerical integration. Or this term is transformed to boundary integration by using multiplex reciprocity method[5,6]. On the other hand, instead of these methods, the approximating way using Dirac's delta function can be developed. Namely, the function is approximated as follows:

$$\nabla^k b = \sum_{i=1}^{m} B_i \delta(x - x_i) \qquad (3)$$

Here, ∇^k is the k-th Nabla differential operator, B_i is the strength of the delta function, x_i is its applied position, and m is their number.

Further, we multiply a new function Z^* defined as

$$\nabla^k Z^* = u^*(p,Q), \quad \text{namely,} \qquad Z^* = \frac{r^4}{256\pi}(3 - 2\ln r) \qquad (4)$$

with the both sides of Eqn.3 and integrate them over the whole domain. Then, the following equation can be derived by integration by part when $k = 2$:

$$\int_\Omega b u^* d\Omega = \int_\Omega b \nabla^2 Z^* d\Omega = \int_\Gamma (b \nabla Z^* - \nabla b Z^*) \mathbf{n} d\Gamma + \sum_{i=1}^{m} Z^*(x_i) B_i \qquad (5)$$

Eqn.5 shows that a given domain integration term can be calculated by using boundary integration and the strength B_i (which is unknown quantity) of concentrated source on discrete points. We call this series of schemes as the discrete integral method, and try to introduce it to identification of heat source distribution.

1.3 *Application to inverse problem*

The strength B_i in Eqn.3 are unknown quantities. In order to determine their values, we use the information of temperature distribution. By substituting Eqn.5 into Eqn.1, we obtain the following equation:

$$u(p)-u(P)=\int_\Gamma\Big[q^*\{u(Q)-u(P)\}-u^*q(Q)\Big]d\Gamma(Q)+\int_\Gamma(b\nabla Z^*-\nabla bZ^*)\mathbf{n}d\Gamma+\sum_{i=1}^{m}Z^*(x_i)B_i \qquad (6)$$

Here, by monitoring $u(p)$ on m-points, we can compose a set of simultaneous equations with the dimension of m. The differential terms of b, exist in boundary integration term on right side of Eqn.6 can be eliminated by the interpolating as shown later.

Then, by using B_i obtained in this way, it becomes possible to interpolate the function b on any point s, and the distribution of heat generation is obtained as follows. Namely, we multiply a function Y^* defined as

$$\nabla^k Y^*=-\delta(x-p), \qquad \text{namely,} \qquad Y^*=\frac{r^2}{8\pi}(1-\ln r) \qquad (7)$$

with both sides of Eqn.3, and integrate them over the whole domain, then, it becomes

$$\int_\Omega\nabla^k bY^*d\Omega=\int_\Omega\sum_{i=1}^{m}B_i\delta(x-x_i)Y^*d\Omega \qquad (8)$$

Eqn.8 is transformed by means of integration by part:

$$b(p)=\int_\Gamma(\nabla bY^*-b\nabla Y^*)\mathbf{n}d\Gamma-\sum_{i=1}^{m}B_iY^*(x_i,p) \qquad (9)$$

Eqn.9 gives the distribution of heat sources. Thus, we can identify the existence of the heat source distribution, its type as well as its number without any a priori assumptions.

2. EXAMPLES

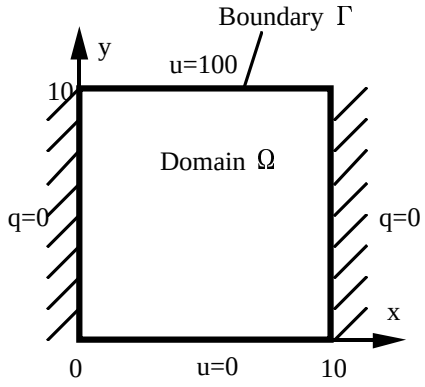

Figure 1: Analysis model and boundary condition

Here shows the practical analysis of the inverse problem by using the scheme mentioned above. In all cases, heat source distribution inside the domain is identified from the given data of boundary conditions and temperature distribution in the domain. Analysis model is a 10×10 square plate, and the boundary conditions are as shown in Figure 1. Furthermore, m, the number of points positioned as point sources is fundamentally 9 in both x and y direction, so the total number is 81. They are arranged at even intervals in the domain excluding the boundary.

2.1 ***Examples for distributed heat source***

First, as an analysis example for distributed heat source, the case of a heat source distribution expressed by $b = -x + y + 13$ applies on the whole domain, namely, on the range of $0 \leq x \leq 10, 0 \leq y \leq 10$ is examined. The result is shown in Figure 2. In this figure (including all of following figures), x-axis and y-axis correspond to those of Figure 1 respectively, and the axis of vertical direction expresses heat source distribution b which is identified by Eqn.9.

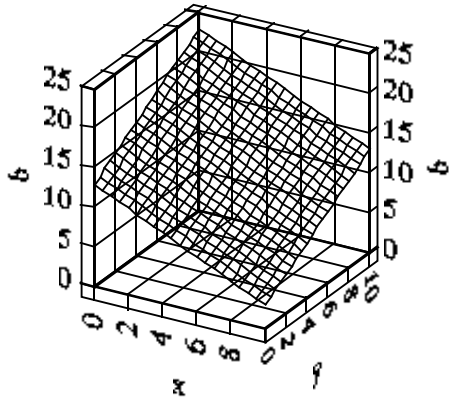

Figure 2: Identification of heat source given by $b = -x + y + 13$

Figure 2 shows that the identified data reappears accurately the given distribution. They agree in 6 decimal places or more. Because it is a case that the distributed shape of heat source becomes 0 by 2nd differential operation, very accurate result can be obtained with $k = 2$ in Eqn.3.

Figure 3 shows the result for a uniform heat source with the magnitude 5 distributes in a rectangular region of $4 \leq x \leq 6, 5 \leq y \leq 7$. The equation with the order of $k = 2$ is not available for this problem because of too big errors, so we use that of $k = 4$ from this problem. From the figure, we can clearly distinguish the heat source distribution in the right region although not any presumption is used. However, it is noticed that a little overshoot appears at the edge of the step. This shows the limit of the scheme and, you may also noticed the unevenness of the distribution of heat source. The amount of the overshoot is about 10% at most. If these identified results are considered to be insufficient, the denser arrange of the points can be employed, or the secondary identification based on the primary identified data can be performed as it will be mentioned hereafter. Besides, the shape of step part in this figure has a little trapezoidal, it depends on the intervals of the point source. If the number of points is increased, the sharper edge will appear.

Instead of a rectangular region, if the heat source has a circular region, almost the same behavior of the

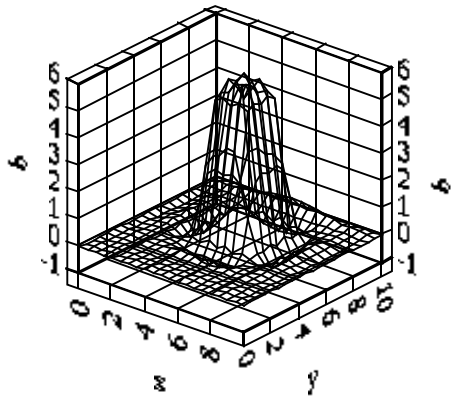

Figure 3: Identification of localized heat source

identified result can be observed.

2.2 ***The secondary identification for distributed heat source***

If the accuracy obtained by the scheme as mentioned above is not enough, it can be improved by using data of the primary identified result. Here, we will discuss the case of the further identification based on the result of Figure 3. From the result in the primary step, we can suppose the region where there is no heat source. Therefore, we try to reidentify the heat source by rearranging the point source on the part where the value from the first calculation is not zero.

From Figure 3 we can presume that a rectangular of $4 \leq x \leq 6, 5 \leq y \leq 7$ is the region where heat source may exist. Therefore, we arrange the point source only in this region, and perform the re-identification (the secondary identification). The results are improved with extremely high accuracy which error is 0.1% or less.

2.3 ***Examples for concentrated heat source and its secondary identification***

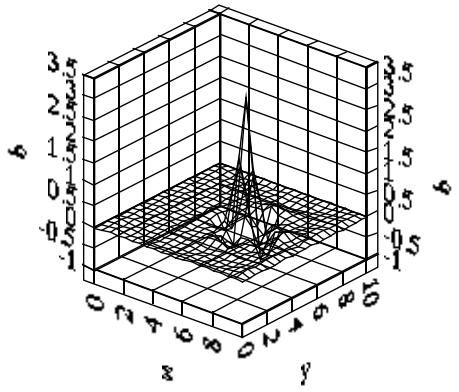

Figure 4: Identification of a concentrated heat source

A concentrated heat source with magnitude 2 applies on the position of $x = 6, y = 5$ is instituted. Identified result for this problem is shown in Figure 4. It can be seen in the figure that the distribution has a sharp peak round $x = 6, y = 5$, so we can consider a concentrated heat source exists there. However, the value of peak is not 2 which was instituted, and its applied region is very indistinct. Such an abrupt change caused because the concentrated heat source is attempted to be expressed in the form of distribution. Therefore, it is impossible essentially for this analysis scheme to distinguish a concentrated source from a distributed one in a very small region by once identification. Nevertheless, it seems that this is not a so serious problem practically. Essentially the distinction is not necessary, and as will be shown later, reasonable value of its magnitude and position also can be obtained.

To obtain the magnitude of the distribution b which is possibly a concentrated heat source as it has a sharp peak, we can integrate it over a circular region with any radius. It is calculated by the following equation which is a direct integration of Eqn.9:

$$F = \int_0^R \int_0^{2\pi} b(p)\rho d\theta d\rho \tag{10}$$

where F is the identified value regarded as the magnitude of concentrated heat source, ρ is the radius of the peak with the center point of p_0, R is the radius of integral region and θ is the angle around p_0. The result is shown at the left side of table 1. It can be seen though the error is large in abrupt changing part when integral region is small, very good value is obtained when the radius R becomes larger.

When the accuracy in Table 1 is not enough, we can perform the secondary identification by using data of the primary identification, as done in the case of distributed heat source, so that it can be distinguished from a distributed heat source more clearly. Further, as a concentrated heat source, its position and magnitude

Table 1: Identified value of the source strength in Fig.4

1st Identification		2nd Identification	
Integral Radius	Result	Integral Radius	Result
0.5	1.6034	0.05	2.1535
1.0	2.6018	0.1	3.2735
2.0	1.1992	0.2	1.0837
3.0	2.0016	0.3	1.9991

can be identified definitely. From the result in Figure 4, the point source is positioned in the region of only $5.5 \leq x \leq 6.5, 4.5 \leq y \leq 5.5$ which is a smaller region, and re-identification (the secondary identification) is performed. We found that the distribution concentrates in a much smaller region than the primary identification, and the value of its peak also becomes about 150 times larger. The same as the primary identification, the computed value for magnitude of concentrated heat source by using Eqn.10 is shown at the right side of table 1. Comparing with the result at the left, it can be seen that extremely accurate identified value is obtained in the region with much smaller radius. On the other hand, now the region where the data changes abruptly at the primary identification becomes 0, and the part with abrupt change is limited in a very narrow region. This behavior can not be considered as a distributed one, so it can be identified sufficiently that it is a concentrated heat source. We think the further study is indispensable, however, it is expected that the identification with sufficient accuracy will be possible by devising how to do the re-identification well.

3. CONCLUSIONS

The discrete integral method utilizing the delta function was introduced, and a new analysis scheme for two dimensional inverse problem based on the discrete integral method was suggested. From the analysis examples, it was shown that the heat source could be identified naturally and accurately without any a priori assumptions such as for the kind of applied heat source, its distributed shape, the number, and so on.

REFERENCES

1. Kubo,(1998) “Inverse Problem”, Baifu-Kan, Japan.
2. Chrles W. Groetch.(1996) Translated by Kaneo and so on, “*Inverse Problem in Mathematical Science*”, Separate Volume: Mathematical Science, Science-Sha, Japan.
3. Kisu, Kondo and Rong,(2000). In: *JSME Lecture Journal,* No.008-1, pp. 95, Japan.
4. Kisu, Kondo and Rong,(2000). In: *JSME Lecture Journal,* No.00-1, Vol.2, pp. 47, Japan.
5. Ochiai, (1993). In: *JSME Journal,* ser.A, 60-571, pp. 756, Japan.
6. Ochiai and Kobayashi, (1998). In: *JSME Journal,* ser.A, 64-621, pp. 1273, Japan.
7. Kisu and Kawahara, (1989). In: *JSME Journal,* ser.B, 55-514, pp. 968, Japan.
8. A. C. Neves and C. A. Brebbia, (1991). *Int. J. Num. Meth. Eng.,* 31, pp. 709.

ORAL REFERENCE:ICF100266OR

FORMATION OF TiO_2 THIN FILM BY ION-BEAM-MIXING METHOD AND ITS APPLICATION AS THE CORROSION PROTECTING FILM

Yuji KIMURA[1] and Hirotsugu SAITO[1]

[1] Dept. of Materials Science and Technology, Kogakuin University,
Nishishinjuku, Shinjuku-ku, Tokyo 163-8677, Japan
kimura@cc.kogakuin.ac.jp

ABSTRACT

One of the n-type semiconductor materials of TiO_2 has been expected to be used as photo-catalytic media in these days. A lot of studies have been conducted for applying TiO_2 film to anti-bacterium, water decomposing, anti-stain and deodorant coatings. The TiO_2's photo-catalytic function can be obtained under the condition of UV light illumination. Purpose of this study is to apply coated TiO_2 thin film as the corrosion protecting film of substrate metals using photocurrent obtained from UV ray irradiation. This implies the cathodic protection employing outer electric source. Therefore, even though when the thin film having some defect distribution in itself, the TiO_2 thin film shows corrosion protecting effects to substrate without a anodic dissolution of film itself. In this paper, formation and characterization of TiO_2 thin film made on AISI 304 stainless steel by Ion-Beam-Mixing method were conducted. Then, the cathodic protection performance of 0.15 μm thick TiO_2 thin film with some defect distribution was investigated in 0.3wt% NaCl aqueous solution. And also, effects of ion source upon the photo-catalytic function of TiO_2 thin film was investigated.

KEYWORDS

TiO_2 thin film, Ion-Beam-mixing Method, photo-catalytic function, corrosion protecting film, UV ray irradiation, defect distribution, cathodic protection performance

INTRODUCTION

Thin film coatings toward various types of materials such as metal and organic compound have been used for protecting substrate surface from harsh environment or adding a lot of functions to them [1]. However, nanometric defects and cracks were always existed in coated thin film from the initial stage [2]. In actual environment, degradation was generated as a result of the corrosive solution coming into substrate metals through the nanometric defect of coating.

Recently, one of the n-type semiconductor materials of TiO_2 has been expected to be used as photo-catalytic media.

And a lot of studies have been conducted for applying TiO_2 film to anti-bacterium, water decomposing, anti-stain and deodorant coatings[3-5] The TiO_2's photo-catalytic effect can be obtained under the condition of UV light illumination as shown in the following equation.

$$H_2O + 2h^+ \rightarrow 2H^+ + (1/2)\, O_2 \qquad (1)$$

Purpose of this study is to apply coated TiO_2 thin film to the corrosion protecting film of substrate metals using photocurrent obtained from UV ray irradiation. This implies the cathodic protection employing outer electric source. Therefore, even though when the film having defect in itself, the TiO_2 thin film shows corrosion protecting effects to substrate without an anodic dissolution of film itself. In this study, formation of TiO_2 thin film was conducted on AISI 304 stainless steel by Ion-Beam-Mixing method. Then, the characterization of the compositions and crystal structure of deposited thin films were conducted by XRD and ESCA. And also, cathodic protection performance of TiO_2 thin film with some defect distribution in itself was investigated under UV ray irradiation condition.

EXPERIMENTAL PROCEDURES

The Specimen

The specimen used in this study was 0.15 μm thick TiO_2 thin film coated on AISI 304 stainless steel plate (25×50 ×1.0mm) by Ion-Beam-Mixing method shown in Figure 1. Because, TiO_2 thin film made by Ion-Beam-Mixing method had superior adhesive strength. In this process ion beams of the inert gas of Ar and He have been used for assisting to obtain TiO_2 thin film with well-crystallized microstructure. The surface of AISI 304 substrate specimen was finished like mirror, and also degreased by methanol. Table 1 showed condition of TiO_2 thin film formation by this method. Chemical compositional profile of thin films was examined by X-ray Photoelectron Spectroscopy and the structure of coated layer was investigated by X-ray Diffraction.

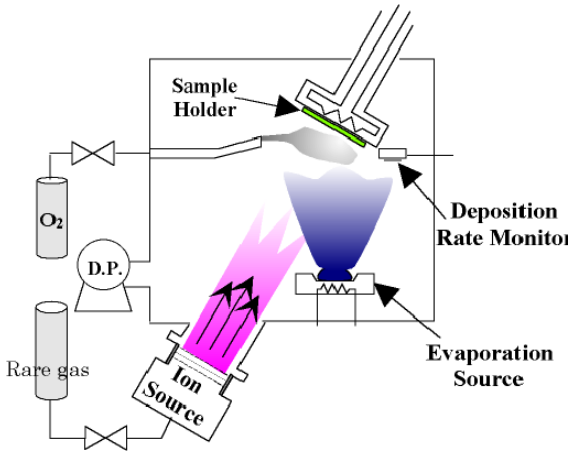

Figure 1: The chamber of Ion-Beam-Mixing equipment

TABLE 1 CONDITION OF TiO_2 FILMS FORMATION BY ION-BEAM-MIXING METHOD

Ion beam gas	Ar^+	He^+
Ar or He gas pressure (mPa)	3.0	4.0E-2
O_2 gas pressure (mPa)	14.0	18.0
Ar or He ion beam current (μ A/cm^2)	20.0	15.0
Ti evaporation rate (μ m/s)	0.5	0.5
Thickness of films (μ m)	0.15	0.15

Electrochemical Measurement

To examine the corrosion characteristics of TiO_2 coated specimen, the corrosion potential measurement and the anodic polarization measurement were conducted with and without the UV ray irradiation employing automatic polarization test system shown in Figure 2. For an electrochemical measurement, the specimen was coated by silicone for insulation from solution with non-coated area of $1cm^2$ left for testing. Each examination was conducted using three electrodes method that composed from specimen (working electrode), Pt (counter electrode) and the saturated calomel electrode (SCE)(referential electrode). Anodic polarization measurement was conducted in 0.3 wt% NaCl aqueous solution of 298K from –700 to 1000mV at a sweep rate of 20mV/min [3]. Natural corrosion potential measurement was conducted initially during 2 hours without UV ray irradiation, next 2 hours with UV illumination and final 2 hours in dark again. The light source was UV ray whose wave length λ =366nm and luminous intensity was $1.70mW/cm^2$. The distance of UV light from specimen was kept to be 60mm during testing.

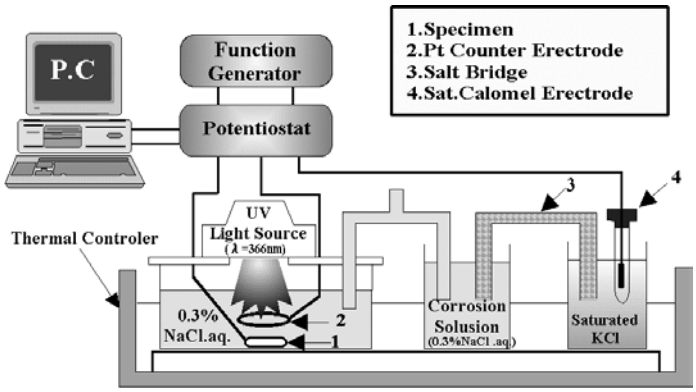

Figure 2: Schematic diagram of the system for electrochemical measurements

EXPERIMENTAL RESULTS AND DISCUSSIONS

Examination of the Compositions and Crystal Structure of Deposited Thin Films

The depth profiles of chemical composition and crystal structure of TiO_2 thin film made by Ion-Beam- Mixing method was investigated by XPS. The correlation between the composition ratio O/Ti and etching time was obtained and shown in Figure 3 together with those of other TiO_2 films made under different Ar ion

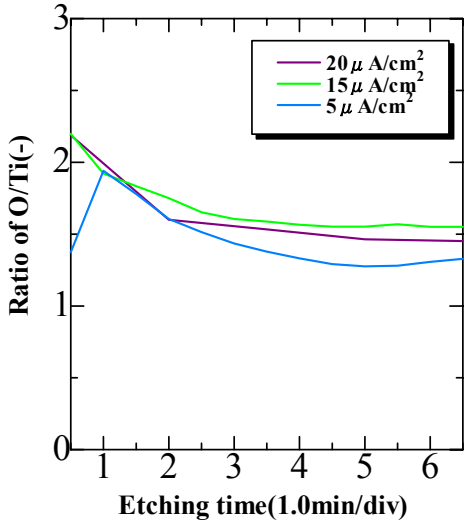

Figure 3: The composition ratio of TiO_2 thin films made under various Ar ion beam current

beam current. Almost of all the TiO_2 thin films made by this method is confirmed that oxygen in the films decreased from surface in the depth direction, and the other element of Ti in the films increase from surface toward the depth direction. Chemical compositional depth profile obtained in this study showed that the crystal structure of TiO_2 film obtained by using He ion beam had relative better crystallized structure.

Then, the crystal structure of the coated TiO_2 thin film was investigated by XRD and shown in Figure 4. From the result of crystal structure examined for thin films by X-ray Diffraction, no sharp peak strength was recognized both in Rutile structure and Anatase one. Therefore, the thin films obtained in this study by Ion-Beam-Mixing method showed relatively amorphous microstructure. However, in case when the TiO_2 thin film was obtained using He ion for assisting comparatively crystallized microstructure of Rutile was obtained .

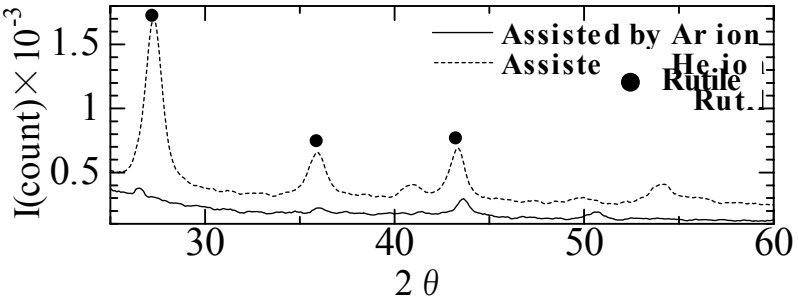

Figure 4: TiO_2 films diffraction pattern by XRD

Natural Corrosion Potentials of TiO_2 Thin Films in 0.3% NaCl Aqueous Solution

Natural corrosion potentials of TiO_2 thin coatings film were measured in 0.3% NaCl aqueous solution of 298K under the conditions of initial 2 hours without UV ray irradiation, next 2 hours with UV illumination and final 2 hours in dark again for both of Ar and He ions assisted films. In Figure 5 obtained results were indicated. From this figure, abrupt drop was recognized in the potential values when UV ray illumination was conducted. And then, gradual recover in the potential was recognized after UV ray was turned off. From these results, it was understood that the potentials gaps between UV ray illumination and dark were about 200mV and 120mV for He and Ar assisted TiO_2 thin films, respectively. Therefor, it is confirmed that the shift of potential was generated in the negative direction. Therefore, TiO_2 thin films showed the photo-catalytic function under UV ray illumination.

Anodic Polarization Measurement of TiO_2 Thin Films Coated Specimen in 0.3% NaCl Aqueous Solution

The polarization curves of TiO_2 thin films coated AISI 304 stainless steel specimen were obtained under UV ray illumination and non-illumination conditions in 0.3% NaCl aqueous solution of 298K and shown in Figure 6. Under UV ray illuminating condition both specimens made by Ar and He ions assisting showed no remarkable current density increase. In contrast, in case of non UV ray irradiated condition abrupt increase in the current density was recognized especially in He assisted TiO_2 thin film and resulted in the pitting corrosion with local exfoliation of thin film. Therefore, TiO_2 thin film has corrosion protecting performance under UV ray irradiating condition, even when TiO_2 thin film has some inherent defect distribution in itself. Under dark condition, however, distributed inherent defects such as pinhole and so on played an important role in the localized corrosion process of TiO_2 thin film coated SISI 304 stainless steel specimen. The adhesion strength between TiO_2 thin film and substrate metal became relatively low especially in case when He ion assisted thin film in spite of having better photo-catalytic function. As a result, the pitting corrosion with local exfoliation was generated in this film.

Cathodic Protection Performance of TiO_2 Thin Film with Some Artificial Defect

In the previous chapter, cathodic protection performance of TiO_2 film was indicated under UV ray irradiation condition. Usually, ceramic coatings inevitably have various defects even when appropriate coating

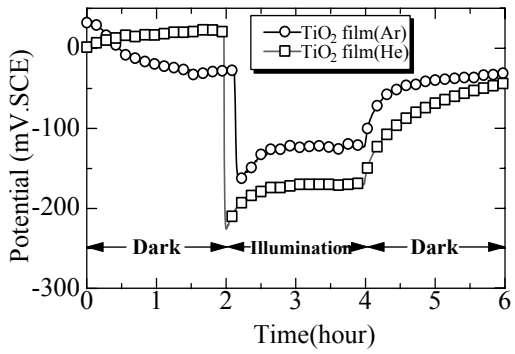

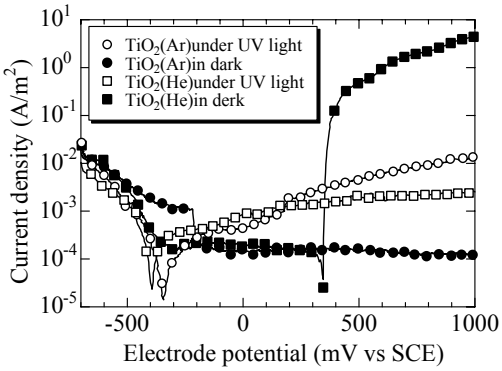

Figure 5:Spontaneous potential shift of TiO_2 films with and without UV illumination

Figure 6: Polarization curves of TiO_2 films (Ar and He) with and without UV illumination

conditions were selected for formation of thin films. For this reason, corrosion resisting property may be affected by distributed defects in thin film itself. Therefore, results shown in the previous section may be obtained from the situation that few large sized defects were existed in the TiO_2 thin film especially made by Ar ion assisted condition.

In this chapter, the dependency of TiO_2's photo-catalytic effect upon defect size that limited the cathodic protection performance of thin film was investigated. For this purpose, artificial scratch defect, whose width and defect ratio were about 200 μ m and about 2 %, was introduced on the coated thin film by diamond cutter as shown in Figure 5. By using Ar ion assisted TiO_2 thin film coated specimens with and without such scratch defect anodic polarization measurements were conducted under UV ray irradiating condition and shown in Figure 6 together with the result obtained using substrate AISI 304 stainless steel specimen. At the same time, above-mentioned measurements were conducted also under non UV ray irradiating condition and shown in Figure 7.

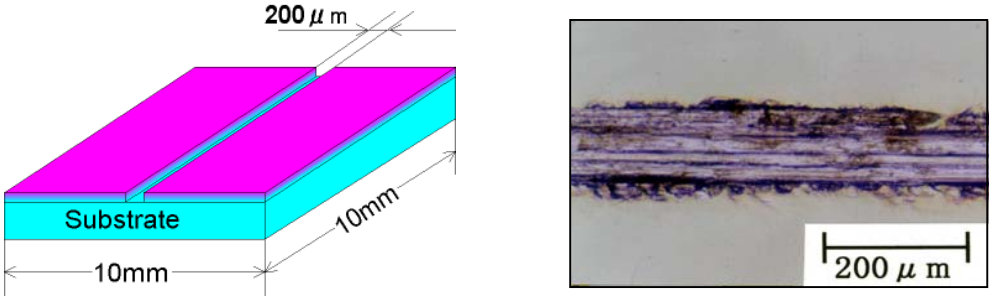

Figure 5: The scratch defect size and surface photograph

Some increase in the current density was recognized in TiO_2 thin film coated specimen with scratched defect when polarization measurement was conducted even under UV ray irradiating condition as shown in Figure 6. However, no localized corrosion was generated on the specimen surface after anodic polarization measurement. In contrast, remarkable increase in the current density was generated in TiO_2 thin film coated specimen with scratched defect when polarization measurement was conducted under non UV ray irradiating condition as shown in Figure 7. In this case, the pitting corrosion was recognized after electrochemical test as shown in Figure 8. Therefore, the cathodic protection performance of 0.15 μ m thick TiO_2 film coated on
AISI 304 stainless steel by Ion-Beam-Mixing method with Ar ion beam assisting can be obtained due to its photo-catalytic effect even when the film has artificially scratched defect whose width was about 200 μ m.

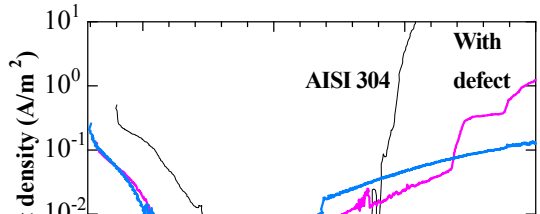

Figure 6: Polarization curves of TiO_2 film under UV ray irradiating condition

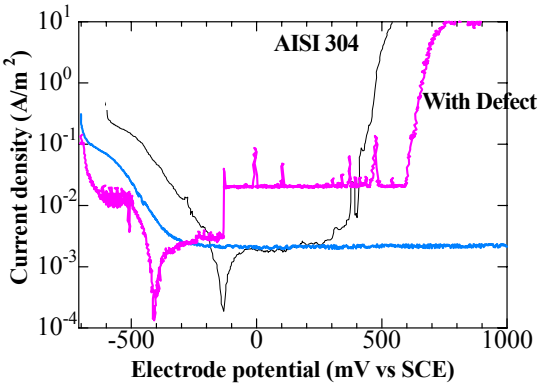

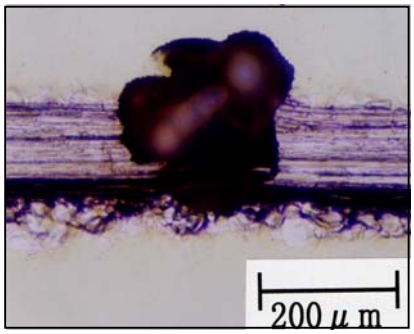

Figure 8:Pitting corrosion recognized after polarization measurement

Figure 7: Polarization curves of TiO_2 films under the dark

.

CONCLUSIONS

In this study, formation and characterization of TiO_2 thin film made on AISI 304 stainless steel by Ion-Beam-Mixing method were conducted. Then, the cathodic protection performance of 0.15 μ m thick TiO_2 thin film with some artificially scratched defect was investigated in 0.3wt% NaCl aqueous solution. And also, effects of ion source upon the photo-catalytic function of TiO_2 thin film was investigated.

The results of obtained were summarized as follows:

1. TiO_2 thin films made by Ion-Beam Mixing method shows the cathodic protection performance due to its photo-catalytic effect even when TiO_2 thin film has some inherent defect distribution in itself.
2. 0.15 μ m thick TiO_2 thin films shows the cathodic protection performance under UV ray irradiating condition in 0.3% NaCl aqueous solution of 298K even when it has artificially scratched defect whose width was about 200 μ m.

This research was supported by Grant-In-Aid for Scientific Research (B) (1999-2000) (Project No.11450048), The Ministry of Education, Science, Spots and Culture, Japan.

REFERENCES

1. Fujishima, A. et.al.(1984). In : Electrochemical Measurement II, Gihodo, Chapter 16.
2. Ohata, M. and Kimura, Y.(2000), Proc. of ECF13, CD Volume, Environmentally assisted cracking, Paper No.2, pp.1-8.
3. Uhlig,H.H.(1971). In : Corrosion and corrosion control, John Wiley & Sons, Chapter 12.
4. Fujisawa, R. and Tsujikawa, S.(1994) Corrosion Engineering, 43, pp.500-504.
5. Tsujikawa, S., et.al.,(1994) Corrosion Engineering, 43, pp.482-486.

ORAL REFERENCE: ICF100663OR

Fractal and Fracture Mechanics Analyses on Fatigue Fracture Surfaces of Metallic Materials

Takashi SAKAI [1], Tatsuo SAKAI [2] and Akira UENO [3]

[1] Department of Mechanical Engineering, Osaka Institute of Technology
5-16-1 Omiya, Asahi-ku, Osaka, 535-8585 JAPAN
[2] Faculty of Science and Engineering, Ritsumeikan University
1-1-1 Nojihigashi, Kusatsu, Shiga, 525-8577 JAPAN
[3] Department of Mechanical System Engineering, Toyota Institute of Technology
2-12-1 Hisakata, Tempaku-ku, Nagoya, Aichi, 468-8511 JAPAN

ABSTRACT

In this study, fatigue crack propagation tests were carried out to obtain the fatigue fracture surfaces on compact tension type specimens of A5052 aluminum alloy and S25C carbon steel, and the fatigue fracture surfaces were observed by means of a scanning laser microscope system. Based on the digital data thus obtained, imaginary fracture surface was reconstructed in a 3-dimensional space by a personal computer. Fractal analysis proposed by B. B. Mandelbrot was applied to such 3-dimensional surfaces and a hyperbola model was accepted to represent the Richardson effect. Due to the Richardson effect thus analysed, the fractal feature was confirmed in the fracture surface irregularity. It was finally found that the geometrical irregularity of the surface was well evaluated by combining the fractal dimension and additional indices termed as "index of fracture surface nature", and that the fractal dimension and the additional indices were successfully connected to the stress intensity factor range of ΔK.

KEYWORDS

Fractal, Richardson Effect, Self-similarity, Fatigue Fracture Surface, Surface Irregularity, Fractography, Fracture Mechanics, SLM Observation

1. INTRODUCTION

In order to analyse the irregularity of shapes and time-dependent phenomena, various methods such as Fourier analysis and some conventional procedures as stochastic process have been developed and used by many researchers. A concept of fractal proposed by B. B. Mandelbrot [1] is useful to quantify the above irregularity and this has been successfully applied to various fields in both science and technology [2-5].

On the other hand, several kinds of high resolution microscopes such as SLM (Scanning Laser Microscope), STM (Scanning Tunnel Microscope) and AFM (Atomic Force Microscope) have been used in recent years to observe the nature of the fracture surface in a 3-dimensional space. However, definite procedures to quantify the irregularity of the fracture surfaces have not been established yet.

As reported in the earlier papers [6, 7], we proposed a new analytical method to quantify the surface irregularity applying the concept of fractal, and the surface irregularity of the tensile fracture surfaces and the mechanically finished surfaces was successfully evaluated by using this method. In the present study, this method is modified and expanded to analyse the surface irregularity of the fatigue fracture surfaces. Moreover, particular attention is paid here to investigate the relationship between the surface irregularity

and the fracture mechanics parameter of ΔK.

2. SPECIMENS AND FATIGUE CRACK PROPAGATION TESTS

2.1 Specimens and Fatigue Crack Propagation Behavior

Materials used in this study are A5052 aluminum alloy and S25C carbon steel in JIS material codes. Mechanical properties of these materials obtained by tensile tests are listed in Table 1. Fatigue crack propagation tests were performed by a hydraulic servo fatigue testing machine to obtain the fatigue fracture surfaces on compact tension type specimen [8, 9] standardized in ASTM. The frequency was fixed to 50Hz, and two different stress ratios of $R=0.1$ and 0.5 were selected. Fatigue fracture surfaces were observed by means of a SLM system explained in other papers [10, 11], whereas the fatigue crack propagation was observed by an optical microscope with the resolution of $\times 100$.

Based on the crack propagation behavior thus observed, relationships between the stress intensity factor range ΔK and the crack growth rate da/dN are plotted as shown in Figure 1. It should be noted that only one specimen was assigned to each series of the fatigue crack propagation test. In this figure, each solid line is determined as to provide the least squares for the respective data points. It is confirmed that the fatigue crack propagation behavior is well represented by the following expression [12];

$$\frac{da}{dN}=C(\Delta K)^m \quad , \tag{1}$$

where

$$\Delta K=\frac{\Delta P}{BW^{\frac{1}{2}}}\times f(\alpha) \quad , \tag{2}$$

$$f(\alpha)=\frac{(2+\alpha)(0.886+4.64\alpha-13.32\alpha^2+14.72\alpha^3-5.6\alpha^4)}{(1-\alpha)^{\frac{3}{2}}} \quad , \tag{3}$$

Table 1: Mechanical properties of materials

Material	Yield stress σ_y (MPa)	0.2% Proof stress $\sigma_{0.2}$ (MPa)	Tensile strength σ_B (MPa)	Elongation δ (%)	Reduction of area ϕ (%)
A5052	-	225	268	19.8	43.4
S25C	333	-	506	35.5	59.8

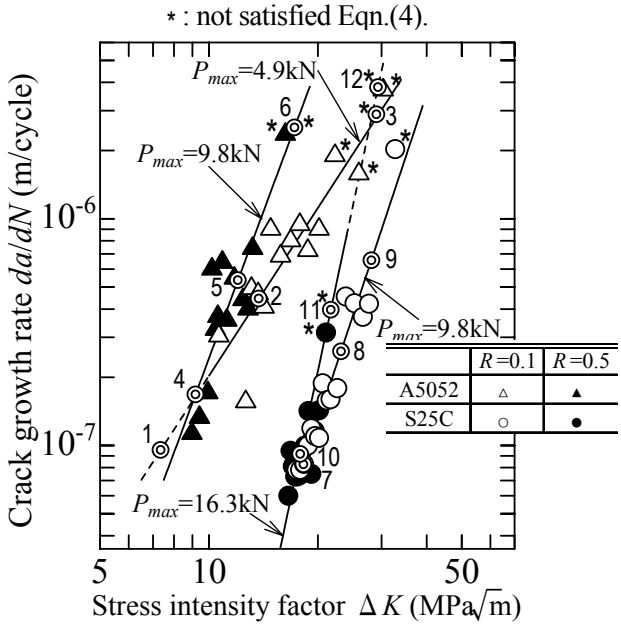

Figure 1: Relationships between stress intensity factor range ΔK and crack growth rate da/dN

and $f(\alpha)$ is the modification coefficient depending on the specimen configuration of $\alpha = a / W$. Furthermore ΔP and a mean the load range and the crack length, respectively. B and W are the specimen thickness and width, and they are B=16mm and W=32mm for the present specimens.

When the linear fracture mechanics is applied to the fatigue crack propagation behavior, the following condition of small scale yielding [13] must be always satisfied;

$$W - a \geq \frac{4}{\pi}\left(\frac{K_{\max}}{\sigma_y}\right)^2 , \tag{4}$$

where σ_y is the yield stress of the materials, and K_{max} is the maximum stress intensity factor calculated by substituting the maximum load P_{max} into ΔP in Eqn. (2). In this study, we have $\sigma_{0.2}$=225MPa for A5052 specimen and σ_y=333MPa for S25C specimen as shown in Table 1. Based on calculation at every stage of the crack propagation, almost all experimental points in Figure 1 satisfy the above condition except for a few points attached the mark of "*", which appear in the high crack growth rate region.

2.2 Observation of Fatigue Fracture Surfaces

Fatigue fracture surfaces were observed by means of a SLM (Scanning Laser Microscope) system. Comparing with SEM (Scanning Electronic Microscope) observations, the present SLM has some advantages such that 3-dimensional numerical data are directly obtained on real-time and these data are fundamentally convenient for the fractal analysis performed in this study.

As examples of SLM observations, micrographs of the fatigue fracture surface of A5052 aluminum alloy taken at the resolution of ×1250 are shown in Figure 2 (a) and (b). For the sake of comparison, SEM micrograph of the same area is also shown in Figure 2 (c), and the striation pattern is again observed with the further high resolution as shown in Figure 2 (d). In these SLM micrographs, a bright part indicates a high position on the real surface, whereas a dark part indicates a low position. The real height (total depth) in Figure 2 (a) is 64 μm and that in Figure 2 (b) is 122 μm , respectively. For the SLM observation with the resolution of ×1250, a square area of 161.5 μm×161.5 μm is defined as a sample space to analyse the fracture surface irregularity. This area is replaced by a 200dot×200dot square on CRT screen. Based on the digital data thus obtained, the imaginary fracture surface was reconstructed in a 3-dimensional space as illustrated in Figure 3. Fractal analysis was performed on the geometrical

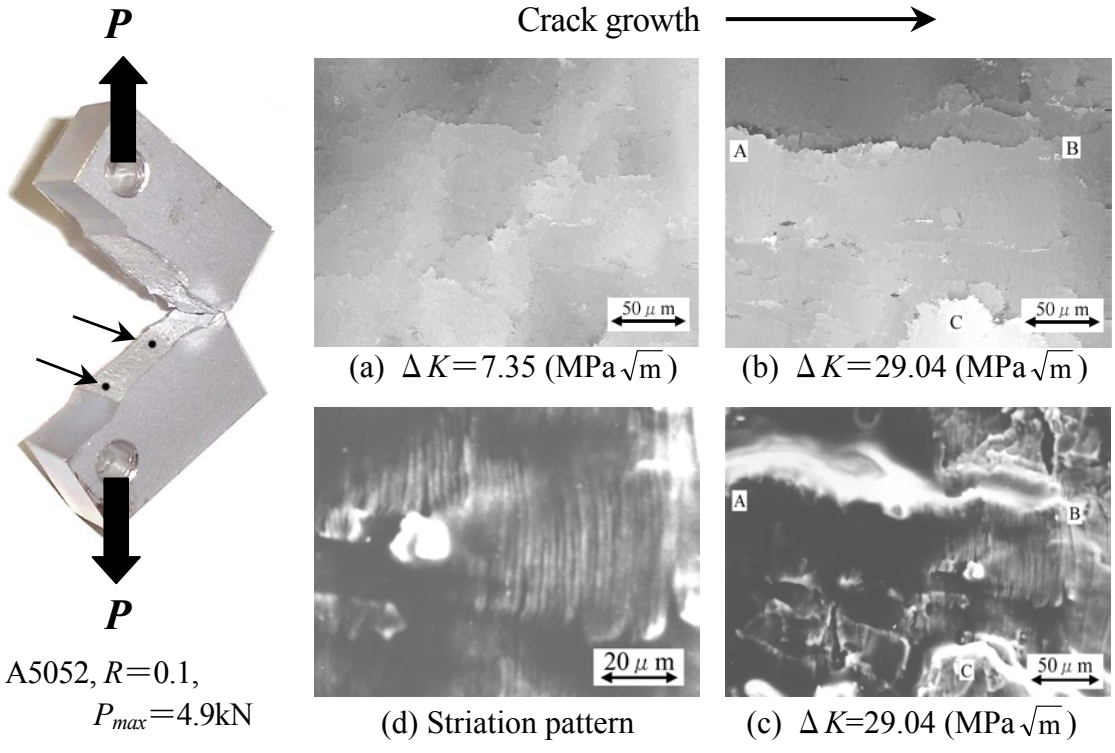

Figure 2: (a), (b)SLM and (c), (d)SEM micrographs of fatigue fracture surface

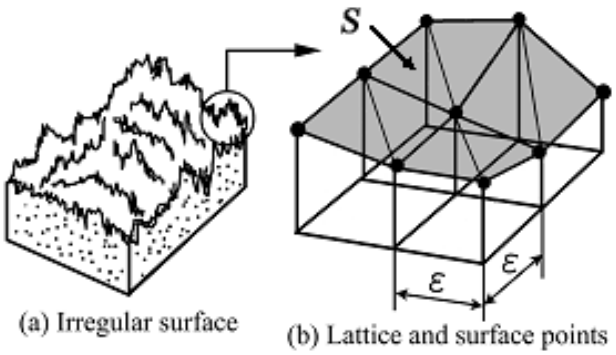

Figure 3: Reconstruction of imaginary fracture surface by multifacet surface

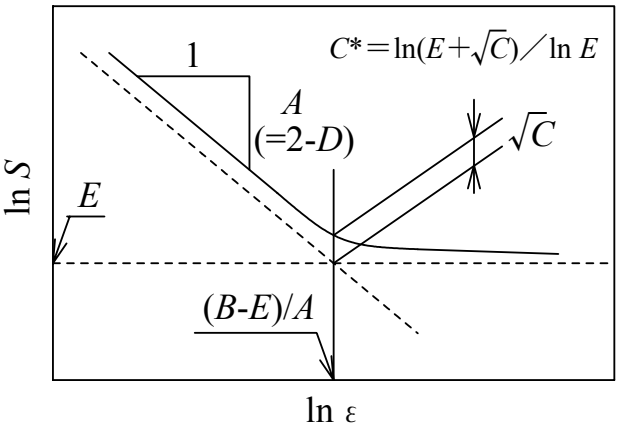

Figure 4: Schematics of ln ε －ln *S* relationship

irregularity of such a imaginary fracture surface.

3. ANALYTICAL PROCEDURE

As reported in the earlier papers [6, 7], geometrical irregularity of the tensile fracture surfaces and the mechanically finished surfaces were well evaluated by using the method of "Fractal". If a surface has the fractal nature, we have the following equation between the total area of imaginary fracture surface *S* and the measuring unit length ε ;

$$\ln S = \ln F + (2 - D) \ln \varepsilon \quad , \tag{5}$$

where *D* is the fractal dimension. Thus this dimension can be calculated from the slope of the regression line for ln ε －ln *S* relationship as shown in Figure 4. The value of *D* is always in $D \geqq 2.0$, since the regression line must have a negative slope. The surface area *S* changes depending on the unit length of ε , and the effect of ε on the surface area *S* is so called "Richardson effect [14]".

Usually, the linear Richardson effect is confirmed within a limited range of ε , so that the effect is no longer represented by the linear expression in other area of ε . Thus the Richardson effect in the entire region of ε should be represented by a different type of expression. Accordingly, the following expression in hyperbola type [15] is proposed here;

$$(\ln S - E)(\ln S + A \ln \varepsilon - B) = C \ . \tag{6}$$

Meanings of all the parameters in this expression are schematically indicated in Figure 4. Fractal dimension *D* can be calculated from the slope of *A* as $D = 2 - A$. Other parameters such as *B*, *C* and *E* are termed as "index of fracture surface nature" in this paper, since these parameters well reflect the geometrical characteristics of the fracture surface.

4. ANALYTICAL RESULTS AND DISCUSSIONS

4.1 Analytical Results and Self-similarity of Fatigue Fracture Surface

As examples of the Richardson effect, the fracture surface area *S* measured on A5052 alloy and S25C steel specimens was plotted as functions of the unit length ε in Figure 5 (a) and (b). For the sake of comparison, the analytical results of the tensile fracture surface [6] were also plotted by using small solid symbols in Figure 5 (b). Fractal dimension and each index of fracture surface nature analysed for the respective SLM micrographs are listed in Table 2. Fractal dimensions are calculated from the slope of each regression line for the individual magnification. Each horizontal dashed line indicates the level of perfect flat surface which has $D = 2.0$ for every magnification of the SLM observation. In these figures, it is found that ln ε －ln *S* relationships for fatigue fracture surfaces of the objective materials are well

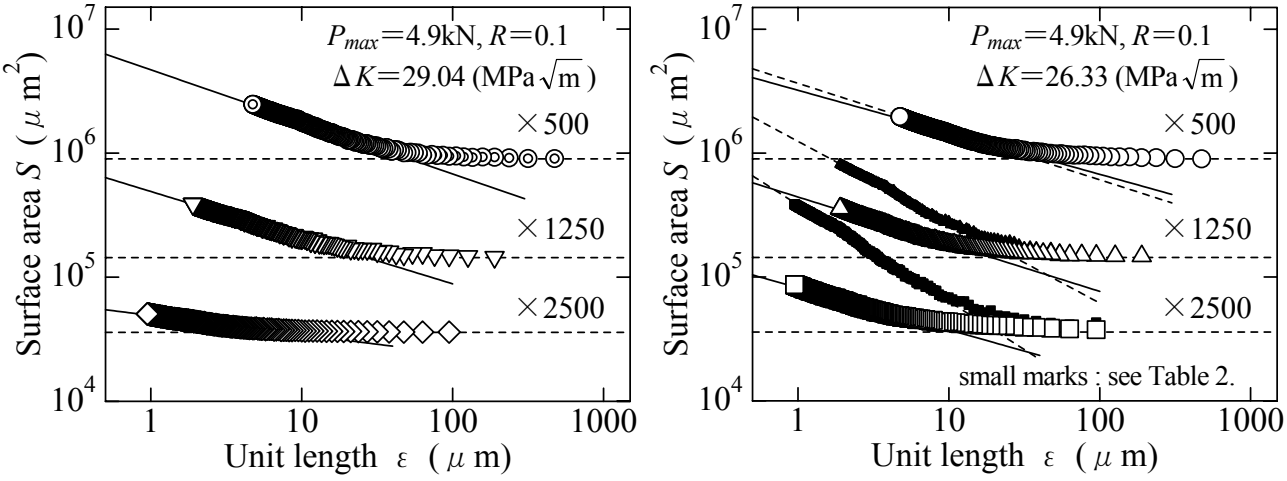

(a) A5052 aluminum alloy (b) S25C carbon steel

Figure 5: ln ε −ln S relationships for A5052 aluminum alloy and S25C carbon steel under R=0.1

Table 2: Numerical list of analytical results (P_{max}=4.9kN)

Material	ΔK	Mag.	Mark	D	$(B-E)/A$	C^*
A5052 (Fatigue) R=0.1	29.04 MPa$\sqrt{m}$	500	◎	2.42	51.5	1.13
		1250	▽	2.37	26.8	1.17
		2500	◇	2.16	7.4	1.04
S25C (Fatigue) R=0.1	26.33 MPa$\sqrt{m}$	500	○	2.34	42.5	1.12
		1250	△	2.38	19.1	1.14
		2500	□	2.34	11.1	1.19
S35C (Tension)	-	500	●	2.39	36.7	1.11
		1250	▲	2.65	27.1	1.34
		2500	■	2.78	20.7	1.36

represented by the expression in hyperbola type in Eqn. (6).

If the analytical object has a fractal nature, then the irregularity is well evaluated by the fractal dimension and must have characteristics of the self-similarity [1]. In Table 2, the values of D are almost constant for the fracture surfaces of S25C carbon steel in wide resolution range. However, in the case of A5052 aluminum alloy, the fractal dimension tends to decrease in the higher magnification of ×2500. Thus the self-similarity cannot be confirmed in the entire resolution range depending on the material. Similar trend was found on the fracture surfaces failed under R=0.5.

4.2 Connection of Surface Irregularity and Fracture Mechanics

Relationships between the stress intensity factor range ΔK and the fractal dimension D were plotted in Figure 6. Each number attached to the bracket is the code number to be linked the corresponding number in Figure 1. In Figure 6 (a), it is found that the fractal dimension tends to increase with an increase of the ΔK in the lower resolution, although the value keeps constant in the higher resolution. This means that the macroscopic irregularity on the fracture surface increases with an increase of ΔK, while the microscopic irregularity has no effect on ΔK. On the other hand, in Figure 6 (b), the fractal dimension tends to increase as the ΔK is increased in the entire resolution range. Thus the macroscopic and the microscopic irregularities on the fracture surface of S25C increase with an increase of ΔK.

Furthermore, in the relationships between the ΔK and index of fracture surface nature $(B-E)/A$, the value of $(B-E)/A$ tends to increase regardless of the resolution range as the ΔK is increased. Especially, this trend is distinct in the lower resolution range. Thus the fractal dimension and each index of fracture surface nature were successfully connected to the stress intensity factor range of ΔK.

5. CONCLUSIONS

(1) Analytical procedure to evaluate the surface irregularity of the fatigue fracture surfaces for A5052

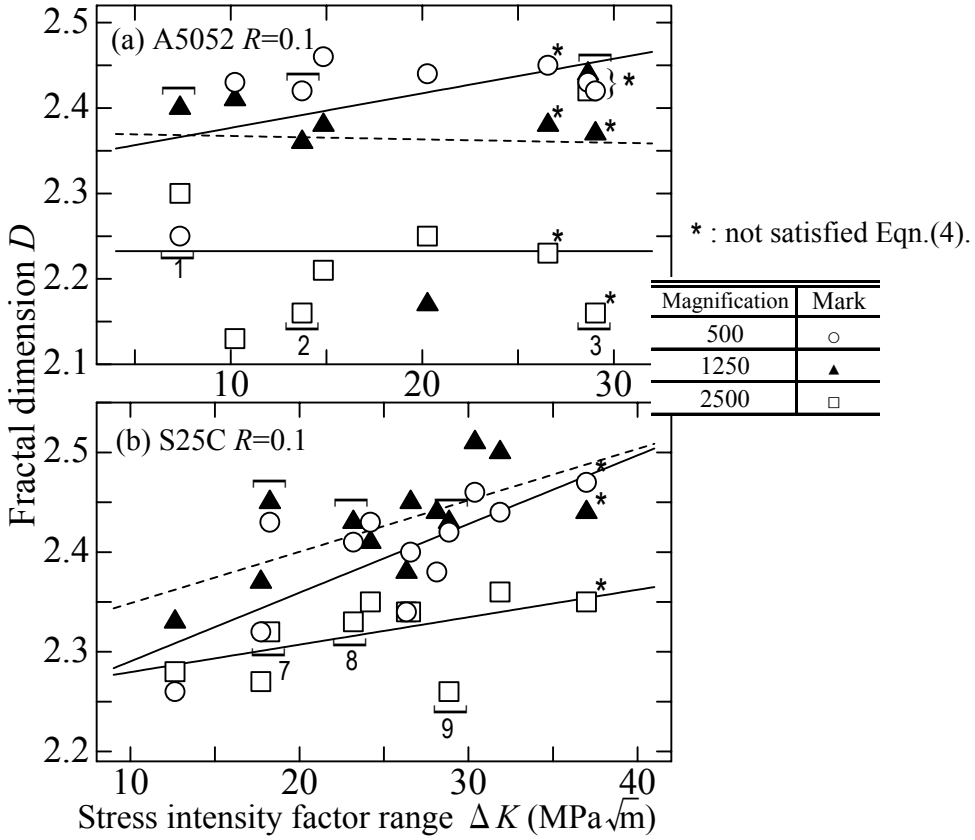

Figure 6: Relationships between stress intensity factor range ΔK and fractal dimension D

aluminum alloy and S25C carbon steel was developed by applying a concept of fractal and a curve fitting technique.

(2) Fatigue fracture surfaces of the present metallic materials have the fractal nature. Especially, the fracture surfaces of S25C carbon steel under the stress ratios $R=0.1$ and 0.5 have the complete self-similarity in wide resolution range.

(3) In order to evaluate the geometrical irregularity of the fracture surface, one should combine the fractal dimension and additional indices termed as "index of fracture surface nature".

(4) Fractal dimension and each index of fracture surface nature were successfully connected to the stress intensity factor range ΔK giving the key parameter in the fracture mechanics approach to the crack propagation.

REFFERENCES

(1) Mandelbrot, B. B. (1983). *The Fractal Geometry of Nature*. W. H. Freeman and Company. 109.
(2) Bazant, Z. P. (1998). *Structural Safety and Reliability*. 2, 1255.
(3) Sakai, T. and Fujikawa, M. (1998). *Trans. Jap. Soc. Mech. Engrs*. A-64, 2271.
(4) Tanaka, M. (1998). *J. Soc. Mater. Sci., Japan.* 47, 169.
(5) Tsuda, M. et al. (1991). *J. Soc. Mater. Sci., Japan.* 40, 1066.
(6) Sakai, T. et al. (2000). *Trans. Jap. Soc. Mech. Engrs*. A-66, 741.
(7) Sakai, T. et al. (1998). *Trans. Jap. Soc. Mech. Engrs*. A-64, 1104.
(8) Srawley, J. E. (1976). *Int. J. of Fract*. 12, 475.
(9) Murakami, K. et al. (1987). *Stress Intensity Factor Handbook*. Pergamon. 1, 18.
(10) Oide, T. (1995). *J. Soc. Mater. Sci., Japan.* 44, 262.
(11) Masubuchi, K. (1992). *Welding J*. 71, 69.
(12) Paris, P. C. et al. (1963). *Trans. of the ASME J. of Basic Engrs*. 85, 528.
(13) ASTM E647-93. (1993). *Standard Test Method for Measurement of Fatigue Crack Growth Rate*.
(14) Richardson, L. F. (1961). *General System Yearbook*. 6, 139.
(15) Nishijima, S. (1990). *Trans. Jap. Soc. Mech. Engrs*. A-46, 1303.

ORAL REFERENCE: ICF100570OR

FRACTAL FRACTURE SURFACES AND FLUID DISPLACEMENT PROCESS IN FRACTURED ROCKS

T. Babadagli[1] and K. Develi[2]

[1]Dept. of Petroleum and Min. Res. Eng., Sultan Qaboos University, Muscat, OMAN
[2]Dept. of Geological Engineering, Istanbul Technical University, Maslak, Istanbul, TURKEY

ABSTRACT

This paper deals with the fractal analysis of the surface roughness of rock fractures and the displacement experiments on these types of surfaces using invasion percolation simulations. Data acquired from natural and synthetic origin (developed under indirect tensional stress) fracture surfaces are subjected to fractal analysis applying different methods. Power spectral density method yields considerably lower fractal dimensions than those obtained by variogram analysis for naturally fractured surfaces. It is observed that the two methods yield more consistent fractal dimension values for synthetically fractured rock samples. The systematic difference between the fractal dimensions of horizontal and vertical profiles indicates that the variogram analysis enables us to asses the anisotropic nature of the fractal behavior. Next, invasion percolation simulations on synthetically generated (fractional Brownian motion) representative fractal fracture surfaces are conducted. It is observed that increasing surface roughness, indicated by increasing surface fractal dimension, causes less efficient displacement. Lower fractal dimension of the surfaces yields more compact cluster of injected fluid.

KEYWORDS

Fractal, fracture surface, invasion percolation, fluid displacement.

INTRODUCTION

In order to assess the transport characteristics of fractured systems, the roughness of fracture surfaces should be characterized quantitatively. For this purpose, first, a measurement technique for mapping the surface should be employed. Then, a quantitative analysis should be performed. The measurement techniques include photographic, the scattering of energy such as neutron and X-ray, laser profilometry, optical and mechanical methods. Develi et al. [1] provided an extensive review of different methods in comparison with their automated scanning device. Data obtained through these measurement methods can be used in the quantification of roughness. Since Mandelbrot *et al.* [2] have observed that the fracture surfaces of metals exhibit fractal characteristics, the fractal concept has been applied in rock fracture surface analysis. Self-affine fractal models were found to be suitable to represent natural rock fracture surfaces [3,4,5]. In this study, a brief description of a system designed to quantify the surface topography by measuring the elevations on the fracture surface was presented. Then, the results of fractal analysis of surface data acquired through this device were summarized. Next, invasion percolation

simulations were applied on the synthetically generated self-affine surfaces with different fractal dimensions. In the generation of synthetic representative surfaces, typical fractal dimension values obtained through the measurements were used. Finally, the simulation results were utilized to relate the surface roughness and the fluid transport in fractures.

MEASUREMENT OF THE FRACTURE SURFACE ROUGHNESS

To map the surface roughness, a computer-controlled surface scanning device designed by Develi et al. [1] was used. The device consists of three main parts, each of them capable of moving in three orthogonal directions. The displacement of each part is supplied by three step motors. The scanning is accomplished by a needle that is capable of moving up and down. The needle is fixed at a known distance over the sample and calibrated based on this distance. Once the needle touches the fracture surface, the number of step motor rounds is counted to calculate the traveled distance from the initial point. Then, the needle moves to next pixel by means of other two step motors. When the 55x55 array of pixels (each pixel is 1 mm) have been scanned, the process is terminated. Detailed description of the system can be found in the relevant reference [1]. 3-D representations of natural and synthetic surfaces mapped using this device are shown in Fig. 1. Natural surfaces are the outcrop marble samples cored 55 mm in diameter. Synthetic surfaces were created by Brazilian tests (indirect tensile fractures) on three different marble samples. During the tests, different loading rates between 0.05 and 0.2 kN/s were applied. The fracture surfaces were 55x55 mm. Only the middle 32x32 mm part of the samples was used in fractal analysis.

FRACTAL DIMENSION CALCULATIONS

Methods Applied to Measure Fractal Dimension

The fractal dimension values were calculated using three methods applicable to self-affine fractal sets.

Variogram analysis

The variogram is defined as the mean squared increment of points:

$$\gamma(h) = \frac{1}{2n}\sum_{i=1}^{n}\left[V(x_i) - V(x_{i+h})\right]^2 \tag{1}$$

where h is the lag distance (distance between two successive points), $\gamma(h)$ is variogram at lag distance h, n is the number of pairs at a lag distance h, and $V(x_i)$ is the sample values at location x_i. Fractal distributions are characterized by a variogram model of the following form:

$$\gamma(h) = \gamma_o h^{2H} \tag{2}$$

where H is called the Hurst exponent. H is related to the fractal dimension by $D = 2\text{-}H = 2 - \beta/2$ where β is the slope of lag distance, h vs. variogram, $\gamma(h)$ plot in log-log scale and equal to $2H$.

The 32x32 points taken from the middle portion of 55x55 data set were used for the analysis. The fractal dimension of each profile with 32 points was calculated for both horizontal and vertical directions. Then the 32 fractal dimensions were arithmetically averaged. It was observed that the optimum lag distance yielding the most accurate results is between 4-6 for 32 data points [6] and therefore, maximum length distance was selected to be 5 in the application of Eq. 1.

Roughness-length method

The profile roughness is measured as the root-mean-square value of the residual on a linear trend fitted to the sample points in a window of length w [7]. Then, the root-mean-square roughness is calculated by

$$RMS(w) = \frac{1}{n_w} \sum_{i=1}^{n_w} \sqrt{\frac{1}{m_i - 2} \sum_{j \in w_i} (z_j - z)^2} \tag{3}$$

where n_w is the total number of windows of length w, m_i is the number of points in window w_i, z_j is the residual on the trend and z is the mean residual in window w_i. The fractal dimension can be calculated from $D=2-\beta$, where β is the slope of the log-log plot of the $RMS(w)$ function vs. the window length w. Fractal dimensions were obtained using 20 mm window lengths in 32 mm profile (between 10th and 30th points). Like variogram analysis, fractal dimensions of 32 profiles in both horizontal and vertical directions were calculated and averaged. This method was applied to only natural fracture surfaces.

Power spectral density analysis

The fractal dimension of 2-D data set can be calculated from the slope of a log-log plot of power $S(k)$ vs. wavenumber k. The relationship between the power, $S(k)$, and the wavenumber, k, is given as [3]:

$$S(k) \propto k^{-\beta} \tag{4}$$

where β is the slope of the log-log plot. The fractal dimension, *D,* is related to the slope as follows:

$$D=(8+\beta) / 2 \quad (5)$$

Results

Results obtained by the above methods are summarized below. The power spectral measurement directly yields fractal dimension for 2-D data set. Whereas other two methods give the fractal dimension of 1-D set and these fractal dimensions were extended to represent 2-D data set by $D_{surface} = D_{profile} + 1$.

For natural fracture surfaces:

- The power spectral method yielded fractal dimensions between 1.70 and 2.25. They were expected to be greater than 2 to be in fractal regime but more than half of the samples yielded values less than 2.
- The fractal dimensions obtained through variogram analysis varied between 2.10 and 2.33 for vertical and 2.25 and 2.62 for horizontal profiles (for maximum lag distance of 5). Roughness length measurement fractal dimensions were between 2.03 and 2.52 for vertical and 2.03 and 2.63 for horizontal direction profiles. In general two methods were observed as consistent. Also, the fractal dimensions of the profiles in horizontal direction were generally greater than vertical ones.

For synthetic fracture surfaces:

- The power spectral method yielded fractal dimensions between 2.00 and 2.50. They were expected to be greater than 2 to be in fractal regime and all the values fell into this interval unlike natural fracture surfaces. The fractal dimensions of upper and lower surfaces were not consistent for any loading rate.
- The fractal dimensions obtained through variogram analysis varied between 2.21 and 2.52 for vertical and 2.43 and 2.59 for horizontal profiles (for maximum lag distance of 5). The fractal dimensions of upper and lower surfaces were consistent at any loading rate. As similar to the natural surfaces, dimensions in horizontal direction were generally higher than the dimensions in vertical direction.

The difference between the fractal dimensions of horizontal and vertical profiles indicates the anisotropic nature of the fracture surfaces. Variogram analysis and roughness length measurement were, therefore, found as suitable methods to assess this feature of the surfaces. Detailed analysis of the fracture surfaces [4-6] and selection and application criteria of the methods [6,8,9] can be found in previous publications. The results gave an idea of the typical range of the fractal dimensions. Based on these observations, computer generated fracture surfaces were created for invasion percolation simulations.

GENERATION OF SYNTHETIC SURFACES

Mid-point displacement and successive random addition algorithm introduced by Voss [10] was used to generate 2-D self-affine fractional Brownian motion (fBm) data. The method relies on the displacements of mid points using a value of independent Gaussian random variable. This process produces 2-D self-affine distributions, which have a fractal dimension *D=3-H*. Fig. 2 illustrates 3-D representation of fBm surfaces generated using the same random number seed with different fractal dimensions. As can be visually observed, increasing fractal dimension yields more tortuous surfaces. As the fractal dimension decreases and approaches Euclidean dimension of 2, smoother surfaces are obtained. Invasion percolation simulations were performed on these lattices to qualitatively analyze the displacement patterns between two fracture surfaces.

INVASION PERCOLATION SIMULATIONS

Invasion percolation generates structures that are similar to patterns obtained during displacement of one fluid with another in porous media [11]. The simulation algorithm is as follows: The invasion starts from the bottom of the lattice and the smallest pixel neighboring the invasion front is occupied first. Both sides are close to flow and once the front reaches the top of the lattice, the process is stopped. In all simulations no trapping rule was applied.

Fig. 3 demonstrates the fractal distribution of aperture divided into 100x100 grids (Fig. 3-a) and the corresponding displacement patterns (Fig. 3-b). It was observed that the aperture between two fracture surfaces yields the same fractal dimension with fracture surfaces if the aperture is defined as the difference between the pixel values of upper and lower fracture surfaces. The invasion percolation simulations represent the displacement through fracture aperture. Note that no contact exists between two walls and all points are open to flow. As the fractal dimension decreases, smoother surfaces are obtained (Fig. 3-a). Typical fractal dimension for both natural and synthetic surfaces (measured by variogram analysis and roughness length measurement) of fracture surfaces lies between 2 and 2.5. Therefore, one has to bring attention to the patterns obtained for the lattices with fractal dimensions lower than 2.5. An extreme and unusual value of fractal dimension (D=2.9) for fracture surfaces was also included to compare the displacement behavior. More compact clusters are obtained with decreasing fractal dimension of fracture surface or aperture. However, no typical shape of the invasion cluster is expected as also observed by Babadagli [12]. Thus, the shape of the displacement pattern is determined by the local heterogeneity which is a random characteristic of the fracture surface. Typically, the displacement patterns follow the same trend for all surfaces with different fractal dimensions but the displacement efficiency increases with an increase in the fractal dimension of lattice.

CONCLUSIONS

The fractal dimensions obtained by power spectral density, variogram analysis and roughness length measurement methods indicated that the naturally and synthetically developed fracture surfaces represent fractal feature with the dimension values between 2 and 2.5. The only exception for this was the fractal dimension values of power spectral method for natural fracture surfaces. The results obtained by the variogram analysis were consistent with the ones obtained by the roughness length measurement method. The systematic difference between the fractal dimensions of horizontal and vertical profiles enables us to asses the anisotropic nature of the fractal behavior. Invasion percolation simulations on synthetically generated fractal lattices revealed that more compact clusters are obtained as the fractal dimension of the surfaces decreases. This implies that the displacement efficiency in the fracture increases with decreasing fractal dimension of the fracture surfaces.

REFERENCES

1. Develi, K., Babadagli, T. and Comlekci, C. (2001) *Comp. and Geosci.,* 27, 265.
2. Mandelbrot B. B., Passoja D. E. and Paullay A.J. (1984) *Nature* 308, 721.
3. Brown S. R. and Scholz C. H. (1985) *J. Geophys. Res.* 90, 12575.
4. Huang S. L., Oelfke S. M. and Speck R. C. (1992) *Int. J. Rock Mech. Min Sci & Geo. Abs.* 29, 89.
5. Develi, K. and Babadagli, T. (1998) *Mathematical Geology,* 30*,* 971.
6. Babadagli, T. and Develi, K. (2001) *Fractals,* 9, March issue.
7. Malinvero, A. (1990) *Geophys. Res. Let.* 14, 1953.
8. Mehrabi, A. R., Rassamdana, H. and Sahimi, M. (1997) *Phys. Rew. E*, 56, 712.
9. Schmittbuhl, J., Vilotte, J.-P. and Roux, S. (1995) *Physical Review E*, 51, 131.
10. Voss R. F. (1985) In: *Fundamental Algorithms for Computer Graphics*. *NATO ASI Series.* Springer-Verlag, Berlin, pp. 805-835.
11. Wilkinson, D. and Willemsen, F.J. (1983) *J. of Physics A: Mat. Gen*., 16, 3365.
12. Babadagli, T. (2000) *Physica A,* 285, 248.

ORAL/POSTER REFERENCE: ICF100925PR

FRACTOGRAPHIC ANALYSIS OF FISH-EYE TYPE FATIGUE CRACK IN TWO KINDS OF HIGH STRENGTH STEELS

KANAME MORI AKIRA UCHIYAMA YOSHIKAZU YAMADA

Department of Materials Science Engineering, School of Science and Engineering,
Teikyo University,
1-1 Toyosatodai, Utsunomiya, 320-8551, Japan

ABSTRACT

In order to clarify the influence of the surface treatment on the fatigue behavior of two high strength steels in long life region, cantilever type rotating bending fatigue tests have been carried out by using the specimen to which three kinds of surface treatments were finally performed. The surface treatments tested were grinding, polishing and shot-peening. Many fish-eye type fracture surfaces in long life region were observed in detail using SEM, EDS, and optical microscopy. Two kinds of inclusions were found often in the fatigue crack initiation site of fish-eye cracking. One is alumina for a low alloy steel, another nitride titanium for a bearing steel. Based on the testing conditions, the distance to crack initiation site, the size of inclusions and the size of fish-eye feature, the fish-eye type fatigue initiation behaviors under the condition of three different surface treatments were analyzed using the method of Fracture Mechanics.

KEYWORDS

fatigue, long life, fractography, surface treatment, shot-peening, fish-eye, crack initiation, inclusion

INTRODUCTION

There are a lot of data [1,2,3] on the influence of the surface treatment on fatigue strength of steels in the range up to ten million cycles. Recently, some important researches [4,5,6,7,8,9] that fatigue strength decreases in high cycle range, which exceeds ten million cycles for several steels, are reported.

The purpose of this study is to clarify the influence of the surface treatment on the fatigue behavior of the high strength steel in high cycle region. The fatigue crack initiation behaviors of two kinds of high strength steels were investigated by using the specimens with three different surface treatments. Especially, fish-eye type fracture images at subsurface fatigue crack initiation site were observed in detail using SEM, EDS and optical microscopy to search for the mechanism of fatigue fracture.

EXPERIMENTAL PROCEDURE

A low alloy steel (JIS SNCM439: 0.40C, 0.22Si, 0.78Mn, 0.02P, 0.013S, 0.18Cu, 1.78Ni, 0.83Cr, 0.2Mo, in mass%, 1123K x 1h gas cooled, 1123K x 1h oil cooled and 433K x 1h gas cooled) and a bearing steel (JIS SUJ2: 1.01C, 0.23Si, 0.36Mn, 0.01P, 0.007S, 0.06Cu, 0.04Ni, 1.45Cr, 0.02Mo, in mass%, 8ppmO, 1108K x 40min oil(353K) cooled, 453K x 2h air cooled) were investigated. The notch parts of specimen shown in Fig.1 were finally finished by 100 mesh grindstone, 1500 mesh emery paper a
l

RESULTS AND DISCUSSION

Effects of surface treatment on fatigue strength

Figures 2 (a) shows the effects of surface treatment on fatigue strength in a low alloy steel, JIS SNCM439. High stress amplitude loading for rough surface finish promotes surface cracking. The influence of surface treatments on the fatigue life under same stress amplitude is large in short life region. Low stress amplitude loading for all surface treatments promote fish-eye type cracking. The influence of surface treatments on the fatigue limit is hardly admitted in long life region.

Figure 2 (b) shows the results of a bearing steel, JIS SUJ2. Most of the specimens finished by 100 mesh grindstone were surface cracking, and the fatigue life under the same stress amplitude has changed a little depending on the processing lot. Fine finish by 1500 mesh emery paper and surface treatments by shot-peening promote fish-eye type, subsurface cracking. Two open circle symbol data with * marking for the specimens polished by 1500 mesh emery paper show the surface cracking, which the cracking start from the inclusion located on the notch surface. There is a tendency to which the fatigue limit decreases in the range that fatigue life exceeds 10^7 cycles, and the tendency is remarkable in the bearing steel. The fatigue life varies remarkably for the 100 mesh grinding finish, because of the grinding processing damage.

Fractographic analysis of fish-eye type fatigue fracture

Figure 3 shows the typical examples of fish-eye cracking on the specimen finally polished by 1500 mesh emery paper in low alloy steel. In the optical microscope image of the fish-eye as shown in Figure 3 (a), the fatigue crack initiation site is

found as a dark area. Y. Murakami et al. [10,11] call this region optical dark area (ODA). Figure 3 (b) is the scanning electron microscope image of the same fish-eye in Fig. 3 (a). The area corresponding to ODA in Fig. 3 (a) is observed in the fatigue crack origin in Fig.3 (b). In this paper, we call this region in Fig.3 (b) granular area (GA).

Figure 4 shows the inclusion observed at the origin of fish-eye cracking on the specimen finally polished by 1500 mesh emery paper in low alloy steel. Figures 4 (a) and (b) show the mating fracture surface images. The image shown in (a) was printed inside out for the convenience of the comparison. Figure 4 (c) shows the Al Kα dot map of the inclusion in (b). It was presumed that this inclusion was an alumina in addition to the information on the shape and size [3,12]., which was grainy and hexagonal. It is a little vague, but GA was also observed in surrounding of the inclusion.

Figure 5 is an unusual observation example in low alloy steel. The inclusion, which was the nucleus of the fish-eye, was presumed as nitride titanium, because of the EDS image, the angular shape and size [3,12]. In this case, GA was remarkably developed in surrounding of the inclusion.

Figures 6 and 7 show the typical inclusions observed at the origin of fish-eye cracking in bearing steel. It was presumed that these inclusions were nitride titanium based on the information of the EDS image, the angular shape and size [3,12]. In Fig.6, GA is hardly observed in surrounding of the inclusion. In Fig.7, GA is remarkably developed in surrounding of the inclusion.

The detailed observation results of the fatigue fracture origin are summarized as follows. The inclusions observed at the origin of fatigue fracture depend on the kinds of steels. Thirteen examples were alumina in the low

alloy steel in the observed inclusion of eighteen samples, four examples was the nitride titanium, and one example was the manganese sulfides. On the other hand, eleven examples were nitride titanium in the bearing steel in the observed inclusion of sixteen samples, four examples were the alumina, and one example was unknown. In both steels, the fatigue fracture has been initiated at the interface of inclusion and matrix. The peculiar fracture area (GA) formed to surrounding of the inclusion develops remarkably under the low stress amplitude and in the long life region. Y. Murakami [10,11] suggested the high possibility that hydrogen takes part in the formation of this GA, but clear evidence has not been obtained yet.

FRACTURE MECHANICS APPROACH

The stress intensity factor range, ΔK_{ini}, corresponding to the defect size which are evaluated on the square root of the area of inclusion or GA, were calculated using the following expression suggested by Y. Murakami et al.[13].

$$\Delta K_{ini} = 0.5\,\sigma_{at}\sqrt{\pi\sqrt{(area)}}$$

, where σat is a stress amplitude value which acts on the position of the crack origin. Figures 8 show the relation between $\Delta Kini$ and cycles to failure, Nf. for both steels. In both results, the tendency that $\Delta Kini$ corresponding to the inclusion size decreases with the increase of Nf is obtained. On the other hand, $\Delta Kini$ corresponding to the GA size almost indicates a constant value without depending on the increase of Nf.

CONCLUSION

The influence of the surface treatment on the fatigue behaviors of two high strength steels in long life region was investigated under the cantilever type rotating bending fatigue testing. The surface treatments tested were grinding, polishing and shot-peening. Many fish-eye type fracture surfaces in long life region were observed in detail using SEM, EDS, and optical microscopy. Main results obtained are as follows.

(1) The influence of the surface treatment on fatigue strength of two high strength steels was remarkably large under high stress amplitude and in short life region. But, the influence becomes small under low stress amplitude and in long life region.

(2) The peculiar fracture area (GA) formed to surrounding of the inclusion developed remarkably under the low stress amplitude and in the long life region.

(3) Two kinds of inclusions were found often as nucleus of the fish-eye cracking. One was alumina for low alloy steel, another nitride titanium for bearing steel.

(4) According to the Fracture Mechanics analysis, the tendency that critical stress intensity factors, ΔK_{ini} corresponding to the inclusion size decreases with the increase of N_f ,was obtained. ΔK_{ini} corresponding to the GA size almost indicated constant value without depending on the increase of N_f and the difference of the surface treatments.

ACKNOWLEDGEMENTS

The authors would like to thank Mr. K. Waguri, Mr. K. Kageyama and Mr. Y. Kakurai for the cooperation of the fatigue testing and the fracture surface observation. This work was financed in part by Japan Society Promotion Science, Research for the Future Program.

REFERENCES

1. N. E. Frost, K. J.Marsh and L. P. Pook (1974) "Metal Fatigue", pp.340-346, Clarendon Press, Oxford.
2. S. Suresh (1991) "Fatigue of Materials", pp.134-135, Cambridge Solid State Science Series, Cambridge University Press.
3. Y. Murakami (1993) "Metal Fatigue : Effects of Small Defects and Nonmetallic Inclusions (in Japanese)", Yokendo LTD. Tokyo.
4. T. Naito, H. Ueda and M. Kikuchi, (1984) , Metal Trans., Vol.15A, pp. 1431-1436.
5. C. Masuda, S. Nishijima and Y. Tanaka (1986) , Trans. JSME, Vol.52A, pp. 847-852.
6. K. Asami and M. Hironaga (1994), J. Soc. Mat. Sci. , Japan, Vol.43, pp. 12-17.
7. M. Nakajima, T. Sakai and T. Shimizu (1999), Trans. JSME, Vol.65A, pp. 2504-2510
8. K. Shiozawa, L.T. Lu and H. Ishihara (1999), J. Soc. Mat. Sci. , Japan, Vol.48, pp. 1095-1100.
9. S. Nishijima and K. Kanazawa, (1999), Fatigue Fract. Eng. Mater. Struct., Vol.22, pp.601-607.
10. A. Koyanagi and M. Kinoshi, (1975), ASTM STP 575 , pp.27-37.
11. Y. Murakami, S. Kodama and S. Konuma, (1988), Trans. JSME, Vol.54A, pp. 688-691.
12. Y. Murakami, T. Nomoto and T. Ueda, Y. Murakami and M. Oohori, (1999), J. Soc. Mat. Sci. , Japan, Vol.48, pp. 1112-1117.
13. Y. Murakami, T. Nomoto and T. Ueda, (1999), Fatigue Fract. Eng. Mater. Struct., Vol.22, pp.581-590.

ICF100158OR

FRACTROGRAPHY OF S.E.N. SOFT SOLDERED COMPOSITE LAMINATES MADE FROM 0.8 % CARBON MANGANESE STEEL UNDER PLANE STRAIN CONDITIONS

M.R. SABAYO

Department of Metallurgical Engineering,
Mehran University of Engineering & Technology,
Jamshoro Pakistan.

ABSTRACT:

An attempt has been made to discuss the design criterion of the composite materials at and during service conditions of engineering structures. The present work supports this and suggests a compromise between the properties of the materials such as strength and fracture toughness with pearlitic and martensic structures of composite laminates by using thin sheets of critical thickness in the form of laminate with crack divider geometry under plane strain conditions. This is supported by the load displacement graph by using an Instron testing machine at a strain rate of 0.05 cm/min and the fractography which supports the same modes of failure during fracture process. Thus suggesting the advanced materials for achieving the structure integrity of engineering structures.

KEY WORDS:

Composite laminates, crack controlling properties, delamination fracture and structural integrity.

INTRODUCTION:

A most serious problem now a days is to be able to build an Engineering structure which can resist the cracks or flaws present in it. Failure may take place in such structures below their yield or ultimate strengths. To over come this, composite materials, particularly laminates have been used, (Embury, (1), 1969). Such materials C not only resist crack propagation more (Sabayo, (2), 1981), than the homogenous materials but also have higher critical crack lengths giving a better chance of crack detention prior to failure and in some cases completely prevented through the thickness cracks (Sabayo, (3), 1982). This has drawn attention to the role of interfaces, their strength, delimitation during and after fracture, and the thickness of elements (layers) used in composite laminates.

Crack controlling properties and lamination have recently been applied in conventional metallurgy. Steel can be made more resistant to crack by cementing together thin sheets of it with soft solder. This laminated steel is of course a composite materials, (Kelley, (4) 1970). Such studies have shown that through proper control of mechanical properties of the bonds, joining the sheets, it is possible to introduce delimitation fracture that markedly improve the over-all toughness of composite and in some cases completely prevented through the thickness cracks, (Sabayo, (5), 1983).

In order to optimize the performance of the composite materials, it is necessary to gain some fundamental understanding of the nature of the components. Even for simple external composite loadings, the state of stress and strain at the interfaces between the components are complex and vary from place to place in the composite. This complexity of conditions at the interface is different from what might be expected from simple loading conditions. Although a precise description of the interface is beyond our present knowledge, and understanding of the role of the interface on composite behaviour and the ability to control the interface are important factors. (Sabayo, 5, 1991).

Strength and toughness are related but different properties. One is generally obtained at the expense of the other where as the lamination provides a means of increasing resistance to fracture that is independent of the structure variables of the materials very much required for achieving the structural integrity. (Sabyo, 6, 1997).

MATERIAL AND EXPERIMENTAL PROCEDURE:

The patented and cold worked pearlitic material with the following compsition and homogenous properties throughout its length in the form of coiled strip was supplied.

C: 0.8%, Si 0.18%, S 0.015%, P 0.007%, Mn 0.55%.

The same material was hardened at 790oC and tempered at 418oC for one hourt to give almost identical strength values corresponds to a hardness of 431 + 16 D.P.N. To make fracture toughness specimens, strips 84x19x1mm were polished down to 30 grade emery paper and then dpped into 70% pb & 30% Sn molten lead tin solder held in graphite crucible at a temperature of 232oC. In this way a uniform layer of solder was maintained on each strip. In order to get the required geometry for the fracture toughness specimens, eight such strips were riveted together and then hot pressed at a temperature of 250oC for one hour. A pressure of 635 MN/m2 was maintained until the temperature dropped to room temperature. The composite specimens were machined and then notched according to the specification. Fig. 1 shows the specimen geometry. For pre-cracking, a high frequency vibraphone was used. All conditions satisfied for pre-cracking were fulfilled, (Brown, 7, 1970).

FRACTURE TOUGHNESS TESTING:

Fracture toughness tests were carried out on an Instron machine at a cross head-displacement rate of 0.05cm/min using the pre-cracked specimens and specimens were mounted in pin type grips loaded in tension. A 1000 ohm BISRA clip guage was located across the notch of the specimens using brass sadles glued on the X-Y recorder was subsequently used for analysis and measurement of fracture toughness. Fig 3 shows the load displacement records, which full-filled all conditions for valid K_{IC}. The results are shown in Table 1 and Table 2.

MICROSCOPY:

To study the modes of failure of the laminates electron fractography was carried out by using EM6G microscope and Cambridge Scanning Electron Microscope. Such details are shown in Fig. 3 (a, b, c) and Fig. 4 (a, b, c) for soft soldered composite laminates tested at a cross head displacement rate of 0.05cm/min, with pearlitic and martensitic and martensitic structures. This includes delamination in the region of slow crack growth, cracking of pearliest and inclusions in the region of fast fracture and ductile failure in the region of fast fracture in either case.

TABLE 1. FRACTURE TOUGHNESS TEST RESULTS OF S.E.N., SPECIMEN MADE FROM 0.8% CARBON MANGANESE STEEL WITH PATENTED AND COLD WORKED SOFT SOLDERED LAMINATES TESTED IN AIR.

Specimen No.	Displacement Rate.	Tagent Line (Degree)	P5 (A) P_{kg}	KQ M_{Nm}-3/2
1.	0.05	51	1530	140.75
2.	0.05	51	1530	140.75
3.	0.05	51	1530	140.75
Mean KQ = $140.75 MNm^{-3/2}$				

ICF100158OR

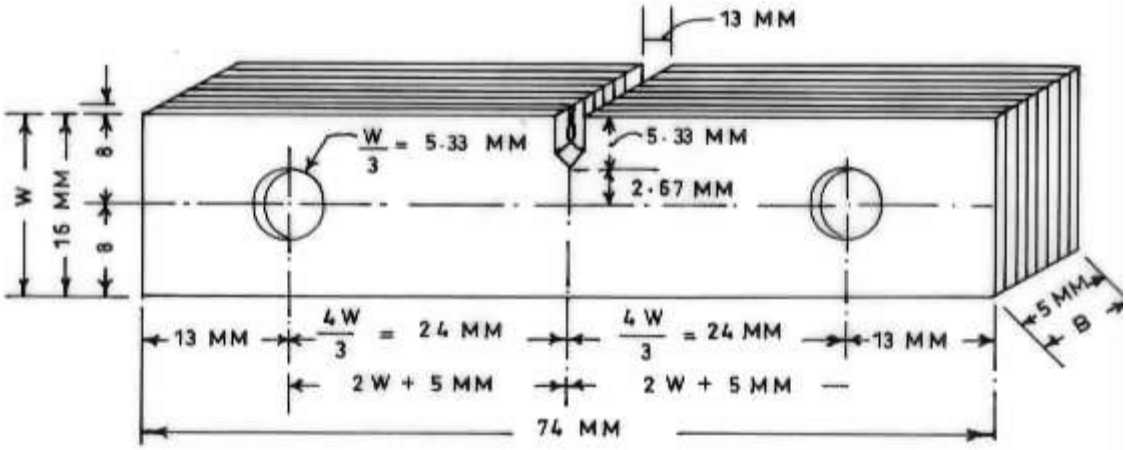

FIG_1 SEN FRACTURE TOUGHNESS TESTING COMPOSITE LAMINATES

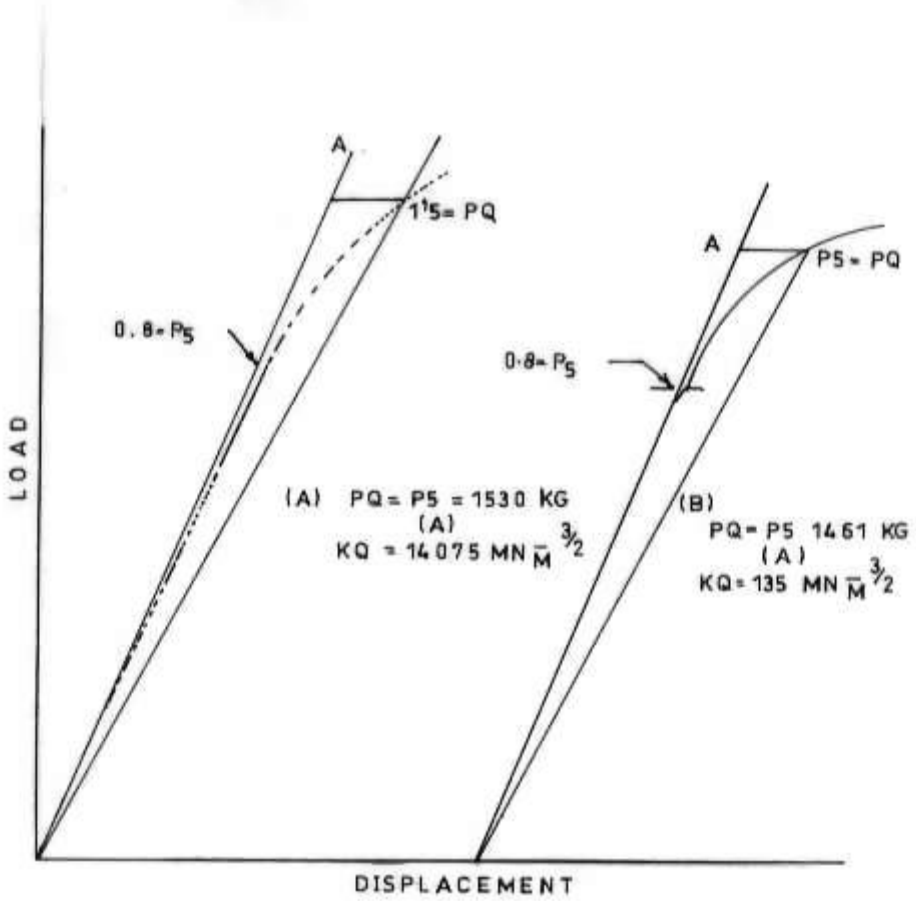

FIG_2 LOAD DISPLACEMENT GRAPH FOR SOFT SOLDERED COMPOSITE LAMINATES WITH (A) PEARLICTIC AND (B) MARTENSITIC STRUCTURES

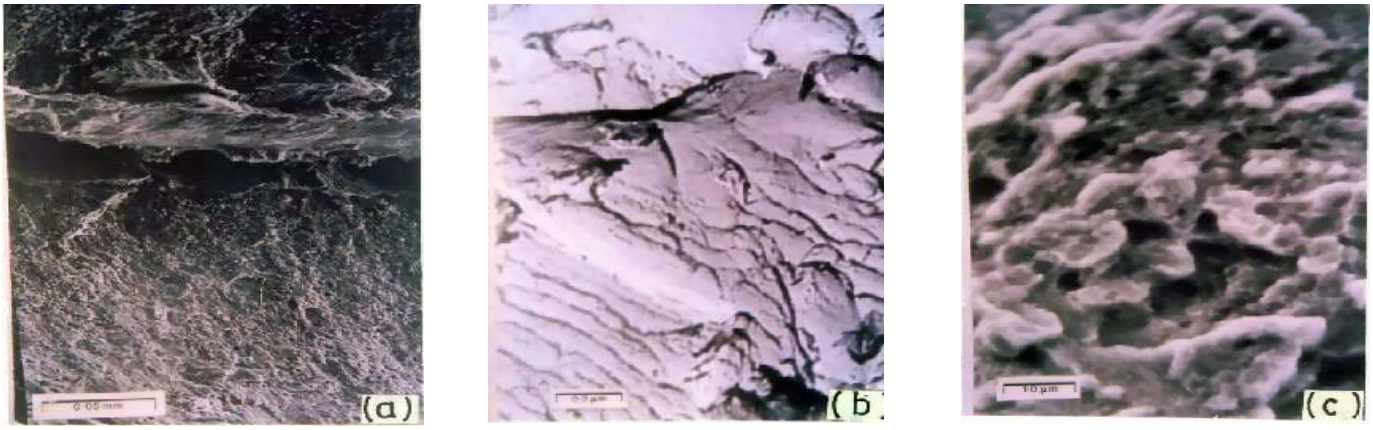

Fig. 3 (a, b, c) Electron fractography for SEN soft soldered composite laminates made from 0.8C% manganese steel with pearlatic structure tested in air at 0.05cm/min

a) Delamination in one layer in the region of slow crack growth.
b) Cracking of pearlites in the region of fast fracture.
C) Ductile failure in the region of fast fracture.

TABLE 2. FRACTURE TOUGHNESS TEST RESULTS OF S.E.N., SPECIMEN MADE FROM 0.8% CARBON MANGANESE STEEL WITH HARDENED AND TEMPERED SOFT SOLDERED LAMINATES TESTED IN AIR.

Specimen No.	**Displacement Rate.**	**Tagent Line (Degree)**	**P5 (A) P_{kg}**	**KQ M_{Nm}-3/2**
1.	0.05	55	1461	135
2.	0.05	55	1461	135
3.	0.05	55	1461	135
Mean KQ = $135MNm^{-3/2}$				

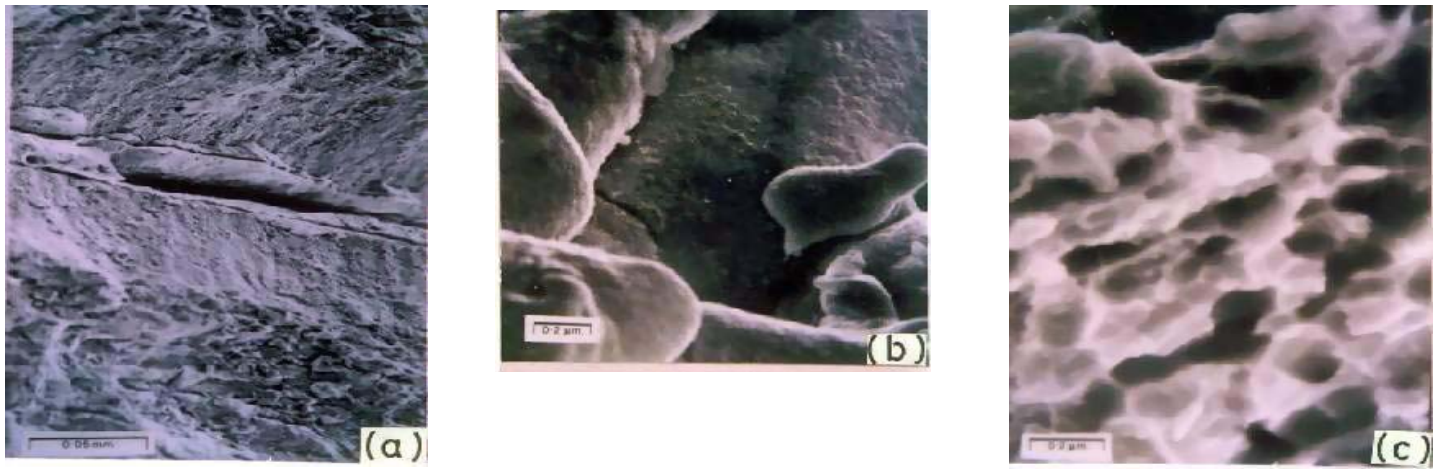

Fig. 4 (a, b, c) Electron fractography for SEN soft soldered composite laminates made from 0.8C% manganese steel with martensitic structure tested in air at 0.02cm/min

a) Delamination in one layer with region of slow crack.
b) Cracking along the inclusions in the region of fast fracture.
c) Ductile failure in the region of fast fracture.

DISCUSSION:

A laminated is a composite in which two or more sheets are bonded together, where crack growth can occur under either stress or plane strain conditions. Interfacial strength plays an important role in laminates. Usually too high an interfacial strength gives no benefits since the material then behaves as a homogenous solid. Similarly a material with negligible strength results if the adhesion is too weak. Even for simple external composite loading, the state of stress and strain at the interfaces between the components are complex and vary from place to place in the composite (Sabayo, 8, 1991).

This all is supported by the load displacement graph plotted by using Instron testing machine under plane strain condition and the fractography which shows similar modes of failures in each case during fracture process. This includes the delamination in the region of slow crack growth, cracking of pearlites / along the inclusions in the region of fast fracture and ductile failure in the region of fast fracture.

The average K_Q values for patented and cold worked were 141 $MNm^{-3/2}$ while hardened and tempered laminates gave an average value of $135MN3^{-/2}$. This showed that patented and cold worked composite laminates were tougher than the hardened and tampered laminates under plane conditions for identical strength values corresponds to hardness values of 431$\pm$ 16DPN.

The work demonstrates that good combination of strength and toughness can be obtained in crack divider laminates of both pearlitic and martenstic structures under plane strength conditions provided the width of the strip is increased. Unfortunately the maximum width of the material that is obtainable not more than 19mm hence before it is impossible to get K_{IC} so far as specification (Brown, 5, 1971) is concerned. Although each element fails by slant fracture at approximately 45^o to the tension of axis Fig. 4 confirms that the individual element making up the laminates were of the thickness t critical corresponding to K_C maximum. It is however interesting to note that the results obtained with a low cost plain carbon steel are at least as good those reported by (Zakay, 9, 1970). Thus encouraging manufacturing technology sectors more to produce the advanced material for achieving the high structural integrity of the structures (Sabayo, 6) 1997.

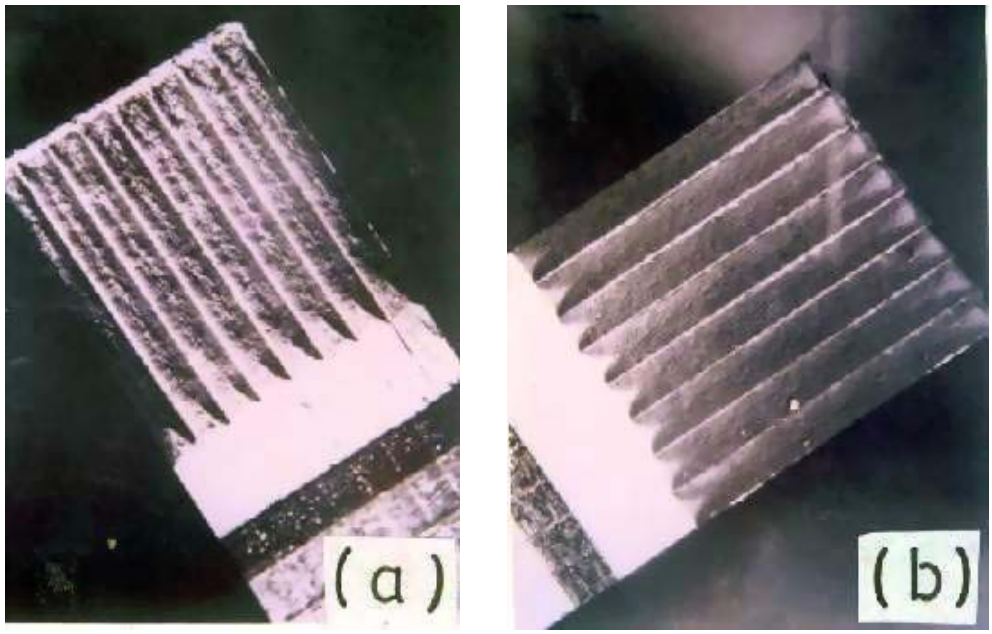

Fig. 4 General view of fracture surface typical of (a) patented and cold worked laminates and (b) hardened and tempered laminates where each elements fails by slant fracture at approximately 45^o to the tension axis.

ACKNOWLEDGEMENT:

The author is grateful to the Administration of Mehran University of Engineering and Technology, Jamshoro, for financial support.

REFERENCES:

1. **SABAYO M.R. (1988) :** Composites and failure of the interfaces, Proceedings, 6NCEFMechanics, Institution of Engineers, Karachi Centre, Pakistan.

2. **EMBURY J.D, (1967) :** N.J. Pethc, A.E. Wraith and E.S. Wright, Transaction of Metallurgists Society of AIME, Vol: 239, p 115.

3. **SABAYO, M.R. (1983) :** The failure of Engineering Structures in the countries of Muslim World, International Conference in Islamic Polity, Ministry of Science and Technology, Islamabad.

4. **SABYO M.R. (1981) :** Fracture Behaviour of CTS crack Divider soft soldered composite laminates made form 4340 steel in the Environments of Hydrogen, 8th International Conference on Metallic Corrosion, Frankfurt, Mianse, Germany.

5. **SABAYO M.R. (1987) :** The Toughness of Composite Laminates, Proceedings, 5th International Conference on Mechanical Behaviour of Materials, Pergamon Press, London.

6. **BROWN, H.F. (1970) :** A.S.T.M., S.T.P., 463, P-49.

7. **SABAYO M.R. (1991) :** Mechanical Behaviour of Soft Soldered Composite Laminates in High Vacuum Atmosphere Under Plane Strain Conditions. Proceedings of the Sixth International Conference Kyoto, Japan.

8. **ZAKAY V.F. ET AL (1970):** C2-35, III International Conference on Strength of Metals and Alloys.

9. **SABAYO M.R. (1997) :** Structural integrity (invited lecture) Proceedings of 12th National Conference on Engineering Fracture Mechanics.
Mehran University of Engineering & Technology, Jamshoro.

FRACTURE AND CREEP RUPTURE BEHAVIOR OF NOTCHED OXIDE/OXIDE AND SiC/SiC CMC

Reji John[1], Dennis J. Buchanan[2] and Larry P. Zawada[1]

[1] Air Force Research Laboratory, Materials and Manufacturing Directorate (AFRL/MLLMN)
Wright-Patterson AFB, OH 45433-7817, USA
[2] University of Dayton Research Institute
Dayton, OH 45419, USA

ABSTRACT

Woven Oxide/Oxide and SiC/SiC ceramic matrix composites (CMC) are targeted for high-temperature aerospace applications such as combustors, combustor liners, exhaust washed structures, exhaust nozzle flaps and seals, and blade outer air seals. Some of these components contain stress concentration sites such as holes and attachment points. During service, these locations will be subjected to long-term exposures. Hence, the knowledge of the effect of sustained (creep) loading on the deformation and rupture of notched Oxide/Oxide and SiC/SiC composites is required for durability assessment. The results from creep tests of unnotched and notched Nextel™720/Alumina-Silica (Nextel™720/AS-0) and Melt Infiltrated (MI) HI-NICALON-Type-S/SiC (MI HI-NICALON-S/SiC) are discussed in this paper. Nextel™720/AS-0 was evaluated at 1100°C and MI HI-NICALON-S/SiC at 1200°C in laboratory air. In the case of large notches, i.e., notch length greater than the average tow size, the notch-sensitivity increased significantly under sustained loading for both composites. Nextel™720/AS-0 specimens with straight-through effusion holes (hole diameter = 0.5 mm) were also subjected to sustained loading at 100MPa/1100°C. In this case, the presence of effusion holes did not affect the overall creep response.

KEYWORDS

ceramic matrix composite, creep, effusion holes, fracture, notch-sensitivity, oxide/oxide, sic/sic, woven cmc

INTRODUCTION

Woven Oxide/Oxide and SiC/SiC ceramic matrix composites are being demonstrated for high-temperature aerospace applications with temperature requirements in the range of 1000-1300°C [1-4]. Current targeted aerospace turbine engine components, such as combustors, combustor liners, divergent flaps and seals, contain bolted attachment points and cooling holes. Local stresses in these regions often exceed the proportional limit of the composite, resulting in damage and crack initiation. Hence, component design using CMC will require knowledge of the notched fracture behavior and damage progression under service thermomechanical loading conditions. Most of the results on the notched behavior of Oxide/Oxide and MI SiC/SiC CMC correspond to monotonic tensile loading [5-14]. Recently, John et al. [8,9] and McNulty et al. [12] studied the effects of long-term loading on notched Oxide/Oxide at 1100°C and MI SiC/SiC at 815°C,

respectively. Based on specimens with large notches (i.e., notch length greater than tow size), these studies [8,9,12] reported an increase in notch-sensitivity when exposed to temperature for 100+ hours.

Components such as combustors are designed to contain effusion holes, which are used to lay down a film of cooling air on the hot wall to create a boundary layer effect and to cool the component by providing more internal surface area. The effusion holes are typically of the order of 0.50 mm diameter, which is approximately half the average fiber tow size. This paper summarizes the results of a recent study [10] on the creep behavior of Oxide/Oxide at 1100°C. The results are compared to the creep behavior of specimens with large notches. In addition, the creep behavior of notched MI SiC/SiC at 1200°C is also discussed.

MATERIAL AND EXPERIMENTAL PROCEDURE

The Oxide/Oxide CMC used in this study was Nextel™720/AS-0, which was manufactured by COI Ceramics, Inc., San Diego, CA. Figure 1(a) shows the microstructure of Nextel™720/AS-0. The matrix consists of a porous alumina-silica (AS) that is weakly bonded to the fibers without an engineered interphase. Approximately 400 Nextel™720 fibers were bundled together in tows and woven into a balanced eight-harness-satin weave (8HSW) cloth. The fiber mat had a (0/90) layup with final CMC volume fraction ≈ 0.46.

The SiC/SiC CMC used in this study was HI-NICALON-S/SiC, which was manufactured by Honeywell Advanced Composites, Inc, Newark, DE. Figure 1(b) shows the microstructure of MI HI-NICALON-S/SiC. The matrix is described as Melt-Infiltrated (MI) SiC. The HI-NICALON-Type-S (HI-NICALON-S) fibers were bundled together in tows and woven into a balanced five-harness-satin weave (5HSW) cloth. The fiber mat had a (0/90) layup with final CMC volume fraction ≈ 0.33.

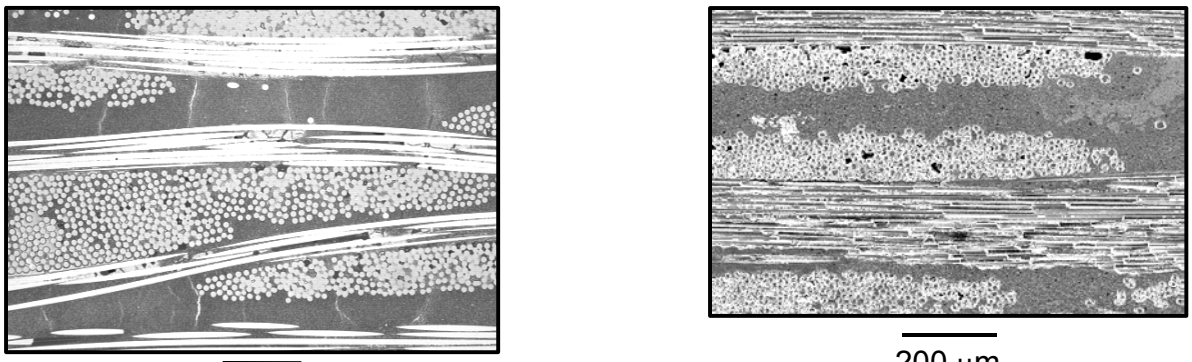

Figure 1: Microstructure of (a) Nextel720/AS-0 and (b) Melt Infiltrated HI-NICALON-S/SiC.

During this study, baseline tensile tests were conducted using dogbone specimens. For the conventional notch sensitivity tests, straight-sided specimens with large notches (notch length greater than the average tow size) were used. Semi-circular notches, DEH(T) and sharp notches, DE(T) were used during this study, Figure 2(a). The semi-circular and sharp notches were machined using a drill and a thin diamond saw (≈ 0.1 mm thick), respectively. In all these tests, the notch mouth opening displacement (NMOD) was measured. Figure 2(b) shows the effusion hole patterns used for this study. The nominal dimensions of the specimens were, width (W) = 10.0 mm in gage section, thickness (B) ≈ 2.5 mm and gage length ≈ 12.5 mm. All effusion holes were 0.5 mm in diameter with the hole axis perpendicular to the loading axis. The hole density studied in this investigation was ≈ 8 holes/cm^2 (≈ 50 holes/in^2).

The specimens were measured and photographed to document the condition of the holes prior to testing. The specimen ends were tabbed with fiberglass tabs to provide a flat uniform surface for the smooth grip surfaces and to minimize the possibility of grip failure. The specimens were mounted in a precisely aligned, rigid grip system that minimized specimen bending and rotation. A clamshell furnace with SiC heating elements and four-zone control were used for the elevated temperature creep tests. Thermal profile maps on the specimen showed that the specimen was uniformly heated, ± 0.6%, over the entire gage section of the specimen. All creep tests were loaded to the maximum stress at a loading rate of 20 MPa/s.

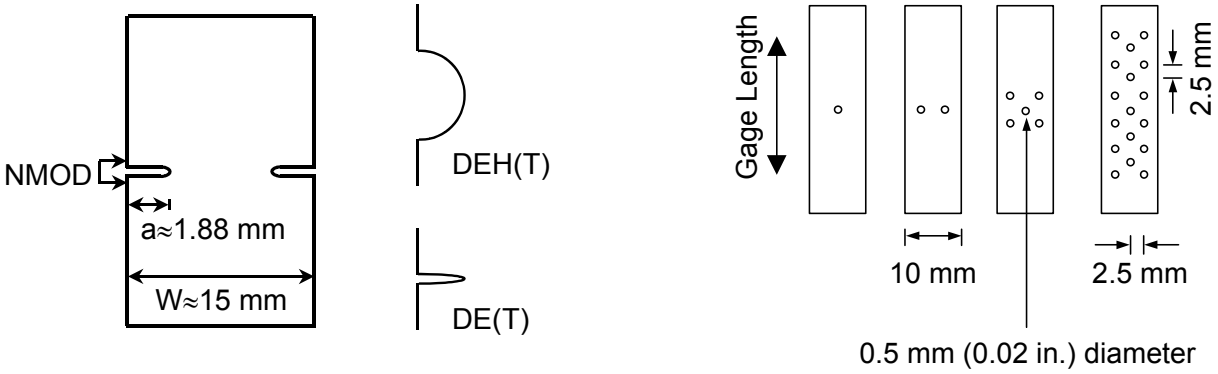

(a) CMC: Nextel™720/AS-0 & MI HI-NICALON-S/SiC (b) CMC: Nextel™720/AS-0

Figure 2: Schematic of (a) double edge notched, and (b) effusion hole specimens.

RESULTS AND DISCUSSION

The unnotched tensile behaviors of Nextel™720/AS-0 and MI HI-NICALON-S/SiC are shown in Figures 3(a) and 3(b), respectively. Nextel™720/AS-0 exhibits nearly linear behavior until failure at 23 and 1100°C with insignificant temperature dependence. The proportional limit (PL), defined as deviation from initial linear response, for Nextel™720/AS-0 was ≈ 75 and 80 MPa at 23°C and 1100°C, respectively. In contrast, MI HI-NICALON-S/SiC exhibits bi-linear response at 23°C and 1200°C with significantly higher ultimate tensile strength (UTS) than that of Nextel™720/AS-0. The PL for MI HI-NICALON-S/SiC was ≈ 145 and 150 MPa at 23°C and 1200°C, respectively.

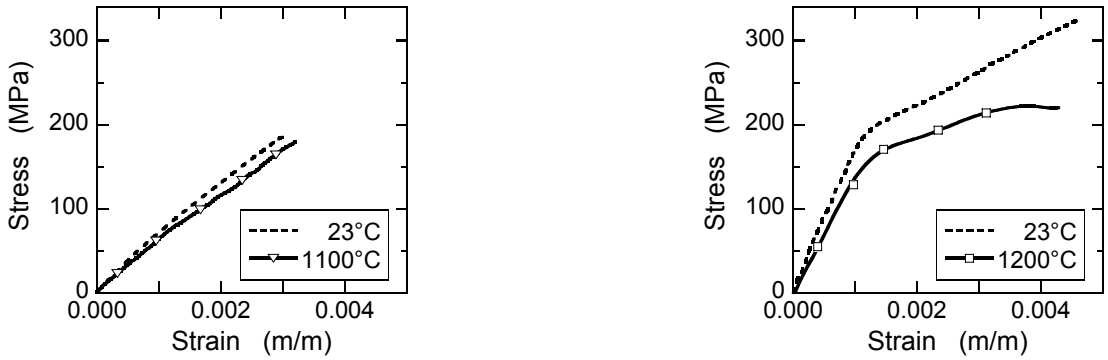

(a) (b)

Figure 3: Tensile behavior of (a) Nextel™720/AS-0 and (b) Melt Infiltrated HI-NICALON-S/SiC.

The net-section strength normalized with respect to the corresponding unnotched UTS versus notch length is plotted in Figures 4(a) and 4(b) for Oxide/Oxide and MI SiC/SiC systems, respectively. At room temperature, Nextel™720/AS-0 [This study, 11] is notch-insensitive while Nextel™610/MA [5] is notch-

sensitive. At 1100°C, Nextel™720/AS-0 exhibits mild notch-sensitivity (≈15%) at notch length (2a) ≈ 4.5 mm. At room temperature, MI HI-NICALON-S/SiC from this study exhibits slight notch-sensitivity, similar to that reported by McNulty et al. [12,13] and Morscher et al. [14] for other SiC/SiC composites. At 815°C, MI Sylramic/SiC exhibited notch-sensitivity similar to that at room temperature [12]. In contrast, MI HI-NICALON-S/SiC was notch-insensitive at 1200°C.

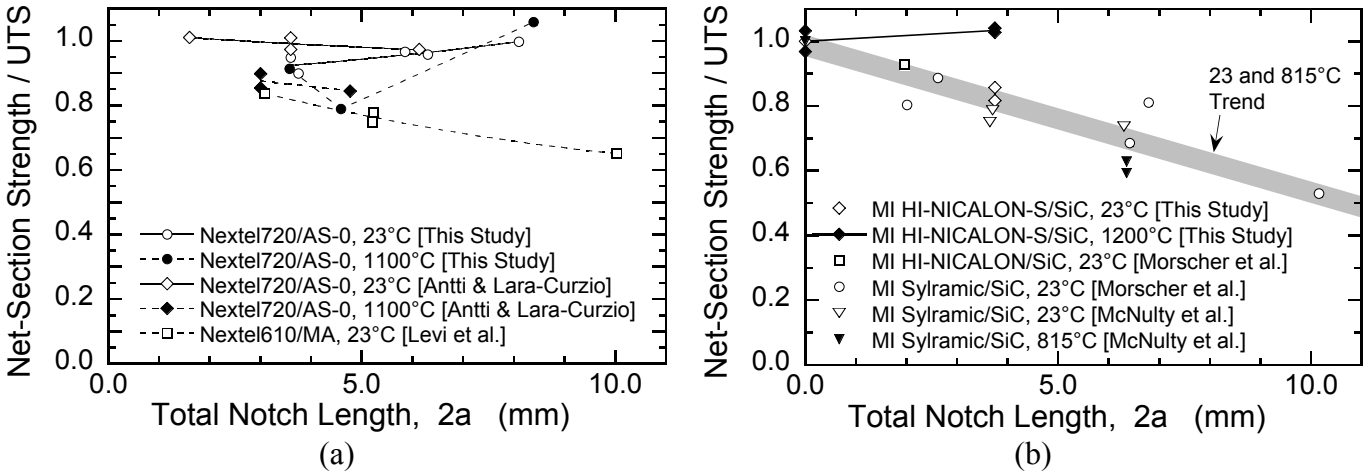

Figure 4: Notch sensitivity of (a) Nextel™720/AS-0 and (b) MI HI-NICALON-S/SiC under tensile loading.

The notched strength data shown in Figure 4 for Oxide/Oxide and MI SiC/SiC systems correspond to short-duration tensile tests. During service, the CMC components will be subjected to long-term thermomechanical loading. Hence, durability assessment of such long-life components require knowledge of the notched behavior under long-duration test conditions. Sustained loading (creep) tests were conducted on unnotched and notched Nextel™720/AS-0 and MI HI-NICALON-S/SiC specimens at 1100°C and 1200°C, respectively, Figure 5.

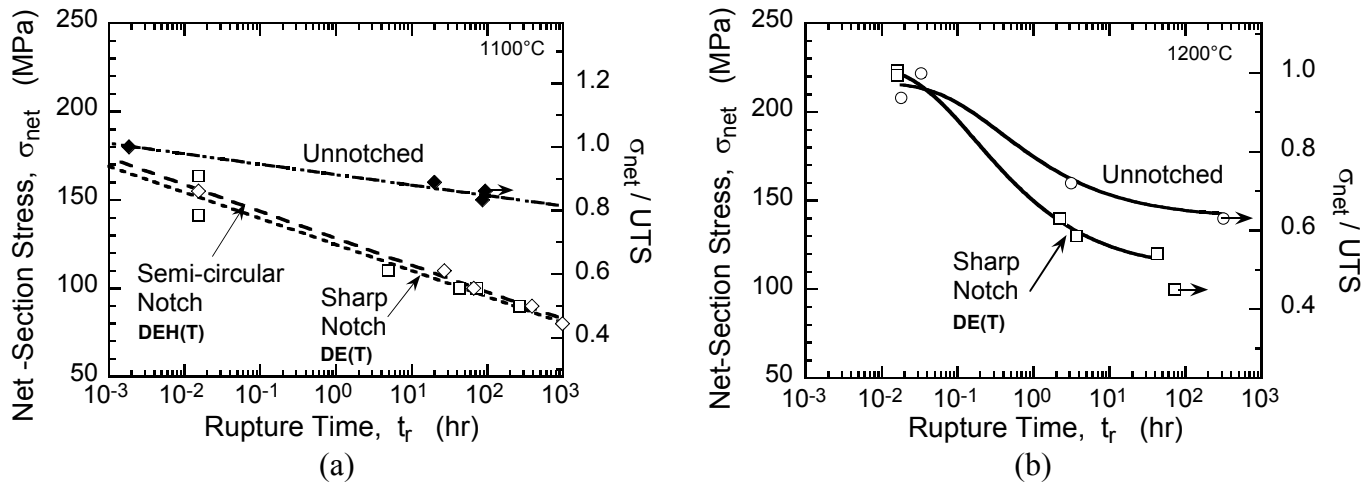

Figure 5: Notch effects on creep rupture behavior of (a) Nextel™720/AS-0 and (b) MI HI-NICALON-S/SiC.

The unnotched Nextel™720/AS-0 shows excellent creep strength of ≈ 150 MPa which is ≈80% of UTS and well above the PL≈80 MPa. Unnotched MI HI-NICALON-S/SiC also shows similar creep strength (≈150 MPa) which is close to the PL. Hence, the maximum design stress for long-life components (with no

notches) is similar for both Nextel™720/AS-0 and MI HI-NICALON-S/SiC. When large notches (notch length ≈ 2 mm) are introduced, the net-section stress that can be sustained by the composite at 100+ hours decreases significantly. For Nextel™720/AS-0, the notch strength decreased to ≈ 85 MPa, which is close to the unnotched proportional limit. This decrease is independent of the type of notch. For MI HI-NICALON-S/SiC, the notch strength decreased to 110 MPa, which is ≈ 73% of PL. These results are summarized in Table 1. Also shown in Table 1 are the 815°C results from McNulty et al. [12] based on low-cycle fatigue tests with a 2 hour dwell time. At 815°C, the reduction in notch strength is greater than that observed at 1200°C. These results show that design of long-life components with stress concentration sites should be based on careful detailed durability assessment studies with sub-elements simulating the actual features.

TABLE 1
CREEP STRENGTH OF NEXTEL™720/AS-0 AND MI HI-NICALON-S/SiC

Creep Strength at rupture time = 100+ hr [This study]			LCF Threshold [McNulty et al.]
Geometry	Nextel™720/AS-0 at 1100°C	MI HI-NICALON-S/SiC at 1200°C	MI Sylramic/SiC at 815°C
Unnotched	≈ 150 MPa	≈ 150 MPa	165 MPa
Notched	≈ 85 MPa	≈ 110 MPa	60-85 MPa

Since the large notch specimens exhibited significantly increased notch-sensitivity under sustained loading in contrast to the short-duration tensile loading, a program was initiated to evaluate the performance of specimens with effusion holes under creep loading. The creep behavior of Nextel™720/AS-0 with effusion holes (8 holes/cm^2) is shown in Figure 6. The overall creep deformation is similar to that of the unnotched specimen. Following the creep tests, retained strength tests were conducted at room temperature and compared with the unnotched tensile behavior in Figure 7. The stress-strain response of specimens with effusion holes is identical to that of unnotched material. The decrease in UTS is similar to that observed for unnotched specimens. Hence, under creep loading conditions, Nextel™720/AS-0 with effusion holes @ 8 holes/cm^2 could be expected to respond similar to the unnotched composite. Additional tests are in progress to understand the effect of higher stress levels on the creep behavior of specimens with effusion holes and the relationship between hole size and notch-sensitivity.

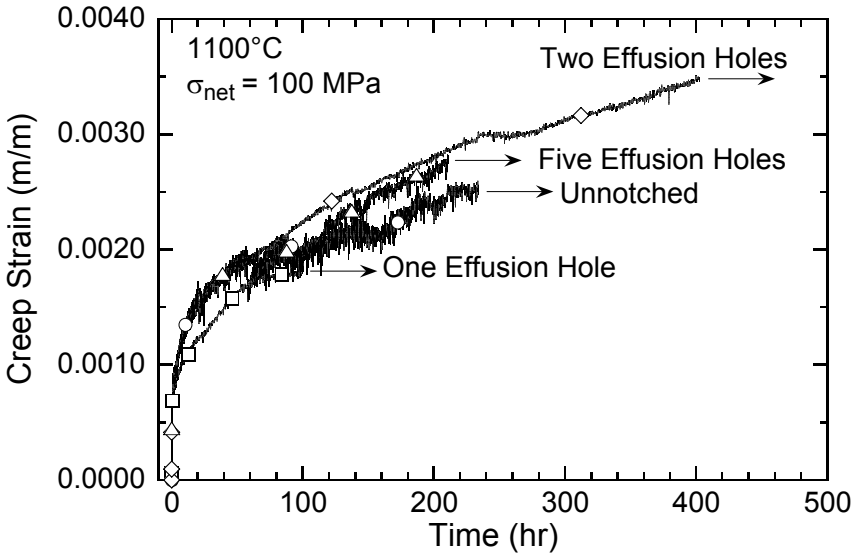

Figure 6: Creep deformation of Nextel™720/AS-0 specimens with effusion holes.

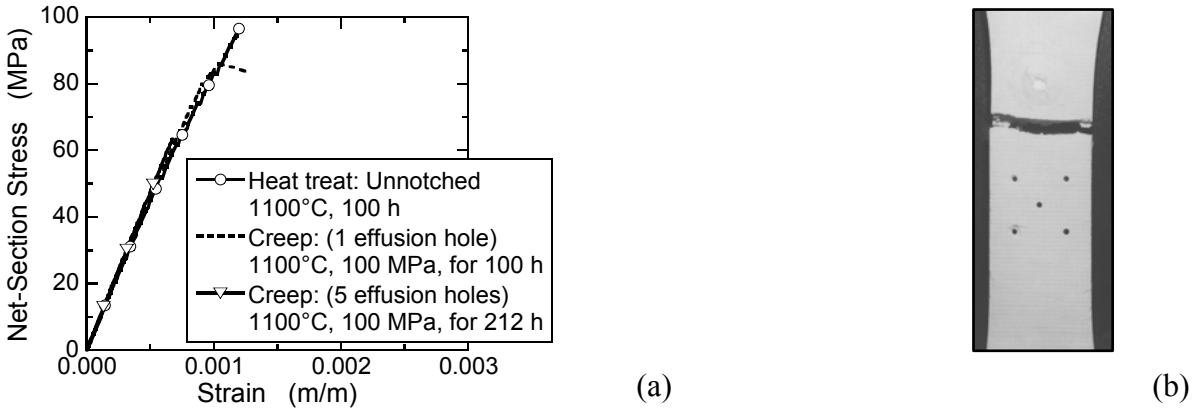

Figure 7: (a) Retained strength (@23°C) of creep-tested Nextel™720/AS-0 specimens with effusion holes. (b) Fracture profile of effusion hole specimen after retained strength test.

CONCLUSIONS

Notch-sensitivity of woven Nextel™720/AS-0 and MI HI-NICALON-S/SiC with (0/90) layup increases significantly under sustained (creep) loading conditions. The creep strength (in terms of net-section stress) decreases ≈ 40% and 27% for Nextel™720/AS-0 and MI HI-NICALON-S/SiC, respectively. The creep behavior of Nextel™720/AS-0 with effusion holes (8 holes/cm^2) was similar to that of the unnotched composite.

ACKNOWLEDGMENTS

This research was conducted at the Air Force Research Laboratory, Materials and Manufacturing Directorate (AFRL/MLLMN), Wright-Patterson Air Force Base, OH 45433-7817 and was supported in part by the Air Force Office of Scientific Research under task 23061P10 (Program Manager: Dr. Craig Hartley). Mr. Buchanan was supported under an onsite contract number F33615-98-C-5214.

REFERENCES

[1] IHPTET Brochure, Turbine Engine Division, Propulsion Directorate (AFRL/PRT), Air Force Research Laboratory, Wright-Patterson Air Force Base, OH, USA.
[2] Brewer D. (1999) *Materials Science and Engineering A* 261, 284.
[3] Ohnabe, H., Masaki, S., Onozuka, M., Miyahara, K., and Sasa, T. (1999) *Composites: Part A* 30, 489.
[4] Zawada, L.P. and Lee, S.S. (1995) *Ceramic Engineering and Science Proceedings* 16, 337.
[5] Levi, C.G., Yang, J.Y., Dalgleish, B.J., Zok, F.W. and Evans, A.G. (1998) *Journal of the American Ceramic Society*, 81, 2077.
[6] Heathcote, J.A., Gong, X.-Y, Yang, J., Ramamurty, U., and Zok, F.W. (1999) *Journal of the American Ceramic Society*, 82, 2721.
[7] Kramb, V.A., John, R., and Zawada, L.P. (1999) *Journal of the American Ceramic Society* 82, 3087.
[8] John, R., Buchanan, D.J., and Zawada, L.P. (2000) *Ceramic Eng. and Science Proceedings* 21, 567.
[9] John, R., Buchanan, D.J. and Zawada, L.P. (2000) *STP 1392 ASTM* 172.
[10] Buchanan, D.J., Kramb, V.A., John, R., and Zawada, L.P. (2001) *Ceramic Engineering and Science Proceedings* Accepted.
[11] Antti, M-L. and Lara-Curzio, E. (2001) *Ceramic Engineering and Science Proceedings* Accepted.
[12] McNulty, J.C., He, M.Y., Zok, F.W. (2001) *Composites Science and Technology* Accepted.
[13] McNulty, J.C., Zok, F.W., Genin, G.M., and Evans, A.G., (1999) *J. of the Am. Cer. Soc.* 82, 1217.
[14] Morscher, G., Gyekenyesi, J.Z., and Gyekenyesi, A.L., (2001) *Proceedings of 46th ASME IGTI.*

FRACTURE AND FATIGUE BEHAVIOR OF TOUGHENED DRA, Al-Be, AND BULK METALLIC GLASS COMPOSITES

J.J. Lewandowski, J. Larose and S. Solv'yev

Department of Materials Science and Engineering
Case Western Reserve University
Cleveland, Ohio 44106, USA

ABSTRACT

The fracture and fatigue behavior of discontinuously reinforced aluminum (DRA) composites, Al-Be composites, and toughened bulk metallic glass systems are presented. Data on the effects of particulate reinforcement additions to an aluminum matrix are presented first and illustrate the decrease in toughness typically observed with reinforcement additions in such systems. The effects of incorporating extrinsic toughening regions on the fracture and fatigue crack growth are subsequently presented and show that both the fracture and fatigue crack growth performance can be improved with such additions. Additional work is presented on the behavior of Al-Be composites produced by powder metallurgy techniques. The fracture and fatigue behavior of the constituents are presented in addition to that of the behavior of the Al-Be composites containing, by volume, 70% Be and 30% Al. The addition of Al to produce the Al-Be composite provides improvements to the toughness and some aspects of the fatigue crack growth behavior in comparison to the monolithic Be. Finally, the effects of the addition of a refractory metal containing toughening phase on the fracture behavior of a bulk amorphous material based on the Zr-Ti-Ni-Cu-Be system is presented

KEYWORDS: ***Discontinuously Reinforced Al (DRA), Ultra-light Al-Be composites, bulk metallic glass/composites.***

1. INTRODUCTION

There is a continuing need for high performance affordable materials with high specific strength and stiffness. The modified Ashby plot shown in Figure 1 illustrates that composites based on a variety of lightweight materials (e.g. Al, Mg, Ti, Be) provide combinations of high specific stiffness and strength which are attractive to the automotive, aerospace, and electronic packaging communities. Recent reviews have illustrated some of the material sources and balance of properties present in the DRA systems [1-3]. While discontinuous reinforcement additions increase the modulus, Figure 2 [1] illustrates the significant decrease in fracture toughness resulting from such additions. The fatigue crack growth characteristics of DRA (Figure 3 – closed symbols) in comparison to the monolithic matrices (Figure 3 – open symbols) are summarized in Figure 3 [1]. The DRA generally exhibits similar/increased fatigue thresholds and higher Paris Law slopes in comparison to the monolithic matrices upon which they are based [1].

Ultra-light materials based on Be also present some interesting combinations of properties. While Figure 1 illustrates that extra-ordinary combinations of specific stiffness and strength are possible with monolithic

Be, these materials often possess relatively low ambient ductility and fracture properties [4]. Compositing with Al and the production of Al-Be composites potentially provides extrinsic toughening approaches [5], which can provide a balance of properties.

Ultra-high strength (e.g. 2 GPa) bulk amorphous materials based on the Zr-Ti-Ni-Cu-Be system have recently been produced [6]. Preliminary fracture toughness [7-10] and ductility [10-13] data have been developed for this system. The bulk amorphous materials possess low ductility in tension [10-13] due to the initiation and propagation of intense localized shear. The addition of a refractory metal containing toughening phase has been shown to provide for multiple initiation and growth of such localized shear regions, thereby increasing the tensile ductility [14]. Little work has been conducted to determine the effectiveness of such regions on the fracture toughness of such systems.

This paper briefly reviews some ongoing work to illustrate the effects of extrinsic [5] toughening approaches on the fracture and fatigue behavior of DRA, Ultra-light materials based on Be, and toughened bulk metallic glass based on the Zr-Ti-Ni-Cu-Be system. In the DRA systems, the incorporation of unreinforced regions of different size/properties have been investigated using powder metallurgy approaches in order to determine the effectiveness of such additions on both the fracture and fatigue crack growth behavior. In the Al-Be system, powder metallurgy approaches have also been utilized to produce Al-Be composites containing 70% by volume Be. In the bulk metallic glass system, the refractory metal containing toughening regions have been produced by controlled devitrification of the metallic glass during solidification processing. The effects of such additions to the fracture and fatigue behavior of these various systems are presented.

2. MATERIALS

The DRA composite consisted of a 7093 powder metallurgy Al matrix reinforced with 15 volume % SiC particles, denoted 7093/SiC/15p DRA (nominal composition of 9 Zn, 2.2 Mg, 1.5 Cu, 0.14 Zr, 0.1 Ni, bal Al reinforced with 10 μm average size SiC particulates) provides the baseline material for the DRA reviewed in this work. "Toughened" DRA was produced at ALCOA via the addition of aluminum/aluminum alloy particles to the powder metallurgy blend at volume fractions of either 10% or 25%. The final product thus consists of DRA and discrete unreinforced Al regions. The global volume fraction of the reinforcement was kept at 15%, while the strength of the toughening region was varied independently in the manner described elsewhere [15]. The material test matrix is shown in Table 1. The behavior and properties of the "toughened" materials are compared to the materials with a conventional DRA structure (i.e. C1, C2, C3). The consolidated billets were extruded at 22:1 ratio to produce 1" x 3" bars, while Figures 4 (a-c) show the three major classifications of materials studied corresponding to the descriptions provided in Table 1. All materials were heat treated to an overaged condition, T7E92, consisting of 490ºC/4 hrs/CWQ, followed by aging at 120ºC/24hrs + 150ºC/8hrs.

The Al-Be composites were produced by Brush Wellman Inc., Cleveland, Ohio. Prealloyed powders containing 62wt% Be were atomized and filtered to below 74 mesh (i.e. 120 – 150 μm). The powders were then cold isostatically pressed to 80% density, degassed, and extruded at 10:1 ratio at 454ºC, followed by annealing at 593ºC/24 hrs. The microstructure of the extruded Al-Be composite is shown in Figure 5.

Both 4 mm and 7 mm thick bulk metallic glass plates and composites were supplied by Howmet Corporation and were produced by solidification processing. The composition of the bulk amorphous alloy was, in at%, 12.0-12.9Ti, 9.3-9.5Ni, 11.9-12.0Cu, 23.8-26.5Be, and balance Zr. Oxygen contents were in the range 1350 – 1600 ppm, respectively [7,8,12,13]. X-ray diffraction and TEM analyses revealed the structure to be fully amorphous [7,8,12]. The "in-situ" toughened bulk metallic glass composites were obtained via dendritic growth of a beta-phase (Ti-Zr-Nb) grown during partial crystallization of a molten alloy during cooling. The remaining matrix was vitrified during solidification to produce the composite structure shown in Figure 6.

3. EXPERIMENTAL PROCEDURES

Fracture toughness testing was conducted in general accordance with ASTM E-399-90 on single edge notch bend specimens for all of the materials listed above. The DRA and toughened DRA utilized dimensions of 65 mm x 14 mm x 4 mm, the Al-Be composites utilized dimensions of 75 mm x 16 mm x 22 mm, and the bulk metallic glass (BMG) and BMG composites used dimensions of either 85 mm x 12 mm x 4 mm or 95 mm x 14 mm x 7 mm. In addition, the BMG specimens were also tested in the notched condition, with notch root radii varying from 65 μm to 250 μm, as reported elsewhere [7,8,13]. Fatigue precracking was conducted in general accordance with ASTM E-399-90, while toughness testing was conducted on an MTS servo-hydraulic testing machine. Load, load point displacement, and clip gage opening displacement were continuously monitored during the test.

Fatigue crack growth experiments for DRA and Al-Be composites were conducted using the MTS testing machine described above. Crack growth was monitored via the use of a foil gage (KRAK gage) bonded to the outer surface of the specimen. The samples were cycled at 20 Hz with a stress ratio of 0.1.

Fracture surfaces were examined in a Hitachi Field Emission Gun (FEG) scanning electron microscope (SEM) to characterize the predominant fracture mode and the fine-scale features on the fracture surface. Operating voltages were generally in the range 10-12 kV.

4. RESULTS AND DISCUSSION

4.1 *Microstructures*

The microstructures of the DRA/toughened DRA, Al-Be composite, and toughened BMG composite were shown in Figures 4,5,6, respectively. Fracture experiments were performed such that fracture propagated perpendicular to the extrusion direction in the DRA and Al-Be composites. The crack growth direction in the BMG and toughened BMG cast plates was perpendicular to the thickness of the original casting.

A: *Fracture and Fatigue Behavior of DRA/Toughened DRA*

Both the size and chemistry of the toughening phase affect the increase in toughness over that of the control DRA. The control DRA (i.e. C1, C2, C3) exhibited toughness in the range 19.0-20.8 MPa-$m^{1/2}$, while that of the SDP1 and SDP2 composites were 19.4 and 20.8 MPa-$m^{1/2}$, respectively. The peak toughness of the LDP1, LDP2, and LDP3 composites were 33.1, 30.4, and 23.3 MPa-$m^{1/2}$, respectively. The toughened DRA containing the small ductile phase reinforcements (i.e. SDP1 and SDP2) provided negligible toughening in comparison to that of the large ductile phases (i.e. LDP1, LDP2). Increasing the alloy content of the toughening phase (i.e. LDP3 vs. LDP1 or LDP2), while increasing the strength of the toughened composite [15,16] in comparison to that obtained in the material toughened with pure Al (i.e. LDP1, LDP2), did not produce as significant increases to the toughness as did the weaker, but more ductile large Al additions. Some of these differences in fracture behavior are related to the constrained flow and fracture behavior of the toughening phases, as demonstrated in other work [17,18].

The fatigue behavior of the DRA and toughened DRA were all similar except for the toughened DRA containing the large Al toughening regions. Figure 7 plots the fatigue crack growth behavior at R=0.1 for the control DRA in comparison to the DRA toughened with the large Al regions, Figure 4c. Although the fatigue threshold of all of the materials tested was similar, the fatigue crack growth characteristics of the toughened DRA shown in Figure 7 are significantly different. Comparison of the crack growth data to the microstructure encountered during fatigue (c.f. Figure 4c) revealed that significant crack deceleration occurred as the fatigue crack approached and entered the large ductile Al regions. Upon exiting these regions, the crack growth rate in the DRA regions was similar to that of the control material, until the next toughened region was encountered, as shown in Figure 7. The higher strength toughening regions did not significantly change the fatigue crack growth characteristics from that exhibited by the control DRA, although fracture of the high strength toughening regions was often along grain boundaries [16] and this may have compromised the fatigue behavior of the toughening phases in those specimens.

B: *Fracture and Fatigue Behavior of Al-Be Composites*

The toughness of monolithic polycrystalline Be is in the range 8-13 MPa-$m^{1/2}$ [4] on both cast/extruded as well as powder metallurgy produced material. The addition of 30 volume % Al in the extruded powder metallurgy product tested presently significantly increases the fracture toughness, as shown by Table 2. Fracture surface analyses revealed a combination of ductile rupture of the Al with brittle fracture of the Be. The fracture toughness values were relatively unaffected by changes in test temperature over the range -125ºC to 225ºC at the testing rates specified by ASTM E-399-90.

The fatigue behavior of the extruded Al-Be composites is also summarized in Table 2 and is accompanied by literature data on both pure Al [19] as well as monolithic Be [4, 20]. Although the monolithic Be has a lower toughness than any of the materials tested, it exhibits a somewhat higher fatigue threshold. The fatigue crack growth rate accelerates rapidly as static modes of fracture intervene near the toughness of Be. In this regard, the fatigue behavior of the Al-Be composites represents an improvement over that of the monolithic Be. Paris law slopes less than 2 were observed for the composite, in comparison to that of 3.8 for the pure Al and 9 – 21 for the pure Be. Fatigue crack growth in the composite extends over a much wider range of ΔK in comparison to both the pure Al and Be. This is due to the higher toughness of the composite in comparison to that of the Be in the latter case, and due to the early onset of net section yielding in the pure Al due to its very low strength, in the former case.

C: *Fracture Behavior of Bulk Metallic Glass and Toughened Bulk Metallic Glass*

The effects of changes in notch root radius on the toughness of the bulk metallic glass are shown in Figure 8. The values for toughness for fatigue precracked bulk metallic glass specimens are in the range 18 MPa-$m^{1/2}$ and no stable cracking was observed in these specimens. The toughness increases dramatically with an increase in notch root radius, as shown in Figure 8 [7,8,13]. As reviewed elsewhere [8], this increase in toughness with increase in notch root radius exhibited by the bulk metallic glass specimens reported presently far exceeds that exhibited by other structural materials. The potential sources of this large increase in toughness with increase in notch root radius are covered elsewhere [7,8,13]. Despite the general lack of tensile ductility in the bulk metallic glass, the presence of extensive shear banding at the notch significantly increases the toughness of the notched specimens, in contrast to that of the planar fracture surface exhibited by the fatigue precracked specimens. The fracture toughness of the fatigue precracked specimens is in general agreement with a model provided by Argon [21], which predicts toughness values in the range of those obtained presently.

The introduction of the toughening phase shown in Figure 6 produces R-curve behavior in the composite. The peak toughness measured on fatigue precracked specimens of the toughened bulk metallic glass was in the range 29.7 – 35.6 MPa-$m^{1/2}$ for tests conducted at room temperature. Analyses of the fracture surfaces revealed ductile behavior of the toughening ligaments. Work is continuing on this system to determine the effects of such toughening phases on the fatigue crack growth characteristics.

5. CONCLUSIONS

1. Significant toughness increases may be obtained in DRA materials via the use of extrinsic toughening approaches. The size and chemistry of the toughening regions are important considerations in the toughness attained. The fatigue crack growth behavior is also affected by the size and chemistry of the toughening regions. In this work, the use of large regions of relatively low strength Al was very effective in improving the fatigue performance, although this will reduce the strength of the material.

2. The Al-Be composites tested presently exhibited toughness values in excess of that of monolithic Be. Fracture occurred via ductile rupture of the Al with brittle fracture of the Be. The improved toughness exhibited by the Al-Be composites enabled the composites to be tested over a wider range of ΔK than that of the more brittle Be. Fatigue thresholds were greater than that exhibited by the pure Al, although slightly lower than that reported for pure Be.

3. The fracture toughness of bulk metallic glass is dramatically affected by changes in the notch root radius. Fatigue precracked specimens exhibited values in the range 18 MPa-$m^{1/2}$, while increasing the notch root radius increased the toughness to values in excess of 100 MPa-$m^{1/2}$. The incorporation of toughening phases in the bulk metallic glass produced R-curve behavior in the fatigue precracked specimens, and increases in toughness to 29.7 – 35.6 MPa-$m^{1/2}$.

ACKNOWLEDGEMENTS

The authors acknowledge the support of various agencies and companies for this work. The work on DRA was supported by Ohio Aerospace Institute and ALCOA with supply of materials by ALCOA and Warren Hunt. The Al-Be composites were supplied by Brush Wellman, Inc. and Mark Svilar with support from ONR-N00014-99-1-0237. The work on bulk metallic glass was partly funded by AFOSR-AASERT-F49620-96-1-0228, Howmet Corporation, Reference Metals Company, and the DARPA SAM program. Supply of bulk metallic glass/composite materials and useful discussions with W. Johnson and Howmet are gratefully acknowledged.

TABLE 1
MATERIAL TEST MATRIX FOR DRA AND TOUGHENED DRA

	Material ID	Type of Ductile Phase Addition	Quantity (vol. %)	Discrete Ductile Phase in Product?
"Control DRA"	C1	None	N/A	No
	C2	commercial purity Al powder	10%	No
	C3	commercial purity Al powder	25%	No
"Small Ductile Phase"	SDP1	small c.p. Al - low strength	10%	Yes
	SDP2	small c.p. Al - low strength	25%	Yes
"Large Ductile Phase"	LDP1	large c.p. Al -low strength	10%	Yes
	LDP2	large c.p. Al - low strength	25%	Yes
	LDP3	large alloyed Al - high strength	10%	Yes

TABLE 2
FRACTURE AND FATIGUE BEHAVIOR OF Al-Be COMPOSITES, PURE Al, PURE Be

Material	K_{Ic} (MPa√m)	ΔK_{th} (MPa√m)	Paris slope
Al [19]	> 45	< 2.5	3.8
Be [4, 20]	8-13	< 8.8	9-21
Al-Be	20.3	5	< 2

6. REFERENCES

1. Lewandowski, J.J. (2000) Comprehensive Composite Materials, A. Kelly and C. Zweben, eds., Volume 3 – Metal Matrix Composites, Elsevier, 151.
2. Miracle, D.B. (2001) *Journal of Metals*, 53(4), 12.
3. Hunt, W.H. (2000) Comprehensive Composite Materials, A. Kelly and C. Zweben, eds., Volume 3 – Metal Matrix Composites, Elsevier, 701.
4. Lemon, D.D. and Brown W.F. (1985) *Journal of Testing and Evaluation,* JTEVA, 13(2), 152.
5. Ritchie, R.O. (1988) *Materials Science and Eng.,* A103, 15.
6. Peker, A. and Johnson, W.L. (1993) *Appl. Phys. Letters,* 63, 2342.
7. Lowhaphandu, P. and Lewandowski, J.J. (1998) *Scripta Metallurgica et Materialia*, 38(12), 1811.
8. Lewandowski, J.J. (2001) *Materials Transactions – JIM*, 42(4), 633.

9. Gilbert, C.J., Ritchie, R.O., and Johnson, W.L. (1997) *Appl. Phys. Letters,* 71, 476.
10. Liu, C.T., Heatherly, L., Easton, D.S., Carmichael, C.A., Schniebel, J.H., Chen, C.H., Wright, J.L., Yoo, M.H., Horton, J.A., and Inoue, A. (1998) *Metallurgical and Materials Trans. A,* 29A, 1811.
11. Bruck, H.A., Christman, T., Rosakis, A.J., and Johnson, W.L. (1994) *Scripta Metall.,* 30, 429.
12. Lowhaphandu, P., Montgomery, S.L., and Lewandowski, J.J. (1999) *Scripta Metall. et Materialia*, 41, 19.
13. Lowhaphandu, P., Ludrosky, L.A., Montgomery, S.L., and Lewandowski, J.J. (2000) *Intermetallics,* 8, 487.
14. Johnson, W.L. (2000) Personal Communication, California Institute of Technology.
15. Ellis, L.Y., Lewandowski, J.J., and Hunt, W.H. (1996) Layered Materials for Structural Applications, JJ Lewandowski, CH Ward, MR Jackson, and WH Hunt, eds.), MRS Proceedings – Volume 434, MRS, Pittsburgh, PA, 213.
16. Ellis, L.Y. (1998) Ph.D. Thesis, Case Western Reserve University, Cleveland, OH.
17. Lesuer, D.R., Syn, C.K., Sherby, O.D., Wadsworth, J., Lewandowski, J.J., and Hunt, W.H. (1996) *International Materials Reviews,* 41, 169.
18. Osman, T.M. and Lewandowski, J.J. (1996) *Metall. and Materials Transactions A,* 27A, 3937.
19. Kapp, J.A., Duquette, D.J. and Kamdar, M.H. (1986) *Journal Eng. Mater. Tech..,* 108, 37.
20. Shabbits, W.O. and Logsdon, W.A. (1973) *Journal of Testing and Evaluation,* 1(2), 110.
21. Argon, A.S. and Salama, M. *Mater. Sci. Eng.,* 23, 219.

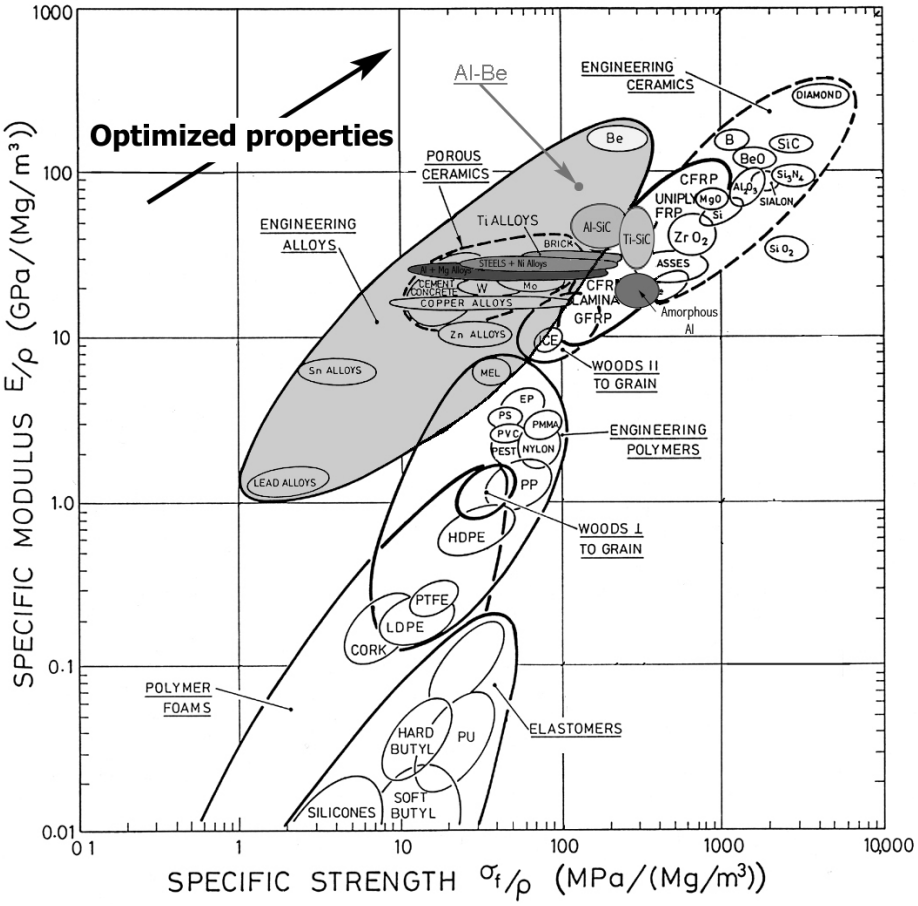

Figure 1: Modified Ashby plot of specific modulus vs. specific strength

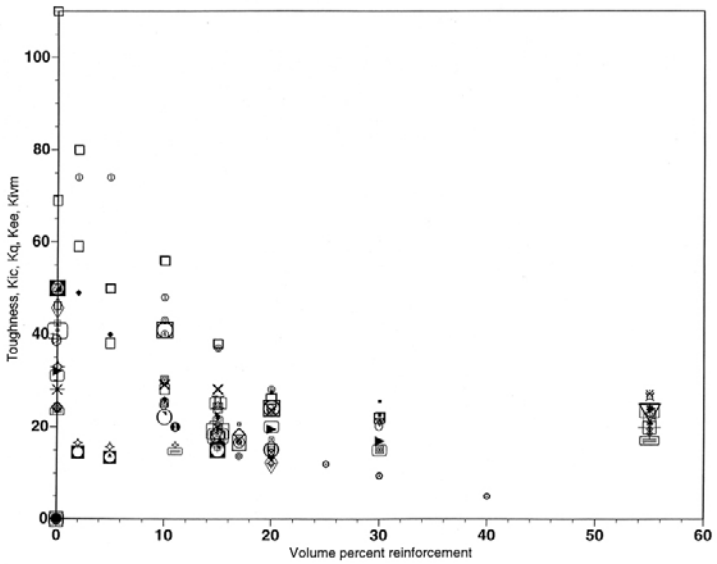

Figure 2: Effects of particulate reinforcement additions on toughness of DRA [1]

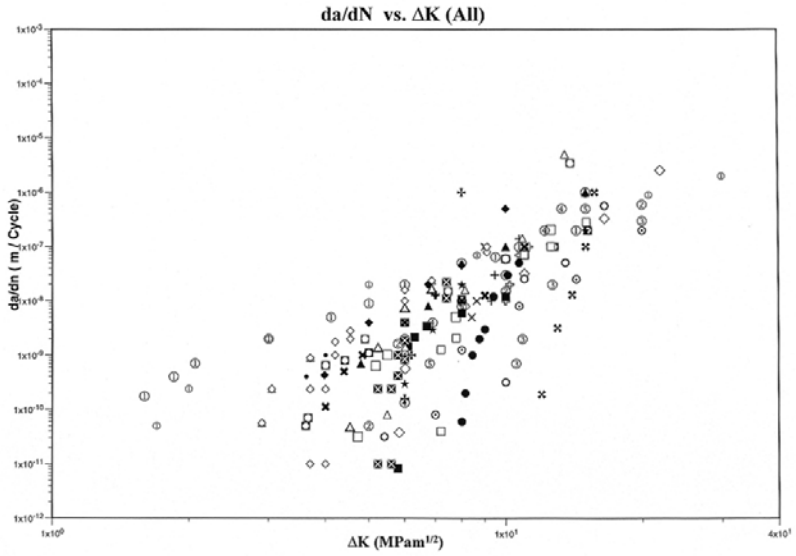

Figure 3: Fatigue crack growth behavior of monolithic (open symbols) and DRA (closed symbols) [1]

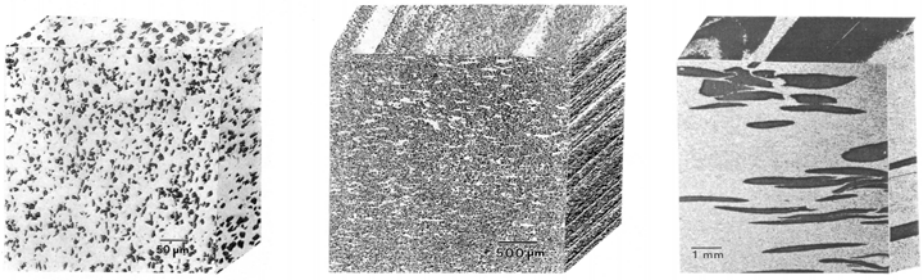

a) b) c)

Figure 4: 3D structures of DRA / toughened DRA a) "Control" (C1, C2, C3); b) SDP-DRA; c) LDP-DRA [15]

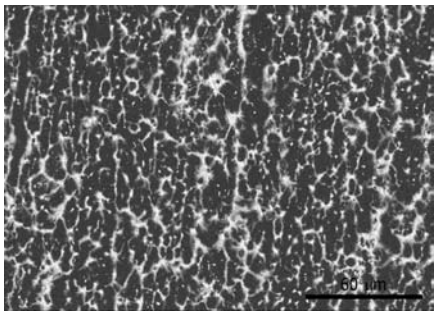

Figure 5: Extruded Al-Be composite

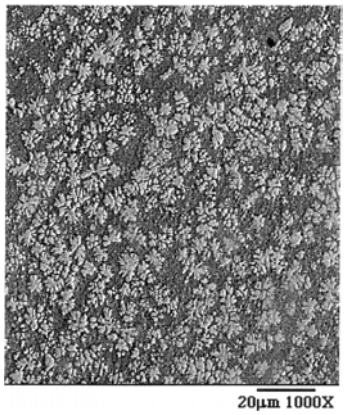

Figure 6: Toughened BMG microstructure [14]

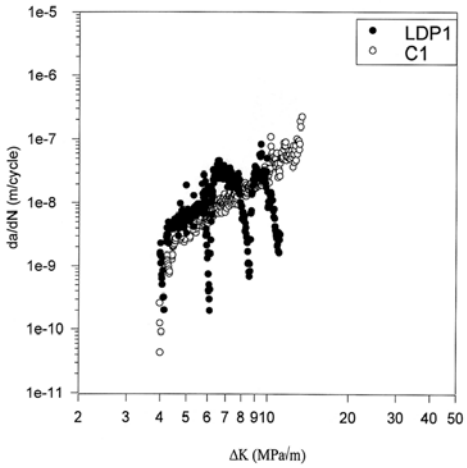

Figure 7: Fatigue crack growth behavior of control (C1) DRA vs. toughened (LDP1) DRA [1,16]

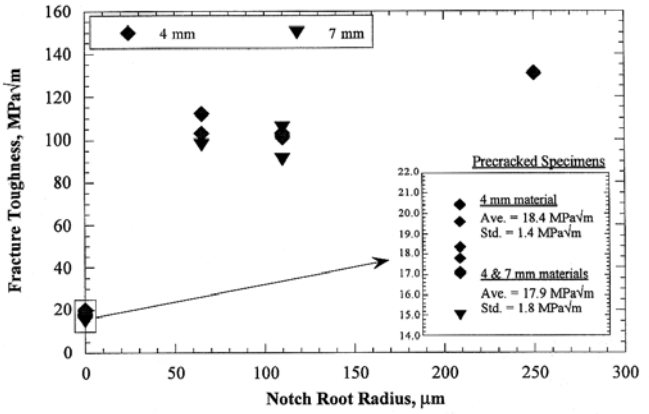

Figure 8: Effects of changes in notch root radius on toughness of bulk metallic glass [7,8,13]

ORAL REFERENCE: ICF10 0176OR

FRACTURE AND FATIGUE CRACK GROWTH FOR MICRO-SIZED SPECIMENS

K. Takashima and Y. Higo

Precision and Intelligence Laboratory, Tokyo Institute of Technology,
4259 Nagatsuta, Midori-ku, Yokohama 226-8503, Japan.

ABSTRACT

Fracture and fatigue tests were carried out on micro-sized specimens prepared from an electroless deposited Ni-P amorphous alloy thin film using a newly developed mechanical testing machine, and the size effects on the fracture and fatigue crack growth behavior have been discussed. Cantilever beam type specimens (10 x 12 x 50 μm^3) with notches were prepared from a Ni-P amorphous thin film by focused ion beam machining. Fatigue crack growth tests were carried out in air at room temperature under constant load amplitude using the testing machine for micro-sized specimens. Fatigue crack growth resistance curves were obtained from the measurement of striation spacing on the fatigue surface. Once fatigue crack growth occurs, the specimens failed after several thousand cycles. This indicates that the fatigue life of micro-sized specimens is mainly dominated by crack initiation. Fracture tests were performed for the specimens with fatigue pre-cracks ahead of the notches. The plane strain fracture toughness, K_{IC}, value was not obtained since the criteria of plane strain were not satisfied for this specimen size. As the plane strain requirements are determined by stress intensity and yield stress of the material, it is rather difficult for micro-sized specimens to satisfy these requirements. Plane stress and plane strain dominated regions were clearly observed on the fracture surfaces and their sizes were consistent with those estimated by fracture mechanics calculations. It is necessary to consider the results obtained in this investigation when designing actual MEMS devices.

KEYWORDS

Micro-sized specimen, MEMS, Fracture, Fatigue, Amorphous alloy, Thin film, Size effect

INTRODUCTION

Micro-sized machines and microelectromechanical systems (MEMS) are expected to be applied to bio-medical and micro-photonics devices such as micro-catheters for brain surgery and optical switches for electro-optical communications. The size of the components used in such MEMS devices is considered to be in the order of microns, and the mechanical properties of such micro-sized materials are considered to be different from those of bulk (ordinary sized) materials. Therefore, the evaluation of mechanical properties including elastic modulus, tensile strength, fracture toughness and fatigue properties are essential for practical applications of such MEMS devices. To date, there have been several studies which investigate the mechanical properties of small sized materials [1-3]. In particular, fracture toughness and fatigue crack growth properties of micro-sized materials are extremely important to enable reliable design of actual MEMS devices. In our previous studies, we have developed a new

type mechanical testing machine for micro-sized specimens, which can apply small amount of static and cyclic loads to the specimens [4, 5], and have obtained fatigue life curves of micro-sized Ni-P amorphous alloy specimens [6]. In addition to fatigue life, fatigue crack growth property and fracture toughness are also important for designing reliable and long-term durable MEMS devices. In this investigation, fracture and fatigue crack growth tests have been performed on Ni-P amorphous alloy micro-sized specimens, and the size effects on the fracture and fatigue crack growth behavior have been discussed.

EXPERIMENTAL PROCEDURE

Material and Specimen Preparation

The material used in this investigation was a Ni-11.5 mass%P amorphous thin film electroless plated on an Al-4.5 mass%Mg alloy. The thickness of the amorphous layer was 12 μm and that of the Al-4.5 mass%Mg alloy substrate was 0.79 mm, respectively. A disk with a diameter of 3 mm was cut from the Ni-P/Al-Mg sheet by electro discharge machining. An amorphous layer was separated from the Al-Mg alloy substrate by dissolving the substrate with a NaOH aqueous solution. The amorphous thin film was fixed on a holder and two types of micro-cantilever beam specimens with dimensions of 10 (B) x 12 (W) x 50 (L) μm^3 were cut from the amorphous layer by focused ion beam machining. This specimen size is equivalent to approximately 1/1000 of ordinary sized bending specimens. Figure 1 show a specimen prepared by the above procedures.

Testing Machine

Fatigue crack growth and fracture tests were carried out using a newly developed fatigue testing machine for micro-sized specimens. Figure 2 shows a block diagram of the fatigue testing machine. A magnetostrictive device is used as an actuator, which is able to produce displacements upto ±10 μm with an accuracy of 5 nm, and the maximum response frequency of cyclic displacement is 100 Hz. The end of the actuator is connected to a metal shaft and a diamond tip of 5 μm in radius is attached to the other end of the shaft. The displacement of the actuator is measured by a laser displacement meter with an accuracy of 5 nm and the displacement signal is used as feed back control. The micro-sized specimen is set in a specimen holder and the holder is placed on a load cell as shown in Fig. 2. Small amount of displacement is applied to the specimen through the diamond tip. The amount of load applied to the specimen is measured by a strain gauge type load cell with a load resolution of 10 μN that is set under the specimen. The horizontal location of the specimen stage can be moved to adjust the loading position precisely by a stepping motor with a translation resolution of 0.1 μm. Further details of the testing machine are described in our previous papers [4, 5].

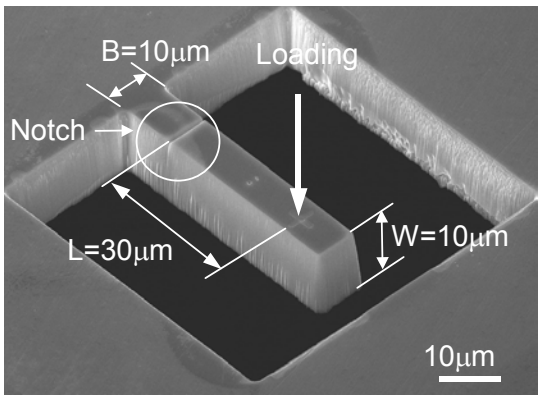

Figure 1: Scanning electron micrograph of micro-sized cantilever beam specimen prepared by focused ion beam machining.

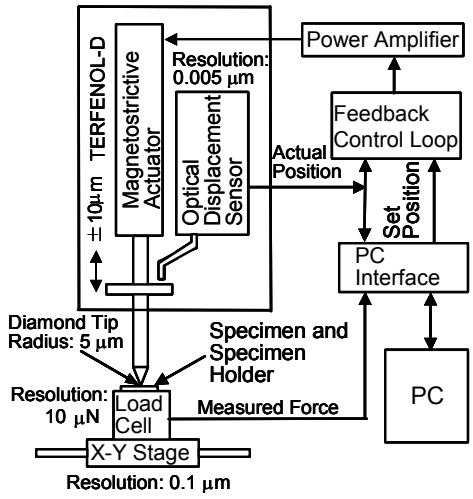

Figure 2: Block diagram of mechanical testing machine for micro-sized specimens.

Fatigue Test

In fatigue crack growth tests, notches with a depth of 3 μm were introduced into the specimens by focused ion beam machining. This notch depth is equivalent to $a/W = 0.25$, where a is notch length and W is specimen width. The width of the notch was 0.5 μm, and the notch radius is thus deduced to be 0.25 μm. The notch position was 10 μm from the fixed end of the specimen. The loading position is set at 40 μm from the fixed end of the specimen. Fatigue crack growth tests were performed in air at room temperature. Fatigue tests were carried out at a frequency of 10 Hz and a stress ratio, R ($R = P_{min} / P_{max}$, where P_{min} is the minimum load and P_{max} is the maximum load applied over the fatigue cycle) of 0.5 under constant load amplitude ($\Delta P/2$, where $\Delta P = P_{max} - P_{min}$) of 2 mN. Although the crack length was not able to be measured directly in this testing machine, the change in specimen compliance can be measured during fatigue tests. The initiation of crack growth was then determined by monitoring the specimen compliance.

Fracture Toughness Test

Fracture toughness tests were carried out on specimens with a notch (depth of 6 μm and notch radius of 0.25 μm) and those with a fatigue pre-crack (length of 3 μm) ahead of a notch (depth of 3 μm). In both the specimens, the total crack (or notch) length was adjusted to be a/W~0.5. The notch position is the same as in the specimens for fatigue crack growth tests. Fracture toughness tests were also carried out using the mechanical testing machine for micro-sized specimens.

RESULTS AND DISCUSSION

Fatigue Crack Growth Behavior

Figure 3(a) shows a scanning electron micrograph of the specimen appearance after a fatigue crack growth test at a stress ratio of 0.5. A fatigue crack initiates from the notch root. The crack did not start to grow immediately after applying cyclic load and the crack started to grow after approximately 20,000 cycles (this was confirmed by a compliance change of the specimen during fatigue test). This indicates that even the notch with root radius of only 0.25 μm is not regarded as a natural crack for micro-sized specimens. Figure 3(b) shows a high magnification of the center region of the fracture surface. The upper part of Fig. 3(b) is a notch and the bottom region is a final fracture surface featured by a vein pattern which is observed on monotonic fracture surface in amorphous alloys [7]. The region between the notch and the final fractured region is thus a fatigue surface. The fatigue surface is relatively flat and very fine equispaced markings are clearly observed on the fatigue surface. The spacing between these markings are approximately 30 nm near the notch and 80 nm near the final fractured region, and increased with the crack extension. It is not certain whether these markings correspond to striations, but these markings are aligned perpendicular to the crack growth direction and were not observed on the

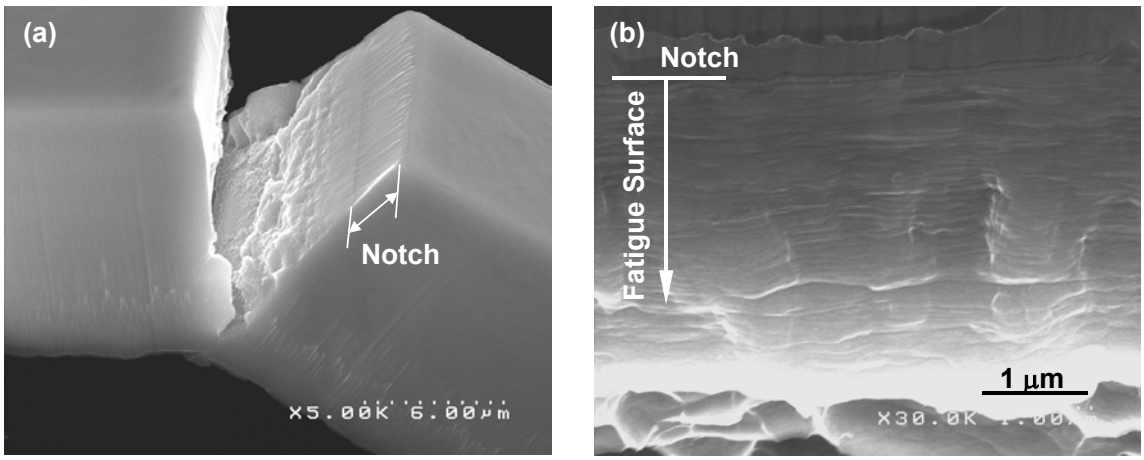

Figure 3: Scanning electron micrographs of micro-sized specimen after fatigue crack growth test. (a) close view near notch and fracture surface and (b) high magnification of fatigue surface.

fracture surface by static bending tests [8], so these markings are deduced to be striations. Such striations have also been observed on fatigue surfaces of metallic glass bulk specimens [9]. The formation of striations suggests that the crack has propagated by cyclic plastic deformation at the crack tip (i.e., blunting and resharpening of crack tip). Actually, shear bands which are considered to be formed by plastic deformation were observed on the side surface of the specimen near the crack tip. Consequently, the fatigue crack growth seems to be based on cyclic plastic deformation at the crack tip even in micro-sized amorphous alloys.

If the spacing between the striations on the fatigue surface is assumed to be equivalent to the fatigue crack growth rate for the specimens, a fatigue crack growth resistance curve can be obtained from the measurement of the striation spacings. Careful measurements of the striation spacings were made and fatigue crack growth rates (da/dN) as a function of applied stress intensity factor range (ΔK) (where $\Delta K = K_{max} - K_{min}$) were obtained. Stress intensity factor (K) is calculated based on the equation obtained for a single edge notched cantilever beam specimen [10]. Figure 4 shows the fatigue crack growth resistance curve at a stress ratio of 0.5. As once a crack started to grow, the specimen failed after only several thousand cycles for the micro-sized specimens, so ΔK_{th} (a stress intensity range at which a crack starts to grow) was not able to be determined. Also, the number of data points is only three, but this is due to the difficulty in the measurement of striation spacings since the spacing is only between 20 - 70 nm. Therefore, It is not certain whether a Paris-Erdogan relationship ($da/dN = A\Delta K^m$, where A and m are material constants) is applicable for these data.

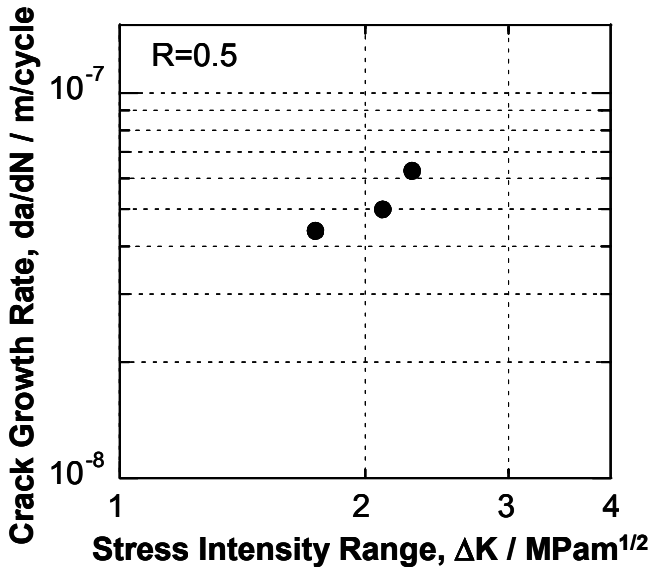

Figure 4: Fatigue crack growth resistance curve of micro-sized Ni-P amorphous alloy specimen.

The final fatigue fracture occurred at the crack growth rate less than 10^{-7} m/cycle. This crack growth rate is much lower compared to that of ordinary-sized specimens. This means that once a fatigue crack starts to grow then the fatigue fracture occurs only after several thousands of cycles. Therefore, the fatigue life of micro-sized specimens is mainly dominated by crack initiation. This also suggests that even micro-sized surface flaws may be an initiation site of fatigue crack growth and this will shorten the fatigue life of micro-sized specimens.

Fracture Toughness Tests

Figure 5 shows typical load - displacement curves for the specimens with a notch only and with a fatigue pre-crack. The fracture behavior is different between these two specimens. The specimen with a notch only fractured in a brittle manner, while the specimen with a fatigue pre-crack fractured in a ductile manner. The maximum load of the specimen with a notch only is approximately twice as that of the specimen with a fatigue pre-crack. This may be due to the difference in stress concentration at the crack

tip. The stress concentration arising at a fatigue crack tip is larger than that of the notch tip. This indicates that even the notch with a root radius of 0.25 μm is not able to be regarded as a crack for micro-sized specimens. In addition, the ion implantation caused by focused ion beam machining may change the mechanical properties around the notch tip. As the depth of ion implantation area is estimated to be less than 1 μm, the influence of ion implantation can be ignored by introducing a fatigue pre-crack of more than 1 μm in length. Therefore, it is essential for evaluating fracture toughness to introduce a fatigue pre-crack for the material used in this investigation.

Figure 6 shows a scanning electron micrograph of fracture surface of the specimen with a fatigue pre-crack. The slant fractured regions which appear to be shear lips are clearly observed near the side surfaces of the crack. The width of the region is approximately 3 μm. If these are shear lips, these areas should be plane stress dominated regions. The width of shear lip is expressed approximately as $2r_y/3$, where r_y is the size of plane stress plastic zone ($r_y = (K/\sigma_y)^2/\pi$, where K is the stress intensity factor and σ_y is the yield stress of the specimen) [11]. The calculated value of shear lip width at the maximum load is 2.8 μm (the value of σ_y = 2.0 GPa in this amorphous alloy thin film was quoted [12] in this calculation). These sizes are very close to the those of slant fractured regions in Fig. 6. Therefore,

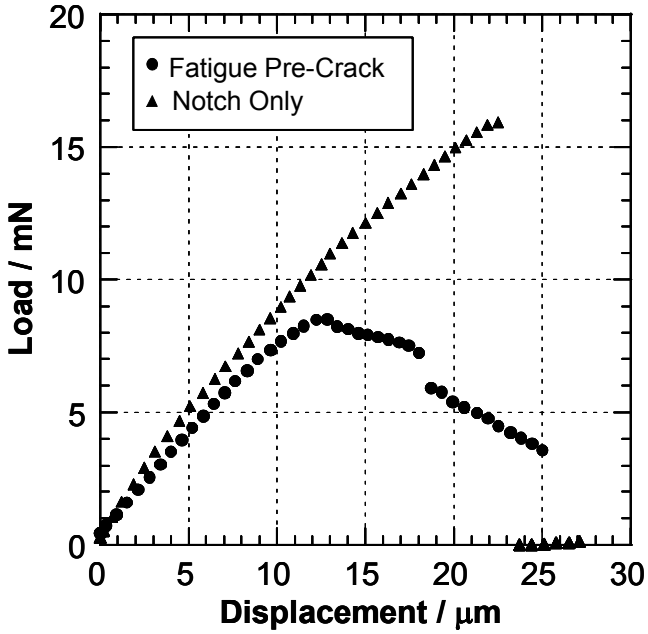

Figure 5: Load-displacement curves for micro-sized specimens with a notch only and with a fatigue pre-crack.

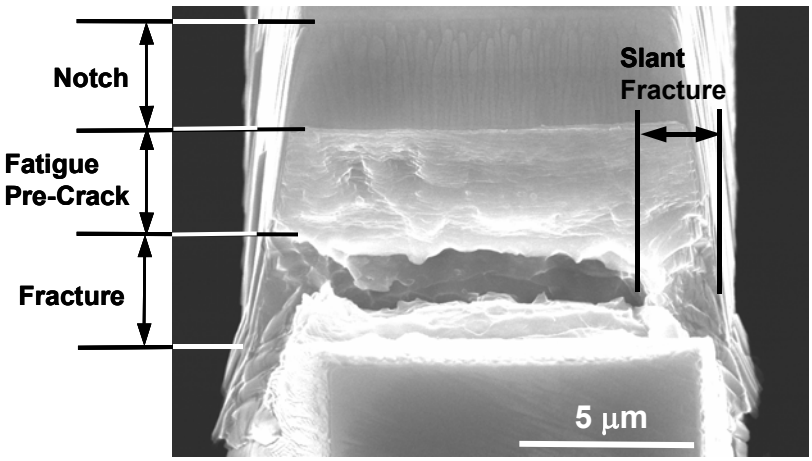

Figure 6: Scanning electron micrograph of fracture surface.

these slant fractured zones are plane stress dominated region and the flat region corresponds to plane strain dominated one. It is very interesting to note that there exists a plane strain region even in such micro-sized specimens.

As crack opening displacement was not able to be measured for this specimen, the crack initiation load was not able to be determined. The maximum load was then assumed to be the crack initiation load and this load was used to calculate a fracture toughness value. The total pre-crack length was measured from Fig. 6. The calculated provisional fracture toughness values (K_Q) for the specimen with fatigue pre-crack is 7.3 MPam$^{1/2}$. However, this value is not a valid plane strain fracture toughness values (K_{IC}), as the criteria of plane strain requirements (a, W-a, $B > 2.5\ (K_Q/\sigma_y)^2$) were not satisfied for this specimen size. As the plane strain requirements are determined by K and σ_y, it is difficult for micro-sized specimens to satisfy these requirements. Consequently, another criterion such as J integral might be required to evaluate fracture toughness of such micro-sized specimens.

CONCLUSIONS

Fatigue crack growth and fracture toughness tests have been performed on micro-sized Ni-P amorphous alloy specimens. Once fatigue crack growth occurs, the specimens failed after several thousand cycles. This indicates that the fatigue life of micro-sized specimens is dominated by crack initiation. This also suggests that even a micro-sized surface flaw may be an initiation site of fatigue crack and this will shorten the fatigue life of micro-sized specimens. It is essential for evaluating fracture toughness to introduce a fatigue pre-crack even for micro-sized specimens. The plane strain fracture toughness, K_{IC}, value was not obtained since the criteria of plane strain were not satisfied for this size of specimens. As the plane strain requirements are determined by stress intensity and yield stress of the material, it is rather difficult for micro-sized specimens to satisfy these requirements. Plane stress and plane strain dominated regions were clearly observed on the fracture surfaces and their sizes were consistent with those estimated by fracture mechanics calculations.

REFRERNCES

1. Shrape, Jr., W. N., Yuan, B. and Edwards, R. L. (1997) *J. Microelectromechanical Systems*, **6**, 193.
2. Ballarini, R., Mullen, R. L., Yin, Y., Kahn, H., Stemmer, S. and Heuer, A. H. (1997) *J. Mater. Res.* **12**, 915.
3. Sato, K., Yoshioka, T., Ando, T., Shikada, M. and Kawabata, T. (1998) *Sensors and Actuators A: Physical*, **70**, 148.
4. Takashima, K., Kimura, T., Shimojo, M., Higo, Y., Sugiura, S. and Swain, M. V. (1999). In: *Fatigue '99 (Proc. 7th Int. Fatigue Cong.)*, pp. 1871-1876, Wu, X-R. and Wang, Z-G., (Eds). Higher Education Press, Beijing.
5. Higo, Y., Takashima, K., Shimojo, M., Sugiura, S., Pfister, B. and Swain, M. V. (2000). In: *Materials Science of Microelectromechanical Systems (MEMS) Devices II*, pp. 241-246, deBoer, M. P., Heuer, A. H., Jacobs, S. J. and Peeters, E., (Eds). The Materials Research Society, Pennsylvania.
6. Maekawa, S., Takashima, K., Shimojo, M., Higo, Y., Sugiura, S., Pfister, B. and Swain, M. V. (1999) *Jpn. J. Appl. Phys.*, **38**, 7194.
7. Misknf, J., Csach, K., Ocelik, V. and Duhaj, P. (1997) *Mat. Sci. Eng.*, **A226-228**, 883.
8. Ichikawa, Y., Maekawa, S., Takashima, K., Shimojo, M., Higo, Y. and Swain, M. V. (2000). In: *Materials Science of Microelectromechanical Systems (MEMS) Devices II,* pp. 273-278, deBoer, M. P., Heuer, A. H., Jacobs, S. J. and Peeters, E., (Eds). The Materials Research Society, Pennsylvania.
9. Gilbert, C. J. and Ritchie, R. O. (1997) *Appl. Phys. Lett.*, **71**, 476.
10. Okamura, H. (1976). *Introduction to Linear Fracture Mechanics*, Baifukan, Tokyo, (in Japanese).
11. Knott, J. F. (1976). *Fundamentals of Fracture Mechanics*, Butterworths, London.
12. Morita, A., Takashima, K. and Higo, Y., to be published.

ICF1001043OR

FRACTURE AT COMPRESSION

R. V. Goldstein

Institute for Problems in Mechanics,
Russian Academy of Sciences,
Prospect Vernadskogo, 101-1
117526, Moscow, Russia

ABSTRACT

Fracture processes under compressive loading are considered from two points of view: 1) specific fracture mechanisms at compression and their influence on the material strength and fracture resistance; 2) an influence of the geometric constraints on the stress-deformation state and fracture conditions of bodies (natural objects) with cracks and cracklike faults (in particular, effects of a crack surfaces contact, friction, loading hystory; features of thin bodies fracture).

KEYWORDS

Compression, microstructure, crack, strength, fracture resistance, friction, loading hystory, thin bodies

INTRODUCTION

Fracture at compression is a rather complex process which occurs by combining some features of fracture at tension and shear complicated by an influence of the microstructure and geometric constraints. The observed relations between the real compressive and tensile strengthes can not be described by classical fracture criteria. To overcome this difficulty Griffith suggested to take into account a cracklike defect behaviour under compression. The theory predicted that the ratio of the compressive strength to tensile one equals 8. This result is not confirmed by experimental data. A new stage of studying the fracture at compression started at the early 60^{th} and was associated with a more detailed analysis of micro- and macromechanisms of fracture at compression. Possibilities of microcrack nucleation near the material nonhomogeneities or near existing cracks, crack surface contact accompanied by friction and dilation effects, and, finally, crack surfaces overlapping in thin bodies create diversity of schemes and forms of fracture at compression. The paper is aimed to demonstrate some characteristic features of fracture at compression and models which enable to describe and predict the observed processes. The models are often related to nonstandard using or generalization of fracture mechanics concepts.

FRACTURE AT COMPRESSION

Macrostrength and microfracture

Brittle fracture in bulk under compression is as a rule related to redistribution of general compressive stresses into local tensile ones at the material structural or textural nonhomogeneities (such as pores, inclusions, etc). The fracture mechanism can be illustrated by the classical example: uniaxial compression of an elastic plane with a single circular hole (pore) by the stresses (σ). The tensile stresses occur at a part of the hole contour and attain their maximum value, σ, at the points of the hole contour intersection with its diameter parallel to the compression direction. The tensile stresses act in the transverse direction and lead to nucleation and growth of two cracks emanating from the hole contour. This fracture scheme was, in particular, observed on the prisms of natural quartz single crystals free of cleakage with a small central cylindrical hole drilled normal to the largest face [1]. The crack growth is stable since an influence of local tension decreases as the crack length increases.

In case of a real porous material each pore is a potential source of microcrack nucleation in the direction of sample compression. The distinct difference from the case of a single hole is related to the transition from the initial stage of the stable crack growth to the stage of the unstable coalescence of cracks growing from the adjacent pores. This process leads to formation of a series of macrocracks which separate the sample on the layers parallel to the compression direction if a friction influence was eliminated along the contact surfaces of the compressed sample. The compression level at the attaing the crack instability determines the material compressive strength, σ_{st}^{c}. The process of the microcrack growth is adjusted by the material fracture toughness at the scale of their sizes. In turn, the microcrack size when it becomes unstable depends on the material porosity. As a result the compressive strength of a porous material depends on both the porosity and microfracture toughness. A quantitative model taking into account the aforedescribed mechanism of porous material brittle fracture under uniaxial compression was developed in [2]. The theoretical dependence of the compressive strength on porosity fitted the available and authors own experimental data for a series of brittle effusive rocks. Note, that a close model was suggested to describe the similar fracture mechanism of fracture of ceramics under compression [3].

One of the key points of the aforedescribed fracture mechanism was associated with occuring an instability stage of microcrack growth in the compression direction. However, this process can be arrested by compression in the transverse direction at a certain length of an elongated cracklike defect formed by an array of pores linked by microcracks. In turn, this cracklike defect causes redistribution of the stresses in a material. An analysis shows that a process of nucleation and growth of another adjacent similar cracklike defect can be initiated near the end zones of this cracklike defect, etc. This mechanism leads to formation of an ordered system of cracklike defects (structure of fracture) under bi-axial compression. An approach to modeling formation of ordered crack (or cracklike defect) systems (structures of fracture) was suggested in [4,5] and [6] and summarized in the review paper [7]. Note, that formation of structures of fracture represents an often observed mechanism of fracture transition from one scale to another (see, [7]).

Ordered crack systems are formed not only at brittle fracture under compression. Let us illustrate this possibility for a porous material. Again consider a plane with a circular pore under uniaxial compression. Remind, that the shear stress concentration occurs at the points of the pore contour interaction with the diameter transverse to the compression direction. The maximal shear acts along the planes inclined by the angle $\pm\pi/4$ to this diameter. In case of shear fracture mechanism slip lines can occur along these directions. As a result a net of cracklike elements of rhombic shape will be formed between the adjacent pores. Such structure of fracture was observed on the plates of a material of high plasticity [8] and modeled (see [7]).

Microcracks along with the considered microstructural nonhomogeneities can initiate macrofracture formation in the direction of compression. The basic element of the appropriate well known mechanism (see, e.g. [9-15]) is a microcrack inclined to the compression direction. Slipping effects along a contact zone of the microcrack surfaces lead to formation of the wing cracks.

One of the possibilities of macrofracture occuring is associated with the wing cracks coalescence. Usually

the compressive strength is evaluated within the framework of this mechanism for a 2D model. An experimental and theoretical study of the 3D effects was performed in [16]. Experiments on uniaxial compression of transparent samples with inner diskshaped cracks demonstrated that macrocrack formation can only result from the interaction of properly oriented and closely located wing cracks. The critical distance for two coplanar cracks is of order four crack radii. This experimental observation was also explained within the framework of a model of 3D wing crack interaction suggested in [16] using the far field asymptotics of the crack induced stress field given in [6].

Another possible scenario of macrofracture initiated, in particular, by wing cracks can be related to the occuring of compression-shear bands formed by ordered (echelon like) wing crack systems [15]. In turn, the compression-shear bands can initiate inner or surface buckling. Note, that mechanisms and models of global compression fracture were summarized in [15] and used for an analysis of the scale effects at compressive fracture.

Brittle fracture of samples by macrosplitting occurs in conditions of uniform compression in the absence of confining stresses at the end surfaces of a sample. The confining stresses, as a rule, cause a transition of the brittle macrofracture scheme from splitting to inclined fracture. However, similar transition is also observed under compression without confining stresses if material fracture is accompanied by some plastic effects (see, e.g. [17]). Experiments on cementitious materials [17] demonstrated both the splitting mode for pure cement samples and inclined (shear) mode for concrete ones under the same loading conditions. To clarify the mechanism of the fracture mode transition, the tests were performed on samples made from hydrated cement paste with filling of different grade [18]. The results of the experiments and modeling showed that in this case the macrofracture mode under uniaxial compression was adjusted by the microplastic behavior of the material. Splitting was a result of formation and growth of cracklike macrofaults with a long process zone being formed because of the material high microplasticity. On the other hand, in case of a short process zone (in microscopically brittle materials) growth of a macrocrack inclined to the compression direction and shear fracture were caused by an influence of a lateral surface of a sample.

Macrocrack with partial contact of its surfaces

The aforegiven analysis was related to the global fracture at compression based on the mechanisms of multiple microcracking. Now let us consider some features of deformation and fracture of an elastic body with a macrocrack or cracklike cavity at compression.

First, for simplicity we will illustrate the effects for a homogeneous, isotropic, linear elastic space with a plane crack. The influence of a body boundary and the behavior of thin bodies will be discussed later on.

Consider a plane crack-cut under compression transverse to the crack plane. Then the crack surfaces contact occurs along the whole crack domain when an analysis being performed within the framework of the linear elastic fracture mechanics. Indeed, in opposite case the stress intensity factor, K_I, becomes negative and, hence, the crack surfaces overlapping needs to occur. The full crack closure is a consequence of the impossibility of crack surfaces overlapping in bulk [19,20].

More complex behavior is inherent to cracklike cavities. For instance, consider a cracklike cavity of the cross-section Ω in the plane $x_3 = 0$ of the x_1, x_2, x_3 coordinate system. The distance between the cavity surfaces, $w_0(x_1,x_2)$ is a single-valued function of (x_1,x_2). The initial cavity opening, $w_0(x_1,x_2)$, is small as compared with the characteristic sizes of the domain Ω. A partial contact of the cavity surfaces can occur under the compressive loading at infinity and/or in bulk. The problem under consideration was analyzed in [21] within the assumption on the friction absence in the contact region. The asymptotics of the solution near an arbitrary smoothness point of the boundary separating the contact region and the opening region was obtained for a rather general geometry of the cavity surfaces. As a result the conditions were obtained which enable to determine a priori, without solving the problem, the regions of cavity surfaces where their contact is impossible. We will illustrate these conditions for the cavities with elliptic cross-sections. The initial cavity opening has the following $w_0(x_1,x_2) = b\,(1-x_1^2/a_1^2-x_2^2/a_2^2)^{\alpha/2}$. The process of contact region formation starts at the cavity's boundary (in plane $x_3 = 0$) if $\alpha \geq 1$, and inside the cavity if $0 < \alpha < 1$. For this specific

geometry of the cavities the contact regions were also studied numerically in [22], where a boundary variational method was suggested for solving the 3D problems of cracks and cracklike cavities with contact regions without friction. Note, that a series of qualitative properties of the problems solution were established in [21,23]. On the basis of these properties another nonvariational numerical method for solving the problems was developed. The method enables to construct a sequence of approximate solutions which monotonically tend to the exact solution from one side.

Note, that in some cases the unilateral constraints of the cavity surfaces displacements related to a possibility of their contact are replaced by the condition implying that these surfaces drawing together $w(x_1, x_2)$ needs to be nonless than the values of a given function $u_0(x_1, x_2) > 0$ such that $w(x_1, x_2) \geq u_0(x_1, x_2)$. For instance, this condition is inherent to the statement of the problem on evaluation of the drawing together of the surfaces of a mine (see, [22]). The regions where the strict inequality or equality in the above condition are fulfilled need to be determined.

Having the solution of the appropriate elasticity problem with unknown boundaries separating the fulfillment the conditions in the form of equalities and inequalities one can calculate the stress state near the cavity (crack) surfaces and analyze possible fracture mechanisms and conditions.

We would like to pay attention to a model of fracture and stability near a mine suggested in [24]. A model is based on the consepts of the LEFM. A mine is modeled as an elongated striplike narrow cavity in an elastic space such that really a 2D elasticity plane strain problem on a cavity of the characteristic height h and length ℓ ($h << \ell$) located transverse to the compression direction is considered. At the scale ℓ the mine can be modeled as an effective crack under compression with additional condition which admits the crack surfaces overlapping less than the half of the mine height (the outer problem). Evidently, the stress intensity factor, K_I, near the tip of this crack will be negative. Further, at the scale h one has an inner problem on a half-infinite mine of height h. The conditions of biaxial loading near its end section (the mine working face) are determined by the stress intensity factor of the outer problem. Solving the inner problem one can search for the characteristic regimes of fracture, rockburst and loss of stability of a mine. Examples of the analysis were given in [24]. An energetic approach based on a concept of a release of the energy stored in the rock massiff was also suggested for an analysis of the similar problems of mining engineering (see, e.g. [15]).

Macrocrack. Friction and loading hystory effects

We considered a partial contact of the cavity (crack) surfaces without friction under the compressive load normal to the plane $x_3 = 0$ along which the cavity is elongated. Friction between the cavity (or crack) surfaces within the region of their contact leads to some new effects in the deformation and fracture processes. In particular, the loading hystory and related stick-slip phenomena become to be essential. The general statement of the 3D problems was given in [25] and their analysis was performed in [25-29]. Some aspects of the crack problems with friction were considered in [30,31] for 3D case and in [32-35] for 2D case. For the sake of definiteness and simplicity consider a crack in the plane $x_3 = 0$ of an elastic space. Assume that the loads acting at infinity and (or) in bulk are slowly varying in dependence on a loading parameter θ (complex loading) such that the inertia effects are negligible. A crack surfaces interaction within the contact region obeys the Coulomb friction law: $F_{3i} = \rho\sigma\, V_i/V$, where ρ is the friction coefficient, $\sigma(x_1,x_2,\theta)$ is the normal stress (pressure), $V_i = \partial U_i/\partial\theta$ are the components of the slipping velocity, $U_i = U_i^+ - U_i^-$ are the components of the displacement jump ($i = 1,2$), $V = (V_1^2 + V_2^2)^{1/2}$. Note, that the sign in the right hand side of the friction law was chosen taking into account that the displacement jump is counted off from the upper surface of the crack-cut.

The problem is subdivided on symmetric and antisymmetric relative to the plane $x_3 = 0$ ones related to the normal displacement jump, U_3, and shear displacement jumps, U_1, U_2, respectively. It is possible to separate the initial problem in spite of its nonlinearity since the normal and shear components of the displacement jumps do not cause shear and normal stresses at the crack plane, respectively. Then the initial problem is solved sequentially. The contact region and distribution of the normal stresses $\sigma_{33}^{\pm}(x_1,x_2,\theta)$ in this region are determined within the framework of the symmetric problem (the normal problem). The antisymmetric problem (the shear problem) implies searching for the regions of slipping, $G_{s\ell}$, and sticking, G_{st}, where

$V_i \neq 0$ and $V_i = 0$, respectively, and the distribution of shear stresses in these regions at the known contact region and distribution of the normal stresses.

Note the essential feature of the crack problem with friction at the complex loading [25]. The sticking region is determined by the condition of vanishing the slipping velocity. Hence, two tipes of the sticking regions can occur: the sticking regions with zero and non-zero shear displacement jumps, $U_i = 0$ (i = 1,2) and $U_i \neq 0$ (i = 1 and/or 2), respectively. Occuring the sticking regions with the fixed shear displacement jump is related to a memory of the loading process. The loading process leads to the evolution of contact, slipping and sticking regions in dependence on the loading hystory. In turn, this evolution determines (through the stress intensity factors) occuring the crack limit equilibrium and its growth.

To solve the appropriate boundary value problem taking into account the loading hystory one needs to know some properties of the normal and shear problem solutions and additional conditions proved in [25, 27, 28]. First of all, the shear displacement jumps, U_1, U_2, are continuously differentiable functions of the loading parameter. The distribution of the shear displacement jumps and the slipping rates are uniguely determined at the end point of the given loading trajectory. Further, denote by $\sigma_{31}^0(x_1,x_2,\theta)$, $\sigma_{32}^0(x_1,x_2,\theta)$, $\sigma_{33}^0 = -\sigma(x_1,x_2,\theta)$ the loading trajectory. Then an increment of the shear displacement jumps δU_1, δU_2 can occur if it exists a point (x_1,x_2) within the crack region Ω such that $\delta\tau(x_1,x_2,\theta)\cos\gamma \geq \rho\delta\sigma(x_1,x_2,\theta)$ where $\tau = [(\sigma_{31}^0)^2 + (\sigma_{32}^0)^2]^{1/2}$, γ is the angle between the vectors $(\delta\sigma_{31}, \delta\sigma_{32})$ and $(\delta U_1, \delta U_2)$, ρ is the friction coefficient. An essential property of the solution is related to a possibility of the slipping continuation at the normal load decreasing, $(\partial\sigma/\partial\theta) < 0$ [27, Part II]. Indeed, it means that an increment of the displacement jumps and stress intensity factors can occur at the unloading stage if the boundary of the slipping region and the crack contour have common points. Hence, a crack can attain a limit equilibrium state at decreasing the normal load. This effect is associated with a possibility of a more fast decreasing of the friction force as compared to the shear load. Note, that this effect is inherent to the problem with friction. It was demonstrated in an explicit form for the problem on an annular crack in an elastic space under the action of a single compressive concentrated load acting at some distance from the crack plane [27, Part II). The properties of the slipping angle were studied in [28]. In particular, it was shown that the slipping angle near the zones of the positive pressure is a continuous function of the loading parameter both in the slipping region and during its extension into the sticking one. This property enables to write the initial nonlinear problem in the increments and to obtain a linear problem relative to the slipping angle increment. Then the slipping angle increment can be calculated by a step-wise procedure at the given slip line field and increments of the external loads.

The slipping process near the regions of the crack opening was also analyzed. It was shown that the slipping angle is not a continuous function near the boundary of the opening region. Hence, generally, two types of the regions were separated relative to the slipping regime: regions of the stable slipping (the slipping angle and slipping rate are continuous functions of the loading parameters) when the problem admits linearization and regions of the unstable slipping (infinitesimal variations of the external loads lead to finite increments of the slipping angle) where the problem does not admit linearization. Numerical algorithms for solving the normal and shear problems were suggested in [27,28] taking into account the aforedescribed properties and conditions determined by the asymptotic behavior of the solutions at the boundaries of the regions of the different types within the crack [25]. These conditions enable to search for the location of the unknown boundaries (in particular, the boundary of the slipping and sticking regions are determined by the condition that the solution needs to be nonsingular at this boundary [25]).

Several analytical and numerical examples demonstrating the efficiency of the suggested methods for solving the crack problems with friction at complex loading were given in [26-28]. In particular, the elliptic crack with interacting surfaces was analyzed in [26] under the uniform loading depending on the loading parameter. In this case the component of the shear displacement jump along each of the main axes of the ellipse only depends on the appropriare component of the shear stress. The slipping angle is independent on the coordinates x_1, x_2 and is determined by an ordinary differential equation of the first order as a function of the loading parameter. A geometric interpretation of the slipping regimes was suggested such that a slipping

cone can be constructed at each point of the loading trajectory. The cone determines the continuity of the slipping process and transition to the sticking state. The geometric interpretation enables before the problem solving to separate a possible slipping regime, a friction force direction and initial conditions at the transition from the sticking state to the slipping one. It is essential that the evolution of the far field is closely related to the processes of continuing loading or unloading at the crack such that the observations of the displacement and stresses far fields can be used for an analysis of a limit equilibrium of a crack. This effect can be used in geophysics.

Let us pay attention to an effect in a simple axisymmetric crack problem. A singular point (the crack center) exists in this problem. Neither displacement nor stress direction are not determined at this point. This circumstance leads to a qualitative effect in the problem with friction. Indeed, a finite sticking zone occurs near the crack center, e.g., at the classical loading trajectory: compression to the value σ and then axisymmetric shear τ (r).

Remarks. I. We considered the behavior of the plane cracks. The compression and friction effects essentially influence the conditions of the curvilinear cracks limit equilibrium and propagation.

Remind, that the contact zones can occur along a curvilinear crack even under uniform tension (e.g. for an arc crack of sufficiently large angle [36]).

Further, the stability of the trajectory of a slightly curved crack is influenced by the compressive loads acting along the initial nonperturbated crack direction. It is essential that the conditions of the stability are determined by a nonsingular term of stresses near the crack tip caused by this compressive load [37].

An analysis of the limit equilibrium of a curvilinear crack taking into account friction in the contact zones at complex loading was recently performed in [38].

II. Fracture at compression of bodies (media) with many cracks is complicated by the crack influence on the effective deformation characteristics of the object under consideration. The crack interaction leads to an induced deformation anisotropy, nonhomogeneity and irreversibility of deformations in the loading-unloading regime, as well as to essential dilatation effects both at compression and shear. These effects were observed experimentally and described theoretically (the references are given, e.g., in [39-41]). Note, that an induced nonhomogeneity causes redistribution of a stress state of a body [41]. For instance, longitudinal compressive deformations occur in a cracked plate at bending; the Euler critical load of a plate loss of stability is also changed for a cracked plate.

Geometric constraints influence the mechanisms of fracture at compression. Thin bodies

First, let us consider a specific mechanism of fracture at compression along a body surface or interface associated with formation and growth of a crack parallel to the surface (delamination in case of an interface). This fracture mechanism is, in particular, inherent to composites, e.g., layered systems and systems with coatings. An energetic approach was suggested in [42,43] (see also [44-46]) to search for the conditions of a dilamination limit equilibrium if its characteristic size is much larger than the thickness of a delaminated layer. According to this approach the energy balance is evaluated by modeling the delamination as a beam (or plate) rigidly clamped at its ends (contour). An asymptotic approach to the problem based on the method of the matched asymptotic expansions was suggested in [47,48]. This approach enables to make more precise the estimates given by the energetic approach by replacing the condition of rigid clamping on a condition of elastic clamping obtained in [47,48]. A similar condition for the 2D case was given in [49].

Effects of loss of stability and breakdown were also observed in systems with coatings (see, e.g., [50,51]). The systems based on polymer (polyethylene terephthalate) with a thin stiff coating (platinum or SiO_2) with a thickness of several nanometers were studied. The samples were loaded by uniaxial tension in the direction parallel to the interface. The fracture process of two stages was observed. First, a system of parallel cracks occured in the coating separating it on a series of strips. Then loss a stability and regular fracture of separate strips appeared under the action of a transverse compression of the deformed polymeric substrate. A model

of the process was also suggested in [50,51].

Possible mechanisms of loss of stability of surface layer on an elastic halfspace or a surface layer of an elastic halfspace with elasticity parameters variable through its thickness under the action of bi-axial compression caused by steady termal loading were studied in [52]. In particular, it was shown that if the substrate (half-space) is more compliant as compared with the surface coating then loss of stability will be accompanied by formation of concavities with a characteristic length essentially exceeding the coating thickness.

In thin bodies with elongated through crack (or cracklike defects) of characteristic length much larger than the body thickness one can observe a specific mechanism of fracture at compression associated with a possibility of crack surfaces overlapping [53-55]. For instance, consider a thin plate with a stright through crack under uniaxial compression transverse to the crack plane. The zone near the crack is more compliant than the initial plate. As a result the crack surfaces can be shifted in the direction transverse to the plate plane. Then an overlapping of the crack surfaces occur at least within the central part of the crack, while the zones of the compressive stress concentration will be localized near the crack edges. The fracture process in these end zones is adjusted by the value of the negative stress intensity factor. Different fracture schemes in the end zones are related to different ranges of the negative stress intensity factor. The aforedescribed fracture mechanism is inherent to the ice cover compression with ridge formation. It was also observed in special experiments performed on thin paraffin plates placed on a rubber substrate when a constraint of the plate displacements in the direction transverse to the plate plane was provided by a special glass plate fixed on a small distance from the paraffin one [53,54]. Models of the observed local fracture schemes were also suggested. Note, considering a crack with overlapping surfaces as a crack of compression one can generalize the LEFM concept for this case. In particular, one can introduce a critical value of the negative stress intensity factor which characterizes the ice cover resistance to the ridge growth, K_r, [53]. The estimates and experiments on thin ice plates showed that the modulus of K_r exceeds the ice fracture toughness K_{Ic} on an order of value. The concept of cracks of compression was also used for description and classification of the regimes of ice cover fracture by icebreaker [56,57].

The aforediscussed features of fracture are inherent to both static and dynamic compression. Additional effects of dynamic compression were considered in the recent review [58].

References

1. Martin, R.J. (1972) *J. Geophys. Res.*. 77, N 8, 1406.
2. Goldstein, R.V., Ladygin, V.M., Osipenko, N.M. (1974) *Fizico-technicheskie problemy razrabotki poleznych iskopaemych.* N 1, 3.
3. Evans, A.G., Fu, Y. (1984). In: *Fracture in ceramic materials,* pp.56-88, Park Ridge, N.Y., *Noyes Publications*.
4. Goldstein, R.V., Osipenko, N.M. (1978) *Reports of the USSR Academy of Sci.*. 240, N 4, 829.
5. Goldstein, R.V., Osipenko, N.M. (1978) *Preprint N 110 IPM AN SSSR.* Moscow.
6. Goldstein, R.V., Kaptsov, A.V. (1982) *Mechanics of Solids.* N 4, 173.
7. Goldstein, R.V., Osipenko, N.M. (1999) *Mechanics of Solids.* N 5, 49.
8. Sobolev, G.A., Asatrjan, H.O. (1990) *Reports of the USSR Academy of Sci.*. 315, N 2, 345.
9. Brace, W.F., Bombolakis, E.G. (1963) *J. Geophys. Res.*. 68, N 12, 3709.
10. Hoek, E., Bieniawski, Z.T. (1965) *Int. J. Fract. Mech.*. 1, N 2, 137.
11. Cotterell, B. (1972) *Int. J. Fract. Mech.*. 8, N 2, 195.
12. Nemat-Nasser, S., Horri, H. (1982) *J. Geophys. Res.*. 87, N B8, 6805.
13. Kranz, R.L. (1983) *Tectonophys.* 100, N , 449.
14. Wang, E.Z., Shrive, N.G. (1995) *Eng. Fract. Mech.*. 52, N 6, 1107.
15. Bazant, Z.P., Planas, J. (1998) Fracture and size effect in concrete and other quasibrittle materials. *CRC Press LLC. N.Y.*.
16. Dyskin, A.V., Germanovich, L.N., Ustinov, K.B. (1996) *Proceedings, First Australasian Congress on Appl. Mech.-ACAM-96. The Institute of Engineers, Melbourne.* 1, 139.
17. Santiago, S.D., Hildsorf, H. (1973) *Cement and Concrete Research.* 3, N , 363.

18. Dyskin, A.V., Sahouryeh, E., Ustinov, K.B. (1996) *Proceedings, 2nd North American Rock Mechanics Symposium: Tools and Techniques in Rock Mech.-NARMS-96. Balkema. Rotterdam.* 2, 1611.
19. Barenblatt, G.I. (1959) *Appl. Math. Mech. (PMM).* 23, N 3, 434; N 4, 706; N 5, 893.
20. Barenblatt, G.I. (1962) *Adv. Appl. Mech.*. 7, 55.
21. Goldstein, R.V., Zhitnikov, Yu.V. (1986) *Appl. Math. Mech. (PMM).* 50, N 5, 826.
22. Balueva, A.V., Goldstein, R.V., Zazovski, A.F. (1984) *Fiziko-technicheskie problemy razrabotki poleznych iskopaemych.* N 6, 3.
23. Goldstein, R.V., Zhitnikov, Yu.V. (1988) *Part I. Mechanics of Solids.* N 4, 75.
24. Lin'kov, A.M., Petuchov, I.M., et al. (1976) A theory of protecting seams. Moscow: *"Nedra" Publishers*.
25. Goldstein, R.V., Zhitnikov, Yu.V. (1987) *Mechanics of Solids.* N 2, 141.
26. Goldstein, R.V., Zhitnikov, Yu.V. (1988) *Mechanics of Solids.* N 4, 126.
27. Goldstein, R.V., Zhitnikov, Yu.V. (1988) *Mechanics of Solids. Part I.* N 4, 75. *Part II*. N 5, 65.
28. Goldstein, R.V., Zhitnikov, Yu.V. (1991) *Mechanics of Solids.* N 1, 139.
29. Goldstein, R.V., Zhitnikov, Yu.V. (1993) *Mechanics of Solids.* N 3, 161.
30. Mossakovskii, V.I., Rybka, V.M. (1976). In: *Hydrodynamics and elasticity.,* N 23, pp.149-156, Dnepropetrovsk: *Univ. Publishers*.
31. Goldstein, R.V., Spector, A.A. (1983) *Appl. Math. Mech. (PMM).* 47, N 2, 276.
32. Walsh, J.B. (1965) *J. Geophys. Res.*. 70, N 2, 399.
33. Berkovich, L.E., Mossakovskii, V.I., Rybka, V.M. (1977) *Mechanics of Solids.* N 4, 137.
34. Zhitnikov, Yu.V., Tulinov, B.M. (1984) *Mechanics of Solids.* N 5, 44.
35. Zhitnikov, Yu.V., Tulinov, B.M. (1982) *Mechanics of Solids.* N 4, 168.
36. Goldstein, R.V., Savova, L.N. (1972) *Mechanics of Solids.* N 2, 69.
37. Cotterell, B., Rice, J.R. (1980) *Int. J. Fract.*. 16, N 2, 155.
38. Andreev, A.V., Goldstein, R.V., Zhitnikov, Yu.V. (2000) *Mechanics of Solids.* N 3, 137.
39. Dyskin, A.V., Salganik, R.L. (1987) *Mechanics of Solids.* N 6, 165.
40. Goldstein, R.V., Zhitnikov, Yu.V. (1993) *Mechanics of Solids.* N 3, 161.
41. Goldstein, R.V., Zhitnikov, Yu.V. (1998) *Mechanics of Solids.* N 6, 38.
42. Kachanov, L.M. (1975) *Mechanics of polymers.* N 6, 1106.
43. Kachanov, L.M. (1976) *Bulletin of the Leningrad State University.* 13, N 3, 77.
44. Bolotin, V.V. (1986). In: *Strength calculations.* N 27, 8. Moscow: *"Maschinostroenie" Publishers*.
45. Bolotin, V.V. (1996) Stability problems in fracture mechanics. N.Y.: *John Wiley and Sons*.
46. Slepyan, L.I. (1981) Mechanics of cracks. Leningrad. "*Sydostroenie" Publishers.*
47. Goldstein, R.V., Konovalov, M.B. (1996) *Mechanics of Solids.* N 3, 62.
48. Goldstein, R.V., Konovalov, M.B. (1997) *Acad. Sci. Paris.* t.324, serie IIb, 419.
49. Dyskin, A.V., Germanovich, L.N., Ustinov, K.B. (2000) *Int. J. Solids Struct.* 37, 857.
50. Volynskii, A.L., Chernov, I.V., Bakeev, N.F. (1997) *Reports of the Russian Academy of Sci..* 356, N 2, 199.
51. Volynskii, A.L., Lebedeva, O.V., Bazenov, S.L., Bakeev, N.F. (2000) *Polymer Sci..* Ser.A, 42, N 4, 438.
52. Morozov, N.F., Paukshto, M.V., Tovstik, P.E. (1998) *Mechanics of Solids.* N 1, 130.
53. Goldstein, R.V., Osipenko, N.M. (1985) *Proc. 8th Int. Conf. POAC'85, Narssarssuaq, Greenland.* 3, 1170.
54. Goldstein, R.V., Osipenko, N.M. (1987) *Mechanics of Solids.* 3, 158.
55. Goldstein, R.V., Osipenko, N.M. (1991). In: *Ice-structure interaction. IUTAM-IAHR Symposium St. John's*, *Newfoundland, Canada*, Berlin, Heidelberg, Springer-Verlag. 251.
56. Goldstein, R.V., Osipenko, N.M. (1983). In: *Mechanics and Physics of Ice.* 31. Moscow. *"Nauka" Publishers*.
57. Goldstein, R.V., Osipenko, N.M. (1983) *Proc. 7th Int. Conf. POAC'83,* 3, 132. Helsinki, Finland.
58. Kanel, G.I., Bless, S.J., Rajendran, A.M. (2000) *Inst. Advanced Technology, Report N 0219.*

Fracture behavior of conductive cracks in PZT-4 piezoelectric ceramics

Tian-Hong Wang, Ran Fu and Tong-Yi Zhang*

Department of Mechanical Engineering
Hong Kong University of Science and Technology
Clear Water Bay, Kowloon, Hong Kong, China

ABSTRACT

The present work experimentally investigates the fracture behavior of conductive cracks in PZT-4 piezoelectric ceramics by using compact specimens under combined electrical and mechanical loading. Finite element calculations were conducted to obtain the energy release rate, the stress intensity factor and the intensity factor of electric field strength of the specimens. The results show that the critical energy release rate under purely either electric or mechanical load is a constant, independent of the ligament length. However, the critical energy release rate under combined electrical and mechanical loading depends on the weight of the electrical load in comparison with the mechanical load. We normalize the critical stress intensity factor by the critical stress intensity factor under purely mechanical loading and normalize the critical intensity factor of electric field strength by the critical intensity factor of electric field strength under purely electric loading. Then, a quadratic function describes the relationship between the normalized critical stress intensity factor and the normalized critical intensity factor of electric field strength, which can serve as a failure criterion of conductive cracks in piezoelectric ceramics.

KEYWORDS

piezoelectric ceramics, intensity factor, energy release rate, combined electrical and mechanical loading.

INTRODUCTION

Piezoelectric ceramics are one kind of smart materials widely used in high-tech industries, such as sonar transducers, electromechanical actuators, controlling devices and smart structures etc. due to their high piezoelectricity, permittivity and pyroelectricity as well as the merit of easy processing and low cost. However, piezoelectric ceramics are essentially brittle and susceptible to cracking at all scales from domains to devices. Therefore, the reliability and integrity of such devices and structures made of piezoelectric ceramics have recently attracted increasing interest from both academics and industrialists. There are voluminous theoretical studies on fracture of piezoelectric materials, and more and more increasing experimental results in the literature. Recently, Zhang *et al*. [1] gave an overview about the advances in fracture of piezoelectric ceramics, involving extensively theoretical and experimental studies.

* Corresponding author, E-mail: mezhangt@ust.hk

Internal electrodes are largely adopted in electronic and electromechanical devices made from piezoelectric ceramics. These embedded electrodes may naturally function as pre-conductive cracks or notches, which may lead to failure of these devices under combined electric and mechanical loads. However, only few experimental observations of conductive cracks in piezoelectric ceramics have been reported so far. Lynch *et al*. [2] carried out indentation fracture tests on electroded surfaces submerged in electrically conducting NaCl solution and in distilled water. In both cases, tree-like damage grew from the indented electrode under the cyclic electric field. Heyer *et al*. [3] studied the electromechanical fracture toughness of conductive cracks in PZT-PIC ceramics. They conducted four-point bending tests on pre-notched bars, in which the poling direction was toward the jig surface and the notch was filled with NaCl solution to make the crack conducting. Wide scattering results were obtained under a large applied electric field ($|K_E| > 50 kv/m^{1/2}$, where K_E is the applied electric intensity factor). The critical stress intensity factor increased as the applied intensity factor of the electric field strength changed from $30 kv/m^{1/2}$ to $-90 kv/m^{1/2}$. When the applied electric intensity factor was relative small, within the range of $-15 kv/m^{1/2}$ to $15 kv/m^{1/2}$, they could explain the experimental data using a domain-switching-based model. Fu *et al*. [4] conducted fracture tests of conductive cracks in poled PZT-4 ceramics, in which only positive electric field was applied. They found that under purely electric loading, there existed a critical energy release rate that was named the electric fracture toughness. The electric fracture toughness is a material property, similar to the mechanical fracture toughness. Furthermore, the electric fracture toughness under positive electric loading is about 25 times higher than the mechanical fracture toughness [4]. The present work studies the fracture behavior of conductive cracks in poled PZT-4 ceramics under negative electric fields and combined electric and mechanical loads as well.

EXPERIMENTAL PROCEDURE

The material used in this study was poled lead zirconate titanate ceramics (PZT-4, Morgan Matroc). Pre-notched or cracked compact samples were adopted in the fracture tests under purely mechanical, purely electric and mixed mechanical and electric loads. All samples had the width *w*=10mm, height *h*=10mm and thickness *t*=3mm. A pre-notch or crack was cut in each sample with a 0.15mm thick diamond saw parallel to the poling direction, and further sharpened by a 0.12 mm diameter wire saw. After the cutting, the samples were cleaned ultrasonically in distilled water for 20 seconds. For conductive cracks, silver paint was filled into the notch (crack) to make it function as an electrode. Figure1 schematically shows the sample

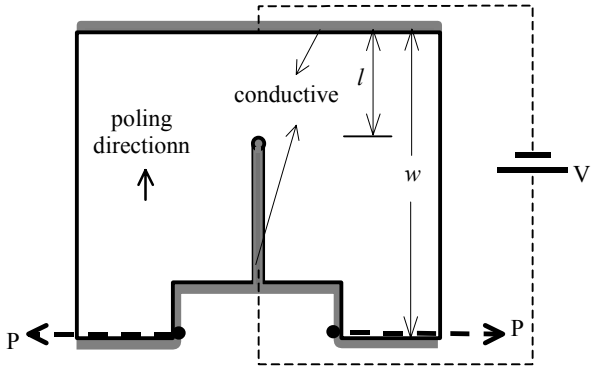

Fig.1 Depiction of the sample geometry and loading.

geometry and loading. The following three types of tests were conducted. 1) Purely mechanical loading (PM). On purpose, the ligament, *l*, varied from sample to sample and ranged from 2.5 to 4.5 mm. The tests were conducted on a mechanical testing machine (Miniature Materials Tester, Polymer Laboratories) at a crosshead rate 0.1mm/min under uniaxial tension. 2) Purely electric loading (PV). A static voltage was applied to a sample and manually increased until the sample was failed. Positive and negative electric fields, which were respectively parallel and anti-parallel to the poling direction, were applied in the tests. 3)

Mixed mechanical and electric loading. The fracture tests were carried out under a constant voltage (CV) or constant load (CM) mode on homemade loading apparatus. A constant voltage was applied first, then, the mechanical load was gradually increased until the sample fractured. In the CM mode, a constant mechanical load was applied first, following by the gradual increasing of the applied electric voltage until the sample fractured. In both modes, positive and negative electric fields were applied also. To avoid electric sparking, the samples were put into the silicone oil during tests under purely electric loading or covered by a thick layer of silicone grease under combined loading. All tests were implemented at room temperature. At least ten samples were tested under each loading condition in the CV or CM mode and 30 samples were tested in the PM or PV mode.

FINETE ELEMENT METHOD (FEM) FORMULATION

The energy release rate is equivalent to the contour-independent J-integral in the linear electro-mechanics [1, 5-8].

$$G = J = \int_{\Gamma} (hn_1 - \sigma_{ij} n_j u_{i,1} + D_i E_1 n_i) d\Gamma, \quad i, j = 1,2,3, \tag{1}$$

where $h = \sigma_{ij}\varepsilon_{ij} / 2 - D_i E_i / 2$ is the electric enthalpy per unit volume, Γ is an integration contour around the crack tip, and $\boldsymbol{n}$ is the unit out normal vector to the contour. In the finite element calculation of J-integral, we used the commercial software ABAQUS and the eight-node plane strain piezoelectric elements, and the material constants of the poled PZT-4 ceramics

Elastic constants ($10^{10}\ N/m^2$):
$c_{11} = 13.9,\ c_{12} = 7.78,\ c_{13} = 7.43,\ c_{33} = 11.3,\ c_{44} = 2.56$;
Piezoelectric constants (C/m^2):
$e_{31} = -6.89,\ e_{33} = 13.84,\ e_{15} = 13.44$;
Dielectric constants ($10^{-9}\ F/m$):
$\kappa_{11} = 6.00,\ \kappa_{33} = 5.47$

where the subscript "3" denotes the poling direction and *N*, *m*, *C* and *F* represent, respectively, Newton, Meter, Coulomb and Farad. The numerical results were fitted into the following formulas for the sample ligament, *l*, ranging from 2.5mm to 4.5mm.

$$G_I^M = \left[1.1783 - 9.8796s + 32.606s^2 - 49.125s^3 + 28.229s^4\right]P^2 \ \text{(N/m)} \tag{2}$$

for purely mechanical loading, and

$$G_I^E = \left[11.83 - 73.34s + 213.18s^2 - 306.53s^3 + 174.67s^4\right]V^2 \ \text{(N/m)} \tag{3}$$

for purely electric loading, where $s = l/w$ and *w*=10 mm is the sample width, *P* is the mechanical load in units of *N*, and *V* is the applied voltage in units of *kV*. The stress intensity factor and the intensity factor of electric field strength were derived from the J-integral under combined loading

$$K^{\sigma} = \frac{P}{t\sqrt{w}} f_1(s), \qquad K^{E} = \frac{V}{\sqrt{w}} f_2(s), \tag{4}$$

where *t* is the sample thickness, f_1 and f_2 are two dimensionless function of *s,* and given by

$$f_1(s) = (-2.861 + 15.076s - 26.612s^2 + 17.328s^3 - 1.603s^4) \times 10^2, \tag{5}$$

$$f_2(s) = 7.116 - 48.142s + 134.323s^2 - 160.043s^3 + 72.244s^4 . \quad (6)$$

Under mixed mechanical and electrical loading, the critical load and voltage at fracture were recorded to calculate the critical intensity factors with Eqs. (4-6).

RESULTS AND DISCUSSION

Fig. 2(a) shows the relationship of critical load versus ligament for purely mechanical loading, where a solid circle represents an experimental datum and hereafter the same symbol is used in the rest figures without notation. The mean of the energy release rate is $G_{IC}^{M} = 8.7 \pm 0.4 N/m$ (95% confidence). Using this mean and Eq. (2) we plot the load versus the ligament again, which is shown as the dot line in Fig. 2(a). On the other hand, a linear regression of the experimental data is shown as the solid line in Fig. 2(a). It can be seen the dotted line almost coincides with the solid one, indicating the existence of the mechanical fracture toughness in terms of the critical energy release rate. To be more straightforward, the calculated critical energy release rate versus the sample ligament is plotted in Fig. 2(b). It is clearly seen that the linear regression of the plot is very approximate to the horizontal line, indicating that the critical energy release rate is a material constant independent of the sample ligament. The mechanical fracture toughness can also be expressed in terms of the critical stress intensity factor, which is $K^{\sigma_0} = 0.934 \pm 0.06 MPa\sqrt{m}$ under purely mechanical loading. Fig. 2(c) shows that the failure probability of the PZT-4 ceramics under purely mechanical loading follows the Weibull distribution

$$F(G_I^M) = 1 - \exp\left[-\left(\frac{G_I^M}{9.0103} \right)^{9.6435} \right], \quad (7)$$

where F is the cumulative distribution function and G_I^M is in units of *N/m*. Under purely mechanical loading, the PZT-4 ceramics has a Weibull modulus of 9.6435, more or less the same as other engineering ceramics.

In the same way, Fig. 3(a) illustrates the critical voltage as a function of the ligament. The mean of the critical energy release rate is $G_{IC}^{E} = 223.7 \pm 17.0 N/m$ (95% confidence). As shown in Fig. 3(a), the dotted line of the theoretical prediction coincides the solid line of the linear regression of the experimental data, indicating the existence of the electrical fracture toughness. We also plot the critical energy release rate versus the sample ligament in Fig. 3(b). As expected, the linear regression of the plot is almost a horizontal line. This feature, in analogy with the mechanical case, indicates the existence of the electric fracture toughness under purely electric loading. The electric fracture toughness is a material property and has the value $G_{IC}^{E} = 223.7 \pm 17.0 N/m$ in terms of the critical energy release rate, which is about 25 times larger than $G_{IC}^{M} = 8.7 \pm 0.4 N/m$. This is because electrical discharge and domain switching may occur at the tip of the conductive crack, forming an electrically plastic zone. Actually, electric discharge was observed during the tests. This kind of electrical plastic deformation accompanies crack propagation and consumes energy, thus leading to the high electrical fracture toughness. The failure probability of the PZT-4 ceramics under purely electric loading, as shown in Fig. 3(c), follows the Weibull distribution of

$$F(G_I^E) = 1 - \exp\left[-\left(\frac{G_I^E - 130}{110.25} \right)^{2.331} \right] \text{ with } G_I^E \text{ in units of } N/m. \quad (8)$$

Comparing Eq. (8) with Eq. (7) indicates that a three parameter Weibull distribution has to be used to describe the failure probability under purely electrical loading, while a two parameter Weibull distribution is sufficient to describe the failure probability under purely mechanical loading. Equation (8) is valid only

when G_I^E is larger than 130 *N/m*. When G_I^E is smaller than 130 *N/m*, no failure will occur under purely electrical loading. The PZT-4 ceramics under purely electric loading has a Weibull modulus of 2.331, as

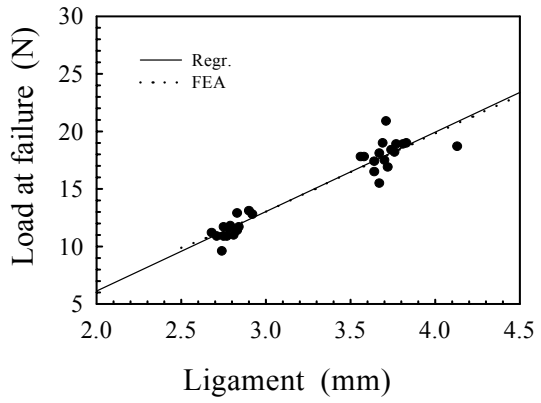

Fig.2(a) Critical force versus ligament under purely mechanical loading.

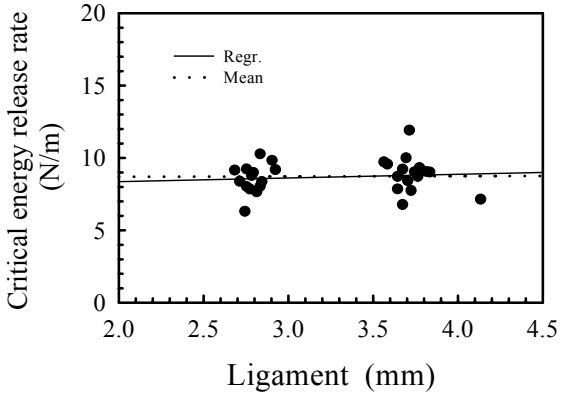

Fig.2(b) Critical energy release rate versus ligament under purely mechanical loading.

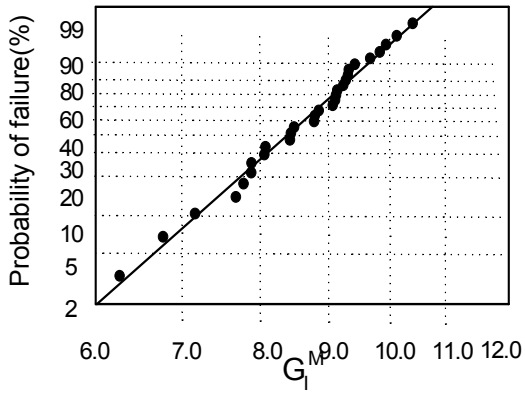

Fig.2(c) Weibull distribution of critical energy release rate under purely mechanical loading.

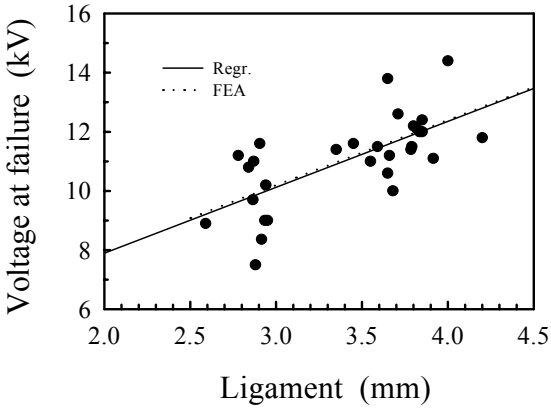

Fig.3(a) Critical voltage versus ligament under purely electric loading.

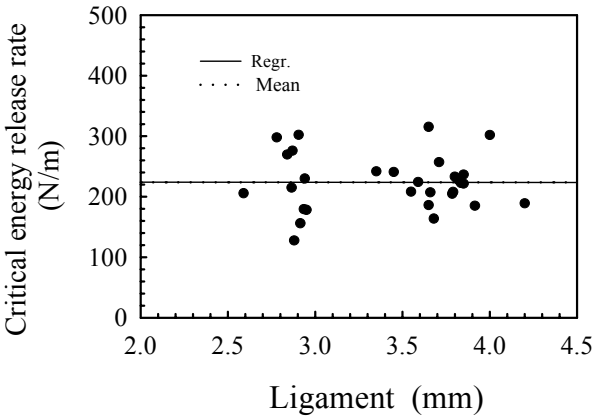

Fig.3(b) Critical energy release rate versus ligament under purely electric loading.

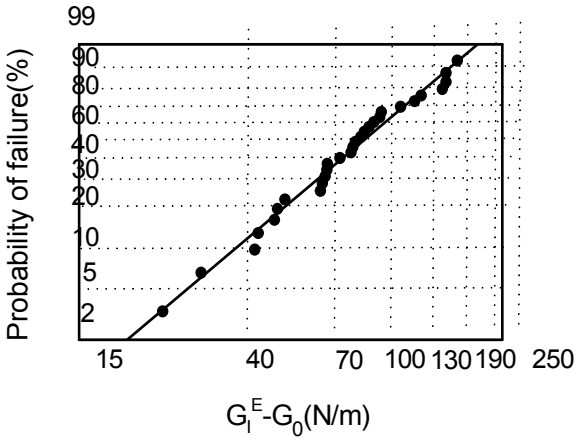

Fig.3 (c) Weibull distribution of critical energy release rate under purely electric loading.

shown in Eq. (8), which is much smaller than that under purely mechanical loading, indicating a larger variability of the electric fracture toughness.

Under combined electric and mechanical loading, we normalize the critical stress intensity factor by the critical stress intensity factor under purely mechanical loading and normalize the critical intensity factor of electric field strength by the critical intensity factor of electric field strength under purely electric loading. Figures 4(a) and 4(b) show the relationships of the normalized intensity factor of electric field strength

versus the normalized stress intensity factor, respectively, for positive and negative electric loading. The experimental data can be approximately described by the equation

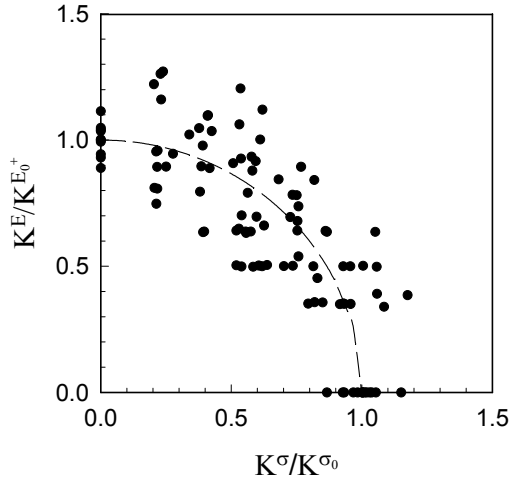

Fig.4(a) The normalized electric intensity factor versus the normalized stress intensity factor under positive electric fields.

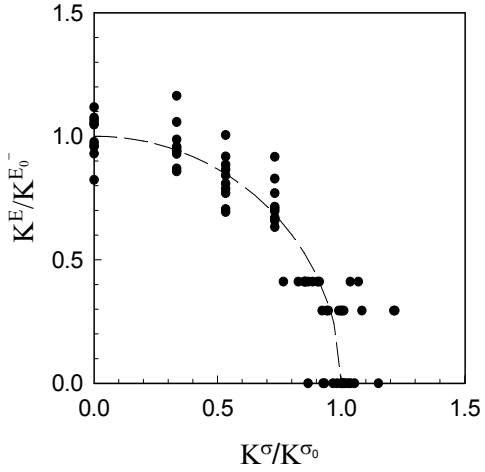

Fig.4(b) The normalized electric intensity factor versus the normalized stress intensity factor under negative electric fields.

$$\left(K^E / K^{E_0^{\pm}}\right)^2 + \left(K^\sigma / K^{\sigma_0}\right)^2 = 1, \tag{9}$$

which is shown as the dashed curve in Figs. 4(a) and 4(b). Equation (9) may serve as a failure criterion for poled PZT ceramics under combined electric and mechanical loading. A model to explain the experimental observations will be given in a separate paper [9].

CONCLUSIONS

This work experimentally investigates the fracture behavior of conductive cracks in PZT-4 piezoelectric ceramics. The results demonstrate the existence of the electric facture toughness under purely electrical loading. The failure probabilities of the PZT-4 ceramics are expressed in terms of three and two parameter Weibull distributions, respectively, for purely electrical and mechanical fracture toughnesses. An empirical criterion in terms of the normalized intensity factors of stress and electric field strength is proposed to describe the fracture behavior of poled PZT ceramics under combined electrical and mechanical loading.

ACKNOWLEDGEMENTS: The work was supported by the Research Grants Council of the Hong Kong Special Administrative Region, China.

REFENRENCES

1. Zhang, T.Y., Zhao, M.H. and Tong, P. (2001) Fracture of Piezoelectric Ceramics, *Advances in Applied Mechanics*, in press.
2. Lynch, C. S., Yang, W., Collier, L., Suo, Z., and McMeeking, R. M. (1995) *Ferroelectrics* **166**, 11.
3. Heyer, V., Schneider, G. A., Balker, H., Drescher, J., and Bahr, H. A. (1998) *Acta mater*. **46**, 6615.
4. Fu, R., Qian, C.F. and Zhang, T. Y., (2000) *Appl. Phys. Lett*. **76**, 126.
5. McMeeking, R. M. (1990) *Int. J. Engng, Sci.*, **28**, 605.
6. Suo, Z. (1993*) J. Mech. Phys. Solids*, **41**, 1155.
7. Zhang, T. Y., Qian, C. F. and Tong, P. (1998) *Int. J. Solids Structures*, **35**, 2121.
8. Cherepanov, G.P. (1979) Mechanics of Brittle Fracture, McGraw-Hill, New York.
9. Zhang, T. Y., Wang, T. H., Fu, R. and Zhao, M. H., unpublished work.

ICF1001038OR

FRACTURE BEHAVIOR OF A CORRODED ANNULAR PLATE UNDER A MULTI-AXIAL STRESS STATE

M.OHASHI

National Research Institute of Police Science
6-3-1, Kashiwanoha, Kashiwa, Chiba277-0882, Japan

ABSTRACT

For the purpose of risk assessment of damaged structure, bend tests were carried out on a corroded annular plate prepared from the oil storage tank. Corrosive attack occurred extensively on the outer surface of the annular plate. Seriously developed cracking was noted in the high deflection region depending upon the degree of corrosion damage. From successive observation of crack growth behavior on the roughened corroded surface, it was clearly recognized that the multiple cracks, initiated around pits, grew rapidly not only by crack growth by itself, but also by coalescence with other neighboring cracks under the influence of plastic constraint derived from the welded joint. Then, it should be emphasized that the development of serious cracking, leading to a catastrophic failure, was expected to occur on a corroded component through the linking up of multiple cracks under a multi-axial stress state.

KEYWORDS

risk assessment, corrosion damage, annular plate, multiple cracks, crack coalescence, stress concentration, plastic constraint.

INTRODUCTION

Some of the existing structures degrade in service resulting from various types of deterioration. The reliability assessment of the damaged structure should be considered to minimize the risk of failures. Research activities are mainly concerned with degradation occurring in high temperature power plants, commonly known as creep damage and temper embrittlement .
However, corrosion of the structural component is the simplest and most common form of degradation, and occurs frequently under normal service condition. Besides, a generally uniform corrosion produces a rough surface on the component in some situations.
In such circumstances, a more serious problem should be supposed to occur under a multi-axial stress state around the welded joint. Hence, the reliability of the corroded component should be considered against various loading or stress state that would be envisaged to be applied in service.
In this study, the fracture behavior of a corroded annular plate, prepared from the oil storage tank, was investigated under bending load, to identify the significance of corrosion damage for risk assessment.

EXPERIMENTAL PROCEDURE

Material and Bend Specimen

L-shaped bend specimens were machined from the welded joint between the shell plate and the annular plate of the oil storage tank. The geometry and dimensions of the bend specimen is given in Fig.1. The general appearance of the corroded surface is a roughened one with a

relatively uniform reduction in thickness. A large number of pits, which had developed to a visible size, are distributed randomly over the corroded surface. The annular plate is made of high strength steel with a tensile strength of 613MPa. It should be noted that the major axis of the bend specimen is transverse to the rolling direction.

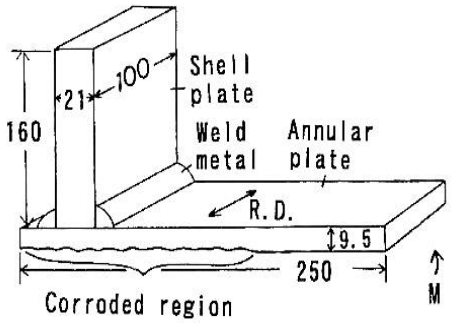

Fig.1. Geometry of L-shaped bend specimen. (dimensions in mm).

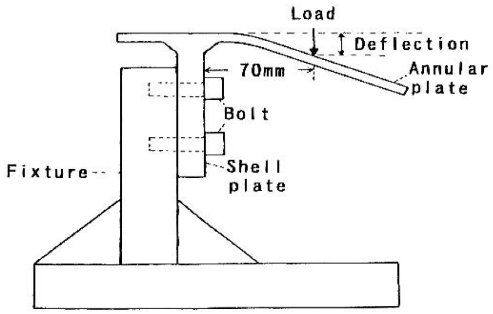

Fig.2. Schematic illustration of setup for bend test.

Fig.2 shows the schematic illustration of setup for the bend test. The axial load was applied on the corroded surface of the annular plate. It was envisaged to be applied in a case of huge earthquake followed by sinking of the foundation of the tank.

Quantitative Assessment of Corrosion Damage

Three specimens with varying degree of corrosion damage were prepared. Each specimen was labeled specimen A to specimen C. The pitting depth distribution over an extent of 10mm in length and 100mm in width adjacent to the welded joint was evaluated stochastically. In addition, the pit root radius and the depth of deepest bottom of the pit was measured for specimen A and C over an extent of 15mm in length and 100mm in width. The stress concentration factor K_t due to a pit is given approximately under bending load by

$$K_t=1+2(d/\rho)^{1/2} \qquad (1)$$

where d is the depth of deepest bottom of pit and ρ is the pit root radius[1].

Observation of Crack Growth Behavior

Crack growth behavior on the corroded surface was observed after attaining every increment of deflection of 5mm. The surface crack length was measured on the photographs, where its length was represented by the projected length in the direction perpendicular to the loading axis.

Notched Tensile Specimen

Notched tensile specimens with different notch acuity were prepared from the annular plate to investigate the effect of stress concentration on the fracture strain. The fracture strain in the minimum section is given by

$$\varepsilon_f=2\ln(d_0/d) \qquad (2)$$

where d is the diameter of the minimum section at fracture and d_0 is the initial value of d.

RESULTS AND DISCUSSION

Distribution of Pitting Depth and Stress Concentration Factor

Fig. 3 shows the probability distributions of pitting depth on Weibull distribution paper.

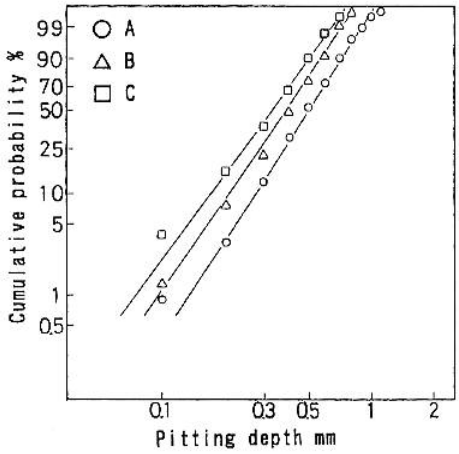

Fig.3. Weibull distributions of pitting depth for specimen A, B and C.

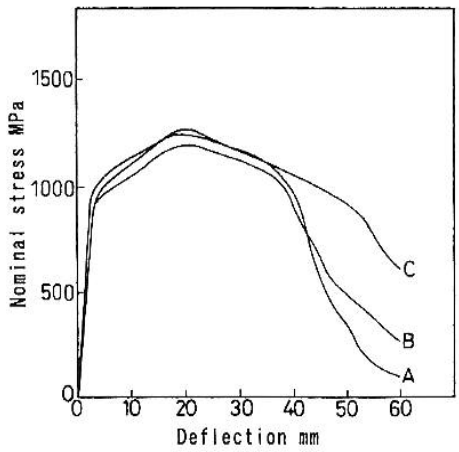

Fig.4. Nominal stress versus deflection curves for specimen A, B and C.

The distribution of pitting depth can be approximately described as a Weibull distribution. Three specimens were found to be corroded to a greater depth in order of specimen A, B and C. While, the probability distributions of stress concentration factors are fitted to log-normal distribution. The median values for specimens A and C were 2.1 and 1.9, respectively.

Nominal Stress-Deflection Curve of Bend Specimen

Fig.4 shows the results of bend tests. The nominal stress σ_n is given by

$$\sigma_n = 6PL/bh^2 \qquad (3)$$

where P is the applied load, L is the span length, b and h are the width and thickness of the bend specimen. The thickness of the specimen was defined here as the difference between the thickness of annular plate in the non-corroded region and the median value of pitting depth. At the early stages of deformation, the stress rises with increasing deflection. Then, the stress reaches a maximum value and thereafter starts to decrease after a deflection of about 20mm. A difference in the stress-deflection curves for three specimens is scarcely recognized at the early and the middle stage of deformation. In contrast, a different response was noted after attaining a deflection of about 35mm, associated with a varying degree of corrosion damage.

Crack Growth Behavior on the Corroded Surface

The reason of different shapes of the stress-deflection curves was successfully explained from successive observation of crack growth behavior on the corroded surface. Photographic evidence showed that the multiple cracks had initiated after a deflection of 35mm on the corroded surface of specimen A and B. Thereafter, rapid crack growth occurred through crack growth by itself and coalescence with other cracks. Typical examples of crack coalescence are shown in Fig.5. Several cracks, initiated around pits, grew rapidly into large crack by

coalescence with neighboring cracks. Hence, it should be emphasized that the linking up of multiple cracks and the subsequent development of extensive cracking is considered to be a characteristic event of the roughened corroded component, and is expected to occur in the high deflection region depending upon the degree of corrosion damage. Plastic constraint, derived from the welded joint, produced a multi-axial stress state, and presumably accelerated crack growth among multiple cracks.

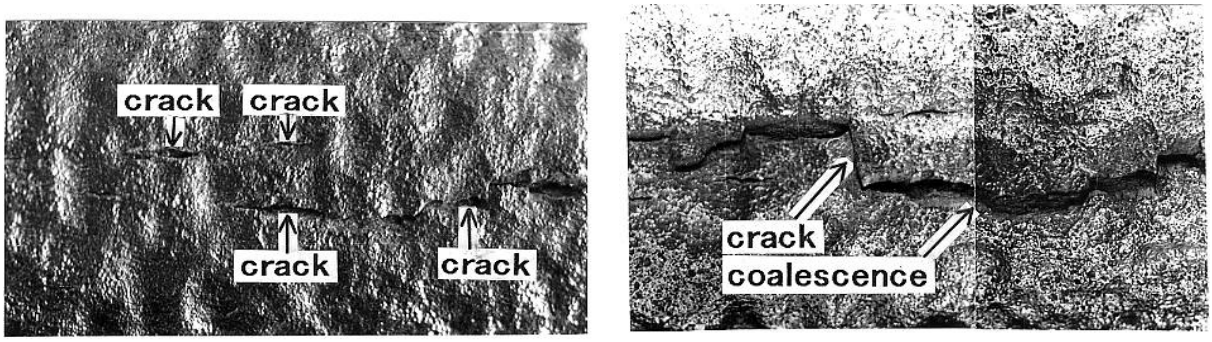

(a)Deflection 50mm. 5mm (b)Deflection 60mm.

Fig.5. Crack coalescence with increase of deflection for specimen B.

Well developed cracks at a deflection of 60mm for specimen A are demonstrated in Fig.6. In contrast, the development of cracks for specimen C is less extensive in concurrence with a lesser degree of corrosion damage. The increase in surface crack length for specimen A is shown in Fig.7. Several cracks had developed on the corroded surface at a deflection of 35mm. These cracks grew rapidly to join other cracks with increase of deflection. A coalescence of crack a and crack b in Fig.7 leads to larger crack c at a deflection of 50mm. As a result, an extensive crack①A and ②A with a length of 64 and 35mm had been formed for specimen A.

Similarly, multiple cracks, initiated on the corroded surface of specimen B, continued to grow and coalesce rapidly into large cracks. Consequently, an extensive crack with a length of 71 mm had been developed at a deflection of 60mm. Whilst, specimen C showed a much lower crack growth rate, and the largest crack①C in Fig.8 is 31 mm long.

The increase in surface crack length for specimen A, B and C were re-plotted in Fig.9 in terms of total crack length. The difference in fracture behavior of each specimen has been clarified in Fig.9. The deeper the pitting depth, the more rapidly the dimension of total crack length has increased. A high pit density and a higher stress concentration factor for

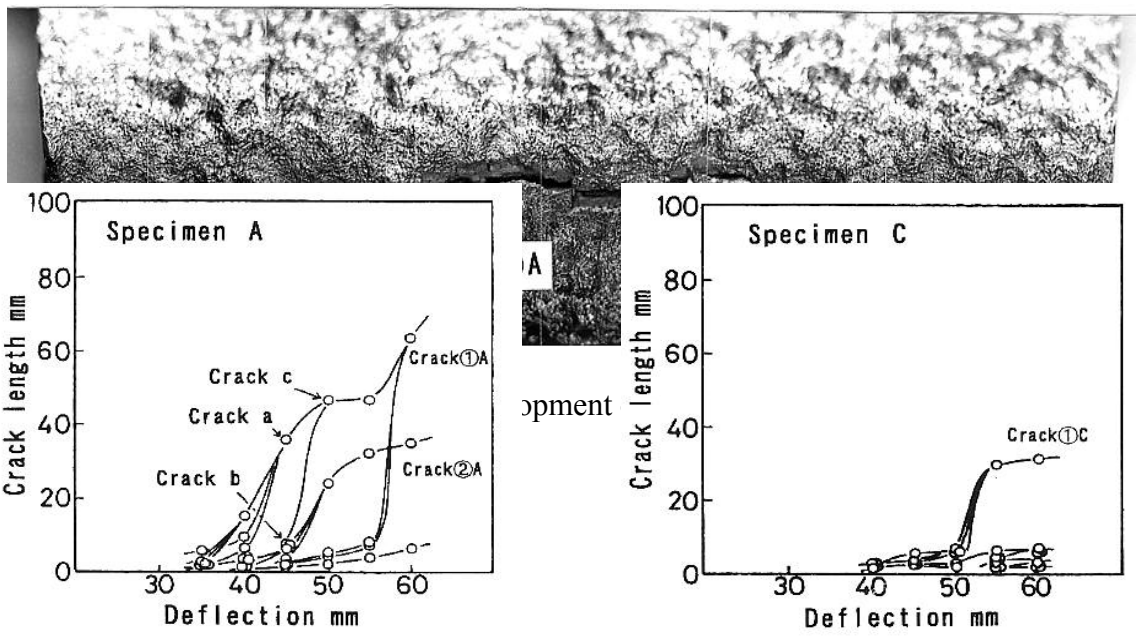

Fig.7. Relation between crack length and deflection for specimen A.

Fig.8. Relation between crack length and deflection for specimen C.

specimen A was also presumed to promote crack growth. The experimental results have led to the possibility that more serious crack growth might occur in a component subjected to a higher degree of corrosion damage. Hence, the fracture behavior of the corroded structure should be considered for the risk assessment to minimize the risk of catastrophic failure.

Ductility of the Annular Plate

Poor ductility of the annular plate in the transverse direction was assumed to promote crack growth. Fig.10 shows the relationship between the fracture strains and stress concentration factors of tensile specimens[2] for both the transverse and longitudinal directions. The fracture strain in the transverse direction was about a half of that in the longitudinal

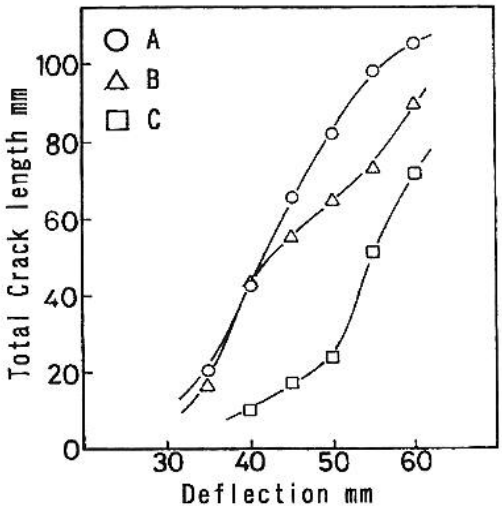

Fig. 9. Relation between total crack length and deflection.

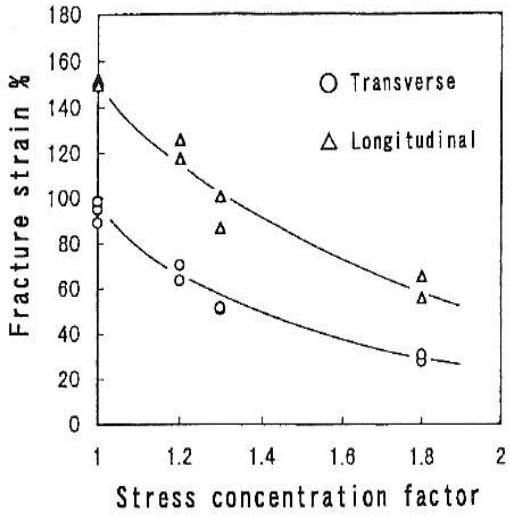

Fig.10. Relation between fracture strain and stress concentration factor.

direction, and was found to be a small value under a high stress concentration factor. Thus, the crack growth behavior was certainly accelerated by low ductility of the annular plate.
Also, poor ductility of the annular plate was well explained from a detailed fractographic examination. A typical fractograph of the annular plate is shown in Fig.11. The fracture surfaces are composed of equiaxed dimple area and featureless zone that is supposed to be caused by cracking and decohesion of non-metallic inclusion. The greater portion of the fracture surface is covered by featureless area. An average value of area fraction covered by dimple for 14 views was found to be a small value of 22% because of low ductility of the annular plate.
The relationship between dimple area fraction and ı the transverse direction was developed in Fig.12. Dim ıe of about 50% for the unnotched specimen, and decrea rain. ate de men . Using f the ely low ction

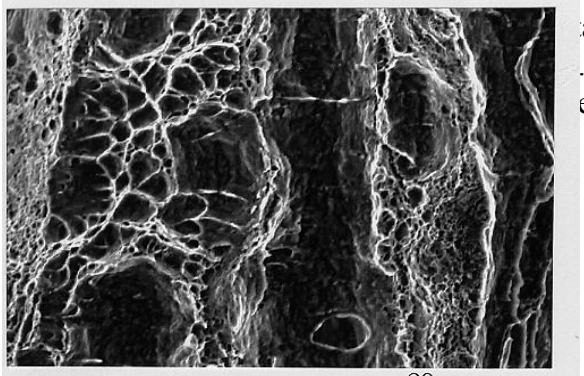

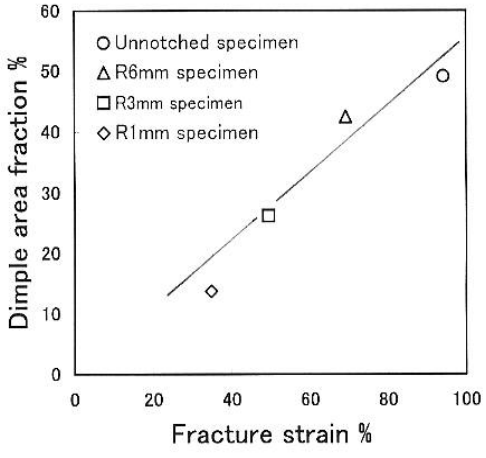

20 μ m

Fig.11. SEM fractograph of the annular plate.

Fig.12. Relation between dimple area fraction and fracture strain.

CONCLUSION

In this study, the fracture behavior of a corroded annular plate was clarified for the reliability assessment of damaged structure. The main conclusions are as follows.

As a result of bend tests, well developed extensive cracking was noted in the high deflection region correlated with varying degree of corrosion damage. From successive observation of crack growth behavior on the corroded surface, it was clearly demonstrated that the multiple cracks, initiated around pits, grew rapidly into large cracks not only by crack growth by itself but also by coalescence with other neighboring cracks under the influence of plastic constraint. Then, it should be emphasized that the development of serious cracking through the coalescence of multiple cracks was considered to be a characteristic event of the corroded component, and was envisaged to occur under a multi-axial stress state depending upon the degree of corrosion damage.

REFERENCES

[1]. R. E. Peterson(1953), “Stress concentration design factors”, John Wiley & Sons, 136.

[2]. R. E. Peterson(1953), “Stress concentration design factors”, John Wiley & Sons, 35.

FRACTURE BEHAVIOUR OF A FIBRE-BRIDGED CRACK

Hong-Yuan Liu [1], Xi Zhang [2], and Yiu-Wing Mai[1,3]

[1] Centre for Advanced Materials Technology, School of Aerospace, Mechanical and Mechatronic Engineering, The University of Sydney, Sydney, NSW 2006, Australia
[2] CSIRO Petroleum, PO Box 3000, Glen Waverley, VIC 3150, Australia
[3] MEEM, City University of Hong Kong, 83 Tat Chee Avenue, Kowloon, Hong Kong

ABSTRACT

The effects of interfacial debonding and sliding on the fracture characterisation of unidirectional fibre-reinforced composites are studied numerically under small-scale bridging conditions in plane strain. The cohesive zone, more commonly called the fracture process zone (FPZ), is characterised by matrix separation and individual fibre pullout. A bi-linear stress-displacement fibre-bridging law is incorporated into the computational model to account for interfacial debonding and sliding and fibre breakage, instead of the line-spring model in which the fibres remain intact. The matrix fracture process is described by a linear stress-displacement cohesive law. Anisotropic elastic constitutive relations are used for the effective properties of the brittle-matrix composite outside the FPZ. A remote boundary condition is also imposed in terms of the elastic solutions for a mode I crack. Crack advance and fibre breakage are direct consequences of the constitutive modelling without any *ad hoc* crack growth criterion. Numerical implementation of the finite element method with the embedded cohesive zone containing fibre bridging and matrix fracture is elucidated. Fracture resistance (R)-curve is obtained for a range of conditions to highlight the debonding and frictional behaviours at the fibre-matrix interface. It is shown that the fracture toughness can be enhanced by optimisation of the fibre-matrix interfacial properties. Numerical results also show that fibre breakage plays an important role on the reduction of the slope of the R-curve.

KEYWORDS

Cohesive zone, Fibre-bridging, Matrix cracking, Interface behaviour, (R)-curve, Finite element method, Fibre pullout, Fibre breakage

INTRODUCTION

In fibre-reinforced composites, the interaction of a fibre with the matrix is of great interest for failure assessment. Interfacial debonding and frictional sliding associated with the fibre pullout process are regarded as two important mechanisms to increase the toughness of unidirectional fibre-reinforced composites. In general, a cell model for a single fibre pullout test is used to evaluate the relationship between pullout force and pullout displacement. The fibre pullout force-displacement curves obtained provide a good approximation of the crack-face bridging law in the wake region [1-3].

Various approximation methods with regard to the bridged-crack have been developed. Aveston, et al

[1] estimated the applied stress at which matrix cracking takes place with the fibres left completely intact. In Marshall and Cox's work [2], a shear lag analysis, i.e., a constant shear frictional stress, is used to deal with interfacial sliding resistance. This is valid for a composite system with a weak or un-bonded sliding interface. Also, different forms of bridging laws have been presented in the past decade to account for the effects of fibre debonding and fibre sliding [4,5]. Further, the effect of interface roughness on the bridging law was analysed by Liu, Zhou and Mai [6]. Even so, the effect of fibre-matrix interface debonding and sliding on the fracture process has not yet been thoroughly investigated.

In low-density fibre composites a crack is bridged by a few fibres, and the smeared-out model cannot be usefully applied without loss of accuracy. Hence, there is a need to understand the bridging effect by discrete fibres over a finite length. Meda and Steif [4] discussed several reasons for poor agreement between experimental observations and theoretical predictions based on the continuous distribution of tractions along the crack-faces. It is desirable to develop an independent model where discrete fibres are analysed explicitly, rather than implicitly as in earlier crack-bridging models. Fibre breaks play an important role in the softening behaviour of fibre-reinforced composites. However, most solutions available for crack resistance (R)-curves are obtained from approximate shear lag analysis and smeared-out representation of the bridged area and do not include fibre breakage. Also, fracture of composites involves more than one physical process. Thus, rupture in unidirectional fibre-reinforced composites is associated with brittle matrix fracture, fibre pullout and fibre fracture [7]. In principle, distinct failure mechanisms cannot be incorporated in a unified cohesive zone model, although attempts have been made to do so. Hence, matrix cracking and fibre bridging should be modelled separately by a two-part description. That is, the coexistence of a fibre bridging zone and a matrix cohesive zone, whose stresses depend on the crack-face opening displacement.

The aim of this work is to study the toughening mechanisms of aligned fibre composites by finite element analysis. Two failure mechanisms, fibre-bridging and matrix cracking, are considered separate entities, rather than by a single smeared-out bridging law. A bi-linear constitutive relation is employed to describe the fibre-matrix debonding and frictional sliding process. A softening cohesive law is used for matrix separation to avoid the stress singularity in conventional bridged-crack models. Numerical results are calculated for a carbon fibre-epoxy unidirectional composite with a low fibre density. The effects of the interface properties and fibre breakage on the fracture toughness of the composite are presented and discussed in detail.

THEORETICAL ANALYSIS

Bridging Law during Fibre Pullout

Consider an infinite uniformly aligned unidirectional fibre composite containing a semi-infinite crack. The crack-face separation and crack growth are restrained by the bridging fibres. Descriptions of the fibre bridging stress and crack-face displacement relationship can be obtained by a theoretical analysis of a fibre pullout process [8] as typified by the stress-displacement curve in Fig.1, in which σ is applied stress at fibre end and δ is pullout displacement. σ_{1f} and δ_{1f} are the initial debonding stress and displacement, respectively. Two parameters, σ_{1f} and the slope κ (see Fig.1) are used as indicative measures of the interfacial bond strength and friction coefficient at the partially debonded interface, respectively. They define the bilinear law of the stress-displacement relation prior to the full fibre pullout from the matrix (which is not shown). Computer simulation [9] study shows that a strong bond gives a high initial debonding stress and a high interfacial friction. However, a very strong bond will increase the full debonding stress but decrease the pullout-displacement due to fiber breaks.

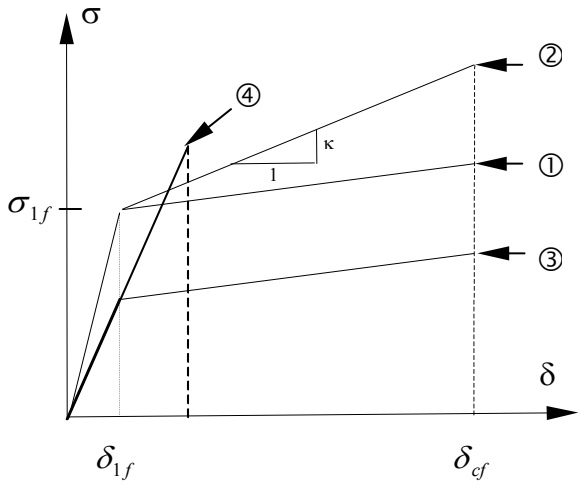

Fig. 1. Schematic representation of fibre-bridging stress with pullout displacement. Four cases are studied in this work are shown here and case 4 is for a very strong bond.

Cohesive Law for Matrix Cracking

The constitutive relationship of the matrix cohesive zone is described by the traction σ and the displacement δ. It is recognised that the specific work of separation, $\Gamma_0 = 2\int_0^{\delta_1} \sigma(\delta) d\delta$, reaches a critical value when crack growth commences. In the numerical results of Xu, Bower and Oritz [10], it was found that fibre debonding occurred as the matrix crack reached a fibre. Hence, we assume that the maximum separation δ_1 across the matrix cohesive zone must equal the fibre pullout displacement δ_{1f} corresponding to σ_{1f} as shown in Fig. 1. The shape of the cohesive law is assumed to be a linear function of the separation displacement and is given by: $\sigma = \sigma_1(1 - \delta/\delta_1)$ so that $\Gamma_0=\sigma_1\delta_1$.

Finite Element Method

Finite element simulations are based on the updated co-ordinate Lagrangian formulation for a dynamic case. For quasi-static cases studied here, the loading rate is assumed to be very small to eliminate the kinetic effect. All physical quantities are functions of a set of moving co-ordinates x^i at time t. Fig. 2 shows the schematic diagram of this small-scale bridging problem of a semi-infinite crack in a uniform unidirectional fibre composite. Due to symmetry only a half cracked specimen needs to be considered. The fracture plane is replaced by the cohesive zone with fibre-bridging and matrix separation. The stresses are related to δ by the assumed cohesive laws.

Numerical method is implemented by displacement-based finite element method and uniformly distributed fine meshes are placed along the fracture plane to simulate crack growth. The size of these elements is assumed to be the fibre spacing. A linear interpolation procedure is carried out to obtain values of δ at four Gaussian integration points. Then the stress can be obtained from the cohesive law. A fourth order Gaussian integration scheme is used to obtain contribution to the fracture work from the matrix process zone. The fibre bridging force is a force at each node due to the small fibre radius. Its magnitude is determined by the crack-face displacement. The results are obtained for a semicircular region with initial radius R_0 = 200 mm. It is chosen such that $R_0 = 4000\Delta$ in which Δ is the size of the smallest mesh element ahead of the crack-tip. $\delta_{cf} = 10\delta_1 = 0.1\Delta$ is selected to determine the

maximum separation of the fibre and $\delta_1 = 0.01\Delta$ is the maximum matrix separation. A fine mesh with length $L_0 = 48\Delta$ is placed ahead of the crack tip to simulate crack growth.

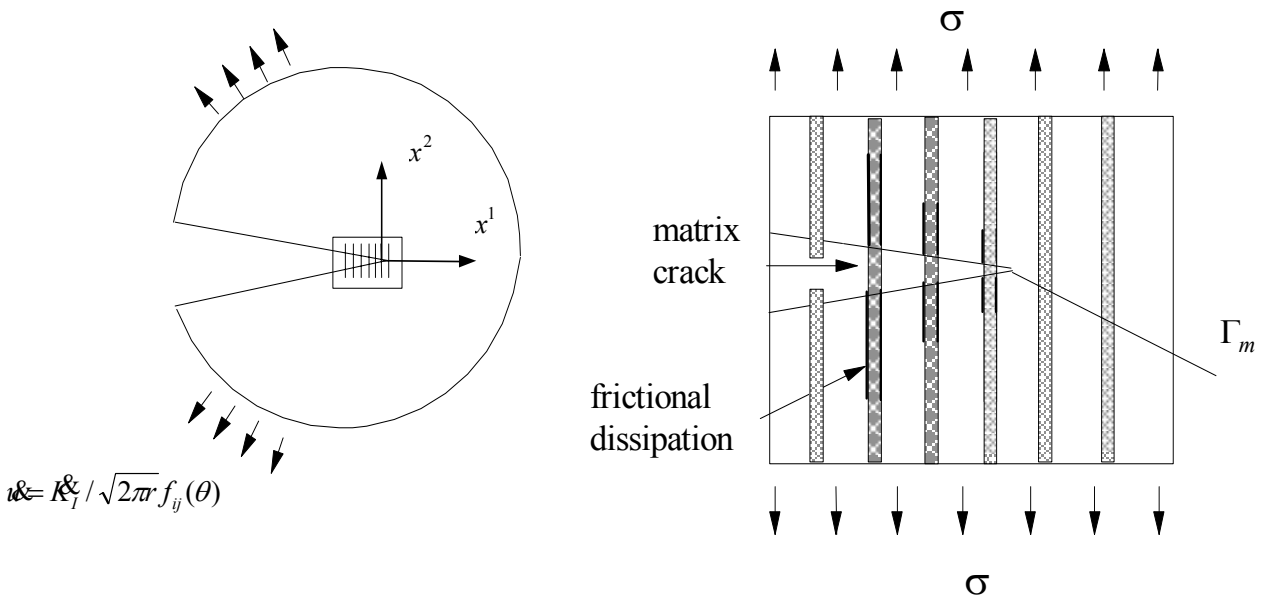

Fig. 2. Schematic diagram of the small-scale bridging problems of a semi-infinite crack in uni-directionally aligned fibre reinforced composites.

Small-scale bridging conditions involve imposing initial and boundary conditions appropriate to the linear transversely isotropic and orthotropic elastic crack-tip fields, respectively. The traction-separation law used to model the fracture process is specified everywhere on the boundary $x^1 > 0$ and $x^2 = 0$ of the region analysed, while zero traction exists on the boundary $x^1 < 0$ and $x^2 = 0$. On the outer semi-circular boundary, the displacements, $\dot{u}_1$ and $\dot{u}_2$ are given by the external stress fields, specified by the incremental rate of the mode I stress intensity factor $\dot{K}_I$. Details of the equations, mesh and FEA procedure are given in Ref. [11].

NUMERICAL RESULTS

Numerical calculations are carried out for carbon fibres in an epoxy matrix with material parameters E_f=230 GPa, $E_m = 3$ GPa, $\nu_f = 0.2, \nu_m$=0.4 and V_f=0.1. Thus, we can obtain the effective elastic modulus and Poisson ratio as $\overline{E} = 25.7$ GPa and $\overline{\nu}$=0.38, as well as the mass density 2000 kg/m^3. The computation is stopped when sufficiently long crack growth occurs. We assume the fibre strength to be uniform and the fibres break at the crack plane. (However, non-uniform fibre strength distribution can be included in our computation model as in [12,13].) Hence, there is no fibre pullout due to frictional sliding from the matrix. For numerical calculations, we give the fibre a small extra pullout displacement, $\delta_{1f}/10$, so that the pullout force can be reduced to zero. This also stabilized the computations. For simplicity, the debonding strength σ_{1f} is normalised by the matrix cohesive strength, i.e., $\eta = \sigma_{1f} / \sigma_1$. In the calculations, we assumed fibre debonding begins when the matrix crack-tip reaches this fibre. The non-dimensional cohesive strength of the matrix $\sigma_1 / \overline{E}$ is assumed to be 5×10^{-3}. Thus, the cohesive energy G_{mc} for the

matrix is 66.25 J/m^2. Based on the relationship: $K_{mc}^2 = E_m G_{mc}/(1-\nu_m^2)$, we obtain the matrix critical stress intensity factor $K_{mc} = 0.486\text{MPa}\sqrt{\text{m}}$.

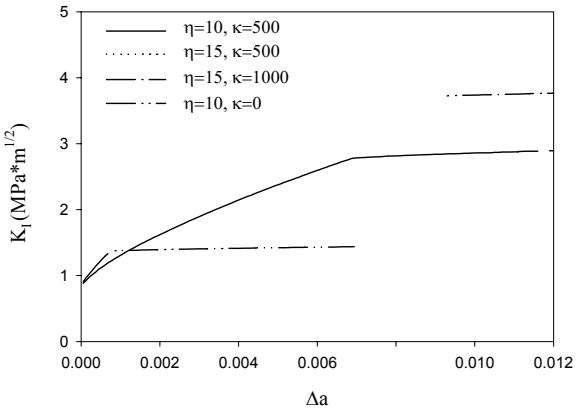

Fig. 3. Fracture resistance curves for several values of parameters η and κ.

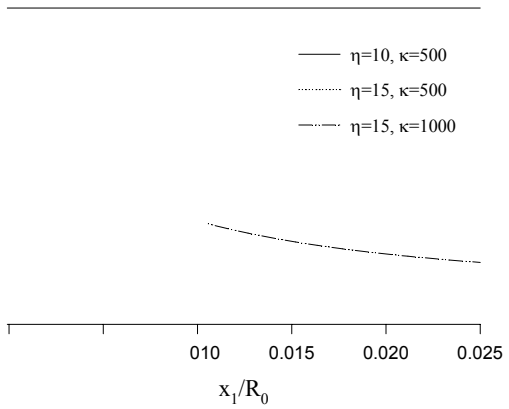

Fig. 4. Fiber stress ($\sigma/\overline{E}$) along the crack-line (x_1/R_0) for several values of parameters η and κ

Figure 3 shows typical R-curves for different debonding energy and interfacial frictional resistance. An increase in σ_{1f} means an improvement in debond toughness and an increase in κ, normalised by $\overline{E}/R_0$, means an increase in frictional sliding resistance. It is clear that crack initiation is delayed by increasing η. Fracture toughness is enhanced as crack advances at a relatively large slope because of the dominant effect of fibre-bridging. An increase in the frictional sliding resistance also increases the fracture toughness. Due to the complexity of the pullout process, the effects of fibre sliding at the debonded interface cannot be separated in the bridging law. However, it is reasonable that an increase in fracture resistance takes place at large κ. There is a transition of the R-curve from an initial rising part to a steady-state in which the length of the bridging zone does not change with subsequent crack extension. This transition occurs when the fibres at the receding edge of the bridging zone begins to break. The very slight rise of crack-resistance in the steady-state region is caused by kinetic effect since extremely large CPU time is required for lower loading rate than that used.

Increasing the interface strength will accelerate fibre breakage due to the stress elevation in the fibres ahead of the crack-tip. The nett effect is a reduction in the fibre pull-out displacement. If we take case 4 in Fig. 1 with η=10 and $\delta_{cf} = 2\delta_1$ for a very strong interface, the steady-state toughness is much lower but slope much larger at the initial stage than that with the same η, Fig. 3. It is unwise hence to increase the interface strength, as the admissible inelastic deformation accompanying fibre sliding is severely curtailed. There are optimal interface properties to obtain maximum fracture toughness.

As fibre stress ahead of the crack-tip is not affected by the amount of crack advance at the stage of steady-state crack growth, the distribution of fibre stress at incipient fibre breaks can be taken as typical for a set of given material parameters. Fig. 4 shows distributions of normalized fibre stresses for three cases studied. With increasing interface strength and frictional resistance, the maximum fibre stress also increases. This corresponds to 0.06, 0.084 and 0.095 for the three cases. Although a large κ can increase the maximum stress in the bridged zone, it decreases rapidly to the same level as low κ's at the crack-tip, as frictional sliding does not come into effect ahead of the crack-tip.

CONCLUSIONS

A finite element analysis was carried out for the failure behaviours of aligned fibre composites in terms of an embedded cohesive zone with matrix cracking and fibre-bridging. These two failure mechanisms, matrix cracking and fibre debond, pullout and fracture, are considered as separate entities, rather than under a single smeared-out bridging law. In describing the properties of fibre debonding and frictional sliding, a bi-linear constitutive law is used and in which, two parameters, η and κ, have been utilised to characterise these two effects on the fracture resistance.

Numerical results show that the composite toughness can be increased by improving the interfacial properties. However, if the interface is too strong, low toughness can be caused by fibre breakage. Hence, high toughness can only be achieved by optimal design of the fibre-matrix interface.

ACKNOWLEDGMENTS

We would like to thank the Australian Research Council (ARC) for their continuing support of this project. H-YL acknowledges an ARC Postdoctoral Fellowship tenable at the University of Sydney. XZ was in receipt of an Overseas Postgraduate Research Studentship from the Australian Government and an ARC Scholarship from the research grant awarded to Y-WM.

REFERENCES

1. Aveston, J., Copper, A. G. and Kelly, A. (1971) The properties of fibre composites. In Conference Proceedings, National Physical Laboratory, Guildford, 15-26.
2. Marshall, D. B. and Cox, B. N. (1985) Tensile fracture of brittle matrix composites, influence of fibre strength. *Acta Metall.* 35, 2607-2619.
3. Zhou, L.-M., Kim, J.-K. and Mai, Y.-W., (1992) On the single fibre pullout problem: effect of loading methods. *Composite Science and Technology* 45, 153-160.
4. Meda, G. and Steif, P. S. (1994) A detailed analysis of crack bridged by fibres. I: limiting cases of short and long cracks, *J. Mech. Phys. Solids* 42, 1293-1321.
5. Xia, Z. C., Hutchinson, J. W., Evans, A. G., and Budiansky, B. (1994) On large scale sliding in fibre-reinforced composites, *J. Mech. Phys. Solids* 42, 1139-1158.
6. Liu, H.-Y., Zhou, L.-M. and Mai, Y.-W., (1994) On fibre pullout with a rough interface. *Philosophical Magazine A* 70, 359-372.
7. Cox, B. N. and Marshall, D. B. (1994) Concepts for bridged cracks in fracture and fatigue, *Acta Metall. Mater*. 42, 341-363.
8. Zhang, X, Liu, H-Y, Mai, Y-W and Diao, X-X (1999) On steady-state fiber pull-out. Part I: stress field, *Composite Science and Technology*, 59, pp.2179-2189.
9. Liu, H-Y, Zhang, X, Mai, Y-W and Diao, X-X (1999) On steady-state fiber pull-out. Part II: numerical results, *Composite Science and Technology*, 59, pp.2191-2199.
10. Xu, G., Bower, A. and Ortiz, M. (1998) The influence of crack trapping on the toughness of fiber reinforced composites, *J. Mech. Phys. Solids* 46, 1815-1833.
11. Zhang, X, "Some Problems Relevant to Crack Propagation in Non-linear Solids", PhD thesis, The University of Sydney, 1999.
12. Zhou, S. J. and Curtin, W. A. (1995) Failure of fiber composites: a lattice Green function model, *Acta Metall. Mater*. 43, 3093-3104.
13. Landis, C.M., Beyerlein, I. J. and McMeeking, R. M. (2000) Micromechaincal simulation of the failure of fiber reinforced composites, *J. Mech. Phys. Solids* 48, 621-648.

FRACTURE BEHAVIOR OF A SICw/6061AL ALLOY COMPOSITE UNDER CYCLIC LOADING

Lei WANG[*1] T. KOBAYASHI[2] Z. M. SUN[3] and H. TODA[2]

[1]Department of Mechanical Engineering, Tottori University, Koyama 4-101, Tottori 680-8552, Japan
[2]Department of Production Systems Engineering, Toyohashi University of Technology,Tempaku-cho 1-1, Toyohashi, 441-8580, Japan
[3]Materials Engineering, Tohoku National Industrial Research Institute, Nigatake 4-2-1, Sendai 983, Japan

ABSTRACT

The fracture behavior of a SiC whisker reinforced 6061 aluminum alloy matrix composite under cyclic loading were investigated at both room and elevated temperatures with total strain controlled method. TEM and SEM were used to examine the microstructure and fracture surfaces of the specimens. The mechanical test results demonstrated that the composite materials maintained initial cyclic hardening. Under cyclic loading, the composite material failures with a mechanism of void‘s nucleation, growth and coalescence, which are near the end of SiC whisker reinforcements.

KEYWORDS: fracture behavior, cyclic loading, SiCw/6061Al, low cycle fatigue

1. INTRODUCTION

In order to reduce the fuel consumption and improve thermal efficiency of engines, aluminum matrix composites have been used for the new engine parts. For instance, the material used in the present study, SiCw/Al composite, is being used in motor parts of Suzuki engines[1]. However, a detailed understanding of the resistance of this material to cyclic deformation and low cycle fatigue fracture is required for further

* Corresponding Author: Associate Professor Lei WANG Phone & Fax: +81-857-31-6786, E-mail: lwang@mech.tottori-u.ac.jp

extending its applications in engineering, particularly where large deformation or thermal shock are unavoidable. Whereas the fatigue strength and the fatigue crack growth behavior of the metal matrix composites have been presented extensively in the literatures[2]-[5], limited results have been reported on the cyclic deformation of this type of materials, especially, at elevated temperature. The present study is to investigate the fracture behavior of a SiCw/6061Al composite and its matrix under cyclic loading.

2. MATERIAL AND EXPERIMENTAL PROCEDURES

2.1 *Material and specimen*

The material used in the present study was a 6061 Al alloy matrix composite(MMC) reinforced with 22vol% SiC whisker, fabricated using a high pressure infiltration technique[2]. For comparison, a 6061 Al alloy(matrix) was also prepared in the same fabrication route as for (MMC). Both MMC and matrix materials were heat treated to the overaging conditions. Solid solution treatment was performed at 803K for 9ks followed by water quenching, then aged at 450K for 180ks to achieve overaged condition. The test specimens were machined with the loading axis perpendicular to the casting direction. The plate-shaped specimens of 80mm long, with gage section of $4\times6\times20$mm, following ASTM (E606-92) recommendations were used for this study. The surface of the uniform-gage section of the specimens was carefully polished.

2.2 *Testing procedures*

A servo-hydraulic testing machine (load capacity: 50kN) was used in the present study. The tensile tests were performed in stroke controlled mode in accordance with ASTM E8M at an average cross head speed of 10^{-2} mm·s^{-1}. The cyclic deformation tests were performed in a fully reversed axial total-strain controlled mode. The strain rate was kept at 10^{-2}s^{-1} for various strain amplitude tests. Since triangular wave was used for the strain controlled testing, a constant strain rate was available during the complete loading cycle. The cyclic stress-strain behavior was studied with the incremental step method at different temperatures. The tests were carried out typically with a initial total strain amplitude, $\Delta\varepsilon_t/2$ of 0.075%. After 10 loading cycles, the total strain amplitude was increased by 0.075%, and the procedure was repeated. The tests were conducted in air at RT(293K), 373K, 423K and 473K. The specimens were heated in a resistance furnace with a temperature accuracy of $\pm$1K, and kept at the testing temperature for 3.6ks before starting a test.

2.3 *Microstructural analysis*

The fracture surfaces and gage section surfaces were examined in a scanning electron microscope (SEM), and an energy dispersive x-ray analysis system was used to determine the chemical compositions on some local area of fracture surfaces. Transmission electron microscope (TEM) was also used to study the microstructure of the specimens for different loading histories. TEM samples were sectioned near the fracture surface along the loading axis of the specimen. Ion-milling was utilized for the final thinning of the samples.

3. EXPERIMENTAL RESULTS AND DISCUSSION

3.1 *Mechanical behavior*

Figure 1 shows the stress-strain curves of MMC under cyclic and monotonic(tensile) loading at different temperatures. It can be seen that the stress response of MMC under cyclic loading were higher that those under

monotonic loading, regardless at the elevated temperatures. Table 1 shows typical stress response to cyclic and

Table 1 The cyclic and monotonic(tensile) stress with a strain of 0.6% at different temperatures.

Fig. 1 The cyclic stress-strain and tensile stress-strain curves at low strain range for MMC at different temperatures.

monotonic straining for MMC and matrix with a strain of 0.60% at different temperatures. Both cyclic and tensile stress responses decreased with the increasing of testing temperatures, while, comparing with the matrix, MMC showed higher stress response and kept less cyclic hardening until 473K. The higher stress response and higher strain hardening exponent in the composite are attributed to the constraint of the matrix flow caused by the reinforcement of SiC whiskers. This has been confirmed by an experimental study [6] and an FEM study [7].

Figure 2 shows the tress response to cyclic straining for both MMC and matrix at RT and 473K. The stress amplitude was taken as the average of the peak values of the stress in tension and in compression during the loading cycles. It is clear that MMC shows initial cyclic hardening at both temperatures during cyclic straining, and the cyclic hardening was more prominent at RT, which was followed by saturation and softening after a few initial hardening cycles. The matrix exhibits cyclic hardening at RT, however, when the temperature increase to 473K, it indicates softening from the starting.

Fig. 2 Cyclic stress amplitude of MMC and its matrix with different total strain amplitudes at RT and 473K.

The cyclic saturation implies that the deformation resistance remains unchanged with further cyclic straining. In other words, the cyclic straining is accommodated by certain reversible micromechanisms in the material during cycling. For MMC, due to the large difference in the coefficient of thermal expansion [CTE] between the reinforcement of SiC whiskers and the matrix, it introduces a tensile residual stress[8] and dislocations[9] in the matrix, especially in the vicinity of the whiskers, as shown in Fig. 3 a). When the material is cycled to saturation, for instance at 473K with total strain amplitude of $\pm 0.45\%$, the planar-array dislocation structure is formed, as shown in Fig. 3 b). The fro-and-to movement of screw dislocations in the

Fig. 3 TEM microstructure in MMC showing: (a) the dislocations in matrix near a SiCw in the deformed sample, and (b) the planar-array type dislocations configuration formed in a specimen after cyclic straining at 473K.

low dislocation density interior of the planar-array accommodates the applied strain. The presence of SiC whisker reinforcements induces changes in the matrix microstructure, *i.e*. high dislocation density, the smaller grain size [10], and the more homogeneous slip during cyclic deformation[11]. On the other hand, the matrix material is actually in an annealed condition with a lower dislocation density. When such a material is cyclically deformed, the increase in dislocation density and subsequent dislocation interactions can give rise to the initial hardening and finally cause cyclic stability. However, when the testing temperature and strain amplitude are increased, it exhibits softening from initial straining (Fig. 2 d)). This may be attributed to the cross slip of dislocations at higher temperatures (Fig. 5 c)), which caused the improvement of deformation flow. Furthermore, in Fig. 5 c) & d) intergranular failure can be noted clearly, which means that the matrix material failed in creep type at 473K. Therefore, it is not surprising that for the matrix cyclic softening occurs at higher temperatures.

3.2 *Fracture behavior*

The fracture surface morphology after cyclic straining (low cycle fatigue) of MMC and the matrix were shown in Figs. 4 and 5, at RT and 473K, respectively. It is notice that the fracture features of MMC are much finer than those of the matrix, regardless the different temperatures. And, for MMC, no evident slip line can be seen at the surface, while the microcracks perpendicular to the loading direction can be clearly seen from Figs. 4 a) and 5 a). It could be considered that since the addition of SiC whiskers introduced high density of dislocation and fine grain sizes, the cross and long distance slip of dislocations can hardly take place, even at high temperatures. Also, it can be seen that the SiC whiskers were exposed on the fracture surface (Figs. 4 b) and 5 b)), and such SiC whiskers were pulled out of the fracture surfaces (which were covered with the matrix

material examined by EDAX). This demonstrates that the failure of MMC was predominantly through the matrix and not along the SiC whisker-matrix interface. The same behavior is reported for A2124 matrix composite[12]. In order to reveal the nucleation sites for voids in MMC material, the samples were sectioned near the fracture surface after cyclic straining and examined with TEM. Fig. 6 showed three kind of voids nucleation in composite. They are around the end of whiskers (Fig. 6 a)), at the corners between the cross whiskers (Fig. 6 b)), and at the whisker break (Fig. 6 c)), in the matrix. This feature seems to be because of large stress concentration at the end of whiskers [7][13], which causes intense plastic straining in the nearby matrix and leads to void initiation at the corners. Moreover, the large precipitates on the SiC whiskers (Fig. 6 c), arrow marks) have a notch effect and cause the whiskers broken[14] when the stress increases up to a certain level, then it will become a void. It is clearly noticed that void growth involves the emission of matrix dislocations from the whisker end. This can be considered as follows. Under the cyclic straining, the matrix around the whiskers has undergone extensive sliding. This observation reveals the possibility of the matrix debonding in the immediate vicinity of the whiskers where the tensile hydrostatic stresses are high enough to cause the whisker pull-out with the coalescence of voids. Therefore, the composite seems to be fractured mainly due to nucleation, growth (include the voids merge) and coalescence of the voids in the matrix around

Fig. 4 SEM micrographs for MMC(a & b) and the matrix(c & d) cyclic deformed at RT, a) & c) specimen surface; b) & d) fracture surface.

Fig. 5 SEM micrographs for MMC(a & b and the matrix(c & d) cyclic deformed at 473K, a) & c) specimen surface; b) & d) fracture surface.

Fig. 6 TEM microstructure in MMC after cyclic straining at 473K, showing the void initiation: (a) near the end of whisker; (b) between cross whiskers and (c) at the whisker breaks.

SiC whiskers.

On the other hand, the fracture of the matrix under cycle straining seems to be associated with slip and creep. When the test is performed at low temperature, the fracture of matrix displays striation and transgranular failure (Fig. 4 c) & d)), while when the testing temperature is raised to 473K (Fig. 5 c) & d)), intergranular cavitation and microcracking generated mainly by the grain boundary diffusion. It can also be said that it is fatigue-creep fracture (Fig. 5 d)).

4. CONCLUSIONS

1) The SiCw/6061Al composite showed initial cyclic hardening with various strain levels from RT to 473K. Incorporation of SiC whiskers improved the cyclic flow stress as well as the monotonic flow stress at elevated temperature. These effects can be attributed to adding of whiskers into the matrix, which introduces high density of dislocations and constrains the matrix flow, aiding the composite to keep initial cyclic hardening and high stress until 473K.
2) Under the cyclic straining, SiCw/6061Al composite was found to fail in a mechanism of initiation, growth and coalescence (include merge) of voids in the matrix around SiC whiskers or at the whisker breaks, finally it makes the whisker pull-out from the matrix to cause the sample broken. While, the 6061Al alloy matrix failed in a manner changing from a pure fatigue to a creep/fatigue when the testing temperature increased.

REFERENCES

1. Yamaucchi, T. (1991) *Proc. 1991 Small Engine Tech. Conf.*, SAE, p. 505.
2. Vyletel, G. M., Allison, J. E. and Aken Van, D. C. (1995) *Metall. Mater. Trans. A*, **26A**, 3143.
3. Toda, H. and Kobayashi, T. (1994) *Proc. 10th Int. Conf. Strength of Mater*., pp.525-530, Oikawa, H. (Ed.), Jap. Inst. Metals, Sendai.
4. Venkateswara Rao, K. T., Siu, S. C. and Ritchie, R. O. (1993) *Metall. Trans. A*, **24A**, 721.
5. Toda, H. and Kobayashi, T. (1993) *Proc. of Int. Mechanics and Mechanisms of Comp. Mater*., pp. 55-60, Bhagat, B, Fishman, S. G. and Arsenault, R. J.(Eds.), TMS, Pittsburgh.
6. Arsenault, R. J. and Wu, . B. (1987) *Mater. Sci. Eng.*, **96,** 11.
7. Llorca, J., Suresh, S. and Needleman, A. (1992) *Metall. Trans.*, **23**, 919.
8. Povirk, G. L., Needleman, A. and Nutt, S. R. (1990) *Mater. Sci. Eng.*, **A125**, 129.
9. Han, N. L., Wang, Z. G. and Sun, L. Z. (1990) *Scr. Metall. Mater.*, **33**, 781.
10. Lloyd, D. J. (1994) *Int. Mater. Rev*., **39**, 1.
11. Poza, P. and Llorca, J. (1995) *Metall. Mater, Trans. A*, **26A**, 3131.
12. Sasaki, M., Lawson, L. and Meshii, M. (1994) *Metall. Trans. A*, **25A**, 2265.
13. Sun, Z. M., Li, J. B. and Wang , Z. G. (1992) *Chin. J. Met. Sci. Technol*., **8**, 107.
14. Lee, S., Kim, T. H. and Kwon, D. (1994) *Metall. & Mater. Trans. A*, **25**, 2213.

POSTER REFERENCE: ICF100238PR

FRACTURE BEHAVIOUR OF BLENDS CONSISTING OF ASYMMETRIC STYRENE/BUTADIENE BLOCK COPOLYMERS

R. Adhikari[1], R. Lach[1], G. H. Michler[1], R. Weidisch[1], W. Grellmann[1] and K. Knoll[2]

[1]Institute of Materials Science, Martin-Luther University Halle-Wittenberg
D-06099 Halle/Saale, Germany
[2]BASF Aktiengesellschaft, Polymer Research Laboratory, ZKT/I-B1
D-67056, Ludwigshafen, Germany

ABSTRACT

Fracture behavior of binary blends consisting of styrene/butadiene block copolymers having star and triblock architectures are studied via instrumented Charpy impact testing. The toughness of the ductile blends is characterized by dynamic crack resistance curves (R-curves). While the lamellar star block copolymer shows nearly an elastic behavior (small scale yielding and unstable crack growth), adding of 20 wt % of a triblock copolymer with dispersed styrene domains leads to a strong increase in fracture toughness. At this concentration, a transition from mechanism of micro-void coalescence to shear deformation takes place. New mechanism of toughness modification (where the transition from a lamellar structure with a long range order to a less ordered structure plays the central role) results in a specific morphology-toughness correlation which differs fundamentally from toughening mechanisms in conventional polymer blends.

KEYWORDS

Block copolymer blends, toughness modification, Charpy impact testing, R-Curves

INTRODUCTION

A large variety of mechanical properties and micromechanical deformation mechanisms are observed in block copolymers attributed to the existence of different highly ordered microphase separated morphologies whose periodicity lies in the range of the radius of gyration, R_g of the copolymer molecules [1-3].
In spite of rapid development of block copolymers with a variety of viscoelastic behavior, only limited investigations have been carried out concerning the influence of morphology on mechanical properties. Only few studies have been reported on the effect of microphase morphology on strength and stiffness of block copolymers [2,4] and blends containing block copolymers [5]. While the application of crack resistance concepts on nanophase-separated block copolymers has not yet been reported, experimental results on crack propagation behavior of other heterogeneous polymers systems under impact loading conditions are well known [6,7]. It should be, however, mentioned that the morphology-toughness correlation observed in the investigated systems are fundamentally different from that found in conventional impact modified or reinforced polymeric systems (matrix-particle morphology). The aim of this paper is to study new toughening mechanisms in binary block copolymer blends using crack resistance concept.

EXPERIMENTAL

Binary blends of a star block copolymer (ST2-S74) and a triblock copolymer (LN4-S65), both based on styrene and butadiene, are used in this study. The characteristics of the block copolymers are given in table 1. After mixing the materials in extruder, the single-edge notched bend (SENB) specimens were prepared by injection molding (mass temperature 250°C and mold temperature 45°C). The blends contain 5, 10, 20, 40, 60 and 80 wt % of LN4-S65.

Table1: Characteristics of the blend components; styrene as hard outer block in LN4 is 32 vol. % while the middle statistical block contains about 50 vol. % styrene.

blend component	M_n (g/mol)	M_w/M_n	$\Phi_{styrene}$	Morphology (TEM)
ST2-S74	109,200	1.69	0.74	lamellar
LN4-S65	116,000	1.20	0.65	PS domains in S/B copolymer matrix

In order to quantify the toughness behavior of investigated block copolymer blends, an instrumented Charpy impact tester IKBV-4J with 4J total work capacity was used. The SENB specimens have following dimension: length L = 80 mm, width W = 10 mm and thickness B = 4 mm. The specimens were notched with a razor blade (notch tip radius = about 0.13 μm). For the measurement of fracture mechanics parameters as resistance against unstable and stable crack growth, the initial crack lengths of 2 mm and 4.5 mm were cut [8]. To minimize the vibration of specimen, the span length was set to 40 mm, and the pendulum hammer speed was 1m/s. The determination of Young's modulus and yield strength as well as the fracture mechanics parameters as resistance against unstable crack initiation is carried out by using the procedures described in ref. [8]. Because blends with LN4 content ≥ 20 wt % reveal stable crack propagation behavior, an equivalent toughness characterization of these blends was only possible by crack resistance (R-) concept of elastic-plastic fracture mechanics. Crack resistance curves (R-Curves) represent the functional dependence of loading parameters (J-integral or δ) with the stable crack growth Δa. These curves allow the determination of fracture mechanics parameters as resistance against stable crack initiation and propagation. The multi-specimen-method in the stop-block-technique is found to be most effective for polymeric materials. Further details on determination and evaluation of R-curves under impact loading conditions are discussed in [8].
A small piece of each sample was cut from the bulk specimen and immersed in an aqueous osmium tetroxide (OsO_4) solution for several hours at room temperature to selectively stain the butadiene phase. Ultra-thin sections were cut using an ultramicrotome (Reichert Ultracut E) equipped with a diamond knife (Diatome). Microphase morphology of the samples was examined using a 200 kV transmission electron microscope (TEM, JEOL 2010).
In order to correlate the microstructure and fracture behavior with micromechanical deformation behavior, fracture surfaces of the specimens were qualitatively as well as quantitatively analyzed by scanning electron microscope (SEM, Jeol JSM-6300). Special attention was paid to quantification of some selected areas on the fracture surfaces like crack-tip blunting zone (stretch zone). For this purpose, the fracture surface of the SENB specimens were mounted on 45° sloped specimen target and sputtered with gold prior to the SEM imaging.

RESULTS AND DISCUSSION

Samples ST2 and LN4 have equilibrium morphologies comprising of alternating lamellae and randomly distributed cylinders [9] respectively. Morphology of the block copolymers and their blends is strongly influenced by shear stress of injection molding. As shown in fig. 1, lamellar structures of sample ST2 are aligned parallel to the injection direction by the shear stress.

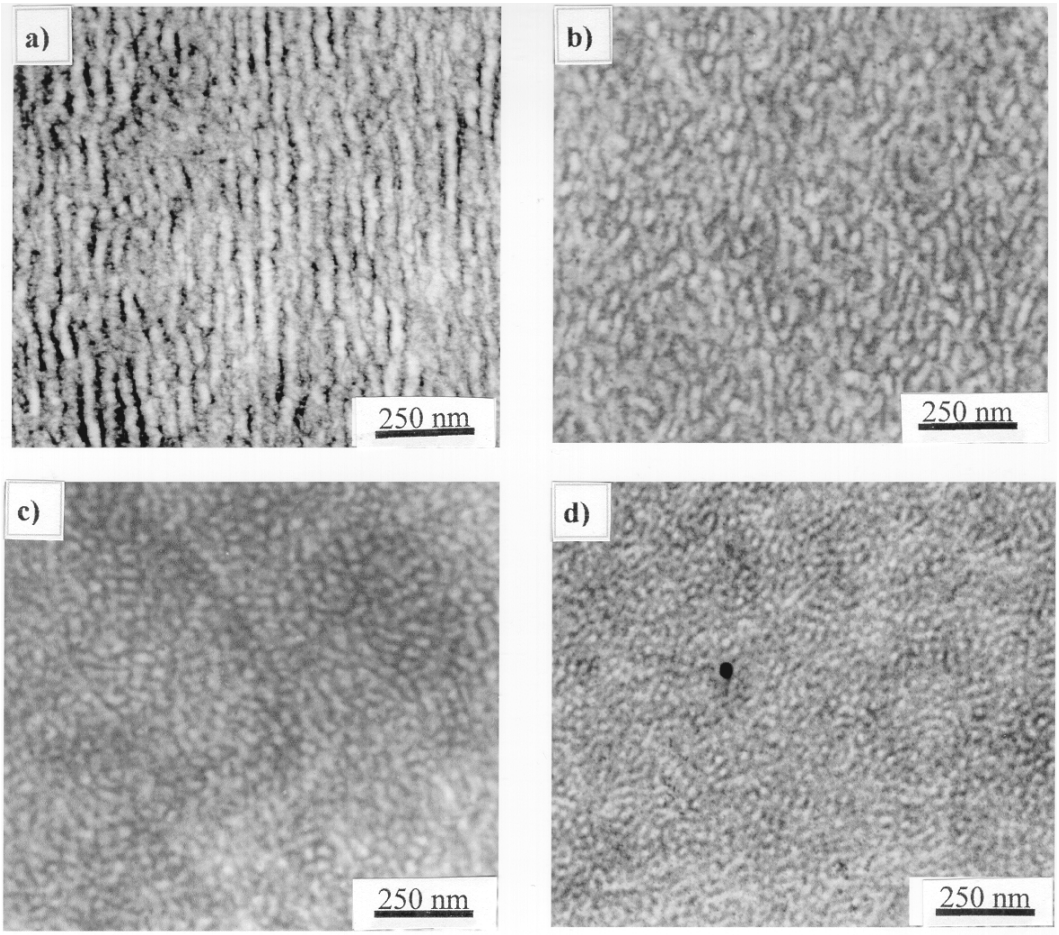

Figure 1: TEM images showing morphology of ST2/LN4 blends: a) pure ST2, b) 20% LN4, c) 80% LN4 and d) pure LN4; injection direction vertical.

Macrophase separation in the blends is strongly suppressed by the shear stress in the melt. Basically, two types of morphologies have been found. At lower LN4 content (0-20 wt % LN4), a lamellar morphology prevails which resemble qualitatively the morphology of pure ST2. At higher LN4 content (40-80 wt % LN4), the morphology of the blends is qualitatively comparable to that of pure LN4. The structural reorganization ("disorder") which occurs with increasing LN4-content has, as will be shown below, a strong influence on the achieved toughness level and underlying crack propagation mechanisms.

Physical crack initiation values (J_i and δ_i) were determined based on the considerations of crack propagation kinetics, i.e. analysis of different phases of crack growth (like crack-tip blunting, stable crack initiation and propagation or the unstable crack propagation) as a function of time. Parameters determined at physical crack initiation points are more structurally motivated than those at technical ones (e.g. $J_{0.1}$ and $\delta_{0.1}$ which are determined for stable crack growth of 0.1 mm, i.e. $\Delta a = 0.1$ mm). The slope of the R-curves at $\Delta a = 0.1$ mm (i.e. measured as $dJ/d(\Delta a)\big|_{0.1}$ and $d\delta/d(\Delta a)\big|_{0.1}$) and resulting tearing modulus $T_J = dJ/d(\Delta a)\big|_{0.1} \times E_d/\sigma_{yd}^2$ and $T_\delta = d\delta/d(\Delta a)\big|_{0.1} \times E_d/\sigma_{yd}$ are determined as resistance against stable crack propagation.

As shown in fig. 2a, R-curves with J or δ as loading parameters exhibit identical behavior. The slope of the R-curves at $\Delta a = 0.1$ mm and the tearing modulus increase with LN4 concentration until 80 wt% (fig. 2b). This indicates that the increasing ductility of the unnotched samples with increasing LN4 content, connected with decreasing elasticity modulus E_d and yield strength σ_{yd}, is also causing an increasing resistance against stable crack propagation. It should be, however, mentioned that this correlation does not have a general validity as shown by our recent results [9]. The physical crack initiation values (J_i and δ_i, fig. 2c) are insensitive to morphology which is in accordance with the previous results obtained for heterophase polymeric systems [7]. It is found that crack initiation values (e.g. $J_{0.1}$ and $\delta_{0.1}$) are generally not (or less pronounced) sensitive to the structure of the materials in contrast to the crack propagation values (like tearing modulus T_J and T_δ, fig. 2b).

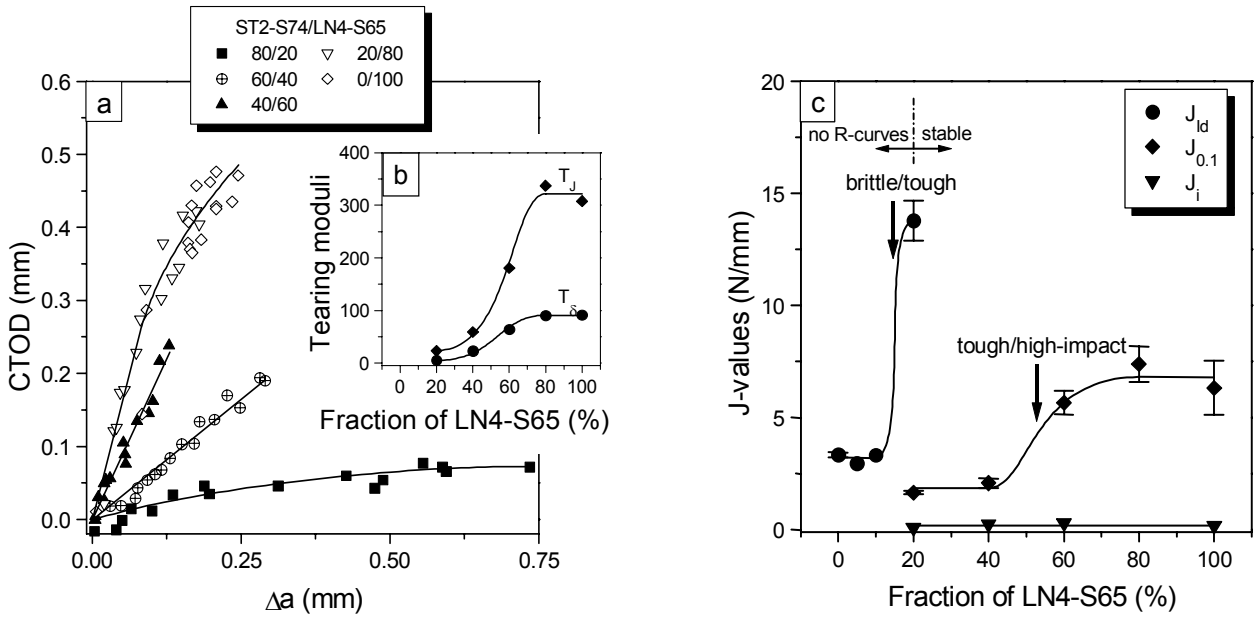

Figure 2: Crack resistance curve (a) and fracture mechanics parameters as resistance against stable crack propagation, tearing modulus (b) as well as resistance against unstable crack initiation J_{Id}; $J_{0.1}$ und J_i (c) as a function of blend composition

The kinetics of crack growth, especially the demarcation of each stage of crack growth, can be described by the crack propagation velocity. Additionally, it may be described by values as resistance against temporal change of fracture mechanics parameters e.g. CTOD-velocity dδ/dt. In fig 3., the stages of crack propagation are represented by the slopes of dδ/dt values. Stage I is correlated with the region of crack tip blunting, where the original razor-sharp crack blunts resulting in a strong increase in dδ/dt values. In stage II, the blunted crack propagates stable but non-stationary, i.e. the dδ/dt values increase with Δa. In stage III, the non-stationary stable crack propagation finally reaches a stationary stable crack growth, and the value of dδ/dt remains constant. The meaning of the constancy of dδ/dt values is equivalent to that of crack tip opening angles (CTOA).

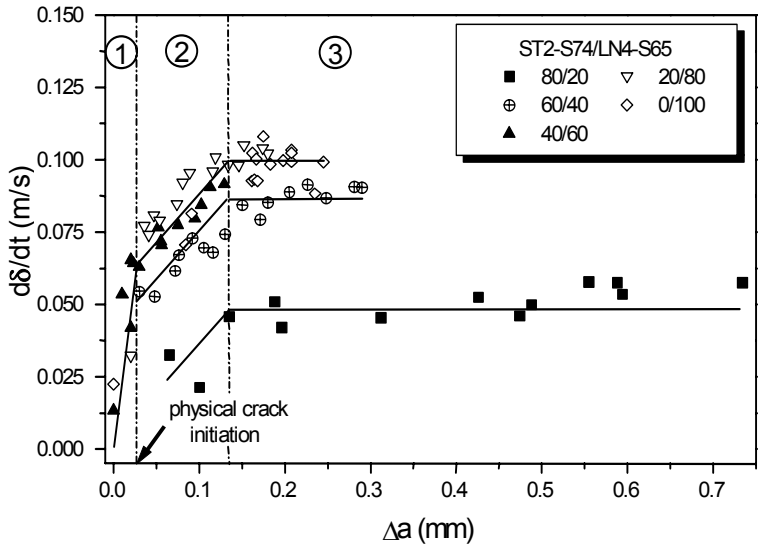

Figure 3: Crack-tip-opening-displacement-velocity dδ/dt as a function of stable crack growth and blend composition

Two different brittle/ductile transitions (BDT) were observed in other heterophase polymers [10,11]: the conventional BDT1 ("brittle/tough" transition) as a measure for the safety against unstable crack initiation

and BDT2 ("tough/high-impact" transition) as a measure for the protection against stable crack initiation. While a pronounced BDT1 can be observed at 10-20% wt of LN4, the quite wide BDT2 is observed between 50 and 60% of LN4 (fig. 2c). As demonstrated in recent studies [10,11], a shift from BDT1 to BDT2 occurs if the crack growth mechanism shifts from stable towards unstable one. As discussed in [10], differences in deformation mechanisms leading to BDT1 and BDT2 may be explained by Wu's percolation theory [12] and Margolina's theory [13] respectively. This classification is, however, impossible in the investigated system where the structural heterogeneity lies on the nanometer scale in contrast to a particle-matrix structure of polymer blends where particles sizes are usually in the μm scale.

In addition to in-situ investigation, examination of fracture surfaces also allows an analysis of crack propagation phenomenon. As shown in fig. 4, the transition BDT1 is associated not only with a strong increase in stable crack growth but also with a principal change in crack propagation mechanism. ST2 undergoes a brittle failure after crack tip blunting via unstable crack propagation. In the blends with 5 and 10 wt % LN4, a small amount of stable crack growth may be observed before the unstable crack growth begins, which is visible in SEM micrographs as structures formed by coalescence of micro-voids (fig. 4a,b). Such a crack propagation mechanism is typical for semicrystalline polymers like HDPE [14], where the structures are in nanometer scale, as well. In a composition range 10-20 wt % LN4, as a consequence of increasing disordered morphology, a sudden change from stable crack propagation via coalescence of micro-voids to the crack propagation via shear-flow occurs (fig. 4c). The individual crack growth areas (fracture parable) are separated by clearly visible shear-lips. Crack growth via shear-flow mechanism is typical for many amorphous polymers like polycarbonate [15]. Here, the crack becomes again sharp after blunting and propagates through the material by translation of the whole crack front [11]. This leads to the stretch-zone at the end of whole fracture surface length in contrast to the stretch-zone in blends containing 5 and 10 wt % of LN4 which is formed at the end of razor-notch.

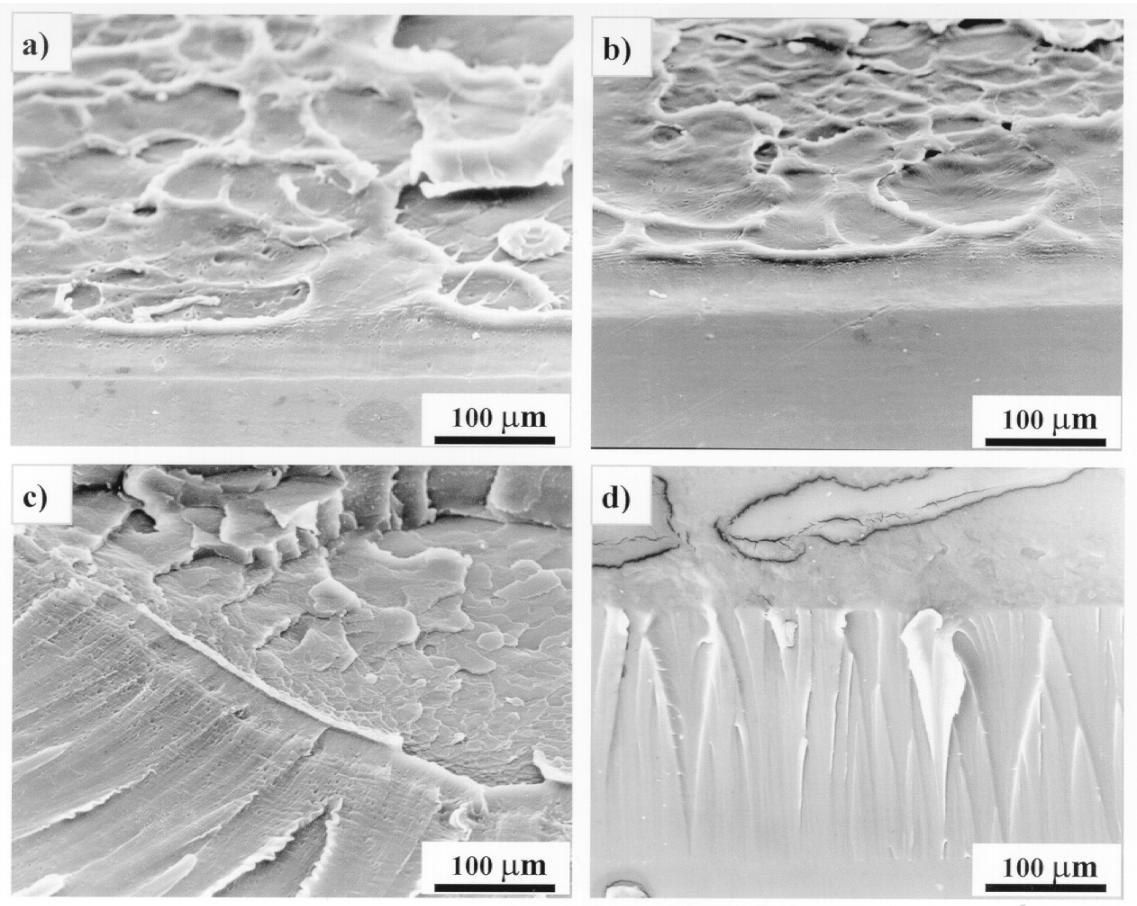

Figure 4: SEM images showing fracture surface morphology as a function of LN4 content: a) pure ST2, b) 5% LN4, c) 20% LN4 and d) pure LN4

The geometry of the stretch-zone can be used as a measure for plastic deformation during crack tip blunting, which is indicated by stretch-zone-width (SZW) and stretch-zone-height (SZH) along and normal to the direction of crack propagation. The decrease of SZW in the blends with increasing LN4 content (fig. 4) may

be attributed to the transition from the behavior of a conventional thermoplastic material (ST2) to that of a thermoplastic elastomer (LN4) i.e. a transition from viscoelastic to an entropy-elastic deformation behavior.

CONCLUSION

In contrast to conventional polymer blends where the toughness modification is achieved through dispersion of a soft phase in a hard matrix (macrophase separation), the investigated binary block copolymer blends represent nanometer-structured materials. New mechanism of toughness modification (where the transition from a lamellar structure with a high long range order to a less ordered structure plays the central role) results in a specific structure-toughness correlation which differs fundamentally from toughening mechanism in conventional polymer blends.

ACKNOWLEDGEMENT

We would like to thank BASF AG for fruitful cooperation and for providing materials and Ms. S. Goerlitz/ Ms. C. Becker for electron microscopic investigations.

REFERENCES

1. Keller, A.; Odell, J.A. (1986) In: *Processing, Structure and Properties of Block Copolymers*, p. 29, Folkes, M.J. (Eds). Elsevier Applied science Publishers, London
2. Weidisch, R. and Michler, G.H., (2000) In: *Block Copolymers*, p.215, Balta Calleja, F. and Roslaniec; Z. (Eds). Mercel Dekker, Inc. New York
3. Quirk, R.P. and Morton, M. (1998) In: *Thermoplastic Elastomers*, 2nd Edition., p. 71, Holden, Legge, Quirk, Schroeder (Eds). Hanser Publishers, Munich
4. Yamaoka, I. and Kimura, M. (1993) *Polymer* 34, 4399.
5. Yamaoka, I. (1998) *Polymer* 39 1765.
6. Castellani, L., Frassine, R., Pavan, A. and Rink, M. (1996) *Polymer* 37, 1329.
7. Grellmann, W., In Grellmann, W. and Seidler, S. (Eds.) (2001). *Deformation and Fracture Behaviour of Polymers*. Springer, Berlin Heidelberg, 3-26.
8. Grellmann, W, Seidler, S. and Hesse, W. (2001). In: *Deformation and Fracture Behaviour of Polymers*, Grellmann, W. and Seidler S. (Eds.). Springer, Berlin Heidelberg, 71-86.
9. Adhikari, R., Lach, R., Michler, G.H., Weidisch, R. and Knoll K., *Polymer*, in preparation.
10. Grellmann, W., Seidler, S., Jung, K. and Kotter I. (2001) *J. Appl. Polym. Sci.*, in press.
11. Han, Y., Lach, R. and Grellmann, W. (2001) *J. Appl. Polym. Sci.* 79, 9.
12. Wu, S. (1985) *Polymer* 26, 1855.
13. Margolina, A. (1990) *Polym. Commun*. 31, 95.
14. Beerbaum, H. and Grellmann, W. (2000). In: *Fracture of Polymers, Composites and Adhesives. ESIS Publication 27*, pp. 163-174, Williams, J.G. and Pavan, A. (Eds.). Elsevier Science Ltd., Oxford.
15. Grellmann, W. and Lach, R. (1997) *Appl. Macromol. Chem. Phys.* 253, 27.

ICF1009740R

FRACTURE BEHAVIOUR OF INJECTION MOLDINGS WITH WELD LINE

H. Hamada[1], K. Yamada[2], K. Tomari[2] and T. Harada[2]

[1] Advanced Fibro-Science, Kyoto Institute of Technology,
Matsugasaki, Sakyo-ku, Kyoto, 606-8585, JAPAN
[2] Plastics Department, Osaka Municipal Technical Research Institute,
Morinomiya, Joto-ku, Osaka, 536-8553, JAPAN

ABSTRACT

Weld lines are fatal defects in many injection moldings. Fracture behaviour of weld line is investigated in double torsion (DT) test using injection-molded polystyrene plates with a circular hole. The load-displacement curve showed irregular fluctuation corresponding to the alternate slow and rapid crack propagation. When the crack propagated rapidly, ripple marks appeared on the fracture surface, which were affected by the weld line. The ripple marks could be classified into two patterns, pattern I the ripple marks indicate that the crack propagated inwardly from the surface, and pattern II the ripple marks indicate the crack propagated from the mechanically introduced pre-notch. Pattern I was assumed to show the effect of V-notch on the weld line surface because the pattern was observed only in the fracture surface with a weld line. However, it was found that pattern I appeared even where there was no V-notch on the surface. It can be concluded that V-notch on the weld line surface does not affect the fracture behaviour, while it affects the visual defects of injection moldings.

KEY WORDS

Injection molding, weld line, polystyrene, fracture toughness, double torsion

INTRODUCTION

Weld lines that occur wherever two or more melt fronts meet cause reduced mechanical properties and visual defects of injection moldings. The reduction of mechanical properties is considered to be caused by poor intermolecular entanglement at the weld line, molecular orientation induced by the fountain flow, and the stress concentration effect of surface V-notch. Although the effect of weld line on the strength of injection moldings can be easily evaluated using dumbbell specimens which are molded in

two-gate mold, the effect on the fracture behaviour in practical injection moldings can not be estimated only by the dumbbell data because there are many types of weld lines and their generation mechanism is not so simple as that in dumbbell specimen. In the case of the dumbbell, as soon as two flow fronts collide head-on at the center of the specimen, a weld line occurs so that the property of weld line is not much affected by the flow behaviour. In the case of injection molded product on the market, after a weld line occurs behind an obstacle, polymer continues to flow and the pressure and temperature at the weld line region varies during the filling process. This means that pressure and temperature histories affect the properties of weld line occurring in injection molded products. The tests using the dumbbell that were used in previous studies are not sufficient to investigate the fracture behaviour of weld lines occurring in complicated mechanism.

In the present study, fracture behaviour of weld line is investigated in double torsion (DT) test using injection-molded polystyrene plates with a circular hole, which is structurally more complicated than a dumbbell. This is because DT test has many advantages, for example, the specimen is simple, crack speed can be easily controlled by loading rate and so on. The influence of V-notch, a factor affecting visual defects as well as mechanical properties, on the behaviour of crack propagation is discussed in particular.

EXPERIMENTAL

Injection Molding

The material in this study was general purpose polystyrene (GPPS), Styron 666, from A & M Styrene Co. Rectangular plates with and without a weld line were injection molded using the mold shown in Fig. 1. The plate dimensions were 100 x 50 x 3 mm^3. When an insert pin whose diameter was 20 mm was located in the center of the cavity, the plate with a weld line can be obtained. When the pin is removed, the plate without a weld line can be obtained. An injection molding machine, TP-80, manufactured by Toyo Machinery and Metal Co., was used, the performance of which was 80 tons in clamping force and 200 MPa at the maximum injection pressure. Molding conditions are listed in Table 1.

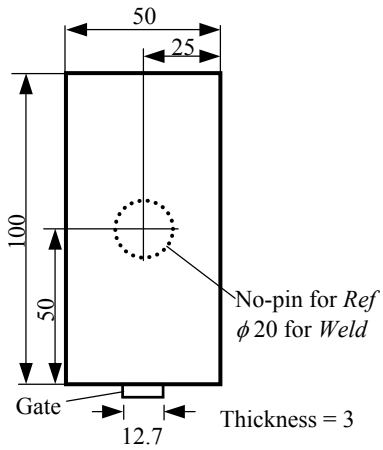

Figure 1: Specimens for double torsion test.

TABLE 1

MOLDING CONDITIONS

Run	Resin temp. (deg. C)	Mold temp. (deg. C)	Injection Speed (%)
1	180	40	30
2	200	40	30
3	220	40	30
4	200	80	30
5	200	40	10
6	200	40	90

Double Torsion Test

Fracture behaviour was investigated in double torsion (DT) test. The specimens were cut from the injection molded plates shown in Fig. 2(a). The specimens without weld lines were called *Ref* and those with a weld line were called *Weld*, respectively. A sharp pre-notch was introduced just at the pin side of the weld line for *Weld* as shown in the circle marked A in Fig. 2(b). A pre-notch was also introduced at an equivalent position for *Ref*. The fracture tests were conducted at a crosshead speed of 0.1 mm/min. at 23±2 ℃ and 60±5% with universal test machine, Autograph AG-50kNE, from Shimadzu Co. The specimen was supported by steel spheres (ϕ 11 mm) at each corner of the specimen and loaded by two spheres positioned over the notch (Fig. 3).

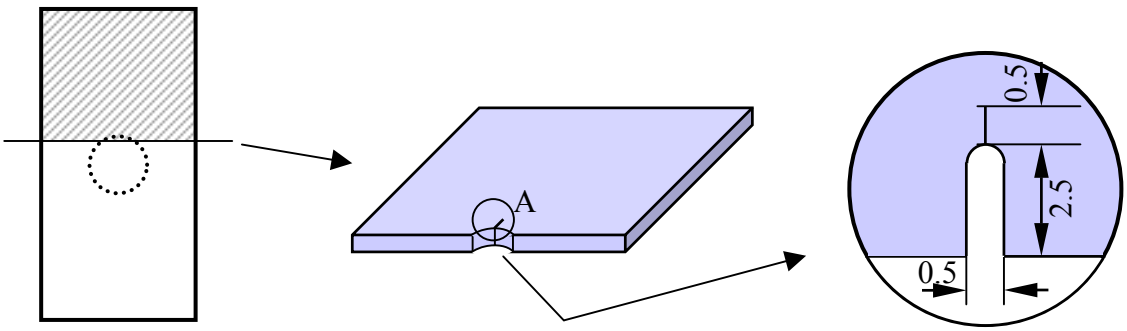

Figure 2: Specimen for double torsion test.

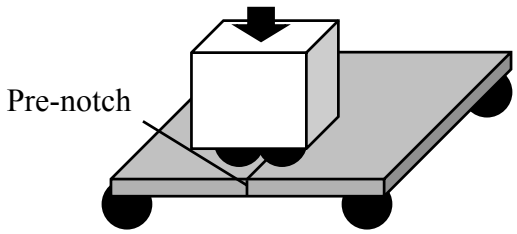

Figure 3: Schematic diagram of double torsion test.

RESULTS AND DISCUSSION

Fig. 4 shows typical load-displacement curves for both *Ref* and *Weld* obtained from the DT test. They exhibited a stick-slip mode. At start of the test the load rose linearly until the pre-notch opens, and rapid fall and linear increase in load were observed alternately. They were found to correspond to unstable crack propagation and crack arrest, respectively. In addition, slow crack propagation was observed with gradual falls in load. Fig. 5(A) shows the micrograph of the whole fracture surface of *Ref*. The fracture surface could be classified into two regions, mirror regions with no marks, and rough regions with ripple marks, indicating that the crack propagated in two kinds of manner. Tracing the crack propagation in the

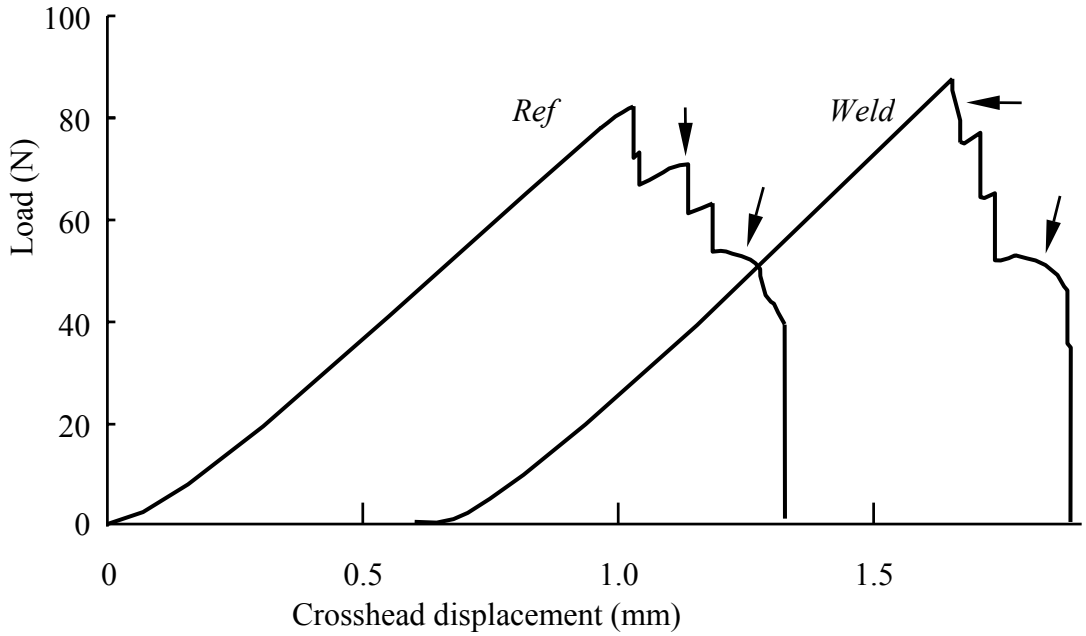

Figure 4: Load-displacement curves of *Ref* and *Weld* in DT test.
Arrows indicate slow crack propagation region.

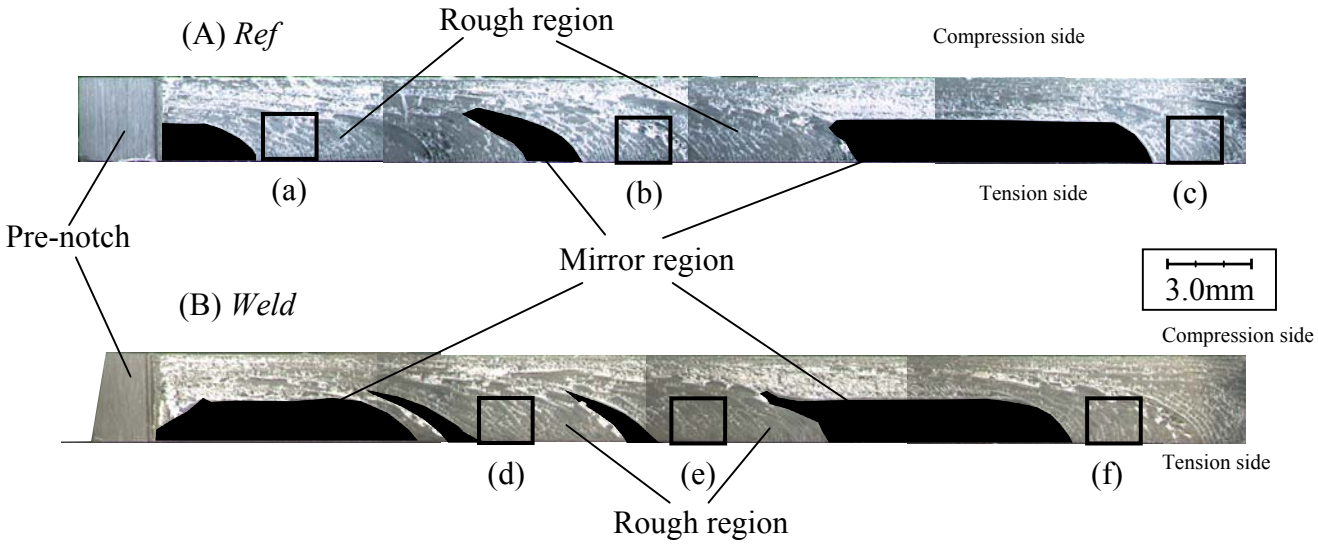

Figure 5: overviews of fracture surfaces. (A) *Ref* and (B) *Weld*.
Six rectangles (a), (b), (c), (d), (e) and (f) correspond to magnified images in Figure 6.

specimen during DT test clarified that the former corresponded to the area in which the crack propagated slowly (0.1 – 1.0 mm/s) and the latter corresponded to the area in which the crack propagated rapidly (ca. 200 mm/s).

Although the fracture surface of *Weld* seemed to be the same as that of *Ref* as shown in Fig 5(B), two different patterns of ripple marks were recognized in the rough region near the tension side surface as can be seen in Fig 6:

Pattern I: Ripple marks were parallel to the tension side surface. This pattern was observed only in the region close to the insert pin of *Weld* as shown in Fig. 6(d).

Pattern II: Ripple marks were perpendicular to the tension side surface. This pattern was observed in the whole of *Ref* and the region remote from the pin of *Weld* as shown in Fig. 6(a)-(c) and (f), respectively.

The fracture surface of *Weld* could be obviously divided into two areas, one having a rough surface with pattern I and the other having one with pattern II. Pattern I implied that the crack propagated inwardly from the tension side surface, while pattern II indicated that the crack propagated simultaneously with the surface crack. It is assumed that pattern I appears where there is a deep V-notch on the surface and pattern II appears where there is little V-notch.

Fig. 7 shows the relationship between the V-notch length and the length of pattern I. The V-notch length was not always equal to the length of pattern I. In particularly, when the mold temperature was 80 deg. C (No. 4 in Fig. 7), the V-notch length was only 6.0 mm, while the length of pattern I was 40 mm. This indicates that pattern I appears even where there is no V-notch on the surface. In other words, the other factors could affect the fracture behavior except V-notch. Although V-notch affects visual defects, it does not affect fracture behaviour.

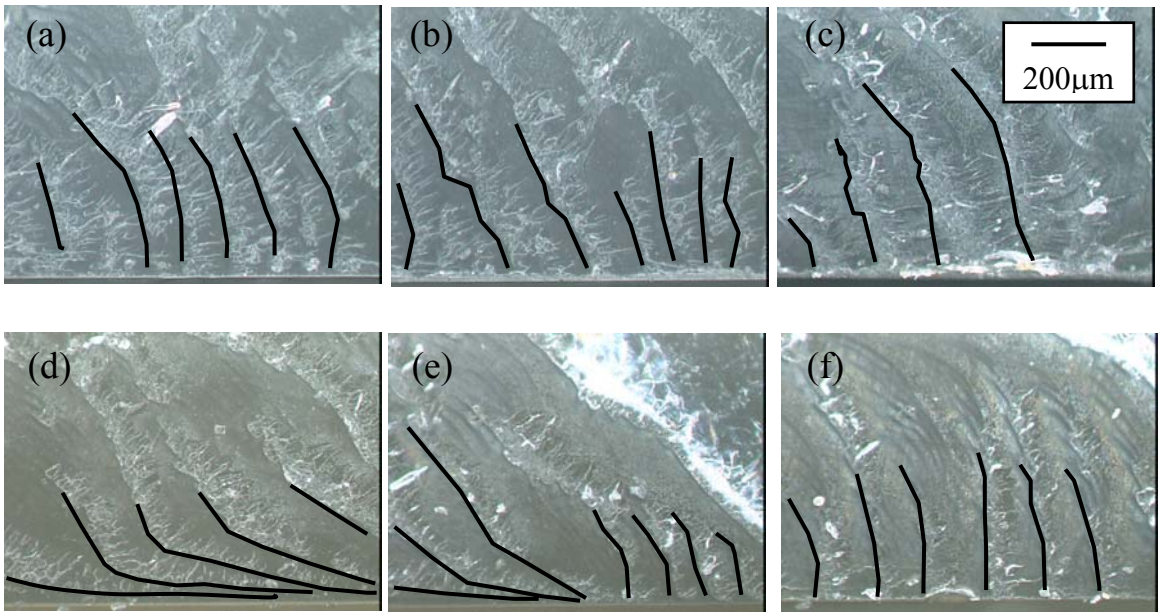

Figure 6: Optical micrographs of fracture surface of *Ref* and *Weld*. The alphabets correspond to those in Fig. 5 (a), (b) and (c) are from *Ref.* and (d), (e) and (f) are from *Weld.* Ripple marks are emphasized by black lines.

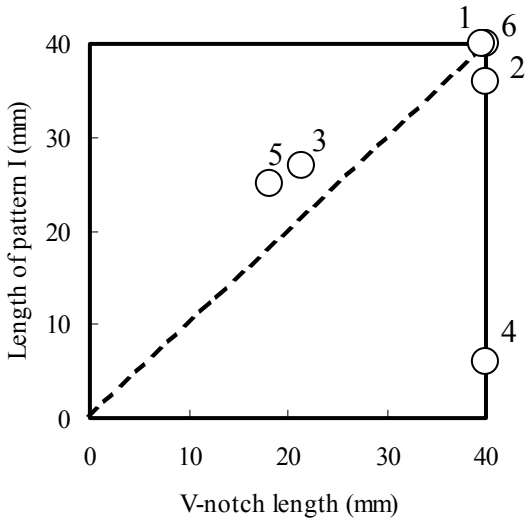

Figure 7: The relationship between the V-notch length and the length of pattern I. The numbers correspond to the run numbers in Table 1.

CONCLUSIONS

The influence of weld line on the fracture behaviour was investigated by tracing the ripple mark patterns appearing on the fracture surface from double torsion test. One of the patterns indicated that the crack propagated inwardly from the surface of specimen. Although the pattern was assumed to show the effect of V-notch on the weld line surface, the pattern was found to appear even where there was no V-notch on the surface. It can be concluded that V-notch on the weld line surface does not affect the fracture behaviour, while it affects the visual defects of injection moldings.

ICF100433PR

FRACTURE CONTROL OF GLASS THROUGH LAMINATION

F.A.Veer[1], S. Benedictus-de Vries[2], C. van Kranenburg[3]

[1]Faculty of Architecture, Delft University of Technology, NL
[2]Netherlands Institute for metals research, NL
[3]Laboratory of Materials science, Delft University of Technology, NL
E-mail : f.a.veer@bk.tudelft.nl

ABSTRACT

The mechanism of fracture in glass has been studied extensively. Through it's brittle nature it is an ideal model material. This suitability as a model material unfortunately also makes it a poor engineering material. The unique characteristics of transparency and chemical durability of glass forces the large scale use of this material in architecture and many other engineering branches. The limitations of glass as an engineering material however are a problem creating a requirement for a transparent material with mechanical properties comparable to metals.

Research into novel laminated glass based composites has resulted in a concept material that combines the transparency of glass with the structural safety of metals. This material is based on the concept of controlling the crack behaviour of the glass and arresting the cracks using crack bridging by the polymer interlayer in the crack wake.

KEYWORDS

Glass, Laminates, Fracture control, Crack bridging

INTRODUCTION

In many design's glass is used because it is the only transparent material available with a sufficiently high E-modulus to achieve adequate rigidity of the structure. Glass is however an extremely brittle material. The fracture mechanics of glass is well known, as the material was used by Griffith to develop the discipline of fracture mechanics. Although the mechanism of fracture in glass has been well understood for decades the only improvement that has been made is laminating the glass to increase the safety by avoiding spalling of glass fragments after failure has started. From the mechanical point of view no safety is obtained because, after failure of a glass pane in a laminated sheet has started, it effectively has no residual strength. Current tendencies in architecture are for increased usage of glass to the point where it is used as a structural material. The lack of residual strength after failure has been initiated requires the use of very high quantities of glass to provide for adequate structural safety by introducing redundancy through overdimensioning the structure. To avoid the extreme overdimensioning of the structure a material that combines the transparency of glass with the ductility of metals is required. This paper will show some of the steps in developing the resulting composite.

THEORETICAL FORMULATION

To develop a transparent structural material it has to be realised that transparency imposes unique restrictions. A material that is transparent must not disperse light. Thus all phase boundaries must be in the plane of the material to assure that all light is refracted in the same way. The requirement of high E-modulus requires the use of glass sheets as a base material. The question thus resolves itself to how to control the fracture behaviour of glass. A pane of glass normally fails by cracks developing from defects on the edges of the material. These edges are the result of processing. The inherent brittleness of glass means that even defects with sizes of 10 μm can lead to cracks developing at low stresses. Pre-stressing the glass can reduce the stress concentrations at these defects by introducing a permanent compressive stress in the surface. The normal thermal pre-stressing methods however stores so much energy in the material that once failure is induced the material disintegrates. Using ion-exchange techniques for pre-stressing allow for exact control of the residual stress. This means that fracture initiation can be delayed but total disintegration can be avoided (1). This means that the problem resolves itself to arresting the cracks and bridging the cracks that are initiated. Successful crack bridging and crack arrest means that the material has potentially enough residual strength to allow it carry loads after accidental overloading has introduced some cracks.

This problems is similar to that faced in concrete. In concrete fibre or rod reinforcements can bridge cracks arresting and bridging the cracks by deformation of the reinforcement in the crack wake (2). Unfortunately these fibres would scatter the light passing through the glass making the material translucent. Crack wake effects must thus be introduced not into the sheet of glass but in a adjacent sheet of a transparent polymer bonded to the glass. If an edge crack starts in a glass pane, the crack will grow until the energy released by crack propagation is equalled by the energy absorbed by deformation of the polymer in the crack wake.

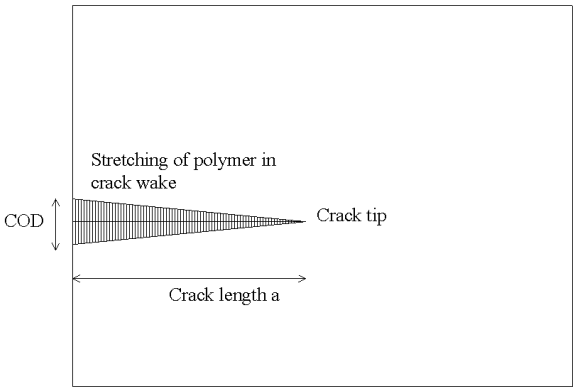

Figure 1: Schematic diagram of crack wake activity in laminated glass

The problem lies in the adhesive layer. If the adhesive is too strong all the energy will be focussed on a small region of polymer adjacent to the actual crack. In theory this means that an almost infinite strain will be placed on a small area of the polymer adjacent to the actual crack. If the adhesive fails locally, local debonding becomes possible allowing for distribution of the strain across a greater volume.

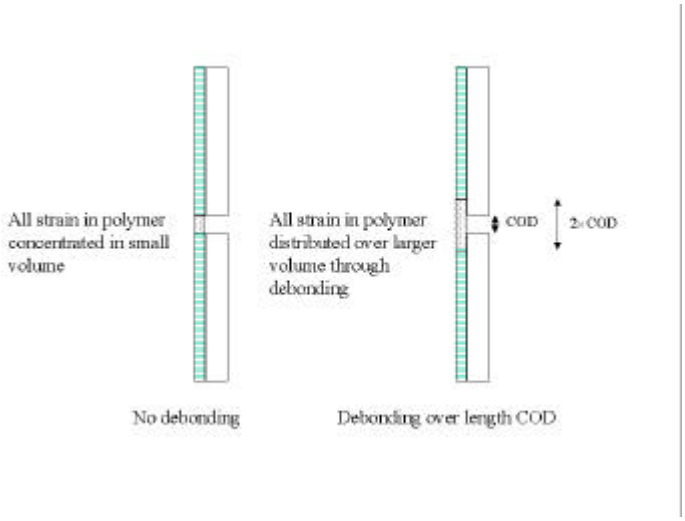

Figure 2: Effect of debonding on strain distribution in the polymer

Assuming that the length of the debonding region is X×COD, at any point in the crack wake a length of 2X×COD is being stretched to (2X+1)×COD. If X is too small the strain in the polymer will exceed the fracture strain and the polymer will fail leading to total failure of the element. If X is too big the composite will delaminate and fail. Achieving a critical value of X allows the possibility of successful crack arrest and crack bridging. This can be solved analytically for a single crack in glass with two sheets of polymer on either side. In a realistic component multiple layers of glass will be used with polymer interlayers. The interaction will be too complex for effective analytical formulation. In addition the possibility of building up large components from smaller plates by an overlapping arrangement complicates the modelling.

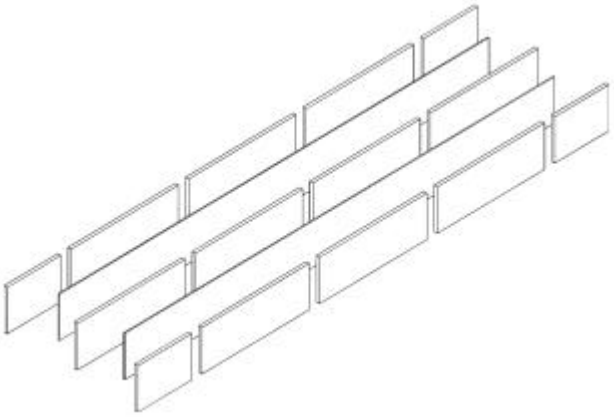

Figure 3 : Beam build up from smaller components

Numerical studies of the concept using the finite element technique are possible. Some studies were conducted using the ANSYS FEM programme. Initial studies suggested the following :

- the theoretical concept should work in real life
- the polymer plies should be much thinner than the glass plies
- the polymer should have a large fracture strain (>50%) for the mechanism to work efficient, polymers with small fracture strains require large debonding lengths, which reduces the properties of the composite to an unacceptable level.
- the individual glass plates should be as large as possible in relation to the thickness to prevent hinges forming in the component

The results of these calculations were interesting and showed that the concept was workable but also showed that very complicated models are required to take account of the following :

- debonding of the adhesive layer
- transfer of compressive and shear loading across the crack face

From these initial results it was decided to use polycarbonate as the polymer due to it's large fracture strain and easy availability. As a result an experimental programme was formulated to test the concept and to determine :

- the required strength of the adhesive to give adequate debonding
- the optimum thicknesses of glass and polymer

RESEARCH INTO THE ADHESIVES

As sufficient is known about the effect of ion-exchange on the residual stress in glass and the fracture properties, the primary problem was to investigate which adhesives are suitable for this requirement. Although several types of transparent adhesive exist, they are not all able to bond polycarbonate which has a low surface energy. Testing different types of polyurethane and acrylic adhesives showed that the polyurethane adhesives were not suitable because they only formed thick adhesive layers. The thickness of the adhesive did allow for quick redistribution of the stresses from the glass to the polycarbonate. In addition the adhesive was too tough to effect delamination. Acrylic adhesives formed thin layers (˜10µm) with a shear strength of 5 MPa and sufficient brittleness to delaminate close to the crack.

Further research used photo-catalytic acrylic adhesives which are easier to use as they only start to cure when illuminated by light of the right frequency. These photo-catalytic adhesive have a shear strength of 5 MPa, can wetten the polycarbonate. They have sufficient bond strength to bond the glass and polycarbonate together and sufficient brittleness to allow for easy local debonding near cracks.

RESEARCH INTO COMPOSITE BEAMS

Prototype beams were made using several configurations based on the general design shown in figure 3. These were tested in 4 point bending. In the test the following phases could be distinguished :

(a) an initial elastic part
(b) a part where cracks start to form in the tensile region, these cracks propagate at angles of about 20º to the loading axis, E-modulus falls but strength remains constant
(c) a part where cracking intensifies and significant displacement of the specimen occurs, the E-modulus falls but the strength remains constant
(d) the final stages where crushing of the glass takes place in the compression zone, strength falls slowly until final failure occurs

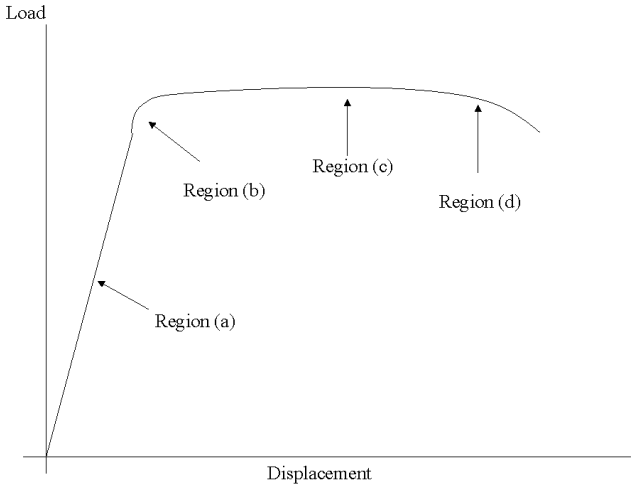

Figure 4: Generalised load-displacement curve of composite beams

The actual strength is dependent on the level of pre-stressing of the glass and the configuration. Ultimate strengths in bending of 80 MPa with a Young's modulus of 50 GPa and a fracture strain of 25% can be achieved reliably. This is similar to the mechanical properties of some aluminium alloys.

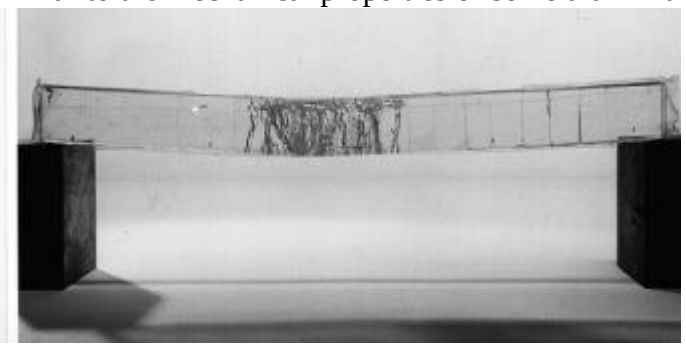

Figure 5: Beam specimen after testing

RESEARCH INTO COMPOSITE PLATES

In a similar way composite plates were produced. The number of layers, number segments in a glass ply and method of overlapping is a design variable that allows for tailoring of the properties. The plates were tested by supporting them at the four corners and loading them in the centre until cracks started to form.

Cracks were always started at the edges of the glass segments in the tensile bottom layer. At a given stress level the cracks were arrested after several mm of growth. Increasing the stress resulted in limited crack growth followed by crack arrest. Study of the arrested cracks under load with microscopes showed that debonding took place over a length of approximately 2× COD at any point in the crack length with variations between 1 and 3× COD depending on bonding quality. Properties are again dependent on the configuration but similar to those found for beams. In addition the plates have a significant anti-penetration capability.

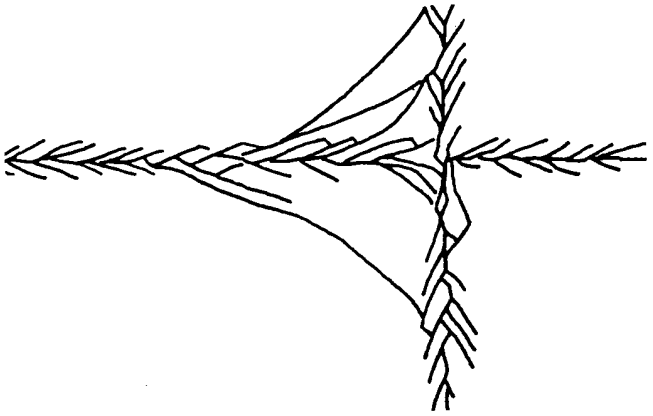

Figure 6: Drawing of arrested cracks at edges of segments in composite plates

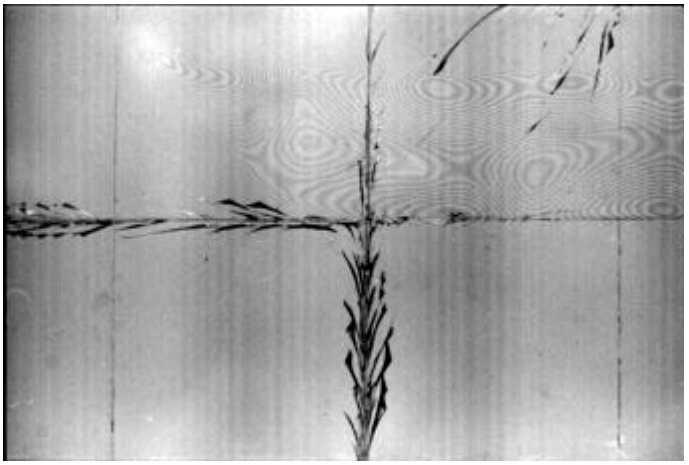

Figure 7: Foto of arrested cracks at edges of segments in composite plates

CONCLUSIONS

Although the brittle nature of glass cannot be changed some toughness can be build into laminated composite glass structures by new methods of lamination. Using a thin ductile polymer interlayer bonded to the glass cracks in the glass can be arrested by stretching of the polymer interlayer in the crack wake. In addition this provides crack bridging.

This stretching can only occur if the adhesive delaminates locally, distributing the strain in the polymer over a greater volume. A brittle and strong adhesive that can be applied in a thin layer is required for this. If the adhesive is too strong or the layer is too thick the mechanism does not work because the strains are not properly distributed to the polymer interlayer resulting in failure of the interlayer of failure of the laminate.

Using this method of obtaining crack arrest and crack bridging transparent composite beams and plates can be made with mechanical properties similar to some aluminium alloys. Although considerable work is yet required to produce a real engineering material the concept provides the basis for an unique material combining transparency with the ability to safely carry loads. Patent for the various developments is being applied for.

ACKNOWLEDGEMENTS

The assistance of the “van Noordenne groep”, in providing us with glass and technical expertise is acknowledged. The assistance of “Siko BV”, in providing bonding agents, equipment and technical expertise, is acknowledged

REFERENCES

1 I.W. Donals et al. , The mechanical properties and fracture behaviour of some chemically strengthened silicate and borate glasses, Glass technology vol 34, p 114, 1993

2 G. Weidman et al. Structural materials, Butterworth Heineman, 1990

FRACTURE CRITERION FOR PIEZOELECTRIC MATERIALS WITH DEFECTS BASED ON ENERGY DENSITY THEORY

Ai Kah Soh[1], Kwok Lun Lee [1] and Dai-Ning Fang [2]

[1] Department of Mechanical Engineering, The University of Hong Kong, Hong Kong
[2] Department of Engineering Mechanics, Tsinghua University, Beijing 100084

ABSTRACT

A failure criterion, which was established based on the energy density factor, is extended for an elliptical cavity or a line crack embedded in an infinite piezoelectric solids, subjected to a combined in-plane electrical and mechanical loading. In the present analysis, the exact electric boundary conditions are applied at the rim of the cavity/crack. The direction of crack initiation or subsequent post-failure, and the critical loads for fracture, can be predicted using the total energy density factor, S. This factor is a function of the aspect ratio of the elliptical cavity, the electromechanical loading, core region outside the crack tip, permittivity of vacuum and material constants. The results obtained agree with the experimental observation, i.e. a positive electric field enhances crack growth while a negative electric field impedes crack growth. Moreover, the results indicate that the critical fracture loads are under-estimated by the assumption of impermeable crack and over-estimated when the crack is assumed to be permeable for $E_z^{app}>0$, where E_z^{app} is the applied electric field. However, the fracture loads are over-estimated by the assumption of impermeable crack and under-estimated when the crack is assumed to be permeable for $E_z^{app}<0$. The energy density criterion has the advantage of possessing the capability to implement the exact electric boundary conditions. This is due to the fact that the criterion can link the behavior of a crack to that of an elliptical cavity by consistent application of this criterion to a thin layer near the cavity/crack boundary.

KEYWORDS

Energy density factor, piezoelectric material, fracture criterion, energy release rate, elliptical cavity, crack

INTRODUCTION

The fracture problems of piezoelectric materials have received much attention in the last ten years. Thus, vast amount of theoretical results have been obtained by many researchers [1-8]. However, nearly all the previous analyses were based on the assumption of impermeable or permeable crack. In fact, these two extreme cases are not realistic. Since the dielectric constant of the air or vacuum inside the crack is neither zero nor the dielectric permittivity of the material [3, 7], the crack problems in a piezoelectric material should be treated as electric inclusion problems. Consequently, Sosa and Khutoryansky [9] used the series expansion method to address the plane problem of a transversely isotropic piezoelectric medium with an elliptical hole.

Many fracture criteria for piezoelectric materials have been proposed in the recent years, e.g., the total potential [4,6], the mechanical [8] and the local [10] energy release rates, and the energy criterion considering domain switching dissipation [11]. Pak [4] found that the presence of applied electric field always reduced the total potential energy release rate. This implies that a crack is impeded by the electric field regardless of its direction. This conclusion contradicts the existing experimental data. Later, Park and Sun [8] proposed to use only the mechanical part of the energy as a criterion by arguing that fracture is a mechanical process and, therefore, it should be controlled by the mechanical part of the energy release rate. But, this argument is unsound because there is no fundamental reason to separate a physical process into an electric part and a mechanical part, in view of the fact that all mechanical forces are of electromagnetic origin. As a result, Gao et al. [10] proposed a criterion based on the local energy release rate of an electrically yielded crack. However, the effect of domain switching cannot be accounted for using this model. In line with Griffith's theory on mechanical fracture, Fang et al. [11] proposed a criterion based on energy balance with the consideration of domain switching dissipation. However, they only proposed an energy balance approach and the results are the same as those of Gao et al [10].

Recently, Shen and Nishioka [12] used strain energy density theory to develop a fracture criterion for piezoelectric materials. Their theoretical result agrees qualitatively with the empirical evidence by assuming impermeable crack. In the present study, the energy density fracture analysis of an elliptic cavity or a crack, in a transversely isotropic piezoelectric solid subjected to remote loading, is carried out. This study adopts the approach and the assumption of exact electric boundary conditions employed by Sosa and Khutoryansky [9]. First of all, a surface layer criterion [13] is used to locate the position where the fracture of the elliptic cavity is expected to initiate. The direction of crack initiation and subsequent post-failure can be described by the total energy density factor, S, from which the critical loads for fracture can be predicted.

SOLUTION FOR AN ELLIPTIC CAVITY

Consider a central elliptic cavity of major and minor semi-axes, *a* and *b*, respectively, embedded in an infinite poled piezoelectric ceramic, which is subjected to a remote in-plane electrical loading, E_z^{∞}, and mode I mechanical loading, σ_{zz}^{∞} as shown in Figure 1. The cavity is assumed to be filled with a dielectric medium of permittivity, ε_0, and it is free of traction force and charge. The ceramic is poled in the positive direction of the z axis.

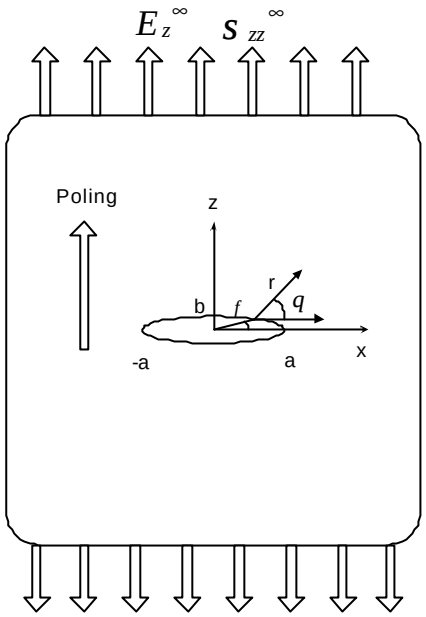

Figure 1: Schematic diagram of an elliptical cavity embedded in a piezoelectric plate

By applying the procedure proposed by Sosa and Khutoryansky [9], the field solutions for two-dimensional problems based on the exact electric boundary conditions can be expressed as

$$\acute{o} = \begin{pmatrix} s_{xx} \\ s_{zz} \\ s_{xz} \end{pmatrix} = \begin{pmatrix} s_{xx}^{\infty} \\ s_{zz}^{\infty} \\ s_{xz}^{\infty} \end{pmatrix} + 2\,\mathrm{Re}\sum_{k=1}^{3} \begin{Bmatrix} m_k^{\,2} \\ 1 \\ -m_k \end{Bmatrix} L_k\,; \qquad \mathrm{D} = \begin{pmatrix} D_x \\ D_z \end{pmatrix} = \begin{pmatrix} D_x^{\infty} \\ D_z^{\infty} \end{pmatrix} + 2\,\mathrm{Re}\sum_{k=1}^{3} \begin{Bmatrix} m_k \\ -1 \end{Bmatrix} l_k L_k\,;$$

$$\mathring{a} = \begin{pmatrix} e_{xx} \\ e_{zz} \\ 2e_{xz} \end{pmatrix} = \begin{pmatrix} e_{xx}^{\infty} \\ e_{zz}^{\infty} \\ e_{xz}^{\infty} \end{pmatrix} + 2\,\mathrm{Re}\sum_{k=1}^{3} \begin{pmatrix} a_{11}m_k^{\,2} + a_{12} - b_{21}\,l_k \\ a_{12}m_k^{\,2} + a_{22} - b_{22}\,l_k \\ -a_{33}m_k + b_{13}\,l_k\,m_k \end{pmatrix} L_k \quad ;\mathrm{E} = \begin{pmatrix} E_x \\ E_z \end{pmatrix} = \begin{pmatrix} E_x^{\infty} \\ E_z^{\infty} \end{pmatrix} + 2\,\mathrm{Re}\sum_{k=1}^{3} \begin{pmatrix} 1 \\ m_k \end{pmatrix} k_k L_k \qquad (1)$$

where Re denotes the real part of a complex valued quantity; complex coefficients, μ_k, λ_k, κ_k, L_k, which are functions of material constants are given in Soh et al [14].

For an elliptical notch, a surface layer criterion proposed by Sih [13] can be employed as a preliminary judgment to locate the position f, at which fracture may initiate from the notch surface. Note that f denotes the angle between the direction of crack propagation and that of the positive major semi-axis of the elliptical notch. Once the angle f is determined, the knowledge of the energy stored in an element outside the core region (near the apex of the elliptical notch) is used as a means for establishing the failure location at some points in the bulk of the solid.

The energy associated with the surface layer can be derived from the mechanics of thin layer. On Γ(surface of cavity), the radial stress is equal to zero. Thus, the element in the thin layer is subjected to uniaxial tension. Therefore, the strain energy per unit area of the surface layer can be expressed as

$$g_e = \left(\frac{1}{2} \sigma_{ss} \varepsilon_{ss} + \frac{1}{2} E_s D_s \right) \delta \tag{2}$$

where δ is a parameter for quantifying the surface condition, and σ_{ss}, ε_{ss}, D_s, E_s are given in Soh et al. [14]. Note that $\gamma_e/\delta\sigma^2\pi a$ is a convenient non-dimensional form for indicating strain energy. A notched specimen may be loaded to failure and the strain energy per unit surface layer can be computed from equation (2). The location of initial failure (i.e., the angle of crack propagation, θ) on the notch boundary is then determined by setting $\partial g_e / \partial \theta = 0$ for g_e to reach its maximum value.

ENERGY DENSITY CONCEPT

For a piezoelectric material containing an elliptical cavity, the surface layer energy criterion is only applicable to the surface of the cavity. The strain energy density criterion is then employed to predict the trajectory of crack propagation or failure path at the interior points near the surface. Similar to the pure mechanical case [13], the energy density function for the electromechanical case in the element dV of a general three-dimensional system can be written as

$$\frac{dW}{dV} = \frac{1}{2} \sigma_{ij} \varepsilon_{ij} + \frac{1}{2} E_i D_i \tag{3}$$

and the strain energy density field, S, is expressed as

$$S = r \frac{dW}{dV} \tag{4}$$

In order to obtain better accuracy, the complete strain-energy density expression is used in the present study rather than that with only singular terms. The fundamental parameter in this theory, S, is direction sensitive in the sense that it predicts the direction of crack propagation. This is accomplished by calculating the stationary value of S or dW/dV, with r being the radial distance measured from the crack front. The minimum S value, i.e., S_{min}, is related to dilatation of material elements and is associated with the creation of a free surface that fracture is expected along the line of crack extension.

For the present two-dimensional problems, the direction of crack propagation can be determined by a single variable θ with different values of r giving the same trend. Hence, the necessary and sufficient conditions for the strain energy density factor S to be minimized are as follows:

$$\frac{\partial S}{\partial \theta} = 0 \qquad \& \qquad \frac{\partial^2 S}{\partial \theta^2} > 0 \qquad at\ \theta = \theta_0 \tag{5}$$

The minimum energy density factor, which occurs at the crack initiation direction, θ_0, can be determined from equation (5).

DISCUSSIONS

In order to demonstrate the suitability of the energy density theory for solving the problem of piezoelectric failure in the case of exact electric boundary conditions, an elliptical crack embedded in a piezoelectric material, PZT-4, is considered. For an infinite plate containing a central elliptical cavity, subjected to remote electro-mechanical loading, failure will occur at around $\phi=-9^0$ for b/a=0.5, around $\phi=-5^0$ for b/a=0.25, and around $\phi=-3^0$ for b/a=0.125 for three different load ratios ($E_z^{¥}/\sigma_{zz}^{¥}$=-0.01,0,0.01). Moreover, for the same remote loading, no matter in which direction the electric field is applied, increase of loading is allowed when the notch tip becomes more blunt. This coincides with the conventional fracture criterion.

Naturally, one would like to know how the crack would extend from the initial failure location on the surface of the elliptical notch. As mentioned above, in order to determine the direction of crack propagation, $\theta = \theta_0$, the stationary values (S_{min}) of the strain energy density for various radius vectors need to be determined. The calculated results show that for different radius vectors, directions of the applied electric field, and permittivity of the medium inside the elliptical cavity, the direction of subsequent fracture is always horizontally outward, i.e., in $\theta = 0$ direction.

Figure 2 shows the effects of the applied electric field on the fracture loads for a crack with half-length a=0.01m for the case of exact, impermeable and permeable boundary conditions, i.e., $\varepsilon_0 = 8.85\times 10^{-12}\ NV^{-2}$, $\varepsilon_0 = 0.0 NV^{-2}$ and $\varepsilon_0 = 5 \times 10^{-9}\ NV^{-2}$, respectively. The critical load of this specimen is 2 MPa when no electric field is applied. It should be noted that b is made approaching zero instead of equal to zero (the crack keeps open). The energy release rate criterion is shown in the same figure for comparison.

It is interesting to note that the effects of the direction of the applied electric field on crack propagation for the case of sharp crack subjected to different electric boundary conditions have the same trend. That is a negative electric field impedes crack propagation while a positive electric field enhances crack propagation. Moreover, the fracture loads are found to be under-estimated by the assumption of impermeable crack and over-estimated when the crack is assumed to be permeable for $E_z^{app}>0$. However, the fracture loads are over-estimated by the assumption of impermeable crack and under-estimated when the crack is assumed to be permeable for $E_z^{app}<0$. In contrast to the energy density criterion, the fracture loads calculated based on the criterion of energy release rate are independent of the direction of the applied electric field, which contradicts many experimental observations. It is physically incorrect for the fracture load to increase with increasing E_z^{app} increases because it is impossible that the load carrying capacity of the cracked specimen increases as the applied load is increased. All the critical stresses must decrease as the load is increased. Note that the four curves intersect at the point of zero applied electric field, which is the case of pure mechanical loading

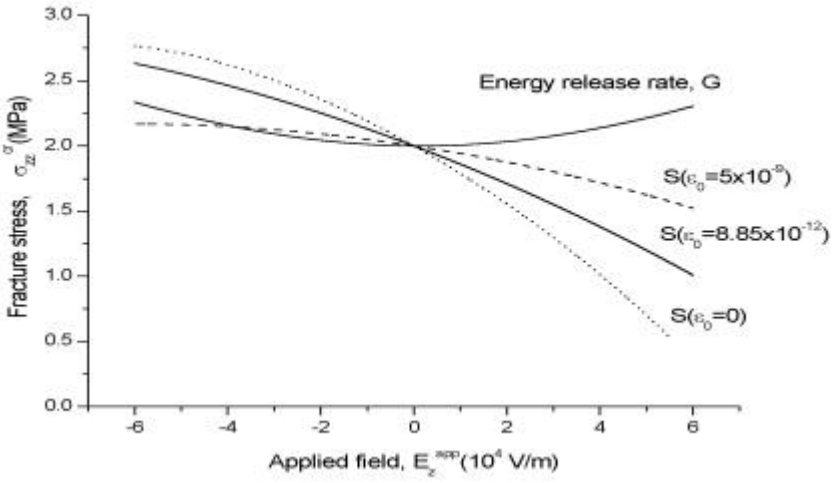

Figure 2: Effect of the applied electric field on the critical stress of a line crack

CONCLUSIONS

The objective of this study is to extend a failure criterion, based on the strain energy density theory, for an elliptical cavity or a line crack embedded in an infinite piezoelectric solid, subjected to a combined in-plane electrical and mechanical loading. This has essentially been accomplished through the consistent application of the strain energy density criterion to a thin layer near the cavity/crack boundary and material element in the interior region of the solid. The total energy density factor, *S*, depends on the material constants, $\boldsymbol{b}$, $\boldsymbol{a}$, polar angle, core region near the apex of the elliptical cavity, and the permittivity of vacuum. The core region on the cavity/crack boundary remains unspecified in size because of different material behavior external to the core region. Unstable crack extension is assumed to occur when some small element just outside the core region has absorbed as much elastic energy as possible and releases it to allow material separation.

As discussed above, the location on the free surface of a cavity, at which the surface layer energy is the maximum, may be postulated to be the location where initial failure occurs. Subsequently, the immediate post-failure crack direction may be determined by minimizing the total energy density factor. The results obtained in this study by introducing the exact electric boundary conditions on the cavity/crack boundary are more realistic because it reflects the practical situation. In short, the superiority of the energy density theory has been clearly shown from its capability of adopting the exact boundary conditions.

ACKNOWLEDGEMENT

Support from the Research Grants Council of the Hong Kong Special Administrative Region, China (*Project No. HKU 7122/99E)*

REFERENCES

1. Parton, Y. E. (1976). *Acta Astronautica* 3, 671-683.
2. Deeg, W.F. (1980). Ph.D. Thesis, Stanford University.
3. McMeeking, R. M. (1989). *J. Appl. Math. Phys.* 40, 615-627.
4. Pak, Y.E. (1990). *Trans. ASME, J. Appl. Mech.* 57, 647-653.
5. Sosa, H.A. and Pak, Y.E. (1990). *Int. J. Solids Structures* 26, 1-15.
6. Suo, Z., Kuo, C.M., Barnett, D.M. and Willis, J.R. (1992). *J. Mech. Phys. Solids* 40, 739-765.
7. Dunn, M. L. (1994). *Engng. Fracture Mechanics* 48, 25-39.
8. Park, S. and Sun, C.T. (1995). *J. Am. Ceram. Soc.* 78, 1475-1480.
9. Sosa, H.A. and Khutoryansky, N. (1996). *Int. J. Solids Structures* 33, 3399-3414.
10. Gao, H., Zhang, T.Y. and Tong, P. (1997). *J. Mech. Phys. Solids* 45, 491-510.
11. Fang, D.N., Liu, B. and Hwang, K.C. (2000). *Int. J. Fracture* 100(4), 401-408.
12. Shen, S. and Nishioka, T. (2000). *Theor. Appl. Fract. Mech.* 33, 57-65.
13. Sih, G.C. (1991). *Mechanics of Fracture Initiation and Propagation*. Kluwer Academic Publishers, Dordrecht.
14. Soh, A.K., Fang, D.N. and Lee, K.L. (2001). *Int. J. Solids Structures* (in press)

ICF100776PR

FRACTURE EVALUATION OF IN-SITU SENSORS FOR HIGH TEMPERATURE APPLICATIONS

Scott C. Forth[1] and Alexander Staroselsky[2]

[1]NASA Langley Research Center, MS 188E, 2 W. Reid St., Hampton, VA 23681
[2]United Technologies Research Center, MS 129-73, 411 Silver Lane, E. Hartford, CT 06108

ABSTRACT

The feasibility of fabricating an in-situ crack sensor for real-time detection of surface cracks propagating in engine components was evaluated using a computational fracture mechanics model. The in-situ sensor system would be required to: (1) be capable of sustaining normal function in a severe environment; (2) transmit a signal if a detected crack in the component was above a predetermined length, but below a critical length that would lead to failure; (3) act neutrally upon the overall performance of the engine system and not interfere with the engine maintenance operations. In this work, fracture mechanics methodologies are used to identify the requirements for an in-situ sensor system that could withstand the engine operating environment, foreign object damage, and minimally degrade engine performance. A computational fracture mechanics model was developed to evaluate the feasibility of fabricating an in-situ crack sensor for real-time damage propagation detection in engine components.

KEYWORDS: In-situ sensor, fracture, thin film, engine, high temperature, aircraft safety

INTRODUCTION

The engine fracture-critical part designation is given to those components with enough energy, due to high rotational speeds and mass, whose failure can have catastrophic consequences. Containment of these potential failures is unrealistic and is not a standard practice due to the excessive weight introduced by a robust containment system would introduce. Therefore, use of a light weight in-situ sensor capable of detecting impending failures will allow timely maintenance actions leading to an increase in overall safety. To implement an in-situ sensor system on an aircraft engine requires several hurdles to be overcome; the operating temperatures of aircraft engines typically exceed 500^{o} C; foreign object damage (FOD) is prevalent in service and manufacturing environments; maintenance actions are driven by safety and cost so the sensor system must not require active attention; and the aircraft engine performance must not be degraded by the inclusion of the sensor, e.g. increased weight or interruption of the gas path.

Currently, high temperature rotating components are inspected visually during routine maintenance with an optical scope, and comprehensively inspected during overhaul using nondestructive inspection (NDI) such as eddy current and ultrasonics. Any new sensor methodology should not increase the frequency of overhaul due to the overwhelming cost of grounding aircraft. An in-situ sensor system, designed and implemented properly, would not require user interaction and may actually reduce the ground time of an aircraft, while increasing overall safety. Current research into in-situ sensor methods for rotating, high-temperature equipment is based on the eddy current method [1, 2]. A sensor capable of inducing eddy currents hovers over the rotating part and detects changes in the signal due to damage. However, these approaches are typically unable to physically monitor a large surface, the diagnostic signals gradually degrade with time, and long-term histories must be stored and analyzed [3, 4]. To address these limitations, a new sensor system must be defined that would function at a high temperature and not require the overhead of current systems. In this paper, the authors address the requirements for and propose a new sensor system based on recent advances in thin film technologies.

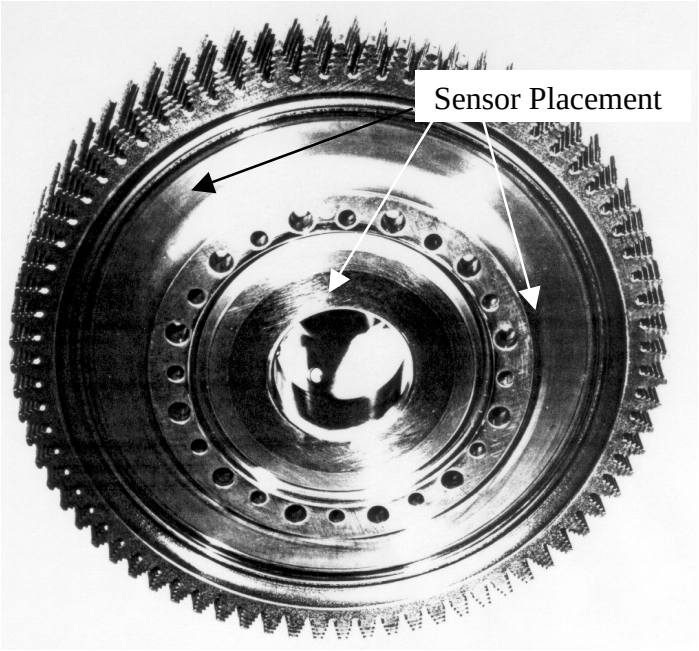

Figure 1: Component schematic and sensor placement location.

SENSOR REQUIREMENTS

An in-situ sensor system designed for high-temperature, rotating applications must conform to the following physical requirements (a schematic of an engine component and proposed sensor placement is shown in Figure 1):

- sensor cannot add significant weight to the structure
- sensor must sense impending component failure without “false alarms” due to FOD, light impact or manufacturing damage.
- coefficient of thermal expansion cannot vary significantly from the base material
- bond for an attached sensor must be able to withstand the thermal expansion of the component and the physical stress of rotation
- sensor must require little user interaction or local data storage
- sensor must not interfere with the continual operation of the engine
- sensor must be cost-effective and readily applicable in a manufacturing environment
- sensor must have tolerances consistent with component design

THIN-FILM SENSOR

Evaluation of current NDI methods and the previously mentioned sensor requirements leads to a sensor design based on thin-film technology. Thin films add little mass to the structure due to small volume; are designed for use in high temperature environments; and can be deposited on an existing structure within current manufacturing tolerances [5]. Choosing the proper material will enable the thin

film to act as an electrical device for sensing systems; absorb impact damage from FOD; and be less susceptible to corrosion than the base component [6]. Recent research in thin film sensors [7] points to tailoring the material properties, such as electrical impedance, to fit the application. For instance, a series of electrically conductive and nonconductive materials could be deposited upon a component. The topmost layer would be designed to withstand damage from FOD, corrosion, impact or manufacturing, and to protect the underlying layer, the conductive material, which would act as the sensor. Another layer would be designed to bond the conductive coating to the component and provide a smooth stress gradient between the sensor and component. An electronics package containing a remote transceiver could then be attached to the stationary portions of the engine to transmit and receive the electrical signals sent through the coating. The electrical system would generate a signal when the conductive material cracks and/or breaks causing an increase in the impedance.

A damage tolerance approach was taken to design the sensor system. First, the sensor must be attachable to the component (shown in Fig. 1). Thin film technology has developed a means of vapor deposition that deposits the coating on rough surfaces with favorable delamination properties [8]. The coating must also be within a given tolerance of the coefficient of thermal expansion (CTE) of the component. If the CTE is significantly different from that of the component, then the thermal cycling of the engine during operation will cause the sensor to delaminate. An idealized loading and temperature spectrum are shown in Figure 2. A simple way for determining if this phenomenon will occur is to assume that the bond between the coating and the component behaves like a crack at a bimaterial interface [9]. If the stresses reach the point that a rogue void or crack stress intensity factor exceeds the local fracture toughness for the bond, then delamination occurs. Also, since the component is rotating, the centrifugal forces of the component must not cause the sensor to delaminate. The stress state at the interface was modeled using the finite element method, and the fatigue crack growth and delamination were modeled using a hybrid finite element/boundary element method [10]. A key advantage of this approach is that only the crack surface has to be discretized and remeshed during crack propagation, while the finite element model remains stable.

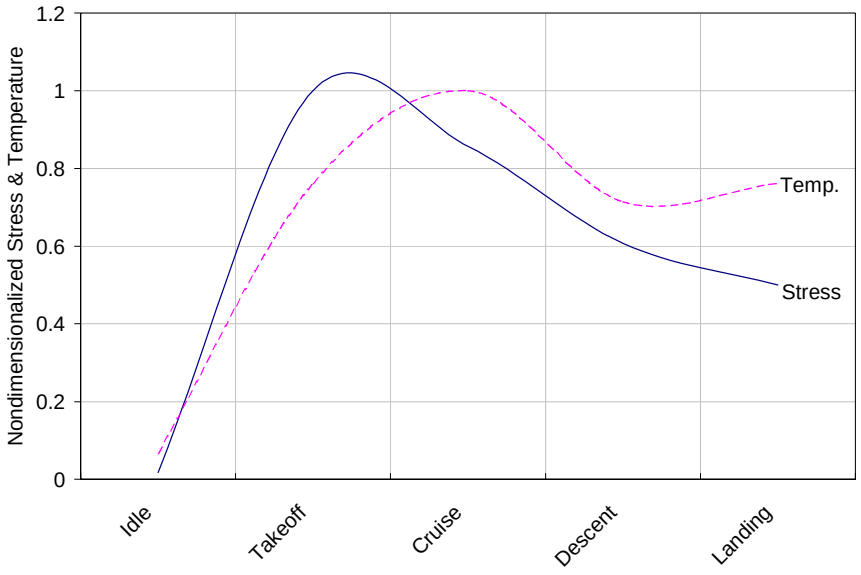

Figure 2: Idealized loading and thermal sequence.

The sensor system is designed to generate a signal when a crack of a given size is present in the base component. A schematic of the system is shown in Figure 3. Tension is applied normally to the plane of the figure. It was apparent that the conductive layer of the sensor would need to be a series of wires, or grid, instead of a continuous layer. This was due to the elastic modulus of the insulating layer being higher than that of the conductive layer. As a crack approaches a more brittle material it will deflect [11]. This was evident because the wires are approximately the same thickness as the topcoat and insulating layer. However, the entire coating is much thinner than the component and does not experience this effect due to scale [12]. Therefore, delamination criterion, where the stress intensities at the interface exceed the fracture toughness of the bond, occurred frequently for all iterations of a crack

approaching the wire/insulation boundary [13]. Therefore, the wire mesh design was introduced to create a discontinuity in the crack path and further to be spatially adaptable to define the crack size resolution the mesh can detect. The wire endings are then connected to induction points that lay at the same radial and axial location along the component surface so that the induction element will hover above all of them as the part spins.

The sensor will consist of at least three layers deposited sequentially onto the surface of the component, as shown in Figure 3. The variables are defined such that: a_0 is the initial crack radius, c is the thickness of coating, d_c is the distance from the crack to the coating, s is the distance between wires, d_w is the distance from the crack center to a wire (0.5 s), h is the height of the wire from the base material, t_w is the thickness of the wire, w is the width of the wire, K_{Td} is the delamination fracture toughness of the sensor/base material bond (assumed to be 0.195 K_{T1}), P is the applied load, E_1, ν_1, α_1, K_{T1} are the Young's modulus, Poisson's ratio, coefficient of thermal expansion and fracture toughness for the base material, E_2, ν_2, α_2, K_{T2} are the material properties of the coating and E_3, ν_3, α_3, K_{T3} are the material properties of the wires.

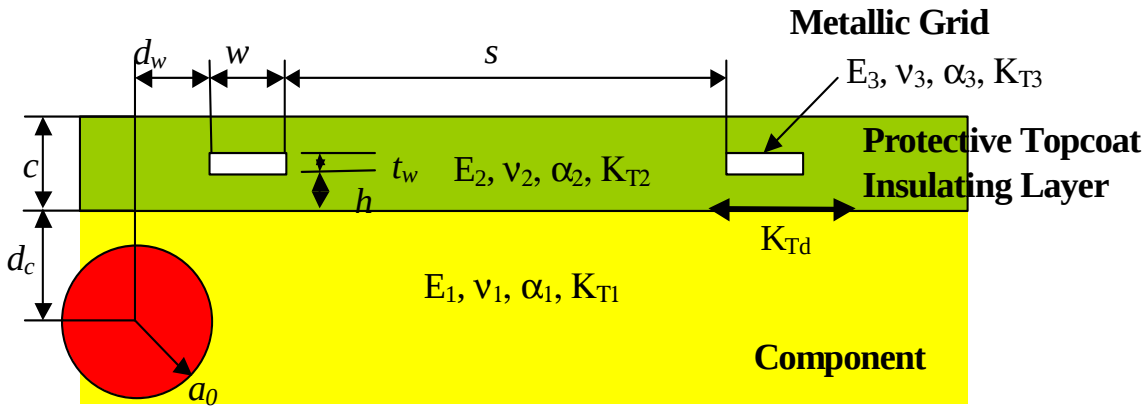

Figure 3: Definition of crack sensor system.

RESULTS

The finite element model was generated such that the displacements, physical and thermal loads (Fig. 2) were input such that the stress field at the crack was similar to that of a rotating engine component (Fig. 1). The initial crack radius was defined as a_0, the base material (E_1, ν_1 α_1) and the wire mesh were assumed to be the same material (E_3, ν_3, α_3) The insulating and protective layers were also assumed to have the same material properties such that ($E_2 = 1.95\ E_1$, $\nu_2 = 0.73\ \nu_1$, $\alpha_2 = 0.89\ \alpha_1$). The initial crack was located equidistant between wires such that the wire spacing would be minimized to detect a crack of a_0 as it propagated. Note that all spatial variables are nondimensionalized to the initial crack length, a_0, and material variables are nondimensionalized to the component material (E_1, ν_1 α_1).

Design of the sensor system to withstand the service conditions (Fig. 2) of a rotating engine component involved determining the principal modes of system failure. The first mode investigated was the catastrophic delamination of the sensor. Initially, the thickness of the coating, c, and the spacing of the wires were varied to determine acceptable stress levels at the component-sensor interface to avoid rapid delamination. For this study, it was assumed that delamination occurred if the stresses at the interface (K_T) exceeded the fracture toughness (K_{Td}) of the bond. Once the onset of delamination was observed, the interface stresses were continually monitored during fatigue crack growth to predict delamination arrest ($K_T/K_{Td} < 1$), stable tearing ($1 < K_T/K_{Td} < 1.5$), or catastrophic failure ($K_T/K_{Td} > 1.5$) [14]. The trend of a thinner coating producing less delamination stress is clearly illustrated in Figure 4.

Also, decreasing the spacing of the wires in the sensor reinforces the system in a manner similar to fibers reinforcing a composite, also depicted in Figure 4. Therefore, the sensor is less prone to delamination if the coating thickness does not exceed 0.166 a_0, and the wire spacing is less than 1.10 a_0.

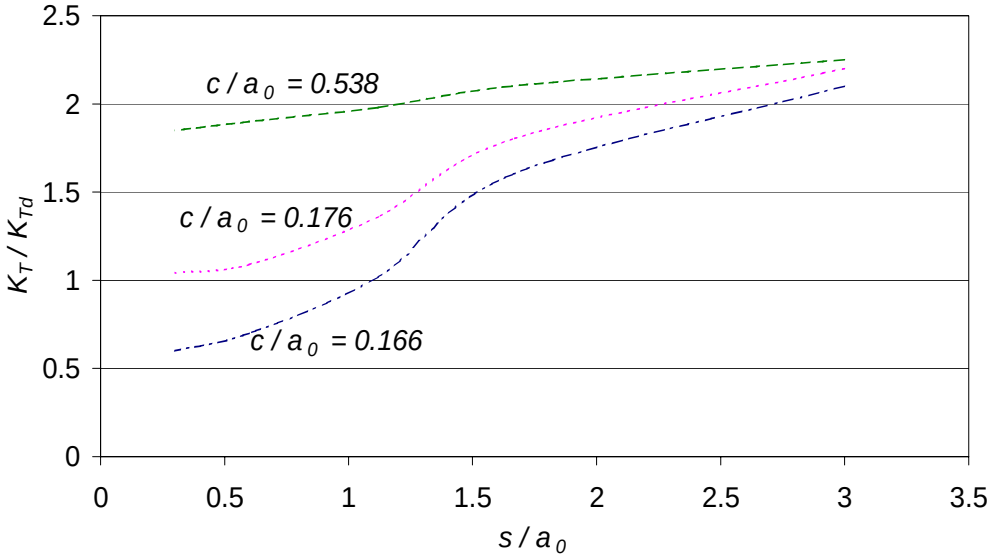

Figure 4: Effect of coating thickness and wire spacing on delamination.

The second mode of failure investigated was fracture of the sensor system due to the fatigue cracking of the component. The sensor material is quite brittle, e.g. a lower fracture toughness, K_{T2}, in comparison to the component material, K_{T1}, and will therefore fracture at a lower stress. The key factors in preventing fracture of the sensor are the position of the wire in the mesh and the size of the crack as it approaches the sensor. If the wire is placed too close to the surface, the insulating layer will simply crack and fall off as the fatigue crack propagates through the part, while the wire remains intact. If the wire is placed too close to the part, then the fatigue crack will break through the insulating layer between the part and the wire causing delamination to occur at the interface. Therefore, the wire in the sensor must be embedded within the coating a minimum of 20% of the coating thickness from either side, as illustrated in Figure 5. This minimum must be then raised to 25% to provide adequate electrical insulation between the component and wire.

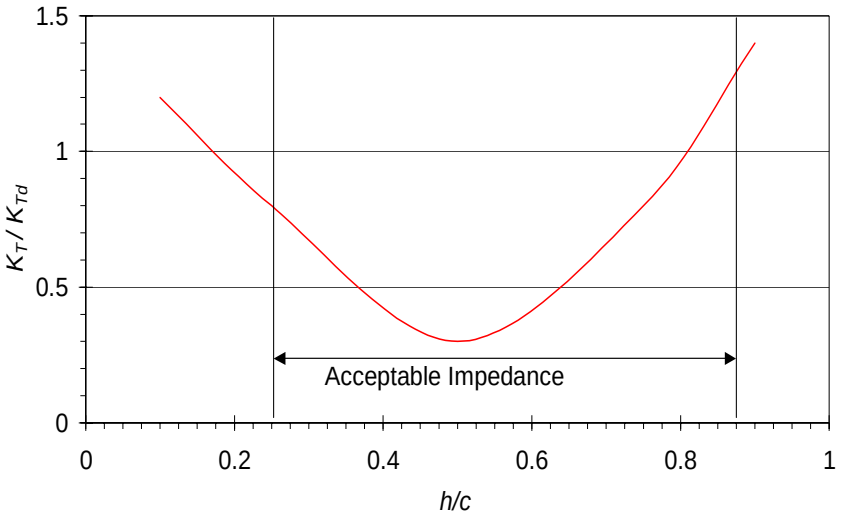

Figure 5: Effect of wire placement on impedance and initiation of delamination.

CONCLUSIONS

The fracture mechanics modeling has shown that it is possible to design a patterned coating on the engine component surface which will be adherent at the stresses and temperatures normally present in operation, and will fracture in a controlled manner when, and only when, there is an underlying crack in the disk. The model has predicted an upper boundary of $c/a_0 = 0.175$ for the total coating thickness, of which at least 25% must be the protective layer covering the conductive grid. Although the model

predicts improved mechanical performance with thinner insulating and metallic layers, the minimum acceptable thicknesses are determined by the required electrical properties of the metallic grid. All the electronic concepts studied required that the insulating film between the component and wires be on the order of $c/a_0 = 0.04$ or greater so that the sensor would have an acceptable impedance. Although the work to date has shown that the proposed sensor is viable, many challenges lie ahead before such a sensor can be demonstrated in an operating engine.

REFERENCES

[1] Barranger, J.P. (1984) "Eddy Current Jet Engine Disk-Crack Monitor", *Materials Evaluation*, Vol. 42.

[2] Chari, M.V.K., Bedorsian, G., Fealey, J.A., Sober, T.J. and Scheibel, J. (1988) "Incipient Failure Prediction of Rotating Electrical Machinery by Eddy Current On-Line Monitoring Method", *IEEE Transactions on Magnetics*, Vol. 24.

[3] Cartz, L. (1995) *Nondestructive testing : radiography, ultrasonics, liquid penetrant, magnetic particle, eddy current*, ASM International.

[4] Tietze, M. (1990) "New aspects in aircraft inspection using eddy current methods", *AGARD, Impact of Emerging NDE-NDI Methods on Aircraft Design, Manufacture, and Maintenance*, N90-28068, pp. 22-38.

[5] Auciello, O. (1999) "In situ process diagnostics and modeling", *Materials Research Society symposium proceedings*, ISSN02729172, Vol. 569.

[6] Elshabini-Riad, A. and Barlow, F.D. (1998) *Thin film technology handbook*, McGraw-Hill, New York.

[7] Lei, J.F., Martin, L.C. and Will, H.A. (1997) "Advances in thin film sensor technologies for engine applications", NASA-TM-107418.

[8] Metev, S. M. (1998) "Laser-assisted microtechnology", *Springer series in materials science*, ISSN0933-033X, Vol. 19.

[9] Dharan, C.K.H. (1986) "Delamination fracture toughness of composite spacecraft structures", *ESA Proceedings of a Workshop on Composites Design for Space Applications*, N86-30758, pp. 159-167.

[10] Forth, S.C. and Keat, W.D. (1998) "A 3D Nonplanar Fracture Model for Life Prediction", *Recent Adv. In Mech. of Aerospace Struct. & Mat.*, ASME Press, AD-Vol. 56.

[11] Selcuk, S., Hurd, D.S., Crouch, S.L. and Gerberich, W.W. (1994) "Prediction of interfacial crack path: a direct boundary integral approach and experimental study", *Int. J. of Fracture*, Vol. 67, pp. 1-20.

[12] Lu, M. C. (1980) "Stress intensity factors in two bonded elastic layers containing cracks perpendicular to and on the interface", NASA-CR-159218.

[13] Keat, W.D. and Forth, S.C. (1997) "Growth of 3D Curved Cracks Towards a Bimaterial Interface", *Developments in Mechanics*, Vol. 19, pp. 2-7 - 2-9.

[14] Knappe, W. and Schneider, W. (1973) "The role of failure criteria in the fracture analysis of fibre-matrix composites", *Deformation and Fracture of High Polymers*, ed. H.H. Kausch, J.A. Hassell and R.I. Jaffee, Plenum Press, New York, pp. 543-556.

ORAL REFERENCE: 100439

FRACTURE IN CHROMIUM: AN ATTEMPT TO IMPROVE DUCTILITY

R. Wadsack[1], R. Pippan[1] and B. Schedler[2]

[1]Austrian Academy of Sciences – Erich Schmid Institute of Materials Science,
Jahnstrasse 12, 8700 Leoben, Austria
[2]Plansee AG, 6600 Reutte, Austria

ABSTRACT

Due to their low neutron-induced radioactivity chromium based materials are considered to be candidates as structure materials in fusion technology. Drawbacks for the application of these materials in industrial design are their brittleness at **R**oom **T**emperature (RT) and their high **D**uctile to **B**rittle **T**ransition **T**emperatures (DBTT). The investigated specimens (pure chromium with a purity of about 99.97%) have been produced in a powder metallurgical route. They have been tested in the as **HIP**ped (Hot Isostatic Pressed) condition and after different pre-deformations. The as HIPped microstructure shows in bending tests and tension tests brittle behavior at RT and a steep increase of ductility in the temperature range between 200°C and 250°C. Fracture toughness investigations reveal a DBTT between 290°C and 300°C. The K_Q value increases from 12 MPa√m at 290°C up to a value exceeding 500 MPa√m at 320°C. Additional to the static fracture toughness investigations also fatigue crack growth tests were performed at RT and above DBTT in order to improve the understanding of the fracture processes. An improvement in ductility and an increase in bending fracture strength have been induced by pre-deformation in tension, in bending, by single passed **E**qual **C**hannel **A**ngular **E**xtrusion (ECAE) and by die compression.

KEYWORDS

ECAE, fracture toughness, cleavage fracture, DBTT, fatigue, ductility, chromium

INTRODUCTION

Due to their low neutron-induced radioactivity chromium based materials are considered to be candidates as structure materials in fusion technology. Drawbacks for the application of these materials in industrial design are their brittleness at **R**oom **T**emperature (RT) and their high **D**uctile to **B**rittle **T**ransition **T**emperatures (DBTT). In this paper mechanical and fractographical investigations are presented of pure chromium (DUCROPUR) with a purity of about 99.97% (N: 19µg/g, C: 51µg/g, O: 40µg/g, H: 2µg/g). The specimens have been produced in a powder metallurgical route by the company Plansee. The density after **H**ot **I**sostatic **P**ressing (HIP) was 7.165g/cm^3 (99.51%) and the grain size was about 100µm. The material has been investigated in the as HIPped condition (recrystallized microstructure) and after different pre-deformations.

EXPERIMENTAL PROCEDURES

Different tests have been performed to characterize the mechanical properties of recrystallized pure chromium (DP-R). Notched and in compression pre-cracked 3-point bending samples (6x6x30mm) have been used to determine the fracture toughness below the DBTT. The span of the rolls was 24mm. Above this temperature J-tests using CT-specimens (W=25mm, B=12mm, a=12mm) have been carried out to measure the value of fracture toughness. To determine the DBTT and the strengths as a function of temperature of uncracked specimens 3-point bending tests (samples 6x6x30mm) and tension tests (samples ∅=3.5mm, l_0=17.5mm), have been performed. All samples have been mechanically polished and electropolished to minimize the surface influence. Furthermore some simple compression tests (samples 6x6x12mm) have been done to determine the yield strengths below the DBTT. To improve the understanding of the fracture processes fatigue crack growth tests (CT-specimens W=25mm, B=6mm, a=12mm) have been performed in air at RT and above DBTT.

Recrystallized (as hipped) tensile and bending specimens have been plastically deformed above the DBTT. These pre-deformed samples have been tested at RT. The crosshead velocity in the bending tests was 0.08mm/min and the strain rate in the tensile tests was $\dot{\varepsilon}=7.6\text{x}10^{-5}\text{s}^{-1}$.

Samples have been pre-deformed by single passed **E**qual **C**hannel **A**ngular **E**xtrusion (ECAE) [1] at 320°C and by die compression at RT. From these resulting samples small specimens have been machined using a diamond wire saw. Subsequently, they have been heat treated in air for 80 minutes at 300°, 500° and 700°C and tested in bending (ECAE: span of the rolls=16.5mm, die compression: span of the rolls=22.5mm) at RT.

RESULTS AND DISCUSSION

Tests on recrystallized samples

Fracture toughness investigations

The obtained fracture toughness values of the performed K- and J-tests are summarized in Tab.1. The specimen size criterion of the ASTM standards was not fulfilled for the toughness values which are marked by a star.

TABLE 1

K_{IC}- OR K_Q-VALUES OF RECRYSTALLIZED PURE CHROMIUM (DP-R) IN MPA√M

T[°C]	DP-R
-196	3.0
25	7.7
100	11.7*
200	11.6*
280	11.8*
290	17.5*
320	~500*
480	500*-660*

From liquid nitrogen temperature (-196°C) up to 290°C the toughness values increase slightly with increasing temperature. No macroscopic plastic deformation has been observed. The fracture surfaces are characterized by cleavage planes. Above 300°C the fracture behavior changes rapidly and dramatically. The samples show large plastic deformations at the crack tip before fracture (CTOD≈1.4mm). The toughness values calculated from the J-tests are 500 MPa√m at 320°C and between 500 and 660 MPa√m at 485°C. The fracture surface of a sample tested at 485°C is depicted in Fig.1a. Similar to the fracture surface of the specimen tested at 320°C it shows an extensive crack tip blunting. The stable ductile crack propagation has

been observed only at 485°C. In spite the large toughness values the final fracture occurs again in a cleavage mode.

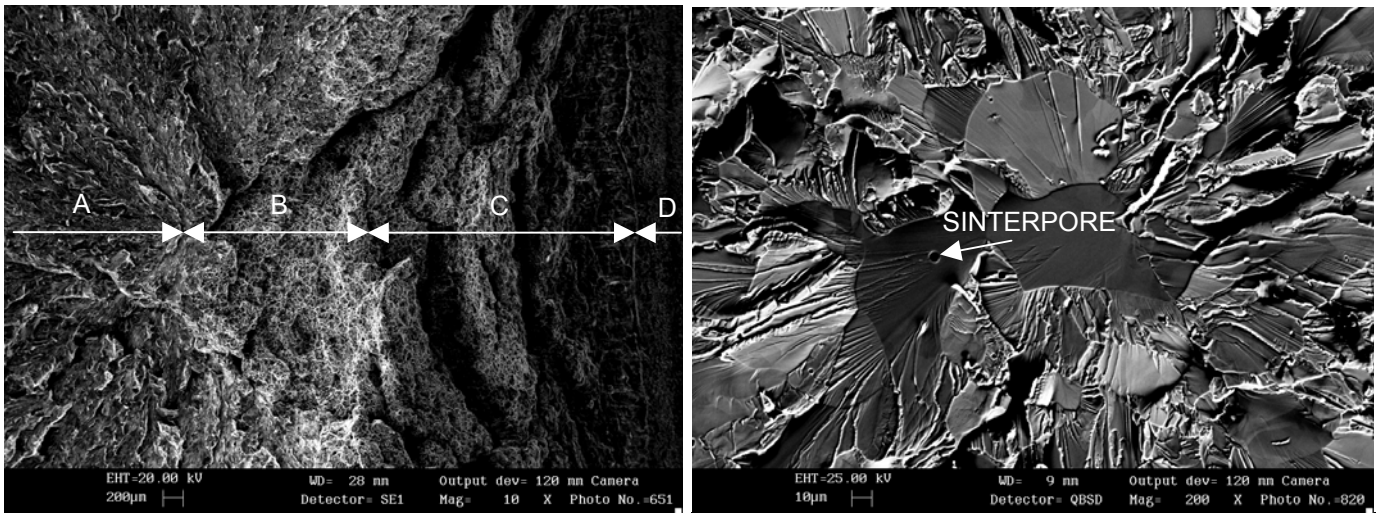

(a) b)

Figure 1: Fracture surfaces of (a) a J-integral sample tested at 485°C (A...final cleavage fracture, B...stable ductile crack growth, C...blunting zone, D...fatigue pre-crack) and (b) a bending sample tested at RT

Bending tests

The obtained results are summarized in Fig. 2. Within the DBTT range (which is here somewhat lower than in the fracture toughness tests) some samples fail in a brittle mode and some show large plastic deflections. Below 200°C no large plastic deflections have been observed. Above DBTT the test has been interrupted after a plastic deflection of about 2mm without final fracture.

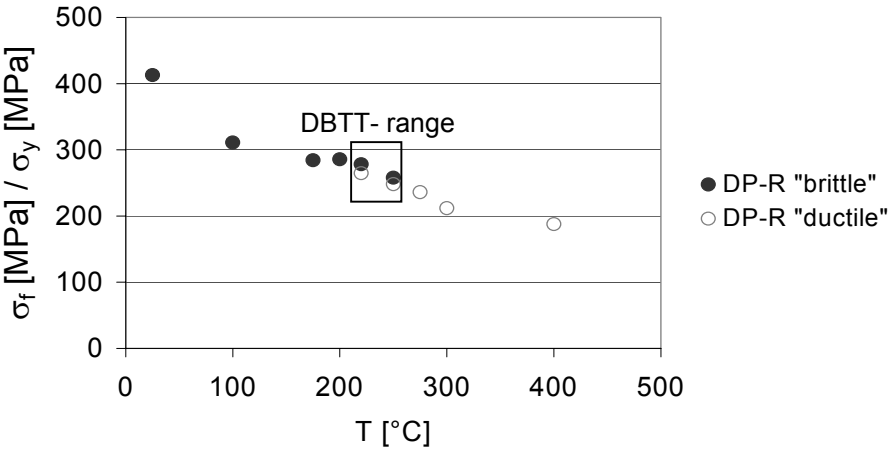

Figure 2: Dependence of bending strengths on temperature; the full symbols indicate fracture strengths (σ_F), the open symbols indicate "yield strengths" (σ_y) at the plastic deflection of 0.01mm

At RT and at a temperature somewhat smaller than DBTT a Weibull characterization has been performed. The Weibull modulus increases from m=20.7 at RT up to m=59.2 at 175°C. In both tests series the initiation points of fracture are usually sinterpores (Fig.1b).

Tension tests

The obtained strengths in MPa and strains in % are listed in Tab. 2. $\sigma_{0.2}$ is the 0.2% offset yield strength, σ_{UYP} the upper yield point and σ_{UTS} the ultimate tensile strength. ε_a is the transversal strain and ε_l the longitudinal strain which is related to 5 times the sample diameter.

TABLE 2
TENSILE STRENGTHS IN MPA AND STRAINS IN %

T [°C]	$\sigma_{0.2}$ or σ_{UYP}	σ_{UTS}	ε_a	ε_l
25	319.0	319.0		0.6
200	*199.3*	195.8	2.9	3.1
300	*121.1*	244.8	79.8	52.6
400	108.5	249.8	84.7	49.4
600	113.1	219.05	87.9	36.9
800	82.6	151.9	95.3	38.3
960	63.1	85.3	84.7	29.7

The fracture surfaces of DP-R below DBTT are again characterized by cleavage planes. Somewhat above the DBTT large plastic deformations take place but beside void formation also cleavage planes are observed on the fracture surface (Fig.3a). With increasing temperature the cleavage planes disappear and the void formation increases (Fig.3b).

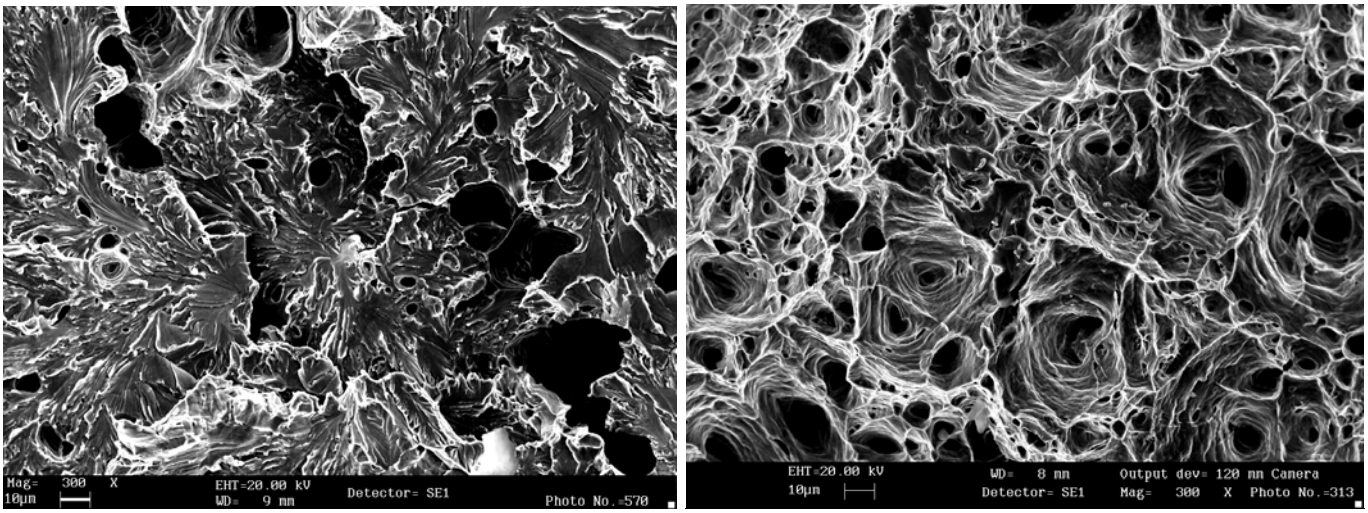

(a) (b)

Figure 3: Fracture surfaces of DP-R tensile specimens (a) tested at 300°C and (b) tested at 400°C

Compression tests

The upper yield point is 402.2MPa and 183.3MPa at RT and 170°C, respectively. At RT the upper yield point is about 25% larger than the fracture stress in tension. In contrast to the tension tests large plastic deformations can be obtained without failure.

Fatigue crack growth tests

Fatigue crack growth experiments were performed at RT and somewhat above DBTT (300°C). The stepwise increasing load amplitude test [2] on compression pre-cracked specimens was applied, which allows to measure fatigue crack growth behavior between the effective threshold and the long crack threshold. At RT the long crack threshold of stress intensity range (at a stress ratio of 0.1) and fracture toughness are approximately the same. However below the long crack threshold the crack propagates over short distances where the fracture surface showed features of a typical ductile metal. This indicates that a certain plastic deformation of the crack tip is possible also at RT. At 300°C a fatigue crack growth behavior typical for ductile metals was observed. An effective threshold $\Delta K_{eff,th} \approx 3.5 MPa\sqrt{m}$ and a long crack threshold $\Delta K_{th} \approx 7.5 MPa\sqrt{m}$ have been determined at a stress ratio of 0.1.

Tests on pre-deformed samples

It had been reported [3-5] that chromium can be ductile at RT. Beside the amount of the interstitial solved impurities (N, C,...) the dislocation density plays an important role. Recrystallized chromium has been found usually brittle at RT whereas pre-deformed samples showed sometimes ductility at RT. Therefore samples have been pre-deformed to investigate the influence of dislocation density on ductility at RT.

Pre-deformation in bending and tension

Bending samples of DP-R have been plastically pre-deformed at 400°C (deflection about 1mm). After that the samples have been tested at RT. In contrast to the tests with DP-R the pre-deformed samples show ductility at RT. A plastic deflection of about 2 mm is obtained before the final fracture occurs in a brittle mode.

Similar to the pre-deformation in bending tension samples of DP-R have been pre-deformed (ε_{pl}= 3%, 5% or 10%) at about 300°C. The stress-strain curve indicates a pronounced yield point and an area of "Lüders strain". This assigns a not negligible amount of interstitial solved impurities. All pre-deformed samples show again ductility at RT. For example a 5% pre-deformed specimen at 300°C exhibits at RT a plastic strain of about 6.5% before the brittle final fracture occurs.

Pre-deformation by ECAE

A 15x15x30mm block was deformed by ECAE at a temperature of about 320°C. The channel angle was 120° which corresponds to a true strain of $\phi \approx 1$. After a single passed deformation the samples were heat treated. The obtained fracture strengths σ_F and fracture bending angles α_F are listed in Tab.3. Samples without heat treatment and after heat treatments up to 500°C show again a limited ductile behavior. The initiation points of fracture are mostly sinter defects (Fig.4a). The specimens after a heat treatment at 700°C fail in a completely brittle mode again. All bending fracture strengths are about 2 times larger than those of DP-R. An attempt to improve the ductility will be a multiple passed ECAE above the DBTT (work in progress). The aim is to obtain a finer grain size which is not the case by single passed ECAE.

TABLE 3

BENDING STRENGTHS (σ_F) IN MPA AND FRACTURE BENDING ANGLES (α_F) AFTER DIFFERENT HEAT TREATMENTS

	E C A E		**DIE COMPRESSION**	
Heat treatment after deformation	**σ_F [MPa]**	**α_F [°]**	**σ_F [MPa]**	**α_F [°]**
none	768.8	0.4	794.7	0.3
none	1031.3	1.9	761.6	0.2
80 minutes at 300°C	854.4	0.6	878.6	0.2
80 minutes at 300°C	932.1	1.0		
80 minutes at 500°C	899.1	0.3	743.7	
80 minutes at 500°C	1053.8	1.2	889.0	1.0
80 minutes at 700°C	727.9	0	641.3	0
80 minutes at 700°C	721.5	0		

Pre-deformation by die compression

A 15x15x30mm block was deformed by die compression at RT (true strain $\phi \approx 1$) and again heat treated. The obtained fracture strengths σ_F and fracture bending angles α_F are listed in Tab.3, too. Again only the samples after the heat treatment at 700°C show completely brittle fracture behavior. The bending fracture strengths

and fracture bending angles are smaller than those of the tested samples after a pre-deformation by ECAE. Pre-deforming by die compression at RT have nucleated cracks, these cracks act as fracture initiator (Fig.4b) and hence no large plastic deflections are possible. To avoid this crack nucleation die compression should be applied above the DBTT (this work is in progress, too).

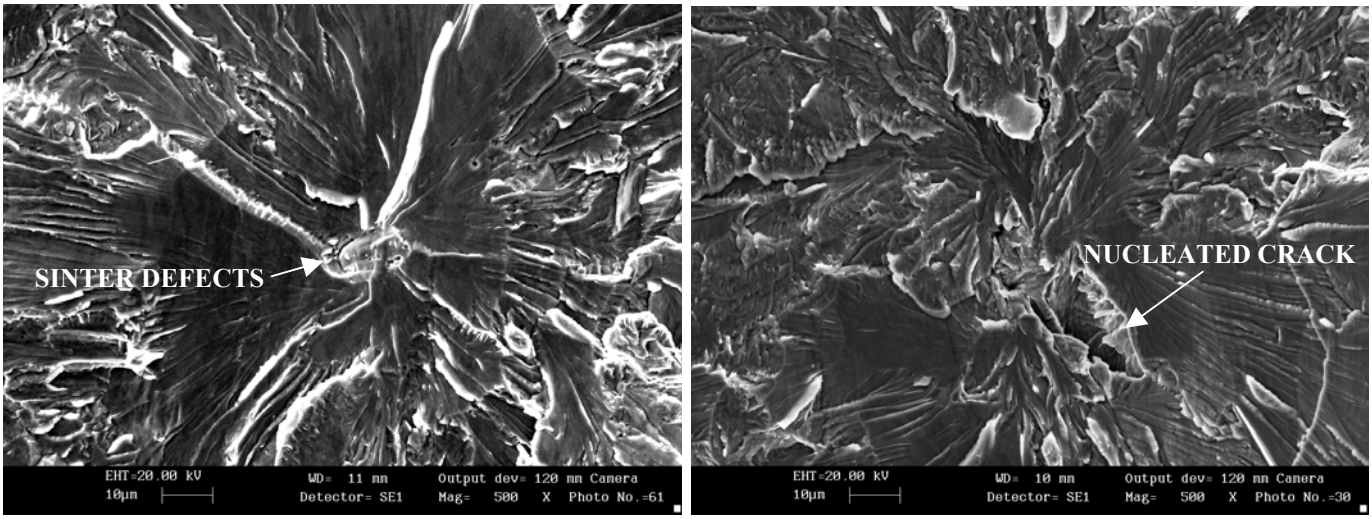

(a) (b)

Figure 4: Fracture point of initiation after pre-deformation by (a) ECAE and (b) die compression

CONCLUSIONS

- The investigated pure chromium in its recrystallized condition shows a rapid increase in fracture toughness between 290°C (17.5MPa√m) and 320°C (500 MPa√m). In the latter case the final fracture occurs after a large crack tip blunting in a brittle mode. Bending tests of smooth specimens show no plasticity at RT, above 220°C large plastic deformations are obtained. Fatigue crack growth tests reveal indications of ductility at RT and at 300°C the typical behavior of a ductile metal.
- A limited ductility in bending and an increase of the bending fracture strength results after different pre-deformations. The best results are obtained by small pre-deformations in bending. The pre-deformation by die compression at RT is characterized by nucleation of small cracks. Therefore no larger plastic deformations can be obtained.

ACKNOWLEDGEMENTS

This work has been carried out within Association EURATOM-ÖAW and is supported by the Bundesministerium für Wissenschaft, Forschung und Kunst.

REFERENCES

1. R. Z. Valiev, A. V. Korznikov and R. R. Mulyukov (1993), *Mater. Sci. Eng. A168*, 141-148

2. R. Pippan, L. Plöchl, F. Klanner, H.P. Stüwe (1994), *Journal of Testing and Evaluation 22, 98-103*

3. H. L. Wain, A. R. Edwards (1960), *Metallwissenschaft und Technik,* 387-395

4. H. L.Wain, F. Henderson, S. T. M. Johnstone, N. Louat (1957), *J. of the Institute of Metals,* 281-288

5. H. L.Wain, F. Henderson, S. T. M. Johnstone (1954), *Journal of the Institute of Metals,* 133-142

FRACTURE IN METAKAOLIN CONCRETE UNDER DIFFERENT LOADING CONDITIONS

B. B. Sabir and S. Wild

School of Technology, University of Glamorgan, Pontypridd, CF37 1DL, UK

ABSTRACT

The study presents the results of fracture tests conducted on concrete in which metakaolin is used to partially replace the cement. The energy required to cause catastrophic failure in concrete cubes containing two symmetrical notches is determined using two approaches. The first is based on the stress intensity factor determined by finite element analysis and the second utilises the energy absorbed by the test specimen up to failure. The test methodology enables estimates to be made of the extent of tortuosity of the fracture surface. The tests are conducted in a stiff testing machine under axial and eccentric loading conditions. The notched samples were allowed to cure in water at room temperature until testing at 28 and 91 days. It is found that increasing cement replacement levels by metakaolin (up to 15%) results in systematic increases in compressive strength and fracture energy. Metakaolin is also found to reduce the tortuosity of the fracture surface. This phenomenon is attributed to the additional strength imparted to the paste component of the matrix and the reduction in the thickness of the interfacial layer, resulting in more composite action between the paste and the coarse aggregates. Visual inspection of the fracture surfaces confirms the role played by the incorporation of metakaolin in causing the fracture to propagate across the coarse aggregates, thus resulting in smother surfaces.

KEYWORDS

Metakaolin, Compact specimen, Fracture, Tortuosity.

INTRODUCTION

There are two main approaches in fracture mechanics for determining the fracture toughness. These are characterised by E_f, which is the fracture energy required to create a crack extension of unit area and K_c, which is the critical value of the stress intensity factor. Several investigations, e.g. [1-3], have been carried out to assess the fracture parameters in concrete using approaches recommended in [4,5]. Despite the testing complexities involved the results of such investigations have not been consistent and controversy exists regarding the applicability of these tests. Furthermore, the tests employ specimens of relatively large sizes, which render them to be impractical and expensive in practice.

A compact compression eccentrically loaded (CCEL) specimen for evaluating the fracture toughness of concrete has previously been reported by the author [6]. The test employs 100 mm concrete cubes modified by introducing two symmetrical notches on opposite faces and loaded eccentrically. The test provides the critical load at fracture, which is employed in a finite element analysis [7] to give the fracture toughness. The testing system was shown to be effective in identifying the differences in the toughness characteristics of concretes of different formulations [6].

The present study utilises this test to determine the fracture energy of concrete using two approaches, i.e. directly from the area under the load-displacement graph and indirectly from the stress intensity factor K. An alternative testing arrangement in which the specimen is loaded along the plane containing the two notches is also used to evaluate the fracture energy of the concretes employed. This test is referred to as the compact compression axially loaded (CCAL) specimen test.

STRESS ANALYSIS

Analyses of the two test geometries have been carried out using isoparametric finite elements [7,8]. Figure 1 gives the variations of the σ_y stress (normal to the crack plane) and the shear stress σ_{xy} along the plane containing the cracks for a unit applied load P on specimens with 30 mm symmetrical notches. The results demonstrate the rapid increase in the tensile σ_y stress along the ligament as the crack tips are approached. The absence of shear stresses along the ligament confirms that the fracture process is predominantly in the opening mode, which is evidenced in the actual tests.

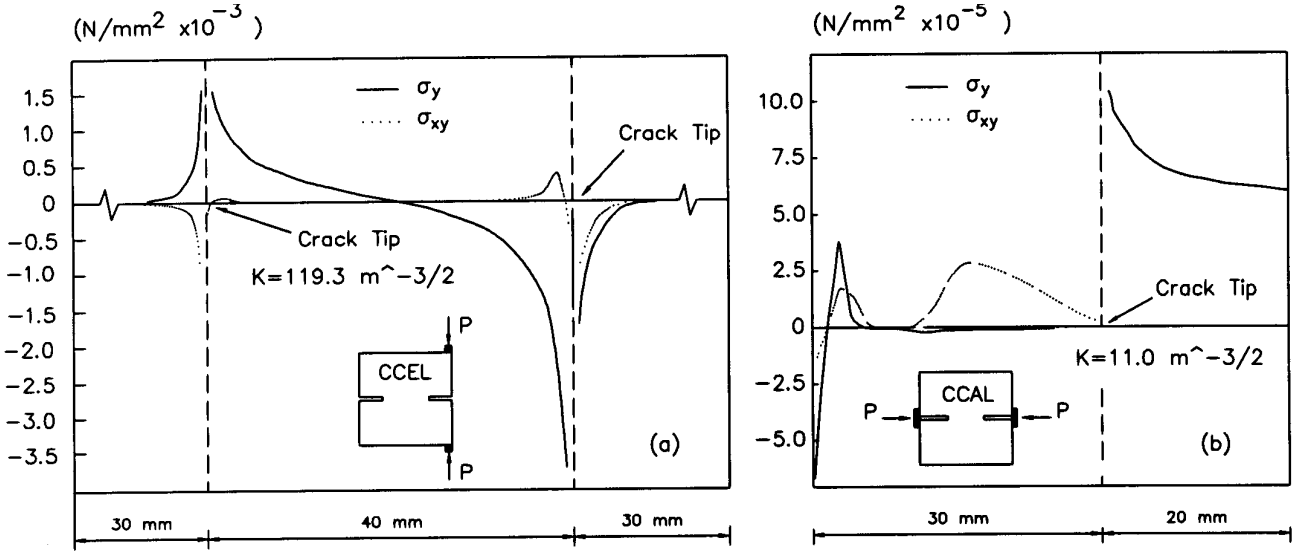

Figure 1. Distribution of σ_y and σ_{xy} along the crack plane
(a) Full CCEL specimen [8] (b) Half CCAL specimen

The fracture toughness K_c is directly related to the stress intensity factor K, which is obtained from the finite element analysis. The fracture toughness K_c is related to the critical value of the strain

energy release rate G_c, or fracture energy, as follows:

$$G_c = \frac{K_c^{\ 2}}{E}\ (1-\mu^2) \qquad (1)$$

Where E is the elasticity modulus and μ is Poisson's ratio.

The fracture energy E_f can be determined from the load-displacement relationship recorded during the test, viz:

$$E_f = \frac{W_s}{d(d-2a)} \qquad (2)$$

Where d is the specimen size, a is the notch size and W_s is the energy consumed in producing the new fracture surface. Full details of the calculation procedure are given in [9].

MATERIALS AND TESTING

Four concrete mixtures were prepared to manufacture the test specimens. Metakaolin (MK) was employed as a partial cement replacement material at 0, 5, 10 and 15%. The mixture without MK is referred to as the control concrete. In all the mixtures, the water to total binder (PC+MK) ratio was kept constant at 0.45. Natural sea-dredged sand of grading M-F complying with BS 882: 1983 and 10mm crushed limestone were used throughout the investigation. The mix proportions of biner:sand:limestone were 1:1.7:3 and the PC content in the control concrete was 395 kg/m^3. A polymeric sulphonate based superplasticiser was added at a dosage of 1 % of the weight of the binder. The concretes produced slumps varying between 15 and 50 mm.

CCEL and CCAL specimens were prepared by means of standard 100 mm steel moulds. Symmetrical notches (30 mm deep) were introduced after curing for 21 days in water at 20^{o}C. After notching, the specimens were returned to the curing tanks until testing at 28 or 91 days. The fracture tests were conducted at ambient room temperature using a 250 kN Instron testing machine.

Further specimens were prepared to evaluate the compressive strength f_c, the modulus of elasticity E and the modulus of rupture MOR. The results of testing at 28 and 91 days are shown in Table 1. It can be seen that in all cases there are systematic increases in the mechanical properties as the MK content increases. This is attributed to the pozzolanic reaction and the filler effect derived

TABLE 1
MECHANICAL PROPERTIES

MK (%)	Results at 28 days			Results at 91 days		
	f_c (MPa)	E (GPa)	MOR (MPa)	f_c (MPa)	E (GPa)	MOR (MPa)
0	63.1	35.1	8.4	64.2	36.2	9.1
5	64.3	37.3	9.2	68.1	37.0	10.1
10	67.2	38.5	10.5	71.5	39.1	10.8
15	73.1	40.1	11.1	74.3	40.5	11.3

from the incorporation of MK. The results also show small increases due to increased curing time. Tables 2 and 3 give the results of the CCEL and CCAL fracture tests respectively for 28 and 91 days of curing .

FRACTURE TOUGHNESS AND FRACTURE ENERGY

It has been reported [9] that the fracture toughness K_c, obtained from the stress intensity factor [7] and the load at failure, did not show significant variation with notch size. This behaviour although not always born out in fracture tests, is in agreement with the notion that K_c is a material property, which should be independent of specimen geometry and notch size. The results presented in this paper were obtained from testing specimens containing symmetrical notches 30 mm deep. It is easily seen (Tables 2 and 3) that K_c increases with increasing MK content for both CCEL and CCAL specimens. This increase is similar to that observed for the compressive strength and is attributed to the pozzolanic activity derived from the MK and the calcium hydroxide liberated during the hydration of the cement and the MK filler effects. The resulting concrete is more densified with the interfacial zones being smaller in thickness thus resulting in more composite action between the paste and the aggregates. The increase in K_c for the specimens tested at 91 days are significantly smaller than those obtained at 28 days. This is not surprising as the pozzolanic activity in concrete due to MK is at its peak at 7-14 days [10].

TABLE 2
FRACTURE RESULTS FROM CCEL SPECIMENS

	MK (%)	K_c (MN/m$^{3/2}$)	G_c N/m	E_f N/m	T_f
28 day tests	0	0.60	9.87	19.2	1.95
	5	0.78	15.8	24.8	1.57
	10	0.87	19.1	28.8	1.51
	15	0.99	23.5	35.0	1.49
91 day tests	0	0.94	23.6	23.0	0.98
	5	0.97	24.4	25.8	1.06
	10	1.07	28.2	30.8	1.09
	15	1.10	29.0	33.8	1.16

The reported values for G_c were determined using Eqn. 1 with μ=2. Similar variations in G_c to those of K_c occur with increasing MK content. The fracture energy E_f was evaluated from the area under the load-displacement curves recorded during the tests. The values for E_f obtained from the CCAL specimens are considerably higher than those recorded from the CCEL specimens. This is attributed to the fact that CCAL specimens are much more rigid than CCEL specimens, which was evidenced by the greater load sustainability before failure in the case of CCAL testing. It has been reported [9,11] that both G_c and E_f converge to the same value as the notch size increases. For short cracks, however, E_f is generally greater than G_c. The differences in the values of the fracture energy determined by G_c and E_f are attributed to the assumption of a planar fracture surface in the determination of E_f. In practice the fracture surface is tortuous and can be several times greater than that assumed [12,13].

TABLE 3
FRACTURE RESULTS FROM CCAL SPECIMENS

	MK (%)	K_c (MN/m$^{3/2}$)	G_c N/m	E_f N/m	T_f
28 day tests	0	0.85	19.8	46.8	2.34
	5	1.01	26.5	67.2	2.54
	10	1.18	35.2	70.7	2.01
	15	1.37	45.1	97.4	2.16
91 day tests	0	1.01	27.2	65.0	2.39
	5	1.11	32.0	71.9	2.25
	10	1.13	31.4	78.8	2.51
	15	1.21	35.1	77.5	2.21

FRACTURE SURFACE TORTUOSITY

The fracture energy E_f is evaluated on the basis of the area of the ligament between the two notches. This overestimates E_f by a factor related to the tortuosity of the newly created surface. A tortuosity, or roughness, factor can be estimated as the ratio of the true surface area to the projected area. This definition was used by Wollrab et al [14] during tensile testing of edge notched specimens. In this paper the tortuosity is estimated by a factor T_f (Tables 2 and 3) given by the ratio of E_f to G_c, as evaluated from Eqns. 1 and 2.

It is seen that in general significant decrease in T_f results with increasing MK content. This is a clear indication that the addition of MK results in smoother fracture surfaces. This is largely attributed to the filler effects of MK, which alter the matrix structure of the concrete. The porosity of the matrix in the region of the interfacial zone reduces resulting in a denser and more homogeneous transition zone [15]. Because the interfacial zone is the 'weak link' within the concrete, the inclusion of MK results in a more effective composite action with a greater role being played by the coarse aggregate in controlling the fracture path. Whereas in normal concrete crack growth usually takes a path around the aggregates, in the case of MK concrete and because of the reduction in the thickness of the interfacial zone the growth proceeds through the aggregates resulting in smoother fracture surface. This phenomenon was very clear on inspection of the actual fracture surfaces of the specimens at fracture.

CONCLUSIONS

The work presented in this paper demonstrated the effectiveness of two testing systems in assessing the changes in the fracture properties of concrete due to the incorporation of metakaolin. The tests employ compact specimens that are easy to manufacture and simple to handle. Significant increases in the fracture toughness and fracture energy results by the incorporation of up to 15% metakaolin. These increases, which surpass those usually obtained for the compressive strength, are attributed to the filler effects and pozzolanic activity of the metakaolin. Improved composite action between the cement paste and the aggregates is obtained resulting in smoother fracture surfaces, which are confirmed by the significant reductions in the tortuosity factors.

REFERENCES

1. Hillerborge, A. (1992) Materials and Structures, 18, No 107, 407.
2. Guinea, G. V., Planas, J. and Elices, M. (1992) Mat. and Struct., 25, No 148, 212.
3. Hu, X. and Wittmann, F. H. (1992) Mat. and Struct., 25, No 123, 319.
4. Draft RELIM recommendation. (1990) Mat. and Struct., 23, No 123, 461.
5. Draft RELIM recommendation. (1990) Mat. and Struct., 23, No 138, 457.
6. Sabir, B. B. (1997) Mag. of Conc. Res., 49, No 179, 139.
7. Sabir, B. B. (1995) Int. J. of Frac., 72, 259.
8. Sabir, B. B. and Asili, M. (1996) Cem. and Conc. Comp., 18, 141.
9. Sabir, B. B., Wild, S. and Asili, M. (1997) Cem. and Conc. Res., 27, No 5, 785.
10. Sabir, B. B., Wild, S. and Khatib, J. M. (1996). In: *Proc: Concrete in the Service of Mankind: Concrete for Environment Enhancement and Protection*, pp. 651-662, R. K. Dhir and T. D. Dyer (Eds), E & FN Spon, Dundee.
11. Nallathambi, P., Karihaloo, B. L. and Heaton, B. S. (1985) Cem. and Conc. Res., 15, No 1, 117-126.
12. Nallathambi, P. and Karihaloo, B. L. (1986), Mag. of Conc. Res., 38, No 135, 67.
13. Swamy, R. N. (1979). In: *Developments in Concrete Technology*, pp. 221-228, Applied Science Publishers, Oxford.
14. Wollrab, C., Ouyang, C., Shah, S. P., Hamm, J. and Konig, G. (1996), Mag. of Conc. Res., 48, No 175, 117.
15. Bentur, A. (1991) In: *Proc: Advances in Cementitious Materials*, Am. Cer. Soc. Publications, 16, pp. 523-532.

ORAL/POSTER REFERENCE: ICF100409PR

FRACTURE INITIATION AND CRACK GROWTH – COHESIVE ZONE MODELING AND STEREOSCOPIC MEASUREMENTS

C.R. Chen[1*], I. Scheider[2], T. Siegmund[3], A. Tatschl[4], O. Kolednik[4] and F.D. Fischer[1]

[1] Institute of Mechanics, Montanuniversität, A - 8700 Leoben, Austria
[2] GKSS Forschungszentrum Geesthacht GmbH, D - 21502 Geesthacht, Germany
[3] School of Mechanical Engineering, Purdue University, West Lafayette, IN 47907-1288, USA
[4] Erich Schmid Institute of Materials Science, Austrian Academy of Sciences, A - 8700 Leoben, Austria

ABSTRACT

The purpose of this paper is to study the application of a cohesive zone model, which is appropriate for the use with 3D-elements, for the numerical simulation of the crack growth in a Compact Tension specimen made of a mild steel. The main problem is how the two parameters which control the crack growth in the model, the cohesive energy Γ_0 and the cohesive strength T_{max}, can be determined. A procedure is proposed to determine the variation of the parameters along the crack front, $\Gamma_0(z)$ and $T_{max}(z)$, by using the local crack growth data in the specimen center and at the side surfaces and 2D modeling under plane strain and plane stress conditions, as well as the measurement of the variation of the critical crack tip opening displacement, $COD_i(z)$, along the crack front. The comparison between the experimental data and the numerical simulation reveals that the parameters of the cohesive zone model change during (the first stages of) crack extension.

KEYWORDS

numerical simulation, 3D cohesive zone model, cohesive strength, fracture initiation, crack growth, critical crack tip opening displacement, automatic fracture surface analysis, stereophotogrammetry

INTRODUCTION

The cohesive zone model has been increasingly applied for the numerical analysis of crack propagation, first, only for brittle materials that exhibit cleavage fracture and, later, also for tough materials which fail in a micro-ductile mode [1]. It uses a traction-separation law, i.e. a special curve relating the separation stress, T, to the displacement, δ, to model the behavior of the material in the process zone in front of the crack tip. The various traction-separation laws for micro-ductile crack growth have a common feature: with the increase of separation the traction increases, reaches the peak value, called the cohesive strength, T_{max}, and then decreases to zero when the separation reaches a critical value, δ_0. The area under the traction-separation curve is the separation energy, Γ_0, which represents physically the specific work required for the formation of the dimple structures on the two fracture surfaces [2]. It has been found that the exact shape of the T-δ curve has little effect on the crack growth behavior [3]; important are the magnitudes of the parameters T_{max} and Γ_0.

In the application of the cohesive zone model to ductile fracture, most studies have been performed under either plane strain or plane stress conditions. However, to model the crack growth in a specimen with smooth

[*] on leave from the Institute of Metal Research,Chinese Academy of Sciences, Shenyang, China

side-surfaces, a tri-dimensional (3D) cohesive zone model is necessary. Although it is conceptually not more complicated, the 3D case is more difficult from the numerical point of view. Some applications of a 3D cohesive zone model can already be found in literature, e.g., [4,5]. However, there still remains the problem how to select the variation of the parameters T_{max} and Γ_0 in the 3D case, since it has been shown in numerical investigations that T_{max} and Γ_0 are no material constants. It has been tried to relate them to either the local equivalent plastic strain [6], the local void volume fraction [7], or the local stress triaxiality, e.g., [8,9,10]. The latter idea seems to be especially promising; however, it is not known whether the stress triaxiality is the only factor influencing T_{max} and Γ_0. The current paper is devoted to this problem.

A 3D COHESIVE ZONE MODEL AND A FRACTURE MECHANICS EXPERIMENT

The experimental data of a multi-specimen J_{IC}-test, [11], shall be used to calibrate the parameters T_{max} and Γ_0 for a 3D cohesive zone model. The specimens were CT-specimens (thickness $B=25$ mm, width $W=50$ mm, initial crack length $a_0=27$ mm), the material was an annealed mild steel (yield strength $\sigma_y=270$ MPa, ultimate tensile strength $\sigma_u=426$ MPa) with a distribution of MnS inclusions which determine the micro-ductile fracture process. It is important to note that no shear lips are seen on the fracture surfaces. The crack extension, Δa, was measured on 9 equidistant positions; near the side surface, additional measurements were made. In total, 14 specimens were analyzed. The experiment was performed to study the near-initiation stage of crack growth; many data were taken at small crack growth values. The test gave a valid $J_{IC} = 120$ kJ/m^2; the physical crack extension in the center region begins much earlier, $J_i = 39$ kJ/m^2 [10].
From these data, curves of the local crack extension can be plotted against the load line displacement, $\Delta a(z)$-v_{LL} curves; z gives the position along the crack front, i.e., the distance from the midsection. Such curves were already used in the past to control the crack extension in conventional 3D-numerical studies where the variation of the crack tip opening displacement[1], CTOD, during crack extension was investigated, e.g. [12].
For the current numerical modeling, a 3D cohesive zone model has been implemented, [13], into the finite element (FE) system ABAQUS [14]. The details can be found elsewhere [15]. It is possible to use different traction-separation laws that consider both normal and shear components of fracture. For the current simulation, a cubic traction-separation law, [1], is applied. As we observe only Mode I fracture in the test, only the normal components of separation are relevant:

$$T(\delta) = \frac{27}{4} T_{\max} \left(\frac{\delta}{\delta_0} \right) \left[1 - 2 \left(\frac{\delta}{\delta_0} \right) + \left(\frac{\delta}{\delta_0} \right)^2 \right] \quad . \tag{1}$$

The integration of the curve yields the separation energy,

$$\Gamma_0 = \frac{9}{16} T_{\max} \delta_0 \quad . \tag{2}$$

The FE model consist of 9 layers of 8-node 3D solid elements through the half-thickness of the specimen. The width of the layers decreases near the side surface. The cohesive elements are placed at the crack plane. The element size in the direction of crack extension near the crack tip is 0.05 mm, further away 0.1 and 0.2 mm, respectively. The loading is performed by prescribing the load line displacement, v_{LL}.

THE CALIBRATION OF THE COHESIVE ZONE PARAMETERS FOR 2D MODELING

For 2D computations under plane strain conditions, the data of the local crack extension in the midsection, $\Delta a(z=0)$, can be used to select the appropriate cohesive element parameters $T_{max}^{(pl\varepsilon)}$ and $\Gamma_0^{(pl\varepsilon)}$, see Figure 1a. Figure 2a demonstrates that an increase of T_{max} (at fixed Γ_0) leads to a flatter Δa-v_{LL} curve; however, it does not influence the load line displacement at the point of fracture initiation, $v_{LL}^{(i)}$. An increase of Γ_0 (at fixed T_{max}) results in both a higher value of v_{LL} at initiation, $v_{LL}^{(i)}$ and a flatter Δa-v_{LL} curve, Figure 2b. This

[1] The crack tip opening displacement measured at the actual tip of (a growing) crack is designated *CTOD*; the value measured at the position of the initial crack front after the pre-fatigue is designated *COD*.

enables us to find the values $T_{max}^{(pl\sigma)} = 1100$ MPa and $\Gamma_0^{(pl\sigma)} = 11.5$ kJ/m^2 which give the best fit to the data. The accuracy of these values is good, say about 5%.

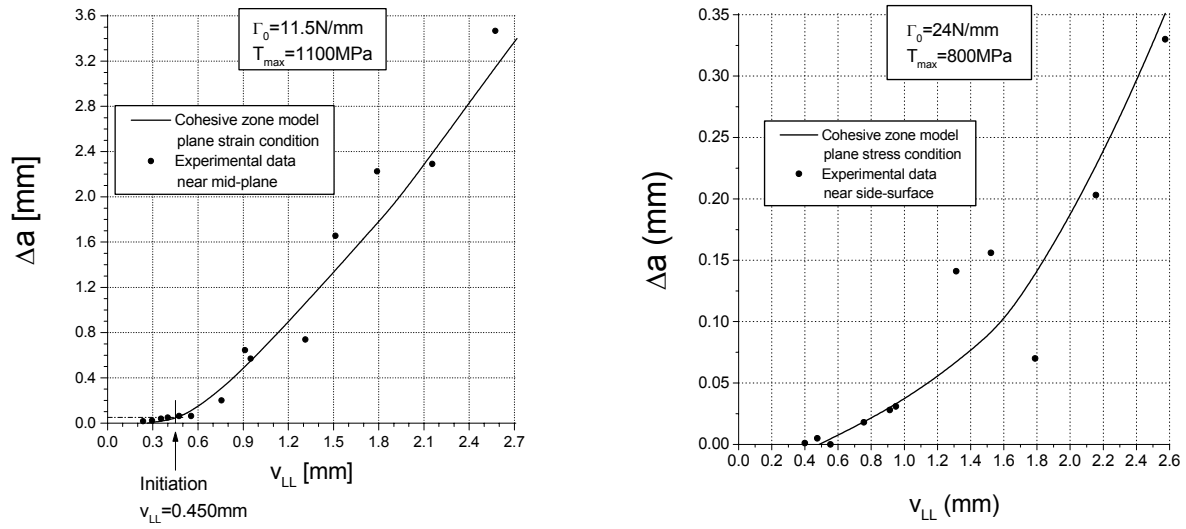

Figure 1: Local crack extension, Δa, versus load line displacement, v_{LL}. (a) Experimental data from the midsection and plane strain computation, (b) data from the side surface and plane stress computation.

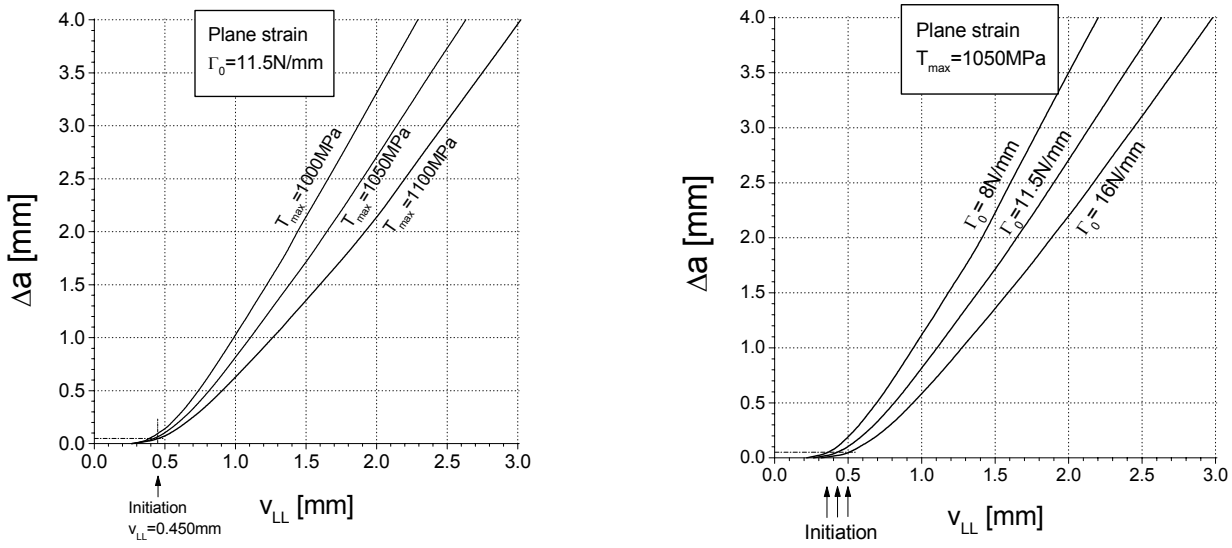

Figure 2: Influence of (a) the cohesive strength, T_{max}, and (b) the cohesive energy, Γ_0, on the Δa-v_{LL} curve for plane strain conditions.

Similarly, a 2D computation under plane stress conditions and the data of the local crack extension near the side surface, $\Delta a(z=12.5)$, can be used to find $T_{max}^{(pl\sigma)} \approx 800$ MPa and $\Gamma_0^{(pl\sigma)} = 24$ kJ/m^2 (Figure 1b). Because of the large scatter of the data, the accuracy is worse than for the plane strain case. T_{max} might be especially inaccurate, as in the plane stress case the separation strength does not have a large effect on the Δa-v_{LL} curve. Figure 3 shows the resulting J-integral versus crack extension (J-Δa) curves. These curves and the J-values at fracture initiation, $J_i^{(pl\varepsilon)} = 40$ kJ/m^2 and $J_i^{(pl\sigma)} = 85$ kJ/m^2, are similar to those obtained by a sandwich layer model [16]. From Eqn. 2, the values of the critical separation can be calculated, $\delta_0^{(pl\varepsilon)} = 0.020$ mm and $\delta_0^{(pl\sigma)} = 0.056$ mm. The J_i-values are much higher than the separation energies. This has been expected because at fracture initiation the plastic zone exceeds the process zone already by 2 orders of magnitude, $r_{y,i}^{(pl\varepsilon)} = 4.8$ mm. It is interesting to note that the ratio $J_i^{(pl\sigma)}/J_i^{(pl\varepsilon)} \approx 2.1$ comes close to the ratio of the separation energies $\Gamma_0^{(pl\sigma)}/\Gamma_0^{(pl\varepsilon)} \approx 2.2$. For the same material, in [17] the energy dissipation rate, i.e., the total non-reversible energy for a unit-area crack growth, was estimated for plane strain conditions assuming the

criterion *CTOA = constan*t and plane strain conditions. It was found that $D \approx constant \approx 1160$ kJ/m^2, i.e., by a factor 100 larger than the separation energy.

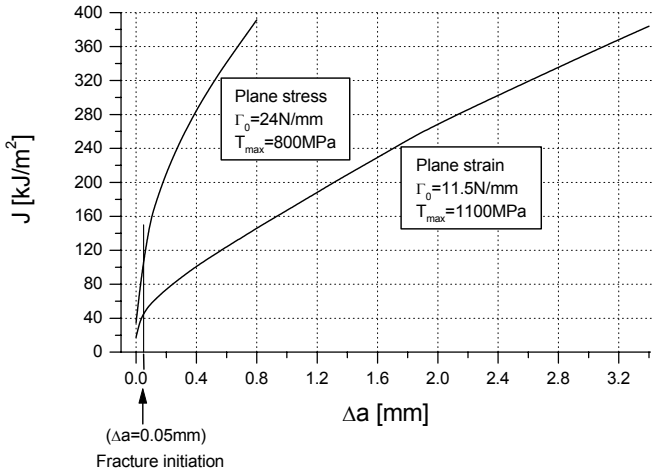

Figure 3: *J*-integral, *J*, versus mean crack extension, Δa, curves computed by the 2D cohesive zone models.

For 2D cohesive zone modeling, the calibration of the parameters poses no serious problem. No hint has been found that for our material the parameters change with the crack extension. However, the maximum Δa values are small, *4* mm in the midsection and *0.34* mm at the side surface.

ON THE CALIBRATION OF THE COHESIVE ZONE PARAMETERS FOR 3D MODELING

In the 3D case, the cohesive parameters are expected to vary along the crack front. An additional variation during crack extension is assumed to be small (see above). The calibration is much more difficult because a change of the parameters in one layer will affect the crack growth in all the other layers.
The first trial is to use cohesive parameters that are constant throughout the whole specimen. In Figure 4a an example is presented for $\Gamma_0 = 17.5$ kJ/m^2 and $T_{max} = 1100$ MPa. In the figure, the experimentally measured $\Delta a(z)$-values for three different load line displacements, v_{LL}, are compared to the computed Δa-distribution. The local crack extension decreases near the side surface but the result is not especially satisfying, see the discussion below.

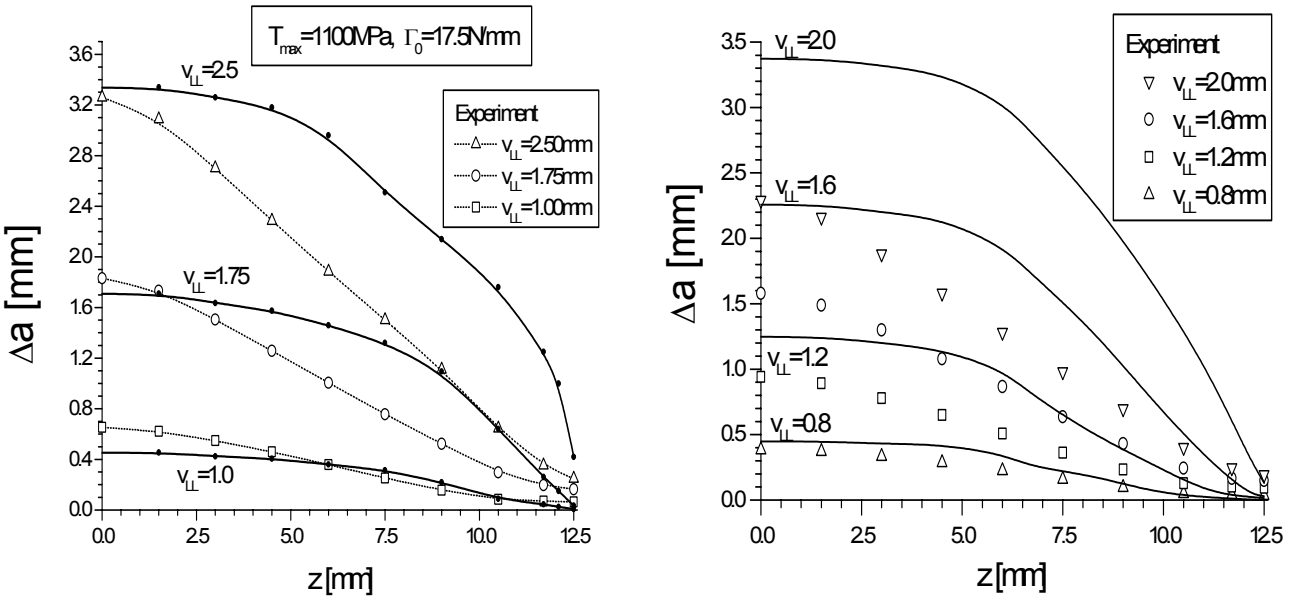

Figure 4: Comparison of the experimentally measured and the computed Δa-distribution along the crack front for three different load line displacements, v_{LL}. (a) for constant cohesive parameters, (b) for constant T_{max} and the variation of the cohesive energy, Γ_0, shown in Figure 6. *z* is the distance from the midsection.

We have seen above that only Γ_0 determines fracture initiation, i.e. $v_{LL}^{(i)}$ or J_i in the 2D case; T_{max} has no influence. As a linear relation exists between J_i and COD_i, the idea is now to measure the critical crack tip opening displacement along the crack front, $COD_i(z)$, to get a hint about the variation $\Gamma_0(z)$. COD_i is measured from corresponding regions of the fracture surface on the two specimen halves [18], applying an automatic fracture surface analysis system [19,20]. The result is shown in Figure 5. There is a midsection region of constant $COD_i^{(M)} \approx 80$ µm for $z \leq 5.5$ mm; near the side surfaces $COD_i^{(SS)} \approx 180$ µm. The ratio $COD_i^{(SS)}/COD_i^{(M)} \approx 2.2$ resembles the ratio of the separation energies $\Gamma_0^{(pl\sigma)}/\Gamma_0^{(pl\varepsilon)}$ noted above.
As a linear relation exists between the J_i and COD_i, we assume a variation of the separation energy depicted in Figure 6: For the center region of constant COD_i, $0 < z \leq 5.5$ mm, we assume $\Gamma_0(z) = \Gamma_0^{(pl\varepsilon)} = 11.5$ kJ/m^2. It seems plausible that for a valid J-resistance curve plane strain conditions prevail in the midsection region. The out-of-plane constraint decreases near the side surface. Therefore, we let the separation energy increase linearly up to a value $\Gamma_0^{(SS)} = \Gamma_0^{(pl\sigma)} = 24$ kJ/m^2 at the side surface. A constant cohesive strength of $T_{max}(z) \approx T_{max}^{(pl\varepsilon)} = 1100$ MPa is assumed for the whole specimen since the difference between $T_{max}^{(pl\varepsilon)}$ and $T_{max}^{(pl\sigma)}$ is not large and the latter value could not be determined accurately.

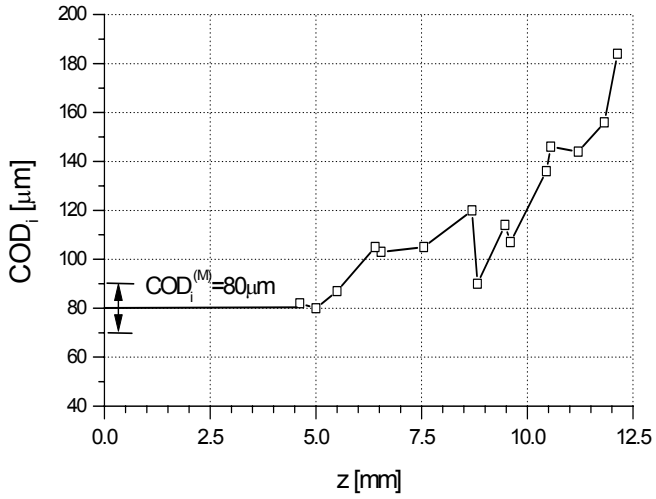

Figure 5: The variation of the critical crack tip opening displacement, COD_i, along the crack front.

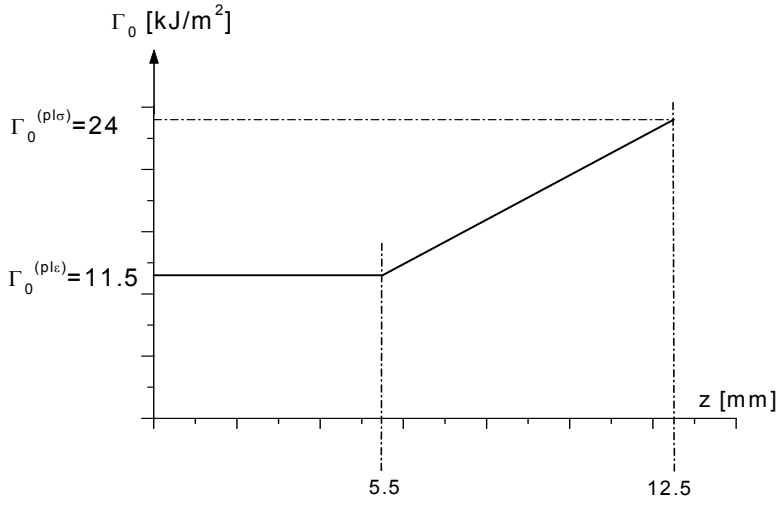

Figure 6: Assumed variation of the cohesive energy, $\Gamma_0(z)$, along the crack front for the computation shown in Figure 4b.

The result of the computation is shown in Figure 4b. The comparison between the experimental data and the computations seems to be even worse than for the case of computations with constant Γ_0. Of course, a distribution of $\Gamma_0(z)$ and $T_{max}(z)$ values could be found that would provide a better fit to the data but that is not the purpose of this paper. However, we think that important conclusions can be drawn from our two "bad" results as should be discussed in the following.

DISCUSSION

First we consider the behavior in the center region of the specimen. The value $\Gamma_0 = 11.5$ kJ/m^2 yields the correct fracture initiation behavior; also the first stages of crack extension are predicted well. With increasing v_{LL}, the crack extension becomes much too high. $\Gamma_0 = 17.5$ kJ/m^2 clearly underestimates the crack growth for small v_{LL}; however, at large v_{LL}, the crack growth rate is still overestimated. It can be concluded that it will be impossible to find any pair of constant $\Gamma_0^{(M)}$ and $T_{max}^{(M)}$ values so that the model reflects the experimental behavior. Either $\Gamma_0^{(M)}$ or $T_{max}^{(M)}$ or both must increase during the crack extension, at least, for the initial stages of crack growth. This could be due to the loss of constraint with increasing deformation [21]. The question, whether a crack growth region of constant cohesive parameters will appear after the initial transition region as it was observed in [8,9], cannot be decided yet.
Directly at the side surface, even a value of $\Gamma_0 = 17.5$ kJ/m^2 leads to a retarded crack extension for small v_{LL}. The reason might be that a too large value of the cohesive strength was taken ($T_{max} = 1100$ MPa, instead of the "correct" value for plane stress, $T_{max}^{(pl\sigma)} \approx 800$ MPa). For large v_{LL}-values, $\Gamma_0 = 17.5$ kJ/m^2 overestimates Δa, $\Gamma_0 = 24$ kJ/m^2 slightly underestimates Δa. It should be noted however, that the experimental determination of Δa is difficult and that the scatter of the data is large.
As a summary we can state that a comparison between the experimental data and the numerical simulation reveals that the parameters of the cohesive zone model depend on the location at the crack front and change during (the first stages of) crack extension.

ACKNOWLEDGEMENTS

The authors acknowledge gratefully the help of Professor W. Brocks of the GKSS Forschungszentrum Geesthacht, Germany, and the financial support of this work by the Materials Center Leoben under the project number SP7 and by the Österreichische Nationalbank under the project number 7744.

REFERENCES

1 Needleman, A. (1987) *J. Applied Mechanics* 54, 525.
2 Stüwe, H.P. (1981) In: *Three.Dimensional Constitutive Relations and Ductile Fracture,* Nemat-Nasser, S. (Ed.). North-Holland, 213.
3 Broberg, K.B. (1995) *Engng Fracture Mech.* 50, 157.
4 Ortiz, M. and Pandolfi, A. (1999) *Int. J. Numer. Mech. Engng.* 44, 1267.
5 de-Andres, A., Perez, J.L. and Ortiz, M. (1999) *Int. J. Solids Struct.* 36, 2231.
6 Tvergaard, V. and Hutchinson, J.W. (1996) *Int. J. Solids Struct.* 33, 3297.
7 Varias, A.G. (1998) *Comput. Mech.* 21, 316.
8 Siegmund, T. and Brocks, W. (1999) *Int. J. Fracture* 99, 97.
9 Siegmund, T. and Brocks, W. (2000) *ASTM STP* 1360, 139.
10 Siegmund, T. and Brocks, W. (2000) *Engng Fracture Mech.* 67, 139.
11 Kolednik, O. and Stüwe, H.P. (1986) *Engng Fracture Mech.* 24, 277.
12 Yan, W.-Y., Shan, G.X., Kolednik, O. and Fischer, F.D. (1998) *Key Engineering Materials* 145-149, 179.
13 Scheider, I. (2001) *Bruchmechanische Bewertung von Laserschweißverbindungen durch numerische Simulation mit dem Kohäsivzonenmodell.* Dissertation, Technical University Harburg, Germany.
14 ABAQUS, Version 5.7, Hibbit, Karlson & Sorenson Inc. Pawtucket, RI, USA.
15 Scheider, I. (2000) Internal Technical Paper GKSS/WMS/00/19. GKSS Forschungszentrum Geesthacht, Germany.
16 Shan, G.X., Kolednik, O., Fischer, F.D. and Stüwe, H.P. (1993) *Engng Fracture Mech.* 45, 99.
17 Kolednik, O., Shan, G.X. and Fischer, F.D. (1997) *ASTM STP* 1296, 126.
18 Kolednik, O. and Stüwe, H.P. (1985) *Engng Fracture Mech.* 21, 145.
19 Stampfl, J., Scherer, S., Berchthaler, M., Gruber, M. and Kolednik, O. (1996) *Int. J. Fracture* 78, 35.
20 Scherer, S. and Kolednik, O. (2001) *Microscopy and Analysis* 70**,** in press.
21 O'Dowd, N. and Shih, C.F. (1991) *J. Mech. Phys. Solids* 39, 898.

FRACTURE MECHANICAL CHARACTERIZATION OF SEMICRYSTALLINE THERMOPLASTICS

H.H. Kausch, Ch. Grein, Ph. Béguelin, R. Gensler

Département des Matériaux, Ecole Polytechnique Fédérale de Lausanne (EPFL)
CH 1015 – Lausanne

ABSTRACT

The different modes of fracture of a (semi-crystalline) polymer are determined by the competition between different *deformation and damage mechanisms*. Their molecular and structural origins and their effect on fracture toughness are discussed using rubber-modified polypropylene (PP/EPR) as main example. Toughness has been assessed using the J-Integral, the Essential Work of Fracture (EWF) and the Linear Elastic Fracture Mechanics (LEFM) concept with plastic zone correction. For relatively ductile, strain-rate sensitive materials the first two methods gave ambiguous results whereas unique values of toughness K_{eff} and strain energy release rate G_{eff} were obtained from properly corrected LEFM data. As an additional advantage the latter approach can be used in a wide range of strain rates extending from slow creep to impact loading (at 7m/s) thus permitting the study of brittle-ductile transitions, often the most sensitive property to characterize the impact performance of a polymer [1].

KEYWORDS

Toughness, semi-crystalline polymers, molecular mechanisms, plastic zone correction, strain-rate sensitive materials, ductile-brittle transitions, impact performance.

INTRODUCTION

High stiffness and fracture toughness are still among the most important mechanical properties. The deformation and fracture behavior of semi-crystalline thermoplastics is strongly influenced by structural features from three different levels of organization: by *molecular configuration* (chain length, tacticity), the physical *structure of the crystal lamellae*, and by their *heterogeneous, frequently spherulitic morphology*. In addition the state of stress (presence of modifier particles, sample geometry) and the rate of loading play an important role. In order to direct the development of these attractive materials and to optimize their application reliable methods of physical and *continuous* mechanical characterization are needed. By *continuous* we understand a method, which works with identical specimen geometry in wide range of strains, strain rates and temperatures.

In this presentation we will mainly deal with polypropylene (PP), which shows an extraordinary breadth of fracture phenomena (*brittle fracture* through unstable rapid crack propagation, *slow creep crack* growth, crazing or macroscopically homogeneous deformation leading to *plastic instability*). The mode of fracture is largely determined by the competition between stress transfer onto backbone chains and the intensity of the different relaxation mechanisms, including segmental slip and disentanglement, void formation and chain scission. The inherent ductility and low glass transition temperature, T_g, of PP give rise to strongly rate dependent *local* plasticity effects, which have to be taken into consideration for a quantitative evaluation of toughness. In the following we will briefly indicate the molecular and structural origins of the different *deformation and damage mechanisms.* Their effect on fracture toughness will then be assessed using three methods (J-Integral, EWF, LEFM).

DEFORMATION AND DAMAGE MECHANISMS AND THEIR EFFECT ON FRACTURE BEHAVIOR

Semi-crystalline polymers are highly heterogeneous on a molecular and microscopic scale. The smallest building-blocks considered here are aggregates of crystal lamellae connected by amorphous regions. These latter consist of a network of non-extended entangled chains, dangling chain ends and/or loops, and more or less taut tie-molecules. When a spherulitic sample is strained, local strains within a lamellar stack will vary considerably, depending on the local Young's modulus, the relative orientation of the lamellar stack with respect to the principal stress direction and the modes of stress relaxation available to a given volume. Above T_g the amorphous regions will account for most of the elastic and anelastic deformation. The regions oriented perpendicular to an applied (uniaxial) stress will initially mainly deform by interlamellar separation.

Evidently, the difference between the crystalline and amorphous moduli and the resulting strain concentration become relatively small at $T<<T_g$. Crack extension in this temperature range occurs by rapid straining and failure of the material ahead of the crack tip following the *plane of least resistance*, i.e. generally through and along the amorphous interlayers. Tie chains are stretched and broken rather than pulled out. Thus, plastic deformation of the bulk material is relatively limited and crack resistance is well quantified by the critical strain energy release rate G_{Ic} (or by the critical stress intensity factor K_{Ic}) using the standard methods of *Linear Elastic Fracture Mechanics* [2, 3].

More extensive anelastic and/or plastic deformation is observed if the drawing process also involves the crystalline regions. *Homogeneous, ductile* deformation through lamellar shear is favored by intense stress transfer between crystal lamellae through strong, well-entangled amorphous regions and a large concentration of tie-molecules. These parameters also increase K_{Ic}. On the other hand, low molecular weight and rigid crystal lamellae favor heterogeneous, localized deformation leading to craze-like features and brittle fracture [4]. However, the mode of fracture is not an inherent property of a given material, it depends strongly on temperature, time scale and state of stress. For an unmodified high molecular weight polypropylene (PP) it changes as a function of loading rate v from full shear yielding ($v < 1$ mm/s) to small scale yielding and multiple crazing (10 mm/s – 1m/s) and to formation of a single crack ($v > 2$ m/s) [5]. The time scale is evidently shifted with molecular weight and temperature (see below).

FRACTURE MECHANICAL CHARACTERIZATION

Essential Work of Fracture (EWF)

The EWF concept is based on the assumption that the total work of fracture, W_{tot}, is dissipated in two distinct regions at the crack tip, in the so-called process zone or inner fracture zone (W_e), and in an outer plastic zone (W_p). A test protocol has been developed by the European Structural Integrity Society (ESIS) [3]. The specific work of fracture, w_{tot}, is obtained by normalizing W_{tot} with the fracture surface $A = \ell \cdot t$ (given by the sample thickness, t, and the so-called ligament length ℓ):

$$w_{tot} = w_e + \beta w_p \ell \tag{1}$$

The quantity w_e is referred to as the specific essential work of fracture (in kJ/m^2) and the parameter w_p is called the specific non-essential or plastic work of fracture (in MJ/m^3). A plot of w_{tot} versus the ligament length results in a straight line, which intersects the ordinate at w_e = 9.05 kJ/m^2 (EWF plot, Figure 1i). An analysis of the stress-strain curve (Figure 1 ii) shows that the energy values obtained for crack initiation and for propagation, both contain contributions to w_e and w_p. Thus, despite the linearity of the EWF plot, there is a notable ambiguity concerning the *fracture* energy. It should be noted, however, that the term βw_p gives a rather sensitive account of the capacity for plastic deformation, thus indicating the effects of e.g. aging much earlier than the yield stress [5].

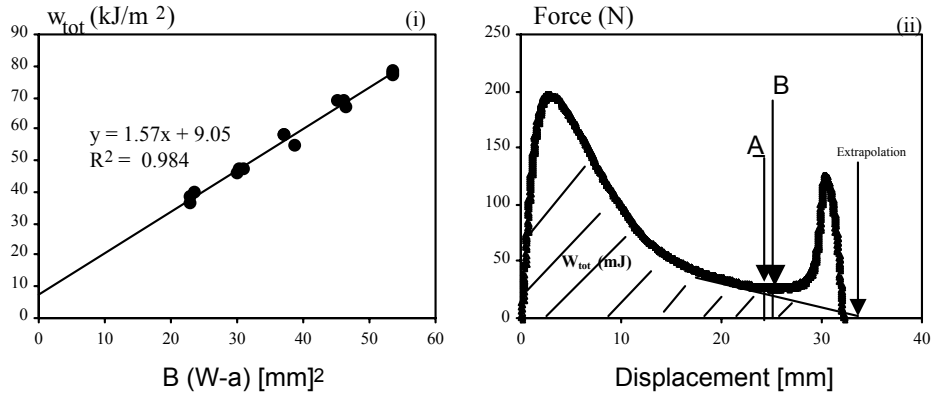

Figure 1: EWF plot (i) and stress-strain curve (ii) of a ductile polymer (β-PP/ 15 vol.% EPR) [1]. Two possible criteria for the determination of W_{tot} are indicated, a fixed displacement (A) and the minimum of force (B).

J-Integral

The J-integral concept has proven its usefulness for a variety of polymers. It relates the dissipated energy *J* to the crack advance Δa. *J* can be calculated for a cracked sample from:

$$J = \frac{\eta U}{B(W - a)} \tag{2}$$

where *U* is the surface under the stress-strain curve, *B* specimen thickness, and *(W-a)* the effective ligament length. The factor η depends on sample geometry [3]. Figure 2 represents the results of a multiple specimen test [1]. The method is not only *laborious* because of the large number of specimens (which could be avoided by the single-specimen J-integral method [3]) but it is also *ambiguous* because of the difficulties to determine Δa with sufficient precision in a non-transparent, tough material.

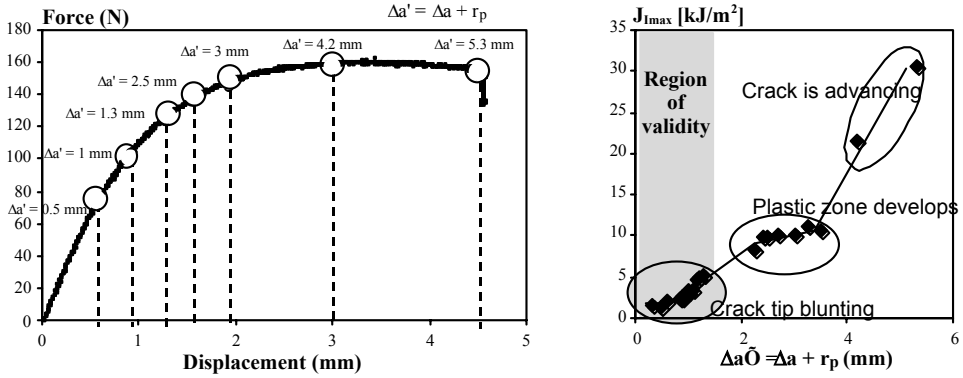

Figure 2 (3.11): Multiple specimen J-integral test on α–PP/ 15 vol.% EPR, *a*/W = 0.5, tested at room temperature and at a displacement rate of v = 0.001 m/s [1]

Linear elastic fracture mechanics (LEFM) analysis with plastic zone correction

From LEFM one derives for a compact tension (CT) specimen a stress intensity factor K_I:

$$K_I = f(a/W)\frac{F_{max}}{B\sqrt{W}} \qquad (3)$$

where F_{max} is the maximum force applied to the specimen and *f(a/W)* a correction function, which depends on sample geometry and is tabulated [6]. In the range of validity of LEFM K_I corresponds to K_{Ic} and a plot of F_{max} over $BW^{1/2}$/f should give a straight line through the origin. If the criteria of LEFM are not met, an *apparent* K_{Imax} is obtained from Eqn. 3 (Figure 3i, bottom curve). In that case K_{Imax} will depend on sample and crack geometry as for instance on *a*/*W* (Figure 3ii). The main reason for such dependence is generally the presence of a small *confined plastic* zone r_p at the crack tip. In the classical models by Irwin [Irwin] for an elasto-plastic material and Dugdale [Dugdale] this has been taken into account by substituting the crack length *a* by $a_{eff} = a + r_p$. The size of r_p is derived from respectively a *yield* or a *line zone* criterion [2]. For a rubber modified polymer Gensler [5] has used a *volume strain* cri-

terion. Grein [1] uses a different procedure to correct for confined plasticity, she proposes to determine r_p by numerical iteration in such a way that all data of a corrected plot F_{max} over $BW^{1/2}$/f(a_{eff}) fall on a line through the origin (Figure 3i, upper curve). The *apparent K* obtained for a ductile (β-crystalline)

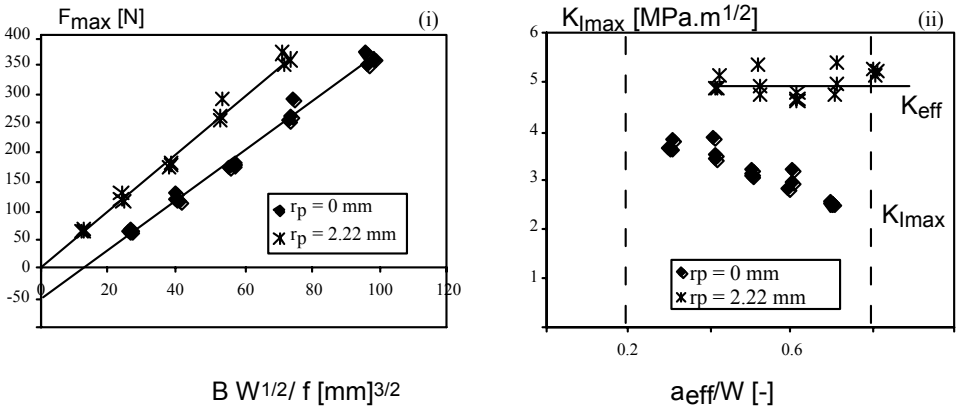

Figure 3: (i) Determination of the size r_p of the plastic zone by an iteration procedure (see text); (ii) evolution of K_{eff} of an unmodified β-PP as a function of a_{eff}/W [1]

material without correction decreases with a/W, whereas K_{eff} vs. a_{eff}/W is constant thus giving credit to the applied procedure (Fig. 3ii) [1].

APPLICATION: TOUGHNESS AS A FONCTION OF LOADING RATE (DUCTILE-BRITTLE TRANSITIONS)

A major advantage of the corrected LEFM method is its applicability in a wide range of strains and strain rates, which permits a homogeneous characterization of ductile-brittle transitions and a convenient comparison of different blends, the principal aim of this investigation. The development of r_p, K_{Imax} and K_{eff} in an α-PP/ 15 vol.% EPR with rate of displacement v is indicated in Figure 4. The transition from ductile to brittle fracture occurs between 0.4 m/s (which corresponds to the maximum of K_{eff}) and 0.7 m/s (where the tenacity decreases notably). A microstructural analysis shows that in ductile fracture three regions ahead of the crack tip can be identified where respectively particle cavitation, interlamellar cavitation leading to craze formation, and large scale matrix plastic deformation dominate. In brittle fracture a single crack propagates with no signs of rubber cavitation or crazing visible [1]. These observations confirm that energy dissipation is triggered by rubber particle cavitation, which contributes to relax the *unfavorable* tri-axial state of stress. Cavitation in itself does not dissipate much energy; for efficient toughening it is essential that the matrix be capable to engage large strains by crystal plastic deformation. The notable influence of the presence of cavitating particles and of matrix ductility are brought out by comparing the fracture behavior of different PP-resins.

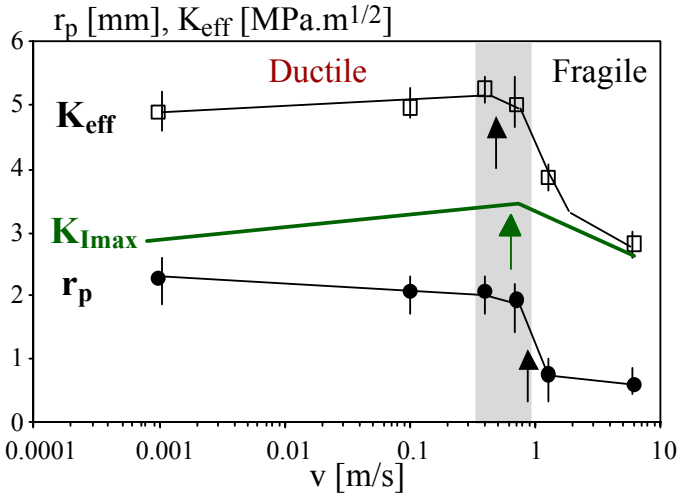

Figure 4: Development of r_p, K_{Imax} and K_{eff} of an α-PP/ 15 vol.% EPR with rate of displacement v [1]

When comparing blends of different composition it is useful to plot *the rate of increase of K* (determined from Eqn.3 by introducing dF/dt) instead of v. This eliminates effects due to differences in sample compliance. A K-rate temperature diagram of the ductile-brittle transitions of three α-PPs is compiled in Figure 5. It clearly shows the important *rate sensitivity* of PP (the fracture transition is shifted by 4 decades of K-rate over a temperature interval of 110 K), the dramatic *toughening effect* caused by the addition of the *first* 15% of rubber particles (the unmodified matrix at +60°C is brittle at loading rates larger than 0.1 MPa.m$^{1/2}$s^{-1}, whereas the transition jumps to 7000 MPa.m$^{1/2}$s^{-1} for the α-15%), and the *large difference* between unmodified α– and β-PP. The latter behavior is ascribed to the increased molecular mobility of the β-phase as evidenced by the fact that the β–transition of β-PP at +5 °C is much more intense than that of α-PP [1]. Unfortunately this difference between α– and β-PP is not maintained after modification with EPR.

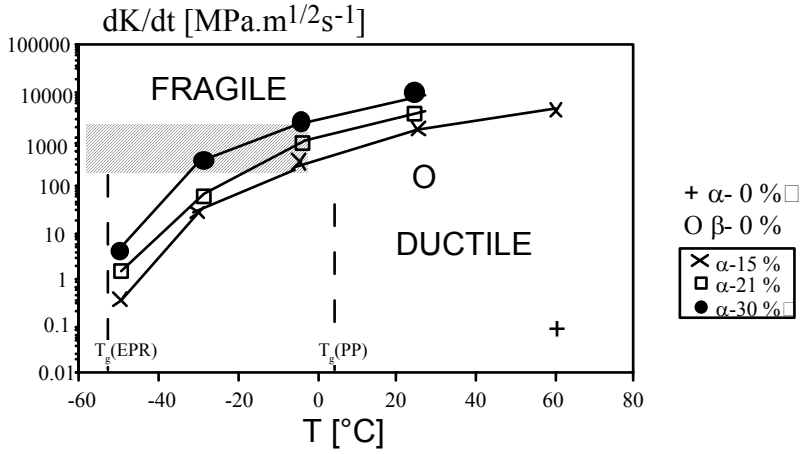

Figure 5: Ductile-brittle transitions of α-PP filled with respectively 15, 21 and 30 vol% EPR as a function of temperature and of rate of increase of *K*. For comparison are also indicated the *K*-rates where the ductile-brittle transition of the pure resins α–PP (+) and β–PP (O) occur.

CONCLUSIONS

Three methods for a quantitative evaluation of fracture toughness have been compared using polypropylene (PP) as an example. Its inherent ductility (low glass transition temperature, T_g) and strain hardening capacity give rise to large, strongly rate dependent local plasticity effects. We have shown that for such materials the J-Integral and the Essential Work of Fracture (EWF) concepts give ambiguous results. From the Linear Elastic Fracture Mechanics (LEFM) approach with plastic zone correction unique values of toughness K_{eff} and strain energy release rate G_{eff} are obtained. Thus one and the same approach can be used in a wide range of strain rates (from creep to impact loading) and fracture modes. The study of brittle-ductile transitions is a sensitive means to elucidate the toughening mechanisms of differently modified PPs and of the influences of the molecular, crystallographic and morphological structure on toughness.

References

1. Grein, C. (2001) PhD thesis No. 2341, Ecole Polytechnique Fédérale de Lausanne, Switzerland
2. Williams J. G (1984), *Fracture Mechanics of Polymers,* Ellis Horwood,Chichester
3. Moore D.R., Blackman B.R.K, Davies P., Pavan A., Reed, P. and Williams J.G., Eds., 2000, *Experimental Methods in the Application of Fracture Mechanics Principles to the Testing of Polymers, Adhesives and Composites*. Elsevier , London,
4. Kausch, H.H., Gensler, R., Grein, C., Plummer C.J.G. and Scaramuzzino, P., (1999) J. Macromol. Sci.-Phys., **B 38**, 803
5. Gensler R., (1998), PhD thesis No. 1863 Ecole Polytechnique Fédérale de Lausanne, Switzerland, (Gensler R., Plummer C.J.G., Grein C. and Kausch H.H., (2000), Polymer **41**, 3809)
6. Williams J. G (1980), *Stress Analysis of Polymers,* Ellis Horwood, Chichester

ORAL/POSTER REFERENCE: 10010590R

FRACTURE MECHANICS AND DURABILITY OF HIGH PERFORMANCE CONCRETE

F. H. Wittmann

Laboratory for Building Materials
Swiss Federal Institute of Technology (ETH) Zürich, Switzerland

ABSTRACT

The crack path through composite materials such as concrete depends on the mechanical interaction of inclusions with the cement-based matrix. Fracture energy depends on the deviations of a real crack from an idealized crack plane. Fracture energy and strain softening of normal, high strength, and self-compacting concrete have been determined by means of the wedge splitting test. In applying the numerical model called „numerical concrete“ crack formation in normal and high strength concrete is simulated. Characteristic differences of the fracture process can be outlined. Finally results obtained are applied to predict shrinkage cracking under different boundary conditions. Crack formation of high strength concrete has to be seriously controlled in order to achieve the necessary durability of concrete structures.

KEYWORDS

composite material, high strength concrete, fracture process, shrinkage cracking

1. INTRODUCTION

Crack formation in concrete is often at the origin of serious damage due to corrosion. The fictitious crack model (FCM) as developed originally by Hillerborg and his co-workers [1] is a powerful tool to predict crack formation in composite materials such as concrete. For a realistic prediction we need fracture energy and strain softening of the material. At present there exists a wealth of data for normal concretes [2,3]. Considerable less data are available for high performance concrete.

Sometimes the term high performance concrete is used for high strength concrete. In fact high performance concrete has a much wider meaning [4]. Strength is an important performance among others such as ductility, self-compacting ability, low shrinkage, high modulus or wear resistance. In this contribution we will consider crack formation of high strength and normal concrete. Fracture energy and strain softening depend on the composite structure of the material. It is essentially governed by the mechanical interaction of the aggregates with the cement-based matrix. In Fig. 1 the influence of maximum aggregate size on the specific fracture energy is given.

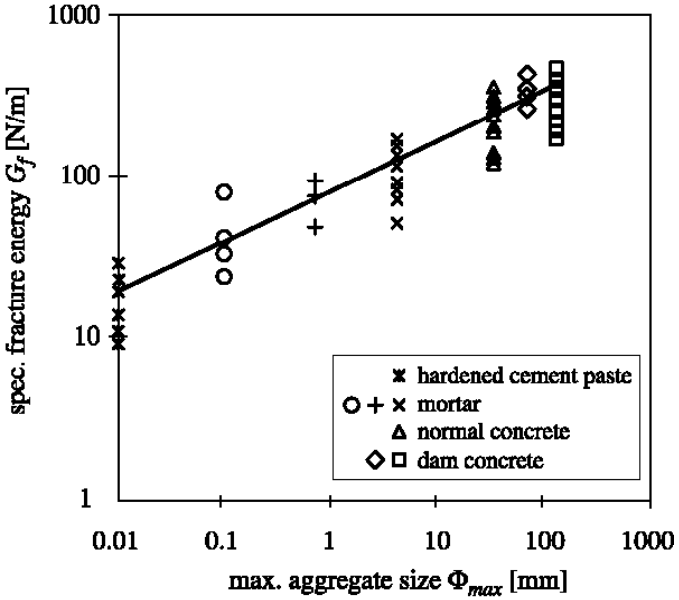

Figure 1: Specific fracture energy of cement-based materials as function of maximum aggregate size.

The lowest fracture energy is measured on pure hardened cement paste. In this case the maximum aggregate size is estimated to be 0,01 mm which corresponds to the dimension of the remaining unhydrated clinker particles. The highest value is observed in dam concrete with a maximum aggregate size of 120 mm [5]. In between the influence of maximum aggregate size on fracture energy can be described by a power function.

$$G_f = a \cdot \Phi_{\max}^{n} \tag{1}$$

From the data shown in Fig. 1 one obtains the following values for the parameters a and n in equ. (1): a = 80,6 and n = 0,32 [5].

In pure hardened cement paste and in fine mortar a crack can develop along a plane. The small and strong particles impose minor deviations from an ideal fracture surface only. In Fig. 2(a) a typical flat fracture surface of a mortar with a maximum aggregate size of 2 mm is shown. In Fig. 2(b) a fracture surface of normal concrete with a maximum aggregate size of 32 mm is shown. As most aggregates (river gravel) are stronger than the cement-based matrix a crack is forced to run around the inclusions. From Fig. 2(b) it can be clearly seen that a crack once it meets an aggregate either has to run out of the plane and leaves a blank aggregate surface behind or it runs in the opposite direction. In the latter case the aggregate is torn out of the matrix. The negative imprints can be seen in Fig. 2(b).

Obviously the necessary fracture energy increases with the maximum aggregate size if the size distribution remains similar. In contrast to the energy consuming crack formation in normal concrete a crack in high strength concrete runs through the inclusions and forms approximately a plane as observed on fine mortars and pure hardened cement paste (Fig. 2(c)). In this case mechanisms of mechanical interaction between inclusions and matrix cannot be activated. This leads to the more brittle behaviour of high strength concrete. By means of the well-known model „numerical concrete“ [6] damage and crack formation in normal and high strength concrete will be simulated. Finally results obtained will be applied to predict shrinkage cracking under different boundary conditions.

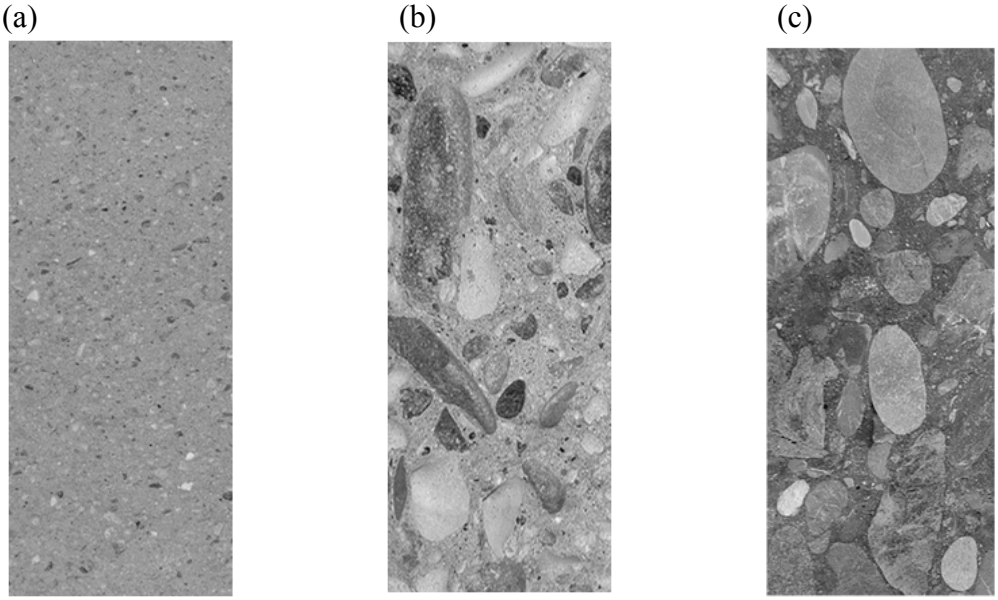

Figure 2: Fracture surface of (a) mortar, (b) normal concrete and (c) high strength concrete.

2. MATERIALS AND EXPERIMENTAL RESULTS

2.1.Concrete Composition

Three types of concrete have been produced. The mix composition is given in Table 1. The maximum aggregate size has been chosen to be 32 mm for all these mixes and the size distribution follows a Fuller curve. In this way the range from a normal concrete to a high strength concrete is covered. Cubes with a side length of 150 mm and cylinders with a diameter of 150 mm have been casted.

TABLE 1: MIX COMPOSITION OF THE THREE DIFFERENT TYPES OF CONCRETE

	Mix A	**Mix B**	**Mix C**
Cement Type	CEM I 425	CEM I 42,5	CEM I 52,5
Cement content kg/m^3	400	400	400
Water/cement ratio	0,55	0,38	0,28
Plasticizer	-	0,5 % Glenium 51	1,5 % Glenium 27
Microsilica	-	-	10%

2.2.Experimental results

In order to be able to simulate shrinkage crack formation a series of material parameters has to be determined. First the compressive strength and the elastic modulus have been measured as function of age. The values obtained at an age of 14 days are compiled in Table 2. Strength has been measured on cubes and the modulus of elasticity on cylinders.

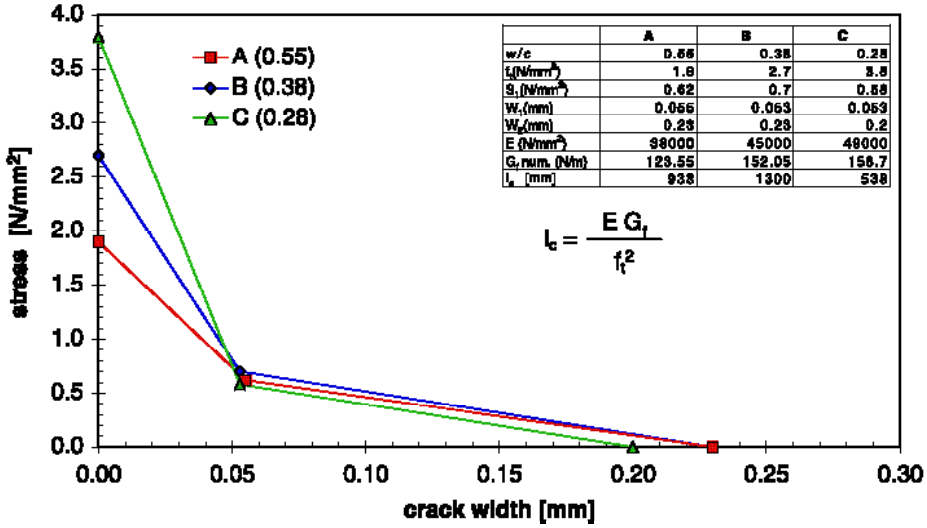

Figure 3: Bilinear relation for strain softening.

TABLE 2: COMPRESSIVE STRENGTH AND ELASTIC MODULUS AT AN AGE OF 14 DAYS

	Mix A	**Mix B**	**Mix C**
Compressive strength N/mm^2	35,3	57,4	112,2
Modulus of elasticity N/ mm^2	38.000	45.000	49.000

Fracture mechanics parameters have been determined by means of the wedge splitting test [7]. These tests have been carried out on cubes with a sawn notch having half the heigth of the cube. Results obtained after inverse analysis are shown in Fig. 3. The insert in Fig. 3 summarizes the obtained parameters of the bilinear model. In the last line the characteristic length l_c is given as calculated by the following equation:

$$l_c = \frac{EG_f}{f_t^2} \tag{2}$$

This length can be considered as an indication of the brittleness of a material. In addition to the mechanical properties we also need the hygral diffusion coefficient and the shrinkage as function of relative humidity. The hygral diffusion coefficient can be calculated from measured drying data [8]. On this basis it is possible to calculate time-dependent moisture distributions in concrete elements prepared with different types of concrete and under different boundary conditions in order to predict crack formation.

3. NUMERICAL SIMULATION OF CRACK FORMATION

In the preceeding section we have outlined all the material parameters which have to be known or determined before the risk of crack formation can be realistically estimated. As a next step we will simulate numerically crack formation in a composite structure such as concrete. We consider concrete to be built up by coarse aggregates embedded in the mortar matrix.

As we want to compare crack propagation in ordinary and high strength concrete we need parameters of two matrixes, i.e. a cement-based mortar with a w/c-ratio of about 0,5 and 0,35 respectively. Based on earlier experiments the data compiled in Table 3 have been used for the numerical simulation. To simulate crack propagation a specimen used for wedge splitting experiments has been chosen. The composite structure of concrete has been simulated by generating randomly dispersed hexagonal

aggregates. The size distribution of the aggregates follows a Fuller curve. The material parameters attributed to the aggregates and the two different matrixes under investigation are all given in Table 3. The composite structure to be analysed is shown in Fig. 4 (a) and (b).

TABLE 3: MATERIAL PARAMETERS USED IN THE NUMERICAL SIMULATION

Materials	Aggregates	Matrix in NC	Matrix in HSC
E (GPa)	60.0	20.0	30.0
υ(-)	0.2	0.2	0.2
f_t (MPa)	10.0	3.0	8.0
w_1 (mm)	0.002	0.02	0.01
σ_1 (Mpa)	1.0	0.5	1.0
w_2 (mm)	0.008	0.03	0.02
G_F (N/m)	14.0	37.5	50.0

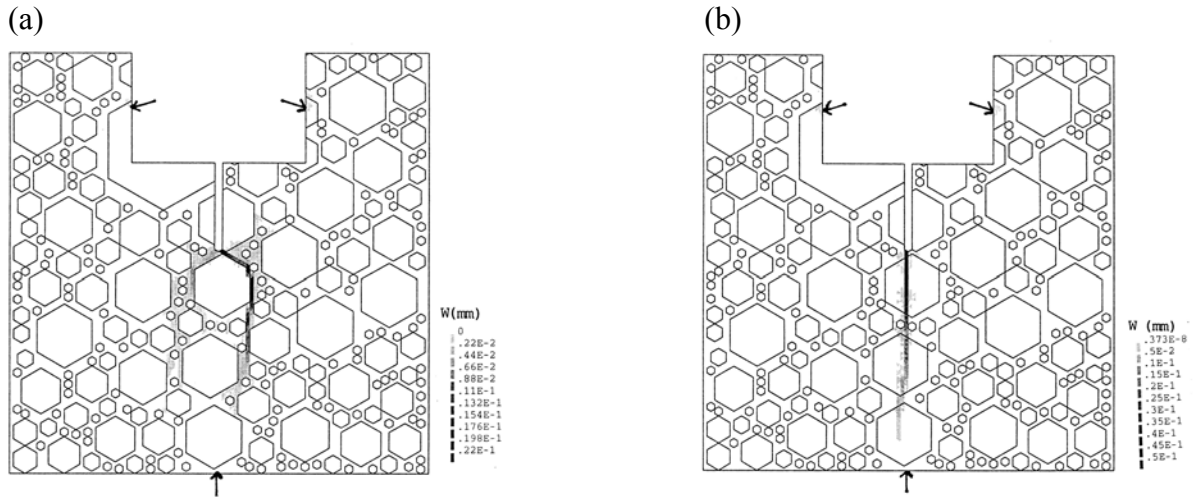

Figure 4: Damage (fictitious cracks) and crack formation in numerically simulated concrete: (a) normal concrete and (b) high strength concrete

If a moderate force F is applied the system reacts linearly elastic. But after a characteristic load is reached a fictitious crack (damaged zone) will be formed in the weaker matrix. The crack propagation in normal concrete is shown in Fig. 4. As the aggregates are stronger than the matrix cracks will run around the aggregates. Finally a damaged band with a width of about twice the maximum diameter of the aggregates is being formed. It is quite clear that due to the mechanical interaction between aggregates and matrix the fracture energy of the composite material becomes considerably bigger than the fracture energy of both the aggregates and the matrix.

If crack propagation in high strength concrete is simulated cracks can run through aggregates as the matrix and the aggregates are mechanically very similar. A typical example is shown in Fig. 4 (b). A comparatively narrow crack band is being formed in high strength concrete. The results shown in Fig. 4 agree well with the photos of crack surfaces as shown in Fig. 2.

4. SHRINKAGE CRACKING

Measured shrinkage is in fact the response of a concrete specimen to the strains and stresses generated by the drying process. If the water loss of a specimen with known geometry is measured the hygral diffusion

coefficient can be determined by inverse analysis [8]. Then time-dependent moisture distributions can be numerically predicted.

The moisture profiles in normal concrete can be realistically predicted by the general diffusion equation [9]. In the case of high strength concrete a sink term has to be added to the diffusion equation because of the endogenous drying. If we compare the moisture profile after 7 days of drying for instance the drying process affects the surface near zone in normal concrete only. In high strength concrete endogenous drying, however, leads to an equilibrium hygral potential of 0,8 in the center of drying elements. This effect has a series of consequences with respect to crack formation. From shrinkage tests infinitesimal shrinkage i.e. shrinkage of an infinitesimal thin layer can be obtained by inverse analysis [10].

Crack formation in reinforced beams made of normal and high strength concrete has been simulated numerically. The entering material properties such as elastic modulus, tensile strength and strain softening, hygral diffusion coefficient, coefficient of hygral dilatation have all been determined experimenteally.

5. CONCLUSIONS

The following conclusions can be drawn from the results presented in this contribution:

- Crack formation and fracture energy depend on the mechanical interaction between inclusions (gravel or crushed stone) and the cement-based matrix.
- High strength means generally low ductility and increased risk for crack formation.
- A numerical model (numerical concrete) can be used to optimise composite materials such as concrete with respect to well-defined requirements: strength, ductility, durability etc.
- Endogenous shrinkage takes place in high strength concrete. This process creates stress states and internal damage which are not covered adequately by most codes so far.

REFERENCES

1. A. Hillerborg, M. Modéer and P.E. Petersson, *Analysis of crack formation and crack growth in concrete by means of fracture mechanics and finite elements*, Cement and Concrete Research, 6, 773-782 (1976)
2. F.H. Wittmann, editor, *Fracture Mechanics of Concrete Structures*, Proc. Second Int. Conf. On Fracture Mechanics of Concrete Structures, Aedificatio Publishers, D-Freiburg (1995)
3. H. Mihashi and K. Rokugo, editors, *Fracture Mechanics of Concrete Structures*, Proc. Third Int. Conf. Of Fracture Mechanics of Concrete Structures, Aedificatio Publishers, D-Freiburg (1998)
4. F.H. Wittmann, editor, *High Performance of Cement-Based Materials*, WTA report series No. 15, Aedificatio Publishers (1997)
5. B. Trunk and F.H. Wittmann, *Experimental investigation into the size dependence of fracture mechanics parameters*, in Ref. 3, pp. 1937-1948 (1998)
6. P.E. Roelfstra, H. Sadouki and F.H. Wittmann, *Le béton numerique*, Materials and Structures 18, 327-335 (1985)
7. E. Brühwiler and F.H. Wittmann, *The Wedge splitting test, a new method of performing stable fracture mechanics tests*, Eng. Fracture Mechanics 35, 117-125 (1990)
8. X.H. Wittmann, H. Sadouki and F.H. Wittmann, *Numerical evaluation of drying test data, Transaction*, 10th Conf. On Struct. Mech. In Reactor Technology (SmiRT-10), Vol Q, pp. 71-79 (1983)
9. A.M. Alvaredo, *Drying shrinkage and crack formation*, Building Materials Reports No. 5, Aedificatio Publishers (1994)
10. G. Martinola, *Rissbildung und Ablösung zementgebundener Beschichtungen auf Beton*, Building Materials Reports No. 12, Aedificatio Publishers (2000)

ORAL REFERENCE: ICF100719OR

FRACTURE MECHANICS CHARACTERISATION OF EPOXY RESINS BY MEANS OF MINI-COMPACT-TENSION-SPECIMENS

C. Bierögel[1], H. Walter[2], W. Grellmann[1], H. Henning[3], B. Michel[4]

[1] Department of Engineering Science, Martin-Luther-University of Halle-Wittenberg, Halle, D 06099, Germany
[2] Angewandte Micro-Messtechnik GmbH, Berlin, D 15834, Germany
[3] Leuna-Harze GmbH, Leuna, D 06233, Germany
[4] Fraunhofer Institute of Reliability and Microintegration, Berlin, D 13355, Germany

ABSTRACT

Epoxy resins typically show a high modulus of elasticity and nearly elastic stress-strain behaviour, but poor resistance to fracture. In case of micro-electronic applications such as chips a complex material behaviour occurs due to different mechanical and thermal properties throughout the sandwich, which can influence the mechanical and thermal reliability as well as the life time. The produced residual stress and material inhomogeneities as well as the high thermal gradients cause local defects such as cracks in the sandwich structure. As a result of this failure behaviour fracture mechanics methods are increasingly used for characterising and optimising the toughness of epoxy resins. Applying fracture mechanics concepts makes it possible to gain much information to characterise fracture toughness of new-developed or modified materials using miniaturised specimens.
In this study the influence of chemical structural parameters, filler content and filler geometry, and test conditions on the crack resistance behaviour and fracture mechanics parameters is examined. The investigation of fracture using small specimens is based upon analysing crack resistance against stable and unstable crack growth behaviour under quasi-static loading of standard specimens by means of experimental fracture mechanics. Furthermore, in this paper fracture properties and toughness behaviour of differently filled and modified epoxy resins for microelectronics applications are investigated.

KEYWORDS

Fracture Behaviour, Toughness, Compact-Tension-Specimen, Crack Initiation and Propagation, Epoxy Resin, Laser double scanner

INTRODUCTION

Epoxy resins are used in a wide range for microelectronics application and electronic packaging [1]. At room temperature crosslinked epoxies typically exhibit a high modulus and a nearly elastic stress-strain behaviour, but they have poor resistance to fracture. A complex material behaviour can often be

observed due to different mechanical and thermal properties of filler and bonded components which can influence the total mechanical-thermal reliability strongly. In these systems local defects such as cracks can appear as a result of inhomogeneities, residual stress of material and high thermal and mechanical loading gradients between the different materials. Consequently the methods of fracture mechanics have an increasing significance regarding the assessment of failure behaviour. The aim is the optimisation of toughness for epoxies under extreme loading conditions of practice. The industrial application of fracture mechanics values for this purpose and the evaluation of structures basically depends on the geometry independence of these parameters. Only under the condition of geometry-independent parameters the structures developed have an optimum of reliability and operation safety in practice. Compact-tension (CT)-specimens normally used require much material and are often unsuitable for experimental investigations. In the future, the application of miniature specimens for determination of fracture mechanics parameters should be enabled so that an efficient toughness evaluation of new-developed materials can be performed [2].

EXPERIMENTAL

Material

The test material chosen for all investigations was epoxy resin Epilox A-1701 from Leuna-Harze GmbH. In accordance to the manufacturer's instructions the curing was carried out at 160 °C. The resin was used both in the unfilled state and reinforced with silica particles (table 1).
The fracture mechanics values of the cured resins were measured by mini-compact-tension-specimens with the dimensions length L = 25.4 mm, width W = 20.4 mm, and thickness B = 1 - 10 mm. For all specimens the ratio of the initial crack length to the width a/W was 0.55. Additionally, to realize a sharpened crack tip, the specimens were notched with an industrial razor blade.

TABLE 1
INVESTIGATED MATERIALS

Filler	Producer	Type of filler	Diameter
Teco Sil 44 L	C-E-Minerals	Glass powder	9 - 13 µm
Sheriglass 5000	Potters Ballotini	Glass balls	3.5 - 7 µm
Sheriglass 2024	Potters Ballotini	Glass balls	100 - 200 µm

Test techniques

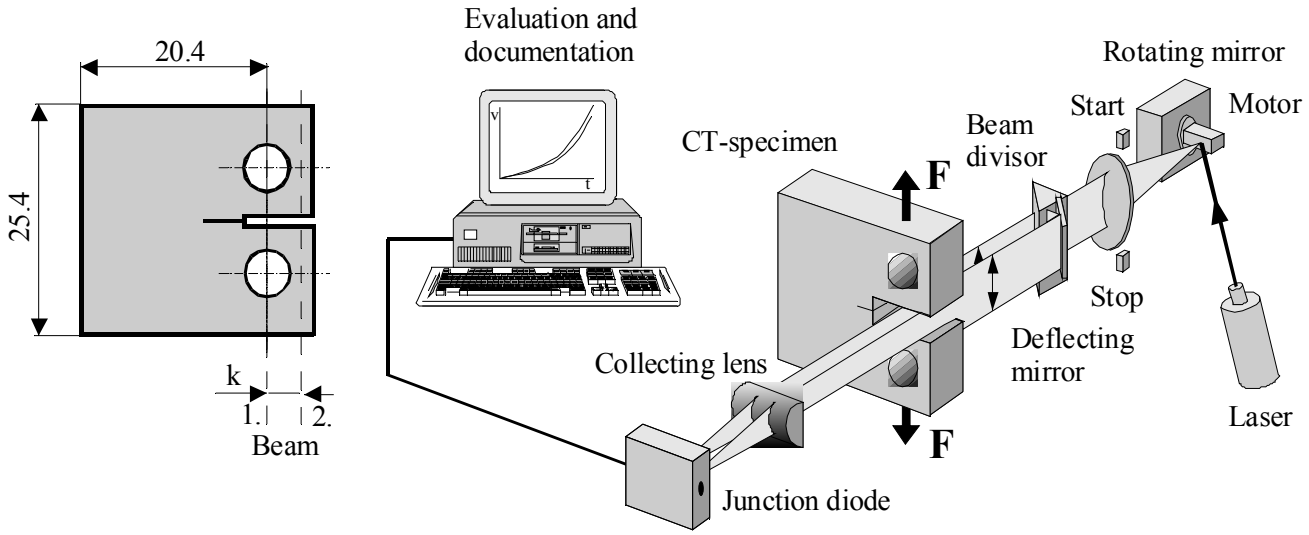

Figure 1: Laser double scanner system and specimen dimensions

All tests were executed on an INSTRON universal testing machine. The load-line displacement was measured by means of a laser scanner system. The laser double scanner used is favoured for the experimental fracture mechanics examination and works in transmission mode with two parallel laser beams. With these two beams the load-line displacement and crack mouth opening displacement can determined by contactless measurements for the shown specimens (fig. 1) [3].

RESULTS AND DISCUSSION

Unfilled and unmodified epoxy resins are brittle and exhibit unstable crack propagation. The estimation of fracture mechanics parameters (stress intensity factor K and J-Integral) by using miniature specimens bases on the analysis of the crack resistance behaviour under quasi-static loading.
Toughness values of epoxy resin depend on specimen thickness. Because the experimental estimation of the minimum thickness B_{min} is very expensive due to the required great number of specimens, of alternative geometry criteria should be used. The empirical geometry criterion (Eq.1) is valid and independent of loading conditions and the nature of materials failure.

$$B_{\min} = \beta\left(\frac{K_{Ic}}{\sigma_Y}\right)^2 \qquad (1)$$

The geometry factor β depends on material and on the loading conditions, but it is often considered to be constant. In case of double-logarithmic plotting of β in dependence on the stress-intensity factor K the value β decrease with increasing toughness independent on the used standard or testing protocol. The experimentally obtained fracture mechanics values will be geometry-independent, if it fulfil this geometry criterion of minimal specimen thickness $B_{min.}$ With increasing thickness of mini-compact-tension specimen geometry independent fracture mechanics values can be found for the epoxy resins. The critical minimum specimen thickness was determined to be 4 mm (fig. 2-filled symbols).Thereby, the fracture mechanics parameters can express the influence of material structure, loading rate, and the test temperature on the toughness by using (CT-) specimens.

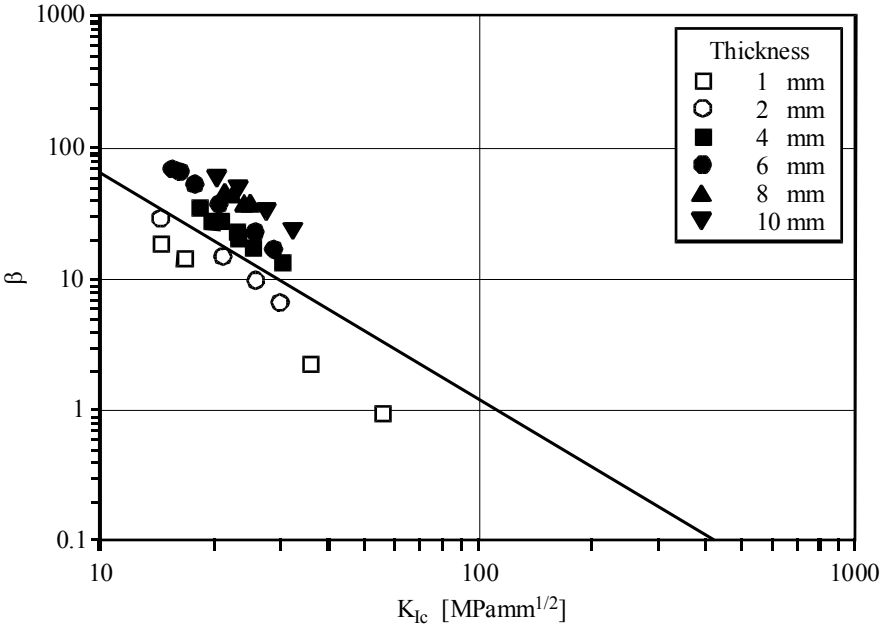

Figure 2: Requirements on specimen geometry for the determination of critical fracture toughness values K_{Ic} with miniature specimens

Under the view of practice, the fixing of employment limits for epoxies is of a special significance and requires the description of the mechanical properties in dependence on temperature. Up to a tempera-

ture of 100°C the toughness behaviour changes insignificantly, but if the temperature is further rising, the fracture toughness increases rapidly (fig. 3). The maximum load reaches the highest value at 140°C just below the glass transition temperature (T_g). This increase of fracture toughness at higher temperatures is caused by an increasing molecular mobility of the network chains. On the other hand, the temperature-induced decrease in the yield stress of the polymers leads to a larger plastic zones in front of the crack tip connected with a crack blunting [4].

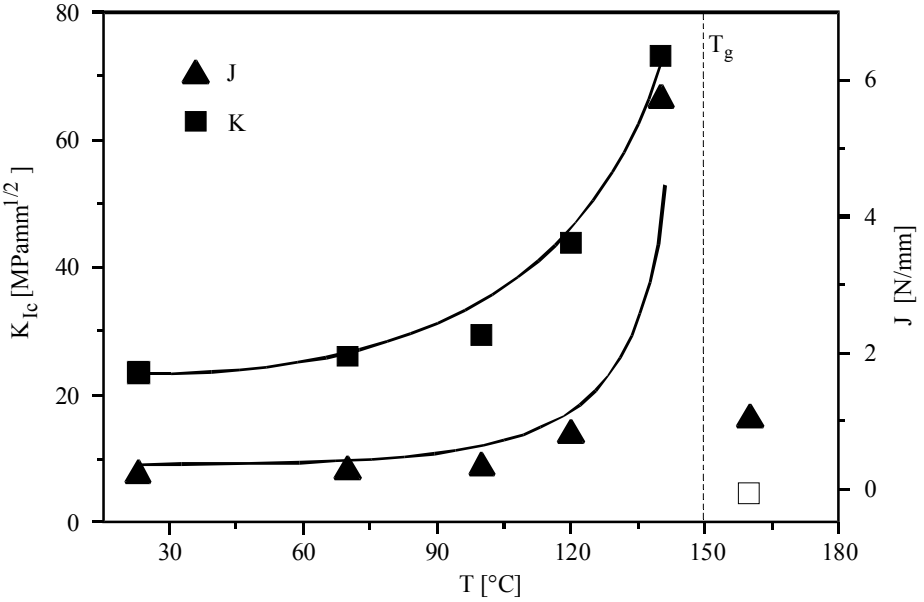

Figure 3: Effect of temperature on fracture toughness for unfilled epoxy resin

The toughness improvement of polymers can be achieved by an enhancement of energy dissipation capability. The efficiency of toughness increase depends on filler geometry, content and chemical bonding. Generally for the materials investigated the coupling to the matrix is insufficient. Because there exist no interaction between matrix and filler, especially the modification with glass balls show a very small effect in toughness behaviour (fig. 4). In opposition to this result the toughness of glass powder filled resin increases essentially, which is caused by the irregular geometry of the powder.

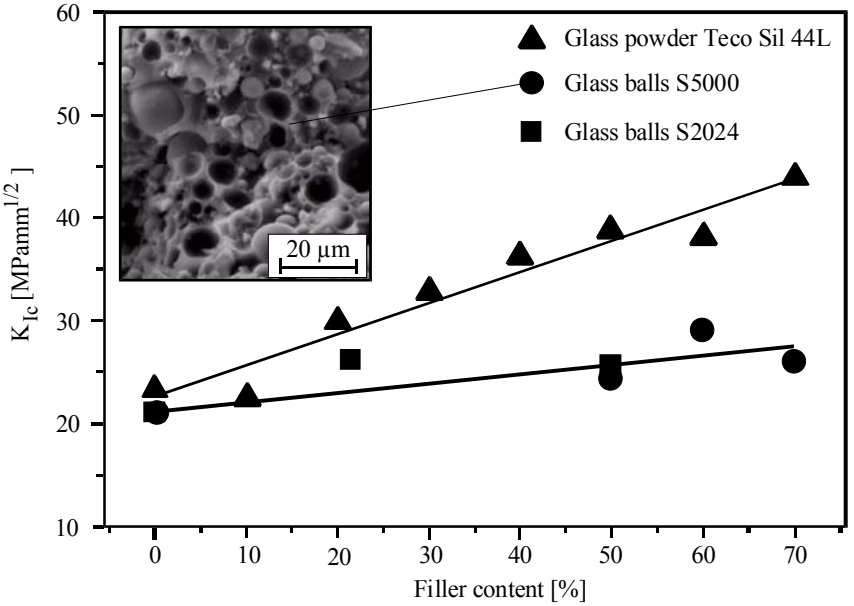

Figure 4: Fracture toughness of differently filled epoxy resin as a function of filler content

If the glass powder filled material is modified with the plasticizer M670 additionally, the chemical activity of this flexibilizier leads to a higher fracture toughness in comparison with the unmodified ma-

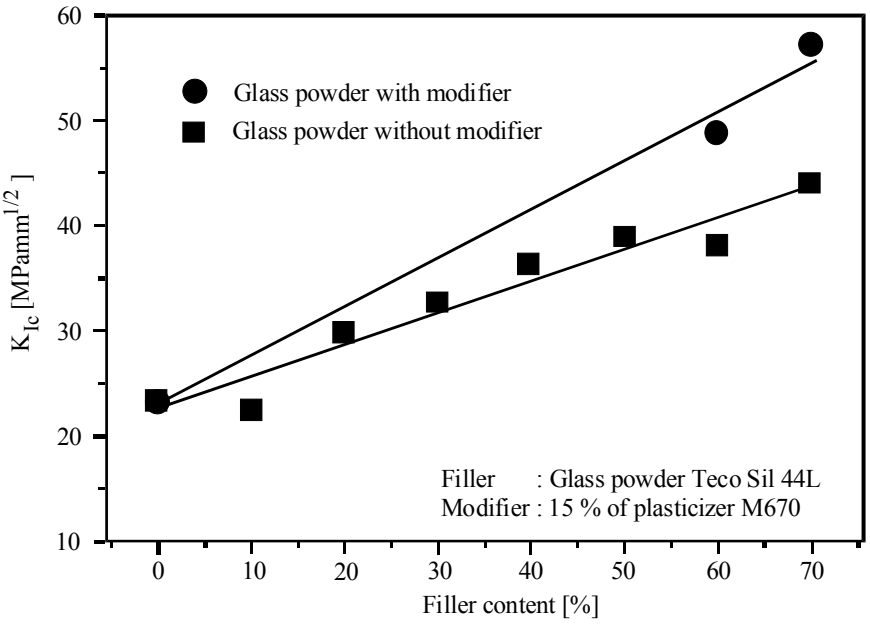

Figure 5: Fracture toughness of differently filled epoxy resin as a function of filler content

terial (fig. 5). Because of the appearing stress distribution the flexibilizier causes an increase of the ductility of the resin matrix and the adhesion between matrix and filler particles is improved simultaneously.

CONCLUSION

The miniature specimens used allow the evaluation of the fracture toughness and the assessment of deformation behaviour. The dependencies of stress intensity factor K on specimens thickness determined using miniature specimens lead to geometry values β those can be introduced into the general dependencies β = f(K). That means, the experimentally determined fracture mechanics values fulfil the geometry criterion and are independent of loading conditions and nature of material failure. At higher temperatures the fracture toughness increases and reaches the maximum near the glass-transition temperature. In the case of filled materials, the fracture toughness is always better if irregular particles such as glass powder are used. Because of the effect of chemical flexibilizier on matrix behaviour and bonding mechanisms the best results were measured for filled and modified epoxy resins. The laserextensometry, used for these investigations, is a successful method for determining the specific material behaviour of epoxy resins by means of miniature test specimens.

REFERENCES

1. Wu, T.Y. and Thiel, G.H. (1995*). Application of Fracture Mechanics in Electronic Packaging and Materials*: ASME EEP-Vol. 11/MD-Vol. 64, pp. 205
2. Walter, H., Bierögel, C., Grellmann, W., Fedtke, M. and Michel B. (2001). In*: Grellmann W., Seidler S. (Eds.) Deformation and Fracture Behaviour of Polymers.* Springer Berlin Heidelberg, p. 519-530
3. Bierögel, C. and Grellmann W.(2001) In*: Grellmann W., Seidler S. (Eds.) Deformation and Fracture Behaviour of Polymers.* Springer Berlin Heidelberg, p. 365-384
4. Lach, R. (1998). *Fortschritt-Berichte VDI-Reihe 18: Mechanik/Bruchmechanik* No.223, VDI-Verlag Düsseldorf

ORAL/POSTER REFERENCE: ICF100137OR

FRACTURE MECHANICS EVALUATION OF POST YIELD FATIGUE CRACK INITIATION AND PROPAGATION

G. S. Wang and A. F. Blom

Aeronautics Division
The Swedish Defence Research Agency, 172 90 Stockholm, Sweden

ABSTRACT

A system of analytical and numerical solutions is developed to deal with fatigue crack initiation and propagation when local yielding occurs. The method is based on the detailed finite element analyses under spectrum fatigue loading. The finite element analyses are used to identify a shakedown condition where a stable residual stress field may be created after a period of fatigue loading. Under the shakedown condition, the analyses of fatigue crack initiation and propagation are performed based on a cycle-by-cycle crack growth evaluation according to a crack closure solution that accounts for both the small and long crack growth behaviour. In this way, the post yield fatigue crack initiation and propagation are evaluated.

KEYWORDS

Post-yield, fatigue, crack growth, strip yield model

INTRODUCTION

For many applications like mechanical or welded joints, local stress concentration is so high that plastic yielding may occur at a very low load level. Similar problems are encountered when residual stresses are introduced by production techniques. The residual stress may significantly increase the local stress such that yielding may occur under service loading. Since most engineering materials have enough resistance to yielding, a field of residual stress is often created to counter the local stress concentration. Significant fatigue life may remain even when local yielding occurs. Many structures are actually sized and used in applications where local yielding is prevalent. When structural weight is a concern, or welding or other advanced production techniques are used, the fatigue after local yield becomes an important issue. It is apparent that gross yield in structural details may prevent success of the use of fracture mechanics methods in evaluating crack initiation and propagation. So far, fatigue tests seem to be the only resort to deal with such a problem.

STRIP YIELD MODEL

When general material responses are considered under fatigue loading, three different cases may be considered as shown in Fig.1. The first case is for the stress less than the yield stress. A linear response will occur under fatigue loading as shown in Fig.1 (a). The second case is for the stress higher than the yield stress. An elastic shakedown state may occur if the range of stress cannot create repeated reverse yielding under fatigue loading. A residual stress field will be created to reduce the peak stress in the material. A linear

material response may appear for the subsequent fatigue cycles. This case is an elastic shakedown case. For the third case, a plastic shakedown may be achieved if the material is subjected to large strain controlled fatigue loading, see Fig.1 (c).

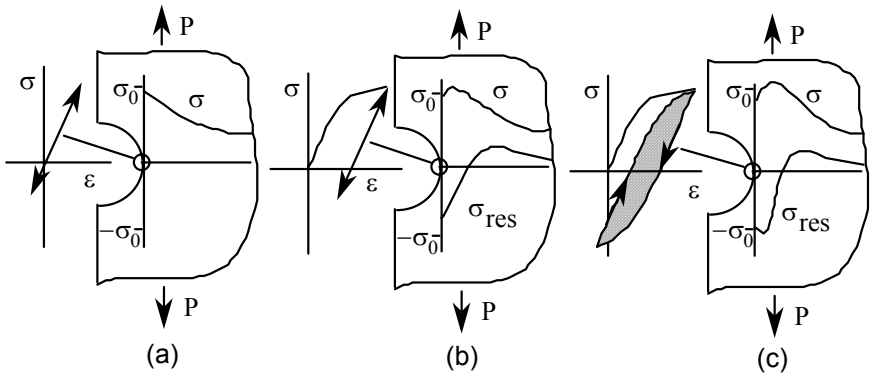

Fig.1: Schematic of various material responses under fatigue loading

Most of the post-yield fatigue problems in application involve the elastic shakedown condition as shown in Fig.1 (b). In this case, the fatigue problem may be solved according to fracture mechanics methods since fatigue life may be determined by considering a single and dominant crack initiation and growth. A possible solution is to consider fatigue crack growth in a residual stress field.

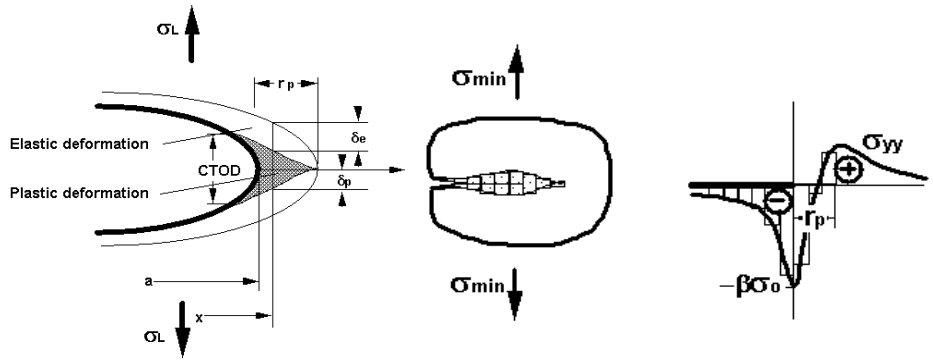

Fig. 2: Schematic of the strip yield crack closure model

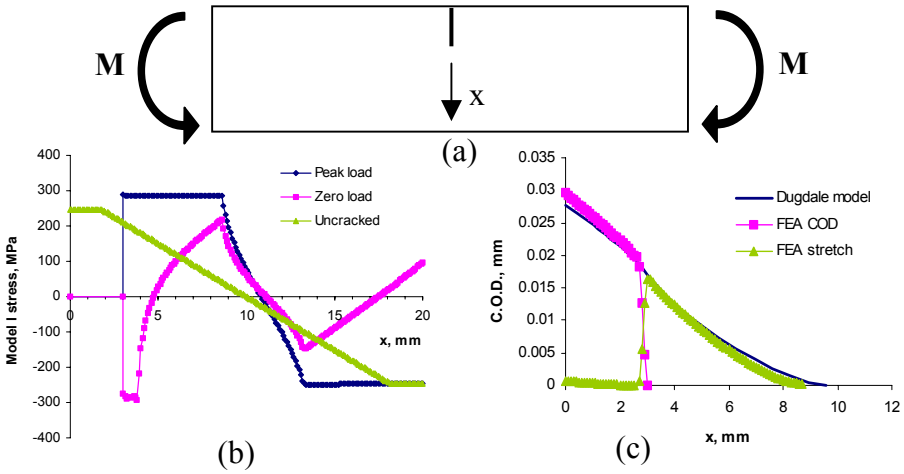

Fig.3: Non-linear finite element verification of the extension of the strip yield model for post yield crack problems.

The Elber's crack closure model [1] is one of the most successful models to account for various aspects of fatigue crack growth under general loading conditions. It may be extended to evaluate the post yield fatigue (PYF) problems. A strip yield model is a practical way to realise the crack closure analyses since the plasticity induced crack closure is often a dominant mechanism for most of the engineering materials, (Wang, 1993 [2]). The strip yield model, as shown schematically in Fig.2, is based on a strip yield assumption in the plastic zone [3]. By assuming an elastic crack located at the elastic-plastic boundary, the

strip yield model is used to determine plastic stretches in the plastic zone so that a system of elements may be created to determine the crack closure, see Fig.2.

The strip yield model has been extended to solve the crack growth problems in residual stress fields created by the plastic yield (Wang, 1999 [4]). Fig.3 shows a verification of the strip yield model when gross yield occurs for a pure bending specimen, Fig.3 (a). Under a gross yield condition, see the stress curve with triangle symbols in Fig.3 (b), the non-linear finite element analyses (FEA) showed that the strip yield solution is a very good approximation for the plastic stretches in the plastic zone when a crack is created. Fig.3 (c) shows a comparison between the results of FEA and the strip yield model for the crack surface profile and pure plastic stretches in the plastic zone. When the plastic stretches are used in the strip yield model as shown in Fig.2, reasonably accurate solution of crack closure may be realised for the analyses of PYF problems.

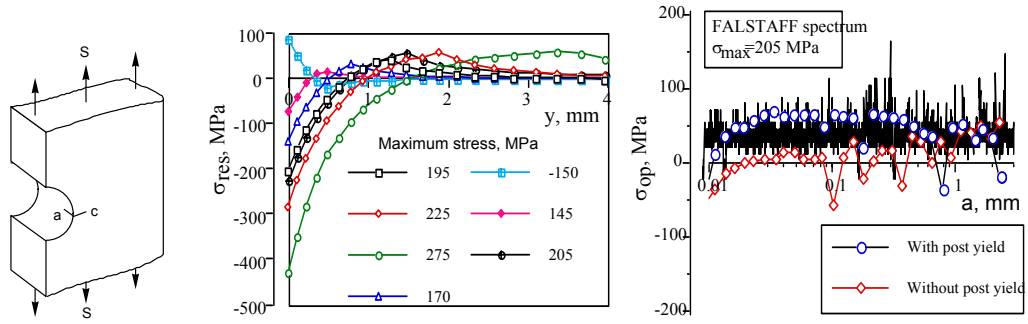

(a) (b) (c)

Fig.4: Residual stress analyses for a single notch specimen.

APPLICATIONS

To demonstrate the necessity and advantage of the PYF analyses, several cases are considered. The first case is for the fatigue life analyses of a single notch specimen, shown in Fig.4 (a), subjected to various spectra and load levels. Most of the fatigue load levels create plastic yield at the notch as shown in Fig.4 (b) for the resulting residual stresses. The PYF effect is particularly strong when a spectrum loading condition are considered. Fig.4 (c) shows an example of the crack closure solution for one case of FALSTAFF spectrum loading with and without post yield effect. When PYF occurs, the crack closure will occur at higher levels due to the residual compressive stress field created by the tensile dominant spectrum. The PYF affects strongly the fatigue life of many small load cycles. The fatigue life may be reduced, on the other hand, for a compressive dominant spectrum.

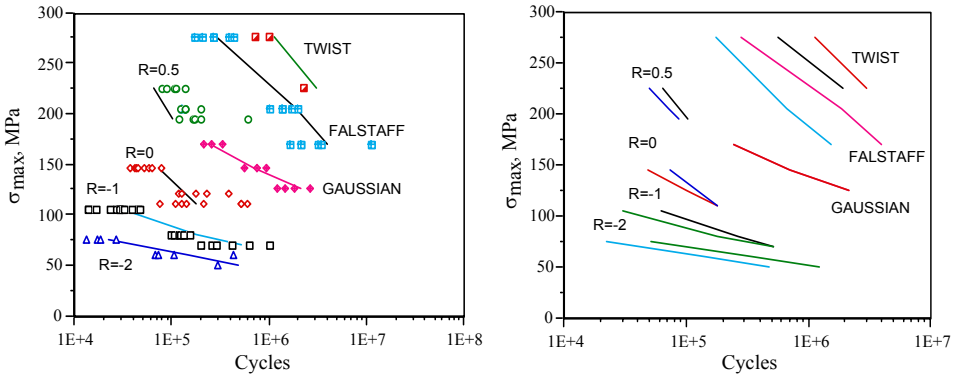

(a) (b)

Fig.5: Comparison of conventional and post yield analytical fatigue lives for various load and spectra.

Fig.5 shows predicted fatigue lives compared to test results for various fatigue load spectra and levels. There are reasonable agreement between predictions and tests, see Fig.5 (a). The PYF effect is obvious as shown in Fig.5 (b) (the curve close to the legends) compared to the analyses when the PYF effect is not considered (the curve away from the legends). The PYF effect can be positive or negative depending on the spectrum

type (tensile or compressive dominant loading). For GAUSSIAN spectrum for example, the PYF effect is negligible since the spectrum is symmetrical at relatively high stress level.

PYF problems are not limited to high loaded details as the example as shown in Fig.4. Residual stresses in the detail may increase the local stress concentration and create PYF problems even when the applied load is low. An example is shown in Fig.6 for a type of cruciform welded specimens with different surface conditions [5]. The specimen has a rather high stress concentration at the as-welded state, but the stress concentration is low for the TIG-dressing condition. There are severe residual stresses due to the welding as shown in Fig.7 for the through-thickness residual stresses measured by the neutron diffraction method for different surface conditions.

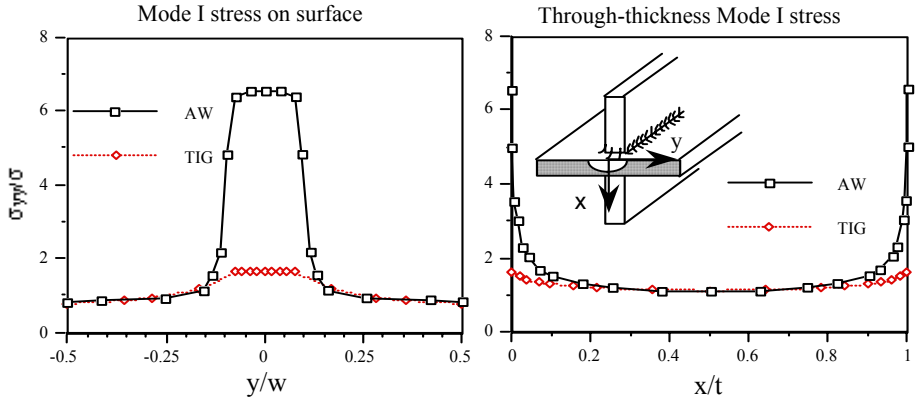

Fig.6: Stress concentration in a cruciform welding specimen.

Measurements of the same specimen after various fatigue cycles are also shown in the figure. The measurements, in agreement with the analyses, showed a possible elastic shakedown condition existing after the initial plastic yield, see Fig.7. At the shakedown condition, the stress concentration combined with the residual stress field creates a much stronger PYF effect as the fatigue results in Fig.8 shows for a comparison between various predictions and fatigue test results for a symmetrical spectrum loading condition. The fatigue lives are nearly two orders of magnitude shorter due to the tensile residual stress. Compared to the PYF effect as shown in Fig.5, the residual stress has a much stronger effect, see the comparison in Fig.8.

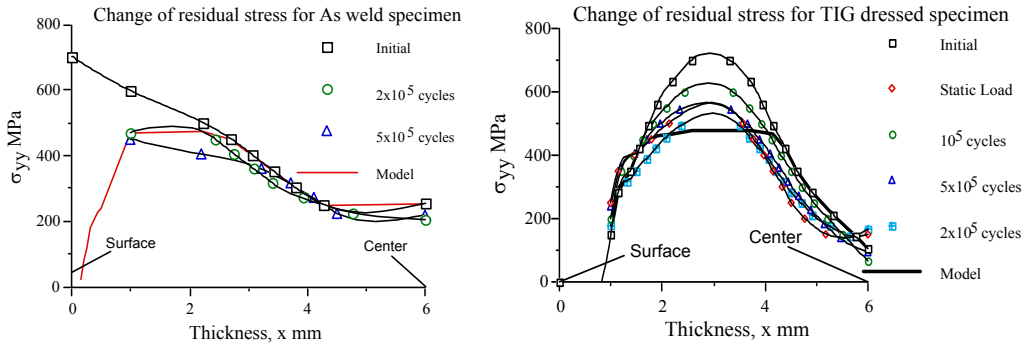

(a) (b)

Fig.7: Neutron diffraction measurements of residual stresses before and after fatigue loading at cruciform welding specimens for as-welded and TIG-dressing condition

For a more complicate case when a mechanical rivet fastener joint is considered as shown on the right side of Fig.9 [6]. The fastener joint has not only a high stress concentration, contact and friction will also be strong at the joint. The right side of Fig.9 shows some stress-strain responses under the fatigue loading condition for various levels of fatigue loads. An elastic shakedown condition is observed in the finite element results even though the stress-strain behaviour is different.

Similar analyses are performed for the fatigue life analyses according to the shakedown stress condition. The analytical results are compared to the test results in Fig.10. In the same figure, the analytical results are also presented for a linear elastic fracture mechanics (LEFM) analysis based on forces computed from a

simplified finite element model using shell and beam elements. It can be seen that there is a significant improvement in prediction capability when the post yield analyses are performed based on the stress analyses when critical fastener parameters are considered.

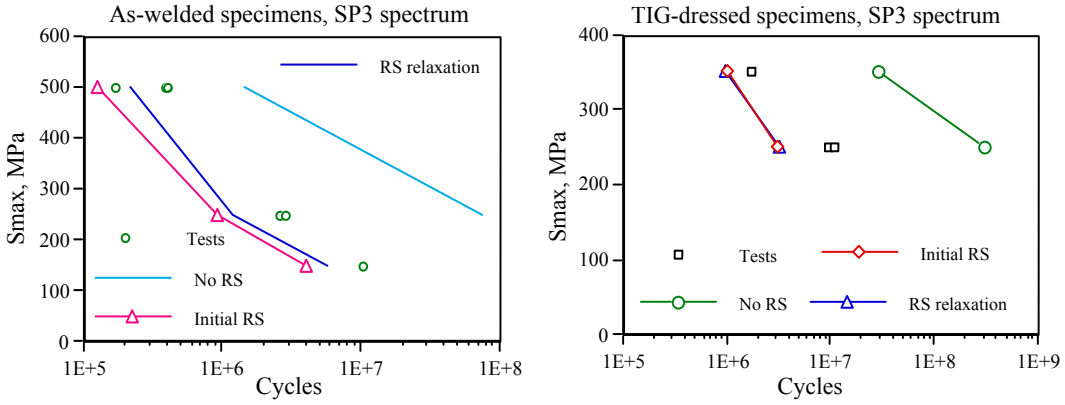

(a) (b)

Fig.8: Comparison of conventional and post-yield fatigue life analyses for as-welded and TIG-dressing condition for cruciform specimens.

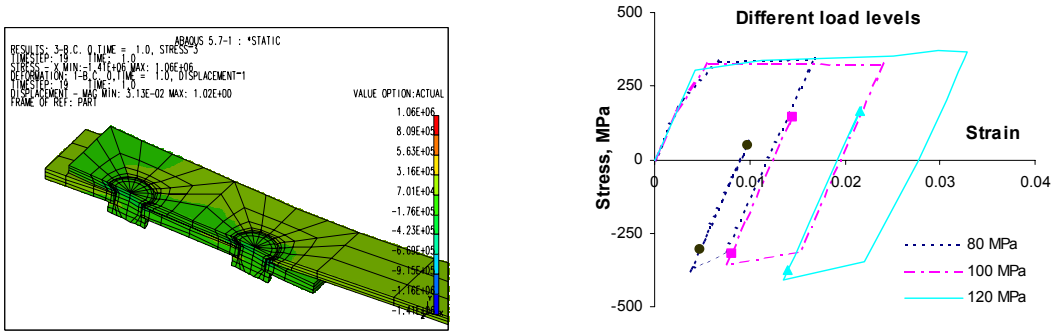

(a) (b)

Fig.9: Shakedown condition at a rivet fastener joint for various load levels.

CONCLUSIONS

The consideration of post yield fatigue is necessary for complicate structural details that may involve plastic yielding under fatigue loading. Without the consideration, it is very difficult to evaluate fatigue problems based on fracture mechanics methods. Under the elastic shakedown condition, a strip yield crack closure model is extended to solve the fatigue problems due to its capability of dealing with load interaction and small crack growth problems. The model is based on the non-linear finite element analyses when cracks are not involved. Extension of the model to the post yield problems is demonstrated and verified with the non-linear finite element solutions. Several practical problems are presented to illustrate the solution and to verify its effectiveness. It is shown that with the correct solution, significant improvements, in at least one order of magnitude, may be achieved in evaluating fatigue life based on the fracture mechanics method even when gross local yielding has occurred. The method is significant in helping to understand fatigue behaviours in complex structural details when local yield occurs, and in promoting the fracture mechanics method into a much wider area of crack growth problems.

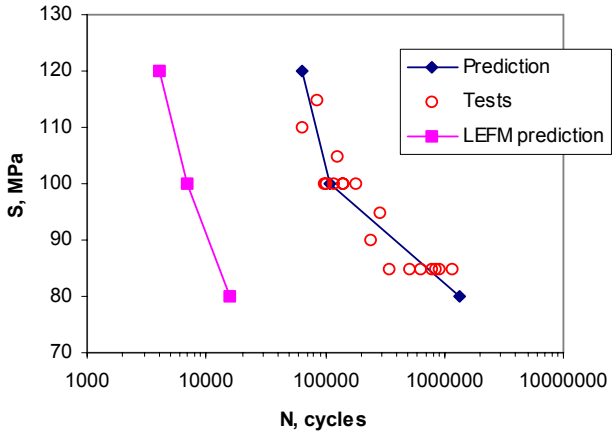

Fig.10: Comparison between analytical and test fatigue lives

REFERENCES

1, Elber, W., (1970) "Fatigue crack closure under cyclic tension," *Engng. Fracture Mech*. Vol. **2**, No.1, pp.37-45

2, Wang, G. S., (1993) "The plasticity aspect of fatigue crack growth," *Engng. Fracture Mech.* Vol.**46**, No.6, pp.909-930.

3, Wang, G. S. and Blom, A. F., (1991) "A strip model for fatigue crack growth predictions under general load conditions," *Engng. Fracture Mech.* Vol.**40**, No.3, pp.507-533.

4, Wang, G. S., (1999) "Post yield fatigue crack growth analyses," *Engng. Frac. Mech*., Vol.**64**, pp.1-21.

5, Wang, G. S., (1999) "A strip yield analysis of fatigue crack growth in the residual stress field," *Int. J. of Fracture*, Vol.**96**, No.3, pp.247-277.

6, Wang, G. S., (2000) "Analysing the onset of multiple site damage at mechanical joints," Int. J. of Fracture, Vol.**105,** No.3, pp.209-241.

FRACTURE MECHANICS MODELS FOR THE ANALYSIS OF COMPOSITE MATERIALS WITH A NONLINEAR MATRIX

A. Carpinteri, G. Ferro & G. Ventura

Department of Structural Engineering, Politecnico di Torino, 10129, Torino, Italy.

ABSTRACT

A model for reproducing the constitutive flexural response of a fiber-reinforced composite material with a non-linear matrix is proposed. The nonlinearity of the matrix is modelled by considering a distribution of closing forces onto the crack faces which increases the fracture toughness of the cross-section with a shielding action. The constitutive flexural response depends on three dimensionless parameters: $\tilde{w}_c^E$, which controls the extension of the process zone, $N_P^{(1)}$ and $N_P^{(2)}$, called *brittleness numbers*, which are related to the reinforcement phases. The role of the specimen size scale is fundamental for the global structural behaviour, which can range from ductile to brittle simply with the variation of the two brittleness numbers. They are functions of matrix toughness, reinforcement yielding or slippage limit, reinforcement volume fraction and global structural size. The application of the model to steel bar reinforced high-performance concrete with fibers is in good agreement with the experimental results.

KEYWORDS

Fracture mechanisms, Fiber-reinforced composite material, High-performance concrete, Bridged crack, Size effects.

INTRODUCTION

The development of high-performance composite materials has been playing a key role in the recent engineering applications. In civil engineering, for example, the introduction of high-strength concretes, characterized by a very brittle behaviour, has required the addition of a secondary phase of reinforcement (fibers) to increase the fracture toughness of the material, so that the cementitious matrix assumes a nonlinear constitutive behaviour. The development of high-performance concretes is emblematic for the modern approach to new composite materials. Despite a large proliferation of experimental tests and papers on the structural behaviour of reinforced elements, there are not theoretical models which describe in exaustive manner these materials. The purpose of this paper is to offer a contribution to the theoretical modelization of the bent elements.

The application of Fracture Mechanics concepts to plain and reinforced concrete structures represents the only way to interpret the collapse behaviour, which shows different rupture modes by varying the size. Two different models have been proposed in the last few years to describe partial damage near a single crack: the *cohesive crack model* and the *bridged crack model*. In the former, the stress-intensity factor K_I at the crack tip is set equal to zero due to the contribution of the applied load and of the softening tractions acting ahead of the notch. The first application to brittle materials is due to Barenblatt [1], while important contributions to relate the cohesive model to the Griffith crack are due to Willis [2] and Rice [3]. In the *bridged crack model* the near tip process is modeled via the stress-intensity factor and a crack propagation condition is reached when the stress-intensity factor equals the toughness of the brittle matrix. Several bridged crack models have been proposed to simulate the structural response of fiber-reinforced materials. These models have been used to describe cracking in brittle-matrix composites [4] and in alloy plates shielded by bonded patches [5], as well as damage zones in concrete [6].

The theoretical model to which we refer determines the problem unknowns by considering the cracked cross-section and by using the local compliance and the stress-intensity factor concepts. It represents an extension of the model proposed by Carpinteri [7] for one single reinforcement, by Bosco and Carpinteri [8] for a discontinuous fiber distribution and by Carpinteri and Massabò [9] for a continuous distribution. The longitudinal

(primary) reinforcements are simulated by the actions of m concentrated forces directly applied onto the crack faces. The nonlinearities of the matrix are instead modelled by the action of a continuous closing traction distribution (secondary reinforcement) onto the cracked zone. Alternatively, the model can simulate a composite material with a brittle matrix and two level of reinforcements, so that it can also be applied to a wider class of composite materials [10]. For the crack propagation condition, both the bridging option as well as the cohesive one are introduced.

The structural response expressed by the functional relationship moment versus local rotation, i.e. M vs ϕ, comes out from Dimensional Analysis [10] of the bridging option to depend on three dimensional parameters:

$$\tilde{w}_c^E = \frac{E w_c}{K_{IC} h^{0.5}} ; \quad N_P^{(1)} = \frac{\rho \sigma_y h^{0.5}}{K_{IC}} ; \quad N_P^{(2)} = \frac{\gamma \sigma_u h^{0.5}}{K_{IC}} , \tag{1}$$

where the symbols are described in the next section. In the cohesive option the third parameter assumes a different expression, as reported later. The parameter $\tilde{w}_c^E$, is a function of the kind of fibers used, and specifically of their length. The other two parameters, called *brittleness numbers*, are related to the two levels of reinforcements. The structural response depends, once all the other mechanical parameters have been set, on the structural element dimension. Theoretical results confirm a transition from brittle to ductile collapse by increasing the brittleness numbers N_P. It is to be observed that the dependence of the brittleness numbers on the structural dimension is represented by a power law with an exponent equal to 0.5, typical for the Linear Elastic Fracture Mechanics stress singularity. A comparison of the theoretical curve vs the experimental one in the case of an high-strength concrete with the two reinforcement phases is discussed at the end of the paper for emphasizing the consistency of the model.

THEORETICAL MODELS

The theoretical model explains and reproduces the constitutive flexural response of a fiber-reinforced concrete element with longitudinal steel bars. Two different options for the model can be used, the *bridging* and the *cohesive*. The scheme of a cracked element is shown in fig. 1.a, where h and b are the height and the width of the cross-section. The normalized crack depth $\xi = a/h$ and the normalized coordinate $\zeta = x/h$ are defined, x being the generic coordinate related to the bottom of the cross-section. In the *bridging option*, the distribution of the discrete actions P_i and of the continuous closing tractions $\sigma(w)$, directly applied onto the crack faces, respectively represent the physical bridging mechanisms of the longitudinal bars (primary reinforcement) and of the fibers (secondary reinforcement), acting at two different scales. Let c_i be the coordinate of the ith reinforcement from the bottom of the beam, and $\zeta_i = c_i/h$ its normalized value. Function $\sigma(w)$ is a constitutive law and defines the relation between the bridging tractions, representative of the action exerted by the fibers onto the crack, and $w(x)$, the crack opening displacement at the generic coordinate x. The cohesive law σ versus w can be extrapoled from experimental pull-out tests on a single fiber. For the sake of simplicity, in the simulation presented herein a perfectly-plastic law with vertical drop for the fibers has been used, Fig.1.c, even if a general law could also be considered. The bridging forces of the secondary reinforcement act on the portion of the crack whose opening displacement is less than the critical value w_c, beyond which the closing tractions vanish (fig. 1.c). In the *cohesive option*, instead, the brittle matrix and the fibers are represented as a single-phase material with homogenized properties. In this case, the closing tractions $\sigma(w)$ describe the combined restraining action of the matrix and of the fibers on the crack propagation and are given by the cohesive law of the composite material.

The assumed rigid-plastic bridging relation for the crack opening displacement w_i at the level of the ith reinforcement is suitable to describe both the yielding mechanism for the reinforcement and the bar-matrix relative slippage (fig. 1.b). The maximum bridging traction is defined for the primary reinforcements by the ultimate force $P_{Pi} = A_i \sigma_y$ and for the fibers by the ultimate stress $\sigma_0 = \gamma \sigma_u$, A_i being the single reinforcement cross-section area, γ the fibers volume ratio, σ_y or σ_u the minimum between the reinforcement yield strength and the sliding limit for the two reinforcement phases. The stress-intensity factors K_{IM} due to the bending moment M, $K_{I\sigma}$ due to the fibers and K_{Ii} due to the ith-longitudinal reinforcement, can be expressed in accordance with the two-dimensional single-edge notched-strip solution [11]:

$$K_{IM} = \frac{M}{b h^{1.5}} Y_M(\xi) \tag{2}$$

$$K_{I\sigma} = \int_0^{\xi} \frac{K_{Ij}}{P_j} \sigma(w(\zeta_j)) b h \, \mathrm{d}\zeta_j = \frac{1}{h^{0.5} b} \int_0^{\xi} \sigma(w(\zeta_j)) Y_P(\xi, \zeta) b h \, \mathrm{d}\zeta_j \tag{3}$$

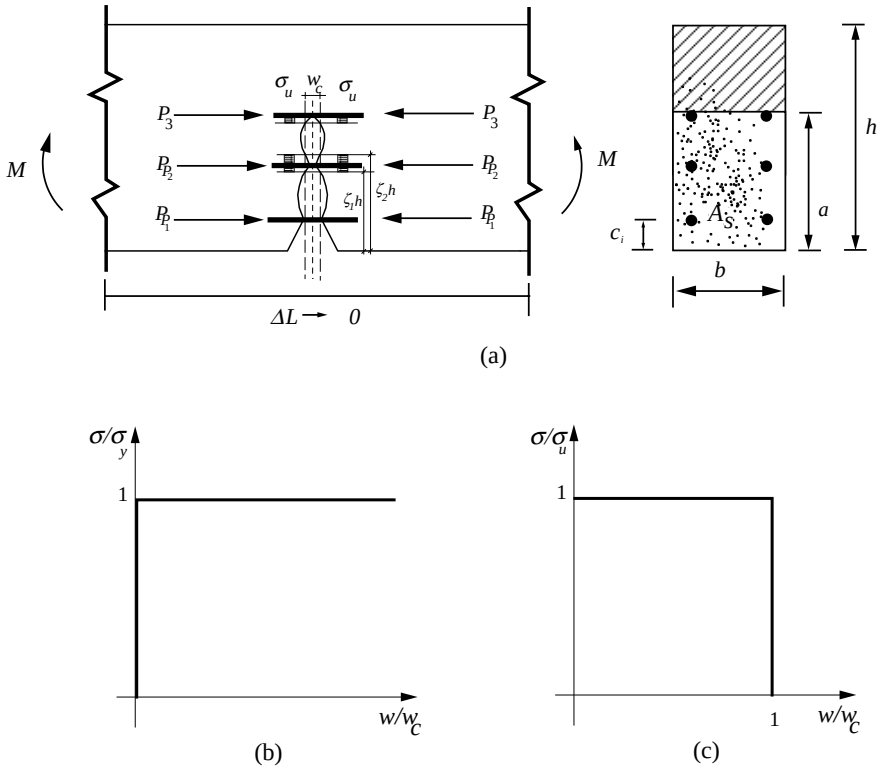

Figure 1: (a) Scheme of a cracked reinforced concrete element containing fibers; (b) rigid-perfectly plastic law for primary reinforcement; (c) plastic law with vertical drop for secondary reinforcement.

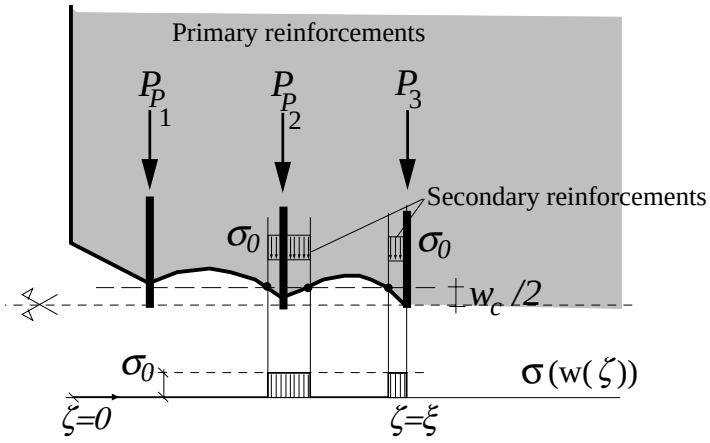

Figure 2: Bridging actions of primary and secondary reinforcements onto the crack faces.

$$K_{Ii} = \frac{P_i}{bh^{0.5}} Y_P(\xi, \zeta_i) \quad (i = 1,\, 2,\, ...,\, m), \tag{4}$$

where $Y_M(\xi)$ and $Y_P(\xi, \zeta_i)$ are functions of the relative crack depth ξ. $K_{I\sigma}$ is obtained by integrating, along the bridged crack zone, the product of the stress-intensity factor due to two opposite unit forces, applied at the generic coordinate ζ_j, times the bridging actions $\sigma(w)$. The integration is extended to the whole crack while function $\sigma(w)$ assumes nonzero values only where $w < w_c$.

The crack propagates when K_I is equal to the matrix fracture toughness, K_{IC}, for the *bridging* option and when K_I vanishes for the *cohesive* one:

$$K_I = K_{IM} - \sum_{j=1}^{m} K_{Ij} - K_{I\sigma} = \begin{cases} K_{IC}, & \text{bridging option} \quad \text{(singular stress field at the crack tip)} \\ 0, & \text{cohesive option} \quad \text{(finite stress field at the crack tip)} \end{cases} \tag{5}$$

The dimensionless crack propagation moment can be obtained from eqs (2-5):

$$\frac{M_F}{K_{IC} h^{1.5} b} = \frac{1}{Y_M(\xi)} \left\{ \frac{N_P^{(1)}}{\rho} \sum_{i=1}^{m} \rho_i \frac{P_i}{P_{Pi}} Y_P(\xi, \zeta) + B \int_0^{\xi} \frac{\sigma(w(\zeta))}{\gamma \sigma_u} Y_P(\xi, \zeta) bh \, \mathrm{d}\zeta + K \right\}, \tag{6}$$

where for $K = 1$ (bridging option) $B = N_P^{(2)} = \frac{\gamma \sigma_u h^{0.5}}{K_{IC}}$, while for $K = 0$ (cohesive option) $B = \frac{1}{s} = \frac{\sigma_u h^{0.5}}{K_{IC}}$, where s is the brittleness number originally defined by Carpinteri [12]. The parameters in the two cases assume different physical meaning. In the bridging option, K_{IC} represents the matrix fracture toughness while in the cohesive option it represents the homogenized toughness of the composite; σ_u represents the ultimate strength of the secondary reinforcement in the former case or the homogenized ultimate strength of the composite in the latter. For a generical relation $\sigma(w)$, the fibers closing tractions onto the crack are indeterminate and depend on the crack opening displacement function $w(x)$. The crack profile (fig.2) can be defined as a function of the mechanical and geometrical properties of the cross-section and of the applied loads, through Castigliano's Theorem:

$$w(\zeta_k) = \lim_{F \to 0} \frac{\partial}{\partial F(\zeta_k)} \left\{ \int_0^{\xi} \frac{K_I^2}{E} bh \, \mathrm{d}y \right\},$$

where $w(\zeta_k)$ is the crack opening displacement at the generic coordinate $\zeta = \zeta_k$, F are two fictitious forces applied in ζ_k and K_I is the global stress-intensity factor:

$$K_I = K_{IM} - \sum_{j=1}^{m} K_{Ij} - K_{I\sigma} + K_{IF}, \tag{7}$$

in which K_{IF} is the stress-intensity factor due to the forces F. The normalized crack opening displacement assumes the following form, by substituting the expressions of the stress-intensity factors:

$$\tilde{w}(\zeta_k) = \frac{w(\zeta_k)}{h} = \frac{2K_{IC}}{Eh^{0.5}} \left\{ \frac{M_F}{K_{IC} h^{1.5} b} \int_{\zeta_k}^{\xi} Y_M(y) Y_P(y, \zeta_k) \mathrm{d}y - \frac{N_P^{(1)}}{\rho} \sum_{i=1}^{m} \left[\frac{P_i}{P_{Pi}} \rho_i \int_{\max[\zeta_i, \zeta_k]}^{\xi} Y_P(\zeta_i, y) Y_P(y, \zeta_k) \, \mathrm{d}y \right] - \right.$$
$$\left. - B \int_{\zeta_k}^{\xi} \left(\int_0^{y} \frac{\sigma(w(\zeta))}{\sigma_u} Y_P(y, \zeta) \, \mathrm{d}\zeta \right) Y_P(y, \zeta_k) \, \mathrm{d}y \right\}, \tag{8}$$

in which the last term represents the displacement at the abscissa ζ_k due to the distribution of tractions $\sigma(w)$ between 0 e ξ. The localized rotation ϕ of the cracked cross-section can be evaluated in the same way by using Castigliano's Theorem and the explicit expression can be found in [10]. Equations (6) and (8) set up a statically indeterminate nonlinear problem. The reactions P_i and $\sigma(w)$ are evaluated by using a numerical procedure based on the assessment of kinematical compatibility and statical equilibrium equations. The complete description of the computational algorithm is reported in [10].

NUMERICAL SIMULATIONS

The numerical procedure under the bridging option has been used to evaluate the flexural behaviour of the cross-section reinforced with two different levels of fibers. The three dimensionless numbers, $N_P^{(1)}$, $N_P^{(2)}$ and $\tilde{w}_c^E$, affect the shape of the curves. Some theoretical diagrams are presented by varying one dimensionless number, the other two being fixed. This is to appreciate the influence of a single group onto the flexural response. A cracked reinforced concrete element containing fibers is considered in the following examples, in which, for the sake of simplicity in the interpretation of the curves, only one primary reinforcement is placed at the normalized coordinate $\zeta_1 = c/h = 0.1$.

As a first case, the evolutive process of crack propagation expressed in terms of the dimensionless crack propagation moment, $M_F/(K_{IC} h^{1.5} b)$, vs the normalized crack depth, $\xi = a/h$, with a fixed value of the primary brittless number $N_P^{(1)}$=1.0 and a fixed dimensionless critical crack opening displacement $\tilde{w}_c^E$=300, is reported in fig. 3.a, for different values of the secondary brittleness number $N_P^{(2)}$ varying between 0 (no secondary phase reinforcement) and 1.9. For $0 < \xi < \zeta_1$, the crack crosses only the matrix of the cross-section. The strain-softening response is controlled by the matrix toughness and by the secondary reinforcements. For crack depths tending to zero, an infinite resistance is provided, as expected form LEFM. In correspondence of $\xi = \zeta_1 = 0.1$, when the crack reaches the primary reinforcement, a loading drop is evidenced. If all the mechanical as well as the dimensional parameters of the cross-section are fixed, the transition from $N_P^{(2)}$=0.0 to $N_P^{(2)}$= 1.9 can be due only to an increment of the fiber content percentage. In such a case, the increment of the fiber percentage increases the toughness of the cross-section, and, secondarily, also the resistance, the curves being translated toward larger values of the crack propagation moment. The circles in the diagram indicate the minimum for each curve, which represents a transition in the evolutive process of crack propagation. For crack depths lower than that corresponding to the minimum, the response is unstable and an uncontrollable crack propagation can be avoided only by progressively decreasing the applied load. On the other hand, for crack depths larger than

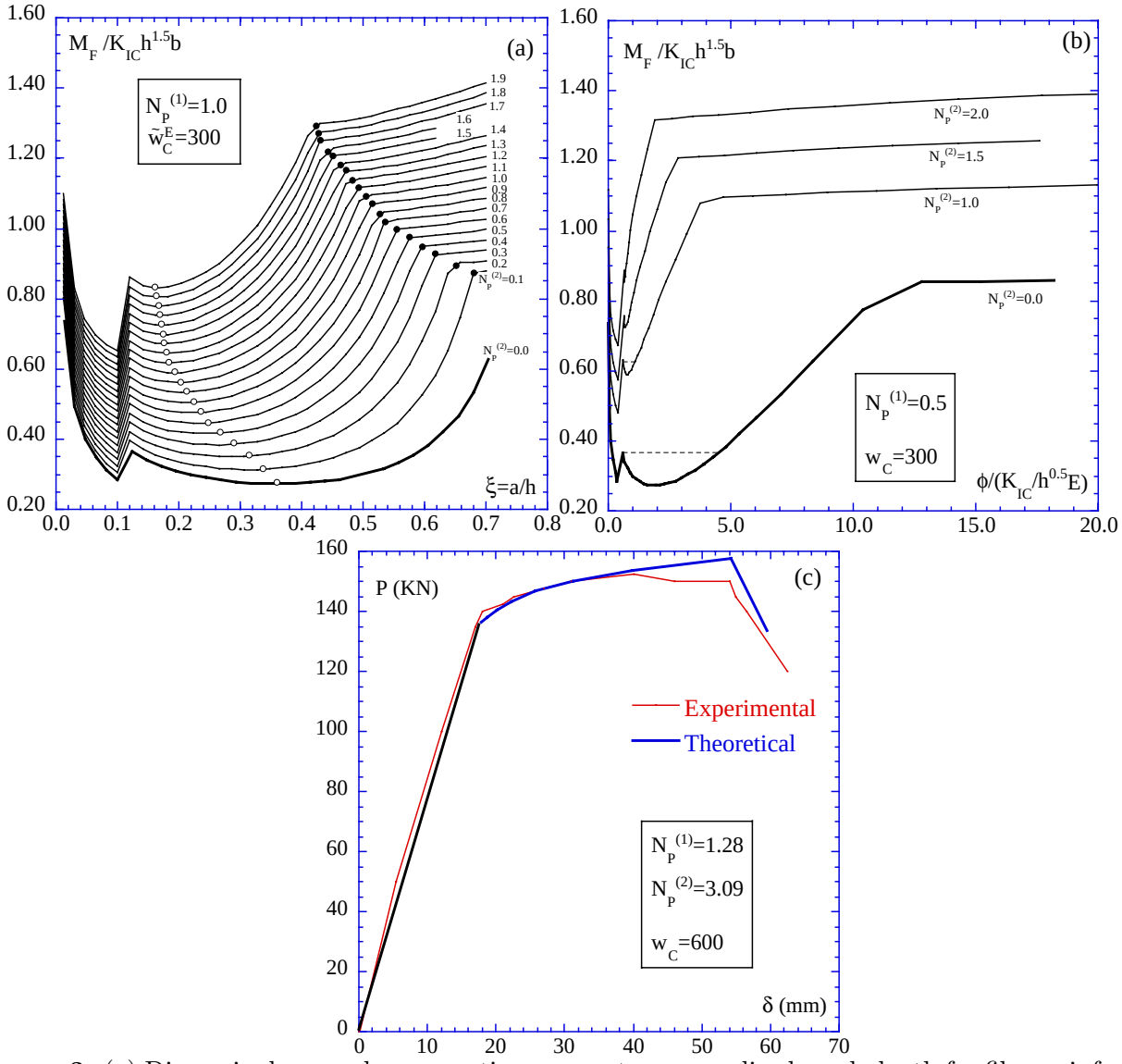

Figure 3: (a) Dimensionless crack propagation moment vs normalized crack depth for fiber-reinforced concrete cross-section with $N_P^{(1)}$=1.0, $\tilde{w}_c^E$=300 and $N_P^{(2)}$ between 0.0 and 1.9. (b) Dimensionless crack propagation moment vs localized rotation diagram for a concrete cross-section as $N_P^{(2)}$ varies, with $N_P^{(1)}$=0.5 and $\tilde{w}_c^E$ =300. (c) Comparison between the experimental load-deflection curve for a fiber-reinforced high-strength concrete [14] and the theoretical results (bridging option).

the limit value, the process is stable, and a slow crack growth is possible also by increasing the applied load. The limit crack depth increases when the brittleness number $N_P^{(2)}$ decreases. This result is consistent with the curves obtained by Carpinteri and Massabò [13] for the cross-section with only secondary reinforcement. The dots in the figure indicate the primary reinforcement yielding points. It can be observed how the yielding point translates by varying the secondary brittless number $N_P^{(2)}$.

From an engineering point of view, it appears very interesting to consider the crack propagation moment vs localized rotation diagram. Fig. 3.b shows the curves for $N_P^{(1)}$=0.5 and $\tilde{w}_c^E$ =300 and four different values of $N_P^{(2)}$. The first one ($N_P^{(2)}$=0.0) is representative of a fiber-reinforced concrete cross-section with no secondary reinforcement. The crack propagation moment shows a vertical asymptote for $\phi \to 0$ ($\xi \to 0$). A vertical drop is achieved when the crack crosses the primary reinforcement. For $N_P^{(2)}$=0.0 and 1.5, a snap-through instability is present after the drop (dotted line), which is less and less evident for increasing values of $N_P^{(2)}$.

The proposed theoretical model has been assessed by simulating an experimental test carried out by Ashour and Wafa [14] on high-strength concrete beams with the presence of two steel bar reinforcements. The beams, loaded in a four-point bending scheme, have a depth × thickness × span of 170 × 300 × 3680 mm. In the testing programme, 20 mm Grade 60 deformed steel bars having yield strength of 437 MPa were used as flexural reinforcement. The concrete mix proportion was 1:0.25:2.5 (cement:sand:coarse aggregate) to produce concrete

with a compressive strength of about 88 MPa. The Young's modulus has been evaluated to be 38,000 N/mm^2, while no information for unreinforced matrix fracture energy is available. Hooked-ends mild carbon steel fibers were used with average length of 60 mm, nominal diameter of 0.8 mm, aspect ratio of 75, and yield strength of 1100 MPa, with a fiber content of 1.5 %. By supposing a matrix fracture toughness equal to 0.14 Nmm$^{-3/2}$ for the present case, we obtain $N_P^{(1)}$=1.276, $N_P^{(2)}$=3.0928 and $\tilde{w}_c^E$ =600, having supposed w_c=1/3 of the length of the fiber. In order to evaluate the load-deflection theoretical curves, the costitutive moment vs localized rotation [10] has been used as a nonlinear hinge placed in the middle of the free span of the four point linear elastic beam [15]. Fig. 3.c shows the relationship between the applied load P and the middle-span deflection δ. The thin curve represents the experimental result, while the thick curve represents the theoretical one. After the linear elastic portion, an hardening behaviour appears due to the yielding of the primary reinforcement and to the bridging action of the fibers. Then, a softening behaviour is evidenced, due to the brittle failure (vertical drop) of the secondary fibers. It can be noticed a very small difference between the two curves, and only in the final portion, when the primary reinforcement yields, an error of 5 % has been achieved.

CONCLUSIONS

The proposed model represents an extension of the bridged crack model to the concurrent presence in a cementitious matrix of longitudinal bars and uniformly distributed fibers. A cohesive crack version can be obtained. It has been shown that the flexural behaviour of geometrically similar structures is governed by three dimensionless parameters. The influence of each parameter has been discussed in the proposed numerical examples, as well as an assessment between the curve predicted by the model and that obtained from an experimental test has been presented. This last result seems very promising for the consistency of the model.

The model reproduces the structural behaviour of high-performance and/or fiber reinforced concrete members in bending. In particular, as the parameters are of easy physical meaning and of simple experimental evaluation, this model represents a very useful tool for the study of mechanical properties (strength and ductility) and of crack propagation regimes, according to concrete composition, typology and density of the fibers, distribution and characteristics of the longitudinal bars.

A very important result of the theoretical formulation is provided by the dependence of the structural behaviour on the member size. Only with the same brittleness numbers it is possible to obtain physically similar structural responses.

ACKNOWLEDGEMENTS

The present research was carried out with the financial support of the Ministry of University and Scientific Research (MURST), the National Research Council (CNR) and the EC-TMR Contract N^o ERBFMRXCT960062.

References

1. Barenblatt, G.I. (1962). In: *Advances in Applied Mechanics*, pp.55-129, Dryden, H.L., von Karman, T. (Eds.), Academic Press, New York.
2. Willis, J.R. (1967) *J. Mech. Phys. Sol.* 15, 151.
3. Rice, J.R. (1968) *J. Appl. Mech.* 35, 379.
4. Mashall,D.B. Cox, B.N. and Evans, G.A. (1985) *Acta Metall. Mater.* 33, 2013.
5. Rose, L.R.F (1987) *Theor. Appl. Fract. Mech.* 7, 125.
6. Jenq, Y.S. and Shah, S.P. (1985) *J. Engng. Mech.* 111, 1227.
7. Carpinteri, A. (1984) *J. Struct. Engng.* 110, 544.
8. Bosco, C. and Carpinteri, A. (1992) *J. Engng. Mech.* 118, 1564.
9. Carpinteri, A. and Massabò, R. (1996) *Int. J. Fract.* 81, 125.
10. Carpinteri, A., Ferro, G. and Ventura, G. (2000). In: Composite Materials & Structures, pp.301-310, de Wilde, W.P., Blain, W.R., Brebbia, C.A. (Eds.). WIT Press, Southampton.
11. Okamura, H., Watanabe, K. and Takano, T. (1975) *Eng. Fract. Mech.* 7, 531.
12. Carpinteri, A. (1981) *Mat. and Struct.* 14, 151.
13. Carpinteri, A. and Massabò, R. (1997) *Int. J. Solids and Struct.* 34, 2321.
14. Ashour, S.A. and Wafa, F.F. (1993) *ACI Struct. J.* 90, 279.
15. Carpinteri, A. and Massabò, R. (1997) *J. Engng. Mech.* 123, 107.

FRACTURE MECHANISM OF A BAINITE STEEL IN PRECRACKED AND NOTCHED SPECIMENS AT LOW TEMPERATURE

C. Yan[1], J.H. Chen[2] and Q. H. Qin[1]

[1]Centre for Advanced Materials Technology, School of Aerospace, Mechanical and Mechatronic Engineering, The University of Sydney, NSW2006, Australia
[2]Department of Materials Engineering, Gansu University of Technology, Lanzhou, Gansu, P.R. China

ABSTRACT

Precracked and notched specimens were used to investigate the fracture mechanism of a bainite steel at low temperature. The critical fracture event was studied using metallographic sectioning method. The results showed that the critical cleavage event was different in the precracked and the notched specimens. At -196^{o}C, all specimens fractured at lower-shelf region without any ductile crack growth. The critical crack tip opening displacement was not sensitive to the depth of precrack. With increasing temperature to –100^{o}C, cleavage was preceded by ductile crack growth for all precracked specimens. A longer ductile crack growth was associated with the shallow crack specimens, which resulted in a higher critical crack tip opening displacement. The ratio of depth to width of micro-dimple on ductile crack surface was decreased with ductile crack growth.

KEYWORDS

Fracture toughness, cleavage fracture, crack depth, ductile crack growth, bainite steel, fracture mechanism

INTRODUCTION

Previous research [1-3] showed that metallic materials, especially low-alloy high-strength (HSLA) steels had the different fracture mechanisms at low temperature in precracked and notched specimens. The work of Lin *et al* [2] in AISI 4340 steel showed that with increasing grain size there was an apparent improvement in fracture toughness (K_{IC}) measured using precracked specimens but a decrease in Charpy V-notch impact energy. They attributed this to the variation of cleavage fracture stress and the characteristic distance over which the cleavage fracture can occur. Recently, the work of Chen *et al* on C-Mn steel [4-6] indicated that the cleavage fracture mechanisms were different in a precracked and a notched specimen. Currently, bainite steels have been increasing used in pressure vessels and piping industries due to superior weldability and fracture toughness. However, the fracture mechanisms of bainite steels are still not very clear. In this study, the fracture mechanism of a bainite steel was investigated using precracked and notched specimen at different temperatures. The cleavage fracture toughness and notch

impact energy were measured. The critical cleavage events in precracked and notched were identified using metallographic sectioning methods.

EXPERIMENTAL PROCEDURE

The test material was a bainite steel (WCF-62) in quench-temper condition. The chemical composition is shown in Table 1. The microstructure is tempered bainite. The yielding strength and hardening exponent were measured using round tensile specimen in the temperature range of –196°C to 20°C.

TABLE 1
COMPOSITION OF THE MATERIAL (%)

C	Si	Mn	Ni	Cr	Mo	V	B	S	P
0.06	0.23	1.36	0.36	0.19	0.21	0.03	0.0017	0.009	0.02

Three-point bend specimens with a/W ratio of 0.23, 0.45 and 0.72 were tested at –196°C and –100°C. Crack tip opening displacement (CTOD) at unstable fracture (δ_c) was obtained according to ASTM standard E1290-93. The impact energy was measure using standard Charpy V-notch test from –100°C to 20°C. To investigate the fracture mechanism in both the precracked and notched specimens, the critical fracture event was identified using metallographic method. The critical fracture event is considered as the most difficult step in the process of cleavage fracture from crack initiation to propagation. For the three-point bend specimen, sections were cut perpendicularly to the front of the precrack tip in the specimens unloaded at 95-98% fracture load at which the specimens were regarded in a critical condition. In this study, double-notched four-point bend specimen with the same notch dimensions of Charpy V-notch was used to investigate the critical event in the notched specimen at –196°C. In the double-notched specimens, when cleavage initiates from one notch, the survived notch must be in the critical state due to the same stress condition. The sections are then cut across the survived notch to observe the arrested cleavage microcracks which are shorter than the critical length for unstable propagation. The fracture surfaces were observed using scanning electronic microscope (SEM) and the composition of particles located in cleavage initiation sites was analyzed using energy dispersive analysis of X-ray (EDAX).

RESULTS AND DISCUSSION

Fracture Mechanism of Precracked Specimens at –196°C

The experimental result of the three-point bend (COD) tests at –196°C is summarized in Table 2. P is the failure load, δ_c is the critical crack tip opening displacement, and K_{IC} is stress intensity factor.

TABLE 2
EXPERIMENTAL RESULTS OF COD TESTS AT –196°C

a/W	P (kg)	δ_c (μm)	K_{IC} (kg/mm$^{3/2}$)
0.23	1240	8.32	136.7
0.23	1580	13.9	176.9
0.45	600	7.6	130.2
0.45	620	7.5	129.8
0.45	680	9.8	148.0
0.45	690	9.5	145.7
0.72	280	9.0	142.4
0.72	320	9.2	143.9
0.72	330	8.9	141.7

It can be seen in Table 2 that the fracture toughness is very low and both the δ_c and K_{IC} are not sensitive to the crack depth (a/W). This indicates that all the specimens fractured in the lower-shelf region. The fracture surface is shown in Fig. 1. There are typical river-pattern marks on the fracture surface and the initiation site is very close to the precrack. The EDAX analysis showed that the cleavage initiated from the second-phase particles (1-2μm) rather than non-metallic inclusions. According to the composition of the steel, the second-phase may be carbide or martensite-austenite constituent (M-A). The metallographic analysis by Ikaw *et al* [7] for the similar steel showed that the majority of the second-phase particles were M-A constituents. Fig.2 shows the metallographic section made from the unloaded three-point bend specimen.

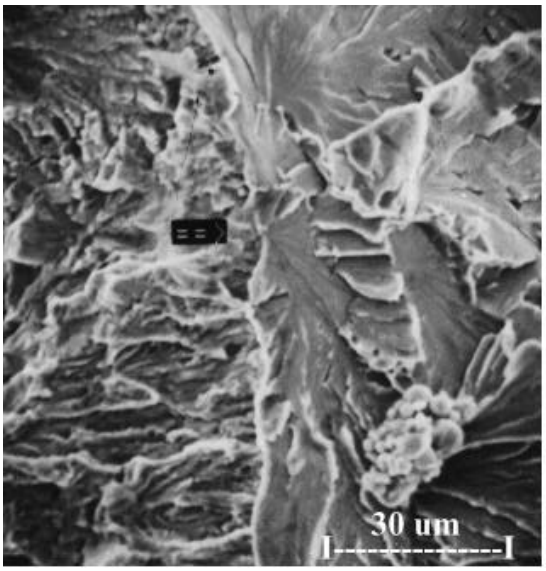

Figure 1: Fracture surface of a three-point bend specimen at –196°C.

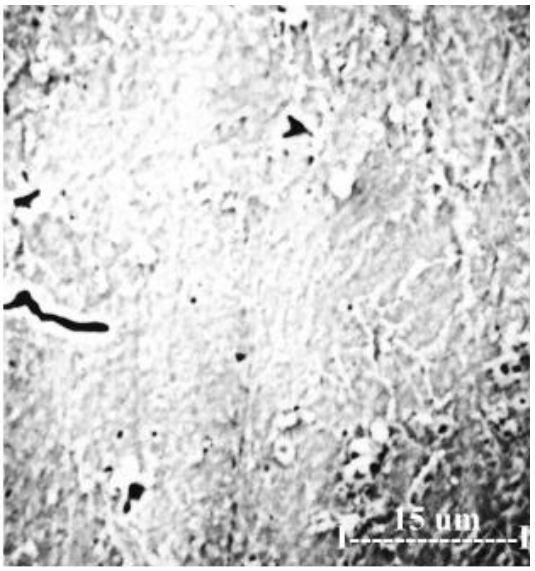

Figure 2: Remaining micro-cracks in the vicinity of precrack tip.

It can be observed in Fig. 2 that the crack tip is only slightly blunted. In the vicinity of the crack tip, some remaining micro-cracks with 1-2μm in length were observed due to unloading prior to fracture. This indicates that the critical fracture event is the propagation of second-phase sized crack to the matrix.

Fracture Mechanism of Precracked Specimen at –100°C

The experimental result of the three-point bend tests at –100°C is shown in Table 3, where δ_u is the crack tip opening displacement at the failure load.

TABLE 3
EXPERIMENTAL RESULTS OF COD TESTS AT –100°C

a/W	P (kg)	δ_u (mm)
0.23	2860	0.635
0.23	2890	0.288
0.23	3280	1.159
0.45	1464	0.413
0.45	1480	0.341
0.72	470	0.096
0.72	510	0.250

In contrast to the fracture at -196°C, for all specimens cleavage was preceded by ductile crack growth. In other words, there was a transition from ductile crack growth to cleavage fracture. It can be seen in the

Table 3 that the average value of δ_u is much higher than the average δ_c (Table 2) due to the ductile crack growth. Also, the δ_u is sensitive to the depth of precrack (*a*/*W*). A high δ_u is associated with a specimen with shallow precrack. Fig. 3 shows the effect of the depth of precrack on the ductile crack growth length (DC). The total length of crack, i.e., precrack plus ductile crack growth (DC+*a*) corresponding to the failure load is also included.

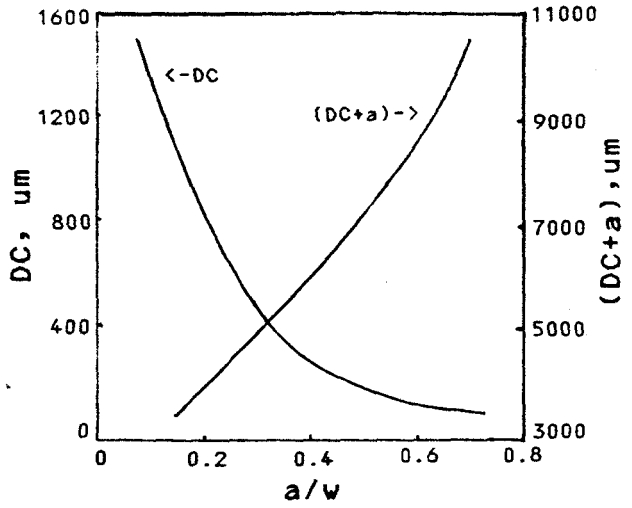

Figure 3: Effect of *a*/*W* on ductile crack growth

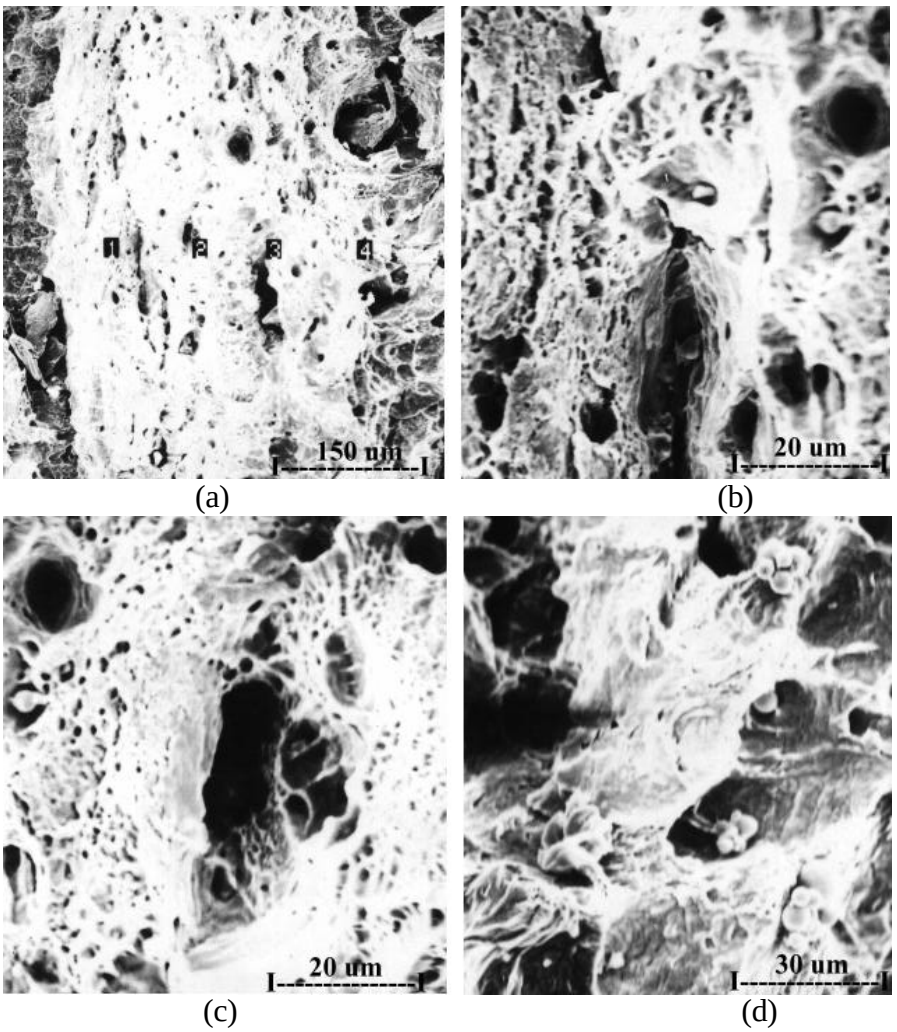

Figure 4: Shapes of microdimples located at different positions of a ductile crack: (a) general view, (b) position 1, (c) position 2 and (d) position 3.

The shallow crack specimen has a greater length of ductile crack growth compared to the deep crack specimen. Normally, fracture toughness is proportional to the length of ductile crack in which the plastic deformation energy is dissipated [8]. The shallow crack specimen has a greater ductile crack growth, thereby having a higher fracture toughness (δ_u). It is well recognized that cleavage fracture is controlled by critical opening stress [9]. Many numerical investigations have demonstrated that the crack depth (a/W) has a significant effect on the stress triaxiality ahead of crack tip [10-11]. The hydrostatic stresses are larger for deeper cracks. On the other hand, Yan *et al* [12] showed that ductile crack growth could elevate the stress triaxiality and opening stress on the remaining ligament. Therefore, a larger ductile crack growth is expected for the shallow crack specimen to raise the opening stress to the critical cleavage stress. The work of Chen *et al* [13] showed that the variation of stress triaxiality could affect the shape of micro-dimples (the ration of depth to width) on the ductile crack surface. High stress triaxiality results a small ratio of depth to width. Fig. 4 shows the variation of microdimples located in different growth length of the ductile crack. In Fig. 4, the dimple becomes flat with the ductile crack growth. This means that the ratio of depth to width of the dimples decreases with ductile crack growth due to an increase of stress triaxiality.

Fracture Mechanism in Notched Specimen

The double-notched four-point bend specimens were tested at –196°C. The fracture surface was typical cleavage fracture without any ductile crack growth. The metallographic sections made from the double-notch four-point bend specimens are shown in Fig. 5. The remaining micro-cracks are much longer than that in the unloaded three-point bend specimens. The typical length of the remaining cracks is about the width of bainite bundle. This implies that the critical cleavage event in the notch specimen is the propagation of grain-sized crack to the matrix, which is, obviously, different from the critical event in the precracked specimen. Cleavage fracture stress can be related to the critical crack size in terms of the well-known Griffith's equation,

$$\sigma_f = \left[\frac{4Er_p}{\pi(1-\nu^2)C}\right]^{1/2}, \qquad (1)$$

where σ_f, E, r_p, ν and C are cleavage stress, Young's modulus, surface energy, Possion's ratio and the critical crack size, respectively. Clearly, a higher cleavage stress can be obtained by decreasing the critical crack size C. As the critical event is the propagation of bainite bundle-sized crack to the matrix, a higher fracture toughness is expected when the size of bainite bundle is reduced.

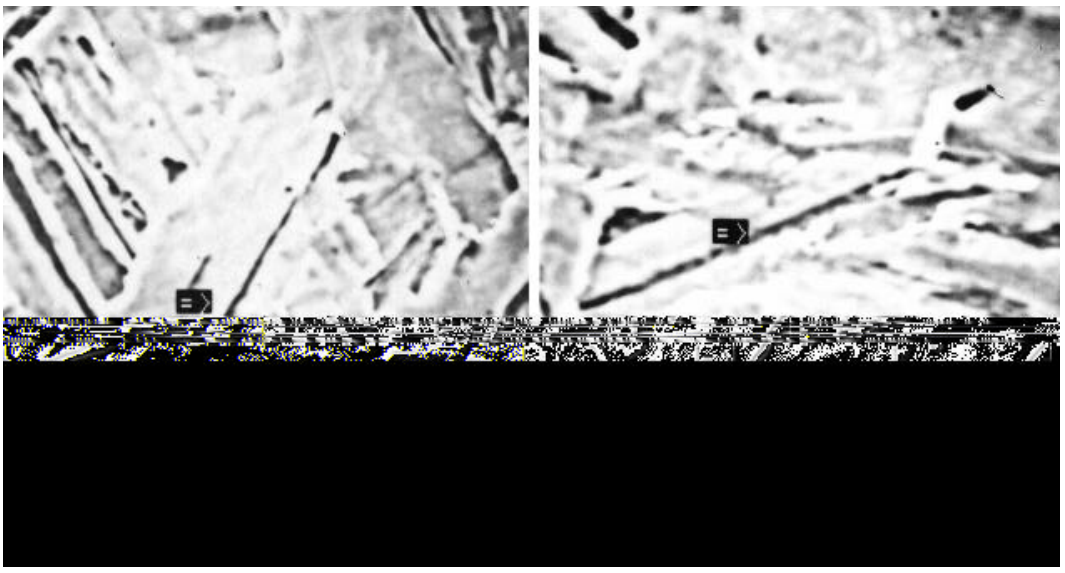

Figure 5: Remaining micro-cracks in the vicinity of notch tip

The impact energy measured in Charpy V-notched specimen from –100°C to 20°C is shown in Table 4.

TABLE 4
CHARPY IMPACT ENERGY (*J*) FROM –100°C TO 20°C

T°C	-100	-80	-60	-40	-20	0	20
	30.8	40.2	40.5	133.9	191.4	184.8	228.0
Impact	32.0	50.6	91.2	1433.0	159.7	187.8	232.1
energy	30.1	49.1	74.9	150.3	181.4	231.6	229.3
	13.1	39.5	86.7	116.2	151.8	203.1	234.0
Average	26.5	44.9	73.3	135.9	171.1	201.8	230.9

It can be seen that there is an increase of impact energy with temperature. The lower-shelf temperature is about –100°C.

CONCLUSIONS

The fracture behaviour of a bainite steel at low temperature was investigated using precracked and notched specimens. Experimental results showed that the critical cleavage events were the propagation of second phase-sized and bainite bundle-sized micro-cracks to the matrix for the precracked and the notched specimens, respectively. At -196°C, both the precracked and the notched specimens fractured at lower-shelf region without any ductile crack growth. The critical crack tip opening displacement was not sensitive to the depth of precrack. At –100°C, for all precracked specimens cleavage was preceded by ductile crack growth. A longer ductile crack growth was associated with the shallow crack specimens, which resulted in a higher critical crack tip opening displacement. The ratio of depth to width of micro-dimple on ductile crack surface was decreased with ductile crack growth, which indicated an increase of stress triaxiality ahead of a growing crack.

REFERENCES

1. Ritchie, R.O. and Horn, R. M. (1978) *Metall. Trans*. 9A, 331.
2. Lin,T., Evans, A.G. and Ritchie, R.O. (1987) *Metall. Trans*. 10A, 641.
3. Zeman, J., Role, S., Buchar, J. and Pokluda, J. (1990) In: *Fracture Mechanics, ASTM STP 1074*, pp396-418, ASTM, Philadelphia.
4. Chen, J.H. and Yan, C. (1992) *Metall. Trans*. 23A, 2549.
5. Yan, C., Chen, J.H., Sun, J. and Wang, Z. (1993) *Metall. Trans*. 24A, 1381.
6. Chen, J.H., Wang, G.Z., Yan, C., Ma, H. and Zhu, L. (1997) *Int. J. Fract*. 83, 105.
7. Ikaw, H *et al* (1980) *Trans. JWS*. 11, 3.
8. Thomason, P.F (1990). *Ductile Fracture of Metals*, Pergamon Press, Oxford.
9. Ritchie, R.O., Knott, J.F. and Rice, J.R. (1973) *J. Mech. Phys. Solids*. 21, 395.
10. Sorem, W.A., Dodds, R.H. and Rolfe, S.T. (1991) *Int. J. Fract*. 47, 105.
11. Ruggieri, C. and Dodds, R.D. (1996) *Int. J. Fract*. 79, 309.
12. Yan, C., Mai, Y.W. and Wu, S.X. (1997) *Int. J. Fract*. 87, 345.
13. Chen, J.H., Wang, G.Z., Yan, C., Ma, H. and Zhu, L. (1997) *Int. J. Fract*. 83, 121.

ORAL REFERENCE: ICF100586OR

FRACTURE MECHANISMS FOR SiC FIBERS AND SiC/SiC COMPOSITES UNDER STRESS-RUPTURE CONDITIONS AT HIGH TEMPERATURES

J.A. DiCarlo, H.M. Yun, and J.B. Hurst

Materials Division, NASA Glenn Research Center
Cleveland, OH 44135, USA

ABSTRACT

The successful application of SiC/SiC ceramic matrix composites as high-temperature structural materials depends strongly on maximizing the fracture or rupture life of the load-bearing fiber and matrix constituents. Using high-temperature data measured under stress-rupture test conditions, this study examines in a mechanistic manner the effects of various intrinsic and extrinsic factors on the creep and fracture behavior of a variety of SiC fiber types. It is shown that although some fiber types fracture during a large primary creep stage, the fiber creep rate just prior to fracture plays a key role in determining fiber rupture time (Monkman-Grant theory). If it is assumed that SiC matrices rupture in a similar manner as fibers with the same microstructures, one can develop simple mechanistic models to analyze and optimize the stress-rupture behavior of SiC/SiC composites for applied stresses that are initially below matrix cracking.

KEY WORDS

SiC fibers, SiC matrices, SiC/SiC composites, creep, rupture, mechanisms, Monkman-Grant diagrams

INTRODUCTION

For long-term structural applications under high-temperature oxidizing conditions, research efforts are ongoing throughout the world to develop SiC fiber-reinforced SiC matrix composites [1,2]. Since these SiC/SiC composites are still in their infancy in terms of selecting and demonstrating the optimum fiber, interphase, and matrix constituents, there currently exists a strong need for studies that mechanistically analyze and predict the fracture-limited envelope of thermostructual capability provided by currently available constituents. Thus the objective of this paper is to present mechanistic models concerning the high-temperature stress-rupture behavior of SiC fibers and SiC/SiC composites of current technical interest. Since the time-dependent fracture of these materials is controlled by creep-induced flaw growth, these models are based on key experimental observations made on the creep-rupture behavior for various SiC fiber types. These observations are important not only because the fibers are the primary structural constituents controlling ultimate composite rupture, but also because SiC fibers display microstructures and fracture behavior representative of SiC matrices, which can also carry structural loads in SiC/SiC composites.

SiC FIBER CREEP-RUPTURE

In terms of providing good thermomechanical reinforcement capability for SiC/SiC composites, small-diameter SiC fiber types with low oxygen content, such as the non-stoichiometric (C/Si >1) Hi-Nicalon fiber from Nippon Carbon and the-stoichiometric (C/Si~1) Sylramic fiber from Dow Corning, have many desirable physical and chemical properties [3,4]. For this reason, considerable creep-rupture property data exist for these two fiber types not only as single fibers [3-8], multifilament tows [9,10], and woven fabric pieces [11], but also as reinforcement for SiC/SiC composites with various types of SiC matrices [12-15]. For example, Fig. 1 shows typical creep strain versus time curves for single Hi-Nicalon and Sylramic fibers as measured at 1400°C in air under a constant stress of 270 MPa. Rupture points are indicated by the symbol ***Fr***. Also shown are typical creep curves measured under the same conditions for the oxygen-containing Nicalon SiC fiber and for the oxygen-free SCS-6 and Ultra SCS SiC fibers from Textron Specialty Materials [5,16]. As will be discussed, although the large diameter of the SCS fibers limit their formability for complex-shaped SiC/SiC components, their microstructures are similar to those of SiC matrices formed by chemical vapor infiltration, a common matrix formation process for SiC/SiC composites.

One important observation from the Fig. 1 data is that all SiC fibers display a primary or transient creep stage that varies in magnitude depending on fiber type. This effect is typically observed in Si-based ceramics in which there exists an initial "anelastic" or recoverable creep component controlled by grain-boundary sliding [17]. Along with the anelastic component, there also exists a 'viscoelastic' or steady-state creep component, which is typically accompanied by creep-induced micro-crack formation, resulting in critical flaw growth and non-recoverable strain. Both components are enhanced by small grain size and by the high diffusion of impurity second phases in the grain boundaries. Thus the high creep behavior of the Nicalon fiber can be explained both by its oxygen content and its very fine grain size (~5 nm); while the high creep of the Hi-Nicalon fiber is primarily due to its fine grain size of ~10 nm. The rather large transient stage for these fibers may also be caused in part by concurrent grain growth during the high-temperature stress-rupture test [7]. Impurity effects also appear to be responsible for the creep behavior of the coarse-grained (~100 nm) Sylramic and SCS-6 fibers, which contain boron sintering phases and free silicon, respectively. This conclusion is supported by the observation that the Sylramic fiber transient stage decreases significantly by post-treatments that remove boron from the fiber bulk [8], and by the Fig. 1 creep data for the Ultra-SCS fiber, which has the same grain size but no boron or excess silicon. Thus microstructure plays a strong role in the creep behavior of SiC fibers in particular and SiC-based ceramics in general.

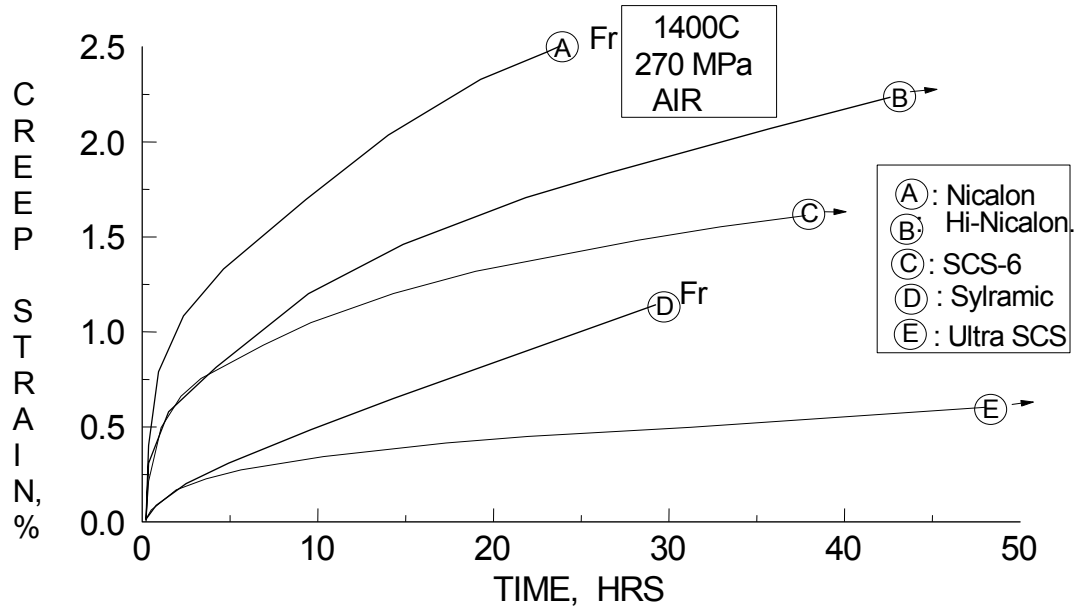

Figure 1. Typical creep curves for SiC fibers tested under high-temperature stress-rupture conditions.

Another point not shown in Fig. 1 is that creep rates and total creep strains for a given time period are typically increased for some fiber types by testing in an argon environment, with the effect being the largest for the Sylramic fiber [6,8]. Although the exact mechanism responsible for this behavior is still unclear, the source appears to be related to decomposition effects. That is, testing in an argon or inert environments should enhance the gaseous volatilization of atomic species (such as silicon or its oxides) from the fiber surface and from within the fiber bulk either along grain boundaries or through open porosity. On the other hand, testing in air can form a silica coating on the fiber surface, which will effectively seal off gaseous volatilization from the bulk. As for possible volatizing species for the Sylramic fiber, this type does contain second-phase impurities, such as boron and TiB_2. However, their removal should only reduce rather than enhance creep. Therefore, at the present time, it would appear that the most likely species for volatilization is silicon from the SiC grains, which in turn can reduce grain size and enhance fiber creep rate. Indeed, this effect should be especially observable in the Sylramic fiber, which has the smallest diameter (~10 μm) and therefore the largest surface to volume ratio of all the Fig. 1 fibers. Thus, from a technical point-of-view, one might expect differences in fiber creep behavior within a SiC/SiC composite, depending on whether the fiber surfaces are exposed to inert or to oxidizing environments. However, for most high-temperature applications of current interest, the typical service environments for the composites are oxidizing; so that even with porous interfacial zones, silica protective layers should eventually form on the SiC/SiC outer surfaces and effectively inhibit further volatilization of gaseous species from the fiber. It follows then that for mechanistic modeling of SiC/SiC creep-rupture behavior, the fiber in-situ environment should be considered; but for most applications, the single fiber data in air should be appropriate.

A final point of interest for Fig. 1 is the rupture life behavior of the various SiC fiber types. In this regard, some important general observations have been made in previous studies [8,18]. These include: (1) the activation controlling high-temperature rupture of the SiC fibers is nearly constant and equal to the activation energy controlling fiber creep; (2) fiber rupture strains for a given test temperature and test environment are fairly independent of the minimum creep rate at rupture, but are dependent on fiber type; (3) when the minimum creep rate is enhanced by argon testing, rupture times are shorter, (4) rupture strains are typically 100% higher in air than in argon; and (5) some of the fiber types rupture before clear attainment of steady-state creep behavior (see Fig. 1). The energy observation confirms that the most important mechanism controlling the high-temperature fracture of SiC fibers (and SiC monolithic ceramics) is creep-induced micro-crack growth. The observations of rupture strain independence on creep-rate and shorter rupture times under higher creep rates in argon indicate that for each fiber type, a certain amount of micro-crack growth is required to create the critical flaw size. Thus lower creep rates are conducive to longer fiber rupture lives. The observation of an approximate doubling of fiber rupture strain in air suggests that the controlling micro-crack growth is primarily on the fiber surface, where silica formation can blunt the stress concentration arising from this micro-crack growth. Finally, the observation of rupture before obvious steady-state creep behavior indicates that viscoelastic creep and micro-crack growth are on going during the transient stage.

The high-temperature creep curves of monolithic Si-based ceramics, such as pressureless sintered Si_3N_3 [19], are very similar to those of the SiC fibers. For the monolithic materials, a convenient empirical approach for modeling rupture time is by use of Monkman-Grant (MG) diagrams that plot the log of average rupture time versus the log of minimum creep rate at various temperatures [20]. On MG diagrams, the log-log results at various temperatures typically fall on a set of parallel straight lines that allow average rupture time $\boldsymbol{t}$ to be described by the simple equation,

$$\boldsymbol{t\,\dot{\varepsilon}^{\,m} = C} \qquad (1).$$

Here $\boldsymbol{\dot{\varepsilon}}$ is the steady state (or minimum) creep rate, and $\boldsymbol{m}$ and $\boldsymbol{C}$ are empirically determined parameters. Using this approach, Fig. 2 shows that the rupture behavior for the five SiC fiber types of Fig. 1 can indeed be best-fit to straight MG lines using data measured at 1200°C in air and at 1400°C in air for the Hi-Nicalon fiber. For these lines, fiber creep rate is equivalent to minimum creep rate or to the instantaneous creep rate at fiber rupture since no tertiary stages were ever observed.

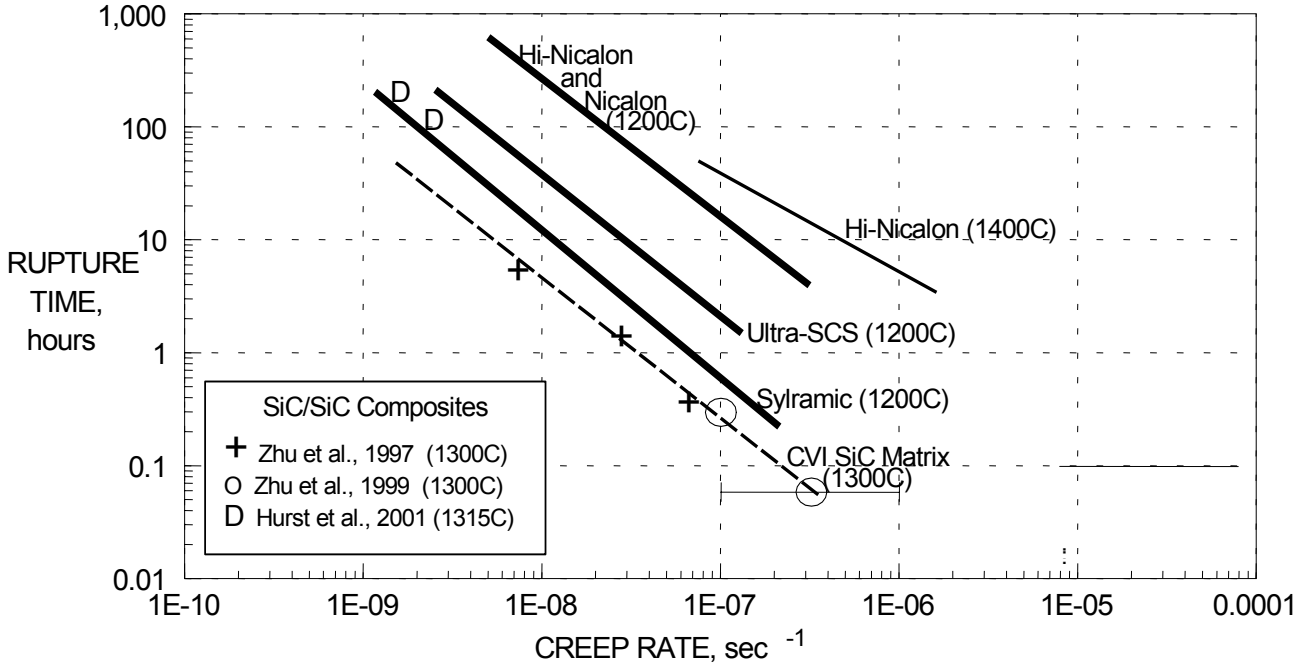

Figure 2. Monkman-Grant lines measured in air for SiC fibers, SiC matrices, and SiC/SiC composites.

Fig. 2 also shows that, except for the Nicalon and Hi-Nicalon fibers, the rupture lines of the different fiber types at 1200°C in air do not fall on one master line as has been observed for various alumina-based fibers [21]. This can probably be attributed in part to the measured creep rates being larger than the viscoelastic creep rates due to the presence of variable anelastic creep components at fiber rupture. However, in relation to Eq. 1, all the lines display approximately the same slope with an $\boldsymbol{m}$ exponent of ~1.2. The fact that the $\boldsymbol{m}$ value is greater than unity indicates that the average fiber rupture strain from the viscoelastic component ($\approx \boldsymbol{\dot{\varepsilon}} \boldsymbol{t}$) increased with increasing rupture time or decreasing stress on the fibers. Also, by increasing test temperature from 1200 to 1400°C, all fiber lines shifted upward (>five-fold increase in rupture time for a given creep rate), like that of the Hi-Nicalon fiber in Fig. 2. However, the Hi-Nicalon line at 1400°C displayed an $\boldsymbol{m}$ value less than unity, implying reduced rupture strain with longer rupture time. This reduction in strain with time may be related to detrimental effects associated with long-term microstructural changes or oxidation. Thus the constant $\boldsymbol{C}$ in Eq. 1 should be dependent both on SiC fiber microstructure and test temperature, but is fairly independent of fiber stress or fiber cross-sectional area since the creep rate variation was obtained by changing the applied load on the fibers. It follows then from Fig. 2 that for a particular SiC/SiC application temperature, *one cannot select fiber rupture time independently of fiber creep rate*. For example, up to 1200°C, the only approach for obtaining a 1000-hour fiber lifetime is to assure that the composite application conditions do not create fiber creep rates more than ~10^{-8} sec^{-1} for the creep–prone Nicalon and Hi-Nicalon fibers and more than ~10^{-9} sec^{-1} for the more creep–resistant Sylramic fiber.

SiC/SiC COMPOSITE CREEP-RUPTURE

The single fiber results presented above indicate that many intrinsic and extrinsic mechanistic factors control the high temperature rupture of SiC fiber types of current interest. As an initial step toward understanding how these factors can in turn affect SiC/SiC composite behavior, the following discussion uses elementary composite theory and the single fiber data to develop simple mechanistic models for composite fracture at high temperatures under typical stress-rupture testing conditions. Common practice for these tests is to first raise the composites to the test temperature in ambient air, and then to increase load to a given level where creep strain is measured versus time until composite fracture. Typically the load is applied in a direction parallel to a set of fiber bundles that have an effective volume fraction of from 15 to 25% in the load direction. In this situation, there are two conditions of practical interest: (A) the maximum applied load is low enough to initially inhibit through-thickness cracking of the matrix, and (B) the maximum applied load is high enough to initially cause through-thickness cracking of the matrix, thereby leaving the fiber bundles

bridging the matrix cracks and exposed to the test environment. For this latter situation, the stress on the bridging fibers can be directly calculated from the composite stress; so that composite rupture can be predicted based on the stress dependence for creep-rupture of the reinforcing fibers. The details of one simple rupture model for condition (B) and its verification data are presented elsewhere [22,23].

For condition (A), a more desirable situation for long-term composite use, the average stresses on the fibers and matrix are not constant; but change with time in a complicated manner due to differences in creep behavior between the two constituents. The initial creep rate of the uncracked composite will generally be controlled by the more creep-prone constituent and the final creep rate by the more creep-resistant constituent. For modeling purposes, one can assume isostrain conditions within the composite, so that the measured creep rate of the composite is equal to that of the fiber and matrix. Assuming near steady-state conditions are reached during composite life, it is proposed that the composite creep rate and the MG lines of Fig. 2 could then be used to predict which constituent will rupture first for a given SiC/SiC creep rate. To determine whether this model has any validity, it is interesting to note that most SiC/SiC composites fabricated today contain SiC matrices produced by chemical vapor infiltration (CVI). Assuming these matrices creep and rupture in a manner equivalent to that of the Ultra SCS fiber, Fig. 2 suggests that at any composite creep rate at temperatures of 1200^{o}C or higher, the CVI SiC matrix should crack before the Nicalon or Hi-Nicalon fibers rupture. This should be the case no matter what the fiber stress or volume fraction within the composite. On the other hand, the Sylramic fibers should rupture before the CVI SiC matrix cracks.

Although there currently exists very little SiC/SiC data to validate the condition (A) model, one can examine two recent papers by Zhu et al. who measured the creep-rupture behavior of two types of SiC/SiC composites containing CVI SiC matrices manufactured by the same vendor. For the first composite type with Nicalon fibers, data taken at 30, 45, and 60 MPa and at 1300^{o}C in air show low composite creep curves and relatively long lives until an abrupt and rapid increase in creep strain occurs, followed by composite rupture within a time period less than 5% of the original creep stage [12]. This behavior supports the prediction described above in which the first abrupt change should be caused by matrix cracking of the CVI SiC matrix, and the final failure by rupture of the fully loaded Nicalon fibers. Assuming this to be the case, one can use the composite creep rates and times at matrix cracking to plot the three [+] data points shown in Fig 2. For the second composite type with Hi-Nicalon fibers, the authors were actually able to measure the times for CVI SiC matrix cracking from periodic hysteresis tests [13]. The two [**O**] data points in the Fig. 2 display these time results versus the composite creep rates at cracking. The observations that all points fall very well on the same straight line and that this line has an ***m*** value of ~1.2 strongly support the assumptions of the condition (A) model. In addition, the matrix cracking line falls below that Ultra SCS fiber at 1200^{o}C, suggesting that the CVI SiC matrix is not pure and stoichiometric like the Ultra SCS fiber. Indeed, recent Raman studies on CVI SiC matrices made by the same vendor have detected free silicon in the matrix bulk [24]. Thus the dashed line can be considered the empirically determined MG line for CVI SiC matrices fabricated by this particular vendor.

Recently, SiC/SiC matrices have been fabricated with Sylramic fibers and with the same CVI SiC matrix from the same vendor as the major structural component of the matrix. Stress-rupture data taken in air at 1315^{o}C and composite stresses from 70 to 105 MPa show composite creep curves with a transient and steady state stage, but with a small tertiary stage before final rupture [15]. Unlike the Nicalon composite of Shi et al. [12], there was no clear evidence that allowed an understanding of which constituent ruptured first or what mechanism controlled final rupture. However, if one plots minimum composite creep rates versus the times at initiation of the tertiary stage, the two [**D**] data points in Fig. 2 show typical results. Since both the Sylramic fiber line at 1200^{o}C and the CVI SiC line at 1300 ^{o}C move up with a temperature increase to 1315^{o}C, the fact that the Sylramic composite data points fall closer to the estimated MG line for the CVI SiC matrix would suggest that the matrix rather than the Sylramic fiber was responsible for composite rupture. Clearly more studies are needed to validate the accuracy of this condition (A) model. Nevertheless, the position of the Fig. 2 MG line for the Ultra SCS fiber, even at 1200^{o}C, would suggest that the rupture lives of these SiC/SiC composites could be significantly improved at any creep rate (or composite stress or constituent volume fraction) if CVI SiC matrices could be developed that displayed a more stoichiometric composition than current versions.

SUMMARY AND CONCLUSIONS

This paper has shown that the high-temperature fracture of SiC/SiC composites is primarily controlled by creep-induced flaw growth in the SiC fibers and matrices. Thus for composite applications requiring long service life, it is very important to reduce effects that enhance constituent creep both from within the microstructure (small grains, impurity phases) and from within the application (high stress, high temperature, inert environment). Despite these complicating factors, it is also shown that empirical rupture models, based on fiber and matrix Monkman-Grant diagrams, offer a simple approach for mechanistic analysis and prediction of creep-induced rupture for SiC/SiC composites and ceramic composites in general.

REFERENCES

1. Brewer, D. (1999). Mater. Sci. Eng., A261, 284.
2. Kameda, T., Itoh, Y., Hijikata T. and Okamura, T. (2000). In: Proceedings of the International Gas Turbine & Aeroengine Congress, The American Society of Mechanical Engineers, New York, N.Y., Paper 2000-GT-67.
3. Ichikawa, H. and Ishikawa, T. (2000). In: Comprehensive Composite Materials, Vol. 1, Eds. A. Kelly, C. Zweben, and T. Chou, Elsevier Science Ltd, Oxford, England, pp.107-145
4. Tressler, R.E. and DiCarlo, J.A. (1993). In: Proceedings of HT-CMC-1, Eds. R. Naslain, J. Lamon, and D. Doumeingts, Woodland Publishing, Ltd., Cambridge, England, pp. 33-49; also (1995). In: Proceedings of HT-CMC-2, Ceramic Transactions, 57**,** 141.
5. Yun, H.M., Goldsby, J.C. and DiCarlo, J.A. (1994). In: Advances in Ceramic Matrix Composites II, Ceramic Transactions 46**,** 17.
6. Yun, H.M., Goldsby, J.C. and DiCarlo, J.A. (1995). In: Proceedings for HTCMC-2, Ceramic Transactions 57**,** 331.
7. Bodet, R., Bourrat, X., Lamon, J. and Naslain, R. (1995). J. Mater. Sci., 30, 661.
8. Yun, H.M. and DiCarlo, J.A. (1999). Ceram. Eng. Sci. Proc., 20 (No. 3), 259.
9. Yun, H.M. and DiCarlo, J.A. (1996). Ceram. Eng. Sci. Proc. 17B, 61.
10. Yun, H.M. and DiCarlo, J.A. (1999). In: Proceedings of ICCM-12, Paris, France, and NASA/TM – 1999-209283.
11. Yun, H.M. and DiCarlo, J.A. (2000). Ceram. Eng. Sci. Proc. 21 (No.4), 347.
12. Zhu, S., Mizuno, M., Nagano, J., Kagawa, Y. and Kaya, H. (1997). Composites Science and Technology 57, 1629.
13. Zhu, S., Mizuno, M., Nagano, Y., Cao, J., Kagawa, Y. and Kaya, H. (1998). J. Am. Ceram. Soc., 81 (No. 9), 2269.
14. Hurst, J.B., DiCarlo, J.A., Bhatt, R.T, Yun, H.M., and Gorican, D. (1999). Presented at 23rd Annual Conference on Composites, Materials and Structures, January 1999, Cocoa Beach, Florida.
15. Hurst, J.B., Calomino, A. and Bakalini, G. (2001). Presented at 25th Annual Conference on Composites, Materials and Structures, January 2001, Cape Canaveral, Florida.
16. Yun, H.M., Goldsby, J.C. and DiCarlo, J.A. (1995). In: HITEMP Review, NASA CP-10178, paper 56.
17. DiCarlo, J.A. (1986). J. Mater. Sci. 21, 217.
18. DiCarlo, J.A., Yun, H.M. and G.N. Morscher (1995). In: Proceedings for HTCMC-2, Ceramic Transactions 57, 343.
19. Wiederhorn, S.M., Luecke, W.E. and Krause, Jr., R.F. (1998). Ceram. Eng. Sci. Proc., 19 (No. 4), 65.
20. Monkman, F.C. and Grant, N.J. (1956). Proc. ASTM, 56, 593.
21. Pysher, D.J. and Tressler, R.E. (1992). Ceram. Eng. Sci. Proc., 13 (No. 7-8), 218.
22. DiCarlo, J.A. and Yun, H.M. (1999). In: Proceedings of ICCM-12, Paris, France.
23. DiCarlo, J.A. and Yun, H.M. (2000). In: Proceedings of the International Gas Turbine & Aeroengine Congress, The American Society of Mechanical Engineers, New York, N.Y., Paper 2000-GT-640.
24. Eldridge, J. (2000). Private communication, NASA Glenn Research Center.

ICF100139OR

FRACTURE MECHANISMS IN B2 NiTi SHAPE MEMORY ALLOYS

Nancy Yang[1], Ken Gall[2], Huseyin Sehitoglu[3], and Yuriy Chumlyakov[4]

[1]Materials & Engineering Sciences Center, Sandia National Laboratories, Livermore, CA, 94550 USA
[2]Department of Mechanical Engineering, University of Colorado, Boulder, CO, 80309 USA
[3]Department of Mechanical and Industrial Engineering, University of Illinois at Urbana-Champaign, Urbana, IL, 61801 USA
[4]Tomsk University, 634050 Tomsk, Russia

ABSTRACT

The fracture mechanisms in single crystal Ti-50.8at%Ni shape memory alloys containing Ti_3Ni_4 precipitates are studied using the scanning electron microscope (SEM). Aged materials with three different precipitate sizes (50 nm, 150 nm, and 400 nm), which have interfaces ranging from semi-coherent to incoherent, are considered. The primary mechanisms of material fracture identified in the single crystal NiTi are: (1) Nucleation, growth, and coalescence of voids from the Ti_3Ni_4 precipitates and (2) Cleavage fracture on {100} crystallographic planes. Cleavage fracture and ductile tearing are found to act in conjunction, and the relative dominance of one over the other depends on the local precipitate size. When the Ti_3Ni_4 precipitates are small and coherent they facilitate mechanism 2. As the Ti_3Ni_4 precipitate size increases to about 400 nm, the overall fracture is dominated by failure mechanism 1, and the cleavage markings become diffuse.

KEYWORDS

NiTi, Single Crystals, Cleavage Fracture, Ductile Tearing.

INTRODUCTION

As evident in a recent review on shape memory alloys [1], the general thermo-mechanical response of NiTi is well characterized for various testing conditions. However, the utilization of NiTi shape memory alloys in long life components requires a thorough understanding of the dominant mechanisms controlling their fatigue and fracture. Under cyclic loading conditions, the failure of NiTi shape memory alloys in service can be caused by either an inability of the alloy to provide the required material response (recoverable displacement or force) or the fracture of the material. Minimal work [2] has been performed on the resistance of NiTi alloys

to fatigue crack growth and fracture. Understanding the fatigue crack growth and fracture behavior of NiTi alloys is imperative for applications where the alloys are subjected to a combination of low cycle fatigue (active use of the transformation) and high cycle fatigue (inactive structural support) conditions. Such loading sequences facilitate the formation of microcracks that can lead to premature fracture of the shape memory alloy component. The present study will consider the fracture mechanisms in single crystal Ti-50.8at%Ni with three different Ti_3Ni_4 precipitate sizes.

MATERIALS AND METHODS

Ti-50.8at%Ni single crystal specimens were grown from a single material batch using the modified Bridgeman technique in an inert gas atmosphere in the temperature range 1773 K – 1893 K. Following growth, the crystals were homogenized at 1273 K for 24 hours in a vacuum furnace and quenched into ambient temperature water, leaving them in the solutionized state. The solutionized single crystal NiTi materials were given subsequent aging treatments of 1.5 hr @ 723 K, 1.0 hr @ 773 K, and 1.5 hr @ 823 K which resulted in Ti_3Ni_4 precipitates with sizes of 50 nm, 150 nm, and 400 nm, respectively.

Mechanical tests were conducted at room temperature (T = 298 K) in laboratory air conditions. Monotonic and cyclic tests (total strain range of 3%, R = 0) were conducted until complete fracture of the specimens. Monotonic tests were conducted on samples aged 1.0 hr @ 773 K with a [100] loading axis orientation. Cyclic tests on the crystals with a [148] loading axis orientation were conducted on materials aged 1.5 hr @ 723 K and 1.5 hr @ 823 K. Material regions on the fracture surface that failed through overload during the monotonic and cyclic tests were examined with the Scanning Electron Microscope (SEM).

FRACTOGRAPHY

The overall fracture surfaces of the three fractured NiTi samples are shown in Figure 1. The crystallographic orientations of the tensile axes (the direction out of the paper) are indicated to the right of the images and the heat treatments are indicated above the appropriate fracture surface image. In general, as the Ti_3Ni_4 precipitate size increases, and the precipitates lose coherency, the fracture surface demonstrates a rougher appearance, indicating a transition to more ductile local fracture mechanisms. In single crystals, the overall orientation of the fracture surface with respect to the applied tensile axis can give insight into the operative fracture mechanisms. The only fracture surface in Figure 1 perpendicular to the applied tensile axis is the sample loaded along the [100] direction. The samples oriented along [148] demonstrated fracture surfaces with a normal misoriented with respect to the tensile axis. Since the specimens loaded along the [100] direction demonstrated fracture surfaces oriented 90 degrees from the tensile axis, it appears that the {100} planes serve as cleavage planes in NiTi. Previous studies on B2 intermetallics have found that both the {100} and {110} planes can act as cleavage planes [3].

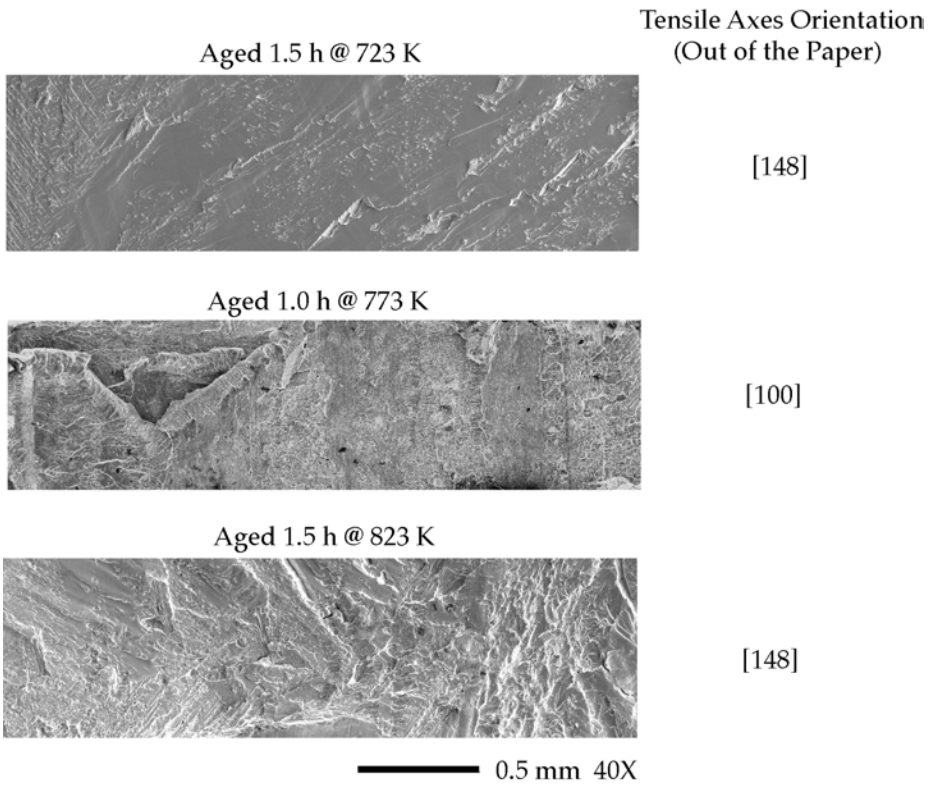

Figure 1: SEM images of the overall appearance of the fracture surfaces.

In order to confirm the above macroscopic observations, higher magnification images of the fracture surface are required. In Figure 2, a SEM image of from fracture surface of the specimen loaded along the [100] orientation demonstrates markings typical of cleavage fracture.

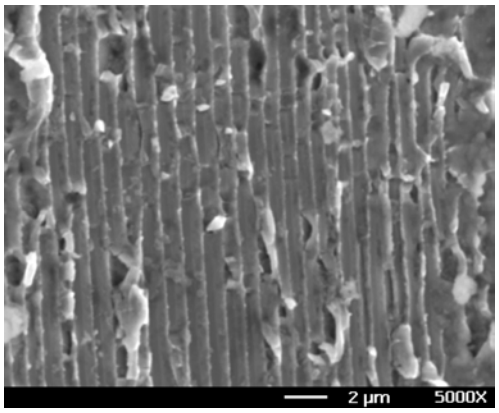

Figure 2: SEM image of the fracture surface of the [100] crystal aged 1.0 hr @ 773 K.

As such, it is confirmed that the NiTi crystals undergo local material cleavage in some regions of the specimen. The markings in Figure 2 have facets on the {100} planes, with crack growth along the $[0\bar{1}1]$ direction and a crack line along the [011] direction. We note that the observed cleavage planes have a correspondence to the highly symmetric B2 parent phase rather than any relation to the habit planes of the low symmetry Type II B19' martensite plates, (-0.88, 0.21, 0.40). Such an observation circumvents any relation between the propagation of overload cracks

and the orientation of the martensite plates; however, it is still possible that the plates nucleate fracture and this is a topic of future research.

Figure 3 shows high resolution images from the [148] crystals, comparing the cleavage markings for samples aged (a) 1.5 hr @ 723 K versus (b) 1.5 hr @ 823 K. The orientations of the markings are the same for samples aged under the two different conditions (they are mirror

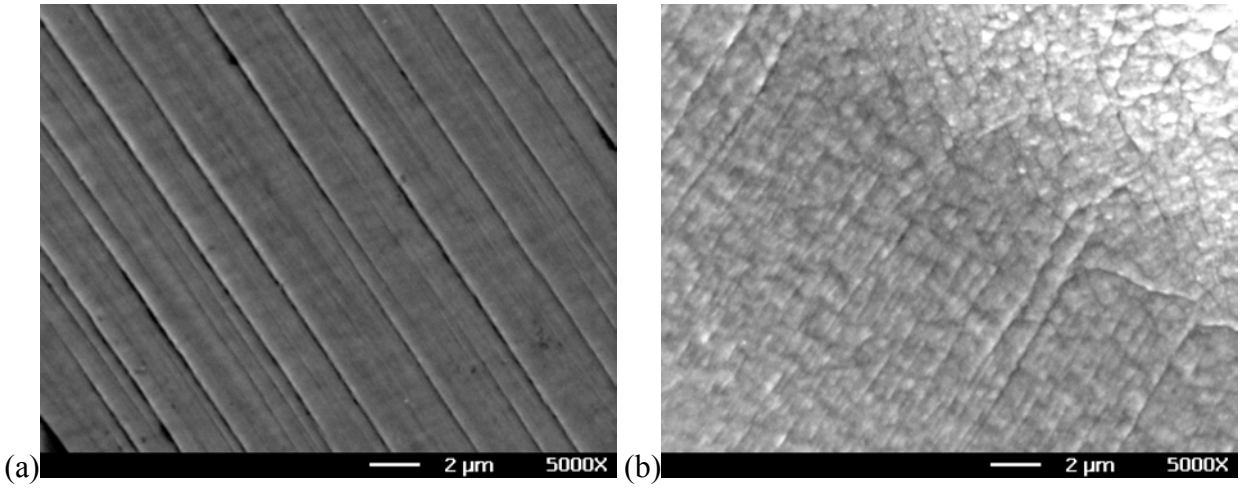

Figure 3: SEM image of cleavage patterns on the fracture surfaces of the [148] crystal aged (a) aged 1.5 hr @ 723 K or (b) 1.5 hr @ 823 K.

images of each other due to the opposite choice of fracture sample halves). However, the cleavage markings in Figure 3b are wavy, and have considerable surface roughness compared to the distinct markings in Figures 3a. In general, a rougher appearance to the fracture surface implies an increased amount of local plastic flow during fracture. In other words, even though the crystallographic aspects of the cleavage fracture are still evident in the samples with the larger Ti_3Ni_4 precipitates, the cleavage occurs with more local distortion than in samples with relatively smaller Ti_3Ni_4 precipitates.

We assert that the increased distortion during cleavage in the samples with the larger precipitates is caused by the local composition changes during the aging process. As Ti_3Ni_4 precipitates coarsen, the local Ni concentration is decreased since the precipitates are Ni rich compared to the matrix. The observations in Figure 3 clearly imply that supersaturated Ni-rich NiTi is inherently more brittle than equiatomic NiTi. Figure 4 lends further support to the above hypothesis on the different fracture mechanisms in the NiTi alloys given the two different aging treatments. The image in Figure 4a was taken in a region of the sample where the Ti_3Ni_4 precipitates are much larger than the average size for the 1.5 hr @ 723 K treatment. Conversely, the visible precipitates in the image in Figure 4b are more typical of the precipitates found in the samples aged 1.5 hr @ 823 K. In the NiTi aged 1.5 hr @ 723 K the cleavage path generally cuts straight through the regions with the large precipitates, leaving negligible voids surrounding them. However, in the alloy aged 1.5 hr @ 823 K the cleavage path is hardly recognizable, except for faint lines, and significant dimples surround the larger precipitates. We note that precipitates much smaller than the ones visible in the holes in figure 4a may exist in the surrounding material. The local deformation characteristics near these smaller precipitates (50-100 nm), coupled with the high Ni concentration of the surrounding matrix, are responsible for the cleavage fracture in Figure 4a versus the ductile fracture in Figure 4b. Such observations are

consistent with previous findings on aluminum alloys where peak aged alloys have a lower toughness compared to overaged alloys [4]. In the aluminum alloys, it has been demonstrated that the finer peak aged precipitates facilitate strong localization and rapid crack extension, rather than crack tip blunting through extensive plasticity [4]. We note that the above observations were typical for the samples given the distinctly different aging treatments.

(a) 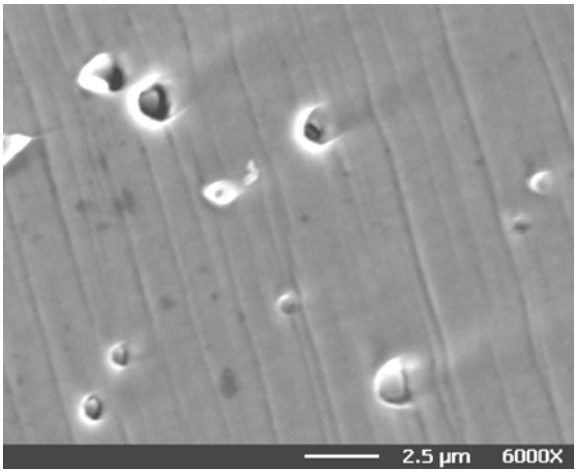

(b) 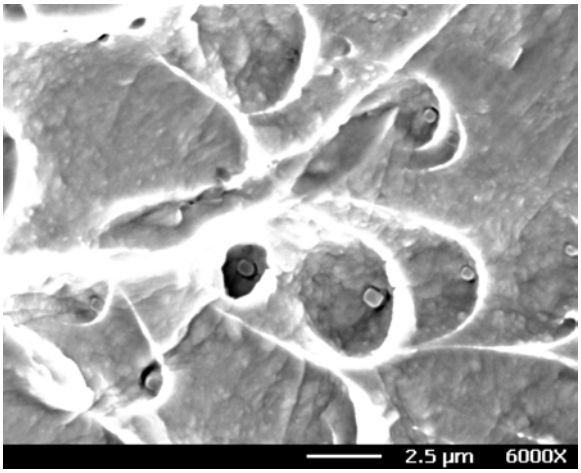

Figure 4: SEM image of dimpled fracture from relatively large second phase Ti_3Ni_4 precipitates on the fracture surfaces of the [148] crystal aged (a) aged 1.5 hr @ 723 K or (b) 1.5 hr @ 823 K.

RAMAFICATIONS AND CONCLUSIONS

The fracture of aged single crystal Ti-50.8at%Ni shape memory alloys containing Ti_3Ni_4 precipitates is controlled by cleavage on the {100} planes coupled with void nucleation, growth, and coalescence from the second phase particles. The two mechanisms of material failure act in conjunction with one another and the dominance of one over the other depends on the relative size of the Ti_3Ni_4 precipitates and the Ni concentration of the matrix. As the average precipitate size increases, the frequency of large dimples near second phase particles also increases.

In materials containing semi-coherent Ti_3Ni_4 precipitates (50 –150 nm), cleavage fracture is distinct and markings appear consistent with markings from traditional intermetallic materials. However, when the Ti_3Ni_4 precipitates are larger (400 nm) and incoherent, the markings are wavy and the cleavage fracture planes become locally distorted. Based on the above observation, it is asserted that the Ni-rich supersaturated NiTi matrix surrounding the precipitates is more brittle than a pure NiTi matrix.

Most drawn wire and bar stock NiTi has a strong fiber texture of the {111} type along the drawing direction. Since the martensitic transformation is triggered at a lower applied tensile stress level as the crystal orientation approaches the [111]-[110] symmetry boundary, such textured polycrystalline alloys are “favorably” oriented for the transformation under tension. Moreover, alloys with such a favorable transformation texture do not have {100} cleavage planes favorably oriented for fracture. Consequently, the well-documented high tensile ductility (along the drawing direction) of bar and wire stock polycrystalline NiTi alloys is partially attributed to the favorable orientation of the transformation coupled with the unfavorable orientation of {100} cleavage planes.

ACKNOWLEDGMENTS

The research of K. Gall and H. Sehitoglu is supported by a grant from the Department of Energy, Basic Energy Sciences Division, Germantown, Maryland, DOE DEFG02-93ER14393. The research of N. Yang is funded by the Department of Energy. The work of Y. Chumlyakov is supported by grants from the Russian Fund for Basic Researches, grant # 02-95-00350, MOPO (MGTU, Moscow) and from fund 99-03-32579a.

REFERENCES

[1] Otsuka, K and Wayman, C. M. (1998) *Shape Memory Materials*, Cambridge University Press, New York, NY.
[2] Melton, K. N. and Mercier, O. (1979) *Acta. Metall*., 27, 137.
[3] Chang, K.-M., Darolia, R., and Lipsitt, H. A. (1992) *Acta. Metall. Mater.*, 40, 2727.
[4] Hahn, G. T. and Rosenfield, A. R. (1975) *Metall. Trans.*, 6A, 653.
[5] Bhattacharya, K. and Kohn, R. V. (1996) *Acta Mater.,* 44, 529.
[6] Shu, Y. C. and Bhattacharya, K. (1998) *Acta Mater.,* 46, 5457.
[7] Gall, K., Sehitoglu, H., Chumlyakov, Y. I., and Kireeva, I. V. (1999) *Acta Mater.,* 47, 1203.

FRACTURE OF CONCRETE CYLINDERS SUBJECTED TO TORSION

G. Lilliu and J.G.M. van Mier

Microlab, Faculty of Civil Engineering and Geosciences,
Delft University of Technology
P.O. Box 5048, 2600 GA Delft, The Netherlands

ABSTRACT

In order to validate the 3D version of the 2D 'Delft' lattice model some torsion tests were conducted on concrete cylinders, both notched and un-notched. A biaxial loading machine with rotational and vertical loading axes was used. Tests were conducted under different axial restraints. It was observed that a perturbation of the stress state induced by the torque may affect significantly the crack pattern. Under axial compressive stress, after a spiralling crack, an axial crack was detected in un-notched specimens. In notched cylinders, the failure surface is conical if an axial load is present, while it appears flat and localized within the notch height in case no axial load is applied.

KEYWORDS

Concrete, 3D fracture, torsion, multiaxial stress.

INTRODUCTION

At the beginning of the 1990's a 2D lattice model was developed in Delft [1]. In the past ten years this model has been used for simulating experiments on concrete specimens subjected to plane stress. Despite the realistic crack patterns, the response of the model in terms of load-displacement diagrams has always been far too brittle when compared with the experimental results. A possible cause is that fracture processes are 3D phenomena. In fact, the presence of randomly distributed inclusions in the material (aggregates) produces curvatures of the crack surface in all directions. As a consequence, the dissipated energy increases. For this reason, a 3D version of the lattice model was developed [2] and torsion tests were designed to validate the numerical simulations.

Several attempts have been made in the past to design a set-up for conducting torsion experiments on cylinders [3,4]. The main reason for conducting torsion tests was that they could likely give insight in the mode III fracture energy, G_f^{III}. The same tests, conducted on notched cylinders, allow measurements of mode II fracture energy, G_f^{II}. In notched cylinders the shear stresses induced by the applied torque should produce a planar crack and, as a result, G_f^{III} and G_f^{II} should coincide. However, it seems that the condition of pure shear stress cannot be achieved in practice. There is experimental evidence that shear fracture tests are very sensitive to axial restraints, such as the axial compressive force arising from presence of friction at the supports. In the torsion tests it has been observed that the failure surface can change drastically from planar to conical [5].

by the axial restraint makes torsion tests particularly suitable for validation of the 3D lattice model and other numerical models in general. In this paper an overview is given of the results of torsion tests on concrete. They form the basis for validation of the 3D lattice model.

EXPERIMENTAL DETAILS

Tests were conducted on concrete cylinders with diameter D=34 mm and height H=68 mm. Both un-notched and notched cylinders were used. The notch, at half height of the cylinder, has a depth d_0=8 mm.

The specimens were drilled from concrete blocks, casted in plywood moulds. The aggregates used for the mixture have maximum size d_a=2 mm. Portland CEM I 32.5R cement was used, with water/cement ratio 0.4. During pouring of the mixture and for other 30 seconds after complete filling, the moulds were vibrated on a small vibrating table. Next, they were covered with plastic sheets. After two days, the concrete blocks were demoulded and placed under water. The cylinders, drilled from the concrete blocks after 28 days, were kept in a climate box, at 20^0 temperature and 90% relative humidity, till the moment of testing.

The tests were conducted with a servo-hydraulic INSTRON 8874. This machine has rotational and vertical loading axes, which can be coupled or de-coupled. The maximum loads which can be reached are 100 Nm and 10 kN, respectively. The feed-back signal during the tests is the rotation, measured with a rotational potentiometer connected to a wire attached to the upper loading platen, as shown in Figure 1.

Different tests with different axial restraint were conducted. The cases considered are: zero axial force, zero axial displacement and constant axial compressive force, corresponding to a nominal stress of -4 MPa. An hour before testing the specimen was glued to the loading platens. After hardening of the glue, the axial load was applied first, whereafter the rotational load was applied at the constant speed of 0.002 deg/sec. During the tests the axial displacement (stroke), the axial load, the rotation and the torque were recorded.

Figure 1: Set-up for measurements of the rotational angle

EXPERIMENTAL RESULTS

For each loading condition, three tests were conducted. The average of the peak torque and of the axial load, with the corresponding standard deviations, are reported in Table 1. There, the tests are named after the applied loading condition: d2**f**, d2**d** and d2**c** refer to tests on cylinders without notch under zero axial **f**orce, zero axial **d**isplacement and constant axial **c**ompression, respectively. In the same way, d2nf, d2nd and d2nc refer to tests on notched cylinders. In Figure 2 and Figure 3, some of the obtained experimental results are reported, together with the crack patterns. The torque versus rotation curves are represented with a continuous line, while the stroke (LVDT in the hydraulic actuator) or the axial load (depending if the experiment was conducted under constant load or fixed displacement) are represented with a dashed line. In the insets in the diagrams, the crack patterns are those photographed after the end of the test, when the upper loading platen was driven far from the bottom platen. The other crack patterns shown in these figures were photographed from different orientations

TABLE 1
EXPERIMENTAL RESULTS

	d2f	d2d	d2c	d2nf	d2nd	d2nc
Avr. Torque [Nm]	66.8	70.0(3.3)	93.6(3.3)	24.4(0.8)	51.7(1.7)	49.0(1.0)
Max. Load [kN]	0	-3.5(0.9)	-3.6	0	-4.7(0.2)	-1.1

Average of three test results and standard deviations (between parenthesis). In d2f the average is computed on two test results.

Un-notched cylinders

Independently from the axial restraint, the crack which can be detected as first with the naked eye is that with label 1 in the subfigures of Figure 2. This crack spirals around the specimen. It is not clear if it starts along the body of the specimen or at one of the ends, since it could be detected only after it covered the whole length of the cylinder. According to the solution of the linear elastic problem, the twisting moment is constant and the crack initiation should be just a consequence of stress concentrations due to the internal structure of the material. However, the specimen is clamped to the loading platens and cannot contract freely. As a consequence, a biaxial tensile stress state might arise at the ends of the specimen causing crack initiation. Other cracks, indicated with the label 2, depart from the spiralling crack as ”wings”. The spiralling crack can be either continuous or consists of more overlapping branches, like shown in Figure 2-a_1. In other cases, more than one of such cracks can be detected (see Figure 2-b_1, b_3 and b_4).

When no axial load is applied, the spiralling crack travels towards the end of the specimen (Figure 2-a_4) and turns, forming a loop (Figure 2-a_3). In case of axial restraint, vertical cracks develop, producing spalling of concrete, as shown in Figure 2-c_1. The cases of zero axial displacement (Figure 2, right top diagram) and constant axial compressive load are similar. In fact, when the specimen cannot elongate freely, a compressive force arises. Thus, the vertical cracks seem a consequence of the axial compressive stresses, although these are of very limited magnitude (4 MPa).

The torque-rotation diagrams have a peak and a softening branch. The tests stop when the external rotation has reached the maximum value, namely 10 deg. When there is no axial load the softening branch is extremely smooth and presents a long tail. The shape of the diagrams is somehow more complex when there is an axial restraint. In case of zero axial displacement, the torque-rotation diagram starts to descend gradually when the compressive force has reached the maximum value. Then, it shows changes of curvature, with corresponding changes of slope in the load-rotation curve. In case of compressive load, as in case of zero axial load, the diagram drops after the peak and the post-peak region is characterized by several changes of curvature, corresponding to a small elongation of the specimen. Afterwards, the cylinder begins to contract and the torque increases with the rotation. The presence of a constant compressive load seems to be a very effective confinement and, thus, strengthens the material. In fact, the peak torque is much higher than in the case of zero axial displacement, where the compression varies during the test.

Notched cylinders

If no axial restraint is applied, the notch causes the localization of the fracture within its height. During the test, it was possible to observe inclined, parallel cracks on the surface of the cylinder’s core. Coalescence of such cracks produced the final failure, as shown in the inset of the torque-rotation diagram (Figure 3).

When an axial restraint is applied cracking also starts at the notch. However, cracks are not localized within the height of the notch, but develop along half or even the complete specimen length. These cracks are similar to the spiralling cracks observed in the un-notched cylinders and seem to start right at the notch, where they show a wider opening. In the tests conducted under constant axial load only one half of the cylinder, namely the top half, was cracked (see Figure 3-b_1, b_2, b_3 and b_4). Two of the tests conducted under zero axial displacement

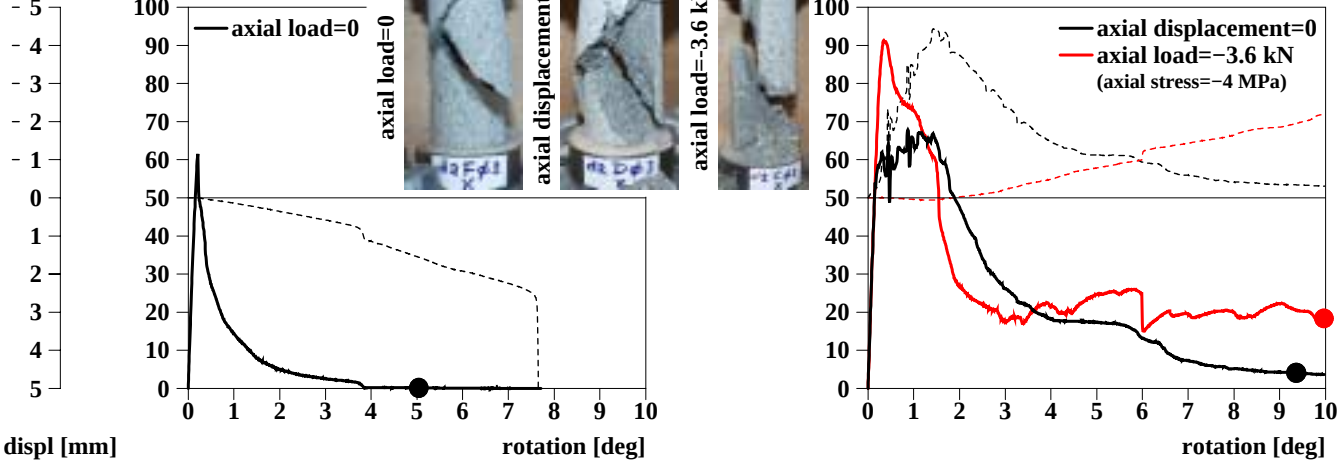

Figure 2: Experimental results obtained with un-notched specimens under zero axial force (a), zero axial displacement (b) and constant compressive load (c)

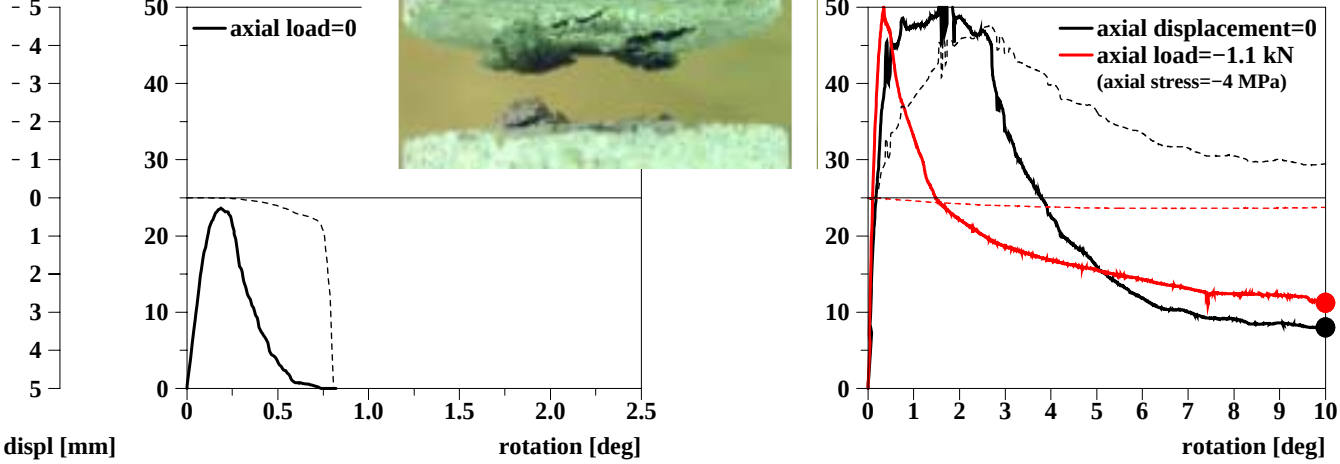

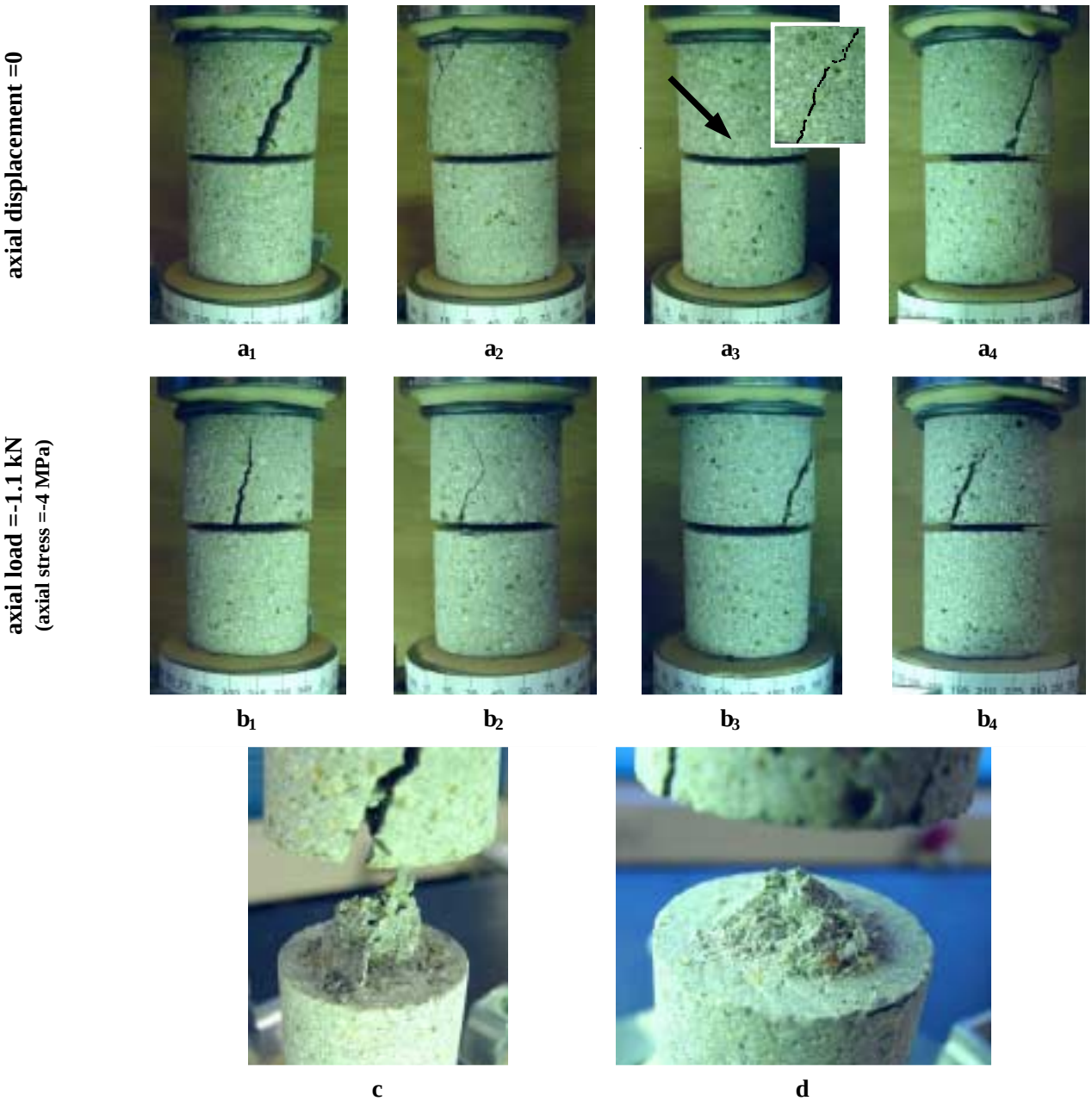

Figure 3: Experimental results obtained with notched specimens under zero axial displacement (a,c) and constant compressive load (b,d)

Figure 3-a_1, a_2, a_3 and a_4). In all the cases considered, a final conical failure surface as reported earlier by Bažant et al. [5] was observed. The cone appeared flatter in the tests conducted under constant compressive force (see Figure 3-d) than in tests under zero axial displacement (see Figure 3-c).

Similar to the tests on un-notched cylinders, in the notched cylinder tests under zero axial displacement a compressive axial force developed. The ascending and descending branch in the load-rotation diagram correspond to an extended zone of nonlinearity and to the softening branch, respectively, in the torque-rotation diagram. The diagrams do not present any change in curvature in the softening branch, as it was observed in the tests on un-notched cylinders. The same happens when the tests are conducted applying a constant compressive force: the torque after the peak decreases gradually without showing changes in curvature. In contrast to the un-notched cylinders, the peak load does not increase when the compressive force is constant during the complete test.

CONCLUSIONS

Torsion tests have been conducted on un-notched and notched concrete cylinders with diameter D=34 mm and height H=68 mm. Different axial restraints were used, namely: zero axial load, zero axial displacement and constant compressive load. The last two loading conditions are somehow similar, since the constrained axial displacement produces as effect a variable axial compression. The crack pattern varies with the adopted axial restraint. In un-notched cylinders the first to develop is a spiralling crack, from which other ”wing” cracks may depart. Vertical cracks appear if a compressive axial stress is applied. Localized failure within the notch height occurs in notched cylinders or a conical crack surface develops depending on the presence of an axial compressive stress. Like the crack pattern, the torque-rotation diagrams differ with axial constraint. In the tests on un-notched cylinders the presence of an axial compressive load produces changes in curvature of the softening branch and, even, a new final increase of torque. No change of curvature was observed in the same kind of tests conducted on notched cylinders. However, in the case of constrained axial displacement the diagram presents an extended zone surrounding the peak where the torque is practically constant. In all cases considered the sensitivity of torsion tests to the presence of an axial stress is confirmed, eventhough only a small amount of constraint is applied. Because of the chosen geometry and the complexity of the final crack pattern, it is difficult at this stage to give an interpretation of the possible fracture mechanism during loading. Currently it is tried to detect propagation of cracks at different loading stages by means of an impregnation technique.

AKNOWLEDGEMENTS

This research has been made possible through a grant from the Priority Programme Materials Research (PPM) and the Dutch Technology Foundation (STW), which is gratefully aknowledged. The authors are indebted to Mr. G. Timmers for his expert help in designing and performing the experiments.

REFERENCES

1. Schlangen, E. and van Mier, J.G.M. (1992) *Cement and Concrete Composites* 14, pp. 105-118.
2. Lilliu, G. and van Mier J.G.M (2000). In: *Proceedings Materials Week*, Münich, Germany.
3. Yacoub-Tokatly, Z., Barr, B. and Norris, P. (1989). In: *Fracture of Concrete and Rock: Recent Developments*, pp. 596-604, Shah, S.P., Swartz, S.E. and Barr, B. (Eds). Elsevier, New York.
4. Xu Daoyuan and Reinhardt, H.W. (1989). In: *Fracture of Concrete and Rock: Recent Developments*, pp. 39-50, Shah, S.P., Swartz, S.E. and Barr, B. (Eds). Elsevier, New York.
5. Bažant, Z.P., Prat, P.C. and Tabbara, M.R. (1990) *ACI Materials Journal* 87, pp. 12-19.

Oral Reference: ICF0677

Fracture of Ferritic Steels; the effects of the Ductile Brittle Transition on Carbides within the Plastic Zone

M. D. Coates, S. G. Roberts

Department of Materials Science, University of Oxford.

Abstract

Ferritic steels undergo a ductile to brittle transition (DBT) with decreasing temperature. The transition temperature may typically be 50°C to 100°C wide, centred around -50°C to 0°C. As temperature falls within this range, the fracture toughness drops from more than 100MPam$^{1/2}$ to less than 40 MPam$^{1/2}$ and the fracture mode changes from rupture to cleavage. The controlling process leading to cleavage is the propagation of a crack from a fractured brittle carbide particle. This work investigates the effects of cracked carbides in the plastic zone ahead of a loaded crack. A heat treatment of 40 hours at 650°C has been applied to A533B steel to produce a homogenous spheroidised microstructure. Carbides have been investigated using TEM. The work has focused on producing experimental data of cleavage fracture around the lower shelf of the DBT. This paper shows the variation of yield stress with temperature and using the 'master curve' approach, the variation in fracture toughness with temperature. It will then be shown that a modelling approach to predicting cleavage behaviour can be coupled with microstructural parameters, and not simply solved empirically.

Keywords

Ductile, Brittle, Transition, Carbides, Fracture, Plastic Zone, Cleavage.

Introduction

Hirsch, Roberts et al at Oxford, over the past ten years, have been very successful in predicting the fracture behaviour of single crystals such as pure silicon, germanium, alumina and molybdenum [1,2,3]. Most recently the models have been extended to materials where the dislocation velocity law contains a significant friction stress, below which the dislocations will not move (i.e. the kind of behaviour expected in steels). It has then been found that the predicted plastic zone sizes and configurations, the crack opening displacement and the crack tip stress fields, follow very closely the 'classic' earlier models based on dislocations [4,5].
This paper presents experimental work aimed at providing experimental data on a material with a model ferrite/carbide microstructure, to correlate modelling of this type.

Experimental Methods

The steel chosen for the investigation was an A533-B pressure vessel steel produced by Ross and Cathedral, Sheffield. It was produced from electrolytic vacuum degassed iron with no single impurity greater then 100ppm. All alloying elements were pure. The composition is given in table 1.

TABLE 1.
Composition of A533-B pressure vessel steel in wt.%

Carbon	Manganese	Molybdenum	Nickel	Silicon	Phosphorus	Sulphur	Copper
0.24	1.37	0.52	0.5	0.23	0.003	0.005	<0.01

The steel was heat-treated 40 hours at 650°C with the aim of producing a microstructure of spherical brittle carbides in a relatively clean ferrite matrix. Fracture specimen dimensions are shown in figure 1.

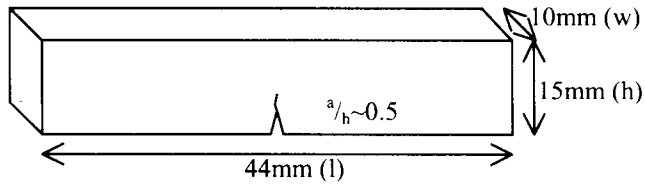

Figure 1. Specimen dimensions.

The total crack length (a) is between 5mm and 6mm leading to an $^{a}/_{h}$ ratio of between 0.46 and 0.53. The crack was introduced into the specimen by fatigue in three point bending. Initial fatiguing was at 10Hz for 50,000 cycles with a surface stress of around 400MPa. Once the crack was initiated the surface stress was reduced to 350MPa for a further 50,000 cycles before being reduced to 250MPa until the $^{a}/_{h}$ ratio reached the desired value. All fatiguing was carried out at room temperature. Samples were then fractured in four point bend under displacement control at 0.25mm/min, over a range of temperatures from -192°C to +120°C. The cold tests used liquid nitrogen; temperatures above ambient were achieved using nitrogen passed through heating coils in a furnace and the use of a high-powered halogen heating lamp. Temperature control was enabled through type K thermocouples attached to the specimen and was stable within $^{+}/_{-}$ 2°C.

At low temperatures fracture loads were measured at the point of catastrophic failure (coincident with initiation). At temperatures above -30°C, no such unstable fracture occurred and the fracture loads were now measured at initiation. The point of initiation could be identified from inflections in the load-displacement curves. The mode of initiation at each temperature was determined by completely fracturing the specimens in liquid nitrogen and examining the fracture surfaces both optically and in the scanning electron microscope.

Uniaxial tensile properties were determined over a similar temperature range by testing modified Hounsfield specimens, figure 2, machined from the fracture specimens. The tests were displacement controlled with an operating actuator speed of 0.5mm/min (strain rate of $6.41 \times 10^{-4} s^{-1}$). Yield stress was measured at the onset of plastic deformation determined by examining the force-displacement data.

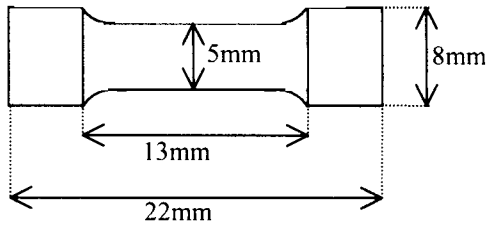

Figure 2. Dimensions of the tensile test specimen.
Radius of curvature of the inner-outer gauge is 1mm

Two sets of fracture tests were completed. Set A was used to gain an overview of the toughness temperature curve. The samples were fatigued at a constant load until the desired crack length was obtained. The crack length was also shorter so that $^{a}/_{h}$~ 0.25-0.35. The samples were also quenched from 650°C to room temperature. In set B the fatigue process was modified to that set out above and quenching was replaced by a slow cool over 12 hours. These specimens were used to study variability of behaviour at two temperatures.

Experimental Results

Many of the test specimens exhibited significant plastic flow before fracture, so fracture data were analysed in terms of the J-integral. ASTM E1921-98 [6] was used for validation J_C analysis. Figure 3 shows fracture toughness, K_{JC}, versus temperature for all specimens tested.

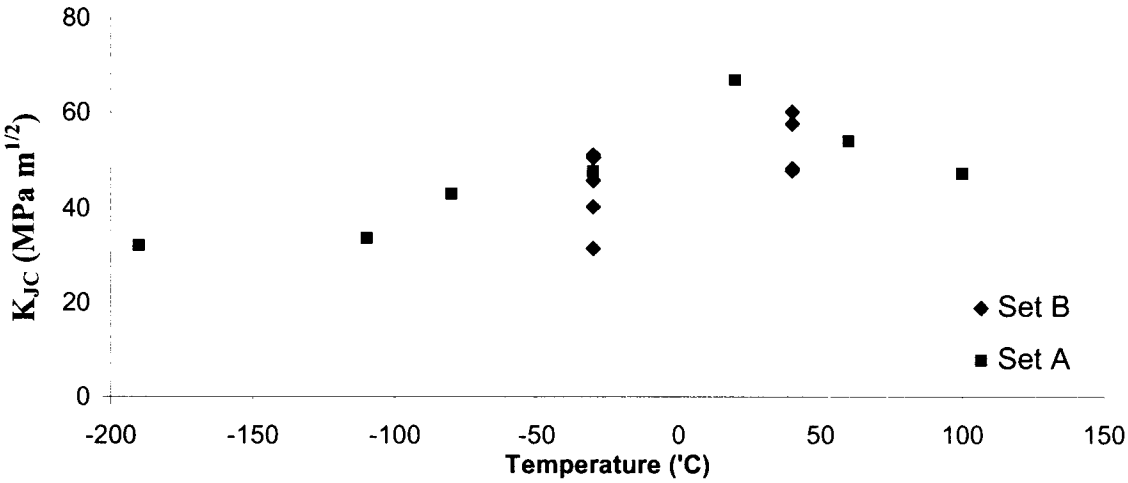

Figure 3. K_{JC} as a function of temperature.

The test results were then analysed using the 'master curve' approach of Wallin et al [7]. In the master curve concept, a universal form of temperature dependence for cleavage fracture toughness is assumed (equation 6), if data are scaled to a material-dependent reference temperature T_0.

$$K_0 = 31 + 77 \cdot \exp\{0.019 \cdot (T - T_0)\} \tag{6}$$

$$\sum_{i=1}^{n} \frac{\exp\{0.019 \cdot [T_i - T_0]\}}{11 + 77 \cdot \exp\{0.019 \cdot [T_i - T_0]\}} - \sum_{i=1}^{n} \frac{(K_{1C_i} - 20)^4 \cdot \exp\{0.019 \cdot [T_i - T_0]\}}{(11 + 77 \cdot \exp\{0.019 \cdot [T_i - T_0]\})^5} = 0 \tag{7}$$

Two methods of estimating the master curve transition temperature T_0 were used. The first method used both set A and set B data. T_0 was calculated from the size adjusted K_{JC} data using a multi-temperature randomly censored maximum likelihood expression given in equation 7 (figure 4). The

second method used data determined to be on the lower shelf (by examining the Force-Displacement curves and where in doubt, the examination of fracture surfaces) and followed the same calculation. Results are shown in figure 5. Results that did not meet the ASTM validity requirements were not included in either master curve calculation.

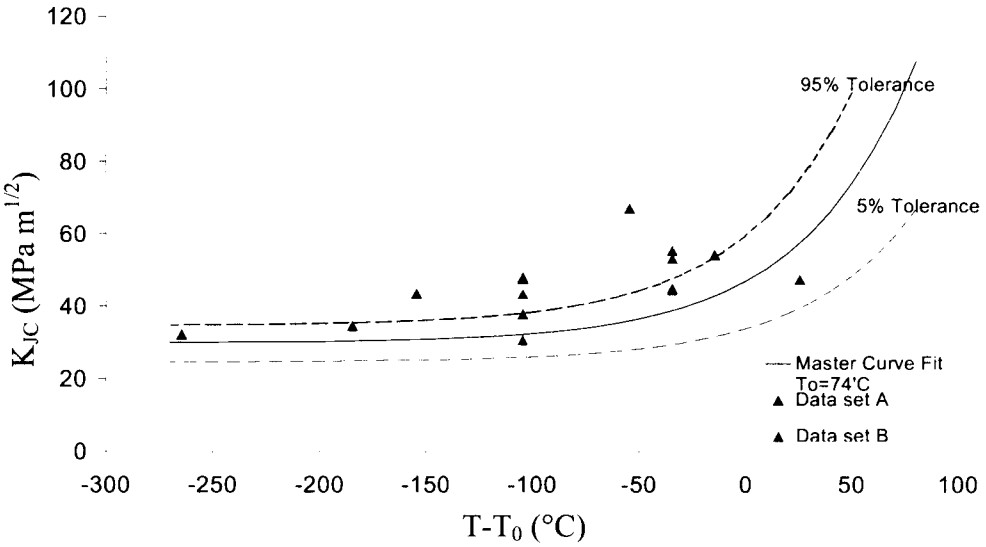

Figure 4. The master curve T_0=74°C using equation 7, with all data present.

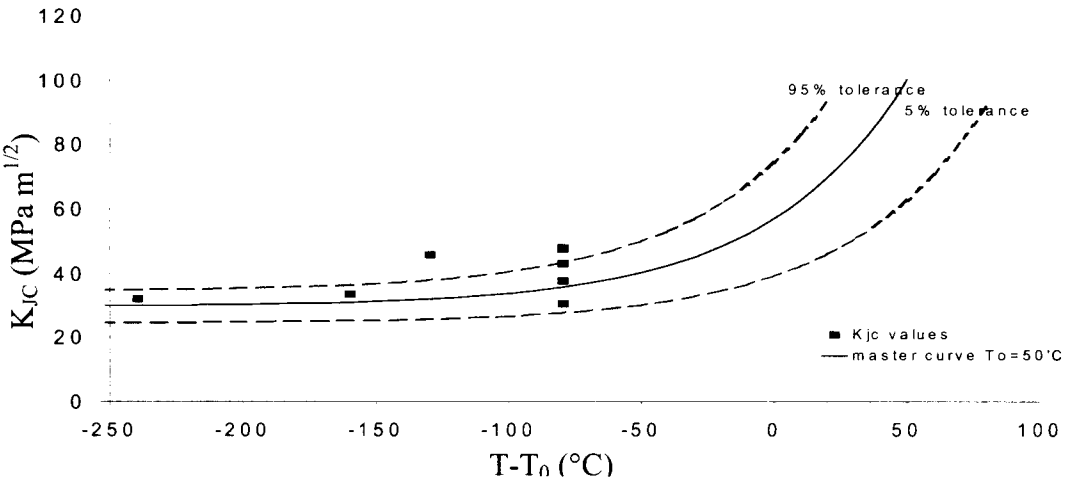

Figure 5. The master curve calculated using cleavage data.

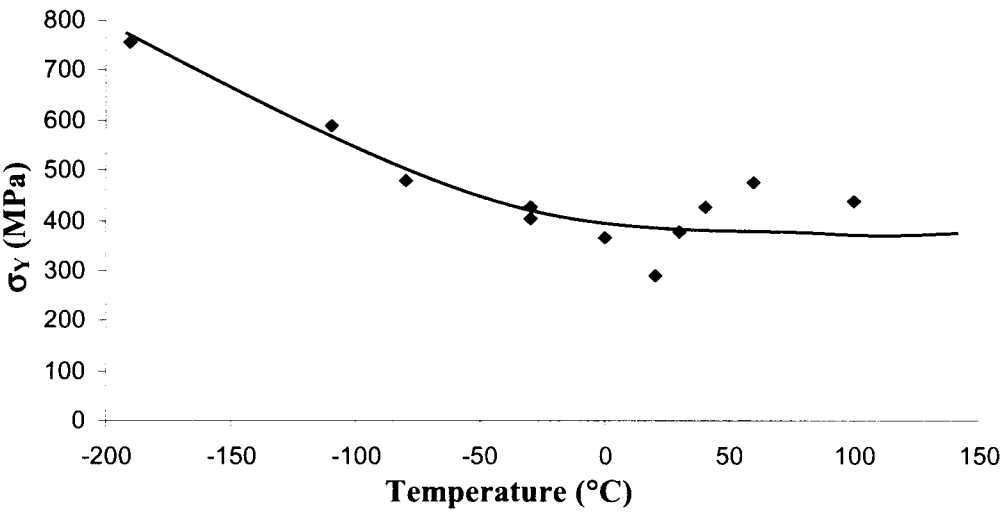

Figure 6. Variation of yield stress with temperature.

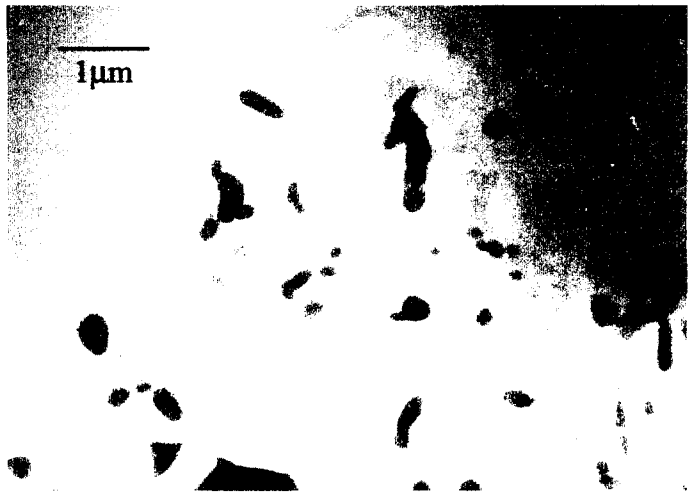

Figure 7. A typical microstructure for a heat-treatment of 40 hours at 650°C.

Image analysis of TEM micrographs was used to determine carbide sizes and spacing. The size was taken as an area measurement and then converted to an equivalent radius. The spacing was taken as the nearest neighbour distance. Carbide size was 0.8μm $^{+}/_{-}$ 0.2μm, and inter particle spacing 0.5μm $^{+}/_{-}$ 0.15μm.

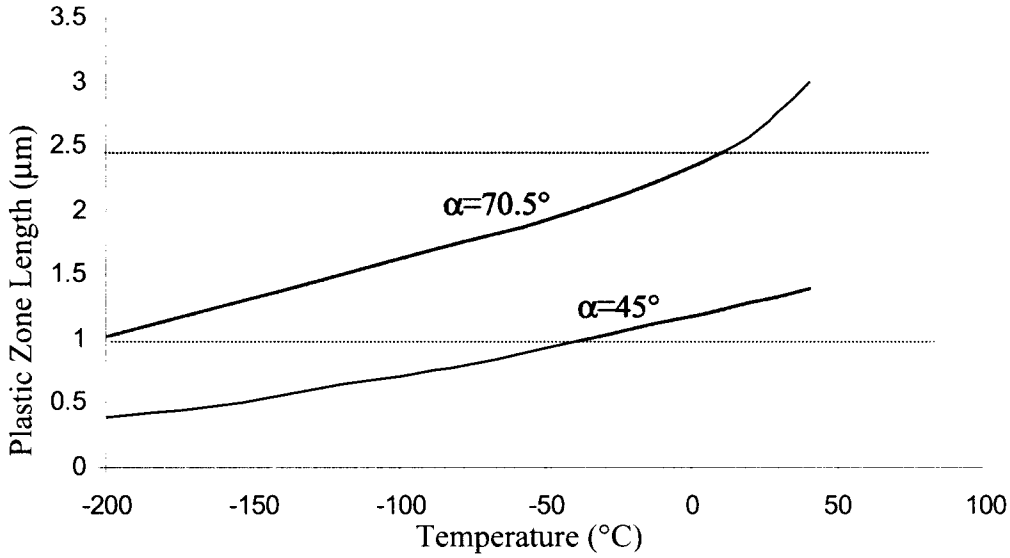

Figure 7. Relationship between the modelled array lengths. α is the slip plane angle and the shading shows the range the transition temperature falls.

These data can be used to link the fracture data presented here and results from dislocation-level simulations of crack tip plastic zones. Figure 7 shows the produced length of crack tip plastic zone size modelled with cracked particles of 0.8μm diameter, as a function of temperature. The modelling simulates the plastic zone as a single slip plane on which dislocations glide away from the crack under the influence of a local stress (the slip plane is at an angle α to the crack plane). Dislocations are assumed to halt at a temperature-dependent friction stress (the yield stress data in figure 6 was used here). Dislocation array/plastic zone length shown in figure 7 is thus achieved just before fracture would propagate from the cracked carbide into the matrix, triggering cleavage of the specimen.

Conclusion

The microstructure of a steel has been modified to produce a simplified microstructure of spherical carbides in a ferrite matrix, better suited to modelling crack tip stress fields around carbides. The changes in microstructure have led to a horizontal shift and flattening of the apparent DBT, with low upper-shelf values for K_{IC}. The J-integral method and the master curve method have been used to identify the transition temperature, T_0. T_0 varies depending on the mode of fracture but this is likely to arise out of a certain invalidity for K_{JC} values above room temperature.

Modelling of plastic zones and crack tips carried out to date correlates well with the experimental data in that, at the transition temperature, the predicted plastic zone length for carbides of the size seen here is roughly equal to its inter-particle spacing. Further work is in progress to investigate this more completely.

Acknowledgements

This work was supported by the Engineering and Physical Sciences Research Council, UK, under grant number M05188, in collaboration with AEA Technology and the Health and Safety Executive.

References

1. Samuels, J. and Roberts, S.G. (1989) The brittle-ductile transition in silicon. I. experiments, *Proc. R. Soc. Lond.* **A 421**, 1-23.
2. Serbena, F.C. and Roberts, S.G. (1994) The brittle ductile transition in germanium, *Acta Metall. Mater.* **42**, 2505-2510
3. Roberts, S.G., Hirsch, P.B., Booth, A.S., Ellis, M. and Serbena, F.C. (1993) Dislocations, cracks and brittleness in single crystals, *Physica Scripta,* **T49**, 420-426.
4. Roberts, S.G. in *Computer Simulation in Materials Science-nano/meso/macroscopic Space and Time Scales,* edited by H.O. Kirchner *et al.* (NATO ASI Series, Series E (Applied Sciences), **308**, Kluwer, Dordrecht, 1996), 409-433.
5. Noronha, S.J., Roberts, S.G. and Wilkinson, A.J. (1999) A multiple slip plane model for crack-tip plasticity. Presented at the MRS Fall 1999 meeting, Boston. Unpublished work.
6. ASTM Standard E1921-98 "Standard test method for determination of reference temperature, T_0, for ferritic steels in the transition range" pub ASTM vol 03.01 1998.
7. Wallin, K. (1998) Master curve analysis of ductile to brittle transition region fracture toughness round robin data. The "EURO" fracture toughness curve. VTT Pulications. Finland.

FRACTURE OF NANOSTRUCTURED FCC METALS

F. Ebrahimi, Z. Ahmed K. L. Morgan and A. J. Liscano

Materials Science and Engineering, University of Florida
P.O. Box 116400, Gainesville, FL 32611

ABSTRACT

Nanocrystalline nickel and nanolayered structures of nickel and copper were produced by electrodeposition techniques. The analysis of the fracture surfaces of tensile specimens from these materials revealed that the low tensile elongation of nanostructured metallic materials is associated with a strong tendency to strain localization and the presence of pores in the microstructure.

KEYWORDS

nanostructures, nanocrystalline, multilayers, electrodeposition, nickel, copper, fracture, ductility

INTRODUCTION

The term “nanostructure” has been used to describe: (1) materials with at least one of their physical dimensions in the nano-range (e.g., particles or wires with nano-size diameters) and (ii) bulk materials (physical dimensions much larger than nano-size) whose microstructural constituents are in the nano-range (e.g., nanocrystalline and nanolayered materials). The nano-size is conventionally referred to lengths less than 100nm [1]. Due to the confinement of dislocations, bulk metallic nanostructures have very high yield strengths. However, the tensile testing results indicate that these materials exhibit low total elongations [2]. Processing defects have been suggested to be the cause of the low ductility of nanocrystalline FCC (face-centered cubic) metals produced via the gas condensation method [3]. We have been successful in fabricating almost defect free nanocrystalline and nanolayered metallic structures from FCC metals using electrodeposition techniques [4]. This paper presents results regarding the fracture behavior of nanocrystalline nickel and nanolayered nickel/copper materials and discusses the low elongation of metallic nanostructures.

EXPERIMENTAL PROCEDURES

The details of the fabrication of the nanomaterials using electrodeposition techniques are given elsewhere [4-7]. The deposits were in the form of discs with a 35mm diameter and were grown on copper substrates, which were subsequently dissolved. The deposits had a thickness between 25 to 40μm. Free-standing tensile specimens with a gage length of 10mm were prepared by hand grinding and were tested at a strain rate of $2x10^{-4}$ s^{-1}. At least two tensile specimens were tested per deposit. The fracture surfaces were studied using scanning electron microscopy (SEM).

RESULTS AND DISCUSSION

Nanocrystalline Nickel

Changing the electrodeposition parameters can vary the grain size of nickel deposits. Table 1 presents the grain size for nickel deposits fabricated at 18 and 25 mA/cm^2 using direct current (DC) and at 25mA/cm^2 by pulse plating. The grain size was measured using x-ray diffraction and applying the Warren-Averbach analysis method. Note that the grain size may vary through the thickness of the deposits. Therefore, the grain size was measured on both the substrate and the solution sides of the deposits. The tensile stress-strain curves for these deposits are presented in Figure 1. The tensile specimens from the same deposit showed similar yield strength and strain hardening rates; however, there was a noticeable scatter in the total elongation.

TABLE 1
GRAIN SIZE OF THE NANOCRYSTALLINE NICKEL SAMPLES

Deposition Condition	Grain Size (nm)	
	Substrate	Solution
25 mA/cm^2 - pulsed	10	9
25 mA/cm^2 - DC	35	17
18 mA/cm^2 -DC	111	11

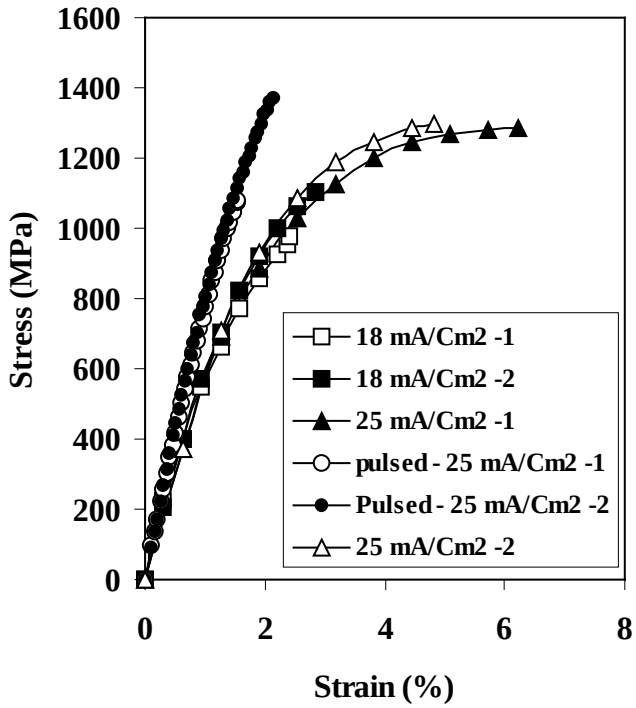

Figure 1: Tensile stress strain curves for three nanocrystalline nickel deposits.

Examples of the fracture surface of the nanocrystalline nickel samples are given in Figure 2. All samples necked before fracture, although none of them showed any post-neck elongation according to the stress-strain curves. This observation shows that the necking process was very localized in these materials. Since such a behavior is not observed in thin samples of metals with conventional grain sizes [8], the strong tendency to strain localization is indicative of a low strain-rate sensitivity of nanocrystalline nickel. Hydrogen incorporation during the deposition may also contribute to this effect . However, the grain boundary sliding mechanism, which has been suggested to operate in nanocrystalline materials at a low homologous temperature [9], is not expected to contribute significantly to the deformation of nanocrystalline nickel samples studied here. The two DC-plated deposits showed similar strength levels, but the deposit made at 18 mA/cm^2 showed a lower ductility than the sample deposited at 25 mA/cm^2. The fractographs presented in Figure 2 show that fracture in the former deposit occurred by microvoid coalescence mechanism while the latter deposit broke by the so-called

knife-edge mechanism, typical of pure defect free metals. During the electrodeposition of nickel hydrogen evolves at the cathode surface and bubbles develop on the deposition front which depending on the cathode surface condition, electrolyte composition and the local hydrodynamic state may get trapped in the deposit. These bubbles act as initiation sites for the microvoids observed on the fracture surface.

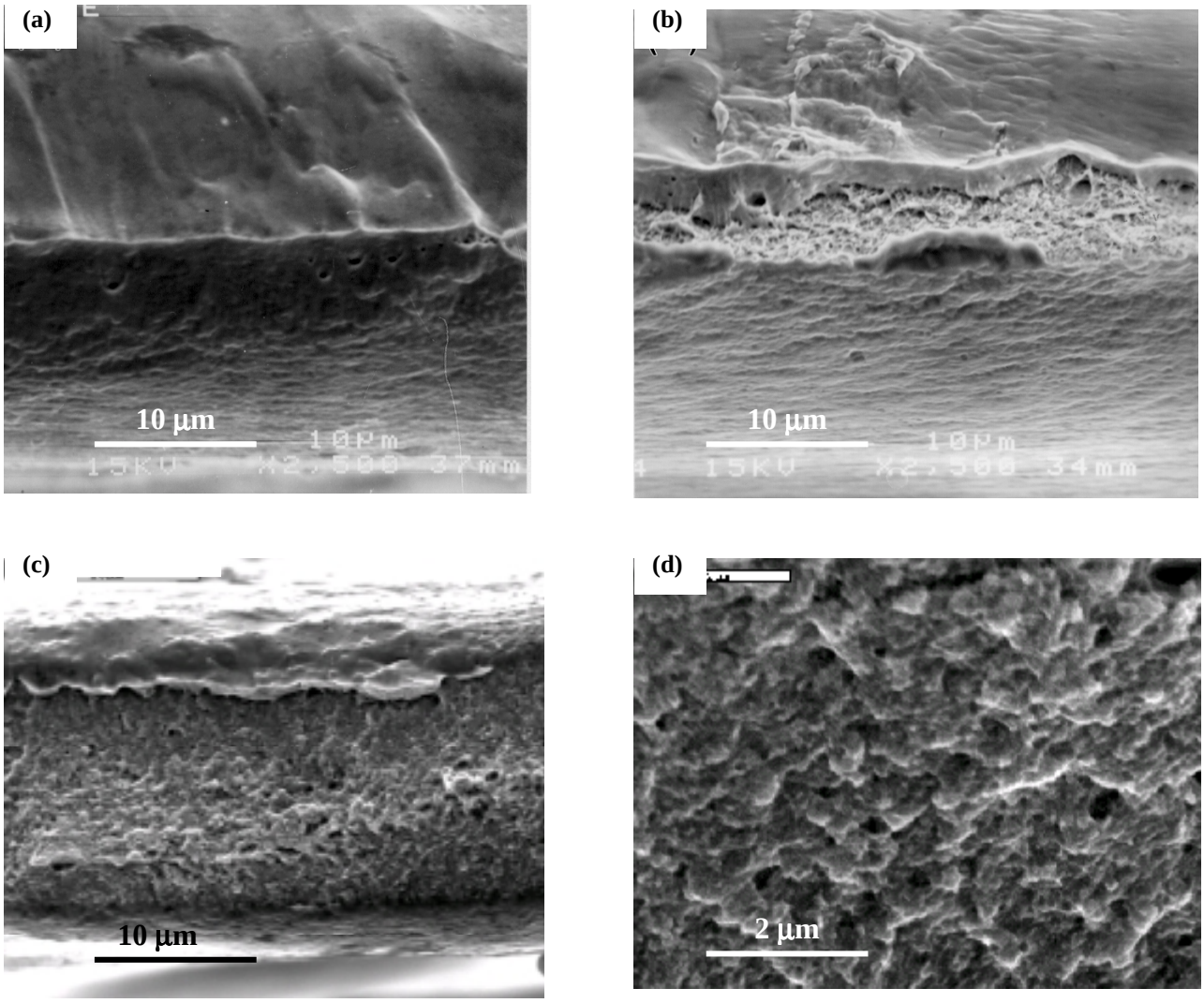

Figure 2: Fracture surfaces of tensile samples from deposits produced at (a) 25 mA/cm^2, DC-plated, (b) 18 mA/cm^2 , DC-plated and (c) 25 mA/cm^2 , pulse plated. A high magnification picture of the fracture surface shown in (c) is presented in (d).

Figure 3 shows the strain-hardening rate as a function of strain for the two DC deposited samples. Note that the Considère necking criterion ($d\sigma/d\varepsilon$ (strain hardening rate)= σ_{UTS} (ultimate tensile strength)) for the high ductility deposit (25 mA/cm^2) is approximately satisfied, however, the necking occurred prematurely in the low ductility deposit (18 mA/cm^2). It is suggested that the pores formed due to the entrapment of the hydrogen bubbles promoted plastic instability.

The deposit produced using the pulse-plating method showed the smallest grain size, the highest yield strength and the lowest ductility. The tensile specimens from this deposit exhibited limited necking (Figure 2c) and the fracture surface resembled the quasi-cleavage fracture behavior usually observed in materials such as high carbon steels (Figure 2d).

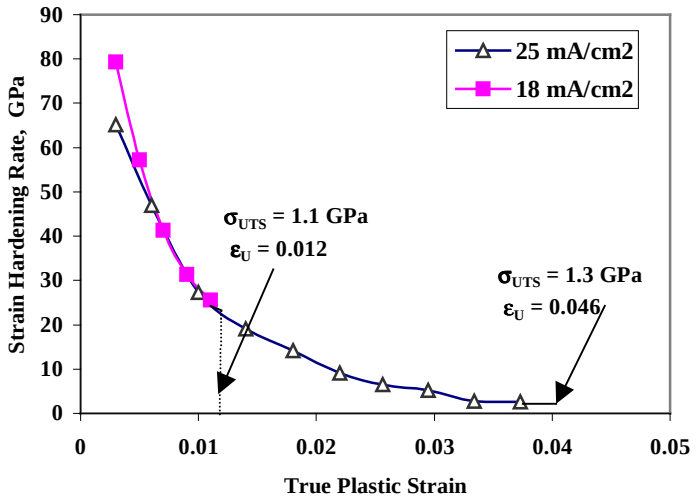

Figure 3: Strain-hardening rate as a function of true plastic strain showing that necking occurred at $d\sigma/d\varepsilon >> \sigma_{UTS}$ in the sample fabricated at 18 mA/cm^2.

Nanolayered Nickel-Copper Structures

The nanolayered Ni/Cu materials showed a variety of fracture behaviors depending on the microstructure and the level of defects of the deposits. Figure 4 shows the stress-strain curve and the fracture surface of a defect-free multilayered Ni/Cu sample with a bi-layer thickness of 7nm. This sample exhibited a low total elongation but it was very ductile as indicated by the knife-edge fracture behavior. It should be noted that at the bi-layer thickness of 7nm, the interface between nickel and copper is most probably coherent and dislocations are not confined by the presence of the interfaces. The low total elongation of this sample indicates that shear localization occurs easily in these metallic nanostructures.

In deposits that hydrogen bubble entrapment was a problem, fracture of the Ni/Cu multilayered structures occurred by microvoid coalescence mechanism. The observation of the microvoid coalescence mechanism was dependent on the stress-state. The plane-stress condition near the edges of the samples decreased the possibility of microvoid growth and resulted in the knife-edge fracture behavior.

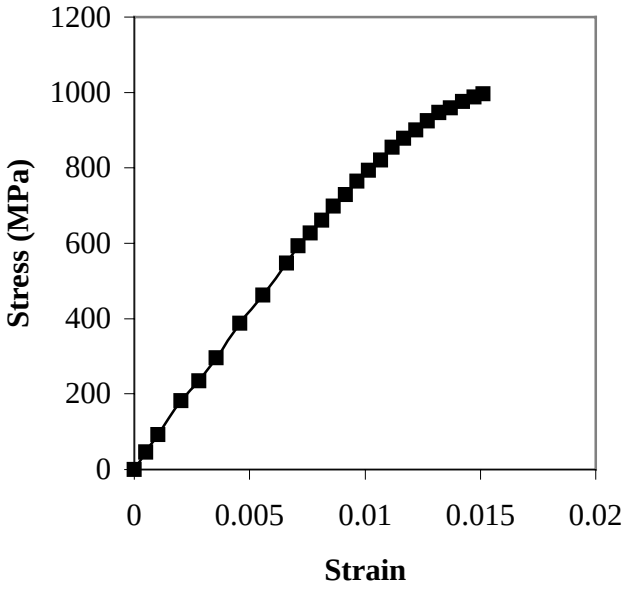

(a)

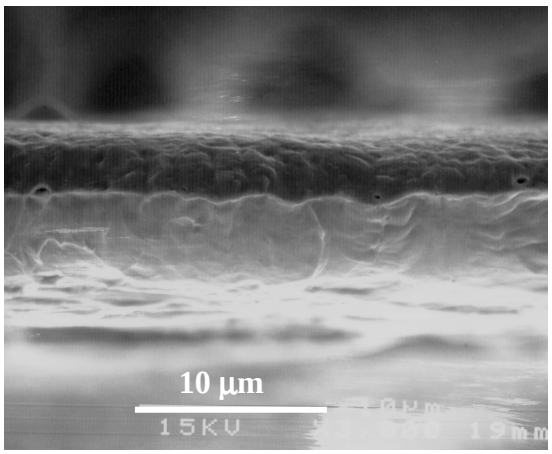

(b)

Figure 4: (a) Tensile stress-strain curve and (b) SEM fractograph of a multilayered Ni/Cu sample showing a low total elongation associated with a ductile fracture behavior.

The fractographs from a relatively brittle multilayered Ni/Cu sample with a bi-layer thickness of 20nm is presented in Figure 5. This sample broke in the linear portion of the stress-strain curve. Several fracture paths can be noticed in these fractographs. The gaps due to the incomplete growth of columns have led to the intercolumnar fracture path. The delamination of the layers is observable near the substrate side of this deposit. The high magnification picture presented in Figures 5b shows the quasi-cleavage facets similar to those observed in the nanocrystalline nickel deposit with the lowest ductility (see Figure 2d).

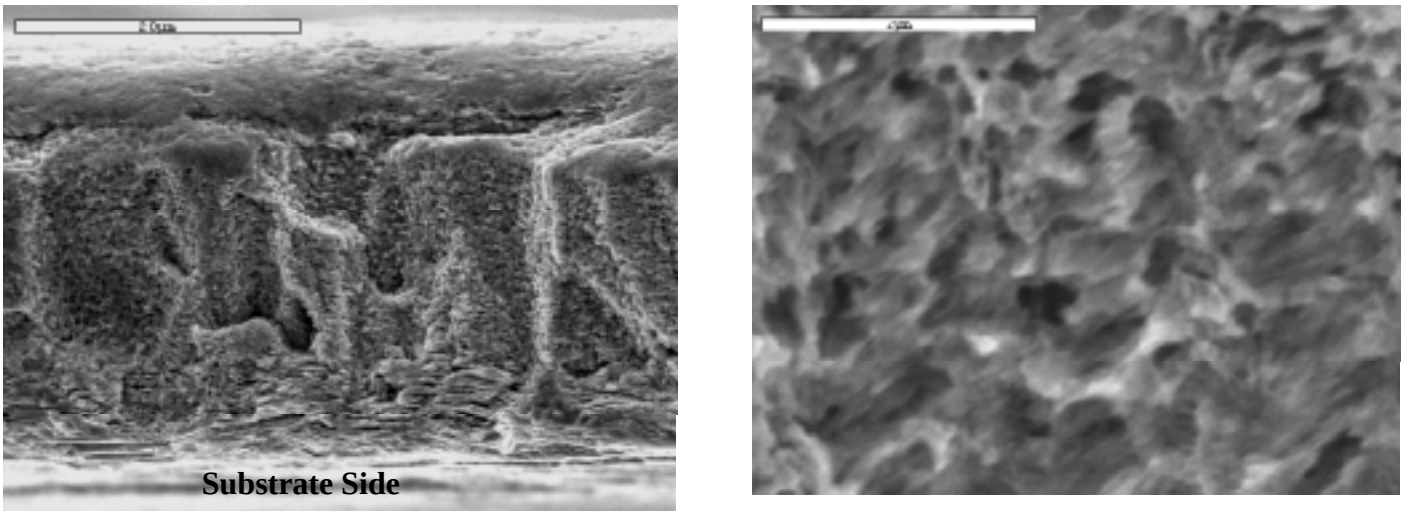

(a) **(b)**

Figure 5: (a) SEM micrograph showing the intercolumnar and the interlayer fracture behaviors in a Ni/Cu nanolayered structure. (b) A high magnification fractograph showing large voids and quasi-cleavage facets.

Brittle Fracture in FCC Metals

Usually, FCC metals do not fracture in a brittle manner. There are two possible mechanisms that can explain the development of quasi-cleavage facets in the FCC metallic nanostructures studied here. One scenario is that the ligaments between the pores, which form by the entrapment of hydrogen bubbles, tear in mode III. Such a process can be envisioned to occur by the generation and motion of screw dislocations from the pore surfaces. Theoretically it has been shown that spontaneous dislocation generation from the crack tip makes the breaking of atomic bonds in FCC metals such as Ni and Cu impossible [10]. However, such models do not take into account the limitation on the size of the dislocation loops that can emerge from the crack tip because of the presence of interfaces and boundaries. Therefore, the other possibility is that due to the confinement of dislocations in metallic nanostructures, the local stresses near the processing defects such as pores can be raised high enough to break the atomic bonds in mode I. We have shown that the quasi cleavage fracture develops in the mid-section of tensile samples under the plane-strain condition and the fracture behavior changes to the microvoid coalescence mechanism under the plane stress condition that develops near the edges [11,12]. These observations suggest that the brittle fracture in FCC metallic nanostructures may occur by the cleavage mechanism, i.e. breaking atomic bonds under mode I loading.

CONCLUSIONS

Naocrystalline nickel and nanolayered nickel/copper structures were fabricated by electrodeposition techniques. Their strength, ductility and fracture behaviors were investigated by tensile testing of dog-bone samples. The results of this study show that the low total elongation of these nanostructures in the absence of any processing defects is associated with a strong tendency to strain localization. It has been suggested that hydrogen gas bubbles form on the cathode surface during deposition. These bubbles become entrapped as pores into the deposits. These pores act as initiation sites for fracture by the microvoid coalescence mechanism. In structures that dislocation generation/motion is inhibited (e.g., nanocrystals with small grain size and nanolayered

structures with incoherent boundaries), fracture in between the pores occurs by breaking atomic bonds, i.e. cleavage mechanism.

ACKNOWLEDGEMENTS

The authors gratefully acknowledge the financial support of National Science Foundation under the contract number DMR – 9980213.

REFERENCES

1. H. Gleiter, *Materials Science Forum* 189-190, 67 (1995).
2. C. C. Koch, D. G. Morris, K. Lu, and A. Inoue, *MRS Bulletin* 24, 54 (1999).
3. P. G. Sanders, C. J. Youngdahl, J. R. Weertman, *Mater. Sci. Eng.* A234-236, 77 (1997).
4. F. Ebrahimi, D. Kong,T. E. Matthews, and Q. Zhai, in Processing and Fabrication of Advanced Materials VII, TMS Publication, Warrendale, PA, 509 (1998).
5. F. Ebrahimi, G. R. Bourne, M. S. Kelly, and T. E. Matthews, *Nanostructured Materials Journal* 11(3), 343 (1999).
6. F. Ebrahimi and D. Kong, *Scripta Materialia*, 40, 609 (1999).
7. F. Ebrahimi and A. J. Liscano, *Mater. Sci. Eng.* A301, 23 (2001).
8. F. Ebrahimi, Q. Zhai and D. Kong, *Scripta matter.* 39, 315 (1998).
9. R. M. Masumura, P. M. Hazzeldine, and C. S. Pande, *Acta matter.* 46, 4527 (1998).
10. J. R. Rice and R. Thomson: *Phil. Mag.* 29, 73 (1974).
11. F. Ebrahimi, Q. Zhai, and D. Kong, *Materials Science and Engineering*, 255, 20 (1998).
12. F. Ebrahimi, Q. Zhai, D. Kong, and G. R. Bourne, in Advanced Materials for 21st Century: The 1999 Julia Weertman Symposium, Edited by Y-W. Chung et al., TMS Publication, Warrendale Pacific, 421 (1999).

FRACTURE OF PIEZOELECTRIC MATERIALS

Tong-Yi Zhang* and Minghao Zhao

Department of Mechanical Engineering, Hong Kong University of Science and Technology
Clear Water Bay, Kowloon, Hong Kong, China, * E-mail: mezhangt@ust.hk

ABSTRACT

The present work studies, theoretically and experimentally, the fracture behavior of piezoelectric ceramics. For an electrically insulating crack, the ratio of α/β plays an important role in the energy release rate, where α is the ratio of the minor semi-axis, *b,* to the major semi-axis, *a,* of the ellipse, and β is the ratio of the dielectric constant of the cavity to the effective dielectric constant of the material. There are three limiting values in the energy release rate, respectively corresponding to $\alpha/\beta \to 0$ for an electrically permeable crack, $\alpha/\beta \to$ a finite nonzero value for general cases and $\alpha/\beta \to \infty$ for an electrically impermeable crack. For an electrically conductive crack, the applied electric field parallel to the crack drives the crack to propagate. When electric yield occurs at a crack tip, the global energy release rate is the same as that derived from linear fracture mechanics, while the local energy release rate shows a linear relationship between the fracture toughness and the applied electric field. The experimental results illustrate that for PZT-841 and PZT-4 ceramics, the degree of scattering of measured data was considerably enhanced by an applied electric field. Either a positive or a negative electric field reduced the fracture toughness. The experimental results also confirmed that there exist mechanical- and electrical-fracture toughness for PZT-4 ceramics and both are material properties. The mechanically- and electrically- critical energy release rates are, respectively, 8.7(±1.1) and 223.7(±45.5) N/m.

KEYWORDS

piezoelectric medium, crack, energy release rate, fracture toughness, polarization saturation

INTRODUCTION

Along with the application of piezoelectric materials in more and more sophisticated structures, their mechanical reliability becomes increasingly important. Thus, many efforts have being made to study the fracture behavior of those materials [1-23]. One of the most interesting aspects is about the effect of electric field on the fracture behavior. Many experimental results are inconsistent or even contradicted, which makes the study of fracture of piezoelectric ceramics more challenging. The present work briefly summarizes the work done at the Hong Kong University of Science and Technology, on this topic.

TWO-DIMENSIONAL SOLUTION

Figure 1 shows schematically a crack of length 2*a* in an infinite piezoelectric medium under remotely

uniform electrical loads and in-plane and anti-plane mechanical loads. Using Stroh's formalism [1-3], the general two-dimensional solution can be written in the form

$$\begin{aligned} &\mathbf{u} = \mathbf{A}\mathbf{f} + \overline{\mathbf{A}\mathbf{f}}, \quad \boldsymbol{\psi} = \mathbf{L}\mathbf{f} + \overline{\mathbf{L}\mathbf{f}}, \quad \boldsymbol{\Sigma}_2 = \boldsymbol{\psi}_{,1}, \quad \boldsymbol{\Sigma}_1 = -\boldsymbol{\psi}_{,2}, \\ &\mathbf{u} = \begin{pmatrix} u_1 & u_2 & u_3 & \varphi \end{pmatrix}^{\mathrm{T}}, \quad \boldsymbol{\Sigma}_1 = \begin{pmatrix} \sigma_{11} & \sigma_{21} & \sigma_{31} & D_1 \end{pmatrix}^{\mathrm{T}}, \quad \boldsymbol{\Sigma}_2 = \begin{pmatrix} \sigma_{12} & \sigma_{22} & \sigma_{32} & D_2 \end{pmatrix}^{\mathrm{T}}, \end{aligned} \tag{1}$$

where $u_i, \varphi, \sigma_{ij}$ and D_i are the displacements, electric potential, stresses and electric displacements, respectively. The two 4×4 matrixes, **A** and **L,** are related to the material properties, with A_{ij} and L_{ij} denoting their elements, repectively. The analytical function vector, $\mathbf{f}(z) = \begin{pmatrix} f_1(z_1) & f_2(z_2) & f_3(z_3) & f_4(z_4) \end{pmatrix}^{\mathrm{T}}$, is determined by the remote loads and the boundary conditions.

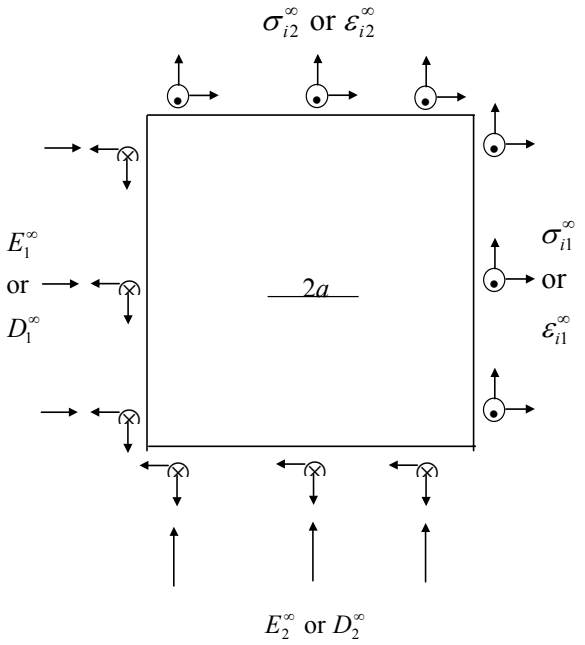

Fig. 1 A crack in an infinite piezoelectric medium under combined remote loadings.

INSULATING CRACK

Zhang *et al*. [3] obtained the solutions for an insulating elliptical cavity using the exact boundary conditions, traction-free, surface charge-free and continuity of electric potential, along the cavity surface. The results depend greatly on the ratio of α/β, where α is the ratio of the minor semi-axis, *b,* to the major semi-axis, *a,* of the ellipse, and β is the ratio of the dielectric constant of the cavity to the effective dielectric constant of the piezoelectric material. When the cavity shrinks into a slit crack, there are three limiting cases, respectively corresponding to $\alpha/\beta \to 0$ for an electrically permeable crack, $\alpha/\beta \to$ a finite nonzero value for general cases and $\alpha/\beta \to \infty$ for an electrically impermeable crack. Only the two cases of electrically permeable and impermeable cracks are discussed in the present paper. From these solutions, the energy release rate for the two cases can be expressed in terms of the intensity factors at the crack tip

$$J = \frac{\mathbf{K}^{\mathrm{T}}\left(\mathbf{B} + \overline{\mathbf{B}}\right)\mathbf{K}}{4}, \tag{2}$$

where $\mathbf{K} = \begin{pmatrix} K_{\mathrm{II}} & K_{\mathrm{I}} & K_{\mathrm{III}} & K_D \end{pmatrix}^{\mathrm{T}}$ with the components being the stress intensity factors of the three modes, K_{I}, K_{II} and K_{III}, and the electric displacement intensity factor, K_D, respectively. **B** is a Hermitian matrix,

$$\mathbf{B} = i\mathbf{A}\mathbf{L}^{-1} = \begin{pmatrix} \mathbf{B}_1 & \mathbf{B}_2 \\ \mathbf{B}_3 & B_{44} \end{pmatrix}, \tag{3}$$

The upper left-hand block $\mathbf{B}_1$ is a 3×3 matrix and the lower right-hand element B_{44} is scalar. For stable materials, **B** has the following properties [1, 2]

$$\mathbf{B}_2 = \overline{\mathbf{B}}_3^{\mathrm{T}}, \quad B_{44} < 0\,. \tag{4}$$

Electrically permeable crack

The electrically permeable boundary conditions correspond to $\alpha/\beta \to 0$ and lead to the intensity factors

$$K_{\mathrm{I}} = \sqrt{\pi a}\,\sigma_{22}^{\infty}, \quad K_{\mathrm{II}} = \sqrt{\pi a}\,\sigma_{12}^{\infty}, \quad K_{\mathrm{III}} = \sqrt{\pi a}\,\sigma_{32}^{\infty},$$
$$K_D = -\frac{\sqrt{\pi a}}{2B_{44}}\left[\left(B_{41}+\overline{B_{41}}\right)\sigma_{12}^{\infty} + \left(B_{42}+\overline{B_{42}}\right)\sigma_{22}^{\infty} + \left(B_{43}+\overline{B_{43}}\right)\sigma_{32}^{\infty}\right] \tag{5}$$

Equation (5) shows that the electric displacement intensity factor is completely induced by the piezoelectric effect rather than by the applied electric loads. Then, substituting Eq. (5) into Eq. (2), we see that the energy release rate is independent of the applied electric field either perpendicular or parallel to the crack. In other words, the energy release rate has nothing to do with the applied electric fields.

Electrically impermeable crack

An electrically impermeable crack ignores the electric field within the crack. Thus, the intensity factors are given by

$$\left(K_{\mathrm{II}} \quad K_{\mathrm{I}} \quad K_{\mathrm{III}} \quad K_D\right) = \left(\sqrt{\pi a}\,\sigma_{12}^{\infty} \quad \sqrt{\pi a}\,\sigma_{22}^{\infty} \quad \sqrt{\pi a}\,\sigma_{32}^{\infty} \quad \sqrt{\pi a}\,D_2^{\infty}\right). \tag{6}$$

Equations (2) and (6) show that the remote mechanical loads, $\sigma_{12}^{\infty}, \sigma_{22}^{\infty}$ and σ_{32}^{∞}, as well as the electrical load, D_2^{∞}, determine the energy release rate, while the applied electric field parallel to the crack contributes nothing to the energy release rate. Furthermore, we can easily see that the applied electric field perpendicular to the crack impedes the crack propagation because B_{44} is negative as given in Eq. (4).

CONDUCTING CRACK

If the crack is electrically conducting, the boundary conditions along crack faces are traction-free and constant electric potential. For simplicity, it is assumed that there are no net electric charges on the crack faces and the constant electric potential on the crack faces is zero. Then, the intensity factors take the form of

$$K_{\mathrm{I}} = \sqrt{\pi a}\,\sigma_{22}^{\infty}, \quad K_{\mathrm{II}} = \sqrt{\pi a}\,\sigma_{12}^{\infty}, \quad K_{\mathrm{III}} = \sqrt{\pi a}\,\sigma_{32}^{\infty}, \quad K_{E_1} = \sqrt{\pi a}\,E_1^{\infty}. \tag{7}$$

The energy release rate is expressed in terms of the intensity factors

$$J = \left(K_{\mathrm{II}} \quad K_{\mathrm{I}} \quad K_{\mathrm{III}} \quad -K_{E_1}\right)\frac{i\left[\mathbf{P}\mathbf{Q}^{-1} - \overline{\mathbf{P}\mathbf{Q}^{-1}}\right]}{4}\begin{pmatrix} K_{\mathrm{II}} \\ K_{\mathrm{I}} \\ K_{\mathrm{III}} \\ -K_{E_1} \end{pmatrix}, \tag{8}$$

where $i = \sqrt{-1}$, and

$$\mathbf{Q} = \begin{pmatrix} L_{11} & L_{12} & L_{13} & L_{14} \\ L_{21} & L_{22} & L_{23} & L_{24} \\ L_{31} & L_{32} & L_{33} & L_{34} \\ A_{41} & A_{42} & A_{43} & A_{44} \end{pmatrix}, \quad \mathbf{P} = \begin{pmatrix} A_{11} & A_{12} & A_{13} & A_{14} \\ A_{21} & A_{22} & A_{23} & A_{24} \\ A_{31} & A_{32} & A_{33} & A_{34} \\ L_{41} & L_{42} & L_{43} & L_{44} \end{pmatrix}. \tag{9}$$

Equation (8) shows that only the electric field parallel to the crack affects the crack propagation. We explicitly demonstrate this result with a mode III conductive crack. When the poling direction of a transversely isotropic piezoelectric medium is perpendicular to the crack, the anti-plane deformation decoupled from the in-plane deformation and the intensity factors for a mode III conductive crack are given by

$$K_{\mathrm{III}} = \sqrt{\pi a}\sigma_{32}^{\infty}, \quad K_{E_1} = \sqrt{\pi a}E_1^{\infty}. \tag{10}$$

Consequently, the energy release rate for the mode III conductive crack is

$$J = \frac{\pi a}{2}\left[\frac{1}{c_{44}}\left(\sigma_{32}^{\infty}\right)^2 + \left(\kappa_{11} + \frac{e_{15}^2}{c_{44}}\right)\left(E_1^{\infty}\right)^2\right]. \tag{11}$$

Equation (11) shows clearly that the applied electric field parallel to the crack drives the crack to propagate.

POLARAZATION SATURATION MODEL

For an electrically impermeable crack, Gao *et al*. [4] proposed a strip polarization model to examine the electrical yielding effect on the fracture behavior of electrically insulating cracks. In this model, piezoelectric ceramics are treated as mechanically brittle and electrically ductile materials. The electrical saturation is analogous to the classical Dugdale model. To emphasize the physical insight, Gao *et al*. [4] considered a simplified piezoelectric material to make the derivation process straightforward. In the present work, the complete governing equations are used. The local intensity factors are the sum of the intensity factors induced by the applied field and the saturation zone

$$\mathbf{K}^{l} = \mathbf{K}^{a} + \mathbf{K}^{d}, \tag{12}$$

where the applied intensity factor vector $\mathbf{K}^{a}$ is given in Eq. (6) and the intensity factor vector $\mathbf{K}^{d}$ caused by the polarization zone takes the form of

$$\left(K_{\mathrm{II}}^{l} \quad K_{\mathrm{I}}^{l} \quad K_{\mathrm{III}}^{l} \quad K_{D}^{l}\right) = \left(K_{\mathrm{II}}^{a} - \frac{\mathbf{L}_1\mathbf{L}_4^{\mathrm{T}}}{\mathbf{L}_4\mathbf{L}_4^{\mathrm{T}}}K_{D}^{a} \quad K_{\mathrm{I}}^{a} - \frac{\mathbf{L}_2\mathbf{L}_4^{\mathrm{T}}}{\mathbf{L}_4\mathbf{L}_4^{\mathrm{T}}}K_{D}^{a} \quad K_{\mathrm{III}}^{a} - \frac{\mathbf{L}_3\mathbf{L}_4^{\mathrm{T}}}{\mathbf{L}_4\mathbf{L}_4^{\mathrm{T}}}K_{D}^{a} \quad 0\right). \tag{13}$$

As a result, the local energy release rate is given by

$$J^{l} = \left(K_{\mathrm{II}}^{a} - \frac{\mathbf{L}_1\mathbf{L}_4^{\mathrm{T}}}{\mathbf{L}_4\mathbf{L}_4^{\mathrm{T}}}K_{D}^{a} \quad K_{\mathrm{I}}^{a} - \frac{\mathbf{L}_2\mathbf{L}_4^{\mathrm{T}}}{\mathbf{L}_4\mathbf{L}_4^{\mathrm{T}}}K_{D}^{a} \quad K_{\mathrm{III}}^{a} - \frac{\mathbf{L}_3\mathbf{L}_4^{\mathrm{T}}}{\mathbf{L}_4\mathbf{L}_4^{\mathrm{T}}}K_{D}^{a}\right)\frac{(\mathbf{B}_1 + \overline{\mathbf{B}_1})}{4}\begin{pmatrix} K_{\mathrm{II}}^{a} - \frac{\mathbf{L}_1\mathbf{L}_4^{\mathrm{T}}}{\mathbf{L}_4\mathbf{L}_4^{\mathrm{T}}}K_{D}^{a} \\ K_{\mathrm{I}}^{a} - \frac{\mathbf{L}_2\mathbf{L}_4^{\mathrm{T}}}{\mathbf{L}_4\mathbf{L}_4^{\mathrm{T}}}K_{D}^{a} \\ K_{\mathrm{III}}^{a} - \frac{\mathbf{L}_3\mathbf{L}_4^{\mathrm{T}}}{\mathbf{L}_4\mathbf{L}_4^{\mathrm{T}}}K_{D}^{a} \end{pmatrix}. \tag{14}$$

Because the polarization zone shields the crack tip electrically and completely, the local electrical displacement intensity factor is zero. The applied electric field contributes to the local energy release rate via the piezoelectric effect. The local energy release rate, as a failure criterion, yields a linear relationship between the applied mechanical load and electric field. But the global energy release rate is the same as that from linear fracture mechanics, which predicts that either a positive or negative electric field impedes the crack propagation.

EXPERIMENTAL RESULTS

Fracture test

Compact Tension (CT) tests and Indentation Fracture (IF) tests were carried out on PZT-841 ceramics under an applied electric field. The material is poled PZT-841 with an average grain size of 4-5 μm. The composition of PZT-841 is near, but in the tetragonal side of the morphotropic phase boundary. In the CT tests, the notch on each sample was cut using a diamond saw with a 0.2 mm-thick blade and the notch tip

was further sharpened with a wire saw of 0.05 mm in diameter. The poling direction was perpendicular to the notch. About 10 samples were tested at each level of the electric fields, except that 33 samples were tested at the electric field of 15 kV/cm to study the distribution of fracture toughness. The energy release rate was calculated by the finite element method and then converted into the mode I stress intensity factor. In the IF tests, the load was 49.0 N and the electric field of 4 kV/cm was applied either parallel or antiparallel to the poling direction of the sample. Under each level of the electric fields, about 10 indentations were performed. Only the fracture behavior of the cracks perpendicular to the poling direction is reported in this paper. Figures 2(a) and 2(b) show the variation of K_{IC} with the applied electric field obtained from the CT and IF tests, respectively. Under purely mechanical loading, the averaged K_{IC}s are $1.12 \pm 0.05 MPa\sqrt{m}$ and $1.01 \pm 0.06 MPa\sqrt{m}$, respectively, from the two methods. The mean value of K_{IC} is reduced by either a positive or a negative applied electric field in both types of testing. In the CT tests, the negative field of 7.5 kV/cm reduces the averaged K_{IC} by $0.25 MPa\sqrt{m}$, while the same strength positive field reduces the averaged K_{IC} by $0.10 MPa\sqrt{m}$. Similarly, in the IF tests, a reduction of $0.21 MPa\sqrt{m}$ or $0.10 MPa\sqrt{m}$ results from the application of a negative or positive field of 4 kV/cm. These facts indicate that a negative field has a stronger influence on the averaged K_{IC} than a positive field does. Applying a positive electric field of 15 kV/cm reduces further the averaged K_{IC} to $0.92 \pm 0.14 MPa\sqrt{m}$ in the CT tests, resulting in a relative reduction of 18%.

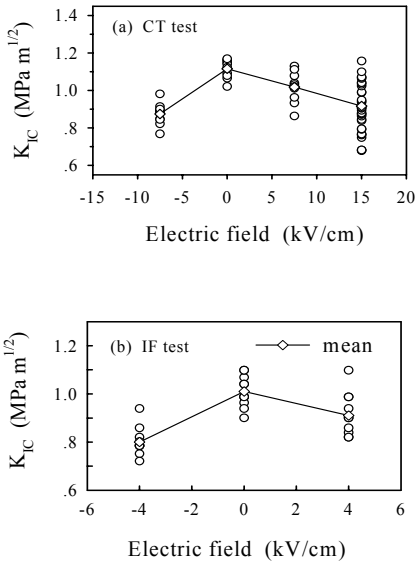

Fig. 2 Effect of an electric field on the fracture toughness.

Conducting crack

CT samples used in this study were made from poled PZT-4 piezoelectric ceramics and the poling direction was parallel to the notch. A 0.25 mm wide notch in every sample was cut and its tip was sharpened further by a wire saw of radius 0.1 mm. Silver paint was filled into the notch to make it function as an electrode. Thus, the crack becomes electrically conducting. Two loading types were applied in this study. One is purely mechanical loading and the other is purely electric loading. In the electric loading tests, a static voltage was applied to a sample at the electrodes and increased until the sample was failed. All tests were carried out at room temperature and 30 samples were tested for each loading type. It was observed that electrical breakdown was usually accompanied by fracture. The fracture surfaces are flat for samples fractured under mechanical loads. A critical voltage causes dielectric breakdown tunnel and rough fracture surfaces. The finite element method was used to calculate the energy release rate for the given samples. The critical energy release rate under mechanical loading was calculated from the fracture load and the corresponding ligament, as shown in Fig. 3(a). The mean of the mechanical critical energy release rate is G_{IC}^{M} =8.7±0.4 N/m. It is clearly seen that the linear regression of the plot is very close to a horizontal line, indicating that the critical energy release rate is a material constant independent on the sample ligament. Similarly, the critical energy release rate under electric loading was calculated from the critical voltage and the ligament. Figure 3(b) presents the electrical critical energy release rate versus sample ligament. The linear regression of the plot is also almost a horizontal line. This fact, in analogy with the mechanical loading situation, means that the

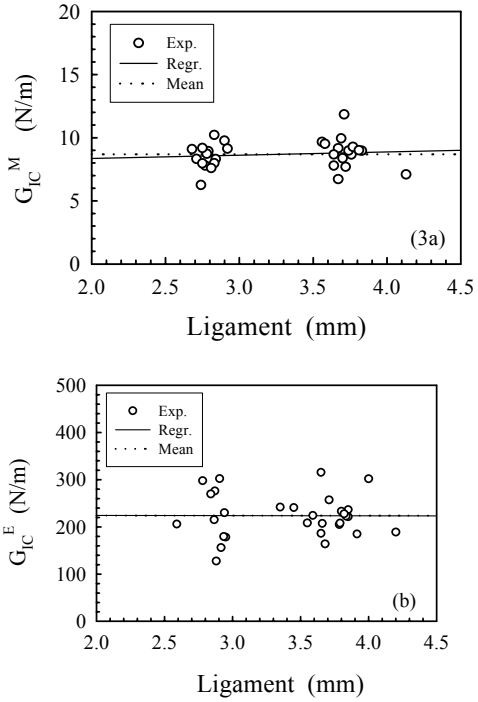

Fig. 3 The energy release rate versus the ligament, (a) mechanical loading and (b) electrical loading.

electrical critical energy release rate is a material property with the value G_{IC}^{E}=223.7±17.0 N/m for PZT-4 ceramics. The significance of the existence of G_{IC}^{E} is that it enables fracture mechanics concepts to be used in understanding dielectric failure, and it provides a useful material property for designers of electronic and electromechanical devices.

CONCLUDING REMARKS

The linear theoretical results show that the electric field has different effects on the energy release rate for different types of cracks. The energy release rate is independent of the applied electric field for electrically permeable cracks. The applied electric field perpendicular to an impermeable crack impedes the crack to propagate, while the applied electric field parallel to a conducting crack drives the crack to propagate. However, the strip polarization saturation model, when electrical yield occurs in front of the crack tip, predicts that the propagation of an impermeable crack is driven by a perpendicular positive electric field and impeded by a perpendicular negative electric field.

The experimental results of both compact tension tests and indentation fracture tests show that either a positive or negative electric field perpendicular to the electrically insulating crack always assists the applied mechanical loads to fracture the sample. For electrically conductive cracks, there is a critical energy release rate under purely electrical loading, just like the case under purely mechanical loading. In terms of the energy release rate, however, the electrical fracture toughness is about 25 times higher than the mechanical fracture toughness.

ACKNOWLEDGEMENTS: This work is supported by a grant from the Research Grant Council of the Hong Kong Special Administrative Region, China.

REFERENCES

1. Barnett, D. M. and Lothe, J. (1975) *Phys. Stat. Sol.* (*b*) **67**, 105.
2. Suo, Z., Kuo, C. M., Barnett, D. M. and Willis, J. R. (1992) *J. Mech. Phys. Solids* **40**, 739.
3. Zhang, T.-Y., Qian, C.-F. and Tong, P. (1998) *Int. J. Solids Structures* **35**, 2121.
4. Gao, H., Zhang, T.-Y. and Tong, P. (1997) *J. Mech. Phys. Solids* **45**, 491.
5. Cao, H. and Evans, A. G. (1993) *J. Am. Ceram. Soc*. **76**, 890.
6. Cherepanov, G. P. (1979). *Mechanics of Brittle Fracture*, McGraw-Hill, New York.
7. Deeg, W.F.J. (1980). The analysis of dislocation, crack, and inclusion problems in piezoelectric solids. *PhD Thesis*, Stanford University.
8. Fu, R. and Zhang, T.-Y. (1998). *J. Am. Ceram. Soc.* **81**, 1058.
9. Fu, R., Qian, C.-F. and Zhang, T.-Y.(2000) *Appl. Phys. Letters*, **76**, 126.
10. Zhang, T.-Y. and Hack, J. E. (1992) *J. Appl. Phys*. **71**, 5865.
11. Zhang, T.-Y.(1994) *Int. J. Fracture* **68**, R33.
12. Zhang, T.-Y. and Tong, P. (1996) *Int. J. Solids Structures* **33**, 343.
13. Lynch, C.S. (1996) *Acta Mater*. **44**, 4137.
14. McMeeking, R. M. (1989) *J. Appl. Math. Phys.* **40**, 615.
15. Mehta, K. and Virkar, A.V. (1990) *J. Am. Ceram. Soc.*, **73**, 567.
16. Pak, Y.E. (1990) *J. Appl. Mech.,* **57**, 647.
17. Sosa, H. and Pak, Y. E. (1990) *Int. J. Solids Structures* **26**, 1.
18. Sosa, H. (1992) *Int. J. Solids Structures* **29**, 2613.
19. Suo, Z. (1993) *J. Mech. Phys. Solids* **41**, 1155.
20. Zhu, T. and Yang, W.(1999) *J. Mech. Phys. Solids*, **47**, 81.
21. Qin, Q. H., Mai, Y. W. and Yu, S. W. (1999) *Int. J. Solids Structures* **36**, 427.
22. Kogan, L., Hui, C. Y. and Molkov V. (1996) *Int. J. Solids Struct.* **33**, 2719.
23. Zhang, T.-Y., Zhao, M. H. and Tong, P. (2001) Fracture of Piezoelectric Ceramics, *Advances in Applied Mechanics*, in press.

ICF1001056OR

FRACTURE OF THERMAL SPRAYED NANOSTRUCTURED COATINGS

Maurice Gell, Leon Shaw, Eric Jordan, Hong Luo and Daniel Goberman
School of Engineering, University of Connecticut
Storrs, CT 06269, USA

ABSTRACT

A nanostructured alumina-13 weight percent titania plasma sprayed coating has been developed with outstanding wear, toughness, adhesion and machinability properties. The optimized properties are associated with a bi-modal microstructure that consists of a fully melted region and a partially melted region. In contrast, a baseline, commercial Metco 130 coating of the same composition contains only the single-phase splat microstructure. The crack growth resistance or "toughness" of each of these materials was investigated using the cracks generated around Vicker's hardness indents.

In Metco 130, long, wide cracks initiate in and propagate along splat boundaries. In the nanostructured alumina-titania, the spherical particles in the bi-modal microstructure serve to trap and deflect the splat boundary cracks. This produces the approximately 100% improvement in the crack growth resistance of the nanostructured coating with the bi-modal microstructure.

The volume fraction of the partially melted regions can be systematically varied by changing the plasma flame temperature. It was found that the crack growth resistance of the nanostructured coatings was optimized when the microstructure contains 15-20% of the partially melted spherical particles.

KEYWORDS

Nanostructured coating, wear resistant coating, plasma sprayed coating, toughness, crack growth resistance.

INTRODUCTION

A nanostructured alumina-13 w/o titania plasma sprayed coating has been developed that has superior wear resistance, toughness, adhesion and machinability properties [1]. The composition, powder preparation procedure, plasma spray processing parameters, microstructure and properties have been described previously [1-4]. The technology for

making this coating has been transferred to the U.S. Navy and an approved supplier. A military specification has been issued and this coating is being deposited on a number of ship and submarine components for service evaluation. This paper describes the microstructural features that give rise to the improved toughness of the coating.

EXPERIMENTAL RESULTS

Crack growth resistance, or pseudo-toughness, measurements were made using a Vickers hardness tester with a 3kg load, and measuring the crack length emerging from the indent corners. The crack growth resistance is defined as the reciprocal of the crack length.

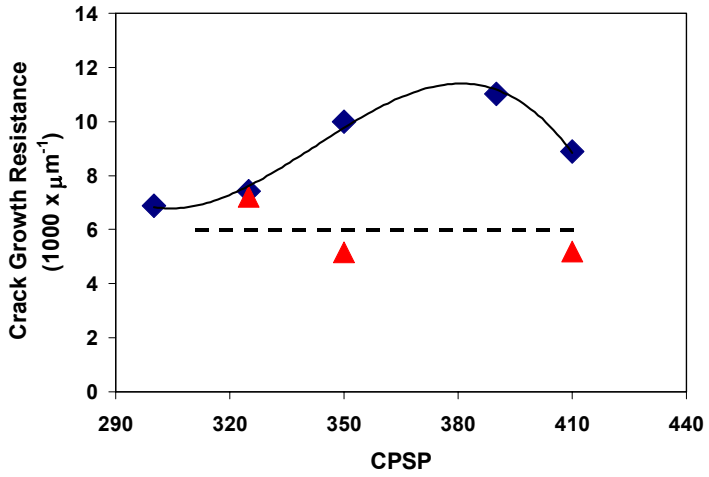

Figure 1. Crack growth resistance as a function of CPSP for Metco 130 coatings (▲) and nanocoatings (◆).

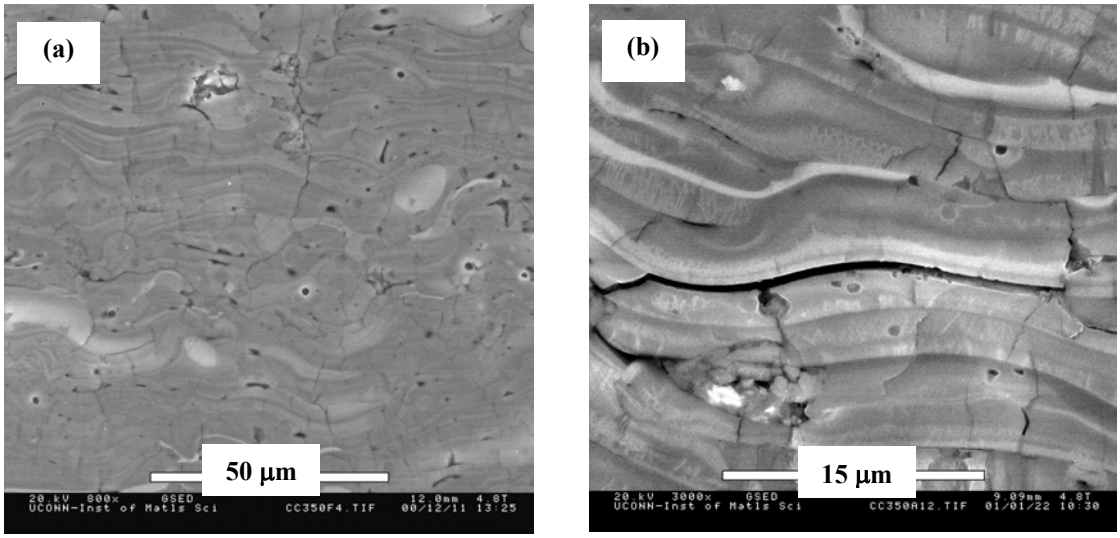

Figure 2. Microstructure and crack characteristics of Metco 130 coatings.

Figure 1 shows the crack growth resistance of the nanostructured alumina-13w/o titania coatings and that of the commercial Metco 130 coating of the same composition. The data is plotted against the critical plasma spray parameter, CPSP, that is a function of flame

temperature, and was found to be the most important processing parameter that controlled the microstructure and properties of the nanostructured alumina-titania coatings [1-4]. The crack growth resistance of the nano-coating increases with increasing CPSP to a peak at CPSP of about 390. By contrast, the crack growth resistance of Metco 130 remains at a constant low value with CPSP. At its peak, the crack growth resistance of the nano-coating is twice that of the Metco 130.

Figure 2a shows the microstructure of the plasma sprayed Metco 130 coating, with its well-defined lamellae or splat structure, associated with deposition and rapid solidification of molten powder particles. Figure 2b shows that the cracks from the hardness indents propagate along splat boundaries.

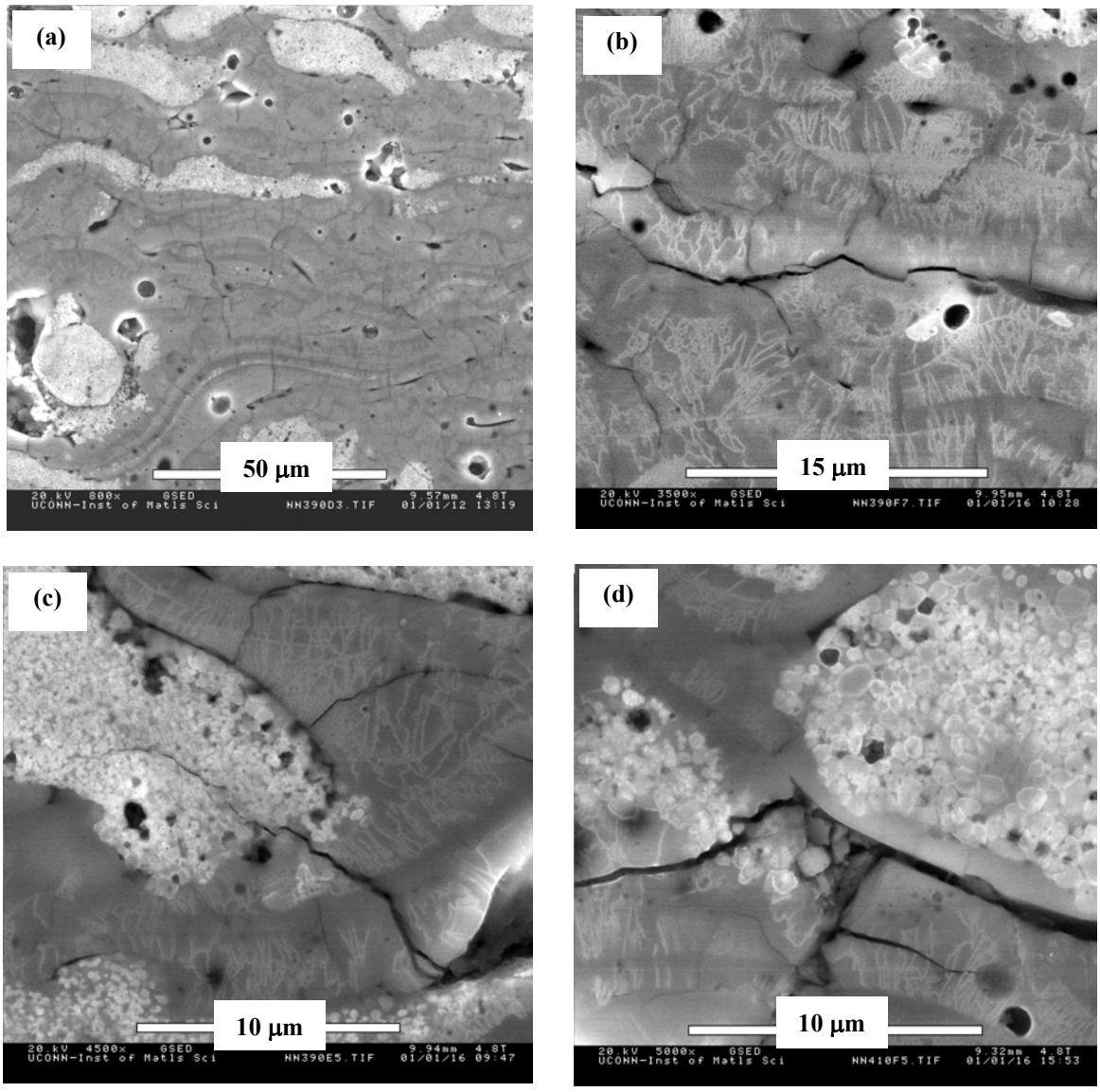

Figure 3. Microstructure and crack paths of nano alumina-titania coatings.

In contrast, Figure 3a shows the microstructure of the nano alumina-titania coating. In addition to the splat structure, there are particulate microstructures (partially melted regions) the shape of which varies from a splat like structure to a round, agglomerate structure depending on the amount of melting that occurred during the thermal spray process. As in the

Metco 130, some cracks also propagate along splat boundaries (Figure 3b). However, in the nanocoatings with the bi-modal microstructure, there are various microstructural features that serve to arrest or deflect cracks and provide toughening. Figure 3c shows a crack being stopped or trapped in the partially melted region. Figure 3d shows a crack being deflected at the interface between the fully melted splat region and the partially melted spherical particles. It is well established that toughening mechanisms such as crack deflection and crack trapping can improve the crack growth resistance of brittle materials [5-8]. Thus, based on these results, we can conclude that nanocoatings should have higher crack growth resistance than Metco 130 coatings because of the toughening mechanisms observed in the nanocoatings.

In order to provide a semi-quantitative determination of the effect of microstructure on crack growth resistance, the microstructural changes with CPSP were determined. Figure 4 shows that the volume fraction of the partially melted regions decreases with CPSP. Based on detailed examination of cracks around at least 10 hardness indentations in each nanocoating, the relative contributions made by various microstructural features, interface boundaries, porosity, partially melted and fully melted regions, to crack growth resistance was assessed. Figure 5 shows the results. By comparing Figures 4 and 5, it can be seen that at CPSP=410 where 90% of the microstructure is fully melted splats, the splats account for only 10% of the crack arrests. By contrast, 64% of the crack arrests in the CPSP=410 specimens are associated with crack arrests in the partially melted regions and by crack deflection at the boundary between partially and fully melted areas.

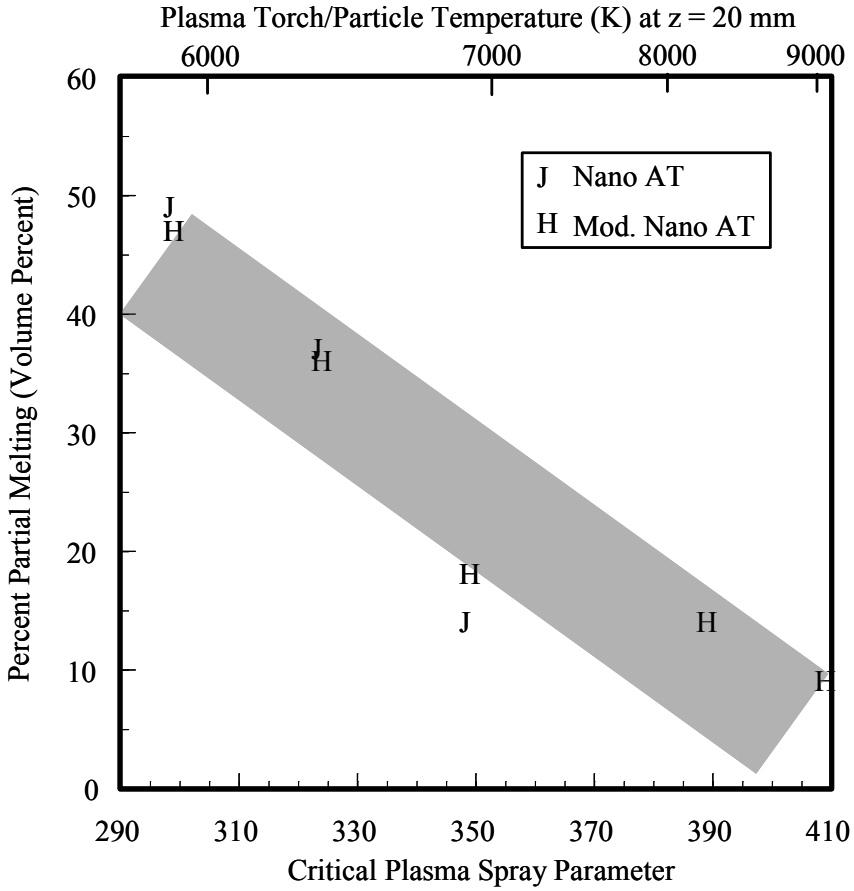

Figure 4. Percentage of coating that is partially melted, determined by quantitative image analysis as a function of CPSP or the plasma torch temperature at a spray distance of 20 mm.

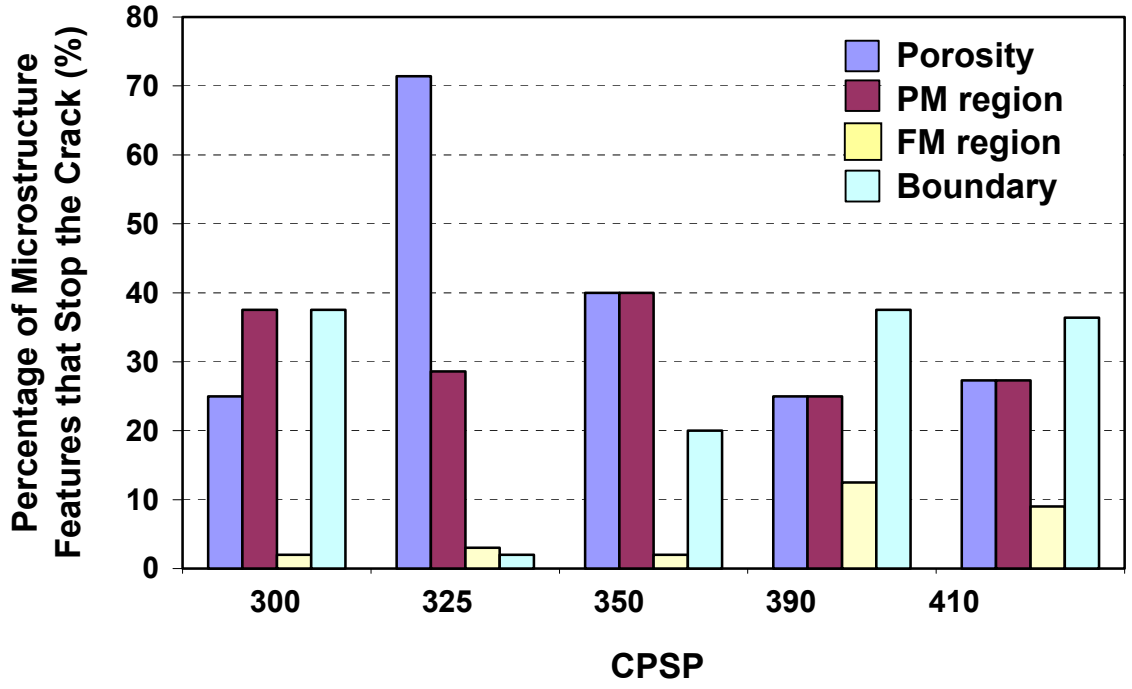

Figure 5. Percentage of microstructure features in the nano alumina-titania coatings that stop the crack as a function of CPSP.

Porosity in the microstructure plays a larger role as the CPSP is reduced. However, for CPSP's less than 350, the porosity level is high (about 10%) because of a high volume fraction of partially melted particles, and this lowers the overall crack growth resistance of these microstructures.

SUMMARY AND CONCLUSIONS

For the nanostructured alumina-titania coatings, optimized crack growth resistance and toughness were obtained for intermediate levels of CPSP. For these CPSP levels between 350 and 390, the partially melted regions represent 15 to 20% of the bi-modal microstructure and provide optimum toughening from a variety of crack arresting and deflection mechanisms. When CPSP is high; e.g., 410, there are insufficient partially melted regions to provide toughening. When CPSP is low; e.g., <350, the coating has sufficient porosity that the toughness of the microstructure is low.

ACKNOWLEDGEMENTS

This work was supported under ONR Contract No. N00014-98-C-0100. The vision and support of Dr. Lawrence Kabacoff, ONR Program Administrator, is greatly appreciated. The efforts of Inframat Corporation in plasma spraying the specimens is noteworthy.

REFERENCES

1) E. H. Jordan, M. Gell, Y. H. Sohn, D. Goberman, L. Shaw, S. Jiang, M. Wang, T. D. Xiao, Y. Wang and P. Strutt, "Fabrication and Evaluation of Plasma Sprayed

Nanostructured Alumina-Titania Coatings with Superior Properties," Mater. Sci. Eng., A301, 80-89 (2001).
2) L. Shaw, D. Goberman, R.-M. Ren, M. Gell, S. Jiang, Y. Wang, T. D. Xiao and P. Strutt, "The Dependency of Microstructure and Properties of Nanostructured Coatings on Plasma Spray Conditions," Surface and Coatings Technology, 130, 1-8 (2000).
3) M. Gell, E. H. Jordan, Y. H. Sohn, D. Goberman, L. Shaw, T. L. Bergman, B. Cetegen, S. Jiang, M. Wang, T. D. Xiao, Y. Wang and P. Strutt, "Development and Implementation of Plasma Sprayed Nanostructured Ceramic Coatings," J. Mater. Process & Technology, in press.
4) D. Goberman, Y. H. Sohn, L. Shaw, E. Jordan and M. Gell, "Microstructure Development of Alumina – 13wt.% Titania Plasma Sprayed Coatings Derived from Nanocrystalline Powders," submitted to Acta Mater., 2001.
5) K. T. Faber and A. G. Evans, "Crack Deflection Processes -- I. Theory", Acta Metall., 31, 565-576 (1983).
6) K. T. Faber and A. G. Evans, "Crack Deflection Processes -- II. Experiment", Acta Metall., 31, 577-584 (1983).
7) R. W. Hertzberg, Deformation and Fracture Mechanics of Engineering Materials, John Wiley & Sons, Inc., New York, NY, 1996, pp. 405-484.
8) R. W. Rice, "Mechanisms of Toughening in Ceramic Matrix Composites", Ceram. Eng. Sci. Proc., 2, 661-701 (1981).

FRACTURE OF VERTEBRAL BONE GOTTEN SURGICAL SCREW INSERTION

Tamotsu Tamaki[1], Son Nguyen[1], Kazuhisa Takahashi[2] and Masatsune Yamagata[2]

[1]Department of Mechanical Engineering, Nippon Institute of Technology 4-1 Gakuendai, Miyashiro, Saitama 345-8501 Japan
[2]Department of Orthopaedic Surgery, School of Medicine, Chiba University, 1-8-1 Inohana, Chuo, Chiba 260-8677 Japan.

ABSTRACT

On spinal surgery, screws execute fixation of the device to vertebral bone mainly. Vertebral bone is composed of cortical bone and cancellous bone. The cortical bone is located on the surface whereas cancellous bone is located in the interior. The cancellous bone has spongy structure and its strength is about one tenth of that of cortical bone. When a screw is inserted to a vertebra, cortical and cancellous bones sustain the screw. The screw dimension is decided as to be average value of surgical screw on the market. Screw was inserted to a bovine lumbar vertebra through a plate with a screw hole, and the binding force between plate and bone was measured. Microstructure of bone before and after the test was examined using reconstructed 3D image by a micro CT machine. The solid model FEM analysis of the bone around the screw was done. The obtained binding forces by experiment and by FEM analysis have good correlation each other. Investigating fractured bone region gotten by micro-CT and von Mieses stress contour by FEM analysis, the fracture is supposed to be induced at the stress excess area of the solid FEM model. And it was suggested that a micro crack initiated in cancellous bone does not affect broader region because it is locally trapped by porous microstructure of the bone.

KEYWORDS

Fracture of cancellous bone, Surgical screw, Micro-CT, FE analysis, von Mieses stress.

INTRODUCTION

On spinal surgery, screws execute fixation of the device to vertebral bone mainly. Vertebral bone is composed of cortical bone and cancellous bone. The cortical bone is located on the surface whereas cancellous bone is located in the interior. The cancellous bone has spongy structure and its strength is about one tenth of that of cortical bone. When a screw is inserted to a vertebra, cortical and cancellous bones sustain the screw. The mechanical role of cortical and cancellous bones on the screw fixation was investigated relating to the cancellous bone fracture [1,2].

MATERIAL AND METHOD

The screw dimension (Figure1) is decided as to be average value of surgical screw on the market1, which is as follows. The effective screw length is 40-mm, major diameter is 6-mm, minor diameter is 4-mm and the screws with different pitches were prepared to test what pitch has the largest binding force between them. The pitches are 2-mm, 3-mm, 4-mm and 5-mm. Specimen of longitudinal direction (long.) is tested applying load parallel to longitudinal directions of bone and specimen of transverse direction (trans.) is done to transverse direction of bone. Material of the screw is stainless steel. Table 1 gives the material property of bone gotten by our experiment. Screw was inserted to a bovine lumbar vertebra through a plate with a screw hole, and the binding force between plate and bone was measured(Figure 2). . Used machine is a material testing machine, Servo-pulsar EHF-ED5 manufactured by Shimadzu Co., Japan (Figure 3a).

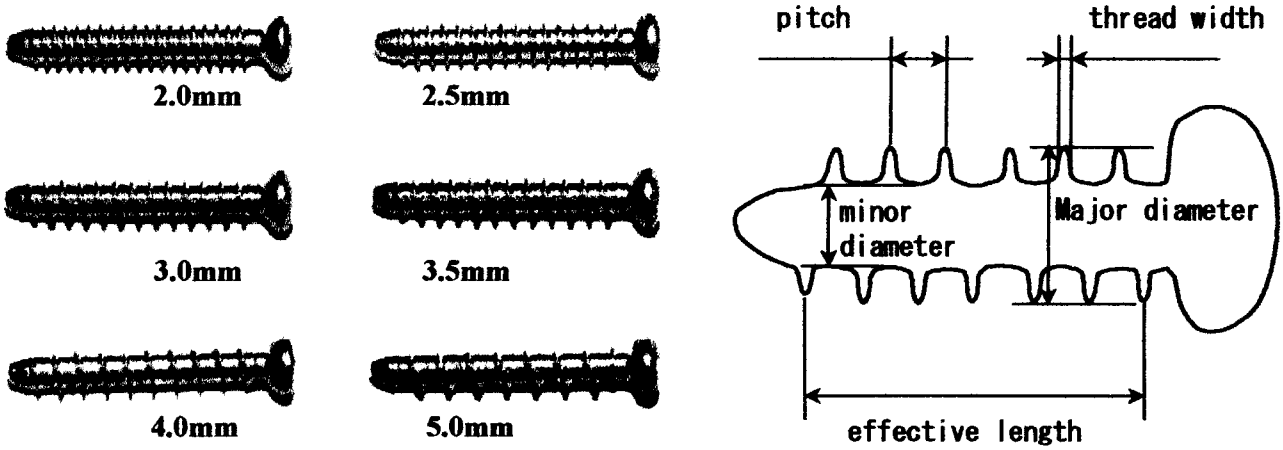

Figure 1: Screws used for of experiment

TABLE 1
MATERIAL PROPERTY OF BOVINE VERTEBRAL BONE [3]

Material property of vertebral bone	Young's modulus (MPa)		Ultimate strength (MPa)		Ultimate strain (mili-strain)		Fracture toughness (MPa(m**0.5))	
Specimen direction	long.	trans.	long.	trans.	long.	trans.	long.	trans.
Cortical bone	8038	3282	31.99	15.64	8.91	7.50	1.8	1.31
(SD of Cortical bone)	(3924)	(1298)	(6.73)	3.85	(3.42)	(4.31)	(0.53)	(0.48)
Cancellous bone	820	498	4.49	1.89	11.10	15.90	0.23	0.37
(SD of Cancellous bone)	(443)	(428)	(1.60)	1.08	(5.45)	(6.30)	(0.12)	(0.25)

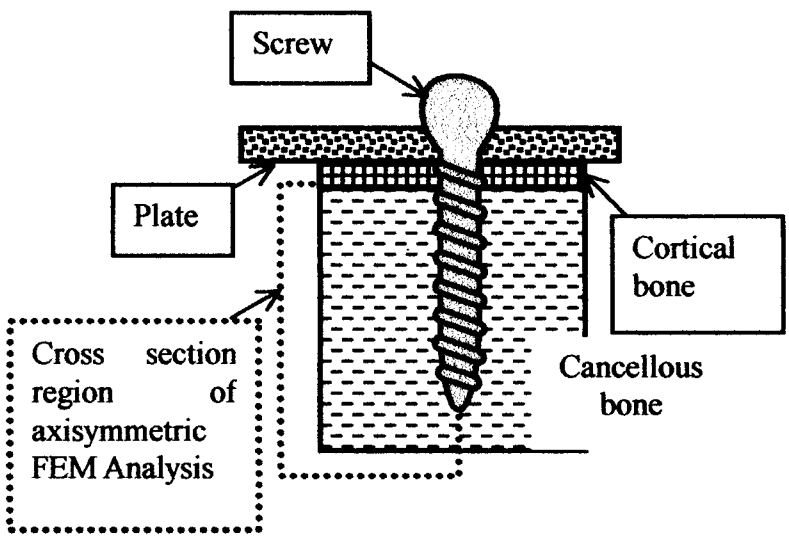

Figure 2: Screw insertion to vertebral bone

The binding force is measured using specially designed load cell of strain gage(Figure 3b). Also the repeated load is applied to vertical to the screw axis until the binding force between plate and vertebra falls to one tenth of initial binding force. The relation of the amplitude of repeated load and the number of cycles was investigated.

Microstructure of bone before and after the test was examined using rconstructed 3D image by a micro CT machine manufactured by Scanco Medical Co., Switzerland. (Figure 4). The solid model FEM (Finite Element Method) analysis of the bone around the screw was done.The used software is ANSYS 5.6 by ANSYS Inc. Pennsylvania, USA

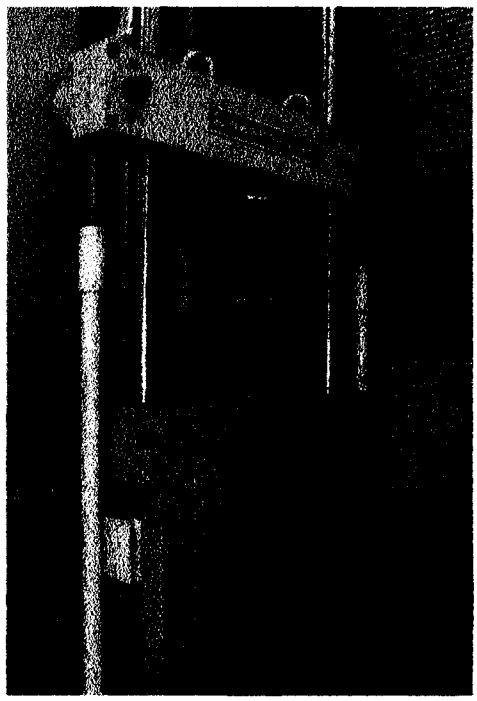

(a) Material testing machine, Survo pulsar EHF-ED5

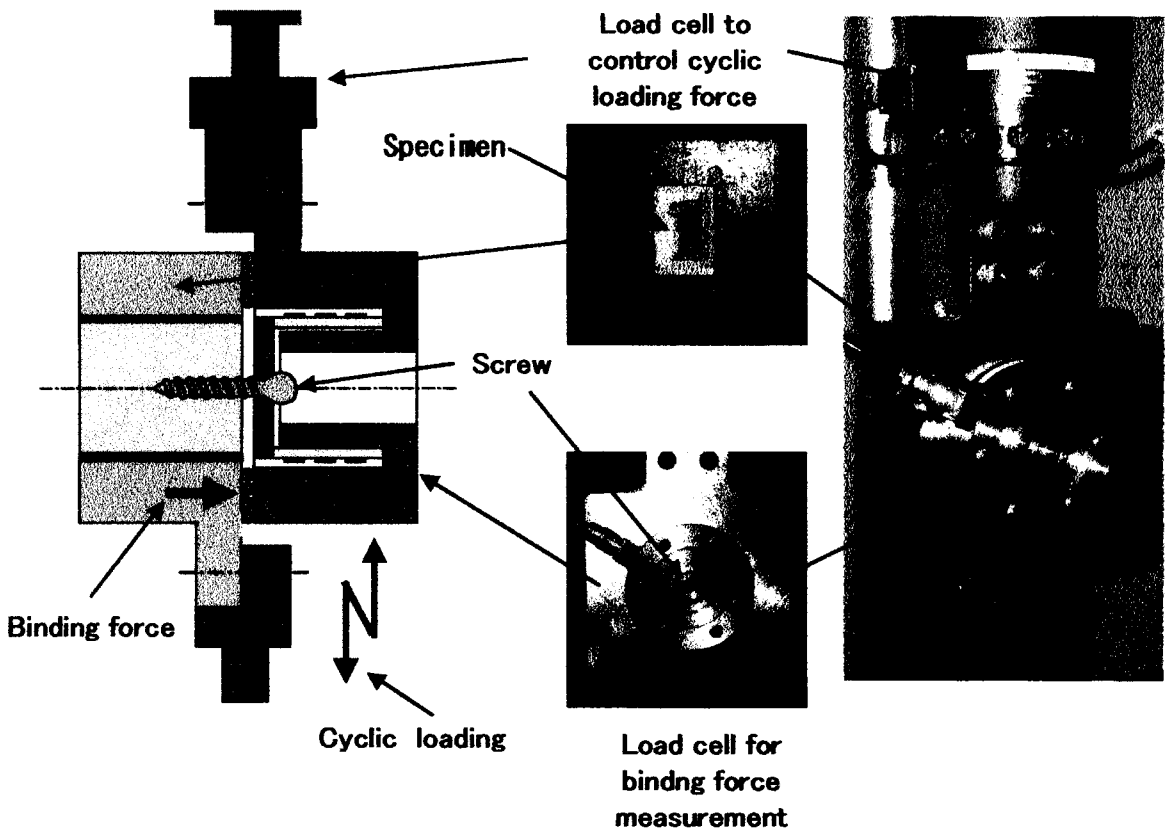

(b) Binding force measurement

Figure 3: Binding force measurement by material testing machine

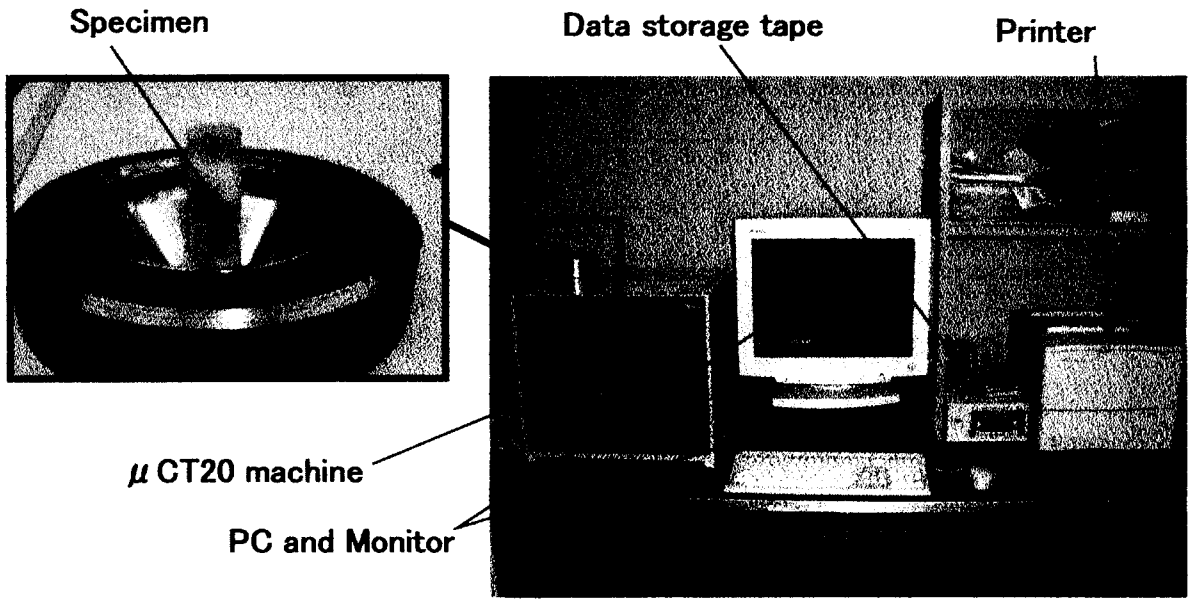

Figure 4: Micro-CT machine, Micro-CT20

RESULT AND DISCUSSION

The obtained binding forces by experiment and by FEM analysis are shown in TABLE 2 and Figure 5. These results show the experiment and FEM analysis have good correlation each other.

Figure 6 is the 3D micro-CT image of bone just after screw hole tapping of pitch 3-mm. The screw insertion test was executed until just after peak-binding force is recorded when the screw insertion was stopped to retrieve the bone for micro-CT observation. Fractured bone region by micro-CT was compared with Von Mieses stress contour by FEM analysis on the screw pitch; 2-mm, 3-mm, 4-mm and 5-mm as shown in Figures 7a, 7b, 7c and 7d respectively and it was found that they have good correlation each other. Then although the structure of cancellous bone is porous and is very complicated, its mechanical property can be understood as a solid material with anisotropy. It was suggested a micro crack initiated in cancellous bone does not affect broader region because it is locally trapped by porous microstructure of the bone.

TABLE 2 Obtained binding forces of pitches from 1 mm to 5 mm by experiment and by FEM analysis.

Pitch (mm)		2	2.5	3	3.5	4	5
Binding force (kN)	Experiment	1.09	1.27	1.33	1.25	1.14	1.07
	FEM-analysis	1.05	1.16	1.18	1.07	0.95	0.63

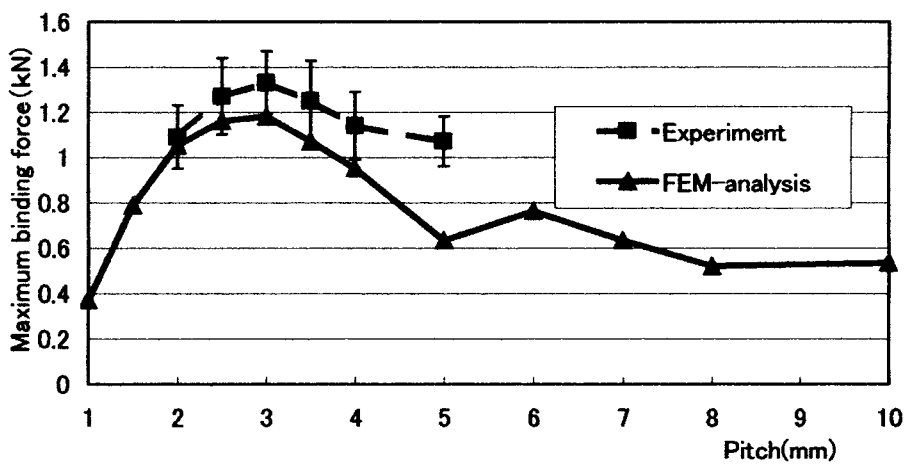

Figure 5 Obtained binding forces of pitches from 1 mm to 10 mm by experiment and by FEM analysis.

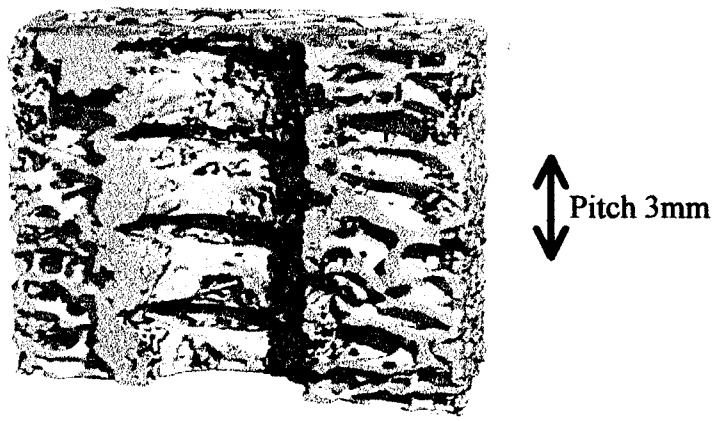

Figure 6: 3D micro-CT image of cancellous bone just after screw hole tapping of pitch 3-mm.

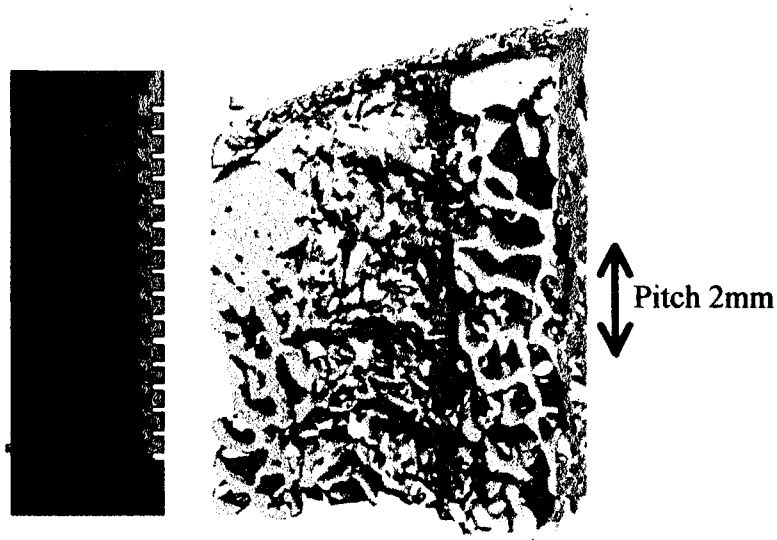

(a) Pitch:2.0mm Maximum stress 3.425MPa

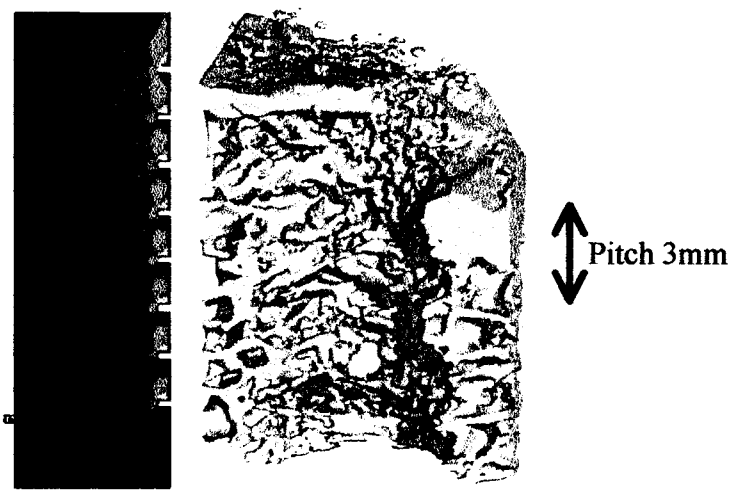

(b) Pitch:3.0mm Maximum stress 3.05MPa

Figure 7ab:The von Mieses stress contour by FE analysis and 3D micro-CT image. The value shows maximum von Mieses stress

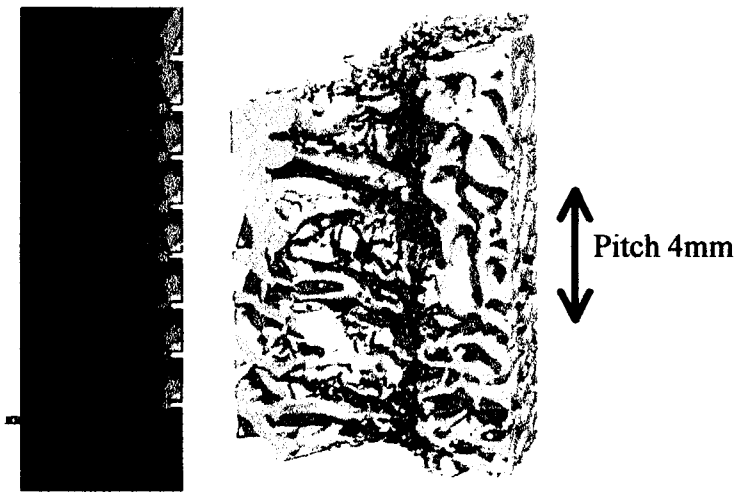

(c) Pitch:4.0mm Maximum stress 3.784MPa

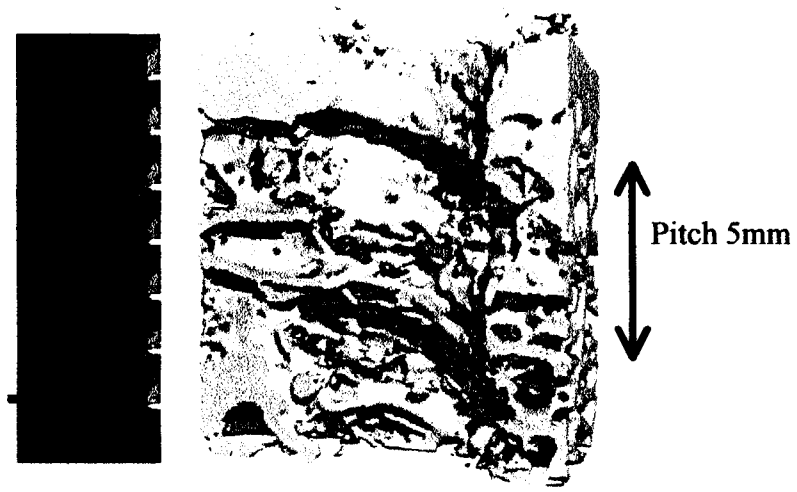

(d) Pitch:5.0mm Maximum stress 5.696MPa

Figure 7cd: The von Mieses stress contour by FE analysis and 3D micro-CT image
The value shows maximum von Mieses stress

CONCLUSION

The result of high stress region of stress distribution by FE analysis was similar to the fractured region by micro-CT image. The mechanical property of cancellous bone can be understood as a solid material with anisotropy and it was suggested a micro crack initiated in cancellous bone does not affect broader region because it is locally trapped by porous microstructure of the bone.

REFERENCES

1. Tamaki, T., Nguyen, S., Maruyama, K., Takahashi, K. and Yamagata, M. (2000), Binding characteristics of screw for spinal fixation relating to the bone structure around it, Proc. 10-th Int. Conf. Biomedical Eng., (Singapore), 622.
2. Nguyen, S., Tamaki, T., Takahashi, K. and Yamagata, M. (1998), Screw shape for spinal fixation and its binding characteristics, Abstract of Third world Congress of Biomechanics (Sapporo), 438b.
3. Nguyen, S., Tamaki, T. (1997), Fracture toughness of bovine vertebra and its comparison with that of bovine long bone, Proc. of Int. Con. on new frontiers in biomedical engineering, (Tokyo), 305-308.

POSTER REFERENCE: ICF100507PR

FRACTURE PREDICTIONS FOR DUCTILE STEEL

G. Pape*, A. Bakker* and M. Janssen*

* Delft University of Technology, Laboratory of Materials Science,
Rotterdamseweg 137, 2628 AL, Delft, The Netherlands

ABSTRACT

Ductile failure predictions have been made for several geometries of notched and smooth tensile specimen. Ductile damage has been accounted for in these predictions using a local failure criterion. This criterion, a Rice & Tracey [1] model for the growth of voids in a triaxial stress field gives a prediction of the relative enlargement of an imperfection with initial radius R_0. Experimental results have been used to compare with numerical predictions of fracture initiation. Damage has been evaluated in every material location as a continuous distribution of a scalar variable. The model has underestimated local damage in the notched tensile specimen. Introduction of a length parameter in the damage calculation accounts for microstructural effects and an appropriate length scale can be related to inclusion distances in the material. Analysing the physical damage in a smooth tensile specimen prior to failure will reveal early stages of fracture initiation. If failure initiates at macroscopic level (small crack) prior to specimen failure, this would result in a better agreement between numerical predictions of ductile damage and results from experiments. A more critical approach was used using the Rice and Tracey damage model. A comparison have been made for smooth round, smooth square and flat notched specimen. The area reduction at fracture has been compared with numerical predictions. These geometries show unexplained discrepancy between numerical predictions and experimental results.
The influence of the strain rate has been taken into account in the numerical simulations by incorporating a strain rate dependent material behaviour derived from experimental data. Only small reductions of the failure strain were calculated using this approach and this compares rather well to experimental results.

KEY WORDS

Ductile Damage, Local Fracture Criterion, Experiments, Numerical Prediction

INTRODUCTION

Research for the Royal Netherlands Navy on the vulnerability of warships has resulted in a detailed study on the failure behaviour of explosively loaded panels inside ship structures. This study contains on the one hand a determination of the material response to high strain rate deformation, and on the other hand an investigation of the failure behaviour of the material. This paper is concerned with experimental and numerical failure investigations of the material; also the influence of the strain rate has been taken into

account. The experimental determination of the flow stress has been presented in an additional paper [2]. First some experiments will be described and results will be presented. Numerical simulations of the experiments including ductile damage have been presented in the next section. Two approaches for failure predictions will be discussed and attention will be paid to the influence of the strain rate on the failure behaviour. Finally, conclusions have been drawn and recommendations for further research have been made.

FRACTURE EXPERIMENTS ON NOTCHED SPECIMEN

The influence of hydrostatic stresses on the failure behaviour of steel has been investigated experimentally. For several geometries of tensile specimen the load-displacement curves have been recorded and the area reduction at failure has been measured. Flat tensile specimen witch notches on both sides have been applied for this research. To vary the level of hydrostatic stress in the specimen, several notch radii have been applied. The influence of the rolling direction of the plate material has been investigated as well as the influence of the strain rate on the failure strain. Figure 1 shows the dimensions of the notched tensile specimen, for high strain rates the specimen width was increased to 15 mm and the gauge length L to 90 mm, also the clamping parts have been modified. This change was made in order to maintain pure elastic deformation outside the notch region.

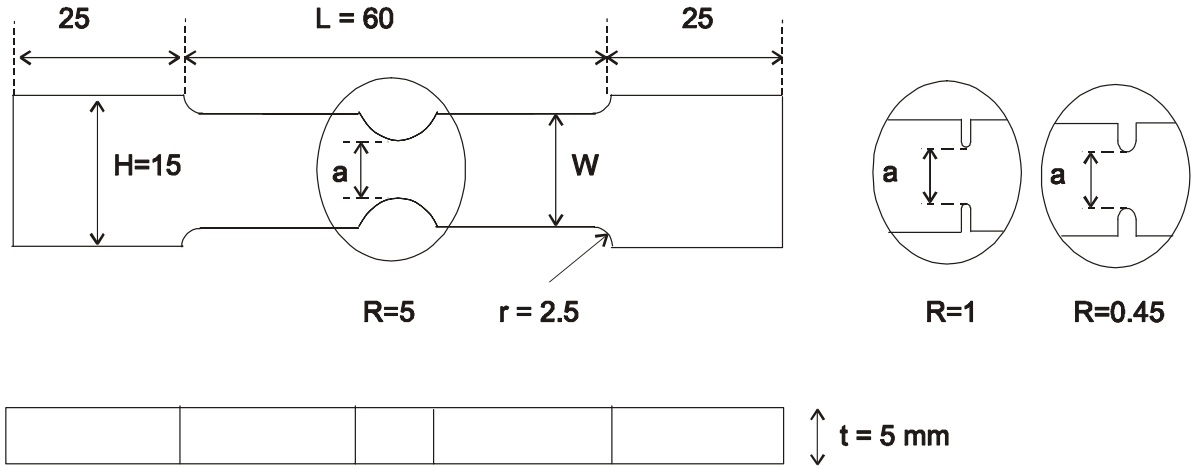

Figure 1: Dimensions of notched specimen [mm]. Notches with radii R=5 mm, 1 mm, and 0.45 mm have been used, a = 5 mm, W = 10 mm.

For low strain rates the experimental curves of load versus displacement have been shown in Figure 2 for three different notch radii. The local strain rate at the notch tip has been calculated using the finite element method and varied from 6.10^{-4} s^{-1} to 1.10^{-3} s^{-1} for these experiments. Displacements have been measured using a strain gauge extensometer with a gauge length of 37.5 mm. As the region outside the notch deforms only elastically, the elongation mainly arises from plastic deformation at the notch. In the figure also arrows have indicated the points of initiation of fracture. A specimen with a notch radius of 0.45 mm was broken in a brittle way just after this initiation point and showed small ductile initiation of fracture at the notch tip. The increase of the maximum load is thought to be caused by increasing hydrostatic stress level at the notch. The area reduction at failure strongly decreases with increasing load level, and this confirms the assumption that hydrostatic stress enhances ductile failure. Figure 3 shows the average values of the failure strain from area reduction at fracture measured from several experiments, and have been computed from:

$$\varepsilon_f = \ln\left(\frac{A_0}{A_f}\right) \tag{1}$$

in which ε_f is the true fracture strain and A_0 and A_f the initial and fracture cross sectional area at the notch, respectively. Several strain rates have been applied in the rolling direction of the material (indicated by curves) and the strain rates in the graph were derived using the finite element method. The influence of the rolling direction is remarkably high compared to the strain rate influence and has been tested only at low strain rates for specimen perpendicular to the rolling direction of the plate material (single points).

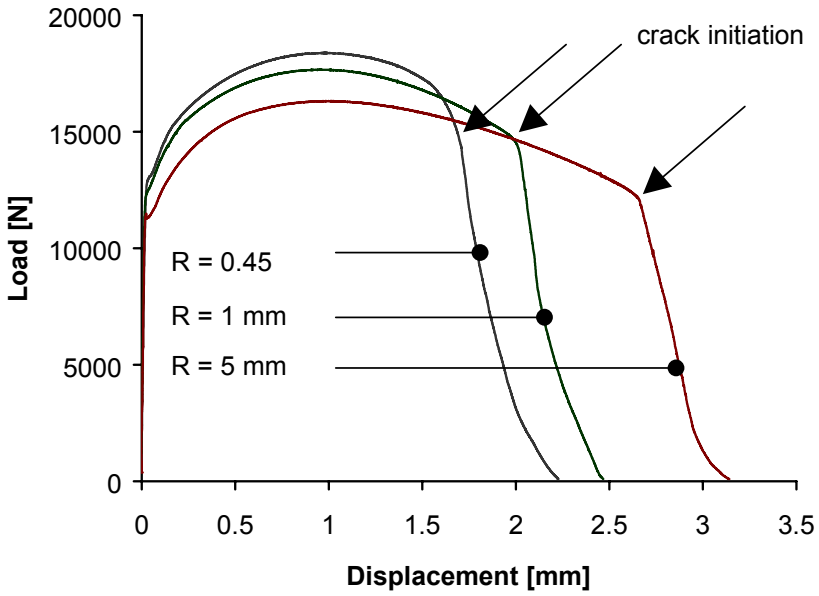

Figure 2: Load – displacement curves for notched specimen in the rolling direction of the plate material at low tensile velocity. Notch radii have been indicated by R.

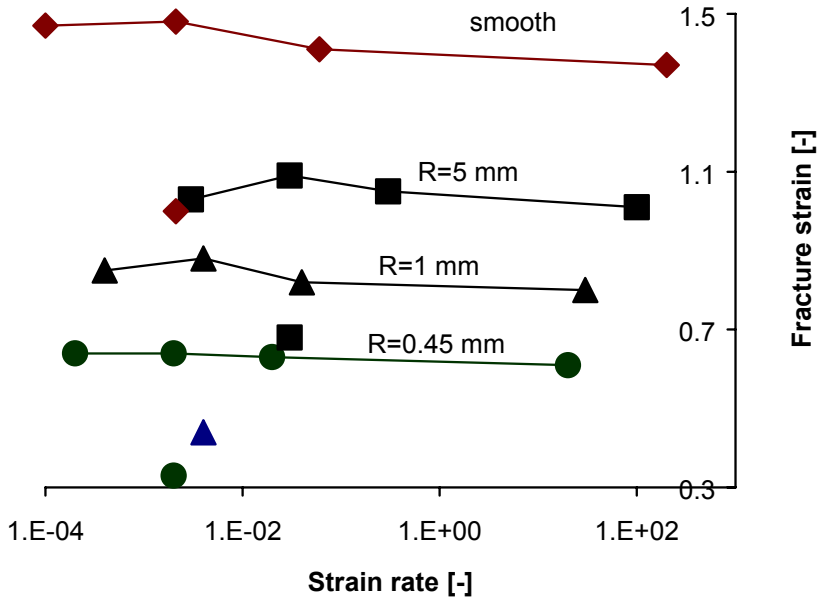

Figure 3: Fracture strains from area reduction for smooth and notched specimen at several strain rates. Strain rates are average values related to area reductions. Standard deviations vary from 0.02 to 0.05.

NUMERICAL PREDICTIONS OF DUCTILE FAILURE

Damage Predictions According to Rice and Tracey

Numerical simulations have been performed using the flow stress of the material, which has been determined experimentally, [2]. The flow stress has been defined as a function of the plastic strain and strain rate. Three-dimensional models have been used to model 1/8 part of each notched specimen, taking into account symmetry conditions. Also a smooth round tensile specimen of 5 mm diameter has been simulated. A preliminary analysis showed that the influence of mass inertia effects is negligible and therefore no dynamic effects have been incorporated into the analysis. A standard plasticity algorithm has been used in the finite element calculations, together with a von Mises yield criterion and isotropic strain hardening. The Rice and Tracey model for ductile damage evolution has been incorporated. The model describes the growth of a void in a plastically deforming material. Assuming an initial void radius R_0 the growth has been given by:

$$\ln\left(\frac{R}{R_0}\right) = 0.283 \cdot \int_{\varepsilon_p} \exp(A_{RT} \cdot \sigma_h / \sigma_e) \quad d\varepsilon_p \tag{2}$$

in which A_{RT} is a constant equal to 3/2, σ_h the hydrostatic stress and σ_e the equivalent von Mises stress. Some results of finite element calculations at low strain rates will be discussed first.

Figure 4 shows local values of the relative hydrostatic stress (triaxiality) σ_h / σ_e . These values have been evaluated at the position of maximum damage, for the R = 1 mm and R = 0.45 mm radius specimen this is at the centre of the notch tip and for the R = 5 mm and smooth specimen at the centre of the minimum cross section. For the specimen with radius R = 1 mm is not quite clear if the initiation position is at the centre of the specimen or at the notch tip. This will be investigated experimentally in the future. As a criterion to stop the numerical simulations the failure strain according to Eqn. 1 has been used. Numerically, the strain from area reduction at the notch equals the experimental fracture strain when the calculation stops.

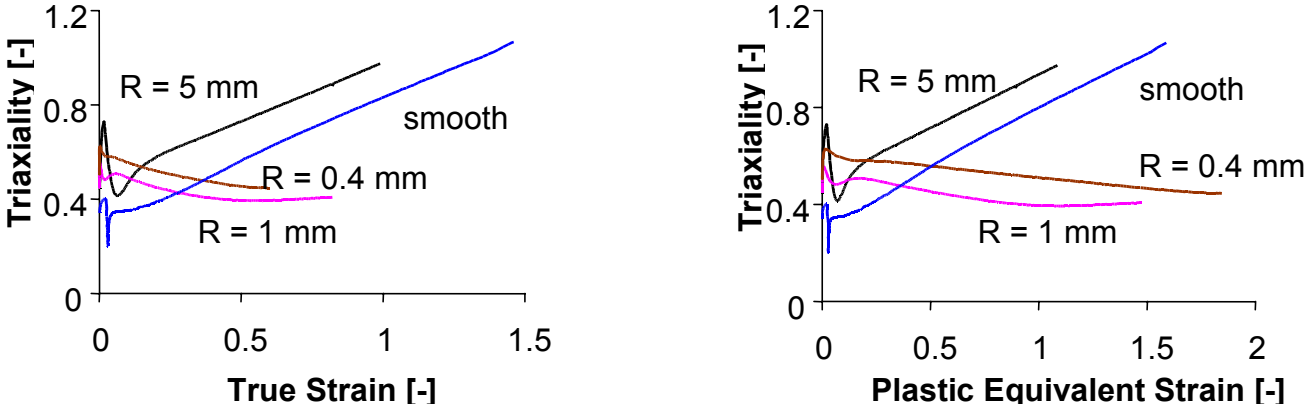

Figure 4: Triaxialities for several geometries at low strain rates. Notched geometries have been indicated by specifying the notch radius R, round tensile specimen is indicated by "smooth". Left figure (a) uses strain from area reduction, right figure (b) uses local plastic strain.

The calculated damage evolution according to Eqn. 2 has been shown in Figure 5 at identical positions in the specimen compared to the results shown in Figure 4. Taking into account the relation for ductile damage, Eqn. 2, together with the calculated hydrostatic stress - plastic strain history, Figure 4, one can conclude that no accordance can be achieved for the smooth and notched R = 5 mm specimen. This applies also for the R = 1 mm and R = 0.45 mm notched specimen. This conclusion becomes clear from Figure 5.

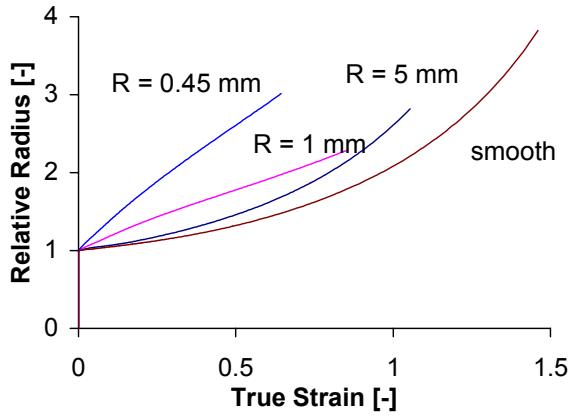

Figure 5. Relative radius predictions according to Rice and Tracey, $A_{RT} = 3/2$.

Influence of the Strain Rate

The damage predictions presented in this work do not include a dependence of the strain rate directly. This can be seen from the formulation used for local failure prediction, Eqn. 2. Implicitly this mechanism is accounted for by strain rate dependence of the flow stress. Experimental results confirmed the choice of this relatively simple approach. No significant dependence of the fracture characteristics has been observed from the tensile tests at different rates of strain. Elongation, reduction of area at fracture, and fracture surface showed no remarkable changes at elevated strain rates. A minor reduction of strain from area reduction might be concluded.

The influence of the strain rate on the local damage prediction in quasi-static analyses has been investigated as well. In these analyses the mass inertia influence has been neglected. In these analyses the strain rate influences the flow stress and will result in strain rate dependent damage evolution. However, physical processes that might influence the void growth on a different basis than the influence of the strain rate on the flow stress have not been taken into account. Reduction of strain at failure has been predicted from the numerical results, applying the same critical damage value for all strain rates. For an increase of the strain rate of 1.10^5 s^{-1} the failure strain reduces about 0.1 for the smooth specimen and about 0.06 for all notched geometries. These values agree with the experimental observations.

Introduction of a Length Parameter

Failure predictions using a characteristic volume might improve the analogy between experimental results and numerical computations. This volume represents a certain process zone in which failure takes place. The characteristic length of the zone can be related to microstructural characteristics, such as the average inclusion size or grain size. The finite element model has been chosen is such a way that the element length in front of the notch tip is equal for all notched specimens. Damage has been evaluated as the average value of each element. As the formulation for strain calculation uses an updating of the incremental displacements (Updated Lagrange), the elements deform in a similar way as the material structure. This can be interpreted as to account for the changing inter-inclusion spacing at proceeding deformation. The element length has been chosen in such a way that the model size would not be excessively large. This element length is approximately 210 µm and might be related to the average inclusion distance of the manganese sulphides, which has been estimated to be 310 µm.

The critical damage value from a smooth tensile specimen changes not significantly using the constant element size approach, as the gradient in damage is small in the specimen centre. A calculation has been performed applying constant element size with similar dimensions as has been used for the notched specimen. From this calculation a damage value of 3.7 has been found. From the finite element results can be concluded that fracture initiation in the notched specimens takes place at lower damage values compared with the smooth tensile specimen. Taking a closer look to the damage curves, the critical value of the relative radius at failure initiation is approximately 2.5 ± 0.35 for all notched geometries. For the smooth specimen this relative void radius corresponds to a strain of 1.2 ± 0.1. Interrupted tests have been

analysed to gain more insight in the process of ductile fracture initiation in the smooth specimen. Table 1 shows the predicted area strains together with experimental results at low strain rates for a critical R/R_0 value of 2.5.

TABLE 1
COMPARISON OF NUMERICAL PREDICTIONS WITH EXPERIMENTAL VALUES
FOR STRAIN FROM AREA REDUCTION AT FAILURE INITIATION.

	smooth	R = 5 mm	R = 1 mm	R = 0.45 mm
experiment	1.47	0.9 – 1.03	0.75 – 0.85	0.55 – 0.64
prediction	1.2	0.97	0.87	0.44

For the notched geometries a more consistent prediction of failure has been obtained. For all notch geometries a damage value of 2.5 has been obtained at fracture initiation. Smooth specimen modelling still results in a larger damage value at failure compared with notched specimen. An approximate failure criterion has been found however, underestimating the failure strain for a smooth specimen with a relative error of 20%. Considering energy absorption in the last stage of deformation prior to fracture of the specimen, this inaccuracy is acceptable.

CONCLUSIONS & RECOMMENDATIONS

From the experimental results has been observed that the failure strain from area reduction at fracture does not change significantly with the strain rate. In a first approximation this effect might be neglected. A decreasing notch radius also decreases the failure strain and increases the hydrostatic stress at the notch. A large influence has been found of the rolling direction of the plate material. The failure strain decreases strongly in the direction perpendicular to the rolling direction.
Application of a ductile damage model according to Rice and Tracey results in inconsistent damage predictions at the experimentally determined fracture strain from area reduction. This is inherent to the applied formulation taking into account the triaxiality – plastic strain path for the points where fracture initiates. Another approach where a certain element volume has been taken into account results in consistent failure predictions for the notched specimen. Comparing this damage prediction at failure with a smooth specimen, an overestimation of damage has been found from the numerical results. However, this approach can be used for a first approximation of the failure behaviour of blast loaded panels in ship structures.

A comparison of void sizes for a notched specimen with notch radius R = 5 mm and a smooth specimen before the onset of failure would be interesting, relating these values to finite element predictions.

ACKNOWLEDGEMENTS

This research was funded by the Technology Foundation STW, the TNO Prins Maurits Laboratory and the Delft University of Technology.

REFERENCES

1. Rice, J.R., Tracey, D.M., (1969) *On the Ductile Enlargement of Voids in Triaxial Stress Fields*, Journal of the Mechanics and Physics of Solids, vol. 17, 201
2. Pape, G., Bakker, A., Janssen, M., (2001) *Flow Stress of Steel at Large Strains and High Strain Rates*, International Conference on Fracture, ICF 10, Conference Proceedings, Honolulu

ORAL REFERENCE : ICF100101OR

FRACTURE PROCESS OF PM Ti6Al4V AT 20K IN PRESENCE OF IMPURITIES

L. Briottet[1], N. Scheer[1] and D. Guichard[2]

[1] CEA/Grenoble, DRT/DTEN, 17 rue des martyrs,
38054 Grenoble cedex 9, France
[2] SNECMA/Division Moteurs Fusée, Forêt de Vernon, BP802,
27208 cedex Vernon, France

ABSTRACT

PM Ti6Al4V is foreseen to manufacture rocket engine components with complex geometry. The major drawback related to this process is the potential presence of impurities mixed with the initial powder. At cryogenic temperature, some of these pollutions lead to a strong decrease of the material ductility. In order to validate the Ti6Al4V powder metallurgy route for critical engine components, it is necessary to understand and quantify the influence of such pollutions. Due to diffusion during the compaction cycle, several layers with different chemical and crystallographic properties are formed. In this paper, an analysis by SEM and TEM of these phases is presented. Moreover, mechanical tests at 20K, including interrupted tensile tests, allow to discriminate the worst potential defects and to propose several fracture processes depending on the initial impurity chemical composition.

KEYWORDS

Ti6Al4V, powder metallurgy, defects, fracture mechanisms

INTRODUCTION

The improvement of rocket engine efficiency necessitates components with an increasing complex geometry. For cryogenic applications, the α/β Ti6Al4V titanium alloy is used owing to its high strength, specific modulus and ductility at such temperatures. To achieve complex geometry, the powder metallurgy route is foreseen with the additional advantage that it provides a good homogeneity of the microstructure. However, a major drawback comes from the possible presence of impurities in the initial powder before compaction. These impurities can be introduced either during the melting operation, during powder production or during subsequent handling. Some defects can be quite large, typically 500 µm diameter including the diffusion affected volume, and lead to a strong decrease of the ductility of the material at low temperature (20K) under monotonic loading. The aim of this study is to investigate the effect of various defects on the ductility as well as to understand the failure mechanisms in order to predict the rupture of a component under in-service conditions.

DEFECTS DESCRIPTION

The Ti6Al4V titanium alloy, widely used in aeronautic and astronautic industries, has the following composition (wt %) : Al 6, V 4, Ti bal. The powder metallurgy alloy microstructure consists of α (hcp) grains with two morphologies, globular or lath shape, embedded in a β (bcc) phase (~10% volume fraction). The potential impurities likely to be found are the following ones (including the composition of the principal elements in wt %) : In718 (Cr 19, Fe 18, Nb 5, Mo 3, Ni bal.), In625 (Cr 20, Mo 8, Nb 3.5, Ni bal.), Astroloy (Cr 15, Mo 5, Al 4, Ti 3.5, Co 1.5, Ni bal.), FeNi (Fe 70, Ni 30), Stellite 21 (Cr 26, Mo 5.5, Ni 2.5, S, 1, C 0.25, Co bal.). After the compaction HIP cycle, followed by a classical heat treatment in order to control the titanium alloy microstructure, the defects present several layers due to cross-diffusion of chemical elements as shown in Figure 1. In these micrographs, displaying the chemical contrast (BSE), the surrounding laths correspond to Ti6Al4V material still affected by diffusion and not yet to the bulk material. By changing the contrast in the bright centre of the defects, more layers can be observed. SEM chemical analysis shows that for the three Ni base alloys analysed, the composition of the initial powder particle completely vanishes, mainly due do Ti diffusion from the matrix and Ni diffusion to the matrix. In the Co base alloy, a similar phenomena is observed with more Ti and a lack of Co in the centre. By contrast, the centre of the FeNi defect remains almost unaffected by diffusion (less than 2% Ti is observed). Of course, these considerations are linked to the unknown size of the initial defect particle of powder, which is at least the diameter of the central layer after compaction.

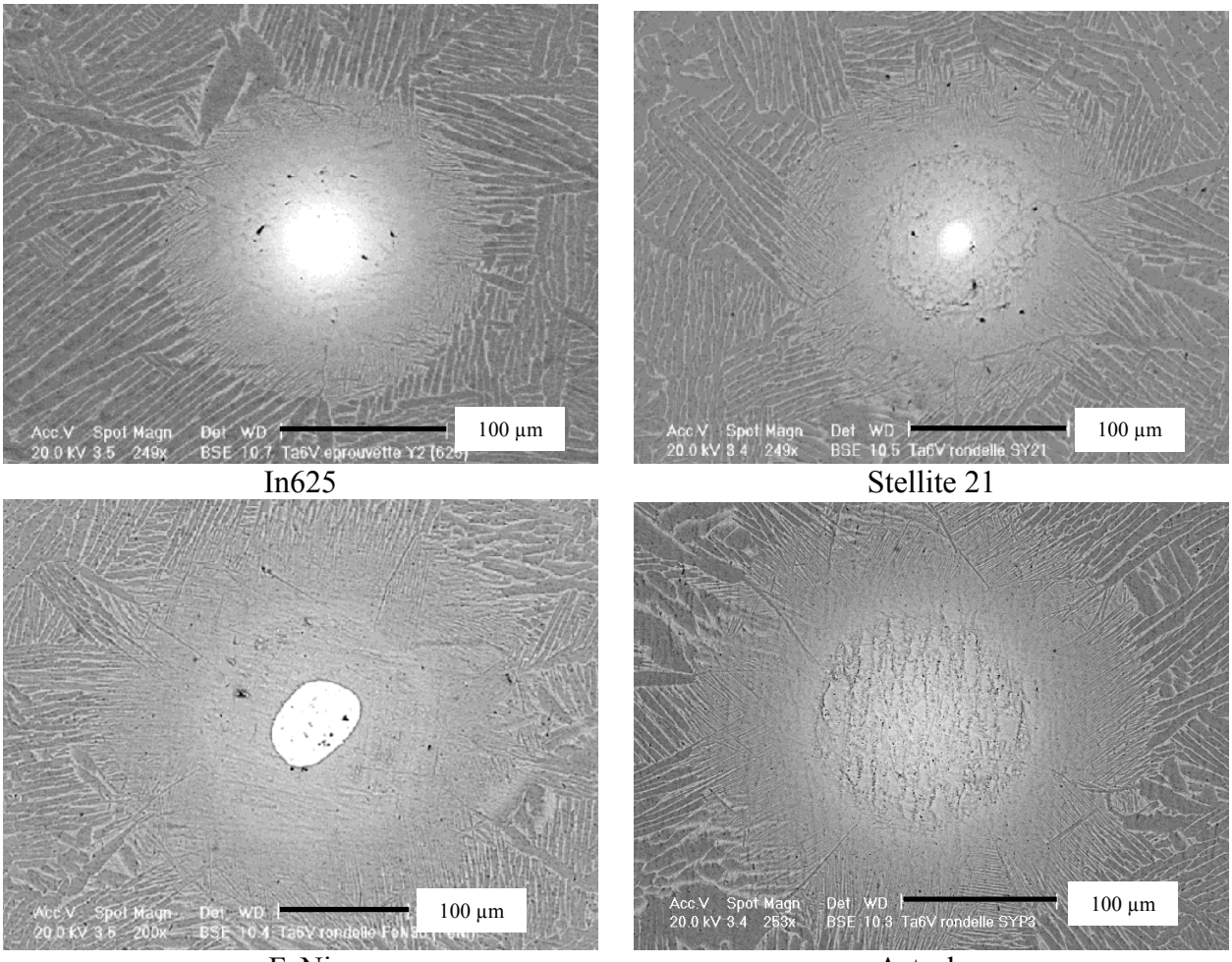

In625 Stellite 21

FeNi Astroloy

Figure 1: Overall aspect of the pollutions

To identify the phases responsible for damage initiation, thin foils have been prepared with care in a In718 pollution for TEM observations (Figure 2). The centre of the pollution is composed of a bcc phase corresponding to Tiβ rich in Cr, and a Ti_2Ni fcc phase with grains of a few µm. The surrounding large layer

consists in large Tiβ grains : a single grain through the whole thickness. The In625 defects are similar to the In718 ones (the main chemical difference is due to the amount of Fe in In718).

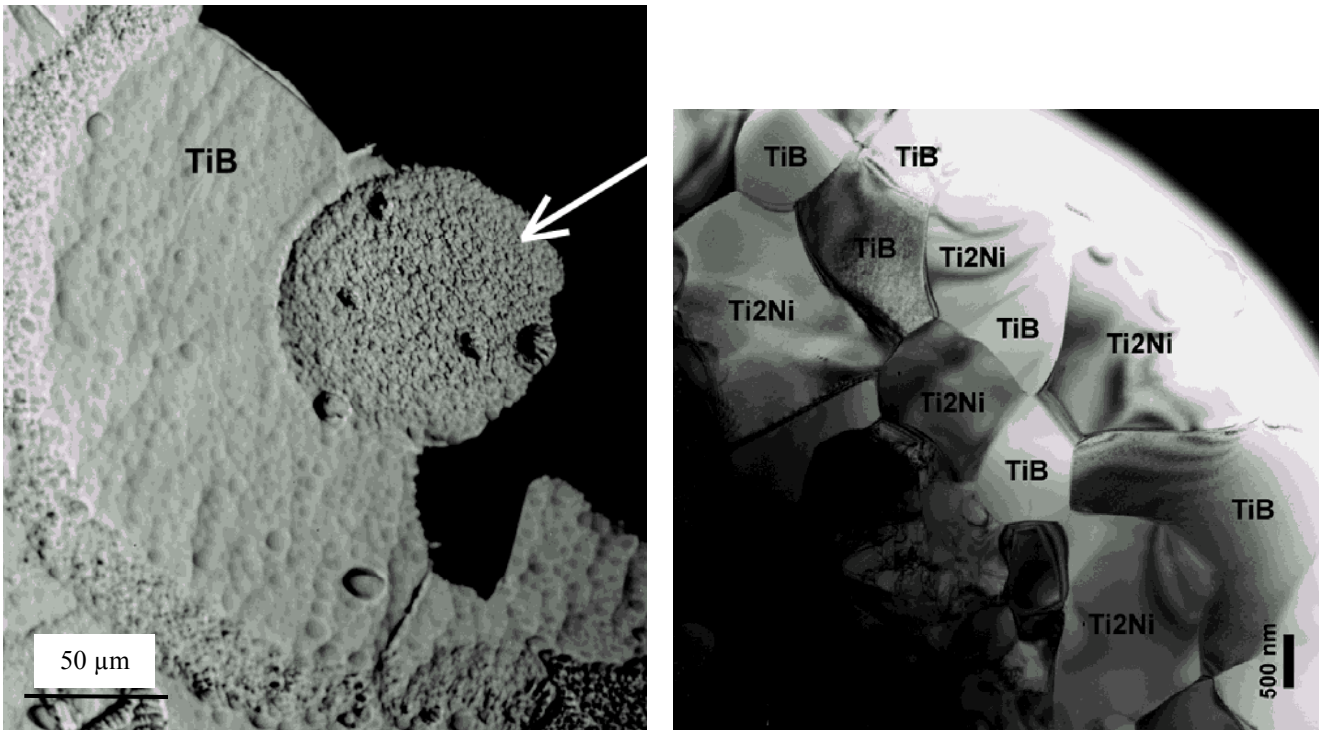

Figure 2: SEM (left) and TEM (right) observation of a In718 pollution in the Ti6Al4V matrix

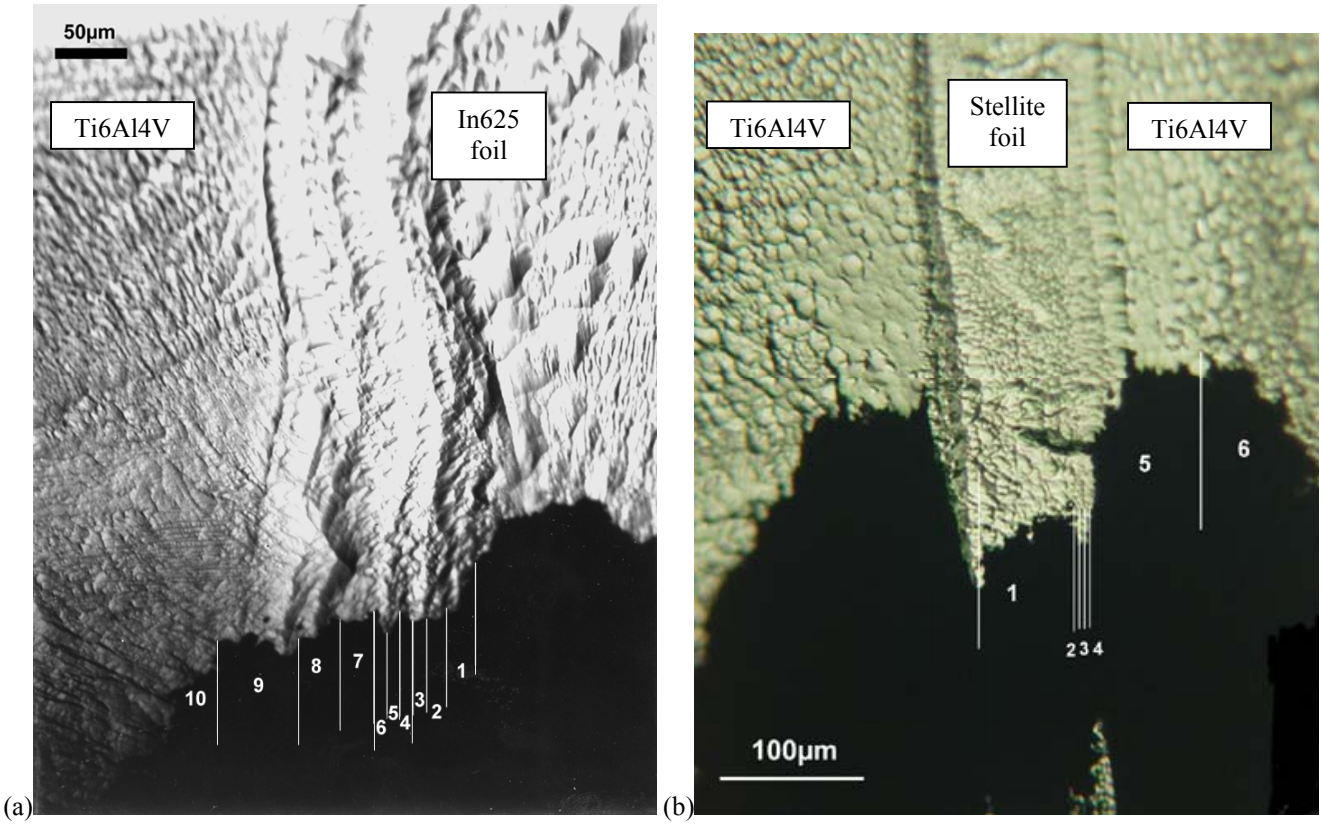

Figure 3: Plane defect (a) In625 foil (b) Stellite foil

Due to the heterogeneous thinning of the thin foil, it was not possible to analyse all the layers observed on spherical defects (Figure 2). Thus, flat defects have been performed by introducing a In625 or a Stellite foil (~100 µm thick) in the Ti6Al4V before compaction. With this defect geometry, thinning crosses the whole layers as seen in Figure 3. All the different phases can here be addressed by TEM analysis. However, the

results have to be handle with care since the diffusion process is not the same for a spherical powder than for a foil. Indeed, some phases observed for one type of geometry may not exist for the second type.

For the Stellite defect a large Tiβ layer is also identified. Moreover, in the small layers close to the defect centre several intermetallics are observed : TiCo, Ti_2Co and CoCr.

MECHANICAL TESTS

In order to analyse the effect of such impurities on the material ductility, tensile tests have been performed at 20K on blocks compacted from voluntarily polluted Ti6Al4V powders. After the compaction cycle, the main pollutions have been localised by X-ray NDE. Smooth and flat tensile specimens have then been machined to settle the impurities in their gage length. A low strain-rate has been imposed in order to avoid thermo-mechanical instabilities likely to occur in this material [1] at that temperature. The main results are displayed in Table 1 showing total elongation in presence of large enough impurities :

TABLE 1
TENSILE RESULTS AT 20K : TOTAL ELONGATION FOR EACH POLLUTION

pollution	no	Astroloy	In625	Stellite	FeNi	In718
TE (%)	~15	~15	~8	~5	~5	~2

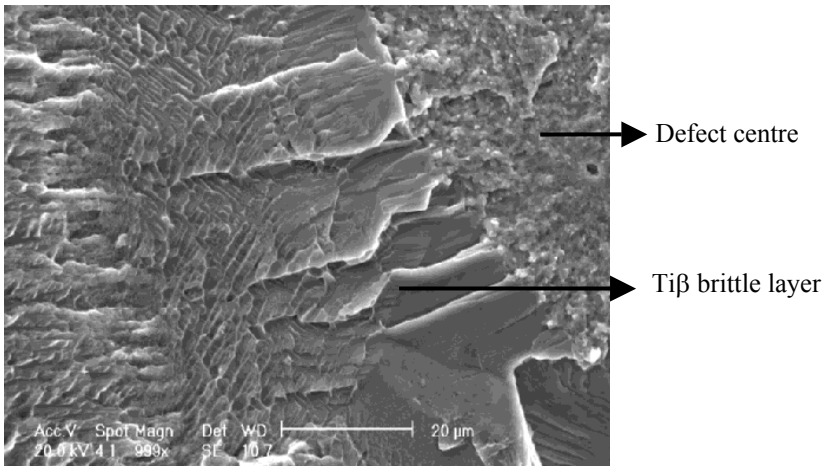

Figure 4: Fracture surface on a In625 pollution at 20K

As can be seen in this Table, Astroloy has no dramatic effect on ductility. By contrast, the other defects lead to a strong decrease of total elongation. Stellite, FeNi and In718 are the more dangerous defects. Tensile tests performed at several temperatures up to 293K emphasize the strong temperature influence on the defect/damage interaction : above 50K, no decrease of ductility is observed whatever the impurity present in the Ti6Al4V blocks.

A fractography of a specimen tested at 20K and containing a In625 pollution is displayed in Figure 4. Some of the layers observed previously by SEM and TEM examinations (Figures 1 and 2) can clearly be identified in this micrograph : the polyphase centre with a rough aspect and the surrounding Tiβ layer known to be brittle as confirmed on this Figure. The outermost layers exhibit a more classical ductile aspect.

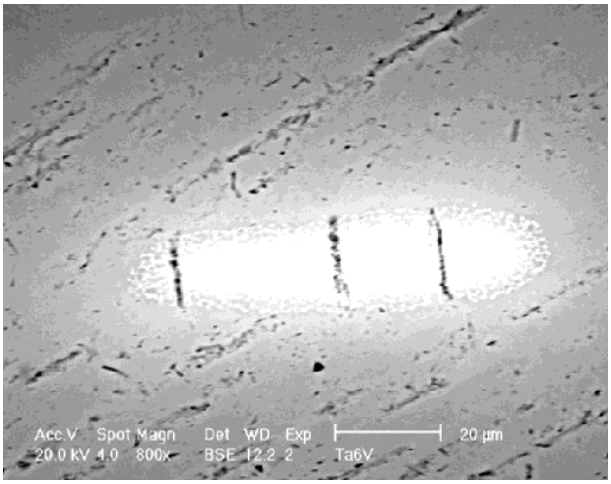

(a) In625 (~4.9%)

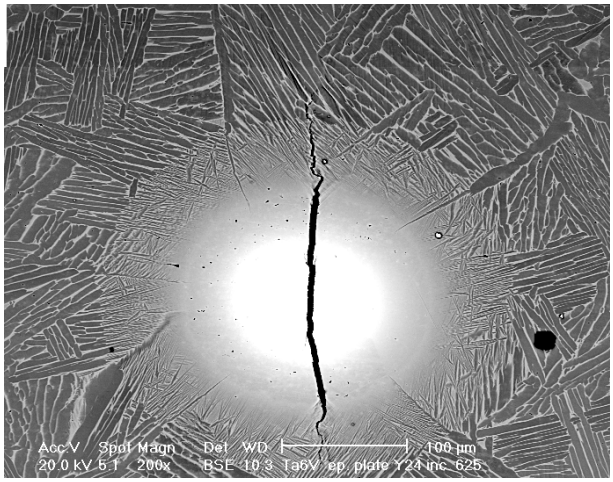

(b) In625 (~1.8%) (flat specimen)

Figure 5: Different stages of damage on In625 pollutions (horizontal loading direction)

Interrupted tests have been performed to analyse damage initiation in presence of such impurities. In Figure 5, different stages of the crack evolution are presented for a In625 pollution. The crack initiates in the centre (Figure 5a) of the defect probably composed of the following brittle phases : Tiβ and Ti_2Ni (as seen in the In718 TEM analysis). Moreover, due to the chemical compositions observed, a Laves phase Cr_2Ti [2] is also expected depending on the diameter of the initial powder. The crack then propagates first in a brittle fashion through the Tiβ layer and finally reaches the unaffected Ti6Al4V material (Figure 5b) where it grows between the α laths. From the very beginning of the damage process, the crack is observed perpendicular to the loading direction. Due to the similarities between In625 and In718 chemical composition and fractographies, the same type of propagation is expected in In718.

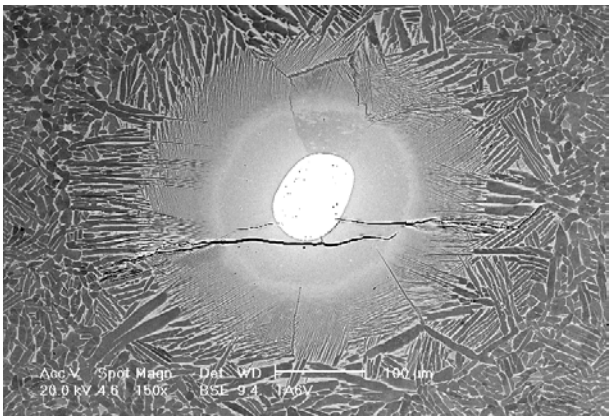

(a) FeNi (1.8 %) flat specimen

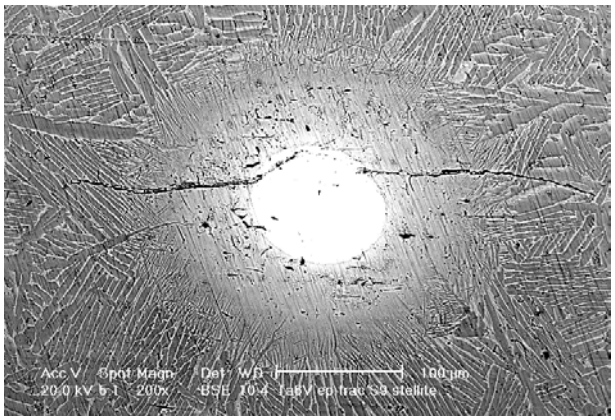

(b) Stellite (3%)

Figure 6: Damage initiation in FeNi (left) and Stellite (right) – (vertical loading direction)

By contrast, for FeNi (Figure 6a) and Stellite (Figure 6b), the crack never propagates through the defect centre. In both cases, the Tiβ brittle layer is broken perpendicularly to the loading direction and the crack pass round the centre.

DISCUSSION

The main conclusion derived from these experiments are presented in Table 2. Interrupted tests at the Ti6Al4V yield stress showed that in the case of FeNi and Stellite, a crack is already present at that stress level. Due to the low ductility observed in presence of In718 defects, it is expected that crack initiation occurs also for an overall stress close to the yield stress. By contrast, in the case of In625, crack initiation is observed after the yield stress.

TABLE 2
MAIN CONCLUSIONS ON THE DEFECTS INFLUENCE ON DAMAGE

pollution		astroloy	In625	FeNi	Stellite	In718
Induced damage	Initiation	-	$\sigma > YS$	$\sigma \leq YS$	$\sigma \leq YS$	$\sigma \leq YS$?
	Min. defect radius	-	$R > 100\mu m$		$R > 50\mu m$	
	TE decrease	-	small	strong	strong	strong

By analysing many samples of In625 and Stellite, a minimum size of the defect centre necessary to induce accelerated damage has been defined. Due to diffusion, the size of the initial defect particle was certainly greater. However, it appears that a pollution of Stellite roughly twice smaller than a In625 one is sufficient to induce damage.

From the above results, we can propose the following fracture processes for the several types of impurities. For In718 and In625, the critical stress for cleavage is first reached in one of the intermetallic compounds present in the central part of the defect. The small grains as well as the polyphase microstructure explain the rough aspect observed on the fractography. In a second step, due to stress concentration at the crak tip and increase of the overall stress, the critical stress in the Tiβ is reached leading to the brittle propagation seen in Figure 4. In718 is found more dangerous than In625 probably due to a particular intermetallic with a lower cleavage stress. The damage stages of FeNi and Stellite are quite different. From the micrographs performed on interrupted tests, it appears that the first stage corresponds to the brittle rupture of the Tiβ layer. The crack then propagates towards the centre following the interface between the centre and the surrounding layer.

This mechanism can explain the effect of temperature by the low sensitivity of the cleavage critical stress σ_c with temperature. If σ_c is considered constant with T, an increase of the testing temperature leads to a decrease of the stresses magnitude in the whole defects. Above 50K, the damage mechanism in the unaffected Ti6Al4V is initiated before cleavage in any of the brittle layers of the defects.

The next step is to quantify the critical stress of the observed brittle layers since in the literature these intermetallics compounds have only been studied at high temperatures.

ACKNOWLEDGEMENTS

The authors are thankful to the Centre National d'Etudes Spatiales for partial financial support of this work, and to I. Chu and S. Pachot for SEM and TEM contributions.

REFERENCES

[1] Ambard, A., Guétaz, L., Briottet, L., and Guichard, D. (1999) IN : *Proc. Of the 9th World Conference on Titanium*, pp. 608-615, Saint Petersburg, Russia.
[2] Van Beek, J.A., Kodentsov, A.A. and Van Loo, F.J.J. (1998) *J. Alloys Comp.* 270, 218.

POSTER REFERENCE: ICF100568OR

CORROSION AND STRENGTH DEGRADATION OF Si-BASED CERAMICS BY MOLTEN SALT

NAOYA MASUDA[1] and YUJI KIMURA[2]

[1]Graduate Student, Kogakuin Univ.1-24-2 Nishishinjuku,Shinjuku-ku,Tokyo,163-8677, Japan
[2]Department of Material Science and Technology, Kogakuin Univ.1-24-2
Nishishinjuku,Shinjuku-ku,Tokyo,163-8677, Japan

ABSTRACT

Several trials have been conducted for applying Si-based ceramics as the materials used for the high temperature structure such as gas turbine components, because of there superior fracture toughness and thermal shock resistance under high temperature condition. However, various problems concerning oxidation and corrosion under high temperature environment have been reported. From among various high temperature corrosion problems, the molten salt corrosion has been pointed out as the most important one which caused serious fracture strength degradation. Purpose of this study is to evaluate the corrosion behavior and the degradation in the mechanical property of SiC and Si_3N_4 caused by molten salt. As a result, the influence of molten salt Na_2SO_4 upon the mechanical property of structural ceramics SiC and Si_3N_4 was made clear to be caused by the progressive corrosion reaction, i.e. the successive repetition of the generation and removal of the SiO_2 membrane under the high temperature condition.

KEYWORDS: SiC, Si_3N_4, gas turbine, molten salt Na_2SO_4, corrosion, oxidation, SiO_2, strength degradation,

INTRODUCTION

The application of Si-based ceramics is expected as the material of the high temperature structure such as gas turbine etc. because SiC and Si_3N_4 have excellent fracture strength, fracture toughness and thermal shock resistance under high temperature condition. It was pointed out that the materials used for the high temperature

gas turbine system were seriously corroded by heavy molten salt such as Na_2SO_4 together with the high temperature oxidation[1]. Therefore it becomes important that the materials used in this system must be basically stable under these corrosive environments. Also, they must have superior thermo-mechanical properties. As mentioned before, non-oxide ceramics such as SiC and Si_3N_4 show excellent fracture strength, fracture toughness and thermal shock resistance when used under high temperature condition. However, these non-oxide ceramics fundamentally have unstable oxidizing character especially under heavy molten salt environment. Therefore, it is important to evaluate the effects of molten salt corrosion upon the mechanical properties of non-oxide ceramics.

Therefore in this paper, corrosion characteristics and degradation of mechanical properties of Si-based structural ceramics such as SiC and Si_3N_4 by molten salt of Na_2SO_4 were investigated. Also, degradation mechanism of Si-based ceramics by molten salt was discussed.

EXPERIMENTAL PROCEDURE

Specimen

Materials used in this study are SiC and Si_3N_4, which are mainly used for various parts of gas turbine engine. Square cross-sectional bar type test specimen ($4 \times 3 \times 40$mm) with a chamfered edge of 0.1 mm is cut from the sintered plate. Surface of specimen was finished by polishing to obtain mirror surface. The sintering method and chemical composition of Specimen are shown in the following Table 1.

Table 1. Specimen Date

Item	SiC	Si_3N_4
Sintering method	Normal pressure sintering	Gas pressure sintering
Chemical Composition	SiC, Na, Mg, Ca, Fe, Ti, Al, Y, B	Si_3N_4, Al_2O_3, Y_2O_3

High Temperature Corrosion Tests and Strength Tests

High temperature corrosion test was conducted employing Na_2SO_4 coated specimens. The Na_2SO_4 coating was conducted as follows. First of all specimen was immersed into the solution that 9.55 g of Na_2SO_4 was mixed to 0.1 litter of pure water. Dip coated layer of Na_2SO_4 was obtained on the surface of the specimen. Then, water molecule in coated layer was evaporated by drying. High temperature oxidation and corrosion tests at 1atm were conducted under various temperature conditions up to 1373K. Holding time for high temperature testing was ranged up to 8 hours. The degrees of progress of high temperature oxidation and molten salt corrosion were evaluated by the change of residual bending strength employing JIS R1601 4 point bending test [2] using each 2 specimens with and without molten salt Na_2SO_4 coating after various high temperature tests. The deflection rate is in bending test selected as 0.5 mm/min. The detailed microscopic observation of specimen surface and fracture surface was conducted by FE-SEM.

EXPERIMENTAL RESURTS AND DISCUSSIONS

The Strength Degradation by Molten Salt Corrosion

The results of 4 point bending test obtain using non-oxidized and oxidized specimens of both SiC and Si_3N_4 under various high temperature conditions were shown in Figure 1. Both SiC and Si_3N_4 specimens without

Na_2SO_4 coated layer showed little change in there bending strength. On the contrary, these specimens with Na_2SO_4 coated layer showed remarkable degradation in bending strength as the corrosion temperature became higher. In case of Si_3N_4, bending strength after high temperature corrosion test under 1273 K and 1373 K with Na_2SO_4 coating dropped down till about the half of that of non-corroded specimen.

Therefore, the oxidation did not play an important role in strength degradation after high temperature test up to 1373K. On the contrary, high temperature corrosion by the molten salt such as Na_2SO_4 play an dominant role in the degradation of Si-based ceramics of SiC and Si_3N_4 under the temperature condition up to 1373K.

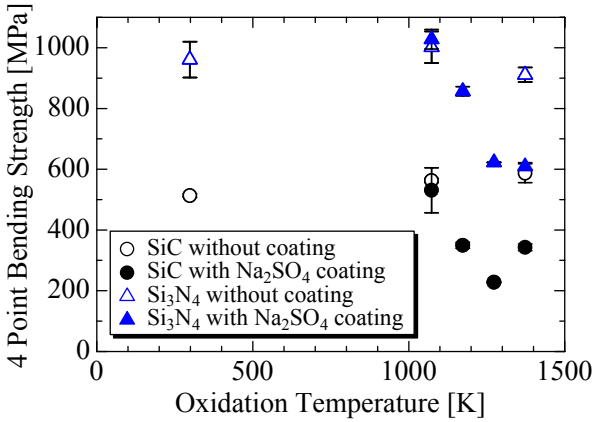

Figure 1: 4 Point Bending Strength after Oxidation Tests under Various Temperature

Also, it was understood that the strength drop of Si_3N_4 is by molten salt corrosion was remarkable compared with that of SiC specimen. Therefore, Si_3N_4 ceramic was more susceptible to molten salt corrosion than SiC.

The results of 4 point bending tests of specimen with Na_2SO_4 coated layer after high temperature corrosion under 1373K with various different holding times were obtained and Shown in Figure 2. These results of bending test after high temperature corrosion showed that the remarkable strength degradation was recognized even after 30 minutes molten salt corrosion. Therefore, molten salt corrosion by Na_2SO_4 was expected to cause serious damage on the Si-based ceramics especially Si_3N_4 even when exposure time of those material to the molten salt is relatively short. Then, no more serious progress in strength degradation was recognized after high temperature corrosion test under longer holding time conditions than 30 minutes. These bending test results showed that the degradation in bending strength caused by Na_2SO_4 corrosion might be saturated in the high temperature test under the above-mentioned conditions.

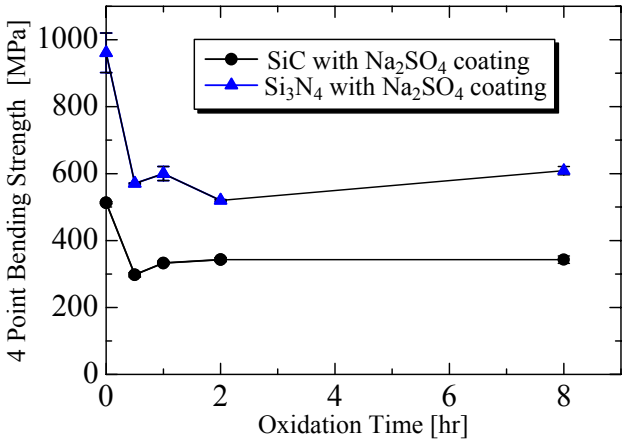

Degradation Mechanism of Si-based Ceramics by Molten Salt Corrosion

To make clear the corroded morphology and to investigate the mechanism of molten salt Na_2SO_4 corrosion in Si-based ceramics, detailed FE-SEM observation of specimen surface and fractured surface was conducted. In Figure 3, the fractured surface morphologies of oxidized and non-oxidized specimen with and without Na_2SO_4 coating were indicated. From Figure 3 it was understood that the fracture of specimen was initiated from original micro-void in specimen when bending test was conducting for non-oxidized specimens. In contrast, on the fracture surface of Na_2SO_4 corroded specimen after high temperature test under 1273K, bubble formation was recognized. Also, crack initiation from these bubbles formed on the specimen surface by molten salt corrosion was observed. The liquid phase $Na_2O \cdot 2(SiO_2)$ formation due to the chemical reaction between molten salt Na_2SO_4 and SiO_2 under the high temperature oxidation condition may play an important role in the high temperature corrosion process of Si-based ceramics caused by Na_2SO_4. Namely the Si-based ceramics are oxidized under high temperature environment and cause the reaction of SiO_2 generation [3] as shown in the following.

$$SiC(s) + 1.5O_2(g) \rightarrow SiO_2(s) + CO(g) \quad (1)$$

$$Si_3N_4(s) + 0.75O_2(g) \rightarrow 1.5Si_2N_2O(s) + 0.5N_2(g) \quad (2\text{-a})$$

$$Si_2N_2O(s) + 1.5O_2(g) \rightarrow 2SiO_2(s) + N_2(g) \quad (2\text{-b})$$

Solid phase SiO_2 formed by the reaction shown by equations (1) and (2-b) reacted with Na_2O and then liquid phase $Na_2O \cdot 2(SiO_2)$ was generated.

$$Na_2SO_4(l) \rightarrow Na_2O(s) + SO_3(g) \quad (3\text{-a})$$

$$2SiO_2(s) + Na_2O(s) \rightarrow Na_2O \cdot 2(SiO_2) \quad (3\text{-b})$$

As a result, oxidation reactions of Si-based ceramics were continued successively. Therefore, continuous formation of N_2 and CO was resulted. These gas formations caused bubble generation that became the initial site for crack formation under bending stress. For this reason, remarkable degradation in room temperature residual bending strength after high temperature corrosion was brought about.

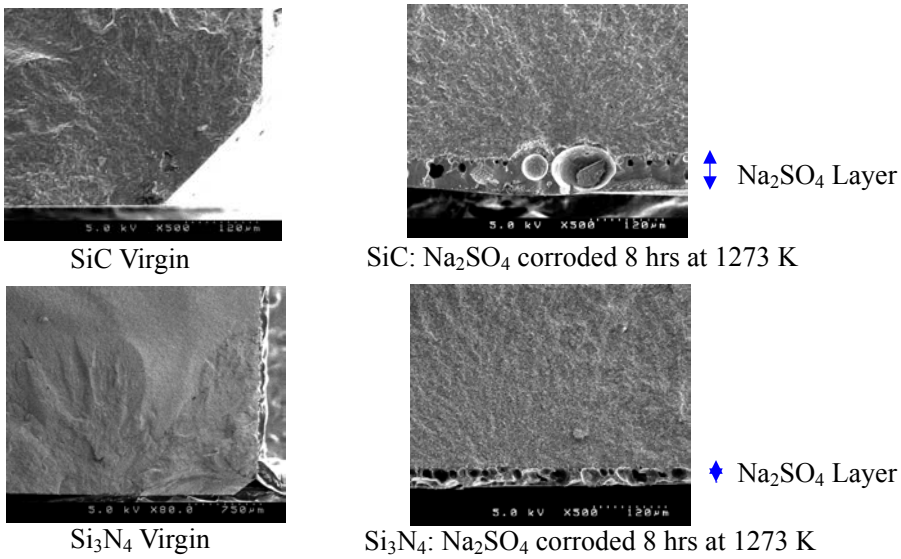

SiC Virgin | SiC: Na_2SO_4 corroded 8 hrs at 1273 K

Si_3N_4 Virgin | Si_3N_4: Na_2SO_4 corroded 8 hrs at 1273 K

Figure 3: FE-SEM Micrographs of Fracture Surfaces

Governing Factor for Residual Bending Strength after High Temperature Corrosion

To investigate the governing factor for residual bending strength of Si-based ceramics after high temperature test from the fracture mechanics view point, correlation between the inverse square root depth (d) of babble

formed layer by Na_2SO_4 corrosion $1/\sqrt{\pi d}$ and residual 4 point bending strength σ_R was investigated and shown in Figure 4. Also in this figure, fracture toughness data [4,5],i.e., K_{IC}=3.5 MPa$\sqrt{m}$ for SiC and K_{IC}=6 MPa$\sqrt{m}$ for Si_3N_4 were indicated by solid lines. As a result, it was indicated that the residual bending strength of Si_3N_4 decreased as the increase of square root depth of babble formed layer in case when the fracture of specimen was initiated from formed babble. For this reason, the residual bending strength of Si_3N_4 ceramic was controlled by K_{IC} value calculated based on depth of babble formed layer. On the contrary, in case of SiC ceramic, the residual bending strength data can not plotted on any straight line which showed $K_{IC}=\sigma_R\sqrt{\pi d}$ =Const, where σ_R means residual bending strength. Therefore, it becomes clear that the residual bending strength after high temperature corrosion can not be uniquely evaluated from the fracture mechanics view point evaluated based on the babble formed layer depth in case of Si-based ceramics.

In the followings, detailed examinations of facture surface morphologies especially bubble shape which governed the residual bending strength after high temperature corrosion test were conducted and shown in Figure 5. From the results shown in this figure, it was recognized that there was clear difference between the corroded morphology and bubble morphology formed on Si_3N_4 and SiC ceramics. In case of Si_3N_4 ceramics corroded by molten salt, continuous bubble formation was usually recognized in entire coated molten salt surface layer. On the contrary, local single bubbles were generated discontinuously in the coated molten salt layer in case of SiC ceramics. Therefore, the fracture of specimen was initiated from the local single bubble. For this reason, in case of SiC ceramics, K_{IC} value evaluation based on fracture origin defect area was introduced employing the following equation [6].

$$K_{IC}=K_{I\ max}=0.629\sigma_0\sqrt{\pi\sqrt{area}} \qquad (4)$$

Then, correlation between K_{IC} values evaluated based on defect area and residual bending strength were obtained and shown in Figure 6. Judging from the results shown in Figure 6, the residual bending strength after high temperature corrosion can be plotted around the straight line showing $K_{IC}=0.629\sigma_0\sqrt{\pi\sqrt{area}}$ =3.5MPa$\sqrt{m}$ in case of SiC. Therefore in this case, it was indicated that the residual bending strength of SiC decreased as the increase of square root defect area. For this reason, the residual bending strength of SiC ceramic was controlled by K_{IC} value calculated based on defect area.

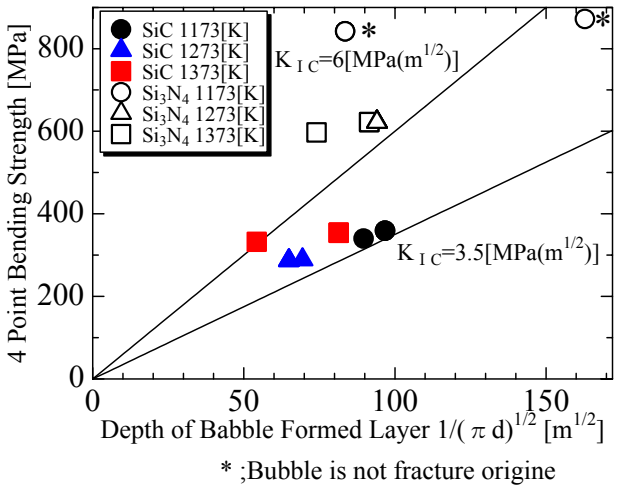

Figure 4: Relation Between Depth of Babble Formed Layer and Strength

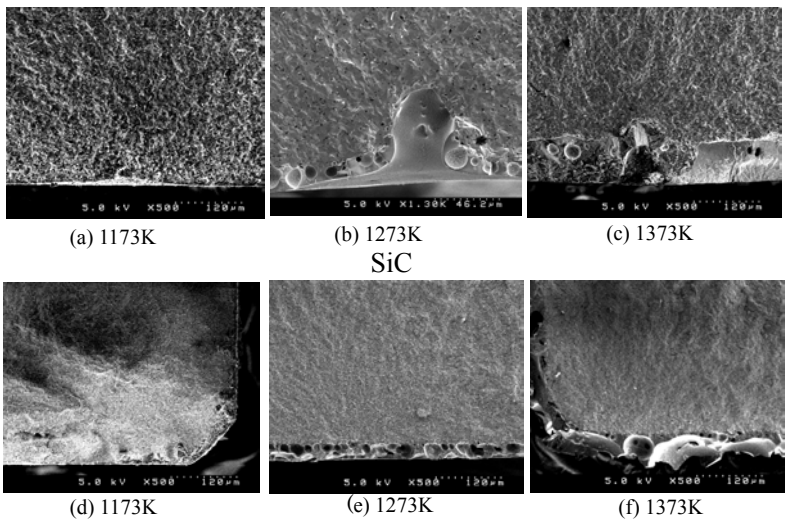

Figure 5: FE-SEM Photographs of Fracture Surface

Figure 6: Relation Between Defect Area and Strength

CONCLUSIONS

Corrosion characteristics and degradation in the mechanical properties of Si-based structural ceramics such as SiC and Si_3N_4 by molten salt of Na_2SO_4 were investigated.

Results obtained are summarized as follows:

1. The influence of molten salt Na_2SO_4 upon the mechanical property of structural ceramics SiC and Si_3N_4 was made clear to be caused by the progressive corrosion reaction, i.e. the successive repetition of the generation and removal of the SiO_2 membrane under the high temperature condition.
2. Also, the degradation of the mechanical property by the progress of the molten salt corrosion under high temperature environment became clear to be saturated within 0.5 hours.
3. Furthermore, the residual bending strength after molten salt corrosion can be investigated on the basis of fracture mechanics view point. In case of Si_3N_4 ceramics, K_{IC} can be evaluated on the basis of square root depth of babble formed layer. On the other hand, in case of SiC ceramics, it can be evaluated based on fracture origin defect area.

Accordingly, it is required to pay sufficient attentions to the existence of the molten salt when Si-baced ceramics such as SiC and Si_3N_4 are used under the high temperature environment.

REFERENCES

1. T Sato, Y Koike, T Endo, M Shimada, (1988) J. Soc. Mat. Sci., Japan, Vol.38, No.424, 39-43
2. JIS R 1601, (1994) Testing method for flexural strength of high performance ceramics
3. Nathan S. Jacobson, (1993) J. Am. Ceram. Soc., 76(1)3-28
4. Catalog of Sintered SiC “CERASIC B”, Toshibaceramics Co. Ltd.
5. Catalog of Gasometrical sintering Si_3N_4, NTK Co. Ltd.
6. Y Murakami, S Nemat-Nasser, (1983) Engineering Fracture Mechanics, Vol.17, No.3, 193-210

ICF1008870R

FRACTURE STRENGTH OF CERAMIC NOZZLE BLADES UNDER THERMAL SHOCK CONDITIONS

Takao Mikami [1], Koichiro Tagashira [2] and Masakazu Obata [3]

[1] Ishikawajima Inspection & Instrumentation Co., Ltd., Yokohama, JAPAN
[2] Ishikawajima-Harima Heavy Industries Co., Ltd., Tokyo, JAPAN
[3] Kanazawa Institute of Technology, Ishikawa, JAPAN

ABSTRACT

The fracture strength of ceramic turbine nozzle blades is evaluated under instantaneous thermal shock working conditions by a newly developed high-temperature thermal cycle cascade tunnel. The facility was designed to be produced an unsteady thermal stress more than 400MPa for ceramic blades and to confirm the fracture strength. The tunnel operates at a constant speed, with heated gas and ambient temperature air, and has the capability to perform thermal fatigue tests. The objective models are SiC and Si_3N_4 blades with a chord length of 33.6 mm and an aspect ratio of 1.05. The heating and cooling conditions of the test blade were confirmed with steady and transient measurements in the hot gas of 1,400 ºC and ambient cooling air. The measurements include surface temperature distributions on the both sides of the blade. The thermal stress distribution of the test blades was predicted by a finite element method under experimental boundary conditions. Typical results of the transient analysis for the test blades are presented and it is shown that the maximum thermal stress occurs at the leading-edge region of the test blades. The two SiC test blades were fractured at a maximum stress range of 550MPa, but any Si_3N_4 blade was not fractured up to 630MPa. A typical fracture mode of ceramic turbine nozzle blades under instantaneous thermal shock conditions is observed and the fracture mode is presented.

KEYWORDS

Thermal shock, Ceramics, nozzle, Fracture probability, Ceramic gas turbine

INTRODUCTION

Gas turbines have attractive characteristics such as low environmental pollution, fuel versatility and high specific power. An increase of the turbine inlet temperature (TIT) enables a significant improvement in the thermal efficiency of a gas turbine. Using metallic materials, further increase in TIT will not be expected without additional cooling air. One of the most effective means to solve this problem is the application of ceramics to gas turbine components. The application of ceramics to the hot section components enables a significant increase of TIT and the reduction of heat losses through the elimination of blade and nozzle cooling, resulting in improved thermal efficiency and fuel savings. The ceramic gas turbines are, therefore, attractive in terms of the conservation of energy resources and the protection of the environment [1,2].
In order to apply ceramic turbine blades to a gas turbine, we have to evaluate their resistance to thermal shock. Especially turbine nozzles are directly exposed to the high-temperature gas from a combustor and they will meet a high thermal shock in case of gas turbine trip and stop operating conditions.
For this purpose, we developed a high-temperature thermal cycle cascade tunnel to simulate the actual gas

turbine operating conditions and silicon carbide (SiC) and silicon nitride (Si_3N_4) nozzle blades were evaluated. This paper describes the developed apparatus and thermal stress evaluation procedures and test results.

THERMAL CYCLE CASCADE TUNNEL AND TEST NOZZLES

To simulate the actual operating condition of gas turbines, we adopted air and helium flows to a rapid cooling system. The apparatus was designed to enable a cyclic thermal shock testing and consists of a high-temperature gas generator (over 1,400℃), a heating and cooling block of ceramic turbine nozzles, a high-speed traverse unit of the nozzles, a control system and a data acquisition system. The main schematic of the apparatus is shown in Figure 1 in which four nozzles are arranged in a retainer block made of fire- brick as shown in Figure 2.

The block is heated up to a required temperature and then the block is rapidly traversed to the cooling air side at a constant speed. An instantaneous thermal shock test is thus completed. In case of cyclic thermal shock testing, following the above procedure, the block is traversed to the heating side contrary and the procedure is repeated. Considering the uniformity of the flow and temperature distribution, two inside nozzles among four nozzles are evaluated in the tests.

After the nozzles were heated up to 1,400℃, they were cooled by the cooling air. The velocity of the cooling air was increased step by step. The thermal stress induced in Si_3N_4 nozzle is lower than that of SiC because of the difference of the material properties. In case of the Si_3N_4 nozzles helium gas was also used for the cooling in order to increase the thermal stress.

Unsteady temperature distributions of the nozzles during the thermal shock test were monitored by scanning type and fiber type pyrometers.

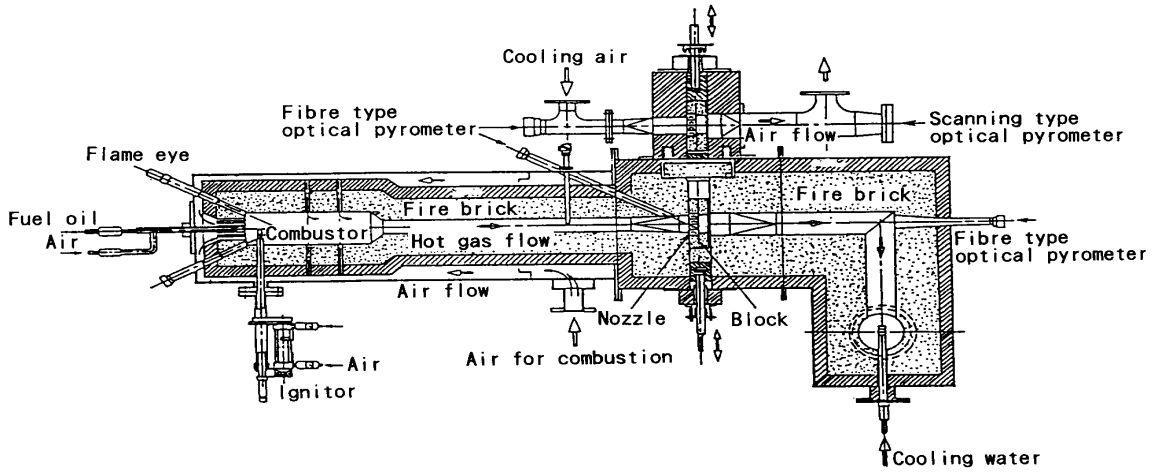

Figure 1: Thermal shock testing facility for turbine nozzle

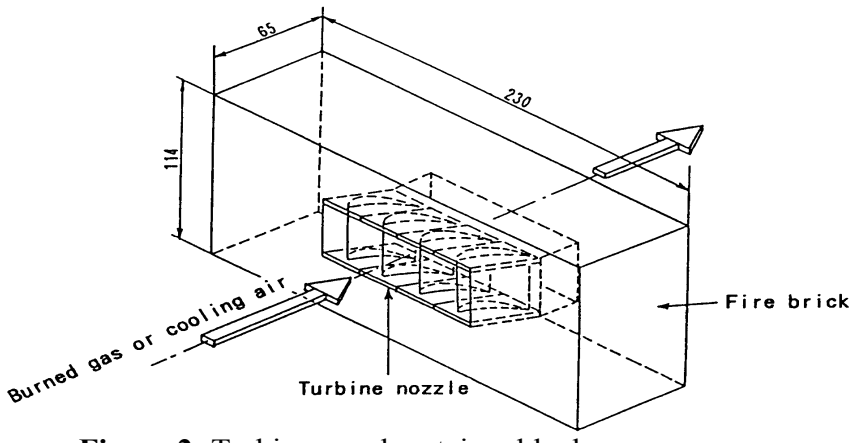

Figure 2: Turbine nozzle retainer block

The configuration of ceramic test nozzles is shown in Figure 3. Two types (Model A and Model B) were designed and were not twisted in considering the easiness of fabrication and analysis.

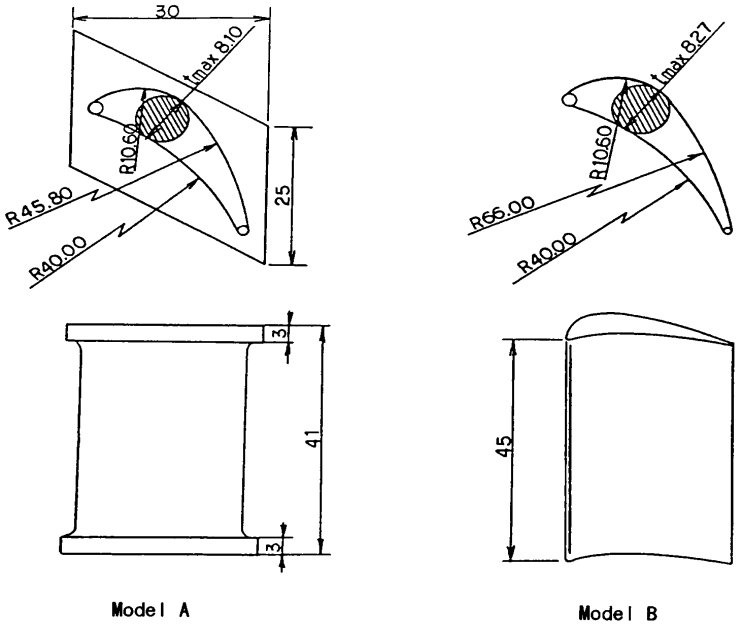

Figure 3: Configurations of turbine nozzle models

UNSTEADY THERMAL STRESS ANALYSIS

Figure 4 shows the flow chart of the test blade design and unsteady stress analysis procedure.
First heat transfer coefficients on the blade surfaces were calculated by a boundary layer approximation method using the specified velocity distribution on the blade surface.
Next, the unsteady temperature and stress distributions of the nozzle are analyzed by the MSC/NASTRAN program.
In the present study, the target strength of the material at 1,400℃was over 400MPa.

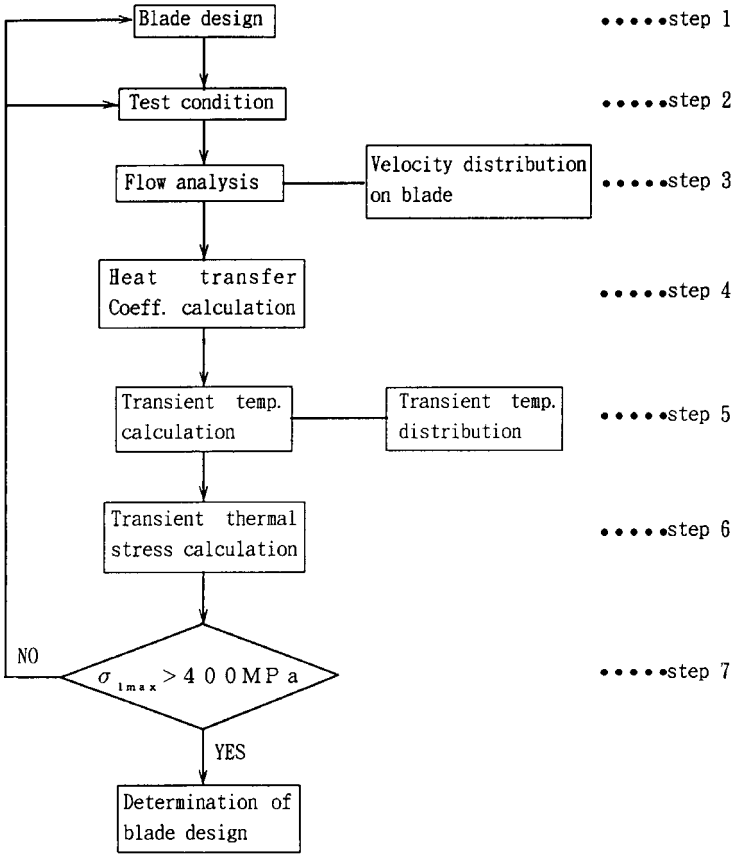

Figure 4: Flow chart of the test blade design and unsteady stress analysis procedure

TEST RESULTS AND DISCUSSION

Results for Model A

Test results for ten pieces of SiC nozzles is shown in Table 1. Any nozzles were not fractured though the cooling air velocity was increased up to 164m/s (630MPa in terms of stress). An analytical result of the thermal stress for one half model is shown in Figure 5(a). The maximum stress occurs at the leading edge. Figure 6 shows a transient thermal stresses with a change of air velocities. As for the leading edge, the stress increases rapidly as soon as cooling starts and after 1 to 2 seconds it reaches a peak value and then it decreases. On the other hand, as for the trailing edge the stress increases gradually and after 5 seconds it reaches a peak value and then it gradually decreases.

TABLE 1
TEST RESULTS OF MODEL A (SiC)

Model NO.	Cooling air		Initial temperature (℃)			Temperature at max. thermal stress (℃)			Max. thermal stress (MPa)
	Flow rate Q (m^3/h)	Velocity U (m/s)	Max. Camber	Trailing Edge	Leading Edge	Max. Camber	Trailing Edge	Leading Edge	
1,2	1,000	106	1,350	1,190	-	1,290	1,140	-	530
3,4	1,015	107	1,380	1,210	765	1,300	1,170	680	530
5	1,030	164	1,370	1,160	-	1,300	1,110	-	630
6	900	144	1,350	1,170	-	1,310	1,100	-	600
7	1,027	164	1,360	1,130	755	1,310	1,090	660	630
8,9	1,027	106	1,380	1,190	-	1,300	1,140	-	530
10	1,030	164	1,370	1,140	780	1,310	1,100	680	630

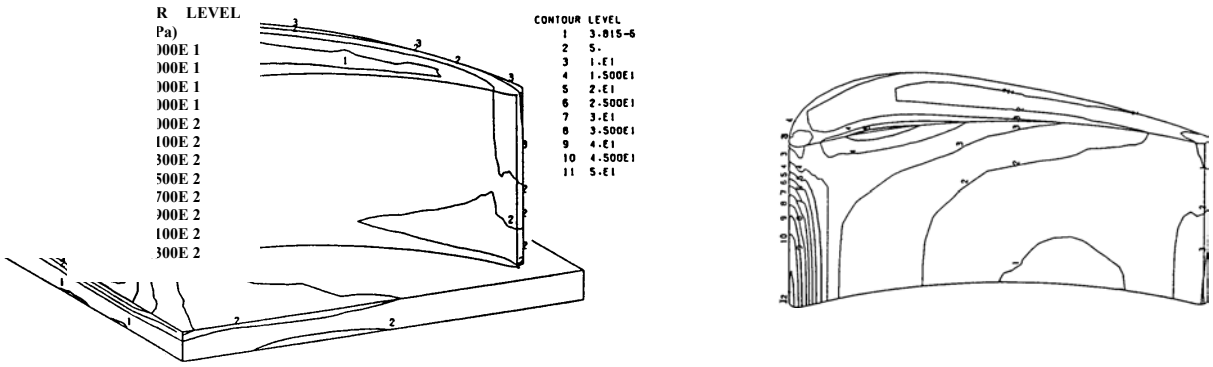

Model A (SiC, U=100m/s with air after two seconds) Model B (Si_3N_4, U=100m/s with air after two seconds)

Figure 5: Thermal stress of Model A and Model B

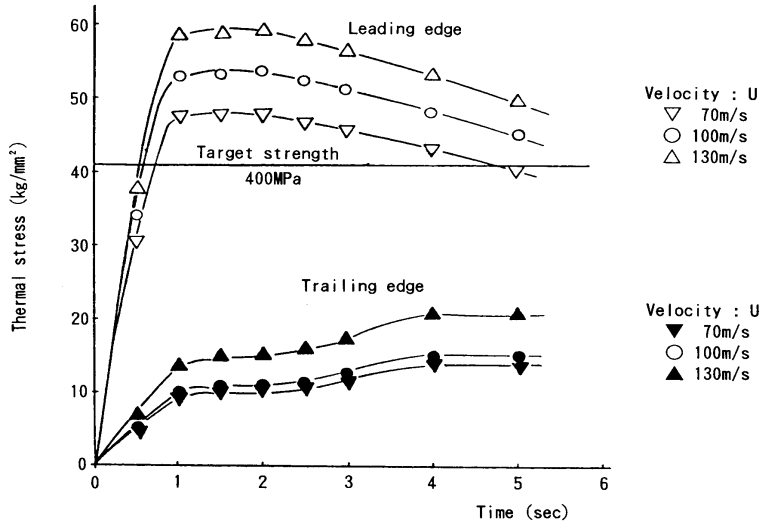

Figure 6: Transient thermal stress of Model A

Results for Model B

Test results for seventeen pieces of SiC nozzles and eight pieces of Si_3N_4 nozzles are shown in Table 2 and Table 3 respectively. As shown in Table 2, two SiC nozzles were fractured at 550MPa and 530MPa.
The fracture mode is shown in Figure 7.
As for the Si_3N_4 nozzles, they were not fractured though the velocity of helium gas was increased up to 160m/s (470MPa in terms of stress). An analytical result of the thermal stress for one half model is shown in Figure 5(b).

TABLE 2
TEST RESULTS OF MODEL B (SiC)

Model NO.	Cooling air		Initial temperature (℃)			Temperature at max. thermal stress (℃)			Max. thermal stress (MPa)
	Flow rate Q (m^3/h)	Velocity U (m/s)	Max. Camber	Trailing Edge	Leading Edge	Max. Camber	Trailing Edge	Leading Edge	
1,2	1,022	109	1,340	1,100	-	1,290	1,070	-	510
3,4	1,027	109	1,380	1,160	-	1,290	1,100	-	510
5	854	130	1,370	1,180	-	1,300	1,120	-	**550(Frac.)**
6	1,000	160	1,360	1,170	780	1,310	1,100	750	600
7	1,039	166	1,380	1,110	-	1,300	1,090	-	630
8	1,000	160	1,385	1,120	800	1,310	1,090	780	530
9	903	144	1,360	1,180	800	1,310	1,025	720	570
10,11	1,010	107	1,380	1,250	-	1,320	1,160	-	510
12,13	1,027	109	1,370	1,200	-	1,300	1,130	-	510
14	700	112	1,370	1,210	-	1,340	1,150	-	**530(Frac.)**
15	1,030	164	1,370	1,200	770	1,320	1,100	750	590
16	840	134	1,340	1,210		1,280	1,170		550
17	1,027	164	1,370	1,150	780	1,330	1,080	760	590

TABLE 3
TEST RESULTS OF MODEL B (Si_3N_4)

Model NO.	Cooling air		Initial temperature (℃)			Temperature at max. thermal stress (℃)			Max. thermal stress (MPa)
	Flow rate Q (m^3/h)	Velocity U (m/s)	Max. Camber	Trailing Edge	Leading Edge	Max. Camber	Trailing Edge	Leading Edge	
1	906	145	1,360	1,160	-	1,290	1,110	-	245
2	900	144	1,380	1,120	-	1,310	1,070	-	245
3	1,040	168	1,370	1,140	-	1,330	1,090	-	265
*4	360	80	1,400	1,355	-	1,340	1,190	-	400
*5	432	96	1,385	1,280	-	1,280	1,130	-	420
*6	576	128	1,385	1,280	-	1,130	875	-	450
*7	720	160	1,370	1,280	-	1,145	920	-	470
*8	617	137	1,355	1,280	-	1,205	995	-	460

*cooling by helium gas

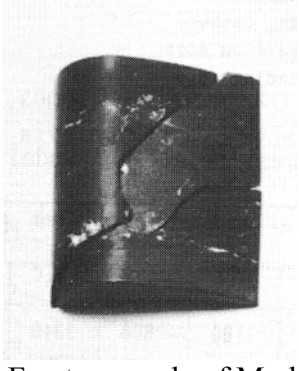

Figure 7: Fracture mode of Model B (SiC)

Fracture Probability

Figure 8 shows the time history of thermal stresses (σ) and the effective volume (Ve), fracture probability (P_f) for a Model A (SiC). It is shown that because of the smaller effective volume, the fracture probability of the nozzle is lower than approximately 10 % and this is considered to be similar to that of other test pieces. It is therefore considered that any Model A were not fractured in the thermal shock tests.

On the other hand, the stress level of Model B is lower than that of Model A, but two nozzles were fractured in the tests. It is because the cause of fracture depended on the difference of fracture probability between Model A and Model B, which gave a higher value. This high fracture probability in Model B resulted from the difference of stress gradient between the two Models as shown in Figure 5(a) and (b).

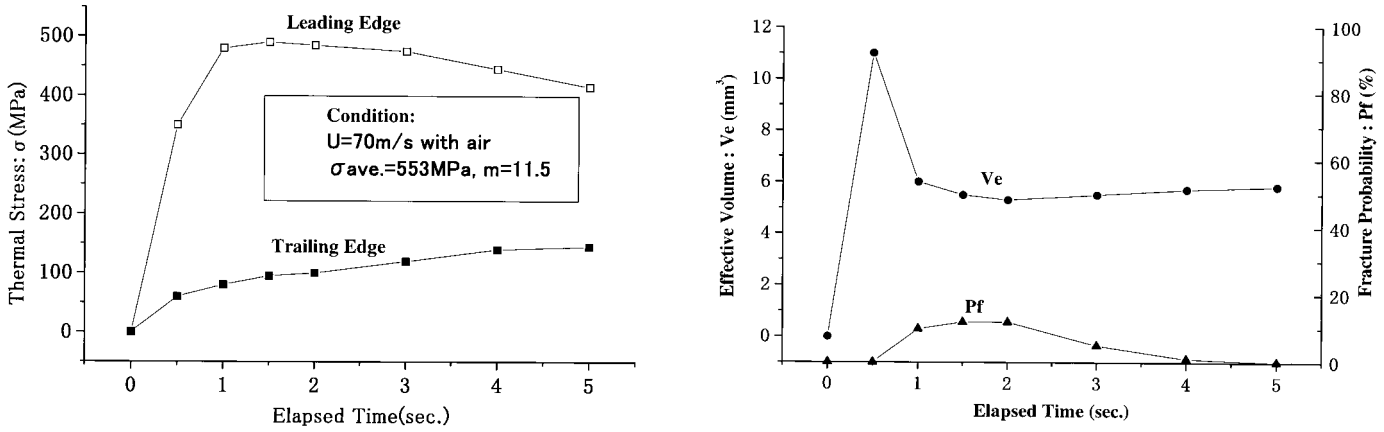

Figure 8: Time history of σ and Ve, P_f of Model A

CONCULUSIONS

A high-temperature thermal shock testing facility and fracture evaluating procedures for ceramic blades were developed. The typical fracture characteristics of ceramic turbine nozzle blade under instantaneous thermal shock condition were clarified and the fracture mode was presented.

ACKNOWLEDGEMENTS

This work was conducted under a contract from the Agency of Industrial Science and Technology of the Ministry of International Trade and Industry (AIST/MITI). We appreciate their advice and support.

REFERENCES

1. Mikami, T. et al (1996). Status of the Development of the CGT301, a 300 KW Class Ceramic Gas Turbine, ASME 96-GT-252, ASME TURBO EXPO'96, Birmingham, UK
2. Mikami, T. et al (1998). Application of Ceramics to the CGT301, a 300 KW Class Ceramic Gas Turbine, CIMTEC 98, Florence, Italy